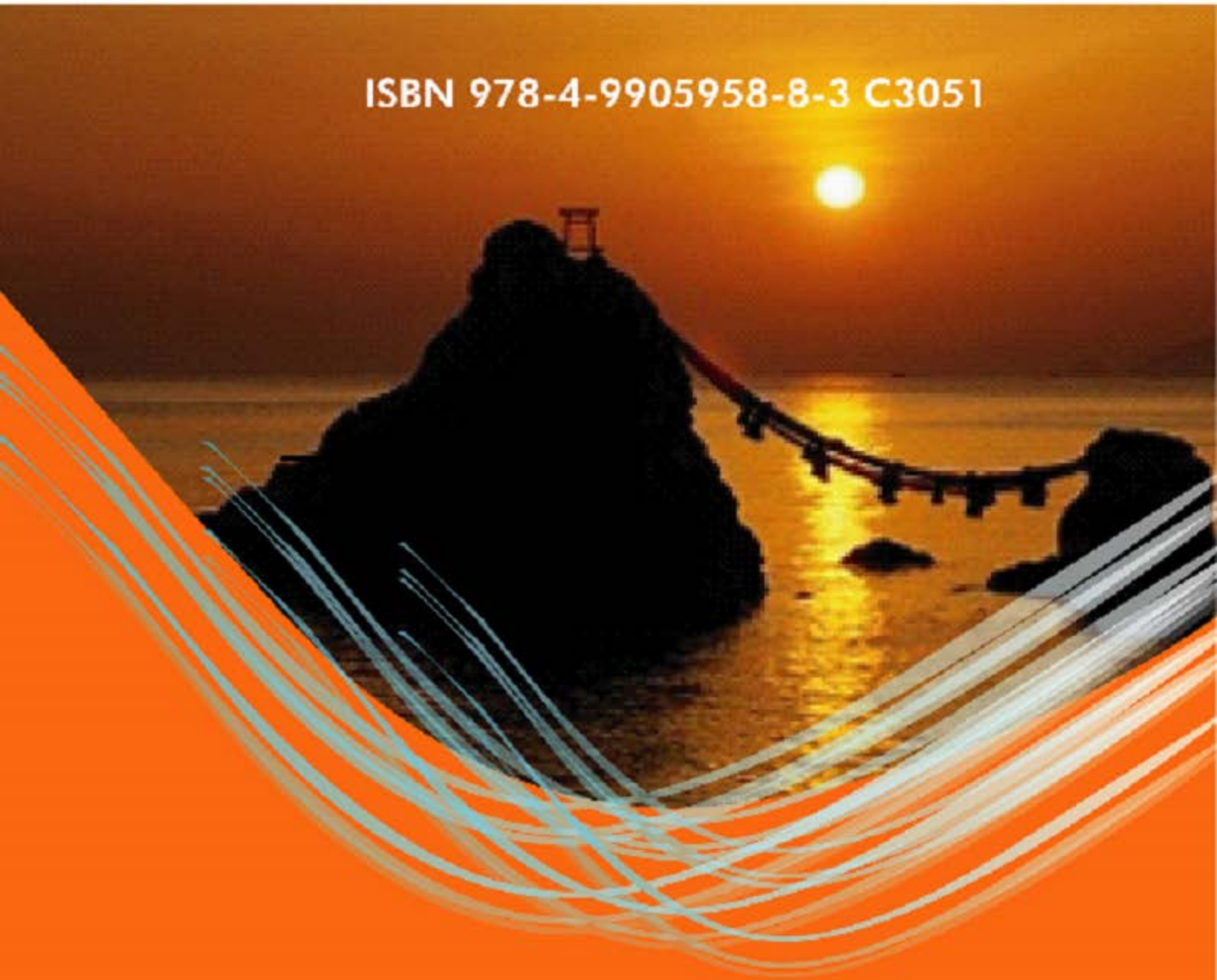


ISBN 978-4-9905958-8-3 C3051



GEOMATE

Geotechnique, Construction
Materials & Environment
Volume 7 (1)

Prof. Dr. Zakaria Hossain
(Editor)



GEOMATE 2017 TSU MIE JAPAN
GEOTECHNIQUE, CONSTRUCTION MATERIALS AND ENVIRONMENT

PROCEEDINGS OF SEVENTH INTERNATIONAL CONFERENCE – GEOMATE 2017
GEOTECHNIQUE, CONSTRUCTION MATERIALS AND ENVIRONMENT, TSU MIE JAPAN
21-24 NOVEMBER 2017

Geotechnique, Construction Materials and Environment

Edited by

Prof. Dr. Zakaria Hossain

Department of Environmental Science and Technology

Graduate School of Bioresources

Mie University, Japan



THE GEOMATE INTERNATIONAL SOCIETY

Copyright @ 2017 by The GEOMATE International Society

All rights reserved. In principle, no part of this publication or the information contained herein may be reproduced in any form or by any means, translated in any language, stored in any data base or retrieval system, or transmitted in any form or by any means without prior permission in writing from the publisher.

Disclaimer: The editors and the publisher have tried their best effort to ensure the integrity and the quality of this publication and information herein. However, they give no warranty of any kind, expressed or implied with regard to the material contained in this book, and will not be liable in any event for the consequences of its use.

Published by:
The GEOMATE International Society
Tsu city, Mie, Japan
E-mail: society@geomate.org
<http://www.geomate.org/>

ISBN Number: 978-4-9905958-8-3 C3051

Table of Contents

	Preface	xiv
	Organization	xv
ID	Keynote Papers	1
1k	FLY ASH GEOPOLYMER STABILIZED RECYCLED ASPHALT PAVEMENT AS A SUSTAINABLE BASE MATERIAL Suksun Horpibulsuk, Menglim Hoy, Runglawan Rachan and Arul Arulrajah	2
2k	EVALUATION OF SLOPE STABILITY BASED ON MONITORING OF RESIDUAL LOADS ON GROUND ANCHORS USING THE SAAM SYSTEM Toshinori Sakai and Yu Fujiwara	10
3k	USING PERMEABLE PAVEMENTS TO REDUCE THE ENVIRONMENTAL IMPACTS OF URBANISATION Terry Lucke	19
4k	ENVIRONMENTALLY GREEN IDEAS FOR SOIL STABILIZATION Bujang B.K.Huat and Afshin Asadi	28
	Technical Papers	34
ID	Geotechnique	35
7105	CHARACTERIZATION OF ENVIRONMENT FRIENDLY GEOTEXTILES EMBEDDED IN SOIL UNDER PULLOUT TEST Md. Aminul Islam, Zakaria Hossain, Jim Shiau and Siti Hanggita Rachmawati	36
7108	THE EFFECT OF VOID RATIO, MOISTURE CONTENT AND VERTICAL PRESSURE ON THE HYDROCOMPRESSION SETTLEMENT OF COPPER MINE TAILING Mary Ann Q. Adajar and Miller DL. Cutora	43
7109	SOIL-STRUCTURE INTERFACE BEHAVIOR OF CEMENTED-PASTE BACKFILL MATERIAL MIXED WITH MINING WASTE Mary Ann Q. Adajar and Wincent Nicole K. Pabilona	49
7114	A NEW TESTING APPARATUS TO EXCAVATE RECTANGULAR SECTION FOR UNDERPASS TUNNEL CONSTRUCTION Yota Togashi , Takashi Nakayama , Sohei Itaya , Takatoshi Hondo and Noriyuki Okano	55
7115	INFLUENCE OF MATRIC SUCTION ON INSTABILITY OF UNSATURATED SILTY SOIL IN UNCONFINED CONDITIONS Ali Murtaza Rasool and Jiro Kuwano	60

7117	PROPERTIES OF RAW AND PROCESSED BUKIT GOH BAUXITE IN KUANTAN, PAHANG IN ACCORDANCE WITH IMSBC CODE Muzamir Hasan, Ahmad Amirul Faez, M. Azizul Moqsud, Tam Weng Long and Phang Biao Yu	66
7121	TEMPERATURE CHANGE AND THE TOTAL STRESS ANOMALY IN PASTE BACKFILL Alsidqi Hasan, Ting Wee Kiet, Fauzan Sahdi, Siti Noor Linda Taib, Norsuzailina Mohamed Sutan, Badhrulhisham Abdul Aziz and Andy Fourie	72
7122	3-D NUMERICAL STUDY ON COASTAL LEVEE REINFORCEMENT USING DOUBLE SHEET-PILES WITH PARTITION WALLS Kousuke Takahama, Yuta Yamanaka, Atsushi Yashima ³ and Kakuta Fujiwara	78
7132	LANDSLIDES AND PRECIPITATION CHARACTERISTICS DURING THE TYPHOON LIONROCK IN IWATE PREFECTURE, JAPAN Thapthai Chaithong, Daisuke Komori, Yoshiya Touge, Yuta Mitobe, Yuto Sukegawa, and Satoshi Anzai	84
7133	SATURATED SHEAR STRENGTH PARAMETERS OF COMPACTED KHON KAEN LOESS BY DIRECT SHEAR TEST Atchariya Saengthongthip, Ratamanee Nuntasarn and Jutaporn Tanok	90
7134	UTILISATION OF ALKALINE ACTIVATED INDUSTRIAL BY-PRODUCTS IN DEEP SOIL MIXING Mohammadjavad Yaghoubi, Arul Arulrajah, Mahdi Miri Disfani, Suksun Horpibulsuk, Myint Win Bo and Melvyn Leong	96
7135	DEEP FOUNDATION REFERENCE FOR METRO MANILA, PHILIPPINES Jonathan R. Dungca, Noel Lester C. Gozum, Jon Arnel S. Telan, Victor Carlo F. Torres and Timothy Scott Y. Uytengsu	102
7143	AN ATTEMPT TO DETERMINE A SUITABLE STABILIZER FOR EXPANSIVE SOILS OF VOLCANIC ORIGIN Rajeshwar Goodary, Avirut Chinkulkijniwat, Vatanavongs Ratanavaraha, Roodheer Beeharry, Anoop Aujayeb	108
7146	LINEAR OPTIMIZATION OF SOIL MIXES IN THE DESIGN OF VERTICAL CUT-OFF WALLS Joanel Galupino, Charlle Sy, Jonathan Dungca, and Anthony Shun Fung Chiu	114
7147	EFFECTS OF CUTTING FACE BOLTS IN THE UNCONSOLIDATED SANDY TUNNEL Yoshifumi Taguchi	121
7149	PHYSICAL MODELING OF PROPOSED POROUS DRAINAGE SYSTEM TO SOLVE INUNDATION PROBLEM Ahmad Rifa'i and Noriyuki Yasufuku	127
7153	EFFECT OF HEATING-WETTING CYCLES ON ROCK PERMEABILITY Ivan Gratchev, Jeremy Stephens and Dong Hyun Kim	133
7154	A SIMPLIFIED METHOD FOR ESTIMATING COEFFICIENT OF EARTH PRESSURE AT REST (K ₀) IN COHESIVE SOILS Premkamol Thuennadee and Kritika Trakoolngam	137
7167	A STUDY ON PERMEATION CHARACTERISTICS OF MICRO PARTICLES INTO SAND Yukoh Hasunuma, Kentaro Uemura, Takamitsu Sasaki, Koichi Nagao, Shunsuke Shimada, Tsuyoshi Tanaka, Naoaki Suemasa	142
7168	OPTIMUM USE OF GEOGRID IN THE UNBOUND GRANULAR LAYER FOR THE PAVEMENT CONSTRUCTION AUNG AUNG SOE, Jiro KUWANO, Ilyas AKRAM and Takaya KOGURE	148
7175	LONG-TIME STRENGTH PREDICTION METHOD OF CHEMICAL GROUT SPECIMEN WITH HEAT CURING Shunsuke Takiura, Naoaki Suemasa and Kazuya Itoh, Takamitsu Sasaki and Shunsuke Shimada	154

7181	FLY-ASH-BASED GEOPOLYMER AS STABILIZER FOR SILTY SAND EMBANKMENT MATERIALS Jonathan R. Dungca, Edward Ephrem T. Codilla II	160
7182	LONG-TERM STRENGTH OF BUBBLE-MIXED SOLIDIFIED SOIL MADE FROM VOLCANIC ASH Atsuko Sato ¹ and Toshihiro Hayashi	167
7199	DEVELOPMENT OF CEMENT-BENTONITE MIXED SOILS BY MIXING SODIUM CARBONATE Ko Hashimoto, Shuichi Kuwahara, Yukio Uchida, Tadaomi Eguchi, Shinya Inazumi	172
7200	DEVELOPMENT OF REAL-TIME CHECKING SYSTEM FOR GROUND IMPROVEMENT WORKS BY HIGH PRESSURE INJECTION Gicheol Lee, Shinya Inazumi, Hiroyuki Hashida, Tadashi Chuman, Keiji Okumura and Kazuhiro Ishimaru	178
7206	THREE-DIMENSIONAL NUMERICAL STUDY OF THE EFFECT OF TUNNELING ON THE SETTLEMENT OF PILE FOUNDATION Mohammad Reza Atrchian, Milad Ghannadzadeh Kermani, Ali Nisari Tabrizi and Hamid Teennejad	184
7208	BEHAVIOR OF MODEL GROUP PILES SUBJECTED TO LATERAL SOIL MOVEMENT IN SAND Saad Farhan Ibrahim, Mohammed Khachi Hatem	188
7215	CHANGE OF DEBRIS FLOW CHARACTERISTICS DUE TO DIFFERENCES IN PHYSICAL CONDITIONS OF LANDSLIDE DAM Naomasa Honda	194
7218	EXPERIMENTAL STUDY ON SOIL BASED SEALING MATERIAL FULFILLING DEFORMATION FOLLOWABILITY AND UNDERWATER PLACEABILITY Yusuke Tadano, Seiichi Ishida and Masanori Shimomura	200
7227	SEISMIC RESPONSE ANALYSIS OF A REINFORCED EARTH WALL USING THE REINFORCEMENTS INCORPORATING BOTH FRICTION RESISTANCE AND BEARING RESISTANCE Hirohisa Muto, Takeshi Kodaka and Akihiko Naganuma	206
7230	EFFECT OF CEMENT TYPES ON STRENGTH DEVELOPMENT OF CEMENT-TREATED SOILS Lanh Si Ho, Kenichiro Nakarai, Kenta Eguchi, Takashi Sasaki, Minoru Morioka	212
7235	ADDITIONAL BEARING CAPACITY OF PILES DUE TO TIME DELAY OF INJECTION Abdul Hakam, M Sofian Asmirza and Heka P Andriani	218
7236	INVESTIGATION ON THE EFFECTS OF PLANT VARIETY AND SOIL SEDIMENT TO THE COASTAL ABRASION IN WEST SUMATRA Abdul Hakam, Bambang Istijono and Taufika Ophiyandri	222
7238	PRELIMINARY STUDY OF LIFT-OFF TEST AND PERFORMANCE EVALUATION FOR ANCHORS ON FREEWAY SLOPES Sao-Jeng Chao, Chia-Yun Wei and Hong-Da Chou	228
7243	INFLUENCE OF LIQUEFACTION ON SOIL-FOUNDATION-STRUCTURE INTERACTION Ryohta Takatoku, Kentaro Uemura, Barrios Gonzalo, Naotaka Kikkawa, Nobutaka Hiraoka, Kazuya Itoh, Naoaki Suemasa, Nawawi Chouw, Thomas Larkin and Rolando Orense	234
7249	ULTIMATE BEARING CAPACITY OF CLAYEY FOOTING UNDER SQUEEZE BREAKDOWN USING RIGID-PLASTIC FINITE ELEMENT METHOD Kazuhiro Kaneda, Masamichi Aoki, Tomohiro Tanikawa and Satoru Ohtsuka	240
7257	CORRELATION AMONG THE SOIL PARAMETERS OF THE KARNAPHULI RIVER TUNNEL PROJECT Khondoker Istiak Ahmad, Masnun Abrar, Hossain Md. Shahin, Sultan Al Shafian and Soumik Nafis Sadeek	246
7258	A STUDY ON COMPRESSION AND SOLIDIFICATION CHARACTERISTICS OF VOLCANIC SAND Katsuhiro Shibano, Naoaki Suemasa, Kazuya Itoh, Tsuyoshi Tanaka, Hiroto Akimoto, Yoshitaka Yanagihara, Yuan Zhang, Kiyoshi Numakami, Yasushi Furugaichi	249

	Katsuya Suzuki, Shun Habara	
7264	NUMERICAL ANALYSIS ON MECHANISM OF LIQUEFACTION NOT ONLY IN MAIN EARTHQUAKE BUT ALSO IN AFTER SHOCK Yukihiro Morikawa, Hide Sakaguchi, Akihiko Taira and Ho Cho	255
7265	EVALUATION OF HEAVING RESISTANCE FOR DEEP SHAFT USING NODULAR DIAPHRAGM WALL Koji Watanabe, Akira Mitsumori, Hidetoshi Nishioka and Masayuki Koda	263
7268	RESEARCH OF DAMAGED CONDITION BY THE 2016 KUMAMOTO EARTHQUAKE AND GROUND INVESTIGATION ON STONE WALLS AND ERATH STRUCTURES IN KUMAMOTO CASTLE Satoshi Sugimoto, Minoru YAMANAKA, Hideki Maeda, Naozo Fukuda and Yuuya Katsuda	269
7283	ESTIMATION OF INITIAL GROUND CONDITIONS UNDER STUPAS BASED ON ONE-DIMENSIONAL CONSOLIDATION THEORY Yuko Ishida, Ayaka Oya, Chaweewan Denpaiboon, Masamitsu Fujimoto and Ryoichi Fukagawa	275
7285	AN EXACT FINITE ELEMENT MODEL FOR AXIAL LOADED PILE IN MULTILAYERED SOIL Chinnapat Buachart, Chayanon Hansapinyo, Piti Pratomkhum and Worsak Kanok-Nukulchai	281
7287	STABILITY ANALYSIS FOR AN AIRPORT EMBANKMENT, EVALUATING SHORT AND LONG TERM TECHNIQUES Ignacio Fructuoso Solís Quispe, José Carlos Solís Tito and Mario Edisson Quilli Apaza	287
7291	DISPLACEMENT OF DIAPHRAGM WALL FOR VERY DEEP BASEMENT EXCAVATION IN SOFT BANGKOK CLAY Wanchai Teparaksa and Jirat Teparaksa	293
7300	THE INFLUENCE OF SOLAR RADIATION ON PAVEMENT PERFORMANCE John Yeaman and Adrian McCallum	298
7301	THE INFLUENCE OF SOLAR RADIATION AND SUBGRADE MOISTURE CONTENT ON PAVEMENT PERFORMANCE John Yeaman and Adrian McCallum	304
7302	THE EFFECT OF LIVE TRAFFIC ON PAVEMENT PERFORMANCE John Yeaman and Adrian McCallum	315
7308	LIQUEFACTION SIMULATION FOR THE OSAKA GULF COAST USING THE LIQCA PROGRAM Tetsuya Okano, Keita Sugito and Ryoichi Fukagawa	321
7320	NUMERICAL SIMULATION OF LIQUEFACTION AND RELATED BEHAVIOR OF UNDERGROUND STRUCTURE ON OSAKA GULF COAST Keita Sugito, Tetsuya Okano and Ryoichi Fukagawa	327
7322	ROBUST POSITIONING OF DRONES FOR LAND USE MONITORING IN STRONG TERRAIN RELIEF USING VISION-BASED NAVIGATION Oleg Kupervasser, Vitalii Sarychev , Alexander Rubinstein and Roman Yavich	333
7329	DEGRADATION OF CEMENT TREATED SOIL DUE TO SULFATE ATTACK Cynthia Debby Heriyani, Sumiyati Gunawan, John Tri Hatmoko, and Luky Handoko	339
7330	CHARACTERIZATION OF PHYSICAL, CHEMICAL, AND COMPACTION PROPERTIES FOR BURIED MUNICIPAL SOLID WASTE AT THREE DUMPING SITES IN SRI LANKA A.B.K.T. Piumali, T. Saito, N.H Priyankara, A.M.N Alagiyawanna, and K. Kawamoto	345
7332	STRESS-STRAIN-DILATANCY RELATIONSHIPS OF NORMALLY CONSOLIDATED DHAKA CLAY Muhammad Abdur Rahman, Hossain Md Shahin and Teruo Nakai	351

7336	MECHANISTIC BEHAVIOR OF OPEN AND DENSE GRADED UNBOUND GRANULAR MATERIALS UNDER TRAFFIC LOADS Ali Alnedawi, Kali Prasad Nepal and Riyadh Al-Ameri	355
7337	STRUCTURAL NUMERICAL ANALYSIS ON AN OPEN-WING-TYPE GROUND ANCHOR Kota Kono, Akihisa Nakahashi , Dong Daicho , Nobuo Fukushima and Ryoichi Fukagawa	361
7340	H/V SPECTRAL RATIO STUDY FOR ESTIMATION OF LOCAL SITE EFFECTS IN VISHAKHAPATNAM CITY Swathi Priyadarsini Putti and Neelima Satyam D	367
7349	STUDY OF GROUND PENETRATING RADAR(GPR) EXPLORATION FOR CAVITY UNDER THE GROUND USING FIELD TEST EXECUTION OF SEWER Daeyoung Lee and Dongmin Kim	373
7359	EFFECT OF CONFINING STRESS AND INCLINATION ANGLE ON THE STRENGTH BEHAVIOUR OF SAND Navid Khayat	377
7363	INVESTIGATIONS OF INTERACTION OF JOINT PILES WITH PROBLEMATIC SOIL GROUND IN KAZAKHSTAN Askar Zhussupbekov, Abdulla Omarov, Asemgul Moldazhanova, Asel Tulebekova, Karlygash Borgekova and Gulshat Tleulenova	383
7365	THE UTILIZATION OF WATER FOOTPRINT TO ENHANCE THE WATER SAVING AWARENESS: CASE STUDY OF A CERAMIC PRODUCT Karin Kandananond	389
ID	<i>Construction Materials</i>	394
7106	MECHANICAL PROPERTIES OF FLY ASH GEOPOLYMER MORTAR CONTAINING RECYCLED GLASS Nattapong Damrongwiriyanupap, Yue Huang, Sangsan Wongchairattana, Sakonwan Hanjitsuwan, Tanakorn Phoo-ngernkham and Prinya Chindaprasirt	395
7116	DEMONSTRATION OF LINER INTEGRITY MONITORING SYSTEM IN A GYPSUM WASTE CONTAINMENT H.B. Ng and Y.Y. Zheng	399
7129	THE USE OF STEEL FIBER EXTRACTED FROM WASTE TYRE AS REINFORCEMENT IN CONCRETE CONTAINING RICE HUSK ASH Fauzan, Febrin Anas Ismail, Rio Sandi and Claudia Lovina A N	405
7141	AN INVESTIGATION ON THE STRENGTH OF AXIALLY LOADED COLD-FORMED STEEL Z-SECTIONS James Matthew L. De Jesus and Bernardo A. Lejano	411
7142	INVESTIGATION OF THE EFFECTS OF DIFFERENT NATURAL FIBERS ON THE STRENGTH OF COMPRESSED STABILIZED EARTH BLOCKS (CSEB) Kyle Solomon D. Pineda and Bernardo A. Lejano	417
7144	USEFULNESS OF ARTIFICIAL BEACHROCK AND GEOTEXTILE TUBE TECHNOLOGY Md. Al Imran, Kazunori Nakashima and Satoru Kawasaki	423
7152	SHEAR BOND STRENGTH OF FA-PC GEOPOLYMER UNDER DIFFERENT SAND TO BINDER RATIO AND SODIUM HYDROXIDE CONCENTRATION Tanakorn Phoo-ngernkham, Sakonwan Hanjitsuwan , Satakhun Detphan , Jaksada Thumrongvut, Cherdasak Suksiripattanapong, Nattapong Damrongwiriyanupap, Prinya Chindaprasirt and Shigemitsu Hatanaka	429

7158	INFLUENCE OF SEAWATER ON THE STRENGTH OF RC BEAMS AND CORROSION BEHAVIOR OF STEEL Bernardo A. Lejano and Cheryl Lyne C. Roxas	435
7170	A COMPARATIVE SETTLEMENT PREDICTION OF LIMESTONE BLENDED MATERIALS USING ASAOKA AND HYPERBOLIC METHOD Erica Elice Saloma Uy and Jonathan Rivera Dungca	441
7171	HYPERBOLIC MODEL PARAMETERS OF PHILIPPINE COAL ASH Erica Elice Saloma Uy and Jonathan Rivera Dungca	447
7172	EXPERIMENTAL STUDY ON MECHANICAL BEHAVIOUR OF CONCRETE BEAMS WITH SHREDDED PLASTICS Richard M. De Jesus, Emmanuel Bastian Pelaez and Moises Carl Caneca	453
7174	PARAMETRIC STUDY OF RESPONSE OF BRICK MASONRY WALL TO OUT-OF-PLANE LOADING Miroslav Mynarz and Lucie Mynarzova	458
7176	MACROCELL CORROSION ASSESSMENT OF STEEL IN COLD-JOINTED CONCRETE MIXED AND CURED IN SEAWATER Cheryl Lyne C. Roxas and Bernardo A. Lejano	464
7192	INFLUENCE OF PRECURSORS AND ACTIVATOR ON STRENGTH AND POROSITY OF ALKALI ACTIVATED BINDERS Nurulhuda Nadziri, Idawati Ismail and Sinin Hamdan	470
7194	CURRENT SITUATION OF CONSTRUCTION AND DEMOLITION WASTE IN VIETNAM: CHALLENGES AND OPPORTUNITIES Nguyen Van Tuan, Tong Ton Kien, Dang Thi Thanh Huyen, Tran Thi Viet Nga, Nguyen Hoang Giang, and Ken Kawamoto	477
7214	IRREPARABLE COMPRESSIVE CREEP DEFORMATION OF CHLOROPRENE BEARING PAD Hidenori TANAKA	483
7221	FE ANALYSIS FOR LATERAL STRENGTH OF CONCRETE WALLS WITH AGGREGATE SEDIMENTATION Mamoru Kawasaki, Tetsuya Ohmura and Ryota ISHII	488
7232	FERROCEMENT - BRICK SANDWICH WALL APPLIED TO NON-ENGINEERED HOUSES Febrin A Ismail, M Sofian Asmirza, Abdul Hakam and Fauzan	494
7305	EXPERIMENTAL STUDY ON MASONRY BUILDING STRENGTHENED WITH FERROCEMENT LAYERS Fauzan, Febrin Anas Ismail, Abdul Hakam, Sindy Harvi Amalia and Siska Apriwelni	499
7310	BIODEGRADABLE POLY(L-LACTIC ACID) MICROCAPSULE CONTAINING HEAT STORAGE MATERIAL: INFLUENCE OF POLYMER MOLECULAR WEIGHT ON ENCAPSULATION EFFICIENCY Primprapa Sangjun and Amorn Chaiyasat	505
7312	COMPOSITE MATERIALS WITH PARTICULAR REFERENCE TO CONCRETE K. K. Ganguly Gangopadhyay	511
7328	ASSESSMENT OF ANTI-RUTTING ABILITIES OF WARM MIX MODIFIED MIXTURES Ivan Syed, Md Amanul Hasan and Rafiqul A. Tarefder	525
7360	LATERAL CYCLIC LOAD TEST AND SEISMIC DESIGN OF PRECAST CONCRETE COLUMNS USING STEEL BOX CONNECTION Nutchanon Siri, Chayanon Hansapinyo and Chinnapat Buachart	531

<i>ID</i>	<i>Environment</i>	537
7110	UTILIZATION OF BUCKLEY-LEVERET THEORY IN BAZARKAMI OIL FIELD IN NORTHERN OF AFGHANISTAN Zabihullah Mahdi and Shigeo Honma	538
7112	THE BEHAVIOR OF WASTE PULLING BY PILE DRIVING THROUGH THE BARRIER CLAY LAYER ON CONTROLLED COASTAL LANDFILL SITE Takayuki Hirao, Yoshiaki Kikuchi Taichi Hyodo Masatsugu Kiko Kouta Katagishi Shohei Namiki Satoshi Matsumura and Makoto Takemoto	546
7119	TOXICITY AND BIOEFFICACY OF WEED ESSENTIAL OILS AGAINST COWPEA BRUCHIDS AND THEIR EFFECT ON MUNGBEAN SEEDS Ruchuon Wanna and Perayos Khangkhun	552
7120	GEOPHYSICAL TOMOGRAPHY BASED ON SPARSE ESTIMATION Takayuki Shuku and Hongyang Cheng	558
7125	LESSONS AND ACHIEVEMENTS FROM THE MERSEY FOREST BY NETWORKING PARTNERSHIP FOR TWENTY YEARS Tomoko Miyagawa, Clare Olver, Noriko Otsuka, Takefumi Kurose and Hirokazu Abe	564
7126	IMPACT OF INCREASE IN SIKA DEER (CERVUS NIPPON) ON INFILTRATION RATE AND SOIL EROSION ON FORESTED HILLSLOPE Taijiro Fukuyama, Shinya Hiramatsu, Keisuke Kase, Masato Kikuchi, Shusaku Shiiba, Hideto Ohmori, Masaaki Hanaoka	571
7127	TSUNAMI RISK MAPPING USING INTEGRATED REMOTE SENSING AND GEOSPATIAL ANALYSIS Abu Bakar Sambah, Fusanori Miura, Guntur, Fuad, and Defrian Marza Arisandi	577
7128	SAFETY AND EFFICIENCY FOR WEEDING WORK AND LEVEE SLOPE'S FORM REQUIRED FOR MOWING MACHINES ON PADDY FIELDS IN STEEP SLOPING AREAS IN JAPAN Yoshiyuki Uchikawa, Masami Matsui, Teruo Arase and Takahiro Tamura	584
7130	OPTIMAL RESTORATION STRATEGY OF A WATER PIPELINE NETWORK IN SURIGAO CITY, PHILIPPINES Agnes Garciano, Lessandro Estelito Garciano, Renan Ma. Tanhueco and Taze Jared Abubo	588
7137	FOREST ROADS CAUSE EDGE EFFECTS ON PLANT SPECIES DIVERSITY IN ARTIFICIAL FORESTS Hiroki Kohmori, Tetsuoh Shirota, Tetsuo Okano and Teruo Arase	593
7138	DRIFTWOOD ACCUMULATION AND FLOOD DAMAGE AREA IN BLOCKED RIVER Takaaki Okamoto, Hiroshi Takebayashi Masato Takenaka Yoshinobu Kashihara and Keiichi Toda	599
7145	PERMEABILITY CHARACTERISTICS OF ROAD BASE MATERIALS BLENDED WITH FLY ASH AND BOTTOM ASH Jonathan R. Dungca and Joenel G. Galupino	605
7148	REVIEWS ON THE APPLICABILITY OF CONSTRUCTION AND DEMOLITION WASTE AND ITS RECYCLED MATERIALS AS LOW-COST ADSORBENTS TO REMOVE HEAVY METALS IN WASTEWATER G.M.P. Kumara, Takashi Saito, Shingo Asamoto, and Ken Kawamoto	611
7150	STUDY ON EXTRACTION AND ADSORPTION OF CESIUM FROM VERMICULITE MIXTURE SAND Shota Nishioka , Keiichiro Shibata, Hidenori Yoshida	617
7156	THE ORIGIN OF GROUNDWATER IN THE KIONOKAWA RIVER CATCHMENT Hiroki Kitagawa, Takuma Kubohara and Hiroyuki Ii	623

7164	STUDY ON THE REMOVAL METHOD FOR CESIUM IN SOIL OF SLOPE Keiichiro Shibata, Hidenori Yoshida and Naomichi Matsumoto	628
7166	NUMERICAL ASSESSMENT OF THE IMPACT OF STRONG WIND ON THERMAL STRATIFICATION IN LAKE BIWA Jinichi Koue, Hikari Shimadera, Tomohito Matsuo, Akira Kondo	634
7169	IMPROVED EFFICIENCY AND FEASIBILITY IN DEVELOPING REGIONAL SCALE OPTIMAL MULTIPLE OBJECTIVE SALTWATER INTRUSION MANAGEMENT STRATEGIES IN COASTAL AQUIFERS UTILIZING NEW SURROGATE MODELS Alvin Lal and Bithin Datta	640
7173	WATER POLLUTION OF KAMATANI-RIVER BASIN IN YOKKAICHI Sachie Takeuchi, Masaaki Takahashi, Yukimasa Takemoto, Maki Oyagi and Satoshi Chiba	647
7177	COMPARISON OF DIFFERENT VEGETATION INDICES FOR ASSESSING MANGROVE DENSITY USING SENTINEL-2 IMAGERY Firman Farid Muhsoni, A.B Sambah, M. Mahmudi and D.G.R Wiadnya	653
7178	ESTIMATING THE ENVIRONMENTAL EFFECTS OF THE CAR SHIFTING BEHAVIOR ALONG EDSA Nicanor R. Roxas, Jr, Alexis M. Fillone, and Krister Ian Daniel Roquel	660
7179	EFFECTIVENESS OF PERMEABLE REACTIVE BARRIER (PRB) ON HEAVY METAL TRAP IN AQUIFER AT SOLID WASTE DUMPSITE: A SIMULATION STUDY Udayagee Kumarasinghe, Y. Sakamoto, T. Saito, M. Nagamori, C. S. Kalpage, G.B. Herath, M.I.M. Mowjood, and Ken Kawamoto	666
7188	ARTIFICIAL PAPER FROM PUTTARAKSA (CANNA INDICA LINN.) AND PLUBPLUENG (CRINUM ASIATICUM) Kanokwan Rudisirisak and Nittaya Ngowattana	672
7193	CRUSTAL THICKNESS OF NORTH-WEST PENINSULAR MALAYSIA REGION INFERRED FROM RECEIVER FUNCTION ANALYSIS Abdul Halim Abdul Latiff and Amin Esmail Khalil	678
7196	ARSENIC CONCENTRATION AND STABLE ISOTOPIC RATIOS OF OXYGEN AND HYDROGEN FOR GROUNDWATER AND RIVER WATER AROUND THE MIDORO AND SHINDENHIGASHISAMI TUNNELS IN GOSE CITY, NARA, CENTRAL JAPAN Hiroyuki Ii, Hiroshi Kono, Yuji Yamashita, Jyunji Uno, Hiroyuki Shimogaki, Sota Ikeda and Toshiki Nishimura	684
7201	GENETIC DIVERSITY OF PSEUDOLABRUS SIEBOLDI, USUAL FISH SPECIES IN A WESTERN JAPAN COASTAL AREA Michiko Masuda, Wataru Kawase and Fumitake Nishimura	690
7207	THE INTEGRATION OF OUTDOOR HUMAN THERMAL COMFORT IN TROPICAL CLIMATE CAMPUS LANDSCAPE: CHULALONGKORN UNIVERSITY, BANGKOK, THAILAND Ariya Aruninta, Yoshihito Kurazumi, Kenta Fukagawa, and Jin Ishii	694
7210	ANALYSIS OF TSUNAMI IMPACT TO COASTAL VEGETATION AND GEOLOGICAL LANDSCAPE AT KUALA TERENGGANU Nurfahana Aisya Anuar and Abdul Halim Abdul Latiff	700
7212	FISH CATCH QUOTA ASSESSMENT FOR SUSTAINABLE MARINE FISHERIES RESOURCES IN EAST JAVA AlfanJauhari, DefrianMarzaArisandi, Abu Bakar Sambah and WildanAlfarizi	706
7213	USE OF INSECTICIDE-TREATED NETS AMONG PIG OWNERS LIVING IN JAPANESE ENCEPHALITIS ENDEMIC AREAS OF NORTHERN MYANMAR Aung Kyaw Soe, Cheerawit Rattanapan, Somsak Wongsawass and Orapin Laosee	713
7223	EFFECT OF ORGANIC BIOPOLYMER ON THE MICROBIALLY INDUCED CARBONATE PRECIPITATION AND ITS MORPHOLOGY Thiloththama Hiranya Kumari Nawarathna, Kazunori Nakashima and Satoru Kawasaki	719

7228	PREDICTION OF SALTWATER INTRUSION PROCESSES USING A WAVELET-FCM-ANFIS HYBRID MODEL Dilip Kumar Roy and Bithin Datta	725
7229	LINKED SIMULATION-OPTIMIZATION MODEL FOR OPTIMUM HYDRAULIC DESIGN OF WATER RETAINING STRUCTURES CONSTRUCTED ON PERMEABLE SOILS Muqdad Al-Juboori and Bithin Datta	732
7231	JOINT BENCHMARKING AND ECO-EFFICIENCY FOR THE SUSTAINABLE PERFORMANCE OF SWINE PRODUCTION IN THAILAND Weerawat Ounsaneha Punthila Janthaphat Thunwadee Tachapattaworakul Suksaroj, Cheerawit Rattanapan	738
7242	EVALUATION OF ATTENUATION OF ULTRASONIC DURING PROPAGATION THE AIR TO MEASURE CONCRETE SURFACE ROUGHNESS BY THE AERIAL ULTRASONIC SENSOR Nagaoka Seiya, Islam Mohammad Raihanul, Okajima Kenji, Ishiguro Satoru, Ito Ryoei, Watanabe Ken and Ito Tetsu	744
7246	A STUDY OF PUBLIC OPINION ON GREEN SPACES USING DATA FROM FREE-TEXT DESCRIPTIVE RESPONSES - A CASE STUDY OF REGIONAL CITY IN JAPAN - Shinya Tsukada and Tetsuo Morita	750
7251	IMPACT OF AGRICULTURAL WATER ALLOCATION ON THE ECOSYSTEMS IN THE INNER NIGER RIVER DELTA Barry Kassambara, Homayoon Ganji and Takamitsu Kajisa	755
7254	A STUDY ON SELECTION FACTORS OF RESIDENCE FOCUSING ON PERSONAL ATTRIBUTES AND DISTRICT CHARACTERISTICS - A CASE STUDY OF REGIONAL CITY IN JAPAN - Tetsuo Morita and Shinya Tsukada	764
7256	REMOVAL OF RADIOACTIVE CESIUM FROM OCEAN SUDLUDGE BY THE BACTERIUM USING PURIFICATION SYSTEM OF CIRCULATION TYPE Tomoe Komoriya, Kyoichi Okamoto and Takashi Toyama	770
7260	GEOCHEMICAL REACTIVE MODELING OF FLOW AND TRANSPORT PROCESS AT A MINE SITE IN NORTHERN TERRITORY, AUSTRALIA Michael S. Hayford and Bithin Datta	775
7267	IMPACT OF LAND LEVELING ON THE WATER BALANCE FOR AGRICULTURE IN EASTERN AFGHANISTAN Shakerullah Hashimi, Pervaiz Ahmad Naseri , Najumuddin Anjum and Takamitsu Kajisa	782
7277	PREDICTORS OF BEHAVIOR INTENTION TO DEVELOP GREEN UNIVERSITY: A CASE OF UNDERGRADUATE UNIVERSITY IN THAILAND Weerawat Ounsaneha, Nahathai Chotklang, Orapin Laosee and Cheerawit Rattanapan	790
7279	GIS BASED IDENTIFICATION OF WATER BORNE DISEASES Hania Arif and Shahid Iqbal	794
7282	ANALYSIS OF RAINFALL IN THE EASTERN THAILAND Wonlee Nounmusig	800
7284	CHANGES IN THE ZOOPLANKTON COMMUNITY BEFORE AND AFTER NUTRIENT DIVERSION AND REVETMENT CONSTRUCTION IN LAKE FUKAMI-IKE, JAPAN Hiromi Suda, Masaaki Tanaka, Maki Oyagi and Akihiko Yagi	805
7286	SPATIAL ASSESSMENT ON THE IMPACT OF FLOOD TO MELAKA'S ECONOMY Rosilawati Zainol, Hanan Elsawahli and Wan Suzita Wan Ibrahim	810
7304	PROPOSAL OF A FLOATING-TYPE ENVIRONMENTAL PURIFICATION FACILITY INCORPORATING THE FUNCTION OF TIDELAND Sato Shinji and Yuji Yamakage	815

7306	WALL OPENINGS AND ITS ABILITY TO MINIMIZE FLOOD INDUCED FORCES ON RESIDENTIAL BUILDINGS Nur Aqilah Ahmad Faisal, Abdul Naser Abdul Ghani and Nuzaihan Aras Agus Salim	821
7309	APPLICATION OF A HYDROLOGICAL LAND SURFACE MODEL TO WATER RESOURCES ASSESSMENT IN PENINSULAR MALAYSIA Chee-Loong Wong , Zulkifli Yusop , Tarmizi Ismail and Raymond Venneker	827
7311	BIFUNCTIONAL MICROCAPSULE FOR HEAT STORAGE AND ANTIBACTERIAL PROPERTIES PREPARED BY MICROSUSPENSION IODINE TRANSFER POLYMERIZATION Amorn Chaiyasat, Siriluk Namwong, Boontida Uapipatanakul, Warayuth Sajomsang, Preeyaporn Chaiyasat	839
7314	KONDO THEORY FOR SPHERICAL SHELL TECTONICS Kazuhei Kikuchi and Hiroyuki Nagahama	845
7315	PHOTOELECTROCATALYTIC CONVERSION OF CO ₂ INTO VALUE-ADDED ORGANIC COMPOUNDS USING Cu ₂ O PHOTOCATHODE Patthanit Thongthep and Chatchai Ponchio	849
7316	DEVELOPMENT AND DESIGN OF PHOTOELECTROCATALYTIC REACTOR FOR DYE REMOVAL FROM INDUSTRIAL SYSTEMS Watcharapong Nareejun and Chatchai Ponchio	854
7317	IMPROVEMENT THE BiVO ₄ PHOTOANODE FABRICATED FOR WATER OXIDATION BY ELECTRODEPOSITION TECHNIQUE Nuanlaor Kiama and Chatchai Ponchio	858
7318	PHOTOELECTROCATALYTIC DETERMINATION OF CHEMICAL OXYGEN DEMAND USING WO ₃ /BiVO ₄ PHOTOELECTRODE Niphawarn Kangkun and Chatchai Ponchio,	863
7326	THE PERFORMANCE RAINFALL DURING RAINY SEASONAL OVER THAILAND BY USING PRELIMINARY REGIONAL COUPLED ATMOSPHERIC AND OCEANIC (WRF-ROMS) MODEL Pramet Kaewmesri, Usa Humphries, Boonlert Archevarapuprok and Sirapong Sooktawee	866
7335	THE LONG TERM CHANGE OF FORM OF NITROGEN IN YAMATO RIVER BASIN Masanobu Taniguchi and Hirayuki Ii	872
7338	HEAVY METAL CONCENTRATION OF SEAWEED BY INFLUENCE ON COPPER MINE AT SADAMISAKI PENINSULA Erika Ueno and Hiroyuki Ii	878
7343	EVALUATION OF IMBIBITION PROCESS IN POROUS MEDIA BY INVASED PERCOLATION PROBABILITY Junichiro Takeuchi and Masayuki Fujihara	884
7351	MEASUREMENT METHOD OF HEAVY METAL CONCENTRATION IN SOIL OF OSAKA PREFECTURE USING CICADA SHELL Satoru Ueda and Hiroyuki Ii	890
7352	PRECIPITATION AMOUNT ON TOPOGRAPHY AT BETWEEN THE OSAKA PLAIN AND THE SOUTH IKOMA MOUNTAINS, OSAKA PREFECTURE, JAPAN Hiroki Nishiwaki and Hiroyuki Ii	896
7353	INFLUENCE OF WASTE LOADING RATE ON BIOGAS GENERATION FROM MUNICIPAL SOLID WASTE Sartaj M., Kennedy K. and Nair A	902
7356	ASSESSING URBAN WATER SUPPLY SYSTEM IN NORTHEASTERN IN THAILAND: WATER QUALITY AND AUTHORITY ORGANIZATION Oranee Roongruang, Pensupa Wirikitkhul, Jareeya Yimrattanabavorn and Sudjit Karuchit	906
7357	COMBINATION COAGULATION AND ADSORPTION PROCESSES FOR TREATING TEXTILE WASTEWATER IN HOUSEHOLD INDUSTRY Tharika Kaenjun, Watcharapol Wonglertarak, Boonchai Wichitsathien and Jareeya Yimrattanabavorn	912

7361	A COMPREHENSIVE METHOD OF EROSION RESISTANCE AND GROWTH PROMOTION FOR PISHA SANDSTONE Zhishui Liang, Zhiren Wu, Caiqian Yang, Mohammad Noori, Xiangyang Wu, Hanbin Ge, Wenyi Yao and Peiqing Xiao	918
7362	PREPARATION AND EVALUTION BY ARTIFICIAL AGING TEST OF SiO ₂ / FLUORINATED POLY-STYRENE-ACRYLATE COMPOSITE MATERIAL Xiaoying Zhang, Dongya Yang, Wenya Wen, Hanqiang Yu, Xiangyang Wu, Jicheng Xu and Qian Chen	924
7364	STUDY ON OUTDOOR THERMAL ENVIRONMENT OF CAMPUS BASED ON GIS Minxue Zheng, Shanwei Li and Hongxiao Liu	929
7367	DEGRADATION OF FAMOTIDINE IN WATER WITH Ag-ZnO UNDER UV LIGHT IRRADIATION Md. Ashraful Islam Molla, Ikki Tateishi, Mai Furukawa, Hideyuki Katsumata, Tohru Suzuki and Satoshi Kaneco	934
7225	ACCELERATING METHANE PRODUCT IN REACTION OF METHANOGENS ARCHAEA WITH COAL IN MUARA ENIM FORMATION Ildo Muhary Putra, Muhammad Ihsan, T.J.L Tobing, Dio Rizqi Irawan and D.A.A. Putri	939
7261	A POST-LIQUEFACTION STUDY AFTER THE 2014 CHIANG RAI EARTHQUAKE AT TUNG-FAH-PAH VILAGE IN CHIANG RAI, THAILAND Sethapong Sethabouppha, Suriyah Tongmunee, Chollachai Kamtawai and Jittanan Kawilanan	945
7183	PRESENCE STATE OF TRACE ELEMENTS IN THE OHTAKIGAWA RIVER WATERSHED FROM THE FOOT OF Mt. ONTAKI Akiko Usami, Megumi Nobori, Akihiko Yagi and Eiji Iwatsuki	951
7239	ASSESSMENT ON THE AEROSOLS VARIATION DURING THE INTENSE HAZE EVENT OF JUNE 2013 OVER MALAYSIA BY UTILIZING THE SATELLITE REMOTE SENSING AND GROUND-BASED MEASUREMENT Nur Atiqah Ainaa Abd Latiff and Takashi Machimura	956
7136	MAT FOUNDATION DESIGN REFERENCE FOR METRO MANILA, PHILIPPINES Jonathan R. Dungca, Raynold Y. Pua and Raynold, Nelson Que	962
7762	PERFORMANCE OF ANN MODEL IN PREDICTING THE BEARING CAPACITY OF SHALLOW FOUNDATIONS Mozaher Ul Kabir, Syed Shadman Sakib, Istiakur Rahman, Md. Sirajul Arefin and Hossain Md. Shahin	968
7180	DEVELOPMENT OF THE TRADITIONAL LOCAL WISDOM INNOVATION USING COCONUT SHELL FOR STRESS RELAXING MASSAGE Peerada Damapong, Pongmada Damapong, Wichai Eungpinichpong and Thanarat Sripongngam	972

7185	SHORT-TERM EFFECTS OF THE AROMATHERAPY TO REDUCE STRESS IN THE ELDERLY Pongmada Damapong, Peerada Damapong and Kanyamanee Koomhangsung	976
------	---	-----

7187	IMMEDIATE EFFECTIVENESS OF TRADITIONAL THAI MASSAGE ON CERVICAL RANGE OF MOTION WITH CHRONIC TENSION-TYPE HEADACHE Chamiporn Kongmong and Peerada Damapong	979
------	---	-----

Authors index

Preface

On behalf of the GEOMATE 2017 Organizing Committee, we would like to welcome you in attending the International Conference on Geotechnique, Construction Materials and Environment held at the Miyako Hotel, Tsu Mie Japan in conjunction with the Japan Geotechnical Society, GEOMATE International Society, Mie University Research Center for Environmental Load Reduction, AOI-Engineering, Useful Plant Spread Society, HOJUN, Cosmo Winds, and Glorious International, Japan

On Friday 11 March 2011, at 14:46 Japan Standard Time, the north east of Japan was struck and severely damaged by a series of powerful earthquakes which also caused a major tsunami. This conference was first dedicated to the tragic victims of the Tohoku-Kanto earthquake and tsunami disasters. The Geomate 2017 conference covers three major themes with 17 specific themes including:

- Advances in Composite Materials
- Computational Mechanics
- Foundation and Retaining Walls
- Slope Stability
- Soil Dynamics
- Soil-Structure Interaction
- Pavement Technology
- Tunnels and Anchors
- Site Investigation and Rehabilitation
- Ecology and Land Development
- Water Resources Planning
- Environmental Management
- Public Health and Rehabilitation
- Earthquake and Tsunami Issues
- Safety and Reliability
- Geo-Hazard Mitigation
- Case History and Practical Experience

This year we have received many paper submissions from different countries all over the world, including Algeria, Australia, Austria, Bangladesh, Brazil, Canada, China, Czech Republic, France, India, Indonesia, Iran, Iraq, Japan, Jordan, Kazakhstan, Libya, Malaysia, Mauritius, Nigeria, Oman, Pakistan, Peru, Philippines, Russia, South Korea, Taiwan, Tanzania, Thailand, Tunisia, Turkey, United Kingdom, United States, Vietnam. The technical papers were selected from the vast number of contributions submitted after a review of the abstracts. The final papers in the proceedings have been peer reviewed rigorously and revised as necessary by the authors. It relies on the solid cooperation of numerous people to organize a conference of this size. Hence, we appreciate everyone who support as well as participate in this joint conferences.

Last but not least, we would like to express our gratitude to all the authors, session chairs, reviewers, participants, institutions and companies for their contribution to GEOMATE 2017. We hope you enjoy the conference and find this experience inspiring and helpful in your professional field. We look forward to seeing you at our upcoming conference next year.

Best regards,

Prof. Dr. Md. Zakaria Hossain, Conference Chairman



Organization

Conference Honorary Chairmen:

Dr. Sohji Inoue, E/Prof., Mie University, Japan
Dr. Teruo Nakai, E/Prof., NIT, Japan
Dr. Fusao Oka, E/Prof. Kyoto University, Japan

Conference Chairman:

Dr. Zakaria Hossain, Prof. Mie University, Japan

General Secretary:

Dr. Shinya Inazumi, A/Prof. Shibaura Ins. of Tech., Japan

Conference Organizing Committee:

Dr. Zakaria Hossain, Prof. Mie University, Japan (Chair)
Dr. Satoshi Kaneco, Prof., Mie University, Japan (Co-Chair)
Dr. Toshinori Sakai, Prof. Mie University, Japan (Co-Chair)
Dr. Takamitsu Kajisa, Prof. Mie University, Japan (Co-Chair)
Dr. Masaaki Kondo, A/Prof. Mie University, Japan (Co-Chair)
Dr. Shinya Inazumi, A/Prof. A/Prof. Shibaura Ins. of Tech. (GS)

National & International Advisory Committee:

Dr. Sittisak Uparivong, Prof. Khon Kaen University, Thailand
Dr. Jirayut Suebsuk, A/Prof. Rajamangala Uni of Tech., Thailand
Dr. Phacharaporn B., A/Prof., Kasetsart Uni., Thailand
Dr. Dolrerddee Hormdee, A/Prof., Khon Kaen Uni, Thailand
Dr. Vanchai Sata, A/Prof., Khon Kaen University, Thailand
Dr. Chinapat Buachart, A/Prof. Chiang Mai University, Thailand
Dr. Mark Jaksa, Prof., University of Adelaide, Australia
Dr. Fumio Tatsuoka, Prof. Tokyo University of Science, Japan
Dr. Jing-Cai Jiang, Prof. University of Tokushima, Japan
Dr. Toshihiro Morii, Prof. Niigata University, Japan
Dr. Kimitoshi Hayano, Prof. Yokohama National Univ., Japan
Dr. Sai Vanapalli, Prof. University of Ottawa, Canada
Dr. M. Bouassida, Prof. National Sch. of Engg. of Tunis
Dr. L.R. Austriaco, Prof. Angles Univ. Found. Philippines
Dr. A.S.M. Abdul Awal, Prof. Univ. Technology Malaysia
Dr. M. Ibn Ibrahimy, Prof. Int. Islamic Univ., Malaysia
Dr. Bujang B.K. Huat, Prof. Univ. Putra Malaysia
Dr. Nemy Banthia, Prof. UBC, Canada
Dr. Ian Jefferson, Prof. Univ. of Birmingham, UK
Dr. John Bolander, Prof. Univ. of California, USA
Dr. Shamsul Chowdhury, Prof. Roosevelt Univ., USA
Dr. Isabel Pinto, Prof. University of Coimbra, Portugal
Dr. Hj. Ramli Bin Hj. Nazir, A/Prof. UTM, Malaysia
Dr. Aly Ahmed, A/Prof. Beni-Suef University, Egypt
Dr. Chang-Yu Ou, Prof. National Taiwan Univ. of Sci. & Tech

GEOMATE Technical Program Committee (TPC):

Prof. Sai Vanapalli, University of Ottawa, Canada
Prof. Alaa Masoud, Tanta University, Egypt
Prof. Aly Ahmed, Beni-Suef University, Egypt
Prof. Aminaton Marto, Universiti Teknologi Malaysia, Malaysia

Prof. Bandari Shankar, Osmania University, India
 Prof. Bashir Ahmed Mir, National Institute of Technology, India
 Prof. Hamidi Abdul, Aziz, Universiti Sains Malaysia (USM), Malaysia
 Prof. Hussein Elarabi, University of Khartoum, Sudan
 Prof. M. Shohidullah Miah, International Univ. of Business Agriculture &Tech., Bangladesh
 Prof. Michele, Casagrande, Pontifical University Catholic of Rio De Janeiro, Brazil
 Prof. Radim Cajka, Technical University of Ostrava, Czech Republic
 Prof. Rajaraman Jambunathan, AMET University, India
 Prof. Reshma Chandran T., Global Institute of Architecture, India
 Prof. Roslan Hashim, University of Malaya, Malaysia
 Prof. Seyed Naser Moghaddas Tafreshi, K.N. Toosi University of Technology, Iran
 Prof. Valeriy Perminov, Tomsk Polytechnic University, Russia
 Prof. Quanmei Gong, Tongji University, China
 A/ Prof. Abdoullah Namdar, Sichuan University, China
 A/ Prof. Abdul Naser Abdul Ghani, Universiti Sains Malaysia, Malaysia
 A/ Prof. Alaeddinne Eljamassi, Islamic University of Gaza, Palestine
 A/ Prof. Alina Paranina, Herzen State Pedagogical University of Russia, Russia
 A/ Prof. Ashraf Elmoustafa, Ain Shams Univeristy, Egypt
 A/ Prof. Bindu C S, Cochin University of Science & Technology, India
 A/ Prof. Chee-Ming Chan, Universiti Tun Hussein Onn Malaysia, Malaysia
 A/ Prof. Chidanand Naik, Anjuman Institute of Technology and Management, India
 A/ Prof. Dahlia Hafez, Cairo University, Egypt
 A/ Prof. Deepa G Nair, Isfahan University of Technology, India
 A/ Prof. Dolrerdee Hormdee, Khon Kaen University, Thailand
 A/ Prof. Farhad Behnamfar, Isfahan University of Technology, Iran
 A/ Prof. Gabriela B. Cazacu, Geotech Dobrogea, Romania
 A/ Prof. Hadi Khabbaz, University of Technology, Sydney (UTS), Australia
 A/ Prof. Homayoon Ganji, Herat Univercity Badghis, Afghanistan
 A/ Prof. Hudson Jackson, US Coast Guard Academy, United States
 A/ Prof. Inazumi Shinya, National Institute of Technology, Akashi, Japan
 A/ Prof. John Smith, RMIT University, Australia
 A/ Prof. Kasinathan Muthukkumaran, National Institute of Technology, India
 A/ Prof. Lindrianasari Lindrianasari, Universitas Lampung, Indonesia
 A/ Prof. Mahdi Karkush, Baghdad University, Iraq
 A/ Prof. Mohamed Redha Menani, Batna University, Algeria
 A/ Prof. Navid Khayat, Ahvaz Branch, Islamic Azad University, Iran
 A/ Prof. Salam, Bash AlMaliky, AlMustansiriya University, Iraq
 A/ Prof. Shailesh Kumar Jha, Indian Institute of Technology, India
 A/Prof. Teodor Lucian Grigorie, University of Craiova, Romania
 A/Prof. Pareshe Dalal, Shri Vitthalrao Shankarrao Naik Arts, Commerce and Science College, India
 A/Prof. Muhammad Qasim, Abdul Wali Khan University Mardan, Pakistan
 A/Prof. R. S. Ajin, GeoVin Solutions Pvt. Ltd., India
 Dr. Abdul Karim M. Zein, University of Khartoum, Sudan
 Dr. Abdull Halim Abdul, Universiti Teknologi MARA, Malaysia
 Dr. Afshin Asadi, University Putra Malaysia, Malaysia
 Dr. Ahmad Safuan A Rashid, Univeristi Teknologi Malaysia, Malaysia
 Dr. Ahmad Safuan Bin A Rashid, Univeristi Teknologi Malaysia, Malaysia
 Dr. Akindele Okewale, Federal University of Petroleum Resources, Nigeria
 Dr. Akinola Johnson Olarewaju, Federal Polytechnic Ilaro, Nigeria
 Dr. Ali Sobhanmanesh, Universiti Teknologi Malaysia (UTM), Malaysia
 Dr. Alireza Bahraie, Semnan University, Iran
 Dr. Allan Manalo, Centre of Excellence in Engineered Fibre Composites, Australia
 Dr. Aniza Ibrahim, National Defence University of Malaysia, Malaysia
 Dr. Arif Ali Baig Moghal, King Saud University, Saudi Arabia
 Dr. Aslan S. Hokmabadi, University of Technology, Sydney (UTS), Australia
 Dr. Ather Ashraf, PUCIT, Old Campus Punjab University, Pakistan
 Dr. Atsuko Sato, Cicil Engineering Research Institute for Cold Region, Japan
 Dr. Ben-Hur Silva, Military Institute of Engineering, United States

Dr. Choy Soon Tan, Univeristi Teknologi Malaysia, Malaysia
 Dr. David Thorpe, University of Southern Queensland, Australia
 Dr. Delsye Ching Lee Teo, Universiti Malaysia Sarawak, Malaysia
 Dr. Domenico Lombardi, University of Manchester, United Kingdom
 Dr. Ehsan, Jorat Newcastle University, United Kingdom
 Dr. Ganesh Kumar Shanmugam, National Institute of Ocean Technology, India
 Dr. Helsin Wang, Institute of Bridge Engineering, Taiwan
 Dr. Hossein Moayedi, Kermanshah University of Technology, Iran
 Dr. Hossein MolaAbasi, Babol University of Technology, Iran
 Dr. James Hambleton, University of Newcastle, Australia
 Dr. James Hambleton, University of Newcastle, Australia
 Dr. Janaka Kumara, Tokyo University of Science, Japan
 Dr. Jirayut, Suebsuk Rajamangala University of Technology Isan, Thailand
 Dr. Juhying Lee, Korea Institute of Civil Engineering and Building Technology, South Korea
 Dr. Jun Sugawara, Advision - WorleyParsons Group, Australia
 Dr. Lamia Touiti Bouebdellah, Ecole Nationale d'Ingénieurs de Gabes, Tunisia
 Dr. Luky Handoko, Universitas Atma Jaya Yogyakarta, Indonesia
 Dr. M. Mohammad Ali, California Public Utilities Commission, United States
 Dr. Marfiah Ab.Wahid, Universiti Teknologi Mara, Malaysia
 Dr. Maryam Naeimi, Semnan University, Iran
 Dr. Mehdi Mokhberi, Islamic Azad University, Shiraz, Iran
 Dr. Mohd Hairy Ibrahim, Sultan Idris Education University, Malaysia
 Dr. Neelima Satyam, International Institute of Information Technology, India
 Dr. Nor Zurairahetty Mohd Yunus, Univeristi Teknologi Malaysia, Malaysia
 Dr. Siavash Zamiran, Southern Illinois University Carbondale, United States
 Dr. Subha Vishnudas, Cochin University of Science and Technology, India
 Dr. Sunggi Jin, SK E&C, South Korea
 Dr. Sunil Pusadkar, Govt. College of Engineering, Amravati, India
 Dr. Teresa Lopez-Lara, Universidad Autonoma De Queretaro, Mexico
 Dr. Usama Juniansyah Fauzi, University of Tokyo, Japan
 Dr. Yusep Muslih Purwana, Sebelas Maret University, Indonesia
 Dr. Ana Almerich-Chulia, Universitat Politecnica de Valencia, Spain
 Dr. Khor Shing Phan, Universiti Malaysia Perlis, Malaysia
 Dr. Afshin Asadi, International College of Auckland, New Zealand

Conference Correspondence:

Prof. Dr. Zakaria Hossain, Conference Chairman,
 Dept. of Env. Sci. & Tech., Mie University, Japan,
 A/Prof. Dr. Shinya Inazumi, General Secretary
 Shibaura Institute of Technology, Japan
 E-mail: conference@geomate.org
 Tel & Fax: +81-59-231-9578

Editorial Committee and Executive Committee:

Dr. Zakaria Hossain
 Dr. Jim Shiau
 Dr. Sinya Inazumi
 Ms. Siti Hanggita Rachmawati
 Mr. Md. Aminul Islam
 Mr. Alex Otieno Owino

List of Universities:

ASEAN Institute for Health Development, Mahidol University
Azad University Of Tehran
Abdul Wali Khan University Mardan, Pakistan
Abubakar Tafawa Balewa University, Bauchi
Acharya Shrimannarayan Polytechnic
Aichi Institute of Tecnology
Al-Mustansiriayah University
Andalas University
Ariel University/Transist Video LLC (Skolkovo)
Bangladesh Agricultural Research Institute
Batna 2 University
Brawijaya University
Can tho university, vietnam
Central building research institute
CHUDEN Engineering Consultants Co.,Ltd.
CMR College of Engineering and Technology
Cal Poly, San Luis Obispo
Centre for Infrastructure Engineering, Western Sydney University
Chiang Mai University
China University of geosciences
Chulalongkorn University
Curtin University
De La Salle University - Manila
Deakin University
Diponegoro University
Disaster Prevention Research Institute Kyoto University
Eastern Mediterranean University
Eurasian National University
GSE Lining Technology Co. Ltd.
Gabes University Tunisia
Geophysical Institute of Vladikavkaz Scientific Center of the Russian Academy of Sciences
Gifu University
Govt. Higher Education Department J&K India
Griffith University
Gunma National College of Technology
Hakeem Water Business Links Nigeria Limited
Hiroshima University
Hokkaido University
Ibaraki University
Indiana University
International Islamic University Bangladesh
Iran University of Science and Technology
Islamic Azad University, Ahvaz, Iran
Isra University,Amman,Jordan
James Cook University, Australia.
Jiangsu University
Kagawa University
Kansai University
Kasetsart University
Khairun University
Khon Kaen University
Kilimanjaro Christian Medical University College
Kindai University Technical College
King Mongkut's University of Technology Thonburi
Kingston University, London
Korea Institue of Civil Engineering and Building Technology

Kyoto University, Japan
 Kyushu University
 L.N.Gumilyov Eurasian National University
 Ladoke Akintola University of Technology, Ogbomosho
 Mahasarakham University
 Maebashi City Office
 Maebashi Institute of Technology
 Mahasarakham University
 Mahidol University
 Meijo University
 Mie University, Japan
 Military Institute of Science and Technology
 Misurata University
 National Institute Of Technology, Calicut, India
 Nagasaki University
 Nagoya Institute of Technology
 National Agronomic Institute of Tunisia
 National Ilan University, Taiwan
 National Institute of Technology, Akashi College
 Nihon University College of Science and Technology
 Nihon University, CST
 Obayashi Corporation, Technical Research Institute
 Okayama University
 Osaka Institute of Technology
 Osaka University
 Pontifical University of Rio de Janeiro
 Pontifícia Universidade Católica do Rio de Janeiro
 Prince of Songkla University, Faculty of environmental management
 Qazvin Islamic Azad University Iran
 Railway Technical Research Institute Japan
 Rajamangala University of Technology Isan, Nakhon Ratchasim, Thailand
 Rajamangala University of Technology Thailand
 Ritsumeikan University
 Roi Et Rajabhat University
 Sungkwang I.T. Inc
 Saitama University
 Shinshu University
 Shridevi Institute of Engineering and Technology
 Sriwijaya University
 Suan Sunandha Rajabhat University
 Suranaree University of Technology
 Swinburne University of Technology
 Syiah Kuala University
 TOKAI UNIVERSITY
 Taisei Corporation
 Takenaka Corporation
 Texas Tech University
 The University of Nottingham Malaysia Campus
 Tohoku University
 Tokushima University
 Tokyo City University
 Tokyu University of Agriculture
 Tomsk Polytechnic University
 Universidad Nacional de San Antonio Abad del Cusco, Peru
 Universidade Federal Fluminense, Instituto de Física, Niteroi, RJ, Brazil,
 Universitas Atma Jaya Yogyakarta
 Universitas Gadjah Mada
 Universiti Malaysia Pahang

Universiti Malaysia Sarawak
Universiti Sains Malaysia
Universiti Teknologi Malaysia
Universiti Teknologi PETRONAS
Universiti Tun Hussein Onn Malaysia
University Normandy
University of Canberra
University of Malaya
University of Msila
University of New Mexico
University of Ottawa
University of Phayao
University of Sriwijaya
University of the Punjab
University of the Philippines
University of the Sunshine Coast, Australia
Université des Mascareignes, Mauritius
VSB - Technical University of Ostrava
Valaya Alongkorn Rajabhat University
Wakayama University
Yahagi Construction Co., Ltd.
Yashwantrao Chavan College of Engineering
Yokkaichi University
Zandjan Azad Slamic Uni, Iran

Keynote Papers

FLY ASH GEOPOLYMER STABILIZED RECYCLED ASPHALT PAVEMENT AS A SUSTAINABLE BASE MATERIAL

Suksun Horpibulsuk¹, Menglim Hoy², Runglawan Rachan³, Arul Arulrajah⁴

¹ School of Civil Engineering and Center of Excellence in Innovation for Sustainable Infrastructure Development, Suranaree University of Technology, Thailand

² School of Civil Engineering, Suranaree University of Technology, Thailand

³ Department of Civil Engineering, Mahanakorn University of Technology, Thailand

⁴ Department of Civil and Construction Engineering, Swinburne University of Technology, Australia

ABSTRACT

This paper presents the results of laboratory evaluation of recycled asphalt pavement (RAP) – fly ash (FA) geopolymer as a base material. A mixture of NaOH and Na₂SiO₃ was prepared as an alkali activator to synthesis FA-geopolymer, while RAP-FA with water (RAP-FA blend) prepared as control material. The strength development and the strength against wet-dry cycles were determined by unconfined compression strength (UCS) test, then the microstructural properties were examined by scanning electron microscopy (SEM) and X-Ray Diffraction (XRD) analysis, while the leachability of heavy metal was measured by Toxicity Characteristic Leaching Procedure (TCLP) test. The results show both RAP-FA blend and geopolymer can be used as a based course as its UCS values meet the minimum strength required specified by Department of Highway, Thailand. The durability test results show the UCS of these materials increase with increasing the number of wet-dry cycles, reaching its peak at 6 wet-dry cycle. The XRD and SME analyses indicate strength development of RAP-FA blend occurs due to a chemical reaction between a high Calcium in RAP with a high Silica and Alumina in FA led to produce calcium aluminate (silicate) hydration formation, while geopolymerization reaction is observed in RAP-FA geopolymer. After 6 wet-dry cycles, the development of the macro- and micro crack propagations caused a strength reduction for both RAP-FA blend and geopolymer samples. The TCLP results demonstrate there is no environmental risk of these stabilized materials. In addition, FA-geopolymer can reduce the leachability of heavy metal in RAP-FA blend.

Keywords: Recycled asphalt pavement, Geopolymer, Durability, Heavy metals, Microstructure.

INTRODUCTION

There is increasing global interest to use recycled materials as a construction and rehabilitation material in infrastructure sectors. Recycled Asphalt Pavement (RAP), a waste material is obtained from spent asphalt extracted from roads that have reached the end of their design life [1]. It was becoming a popular material for pavement application due to its low cost of construction. Though RAP was successful can be reused as pavement material when it mixed with cement, its negative impact on environment due to the product of Portland cement produce a huge amount of carbon dioxide [2], [3]. Exploring alternative green binder material is on attempt. Fly ash (FA)-geopolymer is an environmentally friendly additive, which potentially produce suitable mechanical properties for stabilized material [4].

The RAP stabilized with FA-geopolymer for pavement applications is currently limited due to the lack of laboratory and field evaluation. Therefore, this research aims to study the possibility of using FA-geopolymer stabilized RAP as a pavement material. The laboratory experimental programs were carried out and divided into three main parts. First, the

strength development of these materials were studied, then the durability against wetting-drying (w-d) cycles was undertaken. The strength development with and without w-d cycles process were determined by unconfined compression strength (UCS) test. Scanning electron microscopy (SEM) and X-Ray Diffraction (XRD) analyses were used as a tool to examine those strength changes. Finally, an environmental assessment was carried out by the leachate test to estimate the heavy metal concentration from the RAP-FA blend and geopolymer and compared with international standard. The outcomes of this research will have a positive impact on construction guidelines and specification for using RAP-FA blend and geopolymer in road construction.

MATERIALS

In this research, RAP samples were collected from a mill asphalt pavement stockpile in Nakhon Ratchasima province, Thailand. The gradation and shown in Figure 1 and Table 1, respectively. The chemical and mineral composite of RAP, obtained by X-Ray Fluorescence (XRF) and XRD analyses, are

presented in Table 2 and Figure 2, respectively.

FA, obtained from the largest lignite power plant in the northern region of Thailand, was used in this study. The grain size distribution curve of FA, obtained by a laser particle analyzer, is shown in Figure 1. Table 2 summarizes the chemical composition of FA using XRF analysis. The XRD pattern of FA is also shown in Figure 2.

Liquid alkaline activator (L) is a mixture of sodium silicate (Na_2SiO_3) and sodium hydroxide (NaOH) solution with a 10 M concentration.

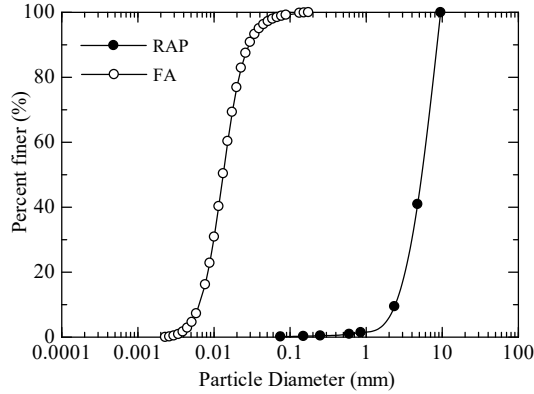


Fig. 1 Grain size distribution of RAP and FA.

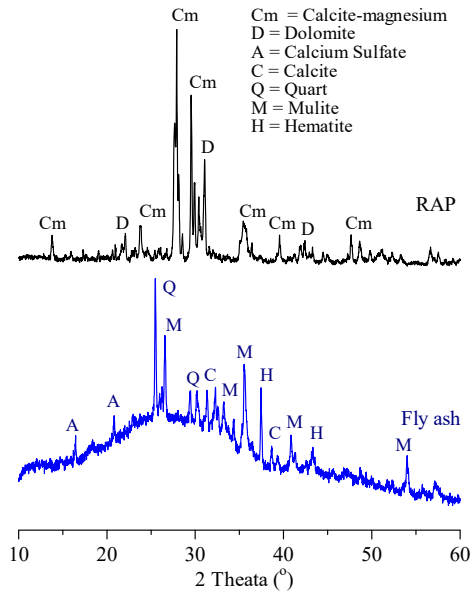


Fig. 2 XRD patterns of RAP and FA.

EXPERIMENTAL PROGRAM

Sample preparation

The RAP-FA geopolymer is a combination of RAP, FA and L ($\text{NaOH}+\text{Na}_2\text{SiO}_3$). The $\text{NaOH}/\text{Na}_2\text{SiO}_3$ ratios studied were 100:0, 90:10,

60:40, and 50:50. The RAP-FA blend, which is a mixture of RAP, FA, and water, was prepared as a control material to investigate the effect of L on strength development. FA replacement ratios are 10, 20, and 30% by weight to RAP.

Compaction and UCS test

The mixtures were compacted in a cylindrical mold (101.6 mm in diameter and 116.3 mm in height) under the modified Proctor energy [7] to determine the optimum water content (OWC) and optimum liquid alkaline activator content (OLC). The sample at the OWC and OLC were prepared for UCS test following the ASTM D1633 [8]. The samples after 7 and 28 days of curing at room temperature (RT), were soaked in water for 2 hours and then were air-dried for 1 hour prior to UCS test according to the specification of the Department of Highway, Thailand [9].

Table 1. Engineering properties of RAP.

Parameter	Values	ASTM
UCS classification	SP	D2487-11
Cu	2.44	-
Cc	1.16	-
Specific gravity	2.70	D1883-07
CBR (%)	10-15	D557-12
Water absorption (%)	6.80	-
Swelling ratio (%)	0.20	-
γ_{dmax} (kN/m^3)	17.50	D1557-12
OWC (%)	4.10	D1557-12

Table 2. Chemical composition of RAP and FA.

Chemical formula	RAP	FA
SiO_2	3.15	40.13
Al_2O_3	4.78	20.51
FeO_3	0.10	5.83
CaO	41.93	12.45
MgO	36.18	3.11
SO_3	0.89	0.42
K_2O	0.04	1.61
LOI	-	0.40

Durability test

The standard wetting-drying (w-d) method for compacted soil-cement mixture [10] was adopted for this study. The samples at 28-day of curing were submerged in water for 5 hours then dried in an oven at 70°C for 42 hours and air-dried for 1 hour. This counted for 1 cycle. The UCS of the samples were measured at 1 to 20 w-d cycles and compared with that of the samples without w-d cycle to investigate the effect of w-d cycles on the UCS changes.

Microstructure analysis

UCS development of the samples before and after w-d cycles test were examined by using XRD and SEM analyses, which performed on the small fragments taken from the broken portion of the UCS samples to investigate the mineralogical and microstructural changes, respectively.

Environmental assessment

The Toxicity Characteristic Leaching Procedure (TCLP) test is the method prescribed by the U.S. EPA guidelines (method 1311) to determine if the solid waste is hazardous. The TCLP test were carried out on 100% RAP, RAP-FA blend and geopolymers for various heavy metal concentrations.

RESULTS AND DISCUSSION

Figure 3 summarizes the UCS results of the RAP-FA blend and RAP-FA geopolymers for various NaOH/Na₂SiO₃ ratios curing for 7 and 28 days at RT. It is noted that the UCS values of both RAP-FA blends and geopolymers increase with increasing curing time. This result is similar to that reported in previous study on the strength development of cement-stabilized RAP and FA-treated RAP [3].

7-day UCS value of both RAP+20%FA blend and RAP+30%FA blend are greater than the strength requirement specified by the Thailand national road authorities in which UCS > 1,723 kPa and UCS > 2,413 kPa for both low and high volume roads, respectively [9, 11]. The UCS of RAP-FA geopolymer at NaOH/Na₂SiO₃ < 10:90 is higher than that of RAP-FA blends and the UCS values of RAP-FA geopolymers increase when NaOH/Na₂SiO₃ ratio is decreased. However, the UCS of RAP-FA blend and geopolymer improves insignificantly when the FA replacement ratios exceeds 20% indicating this to be the optimal ratio. Hence, the RAP+20%FA blend and geopolymer samples curing at 28 days were selected for durability test.

The UCS of RAP+20%FA blend and RAP+20%FA geopolymer at various number of w-d cycles, *C* is presented in Figure 4. The UCS of RAP+20%FA blend and geopolymer increases with increasing *C*, up to *C* = 6 and then decrease when *C* > 6. Previous research on effect of w-d cycles on strength development of FA-stabilized with lime and gypsum indicated that the strength increase due to the development of cementitious compounds during w-d process [12]. The UCS of RAP+20% geopolymer at

L = 100:0 and 50:50 increases sharply after the first w-d cycle and is much higher than that of RAP+20%FA blend for all *C* tested. Although the RAP+20%FA geopolymer sample at *L* = 50:50 possesses higher UCS than the sample with *L* = 100:0 within the first 3 w-d cycles, it has lower UCS when *C* > 6.

The effect of cyclic w-d cycles on the external surface of the RAP+20%FA blend and RAP+20%FA geopolymer at *L* = 100:0, and 50:50 is evident in Figure 5a, b, and c, respectively at a particular *C* = 20. Large macro-cracks and surface deterioration on the RAP+20%FA blend are clearly observed, which leads to strength loss. On the other hand, Figure 5b obviously shows the minimum cracks on the surface of RAP+20%FA geopolymer at *L* = 100:0, while more cracks are observed for the sample at *L* = 50:50 (Figure 5c).

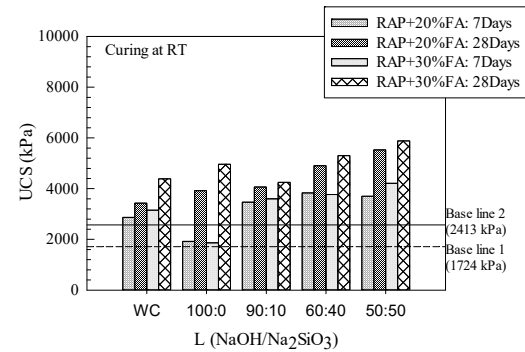


Fig. 3 UCS of RAP-FA blends and RAP-FA geopolymers cured for 7 and 28 days.

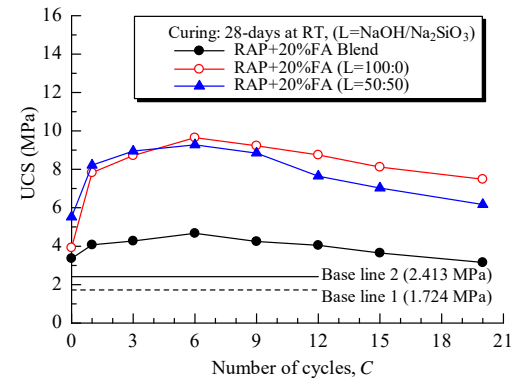


Fig. 4 Relationship between strength and number of w-d cycles of RAP+20%FA and geopolymers.

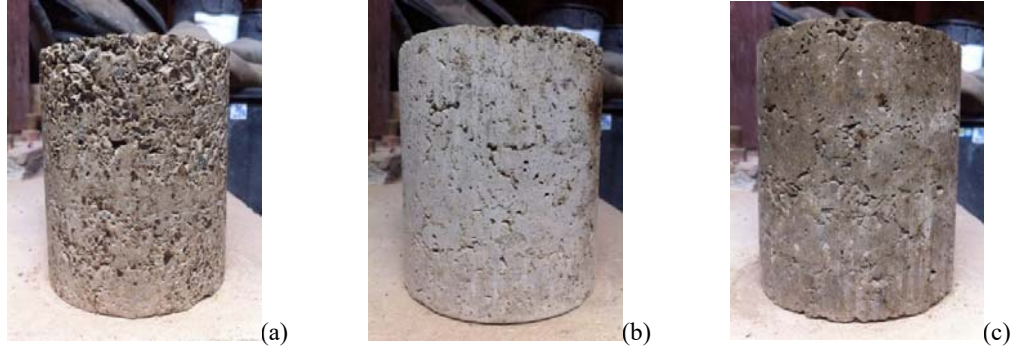


Fig. 5 Photos of (a) RAP+20%FA blend, (b) RAP+20%FA geopolymer at $L = 100:0$, and (c) RAP+20%FA geopolymer at $L = 50:50$ at $C = 20$.

This imply that the samples at $L = 100:0$ has stronger bonding structure than the sample at $L = 50:50$. From the cyclic w-d results and the photos, it is evident that RAP+20%FA blend provides a fairly good durability when subjected to w-d cycles. FA-geopolymer can enhance the durability of RAP-FA material, especially for the sample at $L = 100:0$.

The XRD patterns of RAP+20%FA blend at various C are shown in Figure 6. Without w-d cycle ($C = 0$), the RAP+20%FA blend (Figure 6a) contains the amorphous phases of calcium-magnesium as the predominant minerals (silica- and alumina- products), such as Anorthite, Diopside, Ladradorite, and Ettringite. These new minerals are formed when RAP is mixed with FA (RAP-FA blend). In other words, the chemical reaction between the high amount of calcium of RAP and high amount of silica and alumina of FA results in the formation of Calcium Silicate Hydrate (C-S-H) and Calcium Aluminate Hydrate (C-A-H), or Calcium Aluminate Silicate Hydrate (C-A-S-H), similar to the hydration of Portland cement [13], that can enhance the strength development.

The increase in peaks corresponded to Anorthite, Diopside, and Ladradorite with increasing C up to 6 is observed by comparing Figure 6b ($C = 1$) with Figure 6c ($C = 6$), that indicates the increase of C-A-S-H gel. Drying at 70°C for w-d test evidently enhances the cementitious products (C-A-S-H gel) [14]; i.e., an increase temperature results in a faster moisture diffusivity of the cementitious materials and hence cement hardening [15]. The same is however not true for $C > 6$. The temperature affects the water physical properties (density and surface tension) [16] and causes the coarsening of the pre-structure in relation to Ettringite dissolution and C-A-S-H alteration [14]. Figure 6d indicates the presence of Ettringite and the decreased intensity of Anorthite and Diopside minerals when the samples are subjected to 12 w-d cycles. Ettringite is a hydrous mineral that exhibits expansive behavior upon wetting [17] and makes the RAP-FA blend volumetrically unstable [18].

Besides the XRD results, SEM images of

RAP+20%FA blend at various C are illustrated in Figure 8. The growth of C-A-S-H gel inner and on the spherical surface of FA with increasing C ($C = 0$ to 6, see Figure 7a-c) is observed while reduction in cementitious gel at the $C = 12$ (Figure 7d) is detected, which confirms the XRD results.

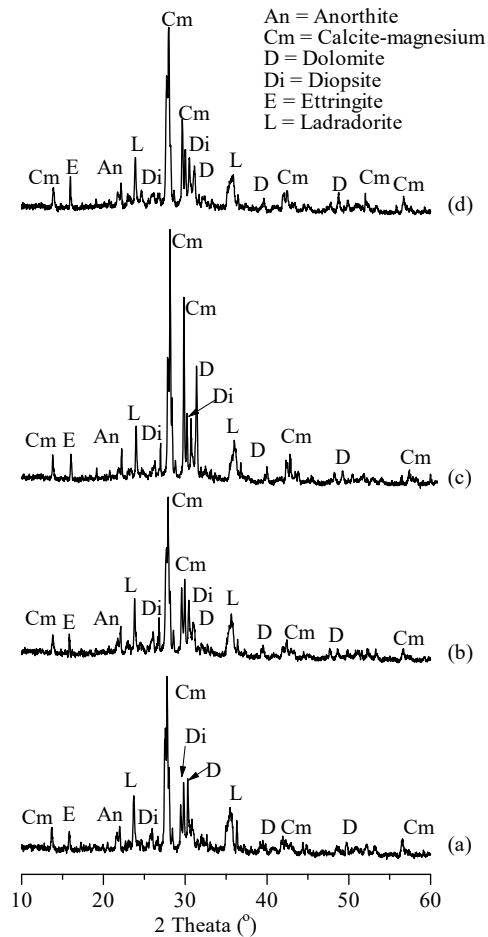


Fig. 6 XRD patterns of RAP+20%FA blend samples at (a) $C = 0$, (b) $C = 1$, (c) $C = 6$, and (d) $C = 12$.

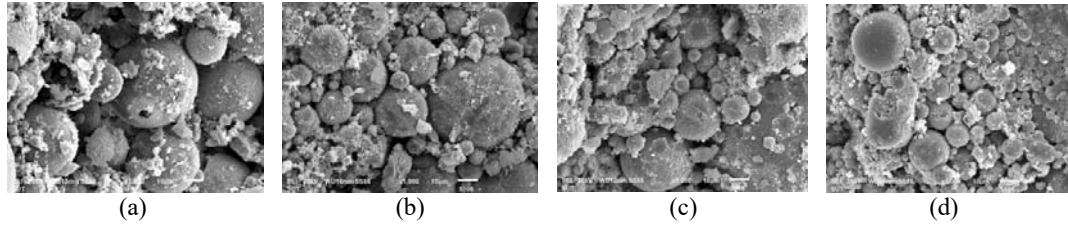


Fig. 7 SEM images of RAP+20%FA blend samples at (a) $C = 0$, (b) $C = 1$, (c) $C = 6$, and (d) $C = 12$.

Figure 8 and 9 presents the XRD patterns of RAP+20%FA geopolymer at $L = 100:0$ and $50:50$ and at various w-d cycles, respectively. As a result of the alkaline activation, new geopolymerization products inclusive of Albite, Nepheline, and Analcime are observed at the broad hump between $22-33^\circ 2\theta$ in the XRD pattern of the sample at $L = 100:0$ (Figure 8a) and at $L = 50:50$ (Figure 9a) for $C = 0$. A good performance of geopolymer was observed when the precursor was in contact with alkali activator at curing temperature of around $40 - 75^\circ\text{C}$ [19]. Therefore, the C-A-S-H from RAP-FA blend co-exist with the geopolymer products and contribute to the additional strength development of RAP+20%FA geopolymer in the first 6 w-d cycles.

The silica presents in sodium silicate is highly soluble and consequently incorporated immediately into the N-A-S-H gel, hence more geopolymer products are detected in the XRD patterns of the geopolymer sample at $L = 50:50$ (Figure 9b and c) compared with those at $L = 100:0$ (Figure 8b and c). consequently, the UCS values of RAP+20%FA geopolymer sample at $L = 50:50$ are higher than those of sample at $L = 100:0$ within the first 6 w-d cycles (see Figure 4).

The SEM images of RAP+20%FA geopolymer at $L = 100:0$ and $50:50$ (Figure 10 and 11) were examined to support the XRD results.

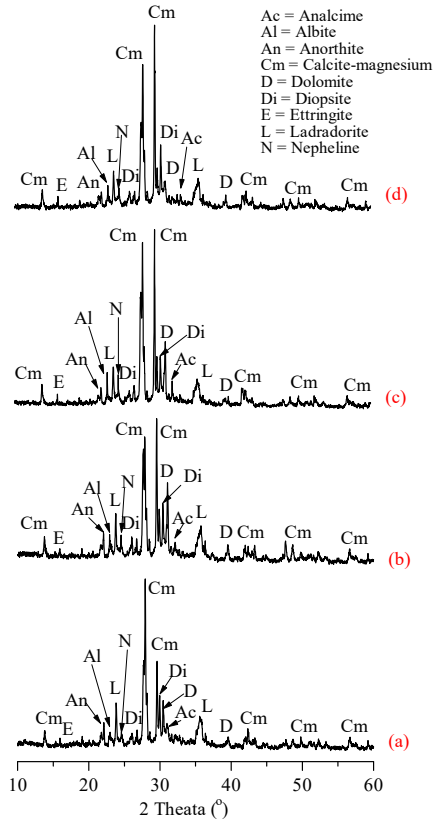


Fig. 8 XRD patterns of RAP+20%FA geopolymer at $L = 100:0$ samples at (a) $C = 0$, (b) $C = 1$, (c) $C = 6$, and (d) $C = 12$.

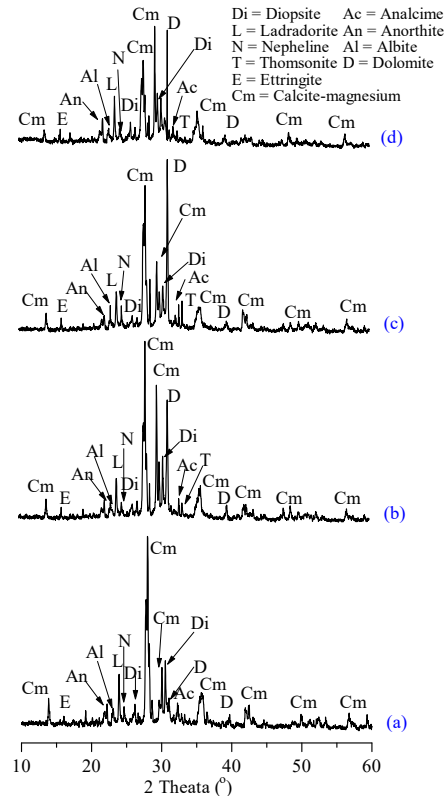


Fig. 9 XRD patterns of RAP+20%FA geopolymer at $L = 50:50$ samples at (a) $C = 0$, (b) $C = 1$, (c) $C = 6$, and (d) $C = 12$.

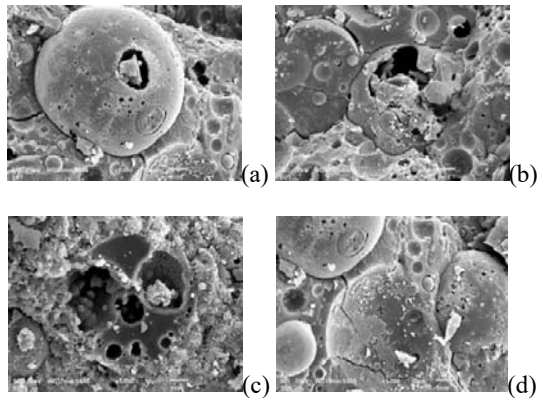


Fig. 10 SEM images of RAP+20%FA geopolymer at $L = 100:0$ samples at (a) $C = 0$, (b) $C = 1$, (c) $C = 6$, and (d) $C = 12$.

The geopolymerization products in the sample at $L = 50:50$ are more than those in the sample $L = 100:0$ for $C < 6$. For $C > 6$, at a particular $C = 12$, the micro-cracks are clearly observed in RAP+20%FA geopolymer samples (Figure 10d and 11d) due to the loss of moisture content result in external surface cracks leading to a strength loss.

It is noted that the sample at $L = 50:50$ (Figure 11d) has more micro-cracks than the sample at $L = 100:0$ (Figure 10d). Consequently, the rate of strength reduction of the sample at $L = 50:50$ is higher than that of the sample at $L = 100:0$ when $C > 6$. This indicates that the RAP+20%FA geopolymer sample at $L = 100:0$ has higher durability against w-d cycles than that sample at $L = 50:50$. This high durability is attributed to the formation of stable cross-linked alumino-silicate polymer structure.

Table 3 shows the leachate analysis of 100% RAP and RAP+20%FA blend and geopolymers using acetic leachate extraction. According to benchmark mandated by the U.S. EPA for storm-water sampling, pH values should in the range of 6 to 9 [20].

Leachate results show that pH level in 100% RAP is 5.12 and 5.59 for RAP+20%FA blend, which are within allowable limits. Table 4 presents the prescribed limits for drinking water and the threshold for hazardous waste defined by the U.S. EPA. Wartman et al. [21] reported that a material is designed as a hazardous waste in according to U.S. EPA if any detected metal is present in concentration larger than 100 times the drinking water standards. Based on this criterion, the comparison of TCLP results between Table 3 and 4 indicated that all metal contaminates are within acceptable limits.

From a geotechnical engineering prospectively, the research results indicate that RAP is mechanically and economically viable for using in pavement base application when it stabilized with FA. Besides having a high UCS, the RAP-FA blend exhibits good durability against w-d cycles, which can be attributed to the growth of C-A-S-H.

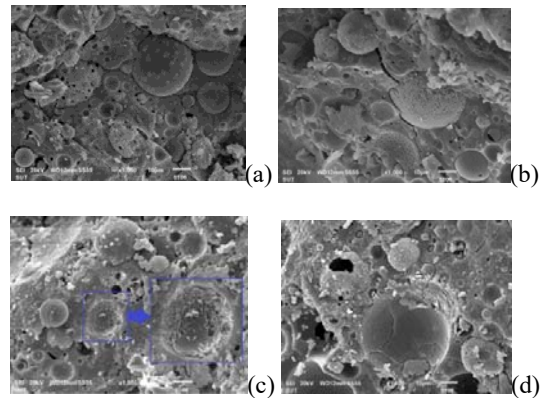


Fig. 11 SEM images of RAP+20%FA geopolymer at $L = 50:50$ samples at (a) $C = 0$, (b) $C = 1$, (c) $C = 6$, and (d) $C = 12$.

FA-geopolymer can significantly improve the strength and durability of RAP-FA blend. Furthermore, these materials provide a positive environmental impact as environmental test results show no significant risk to the ground water.

CONCLUSION

The present study investigated the possibility of using RAP-FA blend and geopolymer as a sustainable pavement material. The 7-day UCS of the compacted RAP-FA blend at OWC for both 20% and 30%FA meets the strength requirement for base course specified by national road authorities, Thailand. The UCS improved insignificantly when the FA replacement ratio exceeds 20%, indicating this to be the optimal content. FA-geopolymer can significantly improves the UCS and durability of RAP-FA blend. The XRD and SEM analyses of RAP-FA blends indicate the growth of C-A-S-H formation, hence its UCS increase over time. The co-exist of C-A-S-H from RAP-FA blend with the N-A-S-H from RAP-FA geopolymer can enhance the durability of RAP-FA blend remarkably.

The TCLP results indicate that RAP-FA blends and geopolymers can be safely used as a sustainable pavement base application as these materials pose no significant environmental and leaching hazard into soil and ground water sources. In addition, FA-geopolymer used can reduce the leachability of met concentration from RAP-FA blend. This study can confirm the utilization of these recycle and waste materials in pavement application results in energy saving and reduction in greenhouse gas emission.

ACKNOWLEDGEMENTS

This work was financially supported by the Thailand Research Fund under the TRF Senior Research Scholar program, Suranaree University of Technology.

Table 3. Leachate analysis results

Parameter	Sample of acid leachate extraction (mg/L)			
	100% RAP	RAP-FA blend	RAP-FA geopolimer	
			L=100:0	L=50:50
pH	5.12	5.59	7.59	7.44
Arsenic	<0.01	<0.01	BDL	BDL
Cadmium	BDL	BDL	BDL	BDL
Chromium	<0.05	<0.05	<0.05	<0.05
Copper	BDL	BDL	BDL	BDL
Lead	BDL	BDL	BDL	BDL
Mercury	BDL	BDL	BDL	BDL
Nickel	<0.05	<0.051	<0.05	<0.05
Zinc	1.348	0.657	BDL	BDL

Note: BDL = Below Detection Limit.

Table 4. Comparison of TCLP data analysis with U.S. EPA requirements.

Contaminant	Drinking water standard (EPA, 1999) (mg/L)	Threshold for solid waste (EPA, 2009) (mg/L)
Arsenic	0.05	0.35
Barium	2.0	35.0
Cadmium	0.005	0.1
Chromium	0.1	2.5
Lead	0.015	0.5
Mercury	0.002	0.05
Selenium	0.05	0.5
Silver	0.05	5.0

REFERENCES

- [1] A. Arulrajah, J. Piratheepan, and M. Disfani, "Reclaimed asphalt pavement and recycled concrete aggregate blends in pavement subbases: laboratory and field evaluation," *Journal of Materials in Civil Engineering*, vol. 26, pp. 349-357, 2013.
- [2] A. J. Puppala, L. R. Hoyos, and A. K. Potturi, "Resilient moduli response of moderately cement-treated reclaimed asphalt pavement aggregates," *Journal of Materials in Civil Engineering*, vol. 23, pp. 990-998, 2011.
- [3] R. Taha, A. Al-Harthy, K. Al-Shamsi, and M. Al-Zubeidi, "Cement stabilization of reclaimed asphalt pavement aggregate for road bases and subbases," *Journal of Materials in Civil Engineering*, vol. 14, pp. 239-245, 2002.
- [4] M. A. Salih, A. A. A. Ali, and N. Farzadnia, "Characterization of mechanical and microstructural properties of palm oil fuel ash geopolimer cement paste," *Construction and Building Materials*, vol. 65, pp. 592-603, 2014.
- [5] M. M. Allam and A. Sridharan, "Effect of wetting and drying on shear strength," *Journal of the Geotechnical Engineering Division*, vol. 107, pp. 421-438, 1981.
- [6] A. Dawson, "Water in road structures. Movement, drainage and effects. Geotechnical, Geological and Earthquake Engineering," ed: Springer. Nottingham, UK, 2009.
- [7] ASTM-D1557, "Standard test methods for laboratory compaction characteristics of soil using modified effort (56,000 ft-lbf/ft³ (2,700 kN/m³)," in West Conshocken, PA, ed, 2012.
- [8] ASTM-D1633, "Standard Test Methods for Compressive Strength of Molded Soil-Cement Cylinders: ASTM International," ed, 2007.
- [9] DOH, "DH-S204/2000 Standard of soil cement base: Department of Highways," ed. Thailand 2000.
- [10] ASTM-D559/D559M-15, "Standard Test Methods for Wetting and Drying Compacted Soil-Cement Mixtures," ed, 2015.
- [11] DRR, "DRR244-2013 Standard of soil cement base: Department of Rural Roads," ed, 2013.
- [12] P. V. Sivapullaiah and A. A. B. Moghal, "Role of gypsum in the strength development of fly ashes with lime," *Journal of materials in civil engineering*, vol. 23, pp. 197-206, 2010.
- [13] N. Cristelo, S. Glendinning, L. Fernandes, and A. T. Pinto, "Effect of calcium content on soil stabilisation with alkaline activation," *Construction and Building Materials*, vol. 29, pp. 167-174, 4// 2012.

- [14] F. Brue, C. A. Davy, F. Skoczylas, N. Burlion, and X. Bourbon, "Effect of temperature on the water retention properties of two high performance concretes," *Cement and Concrete Research*, vol. 42, pp. 384-396, 2// 2012.
- [15] Y. Wang, M. Fall, and A. Wu, "Initial temperature-dependence of strength development and self-desiccation in cemented paste backfill that contains sodium silicate," *Cement and Concrete Composites*, vol. 67, pp. 101-110, 3// 2016.
- [16] M. Wu, B. Johannesson, and M. Geiker, "A study of the water vapor sorption isotherms of hardened cement pastes: Possible pore structure changes at low relative humidity and the impact of temperature on isotherms," *Cement and Concrete Research*, vol. 56, pp. 97-105, 2// 2014.
- [17] E. Celik and Z. Nalbantoglu, "Effects of ground granulated blastfurnace slag (GGBS) on the swelling properties of lime-stabilized sulfate-bearing soils," *Engineering Geology*, vol. 163, pp. 20-25, 8/19/ 2013.
- [18] A. Aldaood, M. Bouasker, and M. Al-Mukhtar, "Impact of wetting–drying cycles on the microstructure and mechanical properties of lime-stabilized gypseous soils," *Engineering Geology*, vol. 174, pp. 11-21, 5/23/ 2014.
- [19] P. Sukmak, S. Horpibulsuk, S.-L. Shen, P. Chindaprasirt, and C. Suksiripattanapong, "Factors influencing strength development in clay–fly ash geopolymer.," *Construction and Building Materials*, 47, 1125-1136. , 2013b.
- [20] EPA, "Benchmarks for storm-water sampling. Business Environmental Resource Center, City of Sacramento, California.," ed, 2005.
- [21] J. Wartman, D. G. Grubb, and A. Nasim, "Select engineering characteristics of crushed glass," *Journal of Materials in Civil Engineering*, vol. 16, pp. 526-539, 2004.

EVALUATION OF SLOPE STABILITY BASED ON MONITORING OF RESIDUAL LOADS ON GROUND ANCHORS USING THE SAAM SYSTEM

Toshinori Sakai¹ and Yu Fujiwara²

¹ Graduate School of Bioresources, Mie University, Japan

² Nippon Expressway Research Institute Company Limited, Japan

ABSTRACT

Ground anchors are constructed every year as a way to stabilize cutting slopes and prevent landslides. After construction, maintenance of ground anchors on a slope is generally conducted on only a portion of anchors. Since anchors are arranged in groups on the slope, it is necessary to evaluate the distribution of tensile loads on the slope. Methods used to determine the tensile loads on anchors are lift-off testing and monitoring using load-cells. In the present study, we propose a new method for evaluating slope stability based on monitoring of tensile loads using the SAAM system. The SAAM system is compact and has high test accuracy. This system can be used to easily evaluate the residual load distribution on the slope and makes it easy to attach or detach load-cells to working anchors. Based on the results, tensile loads on anchors do not converge to a constant level affected by the geological features of the ground. However, the correlation between the measured tensile load obtained by load-cell and temperature is high in stable slopes and low in unstable slopes. It is possible to evaluate slope stability based on monitoring of the correlation between the tensile loads on load-cells and temperature.

Keywords: Ground anchor, Tensile load, Temperature, Correlation, Slope stability

INTRODUCTION

The ground anchoring system was introduced in 1957 in Japan. A number of anchors are constructed every year as a way to stabilize cutting slopes and prevent landslides. Anchors are constructed in natural ground and have complicated structures. Anchor maintenance following construction is important. The tensile loads on an anchor are not constant after introducing the initial tension to the anchor at fixation. The tensile loads on the anchor are reduced due to the effects of soil creep or relaxation of the anchor tendon in a stable slope. On the other hand, when a slope becomes unstable, during a landslide, for example, the tensile loads on the anchor may increase. The anchor has a sensor function, similar to that of a borehole inclination tester or a pipe strain meter.

Anchor inspection is important in order to maintain the stability of the slope. One anchor inspection method involves measuring the tensile load on the anchor. Tensile loads on anchors are measured by lift-off tests or using load-cells. A lift-off test is conducted by pulling the tendon with a hydraulic jack, and conventional hydraulic jacks are large and heavy. Since load-cells must be installed during construction, they are difficult to replace or newly attach to working anchors. For the above reasons, lift-off testing or monitoring using load-cells are typically conducted on approximately 5%

or 10% anchors in a slope^{1),2)}. As shown in Figure 1, a slope may contain numerous anchors, which means that a large number of anchors must be evaluated during maintenance.

We developed a small, lightweight hydraulic jack (SAAM jack) for use in the SAAM system³⁾. The SAAM system enables evaluation of the distribution of tensile loads on an anchor in a slope⁴⁾ and to attach or detach the load-cells to working anchors. In the present study, we propose a new method for evaluating slope stability using the SAAM system.



Figure 1 Ground anchors in a retaining wall.

THE SAAM SYSTEM

The SAAM system was developed in order to properly maintain ground anchors using a SAAM jack, which is comprised of a small, lightweight hydraulic jack, a tension bar, a chair, and a fix-nut. Figure 2 shows the components of the SAAM jack. The SAAM jack is lightweight and compact and has high test accuracy.

There are many anchoring methods. Fixed anchor heads are classified as wedge-fixed, combination wedge-nut-fixed, and nut-fixed anchor. The SAAM system supports all of the anchoring methods and fixation types shown in Fig. 3. The lift-off test is performed by attaching a hydraulic jack to the extra tendon (tension-bar) length of the anchor head.



Figure 2 Components and installation of the SAAM jack.



Figure 3 Anchoring methods.

Figure 4 shows the procedure used to attach a load-cell to a nut-fixed anchor⁵⁾. When a load-cell is attached to a working anchor using the conventional procedure, the tension load on the anchor must be

completely released. If the working anchor is in a hypertonic state, the tendon may be drawn into the ground as the tension released, and the original condition may be difficult to recover. As such, the method used to attach a load-cell may depend on the conditions of the study site. In contrast, the SAAM system makes it easy to attach or detach load-cells to working anchors.

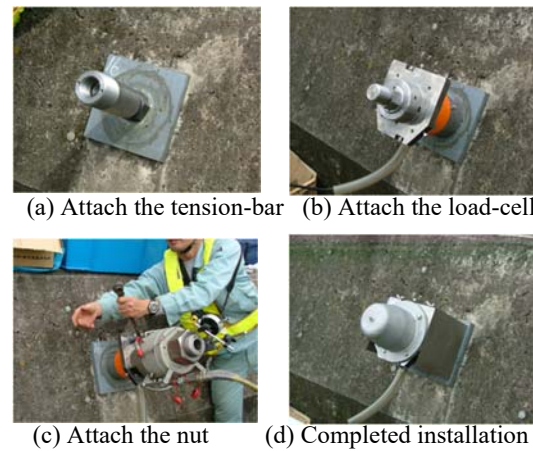


Figure 4 Procedure for load-cell installation in the SAAM system.

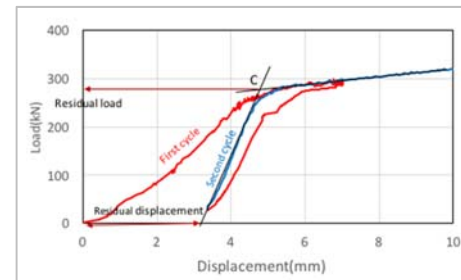


Figure 5 Results of the lift-off test.

Figure 5 shows the typical load-displacement curve obtained by the lift-off test. The initial displacement of the anchor head is small. The slope of the load-displacement curve then increases sharply. When the load increases and becomes equal to the tensile load on the anchor, the anchor head starts to lift away from the bearing plate. This phenomenon is called lift-off. The slope of the load-displacement curve decreases after lift-off because the load is transferred to the long free anchor length. The residual load is defined as the load at intersection of the linear gradients of the load-displacement curve before and after lift-off (point C)⁶⁾. After the residual load is determined, the

unloading process is performed. Residual displacement sometimes occurs during the first loading. The residual displacement of the first cycle is greater than in subsequent cycles. When the lift-off test is performed, preloading should be performed during the first cycle. Actual loading should be performed after confirming the convergence of the small residual displacement in subsequent cycles.

The SAAM system has high test accuracy and can be used to investigate residual loads on anchors in slopes. Figure 6 shows the distribution of residual tensile loads on anchors in a slope obtained by the SAAM system⁷⁾. The distribution in this figure was obtained by determining the residual tensile loads on of the anchors in the slope. Although numerous anchors are usually installed in a slope, it is difficult to investigate the residual loads on all of the anchors in the slope. Figure 7 shows the distributions of residual tensile loads obtained by determining the residual tensile loads on fewer anchors, specifically 1/20, 1/10, 1/4, and 1/2 the total number of anchors. The distributions obtained using 1/4 and 1/2 the total number of anchors were similar to that obtained using all of the anchors.

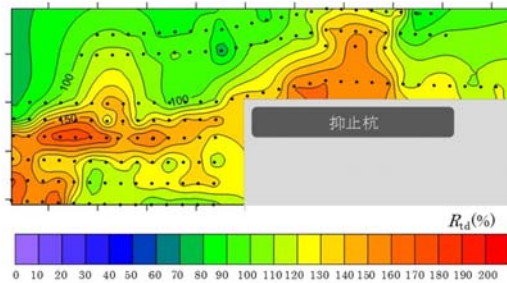


Figure 6 Distribution of residual loads.

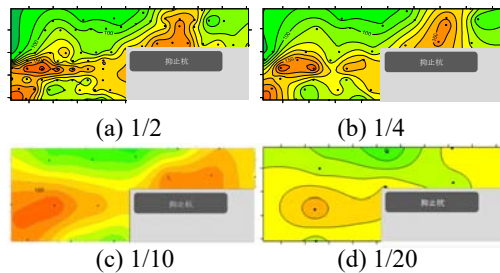
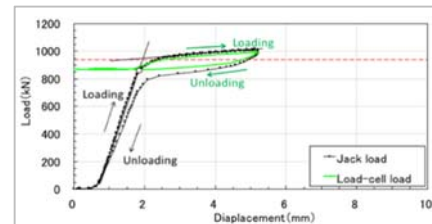


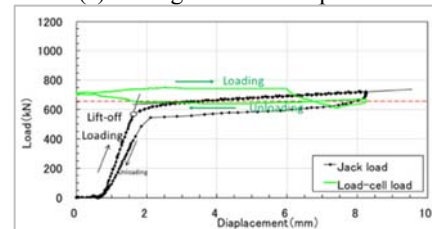
Figure 7 Distributions of residual loads obtained using fewer anchors.

The SAAM system can be used to check the function of load-cells attached to working anchors⁵⁾. Figures 8(a) and 8(b) shows the load-displacement

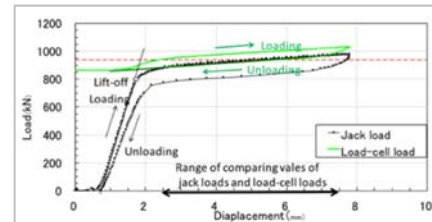
curves obtained by load-cell and SAAM jack. In Fig. 8(a), the values obtained by both load-cell and the SAAM jack were almost identical after lift-off, which indicates that the load-cell is functioning properly. The results in Fig. 8(b) indicate that the load-cell was not operating properly. In Fig. 8(c), the values obtained using the SAAM jack are slightly higher than those obtained using the load-cell, but the results have similar tendencies. Figure 9 shows the relationship between the loads obtained using the SAAM jack and the load-cell. The primary regression equation after lift-off can be obtained.



(a) Taking the identical path



(b) Taking the differences path



(c) Taking the same path

Figure 8 Load-displacement curves obtained by the load-cell and the SAAM jack.

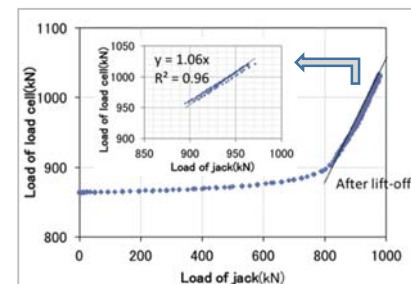


Figure 9 Relationship between the load on the jack and the load on the load-cell.

The values obtained using the load-cell are 1.06 times those obtained using the SAAM jack. Figure 10 shows the results of multiplying the load cell values by 1/1.06. These are referred to as the revised results. The revised results are almost identical to the results measured after lift-off.

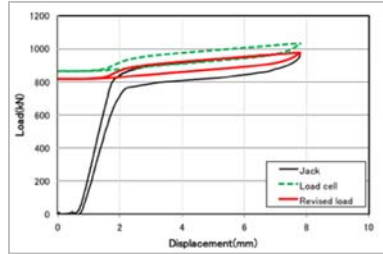


Figure 10 Revised results.

CORRELATION BETWEEN TEMPERATURE AND TENSILE LOAD

The correlation between temperature and tensile load is high in a stable slope. Figure 11 shows anchors in a stable slope. A total of 77 anchors were installed in this slope. The load-cell was attached to a working anchor using the SAAM system, as shown in Fig. 12. A temperature sensor was attached to the surface of the load-cell, as shown in Fig. 13.



Figure 11 Study site.



Figure 12 Load-cell attached to a working anchor.



Figure 13 Temperature sensor attached to a load-cell

Figure 14 shows the variations in tensile load and temperature⁸⁾. The variations reveal that the tensile load changes with the temperature. A difference in temperature of 22°C and a difference in tensile load of 13 kN are observed over the course of a day. Figure 15 shows the relationship between temperature and tensile load throughout the entire measurement period. A very high correlation was observed between temperature and tensile load. Since the measured tensile load is affected by temperature, temperature correction of the tensile load may be performed based on the correlational relationship between the temperature and the tensile load. The corrected load is obtained using the following equation:

$$L_i = L_0 - \{a_i(T_i - T_0)\} \quad (1)$$

where

L_i : Temperature corrected load at time i

L_0 : Load measured at the start time

T_i : Temperature measured at time i

T_0 : Temperature measured at the start time

a_i : Slope of the temperature-tensile load curve

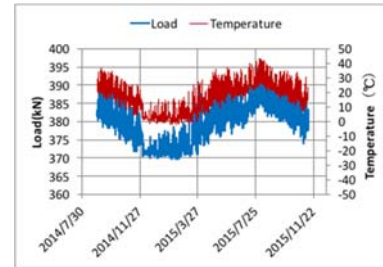


Figure 14 Variations in tensile load and temperature.

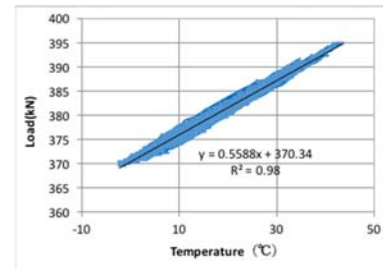


Figure 15 Relationship between temperature and tensile load.

Figure 16 shows the variations in the measured and corrected tensile loads. The measured values are affected by temperature and are not constant. A

difference in tensile load of 25 kN was observed throughout the entire measurement period. The corrected results are approximately constant, and a difference in tensile load of 3 kN is observed throughout the entire measurement period.

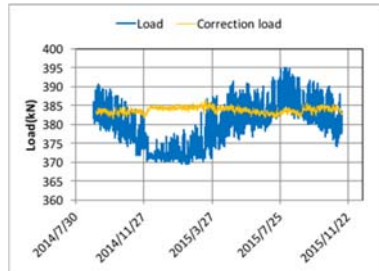


Figure 16 Variations in the measured and corrected tensile loads.

EXPERIMENTAL RESULTS

Study site

Figure 17 shows the study site. A landslide occurred over a wide area at this site, and anchors were installed at the edge of the landslide site⁹⁾. The geological feature is formed from mudstone. A total of 88 anchors were installed in three regions: 33 in the upper region (A3), 30 in the middle region (A2), and 23 in the lower region (A1). The anchor was of the SFL type, and the design load was $T_d = 414.5$ kN. The lock-off load was equal to approximately half the design load ($P_t = 161$ kN to 220 kN). Typhoon 12 struck Japan in September 2011 and caused significant damage. Figure 18 shows the damage to the site and the anchor system. A number of slope deformations appeared on the south side of the slope. The anchor cap of the anchor at A1-13 was broken, and the bearing plate was deformed. At this site, the deformation of the ground was observed using a pipe strain meter at GL -8.5 m, and precipitation for a period of one hour was measured using a rain gauge, and the results are shown in Fig. 19. A landslide occurred at this site after over 400 mm of total precipitation.



Figure 17 Study site.



Figure 18 Damage at the site.

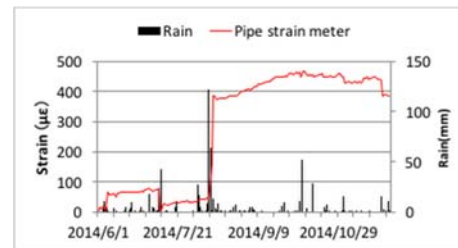


Figure 19 Variations in strain and precipitation.

Distribution of residual load

Figure 20 shows the distribution of residual load obtained by the SAAM system. The number of anchors investigated was 31, which is over to 1/4 (35%) of the total number of anchors installed in the slope. The tensile load was found to exceed 90% of the yield load ($0.9T_{ys}$) at the south side of the site, and the lift-off condition could not be confirmed to have occurred in this region. Lift-off was found to occur on the north side of the site, and the residual loads fell below the design loads. In a stable state, the tensile load on the anchor decreases due to the effects of creep, relaxation, and weathering of the

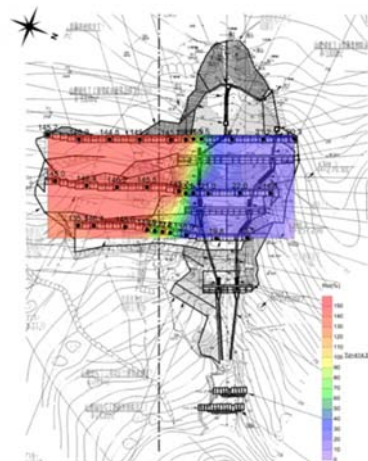


Figure 20 Distribution of residual load.

ground. Based on these results, the landslide appears to have occurred at the south side of the site, where measured tensile loads exceeded $0.9T_{ys}$.

Monitoring of tensile load

The SAAM system can be used to easily attach load-cells to working anchors. Four load-cells were attached to anchors, as shown in Fig. 21¹⁰⁾. The relationship between landslide deformation and tensile loads on anchors obtained by load-cells was evaluated. Figure 22 shows the load-cell attached to the anchor at A3-14. Figure 23 shows the variations in tensile load as determined by load-cell and pipe strain meter. A large change was measured by the

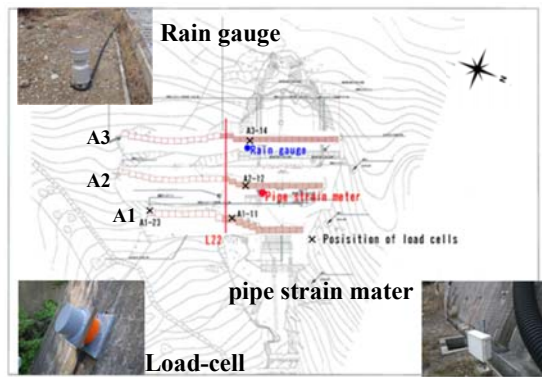


Figure 21 Observation locations.



Figure 22 Load-cell attached to the anchor at A3-14.

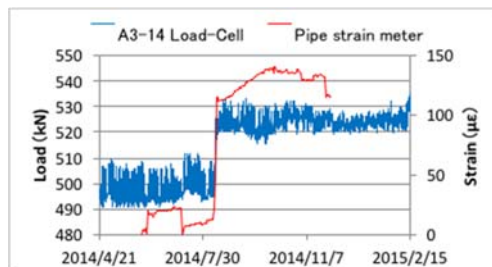


Figure 23 Variations in tensile load as determined by load-cell and pipe strain meter.

pipe strain meter at GL -8.5 m. Changes in the load and strain occur at the same time. Based on these results, the anchor functions as a sensor, in the same manner as the pipe strain meter.

Figure 24 shows the variations in tensile loads on load-cells and precipitation for one-hour periods.

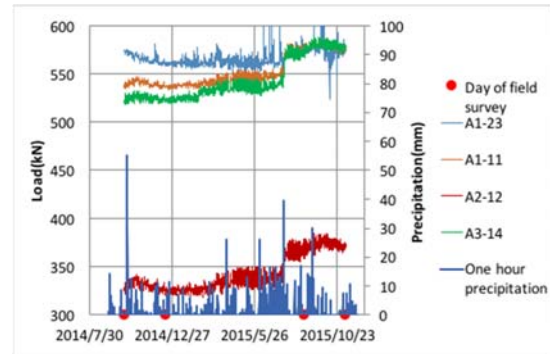


Figure 24 Variations in tensile loads on load-cells and precipitation.

Table 1 List of broken anchors

Anchor No.	2012/9/14	2013/2/19	2013/12/3	2014/9/30	2014/12/15	2015/8/24	2015/11/7
A1-13	○	→	→	→	→	→	→
A1-14	○					○	○
A1-16						○	○
A1-17						○	○
A1-18						○	○
A1-19						○	○
A1-22						○	○
A2-17				○	○	○	○
A2-18				○	○	○	○
A2-21						○	○
A2-22						○	○
A2-29				○	→	→	→
A2-30				○	○	○	○
A3-17						○	○
A3-20						○	○
A3-21						○	○
A3-23						○	○
A3-24						○	○
A3-26						○	○
A3-27				○	→	○	○
A3-28						○	○
A3-29				○	○	○	○
A3-30				○	○	○	○
計	1	1	1	6	6	20	23

○: Broken anchor



Figure 25 Photograph of a jumped out anchor

Landslide deformation was caused by the accumulation of 667 mm of precipitation on 16-17 July 2015, during which time the tensile loads on the anchors increased. Table 1 lists the results of a

survey of the anchor conditions. The number of broken anchors increased after the heavy rain of 16-17 July 2015. Anchors were confirmed to have “jumped out” for a distance of more than 50 m, as shown in Figure 25. Figure 26 shows the locations of broken anchors. All of the broken anchors are located on the south side, where the measured tensile loads exceeded $0.9 T_{ys}$.

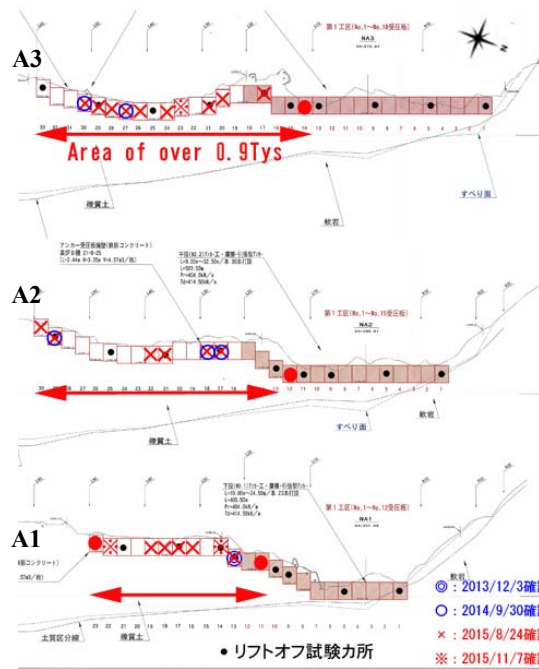


Figure 26 Locations of broken anchors.

Relationship between tensile load and temperature

Figure 27 shows the variations in tensile load and temperature in the anchor at A3-14. The tendency reveals that the tensile load changes with temperature during stable periods. Figure 28 shows the relationship between temperature and tensile load during the stable period of September 2015.

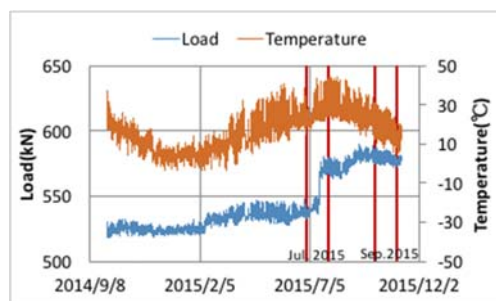


Figure 27 Variations in tensile load and temperature.

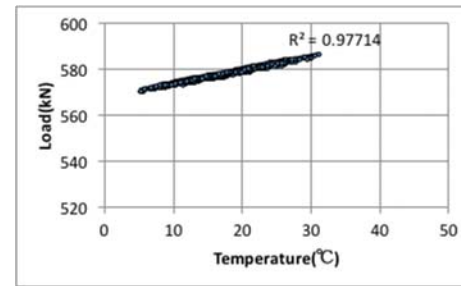


Figure 28 Relationship between temperature and tensile load (during the stable period of November 2015).

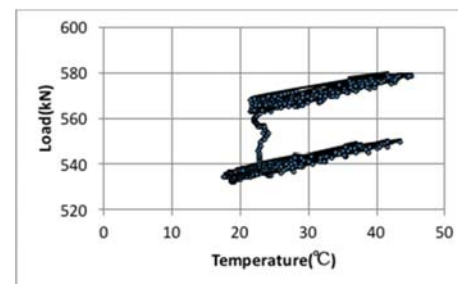


Figure 29 Relationship between temperature and tensile load (during the unstable period of July 2015).

A very high correlational relationship was observed between temperature and tensile load, and R^2 was determined to be 0.98. Figure 29 shows the relationship between temperature and tensile load during the unstable period of July 2015. There was no correlation for this period, during which the landslide occurred.

Figure 30 shows the relationship between tensile load and temperature for one-month periods from October 2014 to October 2015. No correlation appeared for A1-11, A2-12, and A3-14 in 16-17 July. A landslide occurred during this period. The landslide could be evaluated based on the correlation between tensile load and temperature. The correlation between temperature and tensile load is not clear for the anchor at A1-23 during all periods. Figure 31 shows a plan view of the anchors along line A1. Figure 32 shows a cross-sectional view of L22 line shown in Figure 21. The anchor at A1-23 was located at the edge of south side of the site. The landslide clearly spread over this area. A slope failure line appears along anchors of fixed length. Based on these results, the correlation is not clear

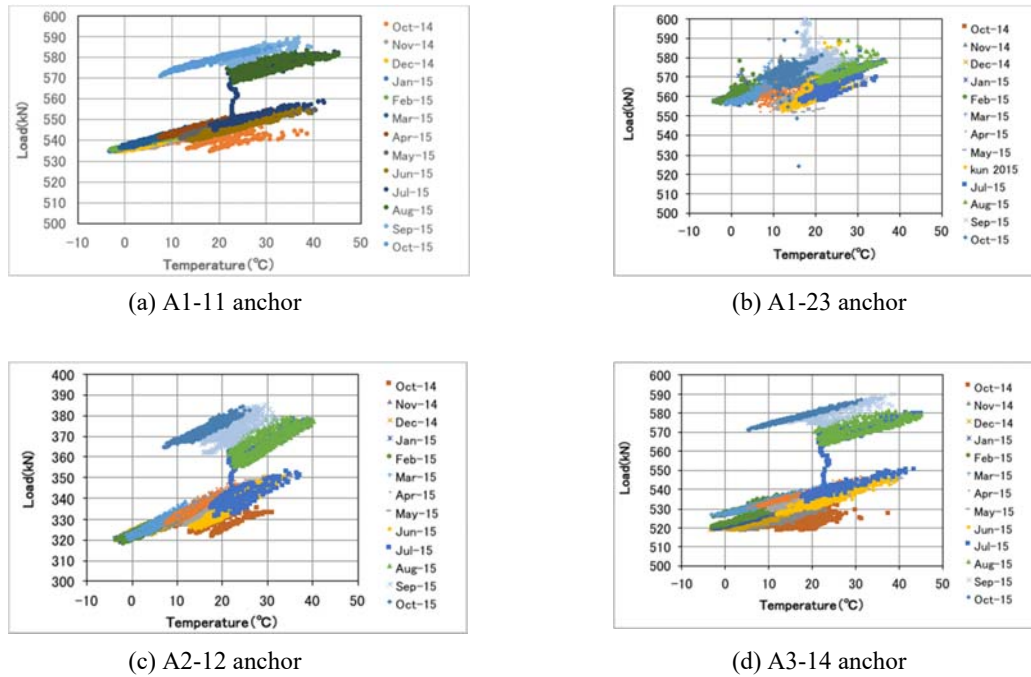


Figure 30 Relationship between tensile load and temperature.

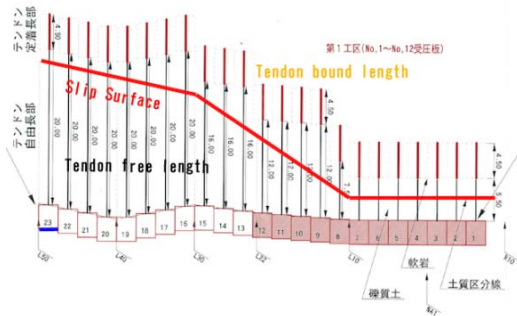


Figure 31 Plan view of anchor locations along line A1.

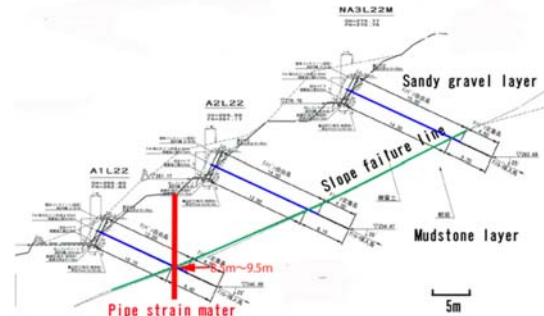


Figure 32 Cross-sectional view of L22 line.

and the tensile load variation in the anchor is unstable at A1-23.

CONCLUSION

We proposed a new method for evaluating slope stability based on monitoring of residual loads using the SAAM system. In the present paper, we obtained the following results.

1) The SAAM system has high test accuracy and can be used to easily investigate the residual loads on numerous anchors and the residual load distribution of a slope.

- 2) The SAAM system can be used to easily attach or detach load-cells to working anchors.
- 3) The SAAM system can be used to confirm the functionality of load-cells attached to working anchors.
- 4) There is very high correlational relationship between temperature and tensile load for a stable slope. However, there is no correlation for an unstable slope. A landslide can be evaluated based on the correlation between temperature and tensile load.

ACKNOWLEDGEMENTS

The present study was supported in part by the Japan Society for the Promotion of Science (JSPS) through a Grant-in-Aid for Scientific Research (No. 26450341). The authors are very grateful to Mr. Kawashima and the members of society of the SAAM for their co-operation.

REFERENCES

- [1] Public Works Research Institute and JAPA Anchor Association, Inspection and Maintenance Manual for Ground Anchor, pp.24-25, 2008.
- [2] Japanese Geotechnical Society, Design and construction standards for ground anchor, pp.122-125, 2012.
- [3] Sakai, T., "Manual of lift off test with SAAM jack for maintenance of ground anchor", Japan Geotechnical Consultants Association, pp.1-72, 2008.
- [4] Sakai, T., "Inspection manual for working ground anchor evaluated by distribution of tensile load using SAAM jack", Committee of maintenance of ground anchor using SAAM jack, pp.1-111, 2010.
- [5] Fujiwara, Y. and Sakai, T., "A study of a monitoring method for residual tensile load of ground anchor", Journal of JSCE, Vol68(3), pp.547-563, 2012.
- [6] Fujiwara, Y. and Sakai, T., "A study of a lift-off test method for ground anchors", Journal of JSCE, Vol.67(4), pp.558-568, 2011.
- [7] Fujiwara, Y. and Sakai, T., "A study of a monitoring method for residual tensile load of ground anchor", Journal of JSCE, Vol68(3), pp.547-563, 2012.
- [8] Sakai, T. and Kawashima, N., "Influence of setting position of thermometer for evaluating of correlation between anchor load and temperature", Proceeding of 50th Symposium of Japanese Geotechnical Society, pp.1387-1388, 2016.
- [9] Sakai, T., Tsunekawa, Y., Taguchi, K., Sakaguchi, K., Fujiwara, Y. and Ichihashi, Y., "Maintenance method of ground anchor using tensile load and temperature of anchor", J. of the Japan Landslide Soc., Vol.51(6), pp.19-24.
- [10] Sakai, T., Tsunekawa, Y., Sakaguchi, K., Isojima, Y. and Yano, M., "Relationship between load of anchor and temperature on the slope confirmed deformation, Proceeding of 28th Symposium of Japanese Geotechnical Society Cyubu Branch, 2016, pp.23-28.

USING PERMEABLE PAVEMENTS TO REDUCE THE ENVIRONMENTAL IMPACTS OF URBANISATION

Terry Lucke

Stormwater Research Group, School of Science and Engineering, University of the Sunshine Coast,
Australia

ABSTRACT

Permeable interlocking concrete pavements (PICPs) are being increasingly utilised in urban developments globally to promote stormwater infiltration, reduce catchment runoff volumes and to improve the quality of downstream receiving waters. Increased interest in permeable pavements from planners, designers and stormwater managers has led to an increase in permeable pavement research to try to address some of the common misconceptions and to investigate new research areas. This paper summarises the results of an international literature review that was undertaken to identify and examine the current state of permeable pavement research worldwide. The study found that the stormwater management and environmental benefits of permeable pavements are irrefutable and they clearly reflect the principals of low impact development. However, there are also misconceptions and barriers to their more widespread implementation which need to be addressed to ensure their future as an effective LID solution. More targeted research is required to address some of the outstanding issues with permeable pavements.

Keywords: Low impact development, Permeable pavements, Stormwater pollution, Urban runoff

INTRODUCTION

Low Impact Development

Altering the natural characteristics of a drainage basin through urbanisation can impose dramatic changes on the movement and storage of water within the catchment. Impervious surfaces such as roofs and pavements can prevent precipitation from reaching the soil and this can reduce infiltration and groundwater recharge, while increasing stormwater runoff volumes and flowrates from the catchment. Increasing impervious areas in urban catchments can also cause flooding during periods of heavy rainfall when stormwater drainage systems are operating at capacity. Increased stormwater runoff can also cause significant reductions in downstream water quality [1, 2]. With approximately 50% of the world's population now living in urban environments impervious surface areas and their associated environmental problems are set to increase [3].

Low impact development (LID) in the USA and Japan is similar to water sensitive urban design (WSUD) in Australia and sustainable urban drainage systems (SUDS) in Europe [4]. All of these initiatives embrace the concept of integrated land and water management and in particular, integrated urban water management [5]. The principles of LID focus on mitigating the adverse effects of urban stormwater

runoff and finding solutions to integrated water cycle management. Pezzaniti et al. [5] defined these principles as being:

- Reducing portable water demand through water efficient appliance, rainwater and grey water reuse;
- Minimising wastewater generated and treatment of wastewater to a standard suitable for efficient reuse opportunities and/or release to receiving waters;
- Treating urban stormwater to meet water quality objectives for reuse and/or discharge to surface waters; and
- Using stormwater in the urban landscape to maximise the visual and recreational amenity of developments.

LID is a relatively recent concept that brings together new technologies, with an increasing interest in urban regeneration, to rethink urban water management and apply solutions to make towns and cities more sustainable.

As part of the LID stormwater management principle, a number of stormwater treatment devices have been developed to improve water quality, such as swales, bioretention basins, settlement ponds and wetlands. However, these treatment devices can require significant land uptake. Highly urbanised areas are often restricted in space, and potential stormwater treatment measures should ideally fit into

the urban area without further land uptake.

Permeable pavements are one type of LID treatment device that is becoming increasingly popular globally due to the many stormwater management and environmental benefits they provide. These will be discussed in the next section.

Permeable Pavements

Pavements are an everyday part of the urban landscape and are rarely thought about yet they have a significant environmental impact. However, for developers and local authorities who have to address stormwater flooding and water quality issues, they are very much at the forefront of the planning process [6]. This is because impervious surfaces such as pavements have such a major impact on downstream flooding, receiving water quality and on the health of natural ecosystems.

Pavements are the most ubiquitous structures built by man and they generally occupy twice the area of buildings. Pavements currently account for approximately 25% of impervious areas within urban environments [7]. Two-thirds of all the rain that falls on potentially impervious surfaces in urban catchments is falling on pavements (Ferguson, 2005) [6]. Pavements are responsible for the generation of excess runoff which is often contaminated with heavy metals and hydrocarbons [8, 9]. They also prevent groundwater recharge and this can result in local water shortages.

The increase in impervious surface accompanying urban development over recent decades has increased both the volume of stormwater runoff, and the amount of pollution flowing downstream to receiving waters [1, 2]. However, the problems associated with pavements are not restricted to water-related issues. They reduce biodiversity by displacing flora and faunal habitats and they cause localised and regionalised temperature increases, known commonly as the "urban heat island" effect [10]. Impermeable pavements also cause street trees to extend their roots in search of water to relieve moisture stress which can result in significant damage to infrastructure. Consequently, the management of stormwater in urban areas has become a priority issue for those responsible for planning and construction of new developments, and maintenance of existing stormwater infrastructure [11].

Conventional pavements designed for use by vehicular traffic typically consist of a sub-grade, one or more overlying basecourses of compacted pavement material and an impervious surface seal.

An integral aspect of conventional pavement design involves preventing the entry of water into the pavement, via the seal or the paving joints, to protect the integrity of the underlying basecourse and sub-grade [12].

Permeable pavements are a relatively new technology and have quite different objectives and design requirements to conventional pavements. They can be used as an alternative to conventional impervious hard surfaces, such as roads, car parks, footpaths and pedestrian areas [13]. Permeable pavements are specifically designed to promote the infiltration of stormwater through the paving and structure where it is filtered through the various pavement layers. The filtered stormwater is then either harvested for later reuse or released slowly into the underlying soil or stormwater drainage system [13]. This results in many stormwater management and environmental benefits. The most common type of permeable pavement is the permeable interlocking concrete paving (PICP) system shown in Fig. 1 [2].

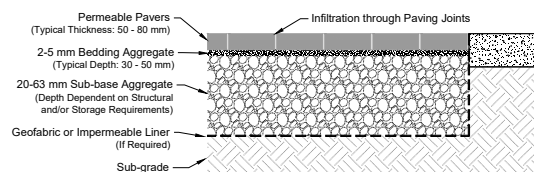


Fig. 1 – Typical PICP Schematic

Even for PICP systems not designed for harvesting and reuse, the storage capacity in the basecourse layers (Fig. 1) can be designed to intercept significant rainfall events. PICPs can therefore reduce runoff volumes and discharge rates from paved surfaces [14-17]. These reductions result in a significantly reduced risk of downstream flooding. PICPs also provide considerable water quality improvements by treating and trapping stormwater pollutants [18 20].

PICPs are one LID treatment option that do not require any increase in land area. They help increase infiltration in urbanised areas and help reduce pressure on existing stormwater infrastructure. They are commonly used as part of a treatment train or as a source control measure [5]. Permeable pavements in good working order have infiltration rates, from 130 mm/h up to several thousand mm/h [2, 21, 27] and can manage the runoff of rainfall events in excess of a 1 in 100-year storm event [22]. However, the performance of a PICP system also depends on the local site conditions. For example, if underlying soils

have low permeability a collection pipe is often needed in the base of the system to divert infiltrated water to the underground drainage network.

Permeable paving provides multiple benefits for managing stormwater runoff at source [2]. They help to reinstate the infiltration capabilities and restore the natural hydrological cycle of urban areas which reduces runoff volumes and the risk of flooding. They filter and treat the infiltrating runoff by trapping pollutants that might otherwise contaminate groundwater and stormwater [7, 23]. It is also thought that permeable pavements can reduce the urban heat island effect and can contribute to a wider range of sustainable water management objectives through rainwater harvesting [13, 24]. Recent research [25, 26] has also shown that the ability of permeable pavements to allow water and air to infiltrate through to the root zone can significantly improve street tree health and minimize pavement damage.

However, there are some common misconceptions associated with the use of permeable pavements systems. These include the belief that they cannot be used in clay soils, that they clog easily which hinders infiltration, and that they do not work well in cold climates due to damage caused by freeze and/or frosting [22]. There are also numerous permeable pavement design guidelines in use worldwide and that the information contained in these design guidelines is often unclear and occasionally conflicting. These issues may have hampered the more widespread implementation of permeable pavement systems.

Increased interest in permeable pavements from planners, designers and stormwater managers has led to an increase in permeable pavement research to try to address some of the common misconceptions [2, 4, 5, 27, 28]. It has also initiated new research areas such as using permeable pavement for stormwater harvesting and reuse and to promote street tree health [13, 25, 26, 29, 30].

This paper summarises the results of an international literature review that was undertaken to identify and examine the current state of permeable pavement research worldwide. It is intended as a practical resource for designers and researchers of permeable pavement systems.

INTERNATIONAL PERMEABLE PAVEMENT RESEARCH

Clogging

Porous Pavements

Research has shown that urban stormwater runoff

contains significant concentrations of suspended sediments and gross pollutants [2, 9, 14, 27, 31]. There is a perception that permeable pavements that are used as source control devices, and designed to infiltrate runoff, will tend to clog quickly and result in high maintenance and replacement costs. This perception has led to a steady increase in the number of research studies into the clogging processes that take place in permeable pavements [4, 5, 9, 28, 31, 32, 33, 34].

Much of the earlier clogging research was conducted on porous concrete materials which have different clogging processes to PICPs [35-38]. The research tended to show that porous pavement materials were more susceptible to clogging, and more difficult to maintain than other systems and their popularity has declined over the last decade.

However, new pavement designs presented by Dierkes et al. [39] demonstrated success with a double layer concrete paver with an impermeable top layer and a porous base layer. The study found that the new pavers could temporarily store water close to the surface which helped promote evaporation of the water back into the atmosphere. This process could help reduce heat island effects. The new paver design was found to be less prone to clogging and the impermeable top layer was also found to be more resistant to damage than typical porous layers. Further research is currently underway to evaluate the new paving design under operational conditions.

PICPs

A significant amount of research has now have been published on the clogging processes that take place in PICPs and the subsequent effects these have on hydraulic performance and how these processes change over time [2, 4, 5, 27, 28, 33]. The key mechanisms that govern clogging in different systems are also now better understood than they were a decade ago.

Pratt [40] undertook a laboratory investigation on small scale, full-size pavement models to investigate pollutant retention within the permeable pavement structure. This study appears to be the first to use an accelerated stormwater sediment dosing program to simulate the long-term performance of PICPs due to clogging. Pratt [40] found that most of the sediment and organic materials tends to get trapped in the upper layers of the bedding aggregate and on the geofabric filter and this prevents them migrating through to the basecourse materials. Pratt predicted that this will lead to eventual total clogging of the system but he conceded that it is difficult to accurately predict the time to failure. Pratt did, however, suggest an

effective life span of between 15 and 20 years in service [40].

Borgwardt [31] reported on the long-term, in-situ infiltration performance of PICPs and presented infiltration test results for over 80 test locations. Borgwardt [31] maintained that the infiltration performance of PICPs decreases significantly within a few years of service due to the entrainment of mineral and organic sediment material retained in the upper 20 mm of the pavement joint material. Comparisons of PSD analyses showed that there were 26% (by mass) more fine particles (less than 63 μm in diameter) trapped in the upper 20 mm of the joint material than in the lower 20 mm. Borgwardt [31] predicted that in practice, the permeability of PICP systems reduces to approximately 18% of the original infiltration value after approximately 10 years' service.

Research to improve understanding of the long-term hydraulic conductivity and the clogging processes in permeable pavements was undertaken by Pezzaniti et al. [5]. The focus of the study, which included both laboratory and field work components, was to quantify the degree of sediment trapping and associated pollutant retention in order to assess the effective life of PICPs. For their laboratory experiments, Pezzaniti et al. [5] applied locally sourced stormwater sediment to PICP testbeds, similar in construction to those used by Pratt [40], in order to simulate 35 years of sediment loading. The study [5] concluded that there are two types of sediment accumulation involved in the clogging process of PICPs, namely coarse and fine sediments. They explained that coarse sediment is retained in a relatively small upper horizon of the pavement joints and this can reduce fine sediment migration to the lower layers. This generally supported by previous research studies [19, 31, 40].

Fassman and Blackbourne [41] investigated infiltration rates and clogging of a 200 m² PICP site that was constructed to form part of a main arterial road in Auckland, New Zealand. The structure was made from PICP blocks (with wide gaps) on a 2 to 5 mm aggregate bedding layer. A geofabric layer was included between the bedding layer and the basecourse. Sub-surface investigations beneath the pavers revealed that a crust had formed above the geofabric and that some of the bedding layer had formed into agglomerated chunks. This in an important finding [41] and demonstrates the significant role that dry periods of no rainfall play in the sediment retention and clogging processes that

potentially occur in PICPs. This finding suggests that results from simulated long-term sediment loading studies that do not include drying cycles, may not be applicable to prototype PICP field installations.

Lucke and Beecham [2] undertook a forensic investigation on a clogged eight-year-old PICP system to determine how sediment had accumulated within the pavement structure. They found that most of the sediment was trapped in the gaps between the paving blocks and on top of the bedding aggregate directly below the gaps. The sediment accumulation pattern that took place on the bedding aggregate beneath pavers is shown Fig. 2. This clearly demonstrates the effectiveness of the bedding aggregate as a filter medium to remove sediment from stormwater runoff.



Fig. 2. Sediment Accumulation Pattern on Bedding Aggregate [2]

It is also clear from Fig. 2 that sediment is only deposited on the bedding aggregate directly below the paving joints. The rest of the bedding aggregate is effectively "as new" and has performed no sediment removal function at all. This suggests that the PICP design is not fully utilising the filter medium properties of the bedding aggregate. Therefore, it was hypothesised [2] that there may be a more effective PICP design which makes greater use of the bedding aggregate area to filter more sediment from stormwater runoff. This was investigated and described in the following sections [28].

The studies outlined above demonstrate the variability of findings from previous research into the clogging processes that occur in permeable pavements and the effects that these processes have on the long-term viability of these systems. While a number of the studies have examined the sediments accumulated in the paving layers in some detail, most of this research did not examine the clogging processes experienced by sediment particle sizes less than 63 μm in diameter. Those studies that did look at particle sizes of less than 63 μm in diameter were conducted on laboratory models and these results may not be applicable to prototype PICP field installations. Further research is required to better understand this process.

Infiltration

Adequate infiltration through PICPs is critical to their hydraulic and stormwater treatment performance. Infiltration is affected by clogging caused by the trapping of fines in the PICP surface, which, over time, reduces treatment performance. It has been shown that clogging can be reduced by periodic maintenance such as vacuum sweeping and/or pressure washing. It has also been suggested that a PICP's maintenance requirements can be identified by measuring reduced infiltration rates. This section examines some of the previous research on PICP infiltration.

Bean et al. [16] evaluated the surface infiltration rates of 40 permeable pavement sites in North Carolina, USA. They measured the surface infiltration rates of different permeable pavement types and tried to relate the infiltration performance to paver type. They used both the Single-ring infiltrometer test method [42] and the Standard test method for infiltration rate of soils in field using double-ring infiltrometer [43] in their study (Fig. 3).

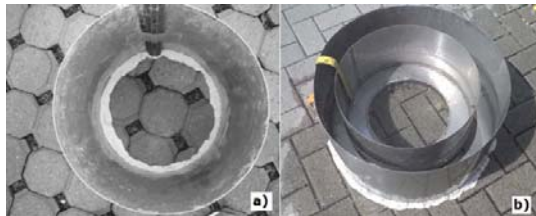


Fig. 3. Modified Ring Infiltrimeters for Permeable Pavement Testing with Waterproof Sealant (a) Single Ring; (b) Double Ring [34]

The study [16] measured infiltration rates between 1,000 mm/h and 40,000 mm/h for PICPs that were not blocked with fine particles. However, the infiltration rate of PICPs that were partially filled by fine soil particles reduced to between 16 mm/h and 2,000 mm/h. They concluded that PICP sites installed for infiltration purposes should not be located adjacent to areas with disturbed soils as accumulations of fine particles can dramatically decrease surface infiltration rates. They also found that higher surface infiltration rates could be sustained by using a vacuum sweeper at regular intervals for maintenance [16].

Lucke and Beecham [2] investigated the infiltration performance of a PICP system that has been in service for over eight years. They developed a new type of double ring infiltration testing apparatus that measured the surface infiltration rate

over one full square metre (1 m²) of paving (Fig. 4). They also found that different areas of the PICP were affected by blockage by fine solid particle and they classified the different areas as either, Fully Blocked (FB), Medium Blocked (MB) or Unblocked (UB).



Fig. 4 Double-ring Infiltration Testing Apparatus Developed by [2]

They [2] found the average infiltration rates for the pavement to be 11 mm/h for the FB areas, 165 mm/h for the MB areas, and 8,530 mm/h for the UB areas. They found that although there was only a maximum difference of 56% in the mass of sediments retained in the paving layers, the infiltration rates varied by five orders of magnitude. These results reinforced previous research findings on how important it is to maintain PICPs to ensure surface infiltration rate performance remains effective.

Due to the difficulty and inconsistencies experienced with PICP infiltration testing using traditional methods, two new experimental test procedures were developed and evaluated [34] to more accurately determine the surface infiltration rate of PICPs. The two new methods were the falling head full-scale (FHFS) method and the constant head full-scale (CHFS) method. Both of the new methods involved inundating a large area of the pavement in order to determine the infiltration rate through the pavement surface (Fig. 5). Double ring infiltrometer tests were also performed to enable a comparison of the results to traditional methods.

While the new infiltration testing methods [34] were found to be more reliable and consistent than traditional methods, there was still a large variation in the results during the testing. It was found that moisture levels in the soil underneath the PICP installation significantly affected test results. This was particularly apparent when multiple tests were performed at the same site as infiltration rates decreased as more tests were performed. Overall, the

study [34] found that the new falling head full-scale testing method produced the most accurate results. This study is continuing the new method has been applied to numerous sites across Europe. It is anticipated that the full results of this study will be published in the near future.

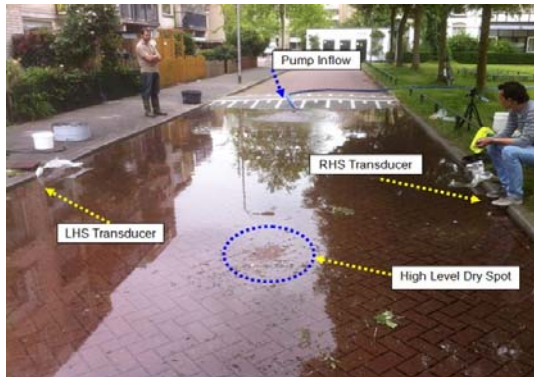


Fig. 5 - Full-scale Infiltration Testing in the Netherlands [34]

Lucke et al. [44] compared infiltration results using the standard test (C1781M-14a – Fig. 3a) with the results of a new stormwater infiltration field test (SWIFT – Fig. 6) developed in Australia to evaluate the maintenance requirements of PICPs. A strong correlation was found between results using the two methods. The study found that the SWIFT was a reliable method for estimating the degree of clogging of PICPs while successfully overcoming some of the problems with the more technical existing test methodology such as horizontal water leakage (use of sealant), unrealistic pressure heads, speed of test, and portability. The SWIFT test [44] is a simple, fast and inexpensive way for asset managers and local government employees to quickly assess the maintenance requirements of PICP installations in the field.



Fig. 6. Stormwater infiltration field test (SWIFT) Infiltrimeter used in this study. (a) SWIFT in use; (b) SWIFT dimensions [44].

Sediment Slots

Previous PICP clogging research [2]

demonstrated that sediment is only deposited on the bedding aggregate directly below the paving joints. The rest of the bedding aggregate is effectively "as new" and has performed no sediment removal function at all. This suggested that current PICP designs were not fully utilising the filter medium properties of the bedding aggregate. It was therefore hypothesised that there may be a more effective PICP design which makes greater use of the bedding aggregate area to filter more sediment from stormwater runoff.



Fig. 7 – Sediment Slots Being Cut into Underside of PICP blocks [28]

A proof of concept study [28] was performed to investigate more efficient use of the bedding aggregate used in PICP systems. Lateral drainage channels (sediment slots) were cut into the underside of PICP blocks (Fig. 7) to allow sediment-laden stormwater to access, and be treated by, a greater surface area of bedding aggregate. Eight different slot designs (Fig. 8) were trialled in the study [28]. Specially fabricated PICP models were tested in the laboratory using semi-synthetic stormwater to determine which of the slot designs made the most efficient use of the bedding aggregate to filter the sediment from the stormwater.

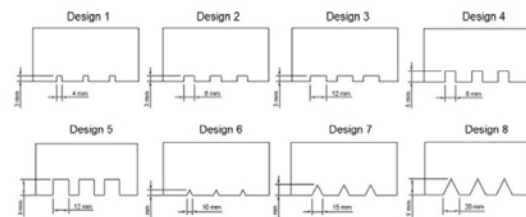


Fig. 8 - Eight Different Drainage Slot Designs Trialled in Study [28]

The study [28] results (Fig. 9) clearly demonstrated that the eight drainage slot designs deposited between 25% and 366% more sediment beneath the pavers than the control pavement (Design 9). The results of the study [28] strongly suggest that PICP systems with drainage slots cast into their bases

would take much longer to clog than unmodified pavers, thereby proving the initial concept of this study. However, more research would be required to verify this fully. More research is also required to optimise the drainage slot designs for use on different paver bedding materials. Finally, a better method of quantifying the amount of sediment that is deposited on the bedding aggregate needs to be developed.

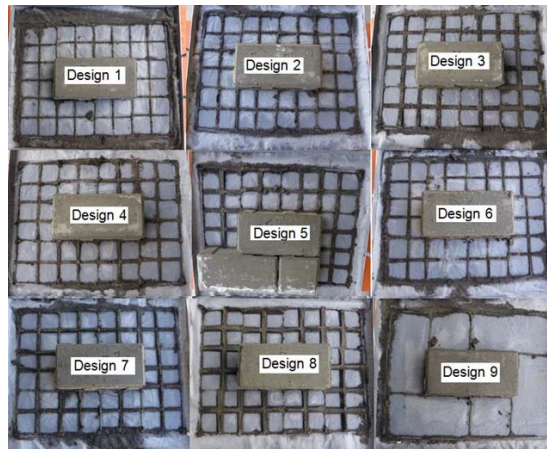


Fig. 9. Study Sediment Distribution Patterns

Summary

Altering the natural characteristics of a drainage basin through urbanisation can impose dramatic changes on the movement and storage of water within the catchment. As permeable pavements are specifically designed to promote the infiltration of stormwater through the paving and structure they can be used to promote infiltration and groundwater recharge, while decreasing stormwater runoff volumes and flowrates from the catchment. The use of permeable pavements can result in many stormwater management and environmental benefits.

The preceding sections have outlined some of the latest international permeable pavement research studies. While there have been other quality studies undertaken, the majority of the research tends to focus on issues to do with surface infiltration and clogging. The stormwater management and environmental benefits of permeable pavements are undeniable and they clearly reflect the principals of low impact development. Uncertainties surrounding surface infiltration and clogging are clearly the main barrier to the more widespread implementation of permeable pavements. If these issues can be satisfactorily addressed, the future of permeable pavements will be assured.

CONCLUSION

This review of permeable pavement research has identified a number of potential solutions to the issues surrounding clogging and reduced surface infiltration capacities. These include:

- A new PICP design using a double layer concrete paver construction with an impermeable top layer and a porous base layer. The new paver design was found to be less prone to clogging, better at evaporating water back into the atmosphere, and more resistant to damage than typical porous layers.
- PICP sites installed for infiltration purposes should not be located adjacent to areas with disturbed soils as accumulations of fine particles can dramatically decrease surface infiltration rates.
- Higher surface infiltration rates can be sustained by using a vacuum sweeper at regular intervals for maintenance.
- Research suggests that PICP's maintenance requirements can be identified by measuring reduced infiltration rates. A number of new methods for measuring surface infiltration capacity were examined.
- New infiltration rate testing methods involving inundating large areas of the pavement were found to be more reliable and consistent than traditional methods, although they were more difficult to implement.
- The SWIFT test is a simple, fast and inexpensive way for asset managers and local government employees to quickly assess the maintenance requirements of PICP installations in the field.
- A proof of concept study to investigate more efficient use of the bedding aggregate used in PICP systems was examined. The study results strongly suggest that PICP systems with drainage slots cast into their bases would take much longer to clog than unmodified pavers.

While all of the potential solutions listed above may be able to resolve some of the issues surrounding surface infiltration and clogging to some extent, more targeted research is required to explicitly address the uncertainties surrounding permeable pavement performance. More positive research results that demonstrate the potential benefits of permeable pavements will secure their future in the LID integrated land and water management philosophy.

REFERENCES

- [1] Dietz, M.E. Low impact development practices: a review of current research and recommendations for future directions. *Water Air Soil Pollution*. 186, 2007, 351-363.
- [2] Lucke, T., Beecham, S. Field investigation of clogging in a permeable pavement system. *Building, Res. & Inform.* 39(6), 2011, 603-615.
- [3] Mullaney, J. and Lucke, T. Practical Review of Pervious Pavement Designs. *CLEAN - Soil, Air, Water Journal*, 42(2), 2014, 111-124.
- [4] Boogaard, F., Lucke, T. and Beecham, S. Effect of Age of Permeable Pavements on Their Infiltration Function. *CLEAN - Soil, Air, Water Journal*, 42(2), 2014a, 46-152.
- [5] Pezzaniti, D., Beecham, S. and Kandasamy, J. Influence of clogging on the effective life of permeable pavements, *Journal of Water Management*, 162(2), 2009, 76-87.
- [6] Ferguson, B. *Porous Pavements*, CRC Press, Boca Raton, 2005, USA.
- [7] Shackel, B. The design, construction and evaluation of permeable pavements in Australia, 24th ARRB Conference, 13-15th October, 2010, Melbourne, Australia.
- [8] Fletcher, T.D., Duncan, H.P., Poelsma, P., Lloyd, S.D. Storm water flow and quality, and the effectiveness of non-proprietary storm water treatment measures-a review and gap analysis, CRC for Cat. Hyd., (Tech. Report 04/8), 2005.
- [9] Hatt, B.E., Fletcher, T.D., Deletic, A. Hydrologic and pollutant removal performance of stormwater biofiltration systems at the field scale, *J. of Hydrology*., 2007, 365(3-4), 310-321.
- [10] Golden, J.S., and Kaloush, K.E. Mesoscale and microscale evaluation of surface pavement impacts on the urban heat island effects, *Int. J. of Pavement Engineering*, 7(1), 2006, 37-52.
- [11] Nichols, P.W.B., White, R. and Lucke, T. Do sediment type and test durations affect results of laboratory-based, accelerated testing studies of permeable pavement clogging? *Science of the Total Environment*, 511, 2015, 786-791.
- [12] Beecham, S., Pezzaniti, D., Myers, B., Shackel, B. and Pearson, A. Experience in the application of permeable interlocking concrete paving in Australia, in Proceedings of 9th ICBP, Buenos Aires, 2009, Argentina.
- [13] Beecham, S., Lucke, T. and Myers, B. (2010) Designing porous and permeable pavements for stormwater harvesting and reuse, in Proceedings of 1st European IAHR Congress, Edinburgh, UK.
- [14] Pratt, C.J., Mantle, J. and Schofield, P. UK Research into the performance of permeable pavement, reservoir structures in controlling stormwater discharge quantity and quality, *J. of Water Sci. & Tech.*, 32(1), 1995, 63-69.
- [15] Hunt, B., Stevens, S. and Mayers, D. Permeable pavement use and research at two sites in eastern North Carolina, in Proceedings of the 9th International Conference on Urban Drainage, Portland, Oregon, 2002, USA.
- [16] Bean, E., Hunt, W. and Bidelsbach, D. Field survey of permeable pavement surface infiltration rates, *Journal of Irrigation and Drainage Engineering*, 133(3), 2007, 247-255.
- [17] Collins, K., Hunt, W. and Hathaway, J. Hydrologic comparison of four types of permeable pavement and standard asphalt in eastern North Carolina, *Journal of Hydrologic Eng.*, 13(12), 2008, 1146-1157.
- [18] Pratt, C.J., Mantle, J. and Schofield, P. Urban stormwater reduction and quality improvement through the use of permeable pavements, *Journal of Water Sci. and Tech.*, 21(8), 1989, 769-778.
- [19] Dierkes, C., Angelis, G., Kandasamy, J. and Kuhlmann, L. Pollution retention capability and maintenance of permeable pavements, in Proceedings of the 9th ICUD Conference, IWA, Portland, Oregon, 2002, USA.
- [20] Brattebo, B. and Booth, B. Long-term stormwater quantity and quality performance of permeable pavement systems, *Journal of Water Research*, 37(18), 2003, 4369-4376.
- [21] Volder, A. Watson, T. and Visawanathan, B. Potential use of pervious concrete for maintaining existing mature trees during and after urban development. *Urban Forestry and Urban Greening*. 8(4), 2009, 249-256.
- [22] Shaffer, P., Wilson, S., Brindle, F., Baffoe-Bonnie, B., Prescott, C., Tarbet, N. Understanding permeable and impermeable surfaces-technical report on surfacing options and cost benefit analysis. 2009, London, Dept. for Communities and local Government.
- [23] Sansalone, J., Kuang, X., Ranieri, V. Permeable pavement as a hydraulic and filtration interface for urban drainage. *J. Irrig. Drain. Eng.* 134(5), 2008, 666-674.
- [24] Frazer, L. Paving paradise-the peril of impervious surfaces, *Environmental. Health Perspectives*. 113(7), 2005, 457-462.
- [25] Mullaney, J., Lucke, T. and Trueman, S.J. A review of benefits and challenges in growing

- street trees in paved urban environments, *Landscape & Urban Plan.*, 134, 2015a, 157–166.
- [26] Mullaney, J., Lucke, T. and Trueman, S.J. The effect of permeable pavements with an underlying drainage layer on the growth and nutrient status of urban trees. *Urban Forestry & Urban Greening*, 14(1), 2015b, 19-29.
- [27] Boogaard, F., Lucke, T., van de Giesen, N. and van de Ven, F. Evaluating the Infiltration Performance of Eight Dutch PPs Using a New Full-Scale Infiltration Testing Method. *Water*, 6(7), 2014b, 2070-2083.
- [28] Lucke, T. Using Drainage Slots in Perm. Paving Blocks to Delay the Effects of Clogging: Proof of Concept Study. *Water*, 6(9), 2014, 2660-2670.
- [29] Morgenroth, J. and Visser, R. Above-Ground Growth Response of *Platanus orientalis* to PPs, *Arboric. Urban Forestry*, 37(1), 2011, 1–5.
- [30] Morgenroth, J., Buchan, G. and Scharenbroch, B.C. Belowground Effects of Porous Pavements – Soil Moisture and Chemical Properties, *Journal of Ecological Eng.*, 51, 2013, 221–228.
- [31] Borgwardt, S. Long-term in-situ infiltration performance of permeable concrete block pavement, in Proceedings of 8th ICBP, San Francisco, 2006, USA.
- [32] Colandini, V., Legret, M., Brosseaud, Y. and Baládes, J.D. Metallic pollution in clogging materials of urban porous pavements, *Journal of Water Sci. and Technology*, 32(1), 1995, 57-62.
- [33] Yong, C.F., Deletic, A., Fletcher, T.D. and Grace, M.R. The drying and wetting effects on clogging and pollutant removal through porous pavements, in Proceedings of 7th International Conference, NOVATECH 2010, Lyon, France.
- [34] Lucke, T., Boogaard, F. and van de Ven, F. Evaluation of a New Experimental Test Procedure to More Accurately Determine the Surface Infiltration Rate of Permeable Pavement Systems. *Urban Planning and Transport Research*, 2(1), 2014, 22-35.
- [35] Hogland, W., Larson, M. and Berndtsson, R. The pollutant build-up in pervious road construction, in Proc. 5th ICUD, Osaka, Japan, 1990, 845-852.
- [36] Larson, R. Swedish experience with design and construction of pervious asphalt constructions, in Proceedings of the Standing Conference on Stormwater Source Control, Volume I, Ed. C.J. Pratt, Coventry University, 1990, UK.
- [37] Legret, M. and Colandini, V. Effects of a porous pavement with reservoir structure on runoff water: water quality and fate of heavy metals, *J. of Water Sci. & Tech.*, 39(3), 1999, 111-117.
- [38] Raimbault, G., Nadjji, D. and Gauthier, C. Stormwater infiltration and porous material clogging, in Proceedings of the 8th ICUD, Sydney, Australia, 1999, 1016-1024.
- [39] Dierkes, D., Lucke, T., Hulsman, H., Vergroesen, T. Permeable pavements as effective method to restore the urban water balance. IWA Water Week, 8-11th July, 2016, Singapore
- [40] Pratt, C.J. Permeable pavements for stormwater quality enhancement, in Proceedings of Urban Stormwater Quality Enhancement – Source Control, Retrofitting and Combined Sewer Tech., Ed. H.C. Torno, ASCE, 1990, 131-155.
- [41] Fassman, E. & Blackbourne, S. Urban runoff mitigation by a PP system over impermeable soils, *J. Hyd. Eng.* 15(6), 2010, 475-485.
- [42] American Standard Testing and Materials (ASTM). Standard test method for surface infiltration rate of permeable unit pavement systems; C1781/C1781M-14a; ASTM International: PA, USA, 2014.
- [43] American Standard Testing and Materials (ASTM). Standard test method for infiltration rate of soils in field using double-ring infiltrometer. ASTM D 3385, ASTM International: PA, USA, 2014.
- [44] Lucke, T., White, R., Nichols, P.W.B. and Borgwardt, S. A Simple Field Test to Evaluate the Maintenance Requirements of Permeable Interlocking Concrete Pavements. *Water*, 7(6), 2015, 2542-2554.

ALKALINE ACTIVATION FOR SOIL STABILIZATION

Bujang B.K.Huat¹, Afshin Asadi²

¹Department of Civil Engineering, Faculty of Engineering, Universiti Putra Malaysia, Serdang, Selangor, Malaysia; ²Department of Civil Engineering, International College of Auckland, Auckland, New Zealand

ABSTRACT

There is a burgeoning interest in the development, characterization and implementation of alternatives to cement and other cementitious binders in ground improvement. This interest is in part because of the technical advantages and related environmental and energy issues, particularly in CO₂ gas emission. The current paper presents a brief history and a review of alkaline activation and carbonation as a greener alternative to cement stabilization. Some recent investigations have been presented in this paper. Alkali-activated binders can constitute interesting materials to fully eliminate traditional cementitious binder (i.e. cement and lime) usage in soil stabilization projects since calcium is not essential in any part of alkali-activated structure. In simple words, alkaline activation binder is generally a synthetic alkali aluminosilicate material that is produced from the reaction of a solid aluminosilicate with a pre-designed concentrated aqueous alkaline hydroxide or silicate solution.

Keywords: Soil improvement, Alkaline activation, Geopolymerisation, Carbonation

INTRODUCTION

Due to robustness and easy adoptability, cement and lime are often employed as stabilizing agents in civil engineering applications (i.e. ground improvement). However, these traditional cementitious binders are not only for their negative environmental effects during manufacture but also for their cost [1].

In the case of cement, it generates around 7% of artificial CO₂ emissions, because of carbonate decomposition. It is estimated that every ton of cement, it produces around one ton of CO₂, a major greenhouse gas implicated in global warming. Beside the emission of CO₂, another by-product of cement production is NO_x. Most of these nitrogen oxides are produced in cement kilns, which can contribute to the greenhouse effect and acid rain [1]-[2]-[3]-[4].

Alkali-activated binder may constitute an interesting option to fully eliminate traditional cementitious binders usage in civil engineering projects since calcium is not essential in any part of alkali-activated structure. Essentially, the synthesis of alkali-activated binders, which are formed by the reaction of any amorphous aluminosilicate source with alkali (usually Na or K) or alkali earth (Ca) metals, involves the dissolution of mineral aluminosilicates, followed by the hydrolysis and condensation of the Al and Si components, resulting in the formation of a three-dimensional, essentially amorphous, aluminosilicate gel. The final product is very much dependent on the calcium availability. Alkaline activation of low-calcium precursors results in a N-A-S-H type gel, while as alkaline activation of high-calcium raw materials forms essentially C-A-S-H gel [1]-[5].

An abundance of papers on alkaline activation

technology can be found in the literature. In this regard, a number of studies were conducted to evaluate the environmental benefits of alkali-activated binder. Moreover, a large and growing body of literature has investigated the mechanism of the alkaline activation (AA) from wide variety of aluminosilicate source materials, and the potentiality of utilizing various alkaline activators for the dissolution of Si and Al oxides through alkaline activation process. A significant body of these studies validate the proposition that alkaline activation provides a promising and sustainable alternative to the use of cement and lime because of (i) the abundant raw material sources and (ii) its lower energy consumption and CO₂ emission [1].

This current paper presents a brief history and a review of alkali-activated materials (new generation of binders) and recent investigation done at Universiti Putra Malaysia.

BACKGROUND

The alkaline activation (also referred as to 'geopolymerisation') can be described as a polycondensation (a reaction that chemically integrates minerals), consisting of aluminum and silica alternately tetrahedrally interlinked by sharing all the oxygen atoms. The process starts when the high hydroxyl concentration of the alkaline medium favors the breaking of the covalent bonds Si-O-Si, Al-O-Al, and Al-O-Si from the vitreous phase of the source material, transforming the silica (SiO₂) and alumina (Al₂O₃) ions in colloids and releasing them into the solution. Under this condition, aluminosilicates are transformed into extremely reactive

materials to form a well-structured alumino-silicate polymerized framework [1]-[2].

In recent years, a large and growing body of literature has investigated the mechanism of alkaline activation using a wide variety of alumino-silicate source materials [2], the role of alkaline activators, which are normally made by mixing a highly alkaline solution (such as sodium hydroxide) [2]-[4]-[9], and the environmental benefits of the alkaline activation method [2].

A significant body of these studies validate the proposition that alkali-activated binders have superior performance in comparison with cementitious binders, such as lower energy consumption, approximately 80% lower carbon dioxide emissions, higher strength and with the principles of sustainable development. Therefore, in a political climate where governments around the world are taxing carbon dioxide emissions and promoting sustainable and environmentally friendly materials, alkali-activated binder can emerge as an important material of the future [2].

In the light of these advantages, research on the synthesis of alkali-activated binder and identification of reaction mechanisms in civil engineering frameworks has intensified over recent years [2]-[4]-[9]. However, using this technology in ground improvement applications is still at the early stage of development.

In very limited attempts, some geotechnical researchers have investigated the effectiveness of alkali-activated fly ash as silica and alumina amorphous sources for soil stabilization [9].

RECENT INVESTIGATIONS AT UPM

Alkaline activation with POFA

One of the well-known agro-wastes, palm oil fuel ash (POFA), was used as a source binder.

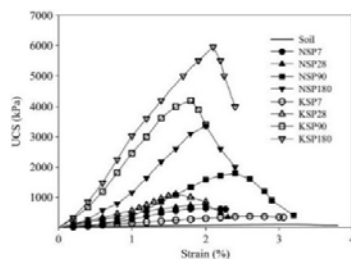


Fig. 1 Stress-strain behavior of treated soil samples using alkali activated POFA (N-KSP) after 7, 28, 90, and 180 days curing.

Fig. 1 shows the stress-strain behavior of the AA-

treated soil after curing times of 7, 28, 90, and 180 days. As can be seen, the AA stabilization induced a drastic increase in strength, either using sodium hydroxide (NaOH) or potassium hydroxide (KOH) as the base element of the activator. For the sodium-soil-POFA (NSP) and potassium-soil-POFA (KSP) mixtures and after 180 days of curing, values of 3,360 and 6,000 kPa were observed, respectively. Nonetheless, a brittle behavior was registered in the case of the 90- and 180-day curing specimens, which was indicated by the sudden drop in strength after a clear peak value was reached. Such behavior was even more accentuated in the K⁺ mixtures (KSP) [10].

The loading procedure was conducted using a hydraulic jack under the stress control condition with an increment of 5 kPa per minute, and the procedure continued until it reached a normalized vertical displacement of nearly 20%, at which small increments in the applied load result in relatively big increase in the settlement, which indicates that the soil has reached the failure condition (Fig. 2) [10].



Fig. 2 Loading procedure.

It can be seen in Fig. 3 that the vertical load in untreated ground (S) increases rapidly with the increase of settlement at first and reaches a plateau at about 0.09 of displacement/footing width. Also, as shown in this figure, the vertical stress–displacement/footing width curve of untreated soil possessed the ductile behavior.

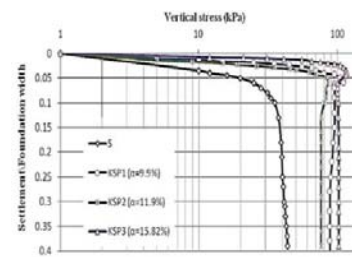


Fig. 3 The relationship between vertical stress and displacement in KSP1–3 group.

It can be clearly seen in Fig. 3 that increasing the replacement area ratio, α , results in more improvement in the q_{ult} of treated columns KSP1 (N=10, $\alpha=9.9$), KSP2 (N=12, $\alpha=11.9$) and KSP3

($N=16$, $\alpha=15.82$) (N and α designate number of columns and replacement area ratio). Other than that, as shown in this figure, compared to untreated soil (S), the q_{ult} increased sharply in treated cases (KSP1–3). This behavior is believed to have been due to the use of alkaline activation process in treated cases (KSP1–3). In this respect, compared to untreated soil (S), higher enhancement was achieved in the case of the KSP3, for which higher increased values of bearing capacities up to 192% was observed at replacement area ratio of 15.82% [5].

From Fig. 3, in treated cases (KSP1–3), the vertical stress increased rapidly at first, and then the model ground exhibited progressive softening since the bearing pressure decrease steadily after the peak.

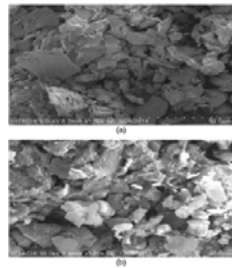


Fig. 4 SEM micrographs of (a) natural soil; (b) KOH-POFA-soil (KSP).

Scanning electron microscopy (SEM) micrographs of the untreated soil (S) and KSP, after curing for 90 days, are shown in Figs. 4(a–b). The more open texture of the untreated soil is clear in Fig. 4(a), whereas the discrete soil particles appear more closely bounded in the stabilized material Fig. 4(b), with the voids seemingly filled.

Wollastonite microfibers were chosen as additive from a pool of several possibilities, based not only on the fact that they fulfil the mentioned requirements but also on their unique chemical composition and microstructure (40.0–50.0% of CaO and 40.0–55.0% of SiO_2), having been formed in nature by the interaction of silica (SiO_2) with calcite (CaCO_3) under high pressure and temperature [5].

Fig. 5 show selected SEM image of the reinforced AA specimens which shows the interaction between the fiber surface and the geopolymeric matrix, contributing to the enhanced behavior of the reinforced mixtures [10].

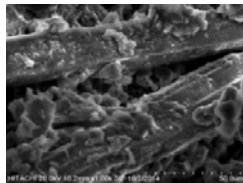


Fig. 5 SEM images of the microfibers inclusion in the stabilized soil mixture.

Alkaline activation with Olivine

Olivine is widely distributed around the world. It has been found everywhere all over the Earth [8].

Fig. 6 shows the stress-strain behavior of soil (S), alkali-activated soil (AS), and alkali-activated soil with different percentages of olivine (A5, A10, A15, and A20) after 7, 14, 28, and 90 days of curing. Untreated soil specimens (S) showed a ductile behavior with the strength of 103.4 kPa at a failure strain of approximately 1.8%. Alkali activation increased the strength of soil to 240.9, 263.0, 370.3, and 521.7 kPa at 7, 14, 28, and 90 days, respectively. The slight increase in the strength of soil specimens observed in the presence of NaOH was attributed to the role of NaOH in promoting the dissolution of Si and Al within soil. The increase in the strength of AS was not significant due to the low reactivity of Si and Al. A progressive increase in strength was observed when different amounts of olivine were used. The strength of samples increased with olivine content (0–20%) and curing time (7–90 days). A20 achieved the highest strength within all alkali-treated soil samples, resulting in 850.3, 1,016.9, 1,210.5, and 3,964.8 kPa at 7, 14, 28, and 90 days, respectively [11].

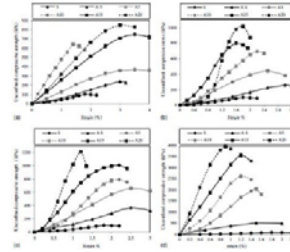


Fig. 6 UCS of alkaline-activated olivine-treated soil at curing times of (a) 7; (b) 14; (c) 28; (d) 90 days.



Fig. 7 Cell setup for carbonating olivine treated soil.

A triaxial reactor was used to carbonate Mix CPTA20 (P =pressure, T =carbonation time) by allowing pressurized gaseous CO_2 (100 and 200 kPa) to permeate through the olivine-treated soil for 12, 24,

48, and 168 h. Immediately after molding, samples were subjected to carbonation under a confining pressure of 400 kPa, during which CO₂ permeated upward. The CO₂ saturation level was detected by the outflow tube placed underwater (Fig. 7) [11].

Fig. 8 shows the stress-strain behavior of alkali-activated soil with 20% olivine (A20) after 90 days of curing and soil treated with 20% olivine in the presence of 10-M NaOH subjected to carbonation at 100 and 200 kPa for up to 168 h. An increase in the UCS was observed with an increase in the carbonation pressure and duration. Strength rapidly increased when the CO₂ pressure and duration increased from 100 to 200 kPa and 12 to 168 h, respectively. When compared with uncarbonated alkali-activated 20% olivine-treated soils at 90 days, the corresponding samples subjected to carbonation (C_(200;168)A20) achieved higher strengths. The results show that olivine is a promising candidate for soil stabilization because alkali-activated olivine treated soils were sufficiently carbonated within a few days to achieve strengths required for ground improvement [11].

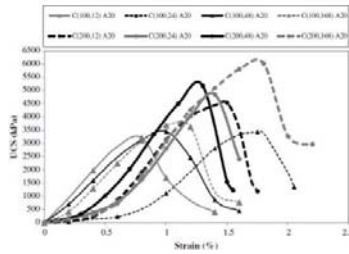


Fig. 8 UCS of carbonated alkaline-activated olivine-treated soil subjected to carbonation for 12, 24, 48, and 168 h at pressures of 100 and 200 kPa.

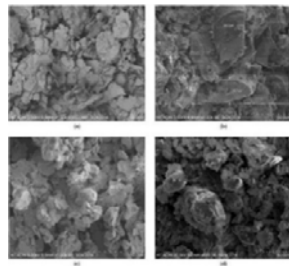


Fig. 9 SEM images of (a) soil; (b) olivine; (c) olivine-treated soil; (d) alkaline-activated olivine-treated soil after 90 days curing.

Fig. 9(a) shows that the microstructure of soil consists of clusters of particles, whereas the irregular shape of olivine particles are seen in Fig. 9(b). Fig. 9(c) illustrates the olivine-treated soil after 90 days of curing. A comparison of Figs. 9 (a & c) reveals how the olivine fills the pores of the soil as a result of its

delayed hydration and pozzolanic reaction within the soil. Fig. 9(d) shows the microstructure of 20% olivine-treated soil in the presence of 10 M of NaOH after 90 days of curing. SEM images demonstrate a compact morphology without any major discontinuities, which is consistent with the mechanical properties observed. The presence of a new amorphous phase is evident in Fig. 9(d), which reveal the formation of a gelatinous structure and crystals on the surface of the samples and around the particles of the starting material. SEM images of samples subjected to carbonation at a CO₂ pressure of 200 kPa for 12, 24, 48, and 168 h shown in Fig. 10 (a & d) demonstrate a denser and more homogenous microstructure with an increase in carbonation duration [6]-[11].

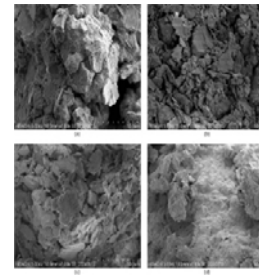


Fig. 10 SEM images of (a) C_(200;12)A20; (b) C_(200;24)A20; (c) C_(200;48)A20; (d) C_(200;168)A20.

Alkaline activation with Fly Ash

Fly ash is a finely divided mineral residue resulting from the combustion of coal in electric generating plants. Fly ash was used as a stabilizer agent to improve gypseous soil. Gypseous soil demonstrates sudden volumetric changes in wetting state due to dissolution of gypsum which causes uneven settlement or collapsing [9].

Fig. 11 illustrates the collapse potentials of gypseous soil samples stabilized with geopolymers fly ash at 7, 28, 90 days of curing. As observed from Fig. 1-a, the gypsum content had a significant influence on the collapse potential of the untreated gypseous soil samples at early ages of curing. The collapse potential increased when the gypsum content was elevated to 45%. In samples with 13% gypsum (G13: natural soil contained 13% gypsum), the collapse potential was 2.86 which can be considered as moderate collapse while for 25% of gypsum content (G25) the collapse potential was 7.95 (moderately severe) and finally for the high gypsum content of 45% (G45), the collapse potential increased to 10.75 and rated as severe. On the other hand, stabilization of soil with geopolymers fly ash decreased the collapsibility in all samples. The increase in the fly ash content from 10 to 30% declined the collapse potential at different rates. As can be seen, the collapse potential for the G45

samples was 10.75 and it reduced to 8.96, 5.88, and 3.7 in KOH activated samples with 10%, 20% and 30% fly ash, respectively. The reduction was to 9.09, 6.64, and 4.48 in samples activated with NaOH at 7 days when 10, 20, and 30% fly ash was used to stabilize the gypseous soil. The mechanism of improvement can be explained as follows: As the content of binder increased the enveloping effect of the crust escalated and consequently the collapsibility potentials declined further [12].

Fig. 12 shows collapsibility potentials of stabilized soil samples soaked in water for 7, 28 and 90 days. It should be noted that the soaking process in water was carried out on samples cured for duration of 28 days. Furthermore, it was observed that within the initial 7 days of soaking, untreated samples were fully dissolved so no data is available. However, the recorded collapse potentials were 4.93, 9.71 and 12.46 for G13, G25, and G45 at 3 days, respectively. In general, the collapse potential for the stabilized gypseous soil with 10, 20, 30% geopolymers fly ash increased as soaking duration prolonged indicating the vulnerability of soil to wetting.

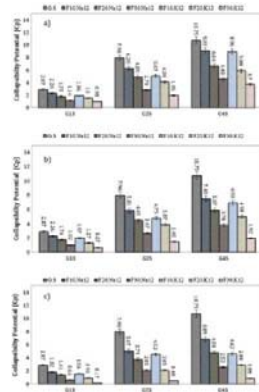


Fig. 11 Collapsibility potentials of soil samples at a) 7 days b) 28 days, c) 90 days.

As can be seen from Fig. 12-a, minimum levels of collapsible potentials were recorded when the gypseous soil samples were stabilized with the fly ash dosage of 30% at 7 days of soaking. However, activation of fly ash with KOH resulted in more resistant samples in terms of collapsibility in short time. The results showed that the collapsibility potentials of samples with 45% gypsum content were lower by 11.6%, 5.5%, and 1.8% when 10%, 20%, and 30% Fly ash activated with KOH was used comparing to its counterparts activated with NaOH. However, it was observed that samples with high content of gypsum (45%) stabilized with 10% fly ash/NaOH disintegrated at 7 days of saturation.

As soaking duration prolonged to 28 days (Fig. 12-b), more series of samples disintegrated namely, samples stabilized with 10% and 20% fly ash /NaOH (12 M) and 10% of activated fly ash with KOH (12

M). For the rest of samples, the collapsibility potential increased by up to 5.7% and 9% in samples activated with KOH and NaOH, respectively. Based on the results, it can be concluded that in gypseous soil samples with low gypsum content the collapsibility potential maintained at a low level especially when activated with KOH. However, when the gypsum content increased to 25% and 45%, higher content of geopolymer fly ash was needed to maintain the collapsibility potential at a controlled range. For example, the collapsibility potential of gypseous soil samples with 25%, 45% of gypsum content stabilized with 30% fly ash / KOH (12 M) increased only by 0.06% and 0.11% as soaking duration increased from 7 to 28 days.

The collapsibility potentials of stabilized soil samples after 90 days of soaking are shown in Fig. 12-c. As can be seen, only samples with lower gypsum content and high percentage of geopolymer fly ash maintained their integrity and the rest dissolved due to gypsum leach out. However, the recorded results showed that the collapse potentials for the G13 and G25 stabilized with 30% fly ash/KOH (12 M) were less affected. The G45 treated with 30% KOH activated fly ash showed slight increase in collapse potential from 1.88 at 28 days to 1.97 at 90 days [9]-[12].

Fig. 13 shows the changes in morphology and microstructure of the gypseous soil samples stabilized with 30% fly ash/KOH (12 M) and 30% fly ash/NaOH (12 M) after 28 days soaking in water. As can be seen, samples activated with KOH (12 M) showed denser matrix and more intact bonds. Increasing the content of gypsum in samples, intensified disintegration of the binder as can be seen from Fig. 13-c, d. Besides, soil grains are easily traceable, though, the presence of the alumina-silicate-hydrate crust cover on the soil particles is observed. As for samples activated with NaOH (12 M), the gaps between the soil grains were greater and the soil particles were more isolated [9]-[12].

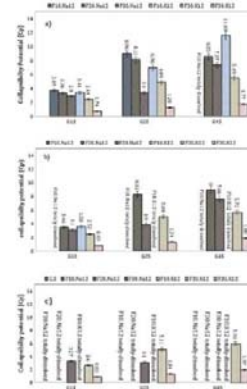


Fig. 12 Collapsibility potentials of the soaked soil samples at a) 7 days b) 28 days c) 90 days.

The microstructure and morphology of the stabilized gypseous soil, G45 with 30% of fly ash activated with KOH (12 M) and NaOH (12 M) are also illustrated in Figs. 14. As can be seen from Fig. 14-a, the SEM image shows the formation of the A-S-H gel binder with a dense texture and highly strong matrix in G45 samples stabilized with KOH activated fly ash. No presence of borders was observed in the gel portion because of the ability of KOH to dissolve the fly ash and soil components. On the other hand, this gel surrounded the insoluble soil grains, which can limit the reactivity of sulfate ions, and their leach out in the gypseous soil. Fig. 14-b shows the SEM image of the G45 treated with 30% fly ash activated with NaOH (12 M). The image is illustrative of a less dense matrix comparing with the gel formed in the KOH (12 M) samples. As can be seen, the soil grains are rather more visible. A denser matrix was also observed in the paste samples with intensive gel when fly ash was activated with KOH (12 M) [12].

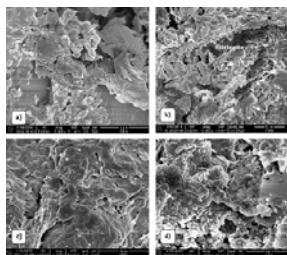


Fig. 13 SEM images of stabilized soil with 30% fly ash after soaking for 28 days a) G13/KOH (12 M) b) G13/NaOH (12 M) c) G45/KOH (12 M) d) G45/NaOH (12 M).

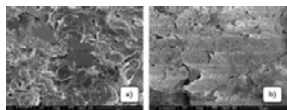


Fig. 14 SEM images of G45 stabilized with 30% fly ash activated with a) KOH (12 M) b) NaOH (12 M).

CONCLUSION

Alkali-activated binders can constitute interesting materials to fully eliminate traditional cementitious binder (i.e. cement and lime) usage in soil stabilization projects since calcium is not essential in any part of alkali-activated structure. In simple words, alkaline activation binder is generally a synthetic alkali aluminosilicate material that is produced from the reaction of a solid aluminosilicate

with a pre-designed concentrated aqueous alkaline hydroxide or silicate solution.

ACKNOWLEDGEMENTS

The authors sincerely thanks Universiti Putra Malaysia (UPM) for providing financial assistance and facilities for this research.

REFERENCES

- [1] Pourakbar, S. and Huat, B. K., A Review of Alternatives Traditional Cementitious Binders for Engineering Improvement of Soils. *Int. J. Geotech. Eng.*, Vol.11, No.2, 2016, pp.206–216.
- [2] Pourakbar, S., Asadi, A., Huat, B. B. and Fasihnikoutalab, M. H., Soil stabilization with alkali-activated agro-waste. *Environmental Geotechnics*, Vol.2, 2015, pp.359–370.
- [3] Pourakbar, S. and Huat, B. K., Laboratory-Scale Model of Reinforced Alkali-Activated Agro-Waste for Clayey Soil Stabilization. *Advances in Civil Eng. Mat.*, Vol.6, Issue 1, 2017, pp.82–105.
- [4] Fasihnikoutalab, M. H., Pourakbar, S., Ball, R. J., and Huat, B. K., The Effect of Olivine Content and Curing Time on the Strength of Treated Soil in Presence of Potassium Hydroxide. *Int. J. of Geosynth. and Ground Eng.*, 2017, 10.1007/s40891-017-0089-3.
- [5] Pourakbar, S., Asadi, A., Huat, B. B., Cristelo, N., and Fasihnikoutalab, M. H., Application of Alkali-Activated Agro-Waste Reinforced With Wollastonite Fibers in Soil Stabilization. *J. Mater. Civ. Eng.*, 2016, 10.1061/(ASCE)MT.1943-5533.0001735.
- [6] Fasihnikoutalab, M. H., Asadi, A., Huat, B. K., Westgate, P., Ball, R. J., and Pourakbar, S., Laboratory-scale model of carbon dioxide deposition for soil stabilization. *J. Rock Mech. Geotech. Eng.*, Vol.8, Issue 2, 2016, pp.178–186.
- [7] Fasihnikoutalab, M. H., Westgate, P., Huat, B. K., Asadi, A., Ball, R. J., Haslinda, N., and Singh, P., New insights into potential capacity of olivine in ground improvement. *Electronic Journal of Geotechnical Engineering*, Vol.20, Issue 8, 2015, pp.2137-2148.
- [8] Fasihnikoutalab, M. H., Asadi, A., Huat, B. K., Ball, R. J., Pourakbar, S., Parminder, S., Utilization of carbonating olivine for soil stabilization. *Environ. Geotech.*, 2015, doi:10.1680/jenge.15.00018.
- [9] Alsafi, S., Farzadnia, N., Asadi, A., Huat, B. K., Collapsibility potential of gypseous soil stabilized with fly ash geopolymer; characterization and assessment. *Const. Build. Mat.*, Vol.137, 2017, pp.390–409.
- [10] Pourakbar, S., The use of alkali-activated palm oil fuel ash reinforced by microfibers in deep mixing method, 2015, pp.1-213.
- [11] Fasihnikoutalab, M. H., Utilization of olivine for soil stabilization. PhD Thesis, UPM, 2015, pp.1-133.
- [12] Alsafi, S., Gypseous soil stabilization by alkaline activation method. PhD Thesis, UPM, 2016, pp.1-25

Technical Papers

Geotechnique

CHARACTERIZATION OF ENVIRONMENT FRIENDLY GEOTEXTILES EMBEDDED IN SOIL UNDER PULLOUT TEST

Md. Aminul Islam¹, Zakaria Hossain¹, Jim Shiau² and Siti Hanggita Rachmawati¹

¹Faculty of Bioresources, Mie University, Japan,

²School of Civil Engineering and Surveying, University of Southern Queensland, Australia

ABSTRACT

Characterizing of a geosynthetic is very essential for its effective use in various field application of reinforced soil structures. The success of reinforced soil structures depends not only on the types of backfill materials but also on the types of the reinforcements used in the structures. In view of this objective, a new type of geosynthetic has been evaluated for its interaction properties for different backfill soils using direct pullout test. The test results are compared based on the type of soils and interface mechanical properties of the reinforcements. Three backfills soils (sandy, clayey, and pure sand) in combination with four different geosynthetics were tested at various loading conditions in direct pullout. Based on the analyses of the experimental data, the pullout strength and the pullout displacement of reinforcements due to the variation of the backfill soils are examined. Test results reveal that the stress-deformation behaviour of the geotextile interfaces with all the backfills can be defined as hyperbolic. GT4 also shows the linear curve with hyperbolic characteristics. Both softening and hardening behavior is found with the pure sand. But with the sandy and clayey soil, no softening behavior is observed. On the contrary; GT1 shows the lowest value of pullout stress with all the backfill soils. For GT2 and GT3, almost the same interface behavior is observed with clayey and sandy soil. It is found that GT4 produces the maximum of 140 kPa pullout stress with the toyoura sand and sandy soil.

Keywords: Geosynthetic; Toyoura sand; Direct pullout test; Interface pullout strength

INTRODUCTION

The fashion of reinforcing the soil with various tensile inclusions has been widely practiced in geotechnical engineering for the last few decades. For the design and performance of reinforced soil structures, the interaction between soil and reinforcement is very important, and this interaction can be very complex depending on the nature and properties of the reinforcement [9]. Various types of geosynthetic materials have been used for soil reinforcement including geotextiles (woven and nonwoven), geogrids and geocells [6,7,8]. Whatever the reinforcement and backfill materials are used for the design of a reinforced soil structure, the interaction properties of soil- reinforcement interface play an important role [1]. The interaction mechanism between the reinforcement and the soil can be classified into two types; sliding of soil over the reinforcement and pullout of reinforcement from the soil [4,5]. The pullout tests and the direct shear are widely used methods to study quantitatively these interaction mechanisms.

To study the interaction between soil and reinforcement, the direct pullout test is a suitable method because it can simulate the pullout mechanism along a potential failure plane in reinforced earth structure [2,3]. The pullout strength of soil-geosynthetic interfaces has been investigated using direct pullout tests by a number of researchers. They used various types of geosynthetic materials like High density polyethylene (HDPE), poly

propylene (PP), Polyester (PET) yarns coated with PVC, etc. The present study dealt with a new type of geosynthetic which is made from basalt fiber. A series of direct pullout tests on the geosynthetic interfaces with different type of backfill soils have been conducted in the laboratory. Based on the test results, the stress-displacement behaviour of the interfaces along with different mechanical characteristics has been evaluated and discussed shortly.

PURPOSE OF THE STUDY

1. To investigate the pullout behavior of a new type of geosynthetic, made of fiber basalt, with different backfill soils, through a series of direct pullout test.
2. Evaluating Soil-Geotextiles interfaces, pullout stress pullout displacement, vertical displacement, cohesion & internal friction
3. Characterizing of Geotextiles

MATERIALS AND METHODS

Backfill Materials

Three types of soils were used as backfill material in this study. Air-dry pure silica sand named as Toyoura sand, one sandy and one clayey soil have been used to evaluate the interface behaviour with the same geosynthetic materials.

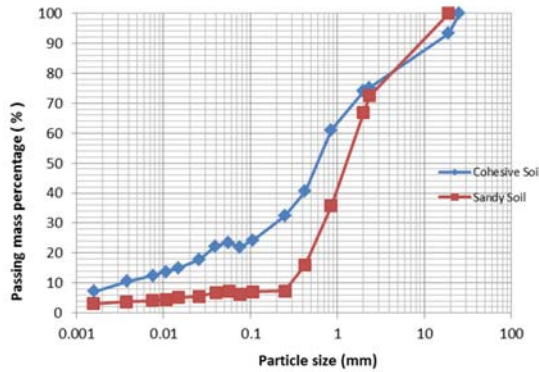


Fig.1 Particle size of the backfill soils

The optimum water content of sandy and clayey soils was 13% and 14%, respectively. Figure 1 represents the gradation curves of the experimental soils. According to JGS engineering classification system, the sandy and clayey soils are classified as SF and CL, respectively. The major physical properties of the soils are listed in Table 1.

Table1. Physical properties of the backfil soils

Properties	Clayey	Sandy
Particle density, ρ_s	2.7 g/cm ³	2.59 g/cm ³
Water content, W_{opt}	14%	13%
Cohesion (c)	5.0	1.5
Angle of internal friction (ϕ)	18.5	23.23
Liquid limit, LL	39%	----
Plastic limit, PL	26.8%	----
Plasticity index, PI	12.2%	----
Sand (75 μ m - 2 mm)	45%	85%
Silt (5 μ m - 75 μ m)	30%	11%
Clay < 5 μ m	25%	4%

Geosynthetic Specimens

The woven geotextiles used in this study are made of Basalt fiber. These materials possess good property of elasticity and stretch tension with good resistance to acid, alkali, heat and vibration. It has also nonconductive and non-magnetic resistance. The physical characteristics of these geosynthetics are listed in Table 2. For the purpose of discussion, the geotextile is noted as GT1, GT2, GT3 and GT4 as shown in fig. 2.

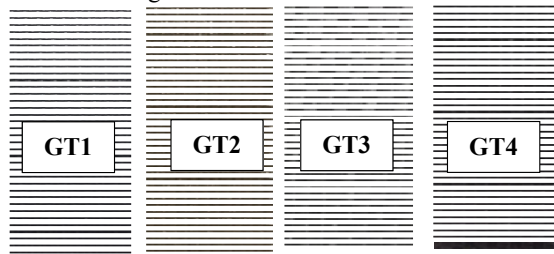


Fig.2 Types of geotextiles used in the direct pullout test

Pullout Apparatus

The pullout box is a rectangular shape of size 150 mm in length, 100 mm in width and 100 mm in height. The box is divided into two parts namely lower box and upper box both are 50 mm in depth. For convenience of the readers, the important components of the testing equipment (Figure 4) are numbered numerically starting from top-left to right-down in the increasing way such as, the number from [1] to [12], where the number [1] is the pullout stress monitoring display, [2] is the supporting plate of reaction of the applied normal stress, [3] is the upper part of the pullout box, [4] is the electrically operated pullout jack, [5] is the pullout stress measuring device, [6] is the reinforcement clamping jack, [7] is the test reinforcement, [8] is the clearance adjusting screw and fixing system of the upper box, [9] is the lower part of the pullout box, [10] is the horizontal displacement measuring dial gauge, [11] is the vertical displacement measuring dial gauge and [12] is the applied normal stress measuring dial gauge.

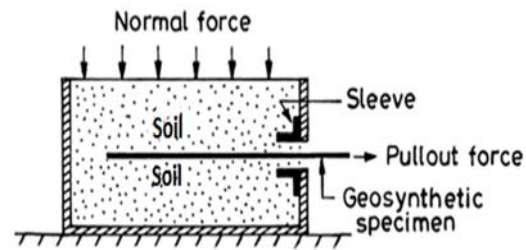


Fig.3 Typical schematic diagram of the pull-out boxes

Setup and procedure

At first, the required amount of soil with desired water content were poured into the lower part of the pullout box (No.9, Figure 4) and compacted uniformly by means of a compactor made of same width as of the pullout box. The lower box was filled completely and the surface of the soil was leveled precisely. The geosynthetic of same width was laid on the soil of lower box and fastened with clamping jack as shown in No. 6 of Figure 4. The upper part of the pullout box (No.3) was placed on the geosynthetic (No.7), and required clearance between the geosynthetic and upper box was set by means of adjusting screw by No.8. In the second stage, the soil was gradually spread over the geosynthetic inside the upper box and compacted uniformly to pour the soil into the geosynthetic. The tests were carried out in the way of pulling out the geosynthetic from the soil with constant speed of 1.0 mm/min by means of screw jack (No.4) under electrically operated constant pressure. The pullout force was

measured using a tension load cell (No.5) with a least count of 5.0 N. The load cell was set between the geosynthetic and the jack to facilitate direct load measurement on the cell avoiding any frictional discrepancy of the machine components. The displacements were measured at the front of the by means of a dial gauge (No.10) with least count of 0.001 mm. The vertical displacement and applied normal loads were measured by the dial gages as shown in figure by Nos. 11 and 12, respectively. The direct pullout tests were conducted using four different normal stresses of 40, 60, 80 and 100 kPa.

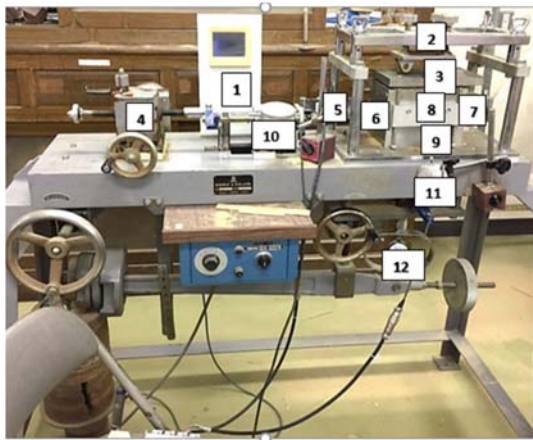


Fig.4. Pullout testing equipment and its components

RESULTS AND DISCUSSION

Pullout Stress-Displacement Relationship

A series of direct pullout tests were performed to obtain the stress-deformation characteristics of the geosynthetic interfaces for different backfill soils. The test results reveal that the relationship between pullout stress and relative displacement depends on both the type of backfill and geosynthetics. It is seen that the stress-displacement relationship of geotextile (GT) interfaces is same for all the backfill soils. The relationship for GT interfaces can be defined as hyperbolic in nature. Before and after the peak pullout stress, displacement hardening and softening behaviour is clearly observed. Maximum pullout resistance mobilizes within 4-7 mm of pullout displacement for geotextiles interfaces with pure sand backfill.

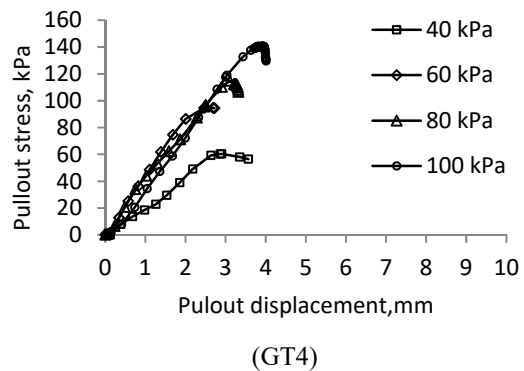
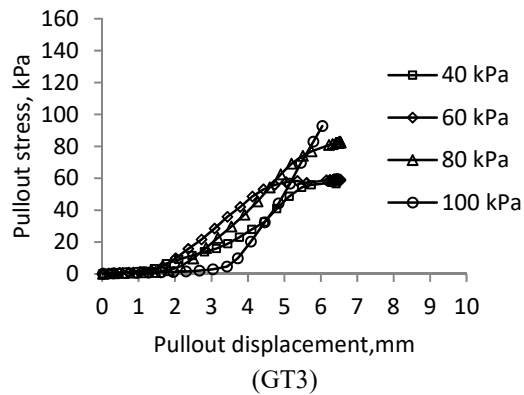
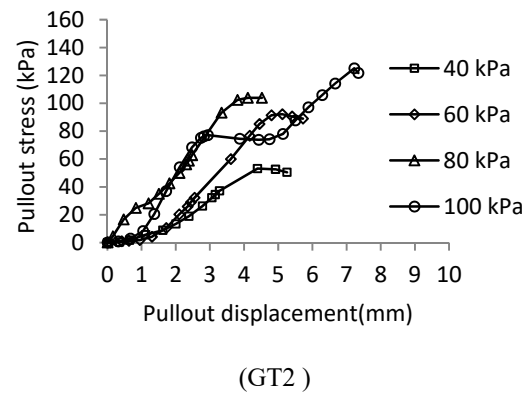
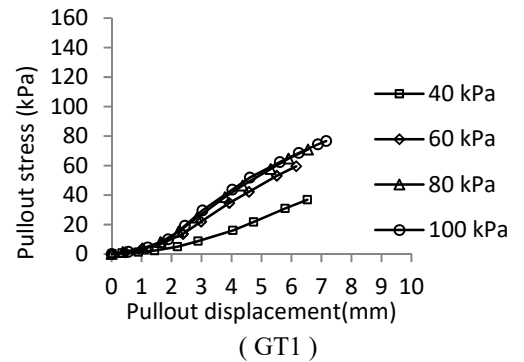


Fig.5 Pullout stress-displacement curve for Toyoura sand

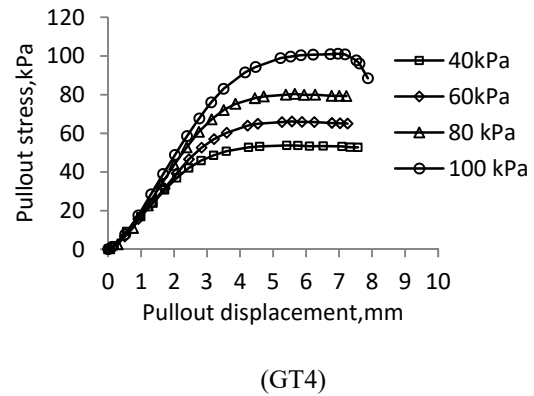
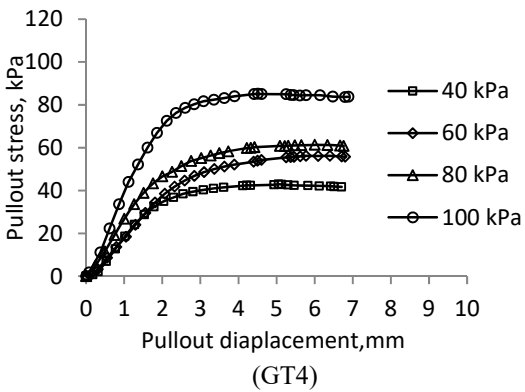
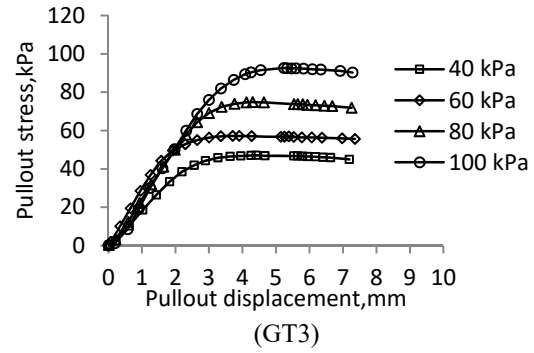
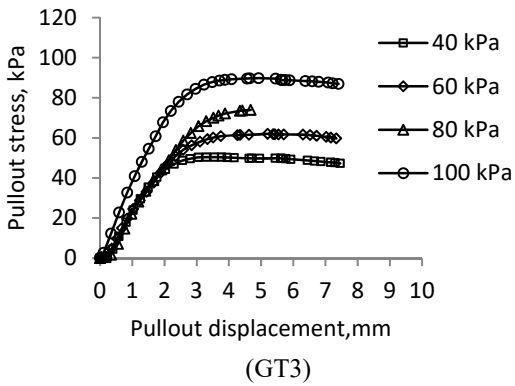
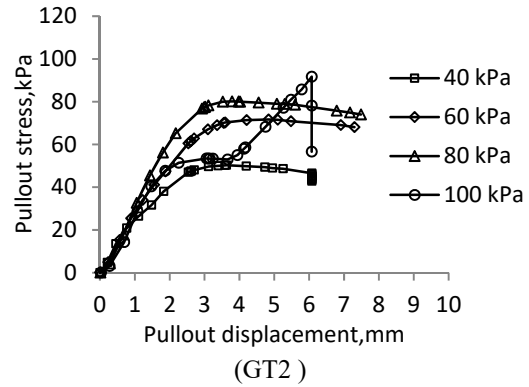
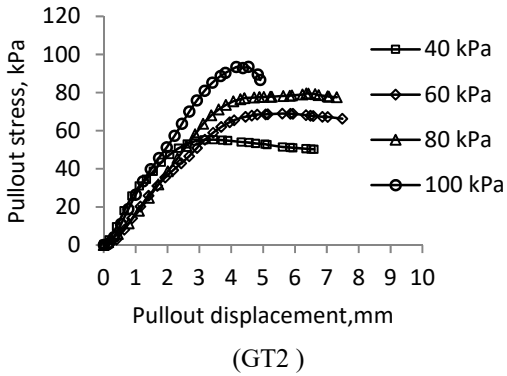
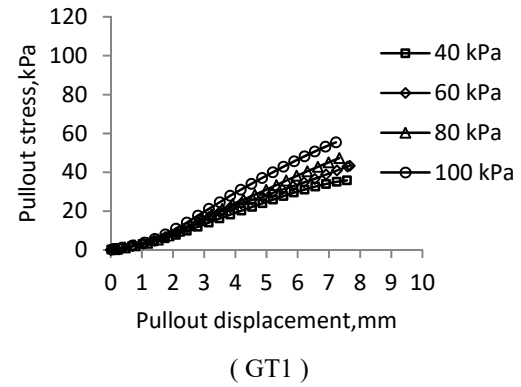
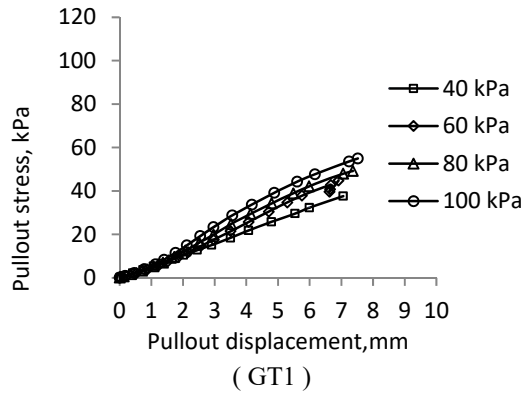


Fig.6 Pullout stress-displacement curve for Clayey soil

Fig.7 Pullout stress-displacement curve for Sandy soil

The pullout strength is found increasing with the increase of normal stress which is a common phenomenon for all soil-geosynthetic interfaces tested in this study.

The relationships between the pulling stress and the displacement of geotextiles under normal stress of 40, 60, 80 and 100 kPa are given in Fig. 5, 6 & 7. It is observed that the difference of the pullout stresses under different normal loading conditions were comparatively smaller at the initial loading till attaining the peak value as compared to the difference of the pullout stresses obtained at the final loading condition after peak value. It is evident that the pullout stresses decreased after attaining the peak value for all the cases.

The Fig.5 shows that GT4 produces the maximum of pullout stress with The Toyoura sand and Sandy soil. On the contrary, GT1 shows the lowest value of Pullout stress with all the backfill soils. For GT2 and GT3, almost the same interface behavior is observed with clayey and sandy soil. But with the Toyoura sand, GT2 produces the higher pullout stress than GT3. The pullout stress mobilizes within 36 kPa to 140 kPa for the applied normal load 40, 60, 80 and 100 kPa. GT1 always shows the straight line curve for every normal load with all the backfill soils. For all the applied normal load, no softening behavior is observed. GT2 shows the fluctuating characteristics with the Toyoura sand and Sandy soil. But with the Clayey soil, it shows the linear behavior. In contrast with GT1, before and after the peak normal stress, both hardening and softening behavior is observed. GT3 shows S stripe curve with the Toyoura sand and linear behavior with the Clayey and Sandy soil. It shows the hardening behavior with all the backfills. GT3 shows the maximum pullout stress with all the backfill soils. GT4 also shows the linear curve with hyperbolic characteristics. Both softening and hardening behavior is found with the pure sand. But with the sandy and clayey soil, no softening behavior is observed

Relationships of Maximum Pullout stress and Normal stress for Soil-Geotextiles

Relationships of maximum pullout stress and normal stress for four types of geotextiles and three types of soils are shown in Figs. 8 to 10. The graphs are drawn with the maximum pullout stress obtained from the applied normal load of 40, 60, 80 and 100 kPa. The angle of the straight line to the X axis indicating the Phai value and its intersection to the Y axis indicating the C value.

It is evident that the maximum pullout stress increases with the increase of normal load in every

cases. But the increasing trend is not the same for all the geotextiles with the clayey and sandy soils. It is observed that GT1 produces the lowest rate of maximum pullout stress with all the soils. In case of Toyoura sand, it is found in Fig. 8 that the GT2 showed the higher rate while GT3 showed the lower rate. Among all the four types of geotextiles, GT4 exhibited the highest rate of maximum pullout stress. On the other hand, in case of clayey and sandy soils, all the geotextiles maintained the similar trend of increasing rate with the increase in normal stress. Figs. 9 and 10 clearly showed that the increasing rate of maximum pullout stress for GT2, GT3 and GT4 is very close to one another.

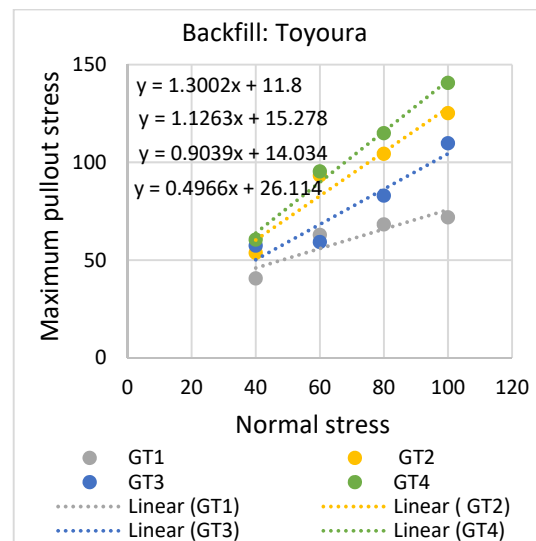


Fig.8 Relationships of maximum pullout stress and normal stress for Clayey-Geotextiles

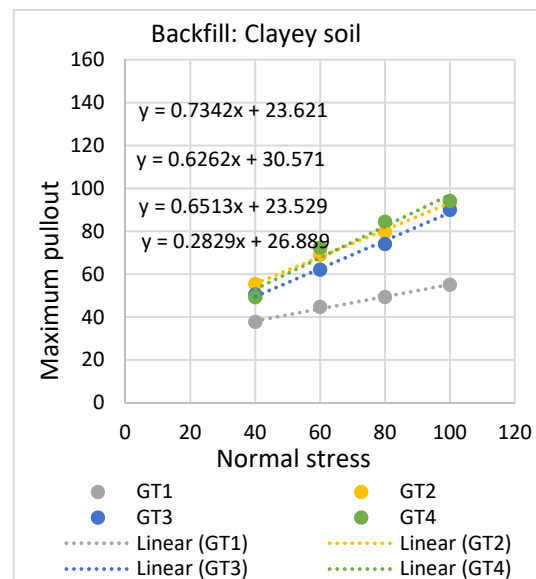


Fig.9 Relationships of maximum pullout stress and normal stress for Clayey-Geotextiles

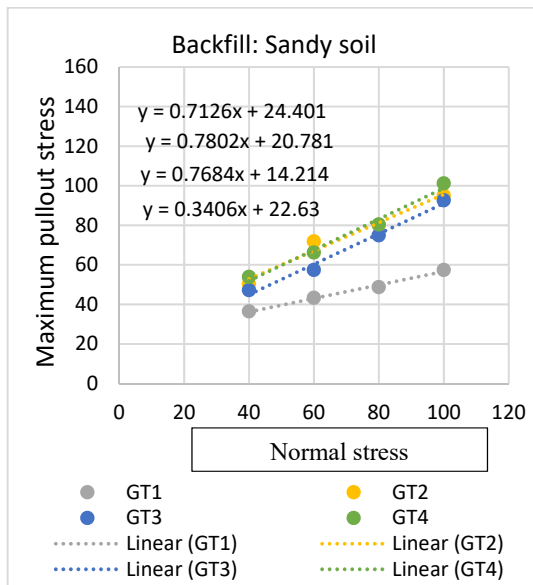


Fig.10 Relationships of maximum pullout stress and normal stress for Toyoura-Geotextiles

Cohesion

Cohesion and internal friction obtained from the relationship of maximum pullout and normal stresses for four types of geotextiles and three types of backfill soils are drawn in Figs. 20 and 21.

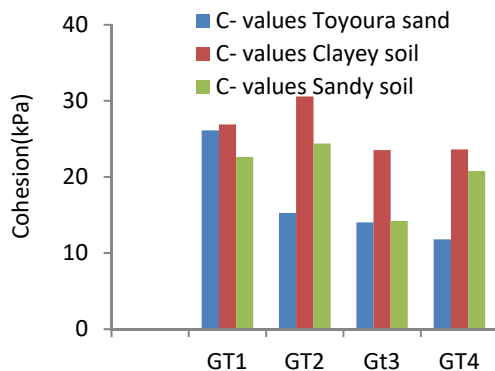


Fig.20 Cohesion of the three types backfills and four type of geosynthetics

Soil-geosynthetic interface friction is an important parameter for designing a reinforced slope (Shukla and Yin, 2006). It is observed in Fig. 4.31 that clayey-GT2 interface obtained the maximum cohesion of 30.5 kPa with the clayey backfill whereas the minimum cohesion of 12 kPa is observed for pure sand-GT4. The maximum cohesion of Clayey- GT1, Clayey- GT2, Clayey-

GT3 and Clayey- GT4 are 26.8 kPa, 30.5 kPa, 23.5 Kpa and 23.6 kPa respectively

Internal Friction

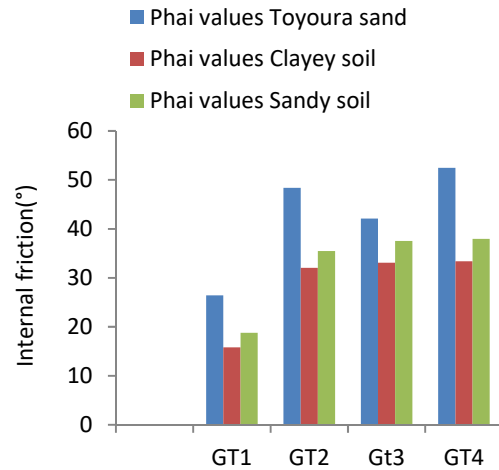


Fig.21 Internal friction of the three types backfills and four types of geosynthetics

The pure sand-GT4 interface obtained maximum friction angle of 52.4° whereas the minimum friction angle of 15.7° is found for Clayey –GT1 interface. The maximum internal friction angles of Toyoura sand-GT1, sand-GT2, sand-GT3 and sand-GT4 interfaces are obtained as 26.4° , 48.3° , 42.1° and 52.4° , respectively. It is observed that among all sand geosynthetic interfaces, the sand-GT4 interface develops the highest frictional resistance whereas sand-GT1 interface develops the lowest frictional resistance. The frictional resistance of sand-GT2 interface is 6° higher than that of sand-GT3 and lower than GT4 interface.

CONCLUSIONS

Finally, it can be concluded that the pullout stress showed its increasing trend with the increase in applied normal stress irrespective of variety of geosynthetics and the different category of backfill soils. The relationship for GT interfaces is defined as hyperbolic. Before and after the peak pullout stress, displacement hardening and softening behaviour is.

It is found that GT4 produces the maximum of 140 kPa pullout stress with the toyoura sand and sandy soil. GT4 also shows the linear curve with hyperbolic characteristics. Both softening and hardening behavior is found with the pure sand. But with the sandy and clayey soil, no softening behavior is observed. On the contrary; GT1 shows the lowest value of pullout stress with all the backfill soils. GT1 always shows the straight line curve for every normal load with all the backfill soils. For

GT2 and GT3, almost the same interface behavior is observed with clayey and sandy soil. pure sand.

It is observed that clayey-GT2 interface obtained the maximum cohesion of 30.5 kPa with the clayey backfill whereas the minimum cohesion of 12 kPa is observed for pure sand-GT4. The maximum cohesion of Clayey- GT1, Clayey- GT2, Clayey- GT3 and Clayey- GT4 are 26.8 kPa, 30.5 kPa, 23.5 Kpa and 23.6 kPa

It is also noticed that the pure sand-GT4 interface obtained maximum friction angle of 52.4° whereas the minimum friction angle of 15.7° is found for Clayey –GT1 interface. The maximum internal friction angles of Toyoura sand-GT1, sand-GT2, sand-GT3 and sand-GT4 interfaces are obtained as 26.4° , 48.3° , 42.1° and 52.4° , respectively. It is observed that among all sand geosynthetic interfaces, the sand-GT4 interface develops the highest frictional resistance whereas sand-GT1 interface develops the lowest frictional resistance. The frictional resistance of sand-GT2 interface is 6° higher than that of sand-GT3 and lower than GT4 interface.

Based on the obtained results of the important parameters for reinforced slope stability like the pullout stress-displacement, vertical-horizontal displacement, cohesion and frictional resistance of the four categories of geotextiles, GT4 can be recommended for the field application.

REFERENCES

- [1] M. B. Hossain, M. Z. Hossain and T. Sakai, Interface Behaviour of Basalt Geosynthetic with Sand Using Direct Shear Device, Proceedings of the 1st International Conference on Geotechnique, Construction Materials and Environment, Mie, 21-23 November 2011, pp. 191-196.
- [2] Jewell, R.A. 1996. Soil strength and bearing capacity. Soil reinforcement with geotextiles, CIRIA, Thomas Telford. 55-83.
- [3] Gurung, N and Y. IWAJO. 1999. Pullout test analysis for georeinforcement. Geotextiles and Geomembranes. 17: 157-170.
- [4] Hossain, M.Z. and Sakai, T.”. A Study on Pullout Behavior of Reinforcement Due to Variation of Water Content of Soil” Agricultural Engineering International: the CIGR Ejournal. Manuscript LW 07 011. Vol. IX. December, 2007.
- [5] M. B. Hossain, M. Z. Hossain and T. Sakai, Interaction Properties of Geosynthetic with Different Backfill Soils” International Journal of Geosciences, 2012, 3, 1033-103.
- [6] Shamsher, F.H. (1992). Ground Improvement with Oriented Geotextiles and Randomly Distributed Geogrid Micro-Mesh. PhD Thesis submitted to Indian Institute of Technology Delhi, New Delhi, India.
- [7] Shukla, S.K. (1997). A study on causes of landslides in Arunachal Pradesh. Proceedings of Indian Geotechnical Conference, Vadodara, India, 1, 613-616.
- [8] Shukla, S.K. (2002). Slopes-stabilization. In Geosynthetics and Their Applications, Shukla, S.K., Ed., Thomas Telford, London, 237-257.
- [9] Shukla, S.K. (2004). Discussion of Applications of geosynthetics for soil reinforcement by M.I.M. Pinto, Ground Improvement, 7(2), 61-72

THE EFFECT OF VOID RATIO, MOISTURE CONTENT AND VERTICAL PRESSURE ON THE HYDROCOMPRESSION SETTLEMENT OF COPPER MINE TAILING

Mary Ann Q. Adajar¹ and Miller DL. Cutora²

¹Faculty, De La Salle University, Manila, Philippines

²Graduate student, De La Salle University, Manila, Philippines

ABSTRACT

Copper mine tailing (CMT) has the potential to be used as embankment material but this waste material contains plasticity. Soils containing plasticity are highly reactive to any form of liquid and considered to have greater compressibility when exposed to water. As an embankment material, CMT is susceptible to different environmental condition which can cause significant settlement. One possible cause of volume loss is the compression due to wetting or hydrocompression. This study aims to determine the consolidation properties and hydrocompression settlement of waste materials with plasticity like copper mine tailing when used as embankment material. One-dimensional consolidation tests were performed on reconstituted specimens. The obtained consolidation properties indicate that CMT is very slightly compressible under over-consolidated condition to moderately compressible under normally consolidated condition. The hydrocompression settlement of CMT in relation to initial void ratio, moisture content and preloaded vertical pressure was investigated. The hydrocompression settlement increases with increasing pressure until the preconsolidation pressure is reached, then decreases with pressure beyond the preconsolidation pressure. Samples with lower density and water content less than its optimum exhibit greater hydrocompression settlement. The determined hydrocompression strain in every condition is less than 5% which means that CMT has a degree of collapsibility classified as low to negligible despite of having plasticity. CMT when used as embankment materials should be prepared with initial moisture content slightly more than its optimum, it should be in its very dense condition and preloaded with vertical stress more than its preconsolidation pressure to make hydrocompression strain negligible.

Keywords: Copper Mine Tailings, Embankment Material, Hydrocompression Settlement, Consolidation Properties

INTRODUCTION

The disposal of the enormous amount of wastes regularly produced from mining processes is one of the most common environmental issues associated in the operation. One possible option to address disposal problem is to utilize these waste materials that do not contain deleterious components as embankment materials. To evaluate the suitability of solid wastes as embankment materials, its geotechnical characteristics have to be established. The determination of the consolidation properties that describe the compressibility and the one-dimensional settlement of mining wastes when subjected to vertical stresses had been covered in the study of some researchers [1]–[3]. However, compressibility and settlement of embankment materials are not only caused by vertical stresses imposed to the earth structure. During service life of embankment or fill materials, environmental changes can lead to an increase in its moisture content which can affect the compressibility and settlement behavior. Waste materials, when use as embankment materials, are susceptible to this kind

of condition where significant settlement can rapidly occur. One possible cause of volume loss is the compression due to wetting or termed as “hydrocompression” or “hydrocollapse”. Some soils can swell, collapse, shrink or experienced extreme settlement if exposed to water or any fluid. Investigation about the hydrocompression of gold mine tailings and wastes from aggregate quarry in the Philippines with non-plastic fines was discussed in previous study [1]. Findings of the study showed that these wastes materials which are non-plastic are less susceptible to hydrocompression.

Copper mine tailing has the potential to be used as embankment material [4] but this waste material contains plasticity, a property prevalent in clay minerals. Soils containing clay minerals are highly reactive to any form of liquid and considered to have greater compressibility when exposed to water. Several studies proved that compressibility and collapsibility of embankment materials are dependent on several factors like amount of moisture, clay mineralogy, density and applied pressure. Increasing the moisture content affects the compaction behavior and compressibility of

municipal solid wastes used as embankment. Its compaction period shortens while compressibility increases when water was added [5]. Clay mineralogy affects the coefficient of consolidation (C_v). The increase or decrease of C_v which describes the compressibility in clays is governed by the mechanical and physicochemical factors [6]. The study of Langroudi and Jefferson [7] investigates the contribution of hydraulic and stress history in collapsibility of excavated calcareous clayey loess re-used as embankment materials. The findings showed that controlled stress-hydraulic paths can guarantee the long-term response of embankments made of excavated calcareous clayey loess.

This research study aims to determine the consolidation properties and hydrocompression settlement of waste materials with plasticity like copper mine tailings through one-dimensional consolidation test. This study verifies if the plasticity of the material is one factor that will lead to greater hydrocompression settlement. It is also the objective of this study to investigate the effect of initial moisture content, initial void ratio in terms of relative density and pre-loaded vertical pressures to the hydrocompression settlement of copper mine tailings. The determination of consolidation properties and hydrocompression settlement are essential steps to completely evaluate the suitability of copper mine tailings for geotechnical application.

EXPERIMENTAL PROGRAM

Preliminary investigation was done to determine the physical properties of copper mine tailing (CMT). The main experimental program consisted of determination of consolidation properties and hydrocompression settlement of CMT. Reconstituted specimen, 50 mm in diameter and 17 mm in height was prepared by moist tamping method to achieve the desired density. An amount of the dry CMT sample that provided the desired density for the specimen was mixed with the small amount of water to produce water content closed to optimum water content. The sample was then stored overnight before being tamped into the consolidometer mold to obtain the desired density.

The Copper Mine Tailing

The waste material used in this study is copper mine tailing (CMT) obtained from Barrio Maglinao, Municipality of Basay, Negros Oriental, Central Visayas in the Philippines. Mine tailing is produced after separating the important ore, which is copper, in open pit mining where blasting and crushing are performed. The copper tailings obtained from tailing dam were somewhat dry. Through visual inspection, dry CMT is grayish brown in color and resemble that of fine sand; when moist, CMT has

soft consistency.

Determination of Consolidation Properties

The consolidation properties of the tailing samples were determined through one-dimensional consolidation test using the procedure described in ASTM D2435. Reconstituted specimen was prepared with a target relative density slightly closed to 90% to simulate the very dense condition of the embankment. Load increments that applied stresses of 12.5, 25, 50, 100 and 200 kPa were used. The tests were conducted with specimen fully submerged in water for the entire duration of the tests. This is to simulate the condition where embankment materials are expected to be at its most compressible state. Consolidation properties such as compression index (C_c), recompression index (C_r) and preconsolidation pressure (σ'_p) were determined using the Modified Strain Energy method [8]. The coefficient of consolidation (C_v) was determined using Taylor's square root of time method [9].

Determination of Hydrocompression Settlement

Variations in initial relative density, initial moisture content, and predetermined vertical stress were incorporated in the experimentation to verify the effect of these factors on the hydrocompression settlement of CMT. Reconstituted specimens were prepared at initial relative density of 60%, 80% and 100% to simulate the medium dense, dense, and very dense conditions of embankment, respectively. Three variations in water content at start of test were used; the dry phase where water content is slightly less than the optimum moisture content (w_{opt}), the optimum phase where water content is equal to w_{opt} , and the wet phase where water content is slightly more than the w_{opt} . Four (4) preloaded vertical stresses (25, 50, 100 and 200 kPa) were used. The preloaded stress simulates the overburden pressure imposed to embankment. A total of thirty six (36) test runs was performed. To evaluate the hydrocompression settlement, the introduction of water to the specimen was delayed until the preloaded stress was reached. At the desired preloaded stress, the specimen was flooded by filling the consolidometer reservoir with distilled water. Hydrocompression strain was observed and recorded for 24 hours, after which, specimen was unloaded and reloaded to complete the consolidation process. Observation was being prolonged when the deformation was still significant. The values of vertical strain of each test samples were plotted in a strain vs. elapsed time graph. Then, the intersection of tangent lines to the curve where flatter slope is observed and to the curve at early stages of plot is determined. The amount of hydrocompression strain (ϵ_h) is then graphically measured [1].

RESULTS AND DISCUSSION

Physical Properties

The values of soil constants of CMT determined from the tests are presented in Table 1. The value of specific gravity showed that CMT has heavier grains as compared to conventional soil. This is because the sample is waste material and found to contain some traces of chemical elements like copper and titanium which are not usually found in conventional soil. Copper mine tailing from this study is considered to have low plasticity based on qualitative manner of plasticity index [10].

Table 1 Soil Constants of CMT [4]

Soil Constants	
Specific Gravity, G_s	2.82
Liquid Limit, LL (%)	32
Plasticity Index, PI (%)	6
Minimum dry density, ρ_{dmin} (kg/m^3)	1,155.42
Maximum dry density, ρ_{dmax} (kg/m^3)	1,436.15
Maximum void ratio, e_{max}	1.441
Minimum void ratio, e_{min}	0.964
D_{10} (mm)	0.003
D_{50} (mm)	0.15
Maximum dry unit weight (kN/m^3)	15.70
Optimum moisture content, w_{opt} (%)	19.47

Consolidation Properties

The relationship between vertical effective stress and vertical strain as expressed by the change in void ratio for the copper mine tailing samples was obtained to determine the consolidation behavior and to measure the eventual magnitude of settlement that sample will experience when they are subjected to one-dimensional compression. Soil exhibiting excessive settlement is not suitable as fill or embankment material because this can be detrimental to the integrity of the supported structure. Consolidation parameters which indicate the compressibility and the amount of settlement that copper mine tailing will experience are presented in Table 2. The preconsolidation stress (σ_p') of fine-grained materials is related to its stress history and significantly affects settlement calculations. The compression index, C_c , and recompression index, C_r , are index values required for primary consolidation settlement predictions. The compression index, C_c is used to classify the compressibility of soils which are normally consolidated. Likewise, the

recompression index, C_r , is used to classify the compressibility of soils which are over-consolidated.

The stress at σ_p' delineates the region of semi-elastic behavior corresponding to over-consolidated states from the region of primarily plastic behavior which is associated with normal consolidation. Hence, if overburden stresses are below σ_p' , the soil is considered as over-consolidated and the irrecoverable deformation is considered to be negligible. If the overburden pressure is quite near of σ_p' , it is classified as normally consolidated and the strain-deformation in this region is somehow tolerable, while far beyond σ_p' , the irrecoverable deformation is expected to be more significant. The compression ratio and recompression ratio were also computed to classify the compressibility of CMT. Copper mine tailing is classified as moderately compressible when it is normally consolidated and very slightly compressible when over-consolidated.

Table 2 Consolidation parameters of CMT

Compression Index, C_c	0.3416
Recompression Index, C_r	0.0263
Preconsolidation Pressure, σ_p' (kPa)	58.3

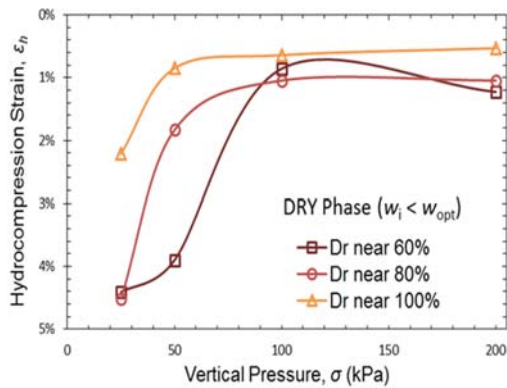
To predict the time rate of settlement, the consolidation characteristics as described by coefficient of consolidation (C_v) was evaluated. It is apparent from test results that values of C_v depend on whether the preconsolidation pressure (σ_p') has been exceeded or not. Values of C_v for each vertical stresses are summarized in Table 3. The typical trend exhibited by the sample is that C_v values are higher in the early stages of over consolidated range specifically at stress near the preconsolidation pressure (σ_p') and showed a relatively rapid decrease for stresses beyond σ_p' . Lower values of C_v are observed at vertical stresses that exceed σ_p' .

Table 3 Values of Coefficient of consolidation, C_v

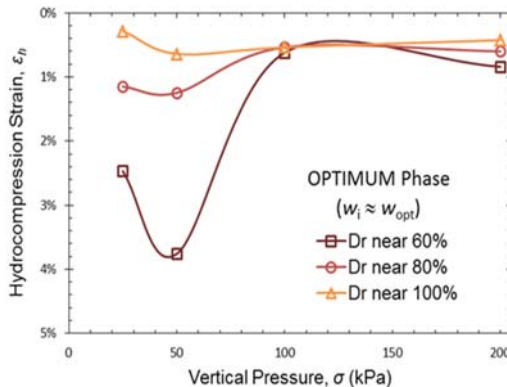
Vertical Effective Stress, σ (KPa)	C_v (cm^2/sec) $\times 10^{-3}$
	Copper Mine Tailings (CMT)
5	3.9465
12.5	7.8671
25	12.4034
50	15.7816
100	11.2129
150	6.7777
200	5.7404

Hydrocompression Settlement

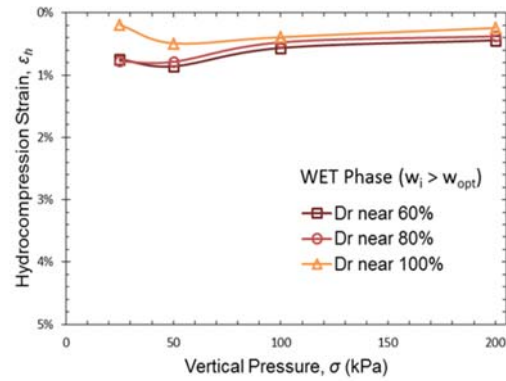
Copper mine tailings like soil have unique geotechnical characteristics including its behavior when saturated. Consolidation tests were performed on reconstituted specimens to determine the collapsibility of copper mine tailings due to intrusion of water or termed as hydrocompression settlement. This study presents the influence of relative density in terms of void ratio, moisture content and preloaded vertical stress on the hydrocompression settlement behavior of CMT. The influence of initial moisture content, w_i (dry phase: $w_i < w_{opt}$; optimum phase: $w_i \approx w_{opt}$; and wet phase: $w_i > w_{opt}$), and the degree of denseness in terms of relative density, Dr (medium dense, $Dr \approx 60\%$; dense, $Dr \approx 80\%$; and very dense, $Dr \approx 100\%$) together with the preloaded vertical stress (Low = 25 kPa, 50 kPa; and High = 100 kPa, 200 kPa) to vertical strain upon saturation were investigated by using varying amount of these factors in the experimentation. The collapsibility behavior of CMT was evaluated according to the amount of hydrocompression strain attained during inundation. Figure 1 shows the influence of these factors to hydrocompression strain.



a.) Dry Phase



b.) Optimum Phase



c.) Wet Phase

Fig. 1 Effect of preloaded vertical pressure and relative density to hydrocompression strain when moisture content is at dry phase, optimum phase and wet phase

Effect of Preloaded Vertical Stress Prior to Inundation

The typical soil response when subjected to stresses lower than the preconsolidation pressure is to exhibit minimal deformation. Preloading the sample with lower stresses before inundation resulted to minimal deformation. However, after the preloading stage and when the sample was inundated with water, it resulted to greater vertical compressive strain. Rearrangement of particles was easily achieved with pressures lower than σ_p' . When the sample experienced sudden flow of water, the dry particles became very responsive due to its plasticity. The inter-assemblage pore spaces allow water to pass through easily that softens the bonds between particles, thus resulted to vertical compressive strain. The water serves as lubricant for the particles to easily rearrange into a denser configuration as manifested by greater hydrocompression strain. When the sample was preloaded with vertical stresses beyond the preconsolidation pressure, the hydrocompression strain decreased even for samples with Dr near 60%. The sample has already achieved its denser and stable condition before the intrusion of water. When the sample was inundated with water, the collapsibility potential was reduced and the hydrocompression strain became negligible.

Effect of Initial Relative Density

The arrangement of the soil skeleton influenced the deformation of CMT due to sudden intrusion of water. During inundation, specimens with greater void ratio (Dr near 60%, medium dense condition) caused the water to easily penetrate the void spaces and increased the collapse potential. At lower relative density, the hydrocompression strain is more significant. As the void ratio decreases (Dr near

100%, very dense condition), the rate of flow of water into the sample also decreases, thus causing minimal disturbance on the particles and the hydrocompression strain became almost negligible.

Effect of Initial Moisture Content

When specimen was prepared with initial moisture content slightly more than its optimum value (wet phase), the collapse potential of the specimen was reduced to negligible value even when the predetermined vertical stresses were below the preconsolidation pressure and at medium dense condition. The hydrocompression strains at wet phase were less than the hydrocompression strains at optimum and dry phase. The presence of water in the void spaces reduces the sudden intrusion of water. Moreover, the pore water pressure aided in supporting the applied vertical load, thus the stress carried by the soil skeleton was reduced.

From test results, the amount of hydrocompression strain experienced by CMT is affected by the applied vertical stress prior to inundation, initial relative density and initial moisture content. To reduce the magnitude of hydrocompression strain to a negligible value, CMT when used as embankment materials should be prepared with initial moisture content slightly more than its optimum value. If the initial moisture content is less than or equal to its optimum value, CMT should be in its very dense condition and it should be preloaded with vertical stress more than its preconsolidation pressure to make hydrocompression strain negligible. The determined hydrocompression strains in every condition is less than 5% which means that CMT has a degree of collapsibility classified as low to negligible despite of having plasticity. The amount of hydrocompression strain obtained is higher than the values obtained for non-plastic mine tailings [1] and within the range of values for mine spoils with low plasticity [12].

Formulation of Empirical Model to Predict Hydrocompression Strain

Using the response surface method (RSM), the relationship of the hydrocompression strain with initial void ratio, e_o , initial water content, w_i , and the preloaded vertical stress, σ , was formulated. The hydrocompression strain, ε_h can be expressed by the equation:

$$\varepsilon_h = \exp(4.8301e_o - 11.4769w_i - 0.0047\sigma - 7.3814) \quad (1)$$

where:
 e_o = initial void ratio

w_i = initial moisture content (e.g. $w_i = 0.10$ for 10% moisture content)

σ = vertical stress before inundation in KPa

To verify the predictive capability of the proposed model, the hydrocompression strain (ε_h) calculated using the proposed model was compared with the measured values from experimentation. Statistical analysis using T-test for paired samples was performed to determine if there is a significant difference between the measured values and the predicted values. The null hypothesis for the T-test states that there is no significant difference between the measured and predicted hydrocompression strain. The results for 36 number of observations with a level of significance equals to 0.05 ($\alpha = 0.05$) showed a t_{stat} value (1.211) is less than t_{critical} (1.689) and the p -value is greater than 0.05. This means that the null hypothesis should be accepted. It can be stated at 95% confidence level that there is no significant difference between the measured ε_h and the predicted ε_h . The strength of association between measured ε_h and the predicted ε_h was verified using the Pearson's correlation coefficient and the data are presented in a scatter plot as shown in Fig. 2. The scatter of data points is nearer to a straight line which means that there is a linear positive correlation between the measured and predicted ε_h . The statistical analysis yielded a Pearson correlation value of 0.82 indicating a very strong association between the two variables (measured and predicted ε_h). It can be concluded that the proposed model (Eq. 1) can be used to predict the amount of hydrocompression strain as a function of initial void ratio, initial moisture content and the vertical stress prior to inundation.

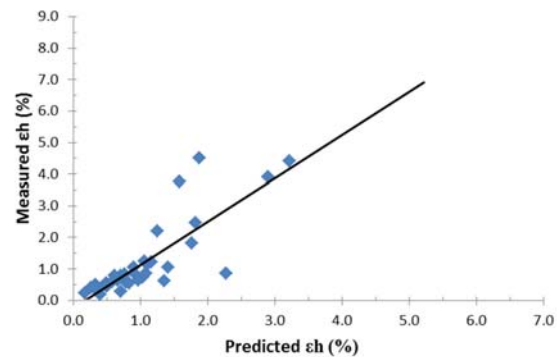


Fig. 2 Correlation of Measured ε_h with Predicted ε_h

CONCLUSIONS

The consolidation behavior and hydrocompression settlement of copper mine tailing were investigated to determine its suitability as

embankment material. Based from laboratory test results, the following conclusions were drawn:

Copper mine tailing is considered to have low plasticity with heavier grains as compared to conventional soil. Based on values of consolidation parameters CMT is classified as moderately compressible when it is normally consolidated and very slightly compressible when over-consolidated.

Coefficient of consolidation (C_v) values are higher in the early stages of overconsolidated range specifically at stress near the preconsolidation pressure (σ_p') and showed a relatively rapid decrease for stresses beyond σ_p' .

The hydrocompression settlement of CMT increases with increasing pressure until the preconsolidation pressure is reached, and then decreases with pressure beyond the preconsolidation pressure. Samples with lower density and water content less than its optimum value exhibit greater hydrocompression settlement. The determined hydrocompression strains in every condition is less than 5% which means that CMT has a degree of collapsibility classified as low to negligible in spite of having plasticity.

To reduce the magnitude of hydrocompression strain to a negligible value, CMT when used as embankment materials should be prepared with initial moisture content slightly more than its optimum value. For cases where the initial moisture content is less than or equal to its optimum value, CMT should be in its very dense condition and it should be preloaded with vertical stress more than its preconsolidation pressure to make hydrocompression strain negligible.

Having good compaction behavior, reasonably stable when dense, with low compressibility and low collapsibility are indications that copper mine tailing despite of having plasticity has consolidation and hydrocompression characteristics suitable as embankment material.

ACKNOWLEDGEMENT

This research study was undertaken through the DLSU-University Research Coordination Office under the new PhD research program.

REFERENCES

- [1] Adajar MQ and Zarco MH, "Estimating Hydrocompression Settlement of Mine Tailings", Philippine Engineering Journal, 2013, Vol. 34, No. 1, ISSN: 0117-5564.
- [2] Germanov T, "Geotechnical Properties of Industrial Waste Deposits in Bulgaria", Proceedings of 13th European Conference on Soil Mechanics and Geotechnical Engineering, Prague, 2003, 1: 95-100.
- [3] Qiu Y and Sego DC, "Laboratory Properties of Mine Tailings", Canadian Geotechnical Journal, 2001, 38: 183-190.
- [4] Uy ES and Adajar MQ, "Assessment of Critical-State Shear Strength Properties of Copper Tailings, International Journal of GEOMATE, April, 2017, Vol. 12, Issue 32, ISSN: 2186-2990, Japan, pp. 12-18.
- [5] Hanson JL, Yesiller N, Von Stockhausen SA and Wong WW, "Compaction Characteristics of Municipal Waste", Journal of Geotechnical and Geoenvironmental Engineering, 2010, pp. 1095-1102.
- [6] Robinson R. and Allam M., "Effect of Clay Mineralogy on Coefficient of Consolidation. Clays and Clay Minerals", 1998, Vol. 46, No. 5, pp. 596-600.
- [7] Langroudi A and Jefferson I, "Collapsibility in Calcareous Clayey Loess: A Factor of Stress-Hydraulic History", Int. J. of GEOMATE, 2013, Vol. 5, No. 1 (Sl. No. 9), ISSN: 2186-2982(P), Japan, pp. 620-627.
- [8] Zarco M, "Modified Strain Energy Method for Determining Preconsolidation Pressures", Proceedings: 32nd Phil. Institute of Civil Engineers National Convention, Iloilo City, 2006.
- [9] Buddhu M, Soil Mechanics and Foundations, 2nd ed., John Wiley and Sons, Inc. USA, 2007, pp 196-197.
- [10] Das B and Sobhan K, Principles of Geotechnical Engineering, 8th ed., Cengage Learning, USA, 2014, pp. 102.
- [11] Prahallada M and Shanthappa B, "Use of Copper Ore Tailings - As an Excellent Pozzolana in the Preparation of Concrete", International Journal of Advanced Research in Engineering and Applied Sciences, 2014, 3(3), pp. 1-10.
- [12] Kalinski ME, Karem WA, and Little LM, "Estimating Hydro-compression Potential of Mine Spoils from a Site in Eastern Kentucky using Dry Unit Weight and Moisture Content", International Journal of Mining, Reclamation and Environment, 2010, 24:4, pp. 350 – 362.

SOIL-STRUCTURE INTERFACE BEHAVIOR OF CEMENTED-PASTE BACKFILL MATERIAL MIXED WITH MINING WASTE

Mary Ann Q. Adajar¹ and Wincent Nicole K. Pabilona²

¹Faculty, De La Salle University, Manila, Philippines

²Graduate student, De La Salle University, Manila, Philippines

ABSTRACT

The use of mining wastes as component of cemented paste backfill provides an environmentally acceptable method of waste disposal at lesser cost as the method does not require tailing dams for storing the large volume of wastes. This study determines the applicability of cemented-paste backfill materials mixed with aggregate quarry wastes as ground support to concrete structures. Aggregate quarry waste with varying fine contents was used as substitute for sand in cemented-paste backfill and the mixture was referred to as cemented-paste tailing backfill (CPTB). Its micro fabric structure was determined through SEM-EDX tests. Test results showed that CPTB with 20% and 40% fine contents has acceptable values of strength properties in terms of its unconfined compressive strength and interface friction angle. The unconfined compressive strength in relation to its curing period is in the range of 120 kPa to 150 kPa which can be described as having stiff consistency. The stress-strain interface behavior between CPTB and concrete structure was evaluated through direct shear test using strain rates that simulate the rapid and slow rates of loading. In both conditions, the stress-strain behavior exhibits strain softening. The average interface friction angle is 38° which can be associated to its dense condition. Modified hyperbolic model was applied to evaluate the soil-structure interface behavior of CPTB. Hyperbolic parameters were formulated to predict the interface shear stress – shear strain behavior of the CPTB when in contact with concrete structure at any value of shear strain and normal effective stress.

Keywords: Cemented-paste Backfill, Unconfined Compressive Strength, Interface Friction Angle, Modified Hyperbolic Model

INTRODUCTION

Cemented paste backfill is a cementitious composite normally made of coarse and fine aggregates mixed with hydraulic binder which is typically Portland cement. It is a means of ground stabilization and for strengthening and solidification of underground foundation of a building which is done at early parts of construction activities. It also provides stable platform and ground support to the structure sitting on it. In mining industry, the extraction of valuable ore creates very large voids which need to be backfilled. The backfill material makes use of waste rocks or tailings mixed with a binder, usually cement, to form a cemented-paste backfill. The use of cemented paste backfill is an increasingly important component of underground mining operations and is becoming a standard practice for use in many cut-and-fill mines around the world [1]. This is an effective means of tailing disposal because it negates the need for constructing large tailing dams at the surface [2].

In the Philippines, sustainable solution to manage wastes being produced by mining industries is essential. Moreover, an effective open-pit mine rehabilitation method is strongly required. Backfilling, which requires large volume of soil

mass, is one of the major activities of open-pit mine rehabilitation to bring back the mined area into beneficial use. The use of mining wastes specifically wastes from aggregate quarry, as component of cemented paste backfill provides an environmentally acceptable method of waste disposal and rehabilitation process at lesser cost. Waste from aggregate quarry is proven to be stable when used as embankment material [3]. It is also a feasible component in concrete mix as substitute for fine aggregates [4]. However, its strength properties when used as component of cemented-paste backfill have yet to be determined. Its interface behavior when in contact with concrete structure has to be evaluated.

Understanding the soil-structure interface behavior is an important tool for use in analyzing, designing, and monitoring geotechnical structures. Several constitutive modeling have been used to obtain accurate solution to many soil-structure interaction problems. The hyperbolic interface model developed by Clough and Duncan [5] presented a systematic approach to model the behavior of the retaining wall-to-soil interfaces in the primary loading stage. An extended hyperbolic model for interfaces was developed that can capture important aspects of interface response under the

type of loading expected to occur in a wall-backfill interface at different stages of construction and operation of a lock wall [6]. In this study, the modified hyperbolic model which was formulated to characterize the stress-strain and volume-change behavior of tailings determined from direct shear tests [3] was applied to evaluate the soil-structure interface behavior of cemented-paste tailing backfill.

This study determines the applicability of cemented-paste backfill materials mixed with aggregate quarry wastes as ground support to concrete structures like footings or retaining walls. The mixture is called cemented-paste tailing backfill (CPTB). Strength properties such as unconfined compressive strength at various curing time and interface friction angle were determined. Hyperbolic parameters were formulated to predict the interface shear stress – shear strain behavior of the CPTB when in contact with concrete structure.

MATERIALS AND TEST METHODS

The material composition of cemented-paste tailing backfill (CPTB) is waste from aggregate quarry (WAQ) as sand substitute with Portland cement as hydraulic binder. WAQ was collected from quarry site in Ternate, Cavite. These quarry wastes are residues of mountain rocks which went through crushing processes to produce fine aggregates. The residues, considered as solid wastes, are produced during the washing of crushed rocks in the siltation pond through the natural process of sedimentation. WAQ has specific gravity of 2.57 and classified as fine-grained soil with no plasticity [4].

The aggregate quarry wastes in the CPTB mixture had varying fine contents ranging from 20%, 40% and 60% by weight. This is done to investigate the effect of fineness of grains on the strength properties of CPTB. The fine content for this experimentation is defined as percent grain particles passing the #200 sieves. Cement consists of 5.5 percent by dry mass of WAQ which is equivalent to 3.8 weight percentage of the entire mixture. The water-cement ratio of 7:1 was used in the mixture. Table 1 shows a typical mix proportion of CPTB.

To determine the strength properties of CPTB, unconfined compression strength (UCS) test in accordance with ASTM D2166 was performed. The cylindrical sample has 63.5 mm diameter with 158.8 mm height. The samples were tested after the 7th, 14th, 28th and 42nd day curing period to determine the effect of curing time on its strength development. The 42nd day curing time was intended to observe the long-term strength of CPTB.

Direct shear test in accordance to ASTM D3080 was performed to determine the interface friction angle and to describe the soil-structure interface behavior of CPTB. The mixture that produced the

maximum unconfined compressive strength was used for the direct shear test. The experimental set-up simulates a concrete structure resting on CPTB material. The lower part of the shear box contains the CPTB mixture while the upper part of the shear box contains the concrete mortar mix to represent a rigid concrete structure. The schematic of experimental set-up is shown in Fig. 1. Samples were subjected to normal stresses of 13.625 kPa, 20.4375 kPa, and 27.25 kPa. Direct shear test was done using the fast strain rate of 1.25mm/min. to simulate the rapid loading condition and slow strain rate of 0.12mm/min to simulate the long term loading condition. From the plot of shear stress vs. shear strain behavior obtained from direct shear test, hyperbolic parameters using the modified hyperbolic model technique were determined to predict the soil-structure interface behavior of CPTB at any value of shear strain and normal effective stress.

Table 1 Typical mix proportion of CPTB for each cylindrical sample for UCS test

% of Fine Contents of WAQ	Cement (g)	Water (g)	WAQ (g)	
			Passing #200 Sieve	Passing #4 sieve, retained on #200 Sieve
20%	15.9	111.5	58.3	233.4
40%	15.9	111.5	116.7	175.0
60%	15.9	111.5	175.0	116.7

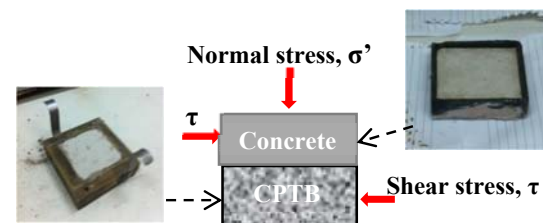


Fig. 1 Schematic of experimental set-up for direct shear test

RESULTS AND DISCUSSION

Unconfined Compressive Strength, q_u

Figure 2 shows the unconfined compressive strength development of CPTB with varying fine contents; the average values are tabulated in Table 2. For CPTB with 20% and 40% fines, the samples exhibited greater q_u at early curing days; however, there is an appreciable decrease in strength beyond the 7th day curing period followed by an almost

constant value of q_u as curing age increases. The observed higher value of q_u at 7th day curing can be explained from the SEM results as shown in Figs. 3 and 4. The microstructure of samples at 7th day curing time showed a more flocculated state with minimum void spaces. This results to a decrease in the total pore volume and a concurrent increase in strength. At 42nd curing day, the micrograph showed a honeycomb structure with intra-assemblage voids depicting an increase in porosity and thus leads to lower compressive strength. The final amount of porosity after the hydration of Portland cement paste depends strongly on the initial water-cement ratio of the paste [7]. The almost constant value of q_u ranging from 120 KPa to 140 KPa for CPTB with 20% fines and 140 KPa to 150 KPa for CPTB with 40% fines can be considered as the suitable value of compressive strength of CPTB that depicts its long-term behavior. The compressive strength is comparable to clay with stiff consistency. The mode of failure exhibited by the samples is diagonal shear as seen in Figures 5a and 5b. Meanwhile, CPTB with 60% fines showed an unpredictable trend in its strength development with respect to curing period. The bonding between Portland cement and WAQ did not work well when the mixture contains more fines. This is further attested from its mode of failure classified as failure by axial splitting (Fig. 5c). It is expected that samples which failed by axial splitting give a lower value of q_u than those that failed by diagonal shear [8].

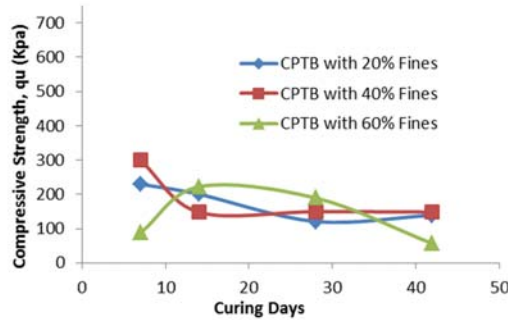
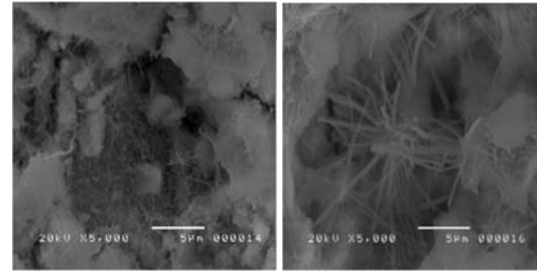


Fig. 2 Unconfined compressive strength of CPTB

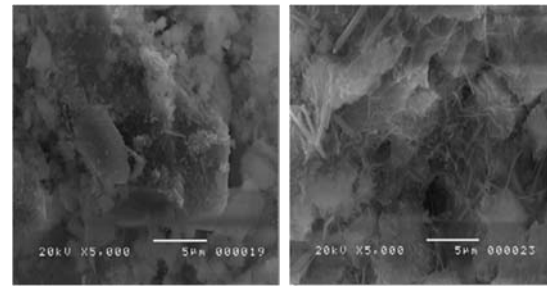
Table 2 Average unconfined compressive strength of CPTB

Curing Days	CPTB with 20% Fine	CPTB with 40% Fine	CPTB with 60% Fine
7	229.81	299.26	88.32
14	200.44	148.03	222.15
28	121.02	149.74	189.38
42	139.07	150.48	56.40



a.) at 7th day curing b.) at 42nd day curing

Fig. 3 Micrographs of CPTB with 20% fines



a.) at 7th day curing b.) at 42nd day curing

Fig. 4 Micrographs of CPTB with 40% fines



a.) 20% fines b.) 40% fines c.) 60% fines

Fig. 5 Modes of failure of CPTB subjected to compressive test a.) and b.) diagonal shear failure c.) axial split

Stress-strain Interface Behavior

The stress-strain interface behavior between CPTB and concrete structure was evaluated through direct shear test using strain rates that simulate the rapid and slow rates of loading. Specimens with 20% and 40% fines were subjected to shear force and normal stress after the 28th day curing period following the experimental set-up described in Fig. 1. CPTB with 60% fines was no longer included in the experimentation since the compressive strength test did not show acceptable results. The typical stress-strain graphs are shown in Figs. 6 to 9. In both conditions, the stress-strain behavior of CPTB

exhibits strain softening. The specimen showed a rapid increase in shear stress reaching a peak value at low shear strains and then decreases with increasing shear strains indicating strain softening until the shear stress at failure is attained. This indicates that specimen failed in brittle manner. The shear stress at failure is described as the shear stress at which continued shearing occurs without change in shear stress for a given normal stress.

The stress-strain curve defines the typical response of dense sample. In this experimentation, the CPTB after 28th days of curing time is comparable to compacted, dense soil. CPTB with 20% and 40% fines, whether subjected to slow or fast strain rates, achieved an almost the same shear stress at failure. The shear stress at failure is greater for specimens subjected to greater normal stress (σ').

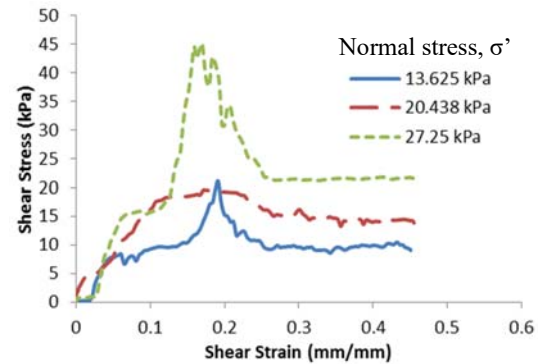


Fig. 8 Shear stress vs. shear strain of CPTB with 40% fines using fast strain rate

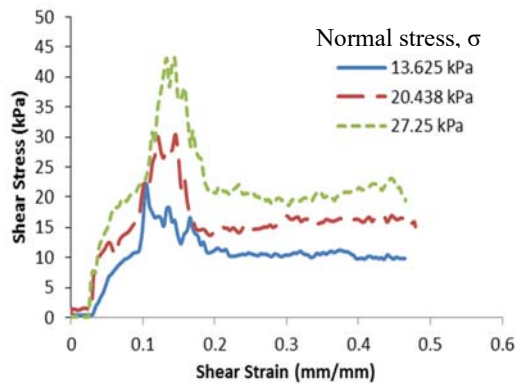


Fig. 6 Shear stress vs. shear strain of CPTB with 20% fines using fast strain rate

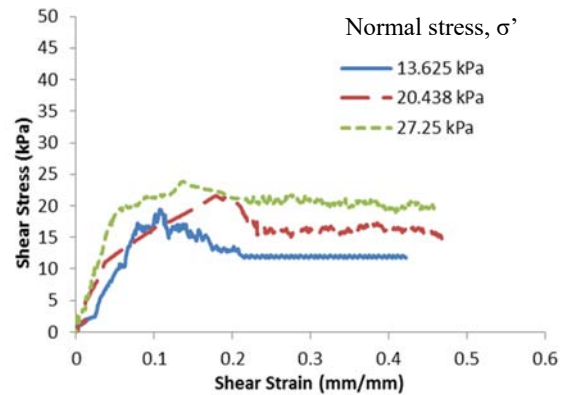


Fig. 9 Shear stress vs. shear strain of CPTB with 40% fines using slow strain rate

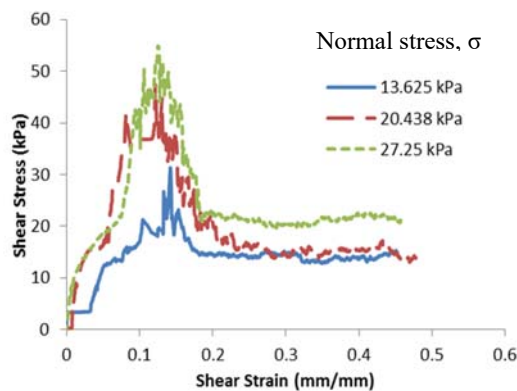


Fig. 7 Shear stress vs. shear strain of CPTB with 20% fines using slow strain rate

The shear stress at failure (τ_f) is plotted against the normal stress (σ') on a graph of τ against σ' . The best fit line joining the τ and σ' can be described by equation $\tau = \sigma' \tan \phi$. This line represents the failure envelope with slope $\tan \phi$. The angle ϕ is referred to as the interface friction angle and is tabulated in Table 3. This friction angle describes the frictional resistance of CPTB when in contact with concrete structure.

Table 3 Interface Friction Angle of CPTB

CPTB with	Interface Friction Angle, ϕ
	(deg.)
20% Fines - Fast Strain Rate	38.8
20% Fines - Slow Strain Rate	38.5
40% Fines - Fast Strain Rate	37.6
40% Fines - Slow Strain Rate	38.7

Hyperbolic Parameters

Shear stress vs. shear strain behavior of CPTB as presented in Figs. 6 to 9 was used to determine the hyperbolic parameters using the modified hyperbolic model. The modified hyperbolic model uses the shear stress against shear strain and volumetric strain against shear strain relations to describe the hyperbolic stress-strain behavior from the direct shear test. The hyperbolic relation between the changes in stress and strains is defined in terms of an initial shear modulus, G_i and the shear strength at failure, τ_f . The modified hyperbolic model concepts and procedure for the determination of hyperbolic parameters are discussed in the study of Adajar and Zarco [3]. Using the modified hyperbolic model, the parameters K (shear modulus number) and n (shear modulus exponent) describing initial shear modulus (G_i), based on hyperbolic fit to the stress-strain curve are obtained. The failure ratio R_f that relates the asymptotic shear stress with shear stress at failure is also determined. R_f is defined as the ratio of τ_f (Eq. 1) and the shear stress at failure. The variation of ϕ' with respect to σ' is described in terms of hyperbolic parameters ϕ_o and $\Delta\phi$. The summary of hyperbolic parameters is presented in Table 4. Applying these hyperbolic parameters in equations (1) to (3) allows the prediction of the interface shear stress – shear strain behavior of the CPTB when in contact with concrete structure at any value of shear strain and normal effective stress.

$$\tau_f = \sigma' \tan \phi' \quad (1)$$

$$\phi' = \phi_o - \Delta\phi \log \left(\frac{\sigma'}{P_a} \right) \quad (2)$$

$$\tau = \frac{\gamma}{\frac{1}{K \cdot P_a \left(\frac{\sigma'}{P_a} \right)^n} + R_f \left(\frac{\gamma}{\tau_f} \right)} \quad (3)$$

Where:

τ = shear stress, KPa

γ = shear strain

σ' = normal effective stress, KPa

P_a = atmospheric pressure = 101.325 KPa

Using the determined hyperbolic parameters, the model's response to the test data was compared with experimental data. The comparison of the test data and the calculated hyperbolic response are shown in Figs. 10 to 12. The modified hyperbolic model provides a good approximation of the interface shear stress – shear strain behavior of the CPTB. The

limitation of the model is that it cannot capture the peak shear stress [3], but it can provide a good prediction of shear stress at failure.

Table 4 Hyperbolic parameters of CPTB

Hyperbolic Parameter	Description	Value
K	Shear modulus number	170.99
n	Shear modulus exponent	0.9809
R_f	Failure ratio	0.9971
ϕ_o	Friction angle parameter	31.021°
$\Delta\phi$	Friction angle parameter	5.126°

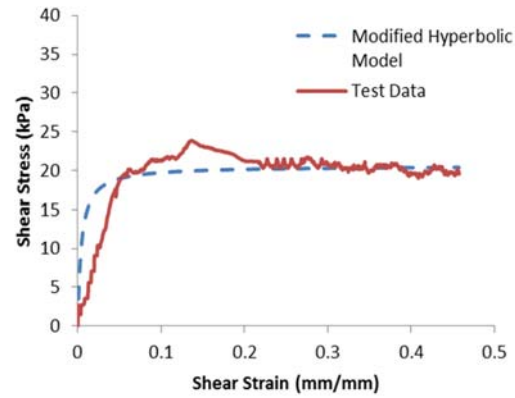


Fig. 10 Comparison of stress-strain curve using modified hyperbolic model and from test data of CPTB with 40% Fines and normal stress of 27.25 KPa

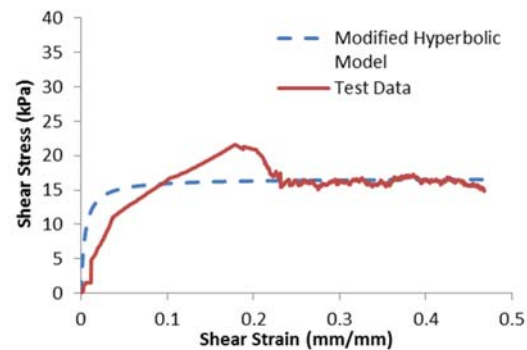


Fig. 11 Comparison of stress-strain curve using modified hyperbolic model and from test data of CPTB with 40% Fines and normal stress of 20.438 KPa

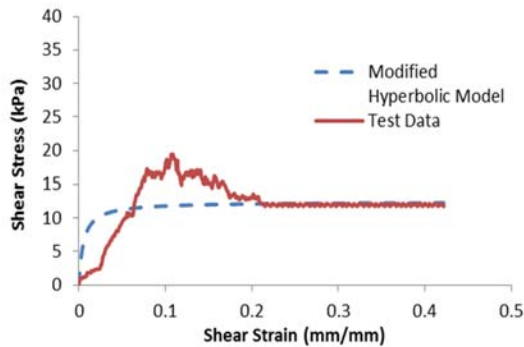


Fig. 12 Comparison of stress-strain curve using modified hyperbolic model and from test data of CPTB with 40% Fines and normal stress of 13.625 KPa

CONCLUSION

Strength properties of cemented-paste tailing backfill with waste from aggregate quarry as sand substitute were determined through unconfined compressive strength test and direct shear test. Its soil-structure interface behavior was evaluated. The following are the conclusions drawn from test results:

Cemented-paste tailing backfill with fine contents up to 40% showed acceptable values of unconfined compressive strength and interface friction angle suitable as ground support to structures. The unconfined compressive strength depicting its long-term behavior is in the range of 120 kPa to 150 kPa comparable to clay with stiff consistency. The mode of failure exhibited by the samples is diagonal shear. Its microstructure showed an increase in porosity as curing age increases. This can be due to the initial water-cement ratio of the paste mixture.

The stress-strain interface behavior between CPTB and concrete structure exhibits strain-softening. The average interface friction angle is 38° which can be associated to its dense condition.

Modified hyperbolic model was applied and hyperbolic parameters were formulated to predict the interface shear stress – shear strain behavior of the CPTB when in contact with concrete structure at any value of shear strain and normal effective stress. The modified hyperbolic model provides a good approximation of the interface shear stress – shear strain behavior of the CPTB. The model cannot capture the peak shear stress, but it provides a good prediction of shear stress at failure.

The CPTB used in this study can be a good alternative to the conventional cemented-paste backfill when used as a free-standing fill if the

design criteria are not requiring a high compressive strength value.

RECOMMENDATION

It is recommended that paste mixture with lower water-cement ratio and using binder other than Portland cement be considered in future test design to verify if the unconfined compressive strength can be improved.

REFERENCES

- [1] Landriault DA, Verburg R, Cincilla W, and Welch D, "Paste technology for underground backfill and surface tailings disposal applications", Short course notes, Canadian Institute of Mining and Metallurgy, Technical workshop – April 27, 1997, Vancouver, British Columbia, Canada, p. 120.
- [2] Sivakugan N, Rankine RM, Rankine KJ, and Rankine KS, "Geotechnical Considerations in Mine Backfilling in Australia", Journal of Cleaner Production, Elsevier, Vol. 14, 2006, pp. 1168 – 1175.
- [3] Adajar MQ and Zarco MH, "Predicting the stress-strain behavior of mine tailing using modified hyperbolic model", Int. J. of GEOMATE, Vol. 10, Issue 21, Japan, May 2016, pp. 1834-1841.
- [4] Adajar MQ, De Guzman E, Ho R, Palma C, and Sindico D, "Utilization of Aggregate Quarry Waste in Construction Industry", Int. J. of GEOMATE, Vol. 12, Issue 31, Japan, March 2017, pp. 16-22.
- [5] Clough GW and Duncan JM, "Finite Element Analyses of Retaining Wall", Journal of the Soil Mechanics and Foundations Division, Proceedings of the American Society of Civil Engineers, Dec. 1971, 97(SM12): 1657-1673.
- [6] Gomez JE, Filz GM and Ebeling RM, "Development of an Improved Numerical Model for Concrete-to-Soil Interfaces in Soil-Structure Interaction Analyses", US Army Engineer Research and Development Center, Technical Report ITL-99-1, August 2000.
- [7] Thomas J. and Jennings H., "The Science of Concrete: Hydration and Microstructure of Cement Paste", Retrieved date: June 17 2016. <http://iti.northwestern.edu/cement/index.html>
- [8] Liu C and Evett J, "An Investigation of the Uniaxial Compressive Strength of a Cemented Hydraulic Backfill Made of Alluvial Sand", Minerals 2017, Vol. 7, Issue 4, pp. 1-13.

A NEW TESTING APPARATUS TO EXCAVATE RECTANGULAR SECTION FOR UNDERPASS TUNNEL CONSTRUCTION

Yota Togashi¹, Takashi Nakayama², Sohei Itaya², Takatoshi Hondo³ and Noriyuki Okano²

¹Disaster Prevention Technology Division, Railway Technical Research Institute, Japan

²Structures Technology Division, Railway Technical Research Institute, Japan

³Railway Dynamics Division, Railway Technical Research Institute, Japan

ABSTRACT

For understanding a mechanical behavior of soils during tunnel excavation, various experiments have been conducted, e.g. trap door test. However, the influence of rectangular shape excavation was not sufficiently investigated by previous studies. In this study, in order to evaluate ground relaxation during underpass tunnel construction by non-open cut method, which include rectangular shape excavation for temporally construction of square pipes to prevent ground relaxation, a new testing apparatus to excavate rectangular section is developed. The testing apparatus is configured by metal lining scaled down by approximately 1 / 5, drilling and its operating devices, and it can be movable corresponding to rectangular tunnel face by three-degree of freedom. For investigate the deformation properties of soils during excavation, jacking and excavation test is conducted by a small sand box using Toyoura soil compacted with water content ratio $w = 10\%$. The results demonstrated that the excavation can be stably conducted using the cutter rotated by a motor and the tunnel face observation can be also stably conducted by a miniature camera. Furthermore, for soil removal amount, the difference between plan and measured values finally become less than 2 %.

Keywords: Underpass, Tunnel, Rectangular shape, Excavating test, Surface displacement

INTRODUCTION

For understanding a mechanical behavior of soils during tunnel excavation, various experiments were developed [1]. For example an earth pressure during tunnel excavation has been investigated by trap door tests using aluminum bars [2, 3], soil relaxation between tunnel face to ground surface were investigated by pull-out test of duplex tube in soil box [4] and an interaction of tunnel construction

with piles were studied by centrifuge model testing using the equipment of decreasing tunnel diameter [5]. These studies were mainly conducted for tunnel construction with circular section combining with some numerical analysis, [e.g. 6, 7]. Furthermore, although there were some studies focused on modeling excavation process [8, 9], the influences of excavating square section were not well studied yet.

In recent years, underpass tunnel, which intersect road or railroad, is increasingly constructed by non-

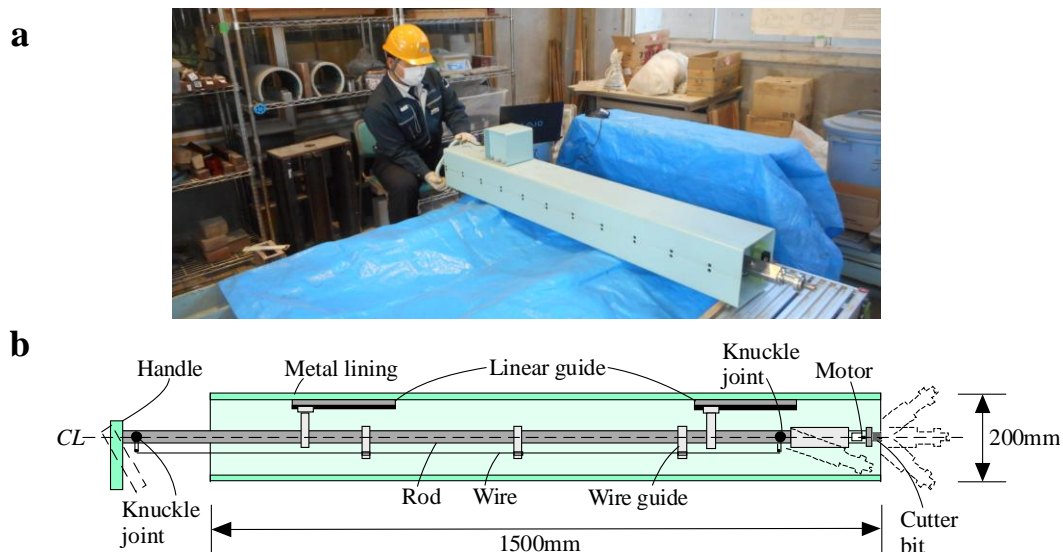


Fig. 1 A new testing apparatus of excavating rectangular section: (a) appearance, (b) cross section

open cut method mainly using jacking method [e.g. 10, 11] and it is strongly important to investigate mechanical behavior of soils during rectangular shape excavation for temporally construction of square pipes to prevent ground relaxation. Although Takahashi et al. [12] conducted FE analysis with modeling of excavating rectangular section in accordance with tunneling process, there were few experimental studies to investigate a mechanical behavior of soils due to rectangular excavation.

In this study, to evaluate mechanical behaviors of soils during underpass tunnel construction, we developed a new laboratory testing apparatus to excavate rectangular section. The structure of the equipment and excavating test using acryl soil box for modeling underpass tunnel construction is reported as following chapter.

STRUCTURE OF TESTING APPARATUS

Fig. 1 shows a new testing apparatus of excavating rectangular section. The apparatus is configured by metal lining scaled down by approximately 1 / 5, drilling and its operating devices as shown in Fig. 1 (b). The cutter can be movable corresponding to rectangular tunnel face by three-degree of freedom, which can be operated by handle via wire connected by knuckle joints to control roll, pitch, and yaw angles separately as shown in Fig. 2. The allowable length of excavation is 20 cm and the maximum inclination angle of cutter is 30 ° as shown in Fig. 3.

By using this apparatus, tunnel excavation with rectangular section is simulated by a laboratory test. In next chapter, excavating and jacking test using soil box is shown.

EXCAVATING AND JACKING TEST

Test condition

For underpass tunnel construction using non-open cut method, steel pipes are propelled by a hydraulic jack after excavating soils. To model the condition of construction, we conducted excavating and jacking test as shown in Fig. 4. The excavating apparatus was fixed on the pedestal, and the soil box was movable to lateral orientation. The soil box is partially opened in the lateral side by 20cm square, and it can be installed the excavating apparatus. The opening is covered before excavation to prevent a collapse of tunnel face and drying soil.

For the testing procedure, the box is first moved to the excavating apparatus and the tunnel face is opened. Soil box is excavated by 20mm and metal lining is installed by lateral movement of acryl soil box by 20mm. The ground surface condition is visually observed and the vertical displacement of

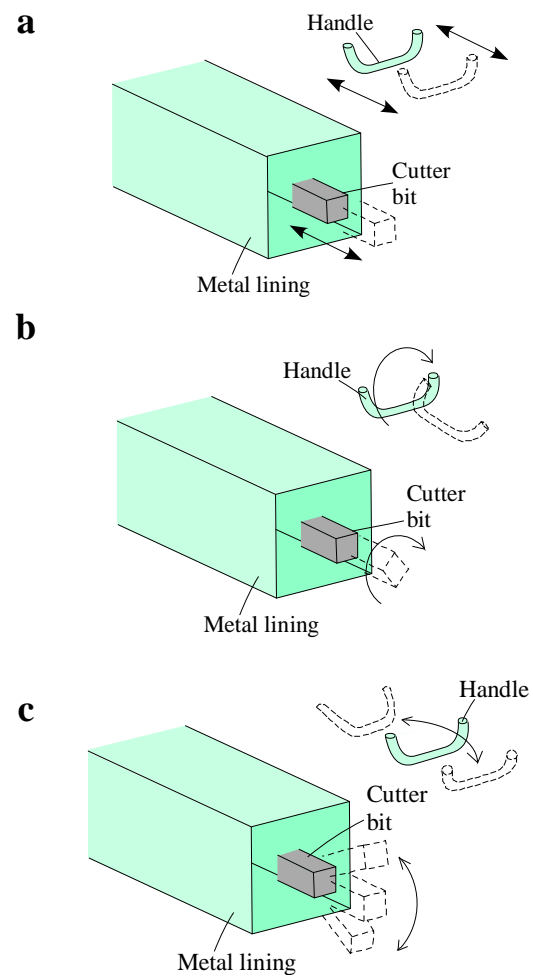


Fig. 2 Movement of cutter due to handle operation: (a) movement to tunnel axis, (b) rotation around tunnel axis, (c) inclination from tunnel axis.

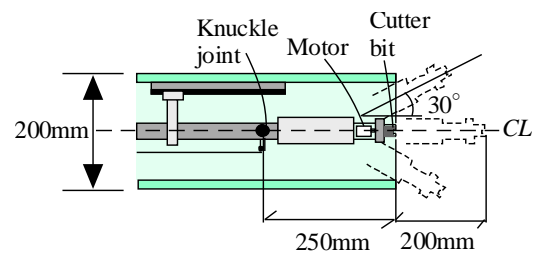


Fig. 3 Structure of the apparatus near tunnel face.

the center of the surface is measured by laser displacement meter on each process. Excavated soils were removed by a vacuum cleaner in each test step, and the weight of soil removal was measured in each step. Tunnel face is also observed by a miniature camera in each excavation phase.

The soil layer in the box is made by Toyoura sand, which properties are shown in Table. 1. Water content w is adjusted by mixing dry sand with water as shown in Fig. 5, and then the layer is compacted

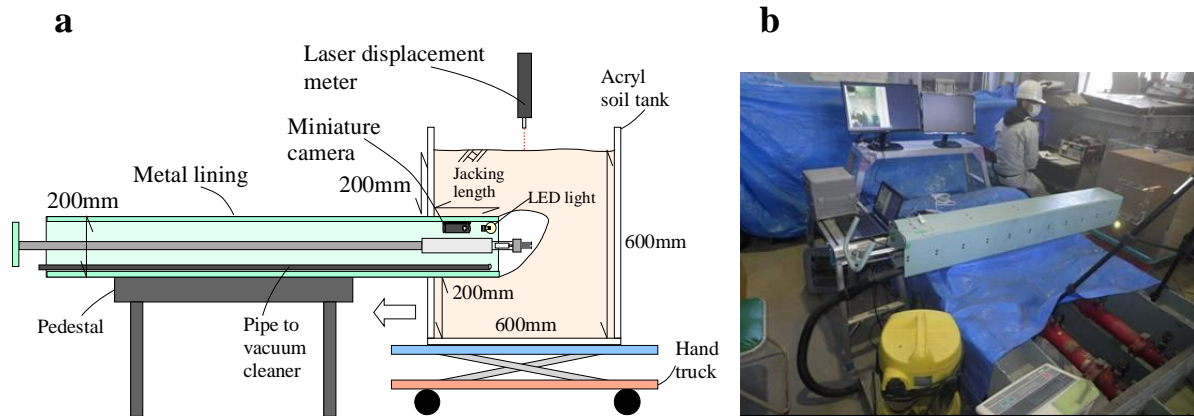


Fig. 4 Excavating and jacking test: (a) settings of equipment, (b) over view.

Table 1 Physical properties of Toyoura sand.

Maximum dry density ρ_{dmax} (g / cm ³)	Minimum dry density ρ_{dmin} (g / cm ³)	Optimum water content ratio w_{opt} (%)	Water content ratio w (%)	Degree of compaction D_c (%)
1.65	1.337	14.3	10	90



Fig. 5 Mixing of sand with water.



Fig. 6 Compacting sand layer in each 50 mm height.

by its ratio $D_c = 90\%$ in every 50 mm to 600 mm height as shown in Fig. 6. As the water content, $w = 10\%$, is a little smaller than optimum water content ratio, it can be expected the stiffest condition of Toyoura sand.

Test results

Fig. 7 shows the relationship between jacking length and testing steps. In the test, the soil box was finally moved laterally by 200 mm. Fig. 8 shows tunnel face changes due to testing step. Tunnel face and its changes can be clearly observed by miniature camera. It demonstrates that a collapse of tunnel face and its mechanical behavior are possibly recorded by the apparatus.

Fig. 9 shows the relationship between soil removal amounts, surface displacements and testing steps. As the planned removal amounts got nearly same values as the excavation test, excavation was appropriately conducted in accordance with the plan. The difference between plan and actual test finally become less than 2% in step 10. The surface displacement got very small values, because the soil condition is very stiffer. Settlements were observed until step 5, and upheaval were then observed after the step. It can be demonstrated that, whereas settlement is occurred in smaller jacking amount due to ground relaxation, the steel lining was approached to measurement points in greater jacking amount, and then positive dilatancy may occurred due to stiffer sand.

As stated above, the applicability of the testing

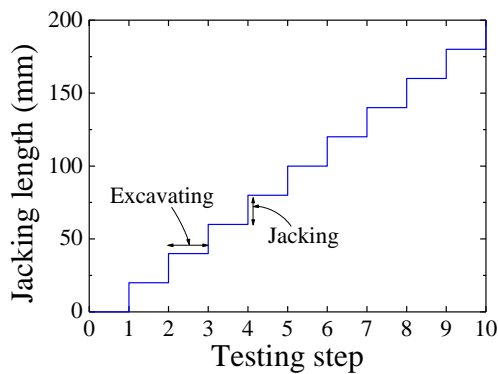


Fig. 7 Relationship between jacking length and testing steps.



Fig. 8 Tunnel face changes by miniature camera.

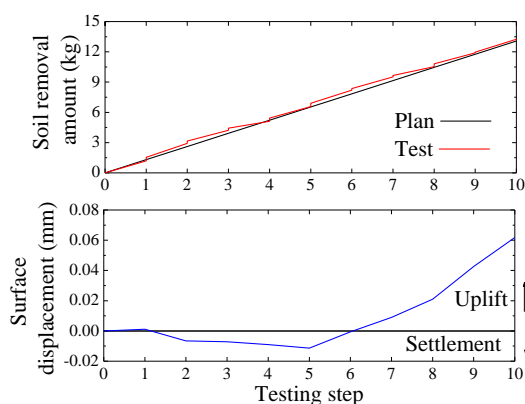


Fig. 9 Relationship between soil removal amounts, surface displacements and testing steps.

apparatus was confirmed. The test using lower water content ratio and using bigger soil box will be conducted and a collapse of tunnel face or relaxation of soils will also be concretely investigated in future.

CONCLUSION

For understanding a mechanical behavior of soils during tunnel excavation, various experiments were developed. However, the influences of excavating square section especially for underpass tunnel construction were not well studied yet.

In this study, to evaluate mechanical behaviors of soils during underpass tunnel construction, a new laboratory testing apparatus to excavate rectangular section was developed. To confirm the applicability of the testing apparatus, jacking and excavation test is conducted. The results of the test using highly compacted Toyoura sand demonstrated that, tunnel face changes due to excavation can be clearly observed by miniature camera and the mechanical behavior of soils during rectangular excavation can be observed by the tests. Furthermore, for soil removal amount, the difference between plan and measured values finally become less than 2 %.

The test using lower water content ratio and using bigger soil box will be conducted to evaluate mechanical properties of soils during rectangular excavation for grasping a mechanism of underpass tunneling.

ACKNOWLEDGEMENTS

Thanks are given to Mr. Yoshiteru Kawakami, Japanese Railway Soken Engineering, for conducting the test.

REFERENCES

- [1] Meguid MA, Saada O, Nunes MA, Mattar J, "Physical modeling of tunnels in soft ground: A review", *Tunnelling and Underground Space Technology*, Vol. 23, 2008, pp. 185–198.
- [2] Adachi T, Kimura M, Kishida K, Ito H, "Mechanical behavior of a tunnel and the ground around it in consideration of the tunnel excavation process through the trapdoor experiments", *J. JSCE*, No. 694, 2001, pp. 277 – 296. (In Japanese with English abstract)
- [3] Kikumoto M, Kimura M, Kishida K, Adachi K, "Three dimensional trapdoor experiments and its numerical analysis on the mechanical behavior during tunnel excavation", *J. JSCE*, No. 750, 2003, pp. 145 – 158. (In Japanese with English abstract)
- [4] Kirsch A, "Experimental investigation of the face stability of shallow tunnels in sand", *Acta Geotechnica*, Vol. 5, 2010, pp. 43 – 62.

- [5] Loganathan H, Poulos HG, Stewart DP, "Centrifuge model testing of tunneling – induced ground and pile deformation", *Geotechnique*, Vol. 50, No. 3, 2000, pp. 283 – 294.
- [6] Davis EH, Gunn MJ, Mair RJ, Seneviratne HN, "The stability of shallow tunnels and underground openings in cohesive materials", *Geotechnique*, Vol. 30, No. 4, 1980, pp. 397 – 416.
- [7] Komiya K, Soga K, Akagi H, Hagiwara T, Bolton MD. "Finite element modelling of excavation and advancement processes of a shield tunnelling machine", *Soils and Foundations*, Vol. 39, No.3, 1999, pp. 37 – 52.
- [8] Shin JH, Choi YK, Kwon OY, Lee SD, "Model testing for pipe-reinforced tunnel heading in agrabular soil", *Tunnelling and Underground Space Technology*, Vol. 23, 2008, pp. 241–250.
- [9] Champan DN, Ahn SK, Hunt DVL, Chan HC, "The use of model tests to investigate the ground displacement associated with multiple tunnel construction in soil", *Tunnelling and Underground Space Technology*, Vol. 21, No. 3, 2006, pp. 1 – 6.
- [10] Nozawa S, "Reduction of the Cost of Construction in the Space Above and Below Rails", *JR EAST Technical Review*, No.4, 2003, pp. 23 – 28.
- [11] Zhang D, Liu B, Qin Y, "Construction of a large-section long pedestrian underpass using pipe jacking in muddy silty clay: A case study", *Tunnelling and Underground Space Technology*, Vol. 60, 2016, pp. 151 –164.
- [12] Takahashi H, Komiya K, Akagi H, Nakayama T, Ohashi Y, "Finite element simulation of construction processes of a mechanized HEP & JES Tunnelling Method", *Proc. EURO:TUN 2009*, pp. 31 – 36.

INFLUENCE OF MATRIC SUCTION ON INSTABILITY OF UNSATURATED SILTY SOIL IN UNCONFINED CONDITIONS

Ali Murtaza Rasool^{1,2}, Jiro Kuwano¹

¹Dept. of Civil & Environmental Engineering, Saitama University, Japan; ²NESPAK Pvt. Ltd., Lahore, Pakistan

ABSTRACT

Rainfall has been recognized as one of the main causes of natural or manmade slope failure in many tropical areas of the world. In order to reduce and mitigate rainfall-induced slope failures, there is a need to develop an understanding of reduction in shear strength of soil due to water infiltration. This research aimed at understanding the influence of matric suction on water infiltration and transformation of shear strength in unsaturated soil in unconfined condition. In the present study, two types of test series have been performed using modern triaxial test apparatus: (1) shear-infiltration test, and (2) pre-wetting shear test. From test results, it was concluded that water infiltration causes the excessive deformations and softening which decreases the cohesion and hence reduces the shear strength of the soil. The more decrease in shear strength was witnessed in case of pre-wetting shear tests and maximum reduction observed was 85% against 36cm³ of infiltrated water.

Keywords: Slope failure, Water infiltration, Suction, Shear strength, Unconfined

INTRODUCTION

A number of shallow depth slope failures have taken place during or just after heavy rainfall. Most of these slope failures are characterized by the fact that they take place in silty and sandy soils. Some of them seem to be caused not only by an increase of pore water pressure in soils resulting from a rise in the groundwater table, but also by the degradation of the strength of soil forming the slopes. In view of these conditions, Yoshida et al. estimated that the cause of the rain-induced slope failure is largely due to a reduction in strength of the slope-forming soil materials caused by the infiltration of water [11]. The amount of rainwater that infiltrates the slope is an important factor. Infiltration of rainwater into a soil slope may impair slope stability by changing the pore water pressure in the soil which in turn controls the water content of the soil. It is important to understand the pore-water pressure changes due to water infiltration in order to calculate the extent of reduction of shear strength under certain rainfall condition. It has implicated that during rainfall, increased water content in the soil decreases the soil suction above the ground water table and, thus, the shear strength of the soil [7].

The stress state in natural slope or the surface layer of an embankment is under very low confining pressure conditions. A triaxial test performed in unconfined conditions can simulate this type of situations. From a practical standpoint, the test performed in unconfined conditions can also play an important role to get a thorough understanding of the mechanical behavior of unsaturated soils and to predict the stability and deformation of the surface layer in natural slopes or embankments. Since no

confining pressure is applied to soil specimen in unconfined conditions, it is primarily the matric suction that controls the measured shear strength. There have been very few studies on unsaturated soils performed in triaxial test apparatus in unconfined conditions. Kato et al. (2002), Pineda et al. (2005), Chae et al. (2010), Kwon et al. (2011) have examined the behavior of unsaturated soil in unconfined conditions and tried to interpret the effects of matric suction and suction stress on shear strength of the soil.

The detailed and fundamental studies on the instability of unsaturated soils due to matric suction have seldom been performed in a laboratory using element test. In the present study, a series of shear infiltration and the pre-wetting shear test has been conducted with the main objective of investigating the mechanical behavior and failure mechanism of silty soil gradually infiltrated by water. The effects of decrease in matric suction on water absorption, volume deformation and shear strength are discussed, and finally, the results of two series are compared.

TESTING PROGRAMME

DL Clay is the commercial name of the soil used in this study, it is a fine material without plasticity. The appearance of freshly and freely deposited DL clay looks yellowish brown. Dried and powdered DL clay consists of Kaolinite and silica. Kaolinite and silica stones are used as agricultural chemicals. According to the Japanese Geotechnical Society (JGS), it is classified as having Medium-Low compressibility (ML) and is composed of 90% silt and 10% clay which show that it is larger in grain size than average clay. Table 1 shows the physical properties of this soil.

Table 1 Physical properties of DL clay

Properties	Unit	Value
Density of soil particle, ρ_s	g/cm ³	2.654
Consistency	-	NP
Maximum dry density, ρ_{dmax}	g/cm ³	1.538
Optimum water content	%	20

The specimens used in the present study were prepared using the static compaction method. Prior to performing the compaction, dry DL clay, with a soil particle density of 2.654g/cm³, was mixed well with water to make up 20% of the water content. Then, the mixed wet DL clay was compacted statically in a cylindrical mold, 5cm in diameter, to obtain a uniform density throughout the length of the specimens. The specimens were compacted in 5 layers, each 2cm thick [10]. The low energy from the static compaction can produce a uniform density that prevents the development of a weaker region in the specimen [8]. The pre-consolidation pressure on a specimen during preparation was approximately 300kPa. The void ratio of the specimens was around 1.1 and the initial degree of saturation was 47.5%. The measured initial matric suction was 19~20kPa for all specimens, which means that the preparation procedure was always followed carefully in order to maintain a suction state of approximately 20kPa. All the specimens had a dry density of 1.3g/cm³ and a degree of compaction 80%.

Two series of experiments with twelve shearing tests on unsaturated soil specimens were conducted under stress states as shown in Table 2 to observe the shear strength of soil due to the decrease of matric suction. The first series involved the infiltration of water during the shearing process in drainage conditions, whereas, in the second series, wetting of specimens was performed before the shearing process.

Table 2 Stress state of specimens

Net normal stress ($\sigma_a - u_a$) kPa	Matric suction ($u_a - u_w$) kPa				
	0	5	10	15	20
0	Shear infiltration (SI) test				
	✓	✓	✓	✓	-
0 20 30	Pre-wetting (PW) test				
	✓	✓	✓	✓	✓
	✓	✓	-	-	-
	-	-	✓	-	-

The relationship between matric suction and water content is generally termed as the soil-water characteristic curve (SWCC). Such curves are usually measured in laboratory through pressure plate tests or pF tests, though the current experimental setup was used to establish the SWCC relation. Several soil specimens with varying water content were prepared and placed on top of a membrane filter and values of initial suction were measured, the same technique to draw SWCC was also used by Farooq et al. (2004). Fig. 1 shows the expected results i.e. the suction decreases as the saturation ratio increases.

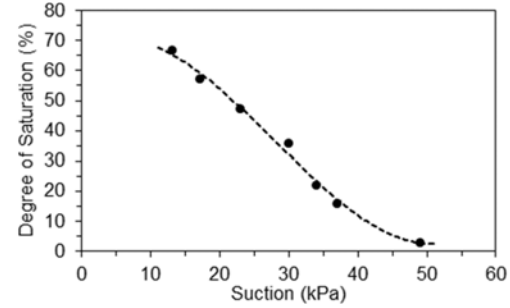


Fig. 1 Variation of suction with degree of saturation

The test apparatus used in this study consists of a double-walled triaxial cell, an axial loading device, pore-air, pore water and cell pressure transducers as shown in Fig. 1(a). The salient feature of this triaxial apparatus is that both pore air and water pressures can be measured separately. The Pore air pressure transducer is installed in the top cap and is connected to the air regulator in order to give a continuous supply of air throughout the test. The change in volume of the specimen during the triaxial tests was measured as the change in the water level in the inner cell through a Low Capacity Differential Pressure Transducer (LCDPT). In order to separate the routes for measurement and control of the pore air pressure and the pore water pressure, a membrane and a PTFE sheet were used. The PTFE sheet was placed in the top cap (Fig. 2(c)) to cut off the flow of water, and the membrane filter was installed in the lower pedestal (Fig. 2(d)) to cut off the flow of air. The thin membrane filter with pores of 0.45mm has an air entry value of 420kPa. In addition, a solenoid controlled valve to control the exhaust air was also installed in the air drainage line inside the top cap to minimize the air volume (in the air drainage line).

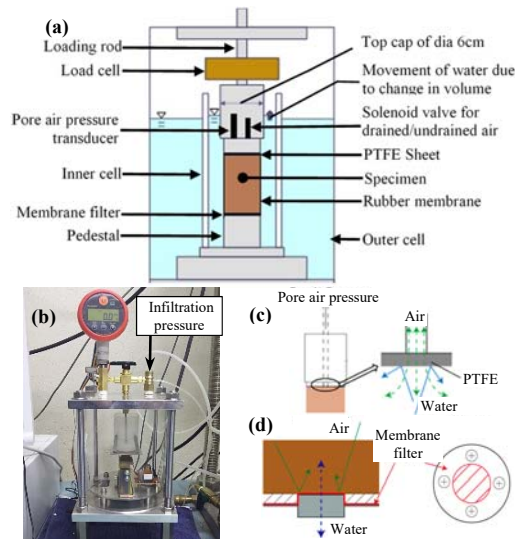


Fig. 2 (a) Schematic figure of triaxial cell; (b) external load cell; (c) top cap; (d) bottom pedestal

Since this study focuses more on shallow slope failure, it was assumed that the pore air pressure remained atmospheric throughout the test and water infiltration increased only the pore water pressure [2]. Water in an unsaturated soil specimen was injected from the bottom pedestal which was connected to a beaker and the pore water pressure transducer through the water line. The beaker was placed on an external load cell and encased in a pressure chamber as shown in Fig. 2(b). The rate of infiltration was controlled by regulating the pressure applied on top of the water surface in the beaker [2], [8].

SHEAR INFILTRATION (SI) TEST

A shear infiltration test simulates the condition and failure mechanisms of slope failures induced by water infiltration. The schematic representation of the test procedure is shown in Fig. 3. After measurement of the initial matric suction, pore air and cell pressures were increased using axis translation technique to keep pore water pressure above atmospheric [4]. Four soil specimens were tested in this series, and before the start of the shearing process each specimen was brought to a matric suction value of 0kPa, 5kPa, 10kPa, and 15kPa by applying an infiltration pressure of 20kPa, 15kPa, 10kPa, and 5kPa. The pore air was drained and controlled throughout the test process, whereas, drainage valve for pore water was kept open during the shear process in order to continuously supply water to the specimen during the shear process.

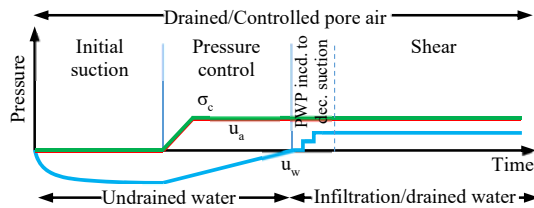


Fig. 3 Schematic illustration of shear infiltration test

Fig. 4 shows the results of the shear infiltration test conducted on unsaturated soil specimens in unconfined conditions. Before the start of the shearing process, an infiltration pressure to individual specimens was applied and the drainage valve for pore water was opened at the start of the shearing process to decrease soil suction as shown in Fig. 4(a). The value of the infiltration pressure was kept the same therefore no further change in suction was observed during the shearing process. Rainfall-induced slope failures are directly related to rainfall intensity in a specific area. Some part of rain water penetrates and some flows as surface runoff. A better parameter to analyze would be the volume of rainwater infiltrating the soil profile as shown in Fig. 4(b), it shows a more direct relation between moisture content and deformation. It can be seen that the water

infiltration continued until the end of the shearing process and the amount of water flow into specimen increases while matric suction decreases. In addition to this, it was observed that most of the water was infiltrated up to peak deviatoric stress (represented as Δ), after which water absorption becomes gradually constant. The bond between the soil particles broke after attaining peak strength, which affects the water infiltration process, it decreases and gradually becomes constant towards the end of shearing.

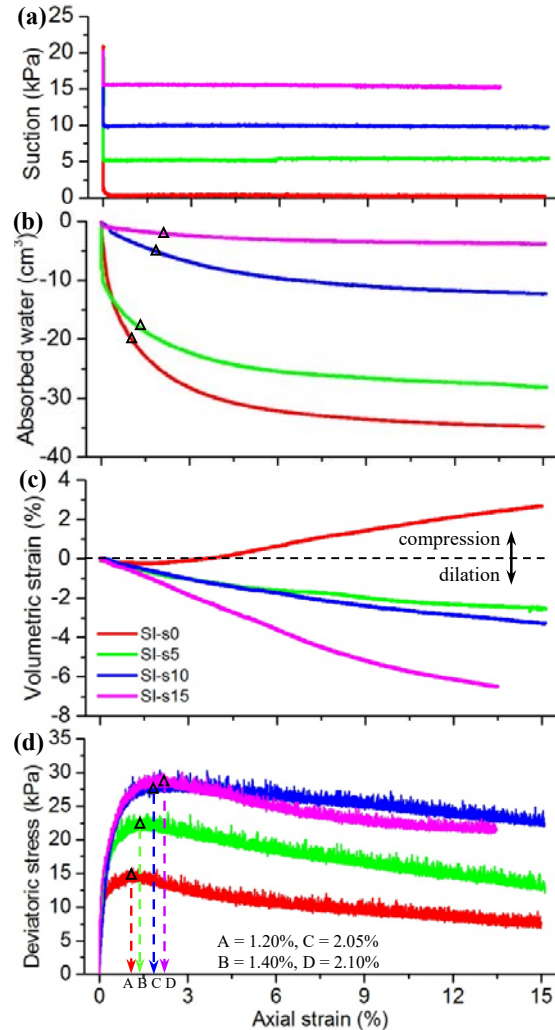


Fig. 4 Shear infiltration test results: (a) matric suction; (b) water flow; (c) volume change; (d) deviator stress

The volumetric strain response during shearing is important to assess or predict the likely field deformations. Hence the monitoring of volume changes during shearing becomes crucial. The volume changes due to water absorption during shearing process are shown in Fig. 4(c). All the test specimens showed dilatative behavior, however, dilatancy decreased with the increase in water absorption. The specimen SI-s0 showed first an initial

dilation followed by compression with an increase in axial strain due to water absorption. As expected, stress-strain curves in Fig. 4(d) show that deviatoric stress decreases with a decrease in matric suction. The axial strain corresponding to the peak strength for all unsaturated specimens ranged between 1.20% to 2.10%. Due to water infiltration during the shearing process, the stress-strain curves showed strain softening at a higher axial strain of above 6%. Following Japanese Geotechnical Society Standard “JGS 0527-1998 Method for Triaxial Compression Test on Unsaturated Soils” the shearing was continued to 15% of axial strain. At the end of each test, it was observed that all the specimens showed failure by bulging. All the specimens had an over consolidation stress history of approximately 300kPa. The impact of over consolidated stress history and imposed suction is clearly seen in the form of first, a peak failure followed by the post-peak softening type of stress-strain response and second, in the form of dilation type of volume change response during the shearing stage.

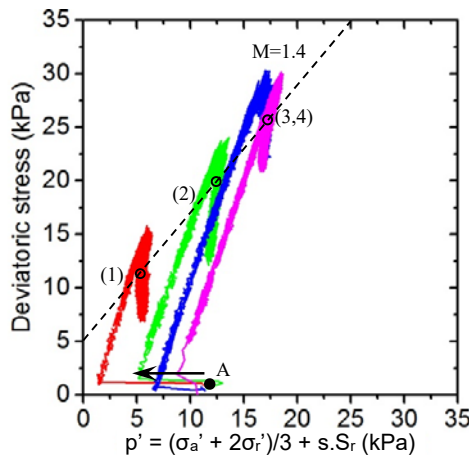


Fig. 5 Stress paths for shear infiltration tests

The stress paths followed by the soil specimens during the shear infiltration test are plotted in p' - q plot as shown in Fig. 5. Since the pore air pressure was exhausted in this series, the stress paths thus sloped at a gradient of 1:3 on the p' - q plot. Initially, the stress path moved towards the left from point “A” due to a decrease in matric suction. The soil used in this study was over-consolidated soil, for such soils, the stress path first crosses the critical state line (CSL) but eventually reverses its direction and fails on a critical state line corresponding to critical state strength (1,2,3,4) and ultimately dropped to residual strength. The gradient M of CSL was 1.4 and intercept q -axis was 5kPa.

PRE-WETTING (PW) SHEAR TEST

A pre-wetting shear test simulates the condition

and failure mechanism of a soil slope after a rainy period where the soil above the water table experienced a wetting process. Such kind of situation has seldom been tested in the laboratory using unsaturated triaxial test apparatus. Initial suction was measured and matric suction was applied using the axis-translation technique [4]. The initial phase of each test consisted of a wetting stage in which five soil specimens were brought to matric suction values of 0kPa, 5kPa, 10kPa, 15kPa and 20kPa respectively. This was achieved by applying an infiltration pressure of 20kPa, 15kPa, 10kPa, 5kPa and 0kPa. The wetting stage of each test was finished when no further change in the flow of water into the specimen was observed. After the wetting stage, the drainage valve for pore water was closed and each specimen was subjected to shear under undrained conditions with measurement of pore water pressure. The pore air was drained and controlled throughout the test process. Fig. 6 shows the schematic diagram of test procedure. In this series, three more tests were carried out by applying low confining stress to make a comparison.

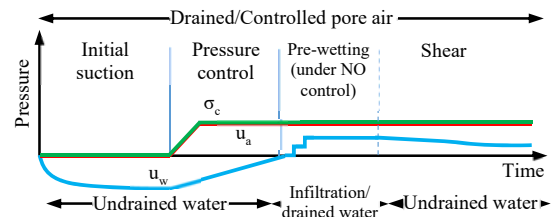


Fig. 6 Schematic illustration of pre-wetting shear test

Fig. 7 shows the flow of water into the specimen due to a decrease in matric suction during the wetting process as a function of time. The volume of water infiltrating the specimen varied from 0cm³ to 36cm³ for specimens which were brought to a suction of 20kPa to 0kPa. At matric suction value of 20kPa no flow of water occurred which shows that a decrease in suction was required to start the infiltration process, the amount of water flow increases with a decrease in suction. However, by just applying a small net confining stress of 20 or 30kPa, the amount of water flowing into the specimen decreases. This is because of a decrease in void ratio due to the confining stress.

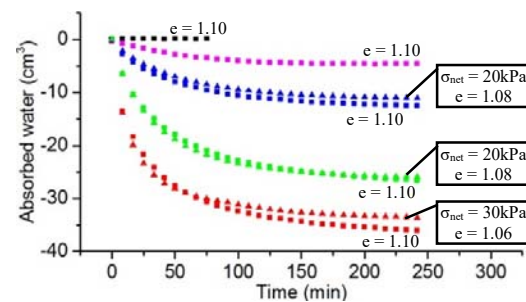


Fig. 7 Flow of water into specimens during wetting

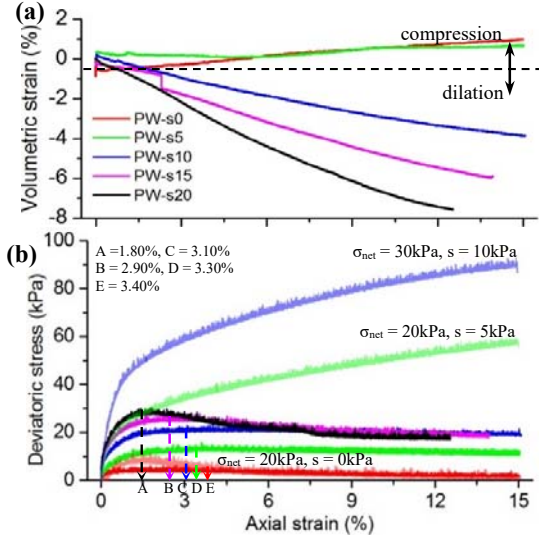


Fig. 8 Pre-wetting shear test results: (a) volume change; (b) deviator stress

The plots of volume change and deviatoric stress versus axial strain relationship for five variable suction pre-wetting shear test is shown in Fig. 8. It can be seen that both stiffness and strength decreases with a decrease in matric suction. This behavior can be related to the influence of matric suction on inter-packet contact forces, which tends to stabilize the soil structure. Specimens with matric suction value of 5kPa or less showed stress-strain behavior typical of normally consolidated soils without a marked reduction of shear strength after attaining peak value, as compared to specimens with matric suction of more than 5kPa which showed stress-strain behavior typical of overconsolidated soils. The different shapes of stress-strain curves during shearing can be explained by looking at how the soil samples were prepared using static compaction technique. The compacted soil behavior was similar to the overconsolidated soil as $\sim 300\text{kPa}$ of vertical stress was applied during sample preparation and tested under zero net stress. This behavior is attributed to dilation of compacted soil [9]. Such specimens show a brittle stress-strain and dilative volume change behavior at a relatively high matric suction as shown by specimen PW-s20, PW-s15 and PW-s10. However, with a decrease in suction the volume of water flow into specimen increases, as a result, stress-strain behavior becomes typical of ductile material and compressive soil behavior was observed in specimen PW-s5 and PW-s0. When specimens with a matric suction of 5kPa and 10kPa were sheared under net confining stress of 20kPa and 30kPa, no peak curve was obtained and specimens showed high strength at the end as compared to unconfined conditions. However, specimens with 0kPa matric suction and net confining stress of 20kPa did not show any remarkable difference. A relationship

between water content, mean net stress and matric suction at failure is plotted in 3D space as shown in Fig. 9. It can be seen that mean net stress decrease with increase moisture content and a decrease in suction, which shows that moisture content and suction independently controls the shear strength of soil.

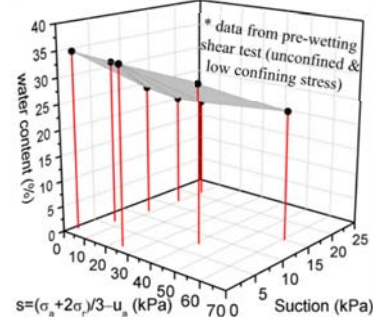


Fig. 9 Relationship between water content, mean net stress, and matric suction

The cohesion of unsaturated soils at a certain level of matric suction can be estimated more efficiently by using extended Mohr-Coulomb failure envelope [3]. The Mohr-Coulomb failure envelope for the study soil was obtained from a series of soil specimen and has a peak angle of shearing ϕ of 32° and apparent cohesion c' (for specimen with 0kPa matric suction) 1.7kPa, shown in Fig. 10(a). The cohesion changed with matric suction, however, ϕ remained constant. The angle of the rate of strength due to matric suction ϕ_b is shown in Fig. 10(b) which is ϕ_b 22° for the study soil. This shows that the cohesion of unsaturated soils is reduced due to water infiltration from the surface.

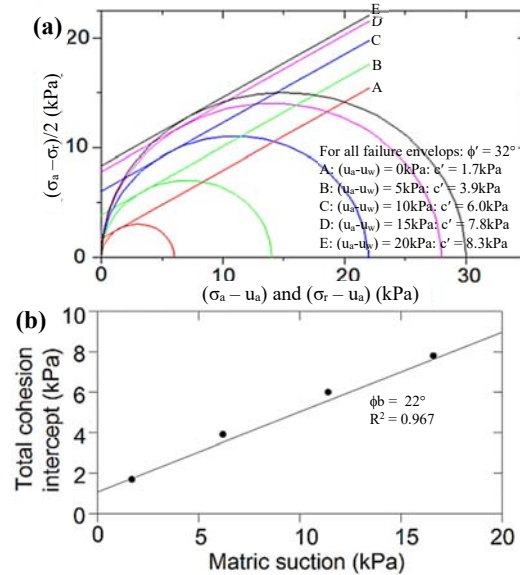


Fig. 10 Pre-wetting shear test results: (a) failure envelope; (b) angle indicating the rate of increase in shear strength with respect to changes in $(u_a - u_w)$

DISCUSSION

The results from the shear infiltration tests are compared with the results from the pre-wetting shear tests and are plotted in Fig. 11. Initially, all specimens have almost the same saturation ratio. In the shear infiltration test, due to the flow of water into specimen during shearing process, the saturation ratio increases till residual stage. Due to this increase in the degree of saturation a decrease in deviator stress was observed, the decrease which is small for matric suction values 15kPa and 10kPa and bigger for 5kPa and 0kPa, can be seen in Fig. 11(b). The change in deviator stress with matric suction is non-linear. In the case of pre-wetting shear test the water infiltration was completed before shearing, therefore, a small change in saturation ratio was observed at the start, peak and residual deviator stress. The amount of water absorbed by the specimen at residual deviator stress stage in shear infiltration test is almost the same as the pre-wetting shear test wetting stage. Due to this, the specimens have almost the same water content and saturation ratio, as a result almost identical peak deviator stresses were observed in pre-wetting shear test as the residual deviator stress in the shear infiltration test, shown in Fig 11(b). The change in the degree of saturation is not only due to the flow of water but also due to the volume of specimen, at matric suction of 15kPa and 20kPa the amount of water infiltration was very small and specimen showed dilatant behavior so a decrease in saturation ratio was observed in both series. When the suction is about zero or at small value, the saturation ratio is between 80% and 85%. That means the specimens could not be fully saturated even at zero suction. The incompletely full saturation at zero suction may be attributed to the trapped air in the pores inside soil specimens or in the testing system.

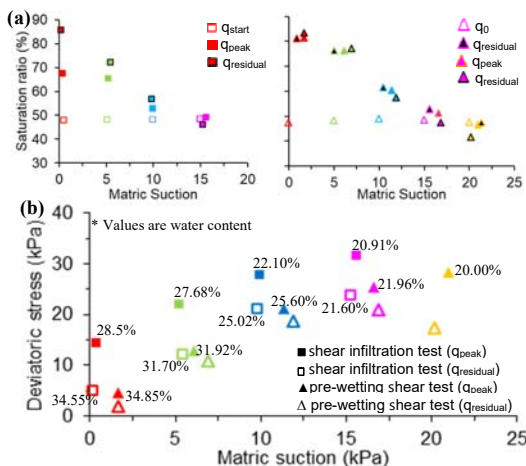


Fig. 11 Comparison of test results: (a) saturation ratio; (b) deviator stress

CONCLUSIONS

A series of laboratory element tests were conducted to examine the instability of unsaturated soil subjected to water infiltration. It was found that under the same matric suction, the soil sheared to failure with pre-wetting condition possessed a lower shear strength than soil sheared to failure under infiltration conditions. The maximum reduction in shear strength due to water infiltration observed in case of SI test was 55% and PW test was 85%. The water infiltration causes excessive deformation changing the soil behavior from dilatant to compression. The slope instability problems, which were always been treated as a shear strength problem, also appeared to be a volume change problem. It seems that a better way of preventing rainfall-induced slope failures is to limit the excessive development of soil deformation rather than just trying to increase the shear strength of slope.

REFERENCES

- [1] Chae et al., "Effect of suction on unconfined strength in partly saturated soils" *KSCE J. of Civil Engineering*, Vol. 14, No. 3, 2010, pp. 281-290.
- [2] Farooq et al., "Response of unsaturated sandy stress under constant shear stress drained condition" *Soils & Found.*, Vol. 44, 2004, pp.1-13
- [3] Fredlund DG, Rahardjo H, *Soil Mechanics for Unsaturated Soils*. New York: John Wiley and Sons Inc., 1993.
- [4] Hilf JW, "An investigation of pore water pressure in compacted cohesive soils" U.S. Dept. Interior Bur. Reclamation tech. Memo. no. 654, 1956.
- [5] Kato et al., "Effect of suction on unconfined compressive strength and undrained shear strength of a compacted silty clay" in *Proc. of the 3rd Intl. Conf. on Unsat. Soils*, 2002, pp. 513-518
- [6] Kwon et al., "Effect of suction on shear strength of unsaturated compacted city sand under low confining pressure" in *Proc. of Intl. Symp. on Def. Charac. of Geomaterials*, 2011, pp. 834-840.
- [7] Meen WG, Yong MW, "Failure of soil under water infiltration" *Engineering Geology*, Vol. 181, 2014, pp. 124-141.
- [8] Melinda et al., "Shear strength of compacted soil under infiltration conditions", *J. of Geotech. Eng. Div. ASCE*, Vol. 130, No. 8, 2004, pp. 807-817.
- [9] Pineda JA, Colmenares JE, "Influence of matric suction on shear strength of compacted kaolin soil under unconfined condition" in *Proc. of Intl. Symp. Adv. Unsat. Soil Mech.*, 2005, pp. 221-226.
- [10] Rasool AM, Kuwano J, Tachibana S, "Behavior of compacted unsaturated soil in isotropic compression, cyclic and monotonic shear loading sequence in undrained condition", in *Proc. of 6th Intl. Symp. on Def. Characteristics of Geomaterials*, 2015, pp. 267-274.
- [11] Yoshida Y, Kuwano J, Kuwano R, "Effects of saturation on shear strength of soils", *Soils and Foundations*, Vol. 31, No. 1, 1991, pp. 181-186.

PROPERTIES OF RAW AND PROCESSED BUKIT GOH BAUXITE IN KUANTAN, PAHANG IN ACCORDANCE WITH IMSBC CODE

Muzamir Hasan^{1,2}, Ahmad Amirul Faez^{1,2}, M. Azizul Moqsud³, Tam Weng Long² and Phang Biao Yu²

¹Centre for Earth Resources Research & Management, Universiti Malaysia Pahang, Malaysia;

²Faculty of Civil Engineering & Earth Resources, Universiti Malaysia Pahang, Malaysia;

³Department of Civil and Environmental Engineering, Yamaguchi University, Ube-Shi, Yamaguchi, Japan.

ABSTRACT

This study focus on the differences of geotechnical properties between raw and processed Bukit Goh bauxite. As bauxite material has high clay content which mostly composed of silicate minerals, it has high risk to cause cargo liquefaction which in turn causes catastrophic incident. This paper includes the analysis of raw and processed bauxite where its fine particle contents has been minimized using beneficiation method to reduce the risk of liquefaction by referring to the International Maritime Solid Bulk Cargoes Code (IMSBC Code) standard. To analyse these characteristics of the bauxite, five samples were selected at Bukit Goh, Kuantan; three of the samples from the Bukit Goh mine and two samples from stock pile were tested to identify the bauxite geotechnical properties by referring to GEOSPEC 3: Model Specification for Soil Testing; particle size distribution, moisture content, specific gravity, morphological properties as well as its elemental and oxide properties. Laboratory tests involved including Small Pycnometer test, Dry Sieve test, X-ray fluorescence test (XRF) and Field emission scanning electron microscopy test (FESEM). The results show that average moisture content of raw bauxite is 24.81% which exceeded the recommended value of maximum 10% while the average moisture content of processed bauxite is only 6.69%. The average fine material for raw bauxite is 38.40% which should not be greater than 30% per IMSBC standard while for processed bauxite is 21.40%. In conclusion, the quality and safety of processed bauxite is better than raw bauxite.

Keywords: Bauxite, Beneficiation, Geotechnical Properties, Soil Liquefaction

INTRODUCTION

Bauxite is the principal ore of alumina (Al_2O_3), which is used to produce aluminum. Hydrated aluminum oxides, hydrated aluminosilicates, iron oxides, hydrated iron oxides, titanium oxide, and silica are the main compound that made a bauxite [1]. Around the globe, approximately 165 million tonnes of bauxite are mined each year and they are usually transported to refineries by conveyor, ship, or rail [2]. Bauxite reserve has been found in Kuantan district and bauxite mining activity has started due to strong demand from China, Malaysia increases the production of bauxite. In 2015, a bulk carrier capsized about 150 nautical miles off the coast of Vietnam with 18 fatalities and only one survivors which were carrying 46 400 tonnes of bauxite. Investigation conducted by International Maritime Organization (IMO) concluded that the loss of the Bulk Jupiter has uncovered evidence to suggest liquefaction of cargo led to loss of stability [3][4]. Liquefaction is a phenomenon where soil experience a process by which water-saturated sediment temporarily loses strength and acts as a fluid [5]. There are some standard and regulation that need to be follow; in this case IMSBC Code to determine the safety of bulk cargoes carrying bauxite and to minimize the risk of

the cargoes to capsize. Figure 1 shows the classification of Bauxite in Group C where it is neither liable to liquefy (Group A) nor to possess chemical hazards (Group B) [6]. If bauxite samples are complied with the specifications as stated in IMSBC Code, the samples are allowed be shipped and exported. Thus, this study is carried out to determine whether Kuantan bauxite samples are in accordance with the IMSBC Code or not; by comparing the parameters stated in the code.

BAUXITE		
DESCRIPTION A brownish, yellow claylike and earthy mineral. Moisture content: 0% to 10%. Insoluble in water.		
CHARACTERISTICS		
ANGLE OF REPOSE	BULK DENSITY (kg/m ³)	STOWAGE FACTOR (m ³ /t)
Not applicable	1190 to 1389	0.72 to 0.84
SIZE	CLASS	GROUP
70% to 90% lumps: 2.5 mm to 500 mm 10% to 30% powder	Not applicable	C

Fig. 1 Bauxite's Group C Classification [6]

Percentages of moisture content of the sample do have a relationship with particle size distribution where the presence of fines particles will influence its water-holding properties [7].

Besides identifying the standard quality of Kuantan bauxite, its morphological characteristic also studied to determine the particles present and its effect. If the particles are found to be harmful, prevention and safety measure should be applied and discussed.

MATERIALS AND METHODS

All laboratory experiments were carried out based on Geospec 3: Model Specification for Soil Testing (as shown in Table 1). The beneficiation process is done in small scale with 100g of samples using a bottle dispenser on 4.25mm passing sieve.

Table 1 Laboratory tests and standard

Laboratory Tests	Standards
Moisture Content Test	Geospec 3: Part 2; 5 Clause 3.2
Specific Gravity Test	Geospec 3: Part 2; 7 Clause 3.4
Particle Size Distribution	Geospec 3: Part 2; 8 Clause 3.5
X-Ray Fluorescence (XRF)	Quantexpress (Full Analysis) by XRF S8 Tiger

RESULTS AND DISCUSSION

There are FIVE (5) samples selected from Bukit Goh in Kuantan; THREE (3) samples are in-situ samples (M2L1B1, M2L2B1 and M2L2B2) and TWO (2) samples are from stockpile (PTSTL1B1 AND PTSTL2B1).

Moisture Content

The result shows moisture content of Bukit Goh bauxite is higher compared to recommended percentage in the IMSBC Code (Table 2). Due to higher moisture content, it clearly shows that Bukit Goh bauxite have large amount of fine particle compared to coarse particle. Based on IMSBC Standard, the allowable moisture content for deposits to be on a cargo ship is 0%-10%. From the comparison in the histogram in Figure 2, it shows that the moisture content of raw Bukit Goh bauxite is higher compared to processed bauxite where it has the average of 24.81% over 6.69% only on the processed bauxite sample. Due to higher moisture content, it clearly demonstrates that raw Bukit Goh bauxite have large amount of fine particle compared to coarse particle. High level of moisture content causes the liquefaction of mineral ores to be occurs and this making the cargo loss of stability during the voyage. If cargoes loaded with too high a moisture content,

liquefaction may occur without warning at any time during the voyage.

Table 2 Moisture content of raw and processed Bukit Goh Bauxite

Sample	Moisture Content (%)	
	Raw	Processed
M2L1B1	27.69	7.31
M2L2B1	22.96	6.12
M2L2B2	23.93	6.47
PTSTL1B1	23.51	6.62
PTSTL2B1	25.95	6.94

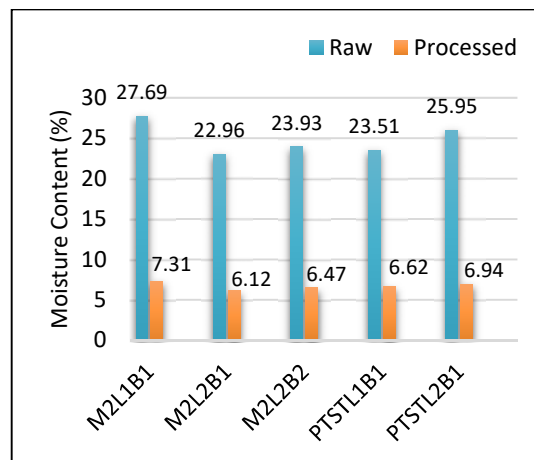


Fig. 2 Moisture content of raw and processed Bukit Goh Bauxite

Based on IMSBC Standard, the allowable moisture content for deposits to be on a cargo ship is 0%-10%. From the comparison in the bar chart, it shows that the moisture content of raw Bukit Goh bauxite is higher compared to processed bauxite where it has the average of 24.81% over 6.69% only on the processed bauxite sample. Due to higher moisture content, it clearly demonstrates that raw Bukit Goh bauxite have large amount of fine particle compared to coarse particle. High level of moisture content causes the liquefaction of mineral ores to be occurs and this making the cargo loss of stability during the voyage. If cargoes loaded with too high a moisture content, liquefaction may occur without warning at any time during the voyage.

Specific Gravity Test

The result from Small Pycnometer Test was collected where there is just a slight difference in specific gravity for both samples (Figure 3). Based on previous studies, the specific gravity values obtained for the bauxites are in the range from 2.70 to 2.87 and specific gravity of bauxite in India is higher compared

to bauxite at Bukit Goh. The specific gravity of bauxite largely depends on the density of the mineral making up the individual soil particle.

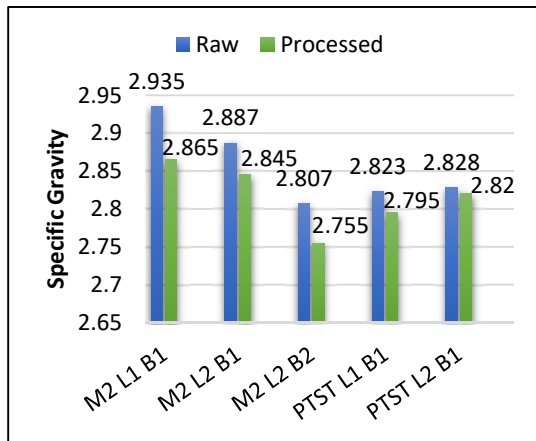


Fig. 3 Specific gravity of raw and processed Bukit Goh Bauxite

Particle Size Distribution

From Table 3, it clearly shows that bauxite sample that undergo beneficiation process have lesser fine particles compare to the raw bauxite sample. Particles that passed through 2.5mm sieve size is consider fine particles. The percentage passing 2.5mm for processed bauxite sample is 20% while for raw sample is 39%. Therefore, this prove that the particle size distribution of raw Bukit Goh bauxites is not in the range of less than 30% fine particle and coarse particle more than 70% as stated in IMSBC Code. Due to higher percentage of fine particle in the raw bauxite, it will cause the moisture content to increase as fine particles absorb more water. Meanwhile, bauxite of the same sample that has been beneficiated has fine particle less than 30% which prove that beneficiation method can reduce the number of fine particles in bauxite.

Table 3 Percentage of fine particles between raw and processed Bukit Goh Bauxite

Samples	Raw (%)	Processed (%)
M2L1B1	39	20
M2L2B1	38	24
M2L2B2	47	18
PTSTL1B1	32	23
PTSTL1B2	36	22
Average fine particles	38.40	21.40

Morphological Properties of Bauxite

Field Emission Scanning Electron Microscopy (FESEM) Test is carried to determine the

morphological properties of both raw and processed Bukit Goh bauxite. The results are shown in Figure 4, Figure 5, Figure 6 and Figure 7 where magnification for each figure is 1000x, 2000x 5000x and 10000x respectively; for both raw and processed bauxite samples. Closer inspection of the particles shows a layer of material coating most of the particle surfaces. The different sizes of particles can be observed with clear image of lump particles and powdery like-structure of fine particles under 2000x magnification. Clear image of particles started to be seen at 5000x magnification and under 10000x magnification, fine particles attached to the bauxite sample are clearly can be seen. Study on morphological properties of Bukit Goh bauxite above displays that the fine particles of raw bauxite is higher than the beneficiated bauxite. Clearly seen that the lesser fine particle attached to the processed bauxite ore. This proved the washing of bauxite can reduce the amount of fine particle in bauxite lump. Bauxite samples collected from Bukit Goh mine are disturbed sample, hence the tendency for this sample to liquefy is higher than undisturbed soil because of the shear force of anti-liquefaction of undisturbed soil is 1.5 to 2 times greater than disturbed soil.

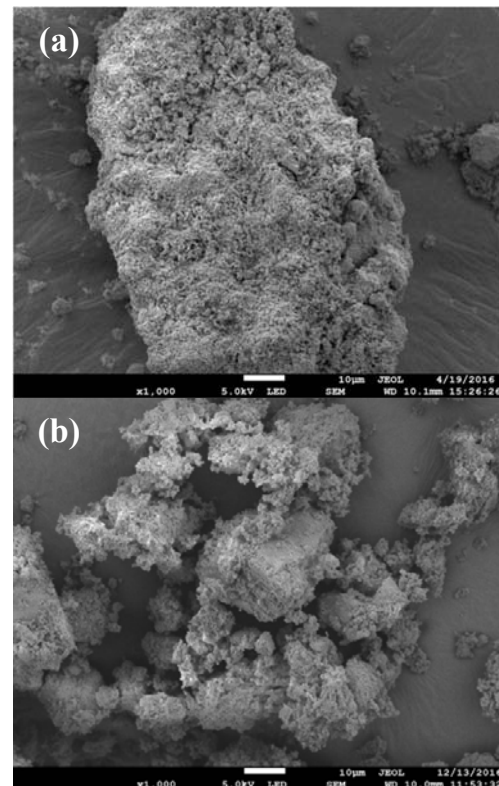


Fig. 4 Magnification of bauxite sample under 1000x magnification for (a) raw and (b) processed bauxite sample

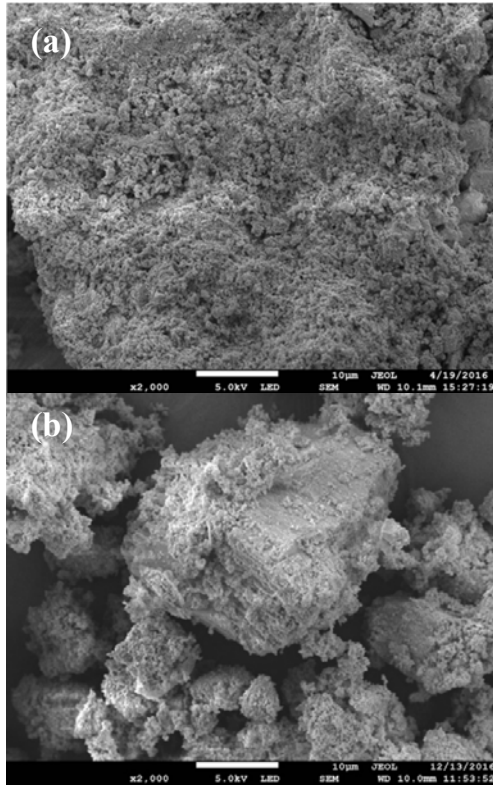


Fig. 5 Magnification of bauxite sample under 2000x magnification for (a) raw and (b) processed bauxite sample

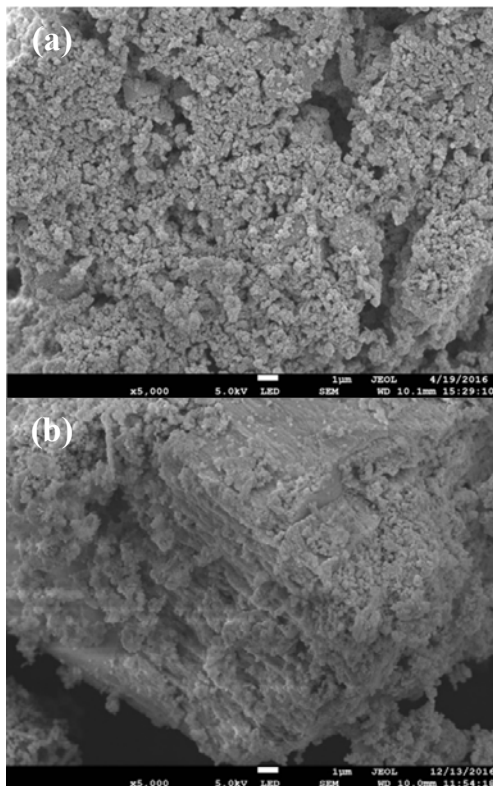


Fig. 6 Magnification of bauxite sample under 5000x magnification for (a) raw and (b) processed bauxite sample

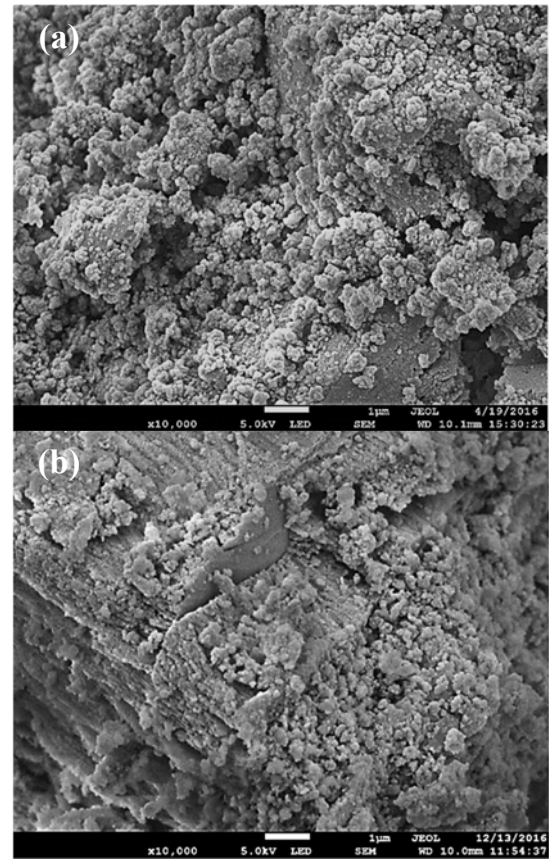


Fig. 7 Magnification of bauxite sample under 10000x magnification for (a) raw and (b) processed bauxite sample

Elemental and Oxide Properties Test

The test of both raw and processed bauxite elements and oxide properties is carried out by X-Ray Fluorescence XFF S8 Tiger machine from the UMP central Laboratory by bombarding a high-energy gamma ray on both M2L1B1 samples. The results are shown in Table 4 and 5.

From Table 4, it shows that the quantity of Silicon (Si) is reduced from 0.50% to 0.44% and from Table 3, the amount of Silicon Dioxide (SiO_2) or also known as silica is minimized from 1.07% to 0.94% after beneficiation process. Unfortunately, the value of aluminium element also decreases slightly from 7.48% to 7.25% although it has not much effects on the bauxite products. As mentioned before, the core target of washing bauxite is to decrease the amount of silica and improve the amount of aluminium. In addition, along with silica, the insoluble iron and titanium oxides in red mud will also be removed that

will abolish lower grade fines and enhance the quality of bauxite.

Table 4 Raw and processed Bukit Goh Bauxite elements

Parameters	Unit	Raw	Processed
Iron (FE)	%	31.38	26.49
Aluminium (AL)	%	7.48	7.25
Titanium (Ti)	%	3.96	3.33
Silicon (Si)	%	0.50	0.44
Phosphorus (P)	%	0.40	0.41
Calcium (Ca)	%	0.09	0.11
Sulphur (S)	%	0.09	0.07
Chromium (Cr)	%	0.08	0.09
Manganese (Mn)	%	0.06	0.05
Zirconium (Zr)	%	0.05	0.05
Strontium (Sr)	%	0.02	0.02
Niobium (Nb)	%	0.02	0.02
Zinc (Zn)	%	0.01	0.02
Gallium (Ga)	ppm	69	79
Yttrium (Y)	ppm	35	48

Table 5 Raw and processed Bukit Goh Bauxite oxides

Parameters	Unit	Raw	Processed
Iron (III) Oxide	%	44.86	37.88
Aluminium Oxide	%	14.13	13.69
Titanium Dioxide	%	6.60	5.55
Silicon Dioxide	%	1.07	0.94
Phosphorus Pentoxide	%	0.91	0.93
Sulphur Trioxide	%	0.22	0.18
Calcium Oxide	%	0.13	0.15
Chromium (III) Oxide	%	0.12	0.13
Manganese Oxide	%	0.08	0.06
Zirconium Dioxide	%	0.07	0.06
Niobium Pentoxide	%	0.03	0.02
Strontium Oxide	%	0.02	0.02
Zinc Oxide	%	0.01	0.02

Comparison with IMSBC Code

The comparison between raw and processed bauxite is shown in Table 6 shows that bauxite that went through beneficiation procedure pass all the requirements whether in particle size or moisture content.

Table 6 Comparison table with IMSBC code

PSD (IMSBC: 30% < 2.5mm passing)		
Sample	Passing (%)	Remarks
M2L1B1 (R)	39	Fail
M2L1B1 (P)	20	Pass
M2L2B1 (R)	38	Fail
M2L2B1 (P)	24	Pass
M2L2B2 (R)	47	Fail
M2L2B2 (P)	18	Pass
PTSTL1B1 (R)	32	Fail
PTSTL1B1 (P)	23	Pass
PTSTL2B1 (R)	36	Fail
PTSTL2B1 (P)	22	Pass
Moisture Content (IMSBC: 0% to 10%)		
M2L1B1 (R)	27.69	Fail
M2L1B1 (P)	7.31	Pass
M2L2B1 (R)	22.96	Fail
M2L2B1 (P)	6.12	Pass
M2L2B2 (R)	23.93	Fail
M2L2B2 (P)	6.47	Pass
PTSTL1B1 (R)	23.51	Fail
PTSTL1B1 (P)	6.62	Pass
PTSTL2B1 (R)	25.95	Fail
PTSTL2B1 (P)	6.94	Pass

*Raw = (R), Processed = (P)

CONCLUSION

The basic geotechnical properties, chemical properties and morphological properties of Bukit Goh bauxite had been determine based on criteria needed in IMSBC Code that focuses on three basic properties which are particle size distribution, moisture content and specific gravity.

The analysis and result from laboratory test shows that the average fine particle size of Bukit Goh bauxite is 38.40% while the average percentage of moisture content is 24.81%. The results obtained was compared with IMSBC Code where each of these basic properties are exceeding the specified value stated in the code. After comparing the results to IMSBC Code, Bukit Goh bauxite cannot be categorized as Group C because the basic properties obtained are not fulfilling the requirement in the standard IMSBC Code. Therefore, it is not suitable to be exported and there will be higher risk in the

transportation of bauxite due to the waves of the ocean. Meanwhile, for the processed bauxite, the average fine particle size is 21.40% which is below the limit of 30% while the average percentage of moisture content is 6.69% which does not exceed the 10% limitation.

In conclusion, the quality of processed bauxite is better than raw bauxite. Bukit Goh bauxite must go through beneficiation process at the site to reduce and eliminate fine particle. The bauxite properties should follow IMSBC Code requirement to prevent liquefaction from occurring.

ACKNOWLEDGEMENTS

The authors would like to acknowledge the Universiti Malaysia Pahang (UMP) for financing this research through the Research University Grant Scheme, Project Number RDU1603122. The cooperation given by all parties involved in this research is greatly acknowledged.

REFERENCES

- [1] Shakhashiri, BZ, "Chemical of The Week": Aluminium. University of Wisconsin: SciFun.org, 2012.
- [2] Donoghue, AM, "Bauxite Mining and Alumina Refining: Process Description and Occupational Health Risks", Journal of Occupational and Environmental Medicine, Vol. 56, No. 5, 2014.
- [3] International Maritime Organization. Retrieved from <http://www.imo.org/en/MediaCentre/PressBriefings/Pages/38-bauxite-CCC.aspx>, 2015.
- [4] World Maritime News. Retrieved from <http://worldmaritimenews.com/archives/172059/imo-bauxite-liquefaction-sank-bulk-jupiter/>, 2015.
- [5] Seed, HB, "Liquefaction of Saturated Sands During Cyclic Loading", Journal of the Soil Mechanics and Foundations Division, pp. 105-134, 1966.
- [6] IMSBC Code. International Maritime Solid Bulk Cargoes Code and Supplement. International Maritime Organization, 2013.
- [7] Freyssinet, P. "Ore forming processes related to lateritic weathering", Economic Geology One Hundredth Anniversary, Vol. 1, 2005, pp. 681-722.

TEMPERATURE CHANGE AND THE TOTAL STRESS ANOMALY IN PASTE BACKFILL

*Alsidqi Hasan¹, Ting Wee Kiet¹, Fauzan Sahdi¹, Siti Noor Linda Taib¹, Norsuzailina Mohamed Sutan¹, Badhrulhisham Abdul Aziz² and Andy Fourie³

¹The Department of Civil Engineering, Universiti Malaysia Sarawak, Malaysia; ²Rare Earth Research Center, Universiti Malaysia Pahang, Malaysia; ³School of Civil, Environmental and Mining Engineering, University of Western Australia, Australia

ABSTRACT

This paper presents preliminary results from a laboratory backfill model test in order to explain the effect of temperature change during the cement hydration on the total stress within cemented paste backfill. It is conducted via temperature control test in the absence of the cement. This investigation is an attempt to resolve an anomalous behaviour reported in recent full scale monitoring reports, where the total vertical stress at the stope base shows a progressive increase after backfilling is terminated. The result in this paper shows that the total vertical stress is not affected by the level of the temperature but rather by the temperature gradient. The empirical relationship between the temperature gradient and the change in the total vertical stress is proposed. The total stress anomaly found in the full scale monitoring of paste backfill could be explained by the finding.

Keywords: Backfill, Temperature, Arching, Total Stress, Anomaly

INTRODUCTION

Paste backfill is a type of material used to fill-up underground mined-out voids (stopes), which improves underground general stability condition. The material has a paste-like consistency made from a mixture of tailings, water, and cement binder to increase the strength of the paste. Figure 1 shows the paste backfill is being tested for its rheology property. The paste backfill or also called cemented paste backfill provides significant advantage in mining production as compared to the other type of backfills (e.g. hydraulic fill), which can be a self-supporting material. The adjacent ore bodies can be mined without the need of leaving some parts to act as underground pillars. Hence, the ore production can be maximized. The cemented paste backfill has been popularly used in the underground mining operations for the last two decades. Figure 2 shows a backfilling sequence in cemented paste backfilling.

During the backfilling, a barricade is constructed to plug the drawpoint. The barricade provides a temporary barrier to prevent the backfill to flow out of the stope until the backfill gains enough strength as a self-supporting material and able withstand pressure from blasting activity of the adjacent stope. As a temporary structure, the barricade has to be cost effective and acceptable in strength. When the barricade fails, a hefty amount of rehabilitation cost has to be spent and more importantly the safety of the underground workers is at serious risk.

In order to design an efficient barricade wall,

the engineers must have a good understanding of the possible mechanisms within the paste backfill during and after backfilling, especially on the horizontal stress exerted by the paste backfill near the barricade. The conservative design practice uses the total vertical stress at the base (bottom) of the stope to estimate the maximum horizontal stress acting on the barricade wall. This assumption is reasonable since the total horizontal stress is equal to the total vertical stress during the backfilling (i.e, the paste is still in liquid phase) and the highest total vertical stress within the paste is located at the deepest location (i.e base).



Fig.1 Paste backfill

According to the overburdened stress theory [1], the total vertical stress (σ_v) is equal to:

$$\sigma_v = \gamma z \quad (1)$$

where, γ is the bulk unit weight of the backfill

(kN/m^3) and z is the depth of backfill (m).

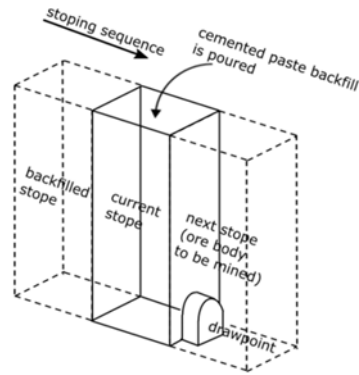


Fig.2 Cemented Paste Backfilling

The equation 1 is valid for a semi-confined area (such as stope) provided that the paste has not been consolidated. During the unconsolidated state, the paste is in liquid phase and the total stress at the base of the stope is then equal to the geostatic stress. After the backfilling is terminated the depth becomes constant and the geostatic stress is also constant. The plot of geostatic stress with elapsed time can be illustrated by a thick solid line in Figure 3. The consolidation appears after the termination of backfilling at which the effective stress starts to generate within the paste. During the consolidation, the interfacial friction between the paste and the stope side walls increases as the effective stress increases. The interfacial friction transfers some of forces in the paste to the side walls (called arching) and therefore, the total vertical stress at base is reduced. The time to consolidate depends of the material properties and the length of drainage path [2]. By considering the arching, the plot of the total vertical stress versus time deviates from the geostatic line as illustrated by the dash lines in Figure 3.

The general observation in Figure 3 is summarized from several full scale monitoring reports [3-10]. However, stress anomalies are found in some reports [3-8], where the total vertical stress increases during the rest period as illustrated by dash dot lines in Figure 3. This is obviously not expected since there is no paste is poured during the rest period. One of the hypotheses is attributed to the temperature increase during the cement hydration. This paper shows some preliminary results to test the hypothesis.

EXPERIMENT

Paste Material

The paste is produced from a mixture of water and silica flour as a replacement of tailings. In

order to isolate the strength gain, the cement is excluded in the paste and the temperature increase is simulated via temperature controller. Therefore, the paste backfill in this experiment is uncemented. The silica flour is sourced from SILVERBOND, Johor, Malaysia. It is inert material with SiO_2 contents of 99.38% and the specific gravity of 2.65.

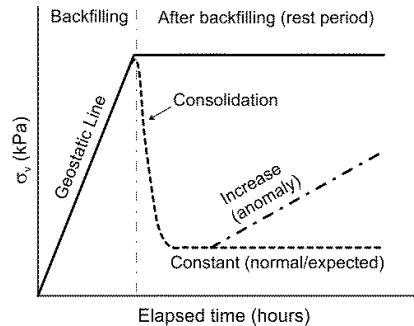


Fig. 3 General plots of total vertical stress at the base of the stope versus elapsed time based on full monitoring reports [3-10].

The particle size distribution (psd) of the silica flour is shown in Figure 4. Two additional points are superimposed to indicate general categories of materials to be used for paste fill and hydraulic fill [12]. The empty square symbol indicates that the paste material should have at least 15% of particles finer than $20 \mu\text{m}$ in order to retain the water in order to achieve reliable paste flow. It is shown that silica flour has more than 15% (i.e. 38%) of particles is finer than $20 \mu\text{m}$, thus it falls within the category. On the other hand, a solid square symbol indicates the category for hydraulic fills material, where it requires a maximum 10% of particles finer than $10 \mu\text{m}$ in order achieve adequate permeability. The silica flour has more than 10% (14.2%) of particles finer than $10 \mu\text{m}$ and therefore it does not fall in this category.

The paste is mixed using 10L portable flour mixer with a solid content of 72% and the unit weight of the paste is 17.5 kN/m^3 . The solid content is defined as the mass of the dry silica flour over the total mass of paste. In mine operations, the solid content is determined by the type of the reticulation system. The higher solid content, the higher energy is needed to transport the paste backfill through the reticulation pipes and vice versa. In some cases, gravity system without pump is sufficient. The range of paste backfill solid content used in some mining paste backfill operation is between 71-82% [2-11].

Apparatus

A laboratory backfill model is built to simulate

stope backfilling. The apparatus has four main parts, namely: a narrow wall, sensors, temperature control system, and data acquisition system. The complete apparatus is depicted in Figure 5.

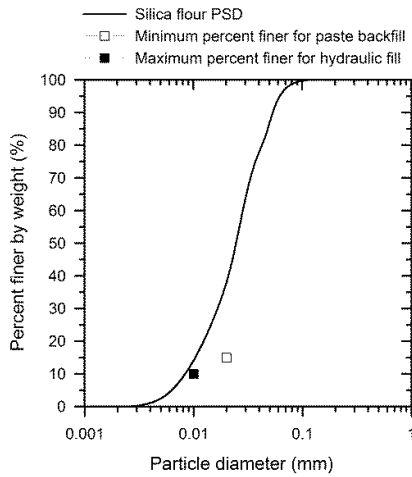


Fig. 4 Particle size distribution

The narrow wall consists of a rectangular aluminum box, two columns and the platform. The box is made of 1 cm thick aluminum measures 15 cm inner length (L), 5 cm inner width (W) and 80 cm inner height (H). The box has a base plate but has no plate at the top. The two columns are made of threaded steel rods fixed vertically on the platform. The rods support the box by fixing its sides via four nuts. The platform is made of thick steel with four legs. In order to ensure the horizontalness, the legs can be adjusted with a spirit level as a reference.

There are two types of sensor used: a load cell and a thermocouple. The load cell is used to measure the weight of the paste transferred to the base of the narrow wall. It is placed right under the base plate. The horizontalness of the load cell can be adjusted. The thermocouple used is type J, inserted into the paste from the above opening of the narrow wall. The temperature control system consists of heating elements and a microprocessor based temperature process control CN7263 manufactured by Omega Engineering. The heating elements are attached to the box using special aluminum holders and connected to the AC 240 volts powerline via temperature controller. The target temperature can be set using “on-off” mode upon receiving signal from the thermocouple. The heating elements will be turned on if the temperature received is lower than the target temperature and vice versa.

The measurements from the sensors are sent to the computer via data acquisition system. The sensors calibration and trial testing are carried out prior to actual test to ensure the test accuracy.

It is important to emphasize the connection between the base plate and the narrow side wall. The base plate and the narrow side wall work independently. This is designed to separate the measurement of force that is transferred to the base of the box and the force that is transferred to the narrow side wall. Therefore, the base plate is not fixed to the narrow side wall. The base plate is simply seats on the load cell and separated by a 3 mm gap from the narrow side wall. In order to prevent flow of paste between the gap, it is closed and secured with latex membrane.

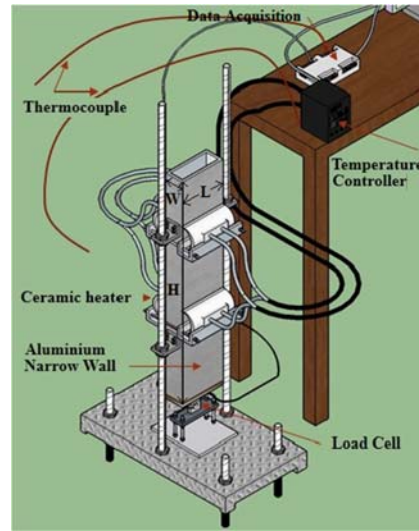


Fig. 5 The laboratory backfill model

Backfilling

The paste is filled (poured) into the box using funnel until about 70 cm in height. The thermocouple is inserted into the backfill from the top opening of the narrow wall. The opening of the narrow wall is then covered with plastic cling wrap to minimize the evaporation from the paste during monitoring. The room temperature during the filling is about 22 °C. At this time, the heating elements are turned off to minimize the risk from electric shock. After the filling is completed, the heating elements are turned on and the temperature control is set to the target temperature of 30 °C.

RESULTS

Figure 6a shows the full observation of vertical stress denotes as σ_v (kPa) and temperature of the paste, T (°C) against the elapsed time. The elapsed time starts from the filling until 78 hours after. The vertical stress, σ_v (kPa) is computed as:

$$\sigma_v = \frac{F}{A} \quad (2)$$

where, F is the downward force measured by the load cell (kN) and A is the base area of the narrow wall (0.0075 m^2). The temperature from the thermocouple is directly registered by the data acquisition in $^{\circ}\text{C}$, therefore there is no additional computation is needed.

Figure 6a is decomposed into Figure 6b-6e that enlarges and highlights specific events in Figure 6a. Figure 6b-6e shows the total vertical stress versus elapsed time during the filling, consolidation, constant temperature after consolidation, and temperature ramp-up,

respectively.

The filling event is highlighted in Figure 6b. The increase in the total vertical stress is as expected until it is terminated at about 40 seconds. The total vertical stress increases from 0 (empty) until about 12 kPa (full). The 12 kPa is equivalent to about 70 cm in height of paste according to equation 1. The vertical stress is kept constant until 0.1 hours. During the filling, the temperature is about 22°C , which indicates the room temperature (not temperature of the paste) since the thermocouple has not been inserted into the paste.

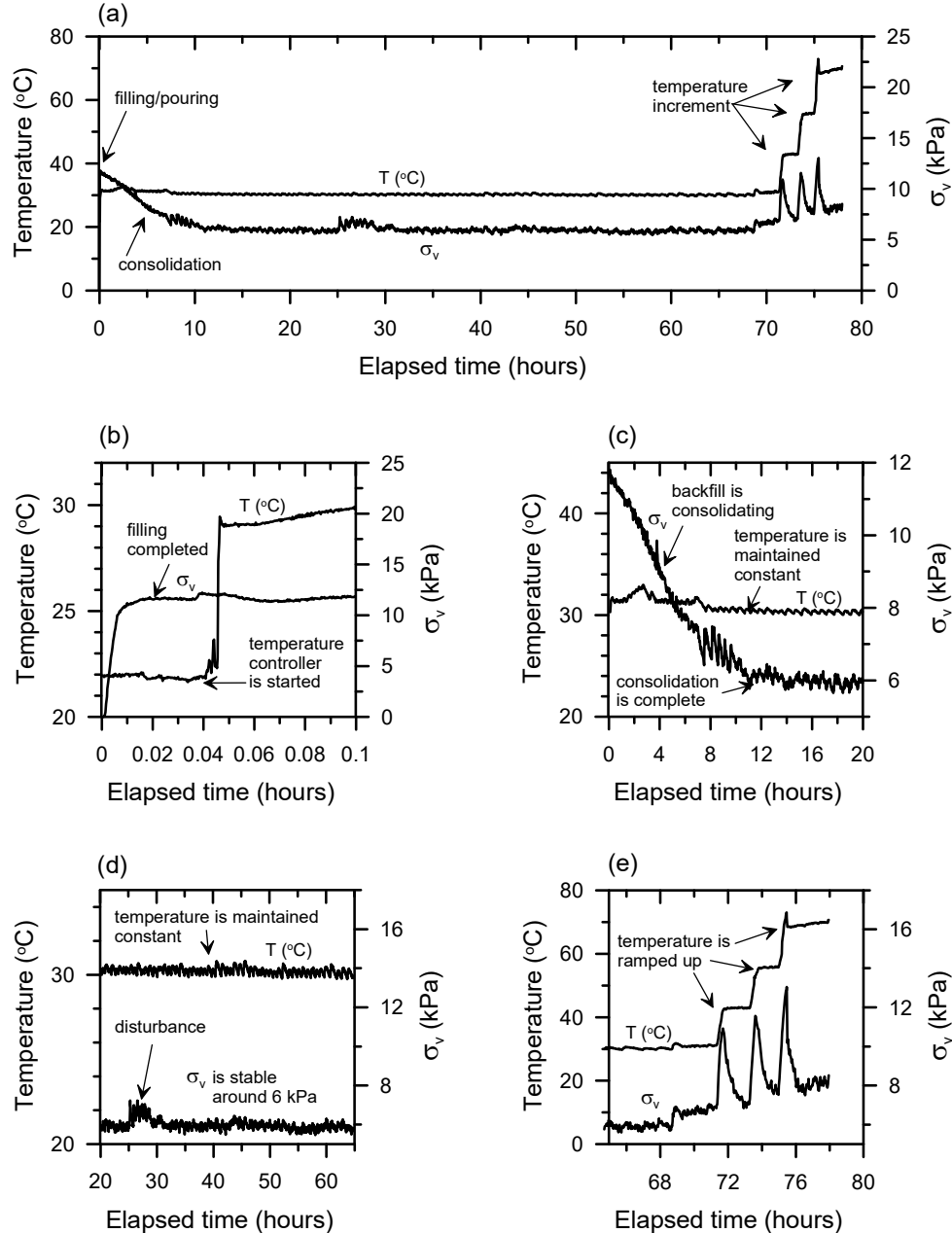


Fig. 6 Backfill monitoring: (a) full observation, (b) filling, (c) consolidation, (d) constant temperature after consolidation, and (e) temperature ramp-up.

About 2.4 minutes after the filling, the thermocouple is inserted into the paste, the heating elements and the temperature control is set to a target temperature of 30 °C. The temperature increases from 22 °C to about 30 °C in about 20 seconds and maintained. There is no effect in increasing temperature on the vertical stress during this filling period is apparent, except a small spike in the total vertical stress at the time the temperature controller starts to ramp up.

Figure 6c depicts the consolidation phase that starts from 6 minutes after the filling and completes at around 12 minutes. The temperature is maintained constant throughout this period. The total vertical stress at base reduces sharply and diminishes when approaching the completion of the consolidation. The consolidation in this process is attributed to the dissipation of pore water to the upper part of the paste and the paste is compressed. The consolidation increases the effective stress within the paste and the friction along the side walls are mobilized that leads to the development of arching. The arching transfers some of the stress within the paste to the side wall and onto the platform. The remaining stress is carried by the base plate. The arching causes the total vertical stress to reduce from 12 kPa to only 6 kPa (50% reduction) in 6 minutes. This consolidation phenomenon has also been found in the full scale monitoring [3-10].

Figure 6d shows that there is no change in the total vertical stress after the consolidation is completed. During this period the temperature is maintained constant. The total vertical stress is constant around 6 kPa. A small disturbance of about 1 kPa is shown as a spike in the total vertical stress, which is located between 26 to 28 hours elapsed time (occurs at daytime). The total vertical stress goes back to 6 kPa after 28 hours.

Figure 6e shows the effect of increasing the temperature (gradient) to the total vertical stress at base. The temperature is ramped-up (increase) and soak (maintained constant) in three step levels. The first step, the temperature is ramped-up from 30 to 42 °C and soaked for about 1.5 hours. During ramp-up, the temperature increases linearly with time in 30 minutes. The calculated temperature rate of increase ($\delta T/\delta t$) is 0.4 °C/hours. Due to this temperature increase, the total vertical stress increases by 4 kPa. It is thought that the increase of the total vertical stress is due to the expansion of the paste. The volumetric strain caused by the expansion is partly resisted by the side wall through friction; hence the arching is reduced and consequently, the additional stress to the base is generated. At the soaking period, the data shows interesting results where the vertical stress decreases and diminishes to its value before the ramped-up. The

second step, the temperature is ramped-up from 42 to 55 °C at the same rate as the first step. The total vertical stress increases by 4 kPa. At the soaking period, the same phenomenon happens where the total vertical stress decreases and diminishes to the original value. The last step, the temperature is ramped-up from 55 to 72 °C with the same rate as the first and the second step. It increases the total vertical stress by 5.5 kPa. During the soaking period, it is noticed from Figure 6e that the temperature slightly drops down to 68 °C after reaching 72 °C, the temperature controller tries to maintain the temperature by heating the narrow wall and the temperature ramps-up again until 70 °C at which the monitoring is terminated. Despite slight drop in the temperature during soaking period, the same phenomenon as the first and the second step reappear.

The relationship between the temperature and the vertical stress is shown in Figure 7. It shows a non-linear increase of vertical stress during the temperature increase. The patterns for the three steps are similar and the empirical formulation of the relationship can be established. In contrast with ramping-up process, soaking process shows vertical drop in the total vertical stress, which brings back the total vertical stress to its consolidated state. This implies that the change in the total vertical stress with respect to its consolidated state equals to zero ($\Delta\sigma_v=0$) if there is no change in temperature ($\Delta T=0$).

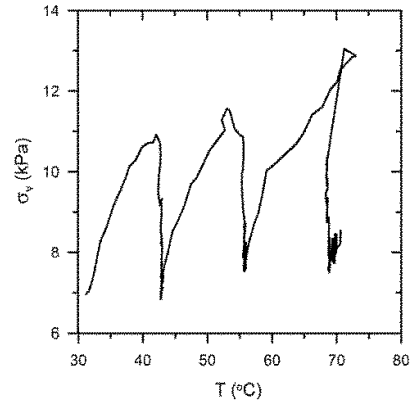


Fig.7 σ_v versus T

Figure 8 shows the relationship between the change in vertical stress ($\Delta\sigma_v$) and the change in temperature (ΔT) for the three steps during the temperature ramp-up period. Attempts have been made to curve fit the experimental data points. The continuous line in Figure 8 represents the best curve fitting to represent the empirical relationship between the change in vertical stress ($\Delta\sigma_v$) and the change in temperature (ΔT). The following form of equation is proposed:

$$\Delta\sigma_v = A \times (1 - e^{B \times \Delta T}) \quad (3)$$

where, A and B are constants. For the curve fitting in Figure 8, the value of A and B are 5 and 0.15, respectively.

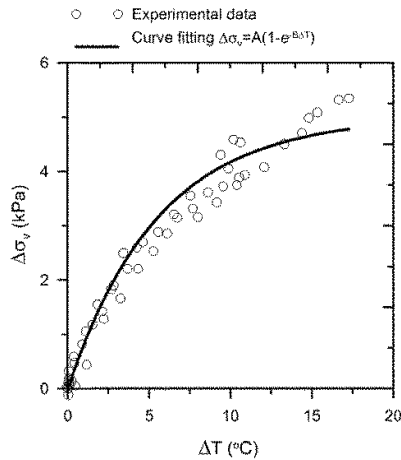


Fig.8 $\Delta\sigma_v$ versus ΔT

CONCLUSIONS

An experiment has been conducted to monitor the effect of the temperature change (gradient) on the total vertical stress within paste backfill via laboratory model. The following conclusions have been made: 1) the total vertical stress is not affected by the level of the temperature, 2) the increase in temperature causes the increase in the total vertical stress at the base of the stope, 3) the empirical relationship between the change in temperature and the change in the total vertical stress fits the exponential function, and 4) the total stress anomaly found in the full scale monitoring of paste backfill can be explained as the change in temperature within the backfill.

ACKNOWLEDGEMENTS

The authors would like to acknowledge financial supports from the Fundamental Research Grant Scheme (FRGS) of the Malaysian Ministry of Higher Education, Grant No. FRGS/TK01(01)/1301/2015(18).

REFERENCES

- [1] Fenner, R., "Untersuchungen zur Erkenntnis des Gebirgsdrucks." Glückauf, Vol. 74, No. 32, 1938, pp. 681-695.
- [2] Terzaghi K., Theoretical Soil Mechanics. New York: Wiley, 1943.

- [3] Doherty, J., Hasan, A., Suazo, G., and Fourie, A. An investigation of some controllable factors that impact the stress state in cemented paste backfill. Canadian Geotechnical Journal, 2015. doi: 10.1139/cgj-014-0321
- [4] Hasan A., Suazo G., & Fourie A, "Full scale experiments on the effectiveness of a drainage system for cemented paste backfill", in Proc. 16th Int. Seminar on Paste and Thickened Tailings (Paste2013), Belo Horizonte, 2013, pp. 381-394. ISBN 978-0-9870937-6-9.
- [5] Hasan A., Suazo G., Doherty J. & Fourie A, "In situ measurements of cemented paste backfilling in an operating stope at Lanfranchi Mine", in Proc. 11th Int. Symposium on Mining with Backfill (Minefill 2014), Perth, 2014a, pp. 327-336. ISBN 978-0-9870937-8-3.
- [6] Hasan A., Suazo G., Doherty J. & Fourie A, "In-stope measurements at two Western Australian mine sites", in Proc. 17th Int. Seminar on Paste and Thickened Tailings (Paste2014), Vancouver, 2014b, pp. 355-370. ISBN 978-0-9917905-3-1.
- [7] Thompson, B, Bawden, W and Grabinsky, M, In situ measurements of cemented paste backfill at the Cayeli Mine', Canadian Geotechnical Journal, Vol. 49, 2012, pp. 755-72.
- [8] Thompson B, Grabinsky M, & Bawden W, "In-situ measurements of cemented paste backfill in long-hole stopes", in Proc. 3rd Canada-US Rock Mechanics Symposium & 20th Canadian Rock Mechanics Symposium, eds. M. Diederichs & G. Grasselli, University of Toronto Press, Toronto, 2009, on CD-ROM.
- [9] Belem T, Harvey A, Simon R, & Aubertin M "Measurement and prediction of internal stresses in an underground opening during its filling with cemented fill", in Proc. 5th Int. Symposium on Ground Support in Mining and Underground Construction, eds. E. Villaescusa & Y. Potvin, Balkema, Rotterdam, 2004, pp. 619-30.
- [10] Yumlu, M., Barricade pressure monitoring in paste backfill. Gospodarka Surowcami Mineralnymi, Vol. 24, 2003, pp. 233-244.
- [11] LeRoux, K., Bawden, W., and Grabinsky M, "Field properties of cemented paste backfill at the Golden Giant mine", Mining Technology (Trans. Inst. Min. Metall. A) Vol. 114, 2005, pp. A66-A80.
- [12] Potvin, Y., Thomas, E., Fourie, A. Handbook on mine fill. ISBN 9780975675625, Perth: Australian Centre for Geomechanics, 2005.

3-D NUMERICAL STUDY ON COASTAL LEVEE REINFORCEMENT USING DOUBLE SHEET-PILES WITH PARTITION WALLS

Kousuke Takahama¹, Yuta Yamanaka², Atsushi Yashima³ and Kakuta Fujiwara⁴
¹Department of Civil Engineering, Gifu University, Japan; ^{2,3} Gifu University, Japan;
⁴Nippon Steel & Sumitomo Metal Corporation, Japan

ABSTRACT

There is fear that coastal levees will sink by liquefaction due to large earthquake such as Nankai Trough Earthquake in Japan. To overcome this damage, as one of major countermeasures, the application of double sheet-piles with partition walls to coastal levees has been proposed. Authors have already carried out 2-D numerical analyses (code:LIQCA2D15) to investigate the effectiveness of the proposed countermeasure. However, the influence of the interval of partition walls has not been discussed in the framework of 2-D analysis. In this study, the applicability and limitation of the 2-D analysis was discussed based on 3-D analyses (code:LIQCA3D15).

It was found that the wider the interval of partition walls becomes, the larger the bending deformation of sheet piles as well as the settlement of coastal levee itself become.

Keywords: Coastal levee, sheet-pile, partition wall, liquefaction, three-dimensional numerical analysis

INTRODUCTION

The severe seismic damage to coastal levees in Japan's Tohoku region was caused by the 2011 Tohoku Region Pacific Coast Earthquake [1]. Large earthquake such as Nankai Trough Earthquake is also concerned to occur in the near future and there is fear that coastal levees will sink by liquefaction. As a countermeasure against a large earthquake and tsunami, the double sheet-piles installation method with partition walls (Fig.1 and 2) has been proposed and its effectiveness has been confirmed by model tests and numerical analyses [2-4]. The more levee damage is reduced, the quicker it is feasible to recover the function of the levee, and as a result, personal and physical damage can be minimized.

Based on the model tests results, the installation of the double sheet-piles in the coastal levee reduced the settlement of the levee significantly during the liquefaction of the foundation ground. Furthermore, if the partition walls were installed with an appropriate interval as shown in Fig.2, the settlement of the top of coastal levee was negligible.

The authors carried out 2-D numerical analysis for the model test with partition walls. The analytical results reproduced model test results quantitatively. In the previous numerical analysis, however, the coastal levee with partition walls were modelled by two dimensional mesh system. If the interval of the partition walls become larger, we have to take into account three dimensional deformation characteristic of coastal levee along the extension direction of the levee. In this study, therefore, we are carrying out 3-D numerical analyses by using LIQCA3D15 [5] to

investigate the applicability and limitation of the 2-D analysis.

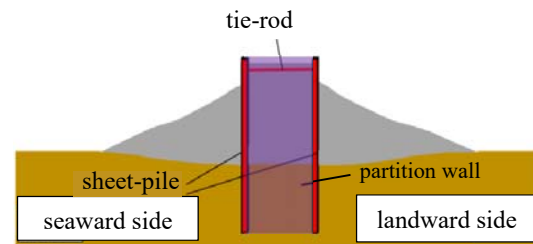


Fig.1 Schematic view of reinforced coastal levee.

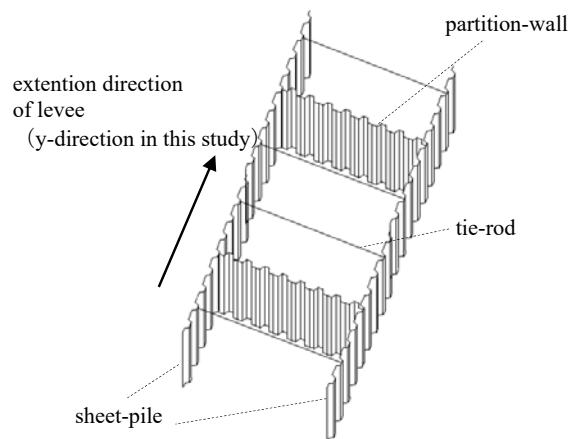


Fig.2 Double sheet-piles with partition walls.

VERIFICATION OF 3-D ANALYSIS

Outline of Numerical Code, LIQCA

We are discussing about the difference between results by 2-D analysis and those by 3-D analysis in this chapter. The model tests carried out by Fujiwara et. al [4] are targeted for the comparative numerical analyses. The experimental results have been reproduced with high accuracy by 2-D analysis [5].

In this study, we are using two-dimensional effective stress analysis program, LIQCA2D15[6] and three-dimensional program, LIQCA3D15[6]. The governing equations for coupling problems between the soil skeleton and pore water pressure were formulated based on two-phase mixture theory [7] and u-p (displacement of solid-phase and pore water pressure) formulation was adopted in both 2- and 3-D analysis. The finite element method (FEM) was employed for spatial discretization of the equation of motion, while the finite difference method (FDM) [8] was employed for spatial discretization of pore water pressure in the continuity equation. In this simulation, a cyclic elastic-plastic model [9] was applied to the coastal levee and liquefiable layer.

Condition for Numerical Model

The shaking table model tests were carried out under the gravity field. The model ground consisted of a levee, liquefiable and unliquefiable layers. The height of the model levee is 300 mm. That condition is approximately 1/25 geometrical scale to the actual structure. Three cases of model tests such as Case-A(without countermeasure), Case-B(with double sheet-piles), Case-C(with double sheet-piles and partition walls) are examined. The model tests have been successfully reproduced by using a two-dimensional effective stress analysis program [10, 11].

In order to compare the performance of 3-D analysis and that of 2-D analysis, 2-D and 3-D numerical mesh systems are prepared as shown in Fig.3. In 3-D analysis, the width is 2800mm, the

height of the levee is 300mm, the thickness of liquefiable layer is 320mm, the thickness of unliquefiable layer is 200mm and the length of the

extension direction of the levee is 170mm which is the half of the model test container due to the symmetric nature along the extension direction of levee. The displacements of the bottom boundary are fixed in all directions. The horizontal displacement of side boundaries is also fixed.

The joint element is not supported in the numerical code, LIQCA3D15. Therefore, the sheet-piles and the interface between sheet-piles and ground are modeled by solid elements. The slipping and separation of the interface between sheet-piles and ground cannot be taken into account. The levee and liquefiable layer are modeled by a cyclic elasto-plastic model, and the unliquefiable layer is modeled by Ramberg-Osgood model (R-O model). As no dilatancy is considered in R-O model, this model is applicable for dense sand or clay layer which generate little build-up of excess pore water pressure during cyclic shear.

The material parameters for a cyclic elastic-plastic model is summarized in Table 1(a). The material parameters of solid element for sheet-pile are shown in Table 1(b). The tie-rod and partition wall are not modeled by the element itself but modeled by the displacement constraint condition of nodes. The interval of tie-rod in the extension direction of the levee is 113 mm and the location is 113 mm below the top of levee. The nodes on both side ends of tie-rod are put on the nodes of the sheet-piles in the same position and they are given equal displacement boundary conditions in the vertical and horizontal directions. As far as the movement of the partition wall concerned, the equal-displacement condition in all directions are set for all nodes located on partition wall. Therefore, shear and bending deformations are not allowed for partition wall.

The levee, liquefiable and unliquefiable layer are modeled by same constitutive models in both 2-D and 3-D analysis. The sheet-piles are represented by linear beam elements (see table 1(c)) in 2-D analysis. A joint element in which the slipping and separation are taken into account is used between the ground and sheet-pile. The joint element values are set referring

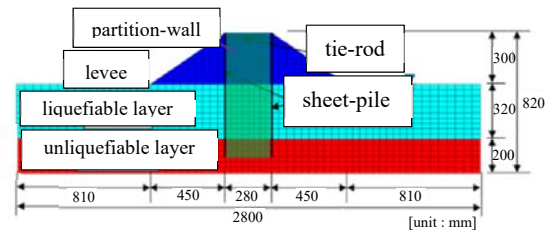
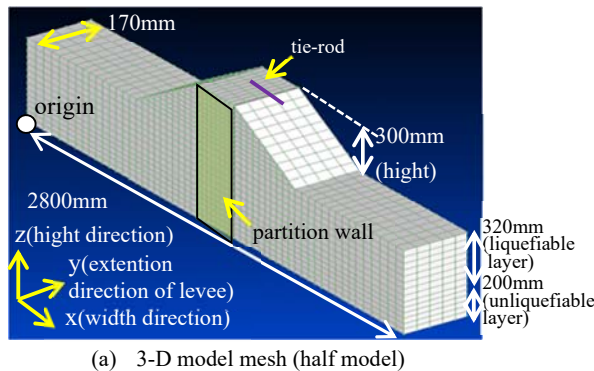


Fig.3 Numerical mesh system

Table 1 Material Parameters for layer

(a) Material Parameters for liquefiable layer		
initial void ratio	e	0.813
compression index	λ	0.015
swelling index	κ	0.002
initial shear modulus ratio	G_0/σ_{m0}	1000
phase transformation stress ratio	M^*_m	0.909
failure stress ratio	M^*_f	1.122
reference strain parameter	γ_P	0.01
reference strain parameter	γ_E	0.02
hardening parameter	B_0	7000
hardening parameter	B_1	50
hardening parameter	C_f	0
dilatancy parameter	D_0	3
dilatancy parameter	n	3
anisotropy parameter	C_d	2000

(b) Material Parameters for sheet-pile (3D)		
Lame' constant (kN/m ²)	λ	1.8×10^9
Lame' constant (kN/m ²)	μ	1.1×10^9
density (t/m ³)	ρ	7.8

(c) Material Parameters for sheet-pile (2D)		
Young's modulus (kN/m ²)	E	2.0×10^8
area of cross section (m ²)	A	3.2×10^{-3}
area moment of inertia (m ⁴)	I	2.7×10^{-9}
density (t/m ³)	ρ	7.8

(d) Material Parameters for joint element (2D)		
spring stiffness in shear direction (kN/m ²)	k_s	1.0×10^4
spring stiffness in shear perpendicular direction (kN/m ²)	k_n	1.0×10^8
cohesion (kN/m ²)	c	0
friction angle (degree)	ϕ	15

(e) Material Parameters for partition wall (2D)		
Young' modulus (kN/m ²)	E	2.0×10^8
shear elastic modulus (kN/m ²)	G	7.8×10^7
thickness (m)	t	6.6×10^{-3}
density (t/m ³)	ρ	7.8

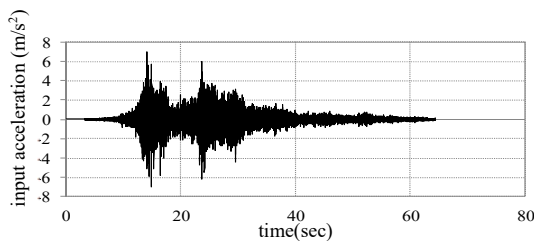


Fig.4 Input acceleration

to example analysis from LIQCA manual (Table 1(d)). The partition wall is modeled by elastic planar elements and arranged so as to be superimposed on the ground elements inside double sheet-piles. The nodes on both side ends of the partition wall are put on the nodes of the sheet-piles in the same position and they are given equal displacement boundary conditions in the vertical and horizontal directions. In the region inside double sheet-piles, thickness of the partition wall and ground element are converted into that per meter in the extension direction of levee and inputted in 2-D analysis. The material parameters for the partition wall are summarized in Table 1(e).

The other boundary conditions are as follows:

- A) The bottom of the ground are fixed in the horizontal and vertical direction.
- B) The side boundary of model are fixed in the horizontal direction.
- C) The water level are adjusted to the surface of the liquefiable layer.
- D) The drainage boundary is set on the surface of the liquefiable layer.

As a large earthquake with high acceleration amplitudes and a long duration, we refer the wave recorded at Kamaishi during the 2011 Tohoku Region Pacific Coast Earthquake (Fig.4). This wave indicates that the maximum acceleration is more than 7m/s², the duration is approximately 240 seconds. We adjust as the input earthquake motion for shaking model tests considering the similarity rule [12], and then extend time duration three times in order to emphasize the effect of countermeasures.

As for the condition of both 2-D and 3-D analysis, the incremental time interval is 0.002 seconds, the coefficient β of the Newmark method is set at 0.3025, and γ is set at 0.6. For Rayleigh damping, a proportional type to the initial stiffness is used. The coefficient is set at 0.003 which corresponds to the 3.0% damping factor to the first natural period of 0.3 seconds of the level ground portion.

NUMERICAL RESULTS

For Case-A and C, the levee deformation together with excess pore water pressure ratio distribution ($t=80\text{sec.}$) in both 2-D and 3-D analyses are shown in Fig.5. In 3-D analysis, the numerical results at the intermediate location of neighboring walls are plotted in Figs.5(a) and (c). It is found that the horizontal ground, P2, reached the liquefaction state. The ground beneath the levee, P1, on the other hand, dose not reach the liquefaction state. Both 2-D and 3-D analyses successfully reproduce the generation of excess pore water pressure observed in the model tests [9, 10].

For Case-A and C, the time histories of the excess pore water pressure at points P1 (beneath the levee) and P2 (horizontal ground) in both 2-D and 3-D analyses are shown in Fig. 6. It is found that time

histories of excess pore water pressure at P1 and P2 are almost identical in both 2-D and 3-D analysis. It is also found that while the foundation ground deforms due to liquefaction, the settlement of double sheet-piles themselves and the ground inside sheet-piles as well as partition walls are significantly reduced both in 2-D and 3-D analyses.

For Case-A ~ C, the time histories of the settlement at the top of the levee in 2-D and 3-D analyses are shown in Fig. 7. The settlement numerically calculated in 3-D analyses is a little bit smaller than that in 2-D analyses. The slipping between sheet-piles and ground is not taken into consideration in 3-D analysis. This is the main reason why the smaller settlement is predicted in 3-D analysis than in 2-D analysis.

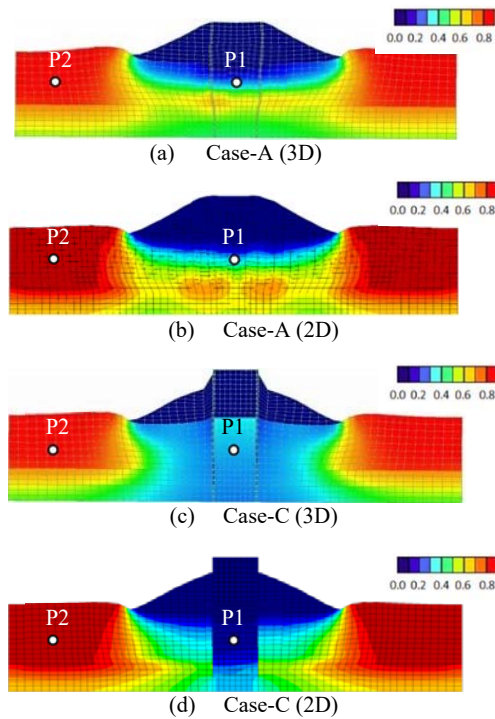
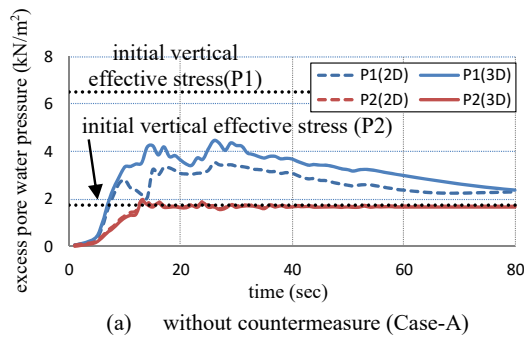
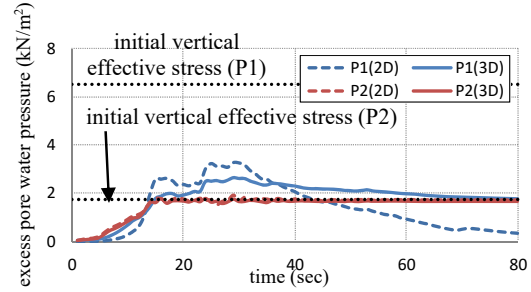


Fig.5 Excess pore water pressure distribution in deformed mesh



(a) without countermeasure (Case-A)



(b) with countermeasure (Case-C)

Fig.6 Time histories of excess pore water pressure

For Case-B and C, the sheet-pile deformation at $t=80\text{sec}$. in both 2-D and 3-D analyses are shown in Fig.8. In 3-D analysis, the numerical results at the intermediate location of neighboring partition walls (at $y=170\text{mm}$) are plotted. In Case-B, 2D and 3D results almost correspond. In Case-C, it is found that there is little deformation in 2-D analysis. There is, on the other hand, a certain horizontal deformation calculated at the intermediate location of the of neighboring partition walls. This deformation pattern can be only predicted in 3-D analysis.

From the above results, 3-D analysis successfully is found to reproduce 2-D analysis. On the other hand, in Case-C, the longer the distance from the partition wall, the larger the horizontal deformation of sheet-piles is expected.

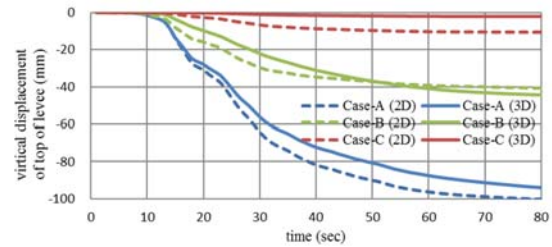
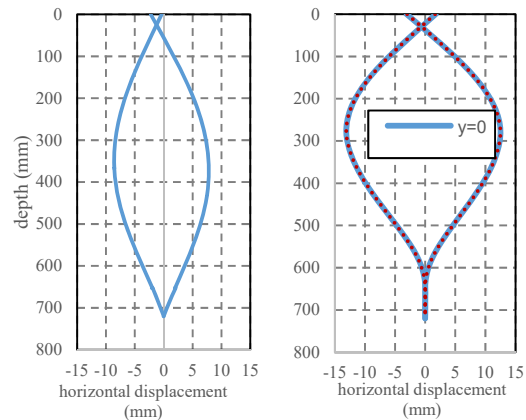


Fig.7 Time histories of settlement at top of levee



(a) 2-D (Case-B)

(b) 3-D (Case-B)

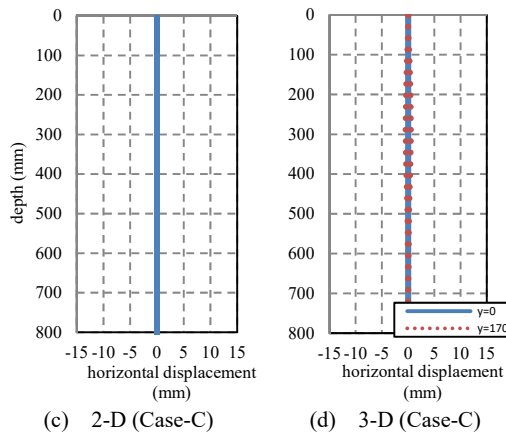


Fig.8 Horizontal displacement of sheet-piles

Discussion on Influence of Interval of Partition Wall

In Case-C, it is expected that the larger the interval of partition walls is, the more vertical settlement at top of levee surrounded by sheet-piles and partition walls in the extension direction of levee will be. We are changing the interval of partition walls under the condition in which all other numerical conditions are same as those employed in the previous chapter. The intervals employed for parametric studies are 170, 226, 280, 510, 680, 1,360, 3,400 and 6,800mm, respectively.

The relationship between the settlement of top of levee at $t=80$ sec. and the interval of partition wall is shown in Fig.9. It is found that the larger the interval of partition wall becomes, the more settlement of top of levee will be. The sheet-piles themselves do not settle because the bottom end of sheet-pile is installed into the unliquefiable layer. The predicted settlement in the present 3-D analysis is thought to be smaller than that predicted in the analysis in which the slipping and separation of the interface between sheet-piles and ground is taken into account.

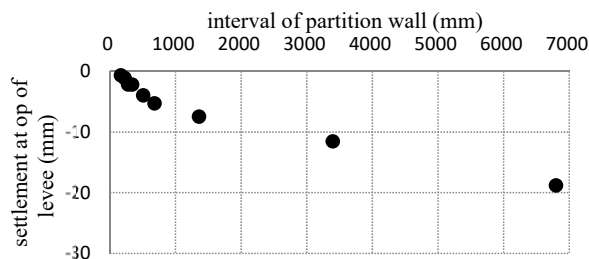


Fig.9 Settlement of levee vs. interval of partition wall

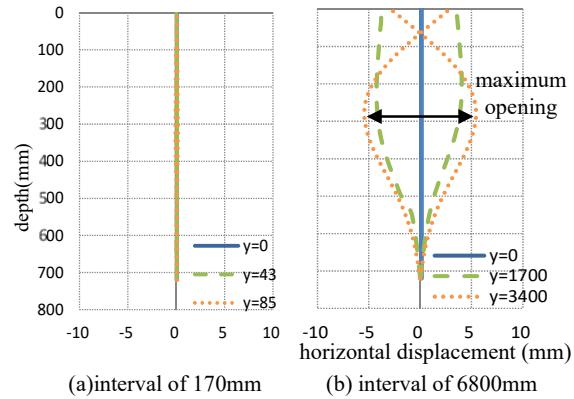


Fig.10 Horizontal deformation of sheet-piles

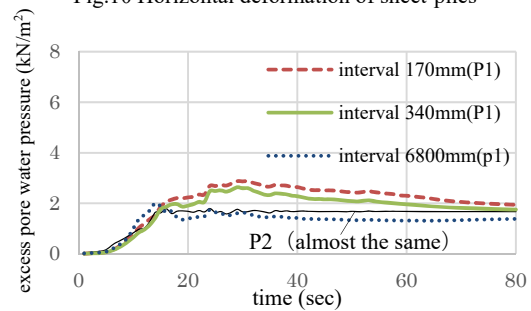


Fig.11 Time histories of excess pore water pressure at the intermediate location of the interval of partition wall

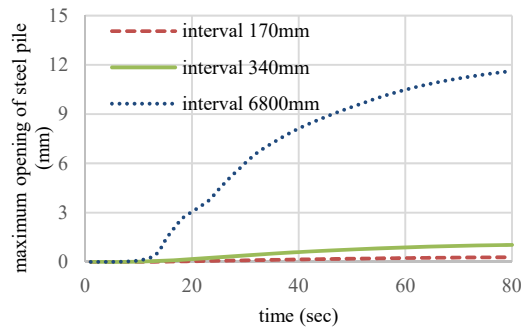


Fig.12 Time histories of maximum opening of sheet-piles

The horizontal deformations of sheet-piles at different distance from the partition wall are shown in Fig.10 for cases of the interval of partition wall with 170mm and 6,800mm, respectively. The value of "y" in the figure represents the distance from the partition wall. It is understood that the horizontal deformation becomes larger if the interval of partition wall becomes larger by comparing the results shown in Fig.8(b). It is found that a large vertical displacement of levee is caused by a large horizontal deformation of sheet-pile. A small horizontal deformation of sheet-pile just beneath the top of levee at $y=3,400$ mm is due to the existence of tie-rod.

The time histories of excess pore water pressures at points P1 (beneath the levee) and P2 (horizontal

ground) are shown in Fig.11 for cases of the interval of partition wall with 170mm, 340mm and 6,800mm, respectively. There is no difference of pore water pressure generation for all cases at point P2. On the other hand, at P2, while the excess pore water pressure generations for all cases almost coincide each other before $t=15\text{sec}$. The dissipation of the excess pore water pressure for narrower interval case is faster than that for wider interval case after $t=15\text{sec}$. The time histories of maximum opening of sheet-pile at the intermediate location of neighboring partition walls are plotted in Fig.12. There is no difference of the increase in the opening of sheet-pile for all cases before $t=15\text{sec}$. On the other hand, the opening of sheet-pile for wider interval case increases larger than that for narrower case after $t=15\text{sec}$. The large opening of sheet-pile induces the expansion of the soil surrounded by sheet-piles. The fast dissipation of excess pore water pressure is partly due to the expansion of soil surrounded by sheet-piles. This typical three dimensional deformation characteristic can only be explained by 3-D analysis.

CONCLUSIONS

Authors investigated the effect of double sheet-piles with partition wall as coastal levee reinforcement method. The following conclusions were obtained by carrying out both 2-D and 3-D numerical analyses (code: LIQCA2D15 and LIQCA3D15).

- 1) It was found that the double sheet-piles with partition wall significantly reduced levee settlement compared to the case without countermeasure.
- 2) It was confirmed that 3-D analysis successfully reproduced 2-D analysis for case with narrow interval of partition walls. It is concluded that 2-D analysis is sufficient to predict the deformation of coastal levee installed by double sheet-piles and partition walls with a certain interval.
- 3) It was found that the larger the interval of partition walls was, the larger the difference between 2-D numerical results and 3-D numerical ones became.

REFERENCES

- [1] Oka, F., Yoshida, N., Kai, S., Tobita, T., Higo, Y., Torii, N., Kagamihara, S., Nakanishi, N., Kimoto, S., Yamakawa, Y., Touse, Y., Uzuoka, R. and Kyoya, T., Reconnaissance Report of Geotechnical Damage due to the 2011 off the Pacific coast of Tohoku Earthquake - Northern Area of Miyagi Prefecture -, *Japanese Geotechnical Journal*, Vol.7, No.1, 2012, pp.37-55.
- [2] Otsushi, K., Koseki, J., Kaneko, M., Tanaka, H. and Nagao, N., Experimental study on reinforcement method of levees by sheet-pile, *Geotechnical Journal*, Vol.6, No.1, 2011, pp.1-14.
- [3] Fujiwara, K., Koseki, J., Otsushi, K. and Nakayama, H., Study on reinforcement method of levees using steel sheet-piles, *Foundation and Soft Ground Engineering Challenges in Mekong Delta*, 2013.
- [4] Fujiwara, K., Taenaka, S., Otsushi, K., Yashima, A., Sawada, K., Hara, T., Ogawa, T. and Takeda, K., Study on coastal levee reinforcement using double sheet-piles with partition walls, *International Journal of Offshore and Polar Engineering*, 2017, (in print)
- [5] Fujiwara, K., Taenaka, D., Otsushi, K., Yashima, A., Sawada, K., Hara, T., Ogawa, T. and Takeda, K., Study on coastal levee reinforcement using double sheet-piles with partition walls, *Proceeding of ISOPE2016*, Rhodes, Greece ; pp.767-774, 2016.
- [6] LIQCA Liquefaction Geo-Research Institute (LIQCARI), Manual of LIQCA2D15 · LIQCA3D15, 2015.
- [7] Biot, M.A., Mechanics of deformation and acoustic propagation in porous media, *Journal of Applied Physics*, 33(4), 1962.
- [8] Oka, F., Yashima, A., Shibata, T., Kato, M. and Uzuoka, R., FEM-FDM coupled liquefaction analysis of a porous soil using an elasto-plastic model, *Applied Scientific Research*, 52, 1994, pp.209-245.
- [9] Oka, F., Yashima, A., Tateishi, A., Taguchi, Y. and Yamashita, A., A cyclic elasto-plastic constitutive model for sand considering a plastic-strain dependence of the shear modulus, *Geotechnique*, 49(5), 1999.
- [10] Fujiwara, K., Taenaka, S., Otsushi, K., Yashima, A., Sawada, K., Ogawa, T. and Takeda, K., Study on levee reinforcement using double sheet-piles with partition walls, *Japanese Geotechnical Society Special Publication*, Vol.5, No.2, 2017, pp.11-15.
- [11] Fujiwara, K., Taenaka, S., Otsushi, K., Yashima, A., Sawada, K., Hara, T., Ogawa, T. and Takeda, K., Study on coastal levee reinforcement using double sheet-piles with partition walls, *Proceeding of ISOPE2016*, 2016, pp.767-774.
- [12] Iai, S., Similitude for shaking table tests on soil-structure-fluid model in 1g gravitational field, *Report of the Port and Harbor Research Institute*, 27(3), 1988, pp.3-24.

LANDSLIDES AND PRECIPITATION CHARACTERISTICS DURING THE TYPHOON LIONROCK IN IWATE PREFECTURE, JAPAN

Thapthai Chaithong¹, Daisuke Komori², Yoshiya Touge³, Yuta Mitobe⁴, Yuto Sukegawa⁵,
and Satoshi Anzai⁶

^{1,2} Graduate School of Environmental Studies, Tohoku University, Japan;

^{3,5,6} Graduate School of Engineering, Tohoku University, Japan

⁴ Faculty of Civil and Environmental Engineering, Tohoku Gakuin University, Japan

ABSTRACT

In August 2016, the typhoon Lionrock made landfall on Japan's northeastern coast and caused floods and landslides. Lionrock brought heavy precipitation to Japan which Shimotokusari station (33201) recorded 24-hour rainfall amount over 200 mm and the peak rainfall intensity was approximately 65 mm/hr. Total cost damage with in the Iwate prefecture is over 700 million dollar, moreover 20 lives were lost and 4 peoples missing. Therefore, the objective of this paper is to present the results of post-disaster investigation, including, the back-analysis of landslides and precipitation due to the typhoon Lionrock. The rainfall and landslides relationship is significantly important for rainfall intensity-duration threshold. In this typhoon, the empirical rainfall intensity-duration threshold has been derived as $I = 20.24D^{-0.33}$. The slope failure could be broadly categorized into the debris flow, surficial erosion, and soil slide, moreover, occurred on slopes ranging from 19 to 58 degrees.

Keywords: Typhoon, Tropical Cyclone, Landslides, Rainfall, Intensity-duration threshold, Critical rainfall

INTRODUCTION

Landslides are one of the serious natural hazards and may lead to the occurrence of the large volumes of rock, wood or the other debris. The mechanism of intense rainfall due to the typhoon (tropical cyclone) induced landslides is well understood. Landslides can be caused by increased pore water pressure or groundwater table during intense storms [1]. Moreover, there are many contributing factor such as, geological, geomorphological, or land use [2].

Numerous studies proposed the model that depicts the criteria and relationship between rainfall and landslides occurrence for early warning development or understanding behavior of rainfall-induced landslide such as empirical rainfall threshold, analytical rainfall infiltration-infinite slope model, and numerical models. The empirical rainfall threshold uses correlation of critical daily rainfall and three day antecedent rainfall for early warning system, in addition, finding the correlation of rainfall intensity and duration of rainfall (I-D critical threshold) [3-6]. The analytical rainfall infiltration-infinite slope model is applied the infiltration model for finding rainwater infiltration volume and also applied the infinite slope model for a factor of safety calculation. The numerical model is a widely used analysis the rainfall seepage through the hillslope.

In 2016, Iwate prefecture is located in the Tohoku region of Japan, experienced extreme events of the Typhoon. Typhoon Lionrock made landfall

near Ofunato city where is a city located in Iwate prefecture on 30 August 2016. This is a cause of flood, landslides, debris flow and the other in Iwate prefecture and vicinity. As a consequence, there are many serious infrastructure damages and loss of lives and property. This study aims to present a post-disaster damage investigation and back analysis of landslides and rainfall characteristic due to the typhoon Lionrock in Iwate prefecture, Japan.

TYPHOON LIONROCK

Typhoon Lionrock was first observed on 15 August 2016 where it was located about 580 km to the west of Wake Island in the western Pacific Ocean. It developed into a tropical depression and was classified by the Japan meteorological agency (JMA) on 16 August 2017 that the wind speed is about 45 km/h. During August 20-21, the wind speed is increased to 65 km/h and became a tropical storm. The lionrock developed into a severe tropical storm on August 23 and tropical storm on August 24. The highest wind speed is 166 km/h on August 28. Table 1 shows the information of the typhoon lionrock. Figure 1 shows the direction of the typhoon lionrock. JMA reported the typhoon lionrock made landfall near the city of Ofunato which this unusual typhoon to directly land in the Tohoku because of typhoons usually approach Japan from the south and southwest before moving northward across the archipelago.

Table 1 The information of the typhoon lionrock

Date (UTC)	Lat	Long	Winds (km/h)	Category
08/21 (12:00)	29.2	133.3	65	Tropical Storm
08/22 (12:00)	28.5	134.1	74	Tropical Storm
08/23 (12:00)	26.6	134	111	Severe Tropical Storm
08/24 (12:00)	24.4	131.8	148	Typhoon
08/25 (12:00)	23.5	130.8	157	Typhoon
08/26 (12:00)	23.2	132.1	148	Typhoon
08/27 (12:00)	24.5	134.6	157	Typhoon
08/28 (12:00)	28.5	138.8	166	Typhoon
08/29 (12:00)	32.3	143.4	138	Typhoon
08/30 (12:00)	41.3	140	111	Severe Tropical storm

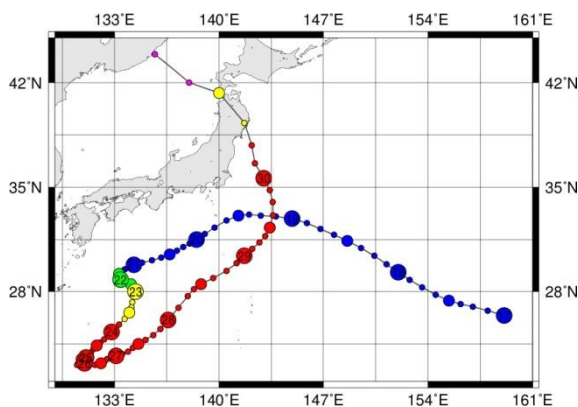


Fig. 1 Direction of the typhoon lionrock [7]

CHARACTERISTICS OF RAINFALL AND LANDSLIDES DURING THE TYPHOON LIONROCK

Rainfall pattern and intensity

There were 50 rain gauges in Iwate prefecture which were used to measure the amount of rain water in this the landslides and debris flow event. Rainfall information for event that triggered the landslides was collected from Automated Meteorological Data Acquisition system (AMeDAS) by the Japanese Meteorological Agency and the rain gauges are operated by Iwate prefecture. The heavy rainfall started on August 30 and the 24 – hour rainfall was

reached 220 mm that was observed at the Shimotokusari station in Kuji city, Iwate. Figure 2 illustrates the intensity and distribution of rainfall on August 30 in Iwate prefecture. The Lionrock typhoon produced the heavy rain covered Iwaizumi town, Tanohata city, Miyako city which the amounts of 24-hour rainfall in these areas were between 155 to 220 mm. This was a cause of the overflow of the riverbanks of Omoto River and landslides and debris flows.

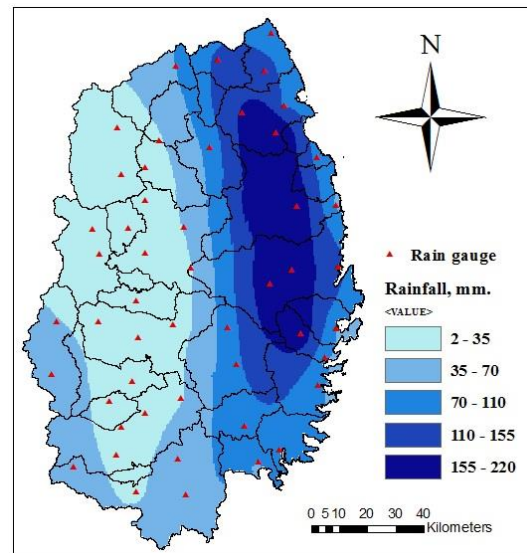


Fig. 2 Distribution of rainfall on August 30 in Iwate prefecture.

Figure 3 shows the hourly rain fall of the five rain gauges in Iwaizumi town on August 30. Considering landslide triggering factors, the intensity and duration of rainfall are the main factors to consider.

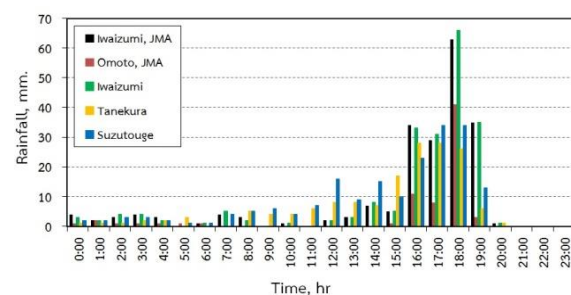


Fig. 3 Hourly rainfall from five rain gauges in Iwaizumi town on August 30.

Therefore, intensity-duration thresholds (I-D critical thresholds), as the empirical threshold, using the rainfall intensity and duration data obtained from this landslide event. Intensity-duration thresholds are the most common type of landslide thresholds and have a general form as the following:

$$I = c + aD^{-\beta} \quad (1)$$

where I is the rainfall intensity, D is rainfall duration, and c, a, β are the parameters obtained from curve. Numerous researchers developed several I-D critical thresholds serves the landslide

warning as shown in Table 2. Figure 4 shows the comparison of I-D critical thresholds obtained from this event and the literature reviews. Fig 4 shows the intensity and duration for the gauge nearest the landslide areas.

Table 2 Intensity-duration threshold for landslides

No	Area	Equation	Range, h	Landslides type	Reference
1	World	$I = 14.82D^{-0.39}$	$0.167 < D < 500$	Shallow landslides, Debris flow	6
2	World	$I = 30.53D^{-0.57}$	$0.5 < D < 12$	Debris flow	6
3	World	$I = 10D^{-0.77}$	$0.1 < D < 1000$	Soil slip	6
4	World	$I = 0.48 + 7.2D^{-1.00}$	$0.1 < D < 1000$	Shallow landslides	6
5	Japan	$I = 39.71D^{-0.62}$	$0.5 < D < 12$	Debris flow	6
6	Japan	$I = 2.18D^{-0.26}$	$3 < D < 537$	Shallow landslides	4

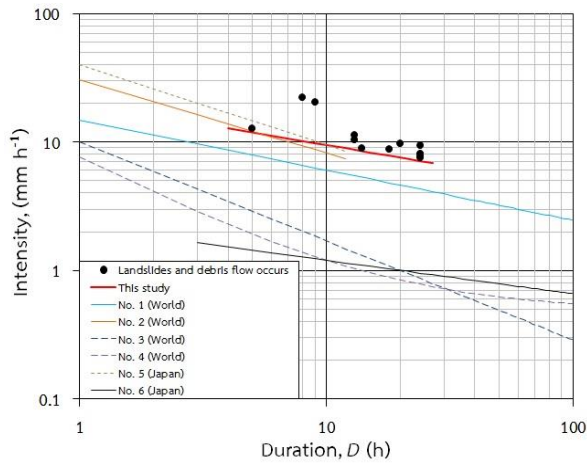


Fig. 4 I-D critical threshold determined by this study and comparison with other I-D critical thresholds

According to the rainfall intensity and duration, the I-D critical threshold for this event can be presented in Eq. (1). This threshold is defined for the rainstorm durations range 5 to 24 hours. The type of failure of the landslide occurrence is to combine shallow landslides with the debris flows.

$$I = 20.24D^{-0.33} \quad (2)$$

As shown in table 1, the previous research studies proposed several I-D critical thresholds for world scale and country scale. Comparison the previous thresholds with the data obtained from this landslide event, it was found that almost of all previous thresholds can serve this event, but only the threshold No. 5 is slightly higher than the one point of intensity and duration this event. Threshold No. 5 was developed to serve the debris flow failure type,

but this event was to combine shallow landslides with debris flow that were observed and surveyed in the field by a team. Considering the threshold No. 6 for Japan, the I-D critical threshold is rather conservative criterion.

In addition to the above mentioned, the relation between the 24-hour rainfall and cumulative soil moisture are also significantly useful for the establishment of the critical rainfall envelope. The 24-hour rainfall criterion can reflect a function of regolith thickness and porosity of soil mass and the antecedent precipitation index, as cumulative soil moisture, can refer a function of interception and evapotranspiration [8]. Figure 5 indicates the plots between the 24-hour rainfall and antecedent precipitation index.

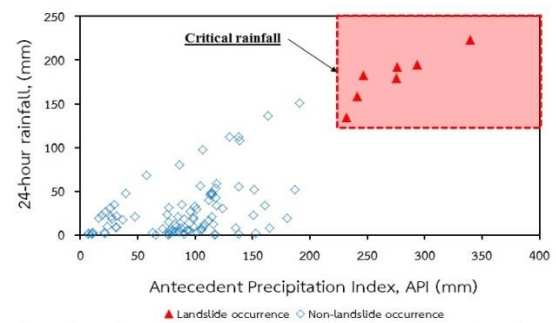


Fig. 5 Critical rainfall envelope obtained from this landslides event

Figure 5 presents the critical zone that is rainfall triggered landslides. The red dots are the 24-hour rainfall and the API that collected from the rain gauges surround the landslide areas. The blue dots are the 24-hour rainfall and the API in the non-landslides occurrence time. The minimum critical 24-hour rainfall is approximately 130 mm and the minimum API is 220 mm.

Landslides characteristics

The catastrophic landslide in Iwaizumi town and Tanohata village are located in Shimohei District, Iwate prefecture, Japan, were serious and large landslide induced Typhoon Lionrock. Geological conditions in these areas were formed an accretionary complex (Mesozoic and Palaeozoic) and some plutonic rocks [10]. Figure 6 shows the bedrock layer of the landslide scar.



Fig. 6 Bedrock layer of the landslide scar

The landslide scars data were obtained from Geospatial Information Authority of Japan and Google Earth website. Figure 7 shows the landslide distribution and slope angle. The failures occurred on slopes ranging from 19 to 58 degrees.

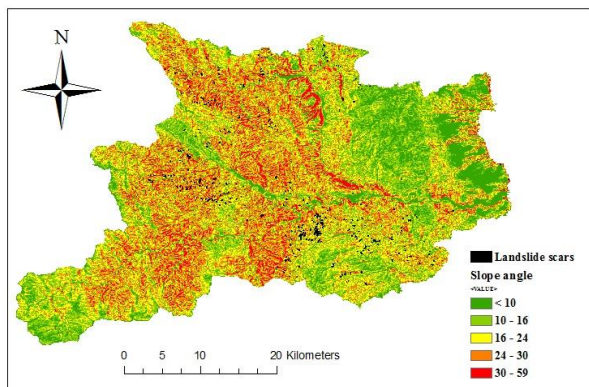


Fig. 7 Landslide distribution and slope angle.

Field investigation revealed that the majority of the slope failures were of complex forms that could be broadly categorized into the debris flow, surficial erosion, and soil slide. Figure 8 shows the debris flow occurrence. Figure 9 shows the aerial photos

showing landslide scars in Iwate. Failure scars usually stretched from the stream banks to uphill at various distances and the depth of failure scars is about 0.5-1.5 meters. Consequences of failure brought the large amounts of debris such as rock, wood, or sediment, into the river or villages and got stuck on the bridge or a house. Fig 10 shows the woody debris trapped the rail bridge.



Fig. 8 Debris flow occurrence in Iwate

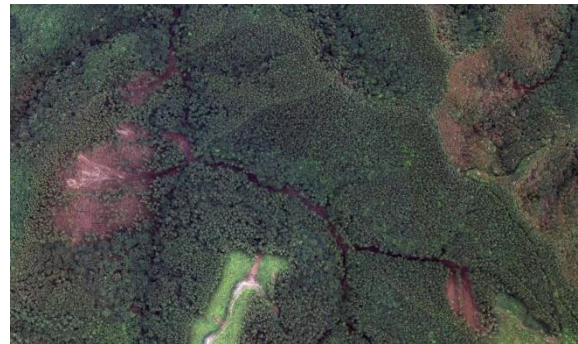


Fig. 9 Aerial photos showing landslide scars in Iwate. [11]



Fig. 10 Woody debris trapped the rail bridge

REGIONAL RAINFALL THRESHOLD

As already discuss the characteristic of precipitation that is the intensity – duration rainfall, and the antecedent rainfall condition as an empirical relationship including the characteristic of the landslide. Hence, the purpose this section is to discuss the critical rainfall threshold at the regional scale which considers the physical properties such as soil permeability, soil strength, and failure mechanism, using the rainfall infiltration and infinite slope model. Conceptual of this critical rainfall threshold is to find the amount of rain that makes the factor of safety less than 1. The critical rainfall threshold is based on two main assumptions. The first assumption is the failure type of landslides is the infinite slope and the saturation of hillslope would destabilize a hillslope. The second assumption is the soil moisture initial condition prior to rainstorm is equal to the volumetric water content at field capacity (suction at 33 kPa).

The wetting front of sloping surface is defined as:

$$z_w = \frac{I}{(\theta_s - \theta_f) \cos \beta} \quad (3)$$

So,

$$I = z_w (\theta_s - \theta_f) \cos \beta \quad (4)$$

So, the critical rainfall threshold is defined as:

$$I_{cr} = z_{cr} (\theta_s - \theta_f) \cos \beta \quad (5)$$

where z_w is the wetting front, I is the amount of rain infiltration, θ_s is the volumetric water content at saturation, θ_f is the volumetric water content at field capacity (33 kPa), I_{cr} is the critical rainfall threshold, z_{cr} is the critical depth, and β is the slope angle. The volumetric water content at field capacity and saturation can be estimated using a soil texture. [12] The soil texture is estimated by the soil classification and grain size distribution curve. The critical depth uses the infinite slope stability model. The factor of safety for an infinite slope model is based on the Mohr-Coulomb failure criterion is defined as:

$$Fs = \frac{c'}{\gamma_t z \sin \beta \cos \beta} + \frac{\tan \phi'}{\tan \beta} \quad (6)$$

where Fs is the safety factor, c' is the effective

cohesion of soil, ϕ' is the effective friction angle, γ_t is the total soil unit weight, and z is the depth.

Hence, from (5) and (6), the critical rainfall threshold can create a new form as follows:

$$I_{cr} = \left[\frac{c'}{\left[\gamma_t \sin \beta \cos \beta \right] + \left[1 - \frac{\tan \phi'}{\tan \beta} \right]} \right] \times \left[(\theta_s - \theta_f) \cos \beta \right] \quad (7)$$

Reference [13] proposed the range of critical depth that is 2-5 metres for a large debris flow and soil slip and 0.7-1.2 metres for small soil slip and local failure. Generally, the critical depth is controlled by the natural soil strata and the other geological condition in each area. Following laboratory results, the type of soil was classified as a loamsand (LSa), so, the volumetric water content at field capacity is 14% and the volumetric water content at saturation is 45%. Figure 11 shows the regional critical rainfall threshold for Iwaizumi town and Tanohata village. Figure 12 shows the rainfall distribution in Iwaizumi town and Tanohata village.

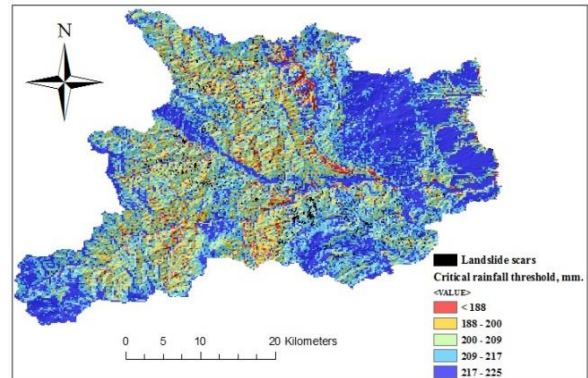


Fig. 11 Regional critical rainfall threshold for Iwaizumi town and Tanohata village.

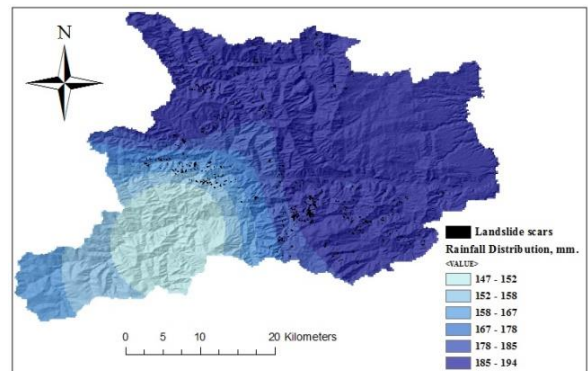


Fig. 12 Rainfall distribution in Iwaizumi town and Tanohata village.

According to the critical rainfall threshold map, the landslides occurred in the red and yellow zone that the critical rainfall is ranging 124 – 192 mm, hence, compared with the rainfall distribution in those zone, it was found that the amount of rainfall is high than the critical rainfall and the excess rainfall is about 5 to 25 mm.

CONCLUSION

Typhoon-triggered landslide is a serious natural disaster. Understanding the characteristics of rainfall and landslides are a very important method for developing the critical criterion of the landslide early warning. This study could be concluded that:

The past I-D threshold can be applied in this case, except the threshold No. 5 that the rainfall is considerably higher than the threshold. Moreover, we create the critical rainfall envelope using the 24-hour rainfall and antecedent precipitation index.

The majority of the failures were could be broadly categorized into the debris flow, surficial erosion, and soil slide, in addition, occurred on slopes ranging from 19 to 58 degrees. One of the consequences of landslide is debris such as rocks, or woody that is cause of property damage.

The region critical rainfall applies the infiltration process and the infinite slope analysis model that can apply in this case.

ACKNOWLEDGEMENTS

This study was supported by Japan Society of Civil Engineering, The Society for the Promotion of Construction Engineering, and The Social Implementation Program on Climate Change Adaptation technology (SI-CAT). The authors gratefully acknowledge the Geotechnical laboratory, Department of civil and environmental engineering, Graduate School of Engineering, Tohoku University, Iwate prefecture, and Geospatial Information Authority of Japan, and National Institute of Informatics of Japan for information and equipment. The authors also gratefully thank Mr. Hiroaki Kabuki for the good suggestion about the laboratory test.

REFERENCES

[1] Tofani V, Dapporto S, Vannocci P, and Casagli N, "Infiltration, seepage and slope instability mechanisms during the 20–21 November 2000 rainstorm in Tuscany, central Italy", *Nat. Hazards Earth Syst. Sci.*, Vol. 6, Issue 6, Dec. 2006, pp. 1025-1033.

[2] Phien-wej N, Nutalaya P, Aung Z, and Zhibin T, "Catastrophic landslides and debris flows in Thailand", *Bulletin of the International*

Association of Engineering Geology, Oct. 1993, pp. 93-100.

[3] Chen CY, "Landslide and debris flow initiated characteristics after typhoon Morakot in Taiwan", *Landslides*, Vol. 13, Nov. 2015, pp. 153-164.

[4] Saito H, Nakayama D, and Matsuyama H, "Relationship between the initiation of a shallow landslide and rainfall intensity-duration thresholds in Japan", *Geomorphology*, Vol. 118, 2010, pp. 167-175.

[5] Godt JW, Baum RL, and Chleborad AF, "Rain fall characteristics for shallow landsliding in Seattle, Washington, USA", *Earth Surf. Process. Landforms*, Vol. 31, 2006, pp. 97-110.

[6] Guzzetti F, Peruccacci S, Rossi M, and Stark CP, "Rainfall thresholds for the initiation of landslides in central and southern Europe", *Meteorol Atmos Phys*, Vol. 98, 2007, pp. 239-267.

[7] Kitamoto A, "Typhoon 201610 (LIONROCK) Detailed Track Information" (Website: <http://agora.ex.nii.ac.jp/digital-typhoon/summary/wnp/1/201610.html.en>)

[8] Gabet EJ, Burbank DW, Putkonen JK, Pratt-Sitaula BA, and Ojha T, "Rainfall thresholds for landsliding in the Himalayas of Nepal", Vol. 63, 2004, pp. 131-143.

[9] Ohtsu H, Chaleiwchalard N, Koga H, and Soralum S, "A study on landslide early warning system considering the effect of antecedent rainfall on slope stability", *The 41th Symposium on Rock Mechanics*, Jan. 2012, pp. 252-257.

[10] Arai K, Nozaki T, Jeong B, and Fukumoto y, "Distribution of landslides and their geological characteristics in Japan-Analysis report based on the data of nation-wide designated landslides-threatened areas", *J. of the Jpn. Landslide Soc*, Vol. 44 No. 5, 2008, pp. 38-43.

[11] Geospatial Information Authority of Japan, Ministry of Land, Infrastructure, Transport and Tourism, (http://www.gsi.go.jp/BOUSAI/H28.ta_ihuu10gou.html)

[12] Saxton KE, and Rawls WJ, "Soil water characteristic estimates by texture and organic matter for hydrologic solutions", *Soil science society of America journal*, Vol. 70, 2006, pp. 1569-1578.

[13] Jotisankasa, A, and Vathananukij, H, "Investigation of soil moisture characteristics of landslide-prone slopes in Thailand", *International Conference on Management of Landslide Hazard in the Asia-Pacific Region*, Nov. 2008, Sendai, Japan .

SATURATED SHEAR STRENGTH PARAMETERS OF COMPACTED KHON KAEN LOESS BY DIRECT SHEAR TEST

Atchariya Saengthongthip¹, Ratamanee Nuntasarn² and Jutaporn Tanok³
^{1,2,3}Faculty of Engineering, Khon Kaen University, Thailand

ABSTRACT

The aim of this study is to investigate shear strength parameters of compacted Khon Kaen loess from UU, CU and CD method. These shear strength parameters were determined by direct shear test. The initial dry density of UU and CU samples was 1.95 t/m³, which was 90% of maximum dry density by modified method. But the initial dry density of CD samples was 2.0 t/m³, which was the maximum dry density by modified method. The shear rate of UU and CU method was 1 mm/min. The shear rates of CD method was determined from consolidation. However, two samples were tested for CD method. The difference between these two samples was the shear rate, which was 0.018 and 0.086 mm/min. The test result showed that total cohesion (c) from UU and CU was 0 and 20 kPa, respectively. Meanwhile, the total friction angle (ϕ) from UU and CU was 36 and 23.5 degree, respectively. The residual friction angle (ϕ_r) from UU and CU method was 34 and 25 degree, respectively. Moreover, the shear strength parameters from CD method, which was tested by different strain rate, showed that were a slightly different. The stress-strain behavior from UU and CU method showed the strain hardening. However, the stress-strain behavior of sample from CD method, which was sheared with a slow rate, showed the strain hardening. The stress-strain behavior of sample from CD method, which was sheared with a quick rate, showed the strain softening.

Keywords: Direct Shear, Unconsolidated Undrained, Consolidated Undrained, Consolidated Drained, Khon Kaen Loess

INTRODUCTION

In the present, there are many constructions in Khon Kaen province. Moreover, Khon Kaen soil was used as construction material for landfill. Therefore the engineering should know the shear strength parameters for design the foundation. The shear strength parameters can be evaluated by unconsolidated undrained method (UU), consolidated undrained method (CU) and consolidated drained method (CD). These methods can test by triaxial and direct shear test. This study used a direct shear test to determine shear strength parameters of three methods as mention previously.

In this study, Khon Kaen loess had been investigated at compacted and saturated condition. Soil samples for UU and CU method were compacted at 95% of maximum dry density by modified method. Moreover, the strain rate of shear for UU and CU method was 1 mm/min. However, the soil sample for CD method was prepared at a different initial dry density from UU and CU. The initial dry density of CD samples was at the maximum dry density by modified method. Moreover, the strain rate of shear CD samples was determined from consolidation test. For this study, the effect of shear rate on the shear strength parameters of CD method was considered. Two strain rate of shears was observed in this study, which was 0.086 and 0.018 mm/min.

BASIC PROPERTIES

Khon Kaen loess, which was used in this study, was classified as silty sand (SM) according to [1]. The results of sieve and hydrometer analysis showed that Khon Kaen loess consists of 55% sand, 30% silt, and 15% clay [1]. The majority of Khon Kaen sand size was a fine grain as illustrated in Fig. 1. The natural density of Khon Kaen loess was 1.65 t/m³, which is the loosed sand. Atterberg's limit results also presented a liquid limit was 16.5% and a non-plastic limit. The specific gravity was 2.65. The basic properties of Khon Kaen loess were present in Table 1.

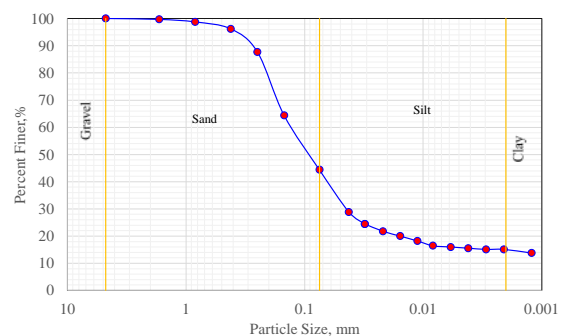


Fig. 1 Grain Size Distribution

In addition, the modified compaction was decided to use in this project because Khon Kaen loess was used in pavement construction rather than an another construction. The maximum dry density was 2 t/m^3 and the optimum moisture content was 9%.

Table 1 Basic Properties of Khon Kaen loess

Properties	
Liquid limit (LL), %	16.5
Plastic limit (PL), %	NP
Plasticity index (PI), %	-
Specific gravity	2.65
Optimum moisture content (OMC), %	9
Maximum dry density (ρ_d), t/m^3	2.0
Sand (%)	55
Silt (%)	30
Clay (%)	15
USCS classification	SM

DIRECT SHEAR

Soil samples were compacted at optimum moisture content by modified method. Soil samples were trimmed by cutting ring and taken into direct shear apparatus as shown in Fig 2 and 3, respectively.



Fig.2 Preparation specimen

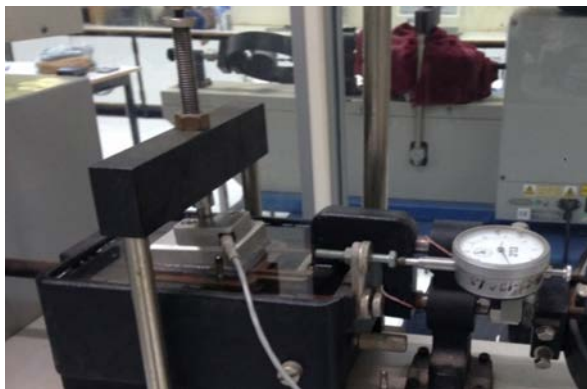


Fig. 3 Direct shear setup

Unconsolidated Undrained Method

After specimen was setup, the specimen was soaked for 24 hr. prior to shear. Then the specimen was shear with rate 1.0 mm/min . Three different vertical stress 144, 286.5 and 572 kPa was used for this method. The test result showed that the total cohesion was 0 kPa and the total friction angle (ϕ) was 36 degrees. The residual friction angle (ϕ_r) was slightly dropped to 34 degree as shown in Fig 4.

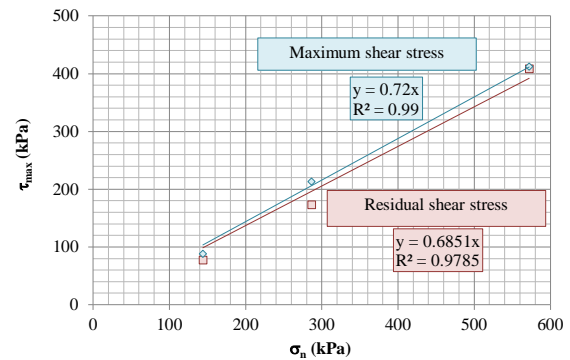


Fig. 4 Unconsolidated Undrained Shear Strength

The relationship between horizontal and shear stress showed a strain hardening except for specimen no.2, which showed a strain softening as shown in Fig. 5. Besides the relationship between the vertical displacement and horizontal displacement presented a dilatation as shown in Fig. 6.

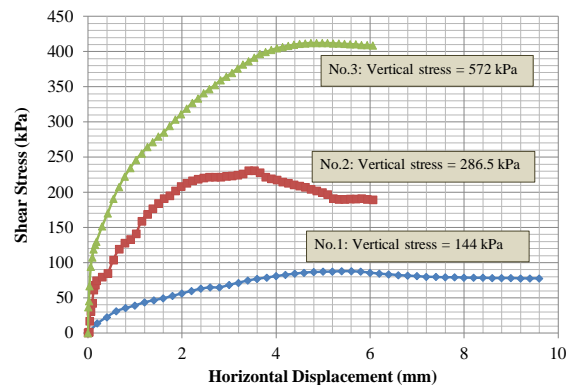


Fig. 5 The relationship between horizontal displacement and shear stress of UU sample

Consolidated Undrained Method

After specimen was setup, the specimen was soaked for 24 hr. and then the specimen had to be consolidated for 24 hr. prior to shear. The specimen was shear with rate 1.0 mm/min . Three different vertical stress 144, 286.5 and 572 kPa was used for this method. The relationship between the shear stress

and normal stress as shown in Fig. 7 presented that the total friction angle of the maximum and residual shear stress equal to 23.5 degrees. However, the residual cohesion was dramatically dropped more than 50% from 20 to 8 kPa.

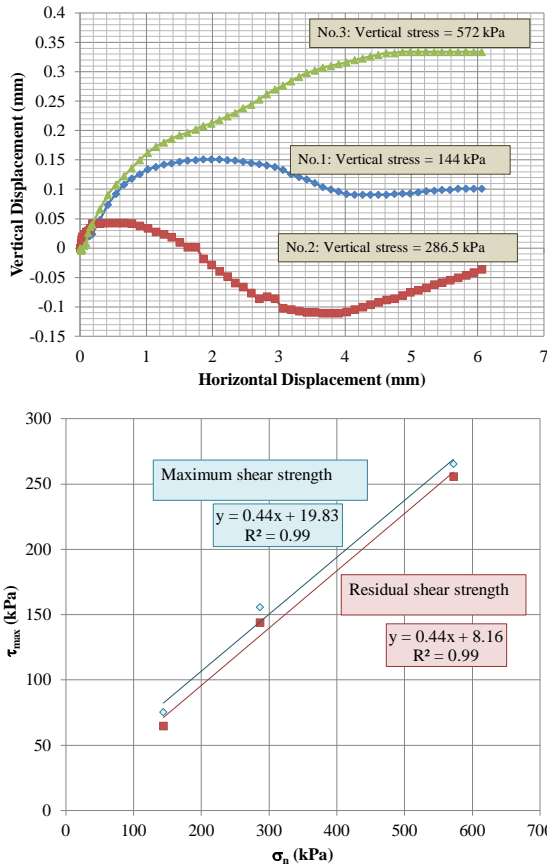


Fig. 7 Consolidated Undrained Shear Strength

The relationship between horizontal and shear stress showed the strain hardening as shown in Fig. 8. Besides the relationship between the vertical displacement and horizontal displacement presented a dilatation as same as UU sample as shown in Fig. 9.

Consolidated Drained Method

After specimen was setup, the specimen was soaked for 24 hr. and then the specimen had to be consolidated for 24 hr. prior to shear as same as CU method. However the shear rate of this method have to determine from consolidation test. Two series was studied in this method. The first series, three vertical stresses 100, 300 and 400 kPa was applied to specimen. Besides the second series, three vertical stresses 100 200 and 400 kPa was applied to specimen.

Consolidation Test

For the first series, the consolidation results found that that pre-consolidation pressure (P_c) was 56 kPa

and OCR was 1.74, which was less than 2. Therefore the failure time has to determine t_{50} or t_{90} as shown in Eq. 1 and 2, respectively. The shear rate was calculated from the maximum value of the failure time as shown in Eq. [3]. This series t_{50} and t_{90} , which was determined from the pressure 200 kPa, was 14 and 9 min, respectively. The failure time, which was calculated from t_{50} was higher than t_{90} . The shear rate of this series equaled to 0.08571 mm/min.

$$t_f = 50t_{50} \quad [1]$$

$$t_{50} = 11.6t_{90} \quad [2]$$

$$R_d = \frac{d_f}{t_f} \quad [3]$$

Where d_f equal to 0.2 inches according [2] because Khon Kaen loess was coarse grain soil. Moreover, t_f is a failure time, which equaled to 60 min.

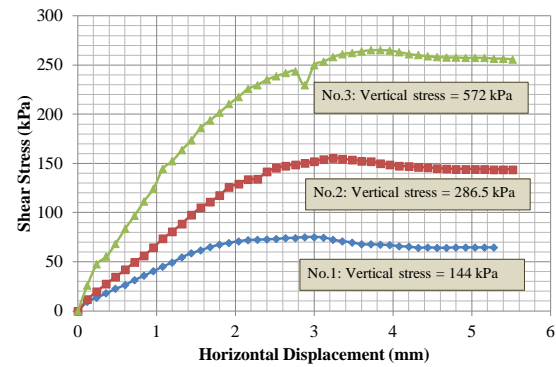


Fig. 8 The relationship between horizontal displacement and shear stress of CU sample

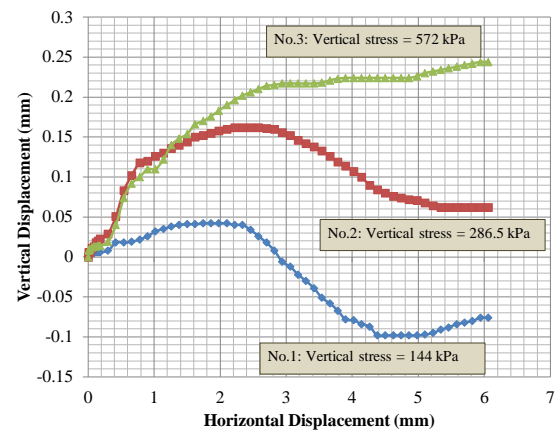


Fig. 9 The relationship between horizontal and vertical displacement of CU sample

For the second series, the consolidation results found that that pre-consolidation pressure (P_c) was 40 kPa and OCR was 1.24, which was also less than 2.

Then the failure time has to determine t_{50} or t_{90} . This series t_{50} and t_{90} , which was determined from the pressure 100, 200 and 400 kPa as shown in Table 2. The failure time which was calculated from t_{50} of 100 kPa vertical stress was highest. Therefore the shear rate of this series equaled to 0.018 mm/min.

Table 2 Failure time of CD series 2

Vertical Stress (kPa)	t_{50} (min)	t_f (min)	t_{90} (min)	t_f (min)
100	5.5	275	7.84	90.944
200	2.5	125	3.24	37.584
400	3.6	180	7.29	84.564

Test Result

The effective friction angle and cohesion of the first series was 30.5 degree and 18 kPa, respectively, as shown in Fig. 10. Moreover, the residual friction angle and cohesion of the first series was 31 degrees and 0 kPa, respectively.

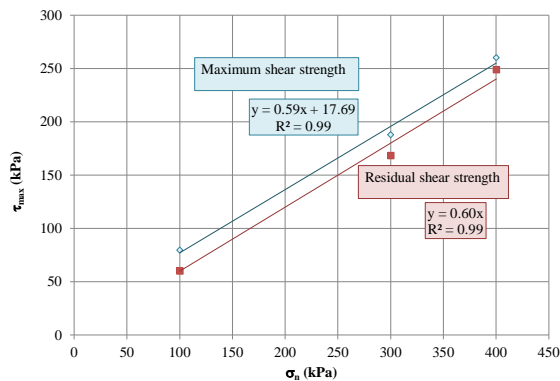


Fig. 10 Consolidated Drained Shear Strength of the First Series

The effective friction angle and cohesion of the first series was 33.5 degrees and 11 kPa, respectively, as shown in Fig. 10. Moreover, the residual friction angle and cohesion of the first series was 34 degree and 4 kPa, respectively.

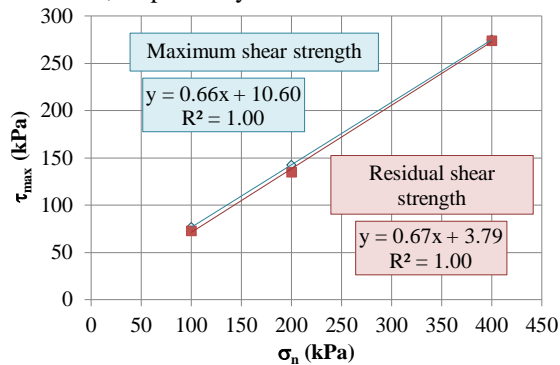


Fig. 11 Consolidated Drained Shear Strength of the Second Series

The effective friction angle of the first series and the second series was slightly different. The effective cohesion of the first series was higher than the second series. The residual friction angle of both series showed slightly increased 0.5 degrees. However, the residual cohesion was dropped dramatically.

The relationship between horizontal displacement and shear stress of the first series showed the strain softening as shown in Fig. 12. Meanwhile, the relationship between horizontal displacement and shear stress of the second series showed the strain hardening as shown in Fig. 13.

However, the relationship between vertical displacement and horizontal displacement of both series showed a dilation behavior except sample no.1 of the second series, which showed the compression.

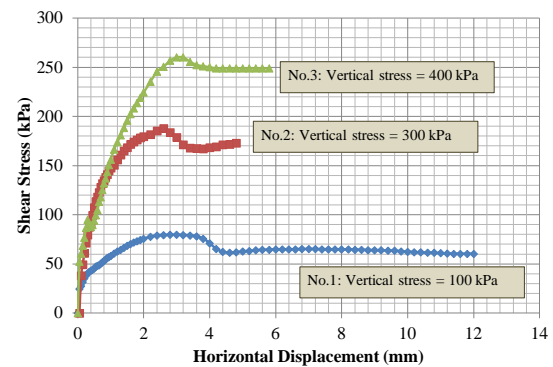


Fig. 12 The relationship between horizontal displacement and shear stress of CD sample (First Series)

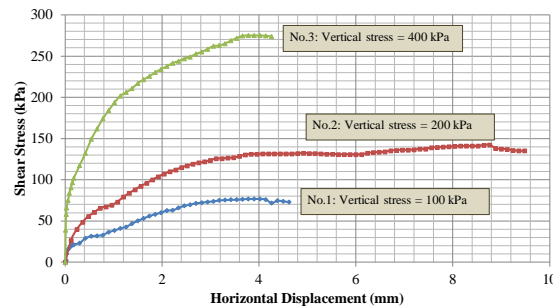


Fig. 13 The relationship between horizontal displacement and shear stress of CD sample (Second Series)

CONCLUSION

All test results were present in Table 3. The residual friction angle (ϕ_r) of all methods was slightly different from the maximum shear stress. However, the cohesion of the residual stress was dropped dramatically (more than 50%) from the maximum shear stress. Moreover, the shear rate has an effect on the stress-strain behavior rather than the shear

strength in term of friction angle. However, the shear rate was impacted on the cohesion of soil.

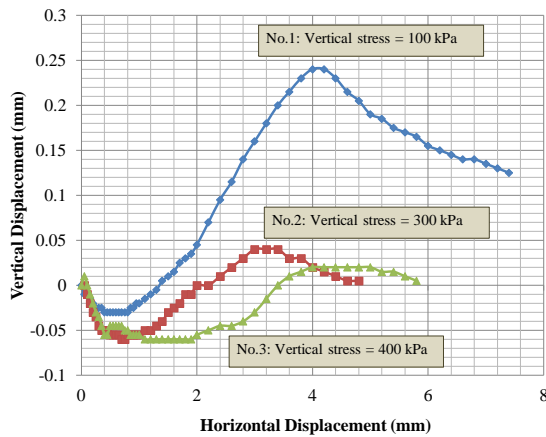


Fig. 14 The relationship between horizontal and vertical displacement of CD sample (First Series)

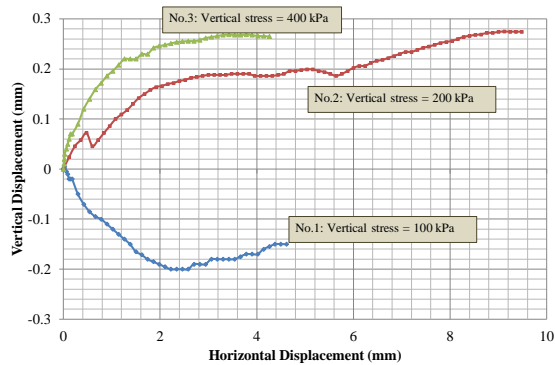


Fig. 14 The relationship between horizontal and vertical displacement of CD sample (First Series)

Table 3 All Test Results

Method	Ini. ρ_{dry} (t/m^3)	Shear Rate (mm/min)	ϕ ($^{\circ}$)	c (kPa)
UU	1.9	1.0		
Max. shear			36	0
Res. shear			34	0
CU	1.9	1.0		
Max. shear			20	20
Res. shear			23.5	8
CD	2	0.086		
Max. shear			30.5	18
Res. shear			31	0
CD	2	0.018		
Max. shear			33.5	11
Res. shear			34	4

ACKNOWLEDGEMENTS

Acknowledgement is given to Faculty of Engineering, Khon Kaen University for the support of this re-search.

REFERENCES

- [1] ASTM - American Society for Testing Material. 2000. Standard Practice for Classification of Soils for Engineering Purposes (Unified Soil Classification System) (ASTM D 2487-00). West Conshohocken. Pennsylvania.
- [2] ASTM - American Society for Testing Material. 2011. Standard Test Method For Direct Shear Test of Soils Under Consolidated Drained (ASTM D3080/D3080M). West Conshohocken. Pennsylvania.

This page has been kept blank intentionally

UTILISATION OF ALKALINE ACTIVATED INDUSTRIAL BY-PRODUCTS IN DEEP SOIL MIXING

Mohammadjavad Yaghoubi¹, Arul Arulrajah², Mahdi Miri Disfani³, Suksun Horpibulsuk⁴, Myint Win Bo⁵ and Melvyn Leong⁶

^{1,2}Faculty of Science, Engineering and Technology, Swinburne University of Technology, Australia;

³School of Engineering, The University of Melbourne, Australia; ⁴Faculty of Engineering, Suranaree University of Technology, Thailand; ⁵Bo & Associates Inc., Canada; ⁶Geofrontiers Group Pty Ltd., Australia

ABSTRACT

The use of deep soil mixing (DSM) technique in deep ground improvement projects has increased over the past decade due to being more cost-effective and easier to implement compared to other techniques such as piling, for structures subject to low to medium loads. Currently, Portland cement, lime and their combination are being used as the most common binders in DSM. However, due to the economic and concerning environmental disadvantages of using these binders, there is a need for new environmentally friendly cementing materials. This research attempts to find a way to use stockpiles of industrial by-products, such as fly ash (FA) and slag (S), as new green binders; consequently, reducing the carbon footprint in ground improvement projects. Different contents of FA and S, activated by liquid alkaline activator (L), were added to a soft marine soil to evaluate the changes in its behaviour as well as its microstructure. In addition, mixtures with cement (C), lime (Li) and their combination were prepared and tested for comparison. Binders were added at contents of 10, 20 and 30%, by dry soil mass, and samples were cured for 7 days. The results revealed that these new binders significantly increased the strength and stiffness of the soft soil, and they can be a suitable replacement for C and Li. The optimum mixture was found to be CIS+5% FA+15% S, within the range of binder, L and water content studied in this research. Moreover, recycling FA and S would substantially limit the expansion of landfill sites.

Keywords: Fly ash, Slag, Geopolymer, Alkaline activation, Deep soil mixing

INTRODUCTION

In the southern part of the Central Business District of Melbourne, Australia, which is located in the Yarra Delta, a highly compressible soft marine soil, known as Coode Island Silt (CIS), with high water contents exists. The vast presence of CIS, with poor engineering characteristics such as low bearing capacity (undrained shear strengths up to 80 kPa depending on the depth), in this area causes geotechnical constraints in construction projects. Proper deep ground improvement techniques need to be implemented to improve these soft soil deposits as they extend up to 30 m in depth [1]-[3]. In the recent years, new deep ground improvement technologies such as deep soil mixing (DSM) have drawn the attention of researchers and engineers. For structures bearing low to medium loads such as road embankments, DSM is faster and cheaper with less practical restrictions compared to traditional methods such as piling [2], [4].

In DSM method, an auger-mixing tool is drilled down to the intended depth while injecting a cementitious material, as binder, to mix with the native soil. The result would be circular columns of treated soil with improved engineering properties

compared to the native soil. Cohesive soils with high moisture contents, such as CIS, are most suited to be treated with the DSM method. Current major binders being used are cement (C) and/or lime (Li) with the contents of 100-500 kg/m³ (up to 30% by mass) of soil [5]-[7]. Due to economic and environmental concerns such as high energy and natural resource consumption and CO₂ emission during the production of these binders, attempts are being made to find alternative binders lowering the aforementioned disadvantages in recent years. There is a great potential in utilizing industrial by-products such as fly ash (FA) and slag (S) as they are available abundantly in landfills; consequently, eliminating the production concerns associated with traditional binders. Moreover, this can be a solution to the mentioned wastes disposal problems. These efforts in recent years have led to the introduction of green binders termed as geopolymers. Geopolymer is an inorganic product of blending precursors, materials rich in alumina and silica such as FA and S, with liquid alkaline activators (L) [8]. FA is a by-product of coal combustion in power plants, and S is a by-product of iron and steel manufacturing.

There has been a great deal of research conducted on the use of DSM method and geopolymers,

especially utilizing FA and S, in the construction industry [2], [6], [8]-[18]. However, since geopolymers are relatively new in civil engineering, there is limited knowledge on the use of these binders in ground improvement, especially in the DSM application. This study investigates utilizing FA and S based geopolymers, as an alternative sustainable material with low carbon footprint, to improve the properties of soft soils in DSM application. The main objective of this research is to study the reliability of using geopolymers, as green binders, compared to traditional binders in implementing the DSM technology in soft soils with high water contents through unconfined compressive strength (UCS) and microstructure analysis. Utilizing FA and S as industrial by-products, which are often discarded to landfills, to produce geopolymeric binders in a sustainable manner could lead to finding proper replacements for traditional binders, both environmentally and economically.

MATERIALS AND METHODS

Materials

The CIS was collected at depths of approximately 3 to 5 m in field, and samples were then put in plastic bags and transferred to the laboratory. Soil classification tests, such as Atterberg's limits tests, were conducted on the CIS to determine its physical properties. Figure 1 presents these characteristics including particle size distribution of CIS, through conducting sieve analysis and hydrometer tests. the

fine fraction of soil was 90% and the coarse fraction was 10%, with the maximum particle size (D_{max}) being 0.15 mm. the soil had a liquid limit (LL) of 50.4% and a plastic limit (PL) of 23.4%, resulting in a plasticity index (PI) of 27.0%. From the results of these tests, the CIS was classified as a silty clay with high plasticity. The FA, S, C and Li were collected from local suppliers in Melbourne.

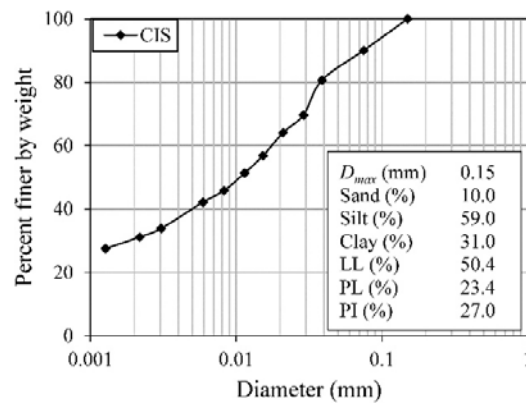


Fig. 1 Properties of CIS.

Figure 1 presents the SEM images of CIS, FA, S, C and Li. It is noted that the CIS particles are almost clustered with irregular shapes, the C and S particles are very similar having irregular shapes and sharp edges, the FA particles are in spherical shapes and have smooth surfaces, and the Li particles show a porous medium.

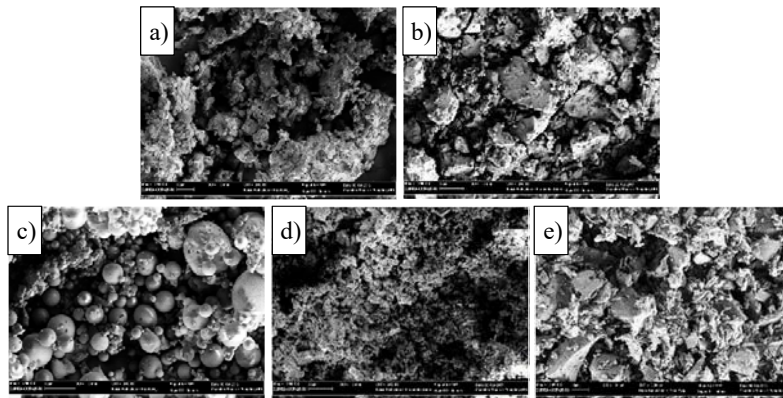


Fig. 1 SEM images of: a) CIS, b) C, c) FA, d) Li and e) S.

A combination of sodium hydroxide (NaOH), obtained in the form of beads, and sodium silicate (Na_2SiO_3), obtained as solution, was used as the L. Following safety and financial factors and previous recommendations, NaOH was prepared to 8 molarity and a Na_2SiO_3 :NaOH ratio of 70:30 was used [3], [14], [16], [18].

Sample Preparation and Testing

Following the range of binder content considered for DSM [6], [7], binder or precursor contents of 10, 20 and 30 %, based on dry CIS mass, were used in this study. The mixtures were prepared as presented in Table 1. For the mixtures where traditional binders,

C and Li, were used, C:Li ratios of 100:0, 50:50 and 0:100 were considered. For the geopolymeric binders, FA:S ratio was considered as 25:75 since S results in higher strengths, and in less time, compared to FA. Nevertheless, FA is needed to achieve a coexistence of Calcium Silicate Hydrate gel, due to the presence of Calcium in S, and Sodium Aluminosilicate Hydrate gel, geopolymer product, for better improvements of the soil properties [3], [11]-[13],

[17]. The ratio of activator to precursor was chosen as 1 based on the recommendations by previous researchers [3], [14]. The water content of the CIS was set at its LL, to replicate the field conditions, before mixing with other materials. Previously, the LL has been reported as the optimum water content for stabilization of high water content clays [3], [6], [10], [14].

Table 1 Mix designs

Mixture	10%				20%				30%			
	C	Li	FA	S	C	Li	FA	S	C	Li	FA	S
CIS+C	10	-	-	-	20	-	-	-	30	-	-	-
CIS+C+Li	5	5	-	-	10	10	-	-	15	15	-	-
CIS+ Li	-	10	-	-	-	20	-	-	-	30	-	-
CIS+FA+S	-	-	2.5	7.5	-	-	5	15	-	-	7.5	22.5

Note: The values are in percent (%) by mass of dry CIS.

For preparation of geopolymer-stabilized samples, first, the CIS and precursors were mixed in a mechanical mixer for 2.5 minutes, before L was added and mixed for another 2.5 minutes, resulting in a total mixing time of 5 minutes. For the feasibility of comparison, traditional binder-treated mixtures were prepared by adding the binder to CIS and mixed for 5 minutes. After mixing the materials, the mixtures were placed into PVC split molds to prepare cylindrical specimens with 38 mm diameter and 76 mm height. Three samples were prepared for each mix to assure the test results were consistent.

Mixtures were put into the molds in two layers, each layer tapped 25 times on the table to remove the entrapped air. The unit weight of the specimens of all mixtures was checked for consistency. The samples were then wrapped with plastic films, put in a humid room with constant temperature (23 ± 1 °C), dismantled the next day, wrapped again, and put in the humid room again to be cured. The overall curing time was 7 days.

After the curing period, UCS tests were conducted on samples with a 1-mm/min (1.32%/min) rate of displacement and stopped manually after the specimens reached a considerable post-peak strength loss. After conducting the UCS tests, small samples were taken from the failed specimens for further analysis by scanning electron microscopy (SEM) imaging tests. The taken samples needed to be dry before being gold-coated and put in the SEM device. Thus, samples were put in the oven at 50 °C overnight before conducting SEM tests.

RESULTS AND DISCUSSION

UCS Tests

Figure 2 presents the results of UCS tests on different mixtures of CIS stabilized with various combinations of binders, C and/or Li, at three contents of 10, 20 and 30%. Puppala et al. [19] suggested a minimum 7-day UCS value of 100 psi (689.5 kPa) for DSM ground improvement using C, which is presented in Fig. 2. As noticed, in the mixtures stabilized with traditional binders, CIS-C mixtures show the highest strength improvement, and as Li content increases, there is a significant decrease in the UCS, as previously observed [20]. Furthermore, while the strength development is almost linear with binder content increment in CIS-C-Li and CIS-Li mixtures, the rate of increase reduces after addition of 20% binder in CIS-C mixtures. This demonstrates that the optimum C content for ground improvement in CIS, with high water content, is 20%, as reported earlier [2], [6], [10], [15].

The UCS values of CIS stabilized with precursors, FA and S, are illustrated in Fig. 3. It is noted that there is a significant increase in the UCS of geopolymer-stabilized mixtures when the precursor content is increased from 10% to 20%, followed by a lower rate of strength enhancement when 30% precursor is added. Previously an increase in strength with precursor content increment has been reported; however, 20-25%, by dry mass of soil, has been reported as the optimum [8], [15]. It can be concluded that, within the range of precursor contents studied here, 20% is the optimum content to use.

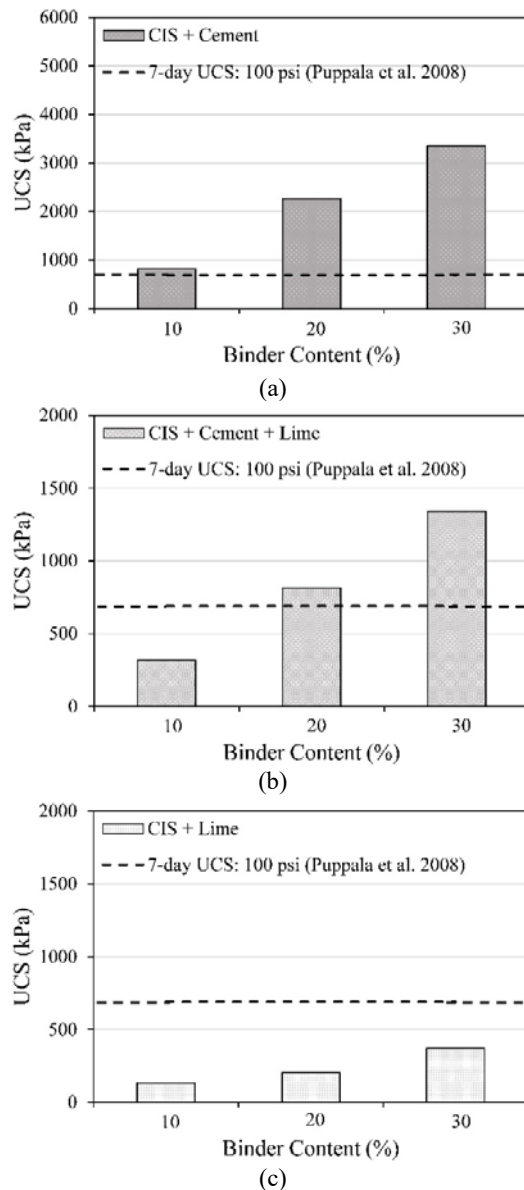


Fig. 2 UCS values for mixtures stabilized with: a) C, b) C+Li and c) Li.

Overall, comparing traditional and geopolymeric binders reveals that, except for 10% binder content, using geopolymeric binders results in considerably higher strengths. Moreover, although CIS+10% C and CIS+10% C+10% Li meet the minimum UCS requirement, it should be noted these are the values achieved in the lab, while the values obtained in the field can be 2 to 3 times lower [9]. Therefore, CIS+20% C and CIS+5% FA+15% S seem to be the optimum mixtures in terms of strength. Considering the economic and environmental factors, mentioned before, using FA-S-based geopolymeric binder in DSM ground improvement of CIS is a beneficial replacement for C and/or Li binders.

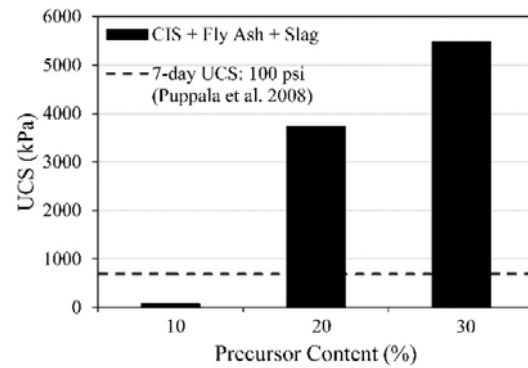


Fig. 3 UCS values for mixtures stabilized with FA and S.

SEM Tests

To analyze the microstructure of the mixtures, SEM tests were conducted on the samples after the UCS tests. The SEM images of CIS stabilized with C and/or Li and geopolymeric binder, with 20% binder or precursor content, are presented in Fig. 3. Figure 3 (a) shows the SEM image of CIS+20% C. It is noticed that the C particles are almost dissolved in the mixture, resulting in a dense medium with strong bonds. As C is gradually being replaced with Li, voids start to appear in the structure, Figs. 3 (b) and (c), to the extent that in Fig. 3 (c) where the binder is merely Li, a completely porous matrix is observed. These images further confirm the considerably higher UCS values of CIS+C mixtures compared to those of CIS+C+Li and CIS+Li mixtures.

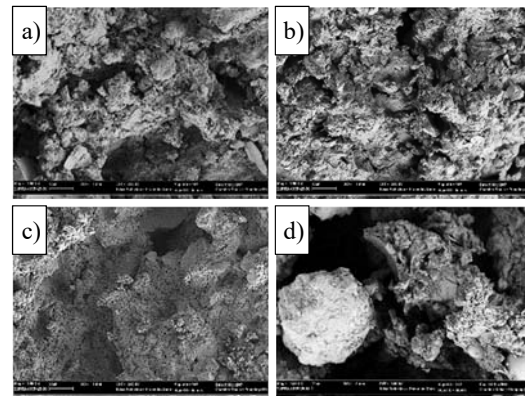


Fig. 3 SEM images of: a) CIS+20% C, b) CIS+10% C+10% Li, c) CIS+20% Li and d) CIS+5% FA+15% S.

In Fig. 3 (d), reacted FA and S particles are clearly evident that leads to a compact morphology with strong geopolymer gel bonds. This strong structure proves proper activation of FA and S with the used L

and water content; and accordingly, the high strength achieved by utilizing geopolymeric binder.

CONCLUSION

A series of UCS and SEM tests were conducted on a clayey soil, CIS, treated with different contents of geopolymeric binders, obtained by activation of industrial by-products such as FA and S, and traditional binders, C and/or Li. The aim was to investigate the performance of utilizing these by-products in DSM application and comparing their reliability with that of the traditional binders.

UCS tests results revealed that increasing the binder content to 30% increased the strength in all mixtures. However, the rate of increase was lower when the binder content was increased from 20% to 30%, especially when using the geopolymeric binder. In terms of strength development, using geopolymeric binder resulted in the highest improvement, followed by using C, C+Li and Li as binders. This was evident from the microstructure of the mixtures using SEM images.

Overall, CIS+5% FA+15% S was found to be the optimum mixture, within the range of binder, L and water content studied in this research. Utilizing stockpiled FA and S in landfills in ground improvement technologies will not only reduce the financial and environmental consequences of using traditional binders, but also will be a solution to the problems regarding the disposal of these wastes.

ACKNOWLEDGEMENTS

This research was supported under Australian Research Council's Linkage Projects funding scheme (project number LP150100043). The fourth author is grateful to the financial support from the Thailand Research Fund under the TRF Senior Research Scholar program Grant No. RTA5980005 and Suranaree University of Technology.

REFERENCES

- [1] Ervin E., "Engineering properties of Quaternary age sediments of the Yarra Delta", *Engineering Geology of Melbourne*, 1992, pp. 245-260.
- [2] Bouazza A., Kwan PS, Chapman G, "Strength properties of cement treated Coode Island Silt by the soil mixing method", *Geotechnical Engineering for Transportation Projects ASCE*, 2004, pp. 1421-1428.
- [3] Phetchuay C., Horpibulsuk S., Arulrajah A., Suksiripattanapong C., Udomchai A, "Strength development in soft marine clay stabilized by fly ash and calcium carbide residue based geopolymer", *Applied Clay Science*, Vol 127-128, 2016, pp. 134-142.
- [4] Porbaha A, "State of the art in deep mixing technology: part I. Basic concepts and overview", *Proceedings of the Institution of Civil Engineers - Ground Improvement*, Vol 2(2), 1998, pp. 81-92.
- [5] Arulrajah A, Abdullah A, Bo MW, Bouazza A, "Ground improvement techniques for railway embankments", *Proceedings of the Institution of Civil Engineers - Ground Improvement*, Vol 162(1), 2009, pp. 3-14.
- [6] Horpibulsuk S, Rachan R, Suddeepong A, "Assessment of strength development in blended cement admixed Bangkok clay", *Construction and building materials*, Vol 25(4), 2011, pp. 1521-1531.
- [7] Bruce MEC, Berg RR, Collin JG, Filz GM, Terashi M, Yang DS, *Federal Highway Administration design manual: deep mixing for embankment and foundation support*, FHWA-HRT-13-046, Federal Highway Administration, Washington, DC, 2013.
- [8] Pourakbar S, Huat BB, Asadi A, Fasihnikoutalab MH, "Model Study of Alkali-Activated Waste Binder for Soil Stabilization", *International Journal of Geosynthetics and Ground Engineering*, Vol 2(4), 2016, pp. 35.
- [9] Horpibulsuk S, Miura N, Koga H, & Nagaraj T, "Analysis of strength development in deep mixing: a field study", *Proceedings of the Institution of Civil Engineers-Ground Improvement*, Vol 8(2), 2004, pp. 59-68.
- [10] Lorenzo GA, Bergado DT, "Fundamental parameters of cement-admixed clay-new approach", *Journal of Geotechnical and Geoenvironmental Engineering*, Vol 130(10), 2004, pp. 1042-1050.
- [11] Yip CK, Lukey G, Van Deventer J, "The coexistence of geopolymeric gel and calcium silicate hydrate at the early stage of alkaline activation", *Cement and Concrete Research*, Vol 35(9), 2005, pp. 1688-1697.
- [12] Kumar S, Kumar R, Mehrotra S, "Influence of granulated blast furnace slag on the reaction, structure and properties of fly ash based geopolymer", *Journal of Materials Science*, Vol 45(3), 2010, pp. 607-615.
- [13] Yang T, Yao X, Zhang Z, Wang, "Mechanical property and structure of alkali-activated fly ash and slag blends", *Journal of Sustainable Cement-Based Materials*, Vol 1(4), 2012, pp. 167-178.
- [14] Cristelo N, Glendinning S, Pinto AT, "Deep soft soil improvement by alkaline activation", *Proceedings of the Institution of Civil Engineers - Ground Improvement*, Vol 164(2), 2011, pp. 73-82.
- [15] Bushra I, Robinson RG, "Effect of Fly Ash on Cement Admixture for a Low Plasticity Marine Soil", *Advances in Civil Engineering Materials*, Vol 2(1), 2013, pp. 608-621.

- [16] Nematollahi B, Sanjayan J, “Effect of different superplasticizers and activator combinations on workability and strength of fly ash based geopolymer”, *Materials & Design*, Vol 57, 2014, pp. 667-672.
- [17] Phoo-ngernkham T, Maegawa A, Mishima N, Hatanaka S, Chindaprasirt P, “Effects of sodium hydroxide and sodium silicate solutions on compressive and shear bond strengths of FA–GBFS geopolymer”, *Construction and Building Materials*, Vol 91, 2015, pp. 1-8.
- [18] Rios S, Ramos C, Viana da Fonseca A, Cruz N, Rodrigues C, “Mechanical and durability properties of a soil stabilised with an alkali-activated cement”, *European Journal of Environmental and Civil Engineering*, 2017, pp. 1-23.
- [19] Puppala A, Madhyannapu R, Nazarian S, Special specification for deep soil mixing, 0-5179, 2008, The University of Texas at Arlington, Arlington, TX.
- [20] Okyay, U, Dias, D, “Use of lime and cement treated soils as pile supported load transfer platform”, *Engineering Geology*, Vol 114(1), 2010, pp. 34-44.

DEEP FOUNDATION REFERENCE FOR METRO MANILA, PHILIPPINES

Jonathan R. Dungca¹, Noel Lester C. Gozum², Jon Arnel S. Telan³, Victor Carlo F. Torres⁴ and Timothy Scott Y. Uytengsu⁵

¹²³⁴⁵ Civil Engineering Department, De La Salle University, Philippines

ABSTRACT

The study focuses on the analysis of the pile capacity and pile length for various cities of Metro Manila. Standard Penetration Test (SPT) N-values from soil reports were used to compute for the geotechnical parameters such as the undrained shear strength and the angle of internal friction which were directly applied in the computation of the allowable pile capacity. The estimation of the pile length, on the other hand, was done by means of determining the depth of the refusal or rock layer. The proposed minimum pile length and the allowable pile capacity values for each city are plotted to establish a contour map. By means of the collected borehole data, the allowable pile capacity was computed, which was shown in the reference as a series of contour maps. The contour maps were provided to show an overview of the soil's pile capacity at various locations in Metro Manila, Philippines. The contour maps presented vary by means of the design of pile, the size of the pile and the proposed pile length for a specific city or municipality and for the entire Metro Manila. A Geographic Information System (GIS) database was made so as to have storage for the collected borehole data and their locations. The database can be updated for the availability of new data.

Keywords: pile capacity, pile length, deep foundation, foundation reference

INTRODUCTION

Metro Manila's buildings are comprised of at least 70% high-rise buildings and skyscrapers, excluding for the cities of Caloocan, Navotas, Las Piñas, Pateros, and Malabon due to the absence of data [1]. High-rise buildings and skyscrapers, compared to low-rise buildings and residential dwellings, would usually require pile foundation. With that, soil exploration or excavation would be needed for every construction.

With such a large amount already allocated to the construction of the structure itself, a great sum of money must again be allotted to the necessary soil explorations, which are not just costly but time consuming. Reducing the total construction expense would greatly benefit the structural engineer and the owner.

There have been some similar studies related to this research [2]-[8], however, there is not one compiled published or commercially available source of data for the entire Metro Manila, just scattered and separate ones. Due to this, if a structural or geotechnical engineer desires a second reference for the soil data of a specific area in Metro Manila, they would need to acquire them from different sources. This, in turn, would take tremendous amount of time and effort. Thus, this paper will try to help structural engineers by giving them a reference for the pile capacity and pile length needed for the construction of a structure in need of pile foundation in any specific place of Metro Manila. The main objectives

of this paper are to estimate the necessary pile lengths for the different areas of Metro Manila and to determine the proposed pile capacity in the entire Metro Manila.

METRO MANILA

Metro Manila, Philippines is bounded by the provinces of Bulacan in the northern part, Rizal in the eastern part, Cavite and Laguna in the Southern part. Manila Bay is located on the western part of Metro Manila, while Laguna de Bay is on the eastern part. Metro Manila has a total land area of 615.39 square kilometers. Basing on geographical coordinate system, the entire Metro Manila lies between 120° 54' and 121° 9' longitudinally and 14° 20' to 14° 47' along the latitude direction.

At some geologic past, the Metro Manila was submerged underwater, which extends up to the mountains in the Eastern part. Intermittent volcanic activities occurred which resulted to the deposition of volcanic materials. During intervening period of inactivity, a layer of sediments are placed on top of the previously laid out volcanic materials which resulted to the common characteristic of the geologic deposit which is alternating beds of tuffaceous materials and transported sediments.

Majority of the sediments present in the geologic deposit of Metro Manila are due to the bodies of water surrounding it which include Manila Bay, Pasig River, and Laguna de Bay. The sediments that were

transported consist of sands, pebbly gravels, silts and clays with various traces of fossil remains or marine shells and several organic particles. The presence of organic particles and fossil remains gives an idea of a swampy environment which prevails during a time which has a shallow water level.

The Guadalupe Tuff formation, the underlying rock formation of Metro Manila, was generally well-consolidated and well-cemented. The tuff formation extends from Quezon City and Novaliches up to the province of Cavite in the south. Majority of its composition is lithified volcanic ash, lapilli and sands. When it comes to the thickness of the tuff formation, it remains to be uncertain. Several areas where the tuff formation is present are overlain by layers of sediments which generally thicken as it approaches the west side of Metro Manila, which is Manila Bay.

Overall, the composition of the geologic deposit can be attributed to its elevation. For highly elevated locations, it is composed of dense sands and tuffaceous clays. For low – lying areas of Metro Manila, it is generally composed of loose sands and soft clays [9].

METHODOLOGY

The aim of this study is to create a deep foundation reference for the district of Metro Manila. Borehole logs with a ratio of one borehole log per square kilometer were collected and compiled accordingly as shown in Figure 1. The borehole logs were accumulated from the different private companies and government institutions in Metro Manila. A total of 677 borehole locations were collected and mapped. For the attained data or soil reports, it already comprised almost 86% of the total target. However, this number of data does not yet include the outskirts of Metro Manila which are from Rizal, Bulacan, Cavite and Laguna. The outskirt data were used to provide accurate mapping even at the near boundaries of Metro Manila. The data are then analyzed and calculated for the depth of rock formation and geotechnical parameters.

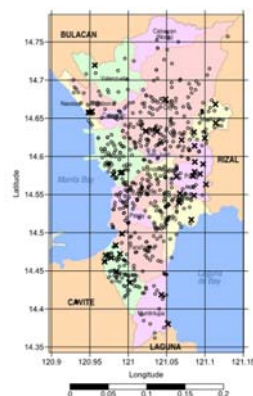


Fig. 1 Map of Manila with borehole locations

The estimation of the pile length and the computation of the allowable pile capacity were performed through an excel program. The soil properties, SPT N-values and RQD were inputted in the program to get some vital geotechnical parameters like the undrained shear strength [10] and the angle of internal friction [11]-[14]. The minimum pile length was estimated depending on the soil condition whether until the refusal layer (SPT-N 50), rock layer (RQD) or even at the last layer of the borehole log in the absence of the refusal or rock layer. The SPT N values that are available in the borehole logs that were collected are the main components used for the computation of the pile capacity. The design of the piles was limited to a range of sizes and shapes. As for the proposed length of the piles, the depth of the rock formation or refusal layer was used as with a one meter embedment on the hard layer or the last soil layer.

The allowable pile capacity, on the other hand, was computed based on the skin friction and end bearing resistance which are both dependent on the geotechnical parameters. The results were summarized in a form of contour maps for easy visualization and interpretation per city. Likewise, to provide a good analysis of the values of the allowable pile capacity, skin-to-tip ratio were also considered and plotted in the maps. This is to provide a support which between the skin friction and the end bearing resistance contributed greater value in the allowable pile capacity, which in turn, describes what kind of soil does a city, in particular, have and how long the pile length is.

The pile capacity was computed by means of the theory of the alpha and beta method. The alpha method is used to estimate the pile capacity especially for clayey soil layers. It uses a factor denoted as α to approximate the value of the skin friction and a coefficient N_c to compute for the end-bearing capacity. The skin friction for any types of piles using the alpha method includes the coefficient, the undrained shear strength and the lateral surface area of the pile [15]:

$$f_s = \alpha_u S_u; \quad (1)$$

$$Q_f = \sum (f_s) \times (\text{perimeter}) \times (\text{length}); \quad (2)$$

where:

f_s = skin friction stress

α_u = coefficient for skin friction

S_u = undrained shear strength .

Beta Method is similar to alpha method in such a way that it uses coefficients but this time, it is denoted as β for skin friction and N_q for end bearing resistance. Unlike alpha method, beta method considers both sandy and clayey soils. The general equations using the beta method is quite similar to alpha method but instead of undrained shear strength, the effective stress is used.

The skin friction for any types of piles using the beta method includes the coefficient, the effective stress and the lateral surface area of the pile [16].

$$q_f = \sum (\beta \sigma_z) \times (\text{perimeter}) \times (\text{length}); \quad (3)$$

where:

β = coefficient for skin friction;

σ'_z = effective stress;

q_f = skin friction .

Some of the borehole data have rock layers designated by RQD or Rock Quality Designation. The computation using the alpha and beta methods are not applicable to rocks anymore. The pile capacity is now based on the end bearing resistance of the rock which is far greater than the soil. Moreover, the skin friction is neglected in the computation of the pile capacity of rock. O' Neill and Reese [7] approximated the ultimate end bearing resistance through the formula:

$$q'_t = 4830 (q_u)^{0.51}; \quad (4)$$

where:

q'_t = end bearing resistance;

q_u = unconfined compressive strength of rock

ϕ' = drained angle of friction

For a better visualization of the acquired data and computed values, the allowable pile capacity values are then mapped out by means of contour maps, implementing the kriging method. Verification for both the data accomplished and the produced contour maps were done as well. The computed values of allowable pile capacity were stored in the GIS database as well.

DEEP FOUNDATION REFERENCE

Proposed Pile Length

The proposed pile length map for the entire Metro Manila can be seen in Figure 2. The map reflects the type of soil present where majority of the area that is underlain by the Guadalupe Tuff Formation has a pile length that ranges from 5 to 10 meters in length. There are regions, which can be seen as areas shaded with white, have pile lengths of 5 meters for the entire region. These regions are recommended for the use of shallow foundation due to the shallowness of the rock layer or refusal layer. For locations composed of alluvial deposits, the range of pile lengths varies significantly depending on the location. For the western part, the pile length ranges from 10 to 15 meters. Several parts of the region show lengths ranging from 20 to 25 meters. The effect of the Manila Bay, in terms of pile length, is manifested through these results. For the eastern part of Metro Manila, the proposed pile length ranges from 10 to 25 meters, which shows the effect of the location with

respect to Laguna de Bay, where majority of the data collected near the said body of water possess thick layers of alluvial deposits, namely sand, silts and clay. Generally, the proposed pile length for Metro Manila ranges from 5 to 15 meters.

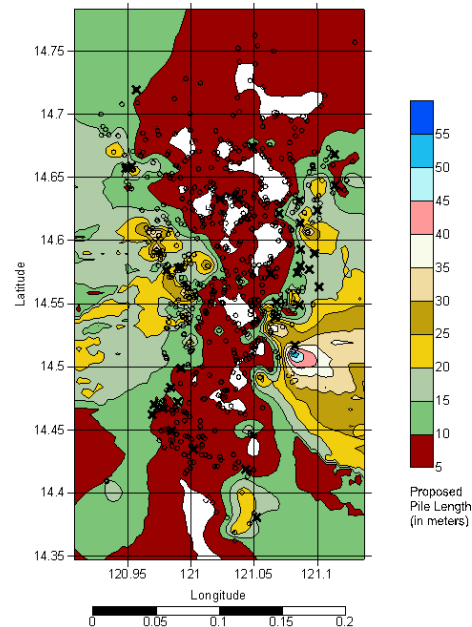


Fig. 2 Proposed Pile Length

Proposed Skin-to-Tip Ratio

The skin-to-tip Ratio is the ratio between the skin friction and the tip resistance or the end bearing resistance. For the skin-to-tip ratio map for Metro Manila, the values can also be reflected by the type of soil present along those areas, as seen in Figures 3 and 4. The areas underlain by the Guadalupe Tuff Formation produces low skin-to-tip ratio whereas a high ratio is observed in areas where alluvial deposits are prevalent. In general, the skin-to-tip ratio has presented that for a certain type of pile, a particular resisting force is dominant over the other, that is, skin friction is greater than the tip resistance, also known as end-bearing resistance, or vice versa. For driven piles, skin friction usually contributes greater resistance than that of the end bearing resistance due to the larger adhesion factors, α and β . Practically, the process of driving the piles really induces greater friction from the soil but the consequence is to use smaller cross-sections only so that the pressure in driving the piles is greater, thus, producing small end-bearing resistance. For bored piles, end bearing resistance dominates the skin friction because the cross-sectional area of the type of pile is quite large. Also, some soil layers are neglected for the computation of the skin friction due to the effect of drilling that make these particular layers disturbed.

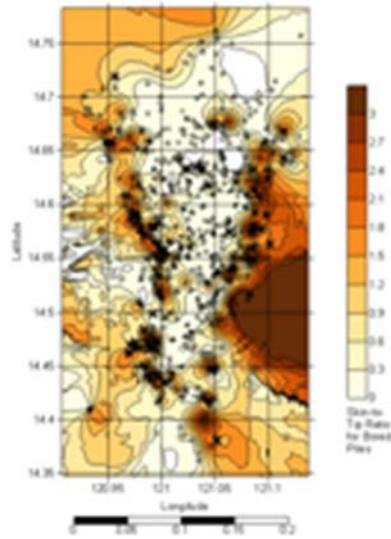


Fig. 3 Proposed Skin-to-tip Ratio (Bored Pile)

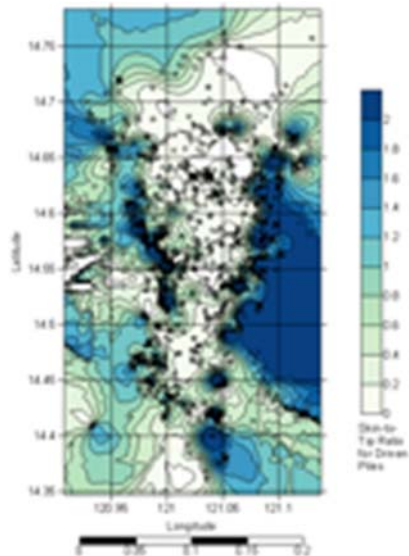


Fig. 4 Proposed Skin-to-tip Ratio (Driven Pile)

Proposed Pile Capacity

The allowable pile capacity maps presented under Figures 5, 6 and 7 show consistency in terms of their distribution of values. A separated sample pile capacity map where the division of the type of soil can be seen under Figure 8 (Guadalupe Tuff Formation) and Figure 9 (Alluvial Deposits). Higher values of allowable pile capacity are found in areas where Guadalupe Tuff Formation is located. On the other hand, areas with alluvial deposits have low allowable pile capacities. Generally, it shows that the pile capacity depends on the type and quality of soil present on a specific area.

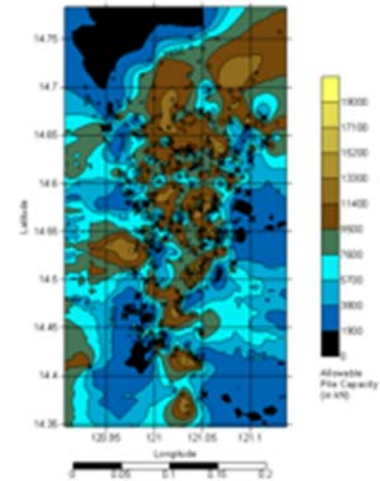


Fig. 5 Pile Capacity (Bored Piles Size 1.50 meter)

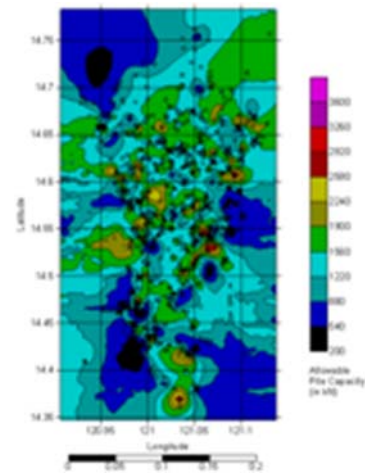


Fig. 6 Pile Capacity (Square Driven Piles Size 0.50 meter)

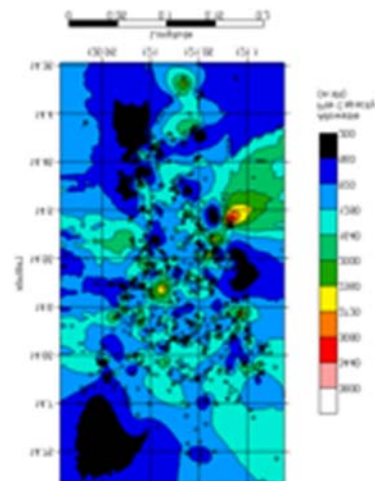


Fig. 7 Pile Capacity (Octagonal Driven Piles Size 0.50 meter)



Fig. 8 Pile Capacity for Bored Pile (Guadalupe Tuff Formation Area)

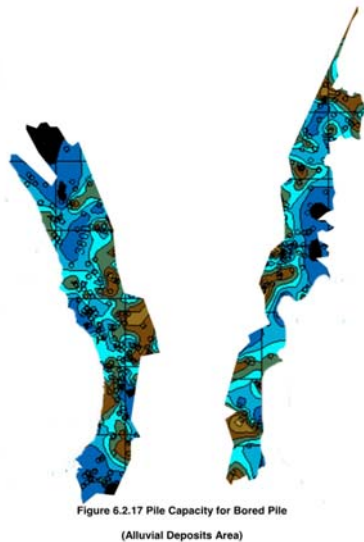


Fig. 9 Pile Capacity for Bored Pile (Alluvial Deposits Area)

CONCLUSION

In this paper, the pile length and allowable pile capacity are determined through borehole logs. For the cities of Las Piñas, Malabon, Navotas, Pateros and Pasig, they have relatively small allowable pile capacities as compared to the other cities for both driven and bored piles. Pile lengths are shorter because they have reach the refusal layers at somehow a shallow depth thus, lesser skin friction is induced. Moreover, based on the skin-to-tip ratio, skin friction

still plays a great contributor over the end-bearing resistance although in totality, the allowable pile capacity is still small as compared to other cities.

The cities of Makati, Mandaluyong, Paranaque, Makati and Quezon are quite remarkable not only due to the high allowable pile capacities that they produce but to the short pile lengths as well. Having a short pile length, in this case, is quite advantageous because it is really cost-effective. Also, it does not affect too much the allowable pile capacity because it majorly relies on the end-bearing resistance. The Guadalupe Tuff formation is actually the factor which makes the end-bearing resistance greater. These cities have shallow rock layers and usually, shallow foundation is recommended for most of the areas of the aforementioned cities. Skin-to-tip ratio has proven that the end-bearing resistance really governs in these cities.

There are cities in Metro Manila which are not recommendable for shallow foundation just because the top layers are weak especially in bearing capacity. These include Manila, Marikina and Pasay. However, when pile foundation is used for these cities, a large allowable pile capacity is computed. This is because a longer pile length is recommended to induce large skin friction from several soil layers and to reach the refusal or rock layer at great depth. In these particular areas, both the skin friction and end bearing resistance greatly contribute to the allowable pile capacity. This means that high loadings from the superstructure can be resisted by piles considering also its length. The trade-off, however, is that it is not cost effective anymore due to the long piles that require great amount of materials.

REFERENCES

- [1] Emporis GmbH. (n.d.). Emporis, "In Building Directory", Retrieved June 10, 2017, from <http://www.emporis.com/city/manila-philippines>.
- [2] Dungca J. R., "Liquefaction Potential Map of Manila", Masteral Thesis, De La Salle University, Philippines, 1997.
- [3] Dungca J. R. and Chua R. A. D., "Development of a Probabilistic Liquefaction Potential Map for Metro Manila", International Journal of GEOMATE, Vol. 11, Issue 25, Sep. 2016, pp. 2461-2467.
- [4] Dungca J. R., Concepcion I., Limyuen M.C.M., See T. O. and Vicencio M. R., "Soil Bearing Capacity Reference for Metro Manila", International Journal of GEOMATE, Vol. 12, Issue 32, Apr 2016, pp. 5-11.
- [5] Dungca J. R. and Macaraeg C. J., "Development of a Reference for Seismic Amplification: The Case of Metro Manila", 19th Congress of International Association for Bridge and

- Structural Engineering, Stockholm, Sweden Sep. 2016.
- [6] Saldivar – Sali, A., “An Earthquake Risk Analysis of Metro Manila from a Foundation Engineering Perspective”, *Journal of the Geological Society of the Philippines*, 50, 1992, pp. 287 – 289.
 - [7] Guevarra E., Santos, J., Sy, Hazel (1999). *Data Aid for the Design of Foundation in Las Pinas City. Manila*”, Thesis, De La Salle University, Philippines, 1999.
 - [8] Mustafa, K. “Evaluation of Soil Bearing Capacities in San Mateo, Rizal,” *Philippines*, 1995.
 - [9] Hosono, T., Siringan, F., Yamanaka, T., Umezawa, Y., Onodera, S., Nakano, T., & Taniguchi, M. “Application of multi-isotope ratios to study the source and quality of urban groundwater in Metro Manila, Philippines”. *Applied Geochemistry*, 25(6), 2010, pp.900–909.
 - [10] Mesri, G. 1989 “A re-evaluation of $s_u(\text{mob}) = 0.22\sigma'$ using laboratory shear tests”, *Canadian Geotechnical Journal*, 26(1): 1989, pp.162–164.
 - [11] Schmertmann, J. H., “Measurement of In-Situ Shear Strength” *Journal of the Proceedings of the American Society of Civil Engineers*, June 1-4, 1975, Vol. II, 1975.
 - [12] Kulhawy, F. H., And Mayne, P. W., “Relative Density, SPT, and CPT Interrelationships”, *Calibration Chamber Testing (Isocct-1)*, Elsevier, New York, 1991, pp. 197-211.
 - [13] Wolff, T. F, “Geotechnical Judgment in Foundation Design. *Foundation Engineering: Current Principles And Practice*”, Vol. 2, American Society Of Civil Engineers, 1989, pp 903 – 917.
 - [14] Hatanaka, M. and Uchida, A. “Empirical correlation between penetration resistance and internal friction angle of sandy soils”, *J. of Soils and Foundations*, 36(4), pp. 1-9 (1996).
 - [15] Budhu, M. “*Soil Mechanics and Foundations*”, 2nd Edition. United States of America: John Wiley & Sons, Inc., 2007.
 - [16] O'Neill, M.W. and Reese, L.C., “*Drilled Shafts: Construction Procedures and Design Methods*,” Publication No. FHWA-AIF-99-025, U.S. Dept. of Transportation, Federal Highway Admin., Washington, D.C., 1999, pp.535.

AN ATTEMPT TO DETERMINE A SUITABLE STABILIZER FOR EXPANSIVE SOILS OF VOLCANIC ORIGIN

Rajeshwar Goodary¹, Avirut Chinkulkijniwat², Vatanavongs Ratanavaraha², Roodheer Beeharry¹, Anoop Aujayeb¹.

¹Université des Mascareignes

Avenue de la Concorde, Rose Hill, Mauritius

²Suranaree University of Technology

Nakhon Ratchasima, Thailand

ABSTRACT

In this study, a family of widespread expansive soil, namely Dark Magnesium Clay of volcanic origin, occurring in Mauritius Island, is stabilized with various stabilizers and their combinations. The strength properties for these mixtures are investigated. The test specimens are prepared at maximum dry density (MDD) value, obtained from the standard Proctor compaction test, in compliance with BS 1377. Lime, Ordinary Portland Cement (OPC), Fly Ash and Coarse Rock Sand and their combinations, that is, lime-cement, coarse rock sand-cement, fly ash-cement, lime-fly ash, lime-coarse sand and fly ash-coarse sand, used as partial replacement of the soil, are used as main stabilizers and their effects on the soil mass strength are investigated. Trial mixes with 0%, 2.5%, 5%, 7.5%, 10%, 12.5% and 15% soil replacement are prepared and tested for Unconfined Compressive Strengths. Specimens 40 mm x 40 mm x 40 mm are prepared in a mold with varying content of stabilizer. The samples are demolded and allowed to cure in a water-saturated and airtight container for 7 days and eventually in ambient laboratory conditions. Hardened samples are tested for their dry Unconfined Compressive Strength at the age of 21 days. Results show that an addition of 2.5% of the combined mix of coarse sand-fly ash and 7.5% fly ash yield acceptable Unconfined Compressive Strengths of 5.2 and 5.5 MPa respectively with a significant decrease in linear shrinkage value

Keywords: Dark magnesium clay, stabilizer, maximum dry density, curing, compressive strength, linear shrinkage

1. INTRODUCTION

1.1 General

An expansive or swelling soil is defined as one which changes volume with change in moisture content of the soil. These soils contain clay minerals of the montmorillonite family as main clay component and they undergo excessive volume change with change in their moisture content, that is from dry to wet state. Deposits of expansive soils occur mainly in dry to moderately dry regions of the globe and are hazardous to engineering structures because of their ability to swell during rainy seasons and shrink as moisture decreases [1]-[5]. Their scattering depends mainly on the geology and genetic of the original material, climate, hydrogeology and other prevailing conditions. Literature review on expansive soils reveal that problems arising are somehow common for all countries and are quite alarming [2]-[4].

Due to the extensive structural damage caused to buildings and structures by expansive soils, it is important that solution to problems related to such soils be investigated on a common platform and regrouping engineers worldwide because if not adequately treated these materials may become a severe potential hazard [6] - [8].

There are several indications associated with the soil behavior that help identifying expansive soils. It may start with a simple visual examination on site. Visual

signs incorporate wide and profound shrinkage cracks and hard consistency when these soils are in a dry state and which becomes soft to liquid with addition of water [9].

1.2 Appropriate additives for stabilization of expansive soils

Lime Stabilization – This technique for ground improvement is the most popular method for chemically changing unstable soils into fundamentally stable construction foundations. The utilization of lime in soil stabilization enhances various critical engineering properties of the material, including compressive strength, imperviousness to crack and decreased swelling.

The addition of lime may not have much effect in kaolinitic clay soils, but rather it can have a significant impact in clay soils containing montmorillonite. Expansive clays have a tendency to respond promptly with lime, losing plasticity instantly. This is due to the fact that montmorillonite display a high cation exchange capacity, while kaolinite has a generally low cation exchange capacity [11]. The addition of lime to a soil initiates a two stage reaction namely short-term and long-term reactions. Short-term reactions show their effect right after the addition of lime, while long term reactions are accompanied by a period of time [12] - [17].

Cement Stabilization - Cement is the most traditional binding agent since the origin of soil stabilization

technology in 1960's. It is considered to be a primary stabilizing agent, as it can be used as a single binder which yields the desired stabilizing reaction [18]. There are several types of cement available in the market namely ordinary Portland cement, blast furnace cement, sulfate resistant cement and high alumina cement. Usually the choice of cement depends on the type of soil to be treated and the desired final mechanical property [19].

Generally the amount of cement used is small in quantity but sufficient to improve the engineering properties of the soil. However, cement increases the strength but may decrease the cohesiveness and compressibility of the soil.

Fly-ash Stabilization - Extensive amount of coal are being burnt in thermal power stations to meet the growing demand for thermal power. About 80% of the ash formed after burning is fly ash. To reduce the problems of disposal of fly ash, expensive and tedious methods are being used and great efforts are being made to utilize fly ash alternately. The use of coal fly ash as a stabilizing agent will on one hand help to mitigate environmental problems associated with fly ash disposal and on the other hand will be beneficial for enhancing the engineering properties of problematic soils [10], [17].

Fly ash is known for its pozzolanic effect. It is a siliceous or alimino-siliceous material with little or no cementitious content but if finely ground it will react with calcium hydroxide to form compounds possessing cementitious properties [20], [21].

Coarse sand Stabilization – Not much research work has been published on the use of sand as a stabilizer but from the few available studies, it has been proved that coarse sand can be used as an additive to modify the particle size distribution in a soil-cement mix [22]. It has been found that an addition of coarse sand to soils, which constitute mainly montmorillonite as clay mineral, increases the values of the compressive strengths at the age of seven days by almost 50 %.

1.3 Background of soil stabilization

When fly ash or lime is added to an expansive soil, the latter reduces its plasticity index and swell potential due to cation exchange which results in an agglomeration of fine clay particles into coarser particles. Furthermore, this activates flocculation of clay particles. On the other hand, cementation process within the soil-additive mass increases shear strength and decreases volume change. Hence, the combined effect of the short term reaction (cation exchange and flocculation) and long term reaction (pozzolanic reaction) leads to a general improvement of the soil behaviour. Generally, the amount of additive required to stabilize an expansive soil may be in the range from

5 to 12% depending upon the soil genetics beyond which strength decreases for obvious reasons.

Cement reaction does not depend on soil minerals as the most important is its reaction with water, already existing in the soil mass, but sometimes the moisture may not be adequate and water has to be added during stabilizing process. This can be the reason why cement is used to stabilize a wide range of soils.

2. MATERIALS AND METHODS

Raw expansive soil was collected from the north western part of the Island of Mauritius or rather the Ring Road Phase 1 project site, located at Pailles, a region which is very well known for problematic soils. The recent problems that have affected the road structures after heavy rainfall justify the choice of the location. From the soil map of Mauritius the sample is classified as Dark Magnesium Clay belonging to the Lauzun family of the Old Volcanic Series deposit [22], [24].

Locally available lime, ordinary Portland cement, coal fly ash and sieved coarse rock sand are used as stabilizers in this research.

Lime - White hydrated lime of the brand Gluex supplied by Cape Lime (PTY) Ltd is used. Table 1 shows the chemical and physical properties of the lime used.

CaO + MgO	80% min
CaO ignited	45% min
CO ₂	5% max at work
Melting point	580°C
pH	11.8
Density	2.5 g/cm ³
Bulk density	0.55 g/cm ³

Table 1: Chemical and physical properties of lime.

Cement - Ordinary Portland Cement of class 42.5, supplied by Lafarge (Mauritius) Cement Limited, is used as binder in the present investigation with compressive strength values of 40.03 and 50.94 MPa after 7 and 28 days respectively, as indicated in supplier specifications.

Fly ash - A high percentage of electricity on the island of Mauritius is produced by burning fossil coal imported mainly from South Africa. Though an insignificant percentage of unburnt coal in the fly ash, the latter is quite responsive when added to soil, as evidenced by results below. Fly ash was acquired from local sugar cane factory, engaged in the production of electricity from fossil coal.

Coarse rock sand - Commercially available rock sand of particle size 0 - 4 mm is sieved through a 2 mm

sieve and as such coarse sand of size 2 - 4 mm is used in the present investigation.

2.1 Sample preparation

The test specimens were prepared at maximum dry density (MDD) and optimum moisture content (OMC) obtained for the adopted soil sample in accordance with BS 1377:1990 [23]. The raw material (dark magnesium clay) is sieved using a 2 mm aperture sieve to avoid any inclusion of gravels and the standard Proctor compaction test method is adopted to determine the compaction properties. Eventually samples for each mix with specific proportion of binder, described below, is prepared and pressed at MDD and OMC. This is achieved by statically compacting the soil in the mold with application of the right amount of energy needed to achieve MDD at OMC [22].

2.2 Mixtures.

Phase I: In the first phase of the investigation, raw lime, fly ash, cement and coarse rock sand acquired from local suppliers in Mauritius are used to prepare various trial mixes. These are used as partial replacement of the soil by 0%, 2.5%, 5%, 7.5%, 10%, 12.5% and 15% additive respectively. The soil is treated with each additive individually

Strength parameter, namely unconfined compressive strength (UCS) is used to assess the effect of the inclusion of each additive in the sample of expansive soil.

As stated above, the soil is sieved through a 2mm sieve to obtain a uniform and homogeneous mix. The constituents, i.e. soil, stabilizers/combinations and water are mixed in a mechanical mortar mixer with a fixed rotational speed of the helix, in the following sequence [22]:

1. soil and stabilizers/combinations for a duration of 5 minutes
2. water is then added and mixed for an additional 10 minutes.

For each mix, a set of three cubical specimens 40 mm x 40 mm x 40 mm are prepared in a mold with dimensions 40 mm x 40 mm and 40 mm high. Specimens are prepared at varying additive content, ranging from 0 to 15 %. The maximum dry density obtained from the standard Proctor compaction test is 1.437 g/cm³, volume of mold is 64 cm³ and the OMC is 30.5%. The mass of soil mix required to fill the mold each time is defined as a function of the maximum dry density, the optimum moisture content and the volume of the mold which gives 120 g (i.e. 64 x 1.437 x 1.305 g) of blended mix to be pressed in the mold at OMC. Table 2 summarizes the mass of dry soil required for each increment of additive. The mass

of water is kept constant with the assumption that the change in OMC for each mix is insignificant.

% additive	Mass of additive g	Mass of dry soil g
0	0	92
2.5	2.3	89.7
5	4.6	87.4
7.5	6.9	85.1
10	9.2	82.8
12.5	11.5	80.5
15	13.8	78.2

Table 2: Mass of additive in each sample.

The samples are demolded and allowed to cure in a water-saturated and airtight container for 7 days at room temperature. After 7 days, the samples are removed from the airtight container and allowed to cure at room temperature in ambient conditions. They are tested for their dry unconfined compressive strengths at the age of 21 days. Fig 1 shows values of the unconfined compressive strengths of the samples.

Phase II: The additives are now used in paired combinations with an aim to investigate the behavior of the mixtures with respect to the characteristic unconfined compressive strengths of the samples. Combinations of 2 additives in the ratio of 1:1 are used. The procedure for sample preparation is kept same as described in phase I above.

3. Results and discussion

3.1 Soil classification parameters

Table 3 summarizes the physical and classification parameters of the selected soil sample. The high values of liquid limit and linear shrinkage are to be noted as they are indicative of swelling and shrinkage behavior.

Soil Characteristics	
Specific Gravity	2.65
Liquid Limit %	53.4
Plastic Limit %	27.2
Plasticity Index %	26.2
Linear Shrinkage %	12.1
Optimum moisture content %	30.5
Maximum dry density g/cm ³	1.437

Table 3: Physical and classification parameters of soil sample.

3.2 Strength properties

Phase I: Single stabilizers by percentage mass used as soil replacement, as shown in Table 4 below, does not show a regular pattern in the strength behavior of the mixtures. However, it is noted that each binder reacts specifically with the Dark Magnesium Clay and likewise there is an optimum content of each stabilizer that yields a maximum characteristic compressive strength. It is noted that 7.5 % lime gives a maximum value of Compressive Strength equal to 5.5 MPa which is explained by the affinity of lime to the montmorillonite clay particles.

% additive	Unconfined Compressive Strength MPa			
	Coarse sand	Lime	Flyash	Cement
0	4.2	4.2	4.2	4.2
2.5	3.5	4.2	3.5	4.0
5	3.6	5.3	4.3	4.1
7.5	4.0	5.5	4.6	1.7
10	4.1	4.5	4.8	2.5
12.5	4.9	5.2	4.5	1.7
15	3.4	4.0	4.6	1.3

Table 4: Strength properties with single stabilizer.

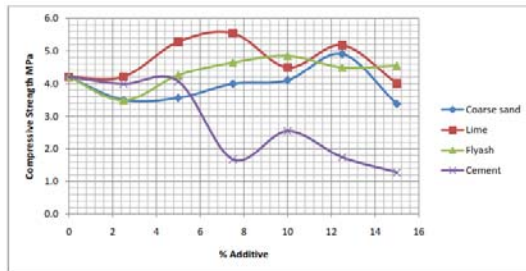


Fig 1: Variation of strength for samples blended with single additives.

Phase II: Combinations of two stabilizers are used to investigate the combined effect of the latter on the strength properties of the trial mixes. As mentioned earlier, samples are tested at the age of 21 days after an adopted curing regime, described above. Here again there is no regular pattern in the strength variation of samples with regards to percentage of binders but each combination has a characteristic maximum compressive strength value as shown in Table 5 below. As evidenced by the results, a combination of 2.5% of coarse sand/fly ash yields a maximum compressive strength of 5.2 MPa. This is explained by the fact that apart from the reactivity effect of the fly ash on the montmorillonite clay particles, coarse sand provides an appropriate skeleton to the overall soil mass. Beyond this optimum percentage, the mutual effect of these binders decreases the characteristic compressive strength value which may be explained by the fact that the constant amount of water in the mix might

have been insufficient for the free migration of clay particles into the voids.

% additive	Unconfined Compressive Strength MPa					
	Coarse sand/Lime	Coarse sand/Cement	Coarse sand/Fly Ash	Lime/Cement	Lime/Fly Ash	Fly Ash/Cement
0	4.2	4.2	4.2	4.2	4.2	4.2
2.5	4.2	4.3	5.2	3.7	3.9	3.7
5	4.3	4.6	4.9	3.4	3.5	3.6
7.5	4.6	4.0	4.8	3.8	4.4	3.9
10	3.5	3.8	4.1	3.9	4.9	4.1
12.5	2.7	3.7	4.1	4.5	4.3	4.6
15	2.5	3.8	3.1	4.2	4.2	4.8

Table 5: Strength properties of combinations of 2 additives

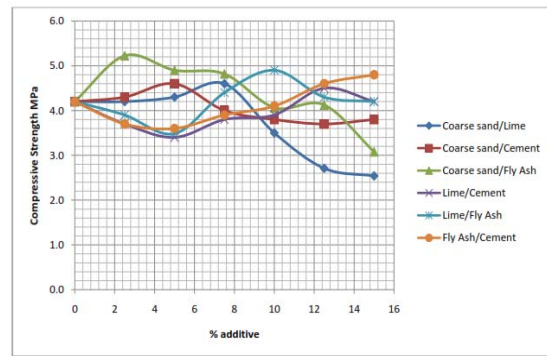


Fig 2: Unconfined compressive strength of samples blended with paired additives.

4. Conclusions

Based on results of the present investigation, the following conclusions are drawn:

1. Dark magnesium clay of the Lauzun family from the ancient lava deposits, sampled from the Port Louis region in Mauritius belongs to the class of expansive soils with liquid limit and linear shrinkage values in the range of 53.4 % and 12.1 % respectively.
2. Single stabilizers when blended with the expansive soil under study, do not show a regular pattern in the strength behavior of the mixtures. The present investigation nevertheless shows that each binder reacts variously with the Dark Magnesium Clay and graphs reveal an optimum content of each stabilizer that yields a maximum characteristic compressive strength. An optimum amount of 7.5 % lime gives a maximum value of compressive strength equal to 5.5 MPa. This is explained by the affinity of lime to react with the montmorillonite clay particles. For cement, fly ash and coarse sand the maximum strength values of 4.2 MPa, 4.8 MPa and 4.9 MPa occur at 4.3%, 10% and 12.4% respectively.
3. In the second part of the present study, the effect of paired combinations of binders in the expansive soil sample has been investigated. As

evidenced by the results of the current investigation, a combination of 2.5% of coarse sand/fly ash blended with the soil under study yields a maximum compressive strength of 5.2 MPa. This may be explained by simultaneous effect of the reactivity of the fly ash with the montmorillonite clay particles and provision of an appropriate skeleton to the overall soil mass by the coarse sand. Further addition of these binders decreases the characteristic compressive strength value which is explained by the constant amount of water in the mix being insufficient for the free migration of clay particles into the voids.

4. Linear shrinkage is found to decrease from 12.1 % for plain soil to 6.1 % for soil blended with additives which is due to the fact that fly ash reduces the soil's plasticity index and swell potential due to cation exchange which results in an agglomeration of fine clay particles into coarser particles.

References

1. Simmons, K.B. (1991) "Limitations of residential structures on expansive soils". *Journal of Performance of Constructed Facilities*, 5 (4), 258-270.
2. Fredlund, D.G & Hung, V.Q. (2001) "Prediction of volume change in an expansive soil as a result of vegetation and environmental changes. Expansive clay soils and vegetative influence on shallow foundations" *ASCE Geotechnical special publications* No.116., 24- 43.
3. Fredlund D.G. and Rahardjo H. (1993) "Soil mechanics for unsaturated soils" John Wiley & Sons, USA.
4. Hyndman, D. & Hyndman, D. (2009) "Natural Hazards and Disasters" Brooks/Cole, Cengage Learning, California
5. Mishra, A.K., Dhawan S., Rao, S.M. "Analysis of Swelling and Shrinkage Behavior of Compacted Clays" *Geotechnical and Geological Engineering*, Vol. 26, No. 3, pp. 289-298, 2008.
6. Al-Rawas, A.A., Taha R., Nelson, J.D., Al-Shab, T.B. and Al-Siyabi, H. "A Comparative Evaluation of Various Additives Used in the Stabilization of Expansive Soils" *Geotechnical Testing Journal*, Vol. 25, No. 2, pp. 199-209, 2002
7. Jones, D. E., and Holtz, W. G. "Expansive Soils - the hidden disaster", *Civil Engineering*, ASCE 43(8), pp. 49-51, 1973
8. Terzaghi, K., Peak R.B. and Mesri, G. "Soil Mechanics in Engineering Practice" 3rd Edition, John Wiley and Sons Inc., New York, 1996.
9. Wayne, A.C., Mohamed, A.O. and El-Fatih, M.A. "Construction on Expansive Soils in Sudan" *Journal of Construction Engineering and Management*, Vol. 110, No. 3, pp. 359-374, 1984
10. Goodary R, et al. "Effect of Fly Ash on Strength and Compressibility of Dark Magnesium Clay" *Proceedings 'Advances in Civil Engineering for Sustainable Development'*. 27-29 Aug 2014: 437-442, Thailand.
11. Ferreira, C., Riberio, A. and Ottosen, L., (2003), "Possible Applications for Municipal Solid Waste Fly Ash", *Journal of Hazardous Materials*, Vol. B96, pp. 201-216.
12. Bell, F.G., (1996), "Lime Stabilization of Clay Minerals and Soils", *Engineering Geology*, Vol. 42, pp. 223-237.
13. Bell, F.G., (1993), "An Examination of the Use of Lime and Pulverized Fly Ash to Stabilize Clay Materials", *Bulletin of the Association of Engineering Geologists*, No. 4, pp. 469-479.
14. Hilt, G. H., and Davidson, D. T. (1960) "Lime fixation in clayey soils" *Highway Res. Board Bull.*, v.262, pp.20-32.
15. Rao, K.S.S. and Tripathy, S., (2003), "Effect of Aging on Swelling and Swell-Shrink Behavior of a Compacted Expansive Soil", *Geotechnical Testing Journal*, Vol. 26, No. 1, pp. 1-11.
16. Kinithua, J.M., Wild, S. and Jones, G.I., (1999), "Effects of Monovalent and Divalent Metal Sulphates on Consistency and Compaction of Lime- Stabilized Kaolinite", *Applied Clay Science*, Vol. 14, pp. 27-45.
17. Nalbantoğlu, Z. and Güçbilmez, E., (2002), "Utilization of an Industrial Waste in Calcareous Expansive Clay Stabilization", *Geotechnical Testing Journal*, Vol. 25, No. 1, pp. 78-84.
18. Sherwood, P. (1993) "Soil stabilization with cement and lime" *State of the Art Review*. London: Transport Research Laboratory, HMSO.
19. EuroSoilStab. (2002) "Development of Design and Construction Methods to Stabilize Soft Organic Soils" *Design Guide for soft soil stabilization*. CT97-0351, European Commission, Industrial and Materials Technologies Programme (Rite-EuRam III) Bryssel.
20. Al-Tabbaa, A. and Evans, W.C. (2005). "Stabilization-Solidification Treatment and Remediation" Part I: Binders and Technologies-Basic Principal. *Proceedings of the International Conference on Stabilization/Solidification Treatment and Remediation* (pp. 367-385). Cambridge, UK: Balkema.
21. ASTM, (1993), "Standard Practice for Characterizing Fly Ash for Use in Soil Stabilization", *Annual Book of ASTM Standards*, D 5239-92, Vol. 04-08, pp. 1277-1279.
22. R. Goodary et al. "Investigation of the strength properties of cement stabilised soils of volcanic origin" *Construction and Building Materials* 2012, 28. Pp. 592-598.

23. British Standards Institution BS1377-4.
“Methods of tests for soils for Civil Engineering purposes” Part 4; Compaction related tests; 1990; 70 p.
24. Proag V. “The geology and water resources of Mauritius” Mahatma Gandhi Institute; Mauritius; 1995

LINEAR OPTIMIZATION OF SOIL MIXES IN THE DESIGN OF VERTICAL CUT-OFF WALLS

Joanel Galupino¹, Charlle Sy², Jonathan Dungca¹, and Anthony Shun Fung Chiu²

¹Civil Engineering Department, De La Salle University, Manila, Philippines

²Industrial Engineering Department, De La Salle University, Manila, Philippines

ABSTRACT

In order to prevent the contamination of surrounding groundwater in a landfill, cut-off walls were recommended. Cut-off walls are walls utilized when there is a need to restrict horizontal movement of liquids. Currently, the factors in designing cut-off walls are effective permeability, and relatively inexpensive materials in containing contaminants. It was suggested to provide a mix of 96% soil and 4% bentonite in the design of cut-off walls, but bentonite is relatively expensive, thus the viability of fly ash as a replacement for bentonite was considered. Soil mixtures were proposed and rigorous laboratory tests were performed to determine the individual properties. Tests such as specific gravity, Atterberg limit (liquid limit, plastic limit and plasticity index), relative density tests, particle size analyses, microscopic characterizations, elemental composition tests and permeability tests were performed to garner data, and were utilized for the model. A linear optimization model was generated to achieve the least cost with the minimum required permeability. The minimum permeability requirement for the cut-off wall was achieved by providing various mixtures for soil-bentonite-fly ash.

Keywords: Permeability, Fly Ash, Bentonite, Optimization, Linear Optimization

INTRODUCTION

Nearly a decade ago, the World Bank found that the San Mateo Landfill located in Rizal Province and Carmona Landfill in Cavite Province of the Philippines containing over 23 million cubic meters of corrupting waste were contaminating the ground water of their nearby vicinities [1]. In order to prevent the contamination of their groundwater, cut-off walls were recommended. In a waste disposal system, cut-off walls and clay liners (also known as contaminant barriers) are used to restrict movement of liquids and gases around waste-disposal facilities or site remediation projects [2]. Cut-off walls are walls utilized when there is a need to restrict horizontal movement of liquids. It is also used to provide an encapsulation for the waste to limit the inward movement of clean ground water in areas where groundwater is being pumped or being treated. It is also used to provide as long-term barrier to impede contaminant transport. The difference between cut-off wall and clay liner is that cut-off wall reduces the contaminant transport in the horizontal direction [3] while clay liner reduces the rate of contaminant transport in the vertical direction.

Currently, one of the factors in designing cut-off walls is to provide an acceptable permeability of containing contaminant. Permeability generally relates to the propensity of a soil to allow fluid to move through its void spaces. Baxter [4] suggested to provide a mix of 96% soil and 4% bentonite in the design of cut-off walls, but bentonite is relatively expensive, thus the viability of fly ash as a

replacement for bentonite was considered. Because of its relatively low permeability, bentonite is usually recommended mixed with non-cohesive soil like silty sand as an encapsulation material [5], however, the utilization of bentonite has made the cost high that is why bentonite is suggested to be replaced. It was proposed that fly ash is a viable replacement for bentonite [5]. It is sustainable, since power plants discharge large amounts of fly ash as waste but only half of them are used and the remaining half is trashed to land and sea, its disposal became an environmental concern. The utilization of fly ash may be a viable alternative for barrier containment material [6] but on the contrary, fly ashes generally consist of silt-sized particles and consequently possess high permeability [7]. Permeability refers to the susceptibility of a material to allow fluid to move through its pores. Tests must be performed to determine if fly ash may be viable for a containment material. The main objective of the study is to determine the most viable permeability characteristic of the various soil mixes of soil, fly ash and bentonite for cut-off wall.

METHODOLOGY

Varying blends were tested to check their response on the vertical and horizontal permeability, shown on Table 1.

Each soil mixture underwent rigorous index tests such as Specific Gravity Test [8], Atterberg Limit Tests [9], e_{\max} test [10] and e_{\min} tests [11] and Particle Size Analysis [12].

The scanning electron microscopy (SEM) was used to evaluate the microfabric of soil, fly ash and bentonite. Scanning electron microscopy (SEM) with energy dispersive X-ray spectroscopy (SEM/EDX) is the best known of the surface analytical techniques. High resolution images of surface topography are produced using these tests. Soil particles were described according to their shape, texture and size.

Table 1. Soil Mixtures of Fly Ash, Soil, and Bentonite

Soil Mixture	Fly Ash (%)	Soil (%)	Bentonite (%)
100FA	100	0	0
75FA25S	75	25	0
50FA50S	50	50	0
25FA75S	25	75	0
100S	0	100	0
100B	0	0	100
96S4B	0	96	4
96S4FA	4	96	0
96S2B2FA	2	96	2

Energy Dispersive X-ray Spectroscopy (EDX) was used to determine the chemical composition of each soil mixture. It is expected to have Oxygen, Silicon, and Calcium elements. The elemental composition was in terms of percent (%).

Permeability of the different soil mixes was determined by the constant head ~~test method~~ and falling head test methods. The direction of flow of water is also important, thus, both the vertical and horizontal orientations of the permeameter were used. A proposed set-up for the permeameter was used and modified to determine the horizontal permeability [13] of the soil mixtures, shown on Fig. 1. The Eq.1 is also used in the analysis. The following were also considered:

1. It was suggested by Baxter (2004) to use a relative density of 90% to provide a very dense soil state, thus, the desired void ratio of each soil mix was determined.
2. It was proposed that the pressure head for constant head permeability test will vary during the experiment to check if there were differences in permeability. Three (3) pressure heads were tested for statistical difference for each soil mix, 200cm, 150cm and the 50cm.
3. The diameter of the soil sample was follow the diameter of the permeameter 2.5in (6.35cm). The length of the specimen is 10cm to accommodate the additional porous stones provided.
4. The standard temperature was 20°C. Results were standardized once the temperature varied.

$$k=Ql/Aht \quad (1)$$

where:

k = coefficient of permeability, cm/s; Q = quantity (volume) of water discharged during test, cm³; l = length between manometer outlets, cm; A = cross-sectional area of specimen, cm²; h = head (difference in manometer levels) during test, cm; t = time required for quantity Q to be discharged during test, s.

A Linear Optimization Model was also proposed to achieve the optimized mixture that will give an acceptable permeability value with the least cost.

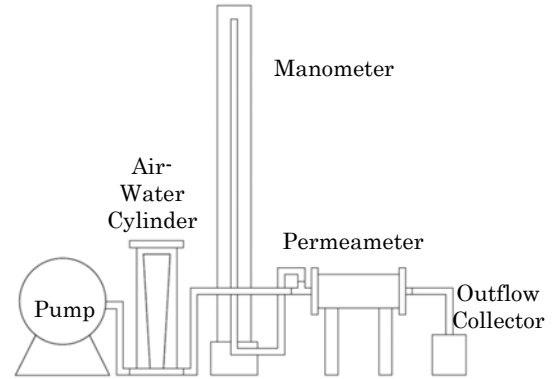


Fig. 1: Horizontal Permeability Set-up

RESULTS AND DISCUSSIONS

Index Properties and Chemical Properties

The specific gravity of each soil blend was determined. The summary of the specific gravity of various soil mixtures are shown in Table 2. The specific gravity of a particular soil shall be reduced by the addition of fly ash [7] since the usual of the specific gravity of fly ash is low. The addition of fly ash reduces the specific gravity of a soil mixture, thus we can agree with the statement of Prabakar [14], this is due to the light weight property of fly ash. Furthermore, it can be noticed that 100B is the heaviest of all the soils. Bentonite being a high density material, an increasing weight by adding bentonite to a soil mix can be noticed.

Table 2. Specific Gravity of Each Mixture

Mixture	G _s
100FA	2.02
75FA25S	2.11
50FA50S	2.31
25FA75S	2.49
100S	2.58
100B	2.75
96S4B	2.61
96S2B2FA	2.60
96S4FA	2.52

ASTM D4253 [10] and ASTM D4254 [11] were used to determine the maximum and minimum void ratios of the different mixes. It can be noticed from Table 3, the Maximum Void Ratio (e_{max}) ranges from 1.78 to 1.99 because the fine contents of the fly ash contributed to the percentage of voids. 100S has the lowest value while 100FA has the highest, also from Table 3, 100S has the lowest fines content, while 100FA garners the highest. Their fines content and microfabric may have contributed to the minimum and maximum void ratio. It can be noticed that the minimum void ratio is much less than the reference [15], this is due to the meticulous laboratory execution. The allotted time for the vibratory table exceeded to determine the extent of the minimum void ratio.

Table 3. Summary of e_{min} and e_{max}

Soil Mixture	e_{min}	e_{max}
100S	0.84	1.78
100FA	0.27	1.99
100B	0.36	1.98
96S4B	0.8	1.80
50FA50S	0.47	1.94
75FA25S	0.37	1.98
25FA75S	0.72	1.93
96S4FA	0.76	1.80
96S2B2FA	0.78	1.81

These minimum and maximum void ratios together with the target relative density of 90% were used to determine the void ratio to be utilized for the permeability specimens.

Summary of results from the particle size analyses are shown on Table 4. 100FA and 100B have the greatest percentage of fines compared with other blends. Both soils are considered fines but the classification differ, fly ash is silt and Bentonite is plastic. It can also be noticed that mixing fly ash with other soils increases the fines content.

Table 4. Summary of Particle Size Analysis Results

Soil Mixture	% Passing #200	D ₁₀	D ₃₀	D ₆₀
100S	21.84	0.01	0.4	1.2
100F	61.83	0.029	0.03	0.04
100B	58.36	0.0022	0.0055	0.032
96S4B	29.33	0.018	0.043	0.125
50FA50S	29.79	0.032	0.0375	0.12
75FA25S	50.78	0.019	0.032	0.06
25FA75S	25.79	0.015	0.042	0.15
96S4FA	22.27	0.035	0.09	0.13
96S2B2FA	23.82	0.03	0.08	0.25

All soil mixture followed the suggested fines content. Geo-con [16] provided the complete

technical specifications on soil-bentonite trench cut-off wall, they stated that the cut-off wall must have at least 15% fines content. Fine materials are particles that passed through #200 sieve during the particles size analysis test (ASTM D422). Evans [17] agreed that the cut-off wall mix must contain at least 15% fines to garner a low coefficient of permeability (commonly less than 9.9×10^{-7} cm/s) because the percentage of fines present affects the hydraulic conductivity [18].

Most of the soil properties and characteristics like strength, compressibility and permeability are ascribed by its microfabric or microstructure. The scanning electron microscopy (SEM) was used to evaluate the microfabric of soil, fly ash and bentonite. Scanning electron microscopy (SEM) with energy dispersive X-ray spectroscopy (SEM/EDX) is the best known of the surface analytical techniques. High resolution images of surface topography, are produced using these tests. Pure soils were initially tested to check their microscopic characteristics, mixed soils were also tested thereafter. In the Energy Dispersive X-ray Spectroscopy (EDX), chemical composition of soil is determined to give information on the elements present in the soil. Oxygen (O) is very abundant, followed by Silicon (for Silty Sand) and Calcium (for Fly Ash). Silicon and Calcium are predominant in the soil elemental composition. Due to the presence of Oxygen and other dominant elements: Silica (from Silicon), Lime (from Calcium) and Alumina (from Aluminum) are the dominant minerals in the soil sample.

As shown in Fig. 2, with 500x magnification for 100S, it is a combination of extremely strandy grains, large angular grains and abundant silt grains formed the micro fabric. The silt grains have a rough surface. The particles are well-graded microscopically. The smaller particles tend to fill the voids created by the larger particles shown in the figure, thus creating a smaller inter-particle void. Looking closer to magnification of 1000x and 5000x, strand-like particles are present, his indicates that these elongated particles also fill the voids, giving small passageways for water to permeate.



Fig. 2. Microfabric of 100S (5000x, 1000x and 500x Magnification)

As shown in Fig. 3, with 500x magnification for fly ash, it is a combination of larger silt grains and smaller silt grains to form the micro fabric. Fly ash is a silt thus normally 0.002-0.05 mm in size. As

seen on the 500x magnification, particles have almost similar size, forming larger inter-particle void, compared with silty sand and bentonite, to allow water to pass through. On the 1000x and 5000x magnification, the surface of the particle is not smooth, this create passageway/voids for water to pass through.

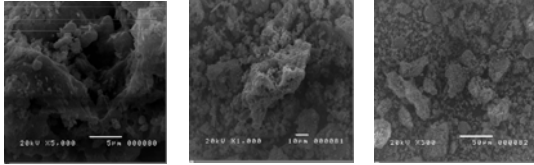


Fig. 3. Microfabric of 100FA (5000x, 1000x and 500x Magnification)

As shown in Fig. 4, with 500x magnification for 50FA50S, it is a combination of extremely strandy grains, large angular grains and abundant larger silt grains and smaller silt grains formed the micro fabric. The silt grains have a rough surface. Looking closer to magnification of 1000x and 5000x, strand-like particles are present but not prevalent compared with the pure soil, the soil particles may contribute to the reduction of permeability but the silt grains of fly ash will counteract to allow water to drain faster.

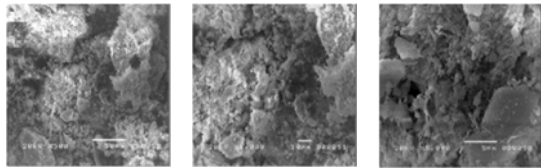


Fig. 4. Microfabric of 50FA50S (5000x, 1000x and 500x Magnification)

As shown in Fig. 5, with 500x magnification for 96S2F2B, it is a combination of extremely strandy grains, large angular grains, silt grains and elongated smooth grains formed the micro fabric. The particles are still well-graded microscopically. Looking closer to magnification of 1000x and 5000x, strand-like particles are present, this indicates that these elongated particles also fill the voids, giving small passageways for water to permeate. Also the smooth surface of bentonite particles gave a smaller inter particle-void which the permeability is reduced but counter-acted by the presence of fly ash's silt grains which contributed to additional drainage.

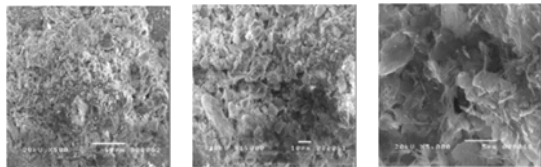


Fig. 5. Microfabric of 96S2F2B (5000x, 1000x and 500x Magnification)

Permeability

A proposed approach utilized in determining the horizontal permeability of the various soil mixtures was referred [13] and was modified. Shown in Table 5 is the range of permeability values gathered for the vertical oriented constant head permeability test.

Table 5. Range of permeability values for vertical oriented permeability test

Soil Mixture	Min K, cm/s	Max K, cm/s
100FA	4.51E-05	5.35E-05
75FA25S	2.93E-05	3.97E-05
50FA50S	2.81E-05	2.98E-05
25FA75S	2.05E-05	2.50E-05
100S	1.66E-05	1.90E-05
100B	6.13E-09	2.48E-08
96S4B	1.16E-07	2.98E-07
96S2B2FA	6.90E-07	7.79E-07
96S4FA	1.93E-05	2.40E-05

It is clear that the permeability is increased when the amount of fly ash is increased. It now agrees with the study by Prashanth [7] that fly ashes generally consists of silt-sized particles and consequently possesses high permeability. Thus, the amount of fly ash increases the permeability of the soil mixes.

Table 6. Range of permeability values for horizontal oriented permeability test

Soil Mixture	Min K, cm/s	Max K, cm/s
100FA	6.15E-05	7.29E-05
75FA25S	4.19E-05	5.46E-05
50FA50S	3.70E-05	4.34E-05
25FA75S	3.39E-05	3.49E-05
100S	2.25E-05	2.66E-05
100B	1.30E-08	3.53E-08
96S4B	1.65E-07	2.72E-07
96S2B2FA	8.04E-07	9.87 E-07
96S4FA	2.52E-05	2.70E-05

The horizontal permeability of the various soil mixtures is important, because for cut-off walls, it can discern how long the contaminated water will penetrate in the horizontal direction. Shown in Table 6, is the range of permeability values gathered for the horizontally oriented constant head permeability test.

Soil is the usual majority component of the soil mixture since the study followed the suggested mix [6] to reduce its cost, the soil excavated from the cut-off wall trench can be utilized as the soil element for the backfill. If the soil is contaminated or does not meet the requirements, the excavated soil can be removed and treated. 100S is not a viable candidate for the cut-off wall. 100S' microfabric having a combination of extremely strandy grains, large

angular grains and abundant rough-surfaced silt grains contributed to the drainage.

Fly ash is the recommended addition to the soil mixtures to form the cut-off wall mix, since waste materials are aimed to be utilized but the addition of fly ash to soils changes the inter-particle void ratio [14], which is prevalent to the microscopic characterization test for 100F. It is a combination of larger silt grains and smaller silt grains to form the micro fabric. Silt particles have almost similar size, forming larger inter-particle void, contributing to a much larger inter-particle voids.

Bentonite has low hydraulic conductivity. Its microfabric usually composed of a combination of smooth elongated grains and smaller grains, thus, smaller inter-particle voids are present.

Baxter [4], 96% soil is mixed with 4% bentonite to form the cut-off wall mix. In the study, 96S4B was used as a control specimen and its permeability is above the minimum requirement of 9.9×10^{-7} cm/s for a cut-off wall. It is a combination of extremely strandy grains, large angular grains and elongated smooth grains formed the micro fabric. In its microscopic structure, strand-like particles are present, this indicates that these elongated particles also fill the voids, giving small passageways for water to permeate. Since, the attained permeability is above the minimum required value, fly ash was incorporated in the mix. Fly ash may increase the drainage but a certain amount of fly ash can be added but still attaining the minimum required permeability.

Linear Optimization Model

To check the effect of fly ash and bentonite when added to soil, the mixtures were tested for specific gravity, soil index property, relative density, microscopic characterizations, elemental composition and permeability. Many models may also be considered [20, 21, 22, and 23]. In the previous study, their permeability values were used to generate linear optimization model. Equations 2 to 7 are considered in the constraint.

Objective Function: Min. x_3 (Bentonite) (2)

Constraints:

$$x_1 \leq 1, x_2 \leq 1, x_3 \leq 1(3)$$

$$x_1 + x_2 + x_3 = 1(4)$$

$$\begin{matrix} - & . & * & - & . & * \\ & & & & & \\ & & & & & \end{matrix} \quad (5)$$

$$\begin{matrix} - & . & * & - & . & * \\ & & & & & \\ & & & & & \end{matrix} \quad (6)$$

$$x_i \geq 0 (7)$$

where:

x_1 = Amount of Soil;

x_2 = Amount of Fly Ash;

x_3 = Amount of Bentonite.

This proposed linear optimization model was used to achieve the optimized mixture, $x_1=38.43\%$ and $x_2=62.57\%$, that will give the permeability value with the least cost.

In order to validate the model, equations 5 and 6 were used. A plot of residuals was considered, shown on Figs. 6 and 7.

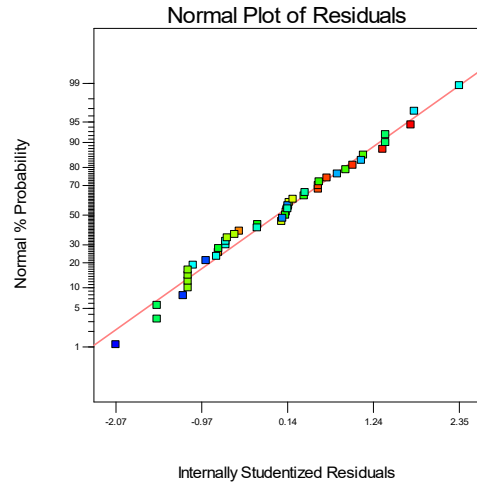


Fig. 6. Normal Plot of Residuals for Equation 5

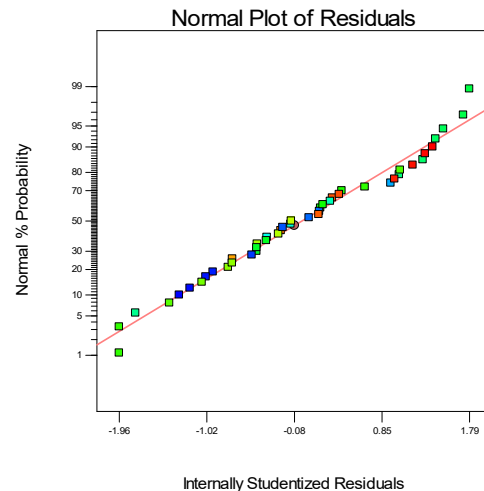


Fig. 7. Normal Plot of Residuals for Equation 6

CONCLUSIONS AND RECOMMENDATIONS

As a criterion in selecting the viable mixture for the cut-off wall, Baxter [4] recommended that the

minimum permeability requirement of $\times 10^{-7}$ cm/s for a cut-off wall. Also, it was suggested to provide a mix of 96% soil and 4% bentonite (96S4B) in the design of cut-off walls, but bentonite is relatively expensive, thus the viability of fly ash as a replacement for bentonite was considered. Fly ash is the recommended addition to the soil mixtures, since waste materials are aimed to be utilized. But the addition of fly ash to soils changes the inter-particle void ratio [14], it increases the permeability, thus, the microscopic characteristics of the soil mixtures may contribute to the increase in permeability. Since, 96S4B's attained permeability is above the minimum required value, fly ash was incorporated in the mix. Fly ash may increase the drainage but a certain amount of fly ash can be added and still attaining the minimum required permeability.

Given the linear optimization model, the optimized mixture, $x_1=38.43\%$ and $x_2=62.57\%$, that will give the permeability value with the least cost was achieved.

REFERENCES

- [1] Caplano, J. (2001, December 30). Closed landfills contaminating groundwater, World Bank warns. (Philippine Star) Retrieved November 2013, from Philippine Star: <http://www.philstar.com/nation/145333/closed-landfillscontaminating-groundwater-world-bank-warns>
- [2] Kansas Health Department. (n.d.). Kansas Health Department Website. Retrieved October 10, 2013, from Kansas Health Department - Waste Management: http://www.kdheks.gov/waste/techguide/EPA_QAQCforWasteContainmentFacilitiesCH7.pdf
- [3] Daniel, D. E., & Koerner, R. M. (2007). Vertical cut-off walls. In A. Press, Waste containment facilities: Guidance for construction quality assurance and construction quality control of liner and cover system (pp. 281-311). Rexton, Virginia, USA: ASCE.
- [4] Baxter, D. Y. (2000, April 14). Mechanical behavior of soil-bentonite cut-off wall. Virginia Polytechnic Institute and State University, Department of Civil Engineering. Blacksburg, Va: Virginia Polytechnic Institute and State University.
- [5] Daniel, D. E. (1993). Clay Liners. Geotechnical practice for waste disposal, 137- 163.
- [6] Yehesis, M. B., Shang, J. Q., & Yanful, E. K. (2010). Feasibility of using fly ash for mine waste containment. Journal of environmental engineering, 682-690.
- [7] Prashanth, J., Sivapullaiah, P., & Sridharan, A. (2001). Pozzolanic fly ash as a hydraulic barrier in land fills. Engineering Geology, 60, 245-252.
- [8] American Society for Testing and Materials. (n.d.). Standard Test Methods for Specific Gravity of Soil Solids by Water Pycnometer. ASTM D854. ASTM D854.
- [9] American Society for Testing and Materials. (n.d.). Standard Test Methods for Liquid Limit, Plastic Limit, and Plasticity Index of Soils. ASTM D4318.
- [10] American Society for Testing and Materials. (n.d.). Standard Test Methods for Maximum Index Density and Unit Weight of Soils Using a Vibratory Table. ASTM D4253.
- [11] American Society for Testing and Materials. (n.d.). Standard Test Methods for Minimum Index Density and Unit Weight of Soils and Calculation of Relative Density. ASTM D4254.
- [12] American Society for Testing and Materials. (n.d.). Standard Test Method for Particle-Size Analysis of Soils. ASTM D422.
- [13] Smith, C. B. (2010). Horizontal Permeameter. Magna Cum Laude Honors Research Project, University of Florida, Department of Civil and Coastal Engineering, Gainesville, Florida.
- [14] Prabakar, J., Dendorkar, N., & Morchhale, R. (2004). Influence of fly ash on strength behavior of typical soils. Construction and Building Materials, 18, 263-267.
- [15] Al-Tabbaa, A., & Wood, D. (1991). Some measurements of the permeability of kaolin. Geotechnique, 499-503.
- [16] Geo-con. (n.d.). Technical specification of soil-bentonite slurry trench cut-off wall. Retrieved from Geo-con: <http://www.geocon.net/pdf/sbswtech.pdf>
- [17] Evans, J. C. (1994). Hydraulic conductivity of vertical cut-off walls. ASTM STP 1142 (pp. 79-94). Philadelphia: American Society for Testing and Materials.
- [18] D' Appolonia, D. (1980). Soil-bentonite slurry trench cut-offs. Journal of Geotechnical Engineering Division, 106(4), 399-417.
- [19] Dungca, J., Galupino, J. (2016). Modelling of Permeability Characteristics of Soil-Fly Ash-Bentonite Cut-Off Wall using Response Surface Methodology, International Journal of GEOMATE 10, 2018-2024.
- [20] Galupino, J., Dungca, J. (2015). Permeability characteristics of soil-fly ash mix. ARPN Journal of Engineering and Applied Sciences, 15, 6440-6447.
- [21] Dungca, J., Galupino, J. (2017). Artificial neural network permeability modeling, International Journal of GEOMATE 12, 77-82.

- [22] Dungca, J.R., Jao, J.A.L. (2017). Strength and permeability characteristics of road base materials blended with fly ash and bottom ash, International Journal of GEOMATE 12, 9-15.
- [23] Uy, E.E.S., Dungca, J.R. (2017). Constitutive modeling of coal ash using modified cam clay model, International Journal of GEOMATE 12, 88-94.

EFFECTS OF CUTTING FACE BOLTS IN THE UNCONSOLIDATED SANDY TUNNEL

Yoshifumi Taguchi ¹

¹Department of Comprehensive Engineering, Urban Environment Course,
Kindai University Technical College, Japan

ABSTRACT

In the tunnel excavating unconsolidated sand layer of urban areas, it is important to stabilize the tunnel cutting face and to control the surface settlement. Therefore, the long face bolts are used frequently. As the effect of the face bolts for the cutting face stability and the surface settlement control, it is thought that reinforcing effects are different according to length and the interval. In this study, we changed the length and the interval of the face bolts by the two-dimensional model test used Toyoura-sand and examined the influence level on the effect of the face stability and the surface settlement. As a result, when the length of the face bolt is longer than $0.3H$ (H : cutting face height), the reinforcing effect of the cutting face becomes higher. It is small in length $0.2H$. For the surface settlement, when the length of the face bolt is longer than $0.5H$, the reinforcing effect becomes higher. Moreover the face stabilizing effect is higher better installation interval of the face bolt is small. In bolt's installation interval $0.2H$, face stabilizing effect and surface settlement control effect is high, but bolt's installation interval $0.5H$ is small. In addition, we examined the reinforcing effect and the mechanism of the face bolts by a numerical analysis using the finite element method.

Keywords: Tunnel, Cutting face bolts, Model test, Numerical analysis, Unconsolidated sandy tunnel

INTRODUCTION

In the tunnel excavating unconsolidated sandy layer in NATM, it is important to stabilize the tunnel cutting face and to prevent the surface settlement. For that purpose, the various auxiliary methods of tunnel construction are used, and it becomes the effective method to drive the long face bolts recently [1]. As the effect of the face bolts for the cutting face stability and the surface settlement control, it is thought that reinforcing effects are different according to length and the interval [2-7].

In this study, we changed the length and the interval of the face bolts by the two-dimensional model test used Toyoura-sand and examined the influence level on the effect of the face stability and the surface settlement [8-9].

In addition, we evaluated the reinforcing effect and the reinforcement mechanism of the face bolts by a numerical analysis using the finite element method [10-11].

OUTLINE OF MODEL TEST

Model Test Equipment

A model test equipment shown in Fig. 1. The size of the soil tank is 65cm in height, 80cm in width, and 15cm in depth. As shown in Fig. 1, Tunnel part of the model is the two-dimensional cross section of

the longitudinal direction taken along the center of the actual tunnel cross section, a rectangular cross-section of the cutting face model is 15cm in height and 15cm in width. In this test, a cutting face bolt modeled with a thin Kent paper thicknesses 0.12mm of a flat plate shape, was placed at a predetermined interval in cutting face, as shown in Fig.2 and Fig.3.

The model test reproduced the excavation by pulling out the tunnel cutting face model by a screw jack. Upon reaching a predetermined pull-out amount was measured the load acting on the tunnel cutting face and the surface settlement. The load acting on the tunnel cutting face sets the load-cell on

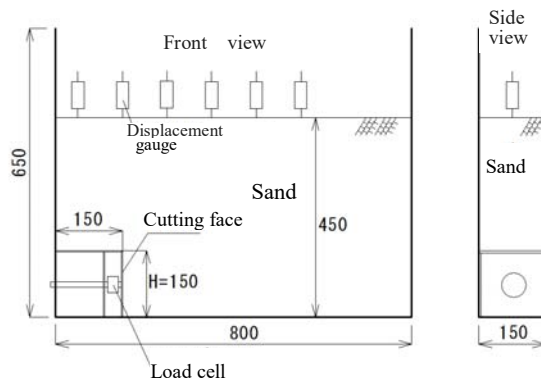


Fig.1 Model test equipment (unit mm)

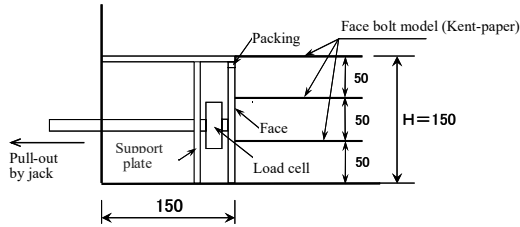


Fig.2 Cutting face part enlarged view (unit mm)



Fig.3 Model test equipment (Photograph)

the back side of the tunnel cutting face, was measured change of the load in accordance with the pull-out.

Table 1 shows the case of the model test. The length of the face bolt model (Kent paper) was changed 15cm (1.0H, H: cutting face height of model tunnel), 7.5cm (0.5H) and 3cm (0.2H). Further, the installation interval was changed 7.5cm (1-stage), 5cm (3-stage) and 3cm (5-stage), it was examined the influence.

Table 1 Case of model test

Test case	length (ℓ)	Installation interval
1	Non-reinforced	
2	15.0cm (1.0H)	1,3,5-stage
3	7.5cm (0.5H)	1,3,5-stage
4	3.0cm (0.2H)	5-stage

Model ground was used Toyoura-sand of the air-dried state. The model sand was free-fall from the outlet of a fixed size at the position of the height 60cm, and the model ground was introduced to overburden thickness 30cm (2.0H). The density of the sand is 1.54g/cm³.

The pull out of the tunnel, one by 0.2mm up to 0 ~ 2mm, one by 0.5mm up to 2 ~ 10mm, one by

1mm up to 10 ~ 15mm was carried out. The measurement of the surface settlement used a displacement gauge. It was placed in five locations in the 10cm interval.

Overview of the Model Test Results

Surface settlement (non-face bolt)

Figure 4 shows the change in surface settlement due to tunnel cutting face pull-out when there is no face bolt. The measurement point just above the face, and front 10cm, 20cm, 30cm and 40cm from the cutting face just above. It is the point of the rear 10cm from the cutting face just above. The surface settlement of the point of the cutting face immediately above and the front 10cm is large. With the pull-out amount of the cutting face increases, the surface settlement is increasing linearly.

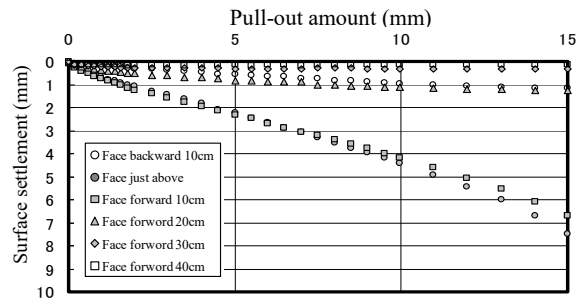


Fig.4 Surface settlement due to the pull-out (non-reinforced)

The reason for this surface settlement has increased because its position is within the range of the sliding surface of the ground. The surface settlement amount at the position of the cutting face behind 10cm and face forward 20cm~40cm is small and the surface settlement is not significantly increased even if the pull-out amount of the cutting face is increased. The reason is because the surface settlement is not significantly increased in order to that position the outside than the range of the sliding surface.

Surface settlement (using face bolts)

Figure 5 shows the change in surface settlement due to cutting face pull-out in the case of the face bolt installed 5-stage at the installation interval 3cm and length 15cm. The settlement measurement points are the same as described above the non-face bolt case. The surface settlement amount of point of

the face above and face the front 10cm is slightly larger. The maximum surface settlement at the time of pull-out 15mm of tunnel face is about 2 mm, the surface settlement than non-face bolt is considerably suppressed.

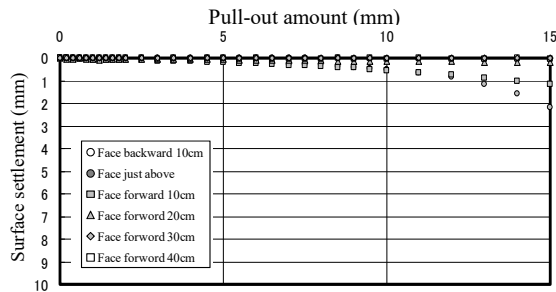


Fig.5 Surface settlement due to pull-out
(Bolt length 15cm, 5- stage)

Surface settlement of the tunnel longitudinal direction

Figure6 to7 shows the surface settlement of the tunnel longitudinal direction in the case of changing the installation interval of the face bolt when the case of face bolt length is 15cm (1.0H). The tunnel cutting face position as 0cm, at the position of the face front 10cm, 20cm, 30cm, 40cm and face backward 10cm, shows the surface settlement value of each case.

Figure6 shows the surface settlement when the cutting face was pulled out 10mm (0.07H). In the case of non-reinforced, at the point of the face front 10cm from the face above, it is about 4mm settlement. On the other hand, in 5-stage and 3-stage hardly subsidence, about 1mm settlement in the face just above even 1-stage, the surface settlement control effect is clearly evident.

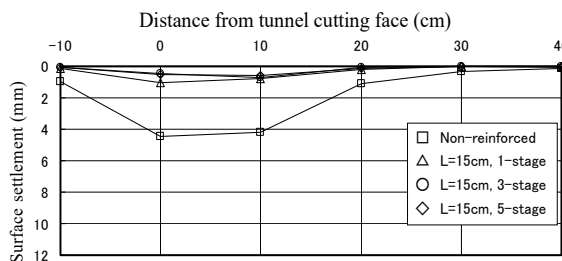


Fig.6 Surface settlement curve
(Longitudinal direction, on 10mm pull-out)

Similarly, Figure 7 shows the surface settlement when pulled out 15mm (0.1H) the cutting face. In the case of non-reinforcement is about 6~7mm settlement at the point of the face front 10cm. Although the 5-stage and 3-stage have been

settlement of about 2mm, increased sharply settlement just above the cutting face in the case of 1-stage, there is no reinforcing effect. In addition, from these figures, the range of influence of surface settlement is about face forward 20 ~ 30cm (1.3 ~ 2.0H).

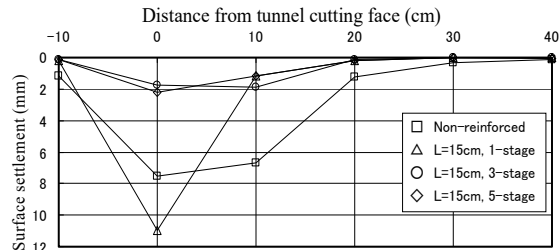


Fig.7 Surface settlement curve
(Longitudinal direction, on 15mm pull-out)

Figure8 show the surface settlement of tunnel longitudinal direction of the case changing the face bolt length 15cm (1.0H), 7.5cm (0.5H) and 3cm (0.2H) in installation interval 5-stages. It shows the surface settlement when pulled out 15mm (0.1H) the cutting face. In the case of non-reinforcement are about 7~8mm settlement at the point of the face front 10cm. Although the settlement amounts of the same degree in the face bolt length 15cm and length 7.5cm are about 2mm settlement, the control effect of settlement is high. On the other hand, in the face bolt length 3cm (0.2H), settlement amount has been increased to about 4mm just above tunnel face, the control effect of the settlement is small.

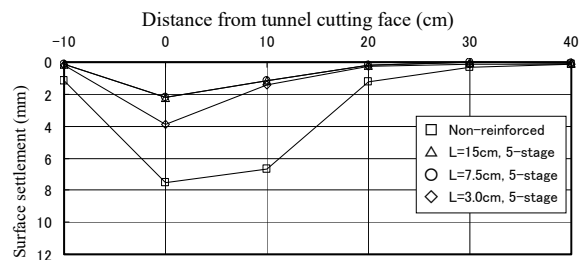


Fig.8 Surface settlement curve
(Longitudinal direction, on 15mm pull-out)

Among the model test results, Table 2 shows a comparison of the surface settlement of each case. The comparison position of the surface settlement is the value of the position of the front 10cm from the cutting face just above. It is shown in detail in reference [8].

Table 2 Experimental results
(Comparison of surface settlement)

№	Test case	Surface settlement (mm)		
		Pull-out 1.5mm	Pull-out 4.5mm	Pull-out 15mm
1	Non-reinforced	0.7	2.0	6.6
2	length15cm, 5stage	0.1	0.2	1.1
3	length15cm, 3stage	0.1	0.2	2.0
4	length7.5cm, 3stage	0.3	0.8	2.4
5	length3cm, 5stage	0.2	0.5	3.8

NUMERICAL ANALYSIS

Analysis Method and Model

The analysis used the two-dimensional plane strain elastic analysis by the finite element method. The analysis model is shown in Fig.9. Although the analysis of the tunnel face portion is inherently three-dimensional, used a two-dimensional cross-section in order to correspond to the model tests described above.

The materials properties used in the analysis are shown in Table 3. The model ground used a quadrilateral element of the 4-node, the face bolt used a beam element. The bending rigidity of the beam element was a small value that can not be resistance to bending due to the use of Kent paper model test.

In accordance with the above-mentioned model test, the tunnel excavation was simulated in a way that extracting the elements of the shaded portion of Fig.9. The stress release ratio as 100% was carried out excavation analysis of the tunnel. For boundary conditions, the soil tank's bottom is a fixed both vertical and horizontal directions, tunnel crown was fixed condition in accordance with the model test.

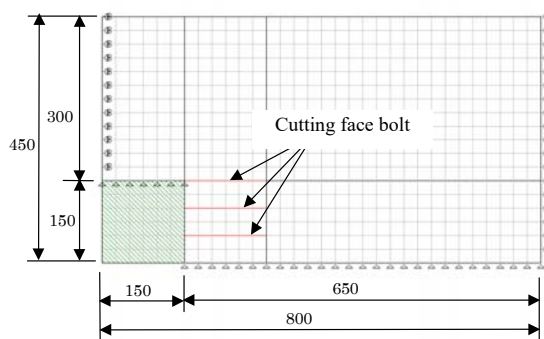


Fig.9 Analysis model and boundary conditions

Analysis Results

Analysis was varied with the length of the face bolts 15cm (1.0H, H: face height) and 7.5cm (0.5H) in correspondence with model test case of Table 1.

Moreover, was changed the face bolt's installation interval in the 3-stages and 5-stages.

Table 3 Material properties

	Deformation Modulus	Poisson's ratio	moment of inertia of area
Ground	1.0MPa	0.3	—
Face bolt	1.0×10^4 MPa	—	1.0×10^{-7} cm ⁴

Non-face bolts

The displacement mode diagram and contour diagram of the horizontal displacement of the analysis results are shown in Fig. 10 to 11. Figure 10 is deformation diagram in the case where there is no face bolt, and Fig.11 is a contour diagram of the horizontal displacement.

From the figure, the cutting face has swelled large, if ground strength is low, is expected to lead to face collapse. In addition, from the contour diagram of the horizontal displacement, it has spread a large area of the horizontal displacement toward the surface in the direction of the obliquely upward 45°.

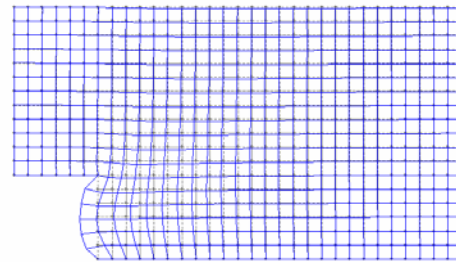


Fig.10 Deformation mode diagram (non-face bolt)

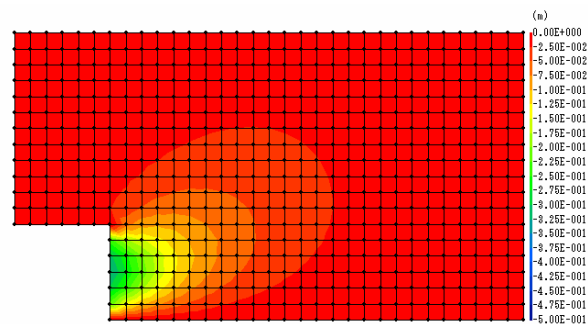


Fig.11 Contour diagram of the horizontal displacement (non-face bolt)

Using face bolts

Figure 12 is a displacement mode diagram of the face bolt's length 15cm (1.0H) in installation interval 5-stages. Figure 13 is a contour diagram of

the horizontal displacement. From this figure, in the face bolt installation position have been suppressed swelling of the cutting face, the amount of horizontal displacement is smaller. Moreover, the contour diagram, a large area of deformation does not extend toward the ground surface, the cutting face is stable, it is expected that the surface settlement is reduced.

Figure 14 is a contour diagram of the horizontal displacement of the face bolt's length 3cm (0.2H) in installation interval 5-stages. From this figure, even if the face bolt has 5-stages, the bolt length is short, so the amount of horizontal displacement of the cutting face is large. The reinforcing effect of the cutting face is small.

Figure 15 is a contour diagram of the horizontal displacement of the face bolt's length 15cm (1.0H) in installation interval 3-stages. From this figure, in the face bolt installation position, the swelling of the cutting face have been suppressed a little. It is almost similar to the case of the face bolt's length 15cm (1.0H) in Fig13.

Figure 16 shows the axial force diagram of the face bolt. From the axial force distribution, the axial force is the largest is near the center of the face bolt, the face bolts are functioning well as the role of the ground anchor. The face bolt does not function as a ground anchor, if the face bolt is pulled out, the axial force distribution dose not become indicating a maximum near the center as shown in the figure, the distribution shape becomes the largest near the cutting face.

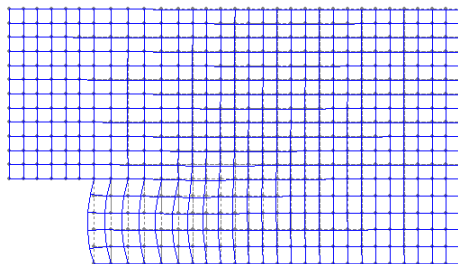


Fig.12 Deformation mode diagram
(Bolt's length 1.0H, installation interval 5-stage)

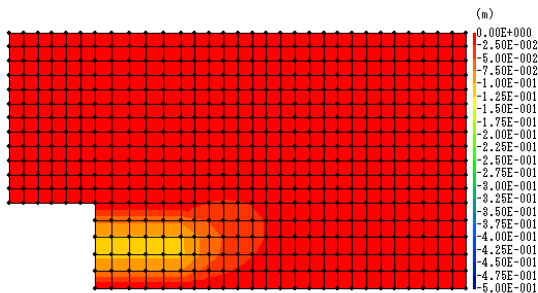


Fig.13 Contour diagram of horizontal displacement
(Bolt's length 1.0H, installation interval 5-stage)

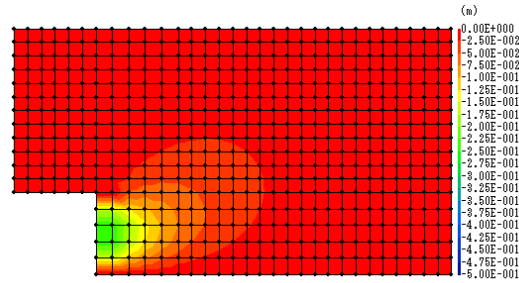


Fig.14 Contour diagram of horizontal displacement
(Bolt's length 0.2H, installation interval 5-stage)

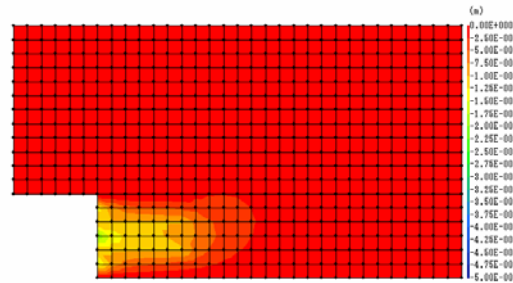


Fig.15 Contour diagram of horizontal displacement
(Bolt's length 1.0H, installation interval 3-stage)

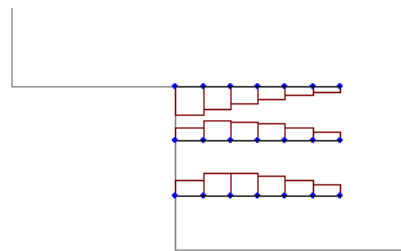


Fig.16 Axial force mode of face bolts
(Bolt's length 1.0H, installation interval 3-stage)

Comparison of the Model Test

Table 4 is the surface settlement and the cutting face's swelling amount in the numerical analysis results. Comparing the position of the surface settlement is the position of the face front 0cm ~ 15cm, was using the maximum value. In the table is also shown the ratio of the case of no face bolt in parentheses. Because it is elastic analysis the amount of deformation of the ground is proportional to the deformation modulus E . Therefore, hereafter we described using the ratio of the no face bolt's case.

From the two Table of Table 2(above mentioned) and Table 4, when inserting the face bolts and the tunnel pull-out amount is small in 1.5mm or 4.5mm, which is an elastic state, the analysis result of the

settlement become larger. The pull-out amount becomes large as 15 mm, the ground is expected to become a plastic state, as compared to the model test, the degree of deformation is well reproducible.

Paying attention to the swelling amount of the cutting face, in the case that the length of the face bolt is short and installation interval is large, it is larger than the trend of surface settlement. However, the tendency of the reinforcing effect of the length and spacing of the face bolt is able to reproduce. From these results, the numerical analysis of the face bolt using the elastic analysis can obtain an analysis result of the safety side with respect to the reinforcing effect of the cutting face bolt.

Table4 Result of numerical analysis

№	Test case	Result of numerical analysis (mm)	
		Settlement	Swelling of face
1	Non-reinforced	0.28(1.0)	3.3(1.0)
2	length15cm, 5stage	0.08(0.3)	1.1(0.3)
3	length15cm, 3stage	0.12(0.4)	2.0(0.6)
4	length7.5cm, 3stage	0.19(0.7)	2.6(0.8)
5	length3cm, 5stage	0.22(0.8)	2.4(0.7)

CONCLUSION

The two-dimensional longitudinal direction of the model tests using Toyoura -sand, was examined influence of the surface settlement by changing the installation interval and the length of the cutting face bolts. Moreover, we examine the reinforcing effect and the reinforcement mechanism of the cutting face bolt using a numerical analysis method by the finite element method. As a result, it was found that the following.

Compared to the model test results, in the region where the tunnel pull-out amount is small and the natural ground seems to be within the elastic range, an elastic analysis result has a bigger ratio of the settlement. When the pull-out amount of the cutting face is as large as 15mm, and the ground becomes the plastic state, the elastic analysis results show the same tendency as the model test results. For the elastic analysis, the swelling amount of the cutting face is larger in the case that the length of the face bolt is short and installation interval is large.

The numerical analysis of the face bolt using the elastic analysis can obtained of the safety side analysis results with respect to reinforcing effect of the natural ground deformation by the cutting face bolt.

REFERENCES

- [1] The Japan Geotechnical Society, "To construction from the design of the mountain tunnel construction method", 2007, pp.140-141. (in Japanese)
- [2] Fukusima S, Mochizuki Y, Kagawa K, Yokoyama A, "Model test on pre-reinforcement of shallow tunnel in sandy ground", Japan Society of Civil Engineers, No.406, III -11, JUN.1989, pp.79-86. (in Japanese)
- [3] Taguchi Y, Kagawa K, Sagara M, Yoshikawa K, "Reinforcing effects of thin flexible pre-lining", Japan Society of Civil Engineers, No. 645, III -50, Mar.2000, pp.125-135. (in Japanese)
- [4] Mitarasi Y, Matsuo T, Tezuka T, Okamoto T, Nisimura S, Matsui T, "Evaluation of effect of long face reinforcement method in tunneling", Japan Society of Civil Engineers, No.743, III -64, SEP.2003, pp.213-222. (in Japanese)
- [5] Miyanomae S, Morita A, Sakai T, Matsui M, Nasimoto Y, Okubo S, "A proposal of the simplified model to evaluate the effect of long bolting", Journal of Japan Society of Civil Engineers, Ser. F, vol.62, No. 2, APR.2006, pp.258-267 (in Japanese)
- [6] Domon T, Seo K, Nishimura K, "Simplified design method for face bolting based on the reinforcing effect", Journal of Japan Society of Civil Engineers, Ser. F1, Tunnel Engineering, vol. 66, No. 1, NOV.2010, pp.29-39. (in Japanese)
- [7] Yokota Y, Yamamoto T, Date K, "Evaluation of reinforcing effects on new face bolts using steel checker pipes by centrifuge model tests and 3D-numerical analysis", Journal of Japan Society of Civil Engineers, Ser. F1, Tunnel Engineering, vol. 67, No. 3, 2011, pp.67-79. (in Japanese)
- [8] Taguchi Y, Tanaka T, "Model test on the effect of reinforcing the face bolt in unconsolidated sand tunnel", Kindai University Technical College Research Reports, vol.4, JAN.2011, pp.79-84. (in Japanese)
- [9] Taguchi Y, Tabira T, "Model test on tunnel face stabilizing effect of the face bolt", Kindai University Technical College Research Reports, vol.6, MAR.2013, pp.71-76. (in Japanese)
- [10] Japan Society of Civil Engineers, "Practice of model experiments and numerical analysis in the mountain tunnel", 2006, pp.22-59. (in Japanese)
- [11] Taguchi Y, "Model Test and Numerical Analysis on the Effect of the Length and Interval of the Face Bolt in Sandy Tunnel", Proceedings of Second International Conference on Science, Engineering & Environment, Nov.2016, pp.328-333.

PHYSICAL MODELING OF PROPOSED POROUS DRAINAGE SYSTEM TO SOLVE INUNDATION PROBLEM

Ahmad Rifa'i¹, Noriyuki Yasufuku²

¹Faculty of Engineering, Universitas Gadjah Mada, Indonesia; ² Faculty of Engineering, Kyushu University, Japan

ABSTRACT

Post rain inundations that occurred in Prambanan Temple yard interfere the visitor's mobility and heavy equipment that operated for restoration activities in the temple. A typical porous drainage system was proposed using waste material from Merapi eruption to reduce the inundations. Research on the characteristics of the waste material becomes important due to the availability of so many supplies from these materials and it has not been utilized optimally. A full scale of physical modeling experimental test, with a modified equipment to determine the performance of the porous drainage system, was proposed in this study. Physical modeling of the porous drainage system is expected to represent the actual conditions in the field. The ground water level was designed in two conditions, deep ground water level based on the natural field condition and shallow ground water level that is an extreme condition that may occur in the field. In this test, rainfall simulator was built to flow the discharge constantly into this physical modeling. The effectiveness of this system amounted to 20% of the drainage capacity in natural field condition during the rainfall duration of 2.183 hours. In the extreme condition, the effectiveness of the system amounted to 75% of the drainage capacity during the rainfall duration of 2.383 hours. It shows that the porous drainage system is quite effective when applied at Prambanan Temple yard that has an average rainfall duration of 2.375 hours. The proposed porous drainage system is expected to solve the inundation problem in Prambanan Temple yard.

Keywords: Post Rain Inundations, Physical Modeling, Porous Drainage System

INTRODUCTION

Prambanan Temple yard is divided into three stages, with the main stage of Prambanan temple complex is located on the first yard. The first yard of Prambanan Temple is the main destination for tourists to enjoy the beautiful view. But in these last few years, the convenience of the tourism activity in the first yard of Prambanan Temple was quite disturbed due to the water inundations that always occur during the rainy season. Inundation that appears after rainfall in certain parts in the first yard of Prambanan Temple, as shown in Fig. 1, is one of issues that must be solved. Cultural Heritage Institution of Prambanan Temple attempted to reduce the inundation problem by adding a special soil above the original soil layer, so that the ground is not expected to quickly become saturated, free of dust, and it is not a growing medium of grass. Moreover, some drainage channels have added on Prambanan Temple yard to reduce the potential inundations of water occurrences, but this treatment is still not effective. To preserve this cultural site and keep the convenience of visitor's mobility, it needed some solution to organize and improve the drainage systems to reduce the inundated area.

According to the soil stratification data, as shown in Fig. 2, the soil layer in Prambanan temple yard is

dominated by sandy soil. The water level condition is on 12 meters under the soil surface. One of solution that can be conducted is by creating a drainage system that able to reduce runoff by infiltration through porous media of a porous material [1].

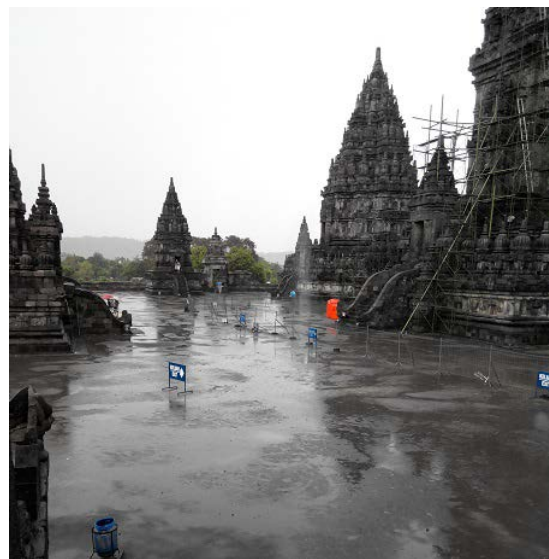


Fig. 1 Inundation that occurs in the yard of Prambanan Temple.

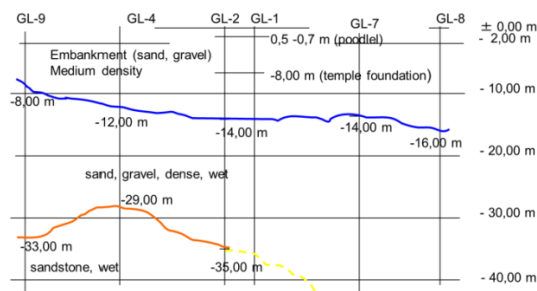


Fig. 2 Stratification of soil layer [2].

In addition, to obtain the high permeability material, a porous medium in the drainage system also serves to reduce the water pressure, prevent erosion, and prevent soil particles transported by the water flow. An alternative porous medium application is the utilization of porous drainage channels and porous paving block as an access road for visitors which considered to solve the inundations. Both of these alternatives are used in this study to optimize the drainage system and to solve the inundations problem. In this study, physical modeling of drainage system based on field condition parameter was conducted. This study focused on the effectiveness of the proposed drainage system with a physical model that has adapted to the conditions in Prambanan Temple yard.

Reference [3] has conducted research on utilization of low strength aggregate or Bantak and volcanic ash for drainage porous. Bantak and volcanic ash are used in no fine concrete as the main substituting material. The materials are used as a basic calculation of the total requirement of drainage material for producing of porous concrete samples. A numerical analysis model of the drainage channel was conducted and the distance between the nearest channels is 7.48 m. In addition to the distance between the channels, a typical channel model was proposed and shown in Fig. 3.

In addition to the porous drainage channels, to reduce inundation that caused by lack of water infiltration into the soil, porous paving blocks can be an alternative construction for pavement, especially for sidewalks, open parking area, etc. Reference [4] has conducted research on utilizing Bantak and volcanic ash to porous paving block in the handling of drainage at Prambanan temple page. The test results of the characteristics of porous paving blocks can be seen in Table 1. In [4], the model testing was conducted in an acrylic box with an area of 50 cm by 50 cm to get the value of the original soil permeability coefficient and porous paving block. This modeling was also performed on the normal paving block as a comparison. The calculation result of infiltration based on the data modeling results can be seen in Table 2.

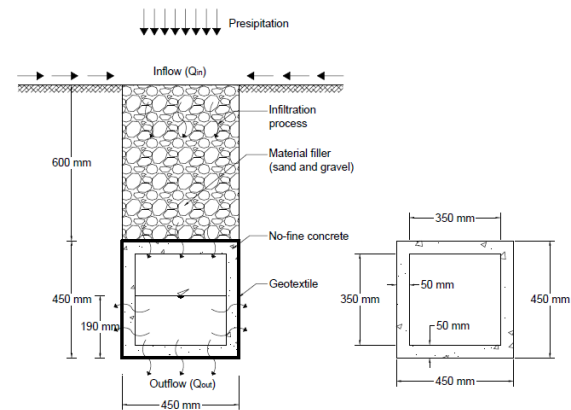


Fig. 3 Proposed drainage system by [3].

Table 1 Characteristics of the porous paving block using volcanic ash [4].

Characteristic	Value
Specific gravity (kN/m^3)	16.80
Compressive strength (MPa)	5.72
Porosity (%)	28.40
Permeability (m/s)	1.93×10^{-2}

Table 2 Hydraulic properties of the soil and paving block [4]

Parameter	Soil	Normal paving block	Porous paving block
Permeability (m/s)	5.8×10^{-6}	1.3×10^{-5}	1.1×10^{-4}
Infiltration capacity (m)	4.2×10^{-2}	1.1×10^{-1}	-
Infiltration velocity (m/s)	7.5×10^{-6}	1.4×10^{-5}	-
Runoff (m)	8.8×10^{-2}	1.6×10^{-2}	-
Inundations time (hour)	3,2	0,3	-

RESEARCH MATERIALS AND METHODS

Three-dimensional physical modeling was conducted in this study to validate theoretical results that have obtained through a mathematical calculation. In the physical modeling, detailed planning with analytical calculations is needed in order to build a physical modeling that represents the actual conditions in the field. Physical modeling can use the full scale or can be scaled from the actual conditions taking into account the scale factor. Detailed figure of a porous drainage system was proposed by [3]. Typical porous drainage channels that have been made by previous researchers then modified into a physical model in a scale of 1:1, that shown in Fig. 4.

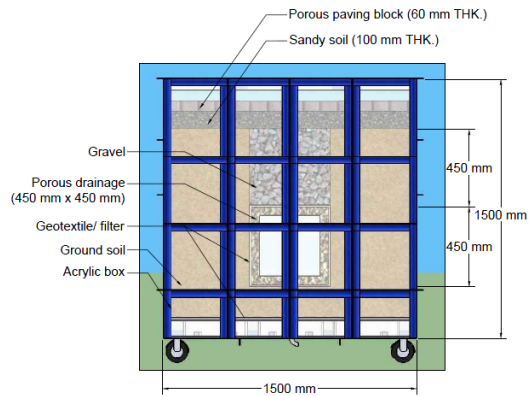


Fig. 4 Physical model of proposed porous drainage system.



Fig. 5 Experimental test apparatus.

Physical modeling testing of the porous drainage process begins with regulating the flow of rain simulation equipment, water discharge arranged until approaching rainfall conditions in the first yard of Prambanan Temple as shown in Fig. 5. Water discharge released from the rain simulation equipment is 14 ml/sec assuming the typical heavy rain. This water discharge represents the rain intensity about 70 mm/hour where it is 5 times higher than normal intensity obtained from the field data that equal to 14 mm/hour. Water discharge flow through a pipe that has been hollowed and the slope of the pipe needs to be taken to ensure that water can flow as expected. There are two conditions in this test, shallow ground water table for the critical condition and deep ground water table that represents actual field conditions.

Conditions of shallow ground water table can be modelled using an impermeable layer on the bottom of the porous drainage. It is made by letting an empty space at the bottom of the modeling box filled with water. The condition is considered to represent

a layer of impermeable because the water does not flow out and the water that seeps through the physical modeling test stuck in the bottom layer. Meanwhile, to simulate actual field conditions, the water valve at the bottom of the box was opened and the flow rate is set in accordance with the soil conditions in the field. Permeable layer conditions on the bottom of the porous drainage are made by making a puddle in advance at the box support as high as the bottom limit of the soil layer, then open the valve outlet of 8.7 ml/sec with assumption that the value of the discharge that comes out of the valve outlet is the same discharge in the modeling test. At the same time simulation of rain still running.

The observations focused on the direction of water flow and time to achieve the highest inundation level at 75% of the drainage capacity in saturated soil conditions. Changes of water content to determine the saturated condition was maintained by using soil moisture sensor devices. Groundwater flow direction can be visually seen when conducting this physical modeling. When the rain simulation equipment conducted, the time monitoring start. Furthermore, every inundation of 2 cm in porous drainage, the elapsed time is recorded until the altitude target. The simulation equipment was stopped when rain inundation on a porous drainage has reached 75% of the porous drainage height, then the elapsed time is recorded.

RESULTS AND DISCUSSIONS

In the shallow ground water level conditions, when rainwater simulation equipment was conducted and the surface of the soil in physical modeling start to wet, at that time the rain time calculation begins. The valve is opened by setting a constant flow of 14 ml/sec. This value is obtained from the calculation using 5 times of the rain intensity on the field that is equal to 70 mm/hour (> 60 mm/hour) and classified as the category of very heavy rain [5]. It used 5 times of the normal intensity because the intensity of rainfall simulation equipment was limited, so it used the higher rain intensity that can be seen visually and the represent the rain in the field. The process of physical modeling test is executed when the soil reaches the saturated condition and based layers as deep as 20 cm below the drainage porous considered impermeable. This impermeable layer is an interpretation of extreme field conditions where the soil is saturated with a high water level.

The results of the physical modeling test are time and water level contained in porous drainage. Observation of the water level in porous drainage every 2 cm to 26 cm, obtained from the 75% of the drainage capacity. The observations are then made in the form of a graph as shown in Fig. 6.

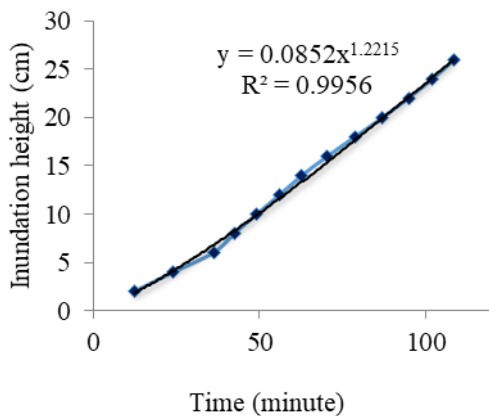


Fig. 6 Recapitulation of physical modeling observations with impermeable layer

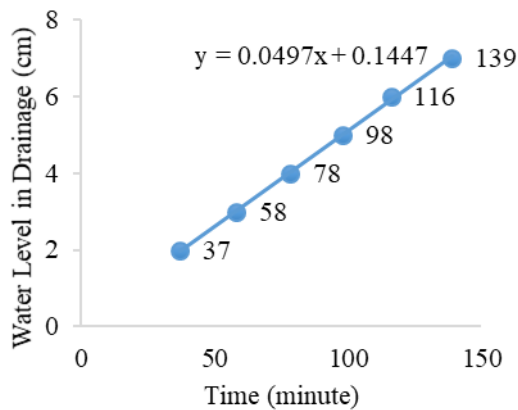


Fig. 7 Recapitulation of physical modeling observations with permeable layer

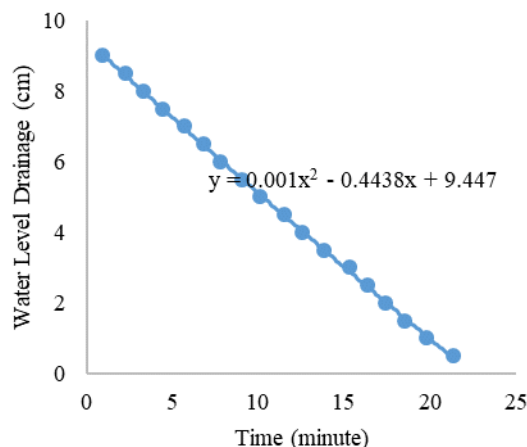


Fig. 8 Testing results of the decreasing water level in porous drainage with permeable layer

From Fig. 6, it can be seen that the time required for the water level every 2 cm is not constant. It appears there was a decrease in significant time when the water level of 6 cm to 8 cm and shows the water flowing into the drainage porous faster. After the water level height above 8 cm time required every 2 cm relatively constant, although there are up and some going down but not too significantly. The test data obtained from the time required for porous drainage inundation heights of 26 cm for 2 hours 23 minutes or 2.383 hours with rainfall intensity 5 times the normal intensity that is equal to 70.55 mm/hour. Data on the average duration of rainfall that occurred in the first yard of Prambanan Temple based on previous research that is over 2,375 hours. Thus the porous drainage system can be said to be effective for the treatment of inundation occurred in the first yard of Prambanan Temple despite heavy rain conditions (intensity of > 60 mm/hour).

On the deep ground water level condition, after the rainwater discharge valve is opened to discharge of 14 ml/sec with the intensity of 72 mm/hour interval of ± 10 minutes the water had penetrated the upper surface of porous drainage. With the soil conditions in the experimental test equipment were saturated and the water level at the bottom has been setting the limit as high as the bottom layer of soil, the results showed after waiting 1.5 hours, ground water level touches the bottom of the porous drainage. After the water reached the base of the porous drainage, then did a calculation of increasing inundation over time as shown in Fig. 7.

Based on Fig. 7, it can be seen every change of time elevation of inundation rose by 2 cm, and then averaged summed it takes about 20 minutes per increment inundation of 2 cm on porous drainage. So the speed of inundation in porous drainage was 0.1 cm/min. Of the total duration of the rain occurs about 2 hours 11 minutes gained inundation height on drainage pore of 7.5 cm from the inner surface drainage. So, in a case of rain with an intensity of 72 mm/hour for 2 hours 11 minutes, the condition is still very efficient drainage as a reservoir and seepage of rain. It is shown at an inundation height still 20% of the total of the level.

Decreasing water level is only performed on a permeable layer, which assumed that the water could flow down. Water level decreasing test in porous drainage, simulating when the rain was stopped but the discharge outlet remains open in accordance flow of water in the soil is 8 ml/sec and the position of the state remain saturated soil conditions. The test results can be seen in the graph shown in Fig. 8 below concluded that the rate of decreasing water level per 0.5 cm takes 1.203 minutes. From the results of this study concluded drainage catchment speed is 0.416 cm/min.

In decrease testing inundation in the porous drainage, rain simulation was stopped but the

discharge outlet remains open in accordance groundwater flow that is 8 ml/sec and the position of the state remain saturated soil conditions. The test results can be seen in the graph below, inundation concluded that the decrease rate every 0.5 cm takes 1.203 minutes. It can be concluded from the speed of the drainage catchment is 0.416 cm/min.

Fig. 9 shows in the direction of flow that occurs in the physical modeling of the porous drainage system. Running physical modeling to determine groundwater flow direction was made during a field dry conditions up to saturated soil conditions. Based on visual observations, the direction of flow on physical and mathematical modeling there is no significant difference, with it can be assumed that the input and output physical modeling and numerical modeling is correct. Conditions on groundwater flow above using rain discharge of 20 ml/sec to the direction of flow as shown above. In the picture, shown in number 1-6 as the change in shape of the flow of time. The initial condition is shown in number 1 and number 6 shows the final condition. In numerical modeling using Finite Element Method is modeled with the same soil conditions such as conditions on the modeling of physical test equipment. Results of running the software SEEP/W is shown in Fig. 10. It was concluded from a comparison of both models show the direction of flow which is not much different shape.

CONCLUSIONS

After testing on modeling of porous drainage system with the condition of the ground water level in accordance with the conditions of the field, the results obtained by 7 cm water level from lower surface drainage within 139 minutes. This shows that the porous drainage system used is quite efficient in streaming and storage of rain water runoff intensity 5 times the average rainfall intensity in the field. The time required for each increase of the water level in the drainage porous 1 cm nearly constant. This is possible because of the influence horizontal water flow coming into the porous drainage changed and influenced also by the already saturated ground conditions. The duration for the decrease in drainage porous inundation with a height of 0.5 cm takes 1.203 minutes. This is possible because the permeability of the non-sand concrete drainage density is very high and the soil density that is not so dense.

On the condition of the shallow ground water table below the drainage system obtained results height of inundation by 26 cm within 2.383 hours of this suggests that the drainage system is porous enough used effectively in reservoir drainage and water runoff. The time required for each increase of the water level in the drainage of 2 cm is not

constant and even tends to decrease. This is possible because of the influence of the horizontal flow of water coming into the porous drainage increased. Comparison of flow direction on physical modeling with Finite Element Method is not too significant.



Fig. 9 Pictures direction of flow in modeling tools experimental test

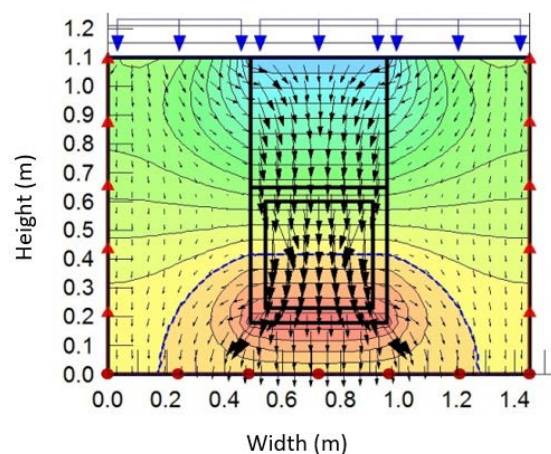


Fig. 10 Vector direction of water seepage on numerical modeling

REFERENCE

- [1] Bhutta MR, Tsuruta K, Mirza J, "Evaluation of High-Performance Porous Concrete Properties", *Construction and Building Materials*, Vol. 31, Jun. 2012, pp. 67-73.
- [2] Rifa'i A, "Sifat Teknis Tanah dan Struktur Fondasi Candi Wisnu dalam Tinjauan Geoteknik, in Proc. PIT-XIII HATTI Development of Geotechnical Engineering in Civil Construction, 2009, pp. 45-53. (In Indonesian Language)
- [3] Rifa'i A, Lestari NP, Yasufuku N, "Drainage System of Prambanan Temple Yard Using No-fine Concrete of Volcanic Ash and Bantak

- Merapi”, International Journal of GEOMATE, Vol. 11, Sept. 2016, pp. 2499-2505.
- [4] Rifa’i A, Yasufuku N, “Utilization of Bantak and Merapi Volcanic Ash for Porous Paving Block as Drainage Control in The Prambanan Temple Yard”, International Journal of GEOMATE, Vol. 12, Mar. 2017, pp. 141-146.
- [5] Sosrodarsono S, Takeda K, “Hidrologi untuk Pengairan”, 9th ed. Pradnya Paramita, 2003, pp. 7-8. (In Indonesian Language)

EFFECT OF HEATING-WETTING CYCLES ON ROCK PERMEABILITY

Ivan Gratchev¹, Jeremy Stephens² and Dong Hyun Kim³

¹ Griffith School of Engineering, Griffith University, Australia; ^{2,3} Griffith University, Australia

ABSTRACT

High temperatures that exist in rock mass can affect the properties of rocks, resulting in the formation of new discontinuities or expansion of the existing cracks. Such changes in the rock structure would likely influence the water flow in rock mass, which may undermine the rock storage capacity. This study seeks to investigate the effect of high temperatures on rock permeability. Fresh and weathered rock samples of argillite were subjected to heating and wetting cycles under the laboratory conditions to simulate the impact of high temperatures on rock mass. After each cycle the rock permeability was determined and compared with its initial value. It was found that as the number of heating-wetting cycles increased the coefficient of permeability of rock specimens also increased. However, this change depended on the initial rock properties and the number of heating-wetting cycles. The observed increase in permeability was attributed to the changes in the rock structure caused by the heating-wetting process.

Keywords: Rock permeability, Heating-wetting procedure, Laboratory testing, Argillite

INTRODUCTION

Variations in temperature and moisture content tend to affect the mechanical properties of rocks through the initiation of new or developing already existing cracks [1]. It is already known that 1) heating and cooling of rock can generate fractures through the thermal expansion and contraction [2], and 2) this process can close or open the existing fractures [3]. A better understanding of the effect of temperature on rock material is extremely important for underground waste repositories including nuclear waste. It is vital to contain the waste by preventing any leakage of hazardous material that can contaminate the surrounding environment. Although rocks are generally considered hard material with very low permeability, it can increase or decrease depending on the behavior of fractures under high temperatures. For example, recent studies [4] indicate that extremely high temperatures of 800-900°C resulted in lower values of permeability (by nearly four orders of magnitude) as the thermal stresses closed the existing fractures.

It is clear that temperature-induced changes in the rock structure would likely influence the fluid flow in rock mass, which may affect the rock storage capacity. This study seeks to better understand the effect of high temperatures on rock permeability.

TESTING PROCEDURE

Rock specimens used

Four borehole core specimens of argillite

(diameter 50 mm) (Fig. 1) from the Neranleigh–Fernvale Beds formation [5-6], Gold Coast, Australia were used in this research. Two fresh specimens (F1 and F2) and two slightly weathered specimens (W1 and W2) were subjected to the same testing procedure that consisted of 3 heating and wetting cycles.



Fig. 1 A view of the fresh and slightly weathered rock used in this study.

Before testing, each specimen was enclosed in a concrete mould (diameter 150 mm) with fiber reinforcement as shown in Fig. 2. Silicone sealant was used to separate the rock from the concrete mould to ensure that the specimen permeability is not affected by the concrete.

Rock permeability tests

To conduct a permeability test, the permeability apparatus with a 50-mm diameter O-ring was positioned on top of the specimen and clamped down to the specimen as shown in Fig. 3. To begin the test,

a pressure of 500 mBar was applied and the volume of water permeated through the rock specimen was measured every minute. The test continued for 15 min when only limited variation in pressure (less than 1%) was observed.

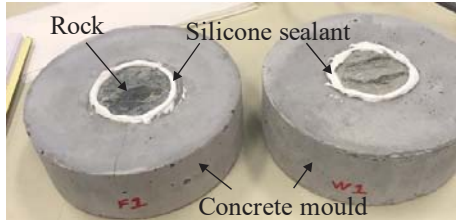


Fig. 2 Specimen preparation for the permeability tests.

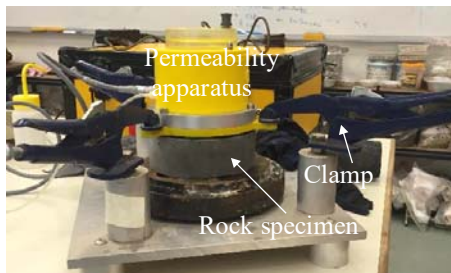


Fig. 3 Experimental setup used for a series of permeability tests.

Heating-wetting cycles

After the initial permeability test was conducted, the specimen was left to dry before starting the first heating cycle. The specimen was placed in an oven for 24 h at a temperature of 105°C. The specimen was then taken out of the oven and left in a controlled environment to cool before being submerged in distilled water (at a room temperature) for 24 h. The final stage of the heating cycle was to remove the specimen from the distilled water and let it dry for 24 h under controlled temperature (20°C) conditions. After each heating-wetting cycle, a permeability test was conducted to investigate the effect of the heating-wetting process on rock permeability. In addition, visual observations of the rock surface were performed after each cycle to study the influence of high temperatures on the crack formation and development.

RESULTS AND DISCUSSIONS

Permeability test results

Three heating-wetting cycles were performed and the obtained results for the fresh specimens of F1 and F2 are given in Fig. 4 as the variation of coefficient of permeability with time. This figure also presents

the data recorded after each heating-wetting cycle. As can be seen in Fig. 4, the initial permeability of the rock was relatively low; that is, about 1×10^{-6} m/s for F1 and 5×10^{-7} m/s for F2. It is also clear from Fig. 4 that the heating-wetting process resulted in higher values of permeability for each specimen. It is interesting to note that for F1, a change in the permeability was much greater compared to F2. It is also evident from this figure that the coefficient of permeability of both specimens (F1 and F2) tends to increase with an increasing number of heating-wetting cycles.

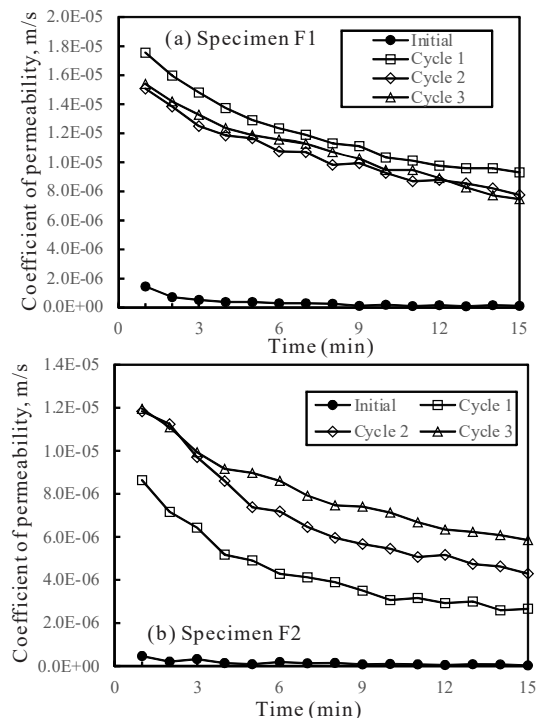


Fig. 4 Results from a series of permeability tests on the fresh specimens of argillite: (a) specimen F1, and (b) specimen F2.

A similar tendency was observed for the slightly weathered rock specimens (W1 and W2). The initial permeability was as low as the one observed for the fresh specimens: W1 – 1.4×10^{-7} m/s, and W2 – 3.5×10^{-7} m/s. In addition, the coefficient of permeability of both specimens increased as the heating-wetting procedure continued. It is noted that for W1, a significant increase in the permeability occurred after the third heating-wetting cycle while for W2, the increase appeared to be more gradual.

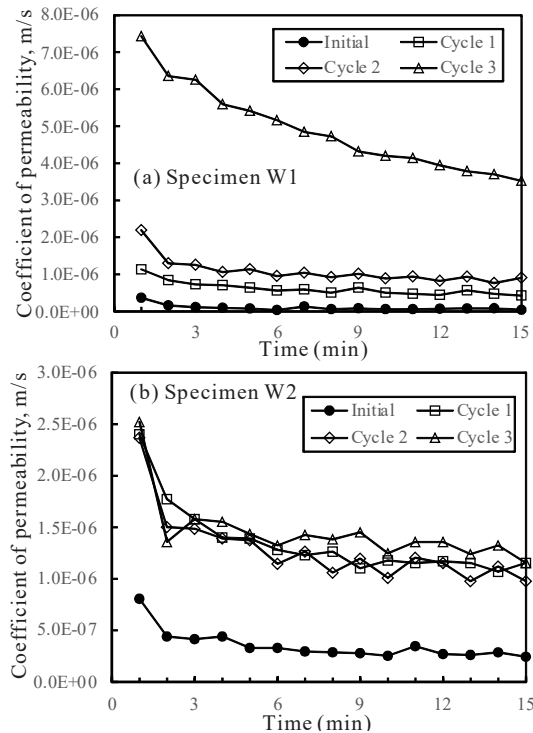


Fig. 5 Results from a series of permeability tests on the slightly weathered specimens of argillite: (a) specimen W1, and (b) specimen W2.

The summary of all permeability tests is given in Fig. 6 as changes in the coefficient of permeability with increasing heating-wetting cycles. It can be inferred from this figure that the initial coefficient of permeability of all specimens (both fresh and slightly weathered) was similar (about $1\text{--}3 \times 10^{-7}$ m/s), and it increased after each heating-wetting cycle.

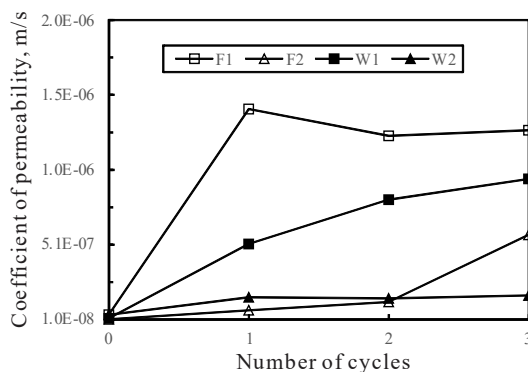


Fig. 6 Summary of permeability tests for the fresh and slightly weathered specimens of argillite.

Visual observations of rock surface

To better understand the effect of the heating-wetting process on the permeability of the tested rocks, the surface of each specimen was visually

examined after each cycle. The surface of F1 (the specimen that exhibited the largest increase in the coefficient of permeability) is shown in Fig. 7a (before the heating procedure) and Fig. 7b (after the third heating-wetting cycle). The change in the rock surface was quite pronounced and can be described as follows: a) a central part of the surface was chipped due to the heating process, b) some minor cracks appeared on the surface as well. Such changes were believed to lead to a higher coefficient of permeability which was observed for F1. For the slightly weathered rock W2 (Fig. 7c), discoloration and some increase in the crack length were observed as a result of heating-wetting (Fig. 7d).

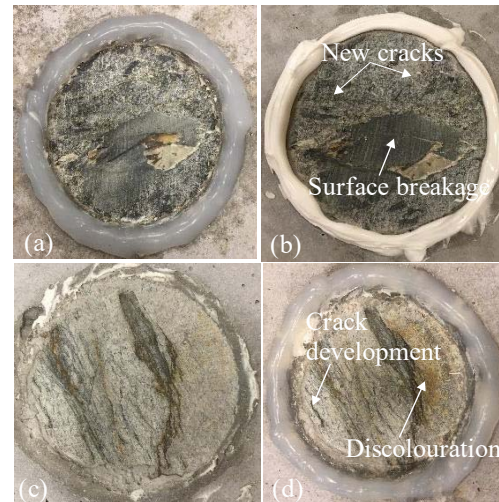


Fig. 7 A view of the specimen surface. F1: a) before the heating-wetting cycles, and b) after the third heating-wetting cycle. W2: c) before the heating-wetting cycles, and d) after the third heating-wetting cycle.

CONCLUSION

A series of permeability tests were performed on core specimens of argillite which were subjected to three cycles of heating and wetting. The following conclusions can be drawn:

- The permeability of the tested rocks, regardless of their weathering degree (fresh or slightly weathered), was found to be low, in the range of 1 to 3×10^{-7} m/s.
- The heating-wetting process caused some increase in rock permeability (approximately by one order of magnitude). This increase was observed for all tested rocks.
- The increase in the coefficient of permeability was mainly attributed to the formation of new cracks or extension of the existing ones. These cracks were observed on the surface of each tested specimen.

REFERENCES

- [1] Takarli M, Prince W, Siddique R, “Damage in granite under heating/cooling cycles and water freeze–thaw condition”, *International Journal of Rock Mechanics and Mining Sciences*, Vol. 45 (7), 2008, pp.1164-1175.
- [2] Fredrich J, Wong T, “Micromechanics of thermally induced cracking in three crustal rocks”, *J. Geophys. Res.*, Vol. 91(B12), 1986, pp. 12743-12764.
- [3] Cooper H, Simmons G, “The effect of cracks on the thermal expansion of rocks”, *Earth and Planetary Science Letters*, Vol. 36 (3), 1977, pp.404-412.
- [4] Gaunt H, Sammonds P, Meredith P, Chadderton A, “Effect of temperature on the permeability of lava dome rocks from the 2004–2008 eruption of Mount St. Helens”, *Bulletin of Volcanology*, Vol. 78 (4), 2016.
- [5] Kim DH, Gratchev I, Balasubramaniam A, “Determination of joint roughness coefficient (JRC) for slope stability analysis: a case study from the Gold Coast area, Australia”, *Landslides*, Vol. 10 (5), 2013, pp. 657-664.
- [6] Shokouhi A, Gratchev I, Kim DH, “Rock slope stability problems in Gold Coast area, Australia” *International Journal of GEOMATE*, Vol. 14, 2013, pp. 501-505.

A SIMPLIFIED METHOD FOR ESTIMATING COEFFICIENT OF EARTH PRESSURE AT REST (K_0) IN COHESIVE SOILS

Premkamol Thuennadee and *Kritika Trakoolngam

Faculty of Technology, Khon Kaen University, Thailand

ABSTRACT

Various geotechnical engineering problems require the value of coefficient of earth pressure at rest (K_0) for determining the in situ stress and designing engineering structures. At present, most available empirical methods for estimating this value are based either on the plasticity index or friction angle. These methods are widely used and proven to be quite accurate. In this paper, we propose a more simplified method to estimate K_0 . The parameters of basic physical properties that influence the value of K_0 were statistically analyzed using data from 3,900 cohesive soil samples. An empirical formula was developed based on the water content, specific gravity, and bulk density. The finalized relationship shows that the value of K_0 is a function of the specific volume. Values of K_0 resulting from the new equation were compared to that from the equation proposed by Massarsch (1979) which is based on the plasticity index. The maximum, minimum, and average error is 5.00%, 0.00%, and 2.00%, respectively. In conclusion, this new empirical method can estimate K_0 values in a much simpler way using the soil's specific volume without the need to determine the plasticity index or the friction angle.

Keywords: Coefficient of lateral earth pressure, Cohesive soil, Empirical method

INTRODUCTION

The coefficient of lateral earth pressure at rest (K_0) is a parameter required for determining the in situ lateral earth pressure which is necessary for designing many underground engineering works. The values of K_0 can be obtained from laboratory tests, in situ tests, theoretical analysis, or empirical method. The latter is the most popular approach since it is most convenient and inexpensive.

Theoretically, the value of K_0 can be determined from an elastic solution based on the Poisson's ratio (μ) as in

$$K_0 = \frac{\mu}{1-\mu} \quad (1)$$

The first empirical solution for determining the value of K_0 was proposed for cohesionless soils by Jaky [1] in 1944 which was then simplified, allowing for some loss in accuracy, in 1948 [2]. Both solutions are based on the friction angle of the material. To date, Jaky's simplified solution is still the most widely used although there have been several authors presenting solutions based on the friction angle of the soil as well [3]-[7].

For overconsolidated clays, the first solution was presented by Schmidt in 1966 [8] which was based on the Overconsolidation Ratio (OCR), the friction angle, and the K_0 in its normally consolidated state. Later on, other formulas were proposed based on the OCR as well but with some

variations using the Rankine active earth pressure coefficient [9] and the Poisson's ratio [10].

Interestingly, very few solutions were proposed for determining K_0 of normally consolidated cohesive soils. The first was proposed by Brooker and Ireland in 1965 [3] based on the Plasticity Index (PI) as

$$K_0 = 0.04 + 0.007 (PI) ; PI = 0 - 40\% \quad (2)$$

$$K_0 = 0.64 + 0.001 (PI) ; PI = 40 - 80\% \quad (3)$$

Later in 1979, Massarsch [11] proposed a more widely accepted formula which was able to determine K_0 at all ranges of PI

$$K_0 = 0.44 + 0.42(PI) \quad (4)$$

RATIONALE

Good predictions of K_0 for cohesionless soils are obtained from solutions based on the friction angle. However, formulas that use friction angles are accurate for only cohesionless soils and those that are accurate for cohesive soils use the plasticity index which are inapplicable to cohesionless soils.

A formula that can solve for both cohesive and cohesionless soils accurately would be preferable. Furthermore, being able to account for OCR would be ideal. This leads to finding a solution that is not dependent on the friction angle nor the plasticity index.

OBJECTIVE AND SCOPE

Our long term goal is to develop a formula which can solve K_0 for both cohesive and cohesionless soils accurately and is based on basic physical properties (independent of friction angle and plasticity index).

In this paper we focus on obtaining a solution for cohesive soils first. The concept is to use Massarsch's 1979 solution as a model and derive a formula that is comparable.

APPROACH

Data Acquisition and Filtering

Secondary data consisting of laboratory tests results were collected from the Geotechnical Engineering Department, Mae Moh Mine, Electricity Generating Authority of Thailand. The data consisted of various soil types, therefore, it had to be filtered to obtain cohesive soil samples. The initial criteria being samples consisting of clay and silt fraction more than 50%. A total of 3,900 records of cohesive soil samples were obtained. According to the USDA soil texture triangle [12] the samples can be classified into 6 types as shown in Table 1. Each sample comprises of laboratory test results which consist of 9 individual parameters as shown in Table 2.

Table 1 Types of soil samples classified according to the USDA texture triangle

Soil type	Number of samples
1. Clay	2,358
2. Clay loam	95
3. Loam	153
4. Silty clay	1,137
5. Silty clay loam	105
6. Silt loam	52
Total	3,900

Data Analysis

Each parameter listed in Table 2 was statistically analyzed compared to the plasticity index which is Massarsch's main variable for determining K_0 .

Three parameters were found to strongly influence the values of plasticity index and K_0 , these are, bulk density (D_b), water content (w), and particle density (used as an alternative to the specific gravity, G_s).

Table 2 Available laboratory test result for each

soil sample.

Soil type	Unit
1 Moisture Content	%
2 Particle Density	kg/m ³
3 Bulk Density	kg/m ³
4 Dry Density	kg/m ³
5 Plasticity Index	%
6 Clay	%
7 Silt	%
8 Sand	%
9 Gravel	%

Note: Parameters not relevant to this study are not listed.

RESULT

Proposed Simplified Solution

The resulting formula for determining K_0 of cohesive soils is found to be based on the bulk density (D_b), water content (w), and specific gravity (G_s) as follow

$$K_0 = 0.38 + 0.102 \left(\frac{G_s (1 + w)}{D_b} \right) \quad (5)$$

The above equation can be written in the form of the specific volume (V') or void ratio whichever is preferred

$$K_0 = 0.38 + 0.102 V' \quad (6)$$

$$K_0 = 0.38 + 0.102 (1 + e) \quad (7)$$

Analysis of the Proposed Solution

Values of K_0 from the new solution is compared to that of Massarsch's solution as shown in Fig.1

The maximum, minimum, and average error of K_0 from the new solution is 5.00%, 0.00%, and 2.00%, respectively. In order to confirm the accuracy of the solution, an analysis of the error was conducted. The dependent variables are plotted against the error of K_0 as shown in Figs.2 to 5.

It can be seen that samples with specific volume between 1.20 and 2.00 do not affect the error of K_0 . However, specific volume values are limited due to the nature of the soil samples, therefore, it cannot yet be concluded that specific volume values higher than 2.00 would result differently. Bulk density, water content, and specific gravity also do not show any influence on the error of K_0 . However, errors may increase at high water content (more than 30%) but this is inconclusive with the available data.

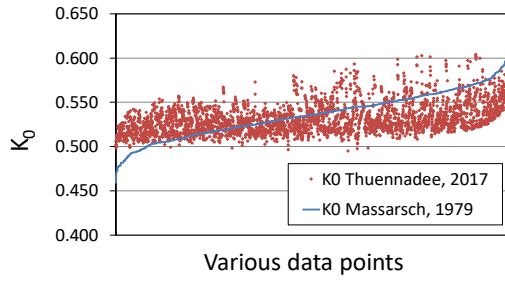


Fig.1 Comparison between values of K_0 obtained from Massarsch's formula and that of the new proposed formula.

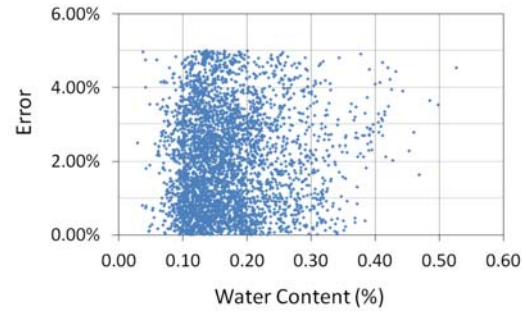


Fig.4 Values of water content and the resulting error of K_0 compared to Massarsch's solution.

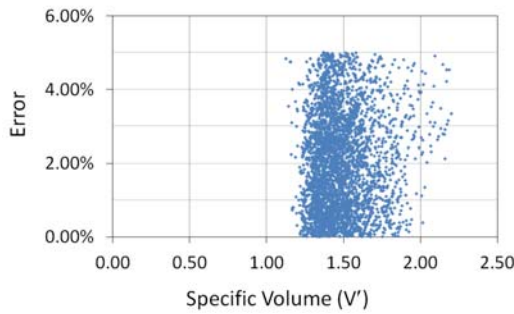


Fig.2 Values of specific volume and the resulting error of K_0 compared to Massarsch's solution.

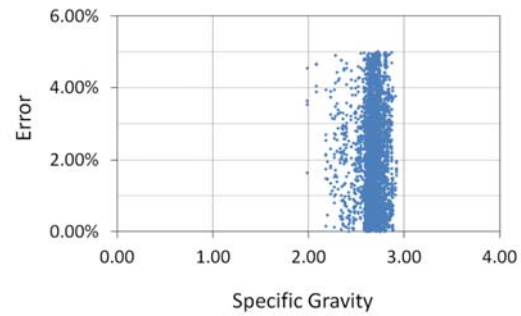


Fig.5 Values of specific gravity and the resulting error of K_0 compared to Massarsch's solution.

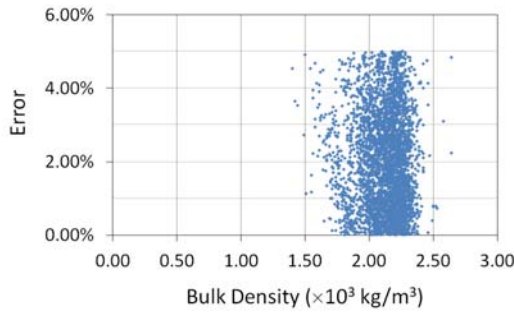


Fig.3 Values of bulk density and the resulting error of K_0 compared to Massarsch's solution.

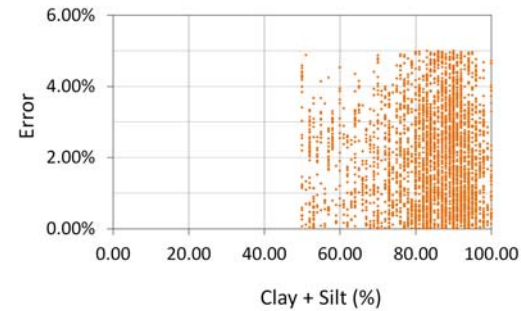


Fig.6 Values of total clay and silt fractions and the resulting error of K_0 compared to Massarsch's solution.

Limitations of the Proposed Solution

5.3.1 Particle Size

The effects of the amount of clay and silt on the error of K_0 is presented in Figs.6 to 8. Fig.6 shows that the error of K_0 is not influenced by the amount of clay and silt of more than 50%. However, Fig.7 and 8 show that error increases with clay fraction less than 20% and silt fraction more than 60%.

5.3.2 Activity

The activity of the clays according to Skempton [13] was calculated from

$$A = \frac{PI}{\% \text{Clay fraction (weight)}} \quad (7)$$

The samples were found to have activity below 1.25. Therefore, the soil samples are categorized as normal clays.

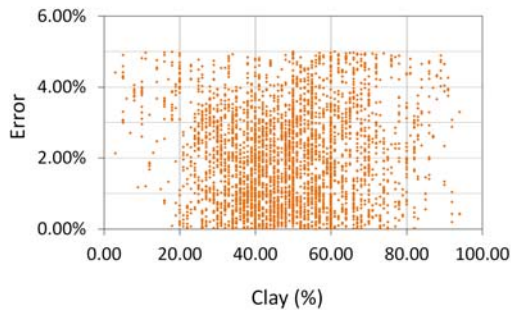


Fig.7 Values of total clay fraction and the resulting error of K_0 compared to Massarsch's solution.

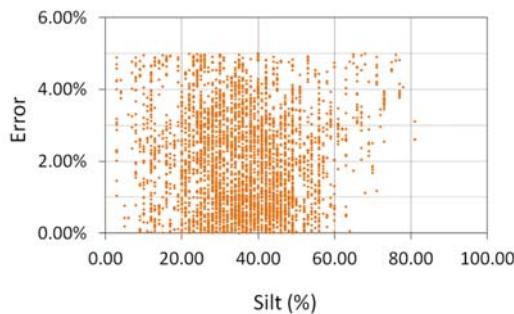


Fig.8 Values of total silt fraction and the resulting error of K_0 compared to Massarsch's solution.

CONCLUSION

A simplified formula for determining the value of coefficient of lateral earth pressure at rest (K_0) is presented in Eq.6. The solution is dependent on the specific volume which can be easily determined in the laboratory. Since it is not dependent on the plasticity index, the application of this formula can be extended to cohesionless soils and especially soils that are ambiguous in its cohesiveness. There are several important notes to be made:

(1) The maximum, minimum, and average error of K_0 from the new solution is 5.00%, 0.00%, and 2.00%, respectively. The accuracy is assumed to correspond with the accuracy of Massarsch's solution and currently applies to cohesive soils.

(2) The formula is applicable to soils with normal clays. Active clays are expected to result differently, therefore, using this formula is not recommended.

(3) Although K_0 values are comparable to those obtained by Massarsch's solution, validation against laboratory or in situ data is necessary and is an ongoing process.

(4) The applicability of this solution to cohesionless soils is still under investigation.

ACKNOWLEDGEMENTS

The authors are truly grateful for the valuable data given by the Geotechnical Engineering Department, Mae Moh Mine, Electricity Generating Authority of Thailand.

REFERENCES

- [1] Jaky J, "The coefficient of earth pressure at rest", Journal of the Society of Hungarian Architects and Engineers, Vol. 7, 1944, pp. 355-358.
- [2] Jaky J, "Pressure in soils", in Proc. 2nd International Conference on Soil Mechanics and Foundation Engineering, Vol. 1, 1948, pp. 103-107.
- [3] Brooker EW and Ireland HO, "Earth pressures at rest related to stress history", Canadian Geotechnical Journal, Vol. 2(1), 1965, pp. 1-15.
- [4] Feda J, "K₀-coefficient of sand in triaxial apparatus", Journal of Geotechnical Engineering-Asce, Vol. 110(4), 1984, pp. 519-524.
- [5] da Fonseca AV and Sousa JAE, "At rest coefficient of earth pressure in saprolitic soils from granite", in Proc. Fifteenth International Conference on Soil Mechanics and Geotechnical Engineering, 2001, pp. 397-400.
- [6] Guo PJ and Stolle DFE, "Fabric and particle shape influence on K₀ of granular materials", Soils and Foundations, Vol. 46(5), Oct 2006, pp. 639-652.
- [7] Wanatowski D and Chu J, "K₀ of sand measured by a plane-strain apparatus", Canadian Geotechnical Journal, Vol. 44(8), Aug 2007, pp. 1006-1012.
- [8] Schmidt B, "Discussion of 'Earth pressures at rest related to stress history' by Brooker & Ireland (1965)", Canadian Geotechnical Journal, Vol. 3(4), 1966, pp. 239-242.
- [9] Pruska MJ, "Effect of initial stress on the stress-strain relation", in Proc. 8th International Conference on Soil Mechanics and Foundation Engineering, Vol. 4, Moscow, 1973, pp. 26-28.
- [10] Wroth CP, "In situ measurement of initial stresses and deformation characteristics", in Proc. In Situ Stress Measurement of Soil Properties, North Carolina State University, Geotechnical Engineering Division, 1975, pp. 181-230.

- [11] Massarsch KR, "Lateral Earth Pressure in Normally Consolidated Clay", in Proc. Seventh European Conference on Soil Mechanics and Foundation Engineering (Design parameters in geotechnical engineering), Vol. 2, Brighton: British Geotechnical Society, 1979, pp. 245-249.
- [12] United States Department of Agriculture, "Texture Triangle and Particle-Size Limits of AASHTO, USDA, and Unified Classification Systems", National soil survey handbook, title 430-VI. USA: United States Department of Agriculture, 2016.
- [13] Skempton AW, "The Colloidal Activity of Clays", in Proc. Third International Conference on Soil Mechanics and Foundation Engineering, Vol. 1, Switzerland, 1953, pp. 57-61.

A STUDY ON PERMEATION CHARACTERISTICS OF MICRO PARTICLES INTO SAND

Yukoh Hasunuma¹, Kentaro Uemura¹
Takamitsu Sasaki², Koichi Nagao³, Shunsuke Shimada⁴
Tsuyoshi Tanaka¹, Naoaki Suemasa¹

¹Tokyo City University Graduate Division, Japan; ²Kyokado Engineering co.,Ltd, Japan;

³Sato Kogyo, Japan; ⁴ Kyokado co.,Ltd, Japan

ABSTRACT

In this study, Bubble White was proposed as a new grouting material for a chemical grouting method, which is a mixture of silica micro-particles and micro bubble water. By injecting the Bubble White into ground, it was expected to increase the effectiveness of preventing ground from liquefaction. However, it is not common to improve granular soil by injecting a suspended grout solution containing micro particles since it is difficult to secure a sufficient improved diameter by this method. Therefore, the penetration properties of micro particles to the ground have not yet been sufficiently clarified. In the previous research, the permeability characteristics under a constant pressure were investigated by the injection experiments using unprepared sand specimens. In this report, therefore, we examined the penetration characteristics when injected at a constant rate. As a result of the experiments, it was confirmed that the permeability of micro particles depended on both injection rate and injection volume.

Keywords: Micro-particles, Micro bubble, Liquefaction countermeasures

INTRODUCTION

Since approximately 75% of Japan is mountains and forests, the Japanese economy has been developed mainly around the coastal areas and landfill was used to supplement lacking developable plains. However, liquefaction strength of the landfill is low. By the Pacific coast of Tohoku Earthquake that occurred in 2011, the landfill such as Urayasu city, Chiba Prefecture suffered from large-scale liquefaction damage and it became a social problem.

Liquefaction has been a serious problem in Japan for a long time and many technical countermeasure methods have been developed until now. However, since most of the methods generally used for liquefaction countermeasures need large-scale construction machinery, it is difficult to improve the grounds in narrow places such as residential land. In addition, the construction in a narrow place requires a high cost per unit area in comparison with that in a large place [1]. Accordingly, it has been demanded to develop a method with a low cost and better operability. In this study, Bubble White is proposed as a new grouting material for a chemical grouting method, which is obtained by mixing silica micro particle and micro bubble water.

It is not common to improve granular soil by injecting a suspended grout solution containing micro particles since it is difficult to secure a sufficient improved diameter by this method. For that reason, it is essential to clarify the injection characteristics of micro particles and the liquefaction strength in sand specimen improved by the micro particles. In the

previous studies, injection experiments were conducted to investigate the injection properties, where silica micro particles were injected into saturated sand specimens at a constant pressure [2]. According to the test results, it was found that when the injection pressure was high, the micro particles flowed in the voids of the soil particles and permeated throughout the specimen, and the concentration distribution became substantially uniform. On the other hand, when the injection pressure was low, the micro particles tended to clog in the voids resulting in an increase in the concentration of the micro particles near the injection port. In addition, it was also revealed that the liquefaction strength improved by injecting Bubble White increased compared to the unimproved case [3]. Since a constant pressure was set for the previous injection experiment, this study focused on the injection rate.

In this report, therefore, a constant rate was provided during the injection experiments to get more detailed information about the permeability.

NEW GROUTING MATERIAL BUBBLE WHITE

Photo. 1 shows micro bubbles pouring in a beaker. As the characteristics of the micro bubbles, the surface area of micro bubbles is quite large in comparison with that of a normal air bubble with the same volume. Also, the bubbles have an advantage that they tend to rise slower and accordingly diffuse horizontally. The micro bubbles can reduce both



Photo. 1 Micro bubbles

saturation degree and pore water pressure in the ground during an earthquake [4].

The silica micro particles are white and powdery, containing silicon dioxide as a main component. The micro particles used for this experiment were industrially produced amorphous silica and classified so that the average particle diameters became about 20 μ m. By injection of the silica particles, the density of ground increases. In addition, the silica particles are viscous enough to stay in the voids of ground. They can increase the density of ground efficiently. Fig.1 shows an image of the improvement effect of bubble white. By combining these excellent materials: the micro-bubble water and the silica micro-particles, it was expected to increase the effectiveness of preventing ground from liquefaction [5].

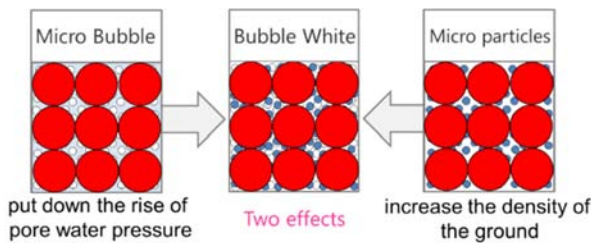


Fig. 1 Improvement effect of bubble white

As described above, although constant pressures were applied to the specimens and the injection behavior was investigated through the previous experiments, the injection characteristics of the micro particles have not yet been sufficiently clarified. This time, therefore, focusing on the injection rate, the purpose of the experiments was set to confirm the injection behavior when the injection rate was constant.

ONE-DIMENSIONAL INJECTION EXPERIMENT

Conditions of Experiment

A series of experiments were carried out with the aim of confirming the difference in injection behavior when different void ratios and different injection rates were provided. During the experiments, silica micro particles were injected into saturated sand specimens at a constant rate. Fig.2 and Fig.3 show the schematic of injection experiment, and grain size accumulation curves of micro particles and silica sand #5. Table 1-3 show the physical properties of silica sand #5, the conditions of specimens and the conditions of experiments, respectively. The specimens were prepared by an air-pluviation method so as to become 50 cm in height and 5.0 cm in diameter, and the void ratios of Case 1 and Case 2 were 0.84, and those of Case 3 and Case 4 were 0.80, respectively.

In order to prevent from clogging of micro particles in pipes of experimental equipment, filter media were installed at the top and the bottom of the specimen, which are constituted of a plurality of glass beads having a diameter of about 1 cm and a plate having a large number of holes with a diameter of about 1.5 mm.

Additionally, the specimens were completely saturated by permeating CO₂ and degassed water into the specimens.

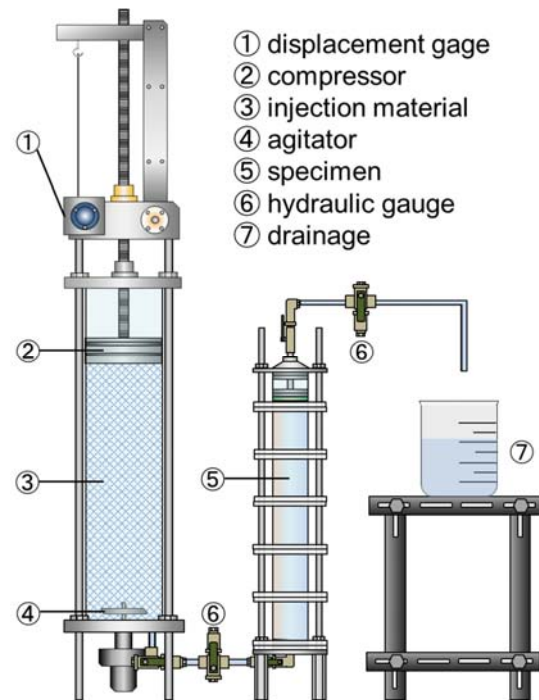


Fig. 2 Schematic of injection experiment

The injection material was a suspended grout solution whose concentration of silica fine particles dissolved in water was adjusted to 6% by weight. Here, the injection rate in Table 2 shows the flow rate of water when draining directly from the injection device. In addition, in order to measure the change of water pressure with time elapsed, water pressure gauges were installed at two places; one was the connection part between the injection device and the specimen and the other was the drain part of the specimen. Columns of the specimens can be divided by 10cm each and concentration distributions of fine particles in pore water were measured after injection experiment was completed.

Table. 1 Physical properties of silica sand #5

	ρ_s (g/cm ³)	ρ_{\max} (g/cm ³)	ρ_{\min} (g/cm ³)
silica sand #5	2.640	1.555	1.300

Table. 2 Conditions of specimens

case	case1	case2	case3	case4
sample	silica sand #5			
diameter (cm)	5.0			
height (cm)	50.0			
void ratio	e=0.84		e=0.80	
void volume (cm ³)	448.19		438.58	

Table. 3 Conditions of experiments

case	case1	case2	case3	case4
injection material	silica micro particles			
concentration of injection material	6.0%			
injection rate (cm ³ /sec)	4.35	22.21	4.35	22.21

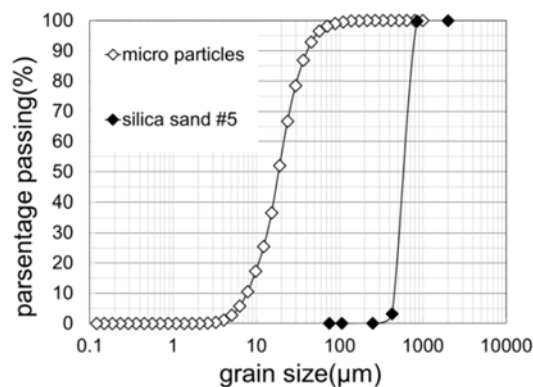


Fig. 3 Grain size accumulation curves of micro particles and silica sand #5

Results of Experiment

(1) Comparison of cases with low injection rate

Fig. 4 shows the relationship between injection volume and pressure head in case of a low injection rate. The chain line shown in the figure is a line drawn to obtain a gradient of the injection volume at the initial stage of injection. At first, the two cases with low injection rates were compared. The comparison between Case 1 and Case 3 showed very similar tendencies, while their void ratios were different. In Case 1, although the pressure increased immediately after injection started, the increase in pressure began to decrease after the injection volume became 300 cm³. The previous studies showed that the injected particles tended to clog more at a low injection pressure rather than at a high injection pressure [2]. Therefore, it was assumed that the micro particles adhered to the voids of the soil particles were swept away due to the high injection pressure at the initial stage in Case 1. As the increase in pressure was also suppressed after the injection volume reached 300 cm³ in Case 3, it was presumed that Case 3 has a similar tendency to Case 1. However, a large pressure fluctuation was seen even after that point in Case 3. It was likely that since the void ratio of Case 3 was smaller than that of Case 1, the particles tended to clog in the voids and flowed intermittently. After that, the pore water was completely replaced with the injection material and the injection behavior became temporarily stabilized. Meanwhile, the micro particles were continuously accumulated and accordingly the pressure kept on increasing until the compressor of the injection device stopped working.

Fig. 5 shows the relationship between concentration ratio and permeation distance in case of low injection rate. In this figure, the index C/C_0 is the ratio of C ; the concentration of pore water to C_0 ; the initial concentration of material in injected mixture. From the comparison between Case 1 and Case 3, it was confirmed that the concentration ratio of Case 3 was lower than that of Case 1. However, almost no difference was seen in the final injection volume between Case 1 and Case 3. Therefore, this result seems to be caused by the fact that the void was small and tended to be clogged by micro particles in Case 3. That is, there is a possibility that they could neither flow through the voids nor sufficiently accumulate in some parts of the specimens because the fine particles clogged in the voids. In addition, high concentration of pore water in the vicinity of the injection port of the specimen was likely to be caused by clogging of the fine particles because the permeability of the micro particles appeared to greatly changed influenced by the characteristics of the experimental apparatus.

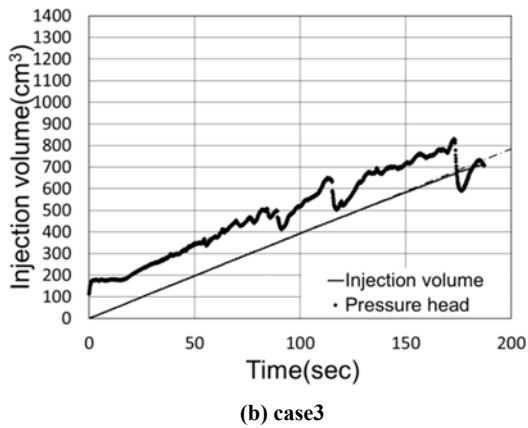
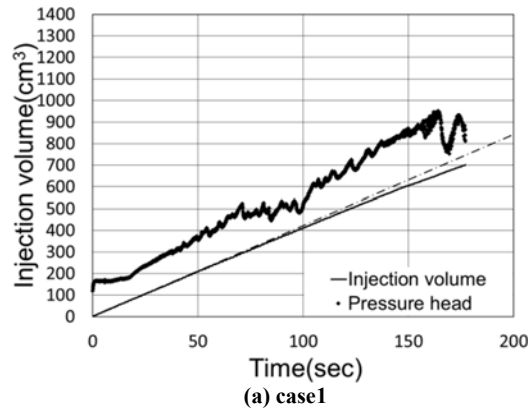


Fig. 4 Relationship between injection volume and pressure head in case of low injection rate

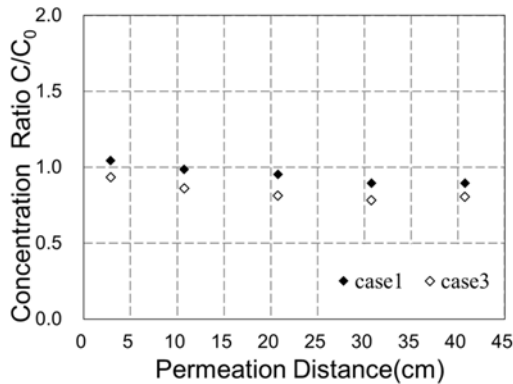


Fig. 5 Relationship between concentration ratio and permeation distance in case of low injection rate

(2) Comparison of cases with high injection rate

Fig. 6 shows the relationship between injection volume and pressure head in case of high injection rate. The injection pressure changed after replacing pore water with injected material in Case 2. After the change of the pressure, although the injection volume decreased slightly, it was possible to keep the

injection volume approximately constant. The total volume of injected material was about 2.7 times as much as the volume of pore water in the specimen of Case 2. In Case 4, on the other hand, sudden pressure fluctuation was seen before replacing the pore water of the specimen and the compressor of the injection device stopped when the pore water was replaced with injected material. According to the result of Case 2, it can be seen that the pressure rose almost constantly until the injected material completely replaced the pore water of the specimen. Thereafter, the pressure fluctuation became large. The pressure fluctuation was likely to be caused by the repeated phenomenon in which injected micro particles were temporarily clogged between sand skeletons, and then removed and transported to another place due to high pressure injection.

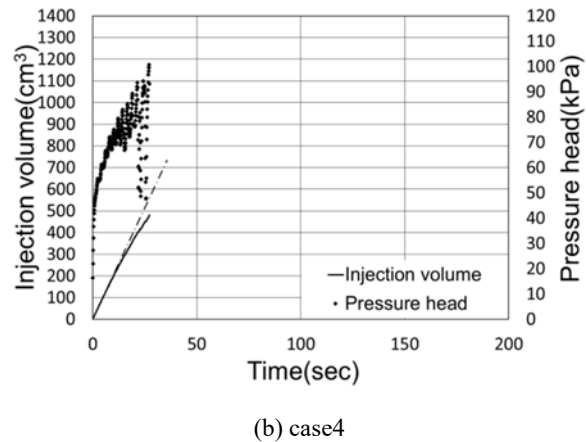
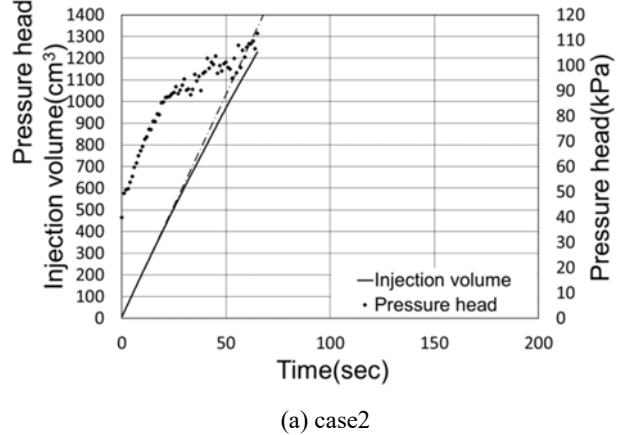


Fig. 6 Relationship between injection volume and pressure head in case of high injection rate

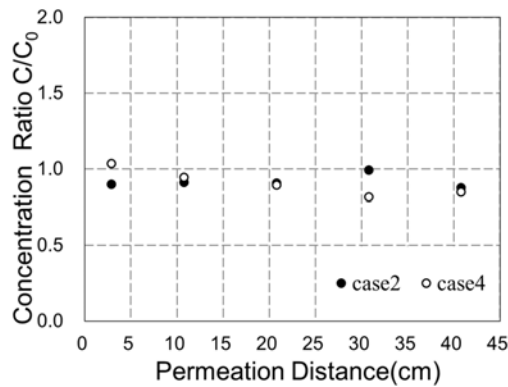


Fig. 7 Relationship between concentration ratio and permeation distance in case of high injection rate

Fig. 7 shows the relationship between concentration ratio and permeation distance in case of high injection rate. As shown in the figure, the variation was large compared with the case where the injection rate was low. In the case where the injection rate was high, it was presumed that the skeleton of the soil particle was disturbed by the flow of the injection material because the injection pressure was high. The tendency of accumulation of micro particles changed due to minute turbulence of the soil particle skeleton and therefore the concentration of pore water became varied. However, it was confirmed that the micro particles penetrated into the specimens sufficiently since the concentration ratios were distributed at around 1.0 as a whole.

(3) Comparison of permeability of injection material

Fig. 8 shows the relationship between injection volume and a coefficient of permeability k' . In this figure, the index k' is defined as the injection rate of the injection material divided by the hydraulic gradient. Since this value is different from the actual coefficient of permeability for water, it is denoted as k' . As shown in the figure, k' tended to depend on injection rate and injection volume. k' tended to be higher as its injection rate became higher. The tendency is considered to be due to the fact that the micro particles are more likely to become clogged because the injection pressure becomes lower as the injection rate is lower. The comparison between Case 1 and Case 3 showed a small difference immediately after the start of injection. However, the two cases showed similar behavior, and the k' value almost agreed with each other. Similarly to the case with low injection rate, the two cases with high injection rate showed similar behaviors. In case 4, however, after k' fluctuated largely, the injection became impossible. It is thought that the pressure fluctuation showed that clogging occurred.

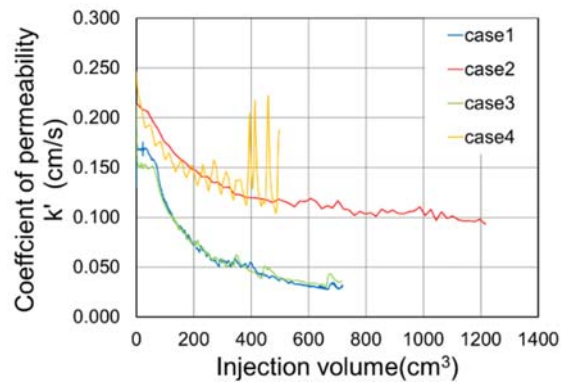


Fig. 8 Relationship between injection volume and coefficient of permeability k'

CONCLUSIONS

In order to investigate the penetrability of micro particles, a series of one-dimensional injection experiments with a constant injection rate was carried out in this paper. The following conclusions were obtained from the experiments.

- 1) Since the pressure increased almost constantly when the injection rate was constant, it is presumed that the micro particles were continuously accumulated.
- 2) It was suggested that the permeability of micro particles varies depending on the injection amount since an increasing tendency was seen in the pressure at the time when the injection volume reached the void volume of the specimen.
- 3) Although the concentration of injection material showed a slightly higher tendency near the injection port, the specimens were uniformly improved in the cases the flow rates were constant throughout the experiments and a sufficient amount of injection material was injected into the specimens.
- 4) It was suggested that there is a possibility that the soil skeleton of specimen could be broken by injection with a high rate.

REFERENCES

- [1] The commission related to earthquake proof countermeasure of residential development in Kanto Branch of The Japanese Geotechnical Society (2013) "The briefing session relate to earthquake proof countermeasure of residential development -a guideline to protect residence from liquefaction-," *Kanto Branch of The Japanese Geotechnical Society*, 84-85
- [2] Uemura K, Naoaki S, Takamitsu S, Koichi N (2016)" The Injection experiment on penetration characteristics of micro particles" *Proceedings of the 71th Annual Conference of the Japan Society of Civil Engineers*, 479-480
- [3] Hasunuma Y, Kentaro U, Naoaki S, Takamitsu S, Koichi N (2016)" A study on injecting micro bubble water mixed with crushed silica" *Sixth International Conference on Geotechnique , Construction Materials and Environment*, Bangkok, GEOMATE, 162-167
- [4] Koichi N, Naoaki S, Tosiya K, Saeki Y(2015),"Applicability of soil improvement with using Micro-Bubbles mixing water against soil liquefaction" *Proceedings of the 70th Annual Conference of the Japan Society of Civil Engineers*, 395-406.
- [5] Shota M, Kentaro U, Naoaki S, Takamitsu S, Koichi N(2015), "Ultrafine particles of silica grouting method for liquefaction countermeasure " *Proceedings of the 50th Annual Conference of The Japanese Geotechnical Society*, 307-308.

OPTIMUM USE OF GEOGRID IN THE UNBOUND GRANULAR LAYER FOR THE PAVEMENT CONSTRUCTION

AUNG AUNG SOE¹, Jiro KUWANO², Ilyas AKRAM³ and Takaya KOGURE⁴
^{1,2,3,4}Department of Civil and Environmental Engineering, Saitama University, Japan

ABSTRACT

The benefits of using geogrid for the pavement construction have been reported by many researchers. The well-known benefits are base course reduction and rut-depth reduction. Currently, the available information is still limited for the geogrid-stabilized pavement construction. In this study, the benefits of geogrid stabilization were investigated through series of laboratory test. Base-course thickness and reinforcement position of geogrid were considered as the control parameters and their influences were analyzed on the surface and subgrade deformations. The tests were performed in a rigid square-tank, and the subgrade and base course were modelled by using the fine and coarse silica sands. Triangular geogrid was used for the reinforcement. Cyclic loading was applied with the variable steps of loading ranging from 100 kPa to 550 kPa. From the test results, it was realized that the surface deformation was mainly contributed from the subgrade deformation in the thin base-course sections. In contrast, the base-course deterioration dominated and resulted in severe surface deformation in the thick base-course sections. This severe deformation was effectively reduced when geogrid location was shifted to the upward position inside base course layer. However, this geogrid position has negligible influence on the subgrade deformation, which is considerably affected by the base-course thickness. In all test cases, a progressive loss in base course thickness was noticed under high footing pressure. This loss is smaller in the thin section, compared to thick one. Test results revealed that the benefit of geogrid stabilization is more obvious in the thin section.

Keywords: Pavement, Base Course, Subgrade, Deformation, Geogrid Position

INTRODUCTION

Geosynthetic materials have been widely used in the geotechnical engineering applications due to their beneficial improvements. Depending on the applications and purposes, there are several types of geosynthetic materials, such as geocell, geotextile and geogrid. Among them, geotextile and geogrid are mainly applied in the flexible pavement constructions in order that the design service life of pavement could be extended and/or the amount of base course materials could be reduced.

The key functions of geotextiles in improving flexible pavement performance are separation, reinforcement, and filtration [1]. Unlike geotextile, the reinforcement function is the main function of geogrid for the flexible pavement. Reinforcement refers to the mechanism(s) by which the engineering properties of the composite soil/aggregate are mechanically improved [2]. Geogrid reinforcement mechanisms can be distinguished into lateral restraint, improved bearing capacity and tensioned membrane effect [3]. From these mechanisms, the lateral restraint, also known as “confinement”, has been identified as the primary reinforcement mechanisms of geogrid [2] [3]. This is the ability of the aperture geometry of a grid to confine the aggregate particles within the plane of the material [3]. Hence, the geometry of geogrid aperture and the average particle

size of aggregate material become important for the lateral restraint mechanism.

Since there are several types of geogrid, such as uniaxial geogrid, biaxial geogrid and triangular geogrid (also called multiaxial geogrid), lateral restraint mechanism will be different depending on the geogrid type. For the recently developed triangular geogrid, there is limited information regarding the reinforcement mechanisms. Therefore, it becomes necessary to know the reinforcement behavior of this triangular geogrid. In this study, a commercially available triangular geogrid (TX160) was selected and its reinforcement behavior was examined by conducting large scale laboratory model test. Regarding the reinforcement position in base-course layer, the optimal placement position of the geosynthetic depends on the thickness of the base-course layer and the applied load magnitude, according to S. W. Perkins [4]. Thus, current study also focused on the reinforcement position in the granular layer in order to know the optimum use of geogrid in the unbound granular layer, together with different base-course thicknesses under the cyclic loading of variable load magnitudes.

EXPERIMENTAL PROGRAM

In this study, seven cyclic loading tests were performed, considering base-course thickness,

geogrid reinforcement position in base-course layer and the applied stress levels. For no reinforcement, base-course thicknesses were 10 cm, 20 cm and 30 cm. In geogrid-reinforced tests, base course thicknesses were 10 cm and 20 cm. For 20 cm thick base course, the reinforcement positions were considered as the reinforcement depth ratios (a/h) of 1.0, 0.75 and 0.5 which were obtained when the depth of reinforcement (a) was divided by the base-course thickness (i.e. $h = 20$ cm). Test conditions are summarized in Table 1.

Table 1 Test conditions

Test ID	*BC thickness (cm)	Reinforcement	** a/h
10X	10	Non	-
20X	20	Non	-
30X	30	Non	-
10T	10	TX160	1.0
20T1.0	20	TX160	1.0
20T0.75	20	TX160	0.75
20T0.5	20	TX160	0.5

* base course

** reinforcement depth ratio

Remarks:

- 1) Subgrade was modelled by fine uniform sand and prepared by sand raining method.
- 2) BC was modelled by coarse uniform sand and prepared by compaction.
- 3) In each test, cyclic load was applied with varying magnitudes ranging from 100 kPa to 550 kPa (500 cycles for each loading step).

MATERIALS

Subgrade and Base Course

Silica Sand No.5 and No.1 were used for the model subgrade and base course preparation. These sands are commercially available in Japan. These sands were selected because they have uniform gradation, and, hence, there would be minimum variation in the particle size distribution in each test.

The model subgrade sand has the following index properties: the specific gravity $G_s = 2.675$, the average particle size $D_{50} = 0.488$ mm, coefficient of uniformity $C_u = 1.98$, coefficient of curvature $C_c = 0.943$, maximum dry density $\rho_{max} = 1.628$ g/cm³, minimum dry density $\rho_{min} = 1.338$ g/cm³. Model base course has the average particle size D_{50} of 3.735 mm, uniformity coefficient C_u of 1.904 and curvature coefficient C_c of 0.879. Since C_u and C_c values of both sands are not in the range ($C_u > 6$ and $1 < C_c < 3$) specified by Unified Soil Classification System (USCS), they can be regarded as poorly graded sand (SP) [5]. The particle size distribution curves of these

sands are presented in Fig. 1.

Reinforcement Material

In this study, the commercially available triangular geogrid (trade name TX160, product of Tensar) was used for the reinforcement purpose. This geogrid has the tensile strength of 10 kN/m in the cross-machine direction and diagonal directions, pitch length of 40 mm along each side of triangular aperture, and unit weight of 245 g/m². The dimensions of TX160 geogrid are illustrated in Fig. 2.

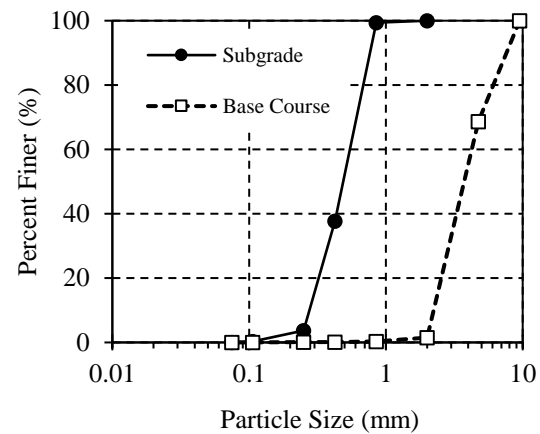


Fig. 1 Particle size distribution curves

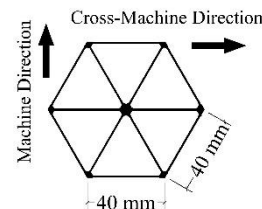


Fig. 2 Dimensions of triangular geogrid (TX160)

EXPERIMENTAL SETUP AND TESTING

In this experimental study, a large square container (100 cm x 100 cm x 80 cm) was used for the preparation of model pavement sections. A rigid circular steel plate, diameter = 17.5 cm, was used as a model footing. Since the total depth of subgrade and base course was greater than 70 cm in each test, the boundary influence from the tank base would be negligible according to Boussinesq Stress Distribution Analysis. In addition to this, the influences from the tank walls would be minimal on the test data because the size ratio between tank and footing diameter is considerably large ($100/17.5 \approx 6$) [6] [7].

In order to model the subgrade soil, the sand raining method was adopted and used in accordance with the literatures [8] [9] [10]. A large raining box

was developed so that the sand raining area covered over the plan area of tank. By using this raining method, the relatively high density was achieved in each test, ranging from 1.54 g/cm^3 to 1.66 g/cm^3 . These densities were calculated from the total mass of sand and the obtained average thickness.

After subgrade layer was prepared, a small plastic plate was placed at the predefined location where subgrade deformation was monitored, directly beneath the footing. Then, a small aluminum tube was set above this plate and was hold in vertical position with the help of supporting system. After that, coarse silica sand was spread over the subgrade layer in case of no reinforcement, while geogrid was placed in case of reinforcement. After the mass of 80 kg coarse sand have been filled, the compaction was manually conducted through the wooden plate in order to minimize the breakage of material. The obtained thickness was about 5 cm as an average after compaction. The same procedure was continued until the desired base-course thickness was obtained. The experimental layout is shown in Fig 3.

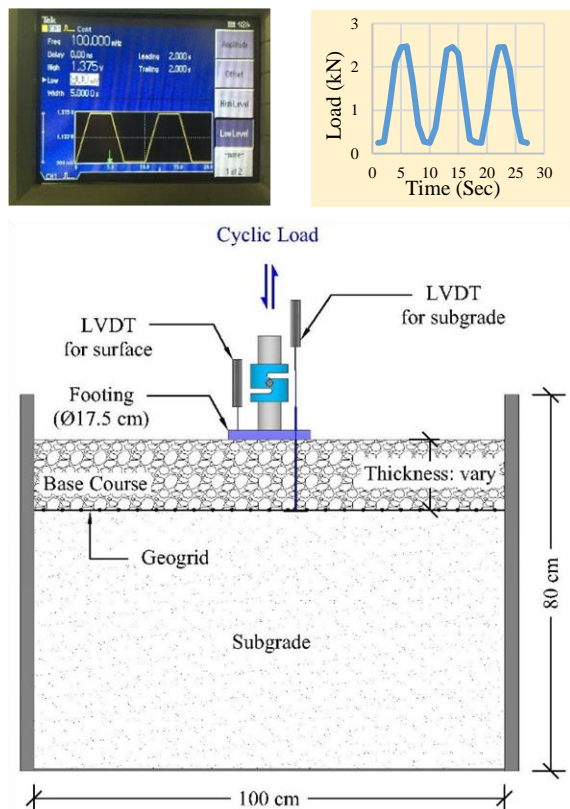


Fig.3 Experimental layout and test setup

The model footing was set after the preparation of subgrade and base course layers. One linear variable displacement transducer was set on the footing to monitor surface deformation, while another transducer was used to monitor subgrade deformation through the small aluminum tube. To simulate trafficked loading, a trapezoidal load pulse with a

frequency of 0.1 Hz was applied with the help of function generator, E-P transducer and pneumatic pressure via Bellofram cylinder. The generated voltage from function generator and the resulting load pulse are shown in Fig. 3. In each test, cyclic load was applied with variable amplitudes ranging from 100 kPa to 550 kPa. Each loading step was allowed until 500 load cycles. Load and deformations at the surface and subgrade were recorded by the data acquisition system at every 1 second.

RESULTS AND DISCUSSION

Influence of Base Course Thickness

The influence of base-course thickness was analyzed on the surface and subgrade deformations of geogrid-stabilized sections and non-stabilized sections. These are shown in Fig.4 and Fig.5, in which the legends represent the test conditions, as presented in Table 1.

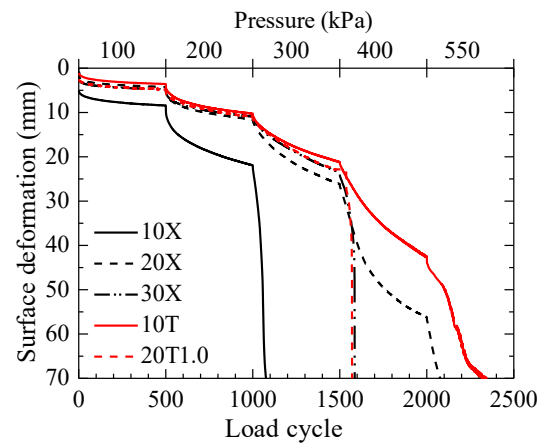


Fig.4 Influence of base-course thickness on surface deformation

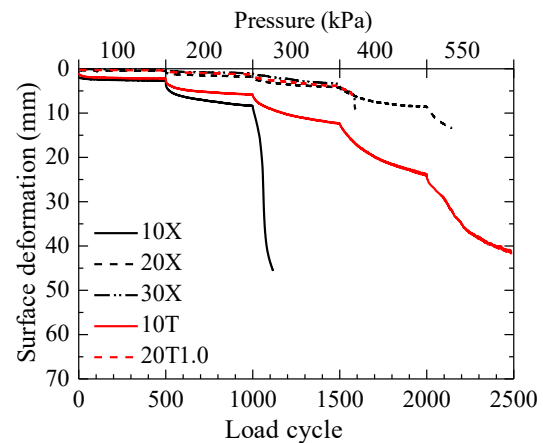


Fig.5 Influence of base-course thickness on subgrade deformation

As seen in Fig.4, the largest surface deformation was observed in the 10cm thick non-stabilized section (10X) since initial loading. Under 300 kPa pressure, this section suddenly failed just after few load cycles. This sudden deformation attributed to the bearing capacity failure of subgrade layer, shown in Fig.5. For 10 cm thick geogrid-stabilized section (10T), the significant improvement was observed under all loading stages, and this became more obvious with the increase in the stress levels. Though the surface deformation of 10T was much smaller than that of the corresponding non-stabilized section 10X, the subgrade deformations were similar to each other under 100 kPa pressure. For this test section, the reduction in subgrade deformation was started notice under 200 kPa pressure together with load cycles, shown in Fig.5. Thus, it can be assumed that the reinforcement action of geogrid might not have been fully mobilized under 100 kPa. However, the smaller surface deformation in 10T revealed that this improvement would have been contributed from the lateral confinement action of geogrid. This also implied that the confinement action of geogrid first appeared as soon as load was applied, and the full reinforcement mobilization would have been achieved with increasing load magnitudes. For 10 cm thick base-course, the benefit of geogrid stabilization was more significant with the increase in pressure and with load cycles.

When base-course thickness was increased to 20 cm, the improvement was noticed in case of non-stabilized sections (10X and 20X in Fig.4). However, this improvement was negligible when the base course was further increased to 30 cm (30X), in which a slight improvement was observed under 300 kPa pressure. Then, this 30cm thick section suddenly failed due to the lateral flow of aggregate materials under 400 kPa pressure. For the geogrid-stabilized sections, there was no obvious improvement when the base course was increased from 10 cm to 20 cm (10T and 20T1.0). Similar to 30X test, the sudden failure was found in 20T1.0 test. That might be due to the lateral flow of aggregate materials under 400 kPa pressure, before the reinforcement action of geogrid was fully mobilized.

Regarding the behavior of subgrade deformation, the deformations were minimal in thick base-course sections: 20X, 30X and 20T1.0, regardless of geogrid-stabilized conditions. Though base-thickness was increased to 30 cm in non-stabilized section, there was no obvious reduction in subgrade deformation, compared to 20 cm thick section (20X). This might be due to the nature of uniformity of aggregate. Because of uniform characteristic of this aggregate, the internal friction angel would be small and, the resulting stress distribution angle might also be small. Qian et al. also reported that the stress distribution angle became smaller with the number of load cycle [11]. Hence, the influence of base-course

thickness might have been smaller with the increasing load cycles.

Interestingly, the geogrid-stabilized section 20T1.0 behaved like 30 cm thick non-stabilized one (30X) in both surface and subgrade deformation characteristics. For the 10cm thick geogrid-stabilized section, it showed even better performance than that of 20X section, especially after 200 kPa stage. Hence, it was realized that the effect of geogrid inclusion in base-course layer was equivalent to the 10cm thickness of the given type of aggregate material. Thus, the required amount of aggregate could be reduced by mean of geogrid stabilization. Due to this aggregate uniformity, however, geogrid stabilization could be effective only in thin base course if geogrid was placed at the boundary between subgrade and base course (10T in Fig.4).

Effect of Geogrid Position in Base-Course Layer

Since a flow-type deformation was observed in 20 cm thick geogrid-stabilized base course, this thickness was selected to investigate the effect of geogrid position in the base course layer. Two more tests were performed; one with geogrid laid in the bottom-third of base course ($a/h = 0.75$) and the other in the middle of base course ($a/h = 0.5$). The surface and subgrade deformations were illustrated in Fig. 6 and Fig.7.

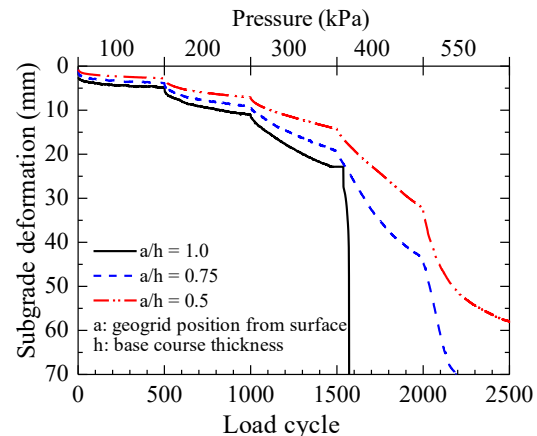


Fig.6 Surface deformation (geogrid position)

From Fig.6, it can be clearly seen that the surface deformation was effectively reduced at all level of loadings when a/h ratio became smaller. The improvement due to the smaller a/h ratio was more pronounced under high pressure levels (400 kPa and 550 kPa). Interestingly, the subgrade deformations were similar in these tests though there were obvious differences between the respective surface deformations. Thus, it was realized that the effect of geogrid position is insignificant on the subgrade deformation behavior.

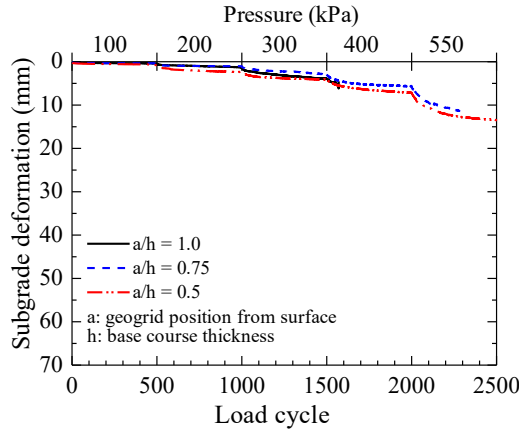


Fig.7 Subgrade deformation (geogrid position)

When geogrid was placed inside base-course layer rather than above the subgrade layer, the geogrid would have confined the aggregate materials on both sides of the layer. As a result, the base course layer became stiffer and the improved bearing resistance would be achieved, sustaining until the end of 550 kPa loading stage, shown in Fig.6. In addition, the lateral flow potential of aggregate material was effectively reduced with smaller a/h ratio due to optimal confinement effect on both sides of geogrid.

Loss in Base Course Thickness

In order to investigate the benefit of geogrid stabilization, the loss in base-course thickness (LBC) was calculated under each pressure level. This was simply formulated considering the difference in the rates of deformation between surface and subgrade, shown in Eq. (1).

$$LBC = \sum (\Delta d_f - \Delta d_{sg}) \quad (1)$$

Where,

Δd_f : rate of surface deformation

Δd_{sg} : rate of subgrade deformation

The variation in the loss of base-course thickness is shown in Fig.8, in which the presented data were taken after 500 cycles of loading. As seen in Fig.8, the loss in base-course thickness was successfully reduced at all pressure levels with the inclusion of geogrid. In all cases, the loss in base-course thickness became more obvious with increasing pressure level. Sun et al. also reported the similar behavior in their study [12].

When LBC values were compared between non-stabilized (10X) and stabilized (10T) sections, the geogrid-stabilized section reduced about 5 mm under given pressure level, though it was known that the

surface deformations were attributed to the subgrade deformations in both tests. On the other hand, the non-stabilized sections: 20X (20 cm thick) and 30X (30 cm thick), and geogrid-stabilized sections: 20T1.0 (20 cm thick, $a/h = 1.0$) and 20T0.75 (20 cm thick, $a/h = 0.75$) showed similar values of LBC under low pressure levels (≤ 200 kPa). Among these tests, the slight reductions in LBC were noticed with base-course thickness (20X to 30X) and geogrid position (20T1.0 to 20T0.5) under 300 kPa pressure, after which the sudden failures were observed in 30X and 20T1.0. These failures were mainly contributed from the lateral flow of aggregate materials.

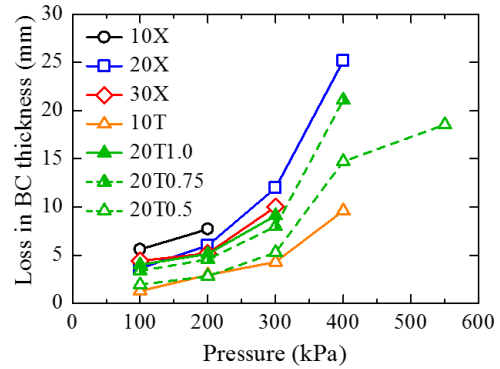


Fig.8 Loss in base-course thickness

For the geogrid stabilized sections: 10T (10 cm thick) and 20T0.5 (20 cm thick, $a/h = 0.5$), LBC values were almost same under the pressures of 100 kPa, 200 kPa and 300 kPa. However, a larger value of LBC was noticed in 20T0.5 than in 10T under 400 kPa pressure. This could be explained from the subgrade deformation behavior. The rate of subgrade deformation in 10T test had been progressively increased under 400 kPa pressure (10T in Fig.5). Hence, the resulting surface deformation was mainly contributed from this subgrade deformation. In addition, the large deformation in subgrade would promote to occur the tension membrane mechanism in geogrid. This behavior is good in agreement with the statement in which the tension membrane effect was recognized when permanent deformation was larger than 33% of the base thickness, reported by Qian et al. [11].

On the other hand, the subgrade deformation of 20T0.5 ($a/h = 0.5$ in Fig.7) was considerably small, compared to that of 10T. Thus, the potential of loss in base-course thickness of 20T0.5, due to lateral flow, was successively increased under 400 kPa pressure. This could result in a linearly increasing trend of surface deformation under 400 kPa pressure, shown in Fig.6 ($a/h = 0.5$). A concave trend of this curve was observed under 550 kPa pressure. This means that the rate of surface deformation became slower with load cycles, unlike the linear trend under 400 kPa. This

slower rate might have been resulted from the certain progressive rate of subgrade deformation ($a/h = 0.5$ in Fig.7). Hence, tension membrane action would have been initiated in the geogrid together with the subgrade deformation, resulting in the larger confinement effect and in the lower rate of increase in *LBC* values, as seen in Fig.8. From these test data, it is generally realized that the loss or deterioration of base course is mainly related to the applied stress level, and this can be effectively reduced by changing the geogrid position inside the base course layer.

CONCLUSIONS

The behavior of geogrid inclusion in the unbound granular layer was studied through large scale model tests. The uniform silica sands No.5 and No.1 were used as model subgrade and base-course layers. The cyclic loading with varying load magnitudes was applied through the circular rigid footing. From this study, the followings were summarized as:

- (1) For the given type of granular material, the effective improvement due to geogrid-stabilization was observed in thin base-course section, if geogrid was placed at the boundary between subgrade and base-course layer.
- (2) The surface and subgrade deformations were optimally reduced with the geogrid stabilization. However, this reduction was insignificant with the increase in base-course thickness.
- (3) In thin base-course section, surface deformation was mainly contributed from the subgrade deformation, while lateral flow dominated in thick section.
- (4) Flow type deformation was obviously minimized with the smaller reinforcement depth ratios. The optimum depth was known when geogrid was laid at the middle of base course.
- (5) The influence of reinforcement position was negligible on the subgrade deformation behavior.
- (6) Loss in base-course thickness (*LBC*) or base course deterioration is smaller in the thinner base course, while this is larger in thick section. This *LBC* can be successfully minimized with the smaller reinforcement depth ratios.
- (7) In all tests, the increase in *LBC* was noticed with increasing pressure levels.

ACKNOWLEDGEMENTS

This study was collaborated with NIPPO CORPORATION and MITSUI CHEMICALS INDUSTRIAL PRODUCTS LTD. Their supports are highly appreciated.

REFERENCES

[1] I. L. Al-Qadi, T. L. Brandon, R. J. Valentine, B.

- A. Lacina and T. E. Smith, "Laboratory Evaluation of Geosynthetic-Reinforced Pavement Sections," *Transportation Research Record*, vol. 1439, no. 1439, pp. 25-31, September 1994.
- [2] R. P. Anderson, "Geogrid Separation," in *Proceedings of International Conference on New Developments in Geoenvironmental and Geotechnical Engineering*, Incheon, Republic of Korea, 2006.
- [3] Stephen Archer, P.E., "Subgrade Improvement for Paved and Unpaved Surfaces Using Geogrids," CE News Professional Development Hours, 2008.
- [4] S. W. Perkins, "Mechanical Response of geosynthetic-reinforced flexible pavements," *Geosynthetics International*, vol. 6, no. 5, pp. 347-382, 1999.
- [5] J.-P. Bardet, *Experimental Soil Mechanics*, Upper Saddle River, New Jersey: Prentice-Hall Inc., 1997.
- [6] H. A. Alawaji, "Settlement and bearing capacity of geogrid-reinforced sand over collapsible soil," *Geotextiles and Geomembranes*, vol. 19, pp. 75-88, 2001.
- [7] T. Yetimoglu, J. T. H. Wu and A. Saglamer, "Bearing Capacity of Rectangular Footings on Geogrid-Reinforced Sand," *Journal of Geotechnical Engineering, ASCE*, vol. 120, no. 12, pp. 2083-2099, December 1994.
- [8] S. Miura and S. Toki, "A sample preparation method and its effect on static and cyclic deformation-strength properties of sand," *Soils and Foundations*, vol. 22, no. 1, pp. 61-77, March 1982.
- [9] Y. P. Vaid and D. Negussey, "Technical Note: Relative density of pluviated sand samples," *Soils and Foundations*, vol. 24, no. 2, pp. 101-105, 1984.
- [10] T. N. Dave and S. M. Dasaka, "Assessment of portable travelling pluviator to prepare reconstituted sand specimens," *Geomechanics and Engineering*, vol. 4, no. 2, pp. 79-90, 2012.
- [11] Y. Qian, J. Han, S. K. Pokharel and R. L. Parsons, "Performance of Triangular Aperture Geogrid-Reinforced Base Courses Over Weak Subgrade under Cyclic Loading," *Journal of Materials in Civil Engineering*, vol. 25, no. 8, pp. 1013-1021, August 2013.
- [12] X. Sun, J. Han, J. Kwon, R. L. Parsons and M. H. Wayne, "Radial stresses and resilient deformations of geogrid-stablized unpaved roads under cyclic plate loading tests," *Geotextiles and Geomembranes*, vol. 43, no. 5, pp. 440-449, 10 2015.

LONG-TIME STRENGTH PREDICTION METHOD OF CHEMICAL GROUT SPECIMEN WITH HEAT CURING

Shunsuke Takiura, Naoaki Suemasa and Kazuya Itoh¹, Takamitsu Sasaki² and Shunsuke Shimada³

¹ Urban and Civil Engineering, Tokyo City University, Tokyo, Japan

² Research and Development, Kyokado Engineering Co., Ltd, Tokyo, Japan

³ President, Kyokado Co., Ltd, Tokyo, Japan

ABSTRACT

In Japan, where many large earthquakes have happened, there has been a growing demand for liquefaction countermeasures. In this study, a chemical grouting method was focused on as a liquefaction countermeasure method because, it is excellent in performance compared to other methods. However, only ten several years have passed since the grout having long term durability was developed and accordingly the proof experiments about its durability have been carried out only during a period equivalent to it. In this study, the possibility to predict the change of long-term strength was examined by a series of short-term laboratory test where heat curing was provided for in promoting time variation of the specimens in a thermostatic tank. Here, the acceleration mechanism by heat curing was based on the chemical reaction rate theory of Arrhenius. As a result, it was confirmed that it was possible to predict the future change of durability with the proposed method in which the Arrhenius plot was adopted with unconfined compression test results from heat cure specimens.

Keywords: liquefaction, chemical grouting method, heat curing, Arrhenius plot, predicted values

INTRODUCTION

Liquefaction is the most significant and urgent concern in Japan and the countermeasures against liquefaction especially for revetments have been executed promptly since the 1995 Hyogoken-Nanbu earthquake caused serious damage to coastal areas. A chemical grouting method was selected as one of them. As a reason of the selection, there is less vibration and noise than other methods during the construction. In addition, this method provides small equipment for space saving, which can drill a hole not only in a vertical but also in an oblique and a curved line. Then, the Pacific coast of Tohoku Earthquake occurred on March 11th 2011. The maximum acceleration of 2933 gal was recorded in Kurihara city in Miyagi prefecture. Liquefaction occurred in many coastal regions from Tohoku to Kanto districts and the total damage throughout Japan reached 42 square kilometers. The liquefaction countermeasures using a chemical grouting method were performed in several places along the Pacific coast in 2008 after the 2007 Niigata Chuetsu-oki earthquake. It was revealed through the damage survey of the 2011 Earthquake that the chemical grouting method was quite effective as a liquefaction countermeasure [1].

The principle of the chemical grouting method is to prevent both contraction of sand skeletons and a rise in excess pore water pressure caused by the seismic vibration by replacing pore water between sand skeletons with a gelatinous silica compound. In addition, the silica compound gives cohesion between sand particles and accordingly increases shear

resistance against earthquake vibration. Fig.1 shows a conceptual diagram of strength development mechanism of a chemical improved body (Sasaki et al. 2011).

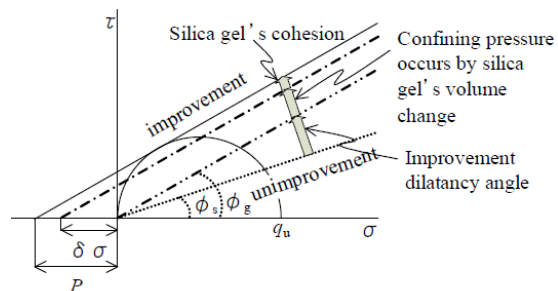


Fig. 1 Mechanism of improvement by active colloidal silica

The strength increase of an improved specimen consists of three parts. In the first place, additional confining pressure (P1) would be generated by that grout material adheres to sand particles and tends to reduce the volume when it is solidified. In the second, confining pressure effect (P2) can be expected by rigidity of solidified grout material when it is deformed by some kind of force. In the third, there is confining pressure effect (P3) added by the cohesion which the solidified grout material originally has.

As mentioned above, although the permanent grout material has been proved to be effective for liquefaction countermeasures, the long-term strength of the improved soil has been unexplained. One

reason is that most of previous studies on chemical grouting have focused on the development or the choice of durable infusion materials [2]. The other reason is that sufficient proof experiments for the materials have not been carried out because it has been only ten and several years since the permanent grout material was developed. Under these circumstances, it is essential to establish a practical way to estimate the strength change of the improved soil with elapsed time.

Therefore, the method in which the long-term strength is able to be verified in a short-term test is suggested in this study. In the method, the improved soil was provided with a special process to promote curing. Additionally, an equation (1) was suggested, which can assume unconfined compression strength, q_{us} , with internal friction angle, ϕ_s , increased by effect of the dilatancy increase with gel in void [3].

$$q_{us} = \frac{2 \sin \phi_s}{1 - \sin \phi_s} (p_1 + p_2 + p_3) \quad (1)$$

In the study, a heat and cure process have been applied to chemical improved specimens in a temperature and humidity testing chamber for 1000 days. Also, unconfined compression strength tests were conducted using the specimens and the strength change was reported. In conclusion, the age of the materials provided with standard cure was calculated from the test results using the specimens provided with promotion cure.

EXPERIMENTAL PROCEDURE

Table 1. Physical properties of Toyoura sand

Density test of soil particle (g/cm ³)	Maximum void ratio e_{max}	Minimum void ratio e_{min}
2.634	0.986	0.621

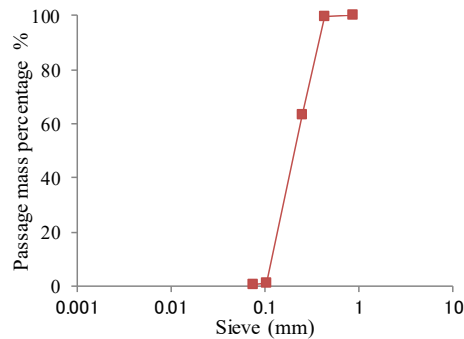


Fig. 2 Grain size accumulation curve of Toyoura sand

Toyouura sand was used for this experiment. Table 1. and Fig. 2 show the Physical characteristics of Toyoura sand.

The grout material used for the experiments was active colloidal silica and silica sol whose concentrations in weight were 29% and 6%, respectively. The active silica colloid is one of permanent grouts used for a permanent work such as liquefaction countermeasures. It is based on the active silica obtained by removing alkali from water glass by an ion exchange technique in order to exclude its deterioration factor. While the silica sol is a grout material for temporary constructions such as the ground improvement for an excavation construction where long term durability is not required. It is based on the non-alkaline water glass solution obtained by neutralizing alkali of water glass with acid [4]. The active colloidal silica has hardly changed in volume for a long time. On the other hand, the silica sol has remarkably changed in volume immediately after it was solidified and therefore, the unconfined compression strength of the improved soil tended to gradually decrease. It seemed to be because the confining pressure and the cohesion of the gel decreased or disappeared by the decrease in volume [5].

Two kinds of specimens; sand gel and plain gel, were prepared as follows. The specimen of sand gel was induration sand infiltrated with chemical grout. Toyoura sand was air-pluviated in a mold of 5cm in inside diameter so as to be a relative density of 60%. The height of samples was set 10cm by putting a weight on the top of the samples and tapping sides of the molds with a wooden hammer. Then the chemical grout deaerated in a vacuum pump was injected into the specimens and removed from the molds after solidification. Photo.1 describes the situation of injecting the chemical grout solution.



Photo.1 Infusion situation

The specimen of plain gel was an indurated gel-formed chemical grout. For the plain gel, 200ml of

chemical grout was poured into a glass container with 5cm in inside diameter and removed from the container after solidification. A process of curing was carried out under the conditions of three different temperatures; 25, 45 and 50 in degrees Celsius. All of the specimens wrapped in a wrap film were covered with wet papers and put in an airtight container to prevent from being dried. As for normal curing, the specimen was cured in the room where the temperature was constantly controlled at 25 degrees with an air conditioner. For heat curing, the specimens in the containers were set in the constant temperature tanks whose temperatures were continuously adjusted at 45 and 55 degrees,

Table 2. Experiment case

Grouting	Test piece	Curing temperature	site
Active colloidal silica	sand gel	25°C	A
		45°C	B
	plain gel	25°C	C
		45°C	D
Silica sol	sand gel	25°C	E
		45°C	F
		55°C	G
	plain gel	25°C	H
		45°C	I
		55°C	J

respectively. Experimental cases are shown in Table 2.

RESULTS AND DISCUSSION

Unconfined compression test result

Fig. 3 and Fig. 4 show the changes in unconfined compression strength of sand gel and plain gel improved by active colloidal silica, respectively. In both cases, the strengths of the specimens became higher when provided with heating curing rather than ordinary temperature curing. From the result, it was confirmed that heating curing was capable to promote the chemical reaction of chemical grout.

Fig. 5 shows the change in unconfined compression strength of sand gel specimens of silica sol. The specimens provided with heating curing showed lower strength than that with ordinary temperature curing and all of them gradually decreased in strength. Fig. 6 shows the change in unconfined compression strength of plain gel specimens of silica sol. In the same way as the sand gel, the specimens provided with heating curing showed lower strength than that with ordinary temperature curing. The specimen with ordinary temperature curing gradually increased in strength. On the other hand, as for the specimens with heating curing, the strength gradually decreased after having increased at the initial stage. Therefore, it is assumed

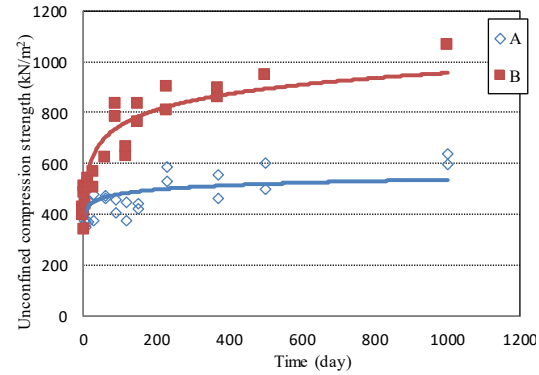


Fig.3 Unconfined compression strength of the active colloidal silica sand gel

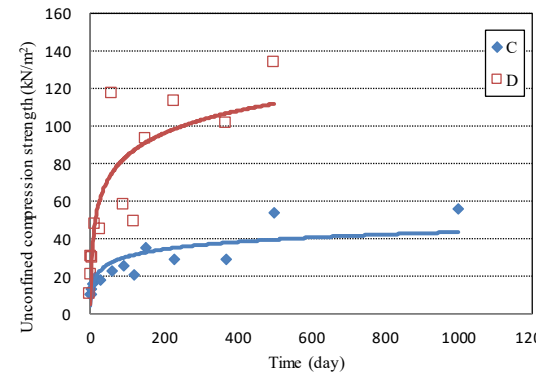


Fig.4 Unconfined compression strength of the active colloidal silica plain gel

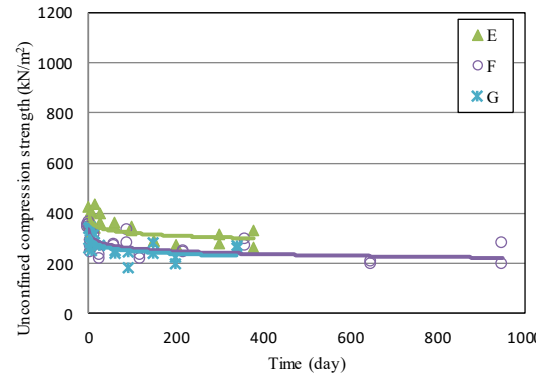


Fig.5 Unconfined compression strength of silica sol sand gel

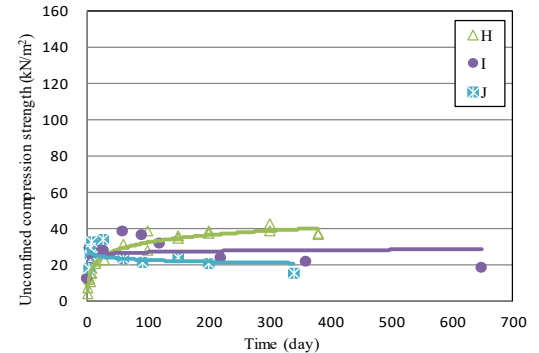


Fig.6 Unconfined compression strength of silica sol plain gel

that the strength with ordinary temperature curing would gradually decrease afterwards as well as the heated ones.

In the sand gel of active colloidal silica, the failure mode of the specimen differed between with and without the heating curing. The left of Photo.2 shows the state of shear failure in the specimen observed in its early period. While the specimen provided with a long-time heat curing had a tendency of tensile failure as shown in the right of Photo.2. The tensile failure in the lengthwise direction seems to be caused by the tensile strength generated when the specimen was compressed in the vertical direction. It is said that the higher the strength of specimen becomes, the more frequently this phenomenon appears.

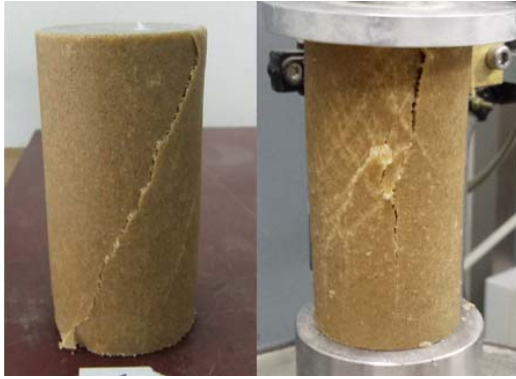


Photo.2 Failure mode of active colloidal silica sand gel

Volume change of plain gel

Fig. 7 and 8 show the changes over time in the volume of plain gel of active colloidal silica and silica sol, respectively. As for the active colloidal silica, the rates of volume change were constantly near -2.5% in all cases of ordinary temperature curing and heating curing. While, as for the silica sol, the rate of volume change in cases of heating curing grew larger than that in case of ordinary temperature curing. In addition, when comparing between the specimens with heating curing at different temperatures, the rate of volume change was larger at a higher temperature. Since the silica sol tends to be changeable in volume, it appeared that heating curing promoted the volume change in silica sol more effectively than ordinary temperature curing.

Long age strength estimation

Kaneko and Ozawa (1977) successfully estimated the deterioration time of insulating material under the condition of standard temperature (by heating curing) using the technique based on the chemical reaction speed theory of Arrhenius in their previous study [6].

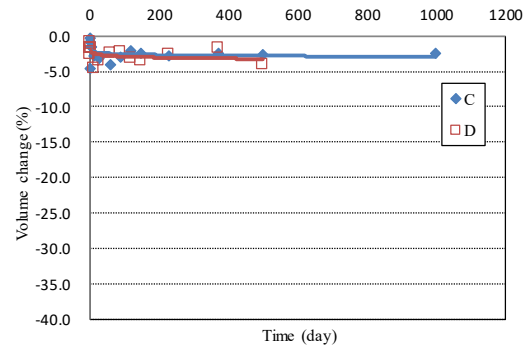


Fig.7 Volume change in active colloidal silica plain gel

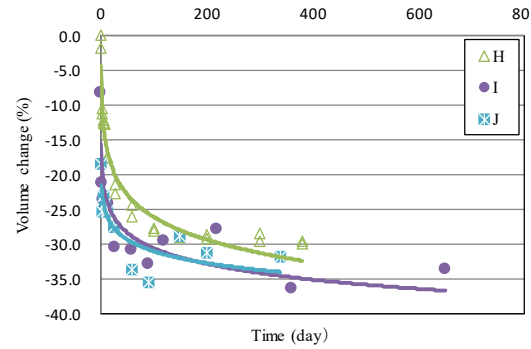


Fig.8 Volume change in silica sol plain gel

It was also supposed by Kaga (1994 and 2000) that it was possible to estimate a strength change with time elapsed by changing curing temperature, assuming that the hardening of infusion compaction sand was influenced by a chemical reaction [7]. Kaga studied the interrelation between a simpler chemical reaction speed and a reaction rate to examine his assumption.

Equations for a chemical reaction speed base on the Arrhenius theory are expressed by logarithm indications as follows.

$$\log \frac{A}{A_0} = -kt \quad (2)$$

$$\log k = \log C - \frac{E}{RT} \quad (3)$$

$$\alpha = \exp \left[\frac{E}{R} \left(\frac{1}{T_1} - \frac{1}{T_2} \right) \right] \quad (4)$$

Where A : density, A0 : initial density, k : rate constant, t : time, C : constant, E : activation energy, R : universal gas constant, T, T1, T2 : absolute temperature, α : acceleration factor.

Equation (2) shows the relationship between reaction rate, (A/A_0) and time. The rate constant, k in the equation (2) is dependent on absolute temperature as seen in the equation (3). Therefore, when temperature at which the chemical reaction is performed rises, the rate constant increases, and then the period required until the same degree of chemical

reaction is achieved decreases. In general, this reaction constant can be substituted with factors such as a volume change, a weight change, an area increment and a strength rate which are directly proportional to a chemical reaction speed [8]. A change rate of specimen strength was adopted for a substitution of k in this paper. Accordingly, strength change rates obtained from the experiment were plotted in a vertical axis of a logarithm indication, and curing temperatures were converted to absolute temperatures and the reciprocals of the factored absolute temperatures, $1000/T$, were plotted in a horizontal axis. Generally, this plot is called "Arrhenius plot". The plot obtained from the experiment results performed at more than two kinds of temperatures gives an acceleration factor shown in the equation (4), which factor is multiplied by time in the heat curing case to predict its future response. In accordance with this theory, the strength change of active colloidal silica provided with standard curing was calculated from the results of promotion curing.

Fig. 9 shows the Arrhenius plot of the same type calculated from the results of this experiment. As showed in Fig.3, the strength of active colloidal silica changed conspicuously from material age of 1 day to 90 days and became relatively stable after 90 days. These two periods, conspicuous change period and

stable change period, were separately plotted in order to get more precise prediction. Fig.10 shows the strength of sand gel of active colloidal silica which was predicted using the acceleration factor obtained from the Arrhenius plot of the same type in Fig.9. The predicted strength change showed a similar tendency to the measured strength changes from materials age 14 days to 1000 days. From the result, it was verified that the predicted values were equivalent to the measured values. Additionally, the strength change applied with standard curing for 3641 days was predicted using the strength change applied with heating curing for 1000-days.

The Arrhenius plot of the same type is shown in Fig.11, which was calculated from the unconfined compression strength of plain gel of active colloidal silica. Also, Fig. 12 shows the strength change of plain gel of active colloidal silica, which was predicted using the acceleration coefficient obtained from Fig.11. In the same way as the sand gel, the measured values and the predicted values of plain gel showed similar tendencies in strength change.

The efficiency of promotion with heating curing was confirmed in all cases through the experiments. In addition, the predictive values of sand gel and plain gel of active colloidal silica were calculated from the

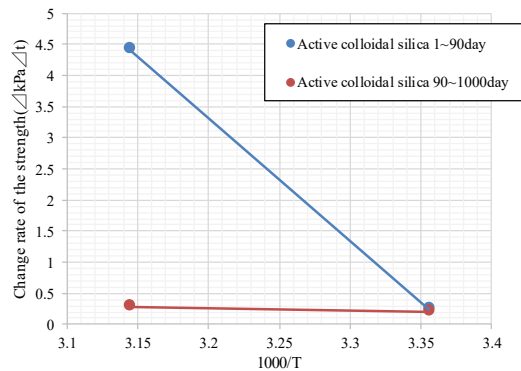


Fig.9 Arrhenius plot of active colloidal silica sand gel

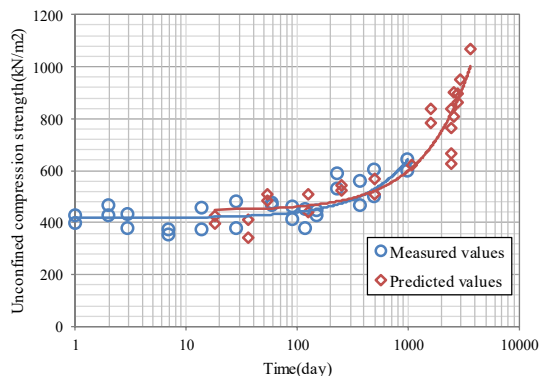


Fig.10 Predictive strength of active colloidal silica sand gel

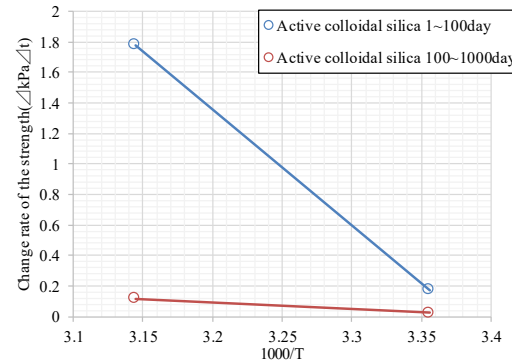


Fig.11 Arrhenius plot of active colloidal silica plain gel

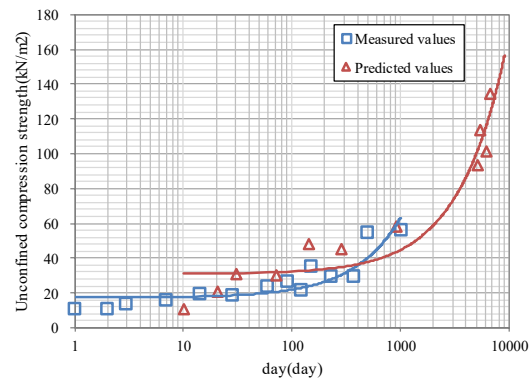


Fig.12 Predictive strength of active colloidal silica plain gel

results of heating curing. Judging from the superimposition of the linear approximate curves of the predicted and measured values, reliability of predicted values are high. Great potential can be expected in the strength prediction method with heating curing using a constant temperature humidistat tank.

CONCLUSION

In the study, a heat and cure process has been applied to a chemical grout in a temperature and humidity testing chamber and attempted predictive calculation in conformity with a chemical reaction speed theory of Arrhenius. The values of predicted strength change were similar to the measured values. In conclusion, long-term prediction was enabled by a short-term examination using a constant temperature humidistat tank.

REFERENCES

- [1] Sasaki, T., Oyama, T., Shimada, S., Suemasa, N (2011). "Influence of Soil Characteristics on Gel Time and Unconfined Compression Strength of Ground Improved by Chemical Grouting Method," The Twenty-first International Offshore and Polar Engineering Conference, 19-24 June, Maui, Hawaii, USA
- [2] Nakayama, T., Sawada, R., Hiraoka, Y., Akagi, H (2013). "Evaluation of Long Term Stability of Chemically Stabilized Sand with Grouting." Japan Society of Civil Engineering Memoirs C (Ground Zone Engineering), Vol69, No.2, pp162-173.
- [3] Sasaki, T., Shimada, S., Oyama, T., Suemasa, N (2011). "Influence of Soil Characteristics On Gel Time And Unconfined Compression Strength of Ground Improved By Chemical Grouting Method," The Twenty-first International Offshore and Polar Engineering Conference, 19-24 June, Maui, Hawaii, USA
- [4] Geo-grouting development Organization
HP: <http://www.jckk.jp/kokyu.php>
- [5] Kaga, M., Mori, A (1994). "Basic Study on Chemical Stability and Strength Durability of Silicate Grout Sand," Japan Society of Civil Engineering Memoirs, No.496/V-24, pp31-40.
- [6] Kaneko, T., Ozawa, T (1977). "The Handling of the Chemical Kinetics of the Deterioration of the Insulating Material Which Increased Heating, Cooling Periodically," The institute of Electrical Engineers of Japan article magazine A, Vol97, No.2, pp48-55.
- [7] Kaga, M (2000). "Physical and Chemical Stability of Pure Silicate Grout and Prediction of the Long-Term Strength of Grouted Sand," Japan Society of Civil Engineering Memoirs, No.652/III -51, pp195-205.
- [8] Hueno, T (1975). "Chemical Reaction Theory," Asakurashoten, pp24-30

FLY-ASH-BASED GEOPOLYMER AS STABILIZER FOR SILTY SAND EMBANKMENT MATERIALS

Jonathan R. Dungca¹, Edward Ephrem T. Codilla II²

^{1,2}Civil Engineering Department, Gokongwei College of Engineering, De La Salle University, 2401 Taft Ave., Malate, Manila 1004, Philippines

ABSTRACT

Fly ash in the recent decades has become abundant resulting to improper waste disposal. However, it is also known to be a precursor to the process of geopolymerization which is categorized under waste utilization. Geopolymer has become known for being on par with cement and other chemical stabilizers in terms of strength. It has been used in numerous studies focusing on concrete and on soil stabilization. This study proposes the use of fly-ash-based geopolymer as a stabilizer for silty sand embankment material wherein the process of synthesizing geopolymer is through the dry-mix method. The dry-mix method is another way of producing geopolymer, requiring the aluminosilicate precursors and alkali activators to be in its dry state, and adding water to the dry-mix would result to geopolymerization. The geopolymer was applied on Silty Sand to verify its reaction with the soil and to obtain the effective mix that would enable the soil to be stabilized for embankment use. The effectiveness of this method in soil stabilization was tested through the following tests, the CBR Test (ASTM D1833) and the UCS Test (ASTM D2166). Results have shown improvements of the geopolymer-stabilized soil in terms of the CBR index and the UCS value. The effective geopolymer concentration was found to be at 30% geopolymer concentration which produced the highest increase for the stabilized soil with a maximum CBR index of 34.32% and a maximum UCS value of 1349.74 kPa.

Keywords: Fly Ash; Dry-mix Geopolymer; Embankment Materials; Soil Stabilization

INTRODUCTION

In geotechnical works, a site is surveyed whether soil conditions meet the design criteria. However, most commonly, sites designated for earthworks do not reach the minimum standards, such as those with soft, highly compressible, or expansive soils lacking the desired strength for loading during construction or for their serviceability [1]. For this reason, such soils are enhanced through soil stabilization, wherein the mechanical properties of the soil are improved by applying materials that have cementitious properties or are considered to be binder materials [2]. The most common soil stabilizers used nowadays are OPC (ordinary Portland cement) and lime. However, due to the CO₂ (Carbon Dioxide) emissions produced during the manufacturing of aforementioned soil stabilizers, which contribute to greenhouse gases, other soil stabilizers are being sought out and recommended. Studies and tests are being conducted in synthesizing alternative and eco-friendly soil stabilizers from waste materials, which can allow decrease in CO₂ emissions and, simultaneously decrease cost in earthwork construction [3], [4].

Fly ash is an industrial waste produced from the combustion of coal into fuel for power generation [5]. Globally, fly ash produced by factories and thermal power plants has been increasing for the past few years. The mass production of fly ash causes disposal

problems and an increase in expenses for storage in available landfills [6], [7]. This eventually poses a threat to the environment if it is not properly managed [8]. Consequently, several studies [9], [10], [11], [12], [13], [14], [15], [16] have been conducted, which is aimed towards recycling fly ash and utilizing it in various applications.

An alternative to stabilizing soil is by introducing geopolymer. Geopolymer is a product of the alkali activation of aluminosilicate materials present in industrial waste materials such as fly ash, red mud, and furnace slag [1]. The waste material used in the study to synthesize geopolymer was fly ash.

MATERIALS AND METHODS

Soil

The soil used in the study was obtained from Taguig City. It has a specific gravity of 2.50. The soil passing the No. 40 sieve has a liquid limit (LL) of 26 and a plasticity index (PI) value of 4, which classifies the soil to be slightly plastic as per ASTM D4318. Referring to Fig. 1, the particle size analysis performed on the soil indicates that the soil has varying grain sizes since it is composed of 18% gravel, 55% sand, and 13% silty fines. According to the Unified Soil Classification System (USCS) and the American Association of State Highway and

Transportation Officials (AASHTO) Soil Classification System, the soil is classified as Silty Sand (SM) with Gravel and as Silty Gravel and Sand (A-2-4), respectively. The standard Proctor test was also performed on the soil to determine its maximum dry unit weight ($\gamma_{d,max}$) and optimum moisture content (OMC), which were 17.61 kN/m³ and 15.15%, respectively.

To determine the corresponding AASHTO rating of the soil, the California bearing ratio (CBR) test was performed. The soil, with a CBR index of 1.68%, was rated as *Poor* for *Subgrade* use. The unconfined compression strength (UCS) test, however, could not be performed as the soil could not form UCS samples; these samples crumbled after being removed from the UCS molds. The two strength tests, UCS and CBR, were later on used as bases in verifying the soil stabilization caused by the geopolymer in comparison to the results of the unstabilized soil.

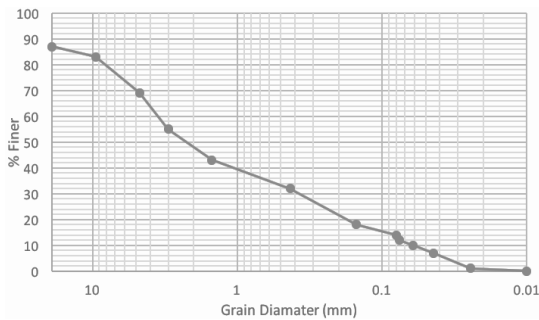


Fig. 1 The particle size distribution of the soil.

Fly Ash

The fly ash used in geopolymer synthesis was obtained from a coal-fired power plant in Mindanao. The X-ray Fluorescence (XRF) test was performed on the fly ash to determine its chemical compounds as shown in Table 1. As per ASTM C168, it is classified as Class F. To test whether the fly ash is safe for use in the environment with regards to leaching, the Toxicity Characterization Leaching Procedure (TCLP) and Heavy Metal test was performed. Table 2 shows that the fly ash is a non-hazardous material as its heavy metal content does not exceed the permissible limits as per TCLP standards.

Table 1 XRF results of the fly ash

Chemical Compounds	Fly Ash (%)
Al ₂ O ₃	26.50
SiO ₂	36.50
Fe ₂ O ₃	16.20
SiO ₂ plus Al ₂ O ₃ plus Fe ₂ O ₃	79.30
SO ₃	8.20
CaO	10.70

Table 2 TCLP results of the fly ash

Heavy Metals	Permissible Limit	Fly Ash
Cadmium	1.000	Not Detected
Chromium	5.000	Not Detected
Lead	5.000	Not Detected
Iron	0.300	0.06
Copper	1.000	0.02
Manganese	0.050	Not Detected
Zinc	5.000	0.008

Geopolymer Synthesis By Dry Mix Method

Soil stabilization should be practical when applied in the field. For geopolymer, this is solved by using the dry mix method. This method requires all materials to be in their dry state when initially mixed together. Afterwards, water is added to this mixture as the final step, which will result to geopolymerization.

The alkali activators used in the study were Sodium Hydroxide (NaOH) pellets and Sodium Silicate (NaSi₂O₃) pellets. In other studies [1], [17], [18], optimal range of values for activators to fly ash ratio, NaSi₂O₃ to NaOH ratio, and NaOH concentration were obtained; the values applied in this study were 0.4, 14 M, and 2, respectively. Three geopolymer concentrations were tested to stabilize the soil. These were in the values of 10%, 20%, and 30% by percent weight of the sample batch.

Prior to preparing the specimens, the geopolymer paste was produced. In the synthesis of the geopolymer paste, the dry alkali activators and the fly ash were initially mixed together using a mixer. Afterwards, water was then added and mixed for approximately 10 minutes. The total water required was considered as the water required to reach the NaOH concentration (14 M) and the OMC (15.15%) of the soil. The said procedure is shown in Fig. 2. This geopolymer paste was then added to the soil to produce that stabilized specimens.



Fig. 2 The dry mix method: (A) dry alkali activators, (B) fly ash, (C) water, (D) geopolymer paste.

Soil Stabilization with Geopolymer and Characterization Tests

UCS and CBR sample preparation and testing

Five samples were made for each geopolymer concentration; a total of 15 samples per strength test was synthesized. The UCS samples of the stabilized soil were compacted into cylindrical PVC molds (40 mm x 100 mm). Prior to testing, these were cured at room temperature for 28 days. For the CBR samples which were unsoaked, the stabilized soil was compacted into the CBR molds at 5 layers with 56 blows per layer to obtain a 95% of the desired $\gamma_{d,max}$ as per ASTM D1883. The CBR samples were cured for 7 days prior to testing.

Statistical analysis of mechanical properties of geopolymer stabilized soil

The statistical analysis of the data was performed in the Design Expert software v7.0. The partial sum of squares Type III analysis of variance (ANOVA) was applied to test the presence of a main effect between the interactions of the model terms in a model equation. The model order (linear, quadratic, or cubic) was selected based on the coefficient of determination (R^2) value; whichever model had the highest R^2 value indicated a great fit for the data points. Each term of the model equation was determined to be significant if its probability p (Prob > F) was less than 0.05. Moreover, the null hypothesis is focused on the lack of fit, as it is assumed that there is no lack of fit for the data points in a linear equation. Small p values, those that are less than 0.05, indicate that the null hypothesis is rejected and that a model of higher order is required. To verify the model equations, equality graphs were made and the correlation value (r) between the predicted and actual values was calculated.

Morphological characteristics

The SEM (scanned electron microscopy) imaging test was applied on the fly ash, the soil, and the samples of the stabilized soil. These were used to verify the formation of geopolymer gels since the dry mix method was used which could affect the rate of geopolymerization. Moreover, the stabilized soil with 28 days of curing was used in the SEM imaging test to better observe the formation of geopolymer gels when compared to the SEM images of the fly ash and the soil. Portions of each sample, with a mass of 10 to 15 grams, were oven-dried before being tested.

Fourier Transform Infrared (FTIR) spectroscopy

The FTIR was performed to further prove the geopolymerization in the dry-mix method. The

samples used in the FTIR tests were the fly ash, the soil, the pure geopolymer, and the 30% geopolymer concentration stabilized soil. The results were used for comparison of the spectra of the samples to check for changes when geopolymer is applied to the soil.

RESULTS AND DISCUSSION

Mechanical Properties of Geopolymer-Stabilized Soil

In the UCS test, the soil being predominantly of sand could not be tested solely due to sand being cohesionless as shown in Fig. 3. When geopolymer was applied starting at 10% geopolymer concentration, UCS samples were able to be produced; these samples started to have cohesive characteristics. The geopolymer acts as a binder for the sand particles and fills the gaps between these particles. Moreover, the geopolymer gel formation creates a network that binds the soil particles and fly ash particles together creating a stronger network of particles. Assessing the results in Table 3, the samples with 10% geopolymer concentration had a UCS (q_u) value of 78.29 kPa (Medium consistency), with 20% it increased to 247.48 kPa (Very Stiff), and with 30% it significantly increased to 1349.74 kPa (Hard).

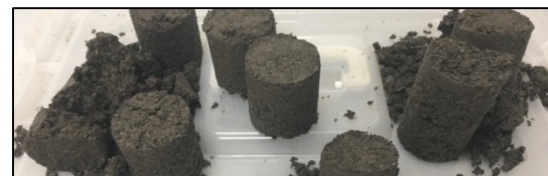


Fig. 3 The UCS samples of the pure soil.

Table 3 UCS testing results of the stabilized soil

Geopolymer Concentration	10%	20%	30%
Unconfined Compressive Strength, q_u (kPa)	78.29	247.48	1349.74
Consistency	Medium	Very Stiff	Hard

These q_u values are comparable to a study using the wet mix approach of synthesizing geopolymer stabilizers. This study [18] used slag-based geopolymer to stabilize clayey soil which resulted to a q_u value of 1223 kPa at 25% geopolymer concentration. Other studies [14], [15] which stabilized expansive soil using fly ash resulted to increase in q_u value by 200 to 1400 kPa. In comparison to a study which used cement stabilization, q_u values ranged from 500 kPa (5% cement) to 2150 kPa (20% cement) [19] for stabilized dredged sediments composed of clay and silt.

Considering that these were stabilized with cement, the fly-ash-based geopolimer can be considered to have advantage over cost since fly ash is free as it is a waste material. At 30% geopolimer concentration, similar UCS values were obtained. Moreover, it is said that the hardness of geopolimer is twice as much higher than cement which indicates that geopolimer is less deformable and has a higher brittle behavior [20]. This behavior was actually observed for the stabilized soil at 30% geopolimer concentration wherein the cured UCS samples were physically similar to concrete during its UCS testing as shown in Fig. 4.

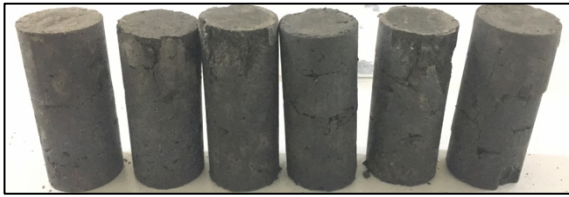


Fig. 4 The stabilized soil samples at 30% geopolimer concentration after UCS testing.

Similarly, the CBR index of the soil improved as it was stabilized with geopolimer. The CBR index of the stabilized soil increased as the geopolimer concentration increased as shown in Table 4. As previously discussed, the geopolimer creates a stronger soil structure since it acts as a binder between the fly ash and the soil. At 10% and 20% geopolimer concentration, the stabilized soil had CBR indices of 9.89% and 16.24%, respectively, which classifies it as subbase material. At 30% geopolimer concentration, the stabilized soil can be used as base material as its CBR index has reached 34.32%. With this said, the highest increase in CBR index is 32.64% when compared to the pure soil, which is 1.68%. This is slightly similar to a local study [11] and, studies in Nigeria [12], Germany [13], Sudan [15], USA [16] which applied fly ash on several types of soil. These studies had results wherein the CBR indices increased by 30% to 55%. This suggests the possible use of the dry mix geopolimer for stabilizing soil based on the improved CBR indices of the pure soil as the improvements are similar to other studies.

Table 4 CBR results of the stabilized soil

Geopolimer	10%	20%	30%
CBR Index (%)	9.89	16.24	34.32
General Rating	Fair	Fair	Good
Uses	Subbase	Subbase	Base, Subbase

ANOVA Analyses and Geopolimer Equations

The factor in the equations is the geopolimer

concentration ranging from 0% to 30%, wherein the 0% value is considered as the pure soil. The independent variables are the strength properties which are q_u and CBR Index.

$$q_u = 3135.75G - 37564.80G^2 + 140365G^3 \quad (1)$$

$$CBR\ Index = 2.77 + 25.64G + 257.66G^2 \quad (2)$$

where q_u is the UCS value (kPa), unsoaked CBR Index (%), and G is the geopolimer concentration (%/100). The data points of both models for Eq. (1) and Eq. (2) have p (Prob > F) values of less than 0.0001 and indicate the rejection of the null hypothesis. This means that the data points for both the q_u and CBR Index have a lack of fit in a linear trend and require a higher order polynomial.

The R^2 value of the model equations were 0.9856 for Eq. (1) and 0.9123 for Eq. (2). These denote a good fit for the data points in terms of their respective model equations. Referring to Fig. 5 and Fig. 6, the equality graphs of both equations are observed to have high r values between the predicted values and the actual values. This implies that the predicted and actual values have a very strong correlation which verifies both model equations.

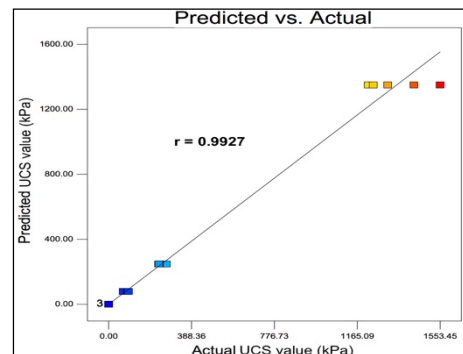


Fig. 5 The equality graph of the UCS values.

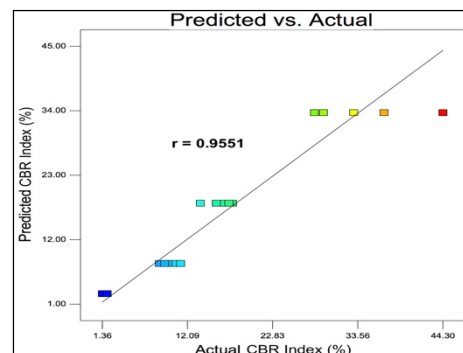


Fig. 6 The equality graph of the CBR indices.

SEM of Geopolimer-Stabilized Soil

The SEM images in Fig. 7 show how the

geopolymer gel formation spread throughout the microstructure as the geopolymer concentration increases. At 10% and 20% geopolymer concentration, the fly ash and the soil particles are still visible with the presence of geopolymer gels. These geopolymer gels have bound the spherical particles of the fly ash together with the soil particles [21]. Notably, the 30% geopolymer gels barely show any particles of both the fly ash and the soil particles. The particles of the precursors have been completely replaced by the geopolymer matrix caused by the increased formation of geopolymer gels. The microstructure shows a compact structure wherein the particles are not separated; they are connected together in the geopolymer matrix. Moreover, the 30% geopolymer concentration shows the crystalline-like structure [1], [22] which is commonly found in geopolymer. These verify that geopolymerization occurs in the dry mix method of synthesizing geopolymer stabilizers.

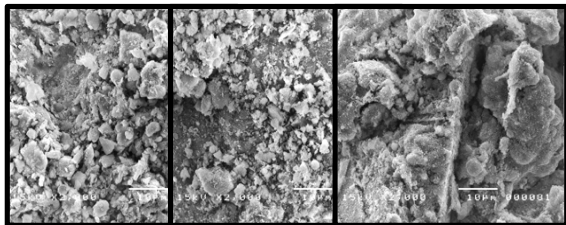


Fig. 7 The SEM images of SM at geopolymer concentrations of 10% (left image), 20% (center), and 30% (right) at 2000x magnification.

FTIR of Geopolymer-Stabilized Soil

The FTIR spectra in Fig. 8 show how the spectra of untreated soil change when geopolymer is applied. The stretched bands at wavenumbers from 800 to 1200 cm^{-1} are considered as the phase change of fly ash when geopolymerization takes place. These peaks of the bands at that range (800-1200 cm^{-1}) show a behavior of shifting to the right or a shifting to lower wavelengths from the untreated to treated soil caused by geopolymerization [22]. Moreover, the bands of the untreated soil at 600 to 800 cm^{-1} , as it is treated with geopolymer, shows the vibrations similar to that of the pure geopolymer. This indicates the reaction of bending and stretching of silicate frameworks [23].

CONCLUSION

The study is aimed towards testing an alternative method of synthesizing a geopolymer soil stabilizer, which can practically be applied in the field of construction. The SEM images have qualitatively verified that geopolymerization occurs in the dry mix method. It has shown the formation of geopolymer gels in the stabilized soil. These gels are characterized by their crystalline-like structure and their binder-like

feature, connecting and surrounding the fly ash particles and soil particles. Moreover, the SEM images of the pure soil and the stabilized soil shows how the geopolymer changes the morphology of the pure soil into a denser soil structure. As for the FTIR results, these have further confirmed the geopolymerization taking place in the stabilized soil which was evident in the change in peaks within the spectra.

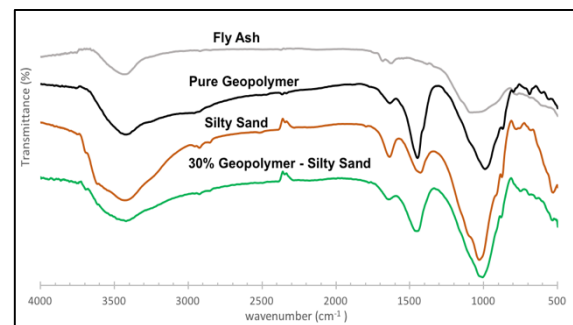


Fig. 8 The FTIR spectra of the fly ash, the pure geopolymer, the soil, and the stabilized soil.

The synthesized geopolymer in the study is considered to be the most effective at the concentration level of 30% since both mechanical properties, UCS and CBR Index, increase as the geopolymer concentration is increased from 10% to 30%. For the UCS results, the improvements are considered to be significant. The application of geopolymer on the soil has allowed the stabilized soil to be molded into UCS samples as the soil does not have cohesive characteristics due to its sand content. The q_u values, from 10% to 30% geopolymer concentration, increase significantly from 78.29 kPa to 1349.74 kPa. As an embankment material, the geopolymer has improved the performance of the soil based on the CBR Index which has increased to a value of 34.32%. The pure soil is rated as *Poor* for *Subgrade* use, whereas the stabilized soil has improved to *Good* for *Base* and *Subbase* use.

The geopolymer, based on these results, has the possibility of being an alternative to conventional soil stabilizers such as cement and lime. The main reason for this is that the geopolymer in the study was synthesized through a different approach rather than the method of using liquid activators, which allows easier application in the field. Focusing on geopolymerization, this further concludes that geopolymerization can still occur in the dry mix method.

RECOMMENDATION

The study has used a limited range of values for geopolymer concentration due to the consideration that higher concentration values are costlier due to requiring more alkali activators. However, since these

are necessary in obtaining an optimal concentration value, it is recommended for future studies to take into consideration concentration values ranging from 40% to 90%. This will produce a geopolymer concentration that can maximize soil stabilization.

The method of testing the CBR property of the stabilized soil was only through the unsoaked CBR. The soaked CBR was not tested due to time constraints. The soaked CBR is significant as it simulates the strength of soil when saturated or during events of flood. This is why it is recommended to test the geopolymer stabilizer in terms of the soaked CBR.

The geotechnical properties of the stabilized soil were not tested in the study. The geotechnical properties such as gradation and permeability are considered to be significant properties. These may change when soils are stabilized with geopolymer. As such, it is recommended to test these properties to further discover the extent of the improvement of geopolymer soil stabilization.

ACKNOWLEDGEMENTS

The authors would like to acknowledge the help of DOST-ERDT for financially supporting this study towards its completion. The help of Dr. Michael Angelo Promentilla and Engr. Roy Alvin Malenab are also greatly appreciated for their aid in the testing and analysis of the SEM and FTIR tests.

REFERENCES

- [1] Zhang, M., Guo, H., El-Korchi, T., Zhang, G., & Tao, M. (2013). Experimental feasibility study of geopolymer as the next-generation soil stabilizer. *Construction and Building Materials*, 1468-1478.
- [2] Makusa, G. (2012). Soil stabilization methods and materials (In engineering practice). Lulea University of Technology, Sweden.
- [3] Thiha, S., & Phueakphum, D. (2015). Shear Strength Enhancement of Compacted Soils using Geopolymer. The 20th National Convention On Civil Engineering, 8-10.
- [4] Dungca, J. R., & Dychangco, L. T. (2016). Strength properties of road base materials blended with waste limestones. *International Journal of Geomate*.
- [5] Dungca, J. R., & Galupino, J. G. (2017). Artificial neural network permeability modeling of soil blended with fly ash. *International Journal of GEOMATE*.
- [6] Ahmaruzzaman, M. (2010). A review on the utilization of fly ash. *Progress in Energy and Combustion Science*. Retrieved March 15, 2017.
- [7] Uy, E. S., & Dungca, J. R. (2017). Constitutive modeling of coal ash using modified Cam Clay model. *International Journal of GEOMATE*.
- [8] Baykal, G., Edinçliler, A., & Saygılı, A. (2004). Highway embankment construction using fly ash in cold regions. *Resources, Conservation and Recycling*, 42(3), 209-222.
- [9] Galupino, J. G., & Dungca, J. R. (2015). Permeability characteristics of soil-fly ash mix. *ARPN Journal of Engineering and Applied Sciences*, 10(15).
- [10] Dungca, J. R., & Galupino, J. G. (2016). Modelling of permeability characteristics of soil-fly ash-bentonite cut-off wall using response surface method. *International Journal of Geomate*.
- [11] Dungca, J. R., & Jao, J. L. (2017). Strength and permeability characteristics of road base materials blended with fly ash and bottom ash. *International Journal of GEOMATE*, 12(31).
- [12] Okunade, E. A. (2010). Geotechnical properties of some coal fly ash stabilized Southwestern Nigeria lateritic soils. *Modern Applied Science*, 4(12).
- [13] Ismaiel, H. H. (2006). Treatment and improvement of the geotechnical properties of different soft fine-grained soils using chemical stabilization.
- [14] Rajakumar, C., & Meenambal, T. (2015). Effect of coal ash in the stabilization of expansive soil for the pavement. *International Journal of ChemTech Research*, 8(1), 170-177.
- [15] Zumrawi, M., & Hamza, O. (2014). Improving the characteristics of expansive subgrade soils using lime and fly ash. *International Journal of Science and Research*.
- [16] Edil, T. B., Acosta, H. A., & Benson, C. H. (2006). Stabilizing Soft Fine-Grained Soils with Fly Ash. *Journal of Materials in Civil Engineering*, 18(2), 283-294.
- [17] Ramezaniapour, A., & Alapour, F. (2013). Compressive strength of fly ash geopolymer paste designed by taguchi method. Third International Conference On Sustainable Construction Materials And Technologies.
- [18] Legrans, R., & Kondo, F. (2015). Strength improvement of dredged soil through solidification by eaf slag-based geopolymer. *Bull. Fac. Agr., Saga Univ.*, 33-41.
- [19] Yusuf, H., Palluh, M. S., Samang, L., & Tjaronge, M. W. (2012). Characteristical analysis of unconfined compressive strength and CBR laboratory on dredging sediment stabilized with Portland cement. *International Journal of Civil & Environmental Engineering*, 12.
- [20] Skvara, F., Kopecky, L., Nemecek, J., & Bittnar, Z. (2006). Microstructure of geopolymer materials based on fly ash. *Ceramics – Silikáty*.
- [21] Sukmak, P., Horpibulsuk, S., Shen, S.,

- Chindaprasirt, P., & Suksiripattanapong, C. (2013). Factors influencing strength development in clay-fly ash geopolymer. *Construction and Building Materials*, 47, 1125-1136.
- [22] Somna, K., Jaturapitakkul, C., Kajitvichyanukul, P., & Chindaprasirt, P. (2011). NaOH-activated ground fly ash geopolymer cured at ambient temperature. *Fuel*, 90(6), 2118-2124.
- [23] Zhang, Z., Wang, H., & Provis, J. L. (2012). Quantitative study of the reactivity of fly ash in geopolymerization by FTIR. *Journal of Sustainable Cement-Based Materials*, 1(4), 154-166.

LONG-TERM STRENGTH OF BUBBLE-MIXED SOLIDIFIED SOIL MADE FROM VOLCANIC ASH

Atsuko Sato¹ and Toshihiro Hayashi²

¹ Civil Engineering Research Institute for Cold Region, Japan; ² Hokkaido Development Bureau, Japan

ABSTRACT

The Civil Engineering Research Institute for Cold Region has been developing a bubble-mixed solidified soil that affords soil pressure reductions on civil engineering structures. This technique is one way to effectively use soil generated at construction sites. The bubble-mixed solidified soil is created by mixing volcanic ash, water, air bubbles, and a soil stabilizer. The volcanic ash is from the suburbs of Sapporo, a city in central Hokkaido, Northern Japan. The strength and density of a roughly 24-year-old specimen of bubble-mixed solidified soil were measured, and the temporal changes in the strength of the specimen were investigated. Previous data on this specimen was examined in comparison with the data from the current measurements. It was found that the material had the strength required for the structure. However, the strength of the material was found to increase and peak in two years, after which the strength decreased and the material deteriorated.

Keywords: Long-term Strength, Bubble-mixed Solidified Soil, Volcanic Ash, Deterioration, Impact acceleration

INTRODUCTION

The Civil Engineering Research Institute for Cold Region (CERI) has been engaging in studies on bubble-mixed solidified soil [1]. In previous studies, the long-term strength of this material has been verified, and it has been reported that the material has sufficient long-term durability for earth works [2]-[3]. CERI measured the strength and density of approximately 24-year-old specimens of bubble-mixed solidified soil, a type of lightweight soil. The measurement results and previous data are reported in this paper.

BUBBLE-MIXED SOLIDIFIED SOIL

Bubble-mixed solidified soil is a plasticized material made by mixing material soil, water, soil stabilizer and bubbles as shown in Fig. 1. Various soil materials, including poor quality soil generated at construction sites, can be used as materials for bubble-mixed solidified soil. Bubble-mixed solidified soil is a plasticized material and does not require compaction, which makes it possible to form

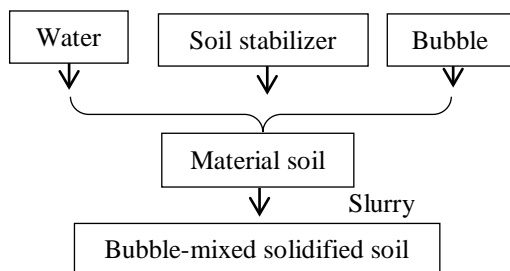


Fig. 1 This is how to make the bubble-mixed solidified soil

it in any shape. The light weight of such soil can contribute to load reductions on the ground. In addition to the above advantages, the solidification of this material progresses with time, and the earth pressure acting on civil engineering structures can be reduced by using this material. Because of these advantages, bubble-mixed solidified soil is a material that can be used in various areas.

TESTING METHOD

Creation of Slurry

In the experiment of this study, bubble-mixed solidified soil was created by using volcanic ash (Shikotsu pyroclastic fall deposit) from a site in the suburbs of Sapporo, a surfactant foaming agent and a cement base solidification material. The basic physical properties of the volcanic ash are shown in Table 1, and the mix proportion of the bubble-mixed solidified soil is shown in Table 2.

Creation of Specimens, and Test Method

To measure the unconfined compressive strength, in 1992 specimens were made by pouring slurry in PVC pipe molds of 5 cm in diameter and 10 cm in height, covering them with plastic wrap and curing them at a constant temperature of 20°C for 1, 7 and 28 days. Part of the above slurry was poured into an experimental soil chamber of 4.5m in length, 4.23m in width, and 2.25m in depth. At 28 days, the generated onsite solidified bubble-mixed solidified

Table 1 This is an basic physical properties of soil

Sample name	Takino
Soil particle density $\rho_s(\text{g/cm}^3)$	2.402
Natural water content $w_n(\%)$	33.7
Grain size $\geq 2 \text{ mm}(\%)$	17.5
distribution $75 \mu\text{m} - 2 \text{ mm}(\%)$	50.2
$\leq 75 \mu\text{m}(\%)$	32.3
Consistency limit	N.P.
Classification symbol of the ground material	SV

Table 2 This is a mix proportion of the bubble-mixed solidified soil

Mixed amount per 1m^3	Volcanic ash (kg)	752.06
	Water (kg)	147.94
	Bubble (l)	395.85
	Soil stabilizer (kg)	100
Target value	Unconfined compressive strength after 7-day curing (kN/m^2)	150
	Wet density (g/cm^3)	1.00
	Adjusted moisture content (%)	60

soil was dug out of the chamber and two blocks were cut out and formed. They were 0.5m in length, 0.5m in width and 0.25 in height. These two blocks were left uncovered in a room with an average annual temperature of about 20°C . This assumes the temperature in the soil where bubble-mixed solidified soil is to be constructed. In 1994, two years after the blocks were created, three cylindrical specimens of 5cm in diameter and 10cm in height were cut out in the perpendicular direction from one of the blocks, and the unconfined compressive

strength was measured. The other block had been left in the room for the roughly 24 years until February 2016. The top surface and one of the side surfaces of a block were made flat. For these two surfaces, the impact acceleration [4] was measured. Soil hardness index was also measured on these two surfaces by using a soil hardness tester [5]. An unconfined compression test was done by using six cylindrical specimens (5cm in diameter by 10cm in height) that were cut out from the block used for the above two measurements. The strength was measured using three specimens cut out in the perpendicular direction and three specimens cut out in the horizontal direction. The unconfined compressive strength was determined as an average for the values of three specimens for each direction. The impact acceleration and Soil hardness index were determined as an average of the values measured at ten points on the two surfaces of the block. The unconfined compressive test was also done on six specimens (three specimens for the perpendicular direction and three specimens for the horizontal direction) after they had been submerged in water. The conditions for each test are shown in Fig. 2.

TEST RESULTS

The Surface of The Bubble-mixed Solidified Soil

A 24-year-old block of bubble-mixed solidified soil is shown in Photo 1. The edges of the block are still intact and the surface has not changed from that at the formation of the block. In the specimen that was cut out from the block for the unconfined compression test, the voids clearly maintained their

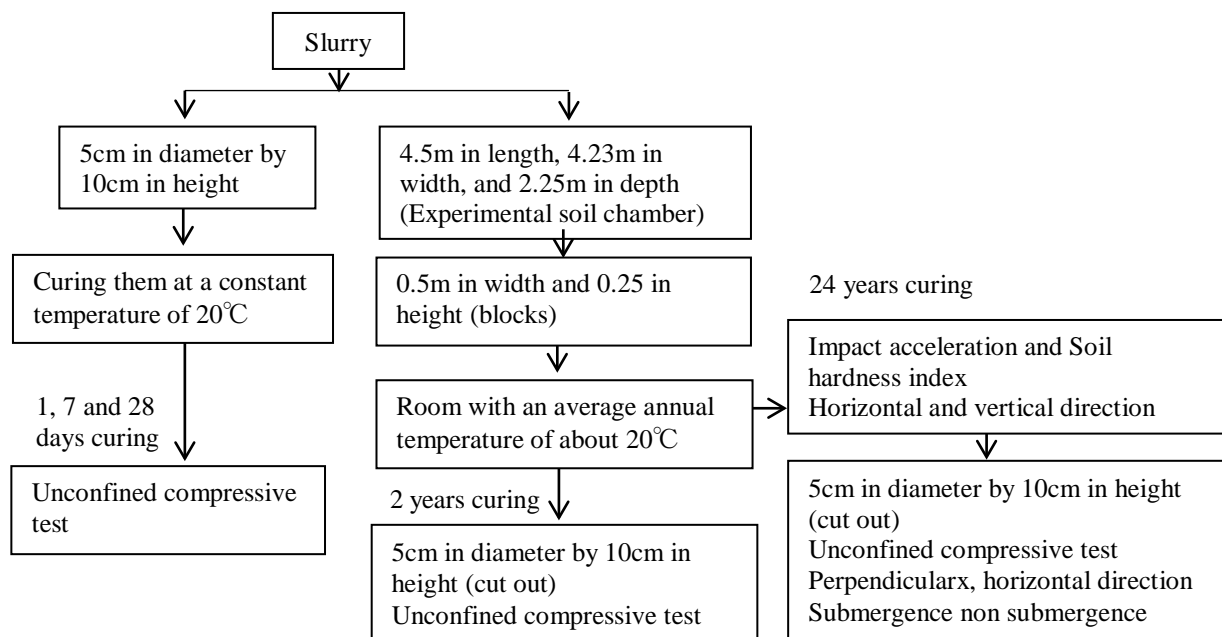


Fig. 2 This is the conditions of each test



Photo 1 This is a block and a specimen of 24-year-old bubble-mixed solidified soil

shapes, and no deterioration was found by visual observation.

Changes in Density

The temporal changes in the wet density of the bubble-mixed solidified soil are shown in Fig. 3. The wet density decreases with time. The wet density of a 24-year-old specimen submerged in water was equal to that of the specimen at its formation 24 years earlier. It is considered that even when the density of bubble-mixed solidified soil on site increases from submergence, a structure near that bubble-mixed solidified soil is unaffected by the changes in the density of the bubble-mixed solidified soil.

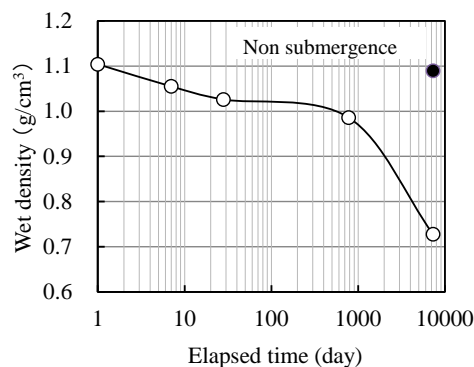


Fig. 3 This is the days elapsed, and wet density

Changes in Moisture Content

The moisture content of the bubble-mixed solidified soil is shown in Fig. 4. The moisture content decreased with time, and became nearly zero in 24 years. When the sample was placed in the

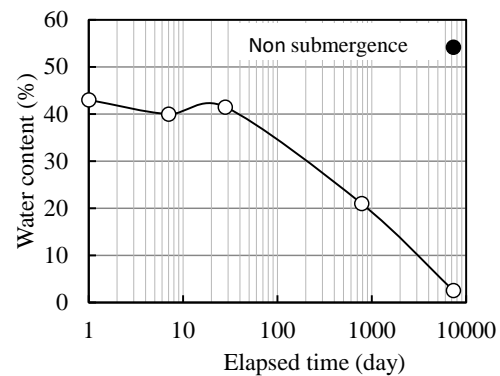


Fig. 4 This is the days elapsed vs water content

water, the sample started to absorb water immediately after being placed in the water and it totally submerged in 10 minutes. The final moisture content of the sample was roughly 60%, which is the adjusted moisture content. The specimen did not collapse when submerged in water. The void ratio remained almost unchanged for 24 years.

Changes in Strength

The unconfined compressive strength of the bubble-mixed solidified soil is shown in Fig. 5. The unconfined compressive strength of the sample increased for the 2 years since its creation. The unconfined compression strength of the 24-year-old sample was about the same as that of the 7-day-old sample. The unconfined compression strength of the sample decreased with time after the initial 2 years. Previous studies have reported that deterioration of cement-treated soil starts at the surface [6] and that the strength of cement-treated coal ash decreases when the coal ash is cured for a long time [7]. In the case of this study, it was thought that the block of bubble-mixed solidified soil had deteriorated from weathering. It is thought that the strength of the cement-treated soil does not decrease as greatly on site as measured in this study, because the cement-treated soil on site is covered with soil to a certain extent. However, in designing cement-treated soil, it is necessary to consider the long-term decrease in strength.

Next, the strength of the 24-year-old block in the perpendicular and horizontal directions was determined, and the strength of an internal part of the block was determined. The results are shown in depending on direction were found. It is thought Table 3. No notable differences in strength that the direction of placement does not greatly affect the

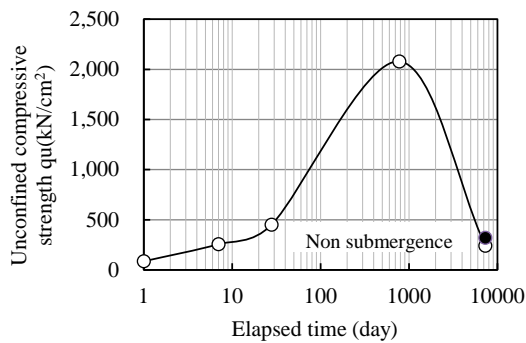


Fig. 5 This is the days elapsed vs unconfined compressive strength

Table 3 This is the direction vs strength

Items	Vertical	Horizontal	Perpendicular
Unconfined compressive strength	258.4	224.1	-
Impact acceleration	48.6	47.5	-
Soil hardness index	27.5	29.4	25.0

strength of bubble-mixed solidified soil. Fig. 6 shows the relationship between the impact acceleration and the unconfined compressive strength of the bubble-mixed solidified soil at placement in a laboratory soil chamber and the relationship between the impact acceleration and the unconfined compressive strength of the bubble-mixed solidified soil at 24 years after placement. The relationship between the impact acceleration and the unconfined compressive strength for the 24-year-old sample is similar to that for the sample at placement. It is possible to estimate the unconfined compressive strength from the impact acceleration even after a long time.

About the bubble-mixed solidified soil made from fly ash, it is reported about elution to the environment [8]-[9]. However, since volcanic ash is a stable material, it is considered that hazardous substances do not elute of bubble-mixed solidified soil made from volcanic ash into the environment.

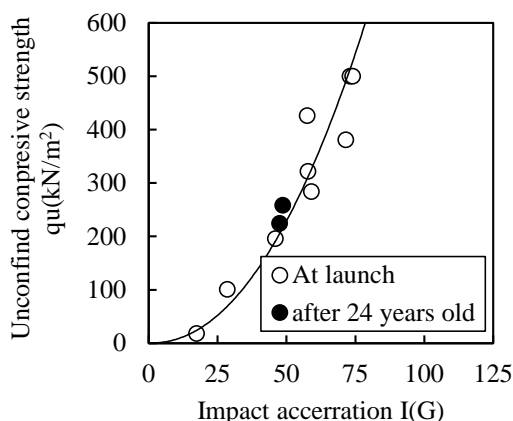


Fig. 6 This is the Impact acceleration vs unconfined strength

SUMMARY

The temporal changes in the properties of bubble-mixed solidified soil were investigated in this study. The investigation revealed the following.

- 1) No marked changes were observed by visual inspection of 24-year-old bubble-mixed solidified soil.
- 2) The water content, wet density and strength of bubble-mixed solidified soil decreases with time. Deterioration was observed in the bubble-mixed solidified soil.
- 3) The strength of bubble-mixed solidified soil is not affected by the direction of placement.

REFERENCES

- [1] Yasuaki Matsuda, Norihiro Mihara and Junichi Nishikawa "An Experimental Study on Foam Mixed Solidified Soil Using Volcanic Ash", Monthly Report of Civil Engineering Research Institute of Hokkaido, No. 482, 1993.
- [2] Yoichi Watabe, Hiroyuki Saegusa, Tomoyuki Ueda, Takashi Tsuchida, Yoshio Mitarai and Hiroshi Shinsha "Long-term Properties of Air-foam Treated Lightweight Soil Placed in Coastal Areas," Proceedings C of JSCE, Vol. 63, No. 1, 2007, pp. 237-248.
- [3] Kazuyori Fujioka, Nagao Kazuyuki, Kitamura Yoshinori and Kato Yoshinori, "Experiment on the Long-term Durability of Bubble-mixed Lightweight Soil", 60th JSCE Annual Meeting, 2005, pp. 725-726.
- [4] The Japanese Geotechnical Society, "Methods of Subsurface Investigation, and Interpretations", 2012, pp. 758-759.
- [5] The Japanese Geotechnical Society, "Methods of Subsurface Investigation, and Interpretations", PP. 758-759, 2012.
- [6] Hirochika Hayashi, Satoshi Nishimoto, Kanta Oishi and Masaaki Terashi, "Long-term Characteristics on Strength of Cement Treated Soil (Part 1) ,Onsite survey of a soil-cement column constructed by using the DJM method", Monthly Report of Civil Engineering Research Institute of Hokkaido, No. 611, 2004, pp. 11-19.
- [7] Atsuko Sato, Satoshi Nishimoto, Takahiro Yamanashi, Teruyuki Suzuki and Shinichiro Kawabata, "Long-term Properties of Solidified Slurried Coal Ash Used for an Artificial Island and Granulated Coal Ash Used for

- Embankments”, Proceedings of the JGS Symposium on Environmental Geotechnics, 2013, pp. 109-112.
- [8] Sivapullaiah PV and Arif Ali Baig Moghal, “Leachability of Trace Elements from Two Stabilized Low Lime Indian Fly Ashes”, Environmental Earth Sciences, Vol. 61, No. 8, 2010, pp.1735-1744.
- [9] Arif Ali Baig Moghal and Sivapullaiah, “PV Retention Characteristics of Cu^{2+} , Pb^{2+} and Zn^{2+} from Aqueous Solutions by Two Types of Low Lime Fly Ashes”, Toxicological and Environmental Chemistry, Vol. 94, No. 10, 2012, pp. 1941-1953.

DEVELOPMENT OF CEMENT-BENTONITE MIXED SOILS BY MIXINGSODIUM CARBONATE

Ko Hashimoto¹, Shuichi Kuwahara², Yukio Uchida³, Tadaomi Eguchi⁴, Shinya Inazumi⁵

¹Advanced Course of Architecture and Civil Engineering, Akashi College, National Institute of Technology, Japan, ²Marushin Co., Ltd., Japan, ³Japan Material Co., Ltd., Japan, ⁴Department of Civil Engineering, Akashi College, National Institute of Technology, Japan, ⁵Department of Civil Engineering, Shibaura Institute of Technology, Japan

Abstract

Cement milk is used as a grout to fill holes which are resulted from pile extraction. Although cement milk has an advantage of being able to perform blending and placing according to circumstance of work on site, cement and water cause segregation, so uniform filling is difficult over the entire length of holes. In addition, there is a disadvantage that cement milk can't perform a predetermined strength when diluted by groundwater erosion. Sodium carbonate is a substance expected to suppress the segregation of cement milk and to speed up the development of strength. In this study, we conducted an indoor mixing test on fillers mixed with sodium carbonate into cement milk which is a mixture consisting of water, cement and bentonite, and examined various characteristics from the viewpoint of physical and chemical aspects. (1) By mixing sodium carbonate, bleeding of cement milk is suppressed. This is considered to be due to increased swelling of bentonite by receiving sodium ions. (2) By mixing sodium carbonate, the strength development time of cement milk is advanced and the long-term strength also increases. This is considered that calcium carbonate is generated at the initial stage of reaction from the reaction of bentonite and sodium carbonate.

Keywords: cement, bentonite, sodium carbonate, bleeding, early strength

1. Introduction

1.1. Background

In demolition work, it is necessary to remove existing piles in the ground. If new land use is planned, existing piles must be removed so as not to interfere with pile foundation of newly built-structures. In addition, existing piles remaining in the ground are industrial waste, so troubles often occur in the land sale transaction. Therefore, removal of existing piles is indispensable. In order to remove an existing piles, a drawing out method is generally adopted. In the drawing out method, holes are formed in the ground, which adversely affect the ground environment. In the vicinity of the hole, it may cause problems such as collapse of earth and sand, subduction of the surrounding ground, weakening, so it is necessary to fill the filling and stabilize the ground quickly. Depending on the construction site, the properties required for the filling are different, but there is no regulation on filling presently. From the above, there is a demand for constructing a filler that can reliably fill and secure stable strength.

1.2. Purpose

We will aim for the development of a filling that exhibits uniform strength without causing material

separation when filling holes generated by pulling out existing piles. We aim at sophistication of cement bentonite typed cavity filling since it is possible to adjust blending filling at the construction site. By mixing sodium carbonate (Na_2CO_3), it is expected that the strength development of the cement bentonite type cavity filling will be promoted and the bleeding will be suppressed. We will examine the improvement and usefulness as cavity filling by conducting an indoor blending test on cement bentonite and sodium carbonate mixed cement bentonite. For examining the improvement and usefulness, a comparative test is conducted in view of strength characteristics, fluidity and material separation.

1.3. Outline

In this research, we carried out uniaxial compression test, penetration test, bleeding test and flow test on cement bentonite and cement bentonite mixing sodium carbonate, and examine usefulness of cement bentonite typed filling by mixing sodium carbonate. In addition, we consider the mechanism of the development of various properties exerted by mixing sodium carbonate from the physical and chemical point of view (Fig.1).

2. Method

2.1. Materials and Mixing Conditions

(1) Cement

The type of cement used in this study is ordinary portland cement, and one is having a density of 3.16 g/cm^3 and a specific surface of $3200 \text{ cm}^2/\text{g}$. Cement is a main component which exerts a curing function as a cement bentonite typed cavity filling because it reaction with hydration and develops initial and long-term strength by the formation of ettringite and calcium silicate hydrate(C-S-H).

(2) Bentonite

The chemical components of the bentonite used on our test are shown in Table 1. Bentonite has the effect of suppressing material separation of cement and water by swelling property due to take water into the one¹⁾. Bentonite is a smectite clay mineral containing montmorillonite as a main component and has a layered structure in which thin plate crystals are stacked. The crystal is negatively charged and electrical equilibrium is maintained by adsorbing cations between crystal layers. The interlayer cations of montmorillonite are mainly composed of sodium ion (Na^+), calcium ion (Ca^{2+}), potassium ion (K^+), magnesium ion (Mg^{2+}), and the properties of bentonite vary depending on the type of the one. The type is divided into two types, one is called Na type where a large number of monovalent cations such as Na^+ and K^+ are adsorbed, and the other is called Ca type where a large number of divalent cations such as Ca^{2+} and Mg^{2+} are adsorbed²⁾. The bentonite used in this experiment is a Na type bentonite having many Na^+ in interlayer cations.

(3) Sodium carbonate

When we mix sodium carbonate as an admixture into a cement bentonite typed cavity filling in this experiment, we use anhydrous salt obtained by heating at a high temperature of 300°C . Table 2 shows the chemical components of the admixture, and it contains Na_2CO_3 of 99.41%. Sodium carbonate is expected to promote the hydration reaction between cement and water and exert the effect of early strength development³⁾.

(4) Mixing condition

Table 3 shows the mixing conditions of each material used in the series of tests. The target strength is set to 0.5 N/mm^2 on the mixing condition. In the precast pile driving method prescribed in the "Public Building Standards Manual"⁴⁾, since the pile circumferential fixing liquid is set to 0.5 N/mm^2 at the compression strength after 28 day material age and is considered to be the same as the ground strength, the strength is generally adopted as a standard. In blend A and B, cement bentonite and cement bentonite mixing sodium

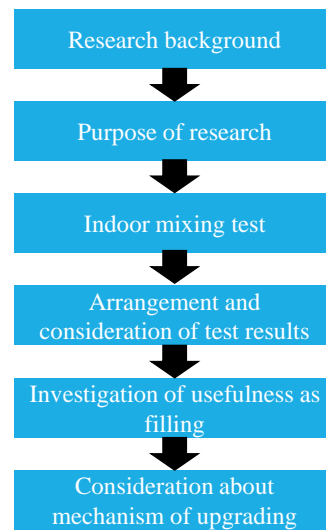


Fig.1 Procedure of study

Table 1 Chemical components of bentonite

Chemical Components	Content (%)
SiO_2	67.1
Al_2O_3	16.8
Fe_2O_3	3.7
MgO	3.3
CaO	2.7
Na_2O	2.2
K_2O	1.3
Ignition loss	2.9

Table 2 Chemical components of the admixture

Chemical Components	Content (%)
Na_2CO_3	99.41
NaCl	0.35
Fe_2O_3	0.003 or less
Insoluble matter	0.001 or less
Ignition loss	0.15

Table 3 Mixing conditions of each material

No.	B (kg/m^3)	C (kg/m^3)	S (kg/m^3)	W (kg/m^3)	W/C (%)
A-1	50	240	0	905	377
A-2	50	240	20	897	374
B-1	50	300	0	886	295
B-2	50	300	20	878	293
C	50	180	20	916	509
D	50	200	20	910	455
E	50	220	20	903	410
F	50	250	20	894	358
G	50	260	20	891	343

carbonate whose weight ratios $\text{C/B}=5, 6$ of cement (C) and bentonite (B) were prepared, and we investigate the properties of cement bentonite mixing sodium carbonate perform. In blend C, D, E, F and G, only the amount of cement (C) is changed to prepare cement

bentonite mixing sodium carbonate and the correlation between sodium carbonate and cement is examined. In the mixing procedure, water (W) and bentonite (B) were added to a stirrer having a rotation speed of 1,500 rpm/min and stirred for 3 minutes, then ordinary portland cement (C) was added and stir for 3 minutes and sodium carbonate was added and stir for 3 minutes (Fig.2).

2.2. Strength Test

The strength development of cement bentonite mixing sodium carbonate will be examined according to the Japanese Industrial Standard (JIS A 1216) "uniaxial compression test". Each material is mixed according to mixing conditions and it is poured into a mold having a diameter of 50mm and a height of 100mm to prepare a sample. Curing is performed for 7, 14, 28, 60, 90, 120 days in a thermostatic chamber at 20°C, and a uniaxial compression test is performed at each curing day (Fig.3).

In order to investigate the change about the action of cement bentonite due to mix sodium carbonate, we conduct a simple penetration test on samples of A and B. Penetration resistance values in immediately after sample mixing and 30 minutes, 1, 2, 3, 4, 5, 6, 7, 8, 12, 24 hours are measured using a simple measuring instrument (Fig.4).

2.3. Bleeding Test

A test is carried out according to the JSCE Standards (JSCE-F522) "Bleeding Rate and Expansion Rate Test Method of grouting Mortar of Prepacked concret (Polyethylene Bag Method)" in order to evaluate material separation of water and cement (Fig.5). The Sample mixing each material put to a height of 200mm in a polyethylene bag with a diameter of 50mm and the amount of bleeding water after 1, 3, 24 hours is measured, and the bleeding rate is obtained using the following formula.

$$Br = \left(\frac{Wb}{V} \right) \times 100$$

Br (%) is the bleeding rate, Wb (ml) is the amount of bleeding water at each elapsed time, and V (ml) is the volume of the whole sample.

2.4. Fluidity Test

The fluidity of cement bentonite mixing sodium carbonate is evaluated according to JSCE-F521 "Fluidity Test Method of grouting Mortar of Prepacked concret (Method of P Funnel)". The Sample mixing each material is filled in a P-funnel tester having an outflow pipe inner diameter of 13mm, an outflow pipe length of 38mm and a funnel portion height of 192mm. The sample is allowed to flow by releasing a finger from the flow pipe, and we measure



Fig.2 Mixing and stirring of materials



Fig.3 Uniaxial compression test



Fig.4 Simple penetration test

the time until the flow of sample is interrupted for the first time with a stopwatch (Fig.6).

3. Consideration

3.1. Consideration on Strength Test

(1) Initial strength development

From the uniaxial compression test results in Fig.8 (a), compare the initial strength of cement bentonite and cement bentonite mixing sodium carbonate. A-1 has the 7th day strength of 0.09N/mm^2 , and A-2 has a seven-day strength of 0.30N/mm^2 , so A-2 is stronger than A-1. Similarly in the comparison between B-1 and B-2, the 7th day strength of B-1 is 0.37N/mm^2 and the 7th day strength of B-2 is 0.59N/mm^2 , so mixing sodium carbonate makes cement bentonite stronger than when it does not mix. Therefore, it can be said that the initial strength of cement bentonite increases by mixing sodium carbonate. In addition, since no significant difference is observed in the strength development behavior up to the 28th day of age, it is thought that sodium carbonate influence the strength development before the 7th day of age.

In Fig.7, the results of the penetration test showed that the resistance values of cement bentonite of A-1 and B-1 rise about 8 hours after mixing and stirring of each material, but the values of cement bentonite mixing sodium carbonate of A-2 and B-2 rise about 1 hour after mixing and stirring. Since the setting initiation time of cement bentonite is accelerating, it can be said that mixing sodium carbonate affects the solidification performance at the one-day of age. Exercising solidification performance in 1 hour after filling prevents the invasion of groundwater in the ground and helps developing stable strength cement bentonite type cavity filling.

From the above, mixing sodium carbonate into cement bentonite promotes the solidification performance immediately after mixing and stirring of each material, and exerts a useful effect as a filling.

(2) Long-term strength

From the uniaxial compression test results in Fig.8 (a), compare the long-term strength of cement bentonite and cement bentonite mixing sodium carbonate. In comparing A-1 and A-2, B-1 and B-2, the strength of mixing sodium carbonate is stronger than not mixing at any age. However, as for the tendency of strength development, there is a tendency that the strength increases up to about the 28th day of age in any samples, and the strength hardly increase after that. In addition, Fig.9 shows the values normalized by the strength of 28th day of age (hereinafter referred to as compression strength ratio). Comparison of each sample from Fig.9 (a) showed no significant difference in long-term strength development behavior after 28th day of age, and the



Fig.5 Bleeding test



Fig.6 fluidity test

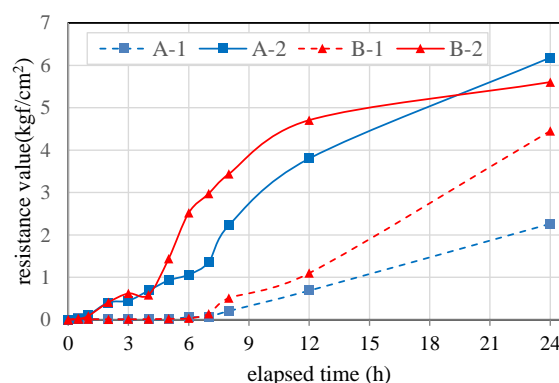


Fig.7 Result of penetration test

compressive strength ratio is around 1.0, except for B-1. There is not effect on the long-term strength development due to mix sodium carbonate, so the reason why the strength is larger on each age at the

time mixing sodium carbonate is considered that the increase of the initial strength affects the long-term strength development.

(3) Increase mechanism of initial and long-term strength

The amount of cement is changed in C, D, E, F, and G of cement bentonite mixing sodium carbonate. From Fig.8 (b), there is a trend that the smaller the water-cement ratio is, the stronger the strength is at each age. In addition, from Fig.9 (b), there is no clear difference in the tendency of strength development in any samples except for C, and the compressive strength ratio at 90th day of age is about 1.15. There is no difference in behavior of initial and long-term strength development of cement bentonite mixing sodium carbonate by difference in cement amount, so it can be said that sodium carbonate has no effect on cement. Therefore, the initial strength increase of cement bentonite by mixing sodium carbonate does not promote the hydration reaction between cement and water, and it is considered that forms a cured body different from cement hydrate.

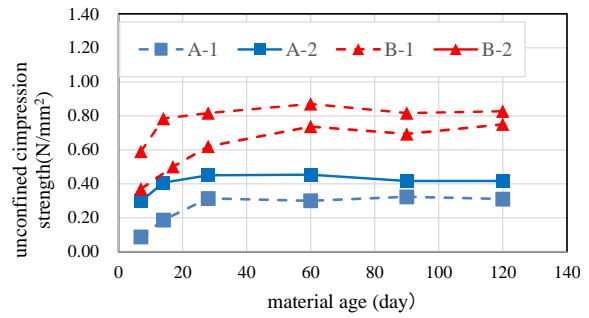
Here, attention is paid to sodium carbonate and bentonite. Bentonite has different properties depending on the type of interlayer cation of montmorillonite, but bentonite easily changes its properties by ion exchange with other types of cations since it has ion exchange properties. The interlayer cation exchangeability increases in the following order⁵⁾.

$$N^+ < K^+ < Ca^{2+} < Mg^{2+}$$

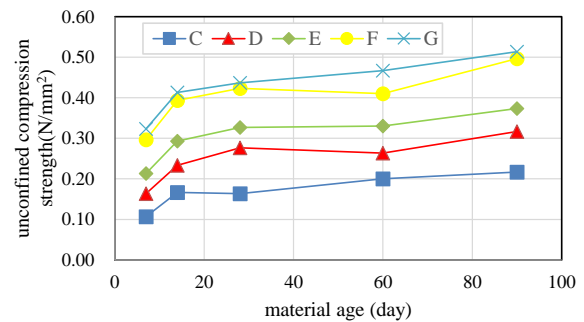
When sodium carbonate (Na_2CO_3) dissolve in water, it ionizes to sodium ion ($2Na^+$) and carbonate ion (CO_3^{2-}). Therefore, Ca^{2+} contained in the interlayer cations in the bentonite and Na^+ ionized from the sodium carbonate perform ion-exchange, and Ca^{2+} and CO_3^{2-} are bonded to form calcium carbonate ($CaCO_3$). Calcium carbonate is a water-insoluble substance, and forms a cured body by binding molecules with each other. The early strength development of cement bentonite by mixing sodium carbonate and the increase in long-term strength are attributed to the formation of a cured body of calcium carbonate immediately after mixing of materials.

3.2. Consideration on Breathing Test

Table 4 shows the results of the bleeding test. In Cement bentonite of A-1 and B-1, the bleeding rate increase with the passage of time, but in cement bentonite mixing sodium carbonate of A-2 and B-2, about 0.5% bleeding is only confirmed after 1 hour, and there is no moisture on the surface of the specimen. Similarly, in C, D, E, F, and G, it can be confirmed that the bleeding rate becomes 0% within 24 hours from the mixing of the materials. The decrease in the bleeding rate of cement bentonite due to the mixing

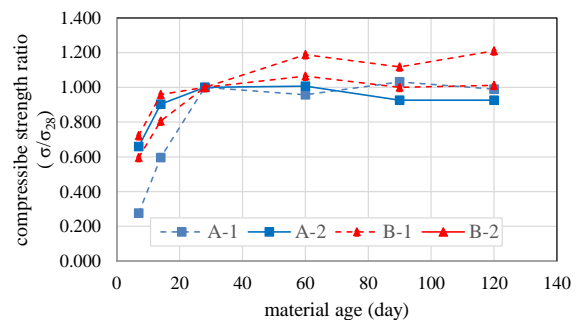


(a) Comparison by mixing sodium carbonate

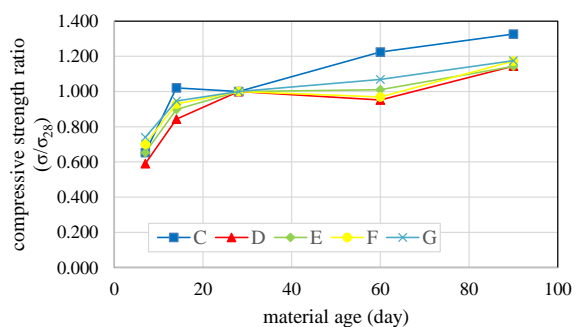


(b) Comparison by changing cement amount

Fig.8 Result of uniaxial compression test



(a) Comparison by mixing sodium carbonate



(b) Comparison by changing cement amount

Fig.9 Compressive strength ratio

sodium carbonate is attributed to the increase in the swellability of bentonite and the initial strength development of cement bentonite. Bentonite exerts swellability by interlayer cations of montmorillonite

Table 4 Results of bleeding and fluidity test

No.	flowing down time (s)	bleeding rate (%)		
		1hour	3hour	24hour
A-1	7.7	3.6	9.3	9.5
A-2	7.6	0.5	0.0	0.0
B-1	7.8	4.0	9.5	9.8
B-2	7.6	0.4	0.0	0.0
C	7.7	0.9	0.8	0.0
D	7.7	0.7	0.5	0.0
E	7.7	0.5	0.0	0.0
F	7.7	0.5	0.0	0.0
G	7.7	0.5	0.0	0.0

adsorbing water molecules. As compared with Ca type bentonite, the Na type bentonite has a weak electrical attraction between the unit layers, and so it is likely to swell when adsorbing water molecules. As described above, sodium carbonate in water is ionized to generate Na^+ , which is exchanged with Ca^{2+} contained in interlayer cations in bentonite. It is considered that the swelling property of bentonite is improved, because the interlayer cations become more inclusive of Na^+ . In addition, a hardened body is formed quickly since calcium carbonate is produced, and movement of water molecules in cement bentonite is inhibited. There is also a decrease of the amount of water due to the hydration reaction with cement. Therefore, it is considered that various phenomena such as increase of swellability with bentonite due to mixing of sodium carbonate, early strength development of cement bentonite, and hydration reaction of cement and water are involved, and the bleeding does not occur after several hours from mixing.

3.3. Consideration on Fluidity Test

Table 4 shows the results of the fluidity test. In each sample, the flowing down time is about 7.7s, and no decrease in fluidity of cement bentonite due to mixing sodium carbonate is observed. As described above, since curing started in about one hour after mixing the materials, the early strength development performance does not affect the fluidity at the time of filling. Although there is a possibility that material separation may occur due to flowing down, since bleeding hardly occurs, it can be said that the samples are having moderate fluidity. Therefore, it is able to say that the cement bentonite mixing sodium carbonate has ensured workability as a cavity filling.

4. Conclusions

In this study, the usefulness of the cement bentonite typed cavity filling mixing sodium carbonate was examined from the viewpoint of strength

characteristics, material separation and fluidity. The obtained results are shown below.

- (1) From the uniaxial compression test, mixing sodium carbonate increases the initial and long-term strength of cement bentonite. The early strength development helps stabilizing the ground as soon as possible.
- (2) From the penetration test, by mixing sodium carbonate, cement bentonite exerts curing performance from about 1 hour after mixing materials. The rapid gelation prevents invasion of groundwater into the filling in the ground, and the filling can stably exhibit the predetermined strength.
- (3) From the bleeding test, bleeding of cement bentonite is suppressed by mixing sodium carbonate. When it fills into the hole made by pulling out piles in the ground, the materials is kept homogeneous and the strength is not differ depending on the depth direction.
- (4) From the fluidity test, the fluidity of cement bentonite is not lost by mixing sodium carbonate. Workability is assured in filling holes in the ground.

In the future, it is necessary to clarify the mechanism of various characteristics development by verifying from a physicochemical point of view.

References

- [1] Kouken Horii, Masaaki Nishi, Tsutomu Yamazaki, Junichi Sakamoto, Michimae Taizou, Yasushi Uta, "Development of cement bentonite complex solidified bodies using concrete recycled materials", Summaries of the Academic Lectures of the Japanese Association of Architectural Conferences, 2007.
- [2] Yashima Takashi, "Estimation of smectite exchangeable cations by powder X-ray regression method", JGCA Technical Forum 2011 lecture collection, No. 40, 2011.
- [3] Kiyoshi Kato, Naoki Kato, Toshio Yuzawa, Isao Masukawa, "A Study on Rapid Evaluation of Long-term Strength and Unit Cement Volume by Ultimate Initial Strength of Rapid Hardening-Promoted Concrete", Report of Concrete Engineering Annual Papers Report, pp. 343 - 346, 1990.
- [4] Ministry of Land, Infrastructure and Transport, "Public Building Construction Standard Specification (Building Construction), Heisei 20th edition, Ministry of Land, Infrastructure and Transport, 2014.
- [5] Masanobu Ogata, "Characteristics of bentonite and its application", Clay science vol. 46, No.2, pp.131-138, 2007.

DEVELOPMENT OF REAL-TIME CHECKING SYSTEM FOR GROUND IMPROVEMENT WORKS BY HIGH PRESSURE INJECTION

Gicheol Lee¹, Shinya Inazumi², Hiroyuki Hashida³, Tadashi Chuman⁴, Keiji Okumura⁵ and
Kazuhiro Ishimaru⁶

^{1,6}National Institute of Technology, Akashi College, Japan, ²Shibaura Institute of
Technology, Japan, ³Sumice Kenzai Co., Ltd., Japan, ^{4,5}Estec Co., Ltd., Japan

ABSTRACT

In contrast to the mechanical stirring method in which the ground soil and the modifying material are mixed and stirred by stirring blades and the improved body is formed in the ground, the high pressure injection stirring method is a method in which the improved diameter is changed due to soil condition, etc. There is a possibility that it can be changed with, and a method for easily confirming the shape, particularly the improved diameter, is highly desired. In this research, we propose and propose a method that can make "visualization" of this improvement situation and confirm the improved diameter in real time. Confirmation was made by measuring water quality in multiple items. From the results, it was confirmed that pH and the values of the other 5 items changed at the same time. And the change was due to the arrival of the cement slurry. Therefore, it can be said that real-time measurement is possible by visualization of improved diameter by water quality measurement conducted this time.

Keywords: real-time checking system, pH, ground improvement, high pressure injection

INTRODUCTION

Currently as a measure against the Nankai Trough Earthquake, strengthening breakwaters is urgent in Japan. The main way of present reinforcement work is to strengthen the ground by making columns with cement. It is an invisible part that a soil-cement column is made, so it is important to check if the soil-cement column is made as planned. Particularly, in contrast to the mechanical stirring method, the high pressure injection stirring method has a possibility that the improved diameter may change depending on the soil conditions and the like, therefore, a method of easily confirming the diameter is desired [1]. In this research, we propose a method to confirm the improvement of the diameter in real time by "visualizing" this situation.

Experiments to confirm the state of improvement construction were carried out at the site where ground improvement is actually carried out. In this research, we focused on improved bodies with double pipe type high pressure injection stirring method. The high pressure injection stirring method is a ground improvement method in which earth and cutting agent are mixed and stirred by cutting the ground by spraying hardening material and air horizontally from an injection nozzle attached to the tip of the injection rod [2]. Normally, the injection

rod is rotated and pulled up by several centimeters at regular time intervals to form a columnar improvement body. Although it is possible to make an improved body with a diameter of 2 to 5 m with a small boring, it is very important to confirm that the diameter of the improved body is made according to the plan as it depends on injection specifications and ground strength.

As an earthquake countermeasure, in addition to reinforcement of the tide bank, reinforcement of the pile foundation can also be mentioned. However, because the reinforcement of pile foundations is in the ground and restrictions on sites and restrictions on heads, reinforcement methods are currently limited. One of the pile foundation reinforcement work performed under such conditions is Confining Pile Reinforcement Method. This method is a construction method that constructs a pile foundation structure resistant to earthquakes by improving the ground near the middle in the depth direction of the pile using cementitious materials. An improved body of the Confining Pile Reinforcement Method is also produced by the high-pressure injection agitation method, but there is a sound confirmation method as a method for confirming this form. The method is a method in which a guide pipe is installed at a planned position to be the outer peripheral portion of the improved body, a microphone underwater is inserted into the guiding

tube, and the arrival of the solidified material is judged by the observed sound [3].

However, in this study, we focused on confirming the arrival of cement directly, so we selected water quality measurement. Measurement was also conducted based on pH, which is strongly related to cement even among water quality.

MATERIALS AND METHODS

Materials

Water quality measurements were conducted twice on the site near a certain river in Osaka Prefecture using the portable multi-item water



Fig. 1 Portable multi-item water quality meter WQC-24

quality meter WQC-24 shown Fig. 1. This is an instrument that can measure multiple items simultaneously [4].

Fig. 2 and 3 show the boring datas of water quality measurement points.

Measurement tool

We used these instruments for the measurement.

- (1) Sensor module WMS-24-1
- (2) Terminal WQC-24-1
- (3) Computer
- (4) Vinyl chloride tubes

Methods

The design of the improved body has a length $L = 8.4$ m and a diameter $\phi 3500$ mm. First, we placed three vinyl chloride tubes of different lengths in advance as shown in Fig. 4 at a point 1750 mm away from the center of the improved body. In the vinyl chloride pipe, 17 holes with a diameter of 10 mm were installed between the length of 5 cm from the bottom, and the strainer portion was provided so that the cement slurry could enter. The measurement



Fig. 2 Boring data (the first point of measurement)

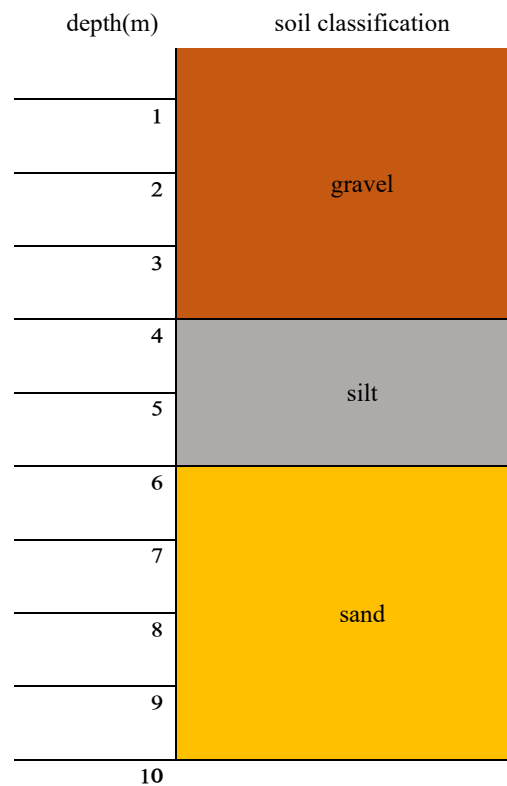


Fig. 3 Boring data (the second point of measurement)

items were pH, dissolved oxygen, electrical conductivity, turbidity, salinity, and water temperature.

In the first measurement, measurements were made by placing three water quality meters throughout three vinyl chloride tubes. In the second measurement, one water quality meter was moved to another vinyl chloride pipe in accordance with the arrival of the injection, and measurement was carried out while using it.

The installation depth of the water quality meter for both the first and second times was set to three places: GL - 9.0 m, GL - 6.0 m, and GL - 3.0 m. The notation was 1CH, 2CH, 3CH in order from the deepest point. The groundwater level exists in the vicinity of 3CH.

RESULTS AND DISCUSSION

Results

The first measurement was pH only, the second measurement was six items of pH, dissolved oxygen, electrical conductivity, turbidity, temperature, and salinity, and a graph was prepared based on the pH measurement value. As expected results, it is difficult to predict dissolved oxygen, but for other

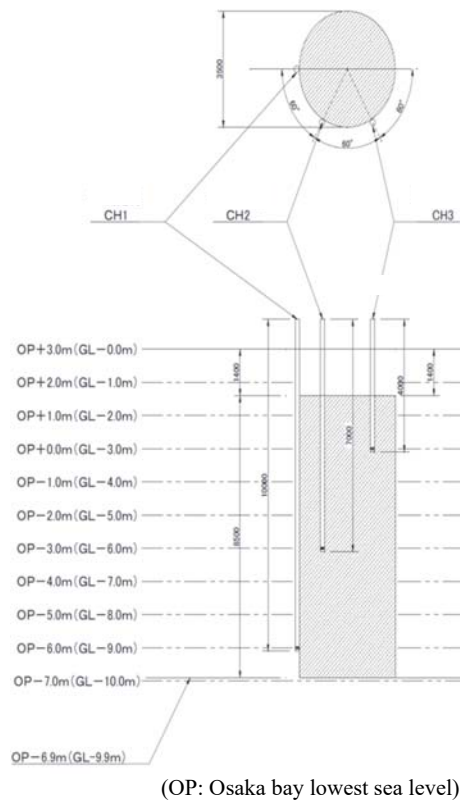


Fig. 4 Arrangement of measuring instrument

five items the pH rises due to cement influence, electric conductivity is difficult to convey electricity by cement slurry mixing due to the properties of cement. As the cement slurry arrives, the turbidity rises rapidly, the temperature rises due to the hydration reaction between cement and water, and the salinity is almost sea water, so if the cement slurry mixes there, the proportion of salt decreases.

The results of the first water quality measurement are shown in Fig. 5. At 1CH, no rise in pH was detected after the cement reached the measurement point. However, in 2CH and 3CH, increase in pH could be confirmed immediately after reaching the measurement point. 2 CH rose to about 11.3 to 13.4, and 3 CH rose to about 10.1 to 12.3.

The results of the second water quality measurement are shown in Fig. 6-10. First, when the change in pH is examined, the pH rises by about 3.0 immediately after the injection arrives in 1CH. However, in 2CH and 3CH, only a small amount of increase in pH immediately after injection was confirmed. Examining the other items, the dissolved oxygen decreased in 1CH, the electric conductivity decreased, the turbidity increased to the upper limit, the temperature increased and the salinity decreased. In 2CH and 3CH, because the rise in pH was small, other values were small changes accordingly.

Discussion

The reason why the pH of 1 CH did not change during the first measurement (Fig. 5)

In 1 CH, no rise in pH was detected after reaching the measurement location. The following can be considered as the cause.

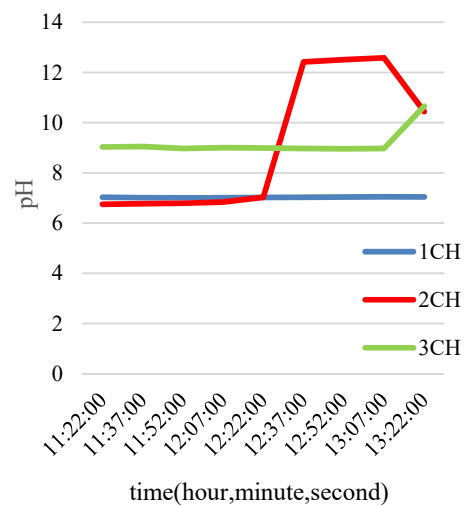


Fig. 5 The results of the first water quality measurement (pH only)

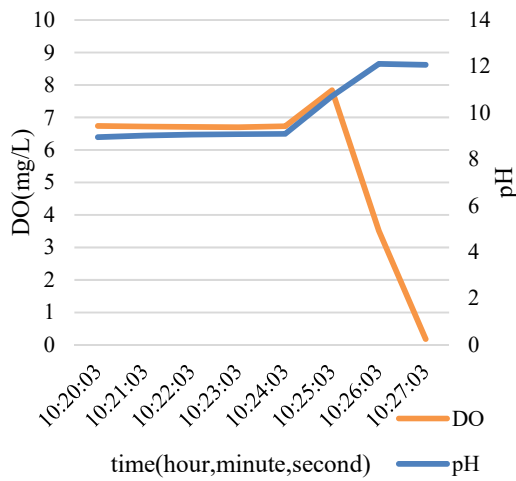


Fig. 6 The results of the second water quality measurement (pH and dissolved oxygen)

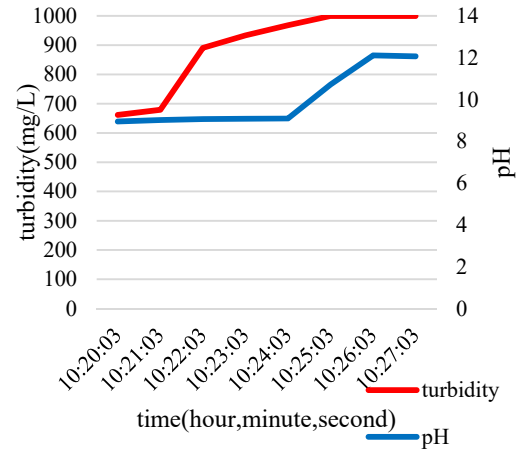


Fig. 8 The results of the second water quality measurement (pH and turbidity)

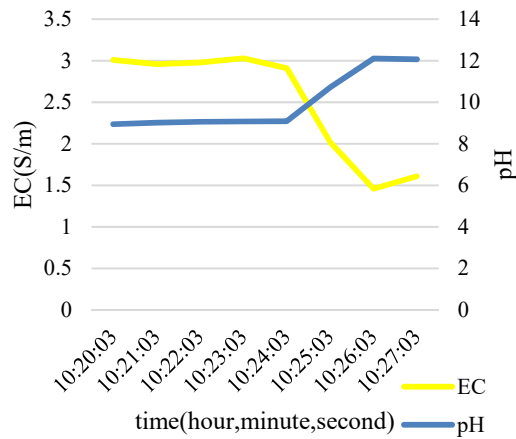


Fig. 7 The results of the second water quality measurement (pH and electrical conductivity)

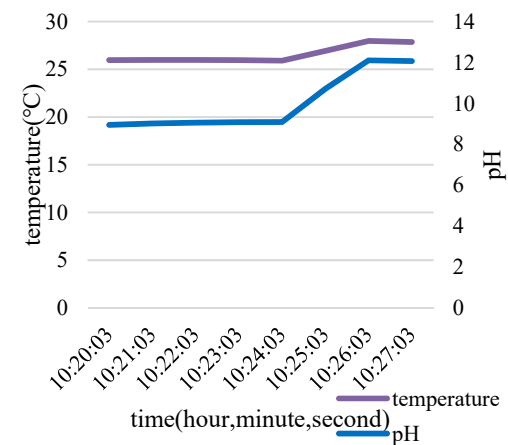


Fig. 9 The results of the second water quality measurement (pH and temperature)

- (1) The solidified material injected at the time of making an existing refinement nearby reached the vicinity of the vinyl chloride tube following the underground water line and closed the tip of the pipe.
- (2) The soil that remained in the ground when we dug a hole to stand vinyl chloride tubes closed the tip of the pipe.

Reason why the pH of 3CH was high from the beginning (Fig. 5)

It is thought that the cause of the pH of 3CH being high from the beginning is the gravel layer and the influence of the already improved ambient groundwater.

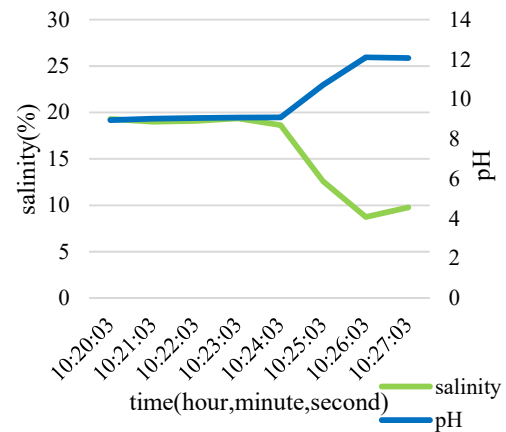


Fig. 10 The results of the second water quality measurement (pH and salinity)

Summary of the first measurement result

No increase in pH could be confirmed with 1 CH. However, in 2CH and 3CH, an increase in pH could be confirmed. And in 2CH and 3CH, after vinyl chloride tubes was pulled out and the tip part was observed, it was confirmed by eyes that cement slurry adhered to vinyl chloride tube and high pressure jet reached. Also, although we checked the diameter by excavating the upper part of the improvement body, we could also confirm that even here it was made almost as planned. From this, it can be said that visualization of improved diameters by pH measurement and real-time confirmation are possible because increase of pH due to arrival of cement slurry can be confirmed in the first measurement.

Cause of pH rise less than 1 CH at 2CH and 3CH in the second measurement

As shown in the figure, the pH rose by about 3.0 immediately after reaching the cement slurry in 1 CH. However, in 2CH and 3CH which are not shown in the figure, only a small amount of pH increase of about 0.5 to 1.0 could be confirmed immediately after reaching the cement slurry. The reasons why the amount of increase in pH immediately after arrival of cement slurry at 2 CH and 3 CH was small may be as follows. Unlike 1 CH where the pH rose sharply immediately after reaching the cement slurry, both 2 CH and 3 CH had already started to raise the pH before cement slurry reached. As a result, the pH increase in 2CH and 3CH became more gentle than the change in 1CH, so the change immediately after arrival of the cement slurry became small. As a fundamental problem, it seems that the reason why the pH rise started before 2CH and 3CH before reaching is because a trace amount of cement slurry began to enter the vinyl chloride tube before reaching the cement slurry. This tendency is considered to be particularly strong in 3CH because the increase in pH was more gradual than 2CH. However, as mentioned in the measurement method, since we used only one water quality meter in the second measurement, it was not clear when cement slurry started entering. But This problem is thought to be avoidable by preparing the water quality meters for the number of tubes and always checking all the CHs at the same time, as in the case of the first measurement, instead of using one water quality meter at a time.

About items examined by the second measurement

Since the measurement results of 2CH and 3CH showed almost no change as described above, mainly the change of each item in 1CH will be considered here. Dissolved oxygen decreased significantly in 1 CH as shown in the Fig. 6. However, in 2 CH, the opposite result was obtained that the pH

risks at a slightly rising timing. Since it is difficult to think that the value will drop to 0 as with 1 CH, dissolved oxygen isn't able to say useful only with this measurement result alone. On the other hand, electric conductivity and temperature can be confirmed to change according to the properties of cement, so it is considered to be useful as a confirmation item for visualization of improved diameter. As turbidity was also confirmed to increase due to arrival of cement slurry and earth and sand, turbidity is also considered to be useful as a confirmation item for visualization of improved diameter. Also, as in this case, when salinity is contained in groundwater, salinity is considered to be a useful confirmation item for visualizing the improved diameter.

Summary of the second measurement result

Although only few results were obtained in the second measurement, useful data could also be reliably obtained. From the results of this research, it is considered that particularly useful items are pH, electric conductivity and temperature. Because these are indices directly related to cement. Other items aren't able to say useful because there are not enough samples or the available conditions are limited.

CONCLUSIONS

In this research, the relationship with the improvement situation was verified by measuring the water quality of six items of pH, dissolved oxygen, turbidity, electric conductivity, temperature and salinity by using the Portable multi - item water quality meter. From the two measurement results, it was confirmed that the timing at which pH and the values of the other 5 items changed, and that the change was due to the arrival of the cement slurry. Therefore, it can be said that real-time measurement is possible by visualization of improved diameter by water quality measurement conducted this time.

In this water quality measurement, visualization and real-time measurement are possible, but there is a possibility of measurement failure such as clogging of the detection tube in 1 CH of the first measurement. Therefore, we need to pursue measurement methods that can compensate for the above weaknesses in the future.

In this research, we focused on preparing an improved body by double pipe type high pressure injection stirring method, but this is not the only way to improve ground. Therefore, in the future, it is necessary to pursue measurement method that can be used not only for the double pipe type high pressure injection stirring method but also for confirming the situation of various soil improvement. In addition to being able to use it not only in various sites but also it must be made cheaply and easily.

ACKNOWLEDGEMENT

In promoting this research, we received polite and enthusiastic guidance from many business people and teachers. I express my appreciation by writing it here.

REFERENCES

- [1] Light Industry Co., Ltd., “high-pressure injection stirring method”, <http://www.raito.co.jp/project/doboku/jiban/kikai/index.html>, Jan. 2017
- [2] Confining Pile Reinforcement Method Study Group, “Confining Pile Reinforcement Method”, <http://www.cpr-m.jp/gaiyou.html>, Feb. 2017
- [3] Urano K, Tsukagoshi K, Sakuma K, et al., “Outline and application example of CPR method of pile foundation seismic reinforcement method”, basic work Vol.44, No. 5, May 2016, pp. 42-45.
- [4] Rex Co., Ltd., “portable multi-item water quality meter WQC-24”, <http://www.rex-rental.jp/sui/wqc-24.html>, Nov. 2016

THREE-DIMENSIONAL NUMERICAL STUDY OF THE EFFECT OF TUNNELING ON THE SETTLEMENT OF PILE FOUNDATION

Mohammad Reza Atrchian¹, MiladGhannadzadehKermani², Ali Nisari Tabrizi³ and HamidTeennejad⁴
^{1, 2, 3} Civil Engineering, Islamic Azad University of Zanzan, Iran; ⁴Civil Engineering, Islamic Azad University of Central Tehran Branch, Iran

ABSTRACT

Problem statement: The issue of transport and mobility of citizens has always been in the town of principal concern cities. However, capacity constraints, traffic urban planning and the use of the available space have pushed below the surface cities. However, we can say use of underground transport, the perfect solution for solving traffic problems and pollution in big cities. Ensure that the loss of the tunnel during and after implementation and lack of surface inappropriate deformation structures, including tunnels are the main objectives of the designers. Thus mutual behavior, understanding and tunnels, soil and surface structures are important and should be examined. With the aid of a numerical model, variations in the tunnel, and tunnel properties were investigated. **Approach/methodology:** Numerical simulation method with software PLAXIS 3D. With the help of a numerical model, various characteristics of the tunnel, soil and foundation were studied. **Results:** The results show that the tunneling drill increases the subsidence and vertical displacements in the model the points on the ground surface have the most displacement and subsidence. As the tunnel is pulled away from the pile, the tunnel effect on the seating and movement is reduced. As the tunnel radius increases, the amount of displacement and settlement has increased. **Conclusions:** By reducing the gap between the tunnel and the pile group the settlement of the pile group increases. Also, the surface subsidence has been increased by increasing the diameter of the tunnel.

Keywords: Tunneling, Pile foundation, Land subsidence, Settlement buildings

INTRODUCTION

Due to urbanization and the need to develop infrastructure and shortage of land for it, inevitably underground space development is considered. An excellent example of this development, urban tunnels, underground car parks and tunnels in urban subway train. On the other hand, many of the structures built on the pile foundation and the tunnel passage near such structures with the blink of computing that such structures based on it were built, would be affected the balance of the settlement [1].

Mohr-Coulomb investigated. Also, considering the pros and cons of different methods and facilities, numerical simulation finite element software PLAXIS 3D chosen for this study. With the help of numerical models feature different variations of the tunnel, the soil around the tunnel and the foundation, were examined. The results show: that the tunnel excavation increased land subsidence and vertical displacement. Points are at ground level have the most displacement and land subsidence. The horizontal and vertical displacement of deep soil less by taking away a tunnel of the pile group tunnel. Effect on land subsidence and displacement is low. By increasing radius of tunnel increased the amount

of displacement and land subsidence [2]. However, in engineering analysis, problems often involve interaction between the construction of tunnels and other structures. Such conditions include surface structures (such as buildings), existing subsurface structures (such as tunnels, urban pipes) or complex underground structures such as tunnels and underground stations are twins. Rock as a continuum that by a limited number of discontinuities is interrupted considered, while in theory the batch, the rock mass as a combination of blocks, which together were considered to be of since the area is bearish in this study for soil and environment is assumed to be continuous, so numerically using finite element method (FEM) is. Plaxis 3D Tunnel finite element software package is exclusively for the analysis of deformation and stability in geotechnical engineering projects have been developed [3].

The identified parameters

Elastic-plastic Mohr-Coulomb model includes 5 parameters E and C and ϕ and ψ for elasticity and plasticity soil and u angle for expansion of the soil. The initial estimate of the behavior of soil or rock does. It is the

model used in the initial analysis issues. For each layer of soil is estimated constant average hardness. Because of the difficulty of constant, rapid calculations and basic understanding of deformation can be achieved. In the 5 parameters mentioned, the initial conditions of soil (Table 1 and 2) had an important role in most of the issues deformation. The initial horizontal stress caused the soil using the appropriate values of K_0 [4].

Table 1: Specifications of soil

Parameter	Name	Clay	DP. Clay	DP. Sand	Unit
Dry soil weight	γ_{dry}	15	16	17	KN/M3
Wet soil weight	γ_{wet}	18	18.5	21	KN/M3
h. permeability	K_x	1.10^{-4}	1.10^{-2}	0.5	KN/M3
v. permeability	K_y	1.10^{-4}	1.10^{-2}	0.5	KN/M3
Young s modulus	E_{ref}	1000	10000	120000	KN/M3
Increase E	E_{inr}	650	-	-	KN/M3
Reference level	Y_{ref}	0	-	-	M
Poisson s ratio	μ	0.33	0.33	0.3	-
Cohesion	C_{ref}	5.5	4	1.0	KN/M3
Friction angle	ϕ	24	25	33	0
Dalliance angle	ω	0	0	3.0	0
Interface strength	R_{inter}	rigid	0.7	0.7	-
Interface perm	perm	neutral	imperm	imperm	-

Also, lining profile is as follows:

Table 2: Specifications of lining

Parameter	Name	Value	Unite
Type of behavior	Material type	Elastic	
Normal stiffness	EA	1.4×10^7	KN/m ³
Flexural rigidity	EL	1.43×10^5	KNm ² /m
Equivalent thickness	d	0.35	m
Weight	w	8.4	KN/m/m
Poissons ratio	v	0.15	-

The geometry of the tunnel

In this study, it is assumed that the tunnel excavation using the TBM Oyster been done immediately after casing drilling as lining installed.

The tunnel excavation is relatively loose soil, the soil and fractured nature does not seem to be converging. For numerical analysis in the study of three-dimensional finite element modeling has been used on the basis of finite element software PLAXIS 3D tunnel works. In engineering analysis, problems often involve interaction between the construction of tunnels and other structures. Such conditions include surface structures (such as buildings), existing subsurface structures (such as tunnels, urban pipes) or complex underground structures such as tunnels and underground stations are twins [1]. Numerical modeling possible to reconcile the different components provides an analysis of the issues involved in the action. Different numerical methods based on the theories of continuous and discontinuous are presented. In theory, continuum rock mass as a continuum that by a limited number of discontinuities is interrupted considered, while in theory the batch, the rock mass as a combination of blocks that together have been put in Taken Since the area is bearish in this study for soil and environment is assumed to be continuous, so the numerical method used a Plaxis 3D tunnel. Is (FEM) and finite element method, finite element software package exclusively for the analyses of deformation and stability in geotechnical engineering projects have been developed [6].

Numerical Modeling

A pile of used computer modeling to evaluate the performance of the group. The method is that first a 4×4 and pile with a diameter of 1 m, 8 m and 1 m intervals modeled in sandy soil. In this study, all piles on all models is constant and equal to the diameter of one meter is assumed loaded onto a pile on a load of 20 KN m wide and done. The time to failure of soil mass gradually increases. This is achieved through the ultimate bearing capacity of pile group. Then dig a tunnel with a diameter of 10 meters at a depth of 10 m above ground level change and displacement following the settlement to examine the group and pile. Of these parameters on the results. The first group of piles in sandy soil modeling with dimensions of 30×20×10 and horizontal and vertical displacements at points A, B, C and D obtained. Location points are: A: ground and left piles B: ground and the right pile group C: 2 m below point A D: 2 m below point Bafter modeling results were presented as follows:

As can be seen from the figure 1 and 2 are for areas near the border cross points B and D the displacement of other points more. It can be seen that at the start of the first swell slightly upward and then starts the settlement that this phenomenon is due to the expansion in the sand. The charts can also be seen on the horizontal displacement of the points where the Earth's surface and are near the head of the

pile the displacement of less than spots that are deep in the soil. This is due to the presence of head pile, which has prevented them from moving too much.

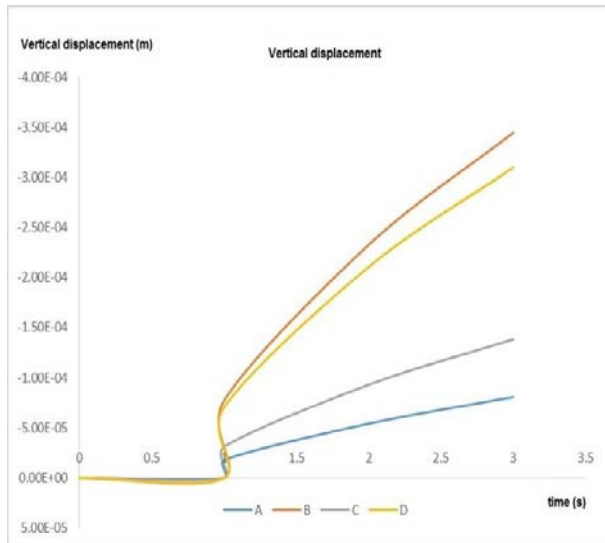


Fig1: Vertical displacement

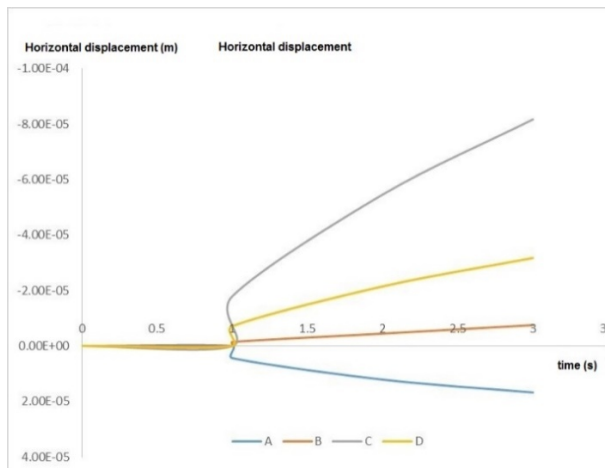


Fig 2: Horizontal displacement

The effect of the tunnel excavation on settlement

In this part of the analysis model was used to dig a tunnel with a radius of 5 meters at a depth of 10 meters at a distance of 9 meters of the pile. Digging tunnels and walls of all sections of drilling with lining was stabilizing. By drilling underground Held settlement curved surface and the central vertical addition to the settlement, [Figure 3] but other sections vertical to horizontal displacement are. When the different parts of the Earth's surface horizontal displacement ratios to acquire land under tension or horizontal compression occurs. The

central portion of the compression curve will be subsidence and settlement of curves on the sides, horizontally placed under tension.

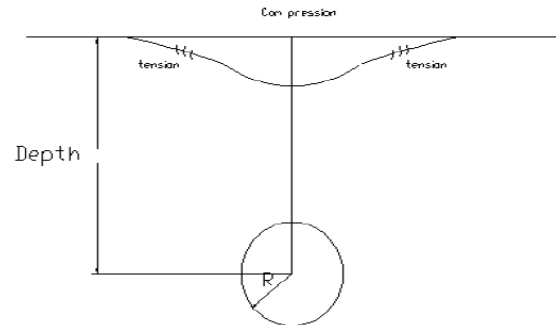


Fig 3: Land subsidence

Mohr Coulomb strength parameters in the model by selecting any change in ductility by increasing the depth of drilling, maximum sat down possible reduction in the earth's sat down. While the maximum surface hardening soil, advanced model with the same selection parameters is possible. The hardening soil model, the model elastoplastic model is hyperbolic. This model can be used to simulate the behavior of granular and cohesive soils used. In the following tables parameters used in both models are provided. Soil elements were prepared such that the lower model boundary condition is closed and there is no displacement in horizontal and vertical direction, but only in the horizontal direction displacement is closed on the flanks. After forming geometric modeling, finite element network is created that can be seen in 3 Figure Build a network of 15 nodes triangular elements were used to model the soil, Accordingly, the average size of each side of the boundary conditions of the soil at least 4 times the diameter of the tunnel and the model has been replaced with proper border [7].

As can be seen from the figure [4] and [5] to point A on the left is a pile group and nearby tunnels land subsidence increased a lot. But elsewhere at a depth of 2 meters above ground level, with a slight increase in their land subsidence occurred. The charts can also be seen on the horizontal displacement to point A on the left is a pile group and tunnels near the land subsidence has increased a lot. But elsewhere at a depth of 2 meters above ground level, with a slight increase in their land subsidence occurred. In this model after the analysis was conducted in the presence of tunnel this time we have dug a tunnel with a radius of 5 meters at a depth of 10 meters at a distance of 11 meters from the ground and the pile. Digging tunnels and walls of all sections of drilling with lining was stabilizing. As can be seen from the

above forms for Point A on the left is a pile group and near the tunnels land subsidence is higher than elsewhere. But elsewhere at a depth of 2 meters above ground level, with a slight increase in their land subsidence occurred.

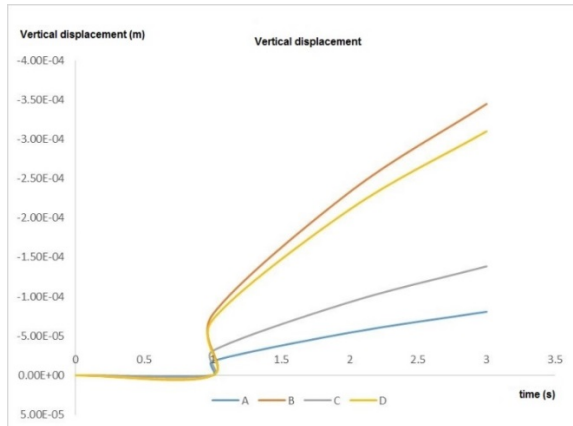


Fig 4 :Vertical displacement

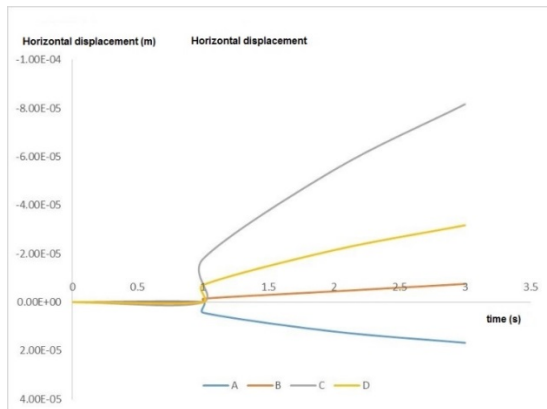


Fig 5: Horizontal displacement

CONCLUSION:

After modeling and model analysis results were presented as follows:

1. Tunnel increases the vertical displacement sat on the model.
2. Points where the Earth's surface is moving further and have a land subsidence.
3. The horizontal and vertical displacement of deep soil less.
4. The tunnel away from the land subsidence and the displacement and pile tunnel effect is low.
5. By increasing the radius of the tunnel and land subsidence increased the amount of displacement.

REFERENCES:

1. Brinkgreve, R. B. J., &Broere, W. The Influence of Tunnel Boring on Foundations and Buildings in Urban Areas -A Numerical Study. *Geotechnics of Soft Soils J.* 2003. pp: 257-263
2. Ng, Cww., Lee, K.M., Tang, D.K. Three-dimensional numerical investigations of New Austrian tunneling method (NATM) twin tunnel interaction. *Canadian Geotechnical J.* 41, 2004. pp:523-539.
3. Blackburn, J. Tanner, and Charles H. Dowding. "Finite-element analysis of time domain reflectometry cable-grout-soil interaction." *Geotechnical and geoenvironmental engineering J.* 130(3), 2004. pp: 231-239.
4. Loganathan, N., and H. G. Poulos. "Analytical prediction for tunneling-induced ground movements in clays." *Geotechnical and Geoenvironmental Engineering J.* 124(9), 1998.pp:846-856.
5. Attewell, P. B., and J. P. Woodman. "Predicting the dynamics of ground settlement and its derivatives caused by tunnelling in soil. *Ground engineering J* 15(8), 1982.
6. Cheng, C. Y., Dasari, G. R., Leung, C. F., Chow, Y. K., & Rosser, H. B. 3D numerical study of tunnel-soil-pile interaction. *Tunnelling and Underground Space Technology J.*19(4), 2004. pp: 381-382.
7. Xiang, Y., Zhiping J., Haijian H. Assessment and control of metro-construction induced settlement of a pile-supported urban overpass." *Tunnelling and Underground Space Technology J.* 23(3), 2008. pp: 300-307.

BEHAVIOR OF MODEL GROUP PILES SUBJECTED TO LATERAL SOIL MOVEMENT IN SAND

*Saad Farhan Ibrahim¹, Mohammed Khachi Hatem²

¹Professor, Faculty of Engineering, Isra University, Amman, Jordan, drsaadfarhan@yahoo.com

² Civil Engineering Department, Faculty of Engineering, Al-Mustansiriyah University, Baghdad, Iraq

ABSTRACT

Laboratory model tests have been carried out to explore the behavior of piles subjected to lateral soil movement in sand. The results of a single pile test and ten tests on of group piles arranged in a row (perpendicular to the direction of soil movement) are presented. Different parameters were utilized in these tests, (e.g., pile spacing, number of piles within a group and pile head condition). Group effect was calculated using group factor (F^m) which is defined in terms of the measured maximum bending moments of an individual with group and that of the single pile. The results showed that the maximum bending moment of group piles decreases from the single pile with decreasing pile spacing and the pile behaves essentially the same as a single pile when the pile spacing is 7d or more. The maximum reduction of the maximum bending moments of about (17%) and (28%) as compared with that for the standard single pile may be observed for a pile spacing of 3d for the free and capped headed condition, respectively. The number of piles does not appear to have significant effect on the group factor F^m of piles, except for the free headed inner piles who's the group factors appear to decrease with increasing the number of piles within a group.

Keywords: Piles, Sand, Lateral Soil Movement, Instrumentations, Bending Moment

INTRODUCTION

Pile foundations are designed to give resistance against active load (i.e., load from structure that is directly transferred to the pile foundation by the cap). However, in many cases, pile foundations are designed to provide resistance against passive load, which that is induced from the lateral soil movements. Earthquakes, landslides and human activities, such as tunneling and deep excavation in the vicinity of piles, might cause irreversible soil movements [1]. These soil movements can generate lateral thrusts on the piles supporting both onshore and offshore structures, in a variety of circumstances. In all these conditions, the externally imposed soil movements will impart extra forces, cause increase in bending moments and lateral deflections in piles which may finally cause problems and even damage to the structure of piles [2] and [3].

In practice, piles are commonly used in groups. When piles are closely spaced in a pile group, the presence of loaded piles nearby affects the behavior of each individual pile [4]. Many researchers [5]; [6];[7] found that the piles within a group may suffer some reduction in capacity compared with single isolated piles due to interaction effects. The behavior of an individual pile within group is different from that of single pile, and several factors may be influenced on the behavior of group piles

[8].

In this study, a series of laboratory tests were conducted on some pile groups subjected to lateral soil movement for investigating the group effect on the lateral response of an individual pile within a group. Different parameters were utilized in these tests, (e.g., pile spacing, number of piles within a group and pile head condition). The piles arranged in one row perpendicular to the direction of lateral soil movement

SOIL PROPERTIES

Dry sand was used in this study and it was sieved on the sieve no. 10 (2 mm) to remove the coarse particles. The specific gravity (G_s), the maximum and the minimum dry unit weights of the soil are 2.65, 16.78 kN/m³ and 14.1 kN/m³ respectively. For 59% relative density, it was found that the angle of internal friction (ϕ) is (35°). Fig. 1 shows the particles size distribution of this sand. The coefficients of curvature (C_c) and uniformity (C_u) are 1.11 and 2.67 respectively. According to the Unified Soil Classification System (USCS), the sand can be classified as poorly graded sand (SP).

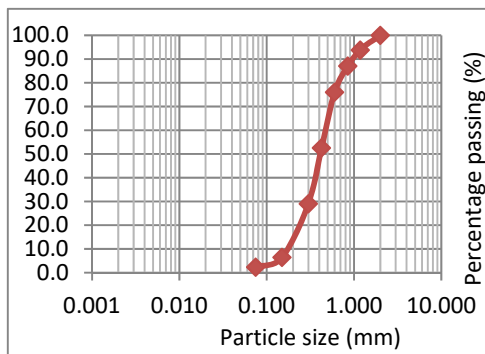


Fig. 1 : Particle size distribution of sand

TEST SET-UP

A special experimental apparatus was designed and manufactured for the current study to investigate the effect of lateral soil movement on pile foundation. It consists of five main parts, (i.e., a steel box, a loading system, a sand raining system, an aluminum piles, and a measurements system). Fig. 2 shows the overall arrangement of the testing apparatus.

The Steel Box

The designed steel box made of thick steel plate having a thickness of (6.5 mm) with internal dimensions of (80cm×80cm) and (80cm) height was used to apply triangular profile shape of lateral soil movements. Across the width of the box, it was divided into two parts, upper part and lower part. The two parts were connected by two hinges at the mid-height of the box. The upper portion is able to rotate while the lower portion is fixed which makes the soil in the box is divided into two layers (movable and stable). Four wheels were welded at the bed of the box in order to allow the box to travel from underneath sand raining to under the pile jacking system.

Loading System

Three mechanical jacks with capacity of 3 tons (for each one) were used to apply vertical and horizontal loadings on the instrumented pile and the box respectively. The vertical jack was used to drive the pile into the model ground. A load cell with a capacity of 5 tons was connected with the vertical jack to measure the load required to install the model pile into the sand. The base of the first horizontal (near) jack was welded perpendicular to the near column of the frame in order to apply horizontal force on the near upper part of the box. A load cell with a capacity of 5 tons was connected

with this near jack to measure the horizontal force acting on the near upper part of the box. By turning the near jack, the near upper moveable part of the model steel box was forced to rotate around its joints, and consequently causes the upper part of the soil in the box to move. The moving soil thus is subjected to a triangular profile of horizontal movement, with the maximum displacement at the soil surface and zero displacement at the level of joints of the upper and lower parts. The base of the second horizontal mechanical jack (rear jack) was welded perpendicular to the rear column of the frame to control on the movement of the rear upper part of the box.

The Details of Pile and Pile Cap

Hollow aluminum pipes of 30 mm outer diameter, 1.4 mm wall thickness and 1000mm total length with a bottom plug were utilized as a model piles in this study. The flexural stiffness of each model pile was calculated by conducting simply supported beam test. By measuring the central deflection under a known load at the center of the beam (model pile), the flexural stiffness of the pile was found (0.91 kN.mm²). The pile caps were designed and fabricated from a solid aluminum block of 60 mm thick. On one face of the pile cap, there were predrilled holes of 30 mm deep, with a diameter to fit the piles. The diameter of each hole was made 0.5 mm greater than the pile diameter to assist the piles to the pile cap connection. The caps were not used just for connecting the pile heads together during the test (capped headed case), but also for helping the jacking system to drive the piles into the sand bed.

Instrumentations and Measurements

The data logger, strain gauges and load cell utilized in this study to determine the strains along the pile shaft and load required causing movement in the upper movable part of the model box. A compact and handheld digital data logger (TC-32K) was utilized to measure and store data from strain gauge measurement for each pile test. TML strain gauges type (FLA-5-23-3L) having a gauge resistance of 120 ± 0.3 Ohm was used to instrument the model piles. The strain gauges were fixed along the model piles using cyanoacrylate adhesive (type CN). The strain gauges were then coated by 1 mm epoxy resin in order to protect from damage during the pile driving and testing under lateral soil movement. Eight pairs of strain gauges were attached along each instrumented pile to measure the developed bending moment caused by lateral soil movement. The number of instrumented piles within the group depends on the number of piles within the group. Due to the limited channels

existing in the current data loggers (maximum ten channels), several separated tests were conducted on pile groups to record the bending moments of the required individual pile, and the number of these separated tests depends on the number of piles.

The Sand Raining

A sand raining device fabricated from timber pieces, having internal dimensions of 790 mm by 790 mm, and 150 mm in height was used to pour the sand in the box. The base of the sand raining consists of two timber plates; the bottom is fixed while the top is moveable. The thickness of the timber plates was 18 mm and 6 mm for fixed and moved respectively. The fixed plate was perforated with 6 mm diameter holes on a 40 mm by 40 mm grid pattern. The moveable plate can slide along the slots on one side of the sand raining. When the top moveable plate is pulled out, the sand is discharged from the sand raining in model box. The falling height of sand was selected as 400 mm, which gave a relative density of sand about 59%, and a unit weight of 15.6 kN/m³.

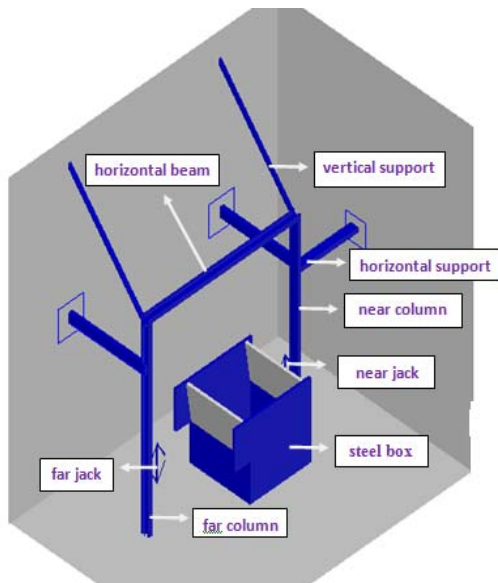


Fig. 2 : Test set-up

COMPRISON METHOD

To explore the group effects on the lateral response of piles, the pile group results were compared with that of the single pile test and hence a suitable comparison method was needed to be adopted. The group factor in term of bending moment (F^m) represents the ratio of the maximum bending moment of individual piles within a group

M_{maxi} to the maximum bending moment of single pile M_{maxs} [9].

THE RESULTS

This section describes the results of free headed single pile (standard) test and the tests of two, three and four piles arranged in one row for free and capped headed cases. The results of the effect of pile spacing and number of piles on response of piles in a row are presented and discussed in the following subsections.

Single Pile (Standard)

This test was performed on free headed single pile of 30 mm in diameter; the box was filled with sand to the top. The pile length in the upper movable part (L_m) was 400 mm, while that in the lower stable part was 350 mm. The falling height of sand raining was (400mm) gave a relative density of about 59%. Fig. 3 shows the response of pile in terms of bending moment. It can be seen that the profiles of the bending moment along the pile shaft at different values of the lateral soil movements are analogous to a parabolic shape. The measured bending moment increases with increasing the lateral soil movement but the rate of the increase reduces, especially when the soil surface movement is greater than 60 mm.

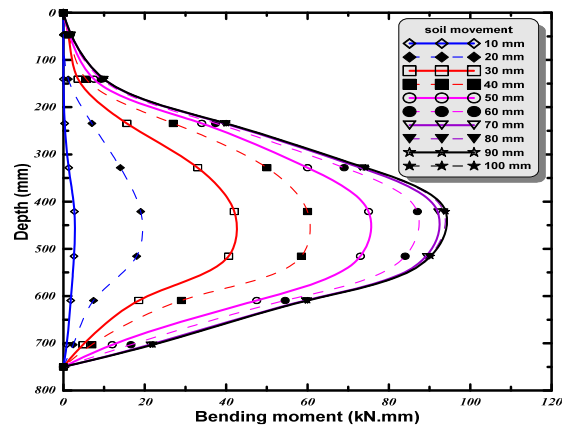


Fig. 3 : Bending moment distributions from the standard test

Pile Group

This test was performed on free headed single pile of 30 mm in diameter; the box was filled with sand to the top.

5.2.1 Effect of pile spacing

For investigating the effect of pile spacing on the lateral response of pile, many tests were carried

out on two piles arranged in a row for both free and capped headed cases. Three different spacing (i.e., 3d, 5d and 7d) were adopted in these tests. Due to symmetrical arrangements of the piles in this type of pile groups, the results of the two piles were suggested to be basically identical and hence only the re results of one pile were presented.

Fig. 4 presents the bending moment profiles for free headed pile group for different pile spacing together with that for the single pile test. It can be seen that the bending moment profiles are very similar in shape for all cases; including the depth of the maximum bending moment, but different in the magnitudes of the bending moments. It can be also seen that the variation of the calculated bending moment with pile spacing is mainly within the middle part of the pile length (which includes the position of the maximum bending moment); while the variation is very small in the upper and lower portions of pile. Also the maximum bending moment decreases from the single pile test with decreasing pile spacing. Since each pile in all cases was subjected to the same magnitude movement, this reduction in the bending moment may be due to a reduction of pile–soil contact pressure resulting from pile-soil interaction. It can be observed from Fig. 4 that a spacing of 7d seems to be large enough to eliminate abolish the group effect. It can be indicated the pile behaves essentially the same as a single pile when the pile spacing is 7d or more.

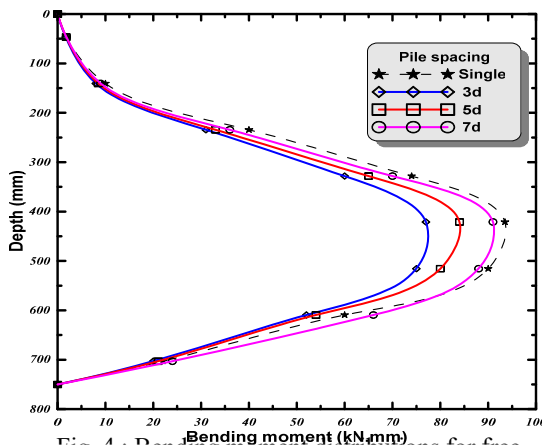


Fig. 4 : Bending moment distributions for free headed two piles

The bending moment profiles for capped headed two piles in a row for different pile spacing together with that for the single pile test are shown in Fig. 5. Although the pile cap tends to develop a negative bending moment at the pile head level, the value of this negative bending moment was very small. Therefore, the bending moment profile for all pile spacing was basically the same as that for the free headed case, but its magnitude appears to be

smaller. It can be noticed that, similarly to the free headed case, the maximum bending moment decreases with decreasing pile spacing.

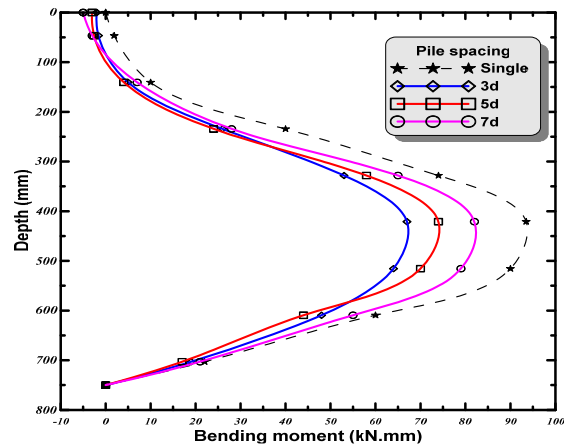


Fig. 5 : Bending moment distributions for capped headed two piles

Fig.6 shows the plot of the group factor F^m for both free and capped headed conditions and different pile spacing. It can be seen that, (F^m) decreases with decreasing pile spacing for both headed cases and capped case, and it is smaller than unity for all cases. The group factor was also seen to be greater for the free headed case than that for the capped case, which may be attributed to a developed negative bending moment and a larger load sharing between the adjacent piles for the capped condition. The maximum reduction of the maximum bending moments of about (17%) and about (28%) as compared with that for the standard single pile may be observed for a pile spacing of 3d for the free headed condition and capped condition, respectively. It seems that the provision of a pile cap for two piles in a row tends to results in a smaller bending moments. Therefore, the provision of a pile cap appears to be an advantage for piles in a row utilized for resisting soils from moving laterally.

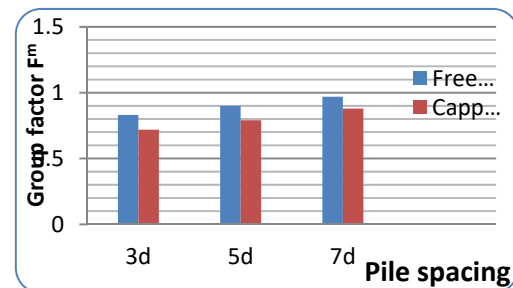


Fig. 6 : The group factor against the pile spacing for two piles

5.2.2 Effect of number of piles

To explore the effect of number of piles on the lateral response of piles in a row, four tests were carried out on three piles and four piles groups for both free head and capped cases with pile spacing 3d. For both the three piles and four piles groups, the outside piles were defined as an outer piles, while the inside pile(s) were defined as inner pile(s).

Fig.7a presents the bending moment profiles for the inner and outer piles for free headed three piles group (for 3d pile spacing), together with that of the single pile test. It can be noticed that, the shape of the bending moment profiles is very similar for each pile, but the maximum bending moment for the outer pile is larger than the maximum bending moment for the inner pile. It can be also seen that the bending moments of the inner pile and the outer pile are smaller than the bending moment of the single pile. The similar trend is also observed for bending moment profiles for the four pile groups, but the differences in the magnitudes of the bending moments for the inner and outer piles appears to be greater than for the three piles group, as presented in Fig.7b. Also, the bending moments of the inner pile and the outer pile are smaller than the bending moment of the single pile.

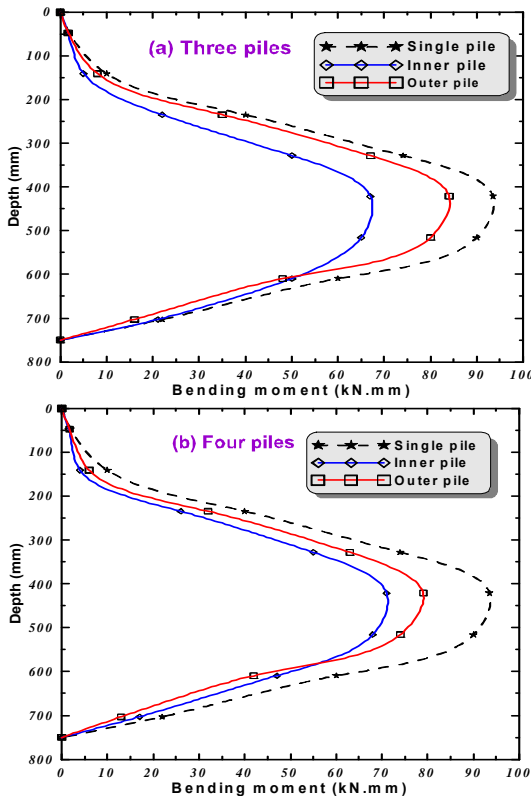


Fig. 7: Bending moment profiles for free headed three and four piles

Fig. 8a presents the bending moment profiles for the inner and outer piles for capped headed three piles group (for 3d pile spacing) together with that of the single pile test. Similar to the test of two piles,

the cap tends to develop a negative bending moments at the pile head level piles, but its value is far less than the maximum positive bending moment. The bending moment profiles for the inner pile and the outer pile for capped headed four piles group (for 3d pile spacing) together with that of the standard single pile test are presented in Fig. 8b. Similar to the case of capped headed three piles group, the cap tends to develop a negative bending moments at the pile head level piles. The negative bending moment appears to increase (but stay less than maximum positive bending moment) with increasing the number of piles with the group, but the maximum positive bending moment is approximately constant.

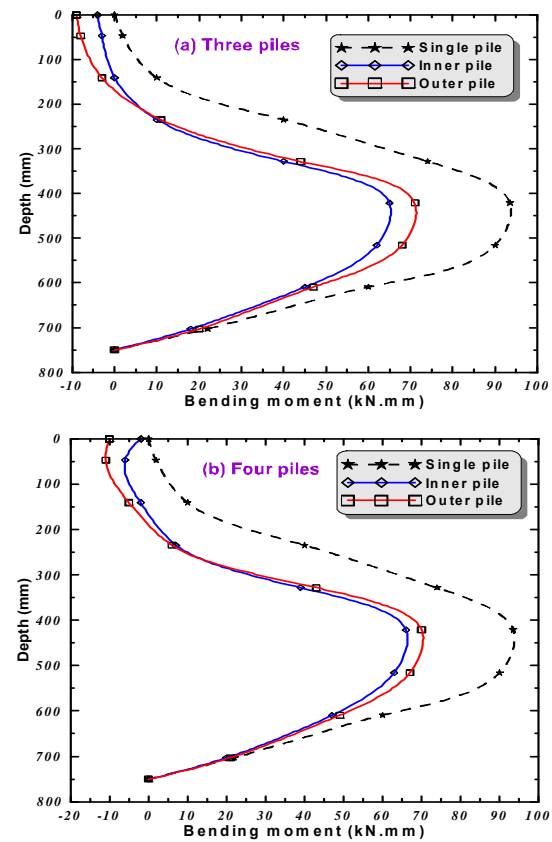


Fig. 8: Bending moment profiles for capped headed three and four piles

The group factor F^m is plotted with the number of piles to explore the influence of the number of piles on the lateral response and the resisting force provided by piles. As shown in Fig. 9 the effect of the number of piles within a group on the group factor F^m , for both the free headed and capped cases is seen to be different for the inner pile and outer pile due to load sharing which develops between the adjacent piles. The number of piles does not appear to have significant effect on the group factor F^m of piles, except for the free headed inner piles (i.e., the

group factors appear to decrease with increasing the number of piles within a group).

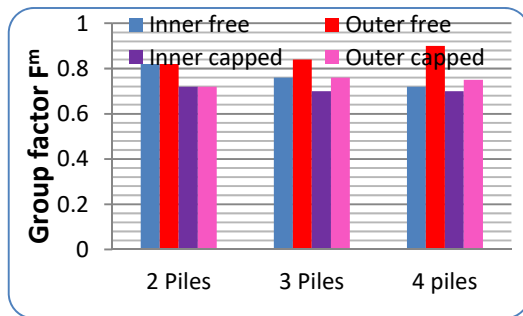


Fig. 9: The group factor against pile spacing for piles in a row

CONCLUSIONS

Laboratory model tests have been conducted on group piles arranged in arrow in addition to single pile subjected to lateral soil movement in sand to investigate the effects of the pile's spacing, number of piles and piles headed condition on lateral response of piles. The results of the tests indicate that the maximum bending moment for both free and capped headed cases decreases from the single pile with decreasing pile spacing and the group piles behaves essentially the same as a single pile when the pile spacing is 7d or more. The maximum reduction of the maximum bending moments of about (17%) and about (28%) as compared with that for the standard single pile may be observed for a pile spacing of 3d for the free and capped headed conditions, respectively. The maximum bending moment for the outer pile was larger than the maximum bending moment for the inner pile. For four piles group, the differences in the magnitudes of the bending moments for the inner and outer piles appears to be greater than those for the three piles group. The number of piles does not appear to have significant effect on the group factor F_m of piles, except for the free headed inner piles whose the group factors appear to decrease with increasing the number of piles within a group.

REFERENCES

- [1] Qin HY. "Response of Pile Foundations due to Lateral Force and Soil Movements". Ph.D. Thesis, Griffith University, 2010.
- [2] Pan JL, Goh AT, Wong KS, Selby AR. "Three-dimensional analysis of single pile response to lateral soil movements". *International Journal for Numerical and Analytical Methods in Geomechanics*. 2002 Jul 1;26(8):747-58.
- [3] Al-Abboodi I, Toma-Sabbagh T, Al-Jazaairry A. "Modelling the response of single passive piles subjected to lateral soil movement using PLAXIS". *International Journal of Engineering Research & Technology*. 2015 Mar 13;4(3):176-80.
- [4] Poulos HG, Davis EH. "Pile foundation analysis and design". 1980.
- [5] Broms BB. "Lateral resistance of piles in cohesionless soils". *Journal of the Soil Mechanics and Foundations Division*. 1964 May;90(3):123-58.
- [6] Randolph MF. "The response of flexible piles to lateral loading". *Geotechnique*. 1981 Jun;31(2):247-59.
- [7] Chen LT, Poulos HG. "Piles subjected to lateral soil movements". *Journal of Geotechnical and Geoenvironmental Engineering*. 1997 Sep;123(9):802-11.
- [8] Kong G, Zhou Y, Yang Q. "Group effect of dragload in pile groups embedded in consolidating soil under embankment load". *KSCE Journal of Civil Engineering*. 2016 Sep 1;20(6):2208-20.
- [9] AlAbdullah S F, Taresh N S. "Evaluation of Soil Reinforcement with Geogrid in Subgrade Layer using FE Techniques". *International Journal of GEOMATE*, 2017 June unpublished yet.

CHANGE OF DEBRIS FLOW CHARACTERISTICS DUE TO DIFFERENCES IN PHYSICAL CONDITIONS OF LANDSLIDE DAM

Naomasa Honda¹

¹ Faculty of Regional Environment Science, Tokyo University of Agriculture, Japan

ABSTRACT

A large-scale collapse can form a landslide dam, which can block a river and create ponds upstream. If a landslide dam outburst occurs, the resulting debris flow and flood can also cause serious problems downstream. In this paper, based on a numerical analysis, we discuss changes in the debris flow characteristics caused by such differences in a landslide dam's physical conditions, as shape and material. We conducted numerical simulations to specify the sediment runoff and the debris flow characteristics, including flow depth, flow velocity and flow discharge along the river's path. Judging from the analytical results, if landslide dams have an identical sediment volume, the debris flow scale is so large that the dam height will be high or the amount of the water overflow will be large. To predict the scale of the debris flow with sufficient accuracy, we must carefully establish the physical conditions that significantly influence sediment mobility.

Keywords: Landslide dam, Dam outburst, Debris flow, Landslide dam's physical conditions, Numerical simulation

INTRODUCTION

A large-scale collapse due to earthquakes or heavy rainfall can form landslide dams, which can block rivers and create ponds upstream: for example, the Imokawa River basin in the Mid Niigata Prefecture Earthquake in 2004, the San-hazama River basin in the Iwate-Miyagi Nairiku Earthquake in 2008, and the Akadani River basin in the Kii peninsula in the typhoon No.12 in 2011 [1] - [3].

If a landslide dam outburst occurs, the resulting debris flow and flooding can cause serious problems downstream. Therefore, many field surveys, experimental studies, and numerical analyses on landslide dams exist: formation, breakdowns, and sediment runoff processes [4] - [6].

Naturally, the debris flow's scale and properties due to landslide dam outburst vary by such conditions as shape and material. But measuring these characteristics at the actual sites is very difficult, because this spot is obviously dangerous during a natural disaster.

In this paper, based on numerical analysis, we discuss the changes in the debris flow characteristics caused by differences in a landslide dam's physical conditions, such as shape and material. We conducted numerical simulations to specify the sediment runoff and such flow characteristics as flow depth, flow velocity and flow discharge along virtual torrents.

RELATIONSHIP BETWEEN LANDSLIDE DAM OUTBURSTS AND DEBRIS FLOW OCCURRENCES

As shown in Fig. 1, when a huge collapse occurs on a mountain slope and a large quantity of sediment flows into a river, the river becomes dammed and

formed a landslide dam. In Japan, earthquakes and heavy rainfalls are often geographically generated, mountain slopes are topographically steep, and the earth's layer is geologically weak. Japan suffers from the conditions under which landslide dams are easily formed.

Landslide dam outbursts are caused by the following reasons:

- (1) sliding failures due to infiltration from ponds
- (2) piping by subsurface backward erosion
- (3) overflow from ponds

Outbursts due to pond overflow cause the large-scale debris flow and serious downstream damage, because overflow occurs when the pond's water level is high. If a landslide dam is formed, draining must be quickly installed and draining channel works must be promptly constructed.

For debris flow hazard mitigation, warning and evacuation measures are as critical as structure measures. The scale and characteristics of the debris flow must be predicted and used to determine warnings and evacuations.

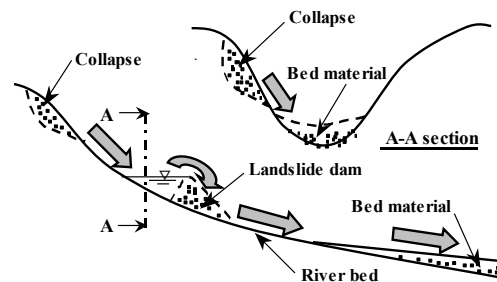


Fig. 1 Debris flow occurrence system due to landslide dam outburst

METHOD AND PROCEDURE FOR STUDY

Governing Equations for Debris flow

The following are the mass conservation equations for the flow mixture and for sediment alone:

$$\frac{\partial h}{\partial t} + \frac{1}{B} \frac{\partial Bvh}{\partial x} = \frac{E}{c_*} \quad (1)$$

$$\frac{\partial \varepsilon ch}{\partial t} + \frac{1}{B} \frac{\partial \varepsilon c Bvh}{\partial x} = E \quad (2)$$

where t is the time, x is the coordinate axis along the flow, h is the flow depth, B is the flow width, v is the flow velocity, E is the erosion velocity (its negative value designates the deposition), c is the sediment concentration by volume, ε is the correction factor (see Egashira et al. [7], where $\varepsilon c = c_t$, c_t is the sediment flux concentration), and c_* is the sediment concentration of the river-bed layer.

The following is the momentum conservation equation:

$$\frac{\partial v}{\partial t} + v \frac{\partial v}{\partial x} = g \sin \theta - \frac{1}{\rho_m h} \frac{\partial P}{\partial x} - \frac{vE}{c_* h} - \frac{\tau_b}{\rho_m h} \quad (3)$$

$$\rho_m = (\sigma - \rho)c + \rho \quad (4)$$

The second term on the right-hand side in Eq. (3) is the pressure gradient and the third is the resistance due to sediment erosion. g is the gravity acceleration, θ is the river-bed slope, P is the pressure, τ_b is the river-bed shear stress, ρ_m is the mass density of the flow mixture defined by Eq. (4), σ is the mass density of gravel, and ρ is the mass density of water.

The mass conservation equation of river-bed sediment takes the following form:

$$\frac{\partial Z_b}{\partial t} = -\frac{E}{c_* \cos \theta} \quad (5)$$

$$\theta = \sin^{-1} \left(-\frac{\partial Z_b}{\partial x} \right) \quad (6)$$

where Z_b is the river-bed elevation, and θ is expressed by Eq. (6).

Even though E and τ_b play an important role in the above governing equations, no general formulas have been developed for them. We used the formulas for E and τ_b developed by Egashira [8], [9]. The following is erosion velocity, E :

$$\frac{E}{v} = c_* \tan(\theta - \theta_e) \quad (7)$$

$$\theta_e = \tan^{-1} \left\{ \frac{(\sigma / \rho - 1)c}{(\sigma / \rho - 1)c + 1} \tan \phi_s \right\} \quad (8)$$

where θ_e is the equilibrium river-bed slope corresponding to the sediment concentration defined by Eq. (8). ϕ_s is the internal friction angle of the sediment in this equation.

The following is the formula for τ_b , developed by Egashira et al. [10]:

$$\tau_b = \tau_y + \rho f v^2 \quad (9)$$

$$\tau_y = \left(\frac{c}{c_*} \right)^{1/5} \rho (\sigma / \rho - 1) c g h \cos \theta \tan \phi_s \quad (10)$$

$$f = \frac{25}{4} \left\{ k_f \frac{(1-c)^{5/3}}{c^{2/3}} + k_g \frac{\sigma}{\rho} (1-e^2) c^{2/3} \right\} \left(\frac{h}{d} \right)^{-2} \quad (11)$$

In Eq. (9), τ_y is the yield stress caused by the particle-to-particle contacts defined by Eq. (10), and f is the friction factor defined by Eq. (11), where e is the restitution coefficient, d is the reference grain size, and k_f and k_g are the coefficients: $k_f=0.16$, $k_g=0.0828$.

Virtual torrents

In actual torrents, the flow width and the riverbed slope change irregularly, and the sediment that becomes the constitution materials of the debris flow are partly distributed on the riverbed. These geographical conditions greatly influence the calculation results of the debris flow characteristics. Therefore, we set two virtual torrents to just focus on the differences of the landslide dam's physical conditions (Fig. 2):

Case 1: $\theta = \text{constant} = 10^\circ$, $B = \text{constant} = 30$ m, total river length, $L = 1,000$ m (horizontal distance = 985 m, relative height = 174 m), no sediment that was entrained in the debris flow exists on the riverbed.

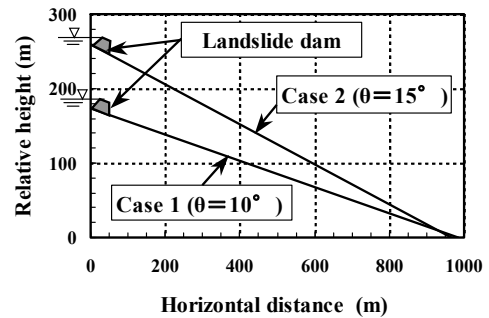


Fig.2 Riverbed profile of virtual torrents

Case 2: $\theta = \text{constant} = 15^\circ$, $B = \text{constant} = 30$ m,
total river length, $L = 1,000$ m (horizontal
distance = 966 m, relative height = 259 m),
no sediment that was entrained in the debris
flow exists on the riverbed.

As shown in Fig. 2, a landslide dam is formed at
the upstream end of the virtual torrent. The landslide
dam outburst occurs due to pond overflow. The
sediment flows downstream and is transported as
debris flows.

Computational Conditions

Shape of landslide dam

In our numerical simulations, our imaged shapes
of the landslide dams are shown in Fig. 3. In all cases,
the sediment volume that constitutes a dam is
approximately $40,000 \text{ m}^3$.

Physical conditions of landslide dam material

The physical parameters of the landslide dam
material necessary for computation are specified as
follows:

- $\sigma = 2.70 \text{ g/cm}^3 = \text{constant}$
- $c_s = 0.50 = \text{constant}$ [5], [6]
- $\phi_s = 30^\circ, 35^\circ, 39^\circ$ (variable conditions)
- $d = 10 \text{ cm}, 5 \text{ cm}, 1 \text{ cm}$ (variable conditions)

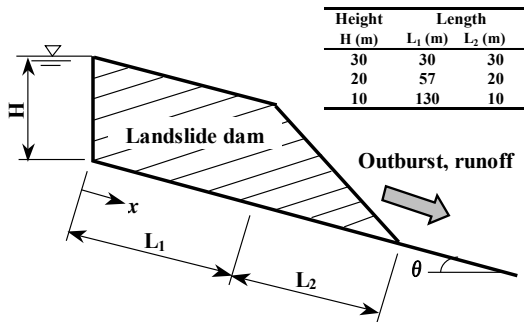


Fig. 3 Shape of landslide dam

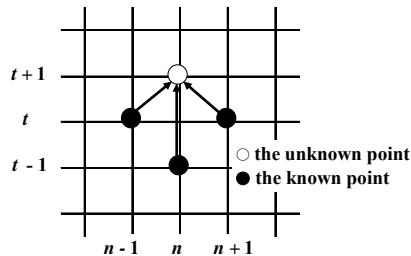


Fig. 4 Schematic diagram of leap-frog scheme

Water supply conditions

The overflow discharge from the pond, Q_{in} , is
assumed as follows:

- $Q_{in} = 10.0 \text{ m}^3/\text{sec}, 1.0 \text{ m}^3/\text{sec}, 0.5 \text{ m}^3/\text{sec}$ (variable
conditions)

Relationship between water density and fine sand concentration in water

The fine sand concentration in water, c_s , is closely
related to a rise in the water's density (muddy water).
Because a rise in the water density increases
buoyancy, our analysis cannot ignore its influence
[11]. Therefore, c_s is assumed as follows:

- $c_s = 10 \%, 20 \%, 30 \%$ (variable conditions)

According to Eq. (4), ρ is calculated follows:

- $\rho = 1.17 \text{ g/cm}^3$ ($c_s = 10 \%$), 1.34 g/cm^3 ($c_s = 20 \%$),
 1.51 g/cm^3 ($c_s = 30 \%$) (variable conditions)

Numerical analytical conditions

We used the finite difference method (leap-frog
scheme in Fig. 4). Time and distance are
discriminated as $\Delta t = 0.025$ seconds and $\Delta x = 5.0$ m,
respectively.

RESULTS AND DISCUSSIONS

Table 1 shows the numerical simulation results of
the debris flow. Figure 5 shows the temporal change
of the debris flow characteristics under the conditions
in Table 1:

- river-bed slope: $\theta = 15^\circ$ (Case 2)
- shape of landslide dam: $H = 30$ m, $\phi_s = 39^\circ$,
 $d = 5$ cm
- water supply conditions: $Q_{in} = 10.0 \text{ m}^3/\text{sec}$,
 $\rho = 1.17 \text{ g/cm}^3$ ($c_s = 10\%$)

Progress of Landslide dam outburst due to overflow water from a pond

As shown in Fig. 5(a), the landslide dam began to
be eroded by the overflow water soon after the water
supply. The eroded rose rapidly toward the upper
reaches of the dam.

Change of debris flow characteristics by differences in landslide dam shape

According to Table 1, the debris flow scale is so
large that river-bed slope θ is so big and dam height

H is so high or the same sediment volume.

Table 1 Results of numerical simulation of debris flow

River-bed slope	Conditions to change											
	H (dam height)				ϕ_s (internal friction angle)				d (reference grain size)			
θ ($^{\circ}$)	H (m)	hmax (m)	Vmax (m/s)	Qmax (m ³ /s)	ϕ_s ($^{\circ}$)	hmax (m)	Vmax (m/s)	Qmax (m ³ /s)	d (cm)	hmax (m)	Vmax (m/s)	Qmax (m ³ /s)
Case 1 ($\theta=10^{\circ}$)	30	4.5	3.8	130	30	3.7	5.0	250	1.0	3.0	3.7	120
	20	2.5	3.3	77	35	4.7	4.1	155	5.0	4.5	3.8	130
	10	—	—	—	39	4.5	3.8	130	10.0	5.0	3.4	135
Case 2 ($\theta=15^{\circ}$)	30	5.7	4.0	215	30	5.4	4.1	330	1.0	5.3	4.5	200
	20	4.5	3.8	170	35	5.7	4.1	265	5.0	5.7	4.0	215
	10	0.2	1.2	6	39	5.7	4.0	215	10.0	6.0	3.8	225
Other conditions	—				H=30 m				H=30 m			
	$\phi_s=39^{\circ}$, d=5.0 cm				d=5.0 cm				$\phi_s=39^{\circ}$			
	$Q_{in}=0.1$ m ³ /s, $c_s=10$ %				$Q_{in}=0.1$ m ³ /s, $c_s=10$ %				$Q_{in}=0.1$ m ³ /s, $c_s=10$ %			

River-bed slope	Conditions to change							
	Q _{in} (water supply)				c _s (fine sand concentration)			
θ (°)	Q _{in} (m ³ /s)	h _{max} (m)	V _{max} (m/s)	Q _{max} (m ³ /s)	c _s (%)	h _{max} (m)	V _{max} (m/s)	Q _{max} (m ³ /s)
Case 1 (θ=10°)	0.1	4.5	3.8	130	10	4.5	3.8	130
	1.0	5.0	4.1	190	20	5.7	4.9	236
	10.0	7.3	5.1	500	30	5.9	5.8	360
Case 2 (θ=15°)	0.1	5.7	4.0	215	10	5.7	4.0	215
	1.0	6.5	4.4	280	20	6.7	5.1	390
	10.0	9.3	5.6	625	30	6.0	6.0	457
Other conditions	H=30 m				H=30m			
	φ _s =39°, d=5.0 cm				φ _s =39°, d=5.0 cm			
	c _s =10 %				Q _{in} =0.1 m ³ /s			

Legend

h_{max}: maximum
flow depth

V_{max}: maximum
flow velocity

Q_{max}: maximum
flow discharge

Legend

hmax: maximum
flow depth
Vmax: maximum
flow velocity
Qmax: maximum
flow discharge

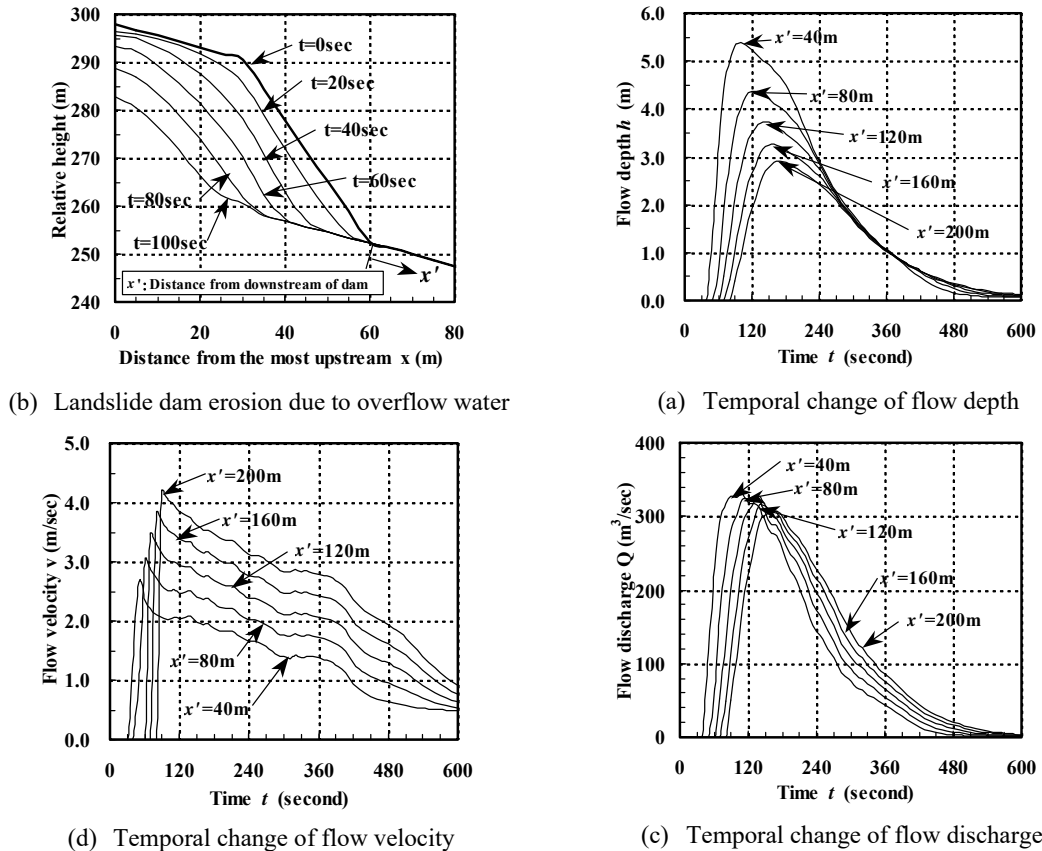


Fig. 5 Example of temporal change of debris flow characteristics

Table 2 Relationship between landslide dam's physical conditions and debris flow characteristics

Physical conditions of landslide dam		Debris flow scale	Influence on debris flow characteristics
Shape of landslide dam	River-bed slope θ	Debris flow scale is so large that θ is big.	• Flow depth h
	Dam height H	In case of same sediment volume, debris flow scale is so large that H is high.	• Flow velocity v • Flow discharge Q
Water supply condition	Overflow water discharge Q_{in}	Debris flow scale is so large that Q_{in} is big.	• Flow depth h • Flow velocity v • Flow discharge Q
	Fine sand concentration c_s	v and Q are so large that c_s is big.	• Flow velocity v • Flow discharge Q
Physical conditions of dam material	Internal friction angle ϕ_s	v and Q are so large that ϕ_s is small.	• Flow velocity v • Flow discharge Q
	Reference grain size d	h and Q are so large that d is big.	• Flow depth h • Flow discharge Q

Figures 5(b), (c) and (d) show that the sediment-water mixture has runoff toward the lower reaches and accelerated.

Change of debris flow characteristics by differences in physical conditions of landslide dam material

According to Table 1, flow velocity v is so large and flow depth h is so small that internal friction angle of sediment ϕ_s and relative grain size d are small. Therefore, the landslide dam embankment body is so loose that ϕ_s is small, and friction factor f , defined by Eq. (11), is so small that d is small, raising the fluidity of the debris flow. However, notice that the influence of ϕ_s on v is so small that θ is big.

Flow discharge Q is so large that ϕ_s is small (v is large and h is small), and since d is big (v is small and h is large) Q is large. Notice that flow width B is constant ($B=30$ m) in this study, because Q is a multiplication of B and v and h . Therefore, the increase and decrease of v directly influence the increase and decrease of h .

When B is constant, the influence of the increase in h by the decrease in v has a bigger d than ϕ_s and influences the tendency to change Q . However, B and θ change irregularly in actual torrents and the sediment, which becomes the constitution materials of the debris flow, is partially distributed on the riverbed. We must consider the influence of changes of ϕ_s and d on the debris flow characteristics.

Change of debris flow characteristics by differences in water supply conditions

According to Table 1, h , v , and Q are so large that overflow discharge Q_{in} and the fine sand concentration in water c_s are also large. Q_{in} especially affects the change of h and c_s affects the change of v .

They collaborate to greatly increase Q .

CONCLUSIONS

Table 2 shows the above considerations:

1) If landslide dams have identical sediment volume, the debris flow scale is so large that dam height H will be high or the amount of overflow water Q_{in} will be large.

2) Such physical conditions of landslide dams as internal friction angle of sediment ϕ_s , relative grain size d , fine sand concentration in water c_s , and overflow discharge Q_{in} lightly influence the debris flow scale. To predict the debris flow scale by numerical analyses with sufficient accuracy, we must carefully establish the physical conditions that significantly influence sediment mobility based on field survey results.

3) Recently, the temporal changes of landslide dam shapes and upstream pond scales can be observed in real time by satellite images. Therefore, it is critical to get the aims of ϕ_s , d , and c_s by numerical analyses of similar examples of landslide dam outbursts, while comparing the local path of the debris flow a calculation of the flow depth.

ACKNOWLEDGEMENTS

Part of the present study was supported by Strategic Research Project from Tokyo University of Agriculture.

REFERENCES

- [1] Kato Y., T. Miyano and T. Mizuyama, "Outburst of a small landslide dam on the Imokawa River (prompt report)", Journal of the Japan Society of

- Erosion Control Engineering, Vol. 57(6), March 2005, pp.47-50 (in Japanese).
- [2] Uchida T., A. Matsuoka, N. Matsumoto, J. Matsuda, K. Akiyama, K. Tamura and K. Ichinohe, "Overtopping erosion of landslide dam at Numakura-urasawa, San-hazama river Miyagi Prefecture, Japan", Journal of the Japan Society of Erosion Control Engineering, Vol. 62(3), Sept. 2009, pp.23-29 (in Japanese).
 - [3] Matsumura K., M. Fijita, T. Yamada, Y. Gonda, S. Numata, D. Tsutsumi, K. Nakatani, F. Imaizumi, T. Shimada, M. Kaibori, K. Suzuki, H. tokunaga, Y. kashiwabara, E. Nagano, O. Yokoyama, T. Suzuki, N. Takezawa, R. Oono, T. Nagayama, T. Ikegima and S. Tsuchiya, "Sediment disasters due to typhoon No.12 at 2011, occurred in Kii peninsula", Journal of the Japan Society of Erosion Control Engineering, Vol. 64(5), Jan. 2012, pp.43-53 (in Japanese).
 - [4] Oda A., T. Mizuyama and Y. Hasegawa, "Experimental study of process and outflow rate when landslide dams outburst", Journal of the Japan Society of Erosion Control Engineering, Vol. 59(1), May 2006, pp.29-34 (in Japanese).
 - [5] Oda A., T. Mizuyama and Y. Hasegawa, "An experimental on a landslide dam outburst", Journal of the Japan Society of Erosion Control Engineering, Vol. 60(2), July 2007, pp.33-38 (in Japanese).
 - [6] Chiba M., T. Mori, T. Uchikawa, T. Mizuyama and Y. Satofuka, "Bursting process of a landslide caused by Typhoon 0514 (Nabi) in the Mimi River, Miyazaki Prefecture, Japan, and suggestions regarding evacuation procedures when a landslide dam bursts", Journal of the Japan Society of Erosion Control Engineering, Vol. 60(1), May 2007, pp.43-47 (in Japanese).
 - [7] Egashira, S., T. Itoh, K. Miyamoto and N. Honda, "Importance of Correction Factor Associated with Sediment Concentration Profile in Debris Flow Simulation", The 2nd International Symposium on Flood Defence 2002, Vol.2, 2002, pp.1658-1666.
 - [8] Egashira, S., "Mechanism of Sediment Deposition from Debris Flow (Part 2)", Journal of the Japan Society of Erosion Control Engineering, Vol. 46(1), May 1993, pp. 45-49 (in Japanese).
 - [9] Egashira, S., "Prospects of debris flow studies from constitutive relations to governing equations", Journal of Disaster Research, Vol. 6(3), June 2011, pp. 313-320.
 - [10] Egashira, S., K. Miyamoto and T. Itoh, "Constitutive equations of debris flow and their applicability", Proc. of 1st Int. Conference on Debris Flow Hazards Mitigation, American Society of Civil Engineering, 1997, pp. 340-349.
 - [11] Egashira, S., N. Honda and K. Miyamoto, "Numerical simulation of debris flow at the Gamaharazawa in the Hime River basin", Annuals of Hydraulic Engineers, Japan Society of Civil Engineering, Vol.42, 1998, pp. 919-924(in Japanese).

EXPERIMENTAL STUDY ON SOIL BASED SEALING MATERIAL FULFILLING DEFORMATION FOLLOWABILITY AND UNDERWATER PLACEABILITY

Yusuke Tadano¹, Seiichi Ishida² and Masanori Shimomura³

^{1,3} Technology center, Taisei corporation, Japan; ³ Civil headquarter, Taisei corporation, Japan

ABSTRACT

For retaining walls composed of structural materials such as steel sheet piles that have been widely used in construction works, long term water cutoff performance is sometimes required; infilling work of an impervious material is additionally necessary at joints/interfaces of these structural members. Though various engineering materials for this purpose have already been developed and put into practice, attempts were made to develop a new material that fill the gaps in the precast concrete (PC) wall piles. The authors focus on a soil based impervious material with appropriate plasticity, generally used for filling larger spaces because of its low fluidity. Its fluidity was improved to maintain sealing performance by optimizing the blending ratio of bentonite, sand, water and dispersing agents. As a result, the developed material has the hydraulic conductivity in the order of 10^{-10} m/s, less consolidation settlement, and capability of underwater placement. To confirm whether the material possessed deformation followability, the authors conducted two types of permeability tests in which deformations caused by shearing and opening of joints/interfaces were taken into account. Underwater placement test with a small pumping equipment was also carried out to demonstrate that the material has a high resistance against material segregation. From these experiments, the mix proportion of the soil based sealing material was optimized and finally established to offer the material fulfilling deformation followability and underwater placeability.

Keywords: Bentonite, Impervious material, Deformation followability, Shear deformation, Boundary separation

INTRODUCTION

Vertical sealing walls built to connect materials such as steel sheet piles have been used as earth retaining structures in which long term water cutoff performance is required. Although these structural members themselves are impermeable, it is difficult to ensure water cutoff capability in their joints/interfaces. Impervious performance at these gaps is a key of overall impervious performance of the earth retaining wall. Hence, a number of impervious materials for this purpose have been already developed and put into practical use [1]. Impervious materials used for vertical sealing walls of important structures that cannot tolerate leakage also need to withstand accidental external forces due to earthquakes and waves. Even when joints/interfaces are deformed by the displacement of the wall member, the material is required to keep the same sealing capability.

This paper deals with a new soil based sealing material recently developed for PC wall piles, demonstrating its applicability through various element tests and underwater placing test by a conventional small grout pump.

BACK GROUND STUDY

Figure 1 summarizes the characteristics of the

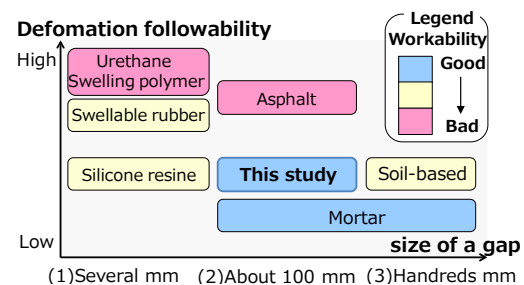


Fig.1 Characteristic of impervious materials

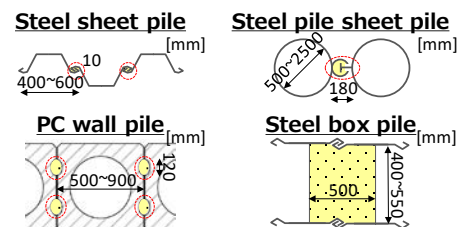


Fig.2 Types of structural members

impervious materials used for gaps between structural members, in terms of the size to be sealed and the deformation followability of the material. The size of sealed parts depends on the types of members used for the vertical sealing wall as schematically shown in Fig.2.

The following are the details of the application of

impervious materials in terms of the gap size:

(1) The gaps with several mm to several tens of mm

High water swelling polymers, water swellable rubbers or silicone resins are generally used for the small gaps such as steel sheet pile joints.[1] These materials expand several times in volume when they come in contact with water to complete the gap filling. Due to chemical effects, its deformation followability is excellent. On the other hand, most of these materials are necessary to be pasted or adhered on the joint surface beforehand. This is only acceptable when the gap size is quite small because the material may peel off during construction of the structural members, and not acceptable in case joint surface is large enough to be exposed to soil during installation works.

(2) The gaps with about a hundred mm

Concrete mortar is generally used for filling the gap of *e.g.*, precast concrete (PC) pile members and steel pipe sheet piles.[1] However, if the structural members deform due to seismic effects after the mortar solidifies, gaps against the members open, and cracks may occur in the mortar. As for the workability, it has high fluidity at the time of mixing, and it can be applied with conventional small pumps.

For steel sheet piles, asphalt may also be used. However, viscosity of asphalt is temperature dependent; its viscosity at normal temperature is very large. Therefore, filling into narrow spaces is difficult without using special pumping facilities equipped with a temperature control system.

(3) The gaps with several hundreds of mm

Soil based impervious plastic materials and a mortar are generally used for relatively large gaps such as those in H joints of steel box piles.[1] Soil based impervious plastic materials have low fluidity, and therefore large pumping facilities as for concrete is necessary. After placing, it may get stiffer due to consolidation, but deformation followability is still high since it does not have a hydration.

Among these impervious materials, the authors focused on the soil based plastic impervious material following the strong points described above.

DEVELOPMENT OF A NEW IMPERVIOUS MATERIAL

Problems of existing soil based impervious materials

Existing soil based impervious materials are dredged soil mixed with bentonite, and added sand or gravel to the mixture for controlling consolidation and improved fluidity [1]. These mixtures have relatively low fluidity, necessitating to be pumped only through a large diameter pipe using a high capacity concrete pump. In order to apply them into narrower spaces, modification of the mix proportion

by increasing the amount of unit water would be effective. However, this leads to lowering its density, resulting in poorer water cutoff performance, dispersion resistance and larger consolidation settlement.

Materials used for development

In order to improve fluidity without increasing the unit water of the material, dispersing agents usually used for the stabilizing solution were implemented to pore walls. To ensure the fluidity with which material can be pumped through a small diameter tube and can avoid segregation, the mixing proportion of bentonite, sand and water was optimized by assessing the blending ratio of the materials.

In the following study, two types of constituent soils were used; a highly swellable powder sodium bentonite and a silica sand. As for silica sand, No.5 (JIS G 5901) was used. The bentonite has many applications for water sealing walls, while silica sand has been used for improving fluidity to suppress consolidation settlement due to its ball bearing effect. As a dispersing agent for improving fluidity, a liquid polyacrylate type was used.

Test procedure

Firstly, the fluidity was evaluated while adjusting the composition of the constituent materials. Cylinder flow test (JHS A 313), table flow test (JIS R 5201) and P type funnel test (JSCE-F521-1999) were used for the evaluation just the same way as for concrete or mortar. In addition, falling head permeability tests (JIS A 1218) were conducted using some of the mixtures to evaluate sealing performance. After selecting two mixtures for the following studies, incremental loading consolidation tests (JIS A 1217) were conducted to optimize a combination which can offer good sealing performance. Furthermore, shear deformation permeability test and interfacial separation permeability test were conducted using the optimized mixture to evaluate the deformation followability. Finally, underwater placement test by a small grout pump was conducted to confirm pumpability and segregation resistance.

Target properties

Fluidity criteria of the mixture were set as follows:

- A) Cylinder flow spread more than 160mm
- B) Capability of natural falling down in P type funnel

The criterion A) is a standard of fluidity used in fluidized soil cement mixture. The criterion B) is an index considering pipe blocking in pumping through a small tube. Both criteria were originally set for the present study.

Table 1 Results of trial mix tests

No.	Fresh water (kg)	Salt water (kg)	Silica sand (kg)	Bento-nite (kg)	Disper-sing agent (kg)	Density (kg/m ³)	Effective clay density (kg/m ³)	Water content (%)	Cylin-der flow (mm)	P funnel time* ² (sec)
1	650	-	748	100	0	1498	0.15	76.7	115	×
2	650	-	748	100	6.5	1498	0.15	76.7	230	71
3	700	-	628	100	0.0	1428	0.14	96.2	147	×
4	700	-	628	100	3.3	1428	0.14	96.2	311	33
5	-	470(1%)	1134	150	3.3	1754	0.28	36.6	104	×
6	-	470(2%)	1134	150	3.3	1754	0.28	36.6	170	200
7	-	470(3%)	1134	150	3.3	1754	0.28	36.6	183	-
8	723	-	480	200	182	1390	0.25	133.1	184* ¹	×

Notes *1: Measured by table flow test, *2: × (No flow down), – (Not implemented)

Numbers are given in the order of the experiment.

TRIAL MIX TEST AND BASIC PROPERTIES TESTS

Trial mix tests

To obtain a combination of mixture satisfying the above criteria, the blending ratios were adjusted on a trial and error basis. The amount of the bentonite was predetermined 100 to 200 kg/m³ based on the authors' previous experience.

Table 1 summarizes the mix proportions tested in the present study. No.1 to No.4 were combination with fresh water for mixing. By adding 0.25 to 0.5 % of the dispersing agent to the whole volume of the mixture, the cylinder flow increased by 100 mm or more, showing the dispersing agent is effective. However, when fresh water is used, montmorillonite took in water and swelled; accordingly, the amount of unit water had to be kept large to maintain the target fluidity.

Instead, salt water was used for mixing to suppress the swelling of bentonite. The salt consisted of sodium chloride with a NaCl concentration of 95 % or more in weight. No.5 to No.7 were the combinations using salt water with concentrations of 1 %, 2 %, 3 % in weight, respectively. In No. 5, the fluidity was low since small concentration of the NaCl was less effective, while No.6 and No.7 satisfied the criteria of fluidity even though the difference is only the NaCl concentration. On the other hand, a previous study pointed out that bentonite flocculates when brought into contact with seawater, resulting in material segregation. However, bleeding ratio additionally confirmed were 0.0 % and 0.5 % for No.6 and No.7, respectively. Regarding this result, the author's hypothesis is as follows: salt water does not contain bivalent cations such as Mg²⁺ and Ca²⁺ which have a high contribution to aggregation of a sodium bentonite unlike seawater [2]; And the effect of dispersion is more predominant than through the aggregation of NaCl. As a result, material

segregation did not occur.

Finally, No.8 with the most bentonite content, equivalent level of effective clay density to No.7 and the less content of silica sand was prepared. This was to assess the contributions of sand to low consolidation settlement and of bentonite to low hydraulic conductivity to be discussed below.

Falling head permeability tests

The sealing performance which satisfied the criteria of fluidity was confirmed for the four combinations by falling head permeability tests. Fresh water was used in ordinary permeability tests, and we also used 3 % salt water, simulating the impervious material used in under sea water environment.

As summarized in Table 2, the combination mixing with 2 % salt water (No.6) had a remarkably low hydraulic conductivity for pure water flow as compared with the combination mixing with fresh water cases (No.2 and No.4). This is because the effective clay density of the combination of mixing with salt water is higher than that with fresh water. When 3 % salt water was passed through the combination No. 6, the hydraulic conductivity rose by about 2 orders of magnitude as compared with pure water flow. It could still keep a hydraulic conductivity on the order of 10⁻⁸ m/s. It was therefore confirmed that No.6 gives sufficient sealing performance even under sea water environment.

Table 2 Results of falling head permeability test

No.	Fresh water (m/s)	3% salt water (m/s)* ³
2	6.31×10 ⁻⁵	—
4	6.79×10 ⁻⁷	—
6	1.80×10 ⁻¹⁰	1.82×10 ⁻⁸
8	9.15×10 ⁻¹⁰	3.06×10 ⁻⁹

*3: — (Not implemented)

On the other hand, clay based No. 8 had high impervious performance when either pure or salt water was passed through.

Incremental loading compression test

Incremental loading compression tests were conducted on No.6 and No.8. The load was incrementally increased to 30, 60, 120, 240 kN/m², and the end of consolidation was judged by \sqrt{t} method.

Figure 3 shows changes in vertical displacements obtained from the mixtures. Both materials settled in the initial stage (30 kN/m²) of loading, however in No.8, mainly composed of clay, continued to settle even after 48 hours, eventually converging at about half the original height. On the other hand, in No.6, mainly composed of sand, settled in about 1 hour from the time of loading, with little consolidation thereafter. Compared to No.8, No.6 had a high blending ratio of sand, so that load might have been supported by sand particles from the early stage.

Based on the above tests, No.6 was selected as a material that satisfies fluidity, sealing performance and consolidation settlement amount.

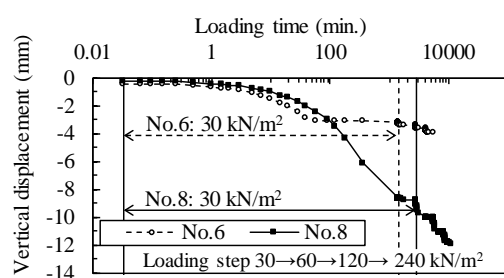


Fig. 3 Results of consolidation tests

PERFORMANCE CONFIRMATION TESTS

Outline

Figure 4 schematically shows deformation modes occurring in the soil based impervious material filled in the joint of the PC wall members. When there is deviation between the members, the impervious material undergoes shear deformation and cracks may occur in the material. On the other hand, when there

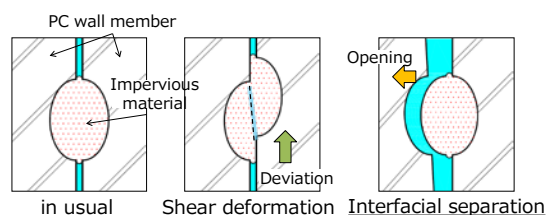


Fig. 4 Deformation of impervious material filled between PC wall members (Plan view, see Fig.2 for overall figure of PC wall members)
is a separation between the members, an opening is

created between the member and the material.

In this study, the following two permeability tests were conducted to reproduce the deformation mode shown in Fig. 4. In addition, aside from the permeability tests, applicability of conventional small pump and underwater placement was examined in a laboratory demonstration.

Shear deformation permeability test

The following three tests have been formerly developed for confirming followability under shear deformation in impervious materials:

- (1) Sampling a specimen at an actual shear plane from a box shear test, and conducting a permeability test [3].
- (2) Conducting a permeability test using a specimen artificially cutting a specimen [4].
- (3) Conducting a permeability test under uniform shear strain generated across the specimen set in a triaxial compression chamber [5].

Since the impervious material of this study does not solidify due to lack of hydration, it is hard to imagine that a clear shear plane occurs. For this reason, the above (3) was adopted in which shear strain was uniformly generated across the specimen.

Based on the results of the incremental loading compression test, it was assumed that the impervious material at a certain depth would deform according to overburden pressure. The test specimen was therefore prepared with a water content that corresponded to the void ratio at 40 kN/m². The specimen size was 25 mm in height and 50 mm in diameter, and the upper and lower ends were set on the pedestals where silicone grease, latex rubber and filter paper were placed in order to reduce end friction.

In the test procedure, firstly deaerated 3 % salt water was thoroughly passed. Secondly it was consolidated at a back pressure of 100 kN/m² and a cell pressure of 140 kN/m². Then the hydraulic conductivity before shearing was measured. Thirdly the specimen was sheared under drainage condition at a strain rate of 0.1 %/min to a predetermined shear strain level stepwisely. During shearing process, the cell pressure was gradually decreased so as not to

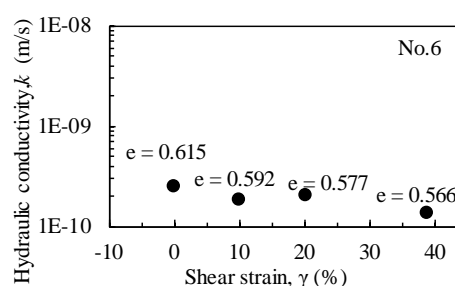


Fig. 5 Relationship between shear strain and hydraulic conductivity

generate any volumetric strain and density change. After shearing, the hydraulic conductivity was measured after the burette water level became constant. After that, the shear process and permeability test were repeated until shear strain of 40 %.

Figure 5 shows the relationship between shear strain and hydraulic conductivity. It was confirmed that the hydraulic conductivity did not increase with increasing shear strain. It became clear that even when shear strain of as much as 40 % occurred, the impervious material effectively followed the shear deformation to maintain sealing performance.

Interfacial separation permeability test

There have been no studies attempting to reproduce the water permeability due to interfacial separation in element tests. Therefore, the authors developed the following new test method.

Figure 6 shows the mold used in the permeability test designed to reproduce interfacial separation due to opening between PC wall members by element tests. Figure 7 shows a setup of interfacial separation permeability test. The acrylic mold, having 100 mm in diameter and 20 or 50 mm in height, was first coated with salt on the inner wall. Once this mold was filled with the impervious material and water flow was started, the salt gradually dissolved and a space would be created between the inner wall and the impervious material. During the process of gradually filling this space by the impervious material, plastic deformation was measured by a change in hydraulic conductivity. 3 % salt water was used for water flow.

For interfacial separation in practice, two modes are possible: one side and two side separations. They were demonstrated both modes by having the salt coating on half the perimeter and the entire perimeter of the inner wall. The coating thickness was set to correspond to 5 % of the mold cross-sectional area in both cases when coating with salt.

Figure 8 shows the change in hydraulic conductivity with increasing quantity of water flow. The height of the mold was 20 mm. In case half the perimeter was coated with salt, the hydraulic conductivity was large immediately after the start of water flow. Then, the impervious material was gradually filled into the space, resulting in the decreased conductivity to about 1×10^{-7} m/s.

In case the entire perimeter of the inner wall was coated with salt, the hydraulic conductivity gradually decreased at the initial stage of water flow, followed by slight increase after water flow exceeded 200 cm^3 .

Because of the test condition in which the height of the specimen was small and the overburden pressure was not applied, the lateral displacement due to plasticity was negligible. Thus, it was thought impossible to fill the space. It was consequently

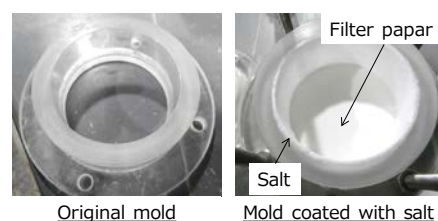


Fig. 6 Mold using for interfacial separation permeability test

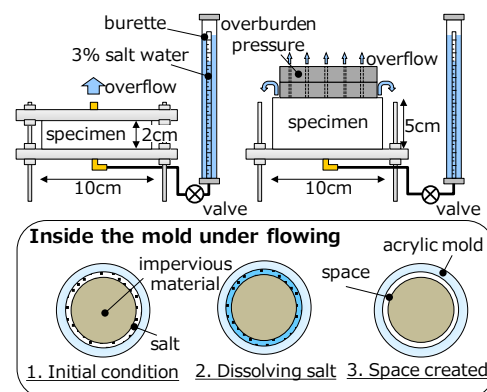


Fig. 7 Set up of interfacial separation permeability test

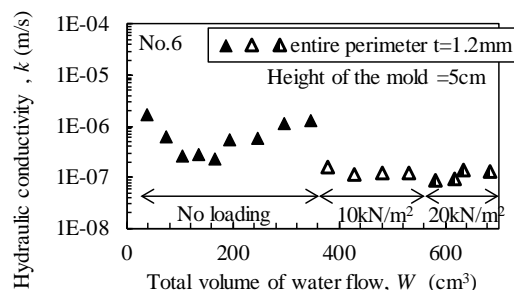


Fig. 8 Hydraulic conductivity by interfacial separation permeability test

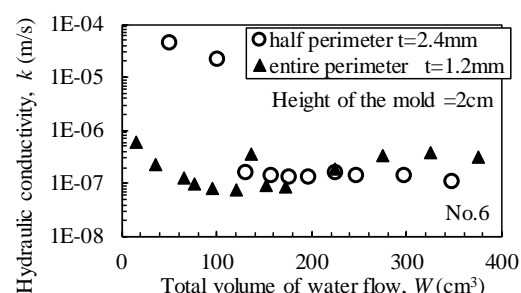


Fig. 9 Hydraulic conductivity by interfacial separation permeability test under loading condition

decided to modify the setup by replacing the top cover by a loading device that could simulate the overburden pressure. The maximum overburden pressure corresponded to the self-weight of the impervious material of about 1m high.

As shown in Fig. 9, the hydraulic conductivity decreased to the order of 10^{-7} m/s. It is confirmed that the impervious material can keep sealing performance by plastic deformation induced by its own weight.

Underwater placement test

The authors conducted underwater placement test by a small grout pump. A squeeze type pump MM 105 manufactured by ShinMaywa Industries, Ltd. was used. The maximum discharge pressure is 2.5 N/mm^2 , and the discharge flow rate can be adjusted in three stages of 40, 75, 100 cm^3/min . Although the tube diameter of the grout pump is 50 mm in general, the diameter was reduced to 25 mm in the middle of the tube line, so that it could be placed in narrower spaces between PC wall piles. Setting tube length as 10 m, the impervious material was pumped through the tube and was placed in an acrylic pipe having 100 mm in diameter and 1.5m in height, which had initially been filled with fresh water. During the placement, the discharging end of the tube was kept in the material.

Before the actual placement, we made sure the impervious material was discharged from the tube. In pumping at 100 cm^3/min which is the maximum discharge rate of the pump, separation and clogging was not observed.

Figure 10 is a photograph to show the state after placing impervious material underwater. When the discharge rate was set at 40 cm^3/min , there was no entrapment of water bubbles, nor segregation of the material. When the rate was increased to 75 cm^3/min , the discharged material around the tube periphery was disturbed because of too high a discharge rate. As a result, the surrounding water was introduced in the material during placement, and water bubbles were formed in the entire material placed underwater.



Fig. 10 View of the impervious material after underwater placement

CONCLUSIONS

In this study, the authors attempted to develop a soil based impervious material to be filled in a submerged narrow space with a gap width of about hundreds of millimeters. Through the laboratory studies the blending ratio of bentonite, sand water and the dispersing agent was optimized. Furthermore, since there were no studies that had attempted to

reproduce the water permeability due to interfacial separation in element tests available in the literature, the authors had devised a new test method and applied it to the developed impervious material. From the results of the study, the following may be summarized:

- (1) *Sealing performance*
Fresh water flow: the order of 10^{-10} m/s
Salt water flow: the order of 10^{-8} m/s
- (2) *Consolidation*
Amount of consolidation settlement was small and it converged early because it contained plenty of sand.
- (3) *Sealing performance in shear deformation*
Even at a high shear strain of 40 %, water barrier was effective, and it effectively followed the shear deformation, and sealing performance was maintained.
- (4) *Sealing performance in opening*
When the overburden pressure that corresponded to its own weight was applied, the impervious material deformed to the sides, filling the spaces.
- (5) *Underwater placement*
By appropriately setting the discharge flow rate, it was possible to construct a uniform impervious material vertically even underwater.

REFERENCES

- [1] Watabe Y, Yoshino H, Kakimoto R, Ukai A, Oki T, Oka Y, Kita H, Nagao N, Mochizuki T, Kinoshita M, "Applicability of impermeable steel seawalls for confined waste disposal site in coastal areas", *Technical Note of the Port and Airport Research Institute*, No.1142, 2006. (in Japanese)
- [2] Katsumi T, Ishimori H, Ogawa A, Yoshikawa K, Hanamoto K, Fukagawa R, "Hydraulic conductivity of nonprehydrated geosynthetic clay liners permeated with inorganic solutions and waste leachates", *Soils and Foundations*, Vol.47, No.1, 2007, pp.79-96.
- [3] Kodaka T, Teramoto Y, Hirate T, Motoyama Y, "Performance evaluation of compacted bentonite buffer material at shear failure", *J. Geotechnical Journal*, No.5, Vol.2, 2010, pp.207-218. (in Japanese)
- [4] Takai A, Katsumi T, Inui T, Kamon M, Araki S, "Long-term durability of soil-bentonite cutoff walls used for containment of ground contamination", *Proc. of the 8AYGEC*, 2016, pp.263-268.
- [5] Imamura S, Goto S, "Experimental study on permeability characteristics of bentonite/sand mixtures", *Report of Taisei Technology Center*, No.22, Extra number, 1989. pp.3-10. (in Japanese)

SEISMIC RESPONSE ANALYSIS OF A REINFORCED EARTH WALL USING THE REINFORCEMENTS INCORPORATING BOTH FRICTION RESISTANCE AND BEARING RESISTANCE

Hirohisa Muto¹, Takeshi Kodaka² and Akihiko Naganuma³
^{1,3} Yahagi Construction Co. Ltd., Japan, ² Professor, Meijo University

ABSTRACT

Past large earthquakes have demonstrated that the seismic performance of reinforced earth walls is considerably high. Although 1g shaking table tests and centrifuge tests of reinforced earth walls have been carried out to study the reinforcing mechanism, there are no sufficient field measurements collected during earthquake. We newly developed a reinforced earth wall using reinforcement members incorporating both friction and bearing resistances. The dynamic behavior of the reinforced earth wall were studied from two relatively large aftershocks of the 2011 off the Pacific Coast of Tohoku Earthquake occurred in the construction area in 2012 and 2013. In this paper, acceleration response and axial forces of the reinforced earth wall are discussed. Numerical simulations of the field measurements were also conducted using a dynamic finite element analysis. The simulated axial forces match the field measurements well. The results also explain the effects of reinforcements by friction and bearing plates accurately.

Keywords: Reinforced earth wall, Seismic behavior, Bearing resistance, Friction resistance

INTRODUCTION

In recent years, large earthquakes occurred frequently in Japan. The Great East Japan Earthquake of M9.0 occurred in 2011. A M9.0 magnitude, wide area and long shaking time were the main characteristics of it. An earthquake occurred in Kumamoto in 2016 exhibited more than once of maximum seismic intensity 6 in a short period. Thus, the characteristics of earthquakes are different. Therefore, it is important to evaluate the seismic performance of each structure. The Great Hanshin-Awaji Earthquake occurred in 1995 became a turning point for seismic designs in Japan. The damages by earthquakes have largely been caused due to collapse of the pier of reinforced concrete structures and slope failures of embankments. There were many cases of collapse of anti-earth pressure structures like block stacking. However, reinforced earth walls have been less damaged. High earthquake performance of reinforced earth walls has been proved in laboratory test such as 1-g shaking table tests and centrifugal model tests [1]. Experiments [1] on gravity retaining wall and reinforced earth wall have revealed that deformation of reinforced earth walls is smaller. They have also indicated that the deformation mechanism of the reinforced soil wall is related to the response acceleration. Therefore, it is necessary to understand the effect of reinforcement to evaluate the seismic performance.

We developed a reinforced earth wall incorporating bearing and friction resistances. Axial force and response acceleration were measured during aftershocks of the Great East Japan Earthquake as the seismic observations in 2012 and

2013. The reinforced earth wall and seismic behavior were modelled using a finite element analysis to study the interrelation between the reinforcement and ground. Then, we compared the field measurements of acceleration and axial force with the results of numerical simulations.

THE EXPERIMENTAL SET-UP

Front and cross-section views of reinforced earth wall are shown in Fig. 1. The reinforced earth wall consists of separate lower and upper parts. The lower part of earth wall was constructed with improved embankment materials by cement to simulate the ground. In addition, the lower part was reinforced by general and reaming type anchors. The cross-section of the general anchors is maintained throughout at 90mm. The diameter of the reaming anchor is equal to that of the general anchor to a predetermined length and the tip end portion is large (see Fig. 2). The improved embankment material was placed to the length of the general anchor. One side of the reinforced earth wall was constructed with a cantilever retaining wall. The other side and the back side have natural gradients.

Lower Part of Reinforced Earth Wall

The reinforcement details of the lower part are given in Table 1. The dimension of the facing panel made of reinforced concrete is 1800mm in width, 1200mm in height and 150mm in thickness. These panels are placed at the front of the reinforced earth wall. A tibar (core material) of high rigidity is fixed o the center of the facing panel by a washer and nut. The grout material is filled around the rod. Similar

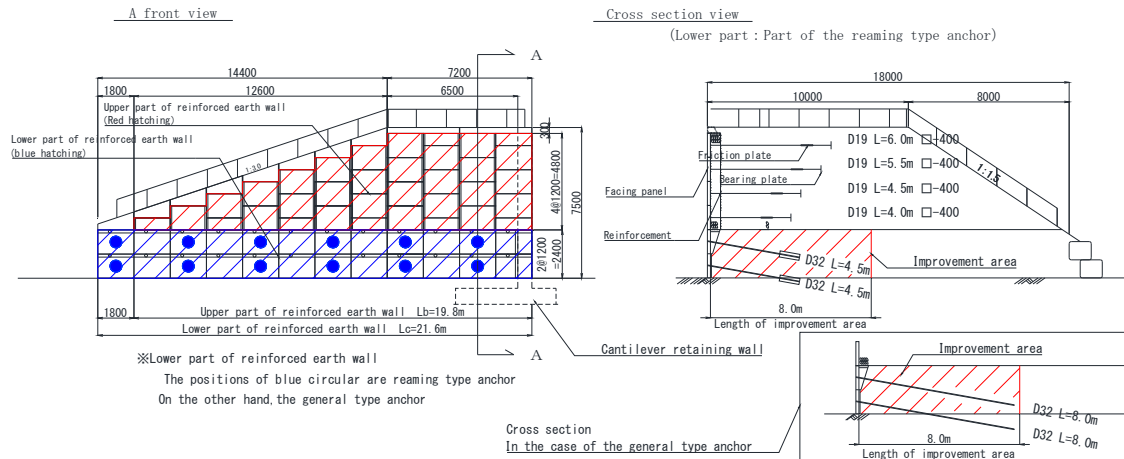


Fig. 1 Front and cross-section picture of reinforced earth wall

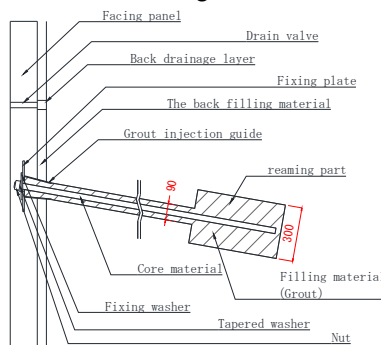


Fig. 2 Lower part of reinforced earth wall

Table 1 Details of the reinforcements

Stage	Height	Tibar		General part	Reaming part
		Diameter	Length		
2 nd	1.8m	D32	4.5m	φ90mm	φ300mm
1 st	0.6m	D32	4.5m		

reinforcements are often used in soil nailing [2]. The reinforcements are stabilized by friction resistance between the fixing material and ground.

The reaming anchor provides both friction and bearing resistances. The reaming anchor has 90mm diameter to 3.5m length and the remaining length of 1.0m is made with 300mm diameter as shown in Fig. 2. However, the general anchors were constructed with 8m length since they provide only frictional resistance. Generally, the soil nailing has a gradient of facing panel from 3/100 to 5/100. However, the wall gradient of this construction is vertical to align the wall gradient of the upper part.

Upper Part of Reinforced Earth Wall

The upper part of the reinforced earth wall is illustrated in Fig. 3. A high rigidity rod (tibar) used as the reinforcement incorporates friction resistance by friction plate and bearing resistance by bearing plate. The same facing panels used in the lower part are used here. The facing panel and reinforcement is connected using a hinge. Therefore, the reinforcement

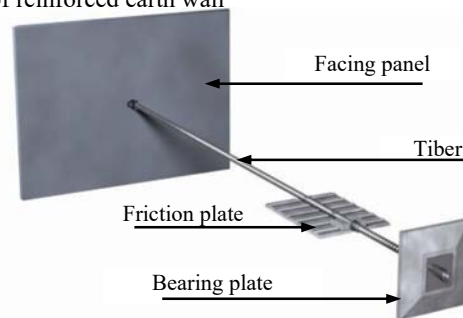


Fig. 3 Upper part of reinforced earth wall

Table 2 Reinforcement specifications

Stage	Height	Tibar		Bearing plate size
		Diameter	Length	
6	6.6m	D19	6.0m	400mm×400mm
5	5.4m	D19	5.5m	
4	4.2m	D19	4.5m	
3	3.0m	D19	4.0m	

reinforcement follows the embankment settlement, and it is possible to reduce stress concentration on the facing panel. The specifications of the reinforcement in the upper part are given in Table 2. The dimension of the friction plate is 450mm wide, 600mm deep and 15mm thick. Also, ribs of 10mm high were placed on the upper surface of the friction plate to increase pull-out resistance. The bearing and friction plates are made of ultra-high strength fiber reinforced concrete.

Embankment and Ground Conditions

An embankment in Tomita-cho, Kurokawa-gun, Miyagi Prefecture was used in this study. The grain size distribution of embankment material is shown in Fig. 4. The material has 1.6kN/m² of cohesion and 35.3 degree of internal friction angle. Soil compaction test gave 1.68g/cm³ of maximum dry density and 18.4% of optimum water content.

Standard penetration tests, borehole lateral load tests and in-situ density tests were performed.

Standard penetration test was carried out at 3m and 8m from the front side of the reinforced earth wall. The results of standard penetration test are shown in Fig. 5. SPT N-value in the upper part varies from 6-17, and increases with depth. SPT N-value in the lower part varies from 42-43 in the near borehole while 12-24 in the far borehole from the facing panel. The results indicate that the SPT N-value increases near the facing panel due to soil improvement. The borehole at 8m can be considered as the boundary between the improved and unimproved grounds.

The positions of the borehole lateral load test (LLT) are shown in Fig. 5. The borehole lateral load test used the same boreholes constructed for standard penetration test. The tests were conducted at depths of 2.7 and 9.3m as shown in Fig. 5. The test was conducted in compliance with JGS (JGS 1421-2003) standard. The tests produced the deformation coefficient of 5.63MPa at LLT No.1, 2.42MPa at LLT No.2 and 4.74MPa at LLT No.3. The N-values calculated using the deformation coefficient are 8.7 for LLT No.1, 3.7 for LLT No.2 and 7.3 for LLT No.3. The calculated N-values agree with the measured SPT N-values as shown in Fig. 5.

In-situ density test was carried out in the upper part of the reinforced earth wall. The measurement position is about 1m from the facing panel, underneath the friction plate and on the front side of the bearing plate. The dry density, ρ_d varies from 1.52 to 1.77g/cm³. The degree of compaction, D_c (the ratio of the dry density, ρ_d and the maximum dry density, ρ_{dmax}) varies from 90.3 to 105.3%. The water content, w varies from 16.6 to 20.3%.

The Field Measurements

Axial forces and accelerations were measured in the constructed reinforced earth wall. The measurement positions are shown in Fig. 6. Both static and dynamic measurements of axial force were measured during and after construction. Deformation such as embankment settlement may induce bending stress in tie bars. A strain gauge was installed on the upper and lower surfaces of the tie bar to cancel such bending stress. However, if bearing plate and facing panel is completely fixed, tension induced by bending of tie bars is calculated as axial force. As shown in Fig. 7, the strain gauges for static axial force ($T_{B3} - T_{B6}$, $T_{C3} - T_{C6}$) was placed at the front of the bearing plate (C3 - C6) and the front of the friction plate (B3 - B6). The strain gauge for seismic axial force was set at the same positions and 500mm from the back of the facing panel (A3 - A6). Friction resistance may mobilize between tie bars and ground during earthquakes [3]. Therefore, the strain

gauges were added since the behavior of axial force at the front of the friction plate and back of the panel are different.

Acceleration sensors were installed on the foundation ground (Acc01), above (Acc02) and inside the reinforced earth wall (Acc03 - Acc05). The Acc04 and Acc05 of sensors were attached to the lid of a U-shaped groove and buried in soil. Acc03 sensor was attached directly to the facing panel. All sensors are water-proof and protected with a steel cover. Static measurement was taken at 1hr intervals. Dynamic measurement can be started and stored automatically when an acceleration sensor exceeds the set value by occurring earthquake.

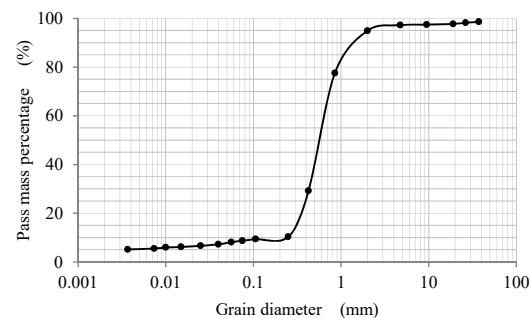


Fig. 4 Grain size distribution curve

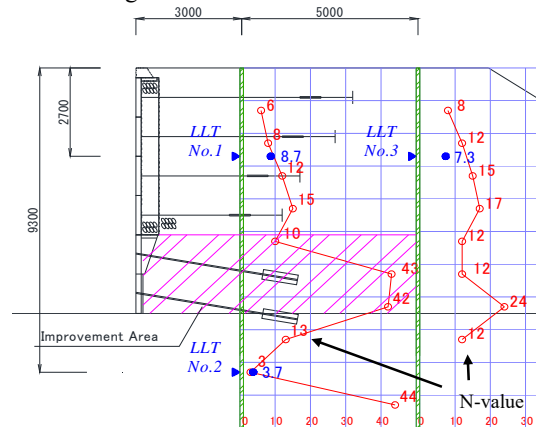


Fig. 5 Results of standard penetration test

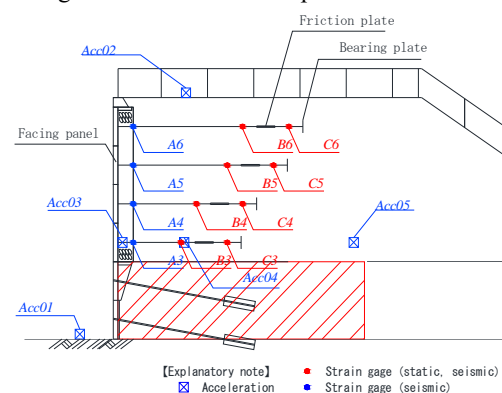


Fig. 6 Measurement positions

NUMERICAL SIMULATIONS

The analytical conditions are given in Table 3. The foundation ground has a height of 5m and a width of 80m. An elastic constitutive model was assigned. The elastic coefficient was calculated assuming a 300m/s of shear wave velocity. It was assumed that the ground is strong and elastic constitutive law was assigned since the lower part of reinforced earth wall is constructed with improved soil. The upper part of the reinforced earth wall was assigned the Mohr-Coulomb law. All the constructional members were considered as elastic bodies. The boundary condition was set as the foundation ground, the bottom of the ground is a free boundary and the side is a viscous boundary. The earthquakes considered in this study occurred on 30 August 2012 (hereinafter H24) and 4 August 2013 (hereinafter H25). The earthquake waves were applied to the bottom of the foundation ground. However, the measurement was taken above the foundation ground (Acc01). Therefore, a pull-back calculation was carried out using K-SHAKE to determine the earthquake waves to induce on the bottom of the foundation ground. Acceleration is measured for 30 seconds or more, but 4s including the maximum acceleration was used in the analysis.

The earthquake waves from the field measurements and the pull-back calculation are shown in Fig. 7. In Fig. 7, the acceleration direction is negative on the embankment side and positive on the facing panel side. The maximum acceleration from at Acc01 is 155cm/s² from H24 and 95cm/s² from H25. The amplitude of the earthquake waves from the pull-back calculation is smaller. However, the phases are almost identical.

Acceleration

The accelerations are shown in Fig. 8. The phase and amplitude of the acceleration on the foundation ground are consistent with each other. The accelerations of the facing panel (Acc01) and the inside of the reinforced earth wall (Acc04, Acc05) are almost identical in phase. However, the numerical simulations gave a slightly higher acceleration. Therefore, we can say that the reinforced earth wall can be modeled with acceptable accuracy.

The results of Fourier spectrum analysis of the acceleration are shown in Fig. 9. The frequencies on the foundation ground shown in Figs. 9(a) and 9(e) are dominated by 5-6Hz and 7-8Hz at H24 and 2-3Hz at H25. The Fourier spectrum results agree well with the field measurements. Therefore, we can confirm that earthquake wave from the pull-back calculation is accurate. The field measurements of the facing panel and the inside of the reinforced

earth wall shown in Figs. 9(b) to 9(h) excluding 9(e) at H25. The numerical results indicate that 5-6Hz is dominant at 5-6Hz at H24, 2-3 and 5-6 Hz and 7-8Hz are dominant at H24. It also suggests that 2-3Hz and 4-5Hz are dominant at H25. Although there is a slight difference in the phase, they tend to agree well.

Static Measurement of Axial Force

The static measurement of axial force is shown in Fig. 10. Axial force during the construction increases with its progress. The axial force after construction suggests a constant value. The axial force is smaller on the front of the bearing plate (C3

Table 3 Analytical conditions

Stage			3	4	5	6
N-value			15	12	8	6
Elastic coefficient	E	MN/m ²	196.2	169.1	129	106.5
	Cohesion	c	10			
Internal friction angle	f	°	40			
	Dilatancy angle	y	10			
Rayleigh damping			α / β	0.02 / 0.02		

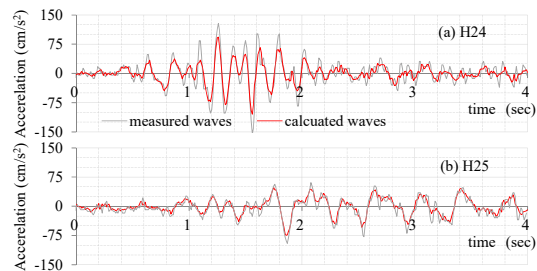


Fig. 7 Field and calculated earthquake waves

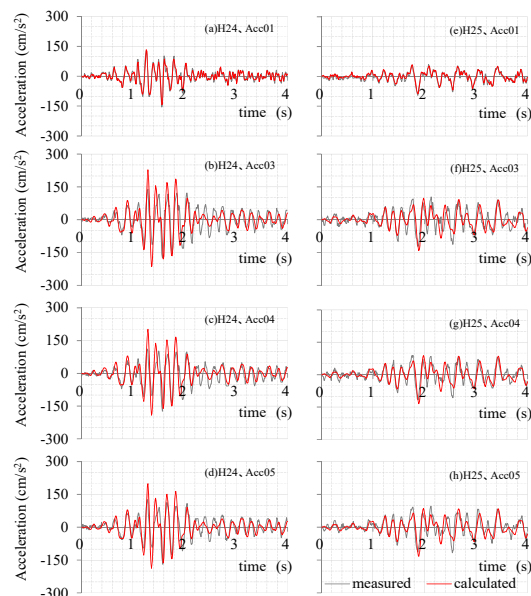


Fig. 8 Accelerations at the measurement points - C6) $T_{C3} \sim T_{C6}$ than the front of the friction plate (B3 - B6) $T_{B3} \sim T_{B6}$. The difference in axial force between the friction and bearing plates is the resistance mobilized by the friction plate. The axial force on the bearing plate is the resistance mobilized by it. It

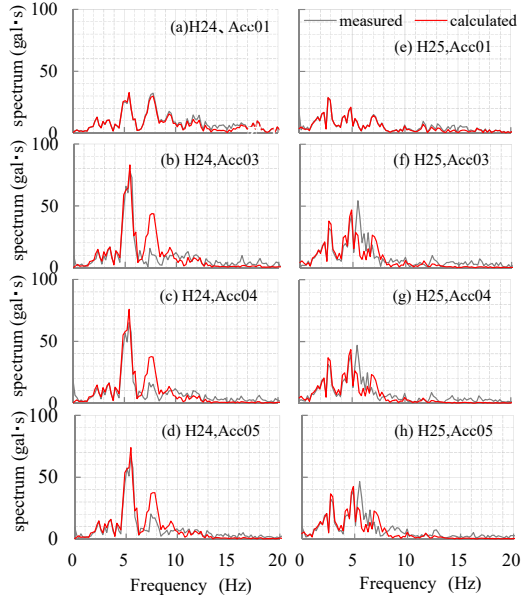


Fig. 9 Results of Fourier spectrum analysis

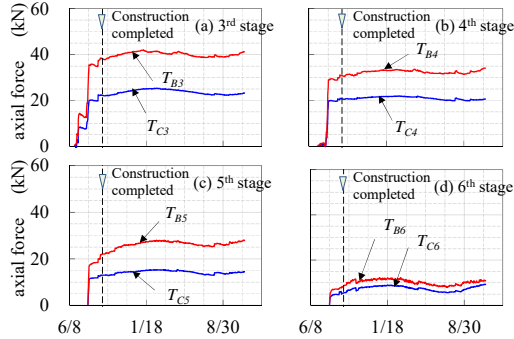


Fig. 10 Static measurement of axial force

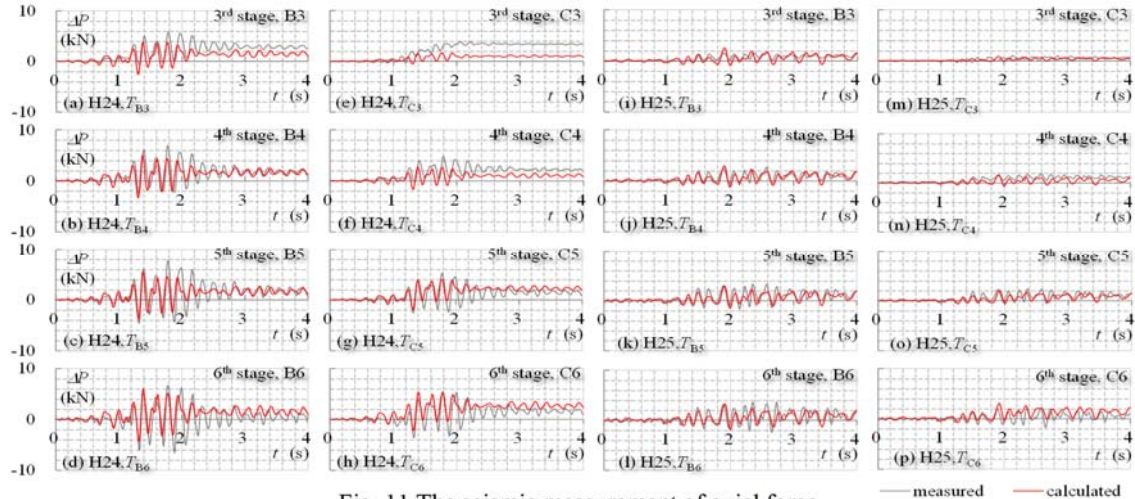


Fig. 11 The seismic measurement of axial force

was confirmed that friction and bearing plates mobilized their resistance force from the start of construction [4]. Here, the burden ratio of the total resistance by the friction resistance after construction has changed from 30 to 50%.

Seismic Measurement of Axial Force

The variation of axial force during an earthquake is shown in Fig. 11. Here, axial force indicates that the change since the earthquake occurred. Also, axial forces $T_{B_i} \sim T_{C_i}$ ($i=1 \sim 3$) are the values measured by $B_i \sim C_i$ ($i=1 \sim 3$). It can be seen that the axial force is larger at sixth stage (T_{B6} , T_{C6}) than third stage (T_{B3} , T_{C3}). It also indicates that the axial force of friction plate is higher than the bearing plate. This trend is similar to the static measurement as well. The axial force on front of the bearing plate suggests a different tendency only at third stage T_{C3} that the phase was different and the value increased monotonously. This may be attributed to the difference in deformation since the improved soil is used in the lower part of the reinforced earth wall. The results also suggest that the numerical simulation gave slightly smaller axial forces, although the phases are generally identical.

Seismic Behavior of Each Resistance

The variation of each resistance with time is shown in Fig. 12. In Fig. 12, the change from $\Delta P_{B3} \sim \Delta P_{B6}$ in bearing resistance is corresponding to the change in axial force from $T_{C3} \sim T_{C6}$ at the front of the bearing plate. The change from $\Delta P_{F3} \sim \Delta P_{F6}$ in friction resistance is corresponding to the change in the difference in axial force between $T_{C3} \sim T_{C6}$ on the front of bearing plate and $T_{B3} \sim T_{B6}$ on the front of

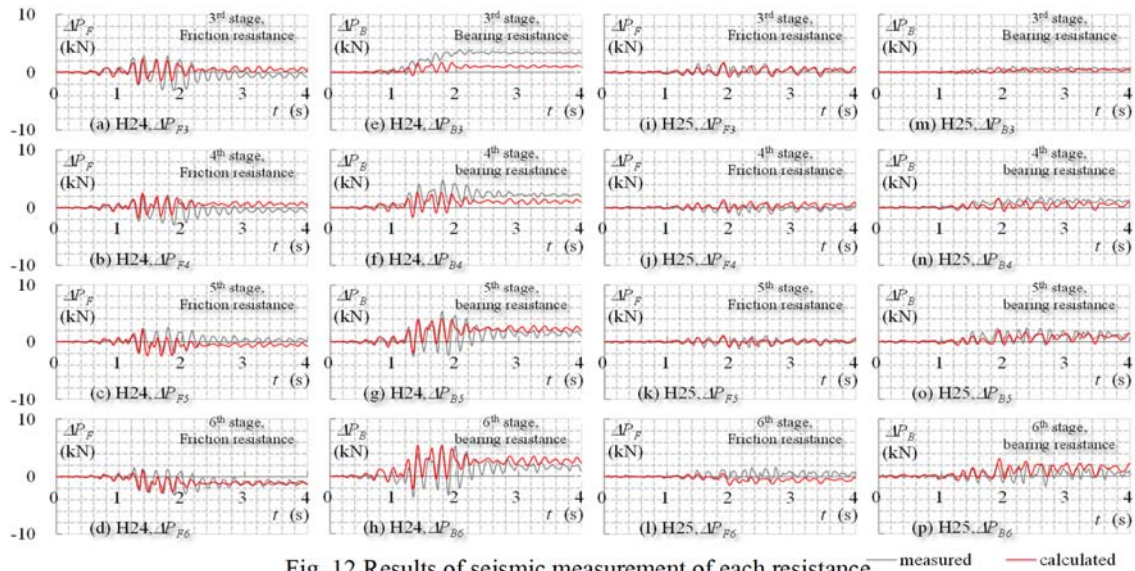


Fig. 12 Results of seismic measurement of each resistance

friction plate. It can be seen that the change in bearing resistance from $\Delta P_{B3} \sim \Delta P_{B6}$ is larger at sixth stage than third stage. The change in friction resistance from $\Delta P_{F3} \sim \Delta P_{F6}$ is larger at third stage than sixth stage. The resistance by the friction plate is larger at third stage than sixth stage. Therefore, we can confirm that bearing and friction plates mobilise their resistance even when an earthquake occurs. It also indicates that the reinforcements at shallow depth increases the resistance by friction plate, and the reinforcements at deep depth increases the resistance by bearing plate.

The numerical simulations give slightly smaller axial forces than the field measurements, although the phases are almost identical. Therefore, we can conclude that it is possible to simulate the resistance of bearing and friction plates by this analysis model quite accurately.

CONCLUSIONS

In this paper, the seismic measurements of axial force of a reinforced earth wall and accelerations from the 2012 and 2013 earthquake were discussed, and compared them with analysis results. In addition, the results from a numerical simulation of the reinforced earth wall were compared with the field measurements. The following conclusions were drawn from the study.

1. The earthquake occurred on 30 August 2012 was dominated by frequencies of 5~6Hz and 7~8Hz. The earthquake occurred on 4 August 2013 was dominated by frequency of 4~5Hz.
2. The results revealed that the resistance forces mobilised by bearing and friction plates during the earthquake effectively demonstrate each

resistance force.

3. The results from the numerical model are consistent with the field measurement of axial force and acceleration. Thus, we can conclude that the reinforced earth wall can be simulated accurately.
4. The numerical model could be validated. In future works, we will examine the stability and seismic behavior of the reinforced earth wall by applying other earthquake motions.

REFERENCES

- [1] Nakajima.S., Koseki.J., Watanabe.K., and Tateyama.M. : Simplified procedure to evaluate earthquake-induced residual displacement of geosynthetic reinforced soil retaining walls, *Soils and Foundations*, Vol.50, No.5, pp.659-677, 2010.
- [2] Fujiwara.Y. : A study on the long-term durability of reinforced cut slopes, *Journal of Japan Society of Civil Engineers*, Ser. C (Geosphere Engineering), Vol.71, No.3, pp.147-162, 2015 (in Japanese).
- [3] Futaki.M., Misawa.K. and Tatsui.T. : Actual size vibration test on the Multi-anchored retaining wall with large-scale shear box, *Proc. of 35th Japan National Conference on Geotechnical Engineering*, pp.2215-2216, 2000 (in Japanese).
- [4] Muto.H., Kamiya.T., Naganuma.A, Kodaka.T., Cui,Y., Nakano.M. and Noda.T. : Construction experiment of reinforced soil wall using reinforcement member incorporating both friction resistance and bearing resistance, *Japanese Geotechnical Journal*, pp.33-46, 2017 (in Japanese).

EFFECT OF CEMENT TYPES ON STRENGTH DEVELOPMENT OF CEMENT-TREATED SOILS

Lanh Si Ho^{a,b}, Kenichiro Nakarai^a, Kenta Eguchi^a, Takashi Sasaki^c, Minoru Morioka^c

^a Hiroshima University, Department of Civil and Environmental Engineering, Graduate School of Engineering, 1-4-1, Kagamiyama, Higashi-Hiroshima, Hiroshima 739-527, Japan

^b University of Transport Technology, Department of Geotechnical Engineering, Faculty of Civil Engineering, 54 Trieu Khuc, Thanh Xuan, Hanoi, Vietnam

^c Denka Co., Ltd., Cement & Special Cement Additives Research Dept., Omi Plant, 2209 Oaza Omi, Itoigawa, Niigata 949-0393, Japan

ABSTRACT

High early strength Portland cement (HPC) generates more hydrated cement products than ordinary Portland cement (OPC) in early age. It suggests that we can utilize the pozzolanic reaction between clay particles and hydrated cement products by using HPC in order to achieve high compressive strength of cement-treated soils in early age. Therefore, the objective of this study is to investigate strength development of cement-treated soils using two types of cement (OPC) and HPC). Two soil specimen types (i.e. sand and sand-loam mixtures) were cured under sealed condition at 20°C and 40°C and then unconfined uniaxial compressive test and thermal analysis were conducted. The results showed that the compressive strength of specimen using HPC under 20°C was 50% and 24% higher than that of specimen using OPC for the sand and sand-loam mixtures, respectively. However, the results by thermal analysis did not provide clear evidence for explaining this unique behavior of HPC. In addition, for the specimen using OPC, the compressive strength under 40°C was 6% and 10% higher than that under 20°C for the sand and sand-loam mixture, respectively; but, for the specimen using HPC, the compressive strength under 40°C was 15% and 48% lower than that under 20°C for the sand and sand-loam, respectively. The further investigations on microstructure and mineralogy are needed to clarify the strength development mechanism of cement-treated soils using several types of cement under various curing temperature.

Keywords: Cement Hydration, Pozzolanic Reaction, High Temperature Curing, Cement Types, Cement-Treated Soils.

INTRODUCTION

Cement-treated soils or cement-mixed soils have been applied popularly to soft soil improvement, especially for deep mixing treatment. It is known that the compressive strength of cement-treated soils still increases considerably for several years [1, 2]. The short-term strength is produced by cement hydration and long-term strength is mostly attributed to pozzolanic reaction. The deep mixing method usually uses big size of soil-cement column. Previous study on temperature history of field deep mixing column revealed that temperature in the core of column generated from cement hydration reached approximately 50°C and maintained at that temperature for several months [3]. It implies that the core of soil-cement column was subjected to high temperature. This high temperature may also promote hydration and pozzolanic reaction process. Previous studies on cement-stabilized clay found that the strengths in both short and long-term increase under high temperature curing [4–6].

In the field of concrete engineering, the high strength at early age was accelerated by high temperature curing because cement hydration process is promoted under that condition [7–9]. However, it was stated that long-term strength of concrete decreases under high temperature curing because main hydrated cement products formed have no time to arrange suitably, and this caused a loss of strength, this behavior had been called as the crossover effect [10–13].

It is known that high early strength Portland cement (HPC) has been applied to concrete and mortar for promoting cement hydration process, the heat generated from HPC at early age is larger than that from ordinary Portland cement (OPC) [14, 15]. As a result, the compressive strength at early age (until 7 days) of the specimens using HPC was 20% higher than that of the specimens using OPC. It suggests that HPC could be applied for cement-treated soils for producing high heat at early age that may activate the pozzolanic reaction between hydrated cement products and soil particles. Thus, we

can use HPC for cement-treated soils to promote cement hydration and utilize pozzolanic reaction in order to achieve high early strength development.

Therefore, the objective of this study is to investigate the strength development of cement-treated soils by using two types of cement (OPC and HPC) cured under the sealed condition at different temperatures (20°C and 40°C). The compressive strength was measured by the unconfined compression test. Thermal analysis was applied to examine the change in chemical reaction progress for explaining strength development.

MATERIALS AND METHODS

Materials

Two types of soil were used in this study including: Toyoura silica sand and Toyoura silica sand–loam mixtures. Toyoura silica sand was chosen because of its recognition as a natural standard sand for experiments in Japan that has low pozzolanic reactivity (166 mg of CaO consumed by 1 g of sand determined by the French standard for the modified Chapelle test NF P18-513). Meanwhile, the Kanto loam produced in Kasama (Japan) is a kind of volcanic cohesive clay that exhibits a high pozzolanic reactivity (580 mg of CaO consumed by 1 g of loam determined by the Chapelle test [16]). Ordinary Portland cement (OPC) and high early strength Portland cement from Denka (Japan) were used. The specific densities of the Toyoura silica sand, OPC/HPC, and loam are 2.65×10^3 , $3.15/3.14 \times 10^3$ and 2.79×10^3 kg/m³, respectively. The designed values of the specimens are listed in Table 1.

Table 1 Designed values of cement-treated soil specimens.

Mixture	Sand content (wt.%)	Loam content (wt.%)	Cement/soil (wt.%)	Water/cement (wt.%)
Sand	100	0	8	100
Sand–loam	95	5	8	100

Specimen preparation

First, soil and water were mixed using a mechanical mixer for 1 min to control the water content. Next, the mixtures were mixed again for 1 min by hand to remove the materials attached to the bowl and paddle of the mixer. Then, the mixtures were mixed again for 1 min by using the mixer. Subsequently, cement was added and mixed for 1 min using the mixer. Finally, the materials were mixed again for 1 min using the mixer after 1 min of mixing by hand to achieve higher homogeneity. In the case

of the sand–loam mixture, before mixing the soil with water, the loam and Toyoura silica sand were mixed together for 1 min by using the mixer. After mixing, cylindrical specimens 50 mm in diameter and 100 mm in height were cast by compaction by using a rammer with a weight of 1.5 kg based on JCAS L-01:2006 standard. Each specimen had three layers; the height of each layer was around 1/3rd the height of the specimen. The rammer was dropped 12 times from a height of 200 mm on each layer of each specimen.

Specimens were cured under the sealed condition. The reproducibility of measurements after five times of curing (1, 3, 7, 14, and 28 days) was tested systematically on three similar specimens. For all specimens obtained after casting into tin molds, the top surfaces were immediately sealed with aluminum tape and cured in a room at a constant temperature of 20°C and 40°C for the prescribed curing period. To ensure the drying and carbonation did not occur, the weights of the specimens under the sealed condition were measured and found to have constant values for the entire curing period.

Methods

The compressive strength of the specimens was measured by the unconfined compression test [17]. At each age of curing under tested condition, three specimens were used for the compression test. The tests were performed at a constant loading rate of 0.1 mm/min using a hydraulic universal system testing machine from Shimadzu Corporation (Japan) with maximum load capacity of 50 kN.

The amounts of chemically bound water and Ca(OH)₂ were measured by TG-DTA. The mass loss due to chemical reactions was taken by the loss of the temperature range (105–1000°C). The amounts of Ca(OH)₂ were determined from the values of mass loss obtained from thermalgravimetry analysis curve (TGA) based on the initial and final temperatures (°C) of the DTA peaks (between 400°C and 460°C).

RESULTS AND DISCUSSION

Compressive Strength

Fig. 1 shows the compressive strength of the sand mixture specimens using different cement types. In the case of OPC specimens, the compressive strength of the specimens cured under 20°C and 40°C increased rapidly until 7 days, then it slightly increased from 7 to 28 days. For that curing period, the compressive strength of the specimens cured under 40°C was 6% higher than that of the specimens cured under 20°C. Thus, we can conclude that high temperature curing could increase the compressive strength of the sand mixture. This increase in strength was caused by pozzolanic reaction between sand

particles and hydrated cement products, which can fill into porous structures of the sand mixture. This will be explained in thermal analysis section.

With regard to the HPC's specimens, the compressive strengths increased quickly until 7 days under both 20°C and 40°C, then they increased slightly. At the age of 1 day the compressive strength of the specimen cured under 40°C was 48% higher than that of the specimen cured under 20°C. However, after 1 day, the tendency was different, at 28 days the strength of the specimens cured under 40°C was 15% lower than that of the specimens cured under 20°C, this behaviour was similar to concrete, which was called as the crossover effect [10–13]. Because the specimens used HPC itself has quick hydration process, and under high temperature curing the hydration process can be promoted more rapidly that leads to crossover effect happened strongly.

It was interesting that the observed compressive strength at 28 days of the specimen used HPC under 20°C was 50% and 42% higher than those of the specimens used OPC under both 20°C and 40°C, respectively. Particularly the compressive strength of the specimen using HPC at 3 days under 20°C was 14% higher than that of the specimens using OPC at 28 days. It suggests that using HPC could achieve high strength at early age.

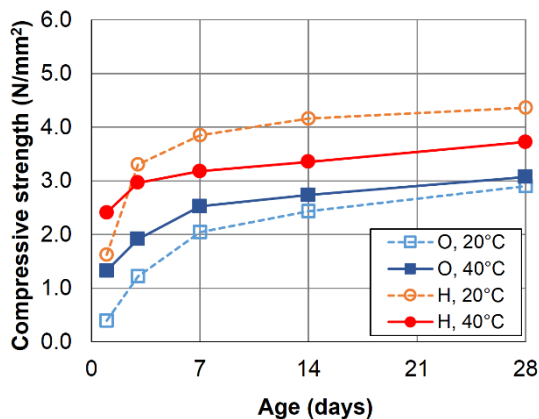


Fig. 1 Compressive strength of the sand mixture specimens used different cement types and cured under different curing temperatures.

The compressive strength of the sand-loam mixture using OPC and HPC cured under 20°C and 40°C is shown as in Fig. 2. Similar to the sand mixture, in term of OPC, the compressive strength increased gradually until 28 days. At 28 days the compressive strength of the specimens under 40°C was 10% larger than that of the specimens under 20°C. It can be explained that under high temperature curing, the cement hydration and pozzolanic reaction could be promoted, leading the increase in compressive strength.

For the case of HPC, the high temperature curing had negative effect on strength development. The

compressive strength under 40°C was not only 48% lower than that under 20°C but also significant lower than those of the specimens using OPC. This may be explained by the combined effect of high temperature curing and rapid hydration process of HPC that could promote crossover effect. At 28 days, the compressive strength of the specimens using HPC under 20°C was 24% and 12% higher than that of the specimen using OPC under 20°C and 40°C, respectively, as observed in the sand mixture.

In both the sand and sand-loam mixtures, the compressive strengths of the specimens using HPC at 28 days under 20°C were 50% and 24% higher than those of the specimens using OPC, respectively. This is a unique behavior that was different from mortar and concrete.

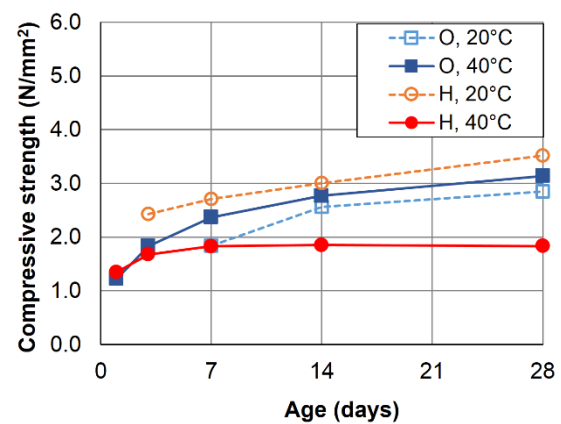


Fig. 2 Compressive strength of the sand-loam mixture specimens used different cement types and cured under different curing temperatures.

Thermal Analysis

The amounts of the chemically bound water and Ca(OH)_2 were measured to examine chemical reaction progresses for explaining strength development.

Fig. 3 shows the chemically bound water of the sand mixture. It was observed that the chemically bound waters increased rapidly until 7 days, then they were almost stable until 28 days. The chemically bound water of the specimen using HPC and OPC under 40°C were 22% and 31% higher than those of the specimen using OPC under 20°C, respectively. The higher chemically bound water are, the more hydrated cement products generated. The higher chemically bound water in the specimens using HPC may explain for the difference between strength of the specimens using HPC and OPC.

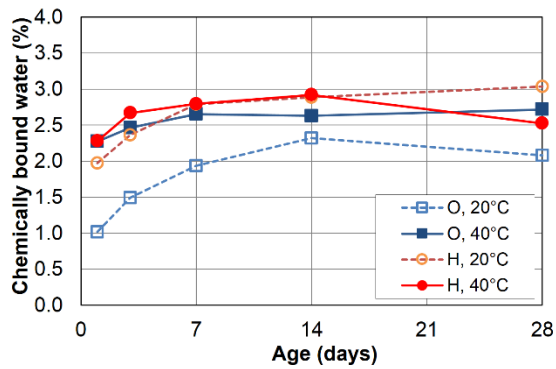


Fig. 3 The chemically bound water in the sand mixture

Fig. 4 presents the amount of Ca(OH)_2 in the sand mixture. In the case of the specimen using OPC, under 20°C, the amount of Ca(OH)_2 increased gradually until 28 days. However, under 40°C, the amount of Ca(OH)_2 increased rapidly until 7 days due to cement hydration caused by high temperature. Then, the amount of Ca(OH)_2 was almost constant from 7 to 28 days. At early age (until 14 days), the amount of Ca(OH)_2 in the specimen under 40°C was 6% higher than that in the specimen under 20°C. Nevertheless, at 28 days the amount of Ca(OH)_2 in the specimen under 40°C was 4% lower than that in the specimen under 20°C. This is explained by pozzolanic reaction between sand particles and hydrated cement products, which can explain for the compressive strength at that age.

Regarding the specimens using HPC, the amount of Ca(OH)_2 increased rapidly until 7 days under both 20°C and 40°C, then it increased slightly in the specimen under 20°C, but it was almost stable in the specimen under 40°C. It is clear that, at 28 days the amount of Ca(OH)_2 in the specimens using HPC under 20°C was 14% greater than that in the specimen using OPC. It implies that cement hydration process in HPC can be 14% larger than that in OPC until 28 days.

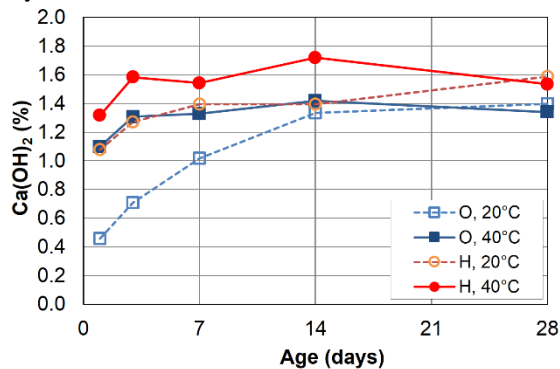


Fig. 4 The amount of Ca(OH)_2 in the sand mixture.

The chemically bound water of the sand-loam mixture is shown in Fig. 5. For the specimen using OPC, at 28 days the amount of chemically bound

water under 40°C was 21% higher than that under 20°C. This is caused by high curing temperature that could promote cement hydration process. Similarly, for the specimen using HPC, the amount of the chemically bound water under 40°C was higher than that under 20°C until 28 days. The amount of the chemically bound water in the specimen using HPC was almost as same as that in the specimen using OPC under 20°C. The chemically bound water and amount of Ca(OH)_2 could not explain for the higher strength in the specimens using HPC under 20°C.

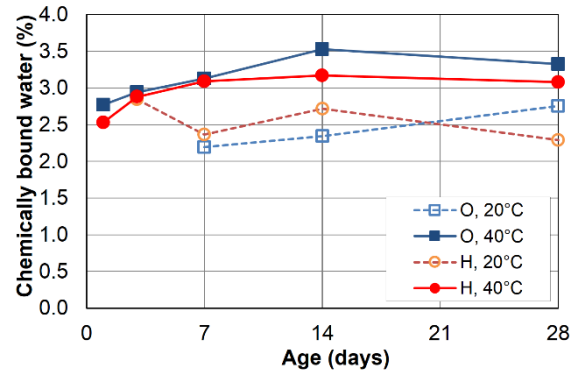


Fig. 5 The chemically bound water in the sand-loam mixture.

Fig. 6 shows the amount of Ca(OH)_2 in the sand-loam mixture. It can be seen that, in both the specimens using HPC and OPC, the amounts of Ca(OH)_2 at 28 days under 40°C were 34% and 13% lower than those under 20°C, respectively. It indicates that pozzolanic reaction was accelerated under high temperature curing. This pozzolanic reaction could explain for the 10% higher strength achieved under 40°C in the specimen using OPC. However, for the specimen using HPC, under 40°C the pozzolanic reaction could not produce an increase in compressive strength because of negative effect of high temperature curing that made strength under this temperature was lower than that in other cases.

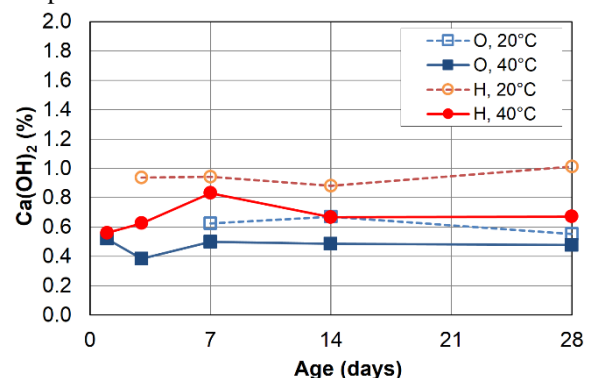


Fig. 6 The amount of Ca(OH)_2 in the sand-loam mixture.

CONCLUSIONS

This study shows the effects of cement types on strength development of cement-treated soils using two types of soil cured under the sealed condition at 20°C and 40°C. The following conclusions could be made from the experimental results.

1. For the sand mixture, the compressive strength of the specimens using HPC under 20°C was 50% and 42% larger than that of the specimens using OPC under 20°C and 40°C, respectively. For the sand-loam mixture, the compressive strength of the specimens using HPC under 20°C was 24% and 12% larger than that of the specimens using OPC under 20°C and 40°C, respectively. But, the results by thermal analysis did not provide clear evidence for explaining this unique behavior of HPC.
2. For the specimen using HPC, the compressive strength under 40°C was 15% and 48% lower than that under 20°C for the sand and sand-loam, respectively. This may be caused by the combined effects of high temperature curing and rapid hydration process of HPC, which could lead to the decrease in compressive strength.
3. For the specimen using OPC, the compressive strength under 40°C was 6% and 10% higher than those under 20°C for the sand and sand-loam mixture, respectively. Because, under high temperature curing, cement hydration and pozzolanic reaction could be accelerated.

The findings in this study suggest that we can use HPC for cement-treated soils to achieve high early strength. The detail evidence is needed to investigate using X-ray diffraction, mercury intrusion porosimetry, and scan electronic microscopy tests to explain the higher strength in HPC. In addition, high temperature curing is recommended to apply for OPC in order to achieve high strength at early age. This study will be extended for long curing age (until 1 year) and higher temperature as well as various soil types.

REFERENCES

- [1] Kongsukprasert L, Tatsuoka F, Takahashi H, "Effects of curing period and stress conditions on the strength and deformation characteristics of cement-mixed soil", *Soils Foundations*, Vol. 47, 2007, pp. 577-596.
- [2] Seng S, Tanaka H, "Properties of cement-treated soils during initial curing stages", *Soils Foundation*, Vol. 51, 2011, pp. 775-784.
- [3] Omura T, Murata M, Hirai M, "the influence of strength due to hydration heat on site measurement results and curing temperature of deep mixing", pp. 732-733, (in Japanese)
- [4] Kitazume M, Nishimura S, "Influence of specimen preparation and curing conditions on unconfined compression behaviour of cement-treated clay." *Proc. of International Symposium on Deep Mixing and Admixture Stabilization*. 2009.
- [5] Zhang RJ, Lu YT, Tan TS, Phoon KK, Santoso AM, "Long-term effect of curing temperature on the strength behavior of cement-stabilized clay", *J. of Geotechnical and Geoenvironmental Engineering*, Vol. 140, 2014, pp.1-12
- [6] Wang D, Zentar R, Abriak NE, "Temperature-accelerated strength development in stabilized marine soils as road construction materials", *J. Materials in Civil Engineering*, Vol. 29, May 2017, pp. 04016281-13.
- [7] Escalante-Garcia JI, Sharp JH, "The microstructure and mechanical properties of blended cements hydrated at various temperatures", *Cem Conc Res*, Vol. 31, 2001, pp.695-702.
- [8] Brooks JJ, Kaisi AF, "Early strength development of Portland and slag cement concretes cured at elevated temperature", *ACI Mater J*, Vol. 87, 1990, pp. 503-7.
- [9] Kim JK, Han SH, Park SK, "Effect of temperature and aging on the mechanical properties of concrete, part I: experimental results", *Cem Conc Res*, Vol. 32, 2002, pp.1087-94.
- [10] Kim J, Moon Y, Eo S, "Compressive strength development of concrete with different curing time and temperature", *Cement and Concrete Research*, Vol. 28, 1998, pp. 1761-1773.
- [11] Kim S, Han S, Song Y, "Effect of temperature and aging on the mechanical properties of concrete Part I. Experimental results", *Cement and concrete Research*, Vol. 32, 2002, pp. 1087-1094.
- [12] Ezziane K, Bougara A, Kadri A, Khelafi H, Kadri E, "Compressive strength of mortar containing natural pozzolan under various curing temperature", *Cement and Concrete Composites*, Vol. 29, 2007, pp.587-593.
- [13] Alexander KM, Taplin JH, "Concrete strength, cement hydration and the maturity rule", Vol. 13, 1962, pp. 277-284.
- [14] JIS R5210: 2009 Japanese Industrial Standard specifies Portland cement.
- [15] Mallow, WA. "Low-cost, high early strength, acid-resistant pozzolanic cement." U.S. Patent No. 5,352,288. 4 Oct. 1994.
- [16] NF P18-513 August 2012, Addition for hydraulic concrete - Metakaolin -Specifications and conformity criteria-Metakaolin, pozzolanic addition for concrete.

- [17] JIS A 1216, Methods for unconfined compression test of soils.

ADDITIONAL BEARING CAPACITY OF PILES DUE TO TIME DELAY OF INJECTION

* Abdul Hakam¹, M Sofian Asmirza² and Heka P Andriani¹

¹Engineering Fac., Andalas University, Indonesia; ² Engineering Fac., North Sumatra University, Indonesia

ABSTRACT

The use of long piles to support construction loads has been recognized for thousands years. At the last century it has been introduced the use of pressure for embedding pile foundations that is named injected piles. In field implementations, if the design depth of the piles is long enough then additional piles are required to be connected. It needs time delay to connect between the earlier embedded pile to the additional one. The time delay can be also caused by other things such as equipment problems, unwilling bad weather etc. Based on the experience of pile injection records, due to the time delay there is a temporary increase in pile bearing capacity, so it takes more effort to continue pile penetrations until the specified length. In this study, the effects of erection time delays on piles are investigated. This study is conducted using experimental injected-pile models at the laboratory. The initial depth of earlier piles prior to further injection is set the relatively same, while the time delays are varied. The injection loads for penetration are recorded as well as the depth of penetration. The results of the experiments in terms of variation of time delays and additional penetration loads show that there are 'jump loads' at the initial last depth due to time delay until a certain period. It can be concluded that the time delay on the pile can increase the bearing capacity and must be limited to a certain time in case of pile connection work on site.

Keywords: bearing capacity, injection pile, time delay, pile foundation

INTRODUCTION

Pile foundations have been used to transfer the building load to the underlying soil layer since the earlier the first century [1]. Based on their load transfer mechanism, piles may be classified by end-bearing and friction piles or combination one. End-bearing piles develop most of their bearing capacity mainly at the tip of the pile. Friction piles transfer the load to the surrounding soil along the pile length by friction between the pile surface and the soil. Piles also can be differed by the method of construction that are driven piles (or displacement) and bore piles (or replacement). The driven pile may be placed into the ground by displaced surrounding soil by hammer, injected, vibrated or screwed. Bored piles are placed into the ground by replacing soil in bore holes with pile materials. In this paper the piles may classified as injected end-bearing piles.

The pile tip resistance can be calculated based on a traditional formula using the cohesion and internal friction angle parameters of the soil. If the soil at the end of the pile consist of sands only, then the cohesion parameter can be avoided in the calculation, so that the end bearing capacity formula becomes:

$$Q_u = q_u A_p \quad (1)$$

with

$$q_u = q' N_q + \frac{1}{2} \gamma B N_\gamma$$

Where: Q_u = ultimate axial load

q' = effective overburden

B = pile tip diameter

γ = unit volume of underneath soil

N_q and N_γ = bearing capacity factors

The effective overburden stress is the difference between total overburden stress with the pore water pressure. Under static conditions, the effective stress may be the result of reduction by hydrostatic pressure. The pore water pressure a dynamic condition may exceed the hydrostatic pressure. The excess pore water pressure in dynamic condition may generated during the pile placement into the ground using dynamic way such as jacking and driving. The effective overburden then can be written as:

$$q' = q_{tot} - u \quad (2)$$

Where q_{tot} = total overburden stress

u = excess pore water pressure

Besides static bearing capacity of pile foundation, there are many problems must be considered during the design. Some problems that might be taken into account in the used of piles are potential consequences of liquefaction, differential settlement, lateral loads and movement and possibility on soil bearing capacity reduction [2]. Pile foundations may not only subjected to static loads but also dynamic loads simultaneously. The study on dynamic response of a single concrete pile in soft clay subjected to static and dynamic simultaneously has been presented [3]. The connection between pile to the cap also may be investigated to understand its behavior respected to the applied loads. The investigation of the moment capacity and load-displacement relationship of laterally loaded the pile to cap connection with different connection details has been reported [4]

On site pile work in order to achieve sufficient bearing capacity at the certain depth, often pile connection work is needed. The pile to pile connection thus become a special consideration in practical works. The required pile to pile connection in some cases are caused by the manufacture limitations at the factory and/or transportation problem of piles from the factory to the site. Extremely long piles will be difficult to be distributed from factory to the site. Very long piles also create difficulties on their mobilization on site.

The pile connection process may need the time and the driving process must be stopped temporarily. The most popular pile connection in Indonesia is mainly done by welding to joint the pile ends. Each pile then has the end that made of steel which may function as a pad/base for pre-stressed wire of pile reinforcement. The steel pads are then to connect the embedded and the subsequent piles on the site.

ON FIELD DATA

The soil sediment in the field consists of a layer of sand and silty sand until 20m of depth and gravelly sand for deeper. Groundwater in the field is at depth 2m from the ground surface. This indicates that the soil beneath the groundwater table is under saturated condition. The mechanical properties of the soil layers are shown in Table 1. Based on standard penetration test data on site (Fig.1), the design depth of the 60cm of diameter piles were about 26 to 30 m.

The spun-piles had been used to support the Public Work Building in Padang. The piles came from the factory have the length of 10m and 12m. Consequently they were needed pile connection work to complete penetration every point on site. During the penetration of piles on site, the applied loads on every single pile was monitored and

recorded (Fig.2).

Table 1 Properties of the soils

Depth (m)	Type (Code)	Mechanical Properties		
		ϕ	c (t/m ²)	γ (t/m ³)
4.0-4.4	Sand (S)	33.6		1.5
14.-14.5	Silty sand (SM)	29	4.5	1.4
24-24.5	Gravelly sand (SG)	35.4		1.9

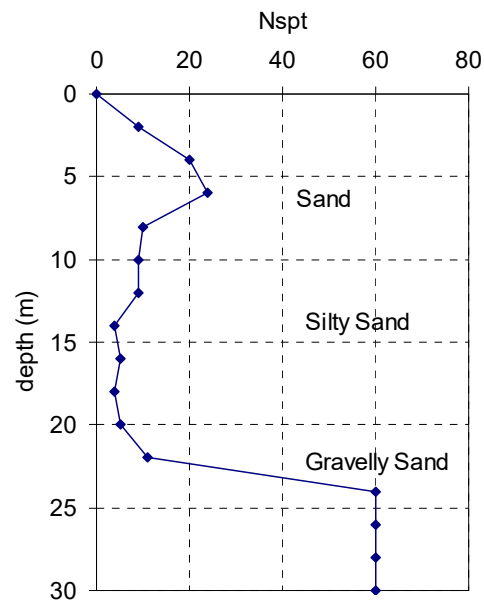


Fig.1 N_{spt} values on the site

It can be seen that the first joining work at the depth of 11m was finished within 16 minutes. The increment of penetration load after 16 minutes increased until 339t then came down to 226t for the next record. It means for 16 minutes delay time, the load of penetration increased until 113t. The same thing happened after pile connection work at the depth of 21m, the penetration load increase by 85t for 14 minutes delay.

There was also a unwilling case due to damage penetration tools that cause penetration process was stopped. The repair work by replacement of broken spare part took a few days. When the penetration was continued, the loads have shown the value that exceeded the maximum capacity of the pile injection tool. The depth of the pile at that point has not reached the specified depth. In order

to continue penetration, the pile the was pulled first, the it pushed again into the ground to continue penetrating to the specified depth. This case indicates that the dissipated pore water pressure within a few days may result in an increase the effective stress in soil mass so consequently increases the pile bearing capacity.

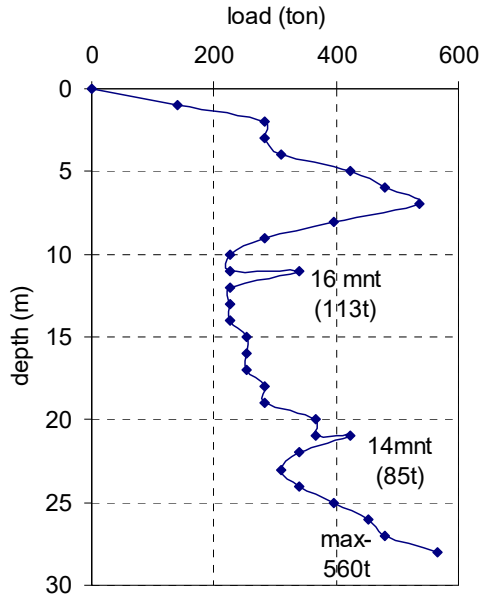


Fig.2 Penetration load record on site

LABORATORY TESTS

In order to understand the increment of load due to the excess pore water pressure during the pile penetration, a series of laboratory test is conducted. This test is carried out using a small scale pile model. A pile model has dimension of length 30 cm and the cone tip with diameter of 1 cm (Fig. 3). The soil is made up of fine sands that sieved pass trough sieve no 40. The soil is in saturated condition with dry unit volume of 1.53 t/m³ which produces relative density of about 30%. The strength parameter of the sand is obtained from laboratory direct shear test, that give internal friction angle of $\phi = 30$ degree. With the purpose to avoid result differences due to soil differences, the tests were conducted using the same soil for every desired time delay.

The pile model is pushed into the soil to have tip resistant. The sleeve of the pile model has casing that keep staying still during the tests. Consequently, the skin friction on the pile model can be ignored in these tests. So, the applied load

to injecting pile is considered equal to the tip resistant of the pile only.

The test procedure of piles are started injecting the pile into the soil to the depth of 25cm. During the initial injection, the given loads for every unit length are recorded. The next procedures are purposed to record the additional load due to the time interval between the first injection to the next one. The results of the test procedure are shown in Table 2 and plotted in Fig.4 as well.

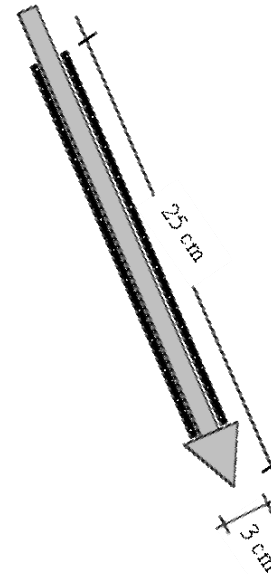


Fig.3 Dimension of the pile model

Table 2 Laboratory test results

Depth (cm)	25.10	25.26	25.44	25.54	25.62
Time interval (mnt)	1	10	20	30	60
Increment (kg)	1.02	4.10	6.15	7.17	7.17

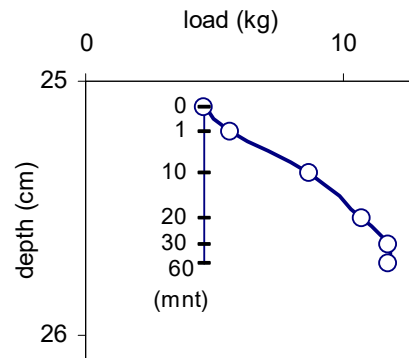


Fig.4 Load increment .vs. time

From the time-load graph it can be seen that the increment load increased with the time delay and reached the maximum after reach time delay about 30 minutes (Fig.5). This graph indicated that the excess pore pressure due to the pile injection was fully dissipated after 30 minutes in this test. In the field, if this delay time may be happened due to the joining work of piles or other injection disturbance. In the real work on site, the delay time may cause the more efforts to continue penetrating the pile are needed.

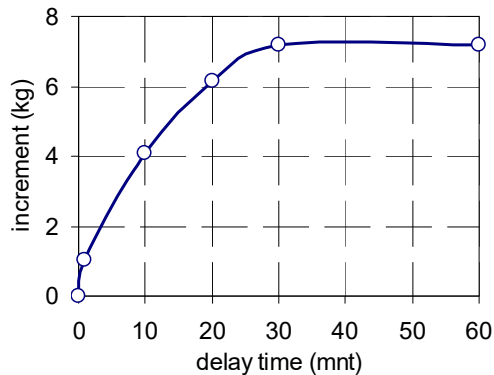


Fig.5 Delay time-load relationship

CONCLUSION

F Due to the time delay on pile injection on site, the pile experienced a temporary increase in the bearing capacity. The effects of time delay on pile bearing capacity then can be understood by a series of laboratory experiments. The experimental work using pile model on saturated sand has succeeded

demonstrating the load increment on penetration due to time delay. The results of the experiments with of time delay variation show that the increment loads will stop until a certain periods. In practical work, the time delay on the pile penetration must be limited to a certain time to avoid difficulty for continuing pile penetration.

ACKNOWLEDGEMENTS

Thanks to our students that have given hands in laboratory work to complete this study.

REFERENCES

- [1] Tomlinson, M. J. and Woodward J., Pile design and construction practice, 5th ed. Fifth Edition, Taylor & Francis, NY, 2008, ch. 1.
- [2] Valley M, S.E., "Foundation Analysis and Design", FEMA P-751, NEHRP Recommended Provisions: Design Examples, 2009, ch. 5, pp. 48.
- [3] Rathod D., Muthukkumaran K. and Sitharam, T.G., "Dynamic Response Of Single Pile, Located In Soft Clay Underlay By Sand", International Journal of GEOMATE, Oct., 2016, Vol. 11, Issue 26, pp. 2563-2567
- [4] Kyle M. Rollins K.M. and Stenlund T.E., "Laterally Loaded Pile Cap Connections", Report No. UT-10.16, Utah Department of Transportation, August 2010

INVESTIGATION ON THE EFFECTS OF PLANT VARIETY AND SOIL SEDIMENT TO THE COASTAL ABRASION IN WEST SUMATRA

Abdul Hakam¹, * Bambang Istijono¹ and Taufika Ophiyandri¹

¹Engineering Faculty, Andalas University, Indonesia.

ABSTRACT

Indonesia has many islands that are suffer from beach abrasion. This phenomenon has been often happening and it categorized in one of the National Disasters. West Sumatra beaches with the total length of about 600 km stretch along the west side of Sumatra Island where directly opposite to the Indian Ocean. The waves from the Indian Ocean in any circumstance may cause abrasion to damage houses and public facilities. Factors that effect coastal abrasion include coastal geometry, wave parameters, soil sediment and beach plantations. An investigation on the plant species and soil sediment on the West Sumatra beach has been done. The effects of the last tow factors on beach abrasion are then elaborated in this paper. It is found that some beach vegetations have shown remarkable role to reduce abrasion impact. Meanwhile the type of soil sediments in which associated to physical properties showed also significant effect. From this study it was found that vegetation roots will protect the beaches together with the soils. This investigation also concludes that coastal endemic plants in the West Sumatra need to be explored as a mitigation action to reduce the abrasion impact.

Keywords: Abrasion, Marine Vegetation, Plantation Effect, Soil Effect, Disaster Mitigation

INTRODUCTION

Indonesia is one of the largest countries with many islands which has very long coastlines. The Indonesian Geospatial Information Agency reported that the total length of the Indonesian coastline reaches about 100,000 kilometers [1]. There are many potential natural treasures and beautiful sceneries along the coastline. Indonesian beaches are often used as tourist destination for local and international tourists. However recent condition of the coastal areas of Indonesia are worrying due to the abrasion. It has been reported that about 100 locations in 17 Provinces with coastline length of approximately 400 km have experienced terrible coastal erosion [2]. The list of coastal areas in Indonesia that are at high risk for abrasion disasters in 2013 including South Aceh, Banda Aceh, Medan City, Surrounding Padang City in Sumatra Island, North Jakarta, Rembang Regency in Java Island, Bali Island, Sikka Regency in East Nusa Tenggara and Selayar in Sulawesi Island [3].

Beach abrasion that is essentially a coastal dynamics influenced by seawater waves has caused many disadvantages such as cutting the accesses, destruction of houses and even the loss of such a beautiful sandy beach (Fig.1). For that reasons the Indonesian government has included abrasion into one of national disaster [4]. Abrasion is part of the phenomenon of erosion and sedimentation cycles along the coastline. To deal with abrasion, beaches can be protected by

providing an engineering construction to reduce the incoming wave energy [5]. However, building such wave protector to prevent abrasion could not restore back the lost of sandy beaches. Further, a hard construction on the beach may also result unpleasant scenery (Fig.2).

Abrasion becomes a research interest and is extensively studied related to the global warming issue. It has been studied relationship between sea levels and coastal damage from the 19th to the 20th centuries [6]. It was strong correlation between the global warming on the damage on beaches. The damage to the beaches has been doubled with the rate of actually sea level rise. It is predicted the coastal abrasion problems that already look severe in the 20th century will be worse in the next century.



Fig.1 Padang Beach in 1890 [7]



Fig.2 The missing sandy beach in Padang

It has been reported there are 14 beaches classified in critical condition [8]. The 14 critical beaches are Air Bangis, Sasak; Pantai Tiku, Pasir Baru, Pariaman, Ketaping, Pasir Jambak, Padang, Bungus, Carocok Painan, Luhung, Surantih, Kambang and Air Haji beaches. From 420 km of the total length of West Sumatra coastline, 45% of them (approximately 180 km) have been damaged by abrasion. With the many of needs on the coastline, the actions are required for protecting beaches from abrasion in West Sumatra.

Abrasion protection has been done by using hard structures, but this way is not natural and resulting bad effect to the environment. A study on the ecological impact to habitat loss due to the presence of hard protective structures along the coastline has been conducted [9]. It was found the surprising drop off the number of seagulls and other seabirds on the protected beach. The study suggested further studies on natural beach protection that including the environmental preservation. The artificial beachrock made of sand solidification for coastal protection may be a prospects of environmental save solution [10].



Fig.3 Simulation of sand-roots interaction

In order to protect beaches from abrasion it is necessary to prevent the sea waves from taking the beach sand particles away from their place. It can be done by constructing wave energy breaker or covering the ground such that the seawater cannot transport the sands away. However, those ways are

not natural and less beautiful. The more natural way is by planting protective vegetations on the beaches. A study to understand the way of those vegetation roots in protecting beaches from abrasion using numerical simulation has been conducted. [11]. The simulations were successfully demonstrated the mechanism of roots for protecting the sandy beaches against seawater erosion (Fig.3).

Besides the numerical study, the field investigation to observe the effect of vegetation and soil sediment to abrasion has also been done. The field investigations were conducted along the West Sumatra coastline. The investigation found that some kind of marine vegetations can withstand against abrasion or seawater erosion. The results of these investigations are further described in this paper.

WEST SUMATRA'S MARINE PLANTS

There are marine vegetations found from field investigation along West Sumatra coastline that empirically can protect beach from abrasion. Mainly there are five kind of marine vegetations exist in the West Sumatra Beaches, that are:

- a. Sea-pine,
- b. Coconut palm,
- c. Mangroves,
- d. Pinago, and
- e. Ketaping (*Terminalia Cattapa*).

The on site captures of those trees can be seen in Fig.4 (a to e). The last two kind of tree seems to be in the same family but different species. However we do not went deeper in to that kind of biological matter.

The abrasion area will be terminated in the zone where there is a vegetation on it. In areas that are not planted, seawater took sand away until several meters into the mainland. Roots are a most important part of vegetation that role the abrasion protection. The marine vegetation roots can creep up to 4 meters from the main wood. The maximum distance of the root extension depends on the soil, planting way and species. For the vegetation where its soil sides have been removed by abrasion, it is found that the roots go only up to about 2.5 meters. This is caused the roots have lost the soil where they need to grow for, are destroyed and taken by the seawater. In order to play as an abrasion protector, the roots and the soil has to take part in symbiotic mutualism.

There are two main types of roots according to

branching pattern as well known: taproot and fibrous root. The taproot is deep-rooted compared to fibrous one. The marine vegetations that are having taproots are Sea-pine, Mangroves, Pinago and Ketaping, meanwhile Coconut palms grow with the fibrous root. It is believed that the taproot may anchor the tree better to the soil and can take water from deeper part from ground surface. However, the fibrous root is found to be denser than the taproot system. This condition give an advantage to the root system to keep the surrounding soil from being taken by the seawater. Then, a coconut tree is better in preventing abrasion than a sea pine tree.



a. Sea pine

b. Coconut palm



c. Mangroves



d. Pinago

e. Ketaping

Fig.4 Marine vegetations in West Sumatra

Based on the study on the mechanism of roots as abrasion protection [11], it is found that the roots give unification effect to the surrounding soil. Further they hold each other and form a bigger mass. The denser roots are the better role in unifying the soil to prevent abrasion. This phenomenon explains the field investigation

results that the Coconut palms with denser fibrous root protecting beaches more than the Sea pines with taproot (Fig.5). Even the field observation also found the row of coconut palms are also found survive better than the sea pine trees (Fig.6). This result proves that taproot roots that capable for penetrating deeper, are not necessarily better to protect abrasion than fiber roots.



Fig.5 On site condition of Sea pine and Coconut



a. Coconut palm beach



b. Sea pine beach

Fig.6 Beaches with marine vegetations

For the same species, the density of vegetation also determines its resistance to abrasion. The vegetations that grow close each other will be more resistant to abrasion than grow in distance. The closer the spacing, the greater the ability to resist abrasion. Clearly that stand-alone tree will be easily demolished by the seawater than they in a group. The same thing happens for plants that grow out of line towards the sea, will easily be turn

down by abrasion. Therefore, planting of vegetations in the purpose of protection against abrasion should be done in groups with a good pattern (Fig.7).

The Field investigation also found that reducing the number of plants in natural growing mangroves will reduced on abrasion resistance (Fig.8). A group of mangroves that experienced a reduction in the number, finally in a critical condition (Fig.9). Eventually that trees will be gone from its original place. So, the density of marine vegetation is an important factor to protect beaches from abrasion. The spacing which is shorter than maximum the root can go, will let the roots cross each other in the form of organic net. This root net will keep the surrounding soil from transported by seawater. While single standing plants with roots are not interconnected, consequently easy to be overturned by seawater.



Fig.7 Plants in group and stand alone



Fig.8 Reduction of mangrove trees for houses



Fig.9 Reduction of mangrove resulting the dead

SOIL SEDIMENT OF BEACHES

In order to investigate the effect of soil sediment for protecting the beach from abrasion, the soil samples have been taken from the beaches along West Sumatra coastline. The samples then are tested in laboratory to elaborate their physical properties. Soil properties are very important engineering as indicator of further engineering behavior such as gradation, strength and stability. Many references have described the testing procedures and the meaning of the engineering properties of soils [12].

The recent study has mentioned that sediments with predominantly non-cohesive materials may be easily transported by seawater. The factor that can keep the soils staying are gravity and internal friction. The coarse grains with greater masses are also more difficult to be mobilized than fine grains [13].

The sand samples taken and analyzed in the laboratory came from 7 beaches in West Sumatra as shown in map Fig.10. The names of each location and the dominant species of vegetation are as follows:

1. Teluk Batang, vegetation Coconut palm
2. Sago Painan, vegetation type: Sea pine
3. Guguk Kuranji Hilir, vegetation Sea pine
4. Tarusan, vegetation type: Sea pine
5. Surantih, vegetation type: Sea pine
6. Tanjung Mutiara, vegetation type: Sea pine
7. Bukit Buayo, vegetation type: Ketaping

The sieve analysis results of the samples are shown in Fig.11. Furthermore, based on the sieve analysis, the sand soils have a low coefficient of uniformity (Table 1). This means that the soils are in uniform gradations. In general, the soil type from the beaches are sandy soil in medium until loose density. In Tanjung Mutiara and Tarusan, the sediment is dominated by fine silty sand. Since those sediments are predominantly non-cohesive materials, then they may be easily transported by seawater. Since those sediments are predominantly non-cohesive materials, then they may be easily transported by seawater.

Based on the findings the sand beaches in West Sumatra are composed of sediments that easily eroded by seawater that is confirmed with the field investigation. The sediments have the relatively small the size of fine to medium sands that are easily transported by seawater. In addition, the

gradations of the soils are uniform which indicates less advantage in terms of stability. It has been explained that the vegetations together with the soil can protect the abrasion, therefore the existing vegetation on the beach must be maintained for the existence of the beaches in the future.

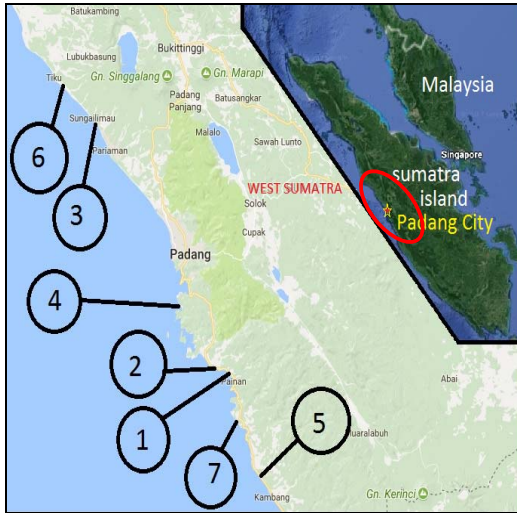


Fig.10 Original sites of the soil samples

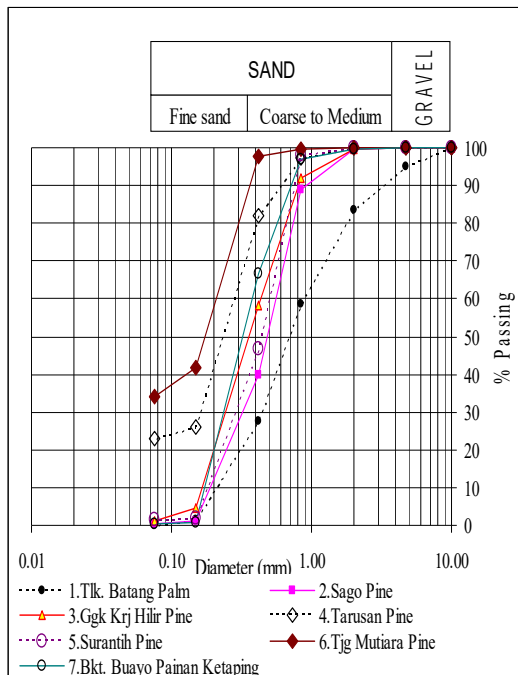


Fig.11 Sieve analysis of sand samples

Table 1 Physical properties of sand samples

Parameter	Symbol	Location number							Unit
		1	2	3	4	5	6	7	
Wet unit volume	γ	1.84	1.95	1.86	1.74	1.85	1.46	1.80	t/m ³
Dry unit volume	γ	1.35	1.48	1.48	1.31	1.42	1.03	1.37	t/m ³
Void ratio	e	0.93	0.87	0.61	0.76	0.76	0.76	0.76	
Saturated water content	w	32.58	31.24	28.14	36.80	32.68	46.77	32.30	%
Sieve analysis	Gravel	4.97	0.10	0.00	0.00	0.00	0.00	0.13	%
	Sand	95.00	98.90	99.43	76.93	98.53	65.80	99.30	%
	Clay	0.03	1.00	0.57	23.07	1.47	34.20	0.57	%
Mean size	D_{50}	0.7	0.49	0.35	0.21	0.42	0.18	0.31	mm
Coef. Uniformity	C_u	4.29	2.89	2.80		2.94		2.11	
Coef. Curvature	C_c	1.07	0.92	0.77		0.92		0.71	

CONCLUSIONS

Indonesian government decided that abrasion has become one of national disasters that resulted in disadvantage coastline changes. Based on the field investigation that has been done there are several marine vegetations that can grow up in decades. The field study also found that the marine vegetations were effectively able to protect beaches against abrasion. At least there are five species of endemic marine vegetations found along the West Sumatra coastline.

This study showed that the beach sediments in West Sumatra are composed of fine to medium sands that easily eroded by seawater. It has been explained using finite element that the roots play a role to unify the soil mass that hold each other to prevent abrasion. Therefore, it is necessary to conserve the existing coastal vegetations as well as planting new specific trees so they will protect the beaches together with the soils. The absence of vegetations on the beaches consequently will result higher vulnerability to abrasion.

ACKNOWLEDGEMENTS

This research is funded by Andalas University under Research Grant No 68/UN.16.17/ PP.HGB /LPPM/ 2017.

REFERENCES

- [1] Badan Informasi Geospasial (BIG), 2013, in: <http://www.bakosurtanal.go.id/berita-surta/show/pentingnya-informasi-geospasial-untuk-menata-laut-indonesia>, accessed on 30 April 2017
- [2] Diposaptono, S., Disaster Mitigation and Climate Change Adaptation (in Indonesia: Mitigasi Bencana dan Adaptasi Perubahan Iklim), Ministry of Marine Affairs and Fisheries, Jakarta 2011

- [3] Hakam, A., Istijono, B., Ismail, FA., Zaidir, Fauzan, Dalrino and Revalin, Report: Deal with Coastal Abrasion in Indonesia (in Indonesia: Penanganan Abrasi Pantai di Indonesia), BNPB, Mataram, 2013
- [4] BNPB, Perka No. 07/2012, Indonesian Disaster Management Data and Information Manual (in Indonesia: Pedoman Pengelolaan Data Dan Informasi Bencana Indonesia), Jakarta, 2012
- [5] Empung, Hiron N. and Chobir A., "Oscillating Water Column (OWE) Building Performance Analysis As Beach Abrasion Reducing", IIOABJ Vol. 7, Suppl. 1, 2016, pp. 515–520,
- [6] Zhang, K., Douglas, B.C. and Leatherman, S.P., "Global Warming and Coastal Erosion", Climatic Change, 64: 41, May 2004, doi:10.1023/B:CLIM.0000024690.32682.48
- [7] Ohgituto, Minangkabau Tempo Doeloe #1 - Padang, <http://ohgituto.blogspot.co.id>, 27 Nov. 2012
- [8] Balai Wilayah Sungai Sumatera (BWSS) V, Project Report: Identification of Critical Coast in West Sumatera Province (in Indonesia: Identifikasi Pantai Kritis di Propinsi Sumatera Barat), Padang, 2009
- [9] Jenifer E. Dugan, David M. Hubbard, Ivan F. Rodil, David L. Revell and Stephen Schroeter, "Ecological effects of coastal armoring on sandy beaches", Marine Ecology 29, Suppl. 1, 2008, pp. 160–170
- [10] Khan Md., N. H., Danjo T. and Kawasaki S., "Artificial Beachrock Formation Through Sand Solidification Towards The Inhibit of Coastal Erosion in Bangladesh". Int. J. of GEOMATE, 9(2), Dec., 2015, pp.1528-1533
- [11] Hakam, A., Istijono B., Ophiyandri T., Darjanto H., Ma'ruf, M.F., "Vegetations as Beach Protection: Simulations of Root Protection Mechanism Against Abrasion". 4th ICEE, accepted, Padang August 2017
- [12] Holtz, R. and Kovacs, W., An Introduction to Geotechnical Engineering, Prentice-Hall, Inc., 1981
- [13] Feagin, R. A., Figlus, J., Zinnert, J. C., Sigren, J., Martinez, M. L., Silva, R., & Carter, G.. "Going with The Flow or Against The Grain? The Promise of Vegetation for Protecting Beaches, Dunes, and Barrier Islands from Erosion", Frontiers in Ecology and the Environment, 13(4), 2015, pp. 203-210

PRELIMINARY STUDY OF LIFT-OFF TEST AND PERFORMANCE EVALUATION FOR ANCHORS ON FREEWAY SLOPES

Sao-Jeng Chao¹, Chia-Yun Wei² and Hong-Da Chou³

¹Professor, National Ilan University, Taiwan; ²Engineer, National Freeway Bureau, Taiwan; ³Master Student, National Ilan University, Taiwan

ABSTRACT

The construction of the freeway system has nearly been completed in Taiwan currently, and many freeways have entered the maintenance stage. Therefore, a series of slope service and maintenance mechanism are established for the National Freeway Bureau for the slope anchors. This paper describes the lift-off test briefly and the performance evaluation of the test results. The purpose of the lift-off test is to obtain the residual tensile load of the existing anchor. The test process is applying tension force in stages, when the pulling out load is greater than the residual tensile load, the load-displacement curve would produce a significant turning point, which is so called the lift-off value. According to the definition proposed by the National Freeway Bureau, the results of anchor lift-off test can be divided into 5 groups, namely D (normal), C (acceptable), B (poor), A (very poor), and X (damage). Through the results of anchor ratings, officers and engineers can be immediately informed of the current conditions of the slope anchors. The results of the lift-off test shows that level D counted for the overall 42.25%, level C counted for the overall 24.72%, level B counted for the overall 12.17%, level A counted for the overall 11.04%, and level X counted for the overall 9.83% in this study. It is found that about 67% of the evaluation results of the lift-off tests are in the decent range, but some anchors need to be further monitored to explore the loss of the pre-stress value as well as the reason. This paper provides clearly and directly understanding on the freeway slope anchor for their service performance.

Keywords: Anchor, Lift-off Test, Slope, Freeway

INTRODUCTION

The effect of frequent activities between the Eurasian plate and the Philippine plate gives birth to a rich and unique terrain condition of Taiwan, which is located in the southeast of Asia. In the distinctive natural environment, there are 2,565 slopes along the freeways, of which there are 1,638 embankment slopes and 927 cutting slopes. In the case of cutting slope construction, a large number of anchors are used to stabilize the slopes in Taiwan, so that the freeway project can be completed smoothly and the safeties of the car drivers are ensured. The construction of the freeway has been nearly completed and many roads have reached the maintenance stage. In order to improve the quality of transportation and guarantee the safety of driver, the freeway bureau has established a series of slope maintenance mechanisms. The government sets up three district engineering office in the north, central and south respectively with a total number of 13 branch stations to perform slope maintenance management. At present, the total number of freeway anchors is 26,802 as shown in Figure 1. With the help of regular slope inspection, ground anchor detection, and the implementation of the maintenance mechanism, the installation rate of the slope anchors is slowed down year by year.

In recent years, the concept of life cycle has been

put forward. Planning, designing, constructing, operating and dismantling of engineering project are considered as a lifecycle. Most of the public construction is currently entering an important stage of operational management and maintenance, and the freeway system is not an exception. Therefore, the establishment of freeway life cycle system, such as recording slope anchor facilities, monitoring systems, and slope inspection data, are implanted under the concept of life cycle at the same time. The anchor detection of the four major groups, including anchor head appearance, anchor head assembly, endoscopic, and lift-off tests, contain all anchor detection data and performance results.

The results of the inspection data are defined to the severity of the development of D level (normal), C level (acceptable), B level (poor), A level (very poor) and X level (damaged). Comprehensive assessment of the anchor appearance as well as the anchor performance provides recommendations based on the follow-up review.

Because the mechanical behavior inside the anchor cannot be seen by the appearance of the inspection, lift-off test is the technique to obtain the residual tensile load of the anchor. When the applied pull-out load is greater than the anchor actually existing load, anchor head with the bearing plate provide obvious displacement to assess the residual

tensile loading. The result of the lift-off test is the most direct representation of the current anchor at this stage, but also the focus of attention from the point view of engineers. This paper describes the test methods and processes of the anchor lift-off test, the classification of the test results for description purpose, the results of the test analysis with comprehensive discussion, to optimize and improve the management measures for achieving the freeway slope sustainable management objective.

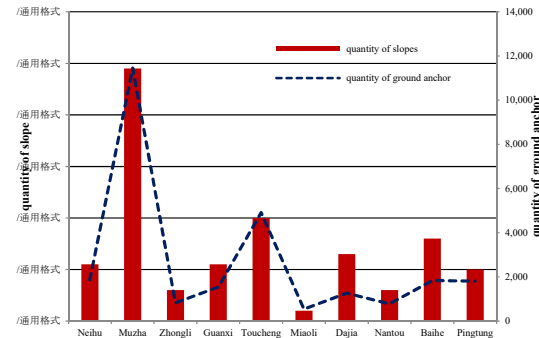


Fig.1 Total number of cutting slopes and anchors

PRINCIPLE AND PROCESS OF ANCHOR LIFT-OFF TEST

During the planning of the slope stability project, the anchor has an initial design load (T_w). After 4 to 5 years of service period, the anchor is re-pulled to find the residual load (T_r), and compared with the design load. In the progressing of lift-off test, when anchor has "lift-off" phenomenon, the displacement-load curve will present a more obvious turning situation (Figure 2, point A), which provides the value of the anchor residual load. The results of the current test and the results of the previous lift-off tests can be compared to obtain the differences in the residual load. The compared result and other monitoring instruments can be used to assess the overall safety of the slope.

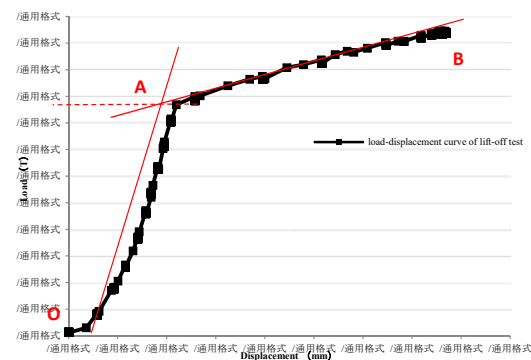


Fig.2 Load-displacement curve of lift-off test

It is an important part for choosing the suitable anchor to carry out the lift-off test. In order to confirm the average and randomness of the anchor samples, it is recommended by the freeway bureau to adopt the characteristics of the "uniform distribution selection" of the anchor selection principle. The main tools of the lift-off test include: anchor head fixture, jack chair, hydraulic jack, load cell, displacement gauge, etc. The lift-off test of anchor is operated according to the process of stage pull out.

Anchor detection frequency is performed for every 4 to 5 years. The anchor detection content includes: anchor head appearance, anchor head assembly, endoscopic, and lift-off test. However, the anchor free-end are filled with cement paste as the second grouting, this work makes it impossible to observe the internal strand by the endoscope anymore. Therefore, the results of the lift-off test are much more significant to show the status of the residual load, and through the lift-off of the test displacement-load curve to understand the situation of the anchor in the slope stratum with the serving time.

Lift-off Test Principle

After the anchor was fixed, in general, some factors will cause the strand and displacement changes. The main reasons include: the sliding loss of the strand during the fixing, the friction loss of the protection tube and the strand, strand relaxation, stratum creep behavior, stratum compaction, influence of proximity to engineering construction, temperature change, various impact, as well as changes in stress state of rock and soil.

There are many possible factors for the loss of anchor force, it is not very easy to point out and explain the exact reason. By employing the lift-off test at the actual site, engineers can obtain the displacement-load curve to interpret the residual load data. The principle of the lift-off the test is based on the existing load (T_r , or the residual load) of the anchor, and the anchor will have obvious characteristics of displacement to evaluate the existing load value of the anchor. An lift-off test of displacement-load curve as an example can be seen in Figure 2 for anchor design load 45T and strand length 25m (anchor fixed length 8m and free length 17m).

During the test process, the fixtures and clips is used to fix the anchor head first, and then the hydraulic jack is installed in the jack chair so that the tensile strand state is set (Figure 4). When the tension of the strand gradually leave out of the pressure plate (Figure 2, \overline{OA}), the drawing the displacement-load curve is plotting at the same time. With the test moving on, we can find the anchor appears "lift-off" phenomenon when the curve has a

significant turning point (Figure 2, A point). Lift-off phenomenon of anchor means the strand load is completely provided by the hydraulic jack at this time, there will be another oblique line (Figure 2, \overline{AB}) after that. The safety and health of the anchor can be evaluated comprehensively, according to the lift-off test results obtained from the displacement-load curve.

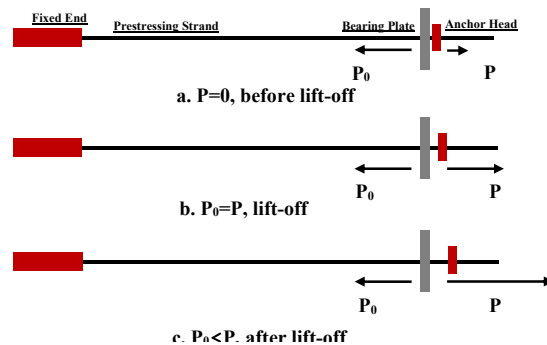


Fig.3 Loading conditions during anchor lift-off test



Fig.4 Lift-off test

In the case where the strand are stressed (Fig. 3-a), P_0 is the original anchor for the existence of the load, which is the anchor of strand pull force so the direction of the direction to the underground anchor section. P is applied by the hydraulic jack to pull out strand for the lift-off test, thus the force direction of P is opposite. Prior to anchor lift-off test, the strand only bears the original anchor load and the appearance of the anchor head is totally attached to the bearing plate.

However, when the lift-off test was progressed (Fig. 3-b), the applied loads of the strand is from two different directions. One, the original load of the original anchor (P_0), due to the initial pre-stressed loading, the steel strand locked to the bearing plate, resulting in the direction of the anchor force for the anchor phase direction. The other force (P) is in the

direction of the hydraulic jack to carry out the test in the direction of the anchor head gradually applied to the load. Therefore, the appearance of the anchor head is not much change until $P = P_0$ (Fig. 3-b and Figure 5). While the load of the hydraulic jack is equal to the original existing load of the anchor, the original position of the anchor head happens to leave the bearing plate by the process of full loading conversion at this moment. This phenomenon is so called the anchor head lift-off.

As a final point, after lift-off (turning point) phenomenon (Figure 3-c), the force behavior of the internal strand of the anchor is provided entirely by the hydraulic jack. When the pull out load, the phenomenon has been lift-off, is less than the anchor design load (T_w), the test load is stop at the 1.1 the design load (T_w) and then record the existing load (T_r). Alternatively, when the pull out load is equal to 1.2 the design load (T_w) but the anchor is still not lift-off, the test is stopped and the existing load (T_r) is recorded as the same.

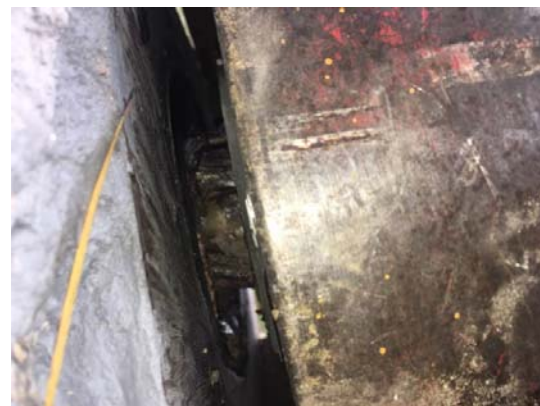


Fig.5 "Lift-off" of phenomenon for anchor head and bearing plate separation

Experimental procedure

The implementation of the anchor lift-off test attempts not to destroy the existing anchor as the principle. Carrying out the test is under the consideration with the principle of selection to the requirements of the "Freeway Maintenance Manual". It is depending on the slope of the anchor by the status of the anchor distribution, with the requirement that at least one per row of each stage with no more than 15 ones per row; and at least 6 lift-off tests per anchored slope. In addition, the abnormal appearance of the anchor head (such as corrosion, rust traces, efflorescence, or pre-cast anchor beam and ground separation) is selected for the priority detection object. Nevertheless, if the appearance can be judged as significant damage (such as the strand has been pulled) would not be tested. The remaining anchors with normal

appearance are randomly sampling to understand the situation of the existing anchor loadings.

In the course of the lift-off test, experimental quality is no doubt the key issue for the residual load of anchor. The test equipment consist of anchor head fixture, clip, pull-out rod, hydraulic jack, load cell, and displacement gauge (Figure 4). Among them, the latter three instruments for the lift-off test need laboratory correction before entering the test site. The procedure of lift-off test as follows:

1. Select the anchor to lift-off test according to the provisions of the maintenance manual or the contract.
2. Open the galvanized protective cover to remove corrosion and grease, and as appropriate, to trim the excess strand.
3. To clamp and clip fixed anchor head, and fitted with support rod and Jack chair.
4. Installation of test equipment, hydraulic jack, load cell and displacement gauge, etc. Pull out strand and measure the initial anchor head displacement as a reference value.
5. According to pull out procedures to start the lift-off test and increase load with the sitting time for recording test data.

The lift-off test is based on the above five steps. During the test process, one needs to consider the different in-situ problems as well as ground anchor has been completed for some time, the function may have some degree of loss, in order to avoid the test load caused excessive anchor damage and to keep construction safety concerns. Therefore, the maximum load is set to 1.25 times the design load (Tw) or the anchor head displacement of 20mm in order to avoid excessive displacement.

If the test result shows that the residual load of the anchor is smaller than the design load, i.e., when the anchor head and the bearing plate has been separated before Tw, it will be the case to insert some different thickness of the steel sheets between the anchor head and bearing plate to effectively increase the anchor force to enhance the anchor function. The test procedure will then be decompressed in 5 steps to the residual load (Tr), and the final step is applied load again to the locked load.

During the process of executing the anchor lift-off test, the load of the internal strand of the anchor is very large and there is a risk of operation. Therefore, it is necessary to pay attention to the procedure of pull out load and the process of pull out load sitting time. The maximum increasing tensile force per minute of the test is not greater than 0.1 times the residual load prior to the test tension (T) exceeding the residual load (Tr). After the strand tensile force exceeds the residual load (Tr), the idea is taking to 5 steps to reach the maximum test strand, and the maintenance time of each step is at least 1

minute. When reaching maximum test load (T), in principle, the test load is supposed to maintain 1 to 15 minutes, if necessary, depending on the status of the situation to extend the sitting time, and record the creep displacement as well.

THE GRADING STANDARDS AND TEST RESULTS OF ANCHOR LIFT-OFF

Anchor inspection is an important part of preservation and maintenance and also responds the concept of slope life cycle. Thus establishing a series of basic information about the anchor facilities associated with the slope is essential. However, before the start of the in-situ test procedure, the slope location, geological condition, slope protection structure and drainage facilities are needed to carry out for the investigation records. The main anchor information, including design load, panel type, ground anchor length, strand, etc. That is to say, the slope conditions and the anchor initial design must be thoroughly understood in the beginning.

The lift-off tests are carried out according to the provisions of the maintenance selection principle by the freeway bureau. The total number of anchors for the lift-off test was 1,323 distributed in five levels, D (normal), C (acceptable), B (poor), A (very poor), and X (damage).

The residual load grading standards is illustrated in Figure 6. If the residual load is between 0.8 ~ 1.2 design load ($0.8 Tw < Tr < 1.2 Tw$), then rated as D (normal). If the residual load is between 0.5 and 0.8, the design load ($0.5 Tw < Tr < 0.8 Tw$) is rated as C (acceptable). If the residual load is between 0.2 ~ 0.5 design load ($0.2 Tw < Tr < 0.5 Tw$), then rated as B (poor). If the residual load is greater than 1.2 design load or less than 0.2 design load ($Tr > 1.2 Tw$ or $Tr < 0.2 Tw$), then rated as A (very poor). If during pull off process of the anchor test, the strand is broken or damaged, then rated as X level (damage).

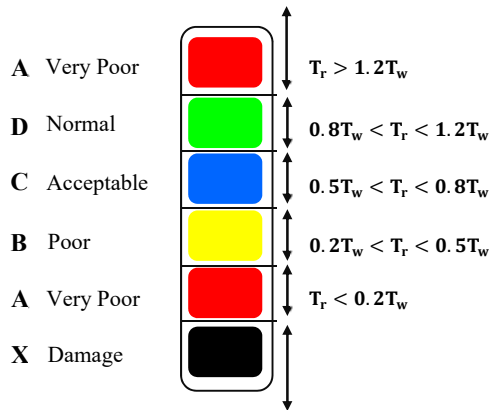


Fig.6 The lift-off test grading standards

The lift-off test results for anchor on the freeway slope are comprehensively assessed in this study. After a detailed statistical data analyzed, it can be found that a total of 1,323 anchors are ranked into 5 levels. There are 559 anchors rated as D (normal), accounting as 42.25%; there are 327 anchors rated as C (acceptable), accounting as 24.72%; there are 161 anchors rated as B (poor), accounting as 12.17%; there are 146 anchors rated as A (very poor), accounting as 11.04%; finally, there are 130 anchors rated as X (damage or function loss), accounting to the overall as 9.83%. The results can be presented into the pie chart to show the proportion of anchor detection project grading situation.

The total number of anchors of the national freeway is 26,802 in our database, while the total number of anchors for lift-off test was 1,323. The residual load in the 1,323 anchor data is divided by the original anchor design load, and the percentage of residual load can be obtained and the percentage of residual load can be clearly seen at the present stage as a pie chart (Figure 7). From the pie chart, it can be learned that the residual load of the anchors is about 67% maintained the values of 51~120% of the anchor design load. The residual load of the anchors is about 12% fell to values of 21~50% of the design load. The residual load of the anchor is about 11% of the total number of anchors larger than the design load of 120% or less than 20%. While about 10% of the anchors are evaluated as damage. This finding indicates that the current anchorage does not seriously affect the safety of the slope, but also shows that the more attention must be paid for national freeway anchored slopes.

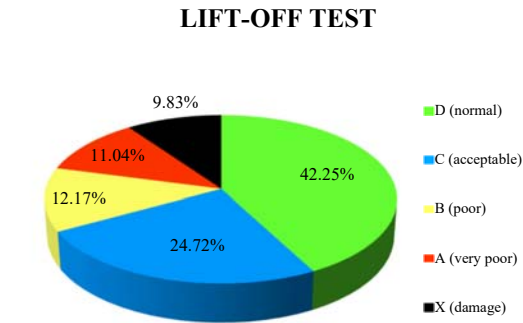


Fig.7 Pie chart for grading of anchor lift-off test

CONCLUSION

The construction of the freeway has been almost completed in Taiwan, and many roads have entered the maintenance stage. At present, the number of existing anchors is 26,802 in total, while the number of new anchors is slowing down year by year. Recently, a total number of 1,323 anchors were conducted the lift-off test. It is found that 559 anchor scores were rated D (normal), accounting for 42.25% of the total; 327 anchor scores were rated as grade C (acceptable), accounting for the overall 24.72%. The percentage number of anchors in the D level and C level (within the design loads of 51% to 120%) is about 67% of the number of tested anchors. This shows that the current anchor performance does not seriously affect the safety of the slope but extra attention is recommended.

REFERENCES

- [1] National Freeway Technical Code, "Freeway Maintenance Manual Chapter 5 Slope", 2013, National Freeway Bureau.
- [2] Liu HS, Preliminary Performance Study of Freeways Soil Anchor and Numerical Simulation for the Pre-stress Attenuation, 2014, Master Thesis, Department of Civil Engineering, National Ilan University.
- [3] Tang TH, Studies of Freeways Soil Anchor Performance and Appropriate Numerical Simulation Computer Programs, 2015, Master Thesis, Department of Civil Engineering, National Ilan University.
- [4] Ye HS, Wei CY, Chao SJ, Wang P, and Tang TH, "Performance Analysis and Application Evaluation of Freeway Anchors", 2016, The

Cross-strait Geotechnical Engineering /
Geotechnical Technology Exchange Conference,
pp. 173-180.

INFLUENCE OF LIQUEFACTION ON SOIL-FOUNDATION-STRUCTURE INTERACTION

Ryohta Takatoku¹, Kentaro Uemura¹, Barrios Gonzalo³, Naotaka Kikkawa², Nobutaka Hiraoka², Kazuya Itoh¹, Naoaki Suemasa¹, Nawawi Chouw³, Thomas Larkin³ and Rolando Orense³

¹ Urban and Civil Engineering, Tokyo City University, Tokyo, Japan

² National Institute of Occupational Safety and Health, Japan

³ The University of Auckland, Auckland, New Zealand

ABSTRACT

Liquefaction occurred in filled grounds and embankments in the 2011 Tohoku-Pacific Ocean Earthquake and in the 2016 Kumamoto earthquake. In New Zealand, medium and small type structures on spread foundations were damaged by uneven settlement and lateral spreading induced by liquefaction in the 2010-2011 Canterbury earthquake sequence. Many studies have been done in the past to elucidate such liquefaction phenomena. Among them, it is necessary to consider the interaction between structures and ground system for liquefaction damage in small and medium type buildings. However, there are many unknown points in the dynamic interaction of the liquefiable ground and structures. In this study, geotechnical centrifuge shaking table tests were carried out to investigate the liquefaction behavior which changed depending on the weight of structures and the distance between neighboring structures. For the cases examined in this study, adjacent structures tended to tilt with respect to each other during liquefaction. In addition, it was confirmed that the inclination of the structures during shaking was different from that after shaking as the distance between the structures changed.

Keywords: Liquefaction, geotechnical centrifuge shaking table test, soil foundation structure interaction, spread foundation

INTRODUCTION

Japan is a nation of earthquakes where many liquefaction-induced damages have occurred on ground and structures every several years. Devastating liquefaction occurred in filled grounds and embankments in the 2011 Tohoku-Pacific Ocean Earthquake. In recent years, wooden small houses were damaged by soil liquefaction in the 2016 Kumamoto earthquake. In New Zealand, small and medium size buildings on spread foundations were damaged by uneven settlement and lateral spreading induced by liquefaction in the 2010-2011 Canterbury earthquake sequence. Methods to predict such liquefaction damage include simplified methods, such as the F_L method shown in the Architectural Basic Design Guidance [1]. However, the assessment method makes judgment on the liquefaction potential of the ground itself. According to the review of the literature conducted on the topic regarding liquefiable soil and structure interaction, liquefaction is less likely to occur in the ground directly under heavy structures [2] and the behavior after liquefaction differs depending on the distance between structures [3]. Several liquefaction countermeasure methods have been actually suggested. For example, Shibata et al. [4] carried out a large-scale shaking table test to verify the effectiveness of a countermeasure which utilizes both the shear deformation suppression effect and the confining pressure increment effect. It is

necessary to examine dynamic interaction between structures and the liquefiable ground since there are still many unexplained issues.

In this study, four cases of geotechnical centrifuge shaking table tests were carried out. One was a free field case and the second has two separated structures with different weights set on top of the soil. The third and the fourth cases involved two adjacent structures with the same and different weights installed. Each behavior was investigated and the mechanism of liquefaction-induced settlement was verified throughout the tests.

GEOTECHNICAL CENTRIFUGE MODEL TESTS

Studying the phenomenon of soil liquefaction is difficult due to the fact that earthquake occurs relatively infrequently and this makes it more difficult to predict the damage that may be caused by the liquefaction with high accuracy. As an alternative to actual earthquakes, dynamic centrifuge modelling can be used to study the effects of shaking on soil and, in particular, the failure mechanism involving liquefaction. In this study, a geotechnical centrifuge facility was used to investigate the mechanism of liquefiable soil and structures interactions. All the tests were conducted on the JNIOH Mark II Centrifuge [5] owned by National Institute of

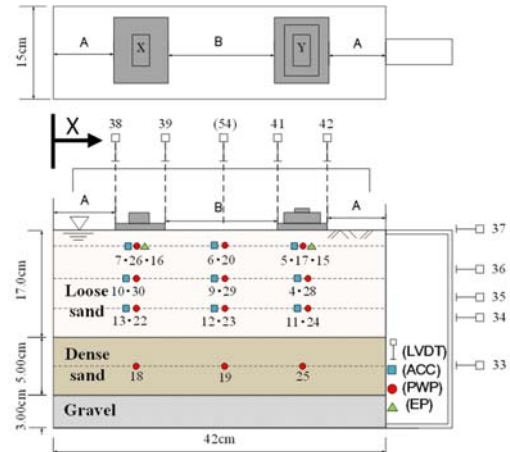
Table 1. Scaling factor

Parameter	Model type	Proto type
Length	1/N	1
Acceleration	N	1
Times (dynamic)	1/N	1
Times (consolidation)	1/N ²	1

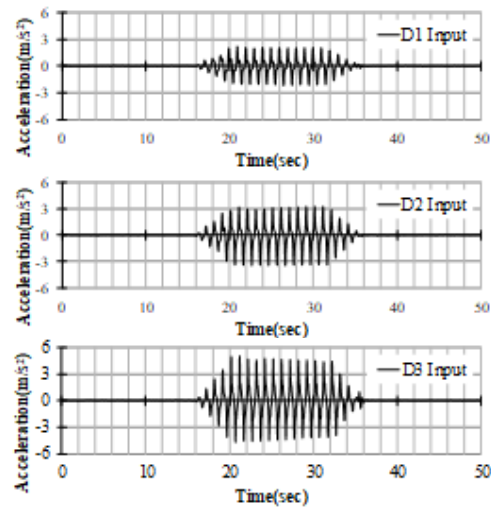
Occupational Safety and Health, Japan (JNIOH). Unlike other centrifuges, its arms (forms) are asymmetric, which is one of its special features. One side of the arm is provided with a bridge plate where a swinging platform is fixed to its inner end plate with the help of a pair of hydraulic suspension jacks when the platform is lifted up (dynamic platform). In order to balance this portion (weight of the end plate) of the dynamic side arm while swinging, two counter weights are overhung on the two sides of opposite arm which is used for non-shaking or static tests (static platform). A model ground was made on a scale of 1/50 and geotechnical centrifuge shaking table tests were carried out under 50G. The results of the experiments were based on the scaling factor shown in Table 1, which theoretically represents the relation between a prototype and a model [6].

EXPERIMENTAL SETUP

In the experiments, liquefaction behavior was examined under four conditions; the ground without any structures (Case 1), two separated structures with different weights (Case 2), two adjacent structures with the same weight (Case 3) and two adjacent structures with different weights (Case 4). Fig. 1 shows a layout of Case 2 where structures and sensors were set in the model ground and Table 2 shows the experiment conditions, including the distance between structures and the values converted to prototype scale. A and B in the positional relationship of the structures shown in Table 2 indicate the locations of A and B shown in Fig.1. A laminar box was used for the model container to reduce refraction waves from side walls as a boundary condition and to reproduce the phenomenon of liquefaction in an infinite ground. The soil used for the model ground was air-dried Toyoura sand. The main properties of this sand are presented in Table 3.

**Fig. 1** Outline figure of model ground**Table 3.** Property of Toyoura sand

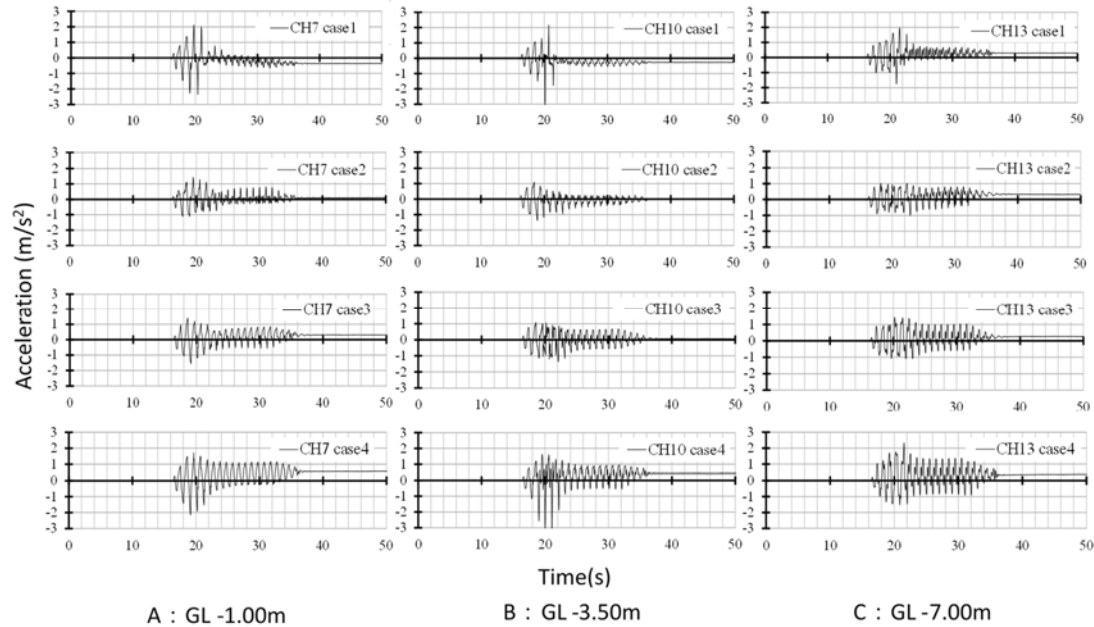
Property	Value
Particle density [g/cm ³]	2.638
Minimum density [g/cm ³]	1.343
Maximum density [g/cm ³]	1.601
Maximum particle size [mm]	0.425
D ₅₀ [mm]	0.106

**Fig. 2** Input waveform**Table 2.** Experiment condition including distance between structures

	Dr [%]		Sr	Bearing pressure		Positioning structure	
	Loose sand	Dense sand		Model scale (kPa) [Prototype scale (kPa)]		A	B
				X	Y		
case1	34.0	91.0	95.0	—	—	—	—
case2	40.0	73.0	93.0	1.40 [70.0]	2.30 [115]	8.00 [4.00]	12.0 [6.00]
case3	34.0	86.0	94.0	1.40 [70.0]	1.40 [70.0]	12.5 [6.25]	3.00 [1.50]
case4	34.0	86.0	97.0	1.40 [70.0]	2.30 [115]	12.5 [6.25]	3.00 [1.50]

Table 4. Number and location of sensors

Height from the ground surface			Accelerometer	Pore water pressure sensor	Earth pressure sensor
Layer	Model type	Proto type			
Loose layer	-2.00cm	-1.00m	3	3	2
	-7.00cm	-3.50m	3	3	—
	-14.0cm	-7.00m	3	3	—
Dense layer	-19.5cm	-9.75m	—	3	—

**Fig. 3** Time history of input acceleration D1 in case1 to case4

The sand was poured from a certain height for consistent production of uniform deposit with an average dry unit weight of 14.04 kN/m^3 and 15.47 kN/m^3 , and corresponding average relative densities of 70% and 40%. Initially, a bottom layer was spread consisting of gravel 30mm thick, then the second layer was dense layer ($Dr_D = 65\% - 75\%$) 50mm thick, and the third layer was loose layer ($Dr_L = 30\% - 40\%$) 170mm thick. These layers correspond to prototype layer thicknesses of 1.5m, 2.5m and 8.5m, respectively. Sensors were installed directly under the structures and at the center of the model ground. Nine accelerometers, nine pore water pressure sensors and two earth pressure sensors in total were installed within the loose layer and three pore water pressure sensors were placed within the dense layer. The setting number and the height from the surface to each sensor are shown in Table 4. Here, the depths from the ground surface in prototype scale are: -1.0m, -3.5m, -7.0m, and -9.75m, respectively. In addition, displacement sensors were installed in the upper part of the model ground to measure the settlement of the surface ground by liquefaction. Five vertical linear

displacement transducers (LVDT's) were set at both edges of the footings and at the middle of the model in Case 2 to Case 4. After setting the sensors, the model ground was saturated by slow-fast penetration with de-aerated silicone oil whose viscosity was 50 times that of water. After completing saturation, the model container was set on the shaking table on the centrifuge platform. All instrumentations were set and centrifugal acceleration was applied up to 50G, allowing self-weight consolidation of the soil. Shaking table tests were carried out in which the dissipation of excessive pore water pressure was confirmed in a 50G centrifugal field before triggering the input waves. The applied vibration of the shaking table is a harmonic sine wave with 50 Hz frequency in model scale. The maximum amplitudes in model scale were 115 m/s^2 for D1, 175 m/s^2 for D2 and 255 m/s^2 for D3, corresponding to 2.2 m/s^2 , 3.2 m/s^2 and 5.0 m/s^2 , respectively, in prototype scale. Hereafter, all the results of the centrifuge tests are presented in terms of prototype scale.

EXPERIMENTAL RESULTS AND DISCUSSION

Response of ground motion during liquefaction

Fig. 3 shows the time histories of input acceleration D1 in Case 1 to Case 4 measured at G.L. -1.00m, G.L. -3.50m, and G.L. -7.00m, respectively. Although several acceleration sensors malfunctioned at some places, all the other sensors in the depth direction worked normally in CH7, CH10 and CH13 located at the left side of the laminar box, as described in Fig. 3. It can be confirmed that while the input waves were constant, the accelerations decreased after $t=20$ seconds in almost all cases. It is assumed that the shear waves became difficult to be transmitted due to the occurrence of liquefaction. The recorded acceleration histories sometimes display a few acceleration spikes around the onset of liquefaction.

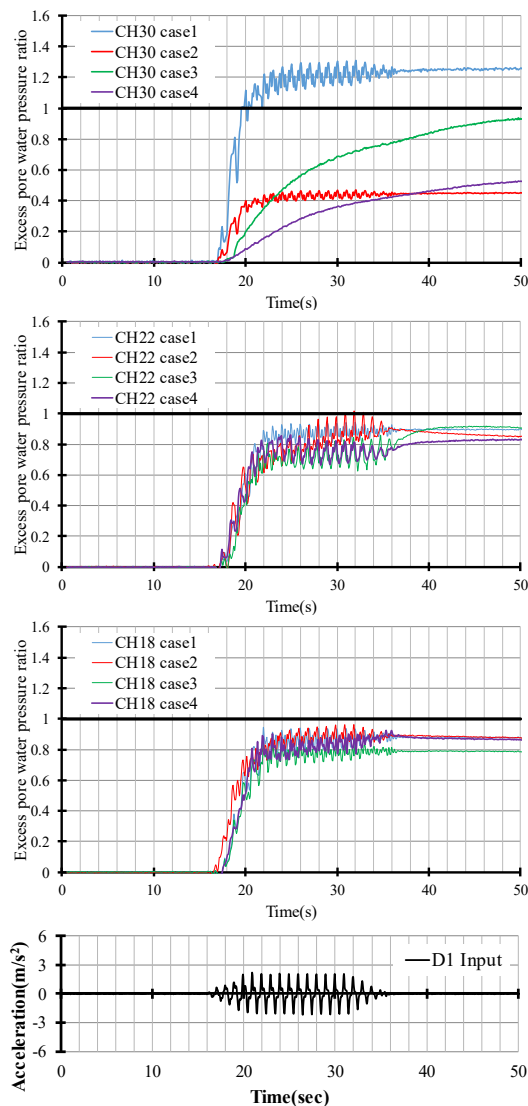


Fig. 4 Time histories of excess pore water pressure

Then the amplitude largely decreased from the $t=20$ seconds in Case 1.

Fig. 4 shows the time histories of the excess pore water pressure when acceleration D1 was the input. As for the cases where the structures were installed, when calculating the excess pore water pressure ratios, the effective stresses were adjusted based on the Boussinesq theory [7]. The excess pore water pressure ratio in Case 1 quickly reached and then slightly exceeded the value of 1.0 during strong shaking. In addition, it is confirmed that the increment of the excess pore water pressure ratio became small at the time when the acceleration decreased, as depicted in Fig. 3. When comparing the three layers in detail: loose layers with $Dr = 30\%$ to 40% at GL-3.50 m, GL-7.00 m, and at dense layer with $Dr = 65\%$ to 75% at GL-9.75 m, it appears that the excess pore water pressure ratios at GL-3.50 m in Case 2 to Case 4 in which the structures were installed were much smaller than that in Case 1. At GL-7.00 m and GL-9.75 m, on the other hand, those in Case 2 to Case 4 showed similar trends to that in Case 1. It is likely that the confining pressure increment effect due to the structure's weight have effect in counteracting liquefaction occurrence. Moreover, as the depth becomes deeper, the more the excess pore water

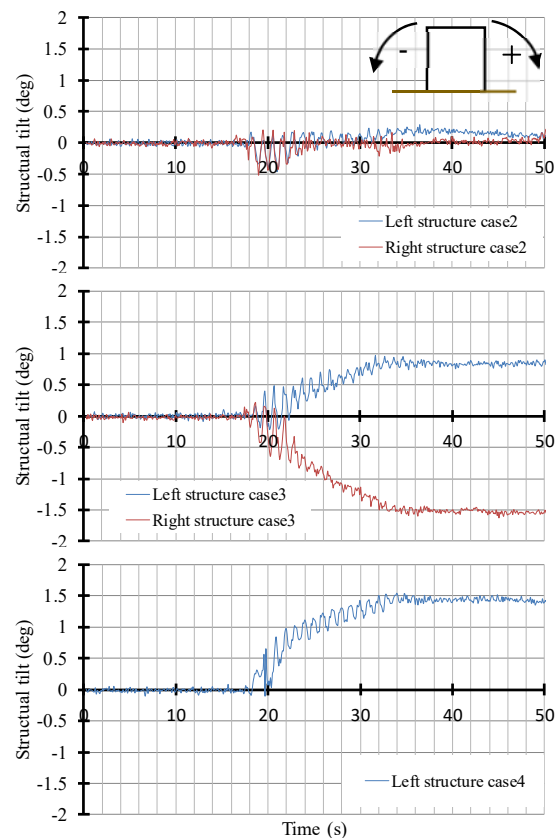


Fig. 5 Time histories of structural tilt in case2 to case4

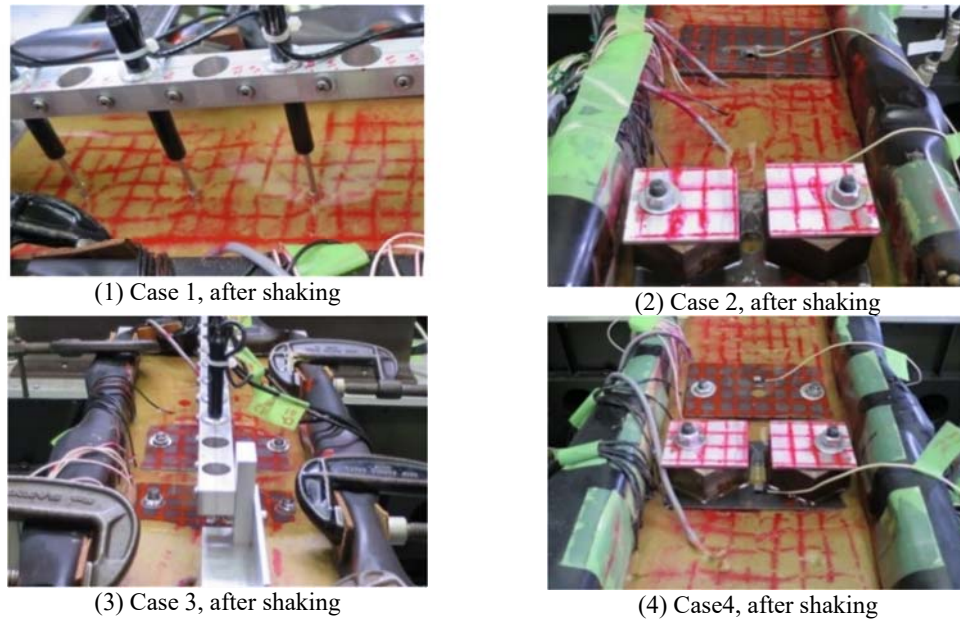


Fig. 6 Photographs of ground settlement and structure after experiment

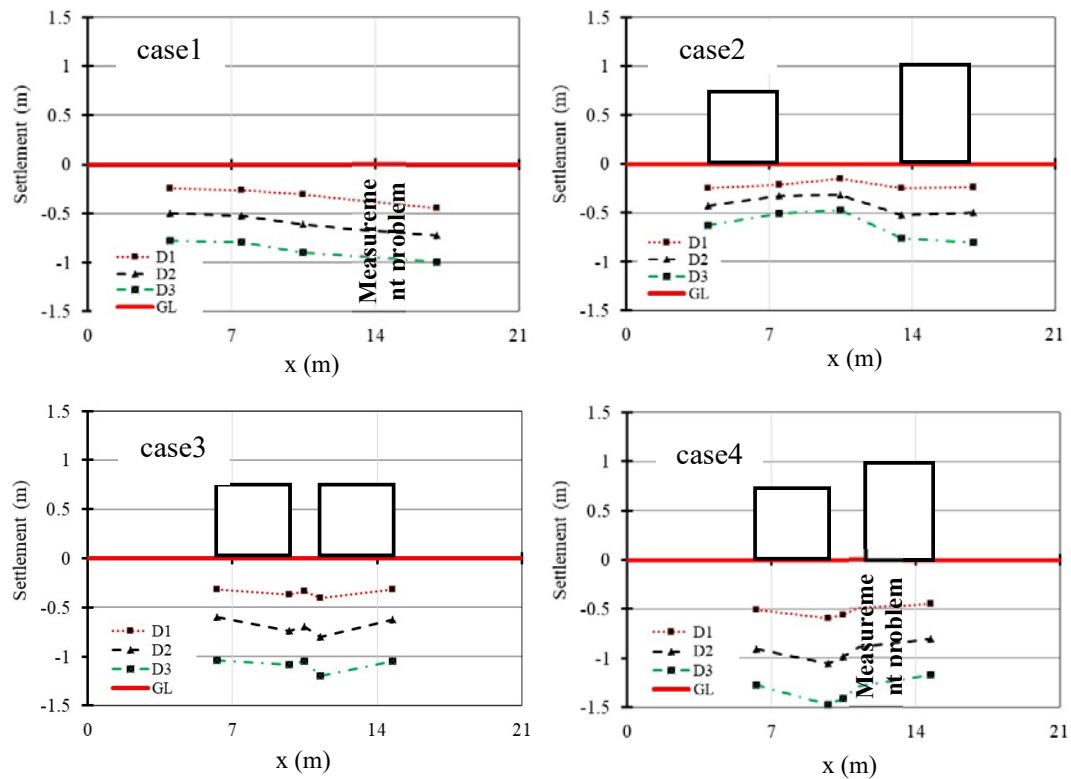


Fig. 7 Tendency of settlement surface ground and structures

pressures tended to decrease. Especially those in Case 2 to Case 4 were the lowest at GL-3.5 m due to the structures' weight.

Structural tilt

Fig. 5 shows the time histories of structural tilt in Cases 2 to 4 when acceleration D1 was the input. It is defined that the tilt to the left is positive and tilt to the

right is negative. In Case 4, measurement of the right structure with heavier weight was not able to be conducted because of defect of the displacement sensor (CH41). In Case 2 where two structures were set separately, it can be seen that the structures were rocked from $t=16$ to 35 seconds during shaking. Since structural tilt was seen after shaking, it is considered that strength loss within the loose soil layer led to partial bearing capacity failure due to liquefaction occurrence. On the other hand, in Case 3 where two adjacent structures were installed, it can be seen that the structures tilted at the same time as shaking. Also, for Case 4 where two structures with different weights were set adjacent to each other, the structures tilted during shaking in the same way as in Case 3. From these results, it was found that the separated structures tilt after shaking and adjacent structures tilt during shaking regardless of the structures' weight.

Settlements

Fig. 6 shows the photos of the amount of ground settlement and subsidence of the structures in Case 1 to Case 4 after each shaking event was completed. It is understood that the structures subsided in all cases, i.e. from Case 2 to Case 4. Fig. 7 shows the settlement trend of the ground surface and structures in Case 1 to Case 4. In Case 1 and Case 4, one of plots were excluded because of malfunctioning of the displacement sensor (CH41). First, when looking at the diagram for Case 1, the amount of vertical displacement on one side was large, which may be due to the influence of the non-uniformity of the model ground and the direction of excitation. In addition, a difference was not observed in the amount of settlement despite the increase in input amplitude D1, D2, and D3. It is likely that this was due to post-liquefaction reconsolidation volumetric strains. Comparing the settlement for D1 of Case 2 and Case 4, the settlement of the adjacent structures in Case 4 was larger than that of the separated structures in Case 2. In Case 3 and Case 4, the weights of the structures were different, however, there was no difference in the settlement after D1 event. When D2 and D3 was applied thereafter, the proportion of vertical displacement was large in Case 4. Comparing case 1 and case 2, the amount of settlement of case 1 on which the structure is not placed was large. The confining pressure increment effect due to structure's weight have effect in counteracting liquefaction occurrence, as shown in Figure 3 and 4. In other words, these results suggest that settlement reduces for large values of bearing pressure.

From these observations, it was confirmed that the inclination of the structures and the amount of vertical displacement of the ground changed after shaking as a result of changing the weights of the adjacent structures.

CONCLUSIONS

A series of geotechnical centrifuge shaking table tests was carried out to investigate the liquefaction behavior which changes depending on the weight of the structure and the distance between neighboring structures. The main observations which were clarified by the centrifuge experiment are as follows:

- (1) The increment of confining pressure due to the weight of structures was effective in preventing the occurrence of liquefaction.
- (2) Adjacent structures tended to tilt with respect to each other during liquefaction.
- (3) It was confirmed that the inclination of the structures during shaking was different from that after shaking as the distance between the structures changed.

REFERENCES

- [1] Japan Institute of Construction and Technology: Basic Structure Design Guidelines, pp. 163-169. 1995.
- [2] Hayden, C. P., Zupan, J. D., Bray, J. D., Allmond, J. D., & Kutter, B. L.: Centrifuge test of adjacent mat-supported buildings affected by liquefaction, *Journal of Geotechnical and Geoenvironmental Engineering*, ASCE, 141(3), 04014118, 2015.
- [3] Yoshida N.: Mechanism of flow accompanying liquefaction, *Symposium on Fluidity and Permanent Deformation of Ground - Soil Structure during Earthquake*, pp. 53 – 70, 1998.
- [4] Shibata K.: Development of liquefaction countermeasures using direct loading on the foundation, *Taisei Construction Technology Center Report No. 45*, pp.1 – 6, 2012.
- [5] Horii, N., Itoh, K., Toyowasa, Y., & Tamate S.: Development of the NIIS Mark-II geotechnical centrifuge. In *Proc. Int. Conf. on Physical Modelling in Geotechnics*, 141-146. 2006.
- [6] Schofield, A. N., & Steedman, R. S.: State-of-the-art report: Recent developments on dynamic model testing in geotechnical engineering, *Proc. 9th World Conference on Earthquake Engineering*, Vol. 8, pp. 813-824, 1988.
- [7] Japanese Geotechnical Society: Introduction to Geotechnical Equations, *Introduction Series 9*, pp.167- 168, 2001.

ULTIMATE BEARING CAPACITY OF CLAYEY FOOTING UNDER SQUEEZE BREAKDOWN USING RIGID-PLASTIC FINITE ELEMENT METHOD

Kazuhiro KANEDA¹, Masamichi AOKI², Tomohiro TANIKAWA³ and Satoru OHTSUKA⁴
^{1,2,3}Takenaka corporation, Japan; ⁴ Department of Civil and Environmental Engineering, Nagaoka University of Technology, Japan

ABSTRACT

The relations of ultimate bearing capacity for foundations are specified in the guideline published by the Architectural Institute of Japan for design of building foundations. The rigid-plastic finite element method developed by Tamura and Ohtsuka has been employed to estimate the ultimate bearing capacity of footings. The characteristic of this method is that, in contrast to deformation analysis, it applies limited soil constants; only the strength parameters, such as cohesion and friction angle, are used since the method deals with the limit state directly by disregarding the deformation of the building and ground. In this study, a series of rigid plastic finite element analyses were performed to compare the ultimate bearing capacities of spread foundation for clayey squeeze breakdown obtained by simulations and the formulae of the Architectural Institute of Japan. The change in the failure mode of the ground was discussed considering the geometrical ratio between the width of the footing and the surface layer. In addition, inclined load was considered for clayey squeeze breakdown. The applicability of rigid plastic FEM to the assessment of ultimate bearing capacity of clayey squeeze breakdown was demonstrated.

Keywords: Clayey squeeze breakdown, Ultimate bearing capacity, Rigid plastic FEM, Inclined load

INTRODUCTION

The calculation of the ultimate bearing capacity of soil (Terzaghi et al., 1967) is important when designing a building. The ultimate bearing capacity formulae for building foundations are specified in the guideline published by the Architectural Institute of Japan (AIJ). These formulae were proposed based on experiments and theoretical considerations avoiding risk. However, the inclined bearing capacity was not adequately investigated. In this research, the bearing capacity of spread foundation with a thin clay layer was analyzed using numerical simulations. First, the clayey squeeze breakdown was simulated (Kaneda et al., 2013), and subsequently, the associated inclined bearing capacity was discussed. The rigid-plastic finite element method (FEM), developed by Tamura and Ohtsuka (T. Tamura et al., 1984 and A. Asaoka and S. Ohtsuka, 1986), was employed to estimate the ultimate bearing capacity of footing. The Drucker–Prager yield function was adopted as the soil constitutive equation and the associate and non-associate flow rules were introduced to establish the configuration relationship of the ultimate state. Using this method, the structural safety assessment or calculation of soil bearing capacity was evaluated. The characteristic of this method is that, in contrast with deformation analysis, it applies limited soil constants; it only uses the strength parameters, such

as cohesion and friction angle, because it deals with the limit state directly by disregarding the deformation of the building and ground. Since RPFEM uses the upper bound theorem of plastic theory, it becomes slightly larger than the true value.

SIMULATION OF CLAYEY SQUEEZE BREAKDOWN WITHOUT INITIAL LOAD

What is clayey squeeze breakdown?

Consider a soft clay upper rigid foundation of height H , as shown in figure 1 (H. Yamaguchi, 1990). When the foundation width B becomes larger than the layer height H , the failure mode shifts from the general failure mode, specified by Terzaghi (Terzaghi et al., 1967), to that of the squeeze breakdown, wherein the upper clay layer is pushed out to both sides in plastic state. The bearing capacity of squeeze breakdown can be expressed as the following equation (Meyerhof et al., 1953).

$$q_f = 4.14c_u + \frac{c_u B}{2H} \quad (1)$$

where q_f , c_u , B , and H are the ultimate bearing capacity of squeeze breakdown (kN/m^2), undrained strength (kN/m^2), foundation width (m), and clay layer height (m), respectively.

When the relationship between B and H is

$$B/H \geq \sqrt{2} \quad (2)$$

squeeze breakdown occurs.

In addition, with regard to the general failure mode, AIJ proposed the following equation for ultimate bearing capacity.

$$q_u = (i_c \cdot \alpha \cdot c_u \cdot N_c + i_\gamma \cdot \beta \cdot \gamma_1 \cdot B \cdot \eta \cdot N_\gamma + i_q \cdot \gamma_2 \cdot D_f \cdot N_q) \quad (3)$$

where q_u is the ultimate bearing capacity (kN/m^2), N_c , N_γ , N_q are the coefficients of bearing capacity, γ_1 is the unit weight of soils (kN/m^3), and γ_2 is the unit weight of the penetration area (kN/m^3). α , β are the shape coefficients, η is the correction factor for the foundation size, i_x , i_γ , i_q are the correction factors of inclined load, and D_f is the penetration length (m).

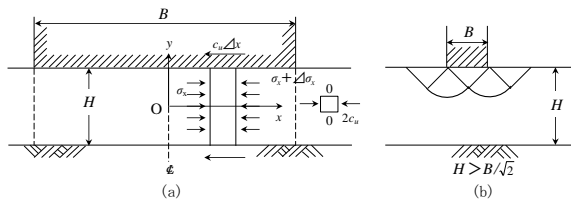


Fig. 1 Outline of squeeze breakdown.

Analysis conditions

In this work, the formulation of the rigid-plastic FEM was omitted; more information can be found in the references (Tamura et.al.,1984, Asaoka and Otsuka, 1986). Figure 2 shows the numerical mesh, which is 150 m wide and 10 m high in the plane condition. The foundation widths were set as 10, 14, 16, 30, 40, and 50 m. Assuming a rigid foundation, the strength of foundation was set as $c_u = 1000000 \text{ kN/m}^2$. The soil layer was assumed to be homogeneous type c material. The inclined load (horizontal load/vertical load (F/V)) was set as 0.1, 0.2, 0.3, 0.4, and 0.5.

Analysis results

Vertical bearing capacity

Table 1 shows the results of the simulation using equation (1). Using equation (2), squeeze breakdown was applied to the 14 m-wide foundation ($B/H=1.4$). Figure 3 shows the relationship between N_c and B/H . N_c is the value of the result divided by $c_u = 10 \text{ kN/m}^2$. From the simulation results, it can be observed that when the foundation width ratio (B/H) is large, N_c is also large for the squeeze breakdown. Figure 4 shows the pattern of the failure mode according the foundation width ratio as per Yamaguchi (Yamaguchi, 1982). The tearing failure was accompanied by tensile cracks. It is important to

clarify the mechanism of tearing; however, it is difficult to evaluate the extension strength using the Drucker–Prager yield function and would thus be future work. In this simulation, it is necessary to consider the extension strength. Without it, the squeeze breakdown was simulated well using the rigid-plastic FEM. Figure 5 shows the contours of the shear strain at the point of failure. The general failure mode occurred at the foundation width of 10 m ($B/H=1.0$), the failure surface touched the bottom for the foundation width of 16 m ($B/H=1.6$), the cross-shaped shear surface occurred at 30 m foundation width ($B/H=3.0$). For the 40 m-foundation width ($B/H=4.0$), the cross-shaped shear surface cannot be seen; squeeze breakdown occurred at both sides of the lower end of the foundation. The calculation of the bearing capacity of squeeze breakdown was performed by assuming that the clay under the foundation was pushed to both sides due to the application of the upper load. Somewhat complicated destruction forms can be seen in figures 5(e) and (f) that show the occurrence of the fan shape failure mode and rigid passive mode at 45° . Although the simulation could not correctly provide the failure mode shown in figure 4, the other bearing capacity values and failure modes obtained with this theory were mostly correct.

Table 1 Comparison of numerical result and theoretical value

	B/H	Bearing theoretical value kN/m^2	Bearing numerical analysis value kN/m^2	Numerical analysis value / Theoretical value	N_c (Numerical analysis value)
General failure mode	-	51.40			
Clayey squeeze breakdown	1.00	46.40	52.71	0.88	5.27
	1.40	48.40	52.53	0.92	5.25
	1.60	49.40	52.93	0.93	5.29
	3.00	56.40	58.78	0.96	5.88
	4.00	61.40	63.91	0.96	6.39
	5.00	66.40	69.23	0.96	6.92
	6.00	71.40	74.47	0.96	7.45

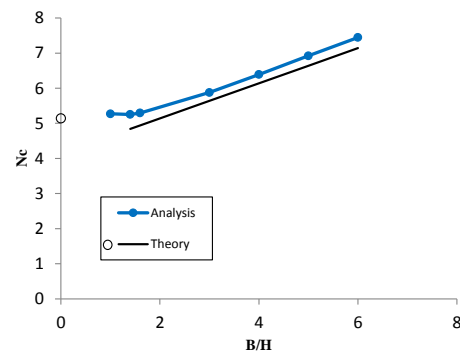


Fig. 3 Relationship between N_c and B/H .

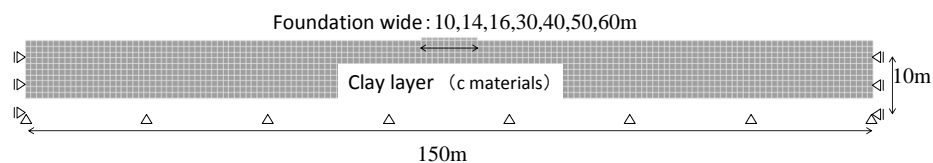


Fig. 2 Analysis mesh.

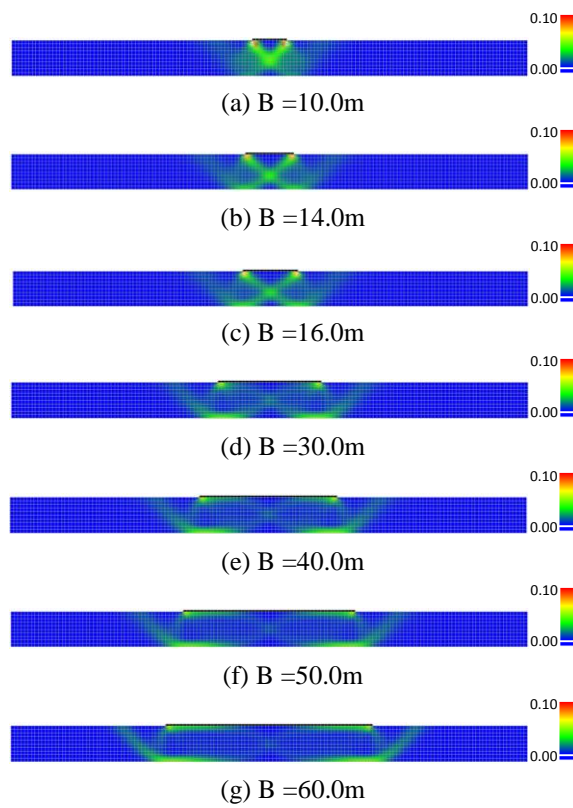
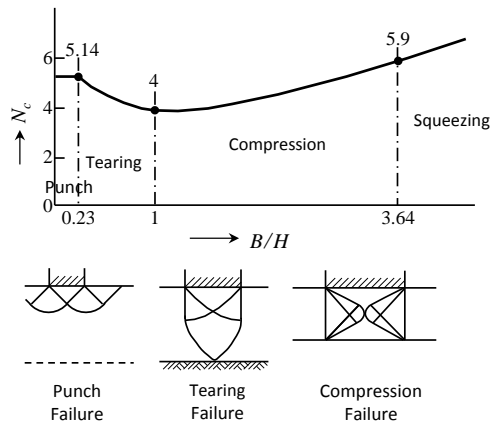


Fig. 5 Contours of shear strain at the failure.

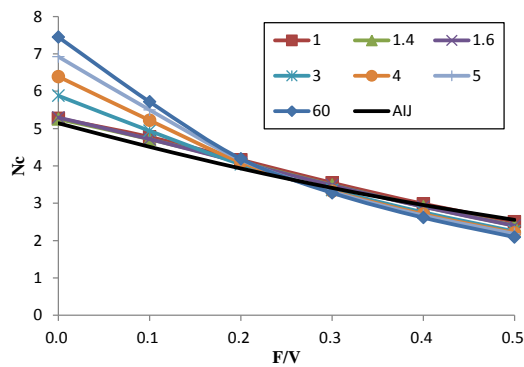


Fig. 6 Relationship between N_c and B/H (Analysis).

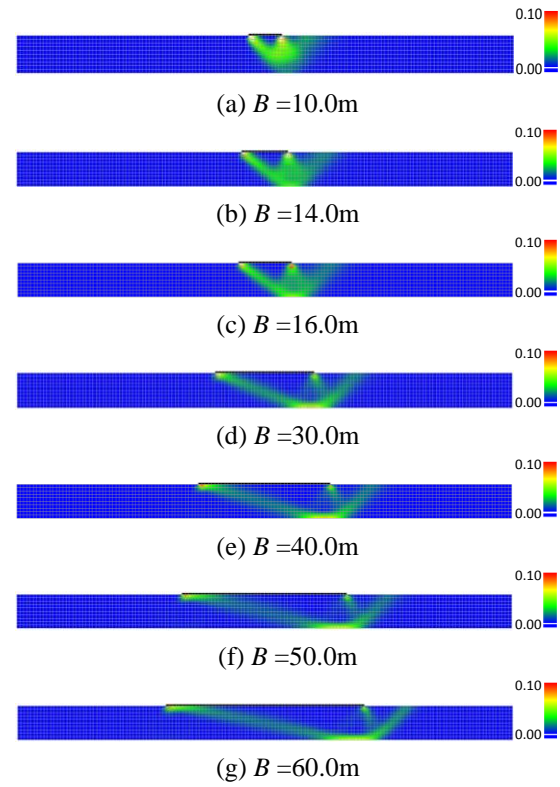


Fig. 7 Shear strain contour at $F/V=0.1$

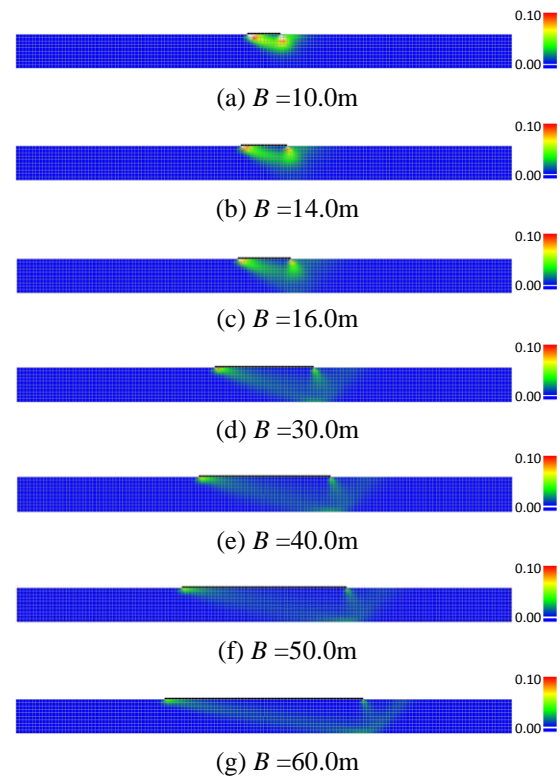


Fig. 8 Shear strain contour at $F/V=0.3$

Inclined bearing capacity

Simulations were performed for both the vertical and horizontal load. Figure 6 shows the numerical results of the relationship between N_c and F/V using AIJ equations; the legend shows the B/H . In the case of $F/V=0$, N_c increases as B/H increases. However, in the case of $F/V=0.2$, the value of each B/H are almost the same. In the case of a larger F/V , a large value of B/H corresponds to a small supporting force. In the AIJ equation (3), the general failure mode was adopted considering the inclined load as the following; however, the inclined load of the squeeze breakdown was not described.

$$i_c = (1 - \theta/90)^2 \quad (4)$$

where θ is the inclination angle ($^\circ$).

For $F/V > 0.2$, the numerical results are nearly equal to those obtained by equation (4). It is therefore indicated that the general failure mode occurred instead of squeeze breakdown. Figures 7 and 8 show the contours of shear strain at the failure point for each foundation width. At large F/V , a large value of B/H is not obtained at the squeeze breakdown because the failure area becomes shallow. However, when both B/H and F/V are large, the failure slip is restricted to the bottom. Therefore, it was considered that the opposite condition occurred, which entails that the bearing capacity associated with a large B/H is smaller than that with small B/H . In earthquake architectural design, the value of $F/V > 0.2$. When detailed bearing capacity analysis is not performed for the case of a large B/H , it is considered better to use the bearing capacity value of the general failure mode obtained by equation (3) for safety.

SIMULATION OF CLAYEY SQUEEZE BREAKDOWN WITH INITIAL LOAD

Analysis conditions

In order to consider the load during an earthquake, the initial vertical load V_0 , horizontal load H_0 , and moment M_0 were introduced as shown in figure 9. Both in-phase and anti-phase moments against the earthquake direction were considered. The ultimate vertical bearing capacity was calculated using rigid-plastic FEM under the initial load conditions listed in table 2. The unit weight of the building (3.3 stories, 10 kN/m² per floor) was assumed as $\gamma = 3$ kN/m³. Three cases with different spread widths (10 m, 30 m, 60 m) and two cases with different heights (1, 1.5 times high were considered. The horizontal force and moment were assumed to be applied at the midpoint of building height. The inclined load was applied to the foundation as the distribution load divided into horizontal and vertical components. "Kh" refers to the horizontal seismic intensity.

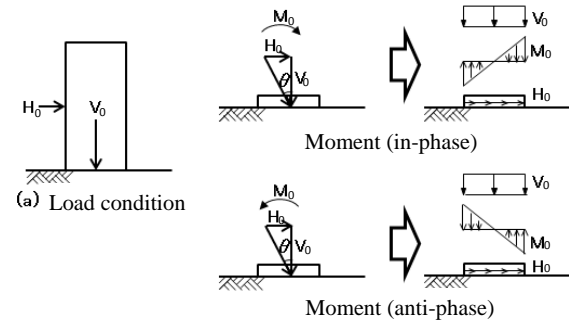


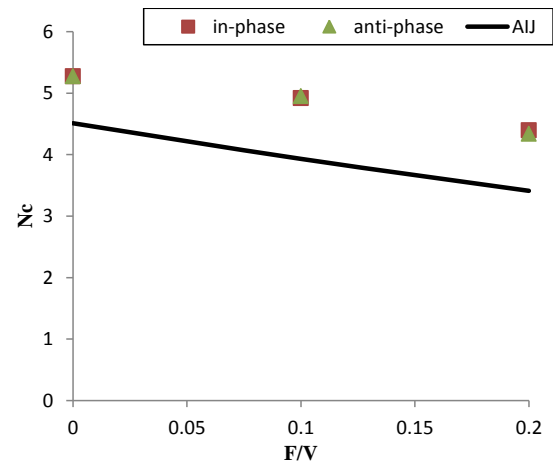
Figure 9 Initial load conditions for rigid-plastic FEM

Table 2 Analysis conditions

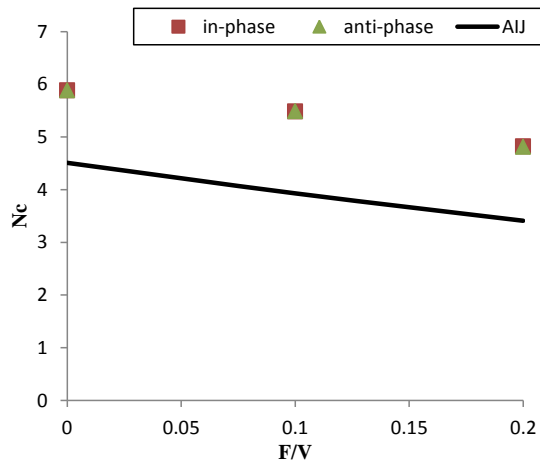
Foundation wide(m)	10	30	60
HeightH(m)	1B	0.3B,0.5B	0.15B,0.25B
Horizontal seismic intensity Kh	0.1,0.2		
Moment direction	in-phase, anti-phase		

Numerical results

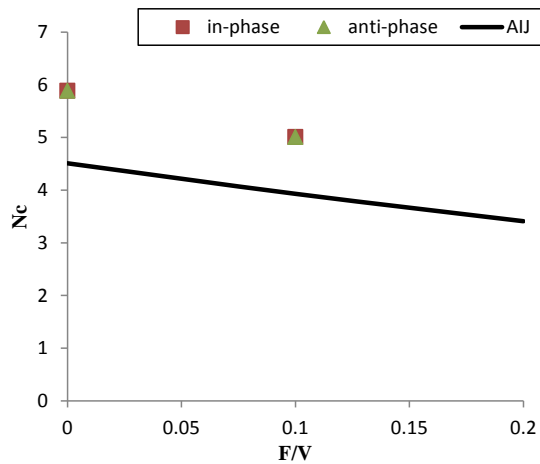
Figure 10 shows the results of the simulation. As with the inclination load consideration, the value of N_c decreased as F/V increased. The values obtained by numerical analysis were larger than those by AIJ. Figure 11 shows the contours of the shear strain at failure at $B=10$ m, $Kh=0.2$, $H=1B$ and $B=60$ m, $Kh=0.2$, $H=0.15B$. For the first condition, each N_c was almost the same. Similar to the shear strain distribution, there are differences in the occurrence of shear faces on the left and right, but general failure mode occurs. In contrast, for the second condition, the value of anti-phase is larger than that for in phase. It is considered that the anti-phase mode is closer to the squeezing breakdown along only the vertical direction. In fact, when assuming a large earthquake, the assumed horizontal force and moment do not change, and the margin of the vertical support force is important. Because the value obtained by the analysis is larger than the value of AIJ including the examination of the previous inclined load, it can be said that the design specification of the AIJ entails lesser risk.



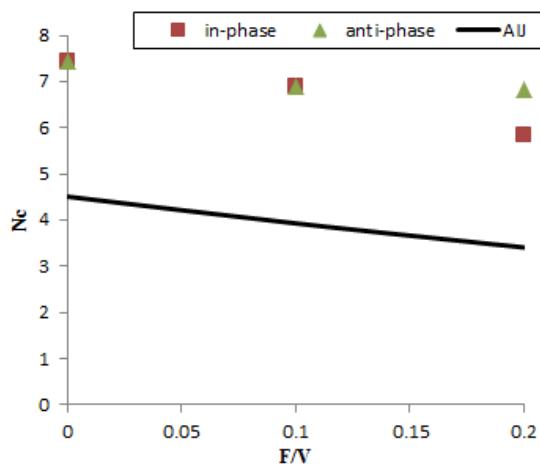
B=10 m, H=1B



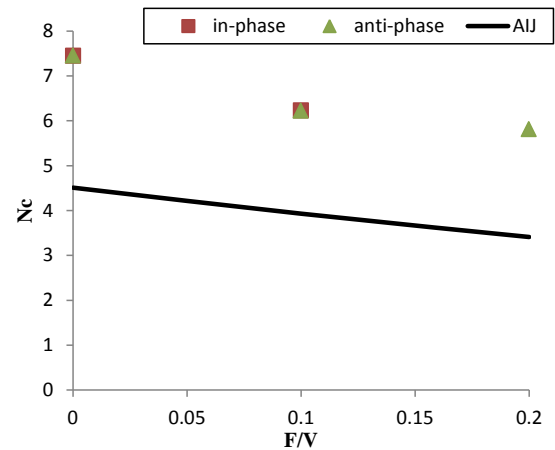
B=30 m, H=0.3B



B=30 m, H=0.5B



B=60 m, H=0.15B



B=60 m, H=0.25B

Figure 10 Relationship between N_c and F/H for in and anti-phase

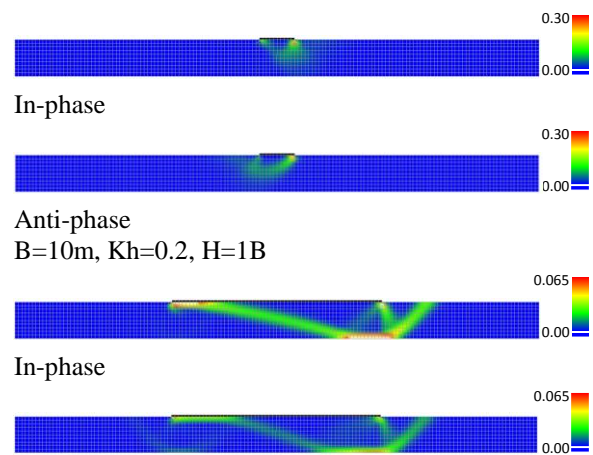


Figure 11 Contours of shear strain at the failure

CONCLUSION

The vertical failure mode changes from the general failure mode to squeezing breakdown with increasing B/H . At $B/H=3$, the cross-shaped failure mode occurred at the ground under foundation. Shearing blocks occurred at both ends of the foundation. For $B/H>4$, the cross-shaped failure mode cannot be seen and shear failure occurred from both sides of the foundation.

In the failure mode with inclined load, at small F/V , the failure mode differed depending on the B/H . For $B/V>0.2$, the failure mode remained the same regardless of B/H . From the results of numerical analysis, it is considered that it is necessary to consider the corrective inclined coefficient for the general failure mode.

In the vertical failure mode with initial load, considering an earthquake, the N_c values were larger than those obtained by the AIJ equation. This further

implies that it is necessary to consider the corrective inclined coefficient for the general failure mode.

REFERENCES

- [1] Terzaghi, K. and Peck, R.B. : Soil Mechanics in Engineering Practice, John Wiley & Sons, pp. 472-569. 1996.
- [2] Tamura, T., Kobayashi, S., and Sumi, T. : "Limit analysis of soil structure by rigid plastic finite element method", Soils and Foundations, Vol.24, No.1, pp.34-42.1984.
- [3] Asaoka, A. and Ohtsuka, S. : "The analysis of failure of a normally consolidated clay foundation under embankment loading", Soils and Foundations, Vol.26, No.2, pp.47-59. 1986.
- [4] Yamaguchi, H. : Theory and applications of bearing capacity and deformation of shallow foundation, Soil Japanese Society of Soil Mechanics and Foundation Engineering, No.2, pp.85-91, 1982. (In Japanese)
- [5] Architectural Institute of Japan, AIJ (1988,2001), Recommendations for design of building foundation , pp.105-111, 2001. (In Japanese)
- [6] Kaneda, K., Tanikawa, T., Hamada, J., Ohtsuka, S., and Aoki, M. : "Analysis of ultimate bearing capacity of footing of two layered clayey soil system by rigid plastic finite element method", AIJ Journal of technology and design, Vol.19, No.43, pp 881-885. (In Japanese)
- [7] Meyerhof, G.G. and Chaplin, T.K., : "The compression and bearing capacity of cohesive layers", British Journal of Applied Physics, Vol.4, No.1. 1953.

CORRELATION AMONG THE SOIL PARAMETERS OF THE KARNAPHULI RIVER TUNNEL PROJECT

Khondoker Istiak Ahmad, Masnun Abrar, Hossain Md. Shahin, Sultan Al Shafian and Soumik Nafis Sadeek
Islamic University Technology, Bangladesh

ABSTRACT

Defining correlation among the soil parameters and strength properties has become a popular research topic among the soil mechanics researchers in recent years. As conducting laboratory test are quite tiresome and time consuming, investigating correlation among the soil parameters using collected data will help to understand the characteristics of soil effortlessly. This research aims at stating a correlation analysis between the strength parameters and index properties of the soils of Karnaphuli river tunnel project site . Around 120 borings were done to determine both the index and strength properties of the soil in the laboratories. Along with the correlation, multiple linear regression analysis was developed for the cohesion and liquid limit along with the collected explanatory variables. This equation supports to adopt different characteristics of the soils of Karnaphuli River, and additionally a statistical significance of correlation among different soil parameters have also been unfolded. Finally the equation is compared with some of commonly used classical soil mechanics equation to determine the acceptability of this correlation.

Keywords: Index Properties, Strength Parameters, Regression Analysis, Correlation.

INTRODUCTION

Determining strength parameters and index properties of a soil sample is a time consuming process. By knowing the strength parameters (e.g shear strength) will help to determine soil characteristics and to be useful for designing future underground structures. Researchers have tried long for stating correlation between strength parameters and index properties of soil. Smith et al. [1] established a correlation among the index properties and other parameters of soil in Israel. Correlation analysis for rock and other marine soils have been established many time by the researchers. But in the developing countries like Bangladesh where soils are characterized as soft soil in a bulk, there are little attempts have been made on correlation analysis. As fas as Authors' knowledge none of the studies have conducted correlation analysis among different parameters of soil in context of Bangladesh.

This study aims at establishing a correlation between the strength parameters and other index properties of the soft soil of Karnaphuli River tunnel project. Around one hundrerd and twenty (120) bore hole samples have been collected for testing and determining various strength and index properties of the soil. Considering depth and other geotechnical properties of soil, first a multivariate statistical analysis i.e. Multiple linear regression is established which comprises the statistical significant variables and then a correlation analysis is established among the soil parameters with proper statistical techniques.

STUDY AREA

The soil samples studied for this project have been collected from the *Karnaphuli River tunnel Project Site of Chittagong*, the first ever underwater tunnel project going to be constructed in Bangladesh. This Multi-lane Road Tunnel project site is located at the sea entrance of River Karnaphuli of Chittagong suburb, and its west coast starting point is connected with Coastal Road.

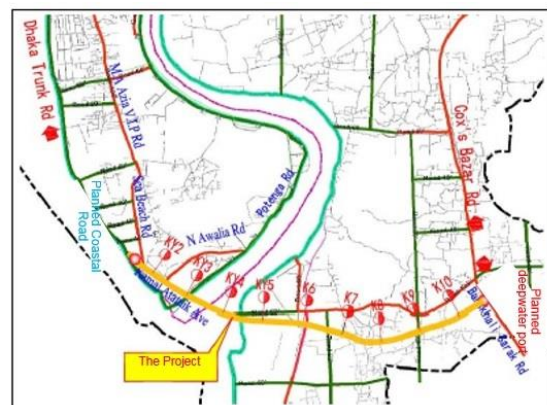


Fig. 1 Location of the Karnaphuli River Tunnel Project Site [2]

Soil samples have been collected from various parts of this project site. The depth of common boreholes is 20 m under the tunnel design bottom surface, while for controlling boreholes, they should be 40 m under the design bottom surface or 5 m into the complete bedrock at least. The number of

controlling boreholes account for 2/5 of the total number of boreholes.[2]

METHODOLOGY

Multiple Linear Regression (MLR) has been used to establish a multivariate equation with statistical significant explanatory variables. MLR has been preferred by many other researchers for establishing suitable relationships among various parameters of both rocks and soils. [3]

Multiple Linear Regression

The most widely used regression model to analyze a dependent variable on the basis of change in more than one independent variables is the Multiple linear regression (MLR) model which is given by

$$y = X\beta + \varepsilon \quad (1)$$

in Eq. (1), where, 'y' is the dependent or response variable, 'X' is the vector of explanatory variables; ' β ' is a vector of parameters to be estimated and ' ε ' is an error term. In this research, an effort has been made to create a relationship among different geotechnical parameters with cohesion and liquid limit. Around 15 variables are selected to formulate this model. In statistics it is very common to conduct hypothesis test to find the statistical significant variables and put it into the model. For this reason, t-test was applied with 5% significance level which means, if the p-value of any variable is less than 0.05, than the null hypothesis will be rejected [4]

Table 1 Summary of the Multiple linear regression (Only statistical significant variables are included)

Variables	Liquid Limit	Cohesion
Stress	0.0091 (<0.001)	0.61 (<0.001)
Void ratio	120.55 (<0.001)	-
*N	102.16 (0.03)	97.37 (0.02)
Dry density	102.16 (0.03)	-
Liquid limit	-	-16.19 (0.017)
Total	75	75
Observation		
R ²	66%	65%
Adjusted R ²	64%	63%
F-statistics	33.33	41.54

*N = Natural mass density
(All the parameters are of 95% of confidence interval, in bracket p-values are given)

Table 1 represents the summary results of the statistical model for two dependent variables (Liquid limit and Cohesion). The model is developed in 'R' - an open source statistical software.

To measure goodness of fit of the model, squared R is taken to show how close the data are to the fitted regression line. Squared R assumes that every predictor in the model explains the variation in the response variable. It gives the percentage of explained variation as if all predictors in the model affect the response variable, whereas the adjusted R-squared gives the percentage of variation explained by only those independent variables or predictor that in reality affect the response variables. To measure the model overall significance F-statistics value tested and evaluated. It can assess multiple coefficients simultaneously.

Correlation

Correlation describes the degree of relationship between two variables. Product moment correlation efficient (r) can be measured to identify the correlation among different important geotechnical parameters. The equation is [4]:

$$r = \frac{s_{xy}}{\sqrt{s_{xx}s_{yy}}} \quad (2)$$

where,

$$s_{xy} = (\sum xy) - nx_{avg}y_{avg}$$

$$s_{xx} = (\sum x^2) - nx_{avg}^2$$

$$s_{yy} = (\sum y^2) - ny_{avg}^2$$

It is also tested whether the correlation between two variables are statistical significant or not. So, a hypothesis test is introduced with 5% significance level following two tailed test. Table 3.2 shows the correlation matrix among different independent variables [5]

Table 2 represents the correlation values of the sample data that has been used for establishing the correlation among the soil parameter

Table 2 Correlation matrix of independent variables

	σ	W	N	e	LL	PL	PI
σ	1						
W	-0.54*	1					
N	0.62*	-0.64*	1				
e	-0.61*	0.93*	-0.86*	1			
LL	0.13	0.56*	-0.21	.5	1		
PL	0.14	0.54*	-0.20	0.49	0.99	1	
PI	0.11	0.57*	-0.21	0.50	0.99	0.98	1

(* represents statistical significant with 5% significance level)

In the following Table 2, the abbreviations of the short terms are :

σ = Stress

W= Water Content

N= Natural mass density

e= Void ratio

LL = Liquid limit

PL= Plastic limit

PI =Plasticity index

RESULTS AND DISCUSSION

Using proper regression analysis, following two equations has been derived.

$$\text{Cohesion} = -158.01 - 16.19(LL) + 0.61(\sigma) + 97.37(N) \quad (3)$$

$$LL = -296.82 + 0.0091(\sigma) + 120.55(e) + 38.33(N) + 102.16(\text{Dry density}) \quad (4)$$

In Eq 3 for one unit increase in LL, the cohesion will decrease by 16.19 unit. For one unit increase of stress, the cohesion will increase by 0.61 unit .For one unit increase in natural mass density, cohesion will increase by 97.37 unit.

In Eq 4, for one unit increase in stress liquid limit will increase by 0.0091 unit. For one unit increase in void ratio the liquid limit will increase by 120.55 unit. For one unit increase in natural mass density, liquid limit will increase by 38.33 unit. and lastly for one unit increase in dry density, the liquid limit will increase by 102.16 unit.

From table 2, we can observe that the best positive relationships exist between liquid limit – plastic limit, liquid limit-plasticity index, plastic limit-plasticity index and void ratio-water content for obvious reasons as there are theoretical relationships among these parameters. Marginal positive degree of relationship exists between natural mass density-stress, liquid limit-water content, plastic limit-water content, plastic limit-water content, void ratio with plastic limit and liquid limit. There are exists some negative correlation among variables that means if one parameter increases in a specific unit others will decreases and vice-versa. There are some statistical insignificant variables i.e. they do belong to the null hypothesis, cannot be rejected.

CONCLUSION

The relation that has been established among the soil parameters is completely based on statistical approach which will be very much helpful for determining the proper characteristics of the soils of Karnaphuli River Tunnel project in future.

REFERENCES

- [1] Smith, C.W., Hadas, A., Dan, J. and Koyumdjisky, H., 1985, "Shrinkage and Atterberg limits in relation to other properties of principal soil types in Israel", *Geoderma*, 35:47-65.
- [2] China Communications Second Highway Survey, Design and Research Institute Co. Ltd., "Detailed Investigation Report of Engineering Geology-Multi lane Road Tunnel Under River Karnaphuli Chittagong Bangladesh", Volume I and II ,October 2016
- [3] Mishra, D.A., Basu, A., "Estimation of uniaxial compressive strength of rock materials by index tests using regression analysis and fuzzy inference system", *Engineering Geology*, Vol. 160, 2013, pp. 54-68
- [4] Montgomery, D.C., Peck, E.A., Vining, G.G. (2012). *Introduction to Linear Regression Analysis* (Fifth Edition), John Wiley and Sons Ltd
- [5] Kottegoda, N.T., Rosso, R. (2008). *Applied Statistics for Civil and Environmental Engineers* (Second Edition), Blackwell Publishing, John Wiley and Sons Ltd

A STUDY ON COMPRESSION AND SOLIDIFICATION CHARACTERISTICS OF VOLCANIC SAND

Katsuhiro Shibano¹, Naoaki Suemasa¹, Kazuya Itoh¹, Tsuyoshi Tanaka¹, Hiroto Akimoto¹
Yoshitaka Yanagihara², Yuan Zhang², Kiyoshi Numakami², Yasushi Furugaichi²
Katsuya Suzuki³, Shun Habara³

¹Urban and Civil Engineering, Tokyo City University, Tokyo, Japan

²Tokyu Construction CO., LTD., Tokyo, Japan

³Nitto Seimo CO., LTD., Hiroshima, Japan

ABSTRACT

In Japan called ‘Nation of volcanoes’, the majority of the land is mountain area and the volcanic activity is still frequent. It is feared that huge amount of eruptive deposits such as volcanic ash could be generated and accordingly serious damage could be caused especially when some of the active volcanos erupts. At present, one of the eruptive deposits, Shirasu has been already variously used as concrete aggregate or road materials. In order to utilize other volcanic sands, however, sufficient investigation has not yet been conducted about the characteristics of eruptive deposits including the base material and the influence of both formation process and sedimentary environment. In this research, an attempt is made to use effectively volcanic ash as a new construction material. If volcanic ash can be compressed and formed in a block body, it can be used in various ways instead of being disposed of as a waste. One-dimensional compression tests were carried out using several kinds of volcanic ashes and the solidification states and the e -log p curves were investigated and compared. In addition, the fragment states of particles of the samples were confirmed after compression to verify the relationship between particle crushing and solidification.

Keywords: Frangible Sand, Volcanic Ash, One-Dimensional Compression, Solidification

INTRODUCTION

In 2003, Meteorological Agency of Japan defined 110 mountains in Japan as active volcanos which have erupted within the past 10,000 years or showed signs of unrest such as significant new gas emissions. Volcanic ash which consists of fine particles of pulverized volcanic rocks is created as eruptive deposit when volcano erupts and high-temperature rocks slide on the hillside of volcano. The appearance of volcanic ashes varies according to ways of eruption or types of volcano, where the color ranges from bright gray to black and the size ranges from almost the same as talc to a pebble. It is seen that thunder or lightning occurs because of collisions between floating small volcanic ash during volcano eruption. Fine volcanic ash spreads on the lee side with smoke and makes serious damage in the around areas.

In general, volcanic ash is disposed as waste because it has difficulty in reuse. At present, one of the eruptive deposits, Shirasu has been already variously used as concrete aggregate or a road material. The major characteristics of Shirasu are light but fragile in water. In addition, mixed with reinforcing materials to make up for its fragile property, Shirasu has been used for lightweight hard

blocks and roadbed. Due to its advantages such as durability, water retention and sound absorption, it is expected to replace asphalt or has potential to be used to reduce temperature rise of road surface [1]. It has been pointed out that sand particle crushing occasionally causes the specific behaviors of structure on sand such as unexpected large settlement of piles [2]. Such particle crush is continual to occur in volcanic soils even in low stress [3]. And also, it is revealed that interlocking effect caused by the particle crushing may develop cohesion of crushed sand although its effect decreases as the applied stress increases [4]. Therefore, if the particle crushing occurs excessively, it is thought that the interlocking effect may weaken. It means that if volcanic ashes are utilized as engineering materials such as Shirasu, it is necessary to grasp their compression and solidification properties.

In this paper, in order to examine the characteristics of several kinds of volcanic ashes, one-dimensional compression tests were carried out to investigate the relationship between particle crushing and solidification. The solidification state of the particles and the extent of particle crushing were evaluated from the result of one-dimensional compression test.

Table. 1. Sample Characteristics

Sample Name	Collection Place	Characteristics		
		Soil Particle Density (g/cm ³)	Cohesion (kPa)	Internal Friction Angle (°)
Hard Kanuma	Tochigi	2.373	15.745	24.313
Shirasu	Miyazaki	2.414	3.223	43.672
Kanuma	Tochigi	2.601	19.781	21.727
Fukushima Volcanic Soil	Fukushima	2.688	19.965	36.859
Pumice	Kagoshima	2.489	22.289	33.465
Lapilli	Akita Lake Towada	2.764	19.699	36.163

SAMPLE CHARACTERISTICS

The samples used in this study were as follows: Hard Kanuma Soil, Shirasu, Kanuma Soil, Fukushima Volcanic Soil, Pumice and Towada Lapilli. All samples were dried sufficiently in a drying kiln until their moisture content became less than 1%. Density soil particle tests, box shear tests and grain size analysis were carried out to measure the characteristics of each sample. The characteristics and the grain size distributions are shown in Table. 1 and Fig. 1, respectively. Shirasu and Pumice mainly composed of silicon dioxide include numerous aluminum oxide and iron oxide as well. Photo. 1 and 2 describe their state observed by an electron microscope. It can be confirmed that both have vitreous and indeterminately squared shapes.

ONE-DIMENSIONAL COMPRESSION TEST

Compression molding was conducted using a compression tester until the pressure reached 10MPa in a constant strain of 1%/min. Each sample was set into a solidification test apparatus so that its height became 5mm after compression. The e-log p curves obtained from the tests were shown in Fig. 2. Solidification by compaction molding of the sample was confirmed in Hard Kanuma, Kanuma and Pumice, although the other samples were fragile enough to crumble with a few shocks. In this paper, therefore, solidification was defined as a condition of self-sustaining without collapsing even if it is lifted up by a hand. As the characteristics of the samples in which solidification was able to be confirmed, the void ratio was large at its initial and greatly decreased beyond its yield point, at which stress the maximum curvature occurs in the e-logp plot. Since it is reported that particle crushing begins at its yield point when void ratio greatly decreases, the appearance of this yield point seems to be related to solidification of particle [5]. As for the samples in

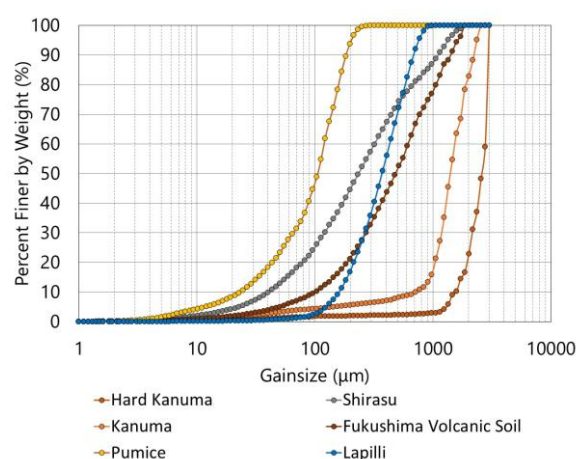


Fig. 1. Grain size distributions



Photo. 1. State observation by the electron microscope: Shirasu



Photo. 2. State observation by the electron microscope: Pumice

which solidification could not be confirmed, the initial void ratios were small and the yield points were unclear.

However, since initial void ratios vary according to the grain size distribution and the method of packing, it is difficult to use the initial void ratio as an indicator for the degree of solidification. Therefore, experiments were performed to grasp the degree of solidification with the decrease in void ratio from yield point. In the experiments, using the pumice in which solidification could be confirmed, applied compression pressure was changed stepwise from 1 to 15 kPa and the solidification state was observed in each step. The curves of e -log p are described in Fig. 3. As seen in the cases of more than 5 kPa of applied pressure in Fig. 3, the void ratios greatly decrease beyond the yield point. On the other hand, in the cases of 1 and 3 kPa of pressure, the void ratios didn't decrease too much and the samples easily crumbled. From the above, it is thought that the solidification of sample is attained by the compression with larger pressure than the yield stress.

Another series of the one-dimensional compression tests was performed using compression testing equipment which can provide a higher compression pressure than the compression tester used before. And as the solidification test apparatus used was not able to endure such high pressure, a compression container was used as shown in Photo. 3. As this testing machine is not suitable for setting constant-speed or detailed loading speeds, loading speed for these tests was roughly set at around 10%/min of specimen height. The sample of Kanuma Soil was excluded in this high-pressure test because of its large compressibility. The applied compression pressure was changed stepwise at 20, 40, 60, 80 and 100 MPa, and the state of solidification were confirmed at each pressure step. As the result of compression tests, the solidification was able to be observed in the specimens of Shirasu at more than 40 MPa. As for Towada Lapilli, although the solidification point was not able to be confirmed since the compression pressures were not applied in steps, solidification was able to be confirmed in the sample compressed to 100 MPa. The tendencies of decreasing void ratio were similar for most of samples, which show the decrease in a reverse S shape curve. It is thought that the particles were crushed with increase in compression stress

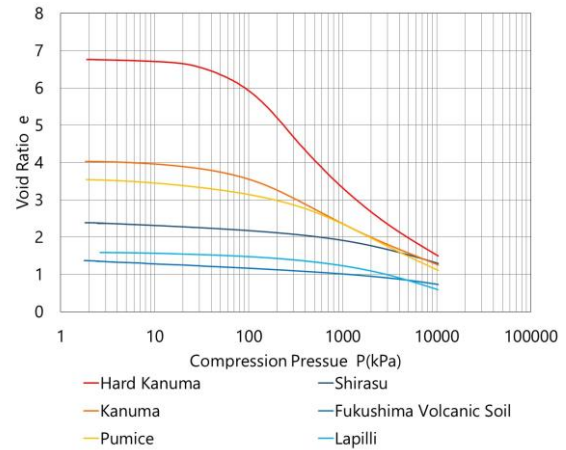


Fig. 2. e -log p relationships for the sample used

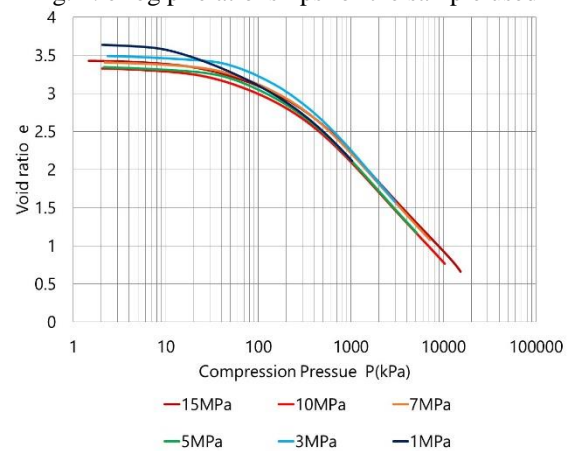


Fig. 3. e -log p relationships for Pumice

beyond the yield stress and particles had been interlocked with each other according as the void ratio decreased and solidified.

It focusses on the three inflection points in the e -log p curve obtained by the one-dimensional compression test. The pressure at which the void ratio in the e -log p curve begins to decrease sharply is named p_1 , the pressure at which the inclination becomes the maximum is defined as p_2 , and the pressure at which the decrease in the void ratio converges and the inclination does not change is called p_3 . For Shirasu, p_1 and p_2 are 1.5 MPa, 15 MPa, respectively, and p_3 cannot be determined yet, but assumed to be 100 MPa. For Pumice, p_1 , p_2 and p_3 are 0.2 MPa, 2 MPa and 60 MPa, respectively. From these results, it is considered that solidification of sample was confirmed at a compression pressure of 60 MPa or more. It is thought that particle crushing was accelerated by high pressure even in the case of the sample in which particle crushing was hard to occur and fine particles engaged each other and caused solidification.

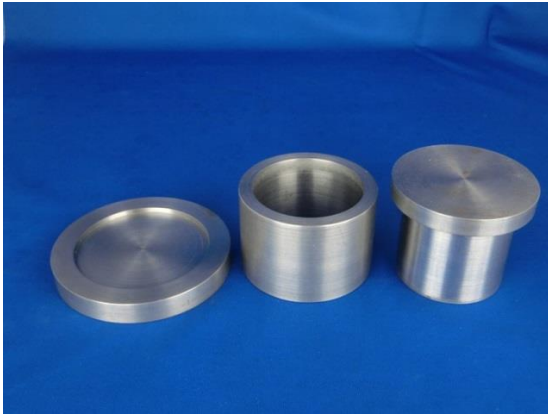


Photo. 3. Compression container

CRUSH EVALUATION FOR SAMPLE

In order to confirm the extent of compressed and crushed particles by one-dimensional compression tests, grain size analysis was conducted. The appearance of crushed particles was observed with a digital microscope (VHX-6000). Particles crush evaluation for the sample was carried out through these two results. The grain size accumulation curves of Shirasu and Pumice which were compressed stepwise describe in Fig. 4 and 5. The grain size distributions of Shirasu and Pumice which were compressed stepwise describe in Fig. 6 and 7. It is understood that the larger compression pressure was added, the more Shirasu particles were crushed. Especially, particles around 300 μ m were crushed into particles of less than 30 μ m. Compression of 100 MPa produced less crushing than that of 80 MPa. It was also found that by the increase in compression pressure, pumice particles of around 100 μ m were crushed into 20 μ m or less. Here, particle-crushing occurred at 40 MPa the most, which is thought to be due to dispersion of particles. For Towada Lapilli, particles of 100 μ m or more were crushed into smaller particles. The conspicuous crush of the particles was able to be confirmed in all samples and it was accordingly confirmed that high pressure compression was effective for crushing.

In order to show the relationship between particle crushing and solidification, crushing of particles has been numerically evaluated and various indexes have been proposed according to changes of particle sizes before and after the crush [6]. Among these indexes proposed, it is said that the reduction ratio of 15% diameter (D_{15} / D_{15}) obtained from grain size accumulation curves is effective as an indicator of particle fragmentation [6]. In this paper, therefore, the comparison of 15% diameter reduction rate and the evaluation of particle crushing were carried out. The relationship between the compression pressure of each sample and the

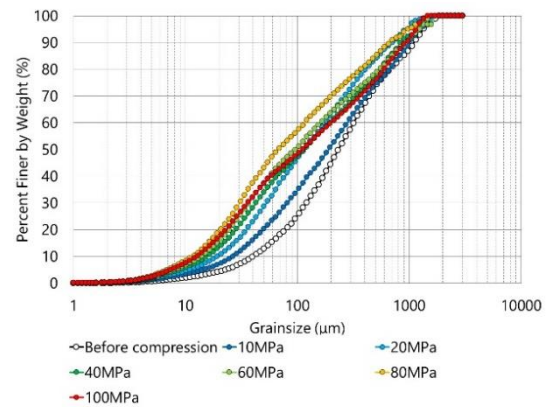


Fig. 4. Grain size accumulation curves of Shirasu

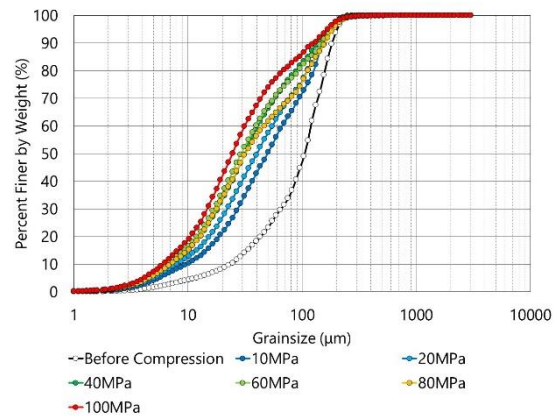


Fig. 5. Grain size accumulation curves of Pumice

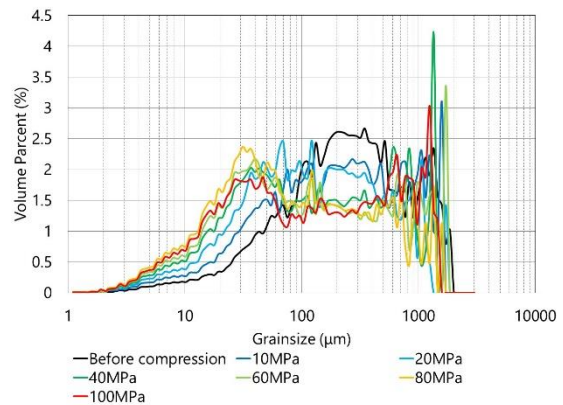


Fig. 6. Grain size distributions of Shirasu

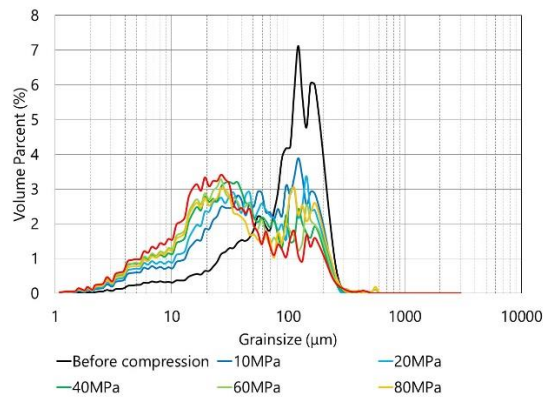


Fig. 7. Grain size distributions of Pumice

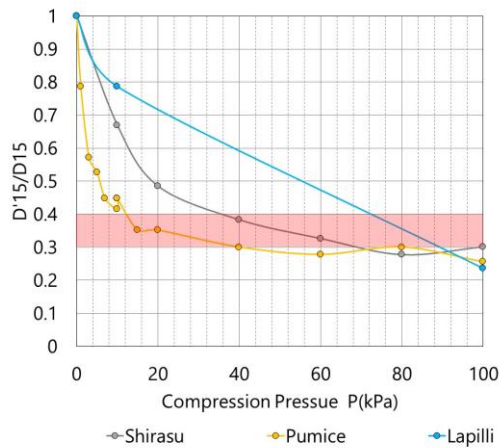


Fig. 8. Curves of diameter ratio to compression pressure

reduction rate D'_{15} / D_{15} is shown in Fig. 8. When checking at the compression pressures of the sample in which the solidification was confirmed, D'_{15} / D_{15} was in values of 0.3 to 0.4. In addition, it was able to be confirmed that the particle crushing was carried out more conspicuously as the compression pressure increased in all samples.

The digital microscope used to observe the crush situation of particles is shown in Photo. 4. Shirasu and Pumice were compared and the appearances of Shirasu and Pumice after the compression are shown in Photo. 5 and 6, respectively. The particle crushing was seen in Shirasu; however, solidification was unperformed because the particles were too large to be interlocked to each other. On the other hand, since the cross section of the particles have irregular shapes in Pumice, it is thought that the particles interlocked each other to perform solidification. Since Photo5 and Photo6 were used for confirming the crush states of the samples, quantitative evaluation can't be conducted.

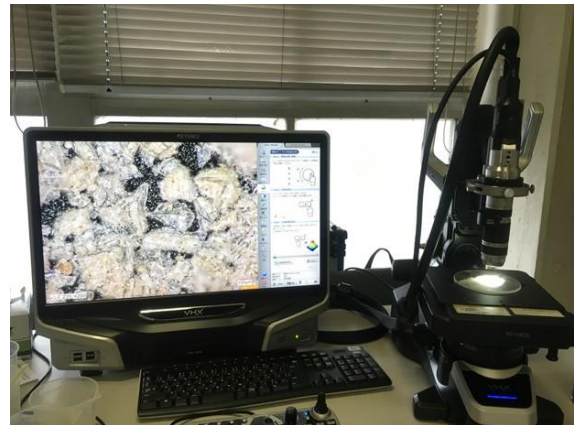


Photo. 4. Digital microscope



Photo. 5. State after the compression: Shirasu



Photo. 6. State after the compression: Pumice

CONCLUSIONS

It was confirmed that particle crushing greatly affected solidification of sand sample. Particle crushing began at the yield point shown in the e-log p curve of the sample that was able to be obtained by one-dimensional compression tests and particle

crushing was promoted as void ratios decreased. It is thought that particle crushing was accelerated by high pressure even in the case of the sample in which particle crushing was hard to occur and fine particles interlocked each other and caused solidification of sample.

Grain size analysis showed that particle crushing was accelerated with the increase in compression pressure. Since the reduction rate of 15% diameter is effective to be an index of particle crushing, particle crushing is likely to be related to the factor that D_{15} / D_{50} is a value of 0.3 to 0.4.

As observed with a digital microscope, the phenomenon that the crushed fine particles stuck into large particles, and interlocked each other contributed to solidification of sample. Easiness of crushing differs depending on the materials and it can be said that it is easier to solidify as the material is more prone to be crushed into the particles. It was confirmed that the minerals are hard to crush and the material with high mineral content is hard to solidify.

ACKNOWLEDGEMENTS

This work was supported by the Space Exploration Innovation Hub Center (TansaX), Japan Aerospace Exploration Agency (JAXA) under the Support Program for Starting Up Innovation Hub promoted by the Japan Science and Technology Agency (JST).

REFERENCES

- [1] Ryoichi, W. Tomoko, M. Hiroki, I. Koreyoshi, Y. "Development and empirical study of highly functional new soil materials with rainwater infiltration and water retention using Silas" Kyushu Engineering Management Association 2010 Results Meeting
- [2] Yukio, N. Yoshinori, K. Masayuki, H. Takayuki, H. Shuiti, M. "Particle fracturing characteristics of sand during one-dimensional compression" The 54th annual academic lecture meeting of Japan Society of Civil Engineers
- [3] Yoshinori, K. Yukio, N. Masayuki, H. Hidekazu, M. "Grains characteristics and one-dimensional compression properties of crushable soils" Journal of Japan Society of Civil Engineers vol. 2002 No. 701 P343-355
- [4] Keiji, K. Haruo, H. Shunji, U. "Bearing force characteristics of crushable ground considering the shape of soil particles" The 59th annual academic lecture meeting of Japan Society of Civil Engineers
- [5] Daisuke, K. Naotaka, K. Yukio, N. Masayuki, H. Norimasa, Y. Hidekazu, M. "Influence of solidification structure and physical properties of particles on one-dimensional compression characteristics of consolidated grain material" The 38th Japan National Conference on Geotechnical Engineering
- [6] Takeaki, F. "Index indicating the degree of the particle crush" Soil mechanics and foundation engineering 29(12), 64-65, 1981-12-25

NUMERICAL ANALYSIS ON MECHANISM OF LIQUEFACTION NOT ONLY IN MAIN EARTHQUAKE BUT ALSO IN AFTER SHOCK

Yukihiro Morikawa¹, Hide Sakaguchi², Akihiko Taira³ and Ho Cho⁴

^{1,4} Department of Civil Engineering, Nagoya Institute of Technology, Japan; ^{2,3} Japan Agency for Marine-Earth Science and Technology, Japan

ABSTRACT

During the 2011 Great East Japan Earthquake, liquefaction occurred in reclaimed ground in wide area of east Japan. In some areas, liquefaction happened in the aftershock was even more serious than that happened in the main shock. For this reason, the liquefaction that happened long time after the earthquake, caused not only by the main shock but also the multiple aftershocks within a short period of time, is intensively investigated in recent years. In this paper, particular attention is paid to the characteristic features of the liquefaction and its consequent consolidation-induced settlement. Based on the observed data, a series of dynamic-static analyses, considering not only the earthquake loading but also static loading during the consolidation after the earthquake shocks, are conducted in a sequential way just the same as the scenario of the earthquake. The calculation is conducted with 3D soil-water coupling finite element-finite difference (FE-FD) analyses based on a rotating-hardening elastoplastic constitutive model. From the analyses, it is recognized that small sequential earthquakes, which cannot cause liquefaction of a ground in an independent earthquake vibration, cannot be neglected when the ground has already experienced the liquefaction after a major shock. In addition, the aftershocks have great influence on the long-term settlement of the soil layers with low permeability. It is confirmed that the numerical method used in this study can describe the ground behavior correctly under repeated earthquake shocks.

Keywords: Repeated earthquake, Liquefaction, FEM, Settlement

1. INTRODUCTION

On March 11, 2011 14:46:18, a 2011 off the Pacific coast of Tohoku Earthquake (The Great East Japan Earthquake) happened with a magnitude of 9.0 in Richter, the greatest earthquake ever recorded in Japan history. Some typical characteristics of the Great East Japan Earthquake can be given, e.g., duration time of the seismic motion was very long, multiple big aftershocks happened in a relative short period of time and so on. According to an investigations after the earthquake [1]-[2], the damages due to tsunami and liquefaction were most serious recorded in Japan. Especially multiple aftershocks in a relative short period of time made damages spread, many existing structures in a wide area along coastal area suffered serious damages. The increase of excess pore water pressure (EPWP) and the development of anisotropy in the ground experienced liquefaction due to the main shock may cause instability of the ground and might cause re-liquefaction in the consequential aftershocks even if the aftershocks are not large. One of the interesting phenomena is that liquefaction not only happened in the main shock of earthquake vibrations, but also happened in the first aftershock whose acceleration was much less than that of main shock. However, it was thought that such a low level of shock was not strong enough to cause liquefaction.

Re-liquefaction happened in a first aftershock was even more serious than that happened in the main shock. This phenomenon indicates a very important fact that the sand boiling was accelerated by the aftershocks and more severe liquefaction occurred during the aftershocks at some sites.

In order to describe and predict correctly the ground behavior in such kind of repeated earthquake vibrations that may occur in future, it is necessary to clarify the mechanism of this geotechnical engineering problem. In this paper, a typical local site of reclaimed ground in Chiba Prefecture Japan, is selected for the numerical analyses. Based on the observed data, a series of repeated dynamic-static analyses, considering not only the earthquake loading but also the static loading during the consolidation after each earthquake shock, are conducted in a sequential way just the same as the scenario happened in the Great East Japan Earthquake.

2. CONSTITUTEIVE MODEL FOR SOILS AND FINITE ELEMENT METHOD

The numerical analyses and prediction are conducted with 3D soil-water coupling finite element-finite difference (FE-FD) analysis based on the Cyclic Mobility model (CM model) proposed by Zhang et al. [3]. CM model is a kind of rotating - hardening elastoplastic model. It can properly

describe the nonlinear behavior of non-cohesive soils under both dynamic and static loadings, especially the cyclic mobility of sand during liquefaction. With CM model and effective stress based FEM code, the mechanical behavior of the ground, such as the change of EPWP, the development of stress-induced anisotropy and the post-liquefaction consolidation, can be properly described not only in the liquefaction stage during the earthquake but also in the post-liquefaction consolidation stage in a unified way.

Numerical simulation is widely used the analyses of earthquake induced liquefaction. The object of the numerical simulation or prediction conducted in this paper is to reproduce or predict the overall mechanical behavior during and after the earthquakes, including the liquefaction and consolidation in repeated earthquake vibrations. The simulation was conducted using a 2D/3D soil-water coupled finite element method program named as DBLEAVES [4]. The applicability and the accuracy of the program have been firmly verified by shaking table tests and other various liquefaction phenomena [5]-[9].

CM model is adopted to simulate the static/dynamic behavior of the non-cohesive soils in the current study. CM model can consider the effect of the stress-induced anisotropy, the density and the structure of soils in a unified way. It can properly describe the mechanical behaviors of non-cohesive soils subjected to monotonic/cyclic loading under drained/undrained conditions. Based on the concepts of subloading [10] and superloading [11], the subloading, normal and superloading yield surfaces in p - q (mean principal stress - deviatoric stress) plane are adopted in the model to take into consideration the influence of density and the structure of soil, as shown in Fig. 1.

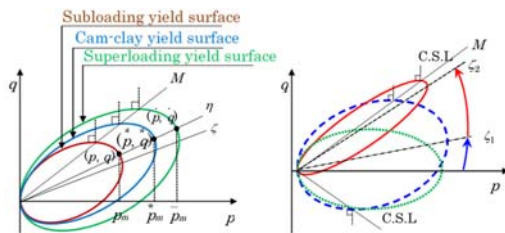


Fig.1 Yield surfaces and its change with the development of anisotropy.

Besides, the elliptical yield surfaces may change with the development of the stress-induced anisotropy. These characteristics enable the model to describe the cyclic mobility of non-cohesive soils. Eight parameters are employed, among which five parameters are the same as those in the Cam-clay model [12]. The others are parameter for controlling the collapse rate of the structure, loosing rate of the overconsolidation ratio and the developing rate of the

stress-induced anisotropy. All parameters have clear physical meanings and can be easily determined by undrained triaxial cyclic loading tests and drained triaxial compression tests. A detailed description and applicability of CM model can be found in the reference [3]-[9].

In the analysis with DBLEVES, the dynamic /static analyses are conducted using the same program, the same parameters throughout the whole calculating process. Newmark- β method is used and the integration time interval is 0.005 sec. Integration time interval is decided from interval time of observed earthquake motion and previous studies. Since it is expected that strong nonlinearity of the soil would occur, Rayleigh type of initial-rigidity-proportional attenuation is adopted and the damping values of the soils, the structure and the piles are assumed to be 2% and 10% for the first and second modes respectively. Before dynamic analyses of earthquake motions, a gravitational stress field analysis is carried out to obtain the initial effective stress of the ground.

3. NUMERICAL SIMULATION DURING AND AFTER EARTHQUAKE

3.1 Earthquake waves

A typical two directions earthquake motion at Simousa 2300m below the ground surface at Chiba Prefecture was recorded and it is selected to be the input earthquake motion in present analyses as shown in Figure 2. It is noted that the earthquake with a main shock followed by two aftershocks shakes in E-W and N-S directions at the same time. The main shock lasted for 300 seconds with a maximum acceleration of 0.85 m/s² and the first aftershock also lasted for 300 seconds with a maximum acceleration of 0.25 m/s² while the second aftershock lasted for 135 seconds with a maximum acceleration of 0.04 m/s². The interval between the main shock and the first aftershock was approximate 24 minutes and the interval between the two aftershocks was approximate 6 minutes. It should be mentioned herein that such a long duration of motions has been expected to be the major cause of the severe liquefaction and ground deformation.

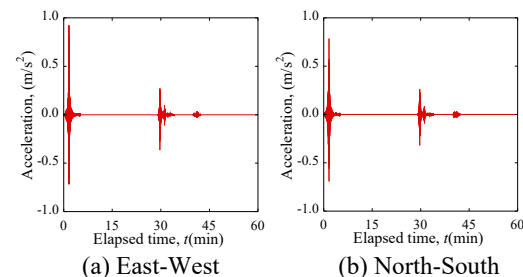


Fig.2 Recorded seismic motions at Shimous

(K-Net, <http://www.k-net.bosai.go.jp>)

3.2 Simulation for one column ground

3.2.1 Simulation scenario

The following 3 cases are considered to evaluate the influence of a main shock on its aftershocks and visa verse:

Case 1: Calculation is conducted in the same way just as the scenario happened in the Great East Japan Earthquake: (1) main shock, (2) 1440 seconds consolidation, (3) first aftershock, (4) 360 seconds consolidation, (5) second aftershock, (6) consolidation until the settlement of the ground ceased completely (50 years).

Case 2: Calculation is conducted only considering the main shock and consolidation after the main shock for a comparison with Case 1: (1) main shock, (2) consolidation until the settlement of the ground ceased completely.

Case 3: Calculation is conducted only considering the aftershock-1 for a comparison with Case 1.

3.2.2 Investigated site and analyses mesh for FEM

The investigated site was reclaimed by dredged soils that consist predominantly of sand or silt from the seabed of Tokyo Bay. Figure 3 shows the result of boring survey in the investigated site and the corresponding FEM mesh used in the calculation. The mesh is coincident with the boring data. It is one column ground with a 1.0m x1.0m horizontal square area. Each mesh has depth of 1m. In the case of dynamic analyses, an equal-displacement boundary, or called as periodic boundary, is applied to two side boundaries in x and y direction respectively to deal with the artificially introduced boundaries that do not exist in reality so that the incident waves are always allowed to transmit freely from the artificial boundaries introduced in FEM analysis in finite domain. The bottom is assumed to be fixed in horizontal and vertical directions. The drained boundary (ground water level) is set at the ground surface.

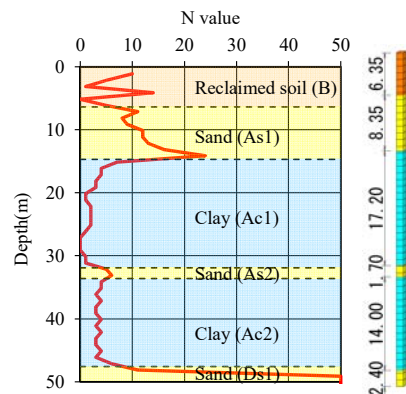


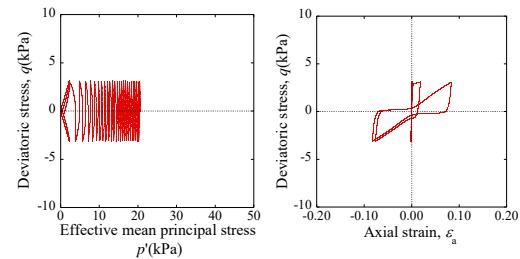
Fig.3 Geological profile and FEM mesh.

3.2.3 Material parameters

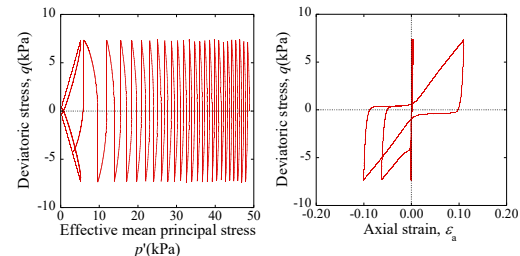
The material parameters used in calculation are shown in Table 1, and Figure 4 shows the theoretical estimation of the element behavior in undrained cyclic loading test. Since no cyclic testing data of soils are available, some of these parameters were determined with reference to the standard penetration tests, and others were estimated with reference to those of *Toyoura* sand. From the results, it is known that the strain accumulates as the number of cyclic loading increases, and liquefaction accompanied by cyclic mobility may occur in the reclaimed layer and loose sand layer at the investigated site. However, liquefaction will not occur easily in the loose silt layer.

Table 1 Material parameters

	B	As1, 2	Ac1, 2
Compression index λ	0.050	0.030	0.043
Swelling index κ	0.0064	0.0060	0.0090
Passion's ratio ν	0.300	0.300	0.300
Stress ratio at critical state R_f	3.650	3.650	3.000
Void ratio e_0 ($p'=98\text{kPa}$ on N.C.L)	0.870	0.870	0.920
Degradation parameter of structure a	2.200	2.200	0.100
Evolution parameter of anisotropy b_r	1.500	1.500	0.100
Degradation parameter of over-consolidation m	0.100	0.100	2.200
Unit weight γ (kN/m^3)	17.64	17.64	16.66
Permeability k (m/sec)	1.0E-4	1.0E-4	1.0E-9
Initial structure R_0^*	0.800	0.800	0.600
Initial degree of over-consolidation $1/R_0$	4.000	2.500	1.500
Initial anisotropy ζ	0.000	0.000	0.000



(a) Reclaimed layer (B layer, GL-3.50m)



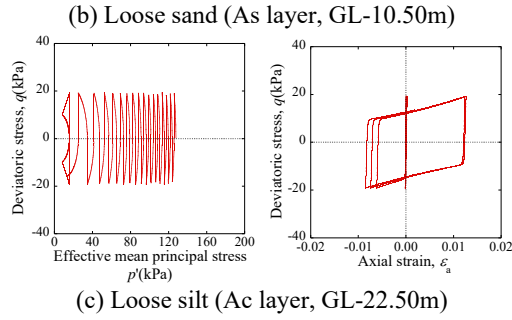


Fig.4 Effective stress paths and stress-strain relations.

3.2.4 Results and discussions

Figure 5 shows analysis results of the excess pore water pressure ratio (EPWPR) in the Case 1 and 3. Case 1 has a history of the main shock before the aftershock-1 while Case 3 did not have a history of the main shock. Here, EPWPR is defined as the ratio of excess pore water pressure to the initial vertical effective stress. Therefore, EPWPR equaling to 1 means liquefaction.

From the result, in the Case 1, for the sand (As1) and the clay (Ac1), liquefaction did not occur in main shock but excess pore water pressure (EPWP) kept increasing after the aftershocks because of the constant water supply from the lower layers. For the reclaimed layer (B), EPWPR increased up almost to 1 both in the main shock. And after the main shock, EPWPR of the reclaimed layer (B) decreased to about 0.70, but liquefaction occurred again in the aftershock-1 even though the maximum acceleration of the aftershock-1 is less than 25 gal. On the other hand, an increasing of EPWPR of Case 3 is much smaller than that of Case 1. Therefore, when a ground has not recovered from damage by main shock, a liquefaction easily occur by small aftershock.

From the above results, it is known that the accumulation of EPWP and development of stress-induced anisotropy induce ground liquefaction.

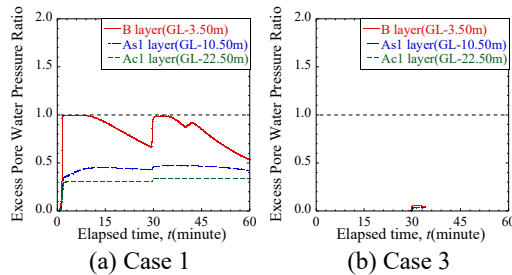


Fig.5 Results of the excess pore water pressure ratio.

Figure 6 shows a comparison of ground surface settlements after earthquake between the Case 1 and 2. In order to investigate the influence of aftershocks on the long-term settlement due to the consolidation

of ground, the simulation was conducted. The Case 1 has a history of the aftershocks but Case 2 did not have that. From the results, ground surface settlement of Case 1 with aftershocks than Case 2 without that. It can be concluded that both the liquefaction and the settlement are significantly affected by the aftershocks.

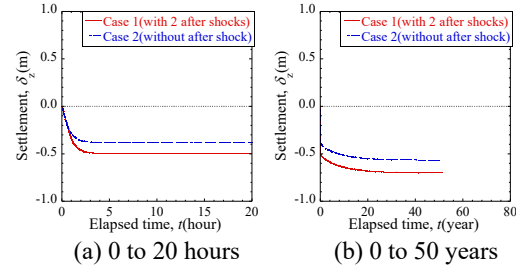


Fig.6 Ground surface settlements in Case 1 and Case 3.

3.3 Simulation for three-dimensional ground

3.3.1 Simulation scenario

In above simulation (Case 1) for one column ground, the calculation is conducted in the same way just as the scenario happened in the Great East Japan Earthquake: (1) main shock, (2) 1440 seconds consolidation, (3) first aftershock, (4) 360 seconds consolidation, (5) second aftershock, (6) consolidation until the settlement of the ground ceased completely (50 years).

3.3.2 Investigated site and analyses mesh for FEM

Figure 7 shows the plan view of the soil distribution based on the results of Swedish weight sounding test by the inhabitants during six months after the earthquake. Soil conditions in this area were also investigated by in-situ boring combined with the Standard Penetration Test (SPT), prior to and after the earthquake. According to the results of SPT and the Swedish weight sounding test, the whole area can be divided into three types of soil, that is, type A, type B and type C. Based on the results shown in Figure 7, the investigated site in the analysis can be divided into four areas shown in Figure 8. The dimension of the calculated area in FEM is 400m in length, 300m in width and 50m in depth. As to boundaries between different types of soil, transition zones were set to link the different types of soil as indicated in soil type AC, type AB, type BC, type ABAC, type BCBA and type CACB, as shown in Figure 8.

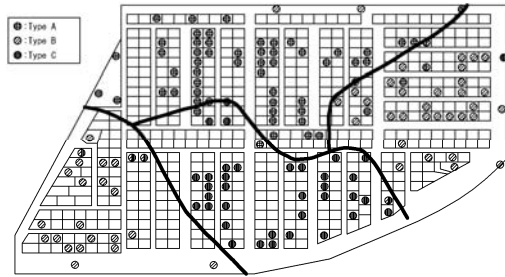


Fig.7 Plan view of the soil distribution based on the results of Swedish weight sounding test.

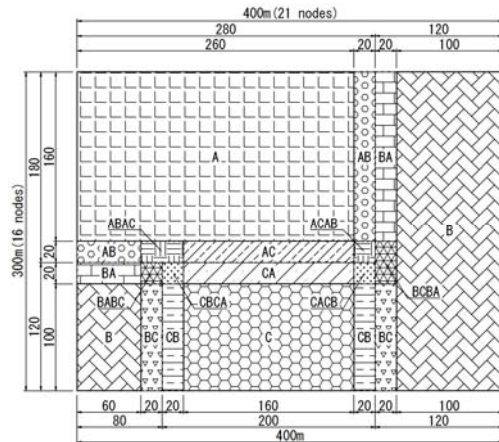


Fig.8 Plan view of the calculated area in FEM

Figure 9 shows the geologic profiles of the calculated area. All geologic profiles consist of loose sand and loose silt above G.L. -15m. The loose sand layer near the surface has a SPT N-value of 5~15 and it easily causing liquefaction.

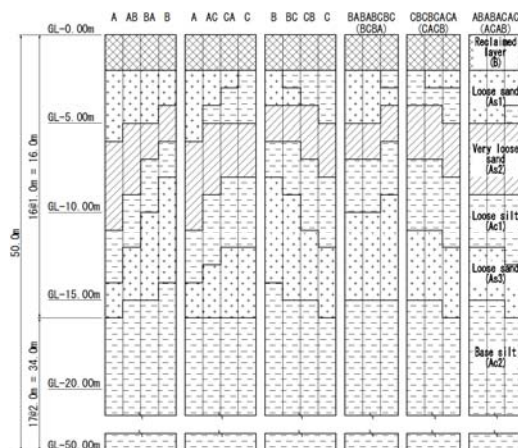


Fig.9 Geologic profiles of the calculated area.

Figure 10 shows the finite element mesh. As for the mesh size, the whole depth of calculation area is 50 m, the top 16 m is divided into 16 layers with each layer of 1m thickness and the below 34 m is divided in to 17 layers with each layer of 2 m thickness. In the analyses, the elements in each soil layer at the center of type A, type B (the larger part) and type C area are selected. In the case of dynamic analyses, an equal displacement boundary condition is applied for two side boundaries in x and y direction respectively to deal with the energy dissipation problem. The bottom is assumed to be fixed in all directions. The drained boundary (ground water level) is set at the ground level of -1 m.

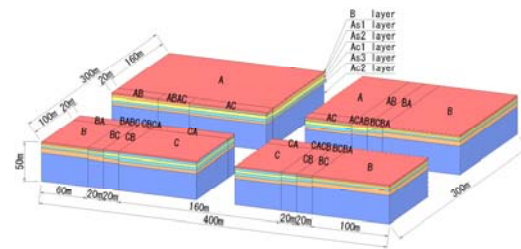


Fig.10 Finite element mesh

3.3.3 Material parameters

The material parameters used in calculation are shown in Table 2, and Figure 11 shows the theoretical estimation of the element behavior in undrained cyclic loading test. Even in this calculation, since no cyclic testing data of soils are available, some of these parameters were determined with reference to the results of SPT, and others were estimated with reference to *Toyoura* sand. From the analyses results, it is known that the strain accumulates as the number of cyclic loading increases, and liquefaction accompanied by cyclic mobility may occur in the reclaimed layer, loose sand and very-loose sand except loose silt land the base silt.

Table 2 Material parameters

	B	As1	As2	Ac1	Ac2
λ	0.030	0.030	0.043	0.207	0.207
κ	0.006	0.006	0.009	0.041	0.041
ν	0.300	0.300	0.300	0.350	0.350
R_f	4.600	4.600	4.600	3.500	3.500
e_0	0.720	0.720	0.880	1.100	1.100
a	2.200	2.200	0.100	0.100	0.100
b_r	1.500	1.500	0.100	0.100	0.100
m	0.100	0.100	0.100	3.800	3.800
γ (kN/m ³)	17.60	18.00	17.00	15.40	17.70
k (m/sec)	1.0E-5	1.0E-5	1.0E-6	1.0E-7	1.0E-7
R_0^*	0.800	0.800	0.600	0.600	0.600
$1/R_0$	5.000	5.000	3.000	2.500	2.500
ζ	0.000	0.000	0.000	0.000	0.000

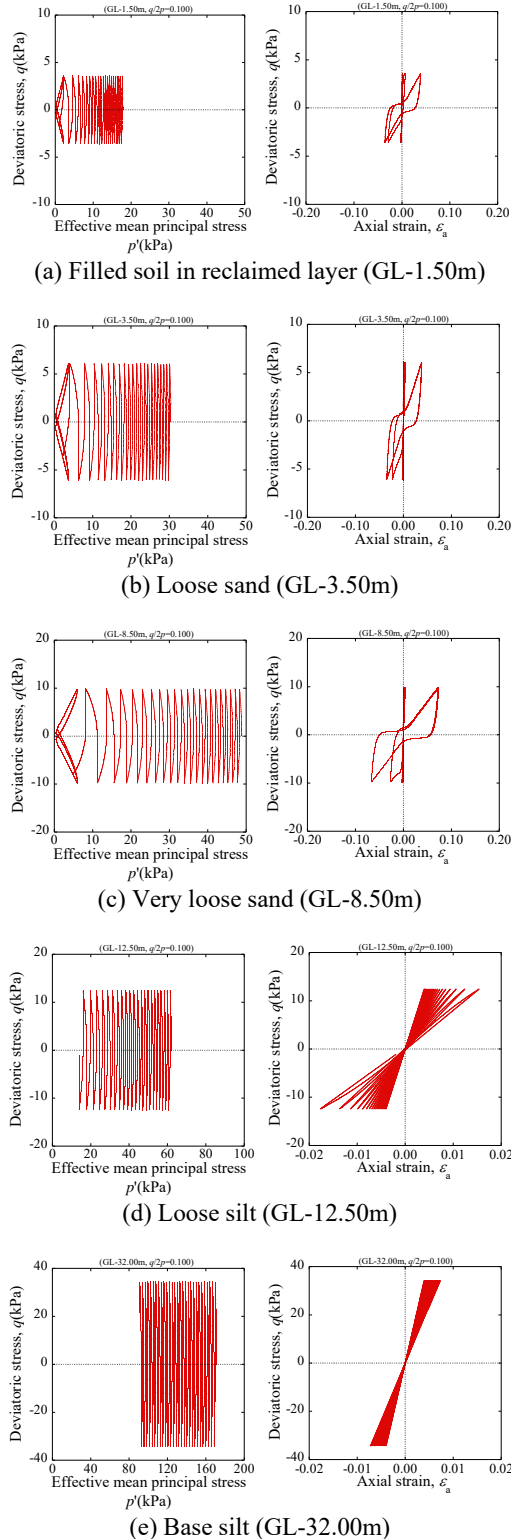


Fig.11 Effective stress paths and stress-strain relations

3.3.4 Results and discussions

Figure 12 shows the EPWPR with time in different soil layers at the center of type A, type B and type C respectively. For the upper loose sand (As1) in the area of type A, liquefaction did not occurred in main shock, but that occurred in after shock. In the area of type B, however, EPWPR in aftershock is smaller than that of main shock. For the very loose sand (As2) in the areas of type A and B, EPWPR raised up almost to 1 in the aftershocks although they were much smaller than the main shock. In the area of type C, however, liquefaction occurred seriously in both the main shock and aftershocks. For the loose silt (Ac1), it did not liquefy anyhow but EPWP kept increasing after the aftershocks because of the constant water supply from the lower layer of whole ground. For the lower loose sand (As3) in the area of type B, liquefaction occurred in the main shock and although EPWP decreased somehow after the main shock the ground liquefied again in the aftershocks. In the areas of type A and C, however, EPWPR was smaller than that of type B.

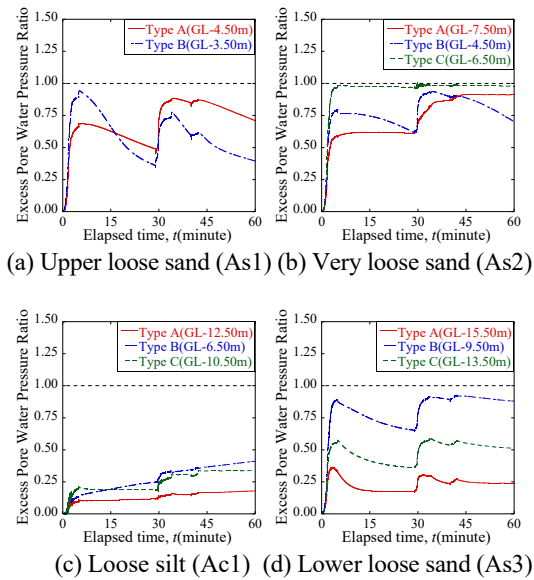


Fig.12 Excess pore water pressure ratios in each area.

Figure 13 shows the distribution of EPWPR at different depths. The left side of the figure is the EPWPR immediately after the main shock and the right of the figure is the EPWPR immediately after the aftershock-1. At the depth of 6m below the ground surface, liquefaction area due to the main shock was clearly smaller than that of the aftershock. In other words, liquefaction occurred in the aftershock was more serious than that of the main shock in the area of type A and type C. At the depth of 8m below the ground, liquefaction only occurred in the area of type

A after the aftershock.

In general, the EPWPR in all areas and soil types may increase again in aftershock.

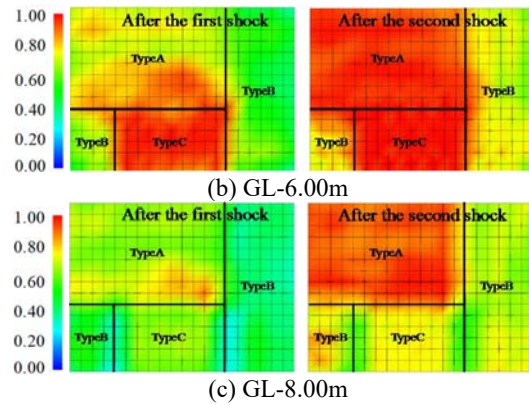


Fig.13 Distribution of EPWPR at different ground levels (Left: main shock, Right: aftershock-1)

Figure 14 shows the calculated distribution of settlement of ground surface. Six hours after the earthquake, an uneven deformation appeared in the area of type C. In this area, maximum amount of upheaval of the ground reach about 0.5m while the ground in types A and B settled about 0.5m. This uneven ground settlement was observed extensively in the field survey. Photo 1 shows the uneven settlement in roadways near the observed site. However, according to the analyses, the ground of all areas will turn out to be settled down 0.25m to 0.90m in 50 years after the earthquake, as shown in Figure 14 (b).

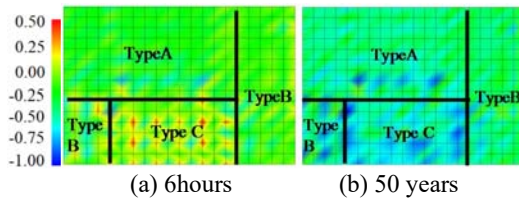


Fig.14 Distribution of settlement of ground surface.



Photo 1 Uneven settlement near the observed sites

3.3.5 X-ray CT image of geological features

Figure 16 shows the photograph and X-ray CT images of core sections drilled immediately after the liquefaction at calculated area [13]. A very important result we have got in this research is that the liquefied soil strata were perfectly identified with X-ray CT images. The pink line next to the CT image indicates the liquefied soil layers that distributed at the depth of 6.2m to 8.6m, where the thin strata of reclaimed ground that was observed clearly at the up strata from 2.0m to 6.2 m, suddenly disappeared due to the liquefaction. This observed phenomenon was remarkably similar to the calculated results showed in Figures 13, 14. It is therefore reasonably to say that the analysis method based on CM model, used in this study, can well describe the actual situation of the liquefaction in main shock, the re-liquefaction in aftershock, and the consolidation and settlement of ground after multiple earthquakes.

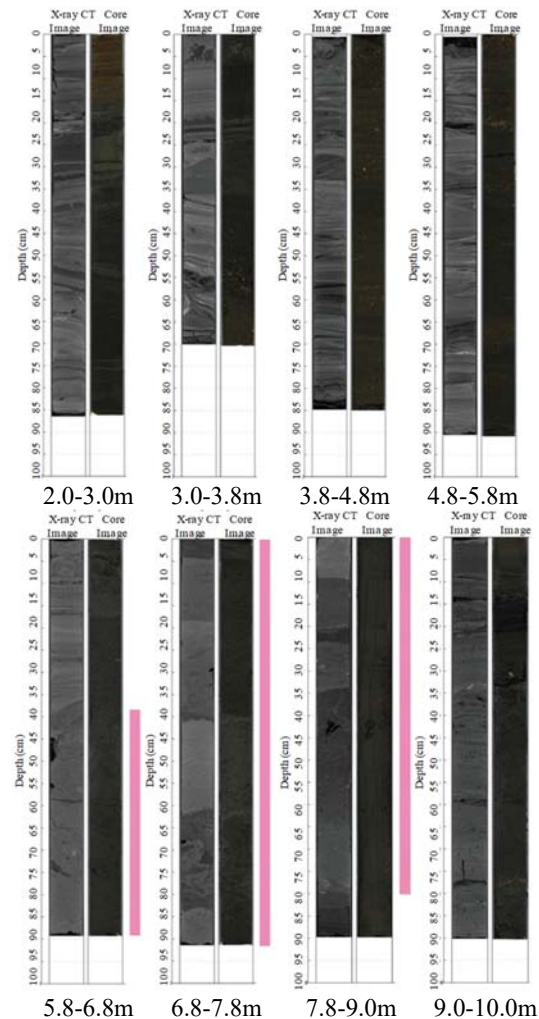


Fig.16 Photograph and X-ray CT images of core sections drilled in calculated area after liquefaction.

4. CONCLUSION

In this study, 3D soil-water coupled finite element-finite difference analyses based on CM model were conducted to investigate the mechanism of liquefaction and consolidation settlement of ground in multiple earthquakes. The following conclusions can be obtained:

1. According to the calculated results of the liquefaction and the settlement in simulation for one column ground and three-dimensional ground, residual excess pore water pressure and stress-induced anisotropy have big influence on the subsequent ground behavior.

2. When a ground receive the damage from main shock and could not recovered promptly, excess pore water pressure in low permeability soil remains high and the stress-induced anisotropy develop to a very large level. As a result, liquefaction may be caused again even by a small aftershock.

3. When an earthquake occurs at ground having low permeability soil, excess pore water pressure may cause not only immediate settlement but also long-term settlement due to consolidation. Furthermore, a ground settlement is significantly affected by the aftershocks.

4. By the comparison between the calculated results and the field observation, it is known that the calculations are consistent well with the real liquefaction and settlement behavior. Therefore, it is confirmed that the proposed numerical method is possible to predict the ground behavior accurately as such multiple earthquakes occur in future.

REFERENCES

- [1] M. Kazama: Overview of the damages of The 2011 Off the Pacific Coast of Tohoku Earthquake and its geotechnical problems, Japanese Geotechnical Journal, Vol. 7, No. 1, pp. 1-11, 2012.
- [2] F. Oka, N. Yoshida, S. Kai, T. Tobita, Y. Higo, N. Torii, S. Kagamihara, N. Nakanishi, S. Kimoto, Y. Yamakawa, Y. Touse, R. Uzuoka and T. Kyoya: Reconnaissance Report of Geotechnical Damage due to the 2011 off the Pacific coast of Tohoku Earthquake - Northern Area of Miyagi Prefecture -, Japanese Geotechnical Journal, Vol. 7, No. 1, pp. 37-55, 2012.
- [3] F. Zhang, B. Ye, T. Noda, M. Nakano and K. Nakai: Explanation of Cyclic Mobility of Soils: Approach by Stress-Induced Anisotropy, Soils and Foundations, Vol.47, No. 4, pp.635-648, 2007.
- [4] Y. Bin: Experiment and Numerical Simulation of Repeated Liquefaction -Consolidation of Sand, Doctoral Dissertation, Gifu University, 2007.
- [5] Y. Morikawa, X. Bao, K. Maeda, T. Imase and F. Zhang: Importance of liquefaction analysis considering re-liquefaction due to aftershock of earthquake, Japanese Geotechnical Journal, Vol. 7, No. 2, pp. 389-397, 2012.
- [6] X. Bao, Y. Morikawa, Y. Kondo, K. Nakamura and F. Zhang: Shaking table test on reinforcement effect of partial ground improvement for group-pile foundation and its numerical simulation, Soils and Foundations, Vol. 52, No. 6, pp. 1043-1061, 2012.
- [7] F. Zhang, R. Oka, Y. Morikawa, Y. Mitsui, T. Osada, M. Kato and Y. Wabiko: Shaking Table Test on Superstructure-foundation-Ground System in Liquefiable Soil and Its Numerical Verification, Geotechnical Engineering Journal of the SEAGS & AGSSEA, Vol. 45, No. 2, pp. 1-6, 2014.
- [8] Y. Morikawa, Y. Tanaka, K. Maeda and H. Cho: Countermeasure against liquefaction using drainage diaphragm wall focused on the effect of dissipation of water pressure, Journal of JSCE, Ser. A2, Vol. 71, No. 2, pp. I_437-I_448, 2015.
- [9] K. Hamayoon, Y. Morikawa, R. Oka, F. Zhang: 3D dynamic finite element analyses and 1 g shaking table tests on seismic performance of existing group-pile foundation in partially improved grounds under dry condition, Soil Dynamics and Earthquake Engineering, Vol. 90, pp. 196-210, 2016.
- [10] K. Hashiguchi and M. Ueno: Elastoplastic constitutive laws of granular material, Constitutive Equations of Soils, Pro. 9th Int. Conf. Soil Mech. Found. Engrg., Spec. Ses. 9, Murayama, S. and Schofield, A. N. (eds.), Tokyo, JSSMFE: pp. 73-82, 1977.
- [11] A. Asaoka, M. Nakano, T. Noda: Superloading yield surface concept for the saturated structured soils, Proc. of the Fourth European Conference on Numerical Methods in Geotechnical Engineering-NUMGE98, pp. 232-242, 1998.
- [12] Roscoe K. H., Schofield A. N. and Thurairajah A.: Yielding of clays in states wetter than critical, Geotechnique 13 (3), pp.211-240, 1963
- [13] A. Taira, K. Iijima, C. Igarashi, S. Sasaki, H. Sakaguchi, A. Sakaguchi, E. Kikawa, T. Kanamatsu, Y. Yamamoto, W. Azuma, T. Tanaka, M. Nishimura, T. Suzuki, Y. Kido, N. Watanabe, M. Okuno, T. Inoue, H. Mayuzumi, T. Oda, T. Hamada, T. Muroyama, I. Takeo, J. Takashina, H. Katsumata, N. Harada, F. Nishida, H. Minamikawa and Y. Kanetaka: Identification of a Soil Liquefied Layer due to the 2011 off the Pacific Coast of Tohoku Earthquake Using X-ray CT Scan Imaging: An Example from Core Samples from Maihama 3-chome, Urayasu City, The Journal of the Geological Society of Japan, Vol. 118, No. 7, pp. 410-418, 2012.

EVALUATION OF HEAVING RESISTANCE FOR DEEP SHAFT USING NODULAR DIAPHRAGM WALL

Koji WATANABE¹, Akira MITSUMORI², Hidetoshi NISHIOKA³ and Masayuki KODA³

¹Technical Research Institute, Obayashi Corporation, Japan; ² Design Department, Obayashi Corporation, Japan; ³ Structures Technology Division, Railway Technical Research Institute, Japan

ABSTRACT

In recent years, an increasing number of plans in Japan have been proposed for large-scale railway structures to be built deep underground. To construct a large-scale railway structure, it is necessary to construct vertical shafts that serve as the starting and ending point for the shield machine during the construction as well as the air vents once it goes into operation. In such situations, it is expected that there will be an increase in the cases where the vertical shafts will be built to reach deep underground. If typical diaphragm walls were used to construct these deep shafts, the embedment depth of the diaphragm walls would have to be made substantially significant in order to control the heaving. Heaving as stated here is a phenomenon in which pressurized water contained in the permeable layer below the impermeable layer close to the bottom of the excavated ground breaks through the impermeable layer owing to the upward force of the water pressure during the excavation process, which then causes the vertical shaft to lose its stability. Using nodular diaphragm walls that have nodular part on the diaphragm walls of the deep shaft could be relied upon for the purpose of supporting the embedment depth of the diaphragm walls. In this research, the influence the nodular part resistivity was examined in resisting heaving when nodular diaphragm walls are used for the deep shaft. The experiments at gravitational and centrifuge acceleration fields were conducted, and their effectiveness were confirmed.

Keywords: Deep Shaft, Heaving Resistance, Nodular Diaphragm Wall, Model Test

INTRODUCTION

In recent years, an increasing number of plans have been proposed for large-scale railway structures to be built deep underground. To construct a large-scale railway structure, it is necessary to construct vertical shafts that serve as the starting and ending point for the shield machine during the construction as well as the air vents once it goes into operation. In such situations, it is expected that there will be an increase in the cases where the vertical shafts will be built to reach deep underground. When typical diaphragm walls were used to construct these deep shafts, the embedment depth of the diaphragm walls would have to be made substantially significant in order to control the heaving. Heaving as stated here is a phenomenon in which pressurized water contained in the permeable layer below the impermeable layer close to the bottom of the excavated ground breaks through the impermeable layer owing to the upward force of the water pressure (uplift force) during the excavation process, which then causes the vertical shaft to lose its stability.

There are two methods to construct deep shafts: the pneumatic caisson construction method and the diaphragm wall construction method. The pneumatic caisson construction method has demonstrated to reach a maximum depth of approximately 40 to 50

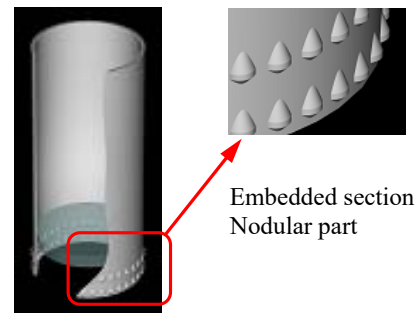


Fig. 1 Schematic View of Nodular Diaphragm Wall

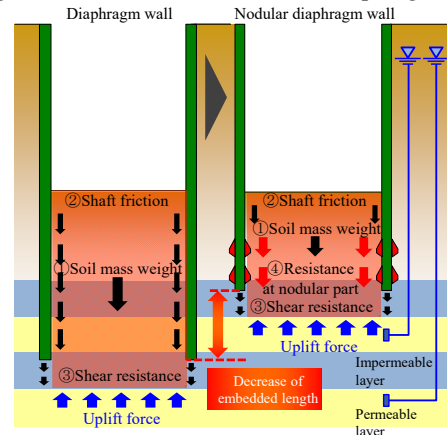


Fig. 2 Effect of Nodular Diaphragm Wall

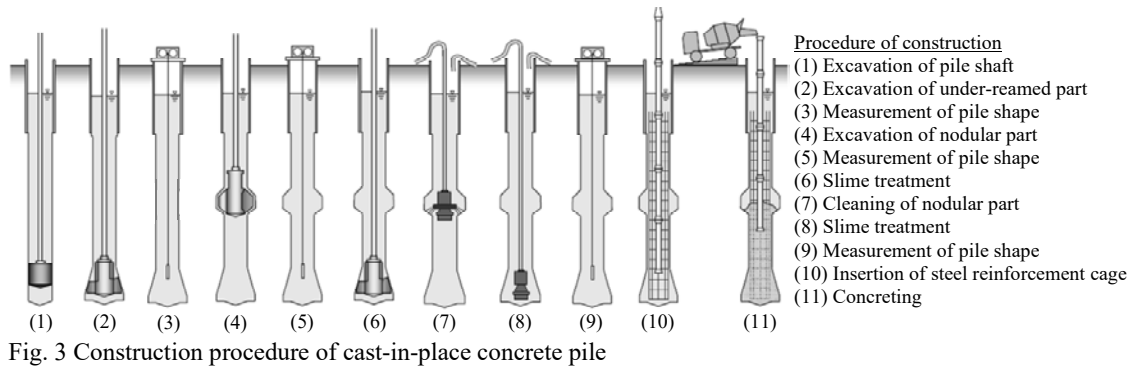


Fig. 3 Construction procedure of cast-in-place concrete pile

m¹⁾, and as there is a need to highly pressurize the air during construction, there are challenges in applying this method to deep underground construction. On the other hand, the diaphragm wall construction method has shown it can reach a maximum depth of approximately 100 to 120 m ^{2), 3)}, but concerning construction deep underground, as some have pointed out, there are chances of pouring deficiencies of concrete due to, for example, the tremie pipes clogging²⁾. Therefore, for this method, it is necessary to make the embedment depth as shallow as possible. Using nodular diaphragm walls that have nodules on the diaphragm walls of the deep shaft, as seen in Fig. 1, could be relied upon for the purpose of supporting the embedment depth of the diaphragm walls (Fig. 2). The nodules of the nodular diaphragm walls are expressively able to bear the pressure and thus possess greater resistance than normal diaphragm walls⁴⁾. In the construction of nodular diaphragm walls, a construction method that expands the mid-section of the diaphragm wall is used in order to create its nodular part. The above-mentioned construction methodology was developed by the Obayashi Corporation and has already been utilized in the field in a few construction projects such as architecture field^{4), 5)}.

In this research, the influence the nodular part resistivity was examined in resisting heaving when nodular diaphragm walls are used for the deep shaft. The experiments at gravitational and centrifuge acceleration fields were conducted, and their effectiveness of heaving resistance were confirmed. This paper reports the results of the model experiment subjected to gravitational and centrifuge acceleration fields.

NODULAR DIAPHRAGM WALL

Figure 3 shows the construction process of the nodular diaphragm wall construction methodology. First, use the diaphragm wall construction method to excavate the trench, and then excavate the bottom of the trench to enlarge. Next, use a specialized bucket for the nodular section to excavate the nodular section. After the excavation, the nodular part and the pile tips are treated for slime and the slurry in the

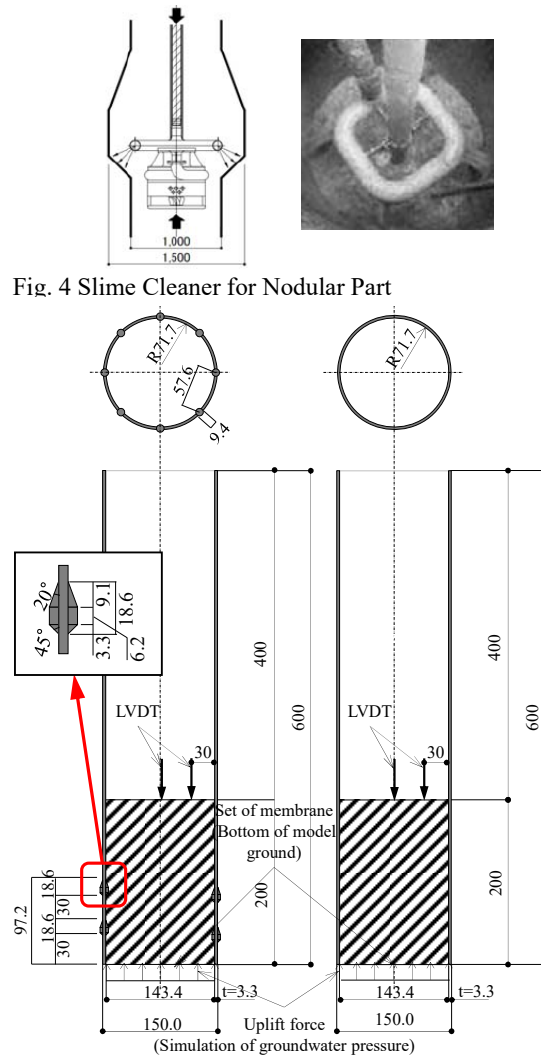


Fig. 5 Shaft Model for Uplift Experiment at Gravitational Acceleration Field

cavity is replaced with good fluids. For the slime treatment of the knuckles, specialized slime cleaner designed for the nodules is used as seen in Fig. 4. After that, a steel reinforcement cage is inserted and set up inside the tremie pipe to pour concrete. The shape of the nodular part is verified by the use of

ultrasound measuring equipment. For the construction experiment conducted here, the result of the ultrasound was compared to the actual measurements of the part that was dug up, and it was verified that the nodular part were indeed in the specified shape⁴⁾.

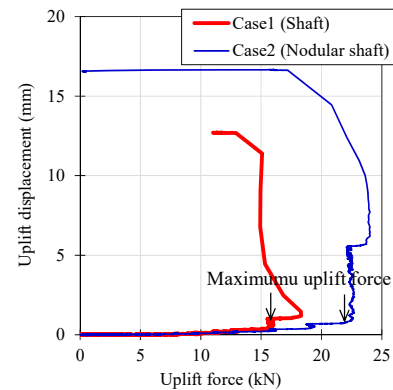
UPLIFT FORCE EXPERIMENT AT GRAVITATIONAL FIELD

Overview of Uplift Force Experiment

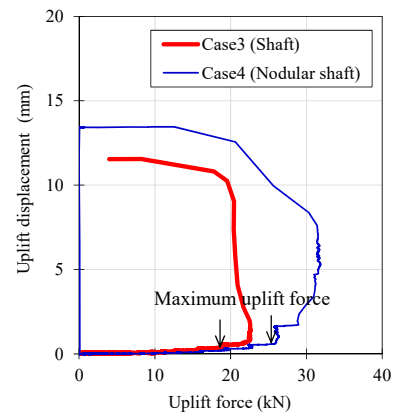
The uplift force experiment at a gravitational field was conducted to verify the heaving resistance of the regular and nodular diaphragm walls. As seen in Fig. 5, two models- one shaped with no nodular part (diaphragm wall model) and one shaped with nodular part (nodular diaphragm wall model)-were used in this experiment. A 200 mm thick foundational ground layer was created in a 600 mm deep cylindrical model. Additionally, the insides of the models were coated with silica sand No. 7 (0.3 ~ 0.08 mm) to create roughness. The ground was created in the model had a solution injection layer and modified concrete ground layer to set up the experimental condition as stated in Table 1. It should be noted that the undrained shear strength in the Table 1 shows the actual strength during the experiment. The chemical grouting soil layer (Cases 1 and 2) was created by mixing soluble glass type chemical grouting to the silica sand No. 7. The target strength for the solution injection layer for the undrained shear strength was $c=100\text{kN/m}^2$. Additionally, the cemented improvement ground layer (Cases 3 to 6) was created by mixing, silica sand No. 7 and blast furnace slag cement type B. The two target strengths for the undrained shear strength were $c=300$ and 500kN/m^2 . The mix for the chemical grouting soil layer and the cemented improvement ground layer were determined through mixing experiments prior to this stage of the experiment. Furthermore, prior to the uplift force experiment, the same materials from the same batch were used that were used to create the ground layer of the models to perform the unconfined compression test to verify they were reaching the specified strength. For the uplift force experiment, the heaving behavior by incrementally applying the uplift force from the bottom of the improvement soil layer was verified. This uplift force mimics the upward water pressure from the pressurized water in the permeable layer below the impermeable layer. For this process, a membrane to simulate the impermeable layer was installed when activating the uplift force. By doing so, the destruction of the ground layer through seepage as well as water filling the interface between the ground and the model was prevented. Measurement items were the uplift displacement on the surface of the ground and the

Table 1 Experiment Condition for Uplift Experiment at Gravitational Acceleration Field

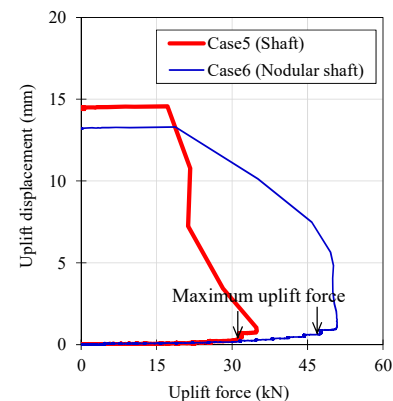
Undrained shea strength c (kN/m ²)		Model shaft
Case 1	105	Diaphragm wall
Case 2	(Chemical grouting)	Nodular diaphragm wall
Case 3	297	Diaphragm wall
Case 4	(Cemented improvement)	Nodular diaphragm wall
Case 5	512	Diaphragm wall
Case 6	(Cemented improvement)	Nodular diaphragm wall



(a) Case 1, Case 2 ($c=100\text{kN/m}^2$)



(b) Case 3, Case 4 ($c=300\text{kN/m}^2$)



(c) Case 5, Case 6 ($c=500\text{kN/m}^2$)

Fig. 6 Relationships between Uplift Displacement and Uplift Force

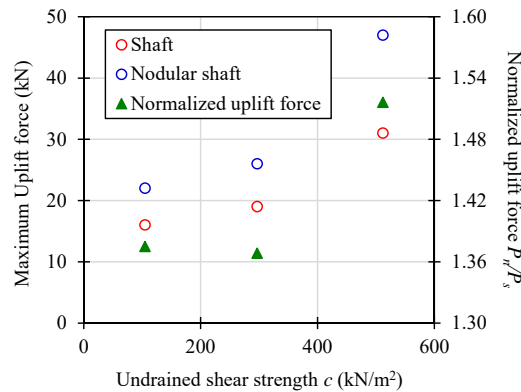


Fig. 7 Relationships between Maximum Uplift Force, Normalized Maximum Uplift Force and Undrained Shear Strength

uplift force. The uplift displacement is measured by checking two-points in the radial direction (the center of the ground surface and 30mm from the wall) in order to see the distribution on the flat surface.

Results of Uplift Force Experiment

Figure 6 shows the relationship between uplift displacement and uplift force obtained through the study of each case. In these cases, two measurement points were used on the topside of the ground to measure uplift displacement, but the differences in the displacement amount were not that different from one another in each case; therefore, they were organized as the average displacement between two points. According to Fig. 6, there is a tendency for the uplift displacement to increase gradually as the uplift force increases. Especially in the case of the diaphragm wall model (no nodular part) which are represented with the red lines, it is seen that the element of resistance against heaving is the peripheral friction between the surfaces where the ground is up against the diaphragm wall model, it is said that once the peripheral friction is triggered, the uplift displacement increases. On the other hand, if the figure is looked upon at the blue line representing the nodular diaphragm walls in each of the figures, since the peripheral friction and nodular resistance is activated, it can be said that it has an improved performance in withstanding heaving. When the uplift force is further increased, then a much greater increase is seen in uplift displacement. This seems to be because the resistivity (bearing resistance) of the nodular diaphragm wall's resistance element against heaving is being expressed in addition to the peripheral friction. The relationship among the maximum uplift force obtained in each of the cases, the normalized maximum uplift force, and the undrained shear strength is plotted in Fig. 7. Here, the normalized

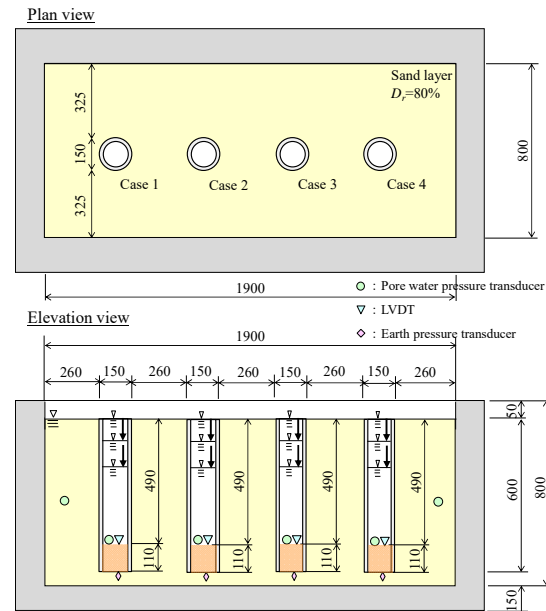


Fig. 8 Summary of Centrifuge Model Test

Table 2 Experiment Condition for Centrifuge Model Tests

	Model shaft	Strength of model ground c (kN/m ²)	Friction at embedded part
Case 1	Diaphragm wall	53	With friction
Case 2	Nodular diaphragm wall		
Case 3	Diaphragm wall		Without friction
Case 4	Nodular diaphragm wall		

maximum uplift force for each case is calculated by dividing the diaphragm wall model's maximum uplift force, P_s , by the nodular diaphragm wall model's maximum uplift force, P_n . It is seen from Fig. 7 that the maximum uplift force increases as the undrained shear strength increases. This tendency is repeated in the diaphragm wall model and the model of the nodular diaphragm wall. From the normalized maximum strength in the Fig. 7, it is seen that each of the undrained shear strengths show a value of approximately 1.37 to 1.51. From this, it can be said that when nodular diaphragm walls are used, owing to the expression of the resistance of nodular part in addition to the peripheral friction, the heaving resistance becomes 30 to 50% greater.

CENTRIFUGE MODEL TEST

Summary of Centrifuge Model Test

A centrifuge model test was conducted to verify the results of the nodular and the diaphragm wall's heaving resistance tested in the gravitational field. Figure 8 covers the overview of the centrifuge model test. The centrifuge model test was conducted by setting up four test pieces inside a large rigid model container (Width 1900mm x Depth 800mm x Height 800mm). The model ground was created by

using silica sand No. 7 ($G_s=2.645$) and using the air-pluviation method to achieve a relative density of $D_r=82\%$, and then soaking the bottom side of the rigid model box in water to saturate the sand. The peripheral ground's ground water level is the same level as the ground surface. The models used in this experiment are the same two shapes as listed in Fig. 5 (diaphragm wall model and the nodular diaphragm wall model), and in a 600mm deep cylindrical model a modified ground layer that is 110mm thick layer was created. Additionally, for the cases where the friction is recreated inside, the model was coated using silica sand No. 7 to create its roughness. The cemented improvement ground placed inside the model used a mixture of silica sand No. 7 and blast furnace slag cement type B with the target of achieving undrained shear strength of $c=50\text{kN/m}^2$. The ratio to create the mixture for the modified ground was decided based on mixing experiments conducted prior to this stage of the study. Before the centrifuge model test was conducted, the same materials from the same batch that were used to create the modified ground in order to conduct the uniaxial compression test to verify when it reached the specified strength. The test was set up to first reach the predetermined centrifugal acceleration (80G) to then simulate the gradual excavation to verify the heaving behavior. To recreate the gradual excavation, the salt water (specific gravity of 1.05) was gradually drained that was covering the cemented improvement ground in the model. The measurement item were the uplift displacement on the surface of the cemented improvement ground, the decrease in the salt water's water level over the cemented improvement ground, and the water pressure of the cemented improvement ground. The experiment condition is shown in Table 2. The ground strength stated in Table 2 is the actual strength at the time of the test.

Results of Centrifuge Model Test

Figure 9 shows the relationship between the uplift displacement and the decrease in the water level. The uplift displacement measured here is the amount of displacement that was measured at the center of the modified ground. Furthermore, both the uplift displacement and the drop in the water level are organized based on the real-life scale calculated by multiplying with the magnification of the centrifugal acceleration (80G). According to Fig. 9, no significant differences are seen in the diaphragm wall or the nodular diaphragm wall in their uplift displacement even when the water level starts to drop. However, there is a sudden increase in the uplift displacement once the water level drops between 10 and 13m. On the other hand, with the

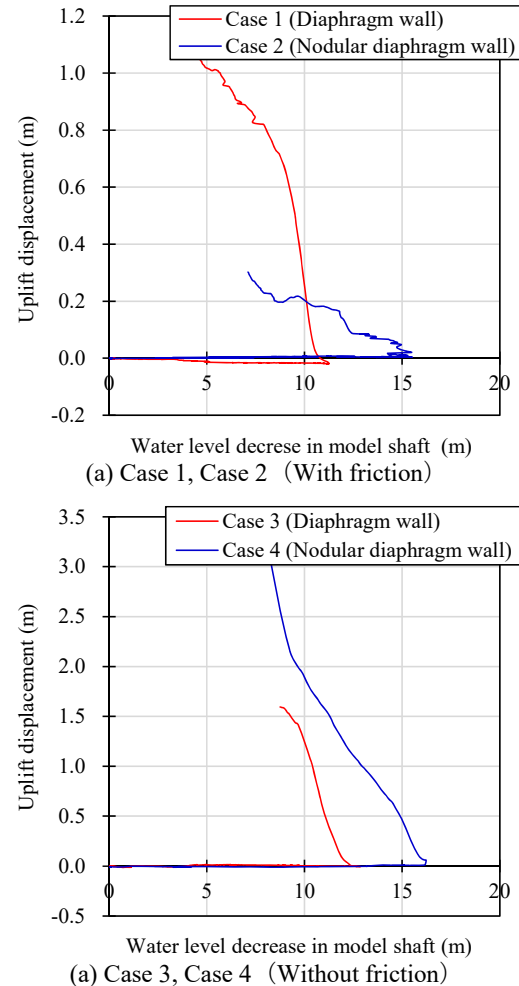


Fig. 9 Relationships between Uplift Displacement and Decrease of Water Surface in Shaft

nodular diaphragm wall, an increase in uplift displacement is seen once the water level drops by 15 to 16m. From this phenomenon, it can be said that in the diaphragm wall model, the resistive element against the heaving behavior is only the cemented improvement ground self-weight and the peripheral friction between the cemented improvement ground and the diaphragm wall model, the uplift displacement occurred at a relatively less significant drop in the water level compared to the nodular diaphragm wall. On the other hand, when it comes to the nodular diaphragm wall, it is said that since there was an additional element of resistance against heaving in the form of nodular part, heaving occurred only after the drop in the water level became significant. For this examination, it was only used the inside of the model's cemented improvement ground and considered the existence or the lack of friction in between the model's boundary surfaces as the parameter. It is said that the influence of the boundary surface's friction, or lack thereof,

between the cemented improvement ground and the model have on heaving resistance is small.

CONCLUSION

The modeled experiments to examine the heaving resistance of nodular diaphragm walls to determine their suitability to be used as the deep shafts for railway structures were conducted. The following findings are obtained from this study:

1) Through the uplift force experiment at the gravitational field is confirmed that when the nodular diaphragm walls are used for the vertical shafts, there would be an increase in the heaving resistance due to the resistance of nodular part in addition to the peripheral friction.

2) It is concluded that in the centrifuge model test, which reproduces the full-scale stress and strain fields, that the vertical shafts using the nodular diaphragm walls had a greater heaving resistance.

REFERENCES

- [1] Uegaki Y, Sawatari T, Tajin M and Miyaji K “Measurement Result on the Largest Circular Pneumatic Caisson Method in the World”, Proceedings of 63th Annual Conference on Japan Society of Civil Engineers, Sep. 2010, pp. 507-508 (in Japanese).
- [2] Kumagai K, Takahashi M and Abe Y “A Report of Methods for the Structural Analysis of High Depth Slurry Wall Supporting the Main Tower of a Suspension Bridge”, Journal of Japan Society of Civil Engineers, No. 504, VI-25, Dec. 1994, pp. 43-50 (in Japanese).
- [3] Mizuno N, Nagashima M, Makino S and Okada T “Prevention of Blocking of Tremie for Slurry Wall Construction”, Concrete Research and Technology, No. 1, Vol. 8, Jan. 1997, pp. 251-265 (in Japanese).
- [4] Watanabe K, Nishiyama T Sei H and Ishii Y “Static Axial Reciprocal Load Test of Cast-in-place Nodular Concrete Pile and Nodular Diaphragm Wall”, Geotechnical Engineering Journal of the SEAGS & AGSSEA, Vol. 42, No. 2, Sep. 2011, pp. 11-19.
- [5] Watanabe K, Sudo T, et al. “Tensile Load Test and Compressive Load Test of Nodular Diaphragm Wall Supporting High-rise Tower”, Proceedings of Annual Conference of Architecture Institute of Japan, Sep. 2009, pp. 545-554.

RESEARCH OF DAMAGED CONDITION BY THE 2016 KUMAMOTO EARTHQUAKE AND GROUND INVESTIGATION ON STONE WALLS AND EARTH STRUCTURES IN KUMAMOTO CASTLE

Satoshi SUGIMOTO ¹, Minoru YAMANAKA ², Hideki MAEDA ³, Naozo FUKUDA ⁴, Yuuya KATSUDA ¹

¹ Faculty of Eng., Nagasaki University, Japan; ² Faculty of Eng., Kagawa University, Japan

³ West Japan Engineering Consultants, Inc., Japan; ⁴ Fukken Co. Ltd., Japan

ABSTRACT

There are a lot of valuable historical structures with stone wall in Japan. Those structures are still active not only as roads and waterways, but also are designated as cultural properties, and in some places, they also play an important role as a tourism resource for the region. However, the current situation is that countermeasures against disasters are delayed like the damage of Kumamoto Castle due to the 2016 Kumamoto Earthquake. In particular, it is considered that it is important to elucidate the earthquake disaster mechanism by the interaction between the ground and the stone wall.

In this research, the tendency of the damage of stone walls and earth structures will be clarified based on the survey team of the Geotechnical Engineering Society and the Kumamoto Castle Research Center, and it is discussed on the mechanism of collapse occurrence by estimating the geological structure under the several sites in Kumamoto Castle by surface wave profiling method and so on.

Keywords: Kumamoto Castle, Earthquake disaster, stone wall, earth structure, investigation

INTRODUCTION

A lot of historical and valuable stone structures continue using for hundreds of years in Japan. These structures have valuable roles as regional tourism resources with registration for cultural heritage and practical usage. Almost structures degraded with age, it is necessary to do maintenance and repair work. However, it is difficult to do them because mechanical evaluation method is never established from an engineering perspective, and information and references are not sufficient about these structures.

Some researchers investigated on the stone walls and embankment in Kumamoto Castle and so on. Kuwahara carried out to survey stone walls of Kumamoto Castle about 30years ago [1]. He collected the data of surface shape on stone walls by surveying tool. These data will be basic and important on comparison of current cross-sectional shape. Yamanaka et.al. carried out to survey embankment of several traditional castles by microtremor in Japan [2][3]. They tried to clarify the distribution of unstable area under the ground surface. It is expected that this method will be able to estimate the intricate geological structure with broken stone, embankment and original ground.

The 2016 Kumamoto earthquake gave huge damage for several structures in Japan. Kumamoto Castle was also damaged on architectural structures, stone wall, embankment and so on. The number of damaged stone walls and embankment is over

hundreds especially. Therefore, the evaluation method of stone wall and embankment stabilization is required from the view of geotechnical engineering quickly. This paper reports the investigation of structures' damaged condition and ground survey around damaged stone walls in Kumamoto Castle after that earthquake with cooperation of Kumamoto Castle Research Center and the survey mission of Japan Geotechnical Society.

CHARACTERISTICS OF KUMAMOTO CASTLE AND OVERVIEW OF GEOLOGICAL STRUCTURE

Kumamoto Castle was constructed by Kiyomasa KATO as a domain head in 1607. Fig.1 shows the landscape around the castle before construction in second hand of sixteenth century [4]. There is Mt. Chausu-yama in center of this picture map, and this mountain was shaped a southern part of Ueki tableland at an altitude about 50 meters. There is a scattering of erosional valleys surrounding here shown in Fig. 2 because an ignimbrite layer exists under the ground surface with humid climate [5].

Fig. 3 and 4 show the geological cross-section based on the past boring survey in the Kumamoto Castle [6]. There are only 12 boring data collections around northern part of the castle tower surveyed in 1958 or 2015. Developed land material and volcanic cohesive soil that N Value is around 10 constitute the ground from the surface to 10meters depth. Volcanic

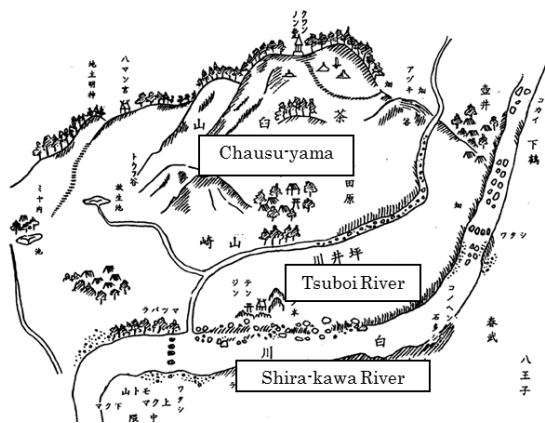


Fig. 1 Picture map of landscape before constructing Kumamoto Castle. [4]

cohesive soil that N Value is under 20 and weathering tuff breccia exist above 50meters depth. The andesite bedrock that N values is over 50 was confirmed under 50meters depth. Fig.4 shows extreme changes of geological structures on the bedrock and the pyroclastic flow layer with the large eruption at Mt. Aso before ninety thousand years (hereinafter called “Aso4”) within just 50meters interval. Furthermore, the reports of 2015 boring survey fingered the existence of discontinuous surface under the castle caused by Tatsuta-gawa geologic fault in northern part of these area. It is estimated that resistance of foundation ground with stone wall and embankment in the castle for huge earthquake because mainly extending Aso4 has low N value under the castle’s site.

GROUND DEFORMATION BASED ON MONITORING DATA

Fig.5 shows the results of 2.5dimensional analysis with Interferometric Synthetic Aperture Radar by Geospatial Information Authority of Japan [7]. Kumamoto Castle is about 9km east of earthquake center on main shock of the 2016 Kumamoto Earthquake. It is estimated that the deformation of ground surface is 10cm subsidence and 30 to 40cm movement to east direction. Fig.6 shows the ground settlement in center of the Kumamoto city and Kumamoto Castle calculated by altitude correction software “PatchJGD” released from Geospatial Information Authority of Japan. This calculation results shows about 20cm settlement in this area.

REPORT OF DISASTER INVESTIGATION ON DAMAGED STRUCTURES

Site Investigation

Several stone walls, embankments and architectural structures were affected by the 2016

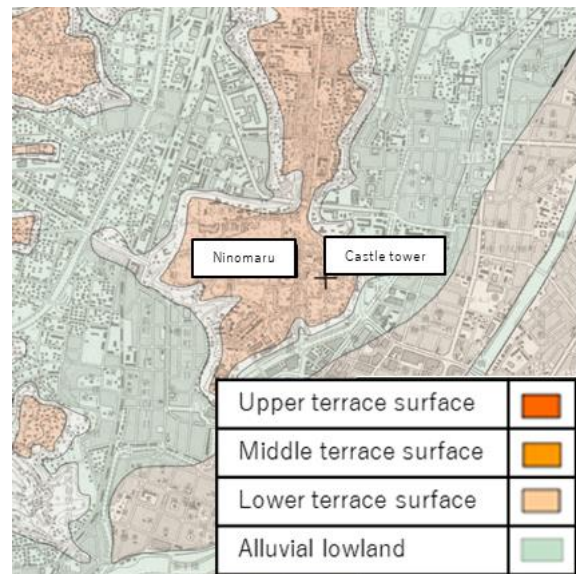


Fig. 2 Topographical structure around Kumamoto Castle. [5]

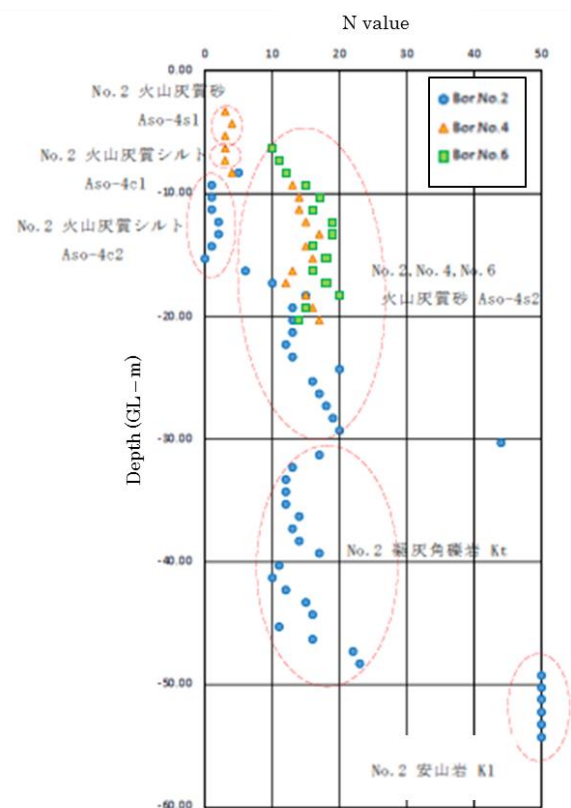


Fig. 3 Distribution of N value under the site of Kumamoto Castle. [6]

Kumamoto Earthquake. Authors especially focused on the damage condition of stone wall and embankment in this report.

Fig. 7 shows the location of damaged stone wall around the castle tower, and Photo 1 shows the damage conditions. The JGS disaster investigating team confirmed the following damages in the whole site of the castle; collapse and destabilization of stone

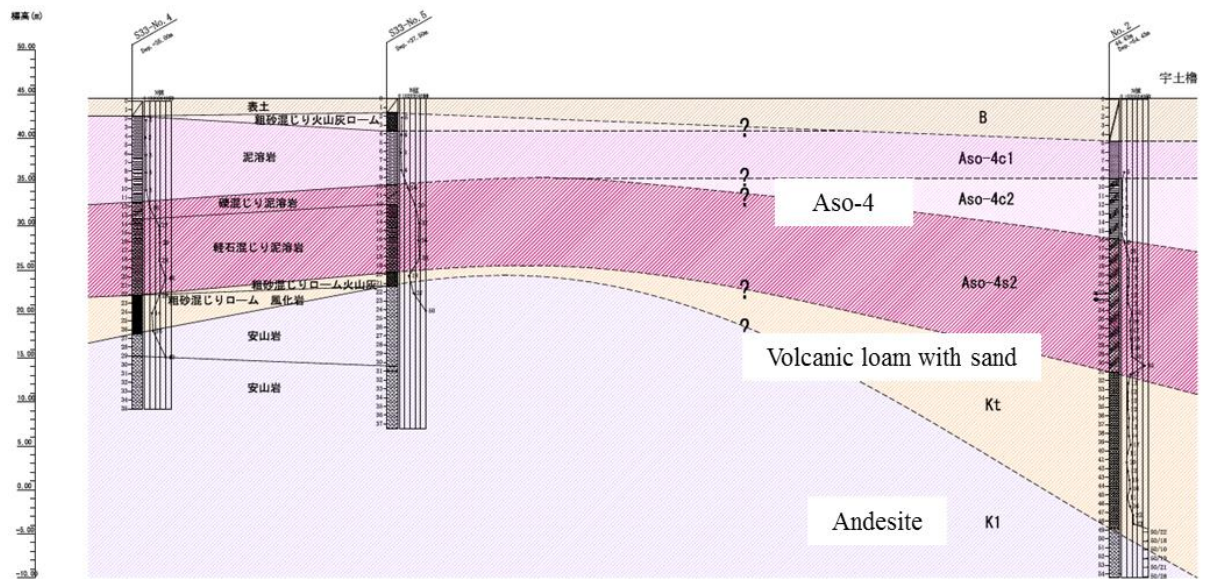


Fig. 4 Geological structure under the tower of Kumamoto Castle. [6]

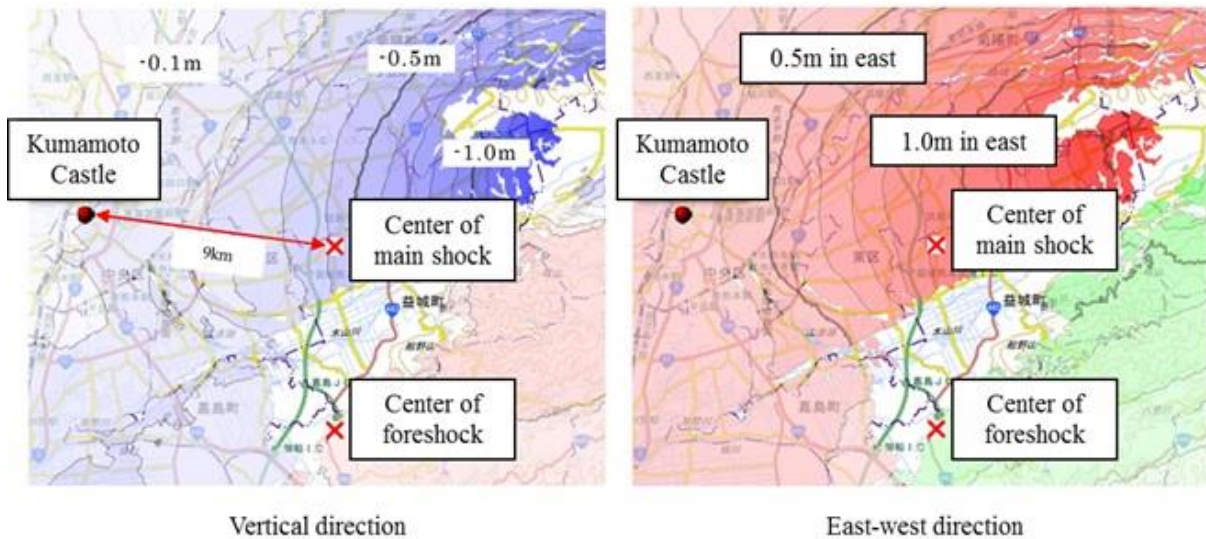


Fig. 5 Ground surface deformation by the 2016 Kumamoto earthquake. [7]

walls, slope failure and surface settlement of embankment and crash of architectural structures.

Fig.8 shows the distribution of damaged stone wall locations, collapse areas, maximum stone movements and directions. It is not clarified that damage scale has causal relation between with height, gradient, width and direction of each stone wall.

Fig. 9 shows the relationship between the maximum stone movements and directions of damaged stone walls in the Honmaru area with the photos by UAV and CAD's plan views. There are a lot of cases that data of stone wall movement in north-south direction are more than the cases in east-west direction. And it is confirmed that maximum movement distance is also longer than in these cases. It is estimated that ground vibrational characteristic under this site has a huge effect because stone walls

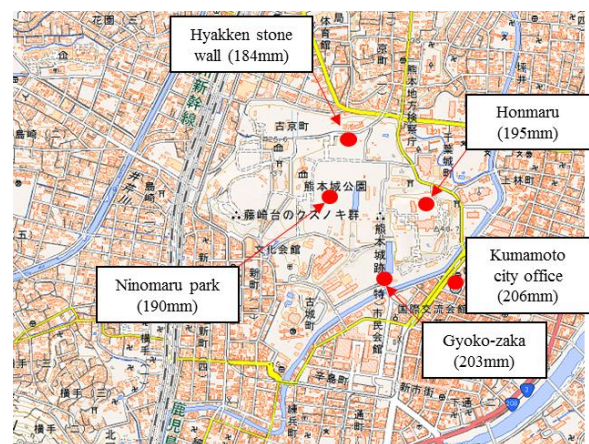


Fig. 6 Ground settlement in center of Kumamoto City and Kumamoto Castle.

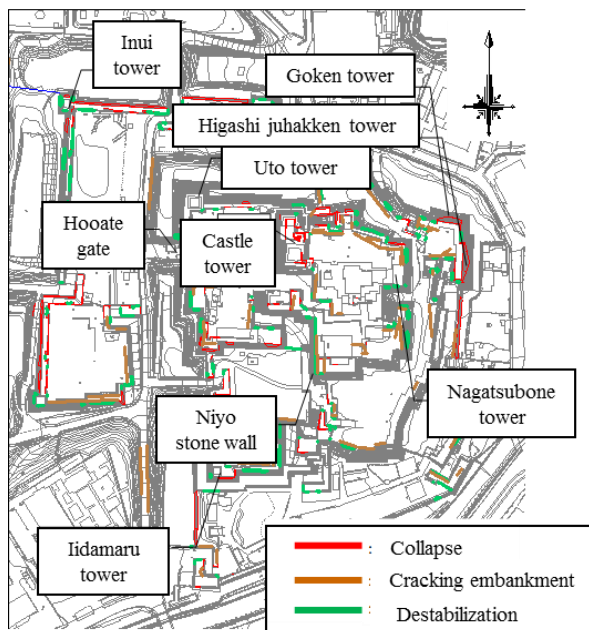


Fig. 7 Distribution of damaged stone wall and embankment.

almost construct equally in the direction of north, south, east and west.

Fig. 10 shows the relationship between the height of stone wall and maximum movement distance. It is confirmed that each parameter has almost linear relation in whole tendency. These results indicate that the more ground investigation of this field will be important on the foundation ground of stone wall and strength of embankment for reconstruction in near future.

Surface wave exploration

Surface wave exploration was carried out by using the high precision surface wave exploration equipment (McSEIS-SXW) in order to discuss on influence a compaction or depth of surface layer for the damage of stone walls. Vibration by hammering interval was 2m and geophone interval was 2m as receiving points. In total 24 seismograph sensors were used. To make

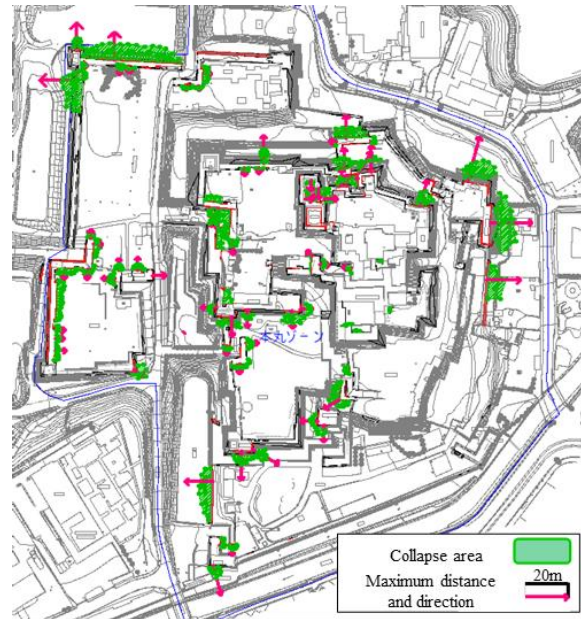


Fig. 8 Collapse area and Stone movements of damaged stone walls in the Honmaru area.

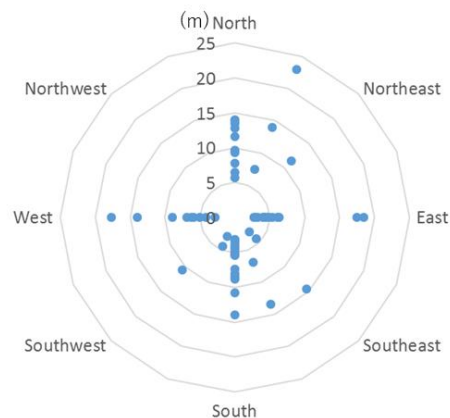


Fig. 9 Relationship between maximum distance and direction.



(a) Northern part of castle tower



(b) Hooate gate



(c) Northern part of Nagatsubone tower

Photo 1 Damaged stone wall and embankment in Kumamoto Castle

good surface connection, the geophones were properly installed in the ground.

Fig. 11 shows survey lines of Surface wave exploration at Heizaemon-maru of Kumamoto Castle. 6 measuring lines are located in a reticular pattern. Fig. 12 shows situation of surface wave prospection at line 6 of Heizaemon-maru.

Fig. 13 shows the distribution of analyzing results of S-wave velocity at line 2 and 4. It is estimated that Aso-4c layer with under $V_s=240\text{m/sec}$ V_s and Aso-4s layer with $V_s=240\text{--}300\text{m/sec}$ locate with indeterminate undulation across a depth of about 8m.

Fig. 14 shows the distribution of N-value calculated from V_s . N-value is calculated by the following equation [8].

$$N=(V_s/97)^{0.314} \quad (1)$$

here,

N : N-value by the standard cone penetration test
 V_s : Surface wave velocity by surface wave prospecting (m/sec)

There is the loosen embankment layer that N-value is about 2 above a depth of 2m. Aso-4c layer has N-value that is from 2 to 8 above a depth of 8m. And Aso-4s extends with N-value from 10 to 25 under the Aso-4c layer.

This result indicates that these soft ground gives

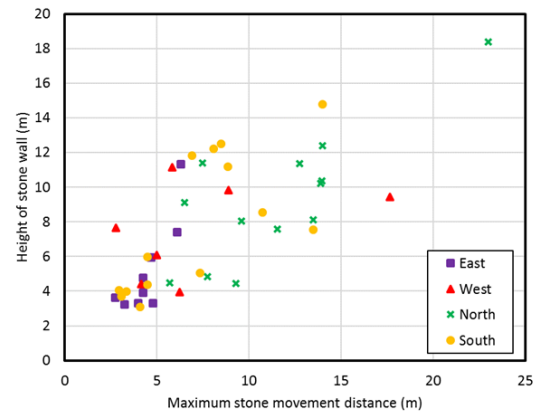


Fig. 10 Relationship between maximum stone movement distance and height of stone wall.

amplification of vibration with earthquake for buildings and structures.

CONCLUSION

The 2016 Kumamoto earthquake caused huge damages for several structures in Kumamoto Castle. These structures almost have high value as cultural assets with past time of about 400years. Hundreds of stone walls and embankments were also damaged or collapsed with the massive earthquake.

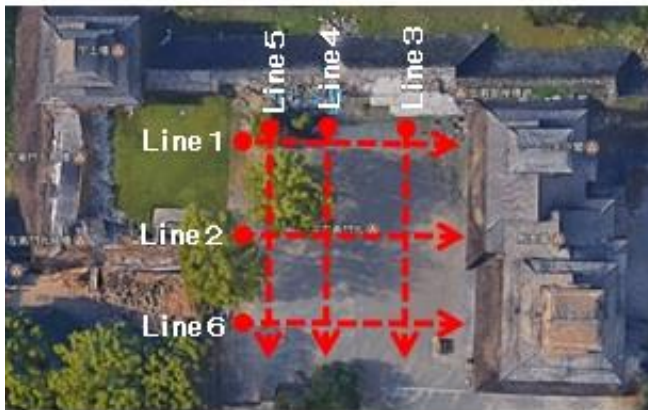


Fig.11 Survey lines of Surface wave exploration at Heizaemon-maru



Fig.12 Situation of Surface wave exploration at line 6

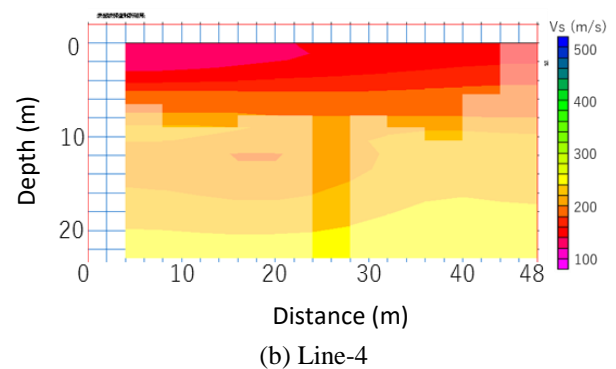
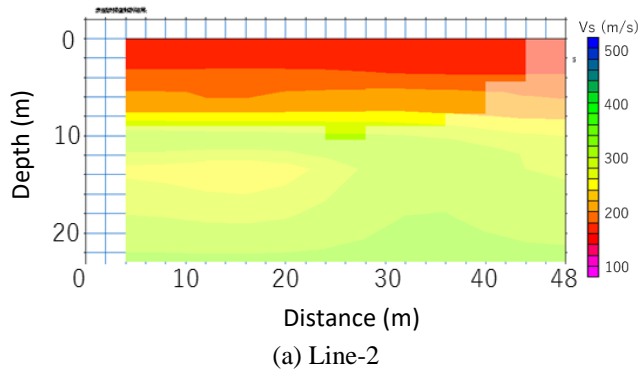


Fig. 13 Distribution of surface wave velocity V_s

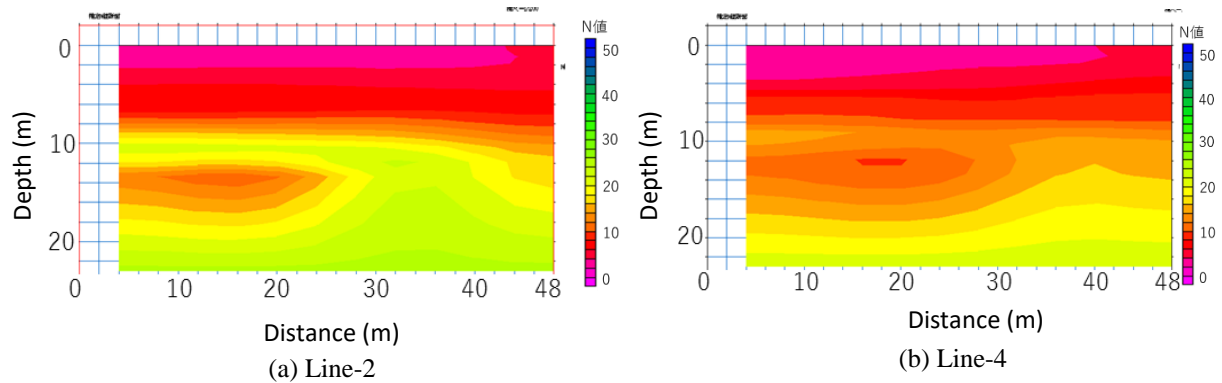


Fig. 14 Distribution of N-value

This investigation carried out with the limited information of ground and geology under the Kumamoto Castle because the boring survey has minimally suppressed due to subsistent as a cultural asset before the earthquake. Therefore, the collection of past limited boring data, site investigation and the method of estimation on geological structure and soil characteristic were combined, and the following results were clarified in this study.

1) There were more cases that stone walls collapsed in north-south direction compared with the cases in east-west direction. This result indicates that the more ground investigation of this field will be important on the foundation ground of stone wall and strength of embankment for reconstruction in near future.

2) It is clarified that the Kumamoto Castle was constructed on the Aso-4 centered volcanic soil layers with low N-value. This result indicates that these soft ground gives amplification of vibration with earthquake for buildings and structures.

ACKNOWLEDGEMENTS

The authors gratefully appreciate a lot support and understanding for this investigation from all officers of Kumamoto Castle Survey and Research Center after shortly after the 2016 Kumamoto earthquake. And our gratitude extends to all cooperators of this investigation with several instruments and information.

REFERENCES

- [1] Kuwahara F., "The gradient of the stone walls in Kumamoto Castle", Report of researches /

Nippon Institute of Technology, 14-2, 1984, pp.59-74 (in Japanese).

- [2] Yamanaka M., Nishiwaki D., Koizumi K. and Hasegawa S. "Detection of dynamic unstable point of stone wall at Kochi Castle by microtremor", Proceedings of 50th Annual Conference of Japanese Geotechnical Society, 2015, pp. 203–204 (in Japanese).
- [3] Yamanaka M., Ishigaki H., Koizumi K., Hasegawa S. and Araki H. "Extracting method of deformed part by microtremor on stone walls of Japanese traditional castle", International Journal of GEOMATE, 2017, Vol.13, Issue 35, pp.73- 79.
- [4] Totsuka S., "The research of advancement history on modern bridges in Kumamoto prefecture", Doctor thesis of Kumamoto University, 1999, p. 90 (in Japanese).
- [5] Geospatial Information Authority of Japan, "Active fault under urban area in Japan", http://www.gsi.go.jp/bousaichiri/active_fault.html, 2016 (in Japanese).
- [6] Kumamoto Castle Survey and Research Center, "The report of outsourcing geological survey for evaluation of seismic capacity on Uto tower in Kumamoto Castle", 2016 (in Japanese).
- [7] Geospatial Information Authority of Japan, "Information of the 2016 Kumamoto Earthquake", <http://www.gsi.go.jp>, 2016 (in Japanese).
- [8] Imai, T. and Tonouchi, K. "Correlation of N-value with S-wave Velocity and Shear Modulus", Proceedings of the Second European Symposium on Penetration Testing, 1982, pp.67-72.

ESTIMATION OF INITIAL GROUND CONDITIONS UNDER STUPAS BASED ON ONE-DIMENSIONAL CONSOLIDATION THEORY

Yuko Ishida¹, Ayaka Oya², Chaweewan Denpaiboon³, Masamitsu Fujimoto⁴ and Ryoichi Fukagawa⁴

¹Research Organization of Science and Engineering, Ritsumeikan University, Japan;

²Graduate School of Science and Engineering, Ritsumeikan University, Japan;

³Faculty of Architecture and Planning, Thammasat University, Thailand;

⁴Department of Science and Engineering, Ritsumeikan University, Japan

ABSTRACT

Many stupas located within the sacred historical site of Ayutthaya, Thailand are inclined. It is important to understand their ground conditions and causes of inclination in order to design appropriate conservation countermeasures for these precious cultural assets. Soil investigations were conducted at four points around the inclined stupa of Wat Krasai, located outside the World Heritage Site "Historic City of Ayutthaya" in 2013 and 2016. Three key soil layers appear to be responsible for the inclination of this stupa: the second soft clay layer, the third loose silty sand layer, and the fourth hard clay layer. The inclination of this stupa increased as the thickness of the second soft clay layer. Thus, we assumed that the cause of stupa inclination and disproportionate settlement of the stupa was only the second soft clay layer. The amount of settlement and the initial void ratio of this second layer were estimated using the consolidation calculation formula based on Terzaghi's one-dimensional consolidation theory. The results of this study indicate that the amount of settlement is not exactly proportional to the thickness of the second soft clay layer, or that the void ratio is inhomogeneous in the layer. Calculation is conducted in four directions, north, south, east and west, and the maximum settlement and the initial void ratio of the second soft clay layer are estimated at approximately 6.9 m and between 1.46 and 2.48 at the north side of the stupa, respectively.

Keywords: Consolidation, Differential settlement, Void ratio, Inclined cultural assets,

INTRODUCTION

The Phra Nakhon Si Ayutthaya Historical Park is located 86 km north of Bangkok, and is surrounded by three rivers: the Chao Phraya, Pa Sak, and Lopburi. This park is one of the most famous World Heritage Sites in Thailand, attracting around one million visitors every year. This important historic city was registered as a UNESCO World Heritage Site in 1991, and encompasses a total area of 289 ha.

The Kingdom of Ayutthaya included one of the largest cities in Southeast Asia, and was an important regional power for 417 years, between 1350 and 1767. During the 16th century, this kingdom encompassed present-day Laos, Cambodia, and Myanmar. Three palaces and more than 400 temples were built during this time. Many of these structures, however, were subsequently almost completely destroyed by Burmese invaders. Many surviving ruins have been painstakingly restored, and two kinds of architecture are visible in Ayutthaya. The first of these comprise cactus-shaped obelisks called prangs that are indicative of Khmer (from the 9th to the 13th century) influence, while the second are more pointed stupas that exhibit Sukhothai (from the 13th to the mid-15th century) influence. Because stupas consist of weathered bricks, some of them have collapsed, and many are

inclined at an angle.

In this study, we focus on the causes underlying the inclination of stupas, which are in need of conservation. Research was carried out on the leaning stupa of the Wat Krasai temple (indicative of Sukhothai influence), located within the World Heritage expansion planning area, with the permission of the 3rd Regional Office of Fine Arts.

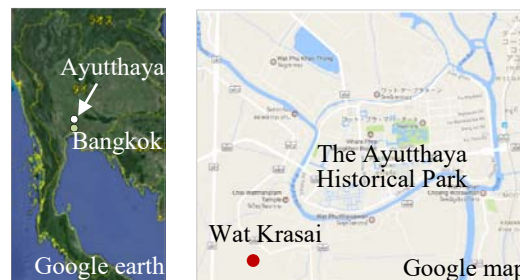


Fig. 1. Location of Ayutthaya and Wat Krasai

PREVIOUS STUDIES AND OUR STUDY OBJECTIVE

Several studies have been conducted investigating the weathering conditions and restoration of cultural assets made of brick,

including the stupas in Thailand. For example, Hatanaka et al. (2013) surveyed the weathered brick stupas at Wat Som and Wat Chaiwatthanaram within the Ayutthaya Historical Area, and developed a restoration method that uses a surface toughening agent [1]. Kuchitsu (1998) surveyed stones used to build historic monuments in Thailand, and concluded that salt efflorescence and bio-deterioration were the causes of brick deterioration [2].

Fujii et al. (2015) monitored the inclined stupa at Wat Langkhakhao using photogrammetry, and confirmed that there was no deformation over the course of approximately 2 years [3]. The National Research Institute for Cultural Properties, Tokyo, investigated the 2011 flood damage of cultural properties in the Ayutthaya Historical Park, and they reported that the 2011 flood did not impact the inclination of these properties [4].

The famous Leaning Tower of Pisa is constructed on three formations. In the past, the cause of creep had been widely attributed to the underlying soft sensitive marine clay, which is normally consolidated. This marine clay is the second layer extending from a depth of 10 m to about 40 m underground. The precision level measurements, which commenced in 1928, revealed the rotation of the tower based on the fact that the center of the foundation plinth had not been displaced vertically relative to the surrounding ground. The cause of the continual long-term rotation of the Tower lies in the first layer. In addition, the most likely cause of the progressive seasonal rotation was a fluctuating ground-water level due to heavy seasonal rainstorms [5]. These studies showed that the inclination of the Tower had multiple causes.

Our project team comprises researchers from Thammasat and Ritsumeikan Universities. We attempted to conduct two studies under the circumstances we are in the lack of accurate information on stupa construction, ground conditions, soil composition, and groundwater levels. Chijiwa et al. (2015) analyzed two cases in Ayutthaya using boring data of the other place in Ayutthaya prefecture, the first of which anticipated the occurrence of two floods over the next 100 years, while the second anticipated no flooding, and subsequently compared the two results after 100 years. The result showed that the stupa are not likely to sink rapidly by floods [6]. Ishida et al. (2016) tried to reproduce the current inclined conditions using a consolidation analysis, working with the assumption that the inclination was caused only due to an imbalance in the stupa weight. The results showed that the cause of inclination does not depend only on the imbalance of stupa weight [7].

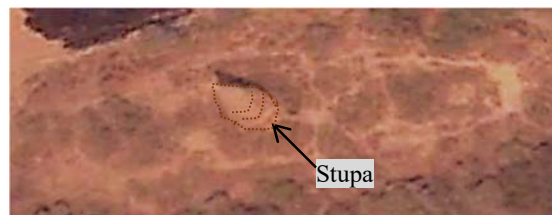
It is possible that the inclination of the stupa may have multiple causes, as in the case of the Leaning Tower of Pisa. However, in this study, we planned

to first attempt to reproduce the current inclination using consolidation analysis from the time of construction of the stupa, assuming that the uneven thickness of the soft clay layer is the cause for inclination. Because physical properties of the soil are change before and after consolidation in general, we have to estimate initial soil parameters. In this study, the methodology of estimating the initial void ratio, which is one of the parameters for consolidation analysis, based on one dimensional consolidation theory is described. The uneven layer thickness and slope angle of the stupa was used in the estimation.

OVERVIEW AND INCLINATION ANGLE OF THE STUPA AT WAT KRASAI

The Wat Krasai site is a long rectangle in the east-west direction. The temple was destroyed and only the stupa remains. The direction of front of the stupa is rotated approximately 8° from east to north. The stupa consists of several parts, an eight-sided pyramid and conical body with a multi-layered structure. This entire structure is hollow, with an approximate height of 27 m and an approximate foundation diameter of 22 m. The stupa is bent, and the inclination of the top and bottom were different, and the base is tilted much more than the head.

Fig. 2 and Fig.3 show the stupa before and after restoration. Before restoration work, the base part of stupa was in a state filled under the ground. Thus, it indicates that the stupa sank below the surrounding ground. The foundation of stupa was excavated, and the octagonal and bottom quadrangular bases were added using a lot of bricks for reinforcement. Additionally, surrounding wall and base of temple was reconstructed.



Before repair (Google earth 2010.3.20 shooting)



After repair (Google earth 2013.2.20 shooting)

Fig.2. Wat Krasai before and after restoration work



Fig.3. Stupa before and after restoration work

The restoration work was carried out on the missing part of the octagonal body, which was below the bell shape in 2013. The entrance of the stupa was closed using bricks, except for small windows on the body in four directions. We observed the internal structure of the small open windows on four sides, and confirmed that the inclination angle of the original bricks and the bricks added during restoration has harmonic relation. Therefore, the inclination of the bricks on the surface of the body can be considered the same as the inclination of the bricks before restoration. The inclination angle of the stupa was obtained by measuring the inclination of the bricks at the yellow and white lines (shown in Fig. 4), using a digital clinometer. Table 1 shows inclination angle measured at 3 points which are the left side, center, and right side in each face.



Fig.4. Inclination measuring station

Table 1. Inclination angle in each face

Direction	Inclination angle (degree)					
	Yellow line			White line		
	Left	Center	Right	Left	Center	Right
North face	2	0	-3	2	0	-1
NorthWest face	-7	-9	-9	-3	-7	-7
West face	-3	-8	-11	-2	-9	-7
SouthWest face	-9	-9	-9	-7	-7	-7
South face	-4	-3	-4	0	0	0
SouthEast face	-2	0	0	2	1	0
East face	1	1	0	0	5	1
NorthEast face	0	1	2	5	5	5

Inclination toward to right is shown in plus and inclination toward to left is shown in minus. Data show that the northern side of the Wat Krasai stupa is the most sunken, followed by the eastern side.

SOIL INVESTIGATION

Standard Penetration Test at 4 points

The topography of the Bangkok plain reflects the fact that it was covered by a shallow marine sea from 3000 to 1000 B.C. Soft clay was deposited in the shallow waters near the shore, and which it is spreading to Ayutthaya [8]. In order to identify ground composition, soil investigations were carried out around the stupa at Wat Krasai. Standard penetration tests (SPTs) at Bor-1 and Bor-2 (shown in Fig. 5) were conducted by the government of Thailand in March 2013, and we carried out additional SPTs at two survey points within Bor-3 and Bor-4 in March 2016.

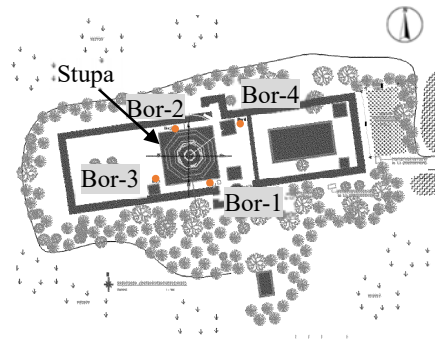


Fig.5. Four points of soil investigation

Relationship between the key soil settlement layer and stupa inclination

We produced four cross-section drawings (Figs. 6–9) of northern side, southern side, eastern side and western side, using data from our soil investigations. Layer thicknesses were prorated by distance from boring points. These drawings illustrate the presence of three key settlement layers. Of these, the second and third layers are soft, while the fourth is hard.

This is illustrated in Fig. 6, where the second layer, a very soft-to-medium stiff clay layer, is much thicker on the northern side than the southern side, and the third layer, a loose-to-medium dense silty sand layer, is also much thicker in the north. In contrast, the fourth layer, a stiff-to-hard clay layer, is much thicker on southern side than the northern side, and it seems to support the stupa. Viewed from west-to-east, the top of stupa is inclined at 2.4° , and the body is inclined approximately 2° to 11° towards the north.

The other orientations are analyzed in the same way, and plotted the difference of the soft layers

thicknesses at the both end sides of the stupa base part as well as the degree of inclination (Fig.10). Results showed that inclination of the stupa correlates roughly with thickness of the soft layers.

ESTIMATION OF INITIAL VOID RATIO

We assumed that the cause of stupa inclination due to disproportionate settlement of the stupa were only the second soft clay layer.

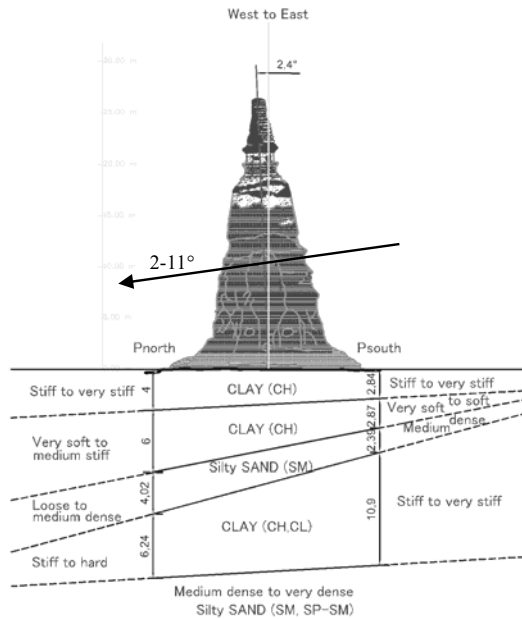


Fig.6. Cross-section drawing of western side

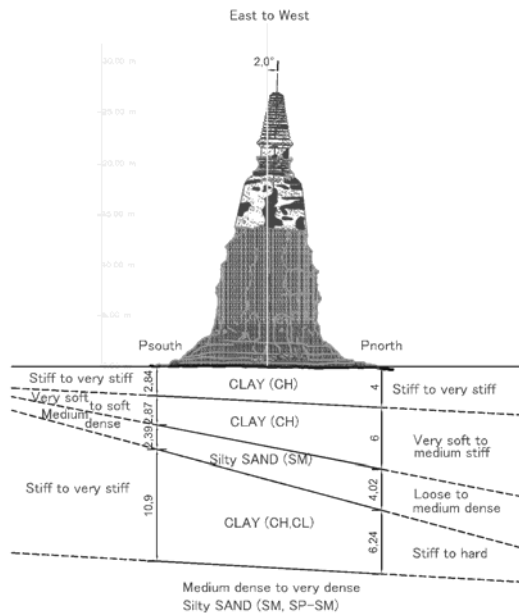


Fig.7. Cross-section drawing of eastern side

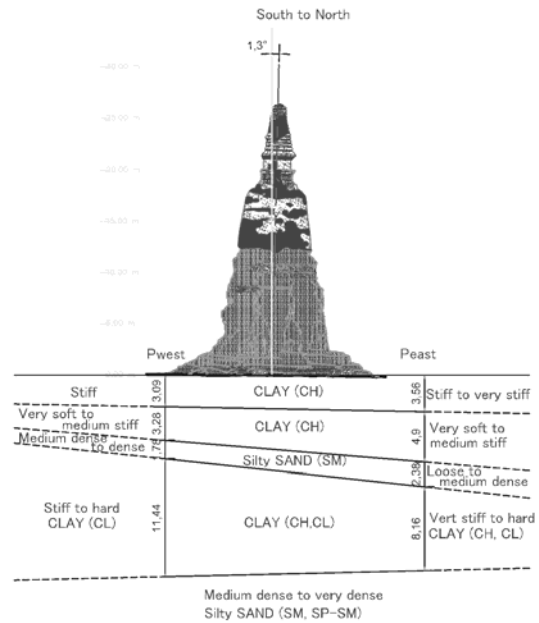


Fig.8. Cross-section drawing of southern side

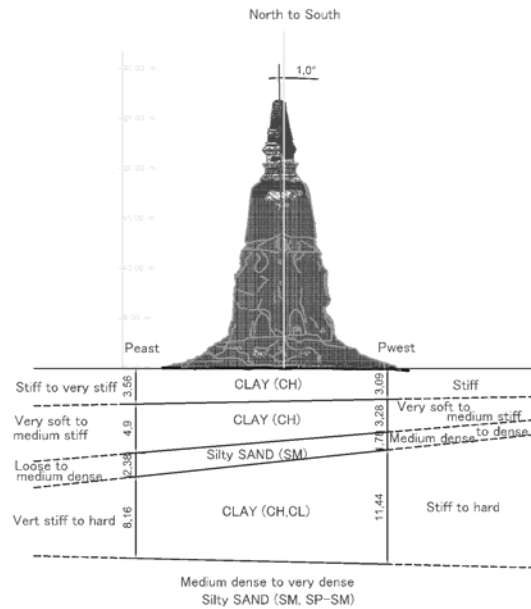


Fig.9. Cross-section drawing of northern side

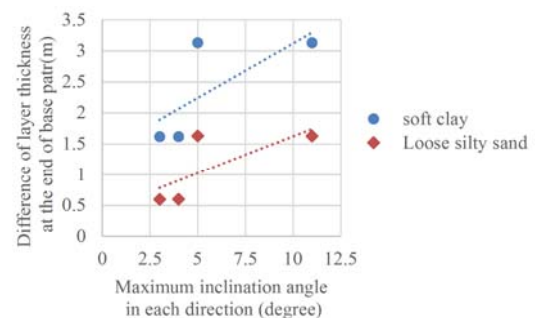


Fig.10. Correlation of layer thickness and inclination

In addition, the amount of settlement due to consolidation and the initial void ratio of the second soft clay layer were calculated using the uneven layer thickness, inclination angle of the stupa, and Eq. (1) based on one dimensional consolidation theory.

$$S = H \frac{\Delta e}{1+e_0} = H \frac{e_0 - e}{1+e_0} \quad (1)$$

In this expression, S refers to the amount of settlement due to consolidation (m), H is the initial thickness of the soft clay layer (m), e is current void ratio (0.62 based on our soil tests), and e_0 is the initial void ratio.

We focused on the difference in layer thickness and the amount of settlement at both ends of the stupa. It was assumed that ground level was horizontal when the stupa built. However, a difference in settlement had occurred over a long period time, caused by the weight of the stupa. It is assumed that the inclination of the stupa is equal to the amount of differential settlement at both ends of the stupa as shown in Fig. 11. In this figure, B refers to the width of octagonal base part, and θ is the inclination angle of the each faces of the stupa. This hypothesis follows Eq. (2), (3), (4), (5), (6), (7).

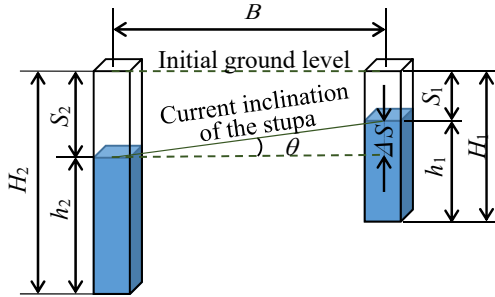


Fig.11. Degree of inclination

$$S_1 = H_1 \frac{e_0 - e}{1+e_0}, \quad e_0 = \frac{S_1 + H_1 e}{H_1 - S_1} \quad (2)$$

$$S_2 = H_2 \frac{e_0 - e}{1+e_0}, \quad e_0 = \frac{S_2 + H_2 e}{H_2 - S_2} \quad (3)$$

$$S_2 = S_1 + \Delta s, \quad \Delta s = S_2 - S_1 \quad (4)$$

$$\Delta s = \tan \theta \cdot B \quad (5)$$

$$H_1 = S_1 + h_1 \quad (6)$$

$$H_2 = S_2 + h_2 = S_1 + \Delta s + h_2 \quad (7)$$

In this expression, S_1 refers to the amount of settlement of the thin layer at the end of the stupa

(m), S_2 refers to the amount of settlement of thick layer at the end of the stupa (m), H_1 refers to the initial thin layer thickness at the end of the stupa (m), H_2 refers to the initial thick layer thickness at the end of the stupa (m), h_1 refers to the current thin layer thickness at the end of the stupa (m), h_2 refers to the current thick layer thickness at the end of the stupa (m), and θ is the inclination angle of the stupa.

S_1 , S_2 , and e_0 were calculated using Eq. (2) and (3) in each directions, north, south, east, west faces. These values are based on the conditions that the initial void ratio of the soft clay layer at both sides of the stupa, differential of the current layer thickness at both sides of the stupa, and settlement differences at both sides of the stupa are the same in each case.

RESULTS AND DISCUSSION

The results of settlement amounts, S_1 and S_2 , as well as e_0 based on maximum inclination angle of each faces are shown in Table 2. As the same way, the inclination angle of 3 cases, average angle, yellow line measurement average angle, white line measurement average angle, were used for calculation. Figure 12 shows settlement amounts in 4 orientations, North, West, South, and East. The maximum settlement amount was estimated 6.90m at western side.

We estimated the initial void ratios in each orientations based on the maximum measurement angle to be within the range of 1.46 to 2.48 as shown in Fig.13. The value of results are in the range of general soft clay.

This estimation method includes some problem, for example in the case of little amount of difference of subsidence. We estimated the inclination angle by measuring on the body bricks. However, because bricks are not perfect shape, the bricks which consists the stupa wall have some minor deviations. In addition, because the inclination is different between top and bottom of the stupa, it is important to decide where sites as the measurement location.

Table.2. Results of the consolidation settlement calculation based on the maximum inclination angle

	North	West	South	East
h_1 (m)	3.28	2.87	3.28	2.87
h_2 (m)	4.90	6.00	4.90	6.00
θ (°)	3.0	11.0	4.0	5.0
B (m)	18.50	18.50	18.50	18.50
Δs (m)	0.97	3.60	1.29	1.62
S_1 (m)	1.96	3.30	2.62	1.48
S_2 (m)	2.93	6.90	3.91	3.10
H_1 (m)	5.24	6.17	5.90	4.35
H_2 (m)	7.83	12.90	8.81	9.10
e	0.62	0.62	0.62	0.62
e_0	1.59	2.48	1.91	1.46

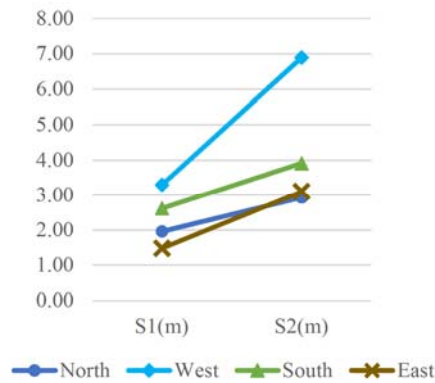


Fig.12. Amount of settlement in 4 orientations

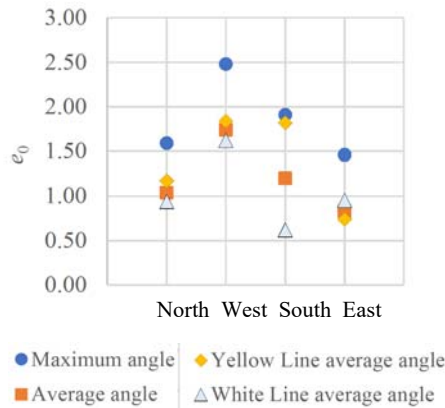


Fig.13. Initial void ratio (e_0) in 4 orientations

CONCLUSION

The settlement due to consolidation under the Wat Krasai stupa was analyzed in this study based on a soil investigation. The result of the soil investigation shows that it is possible that three key layers are responsible for the inclination of this structure, a second soft clay layer, a third loose silty sand layer, and a fourth hard clay layer.

We calculated both the amount of settlement and the initial void ratio of the second soft clay layer. Results indicate that maximum settlement was approximately 6.9 m at the northern end of the stupa, while the initial void ratio falls between 1.46 and 2.48. In the future, consolidation analysis of a model including all soil layers will be required to determine the additional settlement details, and to consider the influence of the other layers.

ACKNOWLEDGEMENTS

We thank the 3rd Regional Office of Fine Arts and the Ayutthaya Historical Park for their cooperation and provision of information. Additionally, we would like to thank Dr. Damrongsak Rinchumphu of Thammasat University, Assistant Professor Weerakaset Suanpaga, and Mr. Chalermchai Trakulphudphong of Kasetsart University for helping with the soil investigations.

REFERENCES

- [1] S. Hatanaka and T. Hasegawa, "Challenge for conservation technique of cultural assets - brick structure-", Concrete Technology, Vol.51(1), 2013, pp.132-136, (in Japanese).
- [2] N. Kuchitsu, "Survey Report on the Stones and Their Weathering at Historic Monuments in Thailand", Conservation Science, No.37, 1998, pp.59-68, (in Japanese).
- [3] Y. Fujii, K. Watanabe, U. Weesakul, N. Poovarodom and B. Bhadrakom, "Measurement of leaning stupas and ground condition in Ayutthaya, Thailand", Proceedings of 50th Japan National Conference on Geotechnical Engineering, Hokkaido, Japan, 2015, (in Japanese).
- [4] National Research Institute for Cultural Properties, Tokyo, "Report on the investigations of the flood damage of cultural properties in the Ayutthaya Historical Park", 2012, pp.1-47.
- [5] John B. Burland, Michele B. Jamiolkowski, Carlo Viggiani, "Leaning Tower of Pisa: Behavior after Stabilization Operations", International Journal of Geoenvironment Case Histories, Vol.1, Issue 3, pp.156-169.
- [6] S. Chijiwa, A. Oya, Y. Ishida, Y. Toyota, M. Fujimoto and R. Fukagawa, "The effect of flood on the differential settlement of the pagoda in Ayutthaya", Journal of Disaster Mitigation for Historical Cities, Vol.9, 2015, pp.17-24, (in Japanese).
- [7] Y. Ishida, S. Chijiwa, A. Oya, C. Denpaiboon, D. Rinchumphu, Y. Toyota, H. Kanegae, M. Fujimoto and R. Fukagawa (2016), "STUDY ON INCLINATION OF PRANG AT AYUTTHAYA, THAILAND", Proceedings of the 6th Vietnam/Japan Joint Seminar on Geohazards and Environmental Issues, 2016, No.S2-5.
- [8] Suksun Horpibulsuk, Satoru Shibuya, Kittitap FuenKajorn, and Wanchai Katkan, "Assessment of engineering properties of Bangkok clay", Canadian Geotechnical Journal, Vol.44, (2), 2007, pp.173-187.

AN EXACT FINITE ELEMENT MODEL FOR AXIAL LOADED PILE IN MULTILAYERED SOIL

Chinnapat Buachart¹, Chayanon Hansapinyo¹, Piti Pratomkhum¹ and Worsak Kanok-Nukulchai²

¹Faculty of Engineering, Graduate School, Chiang Mai University, Thailand

²Asian Institute of Technology, Thailand

ABSTRACT

The nodal exact displacement based finite element method for analyzing axially loaded pile embedded in multi layered of finite depth of elastic soil is presented. The investigation herein is conducted on the condition of shape function by which exact value may be reproduced at the nodal points regarding to a few number of elements. The examined shape functions which satisfy the homogeneous governing equations in each layer of elastic soil are introduced to obtain the so-called exact element stiffness matrix via total potential energy principle. The results obtained from proposed finite element were compared with analytical solution from literature. Axial force and displacement solutions of pile in multi layered soil obtained from proposed finite element model show fairly good agreement with analytical solutions and data from the available literatures.

Keywords: Axially loaded pile, Displacement method, Finite element, Multilayer soil

INTRODUCTION

In this study, the displacement of axially loaded pile embedded in multi-layer soil is solved via proposed finite element procedure. The nodal exact shape function concept suggested in [1]–[4] are used to construct the stiffness matrix and equivalent nodal force incorporate with fixed-point iteration algorithm to solve nonlinear algebraic equations. In each iteration step, the coefficients of differential equation describe pile settlement behavior were estimated easily via component of stiffness matrix and nodal displacement obtained from previous iteration step.

Examples of elasto-static pile embedded in multilayered soil subjected to quasi-static point load on top soil level were analyzed [5]. The results from proposed element are compared with analytical solution obtained from [6] to verify the accuracy of proposed pile element.

MATHEMATICAL FORMULATION

Problem Definition

The analysis considers a single circular cross section pile [5], with radius r_p and total length L_p embedded in a total of N horizontal soil layer (Fig. 1). The pile is subjected to an axial force Q , at the pile head which is flush with the ground surface. The pile itself crosses m layers ($m < N$). All soil layers are assumed to extend to infinity in the radial direction, and the bottom layer (N^{th} layer) also extends to infinity in downwards direction (half-space) as shown in Fig. 1. The soil medium in any layer (i^{th} layer, where $i = 1, \dots, N$) is assumed to be elastic and

isotropic material, with elastic properties described by soil shear modulus G_{si} and Poisson's ratio ν_{si} . The vertical depth from the ground surface to the bottom of any layer i is denoted by H_i . Hence, the thickness of each layer L_i is computed by $H_i - H_{i-1}$ with $H_0 = 0$. The pile is assumed to behave as an elastic column with Young's modulus E_p . The Poisson's ratio of the pile material is neglected.

Governing Differential Equations

Since the cylindrical pile settlement problem in Fig. 1 is axisymmetric. Hence, we use the system of cylindrical coordinates (r - z coordinate) to indicate any position in pile and soil bodies. The origin of cylindrical coordinate coincide with the center of pile cross section at the pile head level. The vertical (positive in downward direction) coordinate z -axis is coincide with pile axis. The non-slip conditions between pile surface and surrounding soil and between soil layers are assumed. The vertical displacement $u_z(r, z)$ at any point in the soil is represented as product of two functions in r and z coordinates as follows:

$$u_z(r, z) = w(z) \cdot \phi(r) \quad (1)$$

where $w(z)$ is the vertical displacement of pile at any point along pile axis, and $\phi(r)$ is the soil displacement decay function in the radial direction.

Then, the calculus of variations are used to obtain the governing differential equation in pile and surrounding soil by define the strains from displacement functions in Eq. (1), and prescribe the

variation of total potential energy with respect to w and ϕ equal to zeros [6]. The governing differential equation for the pile and soil below the pile tip is as follow:

$$-(E_i A_i + 2t_i) \frac{d^2 w_i}{dz^2} + k_{si} w_i = 0 \quad (2)$$

where $E_i = E_p$ and $A_i = A_p$ when $1 \leq i \leq m$ (along pile axis), and $E_i = \lambda_{si} + 2G_{si}$ and $A_i = \pi r_p^2$ when $(m+1) \leq i < N$ (soil below the pile tip). The elastic constant $\lambda_{si} + 2G_{si}$ is a function of Poisson's ratio ν_{si} and shear modulus G_{si} of soil:

$$\lambda_{si} + 2G_{si} = \frac{2G_{si}(1-\nu_{si})}{(1-2\nu_{si})} \quad (3)$$

Note that the coefficients k_{si} , and t_i represent the shear and compressive resistances of soil mass against pile settlement. Both k_{si} , and t_i are a function of decay function ϕ and elastic properties of soil as follow:

$$k_{si} = 2\pi G_{si} \int_{r_p}^{\infty} r \left(\frac{d\phi}{dr} \right)^2 dr \quad (4)$$

$$t_i = \pi(\lambda_{si} + 2G_{si}) \int_{r_p}^{\infty} r \phi^2 dr \quad (5)$$

The governing differential equation for the soil surrounding the pile can be obtained by taking the variation of total potential energy with respect to ϕ equals to zero:

$$\frac{d^2 \phi}{dr^2} + \frac{1}{r} \frac{d\phi}{dr} - \left(\frac{\gamma_r}{r_p} \right)^2 \phi = 0 \quad (6)$$

where

$$\frac{\gamma_r}{r_p} = \sqrt{\frac{n_s}{m_s}} \quad (7)$$

$$m_s = \sum_{i=1}^N G_{si} \int_{H_{i-1}}^{H_i} w_i^2 dz \quad (8)$$

$$n_s = \sum_{i=1}^N (\lambda_{si} + 2G_{si}) \int_{H_{i-1}}^{H_i} \left(\frac{dw_i}{dz} \right)^2 dz \quad (9)$$

and the solution of Eq. (6) with boundary conditions $\phi(r) = 0$ at r extend to infinity, and $\phi(r) = 1$ at $r = r_p$

is a zero order modified Bessel function of the second kind:

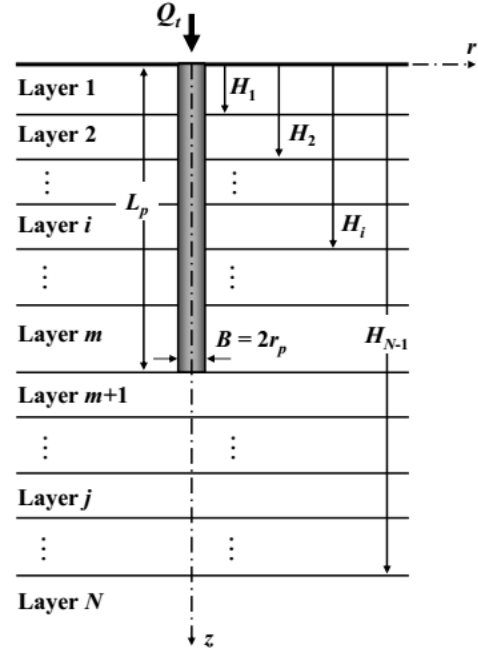


Fig. 1 Axially loaded pile and multi-layer soil [5]

$$\phi(r) = \frac{K_0 \left(\frac{\gamma_r}{r_p} r \right)}{K_0(\gamma_r)}; r_p \leq r \leq \infty \quad (10)$$

Substituting decay function $\phi(r)$ into Eqs. (4) and (5), obtain the explicit formula for coefficients k_{si} and t_i in terms of modified Bessel function of second kind, zero and first orders [6]:

$$k_{si} = \pi G_{si} \left[\gamma_r^2 (1 - \eta^2) + 2\gamma_r \eta \right] \quad (11)$$

$$t_i = \frac{1}{2} \pi r_p^2 (\lambda_{si} + 2G_{si}) (\eta^2 - 1) \quad (12)$$

where the coefficient η is the ratio between the modified Bessel function of the second kind of first order K_1 and zero order K_0 , i.e.:

$$\eta = \frac{K_1(\gamma_r)}{K_0(\gamma_r)} \quad (13)$$

The general solution of Eq. (2) is given by:

$$w_i(z) = B_i \cosh(\alpha_i z) + C_i \sinh(\alpha_i z) \quad (14)$$

where B_i and C_i are integration constant. The characteristic parameter α_i of pile and soil interaction is expressed as follow:

$$\alpha_i = \sqrt{\frac{k_{si}}{(E_i A_i + 2t_i)}} \quad (15)$$

Note that the dimension of parameter α_i is inversion of length. An axial force $Q_i(z)$ at a depth z in the i^{th} layer is obtained defined as:

$$Q_i(z) = -(E_i A_i + 2t_i) \frac{dw_i}{dz} \quad (16)$$

or explicitly in the form:

$$Q_i(z) = -a_i [B_i \sinh(\alpha_i z) + C_i \cosh(\alpha_i z)] \quad (17)$$

where $a_i = \alpha_i (E_i A_i + 2t_i)$, the integration constants B_i and C_i in Eqs. (14) and (17) can be determined analytically from the procedure proposed in [5].

Finite Element Formulation

Consider one-dimensional element in Fig. 2, which represents the portion of pile embedded in any one layer of surrounding soil governed by Eq. (2). Assuming that soil surrounding pile element is in elastic condition for whole length. Shear resistance of soil is represented by equivalent soil spring coefficient k_{si} . Pile element in Fig. 2 compose of two nodes at top and bottom, numbering with node 1 and 2, respectively. The total potential energy of this soil-pile element subjected to an equivalent nodal forces P_1 and P_2 is defined as the sum of internal potential energy (strain energy) and the external potential energy due to external load as follow [4]:

$$\Pi = \frac{1}{2} \left[(E_i A_i + 2t_i) \int_0^L \left(\frac{dw}{dz} \right)^2 dz + k_{si} \int_0^L w^2 dz \right] - P_1 w_1 - P_2 w_2 \quad (18)$$

where $w(z)$ is the vertical pile displacement at depth z where $0 \leq z \leq L$. The first variation of Eq. (18) leads to:

$$\delta \Pi = (E_i A_i + 2t_i) \int_0^L \left(\frac{d\delta w}{dz} \right) \left(\frac{dw}{dz} \right) dz + k_{si} \int_0^L (\delta w) w dz - P_1 \delta w_1 - P_2 \delta w_2 \quad (19)$$

Note that the origin of vertical coordinate along the pile axis in potential function, Eq. (18), is now moved to the top node of pile portion, instead of pile head on ground level. The nodal displacement at top and bottom nodes are denoted by w_1 and w_2 , respectively. Suppose that the pile portion at i^{th} layer is considered, the pile length can be computed from different of bottom depth between nearby soil layer, i.e. $L = H_i - H_{i-1}$.

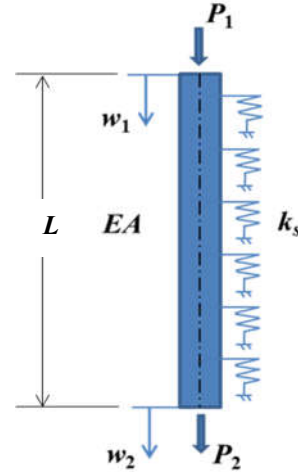


Fig. 2 Axially loaded pile element [4]

Applying the appropriate Gauss-Green theorem to Eq. (19) and setting $\delta \Pi = 0$, gives the differential equation for equilibrium similar to Eq. (2), and a set of natural boundary conditions as follows

$$P_1 = -(E_i A_i + 2t_i) \frac{dw}{dz} \Big|_{z=0} \quad (20)$$

$$P_2 = (E_i A_i + 2t_i) \frac{dw}{dz} \Big|_{z=L} \quad (21)$$

The natural boundary condition at first node, Eq. (20) is similar to axial load expression in Eq. (16).

Interpolation function

To construct the system of algebraic equations with respect to nodal displacement, the trial solution of $w(z)$ in Fig. (2) is introduced in the form:

$$w(z) = w_1 N_1(z) + w_2 N_2(z) \quad (22)$$

The shape functions in Eq. (22) are taken from homogeneous solution of Eq. (2), i.e.

$$N_1(z) = \frac{\sinh[\alpha_i (L-z)]}{\sinh \beta_i} \quad (23)$$

$$N_2(z) = \frac{\sinh(\alpha_i z)}{\sinh \beta_i} \quad (24)$$

where the dimensionless parameter $\beta_i = \alpha_i L$.

In present work, the proposed finite element procedure to solve Eq. (2) for a given load Q_i (Fig. 1) will be explained in next section. Then, the results from proposed nodal exact element will be compared with available analytical solution in [5, 6].

Fixed-Point Iteration

According to Eqs. (8) and (9), the shape parameter of decay function, namely γ_r in Eqs. (6) and (7) depends on pile settlement $w(z)$. Hence, the finite element discretization of Eq. (19) with trial displacement function in Eq. (22) leads to the steady steady-state set of non-linear algebraic equations as follow:

$$\mathbf{K}(\mathbf{w})\mathbf{w} = \mathbf{f} \quad (25)$$

In which stiffness matrix \mathbf{K} is a non-linear function of nodal displacement \mathbf{w} . The external nodal load \mathbf{f} is presented in term of specified vector. The nodal solution \mathbf{w} is obtained by solving an algebraic equation via fixed point iteration technique [7]:

$$\mathbf{K}^{(n-1)}\mathbf{w}^{(n)} = \mathbf{f} \quad (26)$$

where $\mathbf{K}^{(n-1)} = \mathbf{K}(\mathbf{w}^{(n-1)})$, $n = 1, 2, \dots$, is stiffness matrix evaluated from nodal solution \mathbf{w} at previous iteration step. An iteration is repeated until the value of γ_r converged. In this work, the convergence criteria are:

$$|\gamma_r^{(n)} - \gamma_r^{(n-1)}| < 10^{-5} \quad (27)$$

Note that the convergence criteria used in Eq. (27) is similar with criteria used in [5, 6].

Element Stiffness Matrix

Element stiffness matrix in Eqs. (25) and (26) can be derived from first variation of strain energy term in Eq. (19) by substitute the trial solution $w(z)$ and variation $\delta w(z)$ interpolated by the shape functions proposed in Eqs. (22) and (23). Hence, the stiffness matrix of layer i can be defined as:

$$\mathbf{K}_i = a_i \begin{bmatrix} \coth \beta_i & -\operatorname{csch} \beta_i \\ -\operatorname{csch} \beta_i & \coth \beta_i \end{bmatrix} \quad (28)$$

where parameter a_i was already defined in Eq. (17). The element stiffness matrices in Eq. (28) are

assembled to form global stiffness in Eq. (25).

At the bottom most layer (layer N), the thickness is assumed to be infinity, and nodal displacement at bottom most point is prescribed to zero. Hence, the element stiffness matrix in Eq. (28) has to be redefined. Convergence of hyperbolic function when $L \rightarrow \infty$ shows that the element stiffness matrix for N^{th} layer is similar with penalty spring coefficient [8] attached to N^{th} degree of freedom, w_N , with the following form:

$$k_{NN} = a_N = \alpha_N (E_N A_N + 2t_N) \quad (29)$$

The convergence of hyperbolic function also shows that the displacement in N^{th} layer can be interpolated via the form below:

$$w(z) = w_N [\cosh(\alpha_N z) - \sinh(\alpha_N z)] \quad (30)$$

The interpolation of w in Eqs. (22) and (30) are then used to compute axial force according to Eq. (16). Note that coordinate z in Eqs. (22)–(30) is local coordinate defined in i^{th} -layer.

Calculation of Decay Parameter

The value of decay parameter γ_r in any iteration step of Eq. (26) can be evaluated from nodal displacement solution \mathbf{w} in each step. Substituting the displacement function, Eq. (22), into Eqs. (8) and (9) obtained:

$$m_s = \sum_{i=1}^{N-1} \frac{G_{si}}{2\alpha_i} \left[(\coth \beta_i - \beta_i \operatorname{csch}^2 \beta_i) (w_i^2 + w_{i+1}^2) - \right. \\ \left. + \frac{G_{sN}}{2\alpha_N} w_N^2 \right] \quad (31)$$

$$n_s = \sum_{i=1}^{N-1} \frac{\alpha_i \bar{E}_{si}}{2} \left[(\beta_i \operatorname{csch}^2 \beta_i + \coth \beta_i) (w_i^2 + w_{i+1}^2) - \right. \\ \left. + \frac{\alpha_N \bar{E}_{sN}}{2} w_N^2 \right] \quad (32)$$

where $\bar{E}_{si} = \lambda_{si} + 2G_{si}$, the values m_s and n_s are then put into Eq. (7) to compute the parameter γ_r .

NUMERICAL EXAMPLES

In this section, two numerical examples are presented to illustrate the effectiveness of nodal exact finite element proposed in previous section. Results from proposed element are verified using analytical solutions available in [5, 6].

Pile with Ideal Rigid End Bearing

In this example, we study the behavior of pile in homogeneous soil (one layer) subjected to pile head load as shown in Fig. 3. The ratio between pile elastic modulus and soil shear modulus is set to be $E_p/G_s = 3000$, and Poisson's ratio $\nu_s = 0.4999$. The pile tip is assumed to rest on a rigid layer and pile diameter $B = 2r_p = 0.2$ m. Note that this problem was already solved in [6], and repeat hear to verify our proposed finite element model.

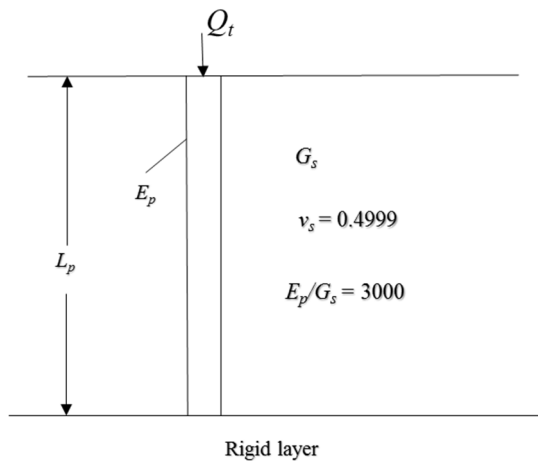


Fig. 3 Pile rest on rigid layer [6]

Figure 4 shows relation between the normalized pile head stiffness K_N versus normalized pile length L_p/B . The normalized pile head stiffness is defined as $K_N = Q_t/(w_0 E_p B)$ where w_0 = settlement at pile head. The plot in Fig. 4 were obtained with the finite element analysis proposed in this work and from analytical method in previous study [5]. The normalized pile head stiffness in Fig. 4 decreases with increasing of normalized pile length. The results of finite element analysis presented in this work is in good agreement with previous study in [6].

Micropile (Italy)

This example present the case of micro-pile, which was installed in a complex soil profile [6]. The soil profile and pile length are shown in Fig. 5. Pile diameter and length are equal to 0.2 m and 19 m, respectively. Modulus of elasticity of pile is approximately 27 GPa. In all soil layers, the Poisson's ratio was assumed to be 0.3. The values of soil depth, shear modulus, and Poisson's ratio of Fig. 5 are listed in Table 1. The numerical test was performed using four proposed nodal exact elements with four active degree of freedom. Figure 6 shows the calculated pile head settlement versus input pile head load. Figure 7 shows measured and calculated load-transfer curves for applied load equal to 50, 250, and 500 kN. These

figures show that there is very good agreement between proposed finite element and analytical solution in literature [5].

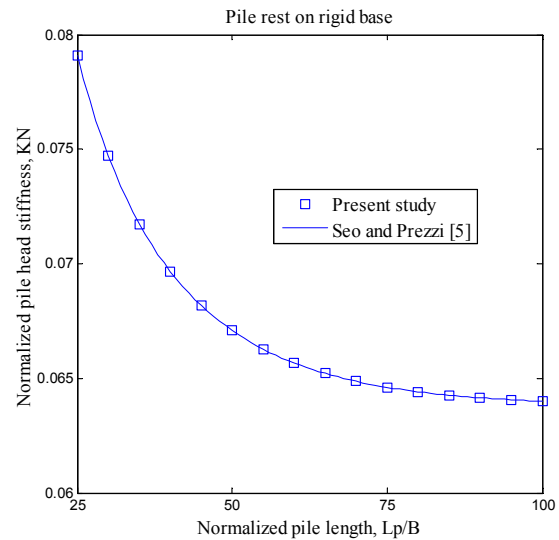


Fig. 4 Normalized pile head stiffness versus normalized pile length of rigid-end pile

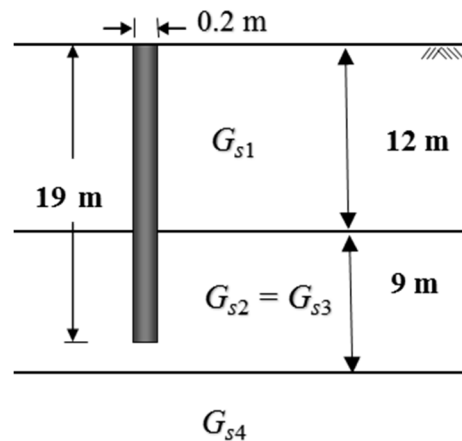


Fig. 5 Soil Profile of Italy case [5]

Table 1 Input properties for the analysis of micropile tested in Italy ($B = 0.2$ m, $L_p = 19$ m, $E_p = 27$ GPa)

Layer	H_i (m)	G_{si} (MPa)	ν_{si}
1	12	19.2	0.3
2	19	45.0	0.3
3	21	45.0	0.3
4	∞	53.1	0.3

CONCLUSION

The finite element model for pile embedded in multilayered elastic soil subjected to axial load is

proposed. The nonlinear algebraic equation has been solved via fixed point iteration. Numerical examples for static load pile embedded in multi layered elastic soil were tested by proposed finite element compare with available analytical solution from literature. Two problems, composed of pile resting on rigid base, and infinite bottom depth were solved to obtain pile settlement and load transfer curves. Numerical test indicates that the proposed finite element method are very good agreement with available analytical solution proposed in literature.

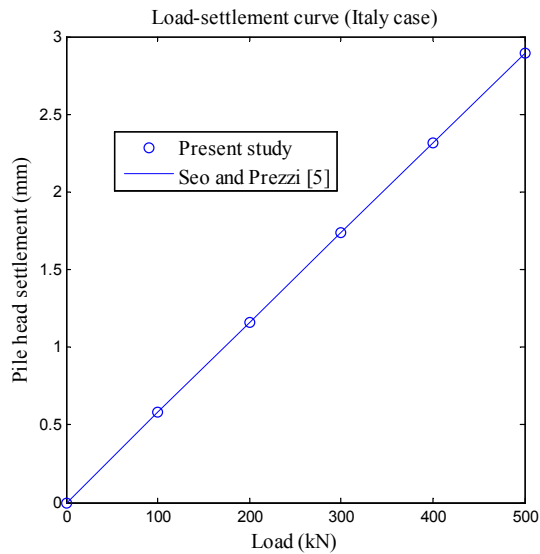


Fig. 6 Load-settlement curve at pile head (Italy case)

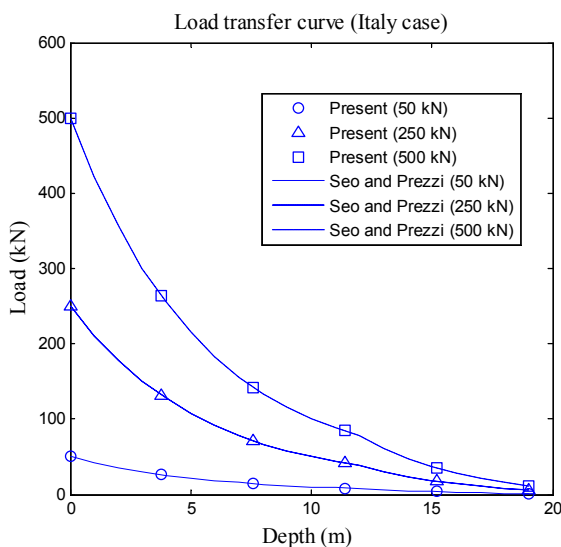


Fig. 7 Load-transfer curve for pile head load equal to 50, 250, and 500 kN (Italy case)

ACKNOWLEDGEMENTS

The author acknowledge the financial support received from Thailand Research Fund (New Researcher Grant TRG5880066).

REFERENCES

- [1] Tong P, "Exact solutions of certain problems by finite element method", AIAA J., Vol. 7, 1969, pp. 178-180.
- [2] Kanok-Nukulchai W, Dayawansa PH, and Karasudhi P, "An exact finite element model for deep beams", Int. J. of Struc, Vol. 1, Jan. 1981, pp. 1-7.
- [3] Ma H, "Exact solutions of axial vibration problems of elastic bars", Int. J. Numer. Meth. Eng., Vol. 75, 2008, pp. 241-252.
- [4] Buachart C, Hansapinyo C, and Sommanawat W, "An exact displacement based finite element model for axially loaded pile", Int. J. of GEOMATE, Sept., Vol. 11(25), 2016, pp. 2474-2479.
- [5] Seo, H and Prezzi, M, "Analytical solutions for a vertically loaded pile in multilayered soil", Geomechanics and Geoengineering: An International Journal, Vol. 2(1), 2007, pp. 51-60.
- [6] Seo, H, Prezzi, M, and Salgado, R, "Settlement analysis of axially loaded pile", International Conference on Case Histories in Geotechnical Engineering, Vol. 27, 2008, pp. 1-8.
- [7] Chapra SC, Applied Numerical Methods with Matlab for Engineers and Scientists. McGraw-Hill, 2005.
- [8] Zienkiewicz OC and Taylor RL, The Finite Element Method. Vol. I. Oxford: Butterworth-Heinemann, 2000.

STABILITY ANALYSIS FOR AN AIRPORT EMBANKMENT, EVALUATING SHORT AND LONG TERM TECHNIQUES

Ignacio Fructuoso Solís Quispe¹, José Carlos Solís Tito² and Mario Edisson Quilli Apaza³

¹Faculty of Civil Engineering, Universidad Nacional de San Antonio Abad del Cusco, Perú; ^{2,3} Universidad Nacional de San Antonio Abad del Cusco, Perú

ABSTRACT

This article discusses the stability analysis corresponding to the construction project of a runway embankment over soft clay, to reach the subgrade level, that conform the foundation of the runway No. 16/34, for the project Aeropuerto Internacional de Chincheros Cusco - Peru (AICC). The safety analysis consists in evaluating the strength reduction of the foundation, considering the effect of the consolidation, for the short term and long-term construction techniques considering the soil improvement with preloading, vertical geodrains and stone columns techniques. The numerical analysis is developed with the Plaxis 2D v8.6 software, considering a typical section corresponding to a critical sector, located on the km 1+180 progressive of the landing strip. According to the results of the definitive geotechnical study, the foundation soil, corresponding to the analysis section, is a saturated soft clay, until a depth of 35 m; then to model its mechanical behavior was used the Soft Soil Model; and for the embankment, that will be constructed of compacted soil obtained from the ground cutting process, was considered the Mohr Coulomb model. The physical and mechanical parameters were established based on the results of field and laboratory test, correlations and referential values established in the specialized bibliography. From the comparative results based on the calculated safety factors, the stone columns technique, presents a higher factor of safety compared to the preloading and vertical geodrains techniques; while considering the short-term construction, the foundation soil fails due to loss of strength before reaching the total embankment height.

Keywords: Stability of Embankment, Numerical Analysis, Stone Columns, Vertical Geodrains.

INTRODUCTION

The construction of the embankment for the runway of the project Aeropuerto Internacional de Chincheros Cusco - Perú (AICC) will allow to reach the level of subgrade, which will form the ground of foundation for the subsequent construction of the runway No. 16/34 (Fig. 1), whose heights vary from 7 m to 13 m according to the site topography [1].

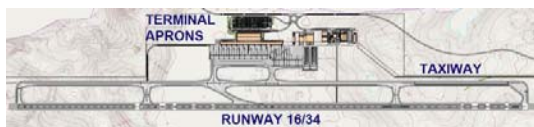


Fig. 1 Location of runway No. 16/34 and Taxiways of the AICC project.

The subsurface exploration (trial pits, borings, drillings) and in-situ testing [5] allowed to identify the type and the geological formation of the soils in the zone, standing out its origin of lakebed (central zone), being this zone an old lake that over time was filled with sediments.

In the longitudinal ground profile corresponding to runway No. 16/34 (Fig. 2), are shown the cut zones (S1, S3) and fill areas (S2, S4). The zone of

the central sector (S2) on which the embankment will be constructed, is considered like a quaternary deposit of lake origin compound for a sequence of fine soils, shaped for silts and organic clays of medium to high plasticity and typical inorganic soils of elevated zones [5].

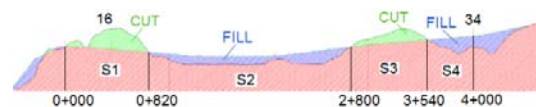


Fig. 2 Longitudinal ground profile corresponding to the runway shaft No. 16/34.

Posterior studies executed [1], concluded that the zone of the central sector of sedimentary origin is composed of fine soft soil permanently saturated due to the accumulation of pluvial water, and mostly correspond to gypsum in saturated state, which gives a whitish color to the surface. According to the USCS, soils are classified as CL, ML and MH.

In the definitive study [8] the longitudinal soil profile of the runway No. 16/34 is presented (Fig. 3), and indicates that the soft soils composed of clays and silts, located between the progressive Km 1+100 to 1+860, with a power of 35m, have weak compressive strengths lower than 0.25 kg/cm².

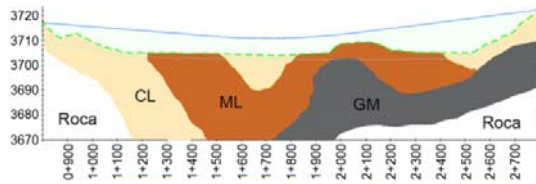


Fig. 3 Longitudinal soil profile of the runway No. 16/34.

In the present paper the stability analysis corresponding to the construction of the runway embankment No. 16/34 on soft clay is developed, in a representative critical section located at Km 1+180 [7], onto the soft soil zone described in the definitive study.

The stability analysis comprises the evaluation of the embankment construction without ground improvement compared with improvement techniques such as preloading, vertical geodrains and stone columns [2]. The analysis is developed numerically using the finite element method, with the Plaxis 8.6 software, considering a 2D analysis with a plane strain model [6]. The numerical analysis provides the results of settlements, consolidation times, factor of safety (FS) expressed in graphs, corresponding to the process of embankment construction, comparing indicated techniques.

METHODOLOGY

The geotechnical parameters of the materials were established based on the results of the field and laboratory tests, correlations and reference values established in the specialized bibliography related to the subject. The results of the site investigation performed in the zone close to the critical section (Fig. 4) allowed to define the soft soil geotechnical parameters to define the constitutive model for the numerical analysis.

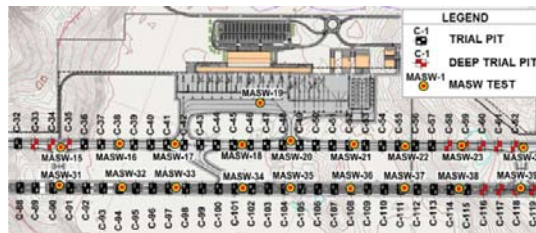


Fig. 4 MASW test and trial pits location plan, in the central zone of the runway No. 16/34.

The definitive study of the project consisted of the execution of field and laboratory tests, as shown in Table 1.

Table 1 Most relevant field and laboratory tests performed to characterize the soil for the AICC.

Test	Geotechnical parameters
Ground Investigation	
Trial pits	LL, IP, G_s
Compaction test	γ_{nat}
DPL	N_{10}
SPT	N_{SPT}
Drilling	sampling
Lefranc Test	k_x
Piezometers	h_p
Geophysical Investigation	
Seismic Refraction	V_p
MASW Test	V_s
MAM Test	V_s
ERT Test	Ohm-meter
Laboratory Investigation	
Sieve analysis	C_u, C_c
Atterberg limits	LL, IP
Unconfined compression test	S_u
Consolidation	e_o, C_c, C_r, P_c, C_v
Proctor Compaction Test and CBR Test	γ_{dmax}, CBR
Triaxial UU	S_u
Permeability (flexible-wall permeameter)	k_y

In the lakebed zones of the profile, the embankment will be formed by filling, with the cutting materials of the elevated zones, as shown in the longitudinal profile (Fig. 2), and mainly the soils correspond to clays with presence of sand, evaluated with the Proctor Compaction and CBR test.

The stability and consolidation analysis for the construction of the embankment were executed with the Plaxis 8.6 software. The method for the safety calculation at each stage of the embankment construction was the phi-c reduction, using the total multiplier factor ΣMsf , which represents the factor of safety [6]. For stability analysis it was considered as a minimum factor of safety $FS = 1.3$, which allows to evaluate the maximum stable elevation of embankment construction.

The consolidation analysis was developed to evaluate soil improvement techniques. For this analysis, the application of load was considered through the option minimum excess pore pressure [6], with a value of 5 KN/m^2 , which is a criterion to finish the analysis of consolidation, then the calculation stops when the absolute maximum excess pore pressure is less than the prescribed value of $|P\text{-stop}|$ [6].

For modeling the embankment construction, it was considered the application of load by means of the option staged construction [3], which allows specifying a new state for each increase of embankment elevation, to be reached at the end of the calculation phase [6]. To each stage was specified a time interval of the calculation phase of 5 days, considering the effect of the consolidation, for each increase of load established by the embankment elevation. The results corresponding to the settlements were evaluated at a point located in the central zone of the base of the embankment, at the ground surface.

The stability analysis of the embankment construction comprises two periods; the first consisted in determining the maximum elevation of embankment construction without considering improvement techniques, evaluating the stability of the embankment by means of the established minimum factor of safety; for this period an embankment elevation of 4.5 m was reached. For the second period of the analysis the improvement techniques of the soft soil were evaluated, applying the improvement techniques elements to the geometry established by the maximum embankment elevation stable without improvement techniques (evaluated in the first period). For this latest geometry, the period of consolidation for the clay was considered, until a minimum excess pore pressure of 5 KN/m² was reached; and later the embankment elevation was gradually increased every 1 m, controlling the minimum factor of safety, until reaching the elevation established by the project of 9.5m. The results corresponding to the settlements and duration times for each construction technique are compared, and allow establishing the advantages of the improvement techniques.

For the geometric model of the embankment (Fig. 5) it was considered to analyze half of its geometry for reasons of symmetry. A length of 60 m at the base, a slope of 1:2 (V:H) and a height of 9.5 m specified in the project were considered.

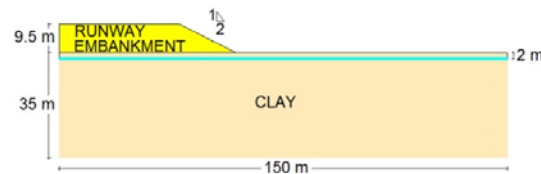


Fig. 5 Geometric model considered for the analysis of section Km 1+180.

The stone columns technique has a distribution of square grid, with columns diameter of 1 m, separated 3 m and an area of influence of 8 m² per column. For its modeling was considered the transformation of its geometry using an equivalent geometry to perform the plane strain analysis [4],

considering each row of stone columns as an equivalent longitudinal trenches with the same area [9], resulting for the numerical modeling, the diameter columns of 0.30 m and the separation between axes of 2.70 m.

For vertical geodrains, a triangular distribution with a separation of 1.5 m and an area of influence of 2 m² for each vertical geodrain were adopted. In the consolidation analysis, drain elements were used, considering a null value of excess pore pressure at all nodes (finite element mesh) along the lines representing the drains in the model [6].

To model the behavior of the materials, constitutive models available in the program Plaxis 8.6 were used. For the embankment, stone columns and drainage layer the linear elastic perfectly plastic Mohr-Coulomb model was used. For the soft clay, the Soft Soil model was used, which provides adequate results in situations of primary consolidation; these parameters are shown in Table 2

Table 2 Geotechnical Properties

Material		Clay	Embankment	Stone column, Drainage layer
Model		Soft Soil	Mohr Coulomb	Mohr Coulomb
Behavior		Undrained	Drained	Drained
General Parameters				
γ_{unsat}	kN/m ³	15.7	19.5	19.0
γ_{sat}	kN/m ³	16.0	20.0	20.0
k_x	m/day	4.41×10^{-5}	2.94×10^{-5}	10.022
k_y	m/day	2.94×10^{-5}	2.94×10^{-5}	10.022
Model Parameters				
E'	kN/m ²		24769	30000
ν'	-		0.3	0.3
c'	kN/m ²	11.0	32.0	1.0
ϕ'	°	2.0	10.0	42.0
ψ	°	0.0	0.0	0.0
e_o	-	1.403		
C_c	-	0.207		
C_s	-	0.026		
Interface				
R_{inter}	-	1.0	1.0	1.0

DISCUSSION OF RESULTS

The embankment construction on the soft clay was considered in stages, with increases of the embankment elevation in layers of 1 m, beginning with a drainage layer of 0.5 m covered by a geotextile at the base of the embankment to allow a better distribution of loads and drainage. Fig. 6 shows the finite element mesh corresponding to the

geometric model for the embankment construction without any soil improvement technique

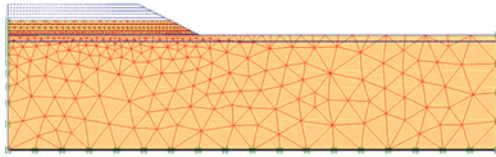


Fig. 6 Finite element mesh for analysis without improvement technique.

Figure 7 shows the result of safety analysis for different embankment elevations and Fig. 8 shows the diagram of settlement increase in function of the elevation of embankment construction and the period of time for each calculation phase, for the construction without improvement technique, reaching a factor of safety of 1.32 and a settlement of 11.1cm, in a period of time of 25 days, for an elevation of 4.5 m. This calculated elevation was the reference for the beginning of the consolidation period for the posterior improvement techniques analyzed.

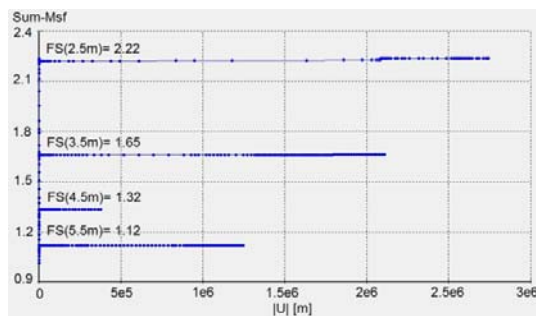


Fig. 7 Factors of safety as a function of construction elevations, for construction without improvement techniques.

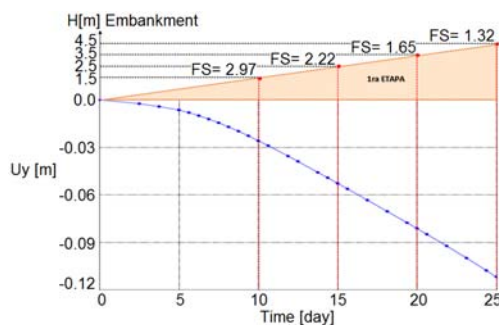


Fig. 8 Settlements vs. embankment elevation with the time, for construction without improvement techniques.

Figure 9 shows the finite element mesh constructed for this analysis.

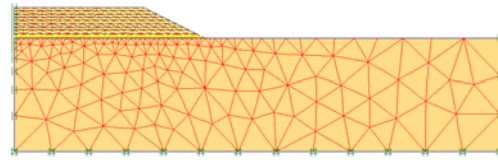


Fig. 9 Finite element mesh for analysis of preloading technique.

Figure 10 shows the result of safety analysis for different embankment elevations and Fig. 11 shows the diagram of settlement increase in function of the elevation of embankment construction and the period of time for each calculation phase, for the construction with preloading technique, reaching a factor of safety of 1.32 and a settlement of 87.5 cm, in a period of time of 31.77 years, for an elevation of 5.5 m.

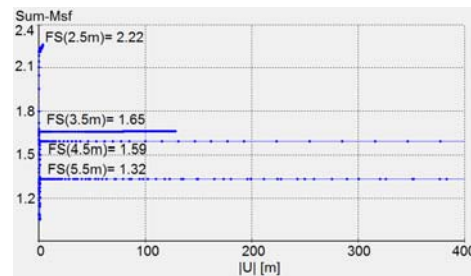


Fig. 10 Factors of safety as a function of construction elevations, for construction with preloading technique.

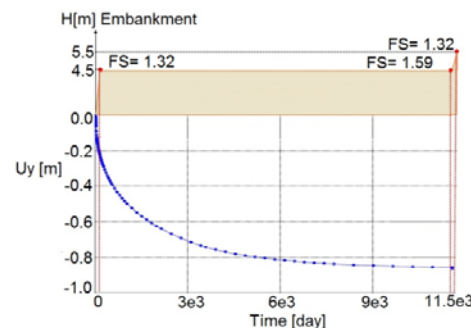


Fig. 11 Settlements vs. embankment elevation with the time, for construction with preloading technique.

In order to accelerate the consolidation and reduce the preloading time, the soil permeability is improved by installing vertical geodrains. Fig. 12 shows the finite element mesh for this analysis considering the drain elements with geometric lines.

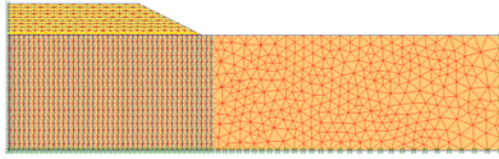


Fig. 12 Finite element mesh for analysis of vertical geodrains technique.

Figure 13 shows the results of the safety analysis for different embankment elevations, and Fig. 14 shows the diagram of settlement increase in function of the elevation of embankment construction and the period of time for each calculation phase, for construction with vertical geodrains technique, reaching a factor of safety of 1.34 and a settlement of 96.6 cm, in a period of time of 220 days, for an elevation of 5.5 m.

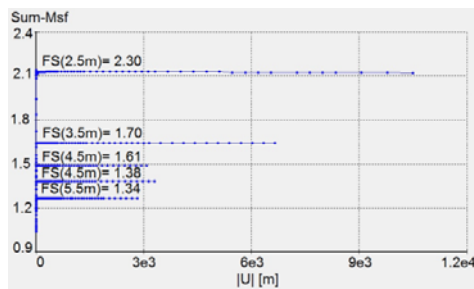


Fig. 13 Factors of safety as a function of construction elevations, for construction with vertical geodrains technique.

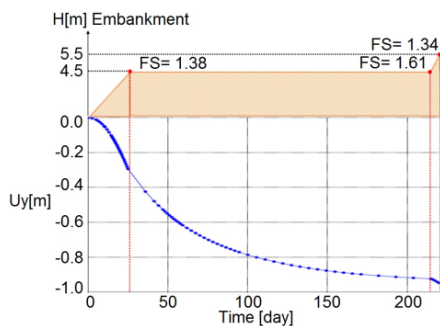


Fig. 14 Settlements vs. embankment elevation with the time, for construction with geodrains technique.

The technique of stone columns improves the soil strength due the rigidization, decreasing the settlement and improves the drainage. Fig. 15 shows the finite element mesh for this analysis.

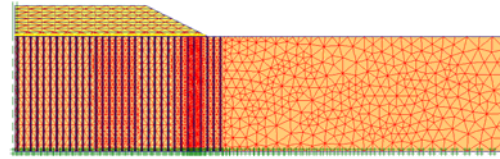


Fig. 15 Finite element mesh for analysis of stone columns technique.

Figure 16 shows the results of the safety analysis for different embankment elevations, and Fig. 17 shows the diagram of settlement increase in function of the elevation of embankment construction and the period of time for each calculation phase, for construction with stone columns technique, reaching a factor of safety of 1.39 and a settlement of 47.1 cm, in a period of time of 315 days, for the projected elevation of 9.5 m.

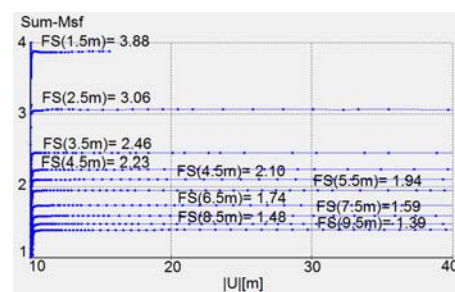


Fig. 16 Factors of safety as a function of construction elevations, for construction with stone columns technique.

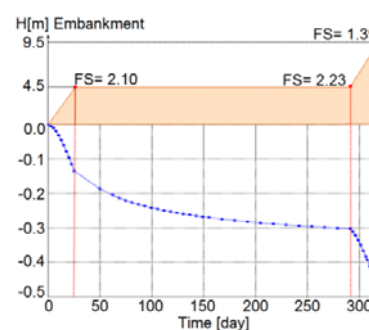


Fig. 17 Settlements vs. embankment elevation with the time, for construction with stone columns technique.

CONCLUSIONS

The construction in stages of the runway No. 16/34 embankment over soft clay, for the section Km 1+180, was modeled with Plaxis 8.6 software, evaluating the stability, settlements and periods of time for each stage; these results were evaluated to compare the benefits of construction techniques without improvement, preloading, vertical geodrains

and stone columns.

The analysis for the embankment construction without improvement technique attained a maximum stable elevation of 4.5 m, with a factor of safety of 1.32, in a period of time of 25 days, with 11.1 cm of settlement in the point of evaluation, located in the central zone of the base of the embankment. This calculated elevation was the reference for the beginning of the consolidation period for the posterior improvement techniques analyzed.

The construction of the runway embankment considering the preloading technique attained a maximum stable elevation of 5.5 m, with a factor of safety of 1.32, in a period of time of 31.77 years, with 87.5cm of settlement in the point of evaluation. The necessary time required to dissipate the excess pore pressure, makes the technique inadequate for the construction.

The construction of the runway embankment considering the vertical geodrains attained a maximum stable elevation of 5.5m, with a factor of safety of 1.34, in a period of time of 220 days, with 96.6cm of settlement in the point of evaluation. This technique reduced the consolidation time making it most effective than the preloading technique.

The construction of the runway embankment considering the stone columns was the only technique that attains the project elevation of 9.5m, with a factor of safety of 1.39, in a period of time of 315 days, with 47.1 cm of settlement in the point of evaluation.

REFERENCES

- [1] Alg - Europraxis. "Anexo 3. Geotecnia y Canteras", Informe 9A-Estudio de Pre Inversión a Nivel de Factibilidad, 2013.
- [2] Bouassida M. and Hazzar L., "Comparison between Stone Columns and Vertical Geodrains with Preloading Embankment Techniques", 6th International Conference on Case Histories in Geotechnical Engineering, 2008
- [3] Bouassida M. and Klai M, "Challenges and Improvement Solutions for Tunis' Soft Clay", J. of GEOMATE, Vol. 3, No. 1, 2012, pp. 298-307.
- [4] Castro et al., "Modelización de columnas de grava", 10 Simposio Nacional de Ingeniería Geotécnica, Vol. 2, 2016
- [5] Consorcio Airways Novoa, "Estudio Técnico Topografía y Geotecnia", Estudios Definitivos de Ingeniería Aeropuerto Internacional Cusco, 1983.
- [6] PLAXIS 2D Version 8, Reference Manual, 2007.
- [7] Quilli A. M. E., "Comparación mediante análisis numérico de métodos de tratamiento de suelo blando bajo un terraplén en Chinchero, Cusco", Tesis de graduación, Facultad de Arquitectura e Ingeniería Civil de la Universidad Nacional de San Antonio Abad del Cusco, 2016.
- [8] Sotelo y Asociados, "Nuevo Aeropuerto Internacional de Chinchero – Cusco. Informe de Geotecnia", Nuevo Aeropuerto Internacional de Chinchero – Cusco. Estudio definitivo de Ingeniería - Estudios Generales. Informe de Geotecnia, 2014.
- [9] Van Impe WF, De Beer E, "Improvement of settlement behaviour of soft layers by means of stone columns", 8th International Conference on Soil Mechanics and Foundation Engineering, Helsinki, 1983, pp. 309 – 312.

DISPLACEMENT OF DIAPHRAGM WALL FOR VERY DEEP BASEMENT EXCAVATION IN SOFT BANGKOK CLAY

Dr. Wanchai Teparaksa¹, Jirat Teparaksa²

¹Department of Civil Engineering, Faculty of Engineering, Chulalongkorn University, Thailand

²Department of Civil Engineering, The University of Tokyo, Japan

ABSTRACT

The Rosewood Hotel Project consists of 6 basements by using the diaphragm wall as a soil protection system. The elevations of Rosewood Hotel basements are -2.9, -6.5 -9.25, -11.95, -14.65 and -18.9m. depth from ground surface. The final excavated depth of this project is -24.2m. from ground surface which is the area of lift pit. Because the final depth of this project was very deep, the effect of water pressure was also considered. The Finite Element Method (FEM) was carried out to predict the behavior and displacement of the diaphragm wall which is used as a soil protection system. In addition, the Mohr-Coulomb soil modeling was used as the failure criteria of FEM analysis. The measured lateral movement of the diaphragm wall by means of inclinometer at all stages of construction is compared with analytical results from FEM prediction. The predicted diaphragm wall displacement by FEM agree well with field performance.

Keywords: diaphragm wall, basement construction, finite element method, wall displacement

INTRODUCTION

The Rosewood hotel consists of six basement floor at -2.90 m, -6.50 m, -9.25 m, -11.95 m, -14.65 m, and -18.90 m. deep below ground surface which is the lift pit of the project. The diaphragm wall is used as the temporary wall during excavation and is used as permanent wall at final stage. During excavation, four temporary steel bracing layer was used at elevation of -1.50 m, -7.45 m, -12.75 m. and -17.50 m. below ground surface. The diaphragm wall is 1.0 m. thick with tip penetrated in the very stiff silty clay layer at -28.0 m. depth below ground surface. The typical section of basement floor is presented in Figure 1 while the detail of temporary bracing system is presented in Figure 2.

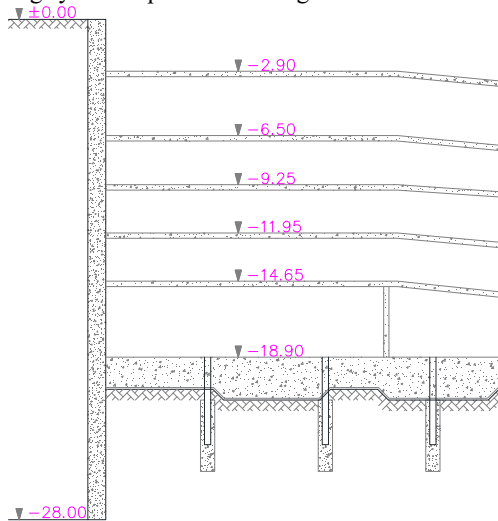


Fig. 1 Typical Section of basement Rosewood Hotel.

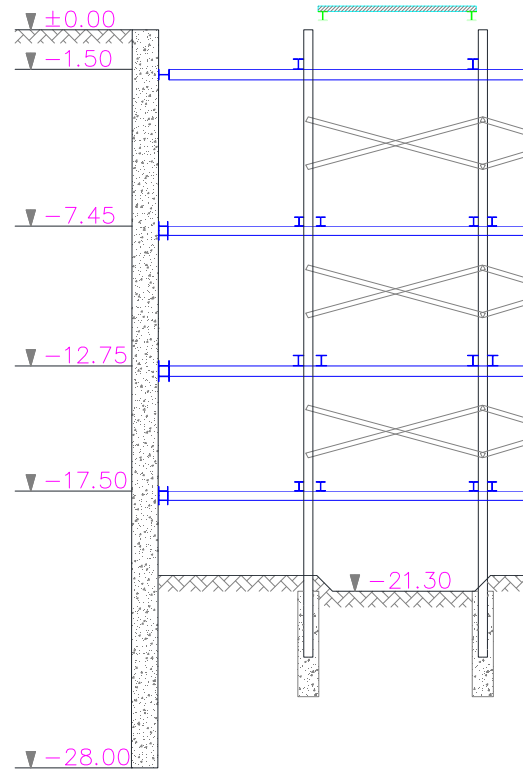


Fig. 2 Detail of temporary bracing system Rosewood Hotel.

The research work for study the behavior and performance of diaphragm wall for basement construction in Bangkok subsoil with various conditions was presented by Teparaksa[1],[2],[3].

This paper presents the performance and

behavior of the diaphragm wall. The lateral displacement of diaphragm wall is predicted by FEM analysis by simulating the construction sequence in the analysis. The lateral wall displacement is monitored during excavation and casting the basement floor. The FEM prediction is compared and discussed with the field performance.

GEOLOGICAL CONDITIONS

Three bored holes of 70 m. depth is carried out to investigate the geological conditions of the project. The soil conditions consists of soft to medium Bangkok clay from ground surface to 14 m. depth. The stiff silty to hard clay is encountered below soft to medium clay up to -45 m. depth. The dense second silty sand layer is found below 45 m. depth below ground surface. At this project site, the first layer of silty sand is no found as the normal Bangkok soil condition which is normally found at about 27 – 30 m. depth. The soil condition as well as soil engineering properties is presented in Figure 3.

Soil Profiles					
+/- 0.00					
-3.0	Top Soil				
	γ _t				
	Su				
-6.5	Soft Clay (CH)				
	γ _t	15.00 kN/m ³			
	Su	16.0 kN/m ²			
-11.0	Medium Clay (CH)				
	γ _t	18.00 kN/m ³			
	Su	25.0 kN/m ²			
-14.0	Medium to Stiff Clay (CH)				
	γ _t	18.40 kN/m ³			
	Su	40.0 kN/m ²			
-18.0	Stiff Clay (CH)				
	γ _t	19.20 kN/m ³	N	10 Blows/ft	
	Su	52.0 kN/m ²			
-22.0	Stiff Sandy Clay (CL)				
	γ _t	19.80 kN/m ³	N	22 Blows/ft	
	Su	146.7 kN/m ²			
-34.0	Stiff Clay (CH)				
	γ _t	20.00 kN/m ³	N	30 Blows/ft	
	Su	200.1 kN/m ²			
-40.0	Hard Clay (CL)				
	γ _t	20.20 kN/m ³	N	52 Blows/ft	
	Su	346.5 kN/m ²			
-45.0	Very Stiff Clay (CH)				
	γ _t	20.00 kN/m ³	N	40 Blows/ft	
	Su	206.7 kN/m ²			
-52.0	Dense Sand (SM)				
	γ _t	20.00 kN/m ³			
	N	44 Blows/ft			
-57.0	Dense Sand (SM)				
	γ _t	20.00 kN/m ³			
	N	60 Blows/ft			
	Very Dense Sand (SM)				
	γ _t	20.00 kN/m ³			
	N	60 Blows/ft			

Fig. 3 Soil properties of Rosewood Hotel.

ANALYSIS BEHAVIOR OF DIAPHRAGM WALL BY FINITE ELEMENT METHOD

Design Criteria of diaphragm wall

The behavior of diaphragm wall can be predicted by Numerical analysis by mean of Finite Element Method (FEM). The result of FEM analysis of diaphragm wall behavior is presented in term of bending moment and shear force induced in the diaphragm wall. The lateral displacement of diaphragm wall is also presented. The soil modeling is one of the main parameter for FEM analysis. The step of soil excavation, bracing installation, as well as preloading in the strut system is simulated in the FEM analysis. The casting of base slab, basement floor and the step of removal of strut system are also have to be designed and combined in the FEM analysis of diaphragm wall. In this project, the PLAXIS 2D [4] program is used as the FEM program analysis to predict the diaphragm wall behavior.

The Mohr-Coulomb soil modeling is used for FEM analysis. The undrained Young's modulus (E_u) of layer is correlated with undrained shear strength (S_u). In the sand layer, the drained modulus (E') is correlated with the Standard penetration SPT N-Value.

The correlation of E_u and S_u as well as E' and N-value can be conducted as follows.

- For soft to medium clay layer, Undrained Young's modulus
 $(E_u) = 500 - 700 S_u$ (Undrained Shear Strength)
- Stiff to very stiff silty clay layer
 $E_u = 1000 S_u$
- Sand layer
 $E' = 2000(N)$ SPT-N-Value (kN/m^2)

The above correlation between E_u - S_u , and E' -N(value) is based on the back analysis from various basement excavation project by means of FEM analysis compared with field measurement proposed by Teparaksa [5]

Surcharge on the diaphragm wall

The ground surface surcharge behind the diaphragm wall during construction is assumed at 10 kN/m^2 . This ground surface is applied during excavation, basement casting and completion of the basement work.

Ground Water Table

The ground water in Bangkok subsoil condition is in the draw down condition due to deep well pumping. Recently, the deep well pumping is not allow, the recent ground water table is at -13 m. below ground surface.

RESULT OF FEM ANALYSIS

The FEM analysis was carried out base on Mohr-Coulomb soil failure criteria by simulating the construction sequence in the FEM analysis. Figure 4 presents the deformed mesh of FEM analysis at final excavation depth -32.30 m. with 4 bracing layers. Figure 5 presents the deformed mesh of FEM analysis at stage of all 6 basement floor is casted. The maximum lateral diaphragm wall deflection is found at 43.34 mm. This maximum diaphragm wall deflection is used as the Trigger Level for monitoring D-wall deflection as the safety control of the project.

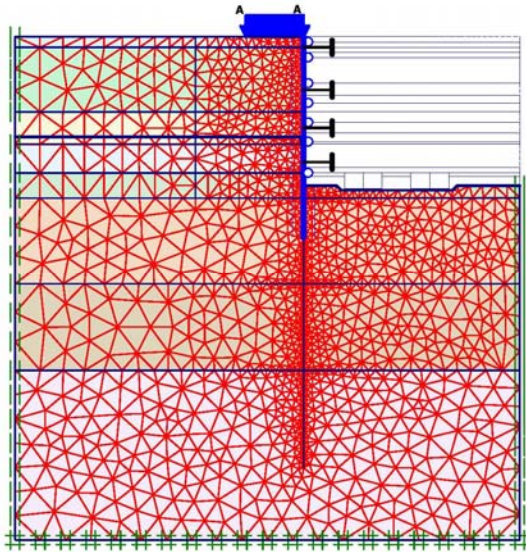


Fig. 4 Deformed mesh from FEM analysis during Final depth excavation.

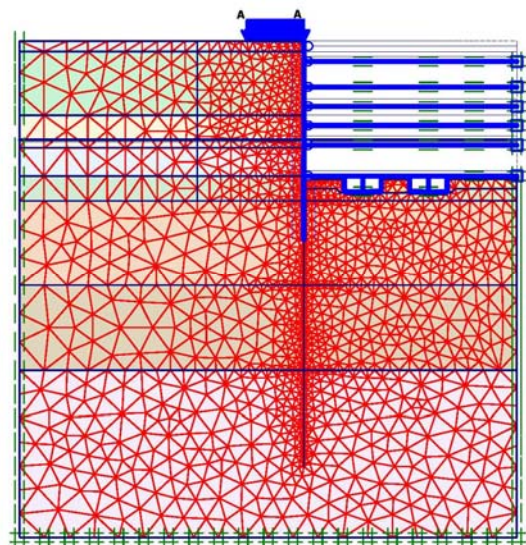


Fig. 5 Deformed mesh from FEM analysis during construct B1 Floor at EL.-2.90 m.

Figure 6 (a) presents the envelop of bending moment diagram induced in the diaphragm wall with all excavation steps including soil excavation and bracing installation until casting the foundation. The upward construction including casting base slab, removing of bracing as well as basement casting is also included in the envelope.

The dotted line outside of the bending moment envelop is the bending moment resistance of the reinforcement. This dotted line of reinforcement is calculated from reinforcement detail presented in Figure 6(b)

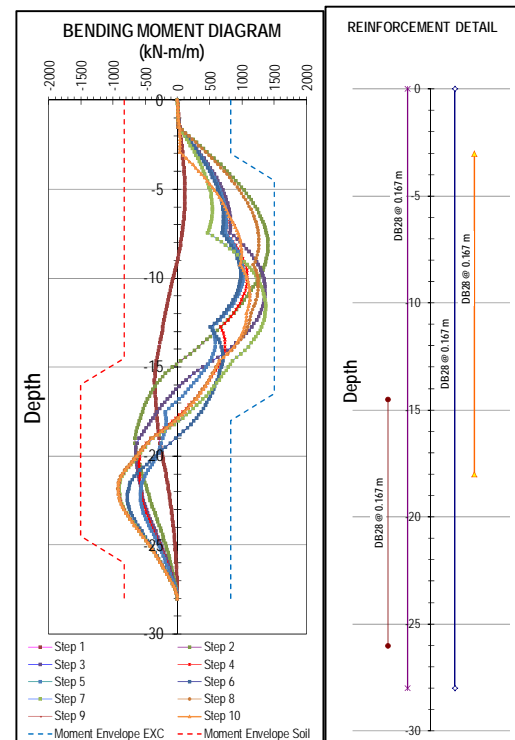


Fig. 6 (a,b) Envelop of Bending moment diagram induced in the diaphragm wall.

TRIGGER LEVEL AND SAFETY CONTROL

The instrumentation for monitoring the diaphragm wall deflection is proposed as inclinometer by installed inside the diaphragm wall panel. The safety control and monitoring criteria is proposed in terms of trigger level as presented in Table 1. The lateral diaphragm wall deflection is monitored at all construction sequence as simulated in the FEM analysis. The safety criteria is only one method to control the behavior and performance of diaphragm wall during construction.

Table 1 Trigger level and safety control

Trigger Level	Inclinometer Movement (mm.)	Safety Criteria
Alarm Level (70 % of design value)	30.34	Inform designer to review construction sequence
Alert Level (80 % of design value)	34.67	Inform all parties to review construction sequence
Action Level (90 % of design value)	39.01	Stop construction and revise the construction sequence.
Maximum	43.34	

FIELD MEASUREMENT OF D-WALL DISPLACEMENT

Figure 7 presents the lateral diaphragm wall displacement by mean of inclinometer reading. At initial stage during first excavation and first strut installation, the D-wall movement is in the mode of cantilever. At other stage the movement of D-wall is changed to be beam on supported shape. This is because the bracing strut is acted as the rigid support of the diaphragm wall. The maximum wall deflection is only 28.41 mm. at final depth excavation. The maximum measured diaphragm wall deflection is less than the prediction of 42 mm. This is because the basement construction period is very fast and can be completed within 4 months. Even the order of maximum measured wall deflection is less than prediction, however, the shape of wall deflection is similar. The FEM prediction of diaphragm wall agree well with field inclinometer measurement.

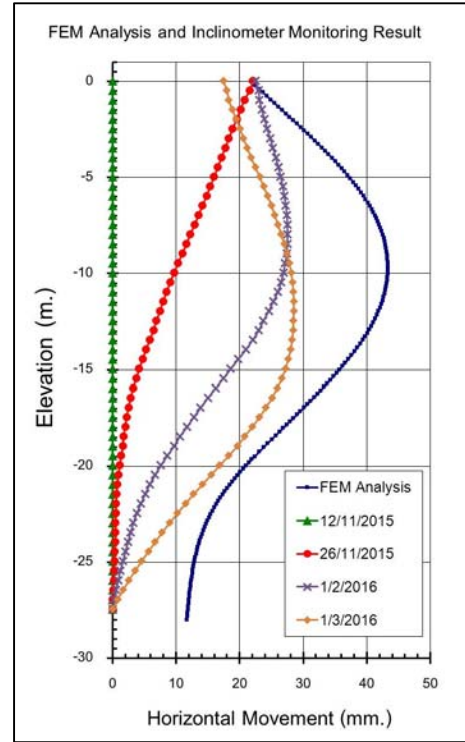


Fig. 7 The lateral diaphragm wall displacement.

SAFTY AGAINST UPLIFT

The deepest basement of Rosewood hotel is at -24 m. below ground surface. The uplift at the final depth excavation is predicted by checking safety factor against uplift. The safety factor against uplift can be estimated as the ratio between weight of overburden stress of soil from final depth to sand layer and uplift pressure as shown in Figure 8. The overburden pressure is estimated at about 410 kN/m² while uplift pressure is at 320 kN/m². The Safety factor against uplift is 1.28.

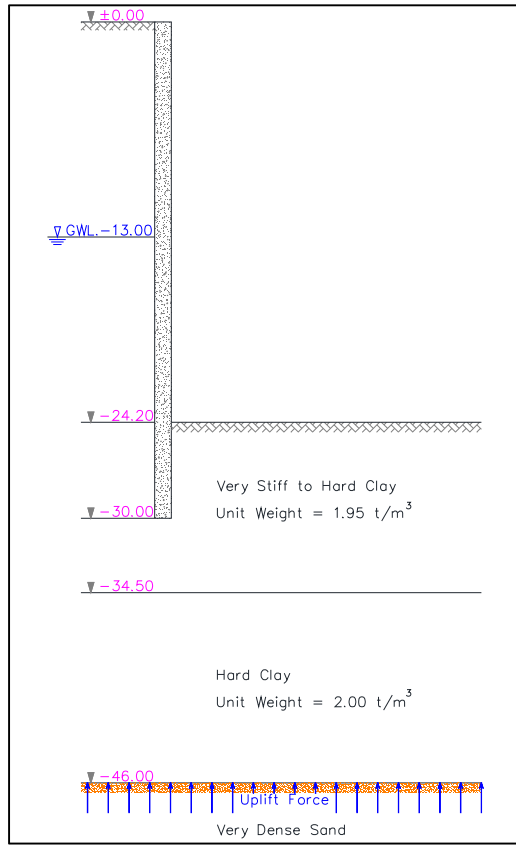


Fig. 8 Layer of soil for estimating uplift.

CONCLUSIONS

The Rosewood hotel consists of six basement floors and constructed by means of diaphragm wall. The maximum depth of excavation is at -24 m. depth below ground surface. The diaphragm wall is 1.0 m. thick with tip penetrated in very stiff clay at -28 m.

below ground surface. Four temporary steel bracing at -1.5 m, -7.45 m, -12.75 m and -17.5 m. is used for excavation work with bottom up construction technique. The behavior of diaphragm wall is predicted by mean of FEM analysis. The Mohr-Coulomb soil modeling is used for FEM analysis with simulating construction sequence in the FEM analysis. The diaphragm wall displacement is predicted. The measurement of D-wall displacement by inclinometer agree well with FEM analysis.

REFERENCES

- [1] Teparaksa W, "Principal and application of instrumentation for the first MRTA subway project in Bangkok", 5th International Symposium on Field Measurement in Geomechanics, Singapore, 1999.
- [2] Teparaksa W, "Deep Basement Construction of Bank of Thailand Along Chao Phraya River closed to Tewavej Palace and Bangkhunphrom Palace", Proc. of the 18th International Conferences on Soil Mechanics and Geotechnical Engineering, Paris, 2013.
- [3] Teparaksa W, P. Sontiprasart, N. Prachayaset and S. Keawsawasvong. "Impact Assessments of the Deep Basement Construction in the MRT Protection Zone", The 28th KKHTCNN Symposium. Civil Engineering, Bangkok, Thailand, 2015.
- [4] Brinkgreve, R.B.J., PLAXIS 2D Version 8 Manual, A.A. Balkema Publishers, 2002.
- [5] Teparaksa W, "Displacement analysis of diaphragm wall for subway construction" The 7th National convention in the Civil Engineering Bangkok, 2001

THE INFLUENCE OF SOLAR RADIATION ON PAVEMENT PERFORMANCE

John Yeaman¹ and Adrian McCallum¹

¹Faculty of Science, Health, Engineering and Education, University of the Sunshine Coast, Australia

ABSTRACT

For the past four years, the University of the Sunshine Coast (USC) has been monitoring the performance of road pavements through “in-situ” monitoring, in association with Sunshine Coast Council and Pavement Management Services. During that time four sites have been built and monitored, wirelessly, minute by minute, 24 hours per day. Each monitoring site is equipped with strain gauge sensors at critical positions within the pavement, moisture gauges and thermocouples. The system is accompanied by a weather station that measures Air Temperature, Wind Speed and Direction, Relative Humidity, Atmospheric Pressure, and Solar Radiation. We have confirmed that pavement stiffness is strongly influenced by pavement temperature, providing the moisture content remains constant, and that for the most part, environmental conditions have a greater influence on pavement behaviour than traffic. This paper examines the influence of solar radiation on pavement temperatures and the subsequent influence on pavement behaviour over a twelve-month study period

Keywords: Solar radiation, Pavement performance

INTRODUCTION

During December 2012, The University of the Sunshine Coast (USC) in association with Sunshine Coast Council (SCC) and Pavement Management Services (PMS) installed an in-situ pavement monitoring site on Sippy Downs Drive adjacent to the University during upgrade of the pavement to dual carriageway configuration. Results from this study have been published by Fairweather (2014), Yeaman (2015) and Azawi (2015), with monitoring continuing. Two other sites consisting of different configurations continue to be monitored with respect to Strain Energy Dissipation and Soil Suction.

As part of this overall research project, Yeaman (2017), at this subject site, postulated that maintenance of the pavement asset can be predicted from in situ strain outcomes as a function of both traffic and the environment but also that pavement temperature has a strong influence on pavement stiffness irrespective of the configuration.

The subject site is situated at Bellevista Boulevard, Caloundra at Latitude S. 26° 47' 41.28" and Longitude E. 153° 05' 49.92" and consists of:

- Yellow Podzol subgrade with a stiffness of 70 MPa
- 100 mm gravel subbase course with a stiffness of 145 MPa
- 270 mm cement treated base with a mean stiffness modulus of 3500 MPa.
- 50 mm Hot Mix Asphalt pavement surface.

Sensors are fitted at the base of the stiff layer at a

depth of 320 mm and in the subgrade at a depth of 420 mm in the following configuration:

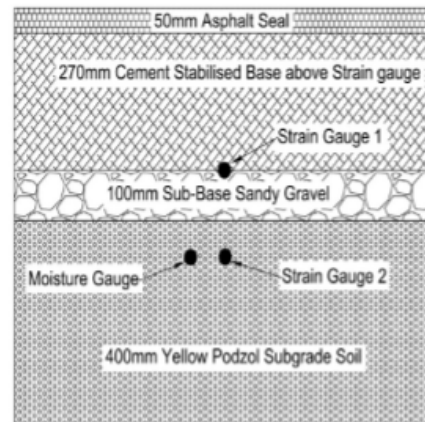


Fig. 1 Pavement and sensor configuration – Bellevista site.

This section of Bellevista Boulevard, Caloundra was constructed in September 2013 and has been instrumented since that date.

Bellevista Boulevard is designed for a 20-year lifespan with an initial high traffic growth of the first five years of 8.3% and subsequent 15 years of 5%. The design traffic is calculated as 5.21 million (5.21×10^6) Heavy Vehicle Axle Groups for the 20-year design life.

This gives Critical Fatigue Strains of $428 \mu\epsilon$ for a cemented layer of 3,500 MPa modulus and $1020 \mu\epsilon$ critical compressive strain for subgrade deformation.

For relationships refer to reference 2 table 8.5.

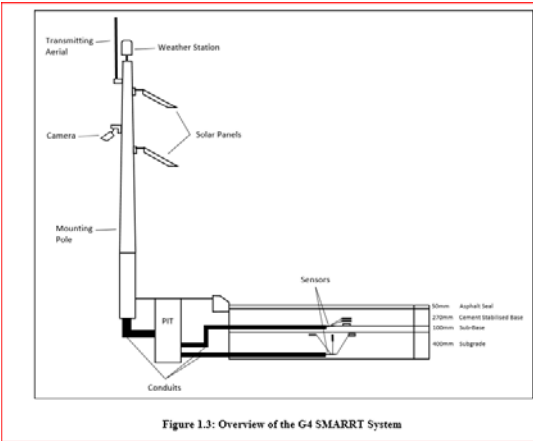


Fig. 2a Configuration of Pavement Management Site (G4SMART)



Fig. 2b Configuration of Pavement Management Site (G4SMART)

Data in the format of Tables 1 and 2, following, is passed from this site by telephone to a central computer at 6:00 am daily.

Strain 1 is the strain measured at the underside of the bound layer (HMA and cemented layer) and Strain 2 is the top of the subgrade (subgrade layer). The negative sign (-) in this instrumentation indicates that the strain is in tension.

Table 1 Example strain and temperature data.
See end of paper

Table 2 Example weather station data.

Wind_Speed _1min (m/s)	Wind_Dir_ 1min (deg)	Rel_Humidity _1min (%RH)	Air_Pressure _1min (HPa)
0.2	306	88.9	1008.3
0.4	166	88.8	1008.3
0.5	218	89	1008.4
0.3	195	88.9	1008.4
0.4	114	88.9	1008.4
0.3	100	88.9	1008.3
0.1	216	88.9	1008.3
0.3	147	88.9	1008.3

SOLAR RADIATION

Solar Radiation is a unique commodity. Solar radiation comes directly to the earth's surface only inhibited by cloud, moisture and dust. It can be predicted (within reasonable accuracy) for any point on the earth's surface for any hour of the day. We are therefore able to use this parameter for evaluating the effect of Solar Radiation on the performance of a pavement.

DISTRIBUTION OF SOLAR RADIATION THROUGHOUT THE YEAR

Clearly, the amount of solar radiation that impacts on the road surface will vary throughout the year, there being much less in mid-winter to mid-summer. Figure 3 suggests the amount of solar radiation accumulated during the hours of sunrise and sunset for Latitude 26° south, Longitude 153° east. At this Longitude, the sun is at its zenith at 12:03 pm daily.

The pattern for December 2015 and December 2016 are similar and that June (mid-winter) experiences much less radiation for each hour of the day, with the accumulated radiation being approximately 10,000 watts per square metre when the sun is at its zenith and 50,000 watts per square metre at sunset. Clearly this must have a significant effect on pavement temperature.

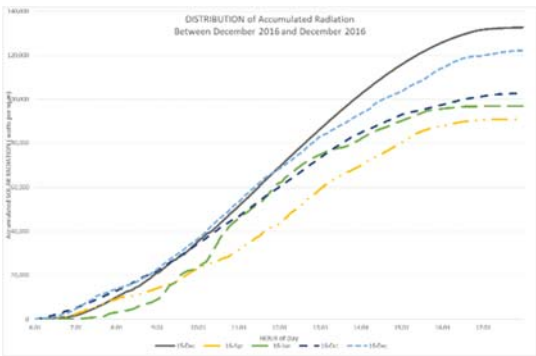


Fig. 3 Distribution of daily accumulated radiation.

THERMAL PROPERTIES OF A PAVEMENT

Figure 4 shows a typical strain and temperature pattern during winter 2016 (23 June; cold & wet). At 6:00 am strain is in compression. At 08:23 something happens that creates a major change in the pavement, here Strain 1 changes to negative (i.e. tension), simultaneously the layer temperature falls below 21 °C. Strain 1 continues to increase in tension until around 5:00 pm (here the temperature is slightly above 21°C). It then stays in compression until 6:00 am the next morning.

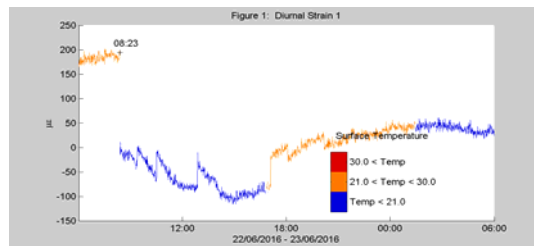


Fig. 4 Diurnal Strain 1 vs time, 23 Jun 2016.

Now consider the following day (24 June 2016). Strain follows on from the same value as the previous day, but with a sudden drop at 08:57 am (peak hour). It then continues to a maximum tension value of 150 µε at around 10:45 am when there is a sudden shift upwards. Here temperature is just under 21°C. Once layer temperature exceeds 21°C strain1 continues to decrease, until it enters a compression mode at about 6:00 pm where it remains until 6:00 am the next day.

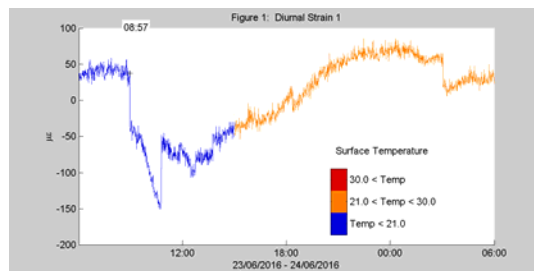


Fig. 5 Diurnal Strain 1 vs time, 24 June 2016.

Clearly this change in behaviour is a function of the pavement layer temperature.

DIURNAL PATTERN OF PAVEMENT TEMPERATURES

Figure 3 shows air, surface and layer temperatures for the Bellevista site on 8 September 2016. From this it can be observed that between 6:00 am and 11:00 the temperature at the underside of the bound layer exceeds the surface temperature and the pavement is

emitting heat. At 11:25 am equilibrium is attained and the structural layer has the same temperature throughout. Between 11:25 am and 11:30 pm the surface temperature is in excess of the layer temperature and the pavement is absorbing heat. Equilibrium is attained at 11:29 pm. From 11:30 pm to dawn (6:00 am) layer temperature is hotter than the surface. Under these conditions where there is a differential in temperature between the surface and the layer then stresses are likely to be building in the pavement.

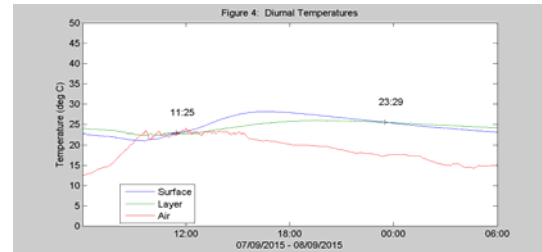


Fig. 6 Diurnal pavement temperatures, 8 September 2016.

SEASONAL VARIATIONS IN TEMPERATURE PARAMETERS

Table 3 demonstrates the Maximum values obtained for Air, Surface and Layer temperatures during the period December 2015 to December 2016.

Table 3 Seasonal variation maximum temperatures.

Period	Air	Surface	Layer
SUMMER	30.0	41.5	41.5
AUTUMN	29.3	35.7	33.6
WINTER	22.1	25.2	25.0
SPRING	31.8	38.6	35.1

Table 4 demonstrates the Minimum values obtained for Air, Surface and Layer temperatures during the period December 2015 to December 2016.

Table 4 Seasonal variation minimum temperatures.

Period	Air	Surface	Layer
SUMMER	17.5	25.8	27.4
AUTUMN	13.5	30.2	21.2
WINTER	10.2	17.8	19.5
SPRING	12.9	22.4	23.4

FIELD STUDIES

Road Surface temperatures are charted against cumulative radiation during sunlight hours for every day of the year example Figure 8c from which it can be seen that there is a defined point of maximum road surface temperature; an example daily report is

appended. At longitude 153°E the sun is at its zenith at 12:03; this maximum occurs between 11:30 am and 1:00 pm each day i.e. the sun's zenith + 1 hour. Oscillations in the solar energy chart are a function of cloud cover.

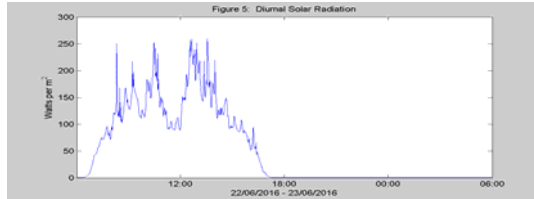


Fig. 7a Radiation parameters (shortest day).

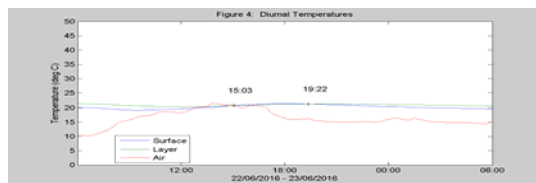


Fig. 7b Temperature parameters (shortest day).

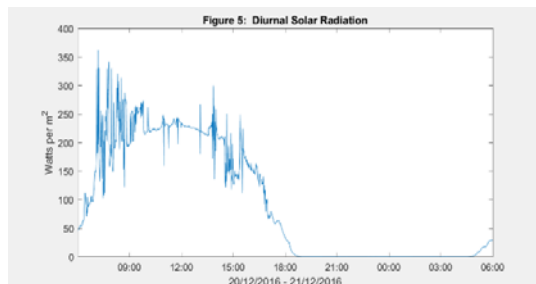


Fig. 8a Radiation parameters (longest day).

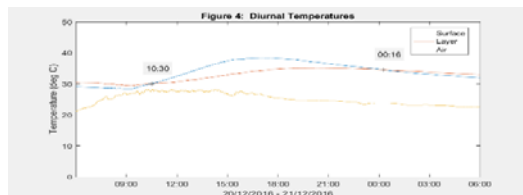


Fig. 8b Temperature parameters (longest day).

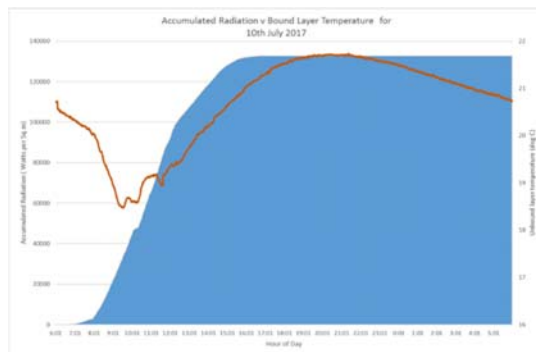


Figure 8(c) Layer Temperature as a function of accumulated radiation

Examination of these data indicates that twice a day there is a point of equilibrium where the pavement is the same temperature at the surface and at the base of the bound layer. Between approximately 11 am and 11 pm the surface temperature is greater than the layer and between approximately 11 pm and 11 am the underside of the bound layer is hotter than the surface

Clearly this is a function of the quantum of solar energy radiating the pavement. Compare the temperature pattern for the shortest day of 2016 (June 21st) and the longest day of 2016 (December 21st) at 3 pm (Table 5).

Table 5 Temperature and Radiation measurements for shortest and longest days.

Date	Surface Temperature (°C)	Layer Temperature (°C)	Air Temperature (°C)	Change in temperature from sunrise (°C)	Accumulated Radiation (watts per m²)
	At 3 pm	At 3 pm	At 3pm	Up to 3 pm	Until 3 pm
Shortest Day	23.6	21.7	20.5	2.0	93,684
Longest Day	37.4	32.8	26.8	5.3	110,389

This is an important consideration when choosing a design temperature for the design of asphalt pavement thickness.

RELATIONSHIP BETWEEN SURFACE TEMPERATURE & STRUCTURAL LAYER STRAIN

In figure 9 we see the distribution of strain as a function of temperature over the full year where the moisture content is below 9%. Here structural layer strain is only in tension at temperatures below 20°C and then only above the critical limit of 248 $\mu\epsilon$ when the temperature is below 18°C. The secondary effect of moisture above 9% is dealt with elsewhere (Yeaman [2]).

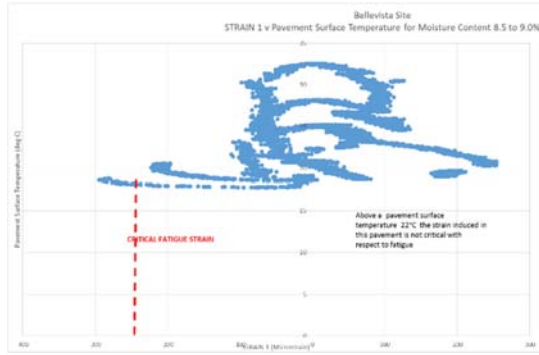


Fig. 9 Distribution of Structural Layer Strain as a function of Pavement Surface Temperature.

LABORATORY STUDIES

Laboratory studies were conducted by Gray (2015), Westerway (2015) and Laws (2015) to better understand the influence of solar radiation on asphalt in a controlled environment (i.e. no wind, no cloud and no dust).

An insulated box (Figure 10) was purpose built to hold a 200 mm square by 450 long billet of Hot Mix Asphalt compacted in the University's Shear box compactor (IPC Global).



Fig. 10 Heat box and thermal lamp constructed to enable pavement insolation to be varied in a controlled manner (Gray 2014).

The Heat Box is designed to simulate thermal radiation from the sun and to measure the temperature changes an asphalt pavement undergoes throughout the day. The Heat Box uses a heat lamp, a servo motor

and microcontroller.

A code is uploaded to the microcontroller that relates the angular degree of the servo motor to a specific solar radiation; the code orders the servo motor to move every five minutes. The code relies on data obtained from the Pavement Monitoring System on Sippy Downs Drive (near Sunshine Coast University). Data from the hottest day on record in 2015 was used (9 February). The microcontroller ran throughout the day simulating the solar radiation.

A datalogger is used to record these temperatures every minute from the thermocouples inserted into the asphalt billet (at depths of 25 mm, 50 mm, 75 mm, 100 mm, 150 mm, 200 mm, 300 mm and 400 mm).

Figure 11 provides an example of the outcome from the heat box comparing the solar radiation and the actual and simulated radiation for the hottest day of 2016 (9th February).

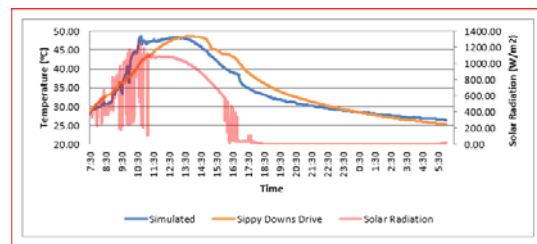


Fig. 11 Simulated Temperature: Solar Radiation for hottest day 2016 (Westaway et al 2017).

Figure 12 demonstrates the effect of thermal radiation on pavement temperatures from the simulation method.

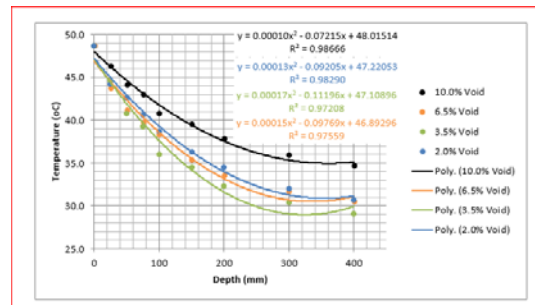


Fig. 12 Relationship between Accumulated Solar Radiation and Pavement Surface Temperature.

Here we see that there is:

- A terminal condition at which the temperature asymptotes to equilibrium and this represents a pavement depth of around 300 mm (noting that this test was run for the hottest day),
- Voids content has a significant influence on

the rate of conduction of heat through the pavement, and

- In a road pavement, 100 mm thick, there is the potential to store thermal energy as heat energy (say 12 °C).

CONCLUSION

Although this study is for a single site and one type of pavement (thin Hot Mix Asphalt on a cemented base) the results are sufficient to warrant further investigation of this technology over a wider range of conditions.

Solar Radiation has a critical influence on both the pavement surface and the structural layer of a cemented base pavement. Further, a road pavement is a potential store for solar energy. Between midnight and midday, the structural layer is hotter than the pavement surface and the pavement is emitting heat,

To date the only values under which a critical level of fatigue is attained is when the structural layer temperature is less than 20°C and at this time (December 2016), the pavement is deemed to be performing according to design criteria.

RECOMMENDATION

Further investigation should be undertaken to evaluate the potential energy source of a large solar

receptor – an asphalt pavement. The Stirling Energy principle has potential in this area.

REFERENCES

- [1] Austroads 2007, “Guide to Pavement Technology”, Part 4B Asphalt, Sydney
- [2] Yeaman 2017 “Managing Pavement Assets through In-Situ Monitoring”, World Conference on Pavement and Asset Management WCPAM 2017 Milan , Italy , June 12/16 2017
- [3] Yeaman 2017 “The Influence of Subgrade Moisture Content on Pavement Performance” under review
- [4] Gray C ,2014 Final Year Capstone thesis, University of the Sunshine Coast
- [5] Westaway K ,2016 “Comparison of asphalt material characteristics as a function of air void content “Final Year Capstone thesis , University of the Sunshine Coast.
- [6] Laws N 2016 , “A Profile of Brisbane City Council Type 3 Asphalt Mix with Varying Air Voids” Final Year Capstone Thesis , University of the Sunshine Coast.

Timestamp	Strain1	Strain 2	Subgrade Moisture	Air Temperature	Surface Temperature	Layer Temperature	Acc. Solar Radiation
6:01	75	137	8.68	21.2	33.7	35.0	29
7:05	568	133	8.70	25.0	33.2	34.7	2912
10:00	5	114	8.70	29.5	32.9	33.8	23988
12:03	-38	110	8.70	30.1	34.9	34.1	49760
15:00	-19	133	8.68	29.4	39.5	35.7	84,689
18:00	66	145	8.65	27.8	40.9	37.5	100,397
21:00	105	124	8.62	26.3	39.1	37.8	101,070
23:59	115	130	8.62	23.6	37.2	37.2	101,080

Figure 1 Example results from Monitoring site (26 January 2017)

THE INFLUENCE OF SOLAR RADIATION AND SUBGRADE MOISTURE CONTENT ON PAVEMENT PERFORMANCE

John Yeaman¹ and Adrian McCallum¹

¹Faculty of Science, Health, Engineering and Education, University of the Sunshine Coast, Australia

ABSTRACT

For the past four years the University of the Sunshine Coast (USC) has been monitoring the performance of road pavements through “in-situ” monitoring, in association with Sunshine Coast Council and Pavement Management Services. During that time four sites have been built and monitored, wirelessly, minute by minute, 24 hours per day. Each monitoring site is equipped with strain gauge sensors at critical positions within the pavement, moisture gauges and thermocouples. The system is accompanied by a weather station that measures Air Temperature, Wind Speed and Direction, Relative Humidity, Atmospheric Pressure, and Solar Radiation. This paper examines the influence of solar radiation on pavement temperatures and the subsequent influence on pavement behaviour over a twelve-month study period from December 2015 to December 2016. Additionally we examine the influence of subgrade moisture content on pavement behaviour at the site, particularly during cyclonic depression “Debbie” in March 2017. We confirm that pavement stiffness is strongly influenced by pavement temperature, providing the moisture content remains constant. Examination of the influence of subgrade moisture content on pavement behaviour shows that critical fatigue strain occurs when moisture content lies above 8.5%. Moisture variation plays a measurable role in pavement strain, fatigue and design life and wide variation in moisture content can occur over a short period. For the most part, environmental conditions have a greater influence on pavement behaviour than traffic.

Keywords: Solar radiation, Subgrade, Moisture, Strain, Pavement performance

INTRODUCTION

During December 2012 The University of the Sunshine Coast (USC) in association with Sunshine Coast Council (SCC) and Pavement Management Services (PMS) installed an in-situ pavement monitoring site on Sippy Downs Drive adjacent to the University during upgrade of the pavement to dual carriageway configuration. Results from this study have been published by Fairweather (2014), Yeaman (2015) and Azawi (2015), with monitoring continuing. Two other sites consisting of different configurations continue to be monitored with respect to Strain Energy Dissipation and Soil Suction.

As part of this overall research project, Yeaman (2017), at this subject site, postulated that maintenance of the pavement asset can be predicted from in situ strain outcomes as a function of both traffic and the environment but also that pavement temperature has a strong influence on pavement stiffness irrespective of the configuration.

The subject site is situated at Bellevista Boulevard, Caloundra at Latitude S. 26° 47' 41.28" and Longitude E. 153° 05' 49.92" and consists of:

- Yellow Podzol subgrade with a stiffness of 70 MPa
- 100 mm gravel subbase course with a stiffness of 145 MPa

- 270 mm cement treated base with a mean stiffness modulus of 3500 MPa.
- 50 mm Hot Mix Asphalt pavement surface.

Sensors are fitted at the base of the stiff layer at a depth of 320 mm and in the subgrade at a depth of 420 mm in the following configuration:

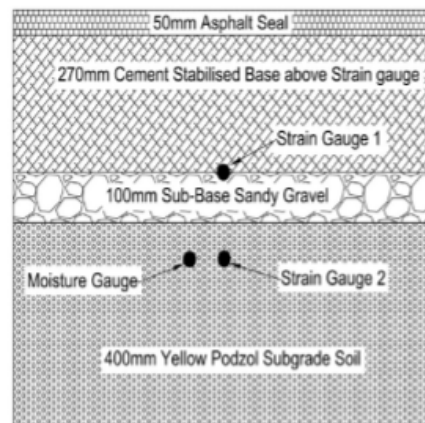


Fig. 1 Pavement and sensor configuration – Bellevista site.

This section of Bellevista Boulevard, Caloundra was constructed in September 2013 and has been instrumented since that date.

Bellevista Boulevard is designed for a 20 year lifespan with an initial high traffic growth of the first five years of 8.3% and subsequent 15 years of 5%. The design traffic is calculated as 5.21 million (5.21*106) Heavy Vehicle Axle Groups for the 20 year design life.

This gives Critical Fatigue Strains of 248 $\mu\epsilon$ for a cemented layer of 3,500 MPa modulus and 1020 $\mu\epsilon$ critical compressive strain for subgrade deformation. For relationships refer to reference 2 table 8.5.

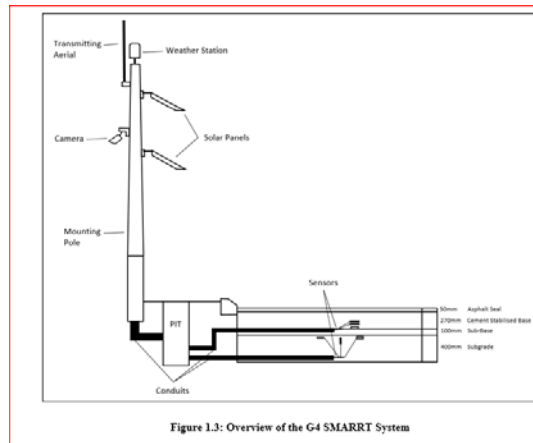


Fig. 2a Configuration of Pavement Management Site (G4SMART)



Fig. 2b Configuration of Pavement Management Site (G4SMART)

Data in the format of Tables 1 and 2, following, is passed from this site by telephone to a central computer at 6:00 am daily.

Strain 1 is the strain measured at the underside of the bound layer (HMA and cemented layer) and

Strain 2 is the top of the subgrade (subgrade layer). The negative sign (-) in this instrumentation indicates that the strain is in tension.

Table 1 Example strain and temperature data.

Time	Strain #1 (ue)	Strain #2 (ue)	Soil-Moisture1 % (by vol)	Air Temp 1min (degC)	Surface Layer Temp (degC)	Road Surface Temp (degC)	Solar_Radiation Corrected (W/m2)	Wind Dir 1min (deg)
1/1	-	56.	32.56	21.1	28.84	27.76	44.46	306
1/2	26.	90	1					
016	96	6						
6:0	9							
1								
1/1	-	64.	32.56	21.1	28.87	27.77	43.74	166
1/2	21.	68	9					
016	68	8						
6:0	8							
2								
1/1	-	59.	32.56	21.1	28.87	27.77	42.99	218
1/2	16.	50	7					
016	43	0						
6:0	8							
3								
1/1	-	59.	32.56	21.2	28.87	27.78	41.92	195
1/2	11.	50	8					
016	21	0						
6:0	9							
4								
1/1	-	54.	32.56	21.2	28.84	27.76	42.32	114
1/2	19.	18	6					
016	09	8						
6:0	4							
5								
1/1	-	59.	32.56	21.2	28.86	27.76	44.04	100
1/2	24.	50	6					
016	40	0						
6:0	6							
6								

Table 2 Example weather station data.

Wind_Speed_1min (m/s)	Wind_Dir_1min (deg)	Rel_Humidity_1min (%RH)	Air_Pressure_1min (hPa)
0.2	306	88.9	1008.3
0.4	166	88.8	1008.3
0.5	218	89	1008.4
0.3	195	88.9	1008.4
0.4	114	88.9	1008.4
0.3	100	88.9	1008.3
0.1	216	88.9	1008.3
0.3	147	88.9	1008.3

SOLAR RADIATION

Solar Radiation is a unique commodity. Solar radiation comes directly to the earth's surface only inhibited by cloud, moisture and dust. It can be predicted (within reasonable accuracy) for any point on the earth's surface for any hour of the day. We are therefore able to use this parameter for evaluating the effect of Solar Radiation on the performance of a pavement.

DISTRIBUTION OF SOLAR RADIATION THROUGHOUT THE YEAR

Clearly, the amount of solar radiation that impacts on the road surface will vary throughout the year, there being much less in mid-winter to mid-summer. Figure 3 suggests the amount of solar radiation accumulated during the hours of sunrise and sunset for Latitude 26° south, Longitude 153° east. At this Longitude the sun is at its zenith at 12:03 pm daily.

It can be seen that the pattern for December 2015 and December 2016 are similar and that June (mid-winter) experiences much less radiation for each hour of the day, with the accumulated radiation being approximately 10,000 watts per square metre when the sun is at its zenith and 50,000 watts per square metre at sunset. Clearly this must have a significant effect on pavement temperature.

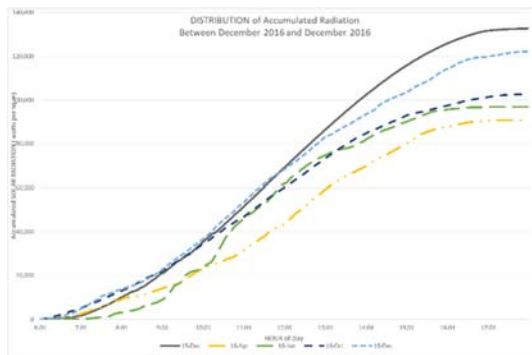


Fig. 3 Distribution of daily accumulated radiation.

THERMAL PROPERTIES OF A PAVEMENT

Figure 4 shows a typical strain and temperature pattern during winter 2016 (23 June; cold & wet). At 6:00 am strain is in compression. At 08:23 something happens that creates a major change in the pavement, here Strain 1 changes to negative (i.e. tension), simultaneously the layer temperature falls below 21 °C. Strain 1 continues to increase in tension until around 5:00 pm (here the temperature is slightly above 21°C). It then stays in compression until 6:00 am the next morning.

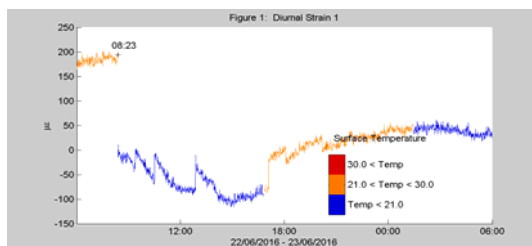


Fig. 4 Diurnal Strain 1 vs time, 23 Jun 2016.

Now consider the following day (24 June 2016). Strain follows on from the same value as the previous day, but with a sudden drop at 08:57 am (peak hour). It then continues to a maximum tension value of 150 µε at around 10:45 am when there is a sudden shift upwards. Here temperature is just under 21°C. Once layer temperature exceeds 21°C strain1 continues to decrease, until it enters a compression mode at about 6:00 pm where it remains until 6:00 am the next day.

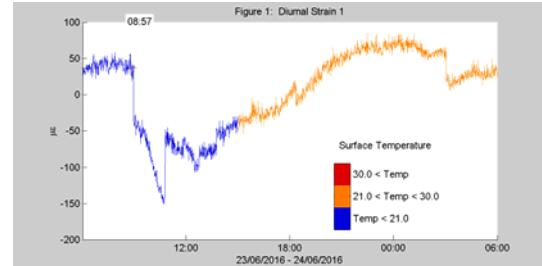


Fig. 5 Diurnal Strain 1 vs time, 24 June 2016.

Clearly this change in behaviour is a function of the pavement layer temperature.

DIURNAL PATTERN OF PAVEMENT TEMPERATURES

Figure 6 shows air, surface and layer temperatures for the Bellevista site on 8 September 2016. From this it can be observed that between 6:00 am and 11:00 the temperature at the underside of the bound layer exceeds the surface temperature and the pavement is emitting heat. At 11:25 am equilibrium is attained and the structural layer has the same temperature throughout. Between 11:25 am and 11:30 pm the surface temperature is in excess of the layer temperature and the pavement is absorbing heat. Equilibrium is attained at 11:29 pm. From 11:30 pm to dawn (6:00 am) layer temperature is hotter than the surface. Under these conditions where there is a differential in temperature between the surface and the layer then stresses are likely to be building in the pavement.

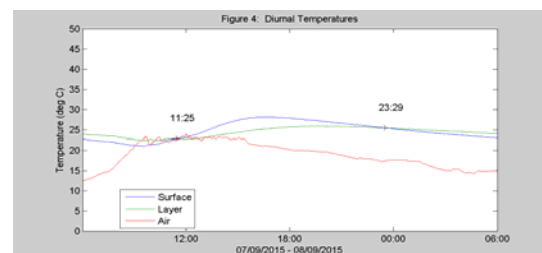


Fig. 6 Diurnal pavement temperatures, 8 September 2016.

SEASONAL VARIATIONS IN TEMPERATURE PARAMETERS

Table 3 demonstrates the Maximum values obtained for Air, Surface and Layer temperatures during the period December 2015 to December 2016.

Table 3 Seasonal variation maximum temperatures.

Period	Air	Surface	Layer
SUMMER	30.0	41.5	41.5
AUTUMN	29.3	35.7	33.6
WINTER	22.1	25.2	25.0
SPRING	31.8	38.6	35.1

Table 4 demonstrates the Minimum values obtained for Air, Surface and Layer temperatures during the period December 2015 to December 2016.

Table 4 Seasonal variation minimum temperatures.

Period	Air	Surface	Layer
SUMMER	17.5	25.8	27.4
AUTUMN	13.5	30.2	21.2
WINTER	10.2	17.8	19.5
SPRING	12.9	22.4	23.4

FIELD STUDIES

Comparison of road surface temperatures with cumulative radiation during sunlight hours shows that there is a defined point of maximum road surface temperature; examples are shown (Figs 7a, 7b, 8a and 8b). At longitude 153°E the sun is at its zenith at 12:03; this maximum occurs between 11:30 am and 1:00 pm each day i.e. the sun's zenith + 1 hour. Radiation oscillates due to cloud cover.

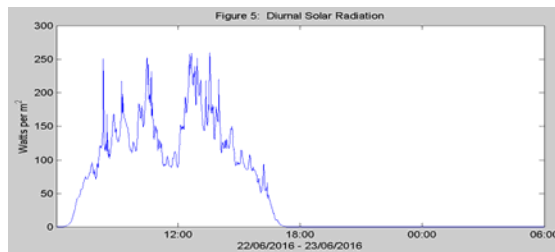


Fig. 7a Radiation parameters (shortest day).

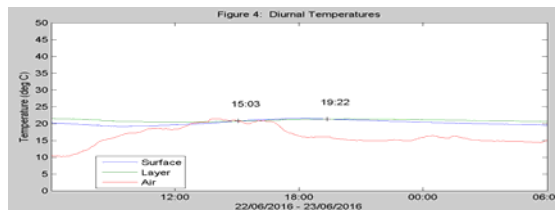


Fig. 7b Temperature parameters (shortest day).

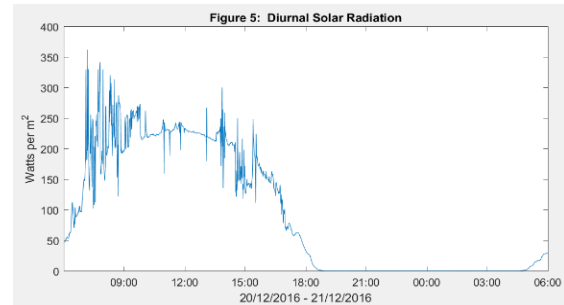


Fig. 8a Radiation parameters (longest day).

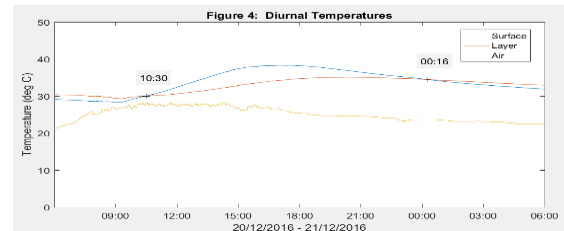


Fig. 8b Temperature parameters (longest day).

Examination of these data indicates that twice a day there is a point of equilibrium where the pavement is the same temperature at the surface and at the base of the bound layer. Between approximately 11 am and 11 pm the surface temperature is greater than the layer and between approximately 11 pm and 11 am the underside of the bound layer is hotter than the surface

Clearly this is a function of the quantum of solar energy radiating the pavement. Compare the temperature pattern for the shortest day of 2016 (June 21st) and the longest day of 2016 (December 21st) at 3 pm (Table 5).

Table 5 Temperature and Radiation measurements for shortest and longest days.

Date	Surface Temperature (°C)	Layer Temperature (°C)	Air Temperature (°C)	Change in temperature from sunrise (°C)	Accumulated Radiation (watts per m²)
	At 3 pm	At 3 pm	At 3pm	Up to 3 pm	Until 3 pm
Shortest Day	23.6	21.7	20.5	2.0	93,684
Longest Day	37.4	32.8	26.8	5.3	110,389

This is an important consideration when choosing a design temperature for the design of asphalt pavement thickness.

RELATIONSHIP BETWEEN SURFACE TEMPERATURE & STRUCTURAL LAYER STRAIN

In figure 9 we see the distribution of strain as a function of temperature over the full year where the moisture content is below 9%. Here structural layer strain is only in tension at temperatures below 20°C and then only above the critical limit of 248 $\mu\epsilon$ when the temperature is below 18°C. The secondary effect of moisture above 9% is dealt with elsewhere (Yeaman [2]).

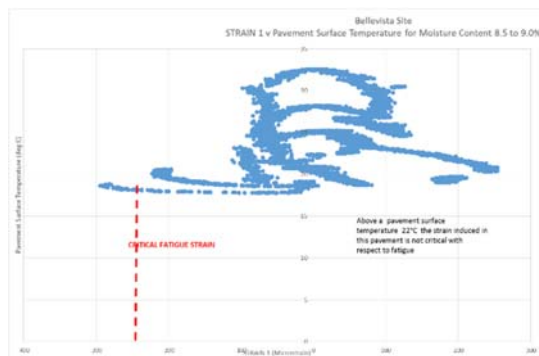


Fig. 9 Distribution of Structural Layer Strain as a function of Pavement Surface Temperature.

LABORATORY STUDIES

Laboratory studies were conducted by Gray (2015), Westerway (2015) and Laws (2015) to better understand the influence of solar radiation on asphalt in a controlled environment (i.e. no wind, no cloud and no dust).

An insulated box (Figure 10) was purpose built to hold a 200 mm square by 450 long billet of Hot Mix Asphalt compacted in the University's Shear box compactor (IPC Global).



Fig. 10 Heat box and thermal lamp constructed to enable pavement insolation to be varied in a controlled manner (Gray 2014).

The Heat Box is designed to simulate thermal radiation from the sun and to measure the temperature changes an asphalt pavement undergoes throughout the day. The Heat Box uses a heat lamp, a servo motor and microcontroller.

A code is uploaded to the microcontroller that relates the angular degree of the servo motor to a specific solar radiation; the code orders the servo motor to move every five minutes. The code relies on data obtained from the Pavement Monitoring System on Sippy Downs Drive (near Sunshine Coast University). Data from the hottest day on record in 2015 was used (9 February). The microcontroller ran throughout the day simulating the solar radiation.

A datalogger is used to record these temperatures every minute from the thermocouples inserted into the asphalt billet (at depths of 25 mm, 50 mm, 75 mm, 100 mm, 150 mm, 200 mm, 300 mm and 400 mm).

Figure 11 provides an example of the outcome from the heat box comparing the solar radiation and the actual and simulated radiation for the hottest day of 2016 (9th February).

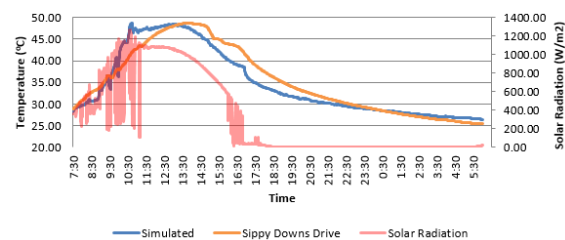


Fig. 11 Simulated Temperature: Solar Radiation for hottest day 2016 (Westerway et al 2017).

Figure 12 demonstrates the effect of thermal radiation on pavement temperatures from the simulation method.

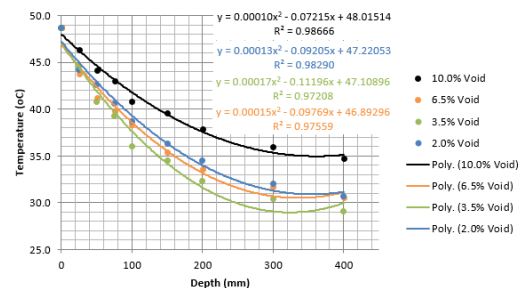


Fig. 12 Relationship between Accumulated Solar Radiation and Pavement Surface Temperature.

Here we see that there is:

- A terminal condition at which the

temperature asymptotes to equilibrium and this represents a pavement depth of around 300 mm (noting that this test was run for the hottest day),

- Voids content has a significant influence on the rate of conduction of heat through the pavement, and
- In a road pavement, 100 mm thick, there is the potential to store thermal energy as heat energy (say 12 °C).

EFFECT OF MOISTURE ON PAVEMENT PERFORMANCE

The presence or ingress of moisture into a pavement structure causes damage, or a loss in the integrity of that pavement structure. The development of damage is often progressive, and can cause sudden failure of a pavement or slow deterioration until the pavement is no longer safe to use. Due to the cumulative nature of moisture damage, it is vital that moisture ingress is understood to ensure a pavement achieves its design life.

Moisture within granular layers reduces the friction between particles and thus the strength of the material by creating large pore pressures. The dynamic loads imposed by moving vehicles makes this even more complicated, as it creates a moving pressure wave with large hydrostatic forces. Moisture conditions can vary from unsaturated to fully saturated. Although pavements are theoretically compacted at the optimum moisture content during construction, the degree of saturation cannot be assumed.

Depending on the situation, the water content may be considered in terms of volumetric water content (in soil science) or gravimetric water content (in geotechnical engineering). In this study, we will examine only the effect of Gravimetric Moisture content on the pavement behaviour.

SOIL MOISTURE RELATIONSHIPS

Figure 13 (after Austroads) demonstrates the various relationships between soil, water and engineering properties. Of importance is the “zero air voids line” or saturation line.

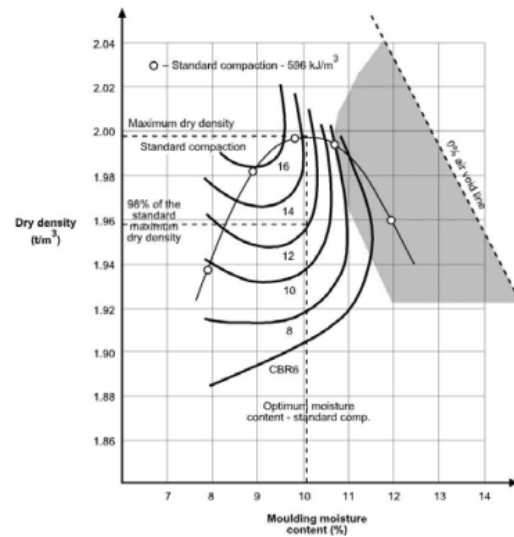


Fig. 13 Soil moisture relationships (Austroads).

Kimmel [8] developed soil moisture relationships for the subgrade at the Bellevista site, as part of his final year undergraduate programme to design and install the pavement monitoring instrumentation at Bellevista Boulevard (Figure 2). Over the past twelve months, the relationships between Gravimetric Moisture Content and rainfall have been established (Figures 14, 15, 16 & 17).

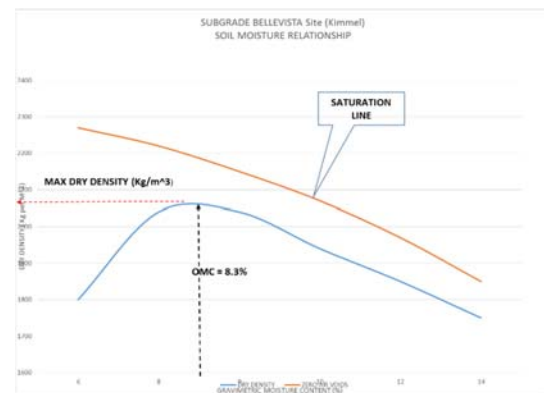


Fig. 14 Moisture density relation Bellevista subgrade (after Kimmel, 2014).

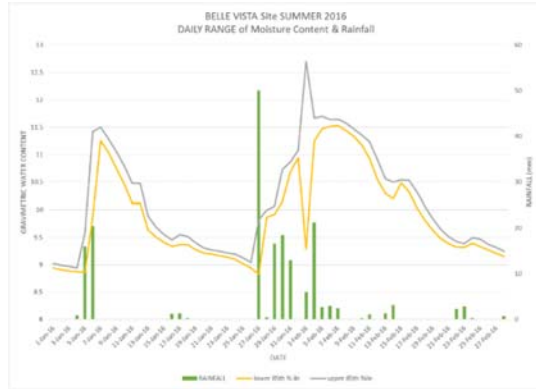


Fig. 15 Distribution of moisture and rainfall, Summer 2016.

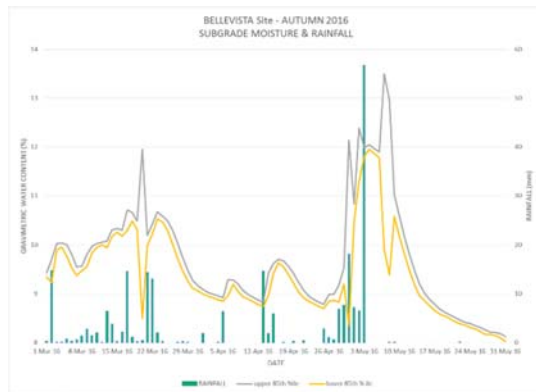


Fig. 16 Gravimetric moisture and rainfall, Autumn 2016.

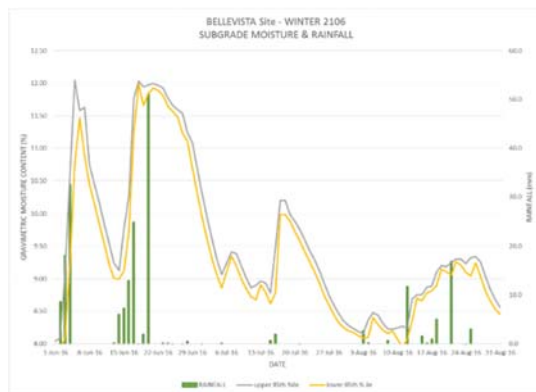


Fig. 17 Gravimetric moisture and rainfall, Winter 2016.

CRITICAL STRAINS AND MOISTURE

Let us consider the Strain conditions over a 7-day period in March 2017 (Figures 18, 19 and 20). In this case, the pavement was very dry on the 14th March with the area being declared in drought. Rain began falling at 1:00pm on the 15th March and

developed into a cyclonic depression with heavy rainfalls and widespread flooding for the following week.

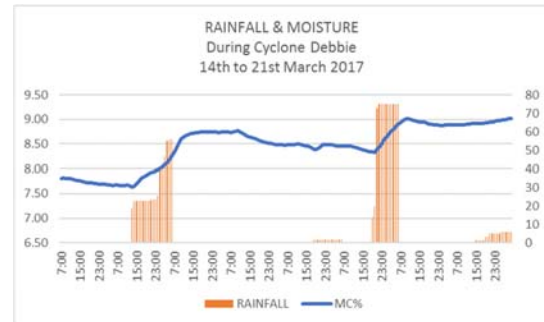


Fig. 18 Rainfall and subgrade moisture - Cyclone Debbie.

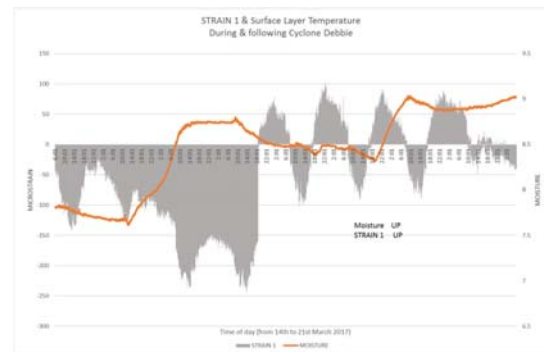


Fig. 19 Bound layer strain and moisture – Cyclone Debbie.

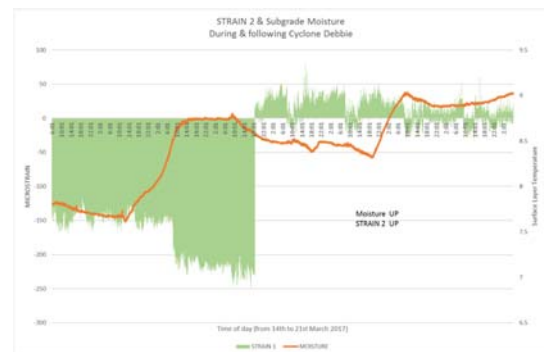


Fig. 20 Bound layer strain and moisture – Cyclone Debbie.

Bound Layer Strain passes from tension to compression whenever subgrade moisture rises above 8.5%. The subgrade strain passes from tension to compression when the moisture content exceeds 8.5% i.e. the optimum of 8.3% (Kimmel [8]). This indicates that moisture contents above optimum in the subgrade will affect the performance of this pavement.

DIFFERENCE IN MOISTURE CONTENT AS A FUNCTION OF RAINFALL

The quantum and intensity of rainfall has a noteworthy influence on the Moisture Content (*vide* Figures 4, 5, 6, 7). In some cases, it can take as long as 3 days for changes in rainfall to be reflected as moisture content. Table 6 shows observed moisture content changes at the Bellevista Site. It is apparent that rainfalls of less than 5 mm have insignificant effect on moisture content. Whereas rainfalls greater than 5 mm may have a significant impact for up to 3 days later.





Table 6 Differences in moisture content with rainfall.

Rainfall	Difference in Moisture Content		
	1 Day	2 days	3 Days
Less than 1 mm	0.31 to 0.43	-1.21 to 0.87	-1.72 to 1.29
1 to 5mm	-0.24 to 0.43	-0.34 to 0.55	-0.45 to 0.57
5 to 15mm	-0.44 to 1.42	-0.34 to 1.58	-0.72 to 2.28
More than 15mm	-0.44 to 1.42	-0.55 to 2.45	-0.5 to 2.40

DAILY CHANGES

A preferred way to examine pavement performance is to compare results obtained every day at 10:00 am. A photograph is taken of the pavement and conditions at that time are recorded (Table 7). For the same conditions the latent strain (no traffic) remains relatively the same. As the subgrade becomes wetter, bearing capacity is reduced and the pavement becomes prone to permanent deformation.

Table 7 Moisture data during and after Cyclone Debbie.

	14 Mar 2017	15 Mar 2017	21 Mar 2017	21 April 2017
				
Strain 1	-92µε	-93µε	-1 µ	-188
Strain 2	-150µε	-142 µε	-17 µε	-155

Moisture Content	7.81%	7.67%	8.91%	7.57%
------------------	-------	-------	-------	-------

In the month following the moisture reduces rapidly and strains correspondingly increase in tension (Figures 21 & 22).

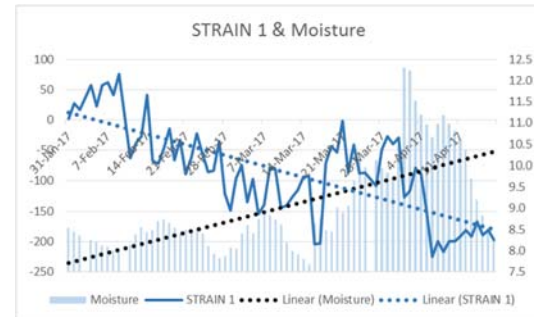


Fig. 21 Influence of moisture content on subgrade strain (Strain 1).

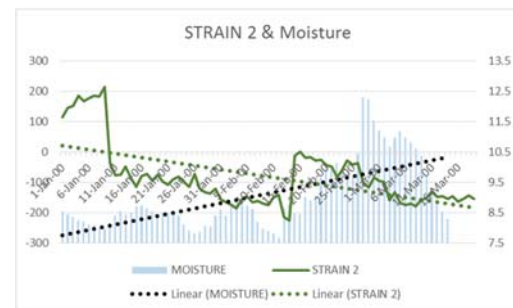


Fig. 22 Influence of moisture content on subgrade strain (Strain 2).

EFFECT ON STIFFNESS

Elastic Modulus with respect to pavements is not applicable to permanent deformation, with the Number of Cycles to Failure (Nf) being defined (in Australia) [1, Table 8.5]; see Eq. (1).

$$Nf = \left[\frac{9300^7}{\mu\epsilon} \right] (1)$$

Where µε is the vertical compressive strain at the top of the subgrade.

In the case of a cemented layer, Nf is derived from the relationship for fatigue of cemented materials (Austroads [1]) as:

$$Nf = \left\{ \frac{\frac{11300}{E^{0.804}} + 191}{\mu \epsilon} \right\}^{12} \quad (2)$$

Where:

Nf = Number of Cycles to failure

E = Modulus of cemented layer (MPa)

$\mu \epsilon$ = compressive strain at the top of the subgrade

Using Boussinesq's Generalised equation (Eq. 3) relating depth of pavement to stress and strain we find:

$$E = \frac{(1 + \mu) \sigma_o a}{\epsilon_z} \left[\frac{1}{\sqrt{1 + \left(\frac{z}{a}\right)^2}} + 1 - 2\mu \left\{ \sqrt{1 + \left(\frac{z}{a}\right)^2} - \frac{z}{a} \right\} \right]$$

Where :

ϵ_z = Strain at depth z

μ = Poisson's ratio - assume 0.45

a = Circular radius of the loaded area - assume 200 mm

σ_o = Stress on the surface

In this case, the stress is derived from the traffic spectrum (Table 8):

Table 8 Traffic distribution and associated tyre pressures.

	% Cars & Trailers	Class 3 Trucks*	Class 4 Trucks	Classes 5-12 Trucks
9500 AADT	92.8	6.1	0.3	0.8
Assumed Tyre Pressure	270 KPa	580 KPa	780 KPa	780 KPa

This results in a calculated site stress of 420 KPa. Therefore, the Dynamic Stiffness Modulus $|E^*|$ can be calculated as $ABS(580,000/(\text{Strain } 1))$.

Using this relationship with the provision that the average tyre pressure for this site is 420 KPa, the depth of the bound layers are 320 mm (fig 1) and the Layer Modulus is 3,500 MPa (design value), we derive the approximate layer stiffness for each of the conditions over the 1 month as follows:

Table 9 Derived layer stiffness for case study days.

Date	14 Mar 17	15 Mar 17	21 Mar 17	21 April 2017
Strain 1 @ 10:00 am ($\mu \epsilon$)	-93	-92	-61	-188
Layer Modulus (MPa)	6237	6304	9508	3.085

Strain at the underside of the cemented layer is constant for March 14 and 15, however, as the moisture content increases on day 7 to 8.9 % (table 7) it decreases by 30 $\mu \epsilon$.

Strain at the top of the subgrade is not a function of layer stiffness, hence the magnitude of this strain indicates the potential to permanent deformation of the subgrade. To date the values of Subgrade layer strain are very much less than design ($\approx 250 \mu \epsilon$ compares with a design value of 1020 $\mu \epsilon$) and will not be discussed further in his paper.

CONDITIONS FOR CRITICAL FATIGUE STRAIN

We now examine data from a 12 month period at the Bellevista Site to examine conditions necessary for critical fatigue strain.

Occasions when Fatigue Strain is critical

Fatigue Strain exceeded the design value of -248 $\mu \epsilon$ on 19 Days between 31st May and 29th August 2016 (Table 10). These data indicate that the lower the bound layer temperature and the lower the moisture, the greater the tensile strain.

Table 10 Traffic distribution and associated tyre pressures.

PARAMETER	MAXIMUM	MINIMUM
Structural Layer Strain ($\mu \epsilon$) *	-253	-492
Subgrade Strain ($\mu \epsilon$) *	-146	-368
Gravimetric Moisture (%)	11.5	8.1
Modulus (MPa)	2560	1320
Air Temperature (°C)	21.3	13.2
Surface Temperature (°C)	19.5	14.7
Layer Temperature (°C)	21.2	16.8

Negative value indicates that parameter is in Fatigue mode.

Relationship between Bound Layer Strain and Moisture Content

The relationships between Bound Layer Strain and moisture content at various pavement temperatures are now examined (Figures 23, 24, 25 and 26).

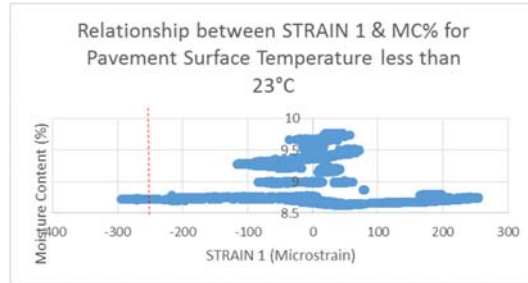


Fig. 23 Moisture content and STRAIN 1 for temperatures below 23°C.

Here strain is evenly distributed for all ranges of moisture with the only critical values ($<-248 \mu\epsilon$) occurring at moisture contents between 8.5 and 9%

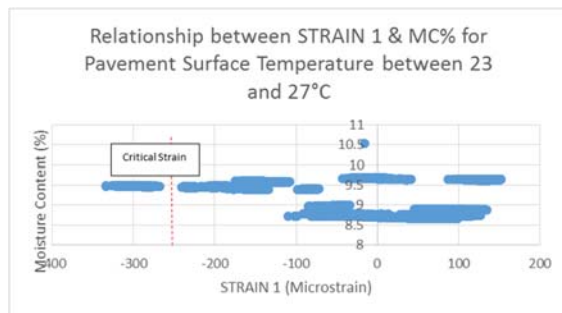


Fig. 24 Moisture content and STRAIN 1 @ temperatures 23°C to 27°C.

Here Bound Layer Strain is critical for moisture contents above 9.5% and temperatures above 23°C.

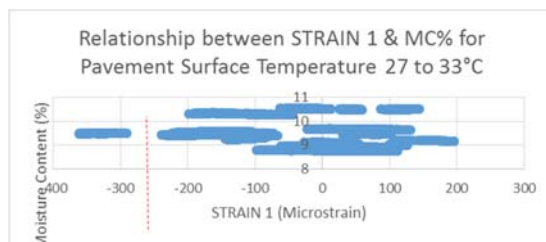


Fig. 25 Moisture content and STRAIN 1 @ temperatures 27°C to 33°C.

Here Bound layer strain is critical for moisture contents above 8.5 % and Surface layer temperatures above 27°C.

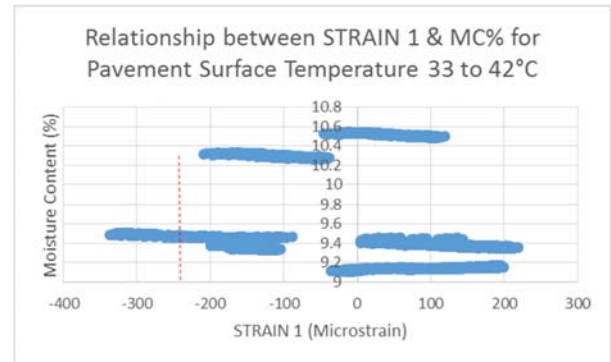


Fig. 26 Moisture content and STRAIN 1 @ temperatures 33°C to 42°C.

Here Bound Layer Strain is critical for moisture contents above 9% and surface layer temperatures above 33°C.

From these relationships, we observe that critical fatigue strain at this site occurs when moisture content lies above 8.5%

CONCLUSION

Although this study is for a single site and one type of pavement (thin Hot Mix Asphalt on a cemented base) the results are sufficient to warrant further investigation of this technology over a wider range of conditions.

Solar Radiation has a critical influence on both the pavement surface and the structural layer of a cemented base pavement. Further, a road pavement is a potential store for solar energy. Between midnight and midday the structural layer is hotter than the pavement surface and the pavement is emitting heat,

To date the only values under which a critical level of fatigue is attained is when the structural layer temperature is less than 20°C and at this time (December 2016), the pavement is deemed to be performing according to design criteria.

At moisture contents above 8.5 % and temperatures above 23°C, for this site, moisture has an influence on fatigue damage of the cemented layer. Therefore, in design calculations, we are not able to adopt one stiffness for the modulus of the structural layer.

RECOMMENDATION

Further investigation should be undertaken to evaluate the potential energy source of a large solar

receptor – an asphalt pavement. The Stirling Energy principle has potential in this area.

REFERENCES

- [1] Austroads 2007, “Guide to Pavement Technology”, Part 4B Asphalt, Sydney
- [2] Yeaman 2017 “Managing Pavement Assets through In-Situ Monitoring”, World Conference on Pavement and Asset Management WCPAM 2017 Milan, Italy, June 12/16 2017
- [3] Yeaman 2017 “The Influence of Subgrade Moisture Content on Pavement Performance” under review
- [4] Gray C, 2014 Final Year Capstone thesis, University of the Sunshine Coast
- [5] Westerway K, 2016 “Comparison of asphalt material characteristics as a function of air void content “Final Year Capstone thesis, University of the Sunshine Coast.
- [6] Laws N, 2016, “A Profile of Brisbane City Council Type 3 Asphalt Mix with Varying Air Voids” Final Year Capstone Thesis, University of the Sunshine Coast.
- [7] Austroads (2008) “Guide to Pavement Technology” Part 2: Pavement Structural Design
- [8] Kimmel B (2014) “The Instrumentation of the entrance to Bella Vista Subdivision at Caloundra” Capstone project thesis University of the Sunshine Coast
- [9] Fairweather, H., and J. Yeaman. A Study of the Parameters Affecting the Performance of Roads Under an Extreme Rainfall Event. International Journal of GEOMATE, Vol. 7, No. 1, 2014, pp. 955-960.

THE EFFECT OF LIVE TRAFFIC ON PAVEMENT PERFORMANCE

John Yeaman¹ and Adrian McCallum¹

¹Faculty of Science, Health, Engineering and Education, University of the Sunshine Coast, Australia

ABSTRACT

For the past four years, the University of the Sunshine Coast (USC) has been monitoring the performance of road pavements through “in-situ” monitoring, in association with Sunshine Coast Council and Pavement Management Services. During that time four sites have been built and monitored, wirelessly, minute by minute 24 hours per day. Each monitoring site is equipped with strain gauge sensors at critical positions within the pavement, moisture gauges and thermocouples. The system is accompanied by a weather station that measures Rainfall, Air Temperature, Wind Speed and Direction, Relative Humidity, Atmospheric Pressure, and Solar Radiation.

Analysis of data accumulated over the past four years has been confirmed that pavement stiffness is strongly influenced by pavement temperature, providing the moisture content remains constant, and that for the most part, environmental conditions have a greater influence on pavement behaviour than traffic.

Examination of the of traffic and no traffic on the pavement and over a twelve-month study period reveals that traffic load does not appear to severely jeopardise pavement life, at least early in the pavement life-cycle.

Pavement fatigue occurs due to a combination of numerous factors, one of which is traffic loading. However, in SE Queensland, traffic loading may play a less significant role than other environmental factors such as pavement temperature fluctuations and moisture ingress.

Keywords: Traffic, Moisture, Strain, Pavement performance

INTRODUCTION

During December 2012, The University of the Sunshine Coast (USC) in association with Sunshine Coast Council (SCC) and Pavement Management Services (PMS) installed an insitu pavement monitoring site on Sippy Downs Drive adjacent to the University during construction of the pavement to dual carriageway configuration. Results from this study have been published by Fairweather (2014), Yeaman (2015) and Azawi (2015), with monitoring continuing. Two other sites consisting of different configurations continue to be monitored with respect to Strain Energy Dissipation and Soil Suction.

As part of this overall research project, Yeaman (2017), at this subject site, postulated that maintenance of the pavement asset can be predicted from in situ strain outcomes as a function of both traffic and the environment .

The subject site is situated at Bellevista Boulevard, Caloundra at Latitude S. 26° 47' 41.28" and Longitude E. 153° 05' 49.92" and consists of:

- Yellow Podzol subgrade with a stiffness of 70 MPa
- 100 mm gravel subbase course with a stiffness of 145 MPa

- 270 mm cement treated base with a mean stiffness modulus of 3500 MPa.
- 50 mm Hot Mix Asphalt pavement surface.

Sensors are fitted at the base of the stiff layer at a depth of 320 mm and in the subgrade at a depth of 420 mm in the following configuration:

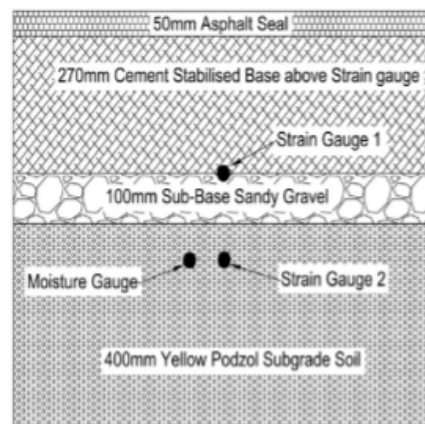


Fig. 1 Pavement and sensor configuration – Bellevista site.

This section of Bellevista Boulevard, Caloundra was constructed in September 2013 and has been instrumented since that date.

Bellevista Boulevard is designed for a 20 year lifespan with an initial high traffic growth of the first five years of 8.3% and subsequent 15 years of 5%. The design traffic is calculated as 5.21 million (5.21×10^6) Heavy Vehicle Axle Groups for the 20 year design life.

This gives Critical Fatigue Strains of $248 \mu\epsilon$ for a cemented layer of 3,500 MPa modulus and $1020 \mu\epsilon$ critical compressive strain for subgrade deformation. For relationships refer to reference 2 table 8.5.

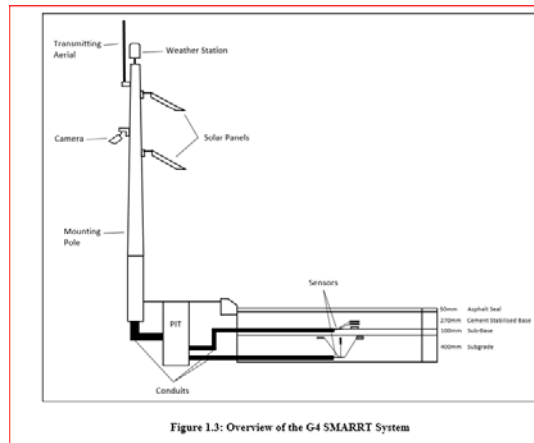


Figure 1.3: Overview of the G4 SMARRT System

Fig. 2a Configuration of Pavement Management Site (G4SMART)



Fig. 2b Configuration of Pavement Management Site (G4SMART)

Data in the format of Tables 1 and 2, following, is passed from this site by telephone to a central computer at 6:00 am daily.

Strain 1 is the strain measured at the underside of the bound layer (HMA and cemented layer) and

Strain 2 is the top of the subgrade (subgrade layer). The negative sign (-) in this instrumentation indicates that the strain is in tension.

Table 1 Example strain and temperature data.

Time	Strain #1 (ue)	Strain #2 (ue)	Soil-Moisture1 % (by vol)	Air Temp 1min (degC)	Surface Layer Temp (degC)	Road Surface Temp (degC)	Solar_Rad Corrected (W/m2)	Wind Dir 1min (deg)
1/1	-	56.	32.56	21.1	28.84	27.76	44.46	306
1/2	26.	90	1					
016	96	6						
6:0	9							
1								
1/1	-	64.	32.56	21.1	28.87	27.77	43.74	166
1/2	21.	68	9					
016	68	8						
6:0	8							
2								
1/1	-	59.	32.56	21.1	28.87	27.77	42.99	218
1/2	16.	50	7					
016	43	0						
6:0	8							
3								
1/1	-	59.	32.56	21.2	28.87	27.78	41.92	195
1/2	11.	50	8					
016	21	0						
6:0	9							
4								
1/1	-	54.	32.56	21.2	28.84	27.76	42.32	114
1/2	19.	18	6					
016	09	8						
6:0	4							
5								
1/1	-	59.	32.56	21.2	28.86	27.76	44.04	100
1/2	24.	50	6					
016	40	0						
6:0	6							
6								

Table 2 Example weather station data.

Wind Speed 1min (m/s)	Wind Dir 1min (deg)	Rel. Humidity 1min (%RH)	Air Pressure 1min (hPa)
0.2	306	88.9	1008.3
0.4	166	88.8	1008.3
0.5	218	89	1008.4
0.3	195	88.9	1008.4
0.4	114	88.9	1008.4
0.3	100	88.9	1008.3
0.1	216	88.9	1008.3
0.3	147	88.9	1008.3

CLASSIFICATION OF VEHICLE TYPE USED IN AUSTRALIA

The following vehicle classifications are adopted for this study (Figure 3).

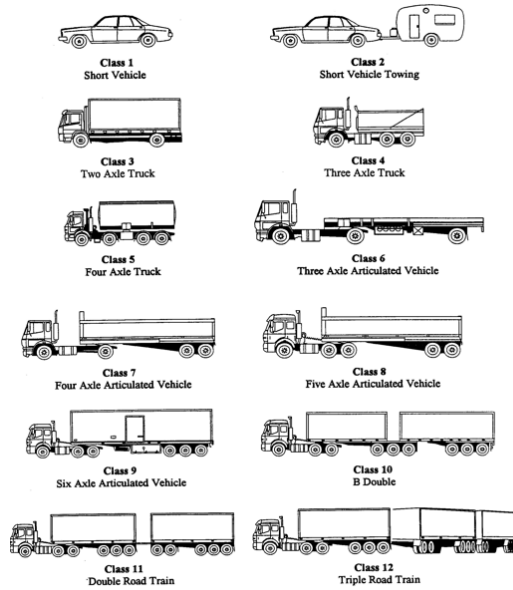


Fig. 3 Australian vehicle classifications (Austroads [1]).

ACTUAL TRAFFIC

Sunshine Coast Council conducts regular traffic counts at the Bellevista site on behalf of the research project. The following data were used in this study (Figures 4).

Speed (km/h)	1	2	3	4	5	6	7	8	9	10	11	12	Speed
10 - 20	216	19	2	3	4	-	-	-	-	-	-	-	301
20 - 30	417	7	22	7	5	1	1	-	1	1	-	-	462
30 - 40	1849	88	155	34	21	8	14	11	19	7	2	-	2204
40 - 50	37412	774	2142	239	116	24	41	25	41	15	2	-	40833
50 - 60	74535	888	1839	94	52	22	23	7	13	6	1	-	77482
60 - 70	11369	87	263	12	7	8	-	1	1	-	-	-	11748
70 - 80	597	5	10	1	-	1	-	-	-	-	-	-	654
80 - 90	49	2	-	-	-	-	-	-	-	-	-	-	51
90 - 100	3	-	-	-	-	-	-	-	-	-	-	-	3
100 - 110	-	-	-	-	-	-	-	-	-	-	-	-	0
110 - 120	-	-	-	-	-	-	-	-	-	-	-	-	0
120 - 130	-	-	-	-	-	-	-	-	-	-	-	-	0
130 - 140	-	-	-	-	-	-	-	-	-	-	-	-	0
140 - 150	-	-	-	-	-	-	-	-	-	-	-	-	0
150 - 160	-	-	-	-	-	-	-	-	-	-	-	-	0
	126505	1849	4452	392	204	68	79	44	75	29	5	2	133704
	94.6%	1.4%	3.3%	0.3%	0.2%	0.1%	0.1%	0.0%	0.1%	0.0%	0.0%	0.0%	
	Class Totals												

Fig. 4 Traffic count for the Bellevista site, 7th to 21st September 2017.

Table 3 lists vehicle class [1] and percentage traffic for 2016.

Table 3 Vehicle class and percentage traffic.

Vehicle class	Traffic (%)
1	91.3
2	1.6
3	6.1
4	0.3
5	0.3
6	0.2
7	0.2

PEAK HOUR AND QUEUING TRAFFIC

Table 4 shows hourly data for 2016. At this site there are two peak periods: 7am to 10 am and 2 pm to 5 pm. In the afternoon the environment is important as the pavement is hot, in this case a static load may cause strains to go to a maximum, as observed, during the calibration of the Sippy Downs East site [3] where a standard axle parked on the sensors caused Strain 1 to go to 600 $\mu\epsilon$ and remain there until the load was removed after 3 minutes.

This can be compared with the 2012 traffic survey from which we note the increase in Class 3 traffic due the development of the “Aura” city, a new development designed to house a population of 300,000 residents [3].

Table 4 Comparison of hourly traffic numbers 2012 to 2016.

Period	2012 survey	2016 survey
7 am to 10 am	1165	1523
2 pm to 5 pm	1349	1645

Figures 5 and 6 are typical of the situation as traffic queues on the site.



Fig. 5 Queuing traffic – morning peak.



Fig. 6 Queuing traffic – afternoon peak.

In the afternoon the pavement is at its most vulnerable with respect to both fatigue cracking and permanent deformation. In this case, the pavement is both hot and wet and the static load may cause strains to increase to a maximum, as observed during the calibration of the Sippy Downs east site (ref 1) where a standard axle parked on the sensors caused the strain1 to go to 600 $\mu\epsilon$ and remain there until the load was removed after 3 minutes.

Observe here (Fig. 7) three different buses, four minutes apart of which two are either standing still or moving very slowly over the sensors with the strains being in compression and the same order of magnitude.







			
Time	08:23 14 Nov 16	08:33 14 Nov 16	08:44 14 Nov 16
Strain 1	31 $\mu\epsilon$	11 $\mu\epsilon$	4 $\mu\epsilon$
Strain 2	288 $\mu\epsilon$	184 $\mu\epsilon$	192 $\mu\epsilon$
Moist.	9.07 %	9.06 %	9.06 %
Layer Temp	30.7 °C	30.4°C	30.3 °C
Sfc Temp	29.4°C	29.1°C	29.0
Condition	Warm & Dry	Warm & Dry	Warm & dry

Fig. 7 Comparison of critical strains for Class 3 vehicle (bus) same day, same time.

And at the same time, three days later (Figure 8).

			
Time	08:23 14 Nov 16	08:33 14 Nov 16	08:44 14 Nov 16
Strain 1	31 $\mu\epsilon$	11 $\mu\epsilon$	4 $\mu\epsilon$

Strain 2	288 $\mu\epsilon$	184 $\mu\epsilon$	192 $\mu\epsilon$
Moisture	9.07 %	9.06 %	9.06 %
Layer Temp	30.7 °C	30.4°C	30.3 °C
Sfc Temp	29.4°C	29.1°C	29.0
Condition	Warm & Dry	Warm & Dry	Warm & dry

Fig. 8 Comparison of critical strains for Class 3 vehicle (bus) same day, same time.

Compare this with the afternoon peak where the last image has the critical fatigue strain in the fatigue mode (Figure 9).




			
Time	14:57; 10 Nov 16	15:10; 10 Nov 16	15:28 10 Nov 16
Strain 1	30 $\mu\epsilon$	36 $\mu\epsilon$	-16 $\mu\epsilon$
Strain 2	234 $\mu\epsilon$	243 $\mu\epsilon$	185 $\mu\epsilon$
Moist.	8.60%	8.60%	8.60%
Layer Temp	33.0°C	33.1°C	33.3°C
Sfc Temp	36.8°C	37.0°C	37.2°C
Condition	Warm & Dry	Warm & Dry	Warm & dry

Fig. 9 Comparison of critical strains for Class 3 vehicle (bus) same day, same time.

‘ROGUES GALLERY’

One of the features of this in-situ monitoring is what we have termed the “Rogues Gallery”. In essence a trigger is set in the data collection software that takes a photograph of the site whenever a strain

exceeds a predetermined value. In this case, we have chosen initially a value of $\pm 180 \mu\epsilon$.



Fig. 10 A concrete pumper has exceeded the 'trigger' strain value.

This method was used over the 12-month study period to classify the strain exerted by various vehicle classes with the following results (Figure 11, 12, 13 & 14).



Fig. 11 Strain for Class 1 & 2 vehicles.



Fig. 12 Strain for Class 3 vehicles.

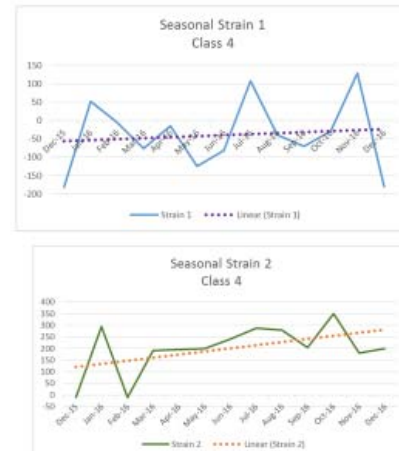


Fig. 13 Strains for Class 4 vehicles.



Fig. 14 Strains for vehicles Class 5 through 12.

Of interest, here is the fact that the strains are increasing from December 2015 to December 2016.

LATENT STRAIN

The ‘rogue’s gallery’ was observed on many occasions to produce multiple photographs without the presence of traffic especially early in the morning.

These following figures (Figs 15 & 16) demonstrate Strains without traffic for the full year.



Fig. 15 Strain 1 for no traffic.

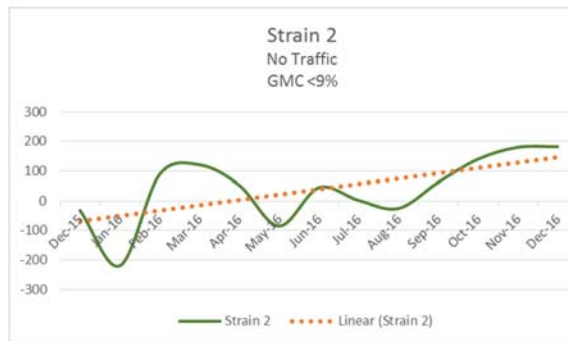


Fig. 16 Strain 2 for no traffic.

The values for these strains have increased with time without the influence of traffic. We have called this “Latent Strain”. Environmental conditions are increasingly observed to play a significant part in pavement fatigue (Yeaman and McCallum, 2017a; Yeaman and McCallum, 2017b).

DIGRESSION – RESILIENT MODULUS

Recall the theory behind the measurement of resilient modulus (Figure 17).

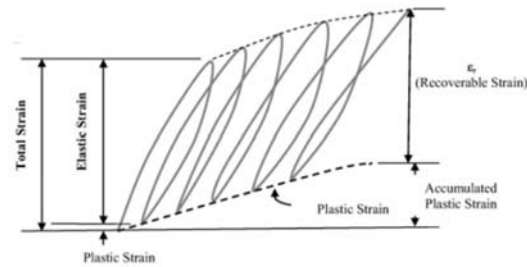


Fig. 17 Resilient Modulus (Mallick and El-Korchi, 2015)

It is the accumulation of this plastic strain that we see incorporated within the Latent Strain. When this value reaches the ultimate critical strain, the pavement will have deemed to be failed.

CONCLUSION

At this time, the Bellevista pavement is performing within the design criteria. Traffic is not a serious issue with this pavement after almost one quarter of the design life. Latent Strain is increasing according to theory but is well below the critical fatigue value for the bound layer of $428\mu\epsilon$ and $1020\mu\epsilon$ for the subgrade layer. Although this study is of a limited nature it does serve to prove that in -situ monitoring can be a useful tool to understand the impact of traffic on a cemented pavement.

REFERENCES

- [1] Austroads (2008) “ Guide to Pavement Technology” Part 2: Pavement Structural Design
- [2] Kimmel B (2014) “The Instrumentation of the entrance to Bella Vista Subdivision at Caloundra” Capstone project thesis University of the Sunshine Coast
- [3] Fairweather, H., and J. Yeaman. A Study of the Parameters Affecting the Performance of Roads Under an Extreme Rainfall Event. International Journal of GEOMATE, Vol. 7, No. 1, 2014, pp. 955-960.

LIQUEFACTION SIMULATION FOR THE OSAKA GULF COAST USING THE LIQCA PROGRAM

Tetsuya Okano¹, Keita Sugito² and Ryoichi Fukagawa³

^{1,2}Graduate School of Science and Engineering, Ritsumeikan University, Japan;

³ Department of Civil Engineering, Ritsumeikan University, Japan

ABSTRACT

A Nankai megathrust earthquake is expected to occur in the Kansai area within the next 30–40 years. According to the worst-case estimations by The Headquarters for Earthquake Research Promotion [1], the earthquake will cause economic losses of approximately 220 trillion yen, and 134,000 buildings will be damaged by liquefaction. To estimate future damage to the Osaka gulf coast, we conduct liquefaction simulations based on the LIQCA program developed by the research group at Kyoto University. The liquefiable layers are composed of relatively loose sand and the underground water level is high. The input earthquake motion is the L2 spectrum I earthquake-resistant standard spectrum, according to the Design Standards for Railway Structures and Commentary [2]. We consider not only the increase of excess pore water pressure, but also its dissipation. The calculated effective stresses in the sand layers approached 0, after which the sand layers liquefied and unevenness occurred at the ground surface. We evaluated the damage due to liquefaction by calculating vertical displacements and unevenness of the ground surface. Countermeasures are proposed for the shallow sand layers to reduce future liquefaction damage.

Keywords: Liquefaction, Simulation, Nankai megathrust earthquake, Gulf coast, Unevenness

INTRODUCTION

A Nankai megathrust earthquake is predicted for the Kansai area within the next 30–40 years. The most recent Nankai megathrust earthquake occurred in 1946 and the recurrence interval of this type of earthquake is over 100 years, according to The Headquarters for Earthquake Research Promotion [1]. If a Nankai megathrust earthquake were to occur, the economic losses would be approximately 220 trillion yen, and 134,000 buildings would be damaged by liquefaction in the worst-case scenario [3], [4]. In addition, a Tokai megathrust earthquake has not occurred for 168 years, even though the recurrence interval of a Tokai megathrust earthquake is also 100 years. It is expected that a Tokai megathrust earthquake would induce the occurrence of a Nankai megathrust earthquake earlier than suggested by its recurrence interval. A Nankai megathrust earthquake would cause huge damage to the Kansai area. Within this area, Osaka city has a significant effect on the national economy and it contains many embankment areas, which tend to liquefy more than other natural ground types. In addition, the high ground water levels of Osaka city would enhance liquefaction.

Therefore, it is important to fully comprehend soil liquefaction characteristics. This paper presents an evaluation of ground liquefaction characteristics for the Osaka Gulf coast. A liquefaction analysis is implemented to assess the liquefaction characteristics. For the scope of this study, the Computer Program for Liquefaction Analysis (LIQCA) is used. This software was developed by the LIQCA Liquefaction

Geo-Research Institute (LIQCARI), consisting of researchers from Kyoto and Gifu universities.

SIMULATION CONDITIONS

The subject of analysis in this research is a site on the Osaka Gulf coast. A cross sectional view of the study area is shown in Figure 1. The cross section contains an embankment layer, which is approximately 0.4 m to 0.5 m thick. The ground water level is GL-2.3 m.

In this study, we consider the effect of a clay layer (Ac1) and a structure on the liquid sand layer. The influence of the Ac1 layer between the sand layers Bs and As1 is evaluated by considering the thickness of the Ac1 layer. In addition, the influence of a structure is evaluated by comparing the point that bears the load of the structure and the point that does not bear any load. Point A is most affected by the load of the structure and the clay layer Ac1 is thinnest at this point. Point B does not bear the load of the structure and the clay layer Ac1 is thick here. Point C bears some of the load of the structure and the clay layer Ac1 is moderately thick at this point. By comparing the results at these three points, we consider the effect of the clay layer between the liquefaction target layers and the liquefaction damage due to the structure.

Table 1 Material parameters of the R-O model

	Bs	Ac1 Ac2 Ac3	Tc1	Tsg2	Tc2	Oc
	Un-sat.	Sat.	Sat.	Sat.	Sat.	Sat.
ρ	1.8	1.6	1.6	1.8	1.6	1.6
k	1.4	9.0	2.6	1.2	1.0	7.5
	$\times 10^{-6}$	$\times 10^{-10}$	$\times 10^{-7}$	$\times 10^{-5}$	$\times 10^{-7}$	$\times 10^{-9}$
e_0	0.658	1.038	0.724	0.777	1.098	1.799
V_s	120	120	200	260	208	208
ν	0.49	0.496	0.494	0.488	0.492	0.492
c (kPa)	0	33	198	0	149	149
ϕ (deg)	30.9	0	0	34.0	0	0
a	6977	2241	4939	8530	4533	4165
b	0.5	0.5	0.5	0.5	0.5	0.5
α	1.89	-	2.3	2	1.4	1.5
r	1.92	-	2.1	3	1.7	1.6

Table 2 Material parameters of the cyclic elasto-plastic constitutive model

	Bs	As1	As2	Tsg1
	Sat.	Sat.	Sat.	Sat.
ρ	1.8	1.8	1.8	1.8
k	1.5E-6	1.5E-6	1.1E-6	5.2E-6
e_0	0.658	0.990	0.673	0.505
V_s	140	120	170	240
λ	0.002	0.002	0.1	0.001
κ	0.025	0.02	0.02	0.001
OCR^*	1.3	1.0	1.0	1.6
G_0/σ'_{m0}	935.5	445.3	646.1	1104
M^*_m	0.909	0.909	0.909	0.909
M^*_f	1.012	0.966	0.958	1.215
B^*_0	3500	2500	5000	10000
B^*_l	80	50	100	200
C_f	0	0	0	0
γ^{P*}	0.02	0.002	0.02	0.005
γ^{E*}	0.001	0.3	0.3	0.001
D^*_0	1	1.5	4	4
n	7	2	6	8
C_d	2000	2000	2000	2000

The cross section in Figure 1 includes a structure in the form of a building, modeled as a point load in the LIQCA program. It is hypothesized that this point load will affect liquefaction damage. We evaluate the effect of the load on liquefaction through the presence and absence of the load.

Analysis parameters are based on the Design Standards for Railway Structures and Commentary [2]. LIQCA specific parameters are based on their operating manual. Dynamic parameters are determined using element simulation.

At first, all soil layers are classified as those that determine the target of liquefaction ('Liquefaction-Layers') and those that determine the non-target of liquefaction ('Non-Liquefaction-Layers') based on [2]. Non-Liquefaction Layers are modeled using the Ramberg-Osgood (R-O) model. Liquefaction-Layers are modeled using the cyclic elasto-plasticity constitutive model. The parameters of these models are shown in Table 1 and Table 2, respectively.

The coefficients of permeability k of Bs, As1, As2, and Tsg1 are determined based on a permeability test conducted in the study area. The rest are determined based on the Creager method. The shear wave velocity, V_s , is determined from the Design Standards for Railway Structures and Commentary [2]. The Oc layer is considered as an engineering base surface. The unit weight γ in the Bs, As1, As2, and Tsg1 layers is determined from a mean density soil test in the study area; the rest are determined from the Design Standards for Railway Structures and Commentary [2]. Other specific parameters and the dynamic parameters are determined using the LIQCA program and element simulation.

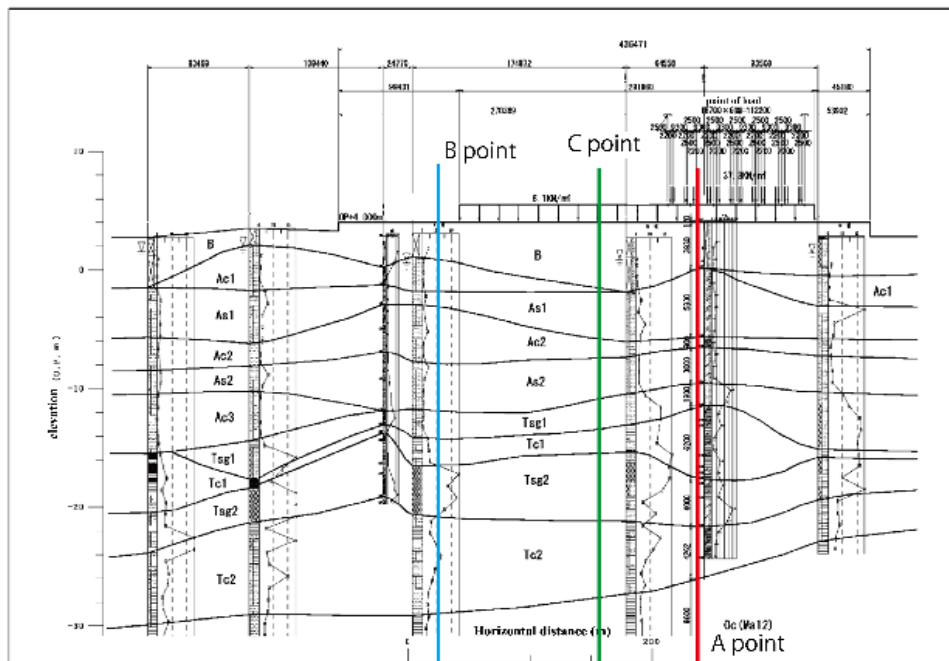


Fig. 1 Cross section of the study area showing the different soil layers.

Input Seismic Vibration

The input seismic vibration is the H24 L2 earthquake-resistant standard spectrum, shown in Figure 2. It is designed by the Design Standards for Railway Structures and Commentary [2].

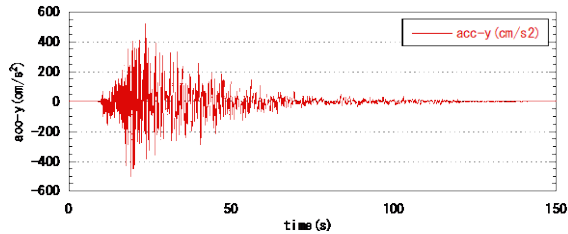


Fig. 2 Input seismic vibration.

Element Simulation

The specific parameters of Liquefaction-Layers are determined by fitting the liquefaction strength curves from the Design Standards for Railway Structures and Commentary [2]. The specific parameters of Non-Liquefaction-Layers are determined by fitting the dynamic deformation characteristics from the Yasuda-Yamaguchi equations [5].

The liquefaction resistance is regulated by the number of cycles. The liquefaction layer is supported in a simple shear test with a double amplitude of axial strain (DA) of 7.5%, and the number of cycles regulating the strength of the liquefaction is 20. The cyclic shear stress ratios of Bs, As1, As2, and Tsg1 are 0.43, 0.35, 0.31, and 0.31, respectively.

Initial Conditions

We conduct an initial effective stress analysis, where the mean effective stress with static overburden pressure is analyzed for the case where the coefficient of earth pressure, K_0 , is 0.5. All layers are modeled using the Drucker-Prager type plasticity models. Poisson's ratios are determined as 0.33 for $K_0 = 0.5$. The Young's modulus, E , was determined by considering the influence of the effective overburden pressure (Eq. 1), as follows:

$$E = E_0 \sigma_{m0}^n \quad (1)$$

E_0 : Constant of proportionality of Young's modulus (kN/m²)

σ'_{m0} : Average effective stress in initial stress state (kN/m²)

The side boundary condition is the vertical roller support and the bottom boundary condition is fixed. After the effective stress analysis, all displacements and pore water pressures are set to 0.

SIMULATION RESULTS

Here, we consider the results in terms of displacements and acceleration, the effective stress reduction ratio, the angle of rotation, and the relationship between effective stress reduction and volume strain, respectively.

Displacements and Acceleration

Figures 3, 4, and 5 show the time series of the horizontal acceleration response, the horizontal displacement response, and the vertical displacement response, respectively. Table 3 shows the maximum absolute values of displacement and acceleration on the ground surface during shaking. Table 4 shows the displacements on the ground surface during the dissipation stage of excess pore water pressure.

Each horizontal acceleration of the output node is converged. Once again, every output node is selected from the ground surface on the longitudinal plane. After all horizontal accelerations are converged, a dissipation stage of excess pore water pressure analysis is conducted. The time series of horizontal acceleration show the same trend and the maximum absolute value of horizontal acceleration is approximately 2.0 m/s² (Figure 3).

Each horizontal displacement of the output node is converged, as with the horizontal accelerations. The maximum absolute value of the horizontal displacement of three output points is approximately 0.847 m. Although the time series of horizontal displacement show the same trend, the final displacements are different (Figure 4). The further to the right the point is on the longitudinal plane, the larger the horizontal displacement.

Again, each vertical displacement of the output node is converged. The vertical sinking was largest at point A, where the clay layer, Ac1, is thinnest (Figure 5). Point B rose slightly due to lateral flow from the thinnest point of the clay layer.

Looking at the time series, when maximum acceleration occurred and the excess pore water pressure rose sharply, the ground surface vibrated slightly. After that, with dissipation of the excess pore water pressure, points A and C experienced vertical sinking. In response to this, the ground surface at point B rose, but subsequently there was slight vertical settlement following dissipation of the excess pore water pressure of the target layer under point B.

Regarding the effect of the structure, the ground surface of point A and point C dropped significantly under the load. Because of this reaction, the ground surface at point B underwent significant flow. Since the ground surface at point A received a larger load than point C, point A dropped further.

After this, the excess pore water pressure

dissipated to between 1×10^4 and 1×10^8 seconds and the ground surface at all points experienced sinking.

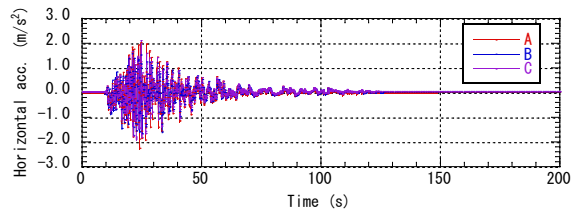


Fig. 3 Time series of the horizontal acceleration response.

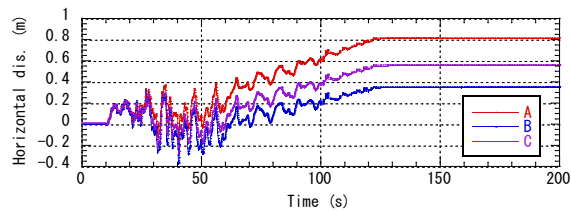


Fig. 4 Time series of the horizontal displacement response.

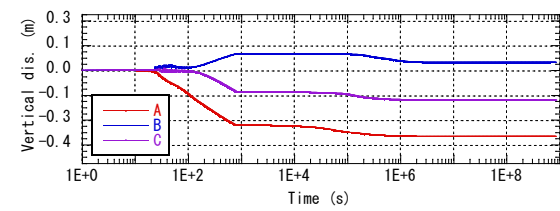


Fig. 5 Time series of the vertical displacement response.

Table 3 Maximum absolute value of displacements and acceleration on the ground surface during shaking

	Displacement (m)		Acceleration (m/s^2)
	Horizontal	Vertical	Horizontal
A	0.847	-0.355	2.020
B	0.440	0.088	1.649
C	0.631	-0.163	2.079

Table 4 Displacements on the ground surface during the dissipation stage of excess pore water pressure

	Horizontal displacement (m)	Vertical displacement (m)
	Horizontal displacement (m)	Vertical displacement (m)
A	0.846	-0.355
B	0.437	0.042
C	0.626	-0.162

Effective Stress Reduction Ratio

Figures 6, 7, 8, and 9 show the effective stress reduction ratio of Bs, As1, As2, and Tsg1, respectively. Table 5 shows the effective stress reduction ratios during shaking. There is no Bs layer at the B output point, so the table does not include the

effective stress reduction ratio of the Bs layer.

The excess pore water pressures of the sand, As1, As2, and Tsg1 layers rose more than that of the Bs layer. Because the Bs layer is closer to the ground water level than other sand layers, the excess pore water pressure of the Bs layer dissipated more quickly than that of the other layers.

Regarding the difference between the output points, point B required more time for dissipation of the excess pore water pressure than other points. We consider that the thickness of the upper clay layer is related to the time required for dissipation of the excess pore water pressure. A thicker clay layer results in a longer dissipation time for the sand layer. Because As1, As2, and Tsg1 layers are above the clay layer, Ac1, their dissipation times are longer than that of the Bs layer.

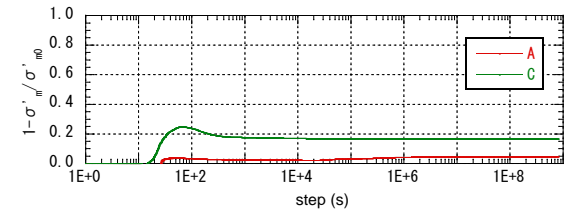


Fig. 6 The effective stress reduction ratio of the Bs layer.

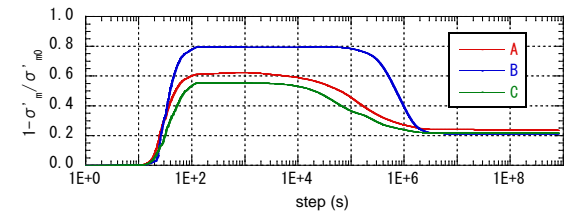


Fig. 7 The effective stress reduction ratio of the As1 layer.

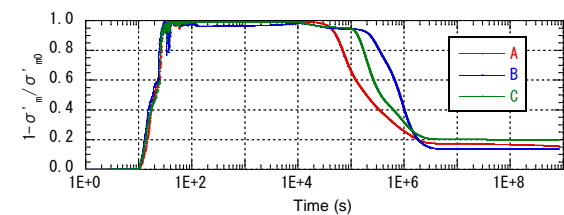


Fig. 8 The effective stress reduction ratio of the As2 layer.

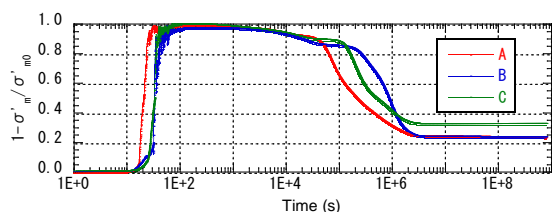


Fig. 9 The effective stress reduction ratio of the Tsg1 layer.

Table 5 Effective stress reduction ratios during shaking

	Bs	As1	As2	Tsg1
A	2.9%	61.3%	98.8%	98.8%
B	-	79.5%	96.1%	96.7%
C	21.1%	55.4%	99.0%	99.0%

Angle of Rotation

Figures 10 and 11 show the angle of rotation at the ground surface and the vertical displacement at the ground surface, respectively.

The angle of rotation is an index indicating the degree of unevenness. It is an angle represented by the absolute value of a certain node and the angle between two adjacent nodes. For example, it is horizontal when it is 180° and vertical when it is 90°.

The angle of rotation decreased the most around the point at which the load was applied. The ground tilted approximately 0.9° at the point that was most severely affected. Ground unevenness when the shaking ended and when the dissipation stage of excess pore water pressure converged showed the same trend. Therefore, it is considered that liquefaction and loss of strength would occur in a relatively short time.

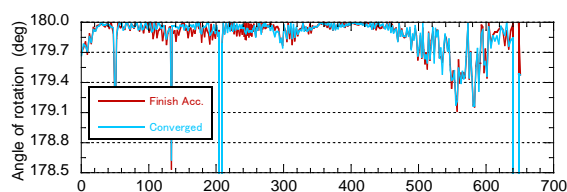


Fig. 10 Angle of rotation at the ground surface.

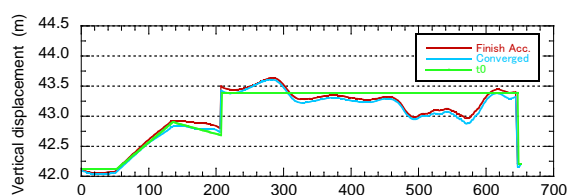


Fig. 11 Vertical displacement at the ground surface.

Relationship between the Effective Stress Reduction Ratio and Volume Strain

Regarding the excess pore water pressure, the effective stress reduction ratio of the As2 and Tsg1 layers reached 1, indicating liquefaction. This result shows that deeper layers can liquefy. However, the As1 layer and the Bs layer were responsible for significant vertical sinking and horizontal displacement. Figure 12, 13, 14 and 15 show the time series of volume strain of Bs, As1, As2 and Tsg1, respectively. Figure 16 shows the relationship between the effective stress reduction ratio and volume strain. As a result, even though the sand layer at a relatively large depth was liquefied, the amount of volume strain is considered small.

In the study area, the Bs and As1 layers, which are the sand layers near the ground surface, are greatly deformed. Therefore, it is necessary to propose countermeasures.

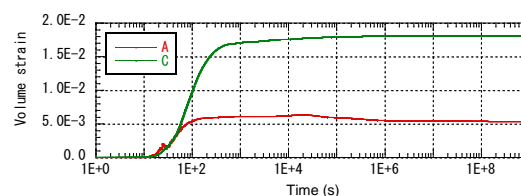


Fig. 12 Time series of volume strain of the Bs layer.

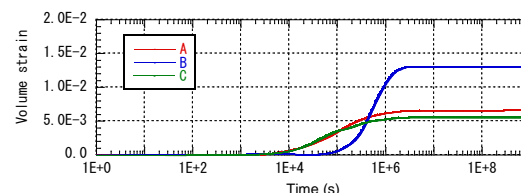


Fig. 13 Time series of volume strain of the As1 layer.

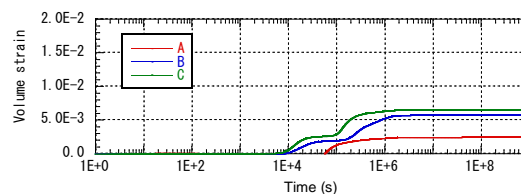


Fig. 14 Time series of volume strain of the As2 layer

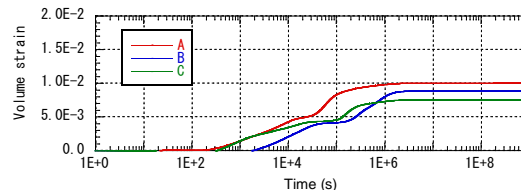


Fig. 15 Time series of volume strain of the Tsg1 layer.

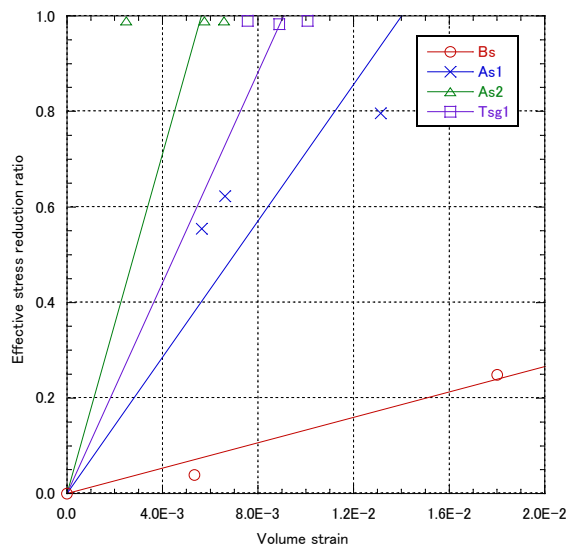


Fig. 16 Relationship between volume strain and the effective stress reduction ratio.

CONCLUSION

Liquefaction simulations using the LIQCA program showed that the ground surface on the Osaka gulf coast would sink by a maximum of 0.355 m and move horizontally by a maximum of 0.847 m due to liquefaction. In addition, if there is a structure on the ground surface, the sand would liquefy due to a sudden loss of strength. Conversely, parts of the ground surface would rise as a reaction to the sinking elsewhere.

Shallow sand layers were displaced more than deep sand layers by liquefaction. Regarding the effective stress reduction ratio, the shallow sand layers did not liquefy much, although they did experience significant sinking. The shallow sand layers moved horizontally because Liquefaction-Layers lose strength due to liquefaction. Therefore, the possibility of damage of liquefaction on the ground at Osaka Gulf Coast is considered high.

REFERENCES

- [1] The Headquarters For Earthquake Research Promotion, "Past earthquake occurrence situation", Earthquakes occurring in the Nankai Trough, http://www.jishin.go.jp/main/yosokuchizu/kaiko/k_nankai.htm (accessed 2017-06-05)
- [2] Railway Technical Research Institute, Design Standards for Railway Structures and Commentary, 2012.
- [3] Nihon Keizai Shimbun, Inc., "Estimated damage amount of the Nankai Trough massive earthquake", Nankai Trough Earthquake, damage amount of up to 220 trillion yen Halved by reduction, http://www.nikkei.com/article/DGXNASDG1802L_Y3A310C1000000/ (accessed 2017-06-05)
- [4] Disaster Management, Cabinet office, "Aspect of Immediate Disaster", About the damage estimate of the Nankai Trough massive earthquake, http://www.bousai.go.jp/jishin/nankai/taisaku_wg/pdf/20130318_shiryo2_1.pdf, (accessed 2017-0605)
- [5] Yasuda S. and Yamaguchi I., "Dynamic soil properties of undisturbed samples.", Proceedings of 20th Japan National Conference on Geotechnical, 1985, pp539:542.

NUMERICAL SIMULATION OF LIQUEFACTION AND RELATED BEHAVIOR OF UNDERGROUND STRUCTURE ON OSAKA GULF COAST

Keita Sugito¹, Tetsuya Okano² and Ryoichi Fukagawa³

^{1,2}Graduate School of Science and Engineering, Ritsumeikan University, Japan; ³Department of Science and Engineering, Ritsumeikan University, Japan

ABSTRACT

The Kansai area has a high possibility of a huge plate-boundary-type earthquake within 30 years. If an earthquake occurs, the Osaka Gulf coast will be struck by severe liquefaction disasters. Therefore, we tried to apply LIQCA, which is often used for liquefaction analysis, to a site on the Osaka Gulf coast. The input earthquake motion is the seismic standard spectrum I, which is commonly used in Japan. The calculation time continued until the excess pore water pressure dissipated. The site has an underground structure, so we investigated not only the liquefaction phenomenon of the ground itself but also the behavior of the underground structure. The results of this analysis indicate that these soil layers of the target area become liquefied. After the excess pore water pressure dissipates, the ground surface settles in the vertical direction and moves in the horizontal direction. In addition, at the vicinity of the underground structure center, it rises in the vertical direction and moves in the horizontal direction.

Keywords: Liquefaction, Numerical Simulation, Tunnel, Float up

INTRODUCTION

A Nankai trough earthquake, which is a plate-boundary-type huge earthquake, has a high probability of occurring within 30 years, and the western part of Japan will be severely damaged by this earthquake. The Osaka Plain is no exception. In particular, the Osaka Gulf coast is predicted to suffer from a severe liquefaction disaster [1]. Therefore, we apply a liquefaction simulation to a typical site on the Osaka Gulf coast. The simulation is based on the LIQCA [2] program, which is widely used as a liquefaction simulation tool in Japan. The target ground has a tunnel beneath the ground, so we investigated not only the liquefaction phenomenon of the ground itself but also the behavior of the underground structure.

OUTLINE OF ANALYSIS

Ground to be analyzed

The analysis target is the ground of a plain on the Osaka Gulf coast. Figure 1 shows the cross section of the ground that is the target of the analysis. The cross section has a length of 100 m in the horizontal direction and a depth of 40 m in the vertical direction. The tunnel is located near the surface in the center of the ground. The soil layers that may liquefy are the As1 layer, As2 layer, and Tsg1 layer.

Other layers are composed of clayey soil and hard, sandy soil. Thus, it is considered that liquefaction barely occurs. Therefore, these layers are not judged for liquefaction.

The groundwater level is set at GL-2.3 m. The Oc layer is the base surface in this cross section. In the B layer, the layer above the groundwater level is considered hard to liquefy, so the R-O model is applied to this layer. The layer below the groundwater level is modeled as a cyclic elastoplastic constitutive model. Table 1 lists the material parameters used in the analysis. The liquefaction layers and non-liquefaction layers are fitted based on the respective standards. The liquefaction layers have liquefaction strength curves based on the *Design Standards for Railway Structures and Commentary* [3]. The non-liquefaction layers are fitted as a Yasuda-Yamaguchi model [4].

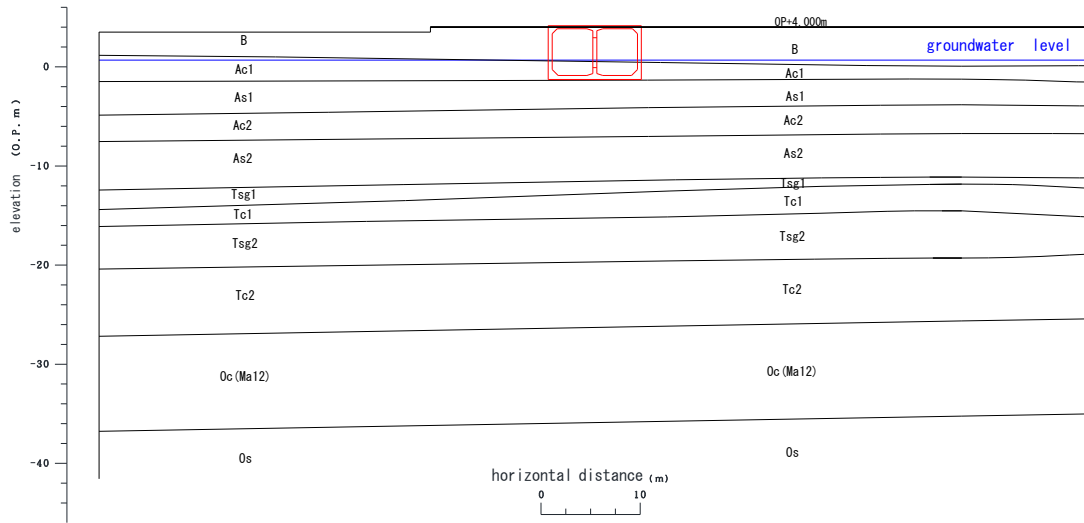


Fig. 1 Target ground of the analysis

Table 1 Material parameters used in analysis

	①		②		③		④		⑤		⑥		⑦		⑧		⑨	
	Bs		As1		Ac1, Ac2		As2		Tsg1		Tc1		Tsg2		Tc2		Oc	
type	Y	X	X		Y		X		Y		Y		Y		Y		X	
γ (kN/m ³)	18.0	18.0	18.0		16.0		18.0		16.0		18.0		16.0		16.0		18.0	
ρ (g/cm ³)	1.8	1.8	1.8		1.6		1.8		1.6		1.8		1.6		1.6		1.8	
k (m/s)	1.47	1.47	1.47		9.00		5.17		2.60		1.20		1.00		7.50		1.12	
e_0	0.658	0.658	0.990		1.038		0.505		0.724		0.777		1.098		1.799		0.673	
Vs (m/s)	120	140	120		120		240		200		260		208		208		170	
λ		0.002	0.002				0.001										0.1	
κ		0.025	0.02				0.001										0.02	
OCR*		1.3	1.0				1.6										1	
G_0/σ'_{m0}		935.5	445.3				1104										646.1	
M^*_m		0.909	0.909				0.909										0.909	
M^*_f		1.012	0.966				1.215										0.958	
B^*_0		3500	2500				10000										5000	
B^*_1		80	50				20										100	
C_f		0	0				0										0	
γ^{P*}_r		0.02	0.002				0.005										0.02	
γ^{E*}_r		0.001	0.3				0.001										0.3	
D^*_0		1.0	1.5				4.0										4	
n		7.0	2.0				8.0										6	
C_d		2000	2000				2000										2000	
ν	0.496				0.496				0.494		0.488		0.492		0.492			
c (kPa)	0				33				198		0		149		149			
ϕ (deg)	30.9				0				0		34		0		0			
a	6977				2241				4939		8530		4533		4165			
b	0.5				0.5				0.5		0.5		0.5		0.5			
α	1.89				16.7				2.3		2		1.4		1.5			
r	1.92				1.78				2.1		3		1.7		1.6			

Notations:

X: cyclic elastoplastic constitutive model

Y: R-O model

γ = unit weight, ρ = density, k = coefficient of permeability, e_0 = initial void ratio, V_s = shear wave velocity, λ = compression index, κ = expansion index, M_f = stress ratio parameter corresponding to failure angle, OCR^* = factoid overconsolidation ratio, G_0/σ'_{m0} = non-dimensional initial shear modulus, M_m = stress ratio parameter corresponding to phase transformation angle, B^*_0 , B^*_1 , and C_f = plastic modulus parameters, γ_r^{P*} = plastic strain, and γ_r^{E*} = elastic strain, D^*_0 , n = dilatancy coefficient, C_d = anisotropy elimination parameter, ν = Poisson's ratio, c = cohesion, ϕ = internal friction angle, and a , b , α , and r = R-O parameters

Tunnel model

Figure 2 shows model of the ground with the tunnel. The green lines indicate the tunnel. The tunnel consists of an upper base plate and a lower base plate, a sidewall, and a center pillar. The tunnel is represented by beam elements. Table 2 lists the tunnel parameters used in the analysis. B is the horizontal length of the element, and H is the vertical length of the element.

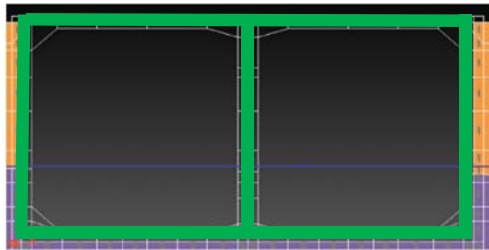


Fig. 2 Tunnel model

Boundary conditions

Soil skeleton

In the analysis model, the bottom of the boundary is an elastic base (viscous boundary). The elastic base is placed as a dashpot on the bottom of the model. The input earthquake motion is a 2E wave. In LIQCA, only the horizontal lower boundary can be set for the viscous boundary. When a consolidation analysis is conducted, the dashpot is automatically replaced with a rigid spring. The side boundary is a method of connecting a wide free ground part, which is not easily influenced by the FEM region, to the side surface when the soil layer configuration of the side boundary is different.

Tunnel

The boundary condition between the tunnel and adjacent ground is free from friction in the vertical direction. The tunnel and its adjacent ground behave similarly in the horizontal direction.

Input earthquake motion

The input earthquake motion is the seismic standard spectrum I, which is commonly used in Japan. The waveform is shown in Fig. 3. The increment of the calculation time is 0.005 s. The Newmark method coefficients are $\beta = 0.3025$ and $\gamma = 0.6$. These values are common in LIQCA simulations. The constant of the Rayleigh attenuation α_1 is equal to 0.001–0.003. The Rayleigh attenuation α_1 in the example of the LIQCA manual is 0.0023. After seismic motion, consolidation analysis is carried out until the vertical settlement converges.

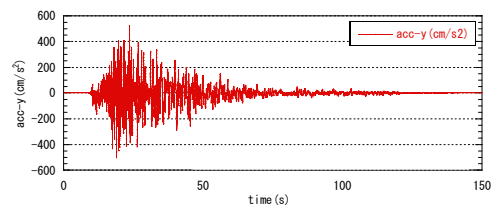


Fig. 3 Waveform of seismic standard spectrum I

Table 2 Tunnel parameters

	B (m)	H (m)	Pitch (m)	Unit volume weight γ (kN/m ³)	Sectional area A(m ²)	Sectional Secondary moment I(m ⁴)	Unit length Weight G(kN/m)
base plate (upper)	1	0.3	1	25	0.30	0.001125	7.5
base plate (lower)	1	0.4	1	25	0.40	0.002667	10
side wall	1	0.4	1	25	0.40	0.002667	10
center pillar	2.3	0.4	4	25	0.23	0.001533	5.75

Initial stress analysis

The initial values of the soil skeleton displacement and excess pore water pressure are all 0. The soil skeleton displacement and excess pore water pressure in LIQCA are the increments from the initial state, that is, the incremental values at the time of the earthquake. What is necessary under the initial conditions is to set the initial effective stress of the ground. Therefore, it is important to estimate the initial stress state in the ground. The initial stress analysis in this paper is a self-weight analysis. The self-weight analysis calculates the initial stress by applying self-weight to the model used for the liquefaction analysis in the zero-gravity state. It considers the increase in ground rigidity and nonlinearity caused by adding weight to the model.

ANALYSIS RESULT

The analysis results are shown below. After the earthquake motion, a consolidation analysis was carried out until the convergence of the vertical displacement was confirmed. The effective stress reduction ratio R is used as an index for determining liquefaction. It is shown in the following equation:

$$R = 1 - \frac{\sigma'_m}{\sigma'_{m0}} \quad (1)$$

σ'_m : average effective stress corresponding to some elapsed time (kN/m²)

σ'_{m0} : average effective stress in the initial stress state (kN/m²)

When this value reaches 1, it can be said that liquefaction occurred in the ground. The nodes and elements that output the analysis results are the vicinity of the tunnel center and the stratum of the point 25 m northward from the tunnel center.

At the stratum of the point 25 m northward from the tunnel center

Figure 4 shows the effective stress reduction ratio of As1, As2, and Tsg1. According to these results, it turns out that these soil layers become liquefied. The effective stress reduction ratio decreases after 10⁸ s (approximately 3 years). This indicates that the excess pore water pressure that occurs by liquefaction is dissipated, and the consolidation settlement converged. Figures 5 and 6 show the vertical displacement and horizontal displacement, respectively. After the excess pore water pressure dissipates, the ground surface settles by 0.5 m in the vertical direction and moves 0.8 m in the horizontal direction.

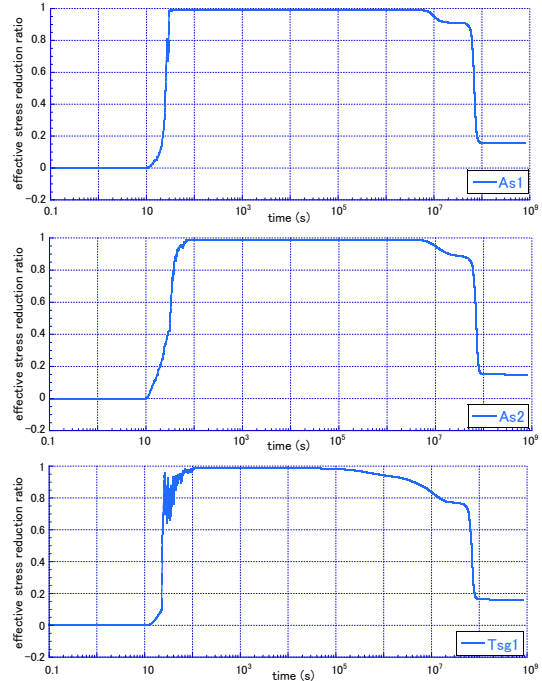


Fig. 4 Effective stress reduction ratio of As1, As2, and Tsg1 (25 m northward from tunnel center)

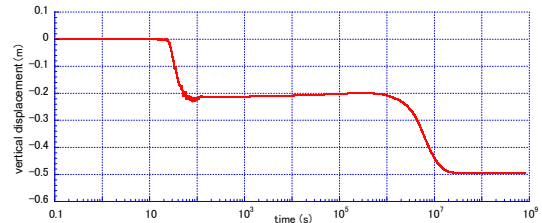


Fig. 5 Vertical displacement (25 m northward from tunnel center)

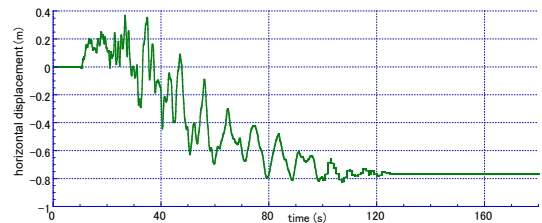


Fig. 6 Horizontal displacement (25 m northward from tunnel center)

At the vicinity of the tunnel center

Figure 7 shows the effective stress reduction ratio of As1, As2, and Tsg1. According to these results, it turns out that these soil layers become liquefied. Figures 8 and 9 show the vertical displacement and horizontal displacement, respectively. After the excess pore water pressure dissipates, the tunnel rises by 0.9 m in the vertical direction, and moves 0.8 m in the horizontal direction.

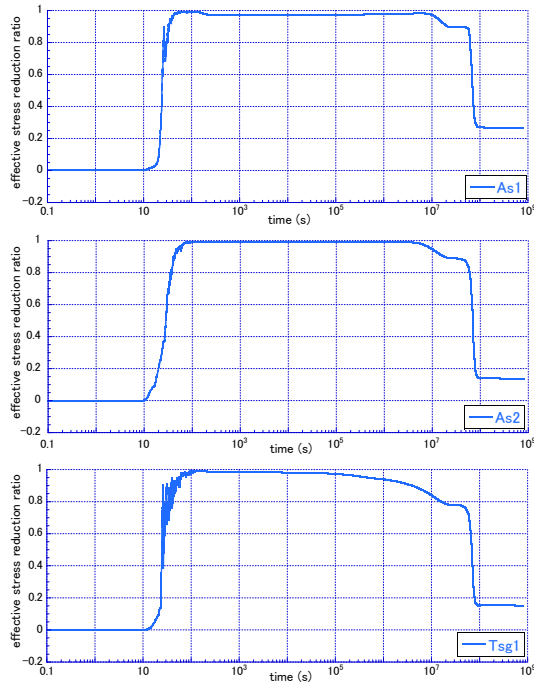


Fig. 7 Effective stress reduction ratio of As1, As2, and Tsg1 (tunnel center)

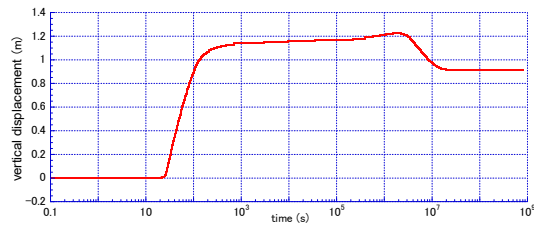


Fig. 8 Vertical displacement (tunnel center)

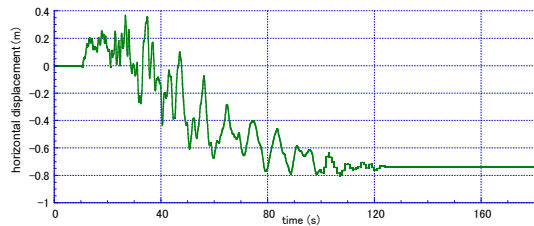


Fig. 9 Horizontal displacement (tunnel center)

Summary of some indices

Table 3 lists the results of the effective stress reduction ratio (just after excitation). Table 4 lists the results of the effective stress reduction ratio (after excess pore water pressure dissipates). Point A corresponds to the stratum, which is 25 m northward from the tunnel center. Point B corresponds to the vicinity of the tunnel center.

Table 3 Effective stress reduction ratio (just after excitation)

	Effective stress reduction ratio (%)		
	As1	As2	Tsg1
A	99.9	99.9	99.9
B	99.9	99.9	99.9

Table 4 Effective stress reduction ratio (after excess pore water pressure dissipates)

	A	B
horizontal displacement (m)	-0.733	-0.758
Vertical displacement (m)	0.898	-0.496

Displacement of the ground surface

Figure 10 shows the vertical displacement for each time history. The data corresponds to the state of the initial coordinate after excitation and after consolidation of the ground surface coordinates. The part from 45 to 55 m of the X coordinate is the tunnel position. When the state, after the excess pore water pressure dissipates, is examined, it can be seen that the tunnel rises by 0.9 m. This phenomenon is caused by the boundary condition between the side surface of the tunnel and the surrounding ground. The boundary was set under a free condition in the vertical direction, which has no friction. Therefore, a settlement of 0.9 m is thought to be the maximum floating amount.

In this analysis, we do not consider the changes in the buoyancy of the surroundings owing to the floating of the tunnel. In other words, the buoyancy around the tunnel remains in its initial state. In addition, this is considered to be a cause of the large level of floating of the tunnel. The other surface part, except for the tunnel position, settles at approximately 0.5 m after the excess pore water pressure dissipates.

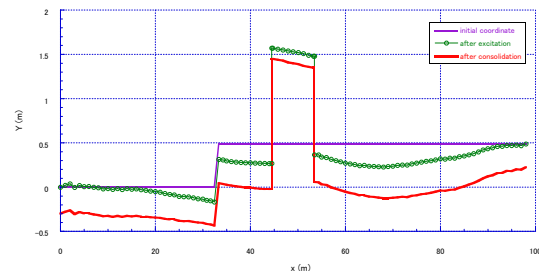


Fig. 10 Vertical displacement for each time history

Deformation map of the ground

Figure 11 shows the deformation of the ground around the tunnel after the excess pore water pressure dissipates. The floating of the tunnel may

depend on how the sediment cuts under the tunnel becomes liquefied. The floating of the tunnel is approximately 0.9 m. However, this value is perhaps the maximum floating amount, as mentioned earlier. In fact, there is friction between the tunnel and the surrounding ground, so it is highly likely that the floating of the tunnel may have a smaller value than that of the analysis result.

CONCLUSION

When an earthquake corresponding to seismic standard spectrum I occurs at the target ground of the Osaka Gulf coast, from the results of a liquefaction simulation based on LIQCA, it turns out that the ground becomes liquefied and the tunnel at the surface of the target ground floats up slightly. It is necessary to investigate the floating amount more precisely, hereafter, because the floating has a serious impact on the restoration process of the target area.

However, a settlement of 0.9 m is thought to be the maximum value of the floating amount. This phenomenon is caused by the boundary condition between the tunnel and the surrounding ground. In

when the As1 layer around the addition, we did not consider the changes in the buoyancy of the surrounding ground. We think that it is necessary to make this phenomenon more realistic. The buoyancy problem may be difficult. Therefore, we will further investigate the boundary condition between the sidewall of the tunnel and the adjacent ground. We will conduct more realistic simulations.

REFERENCES

- [1] Matsuoka S, Wakamatsu K, and Hashimoto K, "Estimation method of liquefaction risk based on topography: Ground classification 250 m mesh map", in Proc. of the Japan Earthquake Engineering Association, 2011, pp. 35–36.
- [2] LIQCA Liquefaction Geo-Research Institute: LIQCA 2 D 15 · LIQCA 3 D 15 material, 2015.
- [3] Railway Technical Research Institute, Design Standards for Railway Structures and Commentary, 2012.
- [4] Yasuda S, and Yamaguchi I, "Dynamic soil properties of undisturbed samples", of the 20th Geotechnical Engineering Research Presentation, 1985, pp. 539–542.

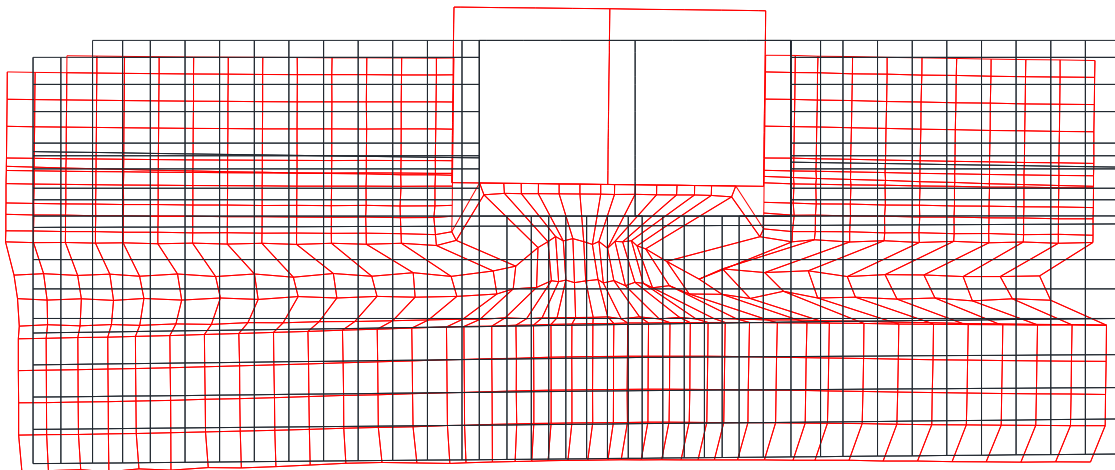


Fig. 11 Deformation around the tunnel

ROBUST POSITIONING OF DRONES FOR LAND USE MONITORING IN STRONG TERRAIN RELIEF USING VISION-BASED NAVIGATION

Oleg Kupervasser^{1,2}, Vitalii Sarychev², Alexander Rubinstein² and Roman Yavich¹

¹ Department of Mathematics, Ariel University, Israel; ² TRANSIST VIDEO LLC, Skolkovo, Russia

ABSTRACT

For land use monitoring, the main problems are robust positioning in urban canyons and strong terrain reliefs with the use of GPS system only. Indeed, satellite signal reflection and shielding in urban canyons and strong terrain relief results in problems with correct positioning. Using GNSS-RTK does not solve the problem completely, because in some complex situations the whole satellites system works incorrectly. We transform the weakness (urban canyons and strong terrain relief) to an advantage. It is a vision-based navigation using a map of the terrain relief. We investigate and demonstrate the effectiveness of this technology in Chinese region Xiaoshan.

Keywords: Vision-based navigation, Robust positioning, Land use monitoring, Urban canyons and strong terrain relief, DTM

INTRODUCTION

Recently International Journal of Geomate has published a very important paper about the integration of Geography Information System (GIS) and Global Navigation Satellite System – Real Time Kinematics (GNSS-RTK) for land use monitoring [1].

Indeed, the authors of [1] write: “limited open space area requires accurate monitoring to maintain changes in land use that is not suitable with city spatial planning. The difference between spatial planning and existing land Use should be minimized”. The main problems are robust positioning in urban canyons and strong terrain reliefs with the use of GPS system only. Indeed, satellite signal reflection and shielding in urban canyons and strong terrain reliefs results in problems with correct positioning. “In urban area study, signal problems become obstacles for determining the position and navigation due to some problems such as shadowing and multipath effects” [1,2].

The paper suggests using GNSS-RTK (full system which is a constellation of current satellites such as GPS (Global Positioning System-USA), GLONASS (Russia), Galileo (Europe), BeiDou (China), and QZSS (Japan)) that can improve positioning [1,3]. However, it does not solve the problem completely, because in some complex situations the whole satellites system works incorrectly.

We need to transform the weakness (urban canyons and strong terrain reliefs) to an advantage. It is a vision-based navigation using a map of the terrain relief. This topic had been recently widely developed by the authors [4-10]. Vision-based algorithms have been a major research issue during

the past decades. Two common approaches for the navigation problem are: the landmarks [11,12]. And the ego-motion integration [13-17].

In [18], the drift is being corrected with the help of a Digital Terrain Map (DTM). The DTM is a discrete representation of the observed ground's topography. It contains the altitude over the sea level of the terrain for every geographical location. A patch from the ground was reconstructed using 'structure-from-motion' (SFM) algorithm and was matched to the DTM in order to derive the camera's pose. The algorithm presented in this work [4-9] does not require an intermediate explicit reconstruction of the 3D world. By combining the DTM information directly with the images information it is claimed that the algorithm is well-conditioned and generates accurate estimates for reasonable scenarios and error sources.

Comparison of the corrected position of the object, measured from the data of Google Earth in China, with the calculated position of the object would estimate the real effectiveness of navigation corrections. The correspondent investigation for the described method was carried out during the flight in Galilee in Israel [19]. The position error was about 25 meter and angle error was about 1.5 degree.

Based on the core theory [4-10], TRANSIST VIDEO LLC (Russian Skolkovo company under the leadership of Kupervasser) developed the computer program “Vision-based navigation of UAV over relief” [20]. This program was tested in Zhejiang Province in east China near the capital Hangzhou using Google Earth data. This work was funded by Hangzhou AVISI Electronics Co. LTD. Currently TRANSIST VIDEO LLC won the grant from the governing body of Hangzhou for creation of the real-time version of the program. This program will

be developed in collaboration with Ariel University in Israel.

METHODOLOGY

Finding of the corresponding characteristic points on the first and second shots (optical-flow field)

Two methods are used to choose the characteristic points on the first shot:

- 1) the characteristic points on the first shot are chosen on the regular grid on the boundaries of the shot. The grid is square of the size of $N \times N$, where N^2 is the general number of the characteristic points.
- 2) the characteristic points on the first shot are chosen with the help of Shi Tomassi corner detector. The Shi Tomassi corner detector [21] (Shi-Tomasi or Kanade-Tomasi, 1993) works as follows: for the given picture let us consider the window (usually the size of the window is 5×5 pixel, but it can depend on the size of the picture) in the centre (x_0, y_0) . Let's determine M – autocorrelation matrix:

$$M_{(x_0, y_0)} = \sum_{(x, y) \in W} w(x - x_0, y - y_0) \begin{bmatrix} I_x^2(x, y) & I_x(x, y)I_y(x, y) \\ I_x(x, y)I_y(x, y) & I_y^2(x, y) \end{bmatrix} \quad (1)$$

where $w(x, y)$ is a weight function (usually the Gaussian function or a binary window is used) (Fig.1).

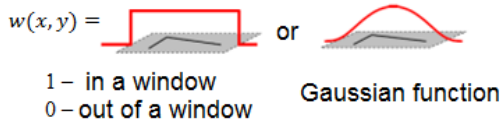


Fig 1. Weight function

A corner is characterized by large absolute values of the matrix eigenvalues M : $M: \lambda_1 \gg 0, \lambda_2 \gg 0$. Shi and Tomassi suggested the measure of corner: $F(x, y) = \min(\lambda_1, \lambda_2)$. The function finds the angles with large eigenvalues.

We use the same equation to analyze the Lucas and Kanade optical flow [22], this local method of optical flow measurement widely used in the computer vision.

The optical-flow field is supplied: $\{u_i(t_k)\}$ ($i=1 \dots n, k=1, 2$). For the i 'th feature, $u_i(t_1) \in P^2$ and $u_i(t_2) \in P^2$ represent its locations at the first and second frame respectively:

$$\begin{bmatrix} u_i^x(t_k) \\ u_i^y(t_k) \end{bmatrix} = M^{-1}(x_i, y_i) \begin{bmatrix} - \sum_{(x, y) \in W'} w(x - x_i, y - y_i) I_x(x, y, t_k) I_y(x, y, t_k) \\ - \sum_{(x, y) \in W'} w(x - x_i, y - y_i) I_y(x, y, t_k) I_x(x, y, t_k) \end{bmatrix} \quad (2)$$

We use affine or translation monitoring of the first shot points on the second shot using pyramid realization (affine or translation) of Lucas and Kanade tracker. [22].

The Navigation Algorithm of DTM usage and optical flow finding

The problem can be briefly described as follows: At any given time instance t , a coordinate system $C(t)$ is fixed to a camera in such a way that the Z -axis coincides with the optical-axis and the origin coincides with the camera's projection center. At that time instance t_1 the camera is located at some geographical location $p_1 = p(t_1)$ and has a given orientation $R_1 = R(t_1)$ with respect to a global coordinate system W ($p(t)$ is a 3D vector, $R(t)$ is an orthonormal rotation matrix). Consider now two sequential time instances t_1 and t_2 : the transformation from $C(t_1)$ to $C(t_2)$ is given by the translation vector $p_{12} = \Delta p(t_1, t_2)$ and the rotation matrix $R_{12} = \Delta R(t_1, t_2)$. Let $q_{1i} = {}^{C_1} q(t_1)$ and $q_{2i} = {}^{C_2} q(t_2)$ be the homogeneous representations of $u_i(t_1), u_i(t_2) \in \mathbb{R}^2$. As standard, one can think of these vectors as the vectors from the optical-center of the camera to the projection point on the image plane. Using an initial-guess of the pose of the camera at t_1 , the line passing through $p_E(t_1)$ and ${}^{C_1} q(t_1)$ can be intersected with the DTM. Any ray-tracing style algorithm can be used for this purpose. The location of this intersection is denoted as ${}^W Q_{E_i}$. The subscript letter “ E ” highlights the fact that this ground-point is the estimated location for the feature point, that in general will be different from the true ground-feature location ${}^W Q_i$ (Fig. 2).

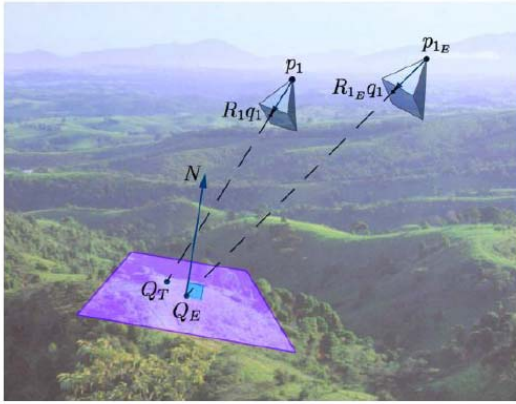


Fig. 2 Ground-feature location

Denoted by N_i the normal of the plane tangent to the DTM at the point Q_{E_i} , one can write:

$$f_i(p_1, \phi_1, \theta_1, \psi_1, p_{12}, \phi_{12}, \theta_{12}, \psi_{12}) = \left(I - \frac{q_{2i} q_{2i}^T}{q_{2i}^T q_{2i}} \right) \frac{p_{12} + R_{12} \Lambda_i (Q_{E_i} - p_1)}{p_{12} + R_{12} \Lambda_i (Q_{E_i} - p_1)} = 0 \quad (3)$$

where Λ_i in the above expression represents:

$$\Lambda_i = \frac{q_{1i} N_i^T}{N_i^T R_{1i} q_{1i}} \quad (4)$$

This constraint involves the position, orientation and the ego-motion defining the two frames of the camera. For each of the n optical-flow vectors, the function $f_i: \mathbb{R}^{12} \rightarrow \mathbb{R}^3$ is defined as the left-hand side of the constraint described in (7). In the above expression, R_{12} and R_{1i} are functions of Euler angles $(\phi_{12}, \theta_{12}, \psi_{12})$ and $(\phi_i, \theta_i, \psi_i)$ respectively. Additionally, the function $F: \mathbb{P}^{12} \rightarrow \mathbb{P}^{3n}$ will be defined as the concatenation of the f_i functions:

$$F(p_1, \phi_1, \theta_1, \psi_1, p_{12}, \phi_{12}, \theta_{12}, \psi_{12}) = [f_1, \dots, f_n]^T$$

According to these notations, the goal of the algorithm is to find the twelve parameters that minimize $M(\theta, D) = \|F(\theta, D)\|^2$, where θ represents the 12-vector of the parameters to be estimated, and D is the concatenation of all the data obtain from the optical-flow and the DTM. If D were error-free, the true parameters would have been obtained. Since D contains some error perturbation, the estimated parameters are drifted to erroneous values. An iterative scheme will be used in order to solve this system. A robust algorithm which uses Gauss-Newton iterations and M-estimator is described in [20]. We begin to use Levenberg-Marquardt method if Gauss-Newton

method after several iterations stops to converge. The applicability, accuracy and robustness of the algorithm were verified through simulations and lab-experiments.

THE FLIGHT TESTING OF THE PROGRAMME

It was decided to carry out the flight testing of the vision-based navigation programme on the terrain relief with the help of Google Earth video data (based on the real data).

We chose the following conditions of the flight, parameters of the trajectory, the video shooting and the inertial navigation:

1) The trajectory parameters: The flight is over Xiaoshan district between 30.0421571732 - 30.0545167923 degrees latitude and 120.1245546341- 120.1479005814 degrees longitude. The picture of the district of the flight and the digital map of the flight district are presented on Fig 3. The flight was at a speed of 50 m/sec during 19,6 sec in a straight line at an altitude of 1000 m above mean sea level from the point (30.05048444, 120.1321713) to the point (30.04588944, 120.1408507). This way is depicted by the red line from the point 1 to the point 50.

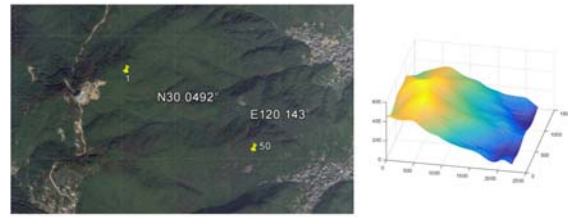


Fig. 3 The district of the flight and the digital map of the flight district.

2) The parameters of the video shooting are as follows:

The 50 images were shot with the 0,4 sec interval between them. The field of view angle of the camera along the short side of the shot are 38,68 degrees; along the long side of the shot - 59,97 degrees. The pixel size of the picture is 4800x2923. The shots are made with the help of the Google Earth. The long side of the shot is perpendicular to the direction of the movement and the airframe, the short side is parallel to the movement, the aircraft flies to the upper side of the picture.

3) The parameters of the inertial navigation system with a random noise are following: the noise results in the average velocity change for the $\Delta V = \pm 20$ m/sec during 1 sec along every axis and average Euler angle change for $\Delta \phi = \pm 0.33$ degrees during 1 sec. Modeling of the inertial system outputs was carried out with the help of the standard

programmes of Matlab INS Toolbox, produced by GPSof [23].

For the vision-based navigation measuring the index shots were chosen with time interval about 3.6 sec and an approximate distance from the previous shot of the pair 175m. The characteristic points (about 300) were presented as a regular grid on the shot, the displacement of these points was measured with the help of Lucas and Kanade method with the use of the series of shots between the pair of the index shots for the vision-based navigation (Fig. 4). The arrows show the found displacement of the characteristic points between the pair of shots, used for the vision-based navigation.

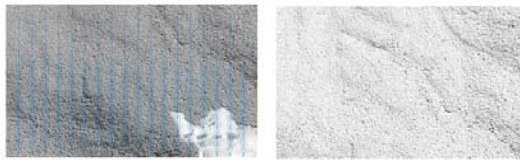


Fig. 4 The pair of shots, used for the vision-based navigation

GRAPHIC RESULTS OF THE VISION-BASED NAVIGATION PROGRAMME TESTING

On Fig. 5 we present three trajectories: the precise trajectory; the trajectory based on the inertial navigation; the trajectory based on the vision-based navigation.

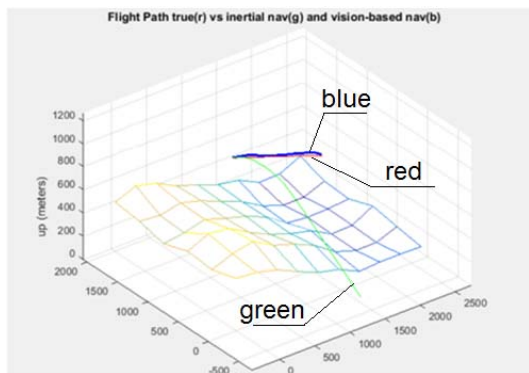


Fig. 5 Three flight trajectories: the precise trajectory is presented in red, the trajectory based on the inertial navigation is presented in green; the trajectory based on the vision-based navigation is presented in blue

The navigation errors are drawn on Fig. 6,7.

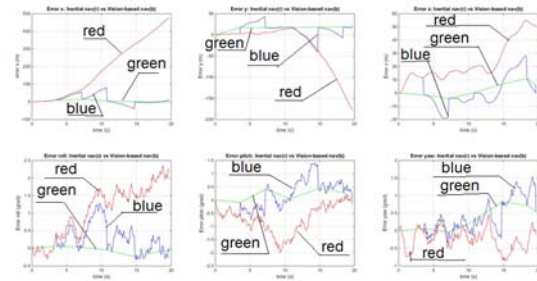


Fig. 6 The navigation errors. The red graphic is based on the inertial navigation; the blue graphic is based on the vision-based navigation with the use of the inertial navigation, the blue graphic is based on the vision-based navigation
The upper graphics – coordinates x,y,z. the lower graphics – Euler angles, roll, pitch, yaw

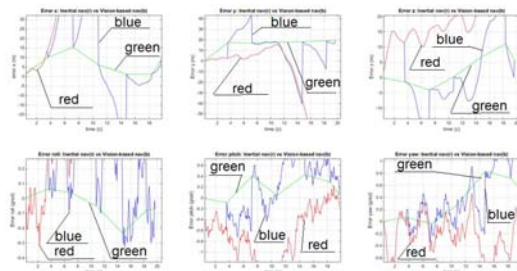


Fig. 7 The same graphic as on Fig 6, but in smaller scale

CONCLUSION

We can make the following conclusions:

1) The methods of vision-based navigation were used for shots, obtained from an independent source – the programme Google Earth (they are obtained from the flight testing). That means that these results of the vision-based navigation are valid because they are obtained not on the basis of synthetical shots of computer simulation but from an independent source on basis of flight testing.

2) The accuracy of the vision-based navigation system corresponds to the expected for these conditions:

a) Maximum position error based on vision-based navigation is 20 m

6) Maximum angle Euler error based on vision-based navigation is 0.83 degree.

3) Also the measurement without INS usage was carried out:

For all the pairs of shots (used for vision-based navigation) every other shot of the previous pair is the first for the next pair except the first and the last shot.

Between the two measurements with the help of vision-based navigation method we consider the camera movement as a straightforward one (without rotation) at a speed found either from positions of the cameras (with the help of the vision-based navigation) for two pairs of shots or from the initial conditions. For this case we got the following results:

a) Maximum position error based on vision-based navigation is 30 m

6) Maximum Euler angle error based on vision-based navigation is 2.2 degrees

The results are worse than with the use of INS.

ACKNOWLEDGEMENTS

We would like to thank Alexander Domoshnitsky, Ronen Lerner, Ehud Rivlin and Hector Rotstein for very useful consultations.

REFERENCES

- [1] K. Djaja, R. Putera, A. F. Rohman, I. Sondang, G. Nanditho, E. Suyanti, "The integration of Geography Information System (GIS) and Global Navigation Satellite System – Real Time Kinematics (GNSS-RTK) for land use monitoring", *International Journal of GEOMATE*, Aug, 2017, Vol.13, Issue 36, pp.31-34
<http://www.geomatejournal.com/sites/default/files/articles/31-34-2768-Komara-Aug-2017-36-g3.pdf>
- [2] A. Bourdeau, M. Sahmoudi, J.-Y. Tournet, "Tight Integration of GNSS-RTK and a 3D City Model for Robust Positioning in Urban Canyons", *Conference Proceedings of the 25th International Technical Meeting of the Satellite Division of the Institute of Navigation (ION GNSS-RTK 2012)*, pp. 1263 – 1269
- [3] Paul D. Grove, "Shadow Matching: A New GNSS-RTK Positioning Technique for Urban Canyons", *The Journal Of Navigation*, Volume 64, Issue 03, July 2011, pp. 417–430
- [4] Kupervasser, Rubinstein "Correction of Inertial Navigation on System's Errors by the Help of Vision-Based Navigator Based on Digital Terrain Map", *Positioning*, 2013, 4,89-108
http://file.scirp.org/pdf/POS_201302281149173_8.pdf
- [5] O. Kupervasser, R. Lerner, E. Rivlin and Hector Rotstein "Error Analysis for a Navigation Algorithm based on Optical-Flow and a Digital Terrain Map", In the *Proceedings of the 2008 IEEE/ION Position, Location and Navigation Symposium*, P.1203-1212
- [6] Oleg Kupervasser, Vladimir Voronov, "A navigation filter for fusing DTM/correspondence updates", *Proceedings of the IEEE International Conference on Robotics and Biomimetics (ROBIO)*, 2011, Page(s): 1591 - 1596
- [7] R. Lerner, O. Kupervasser, E. Rivlin, "Pose and Motion from Omnidirectional Optical Flow and a Digital Terrain Map", In the *Proceedings of the 2006 IEEE/RSJ International Conference on Intelligent Robots and Systems*, P.2251-2256
- [8] Kupervasser O. Yu., Voronov V.V., "Correction of Inertial Navigation System's Errors by the Help of Vision-Based Navigator Based on Digital Terrain Map", presented at XIX St.-Petersburg international conference on the integrated navigation systems (MKINS2012)
- [9] Kupervasser O. Yu., Rubinshtein A.A. "The system of vision-based navigation for unmanned aerial vehicles", IV TRIZ Conference, «TRIZ. Practice for application of methodical instruments», Moscow 19-20 October 2012
- [10] R. Lerner, E. Rivlin and H. P. Rotstein, "Pose and Motion Recovery from Correspondence and a Digital Terrain Map," *IEEE Transactions on Pattern Analysis and Machine Intelligence*, Vol. 28, No. 9, 2006, pp. 1404-1417.
- [11] Y. Liu, M.A. Rodrigues, "Statistical image analysis for pose estimation without point correspondences", *Pattern Recognition Letters*, vol. 22, pp. 1191-1206, 2001
- [12] P. David, D. DeMenthon, R. Duraiswami, H. Samet, "SoftPOSIT: Simultaneous pose and correspondence determination", *ECCV 2002*, LNCS 2352, pp. 698-714, 2002
- [13] D. Shin, S. G. Park, B. S. Song, E. S. Kim, O. Kupervasser, D. Pivovartchuk, I. Gartsev, O. Antipov, E. Kruchenkov, A. Milovanov, A. Kochetov, I. Sazonov, I. Nogtev, S. W. Hyun, "Precision improvement of MEMS gyros for indoor mobile robots with horizontal motion inspired by methods of TRIZ", *Proceedings of 9th IEEE International Conference on Nano/Micro Engineered and Molecular Systems (IEEE-NEMS 2014)* April 13-16, 2014, Hawaii, USA, pp 102-107
- [14] J. L. Barron, R. Eagleson, "Recursive estimation of time-varying motion and structure

- Parameters", *Pattern Recognition* vol. 29, no. 5, pp. 797--818, 1996
- [15] T.Y. Tian, C. Tomashi, D.J. Hegger, "Comparison of approaches to egomotion computation", Department of Psychology and Computer science, Stanford university, CA 94305, 1996
- [16] A.Chiuso, S.Soatto, "MFm: 3-D Motion From 2-D Motion, Causally integrated over time", Washington University Technical Report, 1999
- [17] M. Irani, B. Rousso, S. Peleg, "Robust Recovery of Ego-Motion", *Proc. Of CAIP 93*, pp. 371-378, 1993
- [18] D.G. Sim, R.H. Park, R.C. Kim, S.U. Lee, I.C. Kim, "Integrated position estimation using aerial image sequences", *IEEE transactions on pattern analysis and machine intelligence*, vol. 24, no.1, 2002
- [19] R. Lerner, E. Rivlin, "Direct Method for Vision-Based Navigation Using a Digital Terrain Map", *IEEE transactions on pattern analysis and machine intelligence*, vol. 33, no. 2, 2011
- [20] Computer programs "Vision-navigation of UAV over relief" Part 1, Part 2. The certificates on the state registration of the computer programs № 2016613306, 2016613305. It is registered in the register of the computer programs of Federal service on intellectual property, patents and trade marks, Russia, on March, 24, 2016 (http://leah.haifa.ac.il/~skogan/Apache/mydata1/Oleg_home/2016613306.pdf).
- [21] Shi-Tomasi Corner Detector: <http://aishack.in/tutorials/shitomasi-corner-detector/>
- [22] J. Y. Bouguet "Pyramidal implementation of the affine Lucas-Kanade feature tracker description of the algorithm" Intel Corporation, 2001 http://robots.stanford.edu/cs223b04/algos/affine_tracking.pdf
- [23] Matlab INS Toolbox, produced by GPSof: http://www.navtechgps.com/ins_toolbox_v3_0_for_matlab/

DEGRADATION OF CEMENT TREATED SOIL DUE TO SULFATE ATTACK

Cynthia Debby Heriyani, Sumiyati Gunawan, John Tri Hatmoko, and Luky Handoko
Faculty of Engineering, Universitas Atma Jaya Yogyakarta, Indonesia

ABSTRACT

Ground treatment method by utilizing binding agents has been becoming very popular. Some of the ground treatment were applied at seabed under seawater level. The hardened soil mixture is subjected to sulfate attack contained by sea water. This paper discusses about physical and mechanical degradation of cement treated clay due to sulfate exposure. Grain size distribution, Atterberg limit and Penetration Test were conducted to cement treated clay specimen by varying the initial clay water content, cement content prior to sulfate exposure. In this paper, natrium sulfate (Na_2SO_4) was used as degrading agent to cement treated soil. Based on grain size distribution, the size of particle especially in clay size range is increasing due to the addition of cement and curing time. Furthermore, the plasticity index of cement treated clay decreases when the cement content increases. However, the grain size and Atterberg limit of cement treated clay tends to turn back to original clay properties after exposed with sulfate. The depth of degradation caused by sulfate exposure can be observed from Penetration Test. It increases with the decrease of cement content after immersed to natrium sulfate. Those results indicate that degradation occurs due to loss of binding ability of cement treated clay.

Keywords: Cement Treated Clay, Degradation, Natrium Sulfate, Penetration Test

INTRODUCTION

High water content soil has been utilized as construction materials, recently. Dredged materials from Port of New York and New Jersey was studied to be used for geotechnical application [1]. In Singapore, slurry pond has been used as part of Changi East reclamation project [2]. Dredged soil mixed with cement has been used as filling material for airport construction in Japan [3]. High water content material is available numerously and mostly produced from contaminated sediments at riverbed and seabed [4] and port navigation channel dredging works [1]. In Indonesia, huge volume of high water content volcanic mud existed in East part of Java Island [5]. The volcanic mud has been produced since 2006 and continue until now.

High water content soil is commonly known to have poor characteristics and not suitable for construction materials. It has low strength, high compressibility and low permeability. To be used for construction materials, improvement is required. There are many studies to improve the poor characteristic of high-water content soils. One of the available and famous method is chemical stabilization by mixing high water content soil with binding agent such as lime and cement [6-10]. This method relies on chemical reaction process of employed binding agent, water and soil. There are two reaction that might occur: hydration reaction and pozzolanic reaction. The product of both reaction is strong amorphous materials. Many researches have

focused on finding the influencing factors that can retard the reaction process [11, 12], such as organic content, clay, and sulfate. However, not much researches discuss about the strength degradation of cement treated clay under external corrosive environment attack, such as seawater, sulfate and acid. This paper discusses about the change of physical and strength properties of cement treated clay under sulfate immersion. The physical properties include Atterberg limit and grain size distribution. The strength properties were observed by conducting penetration test to investigate the depth of degradation occurred due to sulfate. Natrium sulfate was selected to represent the corrosive environment.

LABORATORY TEST PROGRAM

Materials

This research utilizes a clayey silt soil as parent material. The soil is derived from Vulcanic mud eruption in Sidoarjo district, East of Java Province, Indonesia. Physically, the soil contains high content of water and 96.62% of the dry weight percentage is fine-grained soil (diameter less than 0.075 mm). The liquid limit (w_L) and plastic limit (w_P) are 60% and 34.08%, respectively. Ordinary Portland Cement was used as chemical binder. The specific gravity (G_s) of soil and cement are 2.785 and 3.00, respectively. Natrium sulfate (Na_2SO_4) is used to represent the corrosive environment which is expected to decrease the strength of cement treated clay.

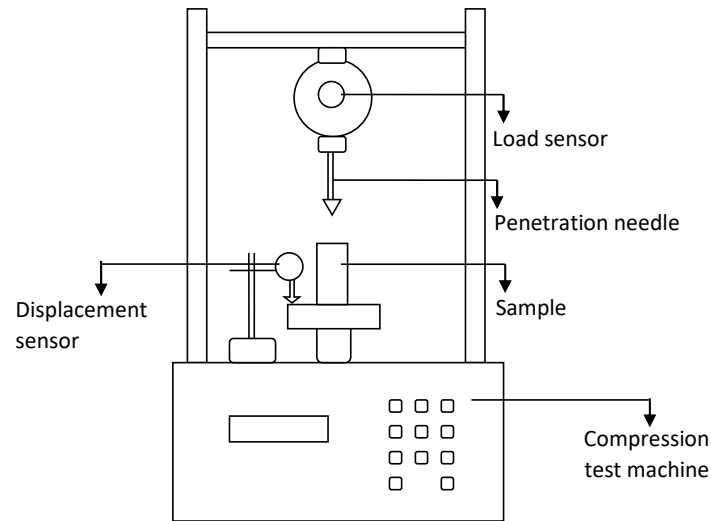


Fig. 1 Sketch of penetration test apparatus

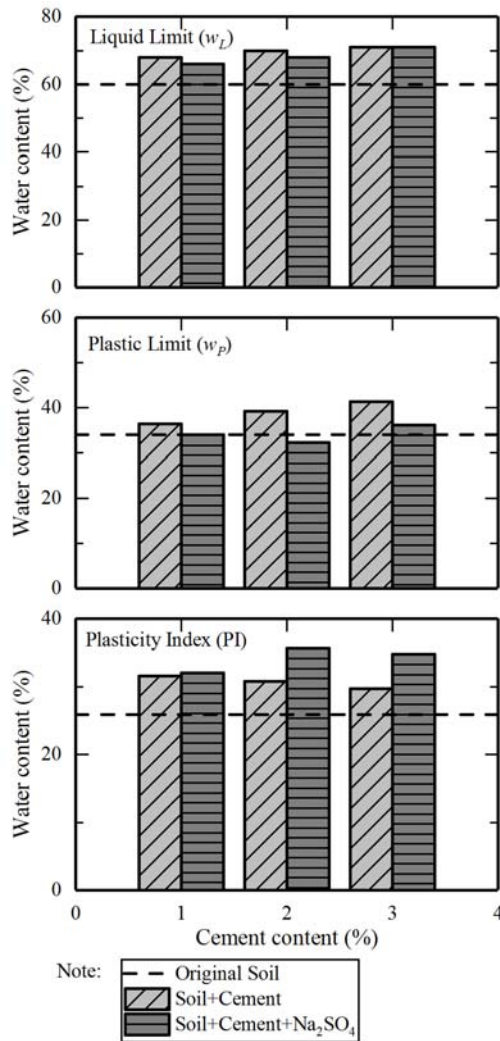


Fig. 2 Evolution of Atterberg limit due to addition of cement

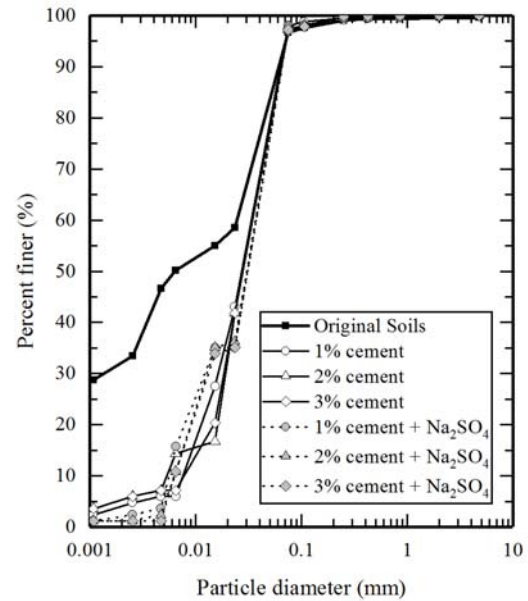


Fig. 3 Evolution of grain size distribution

Specimen Preparation and Penetration Test

Specimen were made by mixing soil, cement and water. Before mixed, soil and cement were placed in the 105°C oven for 24 hours. A certain dry weight of soil, cement and water were mixed thoroughly using automatic hand mixer for 10 minutes to insure the homogeneity of the mixture. The mixture then placed into a cylinder mold with diameter 6 cm and height 10 cm. The specimens were sealed to keep the water inside the specimen by closing the top of the cylinder using lid tightly. During the curing time, the specimens were keep under constant temperature of 30°C. Samples were prepared with a certain water content ($w_c=100\%$) and varied cement content

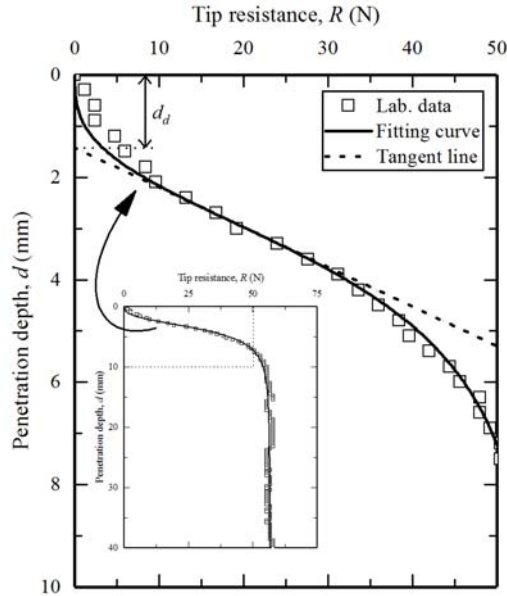


Fig. 4 Penetration test result of specimen without immersed to Na_2SO_4 ($c_c=15\%$ and $w_c=100\%$)

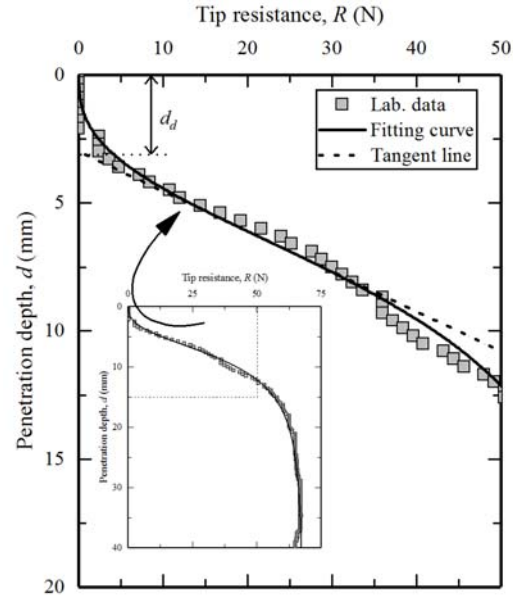


Fig. 5 Penetration test result of specimen without immersed to Na_2SO_4 ($c_c=15\%$ and $w_c=100\%$)

($c_c=10\% - 30\%$). Fig. 1 shows the arrangement of penetration test equipment. This test uses a penetration needle which form a 60° conus at the end. During the test, the needle will penetrate the specimen and the tip resistance was measured for each depth. The penetration rate of the needle is set to be 3 mm/minutes. To investigate the degradation occurred due to corrosive environment, specimens were submerged into Na_2SO_4 solution for 28 days. The concentration of Na_2SO_4 solution used in this research is 10 gr/L. For each specimen, 0.7 L Na_2SO_4 solution was prepared.

RESULTS AND DISCUSSIONS

Atterberg Limit

Change of physical characteristics of cement treated clay due to additional cement and sulfate was observed by conducting Atterberg limit test and grain size distribution test. The tests were conducted on three different soil condition: 1) original soil, 2) original soil added by cement and 3) 28-days age of cement treated clay mixed with Na_2SO_4 .

Figure 2 shows Atterberg limit test results. The results show that Liquid limit is increasing along with the increase of cement content, while the Plasticity Index tends to decrease. When submerged to Na_2SO_4 , the Plasticity Index tends to increase.

Grain Size Distribution

Figure 3 shows the change of particle size distribution due to cement addition with and without Na_2SO_4 . Based on the test results, the mixture

between soil and cement has particle size larger than the original soils. The different of particle size between cement addition 1%, 2% and 3% is not too significant. However, when it is compared with the original soil, the different is significant. When submerged into Na_2SO_4 , the particle size is decreasing at particle size between 0.005 mm – 0.02 mm, while the other range does not change significantly.

Penetration Test

Penetration test result shows the tip resistance at a certain depth measured by load sensor attached at the penetration needle. Figure 4 shows the result of penetration test of specimen without immersed in Na_2SO_4 . Based on the result, the tip resistance at near surface is very low due to the small contact of the needle. The tip resistance gradually increase until a certain constant value which is referred to R_{ref} . Figure 5 shows the result of penetration test of specimen after immersed into Na_2SO_4 with the same water content and same cement content as the specimen at Fig. 4. Comparing the result of specimen with and without immersed into Na_2SO_4 , it is clearly observed that the depth of the zone with low tip resistance is deeper. This results shows that Na_2SO_4 decrease the strength of the cement treated soil. Figure 6 shows the comparison of penetration test for specimen with and without immersed into Na_2SO_4 . The plot data was fitted with the Eq. (1).

$$R = R_{ref} - \frac{R_{ref}}{(1 + (\alpha \cdot d)^\beta)^\gamma} \quad (1)$$

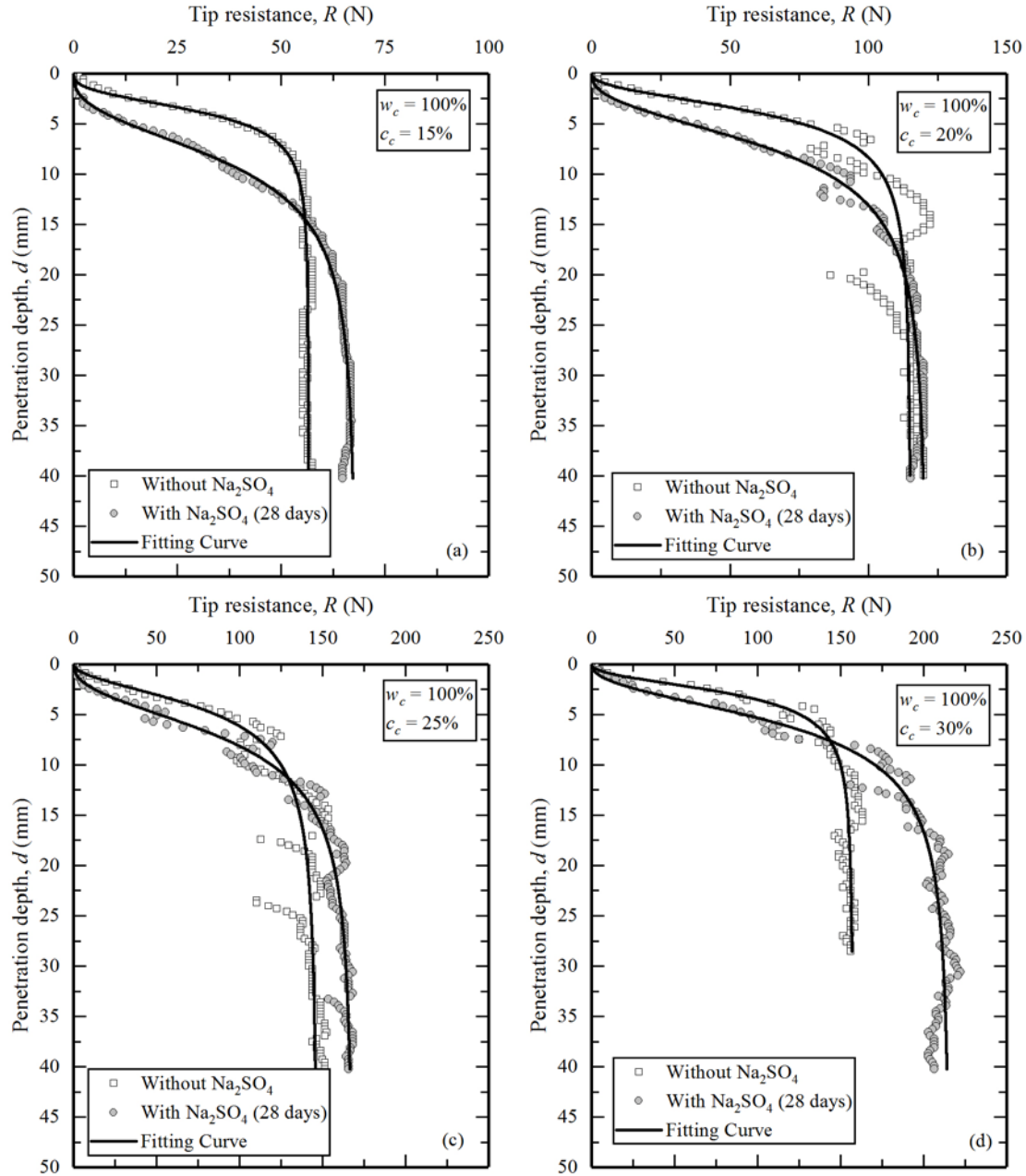


Fig. 6 Comparison of penetration test results for specimen with and without immersed into Na₂SO₄: a) $c_c=15\%$; b) $c_c=20\%$; c) $c_c=25\%$ and d) $c_c=30\%$

Where: R =tip resistance at certain depth, R_{ref} =reference tip resistance where the contact area of penetration needle has been fully work, d =depth of penetration and α, β, γ =fitting constant.

Based on the results shown in Fig. 6, it is clearly observed that the zone which has low tip resistance is getting deeper when specimen is immersed into Na₂SO₄. This results agree with obtained by other researchers [13, 14]. This zone is deeper as the cement content decreases as shown in Fig. 7. Figure 8 shows the R_{ref} value for each specimen. The

results indicated that the tip resistance at undegraded zone for the specimen immersed with Na₂SO₄ is higher than the one not immersed into Na₂SO₄. This results indicate that while the cement treated soil specimen losing the strength at the surface due to Na₂SO₄, the strength of the lower layer keep increasing due to continuous reaction of cement, soil and water. The reaction occurred in this zone is more likely to be the Pozzolanic reaction which take longer time than Hydration reaction.

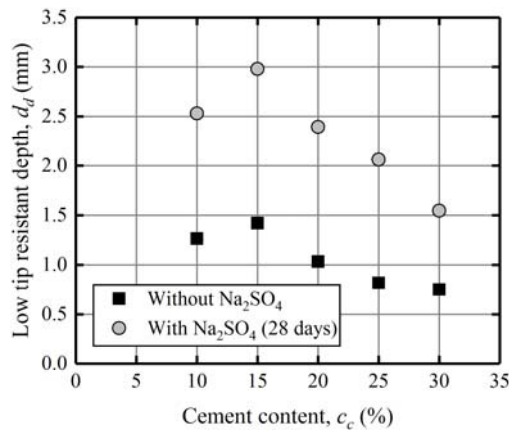


Fig. 7 Penetration test result of specimen without immersed to Na_2SO_4 ($c_c=15\%$ and $w_c=100\%$)

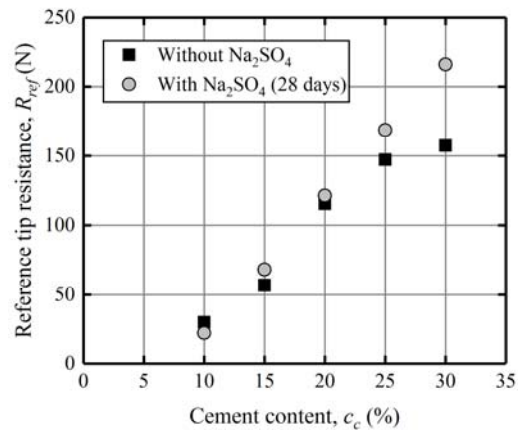


Fig. 8 Penetration test result of specimen without immersed to Na_2SO_4 ($c_c=15\%$ and $w_c=100\%$)

CONCLUSION

This paper shows the comparison of physical properties and penetration test of cement treated soil with and without immersed into natrium sulfate solution. The natrium sulfate solution was selected to represent the corrosive environment.

Based on the test result, the plasticity of cement treated soil tends to decrease as the increase of cement content. After submerged into natrium sulfate, the plasticity index tends to increase. The grain size of cement treated soil is larger than original soils. There is no significant differences of grain size distribution for addition cement from 1-3%. After submerged into natrium sulfate solution, the percentage of particle size between 0.005 mm – 0.02 mm become smaller. The penetration test results clearly show the degradation caused by natrium sulfate solution. As the cement content increases, the degradation depth of cement treated soil due to natrium sulfate decreases

ACKNOWLEDGEMENTS

The authors acknowledge the help from college at Soil Mechanics Laboratory of Universitas Atma Jaya Yogyakarta for their support to this research. The authors also express their gratitude for the financial support from Civil Engineering Department of Universitas Atma Jaya Yogyakarta.

REFERENCES

- [1] Bennert, T.A., et al., *Use of Dredged Sediments from Newark Harbor for Geotechnical Applications*, in *Geotechnics of High Water Content Materials*, T.B. Edil and P.J. Fox, Editors. 2000, American Society for Testing and Materials: West Conshohocken.
- [2] Chu, J., M.W. Bo, and A. Arulrajah, *Reclamation of a slurry pond in Singapore*. Proceedings of the Institution of Civil Engineers - Geotechnical Engineering, 2009. 162(1): p. 13-20.
- [3] Kitazume, M. and T. Satoh, *Development of a pneumatic flow mixing method and its application to Central Japan International Airport construction*. Proceedings of the Institution of Civil Engineers - Ground Improvement, 2003. 7(3): p. 139-148.
- [4] Kamon, M., T. Katsumi, and K. Watanabe, *Heavy-Metal Leaching from Cement Stabilized Waste Sludge*, in *Geotechnics of High Water Content Materials*, T.B. Edil and P.J. Fox, Editors. 2000, American Society for Testing and Materials: West Conshohocken.
- [5] Handoko, L., N. Yasufuku, and A. Rifa'i, *Comparison of consolidation curves for remolded mud volcano of Sidoarjo, Indonesia*. Journal of Geotechnique, Construction Materials and Environment, 2016. 10(22): p. 1978-1982.
- [6] Federico, A., C. Vitone, and A. Murianni, *On the mechanical behaviour of dredged submarine clayey sediments stabilized with lime or cement*. Canadian Geotechnical Journal, 2015. 52(12): p. 2030-2040.
- [7] Antonio, F., et al., *Plasticity of lime/cement-stabilised dredged clayey sediments*. Environmental Geotechnics, 2016. 3(1): p. 17-27.
- [8] Tsuchida, T. and Y.X. Tang, *Estimation of compressive strength of cement-treated marine clays with different initial water contents*. Soils and Foundations, 2015. 55(2): p. 359-374.
- [9] Watabe, Y., et al., *Mechanical characteristics of a cement treated dredged soil utilized for waste reclamation landfill*, in *International Symposium Yokohama*, T. Tsuchida, et al., Editors. 2003, Taylor Francis: Yokohama. p. 739-744.

- [10] Tang, Y.X., Y. Miyazaki, and T. Tsuchida, *Practices of reused dredgings by cement treatment*. Soils and Foundations, 2001. 41(5): p. 129-143.
- [11] Sherwood, P.T., *The Stabilization with Cement of Weathered and Sulphate-Bearing Clays*. Géotechnique, 1957. 7(4): p. 179-191.
- [12] Sherwood, P.T., *Effect of sulfates on cement and lime stabilized soils*. Highway Research Board Bulletin, 1962. 353: p. 98-107.
- [13] Hara, H., et al., *Deterioration Progress of Cement-Treated Ariake Clay under Seawater*. Journal of the Society of Materials Science, 2014. 63(1): p. 49-54.
- [14] Yang, J., et al., *Laboratory test on long-term deterioration of cement soil in seawater environment*. Transactions of Tianjin University, 2016. 22(2): p. 132-138.

CHARACTERIZATION OF PHYSICAL, CHEMICAL, AND COMPACTION PROPERTIES FOR BURIED MUNICIPAL SOLID WASTE AT THREE DUMPING SITES IN SRI LANKA

A.B.K.T. Piumali¹, T. Saito¹, N.H Priyankara², A.M.N Alagiyawanna², and K. Kawamoto¹

¹Graduate School of Science and Engineering, Saitama University, Japan; ²Department of Civil and Environmental Engineering, Faculty of Engineering, University of Ruhuna, Sri Lanka

ABSTRACT

Open dumping of Municipal Solid Waste (MSW) is a common method for waste disposal in most of developing countries. Due to rapid population growth and lack of lands, abandoned waste dumping sites are highly demanded for the redevelopment and construction especially at big cities and their surrounding in developing countries. In order to examine the stability analysis and the construction plan of abandoned waste dumping sites, more studies for characterizing geo-mechanical properties of buried MSW are needed. In this study, a comprehensive laboratory testing program including fundamental physical and chemical properties, and the standard proctor test were performed on buried MSW collected from three waste dumping sites, representing three different climate zones in Sri Lanka. The results indicated that Loss on Ignition (LOI) decreased with the dumped age of tested samples. For all tested samples, measured specific gravities ranged between 2.3 to 2.6 and correlated inversely to LOI values. Electrical conductivities decreased with the age of MSW and pH values ranged between 7 to 8. Based on the results from particle size distribution curves, Uniformity Coefficient decreased and Coefficient of Curvature increased with the age of MSW and the fraction with less than 2mm increased with the age of MSW. Measured maximum dry densities highly correlated to LOI values, suggesting that the LOI is a good indicator to evaluate the particle density and compaction property for buried waste samples.

Keywords: Municipal Solid Waste, open dumping, laboratory testing, Geo-mechanical properties, Loss on Ignition (LOI)

INTRODUCTION

Open dumping of Municipal Solid Waste (MSW) is a common method for waste disposal in most of developing countries and many large dump sites are located in urban and suburban areas. Due to rapid urbanization and increase in population, the generation of MSW is increasing. Available land in urban and suburban areas are becoming scarcer with time. Therefore, the local authorities are forced to strain the existing open dumps to a level which the landfills are reaching to critical heights, causing slope failures or shear failures. Then the operation of dump site is happened to be stopped, it must essentially move to another location near urban or suburban area. The landfills of Cincinnati, Ohio in USA [1], Payatas in Philippines [2] are examples of catastrophic failures of MSW dumps in the world. Sri Lanka is correspondingly facing this problem attributed to the improper MSW management [3], most of collected MSW is dumped at the disposal sites without any engineering considerations such as ground settlement and slope stability. The famous Meethotamulla tragedy occurred on 14th April 2017 in Sri Lanka, is one of the most appropriate examples, which took approximately 30 lives and a huge property damage [4]

Due to the limited available resources of lands in city areas, expanding communities now frequently

encompass waste fill areas and build more frequently in disposal areas and over wasteland. They sometimes operate with a design life of several generations [5]. The post closure use of dump sites was not only limited to the recreational uses, but also other hard end uses [6]. In Sri Lanka where available lands are very much limited for development projects, the abandoned lands are leaned towards use for constructions (i.e. Bloemandhal garbage mountain, Colombo).

In order to take precautions for the safety of structures in designing foundations on such lands and to examine the stability of waste areas, the knowhow of geotechnical properties of MSW is essential. Though some studies have been done on this emerging engineering aspect, more studies for characterizing geo-mechanical properties of buried MSW are needed. One first feasible approach to this study, is to characterize basic physical, chemical and compaction properties to correlate with the geo-mechanical properties of MSW.

Unlike soil, investigation of geo physical, chemical and mechanical properties of MSW is intricate due to high variability of MSW in its composition which is dependent on a variety of factors such as climate, disposal technology, and the demography of the local community. It is therefore essential that the design and stability evaluations of landfills/dump sites in each region be performed

based on the local conditions [7]. However, effects of climate condition and waste age on geotechnical properties of MSW are not well understood [8]. Therefore, this study was formed with the objective of evaluating the climate and aging effect on the geotechnical properties of buried MSW by conducting a comprehensive laboratory testing program. It includes fundamental physical and chemical properties, and the standard proctor compaction test. The tested buried MSW samples were collected from three waste dumping sites, representing three different climate zones in Sri Lanka. Each dump site has three different urbanization statuses. Climate condition controls biological decomposition of buried waste. Level of urbanization controls the fresh MSW composition, and aging cause to change the composition of buried waste. Therefore, it is essential to characterize new MSW and old MSW to identify the aging effect on the geotechnical properties.

However, the benefits of such study are not exclusive to post closure land use and slope stability issues on non-engineered landfills. Prominently they could be utilized for designing, constructing and operating engineered landfill facilities. Additionally, as MSW is a burden to a society, these findings could be used to make recommendations to use MSW as a geo-material/fill material for roads or land reclamations projects, etc. Therefore, this is a sustainable engineering approach on utilizing MSW as a geo-material and the knowledge made by the study would support for preventing slope failure disasters.

METHODOLOGY

Site Selection and Sampling

Table 1 summarizes the details of selected open dump sites in Sri Lanka. Fig. 1 shows the satellite map of Karadiyana dump site which is located in Colombo district. The existing dumpsite is handling

garbage by seven Local Authorities in Colombo Area. The extent of the waste disposal site is 37 acres marking it as the largest dump site in Sri Lanka. This dump site is climatically located in Intermediate zone and it represents the most urbanized locality in Sri Lanka. It has been used as a dump site for more than 30 years. However, it is officially started operation under Waste Management Authority, Sri Lanka in 1996 [9]. The dumpsite consisted of old and new sections. The old section has buried waste more than 25 years old. The samples were collected at the oldest location of the dump site and upon the excavation, up to 8m depth, the buried waste of more than 20 years old was found. Point sampling at each 1m interval from 0-8m were done.



Fig. 1 Site map of Karadiyana dump site (Source:2017 Google Map on 16/5/17 and modified)

Site and sampling information at Udapalatha abandoned open dumping site in Central Province and Hambanthota operating dumping sites in Southern Province are shown in [8].

Table 1 Information of sampling locations

Sampling Site	Local Authority	Population [10]	Site Location	Annual Rainfall and Temperature [11]	Daily Quantity Receiving (T/D)
Karadiyana	Western Province Waste Management Authority	1,185,458	06°48'54.2"N 79°54'08.2"E	>2000mm 25-27.5 °C	632[9]
Udapalatha	Udapalatha Pradeshiya Saba	97,567	07°80'30.1" N 80°34'43.2" E	>2500mm 17.5-25.0 °C	1.78[12]
Hambanthota	Hambanthota Municipal Council	22,691	06°10'36.0" N 81°07'40.5" E	<1250 mm 25-32.5 °C	9.9[12]

Testing Methods

The point samples and core samples taken from boreholes were used to determine basic physical properties including moisture content, Atterberg limits, specific gravity (G_s), and particle size distribution. Importantly the basic chemical properties including Loss on Ignition (LOI), pH and electric conductivity (EC) were performed. Those tests were carried out conforming to Japanese Industrial Standards (JIS) (JIS A 1202, JIS A 1203, JIS A 1204, JIS A 1205) and Japanese Geotechnical Society (JGS) standards (JGS 0211-2009, JGS 0212-2009, JGS 0221-2009). The compositions for buried MSW were characterized by the waste composition analysis in which the waste components were separated visually based on the dry weight of each group. Standard Proctor compaction test was carried out according to (JIS A 1210). The material which has the particle size distribution less than 9.5mm was used in order to conform to the testing methods.

RESULTS AND DISCUSSION

Basic physical and chemical properties

Table 2 shows basic physical and chemical properties of bored core samples taken from the disposal sites of Udapalatha (wet zone), Hambanthota (dry zone) and point samples taken from the disposal sites of Karadiyana (intermediate zone). Field moisture content values are highly scattered depending on the daily weather conditions.

The results indicated that LOI decreased with the dumped age of tested samples and is becoming lesser from wet zone, intermediate zone and dry zone respectively at each new and old site. Inverse trend is shown for the change of G_s with age and the G_s values for buried waste samples were ranged between 2.3 - 2.6, which were lower than that of soil samples. The pH values for waste samples of old site in the wet zone were lower than other samples. The pH values in dry zone is higher than that of intermediate zone. Buried waste samples for all three sites were characterized as having higher EC value compared with soil. Especially, EC values are higher in wet zone, intermediate zone and dry zone respectively

MSW Composition

Many research studies have identified the composition of fresh MSW usually composed of kitchen waste, garden waste, wood, paper and cardboard, plastics, textiles, ceramic, glass, rubber, rock, and soil [12], [13]. The composition analysis of this study showed that after around 1 year fill age, all the kitchen waste and around 80% of garden waste portion is converted to residue by biodegradation. Other materials could be inert and degrade very

slowly with time unless they were subjected to mechanical crushing during dumpsite operation. When the fill age is more than 20 years, in Karadiyana dump site, the composition was basically identified as a combination of a soil like material and other waste materials as defined in [14]. The composition of other waste materials could only be distinguished and soil like materials were hardly identifiable. The results of composition analysis of Karadiyana dump site showed that the contribution from the other waste materials was increased as their fill age was increased.

The paste portion was rich with organic content. The LOI values which give the organic content is high in all three sites compared with those of intact soil samples. The LOI values for wet zone and intermediate zone were higher than those for dry zone. It was clearly identified that the Loss on Ignition was decreasing with age in each site introducing the Loss on Ignition as an indicator parameter of the age of MSW. Due to particle crushing and packing, naturally there should be higher specific gravity values for old buried waste than that of new buried waste. As LOI verifies the exact age of the waste sample, specific gravity showed a higher inverse correlation with Loss on Ignition as shown in Fig. 2.

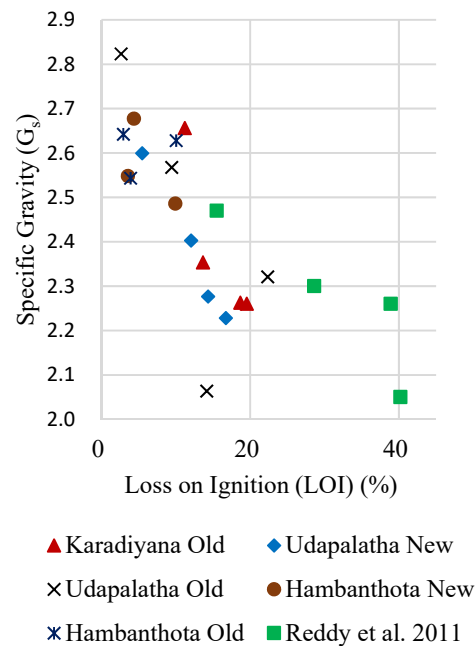


Fig. 2 Graph of Correlation of Specific Gravity with Loss on Ignition.

Table 2 Basic Physical and Chemical Properties for Tested Samples

Location (Age)/ Depth(m)	Description	Field Moisture Content w _f %	Atterberg limits			Specific gravity G _s <2.0 mm	pH	EC mS/cm	Loss on Ignition LOI %
			w _L %	w _p %	I _p				
Karadiyana (Old >20 Years)									
0.00-2.00	Black, dumped waste	45.5	-	-	-	2.26	7.1	1.46	19.5
2.00-4.00		59.0	-	-	-	2.26	7.3	1.63	18.7
4.00-6.00		47.8	-	-	-	2.35	7.3	1.41	13.6
6.00-8.00		65.9	68.2	54.3	13.9	2.66	7.5	1.55	11.2
Udupalatha (New <3 Years)									
0.00-1.00	Black, dumped waste with fine to medium sand	6.7	-	-	-	2.28	7.5	1.43	14.3
1.00-2.00	Black, dumped waste with organic clay, trace of coarse to fine sand	35.8	-	-	-	2.23	7.1	1.98	16.7
2.00-3.20	Black, dumped waste with Coarse to fine sand	27.2	-	-	-	2.40	7.3	1.18	12.1
3.20-4.50	Blackish Brown, coarse to medium sand with organic clay and dumped waste	14.8	-	-	-	2.60	7.7	0.57	5.5
Udupalatha (Old 7-11 Years)									
0.00-1.50	Black, dumped waste	57.1	-	-	-	2.32	6.0	0.84	22.4
1.50-3.00		78.7	-	-	-	2.06	6.1	1.15	14.2
3.00-4.00		13.6	-	-	-	2.57	6.7	0.71	9.4
4.00-4.20		10.1	17.8	-	-	2.82	6.9	0.20	2.7
Hambanthota (New <1 Year)									
0.00-1.00	Blackish dumped waste with clay, trace of fine sand	29.9	25.7	-	-	2.49	7.4	0.64	10.0
1.00-2.00	Blackish dumped waste with clay, trace of fine sand	11.8	40.5	-	-	2.68	7.3	0.69	4.4
2.00-3.00	Reddish brown to yellowish brown lateratic clay, Trace of fine sand	7.0	64.4	25.0	39.4	2.55	8.0	0.29	3.6
Hambanthota (Old7-8 Years)									
0.00-1.00	Blackish dumped waste with clay, trace of fine sand	19.1	29.5	-	-	2.63	7.9	0.37	10.1
1.00-1.50	Blackish dumped waste with clay, trace of fine sand	7.3	30.6	15.5	15.1	2.64	7.6	0.46	2.9
1.50-2.50	Blackish dumped waste with clay, trace of fine sand	4.4	66.5	24.8	41.7	2.54	7.3	0.33	3.9

Particle Size Distribution

Fig.3 shows results of Particle Size Distribution (PSD) curves and Table 3 summarizes the derived values of particle size distribution of buried waste samples from the three dump sites. The coarser fraction higher than 2.0 mm in waste samples was comparatively higher than soil, though to a lesser extent for waste sample from old site in Hambanthota dump site. There was no significant difference in PSD for waste samples except for that of waste sample from old site in Hambanthota and Karadiyana. Hambanthota old samples are mixed with sands reasoning to end up with a finer curve than other locations. Though the sample collected from Karadiyana dump site are more than 20 years old, the particle size distribution is much coarser than other two sites. It is attributed to the urbanization level. As Karadiyana dump site is located in highly urbanized area, the plastic, polythene usage is higher than other two sites. As those materials are non-degradable or take more time to degrade or crushing, despite the age, it has higher coarser fraction. More than 60% of residues of Karadiyana buried waste samples were observed as aggregated together making bigger unite particles larger than 4.75 mm which are easily crushable.

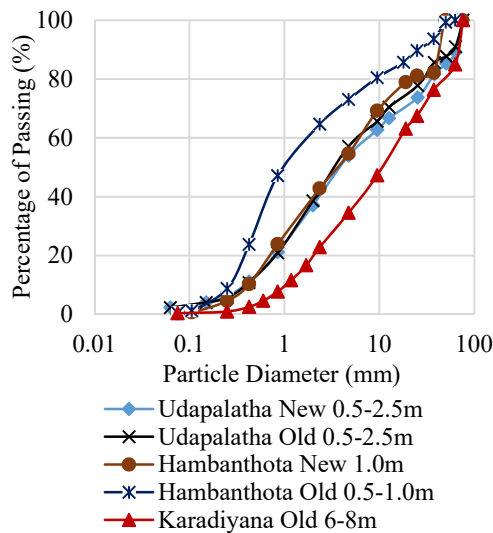


Fig. 3 Graph of Particle Size Distribution.

In wet and dry zones, the residue content below 4.75 mm were high for all waste samples, and that for the new site in dry zone exceeding 60%. Based on the results, it can be found that more variety of waste was mixed in the wet zone samples. The results from particle size distribution curves demonstrates that the uniformity coefficient decreased and the coefficient of curvature increased with the age of MSW and the fraction with less than 2mm increased with the age of MSW.

Compaction

Fig. 4 shows results of compaction tests. It can be found that maximum dry densities (ρ_{dmax}) for dry zone were about 1.5 times higher than those for wet and intermediate zones. There is no any significant difference between compaction curves for both new and old waste samples from wet and intermediate zone. Fig. 5 illustrates the correlations between the ρ_{dmax} values from standard proctor compaction tests and LOI. The ρ_{dmax} values were well correlated with LOI values. This implies that the LOI is a good indicator to evaluate the particle density and compaction property for buried waste samples.

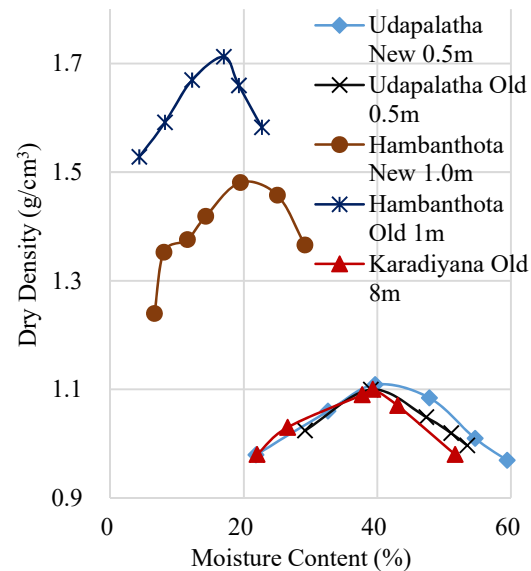


Fig. 4 Compaction Curves.

Table 3 Properties of Particle Size Distribution for Buried Waste Sample

Sample Location	<0.075mm Fraction %	<2mm Fraction %	D ₅₀ mm	Uniformity Coefficient	Coefficient of Curvature
Karadiyana Old	0.4	22.9	11.2	16.5	0.8
Udapalatha New	2.3	37.1	4.0	28.7	0.6
Udapalatha Old	2.3	38.6	4.7	16.7	1.2
Hambanthota New	0.4	42.8	3.5	14.9	0.5
Hambanthota Old	0.6	64.7	1.0	6.4	0.6

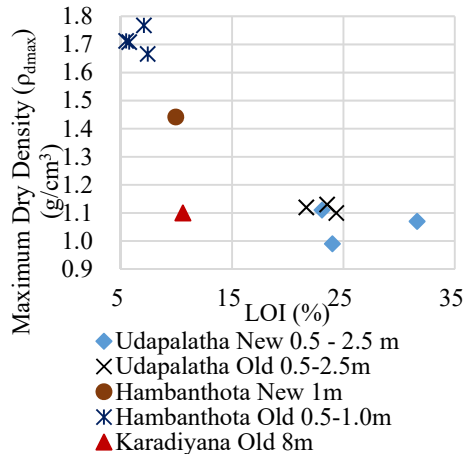


Fig. 5 Graph of correlation of maximum dry density with Loss on Ignition.

CONCLUSION

Using buried waste samples of three different ages from wet, intermediate and dry zone in Sri Lanka, basic physical and chemical properties, and compaction properties were determined in the laboratory. Results showed that buried waste samples were characterized as having high EC and LOI values and Gs values for waste samples in all zones were 2.3-2.6. The Gs values were highly correlated to LOI values, implying the LOI as an indicator parameter to characterize the age and the particle densities of the waste samples. Based on the results from PSD curves, Uniformity Coefficient decreased and Coefficient of Curvature increased with the age of MSW and the fraction with less than 2mm increased with the age of MSW. The ρ_{dmax} values for dry zone became higher than those for wet and intermediate zone, and it is well correlated with LOI. With increasing in LOI, the ρ_{dmax} values decreased, implying that compaction properties for buried waste samples could be well characterized by LOI of samples.

ACKNOWLEDGEMENTS

This study was supported by the SATREPS Project of the Japan Science and Technology agency (JST) and Japanese International cooperation Agency (JICA).

REFERENCES

- [1] Stark TD, Eid HT, Evans WD, Sherry PE, "Municipal solid waste slope failure. II: stability analyses", J. of Geotechnical and Geoenvironmental Engineering, ASCE 126 (5), May. 2000, pp. 408-419.
- [2] Merry SM, E Kavazanjian Jr, Fritz WU, "Reconnaissance of the July 10, 2000, Payatas

- landfill failure", J. of Performance of constructed Facilities, Vol. 19, No. 2, May. 2005, pp. 100-107,
- [3] Sato N, Kawamoto K, Mangalika L, "Current condition and issues of municipal solid waste management in Sri Lanka", in Proc. 7th Asian-Pacific Landfill Symposium (APLAS), 2012, pp OMS 6-58-OMS 6-66.
- [4] <http://blogs.agu.org/landslideblog/2017/04/16/meehotamulla-1/> accessed on 26/05/2017
- [5] Landva AO, Clark JI, "Geotechnics of waste fills", Geotechnics of Waste Fills-Theory and Practice, 1990 pp.86-106, ASTM STP 1070,
- [6] Sharma HD, Krishna RR, "End Uses of Closed Landfills", Chapter 24, Geo-Environmental Engineering, WILEY, 2004, pp. 898-912
- [7] Machado SL, Karimpour-Fard, M, Shariatmadari N, Carvalho MF, Nascimento JCF, "Evaluation of the geotechnical properties of MSW in two Brazilian landfills." J. of Waste Management 30(12), 2010, pp. 2579-2591.
- [8] Ohata H, Saito T, Tachibana S, Balasooriya BLCB, Priyankara NH, Alagiyawanna AMN, Kurukulasuriya LC, Kawamoto K "Geotechnical Properties for Municipal Solid Waste at Open Dumping Sites Located in Wet and Dry Zones, Sri Lanka", International Conference of Geotechnical Engineering, 2015, pp 269-272
- [9] JAICA main report of the data collection survey of solid waste management in Sri Lanka, 2016, pp. 12-20
- [10] Census Department, Sri Lanka accessed on 3/05/2017 <http://www.statistics.gov.lk/PopHouS> at/CPH2011/index.php?fileName=ImpDates
- [11] Climate of Sri Lanka, Department of Meteorology, accessed on 02/05/2017 http://www.meteo.gov.lk/index.php?option=com_content&view=article&id=94&Itemid=310&lang=en
- [12] Satreps project report of Waste Amount and Composition Surveys (WACS) implemented in the Central and Southern Provinces of Sri Lanka. 2014, pp. 36-42, 74-79
- [13] Zekkos D, E Kavazanjian Jr, Bray JD, Matasovic, N, Riemer F, "Physical characterization of municipal solid waste for geotechnical purposes" J. Geotechnical and Geoenvironmental Engineering, 2010, 136(9), pp. 1231-1241.
- [14] Manassero, M., Van Impe, W. F., and Bouazza, A. "Waste disposal and containment." In Proc. 2nd Int. Congress on Environmental Geotechnics, Vol. 2, Balkema, Rotterdam, The Netherlands, 1997, pp. 1425-1474.
- [15] Reddy KR, Hettiarachchi, H, Gangathulasi, J, Bogner, JE "Geotechnical properties of municipal solid waste at different phases of biodegradation." J. of Waste Management, Vol. 31, No. 11, (2011). pp. 2275-2286.

STRESS-STRAIN-DILATANCY RELATIONSHIPS OF NORMALLY CONSOLIDATED DHAKA CLAY

Muhammad Abdur Rahman¹, Hossain Md Shahin² and Teruo Nakai³

¹Lecturer, Department of Civil Engineering, MIST, Mirpur Cantonment, Mirpur, Dhaka-1216, Bangladesh.

²Professor, Department of Civil Engineering, IUT, Board Bazar, Gazipur, Bangladesh.

³Technical Adviser, Geo-Research Institute; Emeritus Professor at NIT, Nagoya, Japan; nakai.teruo@nitech.ac.jp

ABSTRACT

In this paper, stress-strain-dilatancy relationships of normally consolidated Dhaka clay is presented. Here two constitutive models of soils are used - one is Cam clay model (both original and modified) and subloading t_{ij} model. To obtain the model parameters, drained triaxial tests of saturated cylindrical specimens under constant effective confining pressure were conducted. The observed stress-strain relationship of the soil under consideration is presented in the paper which confirms the normally consolidated soils. It is observed from the stress-dilatancy relationship that, subloading t_{ij} model can well describe the stress-dilatancy behavior of normally consolidated Dhaka clay. Therefore, subloading t_{ij} model can be used for the soil with better accuracy for the Dhaka clay.

Keywords: Stress-Dilatancy Relationship, Constitutive Modelling, Stress-Strain Relation, Drained Tri-axial Test.

INTRODUCTION

Usually, geotechnical engineering problems are solved by considering soil as an elastic or rigid plastic material where stress-dilatancy characteristics are not taken into considerations. As in actual soil is an elastoplastic material most of the designs are either over designed or under designed for not taking proper considerations of constitutive model. There is the necessity of a constitutive model which can simulate the soil behavior accurately. On the contrary, most of the constitutive models are not able to simulate total behavior of the soil and does not fit with all the soils. In this paper comparison between two simple constitutive models in terms of stress-dilatancy relationship is made to choose a better constitutive model for Dhaka soils.

The first simple model which considered the soil as an elastoplastic material is the Cam-clay model. In the Cam-clay model (e.g., Schofield and Wroth, 1968) positive dilatancy during strain hardening is not taken into consideration along with some other limitations (Nakai et al., 2011). Subloading t_{ij} model (Nakai et al., 2011) can consider positive dilatancy during strain hardening which has also been used in this paper.

STRESS-DILATANCY EQUATIONS

In this paper, comparison of stress-dilatancy relation is made among the original Cam-clay model, Modified Cam-clay model and subloading t_{ij} model.

Original Cam-Clay Model

Like most of the constitutive models for soils, Cam clay model is formulated using the stress invariants, e.g. mean stress p and deviatoric stress q and the strain increment invariants, e.g. volumetric strain increment $d\varepsilon_v$ and deviatoric strain increment $d\varepsilon_d$ (Nakai et al., 2011).

Yield function of the model is defined by the following equation:

$$\ln p + \zeta(\eta) - \ln p_1 = \ln \frac{p}{p_1} + \zeta(\eta) - \ln \frac{p}{p_1} = 0 \quad (1)$$

Where, $\zeta(\eta)$ is an increasing function of η ($\eta = q/p$) and satisfies the condition $\zeta(0) = 0$, p_0 is the value of the initial yield surface at p-axis, and p_1 determines the size of the current yield surface (the value of p at $\eta = 0$).

The stress ratio function $\zeta(\eta)$ is expressed as follows in Cam-clay model:

Original:

$$\zeta(\eta) = \frac{1}{M} \eta \quad (2)$$

Modified:

$$\zeta(\eta) = \frac{M^2 + \eta^2}{M^2} \eta \quad (3)$$

Here, M is the stress ratio, η at critical state.

The plastic strain increment assuming associated flow rule then can be expressed as follows (Nakai et al., 2011):

$$\frac{d\varepsilon_p^p}{d\varepsilon_d^p} = \frac{\partial f / \partial p}{\partial f / \partial q} = \frac{1 - \zeta'(\eta) \cdot \eta}{\zeta'(\eta)} \quad (4)$$

Using Eq. (2), Eq. (3) and Eq. (4), the stress-dilatancy relation can be derived as follows:
Original:

$$\frac{d\varepsilon_v^p}{d\varepsilon_d^p} = M - \eta \quad (5)$$

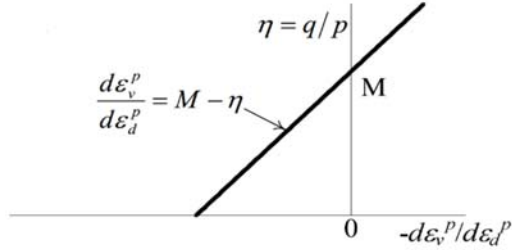


Fig. 1 Stress-dilatancy relation of original Cam clay model.

Modified:

$$\frac{d\varepsilon_v^p}{d\varepsilon_d^p} = \frac{M^2 - \eta^2}{2\eta} \quad (6)$$

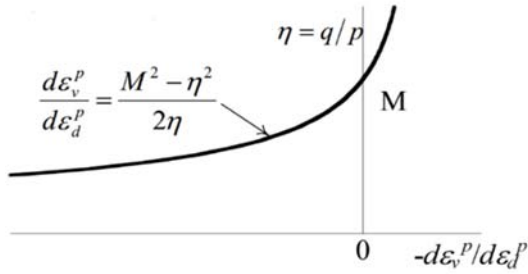


Fig. 2 Stress-dilatancy relation of modified Cam clay model.

Subloading t_{ij} model

In the subloading t_{ij} model (Nakai and Hinoko, 2004) yield function is given by,

$$\ln t_N + \zeta(X) - \ln t_{N1} = \ln \frac{t_N}{t_{N0}} + \zeta(X) - \ln \frac{t_{N1}}{t_{N0}} = 0 \quad (7)$$

The stress ratio function $\zeta(X)$ is then given by the equation below (Chowdhury and Nakai, 1998; Nakai and Hinokio, 2004):

$$\zeta(X) = \frac{1}{\beta} \left(\frac{X}{M^*} \right)^\beta \quad (8)$$

Where $\beta (\geq 1)$ is the parameter which controls the shape function. Finally, the stress dilatancy relation can be expressed as,

$$\frac{d\varepsilon_N^*}{d\varepsilon_s^*} = \frac{1 - \zeta'(X)X}{\zeta'(X)} = \frac{(M^*)^\beta - X^\beta}{X^{\beta-1}} \quad (9)$$

Here, M^* expressed using X_{CS} and Y_{CS} , which are the stress ratio X and Y at critical state ($d\varepsilon_v^p = 0$).

$$M^* = (X_{CS}^\beta + X_{CS}^{\beta-1} Y_{CS})^{1/\beta} \quad (10)$$

X_{CS} and Y_{CS} are expressed as follows (e.g., Nakai and Mihara, 1984):

$$X_{CS} = \frac{\sqrt{2}}{3} \left(\sqrt{R_{CS}} - \frac{1}{\sqrt{R_{CS}}} \right) \quad (11)$$

$$Y_{CS} = \left(\frac{1 - \sqrt{R_{CS}}}{\sqrt{2}(\sqrt{R_{CS}} + 0.5)} \right) \quad (12)$$

Where, R_{CS} is the critical stress ratio and expressed as follows:

$$R_{CS} = (\sigma_1/\sigma_3)_{CS(comp)}. \quad (13)$$

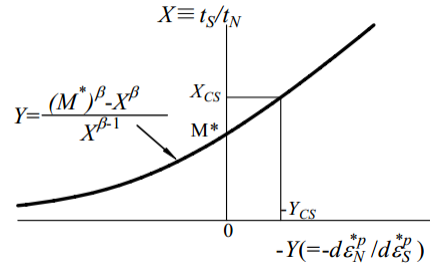


Fig. 3 Stress-dilatancy relation of subloading tij model.

TRIAXIAL COMPRESSION TEST

To evaluate the stress-dilatancy relation, triaxial consolidated drained compression test has been conducted on two saturated specimens of Dhaka clay under constant confining effective pressure of 199 kPa and 397 kPa.

Table 1 Test conditions.

Specimen	Diameter (mm)	Height (mm)	B Value	Effective confining pressure (σ_3'), kPa
A	38	76	0.97	199
B	38	76	0.98	397

RESULTS

Fig. 4 and Fig. 5 show the observed stress-strain, volumetric strain – deviatoric strain relationships in different arrangements.

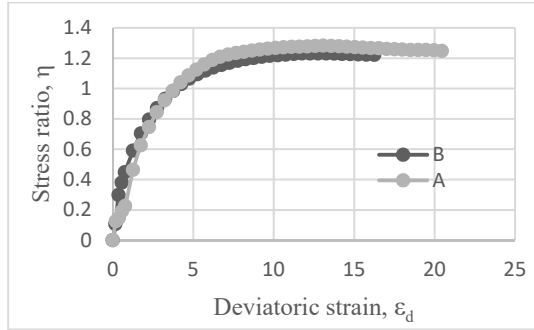


Fig. 4 Observed Stress-strain relation.

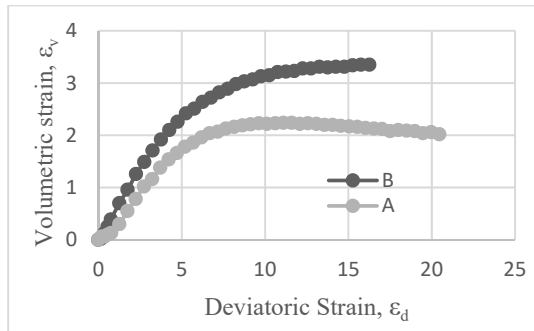


Fig. 5 Observed relation between volumetric strain and deviatoric strain.

Figures 6 – 8 show the observed stress – dilatancy relationship of Cam-clay model and subloading t_{ij} model. In Fig. 6 it is observed that stress – dilatancy relation of original Cam-clay model is linear. In Fig. 7 stress dilatancy relation of modified Cam-clay model does not follow the unique pattern. In case of the specimen A, the shape of the curve does not follow the theoretical pattern as shown in Fig. 2.

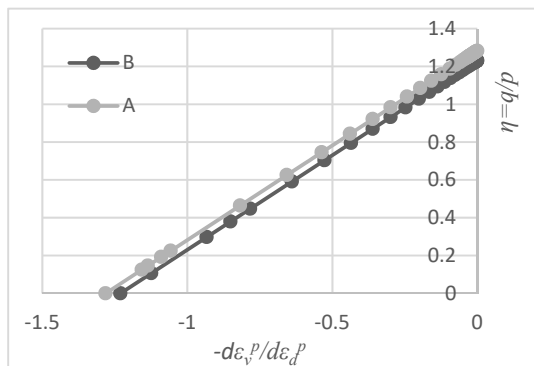


Fig. 6 Observed Stress-dilatancy relation of Cam-clay model

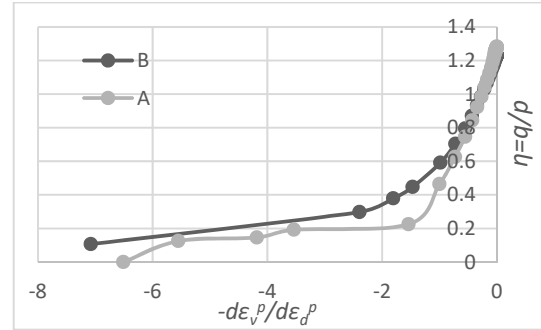


Fig. 7 Observed Stress-dilatancy relation of Modified Cam-clay model.

In Fig. 8 stress – dilatancy relation in subloading t_{ij} model shows that for both the specimens the stress – dilatancy relation follow the identical pattern shown in Fig. 3.

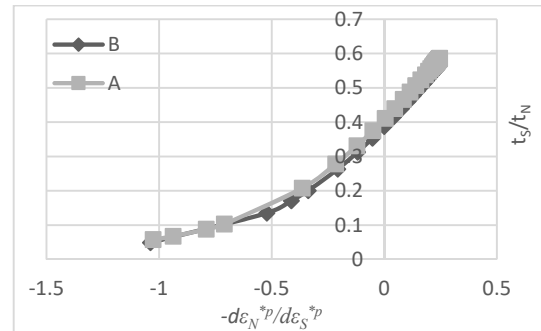


Fig. 8 Observed Stress-dilatancy relation of subloading t_{ij} model.

CONCLUSIONS

From the stress-dilatancy relationship presented above it can be concluded that subloading t_{ij} model fits better than the Cam clay model. Hence subloading t_{ij} model can be used for the Dhaka clay.

REFERENCES

- [1] Teruo Nakai, Constitutive Modeling of Geomaterials, Principles and Applications, ISBN 13:978-0-203-86884-3, CRC Press.
- [2] Schofield, A. N. and Wroth, C. P. (1968) - Critical State Soil Mechanics, McGraw- Hill, London.
- [3] Roscoe, K. H. & Burland, J. B. (1968) - On the generalized stress- strain behavior of wet clay. Heyman and F. A. Leckie (eds.), Engineering Plasticity, Cambridge University Press, pp535-609.
- [4] Nakai, T., Shahin, H. M. Kikumoto, m., Kyokawa, H., Zhang, F. and Farias, M. M. (2011): a simple and unified three-dimensional

- model to describe various characteristics of soils,
Soils and Foundation, 51(6), 1149-1168.
- [5] Nakai, T. (2007): Modeling of soil behavior
based on t_{ij} concept, Proc. Of 13th Asian
Regional Conf. on Soil Mech. And Geotechnical
Eng.m Keynote Paper, 2, 69-89.

MECHANISTIC BEHAVIOR OF OPEN AND DENSE GRADED UNBOUND GRANULAR MATERIALS UNDER TRAFFIC LOADS

*Ali Alnedawi¹, Kali Prasad Nepal¹ and Riyadh Al-Ameri¹

¹ Science Engineering & Built Environment, Deakin University, Australia

ABSTRACT

The absence of natural unbound granular materials (*UGMs*) necessitates investigating alternatives such as processed crushed rock. Extensive use of crushed rock in pavement design requires proper modification of characterization, design and construction practices. Many specifications and standards require adopting of dense gradation of base materials. Although dense gradation has a high dry density, it also has low permeability or voids. This low permeability results in a decrease in material strength when the pavement is exposed to moisture. This research examines the effects of fines content on mechanistic behaviors of *UGMs*, particularly resilient modulus (M_r) and permanent deformation (PD) using repeated load triaxial test (*RLTT*). Class 2 (Victoria, Australia) crushed rock is used in two gradation, dense gradation and open gradation (without filler-passing sieve 0.0075mm). Results from *RLTT* show that open graded Class 2 has an acceptable PD resistance under repeated loads for test's Stages 1, 2 and 3 followed by a significant collapse at Stage 4 as per Australian pavement design guide. This investigation has found that open graded Class 2 has higher M_r than dense graded Class 2. This paper suggests that open graded Class 2 could be used as a porous base material for roads with low traffic volumes.

Keywords: Unbound granular material, Resilient modulus, Permanent deformation, Fines content, Repeated load triaxial test.

1. INTRODUCTION

Unbound granular pavement materials (*UGMs*) are used in many pavement structural systems as base and subbase layers to support the surface layer by distributing the traffic stresses to subgrade. *UGMs* are mainly naturally occurring sourced rocks, gravel or manufactured crushed rock [1].

The absence of natural aggregate necessitates the need of such as processed crushed rock [2]. Crushed rock is the most widely used products in construction materials. It is produced by mining suitable rock and processing it, then by breaking it down to the proper size using crushers [3]. A proper adjustment of characterization, design and construction guides is needed after the extensive usage of manufactured aggregates [4]. In addition, producing fine particles from crushed rock is costly and energy consuming. Some quarries are closed because of the lack of fine particles, and raw rocks in these quarries are robust and difficult to process into fines.

The *UGMs* are nonlinear and have a complex behavior under repeated wheel loads (time-dependent elastoplastic response) [5] [6]. Many researches have been conducted to better understand the behavior and the characteristics of *UGMs* [7-12]. These materials reflect both permanent strain (permanent deformation) and recoverable strain (resilient deformation) as shown

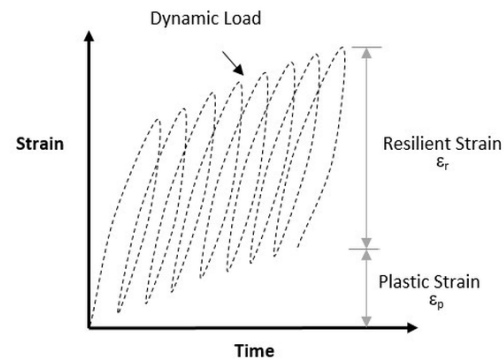


Fig. 1 Plastic strain and resilient strain

in Fig. 1.

The deformation behavior of *UGMs* is essential for performance and stability of the pavement structure [11]. Permanent and resilient deformations usually are tested by using repeated load triaxial test (*RLTT*), which is the best test that simulate the field traffic loads [13]. Both strains are used in flexible pavement structural design through the Mechanistic- Empirical (*M-E*) design methods. For instance, Austroads pavement design method and *NCHRP* design method [14].

Gradation of aggregates is one of the main features when studying the mechanical behavior of

UGMs [15]. Specifications on gradation are intended to guarantee that the designer selects the superlative available combination of materials to achieve the desirable mechanical responses. Many gradation specifications' ambits assure to achieve dense gradation to attain the maximum dry density of the compacted materials such as specification of VicRoads (Roads Corporation of Victoria). Therefore, gradation specifications are so restricted for this purpose. Pavement is susceptible to moisture which comes from variety of sources such as rainfall [16]. As mentioned latterly, dense graded base layer materials have high dry density that coincide with low permeability because of the low voids ratio. If the pavement is exposed to moisture, then this low permeability allow water to get trapped inside the base and subbase layers. Eventually, pore pressure is induced yielding a decrease of material strength [17]. The purpose of aggregate base material in low volume pavement is to protect the surface layer from the contamination of subgrade's fines and do not add much strength to the pavement system [18]. Therefore, high quality gradation with high resilient modulus (M_r) and high permanent deformation (PD) resistance are not needed all the time, low traffic volume pavement can be designed with low mix quality.

Several factors affect the pavement strain response of *UGMs*. These factors can be classified broadly into two categories: stress and materials related factors. Stress related factors include: exerted repeated stresses by tire loads, load duration, frequency of loading and load sequence. Materials related factors include material density, particles gradation, fines content, maximum grain size, aggregate types, particle shapes and moisture content [19].

1.1 Effect of Grading and Fines Content

The significance of identifying proper aggregate gradation has been recognized for achieving suitable performance in pavement design [15].

There are limited studies that investigated the effect of gradation and fines content on the dynamic properties of the *UGMs*. Hicks and Monismith [20] tested two types of materials, partially crushed aggregate and crushed aggregate with different relative densities and percentage of passing sieve number 200 (filler) using *RLTT*. The effect of gradation on M_r was not clear. However, when the fines content (in partially crushed aggregate) increases, M_r decreases. In the other hand, M_r increases with the increase of fines content of crushed aggregates. Raad, Minassian [21] studied the behavior of *UGMs* with different gradations under saturated and undrained *RLTT* conditions. It was recognized that the saturated dense graded aggregates under dynamic loads induce excess pore

pressure which leads to a decrease in the M_r . In addition, open graded aggregates resist higher stresses and strains compared to dense graded aggregates. Type 5 aggregate base was tested by Richardson and Lusher [22] in order to investigate the effect of gradation on M_r . The purpose of the proposed gradation is to help the manufacturer to lower the production cost of said aggregate. A comparison has been made between the proposed gradation (open gradation) and as-delivered gradation. It was concluded that the open graded gradation for the Type 5 aggregate base (without fines passing #200) is better than as-delivered one (dense, high fines content) because M_r is higher and the degree of saturation is low.

Contrary to the previous findings, the variation of M_r is less significant depending on the material gradation. However, the moduli were highest for the open graded specifications than the dense graded specifications for lime stone aggregates [23].

Barksdale [24] observed the effect of fines content in a crushed granite gneiss base after 100,000 load repetitions. Increasing the fines percent from 3 to 11.25 caused 60 percent increase in rut index. Thus, when the fines percentage increase, the plastic strain increase significantly. Kamal, Dawson [25] conducted *RLTT* on *UGMs* at a range of gradations and the results of the tests revealed that the resistance to PD was high for well graded mix in comparison to the open graded one.

A recent study on the deformation behavior of *UGMs* established by Rahman [11] has been suggested to examine the influence of the grain size distribution (gradation) and fines content on the permanent deformation behavior of the *UGMs*.

It can be clearly seen from the previous works that there is no agreement about the effect of gradation and particularly the fines content on the behavior of *UGMs* under repeated dynamic loads. Therefore, this research focused on the fines content effect on the deformation behavior of Class 2 crushed rock under repeated loading. Similarly to Richardson and Lusher [22], open and dense graded crushed rock are investigated. In addition, permanent deformation test is included and different material is used (VicRoads' Class 2). The main objective of this research is to find the response of *UGMs* without filler (particles passing sieve 0.0075 mm) as an approach to design a porous base layer. This research is part of an ongoing study to investigate the response of *UGMs* with different fines content.

2. EXPERIMENTAL INVESTIGATION

2.1 Material

Crushed rock Class 2 is used as *UGMs* for this research. Class 2 is recommended by VicRoads

specifications to be used as base material. Igneous (basalt) rock is the origin of crushed Class 2, which was collected from Mountain View quarry located in Point Wilson, Victoria, Australia and delivered in plastic boxes. Fig. 2 shows Class 2 (as-delivered) particle size distribution. It can be clearly seen that Class 2 is a dense graded material and fits inside the VicRoads specification limitation envelope: upper and lower limits (UL, LL).

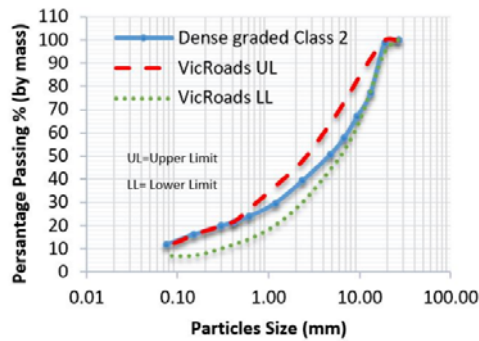


Fig. 2 Class 2 particle size distribution

2.2 Specimen Preparation

To prepare the open gradation, VicRoads' Class 2 (as-delivered dense graded crushed rock) is washed through sieve 0.0075 mm to purge out the fine particles. The specimens from these two gradations are compacted into three split cylindrical mold with respect to optimum moisture content (OMC) and maximum dry density (MDD) of the two gradations as presented in Fig. 3.

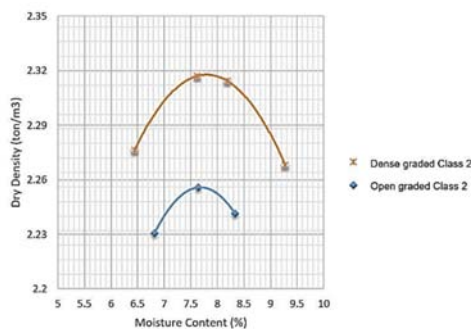


Fig. 3 Dry density-moisture content relationship

Each specimen is compacted into 8 layers using modified compactive effort with 25 blows per layer. The final specimen size is 200 mm high and 100 mm diameter. Rubber membrane is encased the cylindrical specimen as shown in

Fig. 4. The preparation process is applied in accordance with Austroads [26].

2.3 Testing Equipment

Repeated load triaxial test is conducted on the cylindrical crushed Class 2 specimens. The main



Fig. 4 New specimen confined by membrane

parts of the system consist of load frame, actuator motor, triaxial cell, digital control system, pneumatic controller, external displacement transducer and computer control. The actuator is electro-mechanical with maximum dynamic axial load capability of 5 kN, high precision position feedback is provided capable of measuring the axial displacement. The other transducer is used as additional transducer to check the internal axial displacement reading. The range of the LVDTs is ± 11 mm. The system is capable of exerting up to 500 kPa of static confining pressure. Air and water are used as a confining medium. Triaxial cell pressure is controlled via pneumatic controller which controls air pressure. The digital control system is capable of logging data from eight transducers.

2.4 Testing Sequences

Specimens are subjected to 4 stress stages. The first preconditioning stage involves 50 cycles and each permanent deformation stage involves 10,000 cycles. Repeated deviator stress, static confining stress magnitudes and number of cycles are presented in Table 1.

Table 1 Stress sequences for permanent deformation test [26]

Stages	σ_3 (kPa)	σ_d (kPa)	Cycles
1	50	90	50
2	50	350	10000
3	50	450	10000
4	50	500	10000

Note: Preconditioning stage is added by author as described in the European standard [27]

3. RESULT AND DISSCUSSION

In order to investigate the fines content effect on the deformation behavior of the *UGMs*, zero fines content gradation (no particles passing sieve 0.0075 mm) is prepared by using the washing process through sieve 0.075 mm to prepared the open graded Class 2 crushed rock. Both dense and open graded Class 2 were examined under *RLTT* to investigate the deformation behavior.

Fig. 5 compares the axial *PD* behavior for the two gradations of crushed rock materials, dense graded Class 2 and open graded Class 2.

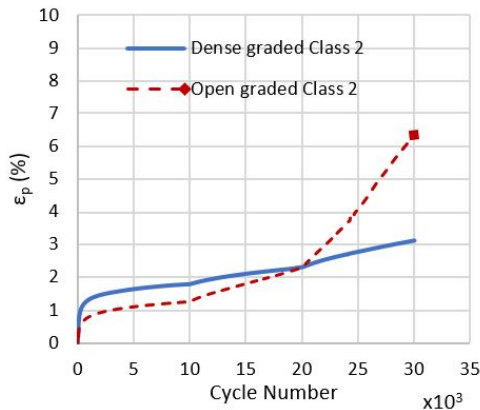


Fig. 5 Permanent deformation

It can be seen that open graded Class 2 has high *PD* resistance in the second stage ($\sigma_d = 350$ kPa) and the third Stage ($\sigma_d = 450$ kPa) of the *RLTT* than dense graded Class 2. This finding is contrary to Kamal, Dawson [25]. Afterwards, when the test entered Stage 4 (after 20000 cycles, $\sigma_d = 500$ kPa), *PD* resistance starts to decrease showing steep upwards trend while *PD* resistance of dense graded Class 2 decreases steadily. A possible explanation of this behavior could be that the open graded Class 2 could not withstand the high deviator stress at Stage 4 ($\sigma_d = 450$ kPa) because of the absence of fine particles, which support the mix by transmitting the loads to other big particles. This preliminary finding suggests that open graded Class 2 could be used as a porous base material but for low traffic volume. Missing fine particles tends to high permeability which minimizes the failure probability from moisture. Even though further tests are required to confirm this result with high degree of confidence.

Fig. 6 shows no significant variation in the *RD* behavior for the two gradations.

Fig. 7 reveals that M_r values of open graded Class 2 are greater than the M_r values of dense graded Class 2, as concluded by Richardson and Lusher [22]. Surprisingly, at Stage 4 of the *RLTT* stress sequence ($\sigma_d = 450$ kPa), M_r of open graded Class 2 remain greater than M_r of dense graded Class 2 despite the dramatic *PD* that happened in

the specimen at this stage as shown in Fig. 7. This finding confirm that pavement design procedures should not only be based on M_r values of pavement materials, the *PD* needs to be examined likewise.

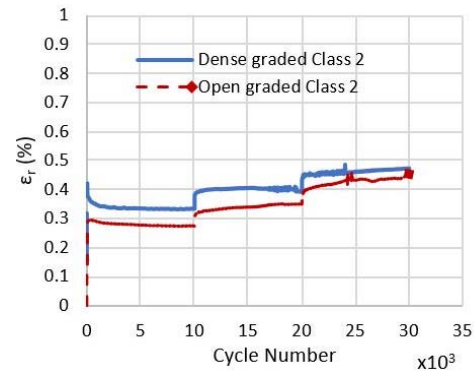


Fig. 6 Resilient deformation

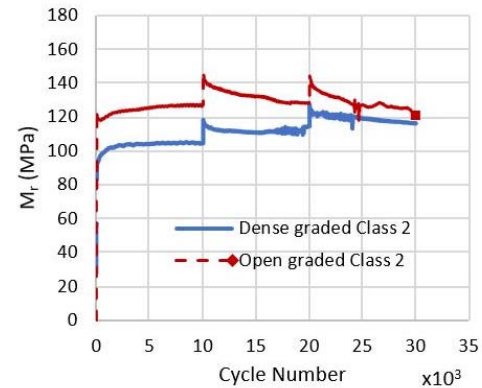


Fig. 7 Resilient modulus

3. CONCLUSION

Results from *RLTT* show that open graded Class 2 has an acceptable *PD* resistance under repeated loads for test's Stages 1, 2 and 3 followed by a significant collapse at Stage 4 as per Australian pavement design guide. Moreover, open graded Class 2 has higher M_r than dense graded Class 2 for all stages. This paper suggests that open graded Class 2 could be used as a porous base material for road pavements with low traffic volumes. Surprisingly, open graded Class 2 has high *PD* in coincidence with high M_r . Therefore, it is recommended to examine both M_r and *PD* for an accurate assessment.

4. ACKNOWLEDGEMENTS

Research material (crushed Class 2) was donated by Mountain View Quarries in Point Wilson, Victoria.

5. REFERENCES

- [1] Huang, Y.H., Pavement Analysis and Design. Pearson Prentice Hall, Pearson Education, Inc., 2004.
- [2] USGS, Mineral Yearbook. 2000, United State Geological Service
- [3] Bowles, O., The stone industries. 1939: McGraw-Hill Book Company.
- [4] Guimaraes, M., et al., Aggregate production: fines generation during rock crushing. International journal of mineral processing, 2007. 81(4): p. 237-247.
- [5] Chazallon, C., et al., Finite elements modelling of the long-term behaviour of a full-scale flexible pavement with the shakedown theory. International journal for numerical and analytical methods in geomechanics, 2009. 33(1): p. 45.
- [6] Uzan, J., Granular Material Characterization for Mechanistic Pavement Design. Journal of Transportation Engineering, 1999. 125(2): p. 108-113.
- [7] Thompson, M. and K. Smith, Repeated triaxial characterization of granular bases. Transportation Research Record, 1990(1278).
- [8] Seyhan, U. and E. Tutumluer, Advanced Characterization of Granular Materials for Mechanistic Based Pavement Design, in Pavement Subgrade, Unbound Materials, and Nondestructive Testing. 2000, American Society of Civil Engineers. p. 51-72.
- [9] Englund, J., Analyses of Resilient Behavior of Unbound Materials for the Purpose of Predicting Permanent Deformation Behavior. 2011: Chalmers University of Technology.
- [10] Cerni, G., et al., Resilient behaviour of unbound granular materials through repeated load triaxial test: influence of the conditioning stress. Road Materials and Pavement Design, 2015. 16(1): p. 70-88.
- [11] Rahman, M.S., Characterising the Deformation Behaviour of Unbound Granular Materials in Pavement Structures. 2015.
- [12] Azam, A.M., D.A. Cameron, and M.M. Rahman, Permanent Strain of Unsaturated Unbound Granular Materials from Construction and Demolition Waste. Journal of Materials in Civil Engineering, 2015. 27(3).
- [13] Witczak, M. and J. Uzan, The Universal Airport Design System, Report I of IV: Granular Material Characterization. Department of Civil Engineering, University of Maryland, College Park, 1988.
- [14] Araya, A.A., Characterization of unbound granular materials for pavements. 2011: TU Delft, Delft University of Technology.
- [15] Xiao, Y., et al., Gradation effects influencing mechanical properties of aggregate base-granular subbase materials in Minnesota. Transportation Research Record: Journal of the Transportation Research Board, 2012(2267): p. 14-26.
- [16] Zaika, Y. and L. Djakfar, GRADATION BAND OF SOME TYPES MATERIAL FOR RESERVOIR BASE OF POROUS PAVEMENT. International Journal, 2016. 11(25): p. 2486-2492.
- [17] Rahman, M.S. and S. Erlingsson, Influence of moisture on Resilient Deformation behaviour of Unbound Granular Materials. Asphalt Pavements, Vols 1 and 2, 2014: p. 571-580.
- [18] Muench, S.T., et al., Best practices for long-lasting low-volume pavements. Journal of Infrastructure Systems, 2007. 13(4): p. 311-320.
- [19] Lekarp, F., U. Isacsson, and A. Dawson, State of the Art.II: Permanent Strain Response of Unbound Aggregates. Journal of Transportation Engineering, 2000. 126(1): p. 76-83.
- [20] Hicks, R.G. and C.L. Monismith, Factors influencing the resilient response of granular materials. Highway research record, 1971(345).
- [21] Raad, L., G.H. Minassian, and S. Gartin, Characterization of saturated granular bases under repeated loads. 1992.
- [22] Richardson, D.N. and S.M. Lusher, Resilient moduli of granular base materials using a modified Type 5 gradation. 2009.
- [23] Heydinger, A., et al., Analysis of resilient modulus of dense-and open-graded aggregates. Transportation Research Record: Journal of the Transportation Research Board, 1996(1547): p. 1-6.
- [24] Barksdale, R.D. Laboratory evaluation of rutting in base course materials. in Presented at the Third International Conference on the Structural Design of Asphalt Pavements, Grosvenor House, Park Lane, London, England, Sept. 11-15, 1972. 1972.
- [25] Kamal, M., et al., Field and Laboratory Evaluation of the Mechanical Behavior of Unbound Granular Materials in Pavements. Transportation Research Record, 1993(1406).
- [26] Austroads, Austroads repeated load triaxial test method: Determination of

- permanent deformation and resilient modulus characteristics of unbound granular materials under drained conditions, AG-PT/T053. 2007, Austroads Publication
- [27] CEN, E.C.f.S., Unbound and hydraulically bound mixtures - Part 7: Cyclic load triaxial test for unbound mixtures. 2004: Brussels.

STRUCTURAL NUMERICAL ANALYSIS ON AN OPEN-WING-TYPE GROUND ANCHOR

Kota Kono¹, Akihisa Nakahashi², Dong Daicho³, Nobuo Fukushima⁴ and Ryoichi Fukagawa⁵
^{1,2,3} Graduate School of Science and Engineering, Ritsumeikan University, Japan; ⁴ Nakakura Inc., Japan; ⁵ Ritsumeikan University, Japan

ABSTRACT

The anchor method involves connecting a structure or a slope with the anchorage zone by using the frictional force between the grouting material and the surrounding ground to stabilize the structure or slope. However, over a long period of time said friction from traditional anchoring methods has been known to decrease, resulting in decreased anchor pullout resistance and ultimately, in anchor pull out. An open-wing type (OW) anchor method developed by our research group is a new type of earth anchor method, in which we use open wings for pullout resistance. Hence, this method can solve problems associated with existing methods. This study suggests an optimum structure for the parts that open in the OW anchor using a numerical analysis, ANSYS (FEM). Three types of 3D analytical models – rotation axis type, bended steel sheet type, and impaction type – are used. The analysis results show the optimum structure to be the impaction type structure, and simulations show that with a base metal yield strength safety factor of 1.5, an OW anchor could generate approximately 4250 N of extreme pullout resistance.

Keywords: Landslide Prevention Work, Anchor Method, OW Anchor, Numerical Analysis, Ansys

INTRODUCTION

The anchor method employs means for connecting a land retaining structure or a slope with the anchorage zone by using the frictional force between the anchor grouting material and surrounding ground. Examples of the many types of anchor methods include the ground anchor method, earth anchor method, and ground reinforcing method. These are applied at many construction sites for maintaining slope stability, preventing overturning of retaining structures, in earth-retaining walls, etc.

The anchor's pullout resistance relies on the functionality of the anchor's main component, grouting material, which is made of mortar. The grouting material works as an adhesive connecting and affixing the anchor via friction to its surrounding ground in the anchorage zone. This friction has been known to decrease over a long time period, ultimately causing the anchor's functionality to be lost as it is pulled out from its anchorage zone. The open-wing type (OW) anchor method is a new type of earth anchor method [1]. In this method, we use open wings for pullout resistance. Hence, this method can solve the problems that are associated with the existing methods.

This study presents an ANSYS (FEM) numerical analysis to suggest an optimum structure for the opening parts of an OW anchor. Then, using the results of preceding studies, values of the cohesion and, the internal friction angle. And this study determines a range of root depths for which the OW

anchor would be well suited to withstand significant pullout resistance and enable practical anchoring.

VERIFICATION OF THE OPTIMUM STRUCTURE BY NUMERICAL ANALYSIS

Method of Numerical Analysis

The pullout resistance of the OW anchor results from wings opened perpendicular to the direction of pull and frictional force between the shaft and surrounding ground. In analysis tool, pullout resistance is expressed load to wings.

In this study, an analysis tool is used to model and compare the pullout resistance of three anchor wing configurations. When the wing or opening parts stresses exceed a criterion, the corresponding load is defined as the extreme pullout resistance for each of the three configurations and the greatest value determines the optimum OW anchor structure.

Points of Attention for Developing Analysis Model

Section size of analysis model

Ground anchors are used in the casing pipe of a borehole, which is placed underground. Hence, the OW anchor must fit into the borehole when the anchor wings are not open. For example, consider "shield casing 85" manufactured by TOHO Underground Inc. as a reference [2]. Its outer diameter is 85 mm and the inner diameter is 69 mm.

Therefore, the outer size of the model must not be more than 69 mm.

Cost of manufacturing

In the ground anchor method, many anchors of ordinary quality are used. Hence, a cheap material is suitable for fabricating an OW anchor. Therefore, it is preferable that the OW anchor structure is simple and expensive materials are not used.

Criterion for Judgment of Practical Application of Model

The pullout safety factor is widely used to determine whether the anchor can be used practically. Table 1 lists the pullout safety factors of different ground anchors.

The OW anchor safety factor is related to wing breakage during pullout, which is a primary consideration when considering the practicality of an OW anchor for use. When planning for long time usage of an OW using pullout safety factor, its safety factor should be at least 2.5. But in this study, we use breakage safety factor. Hence, we consider OW anchors with a safety factor of 1.5.

3D Analytical Model

Three types of 3D analytical models are used in this study. They are the rotation axis type, bended steel sheet type, and impaction type models.

All 3D model have four wings and the angle between shaft and open wing is 60° .

The rotation axis type model

Figure 1 shows the rotation axis type model. In this model, wings are attached to shaft by rotation axis (see Fig. 1 (b) and (c)). In this system, the wings open as a result of rotation.

The bended steel sheet type model

Figure 2 shows the bended steel sheet type model. In this model, wings are attached to shaft by steel sheet. In this system, the wings open owing to bending of the steel sheet.

The impaction type model

Figure 3 shows the impaction type model. This model has wings with a round base (see Fig. 3 (b)) and base part that contains a round hole (see Fig. 3 (c)). This type is used to insert wings in a base part and the wings open as a result of the rotation of wings.

Table 1 Safety factor from pull out of ground anchor [3].

Type of anchor		Safety factor
Short span anchor (less than 2 years)		1.5
Long span anchor (more than 2 years)	Normal time	2.5
	During an earthquake	1.5–2.0

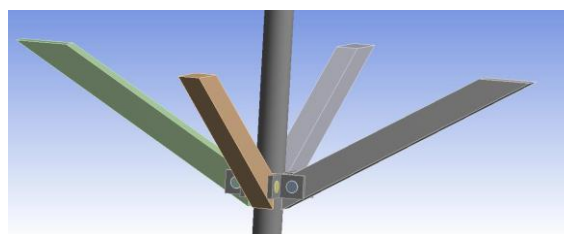


Fig. 1 (a) Rotation axis type model.

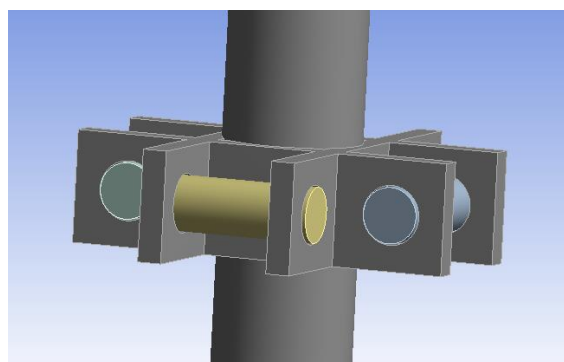


Fig. 1 (b) Rotation axis type model.

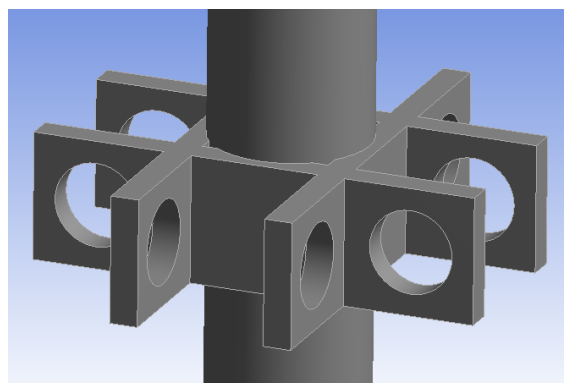


Fig. 1 (c) Rotation axis type model.

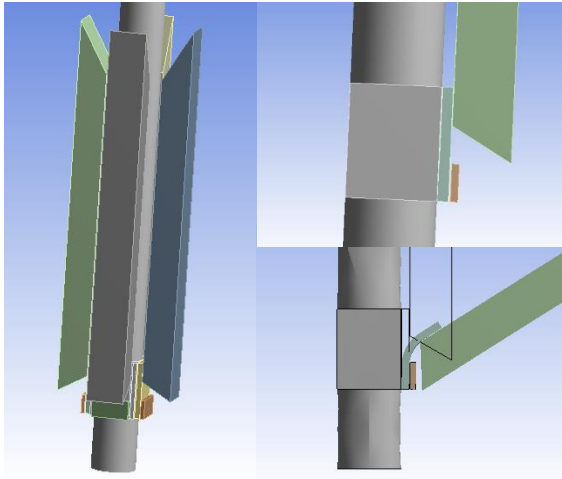


Fig. 2 Bended steel sheet type model.

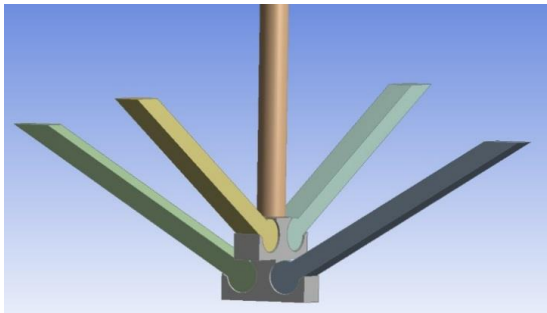


Fig. 3 (a) Impaction type model.

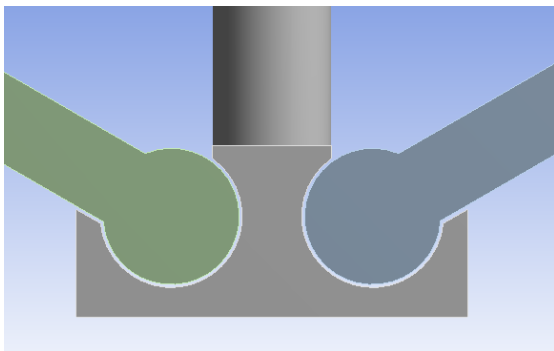


Fig. 3 (b) Impaction type model.

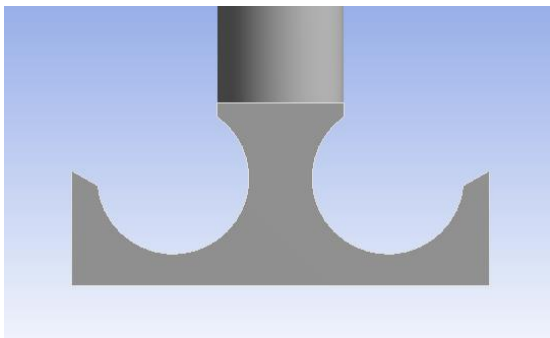


Fig. 3 (c) Impaction type model.

Analysis Results

The rotation axis type

Figure 4 shows the relationship between the safety factor and the extreme pullout resistance. The optimum structure of the rotation axis type model can generate approximately 3350 N of extreme pullout resistance when it is designed with a safety factor of 1.5. Figure 5 shows a colored distribution of safety factor. Red shows the areas with the lowest safety factor; hence, continuously increasing the load would result in the red parts breaking first.

The bended steel sheet type

It can be concluded that the bended steel sheet type model is not suitable for practical use, because some parts have safety factors less than 1 before the wings fully open. Figure 6 (a) and (b) show the distribution of the safety factor. The factor is low when the color is closer to red.

The impaction type

Figure 7 shows the relationship between the safety factor and the extreme pullout resistance. The optimum structure of the impaction type model can generate approximately 4250 N of extreme pullout resistance when it is designed with a safety factor of 1.5. Figure 8 shows the distribution of the safety factor. The safety factor is low when the color is closer to red. When the load is increased, parts of circle in red break first, owing to the low safety factor.

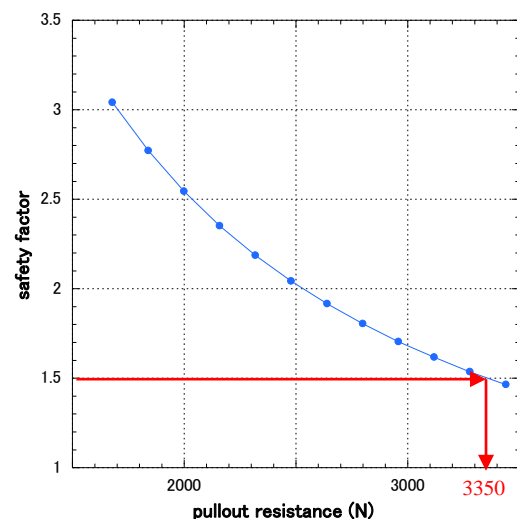


Fig. 4 Relationship between safety factor and extreme pullout resistance of the rotation axis type.

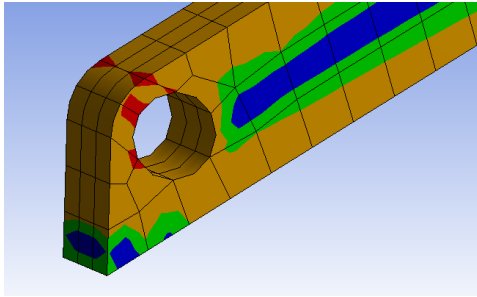


Fig. 5 Distribution of safety factor.

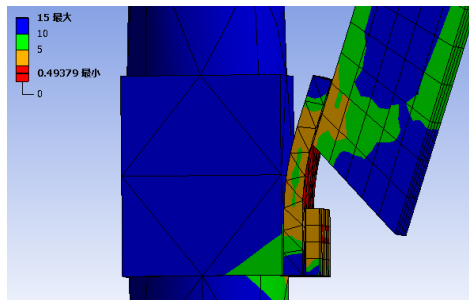


Fig. 6 (a) Distribution of safety factor.

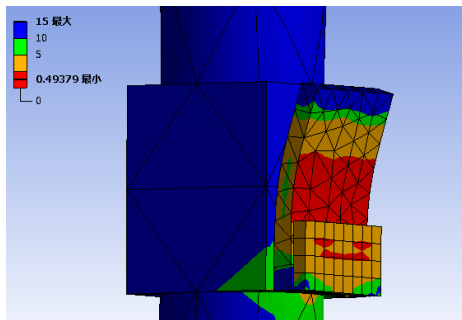


Fig. 6 (b) Distribution of safety factor.

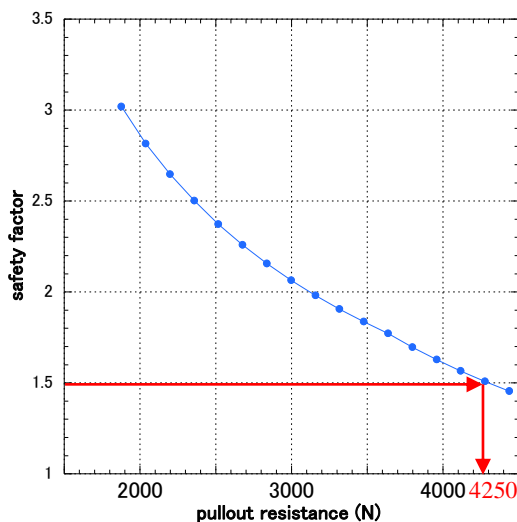


Fig. 7 Relationship between safety factor and extreme pullout resistance of the impaction type.

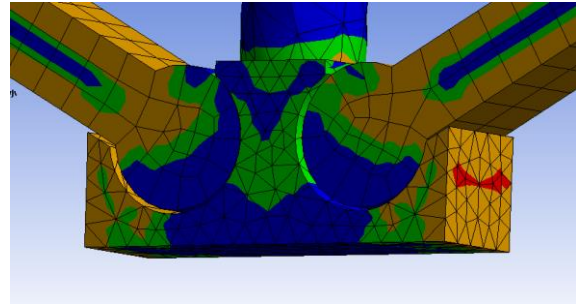


Fig. 8 Distribution of safety factor.

STUDY ON MAXIMUM ROOT DEPTH OF THE OPTIMUM STRUCTURE

Estimation of Maximum Root Depth when using Optimum Structure

The optimum OW anchor structure was the impaction type, owing to the greatest value of extreme pullout resistance. To calculate the maximum root depth that can be withstood by said pullout resistance, we use the results of preceding studies, values of cohesion, and internal friction angle. For estimation and comparison, a formula for the computation of pullout resistance exerted by a disk is used. Then, a series of experiments was conducted to investigate the relationship between the actual pullout resistance exerted by an OW anchor and the actual pullout resistance exerted by disk.

Formula for Computation of Pullout Resistance Exerted by Disk-shaped Earth Anchor

Katsumi and Nishihara (1978) suggested a formula for computing the extreme pullout resistance exerted by a disk as a model of an earth anchor [4]. The formula is based on the formula for computation suggested by Balla [5], Matsuo [6] - [8], Mors [9] and can be expressed as Eq. (1),

$$Q = G_1 + T_v + G_2 \quad (1)$$

Where G_1 is the weight of the soil mass, G_2 is the self-weight of the anchor, and T_v is the summation of the perpendicular component of the shear resistance force that is exerted on a slide plane and the perpendicular component of the force that is perpendicularly exerted on a slide plane.

Experimental Estimation of Pullout Resistance of OW Anchor

We experimentally investigated the relationship between the pullout resistance exerted by the OW anchor and a disk. Figure 9 shows the experiment.

There are four experiment models. The first is the open-wing ground anchor with four wings opened at

45°. The second is the same anchor with the wings opened at 60°. The third is at 90°. The fourth is the disk. The projected lengths of each wing on the horizontal plane are all the same as the radius of the disk. Figure 10 shows the pullout resistance exerted by the OW anchor and the disk. Experimental results show that an OW anchor with four wings opened at 60° exerts 58% of the pullout resistance exerted by the disk.

Calculation of Root Depth

Figure 11 shows the flow chart of the method of calculation of the root depth when using the impaction type OW anchor. The results are shown in Table 2. The root depth of the optimum structure varies between 79 cm and 156 cm when the cohesion value varies between 0–10 and the internal friction angle varies between 15° and 45°.



Fig. 9 Image of the experiment.

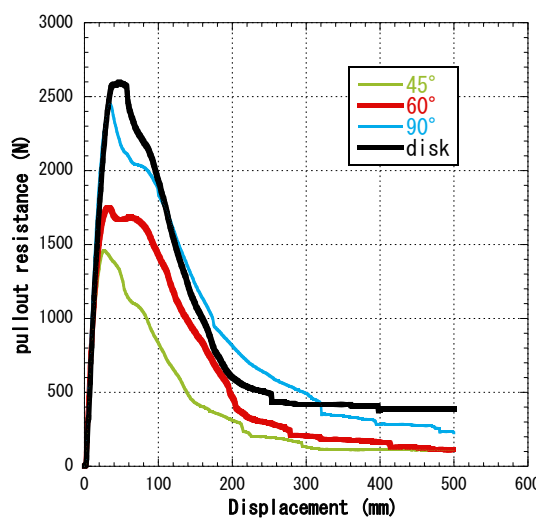


Fig. 10 Pullout resistance exerted by OW anchor and disk.

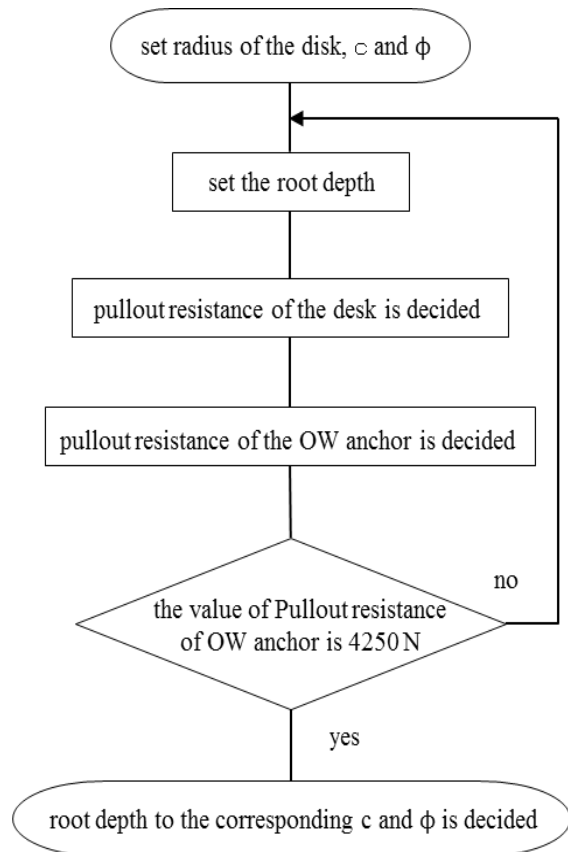


Fig. 11 Method of calculation of root depth.

Table 2 Root depth when using impaction type OW anchor.

c (kN/m ²)	φ (°)	D (cm)
0	15	156
	30	102
	45	83
5	15	146
	30	99
	45	81
10	15	138
	30	95
	45	79

CONCLUSION

Summary

The optimum structure is the impaction type structure, and it can generate approximately 4350 N of extreme pullout resistance. The root depth of the optimum structure varies between 79 cm and 156 cm when the cohesion value varies between 0 kN/m²-10 kN/m² and the internal friction angle varies between 15°-45°.

Future works

It is conceivable that for some use cases, especially in applications with shallow root depths, an OW anchor type, as described and proposed in this study, could be used as a substitute for the existing ground reinforcing type anchors. However, as the root depths increase and approach 2 m, the OW anchor type would not provide the holding abilities of existing ground reinforcing type anchors. For greater root depth applications, it would be essential to improve the proposed OW anchor model or propose a new model that would be capable of exerting more extreme pullout resistance.

REFERENCES

- [1] Danjo T., Teramoto T., Miyajima Y., Fukushima N., Fujimoto M., Fukagawa R., "A series of model experiments for development of Unfolding ground anchor", Proceedings of the 7th Symposium on Sediment-Related Disasters, 2014, Sept, pp. 241-246.
- [2] TOHO underground Inc.
<http://www.tohochikakoki.co.jp/cgi-bin/pdf2.cgi?p=casing.pdf>, 2017/1/16.
- [3] Japan Society of ground Engineers (2012), architectonics, designed and basis on construction of ground anchor, p.64.
- [4] Katsumi T., Nishihara A., "Fundamental studies on pullout resistance of earth anchors", J. Jpn. Soc. Civil Eng., No. 276, 1978, pp. 65-76.
- [5] Balla A., "The resistance to breaking out of mushroom foundation for pylons", Proc. 5th ICSMFE, Vol. 1, pp. 569-576. 1961.
- [6] Matuo M., "On the uplift resistance of transmission tower footings", J. Jpn. Soc. Civil Eng., No. 105, 1964, pp. 9-18.
- [7] Matsuo M., Shinjo T., "Study on the uplift resistance of footings buried in cohesive soil", J. Jpn. Soc. Civil Eng., No. 137, 1967, pp. 1-12.
- [8] Matsuo M., Tagawa S., "On an approximate calculation method and a few specific problems for the uplift resistance of footings", J. Jpn. Soc. Civil Eng., No. 149, 1968, pp. 27-35.
- [9] Mors H., "Das Verhalten von Mastgriindungen bei Zugbeanspruchung", Die Bautechnik, Heft 10, pp.367-378, 1959.

H/V SPECTRAL RATIO STUDY FOR ESTIMATION OF LOCAL SITE EFFECTS IN VISHAKHAPATNAM CITY

*Swathi Priyadarsini Putti¹, Dr. Neelima Satyam D.²

¹International Institute of Information technology-Hyderabad, India; ²International Institute of Information technology-Hyderabad, India

ABSTRACT

Dynamic soil properties have their own impact on ground motion intensity and hence regulate the damage. Local site conditions control the frequency content of ground motions due to amplification or de-amplification. Therefore in the present research an attempt has been made to estimate local site effects in Vishakhapatnam city. The port city Vishakhapatnam comes under seismic zone II according to IS 1893:2002 and is one of those rapidly growing cities of Andhra Pradesh, India. It lies in the midst of Bay of Bengal and Eastern Ghats, occupying an area of about 681.96 sq.km and is positioned at 17°41'18"N latitude and 83°13'07"E longitude. To establish the predominant frequency and investigate the dynamic behavior of soils in the study area, micro tremor testing was carried out in 75 locations of the city. Microtremor has been one among the contemporary advances in geophysical testing techniques and is proved to be quite reliable from past studies. The results from the site study has shown presence of soils with frequency greater than 4Hz in most of the parts of the city and few places has shown frequency of less than 1.9Hz where the predominant soils are clayey soils.

Keywords: Micro tremor, Vishakhapatnam, Local site effects, Spectral ratio

INTRODUCTION

Dynamic soil properties play a prominent role in the estimation of deformations and strains due to cyclic loading during an earthquake event. When the frequency of the soil and the structure equals under cyclic loading, resonance occurs which leads to severe damage. Therefore Frequency, time period, amplitude are the influential parameters of a strong ground motion. These parameters of strong ground motion are highly variable depending on the local site conditions. Hence estimation of local site effects forms a reliable base for site characterization studies. Though the study area Vishakhapatnam city falls under Zone-II as per IS 1893:2002 with a zone factor of 0.1, presence of operational port and rapid development of infrastructure makes the city prominent inspiring current research. The micro tremor testing was therefore done to measure the fundamental frequency and amplitudes of the soils all over the city. Site effects due to sand and clay sediments are characteristic of the study area. Higher frequency values (>4Hz.) are observed in many parts of the city due to presence of rock and gravel and few places in eastern and western parts of the city has shown lower frequency values (<4Hz.) indicating presence of silty sand and stiff clay followed by marine clay with frequency values less than 1.9Hz in few places of the study area.

STUDY AREA

The study area Vishakhapatnam is a port city located in southern part of India at 17°41'18"N latitude and 83°13'07"E longitude. Characterized by Eastern Ghats Mobile Belt

(EGMB) Vishakhapatnam is bounded with Kailasa, Narava and Yarada hill ranges on all the other three sides whereas the other side of the city is bounded with Bay of Bengal. Figure-1 shows the political map of the study area.

Major mineral deposits in the city comprises of charnockites, quartzites, pegmites and khondalites, whereas predominant soil types in the area are red clay, gravel clay, sandy soil, clay, gravel loams. Addressing the seismicity of the study area, the area lies in Stable central region of peninsular India. Though major faults were not in the vicinity of Vishakhapatnam city; abundant number of lineaments covers the area. About 85 seismic events (1828-2017) have been identified in about 300km radius of the city with magnitude ranging from 2.0 to 5.5. Contrariwise, the regions which are deficit in past seismic history are assumed to be prone to seismic risk due to excessive buildup of strain energy. Therefore, the seismic hazard of the city is proposed to be estimated in present research. The quantification of seismic hazard can be done by the parameters such as frequency and amplitude. Therefore it is proposed to carryout micro tremor survey to estimate predominant frequency and amplitude.

MICROTREMOR METHOD

Artificial ground vibrations with low amplitude range are called as micro tremors. Microseisms can be differentiated from micro tremors based on their origin and frequency range. Micro tremors are the ground vibrations with frequencies >1Hz because of man-made activities such as movement of vehicles,

impact loading etc. Heavy wind forces and other

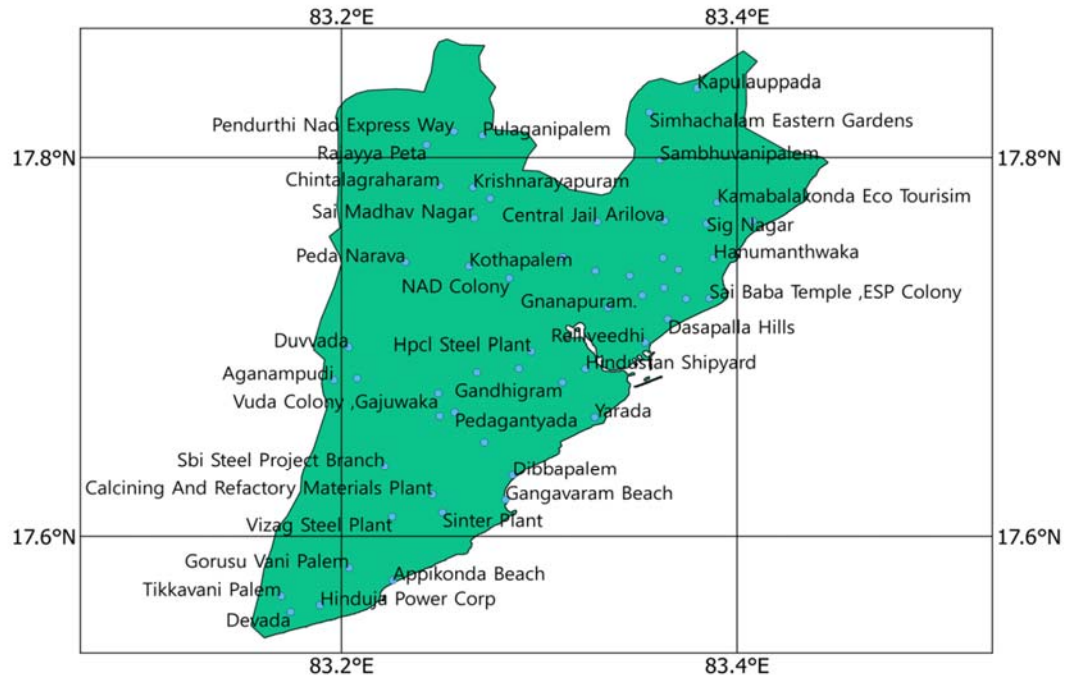


Fig.1 Political boundaries of the study area and marked test locations

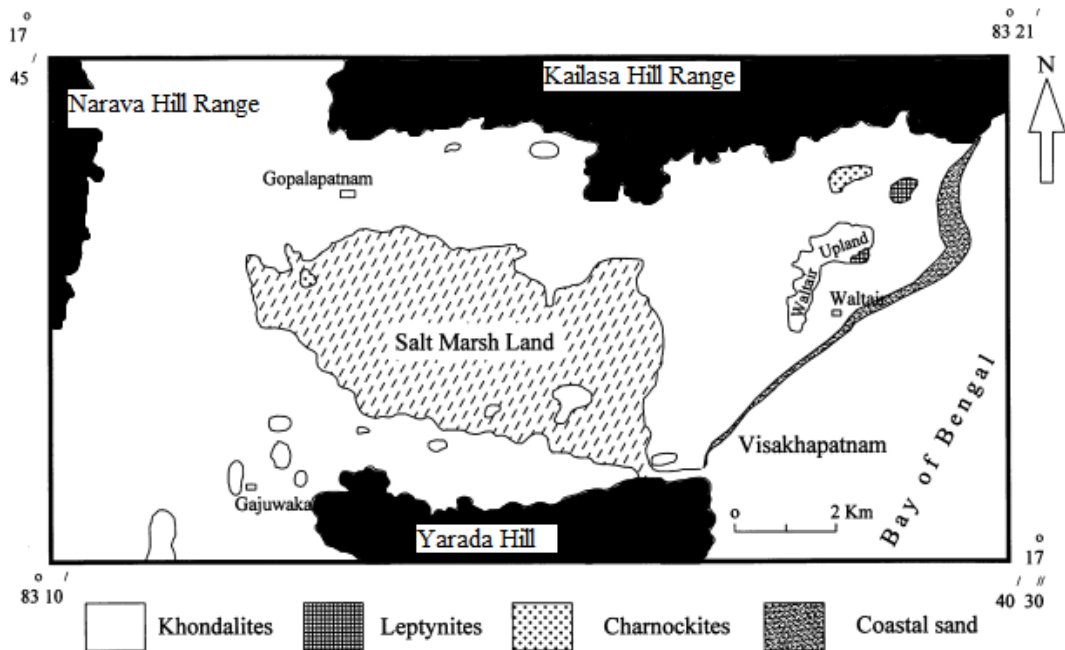


Fig.2 Geological map of the study area (Modified from Subba Rao, 2008) [16]

Oceanic activities causes vibrations with frequencies $<1\text{Hz}$. which are termed as microseisms. Micro tremors are pivotal in dynamic characterization of soil.

The micro tremor peak which denotes the frequency of first mode of vibration can be obtained either from Raleigh wave ellipticity (Bonnefoy - Claudet, Cornou, et. al., 2006)[3] or S-wave resonance (Nakamura, 1989, 2000)[11] or Airy phase of love waves (Bonnefoy-Claudet et al., 2008)[2]. Rayleigh dominate the records in the case of high impedance (I) contrast or frequency range (6-20Hz) and love waves when $I < 3$ or in the case of low frequency (3.6-6Hz) (S.Bonnefoy-Claudet et al., 2008; Chavez-Garcia & Luzon, 2005)[2][6]. Basin geometry can have effects on resonance frequency from HVSr technique (Gueguen et al., 2007) particularly in narrow sediment basins.

Micro tremor method can be best described as an analog of electrically passive magneto-telluric exploration (Asten, 2004)[1]. Micro tremor methods can be array based (ReMi) or single station. Array based methods require more than one sensor and can be used to correlate shear wave velocity using Spatial Auto Correlation (SPAC) or Frequency Wave number (FK) methods resulting in identification of sediments thickness. Single station method is much simple and can be used to estimate dominant earth period, amplitude and vulnerability of an area.

Estimation of dynamic characteristics of soil using micro tremor has been very habitual in the 1980s. But Standard spectral ratio method which was used in earlier practices requires a reference site very near to the site of interest which is not viable in all geological and environmental conditions. The horizontal to vertical spectral ratio (HVSr) method has been introduced by Nakamura (1989)[12] gained prominence in practice. H/V spectral ratio method does not require any reference site for recordings. Identification of a reference site at every survey location will be a herculean task when the testing is to be performed in densely populated cities. The reliability of H/V method has been scrutinized by many researchers by matching the results with the analysis from strong motion records (Ch'avez-Garc'ia & Cuenca, 1996; Teves-Costa et a., 1996; Bour et al., 1998; Jensen, 2000; Ch'avez- Garc'ia & Tejeda-J'acome, 2010; Surve & Mohan, 2010)[4][5][18]. Since 1989, the method has been applied to study dynamic properties and for micro zonation of several cities Dinar-Turkey (Ansal, 2001); Southeastern Iran (Motamed et al., 2007); lower Manhattan-New York (Stephenson et al., 2009); Marmara region- Western turkey (Hasancebi & Ulusay, 2006) ; Hong kong (Pappin et al., 2012)[13]; Izmir- Turkey (Eskisar et al., 2013);

October 6th city- Egypt (Mohamed et al., 2013).

Apart from these applications micro tremor has been used to map collapsed columns in coal mines (Pei-Fen et al., 2009)[15] and for estimation of seismic motion along expressways (Maruyama et al., 2000). Surve & Mohan, (2010)[18] conducted micro tremor testing in Mumbai to demarcate the reclaimed area and actual basaltic islands from the resonant frequencies. Vulnerability index (K_g) from micro tremor can be obtained by dividing the square of amplitude with peak frequency. The index can be used to identify liquefiable sites. Supporting evidence has been provided from case histories (Hardesty et al., 2010; Huang & Tseng, 2002; Saita, Nakamura, & Sato, 2012)[16].

The steps involved in micro tremor survey are data acquisition, data processing and analysis. Important information regarding the site and source of noise can be observed from the type and form of the H/V peaks. Clear peaks in the frequency plots infer distinct impedance between upper soft layer and the bedrock. Lower peaks at higher periods are usually imperative of hard rock. Clear peaks at higher frequencies indicate that the sediment is indicative of weathered soil overlying rock. H/V curves exhibit single peak when the sources are near (4 to 50 times the layer thickness) and surficial. Two peaks show up in case of distant source (more than 50 times the layer thickness) and located inside the sedimentary layer (Bonnefoy-Claudet, S. et al., 2006)[2]. Pappin et al., (2012)[14] from their study in Hong Kong area inferred that the measured frequency values match the calculated values when the soil profile is considered up to a values where $\text{SPT } N > 100$. The limitation of using single station micro tremor is that it is not reliable when the local geology is complex and site effects are not due to single-impedance contrast (Chavez-Garcia et al., 2007)[7].

FIELD TESTING AND DATA ACQUISITION

Though the present study area has experienced no significant earthquakes in the past, from previous earthquake case histories (1997 Jabalpur and 1993 Latur) no region of India is considered to be safe against earthquakes. In case of a linear to low range earthquakes, micro tremor along with non-invasive active source technique best demonstrates the ground response (Hardesty et al., 2010; Molnar et al., 2007). Hence this method can be applied to locations such as Vishakhapatnam with no significant earthquake records.

Micro tremor survey has been conducted in 75 locations well distributed all over the city. Open grounds away from structures, obstructions, wind and underground structures were chosen to carry out the test without any disturbances. During day light the ambient noise will be high that deviates the results of frequency and amplitude. Hence

recordings have been taken at early morning and late evenings to assure reliability. The recorder records microseisms instead of micro tremors if the ambient noise is not avoided. The recording setup consists of a tri axial velocity sensor (MS 2003+), recorder (MR 2002-CE) and a field laptop. Figure-3 shows the setup of the instrument at testing location MVP colony.

The sensor is leveled and noise has been recorded for duration of 60 min with 1 sec pre-event and post-event time. To record the latitude and longitude of recording site global positioning system (GPS) has been used. Three-component recordings for H/V spectral ratio analysis were made at each location stretching from Devada to Kapulauppada. The frequency at maximum H/V ratio is indicative of (among other parameters) presence of soft sediment overlying stiffer materials.



Fig.3 Instrument set up at testing location (MVP Colony)

Summation of two horizontal components in each sample was done to produce the Fourier spectrum of horizontal ground motion for each location. Fourier spectrum for the vertical component was also calculated. The ratio of horizontal to vertical spectral amplitude was calculated to produce H/V spectrum for each location. For the clear identification of peak the curves have been smoothened up to 10%. Each spectrum was used to get the predominant frequency of that location.

RESULTS AND CONCLUSIONS

From Micro tremor test results analysis using Nakamura Horizontal to vertical spectral ratio method, the peak frequency and amplitude has been estimated at all the locations in the study area. Figure5 shows the study area along with marked testing locations. The frequency values are ranging from 0.44-10.1Hz. The H/V plots of the locations

with frequency value greater than 4Hz. has shown a clear distinctive peak indicating high impedance contrast between the bed rock and the soil sediment whereas plots for the locations with frequency range of 2.0-4.0Hz. has two peaks. This indicates that the source of noise has been distant i.e, about 50 times the layer thickness. It was observed that the areas with gravely sand and soft disintegrated rock have shown higher frequency values of greater than 4.0Hz. Whereas locations with soft clay deposits and marine clay deposits near to the coast line has shown lower frequency values of less than 2.0Hz.

Based on the frequency values and response spectrum detailed characterization was carried out. the proposed site classification based on H/V spectral ratio analysis is shown in table-1

Table-1 site classes based on the results

S.No.	Proposed class	Fundamental frequency
1.	Type-1	> 4.0Hz.
2.	Type-2	2.0-4.0Hz.
3.	Type-3	< 2.0Hz.

From the results it was observed that most of the locations where the predominant soils are gravelly soil with pebbles, weathered rock and rock in few places with a thin layer of soil cover has shown higher frequency values as high as 10Hz resulting in lower amplification values. These locations with are classified as Type-1. Few places in southern part of the city and western part of the city with mostly silty sand and clayey sand has shown frequency values of range 2.0-4.0Hz and classified as Type-2. Other locations in eastern part of the city and few locations in the central part has shown frequency values < 2.0Hz indicating presence of soft clay and marine clay. These locations have shown higher amplitude values indicating increased seismic risk in terms of ground motion amplification. Figure 4 shows typical response spectrum for few locations of the study area.

The amplitude values range from 1.11 to 2.46. Amplitude values are dependent on the noise produced and its amplitude. During day time amplitude may be recorded high and during nights it might be low. High amplitude of vibration are distinctive of south western locations (>2) and moderate amplitude values (<1.5) has been recorded all over the city. Iso-frequency maps have been prepared from the frequency values of the study area and can be used in further geotechnical engineering practice.

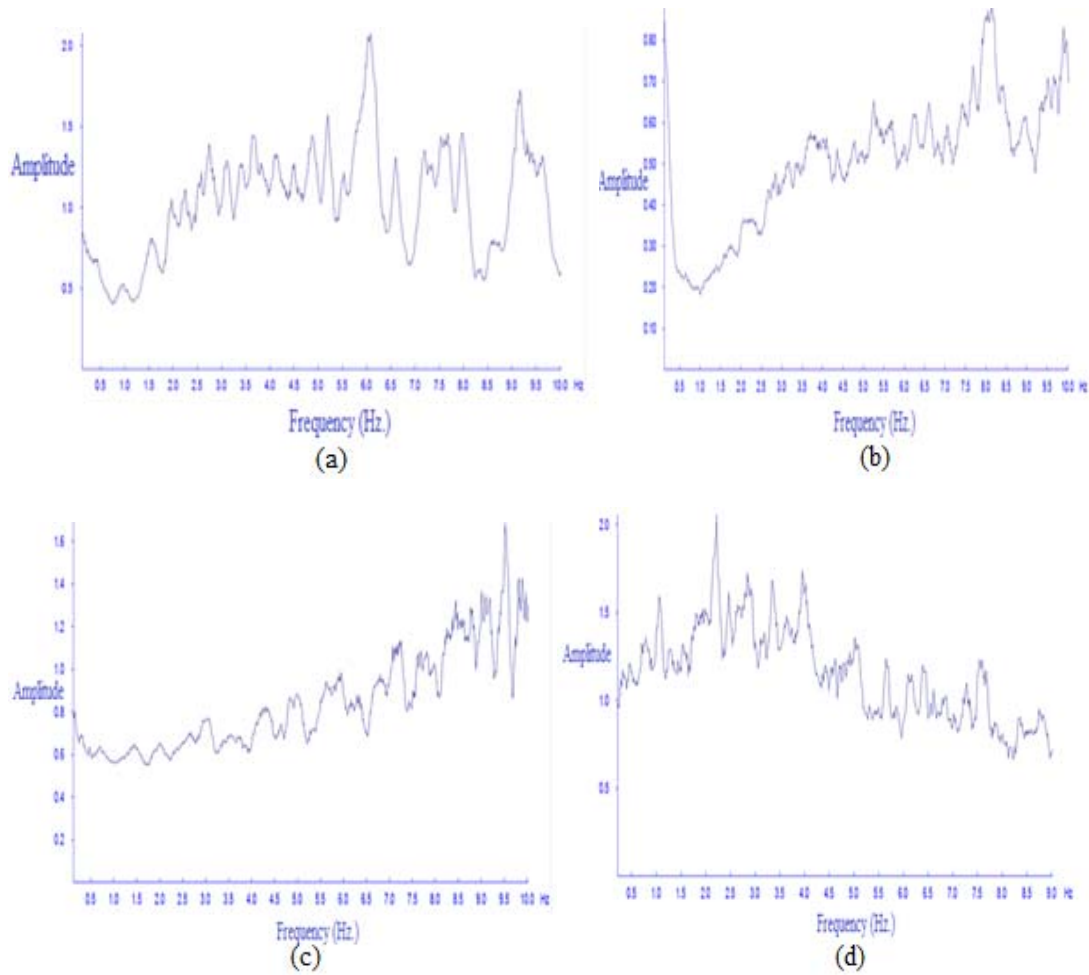


Fig.4 Response spectra for test locations (a) Pendurthi, (b) Pedawaltair, (c) Dasapalla hills, (d) Chinnamushidiwada

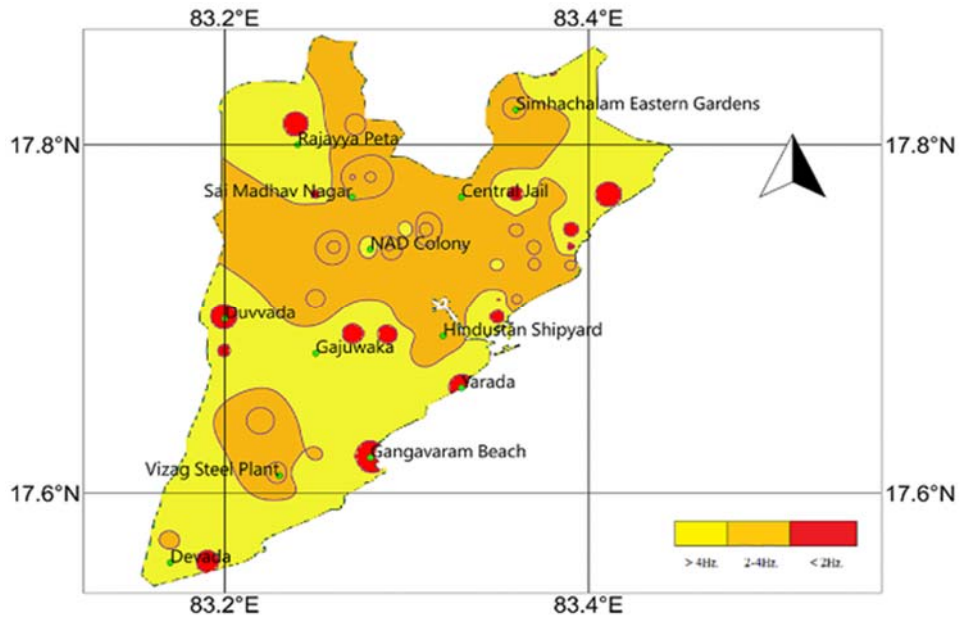


Fig.5 Predominant frequency map of Vishakhapatnam city

Figure 5 shows the frequency map along with site characterization. Vulnerability index has been calculated from the frequency and amplitude values of each location and hazard map was created using the vulnerability index.

REFERENCES

- [1] Asten, M. W. (2004). Passive seismic methods using the microtremor wave field for engineering and earthquake site zonation. SEG 74th Annual Meeting. Denver.
- [2] Bonnefoy- Claudet, S.Kohler, a., cornou, C., Wathelet, M.,&Bard, P-Y.(2008). Effects of Love waves on Microtremor H/V ratio. Bulletin of the seismological society of America, 98(1), 288-300.
- [3] BonnefoyClaudet,Sylvette,Cornou,C.,Bard, P-Y.,Cotton, F., Moczo, p.,kristek,j.,&Fah, D.(2006). H/V ratio. A tool for site effects evaluation. Results from 1-D noise simulations. Geographical Journal international, 167(2), 827-837.
- [4] Bour, M.,Fouissac, d., Dominique,P.,& Martin, C. (1998), On the use of microtremor recordings in seismic microzonation ;J. Soil Dyn.Earthq. Eng. 17,465-474
- [5] Chavez-garcia,F.J., &Tejeda-J.(2010).Site response in Tecoman, Colima, Mexico –II Determination of subsoil structur and composition with observations; j,Soil,Dyn . Earthq. Engg, 30 (8), 717-723.
- [6] Chavez- Garcia F.G.&Luzon , F.(2005) On the correlation of seismic microtremors, Journal of geophysical research 110B11).
- [7] Chavez-Garcea F.J Dominguez, T.Rodriguez, M&Perez F (2007).Site effects in a volcanic environment A comparison between HVSR and array techniques at olima, Mexico. Bulletin of the seismological society of the America.97(2),591-604
- [8] Diagourtas,D, Tzanis,A and Makropolous,K (2002) .Comparative study of microtremor analysis methods. Proc of Earthquake micronizing, 2463-2479
- [9] Gao Y Jiang,Y Li,B &Yamauchi,Y (2012).Study on microtremor spectrum properties on tunnel lining. In 2012 International Conference on Renewable. Energy Research and Applications (ICRERA), IEEE, 1-6
- [10] Maruyama,Y.Yamazaki,F&Hamada,T(2000). Microtremor Measurements for the estimation of seismic motion along expressways. In 6th international conference of seismic zonation ,Palm Springs,California,1361-1366
- [11] Nakamura,Y(1989).A method for dynamic characteristics estimation of subsurface using microtremor on the ground surface. Tokyo, Railway Technical Research Institute/Tetsudo Gijutsu Kenkyujo.
- [12] Neelima Satyam, D. (2006). Seismic Micro zonation of Delhi region. Doctoral Thesis, Indian Institute of Technology Delhi. Delhi. India.
- [13] Neelima Satyam.D and Ikuo Towhata, Site Specific Ground Response Analysis and Liquefaction Assessment of Vijayawada City (India) Natural hazards March 2016, Volume 81, Issue 2, pp 705–724
- [14] Pappin,J, Jirouskova, N,So,M, Jiang,H,Yu, Y.B&Ho, K.K.S(2012), Seismic Microzonation Assessment in Hong-Kong. 15th world conference retrieved from http://www.iitk.ac.in/nicee/wcee/article/WCEE2012_1951.pdf
- [15] Pei-Fen, X., Chuan-Jin, L.Ying-Bing,Z., Yin-Bing , Z., Zhao H.,, & Yong –Jun. S (2009). Mapping collapsed columns in coal mines utilizing microtremor survey methods. Chinese J. geophysics, 52 (7), 1923-1930.
- [16] Saita, J., nakamura, Y., & Sato, T. (2012). Liquefaction caused by the 2011. Off the pacific Coast of Tohoku Earthquake and the result of the prior microtremor measurement. In conference on urban earthquake engineering. Receivedfrom http://www.sdr.co.jp/papers/15wcee_lique.pdf
- [17] Subba Rao,N.(2008). Iron content in ground waters of Visakhapatnam environs, Andhra Pradesh, India. Environmental monitoring and assessment, 136(1-3), 437-47.
- [18] Surve, G., & Mohan, G. (2010). Site response studies in Mumbai using (H/V) Nakamura technique. Natural Hazards, 54(3), 783-795.

STUDY OF GROUND PENETRATING RADAR(GPR) EXPLORATION FOR CAVITY UNDER THE GROUND USING FIELD TEST EXECUTION OF SEWER

Daeyoung Lee¹, Dongmin Kim²

¹Korea Inst. of Civil Eng. & Building Tech., Goyang, Republic of Korea

²Korea Inst. of Civil Eng. & Building Tech., Goyang, Republic of Korea

ABSTRACT

This study, as part of the way to prevent ground settlement by deteriorated sewer, was intended to identify the cause of cavity and soil relaxation and evaluate the cavity exploration technique using GPR (Ground Penetrating Radar) exploration method. To simulate the cavity and ground relaxation caused by sewer leak, field test was conducted. 450mm in diameter and 2,500mm long concrete pipe was used install the sewer for the test and to evaluate the exploration performance by depth, sewer was buried at 1.0m and 1.5m depth. After putting the ice seized 1m×1.0m×0.3m on top and at the bottom of the sewer, hose was connected to promote the thawing. To measure the cavity caused by ice thawing, GPR exploration was carried out in a day, 5 days and 15 days.

In the result of test, Cavity and ground relaxation caused by sewer leakage were simulated using GPR exploration and the cavity and ground relaxation by sewer leakage were monitored. According to GPR analysis, ice thawing caused ground relaxation and the cavity. Given the reflective surface under the ground over time, cavity appeared to have developed upward.

Keywords: Sewer, GPR exploration, Ground settlement, Field test

INTRODUCTION

Ground settlement in downtown is attributable to various factors such as the impact by excavation, soft ground settlement, deteriorated sewer and poor compaction. According to Seoul city office, 2,714 of 3,205 or 84% of road sinking occurred since 2010 were attributable to deteriorated sewer and of 10,392km-long sewer, 73.3% was more than 20 years old, indicating the need for urgent maintenance [1]. According to National Land Technical Policy Institute in Japan which investigated the causes of road sinking from 2006 to 2009, the cases caused by the sewer totaled as many as 4,000 annually [2]. Road sinking resulting from deteriorated sewer is mostly by the soil penetrated into the damaged sewer. Amid ever-increasing road sinking in urban area of Korea, more concern on refurbishing deteriorated sewer has been drawn and in a bid to prevent the ground settlement in urban area, prediction and recovery technology which will prevent the ground settlement in advance becomes more than important [3].

Thus to prevent ground settlement in downtown, it's necessary to develop the detection technique that will evaluate the mechanism and predict the ground settlement by leaked sewer. GPR exploration is used to detect the cavity under the ground but when the cavity is deep or boundary between cavity and loosened soil is unidentified or complicate utilities

and cavity and loosened soil are mixed, it's difficult to detect them. This study, as part of the way to prevent ground settlement by deteriorated sewer, is intended to identify the cause of cavity and soil relaxation and evaluate the cavity exploration technique using GPR exploration method. Cavity simulation and GPR exploration were carried out through field experiment and the possibility of detecting cavity and soil relaxation was reviewed.

SEWER TEST INSTALLATION AND GPR EXPLORATION

GPR exploration is one of the geophysical prospecting technologies for commercial use with highest resolution which has been commonly used domestically for investigating underground utilities, cavity and anomaly zone. For detecting the cavity below heavy traffic road, vehicle-mounted device runs at normal traffic speed which is the optimal method when considering the site condition and safety [4]. GPR exploration is to evaluate the internal state in a way of analyzing the wave refracted, reflected and distracted from other material or structural layer by dielectric constant while electromagnetic wave from the transmitter to the ground passes the pavement structure [5].

To simulate the cavity and ground relaxation caused by sewer leak, field test was conducted.

Table 1. Specification of CCTV

Parts	Specification
Monitor	19 in (48.26 cm)
Main devices	Power, Lighting, Brightness, Forward/ backward, Rotation camera, Side-looking camera, Input power: 220V, 60Hz
Camera	Rotation endless, 1.3 million pixels, Waterproof, Size: ϕ 110, L 250 mm, Weight: 1 kg
Lighting	Camera LED: 12 (1 W) Halogen lamps: 2 (12 V, 35 W)
Self-propelled car	Pipe diameter: ϕ 300~1200 mm Wheel: ϕ 80, ϕ 120, ϕ 50 mm Output: 30 V, 60 W 6 wheel drive Height adjustable (remote control) Size: $621 \times 530 \times 55$ mm Weight: 20 kg
Cable	Size: ϕ 12.5 mm, L 150m Weight : 15Kg

450mm in diameter and 2,500mm long concrete hume pipe was used in stall the sewer for the test and to evaluate the exploration performance by depth, sewer was buried at 1.0m and 1.5m depth. After putting the ice seized $1\text{m} \times 1.0\text{m} \times 0.3\text{m}$ on top and at the bottom of the sewer, hose was connected to promote the thawing. Sand and soil were used to bury the sewer and cavity and ground relaxation were simulated by ice thawing. To measure the cavity caused by ice thawing, GPR exploration was carried out in a day, 5 days and 15 days. GPR equipments used for the test is as Table 1. To evaluate the exploration performance depending on frequency, frequency was varied to 100MHz, 300MHz 500MHz and 1,500MHz during exploration.

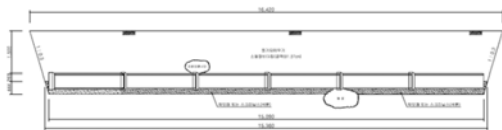


Fig 1. Sewer installed

Table 2. GPR equipment


specification	View
Zond 12e(RADAR Systems, Inc.) Shield Antenna (300MHz, 500MHz) Notebook P/C S/W (Prism2.5) for analysis	



Fig 2. Field test installation process

GPR EXPLORATION OF THE CAVITY UNDER THE GROUND

Ground cavity and relaxation mechanism

Fig 3 shows the result of GPR exploration analysis over time. As a result of sewer cavity exploration with the frequency 300MHz and top soil depth 1.5m, a parabolic reflective surface was distributed above the sewer after installation which was considered made by the ice on top of the sewer. After a day, 5 days and 15 days, a parabolic reflective surface appeared at upper level than immediately after installation, which was attributable to cavity resulting from thawing of ice. According to GPR exploration, the surrounding ground was loosened while the ice is thawing which caused to form the cavity. Reflective surface formed under the ground in 5 days indicated that the cavity was developed upward. Ground surface settlement following the cavity was expected, but no ground settlement occurred thanks to sufficient compaction. And no reflective surface was monitored when the ice was buried below the sewer, which was attributable to the failure of penetration by radar wave into the bottom of the sewer.

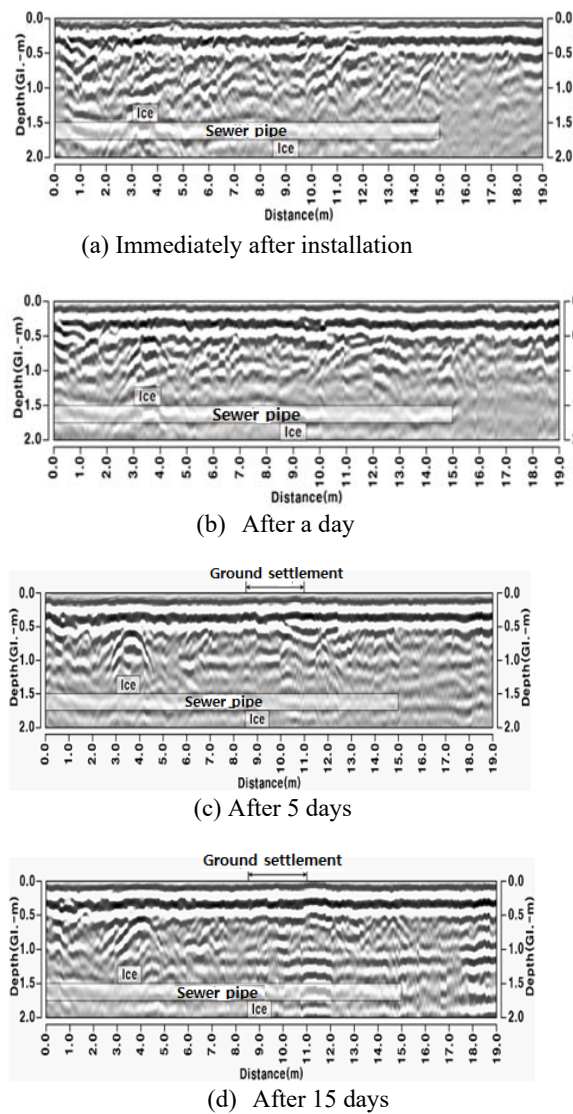


Fig 3. GPR analysis results

GPR exploration performance depending on frequency

Fig 4 shows exploration result varied depending on frequency. No response appeared at 100MHz but a horizontal reflective surface with a little curve along the top of the sewer was extended to sewer length 15.0m. A parabolic reflective surface was distributed above the sewer where the ice was put on which was attributable to the cavity formed when the ice above the sewer was thawing. Reflective surface by cavity was monitored at 500MHz which however disappeared over time, indicating less reliability for road sinking comparing to 300MHz. No reflective surface by the sewer was monitored at 1,500MHz and the signal considered the reflective surface by cavity which was formed when the ice was thawing was very

weak. Generally the higher the GPR frequency the higher the exploration precision and at the depth 1.0m ~ 1.5m, 300MHz ~ 500MHz appeared to be appropriate.

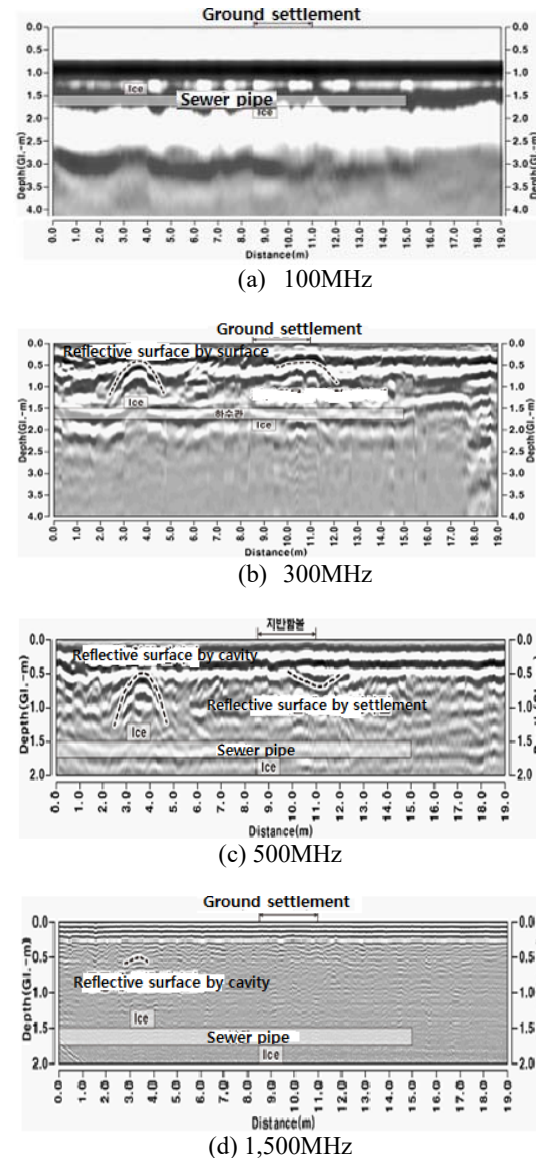


Fig 4. Result of depending on GPR frequency

CONCLUSION

Field test installation and GPR exploration were conducted in a bid to identify the cavity and ground relaxation by sewer leakage and as a result, the conclusion was obtained as follows.

- 1) Cavity and ground relaxation caused by sewer leakage were simulated through field experiment and the cavity and ground relaxation by sewer leakage

were monitored.

2) According to GPR analysis, ice thawing caused ground relaxation and the cavity. Given the reflective surface under the ground over time, cavity appeared to have developed upward. Though ground settlement by cavity was expected, no ground settlement occurred which was attributable to bearing capacity of the well-compacted ground.

3) In case that the ice was buried below the sewer, no reflective surface was monitored which seemed to be attributable to GPR radar wave that failed to penetrate into the bottom of the sewer.

4) According to GPR exploration, reliability to road sinking was higher than others at 300MHz and no reflective surface was monitored at 1,500MHz.

ACKNOWLEDGEMENTS

This research was supported by the Korea Agency for Infrastructure Technology Advancement under the Ministry of Land, Infrastructure and Transport of the Korean government. (Project Number: 17SCIP-B108153-03) and Environment Ministry's Environment Policy Public Technology Development Project (Project Number: 2014000700006)".

REFERENCES

- [1] Road Management Team of Seoul City, *Seoul City's Management of Road Sinking and Manual*, Special Training Manual for Seoul City Officials. 2015
- [2] Yokota, T, Fukatani, W and Miyamoto, T. *The Present Situation of the Road in Sinkholes caused by Sewer System*, National Institute for Land and Infrastructure Management, 2012
- [3] Lee. DY, Choi, YW and Choi, H. "Cavity Detection under Road Structure for Cause Survey of Road Cave-in", *Proc. of 2015 Symposium by Korean Society of Civil Engineers*, 1, 2015, pp. 217-218.
- [4] Park, JJ, Han, JG, Yoo, SK, Hong, KK (2015). "GPR technology for cavity exploration", *Journal of the Korean geosynthetics society*, Vol 14, No 3, pp 12-17
- [5] Baek, JO and Choi, JS (2014). "Road exploration technology using GPR", *Road Engineers*, Vol 16, No 3, pp 11-16.

EFFECT OF CONFINING STRESS AND INCLINATION ANGLE ON THE STRENGTH BEHAVIOUR OF SAND

Navid Khayat¹

¹ Department of Civil Engineering, Ahvaz branch,
Islamic Azad University, Ahvaz, Iran.
Khayat@iauhvaz.ac.ir

ABSTRACT

This study assessed the effects of anisotropy in sands with various confining stresses. The tests conducted in this research include 20 hollow cylinder torsion shear tests conducted on Tehran sand with high angularity. The confining stresses of the samples were 100, 200 and 400 kPa, and the effect of the inclination angle on the major principal stress (α) was investigated. In each confining stress three inclination angle 15, 30 and 60 degree were applied. According to the results, an increase in the α will result in a more contractive behavior in the sands. The effect of anisotropy also becomes more obvious, as the confining stresses increases; however it was found that the mechanical properties of sands changed markedly with confining stress.

Keywords: Sand; Strength; Anisotropy; Confining stress;

INTRODUCTION

The stress-strain behavior of sands under monotonic loading has been the subject of various studies in the past [1-3]. Key parameters-such as density, grain size distribution, particle shape and mineralogy, method of sample preparation, direction of loading, and anisotropy that affect the behaviour of a sand under monotonic loading have been presented widely [3-6].

In addition, Extensive studies have been focused on the effects of inherent and induced anisotropy on the behavior of clean sand [7-9]. In some geotechnical problems, such as the bearing capacity of shallow foundations on sand ground, the confining stress dependency of sand mechanical behavior plays an important role as a stress level effect.

In the geotechnical literature, a large number of intensive experimental studies have been devoted to induced anisotropy of granular material. First, the conventional triaxial apparatus was largely used by Poorooshasb, et al. [10], Poorooshasb, et al. [11], Tatsuoka and Ishihara [12], Ishihara and Okada [13] and Vaid, et al. [14], among others, used to investigate the effects of stress-induced anisotropy on the subsequent drained and undrained behaviour of dense sand. One of the objectives was to recognize the yield surface within the light of the elasto plasticity framework. Therefore, in the following decades, with advances in measurements and control techniques, complex machines such as the true triaxial, by Arthur and Menzies [15]; hollow cylinder torsional shear (HCTS) by Hight, et al. [16]; Khayat, et al. [1]; and plane strain machines by

Park, et al. [17], were used to further explore the role of induced anisotropy, principal stress rotation and intermediate principal stress.

The mechanical properties of sands change notably with a variation of the confining stress. Sugiura, et al. [18] were investigating confining stress dependency of mechanical properties of sands. From their test results, it was found that the mechanical properties of sands changed very markedly with confining stress, and the degree of confining stress dependency diverges with the primary properties.

In this paper, the role of angularity differences in three types of sand with the same initial confining stress and same mineralogical properties was studied. The tests were conducted on Tehran sand (TS), with high angular grains. The effective confining stress was performed in 100, 200 or 400 kPa. In addition, the effects of the inclination angle of the major stress were investigated.

EXPERIMENTAL PROCEDURE

Material Properties

The materials employed in this study was TS with angular grains. The grain size distribution curves for sand is given in Fig. (1), which indicates that influence of particle shape alone is isolated without introducing a possible additional variable in the form of grain size distribution.

Results of the XRD scans of sands indicate that quartz as the main phase is the dominant mineral (>75%) among analyzed sands. The minor amount contains Palygorskite and Kaolinite (<10%). The

minor phases Kaolinite (Table.1).

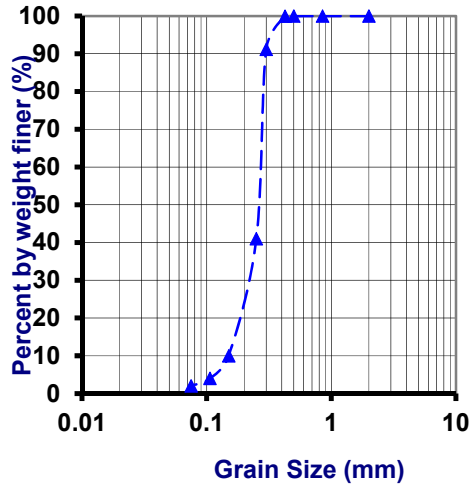


Fig.1 Grain size distribution curves of the Tehran sand.

Table1 Results of semi-quantitative bulk XRD analysis.

Sample No	Main Phase	Minor phase	Trace Phase
Tehran	quartz	Kaolinite	-

In addition one of the important factors in experiments on the sands under high pressure is particle's fracture. If the particles of the sands are broken, under load, the grain size distribution of the sand is changed. Hence, to assessment of the particle fracture, two direct shear tests with 64 kg load (equal 900 kPa) were performed for each type of the sands. The weight of the sands was passed through the sieve No.40 & 100 which measured before and after the test. Results indicated that only one percent of the sand was fractured during the test, which can be neglected. The physical characteristics of studied sand were measured (Coefficient of curvature and uniformity respectively 1.22 and 1.69)

Maximum And Minimum Void Ratios Of Sand

Kandasami and Murthy [19] based on their experimental results, indicated that the influence of sand mechanical response, is a function of the deviatoric stress, relative density and confining stress. Some researcher has extensively described on the non-coaxial behaviour of sand under various stress paths through a series of HCTS tests [1, 16, 19]. The non-coaxial behaviour was found to depend on the type of sand, relative density of the sample

and on the direction of stress increment, and was also found to decrease with increasing strains[20].

An effective factor in the general behaviour of saturated sands in monotonic loading is soil relative density ($D_r = (e_{\max} - e) / (e_{\max} - e_{\min})$), which is a factor that indications the sample's specifications at the end of consolidation stage. The samples prepared at low densities display contractive behaviors in the drained tests; this behavior causes excess pore water pressure in undrained tests, which decreases the effective confined stress. The change of stress-strain from the softening to hardening states is related mostly to the relative density, which is observed and reported by several researchers such as Bishop [21], Castro [22], Castro, et al. [23] and Seed and Idriss [24].

Testing Apparatus And Method

To investigation the inherent anisotropy, a hollow cylinder torsional shear (HCTS) device is used. For a better investigation of the post peak response, the device can perform tests with both stress and strain controls. A closed loop control is applied to the machine to handle any type of desired stress history including major principal stress rotation and intermediary stress ratio. Four electrical/pneumatic [E/P] transducers are used to control the pressure for the inner and outer cell pressures in addition to the torsion and axial load pneumatic actuators. The use of an alternative DC motor for torsional strain control test enables the study of the post peak behavior. In the case of our tests, the motor is utilized because strain control is essential to study the softening response. The motor speed in all of the tests remains constant and equal to one degree per min. Eleven transducers are adjusted to measure the different factors constantly: three water pressure sensors, two for the inner and outer cell pressures and one for the pore pressure; one vertical dislocation sensor to measure axial strain and one rotation angel sensor to measure torsional strain; two differential pressure sensors; two axial and torsional stress sensors; and finally, two limit switch sensors are set up. A computer program is utilized to control all of the test procedures by means of a PID control algorithm. A data logging device is the last part of the control system. The sample dimensions were 16 cm in height, 5 cm in inner diameter and 8 cm in outer diameter.

The maximum inclination of the principal stress (α°), initial confining stress and particle shape are considered the critical parameters in this research. The intermediate stress parameter (b) is constant (= 0.5), for avoid of more variable parameters in tests.

Figure (2) schematically displays details of apparatus, the stresses and their directions in the

hollow cylindrical torsional shear test. In Fig. (2), A_r and A_s are the cross sections area of the axial rod and the sample, respectively.

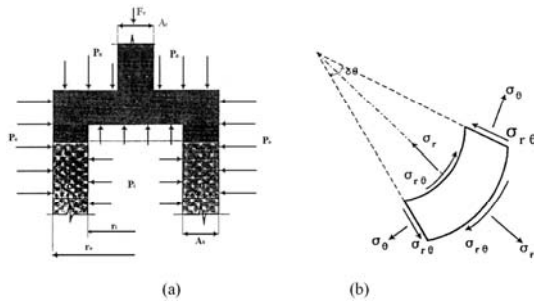


Fig. 2 Schematic details and view of stresses in hollow cylindrical torsional shear test.

- a) Schematic details of HCTS apparatus
- b) Stress distribution

Experimental Program

For sample preparation, the proper amount of sand are deposited into a split mold through a funnel with a long tube after a molding vacuum of 5 kPa is applied to the sample and the split mold is removed. Then the cell parts are assembled. Carbon dioxide (CO₂) and de-aired water are passed through the sample in their saturated states. The circulating time for the CO₂ that is used in the tests conducted by Zlatovic and Ishihara [25] were 30 min for clean sand. This method is applied in the present study. After circulation of the CO₂, the de-aired water enters from the bottom similar to the CO₂, in the opposite direction of gravity and seeps into all of the voids in the sample. The saturation procedure continues as the confining stress increased, and the pore water pressure is measured in several steps. If the B-value exceeded 0.95, then the sample is supposed to be wholly saturated. At this time, the saturation stage is completed and the sample should be consolidated. Since all of the tests conducted in this research are of the Consolidated Undrained (CU) type, all drainage valves should be opened during consolidation and connected to the system. The amount of water discharged from the sample during consolidation can be measured by reading the burette numbers at the beginning and end of this stage. After consolidation, the shear stage starts with one degrees per minute, which is the lowest speed can be applied to the system. During the shearing step the pore pressure is almost uniform.

RESULTS

The stress-strain behaviour of sands under monotonic loading has been the subject of various

studies in the past. Key parameters-such as density, grain size distribution, particle shape and mineralogy, method of sample preparation, direction of loading, and shearing mode which can affect the behaviour of a sand under monotonic loading have been investigated and reported widely [4, 26].

The main goal of this research is to study the effect of grain shapes as well as the confining stress upon anisotropy features. The sand is tested using

different initial confining stresses and various α° , to avoid of another variable parameters effect on tests, the intermediate stress parameter is constant ($b = 0.5$). In the laboratory, the protocol for reconstitution of a sand sample generates an inherently anisotropic fabric structure due to the orientation and morphology of the particles [27]. As a result of different inherent anisotropy of investigated sands, reaching the same void ratio in the similar preparation method of samples is difficult. In equal confining stress, we reach similar relative density in sample sands. For this reason, ASTM 4253 and ASTM 4254[28] (ASTM, 2006b) are used to measure the minimum void ratio (e_{min}) (densest state) and maximum void ratio (e_{max}) (loosest state) respectively.

Test results of stress-strain and effective stress path curves are presented in Figs (3-5). According to these curves, the samples behavior are similar to those of dense sands based on the classification of undrained sand behavior in most conducted tests, which the results are in good agreement with Yoshimine, et al. [8]. The results also indicate that, the samples strength decrease with increasing α° .

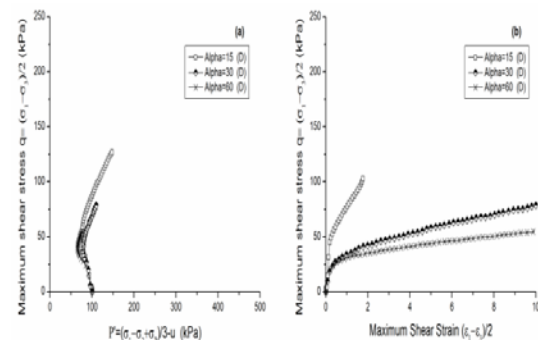


Fig. 3 (a) Stress path and (b) stress-strain curves in Tehran sand subjected to an initial effective stress of 100 kPa.

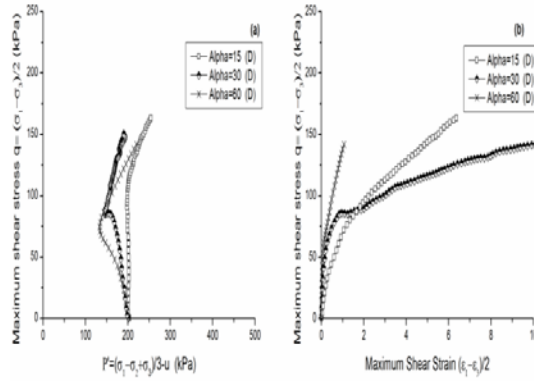


Fig.4 (a) Stress path and (b) stress–strain curves in Tehran sand subjected to an initial effective stress of 200.

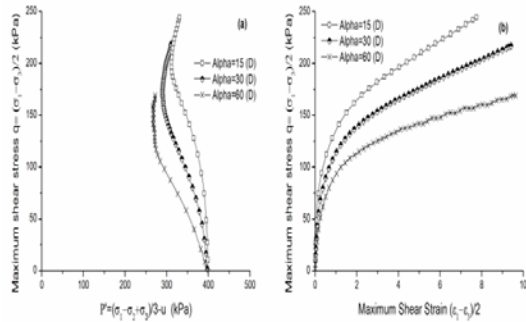


Fig.5 (a) Stress path and (b) stress–strain curves in Tehran sand subjected to an initial effective stress of 400 kPa.

The Effect Of Inclination Angle (α°) On The Sand's Behaviours

In Figs (8-10), the strength of samples in phase transformation point is reduced as α° increases in, which indicates that the soil becomes softer. This behaviour has been confirmed and described by Yoshimine and Ishihara [29] for Toyoura sand and by Khayat, et al. [1] for a Firoozkuh sand-silt mixture.

The changes in the strength and deformation as a consequence of principal stress inclination can be construed as a continuum level indicator of the fabric anisotropy in sands [20, 30]. During shearing, sand particles continuously rearrange and adjust themselves in an ensemble by sliding and rolling so as to form an optimal and unique anisotropic fabric-structure [31] in relation to the loading conditions.

A slow monotonic shearing process is used in experiments to reach the final state, which also shows coincident orientation of the stress and strain increments. While this does not present a detailed

mapping of the network of contact vectors, experiments of this study utilize the principal stress inclination (α) as an ensemble measure of fabric of sands.

In summary, it is especially interesting to study the effects of fabric on very angular particles, such as the ones used in this testing program. Angular sands have a propensity for orienting themselves in a plane normal to the direction of deposition under gravity and exhibit significant interlocking. The inherent anisotropy is especially predominant in very angular sands[32]. Research hitherto reported on various sands such as rounded sands (Ottawa sand—by Dakoulas and Sun [33], sub rounded sands like Nevada sand [30], angular sands by Kandasami and Murthy [19], have significantly enhanced our understanding of sand behaviour. The samples with a different roundness ratio generate different fabric-structures.

Effect Of Initial Effective Confining Stress On The Behaviour Of Sand

As showed in Figs. (5-7), with increasing the confining stress these phenomena is more obvious in investigated sand. In other hand confining stress has a significant effect on the strength behavior of granular materials. Alim, et al. [34], also indicated that confining stress has a significant effect on the strength behaviour of granular materials. Vaid and Negussey [35] showed that, at equal relative densities, angular sand was more resistant to liquefaction at lower confining pressures however, less resistant at higher confining stress than rounded sands. Alim, et al. [34] was defined the average number of contacts per particle, and called it, the coordination number of the particle. The average coordination number of the assembly is defined as the ratio of the total number of contact points within the assembly volume to the total number of particles in the assembly.

CONCLUSIONS

In this study, the following parameters were controlled:

- 1) The grain-size distribution curves of the investigated sands were close to each other.
- 2) The sampling stages for studied sand were similar.
- 3) The comparison samples were consolidated under similar confining stresses (100, 200 and 400 (kPa)).
- 4) With applying same initial confining stress the relative density of studied will be close to each other.

Among the parameters which have effect on sand behaviors the grading curve, sampling stages, relative density, tried to be identical, and results

indicated variation of roundness ratio (r_r), α° and confining stress.

The results can be summarized as follow:

1) With increasing confining stress, anisotropy behavior became remarkable, so the effect of shape more pronounced.

2) For each sand at constant mean effective stress, the decrease in the final state friction angle was a direct consequence of the decrease in final state

shear strength under various inclination angles (α°).

Finally, these experimental results indicated that sands with more angularity, not only cause increasing the shear strength, but also cause increasing the anisotropy. This behaviour has been more pronounce with increasing confining stress. The anisotropic behaviour of sand was a function of the stress ratio, relative density, initial confining stress and particle shape ratios, which could effect on the behaviour of sand samples.

ACKNOWLEDGEMENTS

The author is grateful to the Islamic Azad University Ahvaz branch for their support.

REFERENCES

- [1] N. Khayat, A. Ghalandarzadeh, and M. K. Jafari, "Grain shape effect on the anisotropic behaviour of silt-sand mixtures," *Proceedings of the Institution of Civil Engineers-Geotechnical Engineering*, vol. 167, pp. 281-296, 2014.
- [2] V. Georgiannou, A. Tsomokos, and K. Stavrou, "Monotonic and cyclic behaviour of sand under torsional loading," *Geotechnique*, vol. 58, pp. 113-124, 2008.
- [3] P. Guo and X. Su, "Shear strength, interparticle locking, and dilatancy of granular materials," *Canadian Geotechnical Journal*, vol. 44, pp. 579-591, 2007.
- [4] V. Georgiannou and A. Tsomokos, "Comparison of two fine sands under torsional loading," *Canadian Geotechnical Journal*, vol. 45, pp. 1659-1672, 2008.
- [5] V. Georgiannou, "The undrained response of sands with additions of particles of various shapes and sizes," *Géotechnique*, vol. 56, pp. 639-649, 2006.
- [6] G.-C. Cho, J. Dodds, and J. C. Santamarina, "Particle shape effects on packing density, stiffness, and strength: natural and crushed sands," *Journal of geotechnical and geoenvironmental engineering*, vol. 132, pp. 591-602, 2006.
- [7] M. Symes, A. Gens, and D. Hight, "Undrained anisotropy and principal stress rotation in saturated sand," *Geotechnique*, vol. 34, pp. 11-27, 1984.
- [8] M. Yoshimine, K. Ishihara, and W. Vargas, "Flow deformation of sands subjected to principal stress rotation," *Soils and Foundations*, vol. 38, pp. 179-188, 1998.
- [9] S. Sivathayalan and Y. Vaid, "Influence of generalized initial state and principal stress rotation on the undrained response of sands," *Canadian Geotechnical Journal*, vol. 39, pp. 63-76, 2002.
- [10] H. Poorooshasb, I. Holubec, and A. Sherbourne, "Yielding and flow of sand in triaxial compression: Part I," *Canadian Geotechnical Journal*, vol. 3, pp. 179-190, 1966.
- [11] H. Poorooshasb, I. Holubec, and A. Sherbourne, "Yielding and flow of sand in triaxial compression: Parts II and III," *Canadian Geotechnical Journal*, vol. 4, pp. 376-397, 1967.
- [12] F. Tatsuoka and K. Ishihara, "Yielding of sand in triaxial compression," *Soils and Foundations*, vol. 14, pp. 63-76, 1974.
- [13] K. Ishihara and S. Okada, "Effects of stress history on cyclic behavior of sand," *Soils and Foundations*, 1978.
- [14] Y. Vaid, E. Chung, and R. Kuerbis, "Preshearing and undrained response of sand," *Soils and Foundations*, vol. 29, pp. 49-61, 1989.
- [15] J. Arthur and B. Menzies, "Inherent anisotropy in a sand," *Geotechnique*, vol. 22, pp. 115-128, 1972.
- [16] D. Hight, A. Gens, and M. Symes, "The development of a new hollow cylinder apparatus for investigating the effects of principal stress rotation in soils," *Geotechnique*, vol. 33, pp. 355-383, 1983.
- [17] C.-S. Park, F. Tatsuoka, J. N. Mukabi, T. Sato, Y.-S. Kim, and Y. Kohata, "Measurements of elastic properties of geomaterials in laboratory compression tests," 1994.
- [18] H. Sugiura, M. Ichinose, T. Oyake, Y. Mashito, Y. Ohuchi, N. Endoh, et al., "Role of peroxynitrite in airway microvascular hyperpermeability during late allergic phase in guinea pigs," *American journal of respiratory and critical care medicine*, vol. 160, pp. 663-671, 1999.
- [19] R. K. Kandasami and T. G. Murthy, "Experimental studies on the influence of intermediate principal stress and inclination on the mechanical behaviour of angular sands," *Granular Matter*, vol. 17, pp. 217-230, 2015.
- [20] Y. Cai, H.-S. Yu, D. Wanatowski, and X. Li, "Noncoaxial behavior of sand under various stress paths," *Journal of Geotechnical and Geoenvironmental Engineering*, vol. 139, pp. 1381-1395, 2012.
- [21] A. W. Bishop, "Shear strength parameters for undisturbed and remoulded soil specimens," in *Proceedings of the Roscoe Memorial*

- Symposium, Cambridge University, Cambridge, Mass, 1971, pp. 3-58.
- [22] G. Castro, "Liquefaction of sands, Harvard Soil Mechanics Series No. 81," Cambridge, MA: Harvard University, 1969.
 - [23] G. Castro, J. Enos, J. W. France, and S. Poulos, "Liquefaction induced by cyclic loading," NASA STI/Recon Technical Report N, vol. 83, 1982.
 - [24] H. B. Seed and I. M. Idriss, "Simplified procedure for evaluating soil liquefaction potential," Journal of Soil Mechanics & Foundations Div, 1971.
 - [25] S. Zlatovic and K. Ishihara, "Normalized behavior of very loose non-plastic soils: effects of fabric," Soils and Foundations, vol. 37, pp. 47-56, 1997.
 - [26] A. Tsomokos and V. Georgiannou, "Effect of grain shape and angularity on the undrained response of fine sands," Canadian Geotechnical Journal, vol. 47, pp. 539-551, 2010.
 - [27] Z. Gao, J. Zhao, X. S. Li, and Y. F. Dafalias, "A critical state sand plasticity model accounting for fabric evolution," International journal for numerical and analytical methods in geomechanics, vol. 38, pp. 370-390, 2014.
 - [28] A. Standard, "D4254-91: Standard Test Method for Minimum Index Density and Unit Weight of Soils and Calculation of Relative Density," Annual Book of ASTM Standards, ASTM International, West Conshohocken, PA, 2006.
 - [29] M. Yoshimine and K. Ishihara, "Flow potential of sand during liquefaction," Soils and Foundations, vol. 38, pp. 189-198, 1998.
 - [30] P. V. Lade, N. M. Rodriguez, and E. J. Van Dyck, "Effects of principal stress directions on 3D failure conditions in cross-anisotropic sand," Journal of Geotechnical and Geoenvironmental Engineering, vol. 140, p. 04013001, 2013.
 - [31] J. Zhao and N. Guo, "Unique critical state characteristics in granular media considering fabric anisotropy," Géotechnique, vol. 63, pp. 695-704, 2013.
 - [32] K. Iwashita and M. Oda, Mechanics of granular materials: an introduction: CRC Press, 1999.
 - [33] P. Dakoulas and Y. Sun, "Fine Ottawa sand: experimental behavior and theoretical predictions," Journal of geotechnical engineering, vol. 118, pp. 1906-1923, 1992.
 - [34] M. Alim, K. Suzuki, and K. Iwashita, "Effect of confining pressure on the strength behavior of granular material simulated by the discrete element method," in Proceedings of the 10th IAEG International Congress, IAEG2006, Nottingham, 2006.
 - [35] Y. P. Vaid and D. Negussey, "Relative density of pluviated sand samples," Soils and Foundations, vol. 24, pp. 101-105, 1984.

INVESTIGATIONS OF INTERACTION OF JOINT PILES WITH PROBLEMATICAL SOIL GROUND IN KAZAKHSTAN

Askar Zhussupbekov¹, Abdulla Omarov¹, Asemgul Moldazhanova¹, Asel Tulebekova¹, Karlygash Borgekova¹ and Gulshat Tleulenova¹

¹Department of Civil Engineering, L.N. Gumilyov Eurasian National University, Astana, Kazakhstan

ABSTRACT

At present time the large-scale constructions are built highly in Kazakhstan in particular a building with pile foundations on problematic soils. In this paper are presented the results of pile field test in construction site in Astana and Caspian Sea Port Prorva. In this construction sites were carried out the static load test with ASTM and Kazakhstan standards (GOST) and dynamic load test with GOST. Also using the Pile Dynamic Analyzer testing method need for quickly determination of bearing capacity for single joint piles. These investigations are important for understanding of interaction mechanism of joint piles with problematical soil ground of “Cargo Transportation Route for Facilities of the north-eastern part of the Caspian Sea North Caspian Marine channel with berthing facilities Cargo Offloading Facility” the “Prorva” oilfield, Atyrau region, Western Kazakhstan. Results of static test of steel piles are shown in graphs.

Keywords: joint pile, GOST, bearing capacity, SCLT.

1. INTRODUCTION

In Western Kazakhstan, a mega-project is “Cargo Transportation Route for Facilities of the north-eastern part of the Caspian Sea North Caspian Marine channel with berthing facilities Cargo Offloading Facility” (CaTRO, COF) the “Prorva” oilfield, Atyrau region. Testing of soils by piles was submitted data by engineers of the LLP “KGS-Astana” during November 2016 to May of 2017. This working plan (WP) has been developed for the production of driving operations of precast concrete piles consists of two segments, segment 1 and segment 2 are interconnected that supply the segment 1 length 16 m, segment 2 lengths 9.5 and 11.5 m, the total lengths 25.5 and 27.5 m, the reinforcement diameter of 8 mm with a cross section 400x400 mm. The pile tested areas in construction site were showed on Figure 1.



Fig. 1 The pile tested areas in construction site

Caspian Sea Port “Prorva”.

The project area is situated on the Northern Caspian Shelf. At present the North Caspian Sea has a limited water depth (maximum 5 to 8 m). The water level in the Caspian Sea depends on a balance between the inflow of river water and evaporation (see Figure 2).

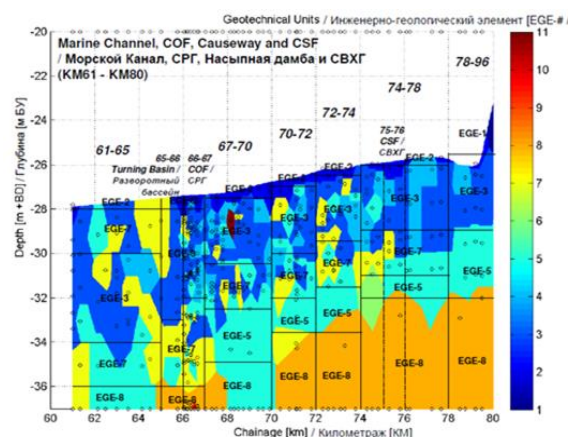


Fig. 2 Geotechnical profile based on Lab Results.

This has resulted in large variations in sea level in the past. This explains the sequence and soil characteristics of the deposits. Table 1 shows engineering-geological structure of the construction site. Eleven engineering-geological elements (units) are identified based on the geological setting and the borehole logs.

Pile driving in EGE-10 material may be difficult. However, this layer is only encountered in one borehole (at the west side of the COF).

Table 1 Engineering-geological elements

(EGE) Soil type	General consistency	C	ϕ , deg	γ_{natural} *, kN/m ³	Su, kPa	E _{oed} , ref
(EGE-1) FILL: SAND, clayey, calcareous	loose to medium dense	0.7	29.4	19.4	25	2,800
(EGE-2) SILT, slightly organic, calcareous	soft to firm	0.7	29.4	19.3	15	2,750
(EGE-3) SAND, silty, calcareous	medium dense to dense	2.7	31.5	19.0	-	30,000
(EGE-7) CLAY, silty, calcareous	stiff	20.8	24.7	19.1	80	2,000
(EGE-8) SAND, silty, calcareous	very dense	2.4	31.8	20.0	-	40,000
(EGE-9) CLAY, sandy, calcareous	very stiff	22.7	23.8	20.6	150	4,000
(EGE-10) CLAY, silty, calcareous	very stiff	25	24.7	20.2	150	2,000

Second Project construction site-Embassy of USA in Astana, Kazakhstan

Construction site located at South-East part of

capital of Republic Kazakhstan. Construction site located at South-East part of capital of Republic Kazakhstan. Territory of Astana city arranged in Kazakh shield so territory isn't seismicity. Loam, clay, eluvia formation presented by loam with inclusion of gruss and ballast stone, sandstone, siltstone. Geology-lithologic cut of construction site shown in Figure 3 [1].

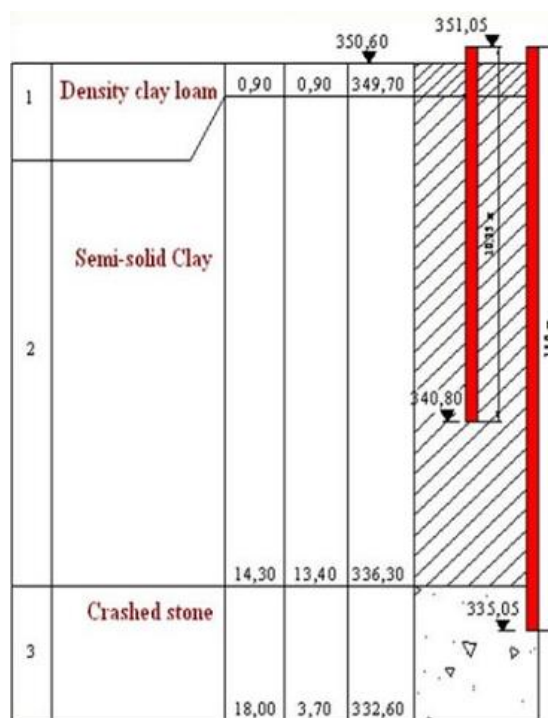


Fig. 3 Geology of construction site-Embassy of USA in Astana, Kazakhstan [1].

2. COMPRESSION STATIC LOAD TEST IN CONSTRUCTION SITE PRORVA

This test is used to measure the axial deflection of a vertical deep foundation when loaded in static axial compression. This vertical compression pile maintained load test is usually carried out to ensure the structural and geotechnical soundness of the pile and also to predict settlement of other piles. The usual procedure is to increase the load in stages until the proposed working load and a certain factor of safety is reached and then to unload and to leave the load off until the rise or rebound substantially ceases, the test is standardized by ASTM D1143 [2].

Testing with a static load (compression) was carried out in accordance with ASTM D 1143 [2]. Vertical static loading of piles using the SCLT method is one of the most widely used field test methods for soil used to analyze pile bearing capacity [2].

Static compression load tests were performed on precast concrete joint piles No. TP-02 and TP-03,

which are driving in COF Area with depth 25.50 and 27.50, from ground level Baltic datum -25,609 m and pre-augering with auger dia. 330 m, depth 11.40 m before driving.

In SCLT testing, the test load on the pile is specified for two cycles (1639 kN and 3274 kN, respectively). Loading and unloading was carried out in the following sequence: 0, 30, 60, 90, 125, 90, 60, 30, 0, 170, 210, 250, 210, 170, 125, 80, 40 and 0% of design. In the first cycle, the experimental pile was loaded to 100% of the design value (1639 kN); during the second cycle, to 200% (3274 kN). The hold time while loading was 60 min; while unloading –10 min. It took 360 min, respectively, to attain peak load [3-6].

Testing platform presented itself system from steel, which consists of metallic beam and 2 platforms located on equidistant distances from the centre main beams (see Figure 4).



Fig. 4 Testing platform for static compression load test.

SLT is a highly accurate and robust system that enables you to monitor static pile tests whilst also ensuring the safety of site operatives.

Davisson's Offset Limit Method (ultimate load) offers the benefit of allowing the engineer, when proofing a pile for a certain allowable load, to determine in advance the maximum allowable movement for this load with consideration to the length and size of the pile (See Table 1 and Figures 5 and 6) [7-11].

Table 1 Pile characteristics and formula's Davisson

	Pile number	TP-02
1	Pile section area	$A=0.16 \text{ m}^2$
2	Approximated pile diameter	$D=45.0 \text{ cm}$
3	Load	$P=3000 \text{ kN}$

4	pile length, L	26,75 m
5	Young's	B 40
6	Econ	45 000 000 kPa
7	Elastic line= $(P*L)/(A*E)$	0.011 m= 11 mm
8	Davisson (ASTM) offset $\Delta=D/120+0.4$	0.78 cm= 7.8 mm
9	Pile Ultimate Capacity (pile number TP-02) F_u	2480 (see Figure 5)
Second pile (Pile number TP-03)		
10	Pile length, L	23,00 m
11	Elastic line= $(P*L)/(A*E)$	0.0096 m= 9.6 mm
12	Davisson (ASTM) offset: $\Delta=D/120+0.4$	0.78 cm= 7.8 mm
13	Pile Ultimate Capacity (pile number TP-03) F_u	2450 kN (see Figure 6)

Figures 5 and 6 shows the results of SCLT testing.

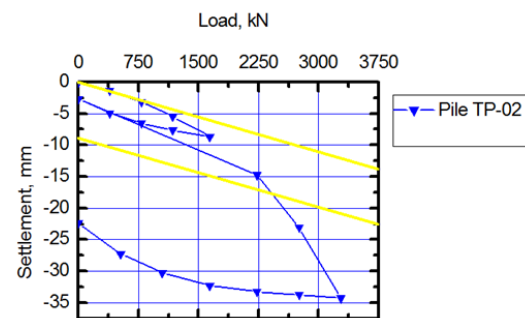


Fig. 5 Results of SCLT pile number TP-02.

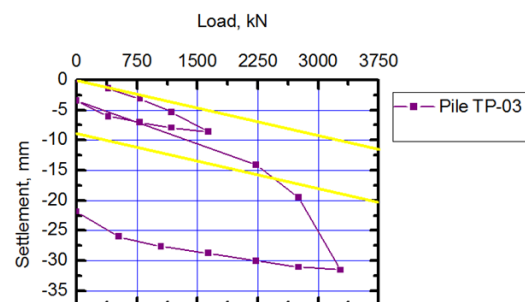


Fig. 6 Results of SCLT pile number TP-03.

A primary advantage of this method is that the actual limit line can be drawn on the load movement diagram already before starting the test. The offset limit load criterion is primarily intended for interpretation of quick testing methods, but it can also be used when interpreting results from the slow methods.

The Davisson Offset Limit is very sensitive to

errors in the measurements of load and movement and requires well-maintained equipment and accurate measurements. However, it is easy to apply and has gained wide acceptance.

3. METHOD OF DYNAMIC LOAD TEST (PDA)

Pile Dynamic Tests were performed on precast concrete joint piles No. G-26 and B-38. Piles were tested with PDA (Pile Driving Analyzer – Model PAX) using hammer JUNTAN PM25LC with a hydraulic hammer HHK-9A of 9 tons of weight and a head-cap of 990 kg. On the tested pile a pair of accelerometers and at least a pair of strain transducers are attached at least two pile diameters below pile head.

The Figure 7 presents CAPWAP analysis results that include plots of measured pile head data obtained under the hammer blows from the end of driving and associated simulated pile head and toe static load-movement relationships.

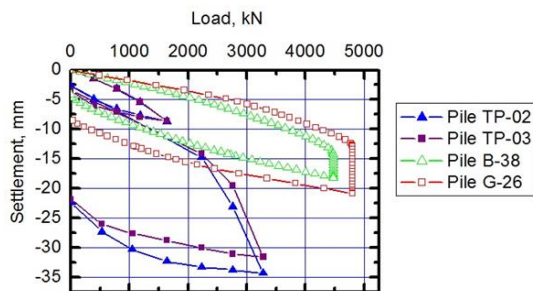


Fig. 7 Results of SCLT and Dynamic load test with PDA.

Difference between performed SCLT and PDA test could be explained partly because time gap between PDA and SCLT is 9 days and also because of driving nearby piles before SCLT test, what produce additional pore pressure and less friction at the time of SCLT. Since high bearing soil layers have large permeability it could be assumed that pore pressure effect and pile set-up are quicker.

We have to be aware that simulation of static load test with CAPWAP (or DLT) does not include any long term effects like creep or long term settlements. This is why in almost all cases CAPWAP load-set curve is little higher than load-set curve from static load test, specially for higher loads and toe bearing piles.

4. STATIC PILE TEST IN CONSTRUCTION SITE-EMBASSY OF USA IN ASTANA

The objective of static pile test is determination of settlement and bearing capacity of pile.

Anchoring-stubborn stand consist with main and subsidiary systems, four anchor pile used for pile test.

Research polygon equipped by driving of testing and anchor piles, mounting of metalwork of anchoring stand, welding of anchor band.

Equipment which used in static pile test as follows:

- hydraulic jack CMZh58A, carrying capacity 2000 kN;
- hand pumping station MNSR with manometer MTP-160;
- two deflectometer - 6 PAO.

Jack with under base hand strain to pile and by up rag of it rod to basic hummer. Steel piles tested for 600 kN bearing load to press load 1200 kN, for 400 kN bearing load to press load 800 kN.

Field static pile test taken as follows [12-15]:

- "rest" pile stand during 7-10 days instant ending of driving pile;
- loading of pile made by load up to 1200 kN and 800 kN;
- size of each step of load equal 50kN and 100 kN;
- unloading of testing piles made step by step;
- removal of samples from the deflectometer was carried out in the following order: first reading - right after the load application, and then sequentially through the four samples every 15 minutes of observation, two samples with an interval of 30 min and then every 60 minutes to conditional stabilization of deformation, ie until the precipitation rate of the pile at a given stage of loading will not exceed 0,1 mm in the last 60 minutes;
- removal of count elastic deformation made on each step on unloading over 15 min.

4.1 Execution of static test of steel piles before heightening of pile length

Graphic of dependence of settlement pile from load and variation of settlement on step of load received in test results.

A static pile test of steel H-piles was carried out after the "rest" of pile after driving. Results of static test of steel piles before heightening of pile length shown in Table 2 and Figure 8

Table 2 - Results of static test of steel H - piles

№	Number of pile	Embedded depth, m	Refusal of pile at driving, cm	Settlement, mm	Design load, kN	Applied load, kN	Max. load, kN
1	LT-1	7,00	1,00	43,03	600	900	1200
2	LT-4	9,25	1,25	42,55	600	900	1200
3	LT-6	10,25	1,25	40,25	600	900	1200
4	LT-7	8,00	1,56	40,88	400	600	800

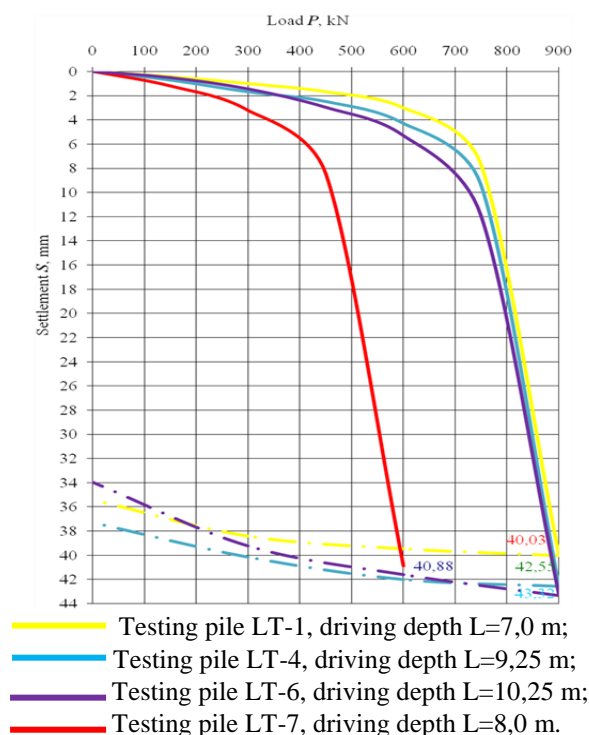


Fig. 8 Graphics of dependence of settlement S from load P regarding results of static pile tests before heightening of pile length (by ASTM D/D 1143M-07).

Results of static test of steel piles after heightening of pile length shown in Table 3 and Figure 9-10. Results of static pile test showed that after heightening of pile length given best results.

Table 3 Results of static test of steel H - piles

№	Number of piles	Embedded depth, m	Driving depth, m	Refusal of pile at driving, after heightening pile, cm	Settlement, mm	Design load, kN	Applied load, kN	Max. load, kN
1	LT-3	10,00	13,00	0,32	7,00	600	1200	1200
2	LT-4	9,25	12,75	0,27	4,96	600	1200	1200
3	LT-5	8,25	11,00	0,27	4,42	600	1200	1200
4	LT-6	10,25	16,00	0,30	6,27	600	1200	1200

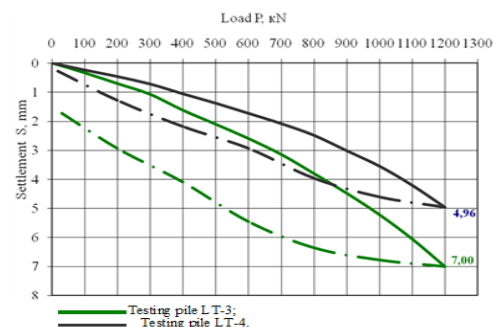


Fig. 9 Results of SLT pile numbers LT-3, 4.

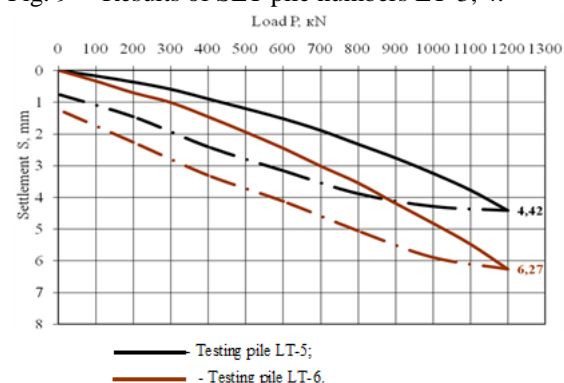


Fig. 10 Graphics dependence of settlement S from Load P for LT-5, 6 (by GOST 5686-94).

CONCLUSION

Since 1994 year Kazakhstan Standard has not changed, ASTM standard was updated in 2007, and therefore takes latest developments in technology and technical terms and provides for the use of more modern equipment.

The purpose of testing is determination of bearing capacity and the penetration depth of immersion of composite piles in problematical ground soils of Atyrau region, Kazkhstan.

According to the results of DLT with PDA of driven piles (40×40 cm and lengths of 23 m and 26.75 m) the bearing capacity of the piles amounted to be 2143 kN. The bearing capacity of driven piles according to the results of SCLT amounted to be 2067 kN and 2042 kN.

The disadvantage of the offset limit load lies in the difficulty of determining the modulus of elasticity E for concrete piles and concreted pipe piles. Davisson's method needs the pile to be loaded to failure to be applicable.

We have to be aware that simulation of static load test with CAPWAP (or DLT) does not include any long term effects like creep or long term settlements. This is why in almost all cases CAPWAP load-set curve is little higher than load-set curve from static load test, specially for higher loads and toe bearing piles.

REFERENCES

- [1] Assel S. Tulebekova. Control Equipment for Pile Test According to American and Kazakhstan Standards. *Modern Applied Science*; Vol. 9, No. 6; 2015, pp. 192-198.
- [2] Standard Test Methods for Deep Foundations Under Static Axial Compressive Load D1143/D1143M – 07'1. ASTM, 2007.
- [3] SNiP RK 5.01-01-2002 "Soil basement and foundations".
- [4] SNIP RK 5.01-03-2002-Pile Foundation, Astana, KAZGOR, 2003.
- [5] Zhussupbekov A.Zh., Lukpanov R.E., Omarov A.R.. "Experience in Applying Pile Static Testing Methods at the Expo 2017 Construction Site". *Journal of Soil Mechanics and Foundation Engineering*. Volume 53, Issue 4, 2016, pp. 251-256.
- [6] Zhussupbekov A.Zh., Omarov A.R. "Geotechnical and construction considerations of pile foundations in problematical soils". *Proceedings of the 8th Asian Young Geotechnical Engineers Conference*, 8th AYGEC. Astana, Kazakhstan, 2016, pp. 27-32.
- [7] Davisson, M. T., "High capacity piles". *Proceedings of Lecture Series on Innovations in Foundation Construction*, American Society of Civil Engineers, ASCE, Illinois Section, Chicago, March 22, 1972, pp. 81-112.
- [8] Zhussupbekov A.; Lukpanov R.; Omarov A.. "The Results of Dynamic (Pile Driving Analysis) and Traditional Static Piling Tests in Capital of Kazakhstan". *13th Baltic Sea Region Geotechnical Conference*. Vilnius, LITHUANIA, 2016, pp. 201-205.
- [9] Poulos, H. G., & Davis, E. H. (1980). *Pile foundation analysis and design // Series in geotechnical engineering*. – John Wiley & Sons, p. 397.
- [10] Zhussupbekov A.Zh., M.K. Syrlybaev, R.E. Lukpanov, A.R. Omarov. "The applications of dynamic and static piling tests of Astana". *15th Asian Regional Conference on Soil Mechanics and Geotechnical Engineering, ARC 2015: New Innovations and Sustainability*, 2015, pp. 2726-2729.
- [11] Abdelrahman G. E., Shaarawi E. M., and Abouzaid K. S. Interpretation of axial pile load test results for continuous flight auger piles. *Proc. of the 9 Arab Structural Engineering Conf.*, Abu Dhabi, UAE,. 2003.
- [12] GOST 5686-1994. Soils. Field test methods be piles. M.: Standards Publishing House.
- [13] Zhussupbekov A.; Omarov A. "Modern Advances in the Field Geotechnical Testing Investigations of Pile Foundations". *Procedia Engineering*. Volume 165, 2016, pp. 88-95.
- [14] MSP 5/01-101-2003-Design and installation of pile foundation.
- [15] Zhussupbekov, A., Omarov, A., Zhukonova, G., Tanyrbergenova, G. *Pile Foundations of Mega Projects: New Railway Station and LRT in Problematical Soil Ground of Astana*. *Procedia Engineering*, Volume 189, 2017, pp.511-518.

THE UTILIZATION OF WATER FOOTPRINT TO ENHANCE THE WATER SAVING AWARENESS: CASE STUDY OF A CERAMIC PRODUCT

Karin Kandananond

Faculty of Industrial Technology, Valaya Alongkorn Rajabhat University, Thailand

ABSTRACT

One of the methods to increase the water saving awareness is the water footprint which is based on the calculation of water usage incurred during the whole life cycle of a product. The case study in this research is the water footprint computation of a ceramic product, a mug. The life cycle of a mug is assessed from the first stage, resource extraction, followed by manufacturing, usage until the last stage, disposal. The calculation of water footprint is based on the ISO 14046: 2014 guidelines. Another objective of this research is to verify that the water footprint can be utilized effectively as a tool to enhance the awareness and the perception of the ceramic business owners towards the water saving issue. According to the research results, the paired t-test statistics was utilized to test the difference of the awareness level before and after introducing the water footprint concept to the business owners. The results indicate that the awareness is significantly built up after the application of water footprint education. This will lead to the sustainable use of water in the ceramic business

Keywords: Awareness, Ceramic, Water footprint, Water saving

INTRODUCTION

The environment issues have come into the attention of people since the last decade and they are ranged from global warming to water drought. Although the society starts to be aware of the importance of the environment, the pathway which leads the conservation of environment in reality is still unclear and not practical. As a result, initiatives, such as carbon footprint, are introduced in order to be used as a tool to assess the carbon emission due to human activities with the objective of having the medium for carbon trade. Similarly, water footprint is the concept introduced by A.Y. Hoekstra from UNESCO-IHE in 2002 and it is the amount of freshwater used to make goods or provide services. The water footprint of every product or service will reflect the tangible amount of used water which is easy to understand for people who are related to any part of the life cycle of product or service. The objective of this research is to study the potential of water footprint as a tool to increase the level of awareness among the people.

REVIEW

According to Badruzzaman, Oppenheimer, Hess, Smith, Upson, Postle, and Jacangelo [1], the purposes of water footprint are differentiated into four categories, the measurement of water consumption, the identification of environmental influence in term of numerical results due to the consumption, the risk assessment regarding the consumption, the

introduction of strategies leading to the reduced consumption. Noga and Wolbring [2] conducted a study on the perceptions of water ownership and water management among one hundred and sixty four individuals. The questionnaires were used as a research instrument and the questions regarding the water footprint were included. The results reveal that the questionnaire respondents are concerned with the water scarcity. Another finding is that education regarding the water conservation and recycling are needed and it is key leading to the raise of awareness. Moreover, most respondents agree that the water footprint might be a potential tool leading to alleviate the awareness. A study by Attari [3] also points out that the accuracy of water use perception (water footprint) is more precise than other means of perception measurement in the similar category, e.g., carbon footprint.

Hoekstra and Chapagain [4] signify that the amount of water consumed for the production of services and commodities is the clear definition of water footprint and this number directly reflects the water use of the population in a nation. Their study is also extended to the identification of four factors affecting the amount of water footprint, namely, volume of consumption, consumption pattern, climate (growth conditions) and agricultural practice. Gerbens-Leenes and Hoekstra [5] identify that there are two parts of water footprint, i.e., operational water footprint and supply chain water footprint. Another way to categorize the water footprint is based on the types of freshwater sources, blue, green and gray water footprint. The blue water footprint is the

amount of water retrieved from the surface and ground water while the green water footprint is the water evaporated from the rainwater in the soil. On the other hand, the gray water footprint is the polluted water due to the manufacturing activities. According to Čuček, Klemeša and Kravanj [6], footprint is a powerful indicator used to measure the level of sustainability in term of environment, society and economy.

METHOD

In this study, there are two folds of processes used to carry on the research, the total water footprint calculation and the increasing level of awareness after the workshop regarding water footprint was introduced. The main concept of water footprint calculation is based on the identification of the framework of life cycle analysis. In term of framework, there are five steps incorporating with the framework creation.

- identify the studied impact
- identify the studied product
- identify the functional unit of product
- identify the period for data collection

The initialization of the framework is shown in the following Fig. 1.

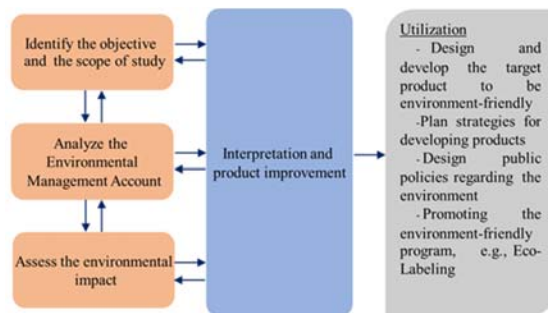


Fig. 1 Research framework.

The life cycle analysis is depicted in Fig. 2 as material flow analysis (MFA) which shows the scope of product life assessment (in this case, cradle to gate). For cradle to gate, the analysis focuses the life cycle only from resource extraction (cradle) to factory gate. However, if it is cradle to grave, the scenario will cover the whole life cycle of product (resource extraction, manufacturing, distribution, use and dispose). Moreover, another critical function of MFA is to identify the flow of materials in the manufacturing process of a certain product. Elaborately, MFA breaks the whole process into sub-processes and each sub-process has inputs (resources), waste (emission) and output [7]. Another important method used to assess the potential of water footprint as a tool to raise the level of awareness is the

questionnaires. They will distributed before and after the workshop regarding the water footprint was carried on. The paired t-test was utilized to signify the different level of awareness after the workshop.

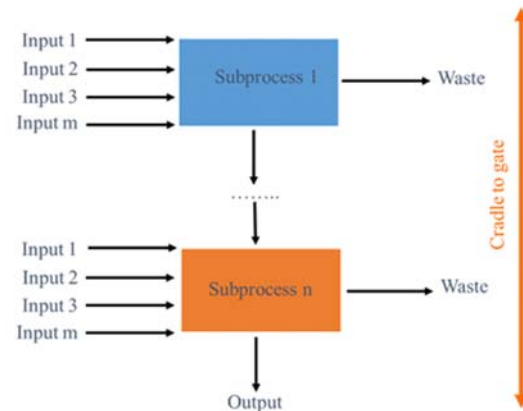


Fig. 2 Material flow analysis.

RESEARCH PROCEDURES

Since the target group of this study is the ceramic business owners and executives, the life cycle analysis of the ceramic product is limited to only cradle to gate which covers the impact from a partial product life cycle, i.e., resource extraction and manufacturing. A ceramic product which is used as the case study is a ceramic yellow jug for serving water. The weight of this jug is 500 gram and it is shown in Fig. 3. Therefore, the function unit of product is a jug. To illustrate the life cycle analysis, the manufacturing flow chart is depicted in Fig. 4 and it composes of six steps as follows: forming and finishing, biscuit firing, glazing, glost firing, polishing and packaging.



Fig. 3 Ceramic jug.

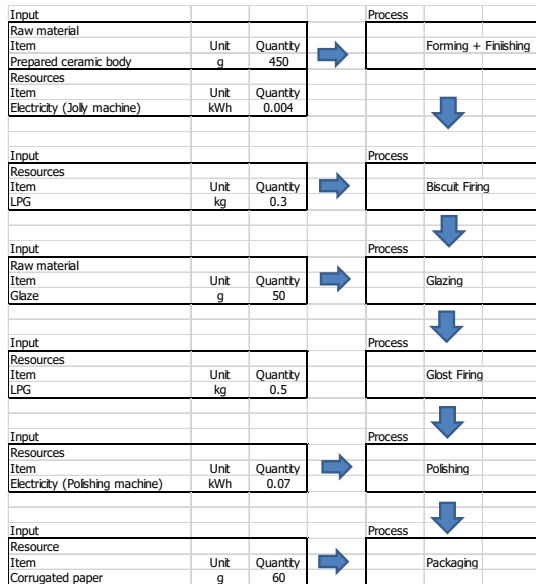


Fig. 4 Manufacturing flow chart.

LIFE CYCLE ANALYSIS

According to the material flow diagram, there are three raw materials required to manufacture a ceramic jug, prepared ceramic body, glaze and corrugated paper (for packaging). Due to Table 1 and 2, the water footprint of prepared ceramic body (l/kg) is equal to 14.4 while the one of glaze is 65 l/kg (the data was forwarded from the suppliers who conducted the in-house experiment to determine the water footprint data). On the other hand, the water footprint of corrugated paper (l/kg) in Table 3 is equal to 38.9 [8]. Therefore, the total water footprint due to the resource extraction equals $6.5 + 3.25 + 2.334 = 12.084$ liter. The forming, finishing and polishing tools are run by electricity which is generated by natural gas. However, the fuel of kiln is LPG (liquefied propane gas). The water footprint calculation for electricity and LPG is shown in Table 4 and 5.

Table 1 Water footprint of raw material extraction (prepared ceramic body)

Resource	Weight (kg)	Water Footprint (l/kg)	Total(l)
Prepared ceramic body	0.45	14.4	6.5

Table 2 Water footprint of raw material extraction (ceramic glaze)

Resource	Weight (kg)	Water Footprint (l/kg)	Total (l)
Glaze	0.05	65	3.25

Table 3 Water footprint of raw material extraction (corrugated paper)

Resource	Weight (kg)	Water Footprint (l/kg)	Total (l)
Corrugated paper	0.06	38.9	2.334

The water footprint calculation shown in Table 4 and 5 obviously show that the generated electricity is contributed to both blue and gray water footprint. Since the blue water footprint equals 5.6 l/kWh while the gray water footprint is 5.7 l/kWh, the generation of electricity causes more polluted water than the used water (the amount of gray one is higher than the blue one.). In conclusion, the electricity used to manufacture a jug leads to the water footprint of 0.8362 liter. According to Table 6 and 7, the blue and gray water footprint are equal to 2.51 l/kg and this implies that the extraction of LPG spends the same amount of surface water as the water it polluted [9]. Totally, the water footprint of LPG for a jug is equal to 4 liter. In conclusion, the total water footprint of the resource extraction and fuel used is shown in Table 8. Therefore, the water footprint of a ceramic jug (cradle to gate) is equal to 16.9202 liter.

Table 4 Total amount of electricity used

Resource	Process	Quantity (kWh)
Electricity	Forming and Finishing	0.004
Electricity	Polishing	0.07

Table 5 Water footprint of electricity used

Process	Blue Water Footprint (5.6l/kWh)	Gray Water Footprint (5.7l/kWh)	Total(l)
Forming and Finishing	0.0224	0.0228	0.0452
Polishing	0.392	0.399	0.791
			0.8362

Table 6 Total amount of LPG used

Resource	Process	Quantity (kg)
LPG	Biscuit Firing	0.3
LPG	Glost Firing	0.5

Table 7 Water footprint of LPG used

Process	Blue Water Footprint (2.51l/kWh)	Gray Water Footprint (2.51l/kWh)	Total(l)
Biscuit Firing	0.75	0.75	1.5
Glost Firing	1.25	1.25	2.5
			4

Table 8 Total water footprint of a ceramic jug

Stage	Material/fuel	Water footprint
Resource extraction	Ceramic prepare body	6.5
	Glaze	3.25
	Material	2.334
	Electricity	0.8362
	LPG	4
Total		16.9202

LEVEL OF AWARENESS

Two groups of samples are selected to be studied. The first group is the business owners and top executives (N=9) while the second group is the mid-level management (N=15). The last group is the operators in the workshop (N=20). All of them is working in the ceramic business. The level of awareness is started from distributing questionnaires by mails to all groups of respondents. Afterwards, all respondents was invited to participate in a one-day workshop. The content covers the life cycle analysis, the water footprint calculation as well as the above case study. After the class, the same set of questionnaires is re-utilized to assess the awareness. The questions are adapted from Carbon awareness questionnaires (available on <https://www.dorsetforyou.gov.uk/media/191602/Carbon-Awareness-Questionnaire/s>) which are designed to assess the following aspects: attitude, environmental impact, water cost and waste, water saving, water usage reduction and motivation. The paired t-test was conducted to assess the knowledge and awareness of experimental group regarding the water footprint by comparing the pre-workshop and post-workshop means. The results signify that there both means differ significantly ($p < 0.01$). Therefore, the conclusion is that the awareness of the top-executive and workforces towards the environment increases dramatically after water footprint has been used a tool.

Table 9 Questions and pre-training scores

Question	Pre-training	
	Mean	S.D.
Q1: To what extent is your general attitude towards reducing your water footprint?	1.21	0.98
Q2: How aware are you of the environmental impact of water usage?	1.58	1.04
Q3: What is your level of awareness of water costs and where water is wasted?	1.96	1.21
Q4: How aware are you of the ways in which you can save water?	1.41	1.44
Q5: Other than reducing your water use, how aware are you of the other ways to reduce your water footprint at work?	1.77	1.13
Q6: How motivated are you to reduce your water footprint?	1.28	1.22
Q7: The life cycle analysis for water footprint is useful for create environmental awareness.	1.15	0.98

Table 10 Questions and post-training scores

Question	Post-training	
	Mean	S.D.
Q1: To what extent is your general attitude towards reducing your water footprint?	3.95	0.81
Q2: How aware are you of the environmental impact of water usage?	3.51	0.78
Q3: What is your level of awareness of water costs and where water is wasted?	4.05	0.89
Q4: How aware are you of the ways in which you can save water?	4.29	0.82
Q5: Other than reducing your water use, how aware are you of the other ways to reduce your water footprint at work?	3.69	0.96
Q6: How motivated are you to reduce your water footprint?	4.41	0.85
Q7: The life cycle analysis for water footprint is useful for create environmental awareness.	4.69	0.91

CONCLUSIONS

Theoretically, environmental awareness is the issue that comes to the interest of many people. Although a lot of information regarding the environment keeps flowing to the society through different mediums, a number of people still finds that

the environmental issue is not tangible. As a result, this study focuses on the utilization of the water footprint concept as an instructional media to raise the environmental awareness of a specific group of people (who works in the ceramic industry). Based on the life cycle analysis, the water footprint of a case study (a ceramic product) is calculated to show a certain amount of water contributed to manufacturing a ceramic jug. Afterwards, the lesson learned from the computation of water footprint was used to train the target group with the objective to raise the environmental awareness. The pre-test and post-test were used to assess the awareness of the corresponding group while the paired t-test shows that the level of awareness before and after the test is significantly different after the water footprint training was introduced to the target group. Therefore, the practical water footprint method is proved to be effective in alleviating the awareness of people towards the environment.

DISCUSSIONS AND FURTHER STUDIES

The accuracy of water footprint calculation heavily relies on the inventory data. However, the preparation of inventory data in Thailand is not standardized. Therefore, most of the data is adopted from the foreign sources. This practice has the influence on the final result of the calculation. Moreover, the water footprint of the energy source might lead to the different results if other energy sources, e.g., biogas is used to fuel the kiln.

Since the target group of this study is the people who works in the manufacturing, the life cycle analysis only covers the manufacturing stage. However, the research study might be interesting to a large group of people if it is extended to the whole life cycle of the product (including distribution, use and dispose).

REFERENCES

- [1] Badruzzaman M, Oppenheimer J, Hess T, Smith H, Upson S, Postle M, Jacangelo GJ, "Water Footprint: A New Concept for Sustainable Water Utilities", Denver: Water Research Foundation, 2014.
- [2] Noga J, Wolbring J, "Perceptions of Water Ownership, Water Management, and the Responsibility of Providing Clean Water", *Water*, Vol. 5, 2013, pp. 1865-1889.
- [3] Attari SZ, "Perceptions of Water Use", *Proceedings of the National Academy of Sciences*, Vol. 111(14), 2014, pp. 5129-5134.
- [4] Hoekstra AY, Chapagain AK, "Water Footprints of Nations: Water Use by People as A Function of Their Consumption Pattern", *Water Resource Management*, Vol. 21(1), 2007, pp. 35-48.
- [5] Gerbens-Leenes PW, Hoekstra AY, "Business Water Footprint Accounting", Delft: UNESCO-IHE Institute for Water Education, 2008.
- [6] Čuček L, Klemeša JJ, Kravanja Z, "A Review of Footprint Analysis Tools for Monitoring Impacts on Sustainability", *J. of Cleaner Production*, Vol. 34, 2012, pp. 9-20.
- [7] Hoekstra AY, "The Water Footprint Assessment Manual: Setting the Global Standard", London: Earthscan, 2011.
- [8] Corrugated Packaging Alliance, "Corrugated Packaging Life-cycle Assessment Summary Report", Grove Village, 2010.
- [9] EPE Empresa de Pesquisa Energética, "National Energy Balance 2011: Base year 2010", Rio de Janeiro: Ministério de Minas E Energia, 2012.

Construction Materials

MECHANICAL PROPERTIES OF FLY ASH GEOPOLYMER MORTAR CONTAINING RECYCLED GLASS

Nattapong Damrongwiriyanupap¹, Yue Huang², Sangsan Wongchairattana¹, Sakonwan Hanjitsuwan³,
Tanakorn Phoo-ngernkham⁴ and Prinya Chindaprasirt⁵

¹Civil Engineering Program, School of Engineering, University of Phayao, Phayao, 56000, Thailand

²Department of Civil Engineering, Faculty of Engineering and Technology,
Liverpool John Moores University, Liverpool, L3 3AF, United Kingdom

³Program of Civil Technology, Faculty of Industrial Technology,
Lampang Rajabhat University, Lampang, 52100, Thailand

⁴Research Center for Advances in Civil Engineering and Construction Materials,
Department of Civil Engineering, Faculty of Engineering and Architecture,
Rajamangala University of Technology Isan, Nakhon Ratchasima, 30000, Thailand

⁵Sustainable Infrastructure Research and Development Center, Department of Civil Engineering,
Faculty of Engineering, Khon Kaen University, Khon Kaen, 40002, Thailand

ABSTRACT

This study presents the development of green and sustainable mortars using novel geopolymer materials as the new binder and recycled glass as part of the aggregates. Recycled glass was used to partially replace fine aggregate at the amount of 0%, 25%, 50%, 75%, and 100% by weight. Sodium hydroxide (NaOH) and sodium silicate (Na_2SiO_3) solutions were used as liquid alkaline activation in all mixtures. The geopolymer samples were prepared with different liquid to solid binder ratios at 0.5, 0.6, and 0.7, and the ratio of Na_2SiO_3 to NaOH were fixed at 2.0. The compressive and flexural strength were determined at the age of 7, 28, 60, and 90 days. The results showed that the compressive and flexural strength of specimens increase with age. The optimum percentage replacement of fine aggregates with recycled glass was observed at 25%. With the proportion higher than optimum level, the compressive and flexural strength of geopolymer mortars were found to decrease with increasing amount of fine aggregate replacement.

Keywords: Geopolymer mortar, Recycled glass, Fine aggregate replacement, Compressive strength, Flexural strength

INTRODUCTION

Recycled glass is increasingly being used in civil engineering applications such as construction backfill material, subbase and subgrade materials, pavement aggregates, trench bedding material, and landfill material. This clearly demonstrates the need for an alternative method of glass recycling, one in which large quantities of waste can be consumed. Thus, the construction industry presents an attractive way for the use of waste glass. One of the principal components of construction is concrete which is widely used in many countries. Several studies have been conducted to utilize recycled glass as aggregates in concrete [1]-[3] as well as using recycled glass powder as partial replacement of cement in concrete [4]-[8]. Only a few have studied the use of recycled glass as aggregate replacement and as cement partial replacement in ultra-high performance concrete. Le [9] and Yang et al. [10] used recycled glass with particle size of less than 600 microns as a replacement of 240 microns silica sand in ultra-high performance

fibre-reinforced concrete. He reported that the samples with recycled glass has 12% lower compressive strength of the ones using silica sand when cured at room temperature and 4% lower when cured at 90C. The average 28 day strength of the samples cured at room temperature was found to be 110 MPa while that of samples cured at 90C was 150 MPa. Wille et al. [11] used very fine glass powder (median particle size of 1.7 micron) in the production of UHPC with a food-type mixer. They reported that glass powder can be used for cement replacement and that the optimum amount of replacement is 25% of cement by weight. Kou and Xing [12] used 45 microns recycled glass powder as a cement replacement in UHPFRC. They reported that the replacement of cement with glass powder helps increasing the long-term strength of the concrete and that 15% replacement performs better than 30% replacement. Higher strengths are observed for the specimens cured at 90C in comparison to those cured at 20C. However, concrete production is highly resource and energy intensive, with the industry

responsible for approximately 5-8% of worldwide greenhouse gas emissions [13]. As such, opportunities to reduce the environmental impacts of the concrete industry are required. Therefore, the use of new binding material i.e. geopolymer concrete is one the ways to reduce CO₂ emissions due to Portland cement production. With natural aggregates within the world being present in limited quantities and decreasing every year, and producing crushed aggregate for use in the construction industry is costly. It can therefore be seen that incorporating recycled glass as an aggregate in structural concrete has the potential to not only produce environmental benefits in the reduction of landfill and the consumption of raw materials, but to also reduce costs for industry costs. In addition, the outcome of this research could help not only Thailand but also the world to divert significant quantity of waste material, i.e. waste glass from landfills and considerably reduce environmental damage caused by carbon emissions due to PC production. Therefore, in this work, the study on the effect of incorporation of recycled glass as fine aggregate replacement on mechanical properties of geopolymer mortar will be investigated.

MATERIALS AND TESTING ANALYSIS

All geopolymer mortars were made of fly ash (FA) from Mae Moh lignite power plant in northern Thailand. The chemical compositions of FA consist of SiO₂ (25.6%), Al₂O₃ (9.1%), Fe₂O₃ (27.8%), CaO (25.0%), MgO (3.0%), K₂O (3.0%), Na₂O (0.2%), SO₃ (6.0%), and LOI (0.3%) indicating that FA mainly consisted of SiO₂ and Al₂O₃ and some impurities. The sum of SiO₂, Al₂O₃ and Fe₂O₃ was 62.5%, and the CaO content was high at 25.0%. This FA was Class C fly ash as specified by ASTM C618 [14]. 10 molar sodium hydroxide (SH) and sodium silicate (SS) with 13.89% Na₂O, 32.15% SiO₂, and 46.04% H₂O were used as alkali activators. The local river sand with specific gravity of 2.62 and fineness modulus of 1.41 was used as fine aggregate. Crushed recycled glass used in this study has specific gravity and fineness modulus of 25.1 and 1.67, respectively.

The abbreviations of FA-100S0G, FA-75S25G, FA-50S50G, FA-25S75G, and FA-0S100G with corresponding to fly ash geopolymer mortar with the amount of sand replacement with recycled glass at 0%, 25%, 50%, 75%, and 100% by weight, respectively. The ratios of liquid to solid binder (L/B) were varied at 0.6 and 0.7. While, the ratio of SS to SH, and sand to binder was fixed at 2.0, and 1.0, respectively.

In mixing process of geopolymer mortars, FA and sand/recycled glass were dry mixed until the mixture was homogenous which took approximately 1 minute. The alkali activator solutions were then added and the mixing was done for another 3 minutes. After mixing,

mortar samples were then placed into 50x50x50 mm cube and 75x75x300 mm prism molds for compressive and flexural strength test, respectively. The specimens were wrapped with vinyl sheet to protect moisture loss and kept in the room temperature. The compressive and flexural strength of geopolymer mortars were measured at the age of 7 and 28 days. The results were the average value of three samples.

RESULTS AND DISCUSSION

The 7-day and 28-day compressive strength of geopolymer mortars with L/B = 0.6 and 0.7 at different amount of sand replacement with recycled glass is summarized in Table 1. Figures 1 and 2 illustrated the compressive strength of geopolymer mortars at 7 and 28 days, respectively. As seen in Figs 1 and 2, the compressive strength of mortar specimens depended on L/B and percentage of recycled glass content in the mixtures. At 7 days, it is evident that compressive strength of specimens decreased with increasing of amount of sand replacement for both L/B = 0.6 and 0.7. And, the highest compressive strength was obtained at the control specimen, 0% replacement, that is 17.8 and 13.2 MPa for L/B = 0.6 and 0.7, respectively. Whereas, at 28 days, samples with 25% sand replacement provided the highest strength that is 32.5 and 29.5 MPa for L/B = 0.6 and 0.7, respectively. This is slightly higher than control specimens about 0.93% and 4.2% for L/B = 0.6 and 0.7, respectively. When the amount of sand replacement exceeded 25%, the compressive strength of geopolymer mortars tentatively decreased. It is obviously noticed that, at L/B = 0.6 and 0.7, the 28-day compressive strength of specimens were higher than 7 days due to the increase of degree of geopolymerization.

The flexural strength of geopolymer mortars exhibited the similar trend to compressive strength and was summarized in Table 2. The flexural strength of mortars at different L/B cured for 7 and 28 days are illustrated as Figs. 3 and 4, respectively. The trend of flexural strength tended to decline with increasing of sand replacement with recycled glass. At 28 days, the flexural strength of the mortar samples was higher than 7 days curing due to the additional geopolymeric reaction. At 7 days, the highest flexural strength of specimens was obtained at 0% sand replacement that was 0.14 MPa for L/B = 0.6. Whereas, at L/B = 0.7, the highest flexural strength of mortars was observed at 25% sand replacement i.e. 0.12 MPa. However, this was not much different obtained from 0% replacement which was 0.11 MPa. Similar to the age of 7 days, L/B of 0.6 yielded the highest 28-day flexural strength of 0.29 MPa.

Table 1 Compressive strength of geopolymer mortars (MPa)

Curing time	7 days		28 days	
	L/B		L/B	
		0.6	0.7	
FA-100S0G		17.8	13.2	32.2
FA-75S25G		16.9	11.9	32.5
FA-50S50G		16.6	11.9	28.2
FA-25S75G		16.4	10.9	26.1
FA-0S100G		14.5	10.8	24.7

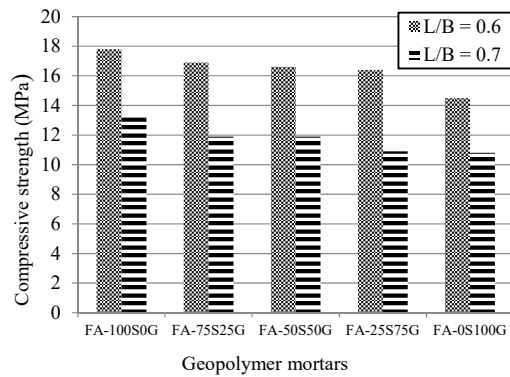


Fig. 1 The 7-day compressive strength of geopolymer mortars containing recycled glass.

Table 2 Flexural strength of geopolymer mortars (MPa)

Curing time	7 days		28 days	
	L/B		L/B	
		0.6	0.7	
FA-100S0G		0.14	0.11	0.75
FA-75S25G		0.10	0.12	0.29
FA-50S50G		0.10	0.11	0.27
FA-25S75G		0.10	0.11	0.19
FA-0S100G		0.09	0.07	0.20

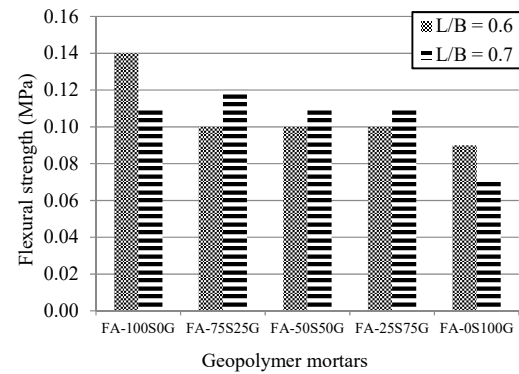


Fig. 3 The 7-day flexural strength of geopolymer mortars containing recycled glass.

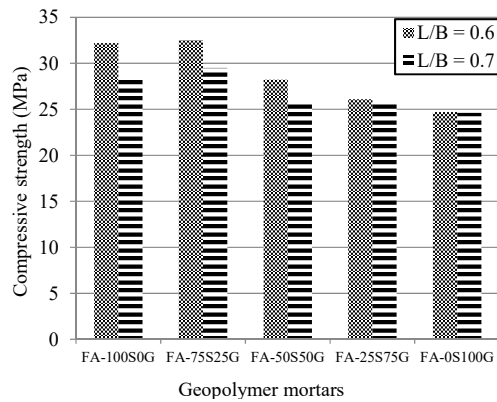


Fig. 2 The 28-day compressive strength of geopolymer mortars containing recycled glass.

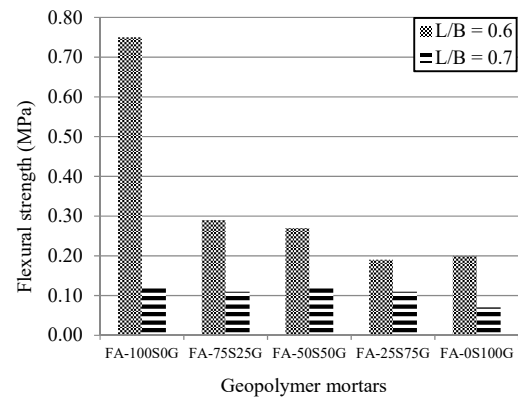


Fig. 4 The 28-day flexural strength of geopolymer mortars containing recycled glass.

CONCLUSION

This study investigated experimental study on compressive and flexural strength of fly ash based geopolymer mortar mixed with recycled glass. Recycled glass was used to partially replace fine aggregate at the amount of 0%, 25%, 50%, 75%, and 100% by weight. The results showed that compressive and flexural strength decreased with increasing of the amount of recycled glass replacement. At 25% replacement, it was found to be an optimal amount of recycled glass to provide 28-day compressive strength slightly higher than control specimens, 0% replacement, which is about 0.93% and 4.2% for L/B = 0.6 and 0.7, respectively. With higher than 25% sand replacement, the 28-day compressive strength tended to decline with the increase of amount of recycled glass in the mixtures. Both compressive and flexural strength at the age of 28 days were higher than 7-day curing due to the increase of degree of polymerization.

ACKNOWLEDGEMENTS

The authors gratefully acknowledge the financial support from European Commission Research Executive Agency, via a research grant (H2020-MSCA-RISE-2015-689857).

REFERENCES

- [1] Jin W, Meyer C, Baxter S, "Glascrete-Concrete with glass aggregate", *ACI Structural J.*, 90(2), 2000, pp. 208-213.
- [2] Meyer C, Egosi N, Andela C, "Concrete with waste glass as aggregate", in *Proc. of the Int. Symp. in Recycl. and Reuse of Glass Cullet*, Conc. Tech. unit of ASCE and Univ. of Dundee, Mar. 2001.
- [3] Park SB, Lee BC, Kim JH, "Studies on mechanical properties of concrete containing waste glass aggregate", *Cem. and Conc. Res.* 34(12), 2004, pp. 181-2189.
- [4] Shayan A, Xu A, "Value-added utilisation of waste glass in concrete", *Cem. and Conc. Res.*, 34(1), 2004, pp. 81-89.
- [5] Shi C, Wu Y, Riefler C, Wang H, "Characteristics and pozzolanic reactivity of glass powders", *Cem. and Conc. Res.*, 35(5), 2005, pp. 987-993.
- [6] Shayan A, Xu A, "Performance of glass powder as a pozzolanic material in concrete: a field trial on concrete slabs", *Cem. and Conc. Res.*, 36(3), 2006, pp. 457-468.
- [7] Schwarz N, Cam H, Neithalath N, "Influence of a fine glass powder on the durability characteristics of concrete and its comparison to fly ash", *Cem. and Conc. Comp.*, 30(6), 2008, pp. 486-496.
- [8] Soroushian P, "Towards board use of recycled glass concrete on MSU campus", *Innovation in Sustainability Seed Grant Report*, Michigan State University, Dec. 2012.
- [9] Le TT "Ultra high performance fibre reinforced concrete paving flags", Ph.D. Dissertation, University of Liverpool, 2008.
- [10] Yang SL, Millard SG, Soutsos MN, Barnett SJ, Le TT, "Influence of aggregate and curing regime on the mechanical properties of ultra-high performance fibre reinforced concrete (UHPFRC)", *Conc. and Build. Mat.*, 23, 2009, pp. 2291-2298.
- [11] Wille K, Naaman AE, Parra-Montesinos GJ, "Ultra-high performance concrete with compressive strength exceeding 150 MPa (22 ksi): A simpler way", *ACI Mat. J.* 108(1), 2011, pp. 46-54.
- [12] Kou SC, Xing F, "The effect of recycled glass powder and rejected fly ash on the mechanical properties of fibre-reinforced ultrahigh performance concrete" *Adv. in Mat. Sci. and Eng.*, Volume 2012, Article ID 263243, 2012, 8 pages.
- [13] Scrivener KL, Kirkpatrick RJ, "Innovation in use and research on cementitious material", *Cem. And Conc. Res.*, 38(2), 2008, pp.128-136.
- [14] ASTM C618-15, "Standard specification for coal fly ash and raw or calcined natural pozzolan for use in concrete", *Annual Book of ASTM Standard*, vol.04.02, 2015.

DEMONSTRATION OF LINER INTEGRITY MONITORING SYSTEM IN A GYPSUM WASTE CONTAINMENT

H.B. Ng¹ and Y.Y. Zheng²

¹GSE Lining Technology Co. Ltd, Bangkok, Thailand; ²CGSE Environmental Lining Technology (Suzhou) Co. Ltd, Shanghai Branch Company, Shanghai China

ABSTRACT

Polyethylene geomembranes have been widely used as primary barriers in environmental containments for decades. A good Construction Quality Assurance (CQA) plays an important role in producing a quality containment. Conventional geomembrane CQA program focuses only on quality of welded seams through traditional destructive and non-destructive seam tests. To ensure the sealing integrity of the installed geomembranes and long-term performance of the liner system, leak integrity surveys and monitoring are implemented so as to serve as validation at post-construction and even when the facilities are in operation. A new generation leak location liner system has been developed to facilitate a comprehensive liner leak testing and long term liner integrity monitoring. This paper presents a demonstration project carried out at a gypsum waste landfill facility in southwest China. Field investigations performed by third party surveyors have successfully and accurately located the blind holes placed by the local authority and owner of the facility. Results from the field tests demonstrated that the improved leak location liner system associated with permanent liner integrity monitoring technology can further reduce the risk of loss of containments, potentially enhances the environmental and economy sustainability of geomembrane lined facilities.

Keywords: CQA, Electrical Liner Integrity Survey, Leak Location Liner, Spark Test, Permanent Monitoring.

INTRODUCTION

Phosphate gypsum, a waste containing calcium sulfate generated during the production of phosphorus fertilizer, should be properly contained due to environmental concerns. A large fertilizer (phosphate gypsum) processing operation located at Guizhou province, Southwest China was selected in this study. It has several large canyon gypsum stack disposal sites with an average height of nearly 100 meters in the mountainous region. The waste disposal sites are lined with HDPE geomembranes and have been operating for almost 10 years.

Today, Guizhou is the only provinces in Mainland China that requires a compulsory engineered geomembrane lining system for general industrial solid waste disposal facilities. This has been imposed by the provincial criteria (DB52/865-2013) particularly due to the local karst geological features, where seepage and ground water contamination in this area could be much difficult to detect and remedy. The existing storage capacity that contains gypsum stack is expected to reach its capacity and hence plans are underway to build vertical expansions that combine two existing gypsum stacks, however leak prevention is a challenge to the design engineers in this particular site condition. It was then decided to construct a test pad to demonstrate the current best available technology and to acquire necessary engineering parameters for inclusion of this liner

system in the final design of the site expansion.

A demonstration project consisting of a preliminary test pad was built on an existing phosphate gypsum stack at the facility in October 2015. The preliminary test pad was lined with high-density polyethylene leak location liner (also known as electrically conductive geomembrane) as the primary barrier. After installation, an electrically spark testing was performed on installed liners at site to inspect for post-installation mechanical damage. A permanent Liner Integrity Monitoring System (LIMS) was conducted after the lined test pad has been covered with water, following with an Electrical Liner Integrity Survey (ELIS) performed on the test pad after covered with gypsum waste.

GEOMEMBRANE PERFORMANCE AND ELECTRICAL LINER INTEGRITY SURVEYS

Polyethylene geomembranes have been widely used as primary barriers in environmental containments for many decades. Many reports revealed that well-stabilized HDPE geomembranes are able to perform satisfactorily for decades if they are protected from mechanical aggressions. A proper geomembrane installation and associated construction quality assurance (CQA) is crucial to the long-term performance of lining system. Many case studies demonstrated that a well-planned and well-executed CQA produces a high quality containment

system; on the contrary, geomembrane will lose parts or all of its functions due to poor CQA. The leakage analysis shows that high quality liner installation associated with a complete CQA program reduces liquid losses by 92% at different hydraulic heads over that of poor installation without an effective CQA program. In addition, an important note regarding geomembrane liners with “low quality” installations: data and in-house surveys suggest that over 30% of such systems experience a failure that requires either a substantial reconstruction or complete replacement of the system (Beck et al., 2009).

Traditional geomembrane CQA program focuses only on weld quality through field destructive and non-destructive tests. To ensure the sealing integrity of installed geomembranes, field monitoring and leak integrity tests are required to serve as verification during and after construction, and even when the facilities are in operation. A case study of a landfill in Victoria, Australia indicated that 57 holes and 350 dimples were found on the installed HDPE geomembrane through electrical survey at post-installation even though a strict construction quality assurance program was executed (Bogoda et al. 2014).

Survey data on occurrence of liner defects reveals that 24% of total amount comes from preliminary construction phase (geomembrane deployment, seam welding, etc.), 73% is related to final construction phase (backfill on geomembrane), defects occurrence at post-construction, early operational phase only takes 2% (Nosko et al., 1996). Figures 1 and 2 are classic examples of such defects. In addition, traditional CQA program is only examining the liner quality during preliminary construction phase. These statistical data clearly indicates that in order to ensure the liner integrity and long-term performance, it is essential to carry out electrical liner integrity survey (ELIS) on the entire installed geomembrane. Electrically spark testing on exposed geomembrane (ASTM D7240) and dipole survey on covered geomembrane (ASTM D7007) are proven technologies for such surveys performed at the final construction stage. Leak location liner featuring a conductive backing is the geomembrane product that has been tested and verified to be able to enhance the efficiency and accuracy of ELIS.



Fig. 1 A defect caused by welding process.



Fig. 2 Liner damage caused by large aggregate.

Today, through combination of leak location liner and combi-modules, the system allows permanent leak monitoring of containments. The following section of this paper illustrates in details the application of ELIS and LIMS technologies in field and the results obtained from the demonstration.

DEMONSTRATION PROJECT

Test Pad Preparation

A test pad of 30m x 30m was constructed above an existing gypsum stack. The test pad was prepared with depth of about 30cm and side slope gradient of 4H: 1V. A 60cm deep trench was also constructed to anchor the geomembrane around the peripheral of test pad. The subgrade was properly compacted and levelling before receiving the geomembrane. Figure 3 shows the cross section of the test pad and Fig. 4 is an overview of the prepared test pad.

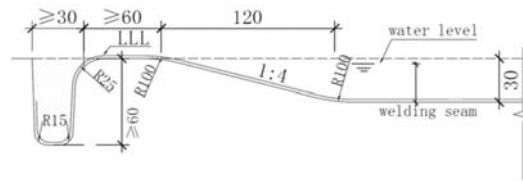


Fig. 3 Test pad cross section



Fig. 4 An overview of the compacted test pad.

Geomembrane Liner Installation

A 2.0mm thick white-surfaced leak location liner was directly deployed on the well-prepared subgrade foundation. Leak location liner has a thin integrated conductive layer at the bottom surface that is installed facing down. An ohmmeter can be used to check and ensure the connectivity of the conductive layer at site. The installation process of leak location liner is identical with that of standard geomembrane installation. Only few measures should be taken to ensure the geomembrane have a well-connecting electrically conductive bottom and a proper isolation of the dual track wedge welded conductive edges, which are the key factors to the success of ELIS and LIMS. These include:

1. Use ISolation-Wedge (Iso-Wedge) for welding the leak location liner. The Iso-Wedge is an improved fusion wedge that breaks the conductivity of the exposed flap from the rest of the sheet at the welded seams to avoid false positive signals when performing ELIS. The installer just have to replace the standard wedge with Iso-Wedge prior to seam welding and perform trial welding to verify that the Iso-Wedge functions as required (Figs. 5 to 7).

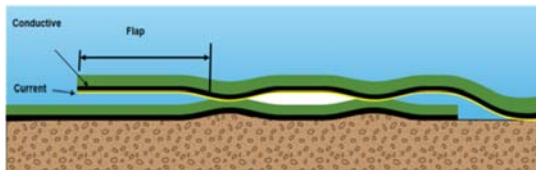


Fig. 5 Welded seam via conventional welder.

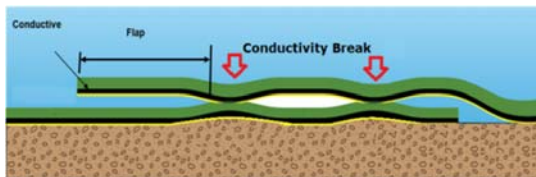


Fig. 6 Welded seam via Iso-wedge welder.



Fig. 7 Trial welding via Iso-wedge welder (left) and check conductivity at weld flap (right).

2. Place an extra piece of 1m x 1m leak location liner at every 15 meters interval under the welding seam with the conductive layer facing up. This is to enhance the electrical connectivity of two adjacent panels (Figs. 8 and 9).



Fig. 8 Extra piece insert and welding in progress.



Fig. 9 Installed White Leak Location Liner.

Field Spark Testing

Leak location liner is an HDPE geomembrane that incorporates an electrically conductive layer and can be utilized for post-installation inspection, i.e., spark testing per ASTM D7240. To perform spark testing, a high electrical voltage of negative polarity (neoprene pad) is applied to the membrane sheet to be tested, and an electrode of positive polarity (test wand) is then passed over the geomembrane. Fig. 10 shows the spark testing on installed geomembrane at site. Spark testing on the entire geomembrane surface was completed within few hours. Few damages caused during installation were found and patched.

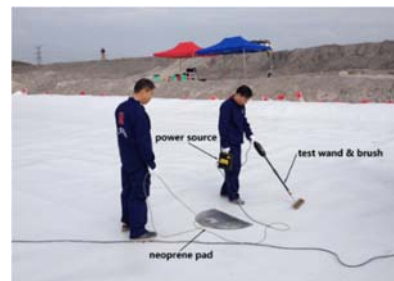


Fig. 10 Field spark testing on installed liner.

Permanent Liner Integrity Monitoring

By integrating combi-modules into Leak Location Liner as shown in Fig. 11, field tests have demonstrated that this advanced technology is capable of performing continuous monitoring and permanent quality control of geomembrane liners during the operation of the facility, which is the highlight of this demonstration project.



Fig. 11 Combi-Module embedded in Leak location liner.

Combi-module is an electronic device that acts both as energy source and as sensor. It is a rare metal plate and encapsulated into a HDPE casing, thus is expected to last as long as the geomembrane. The combi-module is embedded in the liner, for doing so, a hole that is slightly smaller than the combi-module is cut off in the membrane sheet and the sensor's flange is inserted and fixed by extrusion welding along the edge. As shown in Fig. 12, an integrated cable wire is assembled above the liner and connected with the central monitoring unit placed next to the test pad (normally indoor environment). The plugged-in central computer unit is responsible for collecting and analyzing data from the combi-modules located at different positions, supplying power and activates them.



Fig. 12 Installed combi-module with cable wire.

In the early field test that was performed to discover the synergies between the leak location liner and combi-module, it was found that when a hole was drilled on the liner, an electrical circuit between the energy source and sensor was formed, and the combi-module closest to the hole received the most significant levels of energy. It was concluded that the conductive layer of leak location liner, independent from the subgrade soil conductivity, provides "electrical super highway" to the generated current, geomembrane welds does no effect on the survey data, and data is complete reproducible (Weiss et al., 2014).

In this demonstration test pad, three combi-modules were designed and integrated into the installed leak location liner. Leak as tiny as 1 mm², that falls within the triangle area formed by the three combi-modules can be pinpointed. After the installation of leak location liner and combi-modules, and the set-up, calibrations of the central computer unit, a background state was established first. As shown in Fig. 13, the site was then flooded with acid water to a depth of 10-25 centimeters, and a local EPA officer was invited to create a hole of about 1.5 centimeters in diameter through the liner with the absence of all surveyors. The central computer unit responds swiftly within less than 30 seconds after the hole is drilled, receiving data from the three combi-modules to assist in locating the "blind" hole. From the measured data and the subsequent data analysis, the system detected the location of the blind hole with an estimated accuracy within a 1-meter diameter. This calculated location was compared with the actual measured location and was found varied by about 68 centimeters (See Fig. 14).



Fig. 13 Lined test pad flooded with acid water.

The amount and layout of combi-modules designed for leak monitoring depend on the site geometry and the required detection accuracy. When using leak location liner, the area monitored by one combi-module is able to cover up to 3,000m², which will provide a substantial reduction in numbers of combi-modules used for the leak monitoring and hence allowing a more cost-effective solution.

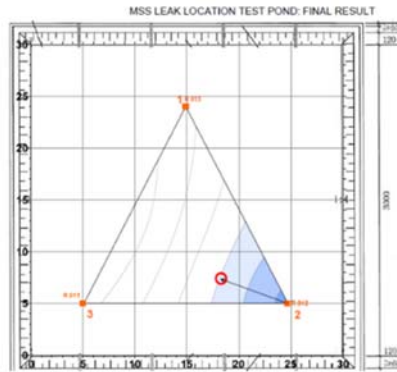


Fig. 14 Leak monitoring results.

Electrical Liner Integrity Survey (ELIS)

With the improvement of installation techniques, today Leak Location Liner also enables ELIS to be effectively performed over entire geomembrane and even with shallow cover soils or water. ELIS as detailed in ASTM D7007 are performed using the concept that if there is a sufficiently conductive medium both above (cover material) and below (subgrade soil or a conductive geomembrane layer) an insulating barrier (geomembrane) and each of these conductive mediums are oppositely electrically charged, electric current will flow towards and through any location where the integrity of the insulating barrier has been compromised. This current flow can then be detected using equipment that measures voltage drop between two measuring points. By taking these voltage drop measurements in a predetermined grid on the cover soil, holes can be pinpointed by finding locations where the current reverses direction (Ramsey B. et al., 2012).

To perform leak survey on a conventional non-conductive geomembrane, the conductive mediums must be in intimate contact with the geomembrane so that an electrical connection can be made through any holes in the geomembrane. For single-lined system using nonconductive traditional liner, an electrical liner integrity survey can only be performed successfully provided that the liner is in intimate contact with the subgrade soil that maintains sufficient natural moisture content. However, in most of the applications, that is not always a guaranteed condition to perform an electrical liner integrity survey on traditional geomembrane liner. In addition, covered ELIS cannot be performed easily on a double lined pond where the primary geomembrane liner is separated from the conductive subgrade by a geonet and a secondary liner. Similarly, even in a single lined

pond, a hole that is located at the peak of a wrinkle in the liner is unlikely to be detected by ELIS on the traditional liner because the electrical connection is broken by the lack of intimate contact between the hole and the subgrade soil. In addition, in cases where there is a dry subgrade or encapsulated geosynthetic clay liner (GCL), the material beneath the nonconductive traditional liner may not be sufficiently conductive to perform the leak survey (Peggs I., 2007). However, when using leak location liner, the conductive layer in the geomembrane will serve as the conductive medium at the base of geomembrane and the aforementioned issues are no longer the concerns (H.B. Ng et al., 2013)

At the demonstration test pad, a dipole test (quadrapole) was conducted by a third party surveyor after the local EPA personnel placed two “blind” holes and test pad was filled up with 30cm thick gypsum. Figure 15 shows the leak survey was in progress. The survey took almost 1.5 hours to complete and managed to identify leaks that were intentionally placed. One of the holes, nearer to the center of the site than the other was very accurately located to a distance of just a few centimeters. The other leak was closer to the edge of the liner and because of some edge distortion effects the accuracy was not quite as good, but still within a 20 to 30 centimeter radius. Figure 16 is the dipole test electric potential diagram with two leaks being detected.

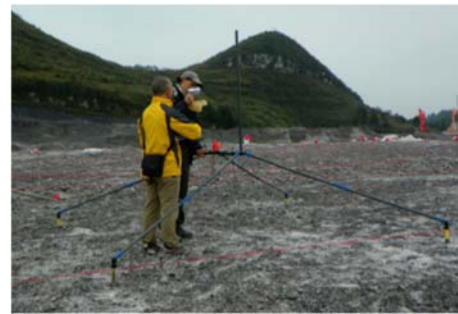


Fig. 15 Dipole (quadrapole) test in progress

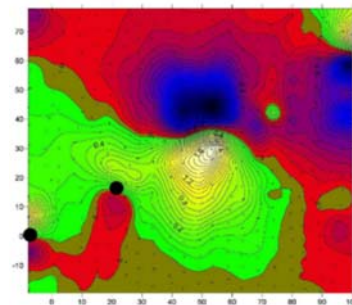


Fig. 16 Dipole test electric potential diagram.

SUMMARY AND CONCLUSION

A series of geomembrane leak tests has been successfully demonstrated at a phosphate gypsum stack in Southwest China. Leak testing was essential at different construction stages, from the initial deployment to the final construction and operation phases. Completion of the field performance tests in this demonstration project has demonstrated the ability of electrically conductive geomembrane (Leak Location Liner) to be used to facilitate an ELIS and permanent LIMS. Few defects on the geomembrane were located accurately, both intentionally placed damage and other damages during construction. Local EPA officers, project owner and design engineers are satisfied with the outcome of the field demonstration, which provides them a complete solution for the leak prevention at their future gypsum stack projects located at the karst topography landscape. Parameters and methodologies obtained from the demonstration project will be served as a reference for future design and construction of environmental containments in the region.

New generation leak location liner system, characterized by the modified welding and installation techniques, facilitates a comprehensive liner integrity tests, inclusive of spark testing on exposed Leak Location Liner, dipole test to be performed after the geomembrane is covered with shallow soils or water, permanent liner integrity monitoring at post-installation and even during the operation of the facility. The new generation leak location liner system has been successfully tested and verified as a reliable and effective technology that significantly enhances the quality of liner leak testing and to ensure a safeguard engineering containment system that potentially improves environmental and economy sustainability of geomembrane lined facilities.

ACKNOWLEDGEMENTS

The authors wish to express their greatest appreciation to Dr. Liu N. of Shanghai Jiaotong University, China; Dr. Geutebrück E of Texplor GmbH; Mr. Yuan Z. and Mr. Guo J. of Shenzhen Shengyi Environmental Co., Ltd. for their support and contribution in this paper.

REFERENCES

- [1] ASTM D7007, "Standard Practices for Electrical Methods for Locating Leaks in Geomembranes Covered with Water or Earth Materials", American Society for Testing and Materials, West Conshohocken, PA., USA.
- [2] ASTM D7240, "Standard Practice for Leak Location using Geomembranes with an Insulating Layer in Intimate Contact with a Conductive Layer via Electrical Capacitance Technique (Conductive Geomembrane Spark Test)", American Society for Testing and Materials, West Conshohocken, PA., USA.
- [3] Beck A., Smith M. and Sample K., "Design considerations for the use of the geomembranes for phosphate tailing impoundments", 3rd International Conference on the Valorization of Phosphates and Phosphorus Compounds (COVAPHOS III), Marrakech, Morocco, 2009.
- [4] Bogoda K. and Bouazza A., "Case study of a geomembrane liner damages in a new landfill cell located in Melbourne, Australia", 10th International Conference on Geosynthetics, Berlin, Germany, 2014.
- [5] DB52/865-2013, "Standard for Pollution Control on the Storage and Disposal Site for General Industrial Solid Wastes in Guizhou Province", Guizhou Environment Protection Agency & Quality and Technical Supervision Bureau of Guizhou Province, Guizhou, China.
- [6] H.B. Ng, D. Gallagher and A. Beck, "Electrically Conductive Geomembrane Enhances Liner Leak Detection Surveys at Post Installation", Third International Conference on Geotechnique, Construction Materials and Environment (GEOMATE 2013), Nagoya, Japan, Nov. 13-15, 2013, ISBN: 978-4-9905958-2-1 C3051.
- [7] Nosko V., Andrezal T., Gregor T. and Ganier P., "SENSOR damage detection systems (DDS) – The unique geomembrane testing method, Geosynthetics: Applications, Design and Construction", Proceedings of the First European Geosynthetics Conference, EuroGeo1, 1996, pp. 743-748.
- [8] Peggs I., "Liner integrity/leak-location survey: The significance of boundary conditions", Geosynthetics, Feb-Mar 2007, pp. 34-38.
- [9] Ramsey B.J., J., Youngblood J, Gallagher D. and Peggs I., "New electrically conductive geomembrane for post installation liner integrity surveys", Proc. Of the 5th European Geosynthetics Conference, Valencia, Spain, September 16-19, 2012, Volume 2, pp. 251-256.
- [10] Weiss B., Geutebrück E., "Next Generation Leak Location in HDPE Liners in Landfills and Other Facilities of Environmental Risk", 10th International Conference on Geosynthetics, Berlin, Germany, 2014.

THE USE OF STEEL FIBER EXTRACTED FROM WASTE TYRE AS REINFORCEMENT IN CONCRETE CONTAINING RICE HUSK ASH

Fauzan¹, Febrin Anas Ismail², Rio Sandi³ And Claudia Lovina A N⁴

¹Engineering Faculty, University of Andalas, Padang City; ²West Sumatera, ³Indonesia

ABSTRACT

The generation and disposal of waste are inherent to life itself and have presented very serious problems to the human community. Waste tyre is one of disposal problem, especially in Indonesia, more than 50 billion waste tyre was generated per year. Recently, some research has been devoted to the utilization of steel fibers extracted from Waste tyre (SFEFWT) in concrete. This study is focusing on the use of SFEFWT with containing rice husk ash (RHA) in concrete mix. Steel fibers was extracted from chips of waste tyres by manual cutting process and cut to 1 inch (25.4mm) length. Number of cylindrical specimen of steel fibers extracted from waste tyre (SFEFWT) with addition of 0%, 0.25%, 0.5%, 0.75%, 1% and RHA with addition 15% by cement weight was used in concrete mix to fabricated and tested. The mechanical properties, compressive strength, flexural strength and tensile strength at 28th day age were studied for concrete prepared. The result show that compressive, flexural and tensile strength was positively affected by the additions of SFEFWT on concrete containing RHA.

Keywords: Concrete; Steel Fiber; Waste Tyre; RHA; Compressive Strength; Flexural Strength; Tensile Strength.

1. INTRODUCTION

Concrete is the most frequently used construction material in the world. However, it has low tensile strength, low ductility, and low energy absorption. An intrinsic cause of the deficient tensile behaviour of concrete is its low toughness and the presence of mentioned defects. Therefore, improving concrete toughness and reducing the size and amount of defects in concrete would lead to better concrete performance. An effective way to improve the toughness of concrete is the addition of a relatively small fraction (usually 0.5–2.0% by volume) of short fibres to the concrete during mixing. Recent research is showing that adding to cement based materials recycled steel fibres (RSF) from wasted tires can decrease significantly the brittle behaviour of these materials, by improving its toughness and post-cracking resistance. The fibers such as steel, glass, polymeric, natural and plastic fibers mixed with concrete at particular cut length and specified aspect ratio and randomly distributed, can effectively be utilized to overwhelm such deficits. However, in developing countries like Indonesia the major problem to utilize steel fibers extracted from waste tyre (SFEFWT) produced from industry is inherent to life itself. In Indonesia, more than 50 billion waste tyre was generated per year.

The use of steel fibers extracted from waste tyre (SFEFWT) is day by day increasing in structural applications because of high stress resistance, toughness and long term strength. Using a little percentage of steel fibers efficiently improve the load-carrying capability of slabs on ground and significantly improve the slab ductility [1]. With the

inclusion of hooked steel fibers with cut length of 6 cm and aspect ratio of 80 and replacement of cement with 0.5%, and 1% improved the mechanical properties of concrete [2]. The inclusion of steel fibers in concrete considerably enhanced the engineering properties of mortar and concrete [3]. The addition of fibers to concrete considerably improves its structural characteristics such as static flexural strength, impact strength, tensile strength, ductility and flexural toughness [4]. The results of ultrasonic pulse velocity revealed that the using of small percentage of steel fiber in concrete improved the quality of concrete [5]. Recent study shows that the utilization of by-products such as fly ash and other materials for example, sawdust and glass powder is frequently used in recent research instead of rice husk ash (RHA). It was found that RHA which is high in silica content can become potential cement replacement material Turgut and Murat Algin [6]. RHA is a consequence of the cultivated industry which contains great amount of silicon dioxide (SiO₂). Ephraim et al [7] conclude that use of Rice husk ash in construction works will decrease the environmental pollution, strengthen the concrete quality and optimize the cost of concrete as well as resolving the problem of agricultural waste management. Khassaf et al [8] determine that workability of fresh concrete fall with the increase of RHA content. Rice Husk Ash concrete gives a durable and good structural concrete for both short term and long term considerations [9]. In this study, the effect of steel fiber extracted from waste tyre on concrete containing rice husk ash was investigated.

II. Materials and Method

II.1 Materials Used

II.1.1 Cement

Ordinary Portland Cement (OPC) commonly available in market was used.

II.1.2 Fine and Coarse Aggregate

Locally available aggregates were used; fine aggregate with size retained on 200 number sieve and passing from 4.75 mm. The specific gravity and fineness modulus of fine aggregate was 2.57 respectively. The coarse aggregate used was locally available quarry having two different sizes; one fraction is passing through 20 mm sieve and another fraction passing through 10 mm sieve. The specific gravity of 20 mm and 10 mm aggregates are 2.70 and 2.60 respectively.

II.1.3 Water

Potable tap water was used in mix preparation.

II.1.4 Steel Fiber Extracted From Waste Tyre

Waste tyres in Indonesia are the low-priced, economical and in abundance available material. In Indonesia there is a lack of appropriate recycling industry of waste tyres, manually a huge amount of Steel fiber are being taken out which includes a little quantity of rubber particles on their surfaces. In this study, the steel fibers taken out from waste tyres are used in the concrete mix to form a composite fibrous material. Steel fibers waste tyre were extracted from chips of waste tyres by manual cutting process (Figure 1 and Figure 2) and cut to 1 inch (25.4 mm) length (Figure 3) and average diameter of fiber was 0.28 mm keeping aspect ratio 90. As waste tyres steel fibers are uniformly and randomly distributed in different proportions from (0-1%) with increment of 0.25% by the weight of cement to prepare the different concrete matrix. The chips of waste tyres available in local market; normally they sell those as scrap to scarp industry.



Figure 1. Waste Tyre



Figure 2. Cutting Process From Waste Tyre to Obtained Steel Fiber Extracted

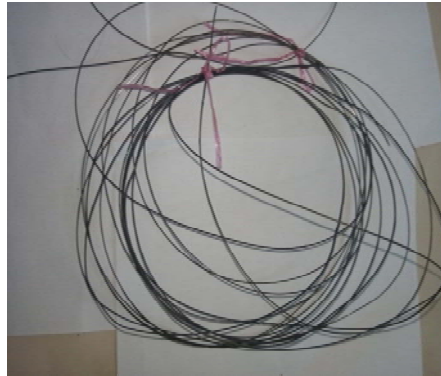


Figure 3. Steel Fiber Extracted From Waste Tyre



Figure 4. Steel Fiber in 1 Inch Cut Length

II.1.5 Rice Husk Ash

RHA is a consequence of the cultivated industry which contains great amount of silicon dioxide (SiO_2). RHA contains about 75 percent of organic content and the remaining 25 percent of husk is transformed into ash during the burning process, is identified as rice husk ash. RHA obtained from rice sheller in Padang. The specific gravity of RHA was 2.30. The chemical composition of RHA was tested at Indarung II, Padang Cement Factory Indonesia and the results is given in Table 1. Figure 4 shows the Rice Husk Ash material.

Table 1. Chemical Composition of Rice Husk Ash

Chemical Composition	Formulae	(%) Content
Silicon Dioxide	SiO ₂	90.13
Aluminium Trioxide	Al ₂ O ₃	1.88
Iron Oxide	Fe ₂ O ₃	0.89
Lime	CaO	0.23
Magnesium Oxide	MgO	0.87
Potassium Oxide	K ₂ O	2.55
Loss of Ignition	LOI	2.65



Figure 5. Rice Husk Ash

II.2 Experimental Program

II.2.1 Mix Proportions of Concrete

The concrete mix is designed as Indonesian Nasional Standar (SNI) for the normal concrete. M35 grade of concrete is used to examine the mechanical properties of concrete with 0.52 water - cement ratio. Five mixture proportions were made. First was control mix (with RHA, without steel fiber), and the other four mixes is steel fiber with percentage of 0.25%, 0.5%, 0.75%, 1% contained rice husk ash.

Table 2. Mix Proportions

Sampel ID	C	SF 0%	SF 0.25 %	SF 0.5 0%	SF 0.75 %	SF 1%
Cement (kg/m ³)	391	332.35	332.35	332.35	332.35	332.35
Water (kg/m ³)	205	205	205	205	205	205
F.A. (kg/m ³)	725.6	725.6	725.6	725.6	725.6	725.6
C.A. (kg/m ³)	108.8.4	108.8.4	108.8.4	108.8.4	108.8.4	108.8.4
SFEFW T (kg/m ³)	-	-	0.976	1.955	2.933	3.910
RHA (kg/m ³)	-	58.560	58.560	58.560	58.560	58.560

Cement was replaced with rice husk ash by weight. The proportions of cement replaced 15%. The ingredients of concrete were thoroughly mixed in a mixer machine till uniform consistency was achieved. Mix proportions are given in Table 2.

II.2.2 Casting of Specimens

Total 27 cylinders were casted, for compressive, tensile and flexural strength test. Cylindrical specimens of length 300 mm and diameter 150 mm and beam specimens of length 500 mm, wide 100 mm, high 100 mm casted with 0%, 0.25%, 0.5%, 0.75% and 1% with used waste tyre steel fibers extracted in Concrete containing rice husk ash addition 15% by weight of cement.

II.2.3 Testing of Specimens

Compressive, splitting tensile and flexural strength tests were conducted on cylindrical specimens and beam specimens using Universal testing machine (UTM) and Flexural test in the concrete laboratory of PT. Semen Padang as per SNI 1974:2011, ASTM C 496-86 and ASTM C 293-08. Figures 6, 7 and 8 show the specimens under compressive, splitting tensile and flexural testing in the laboratory.



Figure 6. Compressive Test on Cylindrical



Figure 7. Splitting Tensile Test on Cylindrical



Figure 8. Flexural Test on Beam

III. RESULT AND DISCUSSION

III.1 Compressive Strength

The results of the tests for compressive strength performed on the samples are shown in Table 3.

Table 3. 28 Days Compressive Strength of Cylinder Specimen

No.	(SFEFWT) Content (%)	Rice Husk Ash Content (%)	Compressive Strength (N/mm ²)
1	0	15	32.60
2	0.25	15	33.40
3	0.50	15	34.40
4	0.75	15	35.30
5	1.00	15	36.20

*SFEFWT : Steel Fiber Extracted From Waste Tyre

The results presented in Table 3, Figure 6 and Figure 9, that the compressive strength of concrete reinforced containing rice husk ash with percentages of SFEFWT slightly increases from 0% to 0.5%, 0.75% and 1% after 28 days. The maximum 11% increase i.e. 36.20 N/mm² as compared to without SFEFWT concrete; at addition of 1.0% SFEFWT.

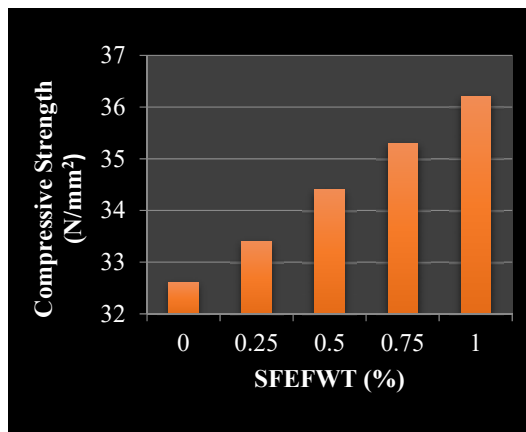


Figure 9. Average Compressive Strength of Ordinary and SFEFWT RHA Concrete

III.2 Splitting Tensile Strength

The results of the tests for splitting tensile strength performed on the samples are shown in Table 4.

Table 4. 28 Days Splitting Tensile Strength of Cylinder Specimen

No.	(SFEFWT) Content (%)	Rice Husk Ash Content (%)	Splitting Tensile Strength (N/mm ²)
1	0	15	2.76
2	0.25	15	2.83
3	0.50	15	2.93
4	0.75	15	2.98
5	1.00	15	3.35

*SFEFWT : Steel Fiber Extracted From Waste Tyre

The Splitting tensile strength in concrete containing rice husk ash mixes made with SFEFWT was determined at 28 days. The results presented in Table 4, Figure 7 and Figure 10, that the splitting tensile strength of concrete reinforced containing rice husk ash with SFEFWT increases with the increase of SFEFWT content. As can be seen from Table 4, the maximum 21% increase i.e. 3.35 N/mm² by addition of 1.0% SFEFWT on RHA concrete.

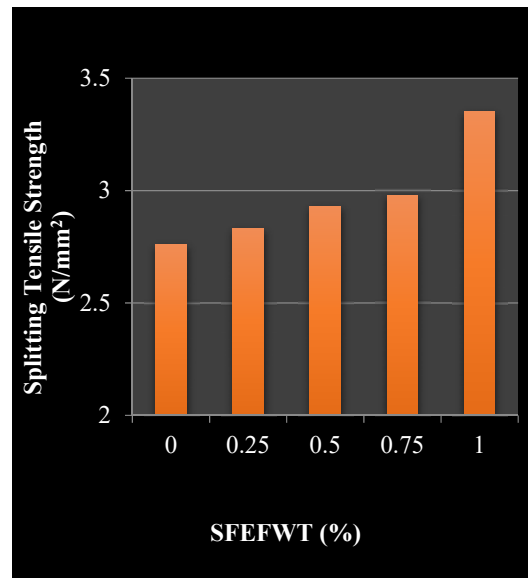


Figure 10. Average Splitting Tensile Strength of Ordinary and SFEFWT RHA Concrete

III.3 Flexural Strength

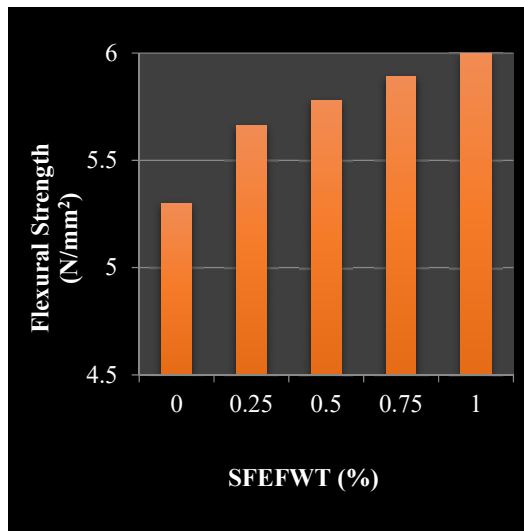
The results of the indirect flexural strength tests performed on the samples are shown in Table 5.

Table 5. 28 Days Indirect Flexural Strength of Cylindrical Specimen

No.	(SFEFWT) Content (%)	Rice Husk Ash Content (%)	Flexural Strength (N/mm ²)
1	0	15	5.30
2	0.25	15	5.66
3	0.50	15	5.78
4	0.75	15	5.89
5	1.00	15	6.00

*SFEFWT : Steel Fiber Extracted From Waste Tyre

The results of flexural strength of concrete containing rice husk ash mixes made with SFEFWT measured at 28 days are given in Table 5, Figure 8 and Figure 11. Test results indicate that the flexural strength increases as the percentage of the SFEFWT from 0% to 0.5%, 0.75% and 1%. The maximum flexural strength in concrete containing rice husk ash with the addition of 1.0% of SFEFWT is 6.00 N/mm², which is 13% increment as compared to conventional concrete.

**Figure 11. Average Flexural Strength of Ordinary and SFEFWT RHA Concrete**

IV. CONCLUSION

The following conclusions could be arrived at from the study:

- Compressive strength, Splitting tensile strength and Flexural strength of steel fiber extracted from waste tyre (SFEFWT) in Concrete containing rice husk ash concrete specimens were stronger than the plan concrete (control mix) specimens at all the percentage.

- At all the concrete investigated, the maximum of compressive strength 11% increase i.e. 36.20 N/mm² as compared to without SFEFWT concrete; at addition of 1.0% SFEFWT in Concrete containing rice husk ash.
- For splitting tensile strength, the maximum 21% increase i.e. 3.35 N/mm² was observed at addition of 1.0% SFEFWT as compared to without SFEFWT concrete.
- The maximum flexural strength with the addition of 1.0% of SFEFWT containing rice husk ash is 6.00 N/mm², which is 13% increment as compared to conventional concrete.

ACKNOWLEDGEMENTS

The authors wish to acknowledge the staffs of the Laboratory of Material and Structure in University of Andalas and the Laboratory of Concrete in Padang Cement Factory for their support.

REFERENCES

- Nili, M. Afrouhsabet, V. "Combined effect of silica fume and steel fibers on the impact resistance and mechanical properties of concrete" *International Journal of Impact Engineering*, Vol 37, pp 879-886. (2010)
- Luca G. S., Meda, A. and Giovanni, A. P. "Steel Fiber Concrete Slabs on Ground: A Structural Matter" *ACI Structural Journal*, Vol 103, pp 551-558 (2006)
- Yet, T.C., Hamid, R. and Kasmuri, M. "Dynamic Stress-Strain Behavior of Steel Fiber Reinforced High-Performance Concrete with Fly Ash" *Hindawi Publishing Corporation, Advances in Civil Engineering* vol. 2012, Article ID 907431, 6pages. (2012)
- Mohammadi Y, Singh SP, Kaushik SK. "Properties of steel fibrous concrete containing mixed fibers in fresh and hardened state". *Constr Build Mater* 2006; doi:10.1016/j.conbuildmat.2006.12.004.
- Nataraja, M.C., Nagaraj, T.S. and Basavaraja. S.B. "Reproportioning of steel fibre reinforced concrete mixes and their impact resistance" *Cement and Concrete Research*, Vol 35, pp 2350 – 2359. (2005)
- P. Turgut, H. Murat Algin, Limestone Dust and Wood Sawdust as Brick Material, *Building and Environment*, 42, 3399-3403 (2007).
- Ephraim M, Akeke GA, Ukpata JO. Compressive strength of concrete with RHA as partial replacement of ordinary Portland cement. *Scholarly Journal of Engineering Research*. 2012; 1(2):32–6.

- [8] Khassaf SI, Jasim AT, Mahdi FK. Investigation on the properties of concrete containing rice husk ash to reduction the seepage in canals. *International Journal of Scientific Technology Research*. 2014; 3:348–54.
- [9] Akeke GA, Ephraim M, Akobo IZS, Ukpata JO. Structural properties of rice husk ash concrete. *International Journal of Advances in Engineering Sciences and Applied Mathematics*. 2013; 3(2):8269.

AN INVESTIGATION ON THE STRENGTH OF AXIALLY LOADED COLD-FORMED STEEL Z-SECTIONS

James Matthew L. De Jesus¹ and Bernardo A. Lejano²

^{1,2}Gokongwei College of Engineering, De La Salle University, Philippines

ABSTRACT

Cold-formed steel (CFS) provides high strength-to-weight ratios that prove efficient in the construction of steel structures. CFS Z-section members exhibit buckling failures that may be difficult to predict due to complexity in geometry. There exists a gap in experimental and computational studies done in the Philippines regarding the structural performance of locally-produced CFS members. The objective of this study is to investigate the load-carrying capacity of Z-section CFS members when subjected to axial compression using experimental and computational methods. The study considers a total of 180 member samples with one section shape, six different lengths and six different thicknesses. Experimentally, the CFS members were subjected to compression loads using a standing steel frame with a hydraulic jack, a load cell and 4 displacement transducers to record the parameters needed for the investigation. High-speed video recordings were used to verify the different failure modes. These are then compared to computational results as per the National Structural Code of the Philippines (NSCP). Furthermore, the study also provides a comparison of experimental and computational results with Finite Element Method (FEM) using ANSYS. The main failure modes were torsional-flexural and distortional buckling. Torsional-flexural buckling was observed in 74.01% of the samples. Although 72.88% of the failure modes were predicted correctly, it was found that the provisions in the NSCP in predicting the strength of the member were relatively high with respect to the experimental and FEM results. This means that the predicted strength was non-conservative. It was also found that a modification factor of 0.52 can be used to achieve similar results between the predicted and actual strength of the member.

Keywords: Cold-formed Steel, Compression Members, Buckling Failures, Z-section

INTRODUCTION

The gap of experimental studies done in the Philippines for CFS may be overlooked by structural designers. The National Structural Code of the Philippines or NSCP (which will also be referred as the Code) stipulates design procedures based on foreign experiments and standards in the application of CFS members in the construction of various types of structures. The use of thinner sections and higher yield strengths can lead to structural design problems [1], [2]. These are due to its complexity that is not routinely encountered by most structural engineers. To allow for safety, the structure must be closely studied in accordance with the Code or other methods such as performance-based analysis.

Currently, there are design provisions for CFS members in the NSCP that can be used by structural designers. It has the capability of computing the compressive strength of Z-section CFS. However, these provisions in the Code were based on design standards formulated in other countries. Although the steel used may be the same, the process of local manufacturing may have slight variation that might affect its performance.

Over the years, the NSCP has been regarded as the sole basis of design of structures all over the

Philippines [3]. The provisions in the Code are assumed to be correct and safe. Confidence in safety is achieved when the provisions in the Code are religiously followed. However, the design provisions of Z-section CFS have not been fully verified in the field. Experimental tests are needed to confirm the accuracy of its design. In axial compression, Z-section CFS can be unstable in different failure modes such as local, distortional and flexural or torsional-flexural buckling [4].

For reference, the typical cross-section of a Cold Form Steel Z-section is shown in Fig. 1.

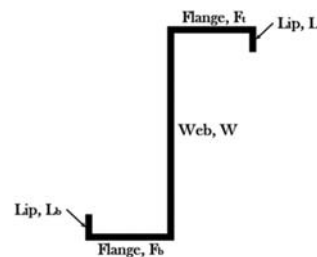


Fig. 1 Cross-section of Z-section CFS

The main objective of this study is to investigate the load carrying-capacity of Z-shaped Cold Formed

Steel when subjected to axial compression. The specific objectives are: (1) to investigate the different buckling modes; (2) to evaluate the axial strength based on the Code and experimental tests; (3) to analyze using Finite Element Method (FEM); and (4) to compare the predictions (Code and FEM) with the experimental results.

METHODOLOGY

This study focused on experimental and computational methods of research. The experimental method of this study is to conduct compressive tests on Z-section cold-formed steel to acquire its strength and mode of failure. The computational aspect of the study is done by using the formulas recommended by the Code in determining the strength and mode of failure of each member. The critical loads obtained from experiment and calculations are compared to verify the reliability of the Code provisions. Furthermore, these critical loads were then compared to the results of ANSYS Finite Element Method (FEM) analysis.

CFS Z-section specimens

The shape of the section is in the form of a Z and is skew symmetric. The section size conform to the limits for unrestrained Z-sections with simple lip stiffeners stipulated in section 553.4 of the NSCP. The Z-section is with a web and two flanges with simple lip stiffeners as shown in Fig. 1. It is also considered as a point-symmetric section. Based on the availability in the market and to conform to the limits, a 2" x 4" (50mm x 100mm) Z-section CFS member was used in the experiment. That is, 2 inches for the flanges and 4 inches for the web. The code adopted for each member sample type is tabulated in Table 1. There were six thicknesses and six lengths considered in the study. Each type has five test samples, for a total of 180 member samples considered in this study.

Table 1 Code used for the test member sample type

Code	Length (mm)	Code	Thickness (mm)
1	800	A	0.80
2	1100	B	1.00
3	1400	C	1.20
4	1700	D	1.40
5	1800	E	1.50
6	2000	F	1.80

The lengths of the members were based on the experiment done before for C-sections [5]. The thickness of the steel was also dependent on the available thickness that are commercially available. To ensure that calculations were accurate, actual

measurements of the dimensions of the samples were taken prior to test of each sample. The measurements were taken using a digital caliper measuring two flanges, two lips, web, thickness and overall height. Each element of the cross-section together with the thickness and length were measured three times at approximately three equidistant sections (e.g. top, middle & bottom). The web height is nominally 100 mm. The flange width is nominally 50 mm. The lip height is nominally 20 mm.

Material properties that were considered to affect the strength and failure modes of the member are the yield strength, f_y , and modulus of elasticity, E . These material properties were determined using ASTM E8: Standard Test Methods for Tension Testing of Metallic Materials where strips of metal were cut and tested from the sample population of Z-section CFS. These material properties together with the dimensions parameters were used in determining the nominal strength and effective dimensions of the web, flange and lip elements.

Experimental test set-up

The experimental set-up is illustrated in Fig. 2. The member sample was placed with its transverse axis at a 45-degree angle with respect to the plane of the steel frame. This is to allow space for the placement of the displacement transducer and to ensure that the displacements in the web and flange are recorded.

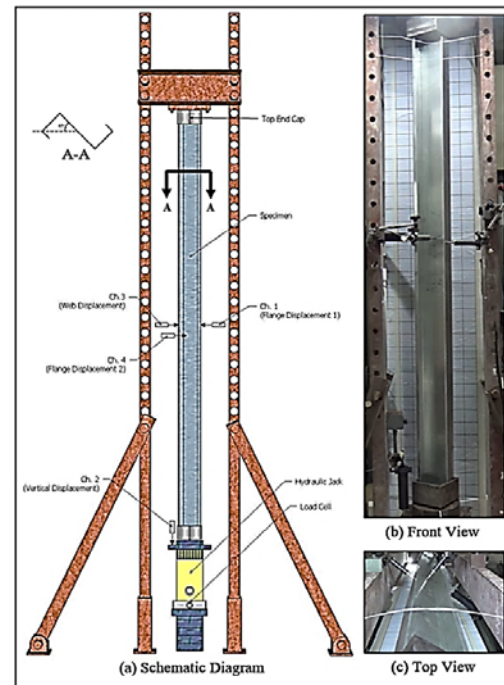


Fig. 2 Experimental set-up

The member samples were loaded axially in compression by the use of a hydraulic jack. The loading was gradual for all samples. Load cell was placed right below the hydraulic jack to monitor the load that was applied. To simplify the calculation of the axial force, the end conditions were designed to be pin-supported, that is, the supports are not restrained from twisting and bending [5]. To simulate the pin-ended condition of the member, steel end caps were placed in both ends of the member with a 20mm diameter bearing ball attached to provide a ball and socket mechanism for the sample to rotate freely about its ends. The ball was positioned so that the line of action of the force will pass through the centroid of the cross-section of the sample so that the members can be said to be concentrically-loaded.

Two displacement transducers were placed in both flanges to record the distortion. Another transducer was also placed in the web to record flexural and/or torsional movement. These three transducers were placed approximately at mid span. Another transducer was placed at the bottom cap to measure the vertical displacement. Data loggers, load cells and transducers were used to measure the experimental data for strength, displacement and deformation to provide accurate results. High-speed cameras were also used to observe the governing failure mode, which is the first buckling failure that occurred. The load, element movements and longitudinal movement were recorded using a data logger which was able to record all four displacements and the load applied to the member.

Failure modes

Evaluation of the failure modes is as important as determining the strength. The modes of failure are mainly of yielding, torsional or torsional-flexural or distortional buckling. The standing steel frame was used with data loggers to determine the movements of the member as it is loaded in compression. Local buckling was usually encountered first. Even if local buckling transpired, it was further loaded to see the buckling mode that the member will exhibit. The different modes of failure are illustrated in Fig. 3. However, the figures just demonstrate the general movements of the elements for each mode. The movement of the elements can either be inward or outward which makes the failure modes more complex. Consequently, a forward or backward movement can also transpire. Furthermore, there exists a local-global interaction in buckling failure modes such that multiple modes can be exhibited by a member sample [6].

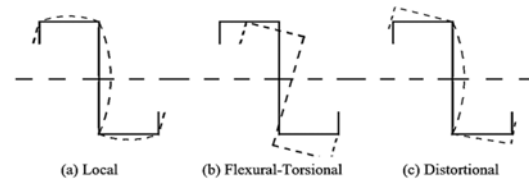


Fig. 3 Section buckling modes of failure

RESULTS AND DISCUSSION

The calculation of strength depends heavily on the values of the yield strength and modulus of elasticity of Galvanized Iron sheets or G.I. sheets from where the Z-section CFS were made from. Test results indicate an average yield strength obtained was 306.04 which is a typical strength for galvanized iron sheets. Furthermore, the average modulus of elasticity from the test was 23.99 GPa.

Evaluation of strength through experiment

The compressive strengths of the Z-section CFS were evaluated from the 180 samples with varying thickness and length. These strengths will be termed as “experimental strengths”. The experimental strength of each sample was taken as the maximum load recorded. The experimental strength results are summarized in matrix form in Table 2. The first column and first row represents the thicknesses and lengths, respectively. Referring from Table 1, codes A to F represent the thickness, while Codes 1 to 6 represents the length, both in ascending values.

Table 2 Experimental strength results (kN)

Code	1	2	3	4	5	6
A	1.64	1.37	0.93	1.19	1.20	0.79
B	2.41	2.06	1.94	1.87	1.39	1.46
C	3.21	2.92	2.73	2.51	2.45	2.13
D	4.96	4.33	4.17	3.31	2.84	2.77
E	5.08	4.13	4.80	4.06	3.36	3.09
F	8.16	6.93	5.84	5.18	4.65	3.73

As seen in Table 2, the experimental strengths were affected by the thickness and the length. The thicker the member the higher the load it can carry. The longer the member, the lower is the strength.

The length and thickness also influence the buckling mode of failure. Thickness governs the local buckling susceptibility of the individual elements. The length influences the global buckling susceptibility of the member. The values in Table 2 provide a more analytic measure on how much both parameters affect the strength of the member.

The observation of the failure modes was done by identifying the movement both locally and globally. Local, torsional-flexural, and distortional

buckling conditions were the main failure modes to be identified. These failure modes can be identified when similar failures are observed as those shown in Fig. 3. As example, Fig. 4 shows torsional-flexural (TF) and distortional buckling (DB). Yielding is not expected to be observed since the GI sheets used in the member are very thin.



Fig. 4 Failure due to torsional-flexural buckling (right) and distortional buckling (left)

Evaluation of strength through computation

The computations of the strength of the members, termed as “computational strength”, were done using the formulas and provisions stipulated in the NSCP for the design strength of Cold-Formed Steel compression members. These provisions are summarized in NSCP Sections 552 and 553. The Code considers three main failure modes for CFS Z-section members. These are yielding, torsional-flexural and distortional buckling. The computational strength considered based on the provisions of the code was taken as the lowest load amongst the three failure modes. Although the yielding strength is generally unattainable, it was still computed for comparison with the buckling strength. The computational strength results are summarized in Table 3.

The same influence of thickness and length is observed in the computational strength, that is: the longer the length, the lower the strength; and the thicker the member, the higher the strength. As seen in Table 3, the shortest length of 800 mm and a thickest GI sheet of 1.8 mm resulted to the largest computational strength.

Table 3 Computational strength results (kN)

Code	1	2	3	4	5	6
A	4.73	4.88	4.03	3.29	3.13	2.77
B	7.42	6.53	4.79	4.01	3.90	3.46
C	8.67	6.97	5.57	4.74	4.42	3.93
D	11.73	8.57	6.55	5.33	4.91	4.42
E	12.50	9.25	7.04	5.72	5.15	4.69
F	14.71	10.90	7.97	6.53	6.20	5.70

Evaluation of strength through FEM

“FEM strengths” is the term used for the strength of the members that were obtained using the FEM analysis. There were three general steps in determining the strength of a member. These are generation of the model and setting up of the boundary conditions, solving the model and gathering and analyzing the results [7]. Prior to analysis, an input for the modulus of elasticity, the yield strength, and density of 8027.28 kg/m³ were inputted in the engineering data. The FEM results are summarized in Table 4.

Table 4 FEM strength results (kN)

Code	1	2	3	4	5	6
A	0.63	0.78	0.78	0.76	0.82	0.71
B	1.54	1.58	1.25	1.47	1.58	1.58
C	2.12	2.34	2.38	2.55	2.50	2.42
D	3.88	4.03	3.74	3.89	3.64	3.76
E	4.57	4.93	4.51	4.83	4.57	4.41
F	7.89	8.30	7.37	7.52	7.08	6.09

The goal of using FEM is to verify further the results of the computational and experimental strength evaluations. The strength was analyzed using the Eigenvalue buckling analysis of ANSYS. A unit axial load was used as the initial load. A sample result of FEM is illustrated in Fig 5. The load multiplier is the strength of sample A1 in Newtons.

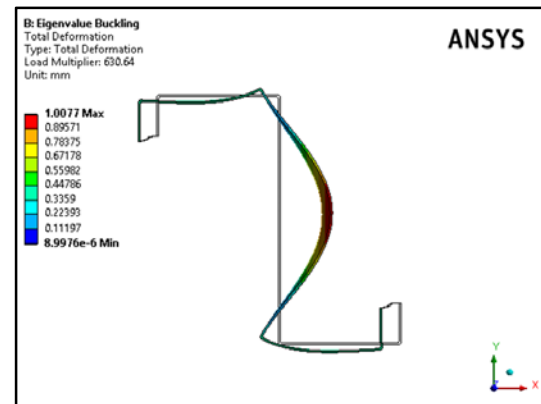


Fig. 5 Cross-section of sample A1 failure using FEM

Analysis of Strength Evaluation Results

The strength results are compared to one another, as shown in Fig. 6. The diagonal line is the equality line that represents the points at which the computational strength is equal to the experimental strength. Majority of the data points fall below the equality line, indicating over-estimate of the computational strength. The FEM/experimental strength was also plotted and showed good

agreement between FEM and experimental strengths. A linear regression was done to show slope for the best-fit line. The FEM strengths show better fit with the experimental results because the R^2 value (0.8379) is higher than the R^2 value (0.7107) of the computational strengths. Moreover, the y-intercept for the computational/experimental strength plot is approximately equal to zero. This means that a relatively direct relationship can be made between the computational and experimental strength, such that the slope of 0.52 can be used as a factor to make computational strength smaller so as to become almost equal to the actual strength.

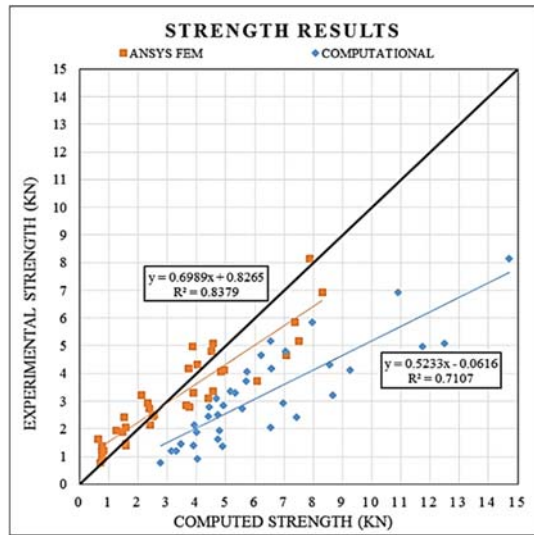


Fig. 6 Comparison of strength results

A comparison between the modes of failures is summarized in Table 5 to check for similarities between the computation and the experimental failure modes. It was calculated that 72.88% of the population are similar. Furthermore, Only 25.99% of the population exhibited distortional buckling failure. Torsional-flexural buckling was the most observed failure, at 74.01%, probably because the Z-section is an open section making it very flexible and weak in resisting to torsion.

The strength ratio is also shown in Table 5. Only the ratio of the experimental strength against the computational strength is shown due to limited space. The values indicated is less than one indicating that the Code does not provide conservative strength predictions. The other strength ratios were also calculated. The experimental against computational strength ratio yielded an average of 0.50 while FEM against computational strength ratio resulted to 0.54. The experimental and FEM agreed well with an average strength ratio of 1.10.

The FEM results were also compared with the computational and experimental results to verify further the reliability of the results. Statistical

analysis using ANOVA was conducted. The p-value for the computational and experimental strength was computed at 4.20×10^{-7} while that of the FEM and experimental was at 0.67. The results indicate that the FEM and experimental strength had no significant difference while the computational strength had significant difference from both the experimental and FEM strength.

Table 5 Compressive strength results.

Code	Expt. Mode Fail.	Comp Mode Fail	Ave. Expt.	Ave. Comp	Same ?	Expt/ Compt Ratio
A1	TF	DB	1.64	4.73	No	0.35
B1	DB	DB	2.41	7.42	Yes	0.33
C1	TF	DB	3.21	8.63	No	0.37
D1	TF	TF	4.96	11.69	Yes	0.42
E1	TF	TF	5.08	12.49	Yes	0.41
F1	TF	TF	8.16	14.71	Yes	0.55
A2	TF	TF	1.37	4.87	Yes	0.28
B2	TF	TF	2.06	6.53	Yes	0.32
C2	TF	TF	2.92	6.97	Yes	0.42
D2	TF	TF	4.33	8.57	Yes	0.51
E2	TF	TF	4.13	9.25	Yes	0.45
F2	DB	TF	6.93	10.90	No	0.64
A3	TF	TF	0.93	4.03	Yes	0.23
B3	TF	TF	1.94	4.79	Yes	0.41
C3	TF	TF	2.73	5.57	Yes	0.49
D3	TF	TF	4.17	6.55	Yes	0.64
E3	TF	TF	4.80	7.04	Yes	0.68
F3	DB	TF	5.84	7.97	No	0.73
A4	DB	TF	1.19	3.29	No	0.36
B4	TF	TF	1.87	4.01	Yes	0.47
C4	DB	TF	2.51	4.74	No	0.53
D4	TF	TF	3.31	5.33	Yes	0.62
E4	DB	TF	4.06	5.72	No	0.71
F4	TF	TF	5.18	6.53	Yes	0.79
A5	TF	TF	1.20	3.13	Yes	0.38
B5	TF	TF	1.39	3.90	Yes	0.36
C5	TF	TF	2.45	4.42	Yes	0.55
D5	DB	TF	2.84	4.91	No	0.58
E5	TF	TF	3.36	5.15	Yes	0.65
F5	TF	TF	4.65	6.20	Yes	0.75
A6	TF	TF	0.79	2.77	Yes	0.28
B6	TF	TF	1.46	3.46	Yes	0.42
C6	TF	TF	2.13	3.93	Yes	0.54
D6	TF	TF	2.77	4.42	Yes	0.63
E6	TF	TF	3.09	4.69	Yes	0.66
F6	TF	TF	3.73	5.70	Yes	0.66

To be able to use the formulas stipulated in the Code that would lead to a safe design, a factor=0.52 must be applied to the computational strength. When this factor is applied, the computational strength would result to a “factored strength” that agrees well with experimental strength as illustrated in Fig. 7. The solid line is the regression line after applying the factor to the original computational strength. On the other hand, the dotted line is the original computational strength.

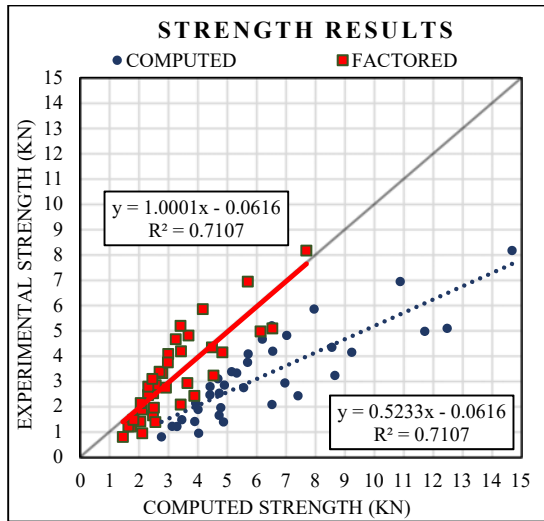


Fig. 7 Strength results with factor = 0.52

CONCLUSION

The local-global interaction of the buckling failure modes was dependent on the thickness and length of the member. The strength increases as the thickness increases. Consequently, it was found that the longer length contributed to the occurrence of global buckling failures. But, smaller lengths exhibit higher strengths.

The comparison of failure modes shows that 72.88% of the experimental results consistently agree with the computational results. It is concluded that the dominant failure mode was torsional-flexural buckling since 74.01% of the samples experienced this failure.

A comparison between the three strength evaluation methods (experimental, computational, and FEM) is done on the averages of the samples' strengths. The predictions made using the Code formulas were too high such that the average ratio between the experimental and computed strength was only 0.50. Thus it may be concluded that the use of the Code formula for this case (in its present form) may be non-conservative. On the other hand, the average ratio between the experimental and FEM results was 1.10 indicating good agreement.

A modification factor of 0.52 may be used by multiplying it to strength obtained based on the Code. This is to achieve a relatively similar result between the predicted strength and actual strength of the member. This may be done to allow for the use of the provisions of the Code without changing the stipulated equations.

ACKNOWLEDGEMENTS

Throughout the duration of this study, there are numerous people that the authors would like to

thank. Acknowledgement is due to De La Salle University – Manila, Civil Engineering Department for the BSMS program. ERDT is also appreciated for providing the scholarship to one of the authors and for providing a research grant. The authors also acknowledge those who helped in the whole research process, especially in doing the experimental tests.

REFERENCES

- [1] Dubina D, Ungureanu V & Landolfo R, Design of Cold-Formed Steel Structures 1st Edition. Berlin: European Convention for Constructional Steelwork, 2012, ch. 4.
- [2] Hancock GJ, "Cold-formed steel structures", Journal of Constructional Steel Research, Vol. 59, April 2003, pp. 473-487.
- [3] Association of Structural Engineers of the Philippines, Inc. (ASEP), National Structural Code of the Philippines Volume 1, 6th Edition, 4th Printing. Philippines: Association of Structural Engineers of the Philippines, Inc. (ASEP), 2010, ch. 5
- [4] Rondal J, "Cold formed steel members and structures: General Report", Journal of Constructional Steel Research, Vol. 55, 2000, pp. 155-158.
- [5] Yu A and Lejano B, "Investigation on the Strength of Cold-Formed Steel C-Section in Compression" in International Conference on Advances on Civil, Structural, Environmental and Bio-Technology CSEB 2014, Kuala Lumpur, Malaysia, 2014.
- [6] Batista E, "Local-global buckling interaction procedures for the design of cold-formed columns: Effective width and direct method integrated approach", Thin-Walled Structures, Vol. 47, April 2009, pp. 1218-1231.
- [7] MacDonald M & Kulatunga M. "Finite Element Analysis of Cold-Formed Steel Structural Members with Performations Subjected to Compression Loading", Mechanics and Mechanical Engineering, Vol. 17, May 2013 pp. 127-139.

INVESTIGATION OF THE EFFECTS OF DIFFERENT NATURAL FIBERS ON THE STRENGTH OF COMPRESSED STABILIZED EARTH BLOCKS (CSEB)

Kyle Solomon D. Pineda¹ and Bernardo A. Lejano²

^{1,2}Gokongwei College of Engineering, De La Salle University, Philippines

ABSTRACT

This study investigates the most effective combination of natural fibers (namely coconut coir, abaca, and maguey) used as reinforcement for Compressed Stabilized Earth Blocks (CSEB). Portland cement and 0.25% fibers by weight were used to stabilize and reinforce CSEB, respectively. The blocks were made primarily with Manila soil and were formed using hand-pressed machine. CSEB without fibers were first tested with varying cement contents of 6%, 8%, 10%, and 12% by weight. This was examined to determine the practical cement content (PCC). Three strength tests namely dry compressive strength, wet compressive strength, and flexural strength were conducted on CSEB at PCC with different fiber combinations of coir, abaca, and maguey fibers to determine the mix producing maximum strength. The highest dry compressive strength was obtained with 100% maguey fiber; the highest wet compressive strength was obtained with 100% abaca fiber; while the highest flexural strength was obtained with 17% coir fiber, 17% abaca fiber, and 67% maguey fiber. Using the Response Surface Methodology (RSM), the maximum strengths were predicted as follows: 100% maguey for dry compressive strength, 100% abaca for wet compressive strength, and 38.4% abaca and 61.6% maguey for flexural strength. However, the optimal mix of CSEB for three the strength tests consists of CSEB with 42.5% abaca and 57.5% maguey. The fibers were found to improve the performance of the block such as the strength and post-crack behavior. Furthermore, the performances of a wall made of fiber-reinforced and unreinforced CSEB were investigated. The test results showed a 33.79% increase in load carrying capacity of the fiber-reinforced wall compared to unreinforced wall.

Keywords: Earth Blocks, Natural Fibers, Abaca, Coir, Maguey, Response Surface Methodology

INTRODUCTION

Agricultural wastes are thrown away every day and if not properly managed, these wastes can have an impact on the general condition of the environment by degrading water quality and contributing to the amounts of pollution that is already present. By utilizing certain wastes such as coconut coir fiber, abaca fiber, and maguey fiber, will not only help protect the environment, but will also help provide alternative housing materials for construction. Given the abundance of these agricultural wastes in the Philippines, this drastically helps the environment through recycling waste materials and utilizing them for different applications such as in construction.

Housing problem exists in both rural and urban areas today; wherein both government and non-government agencies have undertaken measures to provide solutions for this problem, one of which is providing informal settlers with low-cost houses.

A building material that is often underestimated but has immense beneficial effects to society is the compressed stabilized earth block (CSEB). This is a type of construction block primarily made up of mechanically compressed soil stabilized by cement or lime. Cement stabilization is preferable for sandy

soils to achieve immediate higher strength while lime stabilization is used for clayey soils. Soil as a building material has its own advantages such as cost efficiency, virtually soundproof, non-toxic, environmental friendly, durable, abundant, and thermal properties.

Compaction of moist soil, containing 4-20% optimum moisture content (OMC) and often combined with 3-8% cement stabilization by weight of soil, based on economic standard, can significantly improve compressive strength, water resistance, durability, dimensional stability, resistance, and tolerances, in comparison with traditional adobe blocks [1]. To further improve its mechanical properties and, at the same time, reduce waste, researchers are reinforcing it with natural fibers as they show a significant result in post-peak load deformation behavior. The use of fiber reinforcement into CSEB production creates a network of fibers that prevents cracking of the soil resulting from shrinkage and improves tensile and shearing strengths [2], [3]. The inclusion of fibers into CSEB results to resistance towards higher stresses by absorbing high amounts of energy, making them particularly important in earthquake prone regions [4].

The purpose of this study is to evaluate binding

effects of coir, abaca, and maguey fiber; such as increasing strength and improving post-crack behavior. It is hypothesized that using these fibers increase the mechanical properties. The resulting strengths were also expected to vary depending on the fibers used and the characteristics of the chosen soil. Knowing these can increase the efficiency of CSEB usage. However, the long-term behavior and durability of the fibers are not included in this study.

METHODOLOGY

The soil used was obtained from a construction site in Recto, Manila. The soil sample used consists of 2.5% gravel, 69.7% sand, 27.8% fine. With this particle distribution, the soil used was classified as silty sand with shell fragments. The maximum dry density of the soil was 1,530 kg/m³ while the specific gravity was 2.67. Cement stabilization is recommended for soil with a plasticity index of 15% or less [5]. Since the soil was found to have negligible plasticity, cement was used. The OMC of the soil was determined to be 15.19%. Soil at OMC is the recommended condition to produce the blocks. For high strength blocks, additional quantity of water is needed. Therefore, a moisture content of 16% was used in the CSEB mixture.

The length of the fibers considered was based on the studies of [6], [7], where 50-mm fibers were used in the production of their CSEBs. The coir fibers were processed using dry mill while abaca fibers were extracted by hand. Consequently, maguey fibers were retted in the ocean.

Shown in Table 1 are the properties of the fibers used in this study. The coir fiber has the lowest tensile strength, though it is above the average tensile strength of 75.5 N/g.m. set by Philippine Fiber Industry Development Authority (PhilFIDA). Abaca and maguey fibers have almost the same tensile strength, which is relatively high compared to the coir. Although coir fiber has the lowest tensile strength, it has the highest capacity to elongate which is about twice of the standard of PhilFIDA of 10.62%. On the other hand, both abaca and maguey fiber exhibit low elongation.

Table 1 Physical properties of the fibers

Fiber	Grade	Tensile Strength	Elongation
Coir	CH-3	112.6 N/g.m.	20.43%
Abaca	S2	215.9 N/g.m.	2.59%
Maguey	MR-1	232.3 N/g.m.	2.59%

Blocks with varying cement contents of 6%, 8%, 10% and 12% were tested for compressive strength to determine the practical cement content (PCC). The results of the test are shown in Table 2. The strengths obtained were compared to the classification of CSEB that is presented in Table 3.

There are three categories to classify CSEB based on its strength and usage according to [8]. The strengths shown in Table 3 are dry compressive strength, wet compressive strength, and flexural strength.

Table 2 Compressive strength per cement content

Cement Content (%)	Average Compressive Strength (MPa)
6	3.27
8	3.79
10	4.83
12	5.06

Table 3 Classification based on strength [8]

CSEB	Dry	Wet	Flexure
Category I	≥ 2 MPa	≥ 1 MPa	≥ 0.345 MPa
Category II	≥ 4 MPa	≥ 2 MPa	
Category III	≥ 6 MPa	≥ 3 MPa	

The average compressive strength for 6% and 8% cement content suggests that they are classified as Category I. On the other hand, cement contents of 10% and 12% are classified as Category II. Data produced by various researchers show strong, often linear, correlation between compressive strength and cement content [1]. However, handling of blocks with 6% cement content obtained cracks when transferred. This entails that the handling of the blocks need to be considered in choosing the practical cement content (PCC). Therefore, a cement content of 8% was used in this study. This complies with the suggested cement content of 3% to 8% based from an economic stand point [5].

Block Production

The CSEBs were mixed at 16% moisture content, 8% PCC (Category I CSEB), and 0.25% fiber content as shown in the mixes in Table 4.

Table 4 Design mix of reinforced CSEB by weight

Mix Variations of Fibers	Coir, C (g)	Abaca, A (g)	Maguey, M (g)
(1) 100C	15	0	0
(2) 100A	0	15	0
(3) 100M	0	0	15
(4) 50C-50A	7.5	7.5	0
(5) 50A-50M	0	7.5	7.5
(6) 50C-50M	7.5	0	7.5
(7) 67C-17A-17M	10	2.5	2.5
(8) 17C-67A-17M	5	10	2.5
(9) 17C-17A-67M	2.5	2.5	10
(10) 33C-33A-33M	5	5	5
(11) Control Mix	0	0	0

The CSEB used in this study measures 295 mm x 140 mm x 100 mm. The blocks were formed using a hand-pressed machine. The soil weight per block was 6kg, resulting to 15g of fiber that is to be mixed per block. Fifteen block specimens were prepared and tested for each mix shown in Table 4. Five specimens for each of the three strength tests.

Strength Test

The blocks were subjected to three strength tests, namely dry compressive strength, wet compressive strength, and flexural strength, after 28 days of curing, to evaluate the effects of natural fibers on CSEBs. The blocks for dry and wet compressive strength had the same production and testing process. The main difference was that the blocks for wet compressive strength test underwent full submersion in water bath for 24 hours before testing, while the blocks for dry compressive strength test are directly tested after 28 days of curing. A uniform loading rate of 0.0575 MPa/s must be applied for the three strength tests [8].

Drop test was performed to qualitatively test the block's impact strength. The blocks were subjected to fall freely at a height of 3.5 meters. This was done to further highlight the effect of fiber reinforcement and post-crack behavior difference between fiber-reinforced and unreinforced CSEB.

Wall Test

A wall test was conducted on walls made unreinforced CSEB and fiber-reinforced CSEB. It has seven staggered rows with 3 blocks each. As shown in Fig. 1, a proving ring was placed on top of the wall to measure the load applied by the two hydraulic jacks to the wall panel. The hydraulic jacks were situated below the constructed wall. The two dial gauges were placed on opposite sides of the wall to measure the displacement.

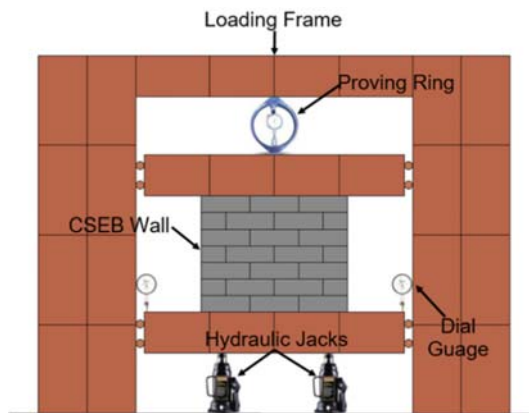


Fig. 1 Wall test set-up

Prior to the wall test, fiber-reinforced CSEBs and unreinforced CSEBs were tested again for their dry compressive strength to be used in the computation of the expected maximum load that can be applied on the wall.

RESULTS AND DISCUSSIONS

The results of the tests of the blocks and the test of the walls will be presented in this section.

Testing of Blocks

The results of testing of blocks are presented in terms of how the fibers influenced the following: strength test, failure mode, drop test, and optimal mix.

Influence of Fiber on Strength Tests

The summary of the strength tests are tabulated in Table 5. The values are the average strength of the test results of 5 CSEB specimens.

Table 5 Experimental strength test results

Mix	Dry (MPa)	Wet (MPa)	Flexure (MPa)
100C	2.83	2.05	0.377
100A	2.99	3.13	0.297
100M	4.27	2.53	0.407
50C-50A	2.71	2.20	0.459
50A-50M	3.16	2.49	0.466
50C-50M	2.84	1.86	0.351
67C-17A-17M	2.08	1.76	0.409
17C-67A-17M	2.15	1.80	0.449
17C-17A-67M	2.13	1.80	0.495
33C-33A-33M	2.93	1.80	0.380
Control Mix	3.00	1.99	0.424

The dry compressive strength test was performed to determine the strength of the blocks that were cured for 28 days. The compressive strength is mainly influenced by the type of soil, compacting procedure, and binding materials used [9]. The control (unreinforced) CSEBs have an average dry compressive strength of 3.00 MPa. This value satisfied Category I CSEB, which has a minimum dry compressive strength of 2 MPa. On the other hand, the highest dry compressive strength for the fiber-reinforced CSEB was obtained from samples with 100% maguey fiber (100M), which is 4.42 MPa or additional 42.33% strength compared to the control.

The RSM was used to plot a 3D surface model for dry compressive strength and the result is shown in Fig. 2. This model was chosen to analyze the data

because of its ability to show the relationship between any fiber combination and its corresponding dry compressive strength. Using this model, the highest value of dry compressive strength was predicted to be 4.19 MPa at 100% maguery fiber (100M).

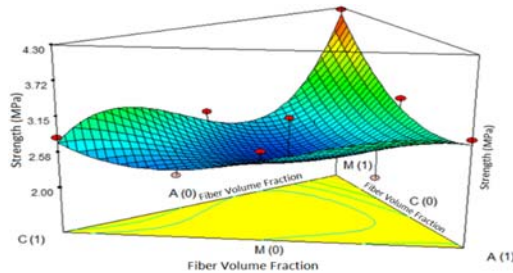


Fig. 2 Dry compressive strength model using RSM

The wet compressive strength test was performed to determine the strength of the blocks that were cured for 28 days and then submerged in water for 24hrs. Unreinforced CSEB has an average wet compressive strength of 1.99 MPa, which satisfy the requirement for Category I CSEB. On the other hand, the highest average wet compressive strength for reinforced CSEB, was found to be 3.13 MPa at 100% abaca fiber (100A). Thus, resulting to an additional 57.59% in strength compared to the control mix.

Similar to dry compressive strength, the RSM was used to plot a 3D surface model for wet compressive strength and is shown in Fig. 3. Using this model, the highest value of wet compressive strength was predicted to be 3.11 MPa and at 100% abaca fiber.

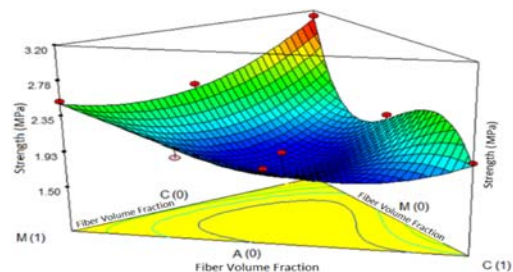


Fig. 3 Wet compressive strength model using RSM

The flexural strength test was performed to determine the 3-point bending strength and the post-crack behavior of the blocks that were cured for 28 days. It was obtained that unreinforced CSEB has an average flexural strength of 0.424 MPa, which satisfies the strength for Category I CSEB. However, the block failed immediately after the peak strength, breaking it in two and discontinues further testing on

said block. On the other hand, the highest average flexural strength of 0.495 MPa was obtained by specimens with 17% coir, 17% abaca and 67% maguery (17C-17A-67M) and this resulted to an additional 16.89% strength compared to the control.

Similar to dry and wet compressive strength, RSM was used to plot a 3D surface model for flexural strength as shown in Fig. 4. Using this model, the highest value of flexural strength was predicted to be 0.483 MPa and at 38.4% abaca and 61.6% maguery (38.4A-61.6M).

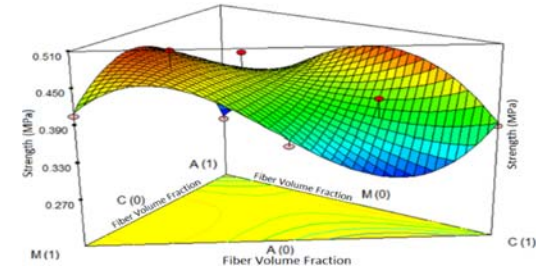


Fig. 4 Flexural strength model using RSM

Influence of Fiber on Failure Mode

The results obtained suggest that the higher the tensile strength of the fiber, the stronger the block is. For dry and wet compressive strength test, it was evident that the fibers provided sufficient resistance towards breakage, holding the block more intact compared to the unreinforced CSEB. This supports the theory where reinforcing fibers in the soil matrices prevent cracking through their adhesion or bonding [6]. Meanwhile, unreinforced CSEB presents noticeable breakage since there is no added fibers that holds the block together. Said breakage occurs roughly 15% of the block population.

For flexural strength, unreinforced CSEBs underwent sudden failure resulting in a total separation of the block in two halves during its 3-point loading test. This sudden failure was present at roughly 1 second of the test, immediately ending the experiment. Meanwhile, fiber-reinforced CSEBs were tested until the fiber reinforcement can no longer sufficiently hold the block for further testing. The presence of the fibers prevented sudden failure or total separation of the block and allowed continuous testing. Upon the removal of the reinforced CSEB from the testing machine, it became apparent that the blocks were split in two but were still held together by the fibers. The observed failure mode was consistent with the findings reported by [1], [10].

Drop Test

A drop test is the simplest way to qualitatively emphasize the advantage of reinforced CSEB

against unreinforced CSEB in terms of the post-crack behavior. The drop test was performed by releasing the block at a height of 3.5 meters above ground. Dropped unreinforced CSEBs disintegrated into many pieces upon impact, which shows a zero-possible recovery. On the contrary, dropped fiber-reinforced CSEBs obtained damages but it did not disintegrate fully. This clearly suggests that fiber inclusion improves post-crack behavior.

Optimal Mix

Using RSM, the optimal mix or most desirable fiber combination based on the 3 strength tests was obtained. The desirability of the fiber mixtures is shown in Fig. 5 using a contour model. The best desirability has a value of 1.0. Based on the figure, it can be deduced that any mixture combining the three fibers results to low desirability. The optimal mix is the combination of 42.5% abaca fiber and 57.5% maguey fiber (42.5A-57.5M), with a desirability value of 0.703. Using this model, the predicted dry compressive strength, wet compressive strength, and flexural strength for the abaca-maguey values were found to be 4.42 MPa, 2.40 MPa, and 0.482 MPa, respectively.

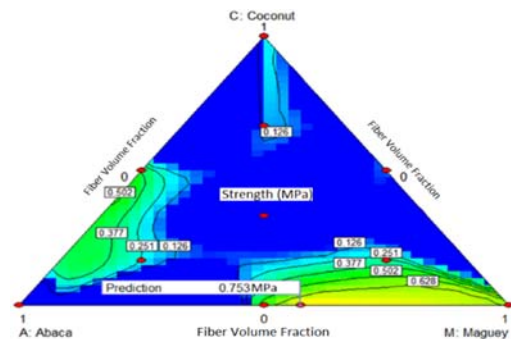


Fig. 5 Optimum mix based on desirability contour

A verification test was performed for the optimal mix (42.5A-57.5M) to compare the resulting data achieved through the RSM with the actual results. The predicted value for the dry compressive strength is 4.42 MPa and the actual value from testing is 4.19 MPa resulting to a 5.48% difference. The predicted value for the wet compressive strength is 2.40 MPa and the actual value from testing is 2.46 MPa resulting to 2.44% difference. Lastly, the predicted value for the flexural strength is 0.482 MPa and the actual value from testing is 0.525 MPa resulting to a 8.19% difference. Thus, the predictions made by RSM are highly reliable.

Wall Test

The blocks in the CSEB wall were arranged in staggered manner. The wall has a dimension of

width, height, and thickness of $W=900$ mm, $H=700$ mm, and $T=140$ mm, respectively. The test was done by gradually applying compressive force on the wall. The failure load was measured and was also predicted by calculating the maximum compressive load (P_c), bucking load (P_e), and shear load (P_v). The formulas used are as follows:

$$P_c = f_{dry} (WT) \quad (1)$$

$$P_e = \pi^2 EI/H^2 \quad (2)$$

$$P_v = A_{sheared} \frac{1}{6} \sqrt{f_{dry}} \quad (3)$$

Where f_{dry} = dry compressive strength of the block at the day of wall testing, E = modulus of elasticity of the wall, and $A_{sheared}$ = area sheared calculated by multiplying the wall width by the product of the block height x the number of rows sheared.

Unreinforced Wall Test

The peak strength was measured to be 142.61 kN. Shown in Fig. 6 is the observed failure pattern of the wall. It can be noticed that the diagonal crack indicates shear failure. The crack passed through 4.5 rows of blocks. The dry compressive strength of these unreinforced blocks is $f_{dry}=3.66$ MPa.



Fig. 6 Complete failure of unreinforced wall

Reinforced Wall Test

The peak load was measured to be 190.79 kN, Almost the same pattern of failure was observed, indicating that the failure mode is also shear. The crack passed through 5 rows of CSEB blocks. The dry compressive strength of these fiber-reinforced blocks is $f_{dry}=4.56$ MPa.

Comparison of Wall Panels

It was clearly observed that the fiber-reinforced CSEB wall was able to carry higher load than the unreinforced CSEB wall. This corroborate with the previously finding that fiber-reinforced CSEB is stronger than unreinforced CSEB. Shown in Fig. 7 are the plots of the load-displacement curves of the two walls. The wall test show that the fiber-reinforced wall exhibit 33.79% increase in load

carrying capacity than the unreinforced wall. The lower stiffness of the fiber-reinforced CSEB wall may be attributed to the elongation of fibers causing larger displacement but with an increase strength.

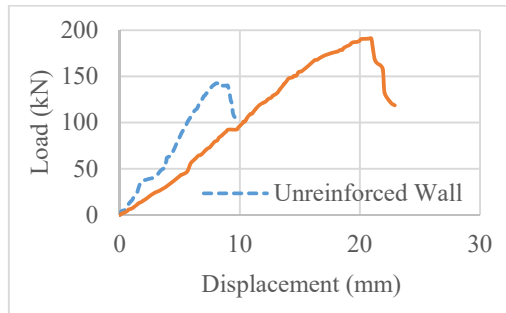


Fig. 7 Load-displacement diagram of CSEB walls

Based from the calculation of strength at failure, both wall panels failed in shear as indicated in Table 6 since the calculated shear load is closest to the actual load. The calculations were done using Eq.(1) to Eq.(3).

Table 6 Calculated load compared to actual load

Wall type	Pc (kN)	Pe(kN)	Pv(kN)	Actual
U-CSEB	457.3	8120.4	129.1	142.6
FR-CSEB	572.5	4634.7	160.1	190.8

Note: U=unreinforced, FR=fiber reinforced

CONCLUSION

The effects of adding coconut coir, abaca, and maguey fibers in CSEB were investigated. The results showed significant strength improvement of CSEB at certain fiber combination may be obtained for all strength tests conducted. RSM was used to model how the strength may be predicted for s given fiber combination or vice-versa. Furthermore, using RSM, a mix of 42.5% Abaca and 57.5% Maguey was predicted and verified to be the optimum mix. The increase in strength may be explained by the bonding effect of the fibers.

The wall test of reinforced CSEB walls shows a 33.79% increase in compressive strength compared to unreinforced CSEB wall, where both walls failed through shear. Due to the establishment of shear failure as the governing mode of failure of the wall, it is recommended that the blocks are best suited for pavements because of their high compressive strength when used individually. It is also recommended to have interlocking blocks for walls instead of plain blocks to enable further reinforcements such as steel, which minimizes shear failure and enables it to be used as load bearing wall.

Lastly, changes in the dimensions of blocks are also recommended to further reduce the shear failure.

ACKNOWLEDGEMENTS

The authors wish to give thanks to Diosdado and Susan Pineda for their financial support of this study. The authors would also like to express their gratitude to the faculty and staff of the Civil Engineering Department of DLSU for all their help. Special appreciation is also due to the staff of the CE Dept., IRTC, TUP for the testing of CSEB walls.

REFERENCES

- [1] Morel J, Pkla A, & Walker P, "Compressive strength testing of compressed earth blocks", *Construction and Building Materials*, Vol. 21, 2007, pp. 303-309.
- [2] American Concrete Institute (ACI), "State-of-the-art Report on Fiber Reinforced Concrete", ACI Committee, Detroit Michigan, USA, 1996.
- [3] Elenga RG, Mabiala B, Ahouet L, Goma-Maniongui J, Dirras GF, "Characterization of clayey soils from congo and physical properties of their compressed earth blocks reinforced with post-consumer plastic wastes", *Geomaterials*, Vol. 1, 2011, pp. 88-94.
- [4] United Nations Centre for Human Settlements (UN-Habitat), *Earth construction technology*, Nairobi, 1992.
- [5] Zami M, & Lee A, "Widespread adoption of contemporary earth construction in Africa to address urban housing crisis", *The Built & Human Environment Review*, Vol. 4, 2011, pp. 85-96.
- [6] Ghavami K, Filho R, & Barbosa N, "Behaviour of composite soil reinforced with natural fibres", *Cement and Concrete Composites*, Vol. 21, 1999, pp. 39-48.
- [7] Danso H, Martinson D, Ali M, & Williams J, "Effect of fibre aspect ratio on mechanical properties of soil building blocks", *Construction and Building Materials*, Vol. 83, 2015, pp. 314-319.
- [8] New Mexico Adobe Code (NMAC), "Chapter 7 Building Codes General: Part 4 New Mexico Earthen Building Materials Code", Housing and Construction, 2009.
- [9] Riza FV, Rahman IA, & Zaidi AM, "Preliminary Study of Compressed Stabilized Earth Brick (CSEB)", *Australian Journal of Basic and Applied Sciences*, Vol. 5, 2011, pp.6-12.
- [10] Donkor P, & Obonyo E, "Earthen construction materials: Assessing the feasibility of improving strength and deformability of compressed earth blocks using polypropylene fibers", *Materials & Design*, Vol. 83, 2015, pp. 813-819.

USEFULNESS OF ARTIFICIAL BEACHROCK AND GEOTEXTILE TUBE TECHNOLOGY

Md. Al Imran¹, Kazunori Nakashima², and Satoru Kawasaki³

¹ Graduate School of Engineering, Hokkaido University, Japan

^{2,3} Faculty of Engineering, Hokkaido University, Japan

ABSTRACT: In recent years, traditional forms of river and coastal structures have become very expensive to build and maintain, because of the shortage of natural rock. As a consequence, the materials used in hydraulic and coastal structures are changing from traditional rubble and concrete systems to cheaper, sustainable, and eco-friendly materials and systems such as artificial rock, gabion, slags, geosynthetics, and so on. Moreover, shorelines are being continually eroded by the wave action of the sea, and the river and coastal structures are frequently damaged by both anthropogenic and natural causes such as over wash and storm. How to deal with eroding coast problems is a main topic of this article. Recently, artificial beachrock and geotextile tube technology has changed from being an alternative construction technique and, in fact, has advanced to become the prime solution of choice. Therefore, the objectives of the present study is to find out the feasibility to protect coastal erosion in Asia along with using artificial beachrock and geotextile tube technology in a cheaper, sustainable and eco-friendly way.

Keywords: Artificial beach rock, Geotextile tube technology, Coastal erosion, Sand cementation, Sustainable, Eco-friendly

INTRODUCTION

The problem of coastal erosion is nothing new, but in recent years, it seems to have increased in speed especially in Asia. Because in Asia there are a lot of islands, long coastal lines and population density is much. So, initially we have focused on Asia and later on we will work on other part of the world regarding coastal erosion. Coastal erosion has long been a significant problem globally, typically due to anthropogenic changes along the coastline, and it poses a hazard for people residing in these areas. Erosion of the sandy shore is often used to refer to changes in the coastline due to the collapse of the sediment balance. In order to prevent, or at least minimize damage from erosion, a combination of various structures and processes has been traditionally used, including embankments, revetments, jetties, artificial reefs, offshore breakwaters, and sand bypassing [5].

The costs of installing hard structures for coastal protection are very high and development within coastal areas has increased interest in erosion problems; it has led to major efforts to manage coastal erosion problems and to restore coastal capacity to accommodate short-and long-term changes induced by human activities, extreme events and sea level rise. The erosion problem becomes worse whenever the countermeasures (i.e. hard or soft structural options) applied are inappropriate, improperly designed, built, or maintained and if the effects on adjacent shores are not carefully evaluated.

Therefore, increased interest in soft structures for coastal protection and a combination of hard and soft structures like geotextile tube technology is predominating and is consonant with advanced knowledge on coastal processes and natural protective functions and researcher showed that, artificial beachrocks (manufacture artificially in the natural condition) have the potential to inhibit coastal erosion [5]. Recently, geotextile tube technology has changed from being an alternative construction technique and, in fact, has advanced to become the prime solution of choice. Geotextile tubes, hydraulically or mechanically filled with dredged materials (woven, non-woven, and composite synthetic fabrics), have been variously applied in hydraulic and coastal engineering fields. The geotextile tube technology is mainly used for flood and water control, but they are also used to prevent beach erosion as well. In additionally, considering the use of artificial rock in order to preserve such submerged-looking islands above sea level, Danjo and Kawasaki [6], [8] conducted several studies in Okinawa and Ishikawa, Japan. They found sufficient information to build artificial beachrock. Considering this importance such type of study is also essential in Asia, as and other vulnerable country to climate change, to inhibit the coastal erosion due to sea level rise using artificial beachrock.

Therefore, the objectives of the present study is to find out the feasible method to protect coastal erosion in Asia along with using artificial beachrock (Microbially Induced Carbonate

Precipitation-MICP method) and geotextile tube technology in a cheaper, sustainable and eco-friendly way.

METHODS

Data used in this study is obtained from literature survey of related works. Data were organized by geographical location of beachrocks and coastal erosion in Asia. Quantitative scenario of coastal erosion and protective measures in Asia was shown in the obtained data.

For the prevention of coastal erosion quantitative information for the prospects of artificial beachrocks formation, their cement components, geotextile tube technology, their prospects, formation and composition etc. were collected, compiled and compared. Since this was the information that we deemed would be essential for the manufacturing of artificial beach rock and at the same time possible protective ways for the control of coastal erosion.

RESULTS AND DISCUSSION

Coastal Erosion in Asia

Coastal erosion has been studied in Viet Nam [3]; Bangladesh [17], [14], [4]; Malaysia [22]; Indonesia [33]; Sri Lanka [25]; India [18], [12]; China [2], Thailand [29] and Japan [6], [8], [16], [19] which is indicated in the Fig. 1 .

From the Fig. 1, it is seen that over 90 % of beachrocks are distributed between the proximity of 40°N and the Tropic of Capricorn. The geographic distribution of beachrocks was not concentrated near the equator. In particular, high concentrations of beachrocks were found at relatively high latitudes areas. This precludes the notion that beachrocks are concentrated only in areas where the temperature of the air or sea is high [6]. Coastal erosion and accretion are natural processes; however, they have become anomalous and widespread in the coastal zone of Asia and other countries in the Indian ocean owing to combinations of various natural forces, population growth and unmanaged economic development along the coast, within river catchments and offshore. This type of erosion has been reported in China, Malaysia, Sri Lanka, India, Japan, Indonesia, Viet Nam, Thailand, and Bangladesh.

Bilan [2] reported that the erosion rate in the northern part of Jiangsu Province in China is serious and as high as 85 metres/year; in Hangzhou Bay the rate is 40 metres/year, while in Tianjin it is 16-56 metres/year. Erosion persists even where preventive measures such as sea dykes are constructed. Beach scour has been found along coasts with sea-dyke protection. This erosion is attributable to many factors such as river damming

and diversion, that leads to less sediment supply to the coast, and the clearing of mangrove forests, which makes coastal areas more susceptible to the hazard.

According to Othman [22] nearly 30 percent of the Malaysian coastline is undergoing erosion.

In Vietnam, most of the coastline in the south that is located in a wide and flat alluvial fan and bordered by tidal rivers fringed by wide mangrove swamps, has been eroded continuously at a rate of approximately 50 metres/year since the early twentieth century. Erosion still occurs in the central coastal zone of Viet Nam and preventive measures such as sea dykes, revetments, and tree plantations have been implemented to prevent further erosion [3].

Sri Lanka's experience with coastal erosion dates back to 1920 and Approximately US\$30 million has already been spent on breakwaters and other construction to combat coastal erosion on southern and western coasts however, coastal erosion still persists in some coastal areas [28].



Fig. 1 Location of beachrock deposition in some Asian countries (google.map)

In India the rapid erosion of the coast of Sagar Island in West Bengal, India, is caused by several processes that act in concert; these are natural processes that occur frequently (cyclones, waves and tides that can reach six metres in height) and anthropogenic activities. The erosion rate from 1996 to 1999 was calculated to be 5.47 square kilometres/year [12]. The areas that are severely affected by erosion are the north-eastern, south-western and south-eastern faces of the island. Malini and Rao [18] reported coastal erosion and habitat loss along the Godavari Delta front owing to the combination of the dam construction across the Godavari and its tributaries that diminishes sediment supply to the coast and continued coastal land subsidence.

In Indonesia, coastal erosion started in the northern coast of Java Island in the 1970s when most of the mangrove forest had been converted to shrimp ponds and other aquaculture activities, and

the area was also subjected to unmanaged coastal development, diversion of upland freshwater and river damming. Coastal erosion is prevalent throughout many provinces [33] such as Lampung, Northeast Sumatra, Kalimantan, West Sumatra (Padang), Nusa Tenggara, Papua, South Sulawesi and Bali.

In Thailand, intensification of coastal erosion came to notice during the past decade overall, the net erosion is approximately 1.3 to 1.7 metres/year along the southern Thailand coastline. Total area losses amount to 0.91 square kilometres/year for the Gulf coast and 0.25 square kilometres/year for the western coast [29].

Khan [17] and Islam [14] studied coastal erosion and accretion activities in Bangladesh. Heavy discharge currents through the GBM (Ganges-Brahmaputra-Meghna) river system, wave action due to strong southwest monsoon winds, high astronomical tides as well as sea level rise (SLR), and storm surges in the Bay of Bengal are the main causes of erosion in the coastal area of Bangladesh [14]. Erosion due to SLR has been discussed by Islam [14] at his study which was done under the U.S. Country Studies Program, and some of the salient features of the study are presented here.

The study was based on the erosion formula given by Bruun [34].

$$x=ab/(e+d) \quad (1)$$

Where x is the shoreline recession due to SLR, a is the rise in water level due to SLR, e is the elevation of the shore, and d is the depth of water at a distance b from the coastline. Islam [14] applied the formula to the eastern region, where the longest continuous sandy beach situated, of Bangladesh.

Coastal Protection

Natural beachrocks, which are formed naturally on beaches, have attracted attention as a model for artificial rocks. Danjo and Kawasaki [5] proposed a new method to protect coastlines from erosion, the use of artificial rock that auto-repairs by means of sunlight, seawater, and bacteria. Their model of artificial rock is beachrock. Beachrock is a type of sedimentary deposit that generally occurs on tropical and subtropical beaches as a result of intertidal lithification of loose beach sands and gravels by carbonate cementation.

Beach rock is generally limited to tropical and subtropical climates, though not every tropical beach has beach rock. Beach rock has also been reported from temperate regions, but such occurrences are rare. Around the world beachrocks have been reported to form over several thousand

years [31] owing to interactions among sand supply, cement precipitation from seawater and coastal erosion by ocean waves [5]. Therefore, it may be possible to slow down the erosion of coasts by making man-made beachrock from coastal sands. Because this artificial rock is made of local materials, it has the potential to be a cheaper and eco-friendly product [5].

Characteristics of Beachrock

The majority of recent beachrock is formed on beaches in the same regions that favour coral reef formation. This is generally below 25° latitude where there is a well-defined dry season and “the temperature of ground water at a depth of about 76 cm in beaches remains above 21°C for at least 8 months of the year” [24]. Several theories have been proposed to explain beachrock formation, which can be divided into physico-chemically and biologically induced precipitation of calcium carbonate. Most of the theories have been formulated to explain occurrences of beachrock.

Physico-chemical models explain marine carbonate cement precipitation by the soaking of beaches during high tides and evaporation of sea water during low tides [11], enhanced by (daytime) solar warming of the beach.

Biological processes may have an important role in beachrock formation. Biological activity controls the partial pressure of CO₂ by its consumption, thus promoting the precipitation of CaCO₃ [13]. Ammonification of amino-acids, sulphate reduction and other bacterial processes taking place during organic matter degradation promote carbonate precipitation by raising the pH, furthermore, organic matter may promote carbonate precipitation [32].

So, there are a number of theories regarding the process of beach sand cementation. Different mechanisms of cementation appear to be responsible at different localities. The primary mechanisms proposed for the origin of beachrock cements are as follows:

- 1) Physicochemical precipitation of high-Mg calcite and aragonite from seawater as a result of high temperatures, CaCO₃ super saturation, and/or evaporation [10],
- 2) Physicochemical precipitation of low-Mg calcite and aragonite by mixing of meteoric and fresh ground water with seawater [26],
- 3) Physicochemical precipitation of high-Mg calcite and aragonite by degassing of CO₂ from beach sediment pore water [30], and
- 4) Precipitation of micritic calcium carbonate as a by-product of microbiological activity [21].

Properties of Beachrock and Beach Sand in Asia

From the Fig. 2 and Table 1, it is shown that, the main component for the formation of beachrock is CaO and SiO₂. But other components like Al₂O₃, TiO₂, and FeO also play a vital role for the beachrock formation.

Table 1: The main component for the formation of beachrock in some Asian countries

Location	Rock Formation Type	Component Materials	References
Bangladesh	Calcareous coral sand, broken coral or limestone	Kaolinite	[17]
India	Calcareous coral sand, limestone	Quartz, Feldspar, Kaolinite	[23]
Sri Lanka		Quartz, Calcite, Dolomite, Aragonite	[15]
Vietnam	Data is not available		
Malaysia	Calcareous, Aragonite		[1]
Indonesia	Data is not available		
China	Calcareous sand, Lime stone		[15]
Thailand	Data is not available		
Japan	Shell sand, foraminifer, sand, gravel	Aragonite, Mg calcite	[5]

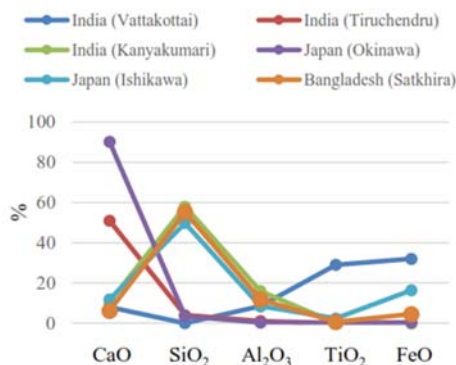


Fig. 2 Beachrock compositions in some Asian countries [17]

Artificial Beachrock Formation through Beach and Sand Solidification

Danjo and Kawasaki [5]-[7] conducted several study in Okinawa and Ishikawa, Japan. They found sufficient information to build manmade beachrock. Danjo and Kawasaki [5] perform coral sand solidification test using ureolytic bacteria (*Pararhodobacter* sp.) and found this type of bacteria has the ability to solidify coral sand precipitating CaCO₃. Considering this importance such type of study is also essential in Asia, and other most vulnerable country to climate change, to inhibit the coastal erosion due to sea level rise.

Danjo and Kawasaki [5]-[7] found that, Column specimens were cemented up to UCS of 10 MPa after 28 days under the conditions (curing temperature; 30°C, injection interval; 1 day, Ca²⁺ concentrations in cementation solution; 0.3 M). Based on formation methods observed by Danjo and Kawasaki [5]-[7] the sand cementation process is very much suitable, eco-friendly, cheaper and sustainable for the areas in Asia where the temperature, sand properties and other conditions is almost same as Japan and the results of this study will contribute to the application of a new technique for coastal sand improvement and bio-stimulation.

Protective Coastal Protection Learned from Beachrock Formation: Through Geo-textile Tube Technology

The recent trend in the mitigation of coastal erosion and costal protection has been shifted now-a-days towards soft novel cheaper, sustainable and eco-friendly methods. Pro-active methods and solutions are being developed and employed, which are not only eco-friendly, construction-friendly and cheaper but also address the root cause of the problem without much adverse effects. Such kind of modern tool is geotextile tube which is one of the geosynthetics structures that are increasingly used in coastal protection. They are made from polypropylene (PP), polyester (PET), polyethylene (PE), polyamide (nylon), olyvinylidene chloride (PVC), and fibreglass. Sewing thread for geotextiles is made from Kevlar or any of the above polymers [20]. Different fabric composition and construction are suitable for different applications.

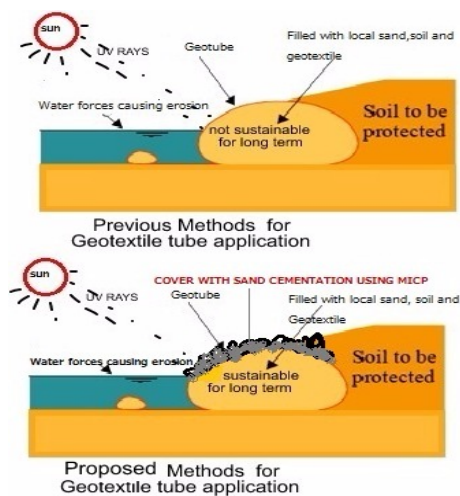


Fig. 3 Proposed Coastal Protection Method

Traditional Geotextile tubes widely used for dewatering, flood control, and coastal protection. Geotextiles are either woven or non-woven permeable fabric or synthetic material which can be used in combination with geotechnical engineering material [27]. But our proposed method is coastal protection along with MICP method and these “Geotube” (Fig. 3). In case of traditional methods, different rays from sun can damage the “Geotube” after a certain time and soil protection may not be sustainable and the cost of re-constructing “Geotube” is much. But, in our proposed method, sand cementation using MICP method can be applied over the “Geotube”. As a result, the surface of the coast and “Geotube” will be strengthened and will remain longer and soil will be protected. In this method, cost is low comparatively and local ureolytic bacteria is used, so this is eco-friendly and sustainable. This method can be applied in a broad range of civil engineering applications including construction, paving, drainage and other applications.

CONCLUSIONS

In conclusion, we can say that, the deposition of beach rock using MICP method is of significance because of the timing of diagenesis and the mode of cementation. Recently, geotextile tube technology has changed from being an alternative construction technique and, in fact, has advanced to become the prime solution of choice. But the method is not sustainable and time consuming and sometimes costly. However, the lower resistance of geotextile to damage needs to be overcome to ensure the longer service period of the geotextile tubes. Covering the tubes with geotextile or rocks can protect the structures from direct contact with sharp objects or vandalism

activities. So, for the protection of coastal erosion geotextile tube technology along with MICP method can be applied which is very much eco-friendly, cheaper, and sustainable. Although, sand cementation and geotextile tube technology procedure is poorly understood till now. However, actual field trials are always recommended prior to final application.

REFERENCES

- [1] Ali CA, and Mohamed KR, “Cementation in Quaternary beach rock in the islands off the East Coast, Peninsular Malaysia: petrographic evidence”, *Warta Geologi*, Vol.23, No.2, 1997, pp. 57-62
- [2] Bilan D, “The preliminary vulnerability assessment of the Chinese coastal zone due to sea level rise”, *Proceedings of the IPCC eastern hemisphere workshop*, 1993, Tsukuba, Japan, pp. 3-6.
- [3] Cat NN, Tien PH, Sam DD, and Bien NN, “Status of coastal erosion of Vietnam and proposed measures for protection”, *FAO forestry report*, 2006, pp.10-21.
- [4] Chowdhury SQ, Fazlul A T M, and Hasan KH, “Beachrock in St. Martin's Island, Bangladesh: Implications of sea level changes on beachrock cementation”, *Marine Geodesy*, 1997, Vol.20, No.1, pp 89-104.
- [5] Danjo T, and Kawasaki S, “A study of the formation mechanism of beachrock in Okinawa, Japan: Toward Making Artificial Rock”, *Int. J. of GEOMATE*, Vol.5, No.1, 2013, pp. 633-638.
- [6] Danjo T, and Kawasaki S, “Characteristics of beachrock based on bibliographical research: toward the development of man-made beachrock”, *J. of Japanese Society of Engineering Geology*, Vol.53, No.3, 2012a, pp. 129-151.
- [7] Danjo T, and Kawasaki S, “Microbially Induced Sand Cementation Method Using *Pararhodobacter* sp. Strain SO1, Inspired by Beachrock Formation Mechanism”, *Materials Transactions ©2016 The Mining and Materials Processing Institute of Japan*, Vol. 57, No.3, 2016, pp. 428-437.
- [8] Danjo T, and Kawasaki S, “Property evaluation of beachrock based on field investigation in Okinawa Island, Japan”, *Harmonising Rock Engineering and the Environment Qian & Zhou (eds)*, Taylor and Francis Group, London, 2012b, pp. 949-952.
- [9] Danjo T, Kawasaki S, Shimazaki S, and Koizuka K, “Coral sand solidification test using ureolytic bacteria”, *Geomechanics from Micro to Macro-Soga et al. (Eds) © 2015*

- Taylor & Francis Group, London, ISBN 978-1-138-0270-7, 2014, pp. 1521-1526.
- [10] Ginsburg RN, "Beachrock in south Florida", *Journal of Sedimentary Petrology*, Vol.23, pp. 85-92.
- [11] Gischler E, "Beachrock and intertidal precipitates Geochemical sediments and Landscapes", © Blackwell Publishing Ltd, 2007, pp. 365-390.
- [12] Gopinath G, and Seralathan P, "Rapid erosion of the coast of Sagar island, West Bengal India", *Environment Geology*, Vol. 48, 2005, pp. 1058-1067.
- [13] Hopley D, "Beachrock as a sea-level indicator", O. Van de Plassche (Ed.), *Sea-level Research: A Manual for the Collection and Evaluation of Data*, Geo Books, Norwich 1986, pp. 157-173.
- [14] Islam SM, Huq S, and Ali A, "Beach erosion in the eastern coastline of Bangladesh", 1999, pp. 71-92.
- [15] Jayasingha P, "Episodic Beach Rock Complex At Bundala Coast Southern Sri Lanka: A Preliminary Study", *Journal of Geological Society of Sri Lanka*, Vol.16, 2014, pp. 119-126.
- [16] Kawata Y, "Methodology of beach erosion control and its application. Coastal Engineering in Japan", Vol.32, No.1, 1989, pp. 113-132.
- [17] Khan NH, Danjo T, and Kawasaki S, "Artificial beachrock formation through sand solidification towards the inhibit of coastal erosion in Bangladesh", *International Journal of GEOMATE*, Dec., Vol.9, No.2 (Sl. No. 18), 2015, pp. 1528-1533.
- [18] Malini BH, and Rao KN, "Coastal erosion and habitat loss along the Godavari delta front a fallout of dam construction", *Current Science*, Vol.87, No.9, 2004, pp. 1232-126.
- [19] Takamura M, Udo K, Sato M, and Takahashi K, "Analysis of Coastal Erosion due to the 2011 Great East Japan Tsunami and its Recovery Using Ground Penetrating Radar Data", *Journal of Coastal Research*, Special Issue 75, 2016, pp. 477-481.
- [20] Mitra A, "Application of geotextiles in Coastal Protection and Coastal Engineering Works: An overview", *International Research Journal of Environment Sciences*, Vol. 4, No.4, 2015, pp. 96-103.
- [21] Molenaar N, and Venmans AAM, "Calcium carbonate cementation of sand: a method for producing artificially cemented samples for geotechnical testing and a comparison with natural cementation processes", *Engineering Geology*, Vol.35, 1993, pp. 103-122.
- [22] Othman MA, "Value of mangroves in coastal protection", *Hydrobiologia*, Vol.285, No.1, 1994, pp. 277-282.
- [23] Ravisankara R, Chandrasekaranb A, Kalaiarsia S, Eswaranc P, Rajashekhare C, Vanasundaria K, and Alok A, "Mineral analysis in beach rocks of Andaman Island: India by spectroscopic techniques", *Archieve of Applied Science Research*, Vol. 3, No.3, 2011, pp. 77-84.
- [24] Russell RJ, "Water-table effects on seacoasts", *Geology Society of America Bulletin*, Vol. 82, 1971, pp. 2343-2348.
- [25] Sato Y, and Mimura N, "Environmental problems and current management issues in the coastal zones of south and southeast Asian developing countries", *Journal of Global Environmental Engineering*, Vol.3, 1997, pp. 163-181.
- [26] Schmalz RF, 'Formation of beach rock at Eniwetok Atoll', In Bricker, O.P., (ed.), *Carbonate Cements*. Maryland: Johns Hopkins University Press, 1971, pp. 17-24.
- [27] Shina EC, Ohi YI, "Coastal erosion prevention by geotextile tube technology", *Geotextiles and Geomembranes*, Vol.25, No.4, 2007, pp. 264-277.
- [28] Swan SB, "The coastal geomorphology of Sri Lanka: An introductory survey", published by Armidale, NSW, Dept. of Geography, University of New England, 1984, pp.125-129.
- [29] Thampanya U, Vermaat JE, Sinsakul S, and Panapitukkul N, "Coastal erosion and mangrove progradation of Southern Thailand", *Estuarine, Coastal and Shelf Science*, Vol.68, 2006, pp. 75-85.
- [30] Thorstenson DC, Mackenzie FT, and Ristvet BL, "Experimental vadose and phreatic cementation of skeletal carbonate sand", *Journal of Sedimentary Petrology*, Vol.42, No.1, 1972, pp. 162-167.
- [31] Vousdoukas MI, Velegrakis AF, And Plomaritis T A, "Beachrock occurrence, characteristics, formation mechanisms and impacts", *Earth-Science Reviews*, Vol.85, 2007, pp. 23-46.
- [32] Webb GE, Jell JS, and Baker JC, (1999). "Cryptic intertidal microbialites in beachrock, Heron Island, Great Barrier Reef: implications for the origin of microcrystalline beachrock cement", *Sedimentary Geology*, Vol.126, pp. 317-334.
- [33] Widayati AYW, and Kim KH, "Improving The Coastal Hazard Management In Indonesia: Lesson Learned From Other Countries", *Proceedings of the 7th International Conference on Asian and Pacific Coasts*, Bali, Indonesia, 2013, pp. 24-26.
- [34] Bruun P, "Sea level rise as cause of shore erosion", *J. of Waterways Harbors Div. Proc. Am. Soc. Civ. Eng.* Vol. 88, 1962, pp. 117-130

SHEAR BOND STRENGTH OF FA-PC GEOPOYLMER UNDER DIFFERENT SAND TO BINDER RATIO AND SODIUM HYDROXIDE CONCENTRATION

Tanakorn Phoo-ngernkham ^{1*}, Sakonwan Hanjitsuwan ², Satakhun Detphan ³, Jaksada Thumrongvut ⁴,
Cherdsak Suksiripattanapong ⁵, Nattapong Damrongwiriyanupap ⁶,
Prinya Chindaprasirt ⁷ and Shigemitsu Hatanaka ⁸

^{1,3,4,5} Faculty of Engineering and Architecture, Rajamangala University of Technology Isan, Nakhon Ratchasim, THAILAND; ² Faculty of Industrial Technology, Lampang Rajabhat University, THAILAND;

⁶ School of Engineering, University of Phayao, THAILAND; ⁷ Faculty of Engineering, Khon Kaen University, THAILAND; ⁸ Faculty of Engineering, Mie University, JAPAN

ABSTRACT

This paper presents the effects of sand to binder (S/B) ratio and sodium hydroxide (NaOH) concentration on setting time, compressive strength and shear bond strength of FA-PC geopolymer binder. Geopolymer binder was manufactured from FA and PC at ratio of 90:10 by weight of binder. The liquid alkali solution used in this study are sodium hydroxide (NaOH) and sodium silicate (Na_2SiO_3) solutions. The $\text{Na}_2\text{SiO}_3/\text{NaOH}$ ratio of 2.0, liquid alkali solution/binder ratio of 0.60, and curing at ambient temperature were fixed in all mixes. The differences in NaOH concentrations of 5, 10 and 15M and S/B ratios of 1.00, 1.25 and 1.50 has been investigated. Test results show that the differences of NaOH concentration and S/B ratio has an effect on setting time, compressive strength and shear bond strength of FA-PC geopolymer mortar. The setting time of mortars are obviously decreased with increasing of S/B ratio whereas the setting time of mortars are obviously increased with increasing of NaOH concentration. The compressive and shear bond strengths of mortar increase as increasing of both S/B ratio and NaOH concentration up to a threshold limit. The highest slant shear strength between PCC substrate and FA-PC geopolymer mortar was found in the mortar with 1.25 of S/B ratio and 10M NaOH concentration which gives 24.1 MPa.

Keywords: Geopolymer, Fly ash-Portland cement blends, Sand to binder ratio, NaOH concentration, Shear bond strength.

INTRODUCTION

The applications of Portland cement (PC) is essential to the rapid urbanization in many developing countries. Advantages of PC are high mechanical performances and low cost; however, increasing of PC manufacture corresponds to energy and environmental issues. An annual publication has reported that approximately 1 ton of CO_2 emissions for each ton of the PC produced [1]. Recently, geopolymer binder is one of the new binders that have been developed by several researchers as an alternative cementing agent to PC [2, 3]. This is because of geopolymer binder is having less CO_2 footprint than PC as reported by McLellan et al. [4].

Geopolymer binder is made from aluminosilicate source materials activated with high alkali solutions [5]. Many researchers [2, 3, 6] have already reported that geopolymer binder could develop as cementing agent because there are many advantages i.e., high strength, excellent durability and high bonding. In Thailand, fly ash (FA) from Mae Moh power station is widely used for making geopolymer binder [7-9]; however, the production of FA geopolymer at ambient temperature gives low strength [10]. Some

researchers [10, 11] reported that the temperature curing at approximately 40-75 °C could enhance the degree of geopolymerization within the matrix and hence reasonable strength FA geopolymer gain. In ideal of real construction, the use of temperature curing is difficult for the construction practice. Nowadays, the materials who consisted of calcium oxide could improve the strength development of FA geopolymer. For example, Pangdaeng et al. [10] studied on the use of PC to replace FA for making geopolymer binder cured at ambient temperature. They reported that the generated heat from hydration products could help the geopolymerization process. Also, Temuujin et al. [12] reported that coexistence of calcium silicate hydrate (C-S-H) and geopolymer gel (N-A-S-H) provides higher compressive strength of geopolymer binder than N-A-S-H gel.

One of the important factor on the strength development of geopolymer binder is alkali solution. Hanjitsuwan et al. [13] claimed that two types of alkali solution viz., sodium hydroxide (NaOH) and sodium silicate (Na_2SiO_3) solutions were widely used for making geopolymer binder. Also, Hanjitsuwan et al. [13] explained that NaOH solution was used for leaching out of Si^{4+} and Al^{3+}

ions whereas Na_2SiO_3 solution was used for condensation process to form aluminosilicate material. In addition, ratio of sand to binder is one of the important factor for considering as repair materials which related to a homogeneous matrix of geopolymer binder as reported by Thakur and Ghosh [14].

In order to utilize geopolymer binder as an alternative repair material, many researchers [2, 3, 15-19] have studied the setting time, strength development and bonding strength for proving their properties compared with commercial repair materials in the market. As mentioned, the 7-day strength requirement of rapid hardening cementitious materials was 28.0 MPa as per ASTM C928-13 [20], and the initial setting time and minimum strength requirements for repair binder were 30 minutes and 35.0 MPa, respectively as per ASTM C881/C881M-14 [21]. Therefore, the aim of this study is to investigate the effects of NaOH concentration and S/B ratio on setting time, compressive strength and shear bond strength of FA-PC blends geopolymer mortar. The obtained results should be very beneficial to the understanding and to the future applications of geopolymer binder as fundamental of alternative repair materials.

EXPERIMENTAL DETAILS AND TESTING ANALYSIS

Materials

The precursors used in this study are fly ash (FA) from Mae Moh power plant in northern of Thailand, and ordinary Portland cement (PC). FA had specific gravity, median particle size and Blaine fineness of 2.65, 15.3 μm and 4300 cm^2/g , respectively. While, PC had specific gravity, median particle size and Blaine fineness of 3.15, 14.6 μm and 3600 cm^2/g , respectively. The liquid alkaline activators are sodium hydroxide (NaOH) and sodium silicate (Na_2SiO_3) with 13.89% Na_2O , 32.15% SiO_2 , and 54.16% H_2O by weight. Fine aggregate used in this study is local river sand with specific gravity of 2.65, and fineness modulus of 2.00.

The chemical compositions of FA and PC are illustrated in Table 1. FA consists of 31.32% SiO_2 , 13.96% Al_2O_3 and 15.64% Fe_2O_3 , and the CaO content is high at 25.79%, thus this FA is Class C as per ASTM C618-15 [22]. In addition, physical properties of FA and PC are illustrated in Table 2.

Mix proportion of FA-PC geopolymer

The mix proportions of FA-PC geopolymer under different NaOH concentration and S/B ratio are shown in Table 3. Constant liquid alkali solution to binder ratio of 0.60, $\text{Na}_2\text{SiO}_3/\text{NaOH}$ ratio of 2.0, and curing at ambient temperature were fixed in all

mixes. Geopolymer binder was manufactured from FA and PC at ratio of 90:10 by weight of binder. FA was replaced by PC because it needs calcium oxide for enhancing the strength development of geopolymer binder when cured at ambient temperature as reported by Pangdaeng et al. [10]. The NaOH concentrations of 5, 10 and 15M, and sand to binder ratios (S/B) of 1.00, 1.25 and 1.50 has been investigated.

For the mixing of mortars, NaOH and Na_2SiO_3 solutions were firstly mixed together before use as liquid solution. The FA, PC, and sand were dry mixed until the mixture was homogenous. Right after, the liquid solution was added and the mixing of mortars was done for 3 minutes.

Table 1 Chemical compositions of FA and PC

Chemical compositions	FA	PC
SiO_2	31.32	20.80
Al_2O_3	13.96	4.70
Fe_2O_3	15.64	3.40
CaO	25.79	65.30
MgO	2.94	1.50
Na_2O	2.83	0.40
K_2O	2.93	0.10
SO_3	3.29	2.70
LOI	1.30	0.92

Table 2 Physical properties of FA and PC

Materials	FA	PC
Specific gravity	2.61	3.15
Median particle size, d_{50} (μm)	15.3	14.6
Blaine fineness (cm^2/g)	4300	3600

Table 3 Mix proportions of FA-PC geopolymer

Mixes	FA (kg)	PC (kg)	Sand (kg)	NaOH (kg)	Na_2SiO_3 (kg)
5M-1.00SB	90	10	100	20	40
5M-1.25SB	90	10	125	20	40
5M-1.50SB	90	10	150	20	40
10M-1.00SB	90	10	100	20	40
10M-1.25SB	90	10	125	20	40
10M-1.50SB	90	10	150	20	40
15M-1.00SB	90	10	100	20	40
15M-1.25SB	90	10	125	20	40
15M-1.50SB	90	10	150	20	40

Experimental details and testing analysis

Setting time of FA-PC geopolymer

After mixing, the setting time of FA-PC geopolymer was tested as per ASTM C191-13 [23].

Compressive strength of FA-PC geopolymer

Fresh FA-PC geopolymer mortar was cast in a 50x50x50 mm³ cube molds for compressive strength test as per ASTM C109 [24]. After that, sample has been wrapped with vinyl sheet to protect moisture loss. The samples were cured for a day and then demolded with immediately wrapped by vinyl sheet and kept in ambient temperature until testing age. The compressive strength of samples has been tested at the age of 28 days. The reported results are the average of five samples.

Shear bond strength between concrete substrate and FA-PC geopolymer

Portland cement concrete (PCC) is a mixture of 500 kg/m³ Portland cement, 510 kg/m³ fine aggregate, 930 kg/m³ coarse aggregate and 238 kg/m³ water, respectively. The 28-day compressive strength and Young's modulus of PCC were 35.0 MPa and 27.5 GPa, respectively, which based on previous study [2, 3]. As mentioned, fresh PCC was cast in a 50x50x125 mm³ prism molds. After curing time for 90 day, the PCC was cut in half at 45° line to the vertical. For preparation of shear bond strength between PCC and geopolymer mortar, fresh FA-PC geopolymer was cast into a 50x50x125 mm³ prism mold with the other half filled with PCC. Then, samples were wrapped with vinyl sheet to protect moisture loss and kept in ambient temperature until testing age. The shear bond strength was calculated as the ratio of maximum load at failure and the bond area. The shear bond strength was tested at the age of 28 days with a constant loading rate of 0.30 MPa/s. The reported results were the average of five samples.

RESULTS AND DISCUSSION

Setting time of FA-PC geopolymer

The results of setting time of FA-PC geopolymer mortar with different NaOH concentration and S/B ratio are shown in Figure 1. The initial and final setting time of FA-PC geopolymer tend to decrease with increasing of both NaOH concentration and S/B ratio. With regard to effect of S/B ratio, the increasing of S/B ratio has an effect on setting time of FA-PC geopolymer mortar. For example, the initial and final setting time of 10M-1.00SB, 10M-1.25SB and 10M-1.50SB mortars are 19, 15, 15 min and 30, 25, 23 min, respectively. This is because increasing of fine aggregate in the geopolymer system is related to decrease in the paste value; therefore, the setting time of mortar is decreased as

increasing of S/B ratio.

For effect of NaOH concentration, the leaching out of Si⁴⁺ and Al³⁺ ions is generally low at low NaOH concentration whereas the leaching out of Ca²⁺ is not interrupted; thus, the solution was filled with calcium as reported by Rattanasak and Chindaprasirt [25]. Also, Guo et al. [26] explained that calcium oxide could react with silica and/or alumina from FA to form C-(A)-S-H gels within geopolymer system. Hence, the setting time of FA-PC geopolymer was thus short. At high NaOH concentration, the leaching out of Si⁴⁺ and Al³⁺ ions is much better than low NaOH concentration; in contrast, calcium oxide was hindered. Thus, the setting time of FA-PC geopolymer with high NaOH concentration is increased.

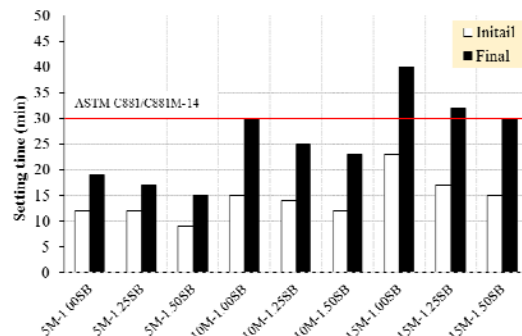


Fig. 1 Setting time of FA-PC geopolymer mortar with various NaOH concentration and S/B ratio.

From this results, it can be concluded that the fast setting of FA-PC geopolymer is very attractive for repair work which the fast setting is normally required. As for ASTM C881/C881M-14 [21] required the initial setting time for repair binder at 30 min; therefore, all mixes meet the requirement of ASTM standard.

Compressive strength of FA-PC geopolymer

The results of 28-day compressive strength of FA-PC geopolymer mortar with different NaOH concentration and S/B ratio are shown in Figure 2. The strength of FA-PC geopolymer mortar increase with increasing of both S/B ratio and NaOH concentration. For example, the 28 day-strength of 5M1.00SB, 5M1.25SB, 5M1.50SB, 10M1.00SB and 15M1.00SB mixes are 40.3, 50.4, 54.3, 46.8 and 45.1 MPa, respectively.

As for effect of NaOH concentration, it has an effect on the strength development of FA-PC geopolymer mortar. At high NaOH concentration, the leaching out of Si⁴⁺ and Al³⁺ ions from FA particles increase which corresponds to increasing of its strength. Hanjitsuwan et al. [13] claimed that the formation of N-A-S-H gel was improved at high

NaOH concentration. Therefore, the coexistence of N-A-S-H and C-S-H gels could enhance the strength development of FA-PC geopolymer mortar [19]. However, at 15M NaOH gives lower strength of FA-PC geopolymer mortar than that of 10M NaOH concentration. This is because the leaching out of CaO from FA and PC was hindered at high NaOH concentration [13]; therefore, 10M NaOH concentration is suitable alkali hydroxide for producing FA-PC geopolymer. According to Figure 2, it can be concluded that the strength of FA-PC geopolymer mortar increase as increasing of S/B ratio and NaOH concentration up to a threshold limit that are 10M NaOH and 1.50 of S/B ratio. The relatively highest strength was found in the 10M1.50SB mix which gives 65.1 MPa of 28-day strength.

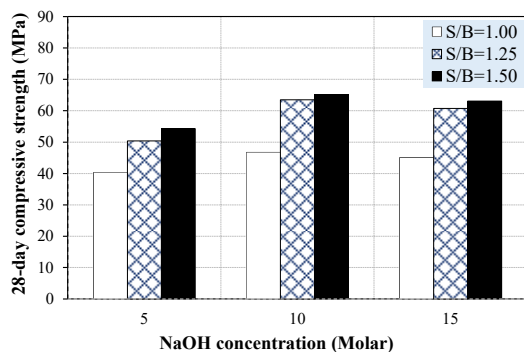


Fig. 2 Compressive strength of FA-PC geopolymer mortar with various NaOH concentration and S/B ratio.

Shear bond strength between PCC substrate and FA-PC geopolymer

Test results of shear bond strength between PCC substrate and FA-PC geopolymer mortar under different NaOH concentration and S/B ratio are summarized in Figure. 3. The increase in both of NaOH concentration and S/B ratio has an effect on shear bond strength between two bonding surfaces. The improvement of shear bond strength is directly related to the behavior of their compressive strength. For instance, the 28 day-shear bond strength of 5M1.00SB, 5M1.25SB, 5M1.50SB, 10M1.00SB and 15M1.00SB mixes are 18.2, 18.6, 15.9, 23.3 and 24.2 MPa, respectively.

With regard to effect of S/B ratio, the slant shear strength between PCC substrate and FA-PC geopolymer mortar tends to increase with increase in S/B ratio up to a threshold limit that is 1.25 of S/B ratio. As mentioned, the slant shear strength at 1.50 of S/B ratio obvious decrease when compared to 1.25 of S/B ratio. As for effect of NaOH concentration, the slant shear strength between PCC substrate and FA-PC geopolymer mortar tends to

increase with increasing NaOH concentration; however, NaOH concentration at 15M seems to be a slight reduction. The CaO from PC could react with SiO_2 and/or Al_2O_3 from FA in the suitable NaOH concentration; hence, additional formation of C-S-H and/or C-A-S-H coexists with N-A-S-H gels [27, 28]. Thus, an enhancement of bonding strength at the interface transition zone between PCC substrate and FA-PC geopolymer mortar was obtained. In contrast, the leaching out of CaO from FA and PC was hindered at higher NaOH concentration [13]. Therefore, bonding at two surfaces slight decrease.

It can be concluded that a mixture of S/B ratio at 1.25 and NaOH concentration at 10M gives the highest slant shear strength between PCC substrate and FA-PC geopolymer mortar.

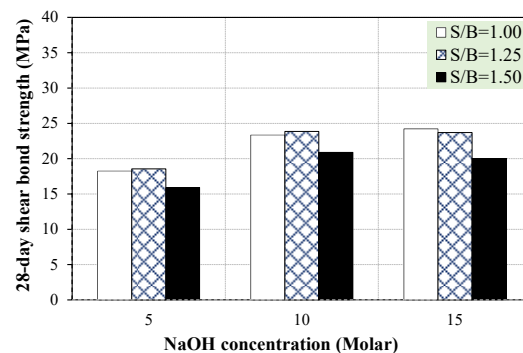


Fig. 3 Shear bond strength between PCC substrate and FA-PC geopolymer with various NaOH concentration and S/B ratio.

CONCLUSION

This paper has provided an experimental study on setting time, compressive strength and shear bond strength of FA-PC geopolymer mortar with various different NaOH concentration and S/B ratio. Based on the obtained experimental results, the following conclusions could be drawn:

1. The difference of NaOH concentration and S/B ratio has an effect on setting time of FA-PC geopolymer mortar. The setting time of mortars are decreased as increasing of S/B ratio. While, increasing of NaOH concentration could delay the setting time of FA-PC geopolymer mortar.
2. Compressive strength of FA-PC geopolymer mortars are increased as increasing of both S/B ratio and NaOH concentration up to a threshold limit. The FA-PC geopolymer mortar manufactured from 10M NaOH and S/B ratio of 1.50 gives the highest 28-day strength of 65.1 MPa.
3. The FA-PC geopolymer mortar with the optimum NaOH concentration and S/B ratio could improve the shear bond strength between PCC substrate and geopolymer mortar. The increase in shear bond strength is due to an enhancement of reaction products at two surfaces. A mixture of S/B

ratio at 1.25 and 10M NaOH gives the highest slant shear strength which is 24.1 MPa.

ACKNOWLEDGEMENTS

The authors gratefully acknowledge the financial supported from the Rajamangala University of Technology Isan, Thailand; and Khon Kaen University and the Thailand Research Fund (TRF) under the TRF Senior Research Scholar, Grant No. RTA5780004.

REFERENCES

- [1] Ferreira LFB, Costa HSS, Barata IIA, Santos Júlio ENB, Tiago PMN, Coelho JFJ, "Precast alkali-activated concrete towards sustainable construction", *Mag. Concrete. Res.*, Vol. 66(12), 2014, pp. 618-626.
- [2] Phoo-ngernkham T, Hanjitsuwan S, Suksiripattanapong C, Thumrongvut J, Suebsuk J, Sookasem S, "Flexural strength of notched concrete beam filled with alkali-activated binders under different types of alkali solutions", *Constr Build Mater.*, Vol. 127, 2016, pp. 673-678.
- [3] Phoo-ngernkham T, Sata V, Hanjitsuwan S, Rittirud C, Hatanaka S, Chindapasirt P, "High calcium fly ash geopolymer mortar containing Portland cement for use as repair material", *Constr Build Mater.*, Vol. 98, 2015, pp. 482-8.
- [4] McLellan BC, Williams RP, Lay J, van Riessen A, Corder GD, "Costs and carbon emissions for geopolymer pastes in comparison to ordinary portland cement", *J. Cleaner Prod.*, Vol. 19(9-10), 2011, pp. 1080-1090.
- [5] Palomo A, Grutzeck MW, Blanco MT, "Alkali-activated fly ashes: A cement for the future" *Cem. Concr. Res.*, Vol. 29(8), 1999, pp. 1323-1329.
- [6] Songpiriyakij S, Pulngern T, Pungpremtrakul P, Jaturapitakkul C, "Anchorage of steel bars in concrete by geopolymer paste", *Mater. Des.*, Vol. 32(5), 2011, pp. 3021-3028.
- [7] Somna K, Jaturapitakkul C, Kajitvichyanukul P, Chindapasirt P, "NaOH-activated ground fly ash geopolymer cured at ambient temperature", *Fuel.*, Vol. 90(6), 2011, pp. 2118-2124.
- [8] Sukmak P, Horpibulsuk S, Shen SL, "Strength development in clay-fly ash geopolymer", *Constr Build Mater.*, Vol. 40, 2013, pp. 566-574.
- [9] Van Jaarsveld JGS, Van Deventer JSJ, "Effect of the alkali metal activator on the properties of fly ash-based geopolymers", *Ind. Eng. Chem. Res.*, Vol. 38(10), 1999, pp. 3932-3941.
- [10] Pangdaeng S, Phoo-ngernkham T, Sata V, Chindapasirt P, "Influence of curing conditions on properties of high calcium fly ash geopolymer containing Portland cement as additive", *Mater. Des.*, Vol. 53, 2014, pp. 269-274.
- [11] Pangdaeng S, Sata V, Aguiar JB, Pacheco-Torgal F, Chindapasirt P, "Apatite formation on calcined kaolin-white Portland cement geopolymer", *Mater. Sci. Eng. C*, Vol. 51, 2015, pp. 1-6.
- [12] Temuujin J, van Riessen A, Williams R, "Influence of calcium compounds on the mechanical properties of fly ash geopolymer pastes", *J. Hazard. Mater.*, Vol. 167(1-3), 2009, pp. 82-88.
- [13] Hanjitsuwan S, Hunpratub S, Thongbai P, Maensiri S, Sata V, Chindapasirt P, "Effects of NaOH concentrations on physical and electrical properties of high calcium fly ash geopolymer paste", *Cem. Concr. Compos.*, Vol. 45, 2014, pp. 9-14.
- [14] Thakur RN, Ghosh S, "Effect of mix proportion on compressive strength and microstructure of fly ash based geopolymer composites", *ARN J Eng Appl Sci.*, Vol. 4(4), 2009, pp. 68-74.
- [15] Hawa A, Tonnayopas D, Prachasaree W, Taneerananon P, "Development and Performance Evaluation of Very High Early Strength Geopolymer for Rapid Road Repair", *Adv. Mater. Sci. Eng.*, Vol. 2013, 2013, pp. 9.
- [16] Pacheco-Torgal F, Castro-Gomes JP, Jalali S, "Adhesion characterization of tungsten mine waste geopolymeric binder. Influence of OPC concrete substrate surface treatment", *Constr Build Mater.*, Vol. 22(3), 2008, pp. 154-161.
- [17] Phoo-ngernkham T, Hanjitsuwan S, Damrongwiriyanupap N, Chindapasirt P, "Effect of sodium hydroxide and sodium silicate solutions on strengths of alkali activated high calcium fly ash containing Portland cement" *KSCE J. Civ. Eng.*, In Press, 2016.
- [18] Phoo-ngernkham T, Hanjitsuwan T, Suebsuk J, Chindapasirt P, "Use of nano-SiO₂ and nano-Al₂O₃ as an additive to improve strength development of fly ash-Portland cement geopolymer", *International Congress on Engineering and Information*, 2016, pp. 623-629.
- [19] Phoo-ngernkham T, Maegawa A, Mishima N, Hatanaka S, Chindapasirt P, "Effects of sodium hydroxide and sodium silicate solutions on compressive and shear bond strengths of FA-GBFS geopolymer", *Constr Build Mater.*, Vol. 91, 2015, pp. 1-8.
- [20] ASTM C928-13, "Standard specification for packaged, dry, rapid-hardening cementitious materials for concrete repairs", *Annual Book of ASTM Standard*, Vol.04.02, 2013
- [21] ASTM C881/C881M-14, "Standard specification for epoxy-resin-base bonding

- systems for concrete”, Annual Book of ASTM Standard, Vol.04.02, 2014.
- [22] ASTM C618-15, “Standard specification for coal fly ash and raw or calcined natural pozzolan for use in concrete”, Annual Book of ASTM Standard, Vol.04.02, 2015.
- [23] ASTM C191-13, “Standard test method for time of setting of hydraulic cement by vicat needle”, Annual Book of ASTM Standard, Vol.04.02, 2013.
- [24] ASTM C109, “Standard test method of compressive strength of hydraulic cement mortars (using 2-in. or [50 mm] cube specimens)”, Annual Book of ASTM Standard, Vol.04.01, 2002.
- [25] Rattanasak U, Chindapasirt P, “Influence of NaOH solution on the synthesis of fly ash geopolymer”, *Miner. Eng.*, Vol. 22(12), 2009, pp. 1073-1078.
- [26] Guo X, Shi H, Chen L, Dick WA, “Alkali-activated complex binders from class C fly ash and Ca-containing admixtures”, *J. Hazard. Mater.*, Vol. 173(1-3), 2010, pp. 480-486.
- [27] Phoo-ngernkham T, Sata V, Hanjitsuwan S, Rittirud C, Hatanaka S, Chindapasirt P, “Compressive strength, Bending and Fracture Characteristics of High Calcium Fly Ash Geopolymer Mortar Containing Portland Cement Cured at Ambient Temperature”, *Arab. J. Sci. Eng.* Vol. 41(4), 2016, pp. 1263-1271.
- [28] Garcia-Lodeiro I, Palomo A, Fernandez-Jimenez A, MacPhee DE. Compatibility studies between N-A-S-H and C-A-S-H gels. Study in the ternary diagram $\text{Na}_2\text{O}-\text{CaO}-\text{Al}_2\text{O}_3-\text{SiO}_2-\text{H}_2\text{O}$. *Cem. Concr. Res.*, Vol. 41(9), 2011, pp. 923-931.

INFLUENCE OF SEAWATER ON THE STRENGTH OF RC BEAMS AND CORROSION BEHAVIOR OF STEEL

Bernardo A. Lejano¹ and Cheryl Lyne C. Roxas²

^{1,2}Faculty, De La Salle University, Philippines

ABSTRACT

The effects of seawater on the strength performance of reinforced concrete (RC) beams were investigated. Four RC beams measuring 150 x 200 x 800 mm were constructed. Two beams were constructed with concrete mixed with freshwater and the other two were constructed with seawater. Center point loading test was conducted on the beams specimens. Load, deflection, and strain of each beam were monitored and recorded. It was found that the difference between the strength test values obtained by using freshwater and seawater were minimal. However, formation of rust in steel when seawater was used was very evident. Hence, the effects of seawater on the corrosion behavior of steel were investigated. Mortar specimens with cold-joint were used as medium to facilitate the investigation of corrosion. Ordinary Portland cement (OPC) Type 1 was used as binder for the mortar and was partially replaced with fly ash at 30% and 50%. Rectangular prism specimens of dimensions 40mm by 40mm by 160mm were cast for macrocell corrosion measurements and compressive strength determination. From the test results, the following were observed: (a) Specimens with fly ash were observed to have lower corrosion rates compared with the ones without fly ash; (b) Specimens mixed with freshwater resulted to the higher strength both at 7th-day age and 28th-day age; (c) Regardless of the type of water used in making the mortar, specimens cured in seawater achieved higher later strength values.

Keywords: Seawater, Corrosion, Reinforced Concrete, Mortar, Fly Ash

INTRODUCTION

Seawater is still currently not allowed to be used in construction as stipulated in the National Structural Code of the Philippines (NSCP) [1] and most of the other codes all over the world. However, there are already studies [2] - [5] that indicate the possibilities of using seawater as a substitute for potable water in concrete; whether for mixing, curing, or both. Results are varying and sometimes contradicting. Studies of Otsuki et al. [2], indicate the countermeasures that can be applied to eliminate the disadvantages that seawater presents. These studies indicate the possibility of using seawater in concrete; but still more studies must be conducted to further validate the usage, especially in reinforced concrete. Establishing criteria in using seawater in reinforced concrete members would benefit places with abundant seawater resources, such as the Philippines.

To investigate the effect of seawater when used in making reinforced concrete (RC) beam, the structural performance of two RC beams constructed with seawater were compared to two control RC beam specimens constructed with freshwater. This is done by testing the RC beams as simply supported beams with center-point loading. The findings of this comparison are presented in this paper. It was observed that the major effect of seawater is in corroding the reinforcing bars. It is also believed that exposing the RC beam to seawater environment

would affect the corrosion behavior of the reinforcing bars.

As a consequence, the effects of seawater on the corrosion behavior of steel in mortar were investigated. In addition, fly ash was also investigated as a possible concrete ingredient that can possibly lower the corrosion rate of steel in concrete. Fly ash is a pozzolan, hence it reacts with calcium hydroxide that is produced during cement hydration resulting to the conversion of larger pores into finer pores [6]. This produces a more compact concrete thereby blocking the flow of seawater or other chemical attacks. As a result, the corrosion risk of reinforced concrete structures in chloride rich environments, such as seawater, can be lowered by fly ash to a satisfactory level [7].

In this study, steel is assumed to undergo macrocell corrosion. Corrosion happens when chemical reaction, specifically oxidation, occurs in steel. The presence of this chemical reaction can be monitored through the flow of electricity when steel bars enclosed in concrete are arranged forming a macrocell circuit, that is, an anode and a cathode that are separated from each other. Usually, the passive film that is formed on the steel surface due to the alkalinity of concrete is broken down due to the presence of chemicals or other environmental factors.

Mortar specimens were used in this research to make it easier to measure to macrocell corrosion, as the presence of coarse aggregate could complicate the flow of electric current. Macrocell corrosion can

be further affected by chloride environment especially when concrete surface has cracks [8]. Since macrocell corrosion may occur at any time to any reinforced concrete structure, it is important to have good awareness of this corrosion process. As seawater is known to increase the probability of corrosion of steel, it is important to determine under what conditions this will happen and what are the possible remedies or solutions that may be applied.

To address the above mentioned problems, the main objective of this phase of study is to determine the effects of seawater on the corrosion density and corrosion rates and the possible countermeasures that fly ash can provide to the macrocell corrosion. In addition, the effects of seawater and fly ash to the compressive strength of mortar are also investigated to provide more information.

METHODOLOGY

This research may be divided into two parts. The first part is the testing of RC beams to evaluate the effect of seawater on their structural performance. The second is the macrocell corrosion test to study the corrosion behavior of steel and find possible way of counteracting it.

Test of RC beams

Four RC beams with dimensions of 150 x 200 x 800 mm with target concrete strength of $f'_c = 21\text{MPa}$ were prepared. Two RC beams used freshwater as mixing water while the other two RC beams used seawater, which will be termed as “freshwater beam” and “seawater beam”, respectively. The seawater used was obtained near seashore at waist-deep with salinity of 30.2 ppt. Other components such as size of aggregates, size of steel reinforcing bars, type of cement, and water to cement ratio were held constant to make the beams identical except for the water used. The diameter of the longitudinal steel reinforcement is 8mm and the stirrup is 6mm. The cross-section detail of the beam is shown in Fig. 1 and the longitudinal dimensions and reinforcing details of the beam is shown in Fig.2.

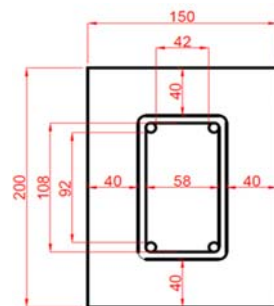


Fig. 1 Cross section of the RC beam specimens

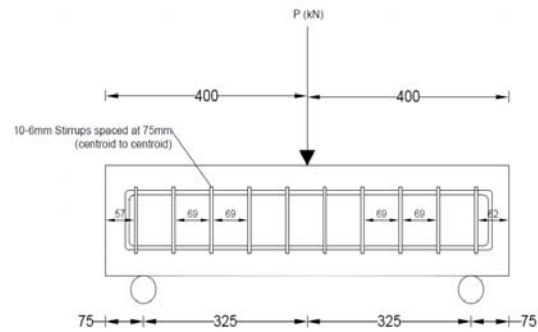


Fig. 2 Longitudinal details of the beam specimens

Testing for the flexural strength of the RC beam was conducted at 56 days after casting. Center point loading on a simply supported beam was adopted. A hydraulic jack was used to apply the load and monitored with a load cell. Clip gages and displacement transducers were used to monitor the strains and deflection, respectively, at the midspan of the beam. Shown in Fig. 3 is the test setup. After the beams were tested, the reinforcing bars were recovered for evaluation of the effect of seawater.

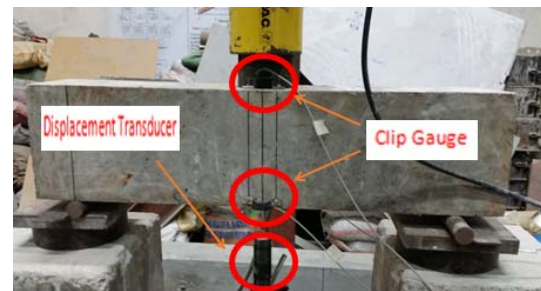


Fig. 3 Experimental test setup of RC beam

Macrocell Corrosion Test

For the macrocell corrosion test, rectangular prism or block specimens measuring 40mm by 40mm by 160mm were used. The water cement ratio used in making the specimens is 0.5 and the cement-sand ratio is 1:2. Fly ash as partial substitute for cement at 30% and 50% by weight was implemented. The seawater used had a salinity of 30.6 ppt. ASTM Type 1 Portland cement was used in combination with class F fly ash. Presented in Table 1 are the specimen codes assigned for the different type of specimens. The specimens were cured in either freshwater or seawater, but the macrocell corrosion test was done only for the specimens that were cured in seawater. To provide more information about the effect of seawater on mortar, compressive strength tests were conducted at the 7th and 28th day age of mortar.

Table 1 Codes used for specimen

Specimen Code	Fly ash (FA) %	Mixing Water	Curing Water
FA0FW-FW	0	FW	FW
FA30SW-FW	30	SW	FW
FA50SW-FW	50	SW	FW
FA0FW-SW	0	FW	SW
FA30SW-SW	30	SW	SW
FA50SW-SW	50	SW	SW

Note: FW=Freshwater, SW=Seawater

For the macrocell corrosion test, reinforcing steel bars, 12 mm in diameter, were arranged in mortar block so that anode and cathode are spatially separated resulting in a flow of electric current over the spatial distance [9]. A 100 mm long deformed bar was cut into three equal lengths and were placed in the mortar blocks as illustrated in Fig. 4. The bars were cleaned by soaking them in 10% diammonium hydrogen citrate to remove rust. Electrical wires were soldered on both ends of the cut steel bars to be connected to the ammeter that will measure the electric current. The divided bars were longitudinally joined together using epoxy. The assembled steel bars were placed in the mortar block maintaining a mortar cover of 10 mm from the surface. Cold-joint was made in the mortar block to ensure penetration of seawater. To do this, only half of the mould was first filled with mortar. Then, the mortar was allowed to set for a whole day before filling the mould to its full capacity. Fig. 5 shows the resulting corrosion specimen with cold-joint. The mortar blocks were then sealed with epoxy on all sides except on the side nearest to the steel bar, the one with 10 mm mortar cover.

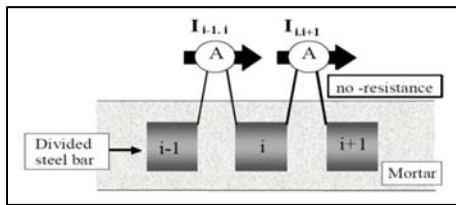


Fig. 4 Macrocell current density measurement [12]

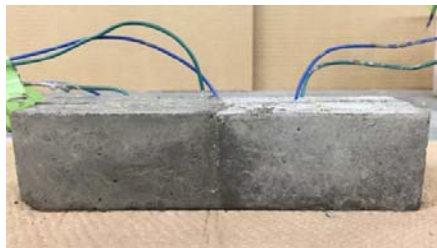


Fig. 5 Corrosion specimen with cold-joint

Cold-joints are incorporated in the specimens to provide a possible passage for the seawater used in curing. This will provide additional chloride ions to reach the steel aside from the ones that are already present in the mortar. The high alkalinity of the mortar creates a thin layer of iron oxide that provides resistance to further oxidation by preventing oxygen from reaching the steel [10]. However, the introduction of chloride ions, oxygen and water into the mortar destroys this protective oxide layer.

As mentioned earlier, macrocell corrosion monitoring was done only to steel in specimens cured in seawater. A zero resistance ammeter (ZRA) was used to measure weekly the macrocell current (refer to Fig. 4). Then the macrocell current densities were calculated from the measured macrocell currents. Macrocell corrosion current is defined as the total electric current flowing through all segmented steel bars in the mortar blocks taken as a unit. The macrocell current density formula is given in Eq. 1 [11]:

$$a_i = \frac{I_{i-1,i} - I_{i,i+1}}{S_i} \quad (1)$$

where: a_i = macrocell current density of steel component i (A/cm^2); $I_{i,j}$ = macrocell corrosion current from steel components i to j (A); and S_i = surface area of steel i .

To evaluate the macrocell corrosion electricity, a graph is made by plotting the macrocell current density against time. An example is shown in Fig. 6. The macrocell current densities are plotted for a period of 8 weeks (56 days). The macrocell corrosion electricity is obtained by integrating the area under the curve in the graph shown in Fig. 6.

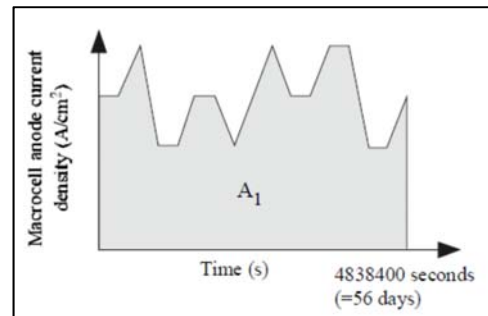


Fig. 6 Macrocell corrosion electricity [11]

According to Miyagawa et al. [12], the corrosion rate may be evaluated as follows: If the maximum corrosion electricity is below 20 Coulomb/cm² in 56 days the corrosion rate is considered “low”, that is, 0.05 mm/year. If it exceeds 50 Coulomb/cm² in 56

days, the corrosion rate is considered “high”, that is, 0.12 mm/year. He also predicted that for “low” corrosion electricity in 30 years, the yield strength of the reinforcing steel may decrease to about 70% of the original strength, while for “high” corrosion electricity, the yield strength may decrease to as low as 35% of the original strength.

TEST RESULTS AND FINDINGS

At the time of testing of the RC beam specimens, the concrete strength was measured using concrete cylinders. The average strength of concrete with freshwater is 27.17 MPa and the strength with seawater is 23.94 MPa, indicating that the compressive strength of concrete with seawater is 11.88% lower than concrete with freshwater.

The yield strength (f_y) of reinforcing bars recovered from the tested RC beam specimens was determined. Freshwater beams had an average $f_y=499.5$ MPa and seawater beams had $f_y=495.7$ MPa. The difference is only 0.76% indicating that the strength of the steel reinforcing bars has not been significantly affected by the seawater. Hence, the decrease in strength of the beam may be due only to the slight decrease in concrete strength.

Fig. 7 shows the visual difference of the steel reinforcement bars taken from the seawater beam specimens and from the freshwater beam specimens. Rust can be clearly observed on the steel reinforcements from the seawater beam specimens while no rust can be observed on the steel from the freshwater beam specimens.



Fig. 7 Steel bar from seawater beam (left), steel bar from freshwater beam (right)

Tabulated in Table 2 are the important values obtained from the test of beam, specifically at the ultimate condition, that is, when the strain of concrete reached 0.003. The average ultimate load obtained from the freshwater beams is a little bit higher than that of the seawater beams. The difference is only 6.10%. The midspan deflection was also almost the same for the two types of beams. The difference is only 12.9%. The load-strain curves of the tested beams are shown in Fig. 8. Curves labeled starting in “F” are for freshwater beams while those starting in “S” are for seawater beams. It can be seen that the curves are almost identical. Differences are very minimal.

Table 2 Values from the test of RC beam specimens

At ultimate condition (strain=0.003)	Specimen Type	
	Freshwater beam	Seawater beam
Ult. Load (kN)	42.11	39.54
Deflection (mm)	0.986	1.113
Mn_{expt} (kN-m)	6.84	6.42
Mn_{calc} (kN-m)	6.72	6.45
Expt/Calc	1.018	0.995

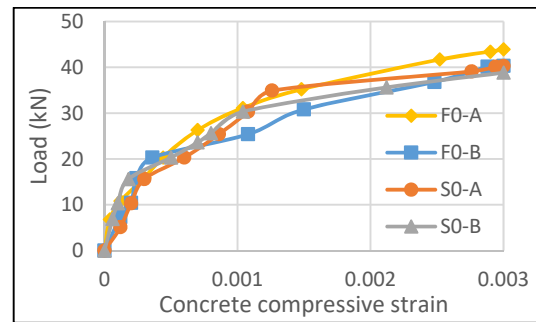


Fig. 8 Load-strain relationship of the RC beams

Comparing the nominal flexural strengths (Mn), the flexural strength of freshwater beams is higher than compared to seawater beams as presented in Table 2. However, the difference between the two groups is again very minimal. The percentage difference is 6.14% only. The comparison between experimental and theoretical nominal moments (Mn_{expt} , Mn_{calc}) yielded very good agreement. The theoretical values were calculated using the formulas stipulated in the code (NSCP).

The test results from the loading test of RC beam specimens indicate that there is very small difference in the structural performance between RC beam specimens with freshwater and that with seawater. The major effect is only in the corrosion of the steel bars, which in the long run may contribute to the deterioration of the structural integrity of the beams.

The macrocell corrosion rate evaluation of steel in mortar provides an insight on the possible corrosion of steel in beams with seawater and exposed to seawater environment. Fig. 9 shows the macrocell current density of the middle steel element for each specimen type.

Although Fig. 9 does not consistently show anodic or cathodic macrocell current densities, it is only an indication that macrocell corrosion measured is non-uniform. The anodic and cathodic reactions may fluctuate throughout the investigation period [8]. Based on corrosion rate calculation of Miyazato [11] and Miyagawa et al. [12], the macrocell corrosion electricity may be calculated from Fig. 9 and can be converted to macrocell

corrosion rate. It is evaluated for the period of 8 weeks (56 days), starting on the 98th-day up to 154th-day of current measurement, when the current measurements are significantly large.

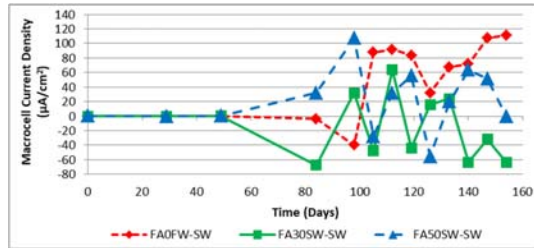


Fig. 9 Macrocell current density variations

Presented in Fig. 10 is the plot of the macrocell corrosion rates of the mortar specimens for the investigation period of 8 weeks. The corrosion rate is calculated per period (per week) so that corrosion development could be observed over the investigation period. The specimens without fly ash (FA0FW-SW) are observed to have the highest corrosion rate. Moreover, the corrosion rate is consistently increasing during the 8-week period and the corrosion rate at the end of the 8-week period is 0.08mm/(8week) which may be projected to one year as 0.51mm/year. For the specimen with 30% fly ash (FA30SW-SW), the corrosion rate is lowest, picking up only at the end of the 8-week period. The corrosion rate at the end of the 8-week period is 0.01mm/(8week) or 0.09mm/year. The lower corrosion rate of specimens mixed with fly ash can be explained by the fine structure of fly ash preventing the penetration of chlorides. However, in the case of the specimen with more fly ash, that is, at 50% cement replacement (FA50SW-SW), the corrosion rate turned out to be higher than the specimens with smaller amount of fly ash. This indicates that the amount of fly ash used as corrosion countermeasure may have a limit and may be at cement replacement lower than 50%. Furthermore, it seems that using seawater as mixing water is a lesser corrosion risk than exposing mortar to chloride-rich environment. Moreover, the existence of cold-joints may have also increased the corrosion activity as surrounding seawater can easily penetrate the mortar.

Regarding the strength investigation of the mortar specimens, the results of the compressive strength test indicate the usual trend that the compressive strength increases with time, as shown in Fig. 11. The strength increased from 7th-day to 28th-day. Furthermore, the compressive strength of specimens mixed with freshwater exhibited higher than those mixed with seawater. This is the same observation in the RC beam test. In general, the increase in fly ash replacement percentage resulted to the decrease in compressive strength of mortar, which was similarly observed by Lim et al. [13].

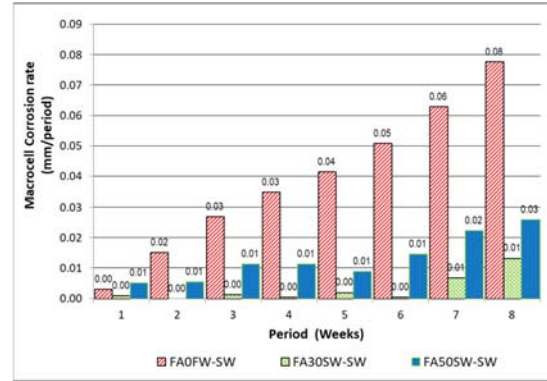


Fig. 10 Macrocell corrosion rate of the specimens

Regardless of the mixing water, specimens cured in seawater resulted to higher 28th-day compressive strength, except for the specimens with 50% fly ash replacement. Results of this study corroborated that mortars with fly ash immersed in seawater tend to have higher compressive strength [14]. However, it seems that the 30% fly ash replacement is the best among the values considered because the increase in strength is higher when cured in seawater.

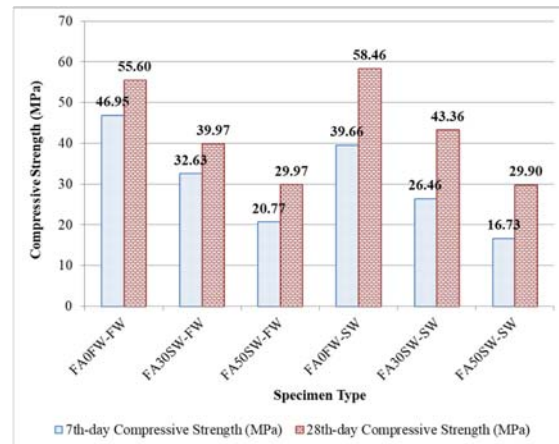


Fig. 11 Day 7 and day 28 compressive strengths

CONCLUSION

Rust was clearly observed on the steel reinforcement recovered from the RC beam specimens mixed with seawater. However, in terms of strength, the steel was not significantly affected.

Although there was a slight strength reduction in concrete with seawater, in general, the seawater did not have any significant effects on the flexural strength of the beam for the period covered in the study. Since the strength performance of RC beams with seawater was not significantly affected, seawater may be used in short term general and minor construction purposes. However, the behavior

of reinforced concrete with seawater must still be studied further on a long-term basis.

To provide insights on the effects of seawater on the corrosion of steel reinforcement in concrete, the effects of seawater and fly ash to the macrocell corrosion behavior of reinforcement in mortar were investigated. Rectangular prism mortar specimens with segmented steel bars were used as specimens. The macrocell corrosion currents were measured every week for a period of 8 weeks in order to compute for the corresponding macrocell corrosion density and corrosion rates. From the results, the following were concluded:

The specimens cured in seawater did not show consistent anodic or cathodic current densities throughout the exposure period, indicating non-uniform corrosion

Mortar specimens with fly ash were observed to have very much lower corrosion rates compared with the ones without fly ash which can be explained by the fine structure of fly ash that reduces the ingress of aggressive elements. However, it was observed that less corrosion rate is obtained when the cement replacement with fly ash is at 30% than when the fly ash is at 50%.

Mortar specimens mixed with freshwater resulted to higher strength both at 7th-day age and 28th-day age. The compressive strength decreases as the fly ash replacement percentage increases. Regardless of the mixing water, mortar specimens cured in seawater seemed to achieve higher 28th-day compressive strength.

ACKNOWLEDGEMENTS

The authors would like to express their utmost gratitude to the faculty members and staff of the Civil Engineering Department of the De La Salle University for their unwavering moral and technical support. Appreciation is also due to students, friends, families, relatives, and other DLSU personnel who contributed in making the experimental tests successful.

REFERENCES

- [1] NSCP 2010, "National Structural Code of the Philippines 6th Ed.", Chapter 4 – Structural Concrete, Vol. 1, 2010, pp. 13-14, pp.
- [2] Mohammed T, Hamada H, & Yamaji T, "Performance of seawater-mixed concrete in the tidal environment", *Cement and Concrete Research*, Volume 34, Issue 4, April 2004, pp. 593–601.
- [3] Otsuki N, Furuya D, Saito T, and Tadokoro Y, "Possibility of sea water as mixing water in concrete", 36th Conference on Our World in Concrete & Structures, Singapore, August 14-16, 2011.
- [4] Wegian FM, "Effect of seawater for mixing and curing on structural concrete", *The IES Journal Part A: Civil & Structural Engineering*, Vol. 3, No. 4, November 2010, pp.235–243.
- [5] Olutoge FA and Amusan GM, "The effect of sea water on compressive strength of concrete", *International Journal of Engineering Science Invention*, Vol. 3, Issue 7, July 2014, pp. 23-31.
- [6] Manmohan D and Mehta PK, "Influence of pozzolanic slag and chemical admixtures on pore size distribution and permeability of hardened cement paste", *Cement Concrete Aggregates*, Vol. 3, Issue 1, July 1981, pp. 63-7.
- [7] Millard SG and Bungey JH, "In-situ assessment of reinforcement corrosion in concrete structures", IABSE Report, 1989.
- [8] Nanayakkara O and Kato Y, "Macro-cell corrosion in reinforcement of concrete under non-homogeneous chloride environment", *Journal of Advanced Concrete Technology*, Vol. 7, No. 1, February 2009, pp. 31-40.
- [9] Subramaniam K and Bi M, "Investigation of steel corrosion in cracked concrete: Evaluation of macrocell and microcell rates using Tafel polarization response", *Corrosion Science*, Volume 52, Issue 8, August 2010, pp 2725-2735.
- [10] Madlangbayan M, Otsuki N, Nishida T and Baccay M, "Corrosion behavior of steel bar in chloride contaminated mortars with fly ash", *Philippine Engineering Journal*, Vol 26, No 2, 2005, pp. 13-24.
- [11] Miyazato S, and Otsuki N, "Steel corrosion induced by chloride or carbonation in mortar with bending cracks or joint", *Journal of Advanced Concrete Technology*, Vol. 8, No. 2, June 2010, pp.135-144.
- [12] Miyagawa T, Takewaka K, Demura K, Masuda Y and Moriwake A, "Technical committee report on the rehabilitation of concrete structures" *Proceedings of the Japan Concrete Institute*, Vol. 20, No. 1, 1998, pp. 39-48. (in Japanese)
- [13] Lim ED, Roxas CLC, Gallardo R and Otsuki N, "Strength and corrosion behavior of mortar mixed and/or cured with seawater with various fly ash replacement ratios", *Asian Journal of Civil Engineering*, (BHRC), Vol. 16, No. 6, Jan. 2015, pp 835-849.
- [14] Donatello S, Palomo A and Fernández-Jiménez A, "Durability of very high volume fly ash cement pastes and mortars in aggressive solutions", *Cement and Concrete Composites*, Vol.38, 2013, pp.12-20.

A COMPARATIVE SETTLEMENT PREDICTION OF LIMESTONE BLENDED MATERIALS USING ASAOKA AND HYPERBOLIC METHOD

Erica Elice Saloma Uy¹ and Jonathan Rivera Dungca¹

¹Civil Engineering, De La Salle University, Philippines

ABSTRACT

The construction industry in the Philippines is predicted to sustain its growth up to 2021 because of the infrastructure plan of the government according to the Philippine Infrastructure Report. With this, the demand in construction materials would increase and as a result an increase in prices is expected. To address this problem, an alternative material must be explored. A promising material is limestone because it is abundant in the Philippines. These materials can be used as a material for structural fill or embankment. In order to determine the material's possible use its capacity to withstand loads must be checked. In this study, its compressibility is the main focus. Its consolidation parameters were first obtained by performing one dimensional consolidation test. Limestone wastes were mixed with a conventional soil and it is proportioned at 0%, 20%, 40%, 60% and 100%. After the consolidation parameters were determined, the data from the consolidation test were used to predicting the settlement behavior of the material. The Asaoka method and hyperbolic method were used in the prediction and the results of both methods were compared. Based on the results, it was observed in the one dimensional consolidation test, the limestone waste used had a minimal effect to the compressibility of the conventional material used. Lastly, the prediction from the hyperbolic method is larger for some mix proportions.

Keywords: Limestone waste, Asaoka Model, Hyperbolic Model

INTRODUCTION

In the recent Philippine Infrastructure Report of 2017, strong growth in the construction and infrastructure industry was predicted to occur in over the next five years. The growth is due to the government's plans to improve transportation infrastructure, residential buildings and social infrastructure. Based on the report, the real growth will reach 12.5% in-between 2017 and 2021 while the average annual growth will reach 11.2% for the construction sector [1]. The Philippine Development Plan was also launched in February of 2017. The plan covers the year 2017 to 2022. The main goal of the plan was to change the Philippine income trend as an upper-middle-income country by 2022 [2]. With this shift, the compound annual growth rate (CAGR) of the construction industry's output value is expected to rise by 9.79% [3]. The continuous growth of the construction industry can result to an increase in demand of construction materials. According to the average construction cost forecast in the Philippines for 2016 to 2020, the average cost of residential is expected to increase by 5.51% [4]. To address this problem, there is a need to explore alternative materials. A promising material is limestone waste because it is abundant in the Philippines. According to the 2013 Minerals Yearbook, limestone quarry production in 2013 reached at 73,359 thousand metric tons and it is the third top quarried mineral commodity. Its production

rate doubled since 2009 [5]. This trend could result to an increase in the production of limestone waste material and this can also lead to a shortage in storage facility. Due to its abundance, possible uses of these materials are as a material for structural fill or embankment.

There were already several researches that showed the material's potential as a construction material. Limestone waste was used as an alternative material for road based material and soil stabilization. Based on their results, the use of limestone waste improved the strength of the road embankment and it was also found to be an economical alternative construction material [6], [7]. Limestone wastes were usually mixed with conventional materials in order to determine the most suitable amount of limestone waste substitution. It was found that a 50% blend of limestone waste mixed with the conventional material was able to produce the optimum strength [6]. Furthermore, limestone waste showed a very high efficiency in improving weak soils and it can also be used as a substitute for lime in soil improvement for engineering construction [8]. However, there is a lack of knowledge on its settlement characteristics. With this, it is the objective of the study to evaluate the compressibility of limestone waste. Limestone wastes were mixed with conventional material and it is proportioned at 0% (L1), 20% (L2), 40% (L3), 60% (L4) and 100% (L5). Its consolidation parameters such as coefficient

of consolidation (C_v), compression index (C_c), recompression index (C_r), coefficient of volume compressibility (m_v), overconsolidation ratio (OCR) and preconsolidation stress (σ'_c) were established by performing one-dimensional consolidation test. After the consolidation parameters were determined, the data from the consolidation test were used in predicting the settlement behavior of the material. The Asaoka method and hyperbolic method were used in the prediction and the results of both methods were compared.

INDEX PROPERTIES OF LIMESTONE WASTES

The limestone wastes used were from a quarry in Guimaras province in central Philippines. The index properties of the five blends were tested following American Society for Testing Materials Standards (ASTM). Its index properties namely, specific gravity (G_s), liquid limit (LL), plastic limit (PL), plasticity index (PI), maximum void ratio (e_{max}), minimum void ratio (e_{min}), maximum dry density (ρ_{dmax}) and minimum dry density (ρ_{dmin}) are tabulated in Table 1. The index properties of L5 were compared with other existing studies. Only this sample was compared because the other samples were blended with conventional material. The conventional material mixed with limestone waste was based on the requirements of the Department of Public Works and Highways (DPWH) Blue Book. The conventional material can be a common material or rock. It must pass a sieve opening of 75 mm or 3 inches. The percentage passing must also be less than 15 mass percent for the number 200 sieve or 0.075 mm opening. Lastly, the material must have a plasticity index less than 6 and a liquid limit of less than 30 [9]. Based on the results of existing studies, the values of their specific gravity for limestone wastes are 2.58, 2.65 and 2.59 [10], [7]. It can be seen that L5 has a value close to their results. For its plasticity, the limestone waste blends tested are classified as samples with medium plasticity [11]. On the other hand for other studies, their limestone has very high plasticity having LL of 72%, PL of 53% and PI of 19%. The difference can be due to the mineralogical composition, origin of the material and its particle shape and size. The effect of blending limestone waste with a conventional material can be seen in the results of the index properties. When the amount of limestone waste is greater the value of the specific gravity, maximum dry density and minimum dry is decreasing. For the result of liquid limit, plastic limit, plasticity index, maximum void ratio and minimum void ratio, it was observed that as the amount of limestone is greater their values increased.

EXPERIMENTAL PROGRAM

Sample Preparation

The ash mixtures were prepared by moist tamping. The target relative density is 90% to 95%. In order to attain a fully saturated condition, the samples were first soaked with distilled water for 16 hours. This was followed by adding distilled water in the consolidation cell. It was made sure that the water would reach the load cap to ensure a fully saturated condition. The amount of distilled water mixed with the sample is close to the value of the optimum moisture content (OMC) as seen in Table 2.

Table 1. Index properties of limestone wastes

Index Property	L1	L2	L3	L4	L5
G_s	2.89	2.77	2.71	2.67	2.63
LL	13.73	14.2	15.82	17.29	19.7
PL	11.84	12.07	13.13	14.42	15.11
PI	1.89	2.13	2.69	2.87	4.59
e_{max}	0.69	0.74	0.87	0.93	1.2
e_{min}	0.32	0.37	0.43	0.48	0.76
ρ_{dmax} (g/m ³)	2.18	2.03	1.89	1.81	1.49
ρ_{dmin} (g/m ³)	1.71	1.59	1.45	1.38	1.19

Table 2. Optimum moisture content (OMC) of limestone wastes [6]

	L1	L2	L3	L4	L5
OMC (%)	5.00	5.56	5.98	6.63	9.54

Consolidation Test

Consolidation test was performed in the study under ASTM D 2435 Standard Test Method for One-Dimensional Consolidation Properties of Soils. The load increments implemented in the experiment were 7, 12, 25, 50, 100, and 200 kPa. A seating pressure of 7kPa was first applied before loading was performed [12]. Reloading was also performed in the experiment and it was initiated at 200 kPa. Reloading was performed until 7 kPa was reached. The settlement was recorded every 0.1, 0.25, 0.5, 1, 2, 4, 8, 15, 30, 60, 120, 240, 480 and 1440 minutes. The load was changed after 24 hours. For this study, a total of 15 samples were tested. Each of the limestone waste blends was tested three times.

OBSERVATIONAL METHODS

Observational methods or also known as graphical method are techniques used to predict the future settlement of a material. These methods use field data or consolidation test data specifically the amount of settlement and time of settlement. Through these methods, uncertainties in soil variability, magnitude and load distribution can be avoided [13]. Some of the widely adopted methods that produces

reasonable estimates are Asaoka method, hyperbolic method and velocity method, just to name a few [14], [15]. For this study, Asaoka and hyperbolic method were used due to its simplicity and accuracy.

Asaoka Method

The Asaoka Method is an observational method that utilizes the settlement data from the field or either from a one-dimensional consolidation test to predict the ultimate settlement (S_{ult}) and the coefficient of consolidation (c_v) [15]. The one-dimensional settlement (S) at a certain time increment (Δt) can be expressed as:

$$S_n = S_o + \beta S_{n-1} \quad (1)$$

Where:

S_n = settlement at time t

S_{n-1} = settlement at time t_{n-1}

β = slope

S_o = intercept

The equation represents the linear trend line in an Asaoka's plot as shown in Fig 1. The figure is the plot of the settlements (S_n, S_{n-1}) having a constant time increment (Δt). The plot is used to estimate the ultimate settlement (S_{ult}) by using the following equation:

$$S_{ult} = \frac{S_o}{1 - \beta} \quad (2)$$

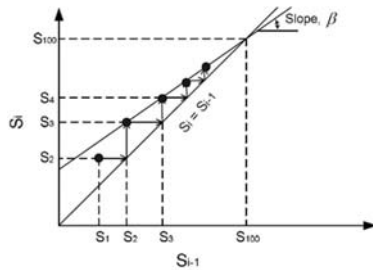


Fig 1 Asaoka's Plot [18].

Another method to estimate the ultimate settlement is by drawing a 45 degree line on the Asaoka's plot. The intersection of both lines is the value of the ultimate settlement [16]. Prior to creating the Asaoka's plot, the settlement must be obtained under a constant time increment (Δt) as seen in Fig 2. The accuracy of estimation is dependent on the time increment employed [17]. The coefficient of consolidation (c_v) can also be estimated by using the following equation [18]:

$$c_v = -\frac{5}{12} H^2 \frac{\ln \beta}{\Delta t} \quad (3)$$

Where

H = thickness of the stratum

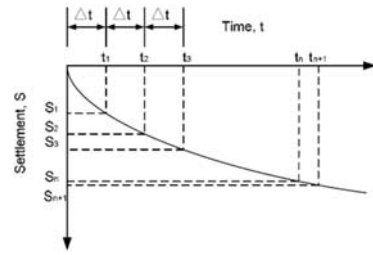


Fig 2 Settlement versus time under a constant time interval [18].

Hyperbolic Method

The hyperbolic method is another observational method that predicts the ultimate settlement of the soil. It also uses the actual settlement data or one-dimensional data in order to perform the prediction. This method replaces the settlement curve with a hyperbolic curve [18]. The hyperbolic curve is a transformed plot of the settlement curve as seen in Fig 3. The ordinate is the ratio of time to settlement while the abscissa is time. When a fitted line is introduced in the plot, the hyperbolic curve is defined as [19]:

$$\frac{t}{s} = \alpha + \beta t \quad (4)$$

Where:

s = settlement at time t

t = time

β = slope

α = intercept

When time in Equation 4 becomes very large or it is approaching infinity, the ultimate settlement (s_{ult}) can be predicted by [20]:

$$\lim_{t \rightarrow \infty} s = \lim_{t \rightarrow \infty} \frac{1}{\frac{\alpha}{t} + \beta} = s_{ult} = \frac{1}{\beta} \quad (5)$$

CONSOLIDATION PARAMETERS

The consolidation parameters for the limestone wastes are discussed and presented in this section. The Casagrande method was used to determine the recompression index (C_r), compression index (C_c), preconsolidation stress (σ'_c) and overconsolidation ratio (OCR). The method uses the consolidation curve in determining the consolidation parameters. The typical result of the consolidation curve is shown in Fig 4. The recompression index is the slope of the recompression curve while the

compression index is the slope of the normal consolidation. The typical values for compression index ranges from 0.1 to 0.8. While for the recompression index, it ranges from 0.015 to 0.35. Both parameters can also be determined from empirical formulas [22]. The results are tabulated in Table 3. Based on the results, the indexes obtained were smaller than the suggested values. This can be due to the fact that the limestone wastes have medium plasticity which means that it has a little potential to compress. It was also observed that as the percentage of limestone waste is increasing the compression index is also increasing. Furthermore, these parameters are also used to classify the soil's compressibility together with the initial void ratio as seen in Table 4. Based on the values of the ratio of compression index and the void ratio, it implies that the limestone waste blends tested are very slightly compressible. The range of values for this classification is 0 to 0.05.

The preconsolidation stress (σ'_c) obtained from the consolidation curve has a value of 25 kPa for L1 and 50 kPa for L2 to L5. For the overconsolidation ratio, larger values were observed for 7 and 12 kPa. On the other hand for 25 to 200 kPa, a decreasing value was experienced. The samples for 7 to 12 kPa except L1 at 25 kPa are overconsolidated while L1 at 25 kPa and L2 to L5 at 50 kPa are normally consolidated. The values of coefficient of consolidation (C_v) are tabulated in Table 6. The parameter was obtained using the early stage log-t method. From the results, no particular trend can be observed. They are compared with the typical values of silts and clays. It was observed that 83.33% of the data are within the range of the typical values. The volume of compressibility is also obtained. Based on the results tabulated in Table 7, the values are very small and when it was compared to the typical values it was classified as a sample with very low compressibility.

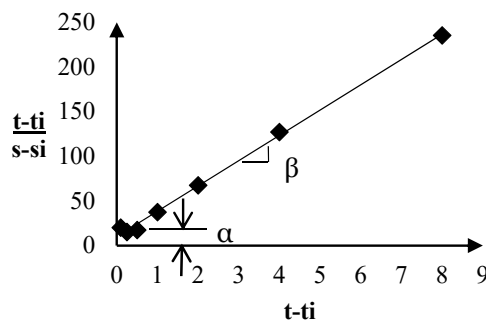


Fig 3 Hyperbolic Curve [21].

The limestone waste tested were compared to another study where a road embankment was constructed over a limestone waste. Specifically, only L5 was compared since it is the only sample

that contained 100% limestone waste. As seen in Table 8, it has a higher σ'_c which means it had experienced a higher effective vertical overburden stress in its loading history. Furthermore, C_c and OCR is higher while C_v is smaller. In the study, their limestone wastes were classified as highly compressible [7]. For this study, the limestone waste tested was considered as very slightly compressible based on values of the ratio of compression index and the void ratio. More so, it is also considered to have a very low compressibility based on the value of its volume of compressibility. The difference in the origin of the material can be the reason why the results of both materials are different.

Table 3. Summary of results for C_c and C_r .

Limestone Waste	Compression Index (C_c)	Recompression Index (C_r)
L1	0.009	0.002
L2	0.015	0.004
L3	0.017	0.003
L4	0.024	0.003
L5	0.03	0.003

Table 4. Classification of soil compressibility.

Limestone Waste	e_0	C_c	$C_c/(1+e_0)$
L1	0.34	0.009	0.0067
L2	0.39	0.015	0.0108
L3	0.45	0.017	0.0117
L4	0.58	0.024	0.0152
L5	0.78	0.03	0.0169

Table 5. Summary of overconsolidation ratio (OCR)

Vertical Stress	OCR				
σ'_z (kPa)	L1	L2	L3	L4	L5
7	3.57	7.14	7.14	7.147	7.147
12	2.08	4.17	4.17	4.17	4.17
25	1	2	2	2	2
50	0.5	1	1	1	1
100	0.25	0.5	0.5	0.5	0.5
200	0.13	0.25	0.25	0.25	0.25

Table 6. Summary of coefficient of consolidation (C_v)

Vertical Stress	C_v (cm ² /sec $\times 10^{-4}$)				
σ'_z (kPa)	L1	L2	L3	L4	L5
7	30.18	28.30	21.57	8.88	8.70
12	1.13	0.45	0.41	0.38	21.57
25	0.27	30.18	0.28	8.70	3.02
50	1.00	8.23	0.15	45.28	45.28
100	14.00	0.30	0.20	30.18	0.90
200	28.83	22.63	45.28	18.12	90.55

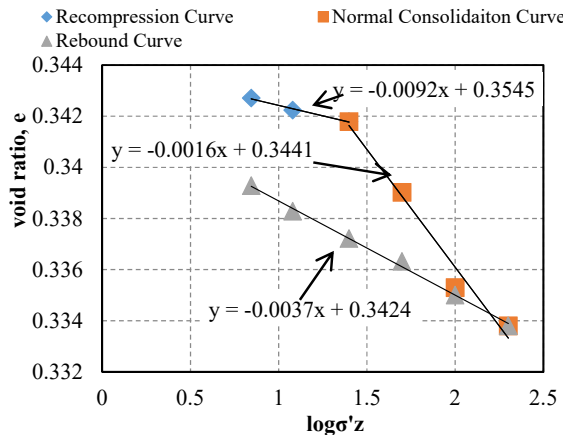


Fig 4 Typical result of the Consolidation Curve.

Table 7. Summary of volume of compressibility(m_v)

Vertical Stress	m_v (mm ² /kN)				
σ'_z (kPa)	L1	L2	L3	L4	L5
7-12	2.0E-3	5.0E-4	3.0E-3	2.0E-3	6.0E-4
12-25	4.0E-5	3.0E-4	3.0E-4	8.0E-5	5.0E-4
25-50	1.0E-4	3.0E-4	5.0E-5	1.0E-4	2.0E-4
50-100	7.0E-5	9.0E-5	3.0E-5	6.0E-5	2.0E-4
100-200	1.0E-5	6.0E-5	5.0E-5	6.0E-5	1.0E-4

Table 8. Consolidation parameters of other limestone waste [7].

Consolidation Parameter	Value
C_c	1.3
C_v	1.25E-04 to 2.33E-04 cm ² /sec
σ'_c	72 to 168 kPa
OCR	0.30 to 0.91

ULTIMATE SETTLEMENT PREDICTION

Two observational methods were used to predict the ultimate settlement of the limestone wastes. For the Asaoka's method, the ultimate settlement was predicted using 4 time interval and these are 10, 20, 30 and 40 minutes. This was done since the result is highly dependent on the value of time increment used. The Asaoka's plot of various time increments is shown in Fig. 5. It can be seen that the plots are overlapping each other which means that the ultimate settlement that will be predicted will have values that are in good agreement with each other. The predicted ultimate settlement resulted to having almost the same values for the time intervals 10, 20 and 30 minutes. A decrease by 0.01% to 0.39% was observed for the 40 minutes time interval. The summary of results for 10 minutes time interval is tabulated at Table 9. The difference in results is because as the time interval is being increased the number of data in the Asaoka's plot is being

decreased. This leads to the change in the value of the slope and the intercept as well. As seen in Table 10, a larger slope was observed for the 10 min. time interval and it continuously decreased when the time interval was increased. The coefficient of consolidation was also computed for each time interval and slope of each Asaoka's plot. The thickness used in the computation is the thickness of the sample which is 20 mm. The results are tabulated in Table 10 and it can be seen that for all time increment, close values were computed from L1 at 50 to 200 kPa and for L2 to L5 for all vertical pressures. For L1 at 12kPa for all time increment, a larger value was computed. The difference in results can be attributed to the trend of deformation or settlement the sample had experienced as it is being compressed. Comparison was also made with C_v from the early stage log-t method and the Asaoka's method. A large difference can be observed because the early stage log-t method is a graphical method that uses the early stage of the consolidation curve which can lead to a larger value of C_v .

Table 9. Ultimate settlement prediction using Asaoka's method at $\Delta t = 10$ minutes.

Vertical Stress	S_{ult} (mm)				
σ'_z (kPa)	0%	20%	40%	60%	100%
7	0.0609	0.0609	0.0658	0.0671	0.0509
12	0.1913	0.1193	0.2981	0.2708	0.2099
25	0.2025	0.1851	0.3230	0.2919	0.2050
50	0.2050	0.2795	0.3677	0.3304	0.3155
100	0.2671	0.3727	0.4000	0.3938	0.4174
200	0.3292	0.4720	0.4832	0.4894	0.6025

Table 10. Summary of coefficient of consolidation (C_v) using Asaoka's method at various Δt .

Δt (min)	Sample	σ'_z (kPa)	β	C_v (cm ² /sec)
10	L1	50 to 200	0.8819	3.49
	L2-L5	All	0.9195	2.33
20	L1	50 to 200	0.7775	3.50
	L2-L5	All	0.878	1.81
30	L1	12	0.803	2.03
	L1	50 to 200	0.6888	3.45
40	L2-L5	All	0.8213	1.82
	L1	50 to 200	0.6145	3.38
	L2-L5	All	0.7703	1.81

For the Hyperbolic method, the hyperbolic curve is shown in Fig.6. It can be seen that the ratio of time and settlement decreases as the pressure is being increased. This was the behavior of the plot for all the samples tested. The predicted ultimate settlement for this method is tabulated at Table 11. Comparing the results of the 2 observational

methods, it was observed that the predicted ultimate settlement for the hyperbolic method is larger than the Asaoka's method except for the ultimate settlement for except for L1 at 100 kPa and L5 at 25 kPa.

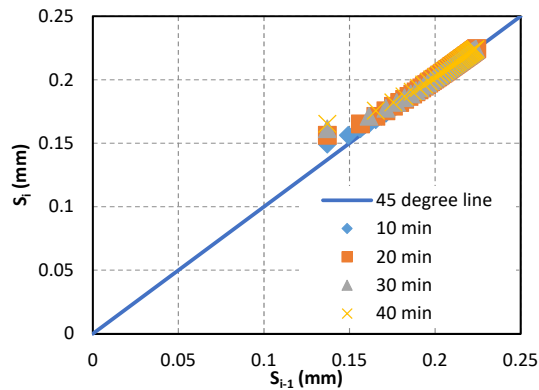


Fig 5. Asaoka's plot of various time increments for L5 at 12 kPa.

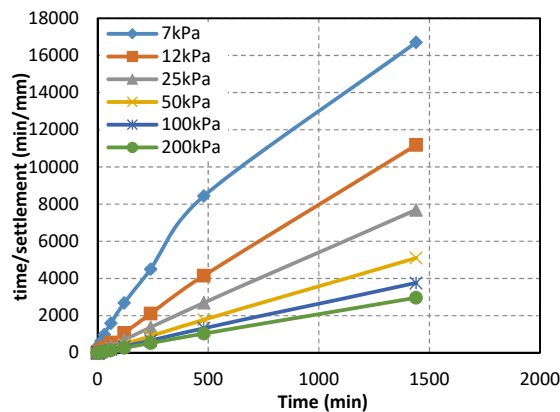


Fig 6. Hyperbolic curve for L2.

Table 11. Ultimate settlement prediction using Asaoka's method at $\Delta t = 10$ minutes.

Vertical Stress	S_{ult} (mm)				
σ'_{vz} (kPa)	0%	20%	40%	60%	100%
7	0.0665	0.0844	0.0812	0.0855	0.0537
12	0.1969	0.1278	0.3013	0.2763	0.2005
25	0.2041	0.1866	0.3289	0.2924	0.2080
50	0.2061	0.2812	0.3727	0.3324	0.3886
100	0.2638	0.3818	0.4074	0.3963	0.4270
200	0.3309	0.4841	0.4865	0.4914	0.6106

CONCLUSIONS

The limestone waste blends' compressibility characteristics were determined by performing one-dimensional consolidation test. The blends tested are

a mixture of limestone wastes and a conventional soil and they are proportioned at 0%, 20%, 40%, 60% and 100%. From the results of the one-dimensional consolidation test, the blends are considered to be very slightly compressible based on the values of the ratio of compression index and the void ratio. More so, based on the values of the volume of compressibility the blends are considered to have a very low compressibility characteristic. From these findings, it can be said that the limestone waste used had a minimal effect to the compressibility of the conventional material. With this, the blends tested have the potential to be used as a material for embankment. For the ultimate settlement predicted using Asaoka's method and hyperbolic method, these values can be used as a reference for the performance of limestone waste blends under a vertical stress of 7, 12, 25, 50, 100 and 200 kPa.

REFERENCES

- (2017). Philippines Infrastructure Report Q3 2017. Retrieved from <https://www.giiresearch.com/report/bmi177867-infrastructure.html>
- National Economic and Development Authority (NEDA). (2017). NEDA board approves Philippine development plan 2017-2022. Retrieved from <http://www.neda.gov.ph/2017/02/21/neda-board-approves-philippine-development-plan-2017-2022/>
- Industry Research Report. (2017). Philippines Construction Industry Trends, Opportunities and Market Report 2021. Retrieved from <http://www.openpr.com/news/532271/Philippines-Construction-Industry-Trends-Opportunities-and-Market-Report-2021.html>
- Philippine Statistics Authority. (2017). Construction materials wholesale price index in the National Capital Region (2000=100) : April 2017. Retrieved from <https://psa.gov.ph/content/construction-materials-wholesale-price-index-national-capital-region-2000100-april-2017>
- Sam, Y. F. (2016). The Mineral Industry of the Philippines. 2013 Minerals Yearbook. 23.1-23.9.
- Dungca, J. R. & Dychanco, L. F. T. (2016). Strength properties of road base materials blended with waste limestones. International Journal of GEOMATE. 11(25). 2493-2498.
- Ramer, D. S. & Wang, M. C. (2000) Performance of roadway embankment on lime waste. ASTM STP 1374. Geotechnics of high water content materials.
- Rahman, N. A., Khoury, H. N. & Suliman, M. R. (2008). Utilization of bituminous limestone ash from El-Lajjun area for engineering applications. Acta Geotechnica. 3. 139-151.
- Department of Public Works and Highways. (2005). DPWH standard specifications for public works and highways, 2004 edition: volume ii, highways, bridges and airports.
- Felekoglu, A. (1980/1981). Utilization of high volumes of limestone quarry wastes in concrete industry (self-compacting concrete case). Resources, Conservation and Recycling. 51. 770-791.
- Burmister, D. M. (1949). Principles and Techniques of Soil Identification. Proceedings, Annual Highway Research Board Meeting, National Research Council, Washington, D.C., 29.402-434.
- Alawaji, H. A. (2001). Settlement and bearing capacity of geogrid-reinforced sand over collapsible soil. Geotextiles and Geomembranes. 19. 75-88.
- Aboshi, H. & Inoue, T. (1986). Prediction of consolidation settlement of clay layers especially in case of soil stabilization by vertical drains. Proceedings of the IEM-JSSMFE Symposium on Geotechnical Problems, Kuala Lumpur, 31-40.
- Asaoka, A. (1978). Observational procedure of settlement predictions. Soils and Foundations, 18(4). 87-101.
- Tan, S. A. & Chew, S. H. (1996). Comparison of the hyperbolic and Asaoka observational method of monitoring consolidation with vertical drains. 36(3). 31-42.
- Whiteley, C. S. (2009). Determining the end of primary settlement using a simple analytical model progressively calibrated to field settlement data. (Unpublished master's thesis). Brigham Young University, Utah, United States of America.
- Edil, T. B., Fox, P. J. & Lan, L. T. (1991). Observational procedure for settlement of peat. GEO-COAST' 91, 2/4, 165-170.
- Kemp, A., Kok, B. W. C., Davis, J. & Menton, P. (2013). The consolidation behavior of alluvial soft clay in Gladstone, Central Queensland. 48(1), 1-17.
- Arulrajah, A., Nikraz, H. & Bo, M. W. (2004). Observational method of assessing improvement of marine clay. Ground Improvement. 8(4). 151-169.
- Huat, B. B. K., Hoe, N. C. & Munzir, H. A. (2004). Observational methods for predicting embankment settlement. Pertanika Journal of Science & Technology. 12(1). 115-128.
- Tan, T. S., Inoue, T. & Lee, S. L. (1991). Hyperbolic method for consolidation analysis. Journal of Geotechnical Engineering. 117(11). 1723-1737.
- Budhu, M. (2000). Soil mechanics and foundations, 3rd edition. United States of America: John Wiley & Sons, Inc. Department of Energy. (2016). 2016 major accomplishments. Retrieved from http://www.doe.gov.ph/sites/default/files/pdf/transparency/annual_report_esar_2016.

HYPERBOLIC MODEL PARAMETERS OF PHILIPPINE COAL ASH

Erica Elice Saloma Uy¹ and Jonathan Rivera Dungca¹

¹Civil Engineering, De La Salle University, Philippines

ABSTRACT

In the 2016 Annual Energy Sector accomplishment report of the Philippine's Department of Energy, power generation in the Philippines relied on coal-fired power plant at 46%. An increase of 19.47% was observed from 2003 to 2016. The increase in demand would result to an increase in production of waste material from the power plant namely, coal ash. Furthermore, the disposal of these waste materials can be an issue because it can cause a shortage in storage facilities. To address this, there is a need to study on the possibility of reusing these waste materials. A probable use of the waste material is by using it as a construction material for road embankments. In the Philippines some of these structures are constructed on areas exposed to seawater in order to address traffic congestion. This study proposes to use coal ash as the material for road embankment. Triaxial test under consolidated drained condition was performed considering the exposure to seawater. Three conditions were implemented namely, no exposure, immediate exposure and prolonged exposure. Based on the results, 100% fly ash had the highest strength. Hyperbolic model was employed to simulate the material's stress-strain response. The hyperbolic model was chosen since it has the capability of predicting load-displacement behavior of the waste material under monotonic loading. The Hyperbolic model prediction shows that the material can still handle higher stresses. With this, the ash mixtures tested has a potential to be used as a construction material for a road embankment.

Keywords: Coal Ash, Hyperbolic Model, Construction Material for Road Embankment

INTRODUCTION

According to the Annual Energy Sector accomplishment report of the Philippine's Department of Energy, power generation grossed at 42,700 Gigawatt hours (GWh) in the first semester of 2016 [1]. Coal-fired power plant generated power at 19,695 GWh. It was followed by renewable energy, natural gas and oil-based power plant at 10,158 GWh, 10,141 GWh and 2, 705 GWh, respectively. In the report, coal-fired power plant remains the major source of electricity at 46 %. In the same year, coal production for the first three quarter reached 8.4 million metric tons (MMMT). In the recent Summary of Installed Capacity, Dependable Capacity, Power Generation and Consumption report of the Department of Energy which was published in March 27, 2017, an increase of 19.47% in contribution to the power generation mix was observed from 2003 to 2016 [2]. The increase in demand would result to an increase in production of waste material from the power plant namely, coal ash. Furthermore, the disposal of these waste materials can be an issue because it can cause a shortage in storage facilities such as ash pond. Using coal ash as a construction material has been a trend in the construction industry due to its abundance. The most frequently used coal combustion by-products (CCB) or coal ash by-products are fly ash and coal ash [3]. Fly ash has been used as a material for cement, concrete and grout production, road embankment, reclamation

and structural fill [3], [4], [5], [7], [20], [21]. It was proven that the partial replacement of fly ash to cement can reduce the demand of water and it improves the concrete's workability. Furthermore, due to its abundance it is an economical material especially for road embankments and reclamation projects [4], [5]. Bottom ash on the other hand was found to have similar performance when compared with typical highway materials. More so, it also meets the conventional materials' specifications and can be used as subgrade and subbase [6]. To further utilize these by-products or waste materials' capability, mixture proportions were tested as a possible construction material for highway embankments. A study investigated 3 mixture ratios such as 50% fly ash and 50% bottom ash, 75% fly ash and 25% bottom ash and 100% fly ash. Based on their results, mixture ratio of 50% fly ash and 50% bottom ash had the highest peak angle of internal friction are suitable for highway embankments. In addition, the results of the study were also in good agreement with the strength and compressibility specifications of a typical fill material [7]. Another study conducted a field performance investigation on a 60% fly ash and 40% bottom ash mixture for a construction of an embankment. The construction was monitored to determine the behavior and performance of the material used. Results showed that the ash mixture adopted is an acceptable material for embankment construction [3]. Although there are several researches on the uses of coal ash, such as road embankment, there is still limited

knowledge on its performance when it is exposed to sea water. This scenario must be considered especially in the Philippines where road embankments are now being constructed on bodies of water, such as the sea, because of traffic congestion. Some projects are the Manila-Cavite Expressway (CAVITEX) and Cebu-Cordova Link Expressway (CCLEX) [8], [9]. With this, there is a need to study on the possibility of reusing these waste materials as a construction material for road embankments exposed to seawater. It is the objective of this study to determine the performance of coal ash as a construction material considering ash mixtures such as 100% fly ash (S1), 100% bottom ash (S2) and 50% fly ash 50% bottom ash (S3). Consolidated drained triaxial test was performed and the waste material will be exposed to seawater. The samples were exposed to seawater under three conditions namely, no exposure (C1), immediate exposure (C2) and prolonged exposure (C3). To simulate the material's stress-strain response hyperbolic model was employed. The hyperbolic model was chosen since it has the capability of predicting load-displacement behavior of the waste material under monotonic loading.

INDEX PROPERTIES OF COAL ASH

The coal ash used in the study is from a power plant in central Philippines. The index properties of S1, S2 and S3 are determined following the American Society for Testing Materials and the results are tabulated in Table 1. It can be seen that all samples are non-plastic. The value of the specific gravity of the ash mixtures are higher than the recommended values ranging from 1.899 to 1.903 [10]. A possible explanation for the difference is both materials came from a different coal-fired power plant. For the results of S3, it is noticeable that the values are in between S1 and S2.

Table 1. Index properties of ash mixtures

Index Property	S1	S2	S3
Specific gravity(Gs)	2.08	2.25	2.11
Liquid limit(LL)	-	-	-
Plastic limit (PL)	-	-	-
Maximum void ratio (e_{max})	1.75	0.94	1.14
Minimum void ratio (e_{min})	1.45	0.85	0.94
Maximum dry unit weight(γ_{dmax}) (kN/m ³)	9.9	13.94	11.7
Optimum water content (w_{opt}) (%)	36.6	15.85	27.1
USCS	ML	SM	

EXPERIMENTAL PROGRAM

Sea water Preparation

The artificial sea water used in the experiment is prepared following ASTM D 1141 – 98 or “Standard Practice for the Preparation of Substitute Ocean Water”. The chemical compositions for the artificial sea water are tabulated in Table 2.

Table 2. Chemical composition of sea water

Compound	Concentration,g/L
NaCl	24.53
MgCl	5.2
NaSO	4.09
CaCl	1.16
KCl	0.695
NaHCO	0.201
KBr	0.101
HBO	0.027
SrCl	0.025
NaF	0.003
Ba(NO	9.94E-05
Mn(NO	3.40E-05
Cu(NO	3.08E-05
Zn(NO	9.60E-06
Pb(NO	6.60E-06
AgNO	4.90E-07

Sample Preparation

The ash mixtures were prepared by moist tamping. Instead of using relative density as the controlled variable for the initial target condition, relative compaction was preferred to properly simulate site conditions. A value of 95% relative compaction was the target initial value in order to satisfy the desired in situ condition [7], [11]. The extent of sea water exposure for the experiment has three conditions. The first condition (C1) has no sea water exposure. Only distilled water was used and the samples were soaked for 16 hours. The second condition (C2) sample preparation is similar with C1. Sea water exposure was performed during consolidation stage of the Consolidated Drained Test. The third condition (C3) is when distilled water was completely replaced with artificial sea water both in the sample preparation step and the consolidation stage of the Consolidated Drained Test.

Consolidated Drained Test

Consolidated Drained Test or slow test was performed in this study following British Standard (BS) 1377-8: 1990. Saturation, consolidation and shear are the stages in this test. For the saturation stage, the sample must reach a fully saturated condition before it is to be consolidated. To ensure a fully saturated condition the B-value or the ratio of

the change in pore water pressure and change in confining pressure must reach a value greater than 0.95. For the consolidation stage, the confining pressures (σ_3) used are 50 kPa, 100 kPa, and 200 kPa. For the shearing stage, a rate of loading of 0.05 mm/min was implemented. This was used for the proper dissipation of pore water pressure. Due to the slow rate, this stage normally performed for a maximum of 7 hours and a minimum of 4 hours.

A total of 51 samples were tested for this study as shown in Table 3. It can be seen that sample S3 was not tested for the C3 condition. During sample preparation when the artificial sea water was mixed with S1 some samples hardened into a rock-like state. This made it difficult for S1 to be mixed with S2.

Table 3. Design of experiment

Ash Mixtures	Sea Water Exposure								
	C1			C2			C3		
	σ_3 (kPa)								
	1	2	3	1	2	3	1	2	3
S1	3	3	3	2	2	2	1	1	1
S2	3	3	3	2	2	2	1	1	1
S3	3	3	3	2	2	2	-	-	-

HYPERBOLIC MODEL

Hyperbolic model or Duncan and Chang model is an incremental stress-dependent model that is based on the stress and strain's hyperbolic relationship (Stark). The soil model can simulate the non-linear response of soil. It is also a variable-parameter model and it is defined in terms of initial tangent modulus (E_i), actual deviator stress at failure ($(\sigma_1 - \sigma_3)_f$) and failure ratio (R_f) [12], [13]. The parameters in this model can be determined by performing a triaxial test [12], [13], [14]. From the variables obtained in the model, prediction of load-displacement behavior of the soil can be performed. The hyperbolic representation of the soil model has the capability to yield acceptable results especially in cases under monotonic loading [14]. A typical result of this model is shown in Fig. 1. The hyperbola in the figure can be mathematically written as [12]:

$$\sigma_1 - \sigma_3 = \frac{\varepsilon}{\frac{1}{E_i} + \frac{\varepsilon}{(\sigma_1 - \sigma_3)_u}} \quad (1)$$

Where:

ε = axial strain

$(\sigma_1 - \sigma_3)_u$ = ultimate deviator stress

The hyperbola produced by the model in Fig. 1 is acceptable only until point A. This point is the actual

deviator stress at failure. It can be used to define the failure ratio together with the ultimate deviator stress. The typical values for the failure ratio range from 0.75 to 1.0 [16]. The failure ratio is defined as:

$$R_f = \frac{(\sigma_1 - \sigma_3)_f}{(\sigma_1 - \sigma_3)_u} \quad (2)$$

The ultimate deviator stress, as seen in Fig. 1, is asymptotic in nature. Its value when compared to the compressive strength of the soil is always larger [14]. In order to establish the parameters needed in the soil model, the stress-strain plot must be transformed in a linearized hyperbolic form. The axial strain must be divided by the deviator stress and it is plotted against the axial stress. The equation of the straight line in the transformed plot is [12]:

$$\frac{\varepsilon}{\sigma_1 - \sigma_3} = \frac{1}{E_i} + \frac{\varepsilon}{(\sigma_1 - \sigma_3)_u} \quad (3)$$

Equation 3 presented is the modified format of Equation 1. In Equation 3, initial tangent modulus is the reciprocal of the y-intercept while ultimate deviator stress is the reciprocal of the slope. In order to perform the prediction of stress-strain behavior of the soil, the primary loading modulus (K) and exponent number (n) must be also established. These parameters are related to initial tangent modulus as seen in the following equation [12]:

$$E_i = KP_a (\sigma_3 / P_a)^n \quad (4)$$

Where:

P_a = atmospheric pressure ($P_a = 101.325$ kPa)

Based on the study of Janbu, the increase in confining pressure is proportional to the initial tangent modulus [14].

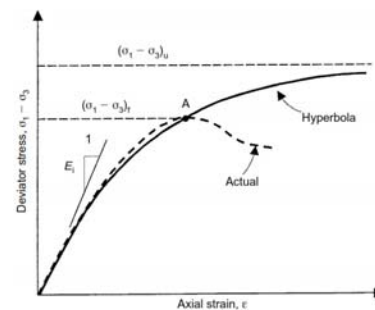


Fig. 1 Hyperbolic model prediction typical result [12].

The parameters primary loading modulus and exponent number can be determined from a

logarithmic plot of E_i / P_a against σ_3 / P_a . The plot is linearized in order to extract the mentioned parameters. The equation of the straight line can be written as follows [12]:

$$\log_{10} \left(\frac{E_i}{P_a} \right) = \log_{10} (K) + n \log_{10} \left(\frac{\sigma_3}{P_a} \right) \quad (5)$$

The slope of Equation 5 is the exponent number while the y-intercept is the primary loading modulus when σ_3 / P_a is equal to 1.0. Once the hyperbolic parameters are established prediction of the load-displacement behavior of the soil can be performed by using the following equation [12], [13]:

$$\sigma_1 - \sigma_3 = \frac{\varepsilon}{\frac{1}{K P_a (\sigma_3 / P_a)^n} + \frac{\varepsilon R_f (1 - \sin \phi)}{2 C \cos \phi + 2 \sigma_3 \sin \phi}} \quad (6)$$

Where:

C = cohesion

ϕ = angle of internal friction

The values of cohesion and angle of internal friction can be determined by plotting the Mohr's Circle. The deviator stress from the stress-strain plot must be at the peak state. If peak state is not experienced, the deviator stress at 15% of the axial strain can be used.

SHEAR STRENGTH OF ASH MIXTURES

The shear strength of ash mixtures was determined from the results of the Consolidated Drained Test. The results are tabulated in Table 4. The results were compared to the typical values of previous researches. The typical values for the angle of internal friction and cohesion for silt is 30° to 35° and 9 kPa, respectively. For silty sand, the typical values for the angle of internal friction and cohesion is 26° to 35° and 50 kPa, respectively [17], [18], [19]. For S1 it was compared to the typical values of silts while for S2 it was compared with silty sand. The results of S3 on the other hand were compared to silty sand. For the results of the ash mixtures in C1, it was observed that all the results are in good agreement for cohesion. For its angle of internal friction, the result of S1 is slightly higher than the typical value by 10%. The increase was due to the amount of relative compaction which contributed to the increase in strength of the ash mixture. It was also observed that S1 has a higher value of angle of internal friction compared to S2. This is because the particle shape of the two was different. A flaky particle shape was observed for S2 while a rounded shape was for S1. The particle shape for S2 is

weaker compared to S1. For S3, its values are in between S1 and S2. For the results of C2, it can be seen that the values of the angle of internal friction decreased for all ash mixtures but the values are still within the typical values. The values for cohesion on the other hand increased. This can be due to the effect of sea water used in the consolidation stage. For the results of C3, the angle of internal friction of S2 is comparable to the results at C1. For cohesion, it dramatically decreased and it is the smallest value when compared to all the results.

Table 4. Shear strength of ash mixtures.

Seawater Exposure	Ash Mixture	ϕ	Cohesion (kPa)
C1	S1	38.53	8.65
	S2	33.77	28.56
	S3	38.94	8.13
C2	S1	31.95	33.32
	S2	27.03	49.91
	S3	31.86	19.06
C3	S1	-	-
	S2	33.91	15.43
	S3	-	-

HYPERBOLIC MODEL PARAMETERS

The hyperbolic model parameters for ash mixtures are tabulated in Table 5, 6, 7 and 8. In order to determine these parameters, the stress-strain plot was linearized as shown in Fig. 2. The plot shown is the typical result for the ash mixtures tested. It was observed that as the confining pressure increases the ratio between the axial strain and deviator stress decreases. This can also lead to the decrease in the value of the slope but the increase in the value of the ultimate deviator stress. From the tabulated results, it showed that as the confining pressure increases the ultimate deviator stress also increases. Comparing the results of the three conditions of sea water exposure, it was observed that the exposure of sea water had an effect towards the ultimate deviator stress of the ash mixtures. Based on the results in Table 7, the values of C3-S2 at 50 kPa and 100 kPa are in between the results of C1-S2 and C2-S2 under the same confining pressure. For C3-S2 at 200 kPa the results are larger than C2-S2 but smaller than C1-S2. At this confining pressure, the exposure to sea water improved the strength of the ash mixture. When the results of C1-S1 and C2-S1 were compared, it was observed that the values of ultimate deviator stress are larger for C2-S1 at 50 kPa and 200 kPa but a smaller value was observed for 100 kPa. For the results of C1-S3 and C2-S3, it can be seen that the ultimate deviator stress decreased due to sea water

exposure. Comparing the results of the ash mixtures in each condition of sea water exposure, for C1 it was observed that there is no particular trend when it comes to the changes in the value of ultimate deviator stress. On the other hand for C2, it was observed that S3 had the smallest values. Knowing the values of ultimate deviator stress can serve as the upper limit or maximum strength of the ash mixtures. There was no consistent trend observed in the result of the ultimate deviator stress. This can be due to the method of sample preparation since preparing the exact replica of the relative compaction is somewhat difficult. For the result of initial tangent modulus, there is also no definite trend. This parameter is highly dependent on the behavior of the stress-strain results. When strain hardening is more pronounced prior to failure the value of initial tangent modulus is smaller. This occurred in C2-S2 at 50 kPa confining pressure. For the failure ratio, it can be observed that almost all the failure ratio is within its acceptable range which except the result from C1-S2. Its value is 0.5335. It was observed that for this ash mixture, the ultimate deviator stress is high and its deviator stress at failure is almost half of its value. This means that for its transformed plot the slope is very steep. A steep plot indicates that strain hardening was present in the stress-strain diagram. Once the hyperbolic parameters are established, prediction can now be performed using Equation 6. The typical results are shown in Fig. 3 and 4. Three trends were observed from the results. First, the prediction seemed less accurate as the confining pressure is increasing as seen in Figure 3. This trend was observed for all results in C1. Second, the prediction was in good agreement with some parts of the stress-strain plot such as the strain hardening portion and the behavior of the plot until it reaches the ultimate shear strength as seen in Figure 4. Third, the model cannot predict the post peak strain behavior of the ash mixtures.

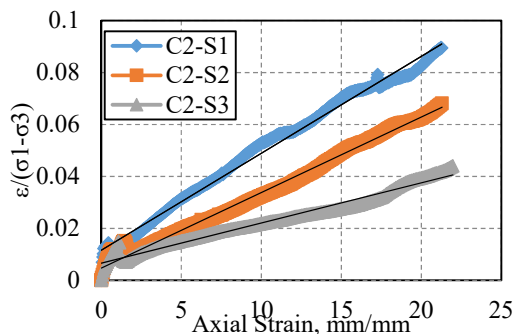


Fig. 2 Typical results for linearized plot.

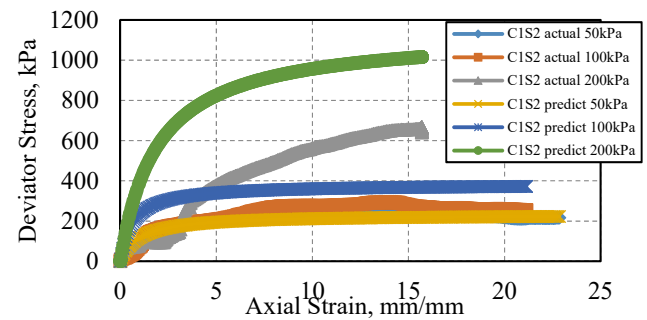


Fig. 3 Hyperbolic prediction for C1-S2.

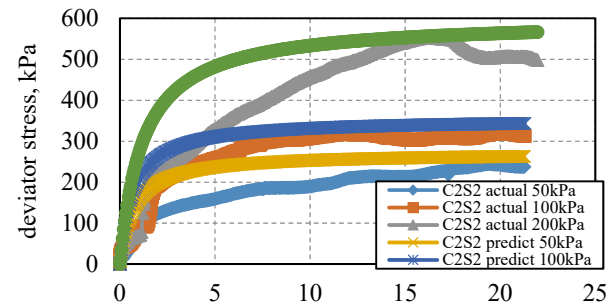


Fig. 4 Hyperbolic prediction for C2-S2.

Table 5. Hyperbolic parameters for C1

Ash Mixture	σ_3 (kPa)	$(\sigma_1 - \sigma_3)_f$ (kPa)	$(\sigma_1 - \sigma_3)_{ult}$ (kPa)	E_i (kPa)	R_f
S1	50	191.93	192.31	217.39	0.9980
	100	398.15	400.00	625.00	0.9954
	200	619.39	625.00	1000.00	0.9910
S2	50	238.04	238.10	277.78	0.9998
	100	274.24	294.12	181.82	0.9324
	200	666.87	1250.00	90.09	0.5335
S3	50	207.25	208.33	769.23	0.9948
	100	470.41	476.19	102.04	0.9877
	200	688.77	909.09	136.99	0.75765

Table 6. Hyperbolic parameters for C2

Ash Mixture	σ_3 (kPa)	$(\sigma_1 - \sigma_3)_f$ (kPa)	$(\sigma_1 - \sigma_3)_{ult}$ (kPa)	E_i (kPa)	R_f
S1	50	239.77	256.41	416.67	0.9351
	100	305.66	344.83	126.58	0.8864
	200	579.76	666.67	185.19	0.8696
S2	50	244.62	270.27	86.21	0.9051
	100	320.07	344.83	250	0.9282
	200	553.92	666.67	149.25	0.8309
S3	50	181.76	181.82	370.37	0.9997
	100	287.47	333.33	116.28	0.8624
	200	474.37	476.19	526.32	0.9962

Table 7. Hyperbolic parameters for C3

Ash Mixture	σ_3 (kPa)	$(\sigma_1 - \sigma_3)_f$ (kPa)	$(\sigma_1 - \sigma_3)_{ult}$ (kPa)	E_i (kPa)	Rf
S2	50	187.66	188.68	185.19	0.9946
	100	248.44	270.27	129.87	0.9192
	200	586.24	714.29	153.85	0.8207

Table 8. Primary loading modulus and exponent number for ash mixtures

Seawater Exposure	Ash Mixture	K	n
C1	S1	461.42	5.57
	S2	5.99	1.34
	S3	25.99	4.50
C2	S1	10.75	1.65
	S2	5.99	1.34
	S3	37.19	1.11
C3	S1	-	-
	S2	4.66	0.22
	S3	-	-

CONCLUSIONS

Ash mixtures were tested under Consolidated Drained test. Three ash mixtures were considered namely, 100% fly ash (S1), 100% bottom ash (S2) and 50% fly ash 50% bottom ash (S3). These ash mixtures were exposed to sea water during the triaxial test. This was done to determine the effect of sea water towards the strength of ash mixtures. Three exposures to sea water conditions were simulated in the experiment namely, no exposure (C1), immediate exposure (C2) and prolonged exposure (C3). Based on the results, the shear strength of the ash mixtures are all within the typical values and are considered to have sufficient strength. For the exposure of sea water, it decreased the strength but the values are still within the acceptable limit. Among all the ash mixtures, S1 had the highest strength. When 50% of S1 was mixed with 50% of S2 to form S3 it showed an improvement in the strength of S3. Furthermore, it was observed that the exposure of sea water had an effect towards the values of the deviator stress at failure and ultimate deviator stress of the ash mixtures. For the C2 condition, both values for S2 and S3 mixtures are smaller compared to C1 and C3 condition. For the hyperbolic parameters, it can be seen that C1-S2 had the highest ultimate deviator stress at 200kPa. The value of the initial tangent modulus ranged from 86.21 to 1000 kPa. The hyperbolic parameters were used in predicting the stress-strain behavior of the ash mixtures. The prediction shows that the material

can still handle higher stresses. The limitation of the model is that it cannot predict the post peak strain behavior. Based on the results from the Consolidated Drained test and Hyperbolic model, they showed that the ash mixtures has a potential to be used as a construction material for a road embankment.

It is suggested that other percentage of ash mixtures be tested in order to determine the most suitable ash mixture. It can be noted that the fly ash specimen has a larger strength, increasing it might improve the strength of the ash mixture.

REFERENCES

- [1] Department of Energy. (2016). 2016 major accomplishments. Retrieved from http://www.doe.gov.ph/sites/default/files/pdf/transparency/annual_report_esar_2016.
- [2] Department of Energy. (2017). Summary of installed capacity, dependable capacity, power generation and consumption report of the department of energy. Retrieved from https://www.doe.gov.ph/sites/default/files/pdf/energy_statistics/summary_2016_power_statistics_final_march_27_2017.pdf.
- [3] Yoon, S., Ph, D., Balunaini, U., Yildirim, I. Z., Prezzi, M., & Siddiki, N. Z. (2009). Construction of an embankment with a fly and bottom ash mixture: field Pperformance study. *Journal of Materials in Civil Engineering*, 21, 271–278.
- [4] Yao, Z. T., Ji, X. S., Sarker, P. K., Tang, J. H., Ge, L. Q., Xia, M. S. & Xi, Y. Q. (2015). A comprehensive review on the applications of coal fly ash. *Elsevier, Earth-Science Reviews*, 141, 105-201.
- [5] Ahmaruzzaman, M. (2010). A review on the utilization of fly ash. *Progress in Energy and Combustion Science*, 36(3), 327-363. Elsevier Ltd. doi:10.1016/j.pccs.2009.11.003
- [6] Huang, W. H. (1990). The use of bottom ash in highway embankments, subgrades and subbases. Retrieved from docs.lib.purdue.edu/cgi/viewcontent.cgi?article=1782&context=jtrp.
- [7] Kim, B., Prezzi, M., & Salgado, R. (2005). Geotechnical Properties of Fly and Bottom Ash Mixtures for Use in Highway Embankments, *Journal of Geotechnical and Geoenvironmental Engineering*, 131(7), 914-924.
- [8] CAVITEX (2016). Cavitec expressway. Retrieved from <http://cavitecexpressway.com/>
- [9] Philippine News Agency (2017). Construction of CCLEX paves way for more bridges linking Visayas islands. Retrieved from <http://news.mb.com.ph/2017/03/04/construction-of-cclex-paves-way-for-more-bridges-linking-visayas-islands/>
- [10] Antonio, O. V. M., & Zarco, M. A. H. (2007). Engineering properties of Calaca Batangas bottom ash, 28(1), 37–56.
- [11] Zabielska-Adamska, K. (2006). Shear strength parameters of compacted fly ash-HDPE geomembrane interfaces. *Geotextiles and Geomembranes*, 24(2), 91–102. doi:10.1016/j.geotexmem.2005.11.006.
- [12] Al-shayea, N., Abduljawwad, S., Bashir, R., Al-Ghamedy, H. & Asi, I. (2001). Determination of parameters for a hyperbolic model of soils from the eastern province of Saudi Arabia. *Proceedings of the Institution of Civil Engineers*. (4). 1-14.
- [13] Stark, T. D., Ebeling, R. M. & Vettel, J. J. (1992). Hyperbolic stress-strain parameters for silts. *Journal of Geotechnical Engineering*. 120(2). 420-441.
- [14] Abdul-kareem, A. H. & Helal, A. (2007). Estimation of hyperbolic stress-strain parameters for gypseous soils. *International Journal of Civil Engineering*. (7).
- [15] Tatsuoka, F. & Shibuya, S. (1991). Modelling of non-linear stress-strain relations of soils and rocks part 1, discussion of hyperbolic equation. *Seisan-Kenkyu*. 43(9). 23-26.
- [16] Chen, W. F. & Saleeb, A. F. (1994). Constitutive equations for engineering materials. Elsevier. 1. 517.
- [17] Das, B. & Sobhan, K. (2014). Principles of Geotechnical Engineering Sixth Edition, United States: Chris Carson.
- [18] Geotechdata (2013). Soil friction angle. Retrieved from <http://www.geotechdata.info/parameter/angle-of-friction.html>.
- [19] Geotechdata (2014). Soil cohesion. Retrieved from <http://www.geotechdata.info/parameter/cohesion.html>.
- [20] Uy, E. E. S. & Dungca, J. R. (2017). Constitutive modeling of coal ash using modified cam clay model. *International Journal of GEOMATE*, 12(31), 88-94.
- [21] Dungca, J. R. & Jao, J. A. L. (2017). Strength and permeability characteristics of road base materials blended with fly ash and bottom ash. *International Journal of GEOMATE*, 12(31), 9-15.

EXPERIMENTAL STUDY ON MECHANICAL BEHAVIOUR OF CONCRETE BEAMS WITH SHREDDED PLASTICS

Richard M. De Jesus¹, Emmanuel Bastian Pelaez², and Moises Carl Caneca³

¹ Faculty of Civil Engineering in De La Salle University (Manila), Philippines

²⁻³ Undergraduate Student of Civil Engineering in De La Salle University (Manila), Philippines

ABSTRACT

In recent years, more attention is being paid to alternative disposal of wastes to lessen the harmful impact of these wastes to the environment. In the construction industry, alternative disposal of waste comes in the form of utilization of waste as a substitute construction material. Plastic, typically in the form of plastic bags and bottles, is one of the most abundant wastes in Manila, and, also among the most problematic when it comes to disposal due to its non-biodegradable nature. Hence, more attention is given to alternative use of plastics as a substitute material in construction. In this study, experimental investigation was conducted to assess the performance of concrete beams with shredded plastics, sourced out locally, as one of its component as a partial replacement to fine aggregates. Strength properties of a concrete beam, in terms of compression, tension, and flexure, were done for both plain concrete and concrete with shredded plastics. Results showed that concrete with shredded plastics were significantly higher than that of plain concrete in terms of tension and compression strength. Flexural strength of concrete with shredded plastic, though the difference were found to be statistically not significant, showed slightly higher strength than that of plain concrete. This study also showed the applicability of elastic flexural theory to concrete beams with plastics as partial substitute to fine aggregates.

Keywords: flexural theory, beams with shredded plastic, alternative material, utilization of wastes

INTRODUCTION

There is a constant, now an increasing, demand for alternative use of waste materials as its management and disposal is worsening with increasing population, continues development, and urban migration. Philippines has not been spared by this and one of the top contributors to this problem in waste disposal is plastics. According to [1], 16% of wastes from Metro Manila are plastics. To make matters worse, Philippines is rated to be among the worst offender in terms of plastic waste disposal as it was ranked 3rd among countries in Asia that disposes plastic wastes into the ocean [2].

Apparently, there is an alarming call for a more effective and environment-friendly disposal of plastic wastes. Environmental Protection Agency (EPA) estimated that 13% of total generated wastes is plastic [3]. Only 9% of the total generated plastic wastes (which are about 869,000 tons of plastic estimated annually) are recycled based on [4].

The government, in order to address rising concerns about plastic waste disposal and management passed and implemented Republic Act 9003 or Ecological Solid Waste Management Act of 2000. This law requires all barangay units to have its own material recovery facility (MRF). However, the implementation of such law had been difficult for many local government units. As reported in [5], many cities find the construction of MRF to be costly,

complicated, and would bring foul odor and eye sore. Hence, most cities still preferred to have all wasted hauled and disposed to a landfill located faraway.

The government needs help in combating waste problem in the country. With regards to plastic in particular, the construction industry has initiated some alternative means of disposing plastics by utilizing it as an alternative material in concrete locally and globally. Several local studies had been done to find an alternative use for plastics in construction [6] to [8].

Globally, studies about alternative use of plastics had gained so much ground already. The studies of [9] and [10] have shown that plastics can be used in concrete for gateway support, tunnel linings, light precast elements, and road pavement applications. Others have explored the possibility of using plastics as partial substitute for sand in concrete for structural applications in the hope that the application of this venture can be extended to a wider range of application. The study of [11] explored the influence of using domestic plastic waste (polythene fibers) in concrete using 0.5% plastic by weight of cement. Results showed that an increase of only 3.84% were observed in compression of concrete cylinders while split tensile strength gained only an increase of 1.63%. Based from [9], where they conducted a critical review of recent studies regarding the use of macro plastic fibers to reinforce concrete, they found that: (1) macro plastic fibres decreases the

workability of fresh concrete but limits plastic shrinkage cracking; (2) it has no obvious effects on compression and flexural strength; (3) and increases ductility of concrete in post-crack region. Reference [12] investigated depolymerized PET plastics used as an alternative binding material in concrete as a partial substitute for Portland cement. Their study compared engineering properties of concrete made up of several variations of PET polymers. According to [13], it investigated the performance of recycled PET fiber reinforced concrete using 0.5%, 0.75%, and 1.0% fiber volume fractions by testing its properties in compression, elastic modulus, and drying shrinkage strain. They compared its performance to that of polypropylene (PP) fiber reinforced concrete. Their study showed that compressive strength and elastic modulus decreases with increasing volume of fiber. However, use of fiber showed improve performance against cracking due to drying shrinkage. Also, structural performance, ultimate strength, and relative ductility were shown to be better with PET fiber reinforced RC beams compared to those without reinforcements. Reference [9] showed that at 1.5% volumetric weight percentage, using PET as fiber reinforcement, resulted to a significant increase in flexural strength.

This study focused on investigating the effect in concrete of partially replacing fine aggregates with combined shredded local plastic bags (low density polyethylene, LDPE) and plastic bottles (polyethylene terephthalate, PET), in terms of its mechanical behavior, particularly its flexural behavior to explore the suitability of its application to beam members. It also investigated the applicability of classic elastic flexural theory to concrete with shredded plastics in conjunction with the transformation procedure as suggested by [14]. Theoretical and experimental estimate of flexural cracking capacity is also assessed.

THEORETICAL BACKGROUND

The elastic flexure theory is proven to be applicable for homogenous materials that behaves elastically. Hence, for flexural capacity, cracking moment, and deflection of plain concrete beam, the elastic theory of flexure is adopted in this study.

Motivated by the transformation procedure suggested by [14] where they transformed FRP-reinforced concrete into a single concrete material using the classic transformation of non-homogeneous elastic beam, this study will follow the same for concrete beams with shredded plastics in calculating for flexural stresses, cracking moment, and deflection.

For concrete with shredded plastics, it is assumed

that the composite section can be transformed into a homogeneous one by transforming the shredded plastics into a concrete equivalent. After transformation, the elastic bending theory will be applied to compute for flexural stresses or flexural capacity. In this study, shredded plastics are uniformly mixed in concrete during mixing, thus, it is assumed that plastics can be represented by a single layer positioned along the centroidal axis. The thickness of the plastic layer is measured, before casting of concrete, by laying down all plastics distributed uniformly in the mold which determines the dimension of plastic in terms of height (or thickness). Modulus of rupture property, or the tensile strength of concrete, is based from actual split tensile test of concrete samples.

The area moment of inertia for the “transformed” shredded plastics mixed into concrete is computed based on the following equation:

$$I_{plastic} = \frac{n \times b t^3}{12} \quad (1)$$

where $I_{plastic}$ = area moment of inertia of a single layer of plastic transformed into concrete, n = modular ratio, b = width of beam, and t = 10mm, the measured equivalent thickness of plastics.

The inertia of the whole section, based on the transformed section, is computed as the sum of the moment of inertia of concrete and (transformed) that of transformed plastic. Flexure formula is then applied to determine flexural stresses.

The following assumptions were further made for this study; (1) the modulus of elasticity for concrete is $4700 \sqrt{f_c'}$; (f_c' is taken from actual compression test); (2) the modulus of elasticity for plastic, which typically is within the range of 2.76 – 4.14 GPa, is taken as 3.45 GPa; and (3) the modulus of rupture is taken equal to tensile strength of concrete from split tensile test.

Theoretical deflection calculations are based on the deflection of a simple beam subjected to concentrated loads applied at third points, and is given by the equation:

$$\delta = \frac{Pa}{24EI} (3L^2 - 4a^2) \quad (2)$$

where: δ = deflection at midspan, P = applied load at third points on a beam, a = 1/3 of span length, L = span length, E = modulus of elasticity of concrete, and I = moment of inertia of concrete and transformed plastic. All specimens were loaded up to failure.

Table 1. Summary of mechanical properties of plain concrete and concrete with 0.5% shredded plastics

Specimen	Compressive strength (MPa)		Tensile strength (MPa)		Flexural strength (MPa)	
	0% plastic	0.5% plastic	0% plastic	0.5% plastic	0% plastic	0.5% plastic
1	21.81	22.28	3.92	4.00	5.44	6.01
2	21.95	22.21	3.95	4.49	5.58	6.29
3	21.71	22.23	3.98	4.25	5.67	6.88
Average	21.82	22.24	3.95	4.25	5.56	6.39

EXPERIMENTAL SETUP

Properties needed for the application of elastic flexural theory on beams, with and without shredded plastics, requires the determination of mechanical properties of concrete. Hence, compression test, split tensile test, and flexural test, were conducted on concrete specimens.

To represent the typical concrete mix composition of beams being used locally, a water-to-cement ratio of 0.4 was adopted in all concrete specimens, and ACI mix design procedure were adopted to determine the proportions. For concrete with shredded plastics, 0.5% plastics by weight of total samples was used. All specimens were cured for 28 days through immersion in a water bath. Concrete cylinders of size 100mm x 200mm, were casted for both plain concrete and concrete with shredded plastics for a total specimen of 3 per test per type. Tests were done after 28 days of curing and in accordance with [15] ASTM C39 (compression test) and [16] ASTM C496 (tension) procedures.

For flexural properties, 3 rectangular specimens of size 100mm x 100mm x 530mm were prepared for each type and tested after 28 days of curing. Testing were done in accordance with [17] ASTM C78 (Flexural strength of concrete using simple beam with third-point loading). To measure deflection, a LVDT (displacement transducer) was attached at midspan of the specimen, and successive deflections were recorded.

DATA AND ANALYSIS

Mechanical properties, in terms of compression, tension, and flexure, derived from experiments for both plain concrete and concrete with shredded plastics, are presented in Table 1. Statistical test for all mechanical properties have shown that the difference in values between plain concrete and concrete with plastics were not significant. Hence, experimentally, addition of shredded plastics in concrete up to 0.5% does not have a detrimental impact to the mechanical properties of concrete.

Flexural behavior of beams made up of plain concrete and concrete with plastics were investigated further by determining the cracking moment (Table 2).

Table 2. Cracking moment of beams

Specimen	Measured cracking moment (kN-m)			
	0% plastic	% diff	0.5% plastic	% diff
1	2.09	6.05	2.56	7.10
2	2.04	8.19	2.50	4.45
3	2.10	5.34	2.51	5.11
Theoretical	2.22		2.39	

Comparison between cracking moment capacity of plain concrete and concrete beam with plastic showed an increase in capacity for beams with plastics. Statistical test showed that this increase is significant.

The gap between theoretical deflection and measured deflection was overwhelmingly large, around 250%. As shown in Eq. (2), the theoretical deflection is calculated based on a transformed section with modulus of elasticity (MOE) estimated to be $4700\sqrt{f_c'}$. This MOE is a code prescribed equation and f_c' is the compression strength from actual tests. The rest of the parameters in Eq. (2) are dependent on the dimension of the section so the gap points out to MOE as the cause of the discrepancy. This, however, was no longer investigated by this study.

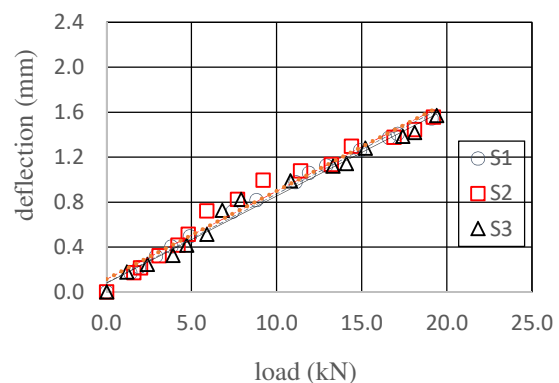


Fig. 1 Load v. deflection for plain concrete beam

Plot of deflection of both beams with plain concrete and concrete with plastics exhibited a linear behavior up to failure. Deflection capacity of beam with plastic was higher (~1.9mm) compared to that of plain concrete beam (~1.5mm).

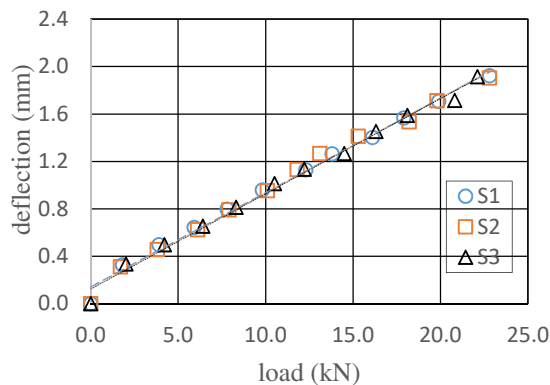


Fig. 2 Load versus deflection for concrete beam with plastics

CONCLUSION

Waste disposal and management is spiraling out of control in response to country's development. The construction industry is in a perfect position to aid in this problem by utilizing waste as alternative construction material. As shown in this study, plastic waste was incorporated as component of concrete. Its mechanical properties were investigated.

It can be seen that all mechanical properties have shown an increase for concrete with shredded plastics compared to plain and summarized as follows:

- compressive strength: 22.24 MPa v 21.82 MPa;
- tensile strength: 4.25 MPa v. 3.95 MPa;
- flexural strength: 6.39 MPa v. 5.56 MPa;

Though, statistical test showed that the increase was not significant, this increase in mechanical strength is a testament that the use of shredded plastics, as a partial substitute, up to 0.5% by weight is not detrimental to the strength properties of concrete.

Improvements were also observed in flexural behavior of beams with shredded plastics, in terms of cracking moment (2.52MPa v 2.07MPa) and deflection. Statistical test showed that the increase in these properties were significant compared to that of plain concrete.

Another important finding from this study is the comparison between the computed values of cracking moment for concrete with shredded plastics using the classical elastic flexural theory and transformation of concrete with plastics following the procedure adopted by [14]. The agreement between experimental and numerical results have shown a maximum difference of only 8.2% for cracking moment implying that the applicability of elastic flexure theory, and that of transformation by [14] can be extended to concrete with shredded plastics.

The deflection needs to be investigated further as disparity between theoretical and measured values was large. On the other hand, consistency was observed in terms of measured deflection for beams

as exhibited by Fig. 1 and 2. For both beams, the one with plain concrete and the one with concrete with plastics, deflection exhibited a linear behavior when loaded up to failure. Measured deflections, for both beams, also showed comparable results with deflection of beams with plastics achieving a slightly higher value than that of plain concrete beam.

REFERENCES

- [1] DENR (2015). Retrieved on October 19, 2015 from <http://newsinfo.inquirer.net/42317/metro-manila-produces-a-fourth-of-philippine-garbage>.
- [2] Jambreck, L. (2015). Worst Plastic offenders. Retrieved from <http://www.motherjones.com/environment/2015/02/ocean-plastic-waste-china>.
- [3] Environmental Protection Agency (2010). Municipal Solid Waste Generation, Recycling, and Disposal in the United States: Facts and Figures for 2010. Retrieved September 29, 2015 from: http://www.epa.gov/epawaste/nonhaz/municipal/pubs/msw_2010_rev_factsheet.pdf.
- [4] National Environment Agency (2014). Waste Statistics and Overall Recycling. Retrieved September 29, 2015 from: <http://www.nea.gov.sg/energy-waste/waste-management/waste-statistics-and-overall-recycling>.
- [5] Ranada, P. (2014, April 25). QC gov't: Garbage law too difficult to implement. *Rappler*. Retrieved on June 5, 2017 from <http://www.rappler.com/science-nature/environment/56378-qc-garbage-management-difficult>.
- [6] Cuartero, M., Villanueva, P., & Oreta A. (2016). Effects of Plastic Wastes as Partial Aggregate Substitute to Concrete Hollow Blocks. *Conference Proceeding*. Workshop on the Utilization of Waste Materials, University of the Philippines, Diliman, QC.
- [7] Alcantara, J. Ayala, P., Santos, V. Yao, E. & Lejano, B. (2016). Effects of Fire on the Compressive Strength of Concrete Hollow Blocks Mixed with Plastic Waste Aggregates, *Conference Proceeding*. Workshop on the Utilization of Waste Materials, University of the Philippines, Diliman, QC.
- [8] Benedicto, M., Eusebio, M., Granada, J., Tuazon, D., & De Jesus, R. (2016). Investigation of Strength and Durability of Paving Blocks Made of Non-Biodegradable Household Waste as Partial Substitute for Fine Aggregates. *Conference Proceeding*. Workshop on the Utilization of Waste Materials, University of the Philippines, Diliman, QC.
- [9] Yin, S., Tuladhar, R., Shi, F., Combe, M., Collister, T., & Sivakugan, N. (2015). Use of macro plastic fibres in concrete: A review. *Construction & Building Materials*, 93, 180-188.

- [10] Ochi, T., Okubo, S. & Fukui, K. (2007). Development of recycled PET fiber and its application as concrete-reinforcing fiber. *Cement & Concrete Composites*, 29(6), 448-455.
- [11] Kandasamy, R., & Murugesan, R. (2011). Fibre Reinforced Concrete using Domestic Waste Plastics as Fibres. *ARPN Journal of Engineering and Applied Sciences*, 6(3), 75-82.
- [12] Mahdi, F., Abbas, H., & Khan, A. (2013). Flexural, shear and bond strength of polymer concrete utilizing recycled resin obtained from post-consumer PET bottles. *Construction and Building Materials*, 44, 798-811.
- [13] Kim, S., Yi, N., Kim, H., Kim, J. & Song, Y. (2010). Material and structural performance evaluation of recycled PET fiber reinforced concrete. *Cement & Concrete Composites*, 32(3), 232-240.
- [14] Mohamed, H., & Masmoudi, R. (2010). Flexural strength and behavior of steel and [14] FRP-reinforced concrete-filled FRP tube beams. *Engineering Structures*, 32, pp 3789-3800.
- [15] American Society for Testing and Materials. (n.d.). Standard Test Methods for Compressive Strength of Cylindrical Concrete Specimens. ASTM C39.
- [16] American Society for Testing and Materials. (n.d.). Standard Test Methods for Splitting Tensile Strength for Cylindrical Concrete Specimens. ASTM C496.
- [17] American Society for Testing and Materials. (n.d.). Standard Test Method for Flexural Strength of Concrete (Using Simple Beam with Third-Point Loading). ASTM C78.

PARAMETRIC STUDY OF RESPONSE OF BRICK MASONRY WALL TO OUT-OF-PLANE LOADING

Miroslav Mynarz¹ and Lucie Mynarzova²

¹Faculty of Safety Engineering, VSB – Technical University of Ostrava, Czech Rep.; ²Faculty of Civil Engineering, VSB – Technical University of Ostrava, Czech Rep.

ABSTRACT

Within the area of explosion prevention and protection, masonry buildings are taking into account considering the danger of explosion of natural gas or other items. For favourable design or assessment of masonry wall exposed to the out-of-plane load, which involves also explosion, it is possible to calculate the structure using some finite element model. Modelling and analysis of masonry seems to be complicated due to two-component material with different properties and dimensions. Out-of-plane loading adds another issue to be solved. Therefore, it is necessary to perform a calibration to evaluate the dynamic properties of the structure. The response of the finite element model is improved by predicting the parameter by performing a non-linear structural analysis. The deformations obtained numerically were compared to that of experimental observations. The experiments were carried out in one of the experimental galleries in the limestone pit. The study deals with the response of the masonry separating walls at various thicknesses, mechanical properties or loading. This contribution compares the effect of variability of particular parameters to the response of the walls.

Keywords: Brick Masonry, Separating Wall, Explosion, Dynamic Response, Nonlinear response

INTRODUCTION

Sorted by their purpose, underground premises involve transportation structures, engineering structures and others (water silo, silo gas, sewerage plant, storage area etc.). Underground galleries interconnecting particular areas are designed with specific aims mainly as transport and airing connections. Purpose and lifetime of underground galleries should be in balance with precautions given on the basis of deep risk analysis. Leakage or formation of flammable gases in such areas certainly represents high risk for interconnected underground locations. Immediate presence of these gases could cause the explosion when open flames or other ignition source are occur at the same time.

To prevent propagation and transfer of the explosion, separating or dam walls are built in the galleries. These structures separate two independent areas with no need to pass through or they close unused halls or premises. In the Czech Republic dam or separating walls are usually built from masonry (Fig. 1) however other materials as plaster or fly ash could be also used.

In the case of accidental event, e. g. explosion, these separating structures are subjected to considerable load therefore they should be designed with sufficient resistance. For effective design and assessment of these walls, in-situ experiments should be carried out to provide useful information about the structures behaviour. Together with the experiments, advanced numerical modelling seems

to be another suitable instrument for separating wall design.



Fig. 1 View of the underground gallery.

EXPERIMENT VENUE

The experiments were carried out [1] in one of the experimental galleries in the limestone pit in Stramberk, Czech Rep. The galleries are used for research and tests in the field of explosion prevention. There are three horizontal parts, two of them are parallel. Concerned gallery measures 300 m (Fig. 2) and its clear section is 10.2 m² in testing part.

Inside the gallery two separating walls were built with the distance of 5.7 m between them. Inside the confined sector, steel frame was embedded in concrete. Loaded structures are placed into this frame with dimensions of 2200 x 2575 mm.

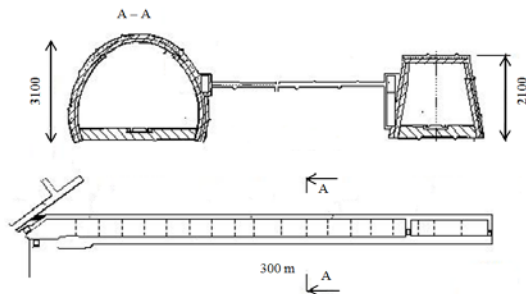


Fig. 2 View of the experimental gallery in Stramberk.

There are two pipes with inner diameter of 800 mm at the edge of the barriers. The pipes provide regulation of applied pressure by changing of their free inner diameter. The confined sector and loaded wall are shown in Fig. 3.

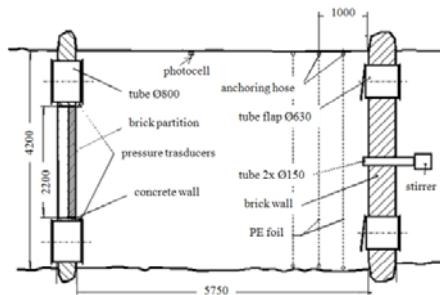


Fig. 3 Confined sector between barriers.

The gassed track is located opposite the loaded wall and it is bounded by the dividing barriers and diaphragm of PE sheeting. This sheeting is fixed by rubber hose to the gallery wall. Pressure tank with methane stands out of the sector. Methane is dosing into the confined sector in parallel with stirring the methane-air mixture. Two ways of stirring were suggested: by ejector straight in the confined sector or by ventilator outside the confined sector which should be connected by pipe with diameter of 150 mm. As ejector did not guarantee the homogeneity of the mixture, only ventilator is used for stirring. During filling and stirring the mixture, methane concentration is measured in different height levels using single gas detectors. The way of ignition affects the final explosion parameters. For these experiments, the electrical ignitor with the ignition energy of 80 J was chosen. The centre of the confined sector, or alternatively the centre of back wall, was chosen as the ignition point. The explosion pressure was recorded by two pressure transducers [2].

Experimental Parameters

The separating walls of three different

thicknesses are dealt with in this paper – 65 mm, 140 mm and 290 mm. This corresponds to the dimensions of used clay bricks (290 x 140 x 65 mm). Their strength is denoted as P10 which corresponds to the compressive strength of the unit 10 MPa; density is considered as $1800 \text{ kg} \cdot \text{m}^{-3}$ and flexural strength is 1.7 MPa. Compressive strength of used cement-lime mortar is between 4 and 5 MPa after 28 days. Used strength characteristics of masonry separating wall result from the standard Eurocode 6 [3]. Other mechanical characteristics of the separating walls are presented in other papers [1], [4]. The dimensions of the walls are approximately 2.2 m width and 2.5 m height, depending on used micromodel or macromodel and particular thickness of the wall.

Each wall was modelled as restrained along all four sides. The load on the structure was considered both as quasi-static action and as real time behaviour measured in the gallery during explosion of methane-air mixture [5]. Corresponding measured load was used for the masonry structure. The explosion pressure is acting like uniform continuous load on the separating wall. For each separating wall of various thicknesses, different values of pressure load were considered according to conducted experiments. Models of the masonry separating walls were created in software ANSYS [6] as it is described later in this paper.

NUMERICAL MODELLING OF MASONRY

Numerical modelling of masonry brings several issues to be solved. Masonry is a heterogeneous and anisotropic material composed of units (bricks, stones) and mortar. These two components differ in material characteristics, behaviour or dimensions. Disposition of units in masonry in a regular pattern or interface between brick and joint could be taken into account as well. Common software usually offer isotropic materials and necessity of simplified – homogeneous – model.

Masonry walls discussed in this paper were modelled using two different approaches according to [7], micromodelling and macromodelling. Detailed micromodel (Fig. 4) consists of bricks and joints. Dimensions and location of bricks correspond to real parameters of clay units. Layers of mortar (bed and head joints) are modelled between the bricks. Two layers with different bonds are changed regularly through the height of the modelled wall. This micromodel could be useful for modelling of details, for better understanding of local masonry behaviour or for determination of homogenized properties of masonry. Density, Young's modulus of elasticity, Poisson's ratio, eventually shear modulus and others are defined for each material. Detailed micromodel represents disposition of bricks in the best way on the other hand it is also very

computationally demanding. It is suitable mainly for academic use or as the first-choice possibility for subsequent calculations.

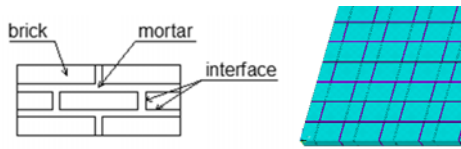


Fig. 4 Detailed micromodel.

In the case of macromodel, neither particular bricks nor mortar layers or their interface are considered. This model is created from one composite (homogenized) material (Fig. 5) which could be isotropic (simplified model) or orthotropic (different strength, stiffness, friction, displacement along the cracks or other parameters could be defined for direction parallel or perpendicular to the bed joints) [8]. The masonry could be homogenized on the basis of constitutive formulas (e. g. modification of models for concrete) or using homogenization techniques (including use of empiric formulas or analysis of detailed macromodel as in [9]). These models are not as precise as macromodel (considering two different materials or units disposition) but they are much less computationally demanding, even for huge structures, and they survey the stress distribution through the whole structure or describe the interaction between particular elements.

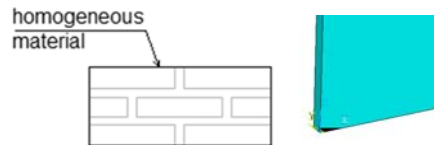


Fig. 5 Homogenized macromodel.

The Concrete Model

For purpose of this paper, all mentioned walls were modelled both as a micromodel and a macromodel. For non-linear solution, several methods are possible. One of them considers the Drucker-Prager plasticity model as it is mention for example in [10]. In our case the “concrete model” was studied. This approach of non-linear solution of masonry structures joins the finite element SOLID65 with the concrete material model available also in ANSYS. The eight-node “reinforced-concrete” element SOLID65 is used for three-dimensional modelling of solids. The concrete element SOLID65 is capable of treating the non-linear material properties such as cracking in tension, crushing in compression, plastic deformations or creep features.

Reinforcement could be also added. A non-linear elasticity concrete model could be used for brittle materials (concrete, ceramics), it is suitable mainly for materials with high compressive load-carrying capacity and low tensile strength.

In ANSYS “concrete model”, both crushing and cracking failure modes are included. The concrete model assumes that behaviour is linear elastic until the failure, than crushing or cracking could appear. Three different colours (red, green, blue) are used for the first, second or third cracks [11].

Tension cracks can occur in three different planes of the element and they are illustrated by a circle outline in the plane of the crack, i. e. perpendicular to the direction of the principal stress in one of the integration point of the element. In the case that more than one integration point has cracked, the circle lies in the average direction of all cracked planes of the element. Cracking occurs when the principal tensile stress in any direction lies outside the concrete failure surface that is shown in Fig. 6. Similarly, when all principal stresses are compressive and lie outside the failure surface, crushing occurs.

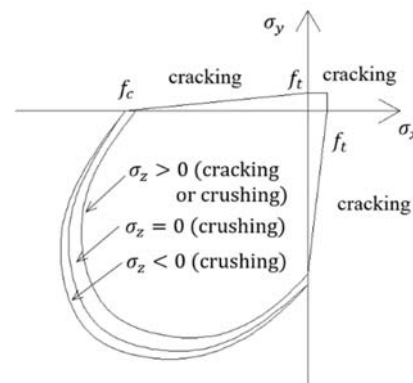


Fig. 6 Concrete failure surface [6].

Behaviour of the model is described, among others, through uniaxial cracking stress, uniaxial or biaxial crushing stress and shear transfer coefficients which take into account sliding across the crack face. Shear transfer coefficient for an open crack β_t varies from 0 to 1. Zero value expresses smooth cracks with complete loss of shear transfer and number 1 represents rough cracks without loss of shear transfer [12]. However, very low values (under 0.1) do not need to lead to convergence. Shear transfer coefficient for a closed crack β_c ranges from 0 to 1 as well. Comparison of cracks in homogenized macromodel is illustrated in Fig. 7. For the illustrative example, both shear transfer coefficients were chosen as 0.1 (left) or 0.9 (right).

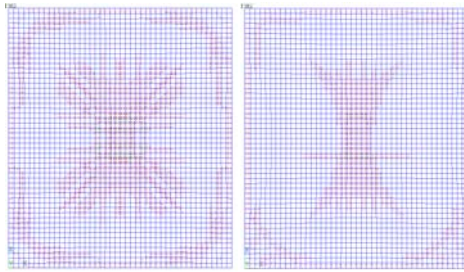


Fig. 7 Illustrative examples of various shear transfer factors.

RESULTS AND DISCUSSION

Masonry wall under out-of-plane load (earthquake, wind, explosion) is subjected to flexure. The cracks occur and develop depending on supports of the wall. In our case, two-way spanning wall is considered with all four sides restrained and it undergoes biaxial bending. Therefore, resulting crack pattern involves a combination of horizontal, vertical and diagonal crack lines [13].

Display of the cracks when SOLID65 element is used could be highly advantageous. Partly, the overview of general behaviour of the structure is given in relation to the presence of the cracks, and moreover the load when the first indications of cracks occur could be pointed out indeed.

Magnitude of pressure at the time of the first cracks appearance is presented on the wall with thickness of 65 mm. The value of pressure load perpendicular to the wall was 6.7 kPa. The first cracks occurred in the middle of the wall at about 10 % of the load (Fig. 8, left) which corresponds to the pressure of 0.7 kPa. After increase of applied load, cracks progressively spread to the corners of the wall. Later phase of cracks pattern at the pressure of 1.1 kPa is shown in Fig. 8, right. Together with cracks in the middle of the numerical model, gradually developing cracks occur also along the supports.

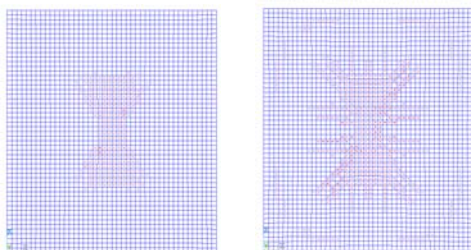


Fig. 8 The first cracks at 10 % (left) and 16 % (right) of applied pressure.

Detail of cracks in the middle of the homogenized macromodel is presented in Fig. 9. The first and the second cracks are outlined with

particular directions.

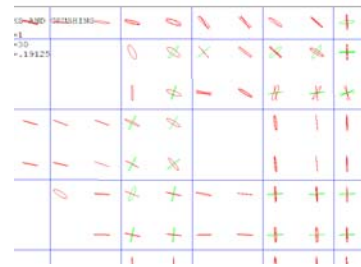


Fig. 9 Detail of crack pattern of homogenized macromodel.

One of the advantage of the detailed micromodel with separately created bricks and mortar is to monitor only one material. Following detail (Fig. 10) shows cracks arrangement in mortar joints in the middle of the wall.

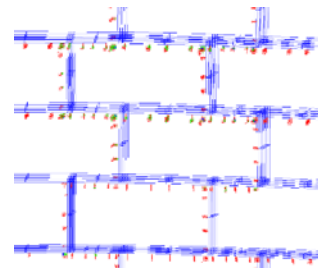


Fig. 10 Detail of crack pattern in mortar joints in micromodel.

Following numerical models illustrate deformations of the wall of thickness of 140 mm. Total value of displacement at micromodel (Fig. 11, left) was calculated as 24.8 mm. The other picture (Fig. 11, right) demonstrates deformations at homogenized macromodel with result of c. 25 mm. Both models are in close agreement with each other and the results also correspond to the conducted experiments.

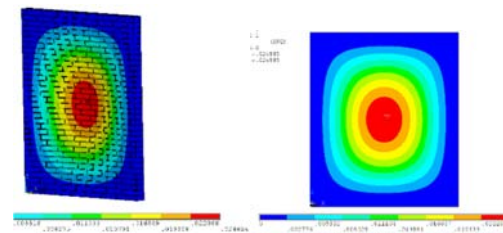


Fig. 11 Total deformations, micromodel (left) and macromodel (right).

Dynamic Load

At real dynamic load, besides dynamic part of the load self-weight is also applied to the masonry separating wall. Such prestress prevents joints and bricks from formation and propagation of cracks. Displacements along the cracks are also limited regarding friction on cracks surface. Ultimate tensile strength, crucial for masonry failure, is – at this type of load – significantly lower compared to compressive strength of masonry. Consequently, the cracks are formed even due to small tensile stresses [14]. The loaded wall is presented on the left side and failure of tested wall is shown on the right side of Fig. 12.



Fig. 12 Masonry wall after explosion [2].

Fig. 13 shows time behaviour of deflection in the middle of the tested partition wall in interaction with the course of explosion load.

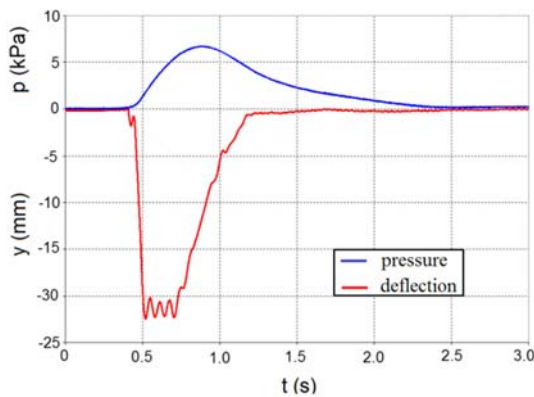


Fig. 13 Measured time behaviour of explosion pressure and deflection during experiment investigation of the wall of thickness 65 mm [15].

Modal Analysis

At dynamic action lateral to the centre-line of the plated structure of separating wall, this wall behaves like a bending slab. Besides load characteristics,

value of dynamic response depends on tune of the structure which is affected by its stiffness and weight. Fig. 14 presents the lowest natural vibration modes of the separating wall. On the left side, the 10th natural mode of homogenized macromodel of the wall of thickness 140 mm is illustrated. 9th natural mode of detailed micromodel of the wall of 290 mm is presented on the right side. Table 1 compares the natural frequencies of the walls created as both micromodel and homogenized macromodel.

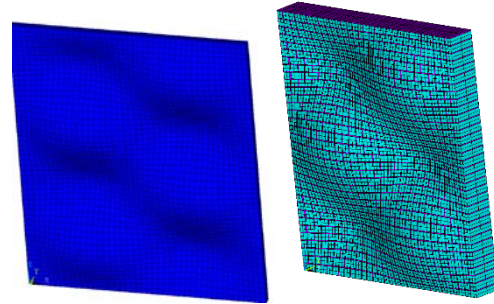


Fig. 14 Natural modes of vibration (left: homogenized macromodel 140 mm, right: micromodel 290 mm).

Tune of the structure is implied in character of the response. If time behaviour of positive phase of the load is significantly longer than the lowest natural vibration frequency, the structure response to the explosion load corresponds to quasi-static deformation of the structure.

Table 1 Calculated natural vibration frequencies $f_{(i)}$ [Hz] of the separating walls

No. of eigenfrequency i	Frequency $f_{(i)}$ for the wall of thickness					
	65 mm	140 mm	290 mm	65 mm	140 mm	290 mm
	macromodel	micromodel	macromodel	micromodel	macromodel	micromodel
1	10.0	10.0	17.2	21.2	48.1	47.4
2	18.4	18.4	31.5	38.6	85.2	85.4
3	22.2	22.3	38.0	45.9	97.5	96.6
4	29.9	29.9	51.1	61.2	127.6	127.3
5	31.7	31.8	54.4	65.6	138.5	138.7
6	40.8	40.8	69.9	82.3	151.6	151.3
7	42.5	42.5	72.7	85.9	159.6	157.7
8	48.0	47.9	82.1	95.9	164.3	162.0
9	49.8	49.8	85.2	100.3	174.1	174.3
10	59.9	59.9	103.	118.5	188.9	187.4

Relatively amplitude low frequency components of motion which corresponds to oscillation in natural frequencies of the structure are superposed to its response.

CONCLUSION

This contribution outlined possible numerical method for solution of masonry separating walls used for partition of underground premises as the explosion prevention. After description of the experimental gallery and conducted experiment, micromodel, macromodel and the concrete model used in software ANSYS were presented and modal analysis was performed. Nowadays non-linear numerical calculations are often used for complex engineering problems but it should be taken into account that many input data are needed to be discussed.

The lack of specific knowledge of the range of values of shear transfer coefficients brings requirements for more experiments as obtain data could be used for further verification of numerical models. On the other hand, micromodels generated from bricks and mortar joints are already in good agreements with homogenized macromodel which could reduce the time for creating the model and computations.

Separating walls as a way of explosion prevention in underground areas could be designed with the help of advanced numerical procedures on condition that input data and used methods are chosen appropriately.

ACKNOWLEDGEMENTS

This paper was financially supported by the project of grant ministry of interior the Czech Republic under the Id. No. VI20152019047, entitled "Development of the rescue destructive bombs for the disposal of statically damaged buildings".

REFERENCES

- [1] Makovicka D, Makovicka D, Jr., Dynamic Response of Thin Masonry Wall Under Explosion Effect. In: Jones, N., Brebbia, C.A., Rajedran, A.M.: Structures Under Shock and Impact VII. WIT Press, Southampton, 2002, pp. 47-56.
- [2] Podstawka T, Janovsky B, Horkel J, Vejs L, Pressure Fields Effects Modelling During Explosions of Gases in Closed Buildings on Engineering Structures, Fire Prevention 2001, 1st Part, VSB-TU, Ostrava, CR, 2001, pp. 333-340.
- [3] CSN EN 1996-1-1: Eurocode 6: Design of masonry structures – Part 1-1: General rules for reinforced and unreinforced masonry structures (in Czech). CEN 2005.
- [4] Makovicka D, Explosion hazard to buildings and design load parameters. In: Jones, N., Brebbia, C.A.: Structures Under Shock and Impact VI. WIT Press, Southampton 2000.
- [5] Mynarzova L, Mynarz M, Study of the effects of transient load on envelope structure Applied Mechanics and Materials, 2014, Vol. 470, pp. 335-339.
- [6] ANSYS® Academic Research, Release 12.1, Help System, ANSYS, Inc.
- [7] Lourenco PB, Computational strategies for masonry structures. Delft University Press, 1996.
- [8] Brozovsky J, Jasek M, Mynarzova L, Maluchova M, Numerical modelling of historical masonry structures, Advanced Materials Research, 2014, Vol. 1020, pp. 182-187.
- [9] Brozovsky J, Kalocova L, Materna A, Constitutive modelling of structural masonry. In Proceedings of VIII. Science conference, technical University of Kosice, 2007. pp. 21 – 25.
- [10] Nguyen CT, Ha HB, Fukagawa R, Two-dimensional numerical modelling of modular-block soil retaining walls collapse using meshfree method, Int. J. of GEOMATE, 2013, Vol. 5, No. 1 (Sl. No. 9), pp. 647-652.
- [11] Brozovsky J, Konecny P, Mynarz M, Sucharda O, Comparison of Alternatives for Remodelling of Laboratory Tests of Concrete, In Proceedings of the Twelfth International Conference on Civil, Structural and Environmental Engineering Computing, 2009, paper 119.
- [12] Kachlakev D, Miller T, Yim S, Chansawat K, Finite Element Modeling of Reinforced Concrete Structures Strengthened with FRP Laminates, Civil and Environmental Engineering, Department California Polytechnic State University, San Luis Obispo, 2001.
- [13] Vaculik J, Unreinforced masonry walls subjected to out-of-plane seismic actions, doctoral thesis, The University of Adelaide, 2012.
- [14] Makovicka D, Kral J, Makovicka D, Jr., Selesovsky P, Brick Masonry Structure Analysis to Gas Explosion on Partition Back Side, Fire Prevention 2002, 1st Part, VSB-TU Ostrava, pp. 221-230.
- [15] Mynarz M, Zdebski J, Mynarzova L, Lepik P, Response of masonry structure to the effects of blast wave induced by deflagration process. In: 5. Magdeburger Brand- und Explosionsschutztag. Magdeburg, 2017.

MACROCELL CORROSION ASSESSMENT OF STEEL IN COLD-JOINTED CONCRETE MIXED AND CURED IN SEAWATER

Cheryl Lyne C. Roxas¹ and Bernardo A. Lejano²
^{1,2}Faculty, De La Salle University – Manila, Philippines

ABSTRACT

Previous research works have been devoted to developing sustainable construction materials. This is due to the potential risk of global warming resulting from the abuse and misuse of natural resources. Therefore, this study aims to address this through the use of abundant and by-product resources in the production of concrete, like seawater and fly ash. If these materials were proven comparable to conventional materials, then problems on freshwater scarcity, fluctuating supply of cement and associated pollutants from its production can be addressed. This research specifically concentrates on the effects of varying water to cement ratios and fly ash content on the macrocell corrosion behavior of steel in cold-jointed concrete. Ordinary Portland cement in concrete was partially replaced with fly ash at 30% and 50%. Water to cement (w/c) ratios of 0.30, 0.35, 0.40, 0.45, 0.55 and 0.60 were tested. Rectangular prism specimens were cast to monitor the macrocell corrosion activity of the reinforcements. Results have shown an increasing trend of corrosion rate with increasing w/c ratios regardless of mixing water, with specimens mixed with seawater having higher values compared to freshwater. Generally, the 0.30 w/c ratio resulted to the lowest corrosion susceptibility. In terms of fly ash content, it was found that corrosion rate decreases with increasing fly ash percentage. Fly ash decreases the permeability of concrete, thus making it less exposed to aggressive environments. Cold-joints showed evident corrosion effects as external elements may penetrate through these planes of weakness in the concrete.

Keywords: macrocell corrosion, seawater, cold-joints, fly ash

INTRODUCTION

Concrete is one of the most widely-used construction materials. The strength and durability of concrete are affected by the properties of its constituents, mix proportions, mixing procedure, curing method and exposure to environment. It is primarily composed of cement, sand, gravel, water and some chemical or natural admixtures. However, due to the potential risk of global warming in the planet resulting from the abuse and misuse of natural resources, the availability of these components for the next generation may be inadequate. Thus, a number of research activities have been devoted to developing sustainable construction materials in order to address this issue. This study focuses on the use of abundant and by-product resources in the production of concrete, specifically the use of seawater and fly ash.

The United Nations Water reported that 1800 million people will be living in regions with absolute water scarcity while two thirds of the world's population could be under water stress conditions by 2025 [1]. Although the Philippines falls under the little or no water scarcity category, it is close to the vulnerability state in terms of freshwater availability [2]. Thus, seawater which surrounds the Philippine archipelago, may be used as an alternative to freshwater. Moreover, people living near coastal

areas, where obtaining freshwater might be difficult, may benefit the most. However, the use of seawater, particularly in the construction sector, is not practiced because of its corrosion effects on reinforced concrete structures.

Meanwhile, the Philippines primarily relies on coal powerplants in generating electricity. With the expected increase of 5.7% electricity consumption on the average between 2015 and 2020, the country is set to open 23 new coal-fired powerplants by 2020 [3]. This increase in the demand for electricity requires a corresponding increase in power generation, thus, additional volume of fly ash is produced. Disposal of this enormous amount of ash becomes a problem to most companies in charge of the operations, coupled with the threat of leaching heavy metals and other toxic chemicals. Therefore, the use of fly ash as partial replacement to cement can help address the management and disposal of accumulated fly ash. During the production of cement, harmful gaseous substances are emitted into the atmosphere, contributing to the global warming effect. Hence, utilization of fly ash can also lessen the amount of cement required in concrete, thereby reducing the demand for production and consequently reducing pollutants.

The main objective of the study is to investigate the effects of using seawater and fly ash in concrete under the influence of cold-joints on a macrocell

corrosion level. Cold-joints are planes of weakness and discontinuity formed when there is a delay in placement of two batches of concrete, i.e., the initially placed and compacted concrete has started to set before the next batch is delivered and placed. Concrete may be difficult to cast monolithically at one time. The delay may result from time gaps in casting or mixing; transportation of concrete from ready-mixed concrete plant to project site; extension of the incomplete construction on next day and inadequate supply of concrete constituents [4]. These cold-joints may become the passageway for aggressive elements that can corrode the reinforcements in concrete and may eventually lead to sudden failure of a structure.

The specific objectives of the study are:

- To determine the effect(s) of different water to cement ratios (w/c) on the macrocell corrosion behavior of steel.
- To determine the effect(s) of different fly ash replacement ratios on the macrocell corrosion behavior of steel.

This paper is organized as follows: First, a literature on corrosion behavior of steel in concrete is presented in order to understand the process and significance of macrocell corrosion assessment. The experimental set-up is discussed next, followed by results and discussion. Finally, conclusions of the research are highlighted.

CORROSION BEHAVIOR OF STEEL IN CONCRETE

The durability of concrete may be compromised through alkali-aggregate reaction, sulfate attacks, freeze-thaw cycles and corrosion, among others. Corrosion of the reinforcing steel in concrete has become a great concern as this may result to sudden failure of structures. The high alkalinity of concrete ($\text{pH} \approx 13$) provides a thin oxide layer that protects the rebar from chemical reactivity [5]. However, the protective film around the reinforcing steel is destroyed when sufficient chloride ions penetrate the concrete and the pH of pore solution drops to low values due to carbonation [6]. Chlorides may be present in the mixing water and aggregates of the concrete at concentrations higher than 0.4-1.0% by cement weight or may penetrate by through cracks and construction joints. It was found that chloride induced corrosion rate is higher than carbonation [7].

The corrosion of steel reinforcement in concrete is an electrochemical process as described in [8]. During the corrosion process, two electrochemical reactions occur simultaneously at two different sites of the steel surface namely: the anodic and cathodic reactions. For these reactions to proceed, electric current must flow in the closed loop between the two sites. An external current also flows through the

pores of the concrete as a result of hydroxide ions (negatively charged) moving the cathode to anode, and also ferrous ions (positively charged) moving from anode to cathode. The water in the concrete pores consists of a dilute solution of alkali and calcium hydroxide which serves as vehicle for ionic flow. The reaction of Fe^{2+} and OH^- forms ferrous hydroxide $(\text{FeOH})_2$ and with further combination with oxygen results to an insoluble product called rust. However, rust is only a byproduct of the corrosion process while actual corrosion means converting metal atoms to ferrous ions dissolved in surrounding aqueous solution.

The loss of metal during corrosion occurs at the anodic sites. The iron atoms are ionized to ferrous (Fe^{2+}) which dissolves in the water solution surrounding the steel. The electrons deposited on the steel raise its electric potential and then flow to a lower potential (cathodic site). At the cathodic site, the electrons combine with dissolved oxygen and water to form hydroxide (OH^-) ions. The number of electrons accepted at the cathodic site must be equal to the number of electrons given up at the anodic site. Hence, two iron atoms must be ionized and dissolved at the anodic site for every dissolved oxygen at the cathodic site. Therefore, for the corrosion process to continue, oxygen and water must be present at the cathodic site.

Depending on the different spatial location of anode and cathode, corrosion of steel in concrete can occur as either microcell or macrocell [6]. However, microcell corrosion of reinforcements must normally co-exist with that of macrocell [9]-[10]. In microcell corrosion, the anode and cathode are located adjacent to each other resulting to a uniform iron dissolution over the whole surface [6]. This type of corrosion produces uniform removal of steel and contains anodic and cathodic sites that are microscopic in size [11]. It was found that microcell corrosion is the major corrosion mechanism for steel in concrete after 3 more than years of testing [12]. This type of corrosion is normally present in laboratory tests on small samples of reinforced concrete [9]. On the other hand, in macrocell corrosion, there is a net distinction between the corroding areas of the rebar and the passive surfaces [6]. Furthermore, macrocell corrosion further occurs when the actively corroding bar is coupled to another bar which is passive, which might be due to its different composition or because of different environment [12]. Macrocells are probable on large dimensions of real structures and often due to large active reinforcement areas that are in contact with passive areas [9].

Macrocell corrosion may be affected by the cover depth and the properties or quality of concrete. Increasing the cover depth resulted to lower the corrosion rate in cracked concrete [13]. The cover depth also increases the barrier to various aggressive

species and corrosion initiation time [14]. The water to cement ratio significantly influence the macrocell corrosion process [15]. A high water-cement ratio leads to high permeability and a low concrete cover reduces the time for corrosive substances to reach the steel reinforcement [16]. This type of corrosion can be further affected by a non-homogeneous chloride environment and when cracks are induced in the concrete surface [17]. Moreover, macrocell pattern formation prevails and that corrosion rate increases when w/c ratio is low and in the presence of defects [7]. Macrocell corrosion investigation of steel in concrete under different w/c ratios and fly ash content mixed with seawater was investigated in this study. Furthermore, the influence of cold-joints was also taken into account. These factors can create a non-homogeneous distribution of chloride ions that may affect the anodic and cathodic transformation of steel through time. As fly ash complements the negative effects of chlorides in the seawater by converting larger pores to finer ones, the study attempts to explain further their influence on a macrocell level.

EXPERIMENTAL SET-UP

Material and Specimen Preparation

Ordinary Portland cement (OPC) Type 1 was used as main binder. Cement was partially replaced by weight with Class F fly ash at 30% and 50%. OPC contained 20.70% silicon dioxide (SiO_2), 5.00% aluminum trioxide (Al_2O_3), 3.36% ferric oxide (Fe_2O_3), 62.80% calcium oxide (CaO), 1.7 magnesium oxide (MgO), and 2.66% sulfur trioxide (SO_3); while fly ash contained 53.30% SiO_2 , 29.10%, Al_2O_3 , 5.44% Fe_2O_3 , 8.00% CaO , 3.70 MgO , and 0.80% SO_3 . W/C ratio was varied at 0.30, 0.35, 0.40, 0.45, 0.55 and 0.60. Freshwater/tapwater and natural seawater were used as mixing water. The salinity of seawater was measured to be 30.60 ppt.

Concrete mixing was done in accordance to ASTM C192 (Standard Practice for Making and Curing Concrete Test Specimens in the Laboratory). Rectangular prism concrete specimens of size 100mm height by 100mm width and 200mm length were cast to investigate the macrocell corrosion activity of the steel reinforcement. Three specimens were cast for each type of specimen. Twelve millimeter diameter deformed steel bars were used as reinforcement. Segmented steel bars (around 60mm in length) were prepared to facilitate the measurement of macrocell current flowing from one element to adjacent elements. Steel bars were submerged in 10% diammonium hydrogen citrate prior to casting to ensure removal of surrounding rust. Lead wires were soldered on both sides of each segment and then attached to one another by epoxy, making sure that no direct electrical connection

exists between the elements except through the wires. The cold-joint in the concrete was formed by casting Section A first followed by Section B after 24 hours. After demolding, each surface of the specimen will be covered by epoxy except for the side with the concrete cover of 10mm. This is to ensure the penetration of outside elements through that surface only. All specimens were then cured by total immersion in freshwater and seawater. For purposes of comparison, control specimens with 0.50 w/c ratio with and without cold-joint were also cast and cured in freshwater. Figure 1 shows the specimen set-up.

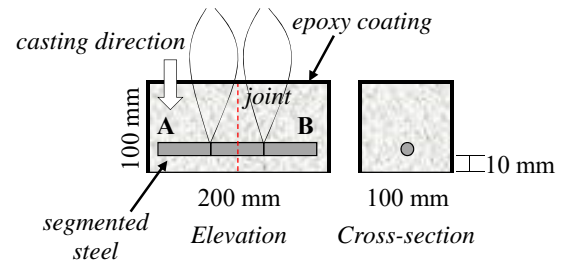


Fig. 1 Specimen set-up

Measurement Methods and Computations

Macrocell currents passing through the segmented steel bars were measured weekly using a zero resistance ammeter. Macrocell corrosion normally occurs in chloride-induced environment and formed along crack and local patch repair areas [18]. Since seawater was used both for mixing and curing concrete with cold-joints, more chloride ions are present for macrocells to occur. Macrocells are characterized by pitting and consists of anodic areas and large cathodic areas situated near or a few distance away from anodes [18]. Formation of macrocells must be considered in designing reinforced concrete structures in aggressive environmental conditions.

The segmented steel bar facilitates the measurement of the actual macrocell current passing from a given element to the adjacent element [17]. Macrocell corrosion current is defined as the total electric current flowing through all steel components taken as a unit. This is given by Eq. (1) considering Fig. 2 [7].

$$I_{macro} = \frac{I_{i-1,i} - I_{i,i+1}}{S_i} \quad (1)$$

Where: I_{macro} = macrocell current density of steel component I (A/cm^2); $I_{i,j}$ = macrocell corrosion current from steel components i to j (A); and S_i = surface area of steel i . For a corrosion density of

100 $\mu\text{A}/\text{cm}^2$, the corrosion rate of steel is equal to 1.16 mm/year [7].

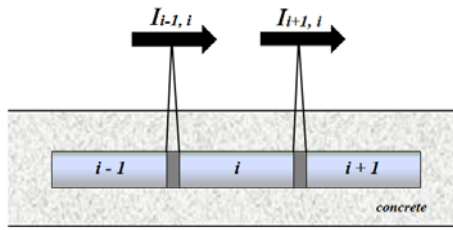


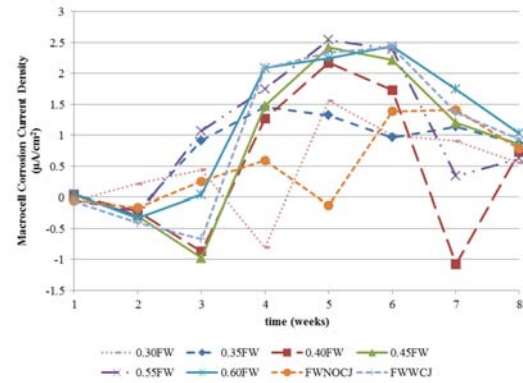
Fig. 2 Macrocell corrosion measurement

RESULTS AND DISCUSSIONS

Effect of W/C Ratio

Three samples were cast to investigate the macrocell current variation in concrete specimens under different w/c ratios. These currents were used to compute for macrocell current densities of the steel elements. Figures 3 and 4 show the macrocell current density variation of freshwater specimens. A uniform variation of macrocell corrosion throughout the exposure period is not evident. The macrocell current variation is acceptable if it behaves either anodically or cathodically throughout the period regardless of its magnitude [17].

Corrosion rates for freshwater and seawater mixed concrete were calculated and presented in Fig. 5 and Fig. 6, respectively. Generally, the values increased with time. In addition, as the w/c ratio increases, the corrosion rate also increases, except in the case of 0.40 w/c ratio. This can be attributed to the higher permeability associated with higher w/c ratio. Higher w/c ratio leads to greater number and size of pores which increased permeability. Increase in permeability means increase in the ingress of external elements which then corrode the steel bar in concrete. As expected, samples mixed with seawater displayed higher corrosion rates. Figure 7 illustrates the effect of cold-joints on corrosion. Samples with cold-joints mixed with seawater resulted to higher corrosion rates. Clearly, the presence of cold-joints resulted to an increase in corrosion activity since surrounding elements can easily penetrate the specimen. At eight week, the 0.30 w/c ratio appeared to be the least corrosive regardless of mixing water.



FW-freshwater; SW-seawater; NOCJ-no cold-joint; WCJ-with cold-joint

Fig. 3 Macrocell corrosion current density variation of freshwater mixed specimens under different w/c ratios

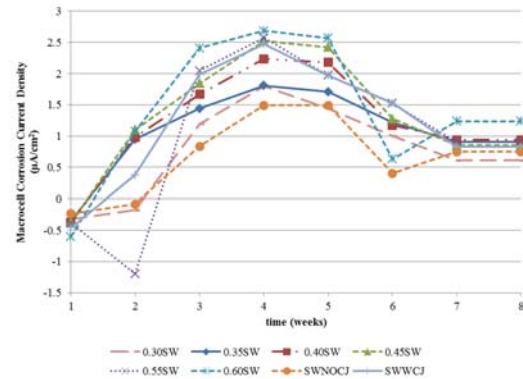


Fig. 4 Macrocell corrosion current density variation of seawater mixed specimens under different w/c ratios

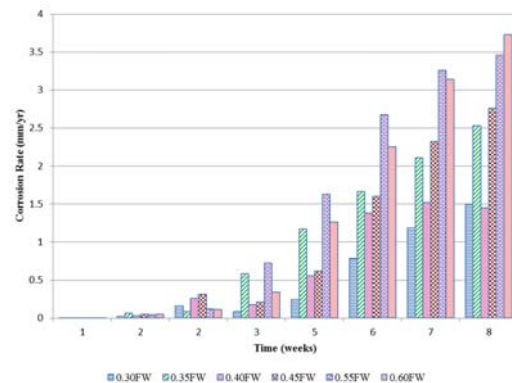


Fig. 5 Corrosion rates of freshwater mixed specimens under different w/c ratios

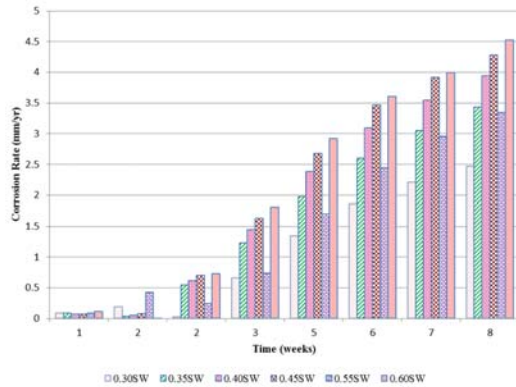


Fig. 6 Corrosion rates of seawater mixed specimens under different w/c ratios

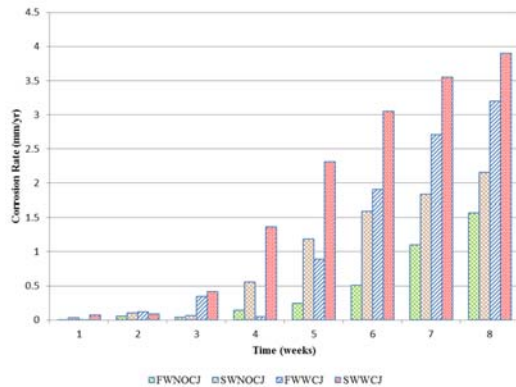


Fig. 7 Effect of cold-joints on corrosion specimens under different w/c ratios

Effect of Fly Ash Replacement Ratios

Figure 8 shows the corrosion rate with respect to varying fly ash replacement ratios. Similar increasing trends of corrosion values can be observed in samples mixed with freshwater and seawater. Generally, those mixed with fly ash exhibited lower corrosion rates. This can be explained by the fine structure of fly ash that reduces the ingress of elements, thereby improving the permeability of concrete. This then delays the occurrence of corrosion. However, 50% replacement displayed higher value compared to 30% replacement. It can also be seen that seawater adds to the corrosiveness of the steel bar. Reinforcement corrosion is initiated when chloride ions from external environment penetrate the concrete and exceed the critical corrosion-inducing limit [19]. With the chloride content of seawater used for mixing and curing, the electrochemical activity of the steel bars is further stimulated.

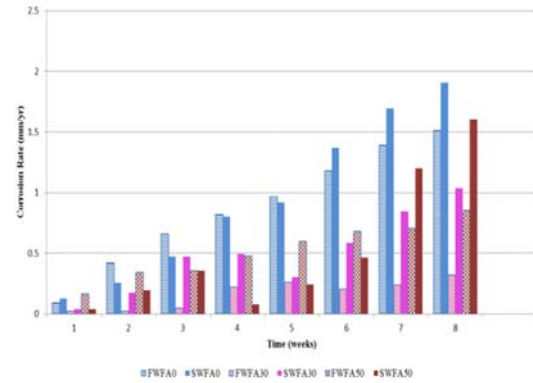


Fig. 8 Effect of fly ash content on corrosion rate

CONCLUSION

This study highlights the utilization of fly ash and seawater as components of concrete in order to address problems on coal ash by-product disposal and global water scarcity. The effects of these materials, specifically on the macrocell corrosion behavior of steel reinforcement in concrete with cold-joints were investigated.

Specifically, this study investigated the influence of water to cement ratio and fly ash replacement ratios to corrosion rate values. Segmented steel bars facilitated the measurement of macrocell corrosion current activities, with cold-joints acting as corrosion catalysts. The following conclusions summarize the results of this research:

1. Using seawater as mixing water showed an increase in the corrosion rate of steel reinforcement compared to specimens mixed with freshwater. Curing specimens with seawater greatly influenced the corrosion rate of the specimens.
2. Specimens without cold-joints obtained lower corrosion rates compared to those with cold-joints.
3. Corrosion rate increases with increasing w/c ratio. A 0.30 water-cement ratio yielded the least corrosion rate. It may be recommended in terms of the low susceptibility corrosion both for freshwater and seawater mixed concrete.
4. Fly ash alters the normal characteristics of concrete when used as partial replacement to cement. It was found that the corrosion rate of steel decreases as fly ash content increases. Specimens containing 30% and 50% fly ash in both freshwater and seawater mixes gained an increase in corrosion resistances. Fly ash decreases the permeability of concrete thus making it less exposed to aggressive environments. Moreover, the fly ash content caused lesser chloride intrusion to the specimens during curing.

ACKNOWLEDGEMENT

The authors would like to thank Christian Huy Dalangin, Jayson Marco Gonzales, John Christopher Ilagan, John Christopher Yu, Joseph Caderao, Raphael Fernandez, Zer Ivan Santos, Juan Philippe Toreja and Kelly Temew for the experimentation and testing. Appreciation is also extended to Pozzolan Philippines for providing the fly ash and De La Salle University faculty and staff; and for the laboratory equipment and facilities.

REFERENCES

- [1] UN Water, Retrieved July 07, 2014, from United Nations Water International Decade for Action: Water for Life 2005-2015: 2014. <http://www.un.org/waterforlifedecade/scar city.shtml>
- [2] IWMI, Water for food Water for Life: A Comprehensive Assessment of Water Management in Agriculture. International Water Management Institute. UK and USA: Earthscan, 2007.
- [3] PEI, Philippines set for 23 new coal-fired power plants. Philippine Engineering International, June 30, 2015, Retrieved February 2017, from <http://www.powerengineeringint.com/articles/2015/06/23-new-coal-fired-power-plants-for-philippines.html>
- [4] Rathi VR & Kolase PK, "Effect of Cold Joint on Strength Of Concrete", International Journal of Innovative Research in Science, Engineering and Technology, 2(9), September 2013, pp. 4671-4679.
- [5] Bolzoni F, Fumagalli G, Lazzari L, Ormellese M, & Pedferri M, "Mixed-in Inhibitors for Concrete Structures" In M. Raupach, B. Elsener, R. Polder, & J. Mietz (Eds.), Corrosion of Reinforcement in Concrete: Mechanisms, monitoring, inhibitors and rehabilitation techniques (Vol. 38, p. 185). Cambridge, England: Woodhead Publishing Limited, 2007.
- [6] Elsener B, "Macrocell corrosion of steel in concrete - implications for corrosion monitoring" Cement & Concrete Composites, 24, 2002, pp. 65-72.
- [7] Miyazato S & Otsuki N, "Steel Corrosion Induced by Chloride or Carbonation in Mortar with Bending Cracks or Joints", Journal of Advanced Concrete Technology, 8(2), June 2010, pp. 135-144.
- [8] Bentur A, Diamond S & Berke NS, "Steel Corrosion in Concrete: Fundamentals and Civil Engineering Practice", Great Britain: E & FN Spon, 1997.
- [9] Andrade C, Maribona I, Feliu S, Gonzales J, & Feliu Jr S, "The effect of macrocells between active and passive areas of steel reinforcements" Corrosion Science, 33(2), 1992, pp. 237-249.
- [10] Ji Y, Zhao W, Zhou M, Mac H, & Zeng P, "Corrosion current distribution of macrocell and microcell of steel bar in concrete exposed to chloride environments", Construction and Building Materials, 47, 2013, pp. 104-110.
- [11] Subramaniam KV & Bi M, "Investigation of steel corrosion in cracked concrete: Evaluation of macrocell and microcell rates using Tafel polarization response" Corrosion Science, 52, 2010, pp. 2725-2735.
- [12] Hansson C, Poursaei A & Laurent A, "Macrocell and microcell corrosion of steel in ordinary Portland cement and high performance concretes" Cement and Concrete Research, 36, 2006, pp. 2098-2102.
- [13] Raupach M, "Corrosion of steel in the area of cracks in concrete – laboratory tests and calculations using transmission-line model", In C. Page, P. Bamforth, & J. Figg (Eds.), Corrosion of Reinforcement in Concrete Construction (pp. 13-23). Great Britain: Royal Society of Chemistry, Information Services, 1996a.
- [14] Shi X, Xie N, Fortune K, & Gong J, "Durability of steel reinforced concrete in chloride environments: An overview", Construction and Building Materials, 30, 2012, pp. 125-138.
- [15] Mohammed TU, Otsuki N, & Hamada H, "Corrosion of Steel Bars in Cracked Concrete under Marine Environment", Journal of Materials in Civil Engineering, 15(5), October 2003.
- [16] Millard S, & Bungey J, "In-situ assessment of reinforcement corrosion in concrete structures", Zurich: IABSE Report, 1989.
- [17] Nanayakkara O & Kato Y, "Macrocell corrosion in reinforcement of concrete under non-homogeneous chloride environment" Journal of Advanced Concrete Technology, 7(1), February 2009, pp. 31-40.
- [18] Raupach M, "Chloride-induced macrocell corrosion of steel in concrete - theoretical background and practical consequences", Construction and Building Materials, 10(5), 1996b, pp. 329-338.
- [19] Al-Attar TS & Abdul-Kareem MS, "Effect of Chloride Ions Source on Corrosion of Reinforced Concrete", Buletinul AGIR. 107-112, 2011.

INFLUENCE OF PRECURSORS AND ACTIVATOR ON STRENGTH AND POROSITY OF ALKALI ACTIVATED BINDERS

Nurulhuda Nadziri^{1,3}, Idawati Ismail¹ and Sinin Hamdan²

¹ Department of Civil Engineering, Faculty of Engineering, Universiti Malaysia Sarawak, 94300 Kota Samarahan, Sarawak, Malaysia

² Department of Mechanical and Manufacturing Engineering, Faculty of Engineering, Universiti Malaysia Sarawak, 94300 Kota Samarahan, Sarawak, Malaysia

³ International College of Advanced Technology Sarawak, 93350 Kuching, Sarawak, Malaysia

ABSTRACT

Pore structure plays an important role in controlling durability and strength of binding materials. The objectives of this study are to characterize porosity and mechanical strength of alkali activated binders and to acquire the major factor that governs the relationship between both properties. Pastes of binder based on POFA and fly ash activated with sodium hydroxide (NaOH) and combination of NaOH with sodium silicate (Na_2SiO_3) were prepared and cured at 80°C for a duration of 7, 28 and 90 days. Mechanical strength was obtained at the same curing condition while porosity was measured via capillary sorptivity test. Coefficient of permeability in alkali activated POFA exhibits the highest porosity while fly ash showed the lowest, in which both types of precursor showed increment in porosity when silicate activator was used. Therefore, there is strong evidence that the choice of raw materials and activator play a major role in controlling pore structures of these materials.

Keywords: Palm Oil Fuel Ash, Fly Ash, Alkali Activated Binders, Porosity, Strength

INTRODUCTION

Production of ordinary Portland cement (OPC) is responsible for the release of anthropogenic carbon dioxide gas and the trend is expected to increase [1],[2]. Alkali activated binders are amorphous materials that have a potential as the alternatives to OPC as cementitious binders. Industrial by products such as fly ash and agricultural waste such as palm oil fuel ash (POFA), rice husk, coconut pitch and sawdust will be used effectively as binders [3],[4].

Pore structure is one of the most important properties that controls durability and strength. Water absorption of the alkali activated concretes is much lower compare to the traditional OPC concretes, depending on hydration products of these materials [5]. The use of supplementary materials such as fly ash and slag which densify concretes can arrest the penetration of “water” to enter inside the materials. Water in alkali activated binders does not present in a similar manner of that in a Portland cement binders [6]. Porosity of cementitious materials depends on many factors, such as curing conditions, use of supplementary materials and types of binding gel. Pores in a cementitious matrix can be classified in various ways. One possibility is the classification as gel pores (<10 nm), capillary pores (10 nm–10 μm) and voids (>10 μm) [7]. Three types of water are related to these types of pores, the pore water, is situated in the capillary pores which mainly govern durability of binders from surrounding environments. The interlayer water held by the gel pores due to

capillary tension and strong hydrogen bonds to the calcium silicate hydrates (C-S-H) [8], a major binding product in the hydration of ordinary Portland cement (OPC). The C-S-H layers consist of physically adsorbed water molecules and interlayer water between the sheet structure. The third type of water is the chemically bound water, which is part of the chemical structure of the hydrated phases. IUPAC also classifies pores according to micropores (<2 nm), mesopores (2–50 nm) and macropores (>50 nm) pores. The latter is generally used for porous materials and is used in the present research.

Limited work has been done on the relationship between capillary porosity and strength in activated materials using POFA and fly ash as the main precursors. Alkali activated POFA was reported to form binder product of calcium-silicate-hydrate (C-S-H) [9] while a fly ash based pastes consists of a sodium-alumina-silicate-hydrate (N-A-S-H) gel [10],[11]. Due to their differences in chemistry and binding products, pore structures in these materials need to be characterized in order to use for durability purposes. Therefore, this study investigates pore structures and strength development of POFA with fly ash activated using sodium hydroxide (NaOH) and the combination of NaOH and sodium silicate (Na_2SiO_3).

EXPERIMENTAL METHODOLOGY

Materials Preparation

To prepare the alkali activated pastes, Palm Oil Fuel Ash (POFA) from palm oil mill in Lundu, Sarawak and fly ash from Sejingkat Fired Coal Power Plant in Kuching were used as raw materials. POFA was pre-dried at 100°C for 24 hours and sieved in 45 micron sieve to remove large particles and to ensure good pozzolanic reactivity. Access carbon on POFA was removed by calcination at 500°C in a furnace for approximately two hours. The removal of excess carbon and other unburnt organic materials contained in POFA is important to avoid their adverse effect on finished product. Particle size of the raw materials was analyzed using CILAS laser particle size analyzer where d_{50} obtained for POFA and fly ash are at 16.7 μm and 9.67 μm respectively.

The chemical composition of POFA and fly ash was shown in Table 1.

Table 1 Chemical composition of raw materials by XRF (%).

Precursors	POFA	Fly Ash
SiO ₂	44.10	55.90
Al ₂ O ₃	1.20	21.80
Fe ₂ O ₃	2.10	6.62
CaO	10.30	4.91
MgO	9.13	2.00
SO ₃	5.80	0.32
Na ₂ O	0.55	0.32
K ₂ O	12.40	2.20
Others	14.95	5.94

POFA was rich in SiO₂ and it has a very little content of Al₂O₃ while fly ash was rich in SiO₂ and Al₂O₃. The composition of fly ash is according to ASTM C 618, "Standard Specification for Coal Fly Ash and Raw or Calcined Natural Pozzolan for Use in Concrete" [12], which is rich in silica and alumina. Two types of alkali solution were used in this study; sodium hydroxide (NaOH), and a combination of NaOH and sodium silicate (Na₂SiO₃). Mix proportions and the water to solid precursor ratio of the alkali-activated POFA/fly ash binder are shown in Table 2. Water to solid precursor ratio was determined based on the workability of the mixes. POFA pastes requires higher water/solid precursor ratio due to its high absorbance properties [13] while fly ash pastes utilizes less water/solid precursor ratio due to its smaller particle size that improves workability [14] which was also observed from 50wt.%POFA/50wt.%fly ash paste.

Table 2 Mix proportions and the water to solid precursor ratio of the alkali-activated POFA/fly ash binder.

Binder ratio (wt.% POFA/wt.% fly ash)	Water/ solid precursor Ratio
100/0	0.55
0/100	0.35
50/50	0.35

The fresh pastes were manually mixed and poured in 25 mm diameter x 50 mm height cylindrical molds. The samples were sealed to prevent any moisture loss and cured at 80°C until age of testing, i.e. 7, 28 and 90 days. The influence of using higher temperature may have some effect properties of the binder [6],[15]. For mechanical strength, the samples were subjected to compression load at 1 mm/s rate until failure. Capillary sorptivity was conducted as described by Fagerlund [16] which measures water uptake until samples become saturated. From sorptivity test, coefficient of permeability, k was calculated using the initial gradient measured. Sorptivity indicates pore structure and their connectivity or capillary network which is a major factor influencing durability towards aggressive ions penetration. A high coefficient of permeability indicates a highly connected porous structure or low tortuosity of the pore network in the binder.

RESULTS AND DISCUSSIONS

Compressive Strength

Figure 1 shows the compressive strength of alkaline activated POFA/ fly ash pastes activated with different alkali solution at 7, 28 and 90 days of curing ages. In sole alkaline activated POFA system (Fig. 1A), samples activated using sodium hydroxide (NaOH) and the combination of NaOH and sodium silicate (Na₂SiO₃) shows continual compressive strength up to 28 days, however decrease at 90 days curing age. POFA activated using NaOH achieved higher compressive strength at younger age (7 days) compared to NaOH with silicate activator. This shows the alkalinity supplied by NaOH is sufficient to promote dissolution of aluminosilicate species and promote hardening [17] while silicate activator suppressed the dissolution process. This is contributed by the high ratio of silicate in the activator. For alkaline activated sole fly ash system with sodium hydroxide as alkali activator (Fig. 1B), the compressive strength at 7 days curing age is slightly higher than other precursor (sole POFA and the combination of POFA and fly ash). This is because of higher content of alumina in the system. In Fig. 1B, the substitution of Na₂SiO₃ as alkaline activator is slowing down the condensation rate between silica and alumina component and this may

influence the compressive strength of the hardened paste. Silva et al. (2007) state that alumina component tends to dissolve easily compared to silica component. This influence the higher rate of condensation between silica and alumina species compared to silica species alone [18]. For sole POFA system with NaOH and combination of NaOH and Na_2SiO_3 as alkaline activator (Fig. 1A), shows the compressive strength at 7 days curing were lowest than other blends. This is because of the lower content of alumina species. Their compressive strength continuously increased at 28 days curing age as the geopolymerization mechanism have been taken place. Substitution of fly ash in alkaline activated POFA (Fig. 1C) leads to a small increment in strength at early age as shown in the 50/50 blends at 7 days of curing age and the compressive strength continuously increase until 90 days curing age. The compressive strength is increase because of the inclusion of fly ash which is rich in alumina. The compressive strength was decrease when Na_2SiO_3 stand-in as the alkali activator which slowing down the condensation rate between silica and alumina component. This is because of the reduction in the reaction mechanism as a result of reduced alkalinity in the system as the raw materials dissolves extensively during the early age [19],[20] which was also shown in sole alkali activated fly ash system (Fig. 1B).

Overall, in sole alkaline activated POFA system showing lower strength compared to the combination of POFA and fly ash geopolymer under this alkaline condition. Calcium species supplied by POFA as shown from XRF data (Table 1) also has significant effect on strength contribution [11],[21], [22]. Ben Haha. et al. (2011) proved that higher MgO content of the POFA (shown in Table 1) influence the compressive strength at 28 days curing age [23]. It is suspected that the co-existence of the calcium with the aluminosilicate geopolymer gel favors the strength development in sole POFA system but upon inclusion of fly ash, aluminosilicate gel became more dominant [24], hence reducing the strength for this binary blend. However, it shows almost the same compressive strength of sole POFA. The higher content of SO_3 in POFA also influence the lower compressive strength compared to fly ash which is also influence the porosity of the geopolymer paste [25]. The silica content in alkaline activator solution also influenced the compressive strength at higher later age. This is because of the polymerized of the silica into an array of small species [26]. Besides that, the formation of a more stable cross-linked aluminosilicate geopolymer structure when the activator used was NaOH and Na_2SiO_3 .

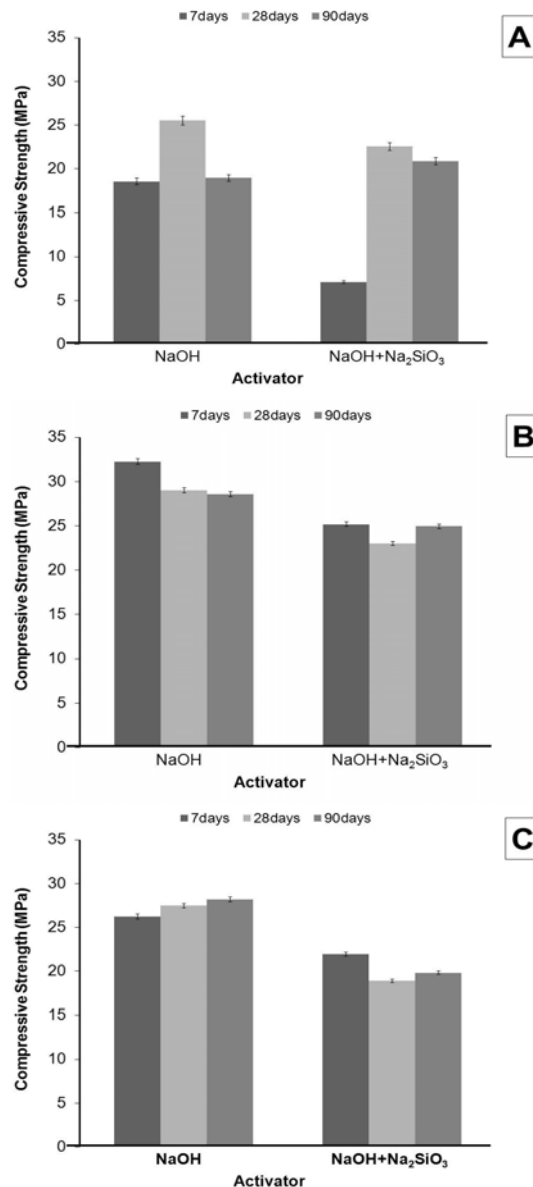


Fig. 1 Compressive strength of alkali activated POFA/fly ash pastes, as a function of the activator type and the time of curing; (A) 100 wt.% POFA, (B) 100 wt.% fly ash and (C) 50wt.%POFA/50wt.% fly ash

Capillary Sorptivity

The rates of water permeability of alkali activated pastes studied here are shown in Fig. 2 and Fig. 3 as a function of precursors and curing age. Sorptivity measurement can be interpreted by the sharp linear increase in water uptake that measures coefficient of permeability, k . This initial water uptake controlled by the larger pores while smaller pores control the capillary suction at later times which can indicate tortuosity or connectivity in a binder. Generally,

NaOH activated POFA shows the highest rate of water permeability by the amount of absorbed water shown in Fig. 2A compared to sample with sole fly ash in Fig. 2B and when both precursors were used as shown in Fig. 2C. This observation shows higher capillary sorptivity in POFA binder as a result of different mechanism that may take place during hardening process due to the chemical characteristics of this material. The physical properties of POFA also contribute to this increased rate of permeability in which POFA are also a high absorbent material [9]. In alkali activated fly ash pastes, lower sorptivity slope and longer time was observed to reach full saturation in the samples indicates a lower porosity and higher tortuosity of this material compared to POFA.

This phenomenon is expected due to the difference in the chemistry of the gel developed in both types of precursors. It has been observed that alkali activated fly ash sample exhibit a sodium alumina silicate hydrate (N-A-S-H) binding gel [11] compared to activated POFA whose gel is mainly composed of sodium rich silica gel with very low calcium [9]. This investigation also allows direct observation of the effect of gel type in porosity measurement by this technique. For sample using both POFA and fly ash (Fig. 2C), a slight difference is shown in the water uptake and saturation time, but with improved permeability compared to sole POFA binder. The measurement of coefficient of permeability, k , is tabulated in Table 3.

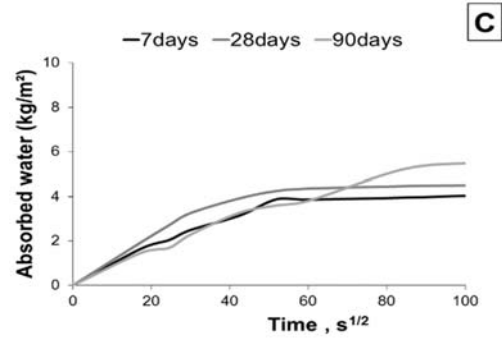
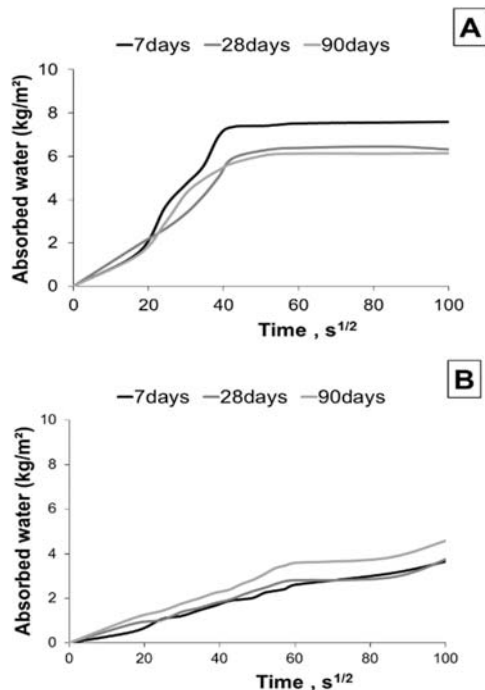
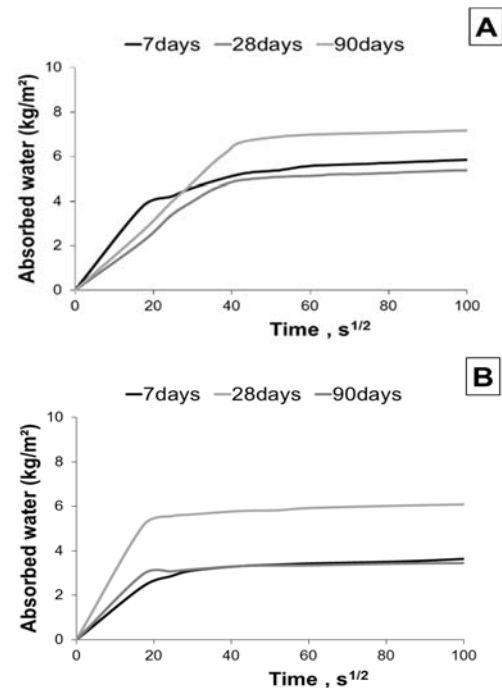


Fig. 2 Capillary sorptivity of NaOH activated pastes as a function of precursors proportions and curing age; (A): 100wt.% POFA, (B) 100wt.% fly ash and (C) 50wt.% POFA/50wt.% fly ash.

The measurement of capillary porosity is also compared with pastes with silicate as activator, shown in Fig. 3. Similar observation was seen where activated POFA (Fig. 3A) exhibits the highest water absorbed while fly ash (Fig. 3B) had the lowest. A combination of both precursor (Fig. 3C) also reduced permeability of alkali activated POFA. The observation from both sets of data implies that there are no significant differences in porosity between activators but strongly influenced by the type of precursor used.



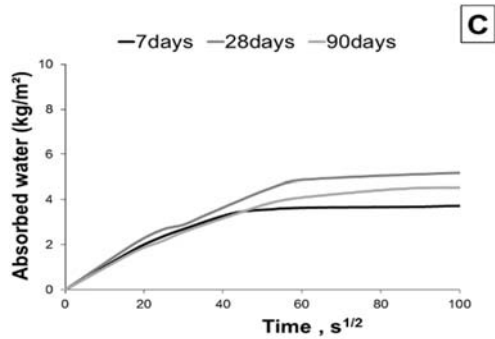


Fig. 3 Capillary sorptivity of NaOH with silicate activated pastes as a function of precursors proportions and curing age; (A): 100wt.% POFA, (B) 100wt.% fly ash and (C) 50wt.% POFA/50wt.%fly ash.

Table 3 summarizes the kinetics of capillary sorption of water by the coefficient of permeability (k) calculated by the initial slope of the sorptivity curves up to saturation limit as a function of precursor proportions and curing age. The lowest k value is shown by fly ash paste in all curing ages, showing a denser matrix in the gel with high tortuosity compared to sole POFA paste which shows highest coefficient of permeability, k value. This observation is true for both types of activator used in this study. It also revealed that the use of silicate as activator increases porosity in these binders.

Table 3 Average capillary absorption coefficient as a function of precursor ratios and curing age.

Precursor proportion (wt.% POFA / wt.% fly ash)	Average Capillary absorption coefficient, k (kg/m ² s ^{1/2})					
	Activator: NaOH			Activator : Na ₂ SiO ₃		
	Curing Age (Days)					
	7	28	90	7	28	90
100/0	0.050	0.079	0.045	0.082	0.121	0.159
0/100	0.024	0.028	0.026	0.183	0.229	0.145
50/50	0.065	0.072	0.065	0.060	0.088	0.068

Coefficient of permeability, k vs mechanical strength

Figure 4 illustrates the coefficient of permeability, k with mechanical strength of these binders. This plot clearly shows the relationship between capillary porosity and strength that is mainly governed by the type of precursor used. There appear a small range of strength obtained between the mixes, which are

between 19 MPa to 32 MPa collected at all curing ages while large range in coefficient of permeability values in these sets of samples (between 0.024 to 0.220), nearly 10 fold. This shows strong influence of raw precursor and the type of binding gel that was formed during hardening process. Fly ash based samples showed the highest mechanical strength with lowest coefficient of permeability compared to alkali activated POFA. In alkali activated POFA paste, the reaction product is sodium silicate gel with a very low calcium gel which has small contribution to strength of the binder. This agrees to lower pozzolanic reaction in POFA compared to fly ash [27]. In addition, water could easily be removed during the drying process prior to the sorptivity measurement which created more pores [6], increasing coefficient of permeability. The hydration product of fly ash alkali activated paste for both types of alkali activator was N-A-S-H gel which has a different water environment compared to calcium based binders. In a N-A-S-H type gel, water is physically bonded in which would not cause significant change in pore structure during drying [6] while water is chemically bonded a calcium based gel binders. It is also observed that NaOH contributes to increment in strength compared to silicate activator for all mixes studied here. This shows the effect of activator in reaction mechanism of these binders. The results for NaOH-activated pastes are in agreement with findings from few researchers [28],[29]. It also suggests silicate activator decelerates reaction mechanism in these pastes [30]. However, the impact on capillary pores is minimal, first time observed in this study.

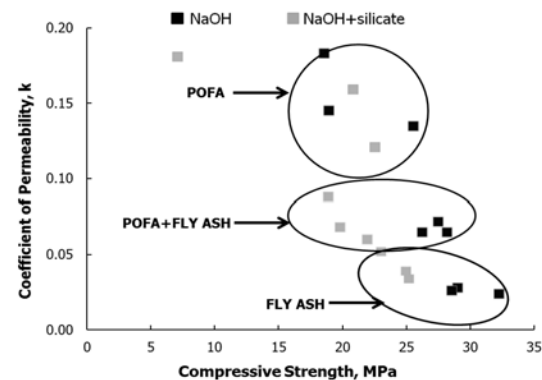


Fig. 4 Correlation between coefficient of permeability and strength as a function of raw materials and activator

CONCLUSIONS

The choice of precursors and type of activator are the main factors in controlling capillary porosity and mechanical strength of alkali activated POFA and fly ash binders. Alkali activated fly ash binder has the

lowest coefficient of permeability with highest mechanical strength compared to POFA binders. When comparing the effect of activator used, NaOH-activated pastes measured lower rate of permeability and improved strength compared to silicate activated paste, for both POFA and fly ash. This implies that these materials have potential applications for strength performance, with differences in porosity which may impact the choice of binder application and environmental exposures. Further works on actual exposure in aggressive environments to test for durability performance of these binders is recommended.

ACKNOWLEDGEMENT

This work was supported by the Ministry of Higher Education Malaysia under MyMaster, MyBrain15 and Universiti Malaysia Sarawak under grant number F02/SpSTG/1389/16/31.

REFERENCES

- [1] Schneider M, Romer M., Tschudin M., and Bolio H., "Sustainable Cement Production-Present and Future", Cement and Concrete Research, Vol. 41, No. 7, 2011, pp. 642–650.
- [2] Gartner E., "Industrially Interesting Approaches to 'Low-CO₂' Cements", Cement and Concrete Research, Vol. 34, No. 9, 2004, pp. 1489–1498.
- [3] Lothenbach B., Scrivener K., and R. D. Hooton, "Supplementary Cementitious Materials", Cement and Concrete Research, Vol. 41, 2011, pp. 1244–1256.
- [4] Juenger M.C.G., Winnefeld F., Provis J. L., and Ideker J. H., "Advances in Alternative Cementitious Binders", Cement and Concrete Research, Vol. 41, No. 12, 2011, pp. 1232–1243.
- [5] Ismail I., Bernal S.A, Provis J. L, San Nicolas R., Brice D. G, Kilcullen A.R, Hamdan S., and Van Deventer J.S.J., "Influence of Fly Ash on The Water and Chloride Permeability of Alkali-Activated Slag Mortars and Concretes", Construction and Building Materials, Vol. 48, 2013, pp. 1187–1201.
- [6] Ismail I., Bernal S.A., Provis J.L., Hamdan S., and Van Deventer J.S.J., "Drying-Induced Changes in The Structure of Alkali-Activated Pastes", Journal of Materials Science, Vol. 48, No. 9, 2013, pp. 3566–3577.
- [7] Aligizaki K.K., Pore Structure Of Cement-Based Materials; Testing, Interpretation And Requirements. New York, 2006.
- [8] Jennings H.M., Thomas J.J., Gevrenov J.S., Constantinides G., and Ulm F.J., "A Multi-Technique Investigation of the Nanoporosity of Cement Paste", Cement and Concrete Research, Vol. 37, No. 3, 2007, pp. 329–336.
- [9] Salih M.A., Abang Ali A.A., and Farzadnia N., "Characterization of Mechanical and Microstructural Properties of Palm Oil Fuel Ash Geopolymer Cement Paste", Construction and Building Materials, Vol. 65, 2014, pp. 592–603.
- [10] Fernández-Jiménez A., Palomo A., and Criado M., "Microstructure Development of Alkali-Activated Fly Ash Cement: A Descriptive Model", Cement and Concrete Research, Vol. 35, 2005, pp. 1204–1209.
- [11] Ismail I., Bernal S.A., Provis J.L., San Nicolas R., Hamdan S., and Van Deventer J.S.J., "Modification of Phase Evolution in Alkali-Activated Blast Furnace Slag by the Incorporation of Fly Ash", Cement and Concrete Composites, Vol. 45, 2014, pp. 125–135.
- [12] American Society for Testing and Materials International, ASTM C 618 Standard Specification for Coal Fly Ash and Raw or Calcined Natural Pozzolan for Use in Concrete, 2013.
- [13] Sata V., Jaturapitakkul C., and Kiattikomol K., "Influence of Pozzolan From Various By-Product Materials on Mechanical Properties of High-Strength Concrete", Construction and Building Materials, Vol. 21, No. 7, 2007, pp. 1589–1598.
- [14] Antoni, Hardjito D., Wibowo F., and Chandra N.W., "Influence of Heat Treatment Temperature , Particle Fineness and Replacement Ratio of Sidoarjo Mud as Pozzolanic Material", in The Fifth Asian Concrete Federation Conference, 2012, pp. 1–4.
- [15] Bakharev T., "Geopolymeric Materials Prepared Using Class F Fly Ash and Elevated Temperature Curing", Cement and Concrete Research, Vol. 35, No. 6, 2005, pp. 1224–1232.
- [16] Fagerlund G., "On the Capillarity of Concrete", Nordic Concrete Research, Vol. 1, 1982, pp. 6.1–6.20.
- [17] Duxson P., Fernández-Jiménez A., Provis J.L., Lukey G.C, Palomo A., and Van Deventer J.S.J., "Geopolymer Technology: The Current State of the Art", Journal of Materials Science, Vol. 42, 2007, pp. 2917–2933.
- [18] Silva P.D., Sagoe-Crenstil K., and Sirivivatnanon V., "Kinetics of Geopolymerization: Role of Al₂O₃ and SiO₂", Cement and Concrete Research, Vol. 37, No. 4, 2007, pp. 512–518.
- [19] Puertas F., Amat T., Fernández-Jiménez A., and Vázquez T., "Mechanical and Durable Behaviour of Alkaline Cement Mortars Reinforced with Polypropylene Fibres", Cement and Concrete Research, Vol. 33, 2003, pp. 2031–2036.
- [20] Bernal S.A., Mejía de Gutiérrez R., Pedraza A.L., Provis J.L., Rodríguez E.D., and Delvasto

- S., "Effect of Binder Content on the Performance of Alkali-Activated Slag Concretes", *Cement and Concrete Research*, Vol. 41, No. 1, 2011, pp. 1–8.
- [21] Garcia-Lodeiro I., Fernández-Jiménez A., Palomo A., and MacPhee D.E., "Effect of Calcium Additions on N-A-S-H Cementitious Gels", *Journal of American Ceramic Society*, Vol. 93, 2010, pp. 1934–1940.
- [22] Mijarsh M.J.A., Johari M.A.M., and Arifin Z., "Cement & Concrete Composites Compressive Strength of Treated Palm Oil Fuel Ash Based Geopolymer Mortar Containing Calcium Hydroxide , Aluminum Hydroxide and Silica Fume as Mineral Additives", *Cement and Concrete Composites*, Vol. 60, 2015, pp. 65–81.
- [23] Ben Haha M., Lothenbach B., Le Saout G., Winnefeld F., "Influence of Slag Chemistry on The Hydration of Alkali-Activated Blast-Furnace Slag - Part I: Effect of MgO", *Cement and Concrete Research*, Vol. 41, 2011, pp. 955–963.
- [24] Garcia-Lodeiro I., Palomo A., Fernández-Jiménez A., and MacPhee D.E., "Compatibility Studies between N-A-S-H and C-A-S-H Gels. Study in the Ternary Diagram $\text{Na}_2\text{O}-\text{CaO}-\text{Al}_2\text{O}_3-\text{SiO}_2-2\text{H}_2\text{O}$ ", *Cement and Concrete Research*, Vol. 41, No. 9, 2011, pp. 923–931.
- [25] Odler I. and Zhang H., "Investigations on High SO_3 Portland Clinkers and Cements", *Cement and Concrete Research*, Vol. 26, 1996, pp. 1307–1313.
- [26] Provis J.L., *Geopolymers: Structure, Processing, Properties and Industrial Applications*, Woodhead Publishing Limited, UK, 2009.
- [27] Ranjbar N, Mehrali M., Alengaram U.J., Metselaar H.S.C., Jumaat M.Z., and Behnia A., "Compressive Strength and Microstructural Analysis of Fly Ash/Palm Oil Fuel Ash Based Geopolymer Mortar Under Elevated Temperatures", *Construction and Building Materials*, Vol. 65, 2014, pp. 114–121.
- [28] Görhan G. and Kürklü G., "The Influence Of The NaOH Solution on The Properties of the Fly Ash-Based Geopolymer Mortar Cured at Different Temperatures", *Composites Part B: Engineering*, Vol. 58, 2014, pp. 371–377.
- [29] Ben Haha M., Le Saout G., Winnefeld F., and Lothenbach B., "Influence of Activator Type on Hydration Kinetics, Hydrate Assemblage and Microstructural Development of Alkali Activated Blast-Furnace Slags", *Cement and Concrete Research*, Vol. 41, No. 3, 2011, pp. 301–310.
- [30] Fernández-Jiménez A., Palomo A., and Criado M., "Microstructure Development of Alkali-Activated Fly Ash Cement: A Descriptive Model", *Cement and Concrete Research*, Vol. 35, 2005, pp. 1204–1209.

CURRENT SITUATION OF CONSTRUCTION AND DEMOLITION WASTE IN VIETNAM: CHALLENGES AND OPPORTUNITIES

Nguyen Van Tuan¹, Tong Ton Kien¹, Dang Thi Thanh Huyen¹, Tran Thi Viet Nga¹, Nguyen Hoang Giang¹, and Ken Kawamoto²

¹National University of Civil Engineering, Hanoi, Vietnam

²Graduate School of Science and Engineering, Saitama University, Japan

ABSTRACT

With the rapid urbanization and economic growth on all the fronts, lots of construction activities are conducted everywhere, especially in big cities in Vietnam (e.g., Hanoi, Haiphong, Ho Chi Minh). All activities such as new construction, renovation, and demolition of buildings and structures generate huge amount of waste, called the Construction and Demolition waste (CDW). According to the State of Environmental Report 2011 on Solid Waste management issued by Ministry of Natural Resources and Environment (MONRE), the total municipal solid waste generation was about 60 thousand tons/day averagely, in which the CDW waste accounts for 10%-12% of total solid waste. In order to maximize the potential positive impacts but at the same time minimize the negative effects of modernization and industrialization in the country, it is necessary to take immediate measures to protect the environment. This paper presents the current situation of CDW in Vietnam and gives challenges and opportunities in the legal and institutional framework for solid waste environmental management. The end solution intended will be to propose suitable CDW management and recycling strategies to suit to these conditions with proven benefits to all stakeholders.

Keywords: Construction and Demolition waste (CDW), Solid waste management, Recycling, Reuse, Vietnam

INTRODUCTION

Like many other developing countries, Vietnam has been experiencing various kinds of environmental problems such as Municipal Solid Waste Management, in which Construction Demolition waste (CDW) management and recycled is one of the most critical engineering issues that need immediate intervention today.

Vietnam is the easternmost country on the Indochina Peninsula in Southeast Asia. It is bordered by China to the north, Laos to the northwest, Cambodia to the southwest, and the South China Sea to the east. The area of Vietnam is approximately 330,000 km² and it is ranked as the 65th largest nation in the world. Currently the national economy heavily relies upon the extraction and use of natural resources. As of July 2016, the population was approximately 91.7 million, making Vietnam the 14th most densely inhabited country in the world and 8th in Asian region, which imposes a constant and long lasting pressure on the country's natural resources.

With the rapid urbanization and economic growth on all the fronts, lots of construction activities are conducted everywhere, especially in big cities in Vietnam (i.e., Hanoi, Hai Phong, Ho Chi Minh). All such activities (new construction, renovation, and demolition of buildings and structures) are generating huge amount of waste, called CDW. According to the State of Environmental Report 2011

on Solid Waste management (issued by Ministry of Natural Resources and Environment - MONRE), the total municipal solid waste generation was about 60 thousand ton/day averagely, in which the CDW waste accounts for 10%-12% of total solid waste. Current generation of CDW in Vietnam can be seen in the Table 1 [1].

Table 1 Current generation of Construction and Demolition Waste (CDW) [1]

Cities	Amount of CDW generated (tons/day)	Percent of CDW collection (%)
Hanoi	1000 – 1500	70
Ho Chi Minh	2000 – 2500	75
Hai Phong	400 – 450	40 - 45
Da Nang	500 - 600	60
Other cities	100 - 200	20 - 30

It is important to minimize CDW generation and maximize reuse/recycling as the construction industry is consumer of tremendous amount of natural resources and energy as well as emitter of GHGs. Establishment of effective strategies and enactment of laws and regulations is essential to achieve this. In addition, provision for some incentives to users of the recycled products seems to be necessary to promote the use. In most of developed countries, for example, they actively introduce “Green Procurement” for newly-construction projects lead by gov-

ernments, i.e., enhancing the use of recycled materials for constructing buildings and infrastructure. It is essential to assess the life-cycle as it provides quantitative tool to assess environmental impact of CDW reuse/recycling [2]. In the move toward green or sustainable environment, Vietnam has to benchmark developed nations like Japan and Hong Kong in handling construction waste issues.

This paper presents the current situation of CDW in Vietnam and gives challenges and opportunities in the legal and institutional framework for solid waste environmental management. The end solution intended will be to propose suitable CDW management and recycling strategies to suit to these conditions with proven benefits to all stakeholders.

CURRENT SITUATION OF CDW IN VIETNAM- CHALLENGES AND OPPORTUNITIES OF RECYCLING

Current situation of CDW generation in Vietnam

In fact, the CDW has great value for recycle. In Vietnam, the amount of solid waste has been being generated more in urban areas. As reported by the national environment agency on solid waste in 2011 [1], the amount of municipal solid waste generated about 12.802 million tons in 2008 and estimated to be 22.352 million tons in 2015. In which, CDW is around 10-15%, mainly arisen from works of construction and demolition. Approximately 2,200 apartments (about 6 million of m²) were built in the 70's - 80's, in which approximately 90% are degraded seriously. In 2007, the Vietnamese Government issued Resolution 34/2007/NQ-CP [3] on a number of solutions to the amelioration and reconstruction of damaged or degraded condominiums by 2015. So in the coming years, a huge amount of CDW will be discharged in the large cities or urban areas.

Furthermore, regardless of compositions of CDW, it has been reported that the compositions of CDW are Soil, Sand, & Gravel (36%), Brick & Building block (31%), Concrete (23%), and others including metal and plastic (10%) [4]. Those major components of construction generated soil, bricks, and concrete can be recycled and reused efficiently and economically in construction and infrastructure systems, which directly contribute to the reduction of CDW land filling.

Because of great value, CDW has been valued subjects for recycle in many countries (Table 2). Especially, Japan has been one of leading countries in promotion of CDW recycle products lines for trade and implementation of related legal regulations such as Construction Recycle Act and Standard for Recycled Construction Waste. These legal approaches taken by Japanese government made the

country become more sustainable in handling construction waste.

Table 2 Recycle of CDW in several countries

Country Region	Waste Generation (million tons /year)	Recycle Rate (%)	Treatment	Reference
Thailand	1.9	Almost no recycle	Dumped and land-fill	[5]
Vietnam	1.9	1-2	Dumped and land-fill	[1]
Malaysia	6.9	5	Reuse and recycle, landfill	[6]
Korea	67	Concrete 36	Reuse and recycle	[2]
Denmark	3	81	Reuse and recycle	[7]
Netherlands	11	90	Reuse and recycle	[7]
Japan	72.7	Concrete (~99), Asphalt (~99), Wood (~90)	Reuse and recycle	[8]

It can be clearly seen that the huge amount of CDW is actually the huge source of energy and saving we can obtain if we know how to take the opportunities. These sources of waste could be used as new recycled materials for infrastructure construction:

- + Production of recycled aggregates (RAs) from CDW and application for Subgrade, base or sub-base layer, laying course and road surface, or for replacement of natural aggregate in mortar and concrete production.
- + Fabrication of sustainable materials for the construction of traffic infrastructure: pervious concrete containing RAs for paving flags; Roof tile embankment, trench plate, blocking barrier; edge restraint; backfill and road embankment; Controlled Low Strength Materials (CLSM) Utilizing Recycled Aggregates, self-leveling CLSM for road base using a combination of all industrial / agricultural wastes (fly ash, gypsum, blast furnace slag, rice husk ash); asphalt containing RAs; recycled aggregate concrete pavement;
- + Sustainable materials for building construction: brick, interlocking concrete block using RAs and industrial/ agricultural wastes (towards cement-less bricks); as raw material or additive for cement production; manufacturing of reinforced concrete piles for reinforcing foundation works; ...

These sources of waste could be used for environmental pollution control:

- + Wastewater treatment: Filter media, Biofilm

- attachment media (Carriers)
- + Remediation of oil-polluted water and sea,
- Remediation of coastal erosion

Current situation of CDW management in Vietnam

Disposal of such CDW in a sustainable manner is a big challenge for the contractors and owners while management of CDW at macro scale is a big task for legal authority. The most common management of CDW at present in Vietnam is dumping indiscriminately and some of CDW are being disposed in landfills. The number of landfills is actually very limited. For instance, there are currently 05 active landfills in Hanoi (Van Noi, Nguyen Khe, Duong Lieu, Van Con, Xuan Son leveling sites). The Van Noi construction landfill in Dong Anh rural district is the largest active one at present (Total 9.5 ha). According to Master map for CDW and sludge management in Hanoi city towards 2030, vision to 2050, there will be 24 CDW landfills and 03 landfills for sewer and fecal sludge treatment. In Haiphong, there is the largest CDW landfill in Hai An district with 29.6 ha including a leveling site for CDW. The management of CDW has been regulated in Master plan on solid waste management in Haiphong city towards 2025 [9]. According to the master plan, Haiphong will have 7 domestic solid waste treatment zones, 7 district treatment zones and 5 landfills for CDW disposing as: Trang Cat (5 ha), Ben Gung (3 ha), Dong Hoa (3 ha), Do Son (3 ha), Lai Cach (3 ha).

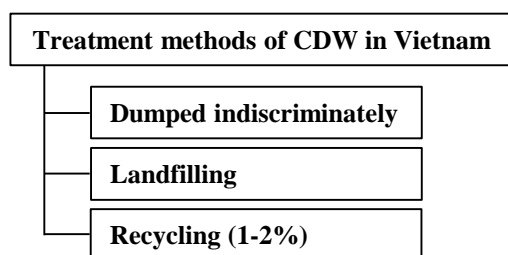


Fig. 1 Treatment of CDW in Vietnam

In the past two decades, Vietnam Government has put in place a sound legal framework for environmental protection that addresses guidelines for the management and disposal of all waste streams. This framework is supported by several National Strategies that apply to solid waste management:

- (i) Strategy for the Management of Solid Waste in Vietnam Cities and Industrial Parks (1999).
- (ii) National Strategy for Environmental Protection (2003).
- (iii) National Strategy for Integrated Management of Solid Waste up to 2025 and vision towards 2050 (2009).

- (iv) National Strategy on Environmental Protection up to the year 2020 and Vision to 2030 (2012).

In the 2009 National Strategy for solid waste management, it is expected that by 2050, all kinds of solid waste will have been collected, reused, recycled and comprehensively treated by advanced, environmentally-friendly technologies, suitable to each locality, thereby limiting the amount of solid waste that needs to be land filled. Together with National Strategies, there have been relevant laws and policy documents such as decree, circular, joint circulation and standards that have been issued to support. Especially, the importance of research and development for the disposal and recycling of waste is emphasized in the newly revised "Law on Environment Protection (2014)": Article 6.6 encourages "Conduct scientific researches, technology transfer and apply the technology for the disposal and recycling of wastes and environment-friendly technologies".

The recycle of CDW has been emphasized once in National strategy for management of solid waste up to the year 2025 and Vision to 2050 (Table 3) in which up to 50% - 60% of collected CDW would need to be recycled [5]. Nevertheless, the detailed instructions such as Construction Recycle Act or Rules for Recycling of CDW are not available. Furthermore, there are no standards and criteria for the use of recycled materials from CDW such as sub-base course materials, concrete aggregate, and construction generated soil in Vietnam. There are only some Directives and Circulars promoting the application of recycled construction materials.

Table 3: National strategy for management of solid waste up to the year 2025 [10]

Targets		In 2020	In 2025
Ratio of cities that have solid waste recycling system %		70	100
% Reduction of plastic bags compare to 2010		65	85
% Collec- tion/ Recycle %	Urban house Waste	90/85	100/90
	Construction and Demolition waste	80/50	90/60
	Urban sludge	50/30	100/50
	Non-hazardous Industrial SW	90/75	100/100
	Hazardous Industrial SW	70/0	100/0

Challenges and Opportunities of recycling CDW in Vietnam

It is obvious that the concept of CDW management has been quite new in Vietnam and it is essentially required to spread the information in order to gain the public and authority support. Vietnam Government indeed is facing a big challenge to deal with MSW (Municipal Solid Waste) management in general and CDW management in particular. The stage wise problems could be identified in the following manners.

Firstly, the *construction technique remains out-of-date*, therefore, it generates huge amount of waste. For instance, instead of underground digging with pipe ploughing technology for pipe installation, it is commonly used the open ditch technique which generates CDW and expense for earth moving. The buildings are constructed with concrete blocks instead of using bricks and mortars will save also lots of money in cleaning the construction waste at sites. The application of new advanced construction technologies would definitely help reduce the CDW at source.

The illegal dumping of CDW, on the other hand, can *cause risks to human health and environment* including transportation obstacle (i.e., CDW on roadsides and pavements) leading to accidents, impact of urban landscape, air pollution (due to dust), degraded infrastructure (i.e., blocking the sewers), waste of lands. It can be seen for the past ten years Hanoi has been a giant construction site and the dust from construction contributes significantly to air pollution in Hanoi. The illegal dumping of CDW on streets happens every day, which cause countless accidents unfortunately. In addition, the improper management of toxic materials including CDW such as gypsum drywall (which can produce hydrogen sulfide) and asbestos (which increase the risk of lung cancer) increases the potential risk to human health. The issues of illegal dumping are mainly due to the cost and project location factors.

Right now, like other developing countries in Asia, Vietnam is facing the *shortage of legal and enforcement in CDW management* as mentioned above. The priority in current solid waste management is for organic waste management and hazardous waste management (health waste and hazardous industrial waste). The CDW, which belongs to non-hazardous solid waste, is considered mostly at research scale and no big investment has been put in so far. At present, there are not any regulations (circulars, guidelines) on classification, collection, transfer and treatment of CDW. The priority policy or investment policy for research, manufacture and business investment in the recycle and management of CDW has not been promulgated. The recycle policy has just mentioned in general solid waste management in *National Strategy on Environmental*

Protection up to the year 2020 and Vision to 2030 approved by Decision No.2149/QĐ-TTg in 2009. In this legal document, one of the big tasks is to increase the reuse and recycling of solid waste by increasingly reuse solid waste; building and developing the waste market and economy; developing the recycling industry, promoting the purchase of recycled products, elaborating and applying incentive policies for recycling activities and forming recycling funds.

Furthermore, there has been not much attention from present *public awareness and attitude towards the waste generated* from construction and demolition sites. This is required to be changed in first possibly the industrial practice. It is required to sensitize not only the Engineers, but all stakeholders including regulatory authorities in construction industry. This also requires full understand the reuse potential of CDW and existing practices in implementation and enforcement for achieving the objectives of national strategy.

In Vietnam, the recycle of CDW has been at research scale only. JICA is one of leading donors in solid waste management (SWM) projects:

- + 2006-2009: 3R initiative project in Hanoi city. This project had been implemented for 3 years from November 2006 to November 2009 aiming at establishing a balanced and unique 3R system centered on the source separation and recycling of biodegradable waste under the 3R Initiative in Hanoi City.
 - + 2005-2013: Haiphong Environmental Improvement Project.
 - + 2014-2018: Project for Capacity Development on Integrated Management of Municipal Solid Waste
 - + 2014- present: DAP Recycle of phosphogypsum in Dinh Vu industrial zone- Haiphong.
- Besides, some SWM and promotion of recycling projects have been done under the support of Ministry of Environment in Japan.
- + 2009: Ichikawa Kankyo Engineering (IKE) CDM Project on SW Composting
 - + 2014: Ichikawa Kankyo Engineering (IKE) D-waste recycle project

Similar projects have also conducted in related Vietnamese Ministries:

- "Investment of CDW recycle line to produce construction materials project" by Ministry of Construction in 2010 - 2012. This project has investigated properties of the recycled aggregates (RAs) from CDW from various CDW sources collected from landfills in Hanoi, as well as some properties of concrete, mortar and concrete bricks and block using RAs. Besides, the project also selected and appropriate technologies for recycling CDW to produce RAs for concrete and mortars applied in Vietnam. How-

ever the project was not entirely successful, RAs is only applied to the base, sub-base layers of rural roads, not for surface layer or highway applications.

- "Treatment and recycle of solid waste in construction of road infrastructure project by Ministry of Transportation in 2010 – 2014.
- "Investigation of management system of CDW in urban areas" by Vietnam Urban Environment and Industrial Zone Association in 2008 – 2010.
- "Research and piloting innovative construction works in the islands" in 2015 – 2020.

The biggest problem with current R&D public investment projects is its limit in application. The R&D manufacture line often stopped when the project finished since the input material and output were not sustainable.

Recently, in 2017, one very important cooperation project between Vietnam and Japan institutional links (Saitama University, Japan and National University of Civil Engineering, Vietnam) was applied successfully, called "*Establishment of Environmentally Sound Management of Construction and Demolition Waste and Its Wise Utilization for Environmental Pollution Control and for New Recycled Construction Materials in Vietnam*". This project is funded by SATREPS, a Japanese government program, that promotes international joint research targeting global issues. The program is collaboration between two Japanese government agencies, i.e. the Japan Science and Technology Agency (JST) and the Japan International Cooperation Agency (JICA). The project proposes to promote the recycling of CDW in Vietnam, which aims (1) to establish guidelines necessary for the environmentally sound CDW management and quality standards for recycled materials produced from CDW; (2) to develop new technologies utilizing recycled materials produced from CDW; and (3) to propose strategic business models designed to promote the CDW recycling in Vietnam and examine their effectiveness and feasibility through on-site pilot projects. The final goal of this project is to contribute to the achievement of a CDW recycling rate of 60%, which meets the Vietnam national strategy for management of solid waste up to the year of 2025, through the application of developed technologies and business models to practical recycling business.

This project is very crucial for Vietnam (1) to take advantage of sharing experience from Japanese side in terms of recycle technology and policy implementation; (2) to strengthen the correlation of stakeholders (research institutions, public authority and private sectors) in implementing a cohesive national program to address waste management issues in Vietnam and (3) to promote the waste recycle business for better energy saving.

CONCLUSION

Taking all facts presented into account, it is obvious that CDW management and recycled is one of the most critical engineering issues that need immediate intervention in Vietnam today. Though there have being some initiatives in the past to address this issue, none has been successful mainly due to the multiplicity of the problem. Therefore a more holistic approach addressing all technical, social, institutional and economical issues is vital to achieve a sustainable solution.

ACKNOWLEDGEMENTS

The authors would like to thank the SATREPS (Science and Technology Research Partnership for Sustainable Development) project, a Japanese government program for the research grant supported by JST-JICA to promote the international joint research targeting global environment issues.

REFERENCES

- [1] Ministry of Natural Resources and Environment (MONRE), 2011, State of Environmental Report 2011 on Solid Waste management (MONRE), Vietnam.
- [2] Vietnamese government, 2007, Resolution No. 34/2007/NQ-CP A number of solutions to the amelioration and reconstruction of damaged or degraded condominiums.
- [3] Shishir Bansal, S K Singh. A Sustainable Approach towards the Construction and Demolition Waste. International Journal of Innovative Research in Science, Engineering and Technology. Vol. 3, Issue 2, February 2014.
- [4] Decision No. 609/QĐ-TTg approved by the Prime Minister of the Socialist Republic of Vietnam dated 24, April, 2014, Master plan on solid waste disposal of Hanoi capital to 2030, with a vision to 2050.
- [5] T. Chinda, W. Engpanyalert, A. Tananoo, J. Chaikong, and A. Methawachananont. The Development of the Construction and Demolition Waste Dynamic Model^[1]. IACSIT International Journal of Engineering and Technology, Vol. 5, No. 5, October 2013.
- [6] Papargyropoulou, E.; Preece, C.; Padfield, R.; Abdullah, A.A. Sustainable construction waste management in Malaysia: A contractor's perspective. Management and Innovation for a Sustainable Built Environment. 2011, Amsterdam, The Netherlands.
- [7] Anton Ming-Zhi, Gao. Construction & Demolition Waste Management: From Japan to Hong Kong. Griffin's View on International and Comparative Law. Retrieved from

- https://papers.ssrn.com/sol3/papers.cfm?abstract_id=1131984 on 21 Jul 2008.
- [8] Ministry of Land, Infrastructure, Transport and Tourism, 2012 (in Japanese).
- [9] Decision No. 1711/QD-UBND on October 11, 2012, Master plan on solid waste management in Haiphong city towards 2025.
- [10] Decision No. 2149/QD-TTg approved by the Prime Minister of the Socialist Republic of Vietnam, 2009, Approving the National Strategy on Integrated Solid Waste Management up to 2025 and Vision to 2050, Hanoi.

IRREPARABLE COMPRESSIVE CREEP DEFORMATION OF CHLOROPRENE BEARING PAD

Hidenori TANAKA¹

¹National Institute of Technology, Gunma College, Japan

ABSTRACT

Rubber is indispensable to fill safety standards against earthquake and vibration. In Japan, this material is normally used to support many concrete structures (bridges, buildings). But, the compressive irreparable creep deformation as time goes by hasn't been considered sufficiently. Generally speaking, rubber is non-compressive and hyper-elastic. This creep would reduce the affect to absorb the horizontal deformation in earthquake. Based on this, we have carried out simple compressive creep test by using cylindrical specimen made of chloroprene rubber as a bearing pad of bridge. At first, we pressed the specimen to equivalent forces which are equal to the self-weight of bridge girders. Secondly, we have kept them under compressive situation for three months. And then, the pressure was released. The residual displacement was measured including unloading elasticity, delayed-elasticity and irreparable creep. The irreparable creep was account for 17 % of the total displacement. Furthermore, we simulated numerical analysis of the cylindrical specimen in 2 dimension based on finite displacement theory. In this analysis, we adopt the hyper-elastic Ogden's model in axisymmetric problem. The result of analysis corresponded with the experimental result well.

Keywords: Bearing pad, Irreparable Creep, Finite displacement, Hyper-elastic, Chloroprene

INTRODUCTION

Seismic isolation rubber has been used for bearing pad of bridges and buildings. The isolated effect would be dependent on the horizontal deformation of rubber under earthquakes. There were many experiments to evaluate the deformation without axial force or axial mechanical properties, for example (stress relaxation, creep, plasticity). It is very important to consider the affection to the isolated effect due to axial irreparable behavior. Therefore, We have carried out simple compressive creep test using chloroprene specimen [1]. Rubber is usually non-compressive and non-volumetric material. In addition, the material will have occurred large displacement even though the applied loads are small. Due to these complicated properties, It has been more difficult to explain mathematical expression in mechanical behavior. In this study, we showed the numerical analysis of compressive deformation by Ogden's model that is the basic theory to explain large displacement behavior in 2 dimensional axisymmetric problem comparing with the result of experiments [2].

COMPRESSIVE TEST

The load-displacement curve

We selected chloroprene rubber that has been used as a bearing pad of bridge. The quasi-compressive loads were applied on the cylindrical specimen (ϕ 80mm, H=80mm) with upper and lower steel plates (refer Fig.1).



Fig 1. Deformation of rubber (compressive test)

The relation between applied loads and longitudinal displacements are shown in Fig.2. In this test, The applied loading speed was 10mm/minute.

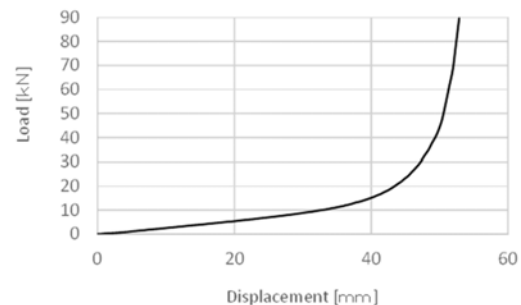


Fig.2 Loads-displacements curve
The curve is typical compressive behavior [3].

Compressive creep test

The Compressive creep test was carried out as following way. At first, we measured the displacements and applied loads until serviceability state which is supporting the self-weight of bridge girders. Secondly, the stress has been holding for 3 months to fix securely upper steel plate by 4 bolts with nuts at the corner (refer to Fig.3).

Finally, we measured the displacements again after releasing stresses unfastening the bolts and nuts (refer to Fig.4). We could evaluate non-linear state that including unloading elasticity, delayed elasticity and irreparable creep to describe the deformation curve after releasing stresses .

We determined serviceability state to consider relationship between real chloroprene pad section area and girders weight.

The serviceability state is shown in Fig.5. The red point in the figure is equivalent to the state.

This curve is approximately linear state comparing with the curve in Fig.2

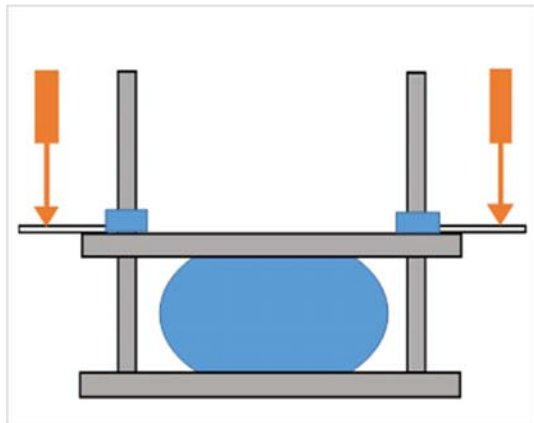


Fig.3 Holding stresses

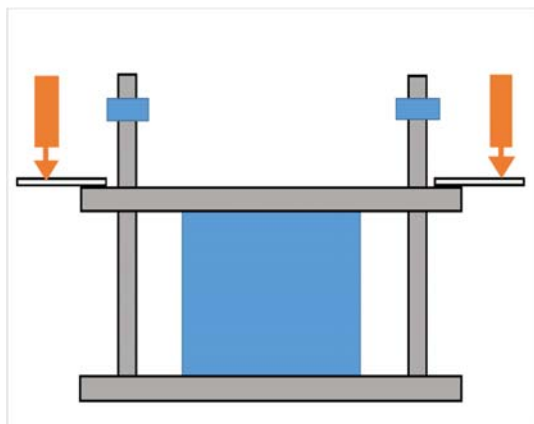


Fig.4 Releasing stresses

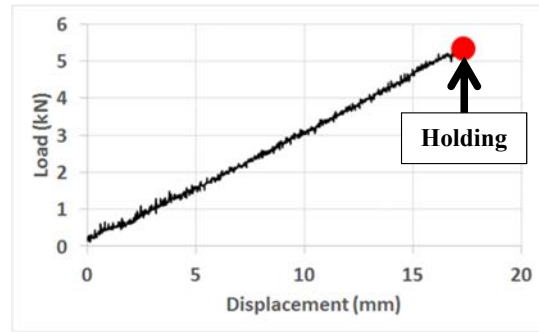


Fig.5 Serviceability state

The curve after releasing stresses reveals creep characteristics (refer to Fig.6). This curve is mainly consist of three parts. The sharp descending line near 0 (hour) is unloading elasticity, by 200 (hours) it showed delayed elasticity, and after 200 (hours) it showed irreparable creep, respectively.

Even though the holding times are less than four months, it was found that the irreparable creep reached about 17 % of total displacement. In addition, The creep would be occurred under the small load that is equal to serviceability state.

The plastic deformation could be visualized the specimen after test (refer to Fig.7).

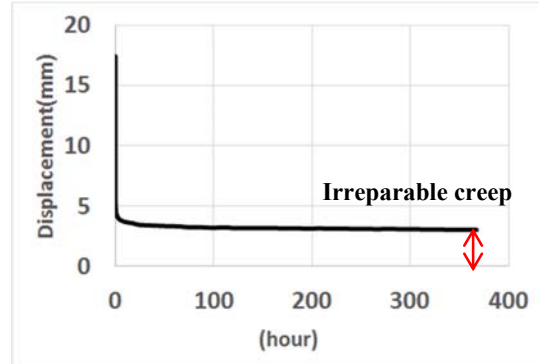


Fig.6 Creep Characteristics



Fig.7 Plastic deformation of specimen

NUMERICAL ANALYSIS

Base of finite displacement theory

Rubber has generally large deformation under compressive loads. So, There are some limitations to apply the infinitesimal deformation theory. The deformation gradient tensor has been used to describe the mechanical properties of rubber. For example, Cauchy stress, Green strain tensor[4]. In this paper, The deformation gradient tensor is defined as follows[5].

$$F = \frac{\partial \mathbf{x}}{\partial \mathbf{X}} \quad (1)$$

F : Deformation gradient tensor

\mathbf{x} : infinitesimal line element vector (after deformation)

\mathbf{X} : infinitesimal line element vector (before deformation)

Green-Lagrange strain tensor

The strain should be described more than second rank orders to apply this analysis. Green-Lagrange strain tensor is reasonable for variational principle [6].

$$E = \frac{1}{2} \frac{d\mathbf{x}^2 - d\mathbf{X}^2}{d\mathbf{X}^2} = \frac{1}{2} \left(\frac{\partial u_i}{\partial X_j} + \frac{\partial u_j}{\partial X_i} + \frac{\partial u_k}{\partial X_i} \frac{\partial u_k}{\partial X_j} \right) \quad (2)$$

E : Green – Lagrange strain tensor

$u_{i,j,k}$: displacement

The Second Piola-Kirchhoff stress tensor

This stress tensor is the best expression corresponding to the Green-Lagrange strain tensor. And then, This form is useful formulation in analysis because of the symmetric form[4].

$$\mathbf{S} = J \mathbf{F}^{-1} \boldsymbol{\sigma} \mathbf{F}^{-T} \quad (3)$$

S : second Piola– Kirchhoff stress

J : det(F)

\mathbf{F}^{-1} : Inverse tensor of F

\mathbf{F}^T : Transpose of F

$\boldsymbol{\sigma}$: Cauchy stress tensor

Ogden's model

Strain energy function has been used to analyze the large deformation of rubber under various loads. Moony-Rivlin and Neo- Hooke models are popular

functions for analysis. But, these models are inadequate for nonlinearity in high strain region. So, here, we adopted Ogden's model to simulate high nonlinearity region in analysis[7].

$$W = \sum_{n=1}^N \frac{\mu_n}{\alpha_n} (\lambda_1^{\alpha_n} + \lambda_2^{\alpha_n} + \lambda_3^{\alpha_n} - 3) \quad (4)$$

W : strain energy function

α_n, μ_n : material constant

$\lambda_1, \lambda_2, \lambda_3$: principal stretch ratio

In this paper, we considered third rank (N=3). The material properties are shown in Table.1.

Table.1 Material properties

Constant value	α	μ
First rank	$\alpha_1=1.3$	$\mu_1=1.491 \text{ (N/mm}^2\text{)}$
Second rank	$\alpha_2=5.0$	$\mu_2=0.003 \text{ (N/mm}^2\text{)}$
Third rank	$\alpha_3=-2.0$	$\mu_3=-0.0237 \text{ (N/mm}^2\text{)}$

Results of analysis

We carried out two dimensional axisymmetric analysis considering the shape of specimen [2]. Fig.9 showed the deformation and the equivalent stress distribution at the quadrilateral point in Fig.8.

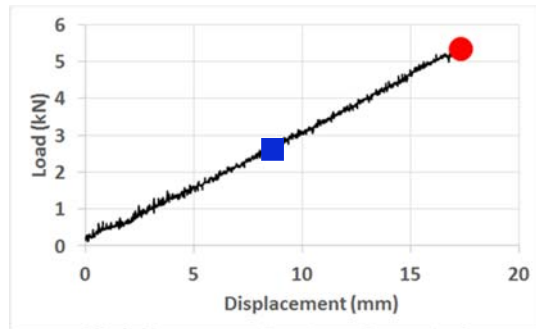


Fig.8 Two example points for analysis

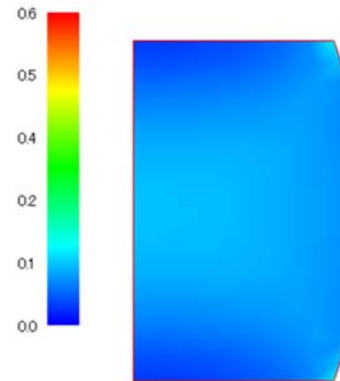


Fig.9 Deformation and equivalent stress No.1

Fig.10 showed the deformation and the equivalent stress distribution at the circular point in Fig.8.

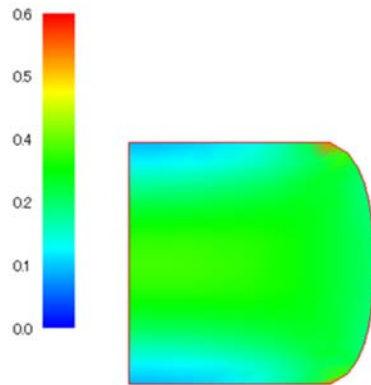


Fig.10 Deformation and equivalent stress No.2

Equivalent stress is defined in equation (5).

$$\sigma_{eq} = \sqrt{3J_2'} \quad (5)$$

σ_{eq} : Equivalent stress (N/mm²)

J_2' : Second invariant of deviatoric stress

We adopted the displacement control method.

The equivalent stress distribution is typical for compression state. The highest stress is distributed at the corner of specimen which is contacted with steel plates (upper and lower). The maximum equivalent stress is approximately 0.6 (N/mm²).

Unsteady thermal conduction analysis

The Thermal analysis was simulated under cyclic temperature change which showed average value in North area in Japan. This is preliminary step to check the evolution of viscoplasticity of this pad under cyclic temperature[8]. The cyclic temperature was shown in Fig.11. This temperature change was determined due to the limit of application of freezing and thawing test machine .

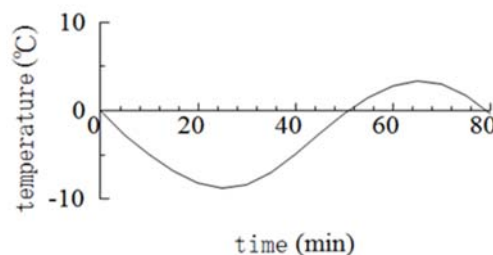


Fig.11 Cyclic Temperature change

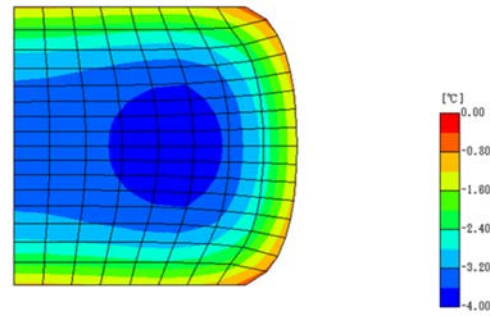


Fig.12 Thermal distribution

In this analysis, We should check the viscoplasticity under serviceability state. We have a plan to carry out the freezing and thawing test keeping the deformation of rubber under serviceability state. So, The compressive final deformation is the initial form for unsteady thermal conduction analysis.

For example, Thermal distribution that the temperature reached zero degree was shown in Fig.12. The center line was heat insulation and the other surface of rubber were heat transfer borders. The material properties are shown in Table 2.

Table 2 Heat properties

Specific heat	1.65 (J/g · K)
Specific gravity	1.39
Heat transfer coefficient	14 (W/m ² °C)

Thermal distribution was changed in about four degrees from the surface to the center of rubber.

CONCLUSION

The knowledge found in this research are as below.

- (1) The irreparable creep would be occurred under the serviceability state even though the elapsed time was only for three months.
- (2) The value of irreparable creep was about 17 % of total displacement.
- (3) Second Piola-Kirchhoff stress and Green-Lagrange strain tensor are suitable expression for large displacement problem of rubber.
- (4) The analysis has a good agreement with the result of experiment.
- (5) We have a plan to adopt F-bar method that is the popular numerical way to describe elasto-viscoplasticity of rubber .
- (6) It was found that the maximum equivalent stress is distributed at the corner of specimen which is contacted with steel plates.

- (7) We would like to research the thermal fatigue behavior keeping serviceability state under cyclic temperature in next stage.
- (8) There are only four degrees thermal distribution changes from surface to center. The thermal fatigue affection may be small.

ACKNOWLEDGEMENTS

The author appreciates Tokyo Fabric Co.,Ltd for providing the chloroprene specimens. In addition, Mr. Kanbe works for Sata Construction Co.,Ltd and Mr. Kitazume works for Oriental Shiraishi Co.Ltd. supported to gather data. And , Research Center of Computational Mechanics, Inc. for supporting two dimensional unsteady thermal conduction analysis.

REFERENCES

- [1] Yoichi Yuki, Hiroki Tamai et al, "Fundamental experiment of shape and confining effect on rubber pieces' cushioning characteristics", Journal of structural engineering, Vol.61A, March,2015, pp. 313–321.
- [2] EA de Souza Neto, D Peric, DRJ Owen," Non-linear finite element method", June, 2012.
- [3] Hisanari Uruta, Kazuhiko Kawashima et al , "Evaluation of stress-strain relation for a rubber rectangular shock absorbing device under an extreme compression stress", Journal of JACE, No.661,Oct,2000,pp.71-83.
- [4] Takashi Kyoya,"Continuum Mechanics ",Japan Association for Non-linear CAE,Dec,2008
- [5] Shigeru Kuranishi,"Introduction to Mathematical Models of Material Characteristics", Subcommittee of Structural Mechanics Committee of Structural Engineering, J.S.C.E.,Aug.,1989
- [6] B.R.Seth, "Generalized strain measure with applications to physical problems", IUTAM Symposium on Second Order Effects in Elasticity, Plasticity and Fluid Mechanics, 1962, pp. 1-14.
- [7] R.W.Ogden,D.G.Roxburgh, "A pseudo-elastic model for the Mullins effect in filled rubber",The royal society, 1999, pp. 2861-2877.
- [8] Hidenori Tanaka, Fimiyasu Makinoshima,"The adhesive characteristic of concrete block with fiber sheets under cyclic temperature", International Conference on the Regeneration And Conservation of Concrete Structures 2015,I-17

FE ANALYSIS FOR LATERAL STRENGTH OF CONCRETE WALLS WITH AGGREGATE SEDIMENTATION

Mamoru Kawasaki¹, Tetsuya Ohmura² and Ryota ISHII³

¹ Graduate school, Tokyo City University, Japan; ²Architecture Department, Tokyo City University, Japan

³The Zenitaka Corporation, Japan

ABSTRACT

Concrete walls are effective earthquake resisting elements for lateral force in concrete buildings. In addition, stiffness and strength of walls are larger than one of columns and girders. As lateral force concentrate on walls, lateral strength of a building would be influenced by that. Therefore a seismic evaluation for walls is significant. However, concrete strength reduction (CSR) would be occurred for the vertical direction due to aggregate sedimentation. Consequently, seismic performance of a whole building might be reduced by CSR. In this paper, lateral strength of concrete walls with CSR was analyzed to get basic behavior by FE analysis. This paper reported that forming compressive strut was influenced by CSR and lateral strength were decreased at concrete wall with the shear span of less than 0.73. That wall was often seen in medium and low buildings, and seismic performance of a building with fewer walls tends to depend on wall strength. Therefore, CSR should be taken into account at a seismic assessment in addition to a conventional concrete survey for an existing building.

Keywords: Concrete wall, Concrete strength reduction, Lateral strength, Shear span ratio, Compressive strut

INTRODUCTION

Seismic evaluation is significantly important in countries where earthquake often occur like Japan. In a concrete building, concrete walls are effective to resist earthquake, and the seismic performance depend on them. Most of the lateral force by earthquake can be concentrated to the walls rather than columns, because the stiffness of the wall is much larger. Therefore the stiffness and strength of the walls must be properly evaluated.

On the other hand, concrete bleeding and aggregate sedimentation often cause concrete strength reduction while concrete casting and concrete curing, because concrete is composed of water, cement and aggregate.

Concrete strength distribution in columns and walls along their height is shown in Fig.1¹⁾. Kasai, et al. concluded that concrete strength was reduced to 80 to 90% in walls and 60 to 90% in columns. Their result indicated that concrete strength can be reduced

at the top of the walls.

Concrete compressive strut is formed in diagonal direction when the wall resists earthquake, and the lateral strength of the wall definitely depends on the concrete compressive strut.

However, seismic performance of a building might be reduced, because of concrete strength reduction as shown in Fig.2. In this paper, concrete walls with concrete strength reduction were modeled and analyzed to have their lateral strength.

ANALYSIS

Analyzed specimen for verification

We modeled and analyzed the wall specimen²⁾ as shown in Fig. 3 and 4 at first to verify our model and analysis. Figure 3 shows the geometric of the wall specimen. The wall is 1/3 scale specimen and has four stories, total height of 3,800mm (12.5 ft.), each height of 1,000mm (3.3 ft.) and the span of 4,000mm (13 ft.). The column section is 300mm (about 1 ft.) square and

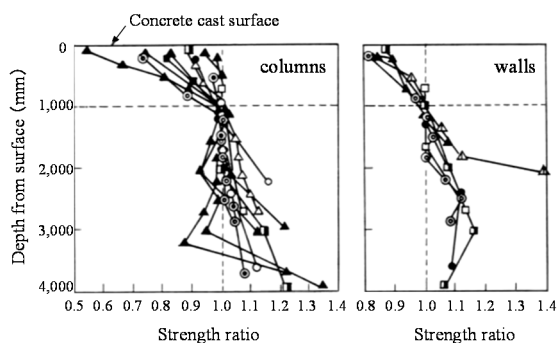


Fig.1 Concrete strength reduction along height¹⁾

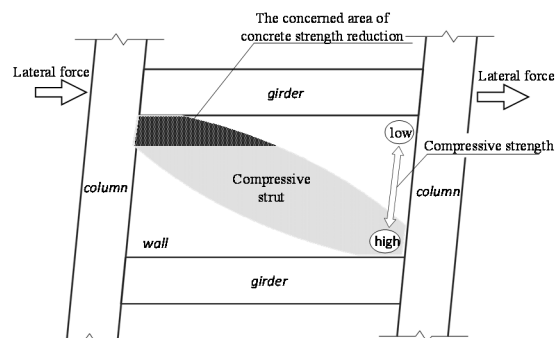


Fig.2 Concrete strength reduction in a concrete wall

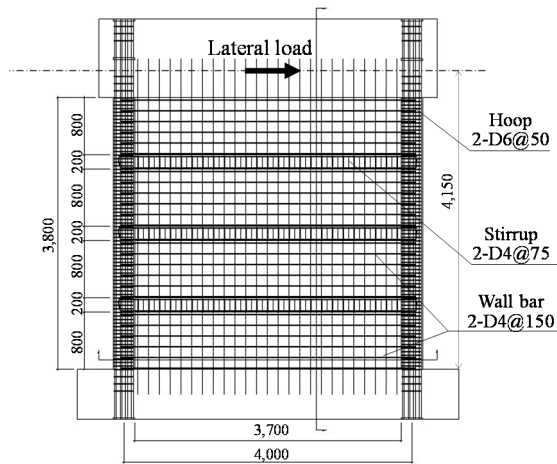


Fig.3 Bar arrangement and the geometry (mm)

the girder section are the wide of 160mm (6 in.) and the depth of 200mm (8in.). Their rebar arrangement are shown in Fig. 3 and 4. Table 1 and 2 show the material property. Table 3 shows Diameter and area of rebar. Concrete strength is 26.6 to 29.4 N/mm² (3.8 to 4.3 ksi.) and the yield strength of the rebar is mainly 323 to 385 N/mm² (47 to 56 ksi.).

Model

Figure 5 shows meshed model. Four nodes and quadrate iso-parametric plan stress element is applied for concrete and each elements are 100mm square. Embedded element is applied for rebar. Bond slip is considered for longitudinal bar, and other bar is assumed to be perfectly bonded. The base stub is fixed, the gravity load and lateral displacement is forced at the top of the wall as shown Fig.5.

Material property

The parabola model of Feenstra³⁾ is applied for the relationship between concrete stress and strain. 0.2% strain of maximum compressive stress is assumed. The fracture energy of 9.5N/mm for column and girder, and 7.2N/mm for wall are considered based on Nakamura, et al⁴⁾. Hordijk⁵⁾ model with 0.1N/mm⁶⁾ of fracture energy is applied for the relationship between tensile stress and strain. The fracture criterion of concrete under biaxial stress is based on Von Mises yield criterion.

Rebar is modeled as bi-linear without strain hardening. Bond slip model is based on Morita, Kaku, and et al. as shown Fig.8⁷⁾.

Concrete strength vertical distribution

The concrete strength vertical distribution is assumed as shown Fig.9 based on Kasai, and et al.¹⁾. Four zones are assumed along the height, and the concrete strength is supposed to be reduced as the height of the zone raise.

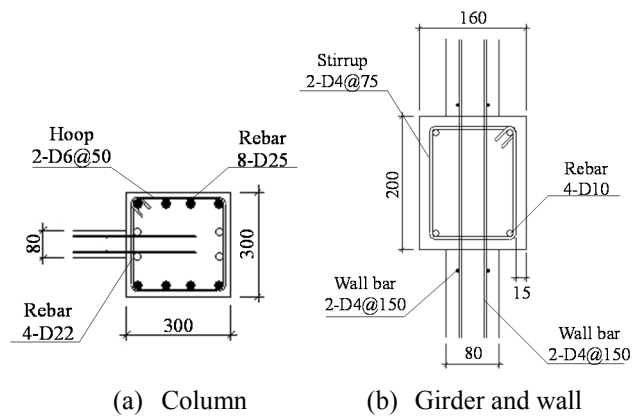


Fig.4 Section of the column and girder (mm)

Table1 Concrete properties

Story	Young modulus (kN/mm ²)	Concrete strength (N/mm ²)	Tensile strength (N/mm ²)
1, 2	21.5	29.4	2.59
3, 4	23.2	26.6	2.36

Table2 Rebar properties

Size (grade)	Location	Young modulus (kN/mm ²)	Yield strength (N/mm ²)	Tensile strength (N/mm ²)
D4(SD295A)	Wall	172	351	518
	Stirrup	163	323	490
D6(SD295A)	Hoop	190	366	491
D10(SD345)	Girder	185	385	594
D22(SD345)	Column	185	563	738
D25(SD345)	Column	185	535	722

Table3 Diameter and area of rebar

Imperial Bar Size	Soft Metric Size	JIS Size	Area (mm ²)
N/A	N/A	D4	14
N/A	N/A	D6	32
#3	#10	D10	71
#4	#13	D13	127
#5	#16	D16	199
#6	#19	D19	287
#7	#22	D22	387
#8	#25	D25	507

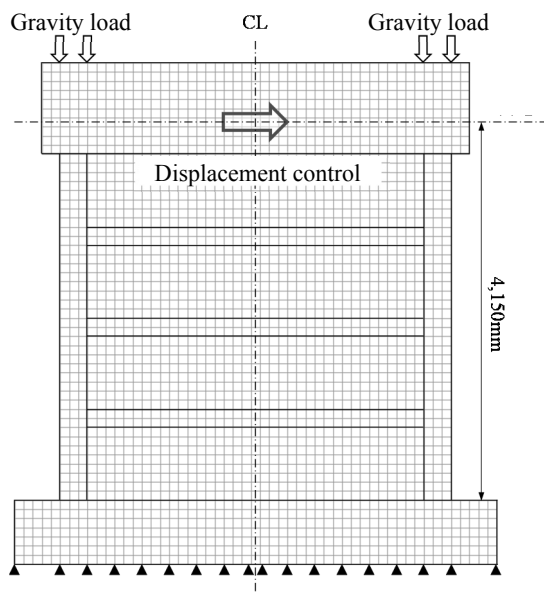


Fig.5 Meshed model

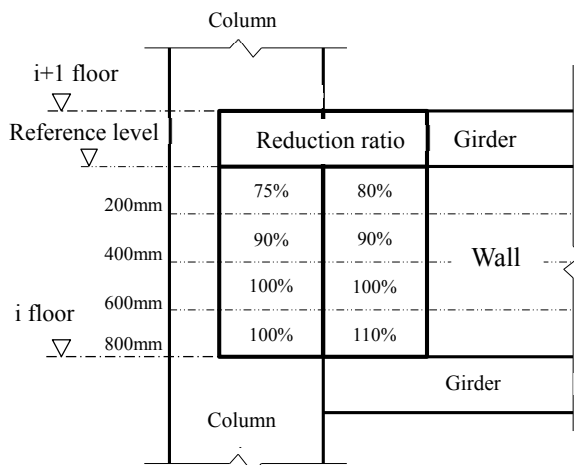


Fig.9 Assumed concrete strength reduction

VERIFICATION

Test result²⁾ and our analysis results are compared to verify our model and analysis. In this verification, the concrete reduction along the height is not considered, because the concrete of the specimen was cast at high accuracy.

Lateral strength and drift angle

Figure 10 shows the lateral force versus drift angle. The maximum lateral force is 1,822kN at 0.37% drift angle in the test and 1,876kN at 0.36% in our analysis. Our analysis result is suited to the test result up to around the maximum lateral force, because the lateral strength in our analysis is 103% of one in the test.

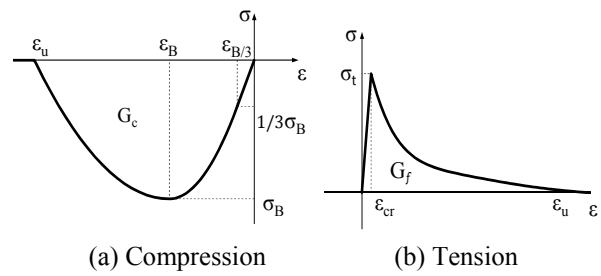


Fig.6 Concrete model

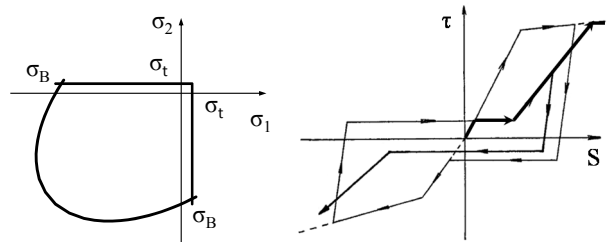


Fig.7 Criterion

Fig.8 Bond slip

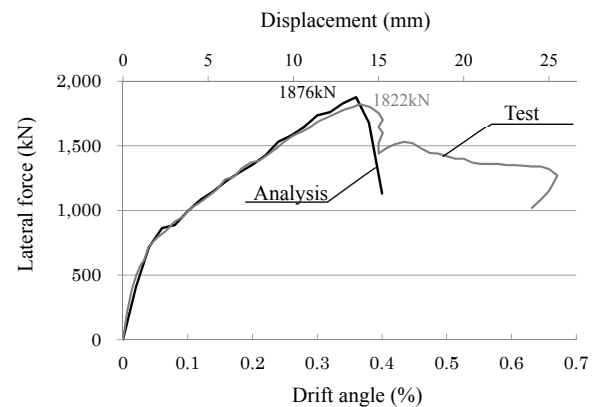


Fig.10 Lateral force versus drift angle

Cracking

Figure 11 shows the cracking in the test²⁾ and crack strain vector in our analysis at 0.4% drift angle. The failure mode was concrete compressive failure at the bottom of the wall in both results. The diagonal crack was observed overall the wall in the test. The crack strain vector was shown overall the wall in our analysis. Good agreement was shown in the test and our analysis results up to around 0.4% drift angle.

RESULTS

Our analysis was verified in the previous section, because our analysis result was approximately suited to the test results. In this section, the same and short height walls with the same section considered concrete strength reduction along the height are analyzed.

Lateral force versus drift angle

The models with / without concrete strength reduction are compared for lateral force versus drift angle.

Figure 12 shows lateral force versus drift angle. Figure (a) shows the result of four stories (shear span of 0.97) model. The maximum lateral force is 1,876kN at 0.36% drift angle in the model without concrete strength reduction, and 1,874kN at 0.36% in the model with concrete strength reduction. The effect of the concrete strength reduction was not seen when the results of the models with / without the concrete strength reduction are compared.

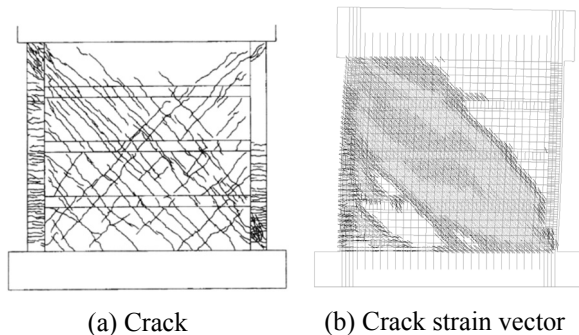
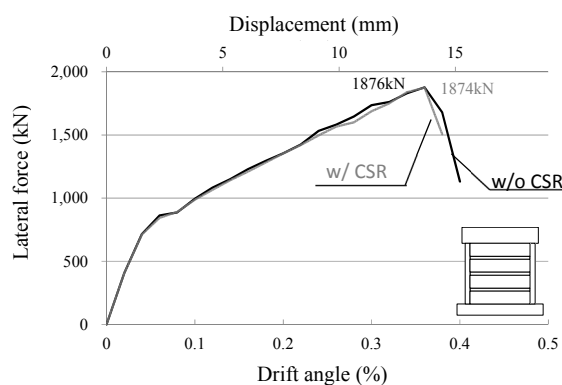


Fig.11 Crack and Crack strain vector at the peak

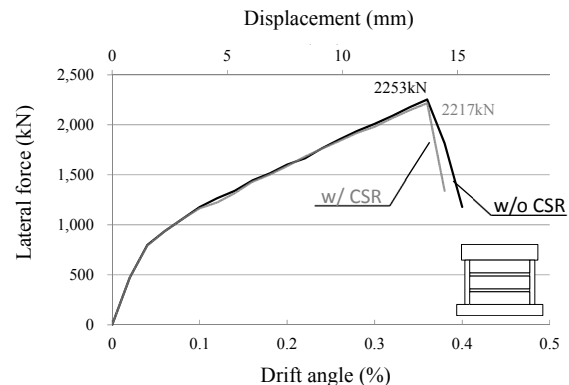
Figure (b) shows the result of three stories (shear span of 0.73) model. The maximum lateral force is 2,253kN at 0.36% drift angle in the model without concrete strength reduction, and 2,217kN at 0.36% in the model with concrete strength reduction. The effect of the concrete strength reduction was not seen when the results of the models with / without the concrete strength reduction are compared as well as four stories (shear span of 0.97) model.

Figure (c) shows the result of two stories (shear span of 0.50) model. The maximum lateral force is 2,826kN at 0.38% drift angle in the model without concrete strength reduction, and 2,592kN at 0.34% in the model with concrete strength reduction. The effect of the concrete strength reduction was seen when the results of the models with / without the concrete strength reduction are compared. The lateral strength of model with concrete strength reduction was decreased to 89.5% of one of model without concrete strength reduction.

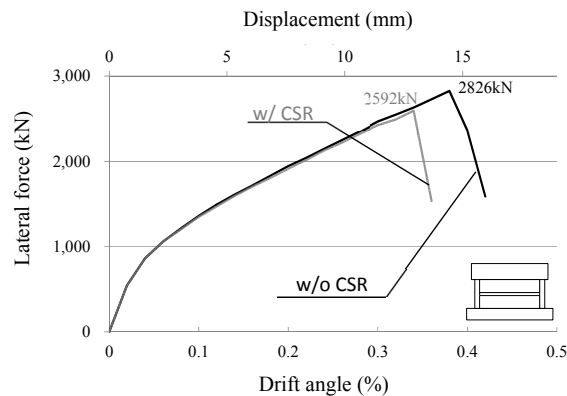
Figure (d) shows the result of one stories (shear span of 0.27) model. The maximum lateral force is 3,756kN at 0.44% drift angle in the model without concrete strength reduction, and 3,215kN at 0.36% in the model with concrete strength reduction. The effect of the concrete strength reduction was seen when the results of the models with / without the



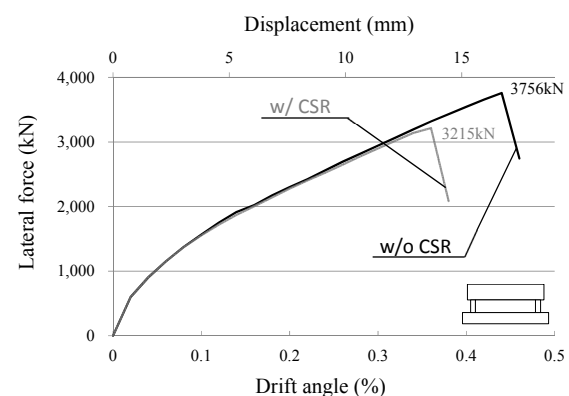
(a) Four stories model



(b) Three stories model



(c) Two stories model



(d) One story model

Fig.12 Lateral force versus drift angle

concrete strength reduction are compared as well as two stories (shear span of 0.50) model. The lateral strength of model with concrete strength reduction was decreased to 85.6% of one of model without concrete strength reduction.

Lateral strength reduction

Figure 13 shows shear span versus reduction ratio. The reduction ratio for lateral strength at the shear span of 0.73 and less was remarkably increased.

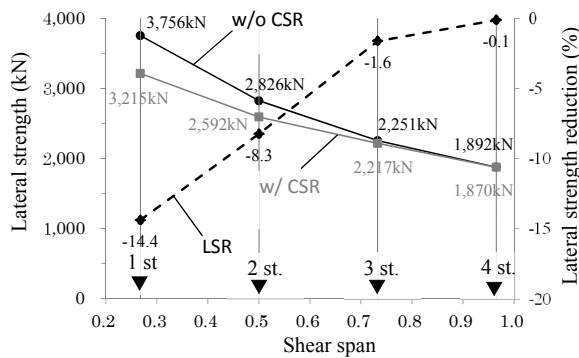


Fig.13 Shear span versus lateral strength reduction

Principal strain (ϵ_2)

Figure 14 shows principal strain (ϵ_2) at the peak of model with CSR. For all models, the angle of compressive strut was about 45 degree. For models with CSR, compressive strut width of ϵ_2 of 0.1% and greater were more increased than models without CSR. Shear span ratio was decreased to 0.97, 0.73, 0.50 and 0.27, those width were 2.0, 1.22, 1.64 and 1.11 times of one without CSR.

CONCLUSION

Two dimensional non-linear FE analyses for concrete walls with / without concrete strength reduction were performed. This paper has reported several conclusions as below.

1. Our analysis was verified to be compared between the test and analysis results.
2. The reduction ratio for lateral strength at the shear span of 0.73 and less was remarkably increased.
3. In models of two and one stories with concrete strength reduction, concrete strength reduction should be considered for the lateral strength evaluation of a concrete wall.

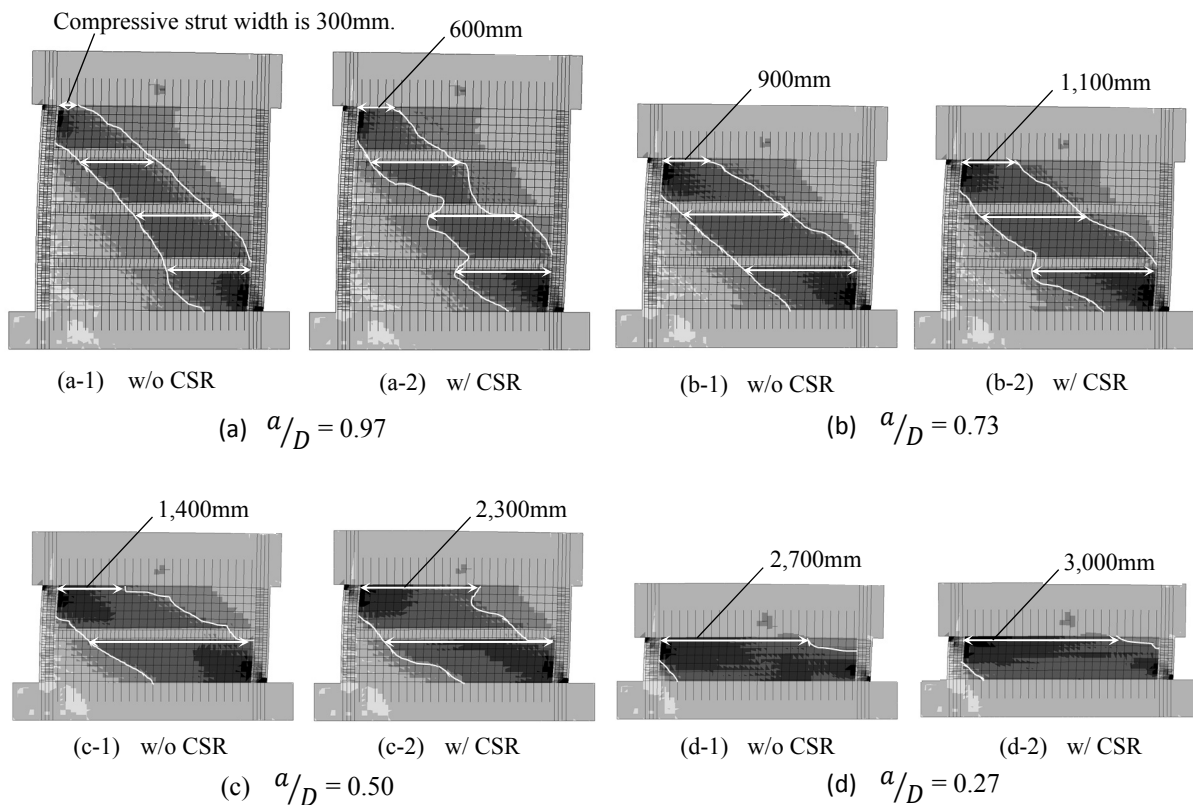


Fig.14 Principal strain ϵ_2

ACKNOWLEDGMENTS

Ryota Ishii is thanked for working much valuable analyses. The support of JIP Techonoscience in NTT DATA group staff is deeply appreciated.

REFERENCES

- [1] Yoshio Kasai, Yuu Matsui. Studies on concrete strength of structure in Japan, RILEM symposium control of concrete structures, 1979, Stockholm Sweden
- [2] Hiroki Tauchi, Masaomi Teshigawara, et al. EFFECT OF INNER BEAMS OF MULTI-STORY SHEAR WALL ON ITS SHEAR STRENGTH, Journal of structural engineering (in Japanese) , Vol.56B, pp61-66, 2010
- [3] Feenstra, P.H., 'Computational Aspects of Biaxial stress in Plain and Reinforced Concrete', PhD Thesis, Delft University of Technology, 1993
- [4] H.Nakamura, T.Higai, 'Compressive Fracture Energy and Fracture Zone Length of Concrete', Seminar on Post-peak Behavior of RC Structures subjected to Seismic Loads, JCI-C51E, Vol.2, pp256-272, 1999
- [5] Cornelissen, H.A.W., Hordijk, D.A., and Reinhardt, H.W. 'Experimental Determination of Crack Softening Characteristics of Normal Weight and Light Weight Concrete', Heron 31, 2, 1986
- [6] Ohoka Takunao, Yoshinori Hitsutaka, Ken Watanabe. INFLUENCE OF SHORT CUT FIBER MIXING AND CURING TIME ON THE FRACTURE PARAMETERS OF CONCRETE, Journal of structural and construction engineering / Architectural Institute of Japan, No.529, pp1-6, 2003
- [7] Shiro Morita, Kaku Tetsuzo. BOND-SLIP RELATIONSHIP UNDER REPEATED LOADING, Journal of structural and construction engineering / Architectural Institute of Japan, No.229, pp15-24, 1975

FERROCEMENT - BRICK SANDWICH WALL APPLIED TO NON-ENGINEERED HOUSES

Febrin A Ismail¹, M Sofian Asmirza², *Abdul Hakam¹ and Fauzan¹

¹Engineering Faculty, Andalas University, Indonesia;

² Engineering Faculty, North Sumatra University, Indonesia

ABSTRACT

Indonesian houses are generally categorized as non-engineered buildings that are constructed without any proper structural analyses. Bricks have long been used for hundreds years as main materials to make houses for the reasons of simplicity and construction speed. Lesson learnt from the Padang earthquake in 2009 concluded many casualties are resulted from the collapsed houses made of bricks. Ferrocement as a construction material that made of wire mesh and mortar plaster become alternative to be used for retrofitting brick-houses. In this paper, structural analyses of a typical non-engineered house and a retrofitted house made of ferrocement-brick sandwich material are described. The ferrocement-brick composite material has role as the main structure in the non-engineered house. The series of tests on that sandwich material has been done prior to the analyses. The results of the tests are then used to determine the strength criteria of the analyzed house. A structural analysis of the house is done by using the finite element computer program. As a comparison, an analysis of an ordinary brick wall house is described. As previously thought, the house with walls made of the ferrocement-brick sandwich material can withstand the given earthquake loads. It is concluded that the ferrocement-brick sandwich material is very useful to build earthquake resistant houses in seismic prone areas such as the West Sumatra.

Keywords: ferrocement, masonry brick wall, composite, non-engineered house, earthquake engineering

INTRODUCTION

The earthquake safe house can be defined as a house that provides security to its occupants in the event of an earthquake whether a weak earthquake or a very strong earthquake. The actual earthquake does not directly cause the victim but the house that collapsed when the earthquake that can cause casualties. This house should be made in such a way that it does not cause accidents or casualties to the inhabitants in it and the people around it. Psychologically secure homes also provide a sense of security to the inhabitants at all times. Small cracks that occur due to small or moderate earthquakes in a house will be very psychological disturbing the people in the house. So the main principle of earthquake safe house may be able to provide security to the occupants at any time, both psychologically and physically.

The earthquake safe house should not has any damage even in case of a weak earthquake (Fig.1). Minor damage is like the small cracks in the wall or loose roof arrangement must be avoided. This should the main the criterion of earthquake safe houses because since the minor damage may cause bad feeling to residents of the house. The earthquake safe house also must not suffer from heavy damage such as the collapse of the wall or the fall of roof construction due to the very strong earthquake. Due to the collapse of the wall and / or

the fall of the roof construction can hurt the occupants of the house and even take a life. During the very strong earthquake, seismic safe house should remain standing and may suffer from minor damage on the construction materials such as wall cracks on the wall. Each element of the earthquake safe house must remain in original place and still be in tied to each other during a very strong earthquake.

The earthquake safe house as well as other buildings can be presented as a good team work of human collaboration between owner, designer and a group of workers. An earthquake safe house in general is ordinary house that may not analyzed with the good science procedures that use of engineered mechanics knowledge, but adopt the principles of earthquake resistance. Dimensions and cost of making a house depends on the desire and ability of the house owner. The final quality of physical engineering work is determined by the builder of the house as a worker who create the house from its raw materials. The role of the house builder has enormous value in generating earthquake safe house. By providing additional knowledge and skills to the builders to create a safe house, earthquake risk reduction can be realized [1].



a. House before earthquake



b. Safe house after big earthquake



c. Un-safe house collapse after earthquake

Fig.1 Earthquake safe house definition

The people still think that the earthquake safe house is a concept of applying advanced technology that is complicated. In addition, earthquake safe house is also a masterpiece of the application of expensive engineering science. That opinion is not entirely wrong, because of some earthquake safety guidelines circulating in the community, tend to feature an addition to the ordinary house so it looks more complex and expensive [2] [3]. The transformation of a house into an earthquake safe house may need up to one third of the overall cost of construction. The extra cost depends on the concept of the earthquake safe house to be adopted. In terms of mechanical

engineering, reinforcement in a house logically provides additional resistance to earthquakes. So the concept of applying additional reinforcement can be justified and applicable to traditional buildings.

Although earthquake-safe houses have the primary mission to avoid casualties from the collapse buildings during the earthquake, people still want a simple and inexpensive concept to be adopted. There is some earthquake-safe housing guidelines that nearly to eliminate the traditional procedure of building a house that are common in society. Some of these concepts have been used in some community in a few sample buildings [4].

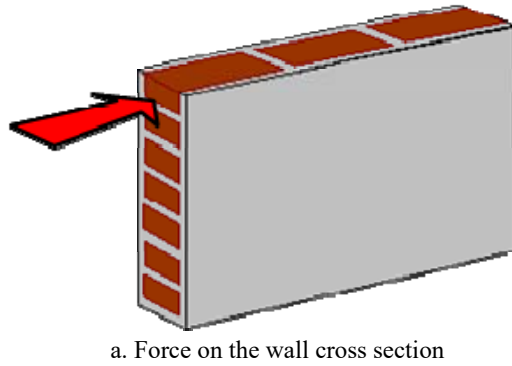
Ferrocement as a construction material that made of wire mesh and mortar plaster become alternative to be used for retrofitting brick-houses to resist the seismic load. The concept of ferrocement material has been applied to almost all structural elements of a building such as floor, roof, water tank including beams [5]. More advance application of ferrocement composites also has been studied by some researcher [6]. In this study an application of ferrocement to ordinary brick wall is done to gain a seismic resistant of the house. In this paper, the tests of brick walls including ferrocement-brick sandwich wall and the structural analyses of a typical non-engineered house are described.

BRICK-FERROCEMENT WALL TESTS

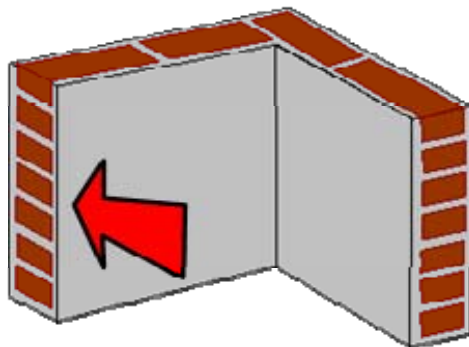
In order to obtain the engineering strength value of ordinary and ferrocement composite brick walls, a series of laboratory tests had been conducted. The specimens included in the tests were:

1. Masonry brick wall
2. Brick wall with wire mesh (Brick wall covered by wire mesh without mortar)
3. Mortared brick wall (Brick wall covered by mortar plaster)
4. Ferrocement brick wall (Brick wall with wire mesh covered by mortar plaster)

The tests were performed by applying single axial force in two different directions, one was parallel to the wall surface, and secondly perpendicular to the wall plane surface (Fig.2). The first one was purposed to obtain the shear strength of the wall in the direction of the wall cross section, and the second direction was for resistant moment as well as shear strength in the wall surface direction.



a. Force on the wall cross section



b. Force on the wall surface

Fig.2 Wall specimen test directions

During the tests, the damage to the specimens in term of crack were monitored. There were two different patterns observed on the tests depend on the direction of applied forces as plotted in Fig.3.

The applied forces and displacement in the same direction are recorded. The results in the terms of forces versus the displacements are shown here (Fig.4 and 5).

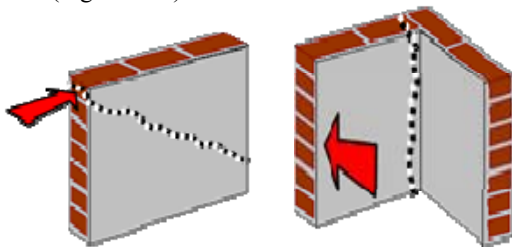


Fig.3 Crack during on tested specimens

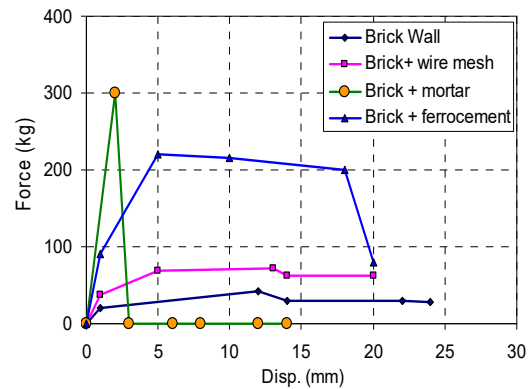


Fig.4 Test results in wall cross section direction

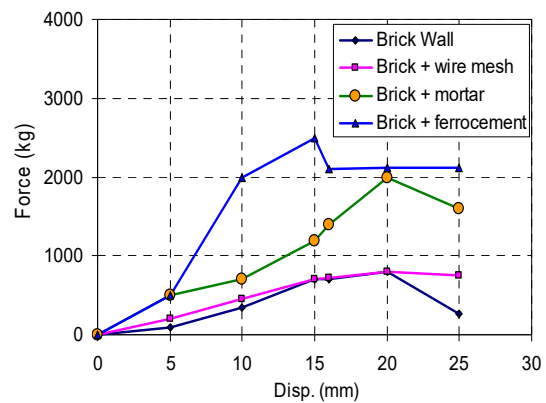


Fig.5 Test results in wall surface direction

Based on those test results, it can be taken the strength values of the walls in terms of the transversal and longitudinal shear forces as well as bending moment resistances as written in Table 1. The mortared brick wall seems almost has the same strength compared to the ferrocement-brick wall, but it is very brittle. This condition is not good for the buildings subject to earthquake load which may experience suddenly collapse. This situation do not give chance for occupants to evacuate from the building.

It also can be seen that the ferrocement-brick wall has the strength about five times compared to the ordinary masonry brick wall. The advantages of the increase strength of ferrocement-brick wall certainly can be used to retrofit brick wall houses such that the earthquake safe houses can be gained.

In order to demonstrate the application of ferrocement-brick wall to a non-engineered house, numerical simulations are performed in the next section. Those values in Table 1 are then used to determine the strength of the analyzed houses subjected to an earthquake.

Table 1 Wall strength to perform under earthquake load

Wall types	Longit. shear force (kg)	Transv. shear force (kg)	Bending moment (kg.m)
Brick Wall	42	800	240
Brick& Mesh	72	800	240
Brick& Mortar	300	2000	600
Brick& Ferroct.	220	2500	750

NUMERICAL SIMULATION

In this section, structural analyses of a typical non-engineered house and a retrofitted house made of ferrocement-brick sandwich material are described. During Padang earthquake on 30 September 2009, many non-engineered houses in the West Sumatra Province suffered from partially (Fig. 6) and totally collapse. This experience must not be happening in the future, thus the existing ordinary brick houses in the West Sumatra need to be retrofitted. The retrofitting model can be performed by using wire mesh and mortar plaster on the houses to present ferrocement-brick sandwich material as the wall. This wall becomes the main structure of the house to subject any forces including seismic loads.



Fig.6 Damaged house due to Padang earthquake

Numerical simulation is a tool can be used to carried out the analysis of houses subjected to an earthquake. Here, the numerical study of a typical house that has experience the damage due to Padang 2009 earthquake are presented. The simulations are carried out first for non-engineered house and then for ferrocement-brick sandwich material retrofitted house (Fig. 7). Seismic loads

are adopted from Indonesian Code for Padang City in transversal and longitudinal to the front side of the house.

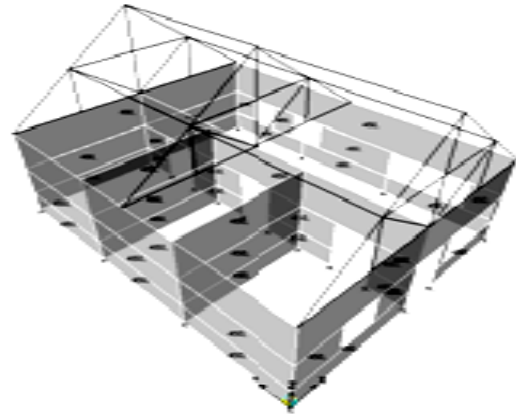


Fig.7 Numerical model of analyzed house

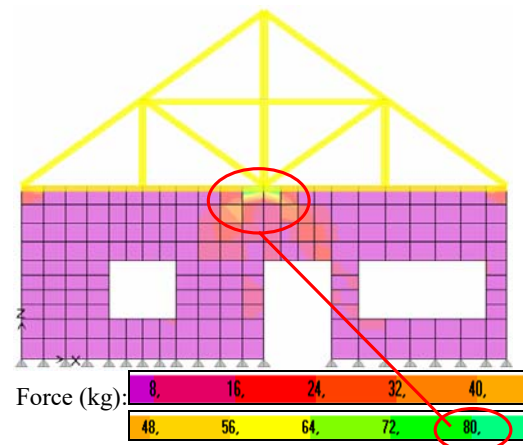


Fig.8 Numerical result for shear forces

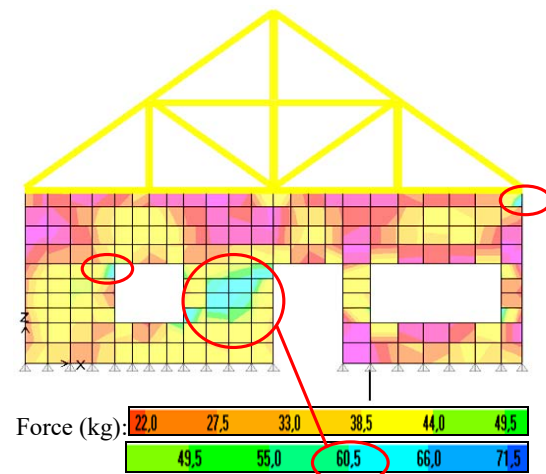


Fig.9 Numerical result in longitudinal shear forces
The simulation results in terms shear forces

due to of transversal and longitudinal seismic loads are shown in Fig.8 and Fig.9. In this paper only the internal shear forces on the front side of house are presented since they have the less strength based on the laboratory tests.

The numerical results are then compared with the results of laboratory testing which are used as strength criteria analyses. The maximum forces acting on the house exceed the strength for ordinary brick wall and this indicates a house damage in reality. The internal shear forces due to seismic loads are about 60 kg and 80 kg which are more than 42 kg for the brick wall. Those internal forces are still under the maximum ferrocement-brick wall strength that is 200 kg.

Thus, the ferrocement-brick sandwich material is very useful to build the strength of the ordinary house due to earthquake. The seismic resistant of houses may increase by applying mortar plaster to the wall, but this way make the wall in brittle condition which may collapse suddenly during the earthquake.

CONCLUSION

Analyses of main structural component of non-engineered buildings have been studied in this paper. The series of tests on that sandwich material has been done. The tests showed that the ferrocement-brick sandwich material increase the strength up to three times compared to the brick wall. The results are used to determine the strength criteria of the analyzed house. Based on comparison study using numerical results and laboratory tests, the ferrocement-brick sandwich material is very useful to build earthquake strength of ordinary brick houses in seismic prone areas such as the West Sumatra.

ACKNOWLEDGEMENTS

Thanks to our students: Mangara, Rido and Siska who have generously involved in this study.

REFERENCES

- [1] Hakam A., Fauzan, Ismail F.A. and Istijono B., "Capacity Building of Local Home Builders on Application of Earthquake Safe House for Disaster Risk Reduction", 4th Annual meeting of Indonesian Disaster Expert Association, will be published in the Proceeding, May 2017, Jakarta
- [2] Boen T., et al., "How to Fix Simple Buildings Damaged by Earthquakes" (in Indonesia: Cara Memperbaiki Bangunan Sederhana yang Rusak Akibat Gempa Bumi), Jakarta: Boen Conslt., 2010
- [3] DirJen Cipta Karya, Indonesian Code No: 111/Kpts/Ck/1993: "Guidelines for Building Earthquake Resistant Construction" (in Indonesia: Pedoman Pembangunan Bangunan Tahan Gempa), Jakarta 28 September 1993
- [4] Imai H., Okubo N., Jamal A.U., Purwoko A., Zahrudin, Hamimie A., Setiyaningsih H., Satyarno I., Manual For Retrofitting Of Brick Masonry Houses For Earthquake Safety: 1st Edition, Jogja, Publisher: Kaliwangi Offset, August 2009
- [5] Paramasivam P., "Ferrocement structural applications, 26th Conference On Our World In Concrete & Structures: 27 - 28 August 2001, Singapore, pp. 99-107
- [6] Sakthivel P.B. and Jagannathan A., "Fibrous Ferrocement Composite with PVC-coated Weld Mesh and Bar-chip Polyolefin Fibers", Int. J. of GEOMATE, Dec., 2012, Vol. 3, No. 2 (Sl. No. 6), pp. 381-388

EXPERIMENTAL STUDY ON MASONRY BUILDING STRENGTHENED WITH FERROCEMENT LAYERS

Fauzan¹, Febrin Anas Ismail², Abdul Hakam³, Sindy Harvi Amalia⁴ and Siska Apriweln⁵

^{1,2,3} Lecture in Engineering Faculty, Andalas University, Indonesia; ^{3,4} Graduate students in Engineering Faculty, Andalas University, Indonesia

ABSTRACT

This present study investigates the behavior of masonry building using ferrocement layers in a non-engineered building. Almost in all regions of Indonesia is an area of frequent earthquakes. In Indonesia, most of masonry building are built with a limitation of finance, skills, building materials, and resulting in poor workmanship and poor quality of construction. When an earthquake happens, the building had collapsed the walls of a sudden, this is caused by the lack of stiffeners of the wall so that the wall is more fragile and vulnerable to tremors for this purpose. Authors conducted a series of experimental study on masonry building strengthened with ferrocement layers in non-engineered building. The specimens were tested above the shaking table (304 x 190) cm² that has simulated earthquake load with variation of ground motions. The specimens was built by masonry wall without main structure elements (column, beam, and sloof). They consist of two models with respective size (90x90x110) cm. The first model does not use ferrocement layers, while the second model given full of ferrocement layers. Experimental results revealed that ferrocement layers can significantly improve masonry walls performance.

Keywords: Earthquake, Masonry, Strengthening, Ferrocement Layers

INTRODUCTION



Fig.1 The collapsed building of unreinforced masonry building [2]

Earthquakes that often occur in the area of West Sumatra, many cause damage to buildings, especially non-engineering building, ranging from minor damage to severe damage of unfit for habitation. In general, non-engineering building are built with unreinforced masonry building as shown in figure 1

This Building is not in accordance with the standards, because if it is built without reinforcement, the wall of engineering building should be arranged with composition of 1 brick. But in reality, there are many people who rebuild the masonry building constructed in 1/2 brick like figure 2, such buildings are very vulnerable and not strong against earthquake loads.



Fig. 2 Unreinforced masonry building

Non-structural components such as walls, roofs and ceilings of a unreinforced masonry building are not part of the main load that works on a structure, but can be a major cause of losses due to the earthquake that occurred.

Most damage buildings are spontaneously constructed buildings (non-engineered building). Where buildings are built on practical experiences whose structural strengths are not calculated. The building is usually built by the general public, in the form of residential houses, school buildings and traditional home buildings. Cracks in brick wall connections occurred during the earthquake in West Sumatra due to the falling brick wall having no stiffener [4].

The causes of this kind of unexpected structural collapse can be explained from several aspects, the uncertainties inherent in the ground shaking [5], feature ground motions with larger damage potentials

[6-9], and deficiencies in our knowledge regarding the collapse resistant design.

The choice for home improvement, certainly influenced by the economic aspect. There are several option to repair a damaged house, some are destroyed and then rebuilt and some are repaired or given strengthened, such as wire mesh.

In this study, authors are interested to perform experimental by modelling a unreinforced masonry building then strengthened with ferrocement layers that are tested on shaking table. So it can be seen how the behavior of unreinforced masonry building which given variation of earthquake loads.

STRUCTURE MODEL

There are two models structure that were built on the shaking table in soil mechanical laboratory, UNAND. Both models have a 1:4 scale of the actual. This is due to the limitation of the table area. The first model (M1) is the original of unreinforced masonry building and plastered, the second (M2) is the same masonry structure strengthened by providing full using ferrocement layers on both of the walls, acting as sandwich structures. In the second model, all strengthened parts are also plastered (figure 3).

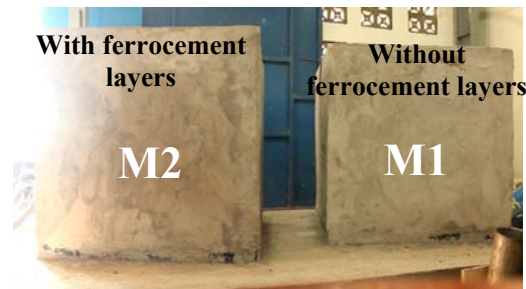


Fig. 3 Two models for shaking table test : Model M1 : unreinforced masonry structure; Model M2: masonry structure strengthened by providing full using ferrocement layers on both sides of the walls, act as sandwich structures.

Each model consisted of four walls with size 0.9m x 1.1m. Figure 4 shows the schematic drawing of masonry walls for model M2. The masonry walls were made brick (200x100x50)mm, bonded with mortar joints (1pc:4ps). The brick were imported from Padang, Indonesia. Figure 5 showed the construction process for installing wire mesh and plastering. Figure 6 showed the detail of wall strengthened with ferrocement layers.

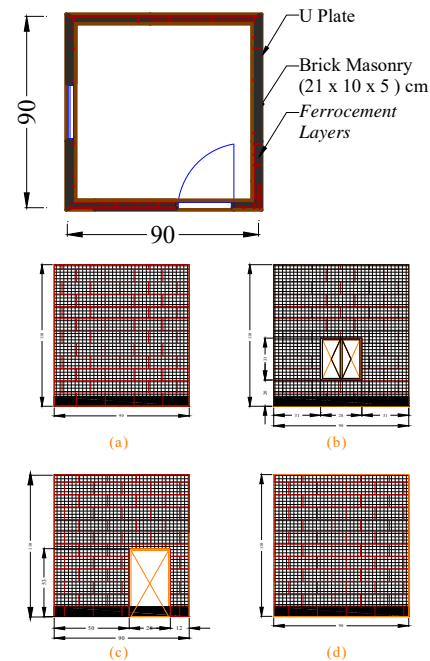


Fig. 4 Schematic drawings of shaking table test for model M2





Fig. 5 Construction process for installing wire mesh and plastering

The specimens are made on the table in a 16° inclined position, this is in accordance with the earthquake loading rule of SNI 1729 - 2012 7.5.3 points, the loading applied separately in all two orthogonal directions. The most critical load effect due to the direction of application of earthquake forces to the structure is considered to be satisfied if its components and foundations are designed to carry the following set load combinations: 100 percent force for one direction plus 30 percent force for perpendicular directions. Based on SNI 2012 earthquake, the slope of the prototype of 16° in the direction of the positive x axis [1].

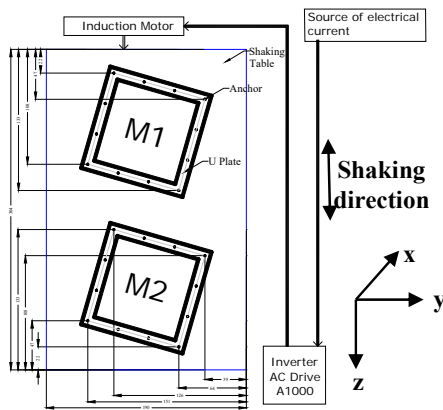


Fig. 6 The specimens are tilted at 16°

INPUT MOTIONS

Tests conducted by varying the frequency of earthquake of small earthquake (SME), medium earthquake (ME) and Strong Earthquake (SE) as shown in table 1.

Table 1 Variation of the motions

Type of earthquake	a (m/s ²)
SME (0.3g)	2.94
ME (0.6g)	5.88
SE (1g)	9.81

EXPERIMENTAL RESULT

The experimental results presented in this section include the acceleration responses of the test specimens and the observed cracks and failure pattern. Testing has been done 3 times with different model variations. Each test is given a weak earthquake load and a medium earthquake, for the third test, tested to a strong earthquake.

Acceleration Responses

A g-trace device mounted beneath the shaking table test that produces a graph showing the amount of vibration that occur in models. The test obtained graphs as in figure 10.

Figure 10 shows the acceleration time histories of the 1st to 3rd test. It seemed that the maximum acceleration responses of the 1st test were generally greater than 2nd or 3rd test. This occurs because the 1st test is not given additional load, so the load on the specimen is lighter than the 2nd and 3rd tests. The specimens on this 1st test received a larger earthquake load, which resulted in the magnitude of the acceleration occurring.

In the 1st test as in figure 7, there is no collapse or cracking of the specimen when subjected to a small earthquake load or a medium earthquake load.



Fig. 7 The specimens of the first test

Because of the limitations of the device capacity, the acceleration of the earthquake load can not be added until it reaches the collapse. Therefore, the 2nd test is given an axial load on the specimen (as in figure 8) so that the earthquake load is greater than the wall capacity and there maybe collapse in the specimen. The load addition is calculated based on the shear stress analysis obtained from SAP2000.

With a small earthquake acceleration and a medium earthquake acceleration given in the second test, the specimen (M1) only had a fine crack in the plaster but was not significant, whereas the M2 specimen did not experience any cracks. This shows that plastering in each specimen contributes the strength of the wall, so that the brick wall is not destroyed.



Fig. 8 The specimens of the second test

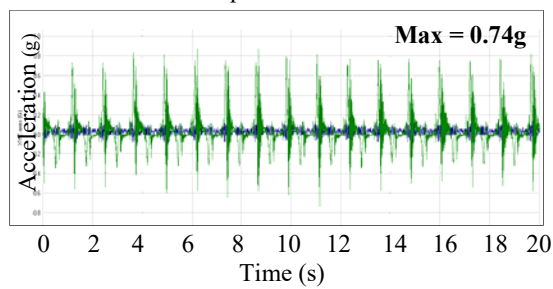
Based on the data of the masonry building in the field, the masonry building is also often made without plastering or with plastering that mixture does not comply with the applicable rules. The researcher then attempts a 3rd test by peeling the plaster on the specimen without ferrocement layers (M1), as shown in figure 9.



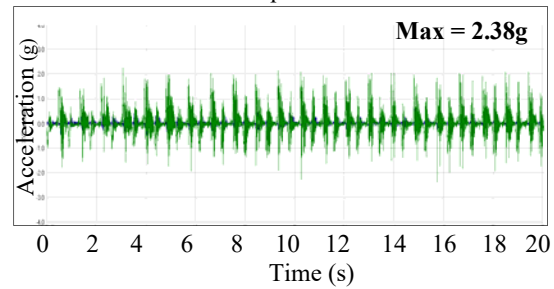
Fig. 9 The specimen of the third test

On a small earthquake acceleration, the specimen did not collapse or cracked, then the acceleration of the earthquake was upgraded to a medium earthquake which resulted in fine cracks on the plaster but not significant. Then the earthquake acceleration is increased until the earthquake load is strong. When a strong earthquake acceleration occurs, the wall of the specimen (M1) is cracked.

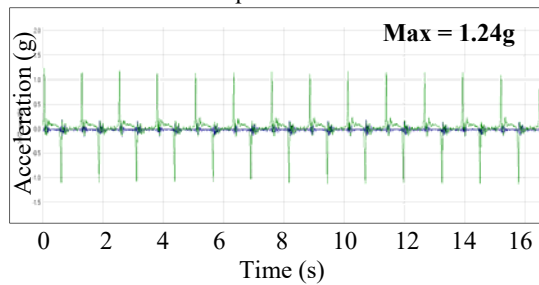
1st Test of small earthquake load



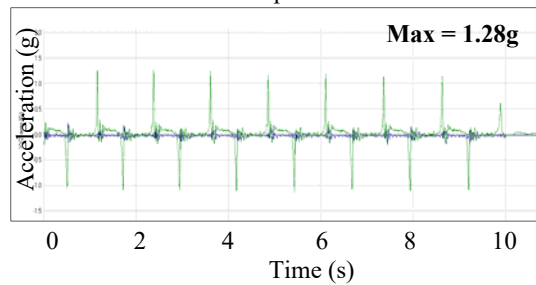
1st Test of medium earthquake load



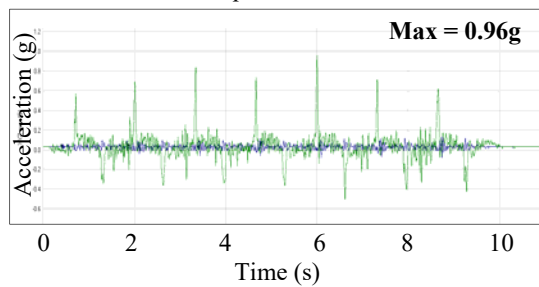
2nd Test of small earthquake load



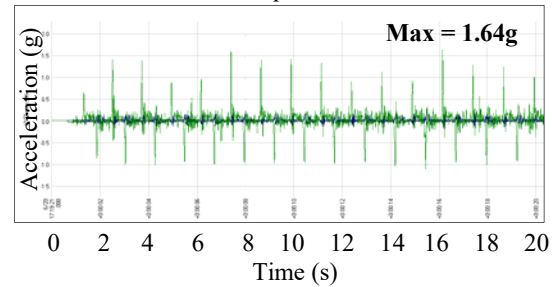
2nd Test of medium earthquake load



3rd Test of small earthquake load



3rd Test of medium earthquake load



3rd Test of strong earthquake load

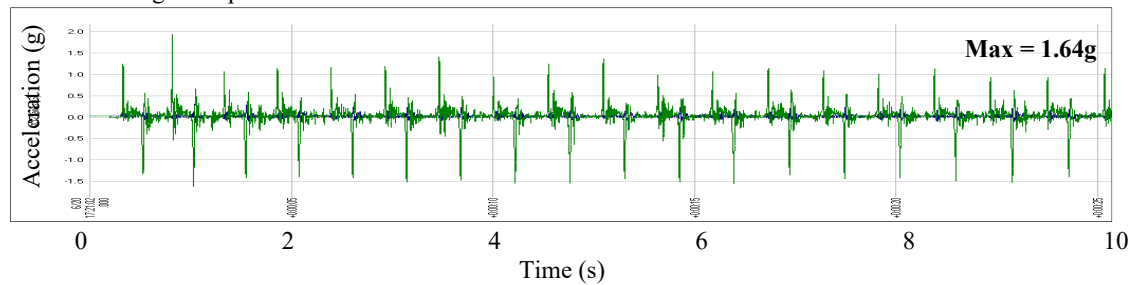


Fig. 10 Acceleration time histories

Observed Cracks and Failure Pattern

Collapse in the specimen occurs in the 3rd test with a strong earthquake load. Specimen collapsed is specimen without ferrocement layers. When the test is carried out, there is a lifting force on the side of the specimen wall (M1) without opening until cracking also occurs in each corner of the specimen as in figure 11, while on the wall having openings, there is also a larger crack may lead to collapse in the building as in figure 12. This means that the opening wall is more vulnerable to collapse in the event of a large earthquake, therefore the design of the house should pay attention to the opening of a wall area and place it not too close to the corners of the building and should be given space from the corner of the building to place the openings such as doors and windows.

While the specimen strengthened with ferrocement layers (M2) did not experience a slight crack during testing from the first test to the last test.



Fig. 11 The crack of the wall without opening.



Fig. 20 The crack in the opening wall

CONCLUSION

Based on data obtained from testing two Based on data obtained from testing two models of masonry building, M1 and M2 given cyclic load it can be concluded that:

1. The specimens does not occur collapse, because the load given does not exceed the capacity of the specimen.
2. After providing an additional axial load. The specimen (M1) had a fine crack in the plaster but it is not significant. It can be concluded that the plaster can reinforce the brick wall if the plaster is made with a good mix and workmanship in accordance with the standards.
3. After providing an additional axial load increase and stripping of wall plastering. There is a crack on the wall of the specimen (M1) with different rift patterns on each side

- of the wall.
4. Throughout the condition, there is no crack at the specimen with ferrocement layers (M2). The shaking table tests demonstrated that the strengthening using ferrocement layers is effective in preventing collapse of masonry walls when shakes by earthquake. This strengthening method has such benefits as more simple and understandable workmanship by the local community, low cost and time saving.

REFERENCES

- [1] Badan Standardisasi Nasional. 2012. "Tata Cara Perencanaan ketahanan gempa untuk struktur bangunan gedung dan non gedung (SK SNI 1726-2012)". Jakarta.
- [2] Boen, T. 2001. "Earthquake resistant design of non-engineered buildings in Indonesia. Kamakura.
- [3] Li Shuang, Zuo Zhanxuan, Zhai Changhai, Xu Shiyu, Xie Lili. 2016. "Shaking table test on the collapse process of a three-story reinforced concrete frame structure
- [4] Sihite, Ivan Darma. 2011. "Kawat anyam sebagai perkuatan pada rumah sederhana tanpa beton bertulang. Padang: Universitas Andalas.
- [5] Takewaki I. "A comprehensive review of seismic critical excitation methods for robust design". *Adv Struct Eng* 2005;8(4):349-62.
- [6] Ni SH, Li S, Chang ZW, Xie LL. "An alternative construction of normalized seismic design spectra for near-fault regions". *Earthquake Eng Eng Vib* 2013;12(2):351-62
- [7] Wen WP, Zhai CH, Li S, Chang ZW, Xie LL. "Constant damage inelastic displacement ratios for the near-fault pulse-like ground motions". *Eng Struct* 2014;59:599–607.
- [8] Raghunandan M, Liel AB. "Effect of ground motion duration on earthquakeinduced structural collapse". *Struct Saf* 2013;41:119–33.
- [9] Ruiz-García J, Marína MV, Terán-Gilmoreb A. "Effect of seismic sequences in reinforced concrete frame buildings located in soft-soil sites". *Soil Dynam Earthquake Eng* 2014;63:56–68

BIODEGRADABLE POLY(L-LACTIC ACID) MICROCAPSULE CONTAINING HEAT STORAGE MATERIAL: INFLUENCE OF POLYMER MOLECULAR WEIGHT ON ENCAPSULATION EFFICIENCY

Primprapa Sangjun¹ and Amorn Chaiyasat^{1,2*}

¹Department of Chemistry, Faculty of Science and Technology, Rajamangala University of Technology Thanyaburi, Pathumthani, Thailand 12110

²Advanced Materials Design and Development (AMDD) Research Unit, Institute of Research and Development, Rajamangala University of Technology Thanyaburi, Pathumthani, Thailand 12110

ABSTRACT

Microcapsule containing heat storage or phase change materials is useful in various applications. It provides a larger heat transfer area and controls the volume change of phase change materials during phase transition. Most polymer shells used in microcapsule are petrochemical-based polymers which is a growing concern about their impact on the environment. Therefore, in this work, biodegradable polymer as a poly(l)-lactic acid (PLLA) was implemented as the polymer shell to encapsulated octadecane (OD), a kind of phase change materials, by a simple emulsion evaporation method. Influence of PLLA molecular weight on the encapsulation efficiency and colloidal stability of microcapsule was studied. The spherical microcapsules with a size range ca. 5-50 μm were obtained in all molecular weights of PLLA. However, at higher molecular weights (54,000, 77,000 and 145,000 g/mol), some OD escaped from the droplets during solvent evaporation due to higher internal viscosity therein where polymer chains hardly diffused to precipitate on the droplet interface. In contrast, using the lowest molecular weight (24,000 g/mol), approximately 86 wt% microcapsule yields with about 100 %encapsulation and high colloidal stability were obtained which were much higher than those (44, 36 and 11% for 54,000, 77,000 and 146,000 g/mol, respectively) of higher molecular weights. In addition, latent heats of the encapsulated OD (200 J/g-OD) were closed to those (230 J/g-OD) of bulk OD. Based on high encapsulation efficiency, this biodegradable microcapsule would enhance environmental sustainability for thermal energy storage applications.

Keywords: *Poly(l-lactic acid); Heat storage materials; Microcapsule; Simple emulsion evaporation method*

INTRODUCTION

Phase change materials are used in many industrial applications such as solar heat storage, air conditioning of building and thermal adaptable fibers[1]. Paraffin wax is one of the most attractive phase change materials. It melts and crystallizes which can absorb and release energy, respectively, at a wide range of temperature. Because of their moderate thermal energy storage and low thermal conductivity, paraffin is then encapsulated within the polymer shell to increase surface area for providing a larger heat transfer before the practical application. Numerous polymer shells are used to fabricate paraffin microcapsules such as polystyrene[2, 3], poly(styrene-co-methyl methacrylate) [4], polydivinylbenzene[5, 6], poly(styrene-co-divinylbenzene) [7], poly(methyl methacrylate) [8] and poly(methyl methacrylate-co-methyl acrylate-co-methacrylic acid) [9]. However, most of them are

petrochemical-based polymers which are a growing concern about their impact on the environment [10, 11]. Biodegradable polymer as PLLA is then the good candidate to be used as the polymer shell of paraffin microcapsules. Because of its non-toxicity and environmental friendly, it is applied for a various applications such as biomedical, pharmaceutical, food packaging and agricultural industries [12, 13]. To the best of our knowledge, there are a few researches using PLLA as phase change materials microcapsule shell. From our previous work [14], we have successfully prepared microcapsule containing urea using PLLA as a polymer shell by a simple emulsion evaporation method. Because urea can soluble in water, water₁ (containing urea) in oil (containing polymer) in water₂ system was prepared in order to increase the encapsulation efficiency. In addition, PLLA was successfully used to encapsulate more hydrophobic material as vitamin E [15] using oil in water

emulsion system with a simple emulsion evaporation method. Therefore, it would be possible to prepare paraffin microcapsule using PLLA as a polymer shell where paraffin and PLLA are dissolved in good solvent as an oil phase before being dispersed in the continuous (water) phase having surfactant. Paraffin microcapsule would be obtained based on an internal phase separation mechanism. Because PLLA is more hydrophilic than that of paraffin, it should diffuse from the polymer solution droplet to the droplet interface during the solvent evaporation to form polymer shell.

In this research, the preparation of paraffin microcapsule with PLLA and octadecane (OD) as a polymer shell and phase change material core, respectively, by oil in water emulsion with a simple emulsion evaporation method will be studied. In addition, influences of PLLA molecular weight and PLLA and OD ratio on the encapsulation efficiency and colloidal stability of microcapsule will be investigated.

EXPERIMENTAL

Materials

PLLA molecular weights of 77,000 and 145,000 g/mol were used as received from B. C. Polymers Marketing Co., Ltd. OD (Sigma-aldrich, USA; purity, 99%), poly(vinyl alcohol) (Aldrich, Wisconsin, USA; degree of saponification, 87-90%) and chloroform (RCI Labscan, Bangkok, Thailand; purity, 99.8%) were used as received. Ethylene glycol (Loba chemie, India; purity, 99.5%) was also used as received.

Preparation of low molecular weight PLLA

Glycolysis of commercial PLLA with molecular weight of 145,000 g/mol employing EG was carried out to break PLLA chains[16]. PLLA and ethylene glycol at 1:1 weight ratio were previously mixed and dissolved in chloroform (finally, 20 wt% of PLLA) before transfer to a round bottom flask and sealed with silicone rubber septum. The solution was purged with five vacuum/ N_2 cycles finally in a N_2 atmosphere. The reaction was started at 175 °C with a stirring rate of 200 rpm and kept at 30 and 60 min. After the completion of reaction, PLLA short chains were purified by precipitation in methanol before dried overnight in a vacuum oven.

Microcapsule preparation

PLLA microcapsules encapsulated OD using various molecular weight s (24,000, 54,000, 77,000 and 145,000 g/mol) were prepared in oil in water

system. Firstly, 2.50 g of PLLA was dissolved in 20 g of chloroform containing 2.50 g of OD as an oil phase. It was added to 45 ml poly(vinyl alcohol) aqueous solution (1% wt) and then homogenized at 5,000 rpm for 5 min to prepare polymer droplets in oil in water emulsion as shown in Fig 1. Thereafter, the obtained polymer droplets emulsion was stirred overnight to evaporate chloroform resulting in the formation of polymer microcapsules.

Table 1 Reagent amounts for the preparation of PLLA/OD microcapsules by a simple emulsion evaporation method

Phase	Ingredients			
Oil	PLLA (g)	2.00 ^a	2.50 ^b	3.00 ^a
	OD (g)	3.00	2.50	2.00
	CHCl ₃ (g)	20.00	20.00	20.00
Aqueous	PVA solution (1 wt%) (g)	45.00	45.00	45.00

^a Molecular weight (g/mol): 24,000

^b Molecular weight (g/mol): 24,000 54,000 77,000 and 145,000

Characterization of PLLA microcapsules

The microcapsules encapsulated OD were observed with an optical microscope (SK-100EB&SK-100ET, Seek, Seek Inter Co. Ltd., Thailand) and scanning electron microscope (JSM-6510, JEOL, JEOL Ltd., Japan) to study the morphology of the particle surface and shape. For scanning electron microscope observation, a few of dried microcapsules were placed on a nickel scanning electron microscope stub and dried before Au-coated. Weight- and number-average molecular weights (M_w and M_n , respectively) and M_w/M_n of PLLA were measured by gel permeation chromatography (Waters 2414, Waters, USA) with two poly(S/divinylbenzene) gel columns (Phenogel 5 x 10³ and 5 x 10⁵ Å (pores), 7.8 mm (i.d) x 30 cm (length), Phenomenex, USA) connected in series and using tetrahydrofuran as eluent. The flow rate of eluent was maintained at 1.0 mL/min with column temperature of 40 °C and elution was monitored with refractive index detector (RI 2414/Waters). The columns were calibrated with six standard PS samples (2.5 x 10³- 6.0 x 10⁵, M_w/M_n = 1.05-1.15). For the measurement of thermal properties, the microcapsules were washed with 2-propanol before dried in vacuum oven. The OD content in the dried washed microcapsules was direction determined by thermogravimetric analyzer (TGA, TGA 4000,

Perkin-Elmer, USA) at a heating rate of 5 °C/min. The latent heats (ΔH_m and ΔH_c) (J/g-capsule) and the melting (T_m) and crystallization (T_c) temperatures of the encapsulated OD were measured with a differential scanning calorimeter (DSC, DSC 4000,

Perkin-Elmer, USA) under a N₂ flow in a scanning temperature range of -20-40 °C and at a heating/ cooling rate of 5 °C/ min and shown as average values of three measurements.

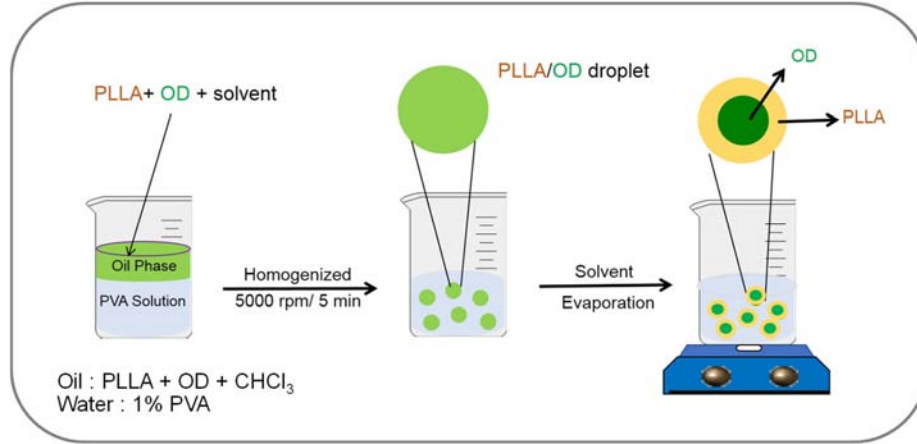


Fig. 1 Schematic diagram for the preparation of PLLA microcapsules containing OD prepared by a simple emulsion evaporation method

ΔH_m^* and ΔH_c^* (J/g-OD) were, respectively, obtained using the following equation (1) from the ΔH_m and ΔH_c (J/g-capsule) and the OD content in each washed microcapsule (% loading) obtained from the thermogravimetric analysis, which did not contain unencapsulated OD.

$$A = [B / C] \times 100 \quad \dots\dots(1)$$

Where

A = ΔH_m^* and ΔH_c^* of the encapsulated OD in unit of joules per 1 g of encapsulated OD (J/g-OD)

B = ΔH_m and ΔH_c of the encapsulated OD in unit of joules per 1 g of microcapsule (J/ g-capsule) measured with differential scanning calorimeter

C = % loading (experiment) of OD in the washed microcapsules measured with thermogravimetric analysis

The theoretical % loading of OD in the washed microcapsules was calculated by equation (2)

$$\% \text{ Loading (theory)} = [W_{\text{wax}} / (W_{\text{wax}} + W_{\text{PLLA}})] \times 100 \quad \dots\dots(2)$$

Where W_{wax} and W_{PLLA} are weights of OD and PLLA, respectively, in the preparation recipes shown in Table 1.

Encapsulation efficiency (%) of OD was calculated using the equation (3).

$$\text{Encapsulation efficiency (\%)} = [\% \text{ loading (experiment)} / \% \text{ loading (theory)}] \times 100 \quad \dots\dots(3)$$

RESULTS AND DISCUSSION

One of the main driving forces for microcapsule

preparation based on internal phase separation mechanism is viscosity inside polymer solution droplet. To the best of our knowledge, when the polymer chains smoothly diffuse to the droplet-water interface, the microcapsule with high encapsulation would be obtained. The amount of polymer chain reached to the droplet-water interface decrease with internal viscosity. In this work, various molecular weights of PLLA were used to encapsulate OD in which using higher molecular weights was expected to obtain high capsule shell strength. However, this parameter was optimized based on both encapsulation efficiency and shell strength. The low molecular weights PLLA were obtained by glycolysis of high molecular weight PLLA (145,000 g/mol) with various times at 30 and 60 min. It was found that the molecular weight of PLLA significantly decreased to 54,000 and 24,000 g/mol for the reaction times of 30 and 60 min, respectively, as shown in Fig. 1. It is due to the depolymerization of PLLA by ethylene glycol to form shorter chain of hydroxyl (OH)-terminated PLLA where PLLA molecular weight decreased with the reaction time [16, 17].

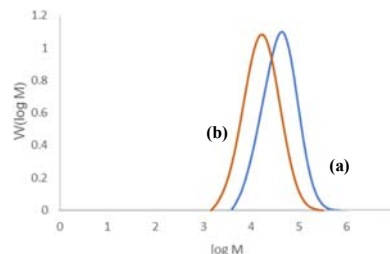


Fig. 2 Molecular weight distribution of PLLA (Mw 145,000) after glycolysis at various times (min): (a) 30 and (b) 60

The PLLA/OD solution droplets dispersed in poly(vinyl alcohol) aqueous solution (1 wt%) were obtained with the homogenization. As seen in Fig. 3, the PLLA chains with higher molecular weights seemed incomplete miscible in CHCl_3 containing OD especially for 77,000 (Fig. 3c) and 145,000 g/mol (Fig. 3d) where the PLLA/OD solution droplets contained dark domains. After CHCl_3 removal, PLLA chains homogeneously distributed throughout the microcapsule due to high internal viscosity. This then resulted in low microcapsule yield where numerous microparticle without OD were obtained. In contrast, for lower molecular weights of PLLA, both PLLA/OD solution droplets, (Fig. 3a and b) and microcapsule (Fig. 3a' and b') were clearly transparent. Based on the theoretical total density of microcapsule (~ 1 ; densities of OD and PLLA are 0.78 and 1.22 g/mol, respectively) at the ratio of PLLA:OD of 1:1, the microcapsule should be floated on the top layer of the suspension. The suspension photos of PLLA/OD microcapsules with various PLLA molecular weights were shown

in Fig. 4. For the three higher molecular weights (Fig. 4b-d), three parts i.e. top, middle and bottom layers of the suspensions were clearly observed where small amounts of microcapsules floating on the top layer were obtained. The PLLA dispersed and precipitated in the medium and the bottom would be the broken particle and the PLLA particle without OD, respectively. In contrast, most of PLLA/OD microcapsules floated on the top layer for the lowest molecular weight (24,000 g/mol) of PLLA (Fig. 4a). The amounts of PLLA/OD microcapsules at the top layer separating from each suspension were measured by gravimetry. It was found that the amounts of PLLA/OD microcapsules prepared by various PLLA molecular weights were 11, 36, 44 and 86 wt% (based on the original of PLLA and OD) for 145,000, 77,000, 54,000 and 24,000 g/mol, respectively. This indicates that the obtained microcapsules increased with the decrease of PLLA molecular weight. From these results, PLLA molecular weight of 24,000 g/mol was selected to be used as the polymer shell for further study. The PLLA:OD ratio will be investigated in order to obtain large amount of PLLA/OD microcapsules.

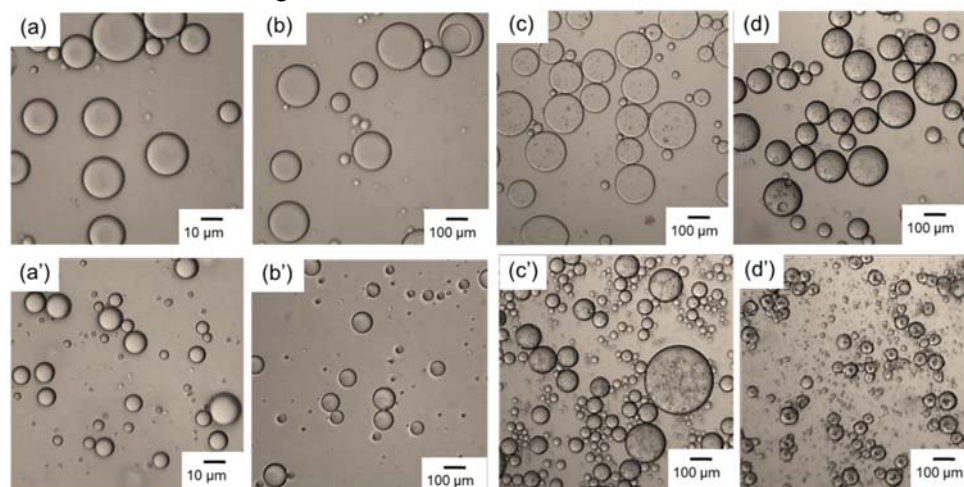


Fig. 3 Optical micrographs of PLLA/OD droplets (a-d) and microcapsules (a'-d') prepared by a simple emulsion evaporation method using different PLLA molecular weights (g/mol): (a and a') 24,000; (b and b') 54,000; (c and c') 77,000 and (d and d') 145,000

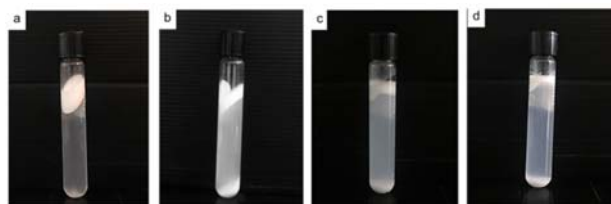


Fig. 4 Suspension photos of PLLA/OD microcapsules after centrifugation at 3,000 rpm using different PLLA molecular weights (g/mol):

(a) 24,000; (b) 54,000; (c) 77,000 and (d) 145,000

PLLA:OD ratio was varied at 40:60, 50:50 and 60:40 wt% using PLLA molecular weight of 24,000 g/mol. The suspensions of three conditions were shown in Fig. 5a-c. The densities of PLLA/OD microcapsule increased with PLLA content in which most (82 % related to original of PLLA and OD) of PLLA/OD microcapsules precipitated onto the bottom layer in the case of 60:40 wt%. However, this phenomenon was also observed for 40:60 wt%

of PLLA:OD (30 % related to original of PLLA and OD). The precipitated polymer is due to the polymer part of the broken microcapsule in which low content of PLLA was not enough to encapsulate OD. The microcapsule size and morphology of all PLLA:OD ratios were then observed by optical microscope as shown in Fig. 5a'-c'. It was found that uneven surface microcapsules (Fig. 5a') were observed with some broken particles in the case of 40:60 wt% of PLLA:OD according to the suspension photo. On the other hands, the spherical microcapsules were formed in the cases of 50:50 (Fig. 5b') and 60:40 wt% (Fig. 5c') without broken particle. This seems that the PLLA shell can completely envelope the OD core.

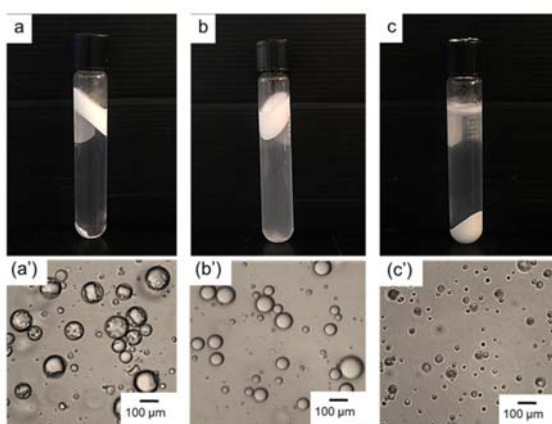


Fig. 5 Suspension photos (a-c) and optical photographs (a'-c') of PLLA/OD microcapsules using PLLA molecular weight of 24,000 g/mol after centrifugation at 3,000 rpm with different PLLA:OD ratios (wt%): (a and a') 40:60; (b and b') 50:50 and (c and c') 60:40

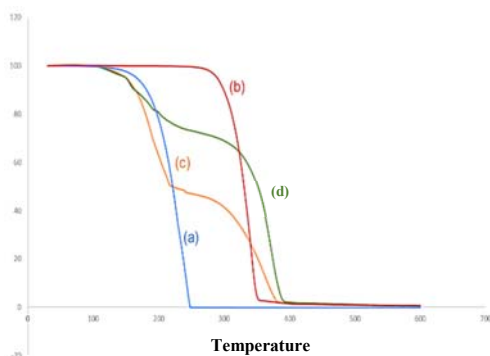


Fig. 6 Thermogravimetric analysis thermograms of (a) bulk OD, (b) PLLA and dried PLLA/OD microcapsules at PLLA:OD ratio (wt%) of (c) 50:50 and (d) 60:40

The degradation temperatures of bulk OD, PLLA and OD encapsulated in the PLLA

microcapsules using PLLA:OD ratio of 50:50 and 60:40 were observed by thermogravimetric analysis and the thermograms are shown in Fig. 6. In the case of dried PLLA/OD microcapsules (Fig. 6c and d), the decomposition temperatures of OD (130-260°C) and PLLA (280-420°C) were shown in two respective steps. The degradation temperature of bulk OD (Fig. 6a) of 140-300°C was closed to that of the encapsulated OD. The thermogravimetric analysis thermograms confirmed that OD existed in the prepared microcapsules. In addition, in the case of 50:50, the experimental percent loading was 50% which was closed to the theoretical ones (50%) giving 100% encapsulation where the experimental percent loading was 27% giving only 65% encapsulation in the case of 60:40 ratio. This indicates that PLLA represented high efficiency to encapsulate OD.

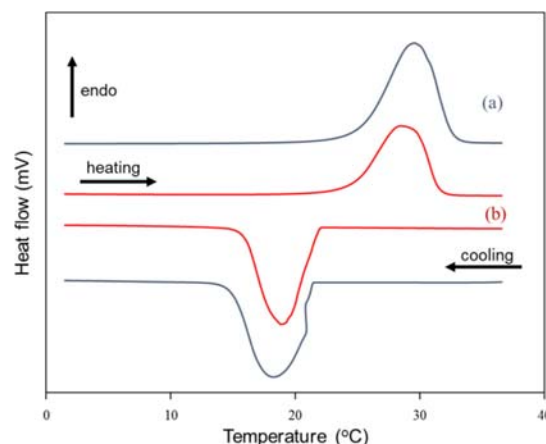


Fig. 7 Differential scanning calorimeter thermograms of (a) bulk OD and (b) the encapsulated OD in dried microcapsules at PLLA:OD ratio of 50:50 %w/w

The latent heats (J/g -OD and J/g -sample for bulk and encapsulated OD, respectively) of bulk OD (Fig. 7a) and the encapsulated OD (Fig. 7b) were obtained from the heating/cooling peak areas of differential scanning calorimeter thermograms. The latent heats ($\Delta H_m^* = 197$ and $\Delta H_c^* = 196$ J/g -OD) of the encapsulated OD were quite closed to those of bulk OD ($\Delta H_m^* = 233$ and $\Delta H_c^* = 234$ J/g -OD). It may be due to the hydrophilicity of PLLA increased the phase separation between polymer shell and OD core where the encapsulated OD behaved similar with bulk OD.

CONCLUSION

The spherical biodegradable poly(l)-lactic acid microcapsule containing octadecane with good colloidal stability was successfully prepared by a simple solvent evaporation method. The molecular weight of poly(l)-lactic acid affected on the formation of the microcapsule shell. The lower

molecular weight poly(l)-lactic acid formed the smoother shell than the higher ones based on lower internal viscosity. The latent heats of the encapsulated octadecane were closed to those of bulk octadecane. Therefore, the prepared polylactic acid/octadecane microcapsules were able to use in heat storage applications in place of petrochemical-based microcapsule.

ACKNOWLEDGEMENTS

This work was supported by the project of Research and Researchers for Industries (RRI), Thailand Research Fund (TRF) and STP Chem Solutions Co., Ltd. (MSD60I0017)

REFERENCES

- [1] Farid M M, Khudhair A M, Razack S A K, and Al-Hallaj S, "A review on phase change energy storage: materials and applications," *Energ Convers. Manage.*, vol. 45, 2004, pp. 1597-1615.
- [2] Sánchez-Silva L, Rodríguez J F, Romero A, and Sánchez P, "Preparation of coated thermo-regulating textiles using Rubitherm-RT31 microcapsules," *J Appl Polym Sci*, vol. 124, 2012, pp. 4809-4818.
- [3] Sánchez P, Sánchez-Fernandez M V, Romero A, Rodríguez J F, and Sánchez-Silva L, "Development of thermo-regulating textiles using paraffin wax microcapsules," *Thermochim. Acta* vol. 498, 2010, pp. 16-21.
- [4] Sánchez-Silva L, Rodríguez J F, Romero A, Borreguero A M, Carmona M, and Sánchez P, "Microencapsulation of PCMs with a styrene-methyl methacrylate copolymer shell by suspension-like polymerisation," *Chem Eng J* vol. 157, 2010, pp. 216-222.
- [5] Supatimusro D, Promdsorn S, Thipsit S, Boontung W, Chaivasat P, and Chaivasat A, "Poly(divinylbenzene) Microencapsulated Octadecane for Use as a Heat Storage Material: Influences of Microcapsule Size and Monomer/Octadecane Ratio," *Polymer - Plastics Technology and Engineering*, vol. 51, 2012, pp. 1167-1172.
- [6] Chaivasat A, Waree C, Songkhamrod K, Sirithip P, Voranuch V, and Chaivasat P, "Preparation of polydivinylbenzene/natural rubber capsule encapsulating octadecane: Influence of natural rubber molecular weight and content," *Express Polymer Letters*, vol. 6, 2012, pp. 70-77.
- [7] You M, Wang X, Zhang X, Zhang L, and Wang J, "Microencapsulated n-Octadecane with styrene-divinylbenzene co-polymer shells," *J Polym Res*, vol. 18, 2011, pp. 49-58.
- [8] Chaivasat P, Noppalit S, Okubo M, and Chaivasat A, "Innovative synthesis of high performance poly(methyl methacrylate) microcapsules with encapsulated heat storage material by micro-suspension iodine transfer polymerization (ms ITP)," *Solar Energy Materials and Solar Cells*, vol. 157, 2016, pp. 996-1003.
- [9] Sanchez-Silva L, Tsavalas J, Sundberg D, Sanchez P, and Rodriguez J F, "Synthesis and characterization of paraffin wax microcapsules with acrylic-based polymer shells," *Ind Eng Chem Res*, vol. 49, 2010, pp. 12204-12211.
- [10] Free C M, Jensen O P, Mason S A, Eriksen M, Williamson N J, and Boldgiv B, "High-levels of microplastic pollution in a large, remote, mountain lake," *Marine Pollution Bulletin*, vol. 85, 2014, pp. 156-163.
- [11] Carr S A, Liu J, and Tesoro A G, "Transport and fate of microplastic particles in wastewater treatment plants," *Water Research*, vol. 91, 2016, pp. 174-182.
- [12] Chen L, Qiu X, Xie Z, Hong Z, Sun J, Chen X, *et al.*, "Poly(l-lactide)/starch blends compatibilized with poly(l-lactide)-g-starch copolymer," *Carbohydrate Polymers*, vol. 65, 2006, pp. 75-80.
- [13] Han X, Wang D, Chen X, Lin H, and Qu F, "One-pot synthesis of macro-mesoporous bioactive glasses/polylactic acid for bone tissue engineering," *Materials Science and Engineering: C*, vol. 43, 2014, pp. 367-374.
- [14] Boontung W, Chaivasat A, and Chaivasat P, "Preparation of poly(l-lactic acid) capsule encapsulating fertilizer," *Adv. Mat. Res.*, vol. 506, 2012, pp. 303-306.
- [15] Chaivasat P, Chaivasat A, Teeka P, Noppalit S, and Srinorachun U, "Preparation of Poly(l-lactic acid) Microencapsulated Vitamin e," *Energy Procedia*, vol. 34, 2013, pp. 656-663.
- [16] Tounthai J, Petchsuk A, Opaprakasit P, and Opaprakasit M, "Curable polyester precursors from polylactic acid glycolized products," *Polymer Bulletin*, vol. 70, 2013, pp. 2223-2238.
- [17] Sukpuang P, Opaprakasit M, Petchsuk A, Tangboriboonrat P, Sojikul P, and Opaprakasit P, "Polylactic acid glycolysate as a cross-linker for epoxidized natural rubber," *Journal of Elastomers & Plastics*, vol. 48, 2016, pp. 105-121.

COMPOSITE MATERIALS FOR CIVIL/STRUCTURAL ENGINEERING

K K Ganguly (Gangopadhyay)

Executive Director

Development consultants Private Limited, Kolkata, India

ABSTRACT

The use of composite materials for concrete is covered briefly starting from metallic reinforcement along with stainless steel bars which have been used in concrete elements by the engineers successfully primarily to improve the strength against tensile loads. The above combination has been further improved by using different types of fibres covering natural, steel, glass, carbon etc. along with fibre reinforced polymers (FRP) in structures. Strengthening structural members for carrying additional loads to meet new requirements have also been done with different wrapping FRP composite materials. Polymer composite materials are manufactured by combining polymer resin with fillers and various types of reinforcing fibres. Concrete as a material is durable and energy efficient. Attempts are made for adopting eco-cement for carbon sequestration and to use alternative material to Portland cement to make the applications more environment friendly. Reference is given to the use of nano and geo-polymer concrete, polymer concrete, high strength and coloured concrete etc. Concrete structures can be repaired and strengthened, if required, and concrete material can be recycled and used with other materials. Concrete material has been found to perform well in fire and against blast. Routine monitoring for assessment of weaknesses, defects and delamination of FRP materials from structural elements and relevant studies are referred. A few applications are included. Further advancements will be more suitable for the projects to come, in the future. This approach is expected to provide satisfactory performance of the structures with added elegance, innovativeness and overall long-term economy at the end.

Keywords: Fibres, Polymer Composites, Different developments, Monitoring, Delamination

INTRODUCTION

Composite materials for concrete had been used by engineers for a long time [1], [2]. Use of different types of fibres along with reinforcement had been tried successfully to overcome weaknesses of concrete. Polymer composite are multiphase materials produced by combining polymer resin like polyester, vinyl ester, epoxy (thermoset) and polyethylene, polypropylene (thermo-plastic) with fillers and reinforcing fibres to produce a material having much superior mechanical and chemical properties than the individual base materials combined. The emphasis was on high strength, low self weight and durability.

TYPES OF COMMON FIBRES [3], [4]

Numerous fibres have been tried. Some of the common types are as mentioned below:

- Natural vegetable or mineral fibres (sisal, jute, bamboo & asbestos)
- Alkali or non-alkali resistant glass fibres
- Aramid fibres
- Polypropylene fibres
- Steel fibres
- Carbon fibres
- Other fibre types - Ceramic, Nylon, Polyester.

FIBRE COMPOSITE MATERIALS

Fibre composite materials have been used for various applications for a long time covering concrete and steel structure. Common fibres may be used.

Requirements of Fibres [5] - The desirable fibre requirements are –

- The variation of strength between individual fibres should be less.
- The fibres should be stable and retain their strength during handling and fabrication.
- The diameter and surface of fibres should be uniform.

Other Important Qualities [3], [5] – Matrix, Interface and Geometrical information

REINFORCING SYSTEM IN CONCRETE

- | | |
|---|-----------------------------------|
| • Mild Steel Bars – Normally not much used | • Cold Twisted High Strength Bars |
| • Galvanised Bars | • Stainless Steel |
| • FRP Bars - FRP is particularly beneficial in highly corrosive environment & electromagnetic [6] applications. | |

Stainless steel may be used in areas directly at the risk of chloride induced corrosion. The

stainless steel bars may be used as the first layer [7] of reinforcement for the structural members. In marine environment where corrosion is more aggressive, use of stainless steel bars may be justified over carbon steel considering reduced maintenance or extended service life of structures [8].

FRP Reinforcing Bars - Reinforcing bars are made using mostly glass and carbon fibres [6] by “pultrusion” method with secondary process for adequate bond properties. Aramid fibres can also be used.

Basalt Reinforcement [9] - Basalt reinforcement has been attempted in concrete beams to use as an alternative to steel bars. Concrete beams with basalt reinforcement have been tested against flexural behaviour.

Special Application of Basalt Fibre Reinforced Polymer Bars - Basalt fibre reinforced polymers (BFRP) have been used as rods [10] for the connections of timber structures instead of steel bars.

STEEL FIBRES

The advantages of steel fibres, in concrete, are for controlled crack width, redistribution of stresses, enhanced load bearing capacity, time savings and added ductility [11]. When steel fibres are added to concrete mix, the performance of the material particularly impact resistance and toughness will be increased. For pile supported floors this toughness will be very important in the load bearing and deformation behaviour [12]. A combination of conventional reinforcement with steel fibres may prove to be a proper solution considering cost and performance. Steel fibre reinforced concrete slabs have been tested successfully. Reasonable agreement between elastic theory and actual test results was observed [13].

Micro-silica & Steel Fibre Concrete [14] - Micro silica with steel Fibres has been selected and used for industrial floors to provide high strength, wear resistant durability and impact resistance.

Construction of Composite Floor Slabs using Steel Fibre Reinforced Concrete - Steel fibre reinforced Concrete is used for the construction of floor slabs in high-rise structures. Full scale tests [12] on suspended slabs have indicated specialist steel fibres increased slab ductility and the yield lines to develop.

GLASS FIBRES

Glass Reinforced Concrete (GRC) is a cement based composite which has been applied successfully in different areas of projects. The resulting material will have high tensile, flexural, impact and abrasion resisting properties [15]. Special e-GRC [16] will be suitable for economy and to produce cleaner and brighter facades of the buildings and will contribute towards reduction of noise and pollution in urban environment.

Permanent Formwork with GRC - GRC panels are of flat sheets or profiled sheets which have been used as permanent formwork [17] for the construction of composite decks.

Arching Action in Concrete Slabs & FRP Reinforcement - Concrete slabs were tested utilising in plane Compressive Membrane Action (CMA) with Glass Fibre Reinforced Plastic (GFRP) bars [18]. The test results indicate higher deflection for simply supported slab with GFRP as compared to equivalent slab with steel reinforcement. However, with lateral restraint the mid span deflection was reduced significantly.

CARBON FIBRES

Short pitch-based carbon fibres may be used in concrete for increasing flexural strength, toughness compressive strength etc.. High modulus (HM20) carbon fibres may be used in conjunction with either a polymer or a cement matrix [5].

ARAMID FIBRES

Aramid fibres are man made organic fibres which have high degree of crystallinity. Higher modulus fibres are used in polymer composites [5].

SYNTHETIC/NON-METALLIC FIBRES

The most relevant ones are polyolefins [5] (Polypropylene and polyethylene), polyamide (nylon) and polyester. The polyolefins are used for the production of cement/mortar composites. The use of structural synthetic fibres will prevent plastic shrinkage cracking in concrete floors slabs and bridge decks and will demonstrate better performance against impact resistance and tensile strength in a more homogenous manner than steel [18]. Non-metallic reinforcement will increase durability of concrete and such reinforcement do not corrode [19].

MACRO SYNTHETIC FIBRES

It had been commented from research [20] that use of macro synthetic fibres, in concrete, was efficient under seismic conditions due to tri-dimensional nature of the reinforcement. Furthermore structural elements performed more ductile and the concrete with these synthetic fibres would be able to absorb high levels of energy. Fibres can be used in external concrete slabs and pre-cast elements [21].

MICRO POLY-PROPYLENE FIBRES

Primarily suitable to control drying shrinkage and settlement cracking including explosive spalling under fire [21]. The health and safety benefits of using polypropylene fibre reinforced concrete will cover construction, maintenance and demolition [22]. It is commented [23] that monofilament polypropylene fibres will provide great advantage in both design and performance for external applications.

INFLUENCE OF GLASS, POLYPROPYLENE & STEEL FIBRES ON PHYSICAL PROPERTIES OF CONCRETE

The following comments are from the investigation carried out [21]

- Concrete workability was least affected by glass fibres and most affected by polypropylene fibres.
- All fibres were efficient for compensating shrinkage cracks.
- All fibres increased abrasion resistance of concrete.
- All fibres increased impact resistance of concrete upto 10 kg./cum.
- Flexure strength increased with glass fibre addition.

POLYPROPYLENE & STEEL FIBRE COMBINATION

It has been commented that combination of polypropylene and steel fibres (i.e. hybrid system) may be suitable for all types of concrete applications but will be more beneficial for ground supported slabs [25].

COMPARISON BETWEEN MACRO-SYNTHETIC & STEEL FIBRE REINFORCED CONCRETE [26]

Comparison between two fibres have been studied specially in respect to limit crack widths in concrete which is generally done by providing

conventional steel reinforcement using reinforcing bars or fabric. Both macro synthetic and steel fibres can perform the same function instead. Micro synthetic fibres can be used to provide control on shrinkage cracks mainly in ground bearing floor slabs, metal decking, sprayed concrete.

POLYESTER FIBRES

Various applications have already been done, in the past, using polyester fibres in cement concrete.

NATURAL FIBRES^[27]

Natural fibre reinforced concrete will consist of small dia-meter discontinuous, discrete natural fibres of different origin randomly mixed in a cementitious matrix.

FIBRE REINFORCED POLYMERS (FRP)

This is basically a combination of fibrous reinforcement held in a polymer matrix to form plates, tubes, rods and other structural profiles [28]. The fibres may be carbon, aramid or glass and the resins may be epoxy, polyester, vinylester or phenolic. FRP materials exhibited good resistance to fatigue and creep and are very durable. FRPs have good fire resistance as they are poor heat conductors and this is advantageous over metals. When the composite and adhesive have been correctly specified, FRP materials will require little or no maintenance during the service life. FRP wrapping can increase the bending and shear strength of an element by a factor around three [29].

GLASS FIBRE REINFORCED POLYMER (GFRP)

Studies have been made to improve the behaviour of the member by using glass fibre reinforced polymer (GFRP), in concrete beams, along with steel as reinforcement for studying the performance at serviceability limit stage. The GFRP reinforced beams had higher failure loads, reinforcement strains, deflections and cracking compared to similar beams with steel reinforcement [30].

Large Diameter Columns Reinforced With WRAPPED Glass Fibre Reinforced Plastic Tubing -

Large diameter (greater than 300 mm) GFRP tubes filled with concrete have been tested at Southampton [31] University, U.K., for both axially and eccentrically loaded columns. As expected centrally loaded columns failed at higher loads than corresponding eccentrically loaded

columns. The failures were sudden and explosive and at failure, located near the centre of columns fibres tended to unwrap themselves from the specimen.

CARBON REINFORCED POLYMER

Carbon fibres reinforced polymer (CFRP) plates have been used for shear strengthening for beams [32]. A large number of beams had been tested at Oxford Brookes University to study the performance of carbon fibres reinforced polymer (CFRP) plates for increasing the shear resistance of the reinforced concrete beams. It was commented that CFRP material was well suited for strengthening, bonding to soffit was effective and beam stiffness increased. Using two horizontal CFRP strips over shear span and tension zone seems to be an efficient method of shear strengthening.

Evaluation of Carbon Reinforced Polymer Plates for strengthening Reinforced Concrete Members -

Experimental study of the strengthened reinforced concrete beams by bonding composite plates has been done [32]. Bonded plates increased ultimate capacity of beams but reduced ductility.

Polymer (CFRP) Composite and Concrete Slab

- A concrete slab was designed with CFRP corrugated sheet as permanent form work and tension reinforcement [33]. Following the test it was commented that the slab was capable of withstanding large plastic deformation. The performance of the slab at serviceability limit state was also satisfactory.

HIGH PERFORMANCE POLYMER FIBRES

High performance polymer (HPP) fibres have been used for design and construction of ground supported slabs. They have high resistance to acidic and alkaline environments [34]. HPP fibres are used in pre-cast housing panels and industrial floor slabs especially external slabs where surface fibres do not corrode.

CREEP TESTS FOR FIBRE REINFORCED CONCRETE

The tests were done on plain and synthetic fibre concrete beams for modulus of rupture, elastic deformation [35] and studied for a period of 12 months. The presence or otherwise of fibres did not influence the flow component of creep. High modulus macro synthetic fibres exhibited creep similar to that of steel fibres [26].

SPECIAL COMMENTS ON FRP STRENGTHENING

Confinement of FRP Jacketed Reinforced Concrete Columns - Following the tests on FRP jacketed reinforced concrete square/rectangular, circular columns with 21 MPa Concrete and using high tensile fibres of Carbon, glass and aramid, some comments are [36] –

- FRP strengthening columns performed better, the failure can be sudden.
- Decreasing the corner sharpness increased both ultimate strength and ultimate axial deformation on square cross sections with carbon fibre reinforced jackets.
- Circular columns experienced uniform confined pressure with significant increase in strength with carbon fibre jacketing

Inspection for FRP Strengthening - The presence of moisture may be the main cause of deterioration of FRP strengthening system [37]. Techniques such as water jetting, grit blasting or steam curing should not be used for cleaning. All strengthened structures should be subjected to routine visual inspections and regular, with more detailed inspections from time to time. The disadvantages of FRP strengthening are –[37]-[38]

- The risk of soffit reinforcement hit by over-weight vehicles. Hence, some kind of protection has to be considered.

OTHER DEVELOPMENTS IN CONCRETE TECHNOLOGY

The development of concrete took place significantly in the following areas -

Ferro-cement [39], [40] - Ferro-cement is actually related to special reinforced concrete work when cement mortar and reinforcement in the form of layers of wire mesh and small diameter steel bars are used to produce, stiff structural form.

High Strength Concrete [1], [2] & [40] - The use of mineral aggregates such as in combination with super plasticisers such as polycarboxylic ethers (PCEs) are responsible for HSC and enhance impermeability, durability and strength.

Nano & Special Concrete [41], [42] - The nano concrete is made with Portland cement with particle size less than 500 nm. [42] as a cementing agent. In recent years it has been observed that concrete can be based on nano technology to improve the properties of conventional concrete. High performance binders reinforced with nano

particles or nano tubes including nano cement may be used [43].

Geo-polymer Concrete [43], [44] - Geo-polymer is an alternative cementitious binder that has been attempted as a substitute for OPC which is comprised of an alkali-activated fly ash. Geo-polymers are inorganic materials rich in silicon (Si) and aluminium (Al) that will react with alkaline activators to become cementitious.

High Performance Concrete [1, 40] - High performance concrete will be high strength concrete with low permeability. Higher doses of super plasticisers may be required to provide desired workability of the concrete mix.

Silica Fume for High Performance Concrete [45] - Silica fume is being used for the production of high quality concrete for its high strength, high chemical and abrasion resistance and durability in marine environment. For high performance silica fume concrete is becoming popular for different applications.

Coloured Concrete [46] – [47] - The colour system can offer excellent pigment dispersion [46], uniform colour, 28 standard [47], colours with colour matching, UV-stable and fade resistant colours in concrete.

Polymer Concrete [1], [40] - As compared to normal concrete the strength and other properties of polymer concrete will be improved along with increased chemical resistance and reduced permeability.

Self Compacted Concrete [40] - Self Compacted Concrete (SCC) will be compacting itself in presence of reinforcement in the form work and suitable for areas with limited access for placement of concrete and vibration. It is flowable, self-levelling, self-developing and cohesive and can be handled without segregation. Self compacting concrete with premix GRC has been tried. Rheology modifier may be required to control segregation in the GRC mix. SCC can provide improved durability and faster construction and innovative design [48].

Sprayed Concrete [49] - Sprayed concrete has been used for various application including new construction strengthening and repair work, fire protection to steel framed structures, tunnel linings etc.

High Performance Light Weight Concrete - High performance light weight concrete (HPLC) is associated with high strength and long durability.

The use of cellular high porous light weight aggregate which is formed from volcanic ash compressed under extreme pressure is made for the preparation of HPLC concrete along with other materials as used for conventional concrete. It is required for modern marine structures [50].

FURTHER ADVANTAGES OF USING CONCRETE

Fire Engineering & Performance of Concrete under Fire [51] - [53] - Concrete has performed very well [2], [51] - [53] during fire over the years and the same has been observed during tests carried out. Performance based approach will provide greater advantages [52]. It has been reported that concrete strength higher than 55 MP [53] are more susceptible to spalling and may show lower fire resistance. In order to reduce spalling, in high strength concrete under fire, fibres may be used in the concrete mix or protecting the concrete surfaces at salient places with thermal barriers.

Design for Blasts - Concrete has performed well against blast loads. Presence of continuous reinforcement [54] with good detailing will provide reserve capacity to develop alternate load path and resistance mechanism under extreme conditions. Steel fibre reinforced concrete (SFRC) can make an important contribution to the integrity and resistance to blast resistant structures [55].

UHPFRC Panel Testing for Explosion and Impact - Studies with the help of experimental work were carried out with steel fibre reinforcement to investigate the properties of ultra-high performance fibre reinforced concrete (UHPFRC) under impact and explosive loading (100 kg TNT equivalent) and found to be suitable [53]. The material exhibited non-linear yielding.

ECO CEMENT [56]

The emphasis now is to find out the alternative materials to Portland cement and the following may be considered in this connection ;

- One alternative is to avoid the use of lime stone altogether from manufacturer process. It will be important to utilise magnesium in cements to have carbon absorption characteristics with greater compressive and tensile strength.
- Eco cements can be produced at low temperature. This means manufacturers have to use renewal sources of energy (i.e. solar furnaces).
- Magnesium cements can have greater compressive and tensile strength and can be

used to build lighter structure with better insulating properties.

RECYCLING CONCRETE MATERIALS [57]

Concrete material after prolonged use when demolished can be recycled for further re-use for different construction activities.

Re-cycled aggregates - Upto 30% recycled concrete aggregates (RCA) as replacement of natural aggregates will have no adverse effect on engineering and durable properties of concrete [57]. RCA will be preferable consisting impact on –

- Potentially reducing transport impacts

DE-BONDING OF FRP COMPOSITES

De-bond problems is a critical issue for proper assessment of performance related to FRP composites in structural strengthening and repair applications. Some comments are made on FRP to steel and FRP to concrete based on experimental and theoretical studies [58] as given below :

FRP Repair to Fatigue Damaged Steel Members [59] - A few important comments from tests on repair of fatigue damaged steel members using FRP steel systems are -

- Notched steel specimens with FRP patches have resulted in significant increases in remaining fatigue life of the specimen.
- Length of the patch (perpendicular to crack orientation) is found to be more effective than its width (parallel to crack orientation)
- Symmetric bonding of the patches is recommended where possible

FRP Strengthening to RC Beams [59] - The comments from studies and research work on debonding failures in FRP strengthened RC beams :

- Assessment of proper de-bonding failures is an essential part of RC beam strengthening using FRP composites.
- Despite brittle nature of de-bonding failures, test results indicated that initiation of FRP de-bonding took place at laminate ends and at crack locations at early load levels.
- Cover of de-bonding takes place along with the re-bar level differs significantly for FRP de-bonding mechanisms in its causes and behaviour. Experimental studies have been carried out [60] to assess the effect of surface profile on the flexural strength of RC sections with FRP. The failure of concrete section strengthened by externally bonded FRP can be due to-
- Failure where composite action is maintained
- Failure where composite action is lost.

The failure plane can be at the surface of concrete or at the level of steel reinforcement.

It is mentioned that the presence of concave surface profile at the soffit of a beam will reduce the degree of flexural strengthening by externally bonded FRP composite.

Debonding Failures in CFRP – Strengthened [61] Steel Structures

Studies including experimental work on the performance of CFRP laminates/plates have been made to assess the performance of the joint, particularly the role of adhesive. De-bonding failures between steel member and CFRP is critical may take place in one of the following modes:

- Within the adhesive (cohesion failure)
 - Between the adhesive and adherends (adhesive failure)
- A combination of adhesion failure and cohesion failure

DETECTING DELAMINATION IN FRP RETROFITTED CONCRETE STRUCTURES [62]

The concern exists for weakening of the bond due to environmental factors such as wet and dry cycles, thermal variation and freeze-thaw cycles as applicable. The failure, if takes place, will be brittle type and will have catastrophic consequences. Traditional ultrasonic methods (linear) have long been used for condition assessment of the materials. In the study for assessment [63] non-linear elastic wave spectroscopy (NEWS) has been used. In NEWS frequency characteristics of the received signal are analysed to understand the condition of the material. Following the laboratory experiments, it is commented that NEWS can not be used as the base line technique for condition assessment. Prior measurements may be compared with new measurements for condition assessment of FRP.

APPLICATIONS - Composite materials have been used successfully, in various projects, in different countries. Only a few are selected as given in the table with some brief details.

No.	Item & Brief Details	Use/Strengthening	Country	Remarks
01.	Tunnel Lining [63]	Steel fibres	Netherlands, Germany	SFRC exhibited reduced crack development
02.	Rock Support, Tunnel [64]	Steel fibres, Sprayed concrete	U.K.	50-100 aspect ratio was used
03.	Suspended floor slab supported on piles [65]	Steel fibres	U.K.	Crack width may be critical than deflection
04.	Pile supported Car Park [66]	Steel fibres	Belfast, U.K.	To withstand 100 KN/m ²
05.	External Cladding [67]	GRC, Single skin panels	Wharf Galleria, U.K.	Stone like finish was required
06.	The Atlantis Hotel, External Cladding [68]	GRC façade Units	Dubai	Ribbed façade panels, Lighter Units
07.	Recladding WestChester County Courthouse [69]	GRC panels	N.Y.	External cladding
08.	Dome Structure, Catholic-Church [70]	GRC	Ukraine	22 m dia dome, 26 m above ground level
09.	Black pool's promenade [71]	Macro Synthetic fibres	U.K.	Strux 90/40 fibres used
10.	Scrabster Harbour Sea Wall [72]	Ground granulated balst furnace slag (ggbs)	Scotland	Largest marine engineering application
11.	Underground Car Park, Tunnel Lining [73]	Macro Synthetic fibres	Sweden, Norway & Japan	Sprayed Concrete
12.	Belfast International Airport, drainage channel [74]	Macro Synthetic fibres	Belfast, UK	Synthetic fibres replaced welded reinforcement mesh
13.	Tunnel lining, Channel Tunnel Rail Link [75]	Steel & Polypropylene fibres	U.K.	Precast Segments, use of PPa
14.	Tunnel linings [76]	Polypropylene Netherlands fibres		
15.	Marine concrete [77]	Monofilament polypropylene fibres	U.K.	
16.	Industrial floors [78]	Steel fibres (SFRC)	U.K.	Jointless, different projects
17.	Hertfordshire Warehouse[79]	Steel fibres (50 mm long 1mm diameter)	U.K.	Large area of 60000 sqm excellent flatness achieved
18.	Biggest SF RC Flooring [80]	Steel fibres	U.K.	250,000 sqm. (approx..) area, Joint-less ground bearing slab
19.	Fibres in floor screed [81]	Polypropylene fibres 60 mm long and 60 micron in dia	U.K.	4 kg drop tests for screed crushing resistance
20.	Rigid pavement [82]	Steel fibres		As reinforcement
21.	Road Tunnel [83]	Steel/Macro Synthetic fibres, sprayed concrete	Hind-Head tunnel, U.K.	Executed quickly
22.	Pre-stressed concrete bridge strengthening [84]	CFRP Plates	Skipton, UK	Pre-stressed concrete beams strengthened
23.	Steel bridge strengthening [85]	Ultra high modulus (UHV) CFRP plates	UK	Job executed without interrupting rail traffic

24.	Concrete Bridges [86]	CFRP Plates, NSM reinforcement.	Park House Bridge(UK); Tay Road Bridge (UK)	Used for different parts of the bridge
25.	Strengthening of Concrete bridges [87]	Carbon fibre Composite Plates, NSM reinf.	Japan, USA, UK	Strengthening Soffit, Shear, top deck
26.	Concrete bridge strengthening [88]	NSM tapes & FRP Bars	USA	
27.	Strengthening bridge columns [89]	Aramid FRP sheets	Middles borough, UK	24 No. tapered columns strengthened on two bridges
28.	Jack-arch beams strengthening [90]	CFRP Composite materials	London UG Ltd. (LUL)	
29.	Harbour City Car Park [91]	Aramid fibre sheets	UK	164 No. Columns strengthened, addition of extra floors
30.	Car park Multi-storied, Merseyside Police [92]	NSM reinf. bars	UK, Liverpool	Car park decks strengthened against flexure
31.	Fertiliser prill tower [93]	CFRP Strips	Qatar	Specially formulated adhesive used
32.	Ribbed floor slab strengthening [94]	Carbon fibre Laminates	UK	Carbon fibre laminates bonded at the bottom
33.	Composite Metal deck applications [95]	Fibre reinforcement	U.K.	Time saving upto 20% may be achieved
34.	Coastal Defence Project Blackpool [96]	Glass fibre(GFRP) reinforced polymer	UK	
35.	Concrete Chimney strength retrofitting [97]	CFRP Composites [97] FRP Composites [98]	USA, Switzerland, Japan USA, Europe	Lower installation and maintenance cost
36.	Soil stabilisation [99]	Geo-polymer injection, Hoxton Property Ecl/Pie Island Innovation	UK	To increase foundation load bearing capacity
37.	Earth Reinforcement [100]	Strips, Sheet reinf. (geotextile), Composite reinf., Anchors	U.K.	Bridge Abantments, Vaults, Land reclamation, Slope stability

DURABILITY OF FIBRE REINFORCED CONCRETE [101]

For durability, corrosion to steel fibres and performance of polymeric fibres under alkaline environment are the main concern. Polypropylene fibre is the only polymeric fibre that has been tested for field applications for a long period. The performance of polypropylene fibres under alkaline environment is found to be satisfactory and unaffected by time and exposure in crack width upto 5 mm, uncracked SRC specimens are largely unaffected by corrosion [101]. Even the fibres do corrode, small volume of each fibre and the fibre being discontinuous will not create problems of cracking like conventional concrete

with corroded steel reinforcement. The durability of fibre reinforced concrete can be considered as good.

STRUCTURAL PERFORMANCE

The performance of the composite materials is expected to be better considering high specific stiffness and strength. Low self weight of the material will provide other benefits such as reduced structural dimensions and reduced cost for transport and erection. It seems that performance of FRP materials specially for strengthening work is satisfactory and reliable when the same is executed properly. However, regular checks and

monitoring for condition assessment will be required.

FAILURE INVESTIGATIONS AND THE FORENSIC PROCESS [102]

Forensic engineering is associated with detective skill as opposed to design skill which will be the key requirement for the investigator. Causation investigation will be the prime item for the forensic approach. The forensic process starts with an investigator collecting and collating physical evidence connected with the failure in an objective manner.

CORROSION TO REINFORCEMENT

This is associated with the de-gradation of the metal by an electro-chemical reaction with its environment. The four essential items are anode, cathode, electrolyte and electrical connection. In the absence of any one of the components, the corrosion reaction will stop [103]. Both oxygen and water must be present for corrosion to occur. Corrosion to reinforcing bars, in concrete members, is responsible for damage and associated repair work.

INSPECTION & MONITORING OF CONCRETE STRUCTURES

The advantages of continuous structural health monitoring are [104] – Early warning of problems, indication of structural current life time, cheaper maintenance and lower running cost, enhanced safety. The items for surveying activities are visual inspection, dimensional measurements, cover depth measurement, rebound hammer tests, carbonation depth measurements and assessment of possible onset of corrosion. The use of sensors is common.

PROTECTIVE COATINGS [105]

Concrete surfaces, in a structure, can be treated with protective coatings for –

- Prevention of direct deterioration due to chemical and physical effects.
- Prevention of indirect deterioration induced by reinforcement corrosion.
- Enhancement or maintenance of appearance

The use of protective treatment on concrete structures is quite common and has increased in recent years.

REPAIR WORK

The repair work to concrete structures is often associated with the following types due to various reasons including environmental factors, constructional deficiencies and poor quality of improper rebar concrete cover. These are –

- Cracking
- Surface Repair
- Strengthening/Retrofitting
- Ground Stabilisation

Non-destructive tests (NDT) are often done on concrete structural elements for diagnosis and for proper assessment prior to repair work. Some comments will be made on fire damaged structures below :

Repairs to Fire Damaged Structures [106] - The main purpose of repairing the structure will be to restore the structure to perform similar to the condition it had before the fire, both in respect of strength and fire resistance in a future fire. The properties of concrete will be altered at high temperature and if the temperature reaches above 500°C and the outer layer of concrete will be much affected when the temperature reaches 900°C. The concrete below the surface may not have suffered much damage in many cases.

Assessment for the effect of fire on structural members [106] - Proper accounting for safety of the affected structural members will be very important. It may be necessary to remove some loads from structural members wherever possible during repair work using proper propping. For repairing materials Cementitious mortar and concrete will be more suitable for fire damaged concrete structures.

Load Tests - It may be necessary to carry out load testing of some selected members of the affected areas after completing the repair work for further confidence and satisfaction.

COST [107]

Fibre composite materials are expensive initially as compared to conventional construction materials. High cost is mainly due to the cost of raw materials. The applications are attractive due to their high strength-weight and stiffness to weight ratios, corrosion resistance, light weight and potentially high durability. With more use of the composite materials the cost is likely to go-down. However, maintenance cost including life cycle cost will be much less as compared to

conventional structural materials. Hence overall economy is expected in the long run.

CONCLUSIONS

A review of composite concrete material has been presented to some limited extent with different reinforcement and fibres. Mostly, steel, polypropylene, carbon and glass fibres have been considered and the behaviour of the same under flexure, shear and other load conditions have been reported. Steel and polypropylene fibres have been used successfully in industrial concrete ground floor slabs. It is commented that glass fibre reinforced composite concrete may be suitable for cleaner and brighter facades of important buildings and will contribute to the reduction of pollution in urban environment. Different test results on the use of composite materials are reported to be reasonable.

It may be concluded that proper use of composite materials, the concrete structures will be able to perform satisfactorily upto the predicted life span with minimum maintenance cost.

ACKNOWLEDGEMENT

The author would like to thank the management of Development Consultants Private Limited (DCPL) for their encouragement in publishing the paper.

REFERENCES

- [01] MEHTA PK, Concrete, Micro-structure, Properties & Materials, ICI, AMBUJA CEMENT, Ch. 11.
- [02] NEVILLE AM, Properties of Concrete, ELBS, 1981, Ch. 7 & 9.
- [03] BEDDAR M, Fibre Reinforced Concrete, Past, Present and future, Concrete, April 2004, PP. 47-49.
- [04] Ganguly KK, Fibre Reinforced Concrete, ACE-2011, K.L. University, Vijayawade, A.P., October 21-23, 2011.
- [05] HOLLAWAY L, Polymer Composites for Civil and Structural Engineering, BLACKIE ACADEMIC & PROGESSIONAL, 1993, Ch. 2.
- [06] CLARKE J, FRP Reinforcement for Concrete, Concrete, May 2000, PP. 21-22.
- [07] JAMES E, SKOVSGAARD T, Sustainable high performance Concrete Structures, Concrete, March 2004, PP.36 - 37.
- [08] WELLS T, Stainless steel – the durable solution in corrosive environments, Concrete, April 2015, PP. 46-47.
- [09] GOHNERT M, VAN GOOL R and BENJAMIN M, Basalt reinforcement in concrete beams in flexure, School of Civil and Environmental Engineering, University of Witwatersrand, South Africa, Structural Engineer, February 2014, PP. 38-43.
- [10] YEBOAH D., TAYLOR S., MCPOLIN D & GILFILLAN R, Pullout behaviour of axially loaded basalt fibre reinforced polymer (BFRP) rods bonded parallel to the grain of glulam elements, The Structural Engineer, May 2012, PP. 42-57.
- [11] GREENHALGH J, Ten years of steel fibre concrete : a manufacturer's view, Concrete, September 2001, PP. 51-52.
- [12] THOOFT H, Structural behaviour of steel fibre reinforced pile supported concrete floors, CONCRETE, September, 2000, PP. 50-54.
- [13] WARD P, SFRC Suspended slabs in flexure, The Structural Engineer, January 2010, PP.16-19.
- [14] MARTIN D, Micro-silica steel-fibre reinforced concrete flooring, Concrete, April 2000, PP. 14-16.
- [15] MORRISON I, Specifying GRC, Concrete, June 2010, PP. 14-15.
- [16] BARTOS PJM, e-GRC – Improving the appearance of concrete buildings and quality of Urban Environment, Concrete, April – 2009, PP. 25-27.
- [17] MCCLELLAND R, Permanent form work for composite bridge decks, Concrete, April 2007, PP. 10-11.
- [18] MULLIN B, Arching Action in Concrete Slabs with novel reinforcement, The Structural Engineer, January 2003, PP. 15-17.
- [19] JOWETT N, Fibre reinforcement the non-metallic way, Concrete, May – 2004, PP. 43-44.
- [20] RIDOUT A, Macro Synthetic fibres replace steel fabric in chilean housing, Concrete, September 2007, PP. 32-34.
- [21] ATKINSON T, Fibres – the traditional method of reinforcement, Concrete, September 2010, PP. 45-46.
- [22] KITCHEN A, New regulations will load to high-fibre diet, Concrete, September 2006, PP. 29-30.
- [23] KITCHEN A, Micro Poly-propylene fibres for external Concrete slabs and hard standings, Concrete, September 2007, PP. 28-31.
- [24] SADEGZADEH M, KETTLE R and VASSOU V, The Influence of glass polypropylene and steel fibres on physical

- properties of concrete, *Concrete*, April, 2001, PP. 12-13.
- [25] CARR K, Polypropylene & Steel Fibre Combinations, *Concrete*, September, 2000, PP. 60-61.
- [26] HATHAWAY B, A Comparison of macro-synthetic and steel fibre reinforced Concretes, *Concrete*, October 2007, PP.43-46.
- [27] SWAMY RN, New reinforced concrete, Surrey University Press, Volume-2, Ch. 3.
- [28] HALLIWELL S, Fibre reinforced polymers in Construction, *Concrete*, May – 2004, PP.41-42.
- [29] SADKA B, Strengthening bridges with fibre reinforced polymers, *Concrete*, February 2000, PP.42-43.
- [30] ROONEY J and TAYLOR S, Flexural behaviour of Steel and GFRP reinforced concrete beams, *Concrete*, May – 2004, PP.38-40.
- [31] MOSS RM, Behaviour of large diameter columns reinforced with wrapped glass fibre plastic tubing, *The Structural Engineer*, July 2001, PP.23-31.
- [32] WALKER P, Carbon fibre reinforced Polymer Plates as Shear Strengthening for Beams, *Concrete*, May – 2004, PP.34-36.
- [33] SZCZERBICKI J, An Advanced Polymer Composite and Concrete Slab System, University of Southampton, *The Structural Engineer*, August 2004, PP.12-13.
- [34] CARR K, Designing with high performance polymer fibres, *Concrete*, September 2001, PP.48-50.
- [35] KHOURY GA, ALGAR S, Fibre reinforced concrete creep tests, Imperial College, *Concrete*, October 2008, PP.40-42.
- [36] BELARBI A, Confinement of FRP Jacketed reinforced Concrete Columns, *Concrete*, June 2001, PP.25-26.
- [37] CLARKE J, Installation, inspecting and monitoring FRP Strengthened Concrete Structures, *Concrete*, February 2002, PP.34-36.
- [38] CLARK J, Design guidance for strengthening Concrete Structures using fibre composite materials, *Concrete*, January 2001, PP. 16-18.
- [39] GANGULY KK, Some Design Issues and Alternative Building Materials – A Brief Review, National Convention of Architectural Engineers, The Institution of Engineers, India, 31st January, 2014.
- [40] REHI SS, NBM Media, Construction Information, An overview of some development in Concrete Technology.
- [41] Nano Concrete, Civil Engineering Seminars (<http://Seminartopics.com>).
- [42] SONOLEV K, SANCHEZ F and FLORES I, The use of Nanoparticle Admixtures to improve the performance of Concrete, University of Wisconsin, Vanderbilt University, PP.1-14.
- [43] One day workshop on Introduction to Geopolymer Composites Technology, Anna University, Chennai, India, February 2017.
- [44] TURNER L K and ZOLLINS F G, Carbon dioxide equivalent (CO₂-e) emissions, a comparison between geo-polymer and OPC Cement Concrete, *Construction and Building Materials* 43(6) : 125-130, January 2013, PP. 1-13.
- [45] LEWIS R, Silica fume for high-performance Concrete, *Concrete*, May 1998, PP. 19-22.
- [46] CHRISTIE I, Adding Colour to Concrete, *Concrete*, July/August 2001, PP. 38-39.
- [47] SHROFF R, Coloured Concrete offers design feasibility, *Concrete*, April 2007.
- [48] GAIMSTER R, Self-compacting Concrete, *Concrete*, April 2000, PP.23-25.
- [49] LEWIS S, Sprayed Concrete, *Concrete*, April 2000, PP. 41-42.
- [50] SHI H, Application of Special Concrete in modern marine structures, *Concrete*, December/January 2012/13, PP.32-34.
- [51] BILOW D N, and KAMARA ME, Fire and Concrete Structures Portland Cement Association 5420, Structures 2008 – Crossing Borders.
- [52] CHUNG KF and WANG AJ, Fire resistance design of composite slabs in building Structures : From research to practice, *The Structural Engineer*, October 2006, PP.30-36.
- [53] KODUR V K R, Fire performance of High-Strength Concrete Structural Members, *Construction Technology update* No. 31, NRC-CNRC, PP. 1-4.
- [54] PCA America's Cement Manufacturers, Design for security with Concrete, Buildings & Structures, Design Aids.
- [55] SCHLEYER G K, BARNETT S J, MILLARD S G, WIGHT G & REBENTROST M, UHPFRC Panel Testing, *The Structural Engineer*, December 2011, PP. 34-40.
- [56] MATHEW J, Eco Cement, the cheapest Carbon sequestration on the planet, AEDT, December 2012, PP. 1 - 4.
- [57] Recycled Concrete Aggregate, Research Information Digest – 1, concrete

- Technology Unit, University of Dundee, Concrete, May 2005, PP. 27-29.
- [58] BUYUKOZTURK O, GUNES O, KARACA E, Progress on understanding de-bonding problems in reinforced concrete and steel members strengthened using FRP Composites, Department of Civil & Environmental Engineering, MIT, USA, Aug 2003.
- [59] BUYUKOZTURK. O., GUNES. O., A Fracture Based Approach to understanding De-bonding in FRP Bonded Structural Members, National Science Foundation, IST Group 2004, PP. 1-6.
- [60] PORTER A, The effect of surface profile on flexural strengthening of R.C. Sections with FRP, The Structural Engineer, March 2003, PP. 17-19.
- [61] TENG J G, FERNANDO D, Yu T and Zhao X L, De-bonding failures in CFRP strengthened Steel Structures, Hong Kong Polytechnic University, China & Monash University, Australia, APFIS 2012, Key 02.
- [62] KRIPAKARAN P, ARMITAGE P, Detecting delamination in FRP retrofitted Concrete Structures using nonlinear ultrasonic, The Structural Engineer, June 2014, PP. 46-50.
- [63] SORELLI L and TOUTLE MONDE F, on the design of steel fibre reinforced concrete tunnel lining segments, 11th International on Fracture, Turin (Italy), March 20-25, 2005, PP. 1-6.
- [64] SWANNELL NG, Fibre-reinforced sprayed concrete for rock support, Concrete, September 2007, PP.35-36.
- [65] VOLLUM R, Design of steel-fibre reinforced pile supported slabs, Concrete, March 2007, PP. 12-15.
- [66] CAMERON G, Steel fibre reinforced pile supported car park in Belfast, Concrete, June 2002, PP. 26.
- [67] SPENCE FE, GRC Cladding at Hays Wharf Galleria, Concrete, January 1987, PP. 5-7.
- [68] HANLEY M, Designing the GRC façade for the Atlantis Hotel, Concrete Engineering International, July 2010, PP.24-26.
- [69] mcdougale Ed, Recladding the Westchester County Court House, New York with GRC panels, Concrete, July/August 2001, PP.24-26.
- [70] PETER ID and CROCKER IA, GRC at height-creating a cathedral dome, Concrete, May 2014, PP. 47-48.
- [71] PERRY B, Synthetic macro fibres storm to the front of Coastal defence innovation, Concrete, November 2006, PP. 72-73.
- [72] JENKINS T, Durable solution for scrabster Harbour Sea Wall, Concrete, November 2006, PP. 84.
- [73] RIDOUT A, The use of macro synthetic fibre reinforcement in underground civil construction, Concrete, April 2007, PP. 39-41.
- [74] MARTIN G, Macro-synthetic fibres take off at Belfast International Airport, Concrete, September 2010, PP. 42-43.
- [75] CRAIG R, Pre-cast tunnel linings in the channel Tunnel Rail Link, Concrete, October 2004, PP. 39-42.
- [76] VERLEY N, Fire protection of Concrete linings in tunnels, Concrete, May 1999, PP. 27-30.
- [77] KITCHEN A, Fibres reduce marine concrete permeability, Concrete, April 2007, PP. 43-44.
- [78] WILLIAMSON N, Steel-fibre-reinforced Concrete fibres, Concrete, April 2011, PP. 20-22.
- [79] EDDY D, SFRC floor slab for Hertfordshire Ware House, Concrete, March 2006, PP. 18
- [80] EDDY D, UK'S biggest ever SFRC flooring project, Concrete, March 2008, PP. 24-25.
- [81] KITCHEN A, Fibres in floor Screeds, Concrete, September 2001, PP. 54-55.
- [82] GAWANDE D S, AA and S P, Innovative use of steel fibres in Rigid pavements, International Conference on Science and Technology for Sustainable Development (ICST SD) – 2016.
- [83] RIDOUT A and MARTIN G, Macro-Synthetic fibres for macro-sized projects, Concrete, April 2009, PP. 15-17.
- [84] LANE J, FASHOLE-LUKE S and SKWARSKI L, Strengthening with Carbon fibre, Concrete, January 1998, PP. 14-15.
- [85] DODDS N, Strengthening a bridge using carbon fibre reinforced plates, The Structural Engineer, March 2003, PP. 17-19.
- [86] LOUDON N, Strengthening of highway structures with fibre reinforced composites, Concrete, June 2001, PP. 16-17.
- [87] CLARKE J, Strengthening Concrete bridges with fibre composites, Concrete, October 2004, PP. 20-22.
- [88] STONE D, TUMIALAN G and NANNI A, Near Surface mounted FRP reinforcement : application of an emerging technology, Concrete, May 2002, PP. 42-44.

- [89] RINZELLI R, FRP Shells for strengthening bridge columns, Concrete, June 2001, PP. 22-23.
- [90] RESEARCH FOCUS, Carbon fibre Composites, Issue No. 46, August 2001, PP. 1-8.
- [91] RUSSEL P, Wrapping the Harbour City Car Park, Concrete, June 2001, PP.24.
- [92] FARMER N, Near-surface-mounted reinforcement preserves car park for Mersayside Police, Concrete, October 2003, PP. 36-38.
- [93] LUKE S and GODMAN S, Strengthening the QAFCO prill tower, Qatar, with FRP Plates, Concrete, February 2002, PP. 32-33.
- [94] FARMER N, using FRP Composites to strengthen Concrete Structures externally, Concrete, February 2000, PP. 47-49.
- [95] EVANS S, The use of fibre-reinforced concrete in composite metal deck applications, Concrete, October 2005, PP. 14-15.
- [96] CUNNINGHAM L and BURGESS A, Composite reinforcement for coastal defence project, Concrete, May 2008, PP. 22-24.
- [97] BALLINGER C, MEADA T and HOSHIJIMA T, Strengthening of Reinforced Concrete Chimneys, Columns and Beams with Carbon Fibre Reinforced Plastics Special Publication, Volume-138, Abstract, PP. 1.
- [98] Chimney – Afzir Retrofitting Company, PP. 9-12.
- [99] BRIERLEY M, Geo-polymer resin and sub-soil injection for soil stabilisation, Concrete, February 2004, PP. 20-21.
- [100] JONES CJFP, Earth reinforcement & soil structures, Thones Telford, ASCE Press, 1998, Ch. 3 & 5.
- [101] WATERBERG R, Durability of fibre reinforced concrete, Part-I – Corrosion, EPC, Aug. 2016, PP.1-5.
- [102] BRADY S, Failure investigations and the forensic process (Part-I), The Structural Engineer, December 2013, PP. 24-25.
- [103] GRANTHAM M and GRAY M, Remediation of St. Mary's multi storey car park, Colchester, Concrete, May 2006, PP. 28-29.
- [104] mccormick N, Structural health monitoring for civil engineered structures, Concrete, August 2009, PP. 40-
- [105] HURLEY S, Coatings for Concrete, Concrete July/August 2004, PP. 24-26.
- [106] LONG W B, Repairs to fire damaged structures, Concrete, May 1984, PP. 13-14.
- [107] VAN L, EINDE D, ZHAO L and SEIBLE F, Use of FRP Composites in Civil Structural applications, Construction and Building materials, Vol.-17, September-October 2003, PP. 389-403.

This page has been kept blank intentionally.

ASSESSMENT OF ANTI-RUTTING ABILITIES OF WARM MIX MODIFIED MIXTURES

*Ivan Syed¹, Md Amanul Hasan² and Rafiqul A. Tarefder³

¹Graduate Research Assistant, University of New Mexico, United States; ²PhD Student, University of New Mexico, United States; ³Professor, University of New Mexico, United States

ABSTRACT

In this study, asphalt binders' rutting resistance were assessed using high temperature rheological properties of warm mix-modified binders. For this evaluation process, frequency temperature sweep and multiple stress-creep recovery tests were conducted on extracted binders at a fixed temperature of 50°C using a dynamic shear rheometer. Two approaches were considered for determining rutting resistance: the Superpave rutting specification parameter ($G^*/\sin\delta$) and multiple stress-creep recovery. By using these specific approaches, the rheological rut properties of modified asphalt binders were determined and then correlated with Hamburg Wheel Track Testing (HWTT) results performed at 50°C. A simple linear regression model was developed to study the relationship between rheological data and pavement rutting potential. It was observed that non-recoverable compliance (J_{nr}) value obtained from the MSCR test demonstrated better correlation with HWTT ($R^2 = 0.96$) compared to Superpave rutting parameter ($R^2 = 0.91$). In addition, the mixture incorporated with both Cecabase® additive and polymer modification exhibited significant enhancement in rutting resistance.

Keywords: Warm mix additives, Rutting resistance, MSCR, Frequency temperature sweep

INTRODUCTION

In perspective of global use, the associated costs for the volume of raw materials used and energy consumption required for asphalt production cost could be astounding. The increasing costs of raw materials and demand for environmentally suitable paving materials in road construction have challenged the asphalt industry to seek and develop alternatives that aid in reduction of production and compaction temperatures of asphalt mixtures without compromising the required performance behavior.

Warm mix asphalt (WMA), pioneered in Europe in the late 1990's [1], is the latest asphalt technology that presents the capability of addressing the practice of environmental sustainability and enhancement of mixture workability without compromising performance. WMA additives can reduce the viscosity of the binder, allowing mixtures to be produced at a temperature grade of 38°C lower than traditional Hot mix asphalt (HMA) [2], [3], which lead to a number of environmental, operational, and economical benefits.

The implementation of WMA has become more widespread with an increasing number of paving contractors employing these sustainable technologies in construction in order to take advantage of reduced mixing and compaction temperatures, lowered energy usage for production and placement, and reduced emissions. However, one of the challenges to implementation is the

uncertainty about how WMA may affect asphalt mixtures' short and long-term field performance. Research has shown that as mixing temperature are reduced for WMA, the mixes show increased tendencies towards rutting and moisture susceptibility [4], [5]. This was attributed to decreased aging of the binder, possible presence of moisture in the mixture incomplete drying of the aggregates due to lower temperatures.

A better understanding of the effects of warm mix additives on the performance of asphalt concrete is a fundamental step towards the effective application of WMA. As part of the structural design processes to optimize field performance of asphalt mixtures, simple performance tests such as Hamburg Wheel Tracking Test (HWTT) has been developed to determine rutting potential. However, the characteristics of the binder component are also important, especially for cases involving binders with modifying agents.

Despite the fact that asphalt bitumen make up 4 to 8 % of a pavement mix structure, it provides a level of rigidity, structural bonding, resilience, and absorbance which holds the total pavement mixture together as a solid body [6]. However, with higher traffic densities and effects of environmental exposure, binder flows and dissipates energy with time [7]. As a result, asphalt binder experience a variety of thermomechanical demands; where pavement defects transpire such as rutting at high temperatures due to thermal susceptibility of asphalt [8].

The asphalt contribution to permanent deformation process has traditionally been handled by observing the asphalt binder's consistency based on softening point and penetration tests [9]. However, with priorities set for environmental conservation and preservation, the integration of polymer modifiers, warm mix additives, and recycling of reclaimed asphalt pavement (RAP) materials into asphalt mixtures have gained popularity [10], [11]. With this in mind, the empirical tests mentioned earlier are insufficient to characterize the rutting resistance behavior of binders. It would be helpful to examine the effects of these modifying agents on the properties of plant produced mixtures. In order to accomplish this task, extraction and recovery of asphalt binder from asphalt concrete were performed.

Thus, this research evaluates the rutting resistance of binders modified with different warm mix additives.

OBJECTIVES

- I. Evaluate the effects of different warm mix additives on the rheological and rutting performance characteristics of asphalt concrete.
- II. Compare rutting resistance of the extracted binders using two different rutting parameters.
- III. Assess the correlation between rheological properties and permanent deformation results obtained from HWTT.

TEST METHODOLOGY

This section of the paper focuses on material selection, experimental plan, and a brief description of each test considered for the purpose of this research. The test methodology is described in Fig.1, where this test program is designed to evaluate the rutting susceptibility of the selected pavements and to see if there are demonstrable differences in test results between control HMA and WMA modified test sections. This study was conducted in two phases: 1) rutting performance evaluation and 2) assessment of extracted binder properties. The rutting potential of WMA modified asphalt mixtures, in comparison to HMA, were evaluated through HWTT device. As samples were collected from the LTPP pavement sections, binders on these plant-produced asphalt mixtures experienced short-term aging during their production stage [12]. The process of laboratory short-term aging was annulled. In order to measure the two rutting parameters, rheological tests were performed on the extracted binders using a Dynamic Shear Rheometer (using a 25 mm diameter plate and 1 mm gap). The average

values of three replicates samples were determined at 50°C, corresponding to the test temperature of the HWTT test.

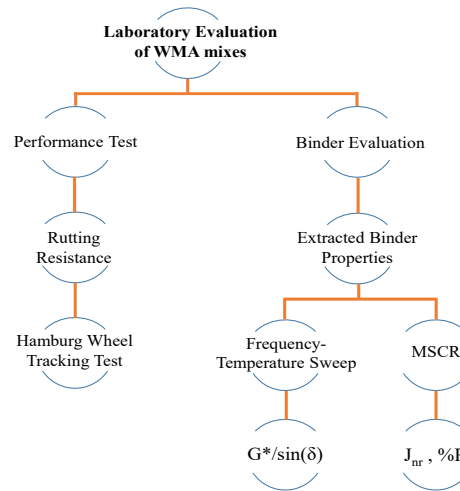


Fig.1 Test methodology implemented in this study

Material Source and Classification

The pavement test sections selected for this research are located in district four of central New Mexico and were constructed in fall of 2014 along the westbound lane of Interstate 40 near Santa Rosa, New Mexico, where designs incorporate approximately 20% RAP materials collected from the Interstate 40 and US 84 highway stockpile.

Material type of sand and gravel with gradation classification of Superpave Mix type III with nominal maximum aggregate size (NMAS) of $\frac{3}{4}$ inches were utilized for design of these AC mixes. In addition, 1% of versabind® were incorporated into the mixes.

The production of asphalt concrete utilized in the second test section were produced with Terex® Foaming technology and WMA chemical additive of Evotherm® was used in the construction of the third test section. Cecabase® chemical additives was considered for the two supplemental pavement test sections in order to perform additional research on the effects of other WMA production methods. The asphalt concrete mixing temperature considered for design of HMA and WMA were 322°F and 270°F, respectively. The first four pavement sections were manufactured using binder grade of PG 70-28. However, the last section was prepared with the same binder grade and enhancement of polymer modifiers, thus resulting in the designation of PG 70-28+.

Based on the different additives used in these test sections, WMA technology is classified into two different technologies namely: (i) water-based and (ii) chemical additive technologies. In the

foaming process, a certain amount of water is added to the hot binder and then the water is turned into steam, which results in a volume expansion of binder and consequently, a reduction of the binder's viscosity [13]. This temporary reduction facilitates aggregate coating and thereby improved workability at reduced temperatures. The expanded volume gradually deteriorates with time and the asphalt binder returns to its original characteristics [14]. This form of technology is currently more popular and widely used compared to other technology categories.

Evotherm[®] and Cecabase[®], for instance, are both chemical additives. Cecabase[®] which do not reduce the asphalt binder's viscosity. They are packaged by surfactant and adhesion agents, which chemically enhance active adhesion and improve the wetting of aggregates by binder without altering considerably the rheological performance [5]. Evotherm[®] is an additive packaged in the form of emulsion, which are introduced into the plant's binder line, allowing for the reduction of mixing temperatures close to 38°C, translating to decreased energy requirements for asphalt production [15].

Mix Performance Evaluation Tests

Mixture rutting performance was done using HWTT following AASHTO T 324-14, a laboratory test procedure which simulates repeated wheel loading on specimens in order to characterize rutting resistance potential and stripping susceptibility. Linear variable displacement transducers (LVDTs) located at the side of each wheel are used to record the rut depth at 11 points along the test samples with 0.01 mm precision. Following the recommendation suggested by Schram et al. [16], the average value of the rut depths at 4th, 5th, 6th, 7th, and 8th points along the wheel path was considered as the HWTT test result for this study.

Plot of rut depth vs. number of wheel passes are analyzed to predict rutting and stripping susceptibility. Fig.2 includes a post compaction consolidation (PCS), a creep slope (CS), a stripping slope (SS), and a stripping inflection point (SIP). PCS occurs within 1,000 number of wheel passes and simulates initial densification of pavement mixtures when traffic movement is allowed on a newly constructed pavement. CS relates the rutting susceptibility through measurement of permanent deformation which occurs due to plastic flow. SS relates the stripping susceptibility of the mixtures. A lower value of CS and SS indicates characteristics of decreased rutting and stripping resistance of tested samples [17]. If the plot does not include a SS or a SIP, the mixture has adequate moisture damage resistance.

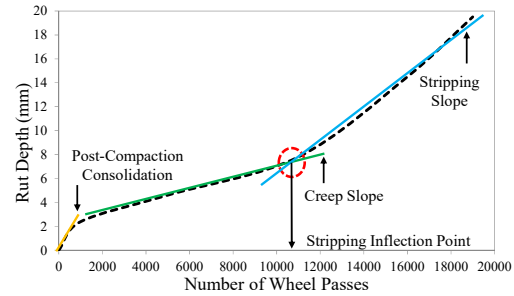


Fig.2 Schematic of HWTT results

3.3 Test Procedures for Binder Evaluation

In order to evaluate the effects of warm mix additives and recycled materials, extraction and recovery of asphalt binder from asphalt concrete was the approach considered. Extraction was performed following AASHTO D2172 and AASHTO D5404, respectively. The solvent used in this process is trichloroethylene.

AASHTO T 315 was followed to perform frequency-temperature sweep tests at 50°C in order to determine the $G^*/\sin\delta$ values of the extracted binders.

In addition, MSCR tests were conducted to determine the percent recovery (% R) and non-recoverable creep compliance (J_{nr}) values of the binders, in accordance to AASHTO TP70.

RESULTS AND ANALYSES

Hamburg Test Results

Fig.3 shows HWTT analysis of the SPS-10 pavement mixtures, where the average rut depth values of four test replicates per mixture has been taken as the symbolic rut depth value.

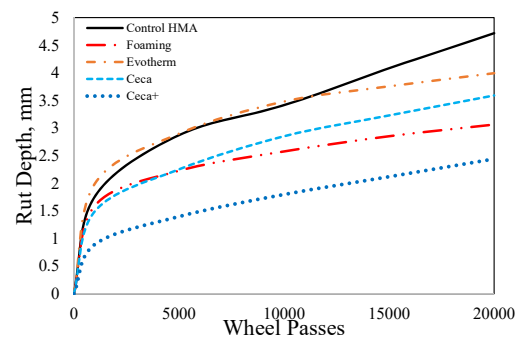


Fig.3 Hamburg test results for evaluated mixes

It is observed that all five mixtures has a representative PCS and CS. However, stripping phase was not reached for any of the mixes, indicating no incidence of damage due to the effects

of moisture. Results display a significant reduction in rutting susceptibility for Cecabase[®]+ (2.44 mm) mixture in comparison to control HMA (4.72 mm). However, between two Cecabase mixtures, Cecabase[®] without polymers exhibited a slightly higher rut depth (3.59 mm). On the contrary, Cecabase[®]+ is polymerized, resulting in a harder mixture. This specific circumstance exhibits the effect of linking warm mix additives with polymers.

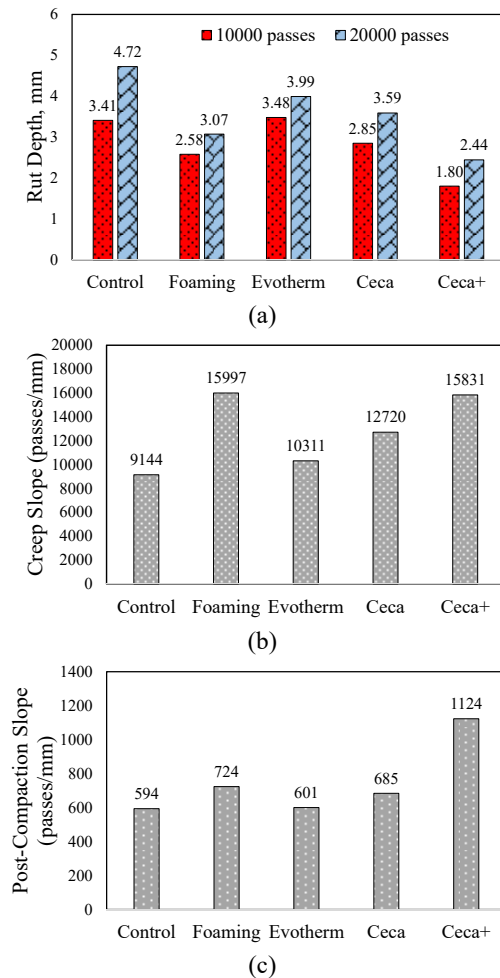


Fig.4 Hamburg test results for evaluated mixes

In reference to Fig.4(a), a comparable trend was observed for permanent deformation measurements at 10,000 number of wheel passes with slightly lower values with respect to values from 20,000 wheel passes. Fig.4(c) indicates that as rut depth increases, PCS decreases. CS of these mixtures also illustrates this similar trend. Since, there is no stripping slope, all mixtures have ample moisture damage resistance. This may be attributed to the incorporation of 1% versabind[®] in these mixtures; a well-known anti-stripping agent. According to research conducted by Hill [18], it was observed

that the incorporation of RAP to WMA has the potential to improve the performance of these type of mixtures at intermediate to high temperatures.

Superpave Rutting Parameter – $G^*/\sin\delta$

The $G^*/\sin\delta$ values of the extracted binders was explored. All forms of warm mix modification was observed to increase the superpave rutting parameter (Fig.5a). For example, $G^*/\sin\delta$ value for binders with Terex[®] foaming, Evotherm[®], Cecabase[®], and Cecabase[®]+ was found to be approximately 27.90, 20.47, 19.90, and 91.83 kPa, respectively, compared to 11.70 kPa for control HMA. Out of the four additives, results show that the addition of Cecabase[®] with polymerization increased $G^*/\sin\delta$ substantially, indicating the highest rutting resistance with this modification arrangement. From these results, Cecabase[®]+ is recognized to be the most effective additive in improving rutting resistance followed by Terex[®] foaming, Evotherm[®], and Cecabase[®] unmodified. Based on the simple regression analysis (Fig.5b), a good correlation of $R^2 = 0.91$ was observed between the maximum rut depth and rheological parameter values of these mixtures.

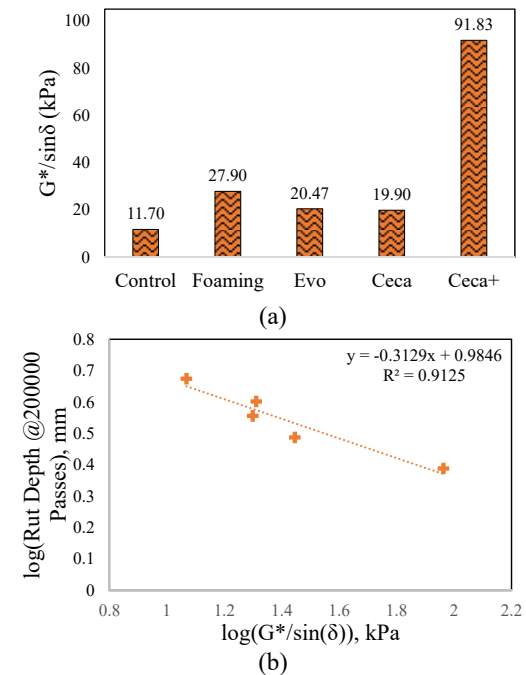


Fig.5 $G^*/\sin\delta$ parameter results

MSCR Rutting Parameters – J_{nr} , %R

As shown in Fig.6a, the J_{nr} value of control HMA was found to be 0.59 kPa^{-1} . The J_{nr} values of the extracted binders with Terex[®], Evotherm[®],

Cecabase[®], and Cecabase[®]+ was found to be 0.15, 0.46, 0.23, and 0.02, respectively. Lower J_{nr} values were observed for all WMA modified mixtures in comparison to control HMA. This indicates increased rut resistance. As shown in Fig.6b, the % Recovery value of the control sample was found to be 13.47. The % Recovery values of the extracted binders with the presence of Terex[®], Evoth[®], Cecabase[®], and Cecabase[®]+ was found to be 32.58, 18.14, 23.71, and 77.54, respectively. This also indicates increased rutting resistance compared to the control sample. Based on the lowered J_{nr} and heightened % Recovery values from the incorporation of Cecabase[®]+, the influence of polymerization is exhibited through the decreased rutting potential.

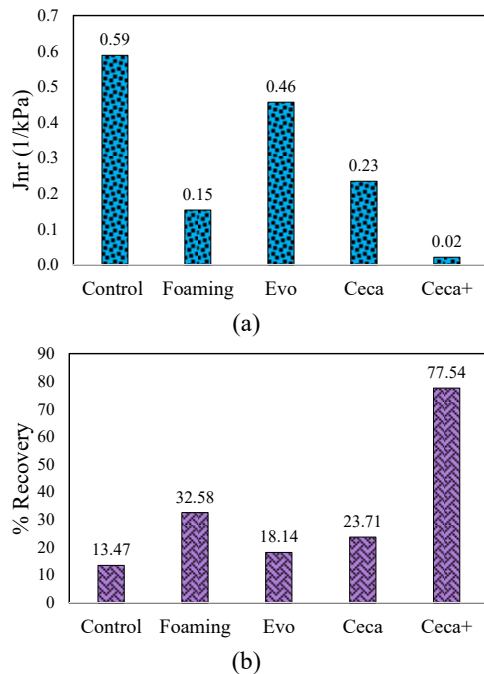


Fig.6 MSCR parameter results

A simple linear regression analyses were performed between the two parameter results obtained from this test method in contrast to HWTT. As shown in Fig.7, a correlation value of $R^2 = 0.96$ and $R^2 = 0.77$ were found for J_{nr} and % Recovery, respectively. Hence, indicating the non-recoverable creep compliance parameter as a reliable measure when it comes to evaluating rutting resistance, out of the MSCR parameters.

Based on the J_{nr} values, the order of rut resistance for the extracted binders can be seen as (i) Cecabase[®]+, (ii) Terex[®] Foam, (iii) Cecabase[®], (iv) Evoth[®], and (v) Control. This ranking order shows that compared to the control HMA sample, WMA modification improves the rutting potential of the mixtures.

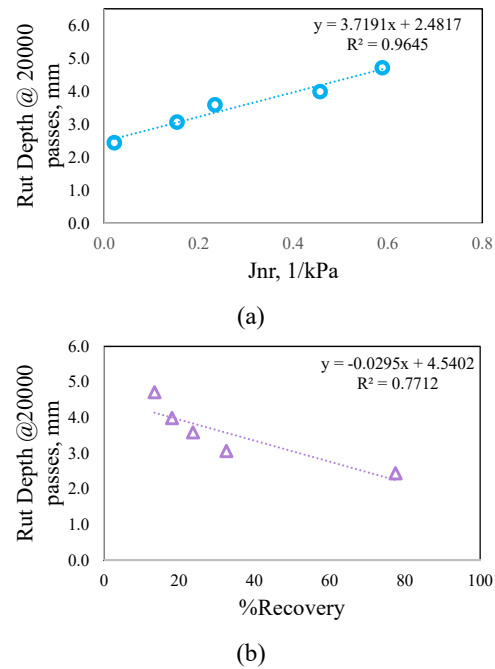


Fig.7 Simple linear regression analysis of MSCR results with respect to HWTT

CONCLUSION

This study has evaluated the anti-rutting abilities of warm mix additives in asphalt concrete mixtures. The key findings drawn from this research are discussed below:

- Based on the simple regression analysis results, J_{nr} presents the best correlation ($R^2 = 0.96$) with rutting results obtained from HWTT. With the absence of MSCR test, the superpave rutting parameter ($G^*/\sin\delta$) may still be considered as a viable option to evaluate rutting resistance.
- Cecabase[®]+ exhibited significant rutting resistance improvement among the five pavement sections. In HWTT mixture testing, stripping phase was not reached for all mixtures, indicating ample damage resistance against the effects of moisture.

It is recommended to conduct another study to evaluate the effects of higher percentages of RAP content. In addition, if the opportunity presents itself, the effects of these select additives on varying binder performance grades and gradation will provide good insight in evaluating the impact of WMA technology.

ACKNOWLEDGEMENT

This project is funded by New Mexico Department of Transportation (NMDOT) and Southern Plain Transportation Center (SPTC). The authors would also like to express their gratitude to the research bureau team of NMDOT.

REFERENCES

- [1] Jones, W., "Warm Mix Asphalt Pavements: Technology of The Future?", *Asphalt*, Vol. 19, No. 3, 2014.
- [2] Button, J.W., Estakhri, C. and Wimsatt, A., "A Synthesis of Warm Mix Asphalt (No. FHWA/TX-07/0-5597-1)", College Station, TX: Texas Transportation Institute, Texas A & M University System, 2007.
- [3] Akisetty, C.K.K., "Evaluation of Warm Asphalt Additives on Performance Properties of CRM Binders and Mixtures", (Doctoral dissertation, Clemson University), 2008.
- [4] Politano, L., "Warm Mix Asphalt-A Greener Alternative to Hot Mix Asphalt", 2012 Conference and Exhibition of the Transportation Association of Canada-Transportation: Innovations and Opportunities, 2012.
- [5] Croteau, J.M. and Tessier, B., "Warm Mix Asphalt Paving Technologies: A Road Builder's Perspective", In Annual Conference of the Transportation Association of Canada, Toronto, 2008.
- [6] Bahia, H.U., Hanson, D.I., Zeng, M., Zhai, H., Khatri, M.A. and Anderson, R.M., "Characterization of Modified Asphalt Binders in Superpave Mix Design", (No. Project 9-10 FY'96), 2001.
- [7] Tabatabaee, H.A. and Bahia, H.U., "Establishing Use of Asphalt Binder Cracking Tests for Prevention of Pavement Cracking", *Road Materials and Pavement Design*, 15(sup1), 2014, pp.279-299.
- [8] Pérez-Lepe, A., Martínez-Boza, F.J., Gallegos, C., González, O., Muñoz, M.E. and Santamaria, A., "Influence of The Processing Conditions on The Rheological Behaviour of Polymer-Modified Bitumen", *Fuel*, Vol. 82, No. 11, 2003, pp.1339-1348.
- [9] Morea, F., Agnusdei, J.O. and Zerbino, R., "Comparison of Methods for Measuring Zero Shear Viscosity in Asphalts", *Materials and structures*, Vol. 43, No. 4, 2010, pp.499-507.
- [10] Yildirim, Y., "Polymer Modified Asphalt Binders", *Construction and Building Materials*, Vol. 21, No. 1, 2001, pp.66-72.
- [11] Moghadas Nejad, F., Azarhoosh, A., Hamed, G.H. and Roshani, H., "Rutting Performance Prediction of Warm Mix Asphalt Containing Reclaimed Asphalt Pavements", *Road Materials and Pavement Design*, Vol. 15, No. 1, 2014, pp.207-219.
- [12] Irfan, M., Waraich, A.S., Ahmed, S. and Ali, Y., "Characterization of Various Plant-Produced Asphalt Concrete Mixtures Using Dynamic Modulus Test", *Advances in Materials Science and Engineering*, 2016.
- [13] Van de Ven, M.F.C., Jenkins, K.J., Voskuilen, J.L.M. and Van Den Beemt, R., "Development of (Half-) Warm Foamed Bitumen Mixes: State of The Art", *International Journal of Pavement Engineering*, Vol. 8, No. 2, 2007, pp.163-175.
- [14] Kristjánssdóttir, Ó., Muench, S., Michael, L. and Burke, G., "Assessing Potential for Warm-Mix Asphalt Technology Adoption", *Transportation Research Record: Journal of the Transportation Research Board*, (2040), 2007, pp.91-99.
- [15] Rashwan, M.H., "Characterization of Warm Mix Asphalt (WMA) Performance In Different Asphalt Applications", (Doctoral dissertation, Iowa State University), 2012.
- [16] Schram, S., Williams, R. and Buss, A., "Reporting Results from the Hamburg Wheel Tracking Device." *Transportation Research Record: Journal of the Transportation Research Board* 2446, 2014, pp.89-98.
- [17] Larrain, M.M.M. "Analytical Modeling of Rutting Potential of Asphalt Mixes Using Hamburg Wheel Tracking Device", (Master's Thesis), 2016.
- [18] Hill, B., "Performance Evaluation of Warm Mix Asphalt Mixtures Incorporating Reclaimed Asphalt Pavement." (Doctoral dissertation, University of Illinois at Urbana-Champaign), 2011.

LATERAL CYCLIC LOAD TEST AND SEISMIC DESIGN OF PRECAST CONCRETE COLUMNS USING STEEL BOX CONNECTION

Nutchanon Siri, Chayanon Hansapinyo* and Chinnapat Buachart
Center of Excellence for Natural Disaster Management,
Department of Civil Engineering, Chiang Mai University, THAILAND
*Corresponding author

ABSTRACT

Due mainly to lacking of skill labor, the precast construction has been widely adopted and increasingly replace the conventional cast-in-place construction. This paper explains experimental investigations on precast concrete columns using steel box connection at the column base under cyclic loading. The test results show satisfactory seismic performance of the precast specimens both in seismic shear capacity, ductility and energy dissipation compared with the identical cast-in-place specimen. The failure of the precast columns, with proper details, was in flexural ductile mode. The shear capacity was respectively 1.16-1.24 times higher than the averaged capacity of the cast-in-place column. The damping ratio was about 18-25 percent in the inelastic range, after the drift ratio of 3.0%. Finally, seismic design of the precast concrete column using the steel box connection is described based on the experimental results.

Keywords: Precast Concrete Column, Seismic Design, Column Steel Box Connection, Lateral Cyclic Load

INTRODUCTION

The increasing rate of the construction industry is related well with the economic growth of country especially for developing countries. Nowadays, the problems about labor shortage and labor cost have become more severe. These problems, as well as high construction industry competition, have led to the application of the precast construction. In addition, the construction technique becomes more popular due to the less time consumption.

In a seismic prone area, failure mechanism of structural elements in a building must be considered to ensure ductile damage under a severe earthquake. Columns and beam-column joint are maintained in elastic range. In other words, a good structure must be able to control the location of damage or plastic hinge under big earthquakes on beam elements for absorbing and dissipating energy. This phenomenon can be achieved by a systematic design for weak beam-strong column. As the column elements are very important, many past researches investigated the shear capacity demand of reinforced concrete columns and beam-column joints under the lateral loading [1-3]. For the precast column, Rejame et al [4] conducted an experimental investigation on precast columns in socket foundations with internal smooth interfaces.

Seismic design of ductile reinforced concrete frames has been developed for a long period of time. A successful design method has been based on the

past lessons learnt from the failed buildings. However, the design of precast concrete element has not been clearly explained, as the existing buildings are mostly reinforced concrete type. The adopted innovative precast connection has then based on experimental result of prototype element. This paper presents lateral cyclic load test and seismic design of precast concrete columns using steel box connection. The technique permits faster construction with use of this bolted connection type, as shown in Fig. 1. Seismic design of reinforced concrete frame buildings is first described to overview demand capacity for design of the precast concrete columns. Then, precast concrete with the steel box connection, as shown in Fig.1(b) and an identical cast-in-place concrete column tests under lateral cyclic load is explained. From the test, seismic performance of the precast columns is discussed compared with the cast-in-place one. Eventually, the design of the precast columns and the steel box connection are described based on the test results.

SEISMIC DESIGN OF REINFORCED CONCRETE FRAME

An overview of seismic design of reinforced concrete frame buildings is described below, as shown in Fig.2. Following the step, damage pattern can be controlled in flexural mode at the beam ends and the collapse of buildings under a strong earthquake can be avoided.

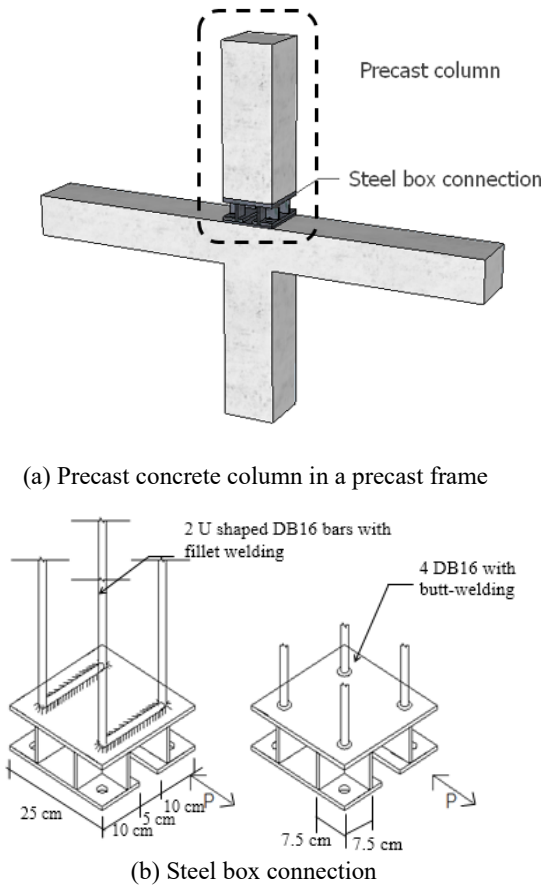


Fig.1 Precast concrete column with steel box connection

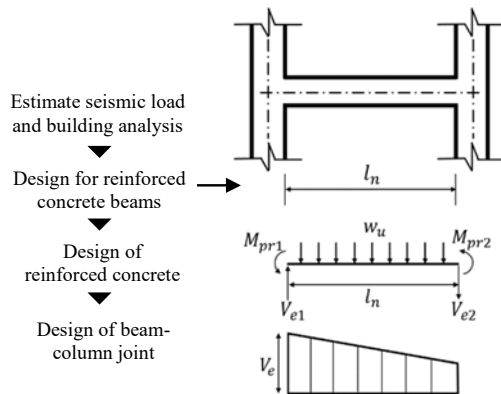


Fig.2 Seismic design of reinforced concrete frames

Estimation of seismic load and building analysis

First, for a regular building, lateral seismic load on building is estimated according to a local standard. The load depends on seismic parameters

including local seismic intensity, type of building, type of soil, building weight and dynamic properties. The calculation starts from base shear force estimation and then distributes the force to each floor of the building. Structural analysis is next performed for element forces induced by all cases of load combination.

Design for reinforced concrete beams

From the envelope flexural force, flexural strengths required for beams are obtained and required longitudinal reinforcement can be determined accordingly. Considering under a strong earthquake forming flexural hinge at the beam ends, shear force (V_e) at the stage is estimated as shown in Eq.(1) and Fig.2. The beam shear strength designed following this procedure ensures the avoiding of shear failure in the beam element.

$$V_e = \frac{M_{pr1} + M_{pr2}}{l_n} + \frac{w_u l_n}{2} \quad (1)$$

Where

M_{pr1} and M_{pr2} are probable flexural strength of the beam ends

w_u is factored load per unit length of the beam

l_n is clear length of the beam

Design of reinforced concrete column

To protect the columns against a strong earthquake, design shear and flexural strengths of the columns must be higher than the flexural strength of the joining beams. According to ACI318 [5], the flexural strengths of the columns shall satisfy

$$\sum M_{nc} \geq 1.2 \sum M_{nb} \quad (2)$$

Where

$\sum M_{nc}$ is sum of nominal flexural strengths of columns framing into the joint

$\sum M_{nb}$ is sum of nominal flexural strengths of beams framing into the joint

The required flexural capacity of the column M_{nc} is then used to determine the column dimension and reinforcement. The required shear capacity of the reinforced concrete column is also determined. Consequently, the steel box connection

is designed which will be explained next.

Design of beam-column joint

Damage of beam-column joint can lead to reduction of redundancy of structure. Hence, elastic performance of the region under an earthquake must be confirmed. Based on the capacity of the designed columns from the previous step, the required strength of the beam-column joint can be determined.

TEST OF PRECAST CONCRETE COLUMNS

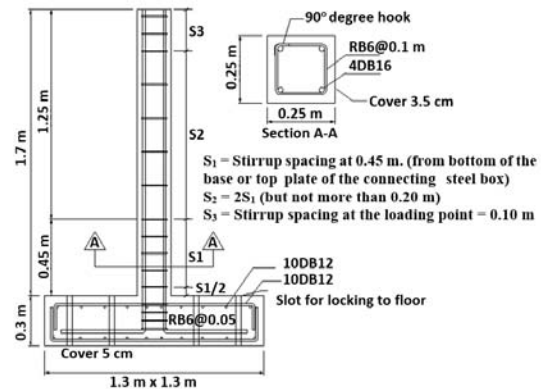
Specimens and Experimental Setup

To verify the applicability of the designed steel box connection, tests of 5 precast columns were carried out at the Structural Laboratory, Department of Civil Engineering, Chiang Mai University [6]. The test results were compared with an identical cast-in-place one. All the columns were 0.25×0.25 m² section and 1.7 m in height from column base to top. 4-DB16 were used as the longitudinal reinforcement for all specimens. For the precast specimens, the steel box connection was used for the base connection. The difference between the precast specimens is based on difference in construction method, e.g. grouting, welding to nuts, welding of the column reinforcement to the steel box. Fig.3 shows the specimen details. For the specimen nomenclature, M and P stand the Cast-in-place specimen and the Precast specimen, respectively. Constant axial load of $0.1f_c' A_g$ was applied to all specimens. Lateral cyclic loading was applied to the tip of the specimen, as seen in Fig.4. While the column bottom was arranged to be a fixed condition, the application of the load induces a cyclic shear and moment as if it is a half-story column in a rigid frame. The deformation control at the loading point, represented as story drift was adopted as recommended in ACI T1.1-01 [7].

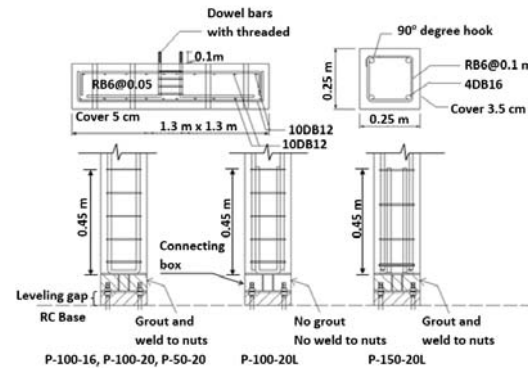
Lateral Load and Deformation Relationship

The cast-in-place specimen failed in flexural failure with yielding of the longitudinal reinforcement at the column base. High ductility and energy dissipation were observed. For all the precast columns, depending on different reinforcement detailing, P-100-20 and P-50-20 specimens were ductile failure and P-100-16 and P-150-20L were brittle failure. The brittle failure was caused by the improper welding details of the column reinforcement on the steel box connection. Under the lateral cyclic loading, the ductile precast

concrete columns with the steel box connection satisfied seismic performances, compared with the



(a) Monolithic specimen M-100



(b) Precast specimens

Fig. 3 Test specimens

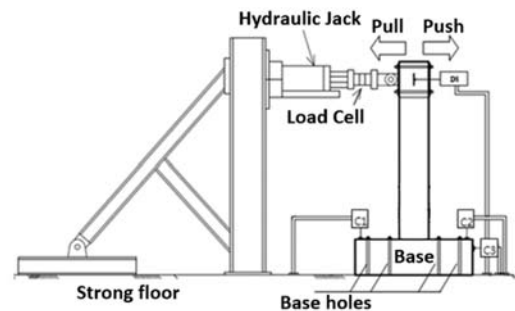


Fig. 4 Lateral cyclic load test

cast-in-place column. The ductile precast columns were failed under flexural mode similar to that of the cast-in-place specimen but at section above the steel box connection. Hence, the ultimate lateral load of the ductile precast is higher than the load of the cast-in-place column due to the shorter moment arm. Figs 5 and 6 respectively show the lateral load-deformation relationship and damping of the ductile precast columns (P-100-20 and P-50-20 specimens)

and the cast-in-place concrete column. As seen in Table 1, the ultimate lateral load capacities of the ductile precast columns are about 1.16-1.24 times higher than the averaged capacity of the cast-in-

place column. The equivalent damping ratios determined from area under the load-deformation curve [8] were between 18-25 percent after drift ratio more than 3 percent.

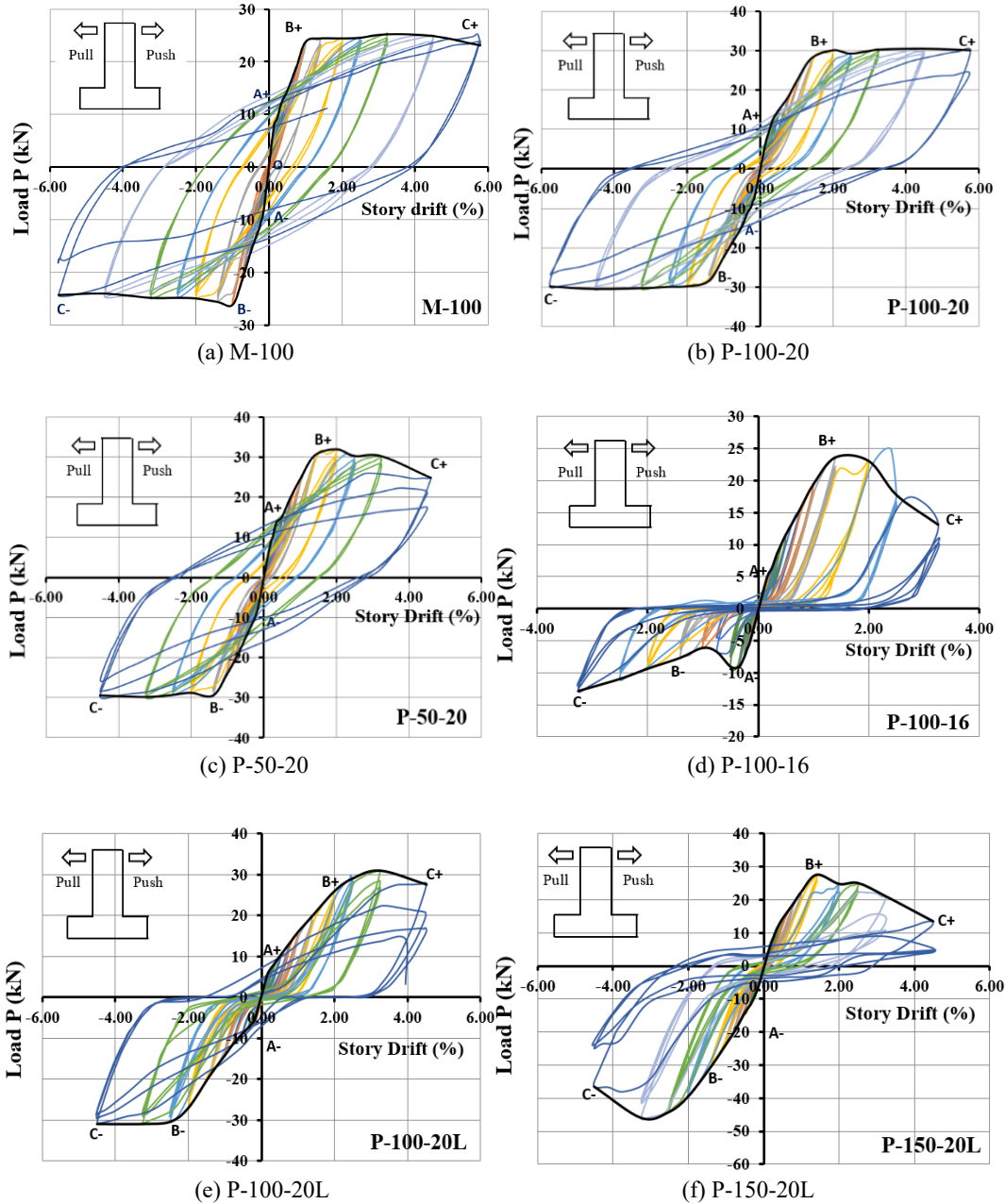


Fig.5 Hysteresis relation of lateral load-deformation

Table 1 Lateral load capacity and damping ratio

Specimen	P_{u_push}	P_{u_pull}	P_{u_Theory} (kN) ³	Failure mode	Damping ratio (%) (Story drift >3%)
M-100	25.26	26.20	25.33	Flexural	22-25
	Avg. (P_{u_Ma}) ¹ 25.73				
P-100-20	30.46 (1.18) ²	30.53 (1.19) ²	39.33	Flexural	15-21
P-50-20	32.00 (1.24) ²	29.86 (1.16) ²	39.33	Flexural	18-22
P-100-16	23.66 (0.92) ²	12.86 (0.50) ²	25.33	Slip of threaded dowel	3-4
P-100-20L	31.00 (1.20) ²	30.93 (1.20) ²	39.33	Fracture of welding	7-15
P-150-20L	27.46 (1.07) ²	45.93 (1.79) ²	39.33	Fracture of welding	5-6

¹ $P_{u,Ma}$ the average of push and pull ultimate capacity of specimen M-100²Numbers in parenthesis and ultimate capacity ratio compared with the P_{u_Ma}

³ $P_{u,Theory}$ is calculated based on ultimate capacity of maximum shear and moment section (at column base). The calculated strengths are controlled by flexure

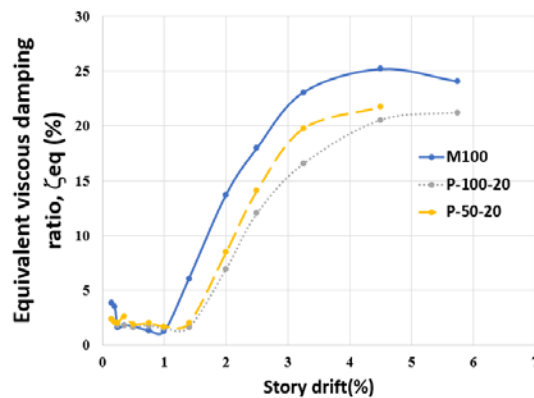


Fig.6 Equivalent damping ratio

DESIGN OF PRECAST CONCRETE COLUMN USING STEEL BOX CONNECTION

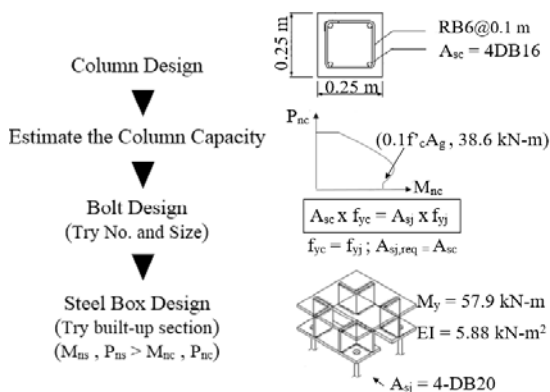


Fig. 7 Design of the steel box connection

After obtaining the designed column section, the steel box connection dimension is determined accordingly. Similarly, to avoid weak points on the connecting steel box, capacity of the connection

must be higher than that of the column section above the connection.

Number of dowel bar and threaded diameter

Under tension load on the column, longitudinal reinforcement resists the entire load. Hence, at the steel box connection, number and threaded diameter of the dowel bars are calculated based on equilibrium, as shown in Eq.(3). It is noted that the buildability also decides size and number of the dowel bars. For this test, as the reinforcement of the column is 4-DB16, 4 dowel bars with the threaded diameter of 20 mm. and same yield strength of the column reinforcement were used. By using this approach, the design under tension becomes conservative. In the real situation, columns will be subjected to combined compressive load and bending. The entire column section will be curved and the stress of the section is under distributed compressive stress or compressive-tensile stress.

$$A_{sc} \times f_{yc} = A_{sj} \times f_{yj} \quad (3)$$

where A_{sc} , f_{yc} and A_{sj} , f_{yj} are sectional area and yield strength of the column reinforcement adjacent to the steel box and dowel bars, respectively.

Section of the steel box connection

This is the additional design procedure compared with the cast-in-place column. As seen in Fig.7, the tested precast concrete columns had the flexural capacity of 38.6 kN-m. associated with the axial load of $0.1f_c'A_g$. Based on AISC steel design [9], flexural yielding (M_y) and stiffness (EI) of the box were 57.9 kN-m and 5.88 kN-m² respectively, providing 1.5 and 2.3 times relatively higher than

the ultimate flexural capacity and non-cracked flexural stiffness of the reinforced concrete column section. With the capacity of the steel box connection is higher than the column above, connection failure can be avoided.

Prevention of premature failure

Premature failure introduces unexpected lower capacity with brittle failure mode. For the design of precast concrete column with the steel box connection, attention should be paid to providing nuts with enough bond-slip capacity. For the column reinforcement, the longitudinal column reinforcements attached to the upper plate of the connecting steel box can be done in either form of welds, e.g. fillet weld with U shape or butt-weld. However, the welding contents should be carefully examined and the welding strength should be guaranteed for the designed purpose. Welding for the built-up steel box is also carefully made.

CONCLUSION

This paper presents the lateral cyclic load test and seismic design of precast concrete column using steel box connection based on capacity design concept. First, seismic design of reinforced concrete frames is reviewed based on capacity design concept. Then, the guideline on how to obtain the seismic design force for the columns is made. The design of precast concrete column with the steel box connection is explained. To illustrate the applicability of the designed steel box connection, lateral cyclic load tests of precast concrete columns was made and the results were compared with a resemble reinforced concrete column. The test results show the good seismic performances of the designed steel box connection. The columns with connection possessing the flexural strength and stiffness higher than the concrete column above the connection performed the ductile behavior. The flexural yielding strength and stiffness of the box were 57.9 kN-m and 5.88 kN-m² respectively, providing 1.5 and 2.3 times relatively higher than the ultimate flexural capacity and non-cracked flexural stiffness of the reinforced concrete column section. It is noted that welding of the column reinforcement to the steel box need to be carefully made. The ultimate capacity of the precast column is

higher compared with the cast-in-place concrete column, due to the relocation of the failure section. Hence, based on the capacity design concept, the weak beam-strong column can be easily achieved.

ACKNOWLEDGEMENTS

The authors would like to express their sincere appreciation to Chiang Mai University for financial supports.

REFERENCES

- [1] Lu, X., Urupak, T. H. Li, S. and Lin, F., "Seismic behavior of interior RC beam-column joints with additional bars under cyclic loading", *Earthquakes and Structures*, Vol.3, No.1, 2012, pp. 37-57.
- [2] Bindhu, K.R., Jaya, K.P. and Manicka Selvam, V.K., "Seismic resistance of exterior beam-column joints with non-conventional confinement reinforcement detailing", *Struct. Eng. Mech.*, Vol.30, No.6, 2008, pp. 733-761.
- [3] Han, S. W. and Jee, N. Y., "Seismic behaviors of columns in ordinary and intermediate moment resisting concrete frames", *Engineering Structures*, Vol.27, No.6, 2005, pp. 951-962.
- [4] Rejame, M. F. C., Eimair, B. E. and Ana, L. H., "Analysing the base of precast column in socket foundation with smooth interfaces", *Materials and Structures*, Vol.42, No.6, 2009, pp. 725-737.
- [5] ACI318, *Building Code Requirements for Reinforced Concrete*, American Concrete Institute, Detroit, Michigan, 2005.
- [6] Hansapinyo, C., Buachart, C. and Wongmetha, P., "Cyclic Performance of precast concrete columns using steel box connection", *International Journal of Civil Engineering*, Vol. 15, No. 4, 2017, pp. 663-676.
- [7] ACI T1.1-01, *Acceptance criteria for moment frames based on structural testing*, American Concrete Institute, 2001.
- [8] Chopra, A. K., "Theory and Applications to Earthquake Engineering: Dynamic of structure (3rd Edition)", Prentice Hall, Englewood Cliffs, NJ, 1999.
- [9] AISC, *Steel Construction Manual*, American Institute of Steel Construction (4th Edition), 2011.

Environment

UTILIZATION OF BUCKLEY-LEVERET THEORY IN BAZARKAMI OIL FIELD IN NORTHERN OF AFGHANISTAN

Zabihullah Mahdi and Shigeo Honma

ABSTRACT

Hydrocarbon resources are important for the rehabilitation and sustainable progresses of Afghanistan's infrastructure. The purpose of this paper is to increase the oil production from petroleum reservoirs of Bazarkami oil field, applying Buckley-Leverett frontal displacement theory, in north part of Afghanistan. In this paper oil displacement is studied by injecting water in to the petroleum reservoir which is known as waterflooding technique. The theory is investigated by laboratory experiment; and graphical study is improved in a horizontal plane model which designed for study of fluid flow properties through porous media. Furthermore, the result of laboratory experiment is compared with graphical calculation, then the theory is applied on the planed oil field, which is now under process of a private petroleum company. The relative permeability of oil and water that obtained by laboratory experiment in reference to the literature by authors, is performed in this study. Based on this study, a considerable amount of oil production obtained from Bazarkami oil field, by determining water-oil displacement characteristic, residual oil saturation, Advance frontal saturation and F_{BL} is determined.

Keywords—waterflooding, petroleum reservoir engineering, two-phase flow, immiscible displacement in porous media, relative permeability, Buckley-Leverett.

INTRODUCTION

Fig. 1 illustrated a naturally general state of a petroleum reservoir where gas is located at the top of the reservoir under cap rock, oil is stored under the gas and there is water in the bed of reservoir [5]-[8].

When water is injected into a petroleum reservoir, oil is displaced toward the production well in a situation of two-phase flow. Buckley and Leverett, in 1942, have studied the mechanism of immiscible displacement of two-phase flow [6].

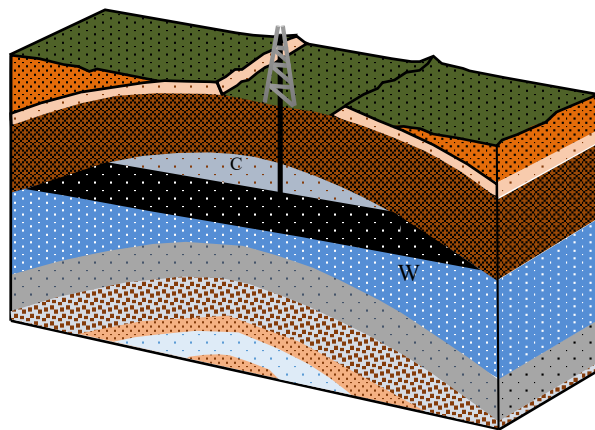


Fig. 1 Typical petroleum reservoir

The Buckley-Leverett frontal displacement theory describes a graphical method to calculate saturation profile based on relative permeability; the effect of capillary pressure between two fluids and the gravitational effects are assumed to be neglected. Based on this theory, the advance of a front saturation by displacing fluid is affected by the oil and water permeability and viscosity ratio between the two fluids [11].

In this paper recovery of heavy oil by water based on the Buckley-Leverett frontal displacement theory has been evaluated. In this study first the oil displacement by water obtained by laboratory experiment then the graphical calculation has been applied. Finally, the result of the laboratory experiment and graphical calculation have been compared. In this paper, the residual oil saturation, irreducible water saturation, S_{BL} , f_{BL} and heavy oil recovery factor were determined.

BUCKLEY-LEVERETT THEORY

Buckley-Leverett is a simple, widely used method of investigating the advance of a fluid displacement front in an immiscible displacement process [3],[8]. The theory is used fractional flow and it is based on flow should be linear and horizontal; water is injected into a petroleum reservoir; oil and water are both incompressible; oil and water are immiscible and the effect of gravity and capillary pressure are negligible [8].

Mostly in petroleum reservoir rocks there is a transition zone between water and oil. Saturation of water is 100% in a true water zone but in the oil zone, there is usually connate water, which counts as an immobile water. Oil and water will produce together from a well if it is in the transition zone. The fractional flow rate at each point will depend on to the water and oil saturation in the reservoir. It is mentioned that Buckley-Leverett advance theory is an application of the law of the mass conservation [8].

Fluid flow through a small volume section with length of Δx and cross-sectional area of " A " may be expressed in terms of total flow rate q_t as in (1):

$$q_t = q_o + q_w$$

(1)

$$q_w = q_t \times f_w$$

(2)

$$q_o = q_t \times f_o = q_t \times (1 - f_w)$$

(3)

In Eq. 3 the q is volumetric flow rate in petroleum reservoir situations, sub-script (o, w, and t) referred to the oil, water, and total rate, respectively and f_w and f_o are water and oil fractional flow respectively.

The one-dimensional flow rate of oil and water by considering of oil displacement by water in a completely saturated porous medium can be investigated by Darcy's law as

$$q_w = -\frac{k_z k_{rw} A}{\mu_w} \frac{\partial p_w}{\partial z}$$

(4)

$$q_o = -\frac{k_z k_{ro} A}{\mu_o} \frac{\partial p_o}{\partial z}$$

(5)

in equation 4 and 5, k_z is the intrinsic permeability of the porous medium, in equations 4 and 5, A the cross-sectional area of the reservoir, and μ_o and μ_w are the dynamic viscosity of oil and water, k_{ro} and k_{rw} are the relative permeability of oil and water, p_w and p_o and pore pressure of water and oil respectively.

As illustrated in Fig. 4 the relative permeability of oil and water (k_{ro} and k_{rw}) are typically given as a function of water saturation S_w and S_{or} and S_{wi} are the residual oil saturation and irreducible water saturation in the petroleum reservoir. The capillary pressure is denoted by $p_{o/w}$, and p_w and it can write as equation (6):

$$q_w = -\frac{k_x k_{rw} A}{\mu_w} \frac{\partial (p_o - p_{o/w})}{\partial x}$$

(6)

subtracting Eq. (4) from Eq. (6), gives

$$-\frac{1}{k_x A} (q_w \frac{\mu_w}{k_{rw}} - q_o \frac{\mu_o}{k_{ro}}) = -\frac{\partial p_{o/w}}{\partial x}$$

(7)

From the relation that explained in equation 1, 2 and 3 into Eq.

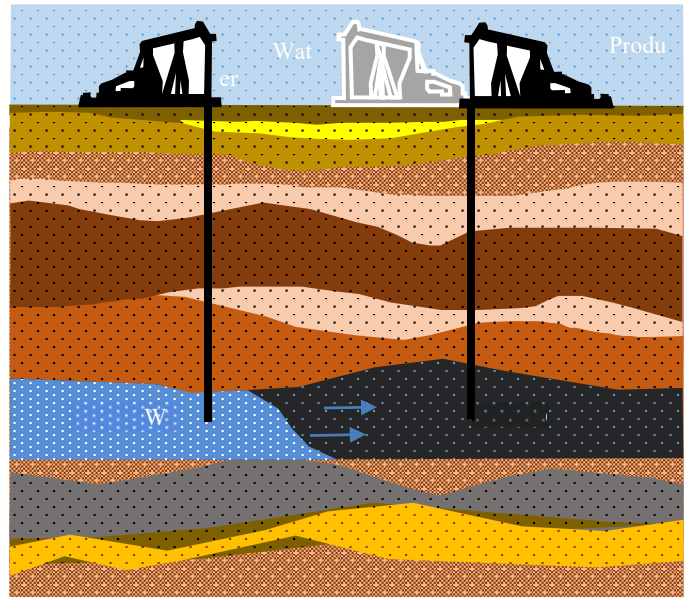


Fig. 2 Displacement of oil by water in a natural petroleum reservoir.

(7) gives

$$q_T = q_w \left(1 + \frac{k_{ro}}{k_{rw}} \frac{\mu_w}{\mu_o}\right) - \frac{k_x k_{ro} A}{\mu_o} \frac{\partial p_{o/w}}{\partial x}$$

(8)

The fractional flow f_w can give as

$$f_w = \frac{q_w}{q_T} = \frac{1 + \frac{k_x k_{ro} A}{q_T \mu_o} \frac{\partial p_{o/w}}{\partial x}}{1 + \frac{k_{ro}}{k_{rw}} \frac{\mu_w}{\mu_o}}$$

(9)

The capillary pressure ($p_{o/w}$) is essentially very small compared with the oil/water pressure when oil displaced by water in the petroleum reservoir. If the effect of capillary pressure neglected, for the horizontal flow, the fractional flow equation is expressed simply as

$$f_w = \frac{1}{1 + \frac{k_{ro}}{k_{rw}} \frac{\mu_w}{\mu_o}}$$

(10)

The continuity equation may be presented to take the conservation of fluid mass [13], and this is expressed as

$$-\frac{\partial q_w}{\partial x} = A \phi \frac{\partial S_w}{\partial t}$$

(11)

In equation (11), ϕ is the porosity of the reservoir rock. Using the relations $q_w = f_w q_T$ and $f_w(S_w)$, Eq. (11) is rewritten as:

$$\frac{\partial S_w}{\partial t} = -\frac{q_T}{A \phi} \left(\frac{df_w}{dS_w} \frac{\partial S_w}{\partial x} \right)$$

(12)

Because $S_w(z, t)$, we can express saturation change as

$$dS_w = \frac{\partial S_w}{\partial x} dx + \frac{\partial S_w}{\partial t} dt$$

(13)

In Eq. (13), if the fluid is at constant saturation during the displacement process, can rewrite it as

$$0 = \frac{\partial S_w}{\partial x} dx + \frac{\partial S_w}{\partial t} dt$$

(14)

Then, it follows that

$$\frac{\partial S_w}{\partial t} = - \frac{\partial S_w}{\partial x} \frac{dx}{dt}$$

(15)

Substituting Eq. (15) into Eq. (12), obtain

$$\frac{\partial x}{\partial t} = \frac{q_T}{A\phi} \left(\frac{df_w}{dS_w} \right)$$

(16)

Equation (16) indicates the Buckley-Leverett theory. This equation illustrates, the rate of the advance plane of fixed water saturation S_w , which is directly proportion to the rate of changes in the stream and is a composition with saturation. Because f_w is not an explicit function of t , so Eq. (16) can be integrated to give the position of a particular saturation value as a function of time.

$$x_{S_w} = \frac{q_T t}{A\phi} \left(\frac{df_w}{dS_w} \right) + x_0$$

(17)

In Eq. (17), x_0 is the position of the water saturation at time $t = 0$.

The saturation profile which explained by Eq. (17) is described in Fig. 3 denoted by the curves “abcd”. The conservation of the mass over the advance position was applied by Morel and Seytoux [9]. Based on this application the hatched area which denoted by A is equal to the hatched area described by B in Fig. 3. The saturation advanced immediately behind the front can be calculated by tangent point c on the fractional flow curve. The tangent point c on the fractional flow curve is explained in Fig. 9. The sudden front in the saturation profile is given by line cf (Fig. 9) [10].

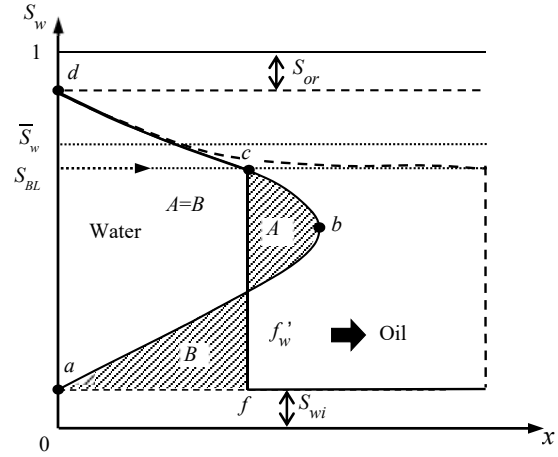


Fig. 3 Tentative saturation profile

RELATIVE PERMEABILITY OF HEAVY OIL AND WATER

Relative permeability is an important parameter that controls the immiscible displacement of two-phase fluids flow in porous media. There are numerous factors that affect the relative permeability such as fluid saturations, the effect of rock pore structure, degree of initial saturation S_{wi} , wettability, and temperature. The relative permeability value is measured through laboratory test by steady-state (SS) methods and unsteady-state (USS) methods [5]. The wetting fluid saturation curves were usually water, S_w , extending from the irreducible wetting-phase saturation to the residual oil saturation. As the relative permeability curve of water, k_{rw} , increases, the relative permeability curve of oil, k_{ro} , gradually decrease with desaturation of oil, and in contrast the relative permeability of water will gradually rises to its maximum value k_{rws} (end-point water permeability) at the time where k_{ro} is 0 because water phase is mobile and at it has maximum saturation [12].

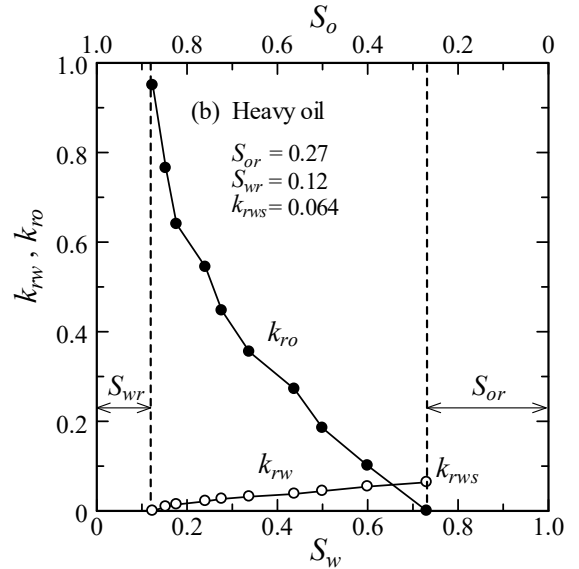


Fig. 4 Relative permeability curves for heavy oil displacement by water [12].

Fig. 4 illustrated the relative permeability curves of heavy oil

and water measured through laboratory experiment by steady state method (SS). In Fig. 4 as relative permeability curves of water, k_{rw} , increases, the relative permeability curve of heavy oil, k_{ro} , gradually decreases. At the left side of the Fig. 4 there is irreducible water saturation ($S_{wr} = 0.12$) and at the right side of the graph, the residual oil saturation ($S_{or} = 0.27$) were demonstrated. It is noticed that displacement of heavy oil by water investigation by Buckley-Leverett frontal displacement theory was calculated by using the relative permeability curves of heavy oil and water illustrated in Fig. 4.

I. EXPERIMENTAL INVESTIGATION OF WATERFLOODING FOR HORIZONTAL DISPLACEMENT

A. Experimental Model

Apparatus illustrated in Fig. 5 was used for horizontal oil displacement by water. Toyoura sand (with the particle diameter, $D = 0.105-0.425\text{mm}$) and the density of soil particle $\rho_s = 2.65\text{g/cm}^3$, was packed in the horizontal square plane with the constant density. It was saturated with heavy oil for the purpose of oil displacement by water.

This apparatus was a regular plane and horizontal square model of 60 cm length and 120 cm² cross-sectional area. At the both sides of the horizontal plane, there was volume area that could keep piezometer pressure at a constant level. There was water supply tank at the left side of the model. The model was designed to study the fluid flow characteristic through porous media. This model made from glass material and has 9 observation wells, with the upstream and downstream level that have been sat to evaluate the hydraulic head from fluid flow pressure. The purpose of this investigation was to evaluate linear horizontal immiscible displacement of fluids flow in

pours media. Water supply tank pushed oil and displaced it from the left side of plain to the right side, displaced fractional fluids discharge were collected at the end of right side of the model.

B. Experimental investigation

Table 1 illustrated the properties of heavy oil, water, sand and experimental model that have been used in the test. Horizontal squire plain model that illustrated in Fig. 5 was packed sand, first saturated by heavy oil. Water pushed through saturated sand plain to displaced heavy oil. Table 2 illustrated piezometer data recorded during the test, from observation wells, it illustrated the hydraulic head verity with the time differences. Fig. 6 illustrated fractional flow discharge of oil and water through horizontal squire plain model. Fig. 6 illustrated heavy oil displacement by water ($q_o = q_T$, q_T is the total input rate). As illustrated in Fig. 6 when soil pore in horizontal squire plain was saturated by heavy oil, the fractional discharge at the outlet f_{od} is 1 until some pore volume, and later some amount of water discharged. Therefore, there was only oil discharged at first 120 min during the operation. After 120 min the oil fractional discharge decreased and water discharge was increased. Finally, after 180 min fluid flow experiment, kerosene discharge was too less, only water is discharged ($f_{wd} = 1$) and fluid flow became the steady state. There was still some amount of heavy oil remained in the plain that can refer to residual oil saturation ($S_{or} = 0.27$).

In this experiment total amount of heavy oil displaced by water until 120 min was 1073 cm³ ($Q_o = 0.39\%$) from total pore volume ($V_v = V \times n = \text{cm}^3$). This experiment was done in 180 min and total discharge of fluids were $Q_T = 1610 \text{ cm}^3$.

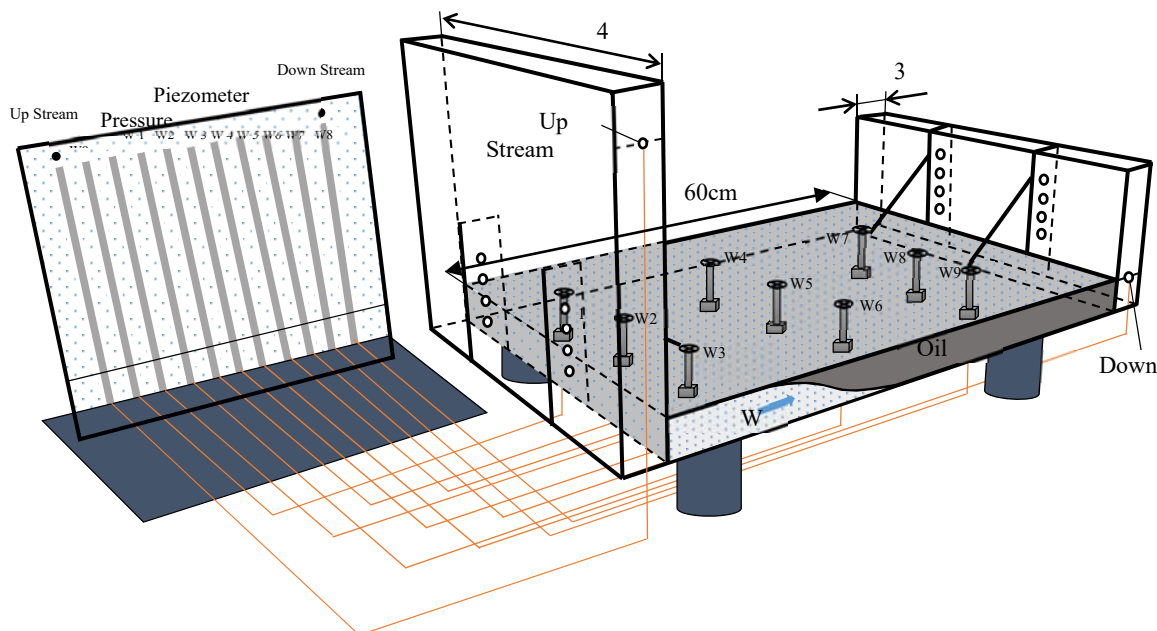


Fig. 5 Experimental apparatus

Table I Properties of heavy oil, water, and test material.

Soil name	Toyoura sand (0.425~0.105mm)	Oil	Heavy Oil (20°C)
Density of soil particle	2.65 (gr/cm ³)	Density	0.837
Column length	60.0 (cm)	Viscosity	0.0107
Column diameter	3.0 (cm)	Volume of soil	0.001
Sectional area	120.0 (cm ²)	Dry density	7200.00
Dry mass of soil	10000.0 (g)	Porosity	1.389
Void ratio	0.908		
Pore volume	3436.42 (cm ³)		
Pumping rate of water	- (cm ³ /s)	Pumping rate of oil	- (cm ³ /s)

Table II Hydraulic head data recorded from the test.

Time : 15 min Time : 30 min Time : 45 min			
Well number	Hydraulic head	Hydraulic head	Hydraulic head
1	13 cm	17 cm	25 cm
2	12.2 cm	24 cm	25 cm
3	13 cm	25 cm	25 cm
4	7 cm	7 cm	14 cm
5	7 cm	7 cm	9 cm
6	6 cm	6.5 cm	9 cm
7	1 cm	1.2 cm	1.5 cm
8	1 cm	1.2 cm	1.5 cm
9	1 cm	1.2 cm	1.5 cm
Upstream	25 cm	25 cm	25 cm
Downstream	0 cm	0 cm	0 cm
Time : 60 min Time : 85 min Time : 110 min			
Well number	Hydraulic head	Hydraulic head	Hydraulic head
1	26 cm	28 cm	28 cm
2	26 cm	28 cm	27 cm
3	26 cm	28 cm	27 cm
4	18 cm	21 cm	21 cm
5	10 cm	21 cm	21 cm
6	16.5 cm	21 cm	21 cm
7	2 cm	14 cm	14.5 cm
8	2 cm	15 cm	15 cm
9	2 cm	1.5 cm	14 cm
Upstream	25 cm	25 cm	25 cm
Downstream	0 cm	0 cm	0 cm

Fig. 7 illustrated the hydraulic head and experimental model during a test at different times. By considering the hydraulic head and piezometer pressure and heavy oil displacement by water in the horizontal square, the plane model is investigated in Fig. 7. As illustrated in Fig. 7 every individual contour line state equipotential line of pressure differences. In fact, the drawing contour line is based on interpolation assumption and approximation method using the observation data recorded during the test.

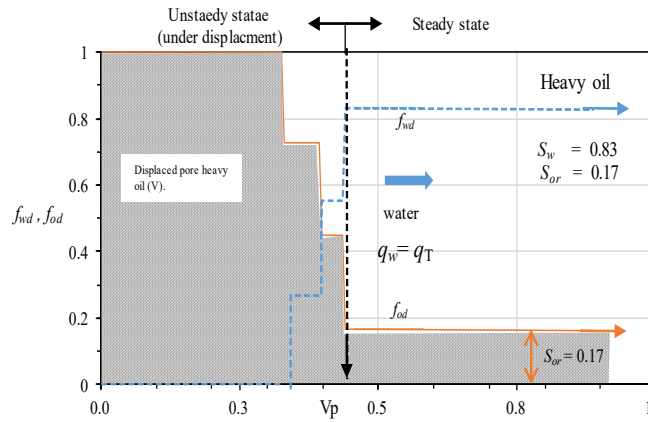


Fig. 6 Experimental result of the fractional discharge of pore heavy oil and water

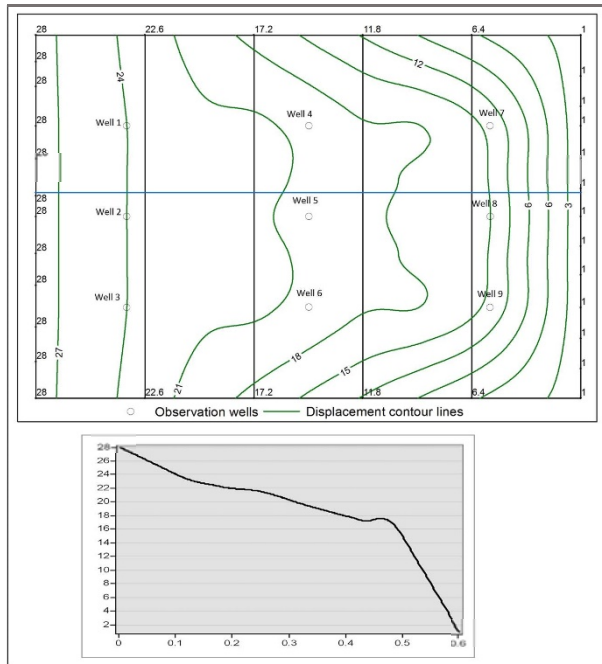


Fig. 7 Contour line for heavy oil displacement by water based on piezometer pressure and it is cross-section.

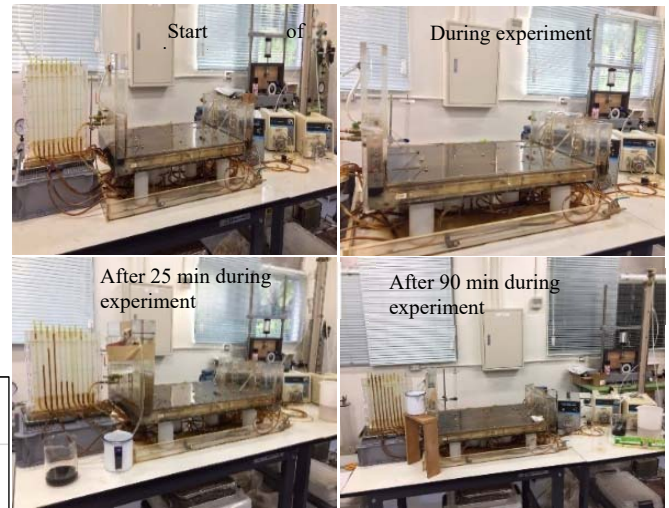


Fig. 8 Experimental apparatus during operation.

II. APPLICATION OF BUCKLEY-LEVERETT THEORY TO EXPERIMENTAL MODEL

The data of table 1 were used for investigation of heavy oil displacement by water through Buckley-Leverett frontal displacement theory. Fig. 5 considered as an artificial petroleum reservoir in this study. In this investigation relative permeability of heavy oil and water that illustrated in Fig. 4 were used. The fractional flow of water and oil may be calculated by equation 10 of section 2. It is known from the experiment that discharge of fluids is 8.94 cm^3 per min, so the water saturation at the front and the average saturation behind the front are found through the graphical method to be $S_{BL} = 0.51$ and $S_w = 0.56$. As illustrated in Fig. 9 the fraction flow of water is an S shape and by using intersection between the tangent line and $f_w = 1$ can calculate the S_{BL} and f_{BL} .

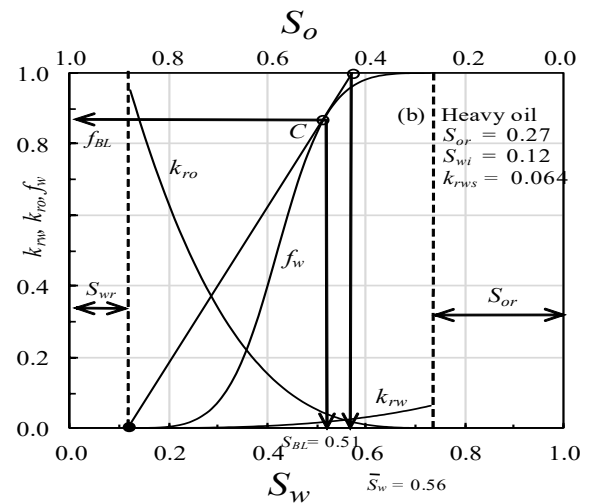


Fig. 9 Relative permeability for heavy oil displacement by water and fractional flow curves.

Fig. 10 illustrated heavy oil displacement by water analyzed based on Buckley-Leverett frontal displacement theory. It has seen the saturation front progresses toward the outlet at a constant speed, and breakthrough occurs at $t = 147$ min. As

shown in Fig. 10 the water displaced heavy oil and reach to the end of a plane model at 147 min and breakthrough occurred, but there is still some amount of heavy oil remained in the column which may be discharged with water together as point out in experiment investigation in section 4. The amount of oil produced may be calculated for a reservoir of area A and distance B by writing Eq. (16) as

$$d x / B = f_w' q_T dt / A \phi B = f_w' q_T dt / V_p = f_w' dv_p \quad (18)$$

where $V_p = A \phi B$ is the pore volume of the reservoir and dv_p is the pore volume of water injected. Because the saturation is steady, the equation can be integrated to obtain the front of swept by water.

$$x = B f_w' v_p \quad (19)$$

where v_p is the pore volume of water injected. When x reaches B , the water saturation at the front is S_{BL} , which makes it possible to evaluate f_w' and calculate v_p , the total amount of oil

displaced by water in units of pore volume [14]. The oil recovery factor of this condition can be calculated by

$$RF = \frac{\bar{S}_w - S_{or}}{1 - S_{or}} \quad (20)$$

$$RFD = \frac{\bar{S}_w - S_{wi}}{1 - S_{wi} - S_{or}} \quad (21)$$

The heavy oil recovery factor is also calculated from Eq. (20) and found to be $RF = 0.40$, from which the amount of water produced up to the breakthrough is $A \phi B \times RF = 1252 \text{ cm}^3$ ($Q_o = 0.45\%$) from total pore volume ($V_v = V \times n$ for the given experimental sand horizontal square plain model).

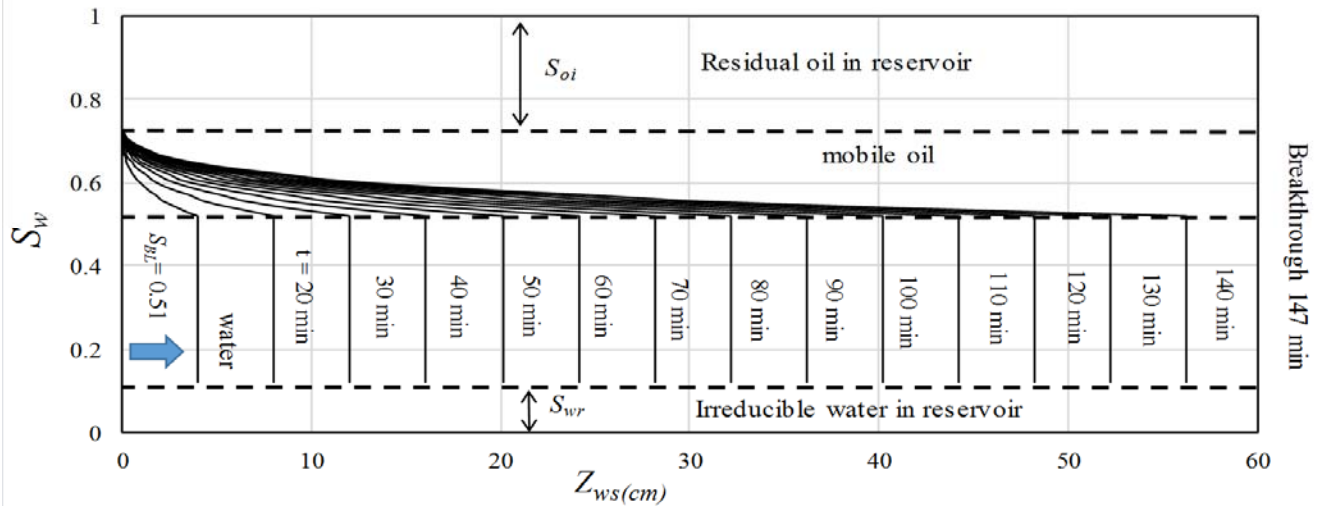


Fig. 10 Calculated results of saturation profile by Buckley–Leverett analysis for heavy oil displacement by water.

RF Recovery factor.

ACKNOWLEDGMENT

The authors are great fully appreciate from Tokai University to provide a comfortable environment for doing the research. We would like to thank from Prof. HONMA who has supported us by his kind advice and sharing his precious experience during this investigation.

REFERENCES

- [1] "Enhanced Oil Recovery", Don, W. Green, G. Paul Willhite, 1998.
- [2] M. Shepherd. Factors Influencing Recovery From Oil and Gas Fields, In M. Shepherd, Oil Field Production Geology, AAPG Memoir 91, p. 37-46.
- [3] R.C. Craft and M. Hawkins, Revised by R.E. Terry, "Applied Petroleum Reservoir Engineering," (Prentice-Hall, 1991), pp.1-35.
- [4] JX. Holdings: Construction of Petroleum Reservoir, <http://www.hd.jx-group.co.jp> (accessed on 03/ 2014). (Translated in English by authors.).
- [5] (CRC Press, 2013), pp.45-83.
- [6] JX. Holdings: Construction of Petroleum Reservoir, <http://www.hd.jx-group.co.jp> (2014) data10. (Translated in English by authors.), accessed on 02/ 2014.
- [7] S.E. Buckley and M.C. Leverett, "Mechanism of Fluid Displacement in Sands, Transactions AIME," Vol.146, (1942), pp.107-116.
- [8] "Principle of applied reservoir simulation", John R. Fanchi.
- [9] H.J. Morel-Seytoux, "Flow through Porous Media," R.J.M. de Wiest ed., (Academic Press, 1969), pp.456-516.
- [10] A. Arabzai and S. Honma "Numerical Simulation of the Buckley-Leverett Problem," Proceedings of School of Engineering of Tokai University, Vol.38 (2013), pp.9-14.
- [11] Hagoort, J "Displacement Stability of Water Drives in Water Wet Connate Water Bearing Reservoirs," 1974. Soc .Pet. Eng. J., February: 63-74. Trans. AI ME.
- [12] J. Nazari, F. Nasiry, N. Seddiqi and S. Honma "Influence of Relative Permeability and Viscosity Ratio on Oil Displacement by Water in Petroleum Reservoir," Proc. School of Eng. Tokai Univ., Vol.40 (2015), pp.15-20.
- [13] Jacob Bear, "Dynamics of fluids in porous Media," 1972, pp 465-479.
- [14] A.Y. Dandekar, "Petroleum Reservoir, Rock and Fluid Properties," (CRC Press, 2013), pp.2-10.

III. CONCLUSION

The conclusion for this study will be explained as follows:

- 1 According to the Buckley-Leverett frontal displacement theory which describes a method of investigating saturation based on the relative permeability and the gravitational effect and capillary pressure effect between the two immiscible fluids are neglected, had been evaluated. It has been identified that fluid flow through porous media should be linear and horizontal. It is mentioned that the saturation advance is largely affected by the permeability of oil and water relativity to collectors and to the viscosity ratio between the two immiscible fluids.
- 2 It is also investigated the rate at which an injected water bank moves through a porous medium. The graphical study is used by fractional flow theory and is based such as flow should be linear and horizontal, water is injected into a petroleum reservoir, oil and water are both incompressible, oil and water are immiscible and the effect of gravity and capillary pressure are negligible.
- 3 Recovery of heavy oil by water is studied in the laboratory, experiments are done to evaluate the residual oil saturation and recovery factor.

APPENDIX

k	Intrinsic permeability
k_{rw}	Relative permeability of water
k_{ro}	Relative permeability of oil
k_{rws}	Endpoint relative permeability
μ_w	Viscosity of water
μ_o	Viscosity of oil
ρ_w	Density of water
ρ_o	Density of oil
p_w	Water pressure
p_o	Oil pressure
q_T	Total pumping rate of oil and water
q_o	Amount of oil
q_w	Amount of water
S_o	Water saturation
S_w	Oil saturation
S_{or}	Residual oil saturation
S_{wi}	Irreducible water saturation
f_w	Fractional water flow
ϕ	Porosity of the reservoir
V_p	Pore volume
A	Cross-sectional area
B	Thickness of reservoir

THE BEHAVIOR OF WASTE PULLING BY PILE DRIVING THROUGH THE BARRIER CLAY LAYER ON CONTROLLED COASTAL LANDFILL SITE

Takayuki Hirao¹, Yoshiaki Kikuchi² Taichi Hyodo³ Masatsugu Kiko⁴ Kouta Katagishi⁵ Shohei Namiki⁵
Satoshi Matsumura⁶ and Makoto Takemoto¹

¹Chuden Engineering Consultants Co., Ltd., Japan; ^{2,3,4,5} Tokyo University of Science, Japan; ⁶ Port and Airport Research Institute, Japan

ABSTRACT

The utilization of coastal waste landfill site remains at low level, up to now. In the consideration of advanced use of these sites, it is necessary to drive some foundation piles through the barrier clay layer. However, there is a concern in the actual field that waste will be pulled into the clay layer by piling. Therefore, a series of experiments were conducted in this research, examining the effect of dragging prevention on pile tip, by model pile penetration experiment and X-ray CT scanning. According to the experiments results, it was found that the pulled-in waste can be reduced by sharpening the tip of the pile. Additionally, with a pile that has an outer edge on the tip, wastes can be easily pulled into between the clay layer and pile, but also found that the pulled-in waste can be reduced by coating a swelling material on the pile surface. Therefore, it is assumed that bring waste can be reduced with a pile that has reinforcement band.

Keywords: pile foundation, pulled-in waste, X-ray CT scanning, absorbent polymer

INTRODUCTION

Like Tokyo bay or Osaka bay, the coastal waste landfill has been executed mainly in the suburbs of metropolis in our country, Japan. These coastal landfill sites have been constructed in offshore. However, after the reclamation is completed, it will become recognized as an important area, as the result of surrounding port areas expansion. In this case, utility value of these landfill site will increase, which is expected to make effective use for as traffic or industrial site. Nevertheless, currently the coastal landfill site is used only horizontally, for such as green space, park or golf course, but there are also cases here and there that many sites are left unused. As described below, the reasons are considered to be largely due to specific circumstance of the landfill site.

When considering effective use for landfill site as an industrial site, many foundation ground of landfill site consist landfilled waste and clay layer as barrier clay layer. Therefore, often the foundation ground is too soft to support the constructions. Also, clay layer is often normal consolidation states in these case, that long term consolidation settlement will become a problem for using the landfill sites. Generally, a pile foundation type structure is consider to be use in this case, and because of the piles are required to install to a ground capable to support the structure, it is necessary to drive some foundation piles through the barrier clay layer. The barrier clay layer is necessary to satisfy structural

standard as waste landfill site after pile driving, however the effect of pile driving through the barrier clay layer on permeability performance has not been cleared in this stage. Also, there is a concern that waste will be pulled into clay layer or taken out of site in some case, while the pile is driving, because of the waste gets tangled and adhere to the pile, However, the effect difference by each pile driving method is also unknown. It is considered that such facts are the cause to not to make advanced use of landfill site.

Against to this situation, Kikuchi and Hashizume [2] or Kamon et al. [3] are doing experimental research about the effect to barrier performances. As a result, it has shown that even if voids are formed between clay layer and the pile surface, if clay layer is normal consolidation state, the voids closed in short time, and there is no influence to barrier of clay layer. Also, about influence by earthquake, Kikuchi et al. [4] have shown that barrier performance is not lowered and pond water (internal water) does not leak to outer site.

On the other side, about waste dragging in to the clay layer, there is an actual case [1] that piles were driven through the barrier clay layer as bridge foundation. In this pile driving method, the steel casing is installed to the ground of landfill site. Then remove the waste in the casing by hammer glove, and make the space that is not filled in waste, then, drive the pile into this space, at the last. With this pile driving method, waste can be completely removed. However, the construction costs are very

high, because it needs triple tubes. Therefore, the inferior of versatility to utilize as general structure foundation is the current subject.

Against to this situation, Kikuchi [5] and Hirao et al. [6] are doing experimental research, an effect for waste type and pile tip shape about behavior of waste dragging by pile driving. And the result shown that is inevitable dragging with close tip piles, and a few dragging with shape tip piles, and it is effective to digging in a pile or coating the swelling material on pile surface in order to prevent the waste dragging.

However, these experimental researches are elemental experiments for finding the effect of pile tip shape qualitatively, and it had carried out under conditions with using the closing tip piles and by simulating the waste with sand. The foundation piles that are mainly used in the actual field are open tip piles made by concrete and steel. It is found that wastes are not homogeneous granules, and have many lumpy items and liner items such as wires include.

From this background, in this research, consider the behavior of waste dragging by installing open ended piles and lumpy items, and investigate the effect of the difference of the pile tip shape and swelling material applied to the pile surface.

METHODOLOGY OF EXPERIMENT

In the experiment for this research, to consider the behavior that waste will be pulled into the clay layer by piling, sands and gravels were laid on clay layer, and drive the piles into this layer, then measured the weight of the sands and gravels that were pulled into the clay layer. The following two methods were used for a method of measuring the sands and gravels that was pulled-in.

The first method is to measure the weight of sands and gravels that has been dragged directly by taking clay layer out from the test vessel after pile driving (hereinafter referred to as “model pile driving test”). The second method is to observe visually for pulled-in conditions of sands and gravels, and to count number of particles, by analysis using the X-ray CT scanner of the test vessel (hereinafter referred to as “X-ray CT scanning test”).

However, in the experiment in this research, barrier clay layer is modeled as clay layer, and wastes are modeled as sands and gravels, then confirmed the pulled-in conditions of sands and gravels by model pile driving to clay, sand and gravel layer. It is considered that the parameter to dominate the pulled-in conditions are friction forces between the piles and ground, or clearance around the piles and particle size. In this experiment, it is modeled by reproducing the stress state and the clearance and the particle size at the realization field. Also, there are various methods for pile driving, and

it is impossible to reproduce these methods in experiments. Therefore, assuming a driving pile method of directly driving into the ground which is considered to be the method pulled-in wastes the most, and then confirm the pulled-in conditions at tip or surface of the piles by experiments.

MODEL PILE DRIVING TEST

CREATE THE MODEL CLAY LAYER

In this experiment, commercial clay called “blue clay” as clay layer that simulates the barrier clay layer was used. It was adjusted by sieving to 106 μ m, considering the separate clay and sand as described later.

Properties of the clay are shown in Table 1. The water content of the blue clay adjusted to slurry states as water content ratio of 100%. It was put into the test vessel shown at the left side on Fig.1. After one and a half day, consolidate with pressure $p=100\text{kN/m}^2$ (equivalent to stress states GL-20m on barrier clay layer). Then continue the consolidation until time to $3T_e$, to create the model clay layer (thickness $h=8\text{cm}$).

LAYING SANDS AND GRAVELS

Silica sand No.5 and gravel No.7 were used as materials that simulate wastes. Silica sand No.5 is simulated as small particle size wastes, using the particles (soil density $\rho_s=2.65\text{ g/cm}^3$, average particle size $D_{50}=0.589\text{ mm}$) left in the sieve with 250 μ m for separate from clay. Also, gravel No.7 is simulated as large particle size wastes, using the particles (average particle size $D_{50}=3.304\text{ mm}$) remain in the sieve with 2 mm. Further, these silica sands and gravels were laid on the clay layer by falling underwater method. It carries out following two type tests to compare the particle size. In case-1, silica sand lay at thickness of 5 cm, this is simulated as small particle size wastes. In other case-2, silica sands and gravels mixed by weight ratio as 3:7. This lay at thickness 1cm, and silica sand lay at thickness 4 cm. These are simulated as the condition with large particle size mixed.

Table 1 Physical Property of BLUE CLAY

Soil Density	2.79 g/cm ³
Liquid Limit	40.1 %
Plastic Limit	24.2 %
Plastic Index	15.9

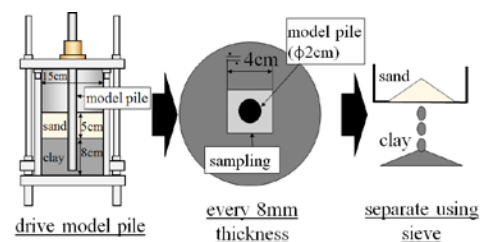


Fig. 1 Experimental Method (outline draw)

DRIVING MODEL PILES

Next, a model pile drives into the model clay layer, using the 4 different type of pile tip shape as shown in Fig.3 for considering the influence of pile tip shape. A model pile drives to the bottom of clay layer statically at driving speed about 10 mm/min, at center of model ground, as shown left side in Fig.1.

Incidentally, model pile diameter is set to $\phi 19\text{mm}$, to secure three times of the pile diameter between pile and vessel inside wall, to not to be affected by lateral conditions at test vessel ($\phi 15\text{ cm}$) when pile driving.

SWELLING MATERIALS

In all of the above experiment cases, experiment case with coating the swelling material on the pile surface, was also conducted. This material is high molecular polymer in solid state in normal conditions, however if it absorbs the water, it swells then becomes to in gel state. It is expected so that the dragging wastes will be reduced by reducing friction forces between the pile and wastes. Prior to this experiment, coat swelling material 5 cm on the tip part of the piles, and let it dry enough. Further, after driving a model pile to the bottom of sand layer (top of the clay layer), in order to absorb and swell enough, standing still for 2 hours, and then driven into the bottom of model ground.

SAMPLING

After driving the pile, clay was sampled around the pile in every 8mm thickness, as shown in the center of the Fig.1. Further, clay and sand were separated using 250 μm sieve as shown on the right side of the Fig.1. And then measure the sands weight that was pulled into model ground per depth.

X-RAY CT SCANNING TESTS

This experiment method is almost the same as the method of model pile driving tests. It carries out with some different conditions, in order to ensure the

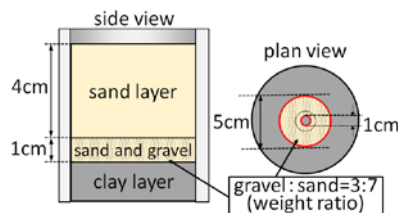


Fig. 2 Laying Method of Sands and Gravels (case-2)

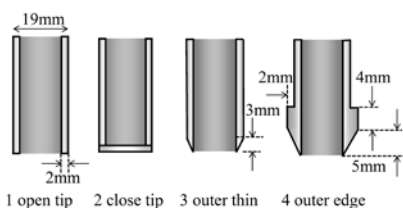


Fig. 3 pile tip shape of model piles(Pile Driving tests)

visibility of sand particle, structural restrictions, and secure experiment time in X-ray CT scanning tests.

For this reason, it is difficult to compare this X-ray CT scanning tests and model pile driving tests directly. However, it can evaluate the mechanism of pulled-in qualitatively by confirmation visually of the pulled-in behavior of sands and gravels caused by pile driving.

First, to create the model ground, mix the clay soil at initial water content of $w=53\%$. And then create by consolidation at pressure $p=100\text{ kPa}$ to shorten the test time and ensure the thickness of test piece using test vessel as shown in the left side of Fig.4.

Next, lay the sands and gravels that is simulated to waste layer on top of the model ground by method of water falling. Sands that was used is YAMAICHI silica sand No.3 ($\rho_s=2.67\text{ g/cm}^3$, $D_{50}=1.276\text{ mm}$), gravels is gravel No.7 as remaining at 4.75 mm sieve.

Same as LAYING SANDS AND GRAVELS, conducted with two case, which is case-1 that laid only silica sands at 5 cm thickness, and case-2 that laid mixed soils (weight ratio of gravels and silica sands is 3:7) at 1cm thickness, and overlay silica sands at 4 cm thickness. After that, drive the three different model type of piles that have different shapes on pile tip (Fig.5) in to the center of model ground till the bottom at driving speed 2 mm/min statically. At that time, stop driving the pile at each certain depth, to scan the test vessel. This is an action to irradiates horizontally X-ray to test vessel, and visualize the absorption of X-ray that catch at sensor through the test vessel. Conduct this action certain times while the test vessel rotates 360 degrees, and reconstruction 3 dimension pictures from 2 dimension pictures obtained by analysis.

With this method, sands and gravels pulled-in behavior by pile driving can be visually confirmed. And count the number of sands and gravels on pictures. Also, in this experiment, coating the swelling material on pile surface is conducted, as same as PILE DRIVING TESTS.

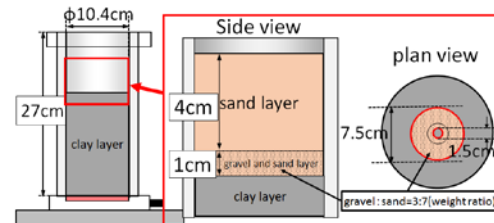


Fig. 4 Test Vessel and Laying method (case-2)

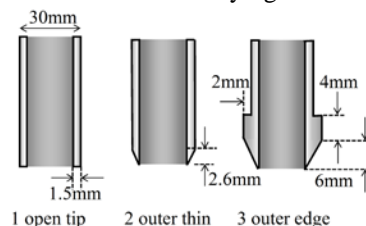


Fig. 5 pile tip shape of model piles (X-ray CT Scanning tests)

RESULT OF EXPERIMENTS

MODEL PILE DRIVING TESTS

MIXTURE OF SANDS AND GRAVELS

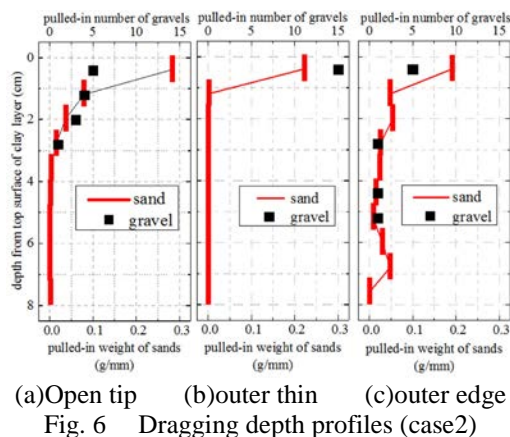
The result (case-2) that was conducted with silica sand No.5 and gravel No.7. A distribution chart of weight of sands and gravels that was pulled into clay layer and its depth is shown in the Fig.6. It shows the vertical axis is depth(cm) from top surface of clay layer, and the horizontal axis is the average weight of the sand contains in the sample collected from thickness 8 mm of clay, and directly count the number of gravels. Incidentally, the thick line on the chart shows average weight within measurement range (8 mm), and the polygonal line is connecting these values at average depth.

As the result, pulled-in sands and gravels adjacent to surface of clay layer, was confirmed on each piles. Also, about (a) open tip pile and (c) piles that has an outer edge on the tip, pulled-in sands and gravels was confirmed from slightly under the clay layer. Particularly, it is remarkable in the case with an outer edge on the tip. Of these, pulled-in sands and gravels up to 3 cm depth was confirmed with (a) open tip pile. Further, it becomes zero at deeper, this fact shows that pulled-in sands and gravels are less.

As shown in the Fig.7(b), in case of close tip pile, behavior that is different from a lot of pulled-in sands at the tip of the piles was confirmed. In case of (c) piles that has an outer edge on the tip, verified pulled-in sands at the bottom of clay layer. Incidentally, in case of (b) with the piles that has thin outside, it was confirmed that pulled-in sands and gravels into the clay layer is almost none. It is suggested to sharpening the tip is effective to reduce the dragging.

DRAGGING REDUCTION EFFECT BY SWELLING MATERIALS

First, the situations of coating and after swelling are shown in the Fig.8. After coating the swelling materials on piles and dried, it becomes to harden state, and it will not peel off from the pile surface.



However, after pile driving, it becomes to gel state by swelling the water from the ground, and expands suddenly. This expanded gel fills the gap between piles surface and surrounding ground, and reduces the friction forces between piles and ground.

Next, among the experiments(case-1) that carried out on the ground made by only sands, by changed the tip shape of the piles, the result that compares with and without swelling materials are shown in Fig.7. As the result, pulled-in behavior adjacent to the surface of clay layer was confirmed at each piles, same as Fig.6. Of these, it is difficult to confirm the effect of reducing the dragging by swelling materials, due to the low volume of dragging by (a) open tip pile and (c) outer thin piles. Also, regarding the (b) close tip pile, it is pulled into the bottom of the clay layer, because of the creation of active wedge on tip of the piles. However, there are no clearly differences because of the existence of swelling materials or no, and the dragging reduction effect by reducing the friction forces around the pile surface, cannot be confirmed.

On the other hand, about (d) piles that has an

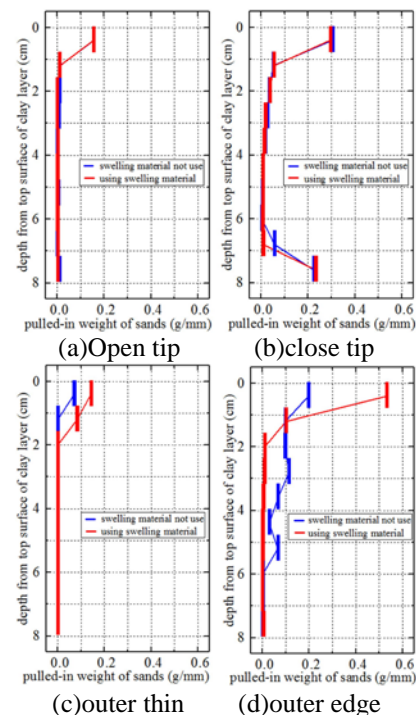


Fig. 7 Dragging depth profiles (case1)

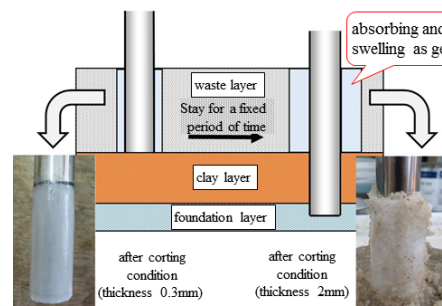


Fig. 8 Effect of Swelling Material

outer edge, reduce of the dragging into the internal clay layer is confirmed, cause of the swelling material fills the gap between piles and ground that was created by an outer edge, which it is considered that the swelling materials are effected to reduce dragging into gap.

X-RAY CT SCANNING TESTS

A sample picture obtained by X-ray CT scanning test is shown in Fig.9. Dragging behavior into the clay layer can be confirmed by this picture.

DRAGGING BEHAVIOR AT THE TIP OF THE PILES

With all of the experimental conditions, sands or gravels adhere to the tip of the piles, and pulled-in into clay layer. To find this behavior, count the number of the sands and gravels at the tip of the piles by horizontal scanning pictures, which is shown in Fig.10.

As the result, in the case of open end pile, it has sands pulled in to the bottom of the clay layer. In the case of the outer thin piles and outer edge piles, pulled-in has remained at the 25 mm depth. Also in the case of gravels, confirmed dragging into the 20 mm depth on the open end piles, though it is up to 10 mm depth on the outer thin piles and outer edge piles. It is considered that particles of sand and gravel are easy to leave (not dragging) from tip of the piles by sharpen the tip of the piles.

Next, about the behavior of sand particles that are adhered to the open tip piles, the three particles

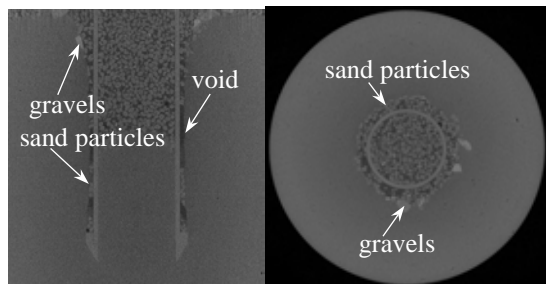


Fig. 9 Picture of X-ray CT Scanning tests

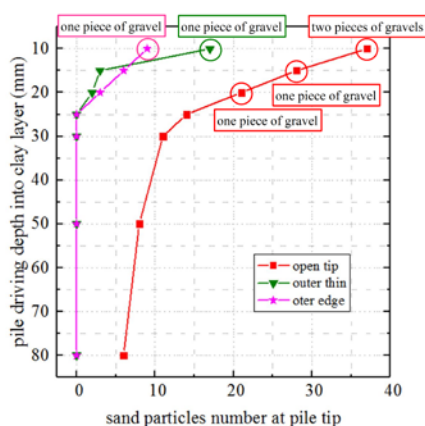


Fig. 10 Dragging in pile tip

were trucked that can be identified before and after the pile driving. In Fig.11, horizontal axis shows penetration amount of the piles, and vertical axis shows the depth which sand particles are pulled-in.

No.1 particle in figure adhere to tip of the pile, and pulled into clay layer while pile driving. It shows that particle leaves from the tip of the pile at the time the pile was driven to 10 mm. Identically, No.2 particle leave from tip of the pile after pulled-in until 35 mm depth, and No.3 particles until 50 mm depth. All of the particles remain at the depth where it left from the tip of the pile. It is unlikely for the particles that was left from tip of the pile, will be pulled-in further more due to the friction force of pile surface.

Further, the enlarged picture of the surrounding of gravels that was pulled-in to the outside of piles is shown in Fig.12. According to this figure, it is confirmed that sand particles adhere to the surface of gravels, which creates a concern of possibility that dragging the large scale particles can promote the small scale particles dragging.

DRAGGING REDUCTION EFFECT BY SWELLING MATERIALS

About the pile with an outer edge at the tip, that had confirmed the effect of swelling materials, will confirm the difference of pulled-in amount, between with or without using the swelling materials. The vertical sectional view after pile driving is shown in Fig.13, and the number of sand particles that had pulled into the gap between piles and surround ground at this time, is shown in Fig.14. On the vertical sectional view, it is confirmed that many sand particles fell in to the gap on an outer edge, when the swelling materials was not used.

Though, this number was confirmed to be reduced

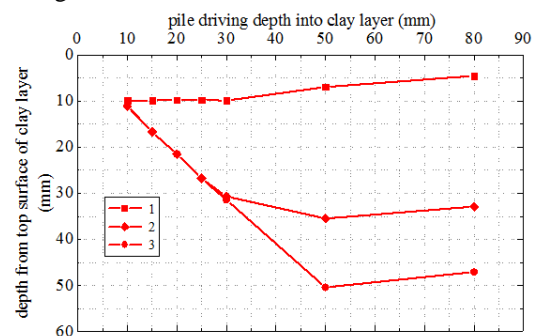


Fig. 11 Behavior of sand particles at pile tip

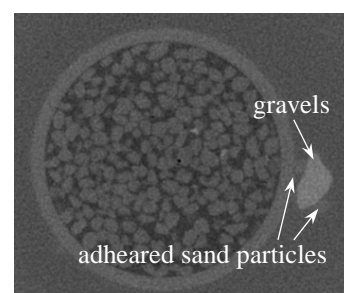
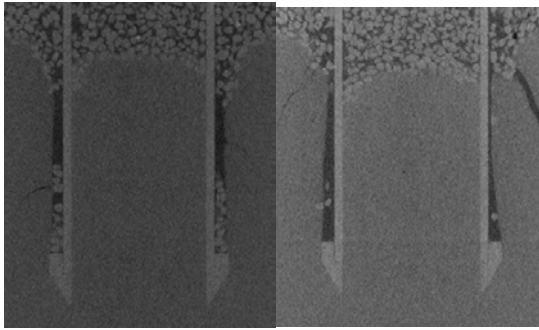


Fig. 12 Dragging in pile tip



(a)no Swelling Material (b)Swelling Materials
Fig. 13 Dragging in pile tip

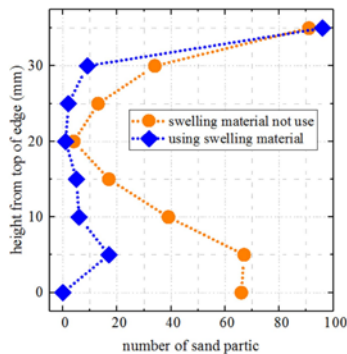


Fig. 14 Dragging number in pile tip

in the case of using swelling materials. This is considered because of the swelling materials fell the gap that was created by an outer edge, which means the piles that has an outer edge, can expect the dragging prevention effect by using swelling materials.

CONCLUSION AND FUTURE ISSUE

In this research, wastes was simulated with sands and gravels, and the behavior of these sands being dragging into the clay layer was investigated experimentally. As a result, in order to reduce the dragging particle wastes into the clay layer, it was suggested, to sharpen the tip of the piles, and the effectiveness of coating swelling materials on the surface of outer edge piles. Also, it was confirmed of the possibility that the dragging large scale waste promote dragging small scale wastes, and the particles that adhere on the tip of the piles, will not be dragging further more after it left from the tip of the piles. In this research, for the convenience of experiment, clay layer was consolidated at pressure 100 kPa, and so, it was in over-consolidation state that is difficult to recover from deformation.

However, actual barrier clay layer of landfill sites is often in the normal-consolidation state, therefore, it is necessary to conduct an experiment in the same state. Additionally, wastes contains

various things, so experiments was not conducted about string state wastes, like wires or bands, because dragging mechanism is different from particle wastes. An experiment of such a case is necessary.

REFERENCES

- [1] Katayama H, Tezuka H, Yamashita K, "Triple Tubular Steel Pile in the Waste Disposal Landfill - The Second Stage Construction of Tokyo Port Coastal Road -", Bridge and Foundation Engineering, Vol. 42, No. 4, 2008, pp. 43-46.
- [2] Kikuchi Y, Hashizume H, "Laboratory test on permeability of ground around a pile", symposium on geotechnical and geo-environmental engineering, vol. 6, 2005, pp. 217-224.
- [3] Kamon M, Katsumi T, Inui T, Hamada S, "Experimental Study on the Interface Transmissivity between Clay Layer and Steel Pile Installed at Waste Disposal Site", Reprinted from Journal of the Society of Materials Science, vol. 54, No.11, 2005, pp. 1100-1104.
- [4] Kikuchi Y, Sugano T, "Construction Possibility of Piles Penetrating Impervious Ground in Offshore Waste Repository", Geotechnical Engineering Magazine, vol. 56, No. 8, 2008, pp. 28-29.
- [5] Kikuchi Y, Moriwaki T, Katsumi T, Hirao T, Tsutakawa T, Hattori A, Okamoto K, Yamada K, Sasaki K, "Influence of pile installation on the barrier performance of natural clay layer at offshore waste landfill", Technical Note of The Port and Airport Research Institute, No. 1252, 2012.
- [6] Hirao T, Tsutakawa T, Sanada K, Moriwaki T, Hattori A, Okamoto K, "A study on the influence of the foundation pile driving to the clay liner in the controlled type seaside landfill site", The 44th Japan National Conference on Geotechnical Engineering, 2009, pp. 1907-1908.
- [7] Watabe Y, Mizutani T, Kaneko T, Masukado K, "Applicability of piled foundation at confined disposal facilities in coastal area - in situ demonstration for pile-driving and impermeable performance at untreated wastes ground", Technical Note of the Port and Airport Research Institute, No. 1321, 2016.
- [8] Okamoto K, Umezaki T, Hattori A, "Development of Absorbent Polymer Materials for Reducing Adhesion and Skin Friction of Underground Structures", Journal of JSCE, Division C : Geotechnics, vol. 67, No. 4, 2011, pp. 407-421.

TOXICITY AND BIOEFFICACY OF WEED ESSENTIAL OILS AGAINST COWPEA BRUCHIDS AND THEIR EFFECT ON MUNGBEAN SEEDS

Ruchuon Wanna¹ and Perayos Khangkhun¹

¹Faculty of Technology, Mahasarakham University, Thailand

ABSTRACT

These investigations aimed to determine toxicity and bioefficacy of weed essential oils Bitter bush (*Eupatorium odoratum* L.), Finger grass (*Limnophila aromatica* (Lamk.) Merr.), and Vietnamese mint (*Polygonum odoratum*) derived by hydrodistillation against cowpea weevil, *Callosobruchus maculatus* (Fabricius) on stored mungbean. Experiments was assessed under laboratory conditions (30±2°C, 70-80%RH and 16L:8D photoperiods). Results showed that weed essential oils from Bitter bush, Finger grass and Vietnamese mint leaves have contact toxicity on cowpea weevil as shown by the impregnated filter paper test. LC₅₀ values were 137.15, 225.17 and 99.12 ppm at 48 h after exposure, respectively. Fumigant toxicity by the fumigation method on cowpea weevil showed all weed essential oils had high efficiency against the cowpea bruchids *C. maculatus* (100% of mortality). Repellency toxicity test showed that weed essential oils from Bitter bush, Finger grass and Vietnamese mint leaves have repellent toxicity on cowpea weevil as LC₅₀ values were 607.23, 141.93 and 109.81 ppm at 6 h after exposure, respectively. The potential of weed essential oils on reproduction of the cowpea bruchids female adults had strong repellent activity for egg laid on mungbean seeds, were 100% at 48 h. Three weed essential oils did not affect the seed germinating. These results suggested that essential oils from three weed plants could be used as potential control agents for cowpea bruchids, and the database can be used for active ingredient studies to develop commercial products in the future.

Keywords: Lethal Concentration, Toxicity, Mungbean Insect Pests, Oviposition Behavior, Seeds Viability

INTRODUCTION

Mungbean, *Vigna radiata* L. Wilczek is one of the most important legume crops in Thailand. Mungbean grown as short rotation crops interspersed with rice and vegetable crops. It provides an inexpensive source of dietary protein to the people and use as protein supplement for meat and fish in animal feed industries. It contains digestible carbohydrate, dietary fiber, calories and lysine [1], [2]. Growing mungbean need to keep seeds for used as seed and consumption. The production of mungbean (*V. radiata*) was restricted by biotic and abiotic factors both in the field and the seed in storage. Among the constraining biotic factors are insect pest. While crops may be infested in the field, infestations are often too low to detect at harvest. Bruchids are most often not detected until seed has been stored for over long periods (e.g. for longer than three months), especially at small scale farming levels. Bruchids are a major and growing problem in stored mungbean in all regions. Bruchids breed rapidly in storage and by the time they are detected, the infested grain is usually unmarketable. The bruchid responsible for most infestations in mungbean is the cowpea bruchids, *Callosobruchus maculatus* (Fabricius). Larvae developing within the grain do the largest damage. Their damage caused

loss of weight, nutritional value and viability of stored grains [3].

Control of cowpea bruchids in the field and store has to be considered in relation to the economic importance of the crop, since it is obvious that these weevils are capable of attacking cowpea both in the field and in storage. In the latter, where feasible, the use of synthetic insecticides is one of the methods used to control cowpea bruchids [4]. Insecticides may be applied as liquid or fumigant formulations. However, continuous use of chemical insecticides may lead to serious problems such as insecticide resistance. Non-chemical methods of bruchid control offer an attractive alternative because the neither leave chemical residues in the commodity no could their use give rise to resistance in the pest. Such methods include periodic exposure of the grains to the sun, coating seeds with cooking oils, or mixing them with ash or sand [5]. Some plant materials have insecticidal properties that could help to control the invading pests [6]. Alternative options for protection cowpea bruchids are using of nature local plant extracts. They can be found and annually growth, such as using of essential oils extracted from the local weeds. Therefore, the most people see weeds and no useful. The objective of this study was to evaluate the lethal toxicity, fumigant toxicity, repellent toxicity and oviposition behavior of weed

essential oils on cowpea bruchids, including their effect on mungbean seed viability.

MATERIALS AND METHODS

Insect Stock Culture

Cowpea bruchids, *Callosobruchus maculatus* was collected from the previously infested mungbean seeds in the grain storage of Department of Agriculture Technology, Faculty of Technology, Mahasarakham University. Insect rearing was carried out inside a glass bottles (\varnothing 15 cm and height 30 cm) covered with mesh netting and kept under laboratory conditions ($30\pm 2^{\circ}\text{C}$, 70-80%RH and 16L: 8D photoperiods). Fifty pairs of male and female of *C. maculatus* adults were isolated and released in a glass bottle having 500 g of mungbean seeds, removed infested seeds and sterile by kept under freezing for 2 weeks and left for 24 h under ambient conditions [7], covered by mesh netting. After 4 weeks, they were separated and used female adults (3-5 days old) in the investigation. Toxicity and bioefficacy bioassays were performed on the adults.

Stored Product

Mungbean obtained from the local market healthy and fresh seeds were used to avoid any pre storage infestation seeds or egg laying of cowpea bruchids and stored followed Ojanwana and Umoru [7]. Mungbean was used in experiments as effect of weed essential oils on the egg laying behavior and mungbean seed germination.

Weed Essential Oils Preparation

Three weed essential oils extracted from Bitter bush (*Eupatorium odoratum* L.), Finger grass (*Linnophila aromatica* (Lamk.) Merr.) and Vietnamese mint (*Polygonum odoratum*), were collected around the Mahasarakham local in the Northeast of Thailand. Bring fresh leave of each weed was washed and air dried in the shade. Using a Steam distillation, the extraction of the essential oils was performed from 1,000 g of fresh weed leaves and 1 liter of distilled water with a rotary evaporator, at the Department of Agricultural Technology, Faculty of Technology, Mahasarakham University. The weed essential oils were desiccated with anhydrous sodium and kept into a vial with the lid closed in the dark at 4°C until use.

Experimental Procedure

The experiment was conducted at laboratory conditions ($30\pm 2^{\circ}\text{C}$, 70-80%RH and 16L:8D photoperiod). Experimental design was Completely

Randomized Design (CRD) with 5 replicates in 5 laboratory experiment.

Contact toxicity bioassay of weed essential oils

Contact toxicity of three weed essential oils against cowpea bruchids were evaluated by impregnated filter paper test, a modified method after Fournet *et al.* [8]. Bioassay was conducted at $30\pm 2^{\circ}\text{C}$, 70-80%RH and 16L:8D photoperiod. The serial solutions of weed essential oils were prepared by dissolving in acetone to achieve the desired concentrations: 5-6 concentrations. For each preparation was dropped and flowed on a disk of filter paper (\varnothing 9 cm) placed in a Petri dish (\varnothing 9 cm and height 1.5 cm) using micropipette. The treated filter paper was air dried and allowed to evaporate the solvent completely before cover petri dish was placed on the petri dish. Ten female adults of cowpea bruchids taken from insect stock culture were released in a petri dish and five replicates were set for each concentration. Acetone was used as controls. The dead cowpea bruchids, no response to blunted needle poking, after 24, 48 and 72 h were recorded. The data were analyzed for the Median Lethal Concentration (LC_{50}).

Fumigant toxicity bioassay of weed essential oils

Fumigant toxicity of three weed essential oils was tested against female adults of the cowpea bruchids *C. maculatus* modified method of Keita *et al.* [9]. Ten female adults taken from the insect stock culture were placed in a glass bottle (\varnothing 5 cm and height 6 cm) and covered with mesh netting and rubber band. Using micropipette dropped weed essential oil inside the center of filter paper (\varnothing 2 cm) in another a glass bottle with various concentrations. Bring a glass bottle contained cowpea bruchids to overlap with a glass bottle dropped of weed essential oil into it. Use clear tape wrapped around a joint of both glass bottles and carried out under laboratory conditions ($30\pm 2^{\circ}\text{C}$, 70-80%RH and 16L:8D photoperiods). Cowpea bruchids *C. maculatus* cannot be directly contact oil because it had a mesh barrier. Dead of adult cowpea bruchids *C. maculatus* were counted after 12, 24 and 48 h.

Repellent toxicity of weed essential oils

Repellency toxicity bioassay was modified method [10] by weighing 10 g of sterile mungbean placed in flask and treated with the solvents of three weed essential oils. Let until mungbean seeds dried to evaporate. Pour the mungbean into plastic cup (\varnothing 5 cm and height 2 cm), had a hole in the bottom so that insect can get through but mungbean cannot, placed on the top a glass bottle (\varnothing 5 cm and height 6 cm). Ten female adults of cowpea mungbean *C.*

maculatus (3-5 days old) were released the middle of plastic cup within contain treated mungbean seeds. It closed with mesh net (size 6 × 12 cm) to prevented insect evasion. Each treatment was replicated five times and the numbers of cowpea bruchids *C. maculatus* settled on each glass bottle were counted and recorded at hourly intervals for 1, 3, 6 and 12 h. Treated mungbean with acetone was used as control.

Impact of weed essential oils on the oviposition behavior

Weighing 10 g of sterile mungbean placed in flask and treated with various the solvents of three weed essential oils. Let until mungbean seeds dried to evaporate. One pair of adults cowpea bruchids placed in a glass bottle within contain treated mungbean seeds for 48 h. Adults were separated and counted the number of eggs on surface of mungbean in each treatment, compared the control with acetone.

Effect of weed essential oils on the mungbean seed viability

Weighing 10 g of sterile mungbean placed in flask and treated with various concentrations (LC₂₀ and LC₄₀) of three weed essential oils. Let until mungbean seeds dried to evaporate. Bring mungbean seeds tested seed germination by each treated mungbean seed was counted and divided into 5 replicates (50 seeds per replicate). Germination test was conducted in a plastic box (size 22 × 33 cm and height 7 cm) within contain 1,000 g of fine sand, was incubated at 150°C for 10 h and separated the other contamination with mesh net, and distilled water 132 ml. Put 50 seeds in a plastic box by a row of five rows along the length of the row of 10 seeds off the plastic covered and kept on the shelf under laboratory conditions. When seed germination was opened the plastic box and keep moisture, add water. Until after 7 days of seed germination were counted seedling in each treatment for checking percentage of seed germination.

Data Analysis

Toxicity bioassay, linear regression analysis was performed from the data obtained to estimate adult mortality for each concentration of three weed essential oils. The mortality was calculated using the Abbott formula [11]. The resulting concentration-mortality data was subjected to probit analysis [12]. Data recorded for percentage of mortality in all toxicity experiments and percentage of seed viability of different treatments were subjected to statistical analysis using CRD design by one-way analysis of variance (ANOVA). Means were compared by using Duncan's Multiple Range Test (DMRT).

RESULTS

Contact Toxicity Bioassay of Weed Essential Oils

Weed essential oil of Vietnamese mint (*P. odoratum*) had the most contact toxicity to cowpea bruchids within 48 h after treatment with the LC₅₀ of 99.12 ppm compare with 137.15 ppm of Bitter bush (*E. odoratum*) and 225.17 ppm of Finger grass (*L. aromatic*), respectively (Table 1). Mortality value exposed with three weed essential oils to cowpea bruchids after treatment at 48 h resulted in adult mortality values between 42-66% and it cause highest significant different (P<0.01) (Table 2).

Fumigant Toxicity of Weed Essential Oils

It is reported that all weed essential oils had efficiency against the cowpea mungbean *C. maculatus*, 100% of adult mortality when comparison with distilled water and acetone treatments and also was high significant different.

Repellent Toxicity of Weed Essential Oils

Result showed that essential oil of Vietnamese mint (*P. odoratum*) has highest against the cowpea bruchids *C. maculatus*. And then Finger grass (*L. aromatic*) oil and Bitter bush (*E. odoratum*) oil had against the cowpea bruchids *C. maculatus*. LC₅₀ at 6 h were 109.81, 141.93 and 607.23 ppm, respectively (Table 3). Repellent value exposed with three weed essential oils to cowpea bruchids after treatment at 6 h resulted in adult mortality values between 34-66% and it cause highest significant different (P<0.01) (Table 4).

Effect of Weed Essential Oils on the Oviposition Behavior

The effect of tested three weeds essential oils on the reproduction of the cowpea bruchids *C. maculatus* female adults were studied using no-choice test. All weed essential oils acted as oviposition deterrent. Egg laid by female on treated seeds with weed essential oils had strong repellent activity (100%) at 48 h (data no representation).

Effect of Weed Essential Oils on the Mungbean Seed Viability

The findings of the present study indicated that mungbean seeds treated with all weed essential oils did not lose their viability and also did not show significant effect on the seed germination rate within 7 days (Table 5).

Table 1 Contact toxicity of weed essential oils against the cowpea bruchids *C. maculatus* at 48 h.

Weed essential oils	LC ₅₀ ^a (ppm)	95%CL ^b (ppm)	χ^2	P-value
Bitter bush (<i>E. odoratum</i>)	137.15 ± 87.63	42.15 – 446.26	0.0086	0.9263
Finger grass (<i>L. aromatic</i>)	225.17 ± 99.43	97.24 – 521.38	0.0245	0.8756
Vietnamese mint (<i>P. odoratum</i>)	99.12 ± 132.90	11.40 – 861.24	0.0003	0.9862

^a LC₅₀ represent the median concentration.^b 95%CL represent the lower and upper fiducially limits.Table 2 Mortality of cowpea bruchids *C. maculatus* with contact toxicity treated weed essential oils at 24, 48 and 72 h.

Treatments	Conc. (ppm)	Mean (±SE) mortality (%)		
		24 h	48 h	72 h
Distilled water		0.0 ± 0.00 g	0.0 ± 0.00 i	2.0 ± 0.45 g
Acetone		2.0 ± 0.45 f	2.0 ± 0.40 h	12.0 ± 1.10 f
Bitter bush (<i>E. odoratum</i>)	100	28.0 ± 0.84 c	50.0 ± 0.63 f	84.0 ± 0.55 e
	200	30.0 ± 1.22 b	50.0 ± 0.89 f	84.0 ± 1.14 e
	300	34.0 ± 0.89 a	56.0 ± 1.02 c	86.0 ± 1.14 d
Finger grass (<i>L. aromatic</i>)	100	24.0 ± 0.55 e	42.0 ± 0.75 g	84.0 ± 1.14 e
	200	34.0 ± 1.34 a	54.0 ± 1.02 d	86.0 ± 0.55 d
	300	34.0 ± 1.14 a	62.0 ± 2.04 b	90.0 ± 1.41 c
Vietnamese mint (<i>P. odoratum</i>)	100	26.0 ± 0.89 d	52.0 ± 0.40 e	90.0 ± 0.71 c
	200	28.0 ± 1.30 c	52.0 ± 0.98 e	98.0 ± 0.45 b
	300	34.0 ± 1.14 a	66.0 ± 1.74 a	100.0 ± 0.00 a

Means within the same column followed by the same letter are not significantly different (DMRT: P>0.05).

Table 3 Repellent toxicity of three weed essential oils against cowpea bruchids *C. maculatus* at 6 h.

Weed essential oils	LC ₅₀ ^a (ppm)	95%CL ^b (ppm)	χ^2	P-value
Bitter bush (<i>E. odoratum</i>)	607.23 ± 145.44	319.82 – 894.64	0.0005	0.9815
Finger grass (<i>L. aromatic</i>)	141.93 ± 42.85	61.61 – 197.77	0.1546	0.6942
Vietnamese mint (<i>P. odoratum</i>)	109.81 ± 51.64	45.06 – 267.61	0.0525	0.8189

^a LC₅₀ represent the median concentration.^b 95%CL represent the lower and upper fiducial limits.Table 4 Repellent Percentage of cowpea bruchids *C. maculatus* with repellent toxicity treated weed essential oils at 1, 3, 6 and 12 h.

Treatments	Conc. (ppm)	Mean (±SE) Repellent Percentage (%)			
		1 h	3 h	6 h	12 h
Distilled water		0.0 ± 0.00 g	0.0 ± 0.00 j	0.0 ± 0.00 i	0.0 ± 0.00 i
Acetone		2.0 ± 0.45 f	4.0 ± 0.55 i	6.0 ± 0.55 h	6.0 ± 0.55 h
Bitter bush (<i>E. odoratum</i>)	100	10.0 ± 0.71 e	14.0 ± 0.55 h	34.0 ± 0.55 g	68.0 ± 0.84 f
	200	18.0 ± 0.45 c	20.0 ± 0.00g	38.0 ± 0.84 f	74.0 ± 1.14 e
	300	20.0 ± 0.71 b	30.0 ± 0.71 e	40.0 ± 1.00 e	94.0 ± 0.89 b
Finger grass (<i>L. aromatic</i>)	100	14.0 ± 0.55 d	22.0 ± 0.45 f	40.0 ± 1.22 e	64.0 ± 1.14 g
	200	20.0 ± 0.71 b	40.0 ± 1.00 b	62.0 ± 1.30 b	86.0 ± 0.89 c
	300	24.0 ± 0.89 a	48.0 ± 0.45 a	66.0 ± 1.14 a	94.0 ± 0.89 b
Vietnamese mint (<i>P. odoratum</i>)	100	18.0 ± 0.84 c	32.0 ± 1.10 d	46.0 ± 0.89 d	78.0 ± 0.84 d
	200	24.0 ± 1.14 a	38.8 ± 1.82 c	60.0 ± 2.00 c	94.0 ± 0.55 b
	300	24.0 ± 1.14 a	40.0 ± 1.58 b	62.0 ± 0.84 b	98.0 ± 0.45 a

Means within the same column followed by the same letter are not significantly different (DMRT: P>0.05).

Table 5 Effect of three weed essential oils in various concentrations on mungbean seeds viability.

Treatments	Conc. (ppm)	Mean (\pm SE) Germination Percentage (%)	
		5 days	7 days
Distilled water		92.0 \pm 1.00 d	92.0 \pm 1.00 d
Acetone		87.6 \pm 3.56 k	87.6 \pm 3.56 h
Bitter bush	100	88.4 \pm 0.84 i	89.2 \pm 1.52 g
(<i>E. odoratum</i>)	200	89.2 \pm 0.55 h	89.2 \pm 0.55 g
	300	91.2 \pm 2.30 e	91.2 \pm 2.30 e
Finger grass	100	90.4 \pm 3.77 f	90.4 \pm 3.77 f
(<i>L. aromatic</i>)	200	95.2 \pm 1.52 a	95.2 \pm 1.52 a
	300	94.2 \pm 1.67 b	94.8 \pm 1.67 b
Vietnamese mint	100	92.0 \pm 1.58 c	93.2 \pm 2.07 c
(<i>P. odoratum</i>)	200	88.0 \pm 2.55 j	89.2 \pm 2.70 g
	300	89.6 \pm 1.92 g	93.2 \pm 1.14 c

Means within the same column followed by the same letter are not significantly different (DMRT: $P > 0.05$).

DISCUSSIONS

Different spice of plant products in the form essential oils (EOs, powders, pellets, extracts or distillates could be harnessed as potential toxicants, deterrents, antifeedants, repellents and fumigants for exclusion of stored-product pests from grain, and have been used, but low toxicity has obtained much attention for alternative control measures of stored-product pest. Diverse essential oils (EOs) and other plant products have been used. Three weed essential oils investigated showed sufficient protection of cowpea grains from damage by cowpea bruchids, *C. maculatus* and these oils acted oviposition deterrent by adult female. Also, we observed not to affect seed germination which confirms non-adverse effect on grain chemistry. This demonstrated the ability of the oils to act as suffocation materials with the possibility of preventing respiration [13]. However, plant natural products that constitute effective safer alternatives to synthetic insecticides without producing adverse effects on the ecosystem have been tested in the management of stored-product pests [14]-[16]. In this study, we evaluated the insecticidal and repellent properties of Bitter bush (*E. odoratum* L.), Finger grass (*L. aromatica* (Lamk.) Merr.), Vietnamese mint (*P. odoratum*) and EO against *C. maculatus*, under laboratory conditions.

CONCLUSIONS

Based on the results obtained in the current study, it may be conclude that Bitter bush (*E. odoratum* L.), Finger grass (*L. aromatica* (Lamk.) Merr.), and Vietnamese mint (*P. odoratum*) weed plant materials have a broad spectrum of activity against cowpea bruchids *C. maculatus*, and the essential oils could have potential as bioinsecticides in stored product protection. However, since plant

products volatilize quickly in the environment and do not persist for longer duration unlike synthetic pesticides, there could be a need for re-application to obtain the desired results. The efficacy of plant-based pesticides could also be enhanced when dissolved or mixed with a slow release fixative material or carrier such as starch or liquid paraffin, and incorporated as an integral part of integrated pest management system especially at a small-scale farmer level. The essential oil from these plants could become a viable alternative to conventional chemical control strategies. However, further studies need to be conducted in order to evaluate the safety of these oils before practical use in stored-product insect control.

ACKNOWLEDGEMENTS

This research was supported by Research Facilitation and Dissemination of Department of Mahasarakham University, Thailand, which is greatly appreciated.

REFERENCES

- [1] Bliss FA, "Cowpea in Nigeria", Nutritional improvement of food legumes by breeding, Milner M, Ed. Rome: PGA/FAO, 1972, pp. 151-153.
- [2] Bressani R, "Nutritive value of cowpea", Cowpea Res. Prod And Util, Singh SR, Rachie. KO, Eds. New York: John Wiley & Son, 1985, pp. 358-359.
- [3] Swella GB, Mushobozy DMK, "Evaluation of the efficacy of protectants against cowpea bruchids (*Callosobruchus maculatus* (F.)) on cowpea seeds (*Vigna unguiculata* (L.) Walp.)", Plant Protection Science, Vol.43, Issue 2, 2007, pp. 68-72.

- [4] Khalequzzaman M, Chowdhury FD, "Evaluation of mixtures of plant oils as synergists for pirimiphos-methyl in mixed formulations against *Tribolium castaneum* (Herbst)", Journal of Biological Sciences, Vol.3, Issue 3, 2003, pp. 347-359.
- [5] Busungu DG, Mushobozy DMK, "The efficacy of various protectants against *Zabrotes subfasciatus* (Boh) Coleoptera, Bruchidae in common beans" Bean Research, Vol.6, 1991, pp. 62-67.
- [6] Jacobson M, Crosby DG, Naturally occurring insecticides. New York: Marcel Dekker Inc., 1971, 585 p.
- [7] Ojanwana CC, Umoru PA, "The use of two indigenous medicinal plant leaf powders (*Cymbopogon citratus* and *Ocimum suave*) applied as mixed and individual powders to evaluate the reproductive fitness of F1 generation (eggs laid and F2 adult) of *Callosobruchus maculatus* (cowpea bruchid)" Journal of Stored Product And Postharvest Research, Vol.3, Issue 2, 2012, pp. 14-18.
- [8] Fournet A, Rojas de Arias A, Charles B, Bruneton J, "Chemical constituents of essential oils of Muna, Bolivian plants traditionally used as pesticides, and their insecticidal properties against Chagas' disease vectors" Journal of Ethnopharmacology, Vol. 52, 1996, pp. 145-149.
- [9] Keita SM, Vincent C, Schmit J, Arnason JT, Bélanger A, "Efficacy of essential oil of *Ocimum Basilicum* L. and *O. Gratissimum* L. applied as an insecticidal fumigant and powder to control *Callosobruchus Maculatus* (Fab.)" Journal of Stored Product Research, Vol.37, Issue 4, 2001, pp. 339-349.
- [10] Mohan S, Fields PG, "A simple technique to assess compounds that are repellent or attractive to stored product insects" Journal of Stored Products Research, Vol.38, 2002, pp. 23-31.
- [11] Abbott WS, "A method of computing the effectiveness of an insecticide" Journal of Economic Entomology, Vol.18, 1925, pp. 265-267.
- [12] Finney DJ, Probit analysis. 3rd ed. Cambridge: Cambridge University Press, 1971.
- [13] Obeng-Ofori D, "Plant oils as grain protectants against infestations of *Cryptolestes pusillus* and *Rhyzopertha dominica* in stored grain" Entomologia Experimentalis Et Applicata, Vol.77, 1995, pp. 133-139.
- [14] Isman MB, "Botanical insecticides, deterrents, and repellents in modern agriculture and an increasingly regulated World" Annual Review of Entomology, Vol.51, 2006, pp. 45-66.
- [15] Ukeh DA, Birkett MA, Pickett JA, Bowman AS, Luntz AJ, "Repellent activity of alligator pepper, *Aframomum melegueta*, and ginger, *Zingiber officinale* against the maize weevil, *Sitophilus zeamais*" Phytochemistry, Vol.70, 2009, pp. 751-758.
- [16] Mao L, Henderson G, "Evaluation of potential use of nootkatone against maize weevil (*Sitophilus zeamais* Motschulsky) and rice weevil [*S. oryzae* (L.)] (Coleoptera: Curculionidae)" Journal of Stored Products Research, Vol.46, 2010, pp. 129-132.

GEOPHYSICAL TOMOGRAPHY BASED ON SPARSE ESTIMATION

Takayuki Shuku¹ and Hongyang Cheng²

¹Graduate School of Environmental and Life Science, Okayama University, Japan

² Multi Scale Mechanics (MSM), ET, MESA+, University of Twente, The Netherlands.

ABSTRACT

In this paper, a new geophysical tomography method based on sparse modeling, where the least absolute shrinkage and selection operator (LASSO) is used as an inverse analysis method, is proposed, and the proposed method is applied to numerical examples of cross-hole seismic tomography designed to reconstruct an image of the ground between two boreholes. Compared with the conventional ridge regression-based method, the proposed method could reconstruct the image with higher accuracy, particularly when the observed data is not sufficient. Therefore, this method is a promising methodology for reconstructing the layered structures of grounds and geotechnical structures in geotechnical practice.

Keywords: Sparse estimation, Geotomography, Inverse problems

INTRODUCTION

Cross-borehole seismic tomography, also called geophysical tomography, is a method of inferring the properties of the ground between two parallel boreholes (Fig. 1). In geotechnical practice, a problem in geophysical tomography is that only a limited number of transmitters and receivers can be used because of the limitations in the construction budget. In addition, the ray paths in geophysical tomography are restricted, which is in contrast to X-ray CT scanning wherein transmitters and receivers can be placed arbitrarily around the targets. These limitations affect the quality of image reconstruction, which in geophysical tomography tends to be an ill-posed problem from the perspective of inverse analysis. Ill-posed problems in geophysical tomography were particularly studied by Honjo and Kashiwagi [1][2], who applied a smoothing filter for image reconstruction and numerically simulated the optimal design of the smoothing filters on the basis of the Akaike Information Criterion [3].

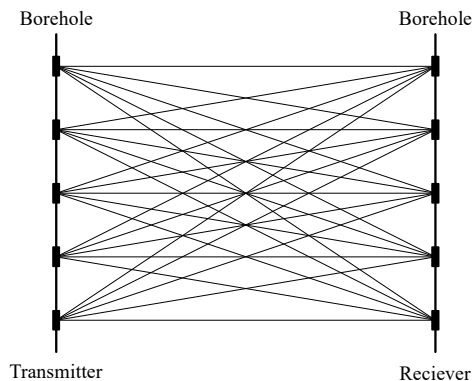


Fig. 1 Cross-hole tomography.

Many methodologies such as smoothing filters and regularization methods have been proposed for managing ill-posed inverse problems. In particular, sparse modeling has received much attention recently in image and vision processing as well as in machine learning (e.g., [4], [5]). According to the general principle of sparsity, a phenomenon should be represented with as few variables as possible.

Similarly, sparse modeling can be useful in geotechnical engineering. This paper proposes a sparse modeling-based geophysical tomography method and reports its effectiveness by applying it to a numerical example of cross-hole seismic tomography: an image of the spatial distribution of the geotechnical parameters of the ground is reconstructed using the proposed method, and the results are compared with those of a current method.

The rest of this paper is structured as follows. In Chapter 2, the theoretical basics of geophysical tomography and inverse analysis are presented. Chapter 3 outlines the least absolute shrinkage and selection operator (LASSO) and a sparse modeling reconstruction algorithm called the Alternating Direction Methods of Multiplier (ADMM). The numerical application of the proposed method and its results are reported in sections “Numerical Experiments” and “Results.” The section “Conclusion” summarizes the method and key findings of the study.

FORMULATION OF GEOTOMOGRAPHY

Reconstruction techniques can be classified into two broad categories: transform methods and series expansion methods. In the transform method, the motion of the target object is described as a

continuous function with a continuous set of projections, whereas in the series expansion methods, the object of interest is comprised of elements, and seismic waves are propagated through the elements to obtain a projection of the element values. The reconstruction of images through the series expansion methods can be theoretically discussed in terms of linear algebra.

This paper focuses on the series expansion methods as they are the most widely used in geotechnical applications [1][2]. In this methodology, the reconstruction area is discretized into cells (Fig. 2). The wave observations at the receivers can be discretely approximated as

$$\mathbf{y} = \mathbf{A}\mathbf{x} + \boldsymbol{\varepsilon}, \quad (1)$$

where \mathbf{y} is an m -dimensional observation vector, \mathbf{x} is an n -dimensional parameter vector, \mathbf{A} is an m -by- n observation matrix, and $\boldsymbol{\varepsilon}$ is an m -dimensional error (noise) vector. These are defined as

$$\mathbf{y} = \{y_1, y_2, \dots, y_m\}^T \quad (2)$$

$$\mathbf{x} = \{x_1, x_2, \dots, x_n\}^T \quad (3)$$

$$\mathbf{A} = \begin{bmatrix} a_{11} & a_{12} & \cdots & a_{1n} \\ a_{21} & a_{22} & \cdots & a_{2n} \\ \vdots & \vdots & \ddots & \vdots \\ a_{m1} & a_{m2} & \cdots & a_{mn} \end{bmatrix} \quad (4)$$

$$\boldsymbol{\varepsilon} = \{\varepsilon_1, \varepsilon_2, \dots, \varepsilon_m\}^T, \quad (5)$$

where the superscript "T" indicates the transpose of the vectors and matrices. In this paper, the error ε_i is assumed an independently and identically distributed random variable that follows normal distribution with mean 0 and standard deviation σ .

Determining the unknown parameter vector \mathbf{x} , that is, reconstruction of the image of the ground between the two boreholes, can be classified into one of three types of problems depending on the

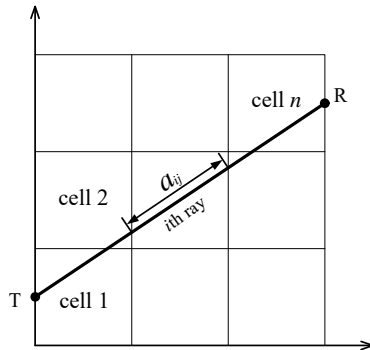


Fig. 2 Cross-hole tomography.

relationship between the dimension of the observation vector m , rank of the observation matrix r , and dimension of the unknown parameter vector n .

When $r = m = n$, the problems are called even-determined problems and can be easily solved. However, most inverse problems in practice are not even-determined.

When $r = m > n$, the problems are said to be overdetermined. The entire vector \mathbf{x} cannot completely fit all the observation data; therefore, the squared error E_D is minimized as follows:

$$\underset{\mathbf{x}}{\text{minimize}} E_D(\mathbf{x}) \quad (6)$$

$$E_D(\mathbf{x}) = \frac{1}{2} \|\boldsymbol{\varepsilon}\|_2^2 = \frac{1}{2} \|\mathbf{y} - \mathbf{A}\mathbf{x}\|_2^2. \quad (7)$$

Eq. (7) can be analytically solved to obtain the estimated vector $\hat{\mathbf{x}}$ as

$$\hat{\mathbf{x}} = (\mathbf{A}^T \mathbf{A})^{-1} \mathbf{A}^T \mathbf{y}. \quad (8)$$

Eq. (8) is called the least squares estimator and is widely used for solving overdetermined problems.

When $r = m < n$, the vector \mathbf{x} cannot be obtained uniquely as it has many possible solutions. To solve the problem, regularization terms are often added into Eq. (7).

$$\tilde{E}_D(\mathbf{x}) = E_D(\mathbf{x}) + \lambda E_W(\mathbf{x}), \quad (9)$$

where λ is the regularization coefficient that controls the relative importance of the data-dependent error $E_D(\mathbf{x})$ and the regularization term $E_W(\mathbf{x})$. One of the simplest forms of the regularization term is the sum-of-squares of the parameter vector \mathbf{x}

$$E_W(\mathbf{x}) = \frac{1}{2} \|\mathbf{x}\|_2^2 = \frac{1}{2} \mathbf{x}^T \mathbf{x}. \quad (10)$$

This quadratic regularizer is called ridge regression. Substituting Eq. (10) into Eq. (9) yields the following error function:

$$\tilde{E}_D(\mathbf{x}) = \frac{1}{2} \|\mathbf{y} - \mathbf{A}\mathbf{x}\|_2^2 + \lambda \frac{1}{2} \|\mathbf{x}\|_2^2. \quad (11)$$

By minimizing Eq. (11) for \mathbf{x} , the ridge estimator is obtained as

$$\tilde{\mathbf{x}} = (\mathbf{A}^T \mathbf{A} + \lambda \mathbf{I})^{-1} \mathbf{A}^T \mathbf{y}, \quad (12)$$

where \mathbf{I} is the identity matrix.

Because the ray paths in geophysical tomography

are restricted, as explained in the introduction, the reconstruction problems in geophysical tomography tend to be underdetermined problems: the number of observations is much less than the number of unknown parameters. Solving the underdetermined problems is thus a central topic in geotechnical practice.

SPARSE ESTIMATION

The regularization term $E_W(\mathbf{x})$ can have many possible forms. Tibshirani [6] proposed the LASSO for solving underdetermined problems, wherein if λ is sufficiently large, some parameters in \mathbf{x} tend to zero, resulting in a sparse model in which the corresponding basis functions play no role.

In the LASSO, the regularization term in Eq. (9) takes the following form:

$$E_W(\mathbf{x}) = \lambda \|\mathbf{x}\|_1 = \lambda |\mathbf{x}|, \quad (13)$$

where $|\cdot|$ indicates the absolute value. By substituting Eq. (13) into Eq. (9), the objective function of the LASSO is obtained as

$$\tilde{E}_D(\mathbf{x}) = \frac{1}{2} \|\mathbf{y} - \mathbf{A}\mathbf{x}\|_2^2 + \lambda \|\mathbf{x}\|_1. \quad (14)$$

The LASSO yields sparse solutions, which implies that many of the estimates are exactly zero because of the geometry of its regularization term. Fig. 3 illustrates the estimation picture for ridge regression and LASSO. The residual sum of the squares, which is obtained from the first term on the right side in Eq. (14), has elliptical contours centered at the least-squares estimates. Both regressions find the first point where the elliptical contours meet the regularization region. Unlike a circle, a diamond has corners; if the solutions lie at the corners, then one of the \mathbf{x} parameters equals zero. In Fig. 3, x_1 becomes zero because of the diamond-shaped regularization term.

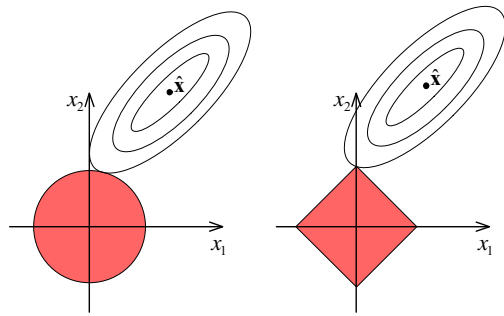


Fig. 3 Estimation picture for ridge (left) and LASSO (right) regression [5].

The LASSO problem is a convex minimization problem, that is, a quadratic program with a convex constraint. For simplicity, the following problem is used to explain the computational procedure for the LASSO solution (e.g., [4]).

$$\underset{x}{\text{minimize}} \left\{ \frac{1}{2} (y - x)^2 + \lambda |x| \right\} \quad (15)$$

The standard approach to this one-dimensional minimization problem is to set the gradient with respect to x to zero. However, one of the central difficulties in solving Eq. (15) is the presence of a non-smooth L1 norm, $|x|$. In other words, the absolute value function $|x|$ does not have a derivative at $x = 0$. Nevertheless, this problem can be solved by applying to x a soft-thresholding operator (e.g., [7]), which is defined as

$$S_\lambda(y) = \begin{cases} y - \lambda & (y > \lambda) \\ 0 & (-\lambda \leq y \leq \lambda) \\ y + \lambda & (y < -\lambda) \end{cases}, \quad (16)$$

where S_λ is a soft-thresholding function (Fig. 4). This operator translates x toward zero by a certain amount and sets it to zero if $|x| < \lambda$. When $\lambda = 0$, the solution of Eq. (15) becomes the solution for the ordinary least squares problem.

The general approach for solving the LASSO problem can be summarized as follows:

Step 1: Minimize the first term in the objective function

Step 2: Apply the soft-thresholding operator to x

Step 3: Repeat steps 1 and 2

OPTIMIZATION METHOD

Of the many reconstruction algorithms proposed for solving convex problems, ADMM [8], which blends the decomposability of the dual ascent method with the superior convergence properties of

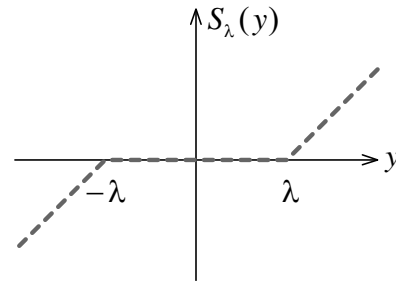


Fig. 4 Soft-thresholding function.

the method of multipliers, is used in this paper to solve the LASSO problem. This algorithm solves problems in the form

$$\underset{\mathbf{x}, \mathbf{z}}{\text{minimize}} \quad f(\mathbf{x}) + g(\mathbf{z}) \quad \text{subject to} \quad \mathbf{Ax} + \mathbf{Bz} = \mathbf{c}, \quad (17)$$

where $f(\mathbf{x})$ and $g(\mathbf{z})$ are assumed to be convex, \mathbf{A} and \mathbf{B} are known matrices of constraints, and \mathbf{c} is a constraint vector. To solve this problem, a vector $\boldsymbol{\mu}$ of the Lagrange multipliers associated with the constraint is introduced to form the augmented Lagrangian

$$L_\rho(\mathbf{x}, \mathbf{z}, \boldsymbol{\mu}) = f(\mathbf{x}) + g(\mathbf{z}) + \boldsymbol{\mu}^T (\mathbf{Ax} + \mathbf{Bz} - \mathbf{c}) + \frac{\rho}{2} \|\mathbf{Ax} + \mathbf{Bz} - \mathbf{c}\|_2^2, \quad (18)$$

where $\rho > 0$ is called the penalty parameter. The ADMM is based on minimizing the augmented Lagrangian (Eq. (18)) successively over \mathbf{x} and \mathbf{z} and then applying a dual-variable update to $\boldsymbol{\mu}$. Thus, it consists of iterations of an \mathbf{x} -minimization step (Eq. 19), a \mathbf{z} -minimization step (Eq. 20), and a dual-variable update (Eq. 21).

$$\mathbf{x}^{k+1} = \arg \min_{\mathbf{x}} L_\rho(\mathbf{x}, \mathbf{z}^k, \boldsymbol{\mu}^k) \quad (19)$$

$$\mathbf{z}^{k+1} = \arg \min_{\mathbf{z}} L_\rho(\mathbf{x}^{k+1}, \mathbf{z}, \boldsymbol{\mu}^k) \quad (20)$$

$$\boldsymbol{\mu}^{k+1} = \boldsymbol{\mu}^k + \rho(\mathbf{Ax}^{k+1} + \mathbf{Bz}^{k+1} - \mathbf{c}) \quad (21)$$

Similar to the method of multipliers, the dual-variable update uses a step size equal to the augmented Lagrangian parameter ρ .

The ADMM framework has several advantages. First, convex problems with non-differentiable constraints can be easily solved by the separation of parameters \mathbf{x} and \mathbf{z} . Second, the ADMM can break up a large problem into smaller problems. For datasets with a large number of observations, the data can be broken into blocks, and each block can be optimized.

Next, the ADMM procedure is illustrated by applying it to the LASSO.

The Lagrangian form of the LASSO can be expressed in an equivalent form as

$$\underset{\mathbf{x}, \mathbf{z}}{\text{minimize}} \quad \left\{ \frac{1}{2N} \|\mathbf{y} - \mathbf{Ax}\|_2 + \lambda \|\mathbf{z}\|_1 \right\} \quad \text{such that} \quad \mathbf{x} - \mathbf{z} = \mathbf{0} \quad (22)$$

When applied to this problem, the ADMM updates take the form

$$\mathbf{x}^{k+1} = (\mathbf{A}^T \mathbf{A} + \rho \mathbf{I})^{-1} (\mathbf{A}^T \mathbf{y} + \rho(\mathbf{z}^k - \boldsymbol{\mu}^k)) \quad (23)$$

$$\mathbf{z}^{k+1} = S_{1/\rho}(\mathbf{x}^{k+1} + \boldsymbol{\mu}^k) \quad (24)$$

$$\boldsymbol{\mu}^{k+1} = \boldsymbol{\mu}^k + (\mathbf{x}^k - \mathbf{z}^k), \quad (25)$$

where $S_{1/\rho}$ is a soft-thresholding operator. $\mathbf{A}^T \mathbf{A} + \rho \mathbf{I}$ is always invertible as $\rho > 0$. The algorithm involves a ridge regression update for \mathbf{x} , a soft-thresholding step for \mathbf{z} , and a simple linear update for $\boldsymbol{\mu}$. Accordingly, the ADMM can be interpreted as a method for solving the LASSO problem through iterative ridge regression.

NUMERICAL EXPERIMENTS

The accurate reconstruction of soil profiles using existing geophysical tomography methods is difficult. Consider the true distribution of the geotechnical parameters depicted in Fig. 5. We attempted to reconstruct this image using the proposed method and ridge regression method, which is an existing geophysical tomography method, for comparison.

Each transmitter individually generates seismic wave, and the receivers observe travel time of the wave between two boreholes. Geophysical tomography estimates elastic modulus of cells based on the observed travel time. Therefore, in this numerical experiment, \mathbf{y} and \mathbf{x} in Eq. 1 mean the travel time and elastic modulus respectively.

We considered two configurations of transmitters and receivers: Case 1 and Case 2 depicted in Fig. 6. Case 1 has 21 receivers and transmitters each, which yield $21 \times 21 = 441$ ray paths in total, and Case 2

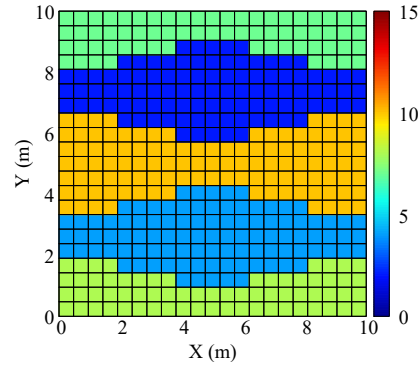


Fig. 5 Schematic view of regularization.

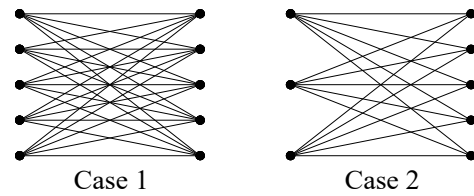


Fig. 6 Configurations of transmitters and receivers.

has 21 receivers and 11 transmitters, which yield $11 \times 21 = 231$ ray paths.

The synthetic observation vector \mathbf{y} used for inverse analysis is generated as follows:

- 1) Assuming that all ray paths are straight, compute the observation matrix \mathbf{A} (Eq. (1)).
- 2) Compute \mathbf{Ax} ; the parameter vector \mathbf{x} is given in Fig. 5. We did not add observation noise to \mathbf{y} for simplicity.

The LASSO is effective when the vector \mathbf{x} has many zeroes, that is, when the solution is sparse. The LASSO cannot function well in this numerical example because most of the parameter vector \mathbf{x} are non-zero. Therefore, the L1 regularization term in Eq. (14) is modified as follows:

$$\tilde{E}_D(\mathbf{x}) = \frac{1}{2} \|\mathbf{y} - \mathbf{Ax}\|_2^2 + \lambda \|\mathbf{Bx}\|_1, \quad (26)$$

where \mathbf{B} represents the matrix for the spatial derivative of parameters in cells called the total variation [9].

The accuracy of the reconstructed image is evaluated in terms of the root mean square error (RMSE)

$$\text{RMSE} = \sqrt{\frac{1}{N} \sum_{i=1}^N (x_i^{\text{est}} - x_i^{\text{true}})^2}, \quad (27)$$

where x_i^{true} is the true value of the geotechnical parameter for the i^{th} cell shown in Fig. 5 and x_i^{est} is the reconstructed (estimated) value for the i^{th} cell as obtained through geophysical tomography.

RESULTS

Fig. 7 presents the reconstructed image, that is, the estimated parameter distribution, obtained through ridge regression and LASSO for Case 1. Both the methods can capture the layered structures of the ground and an accurate image could be reconstructed. However, the LASSO almost perfectly reconstructed the values of the geotechnical parameters of the cells.

Fig. 8 depicts the image reconstructed using the ridge and LASSO-based methods for Case 2. The results prove that reconstruction using the LASSO-based method is more accurate than that using ridge regression, particularly at the left edge where the observed data are not sufficient. The reconstructed image almost completely coincides with the true image shown in Fig. 5. Table 1 summarizes the RMSE for each reconstructed image. The RMSE of the LASSO-reconstructed images are considerably lower than that of the ridge-reconstructed images. Remarkably, the RMSE of the LASSO for Case 1 is

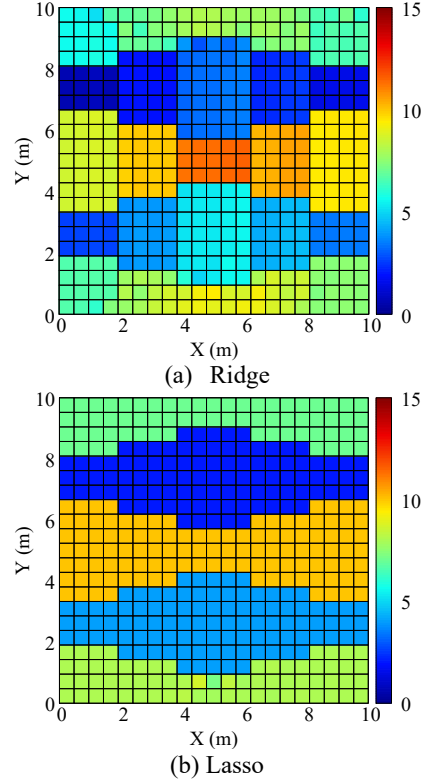


Fig. 7 Reconstructed images for Case 1.

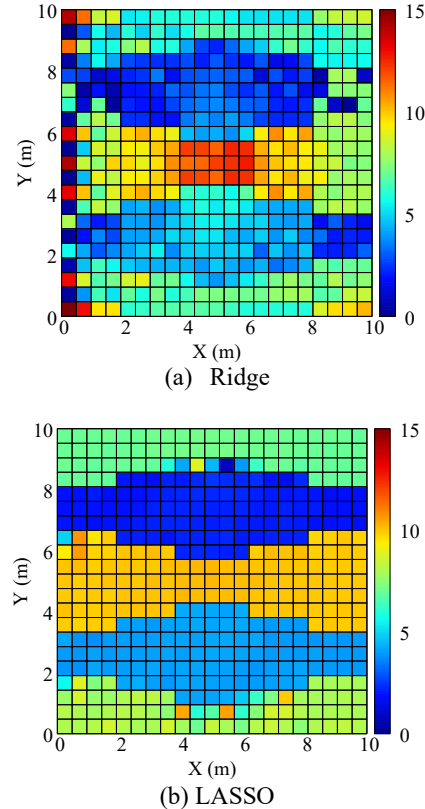


Fig. 8 Reconstructed images for Case 2

Table 1 RMSE in ridge and lasso estimations

	RMSE	
	Case 1	Case 2
Ridge	0.04137	0.09600
Lasso	0.00258	0.02246

much less than that of the ridge regression method. This implies that LASSO can reconstruct images with high accuracy when the number of observed data is not sufficient.

CONCLUSION

This study proposed a geophysical tomography method based on LASSO, which is a method for sparse modeling. The proposed method was applied to the numerical examples of cross-hole seismic tomography designed to estimate soil profiles. To validate the effectiveness of the proposed method, its results were compared with those of ridge regression.

When the number of observed data is large enough, both ridge regression and the proposed LASSO-based method could accurately reconstruct the image of the ground between the boreholes. When the number of observed data is small, ridge regression yields poorly reconstructed images. In contrast, the proposed method yielded accurate images regardless of the insufficient number of observed data. Thus, the proposed method is more robust than ridge regression and is expected to be a useful tool in geotechnical practice.

ACKNOWLEDGEMENTS

This work was supported by JSPS KAKENHI Grant-in-Aid for Young Scientists (B) Grant

Numbers 15K18759.

REFERENCES

- [1] Honjo, Y. (1987): Geophysical tomography: Estimation error and optimum choice of cell size, In Proc. 5th Int. Conf. on the Application of Statistics and Probability in Soil and Structural Engineering, Vancouver, 91-100.
- [2] Honjo, Y. and Kashiwagi, N. (1991): On the optimum design of a smoothing filter for geophysical tomography, *Soils Found.*, 31(1), 131-144.
- [3] Akaike, H. (1973): Information theory and an extension of the maximum likelihood principle, In Proc. 2nd Int. Symp. on Information Theory, Petrov, B. N., and Caski, F. (eds.), Akademiai Kiado, Budapest: 267-281.
- [4] Mairal, J., Bach, F. and Ponce, J. (2014): Sparse modeling for image and vision processing, *Found. Trends Comput. Graph. Vis.*, 8(2-3), 199.
- [5] Hastie, T., Tibshirani, R. and Wainwright, M. (2015): *Statistical Learning with Sparsity*, CRC Press, p. 351.
- [6] Tibshirani, R. (1996): Regression shrinkage and selection via the lasso, *J. Royal. Statist. Soc. B.*, 58(1), 267-288.
- [7] Figueiredo, M.A.T. and Nowak, R.D. (2003): An EM algorithm for wavelet-based image restoration, *IEEE Trans. Image Process.*, 12, 906-916.
- [8] Boyd, S., Parikh, N., Chu, E., Peleato, B. and Eckstein, J. (2011): Distributed optimization and statistical learning via alternating direction method of multipliers, *Found. Trends Machine Learning*, 3(1), 122.
- [9] Rudin, L. I., Osher, S., and Fatemi, E. (1992): Nonlinear total variation based noise removal algorithms, *Physica D*, 60, 259-268.

LESSONS AND ACHIEVEMENTS FROM THE MERSEY FOREST BY NETWORKING PARTNERSHIP FOR TWENTY YEARS

Tomoko Miyagawa¹, Clare Oliver², Noriko Otsuka³, Takefumi Kurose⁴ and Hirokazu Abe⁵

¹Faculty of Systems Engineering, Wakayama University, Japan; ²The Mersey Forest, the UK;

^{3,5}Cyber Media Centre, Osaka University, Japan;

⁴ Faculty of Human-Environment Studies, Kyushu University, Japan

ABSTRACT

In the UK, community forest projects have created an increase of new accessible open green spaces in post-industrial areas. However, there is a scarcity of sustainable funding for long-term management. Therefore, partnership is recognised to be a key mechanism to maximise the benefits and to share the risks with a range of organisation to maintain the quality of green spaces. This study is to clarify the achievements and the roles of the Mersey Forest over the last twenty years in developing partnership approaches in the Northwest of England. The study methods are based on literature reviews regarding on published literature on environmental regeneration and the data provided from MF, and interviews with representatives of the Mersey Forest. The first 10 years from 1994 to 2004 focused on planting trees for creating new and extending woodland. After that opportunities for large scale new planting decreased and there was a need for managing the newly created open green spaces. Therefore, it has entered in the management phase and the role of the Mersey Forest is shifting to strengthen partnership working by providing advice to landowners. It also became clear that community forest approaches have been achieved together with landowners and partners through partnership working led by the Mersey Forest for over twenty years. Thus, the Mersey Forest has evolved from a governmental inspired organisation to a community empowered organisation.

Keywords: Green Infrastructure; Environmental Regeneration; Community Forests; Post Industrial Landscapes

INTRODUCTION

A Creation of Post-industrial Landscapes Through Environmental Regeneration in the UK

In recent years, newly created accessible green spaces have increased by community forest activities in post-industrial areas, particularly in the North of England, and it is necessary to determine the cumulative effects of changes [1], [2]. Through environmental regeneration, activities are becoming area wide and networking surrounding areas to create a landscape with local characters [3]. Newly created open green spaces can be a platform for biodiversity and culture which have possibilities to empower the community in the local area for active participation and to create new socio-economy and culture, thus, activities of environmental regeneration is reflecting the community development [2]. Post-industrial landscapes have blue (water) and green (open spaces) systems. However, in some cases, it is difficult to access due to a lack of infrastructure for people to use and not known by the local community. Therefore, it may be important to manage these newly created open green spaces through a process of creating post-industrial landscapes with a long-term vision, as well as to work in partnership with the community in the local area.

Community forest activities are to create and manage new and existing open green spaces, including derelict under-used and neglected land, in England by forming a network of these spaces into a part of Green Infrastructure (GI), through working in partnership with organisations [3]. In recent years, institutional support for public participation is becoming important in urban regeneration areas for public benefits [4]. Regeneration of post-industrial areas in the UK has been undertaken since 1980, however, with not much provision for covering costs for long-term management [1] which is necessary for maintaining open green spaces. In addition, partnership approach is recognised to be a way forward to balance risks and costs with partner organisations.

Environmental regeneration and post-industrial landscapes with a focus on working in partnership can be seen in the research for conserving and reusing industrial heritage [3], activities of community forests in England since 1994 [4], a way forward to form a partnership as a method of environmental regeneration in a river basin environment [5], and the approach used by environmental regeneration organisations such as Groundwork in the UK an intermediate sector organisation [6]. However, there has been a change for community forests over time particularly for financial support from the central

government in recent years, and there is a scarcity and a need for a further research on recent trends and partnership working as a methodology.

Aims of the study and study methods

This study aims to clarify the achievements and the role of the Mersey Forest (MF) by undertaking environmental regeneration to create post-industrial landscapes over the last twenty years. The Mersey Forest Partnership was set up in 1991 with organisations in Merseyside and North Cheshire in the Northwest of England - an area containing much brownfield land. The study methods are based on literature reviews regarding on published literature on environmental regeneration and the data provided from MF, and interviews with representatives of MF, Clare Olver and Paul Nolan OBE.

HISTORY AND ROLES OF MF

MF and Partner Organisations

MF covers 1370 square kilometers with 1.7 million inhabitants with a vision to create and manage open green spaces in the long term for environmental regeneration and community development in the Northwest of England (Fig.1)[7]. Since 1991, MF has been a leading partnership in Merseyside and North Cheshire enabling community forest activities focusing on urban, suburban and post-industrial areas to provide open green spaces nearby the community [7]. Partner organisations include the local authorities within the MF area, the government organisations within the UK Government's Department for Environment, Food, and Rural Affairs (DEFRA), such as Forestry Commission (FC), Natural England (NE), and Environment Agency (EA), landowners, private companies, and the community in the local area [8]. MF do not hold any



Fig.1 A map of MF[9] with some amendments

land ownership, while promoting community forest activities to create and manage open green spaces on publicly and privately owned land by partner organisations, such as, local authorities, companies and individuals. MF encourages people to become more actively involved with their local trees and woodlands through support to form 'Friends' groups, assistance to obtain funding and by providing trees for community planting [10].

Partnership Working with the Community

MF was established in 1991 as one of 12 community forests in England by the Countryside Commission. However, in recent years, community forest organisations have had to become more financially independent, therefore, activities are becoming more focused on the local area [11]. Thus, networking of a partnership and working with the community in the local area is becoming increasingly important.

Fig.2 illustrates a framework showing the levels of community engagement in creating the MF. There are seven stages from Stage 7: 'Not informed but using MF', to Stage 1: 'Community ownership'. This allows a continuum of levels of participation, therefore, ranges of people can participate and to support participation in various ways.



Fig.2 A creating process of MF with the community [7]

ACHIEVEMENTS OF MF IN PARTNERSHIP

Newly Created Open Green Spaces by MF

Community forest activities led by the MF partnership has created three times of the number of newly planted trees since 1991 to reach 9 million trees in Merseyside and North Cheshire in comparison to the number of whole of England on average at the same time [7]. According to an awareness survey on environmental regeneration with local residents in 2010 (1121 respondents, response rate 65%) said that the environment had improved by MF activities, and two thirds of people had visited newly created open green spaces [7]. It also became clear that newly created open green spaces have been recognised and

visited by local community. In terms of the Woodland Access Standard, suggested by the Woodland Trust (WT), a charity organisation for conserving woodland in the UK, in 2012 23 percent of the population in MF lived within '500m of an accessible woodland of at least 2ha', and 77 percent of the population lived 'within 4km of one of at least 20ha'. This means that access to woodland is higher in MF than in England as a whole [7]. Therefore, it is evident that community forest activities have promoted to create and manage open green spaces since 1990 particularly in the Northwest of England where MF is located.

Plans for The Long term and The Short term

MF reviews The Mersey Forest Plan every ten years based on the agreement between partner organisations, and minor amendments are updated on the MF website [7]. In the plan-making stage, it is compiled with partner organisations through consultation, therefore, it is a 'locally developed plan' which is approved by the local government [7].

The Mersey Forest Plan is a long term and strategic guide to the work of The Mersey Forest team and partners. This is accompanied by an annually updated Delivery Plan which covers how the long term vision of The Mersey Forest Plan will be delivered and considers the resources available at the time [7]. To achieve policies of The Mersey Forest Plan can bring many benefits, and moreover, it is also important to be in accordance with legal framework and policy contexts [7]. For example, at the national level, The Mersey Forest Plan is in accordance with the Government's Forestry and Woodlands Policy Statement, 2013 and the National Planning Policy Framework, 2012 [7]. In addition, policies of the Mersey Forest Plan can be the 'material consideration [12]' on planning permission through planning system to support development control and local area planning [7].

Partnership of Local Authorities for MF

To undertake projects beyond local authority boundaries, such as community forests activities, cooperation of neighbouring local authorities is a statutory requirement stated by Localism Act, 2011 [7]. Local authorities in MF area have a Partnership Agreement among them to exchange knowledge and information, and to share opportunities for solutions [7]. Among local authorities, Cheshire West and Chester Council (formerly Cheshire County Council) is the lead authority providing employment, finance, and treasury for the MF team [7]. In addition, local authorities in the MF Partnership commit to investing resources: 'core funding'. MF is taking a role as a leader to work in partnership with various organisations, to invest in resources to generate

incomes by applying for external funding with partners and by securing resources from the partners to maximise benefits, and to impact on future policy-making [7].

ANALYSIS AND COMPARISON OF TWENTY YEARS OF ACTIVITIES BY MF

Area of New Woodland Planting

This section tries to examine the selected data from MF for the past twenty years of activities. Fig. 3 shows area of new woodland planting in MF area since 1990/1991 to 2014/2015. It became clear that from 1993/1994 to 2003/2004 was a time of significant tree planting increasing new woodland cover from 500ha to 2,500ha. New woodland planting took place at most from 2000/2001 to 2002/2003. Since 2005, the increasing trend has ended and became stable at around 3,000ha. This trend has been seen right across England and the reasons for this are complex, including changes to new woodland grant aid; EU Single Farm Payments acting as a disincentive for woodland planting; increasing numbers of non-farmer landowners; changes to eligibility for new tree planting grants and an increase in commodity prices.

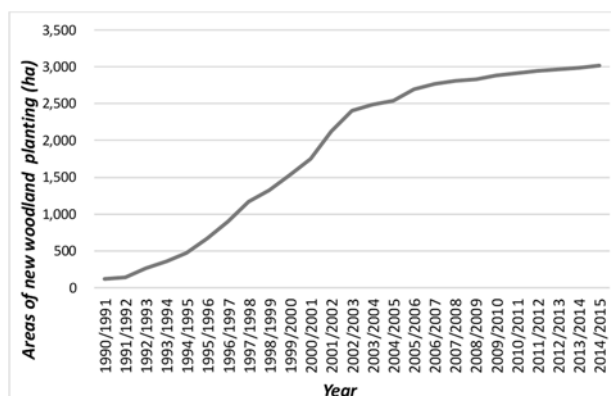


Fig.3 Areas of new woodland planting in MF (cumulative) [13]

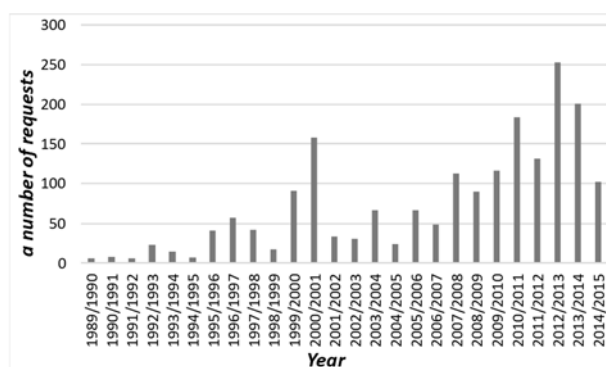


Fig.4 A number of consultations to MF (1989/1990–2014/2015) [14]

Numbers of Consultation to MF

Fig. 4 shows numbers of requests for support by landowners to the MF team between 1990/1991 and 2014/2015. From 1989/1990 to 1999/2000 were in average of 29 cases per year, while 2000/2001 to 2014/2015 rose three times to 108 requests in average per year which may be a result of better monitoring and recording.

Landuses and Landowners Consulted MF

Types of land use

Fig.5 shows types of land use of landowners who requested support by MF between 2001/2002 to 2014/2015. Agricultural land has the highest rate to be a half of all land types during 2001/2002 to 2003/2004. At that time, funding for new planting by WGS was available and many consultations had taken place on transforming farmland to woodland. Since 2007/2008, requests for support to manage existing woodland have increased to 28 percent on average. Likewise requests from schools have also increased since 2008/2009 to be at 28 percent on average.

Enquiries for support to improve and manage public open green spaces remain at 5 percent on average (Fig. 5) [14]. However, there are requests for support from many other types of open green spaces, such as, privately owned estate/church, golf course/sports field, and derelict land after reclamation for greening, it comes up to 13 percent in total. 29 site owners consulted MF during 2001/2002 to 2014/2015 nearly 40 percent out of 71 sites within local authorities in MF area have been selected by Green Flag Award which recognises excellent management and high quality green spaces [15]. The Award is recognised by The UK Government's Department for Communities and Local Government, and managed by environmental charity, Keep Britain

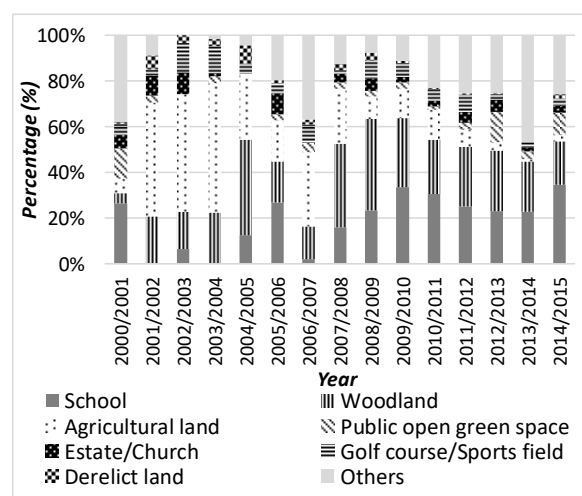


Fig.5 Land use for sites where support requested to MF (2001/2002-2014/2015) [14]

Tidy. It has become a benchmark national standard for parks and green spaces.

Types of landowners

In the case of local authorities and others, where landowners have many parcels of land and woodland, these have only been recorded once: 'Unique Landowners'. These landowners are frequently supported with the management and evaluation of projects at many occasions by the MF team for many separate parcels of land. There are also some sites outside of MF geographical area but participating towards the MF vision. This suggests an extending and growing network of community forests activities in the Northwest of England. Cooperation from landowners is necessary for MF covering a regional area including privately owned land, to work in partnership, and to create a network of GI of open green spaces.

Unique landowners

Fig. 6 shows types of unique landowners from 2001/2002 to 2014/2015 by land use types who contacted MF. Of those 90 percent of the schools were state schools (including nursery, primary school, junior school and high schools), while the remaining 10 percent were privately owned. 70 percent of the woodland owners who contacted MF were private companies, including individual landowners, while 10 percent were owned by national and local government. The remaining woodland owners included charitable organisations such as National Trust and WT, and parish councils. From enquiries around agricultural land, 90 percent were primarily owned by private landowners. Of the 75 percent of support requested for public open green spaces these were owned mainly by national and local government; the remaining 25 percent owned by charity organisations. From support requested for estate/church managed land, 50 percent of enquiries came from church or parish councils, while 20 percent were from private companies and organisations including individual landowners; the remainder from other land owners including national and local government, and charity organisations. Enquiries from managers of golf course/sports fields, 80 percent were private companies and organisations, including individual landowners, the remainder from national and local government, and charity organisations. 90 percent of support requested for derelict land came for land owned by private companies and organisations including individual landowners, with 10 percent from national and local government.

In terms of land owners who contacted MF, schools and public open green spaces are mainly owned and managed by the public organisations,

while other landuse types are mostly owned by the private landowners. This suggests that MF has consulted ranges of partners to provide supports requested.

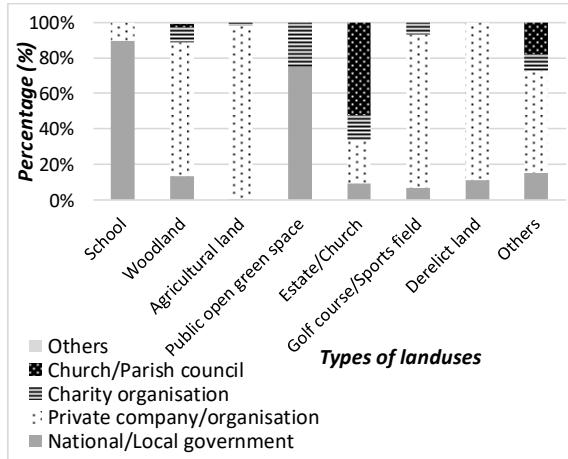


Fig.6 Types of unique landowners by landuse types (2001/2002-2014/2015) [14]

Sources of funding for MF

Core funding from local authorities

Core funding and additional funding secured from other sources between 2008/2009 and 2014/2015 is shown in Fig. 7. This shows 12 percent is core funding (resources from the local authority partners) while nearly 90 percent is funded by EU, the national government, government, charitable and private organisations. By applying for external funding with partners the total budget increased to exceed a hundred thousand pounds from 2011/2012 to 2014/2015.

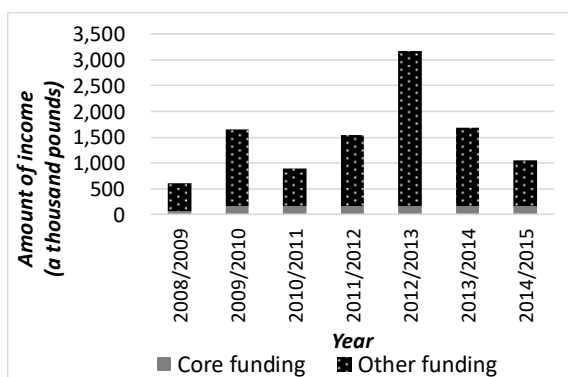


Fig.7 Funding sources (2008/2009-2014/2015)[16]

Funding from other organisations

Funding sources in percentage in total between 2008/2009 and 2014/2015 is shown in Fig. 8, and yearly based details is shown in Fig. 9. 28 percent of

funding is coming from FC with the largest share, while 12 percent of funding is core funding from the local authority, and 11 percent of funding is covered from the EU (Figs. 8 and 9). Funding from the national government and government organisations in total shares a half, while 40 percent of funding is coming from DEFRA and affiliated organisations including EA and NE. About the funding from FC in 2011/2012 and 2013/2014, EA and NE in 2012/2013 has a higher rate (Fig.9), and total funding to exceed three hundred thousand pounds in 2012/2013 (Fig. 7). This is due to special projects to increase funding, such as a river improvement project of EA and a brownfield regeneration project by FC.

Between 2008/2009 and 2011/2012 the Northwest Development Agency (NWDA) funded the creation of new community woodlands on derelict land as part of its urban regeneration policy. However, NWDA was abolished in 2012 and funding for urban regeneration has since decreased. Since 2012, through the Sustainable Transport Fund, the Department for Transport has provided funding for improvements to promote cycling and walking which has enabled the delivery of the MF street tree planting

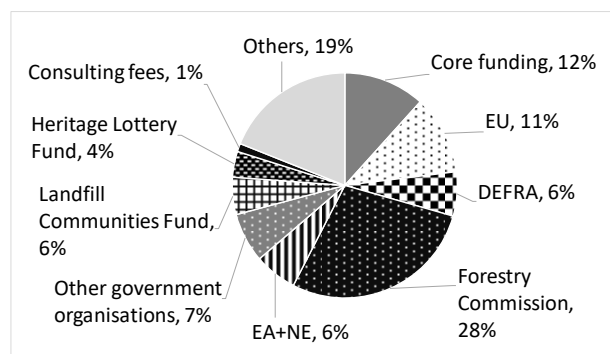


Fig.8 Funding sources (Unit: Percentage (%); 2008/2009-2014/2015)[16]

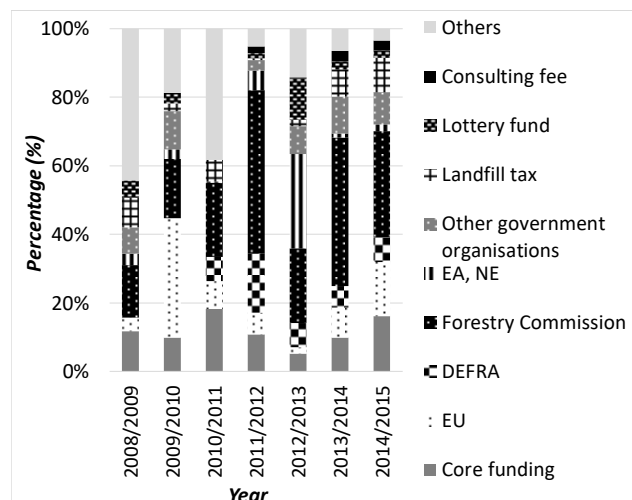


Fig.9 Funding sources in percentage per year (2008/2009-2014/2015)[16]

programme: Green Streets.

The prospects of EU funding are uncertain owing to the Brexit procedure and the need to pay attention to future trends. Other funding from non-governmental organisations includes Landfill Communities Fund [17] by Landfill Tax Regulations, 1996 for community and environment, and Heritage Lottery Fund through profits of the National Lottery in the UK for conserving environment, ecosystem, and heritage to be around 10 percent in total.

CONCLUSION

The data since 1991, when MF was established, has clearly highlighted the role of the MF partnership of leading a network of local governments, government organisations, landowners, private companies and the community in delivering landscape changes. It also became clear the progress of community forestry in the Northwest of the UK.

It can be divided into two phases: the creation phase, from 1994 to 2004, when there was large scale new woodland planting, and after that when opportunities for new planting have decreased. There then became a need to manage the newly created open green spaces and woodlands delivering the MF vision 'to get more from trees' [7]. Thus, it has entered in the management phase and the role of MF has shifted to strengthen partnership working to provide advice and supports to landowners and partner organisations.

The above tendency is also evident from the funding particularly since 2008/2009, nearly 90 percent is funded by the EU, the national government, government and private organisations while 12 percent is funded from resources by the local authority partners. Therefore, MF is applying for a range of external funding with partners and to secure resources from the partners for various activities to invest in resources previously provided by the national government partners.

It also became clear that community forest approaches have been achieved together with landowners and partners through partnership working led by MF for over twenty years. Thus, MF has evolved from a governmental inspired organisation to a community empowered organisation.

Future challenges to work in partnership locally for the needs from the community, to continue the quality of management of open green spaces and to utilise its resources, and to create a further network of these open green spaces into the enhancement of forming GI in the area.

ACKNOWLEDGEMENTS

The authors would like to express our gratitude for the financial support provided by the Japan Society for the Promotion of Science (no. 16H04474).

REFERENCES

- [1] Davies C, "Old culture and damaged landscapes: The new cultural landscapes of post-industrial sites in Britain", in *New cultural landscapes*, Roe and Taylor, Ed., Abingdon: Routledge, 2014, pp.41-58.
- [2] Roe M, "Exploring future cultural landscapes, in *New cultural landscapes*", Roe and Taylor, Ed., Abingdon: Routledge, 2014, pp.241-269.
- [3] Miyagawa T, Olver C, Otsuka N, Kurose T, and Abe H, "The landuse changes and formation of partnerships through the environmental regeneration in Cheshire, the UK", *J. of the Japanese Institute of Landscape Architecture*, Vol.79(5), 2016, pp.555-558 (in Japanese).
- [4] Lawrence A, Anglezarke B, Frost B, Nolan P, and Owen R, "What does community forestry mean in a devolved Great Britain?", *International Forestry Review*, Vol. 11(2), 2009, pp.281-297.
- [5] Mitsuhashi N, Tsutsui Y, and Kamata M, "On implementation for regional environmental regeneration through the partnership with public, private and voluntary sector: A case study of Mersey Basin in the U.K.", *AIJ J. of technology and design*, No.20, 2004, pp.251-254 (in Japanese).
- [6] Mitsuhashi N, and Koyama Y, "On the method of community development with Groundwork in the United Kingdom", *AIJ J. of technology and design*, No.14, 2001, pp.259-264 (in Japanese).
- [7] The Mersey Forest Office, "More from trees, The Mersey Forest Plan", 2014, Available at <<http://www.merseyforest.org.uk/about/plan/>>, undated, [Accessed 2017.3.13.].
- [8] The Mersey Forest, "Who creates the forest?", <<http://www.merseyforest.org.uk/about-the-mersey-forest/who-creates-the-forest/>>, undated, [Accessed 2017.3.13.].
- [9] The Mersey Forest, a provided material, undated.
- [10] The Mersey Forest, "Funding and resources for communities", <<http://www.merseyForest.org.uk/support-we-offer/funding-and-resources-for-communities/>>, undated, [Accessed 2017.3.13.].
- [11] England's Community Forest, "About England's Community Forests", <<http://www.communityforest.org.uk/aboutenglandsforests.htm>>, undated, [Accessed 2017.3.13.].
- [12] Hart T, "The management of development" , in *Town and Country Planning in the UK Fifteenth Edition*, Cullingworth, Nadin, Hart, Davoudi, Pendlebury, Vigar, Webb, and Townshend, Ed., Abingdon: Routledge, 2015, pp.155 -160.
- [13] The Mersey Forest, provided materials, undated, "Master Statistics".

- [14] The Mersey Forest, provided materials, undated, “Cumulative landowner support from 2001 onwards”.
- [15] Keep Britain Tidy, <<http://www.keepbritaintidy.org/greenflagawards2015/2335>>, undated, [Accessed 2017.3.13].
- [16] The Mersey Forest, provided materials, undated, “Finance totals”.
- [17] ENTRUST, <<http://www.entrust.org.uk/landfill-community-fund>>, undated, [Accessed 2017.3.13].

IMPACT OF INCREASE IN SIKA DEER (*CERVUS NIPPON*) ON INFILTRATION RATE AND SOIL EROSION ON FORESTED HILLSLOPE

Taijiro Fukuyama¹, Shinya Hiramatsu¹, Keisuke Kase¹, Masato Kikuchi¹, Shusaku Shiiba², Hideto Ohmori², Masaaki Hanaoka³

¹Faculty of Agriculture, Shinshu University, Japan; ²Tenryu River Upper Reaches River Office, Chubu Regional Development Bureau, MLIT, Japan; ³Civil Engineering and Eco-Technology Consultants Co., Ltd., Japan

ABSTRACT

To assess the impact of increase in Sika deer (*Cervus Nippon*) on infiltration rate on forested hillslope, we conducted a sprinkling experiment at Japanese Alps area, where is recognized as high density deer area. We conducted sprinkling experiment totally 22 times at three experimental plots as follows: 1) plot with animal trail, 2) without animal trail and 3) disturbed by treading. Based on the rainfall intensity and overland flow, infiltration rate was obtained and compared among experimental plots. We compared the gradients of the linear regression between rainfall intensity and the final infiltration rate for three plots. As a result, Final infiltration rates of 3) disturbed plot and 1) plot with animal trail were respectively 6 % and 13 % less than that of 2) plot. Secondly, to assess the Sika deer impact on soil erosion, we monitored soil erosion from late autumn till early winter. We set the 16 sediment collection troughs along the contour on October 10, 2016 and observed rainfall, air and surface soil temperature, and counted the number of deer using sensor cameras. Soil loss increased with increasing the number of deer and with increasing freeze-thaw cycle. At the sprinkling experiment, the maximum value of soil loss per unit width was 6.5 g/m. Soil erosion monitoring showed average soil loss per unit width as 665 g/m. Therefore, soil erosion due to the freeze-thaw cycle and deer-disturbance seemed dominant than that induced by raindrop impact and/or overland flow.

Keywords: Sika deer (*Cervus Nippon*), animal trail, disturbed by treading, sprinkling experiment, soil erosion

INTRODUCTION

Recently, damage by wildlives to agriculture and forestry has been a serious problem especially in mountainous area in Japan. The total damaged area of forest became 90 km² in 2013. In Nagano prefecture, central Japan, damage to agricultural crops and forest, reducing undergrowth in forests, mortality of the trees due to rapid increase in Sika deer were reported. At Mt. Senjougatake, located in the Akaishi Mountains, structural changes in alpine plant communities caused by grazing has been reported [6].

The impact of increase in Sika deer is not limited on the plants. Figure 1 shows that the direct and indirect impact of Sika deer increase on the forested hillslope and the watershed. Decline of the understory vegetation that covers the forest floor accelerate the soil erosion due to the raindrop impact. Exposed soil surface amplify the variation of the earth temperature and increase the cycle of freezing and thawing, which lead to aggregate destruction at the soil surface. These mechanical destruction of aggregate can occur due to the treading by animals. Therefore, recent Sika increase may influence sediment production and transport by fluvial processes. Increase in unstable sediment on the riverbed, off-site impact such as

increase in sedimentation rate in dams, or increase in suspended sediment concentration. Therefore, it is important to assess the impact of Sika increase on the sediment delivery at the hillslope scale and the watershed scale.

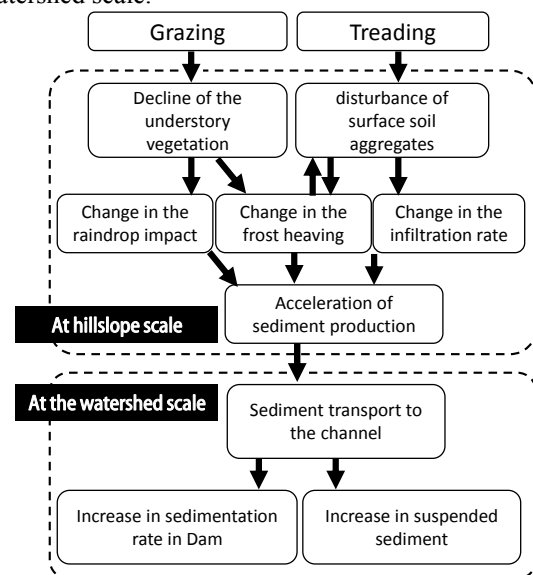


Fig.1 Scenario for the impact of Sika increase on the

sediment delivery at the hillslope scale and the watershed scale.

To assess the impact of the Sika treading on infiltration and soil erosion at forested hillslope, we conducted a sprinkling experiment at Japanese Alps area, where is recognized as high density deer area. Secondly, to assess the Sika deer impact on soil erosion, we monitored soil erosion from late autumn till early winter using 16 sediment collection troughs along the contour.

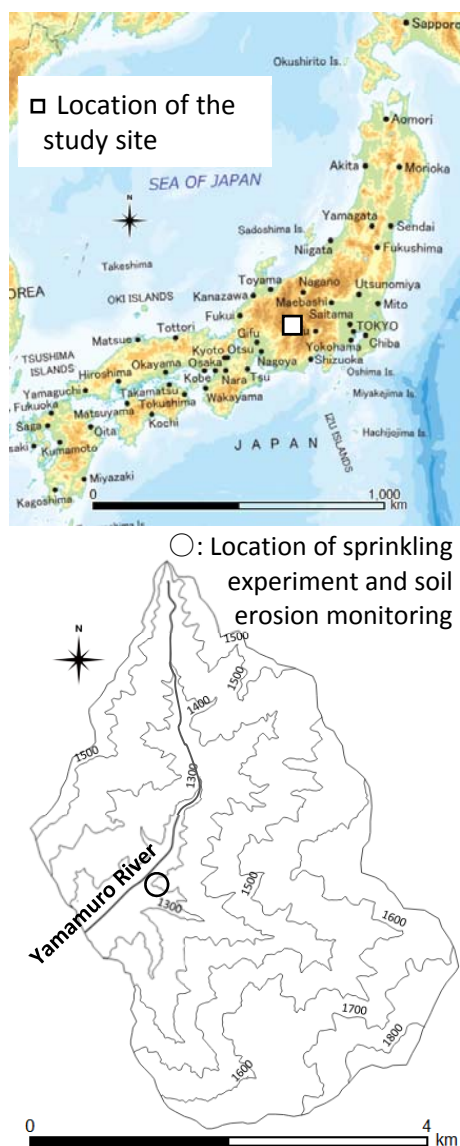


Fig.2 Location of the study site

SITE DESCRIPTION

The study site is located in the watershed of Yamamuro river, which is the upper reach of Tenryu river, at an elevation of about 1,270 m (Fig.2). Dominant tree species are Larch (*Larix kaempferi*)

and Japanese red pine (*Pinus densiflora*). In this watershed, Sika deer activity has been reported using sensor cameras in 2015 by Tenryu River Upper Reaches River Office.

The watershed is located in the east side of Median Tectonic Line (MTL). Along the MTL, there is the Sambagawa metamorphic belt, which contain crystalline schist and serpentinite, and the Chichibu belt, which is consisted with sedimentary rock of the accretionary wedge in the Jurassic period.

SPRINKLING EXPERIMENT

To assess the impact of the Sika deer treading on infiltration rate and surface soil erosion at forested hillslope, we conducted a sprinkling experiment at three experimental plots with different conditions as follows: 1) plot with animal trail, 2) without animal trail and 3) disturbed by treading, as shown in Fig. 3. The plot with animal trail 1) shows poor understory vegetation compared to the 2) plot without animal trail. The disturbed plot 3) is the location with the poor understory vegetation and with disturbed surface soil because of frequent use by Sika deer.

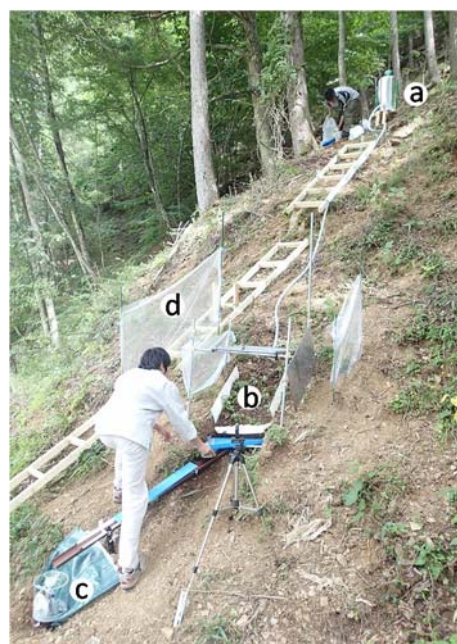


Fig.3 Sprinkling experiment at the plot 1) with animal trail. a: Water tank with level gauge, b: Experimental plot, c: Tipping-bucket raingauge, d: Windshield

We conducted sprinkling experiment totally 22 times: 6 cases of experiment in plot 1, 8 cases in plot 2 and 8 cases in plot 3. The intensity and duration of simulated rainfall were 20 to 110 mm h⁻¹ and 180 minutes, respectively. The size of the experimental plots is 0.5 m width and 0.5 m length. To supply water, water tank with level gauge was set upslope of the

plots. In experiment, we measured the sprinkling intensity (water supply per unit time) and surface runoff. Surface runoff was measured with automated tipping-bucket raingauge. Then we calculated the infiltration rate and compared among plots.

EFFECT OF SIKA DEER TREADING ON SURFACE INFILTRATION RATE

We compared the gradients of the linear regression between rainfall intensity of sprinkling experiment and the final infiltration rate: infiltration rate at the end of 30 minutes, for three plots. As a result, gradients of the linear regression were 0.85 at 2) plot without animal trail, 0.80 at 3) disturbed by treading and 0.74 at 1) plot with animal trail, respectively. Final infiltration rates of 3) disturbed plot and 1) plot with animal trail were respectively 6 % and 13 % less than that of the 2) undisturbed plot as shown in Figure 4.

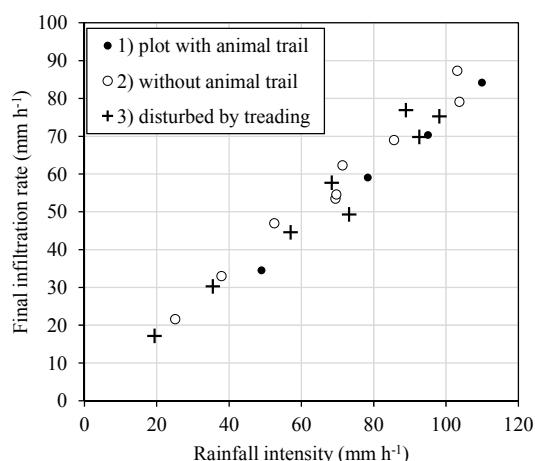


Fig.4 Rainfall intensity of sprinkling experiment and the final infiltration rate, measured at three experimental plots with different conditions of treading

There were no remarkable difference in infiltration rate between 2) plot without animal trail and 3) plot disturbed by treading. This result indicates that the change in infiltration rate, due to surface soil disturbance by Sika deer, is not clear. In contrast, infiltration rate observed in 1) plot with animal trail was less than that of 2) plot without animal trail. Therefore, repeated treading and formation of animal trail may induce soil surface sealing and following decrease in permeability.

Soil compaction, the process by which the soil grains are rearranged to decrease void space, due to treading by grazing animals is one of the factors responsible for the degradation of the physical quality of soils, such as water infiltration [1]. In our study, lower infiltration rate was observed on steep hillslope in contrast with the relatively plain pastureland.

SOIL EROSION MEASUREMENT

To assess the Sika deer impact on soil erosion, we monitored soil erosion from late autumn till early winter. As shown in figure 5, we set the 16 sediment collection troughs along the contour considering the spatial variability of soil properties on forested hillslope on October 10, 2016. The sediment collection troughs No.1, 3, 6, 14 and 16 set bottom of animal trails. Rain gutter of 10 cm-width and 50cm length was used as sediment collection troughs. We collected sediment totally 22 times (2 to 10 days interval). Collected sediment was oven dried at 80 °C and weighed.

Nearby sediment collection troughs, we observed rainfall (throughfall) using tipping bucket raingauge and datalogger (HOBO Pendant, CO-UA-003-64, Onset corp.) since September 28, 2016. Air and surface soil temperature were observed using thermometer (Thermorecorder, TR-71nw, T and D corp.) and counted the number of deer using 4 motion sensor cameras (TrophyCam HD 119736C, Bushnell Outdoor Products).



Fig.5 Static image of Sika deer using a motion sensor camera on December 7, 2016.

White arrows in picture indicate sediment collection troughs

Total sediment yield of all 16 sediment collection trough during monitoring period (October 10, 2016 to January 13, 2017) was 4,787 grams. As shown in Figure 6, soil erosion concentrated in the second half of monitoring period. 88.2 % of total sediment yield was observed during November 11 to the end of period. Especially 56.5 % of total sediment yield concentrated in 10 days since December 8. Total soil loss of each collection trough ranged from 73 to 704 grams. Although the greatest soil loss was observed at No. 14, located at the end of animal trail, location of greater soil loss was not necessarily corresponding the location of animal trail.



Fig.6 Total soil loss of all 16 sediment collection trough during monitoring period (December 10, 2016 to January 13, 2017)

Table 1 Presence of animal trail above the trough, number of deer and total soil loss during monitoring period

Trough No.	1	2	3	4	5	6	7	8
Animal trail	A	N/A	A	N/A	N/A	A	N/A	N/A
Number of deer	42	137	466	38	46	499	276	95
Soil loss (g)	435	449	328	73	97	295	83	668
Trough No.	9	10	11	12	13	14	15	16
Animal trail	N/A	N/A	N/A	N/A	N/A	A	N/A	A
Number of deer	66	10	8	42	40	101	21	7
Soil loss (g)	228	292	88	257	358	704	247	184

Note: "Animal trail" indicates whether the collection trough located at the end of animal trail. N/A in table is an abbreviation for "not applicable". "Number of deer" indicates that the number of Sika deer that passed within 1 meter upslope the sediment collection trough.

RAINFALL AND TEMPERATURE

Daily rainfall, rainfall intensity and air/ground temperature during monitoring period were shown in figure 7. Total rainfall during monitoring period was 341 mm (December 10, 2016 to January 13, 2017). Maximum daily rainfall occurred on November 27 (52.5 mm). Maximum rainfall intensity occurred on December 22 (13.5 mm/h). Snowfall started on November 24, then accumulated after January 8, 2017. Air temperature ranged from -10.2 °C to 15.7 °C. On November 10, minimum air temperature fell below freezing. During the non-snow-cover period after latter half of November, frost heave on surface soil was frequently observed. Although the ground temperature essentially synchronized to the air temperature, it showed smaller amplitude compared to the air, especially during snow-cover period.

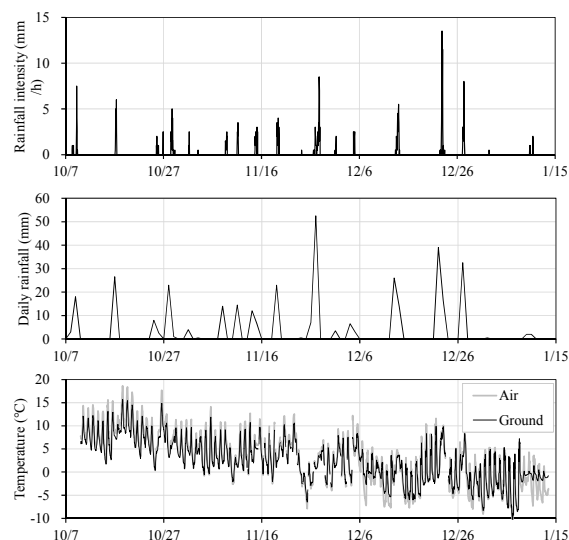


Fig. 7 Daily rainfall, rainfall intensity and air/ground temperature during monitoring period (December 10, 2016 to January 13, 2017)

Relationship between the maximum rainfall intensity and the soil loss shows that the soil loss does not always increase with the rainfall intensity (Fig.8). Soil loss was observed even in case of no rainfall. Similarly there was no clear correlation between total rainfall and soil loss (Fig.9). These results infer that rainfall-induced soil erosion is not dominant process.

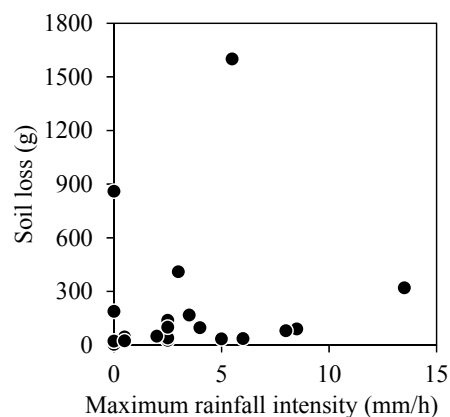


Fig.8 Maximum rainfall intensity and the soil loss
Maximum rainfall intensity means the highest hourly rainfall during each monitoring period of soil loss.

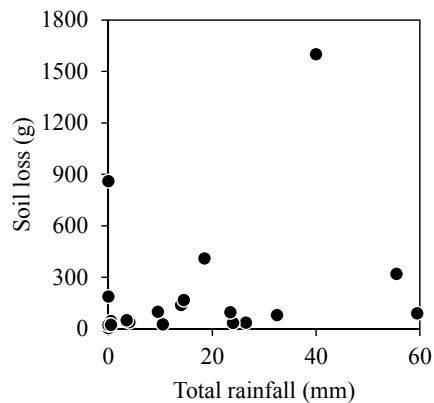


Fig.9 Total rainfall and the soil loss

ESTIMATE OF SIKA DEER IMPACT OF TREADING

Appearance of Sika deer concentrate the latter half of monitoring period as shown in figure 10. Especially, 60.7 % of total was observed during 10 days after December 8, 2016. The number of Sika deer that passed within 1 meter upslope the 16 sediment collection troughs was 1,851 during monitoring period (October 10, 2016 to January 13, 2017). This is a cumulative number of individuals in an image, not actual population of Sika deer. The number of Sika deer ranged 7 to 499 among sediment trap. There were most Sika deer at the end of animal trail (sediment collection trough No.6 and No.3).

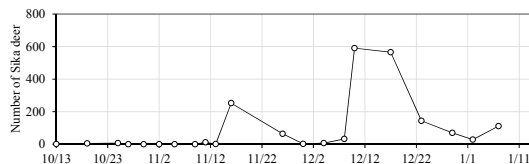


Fig.10 The number of Sika deer that passed within 1 meter upslope the 16 sediment collection troughs during monitoring period (October 10, 2016 to January 13, 2017)

Previous studies on the effect of Sika deer on soil erosion reported that strong negative correlation expressed by an exponential function between the soil loss per unit rainfall and the percentage of the forest floor coverage [2], based on the 5-years monitoring of soil loss in *Fagus* trees with degraded understory vegetation during warm period. At the same site, it is reported that the surface runoff and rainfall intensity strongly affect the amount of soil loss [3].

Although during warm period (April to November), under the condition of degraded understory vegetation due to grazing and treading, erosion process induced by the surface runoff and rainfall is dominant as previous studies shown, our study conducted in cooling season showed different trend.

EFFECT OF FREEZE AND THAWING ON SOIL LOSS

Air and ground temperature (Fig.7) and soil loss (Fig.6) show that the increase in soil loss when the temperature falls at the latter half period. Furthermore, at the timing of minimum temperature was below freezing, remarkable increase in soil loss was observed. The frequency of freeze-thaw cycles (the number of times that the ground temperature go below freezing then above freezing) showed positive correlation to the soil loss of each monitoring period (Fig.11). This result infers that freeze and thawing concern the movement of soil particles.

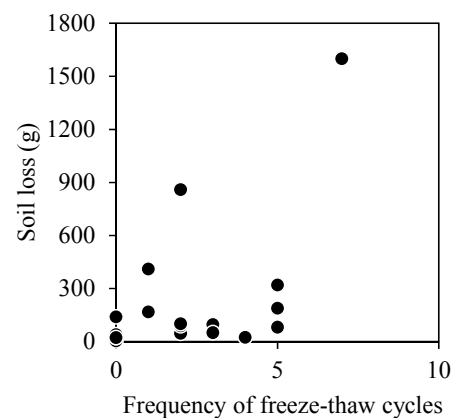


Fig.11 The frequency of freeze-thaw cycles and soil loss

Periglacial soil movements due to frost heaving or freeze-thaw cycle has been measured [4, 5]. Moreover it has been reported that physical weathering [7] or soil creep can occur due to the freeze and thawing under sparse understory, even in case of mountainous hillslope below the forest limit. Study of soil movement [8] on forested slopes with 38 to 43 degrees, elevation of 1,350 meters in Akaishi Mountains, central Japan, showed that the freeze-thawing in winter induces active soil movements as the dry ravel and soil creep.

In the present study, soil loss observed at similar condition to the previous study [7, 8]. We conducted the monitoring at elevation of 1,270 meters, under condition of sparse understory vegetation, at relative steep hillslope ranges from 25 to 41 degrees. During the non-snow-cover period, frost heave on surface soil was frequently observed. Therefore, freeze-thawing and frost heave would partly contribute to the disturbance and movement of surface soil.

EFFECT OF TREADING OF DEER ON SOIL LOSS

Number of deer and the soil loss shown in Figure 12 demonstrate that the soil loss increases with increasing number of Sika deer. This result indicates that the increasing number of deer; more frequent treading induce disturbance and movement of surface soil. Judging from both relationship between the frequency of freeze-thaw cycles and soil loss shown in figure 11, and relationship between number of deer and soil loss shown in figure 12, it was found that the dominant processes of soil loss are both disturbance of surface soil induced by freeze-thawing and treading by deer.

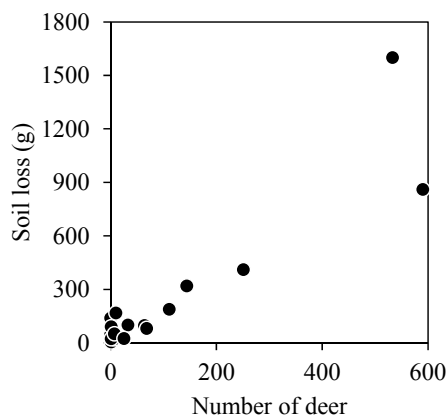


Fig.12 The number of Sika deer and soil loss

CONCUSION

A sprinkling experiment at three experimental plots as follows: 1) plot with animal trail, 2) without animal trail and 3) disturbed by treading showed that the deer-disturbance and/or treading affect the overland flow generation; final infiltration rate on forested hillslope. Soil erosion observation and monitoring of rainfall, air and surface soil temperature and the number of deer, from late autumn till early winter, demonstrated that combination of the frost heaving and disturbance of surface soil by Sika treading accelerates the soil erosion.

ACKNOWLEDGEMENTS

This work was funded by River Planning Division, Water and Disaster Management Bureau, Ministry of Land, Infrastructure, Transport and Tourism, Japan.

REFERENCES

- [1] Hamza MA, Anderson WK, Soil compaction in cropping systems: A review of the nature, causes and possible solutions. *Soil & Tillage Research*, Vol. 82, 2005, pp. 121-145.
- [2] Chu L, Ishikawa Y, Shiraki K, Wakahara T, Uchiyama Y, Relationship between Forest Floor Cover Percentage and Soil Erosion Rate on the Forest Floor with an Impoverished Understory Grazed by Deer (*Cervus Nippon*) at Doudaira, Tanzawa Mountains. *Journal of the Japanese Forest Society*, Vol. 92, 2010, pp. 261-268.
- [3] Biligetu, Ishikawa Y, Shiraki K, Wakahara T, Hai Hu, Yoshimi Uchiyama Y. Relationship between Rainfall Intensity, Rainfall Factor, and Surface Runoff and Soil Loss on the Forest Floor with an Impoverished Understory Grazed by Deer in Doudaira, Tanzawa Mountains. *Journal of the Japanese Forest Society* Vol. 95, 2013 pp. 163-172.
- [4] Matsuoka, N. Solifluction rates, processes and landforms: a global review, *Earth-Science Reviews*, Vol. 55, pp.107-134.
- [5] Matsuoka N. Temporal and spatial variations in periglacial soil movements on alpine crest slopes. *Earth Surface Processes and Landforms* Vol.30, 2005, pp. 41-58.
- [6] Tanaka T, Matsushima K, Tanaka R. Deer Damage and Control in the Nanshin Regional Forest Office. *Water Science* Vol. 58 No. 4, 2014, 39-51.
- [7] Tsutsumi D, Fujita M, Ito M, Teshima H, Sawada T, Kosugi K, Mizuyama T. Fundamental study on sediment yield due to freeze and thaw process, Field observation on bare slope in Tanakami Mountains and its numerical simulation. *Journal of the Japan Society of Erosion Control Engineering* Vol. 59, 2007, pp. 3-13.
- [8] Imaizumi F, Ueji Y. Soil Movement in Artificial Forests Located in Steep Mountain Area and its Countermeasures Using Thinned Woods. *Journal of the Japanese Forest Society* Vol. 94, 2012, pp. 24-30.

TSUNAMI RISK MAPPING USING INTEGRATED REMOTE SENSING AND GEOSPATIAL ANALYSIS

Abu Bakar Sambah^{1,2}, Fusanori Miura³, Guntur¹, Fuad¹, and Defrian Marza Arisandi¹

¹Faculty of Fisheries and Marine Science, Brawijaya University, Indonesia;

²Marine Resources Exploration and Management Research Group, Brawijaya University, Indonesia;

³Faculty of Engineering, Yamaguchi University, Japan

ABSTRACT

Tsunami risk is defined as a combination of the danger posted by tsunami hazard, the vulnerability of people to an event (exposure), and the probability of destructive tsunami or likelihood of the tsunami occurring. Tsunami risk is also defined as the mathematical calculation between tsunami vulnerability and tsunami hazard, and it can be assessed using a spatial multi-criteria. The study applied the combination of element at risk to assess tsunami risk area along coastal area of East Java Indonesia off the Indian Ocean. Remote sensing approach followed by geospatial analysis into tsunami risk assessment along with the existing perspective evolving the role of Geographical Information System. The existing physical vulnerability parameter was analyzed and evaluated. All parameters in both tsunami vulnerability and tsunami risk assessment were analyzed through weighted overlay in geospatial analysis, in which the criteria's weight was calculated through Analytical Hierarchy Process. The results were provided as thematic maps of tsunami vulnerability and tsunami risk. Tsunami risk map described five classes of risk from very low to very high based on the geospatial analysis. It described that coastal area with low elevation identified as highly risk to tsunami. Coastal area with high density of vegetation described a low level of tsunami risk. The existence of river and other water canal along coastal area were also identified as important parameters in generating tsunami risk map. Risk map highlights the coastal areas with a strong need for evacuation capacities, including evacuation route and evacuation building.

Keywords: Tsunami Risk, Remote Sensing, Geo-spatial Data

INTRODUCTION

A tsunami is a series of waves generated in an ocean by a disturbance such as an earthquake, landslide, volcanic eruption, or meteorite impact. An earthquake can generate a tsunami in the overlying water. It can be generated when the sea floor abruptly deforms and vertically displaces the overlying water. When tectonic earthquakes occur beneath the sea, the water above the deformed area is displaced from its equilibrium position. Waves are formed as the displaced water mass, which acts under the influence of gravity, attempts to regain its equilibrium. When large areas of the sea floor elevate or subside, a tsunami can be created [1][2][3]

South coast of Java Island as a part of Indian Ocean is in the confluence of two major plates meet each other, Eurasian and Indo-Australian, where the movement of tectonic plates will create an earthquake and generate tsunami. A potential destructive tsunami in the period of 1991 to 2006, recorded a tectonic earthquake in the Indian Ocean and generated tsunami on the southern coast of East Java, namely on June 3, 1994. A magnitude of 7.8 Mw hit southern coastal areas of East Java and causing casualties of 215 people [4]. Due to the tsunami is a recurring event, create an appropriate

disaster mitigation is important. Tsunami risk mapping is one of the approaches needed for tsunami disaster preparedness.

Tsunami risk mapping combines the results of the tsunami vulnerability and tsunami hazard (Fig. 1). Assessing tsunami vulnerability can provide important information for tsunami disaster risk management plans and mitigation. This also plays an important role in preparing and mitigating for the future events [5][6]. A risk to a tsunami disaster is defined as the mathematical product between tsunami vulnerability and tsunami hazard; it refers to the expected loss from a given hazard to a given element at risk [7]. A disaster is a function of the risk process. Risk results from the combination of hazards, conditions of vulnerability and insufficient capacity to reduce the potential negative consequences of risk. Risk assessment combines the results of the hazard and vulnerability assessments [8][9][10].

Moreover, disaster risk assessment is a qualitative or quantitative approach to determine the nature and extent of disaster risk by analyzing potential hazards and evaluating existing conditions of exposure and vulnerability that together could harm people, property, services, livelihoods and the environment on which they depend.

This includes the identification of hazards, a review of the technical characteristics of hazards (location, intensity, frequency and probability), the analysis of exposure and vulnerability (the physical, social, health, environmental and economic dimensions), and the evaluation of the effectiveness of prevailing and alternative coping capacities with respect to likely risk scenarios [8].

Traditionally risk assessment urges at determining the likelihood of specific losses and damages, which includes population, economy, supporting environment and institutional structures [5].

Satellite remote sensing approach combined with geospatial analysis using Geographical Information System (GIS) for disaster mitigation study provides an important integrated contribution in conducting a tsunami risk assessment. This study assesses tsunami risk area through an integrated satellite remote sensing data and geospatial analysis in the south coastal area of East Java. This is important for tsunami early warning and mitigation. General concepts of the study as shown in Fig 1.

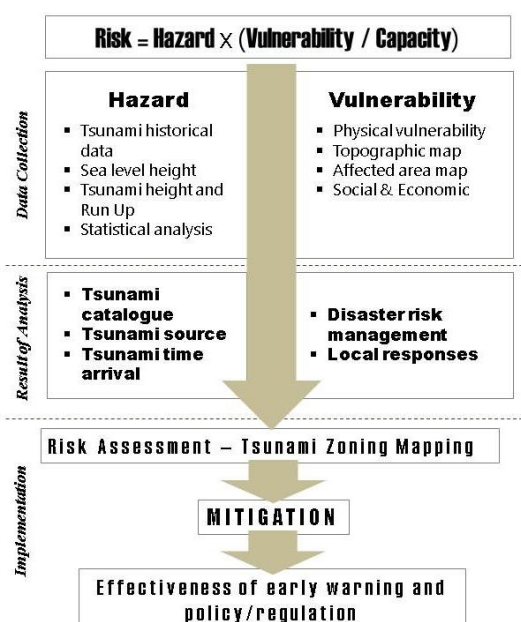


Fig. 1 General concepts of the study

METHODS

Study Area

The study was applied at the south coastal area of East Java, focusing on the coastal area of Jember District, Indonesia (Fig. 1). The coastal area of Jember district was known as one of important marine fisheries resources spot in East Java. This area also affected by 1994 tsunami event along coastal area of East Java. The tsunamigenic earthquake occurred on June 3, 1994 in the Indian

Ocean about 200 km south of Java. The earthquake, which had a surface-wave magnitude of 7.2 and a moment magnitude of 7.8 at 10.51°S and 112.87°E, generated a devastating tsunami that took the lives of more than 200 East Java coastal residents; with maximum runup value of 9.50 m was measured at Rajekwesi area, east part of the study area [11][12].

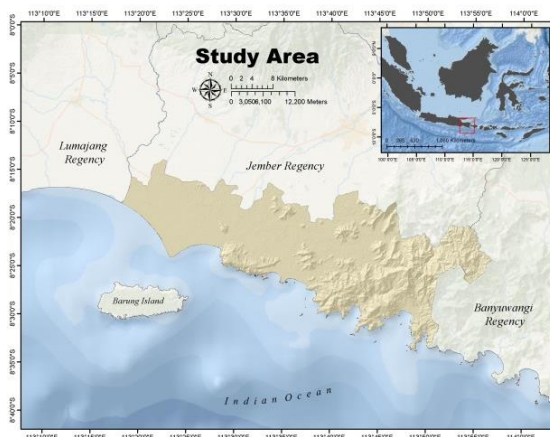


Fig. 2 Study area.

Dataset

Seismic data of the study area from 1992 to 2014 collected from The United States Geological Survey (USGS), and downloaded from <http://earthquake.usgs.gov/earthquakes/search/>. was used as a supporting parameter for tsunami vulnerability in which further will generated seismic map. In order to map the land cover of study area, ALOS satellite imagery with the instrument of the Advanced Visible and Near Infrared Radiometer type 2 (AVNIR-2) with the spatial resolution of 10 m was analysed.

In addition to create tsunami vulnerability map, Digital Elevation Model (DEM) from The ASTER Global Digital Elevation Model (ASTER GDEM) version 2 was applied to generate elevation and slope map. The Advanced Space-borne Thermal Emission and Reflection Radiometer (ASTER) GDEM is a joint product developed and made available to the public by the Ministry of Economy, Trade, and Industry (METI) of Japan and the United States National Aeronautics and Space Administration (NASA). Moreover, vector base map of East Java Indonesia was applied to prepare vector data of coastal morphology, coastal line, and river.

GEOSPASIAL ANALYSIS FOR TSUNAMI VULNERABILITY MAPPING

Vulnerability mapping has been generated using the parameters elevation, slope, coastal proximity, river proximity, coastal type, and land use. Together

with hazard or capacity, tsunami vulnerability is one of the parameters in assessing tsunami risk. Cell-based analysis was applied in combining all parameters through GIS process. The classes of coastal proximity in meter (Fig. 3) was calculated based on the measured run-up and water height in the surveyed area during the last tsunami event in coastal area of East Java, June 3, 1994. It was calculated using algorithm [13][14] :

$$\log X_{\max} = \log 1400 + \frac{4}{3} \log \left(\frac{Y_0}{10} \right) \quad (1)$$

X_{\max} is the maximum reach of the tsunami over land, and Y_0 is the height of the tsunami at the coast.

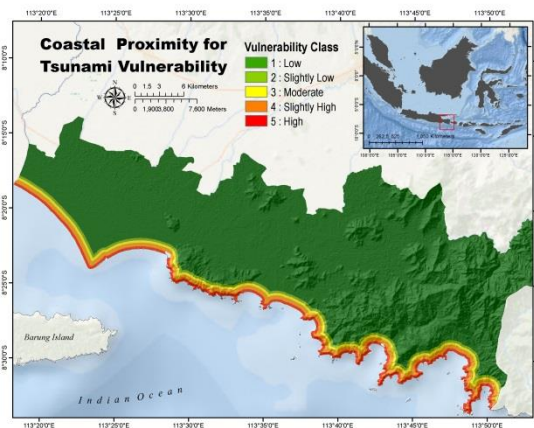


Fig. 3 Coastal proximity map for tsunami vulnerability

Moreover, land use map was generated from supervised classification process of ALOS/AVNIR-2 image. Reflectance value of ALOS image applied in maximum likelihood classification and generated five classes of land use in the study area. Before calculating parameters for tsunami vulnerability mapping, each parameter should be re-classify based on tsunami vulnerability classes, using criteria described in Table 1.

Table 1 Parameter classification based on vulnerability classes. [13][14][15][16]

Parameters	Vulnerability Classes				
	5	4	3	2	1
Elevation (m)	<5	5-10	10-15	15-20	>20
Slope (‰)	0-2	2-6	6-13	13-20	>20
Coastal type	-	Bay	Straight	Cape	-
Land use	Urban	Agriculture	Bare	Water	Forest
Coastal proximity (m)	<293	293-514	514-762	762-1032	>1032
River proximity (m)	<100	100-200	200-300	300-500	>500

Raster overlay for tsunami vulnerability mapping was done based on the weight of parameters. Weights were calculated using Analytical Hierarchy Process (AHP). Weighted overlay is a technique for applying a common measurement scale of values to

diverse and dissimilar inputs to create an integrated analysis. Weighted overlay also one of the suitability analysis based on spatial multi-criteria processing [13][17]. Vulnerability map was generating by applying a weight value to each parameter in raster data format. The calculation applied $[elevation*0.28]+[slope*0.19]+[coastal_proximity*0.18]+[river_proximity*0.12]+[coastal_type*0.13]+[land_use*0.09]$, as the result as shown in Fig. 4.

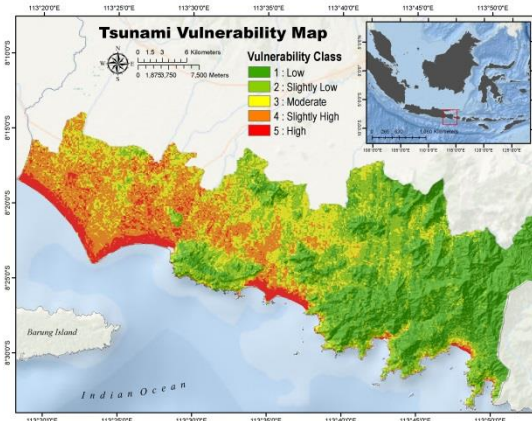


Fig. 4 Tsunami vulnerability map

The use of AHP analysis in generating weight of parameters in which applied in weighted raster overlay describes five classes of vulnerability due to tsunami in coastal area of study area (Fig. 4). It describes that west part of study area, mostly in the class of slightly high to high class of tsunami. This area was identified as flat area with land use class of urban area and agriculture. The associated dataset required for the vulnerability assessment including number of buildings, typologies of buildings, number of floors, or age of building.

The coastal area exposed to tsunami inundation, the buildings and infrastructure are not uniformly at risk within the flood zone [18][19]. The probability of damage is related both to vulnerability and to the tsunami wave energy. Damage level to buildings depends on building type and on inundation depth [20] or could be depend on the density of vegetation around the coastal that assumed will reduce tsunami impact. Assessing tsunami vulnerability in the urban area has to considered that individual buildings will interact differently with a tsunami depending on a number of parameters [18][19]. Various parameters that affect the resistance of the building interact to generate a real class of building vulnerability [20][21].

SEISMIC AND RUN UP ANALYSIS

Seismic data are physical observations or measurements, seismic sources, seismic waves, and their propagating media. The purpose of processing

seismic data is to learn something about the Earth's interior. It needs to figure out some specific relations between the intended targets and measurable parameters in order to understand certain aspects of the Earth [22].

All initial tsunami warnings are based on rapid detection and characterization of seismic activity. Because of the fundamental differences in nature between the solid earth in which an earthquake takes place and the fluid ocean where tsunami gravity waves propagate, the vast majority of earthquakes occurring on a daily basis do not trigger appreciable or even measurable tsunamis. It takes a large event (magnitude >7.0) to generate a damaging tsunami in the near-field and a great earthquake (magnitude >8.0) to generate a tsunami in the far-field [23].

The study area was identified as a high number of seismic point with the depth average of 1 to 5 km and the range of magnitude 1 until >6 . As the result, coastal area of East Java can be classified as a high vulnerable to tsunami. Based on historical data, it was a magnitude of 7.8 Mw in the depth of 18 km and latitude of -10.477° /longitude of 112.835° , caused big tsunami and affected to the coastal area of East Java, including in this study area (Fig. 5).

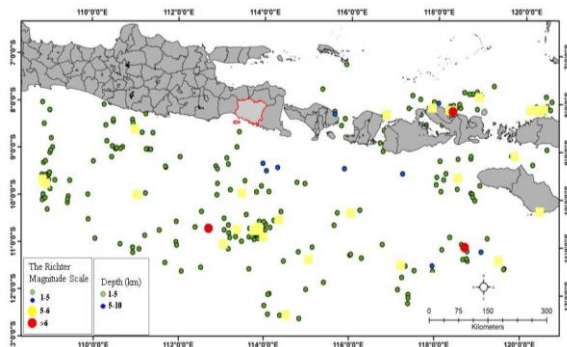


Fig. 5 Seismic data in Indian Ocean close to coastal area of East Java from 1992 to 2004 from U.S. Geological Survey

Fig. 5 illustrated that based on the U.S. Geological Survey data of seismic intensity around Indonesia, it was recorded that the range of magnitude was 1 to 6.3 Mw. It describes the typical effects of earthquakes of various magnitudes near the epicenter. Intensity and thus ground effects depend not only on the magnitude, but also on the distance to the epicenter, the depth of the earthquake's focus beneath the epicenter, the location of the epicenter and geological conditions.

Magnitude of 1 – 6.3 was classified as micro to strong effect or I until VII to X in Mercalli intensity. It was categorized that the damage to a moderate number of well-built structures in populated areas. Earthquake-resistant structures survive with slight to moderate damage. Poorly designed structures receive moderate to severe damage. Felt in wider areas; up to hundreds of miles/kilometers from the

epicenter and strong to violent shaking in epicenter area.

The historical tsunami event of 1994 was used as a basic data for run up analysis. Maximum run up was recorded at Tempurejo district (11.2 m), and minimum run up was 3.1 m in the area of Puger district. Run up analysis described seven points of run up point along coastal area of Jember Regency. Tsunami run up parameter is one of the important parameters in determining tsunami risk due to this parameter is the main parameter in hazard criteria.

Last survey reported by [11] described that in the North West part of study area, Cape Pelindu, a small fishermen village where a fishery created a sort of barrier to the sea water, separating houses from the open sea. The fishery defense wall and three typical straw houses were destroyed. According to eye-witnesses, three big waves followed each other, the third one being the biggest. The measured maximum water height was 3.20 m and the maximum water ingress was about 350 m. The next village was Puger where no evidence of a tsunami could be observed in the harbor. But, just a few kilometers westward, in a place called Tambak Getem, the tsunami left visible marks on the beach: the keeper of a fishery reported that he weakly felt the shock and about 15 minutes later three big waves flooded the beach, the last penetrating about 300 m in land. The measured maximum water height was 5.85 m [11].

Close to the area of Puger, it was a big river. In general, rivers were identified in four different areas. Rivers can play an important role in expanding the impact of the damage during tsunami event. The run-up of the tsunami reaches the hinterland not only through the low elevation of the area, but also through rivers. Rivers also act as flooding strips transporting inundation [13][24].

TSUNAMI RISK MAPPING

Vulnerability refers to the potential for casualty, destruction, damage, disruption or other form of loss in a particular element. Risk combines this with the probable level of loss to be expected from a predictable magnitude of hazard (which can be considered as the manifestation of the agent that produces the loss). Risk is thus the product of hazard and vulnerability. It is an essentially hypothetical quantity, in that it can only materialise in the form of disaster impacts [25][26].

Risk, vulnerability and hazard are the three factors or elements which we are considering here in this pseudo equation. Another definition of risk given by Factor analysis of information risk which may be related to disaster is 'the probable frequency and probable magnitude of future losses. [27]

The numeric value of risk can be calculated as the product between vulnerability and hazard level.

Since vulnerability level ranges from 1 to 5 and hazard level ranges from 1 to 4, risk level of each vulnerable element will be given by:

$$R = V \cdot \frac{H}{4} \quad (2)$$

R is risk, V is vulnerability, and H is hazard. R must be an integer number ranging from 1 to 5, where 5 stands for the maximum risk level. Once risk level has been calculated it will be possible to plot it on a risk map by the process of GIS. Risk map also generated using weighted cell-based overlay. Weighted overlay analysis allows the user to combine weight and rank several different types of information and visualize it, so multiple factors can be evaluated at once [10].

All parameters generated tsunami risk map were displayed in grid cells. Cells were then classified based on its value to five classes of risk; represent low, slightly low, medium, slightly high and high risk. Grouping cells in this raster data followed zonal function operation. Each cell is encoded based on the criteria that make up a zone.

Tsunami risks map (Fig. 6) in the area of East Java, as the result of this study, applied weighted linear combination. This approach processed in a raster GIS in which factors were combined by applying a weight value to each followed by a summation of the results using equation of $\sum (W_i \cdot X_i)$, where W_i is the weight values of the parameter i , and X_i is the potential rating of the factor [28][29].



Fig. 6 Tsunami risk map.

DISCUSSION

Tsunami risk map describes that risk level in the study area divided into five classes. Moderate until high class of tsunami risk were found in the western part. This area mostly covered by flat elevation with rare density of coastal vegetation and high density of urban area. In the previous tsunami event, run up of 4.85 – 5.85 m was recorded in this area.

High density of mangrove in coastal areas and reefs can be a barrier to reduce the effect of tsunami wave, as well as the islands with steep-sided fringing is only at moderate risk from tsunamis. Study about predicting tsunami inundation area using coastal vegetation density was carried out after the 2011 Japan tsunami and found that coastal vegetation also important feature in reducing tsunami wave when hit the coastal area [24]. The high density of mangrove along coastal area has capacity to minimize the negative impact of tsunami wave. Dense mangrove forests growing along coastal areas can help reduce the devastating impact of tsunamis and coastal storms by absorbing some of the waves' energy. When the tsunami struck India's southern state of Tamil Nadu on 26 December, for example, coastal areas in with dense mangroves (area of Pichavaram and Muthupet) suffered fewer human casualties and less damage to property compared to areas without mangroves [30].

Tsunamis waves may undergo extensive refraction and create a process that may converges their energy to particular areas on the coastal areas and increase the heights. High risk of tsunami is depending on the water depth, the coastal geomorphology, the direction of tsunami wave, and the existence of rivers or other water canals. Fig. 8 described that the high class of tsunami risk was identified in the area of Puger district. Total area of tsunami risk in the study area is described in Table 2 and Table 3.

Table 2 Tsunami risk area

No.	Risk level	Cell	Area (m ²)	Area (Ha)
1	Slightly low	2,981	298,100	29.81
2	Low	39,643	3,964,300	396.43
3	Moderate	1,784	178,400	17.84
4	High	153	15,300	1.53
5	Slightly high	-	-	-
Total		44561	4456100	445.61

Table 3 Percentage of tsunami risk level in different district

District	Risk percentage (%)					Total (%)
	Slightly low	Low	Moderate	High	Slightly High	
Kencong	-	92.55	7.44	-	-	100
Gumukmas	-	87.48	10.84	1.66	-	100
Puger	-	81.01	16.81	2.71	-	100
Wuluhan	1.11	97.69	1.16	0.017	-	100
Ambulu	0.69	91.58	7.71	-	-	100
Tempurejo	12.42	87.37	0.18	0.004	-	100

Four district in study area was classified as high risk of tsunami; Gumukmas (0.70 Ha), Puger (0.79 Ha), Wuluhan (0.001 Ha), and Tempurejo (0.001 Ha). Moreover, moderate to low level was in the district of Ambulu, Wuluhan dan Tempurejo. The level of tsunami risk for each district was different

due to the topography or land cover of the area. Puger was an area that most affected based on tsunami risk mapping. Land use in Puger was mostly covered by urban area and the area with low elevation, low density of vegetation, and close to big river. This area is one of the important marine fisheries activities in East Java province.

The use of pair-wise comparison matrix helps in the analysis of multi criteria data where all of the parameters used in this study were calculated based on its weight factor to create vulnerability and also risk map. The calculation of weight as a result of pair-wise comparison matrix was created from expert judgment. Tsunami vulnerability research in Alexandria was applied all parameter in equal weight due to the limitation of knowledge regarding to the study area [31].

The high vulnerability areas were mostly found in the coastal area with the sloping coast type. Elevation and slope play an important role in governing the stability of a terrain. Tsunami vulnerability research in Bali, Indonesia shows the distribution of vulnerability is not uniform and physically it is highly influenced by coastal proximity, elevation, and slope [32][13]. Tsunami risk map that described here based on the integrated approach and to be provided to the people in the study area in the near future due to less information about tsunami risk in the study area.

CONCLUSIONS

Tsunami risk can be assess using the application of multi criteria analysis followed by weighted cell-based processing in which DEM data was applied. The result perform here can be used for the evacuation and reconstruction plan due to tsunami disaster. Also this will be important basic information in determining the evacuation route and evacuation building. Moreover, the final target of tsunami risk mapping is to reduce the effect of tsunami by generating a good mitigation plan.

The combination of raster weighted overlay in the geo-spatial data analysis indicated the vulnerability and risk area due to tsunami and described the possibility area that could be affected by tsunami. The weight of each parameter was calculated by pair-wise comparison matrix of expert judgment, in which every parameter was weighted not equally. By applying overlay process for tsunami risk map and existing land use will describe which area need first to be evacuated when tsunami come.

The result of weighted overlay illustrated that high class of tsunami vulnerability and tsunami risk mostly in the class of urban area, while forest area was indicated in the low class. The more parameters that are applied, the more detailed is the assessment that can be analysed and displayed.

ACKNOWLEDGEMENTS

Authors are thankful to Ministry of Research, Technology and Higher Education Indonesia for financial support, METI and NASA for the Aster GDEM version 2 products, Japan Aerospace Exploration Agency (JAXA) for the ALOS images, BIG Indonesia for providing the basic map of the study area, and U.S. Geological Survey for seismic data. We also thank to Laboratory of Disaster Prevention System, Yamaguchi University, Japan and Laboratory of Marine Resources Exploration, Brawijaya University Indonesia.

REFERENCES

- [1] Cook P, "Tsunami" Third Edition, 2015, Peter Cook
- [2] Ramasamy SM., Kumanan CJ, Sivakumar R, and BhoopSingh, "Geomatics in Tsunami", 2006, New India Publishing Agemcy.
- [3] Damodarasamy SR and Kavitha S, "Basics Structural Dynamics and Aseismic Design", 2009, PHI Learning Priwave Limited, New Delhi.
- [4] Synolakis C, F. Imamura, Y. Tsuji, H. Matsutomi, S. Tinti, B. Cook, Y. P. Chandra, and M. Usman, Damage, "Conditions of East Java Tsunami of 1994 Analyzed", Eos, Transaction, American Geophysical Union, Vol. 76, No. 26, June 27, 1995, p. 257, 261-262
- [5] Strunz, G., Post, J., Zosseder, K., Wegscheider, S., Muck, M., Riedlinger, T., Mehl, H., Dech, S., Birkmann, J., Gebert, N., Harjono, H., Anwar, H.Z., Sumaryono, Khomarudin, R.M. and Muhari, A., "Tsunami risk assessment in Indonesia", Natural Hazards and Earth System Science, Vol. 11 No. 1, 2011, pp. 67-82.
- [6] Papathoma M, Dominey-Howes D, "Tsunami vulnerability assessment and its implications for coastal hazard analysis and disaster management planning, Gulf of Corinth, Greece", Natural Hazards and Earth System Sciences, Vol. 3, 2003, pp. 733-747.
- [7] Dalezios NR, "Environmental Hazaerd; Methodologies for Risk Assessment and Management", 2017, IWA Publishing, London. UK
- [8] UN-ISDR (United Nations International Strategy for Disaster Reduction, <https://www.unisdr.org/we/inform/terminology> , 2009.
- [9] European Commission, "Risk Assessment and Mapping Guidelines for Disaster Management", Commission Staff Working Paper, Brussel, 2010.
- [10] Niekert D, "Introduction to Disaster Risk Reduction", USAID Disaster Risk Reduction

- Training Course for Southern Africa, Creative Commons Attribution-Share Alike 2.5 South Africa, 2011.
- [11] Maramai A, and S. Tinti, "The 3 June 1994 Java Tsunami: A Post-Event Survey of the Coastal Effects", *Natural Hazards*, 1997, Vol. 15, pp.31-49.
- [12] Storchak, D.A., D. Di Giacomo, I. Bondár, E. R. Engdahl, J. Harris, W.H.K. Lee, A. Villaseñor and P. Bormann, "Public Release of the ISC-GEM Global Instrumental Earthquake Catalogue (1900-2009)". *Seism. Res. Lett.*, 2013, Vol 84, 5, pp. 810-815.
- [13] Guntur, Sambah AB, Miura F, Fuad, and Arisandi, DM, "Assessing Tsunami Vulnerability Areas Using Satellite Imagery and Weighted Cell-Based Analysis", *International Journal of GEOMATE*, Vol.12 Issue 34, 2017, pp. 115-122.
- [14] Bretschneider, C.L. and Wybro, P.G, "Tsunami Inundation Prediction", *Proceedings of The 15th ASCE Conference on Coastal Engineering*, Honolulu, July 11-17, 1976, pp. 1006-1024.
- [15] Iida K., "Magnitude, energy and generation mechanisms of tsunamis and a catalogue of earthquakes associated with tsunamis", *Proceeding of Tsunami Meeting at the 10th Pacific Science Congress*, 1963, pp. 7-18.
- [16] Van Zuidam RA, "Guide to Geomorphologic - Aerial Photographic Interpretation and Mapping", *International Institute for Geo-Information Science and Earth Observation*, Enschede, 1983, The Netherlands.
- [17] ESRI, "Environmental Systems Research Institute, Inc. Analyse Site Conditions Using Weighted Overlay", 2015, ESRI.
- [18] Papathoma, M. And Dominey-Howes, D., "Tsunami Vulnerability Assessment and Its Implications for Coastal Hazard Analysis and Disaster Management Planning, Gulf of Corinth, Greece", *Natural Hazards and Earth System Sciences*, 2003, Vol. 3 No. 6, pp733-747.
- [19] Papathoma, M., Dominey-Howes, D., Zong, Y. and Smith, D, "Assessing Tsunami Vulnerability, an Example from Herakleio, Crete", *Nat. Hazards Earth Syst. Sci.*, 2003, Vol. 3 No. 5, pp. 377-389.
- [20] Tinti, S., Tonini, R., Bressan, L., Armigliato, A., Gardi, A., and Guillaude, G : *Handbook on Tsunami Hazard and Damage Scenarios, Schema (Scenarios for Hazard-Induced Emergen-Cies Management)*, Project No. 030963, Specific Targeted Research Project, Space Priority, Irc Scientific and Technical RePort (www.schemaproject.org), 2010.
- [21] Alberico I, V. Fiore D, Iavarone R, Petrosino P, Piemontese, L, Tarallo D, Punzo Michele, and Marsella E, "The Tsunami Vulnerability Assessment of Urban Environments Through Freely Available Datasets: The Case Study Of Napoli City (Southern Italy)", *J. MAR. SCI. ENG.* 2015, 3, pp 981-1005
- [22] Hua-Wei Zhou, "Introduction to seismic data and processing", *Practical Seismic Data Analysis*, Cambridge University Press, 1991, http://assets.cambridge.org/9780521199100/excerpt/9780521199100_excerpt.pdf
- [23] Committee on the Review of the Tsunami Warning and Forecast System and Overview of the Nation's Tsunami Preparedness; Ocean Studies Board, "Tsunami Warning and Preparedness: an Assessment of the U.S. Tsunami Program and the Nation's Preparedness Efforts", *Division on Earth and Life Studies; National Research Council*, 2011, (<https://www.nap.edu/read/12628/chapter/7#111>)
- [24] Sambah AB and F. Miura, "Spatial Data Analysis and Remote Sensing for Observing Tsunami-Inundated Areas", *International Journal of Remote Sensing*, 2016, Vol. 37, Issue 9, pp. 2047-2065.
- [25] Alexander D, "Natural Hazards", *GEOGRAPHY*, 2000, Vol. I, p. 13.
- [26] Wisner B, "Disaster Vulnerability: Scale, Power And Daily Life", *Geo. Jour.*, 1993, 30(2), pp. 127-30
- [27] Smith, K, "Environmental Hazards- Assessing Risk and Reducing Disaster", *Routledge*, 1992, 1st ed, P. 324.
- [28] ESRI, "Environmental Systems Research Institute, Inc. Analyse Site Conditions Using Weighted Overlay", 2015, ESRI.
- [29] Eastman JR, Jin W, Kyem PAK, Toledano J, "Raster procedures for multi-criteria/multi-objective decisions", *Photogrammetric Engineering & Remote Sensing*, American Society for Photogrammetry and Remote Sensing, 1995, Vol. 61(5), pp. 539-547.
- [30] Upadhyay, VP, Rajiv Ranjan, JS Singh, "Human-Mangrove Conflicts: The Way Our", *Current Science*, 2002, Vol. 83 No. 11, pp. 1328-1336.
- [31] Eckert, S., Jelinek, R., Zeug, G. and Krausmann, E. (2012), "Remote sensing-based assessment of tsunami vulnerability and risk in Alexandria, Egypt", *Applied Geography*, Vol. 32 No. 2, pp. 714-723.
- [32] Eddy, "GIS in Disaster Management: a Case Study of Tsunami Risk Mapping in Bali, Indonesia", *Masters (Research) Thesis*, 2006, Jamas Cook University, Australia.

SAFETY AND EFFICIENCY FOR WEEDING WORK AND LEVEE SLOPE'S FORM REQUIRED FOR MOWING MACHINES ON PADDY FIELDS IN STEEP SLOPING AREAS IN JAPAN

Yoshiyuki Uchikawa¹, Masami Matsui², Teruo Arase¹, and Takahiro Tamura²

¹ Academic Assembly Institute of Agriculture, Shinshu University, Japan; ² Faculty of Agriculture, Utsunomiya University, Japan

ABSTRACT

In Japan, land readjustment projects have standardized and expanded the design and size of rice paddy fields. These projects have simultaneously promoted the conversion of levee slopes into stable inclines by expanding the difference in levels between paddy fields, which has expanded levee slopes, i.e. the weeding area. Continuous weeding work is required to prevent erosion and the collapse of steep levee slopes, and serious accidents sometimes occur in the weeding work using brush cutters on such slopes. Brush cutters have been popular for weeding work, but mowing machines are increasingly popular for reasons of safety and work efficiency. However, the levee form was designed based on the assumption of using brush cutters, which recommends small horizontal standing places both at the middle and the bottom of the slope. Therefore, it is necessary to examine whether the form of the levee slope is suitable for mowing machines. We conducted weeding work experiments in two types of levee slopes (with and without standing places) using two types of weeding equipment (mowing machines and brush cutters), and the flora of the levee slopes and the working stress on operators were investigated. Our conclusions are that (1) mowing machines are safer and more efficient than brush cutters and (2) the conventional levee form with standing places will also be effective for mowing machines.

Keywords: Steep Sloping Areas, Paddy Fields, Levee Slope Form, Weeding Work, Mowing Machines

1. INTRODUCTION

Japan is mountainous and not blessed with sufficient flat land – 47% of the country has slopes of 15° or more. Because of typhoons, paddy fields are considered the best available form of cultivation and occupy 50% of cultivated land in Japan. All paddy fields in steep sloping areas have levee slopes. When these paddy fields were developed, they were small-sized rice terraces. However, with recent rapid development of mechanized farming technology, land readjustment of the farmland was required. Land readjustment projects not only standardized and expanded plot design and size but also provided stable inclines for levee slopes, which resulted in expansion of the levee weeding area. Levee slopes are occupied by various plants. Because growth of plants in Japan is excellent due to the climate, if weeding is not carried out in a timely manner, plant succession will continue unchecked.

Many farmers use brush cutters to remove weeds from the slope of these levees (Fig. 1). Brush cutters are useful for irregular slopes, but the incidence of machinery accidents is high. The injuries caused by brush cutter accidents are often serious and are of several types: those from contact with the edge (e.g. cutting off a leg and cuts to a leg); those caused by breakage of the edge; injuries to eyes from broken pieces of stone; and those occurring while removing entangled weeds. Many victims have

mentioned “poor footing”, such as on steep slope surfaces, as the cause of accidents. This problem has been previously examined [1].

The cause of machine work accidents can be categorized into three types: (1) “human factors” (e.g. erroneous operation, poor skills, and failure to check safety); (2) “mechanical factors” (e.g. defects and damage to parts, and abnormal working); and (3) “environmental factors” (e.g. steep slopes and defective safety facilities) [2]. These factors often compound and lead to accidents. For “human factors”, every year the Japanese Government carries out a campaign and training sessions for brush cutters’ work security to prevent accidents. In addressing “mechanical factors”, mowing machines have recently become more popular for reasons of safety and work efficiency. Concerning “environmental factors”, the levee form has been redesigned to have small horizontal standing places (small berms) both at the middle and the bottom of the slope (Fig. 2) [3]. This design was developed about 20 years ago and was based on the assumption of using brush cutters.

Therefore, it is necessary to examine the form of the levee slope that is suitable for mowing machines. In this study, we conducted weeding work experiments on two types of levee slopes (with and without small berms) using two types of weeding equipment (mowing machines and brush cutters). We investigated the flora of levee slopes and the

working stress on operators.



Fig. 1 Weeding work using a brush cutter

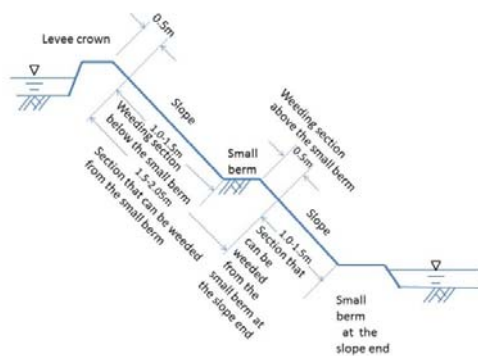


Fig. 2 Levee slope surfaces with appropriate weeding work areas

2. METHODS

In August 2014, we studied vegetation and conducted weeding work experiments at Obasute District, Chikuma City, Nagano Prefecture, Japan [4]. The conditions and the methods follow.

2.1 Working Environment

The four experimental plots had levee slopes with small berms both at the middle and the bottom (Fig. 3). The angle of inclination was 36.3° , the overall slope was 4 m in width by 15 m in length, and the small berms were 60 cm in width.

2.2 Working Machines

The brush cutter was a carried-type model equipped with a steel rotary edge on the end of its rod, with a chip saw attached (230 mm in diameter) (STIHL FS23P, engine output 0.75 kW, mass 3.9 kg, and 1780mm in total length) (Fig. 4).

The mowing machine was a self-propelled-type (OREC SP850B, engine output 2.43 kW, mass 49 kg,

1700 mm in total length, overall width 550 mm, overall height 1100 mm (Fig. 5).

2.3 The Test Subject

The subject was a healthy man (178 cm tall, 78 kg in weight, and aged 41 years) who was an expert with these kinds of machines.

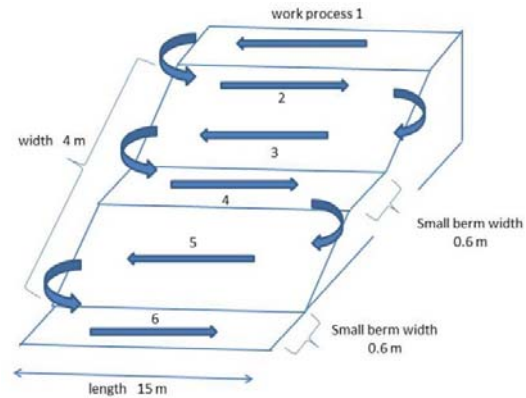


Fig. 3 Plot shape and methods of weeding work used for the experiment



Fig. 4 A brush cutter

Table 1 Plant species and coverage.

	No. small berm	1	2	3	4
species	machine	yes B	yes M	no B	no M
<i>Festuca arundinacea</i>		1	1	1	2
<i>Trifolium repens</i>		1	1	+	1
<i>Equisetum arvense</i>		1	1	1	2
<i>Miscanthus sinensis</i>		3	2	3	3
<i>Erigeron annuus</i>		1	1	1	1
<i>Trifolium pratense</i>		1	1	1	2

B: brush cutter

M: mowing machine



Fig. 5 A mowing machine

2.4 Methods of Weeding Work

Weeding work according to the methods is shown in Fig. 3. The direction of the arrow shows the walking direction of the subject. The work process is 1–6, proceeding from the levee crown, to the upper slope and then to the lower part. When using the brush cutter, the slope surface was entirely cut by the downward weeding method; at the slope end, the upward weeding method was used, so that no grass fell to the plot below.

2.5 Methods of Measuring Physical Burden

The physical influence of weeding work appears

congruent to the shape of the levee slope surface (the working environment), work method, performance of the machine, and the physical condition and skill of the worker. We measured a surface electrode on both deltoid muscles of the shoulder, between the hand and the elbow on the back of the forearm, and the muscle between the knee and the hip on the front of the leg (femur). In addition, we measured the time required for work, and recorded the work using a stationary video camera from two viewpoints.

3. RESULTS

3.1 Vegetation Survey

Table 1 shows the representative common plant species and coverage at the experimental plots.

We employed the following six classes of plant coverage in each plot for the field survey, with the plant species covering: (+) < 1% of the plot area; (1) 1–9%; (2) 10–24%; (3) 25–49%; (4) 50–74%; and (5) 75–100%.

3.2 Work Area and Weeding Time

Table 2 shows the results for the actual working area and time. We calculated the work area per working hour based on this result (Fig. 6). The results clearly showed that the mowing machine had more workload than a brush cutter.

Table 2 Area and work time for each plot

Plot no.	Small berm	Area [m ²]	Work time [s]
1	Yes	105.0	1194
2	Yes	112.5	999
3	No	79.5	794
4	No	82.5	757

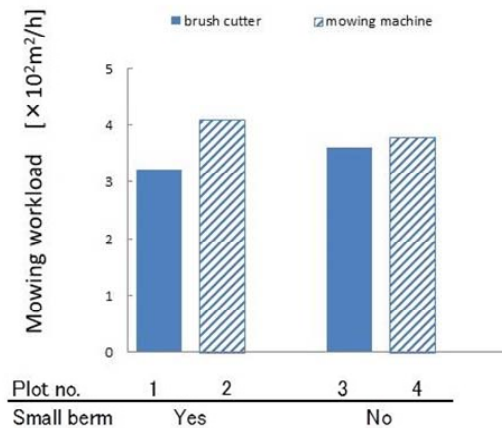


Fig. 6 Mowing workload

3.3 Work Strain Imposed by Machines and Slopes

The work strain results are shown in Fig. 7. During cutting, the work strain imposed by using the mowing machine was 30, 56, and 50% less than the brush cutter for the shoulders, forearms, and thighs, respectively. Notably, the brush

cutter imposed a large strain on the forearms compared with other body parts.

The surface electrode on each muscle does not clearly show according to the availability of footing.

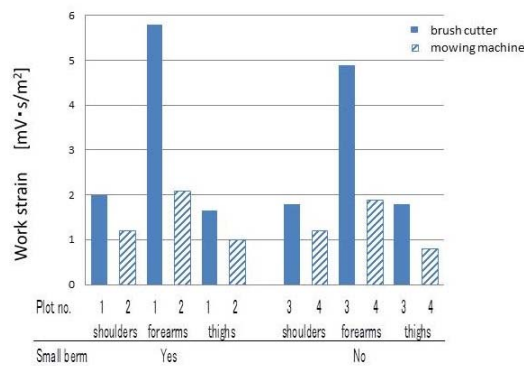


Fig. 7 Work strain on three body parts from using each machine during cutting

3.4 Density of Litter and Work Strain

Table 3 shows the density of cut material (litter) about each plot and work strain on the shoulders and forearms. Regardless of the litter density, the work strain imposed by the mowing machine was less than for the brush cutter.

Table 3 Work area and weeding hours of each plot

plot no.	1	2	3	4
small berm	yes	yes	no	no
machine	B	M	B	M
density of litter[kg/m ²]	0.27	0.19	0.18	0.14
work strain S	1.98	0.87	1.67	0.96
[mV·s/m ²] F	5.55	1.53	4.72	1.32

B: brush cutter M: mowing machine

S: shoulders F: forearms

4. DISCUSSION

The experimental results showed that the physical burden from the mowing machine was less

than from the brush cutter, and the work efficiency was superior. It is self-evident that the mowing machine is safer than the brush cutter, because the cutting edges are not exposed.

Small berms of levee slopes have been provided as a means to secure footing on the slope for safe and efficient weeding work and also as safety zones (stoppers) in the event of slips by brush cutters [1]. On the other hand, from this study, the stability of footing was not necessarily shown to be effective in the work by the mowing machine either. From the walking working conditions in the levee slope, it is expected that the burden would be greater on the lower than the upper thigh. It was thought that the judgment by such a measurement was necessary in future. In addition, it was confirmed that the arm length of the mowing machine suited the position of the small berm according to the current design standard.

5. CONCLUSIONS

The results led to the following conclusions: (1) mowing machines are safer and more effective than brush cutters, since the former had more workload, and less physical burden than the latter; (2) the conventional levee form with standing places did not clearly proved to be effective for mowing machines in the viewpoint of workload and physical stress. However, the mowing machines were confirmed applicable sufficiently to the conventional levee with standing places in this study: the existence of standing places will enable the operators to move safely, with low risk to slide down.

6. REFERENCES

- [1] Kimura, K., Arita, H. and Uchikawa, Y. "Safety and efficiency for weeding work and form of levee slope on paddy field in a steep sloping area - developing farm land consolidation technique in regard to labor efficiency of levee weeding (III)", *Trans JSIDRE*, 170, 1994, pp. 11-18 (in Japanese with English abstract).
- [2] Arita, H. and Kimura, K. *Land Consolidation of Paddy Field*, Association of Agriculture & Forestry Statics, 2003, pp. 187-188.
- [3] MAFF (Ministry of Agriculture, Forestry, and Fisheries). *Design Standard for Land Improvement Project Plans: Planning and Field Development (Paddy Field)*, 2000, pp. 309-314 (in Japanese).
- [4] Kimura, T., Matsui M., Honda, R., Uchikawa, Y., Tamura, T. and Aoyagi, Y. "Difference of influence between Work strain of Mowing Machines", *Journal of the Japanese Society of Agricultural Machinery*, 79(1), 2017, pp. 66-73 (in Japanese with English abstract).

OPTIMAL RESTORATION STRATEGY OF A WATER PIPELINE NETWORK IN SURIGAO CITY, PHILIPPINES

Agnes Garciano¹, Lessandro Estelito Garciano², Renan Ma. Tanhueco³ and Taze Jared Abubo⁴

¹Assistant Professor, Ateneo de Manila University, Philippines; ^{2,3}Associate Professor, De la Salle University, Philippines, ⁴undergraduate student, Ateneo de Manila University, Philippines

ABSTRACT

Quick recovery of water services immediately after an earthquake is critical. This is to minimize hazards to environmental sanitation and consequent health problems caused by the lack of potable water supply. It is necessary therefore that water lifeline operators establish restoration strategies to deal with damage scenarios in their respective concession areas specifically during extreme seismic events. The recent 6.7 magnitude earthquake in Surigao City due to the movement of the Philippine Fault Zone: Surigao segment underscored this need. However due to the complexity of the network a systematic restoration sequence that minimizes restoration time and maximizes delivery of water service should be employed. In this research, the authors employed Horn's algorithm to determine the optimal restoration strategy of a pipeline network in Surigao City, Philippines. The repair sequence starts with the determination of a minimal spanning tree of the given pipeline network. The water source is designated as the root of this tree while the nodes represent the water demand at specific areas. The edges of the tree structure representing the pipelines connect the nodes. The assigned numeric value or weight of an edge (link) denotes the time to repair that specific pipeline. This value is a function of the length of the pipeline. The results show that an optimal job sequence may be carried out by considering maximal ratios of expanding family trees within the network. A least penalty function is a consequence of the optimal repair job sequence.

Keywords: water lifeline, seismic event, Horn's Algorithm, minimal spanning tree, penalty function

INTRODUCTION

The Philippines is frequented by extreme wind speeds (typhoons), earthquakes, extreme floods and thunderstorms due to its geology and geographic setting. Strong magnitude earthquakes which are considered as the most destructive is a constant threat to the country's built environment. The recent earthquakes in the country, e.g., Bohol Earthquake 2013, Batangas Earthquake 2017 and the Surigao Earthquake 2017, have shown that built structures such as schools, hospitals, power supply system (Mallari and Cinco, 2017), historical structures (Lucas, 2013) and water lifeline systems (Crismundo, 2017) can be damaged during strong ground motion events. In this regard, quick recovery of vital lifeline systems damaged by earthquakes is critical for post-earthquake activities. However, it should be emphasized that pre-disaster programs should be established to assess the vulnerability of the system and to manage the risk when a hazard strikes. The recent earthquake in Surigao del Norte that pulled-out some of the pipes from the support underscored the need to prepare contingency plans when ground strains exceed the capacity of buried pipes.

There have been several studies to manage lifelines under earthquake risk (Kameda 2000), optimize restoration of electric power, i.e. (Chi et. al.

2002), utility lifelines (Nojima 2012), redundancy index of lifeline systems (Hoshiya and Yamamoto 2002). In 2004, Ueno et. al. developed fragility curves of components of a gas system in Teheran due to seismic loads. On damage estimation, Toprak and Taksin (2007) estimated the buried pipeline damage relationships using eight scenario earthquakes. On the other hand, a stochastic simulation model of damage and restoration of water supply systems was presented and applied to Bay Area water supply systems under hypothetical earthquake scenarios (Porter 2016). Finally, Khin Aye Mon et al. proposed a simplified seismic design guidelines for buried pipelines for developing countries. In this paper, the authors discuss an algorithm first proposed by Horn [10] and then apply it to a water network system to determine an optimal repair sequencing of the damaged pipeline network.

STUDY AREA

Surigao City is the capital city of Surigao del Norte located in the southeastern part of the Philippines. The city proper is composed of three barangays namely: Washington, Taft and San Juan as shown in Figure 1. The city has a population of about 140,540 with a land area of 245 km².



Fig.1 Study area

Data from the Philippine Institute of Volcanology and Seismology (PHIVOLCS) show that the main earthquake generator around Surigao del Norte is the Philippine Fault Zone: Surigao Segment (see Fig. 2).

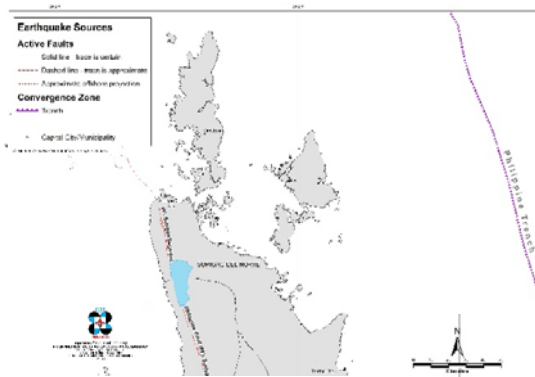


Fig. 2 Active Faults / Trenches in the study area



Fig. 3 SMWD pipe network system

The water system operator of Surigao City is the Surigao Metropolitan Water District (SMWD). The pipeline network of the study area is shown in Figure 3.

Table 1. Link / Length of each pipe

Link	Node i	Node j	Length (m)
448	352	354	1432
564	354	355	425
562	348	347	1531
444	348	349	581

Data of the network provided by SMWD show that pipeline network consists of 416 nodes (junctions) and 415 links (pipes). Table 1 shows a sample data links with connecting nodes i and j and their lengths. The weight of each edge is assumed to be the length of the edge.

Minimum Weight Spanning Trees

Mathematically, a network consisting of nodes and edges linking the nodes may be denoted by a graph. A graph is a pair $G = (V, E)$ of non-empty sets V and E where E consist of two element subsets of V . The elements of V are the vertices or nodes of G and those of E are the edges or links of G . A tree is a connected graph with no closed paths called cycles. A rooted tree is a tree with one vertex designated as a root. A union of trees is called a forest.

A graph $H = (V', E')$ is called a spanning subgraph of $G = (V, E)$ if $V' = V$ and $E' \subseteq E$. If each edge e of a graph is assigned a real number $w(e)$ called its weight, then G is called a weighted graph. In the restoration work of a damaged network, a basic step is to find a minimum weight spanning tree of the network, that is, a tree which contains all the vertices of the network and whose edges have the least total weight. Such minimum weight spanning tree is obtained using Kruskal's algorithm which consists of initially arranging the edges in order of increasing weights. Edges that keep the graph connected and total weight minimum are then chosen. More information on Kruskal's algorithm may be found in [9].

Horn's Algorithm

In applying Horn's algorithm [8] to determine the optimal repair sequence of a damaged network, there are two assumptions: a rooted forest N is given and the vertices follow a precedence relation P . We say that x precedes y or xPy if there is a directed path from x to y in N . To each vertex x in the rooted forest, two nonnegative values $V(x)$ and $T(x)$ are assigned corresponding to the value of the restoration job at vertex x and the time to complete

the job at node x respectively. The best ratio at x , denoted by $r(x)$, is defined as

$$r(x) = \max \left\{ \frac{V(S)}{T(S)} : S \in T[x] \right\} \quad (1)$$

where $T[x]$ denotes the set of all trees rooted in x and

$$V(S) = \sum_{u \in S} V(u) \quad (2)$$

and

$$T(S) = \sum_{u \in S} T(u). \quad (3)$$

A maximal family tree of x , denoted by F_x is an element of $T[x]$ for which the best ratio is achieved.

In order to find an optimal repair sequence, Horn defines a sequencing σ as a bijection $\sigma: V \rightarrow \{1, 2, 3, \dots, n\}$ assigning to each vertex $x \in V$, its position number $\sigma(x)$ in the repair sequence. An allowable sequencing is a sequencing σ with the property that if xPy , then $\sigma(x) \leq \sigma(y)$. Finally a linear delay penalty function is defined as

$$f(\sigma) = \sum_{x \in X} V(x) \left(\sum \{T(y) : \sigma(x) \leq \sigma(y)\} \right). \quad (4)$$

This function is a measure of the penalty caused by delay in completion of the repair job at a node x . Thus, the objective is to find an allowable sequencing σ which gives the least linear delay penalty.

The methodology consists of three components:

1. Given a network, find a minimal weight spanning tree.
2. For each node x in the network, calculate the best ratio $r(x)$ and the maximal family tree F_x .
3. Generate the optimal repair sequence of the network based on the best ratios obtained and calculate the linear delay penalty function.

DATA AND RESULTS

In this study, data on the pipeline network of Surigao City was used to construct a repair sequence scenario in the event of massive earthquake where all pipelines are assumed damaged. The network consists of 416 nodes (junctions) and 542 links (pipes). The nodes represent the water demand in a specific area and the links represent the supply pipes. Each node x has a value $V(x)$ corresponding to the base demand in liters per second. Furthermore we define $T(x)$ to be the time (proportional to the length of the pipe in meters) to supply water to node x . A table of sample data is given in Table 2.

Using Kruskal's algorithm, a minimal spanning tree for the entire network is obtained with root at junction 376. The spanning tree consists of 416 nodes and 415 links, removing 127 links from a

total of 542 pipes as shown in Figure 3. Due to the huge data, only a portion of the minimum weight spanning tree is shown in Figure 4 and Figure 5.

Table 2. Sample nodes with corresponding values of $V(x)$ and $T(x)$

Node (x)	$V(x)$ (in lps)	$T(x)$ (proportional to length in m)
393	0	5691
360	0.89	313
358	0.081	95
357	0.89	234
310	0.79	55
306	0.214	10

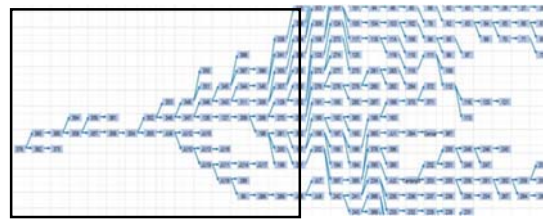


Fig.4 Minimal weight spanning tree

This spanning is rooted at node 376 because this is the water supply source.

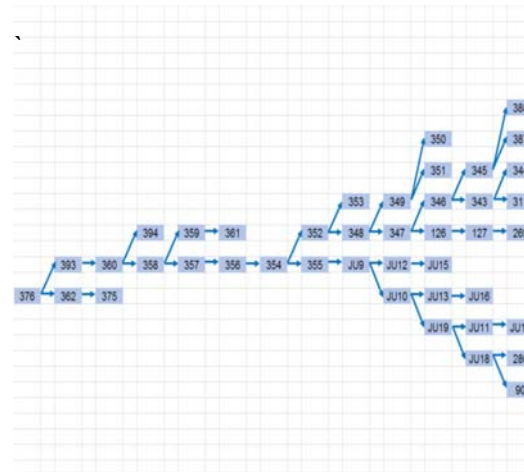


Figure 5. A portion of the minimum weight spanning tree (rooted at node 376)

Applying Horn's algorithm to the rooted tree obtained above yields an optimal repair sequence for in the network. The sequencing of repairs of the first 40 nodes of the network is shown in Table 3. The table indicates that node 393 must be the first to be repaired, followed by node 360, and so on. The value of the least penalty function is $f(\sigma) = 7773252.522$.

Table 3. First 40 restoration jobs in an optimal sequencing

order $\sigma(x)$	node x	order $\sigma(x)$	node x
1	393	21	117
2	360	22	118
3	358	23	114
4	357	24	110
5	356	25	119
6	354	26	115
7	352	27	111
8	348	28	109
9	347	29	104
10	126	30	103
11	127	31	102
12	269	32	106
13	268	33	100
14	129	34	101
15	122	35	94
16	123	36	86
17	124	37	87
18	108	38	91
19	107	39	79
20	105	40	68

Figure 6 below shows the portion of the water pipeline network in the areas of Barangay Canlanipa with node identification numbers. In Figure 7, the same water pipeline network is shown but with the corresponding values of $\sigma(x)$ indicating the number of node x in the cue of the repair work that must be executed.

Restoration curve

Figure 8 shows the restoration process of the water pipeline of SMWD. This restoration curve is a non-decreasing function (Nojima and Kameda, 1992) and shows the repair on a node-to-node basis until the entire network is full operation.

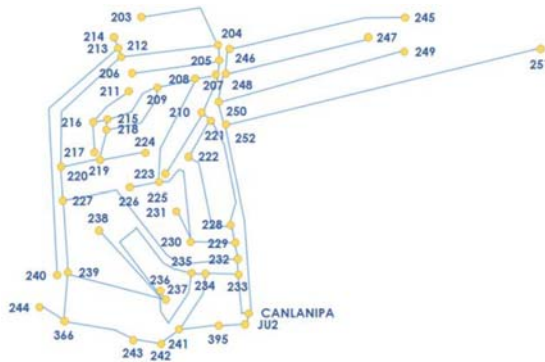


Fig.6 Minimal weight spanning tree of Barangay Canlanipa

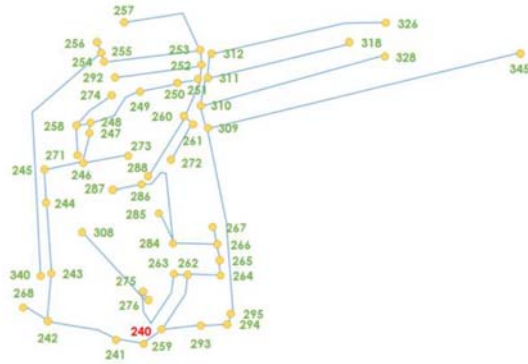


Fig.7: Sequence of restoring the network portion of Barangay Canlanipa

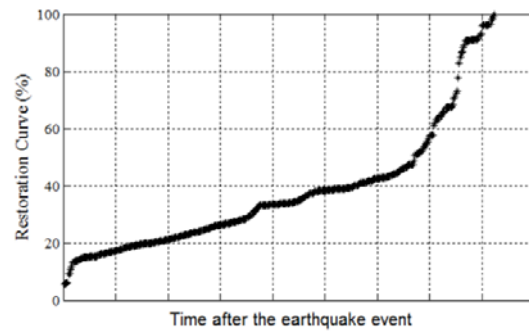


Fig. 8 Restoration Curve

CONCLUSION

A plan for restoring a pipeline network in a post-earthquake scenario takes into account the best ratio $r(x)$ at each node x of the network. This value is the maximum ratio of the demand of water supply associated to the node over the time it takes to repair the pipe leading to the node and is taken over all family trees rooted in node x . In Surigao City, a minimum weight spanning tree is first obtained from the network to ensure that all nodes will be supplied with water using pipes with minimum total length. At each node a best ratio is calculated measuring how urgent the repair of the link to a node is over the time to repair the link. Finally, the optimal sequence of restoring the network is accomplished by starting at the root node and choosing the node with largest best ratio at each step. For future work, it is interesting to calibrate the restoration strategy with actual damage during strong seismic events. The methodology used study can also be replicated to other tree-like systems, e.g. water, electric power, in any area.

ACKNOWLEDGEMENTS

The authors would like to acknowledge the assistance of Engr. Ensomo of the Metro Surigao Water District (MWSD).

REFERENCES

- [1] Luces, K. (2013). From treasure to rubble: Heritage churches before and after the Bohol quake. GMA News Online.
- [2] Crismundo, M. (2017). Panic grips Surigao; Strong aftershocks, water shortage keep quake-affected residents on edge. Manila Bulletin
- [3] Mallari D. and Cinco, M. (2017). 5.6 Magnitude quake causes power outages in Southern Luzon. Phil. Daily Inquirer.
- [4] Kameda, H. (2000). Engineering Management of Lifeline Systems under Earthquake Risk. *Proc. 12th World Conference on Earthquake Engineering*, pp. 2827 – 2843.
- [5] Chi, J. M., Huang, R., and Yang, C. C. (2002). "Practical strategies for post-earthquake restoration of electric power systems," *Proc. 10th World Conference on Earthquake Engineering*, pp. 159 – 164.
- [6] Nojima N. (2012). Restoration Processes of Utility Lifelines in the Great East Japan Earthquake Disaster, 2011. *Proc. 15th World Conference on Earthquake Engineering*, Lisbon, Portugal.
- [7] Hoshiya, M. and Yamamoto, K. (2002). Redundancy Index of Lifeline Systems. *Journal of Engineering Mechanics*, Vol. 128, No. 9, Sept. 1.
- [8] Ueno, J., Takada, S., Ogawa, Y., Matsumoto, M., Fujita, S., Hassani, N. and Ardakani F. S. (2004). "Research and development on fragility of components for the gas distribution system in Greater Tehran, Iran. *Proc. 13th WCEE*, Vancouver, B.C. Canada, Paper No. 193
- [9] Porter, K. (2016). Damage and Restoration of Water Supply Systems in an Earthquake Sequence. *ESM 13-01*, Structural Engineering and Structural Mechanics Program, Department of Civil Environmental and Architectural Engineering, University of Colorado Boulder.
- [10] Toprak, S and Taskin F. (2007). Estimation of Earthquake Damage to Buried Pipelines Caused by Ground Shaking. *Natural Hazards*, Vol. 40, Issue No. 1, pp. 1 – 24.
- [11] Khin Aye Mon, Koike, T., Nishikawa, G., Garciano, L. E. and Kiyono, J., "A Simplified Design Method of Water Lifeline in Developing Countries" In. *Proc. of the 7th China-Japan-US Trilateral Symposium on Lifeline Earthquake Engineering*, Shanghai, China, June 1-4, 2016.
- [12] Horn, W. A. (1972). "Single-machine job sequencing with treelike precedence ordering and linear delay penalties," *SIAM, Journal of Applied Mathematics*, 23(2), 189 - 202.
- [13] Bondy, J.A and Murty, U.S.R. (2008). *Graduate Texts in Mathematics: Graph Theory*. Springer.
- [14] Nojima N. and Kameda H. (1992). Optimal strategy by use of tree structure for post-earthquake restoration of lifeline network system. *Proc. 10th World Conference on Earthquake Engineering*, Balkema, Rotterdam, pp. 5541 - 5546.
- [15] Abubo, T. (2017): Job sequencing with tree-like precedence ordering and linear delay penalties. Undergraduate thesis. Ateneo de Manila University.

FOREST ROADS CAUSE EDGE EFFECTS ON PLANT SPECIES DIVERSITY IN ARTIFICIAL FORESTS

Hiroki Kohmori¹, Tetsuoh Shirota¹, Tetsuo Okano¹ and Teruo Arase¹

¹Faculty of Agriculture, Shinshu University, Japan

ABSTRACT

To evaluate the effects of narrow forest roads on plant species diversity in the forest understory, we analyzed the relationship between distance from the forest road and vegetation structure in young and mature artificial forests of Japanese cedar (*Cryptomeria japonica*). Although exotic species appeared along the side of the forest road, their appearance frequencies and coverage were very small, suggesting that a decline in species diversity due to exotic species did not occur. Although an obvious decrease in vegetation coverage and species number with distance from the forest road was detected in the shrub layer of the young forest, a clear distance-dependency was not observed in the mature forest. However, even though the effects on local species number (α diversity) were unclear, replacement of species was detected with distance from the forest road (β diversity) in association with species' shade tolerance. This replacement of species improved the overall diversity of forest (γ diversity). Thus, it was concluded that narrow forest roads can improve species diversity in artificial forests in association with a diversified environment and the replacement of plant species.

Keywords: Forest Road, Artificial Forest, β Diversity, Edge Effect, Forest Age

INTRODUCTION

Installation of forest roads enables the introduction of high-performance forestry machinery [1], which reduces costs and enhances forestry productivity [2], [3]. Thus, a greater density of forest roads is required in Japan [4]. The construction of forest roads also result in changes to the forest environment, such as temperature, humidity and light [5], [6]. Such environmental changes can impact the species diversity of the forest [6], [7].

Several studies have shown that the existence of forest roads improves species diversity [8]–[10]. However, even if the construction of a forest road initially has positive effects, its impact on the neighboring forest can change over time [8]. On the other hand, the effects of forest road construction are not always positive with respect to species diversity. Road construction enables the invasion and dominance of exotic plant species, which reduce the diversity of native species [7]. Furthermore, the influence on diversity also depends on the road width since the size of the canopy gap is related to the width of the forest road. In the case of narrow forest roads in Iran, the effects on forest species diversity were not obvious [11].

It is generally assumed that Japanese forest roads are narrow (4–6 m); therefore, their effects on species diversity may be slight. In this study, we tested the effects of Japanese forest roads on exotic plant invasion and plant species diversity in forests of different ages.

MATERIALS AND METHODS

Study Site

The survey was conducted in an artificial forest of Japanese cedar (*Cryptomeria japonica*) in Neba Village, Nagano Prefecture in Central Japan. This area is located 35°16'N, 137°35'E. From 2007 to 2016, the annual temperature was 9.6°C and the average annual precipitation was 2,697 mm at the closest observation site (Namiiai Observation Site, Japan Meteorological Agency, 35°22'N, 137°42'E). Two forest roads were surveyed in this study, the Takahashi-Gumino (TK) line, which passes through a young forest, and the Anada (AN) line, which passes through a mature forest (Fig. 1, Table 1).



Fig. 1 Location of the study areas.

Table 1 Outline of the surveyed forests.

	TK line	AN line
Number of plots	5	18
Altitude (m)	919-927	779-829
Road construction year	1999	1970
Road width (m)	4-6	4-5
Forest age (years)	49	63-83
Stand density (trees/ha)	1400	633
Canopy height (m)	21.4	25.9
Canopy coverage (%)	58	65

Field Surveys and Data Collection

To evaluate the effect of forest roads on species diversity in the understory, five and 18 belt plots were established along the TK and AN lines, respectively. The average road width was 4.8 m. For vegetation investigation, belt plots of 10 m wide and 20 m depth were set from the edge of the road to the interior of the forest. Furthermore, each belt plot was divided into four sub-plots, each 10 m wide and 5 m deep, which were named Psub.1, Psub.2, Psub.3, and Psub.4 in order of distance from the forest road. All sub-plots had three major layers including the canopy layer, shrub layer, and herb layer, but lacked a sub-canopy layer. The canopy layer consisted only of planted *Cryptomeria japonica*. The characteristics of the survey area are summarized in Table 1.

We surveyed the vegetation structure of the shrub and herb layers in each sub-plot. We recorded the total vegetation coverage (%) and species coverage (%) along with the names of all vascular plants detected. The scientific name refers to botanical books [12]–[19].

Analysis Method

To characterize the change in vegetation coverage and species diversity with respect to distance from the forest road, we calculated species number and Shannon's diversity index (H') based on the species coverage for each layer of each sub-plot. We compared these characteristics among the sub-plots within each layer of each line using a repeated measure analysis of variance and Holm's multi-comparison method.

To detect the plant species present with distance from the forest road in each layer of each line, we conducted a screening test for all species using the Jonckheere-Terpstra test in each sub-plot according to the distance from road. Species coverage was used for the screening test, and a coverage of 0.1% was used when the coverage was less than 1%. We referred to the species detected along the road side and on the forest interior as "edge species" and "interior species", respectively.

RESULTS

Vegetation Structure

The vegetation survey represents a larger number of plant species in the mature forest compared to the young forest. In the young forest of the TK line, 30 and 114 plant species were recorded in the shrub and herb layers, respectively. On the other hand, in the mature forest of the AN line, 93 and 224 plant species were recorded in the shrub and herb layers, respectively. Vegetation coverage, species richness, and species evenness were larger in the mature forest than the young forest, with the exception of species evenness in the shrub layer (Fig. 2).

Almost all of the plants present were native species, except for the following three exotic species found in the herb layer: *Eragrostis curvula*, *Indigofera bungeana*, and *Phytolacca americana*. Exotic species were found only in sub-plots facing the forest road. However, only one individual of each of the three exotic species was detected and the coverage of each was less than 1%.

Changes in Vegetation Coverage, Species Number, and H' with Distance from Forest Road

Changes in the species number, vegetation coverage, and H' with respect to distance from the forest road are shown in Fig. 2. In the young forest of the TK line, both species number and vegetation coverage in the shrub layer were significantly larger in sub-plots along the road side, whereas these remained unchanged in the herb layer. On the other hand, in the mature forest of the AN line, species number and vegetation coverage in the shrub layer did not show any obvious change along the belt depth, whereas both were slightly larger in the herb layer of sub-plots along the road side. In the herb layer of both the TK and AN lines, vegetation coverage and species number show a non-linear pattern: they were larger in both edge and interior sub-plots, but smaller in sub-plots positioned in the middle. There was no significant difference in H' in any line or in any layer, but H' in the shrub layer of the TK line showed a tendency to increase toward the road side.

Species Appearance Pattern with Distance from Forest Road

The edge and interior species detected along each line are shown in Table 2. In the young artificial forest of the TK line, 30 species were detected in the shrub layer, four of which were edge species; 114 species were detected in the herb layer, two and four of which were edge and interior species, respectively. In the mature artificial forest of the AN line, two of the 93 species detected in the shrub layer were edge species; 224 species were detected in the

herb layer, 11 of which were interior species. Interior species were not detected in the shrub layer of either line. Along the AN Line, two edge species

(*Rubus palmatus* var. *coptophyllus* and *Dioscorea japonica*) were commonly detected along the AN line, whereas any species were commonly detected

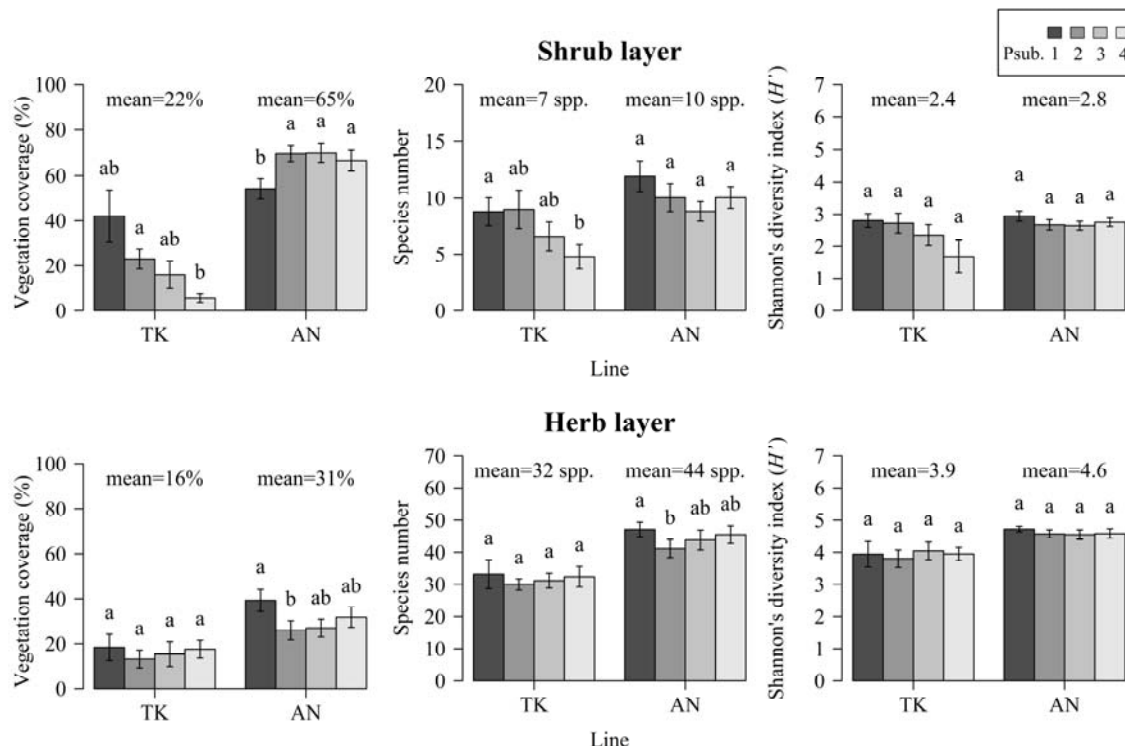


Fig. 2 Vegetation coverage and species diversity with distance from forest road. Vegetation coverage (left), species richness (middle) and species evenness (right) of the shrub layer (upper) and herb layer (lower) of the TK and AN lines are shown. Bars represent standard error. Values with the same characteristics were not significantly different within each line. Mean values of each belt are shown above the four columns and were larger in the mature forest than the young forest with the exception of species evenness in the shrub layer (U-test at 5% level).

Table 2 Edge and interior species detected in the shrub and herb layers of each line.

Layer	TK line		AN line	
	Edge species	Interior species	Edge species	Interior species
Shrub	<i>Styrax japonica</i>	*	NULL	
	<i>Quercus serrata</i>	*	<i>Rubus palmatus</i> var. <i>coptophyllus</i>	*
	<i>Rhus trichocarpa</i>	*	<i>Dioscorea japonica</i>	*
	<i>Clethra barbinervis</i>	*		
	<i>Celastrus orbiculatus</i>	*		
Herb	<i>Rubus palmatus</i> var. <i>coptophyllus</i>	*	<i>Actinidia arguta</i>	***
	<i>Lycopodium serratum</i>	**	<i>Blechnum niponicum</i>	**
	<i>Vaccinium smallii</i> var. <i>glabrum</i>	*	<i>Disporum smilacinum</i>	**
	<i>Disporum smilacinum</i>	*	<i>Tripterispermum japonicum</i>	**
	<i>Tricyrtis affinis</i>	*	<i>Lycopodium serratum</i>	**
			<i>Clinopodium micranthum</i>	*
			<i>Boehmeria tricuspid</i> var. <i>unicuspis</i>	*
			<i>Impatiens textori</i>	*
			<i>Rubus palmatus</i> var. <i>coptophyllus</i>	*
			<i>Carpesium divaricatum</i>	*
			<i>Reynoutria japonica</i>	*
			<i>Carex parviflora</i> var. <i>macroglolla</i>	*
			<i>Polystichum tagawanum</i>	*
			<i>Chloranthus serratus</i>	*
			<i>Diplazium squamigerum</i>	*
			<i>Schisandra nigra</i>	*
			<i>Ampelopsis brevipedunculata</i> var. <i>beterophylla</i>	*
			<i>Stegnogramma pozoi</i>	*
			<i>Wisteria floribunda</i>	*
			<i>Apios fortunei</i>	*
			<i>Pilea hamaoi</i>	*
			<i>Athyrium vidalii</i>	*

Species were detected using a screening test. Asterisks represent the level of statistical significance (*5% level, **1% level, ***0.1% level). NULL means that no species of that type were detected in the layer.

along the TK line. In both the TK and AN lines, three species were commonly detected: one edge species (*Rubus palmatus* var. *coptophyllus*) in the herb layer, and two interior species (*Lycopodium serratum* and *Disporum smilacinum*) in the herb layer.

DISCUSSION

Influence of Exotic Species on Species Diversity

Three major exotic species were detected in this study, as mentioned above. *Eragrostis curvula* and *Indigofera bungeana*, which appeared in the young forest of the TK line, are generally used for artificial greening [20], [21]. All exotic species appeared in the sub-plots facing the forest road, suggesting that these exotic species are likely to invade areas along forest roads. It has been pointed out that wide forest roads are safe sites for exotic species and enhance their dominance, which can negatively impact native species growth and reduce the species diversity of the area [7]. However, the number of individuals and coverage of the three exotic species was very small in this study. Therefore, it is thought that species diversity was not affected by exotic species along the narrow forest roads in this study.

Vegetation Coverage and Species Diversity

Both vegetation coverage and species number were larger in the mature forest of the AN line than the young forest of the TK line (Fig. 2). It is generally reported that thinning has positive effects on understory development and species diversification by improving the light environment [22]–[25]. Repeated thinning over time results in low stand density and a small canopy coverage (Table 1), which enhances species diversification. These findings contradict the results for secondary forests of broadleaf species in France [10], but agree with findings from artificial forests in Japan [26].

In the young forest of the TK line, vegetation coverage and species richness of the shrub layer obviously decreased from the forest edge to the interior. This result is similar to that of other studies [8]–[10]. On the other hand, vegetation coverage, species richness and evenness of the herb layer showed no significant change from the forest edge to the interior. In the young forest, the canopy gap on the forest road was larger. However, the effect of the gap on the herb layer was relatively small due to light interception by the developed shrub layer.

In the mature forest of the AN line, species richness and evenness did not obviously change with distance from the edge in either the shrub or herb layer, as was the case with narrow forest roads in Iran [11]. However, vegetation coverage at the edge of the forest was lowest in the shrub layer and

highest in the herb layer. In mature forests, because the canopy gap along forest roads is reduced, the effect of the gap tends to be small [27]. If canopy closure is in progress, only light-sensitive species of the shrub layer at the forest edge decline, and vegetative recovery is underway in the herb layer.

Enrichment of Overall Diversity by Species Replacement

In total, 20 edge species and 13 interior species were detected by a species screen test. In general, *Rubus palmatus* var. *coptophyllus*, *Clethra barbinervis*, *Boehmeria tricuspidis* var. *unicuspis*, and *Fallopia japonica*, which prefer bright conditions, are detected as edge species. On the contrary, *Huperzia serrata*, *Disporum smilacinum*, and *Chloranthus serratus*, which prefer shaded conditions, are detected as interior species. These differences between edge and interior species suggest that the replacement of plant species occurs in association with their shade tolerances.

The existence of only edge species in the shrub layer (Table 2) agrees with the decline of species number with distance from the forest road (Fig. 2). A lower species number in the shrub layer was clear in the young forest of the TK line where more edge species were detected (Table 2). On the other hand, the existence of both edge and interior species in the herb layer (Table 2) suggests that edge species are replaced by interior species with distance from the forest road. It is thought that this replacement creates a non-linear distribution pattern in species number in the herb layer (Fig. 2). Edge and interior species increase in number in the forest edge and forest interior, respectively. However, both edge and interior species decrease in number in the intermediate position, where the number of species will be the lowest (Fig. 2).

Species replacement can also enhance overall species diversity. Species diversity is classified into α diversity, β diversity, and γ diversity according to a spatial scale [28]–[31]. α diversity is the diversity of one habitat, β diversity is the difference in species composition between habitats, and γ diversity is the diversity of all habitats. The overall γ diversity is a product of α and β diversities [30], [31]. Although the effects of the forest road on the local diversity (α diversity) were not always obvious in this study (Fig. 2), species replacement (β diversity, Table 2) enhanced the overall diversity (γ diversity). This suggests that forest roads have positive effects on γ diversity even if the local species richness does not change with distance from the forest road.

CONCLUSION

In conclusion, narrow forest roads in artificial forests have the following three characteristics.

Firstly, narrow forest roads can inhibit the dominance of exotic species and their negative effects on species diversity. Secondly, the effects of narrow forest roads on local species diversity are small in mature forests. Lastly, narrow forest roads can enhance the overall species diversity through species replacement, even in mature forests. Additionally, our study suggests that the effects of narrow forest roads will dynamically change over time with the forest age. Therefore, a theoretical approach to forest road management that enhances species diversity can be established through quantitative evaluation of age-responsiveness.

ACKNOWLEDGEMENTS

We thank the members of the Laboratory of Silviculture, Faculty of Agriculture, Shinshu University for their help with field surveys. We also thank Dr. Jiro Kodani, the Ishikawa Forest Experiment Station, for his valuable advices. This study was based on a partnership agreement between Shinshu University and Neba Village.

REFERENCES

- [1] Sawaguchi I. (2009) Possibility of low cost logging system by high density road network in mountain forest. Sanrin, (1502), 68-76. *In Japanese.*
- [2] Shiba M., Tobioka J., Yamazaki T. (1995) Studies on the optimization of timber harvesting systems with highly mechanized forestry machines: Case studies of operation practices under moderate slope terrain conditions. Journal of the Japanese Forest Society, 77(5), 486-488. *In Japanese.*
- [3] Iwaoka M. (2007) Introduction of the special issue "forest roads network". Journal of the Japan Forest Engineering Society, 22(3), 119-120. *In Japanese.*
- [4] Japanese Forest Agency (2013) White paper on forests and Forestry. Website of Japanese forest agency, (browsed in June 3rd 2017).
- [5] Kuramoto S. (1997) Spatial distribution of light in a canopy of natural oak (*Quercus mongolica* Blume var. *grosseserrata* Rehd. et. Wils.) stand. Applied Forest Science, 6, 83-86. *In Japanese.*
- [6] Enoki T., Kusumoto B., Igarashi S., Tsuji K. (2014) Stand structure and plant species occurrence in forest edge habitat along different aged roads on Okinawa Island, southwestern Japan. Journal of Forest Research, 19(1), 97-104.
- [7] Watkins R. Z., Chen J., Pickens J., Brososke K. D. (2003) Effects of Forest Roads on Understory Plants in Managed Hardwood Landscape. Conservation Biology, 17(2), 411-419.
- [8] Mullen K., Fahy O., Gormally M. (2003) Ground flora and associated arthropod communities of forest road edges in Connemara, Ireland. Biodiversity and Conservation, 12(1), 87-101.
- [9] Pauchard A., Alaback B. P. (2006) Edge type defines alien plant species invasions along *Pinus contorta* burned, highway and clearcut forest edges. Forest Ecology and Management, 223(1-3), 327-335.
- [10] Avon C., Berges L., Dumas Y., Dupouey J. (2010) Does the effect of forest roads extend a few meters or more into the adjacent forest? A study on understory plant diversity in managed oak stands. Forest Ecology and Management, 259(8), 1546-1555.
- [11] Tehrani B. F., Majnounian B., Abdi E., Amiri Z. G. (2015) Impact of Forest Road on Plant Species Diversity in a Hyrcanian Forest, Iran. Croatian Journal of Forest Engineering, 36(1), 63-71.
- [12] Satake Y., Ohwi J., Kitamura S., Watari S., Tominari T. (1981) Wild Flowers of Japan Herbaceous Plants III. Heibonsha Ltd. Publishers, Tokyo, 259pp. *In Japanese.*
- [13] Satake Y., Ohwi J., Kitamura S., Watari S., Tominari T. (1982) Wild Flowers of Japan Herbaceous Plants I. Heibonsha Ltd. Publishers, Tokyo, 305pp. *In Japanese.*
- [14] Satake Y., Ohwi J., Kitamura S., Watari S., Tominari T. (1982) Wild Flowers of Japan Herbaceous Plants II. Heibonsha Ltd. Publishers, Tokyo, 318pp. *In Japanese.*
- [15] Satake Y., Hara H., Watari S., Tominari T. (1989) Wild Flowers of Japan Woody Plants I. Heibonsha Ltd. Publishers, Tokyo, 321pp. *In Japanese.*
- [16] Satake Y., Hara H., Watari S., Tominari T. (1989) Wild Flowers of Japan Woody Plants II. Heibonsha Ltd. Publishers, Tokyo, 305pp. *In Japanese.*
- [17] Iwaki K. (1992) Ferns and Fern Allies of Japan. Heibonsha Ltd. Publishers, Tokyo, 311pp. *In Japanese.*
- [18] Shimizu T. (2003) Naturalized Plants of Japan. Heibonsha Ltd. Publishers, Tokyo, 337pp. *In Japanese.*
- [19] Hayashi M. (2014) Leaves of Tree -Identify 1100 Kinds of Tree by Scanned Leaves-. Yamakei Publishers co., Ltd., Tokyo, p.184. *In Japanese.*
- [20] Yoshida H., Morimoto Y. (2005) A study on the effects of mixed seeding of Chinese-grown *Indigofera* spp. and evergreen broad-leaved trees. Journal of the Japanese Society of Revegetation Technology, 31(2), 269-277. *In Japanese.*
- [21] Muranaka T., Washitani I. (2006) A Report on the Public Symposium at IMC9: Part 4: Status

- of invasive alien species problems in Japan: current status and ecological effects of aggressive invasion of an alien grass, *Eragrostis curvula*. Mammalian Science, 46(1), 75-80. *In Japanese*.
- [22] Saito M. (1989) The relationship between the amount of undergrowth and solar radiation in *Cryptomeria* plantations. Journal of the Japanese Forest Society, 71(7), 276-280. *In Japanese*.
- [23] Kiyono Y. (1990) Dynamics and Control of Understories in *Chamaecyparis obtusa* Plantations. Bulletin of the Forestry and Forest Products Research Institute, (359), 1-22. *In Japanese*.
- [24] Sugawara M., Kunisaki T. (2011) Hierarchy of factors influencing species diversity of understory trees in Sugi (*Cryptomeria japonica* D. Don) plantations in Takizawa Experimental Forest, Iwate University. Bulletin of the Iwate University Forests, (42), 1-14. *In Japanese*.
- [25] Watanabe M., Yokoi S., Igawahara K. (2011) Changes of the species composition and cover ratio of ground vegetation in Japanese cypress (*Chamaecyparis obtusa*) plantations with poor undergrowth within 5 years after thinning. Bulletin of the Gifu Prefectural Research Institute for Forests, (40), 1-13. *In Japanese*.
- [26] Suzuki W., Suzuki T., Okumura T., Ikeda S. (2005) Aging-induced Development Patterns of *Chamaecyparis obtusa* Plantations. Journal of the Japanese Forest Society, 87(1), 27-35. *In Japanese*.
- [27] Manabe S. (2011) Current Ecology Series 8 Forest Ecology. Kyoritsu Shuppan Co., Ltd., Tokyo, pp.122-135. *In Japanese*.
- [28] Whittaker H. R. (1960) Vegetation of the Siskiyou Mountains, Oregon and California. Ecological Monographs, 30(3), 279-338.
- [29] Whittaker H. R. (1972) Evolution and Measurement of Species Diversity. Taxon, 21, 213-251.
- [30] Miyashita T., Noda T. (2003) Community Ecology. University of Tokyo Press, Tokyo, pp.73-105. *In Japanese*.
- [31] Miyashita T., Isagi Y., Chiba S. (2012) Biodiversity and Ecology –gene, species and ecosystem–. Asakura Publishing Co., Ltd., Tokyo, pp.73-99. *In Japanese*.

DRIFTWOOD ACCUMULATION AND FLOOD DAMAGE AREA IN BLOCKED RIVER

Takaaki Okamoto¹, Hiroshi Takebayashi², Masato Takenaka¹, Yoshinobu Kashiwara¹ and Keiichi Toda³

¹ Department of Civil Engineering, Kyoto University, Japan; ² Disaster Prevention Research Institute, Kyoto University, Japan

ABSTRACT

At the time of heavy rains, a flank collapse occurs. A large driftwood flows into a river and blocks a river, which lead to increased water levels. In Uji city in August 2012, the detour flood-flow occurred around the bridge and the left bank was eroded by high-speed flow. Consequently, the house along Shizugawa River was washed away. However, there is almost no detailed information about the log jam formation and the flood damage by detour flood-flow in a blocked river. In this study, three kinds of laboratory flume experiments (1. Driftwood accumulation experiment, 2. Velocity measurement of Detour flow around a bridge by PIV (Particle Image Velocimetry), 3. Bank erosion experiment) were performed in a 10m and 40cm wide glass-made flume. The results revealed the blockage ratio of driftwood blocking and the flood damage area by detour flood-flow.

Keywords: Driftwood accumulation, blocked river, detour flood-flow, bank erosion

INTRODUCTION

At the time of heavy rains, a flank collapse occurs. A large amount of driftwood flows into a river and blocks a river, which lead to increased water levels (Fig.1). Detour flow around a bridge causes floods and bank erosions. In Uji city in August 2012, the detour flood-flow occurred around the bridge and the house along Shizugawa River was washed away. However, there is almost no detailed information about the flood damage area by detour flood-flow in a blocked river. Some previous research conducted the flume study and investigated a log jam formation.

Bocchiola et al. (2008) investigated jamming of large woody debris in experimental flumes. The results revealed that the probability that large woody debris is entrained in jams increases with its length and decreases with the approaching Froude number. Schmocker & Hager (2011) conducted flume experiments and evaluated the drift-blocking probability at bridge decks depending on (1) driftwood dimensions (single logs and single root stocks) and (2) bridge characteristics. Prister et al. (2013) investigated the interaction between various piano key geometries and woody debris sizes. They found that the floating debris blocking probability is highly influenced by trunk diameter and upstream head. Recently, Rusyda et al. (2014) examined the relationship between a logjam and an obstruction in a channel, and proposed an empirical equation for predicting the volume of a logjam at a bridge.

However, still more works are needed because there is almost no detailed information about the log jam formation around a bridge and flood damage by a detour flood flow in a blocked river. So, in the



Figure 1 Log jam formation around the bridge (Sep. 2014, Fukuchiyama city)

present study, three kinds of flume experiments (1. Driftwood accumulation experiment, 2. Velocity measurement of Detour flow around a bridge by PIV, 3. Bank erosion experiment) were performed. The results of Experiment 1 revealed the accumulation process and backwater rise (blockage ratio of driftwood blocking). After large amount of driftwood models accumulated around the model bridge, the backwater surface rose and the flood-flow occurred around the bridge. The results of Experiment 2 and 3 revealed the flood damage area by detour flood-flow.

EXPERIMENTAL SETUP

Figure 2 shows the experimental set-up and the coordinate system. The flume experiments were conducted in a 10m long and 40cm wide glass-made flume. The x -axis is in the streamwise direction, with $x=0$ at the upstream edge of the model bridge. The y -axis is in the vertical direction, with $y=0$ at the floodplain bed. The z -axis is in the spanwise direction, with $z=0$ at the channel wall. U , V and W are the time-

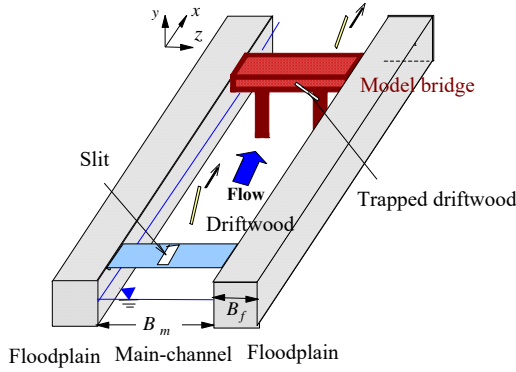


Figure 2 Driftwood accumulation experiment (Experiment D1 and D2)

averaged velocity components in the streamwise, vertical and spanwise velocity components, respectively; u , v and w are the corresponding turbulent fluctuations.

Floodplain models (made of hard vinyl chloride) were placed on both sides of the channel. The width of both floodplains ($B_f=10\text{cm}$) is half the width of Main-channel region ($B_m=20\text{cm}$). The bank height is constant for both bank ($D=10\text{cm}$).

Figure 2 shows the driftwood accumulation experiment set-up. The model bridge was mounted 4.0m from the upstream edge of the floodplain and 9.0cm above the channel bottom. The model bridge was composed of deck and two piers (9.0cm height and 1.0cm width). The bridge roadway is 20cm long, 5.0cm wide and 1.0cm thickness. The model bridge was fixed to the floodplains.

Cylinder wood pieces ($d=6.0\text{mm}$ diameter and $l=6.0, 9.0, 12.0\text{cm}$ length) were used to model driftwood. The wood density is 0.5g/cm^3 . The wood pieces were soaked in water for 1 hour prior to a test. Driftwood models were supplied to the flow at 4.0m upstream from the model bridge ($x=-4.0\text{m}$).

To evaluate the blocking probability at the bridge, Experiment D1 was carried out by adding a single driftwood model to the approach flow. If the driftwood was trapped by the bridge, it was removed before the next test.

To evaluate the effect of the driftwood accumulation on the backwater rise, Experiment D2 was carried out by adding the group of the driftwood models continuously to the approach flow over the test duration. The number of wood pieces was 270 pieces/270s. Over the entire test duration, we measured the temporal development flow depth H in Main-channel at 10cm upstream of the bridge ($x = -0.1\text{m}$) by using a manual point gauge to examine the backwater rise due to driftwood accumulation at the bridge.

After large amount of driftwood models accumulated around the model bridge, the backwater surface rises and the flood water overflows the floodplains. Then, we evaluated the blockage ratio

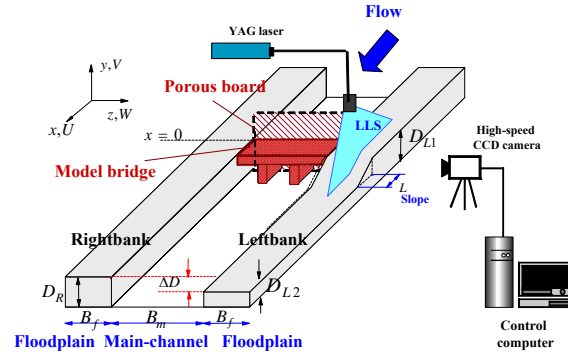


Figure 3 Velocity measurement of Detour flow around a bridge by PIV

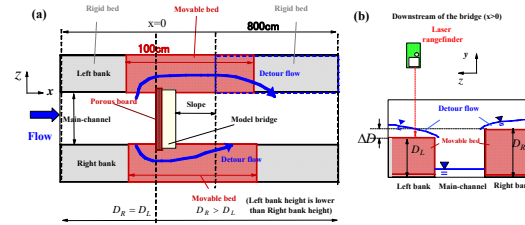


Figure 4 Bank erosion experiment

(porosity) of the driftwood accumulation. The wood pieces accumulated at the bridge were removed and a porous board (15cm height, 20cm width, 3.0mm thickness and 3.0mm hole-diameter) was placed in front of the woody model bridge in Main-channel to mimic a blocked river due to a woody debris jam at a bridge. The blockage ratio of the porous board varied between $A_b/A=0.2$ and 0.91 . We measured the flow depth in Main-channel H at 10cm upstream of the bridge by using a point gauge and compared the measured data with that of the driftwood accumulation test.

Flood-flow velocity around a bridge ($x/B_m=0.0-1.0$) was measure by PIV (see Okamoto & Nezu (2013)). The blockage ratio of the porous board A_b/A was also changed based on the Driftwood accumulation test D2. In order to obtain two velocity-components, i.e., (\tilde{u}, \tilde{v}) on x - y vertical plane ($20\text{cm} \times 20\text{cm}$), a laser-light sheet (LLS) was projected into the water column vertically from the water-surface, as shown in Fig.3. The position of LLS on the right-bank and the left-bank are $z/B_m=0.2$ and 1.8 , respectively. The 2.0mm thick LLS was generated by 3.0W YAG laser using a cylindrical lens. The illuminated flow pictures were taken by a high-speed CCD camera ($1024 \times 1024\text{pixels}$) with 500Hz frame-rate and 60s sampling time. The fluid tracers were Nylon-12 particles of 80 diameter and 1.02 specific density. The instantaneous velocity components on x - y vertical plane (\tilde{u}, \tilde{v}) were calculated by the PIV algorithm.

To examine the effect of the detour flood-flow on the flood damage, the bank erosion experiment was conducted. Figure 4 shows the bank erosion experiment set-up. Near the bridge ($x=-0.2\sim 1.0\text{m}$),

Table 1 Hydraulic condition (driftwood experiment)

Case	Q (l/s)	U_m (cm/s)	H_m (cm)	l (cm)	B_R (cm)	l/B_R	D_{12} (cm)	Fr	Method
Case1.1-1	3.0	21.0	7.0	6.0	1.0	1.0	10.0	0.26	Single driftwood blocking / Driftwood accumulation
Case1.1-2	5.0	36.0	7.0	6.0	1.0	1.0	10.0	0.43	Single driftwood blocking / Driftwood accumulation
Case1.1-3	7.0	50.0	7.0	6.0	1.0	1.0	10.0	0.60	Single driftwood blocking / Driftwood accumulation
Case1.1-4	9.0	64.0	7.0	6.0	1.0	1.0	10.0	0.78	Single driftwood blocking / Driftwood accumulation
Case1.2-1	3.0	21.0	9.0	9.0	1.5	1.5	10.0	0.26	Single driftwood blocking / Driftwood accumulation
Case1.2-2	5.0	36.0	9.0	9.0	1.5	1.5	10.0	0.43	Single driftwood blocking / Driftwood accumulation
Case1.2-3	7.0	50.0	9.0	9.0	1.5	1.5	10.0	0.60	Single driftwood blocking / Driftwood accumulation
Case1.2-4	9.0	64.0	9.0	9.0	1.5	1.5	10.0	0.78	Single driftwood blocking / Driftwood accumulation
Case1.3-1	3.0	21.0	12.0	12.0	2.0	2.0	10.0	0.26	Single driftwood blocking / Driftwood accumulation
Case1.3-2	5.0	36.0	12.0	12.0	2.0	2.0	10.0	0.43	Single driftwood blocking / Driftwood accumulation
Case1.3-3	7.0	50.0	12.0	12.0	2.0	2.0	10.0	0.60	Single driftwood blocking / Driftwood accumulation
Case1.3-4	9.0	64.0	12.0	12.0	2.0	2.0	10.0	0.78	Single driftwood blocking / Driftwood accumulation

Table 2 Hydraulic condition (Velocity measurement and the bank erosion experiments)

Case	Q (l/s)	U_m (cm/s)	H_m (cm)	D_{12} (cm)	D_{12} (cm)	A_b/A	Fr	Method
CaseR10L8-1	7.0	50.0	7.0	10.0	10.0	0.49	0.60	Bank erosion
CaseR10L8-2	7.0	50.0	7.0	10.0	10.0	0.65	0.60	PIV / Bank erosion
CaseR10L8-3	7.0	50.0	7.0	10.0	10.0	0.91	0.60	Bank erosion
CaseR10L8-N1	7.0	50.0	7.0	10.0	10.0	0.2-0.91	0.60	Flow depth measurement
CaseR10L8-N2	7.0	50.0	7.0	10.0	10.0	0.2-0.91	0.78	Flow depth measurement

the floodplain area is mobile. The floodplain models were filled with sand (median size of 0.5mm) to a depth of 0.1m, as shown in Fig.4. In the remaining part, the floodplain area is rigid. Experiment runs were performed for 0.5h when a equilibrium state was attained. The time variation of the bank height around the bridge was measured by the Laser rangefinder (Bosch).

Table1 shows the hydraulic condition of the driftwood accumulation experiment. The driftwood model length l ($l=6.0, 9.0$ and 12.0 cm) and the flow discharge Q were changed. To evaluate the test repeatability, ten times tests were conducted for each case. H_m denotes the initial flow depth in Main-channel. $Fr = U_m / \sqrt{gH_m}$ denotes the approach Froude number.

Table 2 shows the hydraulic condition of the velocity measurement and the bank erosion experiments. Experiments were conducted on the basis of three flow scenarios, in which A_b/A was changed based on the Driftwood accumulation test ($A_b/A = 0.49, 0.65$ and 0.91). Before a flood (without the porous board), the water in Main-channel does not overflow the banks. The bulk mean velocity is $U_m=50.0$ (cm/s) and the flow depth in Main-channel is $H_m=7.0$ cm.

RESULTS

Figure 5 shows the blocking probability of the single driftwood P_b . P_b increases with the relative driftwood length l/B_R . For $l/B_R=1.5$ and $Fr=0.6$, some wood pieces touch a pier, get turned and span between two piers, as shown in Figure 6. The blocking probability of driftwood is $P_b=0.075$. For $l/B_R=2.0$ and $Fr=0.6$, $P_b=0.225$.

No blocking ($P_b=0$) was observed for $l/B_R=1.0$. Some driftwood models are temporally trapped but driftwood models cannot span between two piers. Consequently, the trapped driftwood models are freed.

It is also observed that an increase of Fr results in a decrease of P_b . This result is good agreement with

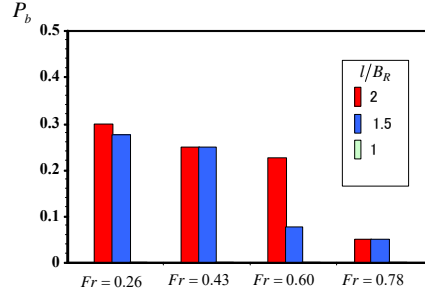


Figure 5 Blocking probability of the single driftwood

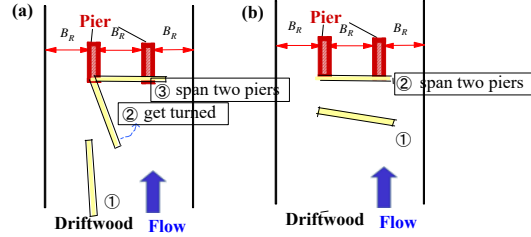


Figure 6 Trapping process of the single driftwood

Schmocker & Hager (2011). They revealed that driftwood transported by high-speed flow touches a bridge but may be freed because of the stream power and the vertical flow components.

To examine the effect of the driftwood accumulation on the backwater rise, we conducted the driftwood accumulation experiment D2. Figure 7 shows the photographic examples of the driftwood accumulation for $l/B_R=1.5$, $Fr=0.6$ and $l/B_R=2.0$, $Fr=0.6$. For $l/B_R=2.0$, $Fr=0.6$, some wood pieces were trapped and accumulated at the bridge. The other pieces passed through the bridge. Once a single driftwood model is trapped by the bridge, the blocking probability increases significantly. The driftwood accumulation resulted in an increase in water level upstream from the model bridge. After large amount of driftwood accumulated at the bridge, the water overflowed the banks and the detour flow occurs around the bridge.

Figure 8 shows the development of the flow depth in Main-channel H at 10cm upstream of the bridge for Test 1 and 2 ($l/B_R=2.0$, $Fr=0.6$). The flow depth values are normalized by the approach flow depth H_m . n_d is number of driftwood models supplied to water.

At the start of the driftwood accumulation, the flow depth increases rapidly with the number of trapped driftwood models. After 70 wood pieces were added to the flow, the backwater rises slower. After 200 wood pieces, the flow depth reaches its final value H_{max} . For $l/B_R=2.0$, $Fr=0.6$, the flow depth is 1.75 times higher at test end.

Due to the random accumulation process, the difference in the increase rate of the flow depth is observed between Test 1 and 2. However, the results of Test 1 and 2 show the almost equal final values at

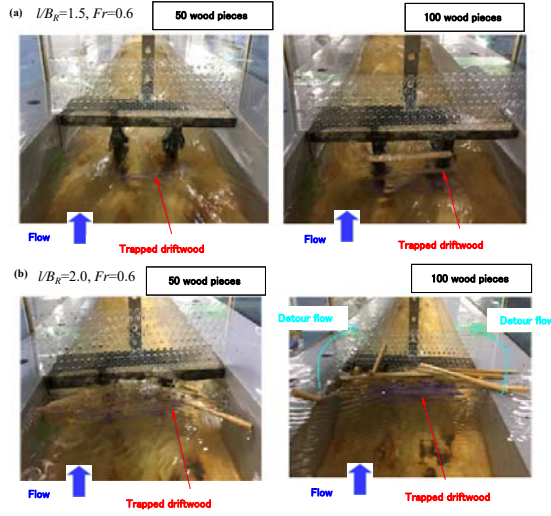


Figure 7 Photographic examples of the driftwood accumulation at a bridge for $l/B_R=2.0$, $Fr=0.6$ (a) and $l/B_R=1.5$, $Fr=0.6$ (b)

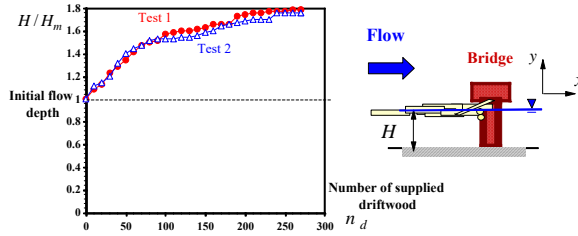


Figure 8 Development of relative flow depth for Test 1 and 2 ($l/B_R=2.0$, $Fr=0.6$)

test end. Therefore, the reproducibility is acceptable.

Figure 8 shows the relative flow depth in Main-channel H/H_m at 10cm upstream of the bridge for $l/B_R=1.5$, 2.0 , $Fr=0.6$ and $l/B_R=1.5$, 2.0 , $Fr=0.78$. The values of the flow depth in ten times tests are averaged for each case.

In Fig.9, the values of the flow depth H for $A_b/A=0.49$, 0.56 , 0.65 (blockage ratio of porous board) are also indicated for comparison.

The values of H_{max} for $l/B_R=2.0$ are larger than those for $l/B_R=1.5$. For $l/B_R=2.0$, $Fr=0.6$, the value of H_{max} is in good agreement with the flow depth H for $A_b/A=0.65$. This indicates that the blockage ratio of driftwood accumulation for $l/B_R=2.0$, $Fr=0.6$ is $A_b/A=0.65$. The blockage ratio of driftwood accumulation for $l/B_R=1.5$, $Fr=0.6$ is $A_b/A=0.56$. This implies that the increase of the driftwood projected area resulted in the increase in the blockage ratio A_b/A of the driftwood accumulation. It is also observed that the flow depth increases with the approach Froude number.

To investigate the occurrence condition of a detour flood-flow around a bridge, we changed the blockage ratio of an obstruction A_b/A for $Fr=0.6$ and 0.78 . Figure 10 shows the flood-flow depth H_f on the left

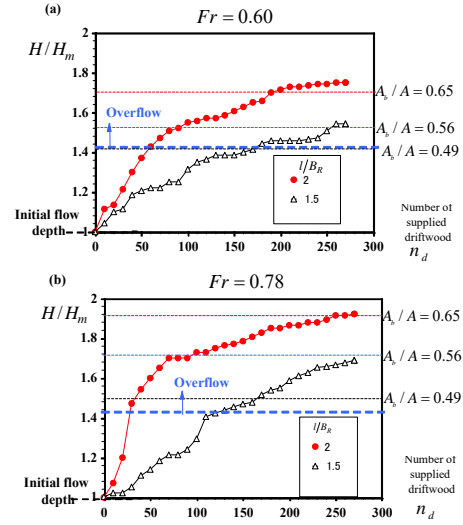


Figure 9 Development of relative flow depth (a) $Fr=0.6$, (b) $Fr=0.78$

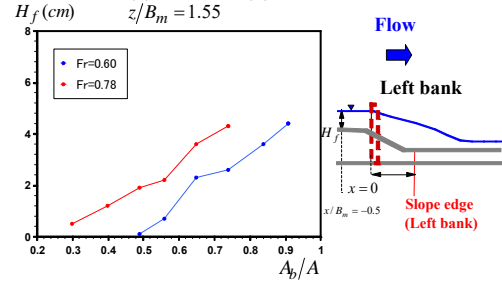


Figure 10 Flood flow depth versus the blockage ratio of an obstruction

bank upstream of the bridge ($x/B_m=-0.5$). The flood-flow depth H_f was measured by a point gauge.

For $Fr=0.6$, the flood-flow depth is $H_f=0$ when $A_b/A \leq 0.49$. This indicates that water in Main-channel does not overflow the banks and the detour flow does not occur when $A_b/A \leq 0.49$. When $A_b/A \geq 0.49$, the water in Main-channel overflows the banks ($H > D$) and the flood-flow depth increases linearly.

The occurrence condition of a detour flood-flow depends on the Froude number. For $Fr=0.78$, the detour flood-flow occurs around the bridge when A_b/A exceeds 0.3 .

Figure 11 shows the contours of the flood-flow depth H_f in $x-z$ plain for CaseR10L8 ($Fr=0.6$ and $A_b/A=0.65$). Upstream of the bridge ($x/B_m \leq 0$), the flood-flow depth H_f is almost constant in the streamwise direction ($H_f=3.0$ cm) and the difference between the left bank and the right bank cannot be observed.

Downstream of the bridge ($x/B_m \geq 0$), the values of flood-flow depth H_f on both banks decrease in the streamwise direction. It is also observed that,

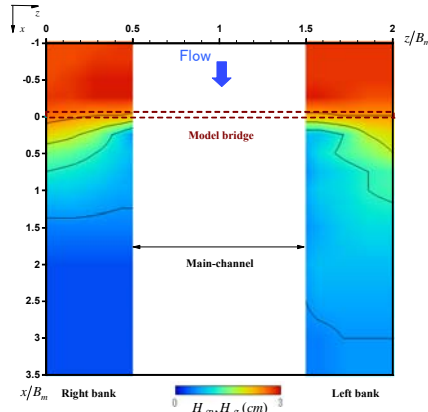


Figure 11 Contour of flood-flow depth on both banks for CaseR10L8 ($Fr=0.6$ and $A_b/A=0.65$)

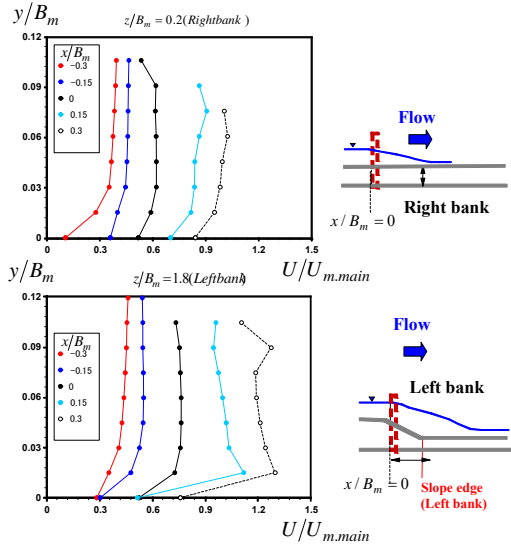


Figure 12 Vertical profiles of the streamwise velocity on the left bank and right bank for CaseR10L8 ($Fr=0.6$ and $A_b/A=0.65$)

the values of the flood-flow depth H_f at $z/B_m=0.5, 1.5$ (floodplain edge) are smaller than those at $z/B_m=0.125, 1.875$ (on the right bank and the left bank). These results imply that the floodwater on both banks flow into the Main-channel for $x/B_m \geq 0$.

The effect of the floodplain shape on the flood prone area is clearly observed for $x/B_m \geq 0$. The values of the flood-flow depth H_f on the left bank decrease in the streamwise direction and become negligibly small for $x/B_m=3.0$. All of the floodwater on the left bank flows into the Main-channel for $x/B_m > 3.0$. On the right bank, the flood-flow depth H_f is negligibly small for $x/B_m > 1.5$.

Figure 12 shows the vertical profiles of the streamwise velocity on the left bank and right bank. The velocity value increases in the streamwise direction. This indicates that the detour flow occurs around a bridge and the flood-flow runs into the both

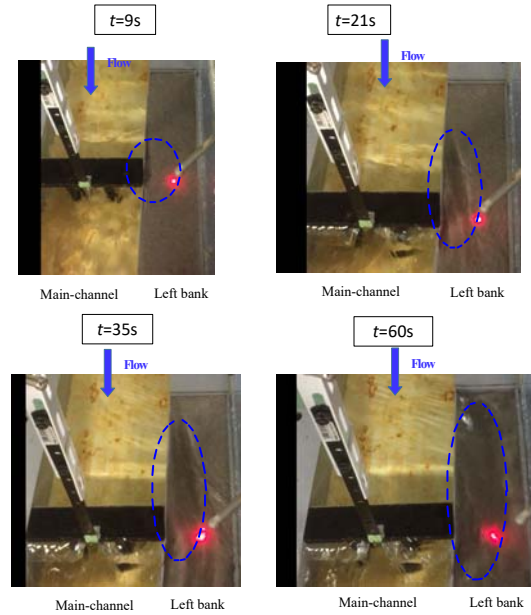


Figure 13 Photographic examples of the bank erosion on the left bank

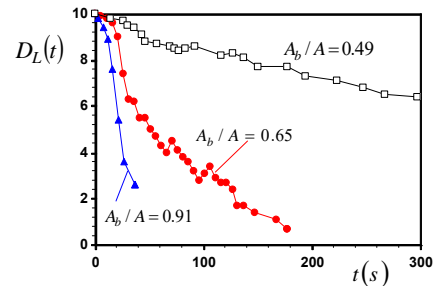


Figure 14 Time variation of the bank height $D_L(t)$

banks. The velocity difference between the left bank and the right bank is not significant upstream of the bridge. In contrast, downstream of the bridge ($x/B_m \geq 0$), the detour flow is concentrated on the left bank and the velocity value increases significantly near the bed. The high-speed flow near the bed may lead to the bank erosion.

Figure 13 shows the photographic examples of the bank erosion on the left bank for CaseR10L8. At $t=0s$, the porous board was placed in front of the bridge. At $t=3.0s$, the detour flood flow runs into the floodplain and the bank erosion occurs around the bridge. The bank erosion area becomes larger with time.

At $t=60s$, the detour flow eroded the left bank at $x/B_m = -1.0 \sim 0.0$ (upstream of the bridge). Downstream of the bridge, the bank erosion is observed at $x/B_m = 0.0 \sim 1.5$.

Figure 14 shows the time variation of the bank height $D_L(t)$ around the bridge for $A_b/A = 0.49, 0.65, 0.91$. The bank height decreases rapidly at $t=3.0-100.0s$ for $A_b/A = 0.65$. An increase of the blockage ratio A_b/A results in an increase of the bank erosion rate.

CONCLUSION

In the present study, three kinds of flume experiments (1. Driftwood accumulation experiment, 2. Velocity measurement of Detour flow around a bridge by PIV (Particle Image Velocimetry), 3. Bank erosion experiment) were performed to investigate the log jam formation around a bridge and flood damage by a detour flood flow in a blocked river. Main findings are as follows:

1. At the start of the Driftwood accumulation (Experiment D2), the flow depth increases rapidly with the number of trapped driftwood models. After 70 wood pieces were added to the flow, the backwater rises slower. After 200 wood pieces, the flow depth reaches its final value H_{\max} . For $l/B_R=2.0$, $Fr=0.6$, the value of H_{\max} is in good agreement with the flow depth H for $A_b/A=0.65$.
2. We changed the blockage ratio A_b/A of an obstruction (porous board) in Main-channel to examine the occurrence condition of the detour flow around the bridge. For $Fr=0.6$, when $A_b/A \geq 0.49$, the water in Main-channel overflows the banks ($H > D$) and the detour flow occurs. For $Fr=0.78$, the detour flood-flow occurs around the bridge when A_b/A exceeds 0.3.
3. The velocity measurement results revealed that the flood velocity increases in the streamwise direction downstream of the bridge. For CaseR10L8, flood-flow is concentrated on the left bank and the velocity values of the detour flow on the left bank become larger than those on the right bank. On the left bank, the detour flow velocity the velocity value increases significantly near the bed at $x/B_m = 0.15-0.3$. All of the floodwater on the left bank flows into the Main-channel for $x/B_m \geq 3.0$. All of the floodwater on

the right bank flows into the Main-channel for $x/B_m \geq 1.5$.

4. The bank erosion experiment revealed that the detour flow eroded the left bank at $x/B_m = -1.0 \sim 0.0$ (upstream of the bridge). Downstream of the bridge, the bank erosion is observed at $x/B_m = 0.0 \sim 1.5$.
5. The bank height decreases rapidly at $t=3.0-100.0$ s for $A_b/A=0.65$. An increases of the blockage ratio A_b/A results in an increase of the bank erosion rate.

ACKNOWLEDGEMENTS

The present study was carried out under the financial support of the Research Project Grant-In-Aid for Scientific Research of Japanese Government (Kakenhi No.15K16311, Principle Investigator= T. Okamoto). The authors greatly acknowledge this support.

REFERENCES

- [1] Bocchila, D., Rulli, M.C. and Rosso, R.: A flume experiment on the formation of wood jams in rivers, *Water Resources Research*, Vol.44, 2008, W02408.
- [2] Okamoto, T. and Nezu, I.: Spatial evolution of coherent motions in finite-length vegetation patch flow, *Environmental Fluid Mechanics*, 13(5), 2013, 417-434.
- [3] Pfister, M., Capobianco, D. and Tullis, B. and Schleiss, A.J.: Debris-blocking sensitivity of piano-key weirs under reservoir-type approach flow, *J. of Hydraul. Eng.*, 2013, pp.1134-1141
- [4] Rusyda, M.I., Hashimoto, H. and Ikematsu, S.: Log jam formation by an obstruction in a river, *Proc. of Rievrfow2014*, 2014, pp.717-724.
- [5] Schmocker, L., and Hager, W.H: Probability of drift blockage at bridge decks, *J. Hydraul. Eng.*, Vol.137, 2011, pp.470-479.

PERMEABILITY CHARACTERISTICS OF ROAD BASE MATERIALS BLENDED WITH FLY ASH AND BOTTOM ASH

Jonathan R. Dungca¹ and Joenel G. Galupino¹

¹Civil Engineering Department, De La Salle University, Manila, Philippines

ABSTRACT

Permeability, being the ability of water to flow through a soil, should be considered when designing roads. Permeability should be employed when designing roads that will provide good drainage as well. Fly ash and bottom ash were utilized as partial substitutes to conventional road base materials in road base construction. The study aimed to prove that employing fly ash and bottom ash would increase the permeability characteristics of road base while also decreasing the disposal costs of the said coal by-products. Series of experiments were conducted to test the horizontal and vertical permeability of pure fly ash, pure bottom ash, pure conventional road base materials, and blends comprising of the said soil components. It was also established that horizontal and vertical permeability had a significant difference wherein the flow of water at the horizontal-direction is greater compared to the vertical-direction.

Keywords: Permeability, Fly Ash, Coal Ash, Waste Utilization

INTRODUCTION

When designing structures, it is very important for engineers to understand the soil underneath because it will affect the way it is designed [1]. Roads, in general, play an important role in the drainage capacity when there is an occurrence of heavy downpour of water. Most of the time, an engineer place focus on the strength characteristics of roads when in fact, permeability also plays an important role in the drainage capacity of these pathways. This study is concentrate on the permeability characteristics of fly ash and bottom ash as road base materials. Permeability is defined as the ability of water to flow through the material. It is also referred to as the “hydraulic conductivity” of the porous material [2].

Permeability can be a fundamental factor in determining the strength and capacity of fly and bottom ashes as road base materials. Through acquiring the size and shape of the ashes’ pores and their connectivity, the researchers will be able to determine their permeability characteristics. With these, they can establish whether fly and bottom ashes will meet the standards of suitable permeability as road base materials. Road base is a blend of gravel and fine materials that will form a hard surface with a high level of mechanical strength when compacted [3]. Good drainage can increase as well as maintain the strength of the subgrade. On the other hand bad drainage would have negative effects in terms of the strength of the subgrade [4,5]. With these, the researches would incorporate fly ash and bottom ashes to the road base materials to ensure the proper and efficient drainage.

Fly and bottom ashes are the two most common

by-products of coal. Fly ash comprises 80% of the total coal by-products left at the boiler, while 20% is composed of bottom ash in fuel gas [6]. This study aim to reduce disposal costs of fly ashes and bottom ashes through utilizing these as road base materials. Through this, they are thriving for a safe disposal of these coal by-products while also providing a new input to how these can be properly and successfully utilized. This will serve as a study on how to reduce disposal of fly and bottom ashes while also putting emphasis on effectively hampering harmful emissions of solid particles and gases into the atmosphere and the improper disposal of hazardous elements.

The study endeavored to present the permeability characteristic of road base materials blended with fly ash and bottom ash. Moreover, the main objective of this proposal is to evaluate the suitability of conventional road subgrade, sub-base, and base materials blended with specific proportion and gradation of fly ash (as partial substitute for fines) and bottom ash (as partial substitute for fine aggregates) for highway embankments with respect to the standard permeability characteristic of road embankments.

METHODOLOGY

The fly ash and bottom ash which were collected from a single and specific thermal power plant in the Philippines. Shown on Table 1 is the soil mixtures that were checked on the effect of specific proportions and gradations of fly ash (as partial substitute for fines) and bottom ash (as partial substitute for fine aggregates) for highway embankments with respect to the standard

permeability characteristic of road embankments.

Table 1. Soil Mixtures used in the Study

Soil Mixtures	Other Notations	Bottom Ash Content (B) %
<i>Blended Samples</i>		
B0 (Pure CRBM)	F0B0C100	0
B20	F10B6.5C83.5	20
B40	F10B13C77	40
B60	F10B19.5C70.5	60
B80	F10B26C64	80
B100	F10B32.5C57.5	100
<i>Controlled Samples</i>		
No Fly Ash	B50F0C0	50
Pure Fly Ash	B0F100C0	0

A microscopic characterization test was done, furthermore, the determination of the index properties of fly ash, bottom ash, and conventional materials through applicable laboratory tests such as Specific Gravity of Soil Solids (ASTM D854) [7], Atterberg Limits (ASTM D4318 and ASTM D427) [8], Particle Size Analysis (ASTM D422) [9] and Maximum and Minimum Index Densities (ASTM D4253 and D4254)[10,11] commenced [12].

Similar ideas of obtaining the horizontal permeability of road base materials had been developed by Roads Division Engineering in collaboration Hydraulics Research Limited, Wallingford and they have also considered designing a horizontal permeameter, there are also other designs of permeameters that may be used [13]. The dimensions used were 1.0m x 0.3m x 0.3m respectively for the length, width and height of the box apparatus while the standpipe was at a length of 0.29 m, shown on Figures 1 and 2. This study scaled down on the dimensions of the apparatus because using similar measures would not only be impractical in terms of time and preparation, but also because it is an in-situ test. As much as possible, the comparison of the the horizontal permeability values with that of the vertical, should be conducted in the study.

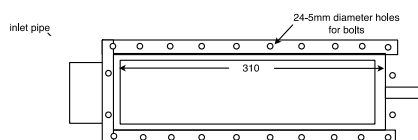


Fig. 1. Top View of Horizontal Permeameter

So as to properly compare the horizontal permeability with that of the vertical permeability, the researchers have thought of incorporating the concept vertical permeameter's design into the horizontal. A design of the horizontal apparatus was

formulated by obtaining the area of the cylindrical vertical permeameter and then converting it into a rectangular box. As for the length of the rectangular box, it was obtained based on the diameter to height ratio of the vertical permeameter and the width to length ratio of the horizontal apparatus.

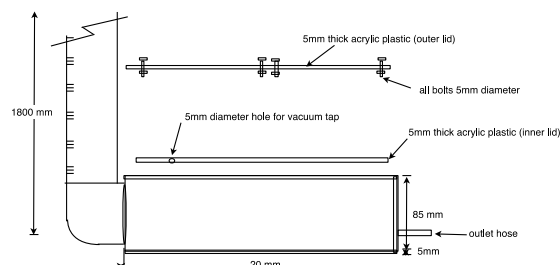


Fig 2. Side View of Horizontal Permeameter

This method was accomplished by comparing the falling-head permeability test results to that of the material requirements. If it passed the requirements by actually exceeding the acceptable values of k , then the results for that certain material blend are considered. On the other hand, if resulting coefficient of permeability values are lower than the basis, the researchers responsible for testing the samples repeated the tests to really verify the permeability values. The permeability characteristics of the blended materials were also related to the obtained index properties of coal ashes for it was used to further analyze the results gathered.

RESULTS AND DISCUSSIONS

Index Properties

Microscopic Characterization

The particle shapes, surfaces, and textures were analyzed on a microscopic level in order to have more appropriate observations and analysis of the behavior of fly ash and bottom ash mainly during the experimental process. Conventional Road Base materials (CRBM) was also subjected to the testing for source of comparison in later analysis. SEM tests were used to analyze the morphology on all the samples.

At first glance it can be observed that bottom ash looks similarly like the sand that can be seen on the beach which is small and angular particles with coarse complexions, shown on Fig. 3. The core of a bottom ash particle is angular in shape and is somehow porous making them easy to crush. These observations were similar to the findings to some studies [14] in where the researchers observed that bottom ash particles exhibited angular and irregular shapes.

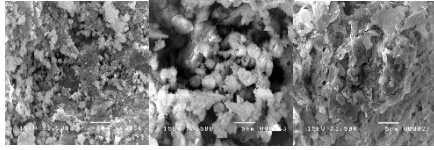


Fig 3. SEM of Bottom Ash, Fly Ash and Conventional Road Base Materials (CRBM)

On the other hand, it was observed that the microscopic characteristics of Fly Ash is quite different that from Bottom Ash. By the naked eye, Fly Ash is brown in color and powder like in texture. They have smaller particles compared to bottom ash. The core of a fly ash particle is possess a more spherical and round shape, shown on Fig. 3. They also possess smoother texture and are more porous. On a same microscopic scale it was observed that it has more voids compared to bottom ash.

SEM was also used to observe CRBM to see its difference from the two coal ashes. Under the naked eye, CRBM are mostly angular and flat in shape. It was observed that on a microscopic level, agglomerate of CRBM are of rough texture more similar but not entirely the same to the Bottom Ash particles. It also is composed entirely of indefinite shapes which are very close to each other, shown on Figure 3.

Grain Size Distribution

In the Grain Size Distribution Curve of pure fly ash, it can be seen that most of the particles are ranging from 0.001 to 0.075 mm which passes the #200 sieve, as such it falls under the classification of the size of silt; thus it can be considered as such. The coefficient of uniformity as well as curvature of fly ash samples were 1.43 and 1.157, respectively; as such it falls under the classification of being poorly graded. On the other hand a similar analysis was made for the pure bottom ash. As such it can be said that Bottom Ash can be considered under the classification that of sand. The coefficient of Uniformity was computed to be 4, while the Coefficient of curvature was 1, therefore it can be said that the bottom ash sample was poorly graded.

Specific Gravity

The specific gravities of the different blends have followed an exponential form, which seems to have been the best fit line that depended on specific bottom ash contents. As the percentage of bottom ash increased in a blend, the specific gravity decreased, shown on Table 2. The reason for this behavior is because of the fact that as the bottom ash content increased, the amount of CRBM decreased. The existence of these CRBM, namely the sand and gravel are denser than that of the bottom ash. The specific gravities of the different blends also largely depended on its morphology.

Table 2. Specific Gravity of the Soil Blends

Soil Mixtures	G_s
<i>Blended Samples</i>	
B0 (Pure CRBM)	2.81
B20	2.78
B40	2.75
B60	2.70
B80	2.52
B100	2.52
<i>Controlled Samples</i>	
No Fly Ash B50F0C0	2.76
Pure Fly Ash B0F100C0	2.33

Atterberg Limits

Liquid limit of the CRBM of around 15.6 was achieved and 13.65 for the plastic limit. Having plasticity index of less than 3 of either the theoretical formula or the polynomial equations, thus fines content of CRBM is considered to be non-plastic. Fly ashes are non-plastic that makes it very difficult to perform the Atterberg test. From observation, experiments and researches, fly ash and bottom ash can be considered as non-plastic.

Compaction Behavior

Proctor test was used to determine the optimum moisture content (OMC) and maximum dry unit weight. These variables were acquired through using the equation of the curve produced when the different water contents and dry densities were plotted. Differentiation of the equation for the curve per blend was done and equated this to zero.

Conventional road base materials demonstrated the highest maximum dry density. However, it also presented the least percentage of OMC. This indicates that with little amount of water, conventional road base materials already reached OMC promptly. This justifies that conventional road base materials reaches OMC even with little amount of water. Also it tends to display the highest maximum dry density because of its relatively high specific gravity that affects the total dry mass at OMC. Pure fly ash and bottom ash exhibited diverse results from each other. Pure bottom ash had low percentage of OMC. Fly ash had a significantly higher percentage of OMC. However, comparing their maximum dry densities, fly ash had a lower value than that of the bottom ash. These results show that fly ash contained more mass of water in the voids distributed among its total dry mass in contrast to that of bottom ash. Since fly ash is considered to exhibit particle size as that of fines, it is characterized to be absorbent of water gradually. Before it can be considered saturated, more water is employed for fly ash than bottom ash. It was observed that as the percentage of bottom ash was increased while the percentage of conventional road

base materials was decreased for a blend, OMC increased also in value, shown on Figure 4. This explains that more bottom ash content with less conventional road base materials made the blend require more water to reach OMC.

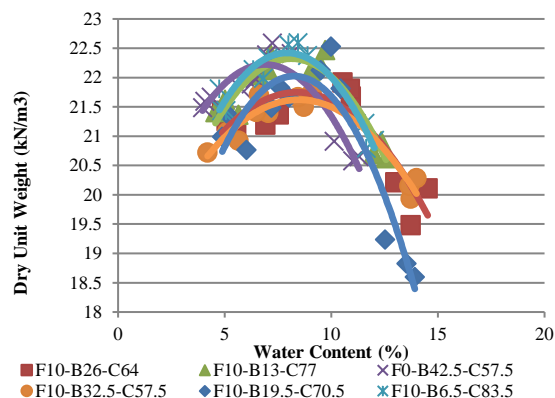


Fig. 4 Dry Unit Weight and Water Content at different blends

Maximum and Minimum Index Densities

The maximum and minimum index densities and void ratio of the blended soil samples and controlled soil samples, which are the CRBM, pure bottom ash, pure fly ash and CRBM blended only with bottom ash (F0-B42.5-C57.5) were determined using standard testing method of ASTM with designations D4253 [10] and D4254 [11]. Pure fly ash has significantly larger values of void ratio compared to bottom ash and CRBM. The results were logical since fly ash is more porous compared to bottom ash and to CRBM that is clearly shown to the SEM photomicrographs. Thus, it tends to increase the volume of voids over the volume of fly ash. The same logic occurs when bottom ash is compared to CRBM. As for the index densities, fly ash obtained the lowest value compared to other control samples. This simply justifies that fly ash produces higher volume of voids over the mass of the ashes. Looking at the controlled blend that has no fly ash content, it produced a higher void ratio and lower dry density when compared to 100% BA-blend. This means that the fines content of bottom ash produces more voids as compared to the fines content of fly ash. This can be defended through the amount of fly ash being mixed to other blends is greater in volume than of the bottom ash. The low specific gravity of fly ash was able to let more fly ash to fill the empty and small spaces of the blended soil samples compared to the fines of bottom ash that has higher specific gravity. For the blended samples, the maximum and minimum void ratios decreases as the bottom ash content increases. Though the morphology of bottom ash particles are more porous compared to CRBM particles, the grain size of bottom ash gives better interlocking property compared to CRBM. This is because of the physical

characteristic of CRBM particles, which are more angular in shape compared to bottom ash.

Hydraulic Conductivity

Vertical Permeability

Among the controlled samples (CRBM, pure bottom ash and pure fly ash), bottom ash has the highest value of coefficient of permeability that ranges from $1.00\text{E-}03$ to $1.00\text{E-}02$. The said values are considered to be a very stable and good to be used as road base material. Pure bottom ash had even surpassed the permeability characteristic of CRBM.

Moreover, pure fly ash has a very poor coefficient permeability that can be considered to use as an impervious layer for other embankment applications but not as a road base material. By looking at Blend F0-B42.5-C57.5, it can be said that replacing bottom ash for the fines content of the soil samples have an effect to the permeability.

By blending bottom ash and fly ash at conventional road base materials, the value of permeability with respect to void ratio, relative compaction and relative density varied at different percentage of bottom ash content. A graphical representation of the coefficient of permeability of bottom ash as a function of void ratio was accomplished, shown on Figure 5. Different proportions of bottom ash, namely 20%, 40%, 60%, 80%, and 100%, were tested using the Falling Head Permeability Test. At these ratios, various coefficients of permeability were attained. A graph showing the relationship between coefficient of permeability and void ratio was then arranged.

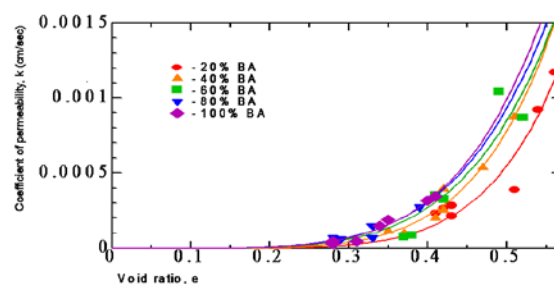


Fig. 5. Coefficient of permeability of different blends at varying void ratio

It can be observed that there was an increasing trend based on the values of coefficient of permeability and void ratio. This explains that as the void ratio, e , increased, the coefficient of permeability, k , also increased. Thus, the soil became more permeable when there was higher void ratio. A specific function was employed in conveying the relationship between k and e . The resulting coefficient of permeability, k is in cm/sec.

The relationship between e and permeability was also influenced by the amount of bottom ash incorporated in the blend. Furthermore, it produced

higher void ratio and permeability when there were greater amount of bottom ash in a blend. The bottom ash content in a blend signified that as one decrease the fraction of bottom ash, void ratio becomes smaller and permeability of the soil also becomes weaker.

Horizontal Permeability

The horizontal permeability was also considered in this study as have been stated in the objectives. An apparatus was devised in such a way that the horizontal permeability of corresponding desired relative compactions can be measured; involved parameters such as the consequent particle sizes' weights for desired relative compaction, void ratios, hydraulic gradient, were also taken into consideration in relation and similar to the vertical set-up.

From the obtained data it was observed that the permeability of all sample tests had a familiar trend in where the permeability decreases as the relative compaction increases. As explained earlier, this trend can be attributed to the reason that due to the increased compaction rate, the voids present in the sample would be lessened as the sample gets more compacted.

Model

Many models may be considered in the study [15, 16, 17, 18]. The experiments conducted for the different blends had been reasonably included within its limits which is $10^{-6} < k < 10^{-3}$ for sand and sandy soils. Looking at the results, it can also be supposed that the blend/s that qualify both Unified Soil Classification System (USCS) recommendations and good permeability are the ones that have around 40% to 60% bottom ash content for a desired relative compaction, blends 3 and 4 for this study.

A multiple regression was also produced so as to predict the permeability at different percent bottom ash content and void ratio. The equation is shown below:

$$k = \exp^{-14.2634+0.88735B+13.361e} \text{ Eq. 1}$$

Where:

B = percent bottom ash content; (%)

e = desired void ratio; and

k = predicted vertical permeability (cm/sec).

Equation 1 produced a coefficient of correlation of above 95% which indicates that it is highly correlated, shown on Figure 6. Further statistical analysis was also done to verify the accuracy of the derived multiple regression equation. The results showed that Equation 1 is acceptable in predicting the vertical permeability given the percent bottom

ash content and void ratio.

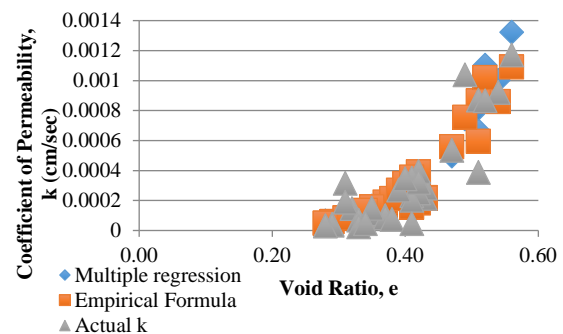


Fig 6. Validation of the Model

Statistical analysis was performed for specific gravity, maximum and minimum index density and void ratio, empirical formulas for vertical permeability and multiple regression. From the analysis, given a level of confidence of 95%, all tStat and P-value was satisfied. Given that there were no value of t-Stat between 1.96 and -1.96 and a P-value greater than 0.005. Thus, all correlation done in the mentioned analyses are considered to be acceptable. In addition, all the graphs for the comparison of the actual and predicted permeability produced a slope almost equal to one of an angle of 45 degrees. From here we could say that using the derived empirical formulas for the different blends would generate consistent results to the actual permeability.

CONCLUSIONS AND RECOMMENDATIONS

This study aimed to present the permeability characteristic of road base materials blended with fly ash and bottom ash and to evaluate the suitability of conventional road subgrade, sub-base, and base materials blended with specific proportion and gradation of fly ash (as partial substitute for fines) and bottom ash (as partial substitute for fine aggregates) for highway embankments with respect to the standard permeability characteristic of road embankments. With thorough researches, analysis with the literatures related to this study and actual laboratory experiments performed by the researchers, the following conclusions are drawn:

1. From SEM tests, fly ash had the most visible voids as compared to bottom ash and CRBM. This had greatly affected the index properties of the soil samples as well as the permeability characteristics of the blended soil samples.
2. Horizontal and vertical permeability of CRBM and pure BA had a significant difference wherein the flow of water at the horizontal-direction is greater compared to the vertical-direction which means that permeability largely depends on the axis of flow and compaction.
3. Blending bottom ash and fly ash has great effect

to the permeability of soils. Among the designed blends, the 40% to 60% substitute of bottom ash to conventional road base materials incurred the highest vertical permeability at different relative compaction but not for the higher relative compaction (RC = 100%) where the amount of bottom ash did not have a significant effect to the permeability.

4. The permeability values obtained for all the blends at the required compaction of 95% range from 1.00×10^{-6} to 1.00×10^{-5} , which is considered to be a fairly stable material as a road embankment according to USCS recommendation for road embankments.
5. Using the derived empirical model for permeability produces good projection of the results, which can also be proven acceptable through statistical analysis.

For future researches, further experiments on different coal ashes of different origins or class may be conducted where the resulting coefficients of permeability may be compared with the outcomes in this thesis. Conducting more researches would not only define the permeability characteristics for the variety of coal ash by-products even more, but also provide engineers with information when it comes to designing road embankments.

It is also recommended for future studies that fly ash content which is ten percent of all blend compositions may be removed and replaced with bottom ash and/or conventional road base material and distinguish if it will have better permeability results than that of the ones conducted in this study.

Moreover, it would be recommendable for future researchers to study the horizontal permeability of the conventional road base materials blended with fly ash and bottom ash. It will be helpful to verify the ratio of horizontal over vertical permeability and confirm if it has satisfactory rate of flow at the x-direction as a good consideration for road base materials.

REFERENCES

- [1] Galupino, J., Dungca, J. (2015). Permeability characteristics of soil-fly ash mix. *ARNP Journal of Engineering and Applied Sciences*, 15, 6440-6447.
- [2] Mordecai & Morris. (1974). Permeability. Retrieved June 22, 2011 from <http://outburst.uow.edu.au/html/permeability.html>
- [3] Pacspi, (n. Understanding road base specifications. Retrieved August 10, 2011, from <http://www.pacspi.com.au/roadbase.html>
- [4] Summers. C.J. (2000) An idiot's guide to highway maintenance. Retrieved August 2011, from <http://www.highwaysmaintenance.com/drainage.htm>
- [5] American Concrete Institute. (2011). What is a subgrade/subbase? Retrieved August 10, 2011, from <http://www.concretenetwork.com/concrete-subgrades-subbases/what-is.html>
- [6] Asilo, M., Pamintuan, C., & Roque, A. (2004). Bottom Ash By-Product from Coal-Fired Power Plant in Pangasinan Used as a Substitute for Fine Aggregates in Concrete. (Undergraduate Thesis) De La Salle University, Manila, Philippines.
- [7] American Society for Testing and Materials.(n.d.). Standard Test Methods for Specific Gravity of Soil Solids by Water Pycnometer. ASTM D854. ASTM D854.
- [8] American Society for Testing and Materials.(n.d.). Standard Test Methods for Liquid Limit, Plastic Limit, and Plasticity Index of Soils. ASTM D4318.
- [9] American Society for Testing and Materials.(n.d.). Standard Test Method for Particle-Size Analysis of Soils. ASTM D422.
- [10] American Society for Testing and Materials.(n.d.). Standard Test Methods for Maximum Index Density and Unit Weight of Soils Using a Vibratory Table. ASTM D4253.
- [11] American Society for Testing and Materials.(n.d.). Standard Test Methods for Minimum Index Density and Unit Weight of Soils and Calculation of Relative Density. ASTM D4254
- [12] Liu, C., & Evett, J. B. (2000). *Soil Properties: Testing, Measurement and Evaluation*. (E. Francis, Ed.) Charlotte, North Carolina, USA: Prentice Hall.
- [13] Smith, C. B. (2010). Horizontal Permeameter. Magna Cum Laude Honors Research Project, University of Florida, Department of Civil and Coastal Engineering, Gainesville, Florida.
- [14] Kim, B., Yoon, S. , Balunaini, L., Prezzi, M. & Salgado, R. (2006). Determination of Ash Mixture Properties and Construction of Test Embankment - Part A.
- [15] Dungca, J., Galupino, J. (2016). Modelling of Permeability Characteristics of Soil-Fly Ash-Bentonite Cut-Off Wall using Response Surface Methodology, *International Journal of GEOMATE* 10, 2018-2024.
- [16] Dungca, J., Galupino, J. (2017). Artificial neural network permeability modeling, *International Journal of GEOMATE* 12, 77-82.
- [17] Dungca, J.R., Jao, J.A.L. (2017). Strength and permeability characteristics of road base materials blended with fly ash and bottom ash, *International Journal of GEOMATE* 12, 9-15.
- [18] Uy, E.E.S., Dungca, J.R. (2017). Constitutive modeling of coal ash using modified cam clay model, *International Journal of GEOMATE* 12, 88-94.

REVIEWS ON THE APPLICABILITY OF CONSTRUCTION AND DEMOLITION WASTE AND ITS RECYCLED MATERIALS AS LOW-COST ADSORBENTS TO REMOVE HEAVY METALS IN WASTEWATER

G.M.P. Kumara, Takashi Saito, Shingo Asamoto, and Ken Kawamoto
Graduate School of Science and Engineering, Saitama University, Saitama, Japan

ABSTRACT

Heavy metal removal from wastewater is of special concern due to the uncontrollable persistency of heavy metals in the environment. The discharge of industries containing heavy metals adversely effects on soil and water resources, aquatic organisms and ecosystem integrity. In addition, it reported high concentrations of heavy metals detected in solid waste landfill leachate in many developing countries due to non-segregated waste dumping. At present, various kinds of adsorbents such as activated carbon, biomass resources, geo materials, and industrial waste products have been used to treat heavy metal-contaminated water. However, the use of construction and demolition waste (CDW) and its recycled materials to treat heavy metal-contaminated water has not been fully examined. Because the generation of CDW is increasing due to the rapid urbanization and high demand of construction works, the wise-use of CDW and its recycled materials can be expected. This paper reviews published journal articles from 2004 to 2016 which studying the applicability of low-cost CDW adsorbents to remove heavy metals from wastewater. In especial, summarizing results from CDW and recycled materials such as cement, concrete, and brick, it compared to those from other various adsorbents such as bio sorbents, geo materials and their industrial products. The potential effectiveness of the applicability of CDW and its recycled materials as heavy metal-adsorbents have been examined based on the comparison table listing material properties, tested conditions and measured adsorption properties.

Keywords: Construction and demolition waste, Recycled materials, Adsorbent, Heavy metals

INTRODUCTION

Conventional wastewater treatment methods such as coagulation, flocculation, reverse osmosis, membrane separation, ion-exchange are long conducted to provide a better water quality and to treat it before being released into the water bodies [1]. However, those methods are expensive and higher cost is needed during the operation [2]. Recently, scientists have been studying on using low cost and abundant adsorbents to remove heavy metals in the wastewater. Natural and industrial geo materials and bio sorbents are well known sorbents and researchers done many experiments to identify the adsorption capacity of those materials [3]. Rapid urbanization, industrialization and population growth in developing and developed countries produce million tons of construction and demolition wastes (CDW) per year. As an example, Malaysia, Thailand and Vietnam produce 1.9, 1.9 and 6.9 million tons of CDW materials per year respectively and common treatment method is landfilling or dumping [4];[5]. About 850 million tons of CDW is generated in the European Union (EU) per year, representing 31% of the total waste generated in the EU [6]. However, the level of recycling and reuse of CDW varies greatly between less than 10% to over 90% across the EU [3]. In 2014 United State produce 534 million tons of CDW materials and out

of that 70% is waste concrete [7]. Then researchers can predict densely populated India and China like countries will produce huge amounts of CDW materials in the future by creating lots of environmental problems. Therefore, the efficient usage of those abundantly available resources for different activities investigation is timely. Therefore, objective of this review is to investigate applicability of CDW and recycle materials as an efficient adsorbent to remove heavy metals from wastewater with respect to geo materials and bio sorbents.

METHODOLOGY

A detailed literature search was carried out by initially selecting several key words. Those used include: heavy metal adsorption, natural and industrial geo materials, bio sorbents, and CDW materials. The search was limited to paper selection criteria given in Figure 1. All papers selected were published in Web of ScienceTM (Clarivate Analytics). A total of 33 references were selected of which most are journal papers from environmental engineering and material science research areas. A careful review of those selected papers has been done by comparing each category of adsorbents for experimental conditions, maximum adsorption capacity, analysis methods, results and suggesting future considerations.

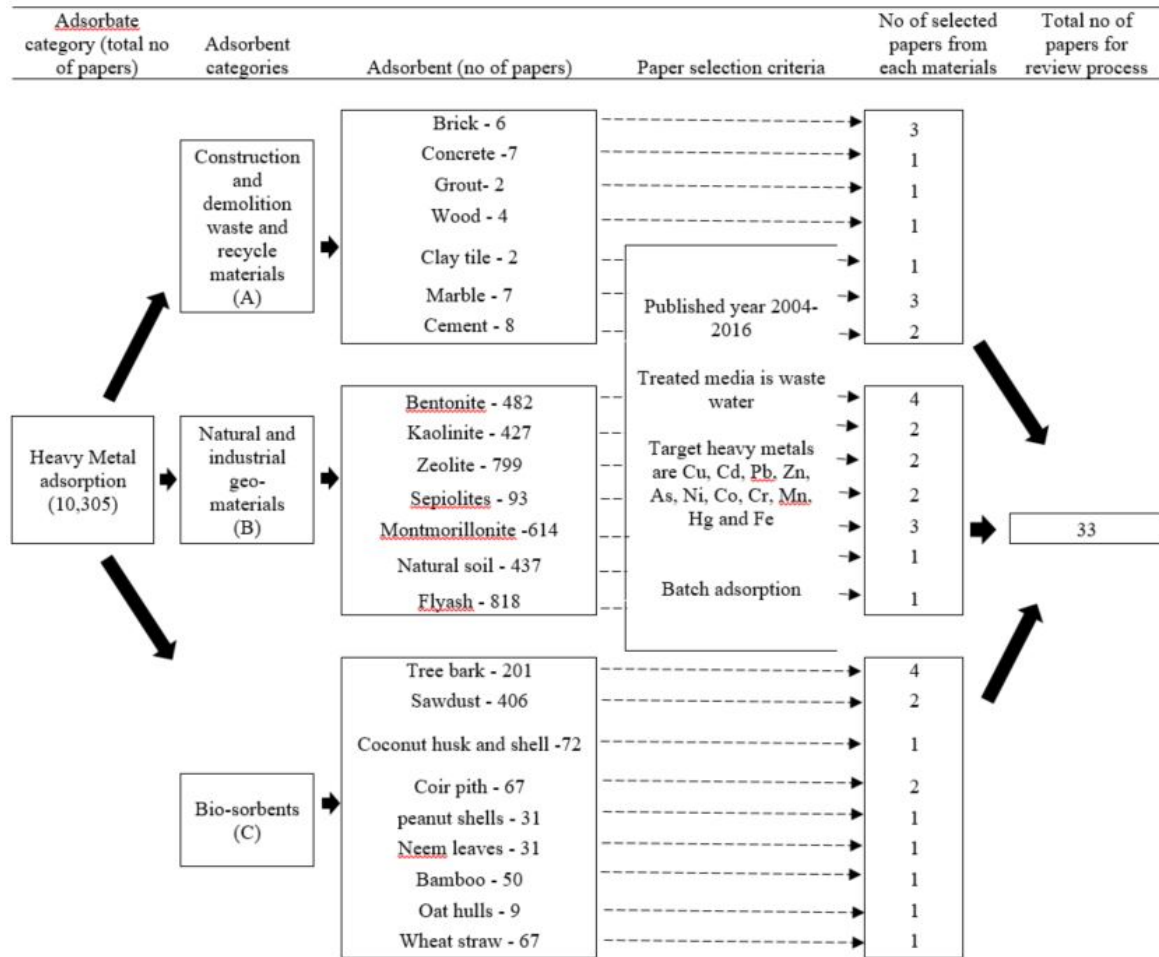


Figure 1: Procedure of journal paper selection for the review in this study

RESULTS AND DISCUSSION

Adsorption has been proved to be an excellent way to treat wastewater, offering significant advantages like the low-cost, availability, profitability and ease of operation. According to Fig. 1, scientist and researchers gave highest priority for geo-materials and bio sorbents (>80%) for adsorption heavy metals with compare to CDW and recycle materials. Furthermore, adsorption study for concrete and cement materials are rare. Hence, investigation, comparison and identification of test conditions, adsorption capacity and analyzing methods of various adsorption materials with respect to CDW materials is beneficial for the next generations.

As shown in the Table 1, all three types of adsorbents, major target metals are Cu, Cd (39.9%), Pb (33.3%), Zn (24%) while less consideration gave for As (12.1%), Cr, Hg and Mn (6.1%) like metals. Used particle size and adsorbent concentration is diverse for each category and for each metal type in reviewed papers. Testing of background electrolytes effect on adsorption process also has

less consideration in each category, and common solution were NaCl, NaNO₃ or NaClO₄ under the concentration range of 0.001-0.1 N. It is clear that CDW and recycle materials need higher equilibrium time than the other two categories of adsorbents. Basically equilibrium time depend on the target metals, adsorbent and its physical conditions and other operation parameters. Higher equilibrium time is one of the main constrain for commercial application of those adsorbents. Therefore, further studies are needed to find out less equilibrium time by changing other testing conditions.

According to Table 2, in all three categories of materials showed lack of data regards to cation exchange capacity (CEC) and point of zero charge of the materials. But, these two parameters are essential to understand the potential of adsorption and to explain adsorption behavior of metals. It revealed that a wide range of initial concentration of metal solutions was tested in the adoption studies. Solution pH is the one of critical parameter in adsorption experiments and especially if adsorbent

Table 1: Summary of followed methodology in each adsorption studies

Category of adsorbent	Adsorbent	Target metals	Particle size (μm)	Adsorbent concentration (g/L)	Back-ground solution	Ionic strength (mol/L)	Equilibrium time for Isotherm (min)	Ref.
A	Brick	As ⁵⁺	≤ 300	10-40	DIW	(-)	60	[8]
	Concrete	Cu ²⁺	63-200	5	NaCl	0-0.34	120	[9]
		Zn ²⁺	45-4760	10	DW	(-)	540-1200	[10]
		Cu ²⁺ , Zn ²⁺ , Pb ²⁺	≤ 250	25	DW	(-)	7200 (Cu ²⁺), >7200 (Zn ²⁺), 2880(Pb ²⁺)	[11]
	Grout	Pb ²⁺ , Cd ²⁺	≤ 80	20	NaCl	0.1	90	[12]
	Wood	Cr ⁶⁺	1-100	1-5	DW	(-)	40	[13]
	Clay tile	Zn ²⁺	45-4760	10	DW	(-)	1200	[10]
	Marble	Cd ²⁺	25-63	2	DDW	(-)	300	[14]
	Cement	Pb ²⁺	25-63	1	DDW	(-)	120	[15]
		As ⁵⁺	50	10-40	DIW	(-)	60	[8]
		Cd ²⁺ , Zn ²⁺ , Cu ²⁺ , Pb ²⁺	2000	40	NaNO ₃	0.01	60	[16]
		As ⁵⁺	1400-3000	10-40	DIW	(-)	60	[8]
B	Bentonite	Cd ²⁺ , Pb ²⁺	≤ 855	10	DIW	(-)	150 (Cd ²⁺), 250 (Pb ²⁺)	[17]
	Kaolinite	Ni ²⁺ , Mn ²⁺	100-500	2-10	DDW	(-)	180	[18]
	Zeolite	Pb ²⁺ , Cu ²⁺ , Zn ²⁺ , Cd ²⁺	90-300	5	NaClO ₄	0.01-0.05	<1440	[19]
	Sepiolite	Pb ²⁺	20-53	2-20	DW	(-)	360	[20]
	Montmorillonite	Co ²⁺	≤ 200	0.2-1.4	NaClO ₄	0.001-0.1	120	[21]
	Alluvial soil	Pb ²⁺ , Cd ²⁺	2000	100	MQW	(-)	Pb ²⁺ 360, Cd ²⁺ 60	[22]
C	Bark	Cd ²⁺	≤ 500	4	Na ₂ SO ₄	0-0.07	25	[23]
	Sawdust	Zn ²⁺ , Cu ²⁺ , Cd ²⁺ , Fe ²⁺ , Ni ²⁺ , Mn ²⁺	400-1000	2-40	DW	(-)	30	[24]
	Coconut shell	Pb ²⁺ , Cd ²⁺	≤ 75	100	MQW	(-)	Pb ²⁺ 360, Cd ²⁺ 60	[22]
	Coir pith	Cd ²⁺	≤ 96	0.25-3	NaCl	0.001-0.1	180	[25]
	Peanut shell	Hg ²⁺ , Cd ²⁺	100-200	8	DIW	(-)	120	[26]
	Neem leaves	Cr ⁶⁺	850-1500	4-16	DW	(-)	4020	[27]
	Bamboo	As ³⁺ , As ⁵⁺	63-125	0.01-0.15	DDW	(-)	1800 for As ³⁺ , 2130 for As ⁵⁺	[28]
	Oat hulls	As ⁵⁺	360-430	0.015	DIW	(-)	1440	[29]
	Wheat straw	As ³⁺ , As ⁵⁺	*	0.5-3	Fe ₃ O ₄	0.5	720	[30]

Note: DW-distilled water, DIW- deionized water, DDW- doubly distilled water, MQW- Milli-Q water, (-) no ionic strength, * No data available

materials are concrete or cement material, careful observation of working pH is essential for maxi-

mum adsorption of heavy metals [8]-[16]. Studies regards to temperature effects on adsorption process

Table 2: Summary of followed methodology in each adsorption studies

Category of adsorbent	Adsorbent	Target metals	Point of zero charge	CEC of adsorbent (mmol/100 g)	Concentration range (mg/L)	Initial pH	Temperature (°C)	Ref.
A	Brick	As ⁵⁺	*	*	0.1-1	2-9	25	[8]
		Cu ²⁺	*	*	200	1.5-6	25-45	[9]
		Zn ²⁺	*	*	40-90	2.5-4.5	25	[10]
	Concrete	Cu ²⁺ , Zn ²⁺ , Pb ²⁺	*	*	873(Cu ²⁺), 837 (Zn ²⁺), 1041(Pb ²⁺)	5-7	20	[11]
		Pb ²⁺ , Cd ²⁺	*	453.2	20 (Cd ²⁺), 200 (Pb ²⁺)	5	25	[12]
		Cr ⁶⁺	*	*	10-50	1-11	10-50	[13]
	Wood	Zn ²⁺	*	*	40-90	2.5-4.5	25	[10]
	Clay tile	Cd ²⁺	8.3	*	20-60	7	25	[14]
		Pb ²⁺	8.3	*	500-1500	7	25	[15]
		As ⁵⁺	*	*	0.1-1	2-9	25	[8]
B	Cement	Cd ²⁺ , Zn ²⁺ , Cu ²⁺ , Pb ²⁺	*	52.2	50-1600	3-9	25	[16]
		As ⁵⁺	*	*	0.1-1	2-9	25	[8]
		Cd ²⁺ , Pb ²⁺	*	61.0	2-500	5.2 (Pb ²⁺), 8 (Cd ²⁺)	0-60	[17]
	Bentonite	Ni ²⁺ , Mn ²⁺	5.5	11.3	100-500	2-8	27-50	[18]
		Pb ²⁺ , Cu ²⁺ , Zn ²⁺ , Cd ²⁺	*	*	5-20	6	25	[19]
		Pb ²⁺	6.4	11.8	300	2-9	20-40	[20]
	Sepiolites	Co ²⁺	*	86.1	9.8	3-12	30-70	[21]
	Montmorillonite	Pb ²⁺ , Cd ²⁺	*	*	100-2000	2-8	25	[22]
	Alluvial soil	Cd ²⁺	5.32	*	25-300	2-5	20-50	[23]
	Bark	Zn ²⁺ , Cu ²⁺ , Cd ²⁺ , Fe ²⁺ , Ni ²⁺ , Mn ²⁺	*	*	5-200	5	25	[24]
C	Sawdust	Pb ²⁺ , Cd ²⁺	*	*	100-2000	2-8	25	[22]
	Coconut shell	Cd ²⁺	5.5	181	25-300	2-8	30	[25]
	Coir pith	Hg ²⁺ , Cd ²⁺	*	*	1-300	1-7	25	[26]
	Peanut shell	Cr ⁶⁺	*	*	40-700	1-11	30	[27]
	Neem leaves	As ³⁺ , As ⁵⁺	5	*	2-38	2-9	25	[28]
	Bamboo	As ⁵⁺	*	*	0.025-0.2	5-9	24	[29]
	Oat hulls	As ³⁺ , As ⁵⁺	*	*	1-28	3-11	30	[30]
	Wheat straw							

Note: *No data available

for CDW and recycle materials is rare and researchers have potential for that. Reported maximum adsorption capacity (Q_{\max}) illustrates in Figs. 2 and 3 for selected adsorbent and all adsorbent show potential for adsorb heavy metals from waste

water. It is clear that less consideration for CDW and recycle materials and limited for few heavy metals such as Pb, Cd and Cu (see, Fig. 1). Furthermore, brick and marble materials show more than 100 mg/g Q_{\max} for Cu and Pb respectively

[9],[15], implying that CDW and recycle materials have a great potential for adsorb heavy metals as

geo and bio sorbents.

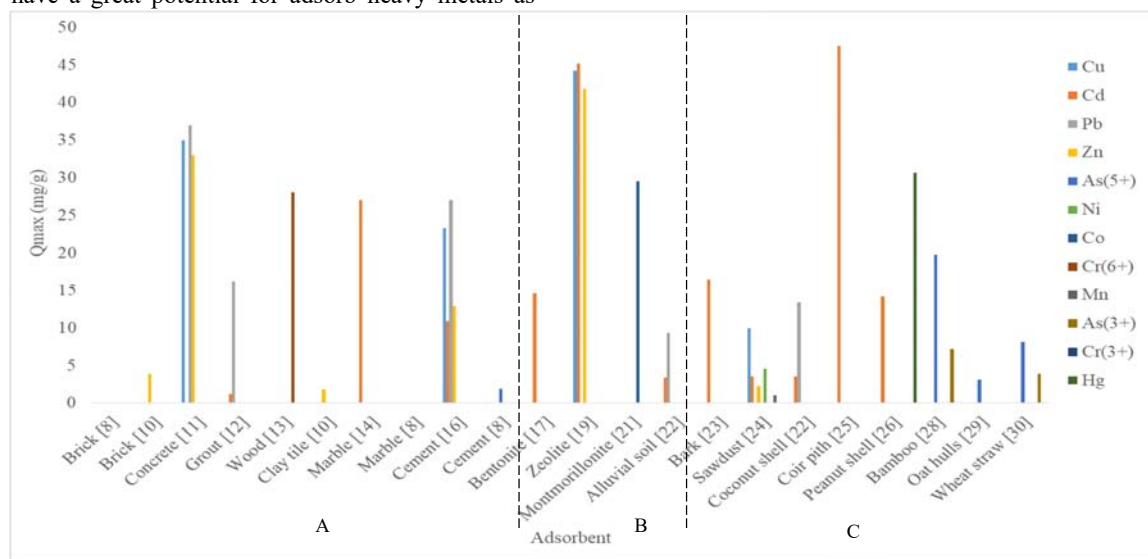


Figure 2: Reported adsorption capacities in selected adsorption studies

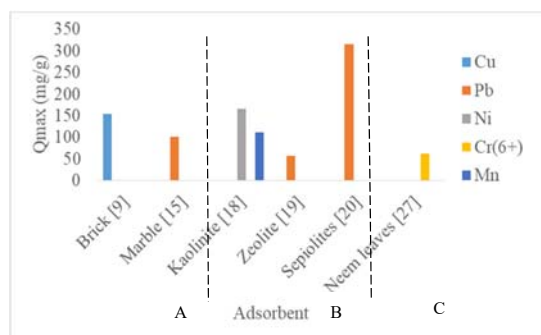


Figure 3: Reported adsorption capacities in selected adsorption studies

According to the data reported, Langmuir and Freundlich models for isotherm studies and pseudo first order and pseudo second order models for kinetic studies are commonly used models and best fit models during the data analyzing process in all three categories. Furthermore, Langmuir model is more than 90% act as a best fit model for CDW and recycle materials by representing mono layer adsorption to adsorbent. There are different types of adsorption mechanisms were reported and for CDW and recycle materials such as ion exchange, chemisorption and film diffusion. Thermodynamic parameters are important to explain adsorption process when changing the temperature of the medium. The Gibbs Free Energy (ΔG) is negative for CDW and recycle materials by indicating the spontaneous nature of the adsorption process and the negative

values of entropy (ΔS) suggest the probability of a favorable adsorption.

CONCLUSION

According to all parameters discussed in this paper, it is clear CDW and recycle materials have same potential as geo and bio sorbents for adsorb heavy metals from wastewater which is marginalized material in current situation. Therefore researchers and scientist have to focus their attention to improve and use this abundantly available material for wastewater treatment process in future.

ACKNOWLEDGEMENTS

This study was supported by the SATREPS Project of the Japan Science and Technology agency (JST) and Japanese International cooperation Agency (JICA).

REFERENCE

- [1] Lim AP, Aris AZ (2013) A novel approach for the adsorption of cadmium ions in aqueous solution by dead calcareous skeletons. *Desalination Water Treat.* doi:10.1080/19443994.2013.798843, pp. 3169-3177.
- [2] Chiban M, Zerbet M, Carja G and Sinan F, Application of low-cost adsorbents for arsenic removal: a review. *J Environ Chem Ecotoxicol*, Vol. 4(5), 2012, pp. 91-102.

- [3] Grace MA, Clifford E and Healy MG, The potential for the use of waste products from a variety of sectors in water treatment processes, *Journal of Cleaner Production*, Vol. 137, 2016, pp. 788-802.
- [4] Papargyropoulou E, Preece C, Rory P, Abdullah AA, Sustainable construction waste management in Malaysia: A contractor's perspective, *Management and Innovation for a Sustainable Built Environment MISBE 2011*, Amsterdam, The Netherlands, June 20-23, 2011.
- [5] Chinda T and Doan DT, Cost Factors of C&D Waste Recycling Program Implementation, the 2nd International Conference on Trends in Multidisciplinary Business and Economic Research (TMBER 2015), At Bangkok, Thailand, 2015.
- [6] Fischer C, Werge M, EU as a Recycling Society: Present Recycling Levels of Municipal Waste and Construction & Demolition Waste in the EU, 2009, Copenhagen.
- [7] United State Environmental Protection Agency, Construction and Demolition Debris Generation in the United States, U.S Office of Resource Conservation and Recovery, 2016, pp 23.
- [8] Sadia et al., Evaluation of industrial based adsorbents for simultaneous removal of arsenic and fluoride from drinking water, *Journal of Cleaner Production*, Vol. 87, 2015, pp. 882-896.
- [9] Rabiaa et al., Sorption of copper(II) from aqueous solutions by cedar sawdust and crushed brick, *Desalination*, Vol. 225, 2008, pp. 95-112.
- [10] Hoda et al., Characterization and Utilization of Clay-Based Construction and Demolition Wastes as Adsorbents for Zinc (II) Removal from Aqueous Solutions: an Equilibrium and Kinetic Study, *Environmental Progress & Sustainable Energy*, Vol. 33(3), 2014, pp. 777-789.
- [11] Nichola et al., Interactions of aqueous Cu^{2+} , Zn^{2+} and Pb^{2+} ions with crushed concrete fines, *Journal of Hazardous Materials*, B121, 2005, pp. 203-213.
- [12] Chen et al., Removal of Pb^{2+} and Cd^{2+} by adsorption on clay-solidified grouting curtain for waste landfills, *J. Cent. South Univ. Technol*, Vol. 13(2), 2006, pp.166-170.
- [13] Jyotikusum et al., Removal of chromium(VI) from wastewater by activated carbon developed from *Tamarind wood* activated with zinc chloride, *Chemical Engineering Journal*, Vol. 150, 2009, pp. 25-39.
- [14] Shaban et al., Cadmium(II) sorption from water samples by powdered marble wastes, *Chemical Speciation & Bioavailability*, Vol. 20(4), 2008, pp. 249-260.
- [15] Shaban et al., Lead separation by sorption onto powdered marble waste, *Arabian Journal of Chemistry*, Vol. 7, 2014, pp. 277-286.
- [16] Yong et al., Heavy metal adsorption by a formulated zeolite-Portland cement mixture, *Journal of Hazardous Materials*, Vol. 147, 2007, pp. 91-96.
- [17] Luz et al., Removal of Cadmium(II) and Lead(II) Ions from Aqueous Phase on Sodic Bentonite, *Materials Research*, Vol. 16(2), 2013, pp 515-527.
- [18] Dawodu et al., Simultaneous adsorption of Ni(II) and Mn(II) ions from aqueous solution unto a Nigerian kaolinite Clay, *Journal of material research tec*. Vol. 3(2), 2014, pp. 129-141.
- [19] Hutaf et al., Natural Jordanian zeolite: removal of heavy metal ions from water samples using column and batch methods, *Environ Monit Assess*, Vol. 157, 2009, pp. 319-330.
- [20] Sharifipour et al., Kinetics and Thermodynamics of Lead Adsorption from Aqueous Solutions on to Iranian Sepiolite and Zeolite, *Int. J. Environ. Res.*, Vol. 9(3), 2015, pp. 1001-1010.
- [21] Guo et al., Enhanced sorption of radiocobalt from water by Bi(III) modified montmorillonite: A novel adsorbent, *Journal of Hazardous Materials*, Vol. 192, 2011, pp.168-175.
- [22] Paravithana et al., Adsorption of Cd^{2+} and Pb^{2+} onto coconut shell biochar and biochar-mixed soil. *Environ Earth Sci*, Vol. 75, 2016, pp. 484.
- [23] Ghodbane et al., Kinetic and equilibrium study for the sorption of cadmium(II) ions from aqueous phase by eucalyptus bark, *Journal of Hazardous Materials*, Vol. 152, 2008, pp. 148-158.
- [24] Bozic et al., Adsorption of heavy metal ions by sawdust of deciduous trees, *Journal of Hazardous Materials*, Vol. 171, 2009, pp. 684-692.
- [25] Anirudhan et al., Adsorption Characteristics of Cadmium(II) onto Functionalized Poly(hydroxyethylmethacrylate)-Grafted Coconut Coir Pith, *Bull Environ Contam Toxicol*, 2010, Vol. 85, pp. 42-47.
- [26] Liu et al., Adsorption of Hg^{2+} and Cd^{2+} by ethylenediamine modified peanut shells, *Carbohydrate Polymers*, Vol. 81, 2010, pp.335-339.
- [27] Babu et al., Adsorption of Cr(VI) using activated neem leaves: kinetic studies, *Adsorption*, 2008, Vol. 14, pp. 85-92.
- [28] Liu et al., Arsenic Removal from Water by Iron-Modified Bamboo Charcoal, *Water Air Soil Pollut*, 2012, Vol. 223, pp 1033-1044.
- [29] Chuang et al., Adsorption of arsenic(V) by activated carbon prepared from oat hulls, *Chemosphere*, Vol. 61, 2005, pp. 478-483.
- [30] Tian et al., Synthesis of magnetic wheat straw for arsenic adsorption, *Journal of Hazardous Materials*, Vol. 193, 2011, pp 10-16.

STUDY ON EXTRACTION AND ADSORPTION OF CESIUM FROM VERMICULITE MIXTURE SAND

Shota NISHIOKA ¹, Keiichiro SHIBATA ², Hidenori YOSHIDA ²

Naomichi MATSUMOTO ² and Yoshihiro SUENAGA ²

¹ Graduate School of Engineering, ² Kagawa University, Japan

ABSTRACT

A large amount of radioactive materials were diffused by the accident at Fukushima Daiichi nuclear power station of Tokyo electric power company, and decontamination has been continued for about six years in Fukushima. The contaminated soil that is stripped on the ground and is collected should be reduced in volume at an intermediate storage facility. However, it takes a long time to operate the facility. The ministry of the environment shows the guidelines that it is possible to dispose the radioactive waste below 8000Bq/kg of radiation dose in an ordinary process. Therefore, it is more desirable that the radiation dose should be reduced below 800Bq/kg in flexible containers filled with contaminated soil than the reduction of radiation dose in the intermediate storage facility. Thus, in this study, the method in which only radioactive materials are collected from the contaminated soil in the flexible containers is proposed. The extraction of radioactive cesium from the soil is investigated so as to check the performance and availability of the proposed method. As a result, it is confirmed that it is possible to collect a certain amount of cesium from cohesive soil like vermiculite in which cesium is strongly fixed.

Keywords: Cesium, Vermiculite, Ammonium acetate, Electrophoresis, Zeolite

INTRODUCTION

A serious nuclear accident at the Tokyo electric power company's Fukushima Daiichi nuclear power station caused the spread of large amounts of radioactive materials. Among released radioactive substances, iodine 131, cesium 134, cesium 137 and strontium 90 have serious influences on the human body and the environment in terms of release amount and half-life [1]. In particular, cesium 137 has a large release amount of 1.5×10^{16} Bq and its half-life is as long as about 30 years. Moreover the detection of radiation still continues over a wide range of Fukushima.

Cesium fixed in clay minerals in soil is known to be difficult to remove from the soil. The soil in Fukushima prefecture is relatively abundant in viscous soils. In general, the viscous soils absorb the cesium well from the environmental point of view. In addition, it has been confirmed that most of radioactive cesium is fixed in mineral particles called vermiculite (weathered biotite) which is unevenly distributed in the soil of Fukushima [2], and it is necessary to establish the efficient removal method of cesium from vermiculite.

In Fukushima, the stripping on topsoil has been carried out for the decontamination of cesium in soil.

The Ministry of the Environment estimates that the amount of generated contaminated soil is about 16 million m³ to 22 million m³ after the volume reduction of the gathered one when all the soil in

decontamination area of Fukushima are stripped. It is currently considered difficult to secure an intermediate storage facility in which these large contaminated soils will be managed over a long period of time. Therefore, the disaster waste safety assessment study meeting organized by the Ministry of the Environment proposed that the polluted soil whose radiation dose is less than 8000 Bq / kg can be reused as construction materials such as embankment [3]. This propose indicates that a certain amount of cesium from the contaminated soil in the temporary storage bag are removed without waiting for the construction of intermediate storage facilities.

As a technology for removing cesium, the method in which the volume of contaminated soils can be reduced by burning the burnable materials after separating soil and organic matter mechanically and with high precision is proposed. Other method in which contaminated soils are classified into fine particles fixed with cesium and regenerated soil by washing the soils is proposed [4]. However, in these methods, the contaminated soils are decontaminated in large-scale facilities such as intermediate storage facilities which is difficult to construct in the present situation due to securing their construction sites. Therefore, it is necessary to reduce the radiation dose of contaminated soil in temporary storage space.

In this study, the artificial soil mixed vermiculite and Toyoura standard sand was prepared as the soil to which cesium could be easily adhered, and a stirring test was conducted using an ammonium

acetate aqueous solution as an extraction solution. Based on the results obtained in these cesium extraction tests, electrophoresis tests were conducted at different current values. In the test, it was aimed to investigate whether it is possible to transfer cesium from vermiculite to the adsorbent and to investigate whether it is possible to reduce the radiation dose of contaminated soil in the flexible container at the temporary houseroom.

MATERIALS AND METHODS

Materials

In this study, the soil mixed with Toyoura standard sand (Fig.1) and vermiculite (Fig.2) was used as an experimental soil to which cesium was added.

The Toyoura standard sand is composed with the soil particle of the uniform grain size. Moreover, it is very smooth, and the soil grains hardly stick each other. Therefore, the difference between experimental samples can be neglected under the same condition, and the reproducibility of experiments are secured.



Fig.1 Toyoura standard sand.

The vermiculite is the silicate mineral that mainly consists of the oxidized silicon, magnesia and aluminum oxide. It is also called leech stone in Japan since it expands at high temperature. The common uses of vermiculite include soil improvement and livestock food in agricultural and horticultural fields, refractory materials and lightweight concrete in construction field, disposable hand warmer and friction materials. It has been confirmed that the vermiculite is unevenly distributed in the soil of Fukushima, which is a major obstacle to the decontamination of radioactive cesium [5]. Cesium present as a monovalent cation in soil adsorbs to negatively charged soil particles in soil. It also has the property of selectively adsorbing to clay particles of small particle size. Cesium is fixed to the soil by the 2: 1 type layered silicate (Fig.3) such as vermiculite among the minerals constituting the clay mineral. The weathering of the soil swells so that the terminal part of the layer of clay mineral gets frayed and releases

potassium ion. As a result, a portion where other cations can enter can be formed. This is called a frayed edge (Fig.4). The cesium ion fixed to this frayed edge becomes difficult to replace by other cations [6]. In this study, 0.7 mm, 1.0 mm, 2.0 mm of grain size of vermiculite was utilized.



Fig.2 Vermiculite (particle size 0.7mm, 1.0mm, 2.0mm from the left).

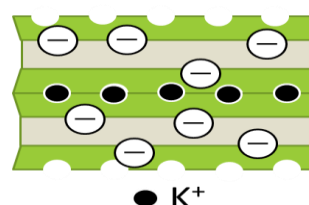


Fig.3 2: 1 type layered silicate schematic.

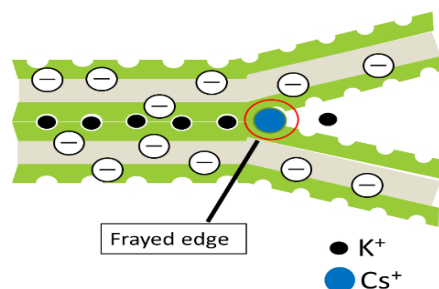


Fig.4 Schematic diagram of the frayed edge in 2: 1 type layered silicate.

The cesium extraction test using decomposed granite soil was conducted by Miyazaki (2016), but the test result tended to vary on account of the size of weathered granite soil. Therefore, in this study, the experimental results with high reproducibility can be secured by preparing the mixed soils mentioned above, because only the Toyoura standard sand and the vermiculite are employed as a soil sample. In the experiment, it was decided to carry out a cesium extraction test on the mixed soil with the Toyoura standard sand and the vermiculite.

Powdered zeolite (Fig.3) was used as adsorbent for cesium in the electrophoresis test. The skeleton structure of zeolite is silicon and aluminum bonded

via oxygen. In the skeleton structure, the periphery of silicon is electrically neutral and the surroundings of aluminum are negatively charged since aluminum and silicon share oxygen with each other. Therefore, the cations are required in the framework to compensate for the negative charge. Since the cation is easily exchanged with other metal ions, the zeolite is known to have ion exchange properties.



Fig.5 Powdered zeolite.

An aqueous ammonium acetate solution as an extra-ction solution for extracting cesium in the soil and as an electrolyte in the electrophoresis test was used. It is known that the ammonium ion of ammonium acetate shows a high ion exchange reaction with cesium ions fixed in the clay mineral. Based on this fact, it is suitable for the extraction of cesium in the mixed soil. From the study of Yoshida (2016), the higher the concentration of the ammonium acetate aqueous solution used as the extraction solution and electrolyte, the higher the extraction ratio of cesium [7]. Since, however, the contaminated soil in which the radiation dose is decreased below the reference value is reused, the ammonium acetate aqueous solution in concentrated form cannot be employed. Therefore, 5% concentration of ammonium acetate aqueous solution (concentration 3.0%) of a saturated aqueous ammonium acetate solution (concentration 59.7%) having a low concentration and an excellent extraction ratio.

Cesium extraction test method

In this study, the experimental sample should be put into solution for the quantitative analysis for cesium with atomic absorption spectrometry. Therefore, it is necessary to separate the cesium in the soil into the solution after the electrophoresis test. In addition, it is difficult to separate only cesium from the adsorbent after the test into a solution. Thus, in order to confirm the adsorption effect for cesium on the adsorbent by electrophoresis, it is necessary to separate cesium into solution and to compare the difference of cesium between the tests with and without the adsorbent. As a separation method, 100

mL of the ammonium acetate aqueous solution whose concentration is same as that used in the test was added to the soil after the test. Then, it is agitated for 10 minutes at 300 rpm of a rotation speed using a stirrer. Moreover, it is sieved with a sieve of 38 μm . Stirring is performed for 40 minutes in total by repeating the solid-liquid separation step of filtering to solution and soil four times. The amount of cesium contained in the solution after the test and the soil is quantified for the solution separated by filtration with each stirring using an atomic absorption spectrometer.

Electrophoresis test

As a test soil assuming contaminated soil, vermicu-lite mixed sand with cesium is placed in a test container and a carbon rod (D 15 mm, L 40 mm) to be an anode is installed on the bottom of container. It is immersed in an aqueous solution of ammonium acetate which is an electrolyte, and an adsorbent is placed on an assumed contaminated soil. The adsorbent was placed in the simple container which consists of a filter paper and a holding cloth for an easy access after testing. Finally, an aluminum plate (W 30 mm, L 90 mm) is installed to serve as a cathode from the top of the adsorbent (Fig.4). Since cesium exists as a cation in solution, it moves to the aluminum plate which is the cathode by energization and is adsorbed by the adsorbent.

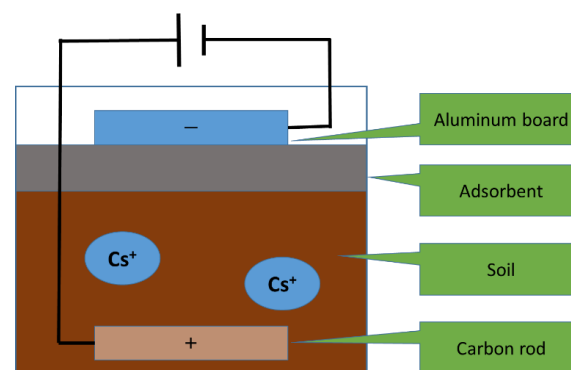


Fig.6 Schematic drawing of electrophoresis test

RESULTS AND DISCUSSION

Cesium adsorption of vermiculite

In order to confirm the adsorption performance of vermiculite to cesium, the results of cesium extraction test using aqueous ammonium acetate solution as an extraction solution are shown. The purpose of the extraction test is to confirm whether cesium can be efficiently extracted from vermiculite by using aqueous ammonium acetate solution. In addition, the

tests are conducted under the conditions where cesium is more easily to be fixed, such as the curing tests in which the curing period of the assumed contaminated soil is varied or the wet state is kept. According to the test results, the compounding ratio of vermiculite and sand for the mixed sand is determined. As a result, 20 g of mass and 0.7, 1.0, and 2.0 mm of particle size of the vermiculite are determined.

In this test, cesium is extracted by washing with stirring. 1 mg of cesium is added to the vermiculite or mixed sand in the test container. 0 hour and 168 hours of curing period are set, 100 ml of ammonium acetate aqueous solution as extraction solution is poured into the assumed contaminated soil, and the washing out by stirring is carried out. The concentration of the ammonium acetate aqueous solution is set to 3.0%, and the stirring is carried out for 10 minutes at 300 rpm of a rotation speed. Four sets of the stirring is conducted, that is to say, 40 minutes stirring is totally carried out. In some tests, the distilled water is added into the assumed contaminated soil before the addition of cesium into the soil so as to reproduce the real condition in Fukushima. In this study, each test is conducted three times under the same condition to ensure a reproducibility.

In the cesium extraction test with 0.7 mm of vermiculite particle size, Fig. 7 shows that about 20% of cesium can be extracted by washing out with distilled water immediately after the addition of cesium. However, compared with Fig. 8, the extraction ratio is reduced to 10% or less due to long curing period. This is because the cesium is not completely absorbed in the flied edge of vermiculite immediately after the addition of cesium. However, the cesium is sufficiently adsorbed in the flied edge of vermiculite due to the long curing period. This face suggests that the washing out with the distilled water against the curing contaminated soil is ineffective.

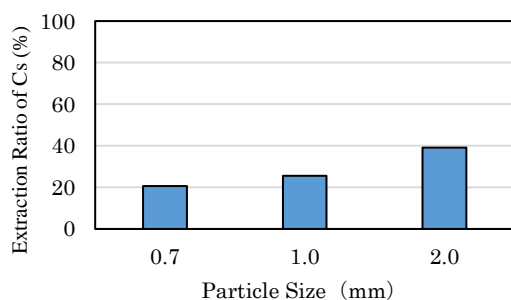


Fig. 7 Extraction ratio of cesium by washing out with distilled water (curing period 0 h).

Figure 9 shows the result of washing out the curing vermiculite with an ammonium acetate aqueous solution. Comparing Fig. 8 with Fig. 9, it can be seen that the extraction ratio of cesium is improved by about 20% by washing with ammonium acetate. Therefore, it was confirmed that the ammonium acetate aqueous solution was effective and efficient extraction of cesium for the curing contaminated soil.

In the cesium extraction test with 1.0 mm of the vermiculite particle size, the cesium extraction ratio is slightly higher than that of 0.7 mm of the vermiculite particle size. The surface area per gram of vermiculite is larger when the particle size is smaller. The vermiculite having 0.7 mm of the particle size contacts cesium more widely than the others, and trend high performance of cesium adsorption.

For the vermiculite having 2.0 mm of the particle size, the extraction ratio is higher than the other two. As mentioned above, the extraction amount of cesium depends on the surface area per gram of vermiculite. However, it is found that the extraction rate by the extraction with distilled water shows about 20% drop due to curing in the case of 2.0 mm particle size.

From the results of these tests, it is confirmed that it is difficult to extract cesium in the case of smaller size

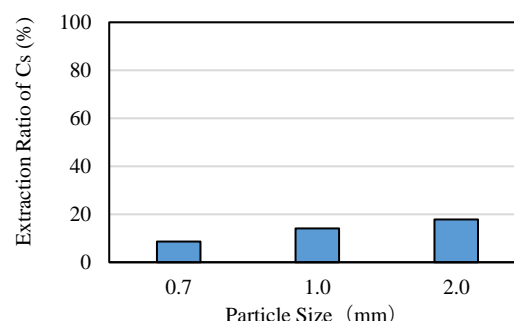


Fig. 8 Extraction ratio of cesium by washing out with distilled water (curing period 168 h).

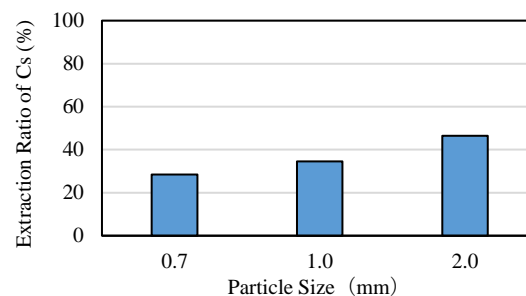


Fig. 9 Extraction ratio of cesium by washing out with ammonium acetate aqueous solution (curing period 168 h).

is difficult to extract cesium in the case of smaller size of vermiculite particle and to extract cesium with distilled water from cured contaminated soil. In these tests, it is found that the vermiculite having 0.7 mm of particle size adsorbs a lot of cesium. Thus, in this study, the vermiculite having 0.7 mm of particle size is mixed with the Toyoura standard sand and employ an ammonium acetate aqueous solution as an extraction solution.

Extraction of cesium from mixed sand

The vermiculite mixed sand is prepared based on the results obtained from the tests in which the cesium is extracted from only vermiculite. The vermiculite with 0.7 mm particle size is employed in order to prepare the mixed soil. The total mass of the mixed soil in the cesium extraction test and electrophoresis test are set to 50 g and 120 g, respectively. The mixing ratios of vermiculite to standard sand are three cases; 3, 5, 10%.

As can be seen from Fig. 10, the lower the cesium extraction rate is, the higher the mixing ratio of vermiculite to standard sand is. Under the condition of constant volume of standard sand, the more the cesium is adsorbed, the higher the mixed ratio of vermiculite to standard sand is.

The extraction ratio of cesium in the case of only the vermiculite and the mixed sand is considered. Comparing Fig. 9 with Fig. 10, there is not much difference between only the vermiculite and the mixed sand in terms of the extraction of cesium.

Figure 11 shows the result of cesium extraction of assumed contaminated soil in the case of 120 g of the mixed sand for electrophoresis test. Comparing Fig. 10 with Fig. 11, it can be seen that there is not much difference between 50 g case and 120 g case in terms of the extraction ratio of cesium. This is because the volume ratio of vermiculite and standard sand hardly changes between them even if their total amount of mixed sand are different. Thus, more or less same

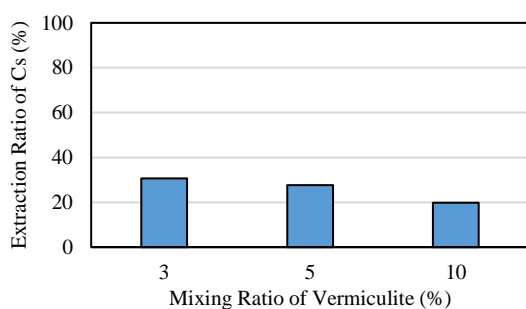


Fig. 10 Extraction ratio of cesium in vermiculite mixed sand 50 g (curing period 168 h).

cesium extraction ratio are obtained in both cases.

From the above test results, the addition of 5% of vermiculite for 120 g of the mixed soil is determined in the electrophoresis test.

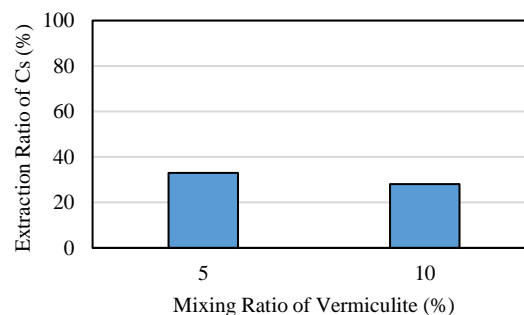


Fig. 11 Extraction ratio of cesium in vermiculite mixed sand 120 g (curing period 168 h).

Electrophoresis test

In the electrophoresis test, the vermiculite having 0.7 mm particle size, which adsorbs cesium most, is employed based on the results of cesium adsorption a performance test of vermiculite. In the assumed contaminated soil used for the electrophoresis test, 1 mg of cesium is added after setting the moisture content to 30% wet state, and the curing period is 168 hours.

In the electrophoresis test, the aqueous solution of ammonium acetate is employed as an electrolyte, and the test is carried out under the conduction conditions of 48 hours of the energization time, 25V or less of voltage, and 0.005, 0.010, 0.015, 0.025, 0.050 or 0.100 A of current. As a result, the most effective condition in which the cesium moves from the assumed contaminated soil to the adsorbent is selected. The adsorption effect is evaluated through the comparison of the cesium extraction ratio in the case of presence or absence of the adsorbent. In this stage, the difference of the cesium extraction ratio between two cases of gives us the adsorption performance of absorbent for cesium.

As can be seen from Fig. 12, it is confirmed that a certain amount of cesium is adsorbed to the zeolite which is employed as an absorbent in this study at 0.015 A or more of current. The cesium is considered to be unmoving because 0.010 A or less of current is not enough or the cesium to move. Compared Fig. 11 to Fig. 12, it is found that extraction ratio of cesium is decreased by carrying on the electrophoresis test. This is thought that the cesium which is not fixed moves to the frayed edge of vermiculite by current application.

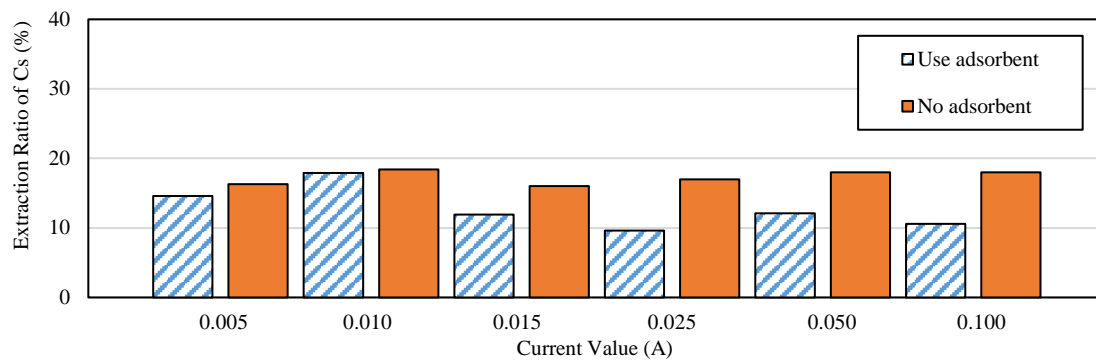


Fig. 12 Cesium extraction ratio (adsorbent: zeolite) in vermiculite mixed sand for 48 hours electricity test.

CONCLUSIONS

The decomposed granite used in our previous studies was heterogeneous in particle size, and there was variability in the result of cesium extraction for each test. The vermiculite which exists a lot in Fukushima soil fixes cesium and causes the removal of cesium from the soil difficult. Therefore, in this study, the vermiculite is employed as an assumed contaminated soil. The aim of this study is to examine the possibility of decontamination of contaminated soil in a flexible control bag through the extraction of cesium test and electrophoresis test with thinking much of reproducible conditions.

First, in order to investigate the cesium adsorption ability of vermiculite used in this study as an assumed contaminated soil, the extraction test in which some size of vermiculite particle are used is conducted under various conditions. The distilled water and ammonium acetate aqueous solution are utilized as an extraction solution to extract cesium from the vermiculite. As a result, it is found that the smaller the particle size is, the more the cesium is absorbed in the vermiculite due to the larger surface area of the particle. In the extraction of cesium test with using 0.7 mm of vermiculite particle size and the distilled water, it is found that the extraction ratio is about 20% without the curing period and about 10% under the curing. Furthermore, it is clarified that extraction of cesium with the distilled water is difficult. However, using an aqueous solution of ammonium acetate as an extraction solution, the extraction ratio of cesium in the case of 0.7 mm of the vermiculite particle size is about 30% without respect to the curing period of an assumed contaminated soil after adding cesium into it. Therefore, it is confirmed that more cesium can be extracted by using ammonium acetate aqueous solution even if the curing period is provided.

Based on the above test results, the cesium extraction test on mixed soil of vermiculite and Toyoura standard sand is conducted. In this test, the extraction of cesium from the assumed contaminated soil with using 0.7 mm of vermiculite particle size is examined. From the tests, it is found that the

extraction ratio of cesium decreases as the mixing ratio of vermiculite is higher.

In the electrophoresis test, it is turned out that a certain amount of cesium is adsorbed to the zeolite which is employed as an adsorbent in this study at 0.015 A or more of current. In addition, it is also confirmed that extraction ratio of cesium declines by carrying out energization. However, there is no need to remove all the cesium from the contaminated soil, so we need to consider how much cesium should be adsorbed by an adsorbent like zeolite. As for future tasks, the containers assuming actual flexible container bags will be prepared and the electrophoresis test is conducted to investigate the amount of adsorption of cesium which is added into the soil in the container.

REFERENCE

- [1] Ministry of the Environment, "Unified basic data on health effects such as radiation", 2014, pp. 32.
- [2] Mukai H, Hatta T, Kitazawa H, et al, "Speciation of Radioactive Soil Particles in the Fukushima Contaminated Area by IP Autoradiography and Microanalyses", *Environmental Science & Technology*, Vol. 48, No. 22, 2014, pp.13053-13059.
- [3] Ministry of the Environment, "The basic concept of the safe use of recycled materials of the removed soil", 2016, pp.1-8.
- [4] Tokyo Sangyo Co., Ltd, "Decontamination and reduction system of radioactive substances", 2014, pp.2-10.
- [5] Ministry of the Environment, "About efforts of technology demonstration projects such as decontamination and volume reduction", 2016, pp.1-7.
- [6] Atsushi Nakao, Noriko Yamaguchi, "Movement of radioactive substance in soil", *Soil fertilizer compilation*, No.23, 2011, pp.85-93.
- [7] Hidenori Yoshida, et al, "Fundamental study on extraction of cesium from soil", *Environmental Geotechnical Engineering Symposium paper*, Vol.11, 2015, pp.453-460.

THE ORIGIN OF GROUNDWATER IN THE KIONOKAWA RIVER CATCHMENT

Hiroki Kitagawa¹, Takuma Kubohara² and Hiroyuki Ii³

^{1,2}Graduate school of Systems Engineering, Wakayama University, Japan

³Faculty of Systems Engineering, Wakayama University, Japan

ABSTRACT

The origin for the shallow and deep groundwater in the Kinokawa River catchment was studied by measuring the depth, water temperature, dissolved ions, and oxygen and hydrogen isotope ratios. $\delta^{18}\text{O}$ and δD values of shallow groundwater are on the meteoric line and thought to derive from precipitation.

The deep groundwater can be divided into two types, high $\delta^{18}\text{O}$ groundwater and low $\delta^{18}\text{O}$ groundwater. Na^+ and Cl^- for high $\delta^{18}\text{O}$ groundwater is similar to modern seawater, however its $\delta^{18}\text{O}$ is between metamorphic fluid and precipitation. Therefore high $\delta^{18}\text{O}$ groundwater is thought to be metamorphic water. Na^+/Cl^- for low $\delta^{18}\text{O}$ groundwater is between the Kinokawa River water and metamorphic water. $\text{Ca}^{2+}/\text{Cl}^-$ and $\text{HCO}_3^-/\text{Cl}^-$ values for low $\delta^{18}\text{O}$ groundwater is also between the Kinokawa River water and metamorphic water. Therefore low $\delta^{18}\text{O}$ groundwater is mixture of precipitation and metamorphic water. High Ca^{2+} concentration deep groundwater is mixture of precipitation and metamorphic water in calcium rich rocks.

Keywords: groundwater, dissolved ions, the stable oxygen and hydrogen isotope ratios, metamorphic water

INTRODUCTION

Groundwater is widely used for agriculture, industry or domestic water all over the world and then its stable use is necessary to conserve source of groundwater and to determine origin of groundwater. Precipitation is a main source for groundwater. However seawater is also a main source of groundwater beside the sea. In recent years the origin for saline hot spring water is studied and its origin is thought not to be precipitation or modern seawater but to be metamorphic dehydrated fluid [1], [2].

The stable oxygen and hydrogen isotope ratios are useful tracers for clarifying the origin for groundwater. Generally oxygen and hydrogen isotope ratios are expressed $\delta^{18}\text{O}$ and δD . They are presented as per mil (‰) of the standard average seawater (SMOW: Standard Mean Ocean Water). The formulas are shown in equation (1) and (2). $\delta^{18}\text{O}$ and δD of SMOW are denoted as (D/H)SMOW, ($^{18}\text{O}/^{16}\text{O}$)SMOW and δD and $\delta^{18}\text{O}$ of the sample are denoted as (D/H)Sample, ($^{18}\text{O}/^{16}\text{O}$)Sample. Measurement error of δD is $\pm 1.0\text{‰}$ and measurement error of $\delta^{18}\text{O}$ is $\pm 0.1\text{‰}$.

$$\delta\text{D} = [(D/H)\text{Sample}/(D/H)\text{SMOW}-1]\times 1000: \quad (1)$$

$$\delta^{18}\text{O} = [(^{18}\text{O}/^{16}\text{O})\text{Sample}/(^{18}\text{O}/^{16}\text{O})\text{SMOW}-1]\times 1000: \quad (2)$$

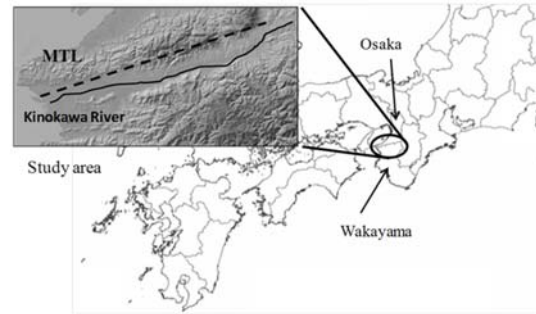


Fig.1 Location of study area.

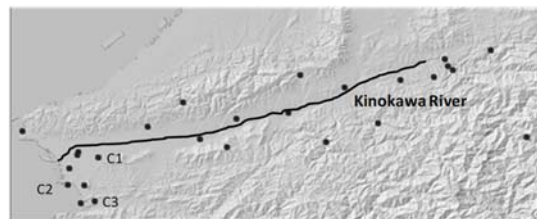


Fig.2 Location map showing Shallow groundwater in the Kinokawa River catchment.

In early period of those studies, one of the important characteristics of meteoric water was found by Craig (1961). Generally $\delta^{18}\text{O}$ and δD values in rain water are located in the vicinity of the meteoric line of equation (3) [3].

$$\delta\text{D} = 8 \delta^{18}\text{O} + 10: \quad (3)$$

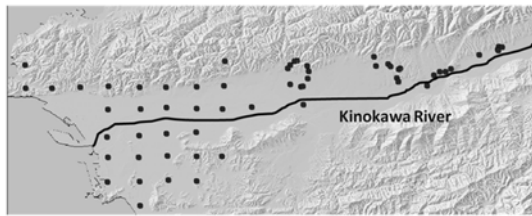


Fig.3 Location map showing deep groundwater in the Kinokawa River catchment.

STUDY AREA

Fig.1 shows the study area. The Kinokawa River, approximately 136 km, flows from east to west in the area. The river flow rate is estimated to be 37.4 m³/s on average [4]. The Median Tectonic Line (MTL) is at the north end of Wakayama prefecture. There are sedimentary rocks and Sambagawa metamorphic rocks under the Kinokawa River catchment. Sedimentary rocks are from 0 m to 600 m in depth, Sambagawa metamorphic rocks are lower than 600 m in the ground [5].

METHOD

Water samples were taken from the Kinokawa River, shallow wells and deep wells (hot spring wells). Sampling was performed from April 2012 to November 2016. The concentrations of Na⁺, Ca²⁺, Mg²⁺, Cl⁻, NO₃⁻ and SO₄²⁻ for the sampled water were measured by ion exchange chromatography. The concentration of HCO₃⁻ for the sampled water was measured by TOC analyzer. Stable hydrogen and oxygen isotopic ratios were measured by mass spectrometer (Sercon Geo Wet System) with dual inlet and equilibrium with CO₂ and H₂ gas method.

RESULT

All groundwater samples were taken from wells in the Kinokawa River basin. The depth range of wells is from 5 m to 1500 m, so groundwater can be divided into two types, shallow groundwater from 5m to 100m in depth shown in Fig.2 and deep groundwater from 100 m to 1500 m in depth shown in Fig.3.

Isotope

Isotope values of shallow groundwater and Kinokawa River water are on the meteoric line in Fig.4. Generally precipitation isotopic values are on the meteoric line. Therefore shallow groundwater is thought to derive from precipitation.

As shown in Fig.5, there are two types of deep groundwater, high $\delta^{18}\text{O}$ (0 ~ 6 ‰) and low $\delta^{18}\text{O}$ (-10

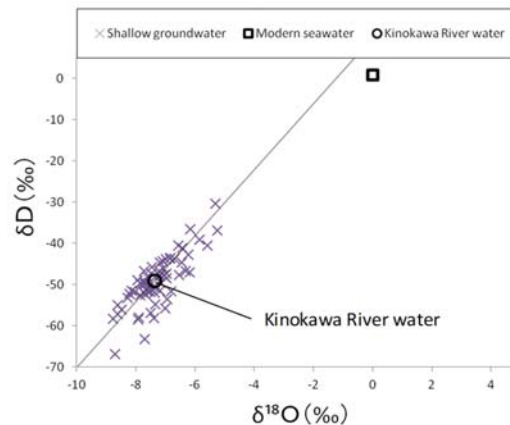


Fig.4 Relationship between $\delta^{18}\text{O}$ and δD for shallow groundwater.

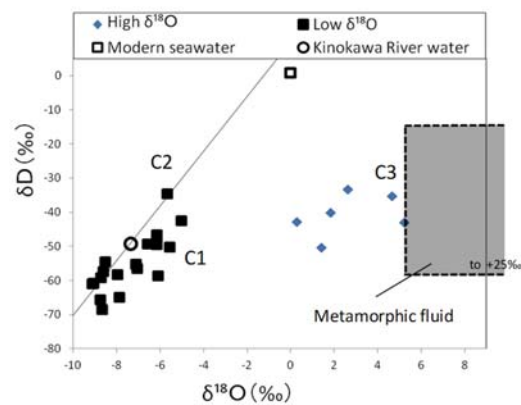


Fig.5 Relationship between $\delta^{18}\text{O}$ and δD for deep groundwater.

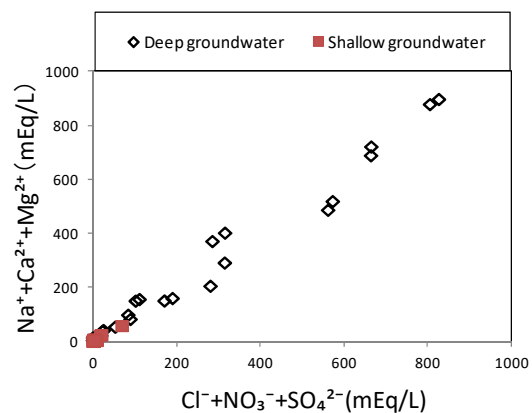


Fig.6 Relationship between anion and cation concentration.

~ -4 ‰). Groundwater with low $\delta^{18}\text{O}$ is close to the meteoric line and groundwater with high $\delta^{18}\text{O}$ is between the meteoric line and the metamorphic fluid. $\delta^{18}\text{O}$ value for the metamorphic fluid is from 5 ‰ to 25 ‰ [6].

Generally $\delta^{18}\text{O}$ values of rocks are higher than those of precipitation and seawater. If water reacts with rocks for a long term under high temperature condition, $\delta^{18}\text{O}$ values of groundwater increase because original silicate mineral contains high $\delta^{18}\text{O}$ values. On the other hand, groundwater with high δD values selectively reacts with rocks and clay mineral is produced and then δD values of residual water decreases [6]. Metamorphic rocks are distributed under the Kinokawa River basin. It is thought that seawater in marine sediments goes into underground with sediments and water squeezed from sea sediments is fossil seawater and furthermore under both high temperature and high pressure condition it becomes metamorphic fluid.

Chemical

Fig.6 shows anion concentration (Cl^- , NO_3^- , SO_4^{2-}) and cation concentration (Na^+ , Ca^{2+} and Mg^{2+}) of shallow groundwater and deep groundwater. Cation and anion values for deep groundwater are high and its shallow groundwater values are low.

If groundwater mixes with seawater or reacts with rocks for a long term, dissolved substances in groundwater increase. However all samples values for shallow groundwater are low, moreover as shown in Fig.4 these isotope values are on the meteoric line, therefore these are thought to derive from precipitation.

Fig.7 shows relationship between Na^+ and Ca^{2+} . Na^+ concentration of high $\delta^{18}\text{O}$ groundwater is higher than 300 mEq. C1, C2, C3 are high Ca^{2+} concentration groundwater (Ca^{2+} concentration are more than 100 mEq).

Low $\delta^{18}\text{O}$ groundwater has two types, high Na^+ concentration groundwater and high Ca^{2+} concentration groundwater. The origin for high Na^+ concentration groundwater is thought to be two things, one is mixture of precipitation and modern seawater or high $\delta^{18}\text{O}$ groundwater, the other one is reaction with rocks.

Fig.8 shows relationship between Na^+/Cl^- ratio and Cl^- concentration. Na^+/Cl^- ratio of modern seawater is 0.9 and that of the Kinokawa river water is 3.2. Na^+/Cl^- ratio of high $\delta^{18}\text{O}$ groundwater is similar to its modern seawater. However as shown in Fig.5 high $\delta^{18}\text{O}$ groundwater is different from modern seawater. Low $\delta^{18}\text{O}$ groundwater is between the Kinokawa River water and modern seawater or high $\delta^{18}\text{O}$ groundwater. Generally Cl^- concentration for groundwater doesn't increase with depth unless seawater is mixed or groundwater reacts with rock salt. However there is no rock salt in Japan. Therefore it is thought that low $\delta^{18}\text{O}$ groundwater is mixture of modern seawater or high $\delta^{18}\text{O}$ groundwater and precipitation. However as shown in

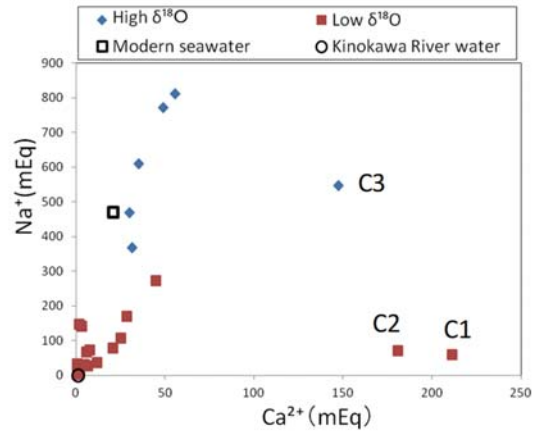


Fig7 Relationship between Ca^{2+} concentration and Na^+ concentration for deep groundwater.

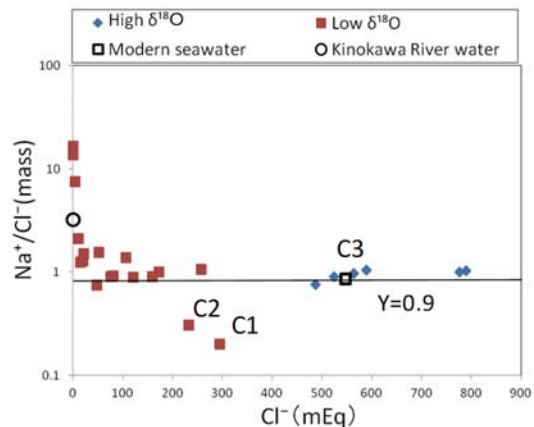


Fig.8 Relationship between $\text{Na}^+/\text{Ca}^{2+}$ and Cl^- concentration for deep groundwater.

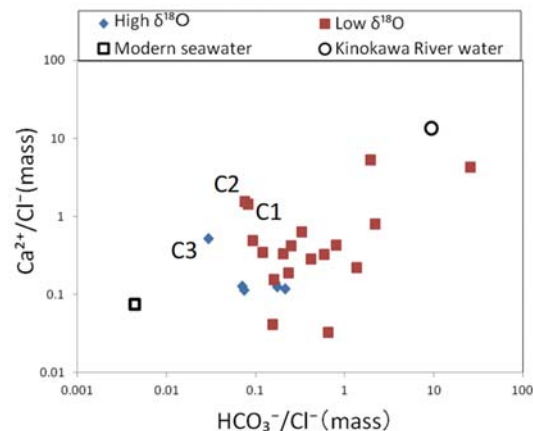


Fig.9 Relationship $\text{HCO}_3^-/\text{Cl}^-$ and $\text{Ca}^{2+}/\text{Cl}^-$ for deep groundwater.

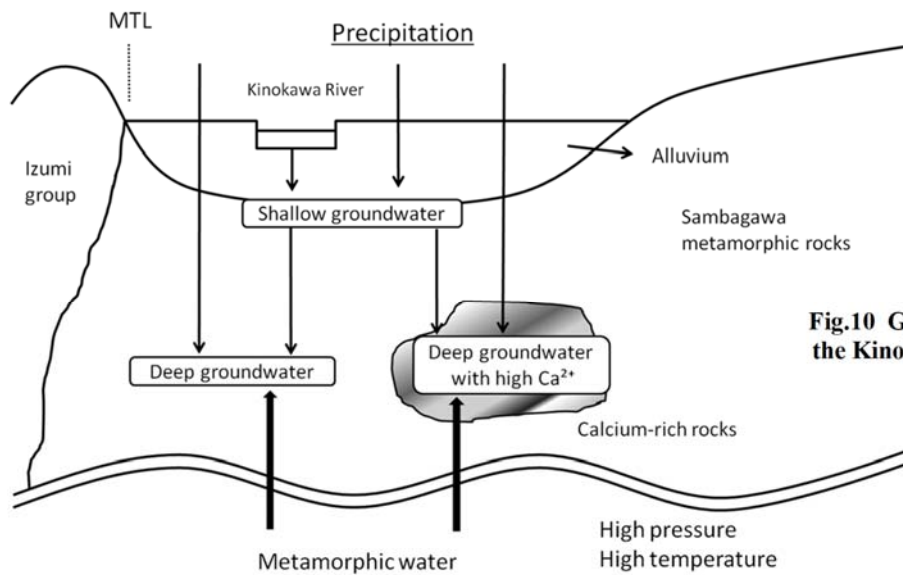


Fig.10 Groundwater flow under the Kinokawa River Catchment

Fig.5, δD values don't change, so low $\delta^{18}O$ groundwater is not mixed with modern seawater.

Fig.9 shows relationship Ca^{2+}/Cl^{-} ratio and HCO_3^{-}/Cl^{-} ratio. In the deep groundwater a decomposition of inorganic matter causes to increase HCO_3^{-} concentrations and pH of the water is getting low, therefore Na^{+} or Ca^{2+} in rocks are dissolved into groundwater.

Ca^{2+}/Cl^{-} values and HCO_3^{-}/Cl^{-} values of high $\delta^{18}O$ groundwater are higher than those of modern seawater, namely high $\delta^{18}O$ groundwater is thought to be in the deep ground. This result indicates that high $\delta^{18}O$ groundwater is metamorphic water. And low $\delta^{18}O$ groundwater is between the Kinokawa River water and high $\delta^{18}O$ groundwater. Therefore low $\delta^{18}O$ groundwater is thought to be mixture of precipitation and metamorphic water.

C1, C2 and C3 are high Ca^{2+} concentration groundwater. As shown in Fig.5, C1 and C2 are on the meteoric line. However they are on the right side for Kinokawa River water in Fig.5. Therefore they are thought to be mixture of precipitation and metamorphic water or modern seawater, and then they are influenced by calcium rich rocks.

CONCLUSION

Fig.10 shows groundwater flow under the Kinokawa River catchment. There are mainly two types of origin for groundwater in the Kinokawa River catchment. One is shallow groundwater derived from precipitation because these isotope values are on the meteoric line and total dissolved substances are low. The other one is metamorphic water because those isotope values are different from seawater and between precipitation and metamorphism. Moreover Relationship between

Ca^{2+}/Cl^{-} and HCO_3^{-}/Cl^{-} shows the difference of between modern seawater and metamorphic water. Beside sea there is high Ca^{2+} concentration deep groundwater. They are the mixture of precipitation and modern seawater or metamorphic water. Also they are influenced by calcium rich rocks.

REFERENCES

- [1] Ohsawa S, Amita K, Oue K, Sakai T and Mishima, T, "Hypersaline hot-spring water with similar hydrochemical facies but different isotopic characteristics from Arima-type Thermal water-Yokawa hot spring, Hyogo prefecture, Japan", J. of Hot Spring Science, 2015, Vol. 64, pp. 369-379.
- [2] Amita K, Ohsawa S, Nishimura K, Yamada, M, Mishima T, Kazahara K, Morikawa N and Hirajima T, "Origin of saline waters distributed along the Median Tectonic Line in south-west Japan: Hydrogeochemical investigation on possibility of derivation of metamorphic dehydrated fluid from subducting oceanic plate", Japanese Association of Hydrological Sciences, 2014, Vol. 44, pp17-38.
- [3] Yamashita M and Ii H "Estimation of evaporation rate of surface water using hydrogen and oxygen isotopic ratios" Int. J. of GEOMATE, Oct., 2016, Vol. 11, Issue 26, pp. 2659-2664.
- [4] Ministry of Land, Infrastructure, Transport and Tourism Kinki Regional Development Bureau <https://www.kkr.mlit.go.jp/river/kasen/kinokawa.html>
- [5] Mizuno K, Tsukuda E, Takahashi, M, Momohara T and Uchiyama T, "Subsurface

geology of the Wakayama Plain, southwestern Japan based on the deep boring survey”, J. of Geology Society of Japan, Vol. 105, March 1999, No.3, pp. 235-238.

- [6] Auther Hugh Richard Rollinson, Using Geochemical Data: Evaporation, Presentation, Interpretation Longman Scientific & Technical. Routledge, 1993.
- [7] Cerling T.E, Pederson BL, Von Damm K.L, “Sodium-calcium ion exchange in the weathering of shales. Implications for global weathering budgets” Geology, Vol. 17, 1989, pp. 522-554.

STUDY ON THE REMOVAL METHOD FOR CESIUM IN SOIL OF SLOPE

Keiichiro Shibata¹, Hidenori Yoshida² and Naomichi Matsumoto³

¹Graduate school of engineering, Kagawa University, Japan, ^{2,3}Faculty of engineering, Kagawa University, Japan

ABSTRACT

Various radioactive materials were spread by the accident at Fukushima Daiichi nuclear power station of Tokyo electric power company. Though 6 years passed since the accident, the decontamination of difficult-to-return zone is not in prospect. The reason why the decontamination has not carried on is the geographic factor around the zone. In particular, there is a lot of forestry area around the zone, and radioactive cesium has been accumulated by a rainfall and a wind all the time from forestry area since the accident. In this way, re-pollution is a serious concern even if the level ground was decontaminated. It is necessary for decontamination of the slope that is the supply source of radioactive cesium from the forestry area to a residential area or farmland. Thus, in this study, the simple decontamination method using running water was proposed to solve the decontamination of forestry area. This method has the characteristics that the vermiculite strongly fixes the radioactive cesium and the decontamination site is a slope. In particular, four different experiments; one utilizes only cesium, one does the standard sand, one does the vermiculite and the other does their combination, were conducted. As a result, it is confirmed that it's possible to reduce by 20% of the volume of contaminated soil because of removal of vermiculites. Since the vermiculite is lighter weight than the sand and water, it is easy to remove only vermiculite from the water. Removal of vermiculite using this method leads to volume reduction of the contaminated soil.

Keywords: radioactive cesium, contaminated soil, decontamination method, slope, vermiculite

INTRODUCTION

The Great East Japan Earthquake which is the most powerful earthquake on record occurred in Sanriku offshore on March 11, 2011. The Fukushima Daiichi nuclear energy plant of the Tokyo Electric Power Company (1F) was hit by the great Tsunami several times after an hour of the earthquake. The power facilities were widely destroyed, and the basement room and the shaft were inundated with the Tsunami. Major quantity of radioactive materials were discharged from the 1F for all of mentioned backgrounds. The radioactive materials is spread to atmosphere, which is fallen down mountain, river and marine by rain breeze. Especially, the radioactive cesium is detected in Tokyo Bay far away. Also, the radioactive materials that have fallen into the mountains are firmly bonded to the clay foods in the soil. Especially, the cesium-137 is extensively detected in Fukushima prefecture because the cesium-137 is vigorously discharged and long half period. The influence is strongly shown around the 1F, and the 12 of municipalities in Fukushima prefecture is designated the evacuation zone still (see Fig. 1). Fig. 1 is developed based on the data by the Reconstruction Agency as in [1]. Okuma town where the 1F is located is designated the difficult to return zone of all municipalities. In Okuma town, the current air dose is lower than the air dose at the time with decreasing of cesium-134 (the half period is two years). However, the cesium-137 continuously emit

the radioactivity because the half period of cesium-137 is about thirty years. Therefore, it is considered to be difficult to decrease the radiation dose. The specific plans in the evacuation zone isn't currently devised regardless of decreasing of radiation dose can't expect. For example, the interim storage facilities are built in the Okuma in order to store the flexible container bag in which the contaminated soil is filled. The amount of contaminated soil estimated to 16~20 million cubic meter, and the securement of interim storage facilities where the contaminated soil is stored is difficult. Therefore, the volume reduction of the contaminated soil is urgent business. Alternatively, the contaminated area is dominated by the mountains and village forest. Even if the radioactive cesium of flatland is removed, the clay particle including the radioactive cesium continues to be carried from the village forest by wind or rain. Thus the re-contamination is concerned by the radioactive cesium. In this way, the slope of the mountainous area is a supply route of the radioactive cesium from the forest area to residential areas and agricultural lands as in [2].

Therefore, it is necessary to remove the radioactive cesium in the soil on the slope and reduce the collected contaminated soil. Previous study is conducted by the faculty of engineering, Ibaraki University in order to settle this problem, and it has two feature as in [3].

1. The bentonite is spread onto the leaf mold in the forest so as to control the resorption of the radioactive cesium to plants.
2. The moving of the bentonite including the radioactive cesium is controlled by polyion-complex (PIC) of excess positive charge and negative charge.

The radioactive cesium in the air and solution is adsorbed into the bentonite. The resorption to the plant is controlled by the adsorption performance of the bentonite. Alternatively, the forestry ecosystem is not destroyed because the elements such as the flow of rainwater is used in this method. Furthermore, the PIC is a harmless because the raw material of PIC is mundanely used as the thickener of ice-cream as in [4]. The moving of cesium is controlled, but the contaminated soil is not reduced in this method. Besides, it takes time to complete the work due to using the rainfall. Thus, in this study, the simple decontamination method is proposed in order to decontaminate the contaminated soil on the slope by flowing water. The surface soil including a lot of cesium [5] is collected in this method, and the method is suitable for the feature of soil in the Fukushima. The cesium is easy to be adsorbed into the vermiculite which is eccentrically distributed in the soil of Fukushima. The specific weight of vermiculite is very small, and the vermiculite floats on water. Consequently, the vermiculite can be separated from the washed soil. Alternatively, both the decontamination and volume reduction of contaminated soil are conducted because the cesium which is not contained in the vermiculite can be washed and collected. In this study, the reproducible slope test in which the Toyoura standard sand and vermiculite are utilized is conducted to examine the usability of proposed method.

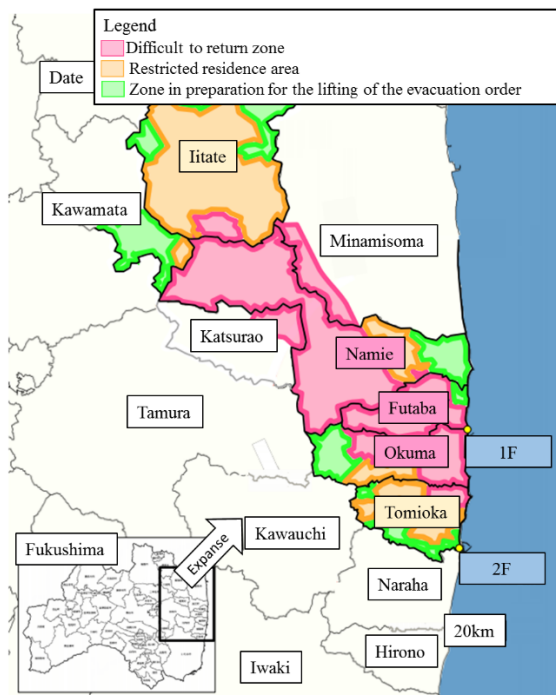


Fig. 1 Conceptual diagram in areas under evacuation orders as in [1]

CESIUM IN THE SOIL

The large amount of radioactive materials was released by the accident in the 1F. Table 1 is the main total amount of the discharged radioactive materials in large quantities and its half-life. Table 1 is developed based on the date by Ministry of Economy as in [6]. Especially, the radioactive cesium has harmful influences for a long-term because its half-life is very long. The volume of spreading of strontium-90 is comparatively small, though the half-life of strontium-90 is long. The cesium exists as the monovalent cation in the soil, and it is adsorbed into the soil particle having a negative charge. Especially, the cesium is selectively adsorbed into the small clay particle. The cesium is adhered to the soil due to the 2:1 types of lamellar silicate. When the part of silicon or aluminum substitute for another element having a few positive charge in the silicon tetrahedron sheet or aluminum octahedron sheet, the negative charge is expressed with the shortage of positive charge in the sheet. Moreover, the cation is adsorbed in order to neutralize the intercalation. The charge in this intercalation shows a high selectivity for the cesium ion. That is because the six-membered ring is nearly equal to the ion radius of the cesium ion in the basal seat of the silicon tetrahedron sheet. Alternatively, the bounding strength with the six-membered ring becomes larger as the hydration energy is smaller, and the bounding strength of cesium ion is the highest. Generally, the six-membered ring is occupied by the potassium ion because the abundance of potassium ion predominantly is major in the soil (see Fig. 2). The terminal of layer in the clay mineral is swelled by the disintegration, and the potassium ion is discharged. Thus, the empty space that another cation gains entry is formed. This space is called the frayed edge (see Fig. 3), and the extraction of cesium ion from the frayed edge is very difficult. It is almost impossible to extract the cesium in the frayed edge only by flowing water.

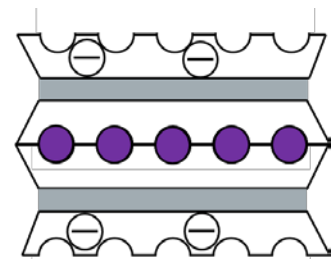


Fig. 2 2:1 types of lamellar silicate

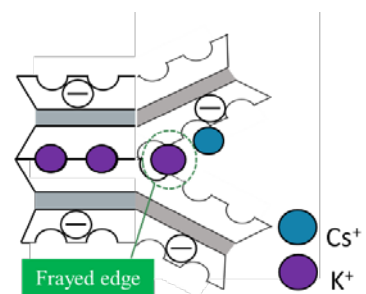


Fig. 3 Frayed edge

Thus, in this study, it is considered that the contaminated surface soil can be collected with the flowing water by utilizing the strong fixation.

Table 1 Compendium of the discharged radioactive materials

Nuclide	Half-life (day)	Total discharge (Bq)
Xe-133	5.2	1.1×10^{19}
Cs-134	766.5	1.8×10^{15}
Cs-137	10950.0	1.5×10^{16}
Sr-90	10621.5	1.4×10^{14}
Ba-140	12.7	3.2×10^{15}
Te-132	3.3	8.8×10^{16}
I-131	8.0	1.6×10^{17}
Sb-127	3.9	6.4×10^{15}

MOCK CONTAMINATED SOIL

In this study, the Toyoura standard sand, vermiculite or their mixed sand is used as the mock contaminated soil that the cesium is added. The Toyoura standard sand consists of uniform size of soil grain (see Fig. 4). Moreover, it is very smooth, and the soil grains hardly stick each other. Therefore, the difference between experimental samples can be neglected under the same condition, and the reproducibility of experiments are secured. The vermiculite is the silicate mineral that mainly consists of the oxidized silicon, magnesia and aluminum oxide. The vermiculite expands with high-temperature heating. The vermiculite has a high adsorption performance for cesium, and the mechanism of adsorption has been clarified as in [7]. The vermiculite is widely distributed to Fukushima soil, and the vermiculite constitutes barriers to the decontamination of cesium from a soil. In this study, the vermiculites of three grain size are used so as to examine the influence of different size of the grain on the adsorption of vermiculites. The actual soil consists of not only vermiculite but also the various minerals whose characterizations are different each other. The actual soil environment is different from the artificial one when the mock contaminated soil consists of only the vermiculite. Therefore, the Toyoura standard sand and the vermiculite are mixed as the mock contaminated soil and the mixed soil is used in the experiments.



Fig. 4 Toyoura standard sand (upper left), vermiculite of 0.7mm (upper right), 1.0mm (lower left), 2.0mm (lower right)

TEST AND ANALYSIS METHOD

In order to imitate the real behavior of cesium in the soil of slope, the slope device is produced (see Fig. 5). The slope device is consisted with two equipment: one is the slope section and another is the flowing water section. A 3D printer is used to produce the slope section (20.0 cm x 20.0 cm x 6.5 cm). 8.0 mm in diameter of drain is set at the bottom of slope section in order to collect the water and soil which contains cesium. The flowing water section is made by connecting the porous rubber hose to the water pump with a tube.

The experiment and analysis methods are explained below in detail. First, the cesium chloride is added to the assumed soil, and the assumed soil is set on the slope of the device. Secondly, the pure water is disembogued from the porous hose set on top of slope until the assumed soil is completely done away from the slope. Finally, both pure water and soil are collected, and the cesium concentration is analyzed by an AAS (Atomic Absorption Spectrometer). The sample must be in a liquid state when the sample is analyzed by the AAS. Therefore, it is necessary to wash out the cesium in the soil after the test. As the washing out method, 200.0 mL of pure water is soured for the collected soil, and the sample is screwed with 300 rpm for the 10 minutes by the stirrer. After that, the solid-liquid separation is conducted four times with 38 μ m of sieve size. The extracted volume of cesium contained in both the solution and the soil after the test is quantitated for each filtrate by the AAS. Alternatively, in this study, all of the tests are conducted three times under the same conditions to ensure repeatability.



Fig. 5 Slope device

PRELIMINARY TEST

The three preliminary tests are conducted as the previous step of slope test. One is the test in which only cesium is flushed out, another is the test in which only standard sand is flushed out, and the other is the test in which only vermiculite is flushed out. As

discussed later, the methods and results of each test are explained in detail.

Cesium flush test

It is necessary to confirm whether added cesium remains or not on the slope after flushing and all cesium can be recovered or not in order to verify the accurate extraction amount of cesium. To begin with, 0.1 mL of cesium chloride solution is added onto the slope and flushed out with pouring 100.0 mL of pure water over the slope. The amount of cesium in the recovered solution is analyzed by the AAS after the cesium is flushed out. The addition amount of cesium is 100.0 μg (1 mg/mL). The extraction amount of cesium in the test is shown in Fig. 6. From the figure, an average 102.3 μg of cesium is detected. It can be said that all cesium is flushed out from the addition amount of cesium. Consequently, it is confirmed that all cesium can be flushed out the slope in this method.

Standard sand flush test

The assumed contaminated soil that mixes with the standard sand and the vermiculite are employed in the slope test discussed in the next section. In this subsection, the flush tests for the standard sand and the vermiculite are conducted in order to ascertain their adsorption properties of cesium. As for the standard sand, 5.0 g and 15.0 g of specimens are prepared. The pure water is poured over the slope until the standard sand in which 0.1 mL of cesium chloride solution is added is completely flushed out. The extraction amount of cesium in the solution is analyzed after collection and stirring by stirrer.

First, the extraction amount of cesium from 5.0 g of standard sand is shown in Fig. 7. The extraction amount of cesium after flushing is an average 21.32 μg , and about twenty percent of cesium is extracted against the addition amount. In addition, an average 35.6 μg of cesium is detected from the solution after stirring, and more than fifty percent is extracted from 5.0 g of standard sand. Secondly, the extraction amount of cesium from 15.0 g of standard sand is

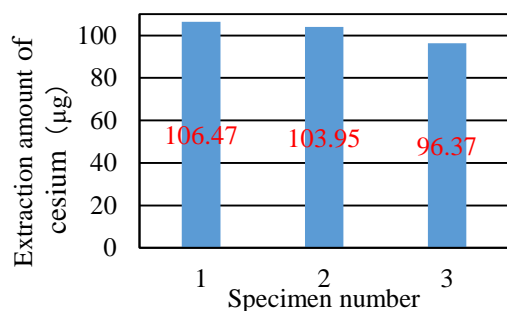


Fig. 6 Extraction amount of cesium in cesium flush test

shown in Fig. 8. An average 25.8 μg of cesium is detected from the solution after flushing. This result is more or less same as that of the test using 5.0 g of standard sand. On the other hand, an average 46.9 μg of cesium is detected from the solution after stirring of the recovered sand and the extraction amount is higher than that of the test using 5.0 g of standard sand. It is confirmed that more than seventy percent of cesium can be extracted from the recovered solution and sand in the test using 15.0 g of standard sand, and the extraction amount in the test using 15.0 g of standard sand is slightly larger than that in the test using 5.0 g of standard sand. When an amount of sample is too small, the sample may accumulate on the bottom of the container and stirring may not be performed well. Therefore, the wash away of recovered sand is not enough in the case of a small amount of the sand. In the future, additional provisions such as the increase of rotation speed of stirring are required.

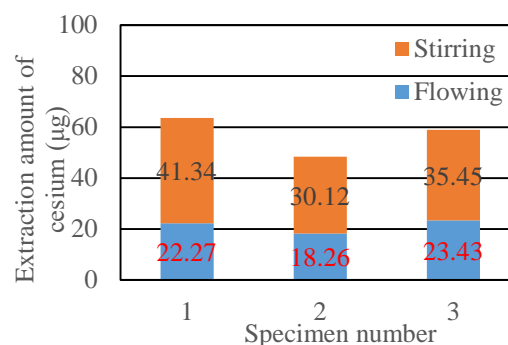


Fig. 7 Extraction amount of cesium in standard sand flush test (5.00g)

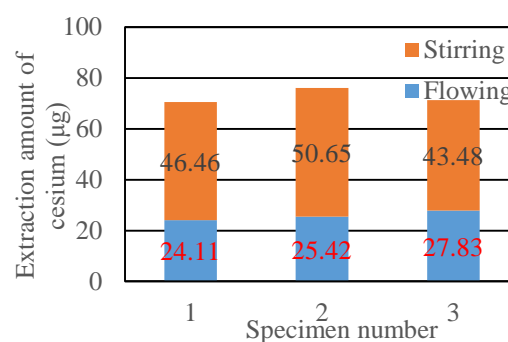


Fig. 8 Extraction amount of cesium in standard sand flush test (15.00g)

Vermiculite flush test

1.0 g of the vermiculite whose particle size is 0.7 mm, 1.0 mm or 2.0 mm is set on the slope and 0.1 mL of cesium chloride solution is added into the vermiculite. Since it is conceivable that the

vermiculite may consist of various particle sizes in the actual one, three particle size of the mixed vermiculite (hereinafter referred to as Mix) that three particle sizes of vermiculite is prepared. Besides the mass of each vermiculite is set to be more or less same in the test.

The extraction amount of cesium from each particle size of vermiculite is shown in Fig. 9. The extraction amount of cesium is an average 11.0 μg from 0.7 mm of vermiculite, 13.2 μg from 1.0 mm, 14.8 μg from 2.0 mm and 13.2 μg from the Mix. The extraction amount of cesium from the different particle size of vermiculite is more or less same, though it increases in proportion as the increase of the particle size. In addition, it is reconfirmed to be extremely difficult for the vermiculite to extract the cesium compared with the standard sand.

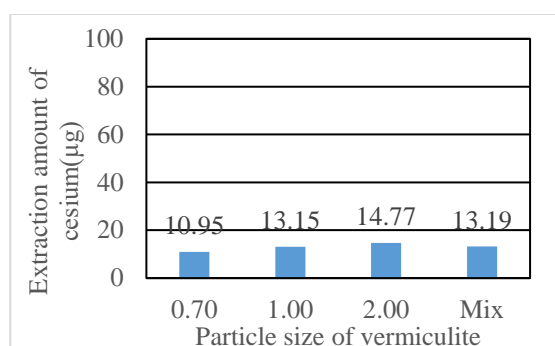


Fig. 9 Extraction amount of cesium in vermiculite flush test

ASSUMED CONTAMINATED SOIL FLUSH TEST

The test which an assumed contaminated soil is flushed out on the slope is conducted in order to make the assumption that the contaminated soil including the cesium on the slope is decontaminated. The assumed contaminated soil is prepared by mixing the standard sand with 1.0 g of the Mix. Besides, three specimens of 10.0 g, 15.0 g and 30.0 g are prepared regard to the standard sand, and each test result is compared.

First, the extraction amount of cesium from the assumed soil using 30.0 g of standard sand is shown in Fig. 10. No more than an average 15.3 μg of cesium is extracted by flushing the soil. By contrast, the total extracted amount of cesium is 46.6 μg on average which is added on the extracted amount from the solution after stirring. There is a same tendency between the test using the MIX and the test using only standard sand.

Secondly, the extraction amount of cesium from the assumed soil using 15.0 g of standard sand is shown in Fig. 11. An average 14.8 μg of cesium is detected from the solution after flushing, and an average 32.1 μg is detected from the solution after

stirring the soil. The total extracted amount is 46.9 μg on average, which is almost same as the extracted amount of the test using 30.0 g of standard sand.

Finally, the extraction amount of cesium from the assumed soil using 10.0 g of standard sand is shown in Fig. 12. The extracted amount of cesium from the solution after flushing and stirring is 55.0 μg on average. In addition, it is confirmed that about fifty percent of cesium is extracted from the assumed soil against 1.0 g of additive cesium regardless of the amount of standard sand. The cesium is extracted from the standard sand, but it is not extracted from the vermiculite. From these results, it is considered that the vermiculite including cesium can be recovered by flushing the contaminated soil out the slope with flowing water and the other cesium can be extracted

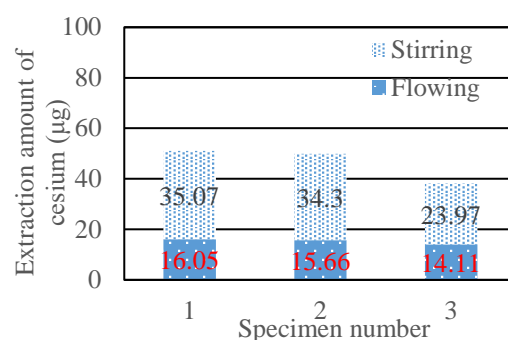


Fig. 10 Extraction amount of cesium from assumed soil using 30.0 g of standard sand

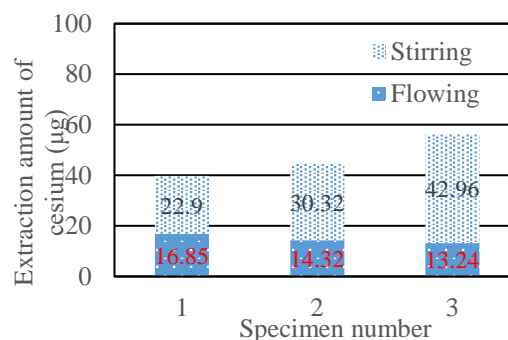


Fig. 11 Extraction amount of cesium from assumed soil using 15.0 g of standard sand

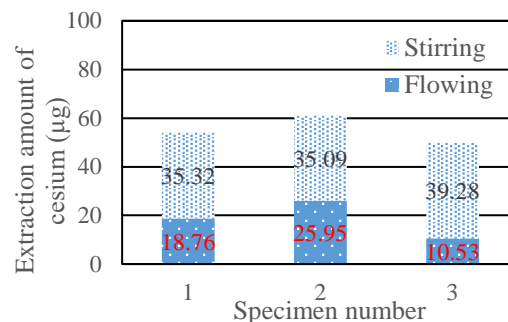


Fig. 12 Extraction amount of cesium from assumed soil using 10.0 g of standard sand

by just flowing the water into the contaminated soil.

CONCLUSIONS

In this study, the simple decontamination method is proposed in order to decontaminate the contaminated soil including cesium on the slope of forest or mountain area, and the flush test on the slope is conducted to examine the performance and availability of the proposed method by which the cesium is recovered from the slope. Specifically, the cesium is added into the assumed contaminated soil in which standard sand and vermiculite are mixed, and the assumed contaminated soil is flushed out the slope by flowing water. Besides, the three preliminary tests are conducted as the previous step of the flushing test of the Mix on the slope. One is the test in which only cesium is flushed out, another is the test in which only standard sand is flushed out, and the other is the test in which only vermiculite is flushed out. In this stage, it is confirmed whether added cesium remains or not on the slope after flushing and all cesium can be recovered or not in order to verify the accurate extraction amount of cesium. From the test results, almost 100.0 % of added cesium is collected by flushing water. In addition, the flushing tests for the standard sand and the vermiculite are conducted in order to examine their adsorption property of cesium. In consequence, approximately 70.0 % of the cesium that added into the standard sand is extracted by flowing water and stirring. Alternatively, three different types of vermiculite which has 0.7 mm, 1.0 mm or 2.0 mm of particle size are used so as to examine the influence of different particle size on the adsorption of cesium. As a result of the test, about 13.0 % of cesium against the added one into the vermiculite is extracted regardless of the particle size of vermiculite. It is confirmed that the extraction of cesium from vermiculite is far hard than that from standard sand.

The flushing test using the assumed contaminated soil is conducted with consideration for the preliminary tests. In the flushing test, the amounts of standard sand are changed and their results are compared. As results, it is confirmed that about fifty percent of cesium against 1.0 g of the additive cesium is extracted from the assumed soil regardless of the amount of standard sand. The cesium can be extracted from the standard sand, but it is not extracted from the vermiculite. From these results, it is considered that the vermiculite including cesium can be recovered by flushing the contaminated soil out the slope with flowing water and the other cesium can be extracted by just flowing the water into the contaminated soil. Furthermore, the vermiculite is easily separated and collected after flushing because the density of vermiculite is lighter than that of water and the vermiculite floats on the water (see Fig. 13). On the other hand, in this study, it is easy to separate the

vermiculite because there are only two constituent substances in the assumed contaminated soil. In near future, it is necessary to verify whether the decontamination by the proposed method is

possible or not for the contaminated soil which consists of various minerals such as the decomposed granite soil.



Fig. 13 Vermiculite floating on the water surface

REFERENCES

- [1] Reconstruction Agency, "Eliminating negative reputation impact –reconstruction from nuclear disaster & the history of safety and revitalization of fukushima-", Aug, 2016, pp. 5-9.
- [2] Ouchi K, "Current measures and challenges on the rehabilitation of radiation-laden farmland and natural land and manmade slopes", *Journal of the Japanese Society of Revegetation Technology* Vol. 38, 2012, No. 2, pp. 282-287
- [3] Ibaraki University, KUMAGAI GUMI CO., LTD. and Japan Atomic energy Agency, "New technology to control the removal of radioactive cesium from forest to living area", May, 2016, pp. 1-4.
- [4] Naganawa H, Kumazawa N, Saitoh H *et al.*, "Removal of Radioactive Cesium from Surface Soils Solidified Using Polyion Complex Rapid Communication for Decontamination Test at Iitate-mura in Fukushima Prefecture," *Transactions of the Atomic Energy Society of Japan*, Vol. 10, 2011, No. 4, pp. 227-234.
- [5] Seki K, "Remediation of Soil Contaminated with Radionuclides Derived from the Fukushima Nuclear Plant Accident", *Journal of business administration of Toyo University*, vol. 78, Nov, 2011, pp. 13-26.
- [6] Ministry of Economy, Trade and Industry, "Evaluation on conduction of reactor of Unit 1, 2 and 3 in The accident of Tokyo Electric Power Company Holdings", 2011, p. 13.
- [7] Motokawa R, Endo H, Yokoyama S *et al.*, "Collective Structural Changes in Vermiculite Clay Suspensions Induced by Cesium Ions", *Scientific Reports (online)*, Vol. 4, Jun, 2014, article number 6585.

NUMERICAL ASSESSMENT OF THE IMPACT OF STRONG WIND ON THERMAL STRATIFICATION IN LAKE BIWA

Jinichi Koue¹, Hikari Shimadera¹, Tomohito Matsuo¹, Akira Kondo¹

¹Graduate School of Engineering, Osaka University, Japan

ABSTRACT

Water temperature near the surface of a lake increases with increasing air temperature, which results in stratification. The strength of stratification substantially influences the transport of dissolved oxygen from the surface to the bottom water of a lake. In recent years, the decrease in dissolved oxygen at the bottom of the northern part of the Lake Biwa, the largest freshwater lake in Japan, has been observed. The main cause of this is considered to be the change in stratification, which depends on weather and climate conditions. In the present study, numerical simulations were carried out to investigate the effect of strong wind on the structure of stratification in Lake Biwa. The baseline simulation was conducted using actual meteorological data, and experimental simulations were conducted using meteorological data with modified wind speed and direction. The numerical experiments showed that if the magnitude of the wind is strong enough, the stratification collapses and the wind can enhance the vertical mixing in the bottom layer even in summer season with strong thermal stratification. In a stratified season, when the strong wind blows predominantly in one direction, the rate of the vertical mixing changes by the wind direction. Moreover, as the duration of the strong wind extends, vertical mixing easily occurs.

Keywords: Strong Wind, Structure of Stratification, Vertical Mixing, Hydrodynamic Model, Lake Biwa

INTRODUCTION

In warm season, water temperature near the surface of a lake increases with increasing air temperature, which results in lake stratification. The thermocline disrupts the transport of substances such as dissolved oxygen between the surface layer and the layer under the thermocline.

In some lakes, a lack of oxygen occurred in the deep layer during a stratified period because of the thermocline [1]. In recent years, the decrease in dissolved oxygen at the bottom of the northern part of Lake Biwa, the largest freshwater lake in Japan, has also been observed. The strength of stratification plays an important role in the varying amounts of dissolved oxygen in the lake. The main cause of the change in the stratification is weather and climate conditions such as air temperature, wind strength, and the precipitation.

Climate change leads to prolonged periods of stratification in lakes [2]. In Lake Zurich, in Switzerland, a continual long term increase in thermal stability resulted in an increase of about 2-3 weeks in the duration of the summer stratification from the 1960s to the 1990s [3]. This impact directly affected the stratification characteristics and mixing processes.

On the other hand, strong typhoons will occur more frequently due to climate change [4], [5]. When strong wind blows, wind stress on the surface layer provokes significant mixing, leading to the weakening of the stratification. Vertical mixing

occurs by strong wind according to the observation.

When wind blows predominantly in one direction, wind driven currents develop in the surface layer and the water in the lower layer proceeds to the opposite direction. Upwelling or downwelling of the water occurs depending on the wind direction toward the coast. In a stratified season, the thermocline oscillates by this movement. This generates internal waves in a stratified lake. Wind driven currents and internal waves were observed by measuring the vertical water temperature and the velocity continuously with using a thermistor chain and an acoustic current profiler [6], [7]. Wind forcing carries the major source of momentum and energy and affects the general circulation in lakes at various scales. However, the processes and the effects of the strong wind on the deep layer remains unclear. Therefore, it is important to understand the effect of the strong wind on the bottom layer in the lake.

In the present study, we investigated the effect of strong wind on stratification in Lake Biwa by using a three dimensional hydrodynamic model. Numerical simulations were carried out for a baseline case using actual meteorological data and experimental cases using meteorological data with modified wind speed and direction.

Hydrodynamic Model in Lake Biwa

Calculation domain

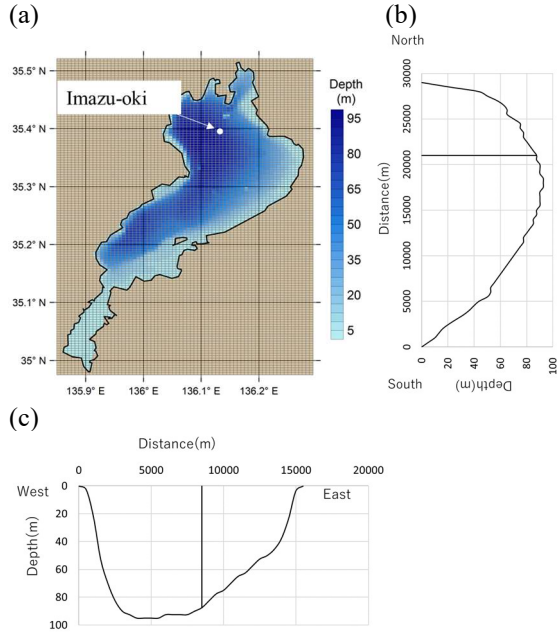


Fig. 1 Calculation domain with topography of Lake Biwa: (a) horizontal domain, (b) south-north and (c) west-east vertical cross sections through Imazu-oki.

This study focused on Lake Biwa, which is the largest freshwater lake in Japan. Fig. 1 shows the calculation domain and water depth in the hydrodynamic model of Lake Biwa. The horizontal domain is $36 \text{ km} \times 65.5 \text{ km}$ with a horizontal resolution of 500 m. The vertical domain consists of 86 layers from the lake surface to the depth of 107.5 m. The vertical grid size is 0.5 m from the surface to the depth of 20 m and gradually increases up to 2.5 m.

Governing equations

The governing equations consist of the momentum equation with Boussinesq approximation, the hydrostatic equation, continuity equation and the conservation equation for temperature. The governing equations are described in the Cartesian coordinate system as follows. The origin of the coordinate axes is in the southwestern edge of the domain on the horizontal plane. The x and y axes are set to west-east and south-north directions, respectively, and the z axis directs upward. Momentum equations (x, y direction) are written by

$$\begin{aligned} \frac{\partial u}{\partial t} + u \frac{\partial u}{\partial x} + v \frac{\partial u}{\partial y} + w \frac{\partial u}{\partial z} - f v = - \frac{1}{\rho_0} \frac{\partial p}{\partial x} \\ + v_h \frac{\partial^2 u}{\partial x^2} + v_h \frac{\partial^2 u}{\partial y^2} + v_z \frac{\partial^2 u}{\partial z^2} - \frac{g}{\rho_0} \frac{\partial \rho}{\partial x} \end{aligned} \quad (1)$$

$$\begin{aligned} \frac{\partial v}{\partial t} + u \frac{\partial v}{\partial x} + v \frac{\partial v}{\partial y} + w \frac{\partial v}{\partial z} + f u = - \frac{1}{\rho_0} \frac{\partial p}{\partial y} \\ + v_h \frac{\partial^2 v}{\partial x^2} + v_h \frac{\partial^2 v}{\partial y^2} + v_z \frac{\partial^2 v}{\partial z^2} - \frac{g}{\rho_0} \frac{\partial \rho}{\partial y} \end{aligned} \quad (2)$$

hydrostatic equation is given by

$$0 = - \frac{1}{\rho_0} \frac{\partial p}{\partial z} - \frac{\rho}{\rho_0} g, \quad (3)$$

continuity Equation is written by

$$\frac{\partial u}{\partial x} + \frac{\partial v}{\partial y} + \frac{\partial w}{\partial z} = 0, \quad (4)$$

conservation equation for temperature is written by

$$\frac{\partial T}{\partial t} + u \frac{\partial T}{\partial x} + v \frac{\partial T}{\partial y} + w \frac{\partial T}{\partial z} = \kappa_h \frac{\partial^2 T}{\partial x^2} + \kappa_h \frac{\partial^2 T}{\partial y^2} + \kappa_z \frac{\partial^2 T}{\partial z^2}, \quad (5)$$

where u , v , and w are the x , y , and z components of current velocity (m s^{-1}), T is the water temperature (K), p is the pressure (N m^{-2}), ρ is the density of water (kg m^{-3}), ρ_0 is the reference density of water ($= 10^3 \text{ kg m}^{-3}$), g is the acceleration due to gravity ($= 9.8 \text{ m s}^{-2}$), f is the Coriolis parameter ($= 8.34 \times 10^{-5} \text{ s}^{-1}$ corresponding to 35°N), v_h is the horizontal eddy viscosity for momentum equations ($= 1.0 \text{ m}^2 \text{ s}^{-1}$ [8]), κ_h is the horizontal eddy diffusivity ($= 1.0 \text{ m}^2 \text{ s}^{-1}$ [8]), v_z is the vertical eddy viscosity ($\text{m}^2 \text{ s}^{-1}$) for momentum equations, κ_z is the vertical eddy diffusivity ($\text{m}^2 \text{ s}^{-1}$).

In summer, a thermocline is typically formed at the depth from 10 m to 30 m. This thermocline suppresses the vertical transport of momentum and heat. To take this effect into account, the parameter values of vertical eddy viscosity and diffusivity are estimated by using Richardson number. Richardson number is a dimensionless number that expresses the ratio of the buoyancy term to the flow gradient term [9] and written by

$$Ri = - \frac{g}{\rho_0} \frac{\frac{\partial \rho}{\partial z}}{\left(\frac{\partial U_w}{\partial z} \right)^2}, \quad (6)$$

where $U_w = \sqrt{u^2 + v^2}$ is the horizontal current velocity (m s^{-1}). Vertical eddy viscosity and diffusivity are respectively given by

$$v_z = \frac{0.0001}{(1.0 + 5.2 Ri)}, \quad (7)$$

and

$$\kappa_z = \frac{0.0001}{\left(1.0 + \frac{10}{3} \times \text{Ri}\right)^{\frac{3}{2}}} \quad (8)$$

Initial conditions

As for the initial condition, the current velocity was set to be 0 m s^{-1} . The initial water temperature on April 1st, 2006 was derived from linear interpolation of observed data on March 20th and April 10th, 2006. The observations were conducted by the Lake Biwa Environmental Research Institute twice a month at the monitoring point Imazu-oki ($35^\circ 23' 41'' \text{ N}$., $136^\circ 07' 57'' \text{ E}$.), the depth of which was 0.5 m, 5 m, 10 m, 15 m, 20 m, 30 m, 40 m, 60 m, 80 m, and about 90 m.

Boundary Conditions

The boundary conditions for the current velocity at the surface of the lake are given by the following formula, taking the wind stress into account.

$$\nu_z \frac{\partial u}{\partial z} = \frac{\tau_x}{\rho_0} \quad (9)$$

$$\nu_z \frac{\partial v}{\partial z} = \frac{\tau_y}{\rho_0}$$

where τ_x and τ_y are the surface wind frictional stresses calculated by

$$\tau_x = \rho_a C_f U_{ax} U_a \quad (10)$$

$$\tau_y = \rho_a C_f U_{ay} U_a, \quad (11)$$

where ρ_a is the density of air (kg m^{-3}), C_f is the wind frictional constant, U_{ax} and U_{ay} are respectively the x and y components of wind velocity (m s^{-1}), U_a is the wind speed from a height of 10 m above the surface (m s^{-1}).

The heat flux through the water surface consists of short-wave solar radiation ($S \downarrow$), latent heat flux (Q_l), sensible heat flux (Q_s) and net long-wave radiation (L_{net}). The heat balance equation on the water surface is given by

$$\rho C_p \kappa_z \frac{\partial T}{\partial z} = S \downarrow + Q_l + Q_s + L_{net} \quad (12)$$

No-slip condition is imposed at the bottom and the side walls. The normal gradients of water temperature are also zero so that there is thermal insulation.

Air temperature, atmospheric pressure, wind direction and speed, and relative humidity over Lake Biwa were derived from the Grid Point Value derived from Meso-Scale Model of Japan Meteorological

Agency (GPV MSM). GPV MSM data have a spatial resolution of 0.0625° (longitude) \times 0.05° (latitude) (approximately 5 km) and a temporal resolution of an hour. The data were horizontally interpolated into each surface mesh of the hydrodynamic model.

Solar radiation was derived from hourly observation data at Hikone local meteorological observatory ($35^\circ 16' 30'' \text{ N}$., $136^\circ 14' 36'' \text{ E}$.). Solar radiation was assumed to be horizontally uniform over the lake.

The boundary conditions for the water volume and temperature associated with inflow from each river and outflow from the lake were calculated by the hydrological model [10].

Simulation cases

The baseline simulation was conducted using actual meteorological data for a period from April 1st, 2006 to March 31st, 2008 including a spin-up period from April 1st, 2006 to March 31st, 2007. In addition, experimental simulations were conducted for the same period using meteorological data with modified wind speed and direction on and after July 15th, 2007 in order to investigate the effect of the strong wind on the change of the stratification. The date was chosen due to strongly developed stratification, and in addition, strong wind associated with a typhoon as shown in Fig. 2. In the numerical experiments, the wind speed was fixed to 10 m s^{-1} or 20 m s^{-1} . The wind direction was fixed to four different directions: northward, southward, eastward and westward. The duration of strong wind ranged from 1 day to 7 days. Another simulation, in which the wind speed was twice as strong as the baseline case and the wind direction was the same as the baseline case, was carried out to analyze the more realistic situation. As shown in Table1, each case was named for speed, direction and duration of strong wind.

Table 1 Wind conditions in numerical experiments

Case name	Wind speed (m s^{-1})	Wind direction	Strong wind duration (day)
s10dS_day	10	Southerly	1,3,5,7
s10dN_day	10	Northerly	1,3,5,7
s10dW_day	10	Westerly	1,3,5,7
s10dE_day	10	Easterly	1,3,5,7
s20dS_day	20	Southerly	1
s20dN_day	20	Northerly	1
sX2dO_day	twice	Original	1,3,5,7

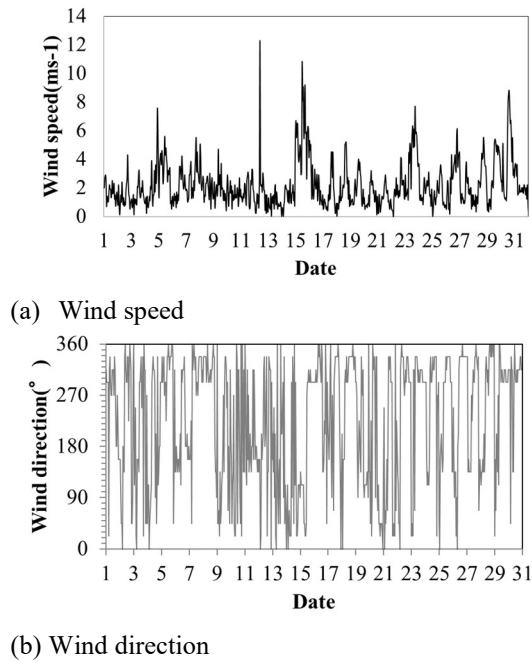


Fig. 2 Hourly wind speed and direction used in the baseline simulation at Hikone local meteorological observatory from July 1st to July 31st, 2007.

RESULTS AND DISCUSSIONS

At first, simulated water temperatures were compared with those of field observations at the monitoring point Imazu-oki as shown in Fig. 3. Although the simulated water temperature of the surface layer was a little lower than the observed one in summer, the simulated water temperature from the surface to the bottom layer agreed well with the observed one. In addition, the stratification was also reproduced well in the simulation.

Next, we examined the effect of the strong wind on the bottom water in the lake. Fig. 4 shows time series of vertical water distribution in Baseline case and some cases at the monitoring point, Imazu-oki from 7th of July to 8th of August. Fig. 5 shows time series of water temperature at a depth of 87.5m in each case.

In s10dS_1, s10dN_1, s10dW_1, and s10dE_1, comparing the change of the vertical water temperature, the wind could not influence the water temperature of the bottom layer in each case right after the wind blew as shown in Fig. 4b and Fig. 5a. Although the difference between Baseline case and s10dS_1 was small in August and September, it suddenly got larger in October. After the overturning in the middle of winter, however, the water temperature in all conditions became similar.

On the other hand, in s20dS_1, the stratification collapsed right after the wind blew, and the vertical mixing occurred, as shown in Fig. 4c. In addition, in sX2dO_1, the stratification also collapsed and the water was mixed between the bottom layer and the

layer above the bottom one (Fig. 4d). Once the stratification collapsed, water temperature at the bottom rose and didn't return to the original water temperature. The destratification depends on the strength of the wind.

The period of the strong wind influencing the water in the bottom layer was investigated. As the period extended from 1 day to 7 days, the duration of the change in water temperature was longer. Fig. 5 shows that the period of strong wind could affect the movement of the water parcel in the bottom layer. And, we could also find the difference in each direction. From Fig. 5b-d, the strong westerly wind would affect the water temperature more than other wind directions. It was because of the position of the monitoring point and the topography. The monitoring point was located at the bottom of the eastern coast (Fig. 1c), thus the water proceeded down along the coast and reached that point. In each direction, water temperature of the bottom layer increased after the strong wind blew. Even if after the overturning occurred, the water temperatures were warmer than the original one, therefore, the bottom water was completely mixed with the water in the upper layer.

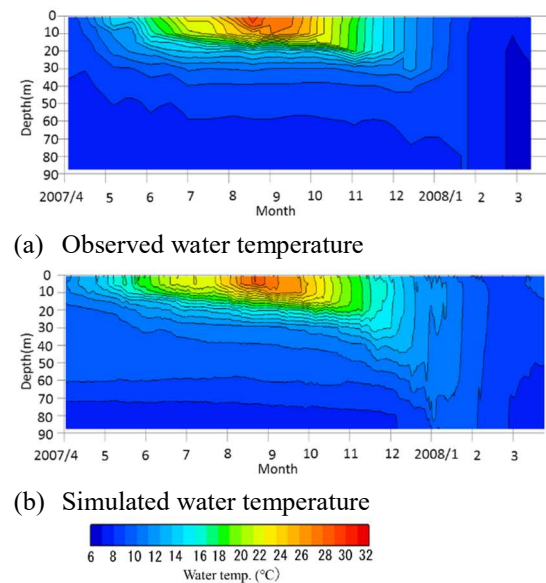
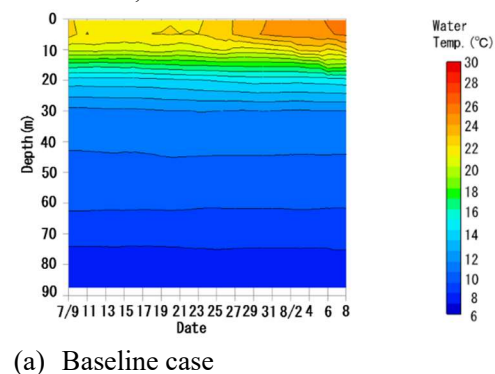


Fig. 3 Time-vertical cross sections of water temperature at Imazu-oki from April 1st, 2007 to March 31st, 2008.



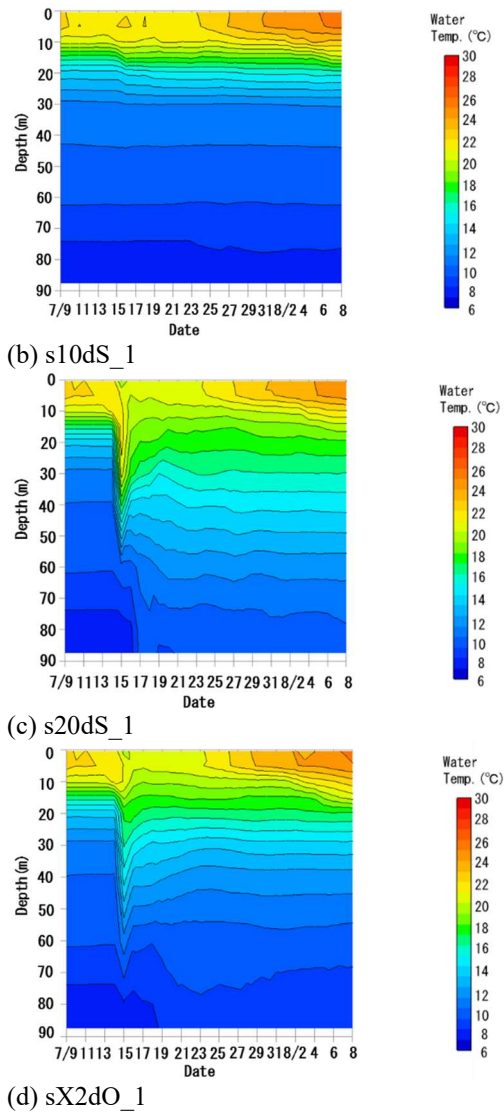


Fig. 4 Time-vertical cross sections of water temperature at Imazu-oki from July 9th to August 8th, 2007.

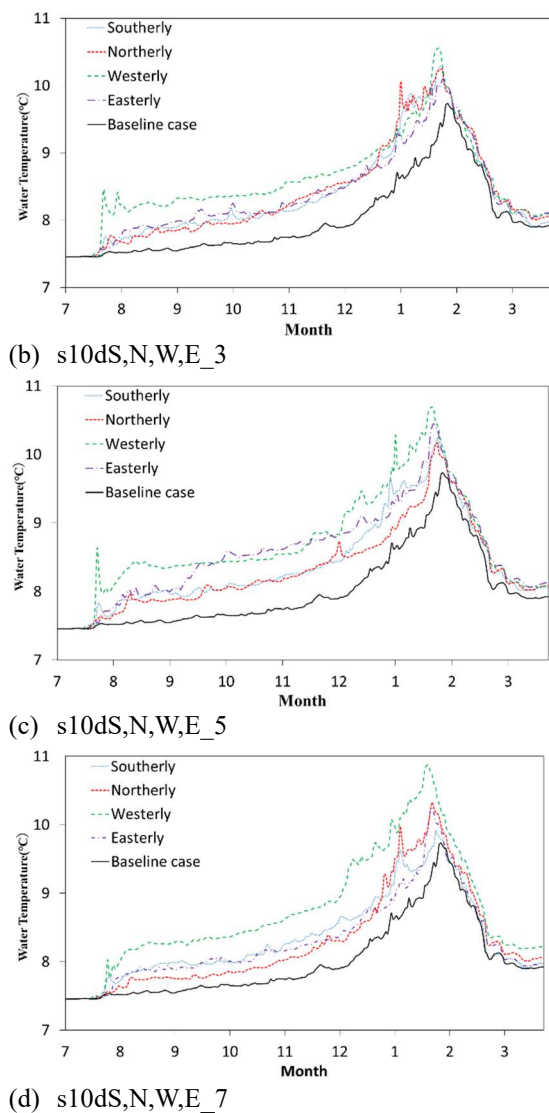
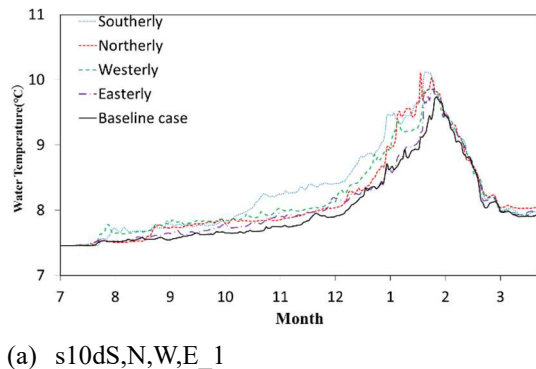


Fig. 5 Time series of water temperature at a depth of 87.5m from July 2007 to March 2008.

Fig. 6 shows the vertical distribution of simulated water temperature and vertical flow speed when the strong westerly winds blew from 15th to 17th of July for 3 days. When strong westerly winds started to blow (eastward), the surface water was driven to the coast. Then, the water in the lower layer moved against the wind, and the thermocline tilted (Fig. 6a). As shown in Fig. 6b, when the thermocline tilted toward the coast, the water flew downward in the coast. After winds ceased, the thermocline returned to the original position and tilted toward the opposite position on the 19th of July as shown in Fig. 6a. With the amplitude of the internal wave being larger, the effect of the wave reached the bottom, and the stratification collapsed. Finally, vertical mixing was enhanced in the bottom layer on July 23th-25th. This similar phenomenon was shown in the observation. When severe winds associated with the passage of three typhoons blew in 1993, the depth of the

thermocline rose deeply. After the wind ceased, it declined suddenly. This movement generated waves that affected the deep layer. The observation showed that the passage of this wave (It is called internal surge) lead to the vertical mixing [7]. The internal wave whose amplitude was larger than usual generated by strong wind became larger during moving, and as the gradient of the wave suddenly became steep and nonlinear, the amplitude of the wave was such a large one. The internal waves broke at the boundaries, and enhanced the turbulence in the bottom layer, which resulted in mixing events.

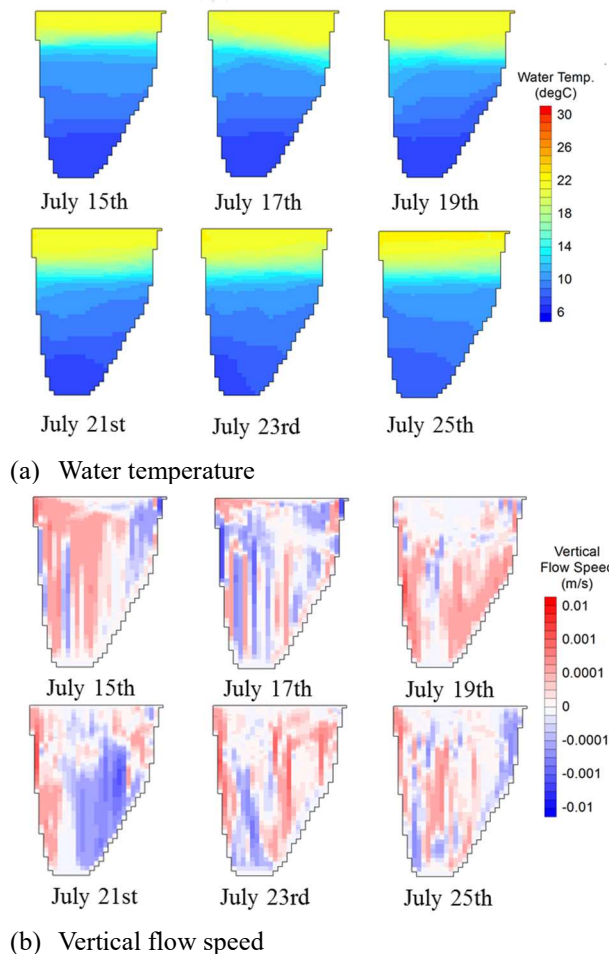


Fig. 6 West-east vertical cross sections through Imazu-oki for (a) water temperature and (b) vertical flow speed from July 15th to 25th in 2007 in the s10dE_3 case.

CONCLUSION

In the present study, we examined the effect of strong wind on the bottom layer by using a three dimensional hydrodynamics model in Lake Biwa.

If the magnitude of the wind is strong enough, the stratification collapses and the wind can enhance the vertical mixing in the bottom layer even in summer season with strong thermal stratification. In a stratified season, when the strong wind blows

predominantly in one direction, the rate of the vertical mixing changes by the wind direction. The rate of the vertical mixing possibly depends on the topography of the bottom of the lake. Once the stratification collapses, the water temperature at the bottom layer increases more than the original temperature even after the overturning. It implies that strong winds can change the water environment surrounding the bottom next year.

In this way, strong winds such as typhoons are energetic enough to tilt the thermocline from its original position. After the wind ceases blowing, the thermocline oscillates at a certain period of time. Internal waves redistribute this energy over different time and length scales. Wind driven currents and waves play an important role in the weakening of stratification and vertical mixing in the lake. These phenomena can influence the transport of substances such as dissolved oxygen and the resuspension of bottom sediments.

REFERENCES

- [1] Matzinger A et al., "Eutrophication of ancient Lake Ohrid: global warming amplifies detrimental effects of increased nutrient inputs.", *Limnology and Oceanography*, Vol. 52, 2007, pp.338-353
- [2] Coats R et al., "The warming of Lake Tahoe.", *Climate Change*, Vol.76, 2006, pp.121-148
- [3] Livingstone DM, "Impact of secular climate change on the thermal structure of a large temperate central European lake.", *Climate Change*, Vol.57, 2003, pp.205-225
- [4] Kishtawal C et al., "Tropical cyclone intensification trends during satellite er, *Geophysical Research Letters*, Vol.39 (10), 2012, pp.810.a (1986-2010)."
- [5] Knutson T et al., "Tropical cyclones and climate change." *Nature Geoscience*, Vol.3, 2010, pp.157-163.
- [6] Saggio A, Imberger J, "Internal wave weather in a stratified lake.", *Limnology and Oceanography*, Vol.43, 1998, pp.1780-1795
- [7] Hayami Y, Fujiwara T, Kumagai M, "Internal Surge in Lake Biwa Induced by strong Winds of thphoon.", *Jpn. J. Limnol.*, Vol.57, 4(2), 1996, pp. 425-444
- [8] Akitomo K, Kurogi M, Kumagai M, "Numerical study of a thermally induced gyre system in Lake Biwa", *Limnology*, Vol.5, 2004, pp.103-114
- [9] Webb EK, "Profile relationships: the log-linear range, and extension to strong stability." *Quarterly Journal of the Royal Meteorological Society*, Vol.96, 1970, pp.67-90
- [10] Shrestha KL, Kondo A, "Assessment of the Water Resource of the Yodo River Basin in Japan Using a Distributed Hydrological Model Coupled with WRF Model." *Environmental Management of River Basin Ecosystems*, Part of the series Springer Earth System Sciences, 2015, pp.137-160

IMPROVED EFFICIENCY AND FEASIBILITY IN DEVELOPING REGIONAL SCALE OPTIMAL MULTIPLE OBJECTIVE SALTWATER INTRUSION MANAGEMENT STRATEGIES IN COASTAL AQUIFERS UTILIZING NEW SURROGATE MODELS

Alvin Lal¹ and Bithin Datta¹

¹Discipline of Civil Engineering, College of Science & Engineering, James Cook University, Townsville, QLD 4811 Australia

ABSTRACT

Coastal aquifers are hydraulically connected to the sea and therefore susceptible to saltwater intrusion problems. This study proposes the utilization of a new surrogate model within coupled simulation-optimization (S/O) model for the management of groundwater use strategies in coastal aquifers subjected to density dependent saltwater intrusion processes. The simulation of the transient 3-dimensional density dependent flow and transport model is based on the solution of an implemented numerical simulation model. The simulation model is coupled with multi-objective genetic algorithm (MOGA) based optimization technique with specified objective functions and constraints. Direct coupling of the numerical simulation model with MOGA is computationally expensive. Hence, the solution of the numerical simulation model with random input variables are used for training and testing the support vector machine regression (SVMR) surrogate models for approximately simulating the flow and transport processes. The performances of the new surrogate models are evaluated using various performance evaluation criteria's. The resulting validated SVMR surrogate models are coupled to the MOGA and implemented for an illustrative coastal aquifer with an aim to develop efficient coastal aquifer management strategies. Based on the objective functions, execution of S/O model presented a set of optimal groundwater withdrawal rates from the simulated aquifer. It also ensured salinity levels at the designated monitoring wells are constrained within specified limits. The efficiency of the new SVMR surrogate models is also demonstrated. Evaluation results suggested that the projected S/O model is an effective way to develop feasible and reliable coastal aquifer management strategies. It also enhances the possibility of solving more realistic large scale problems and developing regional-scale coastal aquifer management methodologies.

Keywords: Coastal aquifers, Density dependent flow and transport model, Multi-objective, Surrogate models

INTRODUCTION

Saltwater intrusion (SWI) is imposing long-term threat to the beneficial use of life sustaining groundwater resources in coastal areas. Sustainable planning and management of coastal aquifers are decisive to ensure future sustainability of these fragile resources. Simulation-optimization (S-O) models are one of the widely used methods for developing management methodologies for coastal aquifers subjected to SWI. The present study demonstrates an integration of a new yet efficient surrogate model into a coupled S-O framework for developing improved, and efficient optimal strategies for groundwater utilization from coastal aquifers.

The S-O approach has been used to develop different coastal aquifer management models [1-6]. In many cases, due to enormous computational requirements and time constraints, numerical simulation models in an S-O model are substituted by surrogate models. Some of the common surrogate models used in developing aquifer management strategies via a S/O model includes Radial Basis Function [7], Artificial Neural Network [8, 9], Modular Neural Network [10], and Genetic Programming [5, 11]. However, the

reliability and accuracy of surrogate model incorporated S/O models are always questionable. The present study focuses on developing and implementing robust support vector machine regression (SVMR) surrogate model assisted S/O model for optimal coastal aquifer management.

In numerous surrogate model performance comparison studies, SVMR has been ranked as an accurate and most efficient predictive modeler [12-14]. Despite several successful applications and numerous benefits, SVMR surrogate model has never been used for predicting SWI into aquifers. It is for the first time, SVMR surrogate models are trained for emulating a numerical coastal aquifer flow and transport simulation model FEMWATER [15] used for predicting impact of variable groundwater pumping patterns. The surrogate model is then integrated into a multi-objective genetic algorithm (MOGA) optimization algorithm within the R2016a MATLAB environment, to develop a multi-objective coastal aquifer management strategy.

METHODS

Coastal Aquifer Management Model for Optimal Groundwater Utilization

The proposed coastal aquifer management model was designed to sustainably pump groundwater from installed production wells (PWs) and barrier wells (BW) in the simulated aquifer system. PWs were installed for withdrawing fresh groundwater for domestic utilization whereas BWs were installed near the shoreline for controlling SWI into the aquifer. Pumping from BWs induces a steeper hydraulic gradient towards the sea, averting encroachment of seawater into the aquifer [6]. Thus, two conflicting objectives i.e. maximizing total pumping from PWs and minimizing total pumping from BWs were considered. Monitoring wells (MWs) were also installed for salinity level monitoring purposes. Limiting salinity levels at respective MWs within specified limits were incorporated as constraints in the SVMR-MOGA optimization framework. The mathematical expressions of the conflicting objective functions, constraints and bounds [16] are given by;

Maximize,

$$F_1(P) = \sum_{n=1}^N \sum_{t=1}^T P_n^t \quad (1)$$

Minimize,

$$F_2(P) = \sum_{m=1}^M \sum_{t=1}^T p_m^t \quad (2)$$

$$\text{Constraints } c_i = \xi(P, p) \quad (3)$$

$$c_i \leq c_{\max} \forall i, t \quad (4)$$

$$\text{Bounds } P_{\min} \leq P_n^t \leq P_{\max} \quad (5)$$

$$p_{\min} \leq p_m^t \leq p_{\max} \quad (6)$$

P_n^t denotes pumping from n th PW at t th time and p_m^t denotes pumping from the m th BW at t th time. c_i represents the saline concentration at the i th monitoring well at the end of management time period. $\xi(\cdot)$ symbolizes the surrogate model replacing the numerical FEMWATER model and constraint (3) denotes coupling of the surrogate model within the S-O framework. M , N and T are the total number of PW, BW and total number of time steps in the management model. Inequality (4) represents the constraints imposed to keep salinity concentrations within specified limits at the respective MWs. Inequality (5) and (6) represents the upper and lower bounds of pumping from PWs and BWs respectively. Pumping bounds for both the PW and BW was set between 0 – 1300 m³/day. The constraints imposed as permissible limits on concentrations (assumed to be a conservative pollutant) were $c_i \leq c_{\max,i}$ of 425 mg/L at MW1, $c_i \leq c_{\max,j}$ of 510 mg/L at MW2 and $c_i \leq c_{\max,k}$ of 625 mg/L at MW3.

The Numerical Coastal Aquifer Simulation Model

The 3D numerical simulation FEMWATER model was used for simulating pumping induced SI processes into an illustrative coastal aquifer system. FEMWATER model (FM) allowed simulation of

density dependent coupled groundwater flow and transport processes in an aquifer system. An illustrative study area containing of a portion of a multi-layered coastal aquifer was modelled using FEMWATER. The length of the coastline (sea side boundary) was 2.13 km and the other two boundaries were of 2.04 km (Boundary A) and 2.79 km (Boundary B) respectively. The 2.53 km² study area incorporated 5 BWs, 8 PWs and 3 MWs. The study area with specific well locations are presented in Fig. 1.

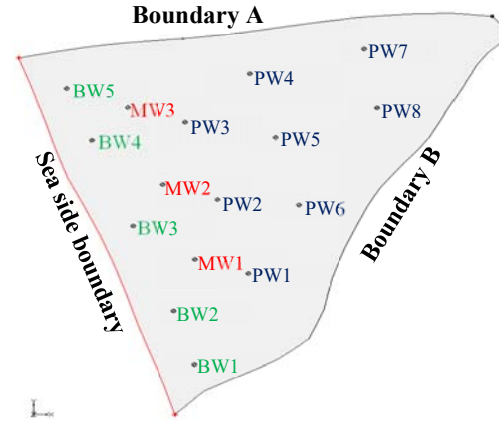


Figure 1: Illustrative study area with specific PW, BW and MW locations after [16].

The sea side boundary was assumed to be a constant head and constant concentration boundary having a concentration of 35000 mg/L. The other two boundaries of the study area were taken as no-flow boundaries. The modelled aquifer was discretized into triangular finite elements having an average element size of 150 m. The element size near the wells were set to 75 m. The total aquifer depth was 60 m, divided equally into 3 layers. A constant vertical groundwater recharge of 0.00054 m/d was specified over the entire study area. The screening interval of all the wells were taken from the second and third layers of the aquifer. The compressibility and velocity of water was taken as 6.69796 X 10⁻²⁰ md²/kg and 131.328 kg.md respectively. Other key parameters used for aquifer simulation are listed in Table 1.

The 3D transient simulation was instigated from an initially steady state condition of the aquifer, achieved via constant pumping of 300 m³/day from 3 of the PWs for a period of 20 years only. The resulting heads and salinity concentrations after 20 years were used as initial conditions for the specified period of 4 years (4th time step) where pumping from all production and barrier wells were instigated.

Table 1: Key parameter values for model development

Properties	Values
Hydraulic Conductivity	<i>x</i> direction 15 m/d
	<i>y</i> direction 7.5 m/d
	<i>z</i> direction 1.5 m/d
Bulk density	1600 kg/m ³
Longitudinal dispersivity	50 m/d
Lateral dispersivity	25 m/d
Molecular dispersion coefficient	0.69 m ² /d
Density reference ratio	7.14x10 ⁻⁷
Soil porosity	0.46
Compressibility	8.5x10 ⁻¹⁵ md ² /kg

Development of Support Vector Machine Regression Surrogate Models

SVMR methodology is a statistical tool employed for numeric data prediction utilizing support vector machines (SVM). SVMs have been applied in various engineering fields because of its attractive features and encouraging empirical performance [17]. A comprehensive discussion on SVM is presented in [18-20] and only a brief theoretical background is given below. For a given training dataset $(\mathbf{x}_i, \mathbf{y}_i)$ where \mathbf{x}_i is the *i*th input pattern and \mathbf{y}_i is the parallel target output and $\mathbf{y}_i \in \mathbf{R}$. The aim of the SVMR is to find a function $f(\mathbf{x})$ that has most ϵ deviation from the targets \mathbf{y}_i for all training data, and also is as flat as possible [21]. A SVM takes advantage of the kernel function to map the input data onto a high-dimensional feature space. Later, linear regression is performed in the high-dimensional feature space. As a result, non-linear problems are addressed in a linear space through non-linear feature mapping. The final prediction function used by an SVM is:

$$f(\mathbf{x}_i) = \sum_{i=1}^l \alpha_i \mathbf{y}_i K(\mathbf{x}_i, \mathbf{x}_j) + b \quad 0 < \alpha_i < C \quad (7)$$

where α_i is Lagrange multiplier, and \mathbf{x}_i is a feature vector corresponding to a training object. The components of vector α_i and the constant b are optimized during training. C is penalty factor, which regulates the trade-off between the flatness of f and the extent up to which deviations greater than ϵ can be accepted. The kernel function is one of the most important parts in the SVMR model. Commonly used kernels are linear, Gaussian, polynomial and sigmoid. The Gaussian function kernel is the most commonly used kernel because of its effectiveness and speed [17]. Mathematical expression of the Gaussian function is given by:

$$K(\mathbf{x}_i, \mathbf{x}_j) \exp(-\gamma |\mathbf{x}_i - \mathbf{x}_j|^2) \quad (8)$$

where γ is the parameter of the kernel function with \mathbf{x}_i and \mathbf{x}_j representing independent variables. Key parameters that control SVMR problems are the cost function C , the radius of the insensitive tube ϵ and the kernel parameter. These parameters are dependent on each other so altering the value of one parameter leads to a change in another parameter. For the present study, Gaussian kernel was used, with ϵ , C and γ having a value of 0.60, 6.49 and 0.001 respectively. Evaluating other values of these fundamental parameters were beyond the scope of this study, although, other parameter values may have provided more accurate results.

500 data sets were generated out which 400 was used for training and 100 were used for testing the trained SVMR models. The training set was used to construct the SVMR models while the testing set assessed the prediction capabilities of the trained model. 500 transient pumping (inputs) were obtained from uniform sampling distribution using Latin Hypercube Sampling (LHS) having an upper bound of 1300 m³/day and lower bound of 0 m³/day. The resulting salt concentration at each monitoring well were obtained from FEMWATER simulation after each set of pumping from all production and barrier wells are fed to the model as inputs. Each FEMWATER simulation took approximately about 4-5 minutes to converge. 500 sets of pumping and resulting output concentration were assembled by running the simulation model 500 times. These input-output patterns were used for surrogate model training and testing purpose. The SVMR models were constructed to learn from the training data presented to them with the intent of capturing the functional relation between the pumping-concentration data sets. 3 SVMR surrogate models namely M^1 , M^2 and M^3 were constructed for predicting salinity concentrations at MW1, MW2 and MW3 respectively.

Performance Analysis of Surrogate Models

The prediction capabilities of the developed SVMR surrogate models were measured using performance evaluation indices (PEI's). Mathematical expressions of these error estimates are presented from Eq. (9) to (12).

$$RMSE = \sqrt{\frac{1}{K} \sum_{k=1}^K (C_k^o - C_k^p)^2} \quad (9)$$

$$MSE = \frac{1}{K} \sum_{k=1}^K (C_k^o - C_k^p)^2 \quad (10)$$

$$C_c = \frac{\sum_{k=1}^K (C_k^o - c^o)(C_k^p - c^p)}{\sqrt{\sum_{k=1}^K (C_k^o - c^o)^2} \sqrt{\sum_{k=1}^K (C_k^p - c^p)^2}} \quad (11)$$

$$NSE = 1 - \frac{\sum_{k=1}^K (C_k^o - C_k^p)^2}{\sum_{k=1}^K (C_k^o - \bar{C}^o)^2} \quad (12)$$

where C_k^o and C_k^p are observed (from FM) and predicted values of saltwater concentrations respectively, \bar{C}^o and \bar{C}^p are observed and predicted saltwater concentration mean values respectively, and K represents total data points.

Linked simulation-optimisation approach

The trained and tested SVMR models were used in the S/O model as a set of binding constraints for salinity concentration prediction purpose. Multi-objective Genetic algorithm (MOGA) was used as an optimization tool. MOGA has been used efficiently in solving multi-objective optimization problems [5, 16]. When using MOGA optimization tool, population size was set to 1500, with 5200 generations, crossover fraction of 0.8 and mutation probability of 0.02. A flowchart for the linked surrogate assisted S/O framework is given in Fig. 2.

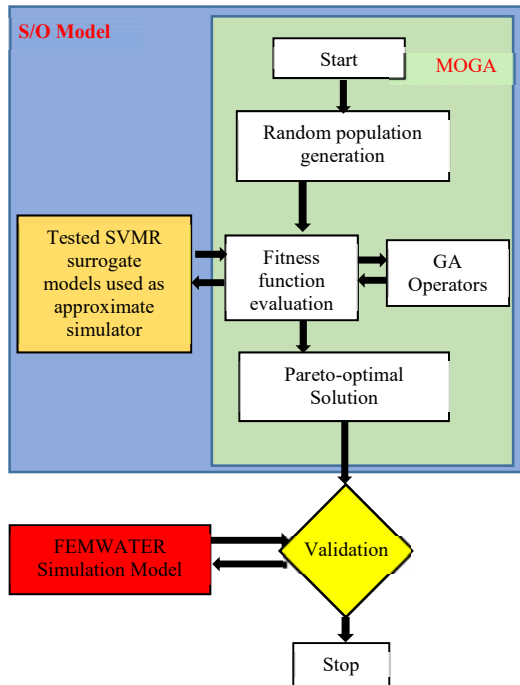


Figure 2: Flowchart for the linked S/O model with optimal solution validation stage.

RESULTS AND DISCUSSIONS

Coastal Aquifer Simulation Model

Fig. 3 presents the simulated coastal aquifer utilizing 1 set of PW and BW pumping.

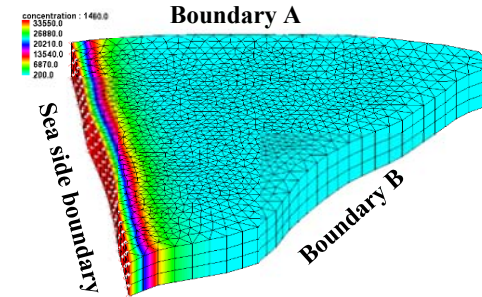


Figure 3: Salinity concentration contours after a period of 4 years (1460 days) using a set of transient pumping pattern.

The numerical coastal aquifer flow and transport model was executed 500 times with each run having different transient pumping values. The obtained pumping-concentration datasets were used to train and test the SVMR surrogate models.

SVMR Model Prediction Capabilities

The error estimates during the training and testing phases are given in Table 2.

Table 2: Performance evaluation results

Phase	PEI's	M ¹	M ²	M ³
Training	MSE	0.164	0.057	0.184
	RMSE	0.405	0.238	0.428
	R ²	0.997	0.997	0.989
	NSE	0.99	0.99	1.00
Testing	MSE	0.202	0.105	0.187
	RMSE	0.449	0.323	0.432
	R ²	0.994	0.993	0.989
	NSE	0.99	1.00	1.00

The performances of the SVMR models at the training and testing phases for M¹, M² and M³ in terms of the 4 evaluation criteria showed similar trends. RMSE, and MSE values for concentrations at M¹, M² and M³ at both the stages were substantially smaller. During the training stage, SVMR model has a smallest RMSE value of 0.238 accomplished for M² and highest RMSE of 0.428 attained for M³. Comparing RMSE values of SVMR models at the testing stage, the lowest 0.323 is obtained for M² and highest value of 0.449 is achieved for M¹. Accordingly, MSE values of the SVMR models are comparatively smaller. R² and NES values do not significantly differ for the three models and have values close to 1. NSE value of 1 presents a perfect estimate with no errors [22]. A model can be considered accurate if the calculated NSE value is greater than 0.8 [23]. The NSE values for M¹, M² and M³ were greater than 0.8 indicating that it can reliably be used for SI prediction. A model's good performance in the testing phase is an indication of its accuracy in prediction and hence its practical

utility [24]. Hence, the observed good performance of SVMR models at the testing stage establishes its credibility, suggesting accurate results when used for prediction purposes.

Optimal Groundwater Pumping Solution Set

After evaluating the prediction performances, the M^1 , M^2 and M^3 replaced the original FEMWATER model in the S-O framework instituted for obtaining optimal groundwater pumping rates from the PWs and BWs installed in the simulated coastal aquifer. The execution of the SVMR-MOGA coastal aquifer management model presented a set of optimal pumping solution. The resulting Pareto-front from the executed S-O model is given in Fig. 4.

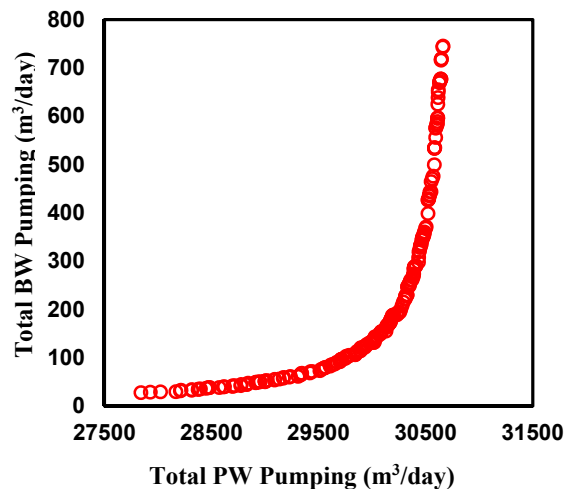


Figure 4: Optimal Pareto-front from the executed SVMR-MOGA model

Depending on the relative importance each of the two objective functions in the management model, a set of pumping solutions can be chosen and implemented for optimal and sustainable utilization of groundwater from the simulated aquifer. The selected optimal pumping solutions from the Pareto-front will ensure optimal pumping and maintaining salinity levels at the MWs within specified limits which was the major aim of the proposed management model. The Pareto optimal solutions also show the conflicting nature of the two objectives. For example, if the pumping for beneficial use increases beyond 30500 m³/day, the marginal increase in barrier well pumping increases exponentially.

Validation of Optimal Pumping Solutions

To establish the validity of the resulting optimal solution, the salinity concentration obtained from the SVMR surrogate models were compared with the salinity concentration obtained from the original FM. Five random solutions from the optimal Pareto-front were chosen and the salinity comparison results are presented in Table 3.

Table 3: Optimal pumping solution validation results

Sol.	$C_{max,i}$ at MW1 ≤ 425 mg/L		$C_{max,j}$ at MW2 ≤ 510 mg/L		$C_{max,k}$ at MW3 ≤ 625 mg/L	
	SVMR	FM	SVMR	FM	SVMR	FM
1	423.8	422.9	509.2	507.9	624.2	623.9
2	424.5	423.5	509.4	508.3	623.6	622.1
3	423.2	422.2	508.9	506.5	624.6	623.5
4	425.0	425.3	508.4	508.9	623.1	622.6
5	424.7	423.6	509.4	508.3	624.7	622.0

It was observed that the salinity concentration values from both the modelling tools were very close to each other. It was also observed that the optimal pumping values satisfied the specified concentration constraints at monitoring locations. Also, the optimal solutions converged to the specified upper bound of the concentrations constraint. The validation results established that the SVMR surrogate models predicted the salinity concentrations at MWs accurately and can be utilized for developing coastal aquifer management strategies.

Conclusion

This paper presents an efficient and feasible SVMR model assisted coupled S/O model for the optimal sustainable management of coastal aquifers subjected to SWI. The S/O model maximizes pumping from PWs, and minimizes pumping from BWs while maintaining salinity concentrations at respective MWs within specified limits. Utilized SVMR surrogate models have effectively approximated density-dependent SWI processes in the simulated aquifer. Hence, SVMR models efficiently predicted salinity concentrations at monitoring wells in response to variable transient pumping patterns. The execution of the developed management model presented a set of optimal pumping patterns for both the PWs and BWs. An optimal pumping solution set can be chosen and implemented for the sustainable utilization of the modelled coastal aquifer. The implementation of the developed management model has the potential to aid in developing regional-scale coastal aquifer management strategies while ensuring computational efficiency, thus making it feasible to address much larger study areas. In future, it would be beneficial to compare the prediction performances of SVMR with other available surrogate modelling methods and also apply the established management model on a real case study area.

REFERENCES

- [1] A. Javadi, M. Hussain, M. Sherif, and R. Farmani, "Multi-objective optimization of different management scenarios to control seawater intrusion in coastal aquifers," *Water Resources Management*, vol. 29, pp. 1843-1857, 2015.

- [2] G. Kourakos and A. Mantoglou, "Development of a multi-objective optimization algorithm using surrogate models for coastal aquifer management," *Journal of Hydrology*, vol. 479, pp. 13-23, 2013.
- [3] B. Ataie-Ashtiani, H. Ketabchi, and M. M. Rajabi, "Optimal management of a freshwater lens in a small island using surrogate models and evolutionary algorithms," *Journal of Hydrologic Engineering*, vol. 19, pp. 339-354, 2013.
- [4] B. Ataie-Ashtiani and H. Ketabchi, "Elitist continuous ant colony optimization algorithm for optimal management of coastal aquifers," *Water resources management*, vol. 25, pp. 165-190, 2011.
- [5] J. Sreekanth and B. Datta, "Multi-objective management of saltwater intrusion in coastal aquifers using genetic programming and modular neural network based surrogate models," *Journal of Hydrology*, vol. 393, pp. 245-256, 2010.
- [6] A. Dhar and B. Datta, "Saltwater intrusion management of coastal aquifers. I: Linked simulation-optimization," *Journal of hydrologic engineering*, vol. 14, pp. 1263-1272, 2009.
- [7] V. Christelis and A. Mantoglou, "Pumping Optimization of Coastal Aquifers Assisted by Adaptive Metamodelling Methods and Radial Basis Functions," *Water Resources Management*, pp. 1-15, 2016.
- [8] R. K. Bhattacharjya, B. Datta, and M. G. Satish, "Artificial neural networks approximation of density dependent saltwater intrusion process in coastal aquifers," *Journal of Hydrologic Engineering*, vol. 12, pp. 273-282, 2007.
- [9] R. K. Bhattacharjya and B. Datta, "ANN-GA-based model for multiple objective management of coastal aquifers," *Journal of Water Resources Planning and Management*, vol. 135, pp. 314-322, 2009.
- [10] G. Kourakos and A. Mantoglou, "Pumping optimization of coastal aquifers based on evolutionary algorithms and surrogate modular neural network models," *Advances in water resources*, vol. 32, pp. 507-521, 2009.
- [11] J. Sreekanth and B. Datta, "Comparative evaluation of genetic programming and neural network as potential surrogate models for coastal aquifer management," *Water resources management*, vol. 25, pp. 3201-3218, 2011.
- [12] Z. A. Khalifelu and F. S. Gharehchopogh, "Comparison and evaluation of data mining techniques with algorithmic models in software cost estimation," *Procedia Technology*, vol. 1, pp. 65-71, 2012.
- [13] Y. Li, S. H. Ng, M. Xie, and T. Goh, "A systematic comparison of metamodelling techniques for simulation optimization in decision support systems," *Applied Soft Computing*, vol. 10, pp. 1257-1273, 2010.
- [14] S. Mukherjee, E. Osuna, and F. Girosi, "Nonlinear prediction of chaotic time series using support vector machines," in *Neural Networks for Signal Processing [1997] VII. Proceedings of the 1997 IEEE Workshop*, 1997, pp. 511-520.
- [15] H.-C. J. Lin, D. R. Richards, G.-T. Yeh, J.-R. Cheng, and H.-P. Cheng, "FEMWATER: A Three-Dimensional Finite Element Computer Model for Simulating Density-Dependent Flow and Transport in Variably Saturated Media," DTIC Document 1997.
- [16] J. Sreekanth and B. Datta, "Coupled simulation - optimization model for coastal aquifer management using genetic programming - based ensemble surrogate models and multiple - realization optimization," *Water Resources Research*, vol. 47, 2011.
- [17] b. Liu, j. hu, f. yan, r. f. turkson, and f. lin, "A novel optimal support vector machine ensemble model for NO X emissions prediction of a diesel engine," *Measurement*, vol. 92, pp. 183-192, 2016.
- [18] M. Welling, "Support vector regression," *Department of Computer Science, University of Toronto, Toronto (Canada)*, 2004.
- [19] A. J. Smola and B. Schölkopf, "A tutorial on support vector regression," *Statistics and computing*, vol. 14, pp. 199-222, 2004.
- [20] S. R. Gunn, "Support vector machines for classification and regression," *ISIS technical report*, vol. 14, 1998.
- [21] G. D. Betrie, R. Sadiq, K. A. Morin, and S. Tesfamariam, "Uncertainty quantification and integration of machine learning techniques for predicting acid rock drainage chemistry: A probability bounds approach," *Science of the Total Environment*, vol. 490, pp. 182-190, 2014.
- [22] Z. He, X. Wen, H. Liu, and J. Du, "A comparative study of artificial neural network, adaptive neuro fuzzy inference system and support vector machine for forecasting river flow in the semiarid mountain region," *Journal of Hydrology*, vol. 509, pp. 379-386, 2014.
- [23] C. Shu and T. Ouarda, "Regional flood frequency analysis at ungauged sites using the adaptive neuro-fuzzy inference system,"

- Journal of Hydrology*, vol. 349, pp. 31-43, 2008.
- [24] A. Khalil, M. N. Almasri, M. McKee, and J. J. Kaluarachchi, "Applicability of statistical learning algorithms in groundwater quality modeling," *Water Resources Research*, vol. 41, 2005.

WATER POLLUTION OF KAMATANI-RIVER BASIN IN YOKKAICHI

Sachie Takeuchi¹, Masaaki Takahashi², Yukimasa Takemoto², Maki Oyagi², Satoshi Chiba², Yuzou Morikawa², Jia Zhou³, Kunihide Miyaoka³, Kaoru Ito⁴, Takanori Terazawa⁵

¹Faculty of Medicine, Mie University, Japan, ²Faculty of Information and Environmental Sciences, Yokkaichi University, Japan, ³Faculty of Education, Mie University, Japan, ⁴Yokkaichi Kanngo Iryou University, Japan, ⁵Mie Prefectural Environmental Conservation Agency, Japan

ABSTRACT

Kamatani-River is a small river which flows down from the Suzuka mountain chain to Ise Bay though the western part of Yokkaichi-Shi. In the catchment area of this river, tea plant fields spread widely, and some waste disposal sites and a cow farm have been constructed. In order to find the influence of this land use on the river water, our investigation was carried out. Some polluted water from these disposal sources was found which contains high values of COD, phosphorus, D-Fe, D-Mn and nitrogen compounds. Especially significant nitrogen pollution has been widely found. The main sources of the nitrogen compounds is considered to be related to the tea plant fields which are widely spread in this area.

Key word: Nutrients, Nitrogen compound, Land-Use, Kamatani-river

INTRODUCTION

Yokkaichi-Shi is well known as one of the industrial city, and also has very wide diluvial hill in the west part, there are cultivated many tea plant fields from the old times because of its warm climate, which is good for them. Recently, a waste disposal site and stock farm were made in advantage of the geometrical condition, and their influence on the environment around them is considered serious matter.

Kamatani-River (extension: 20km) is one of the small branch rivers of Suzuka-River which flows down to Ise-bay through this area. Kamatani-River unites the Utsube-River (other branch rivers of the

The investigation was carried out at 14 sites shown in Fig.1 from the year 2014 till 2016 (three times in year). The investigation sites from St11 to St16 and St3, St8 are situated at the main stream of the Kamatani-River (St11 is situated at the upper stream, and St16 is situated at the most down-stream of the river). St5 and St6 are leaching water from the tea plant fields. St2 is situated at the waste disposal site (damping finished about 10 years ago), St4 is situated at the drainage of the cow farm. St7 and St9 are the leaching water near of the dumping site of the construction waste soil.

Suzuka-River), later, flows down to the Suzuka-River. The catchment area of the Kamatani-River distributes long and narrow from the source till the downstream of the river, therefore, the influences of the waste water from these disposal sites is considered significant compared to other rivers. Therefore, environmental counter measure are very important matter [1], and became an important concern in the community of the drainage basin. In order to help them, we investigated the water pollution in Kamatani-River and around the catchment area [2].

METHODS

Investigation Site and Date

Parameter and Analytical Method

Parameter and analytical method is listed below.
pH: glass electrode, EC: Platinum electrode, COD: acidic manganese method, NO₃-N: ultra purple light absorbance method, PO₄-P: Molybdenum blue method.

As a simple method, D-Fe, D-Mn, NH₄-N, NO₂-N, Cl ion were tested using Simplified chemical analysis product for water quality (Kyoritsu Chemical-Check Lab., Corp.).

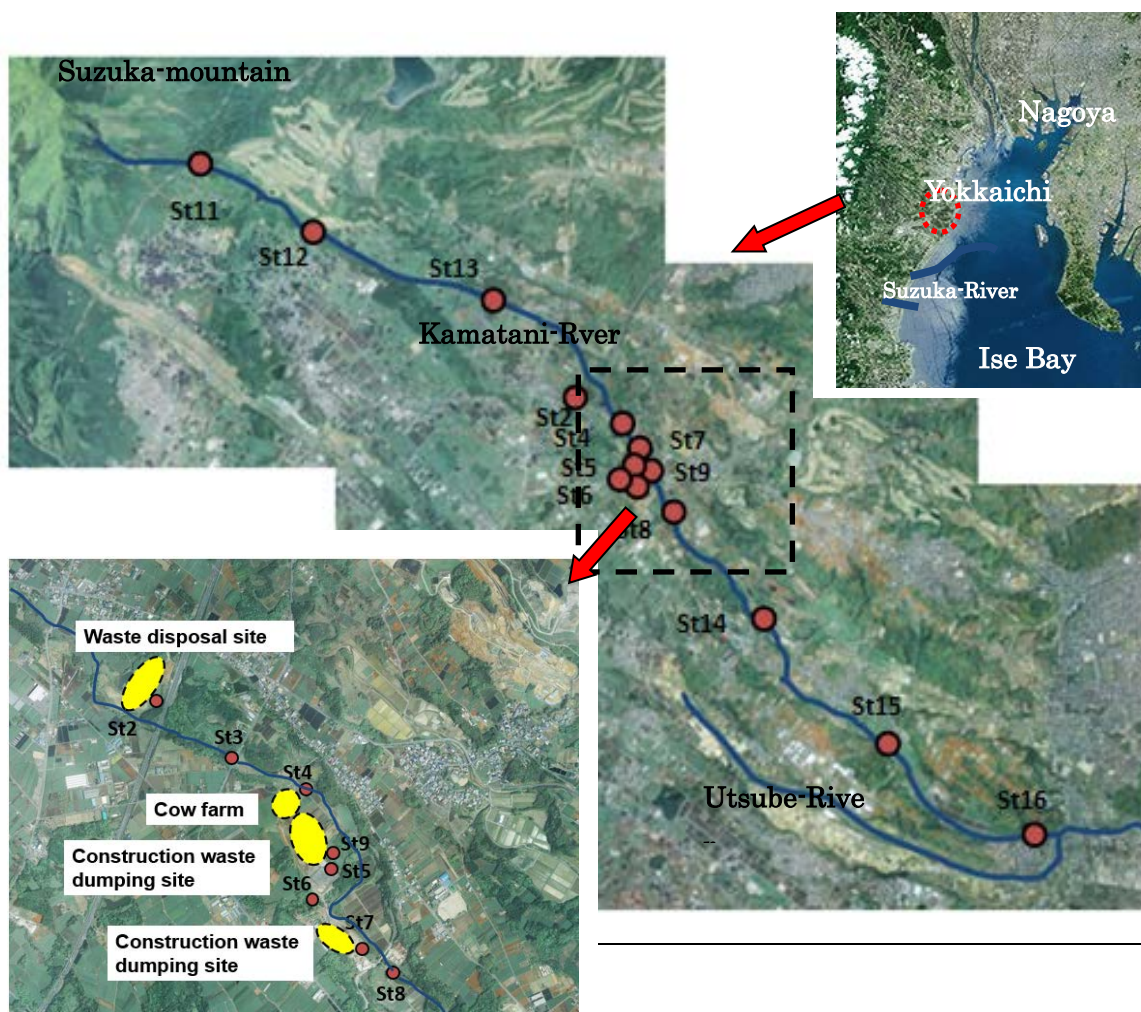


Fig. 1 Investigation site (Using Yahoo Map)

RESULT and DISCUSSION

Pollutants

High values of $\text{NH}_4\text{-ion}$, Cl-ion and D-Fe were found at St2, however, these pollutants were not detected in the down-stream of the river, and the influence from the disposal site is considered to be small. High concentration of $\text{PO}_4\text{-P}$ was found at St4, and was considered to be come from cow farm. These pollutants were not found at the downstream nearby, therefore, this influence was considered to be small. High values of COD were also found at St2, St4 and St9, however, COD values of the main stream are low compared by other rivers in Yokkaichi [3]. COD

tends slightly to be increased toward downstream (St 8 to St15, shown in Fig 2). The concentrations of the $\text{NO}_3\text{-N}$ were low at upstream of the river, and increased toward the down-stream till St8, later, the concentrations tend to decrease toward St16. At St5 or St6, where water is flown out from the tea plant fields, high concentrations of $\text{NO}_3\text{-N}$ were found, and at St2, St4, high concentrations of $\text{NO}_3\text{-N}$ were also found. These values are higher than the main stream of the river (Fig 3). The concentrations of $\text{PO}_4\text{-P}$ were low (under 0.1mg/L) at most of all monitoring stations except for St4 (as mentioned before), however, the concentrations were slightly increased toward St 8 to St15 and St16 (Fig 4).

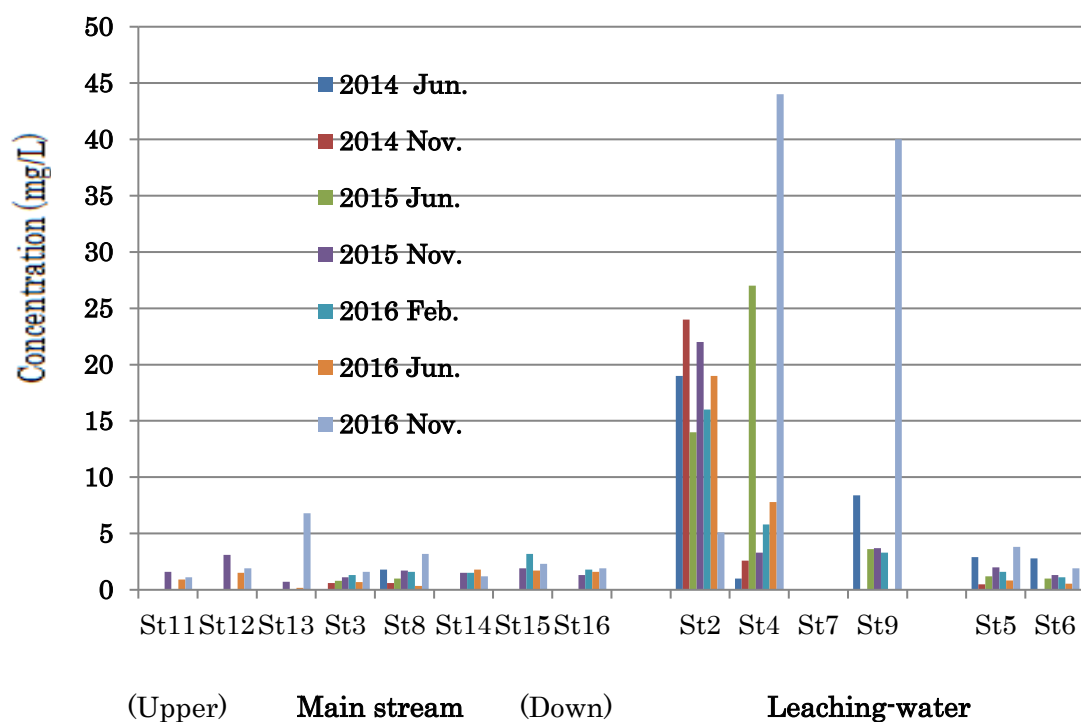


Fig.2 COD at the monitoring stations

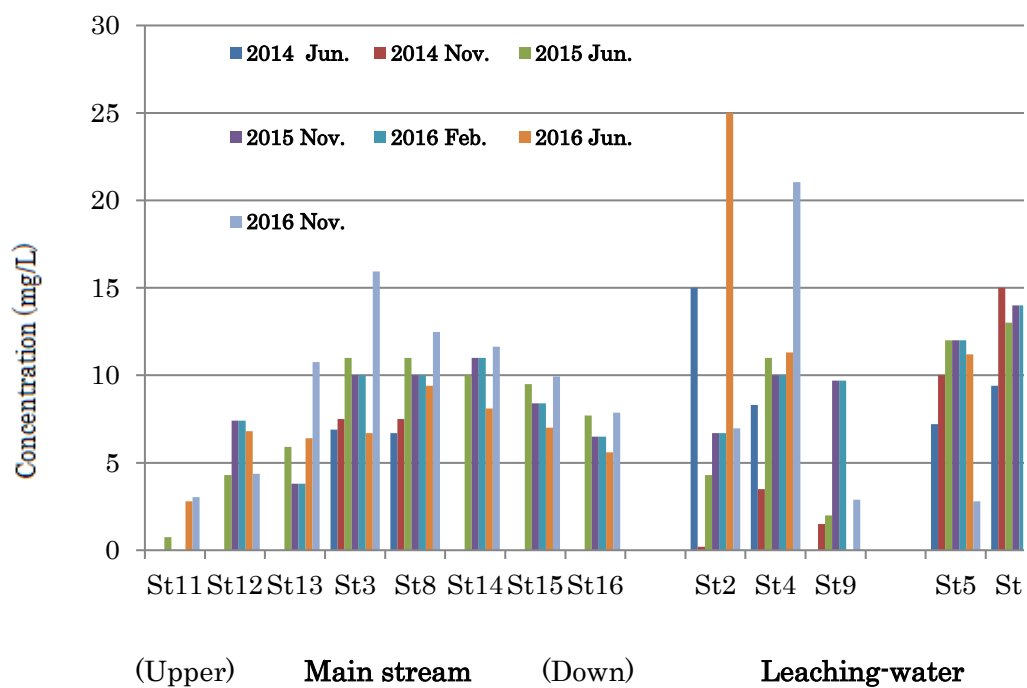


Fig 3 NO₃-N concentration at the monitoring stations

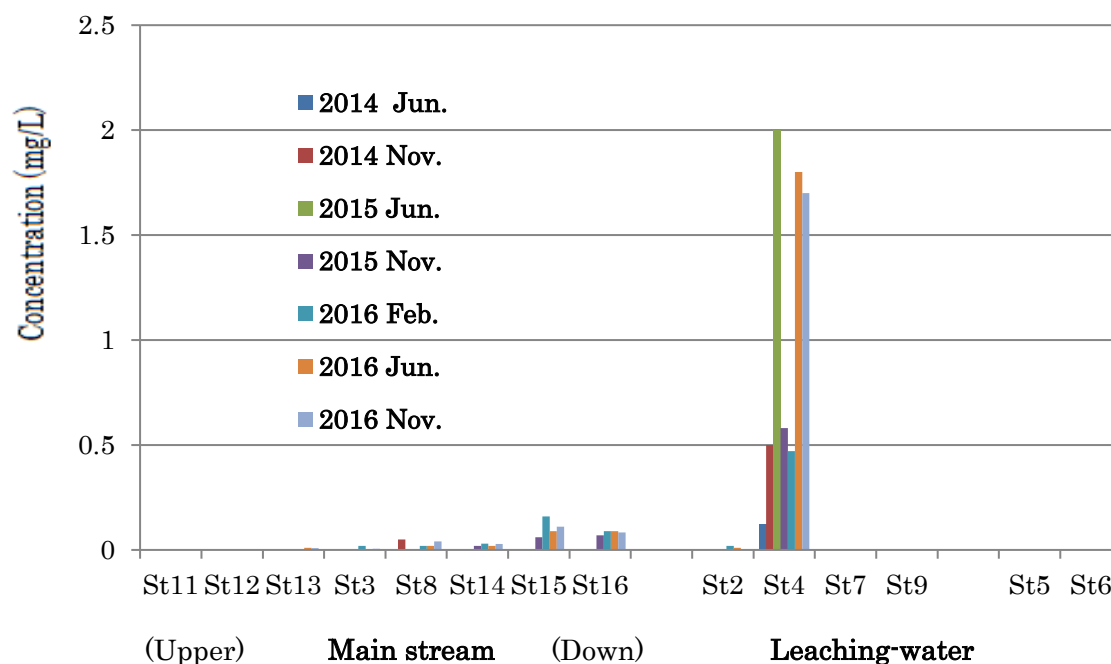


Fig.4 PO₄-P concentration at the monitoring stations

Land Use

In this investigation, high concentrations of the NO₃-N were found, and in order to find a nitrogen flow, land use was investigated using aerial photography [4]. The land use was analyzed in about 4 areas (Fig. 5) with 7 categories as a forest, tea plantation, rice field, farm land, residential area, lake and others (Fig.6).

Area 1: The upstream of St11, where most of the area is covered by forest (Space: 1.45km²). Area 2: The catchment area of St12 to St13, in where the area is mainly covered by tea plant fields and forest (Space: 2.43km²). Area 3: The catchment area from St13 to St14, The half of the area is covered by tea plants and forest, and others are occupied by others (Space: 4.76km²). Area 4: The catchment area from St14 to St16, where, the area is mainly covered by rice fields (Space: 2.35km²). From the result, concentrations of the NO₃-N increased in Area 2 and Area 3 where tea fields spread widely, and NO₃-N pollution is

considered to be related to the tea plant field. In order to clarify the mechanism, further investigation about the flow of nitrogen compounds is needed. It was usual that the outstanding pollution of COD and PO₄-P was not found in main stream of the river. Usually, pollution of nitrogen and phosphorus is related to each other, therefore, further investigation on the source of the nutrients will be needed.

CONCLUSION

In this investigation, high concentrations of NO₃-N were found in the Kamatani-River basin, suggesting the possibility of being a source of the nitrate pollution of the Suzuka-River [5-6]. The main source of the NO₃-N is reconsidered to be related to the tea plant fields by the analysis of land use. Contrarily, COD and PO₄-P were only slightly found in the main stream, and the mechanism of the nutrient flow from these sources should be much more investigated.

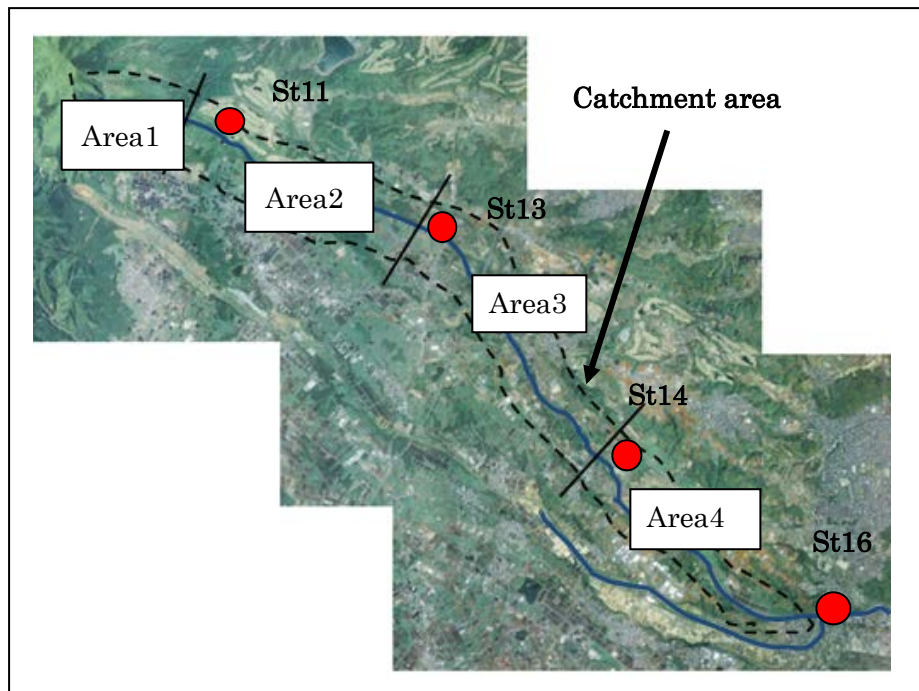


Fig. 5 Situation of the investigated area

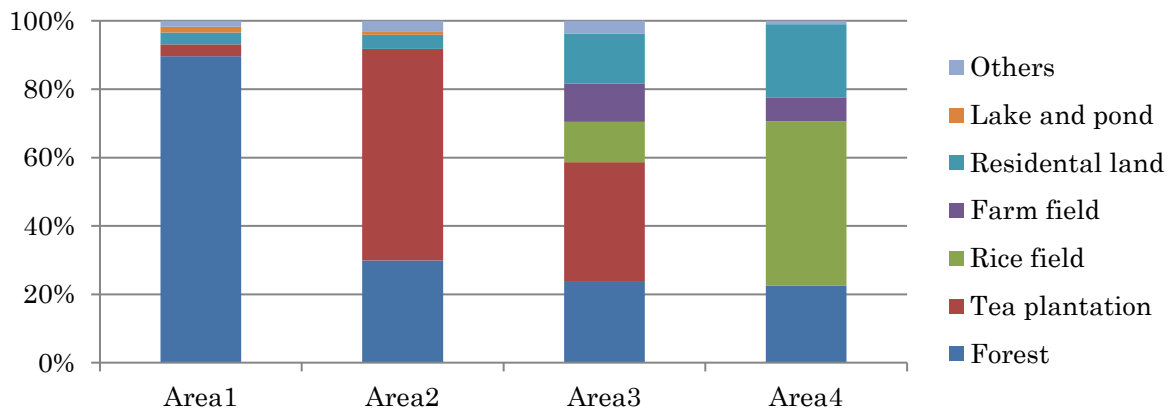


Fig. 6 Land use of the research area

REFERENCE

- [1] Sachie Takeuchi, Yukimasa Takemoto, Masaaki Takahashi, Maki Oyagi, Yuzou Morikawa, Jia Zhou, Kunihide Miyaoka, Kaoru Ito, Takanorii Terazawa "Water pollution of the Kamatani River in Yokkaichi" The proceedings of the 42nd annual conference of Japan Association of Environmental Science, 2016, p124-p125.
- [2] Yukimasa Takemoto, Masaaki Takahashi, Sachie Takeuchi, Maki Oyagi, Yuzou Morikawa, Jia Zhou, Kunihide Miyaoka, Kaoru Ito, Takanorii Terazawa "Water pollution of the Kamatani River in Yokkaichi" Yokkaichi University Journal of Environmental and Information Sciences Vol 20, No2, 2017, p31-p38.
- [3] Yukimasa Takemoto, Peng Guo, Masaaki Takahashi "Water Quality Analysis and Environmental Education (II)" Yokkaichi University Journal of Environmental and Information Sciences Vol 16, No2, 2013, p51-p72.

- [4] Yahoo Map: [https:// map. yahoo. co.jp](https://map.yahoo.co.jp).
- [5] Yokkaichi University “Information System on the River using Internets GIS System” The report of Heisei 14 Nendo Cooperative Research with University and Mie Prefectural Government, 2003, p4-p8.
- [6] Mie Prefecture “Anural Report on Environment in Mie Prefecture” 2016.

COMPARISON OF DIFFERENT VEGETATION INDICES FOR ASSESSING MANGROVE DENSITY USING SENTINEL-2 IMAGERY

Firman Farid Muhsoni^{1,2*}, A.B Sambah^{3,4}, M. Mahmudi³, D.G.R Wiadnya³

¹Marine Science Department, University of Trunojoyo Madura,
Jl.Telang, Bangkalan, Madura 69162, Indonesia

²Post-Graduate Program, Faculty of Fisheries and Marine Science, University of Brawijaya
Jl. Veteran 65145 Malang, Indonesia

³Faculty of Fisheries and Marine Science, University of Brawijaya

⁴Marine and Fisheries Resources Exploration & Management Research Group,
Brawijaya University, Jl. Veteran 65145 Malang, Indonesia

ABSTRACT

Vegetation mapping provides important information for understanding ecological condition through calculation of vegetation density. It based on vegetation indices developed through algorithms of mathematical model within the visible and near-infrared reflectance bands. The indices is an estimate of either leaf density per species, or vegetation types, respectively. This study aimed to evaluate those indices and find best algorithm using Sentinel-2 satellite image. Twenty four algorithms of vegetation indices were analyzed for mangrove density mapping, i.e., BR, GNDVI BR, GR, SAVI, MSAVI, NDRE, NDVI, NDVI2, NDWI, NNIP, PSRI, RR, RVI, VIRE, SVI, VIRRE, MTV1, MTVI2, RDVI, VARI, VI *green*, MSR, and TVI. During pre-processing stage, digital number of Sentinel-2 image was converted into radiance and reflectance value. The analysis resulted in three algorithms that provide highest accuracy, i.e., MSR (*Modified Simple Ratio*), NDVI (*Normalized Difference Vegetation Index*) and RVI (*Ratio Vegetation Index*). All the three methods provided comparable R^2 (0.860, 0.859, and 0.850, respectively). Sentinel-2 satellite image may best using one of those three algorithms, especially applied for mangrove vegetation.

Keywords: Vegetation Indices, Sentinel-2 Imagery, Mangrove Biomass

1. INTRODUCTION

Global warming becomes a global issue. It leads to climate change, due to an increase in atmospheric gas or so-called greenhouse gases. Greenhouse gases occur due to accumulation of carbon in atmosphere accumulation due to burning of fossil fuels (the activity of vehicle and industry) [1].

Mangrove has a function as a carbon sink, although the information and data are still relatively minimal [2]. Mangroves are also called mangroves for tree or shrub communities that grow on the coastal area, or are applied to one type of vegetation species [3]. Mangrove is an intertidal plant found along tropical and non-tropical coastlines [4]. This plant is inundated by tides in the brackish area and has physiological adaptations to salinity [5]. Mangrove ecosystem stored the highest carbon, compared to tropical forests, subtropical forests and boreal forests. Much of the carbon stored in the rich organic underground [5],[6]. Mangroves store carbon four to five times faster than tropical forests [5]. Climate change is closely related to the existence of forest biomass. Biomass plays a role in the carbon cycle. Forest carbon is stored in forest

vegetation. The increase of carbon in the atmosphere caused by the damage or forest fire. More than 50% of the world's mangroves have been destroyed, in the past two decades 35% of damage caused by coastal cultivation and development [7]. Mangrove damage has resulted in the contribution of carbon sequestration in the atmosphere [8]. Mangrove area is only 0.7% of the area of tropical forest, but mangrove destruction will supply 10% of CO₂ from the mangrove deforestation [9].

Remote Sensing, flowed by the application of GIS provide quantitative information to investigate the spatial distribution of vegetation, including mangrove forests in coastal area [10]. The application of satellite image analysis has been applied in various ways to illustrate mangrove ecosystems. Some of the published study includes mapping the distribution of mangrove in coastal area, observing mangrove species by ground survey combination, and estimates it structure such as leaf area, canopy height, and biomass [11].

Satellite imagery data is one of the basic information that could describe the location of deforested or degraded area, also healthy vegetation. Satellite remote sensing approach, due to its

synoptic, multi-temporal, and multi-spectral ability can effectively act as one of methods in providing reliable information on mangrove extent and status of its growth along the coastal areas. The reflectance pattern of the vegetation in red-visible & near infrared spectral region illustrated the density of all vegetation coverage in coastal area.

Moreover, earth observation satellite like Landsat satellite was commonly apply to define the distribution and density of the mangrove forest [12]. In addition to some satellite applied in vegetation density mapping, Sentinel-2 satellite is a relatively new satellite that is assumed can be use in mapping the spatial distribution of vegetation. Sentinel-2 is a European wide-swath, high-resolution, multi-spectral imaging mission. The full mission specification of the twin satellites flying in the same orbit but phased at 180°, is designed to give a high revisit frequency of 5 days (temporal resolution) at the Equator [13]. In this study, we analyze Sentinel-2 satellite imagery to investigate and evaluate the density of mangrove forest by calculation of several vegetation indexes.

Vegetation mapping provides valuable information for understanding the natural and man-made environment. It is important to obtain vegetation cover in the framework of vegetation protection and restoration programs [14]. Mangrove ecosystems have tremendous relevance to the ecological and economic conditions for conservation and restoration measures. The latest information concerning the extent and condition of mangrove ecosystems is essential for management, policy process and decision making. This can be solved using remote sensing technology [15]. The vegetation index approach in remote sensing is commonly used for vegetation mapping [16]. The vegetation index has calculated the vegetation density of green leaf and specifically for vegetation species. The purpose of this study was to evaluate the different vegetation indexes that collected from the Sentinel-2 satellite image analysis.

2. MATERIALS AND METHODS

2.1. Satellite Remote Sensing Data

Sentinel-2 satellite images (Copernicus Sentinel data (2017)) were used in this study in the calculation and mapping of mangrove distribution. The Sentinel-2 satellite has 13 spectral bands from near-infrared to shortwave infrared. Spatial resolution varies from 10m - 60m depending on spectral band [17]. Sentinel 2 image used in this research was December 6, 2016. The bands used in this study were band 2, 3, 4, 5, 6, 8, 8a, with specifications as in Table 1. Moreover, the illustration of Sentinel-2 spectral bands for 10m and 20m spatial resolution as described on Figure 1 and

Figure 2.

Table 1. Sentinel-2 band spesification [4]

No	Band	Wave length (μm)	Spatial resolution
1	Band 2 – Blue	0.490	10m
2	Band 3 – Green	0.560	10m
3	Band 4 – Red	0.665	10m
4	Band 5 – Vegetation Red Edge	0.704	20m
5	Band 6 – Vegetation Red Edge	0.740	20m
6	Band 8 – NIR	0.835	10m
7	Band 8a – Vegetation Red Edge	0.865	20m

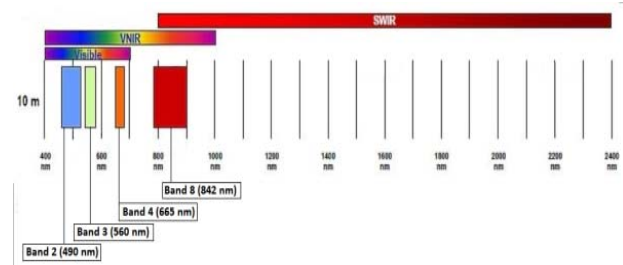


Figure 1. Sentinel-2 10 m spatial resolution bands: B2 (490 nm), B3 (560 nm), B4 (665 nm) and B8 (842 nm) [4]

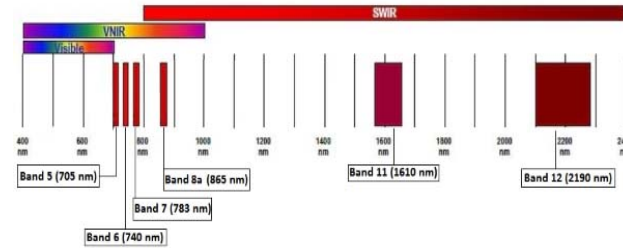


Figure 2. Sentinel-2 20 m spatial resolution bands: B5 (705 nm), B6 (740 nm), B7 (783 nm), B8a (865 nm), B11 (1610 nm) and B12 (2190 nm) [4]

2.2. Radiometry Corrections

The radiometric correction uses the at-sensor reflectance method by changing the pixel value to the radiance-sensor. Then converted to at-sensor reflectance, with the following formula [18]:

$$L_x = offset_x + Gain_x \times (BV)_x \quad (1)$$

$$Gain_x = (L_{maks} - L_{min}) / BV_{maks} \quad (2)$$

Where, L_x is the radiance value; BV is Brightness Value; And Offset, Gain from the mathematical calculation of maximum-minimum

spectral radiance value in image metadata. The radiance value is changed to the at-sensor reflectance value based on the equation:

$$\rho P = \frac{\pi * L_x * d^2}{ESUN_x * \cos \theta_s} \quad (3)$$

$$d = 1 - 0,01674 \cos (0,9856(JD - 4)) \quad (4)$$

Where: ρP = the value of at-sensor reflectance; L_x = radiance value ($Wm^{-2}sr^{-1}\mu m^{-1}$); $\Pi = 3,142857142857143$; D = distance of earth-sun (astronomical unit); $ESUN_x$ = spectral irradiance sun value ($Wm^{-2}\mu m^{-1}$); θ_s = angle sun zenith (degree); JD = Julian Day.

2.3. Transformation of Vegetation Index

The vegetation index method that used is structure vegetation index. The vegetation index method was also adapted to the images band spectral of Sentinel-2 images used in this study. The vegetation index used in mapping of mangrove distribution in this study is described in table 2.

Table 2. An appropriate vegetation index for Sentinel image 2

No	Indeks Vegetasi
1	BR (Blue Ratio)[19] $\left(\frac{R}{B}\right) \times \left(\frac{G}{B}\right) \times \left(\frac{RE1}{B}\right) \times \left(\frac{NIR1}{B}\right)$ (5)
2	GNDVI (Green normalized difference Vegetation index) [20] $\frac{NIR1 - G}{NIR1 + G}$ (6)
3	GR (Green Ratio) [21] $\frac{G}{R}$ (7)
4	SAVI (Soil-Adjusted Vegetation Index) [22], [23] $\frac{(1+0.2) * (NIR1 - NIR2)}{(NIR1 + NIR2) + 0.2}$ (8)
5	MSAVI(modified SAVI) [24] $\frac{1}{2} \left[2 * NIR1 + 1 - \sqrt{(2 * NIR1 + 1)^2 - 8 * (NIR1 - R)} \right]$ (9)
6	NDRE (Normalized difference Red-Edge index) [25]. $\frac{NIR1 - RE}{NIR1 + RE}$ (10)
7	NDVI (normalized difference vegetation index)[26],[27],[20] $\frac{NIR1 - R}{NIR1 + R}$ (11)
8	NDVI2 (normalized difference vegetation index) [26] $\frac{NIR2 - R}{NIR2 + R}$ (12)
9	NDWI (Normalized Difference Water Index) [28]

	$\frac{G - NIR1}{G + NIR1}$ (13)
10	NNIP (Normalized Near Infrared) [19] $\frac{NIR1}{(NIR1 + R + G)}$ (14)
11	PSRI (Plant Senescence Reflectance Index)[29] $\frac{R - B}{RE1}$ (15)
12	RR (Red Ratio) [21] $\left(\frac{NIR1}{R}\right) \times \left(\frac{G}{R}\right) \times \left(\frac{NIR1}{RE1}\right)$ (16)
13	RVi (Ratio Vegetation index) [30] $\frac{NIR1}{R}$ (17)
14	SVI (Sentinel Improved Vegetation Index) [19] $\frac{NIR2 - R}{NIR2 + R}$ (18)
15	VIRE (Vegetation Index based on RedEdge) [19] $\frac{10.000 - NIR1}{RE1^2}$ (19)
16	VIRRE (Vegetation Index Ratio based on RedEdge) [19] $\frac{NIR1}{RE1}$ (20)
17	WVVI (WorldView Improved Vegetative Index) [31] $\frac{NIR2 - RE1}{NIR2 + RE1}$ (21)
18	MTV (Modified Triangular Vegetation Index1) [32] $1, 2 * [1, 2 * (NIR - G) - 2, 5 * (R - G)]$ (22)
19	MTV 2 (Modified Triangular Vegetation Index2)[32] $\frac{1.5 * (1.2 * (NIR - G) - 2.5 * (R - G))}{\sqrt{(2 * NIR + 1)^2 - (6 * NIR - 5 * \sqrt{R})} - 0.5}$ (23)
20	RDVI (renormalized difference vegetation index) [23] $[(NIR - R) / (NIR + R)^2]$ (24)
21	VARI (vegetation atmospherically resistant index)[33] $\frac{(G - R)}{(G + R - B)}$ (25)
22	VI green [33] $\frac{(G - R)}{(G + R)}$ (26)
23	MSR (Modified Simple Ratio) [32] $\frac{\left(\left(\frac{NIR}{R}\right) - 1\right)}{\left(\left(\frac{NIR}{R}\right) + 1\right)^{0.5}}$ (27)
24	TVI (triangular vegetation index) [30] $0.5 * (120 * (NIR - G)) - 200 * (R - G)$ (28)

Description: Blue (B), Green (G), Red (R), Near-infrared 1 (NIR1), Near-infrared 2 (NIR2), Red Edge 1 (RE1), Red Edge 2 (RE2).

2.4 Estimation of Mangrove Biomass

Estimation of mangrove tree biomass in this study was conducted using allometric equations. Allometric equations for above ground biomass [34]; [35] are:

$$W = 0.168 * \rho * (DBH)^{2.471} \quad (29)$$

Meanwhile, biomass measurements below ground level [5]; [35] are:

$$B = 0.199 * \rho^{0.899} * (DBH)^{2.22} \quad (30)$$

Description:

W = above ground level biomass, B = below ground biomass (kg), ρ = Wood density (g / cm³), DNH = diameter at breast height (cm).

Finding the best vegetation index was done by non-linear regression statistical analysis between biomass and vegetation index values. The result of non-linear regression analysis is the coefficient of determination (R^2) to determine the best vegetation index in estimate of mangrove biomass. The best regression equation is used to estimate mangrove biomass.

2.5. Study Area

This research was conducted in Majungan Village, Pademawu Sub-district, Pamekasan Regency. This location is located at the Madura Island which is part of East Java Province. The boundary of the study area is the coordinates of 113°29'48"-113°31'24" E, 7°13'48"-7°15'12" S.

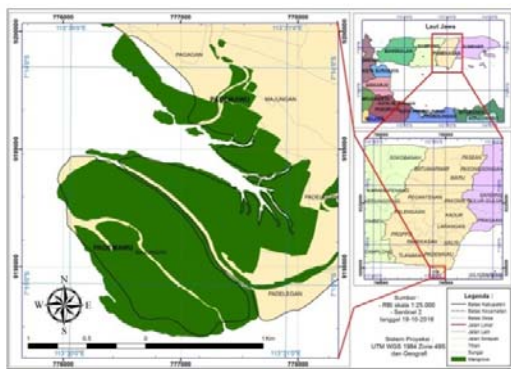


Figure 3. Map of Research Location

3. RESULTS AND DISCUSSION

In this study, the mangrove area was separated by other land cover. The process of mangrove masking was done due to the vegetation index was applied to detect canopy density variation, rather

than differentiate the type of vegetation. The initial stages of the study began with radiometric correction of sentinel-2 images. Radiometric correction was done by converting radian value to at-sensor reflectance. Corrected image then analyzed the vegetation index through the calculation of 24 types of vegetation index (see Table 2). The result of vegetation index analysis is presented in Table 3.

Table 3. Analysis Results 24 Types of Vegetation Index.

No	Index vegetasi	Min	Max	Mean	Stdev
1	BR	-8.79	5.13	-4.56	1.10
2	GNDVI	-0.09	0.52	0.35	0.07
3	GR	0.80	1.32	1.16	0.08
4	SAVI	-5943.31	30299.00	-2.02	230.23
5	MSAVI	-0.23	0.66	0.49	0.08
6	NDRE	-13367.00	10940.00	-4.40	201.74
7	NDVI	-0.07	0.59	0.41	0.09
8	NDVI2	-2442.56	2449.00	1.56	24.39
9	NDWI	-0.52	0.09	-0.35	0.07
10	NNIP	0.30	0.63	0.53	0.04
11	PSRI	-107.94	10.88	0.05	0.91
12	RR	-1138.47	144.26	-2.19	12.31
13	RVI	0.87	3.86	2.48	0.44
14	SVI	-2442.56	2449.00	1.56	24.39
15	VIRE	-15.23	0.0005	0.0017	0.14
16	VIRRE	-829.78	75.02	-0.82	9.25
17	WVVI	-4546.20	25214.00	5.21	310.65
18	MTV	-6573.408	-13520.64	24856.80	5439.40
19	MTV2	-4.59	-0.48	-1.22	0.41
20	RDVI	-0.00005	0.00002	0.00002	0.00005
21	VARI	-0.19	0.33	0.17	0.08
22	VI green	-0.11	0.14	0.07	0.03
23	MSR	-0.001	0.02	0.01	0.003
24	TVI	-136940.00	101924.00	572097.59	160378.89

Field measurements were carried out to obtain biomass values of mangrove trees, i.e. above ground biomass values and below ground biomass values. Sampling point field measurement as on the map Figure 4.

Based on the results of field measurements, biomass mangrove for above ground biomass of 382 kg/100m², below ground biomass was 352,7 kg/100m² and total biomass was 735 kg/100m². In

this study for soil biomass is not taken into account. Table 4 describes the minimum and maximum values of mangrove biomass measured in the field.

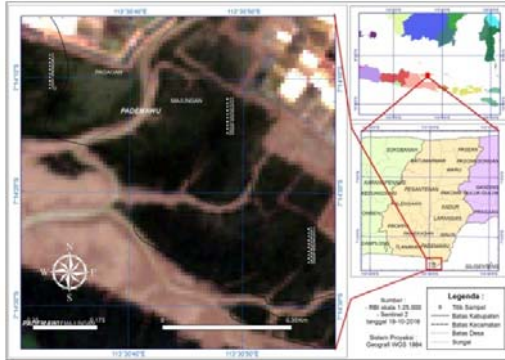


Figure 4. Map of the field measurement sample points

Table 4. Mangrove biomass from field data calculation

	Above ground biomass (kg/100m ²)	Below ground biomass (kg/100m ²)	Total biomass (kg/100m ²)
Min	86.9	84.2	171
Max	817.3	754.4	1572
Mean	382.0	352.7	735

The mangrove species found in the sample location plots are *Rhizophora stylosa*, *Rhizophora mucronata*, *Rhizophora apiculata*, *Avicennia marina*, *Aegiceras corniculatum*, *Sonneratia alba*, *Ceriops decandra*, *Xylocarpus moluccensis*. Composition of dominant mangrove species in the study area *Aegiceras corniculatum* (32%), *Ceriops decandra* (21.2%), *Rhizophora apiculata* (18.9%), *Sonneratia alba* (12.2%) and *Rhizophora stylosa* (10.7 %).

The next step is analyzed the relationship between image vegetation index values that have been produced with field measurement data, using logarithmic, quadratic, and exponential regression. Field measurement was the measurement of mangrove biomass at the sampling point. The model constructed for biomass estimation is based on statistical analysis between vegetation index results of image transformation of Sentinel-2 with the result of biomass calculation value in the field. The regression analysis model used was non-linear regression. Non-linear regression statistical analysis was based on determination coefficient (R^2). The value of R^2 shows the decreasing proportion of variation in the variation of free variables due to the utilization of the dependent variable information. The range of R^2 is between 0 and 1. It depicting how

much dispersion is explained by the prediction. The value of zero means there is no correlation at all, while the value of 1 means the dispersion of the prediction equals the observation. A good R^2 value approaches 1.0 [36].

The Kolmogorov-Smirnov normality test was performed before the independent variable used was normally distributed against the dependent variable or not. Normality test results will show normal distributed data when the value of significance on skewness ratio, and the kurtosis ratio is in the range -2 to 2. Based on statistical analysis of skewness ratio and the kurtosis ratio value, 24 vegetation index is spanned between -2 to 2, only 3 Vegetation indexes greater than 2, i.e. SAVI, NDVI2 and SVI.

Table 5. Regression results of 24 vegetation indexes with $R^2 > 0.8$ value.

Vegetation Index	Regression Model	Regression Equation	R^2
NDVI	Ekspponential	$y = 0.0316e^{22.26x}$	0.859
	Polynomial	$y = 86773x^2 - 62664x + 11397$	0.814
NNIP	Ekspponential	$y = 0.0000001e^{41.24x}$	0.832
RVI	Ekspponential	$y = 0.09e^{3.40x}$	0.850
	Logarithmic	$y = 5534.6\ln(x) - 4538.8$	0.809
	Polynomial	$y = 903.25x^2 - 2542.1x + 1215.4$	0.815
MTV1	Ekspponential	$y = 1,485,906.18e^{0.00x}$	0.813
MTV2	Ekspponential	$y = 180217e^{5.32x}$	0.829
MSR	Ekspponential	$y = 1.7209e^{504.63x}$	0.860
	Polynomial	$y = 48,915,274.97x^2 - 812,817.55x + 3,499.67$	0.815
TVI	Ekspponential	$y = 0.362e^{0.000012x}$	0.821

The best combination of vegetation index results can be seen in Table 5. Consistently, the non-linear regression approach through exponential equation shows higher R^2 value than logarithmic or polynomial equation. The best result of 24 vegetation index is MSR (Modified Simple Ratio), with exponential approach value $R^2 = 0.860$. While the next appropriate vegetation index was NDVI (normalized difference vegetation index) with exponential approach value $R^2 = 0.859$, and then vegetation index RVI (Ratio Vegetation index) with exponential approach value $R^2 = 0.850$. RVI vegetation index has good consistency with exponential, logarithmic or polynomial approach with value $R^2 > 0.8$.

Spatial modeling of mangrove distribution based on vegetation index was done using MSR vegetation index. Mapping of spatial distribution of mangrove biomass in Pademawu Subdistrict of Pamekasan Regency of East Java Province was based on exponential non-linear regression equation

of MSR vegetation index. The results of this mapping as illustrated on the map Figure 3..

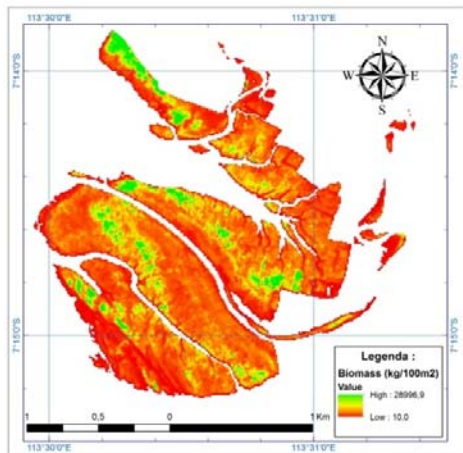


Figure 3. Spatial distribution of biomass in Pademawu Sub-district of Pamekasan Regency of East Java Province based on exponential non-linear regression equation of MSR vegetation index.

The result of spatial modeling of mangrove biomass shows that the average of mangrove biomass at each pixel (10x10m) was 0,9 ton/100m². Total mangrove biomass for above ground and below ground vegetation in the research area was 24,879.6 tons

4. CONCLUSION

The best results of 24 vegetation indices analyzed by exponential regression were MSR (Modified Simple Ratio), NDVI (normalized difference vegetation index) and RVI (Ratio Vegetation index). Spatial modeling of mangrove biomass with MSR approach shows an average of each pixel (10x10m) of 0,9 ton/100m². Total mangrove biomass for above ground and below ground vegetation in the research area was 24,879.6 tons. This research shows that Sentinel-2 image is quite capable of being used in estimation of mangrove distribution through vegetation index calculation and can also be used in analyzing mangrove biomass.

5. ACKNOWLEDGEMENTS

The author would like to thank the doctoral program of Fishery and Marine Science Faculty of Brawijaya University, Indonesia. The Sentinel-2 image used is a product of Copernicus Sentinel Data, the European Space Agency (ESA).

REFERENCES

[1] D. J. Griggs, "Climate change 2001: The scientific basis. Contribution of Working Group

I to the Third Assessment Report of the Intergovernmental Panel on Climate Change," *Weather*, vol. 57, pp. 267–269, 2002.

- [2] P. G. L. Klinkhamer, "Plant allometry: The scaling of form and process," *Trends Ecol. Evol.*, vol. 10, no. 3, p. 134, 1995.
- [3] W. Macnae, "A General Account of the Fauna and Flora of Mangrove Swamps and Forests in the Indo-West-Pacific Region," in *Advances in Marine Biology*, vol. 6, Johannesburg: University of the Witwatersrand, 1969, pp. 73–270.
- [4] P. B. Tomlinson, *The Botany of Mangrove*. New York: Combrige University Press, 1986.
- [5] J. Kauffman and D. Donato, *Protocols for the measurement, monitoring and reporting of structure, biomass and carbon stocks in mangrove forests*. Bogor, 2012.
- [6] S. E. Page, J. O. Rieley, and C. J. Banks, "Global and regional importance of the tropical peatland carbon pool," *Glob. Chang. Biol.*, vol. 17, no. 2, pp. 798–818, 2011.
- [7] I. C. Feller, C. E. Lovelock, U. Berger, K. L. McKee, S. B. Joye, and M. C. Ball, "Biocomplexity in mangrove ecosystems," *Ann. Rev. Mar. Sci.*, vol. 2, pp. 395–417, 2010.
- [8] R. S. DeFries, R. a Houghton, M. C. Hansen, C. B. Field, D. Skole, and J. Townshend, "Carbon emissions from tropical deforestation and regrowth based on satellite observations for the 1980s and 1990s.," *Proceedings of the National Academy of Sciences of the United States of America*, vol. 99, no. 22, pp. 14256–14261, 2002.
- [9] D. Alongi and S. Mukhopadhyay, "Contribution of mangroves to coastal carbon cycling in low latitude seas," *Agric. For. Meteorol.*, vol. 213, pp. 266–272, 2015.
- [10] C. Giri and J. Muhlhausen, "Mangrove forest distributions and dynamics in Madagascar (1975-2005)," *Sensors*, vol. 8, no. 4, pp. 2104–2117, 2008.
- [11] B. W. Heumann, "An object-based classification of mangroves using a hybrid decision tree-support vector machine approach," *Remote Sens.*, vol. 3, no. 11, pp. 2440–2460, 2011.
- [12] S. Sremongkontip, Y. Hussin, and L. Groenindijk, "Detecting changes in the mangrove forests of southern Thailand using remotely sensed data and GIS," *Int. Arch. Photogramm. Remote Sens.*, vol. 33, no. Part B7, pp. 567–574, 2000.
- [13] SUHET, *SENTINEL-2 User Handbook*, no. 1. <https://earth.esa.int/web/sentinel/user-guides/sentinel-2-msi/resolutions/spatial>, 2015.
- [14] Y. Xie, Z. Sha, and M. Yu, "Remote sensing imagery in vegetation mapping: a review," *J. Plant Ecol.*, vol. 1, no. 1, pp. 9–23, 2008.

- [15] L. Wang and W. P. Sousa, "Distinguishing mangrove species with laboratory measurements of hyperspectral leaf reflectance," *Int. J. Remote Sens.*, vol. 30, no. 5, pp. 1267–1281, 2009.
- [16] M. A. El-Shirbeny, B. Abdellatif, A.-E. M. Ali, and N. H. Saleh, "Evaluation of Hargreaves based on remote sensing method to estimate potential crop evapotranspiration," *Int. J. GEOMATE*, vol. 11, no. 23, pp. 2143–2149, 2016.
- [17] M. Drusch, U. Del Bello, S. Carlier, O. Colin, V. Fernandez, F. Gascon, B. Hoersch, C. Isola, P. Laberinti, P. Martimort, A. Meygret, F. Spoto, O. Sy, F. Marchese, and P. Bargellini, "Sentinel-2: ESA's Optical High-Resolution Mission for GMES Operational Services," *Remote Sens. Environ.*, vol. 120, pp. 25–36, 2012.
- [18] T. M. Lillesand, R. W. Kiefer, and J. W. Chipman, *Remote Sensing and Image Interpretation*. Wiley, 2004.
- [19] W.-T. Ng, P. Rima, K. Einzmann, M. Immitzer, C. Atzberger, and S. Eckert, "Assessing the Potential of Sentinel-2 and Pléiades Data for the Detection of *Prosopis* and *Vachellia* spp. in Kenya," *Remote Sens.*, vol. 9, no. 1, p. 74, 2017.
- [20] a. a. Gitelson and M. N. Merzlyak, "Remote estimation of chlorophyll content in higher plant leaves," *Int. J. Remote Sens.*, vol. 18, no. 12, pp. 2691–2697, 1997.
- [21] L. T. Waser, M. Küchler, K. Jütte, and T. Stampfer, "Evaluating the potential of worldview-2 data to classify tree species and different levels of ash mortality," *Remote Sens.*, vol. 6, no. 5, pp. 4515–4545, 2014.
- [22] A. R. Huete, "A soil-adjusted vegetation index (SAVI)," *Remote Sens. Environ.*, vol. 25, no. 3, pp. 295–309, 1988.
- [23] J. L. Roujean and F. M. Breon, "Estimating PAR absorbed by vegetation from bidirectional reflectance measurements," *Remote Sens. Environ.*, vol. 51, no. 3, pp. 375–384, 1995.
- [24] J. Qi, A. Chehbouni, A. R. Huete, Y. H. Kerr, and S. Sorooshian, "A modified soil adjusted vegetation index," *Remote Sens. Environ.*, vol. 48, no. 2, pp. 119–126, 1994.
- [25] A. Ramoelo, S. Dziki, H. Van Deventer, A. Maherry, M. A. Cho, and M. Gush, "Potential to monitor plant stress using remote sensing tools," *J. Arid Environ.*, vol. 113, pp. 134–144, 2015.
- [26] J. W. Rouse, R. H. Haas, J. A. Schell, and D. W. Deering, "Monitoring the vernal advancement and retrogradation (green wave effect) of natural vegetation," *Prog. Rep. RSC 1978-1*, p. 112, 1973.
- [27] N. Pettorelli, S. Ryan, T. Mueller, N. Bunnefeld, B. Jedrzejewska, M. Lima, and K. Kausrud, "The Normalized Difference Vegetation Index (NDVI): Unforeseen successes in animal ecology," *Clim. Res.*, vol. 46, no. 1, pp. 15–27, 2011.
- [28] B. C. Gao, "NDWI - A normalized difference water index for remote sensing of vegetation liquid water from space," *Remote Sens. Environ.*, vol. 58, no. 3, pp. 257–266, 1996.
- [29] M. N. Merzlyak, A. a Gitelson, O. B. Chivkunova, and V. Y. U. Rakitin, "Non-destructive optical detection of pigment changes during leaf senescence and fruit ripening," *Physiol. Plant.*, vol. 106, no. 1, pp. 135–141, 1999.
- [30] N. H. Broge and E. Leblanc, "Comparing prediction power and stability of broadband and hyperspectral vegetation indices for estimation of green leaf area index and canopy chlorophyll density," *Remote Sens. Environ.*, vol. 76, no. 2, pp. 156–172, 2001.
- [31] A. F. Wolf, "Using WorldView-2 Vis-NIR multispectral imagery to support land mapping and feature extraction using normalized difference index ratios," in *Algorithms and Technologies for Multispectral, Hyperspectral, and Ultraspectral Imagery XVIII*, 2012, vol. 8390, p. 83900N–83900N–8.
- [32] D. Haboudane, J. R. Miller, E. Pattey, P. J. Zarco-Tejada, and I. B. Strachan, "Hyperspectral vegetation indices and novel algorithms for predicting green LAI of crop canopies: Modeling and validation in the context of precision agriculture," *Remote Sens. Environ.*, vol. 90, no. 3, pp. 337–352, 2004.
- [33] A. a Gitelson, Y. Zur, O. B. Chivkunova, and M. N. Merzlyak, "Assessing carotenoid content in plant leaves with reflectance spectroscopy," *Photochem. Photobiol.*, vol. 75, no. 3, pp. 272–281, 2002.
- [34] J. Chave, C. Andalo, S. Brown, M. A. Cairns, J. Q. Chambers, D. Eamus, H. Fölster, F. Fromard, N. Higuchi, T. Kira, J. P. Lescure, B. W. Nelson, H. Ogawa, H. Puig, B. Riéra, and T. Yamakura, "Tree allometry and improved estimation of carbon stocks and balance in tropical forests," *Oecologia*, vol. 145, no. 1, pp. 87–99, 2005.
- [35] A. Komiyama, J. E. Ong, and S. Pongparn, "Allometry, biomass, and productivity of mangrove forests: A review," *Aquat. Bot.*, vol. 89, no. 2, pp. 128–137, 2008.
- [36] P. Krause and D. P. Boyle, "Advances in Geosciences Comparison of different efficiency criteria for hydrological model assessment," *Adv. Geosci.*, vol. 5, no. 89, pp. 89–97, 2005.

ESTIMATING THE ENVIRONMENTAL EFFECTS OF THE CAR SHIFTING BEHAVIOR ALONG EDSA

Nicanor R. Roxas, Jr.¹, Alexis M. Fillone², and Krister Ian Daniel Roquel²

¹Manufacturing Engineering and Management Department, De La Salle University – Manila, Philippines;

²Civil Engineering Department, De La Salle University – Manila, Philippines

ABSTRACT

Metro Manila is the most populated region in the country and the largest contributor to the economy of the country at around 40%. Situated in this metropolis is the Epifanio Delos Santos Avenue (EDSA) which currently serves approximately 330,000 vehicles daily, on the average. This number has greatly increased since the early 2000's. Because of EDSA's significance, many transportation related studies have focused on it. Among the largest studies is the Metro Manila Urban Transportation Integration Study (MMUTIS) which was completed in 1999 and has recently been updated through the MMUTIS Update and Capacity Enhancement Project (MUCEP). There is also another ongoing project entitled Integrated and Optimal Scheduling of a Public Transport System in Metro Manila (PUBFix) which is funded by the government (DOST-PCIEERD). The project intends to improve the public transportation system in the metropolis, specifically the operations of the buses along EDSA. In this research, the aim is to formulate SP logit choice models in order to predict the mode choices of commuters along EDSA. Such results are important in order to determine the changes in travel behavior of commuters when certain policies and measures are introduced. An EMME model is also prepared for this study in order to quantify the differences between the baseline and hypothetical scenarios. Aside from quantifying the difference of these scenarios in terms of environmental effects, other traffic parameters were also calculated in order for transport policy makers to be guided in considering more appropriate measures.

Keywords: Logit Choice Models, Urban Public Transport, Stated Preference, Mode Choice

INTRODUCTION

The road network of Metro Manila is defined by ten radial and six circumferential roads which links the region, as seen in Fig.1. Among the region's major thoroughfares, Epifanio Delos Santos Avenue (EDSA), located at the heart of Metro Manila, is one of the busiest roads in the Philippines. It is 24 kilometers long and passes through six of the seventeen cities comprising the metropolis.

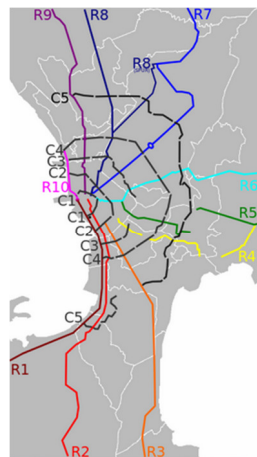


Fig.1 Circumferential and Radials Roads in Metro Manila.

EDSA caters to both private and public transportation for the region and links the North Luzon Expressway at Balintawak in the north to the South Luzon Expressway at the Magallanes Interchange in the south. EDSA serves an average daily traffic of approximately 330,000 vehicles, growing from an approximate number of 195,000 in 2007 [1], [2]. Currently, over 3,700 public utility bus units run along EDSA, while over 60,000 jeepneys and 3,184 AUVs are currently in operation all over the metropolis [3]. Note that all public vehicles are operated by private entities.

Most of the public transportation routes in Metro Manila are concentrated along EDSA because much of the areas of economic activities are adjacent to it. Despite the number of buses and other travel alternatives traversing EDSA, many commuters are inclined to use their own private vehicles which add more volume to the already congested roads of the metropolis brought about by various reasons. Because of the importance of EDSA to the commuters of Metro Manila and the complexity of the problems related to each of the transport alternatives serving the corridor, the road demands much more attention in order to improve its current state. The unorganized public transport system in Metro Manila is one of the reasons that cause commuters to be more inclined to use private modes

of transportation. The inefficiencies caused by a disorderly system are enormous that costs the Filipino people and the economy a huge amount in monetary terms annually. Added to this is the stress and anxiety it brings the commuters on a daily basis. The Department of Transportation (DOTr) and the Metro Manila Development Authority (MMDA) have tried improving the current situation through various means. However, the effects of the measures employed to curb the problem of traffic congestion remains to be felt.



Source: Facebook shared photo at North Ave. Station

Fig. 5 Long queue in one of the MRT stations.

This research is part of the project entitled An Integrated and Optimal Scheduling of Public Transport Operations in Metro Manila (PUBFix) funded by the Department of Science and Technology, Philippine Council for Industry, Energy, and Emerging Technology Research and Development (DOST-PCIEERD). PUBFix is undertaken in order to assess the actual and potential demand of public transport service along EDSA. It also aims to provide a more integrated transportation plan by considering both the existing supply as well as those being planned into the future. In lieu of this, logit choice models are developed in order to aid in planning for the improvement of the transportation network models. Through these logit choice models, the changes in travel behavior of commuters may be estimated when changes in the transportation system are introduced in the transportation network models. Therefore, the effects of certain policies, infrastructure improvements in the network, addition of new transport alternatives, may be estimated and quantified. One of the objectives of PUBFix is to propose, test, evaluate, and recommend, using scenario modeling, possible new high-capacity public transport systems (i.e. LRT, MRT, BRT, and/or city buses) in Metro Manila under 10-year and 20-year planning horizons. Logit choice models, indeed, are very useful in such procedures.

There is an increasing concern for the alarming traffic condition in Metro Manila [4], [5]. It is

imperative that measures are devised in order to alleviate the worsening situation. Several strategies may be implemented in order to achieve the desired result and one of these measures may include reducing the number of private cars from the roads. When introducing strategies, the decision makers should be guided accordingly as to which plan to operationalize in order to save resources. This paper focuses on estimating stated preference (SP) logit choice models for private car users. Various choice situations were presented to the private car users, and they were made to choose between their currently used mode and shifting to a hypothetical public transportation where improvements in the transportation system are introduced. The various significant factors affecting their choice were determined using logit choice models. The models enable transport planners to estimate the sensitivity of private mode users in shifting to public transport modes. The estimated SP logit choice models will then be used to assess the effects of the introduction of hypothetical transport modes in the urban transportation network of Metro Manila. Results from such analyses may aid in devising plans on how to induce the private car users to shift to the public transport modes.

In this study, only the private vehicle users are included in the database which will be the basis for the logit choice modeling. The origin-destination matrix used for the transportation network is taken from the Metro Manila Urban Transportation Integration Study Update and Capacity Enhancement Project (MUCEP) which is funded by JICA.

REVIEW OF RELATED LITERATURE

The transportation sector, specifically road transport, has consistently been cited as one of the leading causes of air pollution [6]–[10]. Reference [11] cited that mobility is correlated with income, add to this the increasing population, resulting in higher demand for passenger transport. The personal mobility offered by the private car makes it more appealing than the other alternatives, thus, the increasing auto use aggravates traffic congestion. This causes the deterioration of air quality in urban and suburban areas where congestion is severe [12]–[14]. There are several schemes that may be introduced in order to reduce emissions. Drastic behavioral and technological changes are needed in order to attain targets. Among those suggested are to encourage active transport, increase car occupancy rates, reduce total urban car kilometers traveled, improve vehicle efficiency, increase public transport's mode share of urban travel [7]. Reference [15] mentioned the implementation of a BRT is considered by many developing countries because of its lower investment cost and flexible

implementation than rail systems. Providing better alternatives to cars make the transport system sustainable [16]. Aside from pollution emissions, public transit also reduces traffic congestion, accidents, parking congestion, excessive energy consumption, road and parking infrastructure costs, and many others [17]. From the experience of British Government in providing a competitive alternative to private cars, several conditions should be implemented in order to increase modal shift to public transportation such as effective marketing and strict implementation of traffic laws. Reference [18] stated that public transit has significant benefits especially when relieving congestion in urban areas, just like Metro Manila.

THEORETICAL BACKGROUND

The multinomial logit model is the simplest, most practical, and most popular discrete choice model available [19]. It adheres to the utility maximization theory [20]. Utilities can be divided into two parts, the systematic or observable component (V) and the disturbance or random component [19], [21], [22]. In specifying the systematic part, the linear combination of the estimated parameters and the attributes of the alternatives are taken. The error terms are assumed to be independent and identically Gumbel distributed where the choice probability is specified as

$$P_n(i) = \frac{e^{V_{in}}}{\sum_{j \in C_n} e^{V_{jn}}} \quad (1)$$

where,

C_n – choice set of respondent, n ,

V_{in} – systematic component of utility of the chosen alternative, i , and

V_{jn} – systematic component of utility of the feasible choices, j .

URBAN TRANSPORT AND SOCIO-ECONOMIC STATISTICS

Survey questionnaires were administered to private car users traversing EDSA where a total of 592 observations were compiled and included for analysis. Table 1 shows the descriptive statistics for the data collected. The usual departure time of the respondents was between 0800 and 0900 in the morning where the average length of travel is approximately 48 minutes and costs 84PHP (≈ 1.75 USD) on the average. The average parking cost for the travelers was 25.20PHP (≈ 0.52 USD). The average age of the respondents was 35 years old. As for the civil status, 32% were married, separated, or widowed, while 68% were single. Seventy three percent of the respondents were male

and 27% were female. Lastly, the average size of the traveling group of the respondents is about 2 persons.

Table 1 Descriptive statistics of the sample

Usual departure time	0800–0900
Usual length of travel	47.43min
Usual sum of costs	84.02PHP
Average parking cost	25.20PHP
Average age (all)	35.01
Male	35.19
Female	34.55
Civil Status	Single: 68% Married: 32%
Gender	Male: 72.97% Female: 27.03%
Average number of people in the group	1.85
Number of observations	592

The majority of the respondents (61%) included in the sample were college graduates. Next is the group of high school graduates with 27%. Respondents with Master's degrees comprise 11% of the dataset and the remaining 1% for vocational training graduates. Almost half of the total trips are going to work. This is understandable because commuters using EDSA are mostly going to their offices especially during the morning rush hours. This is followed by the shop/personal/others trip purpose (19%), and then school trips (18%), and finally business trips (12%).

Majority of the individual incomes are less than or equal to 100,000PHP/month (≈ 2060 USD/month) with an average value of approximately 1100USD/month. This shows that majority of the respondents belong to the high income group according to the income categories of the National Statistics Office.

LOGIT CHOICE MODELING RESULTS

From the 592 observations, SP logit choice models were estimated. The final model is formulated as seen in the following utility equations. Respondents shifting to public transportation are assigned to choice A, whereas choosing to remain using one's private vehicle is assigned to choice B.

$$U(\text{SHIFT}) = ASCA + TOTTIME * (\text{Total travel time}) + AGE * (\text{Age of respondent}) + ACC3 * (\text{Access and egress type 3}) + COMF * (\text{Level of comfort of proposed mode}) + COLL * (\text{College degree holder}) + POST * (\text{MS degree or higher}) \quad (2)$$

$$U(STAY) = TOTTIME * (Total\ travel\ time)$$

(3)

Shown in Table 2 is the final model estimated through the use of NLOGIT software. It can be seen that the model is significant with a corresponding high Chi-squared value. The model performance is acceptable with an *R-sqrd* value of 0.30651. Looking at the final model, the various factors significantly affecting the choices made by the respondents are identified. It can be verified that total travel time, age, access and egress type 3, level of comfort of the new mode, and educational attainment all affect choice. This is indicated by the individual significance values in which all are less than the 0.05 level of significance.

Looking at the TOTTIME parameter which is specified generic for both choices, it can be stated that it negatively affects choice and serves as a disutility to the commuters. As for the age which is specific to choice A, it can be said that older people will be less likely to shift from their private vehicles to a public transport. However, when one looks at the educational attainment variable assigned to choice A, the opposite is true. As the level of educational attainment increases, the more they are likely to shift to public transport modes. This could probably be explained by the fact that when the questionnaires were administered, the current traffic situation is explained to everyone. Most likely, those people with higher levels of educational attainment understand how to contribute in solving the problem of congestion. Access type 3 is a dummy variable assigned to choice A. It takes a value of 1 when the access and egress modes are similar to high-occupancy on-call shared taxis. By inspecting the parameter, it can be noted that when the access and egress modes are upgraded, then the respondents will tend to shift modes. Only this type of improvement in the access and egress modes to and from EDSA was found to be significant among the other three options. It just shows that private car users, indeed, value the comfort and convenience of door-to-door transport and avoid the inconvenience of transfers. Lastly, the comfort and convenience variable has three levels and is orthogonally coded which is assigned to choice A; high level of comfort is designated a value of +1. For the purpose of this study, comfort was represented by the load factor of the mode. Inspection of the COMF coefficient shows that it is positive which only demonstrates that improving the level of comfort of public transportation along EDSA attracts private car users to shift.

Note that when the SP part of the questionnaire was designed, it was assumed that all the improvements in the access, egress, and main modes will not translate to any change in the costs already incurred by the respondents. This is somewhat a limitation of this study. The total cost incurred is the

same for the current private mode of travel and shifting to public transportation combined with all the improvements specified in the questionnaire.

Table 2 SP Logit Choice Model

No. of observations		592
R-sqrd		0.30651
Chi-squared		105.30987
Prob [chi squared > value]		0.00000
Variable	Coefficient	P [Z > z]
ASCA	-1.09028140	0.0007
TOTTIME	-0.02546769	0.0001
AGE	-0.03568077	0.0003
ACCESS3	0.81024906	0.0013
COMF	0.76930538	0.0000
COLL	0.96494867	0.0009
POST	1.09526421	0.0189

The model performance was also checked by the accuracy to estimate the choices made by the respondents. The following table is a crosstab matrix which shows the distribution of the model predictions. It can be verified that 406 or (59+347) out of the 592 choice situations have been correctly predicted by the model. This represents a 68.58% accuracy which is acceptable.

Table 3 SP Logit Choice Model

	A	B	Total
A	59	93	152
B	93	347	440
Total	152	440	592
A – shift B – stay			

EMME MODELING RESULTS

The EMME4 transportation planning software was used in order to incorporate the SP model results in measuring the economic and environmental effects of the mode shifting behavior of travelers in Metro Manila. First, the baseline transportation network of the whole Metro Manila is modeled using the MUCEP data for peak hour traffic. All the necessary data were encoded, the model calibrated and important travel-related statistics obtained. After this, a second scenario was developed incorporating the SP logit choice model and the model was rerun. The differences in travel-related statistics between the results of the two models were then recorded. The following figure shows the EMME baseline model for Metro Manila.

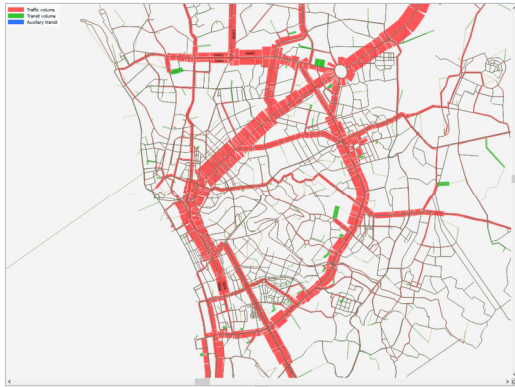


Fig. 1 EMME Model.

Table 4 shows the values of the different parameters measurable in the EMME model when the baseline and with transfer scenarios were run. An increase of 3kph in speed along EDSA, on the average, has been registered. This outcome is a result of the 12% private car users shifting to the new hypothetical transport mode. Along with the increase in average speed are the reductions in vehicle operating costs and value of travel time which are quite significant. Also, quite noticeable are the reduction in environmental pollutants. The differences in the CO₂, NO_x, and SPM values translate to a total of 36% reduction in environmental cost when they are converted to monetary units. This suggests that when a competitive public transport alternative such as a BRT is introduced along EDSA, the current traffic situation will be addressed. The effects are quite significant and should be given ample consideration by the government.

Table 4 Differences between the baseline and with transfer scenarios during the peak hour

	BASELINE	WITH TRANSFER
Average speed (kph)	18.39	21.32
Vehicle operating cost (PHP)	386,382.7	329,641.2
Value of time (PHP)	28,151,511	15,846,214
CO ₂ (g)	2,765,655.92	1,885,906
NO _x (g)	599,308.71	518,045.6
SPM (g)	47,666.68	27,579.6
Environmental Cost (PHP)	198,483.07	126,430.72

CONCLUSION

The PUBFiX project is looking into the current traffic condition in Metro Manila and is formulating strategies in order to improve the public

transportation system along EDSA, as well as lessening the harmful environmental effects of traffic congestion. In order to achieve this, choice modeling is necessary in order to estimate the effects of certain policies on the choices made by the commuters. For this study, SP logit choice models were estimated in order to aid in the planning of the transportation system in the metropolis. The behavior of private car users were investigated and assessed when they were given several hypothetical scenarios which involve several improvements in the public transportation system traversing EDSA. This was done in order to investigate the environmental effects of mode shifting in the metropolis.

Based on the results of the SP logit choice model formulated, it was determined that travel time, age, educational attainment, existence of access type 3, and comfort and convenience significantly affect the mode shifting behavior of private car users in Metro Manila. Interesting to note here is when one looks into the numerical coefficients of travel time, access type 3, and comfort and convenience. The numerical coefficients suggest that the provision of high-occupancy on-call shared taxis to private car users has a similar effect of reducing the disutility of travel time by approximately 32 minutes. This suggests that the convenience of a somewhat door to door travel is particularly desired by the private car users. Also, the provision of a high level of comfort for the hypothetical BRT mode along EDSA is equivalent to a significant amount of reduction in travel time, approximately 31 minutes. The high level of comfort is characterized by load factor less than 1.0, more organized stops, and roomier cabin for passengers. Again, this reinforces the notion that private car users are sensitive to the level of comfort of their mode of travel.

As seen from the EMME modeling results, the shifting of private car users to the hypothetical public transport mode greatly affects the transportation system of the metropolis. The number of vehicles on the road decreases while the average travel speed increases. This not only translates to savings in value of travel time, vehicle operating costs, but savings on environmental pollution, as well. This analysis proves that when the public transport modes are upgraded in terms of their level of comfort, reliability, and speed, then there would be a significant amount of private transport users willing to shift to alternative public transport modes. This is what the future of Metro Manila should be. In order to have a sustainable transportation system, various schemes should be employed in order to attract private car users to shift to the more efficient public transport modes. Strict implementation of laws, major behavioral changes, and technological improvements should be among the government's priorities to improve the current

transportation sector, with emphasis to curbing the worsening environmental pollution. Enormous investments on public transportation are imperative in order to achieve this vision. Current policies such as modifying the number coding scheme are momentary solutions to the serious transportation problem of the metro. What this country needs are long term solutions if the government is really serious. Transportation studies such as PUBFix should not just be encouraged by the government. Their results and recommendations should warrant the consideration of the government, as well.

REFERENCES

- [1] Vallarta B, "With 31 malls near EDSA, Christmas traffic crawls. GMA News", Retrieved from <http://www.gmanetwork.com/news/story/241646/news/nation/with-31-malls-near-edsa-christmas-traffic-crawls>, 2011.
- [2] Kawabata Y and Sakairi Y, "Metro Manila interchange construction project (IV)", Retrieved from: http://www.jica.go.jp/english/our_work/evaluation/oda_loan/post/2008/pdf/e_project22_full.pdf, 2008.
- [3] Land Transportation Franchising and Regulatory Board. <http://www.ltfrb.gov.ph/>.
- [4] ALMEC Corporation, Pacific Consultants International, Yachiyo Engineering Co., Ltd., "Metro Manila Urban Transportation Integration Study, Metro Manila: Japan International Cooperation Agency (JICA)", 1999.
- [5] JICA, "The Project for Capacity development on Transportation Planning and Database Management in the Republic of the Philippines. MMUTIS Update and Enhancement Project (MUCEP)", Retrieved from: http://open_jicareport.jica.go.jp/pdf/12247615.pdf, 2015.
- [6] Hensher D A, "Climate change, enhanced greenhouse gas emissions and passenger transport - What can we do to make a difference?", *Transportation Research Part D*, Issue 13, 2008, pp. 95-111.
- [7] Stanley J K, Hensher D A and Loader C, "Road transport and climate change: Stepping off the greenhouse gas", *Transportation Research Part A*, Issue 45, 2011, pp. 1020-1030.
- [8] Chapman L, "Transport and climate change: a review", *Journal of Transport Geography*, Issue 15, 2007, pp. 354-369.
- [9] Liu Y-H, Liao W-Y, Lin X-F., Li L., and Zeng X-I, "Assessment of Co-benefits of vehicle emission reduction measures for 2015-2020 in the Pearl River Delta region, China", *Environmental Pollution*, Issue 223, 2017, pp. 62-72.
- [10] Chester M et al., "Infrastructure and automobile shifts: positioning transit to reduce life-cycle environmental impacts for urban sustainability goals", *Environmental Research Letters*, Issue 8, 2013, pp. 1-10.
- [11] Dhar S and Shukla P, "Low carbon scenarios for transport in India: Co-benefits analysis", *Energy Policy*, Issue 81, 2015, pp. 186-198.
- [12] Pucher J, "The road to ruin? Impacts of economic shock therapy on urban transport in Poland" *Transport Policy*, 2(1), 1995, pp. 5-13.
- [13] Kamba A N, Rahmat R A O and Ismail A, "Why do people use their cars: A case study in Malaysia", *Journal of Social Sciences*, Issue 3, 2007, pp. 117-122.
- [14] U.S. Department of Transportation, "Federal Transit Administration", [Online] Available at: <https://www.transit.dot.gov/regulations-and-guidance/environmental-programs/transit-environmental-sustainability/transit-role>, 2016.
- [15] Satiennam T, Jaensirisak S, Satiennam W and Detdamrong S, "Potential for modal shift by passenger car and motorcycle users towards Bus Rapid Transit (BRT) in an Asian developing city", *IATSS Research*, Issue 39, 2016, pp. 121-129.
- [16] Davison L J and Knowles R D, "Bus Quality partnerships, modal shift and traffic decongestion", *Journal of Transport Geography*, Issue 14, 2006, pp. 177-194.
- [17] Litman T, "Evaluating Public Transit Benefits and Costs. Victoria: Victoria Transport Policy Institute", 2017.
- [18] Harford J D, "Congestion, pollution, and benefit-to-cost ratios of US public transit systems", *Transportation Research Part D*, Issue 11, 2006, pp. 45-58.
- [19] Ortuzar J dD and Willumsen L G, *Modelling Transport*. 4th ed. United Kingdom: John Wiley and Sons, Ltd, 2011.
- [20] Hess S, "Advanced discrete choice models with applications to transport demand (Thesis)", London: Center for Transport Studies, Imperial College, 2005.
- [21] Ben-Akiva M and Lerman S R, *Discrete Choice Analysis: Theory and Application to Travel Demand*. Cambridge, Massachusetts: MIT Press, 1985.
- [22] Garrow L A, *Discrete Choice Modelling and Air Travel Demand*. Vermont: Ashgate Publishing Company, 2010.

EFFECTIVENESS OF PERMEABLE REACTIVE BARRIER (PRB) ON HEAVY METAL TRAP IN AQUIFER AT SOLID WASTE DUMPSITE: A SIMULATION STUDY

Udayagee Kumarasinghe¹, Y. Sakamoto², T. Saito¹, M. Nagamori³, C. S. Kalpage⁴, G.B. Herath⁴, M.I.M. Mowjood⁵, and Ken Kawamoto^{1,6}

¹Graduate School of Science and Engineering, Saitama University, Japan

²National Institute of Advanced Industrial Science and Technology

³Material Cycles and Waste Management Group, Centre for Environmental Science in Saitama, Japan

⁴Faculty of Engineering, University of Peradeniya, Sri Lanka

⁵Department of Agricultural Engineering, Faculty of Agriculture, University of Peradeniya, Sri Lanka

⁶International Institute for Resilient Society, Saitama University, Japan

ABSTRACT

Open dumping of solid waste causes serious environmental risk of groundwater contamination due to landfill leachate rich in heavy metals. Identification of contaminant flow and implementation of remediation technologies including permeable reactive barrier (PRB) are highly demanded. In this study, Geo Environmental Risk Assessment System (GERAS) has been used to simulate two-dimensional heavy metal transport in an aquifer at solid waste dumpsite and to estimate the effectiveness of virtual PRB on trap heavy metals. For simulation, Cd and Pb were selected as target contaminant based on the results of water quality analyses at an abundant solid waste dump site in Sri Lanka. First, two cases were examined: 1) An open dump of waste located above the aquifer and 2) A buried dump waste inside the aquifer. Concentration changes of heavy metals inside the aquifer beneath the waste unit, inside PRB, upstream and downstream points to PRB were examined by changing the hydraulic gradient in the aquifer and pollution load. Results showed the numerical simulations well captured the wash-out process of heavy metals from the pollutant source. Time period required for full wash-out was highly dependent on the range of hydraulic gradient and pollution load. Next, a virtual PRB was set in downstream of aquifer by installing a section with a high heavy metal adsorption capacity (based on previous studies). Results showed that the virtual PRB well trapped the target metals and reduced the contamination level less than the effluent water quality standards.

Key words: Solid waste dumpsite, Groundwater, Heavy metal, Permeable reactive barrier, Numerical simulation

INTRODUCTION

Open dumping is a common method used for the final disposal of municipal solid waste in most developing countries [1]. Landfill leachate is rich in toxic hazardous heavy metals. The permeation of leachate causes serious soil and groundwater pollution in surroundings [2]. Thus, identification and mitigation of groundwater contamination by heavy metals at open solid waste dumpsites has been highly demanded. Recently, Permeable Reactive Barrier (PRB) system, which is one of in-situ methods for treating contaminated groundwater by immobilization of heavy metal in contaminated groundwater surrounding the open solid waste dumpsites., become an option [3] PRB system does not interrupt the groundwater flow in the treatment process, thus highly suitable to use as *in-situ* pollutant immobilization technique. In this study, a numerical simulation software, Geo Environmental Risk Assessment System (GERAS) [4], has been used to simulate a two-dimensional groundwater flow coupled with heavy metal transport. In the

simulations, the effectiveness of PRB on the heavy metals (Cd and Pb) trap in an aquifer at solid waste dumpsite has been examined.

MATERIALS AND METHODS

Selection of Modeling Area

A conceptual contaminated site was classified based on data collected from an open solid waste dumpsite located in Central province of Sri Lanka. The dumpsite has been used for 7 years of waste dumping [2]. Fig. 1 illustrates the arrangement and setting of the conceptual open solid waste dumpsite model. The conceptual open solid waste dumpsite (waste unit) was fixed as 100m in length and 40m in width and the area of aquifer was set to be 400m x 100m in *x* and *y* direction. The thicknesses of the aquifer and waste unit were set to be 2m. A 4m width and 45m length virtual PRB was installed in the downstream (20 m away from the end point of the dumped waste in *x* direction). In the simulations, two cases were studied: Case 1: An open dump of waste

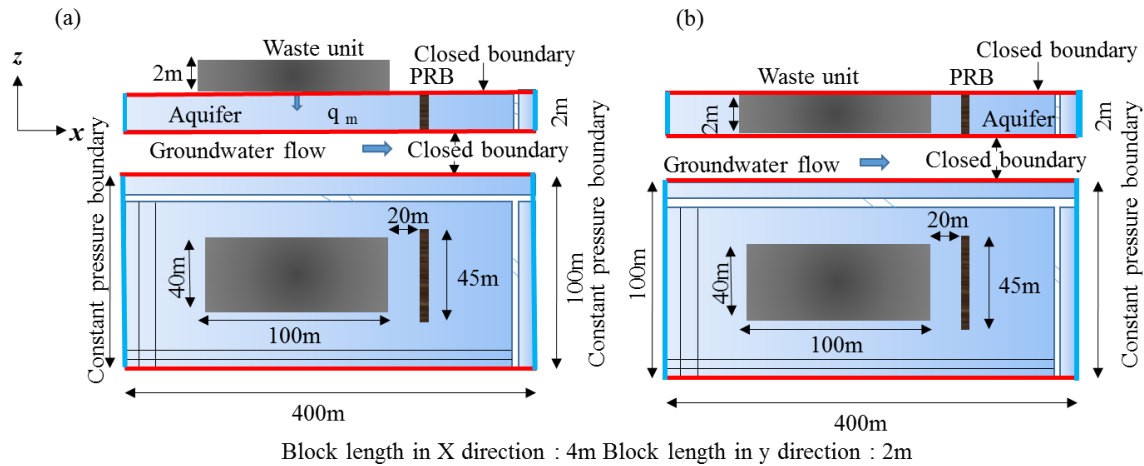


Fig. 1 Scale and initial boundaries of conceptual model for simulation: Case 1 [a] and Case 2 [b]

(pollutant source) located above the aquifer and direct permeation of rainwater into the aquifer through waste layer (Fig. 1a). Case 2: A buried waste dump inside the aquifer, no effect of rainfall, groundwater flow affects the washing out of contaminants (Fig. 1b). Spatial and temporal variabilities of contaminants and the effectiveness of the PRB were evaluated in both cases by analyzing the changes in heavy metal concentrations at upstream, downstream and inside the PRB.

Governing Equations

GERAS simulation model is used to estimate contaminant concentration (heavy metals) in the groundwater as a function of time and space. The model simulation is considered to be two dimensional in horizontal plane. The governing equations has applied for three main zones of the contaminated sites.

Zone 1: Aquifer

The model follows the flow equations as shown in Eqs. (1) and (2) assuming water is an incompressible fluid, fluid pressure created by groundwater is low, and aquifer is homogeneous, and isotropic porous media [5].

$$\frac{\partial^2 \phi}{\partial x^2} + \frac{\partial^2 \phi}{\partial y^2} = 0 \quad (1)$$

$$v_x = \frac{-k_x}{n_a} \cdot \frac{\partial \phi}{\partial x} \text{ and } v_y = \frac{-k_y}{n_a} \cdot \frac{\partial \phi}{\partial y} \quad (2)$$

where ϕ [L] is the pressure head, v_x and v_y [LT⁻¹] are the groundwater velocities in x and y directions, k_x and k_y [LT⁻¹] are the hydraulic conductivities in x and y directions, n_a [-] is the porosity of aquifer.

A solute transport equation used in the simulations was as follows:

$$\frac{\partial C}{\partial t} = \frac{\partial}{\partial x} \left[D_x \frac{\partial C}{\partial x} \right] + \frac{\partial}{\partial y} \left[D_y \frac{\partial C}{\partial y} \right] - \left[V_x \frac{\partial C}{\partial x} - V_y \frac{\partial C}{\partial y} \right] - \left[\frac{1-n_a}{n_a} \right] \rho_s \frac{\partial S}{\partial t} \quad (3)$$

where C [ML⁻³] is the solute concentration, t is the time, D_x and D_y [L²T⁻¹] is the diffusion coefficient in x and y directions, S [MM⁻¹] is the saturated adsorption of contaminant into soil particles. The D_x and D_y are as follows:

$$\begin{aligned} D_x &= \varepsilon D_M + \tau_L |V_x| \\ D_y &= \varepsilon D_M + \tau_T |V_y| \end{aligned} \quad (4)$$

where D_M [L²T⁻¹] is the molecular diffusion coefficient of metal (Cd and Pb) in free water and ε is the tortuosity (used Millington and Quirk model [7] in this study). The longitudinal and transverse dispersivities, τ_L and τ_T [L], were determined with respect to the scale of aquifer in the simulation and τ_T was considered as 0.1 times of τ_L [8]. In the aquifer, linear adsorption model was used for the adsorption of heavy metals into solid phase:

$$S_s = k_{d-w} C_w \quad (5)$$

where k_{d-w} [L³M⁻¹] is the distribution coefficient of target heavy metal in the aquifer.

Zone 2: Waste unit

Few assumptions were made when applying the governing equations to waste unit: 1) heavy metal component in solid waste stocked within the waste unit, 2) dissolution/ desorption of heavy metal due to rainfall permeation and groundwater flow in Case 1, and only by groundwater flow in Case 2. . Saturated adsorption of heavy metals into waste particles: S_{ws} [MM⁻¹] were determined following linear adsorption model using the distribution coefficient of target heavy metal in the waste unit: k_{d-ws} [L³M⁻¹].

$$S_{ws} = k_{d-ws} * C_{ws} \quad (7)$$

The concentration of heavy metal component in porous media of waste (C_{ws}) [ML^{-3}] is considered to be equal to heavy metal concentration of adjacent soil porous.

Inflow flux of heavy metal in Case 1 follows the Eq. (8).

$$q_{hm} = Rq_r C_w \quad (8)$$

where q_{hm} [MT^{-1}] is the inflow flux, R is the permeation ratio, q_r [L^3T^{-1}] is the rainfall intensity, and C_w [ML^{-3}] is the equilibrium concentration of heavy metal in water phase. Inflow of heavy metal in Case 2 is controlled by Eq. (7).

Zone 3: Permeable Reactive Barrier (PRB)

Langmuir adsorption model was applied to characterize the heavy metal adsorption at PRB in the simulations:

$$\frac{C_{ws}}{S} = \frac{1}{bQ_m} + \frac{C_w}{Q_m} \quad (9)$$

where S is the adsorbent amount of heavy metal into reactive material, b [L^3M^{-1}] is the Langmuir constant and Q_m [MM^{-1}] is the maximum adsorption capacity [9].

Setting of Input Parameters

Table 1 summarizes parameters used in the simulations.

Table 1 Input parameters used for model simulation

Zone	Description	Symbol	Unit	Value	Reference
Aquifer	Porosity	n_a		0.4	[10]
	Hydraulic conductivity	k_x, k_y	m/s	1E-03	[10]
	Hydraulic gradient	i	-	0.06 (0.006, 0.12)*	[11]
	Molecular diffusion coefficient	D_M	m ² /s	Cd: 6.0E-10 Pb: 7.9E-10	[10]
	Dispersivity	τ_x	m	Cd: 10 Pb: 10	[12]
	Distribution coefficient	k_{d-w}	m ³ /kg	Cd: 1.3E-02 Pb: 1.4E-01	[12]
Waste unit	Initial concentration of heavy metal component	S_{ws}	mmol/kg	Cd: 3.24E-04 Pb: 2.01E-02	[2]
	Distribution coefficient	k_{d-ws}	m ³ /kg	Cd: 1.3E-03 Pb: 2.7E-03	[13]
PRB	Maximum adsorption capacity of heavy metal	Q_m	mmol/kg	Cd: 2.7E+01 Pb: 4.8 E+01	[12]
	Langmuir isotherm constant	b	m ³ /mmol	Cd: 3.0E-02 Pb: 9.4E-03	[12]
Meteorological parameters	Rainfall intensity	q_r	mm/yr	3.53 E+03	[2]
	Permeation ratio	R	-	1	[14]

*Used for the sensitivity analysis

Aquifer

The hydraulic gradient was calculated based on groundwater level measured at the studied dumpsite. The model use the single value for the calculation and it is assumed that the hydraulic gradient is constant throughout the simulation period. The distribution coefficient of heavy metal in water phase k_{d-w} was determined considering the soil type of studied area. The soil type of the studied dumpsite is Reddish brown latasolic and the distribution coefficient calculated for the same soil type was used [12].

Waste unit

Initial concentration of heavy metal was set by considering monitored metal concentrations at studied dumpsite [2]. Referred values [13] were used for the distribution coefficient of heavy metal in waste. The weight of the dumped waste was considered as 1.07E+07 kg, according to the *in-situ* dry density of waste (= 0.6 kg/m³) and specific gravity (= 2.3) [2].

Permeable reactive barrier (PRB)

The PRB material was selected based on the previous study [12]. In the simulations, the hydraulic conductivity of PRB is assumed to be equal to the hydraulic conductivity of aquifer.

Rainfall data was collected from a rain-gauge station near by studied dumpsite [2].

Sensitivity Analysis

Sensitivity analysis was conducted to analyze the effect of various input parameters. The values chosen were 1, 0.1, 2 times of the actual input parameter for hydraulic gradient (0.06, 0.006, 0.12). Similarly, the scale of the dumpsite (waste unit) was changed into 40 m x 40 m in order to evaluate the effect of pollutant loads. The time taken to peak heavy metal concentration in the monitoring points were compared.

RESULTS AND DISCUSSION

Model Outputs of Sensitivity Analysis

Table 2 exemplifies the model outputs of sensitivity analysis. In both cases output values (peak time and concentration inside the PRB) were highly sensitive to the hydraulic gradient for both heavy metals. For example, the time for peak concentration was mainly controlled by i : the peak time for $i = 0.006$ become 4-6 times higher than that for $i = 0.06$ except for the Pb with low pollution load. On the other hand, the effect of pollution load was significant only for the outputs from Case 2: the peak concentration for the low pollution load became ~20% of the peak concentration for the high pollution load.

As shown in Table 2, the washing out of contaminants (reduction in metal concentration) was much faster in Case 2 than Case 1 for both Cd and Pb. This attributes to the direct exposure of waste unit into the groundwater flow in Case 2. On the other hand, the washing out of heavy metals is

controlled by the rainfall precipitation in Case 1. These results suggest that rapid and higher pollution migration easily occurs in the waste dump site with a buried waste. Furthermore, the heavy metals trapped by the PRB in Case 2 were greater than those in Case 1 due to the higher concentrations of heavy metals in the inflow to PRB.

Evaluation of the Effectiveness of PRB

Figure 2 illustrates the temporal variation of the heavy metal concentration in different places of the aquifer. In most cases, the PRB trapped well heavy metals in the aquifer and reduced the peak concentration at the outflow from PRB. For both Cd and Pb, the heavy metal concentrations observed at the outflow from PRB were less than those of the effluent water quality standards in Sri Lanka which is 8.90E-04 and 4.83E-04 mmol/L respectively for Cd and Pb [15].

Pollution Migration Process in the Aquifer

Figure 3 shows an example for pollutant migration process in aquifer. The simulation was carried out to observe the pollutant plume of Cd in the aquifer, with respect to the Case 2. A rapid washing out process was observed in the upstream to the PRB and the pollutant plume reached to the PRB within six months. Due to the adsorption at the PRB, a drastic reduction of Cd concentration was observed in the outflow from the PRB. However, even after 10 years, contaminants can be found in the aquifer which is 300 m away from the buried waste unit.

Table 2 Model outputs of sensitivity analysis

		i	Cd		Pb	
			Time (Year)	Concentration (mmol/L)	Time (Year)	Concentration (mmol/L)
High pollution load	Case 01	0.060	5.50	2.05E-05	41.7	1.18E-04
		0.120	3.70	1.95E-05	25.3	1.18E-04
		0.006	24.0	2.10E-05	148	1.05E-04
	Case 02	0.060	0.90	1.04E-04	6.70	6.78E-04
		0.120	0.50	1.09E-04	4.20	8.93E-04
		0.006	5.30	1.02E-04	39.7	6.76E-04
Low pollution load	Case 01	0.060	7.50	1.29E-05	78.2	8.06E-05
		0.120	4.60	1.16E-05	45.8	8.23E-05
		0.006	41.9	1.43E-05	N.B.*	N.B.*
	Case 02	0.060	2.80	2.27E-05	30.1	1.26E-04
		0.120	1.70	2.80E-05	17.8	1.99E-04
		0.006	17.7	2.18E-05	N.B.*	N.B.*

*N.B.: No breakthrough.

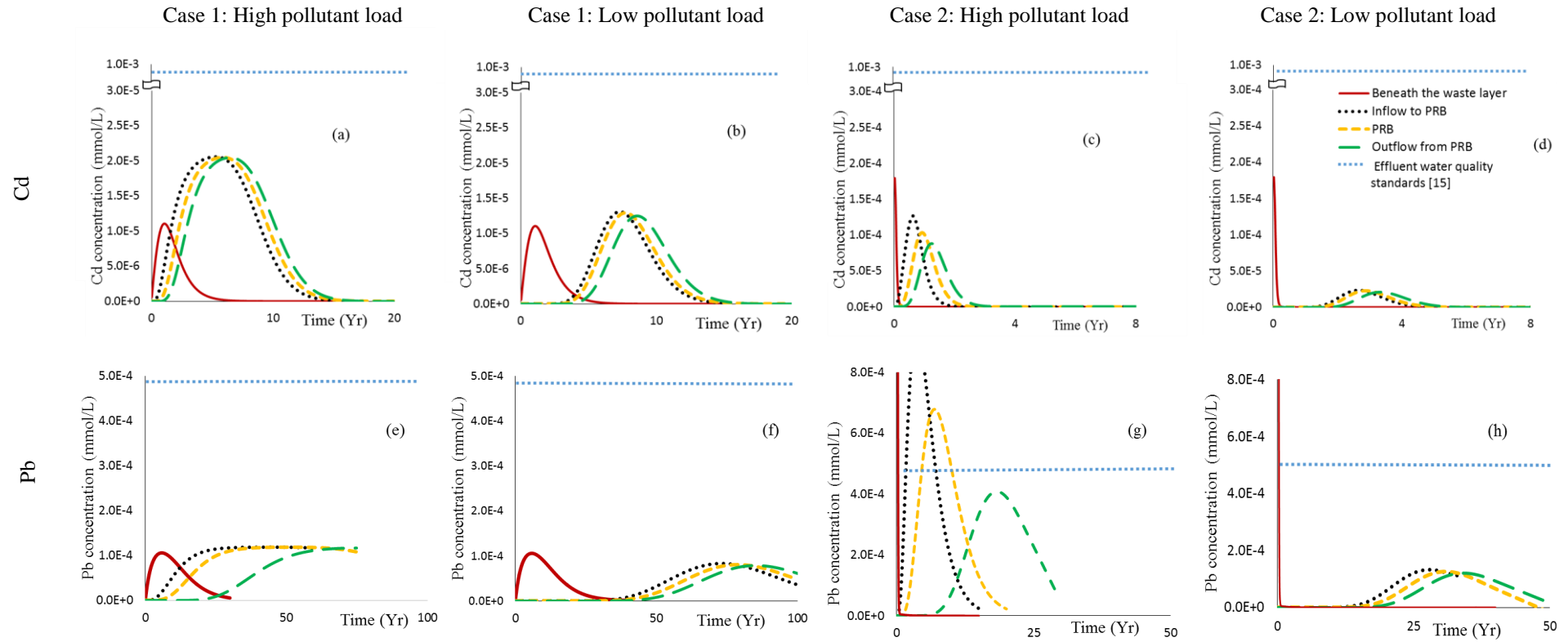


Fig.2 Temporal variation of the heavy metal concentration at the different locations of the aquifer for Cd [(a), (b), (c), (d)] and for Pb [(e), (f), (g), (h)]

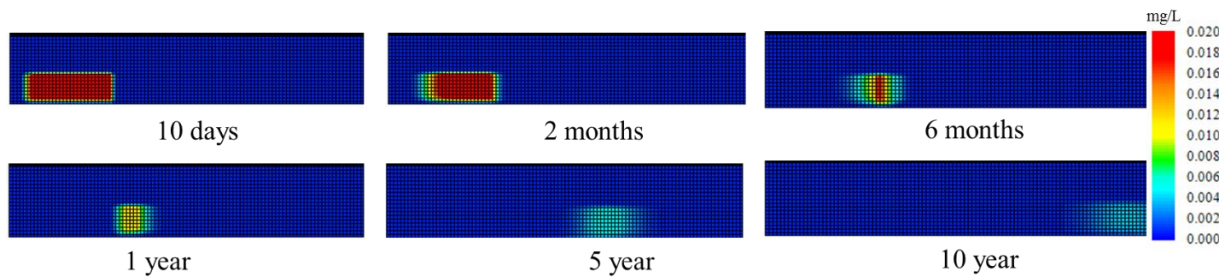


Fig. 3 Pollution migration process in the aquifer

CONCLUSIONS

In this study, numerical simulations were used to understand the washing-out process of heavy metals from the pollutant source (waste unit) and to evaluate the effectiveness of PRB. The time period needed for the full washing-out was highly dependent on the range of hydraulic gradient and pollution load. The PRB well trapped the targeted heavy metals and reduced the contamination level less than the effluent water quality standard.

ACKNOWLEDGEMENT

This study was supported by the SATREPS Project of the Japan Science and Technology agency (JST) and Japanese International cooperation Agency (JICA).

REFERENCES

- [1] Christensen TH, Kjeldsen P, Bjerg PL, Jensen DL, Christensen JB, Baun A, Albrechtsen HJ, Heron G, (2001). Biogeochemistry of landfill leachate plumes. *App. Geochem.*, 16(7-8): 659-718.
- [2] Udayagee Kumarasinghe, Inoue Y, Saito T, Nagamori M, Sakamoto Y, Mowjood MIM, Kawamoto K, (2017). Temporal variations in perched water and groundwater qualities at an open solid waste dumpsite in Sri Lanka. *int. j. geomate*. 13:1-8.
- [3] Park JB, Lee SH, Lee JW, Lee CY (2002) Lab scale experiments for permeable reactive barriers against contaminated groundwater with ammonium and heavy metals using clinoptilolite (01-29B). *J Hazard Mater* 95:65–79.
- [4] National Institute of Advanced Industrial Science and Technology (AIST): [Http://www.aist.go.jp/aist_j/press_release/pr2006/pr20060317/pr20060317.html](http://www.aist.go.jp/aist_j/press_release/pr2006/pr20060317/pr20060317.html).
- [5] Bear J, (1972). Dynamics of fluids in porous media. Elsevier, New York.
- [6] Jury WA, Gardner WR, Gardner WH (1991). Soil physics. 5thed. John Wiley & Sons, New York.
- [7] Millington R J, and Quirk JP, (1961). Transport in porous media. P. 97-106.
- [8] Neuman SP, (1990). Universal scaling of hydraulic conductivities and dispersivities in geologic media. *Water Resour. Res.* 26(8): 1749-1758.
- [9] Bulgariu D, Bulgariu L, (2012). Equilibrium and kinetics studies of heavy metal ions biosorption on green algae waste biomass *Bioresour. Technol.*, 103(1), 489–493.
- [10] USEPA: EPA Region III Risk Based Concentration Table, EPA Region 3(1995).
- [11] Nagamori M, Udayagee Kumarasinghe, Shakila Hettiarachchi, Mowjood MIM, Herath, GBB, Isobe Y, Watanabe Y, Kawamoto K, (2015). Spatiotemporal variation of water quality around and inside an open solid waste dumpsite in Sri Lanka. International conference on Advances in Civil and Environmental Engineering Practices for Sustainable Development Faculty of Engineering, University of Ruhuna, Galle, Sri Lanka.
- [12] Paranavithana GN, Kawamoto K, Inoue Y, Saito T, Vithanage M, Kalpage C. S, and Herath GBB, (2016). Adsorption of Cd²⁺ and Pb²⁺ onto coconut shell biochar and biochar-mixed soil. *Environ. Earth Sci.* 75:484.
- [13] Allison JD, And Allison TL, (2005). Partition coefficients for metals in surface water, soil, and waste. U.S. Environmental Protection Agency, Washington, DC.
- [14] Richards LA, (1931). Capillary conduction of liquids through porous mediums. *Physics*.1 (5): 318.
- [15] Central Environmental Authority, Sri Lanka. (2005). Technical guidelines on solid waste management in Sri Lanka.

ARTIFICIAL PAPER FROM PUTTARAKSA (*CANNA INDICA* LINN.) AND PLUBPLUENG (*CRINUM ASIATICUM*)

Kanokwan Rudisirisak, Nittaya Ngowattana

Department of Chemistry, Faculty of Science and Technology Rajamangala University of Technology, Thunyaburi, Pathumthani, Thailand.

ABSTRACT

Puttaraksa (*Canna indica* Linn.) and Plubplueng (*Crinum asiaticum*) are utilized to decorate landscape. Their branches and leaves are cut and abandoned for beauty and attraction. These parts of the plant are abolished by using fire that cause the greenhouse effect. So this research focused to invent the artificial paper from leaf of Puttaraksa and Plubplueng. We could produce pulp from these leaf by using three bases ; NaOH, KOH and ashes solution in range of concentration 1-5 % (w/v); boiling pulp in range 5-25 minutes. The suitable conditions of Puttaraksa artificial paper were 15 minute of boiling time and 4%(w/v) KOH. The chemical component of this paper were 93.74 % holocellulose, 1.55% lignin and 3.66 % extractive. The physical properties of this paper were 66.43 % brightness, 400 mN tearing resistance and 1.0 kg/cm² bursting strength. The suitable conditions of Plubplueng artificial paper were 15 minute of boiling time and 4% (w/v) ash solution. The chemical component of this paper were 93.25% holocellulose, 5.41% lignin and 4.24% extractive. The physical properties of this paper were 68.08% brightness, 340 mN tearing resistance and 0.5 kg/cm² bursting strength. The chemical properties of the artificial paper from Puttaraksa and Plubplueng were similar to paper from mulberry. The high holocellulose meant the suitable for working.

Keywords: Artificial paper, Puttaraksa, Plubplueng, *Canna indica*, *Crinum lily*, Holocellulose

INTRODUCTION

Puttaraksa(Thailand)



Fig.1 Puttaraksa : *Canna indica*

Puttaraksa is the Thai name of indian shot that has scientific name : *Canna indica* (Cannaceae). *Canna indica* is a perennial rhizomatous herb that grows from a thick, branching, underground rhizome and reaches to 1m. Its leaves are large and up to 50cm long and 25cm wide.[1],[2].



Fig.2 Plubplueng : *Crinum asiaticum* Linn

Plubplueng is the Thai name of crinum lily that has the scientific name : *Crinum asiaticum* Linn. Its common names is Seashore Lily, Poison Bulb, Bakung, Crinum Lily, Asiatic Poison Lily, Spider Lily, Seashore Crinum. Crinum lily is an herbaceous perennial plant that can grow in moist area (swamp, marsh, lake and stream), develops from underground bulbs and reaches 90 to 120 cm at maturity. Crinum leaves are typically long and strap-formed, with light green to green colors. Crinum produces white fragrance and large flowers.[3]

Plubplueng(Thailand)

Puttaraksa and Plubplueng are utilized to decorate landscape. Their branches and leaves are

cut and abandoned for beauty and attraction. These parts of the plant are abolished by using flaming that cause the greenhouse effect. Someone try to explore the process that can take the most useful from their branches and leaves and is the better than using flaming. On the basis of cellulose from plant can use to produce artificial paper, such as mulberry inner bark.[4] So, this research focused to invent the artificial paper from leaf of Puttaraksa and Plubplueng.

EXPERIMENT

Plant Preparation For Artificial Paper

Small pieces of Puttaraksa leaf, 200 g, was boiled for 10 minute in 1,000 mL of NaOH, KOH and ash that varied in range 1, 2, 3, 4 and 5 %w/v. The boiled pulp was adjusted to neutral pH by washing in tap water. These pulp was blended to disperse for 15 minutes then soaked in 5% w/v NaClO₂ for 10 minutes. Artificial paper was produced from dispersed pulp by using 10 cm x 10 cm wire screen frame, 3 hrs. incubated at 100 °C. Artificial paper weight approximately 1.00-1.30 g / sheet. The suitable basis condition was taken to experiment for suitable boiling time ; 5, 10, 20 and 25 minute. Plubplueng leaf was experiment by using the same procedure as Puttaraksa . The artificial paper were photographed by stereomicroscope and analyzed about the chemical component and physical properties.

Microscopic images

Enlarge 51.2X with ZEISS Stemi DV4.

Chemical Component Of Artificial Paper

Extractives : TAPPIT 204 om-88.1988.[4],[5]

Extractives extraction in Soxhlet apparatus by the following ; 3 grams of artificial paper were extracted in Ethanol:Benzene(1:2) for 4-5 hrs. To evaporate the solvent extraction , dry up and calculate the percentage of extractives.

Holocellose : Browing[4], [5]

In 250 mL round bottom flask; 2 grams artificial paper without extractives, 89 mL distilled water, 0.25 mL acetic acid and 0.75 grams sodium chlorite; boiling at 70-80° C in water bath for 30 min in fume hood and always shaking. Add 0.25 mL acetic acid and 0.75 grams sodium chlorite in hot solution at the end of the 1st , 2nd and 3rd hrs. and shaking flask. Take the bottom on ice bath until temperature of solution is below 10⁰C, filter through sinter glass

crucible no.3, washed with cold water and acetone then dry up and calculate.

Lignin : TAPPIT 222 om-88.1988.[4], [5]

In 50 mL beaker in ice bath ; 0.5 grams artificial paper without extractives was added with 7.5 mL of cold 72 %(v/v)H₂SO₄ and well stirred. Covered the beaker with watch glass and placed in water bath 20°C for 1.30 hrs. and stirred every 15 min. Poured the solution in the 500 mL round bottom flask that contained 200 mL distilled water and adjusted to 287.5 mL. Reflux the solution for 2 hrs. then left solution in 500 mL beaker for overnight. Filtered through sinter glass crucible no.3, washed with hot water then dry up at 105⁰C 3 hrs, cool down and calculate percentage of lignin.

Physical Properties Of Artificial Paper

Tearing resistance : Tear Tester[6]

50x65 mm Artificial paper overlapped 4 sheets and test with Tear Tester.

Bursting strength : Burst Strength[6]

8x8 cm Artificial paper and test with Burst Strength.

Brightness : Reflectivity of white light[6]

Take white paper under artificial paper and test by Brightness apparatus.

Table 2 Physical properties of artificial paper from Puttaraksa boiled in various concentration of NaOH for 10 minute

[NaOH] % w/v	Brightness (%)	Tearing resistance (mN)	Bursting strength (kg/cm ²)
1	60.09	300	0.5
2	61.11	360	0.5
3	63.54	380	1
4	65.31	400	1
5	65.93	400	1

Table 1 showed that the amount of NaOH increased as the elimination of lignin and extractives were increased and holocellulose was decreased at 5% w/v NaOH. Table 2 showed that the physical properties of artificial paper were increased because of well-eliminated extractives and lignin.

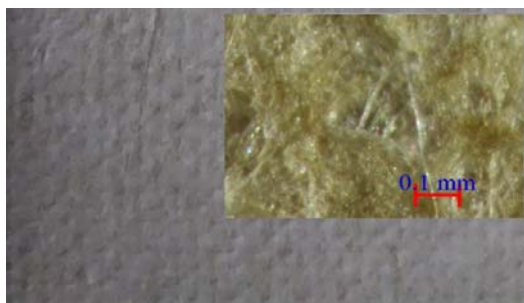


Fig. 3 Puttaraksa artificial paper : 10 minutes boiled in 4%w/v NaOH, 3 hrs. incubated at 100°C

Table 3 Chemical component of artificial paper from Puttaraksa pulp boiled in various concentration of KOH for 10 minute

[KOH] % w/v	Extractive (%)	Holocellulose (%)	Lignin (%)
1	8.86	85.02	4.62
2	7.53	87.70	2.45
3	6.98	88.38	2.06
4	4.93	90.32	1.78
5	4.05	87.43	1.16

Table 4 Physical properties of artificial paper from Puttaraksa pulp boiled in various concentration of KOH for 10 minute

[KOH] % w/v	Brightness (%)	Tearing resistance (mN)	Bursting strength (kg/cm ²)
1	64.33	300	0.5
2	64.37	340	0.5
3	65.80	350	1
4	66.84	400	1
5	66.85	400	1

Table 3 showed that the amount of KOH increased as the elimination of holocellulose was increased and holocellulose was highest at 4% w/v KOH. Table 4 showed that the physical properties of artificial paper were increased as the amount of KOH was increased, too.

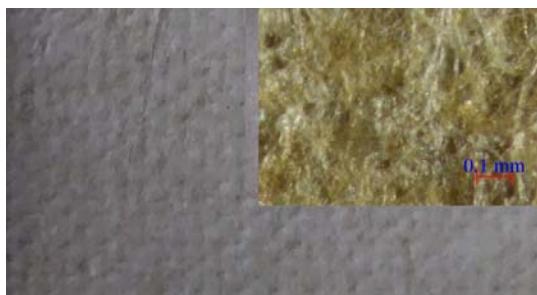


Fig. 4 Puttaraksa artificial paper: 10 minutes boiled in 4% w/v KOH, 3 hrs. incubated at 100°C

Table 5 Chemical component of artificial paper from Puttaraksa pulp boiled in various concentration of ash for 10 minute

[Ashes] % w/v	Extractive (%)	Holocellulose (%)	Lignin (%)
1	12.81	70.72	17.03
2	12.45	73.31	15.88
3	10.51	77.66	13.54
4	8.25	80.29	9.63
5	6.08	74.07	8.51

Table 6 Physical properties artificial paper from Puttaraksa pulp boiled in various concentration of ash for 10 minute

[Ash] % w/v	Brightness (%)	Tearing resistance (mN)	Bursting strength (kg/cm ²)
1	53.24	Nd	Nd
2	54.28	Nd	Nd
3	55.26	Nd	Nd
4	58.92	Nd	Nd
5	58.94	Nd	Nd

Table 5,6 showed that the ability of ashes to eliminate extractives and lignin was worse than NaOH and KOH. Tearing resistance and bursting strength of artificial paper were not evaluate.

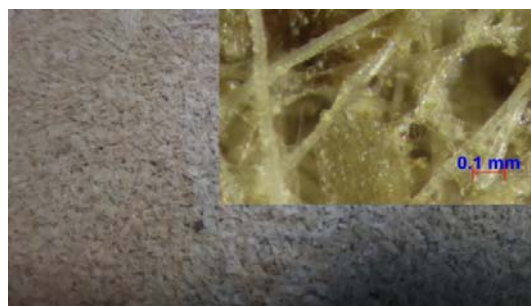


Fig.5 Puttaraksa artificial paper: 10 minutes boiled in 4%w/v ash, 3 hrs. incubated at 100°C. This paper must use more pulp than other paper(fig.3 and fig.4) % Holocellulose

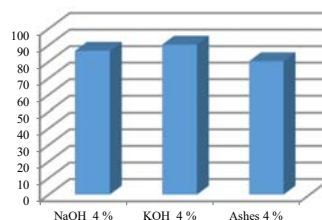


Fig.6 Comparison of holocellulose of artificial paper boiled in 4% NaOH, 4%KOH and 4%ash

Figure 6 showed that amount of holocellulose of artificial paper boiled in 4%KOH was nearby holocellulose of artificial paper boiled in 4%NaOH. It meant that the efficiency of KOH was similar to NaOH and better than ashes. But KOH is safe for environment, so we selected KOH to experiment.

Table 7 Chemical component of artificial paper from Puttaraksa pulp boiled in 4%w/v KOH at any time

Time (min)	Extractive (%)	Holocellulose (%)	Lignin (%)
5	6.36	85.15	3.94
10	4.93	90.32	1.78
15	3.66	93.74	1.55
20	2.84	89.29	1.37
25	2.39	87.21	0.91

Table 8 Physical properties of artificial paper from Puttaraksa pulp boiled in 4%w/v KOH at any time

Time (min)	Brightness (%)	Tearing resistance (mN)	Bursting strength (kg/cm ²)
5	65.43	350	0.5
10	66.24	400	1
15	66.43	400	1
20	66.62	400	1
25	66.69	400	1

Table 7 and 8 showed that boiling time in 4%w/v KOH was longer as extractives and lignin were decreased. Holocellulose was the highest at 15 minute and was decreased. The physical properties were nearby at any time, so the suitable boiling time was 15 minute.



Fig. 7 Puttaraksa artificial paper : 15 minutes boiled in 4%w/v KOH, 3 hrs. incubated at 100 °C.

Plubplueng

Table 9 Chemical component of Plubplueng pulp boiled in NaOH for 10 minute

[NaOH] % w/v	Extractive (%)	Holocellulose (%)	Lignin (%)
--------------	----------------	-------------------	------------

1	6.69	87.33	18.14
2	5.91	86.89	17.72
3	5.83	89.39	13.00
4	5.37	88.76	12.04
5	3.33	88.49	11.81

Table 10 Physical properties of Plubplueng pulp boiled in NaOH for 10 minute

[NaOH] % w/v	Brightness (%)	Tearing resistance (mN)	Bursting strength (kg/cm ²)
1	54.66	300	0.5
2	55.08	300	0.5
3	58.36	320	0.5
4	58.87	320	0.5
5	58.69	320	0.5

Table 9 and 10 showed that all concentration of NaOH could extract holocellulose. Artificial paper from Plubplueng pulp were the same properties.



Fig. 8 Lily artificial paper : 10 minutes boiled in 3%w/v NaOH, 3 hrs. incubated at 100°C

Table 11 Chemical component of Plubplueng pulp boiled in KOH for 10 minute

[KOH] % w/v	Extractive (%)	Holocellulose (%)	Lignin (%)
1	7.92	93.37	10.88
2	6.70	94.15	7.80
3	5.41	94.85	5.39
4	4.91	91.26	4.22
5	4.34	90.92	3.13

Table 12 Physical properties of Plubplueng pulp boiled in KOH for 10 minute

[KOH] % w/v	Brightness (%)	Tearing resistance (mN)	Bursting strength (kg/cm ²)
1	55.71	300	0.5
2	55.43	300	0.5
3	57.36	320	0.5
4	57.78	320	0.5
5	57.61	320	0.5

Table 11 and 12 showed that all concentration of KOH could extract the nearby amount of holocellulose. Artificial paper from Plubplueng pulp were the same properties.



Fig. 9 Plubplueng pulp artificial paper : 10 minutes boiled in 3%w/v KOH, 3 hrs. incubated at 100°C

Table 13 Chemical component of Plubplueng pulp boiled in ash for 10 minute

[Ash] % w/v	Extractive (%)	Holocellulose (%)	Lignin (%)
1	6.56	85.10	7.07
2	5.01	86.84	6.42
3	4.61	88.78	6.22
4	3.91	90.17	5.96
5	3.86	88.74	5.48

Table 14 Physical properties of lily boiled in ash for 10 minute

[Ash] % w/v	Brightness (%)	Tearing resistance (mN)	Bursting strength (kg/cm ²)
1	60.51	300	0.5
2	63.59	310	0.5
3	63.12	320	0.5
4	66.33	320	0.5
5	64.76	320	0.5

Table 13 and 14 showed that ash was well-eliminate extractives and lignin. The amount of holocellulose was high. Artificial paper from Plubplueng pulp were the good physical properties.



Fig. 10 Plubplueng pulp artificial paper :10 minutes boiled in 4%w/v ashes, 3 hrs. incubated at 100°C

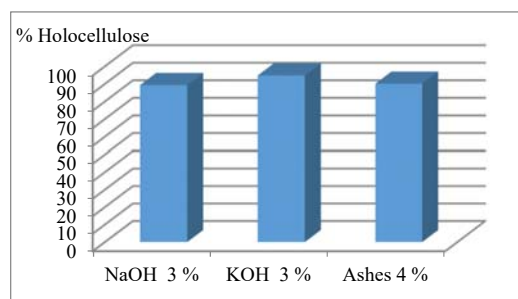


Fig.11 Holocellulose from Plubplueng pulp boiled in 3 % w/v NaOH , 3% w/v KOH and 4% w/v ash

Figure 11 showed that result of holocellulose extraction from lily using 4%w/v ash was similar to result of 3%w/v NaOH and 3%w/v KOH and Plubplueng pulp artificial paper were nearby properties, too. We selected 4% w/v ashes to experiment for boiling time of Plubplueng pulp.

Table 15 Chemical component of Plubplueng pulp boiled in 4%w/v ashes at any time.

Time (min)	Extractive (%)	Holocellulose (%)	Lignin (%)
5	6.16	89.48	8.58
10	4.55	90.17	5.96
15	4.24	93.25	5.41
20	3.91	92.66	5.04
25	3.69	90.59	4.41

Table 16 Physical properties of Plubplueng pulp boiled in 4%w/v ash at any time

Time (min)	Brightness (%)	Tearing resistance (mN)	Bursting strength (kg/cm ²)
5	61.08	310	0.5
10	66.33	320	0.5
15	68.08	340	0.5
20	63.76	340	0.5
25	63.45	340	0.5

Table 15 and 16 showed that 15 minute boiling time with 4%w/v ash could produce the good pulp and artificial paper and not longer time.



Fig.12 Plubplueng artificial paper : 15 minutes boiled in 4%w/v ashes, 3 hrs. incubated at 100 °C.

CONCLUSION

Table 17 Comparison of chemical component between leaf and artificial paper

	Chemical component	
	Holocellulose(%)	Lignin (%)
Puttaraksa leaf	79.62	23.44
Puttaraksa paper at 15 minute boiling time with 4% KOH w/v	93.74	1.55
Plubplueng leaf	73.75	18.35
Plubplueng paper at 15 minute boiling time with 4% ash w/v	93.25	5.41
Mulberry paper [6]	77.55	7.64

The suitable conditions of Plubplueng artificial paper were 15 minute of boiling time and 4% (w/v) ash. The chemical component of this paper were 93.25% holocellulose, 5.41% lignin and 4.24% extractive. The physical properties of this paper were 68.08% brightness, 340 mN tearing resistance and 0.5 kg/cm² bursting strength.

The suitable conditions of Puttaraksa artificial paper were 10 minute of boiling time and 4% (w/v) KOH. The chemical component of this paper were

90.32% holocellulose, 1.78% lignin and 4.93% extractive. The physical properties of this paper were 66.84% brightness, 400mN tearing resistance and 1.0 kg/cm² bursting strength. The chemical component of the artificial paper from Puttaraksa and Plubplueng were similar to paper from mulberry. The high holocellulose meant the suitable for working. As shown in table 17. This result showed that Puttaraksa and Plubplueng were new material to produce artificial paper.

ACKNOWLEDGEMENTS

We appreciated to Faculty of Science and Technology, Rajamangala University of Technology Thunyaburi.

REFERENCES

- [1] https://pediaview.com/openpedia/Canna_indica Author H, A Book. New York: Publisher, Yr, ch. 3.
- [2] <https://www.gardenseeker.com/bulbs/cannas/canna-main-page.html>
- [3] <http://www.floridagardener.com/pom/crinum.htm>
- [4] Vittaya Punsuvon. "Chemical component determination of non wood raw material for pulp and paper industry." Department of chemistry, Kasetsart University, Thailand. Final report the research project for higher utilization of forestry and agricultural plant materials in Thailand (HUFA).
- [5] Browing, B.L. Interscience Publishers, New York, London. Method in Wood Chemistry, 1963, pp.389-407
- [6] Dumrongsak Laoseangtham. "Production of pulp from Vertiver grass. Department of Science service journal. vol 151. sep. 1999.

CRUSTAL THICKNESS OF NORTH-WEST PENINSULAR MALAYSIA REGION INFERRED FROM RECEIVER FUNCTION ANALYSIS

Abdul Halim Abdul Latiff¹ and Amin Esmail Khalil²

¹ Department of Geosciences, Universiti Teknologi PETRONAS, Perak, Malaysia

² School of Physics, Universiti Sains Malaysia, Penang, Malaysia

ABSTRACT

The receiver function analysis has been used in the past 20 years by seismologist in understanding and developing crustal model beneath a 3-components broadband seismometer station. Waveform signal used in the analysis are recorded from the 937 tele-seismic earthquakes occurred in between year 2005 to 2016, from a station located in Kulim, Malaysia. The signal was analyzed by rotating, deconvolving before inverting the waveform based on the IASP91 velocity model, to obtain the local velocity structure and crustal depth to Moho boundary. Unlike in the previous and only crustal study in this region, the receiver function analysis conducted in this study involve more than 800 waveforms, which then separated into different back-azimuth, with the addition to signal-to-noise criterion applied to each individual signal. The waveforms were rotated to ZRT coordinate before the iterative deconvolution was implemented to minimize the noise signal during the rotation. In addition, the H-k stacking analysis were applied to each azimuth quadrants to obtain the estimated crustal thickness. From the results obtained of each azimuth quadrant, the Moho boundary were found consistent at 28 to 32 km from the sea level, which consistent with the result obtained in the previous receiver function study of the area.

Keywords: Receiver function, Crustal thickness, Peninsular Malaysia, Earthquake

INTRODUCTION

In seismically active region, earthquake occurs daily, with some of them are destructive and dangerous in nature. The sudden release of energy, allow seismologist around the world to conduct various studies related to earth system, its tectonic settings and the impact of the earthquake towards human being. The main study area in this paper is located at the north west of the Malay Peninsula, where generally known as a low seismicity region, with relatively low number of earthquakes occurred within the mini-continent while being surrounded by active subduction zone that produce the devastating earthquakes every yearly. Malay Peninsula is the elemental South-east Asian part of Eurasian plate, which commonly known as Sundaland [1].

Within the Peninsula, the general geological setting was divided into three north-south regional zones; eastern belt, central belt and western belt (Fig. 1). Each of the belt region has different tectono-stratigraphic characteristic such as stratigraphies, structural evolution, magmatism and volcanism [2]. The western belt, which contains a northwestern domain, contains mostly lower paleozoic rocks, while the central and eastern belts of the Malay Peninsula are generally were found in upper Paleozoic age. These findings indicate that both central and eastern belt represent the fore-arc, arc and continental basement of the Sukhothai Arc. The arc was developed on the margin of the Indochina Block (can

be derived from Gondwana in the Devonian) which separated from Indochina in the Permian by back-arc spreading, and re-amalgamated with Indochina in the Triassic. These two blocks were separated by a zone, widely known as Bentong-Raub suture zone [3].

The seismological station used in the receiver function analysis, KUM station, is positioned on top of a granite rock, which is part of Bukit Mertajam Kulim (BMK) granite, with STS-2 broadband seismometer and Q330 digitizer is being used to detect the ground motion signal (Fig. 2). The Bukit Mertajam Kulim granite is an isolated body located at north-west Peninsular Malaysia. The granite, which lies to the west of the Bintang batholith, is part of the Western Belt granite of Peninsular Malaysia [4] (Fig. 1). To the west of this granite lies the Penang granite which makes up the whole of Penang Island. The study area which is located south of Kedah, the northern state in Peninsular Malaysia, mapped as the Mahang Formation, with lower Silurian graptolites of Llandovery and Upper Wenlock age have been recovered [5]. Geological work also found Lower Devonian graptolites from the Mahang Formation, belonging to the uniformis, praehercynicus and possibly hercynicus zones, occurring together with numerous tentaculidites.

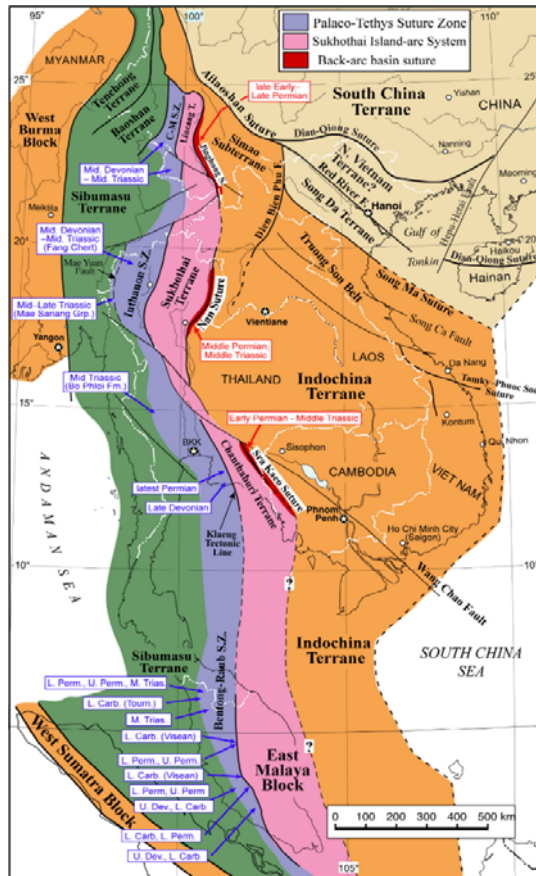


Fig 1. The geological map of Malay Peninsula showing three distinctive North-South belts [2].

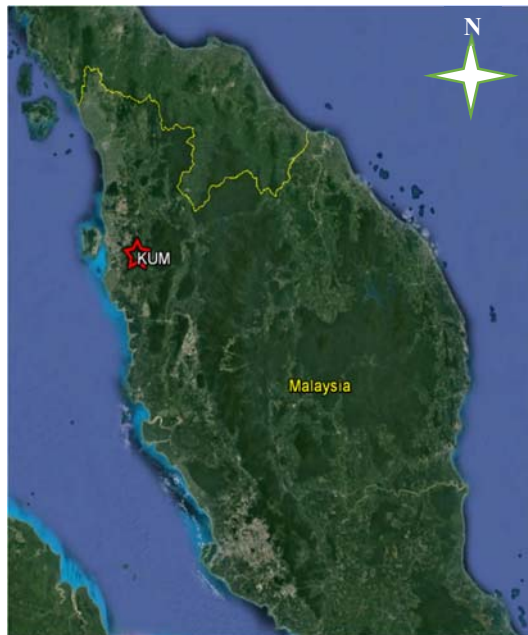


Fig 2. The earth surface map of Peninsular Malaysia with the location of seismological station (red star). Image from Google Earth.

METHODOLOGY

Although the geological characterization of the surface outcrop has been studied extensively, the detail of the subsurface still relatively unknown. Thus, through geophysical data acquisition such as seismic refraction and reflection and potential methods, the earth properties and characteristic can be identified. One of the most reliable method to determine the crustal thickness and velocity properties is through the receiver function method. The general methodology of receiver function is the analysis of P-wave and P-S converted wave signal recorded at the station. The signal must come from an earthquake ruptured at a distance larger than 30° and less than 100° , with a magnitude of 6.0 Mw and higher. Beside the two primary signals, the multiple reverberations such as PpPs and PpSs waveform is also desirable for the higher details of the earth crust and upper mantle. From the waveform recorded, the earthquake delay time difference, i.e. time taken between P-wave and P-S wave to reach the station, as well as amplitudes of direct and multiple phases, will provide the information of crustal – mantle depth discontinuity and the impedance contrast. Throughout the analysis, only 1D structure travel time differences were taken in to account which requires the dependency towards different wave phase type and slowness only.

From the phase determination, the seismograms are rotated to the ZRT-coordinate ray system according to back azimuth incident wave. This step is necessary to isolate the converted S-phase from the direct P-wave. Each seismogram is rotated from the original Z, N-S and E-W components into the Z, radial, R and tangential, T components respectively. As a result, the Z-component points in the direction of the direct P-wave, with the R-component is propagate perpendicular to the Z-component. Meanwhile, the T component is perpendicular to both Z and R components. The Z, R and T components contain mainly P-energy, SV-energy and SH-energy, respectively.

The next step is to remove the source and wave propagation path effect from the recorded waveform through the deconvolution procedure. The deconvolution of the R component from the Z can be conducted in time and frequency domain. By deconvolving the vertical from the radial components of three-component recordings, a time-series that is primarily a function of converted waves is produced. The most common deconvolution method in receiver-function studies is through the frequency domain division with the addition of water level stabilization [6]. Nevertheless, due to the low signal to noise ratios of the tele-seismic earthquake data obtained, the receiver functions were computed using the time-domain iterative deconvolution technique [7] rather than frequency domain deconvolution. In the iterative deconvolution, the differences between the resultant

convolution of the observed vertical component with a spike function, and the recorded radial component were computed and updated iteratively. This method produces a comparably better noise suppression deconvolution outcome compared to frequency domain deconvolution even though the computation process took slightly longer.

While the deconvolution yields receiver function, another algorithm approach is required to determine the earth crustal thickness from the interpreted phases. This was solved by implementing H-k stacking technique, which a grid-search technique approach by incorporating multiple phases amplitude [8]. In the H-k search method, the delay times of P to S conversion Ps and the later arriving multiples crustal reverberations (multiples) such as PpPs and PpPs + PpSs are calculated for each pair of the pre-identified H and k value with the input from mean P-wave velocity above the discontinuity and the average horizontal slowness value. Through the initial experimentation, the suitable P-wave velocity and slowness estimation of the earth crustal thickness and its corresponding velocity ratio is 6.3 km/s and 0.06 s/degree, with the resultant outcome producing a good estimation indicator. However, if the earth structure is complex, e.g. Tibetan Plateau, the H-k grid approach producing ambiguous and low-confidence result.

The Moho boundary thickness found in the H-k analysis, then used as a guide in developing initial P-wave velocity model for the inversion procedure. The inversion process, which involve the forward modelling procedure, requires a synthetic receiver function determination based on a given earth structure model. The problem of this study however is not to find the receiver function, but rather to determine the earth structure that generate the receiver function. Inversion of a waveform is a data-fitting procedure that aims at obtaining estimates of crustal properties from the receiver function. Given an initial model of the subsurface parameters, the data are predicted by solving a wave-equation. The model is then updated through forward modeling in order to reduce the misfit between the observed and predicted data. This procedure is repeated in an iteratively until the misfit between the model and receiver function data is satisfactorily small [7]. To perform the waveform inversion, an initial model needs to be defined. Since the existing model does not provide a good detail of Peninsular Malaysia earth subsurface, the IASP91 velocity was used as an initial model with some modification according to the determined thickness value from H-k method.

DATA AND PROCESSING

The study focused crustal and upper mantle seismic structures of northern Malaysian Peninsula where there is only a single station within the region. Receiver functions were computed in between 2005 till 2016 which involve 889 earthquakes within the epicentral distances of 30°–100° from the station, and with magnitudes, M_w larger than 6.0 were chosen. The vast data availability has allowed a more comprehensive subsurface velocity characterization compare to the previous work in the area which involve only 83 earthquakes [9]. It can be seen from the earthquake tabulation, most of the event distribution were recorded from north-east (back azimuth of 0°–90°) and south-east (90°–180°) earth ruptures. Before the crustal thickness and velocity inversion were carried out, a signal to noise ratio criteria of each of the waveform were analyze individually, with the ratio lower than 5 were discarded from further work. This SNR criterion saw 50% of the data (448 of the erroneous and noisy waveform) were eliminated, with remaining 441 earthquakes signal with good SNR were used in the H-k and velocity inversion analysis.

The resultant receiver functions at station KUM show the good P wave arrival at zero time (Fig. 3a). However, the P-s wave arrival as a result from Moho conversion appears relatively weak, as the earthquake originate from north-west and south-west cause the twin peaks at 3 to 6 seconds. Meanwhile the receiver functions with back azimuth 180° to 360°, a relatively better P-s conversion can be found which indicate a stronger reflection from the north-west and south-west direction. In addition, the PpPs multiple signal is strong at 14 seconds with relatively weaker PpSs multiple at 18 seconds. Beyond 20 seconds of the waveform, several coherent multiple phases can be seen, particularly the 1st and 2nd quadrant earthquakes. However, due to limited waveform available from 3rd quadrant in addition to poor coda wave signal in 4th quadrant, no phase interpretation possible for this station.

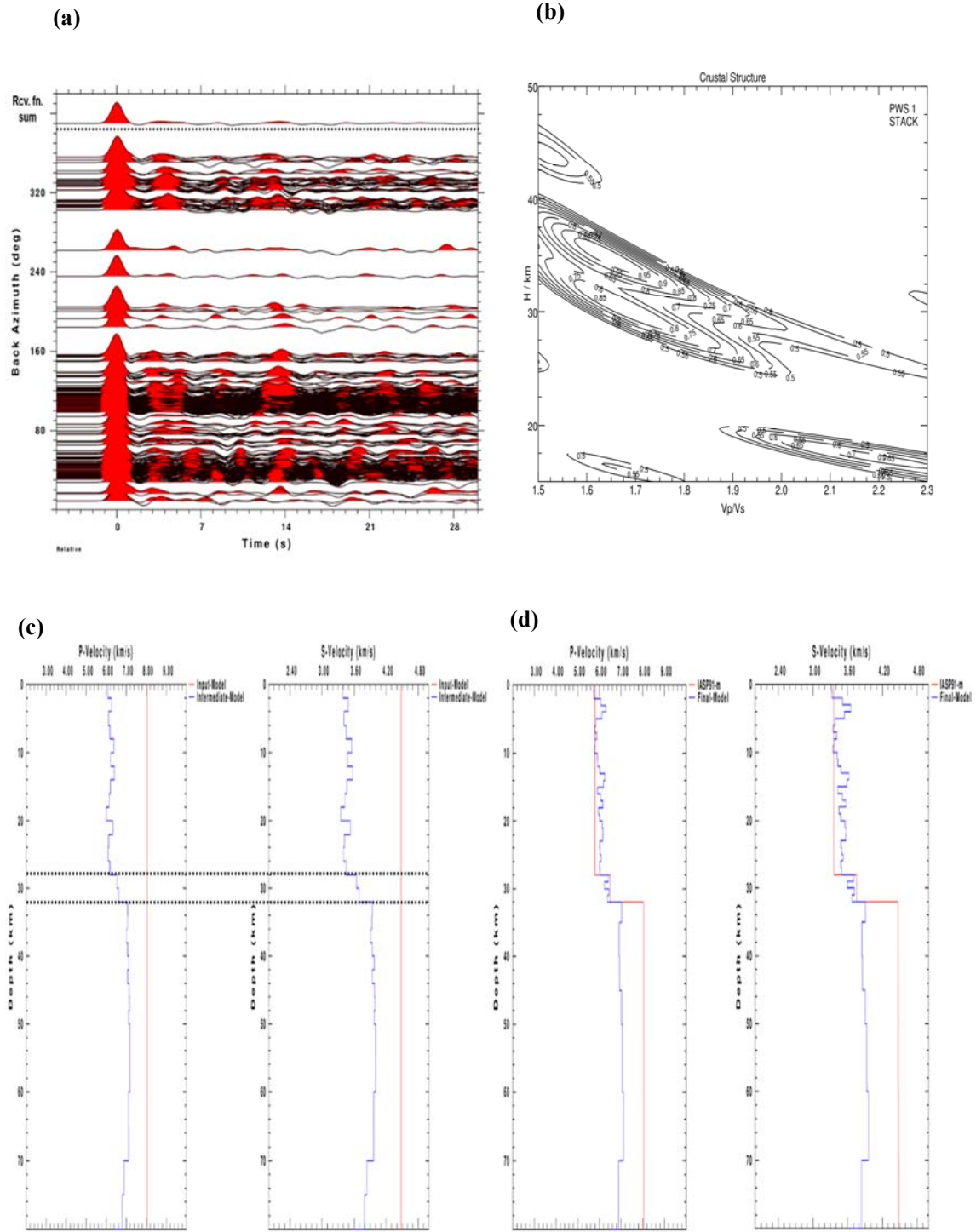


Fig 3. (a) Receiver function analysis for KUM station as a result from tele-seismic earthquake. (b) The H-k analysis from receiver function work indicate the crustal thickness and Vp/Vs ratio of the region. (c) First velocity inversion outcome (in blue) after 100th iteration of initial velocity model (in red). (d) Second velocity inversion using the velocity changes information in (c) with the outcome after 100th iteration (in red) based on the initial IASPP91 velocity model (in blue).

CRUSTAL STRUCTURE ANALYSIS

The H-k stacking analysis use the summation of individual receiver function computed. While the grid-search method shows a few possibilities of crustal thickness and the corresponding V_p/V_s ratio, only two possible thickness were considered, i.e. at 30 km and 35 km (Fig. 3b). Another high confidence H-k result, at 19 km, is highly unlikely true, as the V_p/V_s ratio is very high ($V_p = 2.2 V_s$), and far exceed the global average at 1.78 [10]. Besides these three-high confidence region contour, another two contours can be seen which can be interpreted as coda wave signal from the receiver functions. Since the 95% confidence contour only appear at 35 km depth, this is the highest likely the Moho depth beneath KUM station, north-west Peninsular Malaysia. Another potential interpretation from the grid search analysis is the possibility of slanted crustal-mantle boundary with the depth begin from 28 km on the western side of Kulim and continue to the east with Moho depth at 35 km. This interpretation came from the differences in receiver function signals of the waveform recorded from 1st and 2nd quadrants of back azimuth (east of Kulim), to the 3rd and 4th quadrant of back azimuth (west of Kulim).

The waveform inversion is well known as a non-linear non-uniqueness process, where the resultant velocity model depends on the several trade-in factors, particularly the initial velocity model [10]. To solve this problem, many studies considered the linearized iterative inversion problem, which applies to both synthetic and observed data. There are other approaches, either through different optimization solution such as genetic algorithm, neighborhood algorithm and simulated annealing [11], or by the integration of receiver function inversion with surface wave dispersion procedure [12]. While each of the solution proposed has their advantage, none of them capable to fully solve the non-discriminative solution.

In this study, a two-steps inversion workflow was used to lower the uncertainty from the inversion outcome. The first inversion process used a single and fix velocity value at 8 km/s for P-wave and 4.5 km/s for S-wave, to locate the 'jump' pattern in both P and S-wave velocity function during the inversion process. Since the velocity was fixed from surface level to 100 km depth, the resultant output velocity model was not influenced by the sudden velocity increase in existing velocity model. Throughout the 100 iterations process with damping factor of 0.5 and smoothness value of 0.4, the 1st inversion step allow a validation process of H-k stacking analysis, by locating the sudden velocity increase in both P and S velocity components. From the 1st inversion step, the sudden velocity increase was found at 28 km and 32 km (Fig. 3c). This velocity changes were interpreted as the crustal – upper mantle layer, due to the change in rock type. Another possibility is this represent three distinctive

layers, i.e. Conrad discontinuity at 28 km while Moho discontinuity at 32 km.

We use this information in developing the 2nd and final inversion procedure, by modifying the IASP91 velocity model as the initial velocity model. The IASP91 velocity model was chosen based on the following reading: i) similar initial model used by Malaysia Meteorological Department in their previous hypocenter relocation work, which was found accurate [13], ii) the regular and consistent velocity sampling interval compare to AK135F, PREM and crust1.0 model. In the existing IASP91 model, velocity changes drastically at 20 km (to indicate the Conrad discontinuity) and 35 km (to indicate Moho discontinuity) within the crustal region. Using the findings from the 1st inversion, the IASP91 model was modified to 28 km (first velocity change) and 32 km (second velocity change).

After 100th iteration in the 2nd inversion, with similar coefficients as in the 1st inversion procedure, the final velocity model was found consistent with large velocity difference at 32 km, although the velocity difference at 28 km is not suggesting a separation between upper and lower crust layering, due to lower velocity variation (Fig. 3d). Instead, a gentle velocity gradient increase was identified between 28 km to 32 km, which may indicate the slanted crustal-mantle boundary. These findings consistent with the hypothesis proposed from the receiver function observation, that the crustal thickness and velocity structure in the north-west of Peninsular Malaysia is changing from the west to the east of the Kulim area. Another important observation was found at 70 km depth, as both P and S-waves velocity profile travel slightly slower, which signal the asthenosphere zone of the Malay Peninsula. The relatively high near-surface V_s value of 3.3–3.6 km/s is an indication for plutonic rocks exposed in the region.

CONCLUSION

By incorporating receiver function modelling and inversion method, the crustal thickness and velocity structure underneath the KUM seismic station located at the north-west Peninsular Malaysia were determined. The finding was compared to previous receiver function analysis for KUM station, and found that our analysis shows a close similarity in term of crustal thickness, with 28-32 km in this study compare to 30-34 km in previous published work. In addition, the velocity composition beneath north-west peninsular Malaysia might indicate a distinctive crustal-mantle depth from the west to east side of KUM station. However, a different crustal technique analysis is required, such as surface wave dispersion analysis and ambient noise tomography study, to validate the produced model. In addition, the analysis

for the seismic stations nearby KUM is also needed to obtain a comprehensive 3D velocity tomography of the Malay Peninsula.

REFERENCES

- [1] A. Yan Sze Wah, "Geological assessment of earthquake sources hazard in Malaysia," in *Seminar Teknikal Gempabumi*, Malaysian Meteorological Department, 2011.
- [2] I. Metcalfe, "Tectonic evolution of the Malay Peninsula," *Journal of Asian Earth Sciences*, vol. 76, pp. 195-213, 2013.
- [3] I. Metcalfe, "The Bentong-Raub suture zone," *Journal of Asian Earth Sciences*, vol. 18, pp. 691-712, 2000.
- [4] A. A. Ghani, B. M. Doya, and G. H. Teh, "Age, petrochemistry and modelling of the Bukit Mertajam-Kulim granite, northwest Peninsular Malaysia," *Bulletin Geological Society of Malaysia*, vol. 44, pp. 139-150, 2000.
- [5] C. K. Burton, "The Mahang Formation: A mid-Palaeozoic euxinic facies from Malaya-with notes on its conditions of deposition and palaeogeography," *Geol. en Mijnb.*, vol. 46, 1967.
- [6] R. W. Clayton and R. A. Wiggins, "Source shape estimation and deconvolution of teleseismic bodywaves," *Geophysical Journal International*, vol. 47, pp. 151-177, 1976.
- [7] J. P. Ligorria and C. J. Ammon, "Iterative deconvolution and receiver function estimation," *Bulletin of the Seismological Society of America*, vol. 89, pp. 1395-1400, 1999.
- [8] L. Zhu and H. Kanamori, "Moho depth variation in southern California from teleseismic receiver functions," *Journal of Geophysical Research: Solid Earth*, vol. 105, pp. 2969-2980, 2000.
- [9] K. Kieling, D. Roessler, and F. Krueger, "Receiver function study in northern Sumatra and the Malaysian peninsula," *Journal of Seismology*, vol. 15, pp. 235-259, 2011.
- [10] C. J. Ammon, G. E. Randall, and G. Zandt, "On the nonuniqueness of receiver function inversions," *Journal of Geophysical Research: Solid Earth*, vol. 95, pp. 15303-15318, 1990.
- [11] B. H. Jacobsen and L. Sverningesen, "Enhanced Uniqueness and Linearity of Receiver Function Inversion," *Bulletin of the Seismological Society of America*, vol. 98, pp. 1756-1767, 2008.
- [12] J. Julia, C. J. Ammon, R. B. Herrmann, and A. M. Correig, "Joint inversion of receiver function and surface wave dispersion observations," *Geophysical Journal International*, vol. 143, pp. 99-112, 2000.
- [13] A. H. A. Latiff and A. E. Khalil, "Velocity structure and earthquake relocations at central Peninsular Malaysia region," in *GEOMATE 2016*, Bangkok, Thailand, 2016.

ARSENIC CONCENTRATION AND STABLE ISOTOPIC RATIOS OF OXYGEN AND HYDROGEN FOR GROUNDWATER AND RIVER WATER AROUND THE MIDORO AND SHINDENHIGASHISAMI TUNNELS IN GOSE CITY, NARA, CENTRAL JAPAN

Hiroyuki Ii¹, Hiroshi Kono², Yuji Yamashita³, Jyunji Uno⁴, Hiroyuki Shimogaki⁵, Sota Ikeda⁶ and Toshiki Nishimura⁶

¹Faculty of Systems Engineering, Wakayama University, Japan; ²Ministry of Land, Infrastructure, Transport and Tourism, Japan; ³Takenaka Civil Engineering & Construction Co., Ltd., Japan; ⁴Tekken Corporation, Japan; ⁵Maeda Corporation, Japan; ⁶Undergraduate School, Faculty of Systems Engineering, Wakayama University, Japan

ABSTRACT

During the several tunnel constructions for the Keinawa high way road, arsenic contamination granitic rocks were found at the north of Median Tectonic Line in the Kii Peninsula. Arsenopyrite (FeAsS) was certainly found in granite and then main arsenic source is thought to be arsenopyrite. Arsenic concentrations of tunnel water were found to be over 0.1mg/L, the Japanese Effluent Standard. River arsenic concentration was also found to be widely over 0.01mg/L, the Japanese Environmental Water Quality Standards. Arsenic concentrations of river bryophyte were widely high relative to the normal area. Copper minerals such as chalcopyrite (CuFeS₂) and chalcocite (Cu₂S) were found in both the tunnels. Copper concentration of river bryophyte was 10 to several thousand mg per kg. Some places in the study area were copper contaminated. Molybdenum concentrations of some tunnel waters around molybdenite (MoS₂) occurrence areas were over 0.07 mg/L, the Japanese Monitoring-required Water Quality and then, main molybdenum source is thought to be molybdenite. Arsenic, copper and molybdenum were contaminated in some places of the study area at the north of Median tectonic line and this contaminated zone is thought to spread east and west parallel to Median Tectonic Line. The recharge age of tunnel water is estimated to be less than 12.3 year. River and tunnel waters derive from precipitation however oxygen and hydrogen stable isotope values were different. The isotope difference between river and tunnel waters is thought to be caused by both evaporation and altitude effect of isotope. In forest under high humidity condition isotope effect of evaporation is small.

Keywords: Arsenic contamination, Tunnel water, Metal mine, Oxygen stable isotope, Hydrogen stable isotope

INTRODUCTION

Before the Midoro Tunnel and Shindenhigashisami Tunnel constructions in Gose city for the Keinawa high way road connecting Kyoto with Wakayama through Nara, arsenic contamination rocks around the tunnels were found from field and borehole researches. Figure 1 shows the study area. The Midoro Tunnel at the north side and Shindenhigashisami Tunnel at the south side are 5 to 10 km at the North of Median Tectonic Line in the Kii Peninsula and the tunnel area is composed of fresh granite and sheared granite. Black sheared granite distributed in the south of the area contains often minute arsenic mineral,

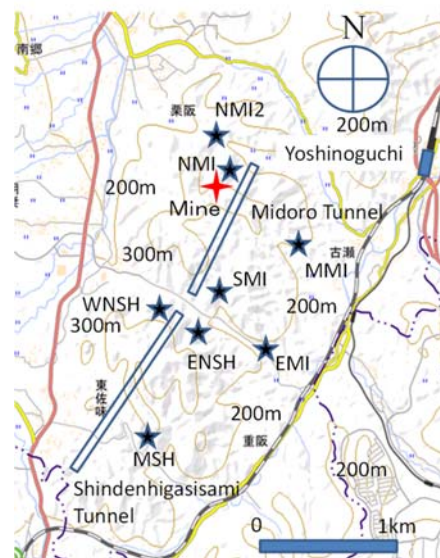


Fig.1 The study area. ★River sampling point.

arsenopyrite (FeAsS). At the north area of the study area, closed copper and molybdenum mine and its tailing were observed in the north area. The tailing contains molybdenite (MoS_2), chalcopyrite (CuFeS_2), chalcocite (Cu_2S) and copper secondary minerals such as malachite $\text{Cu}_2(\text{CO}_3)(\text{OH})_2$ and chrysocolla ($\text{Cu, Al})_2\text{H}_2\text{Si}_2\text{O}_8(\text{OH})_4 \cdot n\text{H}_2\text{O}$. From the valley between two tunnels, tunnel digging started April in 2015 and finished March in 2017. The maximum distance from tunnel to surface is less than 100 m. Then arsenic water contamination was studied using river and tunnel waters during tunnel construction and groundwater migration was traced by stable oxygen and hydrogen isotope for analyzing contaminated water migration. Tunnel water sample is a good indicator for analyzing groundwater migration and groundwater chemistry [1]. Metal concentrations of river bryophyte and river insect are thought to be good indicators for metal contamination [2], [3], [4]. The purpose of this study is groundwater migration analysis using oxygen and hydrogen isotopes and metal concentrations.

METHOD

River water was sampled around the tunnels and tunnel water was also sampled for water migration analysis and then were filtered with 0.45 micrometer filter. Metal concentration of sampled waters spiced with concentrated nitric acid were analyzed by ICP-AES (Inductively Coupled Plasma Atomic Emission Spectroscopy, SPS1700HVR ; Seiko Instruments Inc.). After sampled river insect and river bryophyte were dried then dissolved with concentrated nitric acid solution, metal concentration of the solution was also analyzed by ICP-AES.

^3H concentrations of tunnel and river waters were measured by liquid scintillation counter for estimating recharge age after electrolytic enrichment. The stable hydrogen and oxygen isotopic ratio were measured by mass spectrometer (Sercon Geo Wet System) with dual inlet and equilibrium with CO_2 and H_2 gas method.

RESULTS

Figure 2 shows arsenic concentration of tunnel and river waters. South side from 0 to 1800 m shows the Sindenhigashisami Tunnel. North side from 2000 to 3100m shows the Midoro tunnel. Tunnel length from 1800 to 2000 m is valley and open area. Arsenic concentrations of tunnel water around the valley between both the tunnels are over 0.1mg/L, the Japanese Effluent Standard and reaches 0.9 mg/L. In high arsenic area, arsenopyrite (FeAsS) is certainly found from cracks of granite. In the south of the Shindenigashisami Tunnel, sheared black colored granite with minute chlorite and small amount of arsenopyrite was found.

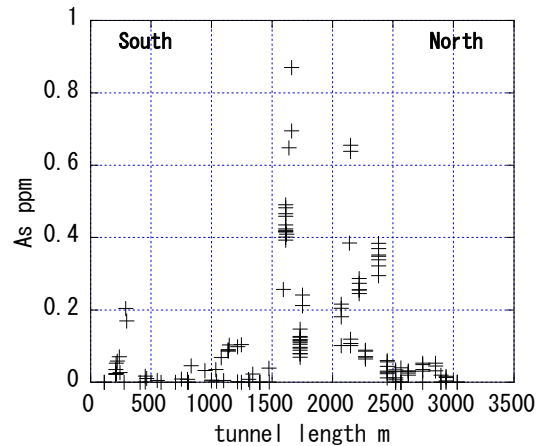


Fig. 2 Arsenic concentration (As) of tunnel waters.

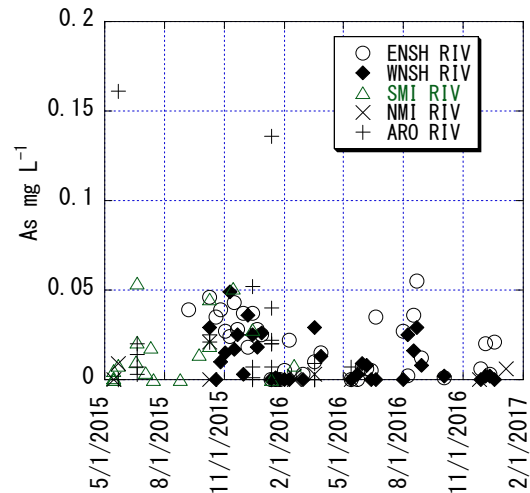


Fig.3 Arsenic concentration (As) of river waters

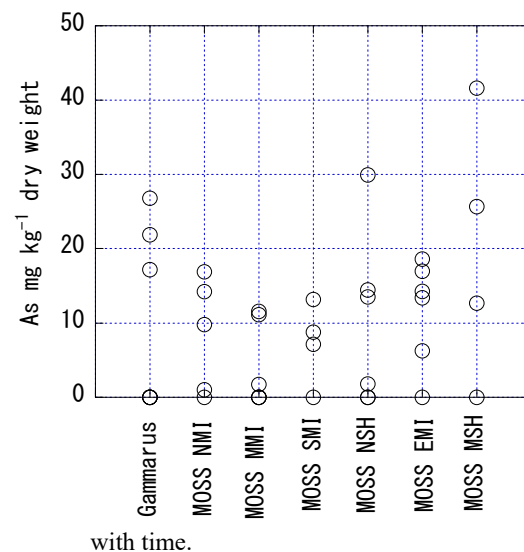


Fig.4 Arsenic concentration (As) of river gammarus and bryophyte with sampled point.

Figure 3 shows arsenic concentration of river waters with time. River sampling points, ENSH, WNSH, SMI, NMI and ARO (MMI, EMI and MSH) were shown as in Fig.1. Arsenic concentrations of river waters were widely over 0.01 mg/L, the Japanese Environmental Water Quality Standards and decreased with wet season. The concentration is thought to depend on amount of precipitation. Figure 4 shows arsenic concentration of river bryophyte and river gammarus. The concentrations of river bryophyte were widely over 10 mg per kg. Arsenic concentration of river gammarus is higher than those of river bryophyte and then gammarus has a higher bioconcentration factor.

Figure 5 shows copper concentration of tunnel waters. Copper concentrations of the tunnel waters in the Shindenhigashisami Tunnel were over 0.02 mg/L and higher than those in the Midoro Tunnel. In the both tunnels, many times copper minerals such as chalcopyrite (CuFeS_2) and chalcocite (Cu_2S) were found as vein and aggregate minerals in granite however copper concentrations of the tunnel waters were low.

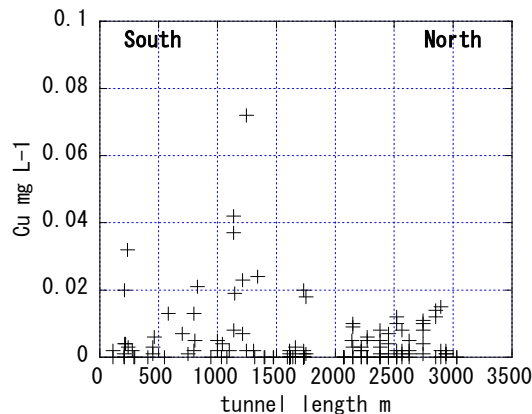
Figure 6 shows copper concentration of river waters with time. Copper concentrations of some river waters were higher than those in the tunnel waters and reached 0.1 mg/L. Generally copper concentrations decrease with pH values and tunnel water is high pH values. Then, copper concentration of tunnel is lower than those of river water.

Figure 7 shows copper concentration of river bryophyte and gammarus. The copper concentration of river bryophyte in the study area was 10 to less than 100 mg per kg and reached several thousand mg per kg. Copper concentration of river gammarus was higher than those of river bryophyte and then gammarus has higher bioconcentration factor.

Figure 8 shows molybdenum concentration of tunnel waters. Molybdenum concentrations of some tunnel waters in the Midoro Tunnel were over 0.07 mg/L, the Japanese Monitoring-required Water Quality Parameters. Molybdenite (MoS_2) was found in crack of the sheared granite and molybdenum concentration of tunnel water was high around molybdenite occurrence areas. Then, main molybdenum source is thought to be molybdenite.

Figure 9 shows δD and $\delta^{18}\text{O}$ values of tunnel and river waters. Although those values were variable, δD and $\delta^{18}\text{O}$ values of tunnel water were higher than those of river water. Only tunnel values can be found under both -55 ‰ for δD and -8.4 ‰ for $\delta^{18}\text{O}$ values. Mainly river water values can be observed over both -55 ‰ for δD and -8.4 ‰ for $\delta^{18}\text{O}$ values.

^3H concentrations of the tunnel and river waters were 1.7 to 1.8 T.U. and 2.5 to 2.8 T.U. The recharge age of tunnel water is estimated to be less than less than 12.3 year from the difference of both



^3H concentrations and then, tunnel water is young.

Fig. 5 Copper concentrations of tunnel waters with distance.

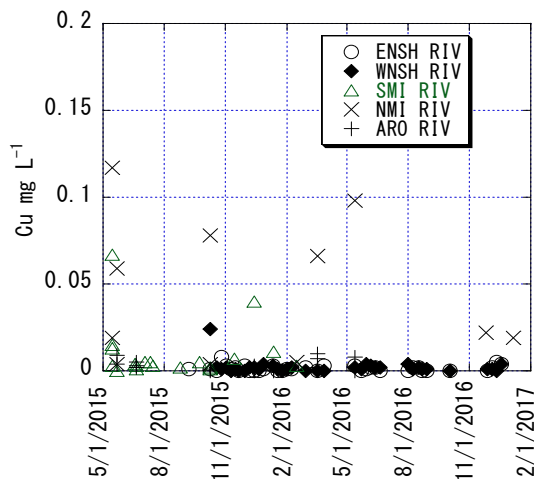


Fig.6 Copper concentration of river waters with time.

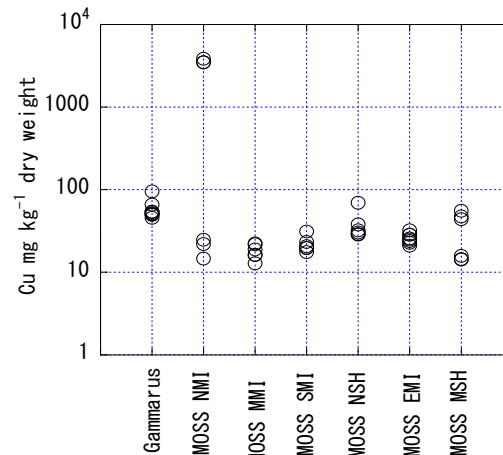


Fig. 7 Copper concentration of river bryophyte and gammarus.

DISCUSSION

Arsenic concentration of the Japanese Environmental Water Quality Standards for river and groundwater is 0.01 mg/L. Arsenic concentrations of many tunnel and river waters are over the Japanese Environmental Water Quality Standards. In particular, arsenic concentrations of tunnel water around the valley between both the tunnels are over 0.1mg/L, the Japanese Effluent Standard and reaches 0.9 mg/L. In high arsenic area, arsenopyrite (FeAsS) is certainly found from cracks of granite. In the south of the Shindenhigashisami Tunnel, sheared black colored granite with minute chlorite and small amount of arsenopyrite was found. Then main arsenic source is thought to be arsenopyrite. River arsenic concentration is found to be widely over the Japanese Environmental Water Quality Standards. Arsenic concentrations of river bryophyte and river gammarus are also widely over 10 mg per kg. Generally, background arsenic concentration of bryophyte is under 1.5 mg per kg [3], [5]. Then, widely arsenic contamination can be found by the concentration of river bryophyte.

Copper concentrations of some river waters were higher than those in the tunnel waters and reached 0.1 mg/L. In both the tunnels, many times copper minerals were found as vein and aggregate minerals in granite however copper concentrations of the tunnel waters were low. Generally copper concentration depends on pH values and tunnel water is high pH values with concrete lining and concrete spraying constructed by the NATM method. Then, copper concentration of tunnel water even contacted with copper minerals is thought to be low because of high pH value of tunnel waters. Generally, background copper concentration of bryophyte is 1 to 50 mg per kg [3], [5] however copper concentration of river bryophyte was 10 to less than 100 mg per kg and reached several thousand mg per kg. Then, some places in the study area were copper contaminated.

Molybdenum concentrations of some tunnel waters in the Midoro Tunnel were over 0.07 mg/L, the Japanese Monitoring-required Water Quality Parameters. Molybdenite (MoS_2) was found in crack of the sheared granite and molybdenum concentration of tunnel water was high around molybdenite occurrence areas. Then, main molybdenum source is thought to be molybdenite.

Arsenic, copper and molybdenum were contaminated in the study area at the north of Median tectonic line and this contaminated zone is thought to spread east and west parallel to Median Tectonic Line because the valley between both the tunnels with high arsenic area spreads parallel to

Median Tectonic Line and the past copper mines in

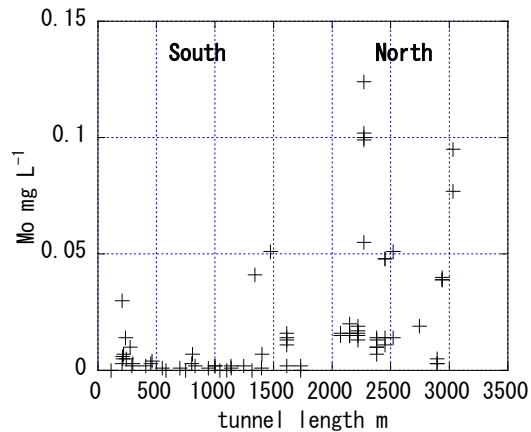
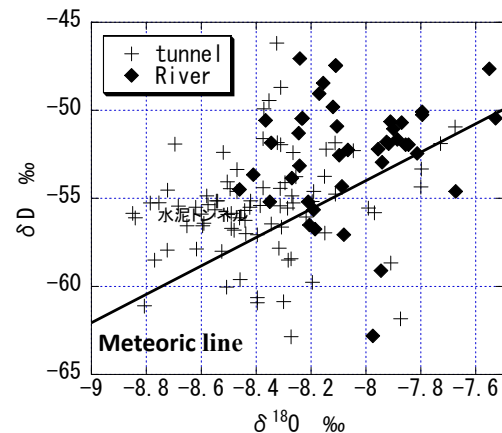


Fig. 8 Molybdenum concentration of tunnel and



river waters with distance.

Fig. 9 δD and $\delta^{18}\text{O}$ values of tunnel and river waters.

the north of study area also were arranged parallel to Median Tectonic Line.

Recharge age of the tunnel waters is estimated to be less than 12.3 year. Therefore, long term contact with metal contaminated rocks is thought to enable high arsenic concentration of tunnel water and actually arsenic concentrations of some tunnel water were higher than those of river waters.

Figure.10 shows schematic diagram for water pass from precipitation to river and tunnel. Tunnel water is groundwater recharged from precipitation and surface run off on the hill. River water comes from precipitation, surface run off derived from precipitation on the hill and groundwater recharged from precipitation on the hill. Therefore, river and tunnel waters derive from precipitation on the hill. However, both their oxygen and hydrogen stable isotope values were not same, the oxygen and hydrogen stable isotope differences between river and tunnel waters were 0.5 ‰ and 4 ‰, respectively

although they were variable values. Therefore, river and tunnel waters derive from precipitation however the isotope values were different.

Tunnel water mainly derives from precipitation on the top of hill and river water comes from precipitation around the hill as shown in Fig.10. Therefore, average altitudes of original precipitation of river and tunnel waters are different, average altitude of original precipitation of tunnel water is higher than that of river water. Generally, oxygen and hydrogen isotope values of precipitation decrease with altitude, $\delta^{18}\text{O}$: $-0.25\text{‰}/100\text{m}$ [6], δD : $-2.0\text{‰}/100\text{ m}$ [6]. In the Kii Peninsula, altitude effect of $\delta^{18}\text{O}$ is -0.15 to -0.4 (-0.23) $\text{‰}/100\text{ m}$ [7] and in the Yakushima Island, the altitude effect of $\delta^{18}\text{O}$ is -0.09 to $0.11\text{‰}/100\text{ m}$ [8].

In this area, although even altitude difference between top of the hill and river level is less than 100m, the oxygen and hydrogen isotope differences between river and tunnel water are 0.5 ‰ and 4 ‰ , respectively and the difference is over twice of altitude effect.

Generally, isotope values of water on the surface increase with evaporation [6], [9]. Surface run off water and soil water evaporate and transpire and then isotope values increase. Then, the isotope difference between river and tunnel waters is thought to be caused by both evaporation and altitude effect of isotope.

The evaporation rate can be estimated from oxygen stable isotope change value during evaporation [6], [9]. When half values of different oxygen isotope value between tunnel and river waters is assumed to be caused by evaporation, the calculated evaporation rate from oxygen isotope values, 0.25 ‰ is 2.5 % using the relation for evaporation rate per oxygen isotope change during evaporation process = 1 % per 0.1 ‰ under high humidity condition, [9]. As annual precipitation of Gojyo in 2015 and 2016 is 1450 mm per year [10], the amount of estimated evaporation from the isotope values is 36 mm per year.

Evapotranspiration for forest in Japan is about 600 to 900 mm per year [11]. Evaporation caused by rainfall interception of trees in Japan reaches 30 to 50 % of total evapotranspiration [11] and is calculated to be 180 to 450 mm per year. Therefore, the estimated evaporation from oxygen isotope values is quite small. If evaporation is large, over 10 %, the isotope value separates from the meteoric line [6], [9]. However the observed isotope values of river and tunnel water are on the meteoric line. Therefore oxygen and hydrogen isotope values are not largely thought to be influenced by evapotranspiration and evaporation of river and groundwater in forest.

Similarly, oxygen and hydrogen stable isotope of river and spring waters at the Izumi Mountain 50 km at the east of the study area were on the meteoric line [12] and the isotope difference between spring and river waters can be estimated from altitude difference between both recharge areas [12]. Therefore, evaporation and evapotranspiration occur during migration from precipitation to river, spring and tunnel water however isotope change caused by evaporation and evapotranspiration does not occur. Generally, oxygen and hydrogen stable isotope change for lake and pond waters during evaporation process occurs [6], [13]. Typically oxygen and hydrogen stable isotope values increase with evaporation rate under low humidity condition however under high humidity condition, over 80 % oxygen and hydrogen stable isotope values do not increase with evaporation rate and sometimes decrease with evaporation rate. Under high humidity condition, isotope values of liquid changes with isotope values of vapor and not always increase with evaporation rate [9]. Therefore forest can keep high humidity condition during and just after rain and then oxygen and hydrogen stable isotope of precipitation water can keep uniform value during evaporation by rainfall interception of trees.

Isotopic fractionation does not occur during absorption water from soil at root and release water from leaves because residual water stays at soil and tree for a long term. Transpiration from soil water to leaves caused by tree also is thought to keep uniform oxygen and hydrogen stable isotope values.

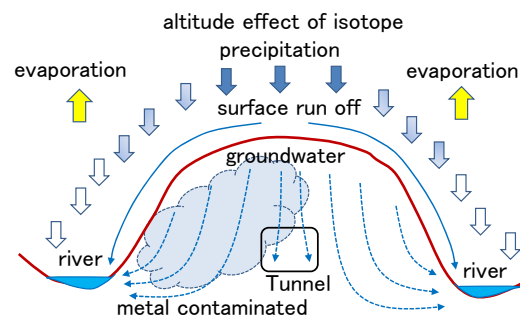


Fig. 10 Schematic diagram for water pass from precipitation to river and tunnel.

CONCLUSION

During the several tunnel constructions for the Keinawa high way road, arsenic contamination rocks composed of granite were found at the north of Median Tectonic Line in the Kii Peninsula. During tunnel construction, arsenopyrite (FeAsS) was certainly found from cracks of granite and in the sheared black colored granite and then main arsenic source is thought to be arsenopyrite. Arsenic

concentrations of tunnel water were found to be over 0.1mg/L, the Japanese Effluent Standard. River arsenic concentration in the study area was also found to be widely over 0.01 mg/L, the Japanese Environmental Water Quality Standards. Arsenic concentrations of river bryophyte and gammarus in the study area were widely high relative to the normal area and then widely arsenic contamination was found.

Most copper concentrations of the tunnel waters with copper minerals such as chalcopyrite (CuFeS_2) and chalcocite (Cu_2S) were less than 0.02 mg/L however copper concentrations of river waters in the study area widely reached 0.1 mg/L. The copper concentration of tunnel water is thought to be low because of high pH control of concrete. Copper concentration of river bryophyte in the study area was 10 to less than 100 mg per kg and reached several thousand mg per kg. Then, some places in the study area were copper contaminated.

Molybdenum concentrations of some tunnel waters around molybdenite (MoS_2) occurrence areas were over 0.07 mg/L, the Japanese Monitoring-required Water Quality Parameters and then, main molybdenum source is thought to be molybdenite. Arsenic, copper and molybdenum were contaminated in some places of the study area at the north of Median tectonic line and this contaminated zone is thought to spread east and west parallel to Median Tectonic Line.

The recharge age of tunnel water is estimated to be less than 12.3 year using ^3H concentration. River and tunnel waters derive from precipitation however oxygen and hydrogen stable isotope values were different. Although even altitude difference between top of the hill and river level is less than 100m, the oxygen and hydrogen stable isotope differences between river and tunnel water are 0.5 ‰ and 4 ‰, respectively and the difference is over twice of altitude effect. Then, the isotope difference between river and tunnel waters is thought to be caused by both evaporation and altitude effect of isotope. Although evaporation and evapotranspiration rates were very large, the isotope difference between river and tunnel waters were too small. Oxygen and hydrogen stable isotope values are not thought to be largely influenced by evapotranspiration and evaporation of river and groundwater in forest because under high humidity condition isotope effect of evaporation is small.

REFERENCES

- [1] Ii H, "Tunnel construction impact on groundwater character over 25 years of observation at Matsumoto Tunnel, Matsumoto city, Japan", *Int. J. of GEOMATE*, Vol. 13, Oct. 2017, pp. 79-88.
- [2] Kubohara T, and Ii H, "Cu, Co and Ni contamination index for using river insects and river plants", *Int. J. of GEOMATE*, Vol. 11, Oct. 2016, pp. 2651-2658.
- [3] Kubohara T, and Ii H, "Evaluation of metal contamination for river using bryophyte in the Kinokawa River catchment", *Int. J. of GEOMATE*, Vol. 13, Sep. 2017, pp. 108-115.
- [4] Ii H and Nishida A, "Effectiveness of using river insect larvae as an index of Cu, Zn and As contaminations in rivers, Japan", *Int. J. of GEOMATE*, Vol. 12, May. 2017, pp. 153-159.
- [5] Fred M. Rhoades "A Review of Lichen and Bryophyte Elemental Content Literature with Reference to Pacific Northwest Species", Forest Service Pacific Northwest Region: United States Department of Agriculture, 1999.
- [6] Sakai H and Matsuhisa Y, *Stable Isotope Geochemistry*. Tokyo: University of Tokyo Press, 1996, ch. 4.
- [7] Ishizuka M, Sone Y, Ii H and Hirata T, "Effect of enriched early dropped rainwater on mesoscale isotopic distribution in surface water on the Kii Peninsula, Japan", *Water Resources Research*, Vol. 42, W12410.2006, pp.1-16.
- [8] Yokota K, Ii H and Taniguchi M, "Effects of altitude and distance from coastline of oxygen stable isotope for precipitation in the Yakushima Island", *Environmental Engineering Research*, Vol. 47, 2010, pp. 667-677. in Japanese.
- [9] Miyahara S and Ii H, "Proposal of simple measurement method for evaporation rate by using oxygen isotopic ratio", *Int. J. of GEOMATE*, Vol. 3, Sep.2012, pp. 318-324.
- [10] Japan Meteorological Agency, <http://www.jma.go.jp/jma/kishou/info/coment.html>, 2017.
- [11] Kondo J, Nakazono M, Watanabe T and Kuwagata T, "Hydrological climate in Japan (3)-Evapotranspiration from forest-", *J.Japan Soc. Hydrol. & Water Resour.*, Vol.5, No.4, 1992, pp8-18. in Japanese.
- [12] Ishizuka M, Ii H, Tsutsumi H and Hirata T, "Characteristics of surface water chemistry in the small forested basin in the Izumi mountains", *Proceedings of hydraulic engineering, JSCE*, Vol.45, 2001, pp1015-1020. in Japanese.
- [13] Allison G.B, Brown R.M and Fritz P, "Estimation of the isotopic composition of lake evaporate.", *Jour. of Hydrol.*, Vol.42, 1979, pp.109-127.

GENETIC DIVERSITY OF *PSEUDOLABRUS SIEBOLDI*, USUAL FISH SPECIES IN A WESTERN JAPAN COASTAL AREA

Michiko Masuda¹, Wataru Kawase² and Fumitake Nishimura³

¹ Department of Civil Engineering, Nagoya Institute of Technology, Japan; ² Shizuoka Prefectural Government, Japan; ³ Department of Environment Engineering, Kyoto University, Japan

ABSTRACT

Pseudolabrus sieboldi is a very common labrid fish at Japan coastal region, so the species wasn't being watched so much up to now. Therefore, the habitats of *P. sieboldi* have been developed easily. But it's pointed out that genetic isolation is easily occurred due to being polygynous in their mating system. In order to investigate the genetic diversity of usual species, we sampled 6 populations of the species from western Japan coastal area, and studied them for allelic variation at 24 enzyme loci. In comparison with other sea fishes, the total genetic diversity is standard. Though sex ratio was inclined to females and inbreeding were easy to be performed, the gene diversity was not decreasing. In fact, there were inbreeding mating within the population. Moreover, standard genetic distance within populations along the Japan Sea is high and standard genetic distance within Pacific Ocean area is low. The fry of the species dispersed to the Pacific or Japan Sea. When they grew adults, they returned along rocky shores for mating. The populations along Pacific Ocean did not return exactly at their birth area. On the other hand, the populations along the Japan sea returned more exactly at their birth area.

Keywords: Genetic Diversity, Genetic Distances, Coastal Conservation, *Pseudolabrus sieboldi*, Mating System

INTRODUCTION

Recently it's thought that the conservation of genetic diversity is very important [1]-[3]. Many researchers have pointed out the importance of the genetic conservation. The maintenance of genetic diversity is important for endangered species. Though the same investigation was also necessary to usual species for genetic diversity to be maintained, few studies were done up to now.

Pseudolabrus sieboldi is very common labrid fishes along rocky shores in the East Asian temperate region. Recently Mabuchi and Nakano showed the species separated from *P. eoethinus* [4], differing in coloration and morphological characters. Mabuchi *et al.*, also investigated the genetic diversity among 3 populations [5]. They collected 5 fishes each population, total 15 fishes, and investigated. There were some differences observed two labrid fishes. But they couldn't analyze the population structure because of low numbers of species. Mabuchi *et al.*, also reported the mating system of the species, and they are polygamous [6]. Polygamous species restricts gene flow and caused population isolation.

Maruyama personal observation (2001) revealed the larva of the species was observed at Pacific Ocean and Japan sea, not at coastal area [7]. The phenomenon suggested the adult fishes breed at coastal area, the larva fishes go to Ocean and growing fishes returned to coastal area. The phenomenon suggests the gene flow easily occurred in Ocean.

In this study, we investigated the genetic structure

and genetic diversity of *P. sieboldi* to know the genetic structure of usual species with 3 questions, 1) Is there a relationship between the location and genetic distance? 2) Is there a difference between Pacific Ocean side and Japan Sea side? 3) Do the adults fishes return to the birth area? The attention was paid at above-mentioned 3 points in our study.

MATERIALS AND METHODS

Study Site

The samplings were carried out on 6 locations of west Japanese seashore (Fig. 1). Specimens (from 26 to 31 fishes) were collected from 6 localities widely distant from each other: 30 samples Nobeoka Bay at Miyazaki Pref., 26 samples Senzaki Bay at Yamaguchi Pref., 30 samples Miho Bay at Shimane Pref., 31 samples Seto Bay at Nagasaki Pref., 28 samples Tasoura Bay at Mie Pref. and 30 samples Miyagawa Bay at Kanagawa Pref.



Fig. 1 Map of sampling localities.

Miyazaki is Seto sea area, Yamaguchi, Shimane, and Nagasaki are Japan Sea area. Mie and Kanagawa are Pacific Ocean area.

The Study Fish

Pseudolabrus sieboldi Mabuchi and Nakano a very common labrid fish at coastal region in Japan (Fig. 2). They have white spits on the dorsal part of the body from initial to terminal phase (IP and TP, respectively). The species is known as the fish which does a sex change, and all larval fish is being born as a female. Within a population the largest female exchanges her sex to male. A matured male makes the territory at sunken rocks and reproduces with a lot of females.

Pair spawning occurred within TP male territories during the daytime. *P. sieboldi* spawned above smaller rocks with seaweed and seagrass, whereas *P. eoethinus*.

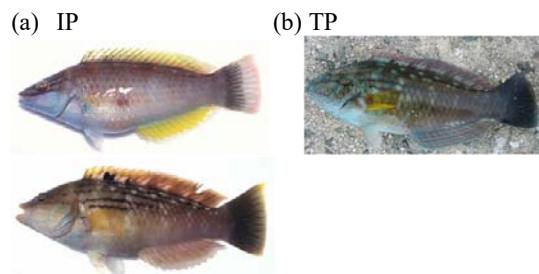


Fig. 2. Different phase of *P. sieboldi*, left side (a) is IP (initial phase female) and right side (b) is TP (terminal phase male).

Electrophoresis

All fresh fishes were collected from 26-31 individuals per population in 2004 and 2005. Fishes were kept on ice during transportation to the laboratory. A part of liver tissues and muscle tissues were cut and homogenized being added with an approximately equal amount of 0.5M sucrose solution. And homogenized tissues were centrifuged at 10,000rpm at 5 minutes. The supernatants were subjected to horizontal starch gel electrophoresis. A tris-citrate buffer system no.5 (Soltis et al. [6]) was used. Starch gels were run for 2 hours at 80mA in a refrigerator at 4°C. After the run, the gel was sliced horizontally. The following enzyme systems were examined: triose-phosphate isomerase (TPI), malate dehydrogenase (MDH), acid phosphate (ACP), mannose phosphate isomerase (MPI), Glycerophosphate dehydrogenase (GPD), 6-phosphogluconate dehydrogenase (6PG), phosphoglucose isomerase (PGI), malic enzyme (ME), Alcohol

dehydrogenase (ADH), aldase (ALD), menadione reductase (MR), phosphoglucumutase (PGM) and glucose 6 phosphate dehydrogenase (G6PDH). Muscle tissues were used to resolve the following 19 loci: tpi-1, tpi-2, mdh-1, mdh-2, mdh-3, mdh-4, acp-1, acp-2, mpi-1, mpi-2, gpd, 6pg, pgi, me, adh, ald, mr, pgm and g6pdh. Liver tissues were correspondingly used for 5 loci mdh, me-1, me-2, pgm and adh. We followed previous works [6][8][9] about staining.

The Statistical analysis

The number of alleles per locus (A), proportion of polymorphic loci (P), and gene diversity (h) were calculated on each population. Additionally, total gene diversity [10] was calculated for species level. The population genetic structure was analyzed by initially calculating Nei's G_{ST} value [10]. Values for standard genetic distance (D) was calculated for each pairwise comparison of all populations. The neighbor joining method [11] based on D was used for constructing a phenogram for *P. sieboldi*.

RESULTS

24 loci were scored (19 for muscle and 5 for liver). All loci have at least two alleles in at least one population. Table 1 summarizes the resultant values of A , P and h for each population.

Table 1 Mean number of polymorphic loci (A), proportion of polymorphic loci (P), and gene diversity within a population (h) at 24 loci for examined populations of *P. sieboldi*

Population	A	P	h
Miyazaki	2.208	0.917	0.206
Yamaguchi	1.583	0.500	0.217
Shimane	1.542	0.542	0.092
Nagasaki	1.792	0.625	0.091
Mie	1.542	0.500	0.028
Kanagawa	1.792	0.750	0.019

And total gene diversity (H_T) of the species was 0.278. The levels of genetic diversity in *P. sieboldi* was high that of other fish species, for example, *Sonoran topminnow* of 0.03 to 0.116 [12].

The mean level of isozyme variation within populations and the total gene diversity of the species are given in Table 2. The resultant hierarchical analysis of population genetic structure is G_{ST} . G_{ST} of Pacific Ocean is 0.03, on the other hand, G_{ST} of Japan Sea is 0.31. That of Japan Sea was higher than that of Pacific Ocean.

Fig. 3 showed the phenogram using the NJ methods based on Nei's standard genetic distance [11].

Table 2. Inbreeding coefficient within a population (F_{IS}), Fixation index (F_{ST}) and inbreeding coefficient among total populations (F_{IT}).

Population	F_{IS}	F_{ST}	F_{IT}
Miyazaki	0.415	-0.262	0.262
Yamaguchi	-0.196	0.347	0.220
Shimane	0.504	0.336	0.670
Nagasaki	0.236	0.570	0.672
Mie	0.703	0.657	0.898
Kanagawa	0.754	0.716	0.930

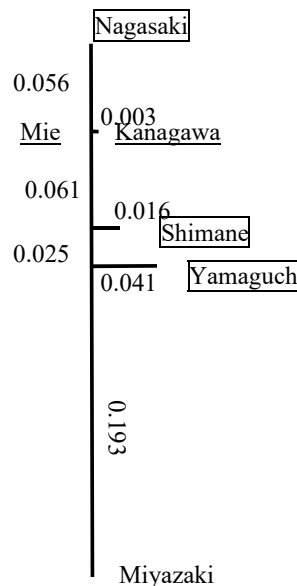


Fig. 2 Phenogram using the neighbor joining method based on Nei's (1987) standard genetic distance. Under line locations are Pacific Ocean area, □ locations are Japan sea locations.

DISCUSSION

Mabuchi and Nakano investigated about the genetic diversity of the species [5]. There were some gene diversity among populations. But the sampling size was 5 each 3 populations. Then they cannot analyze the genetic structure of the species. In this study, we can collect over 25 individuals from 6 populations and analyze the genetic structure.

In comparison with other sea fishes, the total gene diversity is standard [1][2]. But there are some differences about gene diversity among populations. The gene diversity within a population (h) of Mie and Kanagawa (Pacific Ocean side) was lower than those of other population. The value of h is from 1/4 to 1/6 of the expected value. Moreover, the value of the

fixation index at the Pacific Ocean side populations was higher than those of others. The result showed that inbreeding occurred within a population and the effective population size is small at the Pacific Ocean side populations. The inbreeding was expected from the mating system of the labrid species. But there was no inbreeding at other 4 populations.

Our data show another interesting fact. Standard genetic distance within populations along the Japan Sea is high ($D=0.180$). On the other hand, that within the Pacific Ocean side is low ($D=0.000$). It showed the gene flow easily occurred along the Pacific Ocean side, but hardly occurred along the Japan sea side. And there was no relationship between real distance and genetic distance. From the phenogram populations of the Japan Sea side contains the Pacific Ocean side populations.

The fry of the species disperses to the Pacific Ocean or the Japan Sea. When the fry is grown up, they return along rocky shores for reproduction. The populations along the Japan Sea side return their birth area exactly because of the genetic distances over 0.01. But the populations along the Pacific Ocean side did not return to birth area exactly due to the genetic distance value within 0.01, so there were high gene flow among populations.

CONCLUSION

We get three main conclusions.

- 1) There is no relationship between the real distance and genetic distance.
- 2) There is a difference between the Pacific Ocean side population and the Japan Sea side population. The Pacific Ocean side populations have low genetic diversity and easily occurred inbreeding. The Japan Sea side populations have high genetic diversity and isolated each population.
- 3) The matured individuals returned exactly at the Japan Sea side population, on the other hand, mixed return occurred at the Pacific Ocean side populations.

Based on the conclusions, two proposals about the conservation activities are considered

- 1) There is a possibility of inbreeding in the polygamous mating system species, so the investigation should be done at usual species, because of low genetic diversity.
- 2) We should know the differences between the Japan Sea area and the Pacific Ocean area.

ACKNOWLEDGEMENTS

We wish to thank the fishermen advice to us for fishing. We also thank the members of our laboratory for their assistance in the field works.

REFERENCES

- [1] Frankham R, Ballou JD, Briscoe DA. Introduction to Conservation Genetics. Cambridge: Cambridge University Press, 2nd edition, 2010, ch. 3.
- [2] Schonewald CM. Genetics and Conservation: a reference manual for managing wild animal and plant populations. Washington, The Blackburn Press, 2004.
- [3] Avise JC, Hamrick JL. Conservation Genetics: Case Histories from Nature, Chapman & Hall, New York, 1996, ch. 5..
- [4] Mabuchi K, Nakano T, "Revision of the genus *Pseudolabrus* (Labridae) from the East Asian waters", Ichthyological Research, Vol. 44, May, 1997, pp. 321-334.
- [5] Mabuchi K, Kobayashi T, Nakano T, "Genetic Differences between two *Pseudolabrus* species (Osteichthyes: Labridae) from the southern coasts of Japan", Species Diversity, Vol. 5, May, 2000, pp. 163-172.
- [6] Soltis DE, Haufler CH, Darrow DC, Gastony GJ., "Starch gel electrophoresis of ferns: a compilation of grinding buffers, gel and electrode buffers and staining schedules", Amer. Fern J., Vol. 73, Jan. 1983, pp9-27.
- [7] Maruyama T. "Morphology and distribution in larva of labrid fishes", graduate thesis of Ehime University, Feb. 2002, in Japanese.
- [8] Westerbergh A, Saura A. "The effect of serpentine on the population structure of *Silene dioica* (Caryophyllaceae)", *Evolution*, Vol. 46, Oct, 1992, pp. 1537-1548.
- [9] Chepliak WM, Pitel JA, Techniques for starch gel electrophoresis of enzymes from forest tree species., Information report PI-X-42., Petawawa National Forestry Institute, Canadian Forestry Service, 1984.
- [10] Nei M. Molecular evolutionary genetics. New York: Columbia University Press, 1987.
- [11] Saitou N, Nei M, "The neighbor joining method: a new method for reconstructing phylogenetic trees", Molecular Biology and Evolution, Vol. 4, 1987, pp406-425.
- [12] Vrijenhoek RC, Douglas ME, Meffe GK, "Conservation genetics of endangered fish populations in Arizona", Science, Vol. 229, July, 1985, pp. 400-402.

THE INTEGRATION OF OUTDOOR HUMAN THERMAL COMFORT IN TROPICAL CLIMATE CAMPUS LANDSCAPE: CHULALONGKORN UNIVERSITY, BANGKOK, THAILAND

Ariya Aruninta¹, Yoshihito Kurazumi², Kenta Fukagawa³, and Jin Ishii⁴

¹Dept of Landscape Architecture, Faculty of Architecture, Chulalongkorn University, Thailand

²Dept of Human Environment Design, Sugiyama Jogakuen University, Japan

³Dept of Architecture, Kyushu Sangyo University, Japan

⁴Dept of Architecture, Meijo University, Japan

ABSTRACT

The purpose of this research is to study and compare the outdoor spaces with different cooling effects facilities in the tropical climate, city campus in the CBD of Bangkok, Thailand. The study aimed to find the most comfortable outdoor space in a green campus referred to UI GreenMetric World University Ranking indicators, the case study of Chulalongkorn University, tropical wet, in city center/high rise building. The ratio of area on campus covered in planted vegetation (lawns, gardens) provided as percentage of total site area) will be compared, especially, the micro-climatic seems to be an important criteria of the physical design features of an outdoor space: a) with cooling devices – shading, fountain, b) without cooling devices – pavement, open lawn. The cooling effect of these devices which are evaluated by measurement result of thermal comfort responded by tropical environment of the campus. The study will also analyze the human physiological and psychological response in summer / less humidity (in March) and rainy / high humidity (in September) season. The study will explain Micro/Macro-climatic effects from landscape features. The survey measured meteorological condition of the outdoor spaces, skin temperature of the subjects by attaching sensor on skin surface, and then distributed thermal sensation survey to collect psychological thermal comfort of the subjects. The study found out that the shortwave solar-radiation, long-wave radiation from different materials should play an important role in a new paradigm in green design and planning.

Keywords: Thermal comfort, Micro climate, Outdoor environment, Climatic effect, Green campus

INTRODUCTION

UI GreenMetric has been launched in 2010 by Universitas Indonesia, which the key objectives initiated as the cooperative efforts among groups of world universities in order to take steps to manage and improve their sustainability and help combat global climate change. Chulalongkorn University was ranked the world 15th of 'City Center' campus setting category in 2016 and aims for the higher ranking in the next following years. The green campus planning involves the landscape design of campus outdoor environment and while there are still the needs to decrease energy consumption especially for indoor Heating, Ventilation, Air Conditioning (HVAC) system. Thus, it leads to the research questions on campus outdoor thermal comfort as followings: 1) how human sensation responses to each outdoor space in summer and rainy seasons, 2) what cooling effects facilities in the tropical climate should be designed for outdoor space for the best thermal comfort.

Many researches in ergonomics have focused on the thermal comfort in designing and arranging things people use so that the people and things

interact most efficiently and safely, especially in the indoor environment. But methods for making an outdoor environment comfortable are very limited, while outdoor and indoor comfort zones may differ from each other, so adaptation or acclimatization to the outdoor environment should be studied [1]. This paper aims to integrate human thermal sensation and psychological responses as outdoor thermal environment evaluation index in landscape architecture design and planning of an urban campus.

The factors influenced in outdoor environment comfort are included this followings: the albedo, sky temperature and surface temperature, humidity, wind direction, air velocity, shortwave solar-radiation and long-wave radiation heat quantity. In addition, the measurement of sky and green upward and downward ratios from an orthographic photo of each site will be considered in the study. A design of an outdoor space, usually depends on functional and other aesthetic concepts. The authors who are from different research fields have intensively utilized the year long surveys in different seasons for their own aspects. This paper is intended to seek for a new paradigm in green design and planning to remediate the urban heat island effect especially in campus

planning along to improve the thermal environment from harsh to comfortable, in order to draw potential activities to outdoor space and reduce energy consumption in the buildings.

EXPERIMENTAL DESIGN

This research surveys were designed to collect data both from measurements of the meteorological condition of the outdoor spaces in summer and rainy season and the human physiological and psychological response to those outdoor spaces. The surveys were performed during two days in March (summer/dry season) and in September (rainy/wet season) during the day time only from before noon to the afternoon which is usually the peak hours of outdoor space occupancy of the campus. The very simple comparisons of the data aim to seek for the most comfortable condition of the outdoor spaces.

Measurement Procedure

The observation points and route patterns are shown in Fig. 1. For the comparisons, observation points were selected with consideration of the condition of the ground surface, such as paved ground, green areas covered with plants, and water surfaces, and with consideration for the condition of the sky factor due to buildings and trees. Six observation points were chosen in summer season survey and five observation points were chosen in Rainy season survey.

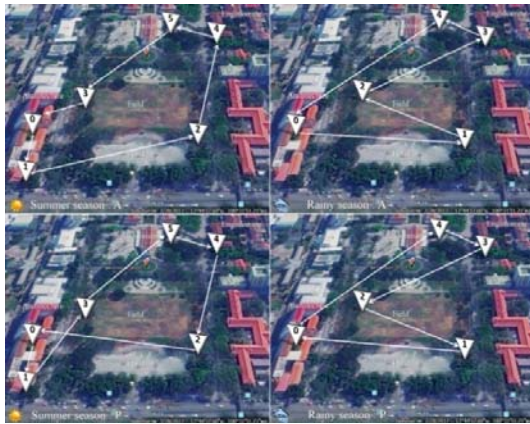


Fig. 1 Sites location maps and patterns of survey routes in summer and rainy season in the peak hours (AM/PM).

Seasonal Related Factors

The observation points in summer season (March) and rainy season (September) were adjusted accordingly with the experiments. Therefore, the point at open-air café was removed in rainy season

survey due to the unavailability of the new construction site, and north playfield was intended to compare the difference between high and low Sky-Factors, identified by the surrounding conditions (Table 1-2).

Table 1 Summary of summer season observation points

Site	Surface		Surrounding			
	Ground	Sky	North	East	South	West
0 Building court	Concrete	Eaves	Building	Building	Building	Building
1 Open-air café	Wooden deck	Awning / Trees	Building	Building	Open	Wall / Tree
2 Pond side	Grass / Pond	Trees	Open	Open	Trees	Trees
3 North playfield	Grass / Bare ground	Trees	Open	Open	Trees	Open
4 Engineering bldg	Concrete pavement	Sunshade / Trees	Open	Building	Trees	Building
5 Auditorium plaza	Concrete pavement	Open	Building	Open	Open	Open

Table 2 Summary of rainy season observation points

Site	Surface		Surrounding			
	Ground	Sky	North	East	South	West
0 Building court	Concrete	Eaves	Building	Building	Building	Building
1 Pond side	Grass / Pond	Trees	Open	Open	Trees	Trees
2 North playfield	Grass / Bare ground	Open*	Open	Open	Open*	Open
3 Engineering bldg	Concrete pavement	Sunshade / Trees	Open	Building	Trees	Building
4 Auditorium plaza	Concrete pavement	Open	Building	Open	Open	Open

Site Related Factors

When considering the thermal sense of humans, it is necessary to include not only air temperature but also the environmental elements of thermal radiation, convection, humidity, and heat conduction. Briefly, a strong solar radiation gives a hot feeling, a strong wind gives a cool feeling, high humidity gives a feeling of an unpleasantly warm and humid (muggy weather), and a heated ground surface that it cannot be touched make us feel so hot. Kurazumi et al. [2]-[5] who revealed the relationship between the physiological and psychological responses of humans and invented the enhanced conduction-corrected modified effective temperature (ETFe) as the outdoor thermal environment evaluation index, clarified in many of their research papers that the variables that affect the thermal sensation are heat conduction, humidity, and short wave solar radiation, air velocity, heat conduction, and humidity.

Air temperature, humidity, wind direction, air velocity, shortwave solar-radiation heat quantity, long-wave radiation heat quantity, and ground surface temperature were measured. The air

temperature and humidity were measured at a height of 90cm above the ground by means of an Assman ventilated psychrometer. For the air velocity, the prevailing wind direction was measured for 5min at a height of 120cm above the ground by means of a three-dimensional ultrasonic anemometer. Concerning when the wind was very gentle, the average air velocity was measured for 5min at a height of 120cm above the ground by a non-directional anemometer and the three-dimensional ultrasonic anemometer.

The short-wave thermal radiation heat quantity in the regions from the visible to the near-and-mid-infrared and the terrestrial thermal radiation in the far infrared region, thermal radiation heat quantities in downwards and upwards directions were measured at a height of 90cm above the ground by long and short-wave radiometer. The ground surface temperature was measured by a radiation thermometer.

The sky factor was measured by a photograph of the sky taken 120cm above the ground at the observation point using a fisheye lens with an orthographical projection format and a 35mmdigital SLR camera. The albedo, sky temperature, and surface temperature were calculated from each directional component of the short-wave thermal radiation heat quantity and the long-wave thermal radiation heat quantity. The abbreviations and the meaning are as followings:

Ta is range of air temperature. Tf is range of ground surface temperature in the vicinity of the human body. RH is relative humidity. Va is air velocity. RSdwn is downward short wave solar radiation. RSup is upward short wave solar radiation. RLdwn is downward long wave radiation. RLup is upward long wave radiation.

The influence of short wave solar radiation in outdoor environment appears to be strong in summer, when the air temperature is higher than the skin temperature of the human body, evaporation is the only means of dissipating heat [2].

Human Related Factors

Subjects moved on foot to the observation points without being planned to reduce mental fatigue at the slow walking speed (around 0.7 m/sec), they were exposed to the thermal environment in a standing posture. Skin temperatures were measured as physiological conditions for the human body by a thermistor thermometer. Skin temperature was measured at the positions of the head, trunk, arm, hand, thigh, lower leg and foot. The subjects freely selected their clothing to be suitable to the weather

on the measurement day. The clothing quantity of the subjects was sought by the clo value by layering the clothing reported by the subjects. As a psychological condition for the human body, the psychological response was measured after staying at the observation point for 5min by means of rating the whole-body thermal sensation (cold-hot) and the whole body thermal comfort (comfortable-uncomfortable) on a linear scale as Kurazumi et al 2011.

The Cooling Effect Conditions and the Thermal Environment Stimuli

Urbanization is a major cause of Urban Heat Island (UHI) phenomenon, relates to a high percentage of low-albedo and impermeable surface, a reduction of the cooling effect of shading, building up areas and especially the urban canyon where heat is reradiated and reflected back to the surrounded environment [6].

Planners always include shade tree wherever possible as a strategy to reduce heat islands and improve outdoor environment in three ways ; through shading, through evapotranspiration, and through wind shielding [7],[8]. The studies in many regions confirm that tree shade is an ecological solution to reduce both mean radiant and surface temperature, tree canopy can filter and absorb solar radiation, whilst be most affects human's thermal comfort or physiologically equivalent temperature (PET) [7],[9]. In macro scale, urban parks have been demonstrated to have a significant cooling effect strongest for land surface temperatures of surrounding urban areas as far as 860 m from the park boundary[6].

While pavements with light-colored surfaces can offset or reverse the heat island, which have high solar reflectance and high thermal emittance can reduce the temperature of the surface, which reduce urban temperature and improve urban air quality in summer season [6],[11],[12],[13].

Human Physiological and Psychological Responses

There was a study that acclimatization will not have significant difference of psychological reaction when the subject could not tolerate the environment at the temperature is greater than 40°C [4]. And Thai people from a tropical region perceive an ETFe of up to around 35°C to be a moderate thermal environment but cannot tolerate the temperature around more than 40°C [5] or 3°C than normal body temperature or normothermia = 36.8 ± 0.7 °C. Therefore, the effective outdoor environment designers should be aware of the harsh environment and consider avoid alternatives and factors that can create heat radiation especially in summer.

RESULTS OF EACH SITE'S THERMAL ENVIRONMENT

After data calibration, the results from measurements were compared in different methods to illustrate the effects site conditions to human thermal comfort. The results after comparing three key issues; seasonal, site, and human related factors; to find the high potential thermal comfort outdoor environment in the urban campus.

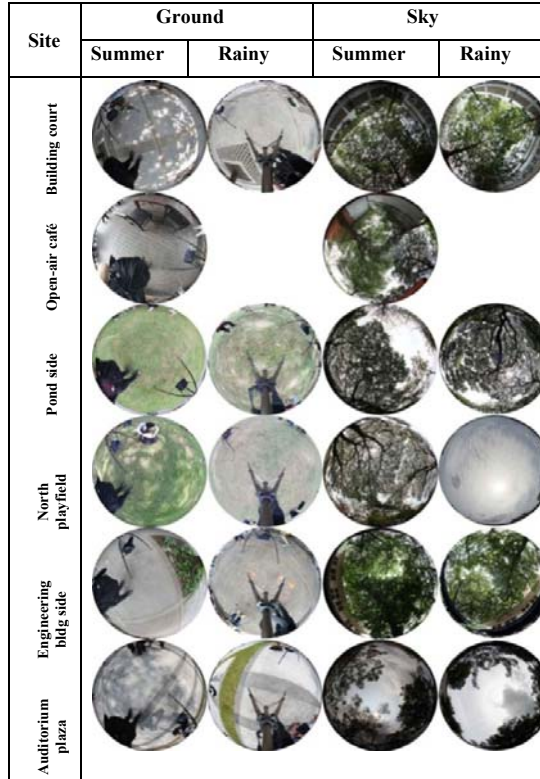


Fig. 2 Ground and sky photos of the sites with different cooling conditions

Site Cooling Effects

The most significant factors to explain site cooling effect are 1) Sky factor, 2) U-green factor, and 3) D-green factor. From Fig. 2, ground and sky orthographic photos of the sites show different cooling conditions of space, especially ground cover and pavement materials from ground photos and building canyon and tree canopy from sky photos.

Thereafter, sky factor and U-green / D-green factor have been simulated. Sky factor is defined as the ratio of configuration factor of sky to semi celestial sphere. U-green factor is defined as the ratio of upward green, water surface and the like solid angles to semi celestial sphere solid angle. D-green factor is defined as the ratio of downward green, water surface and the like solid angles to semi

celestial sphere solid angle. According to Fig. 3 and Fig. 4, the sites with the highest D-green factor are pond site and north play field, where ground is covered with grass, water, and bare ground. U-green factor in each site shows tree canopy coverage ratio. Therefore, at the north playfield site, when the measurement point was moved from under the trees to the field, sky factor is higher more significantly. In addition, the auditorium site has higher sky factor and less D-green factor, thus it tends to directly expose to the radiation.

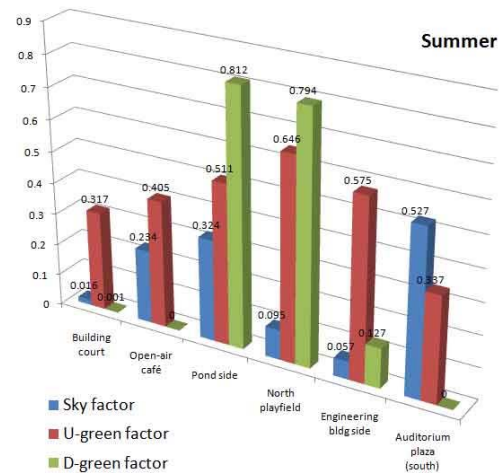


Fig. 3 [Summer season] Characteristics of the sites with different cooling conditions

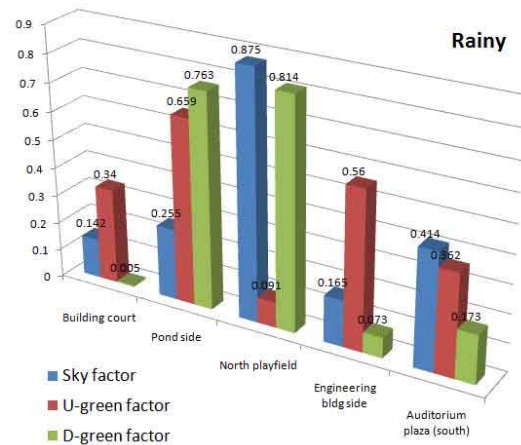


Fig. 4 [Rainy season] Characteristics of the sites with different cooling conditions

Together with the sky factors and green factors, at each site, other factors relates to albedo effect were measured, in order to explain the cooling effect of the sites (Table 3). These included the mean values of RS_{down} (downward short wave solar radiation), RS_{up} (upward short wave solar radiation), RL_{down} (downward long wave radiation), RL_{up} (upward long wave radiation), Ta (air

Table 3 Meteorological condition of the sites with different cooling conditions

	Site[ND]	RSdwn [W/m ²]	RSup [W/m ²]	RLdwn [W/m ²]	RLup [W/m ²]	Mean Va	Mean RH	Mean Ta	Mean Tf	Tf-Ta
Summer	0-Building court	20.32	4.67	484.41	482.61	0.58	61.51	30.10	30.04	-0.06
	1-Open-air café	47.58	<u>3.36</u>	484.24	488.76	0.69	<u>60.87</u>	<u>30.00</u>	<u>31.67</u>	1.67
	2-Pond side	107.24	26.05	478.67	<u>478.92</u>	0.95	61.09	30.20	32.68	2.48
	3-North playfield	136.20	35.64	479.79	489.40	1.52	63.05	30.20	35.28	5.08
	4-Engineering bldg side	28.63	<u>3.60</u>	482.99	484.68	0.79	62.48	30.20	33.72	3.52
	5-Auditorium plaza	437.27	116.06	<u>462.90</u>	530.50	<u>1.61</u>	61.02	30.90	41.08	10.18
Rainy	0-Building court	9.79	0.42	482.76	<u>472.87</u>	0.80	59.36	30.8	<u>27.2</u>	<u>-3.6</u>
	1-Pond side	82.40	17.94	481.67	479.84	0.68	61.44	30.8	29.9	-0.9
	2-North playfield	581.36	96.92	<u>451.17</u>	509.57	<u>1.63</u>	<u>58.47</u>	31.5	37.4	5.9
	3-Engineering bldg side	18.42	<u>-0.82</u>	482.53	479.57	0.83	62.13	<u>30.5</u>	30.4	-0.1
	4-Auditorium plaza	371.61	91.32	467.72	511.83	1.22	59.46	31.4	38.7	7.3

temperature), Tf (ground surface temperature), RH (humidity), Va (air velocity), and Tf-Ta (cooling effect temperature). The underlined numbers are among those with cooling effect presented, and in opposite, the bold numbers are those with harsh thermal effect presented.

DISCUSSION ON INTEGRATION OF HUMAN THERMAL COMFORT AND SITE CHARACTERISTICS

We assumed that site characteristics of how the outdoor spaces and their surroundings have been designed are the key factors influence human thermal comfort. Results from meteorological condition of the sites show that both in summer and rainy seasons, the less cooling condition is significantly presented at auditorium south side plaza, where Tf-Ta is very high.

Table 4 [Summer season] Mean temperature

	Time	Ta[°C]	Tf[°C]	difT	Mean
0-Building court	10-1150	30.1	30.04	-0.06	3.53
0-Building court	10-1330	30.5	35.61	5.11	
0-Building court	10-1533	30.3	30.93	0.63	
0-Building court	10-1716	29.5	34.49	4.99	
0-Building court	11-1045	29.5	32.84	3.34	
0-Building court	11-1226	31.2	35.04	3.84	
0-Building court	11-1417	31.6	35.47	3.87	
0-Building court	11-1604	31.0	37.49	6.49	
1-Open-air café	10-1206	30.0	31.67	1.67	4.70
1-Open-air café	10-1552	31.1	36.52	5.42	
1-Open-air café	11-1104	30.0	35.85	5.85	
1-Open-air café	11-1438	32.1	37.97	5.87	
2-Pond side	10-1224	30.2	32.68	2.48	1.93
2-Pond side	10-1659	29.6	31.82	2.22	
2-Pond side	11-1209	30.8	32.75	1.95	
2-Pond side	11-1456	31.3	32.37	1.07	
3-North playfield	10-1316	30.2	35.28	5.08	5.35
3-North playfield	10-1610	29.9	34.70	4.80	
3-North playfield	11-1120	30.5	34.87	4.37	
3-North playfield	11-1549	31.4	38.55	7.15	
4-Engineering bldg	10-1242	30.2	33.72	3.52	3.80
4-Engineering bldg	10-1642	29.6	34.78	5.18	
4-Engineering bldg	11-1153	30.3	33.68	3.38	
4-Engineering bldg	11-1515	31.5	34.61	3.11	
5-Auditorium plaza	10-1257	30.9	41.08	10.18	12.92
5-Auditorium plaza	10-1628	29.9	41.36	11.46	
5-Auditorium plaza	11-1139	30.8	47.23	16.43	
5-Auditorium plaza	11-1530	32.3	45.92	13.62	

It is interesting that the sites, where surrounded with buildings and pavement such as building court and Engineering building side, have quite high RLdwn radiation. Whilst, the open field area with grass or bare ground such as north play field has very high RS both upward and downward, in addition to quite high RLup but very low RLdwn.

Table 5 [Rainy season] Mean temperature

	Time	Ta[°C]	Tf[°C]	difT	Mean
0-Building court	16-1033	31.1	28.7	-2.4	-3.6
0-Building court	16-1211	31.6	20	-11.6	
0-Building court	16-1336	32.2	29.5	-2.7	
0-Building court	16-1512	30.8	28.5	-2.3	
0-Building court	17-0943	29.4	26.2	-3.2	
0-Building court	17-1107	30.2	27.2	-3.0	
0-Building court	17-1254	30.5	29.2	-1.3	
0-Building court	17-1419	30.5	28.3	-2.2	
1-Pond side	16-1054	31.4	30.8	-0.6	-0.9
1-Pond side	16-1455	31.2	30.6	-0.6	
1-Pond side	17-1050	30	29.1	-0.9	
1-Pond side	17-1312	30.6	29.2	-1.4	
2-North playfield	16-1114	32.5	38.7	6.2	5.9
2-North playfield	16-1441	31.2	34.7	3.5	
2-North playfield	17-1034	30.4	35.3	4.9	
2-North playfield	17-1327	32	40.8	8.8	
3-Engineering bldg	16-1133	31.4	30.4	-1.0	-0.1
3-Engineering bldg	16-1412	30.7	31	0.3	
3-Engineering bldg	17-1017	29.8	29.3	-0.5	
3-Engineering bldg	17-1344	30.2	30.9	0.7	
4-Auditorium plaza	16-1149	32.5	37.1	4.6	7.3
4-Auditorium plaza	16-1356	31.8	41.3	9.5	
4-Auditorium plaza	17-1001	30.4	36.2	5.8	
4-Auditorium plaza	17-1359	30.8	40.2	9.4	

CONCLUSION

Chulalongkorn University aims for the higher ranking of UI GreenMetric in the next following years. The landscape design of urban campus outdoor environment still needs to decrease energy consumption especially for indoor HVAC system. Findings from the research, which integrated human sensation responses to each outdoor space in summer and rainy seasons and the meteorological condition of the sites have shown a significant finding that cooling effects facilities in the tropical climate can be designed for the best thermal comfort, spaces between buildings in the very high

density area would be able to create a comfort zone for outdoor activities. The most interesting finding from this study is the paved outdoor space with less shade can create very harsh thermal condition. Therefore, although the built up area is the major cause of UHI, but a court area between a group of buildings with tree canopies can offer a comfort zone both in summer and rainy season. Open field area is good as an infiltrated ground for Water Sensitive Urban Design (WSUD) and keeps the average temperature cool only being covered with grass. The heat from shortwave solar-radiation, and long-wave radiation ; so called albedo effect and emissivity ; should play an important role in human thermal comfort and landscape design of an outdoor space.

ACKNOWLEDGEMENTS

The corresponding author would like to thanks the Japanese authors who have travelled with all the instruments to Thailand, a hot and humid country, several times throughout the years in order to make this research possible.

REFERENCES

- [1] Honjo T., "Thermal comfort in outdoor environment", *Global Environmental Research*, 13/2009, pp. 43-47.
- [2] Kurazumi Y. et al., "The influence of outdoor thermal environment on young Japanese females", *Int J Biometeorol*, Vol. 58, 2014, pp. 963-974.
- [3] Kurazumi Y. et al., "Evaluation of enhanced conduction-corrected modified effective temperature ETFe as the outdoor thermal environment evaluation index", *Energy and Buildings*, Vol 43, 2011, pp. 2926-2938.
- [4] Kurazumi Y. et al., "Ethnic differences in thermal responses between Thai and Japanese females in tropical urban climate", *American Journal of Climate Change*, Vol. 5, 2016, pp. 52-68.
- [5] Kurazumi Y. et al., "The influence of tropical urban climate upon the human body.", in *Proc. : International Joint-Conference of SENVAR-iNTA-AVAN 2015*, Johor.
- [6] Al-Gretawee H, Rayburg S, Neave M, "The cooling effect of a medium sized park on an urban environment", *International Journal of GEOMATE*, Oct., 2016, Vol. 11, Issue 26, pp. 2541-2546.
- [7] Tukiran J MD, Ariffin J, Ghani A N A, "Cooling effects of two types of tree canopy shape in Penang, Malaysia", *International Journal of GEOMATE*, Aug., 2016, Vol. 11, Issue 24, pp. 2275-2283.
- [8] Huang Y J, Akbari H, Taha H, "The wind-shielding and shading effects of trees on residential heating and cooling requirements", in *Proc. :the ASHRAE Winter Conference*, 1990. pp. 1403-1411.
- [9] Matzarakis A, Mayer H, Iziomon M G, "Applications of a universal thermal index : physiological equivalent temperature", *Int J Biometeorol*, V.43: 1999 pp.76-84.
- [10] Tukiran J MD, Ariffin J, Ghani A N A, "A study on the cooling effects of greening for improving the outdoor thermal environment in Penang, Malaysia", *International Journal of GEOMATE*, June, 2017, Vol.12 Issue 34, pp. 62-70.
- [11] Akbari H, Pomerantz M, Taha H, "Cool surfaces and shade trees to reduce energy use and improve air quality in urban areas", *Sol. Energy*, vol. 70, no. 3, Jan. 2001, pp. 295-310.
- [12] Taha H, Hammer H, Akbari H, "Meteorological and air quality impacts of increased urban albedo and vegetative cover in the Greater Toronto Area, Canada", *Berkeley, Calif.*, 2002.
- [13] Rosenfeld AH. et al., "Mitigation of urban heat islands: materials, utility programs", *Energy and Buildings*, Vol. 22, 1995, pp. 255-265.

ANALYSIS OF TSUNAMI IMPACT TO COASTAL VEGETATION AND GEOLOGICAL LANDSCAPE AT KUALA TERENGGANU

Nurfarhana Aisya Anuar¹ and Abdul Halim Abdul Latiff²

^{1,2}Faculty of Geosciences and Petroleum Engineering, Universiti Teknologi PETRONAS, Malaysia

ABSTRACT

In this study, the impact of potential tsunami occurrences on the Kuala Terengganu coastline, which originated from the Manila Trench is analyzed. The tsunami effects were investigated with the aid of wave simulation models while considering the coastal vegetation and geological factors of the study area. This study was initiated because several seismologist and earth scientist discovered that there is a possibility of an earthquake with the magnitude 9.3 Mw will occur along the Manila Trench. Thus, to identify the potential tsunami impact on the East Coast Peninsular Malaysia area, data were gathered from field study and was used to generate a tsunami wave propagation model and a run-up and inundation model. From the result, a tsunami will reach the coastline by 11 hours with a maximum wave height of 0.143m, a run-up height of 0.5m, and an inundation distance of 4m. However, in consideration of external variables, a new model was constructed with a maximum wave height of 1.5m, a run-up height of 2m, and an inundation distance of 14m. The studied area, Batu Rakit beach coastline was flooded and areas near the coastline have a high risk of getting impacted whereas areas with coastal vegetation have a lower risk of impact.

Keywords: Tsunami; Geological Landscape; Coastal Vegetation

INTRODUCTION

Earthquakes and tsunami have caused countless lives and assets losses throughout the history of mankind. The greatest tsunami that has hit Malaysia recently is the 2004 Andaman seaquake, which holds a magnitude of 9.0. The Andaman Tsunami causes more than 240,000 deaths throughout the Indian Ocean coastline. Later, in 2011, a tsunami of a similar magnitude took place off the Pacific coast of Tohoku, Japan resulting in a death toll of 15,891 whereas 2,500 lives are still missing. Both major earthquakes occur along a subduction zone. The next subduction zone near Malaysia is the Manila Trench (Fig. 1). Researchers are now predicting a potential earthquake of a magnitude of 9.3 occurring from the Manila Trench. Therefore, it is essential to identify the impact of a tsunami originating from the Manila Trench on the coast of Malaysia.

In this study, the potential tsunami impact on the coastline of Batu Rakit beach, Kuala Terengganu will be simulated. The geological landscape of the study area such as the bathymetry, slope of the coastline as well as the shape of the coastline will be identified and used when generating the tsunami simulation. The coastal vegetation of the study area will also be considered. The objectives of this study is to study the geological landscape of Batu Rakit beach coastline as well as to construct a tsunami wave propagation model. Information on the geological landscape of Batu Rakit beach will be analyzed and taken into consideration during the generation of the tsunami

models. Whereas, the tsunami wave propagation model will display the propagation of the tsunami waves originating from the Manila Trench and the time and magnitude of the tsunami impact on the coast of Batu Rakit beach.

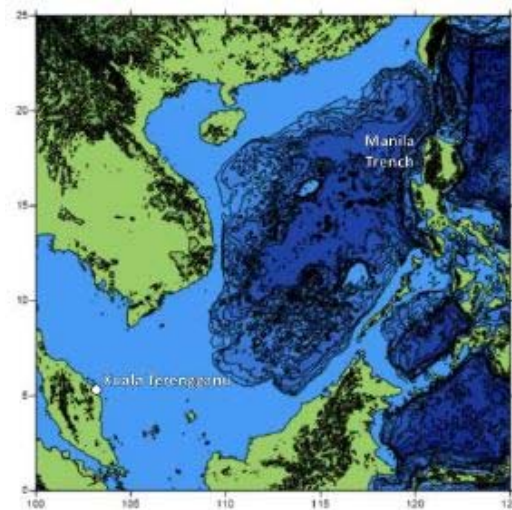


Figure 1: Location of the Manila Trench from Kuala Terengganu

EARTHQUAKES AND TSUNAMI

The Earth's lithosphere is broken into pieces called tectonic plates. These plates are constantly moving due to the tectonic cycle which can be simplified into four stages; formation of new

lithosphere from magma, seafloor spreading, plate collision forming subduction zones and reabsorption of the old plate into the mantle. These subduction processes create tremendous stores of energy, which are released periodically as earthquakes [1]. Tsunami comes from the Japanese word “Tsu” and “Nami” meaning harbour and waves respectively, thus is defined as waves that increase in velocity and height as the waves enter a harbour [1, 2]. As obtained from the Australian Government – Geoscience Australia by Liew [2], 75% of the tsunami are caused by earthquakes, whereas the cause of 10% of the tsunami are unknown followed by 8% due to landslides, 5% from volcanic eruptions and 2% from meteorological impact. However, not all earthquakes can produce a tsunami. Tsunami only develops when an earthquake occurs in the ocean [3] with a vertical fault movement and an earthquake of M7.5 [1]. These earthquakes can also lead to underwater landslides and trigger tsunami.

THE MANILA TRENCH

The Manila Trench is located on the west side of the Philippines. The 1200 km-long subduction zone is formed during the early Miocene and continue active to the present day. Along the Manila Trench, the South China Sea oceanic crust inclines eastward below the Philippines, southern Taiwan and the overriding ocean floor [4]. Several researchers have assessed the tsunami hazard from Manila Trench source and concluded that the worst case scenario is an earthquake with a magnitude 8.2 as there have never been recorded instrumentally an earthquake exceeding 7.6 in the area. However, considering the length of the Manila Trench, other researchers proposed that a larger earthquake with a magnitude up to 9.0 or 9.3 could occur [4]. Considering the fault geometry of the Manila Trench, the Manila Trench is divided into six segments (Fig. 2). Table 1 indicates the parameters of a source model for the Manila Trench proposed by Nguyen et. al [4] sufficient enough to generate an earthquake of 9.3 Mw.

GEOLOGICAL FACTORS INFLUENCING THE TSUNAMI IMPACT

The strength of a tsunami is measured by the wave speed and run-up including how far inland the tsunami can travel. The factors that influence the strength of the tsunami waves are the seaquake magnitude, seaquake depth, shore distance with the epicentre and coastline morphology or bathymetric characteristic as well as the seabed gradient [5]. The deeper the earthquake depth, the weaker the tsunami generated. Whereas in term of the coastline morphology, weak tsunami is generated if the gradient is greater nearing the shore. However, a

constant gradient with a gentle slope will form a tsunami with lower speed compared to the seabed with a sudden change in slope angle [5].

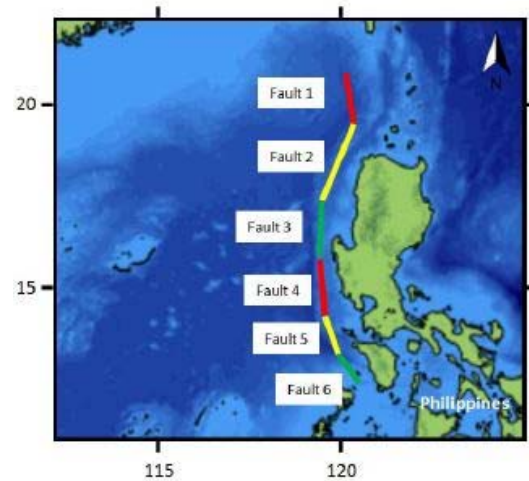


Figure 2: Six segments of the Manila Trench, referred from [4]

ROLE OF COASTAL VEGETATION IN TSUNAMI EVENTS

Coastal vegetation has been proven to ensure the stabilization of the beach and slope areas. Studies have shown damages and impacts from tsunami reduced due to the protection of the coastal vegetation. However, some authors disagree, stating that no real proof existed on the mitigation effects [6]. Despite that, V. Selvam stated that the mangrove forests, a type of coastal vegetation have protected the shore of southern India against cyclones and other storms for thousands of years [7]. Similar in Malaysia, claims have been made on how fishermen were saved during the tsunami of December 2004 due to the existence of mangrove swamps along the Penang coastline. The mangrove forests minimize erosion and sedimentation affects as well as dampening and absorbing the wave energy. The mangrove forests also contribute to the low settlement density in certain areas thus reducing the risks to both human and property [7].

TSUNAMI SIMULATION MODELLING

The Intergovernmental Oceanography Commission, the depth-averaged two-dimensional shallow water equations (SWE) can be used to simulate the tsunami propagation in deep ocean. The conditions of the applicability of SWE is when the wave heights are smaller than the depths of water and the wavelengths. Comparing the 3D and 2D models, 2D models is adequate enough as the 3D models require excessive memory and long computational time [8].

Table 1: The hypothetical fault parameters of Manila Trench source [4]

Fault	Lon.	Lat.	Length (km)	Width (km)	Dislocation (m)	Depth (km)	Strike (°)	Dip (°)	Rake (°)
1	120.5	20.2	190	120	25	30	354	10	90
2	119.8	18.7	250	160	40	30	22	20	90
3	119.3	17.0	220	160	40	30	2	28	90
4	119.2	15.1	170	90	28	30	356	20	90
5	119.6	13.7	140	110	12	30	344	22	90
6	120.5	12.9	95	80	5	30	331	26	90

The tsunami simulation used in the project is TUNA software, which uses the shallow water equations and under normal assumptions, the equations describing the conservation of mass and momentum can be depth averaged and be written as the following equations [8].

METHODOLOGY

First, we conducted a few field studies in order to have a deeper understanding of the geological landscape as well as the coastal vegetation available at Batu Rakit coastline. During the fieldwork, the gradient of the beach will be measured to create the cross-section of the Batu Rakit coast and seafloor. Traversing of the coastline is performed to obtain an accurate image of the coastline. The work conducted similar to the procedure proposed in [9].

Then the tsunami wave propagation was modelled by incorporating TUNA tsunami simulation software. This software will be used to generate tsunami simulation on the area of study. Certain criteria will be taken into consideration during the generation of the simulation such as geological landscape of the study area as well as the fault displacement, fault location and focal depth of the tsunami origin. The input parameters of the TUNA Software are divided into five main controls; domain and output control, source control, boundary control (other control), bathymetry control and time series. The domain and output control defines the computational power required and the output by adjusting the number of iterations, grid size, computational nodes and others [8]. Other controls section defines the boundary conditions, whether the boundary is open or close. In this section, the gravitational acceleration and the Manning's coefficient is also determined [8]. The bathymetry and topography of the area is set in the bathymetry control section. The number and location of observation points to record the wave simulation height of the ocean is adjusted in the time series control [8].

ANALYSIS OF COASTAL MAP

From the initial field study conducted, the coastal map and seafloor cross-section of Batu Rakit coastline was constructed and modelled (figure 3 and figure 4). A total of 11 coordinates were taken along the coastline of Batu Rakit beach with an interval of 100 m. The coastline of Batu Rakit beach is rather straight, facing the South China Sea at a North-East direction. The cross-section is perpendicular to the coastline, with P6 as a starting point. The beach has a width of 30 meters and the coastline elevation rise to almost 6 m above the sea level. The difference between high tide and low tide is around 1.5 meters vertically and 10 meters horizontally. The average slope of the area is of 10^0 thus is considered a gentle slope. There is also a rather thick beach forest located at P1 and continues northwest of the area. Between P3 and P4, more coastal vegetation is observed (figure 5). There are fisherman villages along the coastline. At the end of the study area, starting from P11, large granite boulders are observed. These boulders are used to prevent further coastal erosion to the area. The coastal erosion defense continues up to 2 km eastward of the beach.

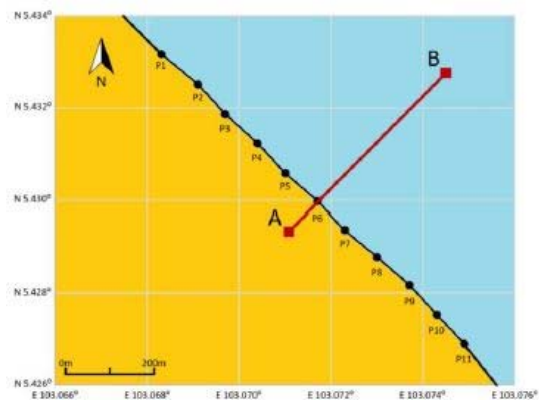


Figure 3: Coastal Map of Pantai Batu Rakit

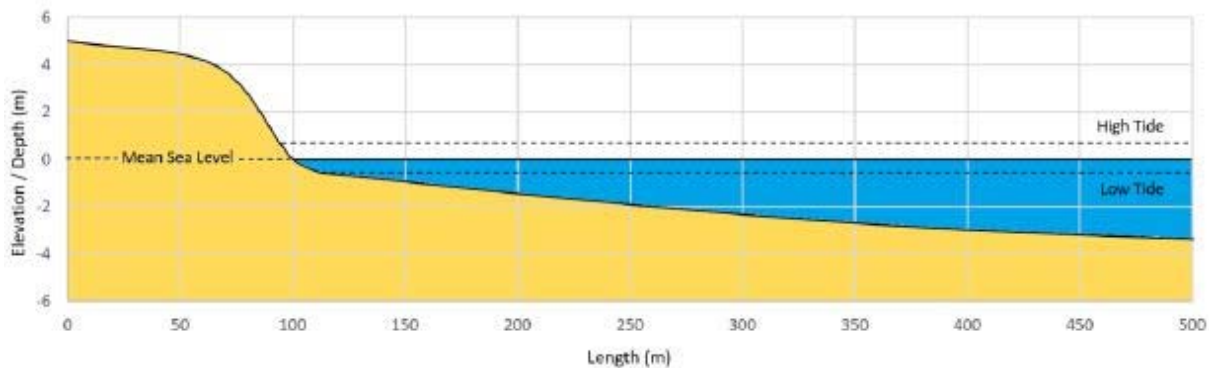


Figure 4: Seafloor Cross-section of the Pantai Batu Rakit Coastline from A to B



Figure 5: Field Map of Batu Rakit beach.

TSUNAMI PROPAGATION MODEL

Seven tsunami wave models are generated using the TUNA-M2 Software. The models are generated according to the parameters in Table 2. The parameters are obtained from Nguyen et. al [4] as the source model incorporated all advantages of two models proposed by Wu and Huang (2009) and Megawati et al. (2009). However, the width of the fault zones is altered to 10km due to the difference in width definition used for the simulation. Six of the models generated simulate the tsunami wave propagation originating from different fault zones; Fault 1 to Fault 6. Whereas one model is generated to simulate the worst case scenario where the tsunami wave propagation originates from all fault zones simultaneously. All the models are run for 40001s of simulation. In all the models, by 11 hours, the tsunami waves reach the coast of Kuala Terengganu but with different wave heights. The maximum wave heights for each tsunami model is recorded in Table 3.

Comparing each individual faults, the tsunami waves originating from Fault 3 shows the highest maximum wave height followed by the waves originating from Fault 2, Fault 4, Fault 1, Fault 5 and Fault 6. Fault 3 has the highest wave height due to its high fault dislocation of 40m as well as the direction of the strike. However, the worst case scenario is when the tsunami waves originates from all the fault zones simultaneously with a maximum wave height of 0.143m. The propagation of the tsunami wave originating from all faults is shown in Fig. 7.

Table 3. Maximum wave height for each tsunami models

Fault	Maximum Wave Height (m)
Fault 1	0.028
Fault 2	0.059
Fault 3	0.082
Fault 4	0.042
Fault 5	0.018
Fault 6	0.006
All Faults	0.143

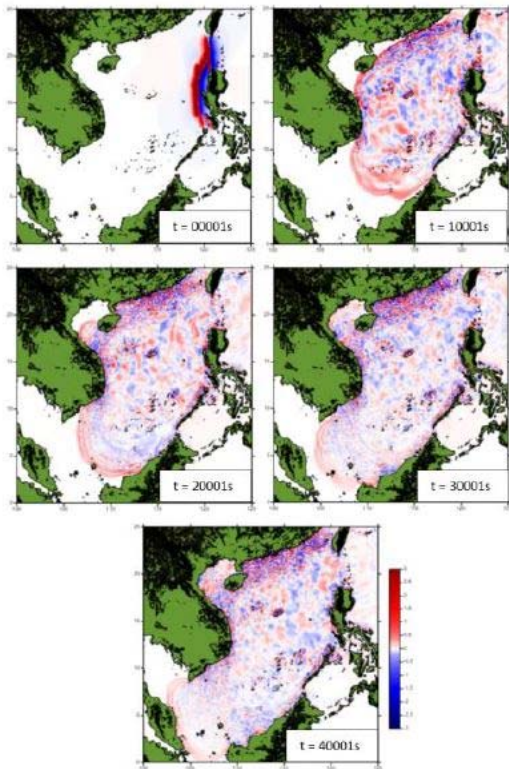


Figure 7: Tsunami wave simulation originating from all fault zones simultaneously.

A tsunami wave run-up and inundation model is generated from the tsunami propagation model originating from all faults simultaneously to illustrate the maximum wave height as well as to identify the run-up height and inundation distance of the tsunami impact. With a maximum wave height of 0.143m, the run-up height of the tsunami impact is 0.5m and the inundation distance is 4m (Fig. 8). Regardless of the 9.3 magnitude earthquake in the Manila Trench, the tsunami has low impact on the coast of Batu Rakit beach.

However, in this study, the propagation model is generated with limited variables. In reality, many more variables can influence the tsunami wave heights. The earthquake in the Manila Trench may reactivate other faults within the area as well as triggering underwater landslides at nearby continental slopes especially along the Palawan Island where the continental slope is fairly steep thus contributing to the impact of the tsunami. In a case where these events may occur, a higher maximum wave height will hit the Batu Rakit coastline. Considering the external variables, a higher maximum wave height may be achieved. In a case where the maximum wave height is 1.5m, a run-up height of 2m whereas the inundation distance of 14m could occur (Fig. 9).

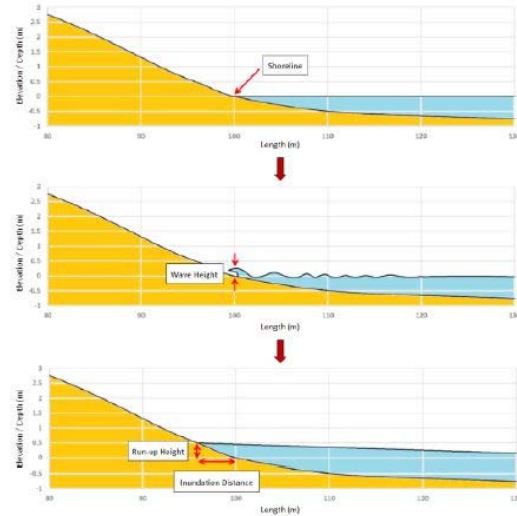


Figure 8: Tsunami Wave Run-up and Inundation Model Originating from All Fault Zones

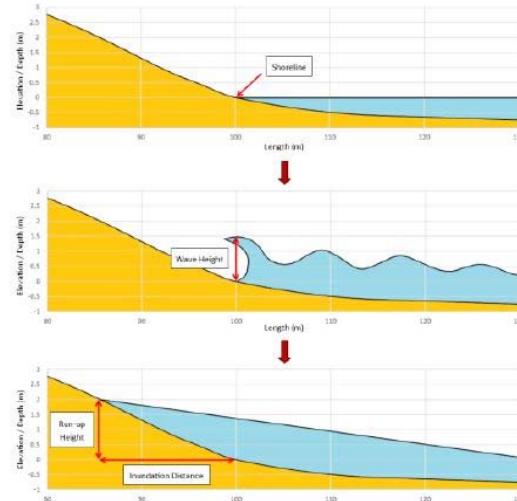


Figure 9: Tsunami Wave Run-up and Inundation Model while Considering External Variables.

Thus, the inundation map of Batu Rakit beach (Fig. 10) indicates that the whole coastline, coloured light blue, will be submerged by the tsunami. As the geological landscape of the coastline is straight and faces the open ocean, the energy of impact along the coastline is constant. Areas in yellow colour have a high risk being effected by the tsunami, whereas areas with coastal vegetation have a lower risk of impact by the tsunami as the vegetation works as a barrier to prevent the tsunami from moving further inland.



Figure 10: Inundation Map of Batu Rakit beach. Blue region indicate the area will be flooded by sea water, while the yellow region is the high risk area.

CONCLUSION & RECOMMENDATION

In this study, the study on the geological landscape of Pantai Batu Rakit Coastline was done. Pantai Batu Rakit is a straight coastline facing the South China Sea in the northeast direction. The coastal slope of the area is gentle with a gradient angle of 10°. Coastal vegetation are present along the coastline, as well as fisherman villages and granite boulders as coastal erosion defence. Several tsunami wave propagation models were constructed. The parameters used in this study generates an earthquake of magnitude 9.3 in the Manila Trench. The models indicate that the tsunami waves will reach the coastline of Pantai Batu Rakit in 11 hours. The model originating from all faults simultaneously shows the highest maximum wave height. A tsunami run-up and inundation models is also generated thus concluding that the tsunami waves with the following parameters have low impact on the coast of Pantai Batu Rakit.

However, many more external variables may contribute to the tsunami wave height. Considering the worst case scenario involving these external variables, a new tsunami wave run-up and inundation model is constructed. From this model, it is identified that the coastline of Pantai Batu Rakit will be submerged. Areas close to the coastline have high risk of tsunami impact except areas with coastal vegetation which will have a lower risk. In conclusion, all the objectives of this study is met. It is recommended a further study of this project is to be done. More possibilities such as the reactivation of

faults and underwater landslide occurring near the Manila Trench are to be considered to identify the worst case scenario for precautionary measures.

ACKNOWLEDGMENT

We would like to Universiti Teknologi PETRONAS for the resources and support in completing this project.

REFERENCES

- [1] P. L. Abbott, *Natural Disasters*, 7th. ed., New York: McGraw-Hill, 2009.
- [2] M. S. Liew. (2015, May). Impact of Tsunami on Oil and Gas Facilities in the Malaysian Waters from Manila Trench. Presented at Universiti Teknologi PETRONAS Sharing Session.
- [3] Nola Taylor Redd. (April, 2015) *Earthquakes & Tsunamis: Causes & Information* [Online]. Available: <http://www.livescience.com/21486-earthquakes-causes.html>
- [4] P. H. Nguyen, Q. C. Bui, P. H. Vu and T. T. Pham, "Scenario-based Tsunami Hazard Assessment for the Coast of Vietnam from the Manila Trench Source," *Physics of the Earth and Planetary Interiors*, vol. 236, pp. 95-108, 2014.
- [5] B. Chatenoux and P. Peduzzi, "Impacts from the 2004 Indian Ocean Tsunami: Analyzing the Potential Protecting Role of Environmental Features," *Nat Hazards*, vol. 40, pp. 289-304, 2007.
- [6] J. C. L. Bayas, "Modeling the Influence of Coastal Vegetation on the 2004 Tsunami Wave Impact", doctoral dissertation, Faculty of Agricultural Sciences, University of Hohenheim, Germany, 2012.
- [7] F. Colbourne, "Tsunami Impact on the West Coast of Penang Island, Malaysia", Research Project Report, Emporia State University, United States of America, 2005.
- [8] H. L. Koh & S. Y. Teh, "TUNA User Manual", Universiti Sains MARA, 2010.
- [9] S.S.S. Singh and A. H. Abdul Latiff, "Tsunami impact analysis to geological landscape in Perak coast, Malaysia", in Proc. 6th Int. Conf. on GEOMATE, 2016, pp. 8-13.

FISH CATCH QUOTA ASSESSMENT FOR SUSTAINABLE MARINE FISHERIES RESOURCES IN EAST JAVA

AlfanJauhari¹, *DefrianMarzaArisandi¹, Abu Bakar Sambah^{1,2}, WildanAlfarizi¹

¹Faculty of Fisheries and Marine Science, Brawijaya University, Indonesia; ²Marine Resources Exploration and Management Research Group, Brawijaya University, Indonesia
Veteran Street Malang east Java

*) Correspondence Author

ABSTRACT

Fish resources Information urgently needed by development planners in fisheries sectors, especially for fisheries development. Quantitative information like the potential assessment number is determined by the presence or absence of basic information such as the results of the surveying research vessel, and also from the information that is collected through a regular monitoring; particularly catch effort data, the fishing season, and the migration of certain species in respective territorial waters. The fisheries resources utilization in East Java tends to be over exploited. This caused uncertainty of fishing activities for the traditional fishermen in the East Java waters. Some studies of population dynamics and fish stock assessment described fisheries resources exploitation in some areas of East Java was on fully exploited to over exploited condition. The aim of this research were; [1] to know sustainable potential and total allowable catch of fisheries resources in the area of Pasuruan regency, Probolinggo regency, and Banyuwangi regency; [2] to know the utilization status of fisheries resources in the area of Pasuruan regency, Probolinggo regency, and Banyuwangi regency; and [3] to determine the empowerment strategy for fishermen community in order to utilize fisheries resources in the area of Pasuruan regency, Probolinggo regency, and Banyuwangi regency. The analyses were done through the calculation of sustainability potential, and total allowable catch, and determine the controlling strategy of fisheries resources utilization. The study described that the comparison analysis of fishing trip data, fish catch and total allowable catch in the sustainable condition was in the over exploited condition. Moreover, based on the analysis of fisheries resources utilization status in the research area, the controlling strategy was created based on the recommendation of all stakeholders. These strategy including the management of fishing area, management of fishing time, and determine of an alternative activities in the scope of both fisheries and non-fisheries sectors. These strategies can be used as a basic data in determining an empowerment strategy for fishermen in the fisheries resources utilization. These strategies including accompaniment approach and information services through community and ecosystem based of fisheries resources management.

Keywords: fisheries resources, sustainability, total allowable catch

INTRODUCTION

Information on fish resources is needed by the special fisheries development planners for the development of capture fisheries. Quantitative information such as potential numbers is largely determined by the presence or absence of information from survey results of research vessels as well as from information collected through the periodic weather system, in particular catch data, fishing seasons, and distribution for certain species of fish in each region see (Purnomo, 2002). The utilization of marine fisheries in East Java can be said to have experienced excessive levels of exploitation. This will impact the uncertainty of fishing effort done by traditional fishermen in East Java responsible area. Various studies of population dynamics and indicator estimates indicate the

pressure of exploitation of fishery resources in some areas such as East Java has experienced full exploitation until more exploitation. This will affect the work being built on the coastal area of East Java, or work as a fisherman. When the level of exploitation of marine fisheries resources in the mouth of East Java has experienced more capture then the catching operation is not possible to be repaired. This situation creates social and economic problems for coastal communities. Arrangement of capture quotas is one of the solutions to regulate excessive exploitation pressure on marine fish stocks in East Java.

METHODS

This research is one of analytical descriptive research that is describing real condition

that exists in field and doing situation analysis to data obtained. Descriptive method of analysis is a method of gathering facts through appropriate interpretation. This method of study is aimed at studying the problems that arise in society in certain situations, including community relations, activities, attitudes, opinions, and ongoing processes and their effects on certain phenomena in society. This method is used to answer the research objectives, namely;

1. To know the amount of sustainable potential and JTB fish in the waters of the study area.
2. To know the status of the utilization of fishery resources in the territorial waters of the study.

The steps taken to answer the first goal are:

1. Collection of captured data
The data collected is data collected from 10 years since 2004-2013, the data is secondary data.
2. Treatment of data
The 10-year data is intended to obtain standard data as input for analysis using Schaefer, fox and Walterhilbern formulas. The treatment technique is using the formula RFP (Relative Fishing Power).

While the steps to answer the second research objectives are:

1. Compare the sustainable potential value calculated in the previous step to the actual utilization rate in 2014.
2. Decision making to determine the status of resource utilization expressed in the sustainable utilization rate..

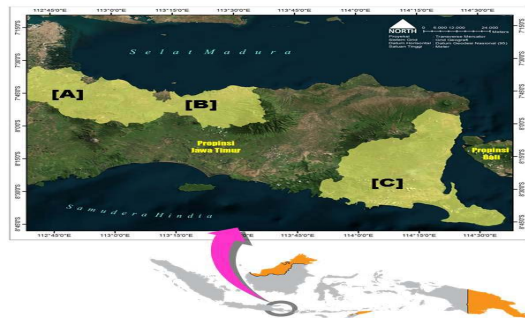


Fig. 1 Study Area

- [A] Pasuruan Regency;
[B] Probolinggo Regency
[C] Banyuwangi Regency

Conversion of the Catching Efforts

The fisheries management model refers to the assumption that fishing gear must be transferred into a standard unit. Thus it can be said that the fishing gear is made into one unit equivalent to the catching equipment that is considered standard. The conversion method used with the equation:

$$CpUE = \frac{Y_i / f_i}{E_{std}} \quad (1)$$

Where :

- CpUE = Capture per unit of effort
= Average portion of fishing gear 1 to total fish production
= Average catch of fish by fishing gear
= Mean Effort of the fishing gear Considered standard (trip).

While the RFP is calculated using the equation:

$$RFP = \frac{Y_i / f_i}{Y_i / f_i \text{ standard}} \quad (2)$$

Dimana :

- RFP = Index type conversion tool Catch
 Y_i / f_i = Catch per unit effort respectively each fishing gear
 $Y_i / f_i \text{ standard}$ = Catch per unit effort from tool standard

Maximum Estimates Sustainable

The estimation of maximum sustainable balanced tuna is done by using holistic approach or surplus production method that is Schaefer model (1954) and Fox (1970) to determine which method is "best fit" which is able to represent actual exploitation level of tuna. The maximum amount of effort sustained (fmsy), and maximum sustainable yield (Ymsy) can be calculated by the formula

(1) According to Schaefer (1954)

$$Y = af - bf^2 \quad (3)$$

$$f_{msy} = \frac{a}{2b} \text{ dan } Y_{msy} = \frac{a^2}{4b} \quad (4)$$

Where :

- Y = Catch
F = Attempts to catch
A = Intercept of Schaefer model
B = Slope of Schaefer model
Ymsy = Maximum sustainable catch (potential Sustainable catch)
Fmsy = Sustainable fishing effort

(2) Menurut Fox (1970)

$$Y = \exp(c - df) \quad (5)$$

$$f_{msy} = \frac{1}{d} \text{ dan } Y_{msy} = \frac{1}{d}(e - 1) \quad (6)$$

Where :

- c = Intercept of Fox model
d = Slope model Fox

To calculate the utilization rate of a fishery resource by the formula:

$$JTB = 80\% Y_{msy} \quad (7)$$

Estimation of the Potential of Sustainable Reserves and Potential Backup

According to Walter and Hilborn (1976) biomass from year $t + 1$, B_{t+1} can be expected from B_t plus biomass growth for one year was reduced by a certain amount of biomass during the year reduced by the amount of biomass released by exploitation of effort (f). The determination of stock biomes follows the calculation by the equation:

$$B_{t+1} = B_t + P_{dt} - Y_t \dots \dots \dots (8)$$

Where :

B_t = biomass stock at time t

$P_{dt} = dB / dt$ = growth rate of biomass, intrinsic (Ton / yr)

K = maximum carrying capacity of natural waters against biomass

R = intrinsic growth rate of population stock

T_0 = time at $B_t = \frac{1}{2} K$

T = time, year, month and so on

The potential for sustainable reserves is obtained from the equation $B_e = \frac{1}{2} K$. While the potential of fish stock in 2013 is obtained by the equation:

$$B_{t+1} = B_t + P_{dt} - Y_t \dots \dots Y_t = f_t \times B_t \times \dots \dots \dots (9)$$

$$P_{dt} = r \times B_t - \frac{r}{K} B_t^2 \dots \dots \dots (10)$$

Preparation of Control Strategies

Fish Resources

The compilation of alternative strategies and the interest analysis of some of these structured alternatives will be based on:

- Identification of potential carrying capacity of non-fishery fisheries in Pasuruan, Probolinggo, and Banyuwangi.
- Identify issues of future utilization, problems and prospects of fishery resources in Pasuruan, Probolinggo and Banyuwangi districts through observation and interview (questionnaire distribution).
- Focus Group Discussion (FGD) with stakeholders in the fishery and non-fishery fields in Pasuruan, Probolinggo and Banyuwangi districts to prepare whether or not alternative strategies have been developed.

Measurement of Interest Scale

One of the measurement of attitude scale in the formulation of alternative interests of control strategy of utilization of Marine Fishery Resources in Pasuruan Regency, Probolinggo Regency and Banyuwangi Regency is analysis in Likert Scale. Likert scale according to Djaali (2008) is a scale that can be used to measure the attitude, opinion, and perception of a person or group of people about a

phenomenon or phenomenon of education. The Likert scale is a psychometric scale commonly used in questionnaires, and is the most widely used scale in research surveys.

Based on the data obtained from respondents' answers, then it is processed by multiplying each point answer with the weight that has been determined with the weighted table of values, using the equation as follows:

$$\text{Total Score} = (\sum \text{Answer} \times \text{Weight strongly agree}) + (\sum \text{Answer} \times \text{Weight agreed}) + (\sum \text{Answer} \times \text{Weight Neutral Weight}) + (\sum \text{Answer} \times \text{Weight not agree}) + (\sum \text{Answer} \times \text{Weight strongly disagree})$$

To get the result of interpretation, must first known the highest score (X) and lowest number (Y) for item of assessment with formula as follows:

Y = highest score likert x number of respondents

(5th highest score) "Notice the Value Weight"

X = Likert's lowest score x number of respondents

(Lowest number 1) "Notice the Value Weight"

So the assessment of respondents' interpretation of the strategy of controlling the utilization of Marine Fishery Resources in Pasuruan Regency is the result of the resulting value using the formula Index% as follows:

$$\text{Formula index\%} = (\text{Total score}) / (Y \times 100)$$

DISCUSSION

Illustration of Concepts

The concept that try to be described in general based on the existing condition is mainly related to the utilization of marine fishery resources obtained through several previous scientific studies and inventory activities of potentials and issues at the field level (location of the study).

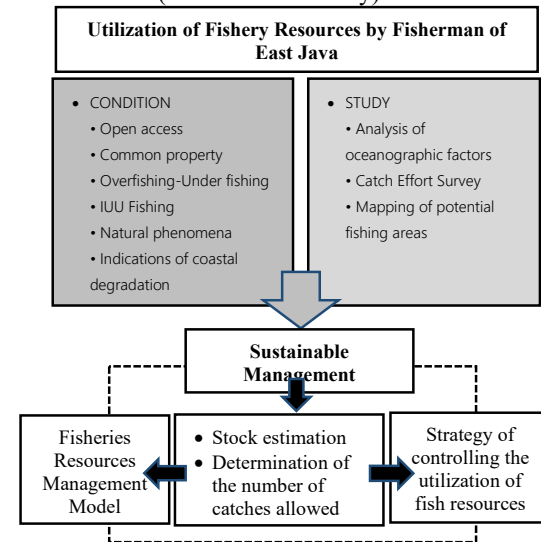


Fig 2. Concept Research Framework

Existing Fishery Potential as a Guideline for Determining the Strategy of Fish Resources Utilization Control.

A preliminary survey related to the production of capture fisheries in the three study areas is presented in Table 1.

Table 1. Production by fishery sub-sector per District (in ton)

Regeency	Total	Catch	
		Sea	Public Waters
Amount For Prov.			
East Java	395.046,8	381.573,9	13.472,9
Pasuruan	7.807,3	7.634,1	173,2
Probolinggo	9.755,7	9.665,2	90,5
Banyuwangi	49.663,1	49.532,0	131,1

(Source: East Java Fishery Statistics Data, 2016)

Based on Table 1, Banyuwangi Regency is the area of study with the largest fishing production in the sea when compared to Pasuruan and Probolinggo districts. Based on this data, the estimation of the utilization status of capture fishery resources in the study area can be based on dominant catch fish production, and into the catch group which has important economic value..

Analysis of marine fisheries resources Pasuruan Regency

Based on the table of fishery production in Pasuruan waters, in Figure 3 presents fluctuations in the production of catches in Pasuruan.

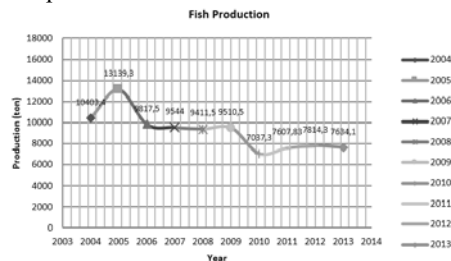


Fig 3. Graph of fish production in Pasuruanwaters (Source: East Java Fishery Statistics Data, 2016)

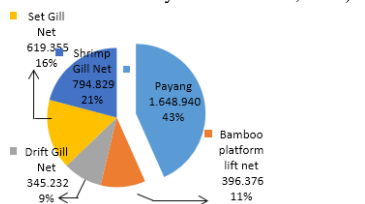


Fig 4. Proportion of trips of four types of fishing gear inWaters of Pasuruan.

The development of the standard payang fishing equipment shows that gear equipment in Pasuruan waters has the highest increase of 235,438 trips from the previous year from 2004 to 2008 there was a decrease of 66,509 trips. In 2009, there was an

increase of 96,539 trips from 2008. Then it decreased 112,822 trips in 2010 and then increased in 2011 With 2013 as many as 128.51 trips. The dominant fishing gear is payang, in this case the prediction of the result of the conversion of fishing gear and the amount of fish catch in Pasuruan waters is needed because this is related to the estimation of both models. The results of the conversion of fishing gear to the standard of fishing gear and the number of fish catch can be seen through Table 2.

Table 2. Data on the number of standard converted tools

Year	Effort standart Payang (trip)	Catch fish in water (ton)	CpUE
2004	561184,6	10403,4	0.018538
2005	550286,2	13139,3	0.023877
2006	391226	9817,5	0.025094
2007	401990,1	9544	0.023742
2008	402027,5	9411,5	0.02341
2009	743624,3	9510,5	0.012789
2010	342852,1	7037,3	0.020526
2011	496436,4	7607,83	0.015325
2012	474066,3	7814,3	0.016484
2013	694523,5	7634,1	0.010992

The highest number of fishing gear was 743,624.3 trips in 2009 with catches of 9,510.5 tons. The Schaefer and Fox models refer to the principle of the Surplus Production Model, the Schaefer and Fox is also called the equilibrium state model. Schaefer and Fox models can predict MSY conditions from optimum production amount (Y_{msy}), optimum catcher (f_{msy}). Fishery status and exploitation rate can be analyzed through comparison of optimum production value with production value in the last year or it can also through the number of fishing gear. Potential Sustainable Reserve (Be) fisheries in waters can be known through the Walter-Hilborn equation approach. This method does not depend on the equilibrium conditions of a stock of fishery biomass as in Schaefer's method (1954) and Fox (1970). In addition, this method is able to estimate the values of population parameters (r = intrinsic biomass stock growth rate (constant), k = maximum natural bearing capacity, q = capture capability (catchability coefficient)) in the model so as to make predictions more dynamic and closer to reality In the field This model is also known as the model of non-equilibrium state model. Based on the results of the analysis on this model obtained the following results:

Table 3. The value of the non-equilibrium state model

Variable	Walter-Hilborn	
Intercept	$B0 = r$	102,5054386
X variable 1	$B1$	2951,977462
X variable 2	$B2 = q$	2,02622
k	7,0359	
Be	3,5179	

Information :

R = Intrinsic population growth rate

K = The maximum carrying capacity of the water (carring capacity)

Q = capability of catch (catchability coeficien)

Be = Potential reserve of sustainable fish

The utilization rate (TP) of fish obtained from the calculation of the average value of effort over the last five years divided by fMSY. The result of the calculation is multiplied by 100 resulting in a utilization rate of 86%. From the calculation of the utilization rate can be said that the status of fishery utilization in the waters of Pasuruan is fully exploited the stock of resources already exploited close to MSY value and the increase in the number of fishing effort is not recommended.

Table 4. Potential sustainable yield data

	Schaefer	Fox	Walter-hilbern
MSY	9.830,9	9,419	31154,84663
JTB	7.864,7	7,535	4,34404E-10
Utilization of Fish Resources in Pasuruan			
The catch (tons)	Number of fishing trips		
7942,9	460868		

Table 5. Potential sustainable yield data

Model Schaefer	Quantity	Year 2014	Result	Utilization rate
Fe (number of trips of catching equipment in sustainable condition) unit	585.231,9	460868	124.363,9	Over
Ye (number of catches of sustainable condition) tons / year	9.830,9	7942,9	1888	Over
JTB	7.864,7	6354,3	1510,4	Over

At the level of pengoprasian fishing gear has exceeded the capacity causing the occurrence of over-fishing or over fishing. Therefore, efforts should be made to formulate strategies for controlling the utilization of fish resources in Pasuruan waters with technical fishing should not exceed MSY and for precautionary action by catching does not exceed JTB.

Analysis of Marine Fisheries Resources Probolinggo District

Participatory mapping is done by involving local fishermen in Probolinggo Regency to create a map of potential marine fisheries in Probolinggo District / City waters. Validation of this map is done through active participation in several trips fishing operations at sea. This active participation also records the main fishing grounds of all fishermen who conducted fishing operations and had a fishing base in Probolinggo District / Town, including mapping the fishing grounds of Probolinggo District / local fishermen as well as local naming tablature and geographical position of fishing areas of Probolinggo

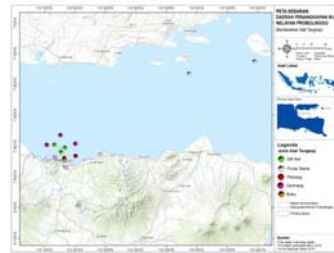


Fig 5. Map of distribution of fishing area Based on fishing gear in Kab / Kota Probolinggo

Production of catches increased significantly from 2004 to 2006 by 56.9%. Production of this catch in 2006 is the largest fish production that is as much as 65,854.50 tons. While the production of the lowest fish is 21,361,7 tons in 2012. In 2008 the production of catch is relatively fixed until 2010, and began to decline until 2013. Fish production in 2006 to the year of 2007 decreased production by 32%, and continues to decline Until 2013. If compared with the highest production (in 2006) then the decline until the year 2013 amounted to 34, 4%

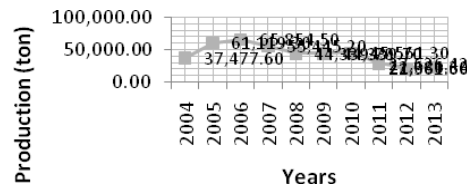


Fig 6. Graph production yield in probolinggo

Potential Sustainable Reserve (Be) fisheries in waters can be known through the Walter-Hilborn equation approach. This method does not depend on the equilibrium conditions of a stock of fishery biomass as in Schaefer's method (1954) and Fox (1970). In addition, this method is able to estimate the values of population parameters (r = intrinsic biomass stock growth rate (constant), k = maximum natural bearing capacity, q = capture capability

(catchability coefficient) in the model so as to make predictions more dynamic and closer to reality. In the field, this model is also known as the model of non-equilibrium state model.

Table 6. The value of the non-equilibrium state model

$b1 = r$	1,014468592
$b2$	0,17940405
$b3 = q$	3,50335E-05
$k = b1/(b2*b3)$	161407,0965
$Be = k/2$	80703,54824
$Pd = (r*k)/4$	1,57129E-06
$Y_{MSY} = (b1*k)/4$	40935,60749
$f_{MSY} = r/(2*q)$	14478,5434
$U_{MSY} = C/E$	2,827329128
$JTB = 80\%*Y_{MSY}$	32748,48599
$TP = (rata2 E / Y_{MSY}) * 100$	79%

Information :

R = Intrinsic population growth rate

K = The maximum carrying capacity of the water (carrying capacity)

Q = capability of catch (catchability coefficient)

Be = Potential reserve of sustainable fish

The utilization rate (TP) of fish obtained from the calculation of the average value of effort over the last five years divided by f_{MSY} . The result of the calculation is multiplied by 100 to yield the utilization rate of 79%. From the calculation of the utilization rate can be said that the status of fishery utilization in Probolinggo waters is fully exploited in the stock of resources already exploited close to MSY value and the increasing number of fishing effort is not recommended.

Table 7. Potential sustainable yield data

	Schaefer	Fox	Walter-hilbern
MSY	65.511,55	59.817,56	40.935,61
JTB	52.409,24	46.053,11	32.748,49
Utilization of Fish Resources			
The results of the catch(ton)	Number of fishing trips		
22.686	159.054		

3.5 Analysis of marine fisheries resources in Regency of Banyuwangi

Mapping of capture areas is done through participatory mapping. This participatory mapping is done by involving local fishermen of Banyuwangi Regency in making map of potential of marine fishery in Banyuwangi Regency waters. Validation of this map is done through active participation in several trips fishing operations at sea. This active participation also records the main fishing grounds of all fishermen who have been engaged in fishing operations and have a fishing base in Banyuwangi Regency, including mapping the fishing areas of local fishermen in Banyuwangi Regency as well as

local naming tabature and geographical position of Banyuwangi fishermen fishing area.

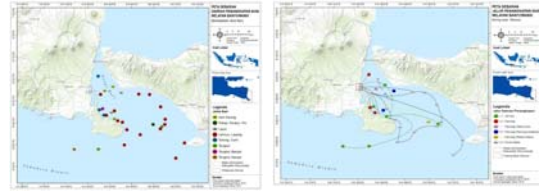


Fig 7. Map of distribution of fishing areas and fish catching line in the Regency of Banyuwangi

Calculation of the result of the conversion of fishing gear and the number of fish catches in Banyuwangi waters is needed because this is related to the estimation of both models. The results of the conversion of fishing gear to the standard of fishing gear and the number of fish catch can be seen through Table 8. While Table 9 illustrates the calculation of the Potential Lestari And Total Allowable Catch / Number of Fishes Captured (JTB).

Table 8. Data on the number of standard converted tools

Year	f (Trip)	Y (Ton)	CpUE
2004	20.443,68	2.406,50	0,117714
2005	101.189,86	13.876,80	0,137136
2006	2.277,46	62.223,50	27,32148
2007	174.374,14	61.801,00	0,354416
2008	7.104,27	51.371,00	7,231004
2009	69.562,34	51.371,00	0,738489
2010	17.163,03	29.264,00	1,70506
2011	226.194,26	31.018,46	0,137132
2012	65.406,91	38.879,95	0,594432
2013	126.123,81	46.366,10	0,367624
2014	460868	7942,9	0,017235

Table 9. Result of sustainable potential calculation and Total Allowable Catch / number of fish that can be caught (JTB)

$b1 = r$	1,778348467	$Y_{MSY} = (b1*k)/4$	1187559,319
$b2$	0,080916473	$f_{MSY} = r/(2*q)$	108070,0588
$b3 = q$	8,22776E-06	$U_{MSY} = C/E$	
$k = b1/(b2*b3)$	2.671.150,99	$JTB = 80\%*Y_{MSY}$	950047,4553
$Be = k/2$	1.335.575,50	$TP = (C_{thntrakhir} / Y_{MSY}) * 10$	32%
$Pd = (r*k)/4$	1.187.559,32		

Analysis of FGD Results on Formulation Strategy

Based on the results of FGD analysis it can be explained that the three alternatives of the compiled strategy are alternative strategies that are

agreed by all FGD groups. This is evidenced by the choice of all groups against the four strategies that have been compiled. Based on the score of interest, then strategy number 2 or is the preferred strategy that ranks first the FGD results. The last strategy is the alternative of other substitution fishery activities in the hope that the stock of marine resources in the waters of the research area is given time to recover naturally. This indicates that it takes a certain period of time for fishermen to be able to try alternative fisheries and other non-fishery activities in response to the catch status of more fish resources in the research area.

Measurement of Interest Scale

Likert scale is done to measure approval and disapproval of respondent to all alternative of strategy which is arranged, with level consist of: [1] strongly disagree; [2] disagree; [3] neutral between agree and not; [4] agree; [5] strongly agree. Likert-scale analysis in this research is based on strategy which have been arranged in FGD and also analysis of Likert scale result using weighted value table.

Table 10. Percentage of values of all alternative strategies

strategy	Response Answer				
	[1]	[2]	[3]	[4]	[5]
1. The strategy for controlling the utilization of fish resources includes: 1. Capture time settings 2. Arrangement of catch areas 3. Alternative fishing and other non-fishery activities	0	0	5	11	7

Information :

[1] strongly disagree; [2] disagree; [3] neutral; [4] agree;
[5] strongly agree

$$\text{Total Score} = (7 \times 5) + (11 \times 4) + (5 \times 3) + (0 \times 2) + (0 \times 1) = 94$$

Based on the total score above, then the interpretation result is calculated as follows :

$$Y = 5 \times 23 = 115$$

$$X = 1 \times 23 = 23$$

Respondent's interpretation of the strategy of controlling the utilization of Marine Fishery Resources are:

$$\text{Rumus Index \%} = \frac{94}{115 \times 100}$$

$$\text{Rumus Index \%} = 81.74$$

(category highly agree)

CONCLUSIONS

Based on the results of the study that has been done can be concluded :

[1] Research on the regulation of capture quota for sustainable management of marine fishery resources

can be done one of them based on the study of potential lestasi and fishery resource utilization status first. [2] Comparison of data analysis on the number of fishing trips in sustainable condition, the number of fish catches in sustainable condition and the number of catches allowed in the research area indicates the utilization level of marine fishery resources experiencing more catching condition. [3] Based on the analysis of the utilization status of marine fishery resources in the research area, the strategy of controlling the utilization of fishery resources is prepared based on the recommendation of all relevant stakeholders. These strategies include setting up fishing grounds, setting up fishing seasons, and setting alternative fisheries / non-fisheries alternatives. This strategy forms the basis for determining the setting of catch quotas for sustainable management of marine fisheries resources in the research area. This strategy includes advisory approach and information services through community-based fishery resource management programs and ecosystems provided to fishermen.

ACKNOWLEDGEMENTS

The researchers would like to thank the East Java Provincial Government, the Faculty of Fisheries and Marine Sciences of Brawijaya University, the Stakeholders, and the Laboratory of Marine Resources Exploration, Brawijaya University Indonesia.

REFERENCES

- [1].Djaali, 2008. *Skalalikert*. Jakarta: PustakaUtama.
- [2].Data Statistik Perikanan. 2014. Potensi Perikanan Kabupaten Pasuruan. Dinas Perikanan dan Kelautan Provinsi Jawa Timur.
- [3].Fox, W.W. Jr., 1970. An Exponential Surplus-Yield Model for Optimizing Exploited Fish Population. *Trans.Am.Fish.Doc.*, 99:80-88.
- [4].Purnomo, H. 2002. Analisis Potensi dan Permasalahan Sumberdaya Ikan Pelagis Kecil Di Perairan Utara Jawa Tengah. Universitas Diponogoro. Semarang.
- [5].Schaefer, M., 1954. Some Aspects of the Dynamics of Pupulations Important to the Management of the Commercial Marine Fisheries. *Bull.I-ATTTC/Bol.CIAT*, 1(2):27-56
- [6].Walters, C. J., and R. Hilborn. 1976. Adaptive control of fishing systems. *Journal of the Fisheries Research Board of Canada* 33:145-159.

USE OF INSECTICIDE-TREATED NETS AMONG PIG OWNERS LIVING IN JAPANESE ENCEPHALITIS ENDEMIC AREAS OF NORTHERN MYANMAR

Aung Kyaw Soe, Cheerawit Rattanapan, Somsak Wongsawass, Orapin Laosee*
ASEAN Institute for Health Development, Mahidol University, Nakorn Pathom 73170, Thailand

ABSTRACT

Japanese encephalitis (JE) virus is the leading cause of vaccine-preventable encephalitis in Asia and the Western Pacific region. This study was carried out to explore the use of insecticide-treated nets (ITNs) to prevent JE among pig owners in the high endemic area of Kachin State, Myanmar. A total of 420 pig owners were interviewed by trained research assistants between March and May 2016. The majority of the respondents were farmers with low family income, living in poor housing conditions. Pig-raising by respondents was mainly categorized as closed-type (75%), however those pigs were kept in sties close to the house at night. Analysis indicated that less than a quarter (21%) of family members slept under insecticide-treated nets at night. Households with five or less members, owning more than two ITNs were more likely to use them at night (AOR: 3.71; 95% CI: 2.07-6.62) (AOR: 5.47; 95% CI: 3.20-9.33). This study highlighted the adequacy of providing ITNs for all family members as a critical issue to prevent JE virus. Initiation of strategies to expand interdisciplinary collaborations and communication in all aspects of health care for humans, animals and the environment could take place. Availability of vaccines must be reconsidered as they are important in prevention and control of JE.

Keywords: insecticide treated nets, Japanese Encephalitis, Pig owner, Myanmar

*Correspondence to: Orapin Laosee, ASEAN Institute for Health Development, Mahidol University, 999 Salaya, Phutthamonthon, Nakorn Pathom 73170, Thailand
Phone: (662) 441 9040-3 ext.43 Fax: (662) 441 9044 Email address: orapin.lao@mahidol.edu

INTRODUCTION

Japanese Encephalitis (JE) is the most important cause of viral encephalitis in Asia and Western Pacific [1], [2]. JE virus is transmitted to humans through the bite of an infected mosquito, primarily *Culex* species. Humans are incidental or dead-end hosts, because they usually do not develop a level or duration of viremia sufficient to infect mosquitoes. *Culex tritaeniorhynchus*, the major mosquito vector, breeds by laying eggs in rice fields, and the pig is considered the most common amplifying host of JE virus [3]. An estimated 67,900 JE cases typically occur annually, of which only 10% are reported to the World Health Organization [4]. Transmission mainly occurs in rural agricultural areas, often associated with rice cultivation and flood irrigation [2], [3], [5].

Myanmar has had one of the highest increases in irrigated rice areas over the past 15 years [1]. Data on JE incidence in Myanmar is limited, and it can be assumed that few cases are reported. According to available data, between 2007 to 2012 there were 74 JE cases in Myanmar, with the highest mortality and morbidity reported in 2012 [6]. There were 113 reported cases in 2015. A report on vaccine preventable disease surveillance from 2006-2011

indicated that the number of reported cases fluctuated [7].

There is no specific treatment for JE, therefore, prevention and control are critically important [1], [6]. The World Health Organization recommends having strong JE prevention and control activities which include ITNs, personal protective equipment, and integrated vector management. Although JE vaccines are available and cost-effective to prevent the disease [8], Myanmar has limited resources and cannot make JE vaccination available through the public sector [9]. There is also no established surveillance system in place [8]. Therefore, Insecticide Treated Bed-nets (ITNs) is one of the most effective methods to prevent mosquito-borne zoonotic disease including JE [10]-[13] in this country. Previous research studies identified several factors related to use of ITNs, these includes socio-demographic factors, availability of bed nets, knowledge, and attitudes towards mosquito-borne diseases [14]-[17]. Lack of information on use and influencing factor on utilizing ITNs to prevent JE in Myanmar. This study aims to examine the use of ITNs and to identify factors associated using ITNs among pig owners the endemic area of Myanmar.

METHODOLOGY

Study design and subjects

This cross-sectional descriptive study was conducted in Moemauk Township, Kachin State, Myanmar, which borders the People's Republic of China. In 2015, the total population was 62,914 within 1,068.95 square meters. It has low land areas in the west and south with a warm-temperate climate. The majority of residents are poor who use agriculture as their main source of family income. There were Japanese Encephalitis outbreaks in this area in 2013, 2015 and 2016. A sample of 420 households (required for 5% precision) around 54% of community residents reported sleeping under an ITN the previous night, with 95% confidence limits and assuming 95% response rate. Simple random sampling was employed to identify pig owners in selected villages of three JE endemic areas. Pig owners responsible for feeding pigs in sampling areas were interviewed from March to May 2016. Interviewers introduced the topic, objectives, and type of questions. Oral informed consent was obtained prior to interview. Household environmental observation was also conducted during each interview.

Research instrument

A questionnaire was developed based on the literature and local context. It was first drafted in English, then translated into the local language, reviewed by a panel of experts and pre-tested in a village with comparable proximity and demographic distribution to the target sample. Observation was used to assess environmental factors related to JE outbreak during data collection time. The questionnaire consisted of four topics; 1) respondents' characteristics, 2) knowledge regarding signs and symptoms of JE and attitude toward the use of ITNs, 3) animals raised and environment surrounding house, 4) use of ITNs by family members-whether they slept under a net the previous night. Approximately 20 to 30 minutes was needed to survey each respondent.

Data analysis

Descriptive statistics were employed to determine central distribution and frequency of the study variables. Bivariate and multivariate logistic regression were conducted to identify the significance of use of ITNs. Use of ITNs refers to whether all family members slept under an ITN on the night prior to being surveyed. A *P* value <0.05 was considered statistically significant.

Ethical considerations

The study was reviewed and approved by the committee for research ethics of the university (COA No.2016/123.2903). The research study was collaborated with the Ministry of Health, Myanmar and Department of Health. Personal data of respondents was coded and kept as confidential information.

RESULTS

Four hundred and twenty pig owners participated in this study. Over three quarters of respondents (76.9%) were female. The median age was 38 years (QD 11). Most participants are Shan, Buddhist. Over half completed primary school and lower, and earn a low level of income. Most respondents (73.3%) were raising pigs for sale, and over half owned at least five pigs. Closed type (74.8 %) was the most common type of pig farming, while half of the pig farms (51.2 %) were located only 6 meters from pig owner's house. For the closed type, pigs were kept in a sty close to the house at night (picture 1). About one-quarter of respondents also owned cows or buffalos. According to environmental observations, rice fields and wild birds were commonly found in the study area (Table 1).

Table 1 Distribution of respondents by demographic characteristics, and environmental factors (n=420)

Respondents' characteristics and environmental factors	n (%)
Sex; Female	328 (78.1)
Age in year <i>Median 40, QD.11, Min. 18, Max. 74</i>	
Ethnicity; Shan	315 (75.0)
Religion; Buddhism	304 (95.0)
Education; Primary school and below	214 (50.9)
Occupation; Farmer	318 (75.7)
Family income (Kyats per month)* <i>Median 100,000, QD. 45,000, Min 50,000, Max 500,000</i>	
Purpose of pig raising	
Sell	308 (73.3)
Consumption	98 (23.3)
Debt	14 (3.3)
Number of pig: <i>Median 4, QD. 2.5, Min. 1, Max. 60</i>	
Type of pig farm	
Closed type	314 (74.8)
Free range	106 (25.2)
Other animal raise	
Own and feed duck; Yes	11 (2.6)
Own and feed cow; Yes	114 (27.1)
Own and feed buffalo; Yes	101 (24.0)
Keep large animals under the house; Yes	6 (1.4)
Environment surrounding household (within 5 km.)	
Rice field; Yes	256 (61.0)
Wild birds; Yes	144 (43.3)
Vegetable field; Yes	80 (19.0)

*1 USD = 1,200 Kyats (As of 18 July 2016)



Picture 1: Closed type of pig farming



Picture 2: Free range pig farming

The majority (88%) of the respondents owned ITNs and approximately one-fifth reported sleeping under the ITNs on the night prior to being surveyed. Nearly one-third (30.5%) had a poor level of knowledge regarding signs & symptoms of JE (Table 2).

Table 2 Use of ITNs, level of knowledge and attitude of respondents

Use of ITNs, knowledge, and attitude	n (%)
Own ITNs	370 (88.1)
Use ITNs prior night	
Yes	88 (21.0)
No	332 (79.0)
Knowledge related to JE signs and symptoms	
Poor	128 (30.5)
Good	292 (69.5)
Attitude toward use of ITNs	
Negative	122 (29.0)
Fair	130 (31.0)
Positive	168 (40.0)

Bivariate analysis indicated that level of family income, family size, number of ITNs owned and presence of rice fields near the house were associated with the use of ITNs (Table 3).

Table 3 Association between independent variables and use of ITNs

Independent variables	Use of ITNs		OR(95%CI)
	Yes (%)	No (%)	
Sex			
Male	23.9	76.1	1.25(0.72-2.16)
Female	20.1	79.9	1
Age in years			
Less than 31	15.7	84.3	1
31-45	23.9	76.1	1.69(0.90-3.15)
More than 45	22.3	77.7	1.54(0.83-2.85)
Ethnicity			
Shan	20.0	80.0	1
Kachin and others	23.8	76.2	1.25(0.74-2.12)
Religion			
Buddhism	20.1	79.9	1
Christianity	23.5	76.5	1.22(0.72-2.08)
Education level			

Primary school and below	24.3	75.7	1.50(0.94-2.44)
High school and higher	17.5	82.5	1
Occupation			
Farmer	20.3	79.7	1
Others	23.7	76.3	1.21(0.67-2.19)
Family income			
High (>100,000 Kyats)	14.5	85.5	1
Low (≤100,000 Kyats)	24.1	75.9	1.87(1.08-3.24)
Number of family member			
More than five	12.6	87.4	1
Five or less	27.3	72.7	2.59(1.54-4.38)
Knowledge level			
Poor (< median)	16.4	83.6	1
Good (≥ median)	22.9	77.1	1.51(0.88-2.60)
Attitude			
Negative	20.3	79.7	1
Positive	21.5	78.5	1.07(0.67-1.72)
Number of ITNs own			
Two or less	12.7	87.3	1
More than two	36.8	63.2	4.01(2.45-6.54)
Own and feed cow			
No	20.6	79.4	1
Yes	21.9	78.1	1.08(0.64-1.82)
Own and feed buffalos			
No	21.3	78.7	1
Yes	19.8	80.2	0.91(0.52-1.59)
Rice field near house			
No	15.2	84.8	1
Yes	24.6	75.4	1.81(1.08-3.02)
Wild bird near house			
No	21.7	78.3	1
Yes	19.4	80.6	0.86(0.52-1.43)
Vegetable field near house			
No	20.3	79.7	1
Yes	23.8	76.3	1.22(0.68-2.18)

Multiple logistic regression revealed that pig owners with low family income are two times more likely to use ITNs compared to those in high income (adjusted odds ratio 2.04, 95%CI: 1.13-3.70). Pig owners with less than five members in their family are nearly 4 times more likely to use ITNs (AOR 3.71, 95%CI: 2.07-6.62). In addition, respondents who own more than two nets are 5 times more likely to use ITNs compared to respondents who own only two nets or less (AOR 5.47, 95%CI: 3.20-9.33) (Table 4).

Table 4 Multiple logistic regression analysis for predictive factors of use of ITNs among pig owners

Independent Variables	Adjusted OR	95% CI	p-value
Family Income			
High	1		
Low	2.04	1.13-3.70	0.018
Number of family member			
More than five	1		
Five or less	3.71	2.07-6.62	<0.001
Knowledge level			
Poor	1		
Good	1.75	0.97-3.17	0.062
Number of ITNs owned			
Two or less	1		
More than two	5.47	3.20-9.33	<0.001

Hosmer and Lameshow Test=8.527, p-value=0.384.

DISCUSSION

In rural areas of Myanmar, the majority of residents work in agriculture as their main source of income. Approximately over half of the households in Moemaik township, Kachin state own at least one pig, while the median ownership is four pigs. This study identified the majority of subjects as farmers, with nearly three-quarters (74%) raising pigs as property which they could sell if financially constrained. In addition, pork is considered an essential luxury food for social and cultural activities such as wedding ceremonies, religious and harvest festivals. The literature indicated that pigs play a central role in the transmission of both Japanese Encephalitis virus and cysticercosis [18]. Expansion of the JE virus-endemic area depends on irrigated rice farming and pig rearing[3]. A higher proportion of rice-planting could therefore predict higher risk of JE [19].

This study found that the majority of pigs (74.8%) are reared in open or unroofed pigpens, close to human dwellings, which hence govern the spread of JE virus. Lindahl, J. (2012) indicated that closed pigpens were associated with the number of vectors to the human dwelling [20]. Furthermore, one-quarter of pigs were raised as free range, and allowed to freely scavenge food from garbage dumps, markets, rice fields, and paddy fields, which could lead to a higher likelihood of disease transmission. Most JE cases were found in rural areas, especially in rice-planting and pig-rearing areas. In Kachin state, a less-developed area of Myanmar, a greater proportion of the rural population was often short of funds for JE prevention and control, a finding similar to a study in China [21].

Systematic review and meta-analysis identified clear evidence that ITNs have the potential to reduce pathogen transmission and morbidity from vector borne disease where vectors enter a house [12].

However, the use of ITNs is related to many factors. A study of the use and maintenance of bed nets and related influence factors in Kachin Special Region in 2015 revealed that residents consist of poor families, living under thatched roofing, with limited knowledge of how to prevent disease transmission [14]. The Ministry of Health, Myanmar began distributing ITNs to prevent vector-borne disease such as Malaria, Dengue, Hemorrhagic Fever, JE, etc. to families in rural endemic areas [14]. Free distribution of ITNs resulted in a higher rate of ownership among the poor. As found in this study, though a high number own ITNs, only 21% use them regularly. The low use of ITNs might be due to the issue of inadequacy. Our study found that families consisting of less than five members are more likely to use ITNs (AOR 3.71, 95%CI 2.07-6.62). However, we found that low income families are more likely to use ITNs compared to high income families, similar to a previous study in eastern Myanmar [17]. This could be explained by the fact that poorer residents were more aware of their risk of being infected by JE due to their work. Most farmers in this area had to sleep in their farm during the harvesting period. They recognized that they could be infected by JE at any time due to the unsafe environment.

Study limitations include the disparity in demographics. More females (78.1%) were interviewed than males, due to the fact that male heads are working in the farm, while females had the role of caring for children, feeding animals and doing household work. Another limitation is that residents in this area consist of different ethnic groups, thus the language barrier could introduce information bias.

CONCLUSION

In the union of Myanmar, especially in high JE endemic areas, an effective surveillance system should be established, along with adequate provision of ITNs for all family members. Introduction of immunization coverage for the prevention and control of JE should be set as high priority agenda, beginning in rural setting. Moreover, mosquito-control efforts emphasizing improved knowledge related to prevention and control should continue, especially before the onset of the rainy season. Community awareness of these issues should be raised by effective use of available resources which all community members can access, in different local languages. In addition, management of household environments could be further targeted to reduce the breeding sites of vectors close to households.

REFERENCES

- [1] Erlanger TE, Weiss S, Keiser J, Utzinger J, Wiedenmayer K., "Past, present, and future of Japanese encephalitis," *Emerging infectious diseases*, vol. 15, no. 1, pp. 1-7, 2009.
- [2] Centers for Disease Control and Prevention. (2016, 8 May 2016). *Japanese Encephalitis*. Available: <https://www.cdc.gov/japaneseencephalitis/index.html>
- [3] Liu W., *et al.*, "Risk factors for Japanese encephalitis: a case-control study," *Epidemiology and infection*, vol. 138, no. 09, pp. 1292-1297, 2010.
- [4] Campbell GL., *et al.*, "Estimated global incidence of Japanese encephalitis: a systematic review," *Bulletin of the World Health Organization*, vol. 89, no. 10, pp. 766-774, 2011.
- [5] Tian HY., *et al.*, "How environmental conditions impact mosquito ecology and Japanese encephalitis: An eco-epidemiological approach," (in English), *Environment International*, vol. 79, pp. 17-24, 2015.
- [6] World Health Organization. (2014). *Japanese encephalitis Fact sheet No 386 March 2014*. Available: <http://www.who.int/mediacentre/factsheets/fs386/en/>
- [7] World Health Organization, "Expanded program on Immunization Multi Year Plan 2012-2016," Central Expanded Program on Immunization, Department of Health, Ministry of Health 2012, Available: http://www.searo.who.int/myanmar/documents/EPImultiyearplan2012_16.pdf?ua=1.
- [8] World Health Organization, "Prevention and Control of Japanese encephalitis (JE), report of the bi-regional meeting, Bangkok, Thailand," 2015, Available: www.searo.who.int.
- [9] Armed Force Research Institute of Medical Sciences, "Japanese encephalitis morbidity, mortality and disability. Reduction and control by 2015," in "PATH, Seattle, WA," Bill & Melinda Gates Foundation2009, Available: http://www.path.org/vaccineresources/files/JE_Reduction_and_Control_by_2015.pdf.
- [10] Hiscox A., *et al.*, "Risk factors for mosquito house entry in the Lao PDR," *PloS one*, vol. 8, no. 5, p. e62769, 2013.
- [11] Alpern JD., Dunlop SJ., Dolan BJ., Stauffer WM., and Boulware DR., "Personal Protection Measures Against Mosquitoes, Ticks, and Other Arthropods," *Medical Clinics of North America*, Review vol. 100, no. 2, pp. 303-316, 2016.
- [12] Wilson AL., Dhiman RC., Kitron U., Scott TW., van den Berg H., and Lindsay SW., "Benefit of Insecticide-Treated Nets, Curtains and Screening on Vector Borne Diseases, Excluding Malaria: A Systematic Review and Meta-analysis," *PLoS Neglected Tropical Diseases*, Article vol. 8, no. 10, p. e3228, 2014.
- [13] Yakob L., Cameron M., and Lines J., "Combining indoor and outdoor methods for controlling malaria vectors: An ecological model of endectocide-treated livestock and insecticidal bed nets," *Malaria Journal*, Article vol. 16, no. 1, p. 114, 2017, Art. no. 114.
- [14] Liu H., *et al.*, "Coverage, use and maintenance of bed nets and related influence factors in Kachin Special Region II, northeastern Myanmar," *Malaria journal*, vol. 14, no. 1, p. 212, 2015.
- [15] Moon TD., *et al.*, "Factors associated with the use of mosquito bed nets: Results from two cross-sectional household surveys in Zambézia Province, Mozambique," *Malaria Journal*, Article vol. 15, no. 1, p. 196, 2016, Art. no. 196.
- [16] Paz-Soldan VA., *et al.*, "Factors Associated with Correct and Consistent Insecticide Treated Curtain Use in Iquitos, Peru," *PLoS Neglected Tropical Diseases*, Article vol. 10, no. 3, p. e0004409, 2016, Art. no. e0004409.
- [17] Aung T., Wei C., McFarland W., Aung YK., and Khin HSS, "Ownership and use of insecticide-treated nets among people living in malaria endemic areas of eastern myanmar," *PLoS ONE*, Article vol. 11, no. 9, p. e0162292, 2016, Art. no. e0162292.
- [18] Misra UK. and Kalita J., "Overview: Japanese encephalitis," *Progress in Neurobiology*, Review vol. 91, no. 2, pp. 108-120, 2010.
- [19] Oya A. and Kurane I., "Japanese encephalitis for a reference to international travelers," *Journal of*

- Travel Medicine*, Review vol. 14, no. 4, pp. 259-268, 2007.
- [20] Lindahl J., Chirico J., Boqvist S., Thu HTV., and Magnusson U., "Occurrence of Japanese encephalitis virus mosquito vectors in relation to urban pig holdings," *American Journal of Tropical Medicine and Hygiene*, vol. 87, no. 6, pp. 1076-1082, 2012.
- [21] Cao M., Feng Z., Zhang J., Ma J., and Li X., "Contextual risk factors for regional distribution of Japanese encephalitis in the People's Republic of China," *Tropical Medicine & International Health*, vol. 15, no. 8, pp. 918-923, 2010.

EFFECT OF ORGANIC BIOPOLYMER ON THE MICROBially INDUCED CARBONATE PRECIPITATION AND ITS MORPHOLOGY

Thiloththama Hiranya Kumari Nawarathna¹, Kazunori Nakashima², Satoru Kawasaki²

¹Graduate School of Engineering, Hokkaido University, Japan

²Faculty of Engineering, Hokkaido University, Japan

ABSTRACT

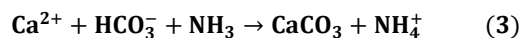
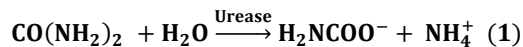
Microbially induced carbonate precipitation (MICP) by using ureolytic bacteria is a novel and environmentally friendly way to treat the un-cemented sand. It was implemented successfully in number of geotechnical applications. Use of organic additives to improve the MICP process is a novel and interesting approach. In this research, effect of the cationic biopolymer poly-L-lysine on the MICP process was investigated by using ureolytic bacteria *Pararhodobacter* sp. Urea hydrolysis by the bacteria in the presence of CaCl₂ was conducted with the addition of the polymer under different conditions. Morphology of the precipitate of CaCO₃ after oven dried was analyzed by using the scanning electron microscope. Bell-shaped curve was obtained for the variation between the amount of the precipitate with the increase of the amount of the poly-L-lysine. Poly-L-lysine gives higher amount of precipitate than conventional MICP process and morphology of the crystals changed drastically from well-developed rhombohedral crystals to ellipsoidal shaped aggregates.

Keywords: Bio-polymer, Calcite, Morphology, Ureolytic bacteria

INTRODUCTION

Today in the world, due to urbanization and rapid growth of population, lands available for the infrastructures and other developments have been decreasing. So people are moving to use loose problematic soils to construct earth structures by using proper ground improvement techniques. Chemical grouting is a most common and effective way to treat weak soils. Cement is the main material use for the chemical grouting, but cement production is more energy consuming and environmental unfriendly method. CO₂ emission from the cement production is 7% from the global CO₂ emissions [1]. So today world is seeking for an environmentally friendly biological approach to treat the loose soils.

Microbially Induced Carbonate Precipitation (MICP) is a one of such kind of novel and environmental friendly ground improvement method. In MICP process, CaCO₃ is precipitated by hydrolysis of the Urea by using ureolytic bacteria and it includes biochemical reactions governed by urease enzyme produced by these ureolytic bacteria as given in the Eqs.(1-3) [2][3][4][5].



Use of organic additives such as biopolymers and protein to improve the weak soil is an alternative biological approach to the MICP process. Biopolymers are organic polymers synthesized by plant or microorganism and it is a natural, non-toxic

and non- petroleum based product. They consist of monomeric units bonded covalently to form large molecules. Number of researches had been done previously to investigate the applicability of biopolymers to improve the weak soil and they concluded that bio polymer have a better ability to improve the weak soils.

Combination of the above two biological processes such as use of biopolymer to the MICP process seems to be novel and innovative idea to improve the efficiency of the MICP process. In this research, effect of the cationic biopolymer on the MICP process was investigated by using ureolytic bacteria *Pararhodobacter* sp.

Poly-L-lysine was used as the cationic biopolymer and it is a kind of basic polypeptide. In neutral pH, its amino group side chains are positively charged [6]. Generally, silica particles have negative charge due to the presence of the silanol group. If we use poly-L-lysine for the MICP process, negatively charged bacteria cell and silica particles could be bound with each other due to positively charged property of the poly-L-lysine. So it can be help to increase the efficiency of the MICP process [7]. Chemical structure of the poly-L-lysine is shown in Fig.1. In this research work, we examined the effect of poly-L-lysine on the MICP process.

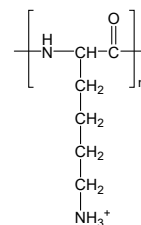


Fig. 1 Structure of the poly-L-lysine.

METHOD

Preparation of Microbial Cell Culture

Ureolytic bacteria *Pararhodobacter* sp. was isolated from the beach sand in Sumuide, Nago, Okinawa, Japan [8] and cultivated using Zobell2216E medium (Polypeptone 5.0 g/L, Yeast extract 1.0 g/L and FePO₄ 0.1 g/L, prepared by using artificial sea water, pH 7.6-7.8). Bacteria cells were precultured using 5ml of Zobell2216E medium and kept in the shaking incubator at 30°C and speed of 160 rpm for 24 hours. One ml of the pre-culture was inoculated into 100ml of fresh Zobell2216E medium and kept in the shaking incubator under the same condition as pre-culture for 48 hours. Finally, bacterial culture was centrifuged to collect the cell pellets, which were dispersed again using distilled water to make bacterial suspension. Cell concentration of the bacterial suspension was measured by UV-vis spectrophotometer and then OD₆₀₀ value was adjusted to one.

Precipitation Test

Effect of the poly-L-lysine on the MICP process

Same concentration (3 mol/l) of CaCl₂ and urea solutions and the stock solution of the poly -L-lysine (0.1g/L) were used for the precipitation test. Two sets of samples were prepared without adding biopolymer and with biopolymer by varying the concentration of bacteria (OD₆₀₀) as shown in Table 1. Total volume of the samples were adjusted to 10ml by using distilled water and after preparation, samples were kept in the shaking incubator under 30°C and 160 rpm speed for 24 hours. Then the reaction mixture was centrifuged to collect the precipitate, and supernatant of tubes were removed separately by using filter paper (11µm).

Both of the filter papers and the tubes with the precipitate were oven dried at 100°C 24 hours and dry weights were measured. Weight of the precipitate was calculated by subtracting the empty weight of the tube and the empty weight of the filter paper from the dry weight of the tube and the dry weight of the filter paper. FTIR analysis was conducted for the sample with and without poly-L-lysine and finally samples were analyzed by using Scanning Electron Microscope (SEM) to identify the morphology of the precipitated calcium carbonate crystals.

Effect of the poly-L-lysine concentration

Samples were prepared by varying the concentration of poly-L-lysine as shown in the Table 2. Sample preparation is same as earlier and samples

were analyzed using Scanning Electron Microscope (SEM).

Table 1 Experimental condition for system with and without poly-L-lysine

Sample No	CaCl ₂ (M)	Urea (M)	Bacteria OD ₆₀₀	Poly-L-Lysine (mg/L)
A	0.3	0.3	0.01	0
B			0.1	
C			0.2	
D			0.3	
E			0.01	10
F			0.1	
G			0.2	
H			0.3	

Table 2 Experimental conditions to evaluate the effect of poly-L-lysine concentration

Sample No	CaCl ₂ (M)	Urea (M)	Bacteria OD ₆₀₀	Poly-L-Lysine (mg/L)
1	0.3	0.3	0.1	0
2				1
3				10
4				30
5				50

RESULTS AND DISCUSSION

Effect of the Poly-L-Lysine on the MICP Process

Variation of the amount of precipitated CaCO₃ with and without adding poly-L-lysine under different bacteria concentrations is given in the Fig.2.

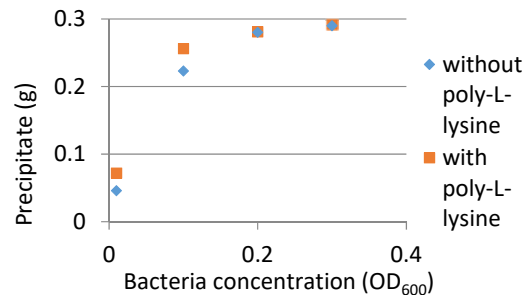


Fig. 2 Variation of the amount of carbonate precipitates with the bacteria concentration (OD₆₀₀)

According to the Fig. 2, it can be seen that in both of the cases, amount of the precipitated CaCO_3 increase with the bacteria concentration. However, considerable amount of increment can be seen only up to the $\text{OD}_{600}=0.2$ after that, rate of the precipitation of CaCO_3 was getting decrease and it is almost become constant for further increase of the concentration of bacteria. So, higher concentration of bacteria inhibits the formation of calcium carbonate. It may be due to the lack of bacteria growth due to higher concentration of the bacteria.

System with the poly-L-lysine gave higher amount of precipitate compared with that without biopolymer. However, for higher bacteria concentration, amount of precipitated CaCO_3 with and without biopolymer were approximately similar. At higher bacteria concentration significant influence from the biopolymer couldn't be identified. However, it can be seen that poly-L-lysine has positive effect on the MICP process.

Figure 3 shows the Scanning Electron Microscopy (SEM) images for the various bacteria concentrations.

According to the SEM images, lower concentration of bacteria gave well-developed rhombohedral calcite crystals. At higher bacteria concentration, agglomeration of rhombohedral crystals can be seen and size of the crystals reduced with the increase of the bacteria concentration. Higher concentration of bacteria inhibits the growth of CaCO_3 crystals. In the presence of the poly-L-lysine, morphology of the crystals change to ellipsoidal shape as shown in Fig. 4. At higher bacteria concentration both of the rhombohedral and ellipsoidal crystals can be seen. This morphology changes may be due to the adsorption of the poly-L-lysine on the crystal surface and formation of new crystal faces.

Effect of the Amount of Poly-L-Lysine

Variation of the amount of the CaCO_3 precipitate with the increase of the amount of the poly-L-lysine is given in the Fig. 5.

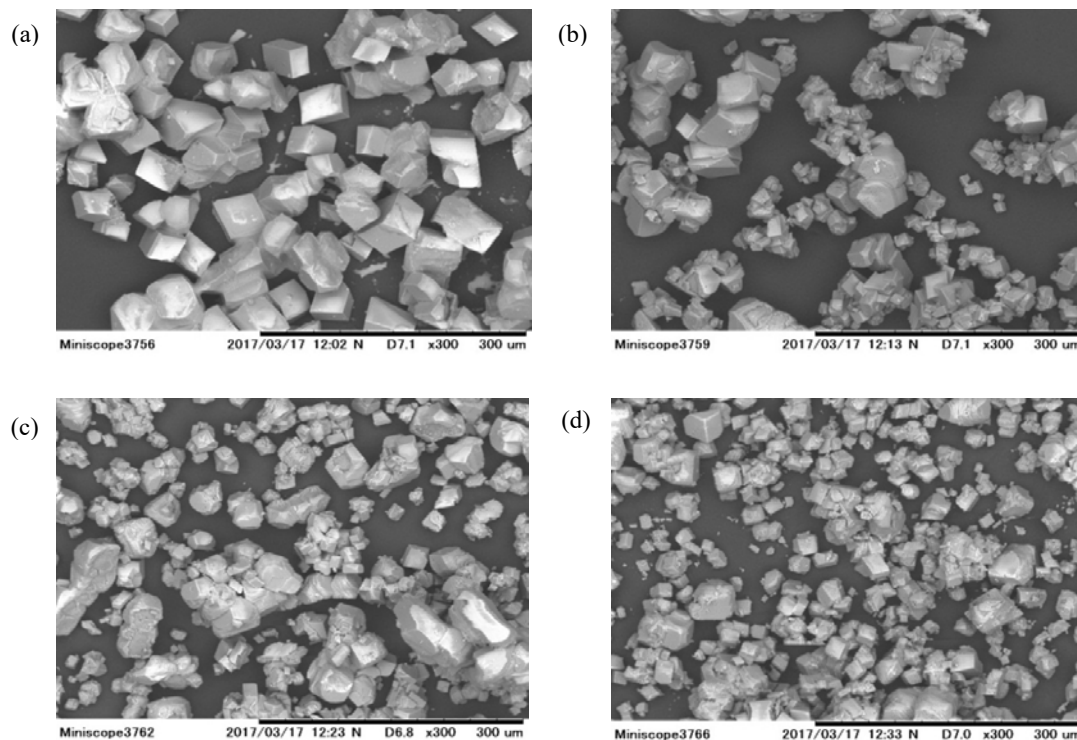


Fig. 3 SEM images of the CaCO_3 precipitate for different bacteria concentration without poly-L-lysine (a) $\text{OD}_{600} = 0.01$ (b) $\text{OD}_{600} = 0.1$ (c) $\text{OD}_{600} = 0.2$ (d) $\text{OD}_{600} = 0.3$

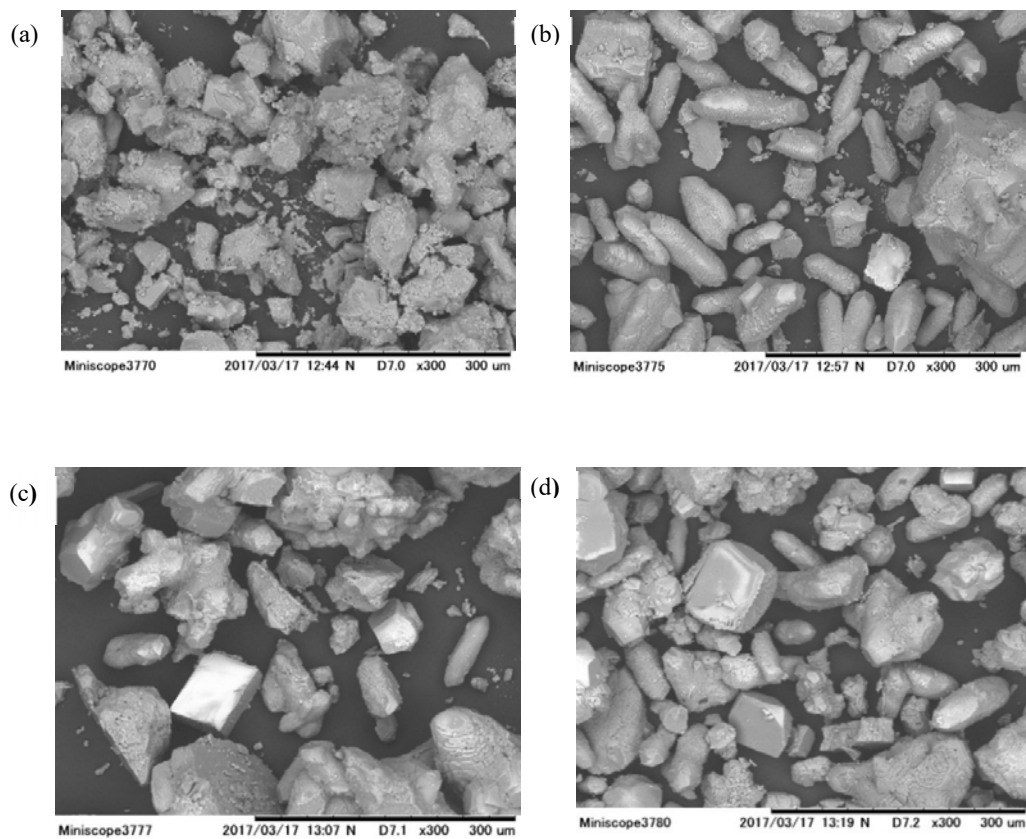


Fig. 4 SEM images of the CaCO_3 precipitate for different bacteria concentration in the presence of poly-L-lysine (a) $\text{OD}_{600} = 0.01$ (b) $\text{OD}_{600} = 0.1$ (c) $\text{OD}_{600} = 0.2$ (d) $\text{OD}_{600} = 0.3$

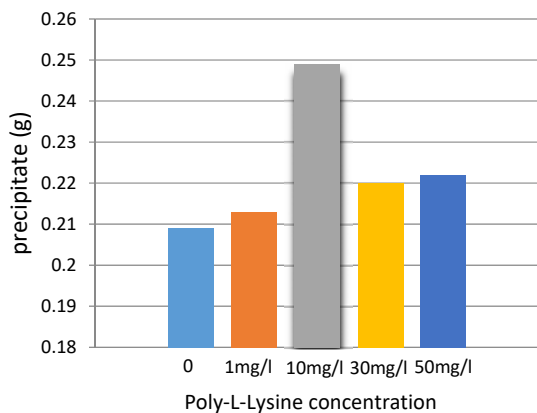


Fig. 5 Variation of the amount of carbonate precipitate with the poly-L-lysine concentration

The amount of precipitate increase with the poly-l-lysine concentration and further increase of the poly-l-lysine concentration leads to reduce the amount of precipitate. This may be due to the excessive amount of poly-L-lysine would reduce the activity of the bacteria. Highest amount of precipitate was obtained at the poly-L-lysine concentration of 10 mg/L. According to the SEM images given in Fig. 6, crystal size was larger compared with the other concentrations when the concentration of the poly-L-lysine was 10mg/L. At lower concentration of poly-L-lysine, combinations of polyhedral crystals were predominant. With the increase of the concentration, morphology of the crystals changed to ellipsoidal shape aggregates. At higher concentration of poly-L-lysine agglomeration of ellipsoidal shaped crystals were obtained.

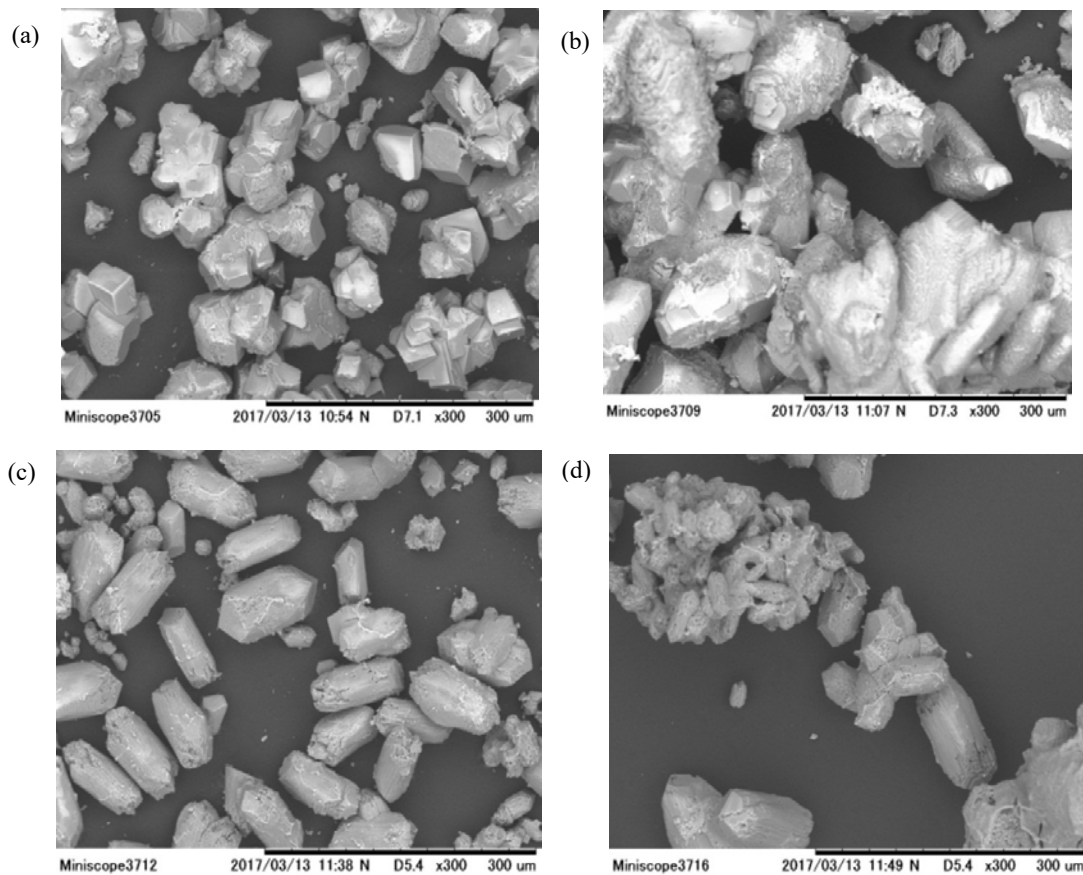


Fig. 6 SEM images of the CaCO_3 precipitate for different poly-L-lysine concentration (a) 1 mg/L (b) 10 mg/L (c) 30 mg/L (d) 50 mg/L

Similar relationship between the amount of precipitate and the poly-L-lysine concentration was found from the previous researches, which reported the precipitation of calcium carbonate using chemical reaction of CaCl_2 and Na_2CO_3 solutions in the presence of calcite seed and poly-L-lysine. They have explained that the increase of the calcite growth at low concentration of poly-L-lysine and growth reduction at higher concentration of poly-L-lysine is a typical behavior of the additives that were weakly, non-selectively, bonded to the surface. This explanation is identical to our research work. Furthermore, they have concluded that the interaction between the poly-L-lysine and the calcite is pure electrostatic and it is between the positively charged polypeptide and the negatively charged calcite surface [6] [9].

FTIR Analysis

Results of the FTIR analysis with and without poly-L-lysine are shown in Fig 7. Both graphs look like similar. However, small peak can be seen at 1200 cm^{-1} in the graph with poly-L-lysine. This peak represents the C-N bond and we can conclude that some amount of poly-L-lysine present in the CaCO_3 precipitate.

CONCLUSION

Effect of the cationic organic biopolymers on the MICP process was investigated by using poly-L-lysine. The results shows that,

- Poly-L-lysine has a positive effect on the MICP process. However with the presence of higher concentration of bacteria significant influence from the poly-L-lysine on the MICP process couldn't be seen.

With the increase of the bacteria concentration, the rate of the formation of calcium carbonate decrease. So, higher bacteria concentration will reduce the crystal growth.

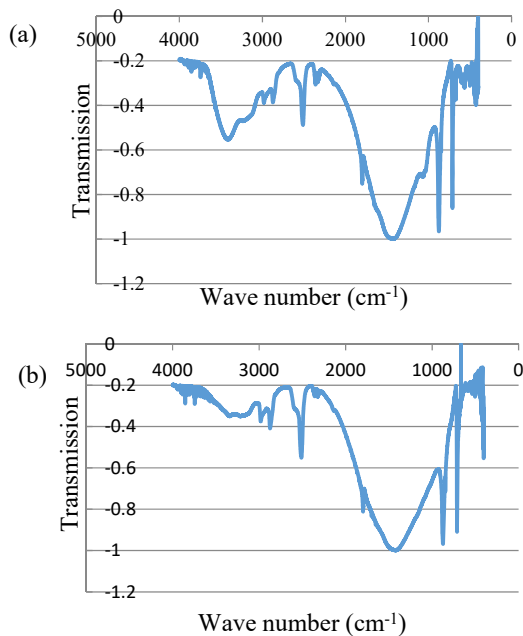


Fig. 7 FTIR spectra for samples (a) with poly-L-lysine (b) without poly-L-lysine

- Relationship between the amount of precipitate and the poly-L-lysine concentration is bell shaped and higher and lower concentrations of the poly-L-lysine concentration inhibit the calcium carbonate precipitation but intermediate concentration give higher amount of precipitate.
- With the increase of the bacteria concentration morphology of the crystals change from well-developed rhombohedral crystals to agglomeration of the rhombohedral crystals and size of the crystals reduces.
- Presence of the poly-L-lysine produces ellipsoidal shape crystals. Morphology of the crystals changes from the polyhedral crystals to agglomeration of ellipsoidal crystals with the increase of the poly-L-lysine concentration.

REFERENCES

- [1] Chang I, Im J, Cho G C, "Introduction of microbial biopolymers in soil treatment for

future environmentally-friendly and sustainable geotechnical engineering", *Journal of sustainability*, Vol. 8, Mar.2016, pp.1-23.

- [2] Akiyama M, Kawasaki S, "Novel grout material comprised of calcium phosphate compounds: In vitro evaluation of crystal precipitation and strength reinforcement", *Journal of engineering geology*, Vol. 125, Jan.2012, pp. 119-128.
- [3] Khan N H, Amarakoon G G N N, Shimazaki S & Kawasaki S, "Coral sand solidification test based on microbially induced carbonate precipitation using ureolytic bacteria", *Journal of materials transactions*, Vol. 56, Aug. 2015, pp. 1725-1732.
- [4] Pacheco T F, Labrincha J A, Diamanti M V, Yu C P & Lee H K, "Production of bacteria for structural concrete", *Biotechnology and bio mimetic for civil engineers*, springer,2015, pp.309-323.
- [5] Fujita M, Nakashima K, Achal V, Kawasaki S, "Whole-cell evaluation of urease activity of *Pararhodobacter* sp. isolated from peripheral beachrock" *Biochemical engineering journal*, Vol. 124, April. 2017, pp. 1-5.
- [6] Dzakula B N, Falini G, Brecevic L, Skoko Z & Kralj D, "Effects of initial supersaturation on spontaneous precipitation of calcium carbonate in the presence of charged poly-L-amino acids", *Journal of colloidal and interface science*, Vol. 343, Dec. 2009, pp.553-563.
- [7] Colville K, Tompkins N, Rutenberg A D, Jericho M H, "Effects of poly(L-lysine) substrates on attached *escherichia coli* bacteria", *Langmuir*, Vol.26,sep.2009,pp. 2639-2644.
- [8] Mitsuyama S, Nakashima K, Kawasaki S, "Evaluation of porosity in biogROUTED sand using microfocus x-ray ct", *International journal of GEOMATE*, Vol. 12, Mar. 2017, pp. 71-76.
- [9] Dzakula B N, Brecevic L, Falini G & Kralj D, "Calcite crystal growth kinetics in the presence of charged synthetic polypeptide", *Journal of crystal growth and design*, Vol.9, Feb.2009, pp.2425-2434.

PREDICTION OF SALTWATER INTRUSION PROCESSES USING A WAVELET-FCM-ANFIS HYBRID MODEL

Dilip Kumar Roy¹, and Bithin Datta²

^{1,2} Discipline of Civil Engineering, College of Science and engineering, James cook University, QLD 4811, Australia

ABSTRACT

Sufficiently accurate and reliable prediction of saltwater intrusion processes can help ensure sustainable groundwater abstraction from coastal aquifers. In this study, a surrogate model based on combination of multi-signal discrete wavelet transforms (MDWT) and adaptive neuro-fuzzy inference system (ANFIS) is proposed to approximate and predict density dependent coupled flow and salt transport processes in a multi-layered coastal aquifer system. MDWT is used as a pre-processing step to improve the ability of the ANFIS model by capturing relevant important information at different resolution levels. The variables used to train and validate the proposed prediction model are the transient groundwater extractions as inputs, and the resulting saltwater concentrations at the end of the simulation period as outputs. To reduce dimensionality of the input space, an additional step of data compression is utilized to prepare data required for ANFIS training. Therefore, input space is divided into a number of clusters by using fuzzy c-mean (FCM) clustering algorithm. The performance of the proposed surrogate model is evaluated for an illustrative study area. It is demonstrated that MDWT in conjunction with FCM can improve accuracy of ANFIS based surrogate model for saltwater intrusion processes prediction. The results of the present study indicates the potential applicability of the proposed MDWT-FCM-ANFIS based surrogate model in approximating and predicting coupled flow and salt transport processes in an illustrative multi-layered coastal aquifer system.

Keywords: Saltwater Intrusion, Multi-signal Discrete Wavelet Transforms, Adaptive Neuro-fuzzy Inference System, Fuzzy C-mean Clustering

INTRODUCTION

Unplanned groundwater extraction is considered as one of the major drivers of saltwater intrusion processes in coastal aquifers [1, 2]. Accurate and reliable prediction of saltwater intrusion processes can be adopted to develop long-term planning and management policy for coastal groundwater resources. Saltwater intrusion phenomena can be predicted by simulating density dependent and non-linear coupled flow and salt transport processes. Saltwater intrusion management models are developed by using repetitive simulation of these complex processes within an iterative simulation-optimization (S/O) approach. Use of the original simulation model is computationally prohibitive (because of multiple calls of the simulation model by the optimization algorithm) in such a linked S/O methodology. Sufficiently accurate approximations of saltwater intrusion processes can be used for developing a regional scale management model to control saltwater intrusion [3]. Present study proposes a fuzzy logic based prediction model to approximate density dependent coupled flow and solute transport processes in a multi-layered coastal aquifer system. Multi-signal discrete wavelet transforms (MDWT)

and fuzzy c-mean (FCM) clustering algorithm are used as preprocessing steps for training of the proposed adaptive neuro-fuzzy inference system (ANFIS) based saltwater intrusion prediction model.

Generalization capability of a trained model to produce similar results from a new pattern of unseen test dataset is an important evaluation criterion. Based on this criterion, quite a few prediction models have been used successfully to predict saltwater intrusion processes in coastal aquifers. Artificial Neural Network (ANN) [4-7], Genetic Programming (GP) [6-8], Evolutionary Polynomial Regression (EPS) [9], Fuzzy Inference System (FIS) [10], Multivariate Adaptive Regression Spline (MARS) [11] and cubic Radial Basis Function (RBF) [12] are the commonly used approximation models for saltwater intrusion prediction. Despite simplicity and reasonable prediction accuracy, most of the surrogate models proposed recently have certain limitations. Therefore, there is still a substantial scope of developing a reliable prediction model with better prediction accuracy. Recently, ANFIS based prediction models have achieved considerable attention as an effective tool to model non-linear systems by capturing non-linear relationships between predictors and response variables [13, 14]. ANFIS combines the concepts of

both neural networks and fuzzy set theory [15]. Present study seeks to propose a MWDT transformed and FCM based ANFIS model as a computationally efficient substitute of complex numerical simulation model to overcome some of the limitations of the commonly used prediction models.

Wavelet transforms (WT) have become a popular preprocessing step for time series analysis in various application domains of water resource engineering and hydrology [16-19]. Wavelet transformed data enhances the prediction capability of a model by extracting important features on various resolution scales of the original data [17]. Discrete wavelet transformation provides approximation (low-frequency) and detail (high-frequency) components after decomposition of the original data to a desired level. Different wavelet components characterize distinct properties of the original data. For instance, high-frequency components capture discontinuities, ruptures, and singularities of the original data. On the other hand, low-frequency components characterize the overall gross structure of the data that helps identify long-term trends. Several previous studies demonstrated the potential benefits of discrete wavelet transforms in improving the capability of prediction models for time series prediction in the domain of river flow forecasting [17], streamflow prediction [19], and lake water level prediction [18]. Wavelet transformed ANFIS has also been used previously in the time series analysis of lake water level prediction [18], precipitation prediction [20], groundwater level prediction [21], and evapotranspiration estimation [22], etc. However, wavelet transformation has not been utilized previously as a preprocessing step to train ANFIS based surrogate models for predicting saltwater intrusion processes resulting from spatial and temporal pumping stresses applied to a multi-layered coastal aquifer system.

However, a major challenge in the application of ANFIS based prediction models to approximate saltwater intrusion processes is to handle high dimensionality of data associated with spatial and temporal groundwater extraction values as input variables. FCM provides a solution to this issue by dividing the high dimensional input space into identical clusters that makes ANFIS generation feasible by limiting the number of rules in the initial FIS for ANFIS generation. This study utilizes FCM clustering approach to generate initial FIS structure for building the final ANFIS model.

Therefore, the contribution of the present study is to develop a reliable and accurate prediction model to

approximate saltwater intrusion processes in a multi-layered coastal aquifer system. Transient input-output patterns generated by using a numerical simulation model are used to train the proposed ANFIS model. MSWT and FCM are used as preprocessing steps of ANFIS model formulation. The performance of the proposed MSWT-FCM-ANFIS based approach is evaluated for an illustrative multi-layered coastal aquifer system. The stratified aquifer system consists of four distinct layers of aquifer materials with different hydraulic conductivity values. Aquifer materials within each layer are considered homogeneous.

METHODOLOGY

The proposed methodology consists of utilizing a numerical simulation model for simulating aquifer processes; and using an ANFIS based prediction model trained and validated using MSWT transformed and FCM clustered modified inputs of transient groundwater extraction values. The following paragraphs provide a brief description of the methodologies.

Numerical Simulation Model

A finite element based numerical simulation model, FEMWATER [23] was used to simulate three dimensional coupled flow and salt transport processes for generating input-output datasets. Governing flow and transport equations are expressed as [23]

$$\frac{\rho}{\rho_0} F \frac{\partial h}{\partial t} = \nabla \cdot \left[K \cdot \left(\nabla h + \frac{\rho}{\rho_0} \nabla z \right) \right] + \frac{\rho}{\rho^*} q \quad (1)$$

where ρ represents water density at chemical concentration C , ρ_0 is referenced water density at zero chemical concentration, F indicates storage coefficient, ∇ stands for del operator, K symbolizes hydraulic conductivity tensor, h is pressure head, z indicates potential head, ρ^* represents density of injection fluid or that of the withdrawn water, and q indicates either a source or a sink.

$$\begin{aligned} & \theta \frac{\partial C}{\partial t} + \rho_b \frac{\partial S}{\partial t} + V \cdot \nabla C - \nabla \cdot (\theta D \cdot \nabla C) \\ & = - \left(\alpha' \frac{\partial h}{\partial t} + \lambda \right) (\theta C + \rho_b S) - (\theta K_w C + \rho_b K_s S) \\ & + m - \frac{\rho^*}{\rho} q C + \left(F \frac{\partial h}{\partial t} + \frac{\rho_0}{\rho} V \cdot \nabla \left(\frac{\rho}{\rho_0} \right) - \frac{\partial C}{\partial t} \right) C \end{aligned} \quad (2)$$

in which θ represents moisture content, C indicates chemical concentration, ρ_b is the bulk density of the medium, V represents discharge, D indicates Dispersion coefficient tensor, α' and β' are respectively the modified compressibility of the water

and the medium, S stands for saturation, K_w is the first order biodegradation rate constant through dissolved phase, K_s is the first order biodegradation rate through adsorbed phase, K_d is the distribution coefficient, and t represented time.

Dataset Preparation

Input-output datasets were obtained from the solution results of the numerical simulation model through repeated simulation of the aquifer processes using a set of transient groundwater extraction values. The input transient groundwater extraction values were generated from a uniform distribution within the range between 0 and 1300 m³/day through Latin Hypercube Sampling (LHS) [24], and is presented in Fig.1. Saltwater concentration values at specified monitoring locations (ML) at the end of the simulation period obtained as solution from the simulation model constitute the output part of the input-output pattern. The study area selected for this research is similar to the one developed in Roy and Datta [10] as shown in Fig.2. The aquifer system has an aerial extent of 4.35 km². The depth of aquifer is 80 m divided into four distinct layers of materials having different hydraulic conductivity values. Materials within each layer were considered homogeneous. Combined operation of a set of production and barrier wells was considered symbolized by PWs and BWs, respectively in Fig. 2. Water was extracted from the 2nd and 3rd layers of the aquifer using the wells, which were assigned a practical extraction limit of 0–1300 m³/day. Saltwater concentrations due to the transient pumping stress applied to the aquifer at the end of the simulation period of five years were monitored at five MLs.

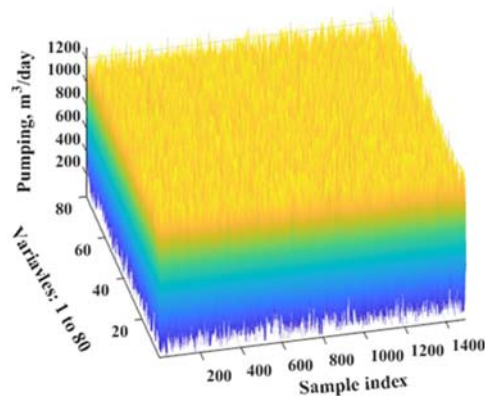


Fig. 1 Three dimensional view of the transient groundwater extraction values

Transient groundwater extraction values and the resulting saltwater concentration at the end of the management period constitute one set of input-output pattern. A set of such patterns was used to train and validate the proposed prediction models. Properly trained models were then presented with a new

realization of the validation sample to check validation performance with new unseen data. For consistency, this validation part was done for all the developed models using the original input values.

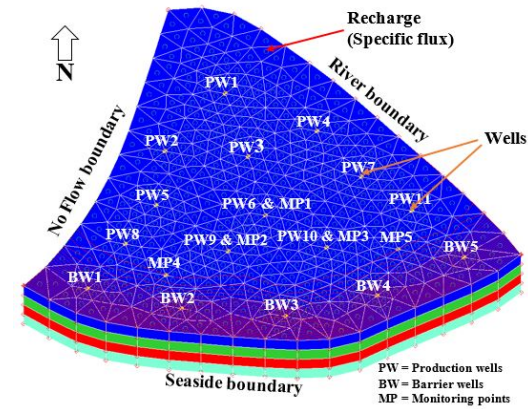


Fig. 2 Three dimensional view of the study area (after Roy and Datta [10])

Multi-signal Discrete Wavelet Transforms (MDWT)

WT is an effective tool in the field of analyzing non-stationary time series data. WT allows decomposition of the original data series into several components with different resolution levels. Each component of the wavelet transformed data has certain characteristics. Present study utilizes Discrete WT (DWT), which is suitable for analyzing signals by decomposing them into progressively finer octave bands. This multi-resolution signal processing enables to recognize unseen patterns of the raw data. Multiple one dimensional signals of input transient pumping variables of same length are stored in a matrix before being decomposed using a one dimensional MDWT. In DWT, the original data series (S) is decomposed into low frequency approximation coefficients (A) and high-frequency detail coefficients (D) after passing through a low-pass and a high-pass filter, respectively. The low-pass filtered signal of any decomposition level acts as input to the next step of decomposition, and the iteration process continues until the specified decomposition level is reached. The A components contain the general trend of the original data series whereas the D components characterize the original signals' local variations. MDWT was performed using Wavelet toolbox of MATLAB [25].

Adaptive Neuro-fuzzy Inference System (ANFIS)

Despite having simple architecture, Sugeno type ANFIS structures have good learning capabilities [26] suitable for non-linear mapping of input-output patterns of non-linear systems [13, 14]. Therefore, a Sugeno type ANFIS has been adopted in the present

study to approximate density dependent coupled flow and salt transport processes in a multi-layered coastal aquifer system. Final ANFIS structure was achieved by tuning the parameters of an initial FIS structure using hybrid algorithm. For a first order Sugeno FIS, the generic form of the fuzzy if-then rule set for two inputs, one output, and two rules can be expressed as

Rule 1: If α is P_1 and β is Q_1 then

$$f_1 = p_1\alpha + q_1\beta + r_1, \quad (3)$$

Rule 2: If α is P_2 and β is Q_2 , then

$$f_2 = p_2\alpha + q_2\beta + r_2 \quad (4)$$

in which P_1 and P_2 represents membership function values for input variable α whereas values of membership functions for input variable β are denoted by Q_1 and Q_2 . Parameters of the output functions f_1 and f_2 are symbolized by p_1, q_1, r_1

and p_2, q_2, r_2 , respectively. Gaussian and linear type membership functions are used as the input and output membership functions, respectively for the initial FIS structure.

The proposed ANFIS consists of five layers, namely, an input fuzzy layer, a product layer, a normalized layer, a defuzzification layer, and an output layer. Detailed description of each of these layers are described in Jang, Sun and Mizutani [26], and is not repeated here.

Fuzzy C-mean (FCM) Clustering

Fuzzy C-mean (FCM) [27] clustering technique was used to reduce dimensionality of the input dataset for generating initial FIS structure. FCM is an important tool for compressing the dataset into a group of identical clusters within the input space. FCM clustering helps reduce number of fuzzy if-then rules as well as limits the number of linear and nonlinear modifiable parameters of a FIS. Desired number of clusters is achieved by minimizing fuzzy overlap between clusters using Eq. 5

$$O_m = \sum_{i=1}^K \sum_{j=1}^N \mu_{ij}^m \|\alpha_i - c_j\|^2 \quad (5)$$

where, O_m = function to be minimized, m = fuzzy partition matrix exponent, K = sample index, N = number of clusters, $\alpha_i = i^{th}$ data point, c_j = center of the j^{th} cluster, μ_{ij} = membership degree of α_i in the j^{th} cluster.

Optimum number of clusters was selected by observing the Root Mean Square Error (RMSE) (Eq. 6) between the actual and predicted data. The

optimum number of clusters was chosen for which the RMSE value was minimum, and the difference in RMSE between the training and test dataset was minimum as well. Based on this criterion, two clusters were found optimal for generating the initial FIS for final ANFIS development. Therefore, this study considered 160 Gaussian input membership functions (80 input variables \times 2 clusters) and 2 (1 output variable \times 2 clusters) linear output membership functions for all developed ANFIS models at each ML.

Conjunction Model (MDWT-FCM-ANFIS)

The hybrid model (MDWT-FCM-ANFIS) developed in the present study utilizes wavelet transformed and FCM clustered input variables. Input variables are the spatial and temporal groundwater pumping values obtained from a uniform distribution using LHS.

Selection of appropriate WT involves adjustment of the three basic parameters, such as selection of a mother wavelet family, an order within that family, and the number of levels of decomposition. Daubechies (db4), Haar (haar), and Symlet (sym4) mother wavelets were used and compared in the present study. Number of decomposition levels was decided based on the number of sample index of the input data. Generally, DWT requires that the decomposition at level k of the input dataset should be an integer value such that 2^k divides evenly into the length of the dataset. As the number of input-output patterns is 1500 in the present study, the number of decomposition levels was restricted to ten [$2^{10} = 1024$; $2^{11} = 2048$]. In the case of 10 levels of decomposition, the original data signal was transformed into an approximation component (A) and 10 detail components (D_1, D_2, \dots, D_{10}).

Thirty five different conjunction models based on ANFIS, FCM, and MDWT have been developed by using the specified mother wavelet families (db4, haar, and sym4). In first step, all the decomposed components from these mother wavelets were separately correlated with the output variables at five MLs. Decomposed details components with lowest correlation coefficients were removed while the remaining details components and the respective approximation components were summed to obtain the input variables for the proposed models. In the second step, all the approximations and details components were summed for obtaining the input datasets. This step is executed because all components of the decomposed signals have certain characteristics of the original data. Therefore, removing any one of them from the input dataset

based on the linear correlation may deteriorate the model performance. The correlation coefficient measure only provides an indication of linear relationship between input and output variables, which is not the case in the present study. In addition, two variables that have a small or no linear correlation might have a strong nonlinear relationship. Present study deals with a highly non-linear relationship between the groundwater pumping input variables and the corresponding saltwater concentration values. Therefore, combining all decomposed components to obtain input variables for the ANFIS models is logical in the context of the present study. Finally, models developed with wavelet transformed input datasets were compared with those obtained by using the original groundwater extraction values.

Performance Indicators

The performance of the proposed prediction models was evaluated using RMSE, Correlation Coefficient (R), and Mean Absolute Percentage Relative Error (MAPRE) criteria.

Root mean square error (RMSE) is given by

$$RMSE = \sqrt{\frac{1}{n} \sum_{i=1}^n (C_{i,o} - C_{i,p})^2} \quad (6)$$

Correlation coefficient (R) is calculated as

$$R = \frac{\sum_{i=1}^n (C_{i,o} - \bar{C}_o)(C_{i,p} - \bar{C}_p)}{\sqrt{\sum_{i=1}^n (C_{i,o} - \bar{C}_o)^2} \sqrt{\sum_{i=1}^n (C_{i,p} - \bar{C}_p)^2}} \quad (7)$$

Mean absolute percentage relative error (MAPRE) is expressed as

$$MAPRE = \frac{1}{n} \sum_{i=1}^n \left| \frac{C_{i,o} - C_{i,p}}{C_{i,o}} \right| \times 100 \quad (8)$$

where, $C_{i,o}$ and $C_{i,p}$ are the observed and predicted saltwater concentrations; \bar{C}_o and \bar{C}_p denotes the mean of the observed and predicted saltwater concentrations; and n represents the number of data points.

RESULTS AND DISCUSSION

Wavelet Decomposition of the Original Data

Transient groundwater extraction datasets were broken down into several sub-sets with different resolution levels by using MDWT. The original dataset S was decomposed into an approximation

coefficient A and details coefficients $D1-D10$ at decomposition level 10. Each component of the decomposed dataset carries different characteristics of the original dataset. While some researchers used those decomposed components of the original dataset that have highest correlations with the original output variable [19, 20], others argued that all of the decomposed components should be summed to prepare the final inputs for the prediction models [18, 28]. The approximate coefficient A captures only the major trends whereas the detail components $D1-D10$ carry abrupt changes, outliers, and short discontinuities in transient groundwater extraction values. Present study chose input data for the ANFIS models by looking at the correlation coefficients between each input subsets and the original saltwater concentration values at specified MLs. However, the correlation coefficients only determine linear correlations, and the datasets are obtained from a highly non-linear system in which non-linear relation exists between the input pumping variables and the output concentration values. For this reason, summing all components of the decomposed datasets were also considered so that non-linearity of the datasets is included in the final inputs. All components (A and $D1-D10$) were summed by reconstructing the decomposed subsets. The reconstruction error was computed, which was negligible in this present study for all considered wavelet families. Summed components all together constitutes a dataset very similar to the original data sets except that the features of the wavelet decomposed datasets are different, which may help improve training of the prediction model compared to when using the original data series. For each monitoring location, seven ANFIS based prediction models (One model developed using the original data, three models are developed using summing all decomposed wavelet components each for three different wavelet families, three models are developed for three mother wavelets based on correlation between the decomposed series and the original output variable) were developed. Therefore, a total of 35 ANFIS based prediction models were developed and compared. At this stage of the model development, all developed models were checked for their prediction error and model overfitting by dividing the dataset into a training (80%) and a test (20%) set. Once the models were developed, they were presented with a new realization of the original test dataset for validation of the prediction results.

ANFIS Models

ANFIS models were developed for each ML using the original input-output patterns obtained from simulation of the aquifer processes as a result of spatial and temporal pumping stress applied to the aquifer. Table 1 shows the performance measures of

the five ANFIS models developed for predicting saltwater concentrations at MLs ML1–ML5. In general, all models produced R values very close to one. This is attributed to very high degree of correlation between the actual and predicted saltwater concentration values. The developed models also had smaller values of RMSE and MAPRE. This indicates the potential ability of the models to capture the trend of the data quite precisely. The MAPRE criterion was used to measure the distribution of errors. The results obtained from these models at five MLs were used as benchmark for comparison with the wavelet-ANFIS models presented in the following sub-section.

Table 1 Performance measures of ANFIS models trained on original data and validated with new test dataset

MPs	Performance Indices		
	RMSE	MAPRE, %	R
MP1	0.242	0.458	0.9986
MP2	5.185	0.281	0.9994
MP3	3.787	0.274	0.9996
MP4	6.541	0.073	0.9998
MP5	3.416	0.043	0.9999

Wavelet-ANFIS Models

Statistical performance measures of the wavelet transformed ANFIS models developed at five MLs were calculated. Totally, 30 different ANFIS structures were developed based on the use of three different mother wavelet families and on the selection of decomposed components. It was observed that R values were very close to 1 for all developed models. Therefore, an R criterion did not provide a good measure of comparison among models in this case. RMSE and MAPRE criteria were used for comparing ANFIS models developed using original data (Table 1) and those using wavelet transformed components of the original datasets. As the input-output patterns come from a highly non-linear system, wavelet decomposed components selected based on linear correlation between decomposed components and the original output may not be the logical way of selecting input variables for the ANFIS models. Moreover, each decomposed components carries distinct and essential characteristics of the original datasets. In this viewpoint, present study used both types of datasets as inputs to the ANFIS models. To make a valid comparison and to reproduce the prediction of the models, random number generator of MATLAB was set to its default value (Mersenne Twister with seed 0). Also, for consistency, all developed models were presented with a totally unseen set of original test data. Results suggested that models developed with different datasets based on

three different mother wavelets produced higher values of R and lower values of RMSE and MAPRE. This implied a good generalization capability of the developed models on unseen datasets. A more precise investigation on RMSE and MAPRE values indicated that for monitoring location ML1, ANFIS model developed using all decomposed components of sym4 decomposed datasets produced the lowest value of RMSE (0.230 mg/l). This result was also better than the RMSE values for ANFIS model developed when original dataset was used for training. Possible explanation for this trend is that WT improves the quality of data at different regions of the input space that helps better training of the ANFIS model. At this monitoring location, db4 decomposed datasets selected using linear correlation produced the worst result (highest RMSE value of 0.560 mg/l). At ML2, haar decomposed datasets produced the lowest RMSE compared to the original datasets. At ML3 and ML5, sym4 decomposed and original datasets produced the similar results. At ML4, all the components decomposed using db4 provided the lowest RMSE (5.898 mg/l) compared to the original datasets (RMSE = 6.5405 mg/l).

CONCLUSION

ANFIS models were developed for approximating and predicting density dependent coupled flow and salt transport processes in a multi-layered coastal aquifer system. Solution results of a numerical simulation model were used for training and validation of all developed ANFIS models. Original datasets as well as the wavelet transformed datasets using db4, haar, and sym4 mother wavelets were used to develop a total of 35 ANFIS models at five MLs. Validation of all the models was carried out by using a new unseen original test data. The results revealed that wavelet transformed datasets helped improve the training of proposed ANFIS based prediction models. Moreover, FCM made it possible to use high dimensional dataset (80 input variables) for developing ANFIS based prediction models. The results also showed that types of mother wavelet selection depended on the actual original non-linear relationship between the transient groundwater extraction values and the resulting saltwater concentration values at different MLs. Wavelet transformed data provided better learning capabilities of the ANFIS based prediction models by capturing important features of the data on different resolution levels. Future research may be directed towards the investigation of possible improvement in the Pareto optimal solution of a saltwater intrusion management model using these wavelet transformed trained ANFIS models.

REFERENCES

- [1] K.A. Narayan, C. Schleeberger, K.L. Bristow, Modelling seawater intrusion in the Burdekin Delta Irrigation Area, North Queensland, Australia, *Agricultural Water Management*, 89 (2007) 217-228.
- [2] Supriyadi, Khumaedi, A.S.P. Putro, Geophysical and hydrochemical approach for seawater intrusion in north Semarang, central Java, Indonesia, *International Journal of GEOMATE*, 12 (2017) 134-140.
- [3] R.K. Bhattacharjya, B. Datta, M.G. Satish, Artificial neural networks approximation of density dependent saltwater intrusion process in coastal aquifers, *Journal of Hydrologic Engineering*, 12 (2007) 273-282.
- [4] R.K. Bhattacharjya, B. Datta, ANN-GA-based model for multiple objective management of coastal aquifers, *Journal of Water Resources Planning and Management*, 135 (2009) 314-322.
- [5] G. Kourakos, A. Mantoglou, Pumping optimization of coastal aquifers based on evolutionary algorithms and surrogate modular neural network models, *Advances in Water Resources*, 32 (2009) 507-521.
- [6] J. Sreekanth, B. Datta, Multi-objective management of saltwater intrusion in coastal aquifers using genetic programming and modular neural network based surrogate models, *Journal of Hydrology*, 393 (2010) 245-256.
- [7] J. Sreekanth, B. Datta, Comparative evaluation of genetic programming and neural network as potential surrogate models for coastal aquifer management, *Water Resources Management*, 25 (2011) 3201-3218.
- [8] J. Sreekanth, B. Datta, Coupled simulation-optimization model for coastal aquifer management using genetic programming-based ensemble surrogate models and multiple-realization optimization, *Water Resources Research*, 47 (2011) W04516.
- [9] M.S. Hussain, A.A. Javadi, A. Ahangar-Asr, R. Farmani, A surrogate model for simulation-optimization of aquifer systems subjected to seawater intrusion, *Journal of Hydrology*, 523 (2015) 542-554.
- [10] D.K. Roy, B. Datta, Fuzzy c-mean clustering based inference system for saltwater intrusion processes prediction in coastal aquifers, *Water Resources Management*, 31 (2017) 355-376.
- [11] D.K. Roy, B. Datta, Multivariate adaptive regression spline ensembles for management of multilayered coastal aquifers, *Journal of Hydrologic Engineering*, 22 (2017) 04017031.
- [12] V. Christelis, A. Mantoglou, Pumping optimization of coastal aquifers assisted by adaptive metamodelling methods and radial basis functions, *Water Resources Management*, 30 (2016) 5845-5859.
- [13] M. Sugeno, T. Yasukawa, A fuzzy-logic-based approach to qualitative modeling, *IEEE Transactions on Fuzzy Systems*, 1 (1993) 7.
- [14] T. Takagi, M. Sugeno, Fuzzy identification of systems and its applications to modeling and control, *IEEE Transactions on Systems, Man, and Cybernetics*, SMC-15 (1985) 116-132.
- [15] J.-S.R. Jang, ANFIS: adaptive-network-based fuzzy inference system, *IEEE Transactions on Systems, Man, and Cybernetics*, 23 (1993) 665-685.
- [16] J. Adamowski, H.F. Chan, A wavelet neural network conjunction model for groundwater level forecasting, *Journal of Hydrology*, 407 (2011) 28-40.
- [17] J. Adamowski, K. Sun, Development of a coupled wavelet transform and neural network method for flow forecasting of non-perennial rivers in semi-arid watersheds, *Journal of Hydrology*, 390 (2010) 85-91.
- [18] M. Shafaei, O. Kisi, Lake level forecasting using wavelet-SVR, wavelet-ANFIS and wavelet-ARMA conjunction models, *Water Resources Management*, 30 (2016) 79-97.
- [19] O. Kisi, M. Cimen, A wavelet-support vector machine conjunction model for monthly streamflow forecasting, *Journal of Hydrology*, 399 (2011) 132-140.
- [20] T. Partal, O. Kisi, Wavelet and neuro-fuzzy conjunction model for precipitation forecasting, *Journal of Hydrology*, 342 (2007) 199-212.
- [21] V. Nourani, M.T. Alami, F.D. Vossoughi, Hybrid of SOM-clustering method and wavelet-ANFIS approach to model and infill missing groundwater level data, *Journal of Hydrologic Engineering*, 21 (2016).
- [22] A.P. Patil, P.C. Deka, Performance evaluation of hybrid Wavelet-ANN and Wavelet-ANFIS models for estimating evapotranspiration in arid regions of India, *Neural Computing and Applications*, 28 (2017) 275-285.
- [23] H.J. Lin, D.R. Reichards, C.A. Talbot, G.T. Yeh, J.R. Cheng, H.P. Cheng, N.L. Jones, A three-dimensional finite element computer model for simulating density-dependent flow and transport in variable saturated media: Version 3.0, US Army Engineering Research and Development Center, Vicksburg, Miss., (1997).
- [24] E.J. Pebesma, G.B.M. Heuvelink, Latin hypercube sampling of gaussian random fields, *Technometrics*, 41 (1999) 303-312.
- [25] MathWorks, Wavelet toolbox: MATLAB version 2017a, The Mathworks Inc, Mathworks, Natick, (2017a).
- [26] J.-S.R. Jang, C.T. Sun, E. Mizutani, Neuro-fuzzy and soft computing: A computational approach to learning and machine intelligence, Prentice Hall, 1997.
- [27] J.C. Bezdek, R. Ehrlich, W. Full, FCM: The fuzzy c-means clustering algorithm, *Computers & Geosciences*, 10 (1984) 191-203.
- [28] S. Lahmiri, Wavelet low- and high-frequency components as features for predicting stock prices with backpropagation neural networks, *Journal of King Saud University - Computer and Information Sciences*, 26 (2014) 218-227.

LINKED SIMULATION-OPTIMIZATION MODEL FOR OPTIMUM HYDRAULIC DESIGN OF WATER RETAINING STRUCTURES CONSTRUCTED ON PERMEABLE SOILS

Muqdad Al-Juboori¹ and Bithin Datta¹

¹ Discipline of Civil Engineering, College of Science and Engineering, James Cook Univ., Townsville, QLD 4811, Australia

ABSTRACT

Hydraulic Water Retaining Structures (HWRS), such as dams, weirs and regulators are important projects and necessary for water management. Seepage analysis under HWRS substantially influences the design of HWRS. One of the biggest challenges in design of HWRS is to determine the accurate seepage characteristics with complex flow conditions, and simultaneously to find the optimum design considering safety and cost. Therefore, this study concentrates on developing a linked simulation-optimization (S-O) model for non-homogenous anisotropic soil properties. This is achieved via linking the numerical seepage simulation (Geo-Studio/SEEPW) with the Genetic Algorithm (GA) evolutionary optimization solver. Since, a direct linking of numerical model with optimization model is computationally expensive and time consuming, accurate surrogate models are integrated instead of a numerical simulation model within the S-O model. A Support vector machine (SVM) based surrogate model is linked with the optimization model to achieve the optimum hydraulic design of HWRS. The seepage characteristics of optimum design obtained by S-O are evaluated by comparing these with the numerical seepage modeling (SEEPW) solutions. The comparison, in general, shows good agreements. Accordingly, the S-O methodology is potentially applicable for providing safe, efficient and economical design of HWRS constructed on a complex seepage flow domain.

Keywords: *Support vector machine, Genetic algorithm, Seepage modeling, Hydraulic structures design*

INTRODUCTION

Construction of Hydraulic Water Retaining Structures (HWRS) is the strategic aim for the most communities around the world to build a strong water management system. Seepage analysis related to HWRS is a critical step of HWRS design [1]. In addition to the direct impacts of hydrostatic water pressures on the structural system of the HWRS, the seepage design parameters such as uplift pressures and exit gradient are the other fundamental factors needed to be incorporated in HWRS design.

The earliest theories and methods, such as Bligh's creep theory, Lane's weighted creep theory, Flow-net method, fragment method and Khosla's theory [1] used to analyse seepage related to HWRS involve many simplifications and are based on many empirical assumptions. These methods are applicable only for simple, symmetrical cases and quite general soil conditions (homogeneous and isotropic), which are rarely found in field soils[2]. Moreover, the solutions of these method are approximation solutions, and these generally display noticeable error compared with experimental observations and the numerical solutions [3].

In contrast, the numerical seepage analysis methods such as the finite element method (FEM) provides accurate solutions for a wide range of the seepage problems encountered in the real field [4, 5]. However, these solutions might not be useful, as the resulting designs may not satisfy the safety requirements and also not optimize the construction costs. Therefore, employing the optimization technique could provide a reliable and optimum solution, especially when accurate numerical seepage simulation responses are integrated in the optimization model. Accordingly, based on linked simulation-optimization S-O methodology [6-8], an ideal HWRS design could be

achieved. This methodology involves developing a constrained optimization model based on Genetic Algorithm (GA) to integrate all design safety factors regarding the wide range of applied forces, i. e. , hydrostatic pressure, uplift pressure, exit gradient, and considering, the minimum cost as the objective function.

The developed optimization model must be linked with the numerical seepage analysis model to concurrently evaluate the candidate designs (solutions) of the HWRS. However, the direct linking of optimization model with the numerical seepage model is a computationally demanding and time consuming task. This is because, the GA calls the simulation model numerous times to evaluate the objective function and the constraints in order to achieve an optimal solution. Alternatively, machine learning technique is used to build a well-trained model (surrogate model), which could be efficiently used instead of the numerical model. A well trained surrogate model can expeditiously and accurately predict the responses of the numerical model for complex problems within the linked S-O model.

Many machine learning techniques could be used in building the surrogate models, such as artificial neural network (ANN), fuzzy logic, multivariate adaptive regression splines (MARS), genetic programming (GP) and support vector machine SVM. In this study, SVM is selected, because SVM is considered a powerful deep-learning tool. SVM is utilized in the classification, function approximation and prediction by which a nonlinear and complex civil engineering problems can be efficiently modeled. Moreover, in addition to the efficiency and predictive accuracy, SVM has a generalization ability to accurately predict data beyond

the training range. Additionally, SVM can overcome the noisy data in the training phase by integrating the most governing support vectors. Hence, SVM has the ability to overcome the over-training phenomena [9].

Recently, SVM has been utilized to model complex civil engineering problems to provide an extensive understanding of the variables involved in the model [9-16]. In the majority of the conducted researches, SVM is utilized to predict specific responses depending on the input variables or to simulate performance of a particular engineering system with special conditions. For example, in hydraulic structure design, SVM has been used to predict the forecasting of the tangential shift of a concrete dam [14], and to predict future dam responses with environmental variables [17]. Nonetheless, SVM has been rarely utilized as a surrogate model within the optimization model in the hydraulic structure design problems. Application of other machine learning techniques for solving optimization problems related to hydraulic structures design incorporating complex soil properties has been very limited as well.

This paper concentrates on developing a linked S-O model based on two different models. The first model is the constraint optimization model based on GA as the optimization solver. The objective function is the minimum construction cost of HWRS and the constraints reflect the HWRS design requirements. The second model is the surrogate model which is based on the SVM. The surrogate model is extensively trained using numerically simulated data generated by a numerical seepage modeling software (Geo_Studio2012/ SEEPW) [18]. The seepage design parameters obtained as the solution of the optimal design by the S-O model are evaluated using SEEPW to investigate the prediction accuracy of the SVM within an S-O model.

NUMERICAL MODEL SOLUTION AND TRAINING DATA GENERATION

In contrast to an experimental study, the numerical model could provide accurate and quick solutions even for complex problems, especially by using high speed processors. The optimization model incorporates the numerical responses, either obtained directly using the numerical model code or approximately by the surrogate models. As it is difficult and computationally very costly to directly link the optimization model with the numerical model, a surrogate model needs to be developed.

To train the surrogate model, Input-output data sets must be generated and solved by the numerical model. Also, a conceptual comprehensive numerical HWRS model shown in Fig.1 is assumed with different variables. These variables represent the decision variable in the optimization model to find the best variables values and best combinations of these variables, which provide the optimum solution.

The conceptual model comprises different sets of design variables randomly varied within assumed ranges. In this study, the proposed design variables are the dimensions and inclination of ten sheet piles (S_1 - S_{10}) (cut-off) and the spacing between them. The symbols for the sheet pile depths are ($d_1, d_2 \dots d_{10}$), for the angles are ($\beta_1, \beta_2, \dots \beta_{10}$) and for the width between the sheet piles ($b_1, b_2, \dots b_{10}$). The subsoil foundation consists of three layers (DL_1, DL_2, DL_3) and their

hydraulic conductivities are (kx_1, kx_2, kx_3) with the anisotropy ratio $(Ky/Kx)_1, (Ky/Kx)_2, (Ky/Kx)_3$ respectively. The total upstream water head (H) is also considered a variable.

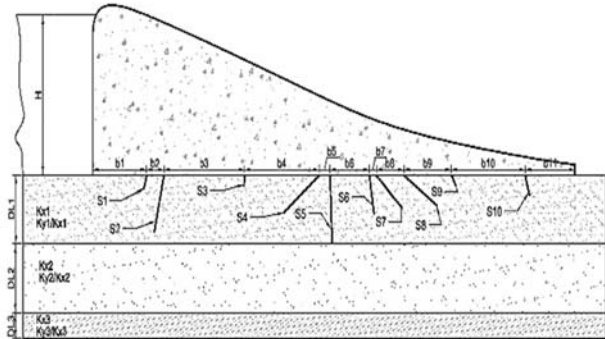


Fig. 1 Conceptual numerical model

All the input sets (1700 sets) are randomly generated using Latin hypercube sampling method (LHS) within specified ranges. LHS provides a uniform periodic random data by which robust training could be achieved in the machine learning process [19]. Each set of input data represents one scenario of the HWRS design. The SEEPW software is utilized to find the resulting seepage characteristics for each scenario. The seepage characteristics include the uplift pressure in front (θE_i) and behind (θC_i) each single sheet pile in addition to the exit gradient at the end of the floor of hydraulic structure (toe). The seepage characteristics resulting from the numerical seepage modeling represent the output data used for training the SVM models.

SUPPORT VECTOR MACHINE

Support vector machine is a deep learning technique used for classification and regression problems. Recently, SVM has been implemented in wide academic applications and engineering problems because the SVM has a good generalization ability, and is less impacted by overfitting phenomena. Generally, the SVM algorithm selects from the training data the best hyperplane (vector) which provides an efficient classification. The SVM algorithm maximizes the distance between the center of the hyperplane and its boundary (margin) to attain the best SVM model. therefore, the ideal SVM must have wider margins, then the SVM model could provide accurate prediction and high generalization ability [20, 21].

The SVM technique is applied to build the models that could accurately predict the numerical responses. Matlab programming language is utilized to develop the SVM models, because Matlab is a versatile tool and provides many options that can be modified to build perfect SVM models. 1700 sets of the simulated data obtained by solving SEEPW numerical code are used to train and build the SVM models. Twenty one models are built to determine the uplift pressure in front, and behind each sheet pile, and the exit gradient near the end of the structure. The SVM is trained on the simulated data where 90% of the data are utilized for training and 10% are used for testing. The coefficient of determination (RSQ) and mean square error (MSE) for the training and testing phases are

listed in the Table A2. The parameter for each SVM model are carefully selected after several iterations of trial and errors until best RSQ and smaller MSE are achieved. It could be concluded that the most influencing parameter on SVM performance is the kernel function type, and the constraint box. The kernel function used in this study is the polynomial kernel with varied order, which provide precise prediction compared to the other kernels.

OPTIMIZATION MODEL

The optimization model integrated in the S-O model is formulated to find the best design of HWRS at a minimum cost. Because of the complexity of the optimization task, the GA is used in this study. GA evaluates the fitness value and the constraints based on the surrogate models responses. Additionally, GA is likely to provide a global optimum solution and has the ability to deal with a complex problem as it does not rely on differentiating the performance equations to find the optimum solution. Instead GA is based on a natural selection principle [22, 23]. The GA is efficient in finding the global solution in such a problem, where the performance function is based on the surrogate model responses. In the S-O model, GA calls the surrogate models (SVM) huge number of times to evaluate the fitness value and the constraints for each individual until the optimum design is achieved. Matlab programming language is used to implement the optimization model. The GA parameters specified in this study are: *Population Size* 2000, *Elite Count* 10, *Crossover Fraction* 0.8, *Function Tolerance* 1e-6, *Constraint Tolerance* 1e-3, and the rest of GA options are left to default Matlab options.

The decision vector (X) involved in the optimization model represents the most important design variable of the HWRS model (conceptual numerical model). The X is modified many times by GA to find the minimum construction cost of the design, and simultaneously to provide safe design that satisfies all design requirements (constraints).

The decision vector is listed as shown below, where the design variables from x_1 to x_{11} represent the width between sheet piles (b_1, b_2, \dots, b_{11}), variables from x_{12} to x_{22} represent the depth of the sheet piles (d_1, d_2, \dots, d_{10}) the variables from x_{23} to x_{32} represent the inclination angle for the cutoffs ($\beta_1, \beta_2, \dots, \beta_{10}$). The optimization problem is formulated as shown below:

$$\text{Find } X = \begin{Bmatrix} x_1 \\ x_2 \\ \vdots \\ x_{32} \end{Bmatrix} = \begin{Bmatrix} b_1 \\ b_2 \\ \vdots \\ b_{11} \\ d_1 \\ d_2 \\ \vdots \\ d_{10} \\ \beta_1 \\ \beta_2 \\ \vdots \\ \beta_{10} \end{Bmatrix}$$

Which minimizes the objective function shown in Eq. (1)

Minimize:

$$f(X) = c_f \sum_{i=1}^{11} T_i x_i + c_c t_c \sum_{i=12}^{21} x_i \quad (1)$$

Where: T_i represent the average thickness of the floor between two sheet piles, c_f = The cost of constructing the body of the HWRS per cubic meter (\$500/m³), c_c = The construction cost of the sheet pile per cubic meter (\$1000/m³), t_c = the thickness of the sheet pile, which is constant = 0.5m.

The decision vector is subjected to the following constraints:

Flotation constrain: The uplift pressure on the foundation of the HWRS along all width of HWR must be safe [24, 25]. Therefore, the value $\emptyset C$ and $\emptyset E$ near each sheet pile must be sufficiently counterbalanced by the floor thickness at these points. The safety factor assumed is 1.3 as shown in Eq. (2).

$$t_i \geq 1.3 \left(\frac{\emptyset E \text{ or } \emptyset C}{G_c - 1} \right), i = 1, 2, 3, \dots, 20 \quad (2)$$

Where G_c is the specific gravity of the concrete.

Exit gradient constrain: If the exit gradient is equal or more than the critical gradient, piping failure is likely. Therefore, it is recommended that the exit gradient value must be at least 3 to 5 times less than critical gradient [26, 27]

Usually, the shortest stream line or the closest point to HWRS toe is the most critical point at which the largest value of exit gradient could be seen. The safety factor of exit gradient is determined by Eq. (3)

$$F.S = \frac{i_c}{i_e} \quad (3)$$

Where i_c is critical exit gradient and given by Eq.(4)

$$i_c = \frac{\gamma_{sub}}{\gamma_w} \quad (4)$$

Where γ_{sub} is the submerged soil density, γ_w is the weight density of water. The soil properties are considered mixed grained sand, which has $\gamma_{sat} = 21.2$ kN/m³ and that results in $i_{cr} = 1.15$ [28].

Other constraints: Many other constraints are also considered in the optimization model, such as sliding constraint and overturning constraint. The preventing eccentric loading state constraints is incorporated also to ensure uniform distribution of the loads on the soil surface.

It is interesting to note that the value $\emptyset C$ and $\emptyset E$ for each sheet pile, and i_e values involved in the S-O model are determined based on the surrogate models responses. The surrogates models within the optimization model are also represents the binding constraints where the decision vector must satisfy the simulation constraints in addition to the design constraints.

RESULTS AND DISCUSSION

The developed methodology was applied to optimize the conceptual model based on the surrogate models responses. Ten different cases having different H values starting from 10 m to 100 m were solved by S-O model as shown the table A1. The other parameters value are left constant, such as

hydraulic conductivity for each layer is 5 m/day, the anisotropy ratio is 1 and the depth of each subsoil layer is 50 m for all cases. For all implemented cases the solution obtained by S-O model satisfy the design requirement and the safety factors.

Generally, the contribution of the variables b_1 to b_8 and d_1 to d_8 on the safety of the HWRS is neglected, where the optimum values for these variables is almost zero. Consequently, as the length of d_1 to d_8 reach their minimum value, their inclination angle become meaningless. Nonetheless, the inclination angle has a noticeable effect on reduction of uplift pressure, especially when β value is less than 90 degrees. In contrast, when β value is more than 90 degree it has a significant effect in reduction of the exit gradient value.

However, the optimum solutions obtained for each case are based more on increasing the width of HWRS to reduce the uplift pressure on the body of HWRS, and less based on the sheet piles lengths to decrease the PWP. This could be attributed to two reasons. First, the uplift pressure value must be counterbalanced by the weight of the construction material of HWRS. Accordingly, even if it is costly solution, it is necessary to provide safe thickness against the uplift pressure. Secondly, some design requirements significantly influenced the design features. For example, to ensure the stability of HWRS against overturning condition, the GA increases the total width of HWRS to provide more stability against the overturning forces and the huge amount of the active moments. Besides, preventing eccentric load state in the foundation of HWRS is another critical design requirement, therefore GA restricts the loads resultant to be located within the second third of the total width. Hence, GA increases the total width to ensure uniform distribution of stress on the soil foundation. Additionally, the construction cost of the sheet piles is more expensive than the construction cost of the HWRS floor.

On the other hand, because of the crucial impact of the exit gradient on the design of HWRS, the d_{10} length has a significant control in reduction of the exit gradient value. As a result, for all optimum solutions the d_{10} values have a considerable length, as shown in Table A3. Additionally, the optimum sheet pile inclination angle of β_{10} is 150 degree toward downstream. The increase of β_{10} value effectively decreases the exit gradient value, as the streamline length of seeping water significantly increases and in turn the exit gradient value decreases. Moreover, another factor which might affect the exit gradient is the length of b_{10} , because increasing the b_{10} reduces the uplift pressure and consequently decreases the exit gradient value.

Mainly, the exit gradient value for all cases reach the maximum allowable value to satisfy a minimum safety factor of five with respect to the critical gradient. Accordingly, the exit gradient parameter plays a critical role in the selection of optimal decision variable values in the optimization process.

Additionally, an extensive evaluation was conducted for validating the S-O optimum solutions. The seepage design variables (θE , θC , exit gradient) were evaluated by solving the optimum solutions using SEEPW, then compared the seepage characteristic obtained by SEEPW with the same values obtained from the S-O model. In general, the

evaluation results showed that maximum percentage of error between the S-O model and SEEPW solutions is around 10%. This figure demonstrates that the SVM generalization ability with unseen and extreme data is good. On the other hand, the prediction of SVM for exit gradient is less accurate, which could be attributed to the large number of input variable for exit gradient surrogate model. However, the most of the exit gradient safety factor for the optimum solution is still within the standard and safe limit, and not less than 3.

CONCLUSION

The optimization based searching process is an expensive and computationally demanding task, especially when the optimization model linked to a numerical simulation to evaluate the fitness value and the constraints. Therefore, the linked S-O model based on SVM surrogate models was implemented to find the optimum design of HWR. Many SVM surrogate models were precisely built to predict the seepage analysis results. Based on the accurate responses of the surrogate models, GA evaluate the fitness value and the constraints. Therefore, a reliable and optimum design of HWRS could be achieved.

The seepage design variable values (θE , θC , exit gradient) obtained as optimum solutions were validated using numerical solutions. The validation process showed that the surrogate models predictions were accurate, even in the solution range beyond the training data range.

In general, the optimum and safe hydraulic design of HWRS must include sufficient floor width (more than H value) and one of the end sheet piles with the optimum length (not less than $0.5H$), with inclination angle attaining up to 150 degrees. Finally the methodology is potentially applicable for funding find the optimum design of HWRS at minimum cost for different scenarios, within the specified training data range. Future studies may include expanded training ranges, and use of different machine learning techniques and optimization solvers to achieve more accuracy.

REFERENCES

1. Garg, S.K., Irrigation engineering and hydraulic structures. 1987: Khanna publishers.
2. Lambe, T.W. and R.V. Whitman, Soil mechanics SI version. 2008: John Wiley & Sons.
3. Shahrbanozadeh, M., G.-A. Barani, and S. Shojaei, Simulation of flow through dam foundation by isogeometric method. *Engineering Science and Technology, an International Journal*, 2015. 18(2): p. 185-193.
4. Mansuri, B., F. Salmasi, and B. Oghati, Effect of Location and Angle of Cutoff Wall on Uplift Pressure in Diversion Dam. *Geotechnical and Geological Engineering*, 2014. 32(5): p. 1165-1173.
5. Moharrami, A., et al., Performance of Cutoff Walls Under Hydraulic Structures Against Uplift Pressure and Piping Phenomenon. *Geotechnical and Geological Engineering*, 2014. 33(1): p. 95-103.
6. Al-Juboori, M. and B. Datta, Artificial Neural Network Modeling and Genetic Algorithm Based Optimization of Hydraulic Design Related to Seepage under Concrete Gravity Dams on Permeable Soils. 2017.
7. Sreekanth, J. and B. Datta, Review: simulation-optimization models for the management and monitoring of coastal aquifers. *Hydrogeology Journal*, 2015. 23(6): p. 1155-1166.

8. Prakash, O. and B. Datta, Optimal monitoring network design for efficient identification of unknown groundwater pollution sources. *Int. J. of GEOMATE*, 2014. 6(1): p. 785-790.
9. Deka, P.C., Support vector machine applications in the field of hydrology: a review. *Applied Soft Computing*, 2014. 19: p. 372-386.
10. Fisher, W.D., T.K. Camp, and V.V. Krzhizhanovskaya, Anomaly detection in earth dam and levee passive seismic data using support vector machines and automatic feature selection. *Journal of Computational Science*, 2016.
11. Mahani, A.S., et al., Hybridizing two-stage meta-heuristic optimization model with weighted least squares support vector machine for optimal shape of double-arch dams. *Applied Soft Computing*, 2015. 27: p. 205-218.
12. Pal, M., N. Singh, and N. Tiwari, Support vector regression based modeling of pier scour using field data. *Engineering Applications of Artificial Intelligence*, 2011. 24(5): p. 911-916.
13. Parsaie, A., H.A. Yonesi, and S. Najafian, Predictive modeling of discharge in compound open channel by support vector machine technique. *Modeling Earth Systems and Environment*, 2015. 1(1-2): p. 1-6.
14. Ranković, V., et al., Development of support vector regression identification model for prediction of dam structural behaviour. *Structural Safety*, 2014. 48: p. 33-39.
15. Su, H., Z. Chen, and Z. Wen, Performance improvement method of support vector machine-based model monitoring dam safety. *Structural Control and Health Monitoring*, 2016. 23(2): p. 252-266.
16. Yu, P.-S., S.-T. Chen, and I.-F. Chang, Support vector regression for real-time flood stage forecasting. *Journal of Hydrology*, 2006. 328(3): p. 704-716.
17. Cheng, L. and D. Zheng, Two online dam safety monitoring models based on the process of extracting environmental effect. *Advances in Engineering Software*, 2013. 57: p. 48-56.
18. Krahn, J., Seepage modeling with SEEP/W: An engineering methodology. GEO-SLOPE International Ltd. Calgary, Alberta, Canada, 2004.
19. Cox, D.R. and N. Reid, The theory of the design of experiments. 2000: CRC Press.
20. Kramer, O., Machine Learning in Evolution Strategies. Vol. 20. 2016: Springer.
21. Alpaydin, E., Introduction to machine learning. 2014: MIT press.
22. Gen, M. and R. Cheng, Genetic algorithm and engineering optimization. John Wiley and Sons, New York, 2000.
23. Haupt, R.L. and S.E. Haupt, Practical genetic algorithms. 2004: John Wiley & Sons.
24. U.S. Army Corps of Engineers, Reliability analysis and risk assessment for seepage and slope stability failure modes for embankment dams 2006.
25. Bligh, W.G., Dams and Weirs: An Analytical and Practical Treatise on Gravity Dams and Weirs; Arch and Buttress Dams; Submerged Weirs; and Barrages. 1915: American Technical Society.
26. Harr, M.E., Groundwater and seepage. 2012: Courier Corporation.
27. Khosla, A.N., N.K. Bose, and E.M. Taylor, Design of weirs on permeable foundations. 1936.
28. Terzaghi, K., R.B. Peck, and G. Mesri, Soil mechanics in engineering practice. 1996: John Wiley & Sons.

APPENDIX

Table A1 optimum solution and the objective function value for different value of H

H (m)	100	90	80	70	60	50	40	30	20	10
Objective Function value (\$)	4385022	3763560	3326936	2236865	1578883	1098975	631827	497585	130951	53324
b ₁	0.0	3.1	0.0	0.7	0.6	0.0	0.0	0.3	0.1	0.7
b ₂	15.1	3.7	0.6	0.3	1.5	1.4	2.6	0.0	1.3	1.2
b ₃	0.5	2.6	1.5	0.7	0.6	0.5	7.1	0.0	1.4	1.1
b ₄	0.1	2.5	1.6	0.9	0.5	0.5	5.8	0.0	1.3	0.2
b ₅	0.7	2.2	0.6	2.3	0.8	0.1	0.0	0.0	0.6	0.5
b ₆	0.7	2.9	1.2	1.6	1.5	0.6	0.1	0.0	1.0	0.5
b ₇	3.9	3.5	4.3	2.3	2.9	0.7	0.3	0.4	0.1	0.5
b ₈	0.1	1.9	1.1	2.7	2.5	2.3	0.7	1.0	3.2	6.0
b ₉	31.2	21.2	36.0	33.4	22.5	15.1	0.9	9.2	2.0	2.8
b ₁₀	113.2	113.1	111.9	72.6	62.7	59.6	37.2	54.6	14.7	7.7
b ₁₁	10.3	11.1	11.3	6.3	6.1	5.8	5.0	8.3	1.0	2.4
d ₁	7.4	1.7	0.2	0.0	0.4	0.0	0.8	0.0	0.0	0.0
d ₂	0.1	0.2	0.1	0.0	0.3	0.0	0.5	0.0	0.1	0.0
d ₃	0.0	1.0	0.4	0.2	0.0	0.0	2.7	0.0	0.0	0.0
d ₄	0.0	0.1	0.2	0.3	0.2	0.0	0.0	0.0	0.2	0.1
d ₅	0.0	0.0	0.0	0.7	0.0	0.0	0.0	0.0	0.0	0.1
d ₆	0.2	0.2	0.3	0.0	0.3	0.2	0.0	0.0	0.0	0.1
d ₇	0.0	0.3	0.0	0.9	1.1	0.0	0.1	0.0	0.0	0.0
d ₈	0.0	0.4	0.5	0.4	0.0	0.0	0.0	0.0	0.0	0.0
d ₉	0.4	0.0	0.5	1.7	0.4	0.0	0.0	0.0	0.0	0.0
d ₁₀	56.2	56.5	55.4	34.4	31.0	29.8	17.5	27.0	7.3	2.5
dd	0.0	0.0	0.1	0.0	0.0	0.0	0.0	0.0	0.0	0.0
β ₁	65.3	67.4	64.4	63.1	66.9	66.2	70.0	70.6	77.9	46.3
β ₂	85.9	85.6	83.8	77.9	84.9	69.0	83.7	84.3	81.6	31.3
β ₃	91.9	89.3	90.0	87.5	88.3	82.1	91.8	89.4	85.9	30.0
β ₄	70.7	70.7	71.6	81.4	79.8	73.3	78.7	79.8	142.9	30.0
β ₅	44.1	46.9	46.1	57.2	61.5	88.4	77.7	30.0	60.0	30.0
β ₆	67.6	76.2	78.1	85.3	89.5	91.8	98.8	117.4	136.0	30.0
β ₇	73.1	61.3	77.0	76.3	83.6	76.0	95.7	30.0	78.8	30.4
β ₈	32.5	100.4	45.0	43.7	93.8	30.0	103.0	30.0	149.5	104.8
β ₉	44.6	30.0	30.0	30.0	30.0	30.0	30.0	30.0	30.0	30.0
β ₁₀	150.0	150.0	128.5	150.0	149.7	135.3	150.0	110.9	121.6	101.9

Table A2 Properties of the developed SVM models

model	RSQ TRAIN	MSE TRAIN	RSQ TEST	MSE TEST	function	ORDER	box constraint	training input variables
Exit gradient	0.95	0.1	0.91	0.17	polynomial	4	1	x8 x9 x10 x11 x19 x20 x21 x22 x30 x31 x32 AB *
0C10	0.97	1.22	0.97	1.08	polynomial	4	10	x11 x21 x32 AB
0E10	0.96	4.57	0.97	3.64	polynomial	3	10	x10 AB
0C9	0.95	7.66	0.95	6.35	polynomial	3	20	x20 x31 AB
0E9	0.99	1.32	0.99	0.96	polynomial	3	15	x9 AB
0C8	0.98	3.74	0.98	2.93	polynomial	4	1	x19 x30 AB
0E8	0.99	0.82	0.99	0.97	polynomial	3	3	x8 AB
0C7	0.99	2.12	0.99	1.59	polynomial	3	1.5	x18 x29 AB
0E7	0.98	5.25	0.99	0.77	polynomial	2	10	x7 AB
0C6	0.99	1.74	0.99	1.46	polynomial	4	5	x17 x28 AB
0E6	0.99	1.08	0.99	0.65	polynomial	3	17	x6 x22 AB
0C5	0.99	0.99	0.99	1.13	polynomial	3	4	x16 x27 AB
0E5	0.99	0.63	0.99	0.54	polynomial	2	4	x5 AB
0C4	0.99	1.21	0.99	1.2	polynomial	3	2.1	x15 x26 AB
0E4	0.99	0.77	0.99	0.74	polynomial	2	1.6	x4 AB
0C3	0.999	0.95	0.99	0.94	polynomial	3	4	x14 x25 AB
0E3	0.999	0.94	0.99	0.93	polynomial	3	2.8	x3 AB
0C2	0.99	1.92	0.99	1.94	polynomial	4	2.7	x13 x24 AB
0E2	0.99	1.11	0.99	1.13	polynomial	3	1.5	x2 AB
0C1	0.99	2.75	0.99	3.2	polynomial	3	8	x12 x23 AB
0E1	0.99	3.2	0.99	2.8	polynomial	2	20	x1 AB

Note: AB equal to $[DL_1 DL_2 DL_3 kx_1 (ky/kx)_1 kx_2 (ky/kx)_2 kx_3 (ky/kx)_3 H]$

Table A3 Evaluation results of the S-O model for different value of H

Seepage design variable		0E1	0C1	0E2	0C2	0E3	0C3	0E4	0C4	0E5	0C5	0E6	0C6	0E7	0C7	0E8	0C8	0E9	0C9	0E10	ie
H=100	S-O	98.7	93.6	91.0	89.4	88.9	88.3	87.3	87.0	86.7	83.2	83.0	81.4	80.9	80.3	77.1	77.2	66.1	65.6	38.7	0.23
	SEEPW	100.0	86.4	81.4	81.2	81.1	80.9	80.9	80.7	80.5	80.4	80.2	80.0	78.6	78.5	78.4	78.3	68.5	68.3	39.7	0.28
	% Error	-1.3	8.3	11.8	10.0	9.6	9.1	7.9	7.8	7.7	3.5	3.5	1.8	2.9	2.3	-1.8	-1.4	-3.5	-4.1	-2.6	-17.94
H=90	S-O	88.3	85.3	83.2	81.4	80.8	80.0	78.9	78.6	78.1	74.9	74.5	73.2	72.6	71.9	69.1	68.3	60.8	60.9	35.7	0.21
	SEEPW	85.5	83.0	81.1	80.7	79.7	78.6	77.7	77.5	76.5	76.3	75.2	74.9	73.6	73.4	72.8	72.5	65.5	65.4	37.7	0.25
	% Error	3.3	2.8	2.5	0.9	1.4	1.8	1.5	1.4	2.1	-1.9	-0.8	-2.3	-1.4	-2.0	-5.0	-5.8	-7.2	-6.9	-5.2	-16.32
H=80	S-O	79.0	76.3	74.3	72.5	72.0	71.2	70.3	69.9	69.4	66.5	66.3	65.1	64.5	63.7	61.4	61.1	53.4	53.5	32.4	0.21
	SEEPW	80.0	78.1	77.2	76.5	75.4	74.5	73.7	73.1	72.9	72.6	72.1	71.7	69.7	69.6	69.3	68.8	57.9	57.7	36.1	0.19
	% Error	-1.3	-2.3	-3.8	-5.3	-4.6	-4.3	-4.5	-4.4	-4.8	-8.4	-8.1	-9.2	-7.6	-8.4	-11.4	-11.3	-7.8	-7.4	-10.3	9.89
H=70	S-O	69.0	66.6	64.6	63.0	62.6	61.9	61.1	60.6	60.0	57.5	57.1	56.2	55.6	54.7	52.9	52.6	46.7	46.3	30.2	0.23
	SEEPW	67.7	67.0	66.6	66.0	65.3	64.6	64.1	63.3	62.2	61.2	60.5	60.2	59.4	58.4	57.6	57.2	46.1	45.4	26.8	0.30
	% Error	-1.3	8.3	11.8	10.0	9.6	9.1	7.9	7.8	7.7	3.5	3.5	1.8	2.9	2.3	-1.8	-1.4	-3.5	-4.1	-2.6	-17.94
H=60	S-O	59.2	56.8	55.0	53.5	53.1	52.5	51.8	51.3	50.7	48.6	48.3	47.5	46.9	46.0	44.5	44.0	40.0	39.8	27.7	0.23
	SEEPW	59.0	56.5	55.4	54.6	54.3	54.0	53.8	53.1	52.7	52.4	51.7	51.2	50.2	49.1	48.3	48.1	40.2	40.1	23.9	0.30
	% Error	-1.3	8.3	11.8	10.0	9.6	9.1	7.9	7.8	7.7	3.5	3.5	1.8	2.9	2.3	-1.8	-1.4	-3.5	-4.1	-2.6	-17.94
H=50	S-O	49.4	47.3	45.7	44.3	44.0	43.3	42.8	42.2	41.7	40.0	39.7	39.0	38.5	37.8	36.7	36.7	33.7	33.3	24.3	0.23
	SEEPW	50.0	48.7	46.6	46.2	45.8	45.4	45.1	44.8	44.8	44.5	44.2	43.8	43.4	43.2	42.0	41.8	36.2	36.0	22.4	0.26
	% Error	-1.3	-3.0	-2.0	-4.0	-3.9	-4.6	-5.2	-5.9	-6.9	-10.0	-10.3	-10.8	-11.4	-12.6	-12.7	-12.3	-6.9	-7.6	8.7	-11.47
H=40	S-O	39.5	37.6	36.2	35.0	34.6	33.8	33.2	32.6	32.1	30.8	30.5	30.0	29.5	28.8	28.1	27.7	25.8	25.1	19.8	0.23
	SEEPW	40.0	36.3	34.8	34.1	31.4	29.2	27.7	27.6	27.6	27.5	27.5	27.3	27.2	27.0	26.9	26.7	26.4	26.3	15.6	0.30
	% Error	-1.3	-3.0	-2.0	-4.0	-3.9	-4.6	-5.2	-5.9	-6.9	-10.0	-10.3	-10.8	-11.4	-12.6	-12.7	-12.3	-6.9	-7.6	8.7	-11.47
H=30	S-O	29.6	28.0	26.9	26.0	25.7	25.0	24.5	23.8	23.4	22.8	22.4	22.0	21.6	21.4	20.8	20.8	19.0	18.1	14.1	0.16
	SEEPW	29.4	28.8	28.8	28.4	28.3	28.0	28.0	27.7	27.7	27.4	27.4	27.2	26.9	26.7	26.3	26.1	23.3	23.2	15.1	0.22
	% Error	0.7	-2.8	-6.4	-8.3	-9.1	-10.5	-12.2	-14.0	-15.4	-16.8	-18.3	-19.1	-19.8	-19.9	-20.9	-20.5	-18.5	-21.7	-6.7	-27.57
H=20	S-O	19.8	18.5	17.7	17.0	16.7	16.0	15.5	15.0	14.7	14.2	13.7	13.4	13.1	12.7	12.3	12.2	11.0	10.3	8.1	0.23
	SEEPW	19.8	18.8	17.5	17.1	16.2	16.0	15.4	15.1	14.9	14.7	14.3	14.2	14.1	14.0	12.8	12.7	12.0	11.9	8.1	0.36
	% Error	-0.2	-1.9	1.1	-0.4	3.1	0.1	0.8	-0.6	-1.7	-3.7	-4.1	-5.4	-7.0	-9.0	-3.8	-3.8	-8.5	-13.4	0.0	-36.17
H=10	S-O	9.9	9.0	8.5	8.4	8.1	7.7	7.2	6.6	6.3	6.5	6.0	6.2	6.2	6.0	5.7	5.6	4.8	4.4	3.2	0.23
	SEEPW	9.2	8.8	8.2	8.1	7.7	7.6	7.5	7.4	7.2	7.1	7.0	6.8	6.7	6.6	5.2	5.1	4.5	4.4	2.9	0.32
	% Error	-1.3	-3.0	-2.0	-4.0	-3.9	-4.6	-5.2	-5.9	-6.9	-10.0	-10.3	-10.8	-11.4	-12.6	-12.7	-12.3	-6.9	-7.6	8.7	-11.47

JOINT BENCHMARKING AND ECO-EFFICIENCY FOR THE SUSTAINABLE PERFORMANCE OF SWINE PRODUCTION IN THAILAND

Weerawat Ounsaneha¹ Punthila Janthaphat² Thunwadee Tachapattaworakul Suksaroj³,
Cheerawit Rattanapan^{3*}

¹Faculty of Science and Technology, Valaya Alongkorn Rajabhat University under the Royal Patronage,
Klong Nuang, Klong Luang, Pathumthani, 13180, Thailand,

²Faculty of Environmental Management, Prince of Songkla University, Hat Yai, Songkhla, 90112, Thailand

³ASEAN Institute for Health Development, Mahidol University, Salaya, Phutthamonthon, Nakhonpathom,
73710, Thailand

ABSTRACT

This research aimed to develop the sustainable performance of swine production through joint benchmarking and eco-efficiency. The economic and environmental performance of fifteen swine farms in Thailand between 2011 – 2013 were evaluated by Gate to Gate sector boundary. The results showed the highest and lowest values of eco-efficiency in the swine farming sector were feed and water consumption respectively. Benchmarking of eco-efficiencies in all indicators demonstrate that best practice for swine farms was obtained with average feed consumption of 1 kg/head-day, average water consumption of 1.17 L/head-day, use of renewable energy from bio-gas of 0.014 kWh/head-day, use of swine fever vaccination and anthelmintics, greenhouse gas emissions of 0.00875 tonCO₂eq/head-day and total amount of waste produced was 6.25 kg/head-day. Lastly, the sustainable development master plan for swine production in Thailand, which includes breeding selection, husbandry management, farm management and attendance, and the environmental management of farms was developed using material flow analysis concepts, in-depth interview and brainstorming with best practice swine farmers.

Keywords: Benchmarking; Eco-Efficiency; Sustainable Performance; Swine Production; Thailand.

INTRODUCTION

The concept of environmental sustainability applies to operations management within food and agricultural systems [1]. In Southeast Asia, Thailand is the largest producer of swine with 13.07 million heads in 2013 [2]. Nuengjamnong and Rachdawong [3] investigated environmental impact issues within the industry, noting that the size of swine farms has shifted from small to large scale operations. Additionally, consumers in developed countries demand safe food of high quality produced with minimal adverse environmental impact [4-7].

A feasible approach to measure sustainability at an individual level, increasingly adopted, is represented by eco-efficiency, which appeared in the 1990s as a practical tool to measure sustainability. The World Business Council for Sustainable Development [8] introduced the term “eco-efficiency”, identifying a management philosophy aimed at encouraging businesses to search for environmental improvements that yield parallel economic benefits. Eco-efficiency studies were used to assess performance and identify opportunities for improvement [9]. This concept, together with integrative design, offers an opportunity to substantially improve eco-efficiency. Various reports [10-11] studied effective methods of linking

benchmarking and eco-efficiency to improve agricultural operations. This study uses benchmarking and the concept of eco-efficiency with the objective of performing an eco-efficiency assessment of swine farms in Thailand. In addition, a joint study was conducted to identify the best performing farms for use in public policy to improve the eco-efficiency of swine farm production.

METHODS

The swine farm production process

According to the previous study [3], verified in a swine farm in the southern part of Thailand, the first step of swine farm production is swine breeding. Pregnant swine are given water and feed for four months. Then, vaccines, energy, water, and feed are needed to care for piglet for one month, or till they have reached 16 kilograms in body weight. Piglets are separated into two groups, those directly sold, and swine grown for a further forty days. In addition, this step in swine production produces significant wastes from swine feces and wastewater from floor and corral cleansing, which can be directed to a biogas system or preliminary treatment before environmental discharge (Figure 1).

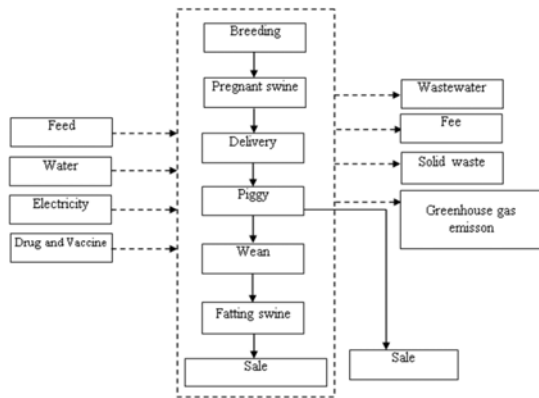


Figure 1. The swine farm production process

Eco-efficiency indicator and data collection procedure

The eco-efficiency assessment of swine farm production required the conclusion of the literature review and farm survey including inputs, outputs and by-products. Eco-efficiency indicators consisted of economic and environmental indicators (Table 1). A questionnaire was developed to collect data on the selected indicators, based on a questionnaire developed by the National Round Table on the Environment and the Economy [12]. This questionnaire was approved by the Social Ethical Committee of Mahidol University.

The environmental and economic performance of fifteen swine farms in the southern and central parts of Thailand between 2011 - 2013 were collected based on farm size recommendations of the Pollution Control Department, Thailand, including small (50-500 pigs), medium (500-5,000 pigs), and large (more than 5,000 pigs) farms.

Table 1 Eco-efficiency indicator of swine production in Thailand

Indicators	Unit
Economic indicator	
Net sale	Baht/year
Environmental indicator	
Feed consumption	Ton/year
Drug and vaccine consumption	ML/year
Electricity consumption	Kwh./year
Water consumption	m ³ /yea
Waste production	Yon/year
Greenhouse gas emission	Ton CO ₂ -eq/year

Eco-efficiency Assessment

The eco-efficiency assessment of swine farm production was modified from key concepts of the World Business Council for Sustainable Development [8] and previous studies [13], with the ratio between swine production value and total environmental impact from the production process.

The eco-efficiency calculation is shown in equation (1).

$$E = EV / \Sigma En \quad (1)$$

Where: E is Eco-efficiency value; EV is the economic value of swine production; ΣEn is the total environmental impact from the material and resource use of swine production.

The master approach of swine production toward sustainable development by joint benchmarking and eco-efficiency concept

The eco-efficiency values of swine farm production were used to identify best practice by benchmarking the value of each indicator. Firstly, indicator units were normalized before benchmarking, then, the eco-efficiency value of each indicator was benchmarked to identify best practice performance. The concept of material flow analysis [13] was used to confirm the process of best practice farm in each indicator. Finally, in-depth interviewing and brainstorming with farm owners were included for approach verification by and then the master plan of swine production toward sustainable development in Thailand was developed.

RESULTS AND DISCUSSION

Eco-efficiency value of swine farm production

The resulting eco-efficiency values of swine farm production are shown in Table 2. The eco-efficiency values of small size farms are highest and lowest for electricity consumption and greenhouse gas emissions respectively. Additionally, the trend for eco-efficiency values increased annually for small farms. However, the net sale of swine production slightly increased due to the increased cost of feed. The main advantage of small size farms was identified as labor cost savings because they are family-run.

The highest and lowest eco-efficiency values for medium size farms were electricity and water consumption respectively (Table 2). These findings show that the swine production process, including heating, ventilation and water pumping in medium-sized farms, requires significant electricity supply. Additionally, the water consumption trend increased annually due to the processes of swine drinking and twice daily corral cleaning.

The highest and lowest eco-efficiency values for large-size farms were water and electricity consumption respectively (Table 2). This finding is consistent with the medium-size farms in the issue of water consumption. Vu et al [14] found that the volume of water consumption was 40 liters/swine for corral and floor cleaning, which was similarity with the result of this study. However, the water supply system and the reuse of treated wastewater were applied in this farm size for reducing water

consumption. Additionally, biogas production systems can be used to reduce electricity consumption in large-size farms with the lowest eco-efficiency value in this study.

Benchmarking value of eco-efficiency for swine production

The results of the eco-efficiency assessment of fifteen swine farms were used to identify best practice performance by benchmarking. This data is shown in Table 4. Regarding feed consumption, the best practice swine production with eco-efficiency values of 58,159.70 baht/ton was farm K, as the tablet type of feed and feed limitation and control at 0.12 ton/head-year with twice daily feeding was used. Regarding water consumption, farm C had the best practice with eco-efficiency values of 14,679.94 baht/m³ and 1.17L/head-day water consumption, as well water was pumped to a large storage tank for supplying swine drinking water needs and once-daily cleaning. Farm O had the best practice regarding electricity consumption, with eco-efficiency values of 5,642.25 baht/kWh and 1.72kWh/head-year. A biogas system using farm wastewater provided all energy needed at a cost of 394 Baht/month. In the case of drug and vaccine consumption, farm A had the best practice with eco-efficiency values of 2,208.77baht/ml and 8.38 ml/head-year. Concerning waste production, an average eco-efficiency of 12,998.90 baht/ton and 6.25 ton/head-year were found in Farm O, as biogas production supported by the government was used to treat both wastewater and solid waste to cover the energy consumption costs of this farm. Finally, farm O also presented the best practice in greenhouse gas emissions, with eco-efficiency values of 9,260.22 baht/ton CO₂-eq and 0.00875 ton CO₂-eq/head-year.

Master approach of swine production toward sustainable development

Using the results of swine production eco-efficiency benchmarking to identify best practices, the master approach of swine production toward sustainable development was developed using material flow analysis, in-depth interviews and brainstorming with the best practice farms within each indicator. The master approach consisted of two paradigms including a technique approach with process improvement and a management approach with farm improvement. The details of the master approach of swine production toward sustainable development are shown in Figure 3 and consist of four components. Firstly, breeding selection should be based on rapid growing, disease-resistance animals. Secondly, the master approach of husbandry management consists of animal health, and feed and water consumption management. For

animal health management, swine farmers should provide drug and vaccine doses based on government regulations. Additionally, pathogen contamination prevention techniques should be implemented as standard. Feed and water consumption management should provide for the demands of swine based on the growing stage. Swine feed can be prepared by farmers, reducing cost. Moreover, feed storage buildings should be separate, protecting from human, insect and pathogen contamination. To provide clean water for drinking, water storage tanks and pipes with nozzles are recommended to reduce water consumption. Thirdly, farm management and attendance including corrals, staff, and document management are proposed as part of the master approach to swine production. The master approach to corral management should be to provide clean, dry, orderly housing, and should be cleaned and sterilize done to two times daily. Regarding staff management, a suitable ratio between personnel/swine is 1 person per 200 swine, together with 1 veterinary specialist. The documentation management of farms, including administration, productivity management, and product and by-product volumes should be developed for data backup and use. Lastly, sound environmental management of farms should be included in the master plan of swine management. All wastewater and feces produced should be collected and treated before environmental discharge. Biogas production systems are recommended as part of the waste management of swine farms, as they produce environmentally friendly energy from waste by-products. The reuse of solid waste in swine farm should be implemented.

Table 2. Eco-efficiency value of swine production

Indicators	Unit	Eco-efficiency value								
		Large Farm			Middle farm			Small farm		
		2011	2012	2013	2011	2012	2013	2011	2012	2013
Feed consumption	Ton/year	26,148.99	22,270.51	23564.67	12,868.14	14,060.16	16,802.43	7,269.69	8,716.32	11,759.55
Drug and vaccine consumption	ML/year	992.49	824.06	1008.67	999.33	1,098.99	1,322.49	460.15	558.26	773.48
Electricity consumption	Kwh./year	3,243.52	2,724.78	3,289.61	333.81	367.55	441.91	196.54	238.96	333.70
Water consumption	m ³ /year	327.12	272.64	332.15	1,046.05	1,150.09	1,379.83	2,468.17	2,985.72	4,103.77
Waste production	Yon/year	11,390.58	9,559.36	11,594.21	5,522.60	6,045.79	7,224.13	2,559.34	3,105.30	4,242.03
Greenhouse gas emission	Ton CO ₂ -eq/year	5,323.36	4,471.99	5,399.00	547.85	603.23	725.27	322.57	329.19	547.61

Table 3. Benchmarking of eco-efficiency for swine production

Indicators	Swine farms														
	A	B	C	D	E	F	G	H	I	J	K	L	M	N	O
Feed consumption (Baht/ton)	31147.90	2529.94	17973.95	2630.20	12011.69	3320.59	4038.11	3415.81	11262.90	19595.18	58159.70	12254.52	22495.51	38930.39	9846.50
Drug and vaccine consumption (Baht/ml)	2208.77	233.67	1095.81	182.83	332.71	713.06	700.29	888.17	1396.84	727.58	1960.98	1071.90	368.44	1499.96	2208.77
Electricity consumption (Baht/kwh)	1208.78	84.11	487.30	87.77	337.48	29.24	147.72	135.75	582.84	242.39	526.53	388.13	1781.87	1285.11	5642.25
Water consumption (Baht/m ³)	5594.65	729.10	14679.94	605.94	7649.04	5419.89	1511.32	1004.24	3513.56	5160.11	3851.03	791.61	7495.14	164.18	232.05
Waste production (Baht/ton)	11326.88	1090.28	6136.69	907.34	2300.12	2255.68	3783.69	1172.60	5433.88	6359.17	7429.58	6964.70	8340.94	7342.65	12998.90
Greenhouse gas emission Baht/tonCO ₂ -eq)	1983.88	138.05	799.77	144.04	553.89	3675.28	2680.97	220.80	956.57	397.82	864.15	637.00	2888.38	2109.16	9260.22

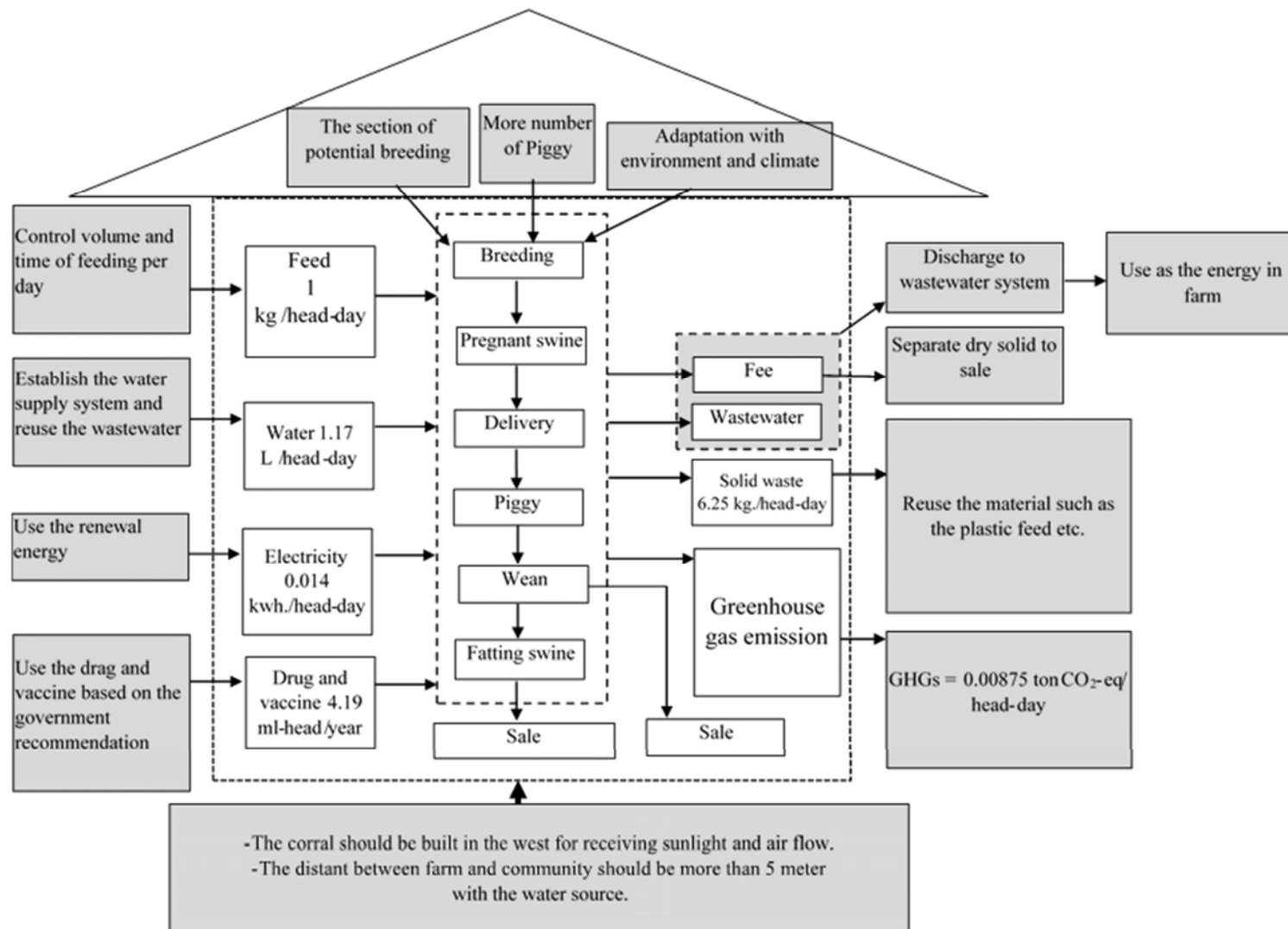


Figure 2. Master approach of swine production toward sustainable development

CONCLUSION

The research objective was to examine the sustainable performance of swine farm production in Thailand using joint eco-efficiency and benchmarking technique. A suitable measure of eco-efficiency values of swine production was developed and used to generate a questionnaire for collecting data on the economic and environmental performance of fifteen swine farms in Thailand. Consequently, eco-efficiency values and benchmarking were combined to identify best practices for a proposed master approach of sustainable swine production. The results showed an evident difference, as small and medium-size farms were concerned with water consumption, and large farms were most concerned with heating and cleaning issues. Then, joint benchmarking and eco-efficiency values were used to ascertain the best practices in swine production. These results identified that best practice attained 1.17 L/head-day water consumption, 0.014kWh/head-day electricity consumption, 0.00875 ton CO₂-eq/head-year greenhouse gas emission, and 6.25 ton/head-year waste production. Finally, best practice in breeding selection, husbandry management, farm management and attendance and the environmental management of farms were identified by material flow analysis, in-depth interviews and brainstorming, then included as part of the master approach to sustainable swine farm production.

ACKNOWLEDGEMENTS

This research was supported by The Thailand Research Fund (contract reference number RDG55520075).

REFERENCE

- [1] Rebolledo-Leiva R, Angulo-Meza L, Iriarte A, Marcela C. "González-Araya MC, Joint carbon footprint assessment and data envelopment analysis for the reduction of greenhouse gas emissions in agriculture production" *Sci Total Environ*, Vol 593-594, 2017, pp. 36-46
- [2] The Office of Agricultural Economics, "Agricultural product data (Swine). [Online]", Available: <http://www.oae.go.th/download/prcai/livestock/swine.pdf>. Accessed April 17, 2015 (in Thai), 2013.
- [3] Nuengjamnong C, Rachdawong P. "Performance analysis of the combined plug-flow anaerobic digester (PFAD) and upflow anaerobic sludge blanket (UASB) for treating swine wastewater in Thailand", *Thai J Vet Med*, 46(3), 2016, pp. 435-442.
- [4] Falguera, V, Aliguer N, Falguera M, "An integrated approach to current trends in food consumption: moving toward functional and organic products?", *Food Control*, Vol 26(2), 2012, pp. 274–281.
- [5] König A, Kuiper, H., Marvin HJP, Boon PE, Busk L, Cnudde F, Wentholt, "The SAFE FOODS framework for improved risk analysis of foods", *Food Control*, Vol. 21, 2010, pp. 1566–1587.
- [6] Styles D, Schoenberger H, Galvez-Martos JL, "Environmental improvement of product supply chains: a review of European retailers' performance", *Resour. Conserv. Recycl*, Vol. 65, 2012, 57–78.
- [7] Vázquez-Rowe I, Villanueva-Rey P, Moreira, MT, Feijoo G, "The role of consumer purchase and post-purchase decision-making in sustainable seafood consumption. A Spanish case study using carbon footprinting", *Food Policy*, Vol. 41, 2013, pp. 94–102.
- [8] World Business Council for Sustainable Development (WBCSD), "Eco-efficiency: Creating more value with less impact", WBCSD, Geneva, 2000.
- [9] Kulak M, Nemecek T, Frossard E, Gaillard G, "Eco-efficiency improvement by using integrative design and life cycle assessment. The case study of alternative bread supply chains in France", *J Clean Prod*, Vol 112, 2016, pp. 2452-2461.
- [10] Iribarren D, Hospido A, Moreira MT, Feijoo G, "Benchmarking environmental and operational parameters through eco-efficiency criteria for dairy farms", *Sci Total Environ*, Vol 409, 2011, pp. 1786–1798.
- [11] Lorenzo-Toja Y, Vázquez-Rowe I, Amores M, Termes-Rifé M., Marín-Navarro D, Moreira MT, Feijoo G, "Benchmarking wastewater treatment plants under an eco-efficiency perspective", *Sci Total Environ*, Vol 566-567, 2016, pp. 468–479.
- [12] National Round Table on the Environment and the Economy (NRTEE), "Calculating eco-efficiency indicators: A workbook for industry", Renouf Publishing Co.Ltd. ON, Canada, 2001.
- [13] Ounsaneha W, Rattanpan C., "Defining the eco-efficiency of rubber glove products manufactured from concentrated latex in Thailand", *Environ Prog Sustain Energy*, Vol 35(3), 2016, 803-808.
- [14] Vu TKV, Tran MT and Dang TSS., "A survey of manure management on pig farms in Northern Vietnam", *Livestock Science*, Vol. 112, 2007, pp. 288–297.

EVALUATION OF ATTENUATION OF ULTRASONIC DURING PROPAGATION THE AIR TO MEASURE CONCRETE SURFACE ROUGHNESS BY THE AERIAL ULTRASONIC SENSOR

NAGAOKA Seiya¹, ISLAM Mohammad Raihanul², OKAJIMA Kenji¹, ISHIGURO Satoru¹, ITO Ryoei¹,
WATANABE Ken³ and ITO Tetsu⁴

¹Graduate school of Bioresources, Mie University, JAPAN

²Department of Farm Structure and Environmental Engineering, Bangladesh Agricultural University, Bangladesh

³Maruei concrete industry Co., Ltd., JAPAN

⁴X-ability Co., Ltd., JAPAN

ABSTRACT

Japan has possessed main concrete agriculture irrigation canals that are total length of about 50,000km. These canals are becoming deterioration over time. Therefore concrete surface of canals have been becoming rough. One method of the roughness measurement is using the aerial ultrasonic sensor. However previous research have been not study about attenuation of ultrasonic during propagation the air using the 42 kHz sensor. The purpose of this study were to evaluate attenuated value of the ultrasonic wave and to correct attenuated value of the ultrasonic wave. Reflected wave of the aerial ultrasonic was measured under the different condition of temperature, humidity and atmospheric pressure with smooth board and roughness board. These were compared measurement value and correction value by ISO9613-1 equation. The relative error of correction value was smaller than measurement value. The result of this study reveal that correction using ISO9613-1 equation for attenuation of ultrasonic wave 42 kHz is effective method.

Keywords: attenuation of aerial ultrasonic, ISO9613-1, concrete surface roughness, aerial ultrasonic sensor

INTRODUCTION

Japan has possessed many concrete irrigation canals mainly used for agriculture that have a total length of 49,239 km. Including lateral canals are about 400,000 km. These canals were constructed since the high economy era of 1954 - 1973 and became too old for work. Reconstruction of canals costs too huge. The government are necessary to be repaired old canals, on other word, they were promoting policy "stock management" in japan. Stock management mean to improve the life of the facility by appropriate inspection.

The concrete surface of canal is worn out by flow-water and flow-sand, and become rough. The roughness of concrete surface causes decline of the water flow function. If canals become decline of the water flow function, causes decreasing the flow velocity and raising the water level. As a result, irrigation water will not reach the end of some lateral canals. However, method of measurement roughness concrete surface of irrigation canals has not been established yet. Roughness of concrete surface is generally by arithmetical mean roughness (ISO 25178).

Over the years, considerable attention has been paid to the study of measurement of the arithmetical mean roughness. Scientists are proposed the

following methods to measure the arithmetical mean roughness.

Sand patch test: This method is one of the most commonly methods used for examination of macrotexture depth of concrete surfaces. This direct volumetric method consists in careful application of a given volume of granular materials (a glass spheres or sand) of given granulometry onto surface and subsequent measurement of the total area covered. The sand patch test is exposed to a greater probability of human error; it is a test that cannot be performed quickly without comprising accuracy [1], [2].

Concrete Surface Profiles: This method is based on the visual inspection of the prepared surface, being this compared with nine standard Concrete Surface Profiles (CSP) of increasing roughness [3].

Outflow Meter: This is a volumetric method used to assess the surface roughness of asphalt and concrete road pavements. The method gives an average value for the surface roughness but no other additional information [1], [4].

Moulage gauge Method: This method is possible to measure the arithmetical mean roughness. This is the simple measurement method, since managers' only pushes the moulage gauge to the concrete surface. However, managers need complication analysis that read displacement from one by one the moulage gauge [5], [6].

Laser Displacement Sensor Method: This method is possible to measure the arithmetical mean roughness. Measurement range of this method is line information of the concrete surface. This method is high precision, but high price to measure irrigation canal [7], [8].

Aerial ultrasonic sensor: This method is possible to measure the arithmetical mean roughness. This was developed by the authors. The frequency was used 42 kHz. Measurement range from 1000 mm can measure diameter 600 mm and from 550 mm can measure diameter 300 mm. This sensor uses to be bought about 25 \$, therefore this is economical to measure canals [10].

Method of the aerial ultrasonic sensor is economical, wide range and simple. However, the amount of the aerial ultrasonic wave during propagation an air is declined by wind velocity over 6 m/s. In the similar, the authors considered that the aerial ultrasonic wave during propagation an air is caused attenuation under different atmosphere condition. The theory of this phenomenon is defined by ISO9613-1 [11]. However, the applicable range of the frequency is defined 50 Hz to 10 kHz. Therefore, the authors have been used sensor 42 kHz is over range in ISO9613-1. Further there is no study focus on reflected wave. The attenuation of the aerial ultrasonic is problem to measure roughness of concrete surface. It is reason that the measurement value change under different condition. The purpose of this study were to evaluate attenuated value of the ultrasonic wave and to correct attenuated value of the ultrasonic wave.

MATERIALS AND METHOD

Aerial Ultrasonic Sensor

The LZ-Maxsonar-EZ1 (MaxBotic, Inc) was used as the aerial ultrasonic sensor. The sensor is designed the ultrasonic range finder. Frequency was selected 42 kHz. Sensitivity of the open type (the sensitivity: min. -80.5dB) and the waterproof type (the sensitivity: min. -58.2dB) were compared. The open type has 13 times higher sensitivity than the waterproof type at each output voltage. So, the open type was selected. But measurement of the aerial ultrasonic wave must limit not to get wet. Other specification shows Table 1. The aerial ultrasonic sensor was attached the horn. The horn was attached due to increase the sound of the aerial ultrasonic. It was made of resin and was made by 3D printer. The Fig.2 shows an example with the horn attached sensor. Measurement value was acquired by the digital oscilloscope TBS1152 (Tektronix, Inc).

Table 1 Specification of the aerial ultrasonic sensor

Frequency	42	kHz
dimension	A	16.4 mm
	B	15.5 mm
	C	19.9 mm
	D	22.1 mm
weight	4.3	grams

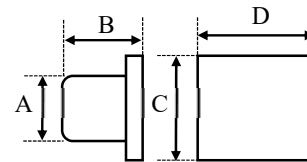


Fig. 1 The aerial ultrasonic sensor



Fig. 2 The horn attached and this size

Thermometer and Hygrometer

The TR-73U and TR-72wf-H (T&D Corporation, Inc) was used as the thermometer and hygrometer. Measuring range of the thermometer is -30 to 80°C, and the hygrometer is 0 to 99 humid. These sensors can record internally and send it to PC with USB connection.



Fig. 3 TR-72wf-H

Concrete Board

The concrete board was made for this experiment by the cooperation of the Maruei concrete industry Co., Ltd. The size of this board is length 700 mm, width 700 mm, height 50 mm. The weight of this board is 45 kg. We prepared two types of roughness. First type of arithmetical mean roughness was 0.04 mm. The condition of concrete surface is smooth. In this study, first type was called smooth board. Second type of arithmetical mean roughness was 1.04 mm. The condition of concrete surface is roughness. In this study, second type was called roughness board.

Experiment Method

Measuring materials was set as Fig.4. The aerial ultrasonic sensor was set 1000 mm height from concrete board. The hygrothermograph was set 0 mm and 500 mm height from concrete board. The ultrasonic data was acquired under different condition of temperature and humidity. We got measurement value of reflected wave, temperature, humidity and air pressure. The measurement value was voltage mV of peak to peak of reflected wave. The roughness of concrete was estimated by the measurement value of reflected wave. Preceding study (2016) showed between the measurement value and roughness of concrete [10].

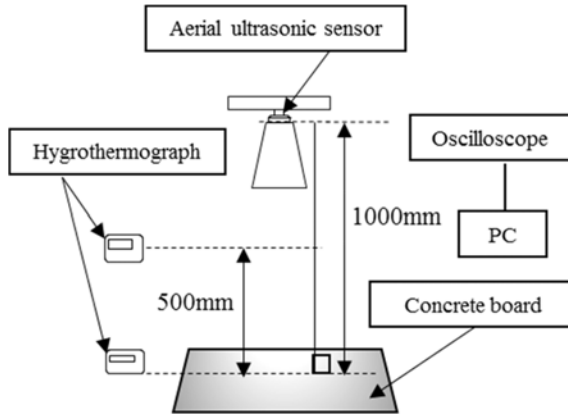


Fig.4 Experiment system

THE ATTENUATION OF ULTRASONIC DURING PROPAGATION THE AIR

The Attenuation of sound during propagation the air has been to be standardized by ISO 9613-1 at 1993. This standard aims noise problems about urban environmental noise and airplane noise. This standard specifies an analytical method of calculating the attenuation of sound as a result of atmospheric absorption for a variety of meteorological conditions when the sound from any source propagates through the atmosphere the air. Absorption of sound through the air is due to shear viscosity, thermal conductivity

or heat dissipation, and molecular relaxation due to oxygen, nitrogen, and water vapor vibrational, rotational, and translational energy. The attenuation of sound varies significantly with temperature, water vapor content and frequency. The range of the standard specifies is as follows.

- Frequency from 50 Hz to 10 kHz
- Temperature from -20°C to +50°C
- Relative humidity from 10% to 100%
- pressure of 101,325 kPa (one atmosphere)

Equation are provided for wider ranges suitable for particular, however frequency 42 kHz of using the aerial ultrasonic is over range.

Symbols

- F : Frequency of the sound, in hertz
- h : Molar concentration of water vapour, as a percent
- p_r : Reference ambient atmospheric pressure, in kilopascals
- p_i : Initial sound pressure amplitude, in pascals
- p_t : Sound pressure amplitude, in pascals
- p_a : Ambient atmospheric pressure, in kilopascals
- s : Distance, in metres, through which the sound propagation
- T : Ambient atmospheric temperature, in kelvins
- T_0 : Reference air temperature, in kelvins
- α : Pure tone sound attenuation coefficient, in decibels per metre, for atmospheric absorption

Calculation

The equation (1) is basic equation of attenuation. The sound pressure p_t is exponentially attenuated from the sound pressure p_i by absorption in the air.

$$p_t = p_i \exp(-0.1151 \alpha s) \quad (1)$$

The attenuation of pressure level δL is described using coefficient α and distance of propagation in the air.

$$\delta L = 10 \log \left(\frac{p_i^2}{p_t^2} \right) = \alpha s \text{ [dB]} \quad (2)$$

$$\alpha = 8.686 f^2 \left(\left[18.4 \times 10^{-11} \left(\frac{p_a}{p_r} \right)^{-1} \left(\frac{T}{T_0} \right)^{\frac{1}{2}} \right] + \left(\frac{T}{T_0} \right)^{-5/2} \times \left\{ 0.01275 \left[\exp \left(\frac{-2239.1}{T} \right) \right] \left[F_{rO} + \left(\frac{F^2}{F_{rO}} \right)^{-1} \right] + 0.1068 \left[\exp \left(\frac{-3352.0}{T} \right) \right] \left[F_{rN} + \left(\frac{F^2}{F_{rN}} \right)^{-1} \right] \right\} \right) \quad (3)$$

$$m = \alpha / (20 \log_{10} e) \text{ [1/m]} \quad (4)$$

The attenuation is the function of the relaxation frequency of molecular oxygen F_{rO} and the relaxation frequency of molecular nitrogen F_{rN} .

$$F_{rO} = \left(\frac{p_a}{p_r}\right) \left(24 + 4.04 \times 10^4 h \frac{0.02+h}{0.391+h}\right) \quad (5)$$

$$F_{rN} = \left(\frac{p_a}{p_r}\right) \left(\frac{T}{T_0}\right) - \frac{1}{2} \left[9 + 280h \exp \left\{ -4.170 \left[\left(\frac{T}{T_0}\right)^{-\frac{1}{3}} - 1 \right] \right\} \right] \quad (6)$$

The h is molar concentration of water vapor in percent. The h is calculated from the relative humidity as follows.

$$h = p_{s0} \left(\frac{h_r}{p_s}\right) \left(\frac{p_{sat}}{p_{s0}}\right) [\%] \quad (7)$$

$$p_{sat} = p_{s0} \times 10^{-6.8346 \left(\frac{T_{01}}{T}\right)^{1.261} + 4.6151} \quad (8)$$

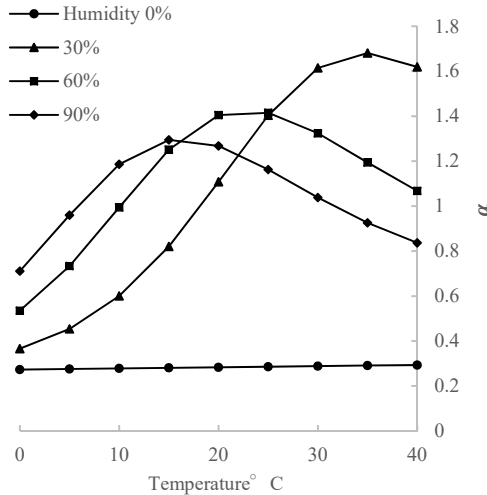


Fig.5 Relation between α and temperature

RESULTS AND DISCUSSION

Measurement Result of Attenuated Ultrasonic Wave

The Fig.6 and Fig.7 shows 71 data under different atmosphere condition. Since the aerial ultrasonic sensor can't measure with rainy weather, the data were acquired mainly with fine weather.

The measurement value was acquired using the aerial ultrasonic with smooth board and roughness board. The measurement value was the peak to peak of reflected wave and was calculated 15 times average. Since the measurement value depended on the temperature, the temperature was taken on the horizontal axis.

The Fig.8 and Fig.9 show that the measurement value was fluctuated by attenuation. When

temperature of atmosphere was under 20°C, attenuation tended to be small. When temperature of atmosphere was over 20°C, attenuation tended to be large. The Fig.6 and Fig.7 shows that when the temperature was over 20°C, the humidity was under 60%. The Fig.5 shows that when the humidity is low, the attenuation coefficient α tend to increase as the temperature increase. There is no research that the phenomenon changes with boundary of 20°C. It is considered to be the relationship between humidity, atmospheric pressure and features of sensor.

The slope of approximation with smooth board is larger than roughness board. It was because the measurement value of smooth board was large than the measurement value of roughness board.

The attenuation rate of change was investigated to due to difference in roughness of concrete. The reference temperature was set to 20° C, and the rate of change was calculated by equation (9). The Fig.10 shows the rate of change was similar between smooth board and roughness board. So the degree of the roughness is not related to the amount of the attenuation of the aerial ultrasonic.

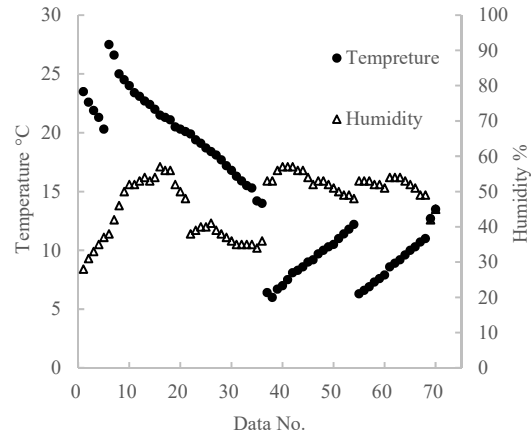


Fig. 6 Atmosphere condition with smooth board

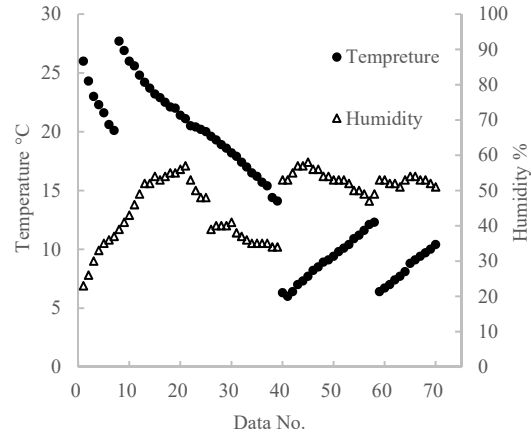


Fig. 7 Atmosphere condition with roughness board

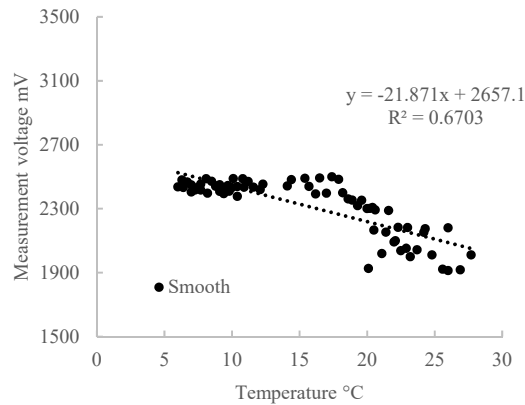


Fig. 8 Measurement data using the aerial ultrasonic with smooth board

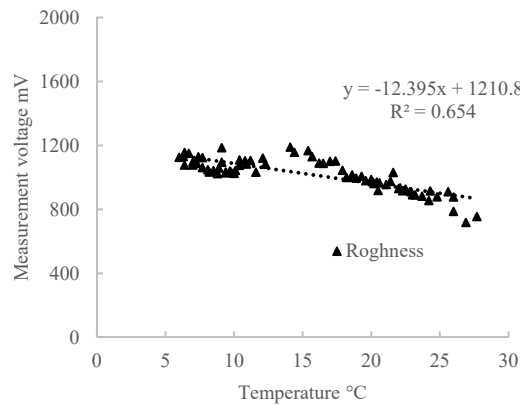


Fig. 9 Measurement data using the aerial ultrasonic with roughness board

$$r = \frac{\text{Measurement Voltage (mV)}}{\text{Ave}_{20} \text{ (mV)}} \quad (9)$$

r : Rate of change, Ave_{20} : Average voltage mV at temperature $20 \pm 0.5^\circ\text{C}$

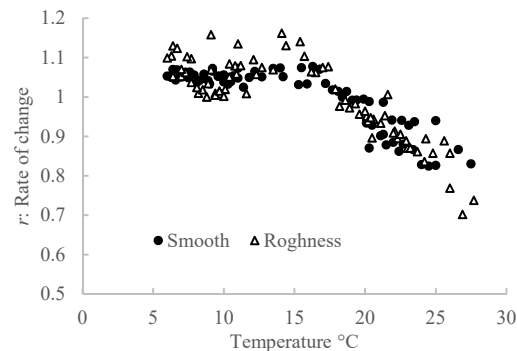


Fig. 10 Relation between rate of change and temperature with smooth board and roughness board

Correction Result of Attenuated Ultrasonic Wave

The Attenuated ultrasonic wave was corrected by ISO9613-1 equation (10). The correction voltage V_0

become approach initial voltage. Fig.11 and Fig.12 shows that the slope of approximation with the correction value become small. This phenomenon was also similar with the roughness board. The relative error was calculated. The theoretical value was taken as the average of all. Table 2 shows that the relative error of the correction value was less than half of the measurement value. This result shows that correction data did not depend on atmosphere condition. However, when it was temperature over 25°C , the correction value tended to become small.

$$V = V_0 \exp(-ms) \quad (10)$$

V : Measurement value mV, V_0 : Correction value mV

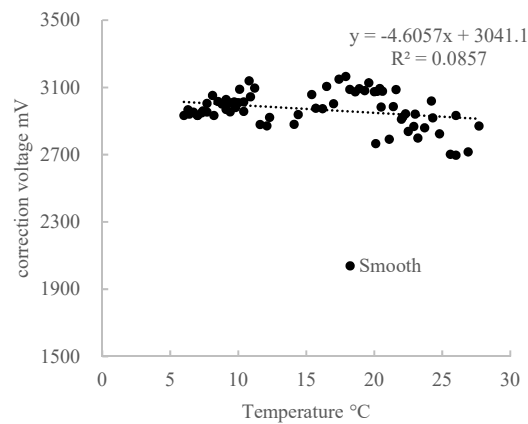


Fig. 11 Correction data by equation ISO9613-1 with smooth board

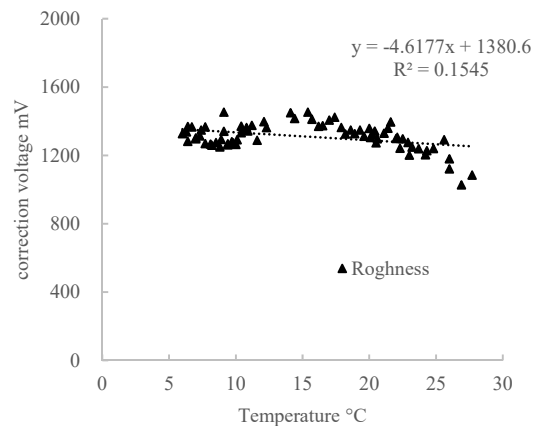


Fig. 12 Correction data by equation ISO9613-1 with roughness board

Table 2 Compare correction value and measurement value with relative error

	Correction value	Measurement value
Average of all mV	2970	2319
Relative error %	2.7	6.4

CONCLUSION

The measurement value was measured using the aerial ultrasonic sensor with 71 data under different atmosphere condition. The measurement value was fluctuated by attenuation. The measurement value depended on the temperature. The attenuation increased at boundary of 20°C. The degree of the roughness is not related to the amount of the attenuation of the aerial ultrasonic.

The measurement value was corrected using ISO9613-1 equation. The slope of approximation with the correction value was smaller than the measurement value. The relative error of the correction value was less than half of the measurement value.

The result of this study reveal that correction using ISO9613-1 equation for attenuation of ultrasonic wave 42 kHz is effective method.

ACKNOWLEDGEMENTS

This study is funded by the Ministry of Agriculture, Forestry and Fisheries, Japan.

REFERENCES

- [1] ASTM E 2380, Standard test method for measuring pavement texture drainage using an outflow meter, West Conshohocken (PA) ASTM International, 2005.
- [2] Courard L, Garbacz A, Bissonnette B, Topography evaluation methods for concrete substrates: parametric study, International Congress on Concrete Repair, Rehabilitation and Retrofitting, 2012.
- [3] Pedro M.D. Santos a, Eduardo N.B.S. Júlio, "A state-of-the-art review on roughness quantification methods for concrete surfaces", Construction and Building Materials, 2013, 38 , pp. 912-923.
- [4] Mokare D, Use of the digital surface roughness meter in Virginia, Research Report VTRC 07-R4, Virginia Transportation Research Council, 2006.
- [5] Kitamura K, Honma S and Kato T, Quantitative Evaluation for Forecast of Irrigation Canal Abrasion, J of Water, Land and Environmental Engineering , Vol 76, No. 9, 2008, pp. 823-828.
- [6] Kawakami A, Asano I, Mori M, Kawabe S and Tokashiki M, Abrasion measurement method Using a Profile Gauge, journal of irrigation, drainage and rural engineering, No.1, Vol.85, 2017, pp. 77-84.
- [7] Nakaya T, Tokashiki M, Mori M and Mori T, Estimation of the Coefficient of Roughness from Surface Characteristics of Abraded Concrete Channel, journal of irrigation, drainage and rural engineering, No. 258, 2008, pp. 501-506.
- [8] Uchida K, Ishida M and Ogawa S, Estimation of the Coefficient of Roughness for Irrigation Canals by Transcription Method for Concrete Surface, presented at JSIDRE, 2008, pp. 432-433.
- [9] Tokashiki M, Studies on Erosion Mechanism and Accelerated Erosion Test of Concrete Irrigation Canal, Bull. Natl. Inst. Rural Eng. Japan, Vol. 52, 2013, pp. 1-57.
- [10] Okajima K, Nagaoka S, Ishiguro S, Ito Ryoei, Watanabe K and Ito Tetsu, Measurement of the Roghness of the Concrete Surface by the Peak to Peak Value of the Aerial Ultrasonic Wave, J of Water, Land and Environmental Engineering, Vol. 84, No. 3, 2016, pp. 233-240.
- [11] ISO9613-1, Acoustics of sound during propagation outdoors-Part 1 : Calculation of the absorption of sound by the atmosphere, 1993.
- [12] Yhoshihisa K, Calculation of the Absorption of Sound by the Atomosphere (ISO9613-1), The Institute of Noise Control Engineering of Japan, Vol. 21, No. 3, 1997, pp. 130-135.

A STUDY OF PUBLIC OPINION ON GREEN SPACES USING DATA FROM FREE-TEXT DESCRIPTIVE RESPONSES - A CASE STUDY OF REGIONAL CITY IN JAPAN -

Shinya Tsukada¹ and Tetsuo Morita²

¹Maebashi City Office, Japan, ²Maebashi Institute of Technology, Japan;

ABSTRACT

The present study analyzed public opinion data from free-text descriptive responses obtained by administering a questionnaire on green spaces to local residents. Maebashi City, the capital city of Gunma Prefecture, was selected as the subject for the study. Maebashi is a standard-sized city in Japan, thus the opinions of its residents can be analyzed and compared to other standard-sized cities. The present study adopted a text mining method for analysis. Text mining can discover the characteristics of words and examine the relationships between words in a large amount of text data objectively and quickly. By exploring the residents' thoughts on green spaces using the data from their free-text descriptive responses, the present study extracted problems with existing green spaces from the viewpoint of the public.

Keywords: Text data, Text mining, Tract, Image

INTRODUCTION

Background

At present, depopulation, low birthrates, aging citizens, and decreased financial resources are serious social problems in Japan, and the appropriate development, maintenance, and management of urban facilities are urgently required. To deal with these social problems and related requirements, new policies on green and open spaces contain strategies to enhance the stock effects of nature spaces, to accelerate the cooperation between the government and private sectors, and to make further use of urban parks.

Social situation

To this end, the Ministry of Land, Infrastructure, Transport and Tourism published an interim summary of the "Review Meeting for the Nature of Urban Parks Corresponding to Urban Management of a New Era." This summary contains three main points.

First, in this new era, green and open spaces that help support cities, including urban parks and private gathering places, must be strategically secured and used.

Second, the multifunctional properties of urban parks must be advertised and exhibited using cooperation between the government and private sectors in order to draw on the power of individual towns and citizens.

Finally, a new framework must be constructed in which the quality of urban parks can be improved through this collaboration between the government

and the private sector, including a wide range of entities such as local councils to support flexible urban park management.

SUTUDY AREA AND STUDY METHODS

Position of this study

Maebashi City, which is a study area, is shown in Fig. 1. Maebashi City is the prefectural capital of Gunma Prefecture, with a population of 340,000 people and a local city located about 100 km from Tokyo. In Maebashi City, motorization is progressing even among local cities, and Maebashi City is studying toward realization of compact city.

Maebashi is a standard-sized city in Japan, thus the opinions of its residents can be analyzed and compared to other standard-sized cities.

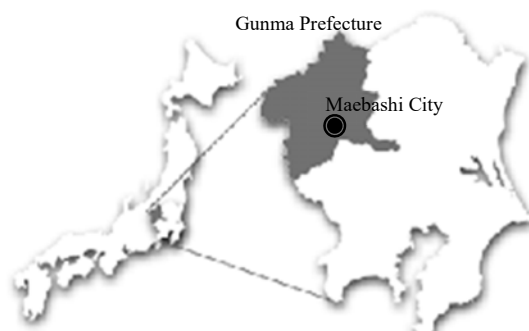


Fig. 1 Location of Maebashi City

Table 1 Details regarding the questionnaire survey

Date of survey	- Distribution: October 14-16,2015 - Collection: October 31,2015
Data collection	Maebashi city area Gunma Prefecture
Data collection method	- Distribution: putting mail box - Collection: Mailing
Question	Please enter your thoughts about the green spaces surrounding you, and your opinions and desires regarding Maebashi City's future policies on green spaces, parks, and street trees. in Maebashi-area (free answer)
Distribution and collection	- Number of questionnaire cards distributed: 1,500 - Number of questionnaire cards collected: 402 - Recovery: 26.8%

Overview of the study

We will review the existing studies related to this study. There are many studies on the quality of life given by green. Morita, Kogure, Sugita, Baba, Tsukada and Miyazato [1] focus on the environment of the water and green for Maebashi City, and evaluate the quality of life. In addition, Tsukada, Morita and Yuzawa [2] analyzed the Relationship between consciousness and environment including water and green of the Tenguiwa-Irrigation in Maebashi City.

There are also many that analyzed free text data as a similar study. Text data must be processed using a particular method so that the data can be analyzed objectively and quantitatively. The field of natural language processing has developed specific software for text mining. As the text mining method can objectively extract important trends in words from statements and free-text descriptive responses, this method has been used in previous studies.

Sasaki, Maruishi [3] studied about Traffic Policy towards the introduction for Fuji-yoshida City, Yamanashi Prefecture. Sasaki attempted to visually analyze public opinions using statements made in workshops transformed into text data.

Kobayashi, Terada and Sato [4] analyze residence selection behavior based on resident preference of residential attribute in for Saiki City, Ooita Prefecture. Kobayashi applied the text mining method to free-text descriptive responses obtained via a questionnaire to analyze the problems peculiar to a local community.

Purpose and method of this study

The present study analyzed public opinion data from free-text descriptive responses obtained by administering a questionnaire on green spaces to local residents, and evaluate the quality of life.

The present study adopted a text mining method for analysis. Text mining can discover the characteristics of words and examine the relationships between words in a large amount of text data objectively and quickly.

By exploring the residents' thoughts on green spaces using the data from their free-text descriptive responses, the present study extracted problems with existing green spaces from the viewpoint of the public. Comparing the problems identified by the study with those recognized by an administrative organization allowed the present study to better examine future policies regarding green spaces.

KH Coder software

The present study used KH Coder software, the technical information of which has been published and which has been used for several existing papers. A morphological analysis function has been incorporated into this software.

Morphological analysis is an operation to divide a statement or a sentence into minimal units that have a syntactic function, and to discriminate each part of speech. This is used instead of artificial data processing to analyze data objectively.

In the present study, we conducted a questionnaire survey on the Table 1. The present study analyzed free-text descriptive answers to the question, "Please enter your thoughts about the green spaces surrounding you, and your opinions and desires regarding Maebashi City's future policies on green spaces, parks, and street trees".

The responses were encoded as text data and then analyzed in order to understand the image that the residents have of green spaces, and evaluate the quality of life.

The initial questionnaire on green spaces was administered by the Maebashi Institute of Technology on October 16, 2015, in which 1,500 questionnaires were randomly distributed to households in Maebashi City. 402 completed surveys were collected by mail. The present study analyzed 181 samples, in which the free-text descriptive responses were examined as text data.

RESULTS AND DISCUSSION

Result of extracted words

The present study examined free-text descriptive responses regarding green spaces, obtained from residents via questionnaire and analyzed as text data.

The researcher performed morphological analysis on the data and created a list of top 50 words with higher frequencies of appearance (Table 2).

Of the nouns and adjectives extracted from these responses, “park” (first place, Fig.2), “suppose” (second place), “greenery” (third place), “roadside tree” (fourth place, Fig.3), “management” (fifth place), “environment” (sixth place), “Maebashi” (seventh place), “many” (eighth place), “tree” (ninth place) and “construction” (tenth place), all symbols of greenery in cities, were the most common.



Fig. 2 Small scale-park, Maebashi-city



Fig. 3 Roadside-tree, Maebashi-city

Table 2 Result of extracted words

No	Extracted Ward	Frequency
1	Park	102
2	Suppose	80
3	Greenery	68
4	Roadside tree	43
5	Management	35
6	Environment	30
7	Maebashi	28
8	Many	26
9	Tree	26
10	Construction	24
11	Road	24
12	Maintenance	21
13	Good	21
14	Near	19
15	Place	19
16	Necessary	18
17	Rose	17
18	Child	17
19	People	17
20	Plant	16
21	Cleaning	15
22	Resident	15
23	Nature	14
24	Tree and shrubs	14
25	Can	14
26	Urban	13
27	Feel	13
28	Cut	13
29	Think	12
30	Few	12
31	Increase	12
32	District	12
33	Flower	11
34	Do	11
35	Go	10
36	Walk	10
37	City	10
38	Citizen	9
39	Live	9
40	Very	9
41	Absent	9
42	Greening	9
43	Beautiful	8
44	Advanced age	8
45	Surroundings	8
46	Housing	8
47	Grass	8
48	Money	7
49	Refuse	7
50	Bad	7

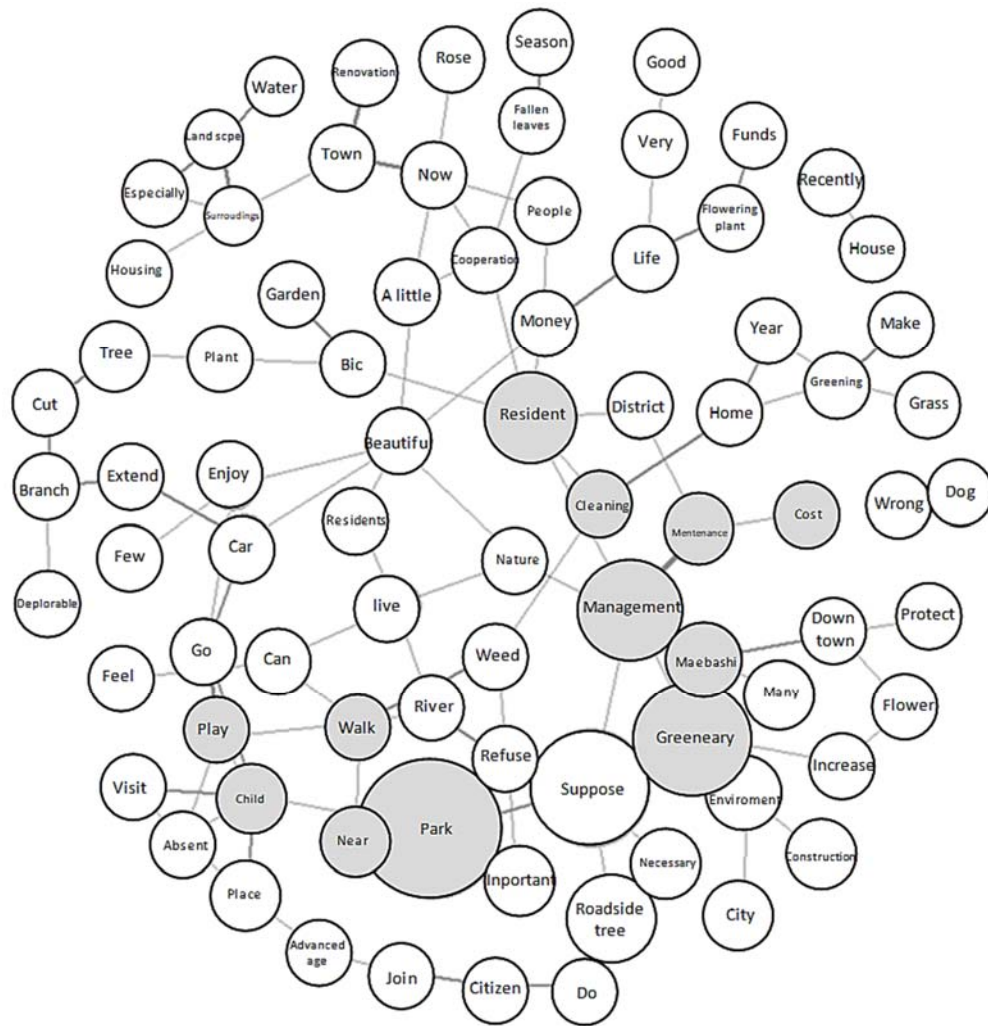


Fig. 4 Co-occurrence network

Result of Co-occurrence network

It was revealed that the residents were more interested in having parks and street trees installed and managed by the public sector rather than in greenery kept on private land. Since “environment,” “Maebashi,” and “many” were extracted in sixth, seventh, and eighth place, respectively, the residents were revealed to feel that the environment of Maebashi City is rich in greenery.

To understand the residents' opinions on green spaces in detail, a co-occurrence network diagram was created using KH Coder, which visually expressed the correlations between words that appeared in the responses.

From this diagram, the rough groups “concerning the use of green spaces” and “concerning the maintenance and management of green spaces” were

created.

First, the group “concerning the use of green spaces” was strongly connected with the words “walk,” “near,” “child,” and “play,” centering on “park.” The trends of these words revealed that the situation of using a park, such as “I can walk in a nearby park,” and the desire for a park, such as “there is no place for my child to play in a nearby park,” were related.

Next, the group “concerning the maintenance and management of green spaces” was strongly connected with the words “management,” “maintenance,” “cleaning,” “resident,” and “cost,” centering on “greenery.” By studying the tendencies of these connections, the desire for maintenance and management of greenery was extracted as, “resident participation and costs are required to maintain and manage abundant greenery in Maebashi City.”

CONCLUSION

The results obtained in the present study can be summarized as follows:

- (1) The present study administered a questionnaire on greenery in Maebashi City, used free-text descriptive responses obtained in the survey as text data, applied the text mining method to the text data, and perform morphological analysis of the residents' opinions on green spaces expressed by word choices in the responses.
- (2) When the residents' opinions on green were visually analyzed using a co-occurrence network diagram, the groups "concerning the use of green spaces" and "concerning the maintenance and management of green spaces" were extracted. Subsequently, opinions such as "there is no place for my child to play in a nearby park" and "resident participation and costs are required to maintain and manage abundant greenery in Maebashi City" were extracted.
- (3) These opinions of the residents were related to political issues, which administrative organizations have attempted to address themselves. Words related to the development of dog runs and the management of greenery by community residents appeared in the minority of responses.

The whole parks in Maebashi City is obsolete and needs renovation. Meanwhile, due to the population decrease and aging, the financial situation of Maebashi City will be severe.

Thus, I think that highly efficient collection is necessary. I think that it will be a new tool to support

quality of life and renovation of parks for the citizen. As mentioned above, the present study will be able to reflect public opinions on the development of parks.

By exploring the residents' thoughts on green spaces using the data from their free-text descriptive responses, the present study extracted problems with existing green spaces from the viewpoint of the public.

REFERENCES

- [1] Tetsuo Morita, Yoshihito Kogure, Hiroshi Sugita, Tsuyoshi Baba, Shinya Tsukada and Naoki Miyazato, "A Study on Evaluation of Quality of Life in Consideration of Water/Green Environment", International Journal of GEOMATE, Vol. 2, No. 2, 2012, pp. 241-246.
- [2] Shinya Tsukada, Tetsuo Morita and Akira YUZAWA, "STUDY ON ASSESSING THE VALUE OF THE TENGUIWA IRRIGATION CANAL, International Journal of GEOMATE, Vol. 10, Issue 22, 2016, pp. 2007-2010.
- [3] Kuniaki Sasaki, Kouichi Maruishi "Summarization and Visualization characteristics of a Workshop Discussion using Text Mining Method", Journal of Japan City Planning Review, 43(6), 20011, pp. 1039-1044.
- [4] Yuji Kobayashi, Akinobu Terada and Seiji Sato, "ANALYSIS OF FREE ANSWER IN QUESTIONNAIRE SURVEY AND EVALUATION OF LIVING ENVIRONMENT BY TEXT MINING", Architectural Institute of Japan, Vol. 77(671), pp.85-93, 2012.

IMPACT OF AGRICULTURAL WATER ALLOCATION ON THE ECOSYSTEMS IN THE INNER NIGER RIVER DELTA

*Barry Kassambara¹, Homayoon Ganji¹ and Takamitsu Kajisa¹

¹Graduate school of Bioresources, Mie University, Japan

ABSTRACT

The Sahel, a transition zone between the humid tropics and the great desert of northern Africa, faces major challenges regarding the survival of its human population and the preservation of its ecosystems. The Niger River, whose source is in Guinea and which crosses much of the Sahel, is a lifeline for humans and biodiversity. Over the past three decades because of climate change and population increase, the inhabitants of the Sahel are witnessing a significant reduction in resources, particularly in the Inner Niger Delta. The main water intake from this river in Mali is the Markala dam, which is located upstream of the Inner Niger Delta. This dam irrigates 118,000 ha of paddy fields and 16,276 ha of sugar cane fields. During the dry season (December - May) some of the paddy fields are used for double cropping (paddy, vegetable etc.). In the recent years, because of the government's policy of developing irrigated agriculture particularly on the land of Office du Niger, a sustained rate of expansion has been seen with an average of 5,000 ha of new land irrigated for agriculture each year. This expansion of agriculture, poor management of water resources, and reduction of the river's hydrologic regime downstream are limiting factors in achieving food self-sufficiency and conservation of the wetland ecosystem in the Inner Niger Delta. The delta covers an area of 41,800 km² with a total catchment area of 130,000 km². In 1987, this Delta was selected as a Ramsar Site because of its wealth of waterfowl.

Key words: Office du Niger, Niger River, Inner Delta, Water Allocation, Irrigation, Ecosystems

INTRODUCTION

The republic of Mali is a landlocked country in West Africa. It is the eighth-largest country in Africa, with an area of 1,241,190 km² and a population of approximately 16.8 million (2013). According to the UNDP¹ report (2015) 50.6% of the population lives below the income poverty line (\$1.25/day) and 10.8% are near multidimensional poverty [1]. With 80% of its population engaged in agricultural activities, this sector is the cornerstone of Mali's economy and shows great potential to drive economic growth. Over 31% of the population is exposed to food insecurity [2] and only 7% of 43.7 million hectares arable land is currently cultivated. Potential irrigable lands that are currently developed correspond to 2.2 million hectares or 14% of the total [3].

The landlocked territory of Mali is very close to the Tropic of Cancer and as result, it has a tropical climate. Mali has distinct periods of summer and winter with three main seasons. Average temperatures range between 24 and 32°C. During the last 50 years, the average temperatures have increased significantly. The annual rainfall is approximately 1400 mm in the south, 1120 mm at Bamako, and 127 mm in the northern part of the country. Central Mali (where

Office du Niger and Inner Delta are located) receives most of its rainfall between June and August.

Around half of Africa's total wetland area comprises floodplains. These include famous large-scale examples that cover several thousand square kilometers such as the Inner Niger Delta in Mali, the Okavango Delta in Botswana, the Sudd of the Upper Nile in Sudan and the Kafue Flats in Zambia [4].

Beyond the town of Ségou, the Niger River forms a vast inland delta (41,800 km²). It joins with its main tributary the Bani at Mopti then forms several lakes. The watershed area of this Inner Delta covers 130,000 km².

The vast majority of the Inner Niger Delta ecosystems are in a state of continuous degradation due to climate change and anthropogenic activities. The rapid expansion of irrigation upstream in the area of Office du Niger (mainly due to paddy and sugar cane production) has had a significant impact on the availability of water resources in the Niger River and associated delta.

To address this problem, this investigation analyzes the historical variation of the Niger River hydrology and the evolution of irrigation areas and crop patterns in Office du Niger. As a result of this analysis, it is hoped that a solution to save water resources and to

¹ United Nations Development Program

overcome the reduction in the floodplain of Inner Niger Delta can be proposed.

ANALYSIS

Climate conditions

The 1960s coincided with a period of increased rainfall. However, during 1970s and 1980s a large rainfall deficit was recorded and this corresponded to a great drought in the Sahel countries. Sahel rainfall has been linked to Atlantic as well as Mediterranean SSTs via evaporation rate and supply of moisture (Giannini et al., 2003; Rowell, 2003). Recently, the variability of rainfall in the Inner Niger Delta has improved, although the level remains below the average of 646 mm/year with a minimum of 390 mm recorded in 1980 and a maximum of 957 mm recorded in 1999 (Figure 1).

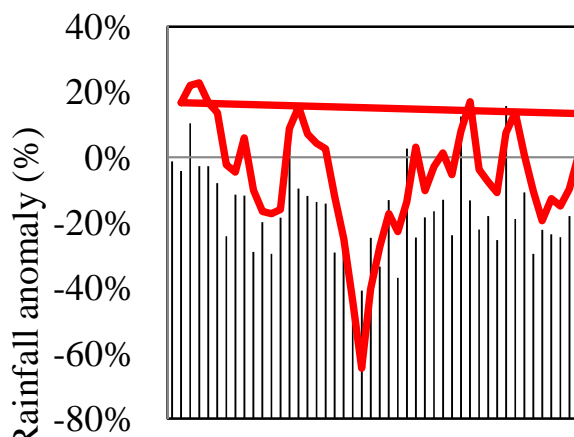


Fig.1 Rainfall and rainfall anomaly shown in relation to average rainfall from 1961 to 2014 (data from Mopti Meteo Station).

The daily ET0 (Reference Evapotranspiration) in the Inner Delta is very high particularly during the dry season (March to May). The annual ETP ranges from 4.72 mm/day in August to 8.63 mm/day in April (Figure 2).

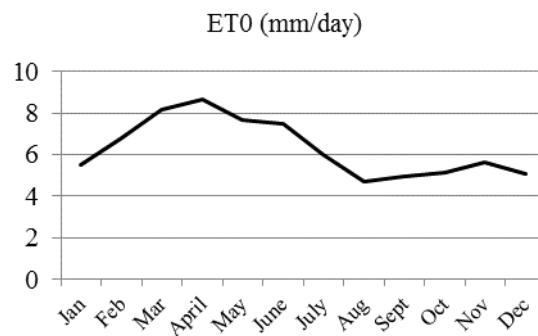


Fig.2 : Reference Evapotranspiration at Mopti Station (Inner Niger River Delta) during 2015 (Source FAO CLIMWAT).

The Niger River and its hydrological potential in Mali

The Niger is the main river in western Africa. It extends approximately 4,185 km (2,600 mi) with 1,700 km (1,060 mi) in Mali (Figure 3). The source is located in the southeastern part of the Guinea Republic and the total catchment area of the Niger River is 2,117,700 km² (817,600 mi²).

In the 1960s, the independent countries of the Niger River Basin decided to coordinate their efforts to exploit natural resources with a priority on water. The Commission of the Niger River was renamed the Niger Basin Authority (NBA) on 21 November 1980. The member countries are: *Benin, Burkina Faso, Cameroon, Côte d'Ivoire, Republic of Guinea, Mali, Niger, Nigeria and Chad.*

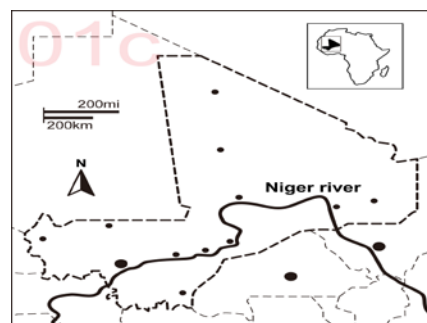


Fig.3 Niger River in Mali

Dams, reservoirs and other water users

The Upper Niger has four dams (Sélingué, Sotuba weir, Markala and Talo) and four dams that are under construction or in the project (Fomi in Republic of Guinée, Kandadji in Republic of Niger, Taoussa and Djenné in Mali).

The Sélingué dam on the Sankarani River has been used for hydropower since 1982. It has a total volume of 2.17 km³, an effective volume of 1.9287 km³ and a

design flood discharge of 3600 m³/s. The Sotuba weir, which has been in operation since 1929, is another very small hydropower plant located directly downstream from Bamako. Because of the limited storage volume of the Sotuba weir, this reservoir does not have a significant hydrological impact on the Niger River flow. The Markala dam which opened in 1947 is a diversion dam just downstream of Ségou with a storage volume of 0.17 km³. This dam is used to irrigate the surrounding area of the Office du Niger. There are two diversion dams on the Bani (tributary of the Niger River), namely Talo which was constructed in 2007 with a storage volume of 0.18 km³ and Djenné, which is under construction.

Data is available for five gauging stations from upstream to downstream of the Inner Delta (Koulikoro, Ke-Macina, Mopti, Akka and Diré) for the period 1960 to 2015. Variation in water flow allows an evaluation of water used and lost between different points (as shown in Figure 4).

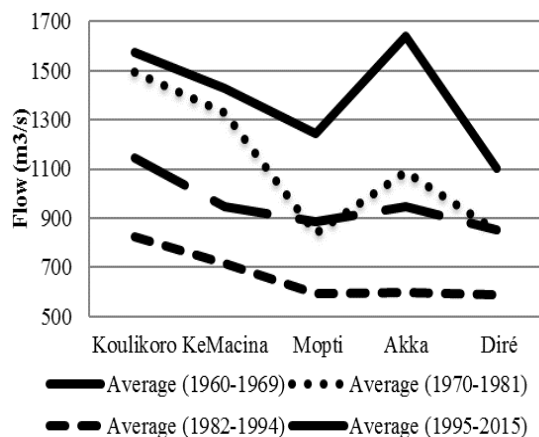


Fig.4 Water flow rate from Koulikoro to the Inner Niger Delta.

From 1960 to 1982 the data recorded by the stations represents the natural flow of the Niger River before the construction and operation of the Sélingué dam in 1982 (Figure 5). This dam is located approximately 200 km upstream of Koulikoro on the Sankarani River, a tributary of the Niger River. It has a catchment area of 33,460 km². The Sankarani River contributes significantly to water supplies during dry periods. This is accomplished through the Sélingué, which regulates the flow of the Niger River provides water to the Office du Niger and other irrigated schemes downstream.

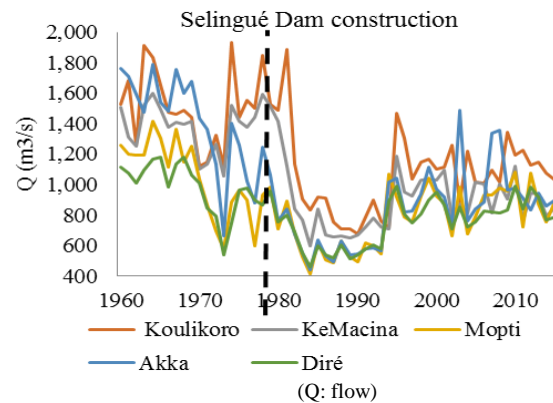


Fig.5 Hydraulicity of the Niger River before and after construction of the Sélingué dam

Agricultural land of Office du Niger

The Government of Mali has adopted several irrigation policies and strategies, in which the development of the Office du Niger land is a priority [5]. At the Second Ordinary Assembly of the African Union (AU) in July 2003 in Maputo, African Heads of State and Government endorsed the “Maputo Declaration on Agriculture and Food Security in Africa” (Assembly/AU/Decl. 7(II)). The Declaration contained several important decisions regarding agriculture, but the most important among these was the “commitment to the allocation of at least 10% of national budgetary resources to agriculture and rural development policy implementation within five years [6]. Moreover, the ministers’ council of 3rd August 2015 of the Malian government decided to allocate 15% of the budget to the rural sector [7].

The irrigation area of Office du Niger is located at the death Delta “delta mort” an ancient branch of the Niger River in the westerly region of the Inner Niger Delta “delta vif”. This irrigation zone covers a gross area of 2,458,506 ha with an irrigable area of 1,947,406 ha. Of this total, 1,445,000 ha is fed by gravity from the Markala dam, and by 2015 only 138,000 ha was developed.

Historically, the regime of paddy field construction in Office du Niger has changed significantly as dictated by the political situation (that is, a change from colonial rule to the present government) (Figure 6). In 1979, because of a high degree of degradation of paddy fields, the Malian government and its technical and financial partners decided to focus efforts on old land improvement. From 1979 till the present, 48,600 ha of paddy fields have been improved. This land improvement has allowed a reduction in water

consumption from 35,000 m³/ha to 15,000 m³/ha with the implementation of new water control equipment, land leveling, land consolidation and water turn between farmers.

In 1965, sugarcane was introduced in Office du Niger with an initial 5,800 ha under cultivation by this crop. This total has increased to 16,276 ha by 2015 with a total of 20,000 ha planned by 2018. Cotton, which was previously the main crop during colonial rule, was banned in 1970.

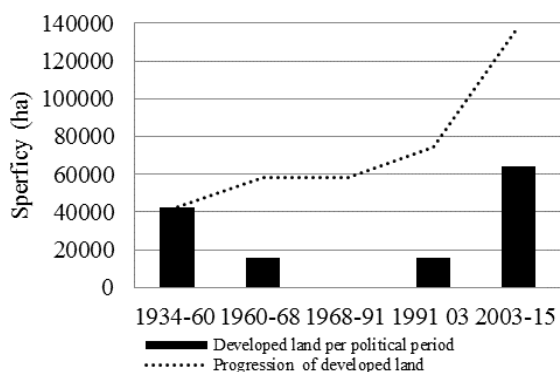


Fig.6 Evolution of irrigated land construction in Office du Niger (Data source: Office du Niger).

Between Koulikoro and Ke-Macina stations there are two main irrigation areas: Office Riz Ségou (ORS) which is comprise of 44,718 ha land irrigated by flooding during the rainy season and Office du Niger (ON) which has 138,000 ha under gravity irrigation (100% of the land is in use during rainy season and 10 to 25% is in use during cool and dry seasons). From 1995 to 2015, which represents the second average hydraulicity period, 17% of the Niger River annual average volume (36 km³) is used mainly by agriculture. The annual flow can be classified as follows: High flow period from June to February and low flow period from March to May.

Crop water production is only governed by transpiration. As it is difficult to separate the effect of transpiration from that of evaporation from the soil surface, defining crop water productivity using evapotranspiration rather than transpiration makes practical sense at field and system level (FAO, 2003). In the Office du Niger area which is characterized by large earthen canals and significant drainage, the amount of water lost is important and the global efficiency is 60% (Adama et al. 2011). This efficiency is used to define the water productivity for different crops. Using, crop evapotranspiration, irrigation efficiency, crop yield and crop price, a comparison is

made between principle crops in term of water productivity and profit-water ratio during the dry period (March to May).

$$WP = CP / WR \quad (1) \quad PWR = WP * CP \quad (2)$$

$$WR = (ETC + Per - R) * 10 * Eff \quad (3)$$

WP: Water Productivity [kg/m³], CP: Crop Production [kg/ha], WR: Water Requirement [m³/ha], PWR: PWR: Profit-Water Ratio [\$/m³], CP: Crop Price [\$/kg], ETC: Crop Evapotranspiration [mm], Per: percolation & seepage [mm], R: Effective Rainfall [mm] and Eff: Efficiency

Ecosystems of the Inner Niger Delta

Some plant species have become very rare such as *Acacia albida*, *Adansonia digitata*, *Boscia senegalensis*, *Balanites aegyptiaca* and *Echinochloa stagnina* locally known as bourgou (Figure 7). Bourgou is distributed in areas persistent flooding with water level 2-5 m in depth. According to Jerome Mari, the bourgou superficies represent 10% (1,613 km²) of the plant material in the floodplain of the delta. Since the great drought of the 1970s and 1980s to the present, 85% of the coverage due to bourgou has disappeared. Bourgou fulfills multiple roles in terms of human and animal populations of the Delta. The seeds of this plant act as a food source for humans while the stems have medicinal applications. Its grass production of 15 to 30 tons/ha, feeds almost 2 million cattle and 3 million small ruminants for 5 to 7 months a year. The vast pastures of bourgou are also favorable zones for the reproduction and growth of the numerous species of fish of the Delta. Furthermore, the large number of Herons species are present owe their survival to the plentiful supply of juvenile fish.

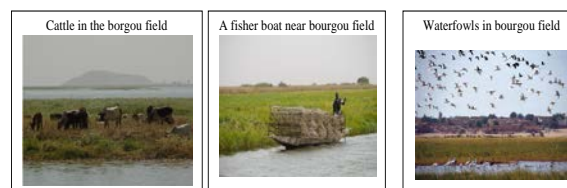


Fig.7 “A vital resource”: *Echinochloa stagnina* (bourgou) in Inner Niger Delta (credit photo OPIDIN)

This wildlife capital was previously the home of wide variety of fauna and flora which included: large herbivores such as gazelle, Hippopotamus amphibious, manatee (*Trichechus senegalensis*), large reptiles such as the Nil Crocodile (*Crocodylus niloticus*), Python (*Python sebae*) and Nile Varan (*Varanus niloticus*) [8]. At present, these floodplains are now poor in animal and plant species as a result of strong human pressure and environmental degradation. Evidence of this is the

fact that large herbivores and large reptiles have almost disappeared.

The number of fishermen in the Inner Niger Delta is estimated at 65,000. This corresponds to an approximate population of 240,000 including children, women and elders depend on fishing as an important part of their livelihood. A large fraction of these fishermen move from their villages to the lakes between December and March and this coincides with the time that the shoals of fish migrate. Due to lack of data it has not been possible to estimate the evolution over a long period. However, according to the Malian National Statistics Institute report on fishery and aquaculture 2010-2015 [9], the quantity of fish caught in the Inner Delta has decreased significantly during this period (Figure 8).

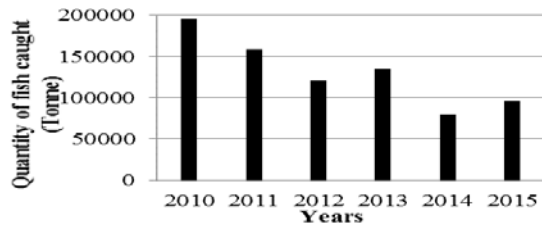


Fig.8 : quantity of fish caught in the Inner Delta (adapted from Ministry of fisheries report 2010-2015)

The Analysis of remote sensing data

Remote sensing data (Landsat images, 2014) and aerial photographs from 1970 (provided by the Malian government hydraulic Service) were analyzed by ArcGIS. As result we found 16,041 km² of maximum flooded area between the period 1970 and 2014 of the Inner Niger Delta with 20,851 km² of flood area, the lost represent 23% during the last four decades (map in Annex). During the same period the irrigated area of Office du Niger increased by 67% (from 58,287 ha to 138,418 ha).

RESULTS

To characterize the hydrological regime of the Niger River, the Koulikoro station was selected for statistical analysis. It is located approximately 200 km upstream from the Markala dam. Koulikoro station has been operational since 1907 and as a continuous data set since its inception. This station therefore allows characterization of the hydrology of the Niger River with an acceptable level of precision.

In the period 1907-1982 before construction of Sélingué dam, the highest flow rate recorded was 7,586m³/s in 1928. After the dam construction

between 1982 and 2014, the highest flow rate recorded was in September 2001 with a corresponding value of 5,500m³/s. According to the historical variation of the hydraulicity of the Niger River from 1960 to 2015 may be classified as follows (Figure 9):

- A period of high hydraulicity for 1960 to 1969 with an annual average flow rate 1,654 m³/s.
- Two periods of average hydraulicity (1970 to 1981 and 1995 to the present) with an annual average flow rate between 1,226 and 1 301 m³/s;
- A period of low hydraulicity from 1982 to 1994 with an annual average flow rate 776 m³/s.

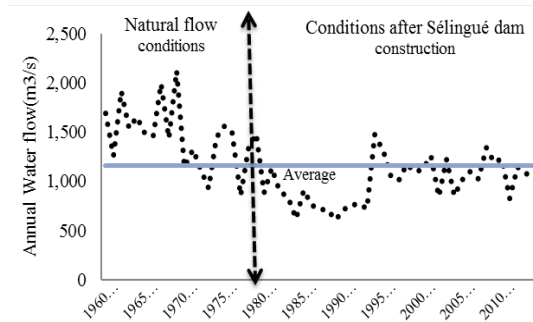


Fig.9 : Hydraulicity of the Niger River before and after construction of the Sélingué dam in Koulikoro

Figure 10 (b) clearly shows the increase in water intake and water lost between Koulikoro and Ke-Macina during the period of low flow despite the improvement in Niger river hydraulicity in comparison with the situation in the 1970's and 1980's. The water loss gap between water inflow and outflow in this section of the river changes from less than 20% in 1960's to 70% today.

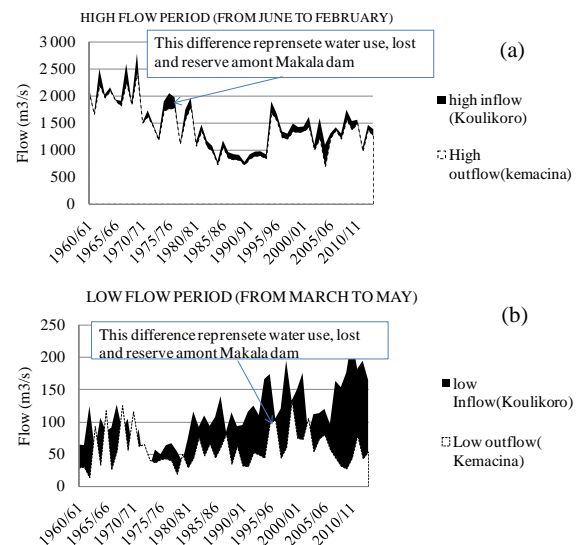


Fig.10 Inflow and outflow of the Markala Dam (for the period 1960 to 2015)

A minimum flow rate of 40 m³/s was established downstream of the Markala Dam through an agreement between the Governments of Niger Basin Authority countries. Despite this agreement, recent hydrometric surveys at the Markala-downstream station show that at the present the minimum flow conditions are not maintained continuously. For the last five years (2011 to 2015), the flows recorded at downstream of the Markala dam is less than 40m³/s for average of 73 days per year (source Office du Niger).

The percentage of water Levy by Office du Niger River ranges from 3% in September to 69% in May. This illustrates the pressure on Niger River water resources during dry periods when the upstream flow rate is below 200m³/s (Figure10b). Despite this situation the cultivation of paddy rice and sugarcane (both high water consumption crops) increases during this period instead of diversification crops (DC) (onion, garlic, tomatoes, corn, potatoes etc.) as shown in the Figure 11. In 2000 the total cultivated area during the dry period increased from 17,102 ha (34% DC, 32% of rice and 34% Sugarcane) to 43 703 ha (24% DC, 39% rice and 37% Sugarcane).

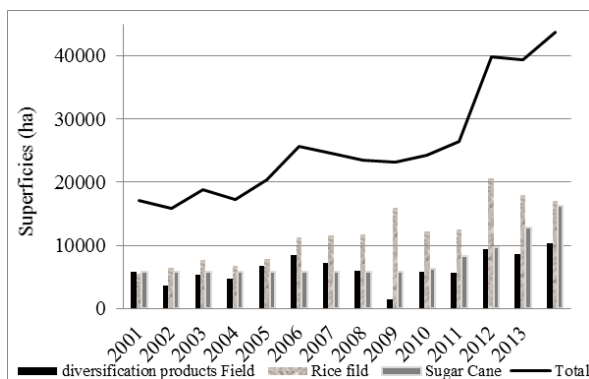


Fig.11 : Evolution of diversification crops, sugarcane and rice cultivation field surface during dry period from 2000 to 2014 (data source, Office du Niger annual activities reports from 2001 to 2014)

From the evapotranspiration, efficiency of irrigation system, crop yield, and crop price data for the dry season 2014, a comparison was made between some principle crops through water productivity and profit-water ratio (Figure 12).

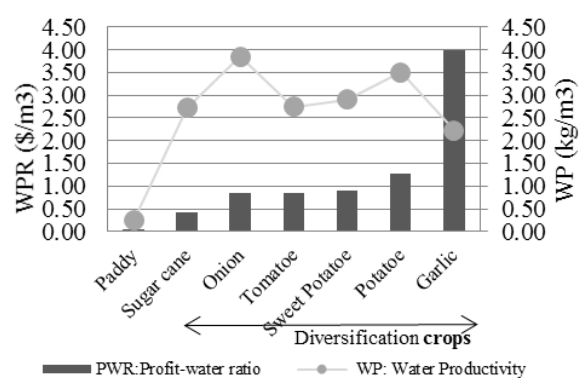


Fig.12 : Profit-water ratio and water productivity for paddy, sugarcane and vegetables (onion, tomato, sweet potato during dry period 2014).

From the Figure 12 it can be clearly seen that paddy and sugarcane are less profitable in terms of water productivity (WP) and profit-water ratio (PWR) than diversification crops. The Paddy rice has the lowest benefit (WP=0.24 kg/m³ and PWR=0.09\$/m³) while onion and potato have the highest water productivity (WP=3.86 and 3.51 kg/m³) and garlic the highest profit-water ratio (PWR=3.13 \$/m³).

DISCUSSION

The rapid development of the large-scale schemes in the area of Office du Niger which is irrigated upstream may have a significant impact on the Niger River's hydrology as well as the floodplain and the ecosystem of the Inner Niger Delta. In this study, changes in the Inner Niger Delta are evaluated as a result of the expansion of the irrigated area and cropping pattern of Office du Niger.

During the high flow season from June to February, almost all the crop is paddy rice in Office du Niger (118 418 ha in 2014) and other irrigated areas upstream of the Inner Niger Delta. Despite the high demand of water for paddy rice and sugarcane, the impact on the Niger River flow remains very low and can reach more than 5 500 m³/s (Figure 10a).

The impact of irrigation is very significant during the low flow season from March to May. This corresponds to a period with flow rate below 250m³/s; (Figure 10b). In the past, the paddy rice cropping was avoided during this season. However, from the year 2000 the Malian government decided to introduce paddy rice double cropping per year. The sugarcane

cultivation area also increased from 5 800 ha to 16 276 ha in 2014.

The cultivated area of diversification crops (vegetables and others) which is the alternative to paddy during the dry season has the highest profit economically and in terms of water saving does not follow the trend, as more farmers prefer paddy. There are four main reasons for this: The farmers use calabash and other container (manual labor) for irrigation and it is very difficult to irrigate a large farm, the access to market is very difficult, the harvest occurs at the same time and prices are very low, there is a lack of refrigerated storage and there is no processing and packaging industry.

How to reverse the trend:

To minimize the impact of Office du Niger particularly and other small-scale irrigated areas located upstream of the Inner Niger Delta, the following actions are required:

- Limitation of rice cultivation during the dry period (March to May)
- Limitation of the extent of sugarcane fields
- Changing of crop pattern during the dry period and opting for diversification crops (vegetable & others)
- Reducing the length of rice growth stage through the use of new varieties.

SUMMARY

At present, It is clear that water has become a constraining factor in the development of irrigated agriculture in Mali and the preservation of the Inner Niger Delta ecosystem.

- After the major drought in 1970's and 1980's, rainfall in the Inner Delta region has improved over the last decade. This condition remains fragile as it is impacted by climate change (Figure 1).
- Despite the recent improvements in upstream hydraulicity of the Niger River, less and less water reaches the Inner Delta. This occurs mainly during the dry season (March to May) and is largely due to water withdrawals for irrigated as a result of paddy cultivation located between Koulikoro and Markala as well as between the recently

constructed dams of Talo and Djenné on the Bani (tributary river)(Figures 5&10).

- During the last three decades, the floodplain of the Inner Niger Delta has been reduced by 23% and the irrigated area increased by 51%. In the Government program for the development of 100,000 ha of irrigated land between 2014 and 2018, 67,850 ha will be realized upstream of the Inner Delta (see sections 2.3 & 2.5).
- To formulate a balance between Inner Niger Delta floodplain and the development of irrigated agriculture, some action needs to be taken. Suggestions include: limiting of rice cultivation especially during the dry period, limiting of area available for sugarcane, changing or reducing rice to vegetable crops during the dry period and the reduction of rice growth stage through the introduction of new varieties (Figures 11 & 12).

ACKNOWLEDGMENT

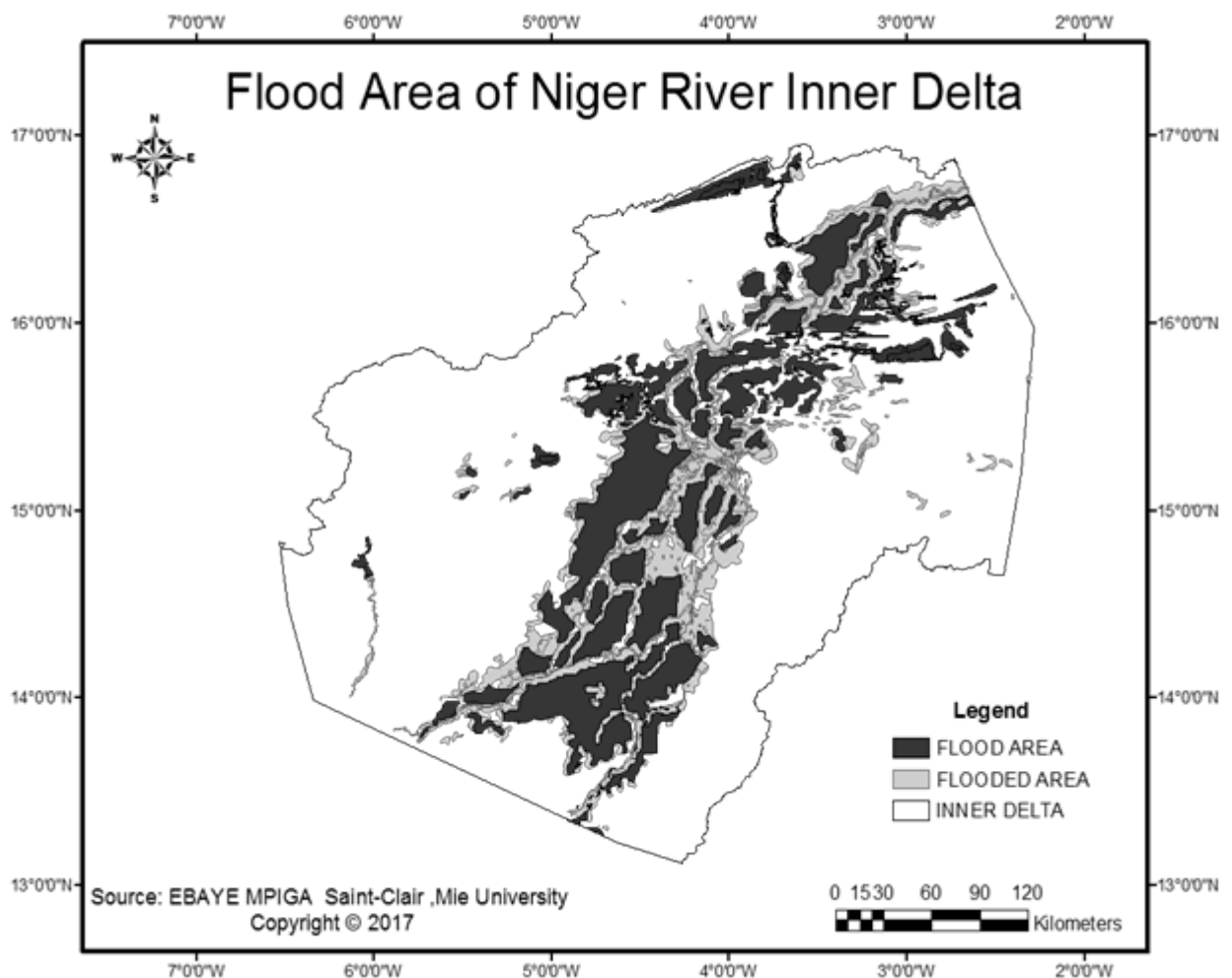
Our warm thanks to Office du Niger, Mali's National Direction of Hydraulic for their supporting in terms of providing some data. Thanks to the Laboratory of Forest Resources of Mie University for their help in term of remote sensing data analyzing.

REFERENCES

- [1] UNDP, 'Human Development Report 2015 Work for Human Development' http://hdr.undp.org/sites/default/files/2015_human_development_report.pdf , 2015, pp 228
- [2] Instat-Mali, "Enquete Modulaire Et Permanente Aupres Des Menages (EMOP), Rapport d'analyse premier passage", http://www.instatmali.org/contenu/eq/rana16pas1_eq.pdf , Août 2016, pp 27
- [3] Cessouma Adama, " l'agriculture irriguee et les perspectives d'economie d'eau au mali", revue HTE n°141, <http://www.anafide.org/doc/HTE%20141/141-2.pdf>, Décembre 2008, pp 04
- [4] " conservation: Conflict on a global scale", Environ. Manage., 25(5), 2000 , pp 485
- [5] Leo Swart& al, "The Niger, a lifeline" wetland International, A&W, 2005, pp 39-77
- [6] INSTAT-MALI, Recueil des données du système d'informations sur la pêche et aquaculture 2010-2015 (SIPA), October 2016, pp 5

- [7] Strategic axes of the agricultural policy of the Government of Mali
<http://ma.gouv.ml/index.php/strategies/vision>
- [8] Conference of ministers of agriculture of the African union Maputo, Mozambique “Report of the ministers of agriculture” , 1-2 july 2003, pp 2
- [9] Presidency of Mali “ Communiqué du conseil des ministres du 03 Août 2015 ”, 2015,
<http://www.koulouba.ml/official-statements/communique-du-conseil-ministres-du-lundi-03-aout-2015>

ANNEX



This page has been kept blank intentionally

A STUDY ON SELECTION FACTORS OF RESIDENCE FOCUSING ON PERSONAL ATTRIBUTES AND DISTRICT CHARACTERISTICS - A CASE STUDY OF REGIONAL CITY IN JAPAN -

Tetsuo Morita¹ and Shinya Tsukada²

¹Graduate School of Engineering, Maebashi Institute of Technology, Japan; ²Maebashi City Office, Japan,

ABSTRACT

In Maebashi City, Gunma Prefecture, Japan like other regional cities, motorization is progressing year by year. Dependence on automobiles has become a major cause of urban sprawl. In Maebashi City, the DID (Densely Inhabited District) is expanding year by year, but the population density is decreasing. In this study, in solving these various problems of local cities, we will consider "Compact City" as one future image of local cities and consider the consolidation of cities. The purpose of this study is three as shown below. The first aim is to analyze the factors of resident consciousness to live in Maebashi City. The second aim is to analyze the reasons for settlement by resident, and to clarify the settlement factors. The third aim is to analyze the factors that define the awareness of residence selection by migrant-oriented persons.

Keywords: Personal Attribute, District Characteristic, Selection Factor of Residence, Maebashi City

INTRODUCTION

Background and purpose of this study

In Maebashi City, Gunma Prefecture, Japan like other regional cities, motorization is progressing year by year. In 2015, 78% of transportation in the central metropolitan area of Gunma prefecture is occupied by automobiles [1]. Dependence on automobiles has become a major cause of urban sprawl. In Maebashi City, the DID (Densely Inhabited District) is expanding year by year, but the population density is decreasing. In this study, in solving these various problems of local cities, we will consider "Compact City" as one future image of local cities and consider the consolidation of cities.

The purpose of this study is three as shown below. The first aim is to analyze the factors of resident consciousness to live in Maebashi City. The second aim is to analyze the reasons for settlement by resident, and to clarify the settlement factors. The third aim is to analyze the factors that define the awareness of residence selection by migrant-oriented persons.

Review of literature

Fujii [2] studied about Traffic Policy towards the introduction of Compact City for Takasaki City, Gunma Prefecture. Nishiyama et al. [3] analyze residence selection behavior based on resident preference of residential attribute in Utsunomiya metropolitan area. Morita et al. [4] analyzed the living consciousness in the mountainous area of Gunma prefecture and proposed compact area creation. In

addition, Morita et al. [5] focused on the environment of the water and green for Maebashi City, and evaluate the quality of life.

As mentioned above, this study is on the line of research on residence selection in local cities. The characteristic of this study is to divide it into people who intend to settle down and those who intend to emigrate, and analyze the factor of choosing a place of residence.

Study Area

The study area, Maebashi City, is shown in Fig. 1. Maebashi City is the prefectural capital of Gunma Prefecture with a population of 340,000 people, and a local city located about 100 km from Tokyo. In Maebashi City, motorization is progressing even among local cities, and Maebashi City is studying toward realization of compact city.

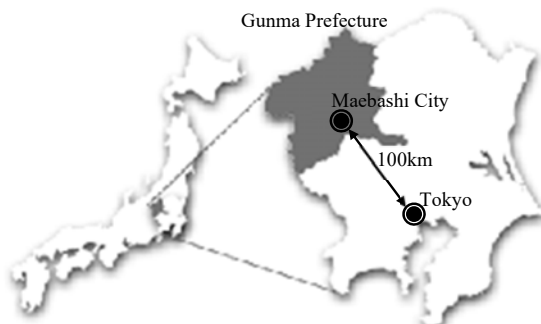


Fig. 1 Location of Maebashi City

RESIDENT CONSCIOUSNESS IN MAEBASHI CITY

The Gunma Person Trip Survey was carried out in 2015, and this data is used in this study. Fig. 2 shows resident consciousness. The percentage of those who want to continue living in the current place is 86.0%, and the proportion of people planning to move to other places or to move is 14.0%. Looking at the proportion of residence by type of age group, those who want to continue living are over 60% in their 10's and 20's. As the age group goes up, the composition ratio of those who want to continue living in the current place tends to be higher.

The reason for continuing living (excluding unknown) is shown in Fig. 3. From this figure, it is found that 19.0% is "easy to go to commercial facility", 16.8% is "easy to go to medical and welfare facility", and 3.3% is "easy to go to child care support facility". The reason for accessibility to daily-related facility accounts for 39.1%. Also, "rich in green and nature" is 12.5%. 7.5% "easy to use railroad and bus", 12.3% "easy to move on foot and by bicycle", 18.9% "easy to move by car", 12.3% "easy to move on foot and by bicycle", 18.9% "easy to move by car".

Figure 4 shows the items that people who want to move and people planning to move from the current location emphasize when choosing a place of residence. Importance degree 1 means "absolutely not important", importance degree 2 means "not very important", importance degree 3 means "neither", importance degree 4 "slightly important" and importance degree 5 means "very important".

When looking at the composition ratio of importance degree 4 (slightly important) and importance degree 5 (very important), the highest is 90.8% in the "district with less risk of natural disasters and fires", 84.0% is district easy to go to medical and welfare facility ". Regarding accessibility to facilities, 73.2% are "easy to go to central shopping area" and 64.6% are "easy to go to shopping center in suburb". Regarding mobility, 74.3% are "district easy to move by car", 73.0% are "district easy to move on foot and by bicycle", 67.4% for "district easy to use railway and bus". From the above, it is assumed that there are people who emphasize mobility by car and accessibility to suburban shopping centers, and people who emphasis mobility on foot and by bicycle and accessibility to central shopping areas.

Next, we will grasp the relationship between the district characteristics of the residential area and the resident consciousness. Fig. 5 shows the resident consciousness by distance range to station, and Fig. 6 shows the resident consciousness by distance range to bus stop. As a result, there is no difference in the consciousness by any district characteristics. There is an influence of individual attributes such as age group

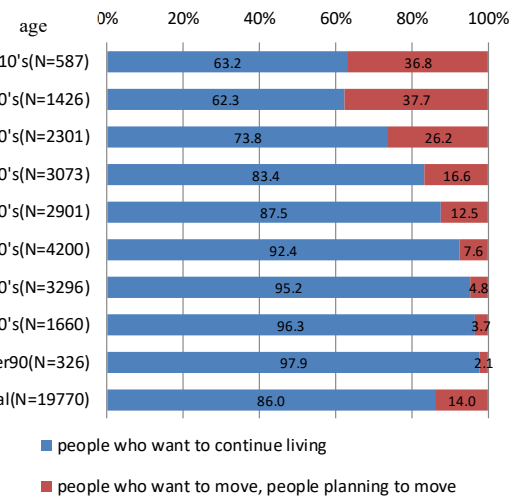


Fig. 2 Resident consciousness by age group in Maebashi City (excluding unknown)

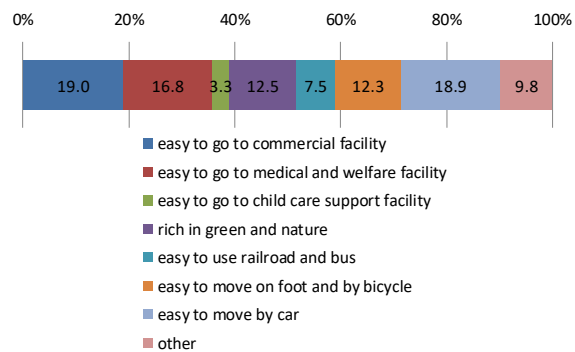


Fig. 3 Reason for continuing living (multiple answers)

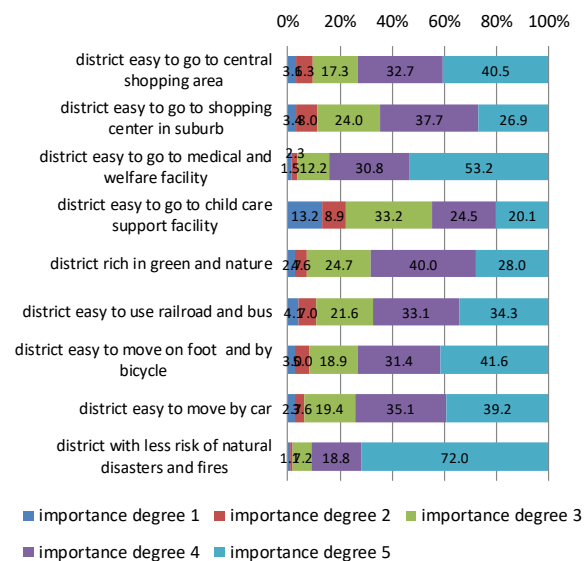


Fig. 4 Items to be emphasized in selecting residence (people who want to move, people planning to move)

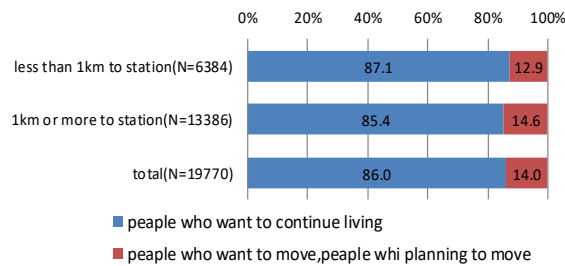


Fig. 5 Resident consciousness by distance range to station

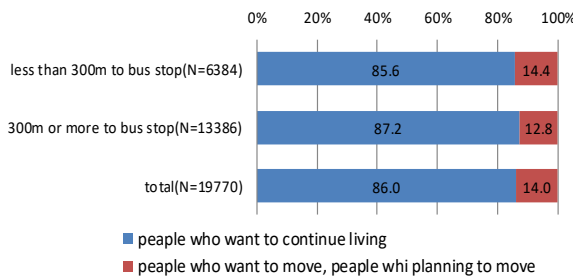


Fig. 6 Resident consciousness by distance range to bus stop

in resident consciousness, and multivariate analysis considering individual attributes and district characteristics is considered necessary.

DISCRIMINANT ANALYSIS ON RESIDENT CONSCIOUSNESS

The analysis results are shown in Table 1 (variable quantification II analysis).

The explanatory variable which most affects resident consciousness is age group, and both the category range and the partial correlation coefficient are higher than other explanatory variables. The explanatory variable that most affects the resident consciousness is age group. The category range and partial correlation coefficient are both higher than other explanatory variables.

Looking at the category score, the higher the age group, the higher the intention of "wanting to continue living" (hereinafter referred to as settlement intention) tends to be higher. Looking at other personal attributes, the variable with the greatest influence after age group is occupation. The settlement intention for people in the primary industry is high, and the intention to "want to move" (hereinafter referred to as migration intention) of students and unemployed people is high. The next most influential variable is car ownership, and there is a certain relationship between car ownership and resident consciousness.

Table 1 Discriminant analysis on resident consciousness (Variable quantification II analysis)

explanatory variable		category	number of samples	category score	range (rank)	partial correlation coefficient (rank)	
individual attribute	age group	10's	273	-1.970	3.384 (1)	0.294 (1)	
		20's	741	-2.221			
		30's	1191	-1.215			
		40's	1597	-0.320			
		50's	1453	0.195			
		60's	2104	0.602			
		70's	1576	0.880			
		over 80	1035	1.163			
	occupation	primary industry	371	0.187	0.353 (3)	0.018 (5)	
		secondary industry	1231	0.066			
		tertiary industry	3985	0.021			
		other occupation	54	-0.166			
		student	375	-0.071			
		housewife /husband	1365	-0.034			
		unemployed	2589	-0.060			
	necessity of attendance	always necessary	470	-0.072	0.137 (6)	0.010 (6)	
		necessary according to circumstances	539	-0.126			
		unnecessary	8961	0.011			
	car ownership	myself only	7041	0.044	0.173 (5)	0.020 (4)	
		family shared	1022	-0.064			
		none	1907	-0.129			
district characteristic	distance range to station	less than 1km	2656	0.158	0.215 (4)	0.030 (2)	
		1km or more	7314	-0.057			
	distance range to bus stop	less than 300m	7814	0.023	0.107 (7)	0.009 (7)	
		300m or more	2156	-0.084			
	city planning area	urbanization promotion area	6474	-0.062	0.384 (2)	0.021 (3)	
		urbanization control area	2080	0.076			
		area where urbanization promotion area and urbanization control area are not distinguished	1006	0.282			
		outside city planning area	410	-0.101			
[objective variable] resident consciousness	people who want to continue living	8585	0.120	correlation ratio 0.300			
	people who want to continue living, planning to move	1385	-0.746				

Regarding district characteristics, the explanatory variable with a great influence is city planning area. People living in urbanization control area and area where urbanization promotion area and urbanization control area are not distinguished are highly likely to settle down. Residents urbanization area and area outside urban planning areas are highly motivated to migrate. It is assumed that residents of urbanization control area, area where urbanization promotion area and urbanization control area are not distinguished have a long residence age and are highly attached to the district. Also, since outside urban planning area is the mountainous area of Mt. Akagi, it seems that there is an intention to migrate to the area with high lifestyle convenience.

Regarding the distance to station, less than 1km tends to settle down, less than 1km tends to be more likely to emigrate. The distance to bus stop is less influential compared to all the other variables, but when it is close to the bus stop, the intention to settle is seen.

ANALYSIS OF THE INTENTION OF RESIDENTS OF SETTLERS (SETTLEMENT INTENTION)

As a result of discriminant analysis of the resident consciousness, it became clear that the variables that greatly influence the residence intention are the age group. For that reason, we analyze the relationship of settlement reasons by age group. For the analysis, we use samples of people who have settlement intention. Correspondence analysis was performed to visualize analysis data.

In conducting correspondence analysis, a composition frequency table of the settlement reasons of people who intend to settle down by age group (respondents who want to continue living) was prepared. The analysis results are shown in Fig. 7.

With respect to the horizontal axis, since it is arranged in the positive direction that "easy to move on foot and by bicycle" and "easy to go to medical and welfare facility" are arranged, "living area is narrow". The negative direction, "easy to move by car" is arranged, so "living area is wide" named. The vertical axis is named "natural" because "rich in green and nature" is a large positive value. We named the negative direction "urban".

Looking at each age group, the area of living becomes narrower as the age group goes up, with respect to the horizontal axis. Looking at each age group individually, the 30's cited it as reason for "easy to move by car". The 40's and 50's cited the reason for "easy to go to commercial facility". The 60's cited the reason for "easy to go to medical and welfare facility". The 70's cited the reasons for "easy to go to medical and welfare facility" and "easy to move on foot and by bicycle". From the above, it became clear that the reasons for settlement differ according to age group. Young people want the convenience of life, people in

their 60's want to have rich green and nature, people over the age of 70 want to go to medical and welfare facilities and to live on foot or bicycle.

ANALYSIS OF THE INTENTION OF RESIDENTS OF MIGRATION (MIGRATION INTENTION)

In this study, we analyze the intention of persons who intends to migrate ((people who want to move, people planning to move). In the survey, people who intend to emigrate are questioned about the degree of importance of choosing a place of residence (hereinafter referred to as residential preference). Table 2 shows the results of applying principal component analysis to these data.

There were two principal components whose eigenvalues exceed 1. The accumulation contribution ratio of the two main components is 52.3%.

Looking at the principal component loading amount of principal component 1, since all variables are positive values, it is regarded as a comprehensive evaluation for selecting residences, and the name of principal component 1 was taken as "living environment". The principal component 2 is positive value for "district easy to move by car" and "easy to go to shopping center in suburb". Also, negative values are "district easy to move on foot and by bicycle" and "district easy to use railroad and buse". Therefore, the name of principal component 2 was "suburb". The negative direction is "city".

By using the principal component scores obtained by principal component analysis, residential preference maps for each attribute were created (Fig. 8). In the residential preference map, the horizontal axis is defined as the principal component 1 "living environment", and the vertical axis as the main component 2 "suburban - urban". By calculating the average value of the principal component scores by attribute and plotting the values on the coordinates, we can visually ascertain the difference of the

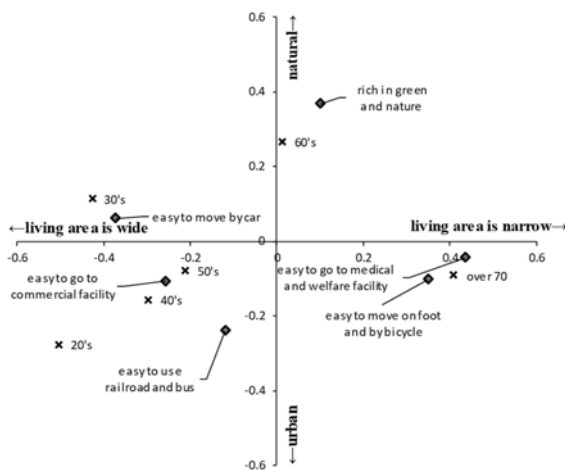


Fig. 7 Analysis of the intention of residents of settlers (Correspondence analysis)

Table 2 Principal component analysis on residential preference

variable	principal component 1	principal component 2
	living environment	suburban (- urban)
district easy to go to central shopping area	0.672	-0.233
district easy to go to shopping center in suburb	0.611	0.251
district easy to go to medical and welfare facility	0.744	-0.022
district easy to go to child care support facility	0.474	0.414
district rich in green and nature	0.595	0.234
district easy to use railroad and bus	0.630	-0.520
district easy to move on foot and by bicycle	0.662	-0.524
district easy to move by car	0.533	0.510
district with less risk of natural disasters and fires	0.682	0.128
eigenvalue	3.542	1.167
contribution ratio	39.4%	13.0%
accumulation contribution ratio	39.4%	52.3%

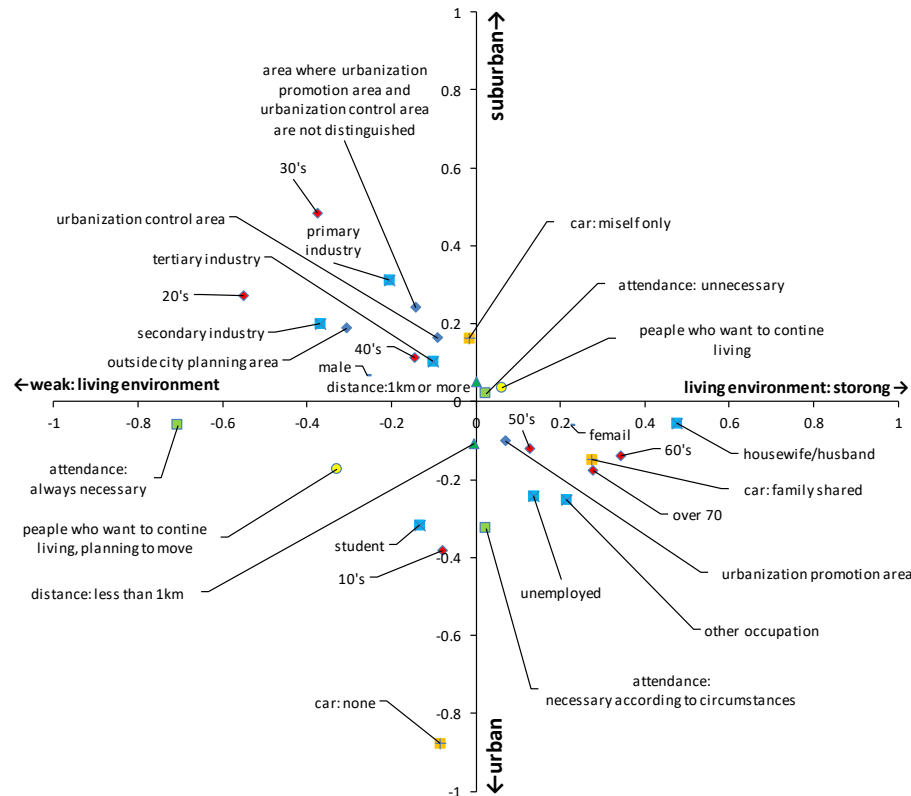


Fig. 8 Residential preference maps for each attribute s (Principal component analysis)

residential preference by the attribute.

Car ownership has great influence on "suburban - urban". People who do not own cars are strongly urban oriented, and those with their own car tend to be suburban oriented. In terms of gender, female tend to have strong feelings for living environment. Looking at by age group, young people are more suburban-oriented, weak in their living environment, the elderly are more urban oriented, and their habitat is strong. However, the tendency of the 10's is urban oriented, and there are trends of students who do not possess cars or students who go to school outside the prefecture. By occupation, people in the primary industry and secondary industry are oriented towards the suburbs, students and unemployed people are urban oriented. People who need attendance depending on circumstances when going out are urban oriented, and those who always need attendance tend to have weak consciousness to living environment.

By the above principal component analysis, we were able to grasp the tendency of intention to migrate by individual attribute.

CONCLUSION

Maebashi citizen's intention to settle is higher, and the tendency is higher for elderly people. People

who want to continue living in the current place give accessibility to facilities and mobility by means of transportation as a reason for settlement. Some people who intend to emigrate are emphasizing mobility by car and accessibility to suburban facilities. On the other hand, there are people who place emphasis on mobility of walking and bicycle and accessibility to the city center.

Maebashi citizens, as a whole, are aiming for automobile use. On the other hand, there is a tendency that people who intend to settle live in the vicinity of station, and the elderly desire "easy to go to medical and welfare facility" and "easy to move on foot and by bicycle". From this, it is thought that there are a certain number of people who are oriented towards public transportation. Among those who intend to emigrate, there are those who do not possess cars, those who need attendance when going out, and urban oriented students. It will be necessary to support the lives of such citizens from the transportation side and to form compact cities that are easy to use for public transportation.

ACKNOWLEDGEMENTS

The data of the Gunma Person Trip Survey used in this research was lent from Gunma prefectural government. We express our appreciation here.

REFERENCES

- [1] Comprehensive City Transportation Planning Council of Gunma Prefecture, Results of Gunma Person Trip Survey in 2015-2016, 2017, <http://www.kendoseibi.pref.gunma.jp/section/to-shikeikaku/gunma-pt/result.html>.
- [2] Fujii S, "An Empirical Test of Hypothesis on Influence of Travel Behavior on Residential Choice Behavior: A Fundamental Study on Transportation Measures for Promoting Compact Cities", *Traffic Engineering of Japan*, Vol. 43, No. 6, 2008, pp. 53-62.
- [3] Nishiyama Y, Nakatani J, Kurisu K, Aramaki T and Hanaki K, "Analysis of residential Choice Behavior Based on Classification of Residential Preference", *Journal of Japan Society of Civil Engineers*, Ser. G, Vol. 67, No. 6, 2011, pp. 1-10, 2011.
- [4] Morita T, Tsukada S, Sano K, "Analysis on Population Trend and Residential Attitude in Depopulated and Aged Area toward the Compact Area: Case Study of Kuni Village in Gunma Prefecture", *Papers on city planning*, No.45-3, 2010, pp. 511-516.
- [5] Morita T, Kogure Y, Sugita H, Baba T, Tsukada S and Miyazato N, "A Study on Evaluation of Quality of Life in Consideration of Water/Green Environment", *International Journal of GEOMATE*, Vol. 2, No. 2, 2012, pp. 241-246.

REMOVAL OF RADIOACTIVE CESIUM FROM OCEAN SLUDGE BY THE BACTERIUM USING PURIFICATION SYSTEM OF CIRCULATION TYPE

Tomoe KOMORIYA¹, Kyoichi OKAMOTO² and Takashi TOYAMA²

¹CIT, Nihon University, JAPAN; ²CST, Nihon University, JAPAN

ABSTRACT

The Fukushima nuclear accident of March 11, 2011 resulted in soil and water contamination by radioactive cesium. Radioactive cesium transported by rivers was also found in the ocean sludge of Tokyo Bay. Cesium adsorbed on the sludge is not easily removed. One of the authors has developed an ocean sludge decomposition system that employs micro-bubble circulation. The circulation of micro-bubbles creates an aerobic state that activates aerobic bacteria, facilitating decomposition and purification of the sludge. The objective of this study was to investigate the effect of the addition of bacteria to the micro-bubble circulation system on the efficient removal of radioactive cesium from ocean sludge. We tested the water purification effect of the system by adding bacteria directly. Results confirmed that the decomposition of the deposited sludge using our system facilitates the elution of the radioactive cesium. Any cesium eluted in the water can be remedied using existing technology such as zeolites. Purification efficiency seems to be greatest when additional bacteria are added directly to the process. With time, bacterial concentration doubles, and 76% of cesium in the liquid phase (dried sludge) and 51% of cesium in solid phase (water) is removed.

Keywords: Decontamination, Radioactive Cesium, Ocean Sludge, Micro-bubble, Bacteria

INTRODUCTION

The 2011 accident at the Fukushima Daiichi nuclear power station led to radioactive cesium contamination of soil and water. Rivers flowing into the Tokyo Bay have transported radioactive cesium into the ocean sediments of the bay [1].

Cesium is reportedly easily adsorbed onto the microscopic particles that constitute soil [1-2]. Most cesium adsorbed by sediments is difficult to remove by external factors, and persists over long timescales. Moreover, closed water environments such as river and bay systems make accumulated organic sludge difficult to decompose. Therefore, radioactive cesium is predicted to be deposited in the sediment of the seabed over time, extending radioactive contamination into the ocean. It is important to decontaminate the sediment.

Okamoto, one of the authors, developed a decomposition system for ocean sludge that employs the circulation of micro-bubbles to promote aerobic conditions that activate aerobic bacteria, facilitating decomposition and purification of the sludge [3]. Moreover, sea-sludge particles were observed to decrease in size through the course of the treatment with our micro-bubbles system and bacteria addition [4].

Radioactive cesium can thus be eluted after the deposited sludge is decomposed by our system. If the cesium is eluted into water, it can then be

remedied using existing technology such as zeolites [5]; resulting in the complete decontamination of sediment.

In this study, to effectively remove radioactive cesium, we added bacteria to break down sludge in the micro-bubble circulation system, and investigated the effect of the addition of microorganisms.

MATERIALS AND METHODS

Decomposition System of the Micro-Bubble Circulation Type

The micro-bubble circulation system comprises two parts, as shown in Fig. 1. The water circulates through two tanks. In one tank (length 40 × width 28 × height 28 cm), highly soluble, micro-bubbles are generated. Consequently, water rich in dissolved oxygen (DO) circulates through these tanks. The experimental tank is 60 × 29 × 35 cm. We used 30 L of seawater and 1 kg of sludge. The micro-bubble generator was based on [6] and the flow rate was 900 L/h. The flow rate of the water pumps connected to each tank was 300 L/h. A cooler for the tank that generates the micro-bubbles was set to 30 °C.

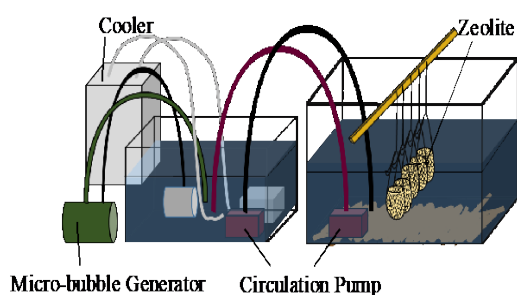


Fig. 1 Circulation purification system

Experiments on Decomposition of Deposited Sludge for Cesium Removal

Fig. 1 illustrates the system used to experimentally remove cesium from ocean sludge. The ocean sludge samples and seawater were obtained from Funabashi Port in Chiba Prefecture, Japan. The first 10 cm of sludge from the seabed was discarded before the samples were taken.

Model sludge was prepared using one kg of ocean-sludge, 30 L of seawater, cesium chloride was mixed. The cesium chloride was included to become 100 mg/L. The model sludge was poured into the system and stirred for 24 h.

Zeolites 4A were placed in the second tank (Fig. 2), and micro-bubbles were generated by a micro-bubble generator using a flow rate of 900 L/h. The flow rate of the water pumps connected to each tank was 2400 L/h. The cooler was set to 30 °C.

After 24 h, bacterial species "*Alcaligenes fecalis*" (15×10^8 cells) [5,7,8] and Glutamic acid (100 ppm) as an activator [9] were added. The activator was added to the experimental tank after 24 and 60 h periods. At 0, 12, 24, 48, 60, 72, 96, and 120 h, DO, water temperature, and pH were measured by a multi-parameter water quality meter. A digital pack test (Kyoritsu Chemical-Check Lab. Corp., Japan) was used to measure ammonium ion (as ammonium nitrogen, $\text{NH}_4\text{-N}$), nitrite ion (as nitrite nitrogen, $\text{NO}_2\text{-N}$), nitrate ion (as nitrate nitrogen, $\text{NO}_3\text{-N}$), total nitrogen (T-N), and hydrogen sulfide (H_2S) concentrations. The seawater was then filtered.

Seawater and sludge samples at 0, 12, 24, 48, 72, 96, and 120 h were collected for DNA concentration and cesium concentration measurements. DNA was extracted from sludge and measured by spectrophotometry. Cesium was measured with energy dispersive X-ray analysis (EDX) in dried sludge and atomic absorption spectrometry in seawater.

Experimental conditions are given in Table 1.



Fig. 2 Zeolites 4A set in experiment tank

Table 1 Experimental conditions

	Micro-bubble	Additive amount of bacteria	Activator
Case 1	○	1.5×10^8 cell	100 ppm
Case 2	—	—	—

RESULTS AND DISCUSSION

Decomposition of Deposited Sludge for Cesium Removal

Results of water temperature, pH, DO and H_2S under varying environmental conditions

Figures 3 and 4 show the pH and DO respectively, resulting from the environmental conditions prevalent in cases 1 and 2 (Table 1). After 24 hrs, the pH of case 1 and 2 was constant at about 8.0. The initial concentrations of DO are 4.9 mg/L and 3.7 mg/L in cases 1 and 2 respectively. The DO of case 1 is saturated at about 7.3 to 7.8 mg/L after 24 h, because the concentration of oxygen saturation is 8.1 mg/L-pure water. The DO of case 2 is saturated at about 3.5 to 4.2 mg/L after 24 h.

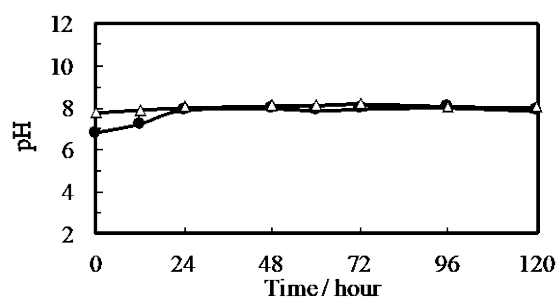


Fig. 3 Change in water pH over time in case 1 (●) and case 2 (Δ).

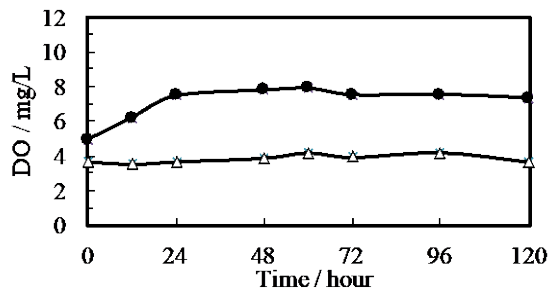


Fig. 4 Change in DO concentration over time in case 1 (●) and case 2 (Δ).

H₂S concentration is shown in Fig. 5. In case 1, H₂S decreases up to 24 h; after which it is no longer detected, before the addition of *A. fecalis* to the experimental tank. *A. fecalis* is not inhibited by H₂S. In case 2, H₂S decreased slightly and remained at 0.16 mg/L at 120 h.

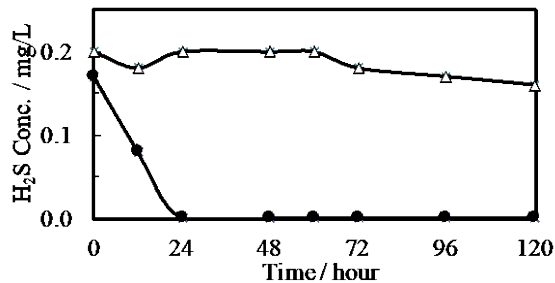


Fig. 5 Change in H₂S concentration over time in case 1 (●) and case 2 (Δ).

Results of NH₄-N, NO₂-N, NO₃-N and T-N

Figure 6 shows the change in NH₄-N (ammonium nitrogen) concentration in the experimental tank over time. In both cases (Table 1), initial concentrations of NH₄-N are approximately 1.5 mg/L. In case 1, NH₄-N decreases and is no longer detected at 72 h. The effect of *A. fecalis* on NH₄-N concentration could not be ascertained because *A. fecalis* was added at 24 h. In case 2, NH₄-N increases to 1.8 mg/L at 120 h.

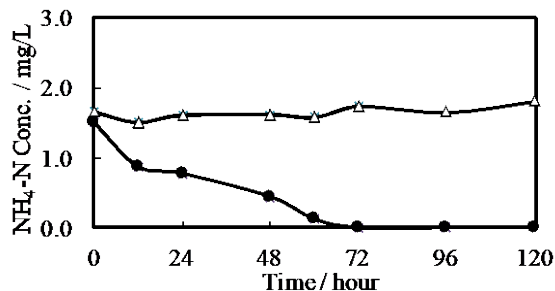


Fig. 6 Change in NH₄-N concentration over time in case 1 (●) and case 2 (Δ).

Figure 7 shows the change in NO₂-N (nitrite

nitrogen) concentration in the experimental tank over time. In case 1, initial concentrations of NO₂-N are approximately 0.28 mg/L. Subsequently NO₂-N constant at 0.01 mg/L up to 48 h, after which it is decreases and remained at 0.02 mg/L at 120 h. In case 2, initial concentrations of NO₂-N are approximately 0.28 mg/L. NO₂-N decreases to 0.13 mg/L at 48 h, then increases to 0.24 mg/L at 120 h.

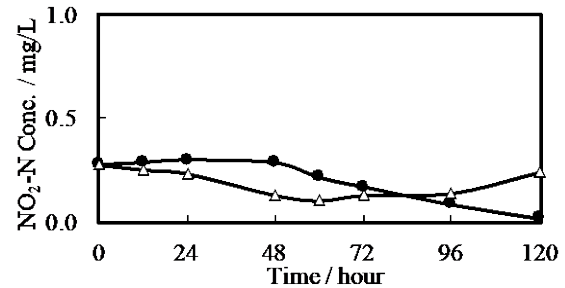


Fig. 7 Change in NO₂-N concentration over time in case 1 (●) and case 2 (Δ).

Figure 8 shows the change in NO₃-N (nitrate nitrogen) concentration in the experimental tank over time. In case 1, initial concentrations of NO₃-N are approximately 3.7 mg/L. Following this, NO₃-N increases to 4.6 mg/L at 6 h, then decreases to 0.60 mg/L at 120 h.

In case 2, initial concentrations are approximately 4.14 mg/L. Following this, NO₃-N increases to 4.7 mg/L at 24 h, then decreases to 2.2 mg/L at 96 h before continuing to gradually increase to 3.3 mg/L at 120 h.

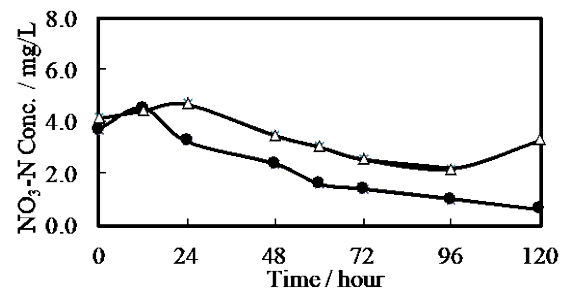


Fig. 8 Change in NO₃-N concentration over time in case 1 (●) and case 2 (Δ).

In case 1, concentrations of NH₄-N and NO₂-N and NO₃-N decreased. Conversely, concentrations of NH₄-N and NO₂-N and NO₃-N increased or remained constant in case 2. It is assumed that the metabolism of the bacteria switched from denitrification to nitrification because the condition of the experimental tank water changed to saturated dissolved oxygen concentration (Fig. 4). Therefore, we assume that the nitrogen source shifts to NH₄⁺ → NO₂⁻ → NO₃⁻ and that this trend of NO₃-N concentration is similar to NO₂-N.

In case 1, dissolved inorganic nitrogen (DIN; NH₄-N + NO₂-N + NO₃-N) shows a 90 % decrease

(Fig. 9). While T-N (total nitrogen, and inorganic and organic nitrogen) decreased and was eventually no longer detected (Fig. 10).

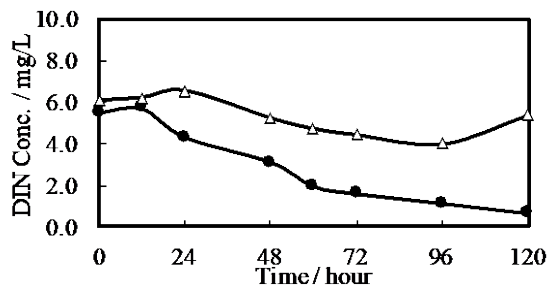


Fig. 9 Change in DIN concentration over time in case 1 (●) and case 2 (Δ).

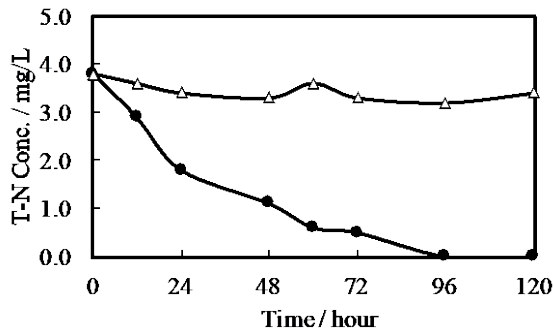


Fig. 10 Change in T-N concentration over time in case 1 (●) and case 2 (Δ).

Results of Bacterium concentration

DNA concentration in sludge was measured as bacterial concentration. Fig. 11 shows the change in DNA concentration. In both cases, initial concentrations of DNA are approximately 2 ug/g-sludge. In case 1, DNA doubled, while in case 2, DNA increased to 2.6 ug/g-sludge at 24 h, then decreased to 1.2 ug/g-sludge at 120 h.

The effect of the addition of *A. fecalis* to a circulation purification system on T-N concentration was investigated.

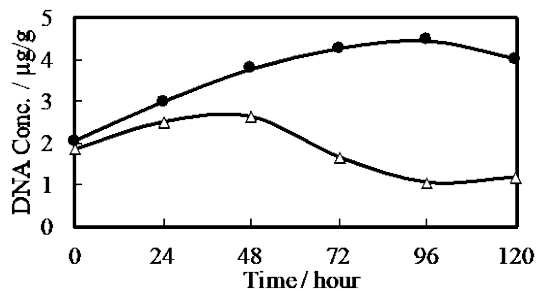


Fig. 11 Change in DNA concentration over time in case 1 (●) and case 2 (Δ).

Results of cesium concentration

Cesium and silica in the sludge were measured with energy dispersive X-ray analysis (EDX). The weight ratios of cesium to silica (Cs/Si) in dried sludge are shown in Fig. 12. The cesium decontamination ratio was calculated from the ratios of cesium content at 0, 6, 24, 48, 72, and 120 h as measured by EDX, using standard values for silica after measuring the weight of the dried sludge. The decontamination ratio obtained in case 1 was about 51 %.

Cesium concentrations in the water are shown in Fig. 13. In case 1, initial concentrations of Cesium are approximately 40 mg/L. Subsequently Cesium decreases to 8.3 mg/L at 120 h indicating that 71 % of cesium was removed.

In case 2, cesium concentrations in the dried sludge and the water did not decrease. Therefore, eluted cesium from the sludge was adsorbed onto the zeolites after the sludge was decomposed by micro-bubbles and *A. fecalis*.

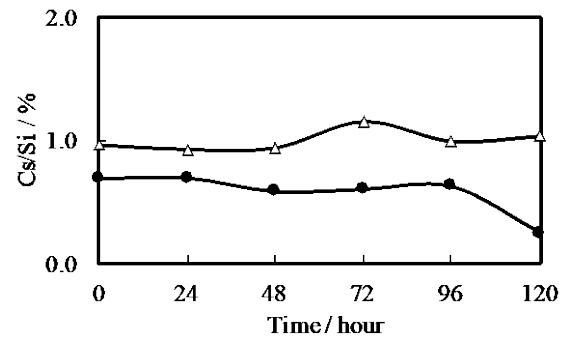


Fig. 12 Change in Cs/Si over time in case 1 (●) and case 2 (Δ) in dried sludge.

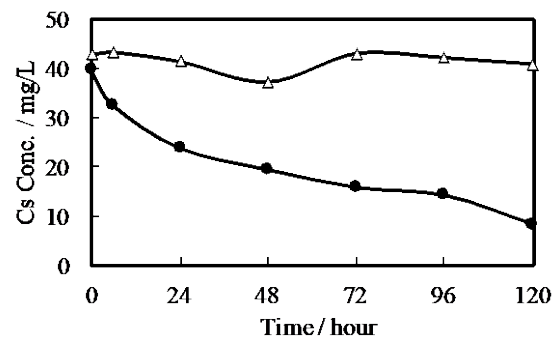


Fig. 13 Change in Cs concentration over time in case 1 (●) and case 2 (Δ) in liquid phase.

The Model sludge was prepared 100 mg/L Cesium chloride in tank and mixed for 24 h. So, at the time of experiment start, Cesium concentration of water was 39.6 mg/L, cesium adsorbed onto sediments was 60 mg/L. After 120 hrs, 31 mg/L

(51%) of cesium onto sediments, and 8.3 mg/L of cesium in water had been remaining. Accordingly, using micro-bubble circulation system with bacteria and zeolite, 61 mg/L of cesium was removed and its removal ratio was 61%.

In case 2, using zeolite only, 42.8 mg/L of cesium in water was removed, while, cesium on sediments was remain unaltered. Therefore, total cesium removal ratio was 42.8%.

Moreover, Okamoto et.al (2015) was reported that cesium concentration of water and sediments was remain unaltered using micro-bubble circulation system with bacteria [4]

These results suggest that after the deposited sludge is decomposed by our micro-bubble circulation system with bacteria and zeolite, the cesium is eluted into water, it can then be remove using zeolites.

CONCLUSION

We carried out elution and fixing of cesium in ocean sludge using a micro-bubble and bacterial circulation decomposition system. From water quality measurements, it can be concluded that after adding *A. fecalis*, T-N decreases and is then no longer detected. *A. fecalis* has a remarkable ability to treat samples through denitrification. The cesium concentrations in sludge and water decreased through treatment with micro-bubbles and bacteria for 120 h. 76% of cesium in dried sludge and 51% of cesium in water were removed. From the results obtained, we can affirm that the system proposed would greatly facilitate cesium removal from ocean sludge.

ACKNOWLEDGEMENTS

The authors would like to express sincere thanks to OSHA Rintarou students of Nihon University, in Japan, for executing the experiments.

This work was supported by KAKENHI C-17K06969 (Grant-in-Aid for Scientific Research).

REFERENCES

[1] Soemori A, Shozugawa K, Nogawa N, Higaki S, Matsuo M, "A change in the concentrations of radioactive cesium in Tokyo-bay's sediments released by the Fukushima Dai-ichi Nuclear Power Station accident", Bunseki Kagaku, Vol. 62(12), 2013, pp. 1079–1086.
 [2] He Q, Walling D E, "Interpreting particle size effects in the adsorption of ^{137}Cs and

unsupported ^{210}Pb by mineral soils and sediments", J. Environ. Radioactivity, Vol. 30(2), 1996, pp. 117–137.
 [3] Okamoto K, Hotta K, Toyama T, Kohno H, "Purification system of ocean sludge by activating microorganisms", Int. J. of GEOMATE, Vol. 6(1), 2014, pp. 791–795.
 [4] Komoriya T, Okamoto K, Toyama T, "Effect of adding of bacteria on the removal of radioactive cesium from ocean sludge in a circulation type purification system", Int. J. of GEOMATE, Vol. 12, 2017, pp. 121–126.
 [5] Okamoto K, Toyama T, "Decontamination of radioactive cesium from ocean sludge by micro-bubble and microorganisms", Int. J. of GEOMATE, Vol. 9(1), 2015, pp. 1390–1394.
 [6] Matsuo K, Maeda K, Ohnari H, Tsunami Y, Ohnari H, "Water purification of a dam lake using micro bubble technology", Progress in Multiphase Flow Research, Vol. 1, 2006, pp. 279–286.
 [7] Inamori Y, Wu X-L, Kimochi Y, "Characteristics of N_2O production by *Alcaligenes faecalis* under aerobic conditions", Journal of Japan Society on Water Environment, Vol. 22, 1999, pp. 904–909.
 [8] Okamoto K, Toyama T, "Ocean decontamination: Removal efficiency of radioactive cesium from ocean sludge by using micro bubbles and activating microorganisms", Int. J. of GEOMATE, Vol. 10(21), 2016, pp. 1924–1928
 [9] Okamoto K, Hotta K, "Purification experiments on sedimentary sludge by microorganism activator", In Proc. of Pacific Congress on Marine Science and Technology (PACON), 2008.

GEOCHEMICAL REACTIVE MODELING OF FLOW AND TRANSPORT PROCESS AT A MINE SITE IN NORTHERN TERRITORY, AUSTRALIA

Michael S. Hayford¹, Bithin Datta^{1, 2}

¹College of Science and Engineering, James Cook University, Australia; ²CRC-CARE, University of New Castle, Australia

ABSTRACT

Subsurface contamination of metals and radionuclides are common problems in abandoned mine sites. Metals and radionuclides are likely to occur in the mobile phase or may bind to soil particles and geologic framework. The transport process for reactive contaminants also include chemical reactions in groundwater aquifers which are complex physical and biogeochemical processes. Accurate tools to reliably predict the movement and changes in concentration of metals and their daughter products (radionuclides) formations in the subsurface environment is important for decision makers to analyze impact, and to evaluate the effectiveness of remediation strategies. An advanced numerical model can provide such useful direction of predictions. A 3-D contaminant transport model for fluid flow, hydrogeologic transport, and biogeochemical kinetic and equilibrium reactions in saturated and unsaturated media was calibrated, validated and implemented to model the hydrogeochemical processes that occur in the subsurface at such a complex contaminated site, consisting of waste rock dumps and flooded mine pits in of this an abandoned uranium mine site. The developed flow and transport simulation model for no longer in use mine site in Northern Territory of Australia is discussed.

Keywords: Reactive Transport, flow and transport modelling, groundwater contamination, Mine site

INTRODUCTION

Groundwater plays an important role in human history and groundwater contamination has attracted intensive investigations in the past 30 years. Contaminants in the aqueous environment undergo changes in concentration resulting from physical, chemical, biological processes, and a capability to understand and model these processes is at the core of assessing the efficacy of environmental remediation strategies. The modeling and prediction of the complex multiple species reactive transport process in mine sites is particularly challenging. The development of an accurate model capable of predicting the transport scenario is very challenging, but a necessity for designing future remediation strategies. Therefore, a robust numerical multiple species reactive transport simulation model HYDROGEOCHEM 5.0 [1] has been calibrated and validated for a study area comprising of an underlying aquifer in a no longer operational mine site in the Northern Territory of Australia. Acid rock drainage (ARD) and heavy metal mobilization at the former mine site have led to significant environment impacts on local groundwater and in the East Branch of the Finnis River [2].

Acid and metalliferous drainage (AMD) also referred to as acid mine drainage or acid rock drainage occurs when sulphidic minerals, such as arsenopyrite, chalcopyrite and pyrite, are exposed to oxygen and water. Although AMD occurs naturally,

the majority of AMD is anthropogenic and originates from reactive sulphide minerals stored in waste rock dumps (WRDs), mine pits, and tailings. Notwithstanding the fact that extensive rehabilitation studies at the mine site exist, a well-defined reactive transport model, with a comprehensive suite of reaction types and reaction rates incorporated into a model aimed at the remediation and rehabilitation of the site, has not been implemented yet. These reaction types includes but not limited to aqueous complexation, adsorption-desorption, ion-exchange, oxidation-reduction, precipitation-dissolution, acid-base reactions, and microbial mediated reactions.

The main sources of pollutants to the environment are the open pit, the waste rock dumps and the tailings dam. The waste rock dumps and tailing dams most often consist of several minerals and geological matrix which are exposed to weathering conditions. Pyrite oxidation is the principle reaction in the leaching of metal and radionuclides into environment. Accurate prediction of the release rate of metal and radionuclides from these sources and their transport into the subsurface environment is a critical factor to the assessment of environmental impacts and to the development of effective remediation strategies. To produce a realistic representation of the system under study with the existing real complex problems, sophisticated models are required. Reactive transport codes are powerful tools in the evaluation of coupled hydrological chemical processes and in the prediction of the long-term performance of remediation

strategies.

A presentation of the application of a reactive-transport model to simulate the transport of reactive multi-species contaminants in heterogeneous, anisotropic, saturated-unsaturated waste rocks damp and mine open pits of the first uranium mine site in Australia is illustrated in this paper. The computer program used to describe the complex hydrogeochemical processes that control the generation of acid drainage and the distribution of solutes between groundwater and waste rock damp is the hydrogeochemical transport model, HYDROGEOCHEM 5.0. This numerical code has been earlier used for modeling a mine site in Queensland Australia [3]. The computer program is a 3-D numerical model of fluid flow, thermal, hydrologic transport, and biogeochemical kinetic and equilibrium reactions in saturated and unsaturated media.

The purpose of this paper is to focus on the solution results of reactive transport geochemical modeling to predict the important complex processes that control the movement and distribution of contaminants in ground water. It is also likely that this calibrated and validated transport model will be utilized for a contamination source characterization study for this contaminated aquifer site. Information gained from these investigations should also provide insight into processes that occur at other sites similarly contaminated.

METHODOLOGY

Study Area Description

The former mine site is located approximately 105km by road south of Darwin in the headwaters of the East Branch of the Finnis River, near Batchelor in the Northern Territory, Australia. This former mine was one of Australia's first major uranium mines and produced approximately 3,500 tonnes of uranium and 20,000 tonnes of copper concentrate between 1954 and 1971 [4]. Uranium was mined from White's and Dyson's open pits from 1954 to 1971, while copper was extracted from the Intermediate pit in 1964. The site underwent rehabilitation from 1983 to 1986 at a total cost of \$18.6 million. Several rehabilitation works have taken place since 1986 and rehabilitation is still on going. [4]

Geological and hydrogeological characterization

The mine areas consist of east branch of the Finnis River about 8.5 km upstream of its confluence with the West Branch of the Finnis River. Surface water enters the mine site from the east via the upper East Branch of the Finnis River and from the southeast via Fitch Creek. River flows vary in response to intra annual variability in rainfall and

changes over the course of a year [5]. The mine area mineral field contains polymetallic ore deposits, such as the Ranger and Woodcutters ore deposits. The mine site includes the Giant's reef fault. The main lithological units are the Rum Jungle Complex and meta-sedimentary and subordinate meta-volcanic rocks of the Mount Partridge Group. The Rum Jungle Complex consists mainly of granites and the Mount Partridge Group consists of sedimentary units: Geolsec formation, the Whites formation, the Coomalie Dolostone, and the Crater formation [6].



Fig. 1 Satellite view of the study site

Numerical Simulation

Flow Model

The general equations for flow through saturated-unsaturated media are obtained based on following fluid continuity, solid continuity, fluid movement (Darcy's law), stabilization of media, and water compressibility [1]

$$\frac{\rho}{\rho_o} F \frac{\partial h}{\partial t} = -\nabla \cdot \left[K \left(\nabla h + \frac{\rho}{\rho_o} \nabla z \right) + \frac{\rho^*}{\rho_o} q \right] \quad (1)$$

Where F = generalized storage coefficient (1/L) defined as

$$F = \alpha' \frac{\theta}{n_e} + \beta' \theta + n_e \frac{dS}{dh} \quad (2)$$

$$K = \frac{\rho g}{\mu} K = \frac{\rho/\rho_o}{\mu/\mu_o} \frac{\rho_o g}{\mu_o} K_s K_r = \frac{(\rho/\rho_o)}{(\mu/\mu_o)} K_{so} k_r \quad (3)$$

and V = Darcy's velocity (L/T), described as:

$$\mathbf{V} = -\mathbf{K} \cdot \left(\frac{\rho_o}{\rho} \nabla h + \nabla z \right) \quad (4)$$

Where: θ : effective moisture content (L^3/L^3); h: pressure head (L); z is the potential head (L), t: time (T); q: source or sink of fluid [$(L^3/L^3)/T$]; ρ_o : fluid density without biochemical concentration (M/L^3); ρ : fluid density with dissolved biochemical concentration (M/L^3); ρ^* : fluid density of either injection ($= \rho^*$) or withdraw ($= \rho$) (M/L^3); μ_o : fluid

dynamic viscosity at zero biogeochemical concentration $[(M/L)/T]$; μ : the fluid dynamic viscosity with dissolved biogeochemical concentrations $[(M/L)/T]$; α' : modified compressibility of the soil matrix (1/L); β : modified compressibility of the liquid (1/L); n_e : effective porosity (L^3/L^3); S : degree of effective saturation of water; G : is the gravity (L/T^2); k : permeability tensor (L^2); k_s : saturated permeability tensor (L^2); K_{so} : referenced saturated hydraulic conductivity tensor (L/T); k_r : relative permeability or relative hydraulic conductivity (dimensionless). The finite element method was used to solve Eq. (1), (2), (3) and (4), and the constitutive relationships among the pressure head, degree of saturation, and hydraulic conductivity tensor, together with the appropriate initial conditions and boundary conditions. The temporal-spatial distributions of the hydrological variables, including pressure head, total head, effective moisture content, and Darcy's velocity were simulated.

Reactive transport Model

Governing equations for the reactive transport of the reactive biogeochemical system is discussed below. The equations for transport were derived based on the continuity of mass and Fick's flux laws. The main transport and fate processes are advection, dispersion/diffusion and biogeochemical reactions (including radioactive decay). The general transport equation governing the temporal-spatial distribution of any biogeochemical species in a reactive system is described below [1]:

$$\frac{\partial \theta C_i}{\partial t} + \theta \alpha' \frac{\partial h}{\partial t} C_i = L(C_i) + \theta r_i + M_i, i \in \{M\} \quad (5)$$

Where L is the transport operator denoting

$$L(C_i) = -\nabla \cdot (\nabla C_i) + \nabla \cdot \left[\theta D \cdot \nabla C_i \right] \quad (6)$$

where C_i is the concentration of the i -th species in units of chemical mass per water volume $[M/L^3]$; r_i is the production rate of the i -th species because of biogeochemical reactions in chemical mass per water volume per unit time $[M/L^3/T]$; $\{M\} = \{1, 2, \dots, M\}$ in which M is the number of biogeochemical species; D is the dispersion coefficient tensor $[L^2/T]$; and M_i is the source/sink of the i -th species in chemical mass per unit volume of media $[M/L^3/T]$.

Conceptualization and Model discretization

A numerical groundwater flow model is constructed to simulate variations in the groundwater flow system at the mine site from December 2010 to

November 2014. This numerical flow model is a mathematical representation of a conceptual model that enables a quantitative representation of real field features. The numerical representation is based on the following assumptions: The aquifer system at the former mine site can be subdivided into hydrostratigraphic units that represent either waste rock dumps or the naturally occurring bedrock aquifer, each hydrostratigraphic unit is represented as a single model layer with representative hydraulic properties and recharge is estimated as a proportion of incident rainfall, mine waste is represented by a single model layer of variable thickness of the waste rock dumps and Dyson's (backfilled) open Pit, whereas the geological aquifer units is represented by model layers with constant thicknesses across the model domain, water movement in the hydrostratigraphic units follows Darcy's law, the flooded open pits is represented by specified head boundary condition that is equivalent to observed water levels in the pits during the simulation period.

Numerical method

The finite element method is used for temporal and spatial discretization of the governing partial differential equations in the flow module. The Galerkin finite element method was used for spatial discretization of the modified Richards equation that governs the distribution of pressure fields. For this model, the critical assumption of this approach is that every element within a particular section of a layer is assigned a set of hydraulic properties to account for heterogeneity. The layers are discretized horizontally into triangular wedge elements but each layer of a finite element mesh is one element thick. The flow of the groundwater is simulated for the observation period 2010 and 2014. Two case scenarios of both steady state and transient flow is simulated for the flow.

Spatial Discretization

The numerical model domain was spatially discretised into a 3-dimensional mesh with a triangular wedge mesh. In planar view, each element is a triangular wedge, whereas the thickness of the elements depends on the number of layers used to vertically discretize the model domain. The thickness of the elements varies depending on lithology. The model is made up of 6 layers and covers a maximum elevation of about 110 m. Surface topography from a recent terrain elevation data was used to define the top of layer 1, including the WRDs and Dyson

(backfilled) pit. Figure 2 shows a plan view of finite element model domain. Layer thicknesses are allocated in this order. Layer 1 which consist mainly of waste rock dumps is assigned variable thickness, layer 2 thickness is from 0 to 7.5 m, layer 3m is 7.5m to 15 m, layer 4 is 15m to 45 m, layer 5 is 45m to 105 m, and layer 6 is 105m to 150 m. The tops and bottoms of layers 3 to 6 are set to thicknesses values listed above which is fixed throughout the model.

Boundary conditions

Specified heads boundary conditions is assigned to elements from layers 1, 2, 3, and 4 that intersects the perimeters of the flooded pits which includes main, intermediate and brown oxide pits. These elements represent the bedrock aquifer that is in contact with standing water within the pits and were assigned a head that is equal to the measured water level in the pits. Flows within the flooded open pits themselves are not simulated by the model so elements within the head boundary are set to be inactive. Pit water levels and groundwater levels at monitoring locations close are used to represent the open pit as a head boundary. The brown's oxide open pit is not completely flooded so heads were only specified for elements in layers 3 and 4. Time varied constant head nodes are set that simulate water level changes in the main, intermediate and brown's pits and the river. The aquifer parameters imputed to model area is shown in Table 1

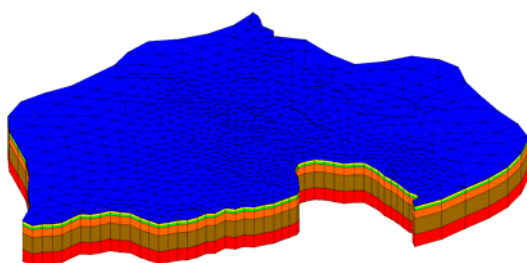


Fig. 2 Three dimension finite element representation of the study site

To model and simulate the reactive transport processes, equations of either the conventional finite element methods or the hybrid Lagrangian–Eulerian finite element methods were used for spatial discretization. The chemical equilibrium equations were solved by the Newton–Raphson method or Picard method. This study considers the possible hydrogeochemical transport of 6 components, including OH^- , Cu^{2+} , Fe^{2+} , Fe^{3+} , Mn^{2+} , UO_2^{2+} and 20 species are considered in this study. These selected sets of components are based on the fact that the primary mining commodities were uranium and

copper. Table 2 shows some chemical reactions incorporated in the model.

Table 1 Aquifer hydrogeologic properties

Aquifer parameter	Value
Number of nodes	6587
Number of elements	10704
Horizontal hydraulic conductivity, K_x K_y	m/d
Layer 1	0.01728 - 5.0112
Layer 2	0.00864 - 0.7776
Layer 3	0.00864 - 0.84672
Layer 4	0.00864 - 0.84672
Layer 5	0.00864 - 0.02592
Layer 6	0.0001728 - 0.0648
Vertical hydraulic conductivity, K_z	m/d
Layer 1	0.00864 - 0.24192
Layer 2	0.00432 - 2.4192
Layer 3	0.00864 - 0.864
Layer 4	0.00864 - 1.296
Layer 5	0.00864 - 0.20736
Layer 6	0.00864 - 0.0648
Effective porosity, θ	0.28
Longitudinal dispersivity, α_L	10 m/d
Transverse dispersivity, α_T	0.1 m/d
Vertical dispersivity (α_V):	0.01
Average rainfall	2372 mm/year

Table 2 Chemical reactions involved in transport

Chemical reactions	Constant rate (log K)
$\text{H}_2\text{O}(\text{aq}) \rightarrow \text{H}^+ + \text{OH}^-$	-13.99
$\text{H}^+ + \text{SO}_4 \rightarrow \text{HSO}_4^-$	1.99
$\text{Cu}^{2+} + \text{H}_2\text{O} \rightarrow \text{Cu}(\text{OH})^+ + \text{H}^+$	-9.19
$\text{Cu}^{2+} + \text{SO}_4^{2-} \rightarrow \text{CuSO}_4$	2.36
$\text{Cu}^{2+} + 2\text{H}_2\text{O} \rightarrow \text{Cu}(\text{OH})_2 + 2\text{H}^+$	-16.19
$\text{Cu}^{2+} + 3\text{H}_2\text{O} \rightarrow \text{Cu}(\text{OH})_3^- + 3\text{H}^+$	-26.9
$\text{Fe}^{2+} + \text{H}_2\text{O} \rightarrow \text{H}^+ + \text{FeOH}^+$	-9.50
$\text{Fe}^{2+} + \text{SO}_4^{2-} \rightarrow \text{FeSO}_4$	2.20
$\text{Fe}^{2+} + 2\text{H}_2\text{O} \rightarrow 2\text{H}^+ + \text{Fe}(\text{OH})_2(\text{aq})$	-20.57
$\text{Fe}^{2+} + 3\text{H}_2\text{O} \rightarrow 3\text{H}^+ + \text{Fe}(\text{OH})_3^-$	-31.00
$\text{Fe}^{2+} + 4\text{H}_2\text{O} \rightarrow 4\text{H}^+ + \text{Fe}(\text{OH})_4^{2-}$	-46.00
$\text{Mn}^{2+} + \text{SO}_4^- \rightarrow \text{MnSO}_4$	2.26
$\text{Mn}^{2+} + \text{H}_2\text{O} \rightarrow \text{MnOH}^+ + \text{H}^+$	-10.59
$\text{Mn}^{2+} + 3\text{H}_2\text{O} \rightarrow \text{Mn}(\text{OH})_3^- + 3\text{H}^+$	-34.08
$\text{UO}_2^{2+} + \text{SO}_4^{2-} \rightarrow \text{UO}_2\text{SO}_4$	3.15
$\text{UO}_2^{2+} + \text{SO}_4^{2-} \rightarrow \text{UO}_2(\text{SO}_4)_2^{2-}$	4.14
$\text{UO}_2^{+2} + 2\text{H}_2\text{O} \leftrightarrow \text{UO}_2(\text{OH})_2 \text{aq} + 2\text{H}^+$	12.15

Conceptual Modelling

The transport model for the mine site was built upon the flow model by including the necessary transport conditions which includes the transport boundary conditions, the total number of components and the species to be simulated. The assumption is that the transport of the contaminants is based solely on the flow fields simulated whereby there is a possible rock interaction or mineral interactions with the aquifer rock bed and formation of daughter products or

additional species.

It is assumed that the oxidative dissolution of pyrite is the driving force in the discharge rate of metal and radionuclides from waste rock dumps. The reactive system is completely defined by geochemical reactions through a network of reactions specifying chemical reactions and the total number of chemical species involved in the reaction. The standard equilibrium expression with a suitable equilibrium constant is used to represent all the fast reactions, such as the aqueous complexation reaction and precipitation of secondary phases. The slow reactions were represented by the kinetic expression and associated rate constants to address the dissolution reactions of key minerals present in the waste rock dumps and pits. The reaction network that describes the evolution of the geochemical system is shown in the Table 2.

RESULTS AND DISCUSSION

The flow model calibration is carried out by running the forward simulation repeatedly, and manually adjusting the input parameters selected for calibration, including those used to define initial and boundary conditions, at each time, until a satisfactory match between model results and field data is achieved. The trial and error procedure is used in this study. This is adopted because it is conceptually straight forward and requires nothing more computationally than making multiple forward simulation runs. This procedure is flexible allowing any adjustment in parameter values and parameter structures, including changes in mesh designs and the representation of the geologic frame work

The main aim of calibration was to obtain the estimation of hydraulic conductivity and groundwater levels for the aquifer based on limited field measurement data. Hydraulic head measurement data from 20 monitoring locations distributed across the mining area were used for the simulation model calibration. The hydraulic head data used for model calibration and validation were recorded in 2010 and 2014. A portion of the average rainfall intensity per year was specified as recharge for calibration of the simulation model also using measured head data from monitoring locations. Calibration targets for the developed model were set to be within 2m intervals of the observed hydraulic head value in monitoring locations with a confidence level of 90%. Exact boundary conditions are difficult to determine with very limited observed measurement data. Hence, realistic boundary conditions need to be specified that matches the site conditions. In the calibration process, one of the most difficult issues is to assign appropriately the correct boundary conditions. Therefore, the boundary conditions need to be determined based on preliminarily calibration results

as well. The model's boundary conditions are adjusted manually to achieve the calibration targets. The measured and simulated heads were compared at selected points.

The developed model was calibrated for flow using observed head data obtained at monitoring points. In the calibration process, estimates of the values of recharge for each recharge zone and the representative hydraulic conductivity of each layer were calibrated. Results of simulated heads calibration are shown in Table 3.

Table 3 Comparison of observed and simulated heads

Location ID	observed head(m)	computed head(m)	Residual (m)
P1a	61.44	62.48	-1.04
P1b	62.65	63.65	-1
P2	63.27	63.12	0.15
P3	60.29	64.9	-0.11
P4	60.41	60.86	-0.45
P5	57	57.14	-0.14
P6	58.33	59.09	-0.76
P7	56.39	59.05	-2.66
P8D	53.96	54.68	-0.72
P9D	56.57	56.69	-0.12
P10	57.63	58.03	-0.4
P11	57.16	57.87	-0.71
P12	56.44	56.91	-0.47
P13	56.89	56.9	-0.01
P14	57.06	57.55	-0.49
P16	56.27	57.16	-0.89
P17	56.45	57.29	-0.84
P18	57.28	58.27	-0.99
P19	57.35	58.23	-0.88
P20	51.01	51.69	-0.68

The flow model is calibrated first to adjust the model input parameters that control the flow process, such as hydraulic conductivity and recharge, sink/sources stress. When the flow model is calibrated to a certain degree, calibration of the transport model is initialized to adjust those parameters specific to the transport model, such as porosity, dispersivity and source concentration. Recalibration of the flow model is done to further adjust the initially calibrated flow parameters. After readjustment of the flow parameters, a new velocity distribution is calculated and used in the transport model where further adjustments in the transport parameters are made. This iterative procedure is repeated until both flow and transport related field data are matched by the simulation results. The results of the calibrated heads

against the observed heads is shown in Table 3. These results show fairly good history matching of the hydraulic heads. The reactive transport model simulation time is 2 years from 2012 to 2014 as of the availability of data. The precipitation/dissolution on the changes of porosity, hydraulic conductivity, and hydrodynamic dispersion of aquifer media may be a key hydrogeochemical mechanism in the transport process. Thus, the effect of precipitation/dissolution reactions on both flow and reactive transport are also considered in the simulations. Moreover, to evaluate the effect of redox processes influencing on the formations of degradation materials, pyrite oxidation, sulfate reduction reactions are also incorporated in the simulation scenarios. Copper (Cu^{2+}), sulphate (SO_4^{2-}), Manganese (Mn^{2+}), Uranium (UO_2^{2+}) and Iron (Fe^{2+}) are introduced as initial contaminants in the waste dump rocks and the open pits, which is assume to be involved in chemical reactions listed in Table 2. The assumed initial conditions for contaminant concentration are specified in the simulation model based on the available data and extrapolation within the area. The sources considered for this study are dysons waste rock dump, dyson open pit, main waste rock dump, intermediate waste rock dump, main pit and intermediate pit. The objective was to demonstrate the flexibility of the model to adapt a known reaction network to an abandon mine site setting and to demonstrate the capability of the code to simulate large complex problems. The results of the simulated concentrations are shown in the Figure 4, Figure 5 and Figure 6.

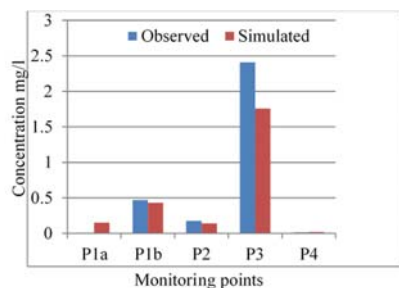


Fig. 4 Comparison of observed and simulated copper concentrations mg/ l at monitoring points

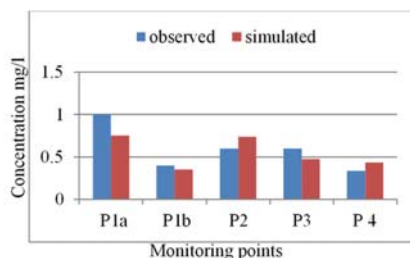


Fig. 5 Comparison of observed and simulated iron concentrations mg/ l at monitoring points

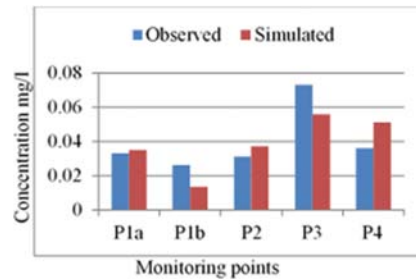


Fig. 7 Comparison of observed and simulated uranium concentrations mg/ l at monitoring points

CONCLUSION

The calibrated flow model, and the developed transport simulation model are capable of simulating the complex flow and multiple species reactive transport processes in the geologically complex multiple layer, heterogeneous aquifer comprising of a no longer in use uranium mine site in NT, Australia. The aquifer processes are considered as 3-dimensional, geologically layered and heterogeneous, with transient flow and transport. It was possible to calibrate the flow model by using sparse spatial-temporal hydraulic head measurements. The contamination simulation scenario resembled the field conditions to a certain extent. The concentrations predicted for the chosen species match with the concentration measurement values available. Therefore, the simulation model, based on HYDRGEOCHEM once calibrated for site conditions, is potentially a good candidate to model the complex flow and transport processes in a geochemically and geologically complex mine site aquifer.

ACKNOWLEDGEMENTS

The authors acknowledge the financial support for this work provided by CRC-CARE, University of New Castle, Callaghan NSW 2308, Australia and James Cook University, Australia.

REFERENCES

- [1] Yeh GT, Sun J, Jardine PM., Burgos WD, Fang Y, Li M., Seigel M.D, ("HYDRGEOCHEM 5.0: A Three-Dimensional Model of Coupled Fluid Flow, Thermal Transport, and Hydrogeochemical Transport through Variably Saturated Conditions - Version 5.0", 2004
- [2] Kraatz M, "Rum Jungle Rehabilitation Site Scoping Study, Environmental Issues and Considerations for Future Management", Report to the Department of Industry, Tourism and Resources, M4K Environmental Consulting, February 2004.

- [3] Esfahani HK, Datta B, “Linked Optimal Reactive Contaminant Source Characterization in Contaminated Mine Sites: Case Study”, *Journal of Water Resources Planning and Management*, Vol 142, Dec. 2016
- [4] Norther Territory Government. “Rum Jungle Conceptual Rehabilitation Plan”, May 2013
- [5] Ferguson PR, Wels C, Fawcett M, “Current water quality conditions at the historic Rum Jungle Mine Site, northern Australia”. *Proceedings of 9th International Conference on Acid Rock Drainage ICARD*), May 20-26, 2012, Ottawa, Canada.
- [6] Robertson GeoConsultants Inc., Phase 3 (Stage 2 Report) “Groundwater Flow Model for the Rum Jungle Mine”, RGC Report submitted to NT DoR, May 2012.

IMPACT OF LAND LEVELING ON THE WATER BALANCE FOR AGRICULTURE IN EASTERN AFGHANISTAN

*Shakerullah Hashimi¹, Pervaiz Ahmad Naseri², Najumuddin Anjum³ and Takamitsu Kajisa⁴

¹Master candidate, Graduate School of Bioresources, Mie University, 514-8507 Kurimamachiya-cho 1577, Tsu, Japan. ²Project Manager of On-Farm Water Management Project, Ministry of Agriculture Irrigation and Livestock (OFWMP/MAIL) Kabul, Afghanistan. ³ Water Management Specialist (OFWMP/MAIL) Kabul, Afghanistan. ⁴Professor of Bioresources, Mie University, 514-8507 Kurimamachiya-cho 1577, Tsu, Japan.

ABSTRACT

The aim of this study was to investigate the effect of laser land leveling (LL-leveling) on the vertical movement of water through soil (seepage rate). Although we could have discussed the use of LL-leveling for crop yield and water efficiency in eastern Afghanistan the difference in seepage was not clear. Therefore, herein, both the water balance at the land surface and the impact of LL-leveling on infiltration rates were investigated. The field experiments were comprised of two parts: Farm-A underwent LL-leveling; and Farm-B was used as the control farm with all other practices maintained the same. The results from Farm-A illustrate that, from a water balance perspective, water seepage was reduced due to smaller water inflow, larger farm size or regular farm shape. By comparing the two farms, we could confirm the linearity of water input to water seepage based on measurements in both areas. Seepage was reduced with increasing field size. In our data, the water input decreased following LL-leveling. This may be strongly related to the water saving mechanisms employed in Farm-A. Further, the areal size of the farm increased following LL-leveling and potentially also contributed to the observed increase in water savings. Simultaneously, we could affirm that the seepage is affected by land cultivation practices and the selection of crop types. Overall, in Farm-A the seepage rates were reduced with LL-leveling by 18%, 77%, and 25% in plots cultivated for wheat, corn, and eggplant, respectively. Thus, it has become clear that LL-leveling will increase water savings.

Keywords: Infiltration, Crop Type, Cultivation Age, Irrigation Interval

INTRODUCTION

The main challenges faced by the Afghan agricultural sector are the shortage of water and the high demand for irrigation water [2]. The country is not self-sufficient in its water requirements nor is it relieved from the impacts of its neighbors'. While undeniably land-locked, the country has five river basins of which four major rivers flow into neighboring countries. However, only a small proportion (around one third) of the water that originates here is utilized within the country. The economy of Afghanistan relies mostly on agriculture, particularly on irrigated agriculture.

Nonetheless, farmers still use traditional farming techniques wherein oxen provide the draught power. The farmers' knowledge of new irrigation technologies and cultural practices is insufficient. Consequently, the efficiency of the irrigation system is quite low (25%–30%) mainly due to high conveyance losses in the traditional watercourses with earth canals, high operational losses in modern schemes with lined conveyance canals, and high on-farm distribution losses (e.g., over-irrigation, poorly leveled land) in both traditional and modern irrigation schemes. The productivity levels are low even by

regional standards. About 20% of both the traditional and modern irrigation systems require an upgrade of the on-farm water management in order to improve the low crop yield or to address water logging and salinization. In fact, the land production potential under low and variable rainfall can be improved by promoting technology transfer [8]-[9]. In traditional as well as modern irrigation schemes, the dominant irrigation method is basin/border irrigation for cereals and furrow irrigation for vegetables and grapes. Farmers are usually not aware about crop water requirements, and over-irrigation is a common practice.

The overall efficiency is only about 25%–30% for both modern and traditional irrigation schemes, resulting in significant water losses and low productivity [4]. The cropping intensity (it is the ratio of net area sown to the total cropped area) varies widely between irrigation systems depending on water availability. It reaches 200% in the upper part of the irrigated area, whereas, in the lower parts, up to-thirds of the crop area remains fallow each year on a rotational basis. In the large schemes supplied by rivers, floods often damage irrigated land as a result of the frequent change in river course due to the high sediment loads and unfavorable geomorphological

conditions [8]-[9]. Traditional management approaches to irrigation supply and conveyance often contribute to high-water losses.

Moreover, low irrigation efficiency is further accentuated by traditional irrigation methods and practices used by farmers, as well as inadequate land leveling [12]. Water scarcity can be overcome by improving water use efficiency at the field level [11]. With traditional applications of water to the fields, crop yields decrease by 75%–85% on average, a percentage that varies widely among farms.

Furthermore, poor farm designs and uneven fields are responsible for 30% of the water losses [6]. About 18 million acre-feet of water are lost while irrigating uneven fields in Pakistan [3]. Due to the low water use efficiency and lack of inputs (chemical fertilizer, improved seed and so on), crop yields are very low. At present, drought has caused a further reduction in crop yields, e.g., the average yield of wheat is 0.8 tons/ha today as opposed to about 1.1 tons/ha in 1978. The total area (irrigated and rainfed) cultivated for cereal crops is about 3.39 million ha. The total cereal production is 4.15 million tons, 2.65 million tons of which are from wheat [8]-[9].

Irrigated agriculture is the mainstay of food security and income for most of the rural population in Afghanistan. It accounts for more than half of the country's GDP and 70% of the total crop production; moreover, it provides a reliable and sustainable production base for several rural communities. The total cultivable area of Afghanistan is about 8 million hectares, which is 12% of the total area of the country. Nearly 3.9 million ha of cultivated land exists in Afghanistan, of which 1.3 million ha is rainfed and 2.6 million ha are irrigated. This irrigated area produces almost 85% of the total agricultural production [10]. LL-leveling and agricultural technology transfer programs were implemented from 2008 to 2011 for wheat crops in the Kama district (Nangarhar and Balkh provinces, Afghanistan). During this period, the maximum reported wheat yield was 6.18 tons/ha and the minimum was 4.01 tons/ha [7].

LL-leveling and layout improvements were conducted in the Bihsud district (Nangarhar province, Afghanistan). Yields of 41, 5.25, and 4.4 tons/ha were noted for eggplant, corn, and wheat respectively. The water savings found in these fields were 17%, 27%, and 21% for eggplants, corn, and wheat, respectively [13]. Seepage is the lateral movement of subsurface water in soil, whereas, percolation is the vertical movement of water beyond the root zone to the water table, and the two are often inseparable [17]. Percolation losses have been reported to vary from 0.1 to several hundred mm/day [16]. These rates can be decreased by increasing the resistance to water movement in the soil and by reducing the hydrostatic pressure of the ponded water [1].

However, studies conducted in eastern

Afghanistan in 2016 on crop yields and water efficiencies in LL-leveled areas did not confirm a difference in the vertical movement of water through soil (seepage rate). Thus, herein, the water balance at the land surface and the effects of LL-leveling on seepage rates have been investigated. The current research was undertaken at the irrigation demonstration site of the on-farm water management project in the Barabad village, (Bihsud district, Nangarhar Province; Fig. 1). The objective of this study is to investigate the vertical movement of water into soil in relation to cultivation age, the durations of the irrigation interval, water inputs, and crop type.

MATERIALS AND METHODS

The field experiments were conducted in the eastern region of Afghanistan from November 2013 to September 2014, shortly after LL-leveling. The experimental farms are located in the Barabad village under the agriculture command area of the Barabad irrigation canal near Jalalabad city, Nangarhar province, Afghanistan (34.27° N, 070.24° E, elevation = 572 m). The region is classified as a semi-arid, Mediterranean-type climate with an annual maximum air temperature of 42°C, an annual minimum air temperature of -2°C, and an annual precipitation varying from 178 mm to 324 mm. The monsoon begins in January and lasts until May, with little rain during the summer season. The wind speed is roughly 30 km/h, and the maximum wind pressure occurs between July and November [5].

Prior to the final selection of the experimental farms, a total of 29 fields, 14 water channels, 39 water inlets, about 116 boundaries and approximately 752 m² of fields were mapped (Fig. 1). Following layout improvements and LL-leveling, a total of 12 fields, 2 water channels, 12 water inlets, and approximately 1925 m² of fields were mapped (Fig. 2). The research was conducted on two separate agricultural farms that were both located along a main irrigation canal. The field experiments included two parts. The first part involved the Farm-A layout improvement, and the second part involved LL-leveling.

LL-leveling is also called laser-guided land leveling or precision-custom farming laser land leveling, and it is a process applied for smoothing a land surface up to ± 2 cm from its average elevation with the help of a laser-guided drag bucket.

The entire Farm-A was investigated before commencing the actual experiment. Permanent benchmarks were installed and a detailed topographic map was created using a total station theodolite (*TST*). Next, the features of Farm-A were designated on the map, and detailed information specified about the slope, the elevations of the low and high spots of the fields, the number and sizes of the fields, the number of water inlets, and the available water channels.

The main and secondary water channels were

surveyed using the same approach, and their profiles were developed. The water channels were designed for earthen lining, and each field in Farm-A was carefully analyzed to improve the farm's layout. With the new layout, the size of each field was expanded, and regular straight boundaries were created across all the fields. Moreover, the water inlets and control structures were considered as suitable points for the installation of the farm's irrigation system. They were selected based on the irrigation demand.

The cut-and-fill soil ratio of the low and high points was calculated for each field and displayed in the site plan to facilitate field leveling for the machinery operators. Both the irrigation channels and the water inlets were adjusted based on the quantity of water required for the fields. In addition, the water channels were earthen improved, and brick water inlets and a control structure were proposed. Following layout improvements, water channels (contour, unwanted bunds, and water inlets) were removed. In the next stage, rough leveling and LL-leveling were applied. To implement LL-leveling, the maximum elevation difference between the different land points should not be above 12–15 cm. In this study, however, most of the selected fields indicated greater differences in elevation.

In order to solve this problem, another tractor was hired to plow and make the soil soft for leveling. All the fields were laser-leveled, and their sizes increased to at least 0.19 ha. Hence, 12 fields were established instead of 29 (Figs. 2 and 3). All unnecessary water channels, undesired field boundaries, water inlets, and ditches were removed, and new straight field boundaries were created. The laser-leveled fields in Farm-A were chosen to observe the impact of LL-leveling, and the un-leveled fields in Farm-B were selected as the controls (Fig. 1).

The soil texture of the experimental farms are predominantly sandy loam soil. Crop fields are arranged in a rectangular shape and are about 2054, 2052, 1924 m² in LL-leveled Farm-A and nearly 1875, 2000, 1680 m² in un-leveled Farm-B. The condition of the crops was kept equal across both farms.

A cutthroat flume was used to determine the water depth (WD) applied to the irrigation. The flume was installed in a uniform, straight, and vegetation-free channel. The flume sides were entirely stoppered with dirt to prevent water leakage from the sides and beneath the flume. The flume was installed at appropriate points to maintain free-flow conditions and to facilitate flow calculations. Whenever, the water flow became stable, constant readings were recorded; five to six readings were taken during irrigation periods. The duration of irrigation was recorded, and the area of the fields was measured by TST. Then, the depth of the applied water was calculated for each irrigation line using the hydrologic formula given in Eq.1.

While the number of irrigation bouts were

recorded 4, 5, and 8 in the both areas, the WD was not equivalent. Farm-A received 283, 334, 570 mm of WD while Farm-B received 319, 394, and 650 mm of WD in wheat, corn, and eggplant fields, respectively. In the next step, the climate parameters needed for the calculation of the water seepage rate were downloaded from the meteorological station of the National Climatic Data Centre (NCDC) [14]. Missing parameters were calculated with the help of the daily Penman-Monteith evapotranspiration equation (FAO-56 method) [15]. The seepage rate for both farms was simulated with the help of the unsaturated water balance Eq. 2.

$$WD = \frac{QT}{A} \quad (1)$$

Where Q is the discharge (m³/s), T is the irrigation duration is seconds, A is the field area (m²), and WD is the applied WD (mm).

$$I = P - E + 1000 \frac{Q_{si} - Q_{so}}{A} - \frac{\Delta Ws}{\Delta t} \quad (2)$$

Where P is precipitation over the time interval Δt (mm), E is evaporation from the land surface (mm/d), Q_{si} is lateral inflow of surface water into the water balance area (A) (m³/day), Q_{so} is lateral outflow of surface water from the water balance area (A) (m³/d), A is the water balance area (m²), and ΔWs is the change in surface water storage (mm).

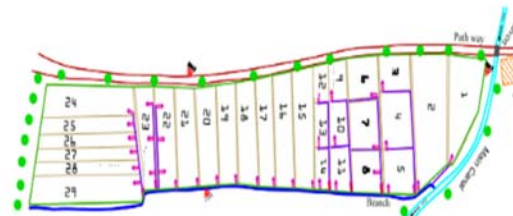


Fig. 1 Layout of Farm-A before LL-leveling [13].

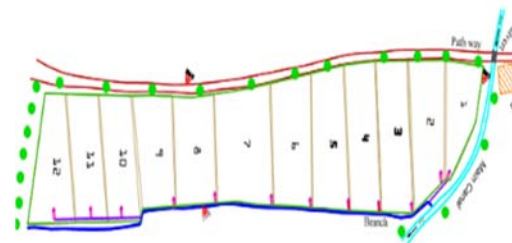


Fig. 2 Layout of Farm-A after LL-leveling [13].



Fig. 3 The location of Farm-A and Farm-B, in Nangarhar, Afghanistan (latitude 34. 27° N and longitude 070.24° E; elevation = 572 m; Source: Google maps, 2016 [13].

Table 1 WD and mean seepage from Farm-A and Farm-B

Crop	Farm-A (Leveled)					Farm-B (Un-leveled)			
	Plot area size (m ²)	Irrigation Method	Irrigation number	Used irrigation depth (mm)	Mean seepage rate (mm/day)	Plot area size (m ²)	Irrigation Number	Used irrigation depth (mm)	Mean water seepage (mm/day)
Wheat	2054	basin	4	283	1.6	1875	4	319	2.0
Corn	2052	basin	5	334	0.3	2000	5	394	1.2
Eggplant	1924	furrow	8	570	3.0	1680	8	650	4.0

RESULTS

Temporal changes in infiltration rates

Figure 4 represents the vertical movement of water through soil (seepage rate) in relation to various times of the year in both the leveled (Farm-A) and in the un-leveled (Farm-B) fields. The seepage rate of used-irrigations was observed shortly after the completion of LL-leveling in the wheat, eggplant, and corn fields.

The first seepage rate in Farm-A was observed in the wheat field. The seepage rate for the very first irrigation, which was applied in November, peaked at about 2.7 mm/day. However, during the next irrigation bout in the following month, the seepage rate declined to around 1.4 mm/day. While during the third irrigation bout the seepage rate stayed constant, the seepage rate dropped substantially to 1 mm/day during the last irrigation bout. Whereas, in Farm-B, the seepage rate was consistently higher across all crop types than that in Farm-A. In Farm-B, the largest

seepage rate recorded was around 3 mm/day, and the lowest was nearly 1.5 mm/day and occurred in November and December, respectively.

In addition, the seepage rates calculated for January and February were 1.6 and 1.9 mm/day, respectively. Hence, in Farm-A, the seepage rate was reduced by 17.5% compared to Farm-B.

Next, the eggplant seepage rate was computed from May to late July for both farms. The highest seepage rate was more than 4 mm/day in May. However, during the next irrigation bout in early June, the seepage rate declined considerably to 1 mm/day and then gradually increased to approximately 4 mm/day by mid-June. After mid-June, the seepage rate steadily declined again and reached about 1 mm/day in late July. Whereas, in Farm-B, the highest seepage rate of 6 mm/day was observed in May and the lowest rate of 2.5 mm/day was observed in June.

The last crop that was planted was corn. The highest seepage rate observed in the corn field was 1.5 mm/day in July and the lowest was -0.6 mm/day in late June. Over the next months, the seepage rate fluctuated throughout the complete season of crops.

In Farm-B, the highest seepage rate calculated was 2.6 mm/day in mid-June and the lowest seepage rate was -0.7 mm/day in late June. In the other months, the seepage rate fluctuated. As a result, the seepage rates in Farm-A were 22% lower than in Farm-B.

Across crop types, the seepage rate was highest in the initial month and then fluctuated throughout the remainder of the growing season in both farms. Further, the average seepage rate of any crop in Farm-A was consistently lower than that of Farm-B. In the days following wheat harvesting and prior to the planting of the eggplant and corn, an increase in seepage rates was observed.

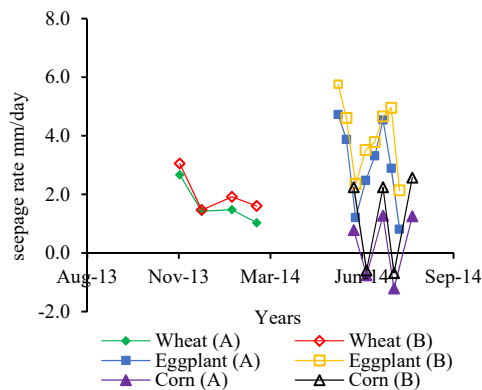


Fig. 4 Cultivation age vs seepage rate (mm/day).

Used-WD

Figure 5 illustrates the relationship between seepage rate and WD in both farms. The colored and uncolored solid shapes of the diamond, square, and triangle markers, represent the seepage rate relative to water intake over the whole growing season for wheat, corn, and eggplant in Farm-A and Farm-B, respectively.

Across all crop types, with an increase in water intake, the seepage rate increased. For instance, the highest observed seepage rate of the eggplant in Farm-B was 6 mm/day concurrent with a peak WD at nearly 90 mm. Likewise, in Farm-A, a similar relation was observed, however, the measured water intake and seepage rate were 15 mm and 2 mm/day lower than in Farm-B, respectively.

In Farm-A, the highest seepage rate for wheat was determined to be 2.4 mm/day concurrent with a WD of 90 mm. While, in Farm-B, the highest seepage rate was around 3 mm/day with the WD being almost 100 mm. During the next irrigations, the applied WDs in Farm-A were computed as about 64, 77, and 55 mm with concurrent seepage rates of 1.5, 1.4 and 1 mm/day, respectively. Whereas in Farm-B, the calculated seepage rates were around 2, 1.7, and 1.5 mm/day concurrent with WDs of 75, 80, and 70 mm, respectively.

In contrast, the corn crop displayed the lowest seepage rates throughout the complete season compared to the other two crops in both farms. In Farm-A, the seepage rate for the WD of 80 mm was calculated as 2 mm/day, and for the lowest WD of about 60 mm the seepage rate was calculated as -0.6 mm/day. Whereas in Farm-B, the equivalent lowest and highest WDs were 65 and 98 mm, respectively. The concurrent highest and lowest seepage rates were 2 mm/day and -0.60 mm/day, respectively. The overall WD and seepage rates of the remaining irrigation bouts were considerably lower in Farm-A than in Farm-B.

As a result, in Farm-A, the seepage rate was reduced by an average of 24%, 17.5%, and 40% in the wheat, eggplant, and corn fields, respectively. The seepage rate was, however, found to be directly linear to water intake.

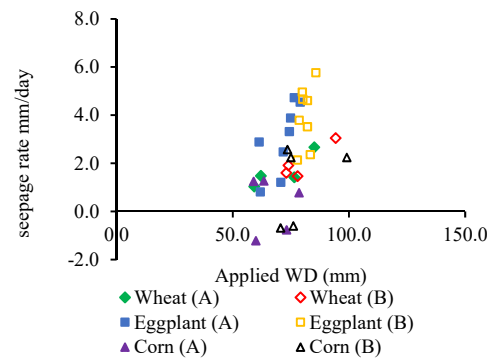


Fig. 5 Relationship between seepage rate (mm/day) and applied WD (mm).

Irrigation Interval

Figure 6 indicates water seepage rates relative to the duration (in days) of the irrigation interval over the period of growing season of wheat, eggplant, and corn in both farms. The duration intervals between irrigations were maintained equivalent across all crops.

In general, the most and the least number of days between irrigations among crops were noted for the wheat and eggplant crops as 33 days and 9 days, respectively. Conversely, the lowest seepage rate measured was less than 1 mm/day for an 11-day interval and the highest was about 6 mm/day for a 10-day interval in corn and eggplant fields in Farm-A and Farm-B, respectively. Overall, the highest seepage rates per number of interval days were always observed in Farm-B.

In the wheat field in Farm-A, the lowest irrigation interval was 24 days and the highest 33 days. However, the lowest seepage rate of 1 mm/day was observed in the 26-day irrigation interval. On the other hand, the highest rate of 2.7 mm/day was

observed in the 24-day irrigation interval. Whereas, in Farm-B, the lowest seepage rate of 3 mm/day, was observed in the 33-day irrigation interval.

During other irrigation bouts, the interval between irrigations and the seepage rate either remained equal or fluctuated slightly. In Farm-A, the seepage rate decreased by an average of 23%.

Similarly, in the corn fields of both farms, the number of irrigations were five and the highest and lowest irrigation intervals were 20 days and 11 days, respectively. Remarkably, the seepage rates did not remain equal. In Farm-A, the highest seepage rate was 1.27 mm/day and occurred in the 12-day irrigation interval, and the lowest rate of -1.22 mm/day was observed in the 20-day irrigation interval. Nonetheless, for the 11-day irrigation interval, the seepage rate was 1.25 mm/day. Whereas, in Farm-B, the highest seepage rate discovered was 2.6 mm/day and occurred in the 11-day irrigation interval and the lowest as -0.6 mm/day and occurred in the 18-day irrigation interval. In both farms, for the next irrigation bouts, the irrigation intervals, and the seepage rates did not remain stable. In Farm-A, the seepage rate was considerably lower than in Farm-B.

The number of irrigations counted in the eggplant field was eight. The highest irrigation interval recorded was 12 days and the lowest recorded was 9 days in both farms. In Farm-A, the lowest seepage rate of 0.8 mm/day occurred in the highest irrigation interval, and the highest seepage rate of 4.7 mm/day occurred in the lowest irrigation interval. Whereas, in Farm-B, the highest seepage rate of 5.8 mm/day occurred in the 9-day interval and the lowest rate of 2.1 mm/day occurred in the 12-day irrigation interval. During the remaining irrigations, the interval days were all similar, while the water seepage rate differed. In Farm-A, the seepage rate decreased by an average of 26% during each irrigation.

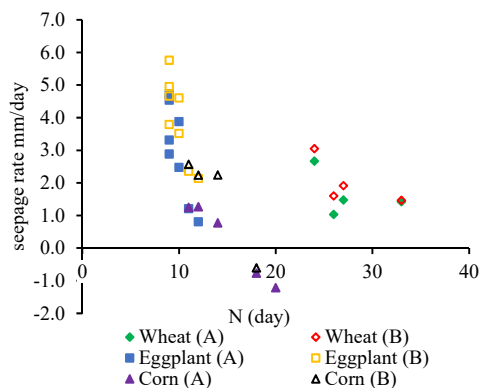


Fig. 6 Duration of irrigation interval (days) vs seepage rate (mm/day).

Land area size

Figure 7 depicts the effect of different land areal size on seepage rates in fields for three different crops, namely wheat, corn, and eggplant across both farms. The field size is shown in m^2 and the water seepage rate in mm/day.

The lowest seepage rate (1 mm/day) was observed in the larger sized field ($2000 m^2$) and the highest seepage rate (6 mm/day) was observed in the smallest sized field ($1680 m^2$).

In Farm-A the highest seepage rate (2.7 mm/day) was observed in the smallest sized field ($1900 m^2$) of the eggplant crop. In addition, the lowest seepage rate (1.31 mm/day) was found in the biggest sized field ($2054 m^2$).

Similarly, in Farm-B, the highest seepage rate (3.7 mm/day) was recorded in the smallest sized field ($1680 m^2$) and the lowest seepage rate (0.9 mm/day) was observed in the largest sized field ($2000 m^2$).

Hence, the areal land size has a relation to the seepage rate, with increasing field size corresponding to lower seepage rates.

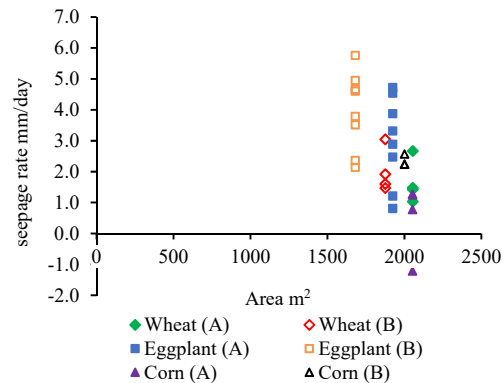


Fig. 7 Relation between land area (m^2) and seepage rates (mm/day).

DISCUSSION

The simulation results of this study provide information regarding the losses of water through seepage from irrigated wheat, corn, and eggplant fields of both farms. These results highlight important aspects of seepage rates relative to temporal changes, seasonal fluctuations of WD, different field sizes, and the variation in the duration interval between irrigation bouts. The findings of this research indicate that seepage rates could differ with WD in the fields affected by seasonal fluctuations in the field water content.

Consequently, the same field may lose different volumes of water at different times of the year; strong, dry soil conditions could rapidly increase water seepage losses in the field, and conversely, strong,

wet soil conditions can cause very low, even negative, seepage losses. In our data, across all crop types, the seepage rate was higher just after LL-leveling and then quickly decreased during the following irrigations. We think that this fast reduction in seepage rate may be due to high antecedent water content in the soil from the previous irrigation. Before LL-leveling, the fields were not irrigated for more than three months nor was there any rainfall, hence, the soil was very dry.

In addition, the seepage rates in Farm-A were consistently lower than those in Farm-B, across all crop types. It could be suggested that this may have resulted from a positive effect of LL-leveling because in the laser-leveled field, moisture was more uniform and lasted for a longer time than in Farm-B. Moreover, it may also be a result of the development of a hardpan layer under the plow layer in the laser-leveled fields.

Further, as the LL-leveling increased the size of each field in Farm-A the water intake and the seepage rates decreased. The seepage rate dropped with increasing field size in both farms. In our results, the intake of water declined and the irrigation duration became shorter because of LL-leveling. There were understandable variations between the two operations at the time of irrigation and after irrigation. These changes, even though small, may be an indication of the advantages brought by LL-leveling. We could purpose that with an increase in field size, water intake and water seepage rates may become lower.

Furthermore, seasonal WD, that was measured separately, resulted in a difference in the amount of irrigation water applied in both farms. Farm-A received 283, 334, and 570 mm WD, while, the Farm-B received 319, 394, and 650 mm WD in wheat, corn, and eggplant fields, respectively. We believe that these reductions in water intake could be a result of the leveled land surface in Farm-A, which provided a more appropriate environment for water to flow across the surface and to reach all corners of a field equally. The total number of irrigation bouts used for the crops were considered the same (4, 5 and 8) in both farms because the farmer did not separate out the irrigations. By comparing this variation, we could verify both the smaller WD in Farm-A and the linearity of WD to the seepage rate that was measured in both farms (Table 1).

Toward the end of the experiment, reports from the farm's irrigator indicated that the water was becoming difficult to manage in Farm-B, despite the small visual changes in, for instance, plant growth, plant height, canopy cover, tillers, and grain sizes. This may also be attributed to LL-leveling. Since the same varieties were sown in both places, differences in yield are most likely due to the optimal crop soil moisture in laser-leveled fields. At the same time, it could be suggested that the order of the seepage rate is affected by both land cultivation practices and the

choice of crop types. For example, the water seepage rates for wheat, corn, and eggplant were, on average, 1.6, 0.3, and 3 mm/day in Farm-A, respectively. Whereas, in Farm-B, the rates were 2, 1.2, and 4 mm/day, respectively (Table 1).

Therefore, it has become clear that the LL-leveling contributes to increased water savings and can decrease seepage rates through the soil by maintaining slow seepage rates, small water inputs, and longer soil moisture conditions.

CONCLUSION

LL-leveling plays a substantial role in decreasing the loss of water in soil due to seepage, by manipulating the high-water input. In addition, LL-leveling can precisely level land and allow for the establishment of larger fields than usual in those areas. The larger field size can help reduce irrigation duration and the amount of water required, by slowing the seepage rate in the soil. Additionally, LL-leveling can distribute water more uniformly in soil, which can support moisture in the soil for longer periods of time.

Moreover, in the laser-leveled field a crop can resist a longer period without water than in an un-leveled field. This implies that the duration of the irrigation interval in days between irrigations can be longer, which can assist farming communities, especially where water intensive practices last for extended periods of time. Furthermore, in a laser-leveled field, the seepage rate can decrease with an increase in crop cultivation age, which is not clear for an un-leveled field. However, the application of traditional land practices can adversely affect water inputs, irrigation duration, cultivation age, and seepage rates.

The results of the present study indicate that, from a water balance perspective, seepage rates were lowered across crop types in the leveled fields. Such practices can, further result in increased water savings, the tackling of water shortage problems, the delivery and access to adequate and reliable water, and increased crop production per unit water and per unit area. More importantly, it could provide an opportunity to downstream farmers to have access to irrigation water, thus, minimizing water conflicts and expanding cultivable area.

In summary, LL-leveling is a proper practice that can save water by reducing seepage losses, minimizing irrigation duration, decreasing water inputs, maintaining uniform soil water distribution, preserving soil moisture for longer periods of time, and by creating a hardpan layer that is more resistant to water movement in the soil. This is a promising approach to using available water more efficiently and effectively in areas where water scarcity is a serious problem for agricultural production. These practices should be the best options to produce more

with less water.

ACKNOWLEDGEMENT

The authors appreciate the tireless support from the technical team of On-Farm Water Management Project and the Ministry of Agriculture Irrigation and livestock of Afghanistan for giving chance for conducting this study.

REFERENCES

- [1] Anbumozhi, V., E., Tabuchi, T. Rice crop and yield as influenced by changes in ponding water depth, water regime and fertigation level. *Water manages.* 1998.37, pp 241-253
- [2] Azimi, A. & McCauley, D. Afghanistan natural Resources comprehensive need assessment final Report. Published by Asian Development Bank. No.010103. Afghan Digital Libraries, 2002, pp 9.
- [3] Gill, M. water for life. Proceeding of seminar on world food day. Directorate of Agriculture Information. Dept. Agric. Govt. Panjab, India.
- [4] National Development Strategy Article No. 114, Afghan water law, 2005.
- [5] Khaurin, E. Trees and Bushes of Afghanistan. Forest National Coordination Office, FAO, Kabul, 2003, pp 9-13.
- [6] Asif, M., Ahmad, M., Gafoor, A. & Aslam, Z. Wheat productivity, land and water use efficiency by traditional and LL-levelling techniques. *Online Journal of Biological Sciences (Pakistan)*, Vol. 3, No. 2, 2003, pp 141-164.
- [7] Prepared by New Mexico State University final report of Afghanistan water, agriculture, and technology transfer, 2011, pp 13.
- [8] Qureshi, A.S. Water resources management in Afghanistan. The issues and options. International water resource institute. Working paper 49, Pakistan country series No. 14, IWMI, 2002.
- [9] Qureshi, A.S. Water resources management in Afghanistan. The issues and options. International water resource institute.
- Working paper 49, Pakistan country series No. 14, IWMI, 2002.
- [10] Rout, B. Water management, livestock, and the opium economy. How the water flow: A typology of irrigation systems in Afghanistan Research and Evaluation Unite (AREU). Synthesis paper series. Kabul, Afghanistan, 2008.
- [11] Rana, M., Arshad, M., & Mauds. Effect of basin, furrow and rain gun sprinkler irrigation system on irrigation efficiencies, nitrate-nitrogen leaching and yield of sunflower. *Pakistan Journal of water resources.* Vol. 10, No.2, 2006, pp. 1.
- [12] Wolf, P., & Stein, T. Improving on farm water management. A never-ending challenge. *Journal of Agriculture and Rural Development in the tropic sand and sub tropic.* Vol. 104, No. 1, 2003, pp. 34.
- [13] Shakerullah Hashimi, Homayoon Ganji, Kondo, Ryoei Ito and Takamitus kajisa, Laser land levelling for crop yield and water efficiency in eastern Afghanistan. *International Journal of GEOMATE, Tsu, Mie, Japan.* Vol. 13, Issue. 36. 2017, pp 116-121.
- [14] National Climate Data Centre (NCDC), country Afghanistan, Jalalabad station No. 691166.
- [15] FAO Irrigation and Drainage Paper No. 56, Chapter 2, Equation 6, pp 24.
(<https://www.ncdc.noaa.gov/CDO/cdosubqueryrouter.cmd>).
- [16] Sharma, P.K., De Datta, S.K. Effects of puddling on soil physical properties and processes. *Soil physics and Rice.* IRRI, Los Banos, Philippines, 1985, pp 217-234.
- [17] Wickham, T.H., Singh, V.P. Water movement through wet soils. *Soils and rice.* IRRI, Los Banos, Philippines, 1978, pp 337-357.

Copyright © Int. J. of GEOMATE. All rights reserved, including the making of copies unless permission is obtained from the copyright proprietors.

PREDICTORS OF BEHAVIOR INTENTION TO DEVELOP GREEN UNIVERSITY: A CASE OF UNDERGRADUATE UNIVERSITY IN THAILAND

Weerawat Ounsaneha¹, Nahathai Chotklang¹, Orapin Laosee², Cheerawit Rattanapan²

¹Faculty of Science and Technology, Valaya Alongkorn Rajabhat University under the Royal Patronage,
Klong Nuang, Klong Luang, Pathumthani, 13180, Thailand,

²ASEAN Institute for Health Development, Mahidol University, Salaya, Phutthamonthon, Nakhonpathom,
73710, Thailand

ABSTRACT

The aim of this study is to identify the level and predictor of behavior intention to develop green university in a case of undergraduate university in Thailand. The university students and staffs in Valaya Alongkorn Rajabhat University under the Royal Patronage, Thailand were included as the participants in this study by structure questionnaire with the six major criteria of the UI GreenMetric World University Ranking. The best predictor factors of dependent variable was performed and find out by multiple logistic regression. The results showed that that positive attitude towards transportation and education were found to be the significant predictors of intention to develop green university behavior. This finding implied that the preparation stage with identification of behavior intention to develop green university of UI GreenMetric World University Ranking should be promoted and provided the opportunity for succession of green university.

Keywords: Behavior Intention to develop Green University, Undergraduate University, Valaya Alongkorn Rajabhat University under the Royal Patronage, Thailand, UI GreenMetric World University Ranking.

INTRODUCTION

For almost three decades, the sustainability society concept was recognized and highlighted for the significant role of higher education organization and then represented the opportunity for generating the behavior change based on the daily life attitude toward sustainable development [1,2,3]. Besides, the enhancing concern on many environmental problems should be generated knowledge and integrate sustainability performance in educational and research programs, as well as promoting environmental view to the society [4]. Hordijk [5] identified that the knowledge of the university community was the key role of sustainable campus with ecological and social challenges in the future. Currently, the concept of green university have been initiated in the worldwide. Universitas Indonesia (UI) developed the UI Green Metric World University Ranking for universities to share information about their sustainability practices with the basis of Sustainability for Higher Education [6]. However, a green university initiative may be the best tool for everyone when universities are well-prepared for it. Hence, only 15 universities in Thailand involved in this ranking on the process in 2014 [7]. Lack of researches was found on the preparation stage of green university development in Thailand. Therefore, this study was to identify the level and best predictor of behavior intention to develop Green University in a case of undergraduate university in Thailand.

METHODS

A Case Study Setting

Valaya Alongkorn Rajabhat University (VRU) under the Royal Patronage, Thailand was included as a case study of this research. This university located at Pathum Thani province and northern border of Bangkok. The main type of VRU students is the undergraduate degree. VRU had not yet entered and will strongly purpose to participate in the ranking system of UI green in 2018. Hence, the behavior intention to develop green university assessment was the preparation stage of UI green participation for this university.

Sample size calculation and procedure

Taro Yamane's equation [8] was used to calculate the sample size of VRU participants and presented in (1)

$$\begin{aligned}n &= N / 1 + N (e)^2 \quad (1) \\n &= 14,000 / 1 + 14,000(0.05)^2 \\&= 700 \text{ people}\end{aligned}$$

Where n is the sample size; N is population size, and e is level of precision; 95 % confidence level with a precision rate of ± 5 % and 0.5 of degree of maximum variability. Therefore, the sample participation in this study was 700 people including 280 staffs and 420 students by the proportion to size. For sample size procedure, VRU staffs or students

who had been worked or studied in this university for at six months were invited to fill the questionnaire with no incentive. The simple random sampling was used to include the participant in this research in the main cafeteria of VRU during 1 weeks.

Data collection tool and analysis

The data collection questionnaire of this study consisted of three sections. The general information of participant including eight question was collected in the first section of questionnaire. The second and third sections were the forty-three questions of attitude and fourth questions of behavior intention to develop green university, respectively based on the UI green categories including (1) Setting and infrastructure; (2) Energy and climate change; (3) Waste management; (4) Water management; (5) Transportation; and (6) Education. Reliability tests of attitude and behavior parts were 0.7 of Conbrach's Coefficient-Alpha formula.

Statistical analysis of this study was performed by SPSS software. The descriptive statistics was used to assess the level of knowledge and behavior intention to develop green university. Association and strength of the relationship between factors was determined by Chi-square and logistic regression. Finally, the best predictor factors of dependent variable was performed and find out by multiple logistic regression.

RESULTS AND DISSCUSSION

Based on the data of questionnaires (Table 1), more than 67 % of participants were female. Most of them (50.10 %) were in the age group of 18 – 20 years old. Concerning the participants' background, most of them (68.7 %) were educated in undergirded level. Almost of participants (31.9 %) lived at home and more than 45.6 % used the public transportation. Besides, the results presented that the knowledge levels in the six categories of UI green university were moderate. Most of the participants (52 %) had good behavior intention to develop green university. Participants who were female, having positive attitude toward setting and infrastructure, energy and climate change, waste management, transportation and education intended to support green university. This finding was according to the results of Mamat et al. [9]. This study mentioned that green office practices have the highest in the categories of solid waste management, water resources management and education and awareness. By multiple logistic regression analysis revealed that female were 1.4 times more likely to support green university (Adj. OR 1.21; 95%CI: 1.00-2.01) because males were considered as primary destroyers of the environment, while females were deemed as secondary users of the environment [10]. In addition, those who had positive attitude towards transportation and

education were nearly two time more likely to support green university (Adj. OR 1.55; 95%CI: 1.09-2.18, 1.86; 95%CI: 1.33-2.59) (Table 2) because the public transport promotion in the university should be the potential of UI green implementation [6].

It can be concluded that the identification of behavior intention to develop green university of UI GreenMetric World University Ranking should be promoted for the preparation stage. More positive attitude and behavior would be the increase the potential of green university implementation. The initiative would be planed the successful strategy and encouraged the world sustainability.

Table 1 Demographic information of the participant

Information	Number	Percent
Sex		
Male	228	32.6
Female	472	67.4
Age (Year)		
18-20	351	50.1
21-30	218	31.1
31-40	102	14.6
41-50	29	4.1
Education		
Bachelor	481	68.7
Master	199	28.4
Ph.D	20	2.9
Status		
Student	420	60.0
Staff	280	40.0
House type		
Home	271	38.7
Condominium	102	14.6
University dormitory	47	6.7
Rent home	57	8.1
Private dormitory	223	31.9
Transportation to university		
Car	63	9.0
Motorcycle	187	26.7
Bicycle	49	7.0
Public transport	319	45.6
Other	82	11.7
Transportation in university		
Car	37	5.3
Motorcycle	155	22.1
Bicycle	67	9.6
Public transport	41	5.9
Other	400	57.1

Table 2. Association and predictor with behavior intention to develop green university

Factor	Behavior			OR	95% CI	Adjusted OR	95% CI
	Number	Good (%)	Bad (%)				
Sex							
Male	228	58.8%	41.2%	1.00		1.00	
Female	472	50.2%	49.8%	1.41	1.02-1.94	1.42	1.00-2.02
Age (Year)							
18-30	569	53.4%	46.6%	1.00		1.00	
30-50	131	51.1%	48.9%	1.09	0.74-1.60	1.17	0.72-1.91
Education							
Bachelor	481	52.6%	47.4%	1.00		1.00	
More than bachelor	219	53.9%	46.1%	0.95	0.68-1.30	1.11	0.61-2.01
Status							
Student	420	52.6%	47.4%	1.00		1.00	
Staff	280	53.6%	46.4%	0.96	0.71-1.30	0.77	0.42-1.42
House type							
Home/Condominium	373	55.8%	44.2%	1.00		1.00	
Dormitory/rent house	327	49.8%	50.2%	1.26	0.94-1.70	1.22	0.88-1.68
Transportation to university							
Public	319	54.9%	45.1%	1.00		1.00	
Owner	381	51.4%	48.6%	1.14	0.85-1.54	1.20	0.82-1.73
Transportation in university							
Public	192	53.1%	46.9%	1.00		1.00	
Owner	508	53.0%	47.0%	1.00	0.72-1.40	0.93	0.61-1.41
Attitude to Green University							
Setting and infrastructure							
Low	551	55.5%	44.5%	1.00		1.00	
High	149	43.6%	56.4%	1.61	1.12-2.32	1.27	0.86-1.88
Energy and climate change							
Low	597	54.8%	45.2%	1.00		1.00	
High	103	42.7%	57.3%	1.62	1.06-2.47	1.13	0.71-1.80
Waste management							
Low	526	56.1%	43.9%	1.00		1.00	
High	174	53.0%	47.0%	1.54	1.16-2.32	1.22	0.82-1.82
Water management							
Low	274	55.5%	44.5%	1.00		1.00	
High	426	51.4%	48.6%	1.17	0.86-1.59	0.85	0.60-1.19
Transportation							
Low	415	59.3%	40.7%	1.00		1.00	
High	285	43.9%	56.1%	1.86	1.37-2.52	1.55	1.09-2.18
Education.							
Low	420	60.2%	39.8%	1.00		1.00	
High	280	42.1%	57.9%	2.08	1.53-2.82	1.86	1.33-2.59

CONCLUSION

This study was to identify the level and predictor of behavior intention to develop green university: A Case of Undergraduate University in Thailand. The students and staffs at Valaya Alongkorn Rajabhat University under the Royal Patronage, Thailand was included as the sample size of this study. A questionnaire for collecting data was developed by the six major criteria of the UI GreenMetric World University Ranking. Association and strength of the relationship between factors was determined by Chi-square and logistic regression and the best predictor factors was performed by multiple logistic regression. The results showed that that positive attitude towards transportation and education were found to be the significant predictors of intention to develop green

ACKNOWLEDGEMENTS

This research was supported by Valaya Alongkorn Rajabhat University under the Royal Patronage.

REFERENCE

- [1] Wright T, "University presidents' conceptualizations of sustainability in higher education", *Int. J. Sustain. High. Educ.*, Vol 11, 2010, pp. 61–73.
- [2] Seitzinger SP, Svedin U, Crumley, CL, Steffen W, Abdullah SA, Alfsen C, Broadgate WJ, Biermann F, Bondre NR, Dearing JA, "Planetary stewardship in an urbanizing world: Beyond city limits", *Ambio*, Vol 41, 2012, pp. 787 –794.
- [3] Tukker A, Emmert S, Charter M, Vezzoli C, Sto E, Andersen MM, Geerken T, Tischner, U, Lahlou S, "Fostering change to sustainable consumption and production: An evidence based view", *J. Clean. Prod.*, Vol 16, 2008, pp. 1218–1225.
- [4] Geng Y, Liu K, Xue B, Fujita T, "Creating a "green university" in China: a case of Shenyang University", *J. Clean. Prod.*, Vol 61, 2013, pp. 13-19.
- [5] Hordijk I, "Position paper on sustainable universities", *J. Clean. Prod.*, Vol 14, 2014, pp.810–819.
- [6] Tiyyarattanachai R, Hollmann NM., "Green campus initiative and its impacts on quality of life of stakeholders in Green and Non-Green Campus universities" *SpringerPlus*, Vol 5, 2016, pp. 84.
- [7] Universitas Indonesia, "UI GreenMetric World University Ranking", <http://greenmetric.ui.ac.id/>. Accessed 17 April 2015.
- [8] Yamane T, "An introductory analysis", Harper and Row, New York, 1967.
- [9] Mamat L, Basri NEA, Zain SM, Rahmah E., "Determining the level of environmental sustainability practices at campus dormitories using green indicators", *Asian Social Science*, Vol 11(12), 2015, pp. 25-31.
- [10] Omoogun AC, Odok AO, "Influence of gender and environmental awareness on attitude of people towards forest conservation in Ekuri communities in Akamkpa local government area of cross river state", *J Public Admin Gov*, Vol 3(2), 2013, pp.219–225.

GIS BASED IDENTIFICATION OF WATER BORNE DISEASES

*Hania Arif¹, Shahid Iqbal²

Research Scholar, University of the Punjab, Pakistan; ^{1,2}

ABSTRACT: In Pakistan, water contamination is one of the most threaten health hazard. There is no check and balance for its management and monitoring. In our country, Surface and Ground water both are contaminated with toxic metal, pesticides and artificial organic materials. World Health Organization (WHO) set the standards for drinking water but unfortunately no one follow them. Main causes of water contamination are industrial wastes, higher concentration of pesticides and other human induced activities mainly due to inappropriate sites for dumping/land fill. Toxic elements are the main factors to pollute the ground water which have direct impacts on the human health. In this present research quality of drinking water and their borne diseases are discussed. If the concentration of these toxic elements increase above their threshold limit then they became a cause of sewer diseases like skin cancer, lung cancer, affects the teeth and bones directly. GIS is a powerful technique for geographical representation and spatial analysis of groundwater. Spatial distributions of ground water quality in the Gujranwala District of Punjab Province is monitored. The data for ground water quality of the study area is prepared using spatial interpolation technique against each parameters. Measured values of the each parameters are classified as per WHO standards for developing countries. The final result conclude that, groundwater of the study area need proper treatment for its usage as drinking water.

Keywords: Health Hazard, WHO, Toxic Elements, GIS

INTRODUCTION

Water borne diseases are among one of the major public health problems in developing countries like Pakistan. They are the leading causes of morbidity and mortality in all age groups particularly in children under 5 years of age. According to the World Health Organization (WHO) 3 million deaths occur every year from diarrheal diseases worldwide. The problem of water borne diseases is especially prevalent where general hygiene and environmental sanitation are poor and where there is a shortage of protected water supply [1, 5]. It is believed that 80% of all diseases in the world are caused by inadequate sanitation, polluted water or unavailability of water (WHO Monica II). Poverty, illiteracy, overcrowding and low health services are contributing factors that directly or indirectly affect the prevalence of water borne diseases. Therefore an integrated prevention and curative approach with community participation is required in order to tackle this prevalent public health problem.

Water borne diseases are viral, bacterial and parasitic diseases which use water as a common means of transmission. In this module we will discuss those water borne diseases in which the mode of entry of their etiologic agents into a susceptible host is oral. The connection between human health and water quality has been well recognized. Use of contaminated water has its health and financial cost. In terms of health cost, it is reported that 80% of all diseases, in developing countries, may be attributed to the use of contaminated water [1]. Poor water quality is responsible for the death of an estimated 5

million children in developing countries for annum. In terms of financial cost, the UN estimates that \$7.3 billion may be saved in healthcare costs by improving water quality and sanitation conditions [2]. Rapid increase in population, especially in urban areas, has led to poor water quality management, which is further aggravating the problem [3]. The recently approved National Drinking Water Policy also recognizes the need to "provide access to safe and sustainable drinking water supply to the entire population of Pakistan by 2025" and the safe water refers to the water complying with National Standards for Drinking Water Quality[4].

LITERATURE REVIEW

Water naturally contains largely suspended and dissolved substances both inorganic and organic in nature. Surface water (Rivers, springs, streams, Lakes, etc.) carries suspended particles of sand, silt and clay and microorganisms both nontoxic and disease causing especially bacteria, protists, algae, protozoa and parasites etc. Ground water includes dissolved substances like dissolved minerals e.g., Calcium, Magnesium, Sodium, Potassium, and dissolved salts of these minerals like sulphates, chlorides, carbonates, bicarbonates, and dissolved metals. Nutrients like phosphorous -and nitrogen etc. are also present in water. There are a variety of trace elements like heavy metals e.g. Arsenic, Chromium, etc. which are also there in ground water.

Composition of water is determined by natural influences in addition to human actions. Under natural influence, water undergoes diverse physical,

biological and chemical processes. For example, surface water composition is a function of natural weathering of rocks, presence of plant roots and leaves, rock minerals and deposition of soil and salts by wind. As water moves on such surfaces, materials like particles of sand, clay and silt, which makes water turbid or mucky, organic materials and minerals are added up in the water. This determines the physical and chemical composition of surface waters. In addition the biological composition of these waters is determined by presence of microorganisms like algae, bacteria, etc. These are naturally in attendance in environment like soil, air, attached to plant leaves and roots. The ground water composition is a function of nutrients and microorganisms present in the plants, leaching of natural organic substances, and the soil naturally. Moreover surface run-off in case of rain storms (ground water recharge) passes through different land surfaces, carrying plant nutrients and minerals, different types of soil particles, eventually seeps through soil. Suspended impurities of percolating water find naturally filtered when the water seeps through diverse soil strata. Nevertheless, dissolved impurities get mixed by means of ground water.

The natural influences are both spatially and temporally altered. Surface water quality depends on kind of rocks and soil on which it moves. Ground water quality is a function of composition of form of bed rock, recharge water, minerals and underground strata present underneath. By and large, normal water quality varies from place to place, depends on climate change and seasonal variation.

Human activities, conversely, affect water significantly and in diverse ways. Included in this are agricultural or farming practices, disposal of urban and industrial waste water in the natural water bodies. Like use of pesticides, fertilizers and insecticides which can mix by storm or rain water and get mixed with ground water during seepage. Mining operations can too contaminate water bodies. Water quality is measured in relation to its anticipated utilization. There are different uses of water i.e. irrigation and agriculture, recreational use, industrial, constructional domestic use, etc. standards or permissible / acceptable limits and Guidelines depend on the anticipated use of water. For example, potable water or water used for drinking will have dissimilar standards as compared to water which is used in industries and agriculture. The subsequent segment is focused on water quality relating to human health.

DISTRICT OVERVIEW

i. BOUNDARY

Gujranwala is 226 meters (744 ft) above sea level, sharing borders with Ghakhar Mandi and several towns and villages. About 80 kilometers (50 mi)

south is the provincial capital, Lahore. Sialkot and Gujrat lie to its north. Gujrat connects Gujranwala with Bhimber, Mirpure Azad Jammun and Kashmir, and Silakot connects it with Jammun. About 160 kilometers (99 mi) southwest is Faisalabad. To its west are Hafizabad and Pindi Bhattian, which connect Gujranwala to Jhang, Chiniot and Sargodha.

HEALTH FACILITIES

Health Medical facilities are on average available in the city. The main government hospital established in the city is THH (Tehsil Headquarters Hospital). There are several other private hospitals, Health centre and Clinics at different locations within the city.

WATER SOURCE

Good quality water source is the main component for the development of water supply system in the city and selection of water source depends upon the quality and availability of adequate water to meet the future requirements. Water source i.e. surface water in the form of canal or ground water can be selected keeping in view the adequate availability of water that has to be required for the town and must meet the future requirement.

WATER RELATED DISEASES

The water related diseases can be classified into 4 categories.

- i. Water-borne diseases
- ii. Water-washed diseases
- iii. Water-based Diseases
- iv. Water-related Diseases

i. Water-borne disease is a disease which is a communicable one caused by drinking contaminated water or eating food cooked with such water contaminated with human or animal excreta (faces or urine). So both water and food can be the source or way of transfer of water-borne diseases.

ii. Water-washed disease is the one that is caused by skin or eye contact with contaminated water. Including in this are Trachoma, Scabies and flea, Lice and tick borne diseases include diarrheal diseases, typhoid, paratyphoid, cholera, Dysentery (both amoebic and bacillary), infectious hepatitis etc.

iii. Water-based disease is the one caused by the Parasites found in organisms living in water. Diseases like Schistosomiasis, Dracunculiasis, Helminthes etc., fall in this type. Schistosomiasis is caused by a small worm, a parasite recognized as Fluke which enters human body by drinking contaminated water. Or it may also enter through skin if one swims or baths in contaminated water. It is one of the most widespread parasitic diseases.

- iv. **Water-related diseases** are caused by breeding of insect vectors like mosquitoes in the water. Common water associated diseases are Dengue, Malaria, Trypanosomiasis, Filariasis, Onchocerciasis, Yellow fever etc.

WATER BORNE DISEASE OF DIFFERENT PARAMETERS

i. pH:

High pH (more than 11) values cause skin disorders, eye irritation and mucous membranes. pH from 10 to 12.5 cause hair fiber swell. Receptive individuals may undergo gastrointestinal problems due to elevated pH. pH of potable water is 7. Low pH has also health impacts. pH below 2.5 may cause irreversible damage to epithelium. Below 4 pH redness and eye irritation may happen which can become cruel with extra lowering of pH. NSDWQ permissible limits for pH ranges from 6.5 to 8. NSDWQ has no health based guidelines for pH.

ii. Total Dissolved Solids (TDS):

It is a chemical property of water. Water having elevated TDS levels may become unpleasant to the consumers. Lofty TDS can cause taste trouble. The palatability of water as per recommended by tasters ranges from Excellent (TDS less than 300 mg/L) to Good (between 300 to 500 mg/L) and Unacceptable if TDS measures more than 1500 mg/L. WDS may be affected by corrosion if sulphates, chlorides, carbonates are present in water. TDS in excess of 500 mg/L can cause scaling of boilers, pipe lines and home appliances like kettles, heaters and steam irons etc. (WHO, 1996).

iii. Arsenic (As):

Arsenic is a metal-like substance found in small amounts in nature. Arsenic is widely distributed throughout the Earth's crust, most often as arsenic sulfide or as metal arsenates and arsenides. (IPCS, World Health Organization, 2001). Drinking water containing elevated levels of arsenic may cause grave health problems mostly skin problem.

iv. Fluoride

Fluoride is found in all natural waters at some concentration. Seawater typically contains about 1 mg l⁻¹ while rivers and lakes generally exhibit concentrations of less than 0.5 mg l⁻¹. In groundwater, however, low or high concentrations of fluoride can occur, it's directly effect on bone.

v. Nitrate & Nitrite

Nitrate (NO₃) is found naturally in the environment and is an important plant nutrient. It is present at varying concentrations in all plants and is a part of the nitrogen cycle. For drinking water 1mg/L is limit for nitrite. Nitrate can reach both surface water and groundwater as a consequence of agricultural activity (including excess application of inorganic nitrogenous fertilizers and manures), from wastewater disposal and from oxidation of nitrogenous waste products in human and animal excreta, including septic tanks. Surface water nitrate

concentrations can change rapidly owing to surface runoff of fertilizer, uptake by phytoplankton and denitrification by bacteria, but groundwater concentrations generally show relatively slow changes.

Sr #	Parametrs	WHO Standard s
1	pH	6.5-8.5
2	Total Dissolved Solids (TDS)	1000 mg/L
3	Arsenic (As)	0.05 ppm
4	Fluoride	1.5 mg/L
5	Nitrate	50 mg/L
6	Nitrite	0.3 mg/L

Table 1: WHO Standard

METHODOLOGY

In case of present study we digitize the main features (Road Network, Settlements, and Irrigation Network) of district Gujranwala. The data from hospitals/clinics were also collected to investigate the water borne diseases related to drinking water available in the study area. This study has conducted to investigate such pollutants of drinking water which damaging human health. We conduct the GPS survey to collect the water sample and hospital data. Collect the Water samples of different sources and depths.

Settlements	Source of Wat	Depth of s	Arsenic	Fluoric	Nitrate	TDS	Latitude	Longitude
Ladhy wala, Che	Hand pump	70	0	0	177.2	1298	32.2778	74.0177
Gakhar	Hand pump	50	0	1.4	177.2	793	32.3028	74.1506
Chak Balig	Motor pump	85	0	1.07	133	612	32.2162	74.0281
Tahliwala	Hand pump	50	0	1.5	132.9	560	32.501	74.1895
Ladhy wala, Che	Motor pump	80	0	1.4	132.9	803	32.2804	74.0209
Kashir kiran	Hand pump	30	0	1.5	132.9	789	32.3832	74.0228
Kallianwala	Hand pump	40	0	0.6	132.9	474	32.2737	73.7546
Kalaski	Hand pump	70	0	1.5	132.9	591	32.2416	74.0188
Jorah siyan	Hand pump	50	0	0	132.9	455	32.3594	74.2132
Banka cheema	Hand pump	250	0	0.6	132.9	335	32.2917	74.0908
Alipurchatha	Motor pump	190	0	1.4	132.9	597	32.2695	73.8189
Qilla Jagger	Hand pump	50	0.3	5.4	132.9	900	32.1369	73.9045
gagewali	Hand pump	70	0.01	0.2	132.9	110	32.2468	74.257
Eimnabad	Hand pump	200	0.02	1.09	132.9	280	32.042	74.2575
Sahensra Goraya	Hand pump	50	0.01	0.5	132.9	620	32.0989	74.2202
Mandiala	Hand pump	60	0	0.6	132.9	680	32.1252	74.3148
Eminabad	Motor pump	100	0.04	1	132.9	1190	32.0372	74.2576
Nadalia Sandhu	Hand pump	60	0.01	0.7	132.9	780	32.1552	74.3679
Sada chak khurd	Motor pump	60	0	1.07	132.9	579	32.2413	74.0443
Pandoki khurd	Hand pump	45	0	1.07	132.9	1108	32.2745	73.8554
Kot Bangliah	Motor pump	60	0	1.07	132.9	434	32.2313	74.014
Kalaski	Hand pump	70	0	1.07	132.9	329	32.245	74.0207
Matu Bhaik	Hand pump	60	0.04	1.2	132.9	420	31.9818	73.9916
naikarain	Motor pump	100	0.02	0.4	132.9	500	32.1002	73.9582
dohgan wala	Hand pump	60	0	0.5	132.9	800	32.219	74.0925
chak beg	Motor pump	120	0.02	0.25	132.9	480	32.2157	74.0268
baljuu muli	Hand pump	80	0.01	0	132.9	520	32.2052	74.0229
bugga	Motor pump	100	0.03	0.7	132.9	480	32.0286	73.8228

Figure 1: Water Sampling

Hospital data collected for getting the all information regarding toxic elements diseases, major diseases, etc. we just do the GPS survey for knowing the location of water sources and hospitals. After collecting and preparing the data water sample data, generate the surface with the help of GIS interpolation method. In this method, we used the special Kriging technique to generate the surface which have some own parameter to define its correlation between values. When we get the final surface of water samples parameter then we correlate this with hospital data and location. In the results we see how contaminated water effect on people health

badly.

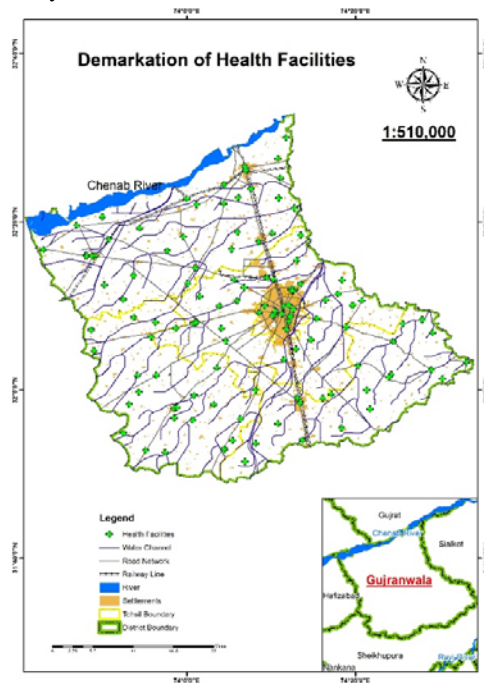


Figure 2: Hospital Data Collected by GPS

And these water sources generate the water borne disease due to the toxicification. In addition to harming animals water pollution can also affect plants, trees, the soil and other natural materials and resources of the earth.

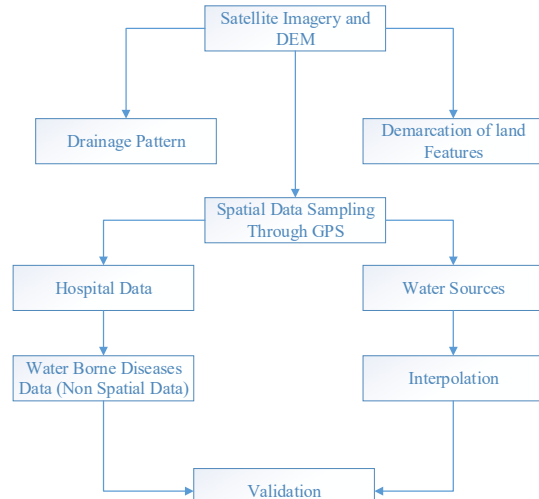


Figure 3: Flow Chart

ANALYSIS

We perform krining analysis using interpolation technique. With the help of GIS, we identify the contaminated area of polluted water and that flows from different sources which are causes of water pollution. Against each parameter interpolation is being done upon which we are able to highlights those areas having higher concentration of toxic materials. Below Maps shows the vulnerability of drinking water which is contaminated by toxified elements.

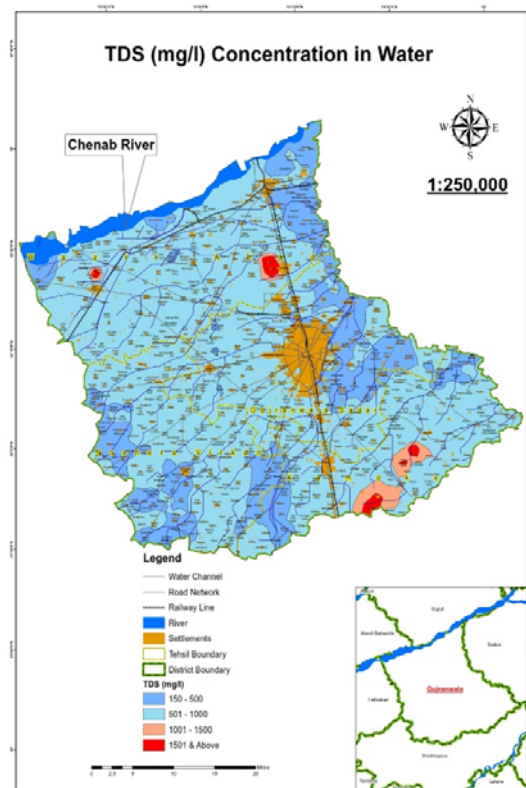


Figure 4 TDS Concentration in Water

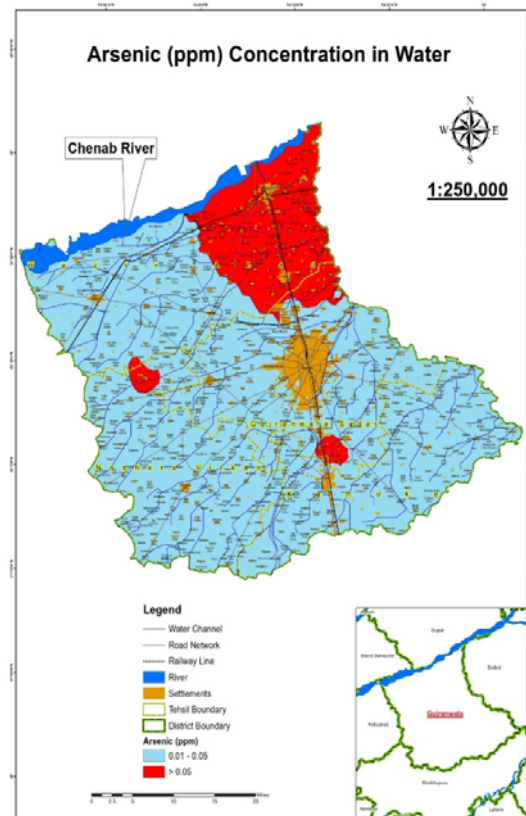


Figure 5: Arsenic Concentration in Water

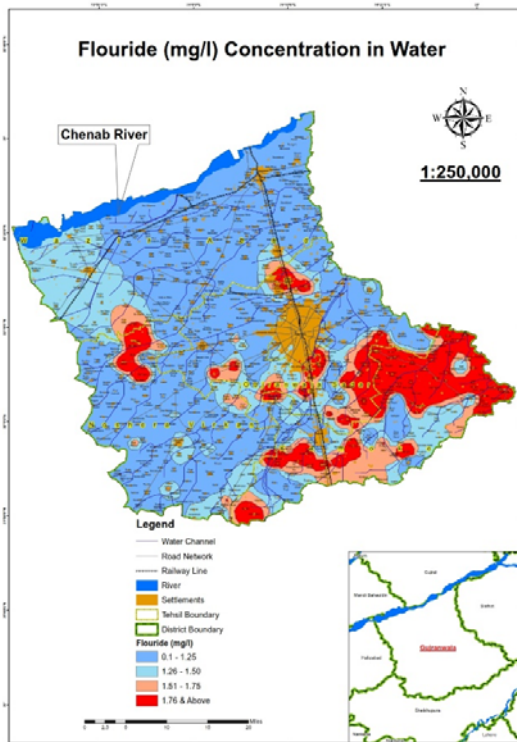


Figure 6: Fluoride Concentration in Water

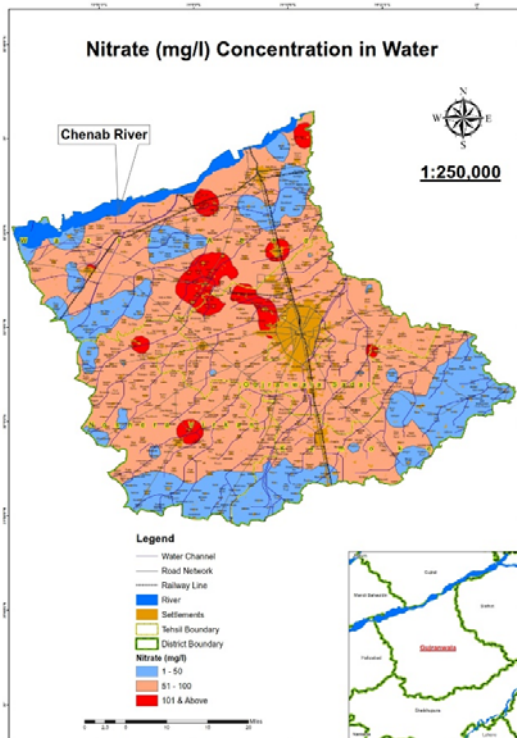


Figure 7: Nitrate Concentration in Water

It indicates the impact in near area that how containment area effect water pollution directly which not only affect the surface water but also disturb the ground water because these toxic elements penetrate by soil, and other ways. And drinking water

also effect by this pollution badly. And people used this water for drinking, farming etc. For the validation of this data, we collect the hospital data, we perform the overlay analysis. We have seen the relationship of containemeted water with hospital data. And its shows the 80% people are affected by toxic water directly.

CONCLUSION

The results indicated that the concentrations of all parameters were higher in groundwater samples of Gujranwala District. They were found toxic elements in water samples which is collected by survey, among different parameters studied in water samples, TDS, As, F, NO_3 , NO_2 was found within the permissible limits for drinking. The results of the water samples indicated that most of the area is effected by these elements and its effect on ground water and the surface water. It's just not polluted the water it's also effect the people health badly. These elements have long term effect on people health and its damages the bones, skin and other features of human body.

RECOMMENDATION

We identify source of pollution and control is on serious note. Finding a way to develop cheap filtration systems and better waste disposal management systems is going to be a vital step towards improving the health of our drinking water and the bodies of water that surround us. To make awareness among People about drinking water standard and water borne diseases. All water sources supervised on regular basses.

REFERENCES

- [1] Leeuwen F. X. R. Van. 2000. Safe drinking water: the toxicologist's approach. Food and Chemical Toxicology, 38: 51-58.
- [2] NDRC. 2014. Safe water: Keystone of environment, health, economy and security. Retrieved October 30, from <http://www.nrdc.org/international/safewater.asp>
- [3] Huang, G. H. and Xia, J. 2001. Barriers to sustainable water-quality management. Journal of Environmental Management, 61: 1-23Kimura S, "Journal paper title", J. of Computer Science, Vol. 1, Aug. 1987, pp. 23-49.
- [4] Govt. of Pakistan, SRO-1062(I)-2010. National Standards for Drinking Water Quality.
- [5] CENSUS ORGANIZATION, District Census Report Rawalpindi 1998, Buru of Statistics, Gujranwala.
- [6] "Planning and Development in a Hill Side City, A Case Study of Murree", Pakistan Journal of Geography, Vol. 2- No. 1&2. 1992. Pp. 145-161.
- [7] World Health Organisation 1996, Guidelines for drinking water quality, 2nd Ed, Vol. 2 Health

- criteria and other supporting information, Geneva, World Health Organization
- [8] Krajnc EI et al. (1987) *Integrated criteria document. Cadmium — Effects. Appendix.* Bilthoven, National Institute of Public Health and Environmental Protection (Report No. 758476004)
- [9] WHO 1972-73 Technical Reports Series No. 505, 532. World Health Organization, Geneva.
- [10] Harlan WR et al. (1973) Blood lead and blood pressure. Relationship in the adolescent and adult US inactivated delta-aminolevulinic acid dehydratase of whole blood and the blood lead level. *Biochemical medicine*, 1973, 8:149-159.
- [11] Risebro, H.L.; Breton, L.; Aird, H.; Hooper, A.; Hunter, P.R. Contaminated small drinking water supplies and risk of infectious intestinal disease: A prospective cohort study. *PLoS One* 2012, 7, doi: 10.1371/journal.

ANALYSIS OF RAINFALL IN THE EASTERN THAILAND

Wonlee Nounmusig¹

¹Faculty of International Maritime Studies, Kasetsart University, Thailand

ABSTRACT

Understanding of rainfall pattern in eastern Thailand is required to support the planning of water management. In this study, the patterns of rainfall in eastern Thailand are analyzed by using statistical analysis. The data used from rain gauge stations in 15 stations (period in 1969-2008). The results show that the yearly rainfall has been a tendency to decrease. The significant correlation between monthly rainfall and ENSO indices has the largest number in the transitional period (April, May and October).

Keywords: Rainfall, Eastern Thailand, Correlation, ENSO

INTRODUCTION

Eastern Thailand is a region of Thailand lying between the Sankampaeng Range to the north and the Gulf of Thailand to the south. The border of the region is Cambodia on the east and central Thailand on the west. Eastern Thailand consists of 7 provinces (Chachoengsao, Chanthaburi, Chonburi, Prachinburi, Rayong, Sa Kaeo and Trat) covering an area of 34,381 km² and account for 6.7% of country. In 2010, approximately 62.49% is an agricultural land proposes, 22.92% for forest land, 6.84% for urban and built-up land, 2.46% for water body and 5.29% for miscellaneous land as shown in Fig. 1 [1]. In addition, a major industrial zone (the Eastern Seaboard) which plays a key role in Thailand's economy is also located in the region. Thus, the need for water in the region increases daily due to population growth, economic developments and urbanization.

The main source of water in the region is mainly from rain. Too much or too little rain can have disastrous effects on the agricultural, industrial, and others consumption sectors. For example, severe drought of the region in 2005 led to a conflict in water resource allocation caused a fall in crop production and the industrial sector shipping water by truck from nearby regions [2].

In general, the climate in Thailand is dominated by northeast monsoon and southwest monsoon [3]. The monsoons are controlled by the Inter Tropical Convergence Zone (ITCZ). Anomalies in the ITCZ and monsoon rainfall are typically in phase with the anomalies in central and eastern Pacific Ocean. The variations in the position and intensity of the ITCZ are associated with climate phenomena known as the El Nino – Southern Oscillation (ENSO) [4-5]. Therefore, the study and understanding of relationships between rainfall and ENSO in eastern Thailand is required to support the planning of water management.



Land use type	Area	
	km ²	%
Urban and built-up land	2,353.02	6.84
Urban and built-up land	2,353.02	6.84
Agricultural land	21,485.01	62.49
Paddy field	4,876.80	14.18
Field crop	5,560.24	16.17
Perennial	6,385.67	18.57
Orchard	3,197.02	9.30
Horticulture	41.27	0.12
Pasture and farm house	154.28	0.45
Aquatic plant	1.08	0.003
Aquaculture land	1,268.47	3.69
Integrated farm/Diversified farm	0.17	0.0005
Forest land	7,879.94	22.92
Dense forest	433.92	1.26
Disturbed forest	7,446.02	21.66
Water body	844.49	2.46
Water body	844.49	2.46
Miscellaneous land	1,818.04	5.29
Other miscellaneous land	1,604.50	4.67
Marsh and swamp	213.54	0.62
Total	34,380.50	100.00

Fig. 1 Land use map in eastern Thailand [1].

DATA AND METHODS

Data used

Rainfall data

15 rain gauge stations during 1969 to 2008 from the Thai Meteorological Department (TMD) were used to analyze rainfall distribution pattern. Table 1 shows the description of the 15 rain gauge stations used in this study. The mean annual rainfall and rain day in eastern Thailand was shown in Table 2. The maximum of rainfall and rain day found at Khlong Yai (Station ID. 501201) with 4713±701mm. and 192±19day, respectively.

Table 1 Description of the 15 rain gauge stations

Station ID.	Station Name	Lat. (°N)	Long. (°E)	Elv. (m)
440201	Aranyaprathet	13°42'00"	102°35'00"	47.0
423301	Chacherngsao*	13°33'57"	101°27'30"	69.4
480201	Chanthaburi	12°37'00"	102°06'48"	2.9
459201	Chon Buri	13°22'00"	100°59'00"	0.9
478301	HuaiPong*	12°44'00"	101°08'00"	43.3
430401	Kabin Buri	13°59'00"	101°42'26"	10.2
501201	Khlong Yai	11°46'00"	102°53'00"	2.0
459202	Ko Sichang	13°09'42"	100°48'07"	24.9
459205	Lam Chabang	13°04'37"	100°52'33"	80.7
459203	Phatthaya	12°55'12"	100°52'10"	58.9
480301	Phriu*	12°31'00"	102°10'00"	22.3
430201	Prachin Buri	14°03'00"	101°22'00"	4.1
478201	Rayong	12°38'05"	101°20'45"	2.6
459204	Sattahip	12°41'00"	100°59'00"	16.0
440401	Sa Kaew	13°47'20"	102°02'05"	40.9

Table 2 Mean annual rainfall and rain days with standard deviation

Station ID.	Recording Period	Mean annual			
		Rainfall (mm)	Std.	Rain days (Day)	Std.
440201	1969-2008	1372	175	130	13
423301	1989-2008	1323	200	120	14
480201	1969-2008	2917	484	167	14
459201	1969-2008	1276	216	118	13
478301	1969-2008	1392	277	119	16
430401	1970-2008	1653	238	132	11
501201	1969-2008	4713	701	192	19
459202	1969-2008	1222	320	102	13
459205	1993-2008	1160	200	103	12
459203	1981-2008	1119	234	106	11
480301	1969-2008	3166	636	171	23
430201	1969-2008	1862	286	134	13
478201	1981-2008	1362	288	114	15

Climate in Thailand

Climate in Thailand is divided into three seasons as follows: 1) southwest monsoon season (mid-May to mid-October). The southwest monsoon prevails and brings warm and wet air from the Indian Ocean to Thailand. Eastern Thailand has also abundant rain occurs in this period. The wettest month in the region is in July to August. 2) Winter or northeast monsoon season (mid-October to mid-February). The northeast monsoon brings cold and dry air from China to upper Thailand. 3) Summer or pre-monsoon season, mid-February to mid-May. This is the transitional period from the northeast to southwest monsoons. The weather becomes warmer, especially in upper Thailand. April is the hottest month for all regions of Thailand.

ENSO indices

Sea surface temperature anomaly (SSTA) data for equatorial regions of the Pacific Ocean which calculated from the HadISST1 [6] were used for this study. The regions included here were Nino3 (the area averaged SST from 90°W–150°W and 5°S–5°N), Nino4 (the area averaged SST from 160°E–150°W and 5°S–5°N), and composite region Nino34 (the area averaged SST from 120°W–170°W and 5°S–5°N).

The Indian Ocean Dipole (IOD) intensity is represented the gradient in the difference between sea surface temperatures of the western equatorial Indian Ocean (50°E–70°E and 10°S–10°N) and the south eastern equatorial Indian Ocean (90°E–110°E and 10°S–0°N). This gradient is named as Dipole Mode Index (DMI). When the DMI is positive then, the phenomenon is refereed as the positive IOD and when it is negative, it is refereed as negative IOD [6].

The Southern Oscillation Index (SOI) is defined as the normalized pressure difference between Tahiti and Darwin. There are several slight variations in the SOI values calculated at various centre. The SOI data used here were calculated using the method given by Ropelewski and Jones [6-7].

Data Analysis

The Pearson correlation coefficients (r) were used for investigation significant relationships between rainfall data and ENSO indices (SSTAs, SOI, IOD) as shown in Eq. (1).

$$r = \frac{\sum_{i=1}^n (x_i - \bar{x})(y_i - \bar{y})}{\sqrt{\sum_{i=1}^n (x_i - \bar{x})^2} \sqrt{\sum_{i=1}^n (y_i - \bar{y})^2}} \quad (1)$$

where n is the number of data, x_i and y_i are the data set at time i , and \bar{x} is defined as in Eq. (2),

$$\bar{x} = \frac{1}{n} \sum_{i=1}^n x_i \quad (2).$$

The significance test of correlation can be calculated with a t statistic using the Eq. (3).

$$t = \frac{r\sqrt{n-2}}{\sqrt{1-r^2}} \quad (3)$$

The null hypothesis was rejected at a significant level of α when $|t|$ is more than or equal to $t_{\frac{\alpha}{2}, n-2}$.

RESULTS AND DISCUSSION

Rainfall

Annual rainfall and rain day

Fig. 2 shows an average annual rainfall in eastern region of Thailand. The 40-year average of rainfall is 1921mm. The annual rainfall has been a tendency to decrease. When El Niño (La Niña) phenomenon is identified, the SSTAs in the Niño34 region is above the threshold of $+0.5^\circ\text{C}$ (-0.5°C). The correlation between average yearly rainfall and Niño34 is weak ($r=-0.28$). During El Niño year, most of the yearly rainfall is below normal especially in 1992 and 1997 (1577 and 1613mm, respectively). During La Niña year, the yearly rainfall is mostly above the average as in 1974, 1975, 1988, 1999 and 2000 with each year exceeding 2000mm. When Consider only in the ENSO year, it is found that the yearly rainfall has the significant correlation with Niño34 ($r=-0.46$).

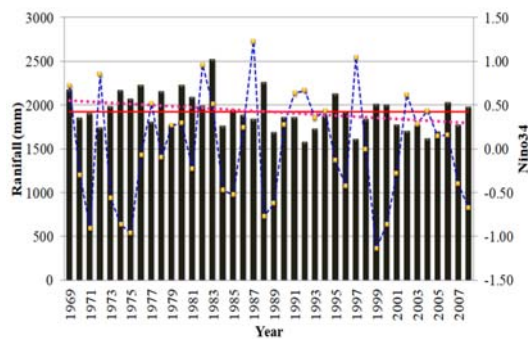


Fig. 2 Average yearly rainfall in eastern Thailand (— represent 40-year average of rainfall, ... represent linear trend, bar represent amount of rainfall, and —■— represent the sea surface temperature anomaly region Niño34)

Table 3 and 4 summarize the significant correlations between ENSO indices and average annual rainfall and rain day, respectively at 15 stations. The correlation between average yearly rainfall and all of ENSO indices is mostly weak ($r \leq -0.51$). The rainfall has only the significant correlation with Niño and SOI Correlation in station ID 440201 and 459202. When consider the correlation between the ENSO indices and rain day, rain day in most of the station has the significant correlation with ENSO indices.

Table 3 Correlation between the ENSO indices and Average Yearly rainfall at 15 stations

Station ID	NINO3	NINO34	NINO4	SOI	DMI
440201	-0.33	-0.45	-0.49	0.52	0.10
423301	-0.16	-0.25	-0.26	0.36	0.21
480201	-0.03	-0.08	-0.01	0.03	0.05
459201	-0.29	-0.33	-0.31	0.32	-0.08
478301	-0.13	-0.20	-0.20	0.24	-0.20
430401	-0.08	-0.18	-0.23	0.21	0.00
501201	-0.02	-0.09	-0.11	0.02	0.24
459202	-0.33	-0.39	-0.37	0.37	-0.26
459205	-0.44	-0.42	-0.30	0.44	-0.51
459203	-0.16	-0.20	-0.14	0.23	-0.26
480301	0.15	0.05	0.05	-0.08	0.22
430201	-0.29	-0.31	-0.31	0.31	-0.06
478201	-0.20	-0.25	-0.21	0.25	-0.23
459204	-0.12	-0.18	-0.24	0.25	0.02
440401	-0.07	-0.29	-0.38	0.48	0.56

Note: Correlations in bold are significant at the $p=0.05$ level

Table 4 Correlation between the ENSO indices and average annual rain day at 15 stations

Station ID	NINO3	NINO34	NINO4	SOI	DMI
440201	-0.26	-0.28	-0.33	0.27	-0.06
423301	-0.55	-0.61	-0.54	0.64	0.10
480201	-0.44	-0.45	-0.39	0.42	0.10
459201	-0.56	-0.60	-0.55	0.61	-0.21
478301	-0.31	-0.33	-0.25	0.36	-0.17
430401	-0.39	-0.46	-0.49	0.49	0.00
501201	-0.36	-0.39	-0.38	0.35	0.25
459202	-0.33	-0.34	-0.32	0.30	-0.09
459205	-0.58	-0.70	-0.68	0.71	-0.50
459203	-0.18	-0.20	-0.17	0.22	-0.15
480301	-0.15	-0.23	-0.22	0.19	-0.07
430201	-0.45	-0.54	-0.60	0.50	-0.13
478201	-0.38	-0.40	-0.32	0.41	-0.27
459204	-0.29	-0.38	-0.41	0.40	0.03
440401	-0.42	-0.65	-0.77	0.82	0.62

Note: Correlations in bold are significant at the $p=0.05$ level

Seasonal Variation in Rainfall

Fig. 2 and Fig. 3 show mean monthly rainfall and rain day, respectively at 15 stations in East Thailand. During May to September has abundant of rainfall. The maximum of rainfall and rain day found in August at Khlong Yai (Station ID. 501201) with exceed 1000mm and exceed 25day, respectively. All of stations have a number of rain days exceed 10day during May to October.

When consider the correlation between the ENSO indices and average monthly rainfall, the rainfall has the largest number of significant correlation with ENSO indices in the transitional period (April, May and October) as shown in Fig. 4. The highest number of significant correlations is found at station ID 440401 in April and May with $r=-0.71$ and $r=-0.52$, respectively. For the rain days, it is also found that the largest number of correlation with ENSO indices is in the transitional period (April, May and October). But, the rain days along the near shore station have no significant correlation with Nino34.

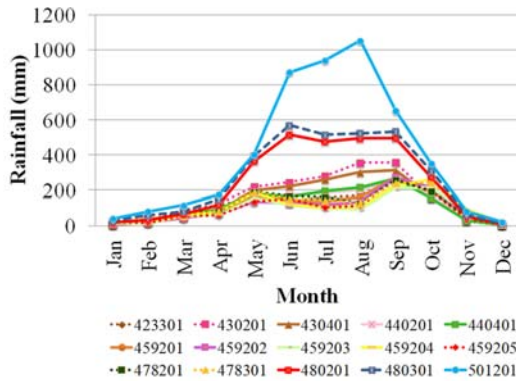


Fig. 2 Mean monthly rainfall in eastern Thailand

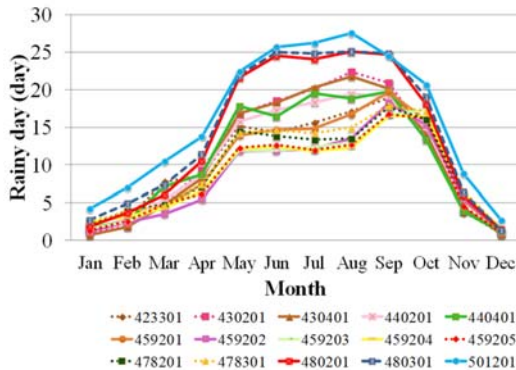


Fig. 3 Mean monthly rainy day in eastern part of Thailand

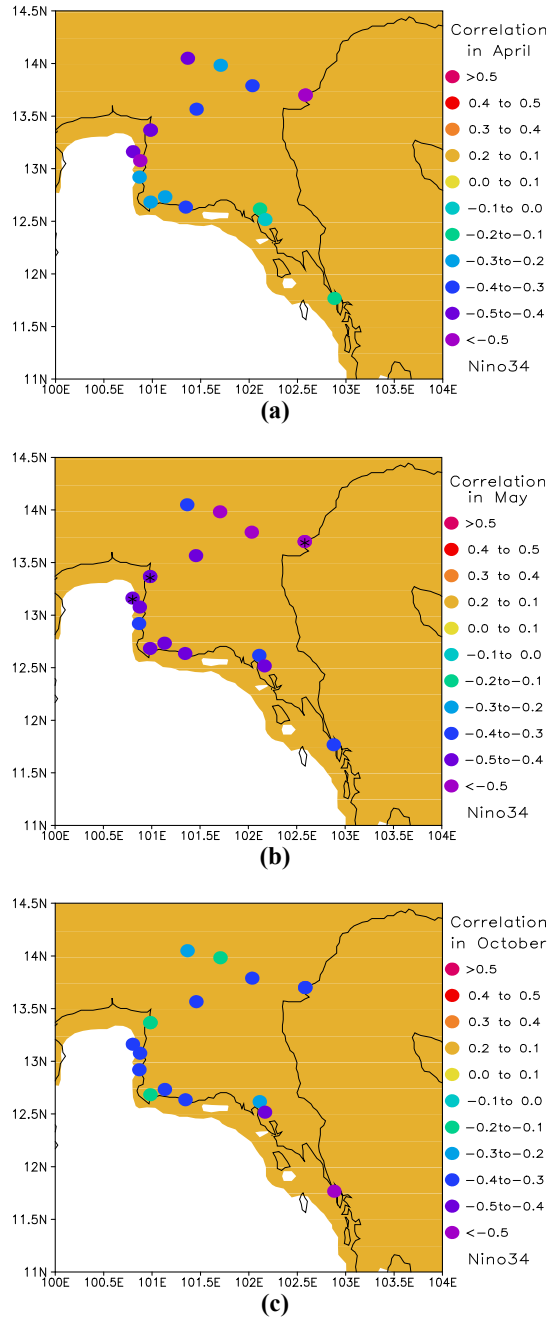


Fig. 4 Correlation map between the Nino34 and average monthly rainfall of 15 stations in (a) April, (b) May and (c) October.

CONCLUSION

The 15 rain gauge stations data during 1969 to 2008 from the Thai Meteorological Department (TMD) were used to analyze rainfall distribution pattern. The main source of rainfall in the region comes from southwest monsoon which brings abundant rain during May to October with a number of rain days exceed 10day. The 40-year average of

rainfall is 1921mm. Since 1969, the annual rainfall has been a tendency to decrease.

The correlation between yearly rainfall and Nino34 is weak ($r=-0.28$). When consider the correlation between the ENSO indices and monthly rainfall, it is found that the rainfall has the largest number of significant correlation with ENSO indices in the transitional period (April, May and October). For the rain days, it is also found that the largest number of correlation with ENSO indices is in the transitional period (April, May and October). But, the rain days along the near shore station have no significant correlation with Nino34.

In future work, the atmospheric model will be applied to study the rainfall pattern in Eastern Thailand and mechanism of atmosphere during the transitional period.

ACKNOWLEDGEMENTS

The rainfall data used in this study were obtained from the Thai Meteorological Department (TMD), Ministry of Digital Economy and Society Thailand.

REFERENCES

- [1] Land Development Department (LDD), http://www.ddd.go.th/ddd_en/en-US/map/map-details/land-use-in-eastern-region/6/, 2014.
- [2] Chitradon R, Boonya-aroonnet S and Thanapakpawin P, "Risk Management of Water Resources in Thailand in the Face of Climate Change", *Sasin Journal of Management*, 2009, pp. 64-67.
- [3] Zhang Y, Li T, Wang B and Wu G, "Onset of the Summer Monsoon over the Indochina Peninsula: Climatology and Interannual Variations", *J. Climate*, Vol.15, Nov. 2002, pp. 3206–3221.
- [4] Lau KM and Yang S, "Climatology and interannual variability of the southeast asian summer monsoon", *Adv. Atmos. Sci.*, Vol. 14, Jun. 1997, pp. 141-162.
- [5] Waliser DE and Jiang X, "Tropical Meteorology: Intertropical Convergence Zones (ITCZ)", *Encyclopedia of Atmospheric Sciences*, 2th ed., Academic Press.
- [6] Smith C, "Climate Time series", NOAA ESRL Physical Sciences Division, <http://www.esrl.noaa.gov/psd/gcos wgsp/Timeseries/index.html>, 2017.
- [7] Ropelewski CF, and Jones PD, "An extension of the Tahiti-Darwin Southern Oscillation Index", *Monthly Weather Review*, Vol. 115, 1987, pp. 2161-2165.

CHANGES IN THE ZOOPLANKTON COMMUNITY BEFORE AND AFTER NUTRIENT DIVERSION AND REVETMENT CONSTRUCTION IN LAKE FUKAMI-IKE, JAPAN

Hiromi Suda¹, Masaaki Tanaka², Maki Oyagi² and Akihiko Yagi³

¹Faculty of Science and Technology, Meijo University, Japan

²Faculty of Environmental and Information Sciences, Yokkaichi University, Japan

³Faculty of Civil Engineering Department of Urban Environment, Aichi Institute of Technology, Japan

ABSTRACT

Lake Fukami-ike is a small eutrophic lake, to improve the water quality of the lake, a lake management project was carried out in 1992. This project involved nutrient diversion and revetment construction along the lake shore. A biotope was built near the lake in 2000. As a result, although the inorganic nitrogen in the lake decreased considerably, chlorophyll-a (phytoplankton) increased slightly.

The zooplankton community in the lake before the project in 1978-1979 predominantly comprised large-sized species (about 1.8 mm), however, small-sized species (about 0.1-0.2 mm) were dominant after in 2013-2015. The reason for the decrease of the large-sized zooplankton was thought to be the possibility of losing habitat space because aquatic macrophytes of the littoral zone were filled up when revetment construction built in 1992. We compared the body length and composition of zooplankton community between the lake (nearly emergent plants on the lake shore) and the biotope (emergent and floating-leaved plant cover). Large-sized zooplankton (about 0.9-1.2 mm) were dominant in the biotope, and size distribution did not differ in 1978-1979. The presence of developed aquatic macrophytes was suggested to promote the survival of large zooplankton.

Keywords: Zooplankton community, aquatic macrophytes, body length

INTRODUCTION

Lake Fukami-ike is a small monomictic and eutrophic lake, located in southern Nagano Prefecture in central Japan. In 1992, a lake management project was carried out to improve the water quality of the lake; this project involved a reduction in external nutrient loadings from surrounding paddy fields into the lake (nutrient diversion), revetment construction along the lake shore (Except for some, the aquatic plants disappeared) [1]. This project was expected to improve the water quality of the lake, but only inorganic nitrogen, and not inorganic phosphorus, was found to be decreased significantly. Moreover, chlorophyll-a (chl-a) increased slightly after the project [2]. In June 2000 and July 2016, blue-green algae (Cyanophyceae, *Microcystis aeruginosa*, *Anabaena affinis*, respectively) blooms occurred, which was not observed before the project. Although more than 20 years have passed since the project, it is difficult to say whether it effectively improved the water quality by nutrient diversion.

Studies on Lake Fukami-ike began from 1978 onwards, and investigations are still being conducted mainly on water quality roughly once a month. However, zooplankton and phytoplankton have not been investigated in detail. Chl-a have been

measured, but its species composition as phytoplankton has not been clarified continuously.

Reference [2] shows the difference in species composition between zooplankton and phytoplankton before and after the project, which also reports that chl-a increase slightly despite the nutrient diversion and large-sized species (body length about 1.8 mm, e.g., *Cyclops vicinus*) dominated the lake in 1978-1979 (before the project), whereas small-seized species (body length about 0.1 mm e.g., *Keratella cochlearis*) dominated the lake in 2013-2014 (after the project).

In addition to the results of reference [2], results from 2014 to 2015 are also included, and the body lengths of zooplankton before and after the project have been extensively compared in this paper. Furthermore, in order to clarify the influence of aquatic macrophytes of the lake shore which was used for zooplankton as a habitat space and an evacuate space from fish, which is considered as one of the factors in the reducing of large-sized zooplankton, we decided to compare the appearance situation of biotope (Adjacent to the west side of the lake) to lakes with different vegetation and lake.

METHODS

Study Site

Lake Fukami-ike

The lake is located at a north latitude of 35°32'55"77 and east longitude of 137°81'93"56. Its short diameter is 150 m, diameter is 300 m, area is about 2.2 ha, and volume is $1.0 \times 10^5 \text{ m}^3$ (Fig.1). The lake has six inflows and an outflow [2, 3]. In 2016, the maximum depth of the water was observed to be 7.6 m.

The dominant macrophytes communities on the lake shore have been established as follows: *Zizania latifolia* and *Phragmites australis*, (both species belong to Poaceae). Among them, *Z. latifolia* were planted after the project [1].

The fish community is dominated by *Lepomis macrochirus* (Centrarchidae) and *Micropterus salmoides* (Centrarchidae), which are piscivorous fish [4].

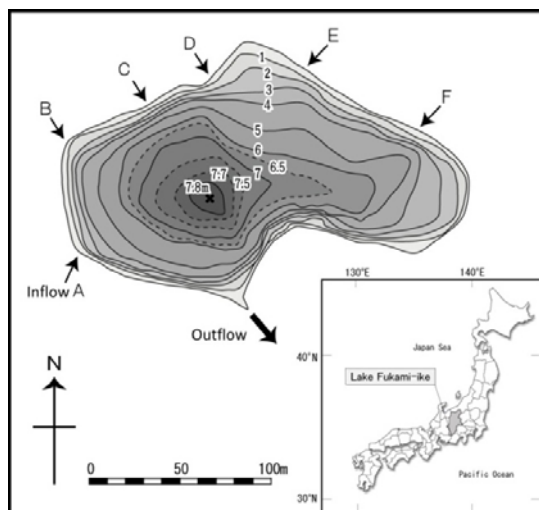


Fig. 1 Location of the Lake Fukami-ike.

Biotope

The biotope is on the west side of the lake and built by local residents in 2000. The biotope is connected to the lake by a hose filled in the ground. The range of water depth is about 0.1-0.3 m, water in the biotope will dry out in the midsummer and freezing in the midwinter temporarily.

In summer, the biotope was found to be covered with *Nelumbo nucifera* (Nelumbonaceae), *Z. latifolia*, and *P. australis* (<http://fukami-ike.jp/page012.html>). *Pelophylax nigromaculatus* (Ranidae) was also found in the biotope.



Fig. 2 The biotope on July 6, 2013.

Sampling and Analysis

Field observations in the lake were conducted from March 2013 to February 2015, including the observations in the biotope from May 2013 to June 2014, roughly once a month.

Lake plankton samples were collected at the deepest point with a Van Dorn water sampler (10L, Rigo Co., Ltd., Tokyo, Japan) from every 0.5m. Biotope plankton samples were collected with polyethylene bottle by scooping water directly.

All the samples were preserved in 1% formalin in the field immediately. Zooplankton were identified using an optical microscope (BX51, Olympus Optical Co., Ltd., Tokyo, Japan) in the laboratory.

RESULTS AND DISCUSSION

Comparing body length of zooplankton before and after project

Reference [5] shows that the zooplankton were collected using plankton-net (mesh size 0.1 mm, Rigo Co., Ltd., Tokyo Japan) from 1978 to 1979. Therefore, we compared the length of zooplankton before and after project, excluding the size smaller than 0.1 mm.

The species with high frequency before and after the project is shown in Table 1.

Before the project, the frequencies of large-sized zooplankton are as follows: *Cyclops vicinus* (36.2%), *Bosmina longirostris* (20.6%), and *Cyclops* sp. (11.8%), respectively. On the other hand, the small-sized zooplankton that appeared after the project are as follows: *Keratella cochlearis* var. *tecta*, *Keratella cochlearis* var. *micracantha* and Nauplius of Cyclopoida (15.6% in total), *Brachionus angularis* and *Polyarthra dolicoptera* (13.4%), *Filinia longiseta* (11.2%).

While there were many large species in the species with high occurrence frequency before the project, there were many small species after the project.

Table 1 Comparison of high frequency species and body length before and after the project.

Project	Species	Body length (mm)	Frequency (%)
Before (1978-1979) [5]	<i>Cyclops vicinus</i>	1.8	36.2
	<i>Bosmina longirostris</i>	0.5	20.6
	<i>Cyclops</i> sp.	1.5	11.8
After (2013-2015)	<i>Keratella cochlearis</i> var. <i>tecta</i>	0.10	15.6
	<i>Keratella cochlearis</i> var. <i>micracantha</i>		
	Nauplius of Cyclopoida		
	<i>Brachionus angularis</i>	0.125	13.4
	<i>Polyarthra dolicoptera</i>		
	<i>Filinia longiseta</i>	0.25	11.2

Figure 2 shows the comparison of the body length of zooplankton collected before and after the project. This finding indicates that many large species inhabited the lake before the project, while the small species mainly inhabited the lake after the project.

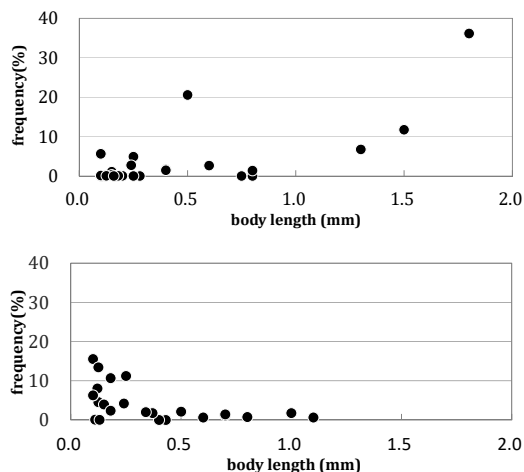


Fig.2 Comparison of the body length and frequency of the zooplankton in Lake Fukami-ike before (upper figure) and after (lower figure) the project.

Factors responsible for reducing the large species in the lake

In general, an increase in grazing pressure of planktivorous fish led to the loss of large-sized zooplanktons [6, 7].

Zooplankton behavior that escapes from predation from fish is well known, it is necessary to move vertically to the layer where light does not reach easily visible during the day [8, 9]. In addition, it is known that zooplankton moves horizontally to aquatic macrophytes community on the lake shore in order to conceal it from fish [10, 11].

The aquatic macrophytes communities are classified in emergent plant, floating-leaved plant, and submerged plants mainly by their form and life-

type. They are distributed in gently sloping places, generally called “lake-shelves”, in strips at different water depths, and established aquatic macrophytes community.

Aquatic plants play an important role in the ecosystem of the lake. They provide habitats for living things, absorb nitrogen and phosphorus so as to maintain water quality, and so on [12]. The developed aquatic macrophytes in the lake shore provides habitats for zooplankton and other organisms because there are three-dimensional structures. The developed aquatic macrophytes in the lake shore also helps the zooplankton to escape from predators such as fish. Emergent plants are shallowly submerged in water while the floating-leaved plants have only the leaves floating on the surface; both these categories of plants are less likely to form complex structures. However, the submerged plants have their whole body submerged in the water, so they have a high hiding effect from fish [10,12]. For this reason, the existence of a submerged plant community is considered important in places where large sized zooplankton exists so as to help hide them from their predators.

In the Lake Fukami-ike, some of the aquatic macrophytes communities in the littoral zone on the shore were left behind before the revetment construction in 1992. But later, many of these macrophytes communities disappeared during the construction process.

To see the influence of macrophytes community, species composition of zooplankton from biotope (emergent and floating-leaved plant cover) was compared with the lake (nearly emergent plants on the lake shore) after the project.

Relationship between macrophytes community and species composition of zooplankton1

Macrophytes community of the lake and biotope

Table 2 shows the macrophytes community of the lake and biotope. Before the project in the lake, the macrophytes community included emergent plants, floating-leaved plants, and submerged plants.

Although there is no data on the area to prove that the community disappeared by revetment construction, the macrophytes community of the lake became simpler with emergent plants on the lake shore.

Table 2 Main macrophytes community of the lake and biotope.

Species	Living Forms*	Area		
		Before [13]	Lake After	Biotope After
<i>Zizania latifolia</i>	E	○		○
<i>Phragmites australis</i>	E	○	○	○
<i>P. japonica</i>	E	○	○	
<i>Typha latifolia</i>	E	○		
<i>Nelumbo nucifera</i>	F			○
<i>Potamogeton cristatus</i>	S	○		

*E: emergent plants, F: floating-leaved plants, S: submerged plants

*Before: before the project, After: after the project

Comparing body length of zooplankton in the lake and biotope after the project

To see the difference in zooplankton composition and macrophytes, the body size of the zooplankton collected from the biotope and the lake were compared (Fig. 3). The size of the circle indicates that the number of zooplankton corresponded to that position.

From the biotope, most cases were dominated by large zooplankton (*Cladocera*, *Scapholeberis kingi*) with a body length of about 0.9 to 1.2 mm during the study period. The distribution of the body size was different from the sample collected from the lake after the project. The size distribution of zooplankton collected from the biotope was similar to that of the lake before the project, and large-sized zooplankton were mainly obtained.

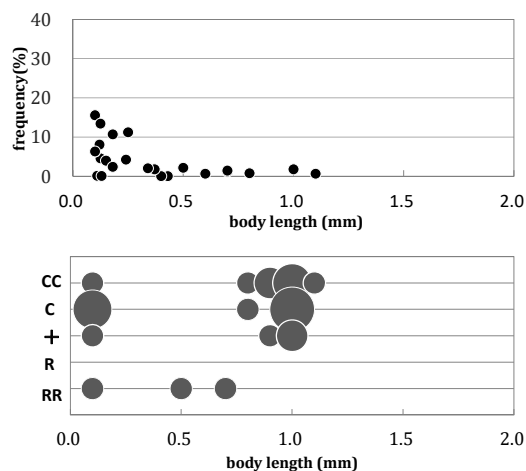


Fig.3 Comparison of body length and frequency of the zooplankton in Lake Fukami-ike after the project (upper figure, refer to Fig.2) and biotope (lower figure).

Reference [10] shows the difference between the living types of aquatic plants and the abundance of *Daphnia*. The abundance of *Daphnia* in the submerged plants community shows that the population density has increased significantly compared with the floating-leaved plant group, the emergent plant group, and the control group (without water plants).

These results suggested that the presence of developed aquatic macrophytes suggested the promotion of the survival of large-sized zooplankton.

CONCLUSION

With the lake management project in 1992, the amount of nitrogen in the lake was decreased significantly; however, the amount of chl-a did not decrease but increased slightly. Although this phenomenon was one of the question, this may be due to the low prey pressure for chl-a (phytoplankton) with remarkably small number of large-sized zooplankton. Moreover, the decrease in large-sized zooplankton was believed to be due to the lack of developed macrophytes for cover from predators as a result of the large landfilling of the lake shore by the revetment construction.

In order to reduce the amount of chl-a in the lake, it is important to increase the predation pressure against them. Developing aquatic macrophytes community on the lake shore is thought to promote the population of large-sized zooplankton, and it also has the effect of stable absorption of nitrogen and phosphorus in the lake.

Although it is still an issue to examine the influence of predatory pressure of fish against zooplankton, restoring the developed community seems to have the potential to improve the ecosystem of the Lake Fukami-ike.

ACKNOWLEDGMENTS

We are grateful to the Anan-cho authorities in Shimoina-gun, Nagano Prefecture, who generously provided research facilities. We also thank Megumi Nobori, Sohey Hane, Seiya Kato, Ryosuke Nakagami, Goto Hironori, Takuya Yokoyama in Yagi laboratory for their help in the field.

REFERENCES

- [1] Limnology of committee of Shimoina kyoiku-kai, "Shimoina-shi", Shimoina Editorial Committee of Shimoina-shi edited, (in Japanese), [Translated from Japanese], 2009, 353pp.
- [2] Suda H, Tanaka M, Oyagi M, Nobori M, and Yagi A, "Water quality and compositions of the phytoplankton and zooplankton before and after building a bulkhead maintenance construction in

- Lake Fukami-ike, Japan”, International Journal of GEOMATE, Vol. 10, Jun. 2016, Issue 22, pp. 1983-1988.
- [3] Yagi A, “Biological manganese cycle in the oxic and anoxic layers of Lake Fukami-ike” (in Japanese), Limnology in Tokai Region of Japan, Vol. 43, 2010, pp.51-60.
- [4] Kawanobe M, Hosoe A. “Extermination of the alien fishes in the Fukami Pond”. Annual Report of Nagano prefectural fisheries experimental station, (in Japanese) [Translated from Japanese] 2008, p.15.
- [5] Tanaka M, “11-18. Lake Fukami-ike”, The lakes in Japan (in Japanese), 1th ed. Nagoya, The University of Nagoya Press., 1992, pp.417-421.
- [6] Brooks, J. L., and S. I. Dodson, “Predation, body size, and composition of plankton.” Science, 1965, 150, 3962, pp.28-35.
- [7] Dahl-Hansen, G. A. P., “Long term changes in crustacean zooplankton - the effect of mass removal of arctic charr, *Salvelinus alpinus* (L), from an oligotrophic lake.”, Plankton Research, 1995, 17, pp.1819-1833.
- [8] Kikuchi, K., “Diurnal migration of plankton crustaceae.”, The Quarterly Review of Biology, 1930, 5, pp.189-206.
- [9] Sekino, T., and N. Yoshioka, “The relationship between nutritional condition and diel vertical migration of *Daphnia galeata*.” Japanese Journal of Limnology, 1995, 56, pp.145-150.
- [10] Hayashi N, Nakano Y, Ozaki Y and Inamori Y., “Influence of Aquatic Plant Communities for Planktonic Biomass.”, Japanese journal of water treatment biology. 2007, 43, pp.113-119.
- [11] Burks, R. L., D. M. Lodge, E. Jeppesen, and T. L. Lauridsen, “Diel horizontal migration of Zooplankton: costs and benefits of inhabiting the littoral.”, Freshwater Biology, 2002, 47, pp.343-365.
- [12] Sakurai Y. and Ministry of Land, Infrastructure and Transport Kasumigaura River Office (editing), “Aquatic organisms of Lake Kasumigaura: records of changes from 1972 to 1993”, (in Japanese) [Translated from Japanese], Shinzansya Publisher Co., Ltd., 2007, 307pp.
- [13] Environmental Science Society (Ueda), “Lake Fukami-ike”, Inland water of Shinshu, (in Japanese) [Translated from Japanese], 1974, pp.117-128.

SPATIAL ASSESSMENT ON THE IMPACT OF FLOOD TO MELAKA'S ECONOMY

Rosilawati Zainol¹, Hanan Elsawahli² and Wan Suzita Wan Ibrahim³

¹Centre for Sustainable Urban Planning and Real Estate, Faculty of Built Environment, University of Malaya, Malaysia; ²The National Ribat University Sudan; ³Universiti Kebangsaan Malaysia, Malaysia

ABSTRACT

Melaka was a significant trading state in the 16th century. It had attracted traders from various continents to be its trading partners. Many of these traders had left their footprint enormously. Over the years, these tangible and intangible historical assets have been an attraction to tourism sector which contributes significantly to Malaysian GDP. However, due to the impact of climate change and rapid urban development in Melaka, the flood has posed a risk to Melaka's economy especially in the tourism sector. To protect its interest, Melaka has taken proactive measures in mitigating flood incidences. Thus, this study intends to examine the impact of the flood on Melaka's economy from 2012 to 2016 using spatial assessments. This study employs a quantitative approach by using secondary data obtained from the Department of Statistics Malaysia and the Department of Irrigation and Drainage. Moran's I, Local Indicator and Spatial Association and Bivariate Moran's I were used to analyse the data spatially. Findings show the mitigation measures taken have relieved the risk posed by floods towards economic activities in Melaka as a whole.

Keywords: Moran's I, Bivariate Moran's I, Local Indication Spatial Association, Flood Modification

INTRODUCTION

Flood has become a global concern, as flood risks caused extensive damage and threatened the lives of many people around the globe. Climate change is causing increased flood damages [1], making flood risks no more associated with underdeveloped countries. Hurricane Katerina hit the Gulf Coast in the USA and caused serious damages to people and property [2]. In 2012 the city of New York was also hit by a hurricane. In Austria, Germany and Hungary excessive heavy rains caused serious damages and losses in billions of Euros. In 2007, England suffered a major flood which caused the destruction of property and loss of lives [3].

Malaysia, being a tropical country suffers flood risks. Flooding is one of the major hazards facing by several cities in Malaysia. However, debates around possibilities of flood occurrence, do not take place against the background of climate change only, but also against the background of rapid urbanisation, resulting in 4.8 million people living in flood-prone areas [4, 5]. The Malaysian government has initiated several programs at both local and national levels to improve flood risk management. However, the effectiveness of these measures has yet to be measured using various assessment tools. Thus, this study intends to examine the impact of mitigation measures taken on economic activities using spatial analysis. The area for this study is Melaka.

BACKGROUND

Flood is the most devastating natural disaster experienced in Malaysia. It has a terrible impact socially and economically and its likelihood to occur in the future is high. There are about 189 river basins in Malaysia, and 85 of them are prone to flood. Flood disaster in Malaysia affects an area of approximately 28,800 km² and almost 4.82 million people are affected by this disaster (DID, 2009). There are two categories of flood that affect Malaysia. First is a flash flood and the other is monsoon flood. The difference between these two is the time taken to recede. Flash flood will only take hours to return normal level, and monsoon flood can last a month.

Mitigation Measures

There are various approaches used by various countries to mitigate flood impact. Among others include flood modification, property modification and response modification.

Flood modification is a traditional method of mitigation that deals with the use of structural measures to keep water away from development. It requires the government to allocate some funding which involves modifying the flow of flood water. Examples of measures are levees, dams, diversions

and channel improvements, flood gates and detention basins.

Property modification measure, a non-structural measure, refers to the placement of development by keeping away from flood prone area using land use planning or building design. Examples of this measure are zoning and land use planning, voluntary purchase or acquisition, building regulations and house raising.

Response modification places more emphasis on risk management as it seeks to modify human behaviour through activities such as planning, warning system, education and awareness campaign. Examples of this measure are state and national emergency services response, forecasts and warning systems, preparedness (planning for emergency) and information and education programs.

Nevertheless, each approach has its strengths and weaknesses. Flood modification requires a hefty amount of funding to be implemented. Usually, the responsibility of this approach lies on the government to prepare for a big budget to tackle areas that are currently located in flood prone areas. Property modification will only be effective in a new development area. However, most of the flood incidences occurred in an area in which the development had been completed. Sometimes it may affect areas which had never experienced flood before. Response modification will be a reactive measure in life-saving. Nevertheless, all these approaches should be implemented in countries that are facing flood risks.

Impact of Flood on Economy

Floods have coast a lot of damages socioeconomically [12]. It is most pronounced in urban areas which have high densities of people, assets, economic activities and vulnerable infrastructures. Malaysia experienced massive flood damages in floods that occurred in 2011 and 2015. However, according to [13] the estimated cost of damages in the 2014 flood in Malaysia is the worst which is within RM 1 billion.

METHODOLOGY

This study employs a quantitative approach. It uses secondary data which are basic data retrieved from Melaka State Government official website, flood and mitigation measures from the Department of Irrigation and Drainage (DID) Melaka Tengah, mitigation measures from Melaka State Structure Plan and also demographic data from the Department of Statistics Malaysia.

Melaka

In this study, Melaka was selected as its study area. This is because Melaka has a lot of tourism areas and flood posts high impact on its wellbeing, economically and socially. The worst flood that ever occurred in this state was in December 2006. Areas that were affected are Sungai Melaka river basin, Sungai Duyung and Sungai Kesang. Almost 70.4 hectares of its area was flooded with a height of 1.5 meters. Almost 19000 families were evacuated. Loss of properties and public facilities reached almost RM54.139 million. [6].

Melaka is one of the states in Malaysia that experiences flood annually. It has three main districts namely Alor Gajah, Melaka Tengah and Jasin. Most of the tourists' attractions are located in Melaka Tengah District. Figure 1 shows the location of the districts in Melaka.



Fig. 1 Districts in Melaka.

Melaka experiences flood annually. According to Melaka State Structure Plan Report (2011) these floods occurred to heavy rains, overflow river stream and high tide. Table 1 shows the number of areas that were affected by flood annually according to districts [6] from 2011 until 2015.

Table 1 Number of Areas Affected by Flood in Melaka by Districts from 2011 to 2015 [6]

Districts	'11	'12	'13	'14	'15
Alor Gajah	5	7	2	15	14
Jasin	2	5	2	21	18
Melaka Tengah	2	15	1	40	36

Figure 2 shows the flood area in Melaka. Most the affected areas are located in Melaka Tengah and Jasin districts.

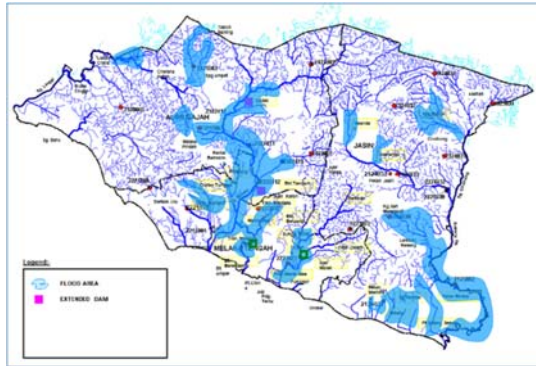


Fig. 2 Rivers and flood affected area (DID Melaka Tengah, 2016)

FINDINGS

This study employs a quantitative approach. Both data and information on flood and mitigation measures obtained from the Department of Irrigation and Drainage, Melaka Tengah were analysed. Similarly, data and information on economic indicators from Melaka State Government official website were also analysed.

Mitigation Measures in Melaka

Melaka has taken a drastic measure to address flood issues in its state. Two main approaches are being used which are flood modification and response modification.

Flood modification: Water Reservoir, Detention Ponds and Warning System

Melaka through the Department of Irrigation and Drainage builds a water reservoir and detention ponds to alleviate the flood water from overflowing into the city and build up areas. These reservoirs and detention ponds are controlled by water gates. Figure 3 shows the water reservoirs and water gates in Melaka.

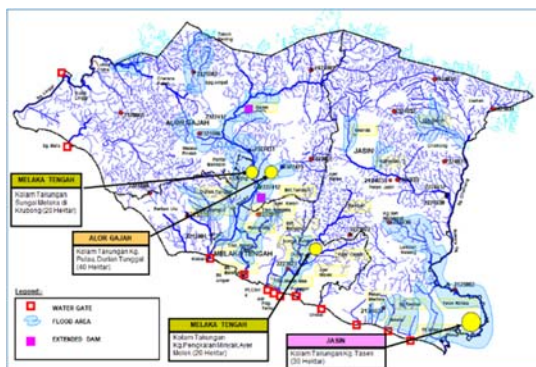


Fig. 3 Water reservoirs in Melaka (DID Melaka Tengah, 2016)

Warning systems are also placed at strategic areas along the rivers that often overflow. Once water level reaches a danger zone, the warning system will signal a siren to the water station. Melaka has five flood warnings systems which are placed in Lubok China, Kg Gadek, Pekan Jasin, Parit Sidang Seman (Sg Rambai) and Taman Malim Jaya.

Mitigation measure: Melaka State Town and Country Planning Department and Local Authority

Flood areas are considered as sensitive areas for development by the State Town and Country Planning Department [7, 8]. Most of these flood affected areas are located in the buildup areas, especially in Melaka Tengah. The only mitigation measures that are documented in the structure and local plan include increasing drainage capacity to handle the flood, to control flood affected areas effectively [8] and to provide a complete irrigation system to overcome flood issues [7].

Population Distribution in Melaka

Melaka has a population of 790,136 people distributed in its three districts; Alor Gajah with 173,712; Jasin with 131,539; and Melaka Tengah with 484,885 [9]. Melaka Tengah has the highest number of the household of 119,120. Alor Gajah ranked second with 40,385 and finally Jasin with 31,888. According to Moran's I analysis, the distribution of households is slightly significant with a p-value < 0.05 (0.03), $z = 2.14$. Local Indicator Spatial Association (LISA) analysis shows that its working population is concentrated in Melaka Tengah. Figure 4 shows the output of this analysis.

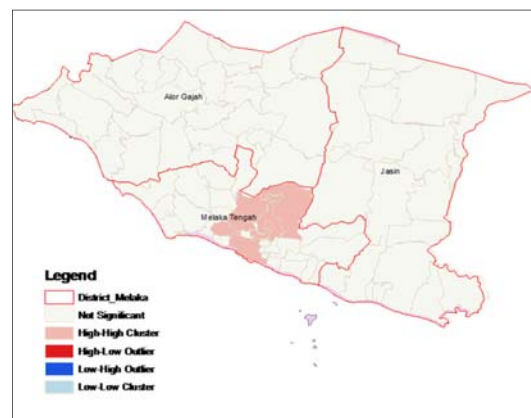


Fig. 4 LISA Analysis on working population

Economic Indicator in Melaka from 2011 to 2015

Melaka relies heavily on three main economic sectors namely services, manufacturing, and agriculture. However, services and manufacturing contributed more than 75% in its gross domestic product (GDP) annually for the past six years [10]. The outcome reflects the importance of tourism related products such as attractions, accommodations and eateries. Table 2 shows the gross domestic product for Melaka from 2011 to 2015.

Table 2 Gross Domestic Product (%) by Sector, Melaka from 2011 to 2015

Sector	'11	'12	'13	'14	'15
Services	46.2	52.5	53.2	53.4	53.5
Manufacturing	41.6	23.2	22.9	23.0	23.0
Agriculture	9.3	9.8	9.5	9.2	8.9

Floods that occurred in 2011 and 2015 were quite bad. These two floods hit many states in Malaysia including Melaka. Costs in damages in these floods were not revealed to the public and unknown to researchers. The only analysis that can be done is by using the percentage of gross domestic product (GDP) disclosed yearly. Since the available data is only until 2015, it is quite difficult to observe the impact of the flood in 2015. As shown in Table 2, a flood that occurred in 2011 does not give any negative impact to Melaka's GDP. Similarly to floods that occurred in 2014. GDP for both services and manufacturing sectors are on the increasing side. However, agriculture sector experienced a declining percentage in 2015.

Due to limited data availability, a Bivariate Moran's I analysis was carried out to only examine the correlation between flood affected areas from 2011 to 2015 and the total household. Melaka was hit badly in flood Table 3 shows the Moran's I score accordingly.

Table 3 Results of Bivariate Moran's I Analysis

Flood	Morans'I Score
2011	0.191
2012	-0.499
2013	0.496
2014	-0.467
2015	-0.477

The negative correlations can be observed in flood affected areas in 2012, 2014 and 2015. The result shows the higher number of affected areas is located in areas with a low number of households. Thus, these results show the mitigation measures

used have been effective in reducing the cost of damages among the household.

DISCUSSION AND CONCLUSION

Do the mitigation measures heavily taken by the Department of Irrigation and Drainage, Department of Town and Country Planning and the local authority make any difference to Melaka's GDP? The results of Bivariate's Moran's I show a negative correlation between 2012, 2014 and 2015 flood affected areas. This is also reflected in GDP. Mitigations measures taken by the authorities have helped minimise the negative impact of flood although the numbers of affected areas are more from the previous years.

However, development in any areas should be carried out sustainably. The United Nations has proposed the Sustainable Development Goals to demand all the countries in the world to be committed to handling climate change issues and flood is one of them [11]. Although some of the mitigations measures seem to be effective, developments should be controlled sustainably. The mitigations employed today might not be able to handle future disasters if preventive measures regarding sustainable developments are not handled properly.

ACKNOWLEDGEMENTS

Authors wish to thank the University of Malaya for grant no. BKP011/13 and Department of Irrigation and Drainage Malaysia Melaka for their strong supports.

REFERENCES

- [1] Millard-Ball, A, "The limits to planning: causal impacts of city climate action plans", J. of Planning Education and Research, 2012. Vol. 33(1), 2012, pp. 5-19.
- [2] Burby, RJ, "Hurricane Katrina and the paradoxes of government disaster policy: bringing about wise governmental decisions for hazardous areas", The ANNALS of the American Academy of Political and Social Science, 2006, Vol. 604(1), pp. 171-191.
- [3] Eliasa Z, Hamin Z, and Othman, MB, "Sustainable management of flood risks in Malaysia: some lessons from the legislation in England and Wales", Procedia - Social and Behavioral Sciences, 2013, Vol. 105(2013), pp. 491-497.
- [4] Diya, SG, et al., "Floods in Malaysia: historical reviews, causes, effects and mitigations approach", Int. J. of Interdisciplinary Research and Innovations, 2014, Vol. 2(4), pp. 59-65.

- [5] Chan, NW, Impacts of disasters and disasters risk management in Malaysia: the case of floods, in Economic and Welfare Impacts of Disasters in East Asia and Policy Responses, in Sawada, Y and Oum, S, Editor. 2012, Jakarta: ERIA, pp. 503-551.
- [6] DID, Urban storm water management manual for Malaysia, 2000a Kuala Lumpur: Department of Irrigation and Drainage Malaysia.
- [7] Jabatan Perancangan Bandar Dan Desa Negeri Melaka, *Rancangan Struktur Negeri Melaka*. 2005, Jabatan Perancangan Bandar dan Desa Semenanjung Malaysia: Melaka. p. 1 - 298.
- [8] Majlis Bandaraya Melaka Bersejarah, Rancangan Tempatan Daerah Melaka Tengah 2005 - 2015, M.B.M. Bersejarah, 2005, Majlis Bandaraya Melaka Bersejarah: Melaka
- [9] Department of Statistics, Population distribution by local authority areas and mukims. 2010, Putrajaya: Malaysian Department of Statistics.
- [10] Melaka State Government. Basic Data. 2017 [cited 2017 20 April]. Available from: https://www.melaka.gov.my/en/media/publications/basic-data?set_language=en.
- [11] United Nations. Sustainable Development Goals. Sustainable Development Knowledge Platform 2015 [cited 2017 27 February]; Available from: <https://sustainabledevelopment.un.org/sdgs>.
- [12] Svetlana, D., D. Radovan, and D. Ján, The Economic Impact of Floods and their Importance in Different Regions of the World with Emphasis on Europe. *Procedia Economics and Finance*, 2015. 34: p. 649-655.
- [13] Akasah, Zainal Abidin, & Doraisamy, Sunitha V. (2015). 2014 Malaysia flood: impacts & factors contributing towards the restoration of damages. *Journal of Scientific Research and Development* 2(14), 53-59.

PROPOSAL OF A FLOATING-TYPE ENVIRONMENTAL PURIFICATION FACILITY INCORPORATING THE FUNCTION OF TIDELAND

Sato Shinji¹, Yuji Yamakage²

¹ Department of Oceanic Architecture and Engineering ,College of Science and Technology,
Nihon University,Japan

²Daiwa House Industry Co., Ltd., Japan

ABSTRACT

Landfill in Tokyo Bay has a direct effect on the disappearance of tideland and shallow waters. Former tideland is a habitat for benthic creatures with the function of decomposing organic substances flowing out from the land area, which were eaten by small fish and served as a feeding point for migratory birds feeding them. Also, in recent years, aquatic plants such as combs forming seaweed beds are being reviewed as being superior to onshore plants in function to absorb CO₂ and produce oxygen. In addition, since seaweed is also expected as a fuel for biomass power generation in recent years, this economic value is great.

In other words, regenerating tidal flats and seaweed beds in Tokyo Bay will contribute not only to environmental improvement of the sea area, but also to CO₂ reduction as well as alternative energy source, which will greatly contribute to our lives.

In this study, we propose a floating type purification facility incorporating the functions of tideland and shallow waters in the northwestern coast of Tokyo Bay and proposing artificial tideland and seaweed bed regeneration.

Keywords: Tideland, Seaweed, bed, Environmental improvement, Alternative energy source, Floating type purification facility

1. INTRODUCTION

Japan has become a blessed country by the high economic growth of the 1960s. As a result, various forms of land use such as logistics, transportation, commerce, residential, heavy industry and park were extensively conducted. On the other hand, it faced many environmental problems such as air pollution, global warming, marine pollution, illegal dumping of waste, exhaustion of resources, etc.

In Tokyo Bay, reclamation in the coastal area was activated for land use from the 1960s, and 15% of the surface area was landfilled [1]. On the land landfilled, environmental problems such as red tide and blue tide caused by domestic wastewater and industrial wastewater have become frequent in the waters while logistics and industries are developing.

Landfill in Tokyo Bay has a direct effect on the disappearance of tideland and shallow waters [2]. Former tideland is a habitat for benthic creatures with the function of decomposing organic substances flowing out from the land area, which were eaten by small fish and served as a feeding site for migratory birds feeding them. In these waters, fish and shellfish played an important role as a spawning place for laying eggs. Furthermore, decomposition of phosphorus and nitrogen was carried out in algae formed by seaweed spreading in shallow waters.

In response to these circumstances, the Tokyo Metropolitan Government has been implementing policies for water quality purification through the expansion of sewage treatment plants in the land area to improve the quality of water in Tokyo Bay. However, such measures to improve water quality only in the land area are currently not a direct countermeasure for the entire sea area.

Also, in recent years, aquatic plants such as alga forming seaweed beds are being reviewed as being superior to onshore plants in the function to absorb CO₂ and produce oxygen. In addition, seaweed is also expected as a fuel for biomass power generation in recent years, so this economic value is great.

In other words, regenerating tidal flats and seaweed beds in Tokyo Bay will contribute not only to environmental improvement of the sea area, but also to CO₂ reduction as an alternative energy source, which will greatly contribute to our lives. In this research, we propose a floating type purification facility incorporating the functions of tideland and shallow waters in the north west of Tokyo Bay. This aims to improve the environment including the ecology of Tokyo Bay. In addition, the tideland and seaweed bed of this floating structure are planned to be an offshore resort of Tokyo Bay. There, it becomes a new type of accommodation type resort facility that can experience and learn the environment through various researches and power

generation using seaweed. These proposals are investigations considering feasibility study.

2. Background of the plan

2.1.1 Transition of Tokyo Bay by Reclamation

The area of the bay in Tokyo Bay is 138,000 ha, but due to various developments about 26,000 ha has been landfilled so far. It is said that it decreased by 20% from the former area[1].

Table 1 Landfill area by Tokyo Bay birthday

Age	1968 ~1911	1912 ~1926	1926 ~1935	1936 ~1945	1946 ~1955	1956 ~1965	1966 ~1975	1976 ~1985	1986 ~1989	1990 ~1996	Not started
Kanagawa Pref.	165	1,001	1,443	2,056	2,225	3,695	5,219	6,448	6,732	7,067	7,363
Tokyo	332	332	1,338	1,477	1,545	1,969	3,562	4,449	5,242	5,812	6,606
Chiba Pref.	63	63	63	187	370	1,671	7,891	11,975	12,076	12,076	12,151
Area by age	560	836	1,448	876	420	3,195	9,337	6,200	1,178	905	1,165
Total area	560	1,396	2,844	3,720	4,140	7,335	16,672	22,872	24,050	24,955	26,120

unit(ha)

2.1.2 Reduction of tideland / shallow area by landfill

In the Meiji era (1868 - 1912's), tidal flats spread continuously from the bay to the mouth of the mouth. However, to date, 26,000 ha, which is 20% of the area of the bay (138,000 ha), is landfilled, the tidal area has been lost to 8,000 ha (6% of the bay area) since the 1950s, .

Tidal flats have inhabited a wide variety of benthic organisms and have been responsible for the spawning and growing areas of living creatures in the sea, the role of migratory birds' important feeds and the function to purify sewage in rivers. The functions of this tidal flats are now reviewed, and the movement of tideland function conservation is increasing among citizens to conserve the rich ecosystem.

In addition, it has been found that there is a big difference between simply purifying water quality and the environment where living things are easy to live. Furthermore, recent studies have revealed that creatures do not increase in Tokyo Bay as long as it increases not only tidal flats but also algae fields and shallows of seaweed.

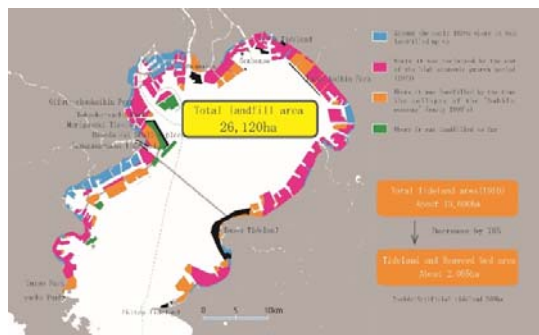


Fig.1 Landfill distribution in Tokyo Bay[3]

2.2.1 Importance of tideland

Wetlands such as tidal flats have become effective on 1975 (December 21), with the Ramsar Convention, meaning that it is very important as a waterfowl habitat, nurturing diverse organisms. Concluding countries have registered 2208 wetlands in 168 countries. In Japan, 50 places are registered, and only Yatsu tidal flat is registered in Tokyo bay.

2.2.2 Reduction of migratory birds

Sea birds with wetlands as a place to relax have been confirmed to decrease by 40 to 50% due to landfill. Moreover, the data of only Yatsu tidal flats according to the data of "Tokyo Bay Sigi, Tidri all over the same survey" shows a clear declining tendency in which 108 birds were confirmed in 2012, 14 birds in 2016.

2.2.3 Changes in Catches

In Tokyo Bay, various fisheries such as shellfish fishing, fishery and algae fishery are still being conducted. However, it is far less than the catch as in the past, making it difficult to continue fishing. In recent reports by the Tokyo Bay Study Group, the yield has been decreasing for many fish species, suggesting the possibility that the lumps of water caused by poor oxygen have an adverse effect on the growth environment of the fish species ing. In addition to the lump of poor oxygen, "Reduction / disappearance of habitats such as shallow and tidal flats" is considered to be one of the causes of the slump of biological resources.

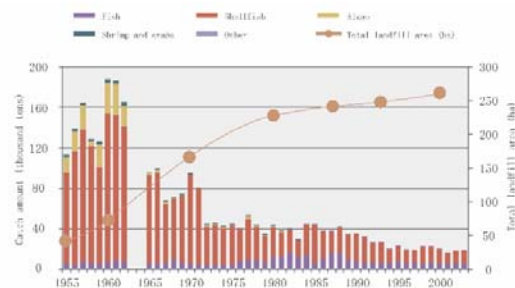


Fig.2 Changes in catches and landfill area[4]

2.3.1 Forest of the sea

In recent years, the phenomenon "sea breeze" which seaweed in the sea has disappeared and the surface of the rock of the sea bed is covered with

white or pinkish lime algae has become remarkable. This may be caused by artificial effects such as rising seawater temperature and water pollution, supply shortage of iron required for algae growth and damage of algae useful due to sea urchins and fish.

Because seaweed beds are also the habitat for fish spawning and frying, it is easy to imagine that it will have a major impact on the underwater ecosystem. This directly leads to a reduction in catches. The "sea forest" in Tokyo Bay, which has been rich, is said to be "desertification of the sea" in recent years. This is because natural purification action of seawater is not properly performed, which indicates that artificial environmental conservation measures are indispensable.

2.3.2 Regeneration of "Sea Forest" by human intervention

In recent years, seaweed beds are not sufficient for natural purification action, and artificial measures for environmental conservation are required. Therefore, since 2010 Kobe Steel Group, which is a steel company, has begun to develop marine area utilization of artificial reefs by steelmaking slag in Okinawa Prefecture and Kobe City. As a result of this marine area development by this artificial reef, the effect as a population reef is demonstrated, such as the glimpse of use as a habitat for frying fish one month later.

2.4 About how to use environmental load

2.4.1 About fixed amount of CO₂ by algae culture device

In the "CO₂ marine immobilization / effective utilization technology survey project[6]" participated by Takenaka Corporation and the authors, the Ministry of Economy, Trade and Industry's subsidiary research research project, CO₂ fixation using seaweed culturing equipment ,investigated. The results are shown in the table.

In estimating the amount of CO₂ fixation accompanying the cultivation of algae, the case where only green algae (Minamionori) was produced (44.3 t-dry / day), the case where only red algae (onia manori) was produced (23.0 t-dry / day) , When green algae, red algae and brown algae were produced at a ratio of 2: 1: 1 (32.1 t-dry / day) when only brown algae (seaweeds) were produced (16.8 t-dry / day), green algae In the case of producing brown algae at a ratio of 1: 1 (30.6 t-dry / day), a

total of five scenarios were set and examined.

As a result, the CO₂ fixed amount is the highest at about 17,500 t-CO₂ per year when only green algae (Minami aonori) are produced, and it is the smallest at approximately 8,300 t-CO₂ per year when only brown algae (seaweed) are produced I found out.

Table 2 Annual carbon dioxide fixed amount by seaweed culture [6]

scenario	Production volume (t - dry / day)	Production days (day / year)	Carbon content (%)	CO ₂ fixed amount (t - CO ₂ / year)
Green algae (Minami Aonori)	44.3	365	29.5	174,900
Red algae (Onia manori)	23	365	30	9,235
Brown algae (Seaweed)	16.8	365	37	8,319
Green algae: red algae: brown algae (2: 1: 1)	32.1	365	-	13,533
Green algae: brown algae ² (1: 1)	30.6	365	-	13,617

Note: CO₂ fixed amount = production amount × carbon content × 44/12

2.4.2 New biomass energy

Regarding the use of renewable energy and renewable energy, development of more effective production technology is definitely required. In recent years, bioethanol made from seaweed has been recognized as renewable energy, and attracts attention as it contributes to maintenance of the global environment and reduction of GHG (greenhouse gas).

2.4.3 Biofuel production

Biofuel production from soybean is 1,900 L per hectare per year and palm oil 5,950 L per year. On the other hand, biofuel production from seaweed is remarkably high at 98,500 L, and it is known that it has the ability to absorb ten times more CO₂ than trees.

2.4.4 Green tide

In recent years, environmental problems called "green tide" have occurred in various coastal areas. This is a phenomenon in which the seaweed Aoshia grows abnormally and accumulates on the coastline, and various adverse effects such as the deterioration of the landscape of the coastal area, the bad smell accompanying the decomposition of the seaweed, the death of shellfish such as clams are occurring. As shown in 2.4.1, it is thought that it is useful for the global environment in a dual sense that energizing environmental problems can reduce expenses for removal and further produce profits through production.

2.4.5 Thalassotherapy

By introducing a facility incorporating natural remedies such as seaside bathing seawater, blood circulation promotion massage using seaweed and esthetics using sea mud, the effect of deepening interest in the ocean by guests is there.

3. Planning policy

3.1.1 Floating Flats

- Floating function -

- ① Artificial tidal land: Improve the migration of migratory birds and the work of natural purification
- ② Seaweed bed: Water purification and recovery of DO value Creation of ecological environment
- ③ securing solar radiation: securing solar radiation to the sea area by subdividing the floating body

- Supposed introduction function -

- ④ Resort hotel: induce publicity of Tokyo Bay problem and measures
- ⑤ Company: Make maritime countermeasures by entering business in similar fields
- ⑥ Research: artificial tidal flats, biomass, plankton, seaweed
- ⑦ Biomass: regenerate seaweed as a useful resource

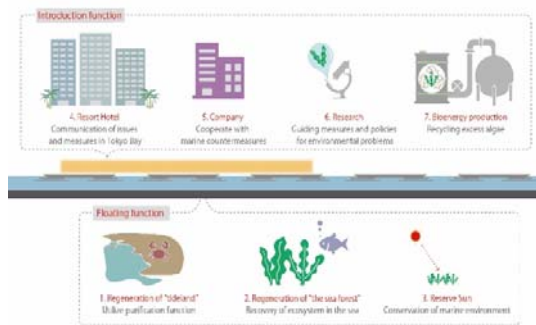


Fig.3 Conceptual diagram of green floating

3.1.2 Introduction function

By using the floating function in 3.1.1 as the central function of this plan, the functions to be introduced in other places can have diversity.

We plan to introduce facilities to produce bioethanol from seaweed using biomass power generation as well as commercial and tourist

facilities such as aquarium and hotel as assumed use.

4. Basic plan

4.1 Calculation of the size of artificial tidal flats

In this project, we plan a floating body of 300 m × 300 m, assuming that the area of the tidal flat is 9 ha. By doing so, we plan to recover 0.005% of the area of tidal flats lost in Tokyo Bay so far. As stated above, by installing floating bodies having various

	100m	150m	200m	250m	300m
	Diameter 100m	Diameter 150m	Diameter 200m	Diameter 250m	Diameter 300m
Piece (ha)	1.00	2.25	4.00	6.25	9.00
Increase rate(%)	0.06	0.13	0.24	0.37	0.54
Recovery rate(%)	0.001	0.001	0.002	0.003	0.005
Five pieces (ha)	5.00	11.25	20.00	31.25	45.00
Increase rate(%)	0.30	0.67	1.19	1.86	2.68
Recovery rate(%)	0.042	0.094	0.168	0.262	0.377

	350m	400m	450m	500m	1000m
	Diameter 350m	Diameter 400m	Diameter 450m	Diameter 500m	Diameter 1000m
Piece (ha)	12.25	16.00	20.25	25.00	100.00
Increase rate(%)	0.73	0.95	1.21	1.49	5.96
Recovery rate(%)	0.103	0.134	0.170	0.210	0.839
Five pieces (ha)	61.25	80.00	101.25	125.00	500.00
Increase rate(%)	3.65	4.77	6.04	7.45	29.82
Recovery rate(%)	0.514	0.671	0.849	1.048	4.194

functions at ten locations, it is assumed that 0.75% of the area of the tidal flat is recovered.

Fig.4 Increase due to tidal flats size in Tokyo Bay, Calculation of Recovery Rate

4.2 Site selection criteria

- ① Area where river exists and inland water crosses sea water
- ② waters where characteristic landscapes exist
- ③ Area where the DO value is low, poor oxygen water mass is generated
- ④ Sea area with floating structure possible depth of water
- ⑤ waters where concern about environmental impacts such as sewage treatment plants are concerned

Based on the above conditions and the consideration of the marine environment based on the "Tokyo Bay Water Quality Survey Report", we will select the sea area off the Tokyo Disneyland at the B type T22 point described in the report as the site of this project.

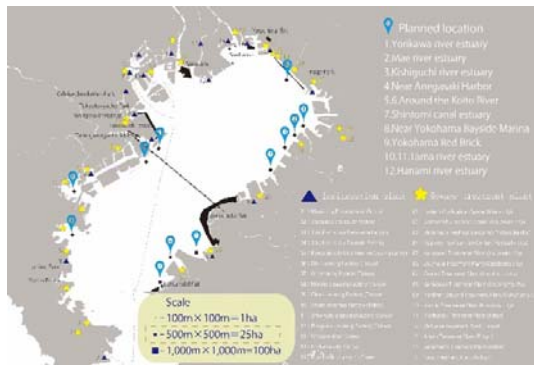


Fig.5 Plan map in Tokyo Bay[5]

4.3 Overall plan

The whole floating body is zoned into L letters, and it is classified into three types of migratory birds, tideland, and architecture. By doing so, we plan to place restrictions on the rate at which human intervention is intervened. As a result, shellfish such as clams in areas for migratory birds will be protected from the collection of human beings. In the tideland, it is planned that tourists can observe the ecological system of valuable Tokyo Bay closely. The second level headings should be in 10pt, bold, justified, and First Characters of Each Word are in Capital font. Leave one blank line both before and after the heading, respectively.

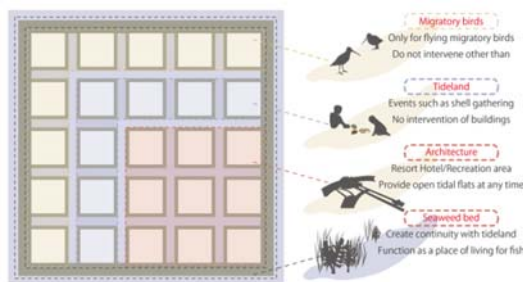


Fig.6 Conceptual diagram of floating body plan

5. Building plan

5.1 Introduction function and scale calculation

In this project, we plan to classify it into 3 buildings, hotel building, research building, power generation building. We calculated the scale by referring to the area ratio of various categories of existing resort hotels and other departments responsible for functions such as drinking, banquet, kitchen and management. The number of rooms is

assumed to be 128 rooms, and a thalassotherapy function incorporating marine resources is introduced.

Table 3 Introduction function and scale

Introduction function and scale		Major room name				
Hotel Faculty	21,091 m ²	Room	Banquet hall	Restaurant	Pool	Gym
Power generation Faculty	1,709 m ²	Power generation room	Boiler room	Processing room	Sewage treatment room	Drying room
Research Faculty	1,905 m ²	Laboratory	Incubation room	Lecture room	Library	Nature observation room
BackSide Faculty	4,085 m ²	Office Room	Central Monitoring Room	Reception Room	Restroom	Warehouse
total scale	28,790 m ²					

5.2 Securing an area to deliver light to the ocean floor

By planning a large floating body of 300 m × 300 m, a wide area shadow appears in the waters under the floating body. For this reason, the floating body is subdivided into 25 squares, and each is shifted at regular intervals, thereby securing an area for delivering light to the seabed. In this project, when the floating body of 60 × 60 m is moved 3 m at a time, the area where light is delivered is calculated, and when it is shifted by 12 m, the strength of the floating structure and the area where light is delivered to the seabed are optimal I found out something. Other seaweed beds are supposed to illuminate the ocean floor by providing LED light as an alternative function of sunlight.

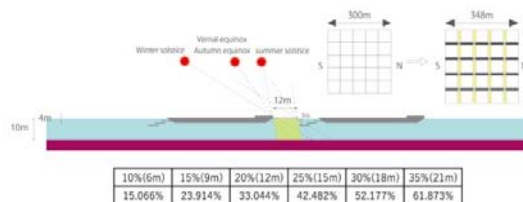
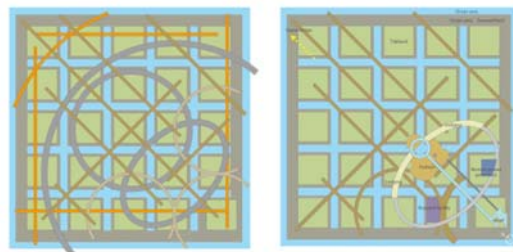


Fig.7 Percentage of appearance of light-transmitting layer when 25 masses are separated by 5%



5.3 Incorporate artificial tidal of tideland

By adopting the water depth adjustment function by ballast water for the floating type structure, we made it possible to artificially create tidal difference which is characteristic of tideland. This will be a

directing to the guests to see the tide difference as a landscape while staying in the center of Tokyo Bay.

5.3 Arrangement plan for seaweed bed

Place a 25 m wide seaweed bed on the outer side of the 16 squares located on the outer periphery of the floating structure. Also, in the 9 squares arranged in the center, seaweed beds are spirally arranged on each of the four sides. These seaweed beds are supposed to adhere to the larvae flowing from the surrounding seas and have a floating structure with continuity with the tidal flats.

5.4 Flow line planning

The flow line of general customers and the flow line of loading goods are done from the same docking station, but we plan to separate them into a hotel flow line and a carry-in flow line extending in straight line. In the interior of the building, we arranged plans that divide the categories and other functions such as drinks, banquets, kitchens, management, etc., into plans that emphasize the privacy of the resort hotel.

5.5 Planning of planning and arrangement of watersheds

We designed a plan for connecting floating bodies subdivided into 25 squares based on the overall plan of 4.3 and introduced the necessary functions for construction purpose to it.

We arranged rooms to provide both the urban dynamic landscape of Tokyo spreading to the north side and the natural landscape of the sea spreading to the south. The accommodation building, the power generation building, and the research building to be introduced in this program are connected by a corridor integrating solar power generation units. Moreover, by making production and research facilities publicly available, it becomes a facility that will be utilized not only as a resort but also as a place for learning. In addition, the tidal flat on the front of the hotel is open to guests all the time, and in addition to enjoying maritime recreation in places facing the sea area, it also functions as a place to conduct educational experiences through lectures by researchers.

Fig.8 Left : Floating bodies to Connecting circuit
Right : Placement plan

5.6 Section planning

In the center of the guest room etc, plan a large

void to incorporate solar radiation into the seaweed bed. Also, as the difference in level between construction and water level changes due to the change in water level due to tides, we planned the entire building as a high floor type like a pier.

Considering the influence of the sea breeze on the accommodation building, we adopted a design that blows the wind upward by raising the building of other functions.

6. CONCLUSIONS

1. Coastal areas are already under development by landfilling of tidal flats and shallow fields, and there is little room for regenerating these.

2. In the central part of Tokyo Bay there is plenty of room to build tidal flats and shallow spaces if you remove the shipping routes for ship navigation.

3. When building floating tidal flats in the central part of Tokyo Bay, it is necessary not to disturb the ship's sailing and consider consideration to the seabed part so that there is no influence on the natural environment and fishery.

4. In order to transmit light to the bottom of the sea while sufficiently satisfying the function of tideland and shallow, it is necessary to devise arrangement and design of facilities.

5. It is quite promising in Japan to use seaweed to fix carbon dioxide. Because Japan's land area is about 380,000 square kilometers, which is 60th in the world, it has eleven territorial waters and EEZ.

REFERENCES

- [1] Ports and Harbours Bureau MLIT/MOE : Towards the reclamation of tideland network
- [2] Fisheries Agency : Conservation of algae, tideland and coral reefs
- [3] NILIM : Outline of Tokyo Bay and its watershed and issue on water environment
- [4] Fisheries and the environment in Tokyo Bay : Current situation of the water environment in Tokyo Bay
- [5] Tokyo Bay Environment Information Center : The environment surrounding Tokyo Bay
- [6] Takenaka Corporation、 Heisei 24th Survey business of carbon dioxide ocean immobilization / effective utilization technology、 Department of Japanese METI、 2013.Feb.28 、 .pp.552-563
http://www.meti.go.jp/meti_lib/report/2014fy/E003661.pdf

WALL OPENINGS AND ITS ABILITY TO MINIMIZE FLOOD INDUCED FORCES ON RESIDENTIAL BUILDINGS

Nur Aqilah Ahmad Faisal¹, Abdul Naser Abdul Ghani² and Nuzaihan Aras Agus Salim³

¹Postgraduate; ^{2,3} School of Housing Building and Planning, Universiti Sains Malaysia, Malaysia

ABSTRACT

Flood induced forces could threaten the stability of residential building during flooding event. The building will have to face the hydrodynamic pressures and sometime impact load from the debris carrying floods. A study on the behavior of flood water movement through external wall were carried out to identify the various wall opening dimensions and its capability to minimize the flood water forces on buildings. Two types of experiments were carried out. First, a water flow table was used to visualize the water pattern diffusion. Next, flood tunnel was used to measure the water velocity reduction response of the various walls. The wall opening configurations were based on the common types of wall opening found in Malaysia. Generally, the results show that walls with bigger openings could withstand the water forces better. This is indicated by the smaller velocity reduction and diffusion when the flowing water passes through the wall. However, the level of opening from the ground could change the overall performance of the various opening sizes as shown by some of the models. Therefore, further studies should be carried out to determine suitable dimensional characteristics and level of the wall openings from the ground. This could produce an optimum impact reduction wall design for residential building in flood prone area.

Keywords: Flood, Residential Building, Wall Opening, Water Velocity

INTRODUCTION

Floods are considered as the worst calamity experienced in Malaysia [1]. As the most frequent natural disaster in Malaysia it affected many areas and cause annual catastrophe and damages to infrastructure, property, crops and other intangible loss. There are no official categories of floods in Malaysia but is often broadly categorized as monsoonal, flash and tidal floods.

A study conducted by Kong et al.[2], on urban flooding found that, 28% of respondents concurred that flood is due to improper drainage system, 20% cause is pollution, 18% the management of urbanization and 16% cause is environment factor and 11% weather while 7% because of dam break [2]. Figure 1 below shows the results of their research.

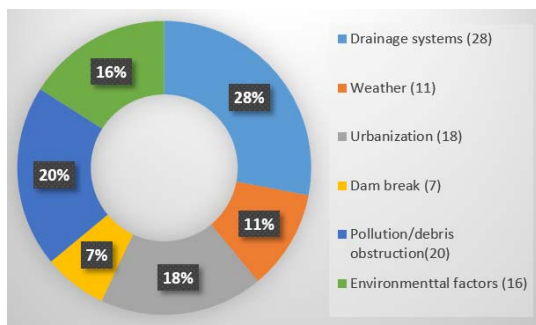


Fig. 1: Public perception of causes of flooding[2]

It can be seen that most Malaysians are less concerned regarding environmental issues especially natural disasters because they assume the issue is a trivial issue which ought to be resolved by the authorities and government[3] and have made little effort to face possible property damage in case of flooding. Flood induced forces could threaten the stability of residential building during flooding event. The building will have to face the hydrodynamic pressures and sometime impact load from the debris carrying floods. Flood impact proofing or reduction can be achieved by making adjustments to building design and building components that could withstand flood forces.

Building Response and Flood Damage

A research by Vinet [4] concluded that the effects of flooding caused damage to home, shops and industries. Sani et al.[5] research concluded that, there are at least 4 effects of flooding which comprise water damage to houses, disruption of transportation, reduction of income and damage of furniture and other appliances. However, majority of the population strongly believes that, water damage to houses is the main effects of flooding. Hence, it is recommended that buildings should be properly built to avoid building on the floodplain and on the flood prone zones [5]. The main idea in the traditional approach for estimation of direct flood damage

monetary terms is the concept of loss functions or depth-damage functions [6]. In actual event, flood damage is influenced by other factors such as flow velocity, debris concentration, flood duration, lead time and information content of flood warning, and the quality of external response in a flood situation [7] [8] [9].

Distributed resistance parameters are needed for local prediction of velocity [10] [11] which might be required for damage assessment or predictions of sediment erosion and deposition [12]. Based on Becker et al. [13] findings, he concluded that structural failure comprises a large portion of the response space for higher depth and velocity combination under flood response scenarios. Thus, by developing a greater understanding of building response to high-velocity floodwaters through this type of behavior modeling, actions could be investigated that may improve resistance of buildings in flood-prone areas. A study by Grundy et al. [14] determine that a large proportion of deaths could be linked to structural failure of buildings since this prevented vertical evacuation from the floodwaters, and damaged buildings created dangerous debris impacts. However, in addition to depth, water velocity has been shown to be a crucial parameter with the potential to cause significant damage [15]. The relationship between the ($d \times v$) factor and flood damage of buildings is the most widely acknowledged predictor of the effect of water velocity. Yet, no further applied theoretical analysis of how swiftly moving floodwaters affect buildings, in terms of structural damage or in terms of their ability to provide for human safety [16].

This study is set out to identify the various wall opening configurations and its capability to minimize the flood water forces on buildings.

METHODOLOGY

This study utilizes laboratory scale experiments to generate data for the parametric analysis. The experiments and setups are based on several previous related works in the study of flooding. Ramsden [17] directly measured the lateral forces on a vertical wall due to long waves, bores, and dry-bed surges instead of calculating the force from pressure measurements. A study focuses on qualitative observations regarding the structures response to wave loading was conducted by Arnason [18] in a small hydraulic wave flume with long aspect ratio (the controlled environment), theoretical predictions of wave height and force aligned well with theory. Thusyanthan and Madabhushi [19] have run a research utilizes a small 4.5 m long tsunami wave tank with waves generated by dropping a 100-kg block in the water. One model of coastal structure was designed similar to a common Sri Lankan house and another one structure designed attempted to

model a new tsunami resistant structure. This research concludes a need to study on how building configuration could be used to better withstand wave loading.

A study on the effect of flood water diffuser on flow pattern using flow water table by Ghani and Kasnon [20] have concluded that the longer the wave diffusion or the higher the wave amplitude, the more velocity can be reduced. Most closely related to this study is the recent work of Ghani et al. [21] which utilized a hydraulic flume tank with sensors placed before and after the diffusing objects to study the velocity reduction effect in a 3-dimensional hydraulic environment. The research conducted identified suitable shape and dimension of objects and its capability to reduce flow velocity across the road. In order for a building to survive loading forces from moving floodwater exerts on wall have to be reduced. This comprises the external and internal wall of a building. Debris resulted from high impacted external wall may produce a greater load compared to original moving water velocity. Thus, laboratory experiments will be conducted to study the effect of wall opening configuration towards its velocity reduction through walls.

Laboratory Experiment

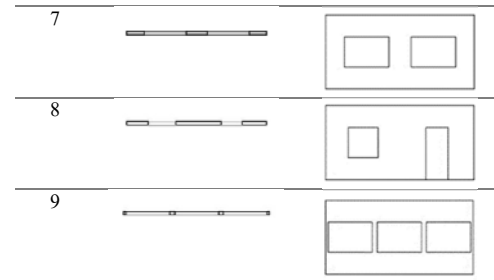
In this laboratory experiment, the equipment must be set up and functions properly include the water visualization table, flood tunnel and camera to take video of the test. The various wall configuration models have been prepared for the experiment purpose. The experiment will be conducted using every type of typical configuration of wall opening of houses in Malaysia and the result gained by observation of the experiment. The wall panel will be varying in configuration of its door(s) and window(s), including their size(s). The size of the model will use scale of 1:50 of the living size. The experiment will only focuses on qualitative observations regarding the flood water breaking, response, or diffuse through wall opening. This research will run two types of experimental test which are (1) flow water table to observe water response pattern through wall opening configuration, and (2) flood tank to measure the velocity response by wall opening configuration. The flow water table experiment will only use the horizontal section of the wall, whilst the flood tunnel experiment will utilized a full height model. Observation method will be used for data collections, which when the execution of laboratory test is running, data will be recorded from the start until the end of the test. The outcome of the water response and diffusion will be witnessed and recorded as collecting data.

Development of the Wall Model

A series of typical elevation of houses in Malaysia especially in flood prone and affected areas was selected and illustrated in accordance to laboratory suitability. Flood affected area selected for this case study is in Perak Tengah region which merely inundated by flood in December 2014. Following are the typical elevations in Table 1.

Table 1: Wall Elevation Model

Model	Plan	Elevation
1		
2		
3		
4		
5		
6		



Flood Diffusion Pattern Experiment

The equipment used in this experiment were water flow table, adjustable stand, water color, camera and double cello tape to represent the section of the walls. See Fig. 2 for the flow pattern laboratory testing instrumentation details.

As the configuration and size of opening are expected to influence the breaking of the flood water, 9 models of different configurations were established for experimenting the performance and reduce the impact towards opposite walls. The experiment were carried out using the 9 patterns of models' sections as shown in Table 1 and the result were acquired by observing the processes. The result outcome will be recorded by video to observe it more clearly without repeating the experiment.

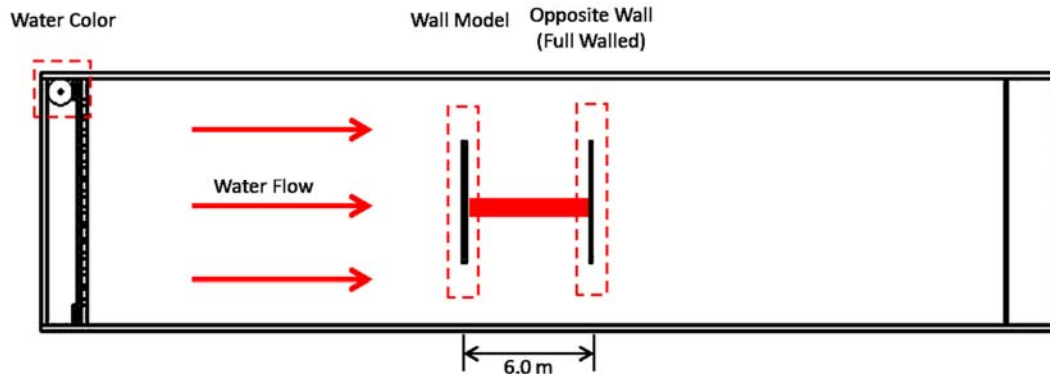


Fig.2: Flow pattern testing

Flood Tunnel Model Experiment

Creating a flood event under laboratory conditions requires a hydraulic flume and continuously flowing water. The flood tunnel was set up as in Fig. 3 and Fig. 4 in which all the 9 3-dimensional wall models were used to study the velocity behavior effect in 3-dimensional hydraulic condition. Water were circulated into hydraulic

flume as configure and time is taken at the external and internal side of the wall to study the behavior of flow occurred when the flood water broke and hit another wall. Velocities (V) of two points were recorded and all the data obtained were compared for every model. This research make use of a small flood tank measuring 1.15m long, 0.3m deep, and 0.25m wide (Fig. 4). Water was allowed to pass through the models whilst data was being collected.

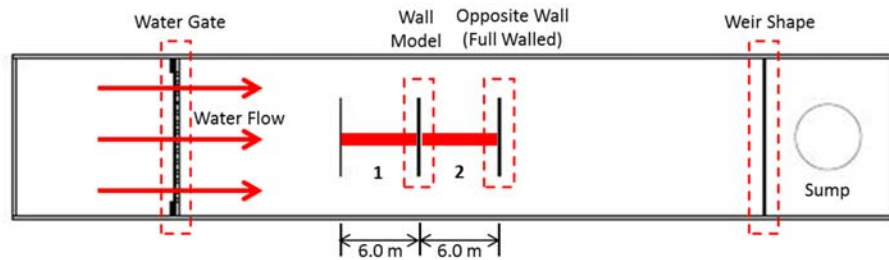


Fig. 3: Plan of flood tunnel model

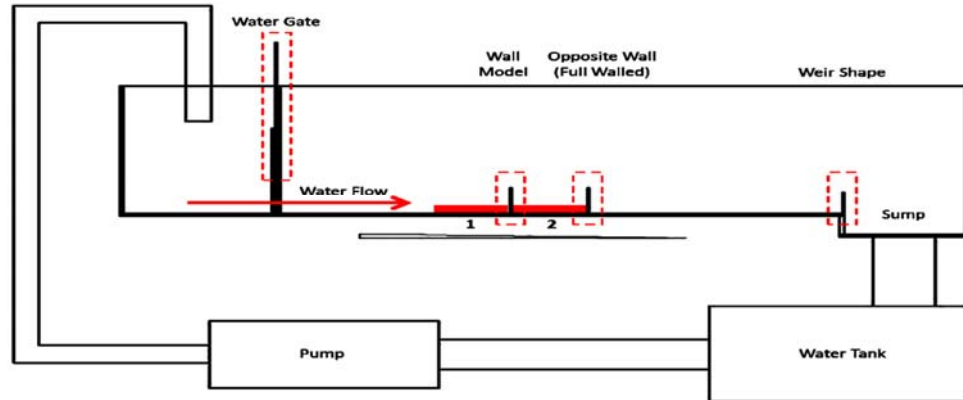


Fig. 4: Flood tunnel model instrumentation
diffusion category.

DATA COLLECTION AND ANALYSIS

Based on the two approaches, data were observed and recorded for the 18 different models; nine numbers of 2-dimensional models for diffusion pattern, and another nine 3-dimensional models for velocity testing.

Flood Diffusion Pattern

By using the flow visualization table, the experiments were conducted on 9 models of different wall configurations. The pattern of diffused flow were then divided into 5 point. Each point of diffusion will be measured, and given a score of 0 until 3 (0-3) which indicates; 0- Not Affected (0.00cm), 1- Poor (0.10-0.60cm), 2- Intermediate (0.70-1.30cm), 3- Good (1.40-2.00cm). The cumulative value of all five points then resulted to diffusion pattern category of each model. The diffusion pattern can be categorized into three categories; (1) low, (2) moderate, and (3) high. The first category which is low diffusion category which obtained less than 7 total value of flow categories score. The second category is moderate diffusion that obtained total value of 8 to 12 score on cumulative flow categories. High category of diffusion described the most diffused flow pattern which cumulated more than 13 score of flow categories. Thus, the experiments observation were been interpreted based on

Table 2: Score and diffusion category

Model	Score	Diffusion Category
1	6	Low
2	10	Moderate
3	13	High
4	10	Moderate
5	8	Moderate
6	11	Moderate
7	12	High
8	12	High
9	9	Moderate

Based on the 9 models experimented, one produced low diffusion, five models categorized as moderate diffuser, and three of them indicated high diffusion pattern. Out of the nine wall configurations, 3 configurations can be considered as the most capable in defusing water flow. Model 3, 7, and 8 are the configuration models that produced the most diffusion. This is because these configurations produced high deflection on most points and have high number of wave amplitude. As a general indicator, the higher the wave amplitude, the more the velocity reduces. However, in this experiment, the magnitude of velocity reduction cannot be verified numerically.

Flood Velocity Reduction

This experiment focused on the flood water velocity behavior before and after passing through all the nine models. Table 3 shows the before and after velocity.

It can be seen that all nine models produced velocity reduction. The result showed based on those models, the least reduction produced is 2.3% by model 9, and the most reduction by model 8

which is 75.3%. From these results it also can be seen that the reduction can be categorized in few groups. 2 of them which are model 3 and 9 produced a very low reduction, model 1 and 2 produced a reduction in range of 28-30% considered as low reduction, model 4, 6, and 7 with a reduction range of 47-50% which are quite high, and the remaining 2 models, 5 and 8 produced a very high velocity reduction.

Table 3: Velocity reductions

Model	Velocity Before (cms ⁻¹)	Velocity After (cms ⁻¹)	Velocity Reduction (%)	Reduction Category
1	18.0	12.61	29.7	Low
2	18.0	12.97	27.9	Low
3	18.0	17.07	5.12	Very Low
4	18.0	9.13	49.3	High
5	18.0	5.69	68.3	Very High
6	18.0	9.49	47.3	High
7	18.0	9.55	46.9	High
8	18.0	4.44	75.3	Very High
9	18.0	12.94	2.3	Very Low

DISCUSSION

Based on all the data that have been obtained from flow diffusion experiment, we can conclude that the wall configurations that give the most diffusion are model 3, 7, and 8. However, for velocity reduction of those models are not in the same category. Model 3 produced very low reduction, model 7 produced high reduction whilst model 8 very high. It can be seen too that model 5 resulted a very high velocity reduction while it is only categorized as moderate diffuser. We can conclude that the diffusion performance is not tally with the velocity reduction. This may cause by other factors or parameters itself such as area and width of opening, that will affect the amount of water passed through in a time, or gap between opening such as wall between windows or doors that will act as barrier that diffuse the flow and velocity, etc. Becker et. al [16] suggested that application of uncertainty investigation is favored to gain further perception into how significant building and flood parameters influence response. Nevertheless, many uncertainties in the analysis remain. Building response parameters have been significantly generalized for this research. More detail and reliable damage estimates could be obtained by acquiring more accurate estimations of building strength and response properties [13]. Further study on diffusion versus velocity should be conducted. High reduction of velocity may result from high amount of impact act on walls. Study on

suitable impact may exert on walls to produced suitable diffusion and reduce optimum velocity should be done.

CONCLUSION

Generally, the results show that walls with bigger openings could withstand the water forces better. This is indicated by the smaller velocity reduction and diffusion when the flowing water passes through the wall. However, the level of opening from the ground could change the overall performance of the various opening sizes as shown by some of the models. Therefore, further studies should be carried out to determine suitable dimensional characteristics and level of the wall openings from the ground. This could produce an optimum impact reduction wall design for residential building in flood prone area.

ACKNOWLEDGEMENT

This work is supported by Universiti Sains Malaysia RUI Grant No. 1001/PPBGN/814283.

REFERENCES

- [1] Chan, N. W. (2012), 'Impacts of Disasters and Disasters Risk Management in Malaysia: The Case of Floods', in Sawada, Y. and S. Oum (eds.), *Economic and Welfare Impacts of Disasters in East Asia and Policy Responses*.

- ERIA Research Project Report 2011-8, Jakarta: ERIA. pp.503-551.
- [2] Kong Yoke Yoon, Noor Azima Binti Bahrin, and Yew Kun. (2010). A study on the urban flooding. October 2010.
 - [3] Mohamad Sukeri Khalid and Shazwani Shafiai. (2015). Flood Disaster Management in Malaysia: An Evaluation of the Effectiveness Flood Delivery System. *International Journal of Social Science and Humanity*, Vol. 5, No. 4, April 2015. School of Law, Government and International Studies, Universiti Utara Malaysia, Malaysia. DOI: 10.7763/IJSSH.2015.V5.488.
 - [4] Vinet, F. (2008). Geographical analysis of damage due to flash floods in southern France: The case study of 12-13 November 1999 and 8-9 September 2002. *Journal of hydrology*, 361(1-2), 199-213.
 - [5] Sani G. Diya, Muhd Barzani Gasim, Mohd Ekhwan Toriman and Musa G. Abdullahi. (2014). FLOODS IN MALAYSIA Historical Reviews, Causes, Effects and Mitigations Approach. *International Journal of Interdisciplinary Research and Innovations* Vol. 2, Issue 4, pp: (59-65), Month: October - December 2014.
 - [6] Pistrika, A. (2010). "Flood Damage Estimation based on Flood Simulation Scenarios and a GIS Platform". National Technical University of Athens. *European Water* 30: pp. 3-11.
 - [7] Smith, D. I. (1996). "Flood damage estimation – A review of urban stage-damage curves and loss functions. *Water SA*, 20(3), pp. 231-238.
 - [8] USACE. (1996). Engineering and Design. Risk – based Analysis for Flood Damage Reduction Studies. Manual No. 1110-2-1619.
 - [9] Kelmen, I. and Spence, R. (2004). An overview of flood actions on buildings. *Engineering Geology* 73 (3-4), pp. 297-309.
 - [10] Bates, P. D., Horritt, M. S., Smith, C. N., et. al. (1997). Integrating remote sensing observations of flood hydrology and hydraulic modeling. *Hydrol Process* 1997;11 (14):1777-95.
 - [11] Horritt, M. J. and Bates, P. D. (2002). Evaluation of 1D and 2D numerical models for predicting river flood inundation. *J Hydrol* 2002;268:87-99
 - [12] Humberto, A. G., Jochen E. S. and Brett, F. S. (2009). Two-dimensional, high-resolution modeling of urban dam-break flooding: A case study of Baldwin Hills, California. *Advances in Water Resources* 32 (2009) 1323-1335.
 - [13] Becker, A. B., Johnstone, W. M. and Lence, B. J. (2011). Wood Frame Building Response to Rapid-Onset Flooding. *Natural Hazards Review*, Vol. 12, No. 2, May 1, 2011. ©ASCE, ISSN 1527-6988/2011/2-85–95. DOI: 10.1061/(ASCE)NH.1527-6996.0000029.
 - [14] Grundy, P., Thurairaja, A., and Walker, G. (2005). Some reflections on the structural engineering aspects of tsunami damage. *Proc. Earthquake Engineering in Australia Conf. 2005*, Albury, New South Wales, Australia.
 - [15] Kelmen, I. (2002). Physical flood vulnerabilities of residential properties in coastal, eastern England. Ph.D thesis, University of Cambridge, United Kingdom.
 - [16] Becker, A. (2008). Wood Frame Building Response to Rapid Onset Flooding. A Thesis Submitted in Partial Fulfillment of The Requirements for The Degree of Master of Applied Science in The Faculty of Graduate Studies (Civil Engineering). Master of Applied Science. The University of British Columbia (Vancouver) September 2008.
 - [17] Ramsden, J. D. (1993). "Tsunamis: Forces on a vertical wall caused by long waves, bores, and surges on a dry bed." Rep. No. KH-R-54, W. M. Keck Laboratory, California Institute of Technology, Pasadena, Calif.
 - [18] Arnason, H. (2005). "Interactions between an incident bore and a freestanding coastal structure." Ph.D. thesis, Univ. of Washington, Seattle.
 - [19] Thusyanthan, I. and Madabhushi, G. (2008). Tsunami wave loading on coastal houses: a model approach. *Proceedings of ICE Civil Engineering* 161 May 2008 Pages 77–86 Paper 07-00037. doi: 10.1680/cien.2008.161.2.77
 - [20] A.N. Abdul Ghani and N. Kasnon (2014). Effect of Flood Water Diffuser on Flow Pattern of Water during Road Crossing. *MATEC Web of Conferences* 10 06006 (2014). DOI: 10.1051/mateconf/20141006006
 - [21] Abdul Naser Abdul Ghani, Ahmad Hilmy Abdul Hamid and Nursriaftah Kasnon. (2015). Study on The Use of Obstructing Objects to Diffuse Flood Water Velocity During Road Crossing. *Int. J. of GEOMATE*, March, 2015, Vol. 8, No. 2 (Sl. No. 16), pp. 1245-1249.

APPLICATION OF A HYDROLOGICAL LAND SURFACE MODEL TO WATER RESOURCES ASSESSMENT IN PENINSULAR MALAYSIA

Chee-Loong Wong^{1,2}, Zulkifli Yusop^{1,3}, Tarmizi Ismail^{1,3} and Raymond Venneker⁴

¹Faculty of Civil Engineering, Universiti Teknologi Malaysia, 81310 Johor Bahru, Malaysia

²Department of Irrigation and Drainage Malaysia, Jalan Sultan Salahuddin, 50626 Kuala Lumpur, Malaysia

³Centre for Environmental Sustainability and Water Security, Research Institute for Sustainable Environment, Universiti Teknologi Malaysia, 81310 Johor Bahru, Malaysia

⁴UNESCO-IHE Institute for Water Education, PO Box 3015, 2601 DA Delft, The Netherlands

ABSTRACT

This paper presents a land surface model application to water resources assessment in Peninsular Malaysia. The approach enables to capture the spatial and seasonal temporal variability of the terrain characteristics, and can be applied for time scales of one year or longer. The spatial resolution used here is 0.05 degrees (approximately 5.5 km). The results are presented in terms of mean annual evaporation and runoff for the period 1999-2004. The model performance in simulating mean annual runoff for this period is evaluated using observed discharge data from 31 hydrological stations across Peninsular Malaysia, with drainage areas between 450 and 25,600 km². A mean absolute error of 10% in the simulated mean annual runoff was found, after excluding three stations that are known to have significant upstream offtakes. A simple and mostly illustrative regional analysis is carried out to assess the spatial and inter-annual variability of the available water resources and the relation with population distribution. While a major part of the population is living in urban centres along the coast, water resources must be drawn from a limited number of relatively small inland basins. The results are discussed and compared with those of previous studies carried out for Peninsular Malaysia, where available. It is shown that for annual time scales, the model configuration is able to assess the amount and spatial variation of natural water resources, and has potential for application within a complex arrangement of multiple river basins or, if required, arbitrarily-defined administrative regions.

Keywords: Water resources assessment, Land surface models, Water balance, Regionalization, Peninsular Malaysia

INTRODUCTION

Water resources assessments are essential to the sustainable development and management of water resources. Information about the extent and variability of water resources is required to evaluate the potential for utilization and control. A combination of factors related to development, human activity, population growth, and changes in land use and climate result in changing hydrological patterns and trends that need to be monitored and assessed for future planning and development [1]. An early investigation in the water balance of Peninsular Malaysia was carried out by [2]. Comprehensive studies by the Department of Irrigation and Drainage (DID) provided further insight in the regional water resources [3,4]. Other studies have focused on understanding the small scale hydrological processes related to land use and agricultural practice [5-9], the hydrological behaviour at river basin scales [10-13], and water use aspects [14].

A basic water resources assessment programme involves collection and processing of hydrological,

hydrogeological and physiographic data, followed by regionalization to assess the spatial distribution and temporal variation [1]. For Peninsular Malaysia, the above-mentioned studies by Scalf [3] and Teh *et al.* [4] produced interpolated maps of potential evaporation and runoff, respectively, using Penman and Hargreaves evaporation methods and a simple Thornthwaite-Mather water balance model with observation data for 1960-1970. Although comprehensive, the procedure was time-consuming and involved. The results are still being used in many current applications. A reassessment has not been carried out since.

Continuous monitoring and assessment of water resources are important in relation to environmental changes that occur at local, regional and global scales due to economic development and population growth. A review of the hydrological impacts from changes in land cover for Southeast Asia has been presented by [15]. In-depth analysis of flow records in relation to the Malaysia water resources master plan for 2000-2050 could not result in conclusions on possible impacts of climate change and/or short-term land-use changes on the water resources

[16]. Xu and Singh [17] present a review of representative model approaches for assessment of regional water resources under stationary and changing conditions. An essential issue is the role of the land surface in partitioning the precipitation between evaporation, rapid runoff and recharge to groundwater.

The objective of this study is to explore the use of a hydrological land surface model (LSM-A) to assess regional mean annual water resources over relatively short time periods for humid tropical conditions in Peninsular Malaysia. It also provides a simple, illustrative, assessment to obtain insight in the variability of the water resources and available water for the peninsula. The study is carried out for the period 1999-2004.

Section 2 describes the general methodological approach, introduces the LSM-A model computations relevant to this study and presents an overview of the data. Overall results and validation of the model performance against discharge observation records are presented in Section 3. A baseline analysis of the water resources availability and variability are presented in Section 4. In Section 5, a discussion of the approach and conclusions are given.

METHOD AND DATA

Methodology

The administrative system in Malaysia is arranged as a federation of states, see Fig. 1, which has implications for conducting water-related assessments. The land mass of Peninsular Malaysia, also referred to as West Malaysia, comprises 11 States and two Federal Territories with a total area of 135,000 km², and a total population of 17,726,283 in 2000 [18]. For simplicity, this study includes the Federal Territories Kuala Lumpur and Putrajaya with Selangor State. Located between latitudes 1°N and 7°N, a humid tropical climate characterized by two monsoon periods prevails. Mean annual rainfall is in the order of 2350 mm [19].

The LSM-A model computations provide daily energy and water balance output on a 0.05 degree (approximately 5.5 km) spatial grid, taking account of spatial variability in land cover and soils. The atmospheric input data are obtained from the gridded daily hydrometeorological data set described by Wong *et al.* [19]. The daily sum of the surface runoff production and the soil water percolation are subsequently accumulated and spatially averaged to obtain mean annual runoff for the period 1999-2004. For time scales of several years or longer, short-term and seasonal variations in surface and subsurface water storage are assumed to cancel out and the computed runoff production Q should represent the difference between rainfall P and evaporation E , i.e.

$$Q = P - E \quad (1)$$

which is taken to represent an estimate of the mean available water resources [17]. The procedure can be applied to river basins delineated by the upslope drainage area at any point in the model grid, or to arbitrary regions such as a State.

The model performance is evaluated using observation records from discharge stations across the peninsula. Subsequently, the model results are used to assess the regional mean annual water resources availability and inter-annual variation for the individual States, and for several of the major river basins in Peninsular Malaysia. We report computed mean values as complete figures with an uncertainty at the 95% confidence interval, obtained by applying a scale of ± 1.96 to the standard errors about the sample mean, assuming a Gaussian distribution.

Model Description

The LSM-A land surface model is composed of grid-distributed land cover and soil components. Land cover is classified according to the International Geosphere-Biosphere Programme (IGBP) legend [20]. The leaf area index varies with space and time according to an annual cycle of mean monthly values. Soils vary spatially according to the USDA soil texture classification [21]. The soil profile is subdivided into five layers of downward increasing thickness up to 2 m depth. The atmospheric forcing consists of downward shortwave and longwave radiation, precipitation, windspeed, and air temperature, pressure and humidity. The computed fluxes include the upward radiation, the latent, sensible and ground heat fluxes, the potential and actual evaporation, the surface runoff production from infiltration or saturation excess, and the soil percolation flux at the bottom of the soil profile. In addition, the model also computes the soil water content and soil temperature for the soil layers.

A general characteristic of land surface models is that model parameter values are prescribed depending on land cover or soil types, and can be obtained from the literature. As such, calibration is not commonly carried out. This may be considered a useful feature but on the other hand it is noted that validation of land surface model output is not straightforward since measurements of model variables at grid scales are mostly unavailable. For grid boxes with a vegetative cover, the effective areal vegetation cover fraction c_v (m² m⁻²) is obtained from the Bouguer-Lambert-Beer relation

$$c_v = 1 - \exp(-K_0 L_{AI}) \quad (2)$$

where K_0 is an optical attenuation coefficient, ranging 0.4–0.6 [22], and L_{AI} is the leaf area index (m² m⁻²).



Fig 1 Major administrative division of Malaysia

The surface energy balance is written

$$C_v \frac{dT_{sk}}{dt} = R_n - H - LE - G \quad (3)$$

where C_v is the surface heat capacity ($J m^{-2} K^{-1}$), T_{sk} is the skin temperature (K), t is the time (s), R_n is the net radiation flux ($W m^{-2}$), H is the sensible heat flux ($W m^{-2}$), L is the latent heat of vaporization ($J kg^{-1}$), E is the evaporation flux $kg m^{-2} s^{-1}$ and G is the ground heat flux ($W m^{-2}$). The surface heat capacity for the vegetated part of a grid box is parameterized from the water in the biomass and the water intercepted by the canopy, i.e.

$$C_v = \frac{C_w}{\rho_w} (w_l L_{AI} + W_v) \quad (4)$$

where C_w is the volumetric heat capacity of liquid water ($J m^{-3} K^{-1}$), ρ_w is the density of water ($kg m^{-3}$), w_l is the mass of water per unit leaf area (set to $0.5 kg m^{-2}$ and W_v is the intercepted water ($kg m^{-2}$). The heat capacity for the unvegetated part of a grid box is assumed zero. The net radiation is described by

$$R_n = (1 - \alpha) R_s \downarrow + \varepsilon R_L \downarrow - \varepsilon \sigma T_{rad}^4 \quad (5)$$

where α is the surface albedo, ε is the surface emissivity, $R_s \downarrow$ and $R_L \downarrow$ are the downward shortwave and longwave radiation fluxes ($W m^{-2}$), σ is the Stefan-Boltzmann constant and T_{rad}^4 is the radiative temperature (K). The sensible and latent heat fluxes are obtained from

$$H = c_p \rho C_H U (T_{sk} - T_a) \quad (6)$$

$$LE = L \beta C_H U (q^* - q_a) \quad (7)$$

respectively, where c_p is the specific heat capacity of dry air ($J kg^{-1} K^{-1}$), ρ is the density of the moist air ($kg m^{-3}$), C_H is the dimensionless heat transfer coefficient, U the magnitude of the horizontal wind speed ($m s^{-1}$), T_a is the temperature of the air (K),

$q^* = q^*(T_{sk})$ is the saturated specific humidity ($kg kg^{-1}$) of the evaporating surface and q_a is the specific humidity of the air ($kg kg^{-1}$). Furthermore, a dimensionless surface resistance factor β is applied in Eq. (7) to partition the latent heat flux between evaporation from the wet canopy and bare soil, and transpiration from the soil-vegetation root complex using a resistance scheme as described by Essery *et al.* [23].

The soil heat transport is described by

$$C_T \frac{\partial T}{\partial t} = \frac{\partial G}{\partial z} \quad (8)$$

where C_T is the volumetric heat capacity of the soil ($J m^{-3} K^{-1}$), T is the soil temperature (K) and z is the depth below surface. Parameterization of C_T is carried out following [24]. The soil heat flux is described by Fourier's law, i.e.

$$G = -k(\theta) \frac{\partial T}{\partial z} \quad (9)$$

where k is the thermal conductivity of the soil, which depends on soil water content θ ($m^3 m^{-3}$) and is parameterized following [25]. A zero heat flux at the bottom of the soil profile is assumed.

The energy balance is solved numerically by linearizing the surface fluxes to obtain an extended Penman-Monteith formulation for the evaporation potential. The actual evapotranspiration is subsequently derived by limiting the evaporation flux to the available water in the soil and vegetation storages [cf. 23].

The vegetation water balance is described by Rutter *et al.* [26]

$$\frac{dW_v}{dt} = c_v P - Q_v - E_w \quad (10)$$

where P is the above-canopy precipitation rate ($kg m^{-2} s^{-1}$), Q_v is the canopy interception drip rate (kg

$\text{m}^{-2} \text{s}^{-1}$) and E_w is the wet canopy evaporation rate ($\text{kg m}^{-2} \text{s}^{-1}$). The interception storage is capped by a limiting storage, which is proportional to the leaf area index. The soil profile water balance per unit surface area is described by the Richards equation

$$\rho_w \frac{\partial \theta}{\partial t} = -\frac{\partial Q_w}{\partial z} - \rho_w S \quad (11)$$

where ρ_w is the density of water (kg m^{-3}), θ is the volumetric soil water content ($\text{m}^3 \text{m}^{-3}$), Q_w is the soil water flux ($\text{kg m}^{-2} \text{s}^{-1}$) and S is the plant root extraction flux ($\text{m}^3 \text{m}^{-3} \text{s}^{-1}$). The soil water flux is described by Darcy's law for unsaturated conditions, i.e.

$$Q_w = -\rho_w \left(D \frac{\partial \theta}{\partial z} + K \right) \quad (12)$$

where D is the hydraulic diffusivity ($\text{m}^2 \text{s}^{-1}$) and K is the hydraulic conductivity (m s^{-1}). The dependencies of both diffusivity and conductivity on soil water content are parameterized using empirical relations [27]. Subgrid infiltration and surface runoff production are modelled using the method of Schaake *et al* [28], which is based on a stochastic distribution of time step accumulated fluxes. The spatially averaged mean infiltration flux ($\text{kg m}^{-2} \text{s}^{-1}$) is given by

$$I_{\text{sf}} = \frac{1}{\Delta t} \frac{P_n I_c}{P_n + I_c} \quad (13)$$

where $P_n = Q_v \Delta t$ is the time step accumulated input of water to the ground surface (kg m^{-2}), i.e. the sum of the canopy drip and free throughfall from precipitation, and I_c is the cumulative infiltration capacity (kg m^{-2}). The latter is obtained here from the advancement of the wetting front and the non-saturated fraction of the pore space, viz.

$$I_c = \rho_w \frac{K_{\text{sat}}}{\theta_{\text{sat}}} (\theta_{\text{sat}} - \theta_1) \Delta t \quad (14)$$

where K_{sat} is the saturated conductivity (m s^{-1}), θ_{sat} is the saturated soil water content ($\text{m}^3 \text{m}^{-3}$), and θ_1 is the soil water content of the top layer ($\text{m}^3 \text{m}^{-3}$). The soil hydraulic properties are obtained from [27]. The surface runoff production is obtained from

$$Q_{\text{sf}} = Q_v - I_{\text{sf}} + R_{\text{sf}} \quad (15)$$

where R_{sf} is the saturation excess flux ($\text{kg m}^{-2} \text{s}^{-1}$), obtained from accumulating any oversaturated soil water through the layers at the end of each time step. The soil water percolation flux at the bottom of the

soil profile towards groundwater is parameterized as gravity flow from the lowest soil layer, reduced by the fractional soil water content above field capacity reference conditions

$$Q_s = \rho_w K (\theta_N) \left(\frac{\theta_{\text{sat}} - \theta_N}{\theta_{\text{sat}} - \theta_{\text{ref}}} \right) \quad (16)$$

where θ_N is the soil water content of the bottom soil layer and θ_{ref} is the soil water content at field capacity ($\text{m}^3 \text{m}^{-3}$). Soil water percolation is assumed to stop for conditions below field capacity. Percolation also ceases for very wet soil bottom conditions that are taken to indicate high groundwater levels. In effect, the groundwater behaviour is unknown.

In the present application, the runoff for a specified area Eq. (1) is computed as the time-integrated spatial average sum of the surface runoff production Eq. (15) and groundwater percolation Eq. (16) over the target area.

Data

The land cover type distribution is derived from MODIS 1km MOD12Q1 V004 products, based on majority of occurrence in the period 2001-2004. Table 1 shows the areal proportion of the cover types after aggregation into the 0.05 degree model grid. The IGBP legend class for agricultural lands is restricted to crops less than 2 m height. Malaysia has extensive oil palm and rubber plantation stands, which are classified together with natural tropical forest as broadleaf evergreen forest. The mean monthly leaf area index is derived from MODIS 8-day 1km MOD15A2 V005 products for the period 2003-2007. The 8-day data were averaged into mean monthly fields at 0.05 degree spatial resolution. Table 1 shows the model grid average and range distribution of leaf area index. Grid box-scale effective values are evidently smaller than those typically observed inside a forest stand or crop field.

The USDA soil texture type distribution is obtained from global 5 arcmin resolution maps of sand, silt and clay separates that have been extracted from the ISRIC-WISE global soil properties data base linked to the FAO-UNESCO Digital Soil Map of the World [29]. The data have been resampled into grid resolution based on majority grid box area fraction. Table 2 shows the areal distribution in the model grid, with most of the area covered by loamy types of soil. The areal distribution of separate fractions and the resulting texture type classification should be considered best-estimates on the basis of the availability of soil profiles in the data base [29].

Table 1 Distribution of IGBP land cover type characteristics obtained from MODIS MOD12Q1 and MOD15A2 products aggregated on a 0.05 degree spatial grid. Coverage is tabulated as areal percentage for Peninsular Malaysia. Leaf area index is tabulated as the mean and uncertainty at the 95% interval, and the minimum and maximum of the mean monthly values, as applicable for the cover types.

Land cover type		Area (%)	Mean monthly leaf area index		
			Mean	Min	Max
1	Evergreen Needleleaf Forest	0.3	1.83 ± 0.12	1.45	2.26
2	Evergreen Broadleaf Forest	86	3.60 ± 0.31	2.48	4.44
3	Deciduous Needleleaf Forest	—			
4	Deciduous Broadleaf Forest	—			
5	Mixed Forest	0.4	2.82 ± 0.25	1.46	2.80
6	Closed Shrublands	—			
7	Open Shrublands	—			
8	Woody Savannas	—			
9	Savannas	0.1	1.39 ± 0.18	0.96	1.90
10	Grasslands	—			
11	Permanent Wetlands	0.1			
12	Croplands	5.8	1.37 ± 0.10	1.18	1.79
13	Urban and Built-Up	1.0			
14	Cropland/Natural Vegetation Mosaic	6.6	2.11 ± 0.14	1.65	2.59
15	Snow and Ice	—			
16	Barren or Sparsely Vegetated	—			
17	Water Bodies	0.2			

Table 2 Distribution of USDA soil texture types aggregated on a 0.05 degree spatial grid as areal percentage for Peninsular Malaysia, as derived from the ISRIC-WISE [29] data.

Soil texture type	Area (%)	Soil texture type	Area (%)
1 Sand	—	7 Sandy clay loam	56
2 Loamy sand	—	8 Clay loam	14
3 Sandy loam	0.3	9 Silty clay loam	—
4 Loam	6.2	10 Sandy clay	19
5 Silt loam	—	11 Silty clay	—
6 Silt	—	12 Clay	4.5

The hydrometeorological input data used in this study are provided by the gridded data set described in Wong *et al.* [19], in which daily data fields of pressure, temperature, humidity, wind speed and precipitation were obtained from interpolating station data, taking account of elevation and land cover characteristics as appropriate. Elevation data are derived from SRTM 30 version 2 data [30]. Daily input fields for downward shortwave and longwave radiation are estimated from the gridded

surface meteorological parameter values in combination with satellite observation-derived radiation and cloud properties obtained from the NASA/GEWEX Surface Radiation Budget (SRB) Release-3.0 data archive. Fig. 2 shows the location of rainfall observing stations and the interpolated mean annual rainfall field for the six years of this study. An average number of 159 daily rainfall observations from 175 rainfall observing stations were available. The largest mean annual rainfall amounts of more than 3400 mm occur along the northeastern coast, mostly during the northeast monsoon period from October to March. The smallest mean annual rainfalls of 1800 – 2000 mm are present in the southern inland and southwestern coastal areas, and in the northern parts of the country. Refer to Wong *et al.* [19] for further analysis of the atmospheric input data set.

SIMULATION RESULTS

Spatial Evaporation and Runoff

Fig. 3 shows the spatial distribution of the computed mean annual potential and actual evaporation for Peninsular Malaysia over the six-year study period. The potential evaporation shows a similar pattern to the interpolated maps for forest and grass cover presented in the earlier study by

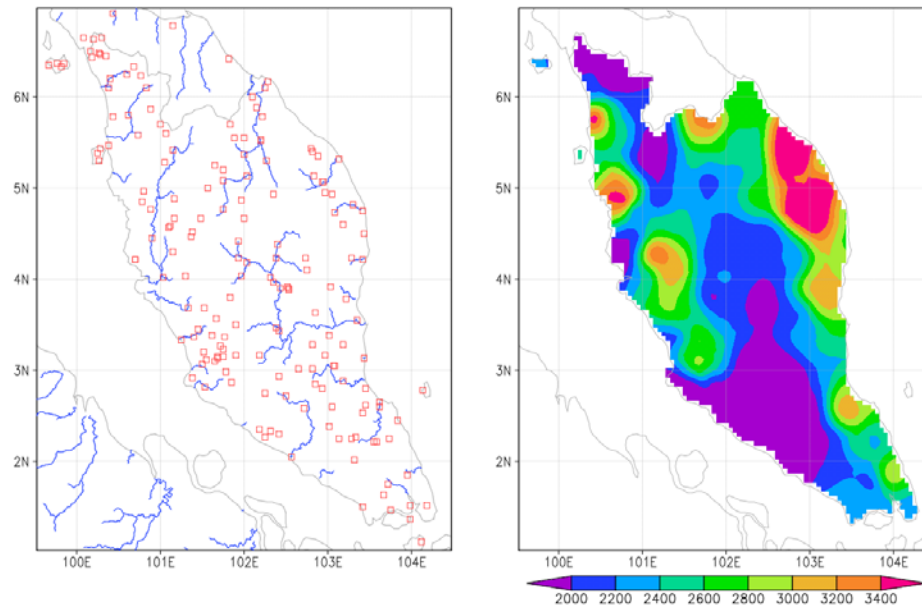


Fig 2 Location of rainfall observing stations (left panel) and the distribution of mean annual rainfall (mm) for 1999-2004 (right panel).

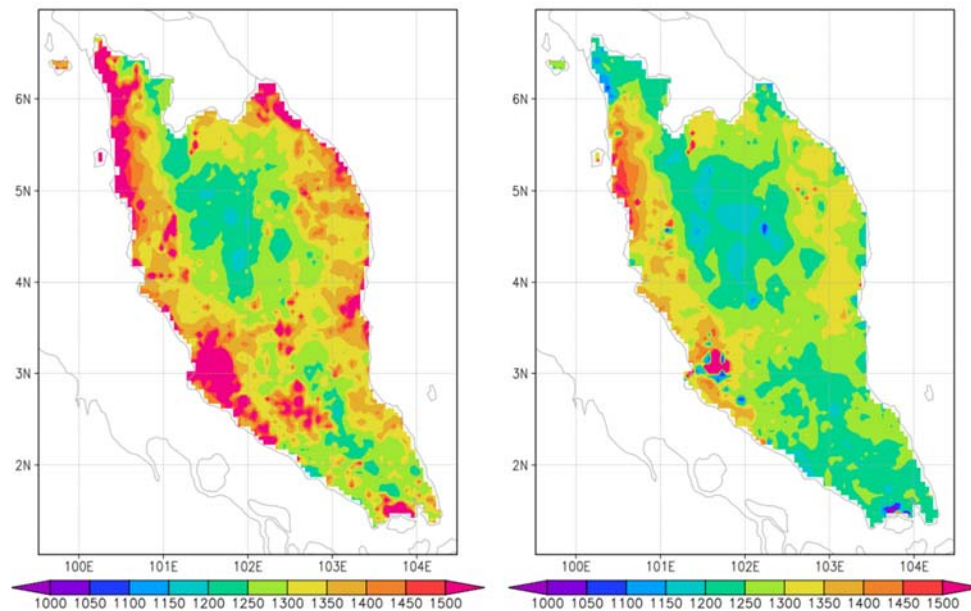


Fig3 Estimated mean annual evaporation (mm) in Peninsular Malaysia for 1999-2004. The left panel displays the potential evaporation, the right panel displays the actual evaporation.

Scarf [3]. The highest potential evaporation values of 1500 – 1700 mm are computed for the coastal zone areas, where relatively high wind speeds occur over low cropland vegetation.

The presence of tall forest in the inland areas reduces the interpolated windspeed [19], resulting in reduced mean evaporation potential. The potential evaporation of 1100 – 1150 mm in the most central mountainous inland areas computed here are

somewhat larger than those of 1000 – 1100 mm estimated by Scarf [3], which may be due to a less accurate representation of the orography on the 5.5 km model grid. The maps in Fig. 3 also show that the mean annual actual evaporation estimate compares close to that of the potential evaporation, as can be expected for humid tropical conditions.

Given the relatively small spatial variation in mean annual evaporation, the spatial distribution of

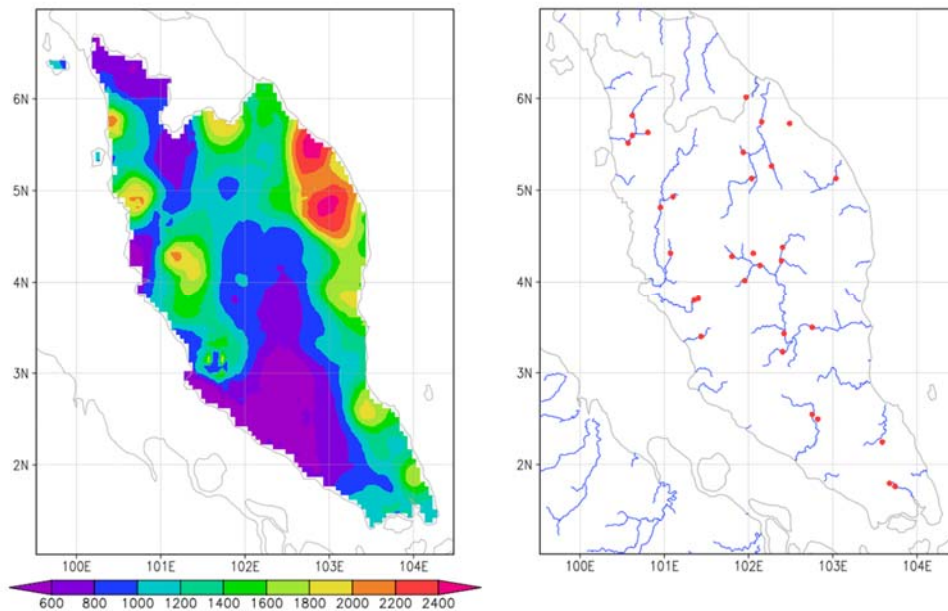


Fig 4 Left panel: estimated mean annual runoff (mm) in Peninsular Malaysia for 1999-2004. Right panel: location of 31 discharge stations that were used for validation of the model simulation results.

mean annual runoff, i.e. the time-integrated sum of the surface runoff production and groundwater percolation, shown in the left panel of Fig. 4 resembles that of the rainfall (Fig. 2). The right panel of Fig. 4 shows the location of discharge stations that were selected for validation of the computed runoff, which is further detailed in the next section.

Model Validation

Table 3 summarizes the runoff validation results by comparison with 31 hydrometric stations that could be included in this study. Criteria for station selection were: a minimum record of five years with 85% of available daily discharge data in the period 1999-2004; a catchment area larger than 450 km² to comprise a minimum of 14-15 grid boxes; and that the catchment area resolved by the model grid matches within 20%. Two stations with known rating curve problems during the simulation period were also excluded. Nine stations lack one year of data, indicated by '(5)' after the station location in Table 3. For all station observation records, an average proportion of 8% of daily data are missing. Only two stations (Sg. Pahang at Lubok Paku and Sg. Muda at Jam. Syed Omar) have a complete record without missing data. The mean absolute error in gridded catchment area for all stations is 6%. The observed annual runoff for the stations was computed from daily discharge values as archived in the DID database and the catchment area as listed in the station registry. The simulated annual runoff is

based on the catchment area as resolved by the model grid using a steepest descent delineation method [31].

Sg. Johor and Sg. Muar are known to be extensively used for water supply purposes [16], which results in an overestimation of model runoff. For the latter station, the discrepancy between observed and simulated runoff is justified by the the match for Sg. Segamat, a tributary downstream of the offtake. The Sg. Muda basin in Kedah State (see Fig. 1) is a complicated area as it supplies part of its water for the Muda Irrigation Project along the west coast [10,16]. Water is diverted from the most upper areas of the basin, which explains the overestimation at Jeniang and to a smaller extent at Jam. Syed Omar. However, at the most downstream station Ldg. Victoria, the simulations match the observations, suggesting potential inconsistency in observation records. Minor abstractions for water supply and/ or irrigation water are known to affect Sg. Selangor, Sg. Bernam and Sg. Lipis, Sg. Perak and Sg.~Besut [4,16]. Two relatively large reservoirs regulating Sg. Perak and Sg. Terengganu are mostly used for hydropower generation and to some extent for flood control. It is therefore assumed that besides possible increase of open water evaporation the operations do not significantly affect water quantities at annual time scales.

The 18% underestimate at Sg. Triang is likely explained by lack of rainfall data. The records for two years from nearby rainfall stations did not pass quality control as described in Wong *et al.* [32]. The underestimate at Sg. Tembeling (18%) may possibly

Table 3 Simulation validation results for 31 stations with minimum five years of sufficient data during 1999-2004. The Data column gives the amount of daily observations and Δ denotes the difference between simulations and observations.

Station location	Area (km ²)	Data (%)	Mean annual runoff (mm)		
			Observed	Simulated	Δ (%)
Sg. Johor di Rantau Panjang (5)	1130	94	740 \pm 200	983 \pm 184	+33*
Sg. Sayong di Jam. Johor Tenggara	624	86	898 \pm 211	1001 \pm 154	+11
Sg. Kahang di Bt. 26 Jln. Kluang	587	90	1253 \pm 214	1262 \pm 97	+1
Sg. Muar di Buloh Kasap	3130	92	410 \pm 97	554 \pm 100	+35*
Sg. Segamat di Segamat	658	96	792 \pm 135	746 \pm 225	-5
Sg. Selangor di Rantau Panjang	1450	95	1028 \pm 134	1223 \pm 116	+19
Sg. Bernam di Jam. SKC	1090	98	1360 \pm 127	1413 \pm 112	+4
Sg. Slim di Slim River Town (5)	455	91	1660 \pm 440	1428 \pm 104	-14
Sg. Pahang di Lubok Paku	25600	100	850 \pm 181	894 \pm 114	+5
Sg. Pahang di Temerloh	19000	96	943 \pm 123	967 \pm 135	+3
Sg. Triang di Jam. Keretapi (5)	2000	87	864 \pm 185	709 \pm 121	-18
Sg. Lipis di Benta	1670	96	919 \pm 241	980 \pm 174	+7
Sg. Jelai di Jeram Bungor (5)	7320	85	997 \pm 203	1019 \pm 227	+2
Sg. Jelai di Kuala Medang	2630	88	1294 \pm 119	1190 \pm 251	-8
Sg. Tembeling di Kg. Merting	5050	88	1094 \pm 112	1060 \pm 238	-3
Sg. Tembeling di Kuala Tahan (5)	2700	94	1439 \pm 124	1187 \pm 315	-18
Sg. Kecaui di Kg. Dusun (5)	497	94	1025 \pm 184	867 \pm 201	-15
Sg. Perak di Jam. Iskandar	7770	94	979 \pm 160	1018 \pm 193	+4
Sg. Kinta di Weir G di Tg. Tualang (5)	1700	87	1394 \pm 181	1284 \pm 259	-8
Sg. Plus di Kg. Lintang	1090	92	996 \pm 251	949 \pm 171	-5
Sg. Terengganu di Kg. Tanggol	3340	96	2608 \pm 307	2144 \pm 364	-18
Sg. Muda di Ldg. Victoria	4010	99	982 \pm 279	996 \pm 228	+1
Sg. Muda di Jam. Syed Omar	3330	100	782 \pm 236	946 \pm 223	+21
Sg. Muda di Jeniang	1710	88	583 \pm 185	850 \pm 228	+46*
Sg. Ketil di Kuala Pegang (5)	704	88	786 \pm 271	853 \pm 262	+9
Sg. Kelantan di Jam. Guillemard	11900	97	1188 \pm 252	1291 \pm 168	+9
Sg. Nenggiri di Jam. Bertam	4130	93	1134 \pm 135	1122 \pm 178	-1
Sg. Lebir di Kg. Tualang	2430	85	1581 \pm 300	1413 \pm 255	-11
Sg. Pergau di Batu Lembu	1290	91	2040 \pm 278	1761 \pm 293	-14
Sg. Besut di Jam. Jerleh (5)	787	95	1945 \pm 523	1713 \pm 332	-12
Sg. Golok di Rantau Panjang	1075	92	1502 \pm 263	1555 \pm 261	+4

arise from lack of orographic rainfall representation in the input data set. For Sg. Terengganu, possible overestimation of evapotranspiration by the model in the northeastern part of the peninsula (see Fig. 3) may be the cause of the 18% deficit in simulated runoff.

Stations with extensive abstractions as described above are marked by an asterisk in the last column of Table 3 and have been discarded from overall error analysis. For the remaining 28 stations, the mean absolute error between observation and simulation of mean annual runoff during 1999-2004 is 8.8%. From this result, it is inferred that the model error in simulating natural mean annual runoff for

periods of five to six years is equal to or better than $\pm 10\%$. This figure compares favourably to the $\pm 15\%$ error that was determined for the procedure used by Teh *et al.*[4]. The mean absolute error in annual runoff for any year for the 28 stations during the simulation period is 199 mm, which amounts to 16% of the mean observed annual runoff value. It should be noted, however, that the rainfall stations are not evenly distributed over the peninsula (Fig. 2) and that the number of reporting rainfall stations also varies from one day to another Wong *et al.*[32], which may have an influence on the results for some parts of the model grid.

APPLICATION TO REGIONAL WATER RESOURCES

The water laws in Malaysia stipulate a shared Federal and State governance of water resources with a large responsibility at State level. Details of the legislative and institutional framework for water resources management are described in Tan and Mokhtar [33]. As a consequence, studies carried out to inform water resources management, development and planning in Malaysia generally need to summarize findings per State, as applicable. The State boundaries do only partly coincide with basin boundaries, whereas in some cases the rivers are the boundaries.

The left graph in Fig. 5 presents the mean annual runoff aggregated over the area of each State. There is a significant difference in available annual water resources ranging from around 500 mm for Melaka in the southwest to more than 2000 mm for Terengganu on the northeastern coast. States with substantial coastal area exposure, i.e. Kedah, Pulau Penang, Perak, Selangor, Johor, Pahang, Terengganu and Kelantan, have abundant runoff. The States of Negeri Sembilan and Melaka, although located along the coast, are part of the dryer zone extending inland into the centre of the peninsula, which is caused by rainfall shading from the mountain ranges in Sumatra [32]. Inter-annual variability ranges $\pm 10\%$ to $\pm 28\%$, with the largest variations occurring in Pulau Penang and Melaka that are confined in narrow zones on the west coast. Comparison with the results in Teh *et al.* [4] suggests a reduction in mean annual runoff with respect to the period 1960-1970. It is impossible at this stage to judge if this is related to short-term climate variation, long-term

climate change, and/or human interference in the environment. However, in thirty years the population must have significant grown. The right graph in Fig. 5 shows the water availability per person, based on population statistics for the year 2000 [18]. The smallest mean annual water availability per capita for Pulau Penang, Selangor and Melaka is less than 1700 m³, which is generally taken indicative for water stress conditions. These States contain some 40% of the population on only 8% of the total area for Peninsular Malaysia. Many of the major urban centres are located in the coastal zones that need to fulfill their water demand from upstream sources. Groundwater is hardly being utilized in Peninsular Malaysia [16]. In reality, States such as Pulau Penang and Melaka draw their water from outside their boundaries, either naturally from a transboundary river basin or through water supply. The shortage in Selangor is currently being addressed by the development of the Pahang-Selangor Interstate Raw Water Transfer system, involving a 45 km tunnel through the central mountain range [16,33]. Water transfers are also foreseen for the southern part of the Peninsula [16].

Characteristic for Peninsular Malaysia is the presence of many smaller river basins along the coast, which are less favourable for large-scale water resources development due to either lack of capacity, vulnerability, or marine influence. It is more efficient to satisfy demand from the larger inland basins. To assess this, five inland river basins have been selected, using the hydrometric stations as basin outlet for the sake of simplicity (Table 3).

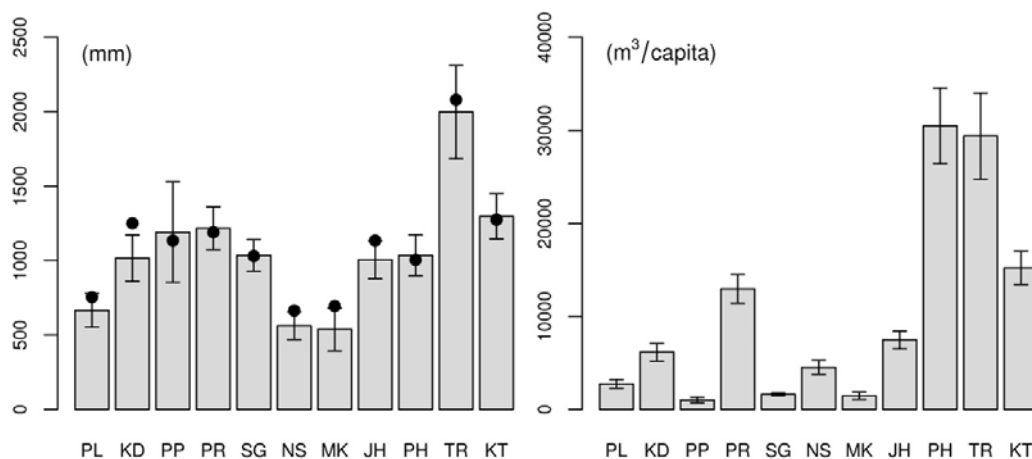


Fig 5 Computed mean annual runoff (mm, left panel) and the available water resources (m³/capita, right panel) for the States of Peninsular Malaysia during 1999-2004. The error bars indicate the 95% confidence level inter-annual variability. The estimated mean annual runoff (mm) as assessed by Teh *et al.* (1976) for 1960-1970 are indicated by black dots. PL: Perlis, KD: Kedah, PP: Pulau Penang, PR: Perak, SG: Selangor, NS: Negeri Sembilan, MK: Melaka, JH: Johor, PH: Pahang, TR: Terengganu, KT: Kelantan.

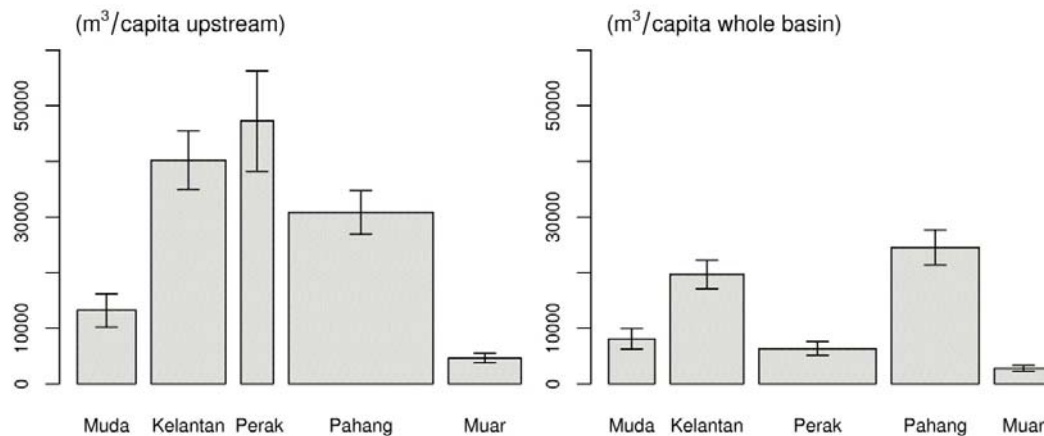


Fig 6 Estimated mean annual water availability per person for selected basins in Peninsular Malaysia during 1999-2004. The left panel considers only the population upstream of the hydrometric station. The right panel considers the population in the entire basin up to the coast. The bar width is scaled by population proportion.

These are the Muda basin at Ldg. Victoria, the Kelantan basin at Jam. Guillemard, the Perak basin at Jam. Iskandar, the Pahang basin at Lubok Paku, and the Muar basin at Buloh Kasap, and are the major inland basins in the peninsula. The population within the basin upstream of the stations and for the whole basin were estimated using district population statistics for 2000 [18]. The left graph in Fig. 6 shows the mean annual available water per person considering only the population upstream of the gauging station. The right graph shows the mean annual available water taking account of the entire population living in the basin up to the coast. The simulated mean inter-annual variability for the basins is $\pm 17\%$. Comparing the height of the bars for the same basin in the two graphs, it is clear that the ratio of whole-basin population to upstream population varies considerably among the basins, ranging from 1.25 for the Pahang basin to more than 7 for the Perak basin. This is again related to the location of the major urban centres along the coast. It should be noted, however, that there may exist additional demand from coastal cities outside the strict basin boundaries. Fig. 6 also indicates that the per capita available water varies considerably per basin. Provisionally, it would appear that the Kelantan and Pahang basins have the largest potential for development of their water resources. However, it needs to be stressed that the simulations provide natural runoff. Currently implemented operations for irrigation, water supply and other uses, are not reflected in the results shown here.

CONCLUSION

This study presented the implementation and application of the LSM-A hydrological land surface model to assessment of annual water resources in

Peninsular Malaysia during the period 1999-2004. The simulations were carried out at daily time steps using input from a previously developed gridded hydrometeorological data set [19]. The simulation results were integrated to annual time scales and averaged over area as required.

The model is based on commonly used parameterizations found in land surface schemes of atmospheric models, with minor adaptation towards hydrological application at smaller grid scales of approximately 5.5 km. One advantage of land surface schemes is that model parameters can be regionalized by simply applying land cover and soil type-prescribed parameter values reported in the literature. As a consequence, the requirement for calibration is absent, which is a major point of practical interest in application over large areas. The land cover, seasonal variation in biomass and soil description for the model are derived from global data sets that are becoming more widely available. On the other hand, the global character of such data sets distinguishes a rather limited selection of generic soil and land cover types, which may be insufficient for some applications, such as those related to agriculture. The grid-based structure, in combination with regionalized parameters, provides a direct means for water balance simulations in ungauged (parts of) river basins, which is essential in water resources assessment [1]. Moreover, in the present annual application, the results can be aggregated over arbitrarily defined units, which is useful within a water resources management framework such as implemented in Malaysia.

For the purpose of validation, the model simulation results were qualitatively compared with findings in the literature and quantitatively evaluated against observation records from 31 hydrometric stations across the peninsula. A mean absolute error

in spatial runoff prediction of 10% was found. An example application to water resources assessment illustrated the variability of water resources, as well as the complex relation between the water resources and the uneven population distribution for Peninsular Malaysia. It is also shown that this particular type of models can be used with relative ease within a rather complex basin arrangement.

The utility of models in water resources assessment and management programmes is generally acknowledged [17]. The model described here can be applied to analyze the natural runoff, which in turn can be used with stream flow observations to monitor the effects of water operations, such as for example water supply and irrigation offtakes, and diversions. Regular application in continuing assessment programmes provides a means to follow the effects and variations in hydrological regime due to short and long-term climatic change and structural change in the environment.

A major limitation is that the present configuration does not permit to assess seasonal and monthly water cycle dynamics, which could be useful for certain water resources management applications. To this end, an extension of LSM-A with a grid box-based runoff storage and routing scheme has been investigated for three large basins in Peninsular Malaysia (submitted for publication). Further studies are being carried out to assess whether the water resources in Peninsular Malaysia have been impacted by climatic or physical environmental changes during the last decades.

ACKNOWLEDGEMENTS

The authors thank the Department of Irrigation and Drainage Malaysia (DID), Malaysia Meteorological Department (MMD), and NOAA/NCDC for providing the data.

REFERENCES

- [1] WMO. *Guide to hydrological practices, volume ii management of water resources and application of hydrological practices*. sixth edition ed.; World Meteorological Organization, Geneva: 2009; Vol. WMO-No. 168.
- [2] Nieuwolt, S. Evaporation and water balances in malaya. *Journal of Tropical Geography* 1965, 20.
- [3] Scarf, T. *Evaporation in peninsular malaysia*; Water Resources Publications No.5; Department of Irrigation and Drainage: Kuala Lumpur, Malaysia, 1976.
- [4] Teh, S.K.; Still, D.C.; Scarf, T. *Average annual surface water resources of peninsular malaysia*; Water Resources Publication No.6; Department of Irrigation and Drainage: Kuala Lumpur, Malaysia, 1976.
- [5] Abdul Rahim, N.; Harding, D. Effects of selective logging methods on water yield and streamflow parameters in peninsular malaysia. *Journal of Tropical Forest Sciences* 1992, 5, 130-154.
- [6] Noguchi, S.; Abdul Rahim, N.; Baharuddin, K.; Tani, M.; Sammori, T.; Morisada, K. Soil physical properties and preferential flow pathways in tropical rain forest, bukit tarek, peninsular malaysia. *Journal of Forest Research* 1994, 2, 115-120.
- [7] Ziegler, A.D.; Negishi, J.N.; R.C., S.; Abdul Rahim, N. Impacts of logging disturbance on hillslope saturated hydraulic conductivity in a tropical forest in peninsular malaysia. *CATENA* 2006, 67, 89-104.
- [8] Henson, I.E.; Yahya, Z.; Noor, M.R.; Harun, M.H.; Mohammed, A.T. Predicting soil water status, evapotranspiration, growth and yield of young oil palm in a seasonally dry region in malaysia. *Journal of Oil Palm Research* 2007, 19, 398-415.
- [9] Chow, M.F.; Yusop, Z.; Shirazi, S.M. Storm runoff quality and pollutant loading from commercial, residential, and industrial catchments in the tropic. *Environmental Monitoring and Assessment* 2013, 185, 8321-8331.
- [10] Ali, M.H.; Lee, T.S. Potential evapotranspiration model for muda irrigation project, malaysia. *Water Resources Management* 2009, 23, 57-69.
- [11] Ab Ghani, A.; Ali, R.; Zakaria, N.A.; Hasan, Z.A.; Chang, C.K.; Ahamad, M.S.S. A temporal change study of the muda river system over 22 years. *International Journal of River Basin Management* 2010, 8, 25-37.
- [12] Julien, P.Y.; Ghani, A.A.; Zakaria, N.A.; Abdulla, R.; Chang, C.K. Case study: Flood mitigation of the muda river, malaysia. *Journal of Hydraulic Engineering* 2010, 136, 251-261.
- [13] Tan, M.L.; Ibrahim, A.L.; Yusop, Z.; Duan, Z.; Ling, L. Impacts of land-use and climate variability on hydrological components in the johor river basin, malaysia. *Hydrological Sciences Journal* 2015, 60, 873-889.
- [14] Ali, M.H.; Lee, T.S. Optimal allocation of monthly water withdrawals in reservoir systems. *Water Resources Management* 2001, 15, 323-341.
- [15] Douglas, I. Hydrological investigations of forest disturbance and land cover impacts in southe-east asia: A review. *Philosophical Transactions of the Royal Society of London* 1999, B354, 1725-1738.

- [16] EPU. *Masterplan for the development of water resources in peninsular malaysia 2000-2050*; Economic Planning Unit, Prime Minister's Department: Kuala Lumpur, 1999.
- [17] Xu, C.-Y.; Singh, V.P. Review on regional water resources assessment models under stationary and changing climate. *Water Resources Management* 2004, 18, 591-612.
- [18] DSM. *Yearbook of statistics malaysia, 2009*; Department of Statistics Malaysia: 2010.
- [19] Wong, C.L.; Venneker, R.; Jamil, A.B.M.; Uhlenbrook, S. Development of a gridded daily hydrometeorological data set for peninsular malaysia. *Hydrological Processes* 2011, 25, 1009-1020.
- [20] Loveland, T.R.; Reed, B.C.; Brown, J.F.; Ohlen, D.O.; Zhu, Z.; Yang, L.; Merchant, J.W. Development of a global land cover characteristics database and igbp discover from 1km avhrr data. *International Journal of Remote Sensing* 2000, 21, 1303-1330.
- [21] US, D.o.A. National soil survey handbook. USDA Natural Resources Conservation Service, URL <http://soil.usda.gov/technical/handbook>: 2007.
- [22] Dorman, J.L.; Seller, P.J. A global climatology of albedo, roughness length and stomatal resistance for atmospheric general circulation models as represented by the simple biospher model (sib). *Journal of Applied Meteorology* 1989, 28, 833-855.
- [23] Essery, R.L.H.; Best, M.J.; Betts, R.A.; Cox, P.M. Explicit representation of subgrid heterogeneity in a gcm land surface scheme. *Journal of Hydrometeorology* 2003, 4, 530-543.
- [24] McCumber, M.C.; Pielke, R.A. Simulation of the effects of surface fluxes of heat and moisture in a mesoscale numerical model. *Journal of Geophysical Research* 1981, 86C, 9929-9938.
- [25] Peters-Lidard, C.D.; Blackburn, E.; Liang, X.; Wood, E.F. The effect of soil thermal conductivity parameterization on surface fluxes and temperatures. *Journal of Atmospheric Sciences* 1998, 55, 1209-1224.
- [26] Rutter, A.J.; Kershaw, K.A.; Robins, P.C.; Morton, A.J. A predictive model of rainfall interception in forests, 1. Derivation of the model from observations in a plantation of corsican pine. *Agriculture Meteorology* 1972, 9, 367-384.
- [27] Clapp, R.B.; Hornberger, G.M. Empirical equations for some soil hydraulic properties. *Water Resources Research* 1978, 14, 601-604.
- [28] Schaake, J.C.; Koren, V.I.; Duan, Q.-Y.; Mitchell, K.; Chen, F. Simple water balance model for estimating runoff at different spatial and temporal scales. *Journal of Geophysical Research* 1996, 101D, 7461--7475.
- [29] Batjes, N.H. *Isric-wise global data set of derived soil properties on a 5 by 5 arc-minutes global grid (version 1.0)*; ISRIC - World Soil Information, Wageningen, Netherlands, Available through <http://www.isric.org>: 2006.
- [30] Farr, T.G.; Rosen, P.A.; Caro, E.; Crippen, R.; Duren, R.; Hensley, S.; Kobrick, M.; Paller, M.; Rodriguez, E.; Roth, L., et al. The shuttle radar topography mission. *Reviews of Geophysics* 2007, 45, RG2004.
- [31] Jenson, S.K.; Domingue, J.O. Extracting topographic structure from digital elevation data for geographic information system analysis. *Photogrammetric Engineering and Remote Sensing* 1988, 54, 1593-1600.
- [32] Wong, C.L.; Venneker, R.; Jamil, A.B.M.; Uhlenbrook, S. Development of a gridded daily hydrometeorological data set for peninsular malaysia. *Hydrological Processes* 2010.
- [33] Tan, K.W.; Mokhtar, M.B. An appropriate institutional framework towards integrated water resources management in pahang river basin, malaysia. *European Journal of Scientific Research* 2009, 27, 536-547.

BIFUNCTIONAL MICROCAPSULE FOR HEAT STORAGE AND ANTIBACTERIAL PROPERTIES PREPARED BY MICROSUSPENSION IODINE TRANSFER POLYMERIZATION

Amorn Chaiyasat^{1,2}, Siriluk Namwong¹, Boontida Uapipatanakul¹, Warayuth Sajomsang³, Preeyaporn Chaiyasat^{1,2 *}

¹Department of Chemistry, Faculty of Science and Technology, Rajamangala University of Technology Thanyaburi, Pathumthani 12110

²Advanced Materials Design and Development (AMDD) Research Unit, Institute of Research and Development, Rajamangala University of Technology Thanyaburi, Pathumthani 12110

³National Nanotechnology, 111 Innovation Cluster 2 (INC2 Building), Thailand Science Park, Paholyothin Road., Khlong Nueng, Khlong Luang, Pathumthani 12120, Thailand

ABSTRACT

It is well known that the microcapsules encapsulating heat storage or phase change materials are coated onto the fabrics for thermoregulating property. To increase their function on textile application, in this work, bifunctional microcapsules having both thermal energy storage and antibacterial properties were fabricated. Chitosan was used as surfactant of poly(methyl methacrylate-divinyl benzene) microcapsule encapsulated octadecane (OD) prepared by microsuspension iodine transfer polymerization. The nonspherical with dent microcapsules were prepared in acidic condition without any free polymethyl methacrylate particles nucleated by emulsion polymerization. Due to amino groups in chitosan chains were protonated in which presented positive charge, the microcapsules stabilized with such molecules were then obtained without any coalescence. In addition, percent yield of microcapsules decreased with chitosan concentration in aqueous medium. It may be due to high viscosity of the aqueous medium where the monomer droplets are unable to maintain the shape in early stage of the polymerization. For thermal properties, the latent heats of the encapsulated octadecane (234 J/g-OD) were closed to those (233 J/g-OD) of bulk octadecane. For antibacterial property, 2 millimetres over control sample of the resulting inhibition zones of both *S. aureus* and *E. coli* were observed. Based on bifunctional feature derived from both microcapsule core and shell for thermal energy storage and antibacterial properties, respectively, the developed microcapsules would express a great potential for textile application.

Keywords: Heat storage materials; Antibacterial property; Microcapsule; Microsuspension iodine transfer polymerization

INTRODUCTION

Because all seasons of Southeast Asia are hot and humid, thermoregulating fabrics or thermal adaptable cloths and antibacterial fabrics are then interested in the commercial production. For the former case, microcapsules containing phase change materials are often coated onto the fabrics [1, 2]. Because Paraffin waxes can melt and crystallize at a wide range of temperature to absorb and release energy, respectively, they then are preferably used as phase change material and encapsulated in the microcapsules. Encapsulation of paraffin waxes not only increases surface area for providing a larger heat transfer but also prevents phase change material reactivity to the outside environment and controls the volume change as

phase change occurs [3]. One of the most famous techniques for phase change material microcapsule preparation is microsuspension conventional radical polymerization due to high encapsulation efficiency of phase change material [4, 5]. Various kinds of polymer shell are used for the encapsulation based on microsuspension conventional radical polymerization such as polystyrene [6], poly(styrene-co-methyl methacrylate) [7], polydivinylbenzene [8, 9], poly(styrene-co-divinylbenzene) [10], poly(methyl methacrylate) [11] and poly(methyl methacrylate-co-methyl acrylate-co-methacrylic acid) [12]. To the best of our knowledge, among these polymer shells, polymethyl methacrylate is the best one to provide high latent heats of phase change material due to completion of phase separation between polymethyl

methacrylate shell and wax core [13]. However, using microsuspension conventional radical polymerization, approximately 35% of free polymethyl methacrylate particles respects to total monomer used were formed competition with microcapsules. In previous work, such phenomenon can be overcome with microsuspension iodine transfer polymerization which reduced radical exit from the monomer droplets to an aqueous medium [11, 14]. Chitosan is one of the most famous biopolymer because its beneficial properties include antifungal and antibacterial [15, 16], neuroprotective [17], anti-inflammatory [18] and so on. Since chitosan contains amino group in its chain which was protonated to give positive charges in acidic condition, it may able to be used as the surfactant of microsuspension polymerization in place of the conventional one as polyvinyl alcohol. To the best of our knowledge, there is a lack of research for phase change material microcapsule preparation using chitosan as a surfactant in microsuspension iodine transfer polymerization.

Therefore, in this research, the preparation of bifunctional microcapsule for both heat storage and antibacterial properties by microsuspension iodine transfer polymerization using octadecane, polymethyl methacrylate and chitosan for phase change material core, polymer shell and surfactant, respectively, was studied in the first time. The influence of chitosan concentration on the encapsulation efficiency was investigated.

2. EXPERIMENTAL

2.1 Materials

Methyl methacrylate (Aldrich, Wisconsin, USA; purity, 99%) was purified by passing through the column packed with basic aluminum oxide to remove the polymerization inhibitors before use. Octadecane (Merck, Munich, Germany; 99.5%) was used as received. Reagent-grade benzoyl peroxide (Merck, Munich, Germany) was purified by recrystallization. Iodoform (CHI_3 ; Aldrich, Wisconsin, USA; purity, 99%), poly(vinyl alcohol) (Aldrich, Wisconsin, USA; degree of saponification 87-90%, molecular weight $3\text{-}7 \times 10^4$ g/mol) and Chitosan were used as received.

2.2 Microcapsule preparation

The preparation of polymethyl methacrylate/octadecane microcapsules by microsuspension iodine transfer polymerization using chitosan as the stabilizer was carried out as follows. Firstly, 2.50 g of methyl methacrylate (or methyl methacrylate/divinyl benzene) was

homogeneously dissolved in 2.50 g of octadecane, 0.02 g of CHI_3 and 0.20 g of benzoyl peroxide as oil phase. It was then added to 45 g aqueous solution containing either 1%wt of poly(vinyl alcohol) or chitosan before homogenized at 5,000 rpm for 5 minutes to prepare monomer droplets in oil in water emulsion. Thereafter, the obtained polymer suspension was subsequently transferred to a round bottom flask, sealed with a silicone rubber septum and purged with a vacuum/ N_2 cycle for five times (finally in N_2). It was finally polymerized at 80 °C for 3 hours and following at 90°C for 5 hours at a stirring rate of 500 rpm. The concentration of chitosan was varied as shown in Table 1.

Table 1 Recipes for the preparation of polymethyl methacrylate/octadecane (50:50 wt%) microcapsules prepared by microsuspension iodine transfer polymerization

Phase	Ingredients		
Oil	MMA (g)	2.50	2.25
	DVB (g)	0.00	0.25
	OD (g)	2.50	2.50
	BPO (g)	0.20	0.20
	CHI_3 (g)	0.02	0.02
Aqueous	Surfactant solution ^a (g)	45.00 ^a	45.00 ^b

Abbreviations: MMA, methyl methacrylate; OD, octadecane; BPO, benzoyl peroxide; CHI_3 , iodoform; CS, chitosan; PVA, polyvinyl alcohol

^a PVA solution 1 wt% or CS solution at 0.25, 0.50 and 1.00 wt%

^b 1 wt% of CS

2.3 Characterization of microcapsules

The microcapsules encapsulated octadecane were observed with an optical microscope (SK-100EB&SK-100ET, Seek, Seek Inter Co. Ltd., Thailand) and scanning electron microscope (JSM-6510, JEOL, JEOL Ltd., Japan) to study the morphology of the particle surface and shape, respectively. For scanning electron microscope observation, a few of dried microcapsules were placed on a nickel stub and dried before Au-coated. For the measurement of thermal properties, the microcapsules were washed with 2-propanol before dried in vacuum oven. The octadecane content in the dried washed microcapsules was determined by thermogravimetric analyzer (TGA 4000, Perkin-Elmer, USA) at a heating rate of 5 °C/min. The latent heats (ΔH_m and ΔH_c) (J/g-capsule) and the melting (T_m) and crystallization (T_c) temperatures of the encapsulated octadecane were measured with a differential scanning calorimeter (DSC 4000, Perkin-Elmer, USA) under a N_2 flow in a scanning

temperature range of -20-40 °C and at a heating/cooling rate of 5 °C/min and shown as average values of three measurements. The ΔH_m^* and ΔH_c^* (J/g-OD) were, respectively, obtained using the following equation (1) from the ΔH_m and ΔH_c and the octadecane content in each washed microcapsule (% loading) obtained from the thermogravimetric analyzer, which did not contain unencapsulated octadecane.

$$A = [B / C] \times 100 \quad \dots\dots\dots(1)$$

Where

A = ΔH_m^* and ΔH_c^* of the encapsulated octadecane in unit of joules per 1 g of encapsulated octadecane (J/g-OD)

B = ΔH_m and ΔH_c of the encapsulated octadecane in unit of joules per 1 g of microcapsule (J/g-capsule) measured with differential scanning calorimeter

C = % loading (experiment) of octadecane in the washed microcapsules measured with

thermogravimetric analyzer

The theoretical % loading of OD in the washed microcapsules was calculated by equation (2)

$$\% \text{ Loading (theory)} = [W_{\text{wax}} / (W_{\text{wax}} + W_{\text{P}})] \times 100 \quad \dots(2)$$

Where W_{wax} and W_{P} are weights of octadecane and polymethyl methacrylate, respectively, in the polymerization recipes shown in Table 1.

Encapsulation efficiency (%) of octadecane was calculated using the equation (3).

$$\text{Encapsulation efficiency (\%)} = [\% \text{ loading (experiment)} / \% \text{ loading (theory)}] \times 100 \quad \dots(3)$$

2.4 Antibacterial property

The antibacterial property of the prepared microcapsules was tested for *Staphylococcus aureus* (*S. aureus*) and *Escherichia coli* (*E.coli*) using disk-diffusion method at 35°C for 24 h.

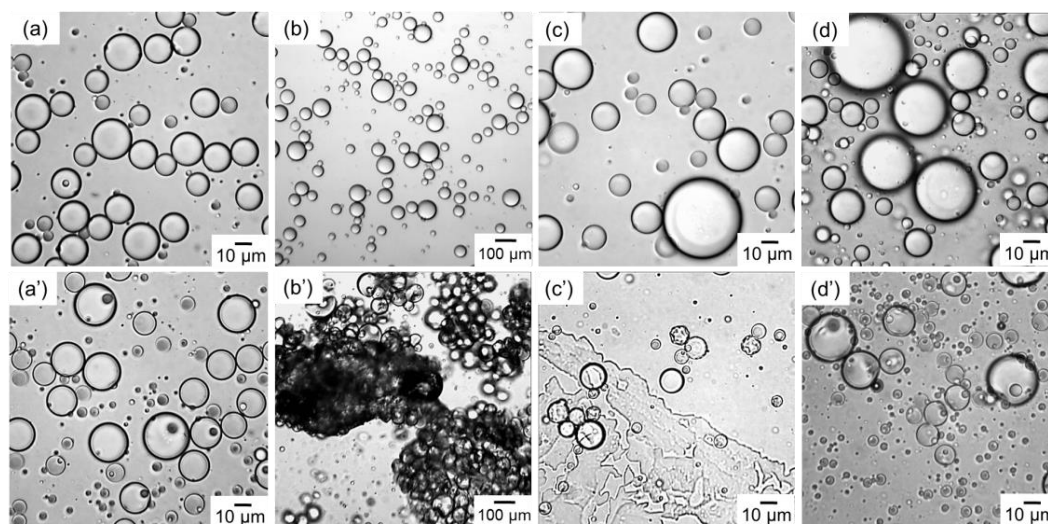


Fig. 1 Optical micrographs before (a-d) and after (a'-d') polymerization of polymethyl methacrylate/octadecane (50:50 w/w%) microcapsules prepared by microsuspension iodine transfer polymerization with 1 wt% of poly(vinyl alcohol) aqueous solution (a, a') and various concentrations of chitosan in aqueous solution (wt%): 0.25 (b, b'); 0.50 (c, c') and 1.0 (d, d')

3. RESULTS AND DISCUSSION

In general, poly(vinyl alcohol) is used as a surfactant in microsuspension polymerization. The obtained microparticle/capsules represented high colloidal stability without coalescence. In this work, chitosan was used in place of poly(vinyl alcohol) to increase antibacterial property where the various concentrations of chitosan were studied compared with poly(vinyl alcohol) as shown in Fig. 1. It was found that at all chitosan concentrations (Fig. 1 b-c), monomer droplets were spherical with micrometer-sized. After polymerization, the

polymethyl methacrylate/octadecane microcapsules were unstable and broken in both cases of 0.25 (Fig. 1b') and 0.50 (c') wt% of chitosan. In addition, most of the obtained microcapsules (~75% based on monomer/octadecane in the recipe) were coagulated as shown in Fig. 2a and b. After left overnight, a lot of unencapsulated octadecane dispersed in the aqueous medium (Fig. 2c) whereas octadecane was not detected by thermogravimetric analyzer (Fig. 2d) in the remained polymer particle precipitated in the bottom. It may be due to insufficient chitosan amount to maintain the microcapsule stability. However, such phenomenon was improved by the

increase of chitosan to 1 wt% (Fig. 1d') in which the obtained polymethyl methacrylate/octadecane microcapsules shape was similar to those of using poly(vinyl alcohol) 1 wt% (Fig. 1a'). In addition, microsuspension iodine transfer polymerization represented high performance to reduce free polymethyl methacrylate particles nucleated in aqueous medium. The aqueous medium of the obtained polymethyl methacrylate/octadecane microcapsule using 1 wt% of chitosan was changed from milky (Fig. 3a) to transparent (Fig. 3b) after centrifugation at about 3,000 rpm. It accorded with the previous articles [11, 14] where most of the obtained polymethyl methacrylate/octadecane microcapsule having total density lower than that of the water floated on the top of the suspension.

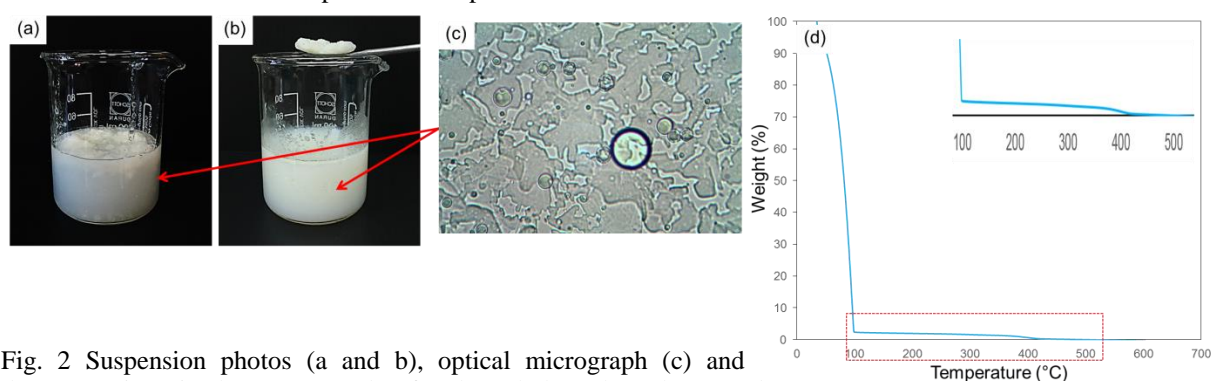


Fig. 2 Suspension photos (a and b), optical micrograph (c) and thermogravimetric thermogram (d) of polymethyl methacrylate/octadecane microcapsules prepared by microsuspension iodine transfer polymerization using various concentrations of chitosan in aqueous medium (wt%): 0.25 (a) and 0.50 (b)

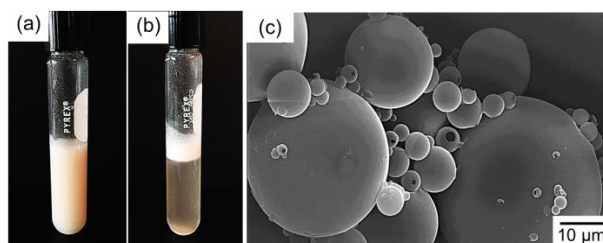


Fig. 3 Suspension photos before (a) and after (b) centrifugation at 3,000 rpm for 15 minutes of polymethyl methacrylate/octadecane microcapsules and scanning electron micrograph (c) polymethyl methacrylate/octadecane microcapsules washed with 2-propanol

The monomer droplets of methyl methacrylate/divinyl benzene/octadecane were spherical (Fig. 4a) similar with methacrylate/octadecane monomer droplets. After polymerization, the obtained poly(methyl methacrylate-divinyl benzene)/octadecane microcapsules represented nonspherical shape with a big dent (Fig. 4b and c). The dent formation is due to the encapsulated octadecane volume shrinkage based on the decreasing of temperature

However, after washing polymethyl methacrylate/octadecane microcapsules with 2-propanol (Fig. 3c), some microcapsules were broken and having a hole on their surface in which reduced the encapsulation efficiency (~80%) of octadecane. This finding may due to some of chitosan having high molecular weight absorbed on some microcapsule surfaces as chitosan-rich surface obstructed the polymethyl methacrylate chains to adsorb at the interface. The shell strength then decreased giving a hole after washing. Therefore, to improve the polymer shell strength, polymethyl methacrylate was then copolymerized with 10 wt% related to monomer of crosslinking monomer as divinyl benzene.

from 90 °C (polymerization temperature) to room temperature. The polymer shell with complete enveloping octadecane core would not withstand the external pressure leading to the formation of dent on their surfaces. In contrast, polymethyl methacrylate/octadecane microcapsules can reduce the external pressure via a hole where they can maintain their shapes without any dents. Therefore, the encapsulation efficiency (~100%) was improved by copolymer shell where the exited octadecane floated on the top of the suspension after polymerization was not observed.

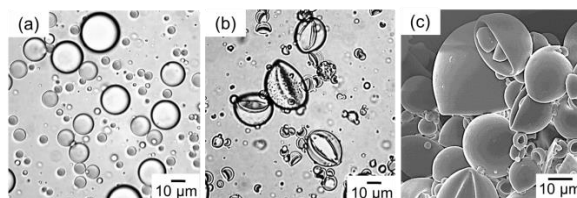


Fig. 4 Optical micrographs of (a) monomer droplets and (b) poly(methyl methacrylate-divinyl benzene)/octadecane microcapsules and scanning electron micrograph of poly(methyl methacrylate-divinyl benzene)/octadecane after washing with 2-propanol

The degradation temperatures of bulk octadecane, poly(methyl methacrylate-divinyl benzene) and the encapsulated octadecane in the poly(methyl methacrylate-divinyl benzene) microcapsules were observed by thermogravimetric analyzer as shown in Fig. 5. The decomposition temperatures of poly(methyl methacrylate-divinyl benzene)/octadecane microcapsule (Fig. 5b) were shown in two respective steps which were octadecane core (130-260°C) and poly(methyl methacrylate-divinyl benzene) shell (220-430°C), respectively. The degradation of bulk octadecane (Fig. 5a) at 140-250°C was closed to that of the encapsulated octadecane. The thermogravimetric thermograms confirmed that octadecane existed in the prepared microcapsules in which about 50% loading of octadecane in poly(methyl methacrylate-divinyl benzene)/octadecane was obtained. In addition, it was close to the theoretical value (50% for 50:50 of monomer:octadecane ratio). This indicates that high encapsulation efficiency (ca. 100%) was obtained.

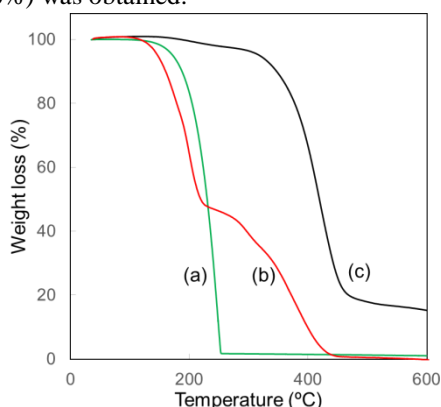


Fig. 5 Thermogravimetric thermograms of bulk octadecane (a), poly(methyl methacrylate-divinyl benzene)/octadecane microcapsules using methyl methacrylate:divinyl benzene ratio of 90:10 (w/w%) (b) and poly(methyl methacrylate-divinyl benzene) particles (c) prepared by micro-suspension iodine transfer polymerization

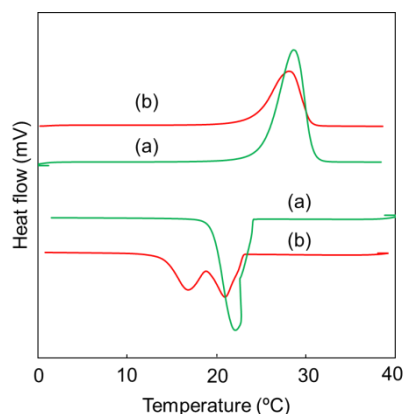


Fig. 6 Differential scanning calorimeter thermograms of bulk octadecane (a) and poly(methyl methacrylate-divinyl benzene)/octadecane microcapsules (b)

benzene)/octadecane microcapsules using methyl methacrylate:divinyl benzene ratio of 90:10 (w/w%) prepared by micro-suspension iodine transfer polymerization (b)

The latent heats of bulk octadecane (J/g) (Fig. 6a) and the encapsulated octadecane (J/g-sample) (Fig. 6b) were obtained from the heating/cooling peak areas of differential scanning calorimeter thermograms at T_m and T_c , respectively. The latent heats ($\Delta H_m^* = 234$ J/g-OD and $\Delta H_c^* = 236$ J/g-OD) of the encapsulated octadecane calculated from equation 1 were quite closed to those of bulk octadecane ($\Delta H_m^* = 233$ J/g-OD and $\Delta H_c^* = 234$ J/g-OD). Because main polymer shell is a hydrophilic polymer as polymethyl methacrylate containing only 10 wt% of hydrophobic polymer as divinyl benzene, it would increase the phase separation between polymer shell and octadecane core where the encapsulated octadecane behaved similar to bulk octadecane.

Antibacterial property of the obtained poly(methyl methacrylate-divinyl benzene)/octadecane microcapsules using chitosan as the stabilizer was performed on a bacterial culture of *S. aureus* and *E. coli* by measuring the size of the inhibition zones. It was found that a few antimicrobial activity of poly(methyl methacrylate-divinyl benzene)/octadecane microcapsule was observed based on the small size (2 millimeters) of the resulting inhibition zones of both bacteria. This indicates that amino groups in chitosan chains represented low performance of antibacterial property. Therefore, in the future work, amino groups in chitosan chains will be functionalized to be ammonium salt having high performance antibacterial activity and used as the surfactant in micro-suspension iodine transfer polymerization.

4. CONCLUSION

The nonspherical shape with a dent poly(methyl methacrylate-divinyl benzene) microcapsules containing octadecane was prepared by micro-suspension iodine transfer polymerization using chitosan as a stabilizer without any coagulation. Using polymethyl methacrylate as a polymer shell, microcapsules with a hole were obtained resulting in about 80% encapsulation efficiency. The encapsulation efficiency (100%) was improved by poly(methyl methacrylate-divinyl benzene) copolymer shell. The latent heats of the encapsulated OD were close to those of bulk octadecane. The antibacterial activity of chitosan absorbed on the microcapsule surface was still low (2 millimeters inhibition zone) which needed to be improved in the future work.

ACKNOWLEDGEMENTS

This study was supported by the RMUTT

annual government statement of expenditure in 2016 (NRMS No. 2560A16502037 given to P.C., A.C. and W.S.)

5. REFERENCES

- [1] Sánchez-Silva L, Rodríguez J F, Romero A, and Sánchez P, "Preparation of coated thermo-regulating textiles using Rubitherm-RT31 microcapsules," *J Appl Polym Sci*, vol. 124, 2012, pp. 4809-4818.
- [2] Sánchez P, Sánchez-Fernandez M V, Romero A, Rodríguez J F, and Sánchez-Silva L, "Development of thermo-regulating textiles using paraffin wax microcapsules," *Thermochim. Acta* vol. 498, 2010, pp. 16-21.
- [3] Sharma A, Tyagi V V, Chen C R, and Buddhi D, "Review on thermal energy storage with phase change materials and applications," *Renew Sust Energy Rev*, vol. 13, 2009, pp. 318-345.
- [4] Namwong S, Islam M Z, Noppalit S, Tangboriboonrat P, Chaiyasat P, and Chaiyasat A, "Encapsulation of octadecane in poly(divinylbenzene-co-methyl methacrylate) using phase inversion emulsification for droplet generation," *Journal of Macromolecular Science, Part A: Pure and Applied Chemistry*, vol. 53, 2016, pp. 11-17.
- [5] Namwong S, Noppalit S, Okubo M, Moonmungmee S, Chaiyasat P, and Chaiyasat A, "Latent Heat Enhancement of Paraffin Wax in Poly(divinylbenzene-co-methyl methacrylate) Microcapsule," *Polymer - Plastics Technology and Engineering*, vol. 54, 2015, pp. 779-785.
- [6] Sánchez L, Sánchez P, de Lucas A, Carmona M, and Rodríguez J F, "Microencapsulation of PCMs with a polystyrene shell," *Colloid and Polymer Science*, vol. 285, 2007, pp. 1377-1385.
- [7] Sánchez-Silva L, Rodríguez J F, Romero A, Borreguero A M, Carmona M, and Sánchez P, "Microencapsulation of PCMs with a styrene-methyl methacrylate copolymer shell by suspension-like polymerisation," *Chem Eng J* vol. 157, 2010, pp. 216-222.
- [8] Supatimusro D, Promdsorn S, Thipsit S, Boontung W, Chaiyasat P, and Chaiyasat A, "Poly(divinylbenzene) Microencapsulated Octadecane for Use as a Heat Storage Material: Influences of Microcapsule Size and Monomer/Octadecane Ratio," *Polymer - Plastics Technology and Engineering*, vol. 51, 2012, pp. 1167-1172.
- [9] Chaiyasat A, Waree C, Songkhamrod K, Sirithip P, Voranuch V, and Chaiyasat P, "Preparation of polydivinylbenzene/natural rubber capsule encapsulating octadecane: Influence of natural rubber molecular weight and content," *Express Polymer Letters*, vol. 6, 2012, pp. 70-77.
- [10] You M, Wang X, Zhang X, Zhang L, and Wang J, "Microencapsulated n-Octadecane with styrene-divinylbenzene co-polymer shells," *J Polym Res*, vol. 18, 2011, pp. 49-58.
- [11] Chaiyasat P, Noppalit S, Okubo M, and Chaiyasat A, "Innovative synthesis of high performance poly(methyl methacrylate) microcapsules with encapsulated heat storage material by microsuspension iodine transfer polymerization (ms ITP)," *Solar Energy Materials and Solar Cells*, vol. 157, 2016, pp. 996-1003.
- [12] Sanchez-Silva L, Tsavalas J, Sundberg D, Sanchez P, and Rodriguez J F, "Synthesis and characterization of paraffin wax microcapsules with acrylic-based polymer shells," *Ind Eng Chem Res*, vol. 49, 2010, pp. 12204-12211.
- [13] Chaiyasat P, Noppalit S, Okubo M, and Chaiyasat A, "Do encapsulated heat storage materials really retain their original thermal properties?," *Physical Chemistry Chemical Physics*, vol. 17, 2015, pp. 1053-1059.
- [14] Chaiyasat P, Namwong S, Okubo M, and Chaiyasat A, "Synthesis of micrometer-sized poly(methyl methacrylate) particles by microsuspension iodine transfer polymerization (ms ITP)," *RSC Advances*, vol. 6, 2016, pp. 95062-95066.
- [15] Fernandes J C, Tavaría F K, Soares J C, Ramos Ó S, João Monteiro M, Pintado M E, *et al.*, "Antimicrobial effects of chitosans and chitooligosaccharides, upon *Staphylococcus aureus* and *Escherichia coli*, in food model systems," *Food Microbiology*, vol. 25, 2008, pp. 922-928.
- [16] Cheng X, Ma K, Li R, Ren X, and Huang T S, "Antimicrobial coating of modified chitosan onto cotton fabrics," *Appl. Surf. Sci.*, vol. 309, 2014, pp. 138-143.
- [17] Pangestuti R and Kim S-K, "Neuroprotective Properties of Chitosan and Its Derivatives," *Marine Drugs*, vol. 8, 2010, p. 2117.
- [18] Yang E-J, Kim J-G, Kim J-Y, Kim S C, Lee N H, and Hyun C-G, "Anti-inflammatory effect of chitosan oligosaccharides in RAW 264.7 cells," *Central European Journal of Biology*, vol. 5, 2010, pp. 95-102.

KONDO THEORY FOR SPHERICAL SHELL TECTONICS

Kazuhei Kikuchi^{1,2*} and Hiroyuki Nagahama²

¹Research Center for Earthquake Prediction, Disaster Prevention Research Institute, Kyoto University, Japan;

²Department of Earth Science, Graduate School of Science, Tohoku University, Japan;

*K. Kikuchi's present affiliation is Kyoto University.

ABSTRACT

The buckling phenomenon of a flat or spherical shell lithosphere (tectonic plate) has been investigated in previous research. However, previous research cannot give us a curvature effect in the buckling phenomenon. Kondo applied Riemannian geometry to the yielding or buckling of curved materials. When the Riemannian manifold (V_n dimensional manifold) with a nonzero Euler-Schouten curvature tensor is manifested in the enveloping manifold (Euclid space: V_m dimensional manifold), the included Riemannian manifold (dimension V_n) protrudes into the enveloping manifold (dimension V_m). The curvature effect for the buckling phenomenon of materials can be formulated by a force-balance equation from mechanics and the Euler-Schouten curvature tensor from differential geometry. In this paper, using the Euler-Schouten curvature tensor from differential geometry, the authors derive a formulation for the buckling phenomenon with the curvature effect for a spherical shell lithosphere as a buckling equation with high-order strain for lithosphere deformation.

Keywords: Buckling phenomenon; Spherical shell lithosphere; Riemannian geometry; Euler-Schouten curvature tensor

INTRODUCTION

The mechanism of flat or spherical shell lithosphere deformation is presented by using buckling theory [e.g., 1–4]. Yamaoka et al. [5] pointed out the buckling phenomena of the subducting lithosphere due to the sphericity of the earth. Moreover, Fukao et al. [6] and Yamaoka [7] denoted the similarity of lithosphere buckling with cylindrical buckling of spherical shells through experiments and numerical simulations based on the nonlinear finite element method. Kikuchi and Nagahama [8] found a new linear relationship between the Batdorf parameter and normalized hydrostatic pressure along the bottom circumferential edge of a hemisphere in spherical shell tectonics. The Batdorf parameter for a subducting lithosphere is equivalent to the length of the slab and is also related to the wavelength (length of the island arc) of buckling. However, previous research has not revealed the buckling equation with high-order strain for the curvature of the lithosphere.

The buckling equation with the high-order strain effect has been addressed in the field of engineering science [9], in which Riemannian geometry has been applied to the yielding and buckling of curved material. Kondo used the concept of dimension protrusion, in which buckling in the two dimensions of a flat plate can occur in three-dimensional space (Fig. 1). In general, when the Riemannian manifold of dimension V_n with a nonzero Euler-Schouten curvature tensor exists in

the enveloping manifold (Euclid space) of dimension V_m , the included Riemannian manifold of V_n protrudes into the enveloping manifold of dimension V_m . From the Euler-Schouten curvature tensor and the force-balance equation, material science is exhibited by the use of the curvature effect for the buckling phenomenon in differential geometry. In this paper, the authors derive the buckling phenomenon with the curvature effect for a spherical shell lithosphere. The authors can apply the Euler-Schouten tensor to the buckling equation with high-order strain for lithosphere deformation. Using deformation theory based on Riemannian space for the buckling system of the flat plate and spherical shell, the equation for the lithosphere deformation and buckling can be derived from the Euler-Schouten curvature tensor. Therefore, this curvature tensor is an important tensor for lithosphere deformation.

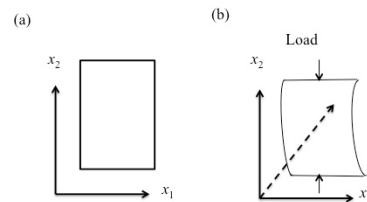


Fig. 1 Two-dimensional pre- and post-buckling of the flat plate. (a) Pre-buckling of material is in two dimensions. (b) Post-buckling of material is in three dimensions.

PREVIOUS BUCKLING THEORY

The authors briefly introduce the previous buckling theory used in earth science. The mechanism of geological folding (flat crust buckling) was described by use of buckling theory [1]. First, the authors introduce the balance equation of the flat crust as follows (Fig 2):

$$\frac{dV}{dx} = -q(x), \quad (1)$$

$$\frac{dM}{dx} = V, \quad (2)$$

where V is the shearing force, x is the coordinate of the system, $q(x)$ is the load, and M is the moment. Moreover, the authors can derive a relationship between the load and moment using Eq.(1) and Eq.(2),

$$\frac{d^2M}{dx^2} = -q(x). \quad (3)$$

Then, the authors can use the proportion of curvature to describe the flexure moment and curvature equations,

$$EI\kappa = M, \quad (4)$$

$$\kappa = -\frac{d^2w}{dx^2}, \quad (5)$$

where E is Young's modulus, I is the second moment, κ is curvature, and w is deflection. Next, from Eqs. (1)–(5),

$$EI \frac{d^2w}{dx^2} = -M, \quad (6)$$

$$EI \frac{d^3w}{dx^3} = -V, \quad (7)$$

$$EI \frac{d^4w}{dx^4} = q(x). \quad (8)$$

Eq. (8) is the crust buckling equation. If the crust undergoes axial compressive force, the authors can write the equation as follows:

$$EI \frac{d^4w}{dx^4} + P \frac{d^2w}{dx^2} = q(x), \quad (9)$$

where P is the axial compressive force.

The mechanism of spherical shell lithosphere deformation is presented, assuming buckling theory [e.g., 2–4]. Turcotte and Schubert [4] showed that lithosphere deformation is given by:

$$D \frac{d^4w}{dx^4} + P \frac{d^2w}{dx^2} + (\rho_c + \rho_m)ghw = q(x), \quad (10)$$

where D is the shear modulus, ρ_c is crust density, ρ_m is mantle density, g is gravity, and h is height (Fig. 3). However, previous studies have not demonstrated a high-order curvature effect in the buckling phenomenon.

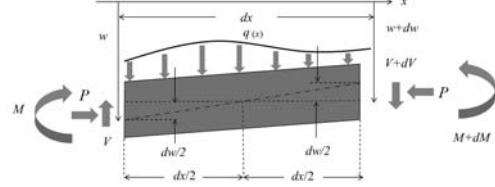


Fig. 2 Buckling of flat crust deformation, where x is the coordinate of the system, $q(x)$ is the load, w is deflection, M is moment, P is axial compressive force, and V is shearing force.

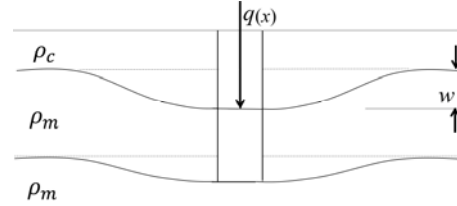


Fig. 3 Buckling of lithosphere deformation, where ρ_c is the crust density, ρ_m is mantle density, w is deflection, and $q(x)$ is the applied load [modified from 4].

KONDO THEOREM

In a previous paper [9], Kondo provided some important information regarding materials science. By using differential geometry in the study of the buckling of plate and shell, Kondo [9] proceeded as follows: The object was placed in Cartesian coordinates and m -dimensional Riemannian space (envelope space V_n ; i, j are frames of reference in Fig. 4).

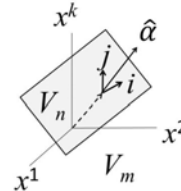


Fig. 4 Riemannian manifold of dimension V_n with a nonzero Euler-Schouten curvature tensor in the enveloping manifold (Euclid space) of V_m , with coordinates $x^{(1,2,\dots,k)}$, and frames of reference i, j . $\hat{\alpha}$ is the normal vector of V_n .

Moreover, the deformation of the normal direction α of the object can be expressed using strain and Christoffel symbols

$$y^{\alpha}_{;ij} = O(\varepsilon), \quad (11)$$

$$\left\{ \begin{matrix} k \\ i \ j \end{matrix} \right\} = O(\varepsilon), \quad (12)$$

where y is the deflection in V_n space, and $O(\varepsilon)$ is order ε of the Landau symbol. In this case, the object deformation is expressed by normal direction ($\hat{\alpha}$):

$$y^{\hat{\alpha}}_{;k} = O(\varepsilon). \quad (13)$$

Then, the subspace of the enveloping protrusion (V_n to V_m space protrusion) is defined by the Euler-Schouten curvature tensor $H^{\hat{\alpha}}_{ij}$ [10]:

$$H^{\hat{\alpha}}_{ij} (\equiv y^{\hat{\alpha}}_{;ij}) = \frac{\partial^2 y^{\hat{\alpha}}}{\partial x^i \partial x^j} - y^{\hat{\alpha}}_{;k} \left\{ \begin{matrix} k \\ i \ j \end{matrix} \right\}. \quad (14)$$

The second term of the components of the curvature tensor is $O(\varepsilon^2)$ order. Hence, the authors omitted the second term in the small deformation theory:

$$H^{\hat{\alpha}}_{ij} \approx \frac{\partial^2 y^{\hat{\alpha}}}{\partial x^i \partial x^j}. \quad (15)$$

The approximate expression is compared to expression (11). It is configured by omitting a very small amount. Metrics are defined by the following:

$$g_{ij} = \delta_{ij} + O(\varepsilon), \quad (16)$$

where g_{ij} and δ_{ij} are matrix elements. The authors use the equation of equilibrium of forces and equations of equilibrium with a small strain,

$$(J - F)^i = \frac{\partial \Sigma^{ij}}{\partial x^j}, \quad (17)$$

$$(L - \varrho)^{\hat{\alpha}} = \frac{\partial^2 G^{\hat{\alpha}ij}}{\partial x^i \partial x^j} + H^{\hat{\alpha}}_{ij} \Sigma^{ij}, \quad (18)$$

where J is the tangential force per unit m volume, F is the difference in the tangential frictions at the upper and lower boundaries, Σ^{ij} is the stress components in the shell space, L is the normal force per unit m volume, ϱ is the difference in the tangential frictions at the upper and lower boundaries, and $G^{\hat{\alpha}ij}$ is the Euler-Schouten curvature contravariant tensor.

The coordinate transformation law is expressed by:

$$G^{ij}_{\alpha} = B^{\cdot i j k l}_{\alpha \beta} H^{\beta}_{\cdot k l}, \quad (19)$$

$$G^{\alpha ij} = \alpha^{\alpha \beta} G^{\cdot ij}_{\beta}, \quad (20)$$

$$B^{\alpha \cdot i j k l}_{\beta} = \alpha^{\alpha \gamma} B^{\cdot i j k l}_{\gamma \beta}, \quad (21)$$

where B is the contravariant tensor in n -space and β and l are indices. From Eq. (15), the balance equations (Eqs. 17–18) and the coordinate transformation (Eqs. 19–21), the authors can write:

$$(L - \varrho)^{\hat{\alpha}} = \frac{\partial^2}{\partial x^i \partial x^j} (B^{\hat{\alpha} \cdot i j k l}_{\beta} \frac{\partial^2 y^{\beta}}{\partial x^k \partial x^l}) + \frac{\partial^2 y^{\hat{\alpha}}}{\partial x^i \partial x^j} \Sigma^{ij}. \quad (22)$$

Moreover, when the material is isotropic, the B^{ijkl} tensor can be expressed with the constant B ,

$$B \Delta \Delta y + \Sigma^{ij} \frac{\partial^2 y}{\partial x^i \partial x^j} = L - \varrho. \quad (23)$$

DISCUSSION

The authors consider the relationship between previous research and Kondo theory. DiDonna [11] presented the buckling equation for an elastic sheet,

$$\frac{E h^3}{12(1 - \nu^2)} \frac{d^2}{dx^2} \left(\frac{d^2 w}{dx^2} \right) - \frac{\partial}{\partial x} \left(\sigma_{ij} \frac{\partial w}{\partial x} \right) = P_e, \quad (24)$$

where h is thickness, ν is Poisson's ratio, σ_{ij} is the stress, and P_e is an external pressure field. The curvature tensor can be written as the derivative of a continuous curvature potential f [11]

$$C_{ij} = \frac{\partial}{\partial x} \frac{\partial f}{\partial x}, \quad (25)$$

where C_{ij} is the curvature tensor. Here the potential f is not identical to the local function w used above, but is approximately equal to w for nearly flat surfaces [11]. The parameter C_{ij} is the Euler-Schouten curvature tensor. Hence, this buckling equation for an elastic sheet is a low-order strain equation. Furthermore, the authors write σ_{ij} in terms of the stress potential χ

$$\sigma_{ij} = \epsilon_{ik} \epsilon_{jl} \frac{\partial}{\partial x} \frac{\partial \chi}{\partial x}, \quad (26)$$

where ϵ_{ik} and ϵ_{jl} are antisymmetric tensors. In terms of the potentials χ and f , the von Karman equations [12] can be expressed by

$$D \nabla^4 f = [\chi, f] + P_e, \quad (27)$$

$$\nabla^4 \chi = -\frac{1}{2}[f, f]. \quad (28)$$

This von Karman equation is a generalized buckling equation (23) for low-order strains. Moreover, the buckling can be described by a simplification of Eq. (9). It is apparent that Eq. (23) is the extended two-dimensional version equation of Eq. (9) with constant vertical forces (i.e., $q = \text{const.}$) and without body forces. It is also apparent that a two-dimensional version equation (e.g. [4]) is included in the kind of equations reduced from Eq. (23). Thus, various kinds of geological deformations can be described by the simplification of the generalized buckling equation. For example, the mechanism of geological folding occurs by plate motion. In this case, three-dimensional flat plate buckling (geological folding) can be described by Eq. (23), the buckling equation of the flat plate.

The buckling phenomena of the subducting lithosphere due to the sphericity of the earth have been studied in the context of spherical shell tectonics [5–7]. The slab length is approximately proportional to the arc length, and the lithosphere thickness is related to the lithosphere age. Moreover, the length of the deformable portion of the shell corresponds to the length of the subducting slab. The lithospheres defined by the length of the Wadati-Benioff zone and the thickness of the shell which corresponds to the effective elastic thickness of the lithosphere. From the dataset of geometrical parameters for subducting lithosphere, Kikuchi and Nagahama [8] presented a new linear relationship between the normalized hydrostatic pressure and the Batdorf parameter as the dimension of the shell (i.e., the flatness). Therefore, in this case, Eq. (23) becomes the buckling equation of the spherical shell lithosphere as a three-dimensional Riemannian manifold (V_n).

CONCLUSIONS

Buckling of the plate and shell in the field of materials science is considered, using differential geometry [9]. From the Euler-Schouten curvature tensor of the shell as a Riemannian manifold and the force-balance equation for the shell, the authors derived a unified theory for buckling of spherical shells. When the Riemannian manifold of dimension V_n with a nonzero Euler-Schouten curvature tensor exists in an enveloping manifold (Euclid space) of dimension V_m , the including Riemannian manifold of V_n protrudes into the enveloping manifold of dimension V_m . From the Euler-Schouten curvature tensor on the shell as a Riemannian manifold and the force-balance equation

for the shell, the authors derived a unified theory for buckling of flat plates or spherical shells in Eq. (23).

ACKNOWLEDGEMENTS

One of the authors (K.K.) is supported by the Institute for International Advanced Research and Education, Tohoku University and the Disaster Prevention Research Institute, Kyoto University. This work was supported by JSPS KAKENHI (15J00934). The authors would like to thank Editage for English language editing.

REFERENCES

- [1] Biot MA, Ode H, and Roever W, “Theory of folding of stratified viscoelastic media and its implications in tectonics and orogenesis”, *Bull. Geol. Soc. Am*, Vol. 72, November 1961, pp. 1595–1620.
- [2] Tanimoto T, “Bending of spherical lithosphere-axisymmetric case”, *Geophys. J. Int.*, Vol. 129, May 1997, pp. 305–310.
- [3] Tanimoto T, “State of stress within a bending spherical shell and its implications for subducting lithosphere”, *Geophys. J. Int.*, Vol. 134, July 1998, pp.199–206.
- [4] Turcotte DL, and Schubert G, “Geodynamics 3rd ed.”, Cambridge: Cambridge University Press, 2014.
- [5] Yamaoka K, Fukao Y, and Kumazawa M, “Spherical shell tectonics: Effects of sphericity and inextensibility on the geometry of the descending lithosphere”, *Rev. Geophys.*, Vol. 24, February 1986, pp. 27–53.
- [6] Fukao Y, Yamaoka K, and Sakurai T, “Spherical shell tectonics: buckling of subducting lithosphere”, *Phys. Earth Planet. Inter.*, Vol. 45, January 1987, pp. 59–67.
- [7] Yamaoka K, “Spherical shell tectonics: On the buckling of the lithosphere at subduction zones”, *Tectonophysics*, Vol. 147, April 1988. pp. 179–191.
- [8] Kikuchi K, and Nagahama H, “Spherical shell tectonics: Batdorf parameter of subducting lithosphere”, *Asia Oceania Geosciences Society 2016 Abstract*, AOGS 13th Annual meeting, SE18-D4-PM2-P-022.
- [9] Kondo K, “Theory of metaphorical plates and shells”, *RAAG memoirs* Vol. I, Kondo Ed. Gakujutsu Bunken Fukyu-kai, 1955, pp. 47–60.
- [10] Schouten JA, *Ricci-calculus*. Berlin: Springer-Verlag, 1954.
- [11] DiDonna BA, “Scaling of the buckling transition of ridges in thin sheets”, *Phys. Rev. E*, Vol. 66, July 2002, 016601.
- [12] von Karman T, “Collected Works of Theodore von Karman”, London: Butterworths Scientific Publications, 1956.

PHOTOELECTROCATALYTIC CONVERSION OF CO₂ INTO VALUE-ADDED ORGANIC COMPOUNDS USING Cu₂O PHOTOCATHODE

Pattranit Thongthep¹, Chatchai Ponchio^{1,2*}

¹Department of Chemistry, Faculty of Science and Technology, Rajamangala University of Technology Thanyaburi, Pathumtani 12110, Thailand

²Advance Materials Design and Development (AMDD) Research Unit, Institute of Research and Development, Rajamangala University of Technology Thanyaburi, Pathumtani 12110, Thailand

*Corresponding Author; E-mail address: chatchai@rmutt.ac.th

ABSTRACT

The global warming from CO₂ emission effect and finding renewable energy are two major issues in today's environmental and energy problems. The conversion of CO₂ into value-added chemicals to achieve an energy-saving and low-carbon economy is needed to be developed. Photoelectrocatalytic technology is one of the most alternative ways to reduce CO₂ under the advantage of high efficiency and inexpensive resembles of the artificial photosynthesis process. This research focuses on photoelectrocatalytic reducing CO₂ solution into organic compounds at a Cu₂O photocathode. The Cu₂O electrode fabrication was developed by electrochemical deposition method to enhance the reduction catalytic activity under visible light irradiation. The effects of light intensity, applies potential, pH and catalytic mechanism parameters were studied in order to enhance the CO₂ conversion to organic compounds efficiency. Carbonyl and methanol compounds were produced at the applied potential of 0.2 V and -0.4 V (vs. Ag/AgCl), respectively with the suitable pH in a solution of carbonate under visible light irradiation. This results illustrate that an applying potential and pH adjustment are the key factors of organic compounds production. This developed photoelectrocatalytic cell shows that the interesting method for reducing CO₂ from air pollutant and also producing value-added chemicals for alternative energy supplying.

Keywords: Photoelectrocatalytic cell, CO₂ reduction, Organic compounds, Cu₂O, Electrodeposition

1. INTRODUCTION

The global warming is main problems of the world by the effect of CO₂ emission to an environment from the combustion of industrial plants or fossil fuel [1]. The methods to convert CO₂ into value added production has attractive been developed to solve the air pollutant and value creation of waste. There are many methods to convert a CO₂ compound into a fuel or a valuable chemical especially photocatalytic, electrocatalytic and photoelectrocatalytic methods [2-4]. The photoelectrocatalytic method has been attracted with many advantages of reducing the recombination effect of the photocatalyst and using low bias potential than the electrocatalytic method [5]. The performance of the photoelectrocatalytic method is depended on the semiconductor selection and the efficiency of semiconductor deposition on the substrate. Cu₂O has been selected to develop for several reduction reaction applications with the narrow band gap energy and high negative potential of conduction band [6]. Recently Cu₂O photocathodes were also applied in

photoelectrocatalytic CO₂ reduction with good properties for hydrocarbon formation [4]. The photocatalytic activity of Cu₂O photoelectrode is also related to the efficiency of semiconductor deposition on the substrate. The electrodeposition is one of the most attractive methods to deposit Cu₂O on the substrate which the advantage of simple, rapid methods, and suitable to scaling up for the large scale applications. This research is developed the electrodeposition method of the Cu₂O semiconductor on fluorine-doped tin oxide (FTO) conductive glass by using cyclic voltammetry deposition method (CVD). The developed FTO/Cu₂O photoelectrode was used to reduce CO₂ solution into organic carbonyl and methanol compounds.

2. EXPERIMENTAL

2.1 Preparation of FTO/Cu₂O electrode

FTO/Cu₂O electrode fabrication was developed by cyclic voltammetry deposition method (FTO/Cu₂O (CVD)) which is a new method for Cu₂O deposited on FTO substrate. The electrochemical cell

containing three electrodes system consist of FTO substrate as a working electrode, Ag/AgCl as a reference electrode and Pt as a counter electrode that immersed in the electrolyte solution of 0.01 M $\text{Cu}(\text{NO}_3)_2$ and 0.1 M KNO_3 . The potential range in cyclic voltammetry mode at -0.5 V to 0.5 V for 20 cycles, scanning rate 50 mV/s and keep the temperature of an electrolyte at 55 °C were performed with the optimum condition for FTO/ Cu_2O preparation. The FTO/ Cu_2O (CVD) was compared with the previous research of fix potential deposition method (FTO/ Cu_2O (FPD)) by considering the photoelectrocatalytic reduction properties [6].

2.2 Characterization and photoelectrocatalytic properties of FTO/ Cu_2O electrodes study

An optical absorption of the FTO/ Cu_2O electrodes were studied by UV-Vis spectrophotometer (Shimadzu, UV-1601) in the wavelength range of 200 – 1,000 nm. The photoelectrocatalytic performance of FTO/ Cu_2O photocathodes were performed by measure the photocurrent response from water reduction at the applied potential of -0.2 V (vs. Ag/AgCl) in 0.1 M Na_2SO_4 solution under visible light irradiation. Electrochemical impedance spectroscopy (EIS) with VersaSTAT3 (Princeton Applied Research, Inc.) was introduced to study the charge transfer resistant of electrode surface which carried out under the frequency range from 100 kHz to 0.1 Hz with -0.2 V.

2.3 Photoelectrocatalytic conversion of CO_2 to carbonyl compound study

The photoelectrocatalytic cell for CO_2 compound conversion to carbonyl compound study was performed by using the FTO/ Cu_2O electrode as working electrode, Ag/AgCl as a reference electrode and Pt wire as a counter by using an amperometry mode with VersaSTAT3 (Princeton Applied Research, Inc.). The effect of bias potential, pH of electrolyte and the intensity of light were studied with the optimum condition for highest photoreduction current of the fabricated FTO/ Cu_2O electrode. The three electrodes were immersed in the $\text{Na}_2\text{CO}_3/\text{NaHCO}_3$ buffer solution which used as the CO_2 saturated solution to study the CO_2 conversion to carbonyl compounds. UV-Vis spectrophotometer was used to confirm carbonyl compound production at the wavelength (λ) of 280 nm [4, 7].

2.4 Photoelectrocatalytic conversion of CO_2 to methanol (MeOH) compound study

The experimental was set up similar to the carbonyl compound production process except for the bias potential and electrolyte solution. 0.1 M Na_2CO_3 solution was performed as the saturated CO_2 solution

which used to study the CO_2 conversion to methanol compound. The cyclic voltammetry technique was used to determine the methanol production at the potential range of -0.5 V to 0.5 V (vs Ag/AgCl) using Pt wires as working and counter electrode [8].

3. RESULTS AND DISCUSSION

3.1 Characterization and photoelectrocatalytic properties of the fabricated FTO/ Cu_2O electrodes

3.1.1 Absorption properties

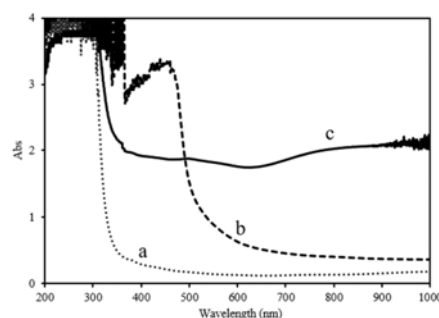


Fig. 1. UV-Vis spectra of (a) FTO and the FTO/ Cu_2O films prepared by different method of (b) FPD (c) CVD.

Fig. 1 shows that the UV-Vis spectra comparison of FTO/ Cu_2O prepared by CVD and FPD method. The absorption edge of FTO/ Cu_2O (FPD) electrode was set at 650 nm corresponding to the band gap of 2.2 eV. While the absorption of FTO/ Cu_2O (CVD) electrode was red shifted to 700 nm indicates that the narrower band gap corresponding to the higher visible light absorption properties.

3.1.2 Photoelectrocatalytic activity

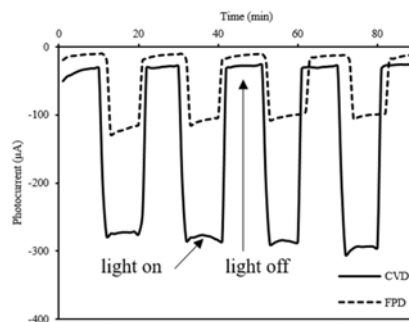


Fig. 2. Photocurrent responses of FTO/ Cu_2O electrodes under the chopped visible light illumination.

The photocurrent response of FTO/ Cu_2O electrodes from water reduction at the applied potential of -0.2V vs Ag/AgCl and under the chopped

visible light illumination were operated to study the photoelectrocatalytic activity of photoelectrode. Fig. 2 shows that the photocurrent of the FTO/Cu₂O electrode prepared by CVD method higher than that the FPD method about 2 times. The enhancing photocatalytic activity of FTO/Cu₂O (CVD) is related to a narrower band gap energy properties caused to the increasing of the photoelectron generated efficiently to enhance water reduction efficiency.

3.1.3 Charge transfer resistant properties

The electrochemical impedance spectroscopy (EIS) was carried to verify the FTO/Cu₂O electrodes performance of interfacial charge transfer properties at the bias potential of -0.2 V vs Ag/AgCl under visible light illumination. Fig. 3 shows the Nyquist plots of FTO/Cu₂O (CVD) electrode has a smaller semicircle than that of FTO/Cu₂O (FPD) electrode related with charge transfer resistant (R_{ct}) values of FTO/Cu₂O electrodes prepared by CVD and FPD methods were 364.8 and 1,754 ohm, respectively. It could indicate that the FTO/Cu₂O electrode prepared by CVD method obtained the high efficiency for charge separation at the interfacial electrode electrolyte caused to improve the photoelectrocatalytic activities for water reduction.

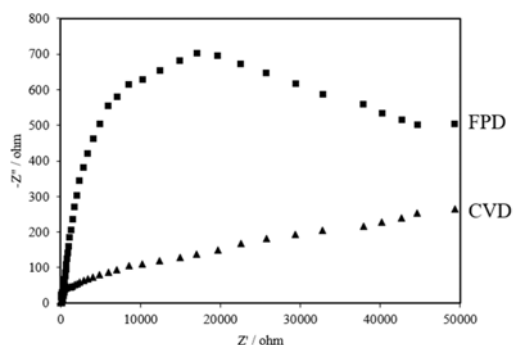


Fig. 3. Nyquist plots of FTO/Cu₂O electrodes prepared by different methods of CVD and FPD in 0.1 M Na₂SO₄ under bias potential of -0.2 V vs Ag/AgCl and visible light illumination condition.

The results show that the FTO/Cu₂O electrode fabricated by CVD method have many good characteristics and photoelectrocatalytic activities for water reduction suitable to further apply to the CO₂ reduction to carbonyl and methanol compounds.

3.2 The CO₂ conversion to carbonyl compound performance using the developed FTO/Cu₂O photocathode

Based on the comparison of the electrodes properties, FTO/Cu₂O (CVD) electrode was selected to study the optimum condition for CO₂ compound

conversion to carbonyl compound by using photoelectrocatalytic process. The photoelectrocatalytic cell was contained with FTO/Cu₂O as a working electrode, Ag/AgCl as a reference electrode and Pt wire as a counter electrode in the Na₂CO₃/NaHCO₃ buffer solution. The effects of bias potential, pH of electrolyte, the power of light intensity were studied for the optimum condition of carbonyl compound production. The absorbance band at 280 nm which related with the formation of carbonyl compounds [4] was monitored for considering the optimum condition (Fig.4).

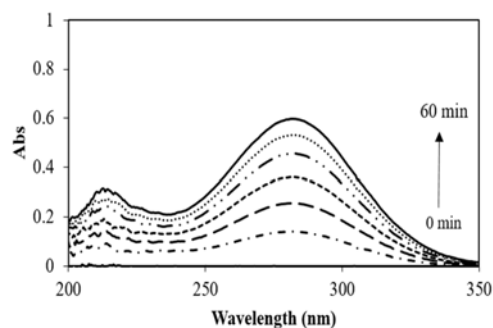


Fig. 4. UV spectra of carbonyl compound functional with the time of photoelectrocatalytic CO₂ reduction process.

The effect of applied potential is studied at -0.1, 0.0, 0.1, 0.2 and 0.3 V vs Ag/AgCl and observed the absorbance value at the λ of 280 nm. Fig. 5 shows that the applied potential significantly affects with the CO₂ conversion to a carbonyl compound. The specific bias potential of 0.2 V presented the highest performance for carbonyl compound production and was selected for next study.

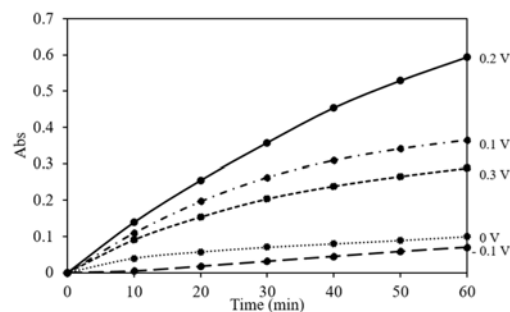


Fig. 5. Absorbance value of carbonyl compound production ($\lambda=280\text{nm}$) with the different bias potential in range of -0.1 to 0.3 V vs Ag/AgCl.

The pH of the electrolyte was varied from 9 to 11 at an applied potential of +0.2 V under visible light irradiation. Fig. 6 shows the proper pH value of 9 for CO₂ compound conversion to the carbonyl compound. The power of light intensity was directly

related to the carbonyl compound production due to the high power of light intensity irradiate at the photosemiconductor cause high efficient to generate photoelectron for reducing CO_2 to carbonyl compound as well.

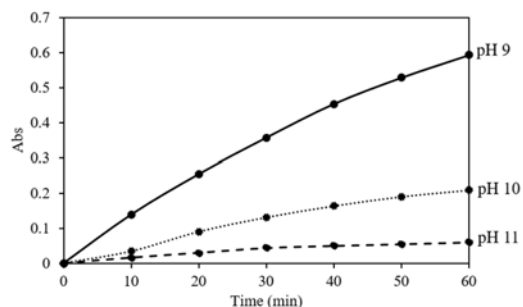


Fig. 6. Absorbance value of carbonyl compound production ($\lambda=280\text{nm}$) with the different pH value of 9, 10 and 11.

Moreover, the catalytic mechanisms to induce FTO/ Cu_2O photoelectrode for carbon dioxide conversion to carbonyl compounds were studied under photoelectrocatalysis (PEC), photocatalysis (PC) and electrocatalysis (EC) process. The result shows that the photoelectrocatalytic process (PEC) presented the highest efficiency for the CO_2 compound conversion to carbonyl compound (Fig. 7). This result confirms that the highest efficiency of PEC process due to the catalytic action applied potential and light irradiation at photoelectrode cause decreased the recombination effect of the electron-hole pair at the Cu_2O semiconductor efficiently induce photoelectron to reduce CO_2 to carbonyl as well.

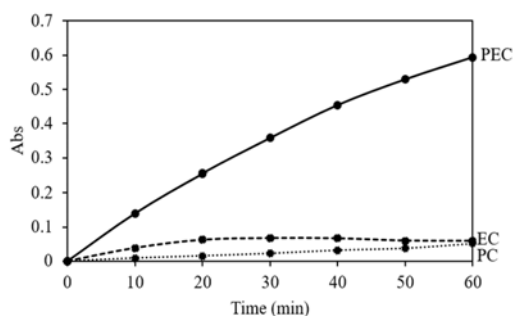


Fig. 7. Absorbance value of carbonyl compound production ($\lambda=280\text{nm}$) with the different catalytic mechanism of photoelectrocatalysis (PEC), photocatalysis (PC) and electrocatalysis (EC) process.

3.3 The CO_2 conversion to MeOH compound performance using the developed FTO/ Cu_2O photocathode

The CO_2 conversion to MeOH was performed by

using photoelectrocatalytic process with the working electrode of FTO/ Cu_2O . The effects of applied potential, the power of light intensity and catalytic mechanism were studied with the optimum condition for MeOH production. A cyclic voltammetry method was introduced to analyze the methanol concentration from the process using Pt wire as working and counter electrode and Ag/AgCl as a reference electrode. The correlation of methanol oxidation current at 0 V as a function of methanol concentrations range of 0 (blank) - 5,000 ppm (MeOH) were performed to use as the standard calibration curve (Fig. 8).

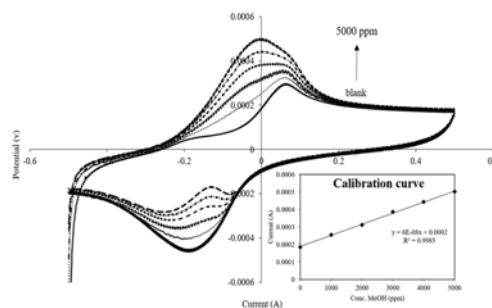


Fig. 8. Cyclic voltammograms of methanol oxidation reaction at Pt wire electrode in 0.1 M Na_2CO_3 and the inset shows the standard calibration curve as a relation of oxidation current versus methanol concentrations.

The effects of applied potential at -0.3, -0.4 and -0.5 V vs Ag/AgCl in 0.1 M Na_2CO_3 (CO_2 saturated) under PEC process with 20 W tungsten lamp for 60 minutes were studied. Fig.9 shows that the applied potential of -0.4 V presented the highest methanol generation to 575 ppm for 1h.

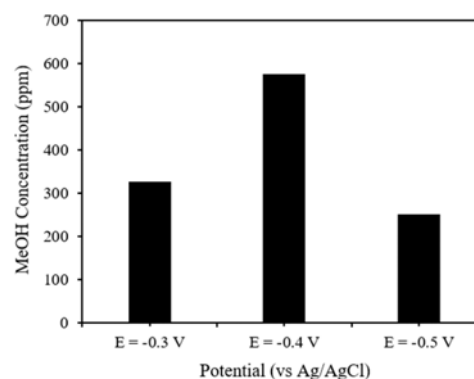


Fig. 9. Methanol production by PEC process with the different of applied potentials for 1 h.

The result indicates that the applied potential is specific to the kind of product from CO_2 reduction process. The power of light intensity is one of the parameters affected by the CO_2 conversion to MeOH.

The light intensity is direct related to the MeOH production efficiency. Therefore, the position and power of light source to irradiate at the photoelectrode have to consider the optimum condition. Furthermore, the catalytic mechanisms of FTO/Cu₂O photoelectrode for CO₂ compound reduced to methanol were studied with the process of PEC, EC, and PC. The result shows that the PEC process has the highest efficiency for the reduced CO₂ compound to methanol production of 726 ppm for 1 h.

3.4 Comparison of FTO/Cu₂O prepared by CVD and FPD methods for CO₂ compound conversion to carbonyl and methanol compounds

The carbonyl and MeOH compound production efficiency were compared to confirm the CO₂ reduction performance of FTO/Cu₂O(CVD) and FTO/Cu₂O(FPD) photoelectrodes. The results show that FTO/Cu₂O electrode prepared by CVD method presented the higher performance for converting CO₂ compound to both carbonyl (Fig.10a) and methanol (Fig.10b) compounds than that the FPD method.

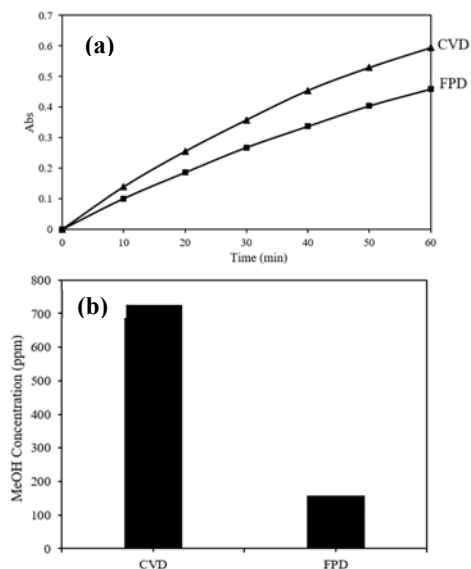


Fig. 10. Comparison the performance of FTO/Cu₂O electrodes prepared by CVD and FPD for CO₂ compound conversion to (a) carbonyl and (b) methanol compounds.

4. CONCLUSIONS

The developed cyclic voltammetry deposition method (CVD) electrodeposition method successfully for the Cu₂O semiconductor fabricated on fluorine-doped tin oxide (FTO) and presented the good characteristic and more photoelectrocatalytic activities than that the previous research. The

developed FTO/Cu₂O photoelectrode was performed high efficiency to reduce CO₂ solution into organic carbonyl and methanol compounds as well. This developed photoelectrocatalytic cell indicates that the powerful method for reducing CO₂ from air pollutant and also producing value-added chemicals for alternative energy supplies.

5. ACKNOWLEDGEMENTS

This work was supported by the RMUTT annual government statement of expenditure in 2017 (NRMS 2560A16502099 ; given to C.P)

6. REFERENCES

- [1] Kiewchaum A, Thepanondh S, Sirithian D, Mahavong K, and Outapa P., "Evaluation of the effectiveness and appropriateness of Bangkok action plans on global warming mitigations" Int. J. of GEOMATE, Vol. 12 (Issue33), 2017, pp. 14-21.
- [2] Boxun H, Curtis G, Steven L. S, "Thermal, electrochemical, and photochemical conversion of CO₂ to fuels and value-added products" J. CO₂ Utilization, Vol. 1, 2013, pp.18–27.
- [3] Kendra P. K, Toru H, Etosha R. C, David N. A, Jakob K, and Thomas F. J, "Electrocatalytic Conversion of Carbon Dioxide to Methane and Methanol on Transition Metal Surfaces" J. Am. Chem. Soc., Vol.136, 2014, pp.14107–14113.
- [4] Juliana F. de B, Angela R. A, Krishnan R, Maria V. B. Z, "Photoelectrochemical reduction of CO₂ on Cu/Cu₂O films: Product distribution and pH effects", Chem. Eng. J., Vol. 264, 2015, pp. 302–309.
- [5] Peiqiang L, Jinfeng X, Hua J, Chenxiao W, Hui P, Jing L, and Hongzong Y, "Wedge N-doped CuO with more negative conductive band and lower overpotential for high efficiency photoelectric converting CO₂ to methanol" Catal. B-Environ. Vol. 156–157, 2014, pp. 134–140.
- [6] Ponchio C, Atsuko Y N, Yoshio N, "The Effect of Platinum Deposition on the Water Photo-Reduction at p-Cu₂O Semiconductor Electrodes with Visible Light Irradiation", Electrochemistry, Vol.79 (10), 2011, pp. 821-825.
- [7] Juliana F. d. B, Alexander A. d. S, Alberto J. C and Maria V. B. Z, "Evaluation of the Parameters Affecting the Photoelectrocatalytic Reduction of CO₂ to CH₃OH at Cu/Cu₂O Electrode" Int. J. Electrochem. Sci., Vol. 9, 2014, pp. 5961 – 5973.
- [8] Polyana F. P, Raquel M.F.S, Rodrigo A.A. M, and Eduardo M. R, "Simultaneous determination of ethanol and methanol in fuel ethanol using cyclic voltammetry" Fuel, Vol. 103, 2013, pp.725–729.

DEVELOPMENT AND DESIGN OF PHOTOELECTROCATALYTIC REACTOR FOR DYE REMOVAL FROM INDUSTRIAL SYSTEMS

Watcharapong Nareejun¹, Chatchai Ponchio^{1,2*}

¹Department of Chemistry, Faculty of Science and Technology, Rajamangala University of Technology Thanyaburi, Pathumtani 12110, Thailand

²Advance Materials Design and Development (AMDD) Research Unit, Institute of Research and Development, Rajamangala University of Technology Thanyaburi, Pathumtani 12110, Thailand

*Corresponding Author; E-mail address: chatchai@rmutt.ac.th

ABSTRACT

Organic dye is a toxic and carcinogenic substance, it is extensively used as the colorant in industries. There is a need to develop the efficient technique to eliminate the dye wastewater and control this environmental problem. The study is developed and designed the photoelectrocatalytic (PEC) reactor with the high efficiency, rapidity and simple method to remove dye from the industrial systems. The $\text{WO}_3/\text{BiVO}_4$ electrode was applied as the photoanode under visible light irradiation. The effects of batch and flow system, electrodes size, electrode position, light intensity, applied potential, pH of the solution and mechanism were studied for development and design reactor with the highest dye degradation efficiency. The optimum condition could be degraded methyl red dyes up to 85% for 3 hours. Significantly, this condition also applied to degrade dye wastewater from the industrial factory up to 93% for 3 hours. It could be reduced the chemical oxygen demand (COD) over 50% confirms high efficiency of PEC reactor with simple and short duration of the operation for dye degradation system. It is appropriate to scale up and apply for remove dye from industrial system.

Keywords: Photoelectrocatalytic reactor, Dye degradation, Visible light irradiation, $\text{WO}_3/\text{BiVO}_4$

1. INTRODUCTION

The textile industry has been released the wastewater containing a variety of organic content, toxic and carcinogenic compounds to the environment. The high-efficiency method to remove this dye wastewater has been expected considering with a simple and low-cost process [1]. Photoelectrocatalytic (PEC) method is one of the most interesting choices to overcome this advantage requirement. The key factors to improve the efficiency of PEC method are electrode development and PEC reactor designation. The previous work, a $\text{WO}_3/\text{BiVO}_4$ electrode was developed to enhance the photoelectrocatalytic activities of water oxidation [2] and dye degradation [3] under visible light irradiation. However, the previous work just studied only laboratory level. The development of the prototype of PEC reactor was expected to study for the scaling up with industrial application. Therefore, the PEC reactor designing is required to improve the efficiency of the PEC cell [4, 5]. This research focuses on the development of visible light PEC reactor for dye degradation with the high efficiency, simple and short time operation method.

2. EXPERIMENTAL

2.1 $\text{WO}_3/\text{BiVO}_4$ electrode preparation

The $\text{WO}_3/\text{BiVO}_4$ electrode fabrication was described in our previous work [2]. A precursor of 0.1 M BiVO_4 solution was prepared by the mixing solution of 0.2 M Vanadium (IV) oxide acetylacetonate in acetyl acetone solution and 0.2 M bismuth (III) nitrate penta hydrate in acetic acid solution. A 0.1 M WO_3 solution was prepared by the mixing solution of 0.1 M tungstic acid in 30% NH_4OH solution and then refluxing at 60°C for 1 hour. The $\text{WO}_3/\text{BiVO}_4$ thin films were deposited on fluorine doped tin oxide (FTO) substrate by spin coating technique. The WO_3 solution was deposited at first layer by spin coating method and covered with 5 layers of BiVO_4 . Each layer deposition was dried at 150°C for 5 minutes. The FTO/ $\text{WO}_3/\text{BiVO}_4$ film electrode was calcinated at 550°C for 1 hour.

2.2 PEC reactor set up for dye degradation study

Figure 1 shows that the PEC reactor set up for dye degradation. The PEC reactor consisted of a beaker 250 mL using the FTO/ $\text{WO}_3/\text{BiVO}_4$ (35x40 mm) as an anode and Cu sheet (40 x 40 mm) as a cathode

and the electrodes were connected to a DC power supply. An 11W tungsten lamp was placed parallel to the FTO/WO₃/BiVO₄ anode. The synthetic methyl red dyes in 0.05 M NaCl and real dye without adjusting condition from paint industry were introduced to study the efficiency of dye waste water degradation. The wastewater in a container was circulated by a pump to study the effect of flow and batch system. The electrodes size, the angle of electrode position, light intensity, applying potential, pH of the solution and catalytic mechanism process were studied. The dye degradation efficiency was monitored by sampling the treated solution from PEC reactor every 10 minutes and measured an absorbance by UV-Vis spectrophotometer (UV-1601, Shimadzu Co., Ltd, Japan) at 420 nm for methyl red and 660 nm for real dye samples. The percentage of dye degradation was calculated by using:

$$\% \text{ Degradation} = \frac{(A_0 - A_t) \times 100}{A_0}$$

where, A_0 = absorbance at $t = 0$ min, A_t = absorbance at t minutes after the treatment process [3]. In addition, chemical oxygen demand (COD) was determined to confirm the mineralization of dye degradation efficiency using standard dichromate method.

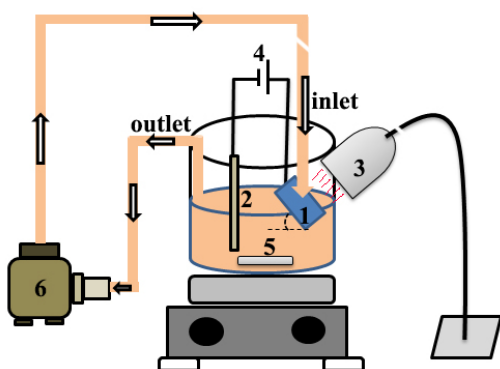


Fig. 1. Schematic diagram of PEC reactor for study dye degradation 1: WO₃/BiVO₄ anode 2: Cu sheet cathode 3: Tungsten lamp 4: DC power supply 5: stirrer 6: flow pump

3. RESULTS AND DISCUSSION

3.1 Evaluation of the optimum condition on dye degradation

The effects of batch and flow system, electrodes size, electrode position, light intensity, applied potential, pH of the solution and mechanism were studied with the highest dye degradation efficiency. Figure 2 shows that the flow system presents higher dye removal than that the batch system due to the effect of surface refreshing

improves the high oxidizing frequency of organic dye at the electrode surface. The larger electrode size of 35×40 mm shows significant higher % degradation for 9 times than the smaller electrode size of 2×2 cm which demonstrated that the active surface area is the key factor to enhance the dye oxidation efficiency proposes considering for further scaling up.

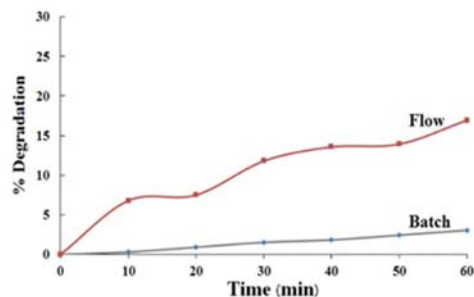


Fig. 2. Comparison % dye degradation between Batch and Flow system. Using FTO/WO₃/BiVO₄ photoanode electrode at 1.0V under 25W tungsten lamp in solution of 5 mg/L Methyl Red and 0.05M NaCl

Based on the effect of the electrode position for dye removal, the degree of electrode placement 30, 45, and 90 degrees were studied. The experiments show that the electrode angle of 45 degrees has the highest removal potential due to at 45 degrees the dye solution flows through contact with the semiconductor surface better than 30 degrees and 90 degrees. The effect of light intensity was studied at 5W, 11W, 20W and 28W that classified by the power of tungsten lamp. The intensity of light is direct depended with the dye removal efficiency due to the fact that high light intensity stimulates semiconductor electrodes induces high hole (h^+) generated at valence band, resulting in increasing the efficiency of dye oxidation process. However, at high light intensity irradiation may effect with electrode lifetime. Therefore, the suitable condition for high photocatalytic activity, long electrode lifetime and low energy consumption are considered. The light intensity of 11 W was selected with the optimum condition for next step. The effect of applied potential was studied in range of 0.5 to 2.0 V. The % dye degradation on PEC oxidation was significantly enhanced with more positive bias potential. This can be explained by increasing the positive bias potential induce to enhance the electron flow rate from the anode electrode to the cathode electrode, caused the h^+ increasing at the surface of the anode electrode and resulting in the oxidation reaction. However, increasing the voltage too much affects the lifetime of the electrode. Therefore, the optimum voltage condition was selected of 1.5 V. The initial solution pH is a key factor influencing the dye degradation

process. Figure 3 shows that the dye removal significantly increasing in the acidic condition. The result is related to the researched by Galenda et al. which pH 3 and 4 obtained highest methyl red degradation efficiency due to high adsorption ability of dye at semiconductor surface under light irradiation [6].

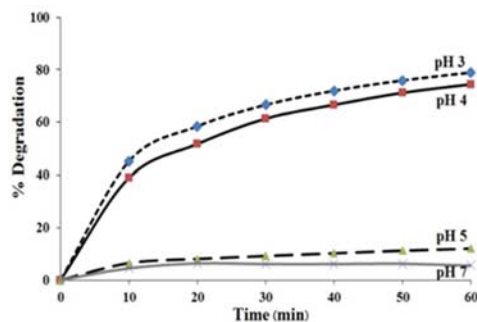


Fig. 3. Effect of pH value in the solution of 5 mg/L of Methyl red and 0.05 M NaCl for dye degradation by using FTO/ $\text{WO}_3/\text{BiVO}_4$ as photoanode, applied potential of 1.5 V.

The efficiency of synthetic methyl red dye removal was optimized at pH 4 with 11W and 1.5V. This optimum condition could be degraded methyl red dyes up to 85% for 3 hours.

3.2 Catalytic mechanism of FTO/ $\text{WO}_3/\text{BiVO}_4$ photoelectrode for dye degradation

The dye removed under various catalytic mechanism at FTO/ $\text{WO}_3/\text{BiVO}_4$ photoelectrode were presented in figure 4 with photoelectrocatalytic (PEC), photocatalytic (PC) and electrocatalytic (EC). It can be clearly observed that the PEC is the most powerful process to degrade the methyl red in aqueous solution. The highest dye removal (75%) is detected after 60 min in PEC method, while only 49% and 40% of the dye degradation at the same degradation time are found in the PC and EC process, respectively.

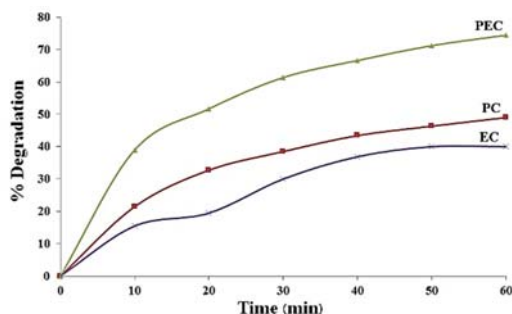


Fig. 4. Methyl red degradation using difference process of FTO/ $\text{WO}_3/\text{BiVO}_4$ stimulation mechanism (potential 1.5 V, 11 W tungsten lamp, pH 4)

3.3 The performance of PEC reactor for real dye wastewater treatment

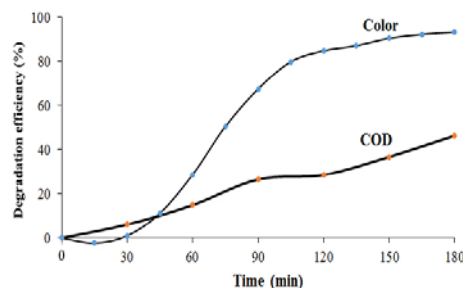


Fig. 5. Decolorization of dye and COD degradation of real dye wastewater effluent treated by $\text{WO}_3/\text{BiVO}_4$ thin-film PEC reactor as a function of degradation time (applied potential of 1.5 V, pH = 4 and 11 W of tungsten lamp)

Figure 5 shows the color removal and COD reduction at 180 min intervals during the entire experiment. The optimum condition of PEC reactor was applied for removal the real dye waste water from industry. The developed PEC reactor presents dye removal up to 93% for 180 minutes can be achieved the efficiency for dye decolonization from dark blue until it becomes a clear solution. Especially, the result shows that the COD reduction up to 50% able confirm the mineralization efficiency of this technique. The results demonstrate that the PEC reactor can degrade practical dye wastewater efficiently.

4. CONCLUSIONS

The developed PEC reactor using FTO/ $\text{WO}_3/\text{BiVO}_4$ photo anode presents high efficiency for 85% synthetic methyl red and 93% real dye degradation under visible light irradiation. This work demonstrated a high efficiency of PEC reactor with a simple and rapid method for dye degradation system suitable to scaling up and apply for dye removal from the industrial system.

5. ACKNOWLEDGEMENTS

This work was supported by the project of Research and Researchers for Industries (RRI), Thailand Research Fund (TRF) and STP Chem Solutions Co., Ltd. (MSD59I0017)

6. REFERENCES

- [1] Akio T, Keiichi K, Takashi N, Ryota S and Hiromu T. "Landfill waste water treatment by application of pulsed high voltage" Int. J. of GEOMATE, Vol. 9 No. 1 (Sl. No. 17), 2015, pp. 1375-1379

- [2] Ponchio C, Yoshinori M, Shin-ya K, Atsuko Y N, Yoshio N, “Efficient photocatalytic activity of water oxidation over $\text{WO}_3/\text{BiVO}_4$ composite under visible light irradiation”, *Electrochim. Acta*, Vol. 54, 2009, pp. 1147-1152.
- [3] Ponchio C, Atsuko Y N, Yoshio N, “Photoelectrocatalytic performance of $\text{WO}_3/\text{BiVO}_4$ toward the dye degradation”, *Electrochim. Acta*, Vol. 94, 2013, pp. 314–319.
- [4] Xua Y, Jia J, Zhongb D, and Y Wanga, “Degradation of dye wastewater in a thin-film photoelectrocatalytic (PEC) reactor with slant-placed TiO_2/Ti anode ”*Chem. Eng. J.* Vol.150, 2009, pp.302 –307.
- [5] Mengb X, Zhanga Z, and Li X, “Synergetic photoelectrocatalytic reactors for environmental remediation: A review ”*J. Photoch. Photobio. A : Photoch. Reviews*, Vol. 24, 2015, pp. 83–101.
- [6] Galenda A, Crociani L, El Habra, Favaro M, Natile M M, Rossetto G, “Effect of reaction conditions on methyl red degradation mediated byboron and nitrogen doped TiO_2 ” *Appl. Surf. Sci.*, Vol. 314, 2014, pp. 919–930.

IMPROVEMENT THE BiVO_4 PHOTOANODE FABRICATED FOR WATER OXIDATION BY ELECTRODEPOSITION TECHNIQUE

Nuanlaor Kiama¹, Chatchai Ponchio^{1,2*}

¹Department of Chemistry, Faculty of Science and Technology, Rajamangala University of Technology Thanyaburi, Pathumtani 12110, Thailand

²Advance Materials Design and Development (AMDD) Research Unit, Institute of Research and Development, Rajamangala University of Technology Thanyaburi, Pathumtani 12110, Thailand

ABSTRACT

Photoelectrocatalytic (PEC) technique for water oxidation technologies could become important components in the renewable energy sector. BiVO_4 has been receiving attention for applications in PEC cell for O_2 evolution with high photoelectrocatalytic activity and the advantage of visible radiation absorption. The simple and high efficiency BiVO_4 thin film fabrication for large scale is very important for scaling up to the industrial application. This research describes the BiVO_4 thin films fabrication on fluorine doped tin oxide (FTO) by electrodeposition technique as simple, fast and suitable for scaling up of electrode preparation. Cyclic voltammetry deposition was developed by studied the effect of potential range, scan rate, number of scan, temperature and pH of solution to enhance the photoelectrocatalytic activity of water oxidation under visible light irradiation. The fabricated FTO/ BiVO_4 thin films were characterized by scanning electron microscope (SEM), X-ray diffractometer (XRD) and UV-Vis spectrophotometer. The developed FTO/ BiVO_4 present the photocatalytic activities for water oxidation improvement more than 10 times when comparing with the previous spin coating techniques. Therefore, this developing technique show that the high efficiency, fast, simple and suitable in scaling up able to approach for water oxidation in the industrial application.

Keywords: Photoelectrocatalytic properties, Water oxidation, BiVO_4 , Electrodeposition

INTRODUCTION

Photoelectrochemical (PEC) water splitting is an alternative way to produce hydrogen and oxygen supporting the hydrogen fuel cell which an important choice in the renewable energy and green technology sector [1, 2]. The development of photoelectrocatalytic activity based on semiconductor materials with appropriate narrow band-gap energy is the key factor to energy conversion efficiency driven by sunlight. Recently, many metal oxide semiconductor materials such as Co_3O_4 , Fe_2O_3 , WO_3 , and BiVO_4 have been employed as photocatalysts for visible light driven water splitting [3-6]. Among them, BiVO_4 has recently been extensively investigated as a photoanode for the generation of oxygen from water due to its favorable optical band gap (~ 2.4 eV), non-toxicity, and stability [7-9]. Especially in the last few years, the PEC performance of BiVO_4 photoanode has been significantly improved via the building of nanostructures [10, 11]. One of the most selected BiVO_4 thin film fabrication is electrodeposition method due to the advantages of high efficient, simple, rapid method and practicable to scaling up.

In this work, the FTO/ BiVO_4 fabricated thin films using cyclic voltammetry electrodeposition method (CVD) was developed by the study of the effects of apply potential range, scan rate, number of cycle scan, temperature, and pH of the solution. The developed BiVO_4 prepared by CVD method was compared with the other electrodeposition technique and classical spin coating method.

EXPERIMENTAL

Materials

Fluorine doped tin oxide (FTO, $\sim 7 \Omega/\text{sq}$, Sigma-Aldrich) was used as a bare electrode substrate. The chemicals used in this study was $\text{Bi}(\text{NO}_3)_3 \cdot 5\text{H}_2\text{O}$ ($\geq 98.0\%$, Sigma-Aldrich), $\text{VOSO}_4 \cdot x\text{H}_2\text{O}$ (97%, Sigma-Aldrich), HNO_3 (70.0%, Sigma-Aldrich) CH_3COONa ($\geq 99.0\%$, Sigma-Aldrich), and Na_2SO_4 (Univar).

Preparation of BiVO_4 thin films

The BiVO_4 thin films were fabricated on FTO substrate by electrodeposition technique. A precursor solution was prepared by mixing

solution of 10 mM $\text{Bi}(\text{NO}_3)_3$ and 35 mM VOSO_4 and adjusted pH < 0.5 with HNO_3 [7]. Then 2 M of sodium acetate was added for adjusting pH of the solution to study the effect of pH at four pH values of 3.0, 4.0, 4.5, and 5.0. Cyclic voltammetry was introduced for BiVO_4 thin film fabrication by using potentiostat (Metrohm 663VA Stand). A typical three-electrode system was comprised of the FTO as working electrode, the Ag/AgCl (3 M KCl) as a reference electrode and a platinum wire as a counter electrode. The amorphous Bi-V-O film deposition was studied with the effect of several parameters; the apply potentials of +1.5 to +2.5 V, the precursor solution temperatures of RT (25°C), 40°C, 50°C, 60°C, and 70 °C, the scan rate of 25, 50, 100, and 250 mV/s and the number of cycle scan of 1, 3, 5, and 7 cycles. The crystalline BiVO_4 thin film was carried out by annealing the amorphous Bi-V-O at the temperatures of 500°C. The optimum condition was considered with the highest photocurrent from the photoelectrocatalytic water oxidation depending with the FTO/ BiVO_4 photoanode from each condition. The photocurrent was measured at a fixed potential of 1.0 V vs. Ag/AgCl in 0.5 M Na_2SO_4 aqueous solution under chopped visible light illumination.

Characteristic and photoelectrocatalytic properties of BiVO_4 thin films

The morphologies of the BiVO_4 thin films on FTO were investigated by using scanning electron microscopy (SEM, JEOL, JSM -5410LV). X-ray diffraction (XRD, JEOL, JDX-3530) analysis was carried out (Cu K α radiation) to confirm the crystallinity of the prepared BiVO_4 electrodes. The optical absorption spectra of the electrodes were measured by using a UV/vis spectrophotometer (Shimadzu, UV-1601). The photoelectrocatalytic activity and the electrochemical impedance spectroscopy (EIS) were performed with a VersaSTAT3 (Princeton Applied Research, Inc.) at the potential of 1.0 V vs. Ag/AgCl under visible light illuminated and frequencies ranging from 100 kHz to 0.1 Hz. The characteristic and photoelectrocatalytic activities of BiVO_4 thin films electrode prepared by CVD method were compared with the other BiVO_4 thin films fabrication by the amperometry (keep the potential of 1.9 V) [7] and spin coating methods (5 layers of BiVO_4) [12].

RESULTS AND DISCUSSION

Evaluation of the optimum condition for BiVO_4 thin films fabricated by CVD method

3.1.1 Effect of pH

After dissolving $\text{Bi}(\text{NO}_3)_3 \cdot 6\text{H}_2\text{O}$ with concentrated HNO_3 , VOSO_4 was added in the chemical bath solution and adjusted pH again by sodium acetate to study the effect of pH value of 3.0, 4.0, 4.5 and 5.0. At pH 3.0 the precursor solution was turbid and presented reddish brown peeling out occurring of BiVO_4 film from FTO substrate because Bi(III) is soluble at a very low pH value, there is no film formation on the substrate. When pH of the electrolyte solution increases to the middle acidity rank, the BiVO_4 film could be completely deposited on the FTO substrate which improved the photoelectrocatalytic activity at pH 4.5. At the pH 5.0, the BiVO_4 was also deposited on the FTO substrate but the photoelectrocatalytic activity was decreased due to the V(IV) precipitates from the solution at the pH above 5 [7]. This result indicates that the specific pH value of a precursor solution is very important to control the quality of BiVO_4 thin film fabrication at FTO substrate.

3.1.2 Effect of precursor solution temperature

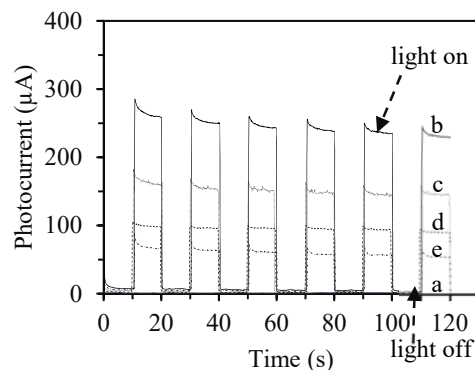


Fig. 1. Amperograms of FTO/ BiVO_4 prepared with the different precursor solution temperatures of (a) Room Temperature (b) 40 °C (c) 50 °C (d) 60 °C and (e) 70 °C

The photoelectrocatalytic water oxidation of the BiVO_4 photo anode obtained at the different precursor solution temperatures during cyclic voltammetry electrodeposition process are shown in Fig. 1. It was found that at room temperature BiVO_4 film could not be deposited on FTO substrate and did not present the photoelectrocatalytic activity. When the temperature was increased to 40°C a BiVO_4 film was completely immobilized onto the substrate cause to the increasing photo current from the water oxidation.

However, the BiVO_4 was agglomerated on the substrate surface and decreased photo current when the temperature is higher than 40°C . This effect due to the increasing temperature would create many ions on the surface that may resulted in the agglomerated and peeled BiVO_4 [13]. Therefore, the temperature of a precursor solution for BiVO_4 electrodeposition was selected at 40°C .

3.1.3 Effect of scan rate

Figure 2 shows that the effect of scanning rate on CVD technique for BiVO_4 thin film fabrication related with the photocurrent from water oxidation. As a result, the low scan rate values of 25 and 50 mV/s presented high photoelectrocatalytic water oxidation of FTO/ BiVO_4 electrode. The increasing scan rate to 100 and 250 mV/s were performed the decreasing of photoelectrocatalytic activity. It indicates that faster scan rate affects the speed of a precursor deposition to incompletely grow the BiVO_4 on FTO while slower scan rate with more diffusion time of a BiVO_4 precursor to deposit completely on the substrate. Based on this experiment, the scanning rate of 50 mV/s was selected with the highest photocurrent from water oxidation.

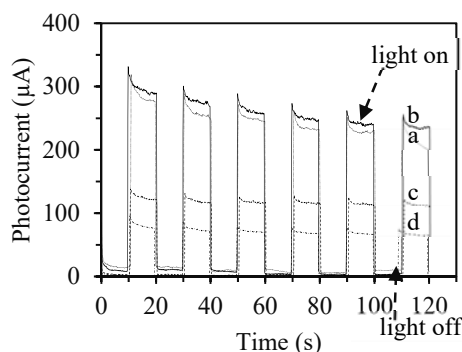


Fig. 2. Amperograms of FTO/ BiVO_4 prepared by the different scan rates of (a) 25 (b) 50 (c) 100 and (d) 250 mV/s

3.1.4 Effect of scanning cycle number

The experiment shows that the photocurrent enhance with the increasing number of scans from 1-5 cycles and decrease when the cycle is more than 5 cycles (Fig. 3). Moreover, the photocurrent was related with the EIS results which the charge transfer resistance decreased at the cycle scan 1 to 5 and increased at 7 cycles. This result indicates that the photocurrent of BiVO_4 depended on the film thickness that related with the number of the scan. However, high film thickness may affect with the charge transfer rate resistance at the electrode surface.

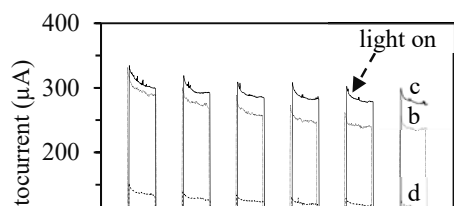


Fig. 3. Amperograms of FTO/ BiVO_4 electrode prepared by CVD method with the study of scanning cycle number (a) 1 (b) 3 (c) 5 and (d) 7 cycles

Comparison BiVO_4 electrode with different deposition method

The characteristic properties and photoelectrocatalytic water oxidation of different BiVO_4 electrode fabrication methods were studied. The BiVO_4 electrode prepared by CVD (applied potential of 1.5-2.5 V) method was compared with the previous research of the amperometry method (keep the potential of 1.9 V) [7] and spin coating method (5 layers of BiVO_4) [12]

3.2.1 Absorption properties

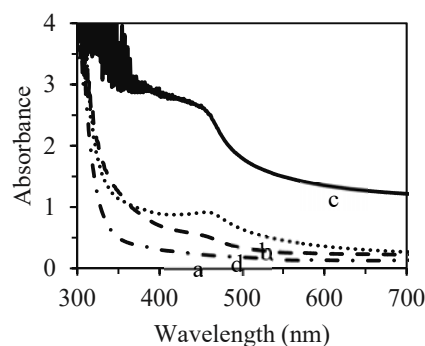


Fig. 4. The UV-visible spectra of (a) FTO and FTO/ BiVO_4 electrodes prepared by different method of (b) Cyclic voltammetry (c) Amperometry and (d) spin coating

The absorption edge of electrodes were used to calculate a band gap energy with equation 1.

$$E_g = \frac{1240}{\lambda} \quad (1)$$

Where, E_g is band gap energy and λ is absorption edge (nm)

The band gap energy of BiVO_4 from CVD, spin coating, and amperometric method were calculated

of 2.21, 2.38 and 2.29 eV, respectively (Fig.4). The results show that BiVO₄ prepared by CVD have a narrower band gap energy than that other technique indicates that higher visible light absorption property.

3.2.2 Photoelectrocatalytic properties

The photoelectrocatalytic properties were studied by measure the photocurrent from water oxidation reaction at the FTO/ BiVO₄ electrode surface. The photocurrent from FTO/ BiVO₄ prepared by CVD technique shows the significantly higher photocurrent than that the amperometry and spin coating technique about 2 and 15 times, respectively (Fig. 5). The result can use to confirm the photoelectrocatalytic improvement of the introduced CVD method for BiVO₄ film fabrication. There are related with high absorption property of the electrode could be produce high photo hole(h⁺) at valent band efficient to oxidize water to oxygen cause present high photocurrent from this reaction.

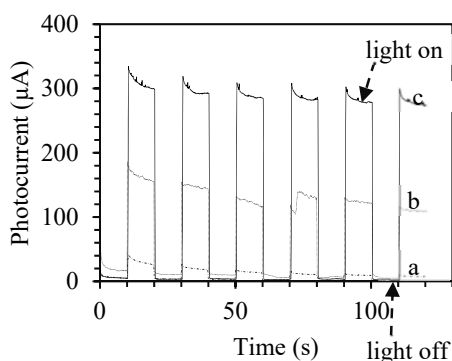


Fig. 5. Photocurrent of BiVO₄ electrode prepared by different methods (a) spin coating (b) amperometry (c) cyclic voltammetry

3.2.3 Charge transfer resistant properties

An EIS measurement was applied to characterize electrochemical interfacial reaction of FTO/ BiVO₄ electrode for water oxidation under visible light irradiation that shows in Fig. 6. The narrowest semi-circle of the Nyquist plot of BiVO₄ electrode prepared by CVD method represents the lowest charge transfer resistant or highest electron transfer rate at the electrode surface. The result can be support the highest photocurrent of the electrode due to the reason of high photo e⁻-h⁺ generation and low e⁻-h⁺ recombination effective with the highest photoelectrocatalytic activity of the developed BiVO₄ electrode.

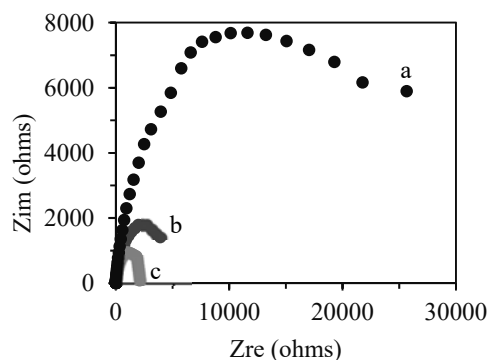


Fig. 6 Nyquist plot of BiVO₄ electrode prepared by different methods of (a) spin coating (b) amperometry (c) Cyclic voltammetry

3.2.4 Morphology and crystalline structure

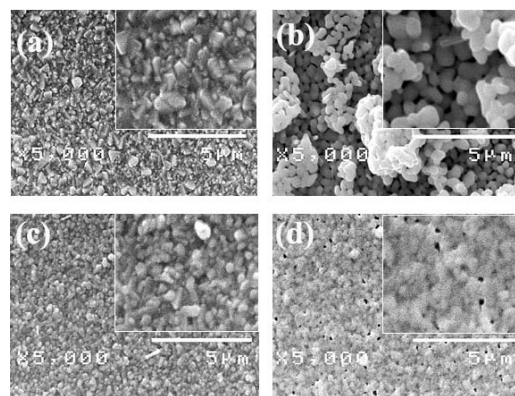


Fig. 7. SEM images of (a) bare FTO substrate and FTO/BiVO₄ electrode prepared by the different methods of (b) Amperometry (c) Cyclic voltammetry and (d) Spin coating

Figure 7 shows the morphology of bare FTO was changed by the covered BiVO₄ and different characteristic depended on the deposition method. The morphologies of BiVO₄ electrodes prepared by CVD method presented the small particle size and well distribution. The particles are clustered together and the size is different when BiVO₄ was prepared by the amperometry method. While the spin coating method shows flat surface by the fused together of BiVO₄. As a result, it can support that the uniform morphology given a good photoelectrocatalytic properties. Figure 8 shows the XRD patterns of BiVO₄ film fabricated with applied potentials after annealing at 500 °C for 1 h. The XRD peaks observed at 2θ = 18.8°, 28.9° and 30.6° were indicated to the diffractions monoclinic BiVO₄ plane of (011), (121) and (040), respectively. As the results show that the monoclinic BiVO₄ crystalline structure can be performed by all methods preparation after annealed at 500°C.

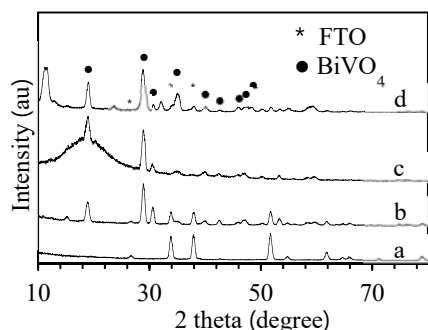


Fig. 8. X-Ray diffraction patterns of (a) FTO and the FTO/BiVO₄ prepared by the different methods of (b) Cyclic voltammetry, (c) Amperometry (d) Spin coating

CONCLUSIONS

The BiVO₄ thin film deposited on FTO using cyclic voltammetry method were successful optimized and presented the photoelectrocatalytic for water oxidation improvement under the good characteristic of films properties. This developed CVD method for FTO/BiVO₄ fabrication shows the high efficiency, fast, simple method and suitable in scaling up able to approach for water oxidation in the industrial application.

ACKNOWLEDGEMENTS

This work was supported by the project of Research and Researchers for Industries (RRI) , Thailand Research Fund (TRF) and Alliance environmental conservation Co., Ltd. (MSD60I0025)

REFERENCES

- [1] Von D, Krol R, Grätzel M, "Photoelectrochemical Hydrogen Production" *Electron. Mater. Sci. Technol.* Vol. 102, 2012, pp.13–21.
- [2] Klabsong M, Kungskulniti N, Puemchalad C, Charoenca N, and Punsuvon V, "Feasibility study of biodiesel production from residual oil of palm oil mill effluent" *Int. J. of GEOMATE*, Vol. 12, 2017, pp. 60-64.
- [3] Zhao J, Zou Y, Zou X, Bai T, Liu Y, Gao R, Wang D, Li G.D, "Self-template construction of hollow Co₃O₄ microspheres from porous ultrathin nanosheets and efficient noble-metal-free water oxidation catalysts" *Nanoscale*, Vol.6 , 2014, pp. 7255–7262.
- [4] Sivula K, Zboril R, Formal F.L, Robert R, Weidenkaff A, Tucek J, Frydrych J, Grätzel M, "Photoelectrochemical Water Splitting with Mesoporous Hematite Prepared by a Solution-Based Colloidal Approach" *J. Am. Chem. Soc.*, Vol.132, 2010, pp.7436–7444.
- [5] Cristino V, Caramori S, Argazzi R, Meda L, Marra G. L, Bignozzi C. A, " Efficient Photoelectrochemical Water Splitting by Anodically Grown WO₃ Electrodes" *Langmuir*, Vol. 27, 2011, pp. 7276–7284.
- [6] Li R, Zhang F, Wang D, Yang J, Li M, Zhu J, Zhou X, Han H, Li N.C, "Spatial separation of photogenerated electrons and holes among {010} and {110} crystal facets of BiVO₄" *Commun.* Vol. 4, 2013, pp.1432-1438.
- [7] Jason A, Seabold and Kyoung-Shin C., "Efficient and Stable Photo-Oxidation of Water by a Bismuth Vanadate Photoanode Coupled with an Iron Oxyhydroxide Oxygen Evolution Catalyst", *J. Am. Chem.Soc.* Vol. 134, 2012, pp. 2186-2192.
- [8] Conrado M.S, Simelys H, and Nunzio R, "BiVO₄ as photocatalyst for solar fuels production through water splitting", *Applied.Chem.*, Vol. 504, 2015, pp. 158-170.
- [9] Park Y, McDonald K.J, and Choi K.-S, "Progress in bismuth vanadate photoanodes for use in solar water oxidation" *Chem. Soc. Rev.*, Vol. 42, 2013, pp. 2321-2337.
- [10] Liu Y, Guo Y.H, Schelhas L.T, Li M.T, Ager J.W, "Undoped and Ni-Doped CoOx surface modification of porous BiVO₄ photoelectrodes for water oxidation", *J.Phys. Chem. C.*, Vol. 120, 2016, pp. 23449–23457.
- [11] He H.C, Berglund S.P, Rettie A.J.E, Chemelewski W.D, Xiao P, Zhang Y.H, Mullins C.B, "Synthesis of BiVO₄ nano flake array films for photoelectrochemical water oxidation", *J. Mater. Chem. A*, Vol. 2, 2014, pp. 9371–9379.
- [12] Ponchio C, Yoshinori M, Shin-ya K, Atsuko Y N, Yoshio N, "Efficient photocatalytic activity of water oxidation over WO₃/BiVO₄ composite under visible light irradiation", *Electrochim. Acta*, Vol. 54, 2009, pp. 1147-1152.
- [13] Kim H.R., Kim G., In S, and Park Y., "Optimization of porous BiVO₄ photoanode from electrodeposited Bi electrode: Structural factors affecting photoelectrochemical performance", *Electrochim. Acta.*, Vol. 189, 2016, pp. 252–258.

PHOTOELECTROCATALYTIC DETERMINATION OF CHEMICAL OXYGEN DEMAND USING WO₃/BiVO₄ PHOTOELECTRODE

Niphawarn Kangkun¹, Chatchai Ponchio^{1,2*}

¹Department of Chemistry, Faculty of Science and Technology, Rajamangala University of Technology Thanyaburi, Pathumtani 12110, Thailand

²Advance Materials Design and Development (AMDD) Research Unit, Institute of Research and Development, Rajamangala University of Technology Thanyaburi, Pathumtani 12110, Thailand

ABSTRACT

Chemical Oxygen Demand (COD) is one of the most extensively used parameter for water quality monitoring with the present of organic level as it can be used to predict a wastewater treatment. The COD determination method is based on as simple, rapid and non-toxicity method has been attracted. The photoelectrocatalytic (PEC) technique could covered the previous mentioned advantage and be an efficient method for determination of COD. A visible light responsive WO₃/BiVO₄ photoelectrode as COD sensor was proposed. A COD detection limit (a signal-to noise ratio of 3) of 1.66 mg L⁻¹ COD with a linearity range of 10 –200 mg L⁻¹ COD were achieved at the optimum condition of applied potential of 1.0 V (vs. Ag/AgCl) and 100 W visible light illumination. This method exhibit high precision and accuracy with the percentage of the relative standard deviation and recovery of 3.17 and 100.87, respectively. The proposed PEC technique for COD sensor represents the simple, rapid and environmental friendly method for the COD monitoring in the wastewater system.

Keywords: Chemical oxygen demand, photoelectrocatalytic cell, photoanode, Visible light responsive

INTRODUCTION

Chemical oxygen demand (COD) is widely used for water monitoring as it can be used to represent the organic pollution level in wastewater [1]. The traditional dichromate method for COD determination is obtaining many drawbacks of a long time-consuming process, highly corrosive and toxic reagents in used [2, 3]. The COD determination method is based on as simple, rapid and non-toxicity method has been attracted [4]. The photoelectrocatalytic process (PEC) is one of the candidate methods with the several advantages of high oxidation ability, non-toxicity, and low cost [5]. TiO₂ usually used in PEC with high photocatalytic activity and stable but it only responding with UV light cause low activity in the solar light application. The narrow band gap energy semiconductors have been investigated for the photooxidation under visible light region [6, 7]. In this work, a visible light responsive WO₃/BiVO₄ photoelectrode was performed for COD determination using photoelectrocatalytic process.

EXPERIMENTAL

Preparation of WO₃/BiVO₄ photoelectrode

The FTO/WO₃/BiVO₄ film photoanode electrode was prepared by using precursor solutions of 0.05 M BiVO₄ and 0.10 M WO₃ as described in the previous research [6]. Fluorine-doped tin oxide (FTO) was used as the substrate for deposited WO₃ at 1st layer and 5 layers of BiVO₄ at outer side by using spin coating method at the condition of 1000 rpm for 60 s. Each layer deposition was dried at 150 °C for 5 min and calcined at 550 °C for 1 h with the last layer.

The photoelectrocatalytic activity of FTO/WO₃/BiVO₄ photoelectrode and characterization study

The fabricated FTO/WO₃/BiVO₄ electrode was studied the absorption properties by UV/Vis spectrophotometer (Shimadzu, UV-1601) in the wavelength of 300-800 nm. The photoelectrocatalytic activity for water oxidation was performed by a VersaSTAT3 (Princeton Applied Research, Inc.) with amperometry at the potential of 1.0 V vs. Ag/AgCl under visible irradiation.

The photoelectrocatalytic performance of FTO/WO₃/BiVO₄ photoelectrode for COD determination study

The fabricated FTO/WO₃/BiVO₄ was

introduced to the photoelectrocatalytic cell as working electrode combining with Ag/AgCl as a reference electrode and Pt wire as a counter electrode. The three electrode system was immersed in the electrolyte solution of 0.1 M Na₂SO₄ using cyclic voltammetry deposition technique (CVD) for determining the photocurrent from the organic glucose oxidation at the electrode surface. The COD value was calculated by the mole ratio of organic glucose and O₂ by the equation of 1.1.



The standard calibration curve was operated by measure the photocurrent depending on the COD value in the range of 10 – 200 mgO₂/L. The effect of supporting electrolyte, pH and electrode size were studied for the optimum condition. The characteristic of the standard calibration curve for COD determination was performed by using glucose as the organic sample and considered with the optimum of sensitivity by slope, interference by y-interception value and linear regression (r) parameters. The figure of merit consist of linearity range, limit of detection (LOD), precision (% Relative standard deviation; % RSD) and accuracy (% Recovery) were performed to confirm the efficiency of PEC method for COD determination.

RESULTS AND DISCUSSION

Characterization and photoelectrocatalytic activities of FTO/WO₃/BiVO₄ photoelectrode

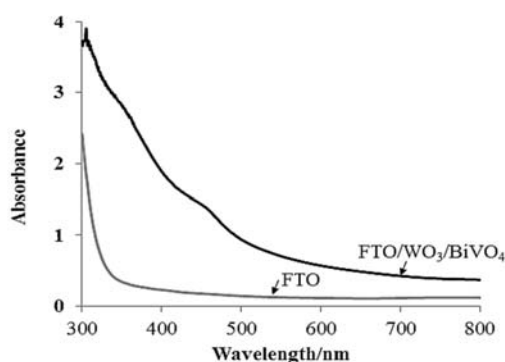


Fig. 1. the absorption spectra of FTO and FTO/WO₃/BiVO₄ electrode

Fig. 1 shows the optical property of the fabricated FTO / WO₃/ BiVO₄ electrode over FTO substrate. It was found that the absorption edge was at 540 nm corresponding to the band gap energy (E_g) value of 2.30 eV, which agree to the E_g value of the BiVO₄. The result can use to confirm the BiVO₄ existent on the FTO surface and facility to absorb visible light. The oxidation efficiency of FTO / WO₃ / BiVO₄ was studied to confirm the photoelectrocatalytic of the

fabricated electrode. Figure 2 shows that the photocurrent under the light on significantly higher than light off condition corresponding with high photoelectrocatalytic water oxidation activity of the FTO / WO₃ / BiVO₄ photoelectrode .

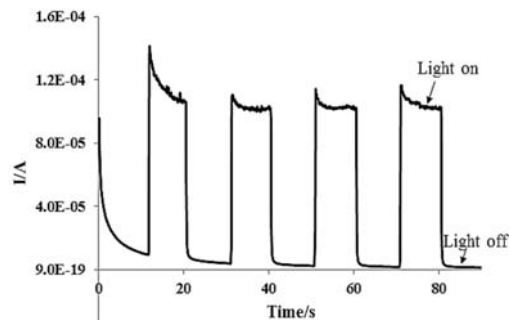


Fig. 2. The photocurrent of FTO/WO₃/BiVO₄ electrode in 0.1 M Na₂SO₄ at an applied potential of 1.0 V vs Ag/AgCl and under the chopper of visible light irradiation.

Evaluation the photoelectrocatalytic COD determination using FTO/WO₃/BiVO₄ electrode

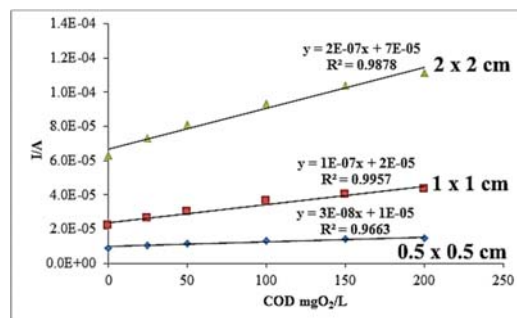


Fig. 3. Standard calibration curve of COD determination by PEC method with the different FTO/WO₃/BiVO₄ electrode size of 0.5x0.5, 1x1 and 2x2 cm

Figure 3 shows that the standard calibration information for COD determination , which considered with the higher slope, low y-intercept value and r closest to 1.00 (Figure 3). The effect of pH value of the solution is a very important parameter in the photoelectrocatalytic COD determination process. The result shows that the pH value of 4 is the specific condition for high sensitivity and good correlation photocurrent and COD value. Therefore, the pH should be kept constant by the buffer solution with the further work. The supporting electrolyte is crucial to the charge transfer process between anode and cathode electrode. In order to select a suitable electrolyte and concentration of sodium salts were tested in the photoelectrocatalytic

process. However, this experimental the electrolyte solution of NaCl and Na₂SO₄ have no different result. The electrode size is one of the important parameter effects with the performance of COD determination. At the larger surface area shows higher sensitivity but more interference. The suitable surface size of 1x1 cm was selected with the optimum of sensitivity, interference and good correlation of photocurrent and COD concentration.

At the optimum condition with applied potential of 1.0 V (vs. Ag/AgCl) and 100W visible light illumination could also be applied for COD determination using potassium hydrogen phthalate (KHP) as another organic sample. Fig. 4 shows that this condition can be used for COD determination with several organic samples. However, the sensitivity is depended with the kind of organic sample. The COD detection limit (a signal-to-noise ratio of 3) and linearity ranges were 1.66 mgO₂.L⁻¹ and 10–200 mgO₂.L⁻¹, respectively. Moreover, the % RSD and % recovery were achieved of 3.17 and 100.87, respective. The result indicates that the developed PEC method using FTO/WO₃/BiVO₄ photoanode exhibited high performance for COD determination with high precision, accuracy, and low detection limit.

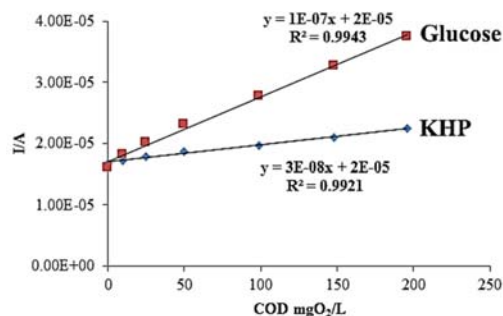


Fig. 4. Standard calibration curve of COD determination by PEC method with the different organic samples of glucose and KHP.

CONCLUSIONS

The proposed PEC method using FTO/WO₃/BiVO₄ electrode represents a good performance for COD determination under visible light irradiation. This method shows a simple, rapid

and environment-friendly technologies for the COD monitoring in the wastewater system.

ACKNOWLEDGEMENTS

This work was supported by the project of Research and Researchers for Industries (RRI), Thailand Research Fund (TRF) and Alliance environmental conservation Co., Ltd. (MSD59I0016)

REFERENCES

- [1] Jin B.H, He Y, Shen J.C, Zhuang Z.X, Wang X.R, Lee F.S.C, "Measurement of chemical oxygen demand (COD) in natural water samples by flow injection ozonation chemiluminescence (FI-CL) technique" *J. Environ. Monit.*, Vol. 6, 2004, pp. 673-678.
- [2] Dan D.Z, Dou F.L, Xiu D.J, Qin Y.Q, "Chemical oxygen demand determination in environmental waters by mixed-acid digestion and single sweep polarography" *Anal. Chim. Acta*, Vol. 420, 2000, pp. 39-44.
- [3] Dharmadhikari D.M, Vanerkar A.P, Barhate N.M, "Chemical oxygen demand using closed microwave digestion system" *Environ. Sci. Technol.*, Vol. 39, 2005, pp. 6198-6201.
- [4] Akio T, Keiichi K, Takashi N, Ryota S, and Hiromu T, "Landfill waste water treatment by application of pulsed high voltage" *Int. J. of GEOMATE*, Vol. 9, No. 1, 2015, pp. 1375-1379.
- [5] Chao W, Jiancheng W, Peifang W, Yanhui A, Jun H, and Jin Q, "Photoelectrocatalytic determination of chemical oxygen demand under visible light using Cu₂O-loaded TiO₂ nanotube arrays electrode" *Sensors and Actuators B*, Vol. 181, 2013, pp. 1–8.
- [6] Ponchio C, Yoshinori M, Shin-ya K, Atsuko Y N, Yoshio N, "Efficient photocatalytic activity of water oxidation over WO₃/BiVO₄ composite under visible light irradiation", *Electrochim. Acta*, Vol. 54, 2009, pp. 1147-1152.
- [7] Ponchio C, Atsuko Y N, Yoshio N, "Photoelectrocatalytic performance of WO₃/BiVO₄ toward the dye degradation", *Electrochim. Acta*, Vol. 94, 2013, pp. 314–319.

THE PERFORMANCE RAINFALL DURING RAINY SEASONAL OVER THAILAND BY USING PRELIMINARY REGIONAL COUPLED ATMOSPHERIC AND OCEANIC (WRF-ROMS) MODEL

Pramet Kaewmesri¹, Usa Humphries^{1*}, Boonlert Archevarapuprok² and Sirapong Sooktawee³

¹Department of Mathematics, Faculty of Science, King Mongkut's University of Technology Thonburi (KMUTT), 126 Pracha-Uthit Road, Bang mod, Thung khru, Bangkok 10140, Thailand;

²Thai Meteorology Department, Bangkok, Thailand;

³Environmental Research and Training Center, Department of Environmental Quality Promotion, Ministry of Natural Resources and Environment, Thailand

ABSTRACT

A coupled regional climate between atmosphere-ocean coupled model systems is developed using the regional model Weather Research and Forecasting (WRF) and Regional Ocean Modeling System (ROMS) to simulate performance rainfall during the rainy season over Thailand. The processes of the atmospheric model is provided to the ocean model. The wind (Uwind, Vwind), the atmospheric pressure (Patm), the relative humidity (RH), the atmosphere surface temperature (Tair), the cloud fraction (Cloud), precipitation (Rain), the short wave (SW), the long wave (LW). The processes of the oceanic model provides sea surface temperature (SST) to atmosphere model. The simulation period is during June-July-August (JJA) in 2014, and the results are compared with rainfall gauge station from Thai Metrology Department (TMD). The results show a good trend performance rainfall and can capture large amount rainfall in June, July and JJA 2014. The average rainfall and Mean Absolute Error (MAE) were show good value in June, July and JJA 2014, especially in June was shown good value average (236.25 mm) and MAE (4.389) than other months.

Keywords: Coupled Model, Rainy Season, Regional Ocean Modeling System (ROMS), Thailand, Weather Research and Forecasting (WRF)

INTRODUCTION

Seasonal prediction of the Asian Monsoon System (ASM) rainfall in advance with high spatial resolution is a major challenge due to influence of multiple factors, including the topography of the subcontinent and the impact of the surrounding oceans [1]. The ASM is regarded to be separate into two subsystems the Indian Ocean monsoon system and the East Asian Monsoon System (EAMS) [2]. The two main points of AMS has impact over Thailand, that regimes are the northeast monsoon (winter season) during November to March and the southwest monsoon (summer season) during mid-May to mid-October. The one important feature of climate in Thailand is rainfall. It is the main source of fresh water on the earth and is a major component of the hydrologic cycle on the earth's surface. Hence, in every annual year, the southwest monsoon (summer season) is blow wet air form the Indian Ocean to over country. So it make the rainfall over Thailand in this period. Sometime the rainfall events occurred in Thailand producing breaking flash flood and enormous amount of property damage. Therefore we can say, the rainfall is the main factor for agriculture, industrial, irrigation and etc. in

Thailand. However a good simulation and forecasting rainfall are main factor for improving water management. Because a good water management can prevent and decrease the damage from the natural disasters.

A majority of the Atmospheric General Circulation Model (AGCMS) has difficulty in simulating the mean well as the intra-seasonal variability of monsoon rainfall mainly due to the lack of air-sea interactions [3]. On the other hand, coupled models are powerful tools for enhancing the skill of seasonal simulation and forecasting. It's providing realistic simulation and forecasting over tropical phenomenon [4].

However, the researches in Thailand are based on rainfall event. They were used AGCM and standalone regional model to simulation rainfall events that were neglected of air-sea interactions. In this study, to use a regional couple modeling system by the Coupled Ocean Atmosphere Wave Sediment Transport (COAWST) to simulate rainfall in rainy season of Thailand. The simulation period was during June, July and August (JJA) in 2014. The results was basic compared with rainfall gauge station from Thai Metrology Department (TMD) data.

METHODOLOGY

The atmospheric model part

The atmosphere part of the coupled model is the Weather Research and Forecasting model (WRF). This model was developed by the National Center for Atmosphere Research (NCAR). The model is contained with a terrain following sigma coordinate in the vertical coordinate, Arakawa C-grid staggering for horizontal grid, initial conditions, boundary condition, multiple-nested domain and full set of physical parameterisation options. The more detailed description of WRF in [5]. The physics parameterizations used in this study that is: WSM3-class scheme for microphysics scheme, the Betts-Miller-Janjic (BMJ) for cumulus scheme, the Rapid Radiative Transfer Model (RRTM) for long wave radiation scheme, the Duhia for short wave radiation scheme, the Noah Land-Surface Model for surface and the Yon-Sei University (YSU) Planetary Boundary Layer (PBL) scheme PBL scheme. The model domain is covers over Thailand and neighbor with horizontal grid spacing of 30 km, 28 layers in vertical levels and the model top of 50 hPa.

The oceanic model part

The oceanic part of the coupled model is the Regional Ocean Modeling System (ROMS). This model is a general class free-surface, terrain-following numerical model that solve the three dimensional Reynolds-averaged Navier-Stokes equations using the hydrostatic and Boussinesq approximations. This model is based on primitive equation ocean model and uses finite-difference approximations on the Arakawa-C staggering in the horizontal with on a vertical stretched terrain-following coordinate. The basic ideal case study the values of thetas, thetab and Tcline in this study are 3.0, 0.4, and 50.0 respectively. The initial values of u wind (wind direction from east to west), v wind (wind direction from south to north), temperature, and salinity before transfer in coupled model are 0, 0, 35, and 18 respectively. The oceanic model domain is the same as the regional atmospheric model. The horizontal grid spacing is 30 km. But the vertical level of oceanic model is 21 levels. The model domain is shown in Fig.1.

The coupled and experiment configuration

In this study was used the Coupled Ocean Atmosphere Wave Sediment Transport (COAWST) model system. The COAWST model system is an agglomeration of open source modeling components that has been tailored to investigate coastal processes of the atmosphere, ocean, waves and coastal environment [6]. The coupler is the Model Coupling

Toolkit (MCT) that allow the transmission and transformation of various distributed data between component models using parallel coupled approach. MCT is a program written in Fortran90 and works with the MPI communication protocol. In this study used the COAWST coupled model to simulate WRF-ROMS over the rainy season in 2014 year. In the processes of the atmospheric model is provided to the ocean model. The wind (Uwind, Vwind), the atmospheric pressure (Patm), the relative humidity (RH), the atmosphere surface temperature (Tair), the cloud fraction (Cloud), precipitation (Rain), the short wave (SW), the long wave (LW). In the processes of the oceanic model provides sea surface temperature (SST) to atmosphere model [6]. The Fig.2 is represent a transfer parameter between atmosphere model and ocean model.

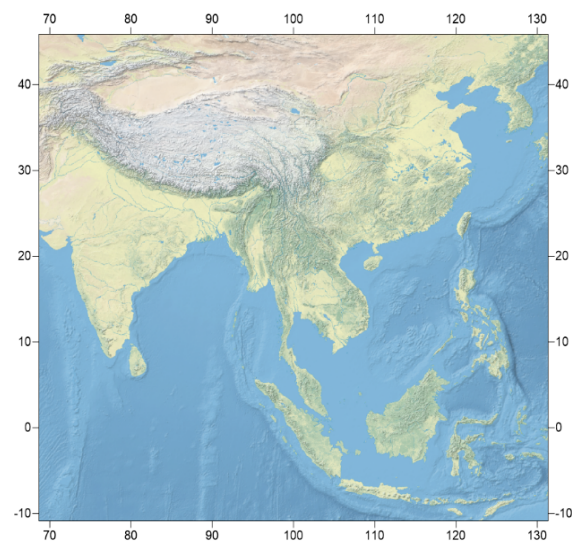


Fig. 1 The domain was used in this study. This domain has 179×179 grids spacing covering at latitude -10.86 degree north to 45.89 degree north and longitude 68.65 degree east to 131.35 degree east

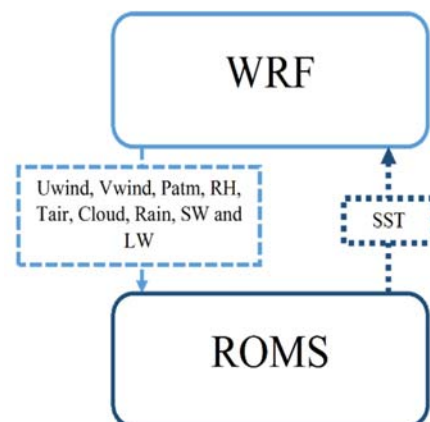


Fig. 2 The application was showed configurations of data exchanged WRF and ROMS model

The model runs were initialized at 0000 UTC 1 May 2014 and ended at 0000 UTC 31 August 2014 for a three month simulation. The first month simulation (May 2014) was regarded as model spin-up and excluded from comparison with observation, as show in Fig. 3.

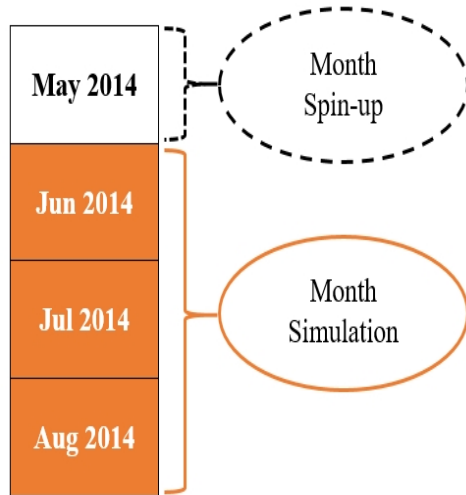


Fig. 3 The period month spin-up and month simulation in this study.

In this study was used the National Centers for Environmental Prediction (NCEP) Final Operational Global Analysis (FNL) data for initial data. The NCEP-FNL product is from the Global Data Assimilation System (GDAS). The grid spacing data are in 1-degree by 1-degree and 6-hourly intervals. The period of data during 1800 UTC 30 July 1999 to the present and the surface area covered longitude 180 degree east to 180 degree west and latitude 90 degree south to 90 degree north. Table 1 was concluded the physics parameterization schemes and scenario configuration.

The observation data used to verify the results from the model. In this study are measurements made at 118 gauge stations from the Thai Meteorological Department (TMD). The location of 118 gauge stations are covered Thailand, as shown in Fig 4.

Table 1 The physics parameterization schemes and scenario configuration.

Physics	Details
Cumulus scheme	BMJ
Microphysics scheme	WSM3
Short wave radiation scheme	RRTM
Long wave radiation scheme	Duhia
Planetary boundary Layer scheme	YSU
Land surface	Noah
Run period	3 Mon (JJA)

118 Gauge Station Data (TMD)

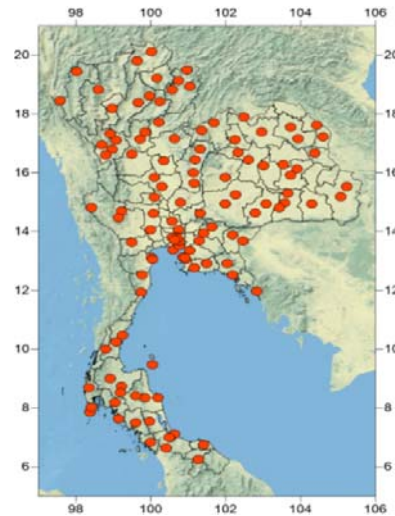


Fig. 4 The station locations used for model evaluations.

RESULT AND DISCUSSION

Fig 5 shows the month accumulate rainfall from TMD station data and month accumulate rainfall simulation from WRF-ROMS coupled model in June 2014.

The TMD station data show the rainfall distribution (in the rage of 0 mm to 400 mm) almost over the country. But the rainfall distribution with large amounts rainfall is (more than 500 mm) over Ubon Ratchathani and Nakhon Phanom province in the northeastern Thailand, Trat province in the coast eastern Thailand and Ranong province in the southern Thailand, as shown in Fig 5(a).

The WRF-ROMS coupled model shows the rainfall distribution (in the range of 0 mm to 400 mm) almost over the country. But the rainfall distribution with large amount rainfall is (more than 500 mm) over Ubon Ratchathani and Nakhon Phanom province in the northeastern Thailand, as shown in Fig 5(b).

Fig 6 shows the month accumulate rainfall from TMD station data and month accumulate rainfall simulation from WRF-ROMS coupled model in July 2014.

The TMD station data show the rainfall distribution (in the rage of 0 mm to 400 mm) almost over the country. But the rainfall distribution with large amounts rainfall is (more than 500 mm) over Ubon Ratchathani, Bung Kan and Nakhon Phanom province in the northeastern Thailand, Trat province in the coast eastern Thailand and Ranong province in the southern Thailand, as shown in Fig 6(a). The

WRF-ROMS coupled model shows the rainfall distribution (in the range of 0 mm to 400 mm) over center, lower northeastern and lower southern Thailand.

But the rainfall distribution with large amount rainfall is (more than 500 mm) over northern, upper northeastern, western, Rayong and Trat province over coast eastern Thailand, as shown in Fig 6(b).

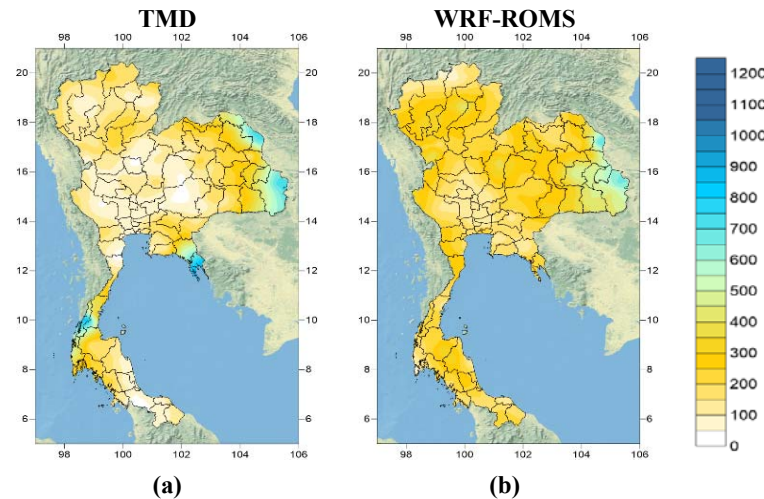


Fig. 5 Spatial rainfall pattern of month accumulate rainfall (mm) in June 2014: a) TMD and b) WRF-ROMS.

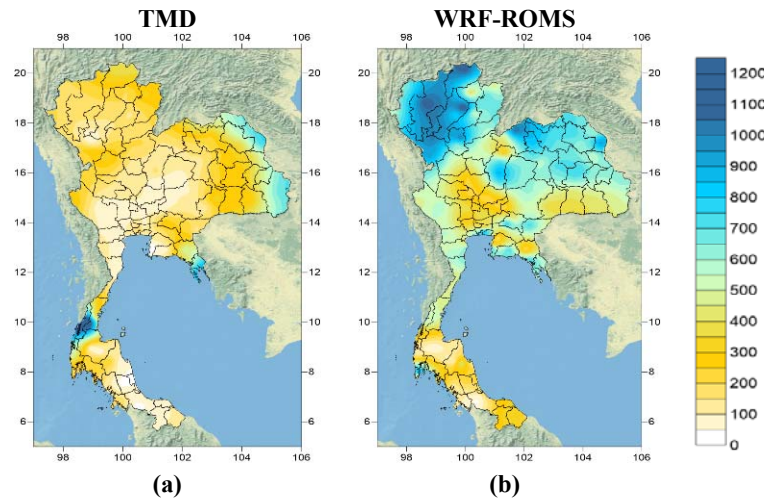


Fig. 6 Spatial rainfall pattern of month accumulate rainfall (mm) in July 2014: a) TMD and b) WRF-ROMS.

Fig 7 shows the month accumulate rainfall from TMD station data and month accumulate rainfall simulation from WRF-ROMS coupled model in August 2014.

The TMD station data show the rainfall distribution (in the range of 0 mm to 400 mm) almost over the country. But the rainfall distribution with large amounts rainfall is (more than 500 mm) over Mae Hong son in northern and Trat province in the coast eastern Thailand and Ranong province in the southern Thailand, as shown in Fig 7(a).

The WRF-ROMS coupled model shows the rainfall distribution (in the range of 0 mm to 400 mm) almost southern and center of Thailand. But the rainfall distribution with large amount rainfall is

(more than 500 mm) over northern, Bung Kan, Sakon Nakhon, Nong Khai and Udon Thani province in northeastern, Sa Kaeo province in coast eastern and Kanchanaburi province in western Thailand, shown in Fig 7(b).

Fig 8 shows the month accumulate rainfall from TMD station data and month accumulate rainfall simulation from WRF-ROMS coupled model in June-July-August (JJA) 2014.

The TMD station data show the rainfall distribution (in the range of 0 mm to 400 mm) almost over the country. But the rainfall distribution with large amounts rainfall is (more than 500 mm) over Ubon Ratchathani and Nakhon Phanom province in

the northeastern, Trat province in the coast eastern Thailand and Ranong province in the southern Thailand, as shown in Fig 8(a).

The WRF-ROMS coupled model shows the rainfall distribution (in the range of 0 mm to 400 mm) almost southern and center of Thailand. But the

rainfall distribution with large amount rainfall is (more than 500 mm) over almost northern, Loei, Nong Bua Lamphu, Amnat Charoen, Yasothon, Nakhon Phanom and Udon Thani province in northeastern Thailand, as shown in Fig 8(b).

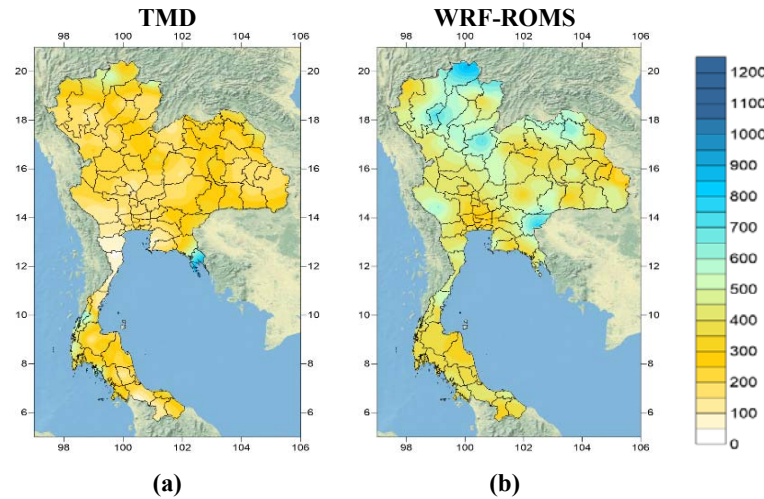


Fig. 7 Spatial rainfall pattern of month accumulate rainfall (mm) in August 2014: a) TMD and b) WRF-ROMS.

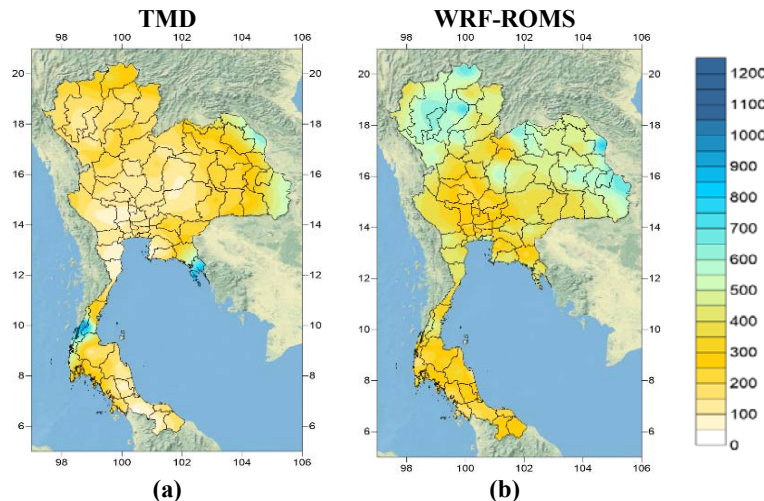


Fig. 8 Spatial rainfall pattern of month accumulate rainfall (mm) in JJA 2014: a) TMD and b) WRF-ROMS.

Table 2 was shown the average rainfall. It was shown overestimate average rainfall than the TMD data in all cases. The Mean Absolute Error (MAE) was shown good performance in June (4.389). But show a more MAE value in July (12.126). In summary, the results was overestimated in average rainfall and the MAE results shown good performance with TMD data.

Fig. 10 shows the temporal MAE over Thailand. It's shown less significant (more than 12) over Chiangmai, Lamphun, Lampang, Phetchabun and Chiangrai in northern, Loei in northeastern, Trat in

eastern, Ranong and Phang Nga in southern Thailand. However, the overall of temporal MAE was shown good performance (less than 12) in many part of Thailand. For example over central, western, lower southern and northeastern Thailand.

CONCLUSION

In this research used a preliminary coupled model between atmospheric model WRF and Oceanic model (Regional Ocean Modeling System (ROMS)) to simulation performance rainfall during

the rainy season over Thailand.

Table 2 Comparison TMD and WRF-ROMS

	Average (mm)		MAE
	TMD	WRF-ROMS	
Jun	186.45	236.25	4.389
Jul	214.77	540.04	12.126
Aug	237.98	416.32	7.150
JJA	213.07	397.54	7.201

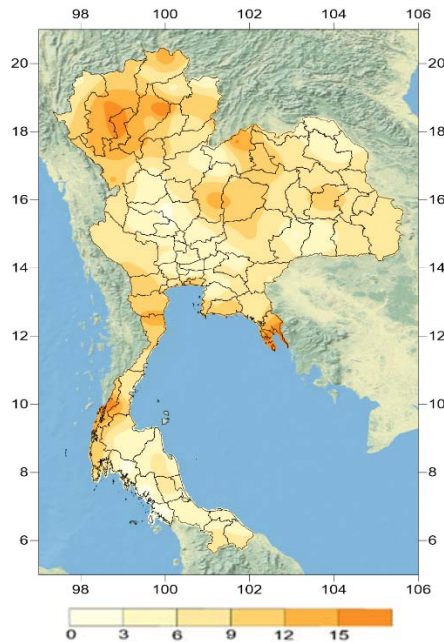


Fig. 10 The temporal MAE in JJA 2014 over Thailand.

The simulation period is during June-July-August (JJA) in 2014. The results from coupled models were shown overestimate accumulate rainfall in June, July, and August 2014. Table 2, the average rainfall were confirmed the coupled model overestimating in all cases.

However, it can capture the large amount rainfall similarly TMD data. In June 2014, the coupled model can capture large amount rainfall similar TMD over Ubon Ratchathani and Nakorn Phanom province in northeastern. In July 2014, the coupled model can capture large amount rainfall similarly TMD over Ubon Ratchathani and Nakorn Phanom province in northeastern and Trat province in eastern. In June-July-August (JJA) 2014, the coupled model can capture large amount rainfall similar TMD over Ubon Ratchathani and Nakorn Phanom province in northeastern.

Therefore, the WRF-ROMS coupled model performed overestimate in simulating spatial

distribution, compared with the TMD. However, the results show in a good trend performance rainfall and can capture large amount rainfall in June, July and JJA 2014. When comparison rainfall gauge stations by using MAE method over Thailand. The MAE shown the relation between TMD and the coupled model similar average rainfall value. The temporal MAE was shown good performance over Thailand. Future work, we will improve the result from the coupled model (WRF-ROMS). We will update the initial boundary condition from ideal case to real case in Oceanic model (ROMS).

ACKNOWLEDGEMENTS

The authors are also grateful NCEP for the FNL data sets, TMD for the station data sets, NCAR for the WRF model and the Department of Mathematics, Faculty of Science, King Mongkut's University of Technology Thonburi (KMUTT). This research was fully supported by the International Research Network (IRN) (IRN5701PDW0002).

REFERENCES

- [1] Salama BK, Nagaraju C, Banerjee S, Kagainalkar A and Dalvi M, "Study of the Indian summer monsoon using WRF-ROMS regional coupled model simulation", *Atmospheric science letters*, Vol. 14, Aug. 2012, pp. 20-27.
- [2] Pokhrel S, Chaudhari HS, Subodh KS, Dhakate A, Yadav RK, Salunke K, Mahapatra S, Suryachandra AR, "ENSO, IOD and Indian Summer Monsoon in MCEP climate forecast system", *Clim Dyn*, Vol. 39, Mar 2012, pp. 2143-2165
- [3] Rajendran K, Kitoh A and Arakawa O, "Monsoon low-frequency oscillation and ocean-atmosphere coupling over the Indian Ocean", *Geophysical Research Letters*, Vol. 31, L002210, DOI:10.1029/2003GL019031
- [4] Kristma KK, Hoerling M, Rajagopalan B, "Advancing dynamical prediction of Indian monsoon rainfall", *Geophysical Research Letters*, Vol. 32, L0874, DOI:10.1029/2004GL021979.
- [5] Skamarock WC, Klemp JB, Dudhia J, Gill DO, Barker DM, Duda MG, Huang XY, Wang W, and Powers JG, A description of the Advance Research WRF Version 3. National Center for Atmospheric Research, Boulder, Colorado, 2008.
- [6] Warner JC, Armstrong B, He R, and Zambon, JB, "Development of a Coupled Ocean-Atmosphere-Wave-Sediment Transport (COAWST) modeling system", *Ocean Modeling*, Vol. 35, July 2010, pp. 230-244.

THE LONG TERM CHANGE OF FORM OF NITROGEN IN YAMATO RIVER BASIN

Masanobu Taniguchi¹ and Hiryuki Ii¹

¹ Faculty of System Engineering, Wakayama University, Japan

ABSTRACT

The long term of the amount of pollutant load was estimated by relation between water level and water quality. The long term data is not enough to the calculation of the amount of pollutant load. The pollutant load in floods is not cleared, so the pollutant load in flood condition is important for the annual pollutant load. The water quality is improved, and the water quality target is being achieved in the Yamato River. To improve the water quality, the sewage systems had been constructing from 1970's in Yamato River Basin. The amount of annual nitrogen load in 2011 was estimated in 2016 by Taniguchi et al. However the long term change of amount of annual load is unclear. It is estimated that the form of nitrogen load was changed. This research is consider the influence for water quality of the construction of sewage system, improvement of riverbed and the River purification facility. It is estimate that the treatment systems had change the environment of the oxygen in the river bed.

Keywords: Annual load, Water quality, Nitrogen, River flow rate, Sewage system

INTRODUCTION

The Yamato River had problems of waste water from sewage. The river water was polluted in 1970's, as the city developed rapidly. The sewage system in the Yamato River Basin had established while each year. The condition of the water quality in the Yamato River was improved from 1970 to 2017. It is estimated that the nitrogen form in the river water was changed by the oxygen condition. The water quality and water flow of the database system was published by Japanese governments. Resultingly, there was not enough data to calculate the amount of nitrogen load in Yamato River Basin[1] It is necessary that clear the relation between everyday data of water quality example EC and nitrogen concentrations. The research purpose is clear the relation between the everyday data and the monthly data. Moreover estimate the nitrogen load form change from 1970 to 2016.

RESEARCH AREA AND METHOD

Fig.1 shows the map of the Yamato River Basin. Fig.2 shows the population of the Yamato River Basin. River basin is 1070km². Green, yellow, pale blue and purple colors show forests, orchards, rice fields and housing sites. The population of the basin is about 2 million people in 2015. The basin has big cities in its upper stream, and the population of the Nara basin is 1 million people. Population increased significantly in high-growth period. The sewage system has been in use since 1970s. The cover area of

the sewage system was 7.4% in 1975, 33% in 1990, 58.7% in 2000 and 85.3% in 2013[3]. The analysis of nitrogen load was performed using data for the water information system of Ministry of Land, Infrastructure, Transport and Tourism, Japanese Government. However there was not enough data to calculate the amount of nitrogen load in Yamato River Basin, so some estimation methods were applied for making this calculation[4].

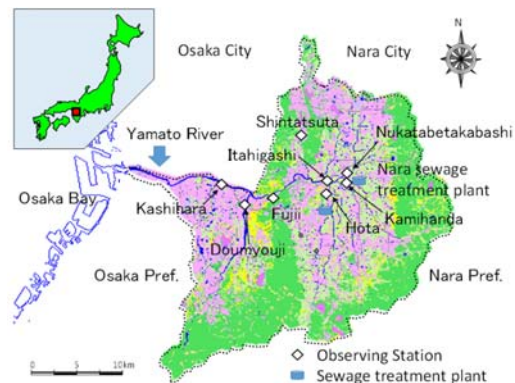


Fig. 1 Map of the Yamato River Basin

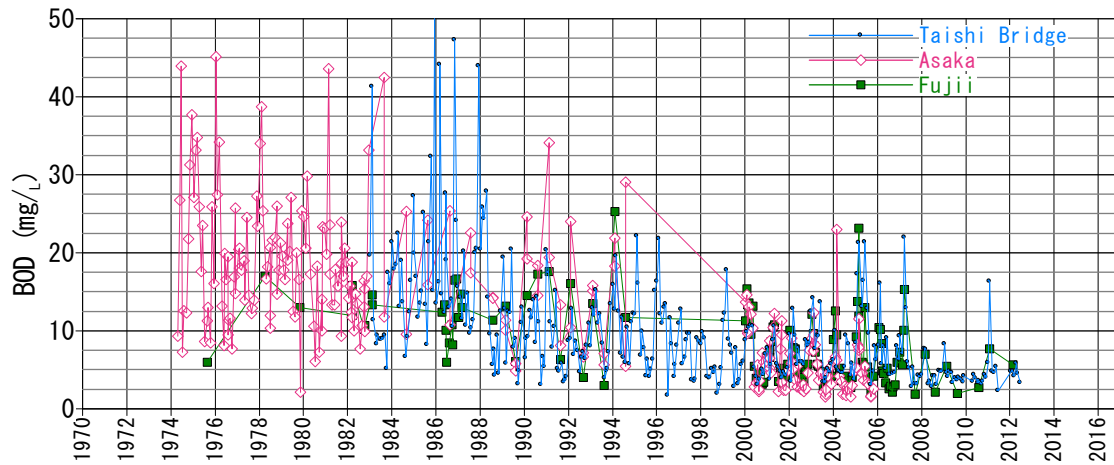


Fig. 3 Time series of BOD concentration

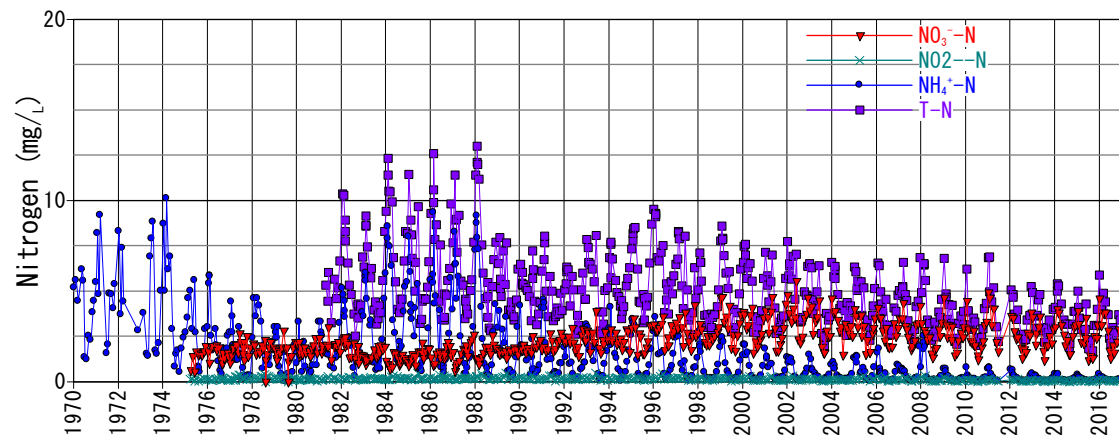


Fig. 4 Time series of nitrogen concentration at Fujii

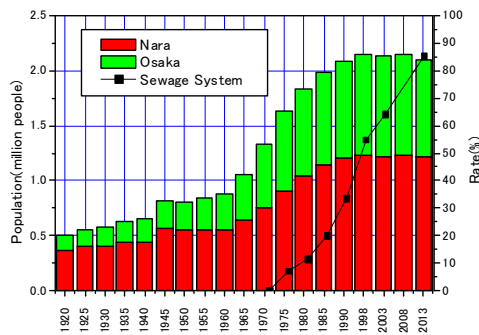


Fig. 2 Population of the Yamato River Basin

TIME SRIES OF WATER QUARLTY AND FLOW RATE

Fig. 3 shows a time series of BOD concentration at Fujii, Asaka and Taishi Bridge. The graph used data of Ministry of Land, Infrastructure and Transport. The BOD concentration was high from

1974 to 1988. And the BOD concentration in 2012 decreased about the one-fourth of 1970's. The Taishi Bridge is located at lower stream of the out flow point of Sewage System in Nara. And Fujii is located in lowest point of the Nara Basin, The water in the Nara Basin is collected at the point. Asaka is lowest point of the Yamato River Basin. The BOD concentration is not measured in all years. So it is difficult to know the annual BOD load, and estimate the influence of decompose the Organic compound by the data only. However the BOD change tends several year is similar, the BOD concentration range is same in 3 points. Therefore it is estimated that the BOD concentration is not almost change at the 3 point in the River. The trends of the BOD concentration is analyzed at the follow in detail.

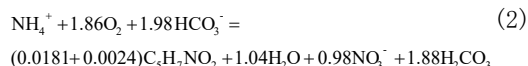
Fig. 4 shows the time series of nitrogen concentration at Fujii. The Total-Nitrogen is high from 1982 to 1988, same as BOD concentration tends. The T-N concentration is not measured before 1981. The ammonia nitrate concentration is high from 1970 to 1988. The ammonia nitrogen concentration decrease from 1989 to 2012. The nitrate nitrogen

concentration tends to increase year by year from 1976 to 1999, and not change after 2000. Nitrite nitrogen concentration is always low.

Generally, organic compounds in an anaerobic condition were decomposed to ammonia by bacteria. The reaction formula is given by the following equation (1).

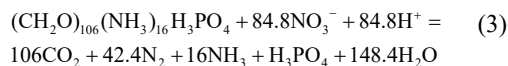


The Nitrification in an aerobic condition is shown by the following equation (2).

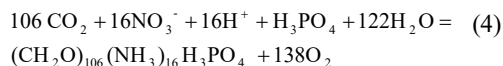


Generally Ammonia changes into nitrate in aerobic conditions and then finally organic compounds change into nitrate. These reactions depend on activity of living organisms. Temperature is important for the activity of the organisms. However nitrate nitrogen concentration did not change with temperature. Nitrate acid was consumed by photosynthesis or denitrification and the biological activities of photosynthesis or denitrification were also dependent on temperature.

Denitrification reaction is shown by the following equation (3).



Photosynthesis reaction is shown by the following equation (4).



As the form of nitrogen is change by the reactions, the nitrogen concentration is

INFLUENCE OF DECOMPOSITION OF ORGANIC COMPONENT

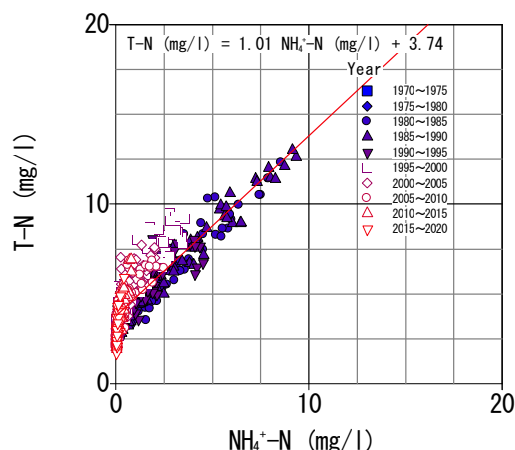


Fig. 5 Relation between T-N and ammonia nitrate concentration at Fujii

Fig. 5 shows the relation between T-N and ammonia nitrate concentration at Fujii. T-N concentration was increased with ammonia nitrate concentration, and T-N concentration was decreased in recent years. The ammonia nitrogen concentration is different by period. The cause is the sewage system is constructed constantly in the period, and it is estimated that the sewage water had become gradually not directly inflow the river. As the ammonia is created by organic compound decomposed, the cause of ammonia rich is that organic compound become ammonia in the river, or not inflow ammonia directly. It was estimate that the ammonia nitrate concentration has been tend to include by constant ratio against T-N. In recent years, as the ammonia nitrogen concentration is low, it was estimate that organic compound did not flow into river, or ammonia was change to nitrate. The ammonia nitrogen concentration before 2000 is increased with T-N concentration. The T-N concentration 1970s was estimated from ammonia nitrogen concentration.

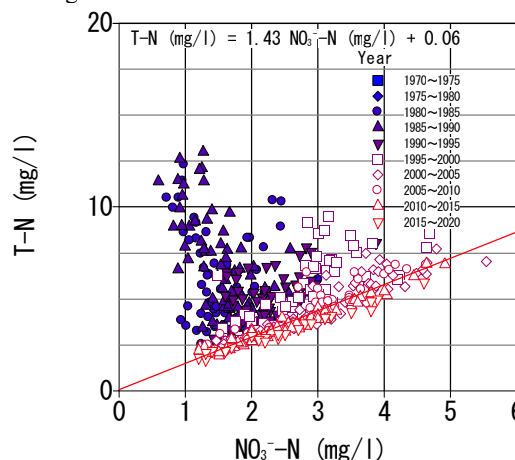


Fig. 6 Relation between nitrogen nitrate concentration

and T-N at Fujii

Fig. 6 shows the relation between T-N and nitrate nitrogen concentration at the Fujii. The nitrate nitrogen concentration is clearly increased with T-N concentration after 2000. However the nitrate nitrogen concentration is not related to T-N concentration before 2000. Moreover T-N concentration is high in low nitrate nitrogen concentration. It is estimated that the nitrate nitrogen change became clearly by construction of the sewage system. Recent years, the 80% of amount of river water in the Yamato River Basin is treatment water of sewage system. It is estimated that the water quality of the river water is almost due to the sewage system condition. However before 2000, the housing water of sewage is inflow directly into the river, in the river, the organic compound of nitrogen is change to ammonia, finally change nitrate. The chemical change of nitrogen is due to the fungus, the reaction is different by water temperature, therefore it is estimated that nitrogen concentrations is not stable.

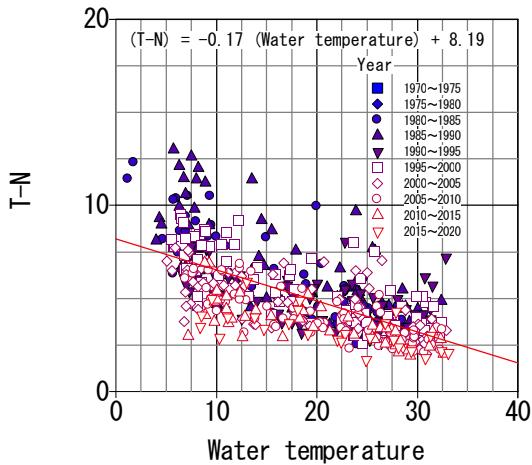


Fig. 7 Relation between water temperature and T-N at Fujii

Fig. 7 shows the relation between water temperature and T-N at Fujii. The T-N concentration is decreased with Water temperature. The T-N concentration before 2000 is tend to higher than its after 2000. It is estimated that the cause of high T-N concentration is due to high ammonia concentration exist, it is considered that more actually nitrogen load can be calculated. Moreover it was estimated that the nitrogen concentration can be calculated using by temperature before and after 2000.

WATER LEVEL CHANGE AND NITROGEN CONCENTRATION CHANGE

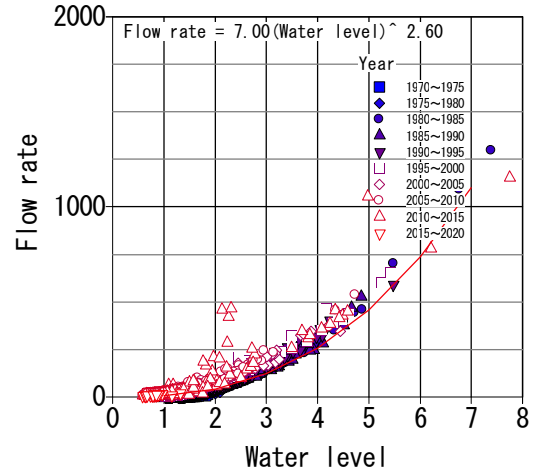


Fig. 8 Relation between Water level and flow rate at Fujii

Fig. 8 shows the relation between water level and flow rate at Fujii. The water level is measured every day, however flow rate is not measured every day, and moreover flow rate in flood time cannot measured direct. Therefore the flow rate is calculated using next formula by the water level.

$$F = 7.00W^{2.60} \quad (5)$$

F : Flow rate (m^3/sec) W : Water level (m)

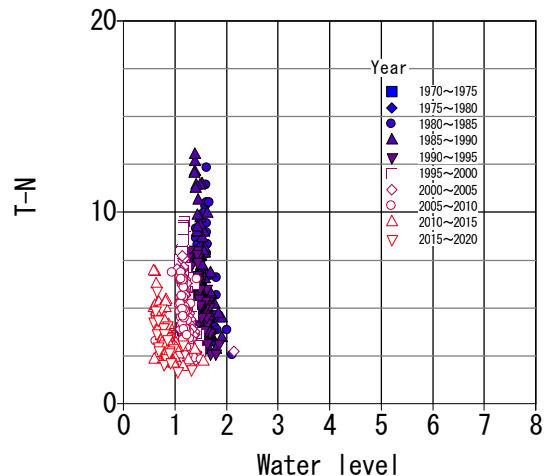


Fig. 9 Relation between water level and T-N concentration at Fujii

Fig. 9 shows the relation between water level and T-N concentration at Fujii. The T-N

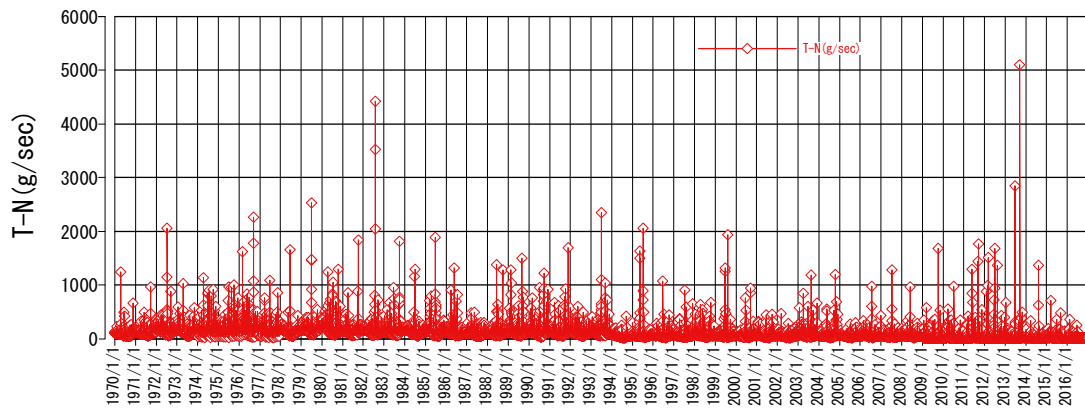


Fig. 11 Time series of T-N load (g/sec)

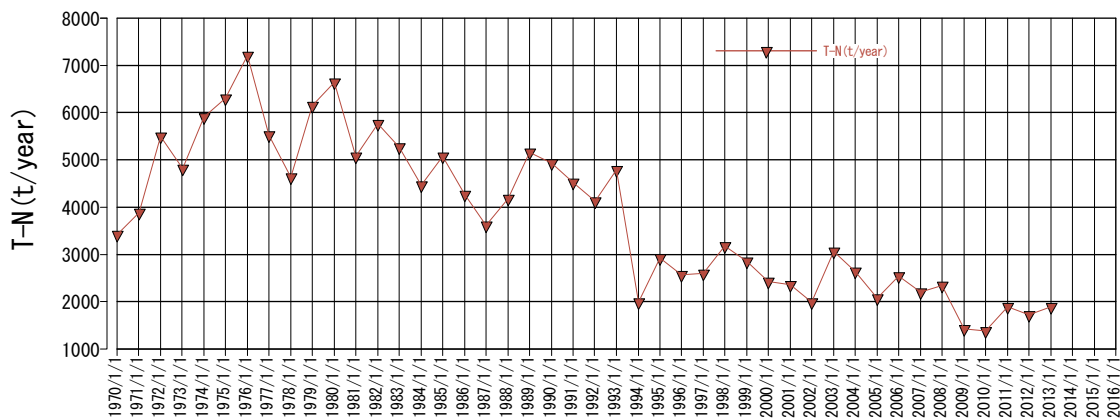


Fig. 12 Time series of T-N load (t/year)

concentration is not change by the water level. The range of water level is narrow, and the range of seasonal change of T-N concentration is tend to large compared with range of water level. It was estimated that the T-N concentration is not influenced by the increased the flow rate by precipitation et.al. Generally it is considered that the T-N concentration is decreased with cause of dilution of precipitation. However T-N concentration is not decreased by dilution, moreover it is estimated the nitrogen is supply from other source example farmland or rice field. Therefore it was considered that the T-N concentration is small influenced by dilution.

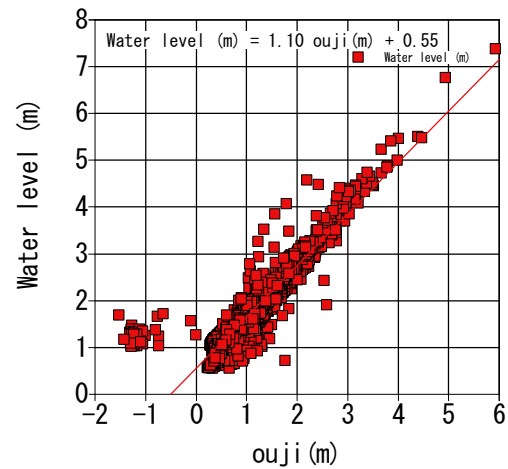


Fig. 10 Relation between the water level at the Uji and the water level at the Fujii

Fig. 10 shows the relation between the water level at Uji and the water level at Fujii. Uji is located upper about 2.7km distance from Fujii. The section from Uji to Fujii has only little stream, the flow rate of the little stream is not influence. The water level at Fujii was no data in several year, so the water level at Fujii was interpolated by the water level

data at Uji. The water level at Fujii was calculated by next formula.

CALCULATION OF ANNUAL LOAD

Fig. 11 and 12 show the time series of T-N load. The T-N concentration was related to water temperature. The T-N load could be calculated roughly. The flow rate was calculated from the water level. The T-N load was multiplied flow rate and T-N concentration. Generally, in the case of calculation of the load amount, the influence of the flow rate is larger than the concentration. Annual total nitrogen load at Fujii station was calculated to be maximum 7208t/year in 1976, minimum 1334t/year in 2010. The T-N load was decreased less than 3500t/year after 1994. It is estimated that the cause of T-N load of decrease is influence of construction of the sewage system and the river purification facility.

CONCLUSION

The amount of nitrogen load was estimated and the distribution of nitrogen load was analyzed in Yamato River Basin from 1970 to 2016. Although there was not enough data to calculate nitrogen load in the basin, some estimation methods were applied for calculation. At Fujii station, flow rate is calculated by water level. Total nitrogen load is estimated using water temperature. Annual total nitrogen load at Fujii station was calculated to be maximum 7208t/year in 1976, minimum 1334t/year in 2010. The T-N load was decreased less than

3500t/year after 1994. It is estimated that the cause of T-N load of decrease is influence of construction of the sewage system and the river purification facility. The main nitrogen form before 2000 was ammonia, the main after 2000 was change to nitrate.

As against the ratio of T-N is cleared, it was estimated that the nitrate nitrogen load was about 70% of T-N after 2000, and the ammonia nitrogen load was more than 50% of T-N before 2000 when there are many.

REFERENCES

- [1] Masanobu Taniguchi, Hiroyuki Ii, Tatemasa Hirata, Analysis of organic nitrogen compound in domestic sewage in Yamato River using a social experimental test, 2010, vol. 30, Part 10, p. 1587-1590, Stuttgart, April 2010
- [2] Ministry of Land, Infrastructure and Transport, Japan, Water information system, <http://www1.river.go.jp/>
- [3] Yamato River construction office, <http://www.yamato.kkr.mlit.go.jp/YKNET/index.html>
- [4] Masanobu Taniguchi, Hiroyuki Ii, Tatemasa Hirata, The development of water resource system – The Water balance of Yamato River Basin, Environmental Engineering Research Papers Vol. 48, 2011.
- [5] Isamu Munemiya, Hiroshi Tsuno: Environmental Water Quality Studies, CoronaSy, in Japanese, p48, 2001.
- [6] Mikio Hino: Clear hydraulics, p138-152, in Japanese, 1983

HEAVY METAL CONCENTRATION OF SEAWEED BY INFLUENCE ON COPPER MINE AT SADAMISAKI PENINSULA

Erika Ueno¹ and Hiroyuki Ii²

¹Graduate School of Systems Engineering, Wakayama University, Japan;

²Faculty of Systems Engineering, Wakayama University, Japan

ABSTRACT

There were about 66 copper active mines in the Sadamisaki Peninsula from middle Meiji to Taisho era although all mines closed. It is important to evaluate influence of waste water and tailings from mines accompanied with past copper mine activity on environment for surrounding area. Sea water heavy metal concentration is low and changeable however heavy metal concentration of seaweed is generally high because of bio-concentration and depends on long term surrounding condition. Therefore, it is easy to measure heavy metal concentration and to evaluate long term environment. Then, seaweeds were sampled at both the Sadamisaki Peninsula and the surrounding non copper mine areas, the Yashiro Island in Yamaguchi prefecture and Kada in Wakayama prefecture and copper, iron, manganese, lead, zinc and arsenic concentrations of seaweeds were measured. As a result, copper and iron concentrations of green seaweed at sampled at the Takaura Bay in the east of the Sadamisaki Peninsula were 100 to 350 ppm and 100 to 1000 ppm respectively and ten times higher than those of the other samples. Manganese, lead, zinc and arsenic concentrations for seaweed sampled at the Sadamisaki Peninsula were almost the same as those sampled at the other areas. As ore minerals of the copper mines were mainly pyrite FeS_2 and chalcopyrite CuFeS_2 , the waste water and tailing contained iron and copper. The biggest mine, the Takaura mine in the Sadamisaki area faced the Takaura Bay. High copper and iron concentrations of seaweed sampled at the Takaura Bay were thought to indicate contamination caused by activity of copper mine.

Keywords: Heavy metal, Mine, Seaweed, Contamination

INTRODUCTION

Seaweed contains 15 kinds of trace elements besides various kinds of minerals taken from sea water. The elements are indispensable for human beings and humans and marine creatures [1]. Seaweed gets nutrition and heavy metal by taken in seawater. Then, seaweed reserves the heavy metals such as arsenic in the body for long term. This characteristic is bioconcentration. It is clear that heavy metal concentration in seaweed is higher than that in seawater by bioconcentration. In previous studies, characteristics of trace element concentration in each region were studied [2]-[6].

The one of the study area is the Sadamisaki Peninsula located in the western part of Ehime prefecture and the area is famous for many closed copper mines operated in Taisho to beginning of Showa era [7]. And development of mines was actively carried out in Taisho era.

Figure.1 shows points of mining trace in the Sadamisaki Peninsula. There were 66 mine traces operated during the heyday. Although at present all mines closed, waste water from some closed mines and from tailings of mines still flows into sea. As the most area of the Sadamisaki Peninsula is mountainous and its coast is steep slope and cliff, waste water directly flows into sea.

Therefore, seaweed sampled around the



Fig.1. Points of mining trace

Sadamisaki Peninsula can be assumed as seaweed in metal contamination sea. Then, seaweed in the Sadamisaki Peninsula and the other areas are sampled and their metal contaminations are measured for evaluating metal contamination in sea.

METHOD AND STUDY AREA



Fig.2. Sampling area

Fig.2 shows sampling area, the Sadamisaki Peninsula, Yashiro Island in Yamaguchi prefecture and Kada in Wakayama Prefecture.



Fig.3. Sampling points at the Sadamisaki Peninsula

Fig.3 shows 14 sampling points around the Sadamisaki Peninsula, 8 points along the Seto Inland Sea and 6 points along the Uwakai Sea.

8 sampling points along the Seto Inland Sea are Lighthouse, Yobokori, Myoujin, Kojima, Ooe, Ikatagoshi, Mue and Izumi, 6 points along the Uwakai Sea are Uchinoura, Takaura, Inoura, Natori, Futami and Mekkomisaki.

The seaweed are collected at the time of the ebb tide.

The collected seaweeds are dried and then dissolved with concentrated nitric acid. Heavy metal concentration of solution is measured by ICP-AES. Heavy metal concentration in seaweed was calculated according to equation (1)

$$\text{Concentration in dry weight(ppm)} = \frac{\text{Concentration in liquid(ppm)} \times \text{Weight of nitric acid(g)}}{\text{Dry weight of sample(g)}} \quad (1)$$

RESULTS

The heavy metal concentrations in seaweed at the Sadamisaki Peninsula

In the previous study, heavy metal concentration in seaweed at the Kii Peninsula was measured and heavy metal concentration pattern for each seaweed species was also clarified. It's known that Cu, Fe and Mn concentrations in green seaweed were higher than those in brown and red seaweed and that there was no clear difference of Pb and Zn concentrations among green, brown and red seaweeds and that As concentration in brown seaweed was higher than those in green and red seaweed. In this research, to clarify the tendency around the Sadamisaki Peninsula based on the previous study.

Cu concentrations in seaweed

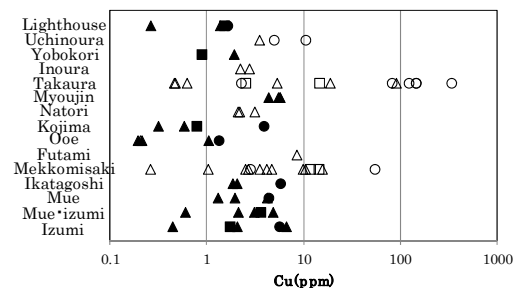


Fig.4.1 Cu concentration in seaweed at the Sadamisaki Peninsula

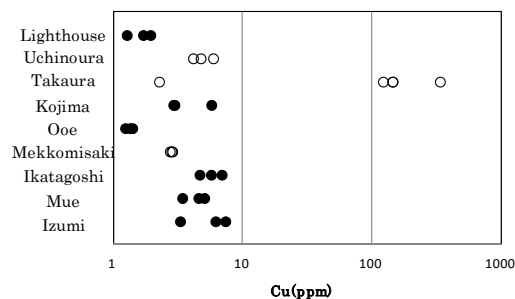


Fig.4.2 Cu concentration in Ulvaes at the Sadamisaki Peninsula

Fig.4.1 shows Cu concentration of seaweed. Green seaweed, brown seaweed, and red seaweed are shown as circle, triangle and square. The Seto Inland Sea and the Uwakai Sea are shown as solid and open symbol. Cu concentrations in seaweed along the Seto Island Sea were 0.19 to 6.57 ppm, Cu concentrations in seaweed along the Uwakai were 0.26 to 337 ppm.

Fig.4.2 shows Cu concentrations in Ulvaes. Cu concentrations in most green seaweed were 1 to 10 ppm. Especially, Cu concentration in green seaweed at Takaura was 121 to 334 ppm.

Fe Concentration in Seaweed

Fig.5.1 shows Fe concentrations in seaweed at the Sadamisaki Peninsula. Fe concentrations in seaweed along the Seto Inland Sea were 30 to 1676 ppm, and along the Uwakai were 30 to 8196 ppm.

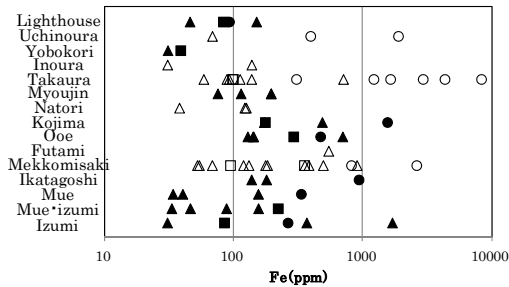


Fig.5.1 Fe concentrations in seaweed at the Sadamisaki Peninsula

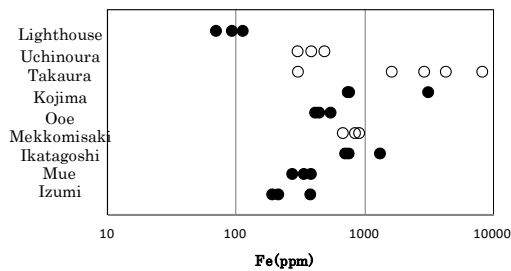


Fig.5.2 Fe concentrations in Ulvaes at the Sadamisaki Peninsula

Fig.5.2 shows Fe concentration in Ulvaes. Fe concentrations at Kojima and Ikatagoshi were 3109 ppm and 1313 ppm, Fe concentrations at Takaura and Mekkumisaki were 1619 to 8195 ppm and 3082 to 4102 ppm.

Mn Concentration in Seaweed.

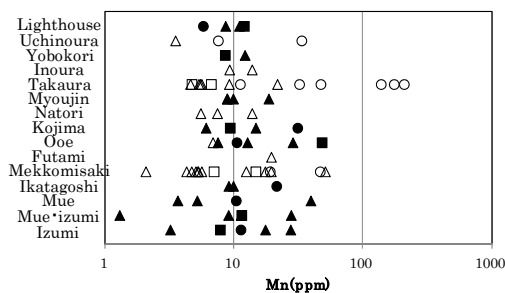


Fig.6 Mn concentrations in seaweed at the Sadamisaki Peninsula

Fig.6 shows Mn concentrations in green seaweed along most points were several to several 10 ppm. Especially Mn concentrations in Ulvaes at Takaura were 136 to 206 ppm.

Pb Concentration in Seaweed

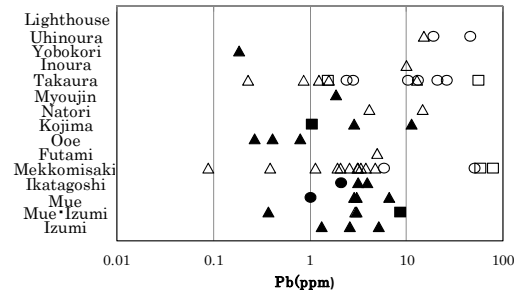


Fig.7 Pb concentrations in seaweed at the Sadamisaki Peninsula

Fig.7 shows Circles show green seaweed, triangles show brown seaweed, and squares show red seaweed. Pb concentrations in green, brown and red seaweed at 8 points along the Seto Inland Sea were 0.1 to 10 ppm. On the other hand Pb concentrations in green, brown and red seaweed at 7 points along the Uwakai Sea were 0.1 to several 10 ppm. Therefore Pb concentrations at the Sadamisaki Peninsula were no clear difference between green, brown and red seaweed.

Zn Concentration in seaweed

Fig.8 shows Circles show green seaweed, triangles show brown seaweed, and squares show red seaweed. Zn concentrations in green, brown and red seaweed at all 15 points were 10 to 100 ppm. Therefore there was no clear difference in 15 points.

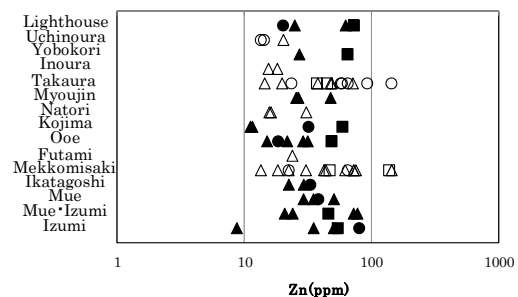


Fig.8 Zn concentrations in seaweed at the Sadamisaki Peninsula

As Concentration in Seaweed

Fig.9 shows As concentrations in brown seaweed at all fifteen points were several to 100 ppm. Therefore there was no clear difference in 15 points.

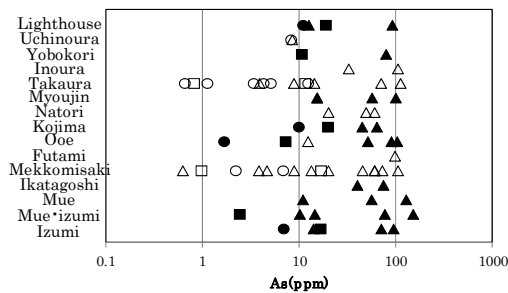


Fig.9. As concentrations in seaweed at the Sadamisaki Peninsula

The heavy metal concentrations in seaweed at the three sampling areas

The heavy metal concentrations in seaweed at the Sadamisaki Peninsula were compared with the Yashiro Island and Kada. The Yashiro Island is along the Seto Island Sea, Kada is along the Osaka bay.

Cu concentrations in seaweed

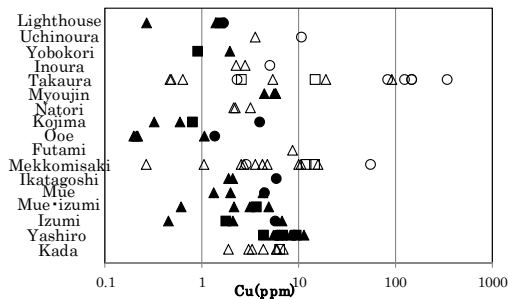


Fig.10 Cu concentrations in seaweed at the three sampling area

Fig.10 shows Cu concentrations in seaweed at the three sampling area. Cu concentrations in seaweed at Takaura were higher than those of the other area.

Fe concentrations in seaweed

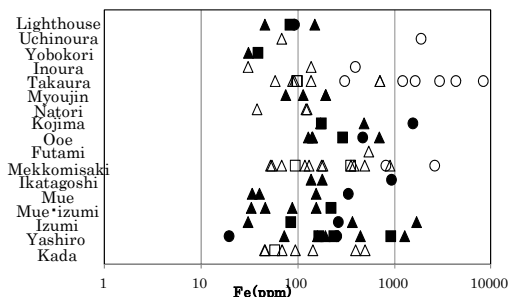


Fig.11 Fe concentrations in seaweed at the three sampling area

Fig.11 shows Fe concentrations in seaweed at the three sampling area. Fe concentrations in seaweed at Takaura were higher than those of the other area.

Mn concentrations in seaweed

Fig.12 shows Mn concentrations in seaweed at the three sampling area. Mn concentrations in seaweed at the Yashiro Island were higher than those of the Sadamisaki Peninsula.

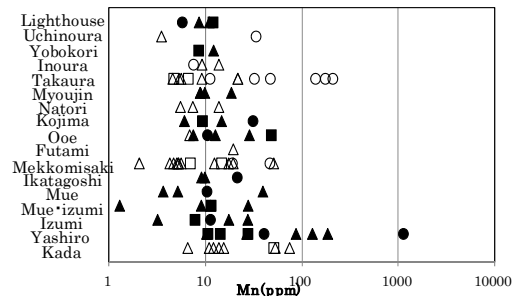


Fig.12 Mn concentrations in seaweed at the three sampling area

Pb concentrations in seaweed

Fig.13 shows Pb concentrations in seaweed at the three sampling area. Pb concentrations in seaweed at Takaura and Mekkomisaki were higher than those of the other area.

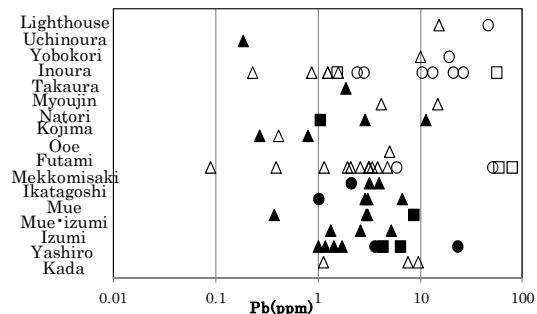


Fig.13 Pb concentrations in seaweed at the three sampling area

Zn and As concentrations in seaweed

Fig.14 and 15 show Zn and As concentrations in seaweed at the three sampling area. Zn and As concentrations in seaweed at the Sadamisaki Peninsula were not higher than those of the other area.

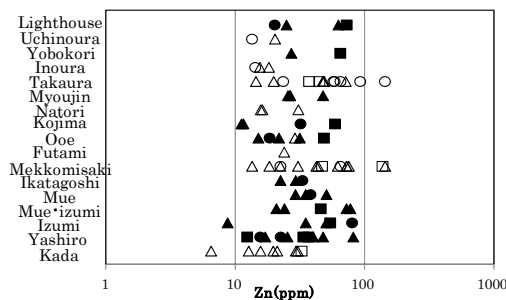


Fig.14 Zn concentrations in seaweed at the three sampling area

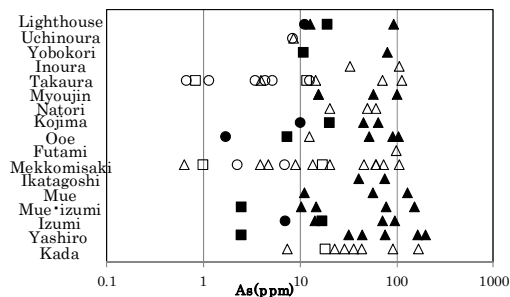


Fig.15 As concentrations in seaweed at the three sampling area

DISCUSSION

Cu and Fe concentrations in Ulvales at Takaura were higher than those of the other areas.

The heavy metal concentrations were studied about seaweed species at Takaura. Cu, Fe and Mn concentrations in Ulvales at Takaura were about 10 to 20 times higher than those of the other kinds of seaweed at Takaura although Pb, Zn and As concentrations in Ulvales at Takaura were not higher than those of the other kinds of seaweed at Takaura.

The heavy metal concentrations in Ulvales at Takaura were compared with the other areas.

Cu concentrations in Ulvales at Takaura were about 100 times higher than those of the other areas at the Sadamisaki Peninsula, Fe concentrations in Ulvales at Takaura were about 10 times higher than those of the other areas at the Sadamisaki Peninsula.

Also Cu concentrations in Ulvales at Takaura were about 10 times higher than those at the Yashiro Island. And Fe concentrations in Ulvales at Takaura were 100 times higher than those at the Yashiro Island.

The other hand, the heavy metal concentrations in Hijiki and Ishige at Takaura were not higher than those in Ulvales at Takaura. The heavy metal concentrations in Hijiki and Ishige at Takaura were compared with those in Hijiki and Ishige at the other areas. Cu, Pb, Zn and As concentrations in Hijiki were about the same as those at the other areas. Fe

and Mn concentrations in Hijiki at Takaura were lower than those at some areas. Cu, Fe, Mn, Pb, Zn, and As concentrations in Ishige were about the same as those at the other areas.

So, Cu, Fe and Mn concentrations in Ulvales were considered to be a sensor for finding contaminated area.

CONCLUSION

There were about 66 closed copper mines in the Sadamisaki Peninsula from middle Meiji to Taisho era. The Takaura Mine was the biggest copper mine in the Sadamisaki area operated from middle Meiji to Taisho era. As ore minerals of the copper mines were mainly pyrite FeS_2 and chalcopyrite CuFeS_2 [8], the waste water and tailing contained iron and copper. The Takaura mine faced the Takaura Bay. At Takaura, Cu, Fe and Mn concentrations in green seaweed were very high. High copper and iron concentrations of seaweed sampled at the Takaura Bay were thought to indicate metal contamination caused by activity of now closed copper mine. Also Fe concentrations in green seaweed at Kojima were higher than those sampled at the other areas. It is faced inside the bay, so sampling point is not influenced by ocean current.

The heavy metal concentrations in seaweed at the Sadamisaki Peninsula were compared with the Yashiro Island and Kada.

Cu and Fe concentrations in green seaweed at Takaura were 100 to 350 ppm and 100 to 1000 ppm respectively and about 10 to 20 times higher than those sampled at the Yashiro Island and Kada. The other metal concentrations in seaweed at the Sadamisaki Peninsula were not higher than those of the Kada and Yashiro Island. Takaura area is concluded to be Cu and Fe contaminated area using seaweed heavy metal concentrations comparing normal area such as the Kada and Yashiro areas.

REFERENCES

- [1] Oishi K, Science of seaweed: Asakura Bookstore, 1933.
- [2] Abe N, Sudo S, Sera K, Saitou Y, Yoshida N and Kudo T, "PIXE analysis of trace heavy metal elements concentrated in seaweed" Report on NMCC Collaborative Research Results 11, 2003, pp.70-77.
- [3] Ii H, "AS, SR, ZN, FE, MN, PB AND CU CONCENTRATIONS OF SEAWEED AT THE KII PENINSULA, JAPAN" International Journal of GEOMATE, June, 2016, Vol. 10, Issue 22, pp. 2036-2042.

- [4] Li H, "CU, ZN AND AS CONTAMINATION OF SEAWEED BESIDE SHIZUKI AND KANAYAMA METAL MINES IN JAPAN" Int. J. of GEOMATE, Sept., 2015, Vol. 9, No. 1 (Sl. No. 17), pp. 1411-1417.
- [5] Yamamoto T, and Ishibasi M, "The Content of Trace Elements in Seaweeds", in Proc. 7th Int. Seaweed Symposium, 1971, pp. 511-514.
- [6] Yamamoto T, "Chemical Studies on the Seaweeds (27) The relations between Concentration Factor in Seaweeds and Residence Time of Some Elements in Sea Water", Records of Oceanographic Works in Japan., Vol. 11, No.2, March. 1972, pp. 65-72.
- [7] Fujioka K, Human geography of the Cape Peninsula - Ehime Prefecture Sadamisaki Peninsula Scientific Research Report -: Taimeido, 1966.
- [8] Kimura T and Kobayashi K, "Report on copper sulfide iron ore floor survey in the western part of Ehime prefecture" Geological Surveyor Monthly Report, 1954, 5(10) pp.505-528.

EVALUATION OF IMBIBITION PROCESS IN POROUS MEDIA BY INVADDED PERCOLATION PROBABILITY

Junichiro Takeuchi¹ and Masayuki Fujihara¹

¹Graduate School of Agriculture, Kyoto University, Japan

ABSTRACT

Water retention property of soil is determined by soil texture, soil structure, and physical properties of grain surface. Specifically, it is influenced by various factors such as pore size, pore shape, connectivity to neighbor pores, and contact angle of grains in a bottom-up manner. The water retention curve, which is a relation between retained water in soil and matric potential, can exhibit different shape depending on such factors. However, from our previous numerical experiments with a pore-network model, it was suggested that the various water retention curves can be integrated into an almost identical curve irrelevantly to different pore-size distributions when variously saturated porous media is evaluated by an evaluation index derived from the percolation theory. The evaluation method is called invaded percolation probability here, and it is extended from the percolation probability, which is the one that evaluates a degree of connectability of a network. In this study, more detailed numerical experiments for imbibition process are conducted and the applicability of the invaded percolation probability is investigated. It is found from the obtained results that a common curve of the invaded percolation probability is obtained if pores in the pore-network do not have any correlation with their neighbor pores. In a case where the pore-network has some spatial structure, it was found that a different curve of the invaded percolation probability is obtained, and that this evaluation method is applicable unless the structure is disturbed.

Keywords: Water Retention Property, Pore-network, Percolation Theory, Invasion Percolation

INTRODUCTION

Soil is essential for not only agriculture but also all terrestrial flora and fauna including humankind. Among various soil properties such as physical, dynamic, and chemical ones, hydraulic properties are quite important for crop production since water retention characteristics and permeability have a large influence on crop growth. So far, many models such as van Genuchten-Mualem model [1], [2], which is one of representative functional ones based on the bundle of capillary tubes model, have been utilized. In addition, to reproduce the hydraulic properties of soil in a bottom-up manner, an approach with a network of pores has been conducted focusing on the importance of connectivity of pores [3] after Fatt et al. proposed a pore-network model [4], and this approach was employed to analysis pore structure [5], [6]. Recently, detail shape of pores and frequency of pore size is being directly grasped due to the development of observation apparatus such as a high-resolution X-ray CT (computed tomography) scan [7].

On the other hand, it was reported that invasion phenomena such as imbibition and drainage processes can be put together into a single curve based on the percolation probability from the analysis with the percolation theory [8]. The curve, which is referred to the invaded percolation probability in this study, shows a relationship between invadable and invaded pores, and resembles the water retention curve, which shows a relationship between matric potential and saturation or water content in soil.

While physical indices are used in both axes in the water retention curve, proportions of invadable and invaded pores to total pores are used in the invaded percolation probability. The matric potential in the water retention property corresponds to the proportion of invadable pores in the invaded percolation probability, and saturation to the proportion of invaded pores. By introducing this evaluation method, there is a possibility various water retention curves obtained from different soil type is treated in a unified way, and this deepens understanding of invasion processes as a basic principle. In this study, applicability of the evaluation method and factors that determine the shape of the invaded percolation probability are investigated through numerical experiments.

MODEL

Pore-network Model

To conduct numerical experiments in the following section, a pore-network model is utilized, and it is extracted from a virtual porous medium which is made by the discrete element method. A virtual porous medium is composed of equal-size spherical grains packed randomly in a cubic container. From the porous media, a pore-network is extracted with the modified Delaunay tessellation method [9]. In Fig. 1, a virtual porous medium, which is formed by about 5800 spherical grains of 0.2 mm in a 3mm×3mm×3mm container, and a pore-network extracted from the porous medium are shown.

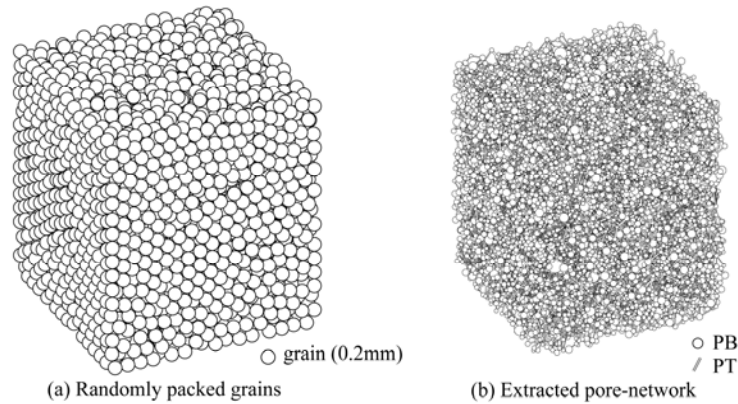


Fig. 1 Virtual porous medium (Network1)

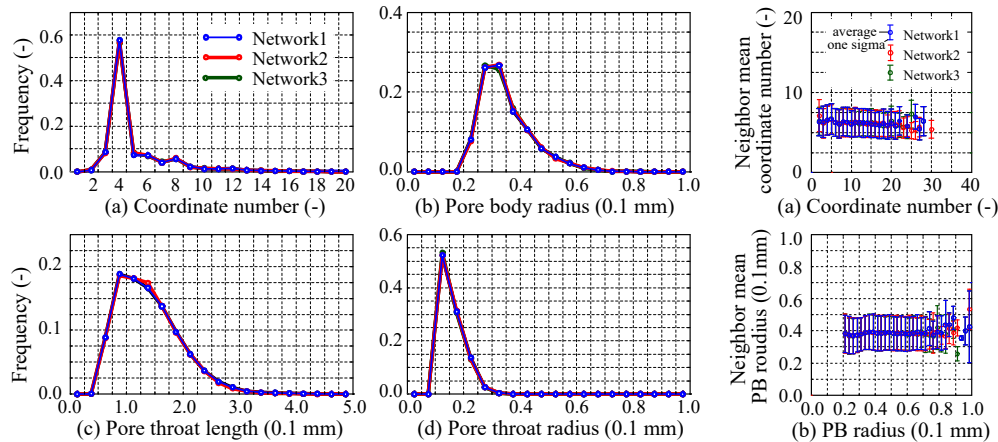


Fig. 2 Histograms of coordinate number and pore sizes

A pore-network consists of pore bodies (PBs) and pore throats (PTs). Pore bodies are relatively large pores and are represented by circles in Fig. 1. Pore throats are relatively small pores that connect two PBs, and are represented by tubes here. The extracted pore-network, which is referred to Network1 here, in Fig. 1 (b) has about 14,000 PBs and 35,500 PTs, and frequency distributions of pore sizes and coordinate number, which is the number of PTs that a single PB connects, are shown in Fig. 2. Figure 3 shows the correlations between coordinate numbers and between pore body radii of PBs and other PBs surrounding them. Except for the vicinity of the right ends of both graphs, where values disperse since the number of samples in each dot is small, the shape of the graphs is generally flat, which shows that neither coordinate number nor PB size have strong spatial correlation with their neighbors. But the level of low radii is a little lower compared with others, which means that small PBs tend to connect small PBs.

Percolation Probability

In the percolation theory, a network is represented by sites and bonds, which correspond to PBs and PTs, respectively, in a pore-network model. In an analysis

using networks, two processes are considered on a network: One is a site process, in which sites play a main role, and the other is a bond process, in which bonds play a main role. In a case of a site process, each site takes one state from two states: 'open' or 'close'. When a site is open, the open site can convey something, which depends on an objective system and information, electricity, and infectious disease are given as an instance [10]. In this study, open sites represent invadable pores that are small enough, and close sites represent non-invadable pores that are large in a case of imbibition process. Then, conveyed matter is water. In a case of drainage process, open (invadable) pores are the ones that are large enough, and conveyed matter is air. Basically, the imbibition process into normal (hydrophilic) soil can be treated as a site process, because PBs regulate water invasion. This means that if water can invade into a certain PB, water can inevitably invade into the PTs connecting to the PB since the connecting PTs are smaller than the PB. And the drainage is treated as the bond process for the same reason.

The percolation probability is an index of connectability inside a network, and is represented by a relation between the proportion of all open elements (sites or bonds) in a network and that of the largest

Fig. 3 Correlation of neighbor PBs

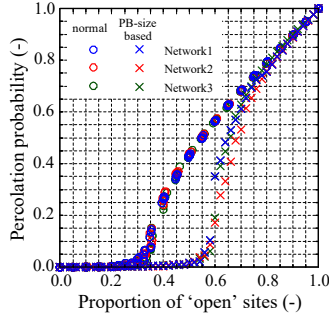


Fig. 4 Percolation probability

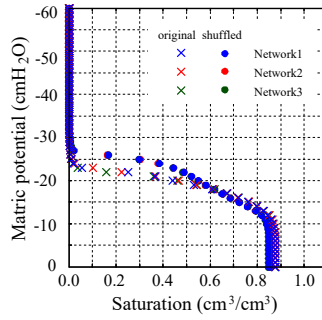


Fig. 5 Water retention curves

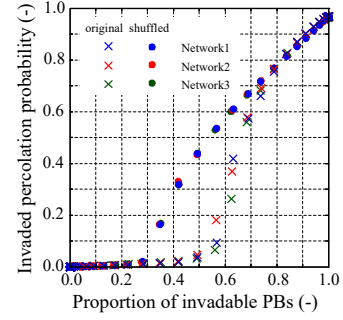


Fig. 6 Invaded percolation probability

open cluster, which is the maximum subnetwork formed by open elements, among all open clusters in the network. Normally, as the proportion of open elements increases, the number of open clusters decreases, and one large subnetwork is formed eventually by connecting each other.

In Fig. 4, two types of percolation probability of the site process are shown: one is a normal percolation probability as a network, in which the percolation probability is computed based on random numbers given to sites. The other is a percolation probability that is computed based on the PB size. These show a typical shape of the percolation probability. As the proportion of open sites increases, the percolation probability rises suddenly at a point, and approaches a diagonal line asymptotically. The point of sudden rise is referred to the percolation threshold, and it shows phase transition since the system changes from non-conveyable to conveyable at this point. In soil physics, the transition point has an important meaning. In a case of imbibition process, it corresponds to the point where water begins to invade into soil at the water-entry pressure of the soil. It can be interpreted in the following way. When the pressure passes across the water-entry pressure, the proportion of invadable pores becomes large enough so as to form a large subnetwork that spreads from one side to the opposite side. In a case of drainage process, it corresponds to air-entry pressure.

Invasion Percolation and Invaded Percolation Probability

The dynamic process of water- or air-invasion is modeled by the invasion percolation [11]. The invasion percolation is a temporally and spatially discretized model, and invading fluid proceeds into invadable pores step by step satisfying the continuity rule. Hence, each pore takes one state from three states in addition to open (invadable) and close (non-invadable). The third state is 'invaded', which means an invadable pore invaded by invading fluid literally.

As reported by Takeuchi et al. [8], the number of pores invaded in one time step has an effect on the invading mode. When the number is large enough,

fluid invades uniformly forming an invading front, and the amount of remains that are not invaded is small. When the number is small enough, fluid invades in a fingering manner, and the amount of remain is large even if all pores are invadable.

After the invasion process is finished, the invaded percolation probability, which is a relation between the proportion of invadable pores and that of invaded pores, is calculated from the obtained final state of the network in the same way with the percolation probability [8]. The invaded percolation probability never exceed the percolation probability from its definition.

NUMERICAL EXPERIMENTS

Based on the extracted pore-networks, various pore-networks with different frequency distribution of pore sizes are generated, and two numerical experiments of the imbibition process are conducted in this study. In an imbibition process, pores that satisfy the following inequality are classified as invadable.

$$p_{we} > p_c \quad (1)$$

with

$$p_c = p_{air} - p_{water}, \quad p_{we} = P \sigma \cos \theta_{adv} / A \quad (2)$$

where p_{we} is the water-entry pressure of an objective pore, and p_c is the capillary pressure, p_{air} and p_{water} are the air and water pressures at the vicinity of the air-water interface, P and A are the wetted perimeter and the cross-sectional area of the pore, σ is the interfacial tension, and θ_{adv} is the advance contact angle of the grain surface. The air pressure is assumed to be constant, and the water pressure is to be hydrostatic from the pressure at the pore-network bottom, to which desired pressure is imposed. The top and bottom are open to air and water, respectively, and the four side faces are enclosed by walls. Then, air and water cannot go in and out through side faces. Water is supplied from the bottom, and air is discharged from the top freely in an imbibition process. The maximum number of pores invaded in one time step is set as 10,000, which gives no limit substantially.

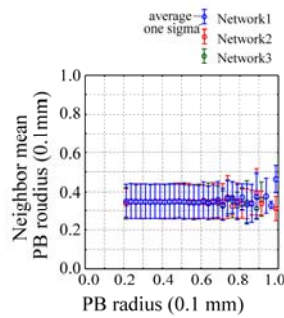


Fig. 7 Correlation of neighbor PBs (shuffled)

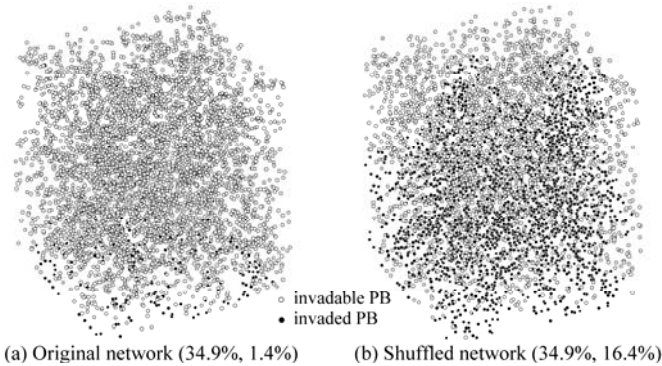


Fig. 8 Invadable and invaded PBs in Network1 (percentages of invadable and invaded PBs to total PBs)

Different Packings of Grains

Three pore-networks extracted from different porous media, which are made from randomly-perturbed initial position of grains, are used to investigate the individual difference of the pore-network. As shown in Figs. 2 through 4, the frequency distributions of the coordinate number and pore sizes, the correlation with neighbor PBs, and the percolation probability are almost identical, although these three pore-networks have different topology. Besides, the computed results of the water retention property and the invaded percolation probability shown in Figs. 5 and 6, respectively, are also almost identical. These results assure that the volume of porous media employed in this study is sufficient, and that this volume exceeds the representative elementary volume (REV).

In addition to the verification of porous media volume, another experiment is conducted to investigate the effect of the arrangement of PBs. In the normal percolation probability, each site is treated equally. Hence, whether a site is open or close is given stochastically. On the other hand, the size of each PB is used as a value in the PB-size-based percolation probability. That is, 0.3 in the horizontal axis in Fig. 4 means that 30% of sites (pores) from the smaller ones are open. Figure 4 shows that the arrangement of PBs makes discrepancy between normal and PB-size-based percolation probability. The percolation threshold of the normal percolation probability is about 0.35, and that of the PB-size-based one is about 0.55. From this result, it is found that the networks as a pure network have potential to form an open subnetwork which expands sufficiently if about 35% of sites are open, and however the network as a pore-network need about 55% of open sites (invadable PBs). This implies that small PBs do not exist uniformly in the pore-network. This inference is supported by the fact that the small PBs whose radius is about 0.03 mm or less tend to connect to small PBs from Fig. 3.

Another three virtual pore-networks in which PB size is randomly shuffled in each network are made

from the three pore-networks, respectively. The generated pore-networks are referred to 'shuffled', and the original ones are to 'original' here. The computed water retention curves and invaded percolation probability are shown in Figs. 5 and 6. These figures show that the difference between each type of pore-network is small enough, and that the water entry pressure of the original pore-networks is larger than that of the shuffled pore-networks reflecting the large percolation threshold of the original pore-networks.

In Fig. 7, the correlation of neighbor PBs of the shuffled pore-networks is shown. Unlike that of the original pore-networks in Fig. 3 (b), totally flat graphs except for the right end are obtained, which shows each size of PBs connect to all size of PBs evenly. In Fig. 8, spatial distributions of invadable and invaded PBs in the original and shuffled pore-networks of Network1 are shown when the percentage of invadable PBs is 34.9%. At this time, the water pressure applied to the bottom of the pore-network is -26 cmH₂O, and only little water invades from the bottom face in the original pore-network while water spreads in the shuffled pore-network as shown in Figs. 5 and 8. Table 1 shows that invadable PBs forms separate small clusters in the original pore-network, and that a big cluster is formed in the shuffled pore-network.

Table 1 Properties of invadable clusters

	original	shuffled
the number of pores	14060	
the number of invadable pores	4907	
the number of clusters	1860	1045
the minimum of NIP [†]	1	1
maximum of NIP	54	2364
mean of NIP	2.7	4.8
standard deviation of NIP	4.1	73.6

[†]NIP is the number of pores in an invadable cluster.

Various Distributions of Pores

In this subsection, three different types of pore-

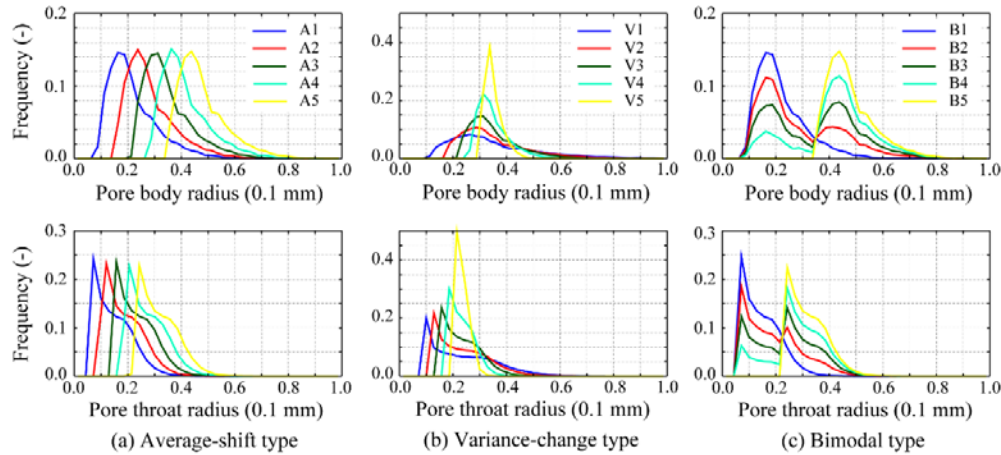


Fig. 9 Pore-size distributions

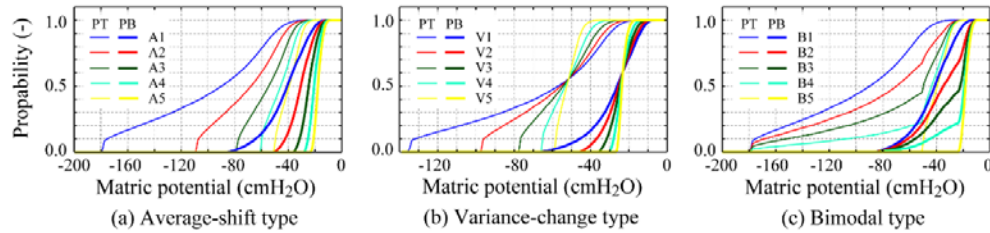


Fig. 10 Cumulative distributions of invadable pores

size distribution, such as average-shift type, variance-change type, and bimodal type, are given to PBs and PTs of Network1 (Fig. 9) to investigate the effect of pore size distributions on water retention property and invaded percolation probability. In the average-shift type, the distributions are shifted upward or downward without changing its shape from the original distribution (A3), and in the variance-change type, the variance of distributions are changed larger or smaller from the original distribution (V3). A3 and V3 are equal to Network1. In the bimodal type, bimodal distributions are generated by mixing two different distributions of B1 (=A1) and B5 (=A5) at various rates. The cumulative distributions of invadable pores to the matric potential of each distributions type are shown in Fig. 10. In the same way with the previous subsection, pore-size-shuffled versions of each pore-network are also generated.

The computed water retention properties and the invaded percolation probabilities are shown in Figs. 11 and 12. It is found from these figures that although the shape of water retention curves changes variously depending on the pore-size distributions, all the obtained invaded percolation probability are almost identical except for the bimodal distribution in the original pore-network, and that the shapes of the invaded percolation probability is the same with those in Fig. 6 and derives from the percolation probability of the site process shown in Fig. 4.

In the original pore-network with the bimodal distribution, the invaded percolation probability of B2, B3 and B4 deviate from others. This is because the

structure of small pores, which form many clusters of several pores in the pore-network, was destroyed by mixing different size of pores. But even in a case of the shuffled pore-network, the obtained invaded percolation probability of the bimodal distributions is almost identical to those of other distributions since shuffled one does not have such structure.

Further, it is also found that the water-entry pressure of a pore-network can be estimated from the percolation probability of the site process (Fig. 4) and the cumulative distribution of invadable pores (Fig. 10). As an example, a case of A1 is explained here. It is found from Fig. 4 that the percolation thresholds of the original and shuffled pore-networks are about 0.55 and 0.35, respectively, and it is found from Fig. 10 (a) that the values of the matric potential of both is about -39 cmH₂O and -48 cmH₂O when the cumulative probability of those are 0.55 and 0.35. This value is identical to the water-entry pressure of A1, which is about -38 cmH₂O and -48 cmH₂O from Fig. 12 (a).

CONCLUSIONS

In this study, two types of numerical experiment were conducted using extracted pore-networks from virtual porous media to investigate the applicability of the evaluation method termed invaded percolation probability. From the first numerical experiment, it was shown that porous media randomly packed with equal-size spherical grains have a spatial structure that small pores form separate clusters compared with

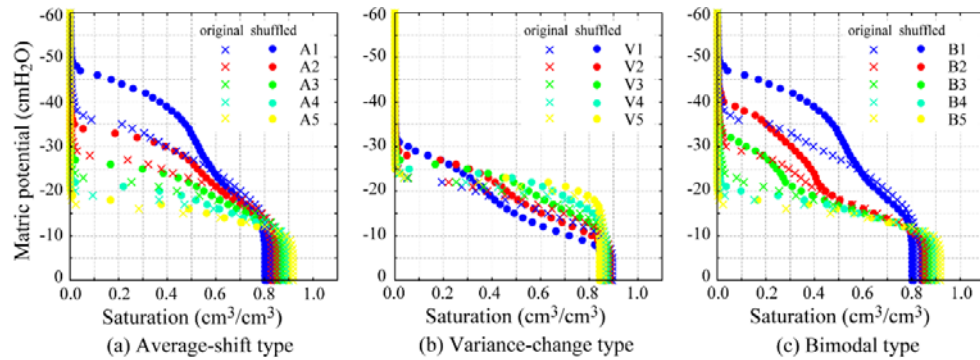


Fig. 11 Water retention curves of different pore-size distributions

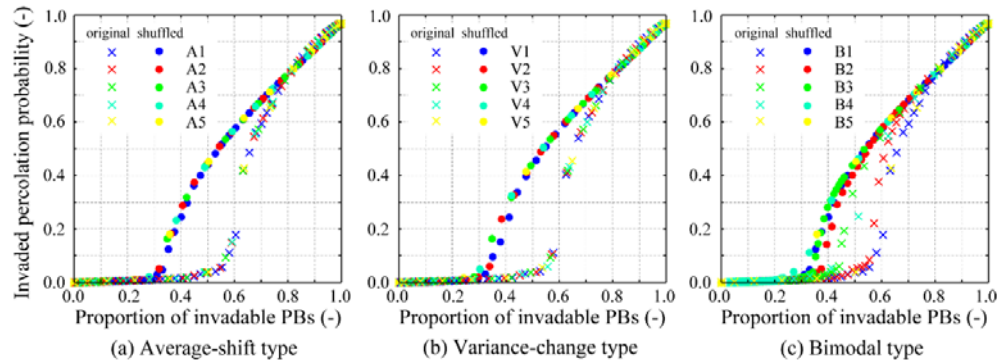


Fig. 12 Invaded percolation probability of different pore-size distributions

the uniformly distributed pore-network, and that the shape of the percolation probability and the invaded percolation probability depend on the structure. In addition, it was also found that the structure obstructs water invasion and makes the water-entry pressure higher as a result. From the second experiment with various pore size distributions, it was shown that almost identical invaded percolation probability in each type of pore-network are obtained unless the pore structure is destroyed, while various water retention curves are obtained depending on the different pore size distributions. This shows the feature of the evaluation method that the same type of network has the same shape of invaded percolation probability. Hence, it is concluded that this evaluation method based on the percolation theory is applicable, but the shape of the percolation probability is valid only in the same type of soil.

REFERENCES

- [1] van Genuchten MT, "A closed form equation for predicting the hydraulic conductivity of unsaturated soils", *Soil Sci. Soc. Am. J.*, Vol. 44, 1980, pp. 892–898.
- [2] Mualem Y, "A new model for predicting the hydraulic conductivity of unsaturated porous media", *Water Resour. Res.*, Vol. 12, 1976, pp. 513–522.
- [3] Reeves PC and Celia MA, "A functional relationship between capillary pressure, saturation and interfacial area as revealed by a pore-scale network model", *Water Resour. Res.*, Vol. 32, 1996, pp. 2345–2358.
- [4] Fatt I, "The network model of porous media", *Trans. AIME*, Vol. 207, 1956, pp. 144–181.
- [5] Takeuchi J, Sumii W, and Fujihara M, "Modeling of fluid intrusion into porous media with mixed wettabilities using pore-network", *Int. J. GEOMATE*, Vol. 10, 2016, pp. 1971–1977.
- [6] Takeuchi J, Tsuji H, and Fujihara M, "Modeling of permeability of porous media with mixed wettabilities based on noncircular capillaries", *Int. J. GEOMATE*, Vol. 12, 2017, pp. 1–7.
- [7] Mukunoki T, Miyata Y, Mikami K, and Shiota E, "X-ray CT analysis of pore structure in sand", *Solid Earth*, Vol. 7, 2016, pp. 929–942.
- [8] Takeuchi J, Tsuji H, and Fujihara M, "The effect of capillary radius distribution on the hydraulic properties of porous media", *Precision Farming and Resource Management*, Excel India Publishers, New Delhi, 2016, pp. 292–304.
- [9] Al-Raoush R, Thompson K, and Willson CS, "Comparison of network generation technique for unconsolidated porous media", *Soil Sci. Soc. Am. J.*, Vol. 67, 2003, pp. 1687–1700.
- [10] Hunt A and Ewing R, "Percolation theory for flow in porous media", Springer, Heidelberg, 2009, p. 319.
- [11] Wilkinson D and Willemsen JF, "Invasion percolation: a new form of percolation", *J. Phys. A: Math. Gen.*, Vol. 16, 1983, pp. 3365–3376.

MEASUREMENT METHOD OF HEAVY METAL CONCENTRATION IN SOIL OF OSAKA PREFECTURE USING CICADA SHELL

Satoru Ueda¹ and Hiroyuki Ii²

¹Graduate School of Systems Engineering, Wakayama University, Japan

²Faculty of Systems Engineering, Wakayama University, Japan

ABSTRACT

Shell of cicada is useful for evaluating heavy metal contamination because heavy metal concentration of cicada is high and has long term information. Soil heavy metal concentration is variable and each soil mineral is quite different chemical composition and its concentration is not always bioavailable concentration. Adult cicada flies after emergence and then it is difficult to determine original metal source. Then, cicada shell is easy to determine original metal source area. In order to investigate effectiveness of using shell of cicadas for evaluating the heavy metal concentration of the soil, heavy metal concentration of shell of popular cicada, *Cryptotympana facialis* in metropolitan parks and factory site was studied. It is thought that heavy metal concentration is high in factory site, and urban park is not so. Cicada larvae absorb nutrients from trees. Cherry is very popular at both parks and factory sites and many shells of cicada were sampled surface of cherry tree. Heavy metal concentrations of leafs and flower of cherry were concluded to be also high and heavy metal of shell of cicada was thought to derive from soil through trees.

Keywords: Heavy metal, Cicada, Cherry, Contamination, Park

INTRODUCTION

Chemical substances such as metals will affect ecosystems and the environment when excess amount of metal is released into environment. As heavy metals in the soil increase, it also affects ecosystems, groundwater and plants. Therefore, it is necessary to grasp the heavy metal concentration of the soil [1].

However, it is not a good idea to directly measure metal concentration of soil because all amount of heavy metal in soil is not soluble and organisms cannot use all amount of heavy metal in soil. Then, bioavailable heavy metal concentration is important for health of organization. Then, heavy metal concentration of organization is thought to depend on bioavailable heavy metal concentration. Cicada larva live for long term underground and get nutrient from tree root [2]. Adult cicada flies and then it is difficult to determine its original ground where its cicada lives. Cicada shell is useful for measuring the soil heavy metal concentration. Cicada shell is found on the tree around the ground. Tree gets nutrient and metal from soil. Therefore, metal concentrations of tree leaves, tree flowers and cicada larva are used for evaluation of metal contamination. The habitat of cicada larvae depends on trees [3]. Cicada shell was seen most often on the surface of cherry tree and then cherry flower and leaves were also analyzed.

Cicada shells were sampled at metropolitan parks and cherry trees are also found in the parks. Cu, Zn, Fe, Pb and Mn were studied for evaluation of heavy metals.

METHOD AND STUDY AREA

Fig.1 shows 12 sampling points in Osaka, Japan. Osaka is an urban area.



Fig.1 sampling points in Osaka, Japan.

No.1 sampling point is site after chemical factory. Many factories are lined up around the No.1

sampling point. There is a possibility that the waste discharged at the factory is absorbed by the soil. No.2 to No.12 sampling point is metropolitan parks. There are no factories in the surrounding area, and it is a place where artificial environmental burden is difficult to apply. Therefore, soil contamination is considered to be small. The heavy metal concentrations of soil are expected to differ between No. 1 and No. 2 to No. 12. By comparing concentrations of cicada shell sampled at No. 1 and No. 2 to No. 12, heavy metal contamination and effectiveness of using cicada shell were evaluated.

Cicada shell, cherry flowers and cherry leaves are collected. The shell of the cicada collected is a black cicada (*Cryptotympana facialis*). The cicadas that inhabit the most in Osaka are black cicadas[4]. Therefore, black cicada was selected. The shell of the black cicada was attached to the cherry tree the most. The cherry tree chose a *Cerasus yedoensis* which is the tree with the most number of shells of black cicadas. At least 20 cicada shells were sampled in each place. A cherry flower was taken 1 g in each place. A cherry leaves was taken 3 leaves in each place. Cicada shells were collected in July of 2016, cherry flower and cherry leaves were collected in May of 2017.

The concentration of heavy metals for each piece of cicada shell was measured. At least 10 pieces (13 pieces in No.1 sampling points) in one place were measured. Cherry flowers and leafs measured the heavy metal concentration per 0.02 g. Cherry flowers were measured in 0.2×4 pieces (0.2×5 pieces in No. 1 sampling point, 0.2×3 pieces in No. 6 sampling point). Cherry leaves were measured 0.2×5 pieces per place. As a pretreatment, the cicada shell was washed with an ultrasonic washer and then dried. Cherry flowers and leaves only dried. Then, they were dissolved in concentrated nitric acid, filtered, and ICP plasma emission spectrometer was used to measure the concentration of heavy metal in nitric acid. The concentration of heavy metal in nitric acid was converted into heavy metal concentrations of cicada shell, cherry flowers and cherry leaves using the formula shown below.

$$A(\text{ppm}) = B(\text{ppm}) * \frac{C(\text{g})}{D(\text{g})} \quad (1)$$

A= Concentration in dry sample

B= Concentration in nitric acid

C= Weight of nitric acid

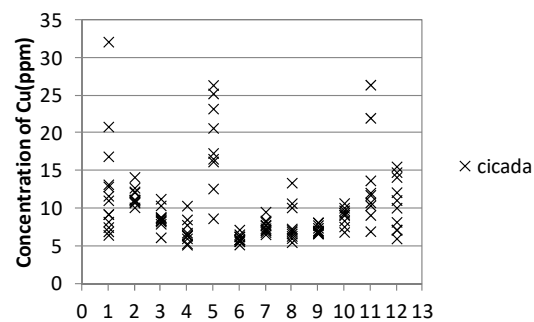
D= Weight of dry sample

The dry sample is a cicada shell, a cherry flowers and a cherry leaf. Measurement items are Cu, Fe, Mn, Zn, Pb.

RESULTS

1. Cu Concentration in cicada shell, cherry flowers and cherry leaves

Fig.1 shows Cu concentration in cicada shell. The maximum value is 32 ppm. The minimum value is 5 ppm. The average value is 11 ppm. Cu concentrations in No. 1, No. 2, No. 5 and No. 11 sampling points are high. Cu concentrations in No. 6 and No. 9 sampling points are low. Cu concentration in No. 1 sampling point is 6 to 32 ppm. Cu concentration in No. 2 sampling point is 10 to 14 ppm. Cu concentration in No. 5 sampling point is 9 to 26 ppm. Cu concentration in No. 11 sampling



point is 7 to 26 ppm. Cu concentration in No. 6 sampling point is 5 to 7 ppm. Cu concentration in No. 9 sampling point is 6 to 8 ppm.

Fig.1 Cu concentration in cicada shell

Fig.2 shows Cu concentration in cherry flower. The maximum value is 26 ppm. The minimum value is 4 ppm. The average value is 12 ppm. Cu concentrations in No. 2, No. 5 and No. 9 sampling points are high. Cu concentrations in No. 11 and No. 12 sampling points are low. Cu concentration in No. 2 sampling point is 19 to 26 ppm. Cu concentration in No. 5 sampling point is 13 to 18 ppm. Cu concentration in No. 9 sampling point is 12 to 15 ppm. Cu concentration in No. 11 sampling point is 4 to 8 ppm. Cu concentration in No. 12 sampling point is 6 to 8 ppm.

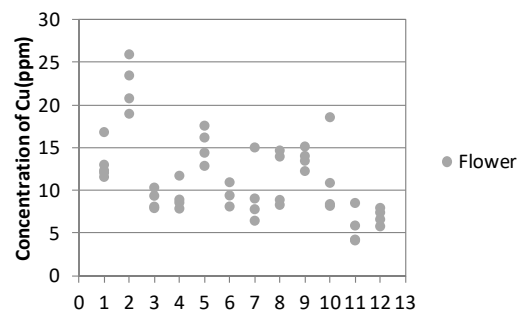
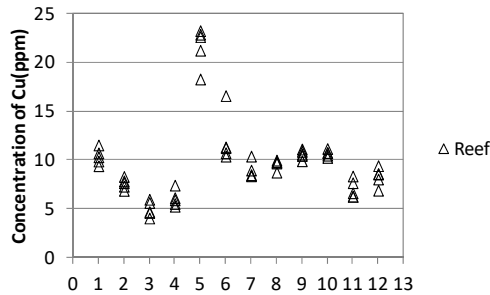


Fig.2 Cu concentration in cherry flower

Fig.3 shows Cu concentration in cherry leaf. The maximum value is 23 ppm. The minimum value is 4 ppm. The average value is 10 ppm. Cu concentrations in No. 5 and No. 6 sampling points are high. Cu concentrations in No. 3, No. 4, No. 11 and No. 12 sampling points are low. Cu concentration in No. 5

Fig.3 Cu concentration in cherry leaf



sampling point is 18 to 23 ppm. Cu concentration in No. 6 sampling point is 10 to 17 ppm. Cu concentration in No. 3 sampling point is 4 to 6 ppm. Cu concentration in No. 4 sampling point is 5 to 7 ppm. Cu concentration in No. 11 sampling point is 6 to 8 ppm. Cu concentration in No. 12 sampling point is 7 to 9 ppm.

Cu concentration in cicada shell, cherry flower and cherry leaf is high in No. 5 sampling point. Cu concentrations in shell of cicadas were 5 to 32 ppm. Cu concentration in cherry flower were 4 to 26 ppm. Cu concentrations in cherry leaf were 4 to 23 ppm. Cu concentration in cicada shell, cherry flower and cherry leaf is similar.

2. Fe Concentration in cicada shell, cherry flowers and cherry leaves

Fig.4 shows Fe concentration in cicada shell. The maximum value is 3300 ppm. The minimum value is 638 ppm. The average value is 1632 ppm. Fe concentrations in No. 10 sampling points are high. Fe concentrations in No. 2 sampling points are low. Fe concentration in No. 10 sampling point is 1440 to 3300 ppm. Fe concentration in No. 2 sampling point is 770 to 1012 ppm.

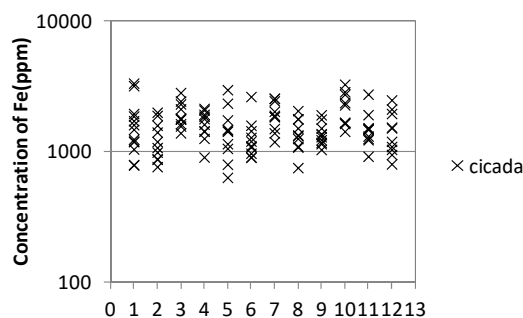
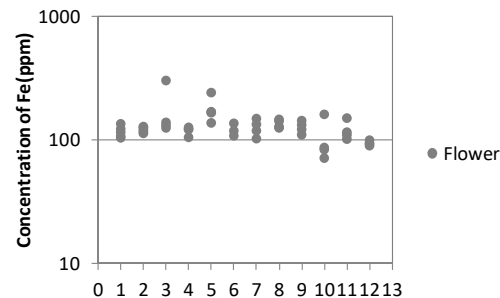


Fig.4 Fe concentration in cicada shell

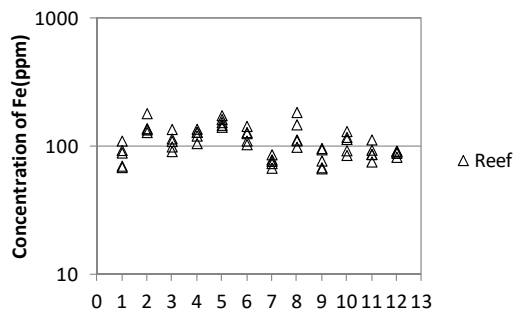
Fig.5 shows Fe concentration in cherry flower. The maximum value is 305 ppm. The minimum value is 72 ppm. The average value is 128 ppm. Fe concentrations in No. 3 and No. 5 sampling points are high. Fe concentrations in No. 10 and No. 12 sampling points are low. Fe concentration in No. 3 sampling point is 125 to 305 ppm. Fe concentration in No. 5 sampling point is 138 to 244 ppm. Fe concentration in No. 10 sampling point is 72 to 162 ppm. Fe concentration in No. 12 sampling point is



90 to 100 ppm.

Fig.5 Fe concentration in cherry flower

Fig.6 shows Fe concentration in cherry leaf. The maximum value is 185 ppm. The minimum value is 67 ppm. The average value is 115 ppm. Fe concentrations in No. 2, No. 5 and No. 8 sampling points are high. Fe concentrations in No. 1, No. 7



and No. 9 sampling points are low.

Fig.6 Fe concentration in cherry leaf

Fe concentration in No. 2 sampling point is 130 to 182 ppm. Fe concentration in No. 5 sampling point is 142 to 175 ppm. Fe concentration in No. 8 sampling point is 100 to 185 ppm. Fe concentration in No. 1 sampling point is 70 to 111 ppm. Fe concentration in No. 7 sampling point is 70 to 86 ppm. Fe concentration in No. 9 sampling point is 67 to 97 ppm.

Fe concentration in cicada shell is 10 to 25 times higher than Fe concentration in cherry flower and cherry leaf.

3. Mn Concentration in cicada shell, cherry flowers and cherry leaves

Fig.7 shows Mn concentration in cicada shell. The maximum value is 1655 ppm. The minimum value is 159 ppm. The average value is 533 ppm. Mn concentrations in No. 5, No. 8 and No. 9 sampling points are high. Mn concentrations in No. 11 and No. 12 sampling points are low. Mn concentration in No. 5 sampling point is 387 to 917 ppm. Mn concentration in No. 8 sampling point is 336 to 1655 ppm. Mn concentration in No. 9 sampling point is 230 to 964 ppm. Mn concentration in No. 11 sampling point is 184 to 821 ppm. Mn concentration in No. 12 sampling point is 159 to 713 ppm.

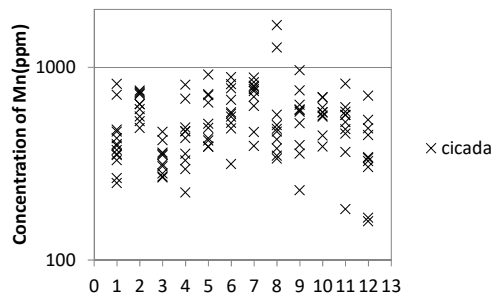


Fig.7 Mn concentration in cicada shell

Fig.8 shows Mn concentration in cherry flower. The maximum value is 120 ppm. The minimum value is 10 ppm. The average value is 38 ppm. Mn concentrations in No. 6 and No. 9 sampling points are high. Mn concentrations in No. 7 and No. 11 sampling points are low. Mn concentration in No. 6 sampling point is 100 to 120 ppm. Mn concentration in No. 9 sampling point is 78 to 104 ppm. Mn concentration in No. 7 sampling point is 11 to 18 ppm. Mn concentration in No. 11 sampling point is 10 to 15 ppm.

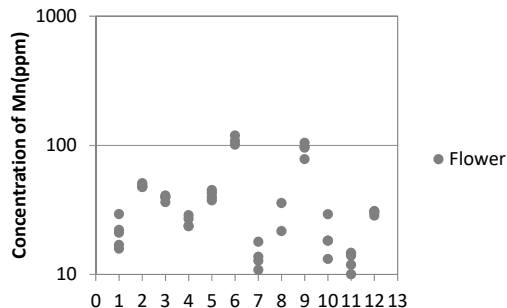


Fig.8 Mn concentration in cherry flower

Fig.9 shows Mn concentration in cherry leaf. The maximum value is 300 ppm. The minimum value is 15 ppm. The average value is 119 ppm. Mn

concentrations in No. 2, No. 3, No. 6, No. 9 and No. 12 sampling points are high. Mn concentrations in No. 8 and No. 11 sampling points are low.

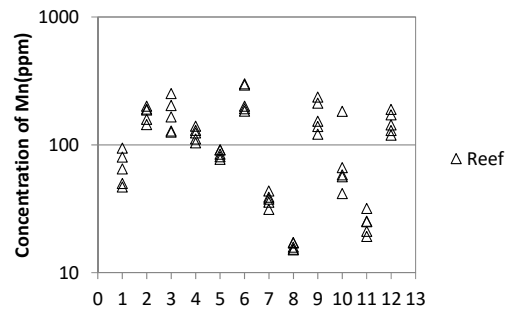


Fig.9 Mn concentration in cherry leaf

Mn concentration in No. 2 sampling point is 144 to 200 ppm. Mn concentration in No. 3 sampling point is 125 to 252 ppm. Mn concentration in No. 6 sampling point is 183 to 300 ppm. Mn concentration in No. 9 sampling point is 121 to 236 ppm. Mn concentration in No. 12 sampling point is 119 to 188 ppm. Mn concentrations in No. 8 sampling point is 15 to 17 ppm. Mn concentration in No. 11 sampling point is 19 to 32 ppm.

Mn concentration in cherry flower and cherry leaf has variation. However, Mn concentration in cicada shell has no variation. Mn concentration in cicada shell is more than 10 times higher than Mn concentration in cherry flower. Mn concentration in cicada shell is more than 5 times higher than Mn concentration in cherry leaf.

4. Zn Concentration in cicada shell, cherry flowers and cherry leaves

Fig.10 shows Zn concentration in cicada shell. The maximum value is 1377 ppm. The minimum value is 11 ppm. The average value is 146 ppm.

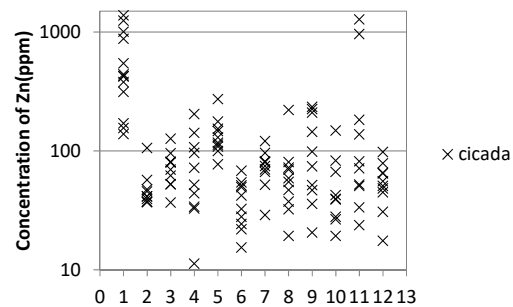


Fig.10 Zn concentration in cicada shell

Zn concentrations in No. 1, No. 5 and No. 11 sampling points are high. Zn concentrations in No. 4 and No. 6 sampling points are low. Zn concentration in No. 1 sampling point is 138 to 1377 ppm. Zn concentration in No. 5 sampling point is 77 to 272 ppm. Zn concentration in No. 11 sampling point is 25 to 1276 ppm. Zn concentration in No. 4 sampling

point is 11 to 203 ppm. Zn concentration in No. 6 sampling point is 15 to 68 ppm.

Fig.11 shows Zn concentration in cherry flower. The maximum value is 211 ppm. The minimum value is 28 ppm. The average value is 75 ppm.

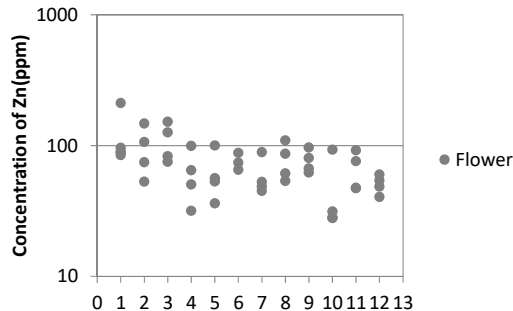


Fig.11 Zn concentration in cherry flower

Zn concentrations in No. 1, No. 2 and No. 3 sampling points are high. Zn concentrations in No. 10 and No. 12 sampling points are low. Zn concentration in No. 1 sampling point is 85 to 211 ppm. Zn concentration in No. 2 sampling point is 53 to 147 ppm. Zn concentration in No. 3 sampling point is 75 to 152 ppm. Zn concentration in No. 10 sampling point is 28 to 93 ppm. Zn concentration in No. 12 sampling point is 40 to 60 ppm.

Fig.12 shows Zn concentration in cherry leaf. The maximum value is 71 ppm. The minimum value is 20 ppm. The average value is 41 ppm. Zn concentrations in No. 4, No. 5 and No. 9 sampling points are high. Zn concentrations in No. 3 and No. 11 sampling points are low. Zn concentration in No. 4 sampling point is 38 to 63 ppm. Zn concentration in No. 5 sampling point is 59 to 71 ppm. Zn concentration in No. 9 sampling point is 34 to 66 ppm. Zn concentration in No. 3 sampling point is 20 to 47 ppm. Zn concentration in No. 11 sampling point is 24 to 37 ppm.

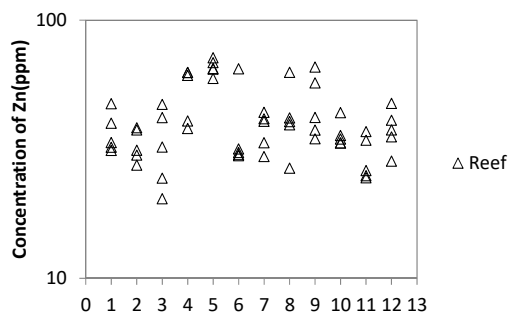


Fig.12 Zn concentration in cherry leaf

5. Pb Concentration in cicada shell, cherry flowers and cherry leaves

Fig.13 shows Pb concentration in cicada shell. The maximum value is 339 ppm. The minimum value is 1 ppm. The average value is 31 ppm. Pb concentrations in No. 1 sampling points are high. Pb concentrations in No. 3, No. 6 and No. 7 sampling points are low. Pb concentration in No. 1 sampling point is 12 to 339 ppm. Pb concentration in No. 3 sampling point is 1 to 3 ppm. Zn concentration in No. 6 sampling point is 1 to 2 ppm. Zn concentration in No. 7 sampling point is 1 to 3 ppm. Pb concentration in cherry flower and cherry leaf could not be detected.

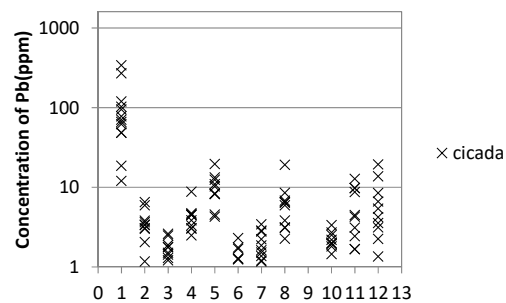


Fig.13 Pb concentration in cicada shell

Pb concentration in cicada shell of No. 1 sampling point is high.

Consideration

Cu concentration in the cicada shell, cherry flowers and cherry leaves was high at No. 5 sampling point. No. 5 sampling point is the Osaka Castle Park. In 1945, there was an air raid at the Osaka Castle Park. At that time, bombs and bullets were dropped. Dropped bullets accumulated in the soil, and the concentration of Cu was thought to be high[5].

The concentration of Fe contained in the cicada shell is very high. Therefore, it is thought that larva of cicada absorb a large amount of Fe.

Mn concentration in the cicada shell is very high. Therefore, it is thought that larva of cicada absorb a large amount of Mn. In addition, Mn concentration in the cherry flowers and cherry leaves has a large difference between the maximum value and the minimum value. However, the Mn concentration in the shell of the cicadas has a small difference between the maximum value and the minimum value. Therefore, there is no correlation between Mn concentrations of cicadas and cherry trees.

Zn and Pb concentrations in cicada shell, cherry flowers and cherry leaves at sampled No.1 were higher than those at sampled other areas. Then, Zn and Pb concentrations in soil at No.1 were thought to be higher than those at the other areas.

Conclusion

In this study, the heavy metal concentration of the soil from cicada shell, cherry flowers and cherry leaves were estimated.

As a result, it was found that some heavy metal concentrations in the cicada shells were higher values than heavy metal concentrations contained in cherry flowers and cherry leaves.

In addition, heavy metal concentrations in the cicada shell, cherry flowers and cherry leaves were variable with places. Heavy metal concentrations in plant are thought to depend on those in soil as generally plant absorbs heavy metal from soil.

As well as heavy metal concentrations in plant, heavy metal concentrations in cicada are thought to be influenced by soil heavy metal concentration and then cicada shell is also depend on soil heavy metal concentration.

Therefore, shell of cicada is effective for estimating heavy metal concentration from soil.

REFERENCE

- [1] Kenichi Ito, "Soil, Clay and Minerals on Metals Contaminated Groundwater and Soil", Journal of the Clay Science Society of Japan (in Japanese), Vol. 50 (2011) No. 3 pp. 144-153
- [2] K Hirose, Y Ito, "On an ecological note of cicada", Proceedings of the Kanto-Tosan Plant Protection Society, Vol. 1961 (1961) No. 8 pp. 59
- [3] Yoshihiro Tokue, Fumiko Imamura, Satoshi Osawa, "Factors Influencing Cicada Distribution in Urban Forests", Journal of The Japanese Institute of Landscape Architecture, Vol. 76 (2013) No. 5 pp. 465-46
- [4] Toshiyuki Minami, "On Global Warming and Predicting Occurrence of Heatstroke", JAPANESE JOURNAL OF BIOMETEOROLOGY, Vol. 41 (2004) No. 1 pp.41-44
- [5] Sinya Inano, Hideo Yamazaki, Shusaku Yoshikawa, "The History of Heavy Metal Pollution during the Last 100 Years, Recorded in Sediment Cores from Osaka Castle Moat, Southwestern Japan", The Quaternary Research (Daiyonki-Kenkyu), Vol. 43 (2004) No. 4 pp. 275-286

PRECIPITATION AMOUNT ON TOPOGRAPHY AT BETWEEN THE OSAKA PLAIN AND THE SOUTH IKOMA MOUNTAINS, OSAKA PREFECTURE, JAPAN

Hiroki Nishiwaki¹ and Hiroyuki Ii²

¹Graduate School of Systems Engineering, Wakayama University, Japan

²Faculty of Systems Engineering, Wakayama University, Japan

ABSTRACT

Rain cloud direction is important for high precipitation around the mountains. The cloud direction is to determine how many times cloud meets mountains. When cloud or wet air from sea crosses mountain in land, updraft brings out at the mountain and new cloud occurs. As a result, at the mountain, amount of precipitation is higher than that around the area. However, when cloud or wet air passes through other mountain before it comes to the mountain, it rains heavily at the first mountain and then it rains little at the second mountain. Wet air or cloud from the Osaka Bay can go to the Ikoma Mountains directly from west to northwest direction and in this case, at the Ikoma Mountains, we have a lot of rain relative to Osaka Plain. However, wet air or cloud from southwest to south firstly meets the other mountain and we have small rain at the Ikoma Mountains because wet air or cloud precipitates before they arrive at the Ikoma Mountains.

Keywords: Amount of Precipitation, Topography, Cloud Direction, Osaka Plain, Ikoma Mountains

INTRODUCTION

About 60 present area of the Japan's land is the mountain. Since heavy rain leads to landslides [1], it is necessary for safety to estimate amount of precipitation in mountain. It has been recognized that amount of precipitation increased with altitude in mountain [2]. In other hand, it has been reported that amount of precipitation didn't increase in mountain. For example, Yamada et al (1995) [3] has been reported that relational expression between altitude and amount of precipitation estimate from precipitation sample in the Yubari Mountain, Hokkaido, and the Gozaishyo Mountain, Mie prefectural, Japan. However, sample gathered in the Owase, Mie prefectural didn't increase with altitude. Yamada (1984) [4] has reported from samples gathered by 28 typhoons in the upper stream of Tone River that amount of precipitation increased with altitude when wind was blocked by mountain. When wind crosses mountains in land, updraft brings out at the mountain and new cloud occurs. New cloud can make new precipitations. Wakimizu et al (1991) [5] has reported that topography on windward side of the mountain can change distribution of precipitation. A number of studies reported relationship between topography and wind is the important factor for amount of precipitation. Relationship topography and precipitation has not been clarified because topography of mountain is complicated. Therefore, in this study, the purpose is to clarify the relation between precipitation amount and topography and then rain sample was sampled from the Osaka Plain to the Ikoma Mountains covering big topography

change.

METHOD

Sampling and Analysis

Fig. 1 shows location of sampling points. Fig.2 shows location of sampling point and cross-section from the Osaka Plain to the Ikoma Mountains. The Ikoma Mountains is located in the north-south direction on the border of Osaka and Nara in Japan. There were 7 rain gauges points at the east of Osaka, Plain, East Plain, Foot, Hillside Top, East Top and East Hillside in east side of the Ikoma Mountains.

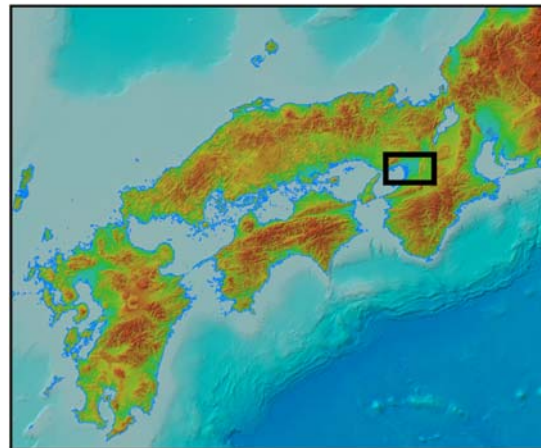


Fig.1 Location of sampling points

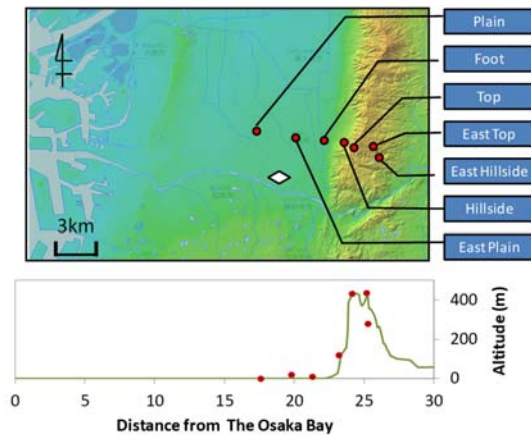


Fig.2 Location of sampling point and cross-section view. Circles are sampling points and names are Plain, East Plain, Foot, Hillside, Top, East Top and East Hillside from west point. Diamond is the meteorological observation stations at Yao.

Rain sampling was performed 43 times by every precipitation from May in 2014 to December in 2015. 500ml bottle made of polyethylene with wide mouth, 43.6 mm in diameter was used for sampling. It was put on the ground at each sampling points. Precipitation amount was measured by the following equation.

$$P = (W/\rho)/((C/2)^2 \times \pi)$$

P: Precipitation amount (mm), W : Weight (g),
 ρ : Density of water (10^{-3} g/mm³), C : Caliber of Sampler (43.6 mm)

Data of wind direction and wind speed were obtained from Japan Meteorological Agency (JMA) at Yao point. Yao point is the closest observation station from sampling area. Wind direction of each event was selected the most numerous direction and was shown by 8 directions. Cloud direction was estimate by weather chart. Cloud direction shows direction where rain cloud coming from and was shown by 8 directions. Weather chart was announced by Japan Weather Association.

RESULTS AND DISCUSSION

Precipitation ratio in each event

Fig.3 shows precipitation ratio in each sampling points. Precipitation ratio is the value obtained by dividing amount of precipitation on each sampling point by amount of precipitation on East Plain for comparing amounts of precipitation between Plain to East Top. Altitude of three sampling points, Plain,

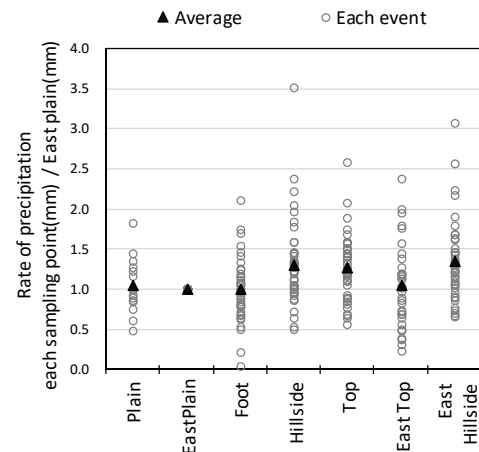


Fig.3 Precipitation ratio in each sampling point. Circle is the value in each event. Triangle is the average ratio of each event.

East Plain, and Foot are 0, 0, 10 m and their sampling points were called flat area. Precipitation ratios for three sampling points, Plain, East Plain and Foot varied 0.5 to 1.5 and their average ratios were 1.0. Amount of precipitation in the flat area was constant. Altitude of four sampling points, Hillside, Top, East Top, and East Hillside are 120, 430, 440, 280 m and their sampling points were called mountain area. Average of precipitation ratios for three sampling points, Hillside, Top and East Hillside were 1.3 however average of precipitation ratios for East Top was 1.0. It was thought that amount of precipitation on mountain area was higher than those of flat area excluding East Top. Each precipitation ratio for Hillside, Top and East Hillside were not always over 1.0. Therefore, it was found that precipitation on the mountain was not always high. In particular for East Top, amount of precipitation is less than those of another mountain area. For mountain area, high precipitation phenomenon was not simple and very complicated.

Characteristic of high precipitation in mountain area

From Fig.3, precipitation ratios in each sampling points were variable and complicated. The sampling point Top is the mountain peak and then each event was grouped into two types based on precipitation ratio of sampling point Top. Precipitation ratio for Top of over 1.5 was defined as A group events. Precipitation ratio for Top of less than 1.1 was defined as B group events. A group events have 12 events. B group events have 9 events.

Fig.4 shows precipitation ratio of A group events classified based on Top precipitation ratio. Average precipitation ratio of A group events in Hillside, Top and East Hillside was about 1.6. Precipitation ratio for East Top varied from 0.4 to 2.4 and the average

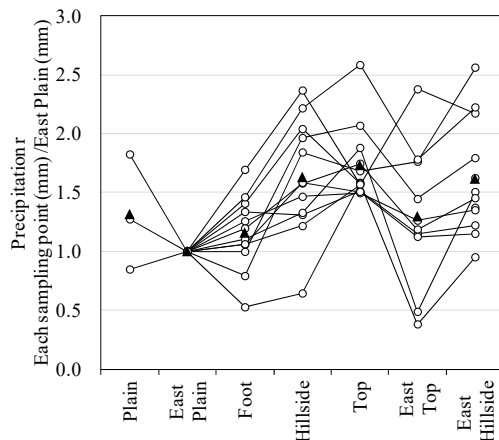


Fig.4 Precipitation ratio of A group events. Circle is the value in each event. Triangle is the average ratio of each event.

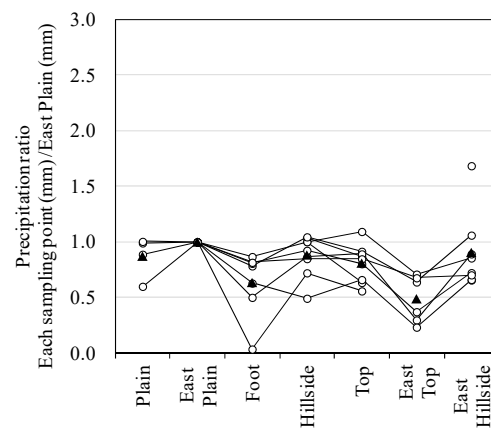


Fig.5 Precipitation ratio of B group events. Circle is the value in each event. Triangle is the average ratio of each event.

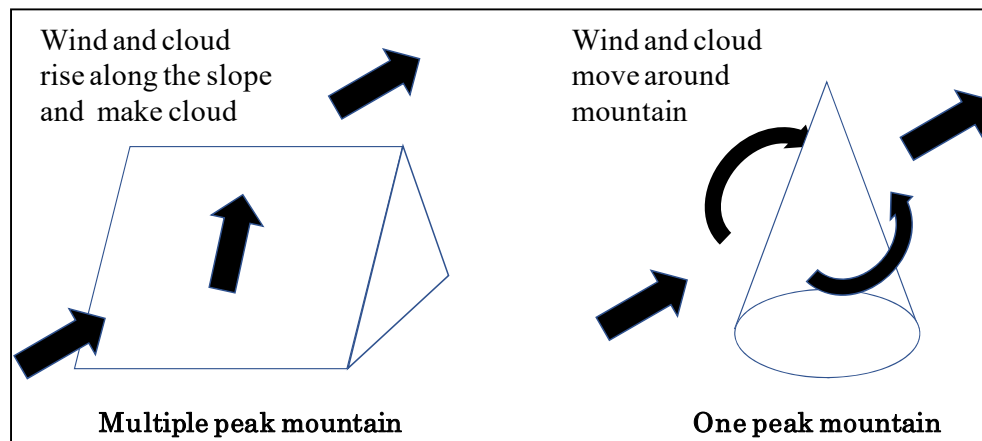


Fig.6 Air motion types based on peak shape, one peak or multiple peaks.

was 1.3. For A group events, precipitation ratio increased with altitude from foot via Hillside to Top along the mountain slope. However for the east side of Top, precipitation ratios for East Top were clearly low and precipitation ratios for East Hillside also were lower than those for Top.

Fig.5 shows precipitation ratio of B group events classified based on Top precipitation ratio. Precipitation ratios for four sampling points, Hillside, Top and East Hillside varied 0.5 to 1.0. Precipitation ratios for Top were almost same as those for Hillside and East Hillside and higher than those for East Top.

Average precipitation ratio of B group events for Hillside, Top and East Hillside was about 0.9. Average precipitation ratio for East Top was about 0.5. In mountain area from Hillside to East Hillside, precipitation ratio of A group events was higher than those of B group events. Precipitation ratio of both A and B group events in East Top were lower than those around another mountain sampling points.

Fig.6 shows air motion types based on shape of

mountain, one peak or multiple peaks. When shape of mountain is multiple, air moves around mountain. When air meets slope, air rises along slope. Air temperature decreases with elevation by adiabatic expansion and then saturated vapor pressure decreases. When air vapor pressure is over the saturated vapor pressure, raindrops occur and make rain cloud. When shape of mountain is cone, air moves around mountain. Cloud is moved by air. Thus, small precipitation ratio for East Top was thought to be caused by cone shape of mountain peak, because rain clouds move to around mountain and updraft does not occur.

Relationships between wind direction and high precipitation of mountain area

Table.1 shows weather conditions of A group events. Table.2 shows weather conditions of B group events. Amount of precipitation in table.1 and 2 are value for the sampling point Plain. Precipitation

Table.1 Weather conditions of A group events

A group events	Amount of Precipitation (mm)	Precipitation Ratio	Wind Direction	Wind Speed (m/s)
	Sampling for Plain	Sampling for Top	obtained by JMA at Yao point	
13-Jul-14	18.2	1.6	SW	2.6
6-Aug-14	196.9	1.6	NE	4.6
11-Dec-14	10.0	2.1	W	2.4
15-Jan-15	34.4	1.5	N	3.5
22-Jan-15	23.3	1.6	W	2.7
1-Mar-15	29.2	1.5	NW	3.2
1-Apr-15	8.7	1.9	N	3.2
3-Apr-15	21.6	1.7	N	3.2
19-Apr-15	25.8	1.5	SW	3.2
16-Sep-15	8.9	1.7	N	3.2
1-Oct-15	47.2	2.6	W	3.2

Table.2 Weather conditions of B group events

B group events	Amount of Precipitation (mm)	Precipitation Ratio	Wind Direction	Wind Speed (m/s)
	Sampling for Plain	Sampling for Top	obtained by JMA at Yao point	
30-Mar-14	35.8	0.9	E	3.4
29-Apr-14	18.3	0.6	E	3.1
15-Aug-14	5.6	0.6	E	1.6
28-Dec-14	12.0	0.8	W	1.2
29-Mar-15	7.5	1.1	N	2.2
8-Jun-15	29.8	0.9	E	2.6
26-Jun-15	22.8	0.9	E	2.8
16-Jul-15	143.2	0.8	NE	1.9
27-Oct-15	6.7	0.7	SE	2.0

ratio in table.1 and 2 are value for the sampling point Top. Both A and B group events had all season. Seasons of A and B group events were variable.

Amount of precipitation of A group events for the sampling point Plain were from 4.6 to 124.8 mm. Amount of precipitation in B group events for the sampling point Plain were from 6.8 to 178.1 mm. August 6, 2014 of A group events and July 16, 2015 in B group events were both Typhoon rain. A and B group events were variable types of rain. Thus, the difference between A and B group events do not depend on rain scale and then increase of precipitation with altitude is not thought to be caused by scale effect.

Most of wind directions in A group events were north to west. Most of wind directions in B group events were east. Some wind directions of A group events were east and north east. Similarly one wind direction of B group events was west. Then, wind direction is not absolute parameter to determine whether A or B group events. However, western and northern wind can easily come up the Ikoma Mountains slope because the mountain direction is south to north and most of events was thought to depend on wind direction.

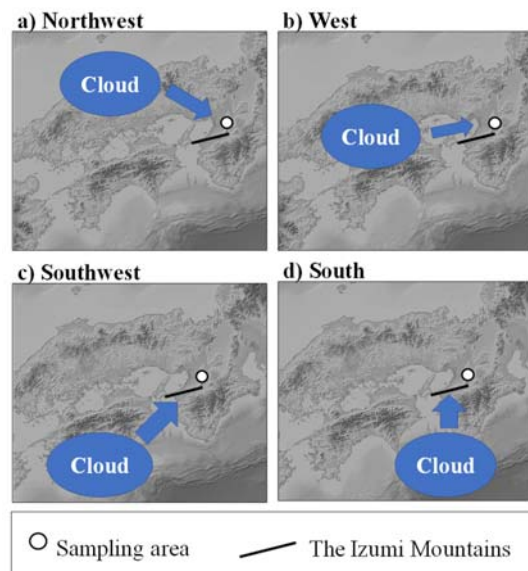


Fig.7 Schema diagram of cloud direction. a), b), c) and d) indicate that rain clouds come from the northwest, west, southwest and south respectively.

A group events	Cloud Direction	B group events	Cloud Direction
26-May-14	W	30-Mar-14	SW
13-Jul-14	W	29-Apr-14	SW
6-Aug-14	NW	15-Aug-14	SW
11-Dec-14	NW	28-Dec-14	SW
15-Jan-15	W	29-Mar-15	SW
22-Jan-15	NW	8-Jun-15	S
1-Mar-15	W	26-Jun-15	W
1-Apr-15	NW	16-Jul-15	S
3-Apr-15	NW	27-Oct-15	NW
19-Apr-15	W		
16-Sep-15	W		
1-Oct-15	W		

Relationships between raincloud direction and high precipitation

Wind direction can cover the phenomenon of most precipitation. Then, cloud direction during rain time was studied.

Fig.7 shows schema diagram of cloud direction. a), b), c) and d) indicate that rain clouds come from the northwest, west, southwest and south respectively. Table.3 shows direction of rain clouds for each event. A group events had only northwest and west. B group events were Southwest, south, west and northwest directions and many events of B group were southwest directions. If rain clouds come from northwest or west, rain clouds move from the Osaka Bay to the Ikoma Mountains across the Osaka Plain.

Rain clouds go up along the slope of the Ikoma

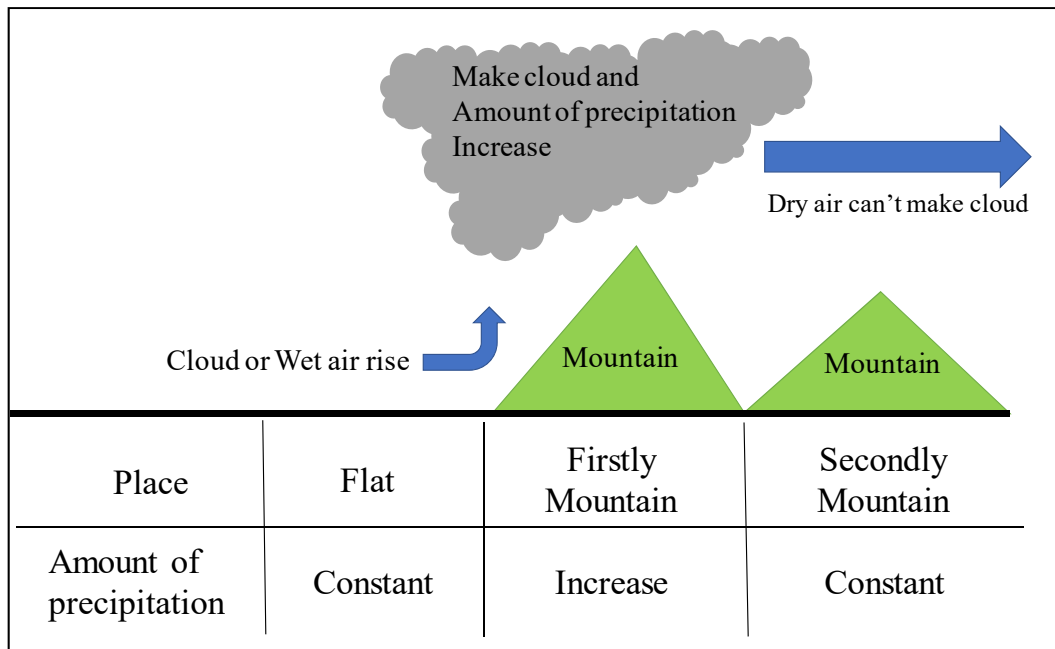


Fig.8 Relation between Amount of precipitation and topography

Mountains and new rain clouds occur around the mountains and amount of precipitation increases around the mountain area. If rain clouds come from southwest or south, rain clouds cross the Izumi Mountains before the Osaka Plain. When rain clouds cross the Izumi Mountains, new rain clouds occur around the Izumi Mountains and amount of precipitation increase around the Izumi Mountains. After passing through the Izumi Mountains, some clouds disappear and wet air is dried because of rain around the Izumi Mountains. Then, rain cloud direction is important for high precipitation around the mountains.

The cloud direction is to determine how many times cloud meets mountains. For the sampling site at the Ikoma Mountains cloud from northwest to west meets firstly the Ikoma Mountains and precipitation around the sampling area is high. However cloud from southwest to south meets firstly the Izumi Mountains and secondly meets the Ikoma Mountains and then, precipitation around the Ikoma Mountains is not high as shown in Fig. 8.

CONCLUSION

The purpose of study is to clarify the relation between precipitation amount and topography. Then rain sample was sampled from the Osaka Plain to the Ikoma Mountains covering big topography change. As a result, amount of precipitation in the flat area was constant. Amount of precipitation on mountain area was higher than those of flat area however it was not always higher than flat area. The sampling point Top is the mountain peak and then each event

was grouped into two types based on precipitation ratio of sampling point Top. Precipitation ratio of over 1.5 for Top was defined as A group events. Precipitation ratio of less than 1.1 for Top was defined as B group events.

Most of wind directions in A group events were north to west. Most of wind directions in B group events were east. Some wind directions of A group events were east and north east. Similarly one wind direction of B group events was west. Then, wind direction is not absolute parameter to determine whether A or B group events. However, western and northern wind can easily come up the Ikoma Mountains slope because the mountain direction is south to north and most of events was thought to depend on wind direction.

Wind direction can cover the phenomenon of most precipitation. Then, cloud direction during rain was studied. Cloud directions in A group events were northwest or west. The other hand, cloud directions in B group events were southwest or south. If rain clouds come from southwest or south, rain clouds cross the Izumi Mountains before the Osaka Plain. When rain clouds cross the Izumi Mountains, new rain clouds occur around the Izumi Mountains and amount of precipitation increases around the Izumi Mountains. After passing through the Izumi Mountains, some clouds disappear and wet air is dried at the Ikoma Mountains because of rain around the Izumi Mountains.

Therefore rain cloud direction is important for high precipitation around the mountains. The cloud direction is to determine how many times cloud meets mountains. When cloud meets firstly the

mountain, amount of precipitation is high around the mountain. However when cloud meets secondly the mountain, amount of precipitation is not high around the mountain.

REFERENCES

- [1] I. M. Patuti, Ahmad R, K. B. Suryolelono, "Mechanism and Characteristics of The Landslides in Bone Bolango Regency, Gorontalo Province, Indonesia", International Journal of GEOMATE, Vol. 12, Issue 29, pp. 1-8, Jan., 2017.
- [2] Yabusaki S, Kono T, "Characteristics of stable isotopes in precipitation at Kyoto basin", Bulletin of geo-environmental science, Vol. 14, 2010, pp23-30.
- [3] Yamada T, Hibino T, Araki T, "Statistical Characteristics of Rainfall in Mountainous Basins" Journal of Japan Society of Civil Engineers, No. 527, 1995, pp1-13.
- [4] Yamada K, "Special Distribution of Heavy Rainfall in Mountainous area", Proceedings of The Japanese Conference on Hydraulics, Vol.28, 1984, pp.509-513.
- [5] Wakimizu K, Kobayashi T, Hyashi S, "On Characteristics of the Rainfall Distribution on the Isolated Conical Mountain", Science bulletin of the Faculty of Agriculture, Kyushu University, Vol. 46, Feb. 1992, pp. 237-242.

INFLUENCE OF WASTE LOADING RATE ON BIOGAS GENERATION FROM MUNICIPAL SOLID WASTE

Sartaj M.¹, Kennedy K.¹ and, Nair A.¹

¹ Civil Eng. Dept., University of Ottawa, Canada K1N6N5

ABSTRACT

Higher growth rate for acidogens compared to methanogens in Anaerobic Digestion (AD) process could result in Volatile Fatty Acids (VFAs) accumulation, pH drop, and process instability. The organic waste loading rate and its distribution could alleviate this problem. The objective of this study was to evaluate the effect of organic waste loading rate and load distribution on biogas generation from organic fraction of municipal solid waste (OFMSW). Biomethane potential (BMP) tests were carried out in 2 phases. In phase 1, the effect of 3 different organic waste loading rates was investigated by adding 3, 6, or 9 g of OFMSW to each BMP bottle. In phase 2, the objective was to analyze the effect of distributed loading of OFMSW. The results from phase 1 showed that the lower the organic load, the higher was the methane generation. The specific biogas generation for all three loading rates was 297 mL/g for 3 g organic load, 155 mL/g for 6 g organic load, and 142 mL/g for 9 g organic load, respectively. The results from phase 2 showed that there was a distinct advantage in a staged fed (distributed organic waste loading) BMP assay with faster biodegradation and a higher yield with increasing intervals of loading. It was observed that the reactors with three loads of 1 g (3 X 1 g) spread over the duration of the test produced higher total biogas at a faster rate compared to the 1 X 3 g and 2 X 1.5 g OFMSW loading.

Keywords: Anaerobic Digestion, Biogas, Municipal Solid Waste, Organic Loading Rate, Leachate.

INTRODUCTION

OFMSW is mainly the waste contained in kitchen waste and yard waste which contain organic content from which gas and energy can be tapped and utilized. The methane generated from the OFMSW is of significance, since this is utilized to generate energy. Methane constitutes to anywhere from 40%-60% of landfill gas generated [1]. By better understanding of landfill decomposition processes, a shift in the philosophy of landfill design from the storage concept towards a process-based (or bioreactor) approach was inevitable in the recent decades.

An anaerobic Bioreactor LandFill (BLF) has a shorter stabilization time compared to conventional engineered landfills and is more of a treatment system than a typical landfill. In BLF technology, the entire landfill works as an anaerobic digester and accelerates the waste decomposition by maintaining a healthy anaerobic bacterial consortium. During the acid formation phase of AD of OFMSW, the hydrocarbons that were broken down by hydrolysis are converted into VFAs, mainly acetic acid, butyric acid and also hydrogen gas with a drop in pH. This along with high concentrations of ammonia inhibits methanogenic bacteria and restricts the potential biogas and methane production [2]-[3]. Since the specific growth rate for acidogens are significantly higher than methanogens, VFA accumulation causes the pH to drop which proves detrimental to the methanogens. Leachate recirculation with supplemental water addition employed in BLFs

dilutes the total VFAs and moderates the pH which makes the substrate and conditions in the landfill more conducive for the methanogens [4].

Since the concentration of VFAs is a function of the rate of hydrolysis of carbohydrates and lipids, it was decided to evaluate the effect of organic waste loading rate and load distribution on biogas generation from OFMSW. It was hypothesized that the organic loading rate would have an effect on the performance of AD process. Also, it was hypothesized that by distributing the organic waste load over time would result in a more stable AD process and an increase in methane yield.

MATERIALS AND METHODS

To achieve the objectives, a series of BMP assay experiments under a controlled environment was conducted as explained below. Two hundred and fifty mL Kimax® glass bottles capped with butyl rubber stoppers were used to perform mesophilic BMP assays. BMP tests were carried out in 2 phases. In phase 1, the objective was to determine the effect of 3 different organic waste loading rates by adding 3, 6, or 9 g of prepared OFMSW waste to each bottle, each duplicated. In phase 2, the objective was to analyze the effect of distributed loading of OFMSW with the best loading obtained from batch phase 1, which was 3 g. A total organic load of 3 g of prepared OFMSW was added to reactors in different time intervals. In the first case, the entire 3 g of organic load was applied right at the start of the batch test, in the second case; the initial

load of 1.5 g was supplemented by a second load of 1.5 g at the end of day 16. And finally in the third set of reactors, the initial load of 1 g was supplemented by two loads of 1 g each at the end of day 16 and day 29. All BMP tests were duplicated. Total working volume for all BMP tests was 200 mL consisting of OFMSW (as discussed above), 30 mL of leachate, 70 mL of mesophilic anaerobic inoculums, and 100mL of

distilled water added for dilution. The leachate blend (30 mL) used was a mix of young leachate and old leachate. Anaerobic sludge collected from a local wastewater treatment plant was used as inoculum. The characteristic properties of the anaerobic inoculums obtained from R.O. Pickard Environmental Center, Ottawa, are also given in Table 1.

Table 1. Properties of prepared OFMSW and Inoculums

	Alkalinity mg/L	COD mg/L	Ammonia as N mg/L	Moisture Content %	TS mg/L	VS mg/L	pH
OFMSW	1,600	536,317	779	65.4	305,100	268,200	4.9
Inoculums	4,250	26,500	990	na	20,900	11,800	7.3

A mixture simulating the OFMSW was prepared in the lab to be used in the experiments as a model waste to minimize compositional variation seen in a real OFMSW. The model waste composition was intended to simulate kitchen waste and industrial food processing waste and had a similar composition as the Canada Food Guide, thus was representative of Canadian kitchen waste [1]. To reduce the particle size, the model waste was placed in a food processor for 30 s at high speed and stored at 4°C until being used. Equal portions of NaHCO₃ and KHCO₃ were added to each bottle to achieve an alkalinity concentration of between 4,000 and 6,000 mg/L (as CaCO₃). This buffered the pH in the bottles between 7.8 and 8.1. The bottles were subsequently sparged with nitrogen gas for two minutes to produce anaerobic conditions and then sealed. The measurement of the gas produced by the batch BMP bottles were monitored on a daily basis using a tube in tube manometer. Bottles were incubated at 35 ± 1°C in a New Brunswick Scientific Controlled Environment Incubator Shaker at 80 rpm, to keep bacteria and substrate in suspension. The measurement of the gas produced by the batch BMP bottles were monitored on a daily basis using a tube manometer. Gas samples were analyzed for gas composition with thermal conductivity gas chromatograph (series 400, Gow-Mac Instrument Co., USA). VFAs were measured using the gas chromatographic method (5560-D, APHA, 2005) with an Agilent-6890 gas chromatograph.

RESULTS AND DISCUSSIONS

The results from the BMP tests, phase 1, are shown in Fig. 1, which shows the total biogas generated (average of the two duplicates) for 3 different organic waste loading. The total biogas yields were used to compare the performances of the reactors with the three different organic loads of 3 g, 6 g and 9 g. The biogas produced from the reactors with 9 g of prepared food waste had an initial surge in gas production which saturated after day 21 producing nearly 1200 mL of biogas in total. The reactors with 6 g of OFMSW waste on the other hand produced nearly 900 mL of gas.

Based on the data for 6 g and 9 g and after deducting the biogas contribution from the leachate and inoculum, the average gas production under these conditions per gram of OFMSW waste was anywhere between 142 mL and 154 mL. Based on this, the reactor with 3 g should technically have produced only 450 mL of gas. On the contrary, the reactor with 3 g of waste actually produced 890 mL of gas. This indicates that the biodegradable portion in the reactors with 6 g and 9 g of waste was not completely utilized. The specific biogas generation for all three loading rates was as follows:

Batch bottle with 3 g organic load: 297 mL/g

Batch bottle with 6 g organic load: 155 mL/g

Batch bottle with 9 g organic load: 142 mL/g

This meant that in terms of performance, the lower the organic load, the higher was the performance in terms of methane generation. One possible reason for this is that as the amount of food waste increases, the methanogenic bacteria experience a lower pH because of the increased acidogenesis in case of higher organic loading and as a result do not perform to the full potential. Methanogenic bacteria have a lower specific growth rate compared to acidogenic bacteria and due to this, the acid formation happens quicker which in turn drops the pH. This also makes available an excess substrate for methanogenic bacteria in cases of higher organic loads and this shock loading cannot be well received by the methanogenic bacteria. This explains why the initial rate of gas production was higher for the higher organic loads of 9 g and 6 g bottles while the 3 g reactors had a more consistent production curve. The results observed in this study indicated that the reactors having an organic loading rate of 3 g had the highest efficiency in terms of biodegradation. This however, is not to be mistaken as a standard value of organic loading or optimal loading for all bioreactor landfills. From this set of batch tests, it can be observed there is a limit on the amount of loading which can be effectively utilized by the methanogenic bacteria within the bioreactor landfill. This is more or less a threshold beyond which there is an inhibitory effect caused by the either the additional organic load which increases the VFA content and drops the pH or

possibly even the increase in ammonia to inhibitory levels. The concentration of acetic acids at the beginning, 3 weeks after the start, and at the end of test was 280, 1160, and 140 mg/L, respectively, showing the increase in VFA content discussed above.

COD concentrations of these bottles at the start, after week 3 and at the end of day 60 of the BMP bottles is presented in Fig.2. During the start-up of the reactors, the average initial COD concentration in the bottles was found to be 3,690 mg/L. After 3 weeks of biodegradation, the COD concentration had dropped down to 2,770 mg/L of COD. Though the decrease is not very high till the end of the third week, the biogas generation curve gives an explanation as to why the decrease is not that high. The biogas generation rate till the end of the third week is comparatively lower (452 mL of biogas for 3 g loading) which explains why there is not much of decrease in the COD concentration.

Ammonia concentrations of these bottles at the start, after week 3 and at the end of day 60 of the BMP bottles are presented in Fig.2. During the start-up of the reactors, the average initial ammonia concentration in the bottles was found to be 405 mg/L. The average ammonia concentration in these batch bottles was noted to be 479 mg/L at the end of 3 weeks of operation. There is a significant amount of hydrolysis of proteins taking place as a result of which the ammonia concentration is comparatively higher at this.

The results from the BMP tests, phase 2, are shown in Fig. 3, which shows the total biogas generated (average of the two duplicates) for 3 different distribution of organic waste loading investigated in this study. The same total organic load of 3 g of prepared OFMSW waste was added to all reactors in different time intervals as explained above. The test results shown in Fig. 3 indicate that there is a distinct advantage in a staged fed (distributed organic waste loading) batch BMP assay with faster biodegradation and a higher yield with increasing intervals of loading. It was observed that the reactors with three loads of 1 g (3 X 1 g) spread over the duration of the test started producing biogas at a rate corresponding to the total biodegradable portion of the food waste. Immediately after a loading, the biogas generation curve for 3 X 1 g showed much steeper curves and by day 30 the reactor had produced the same biogas yield (618 mL) as the reactors loaded once with 3 g (1 X 3 g) of food waste. In calculating the biogas production for each case the biogas contribution from the leachate and inoculum is deducted. With every subsequent loading, the rate of gas production had increased and by day 45, the reactor with 3 X 1 g loading rate had yielded the same amount of gas (1400 mL) produced by the reactor with 2 X 1.5 g loading rate. In addition to producing biogas faster, the reactor with 3 X 1 g loading also produced a higher total biogas generation of 1530mL compared to the 1 X 3 g and 2 X 1.5 g loading which produced a total of 896 mL and 1367 mL, respectively. The reactors with the 2 X 1.5 g loading showed similar characteristics to

the 3 X 1 g loading reactors with the exception that the biogas production rate was very high after the second loading. These reactors equaled the biogas yield (560 mL) from the 1 X 3 g reactors on day 24; soon after the second loading was applied. The reactors with the 1 X 3 g single loading reactors showed a very smooth and consistent curve with the least yield and the slowest rate compared to the other reactors. The cumulative biogas generation curve resembles a standard batch BMP assay curve.

A possible explanation for this increased performance with smaller loads spread out over time is that the bacteria responsible for biodegradation have already acclimatized to the food waste. In addition to this, the acidogenic and methanogenic bacterial consortia are at a better balance which results in more conducive pH stability and a good VFA balance. The methanogens would have been able to utilize the substrate since the methanogenic bacterial population would be well acclimatized which is the rate limiting step for organic biodegradation. No VFA measurement was available for this set of test due to a malfunction of the equipment.

CONCLUSIONS

The test results indicated that a lower the organic loading rate of 3 g had the highest efficiency in terms of biodegradation compared to the higher organic loads of 9 g and 6 g of OFMSW. The results observed in this study also indicated that there was a distinct advantage in a staged fed batch BMP assay with faster biodegradation and a higher yield with increasing intervals of loading.

REFERENCES

- [1] Nair A, Sartaj M., Kennedy K., Coelho NMG. (2014) Enhancing biogas production from anaerobic biodegradation of the organic fraction of municipal solid waste through leachate blending and recirculation. *Waste Management & Research*, 2014, Vol. 32(10) 939–946.
- [2] Dong S., Sartaj M. (2016). Statistical analysis and optimization of ammonia removal from landfill leachate by sequential microwave/aeration process using factorial design and response surface methodology, *J. of Environmental Chemical Engineering*, 4, no. 1, 100-108.
- [3] Berge N.D., Reinhart, D.R., Dietz, J., Townsend, T. (2006) In situ ammonia removal in bioreactor landfill leachate. *Waste Management*, 26, 334–343.
- [4] Sanphoti N., Towprayoon S., Chaiprasert P., Noparatana, A. (2006). The effects of leachate recirculation with supplemental water addition on methane production and waste decomposition in a simulated tropical landfill. *Journal of Environmental Management*, 81(1), 27-35.

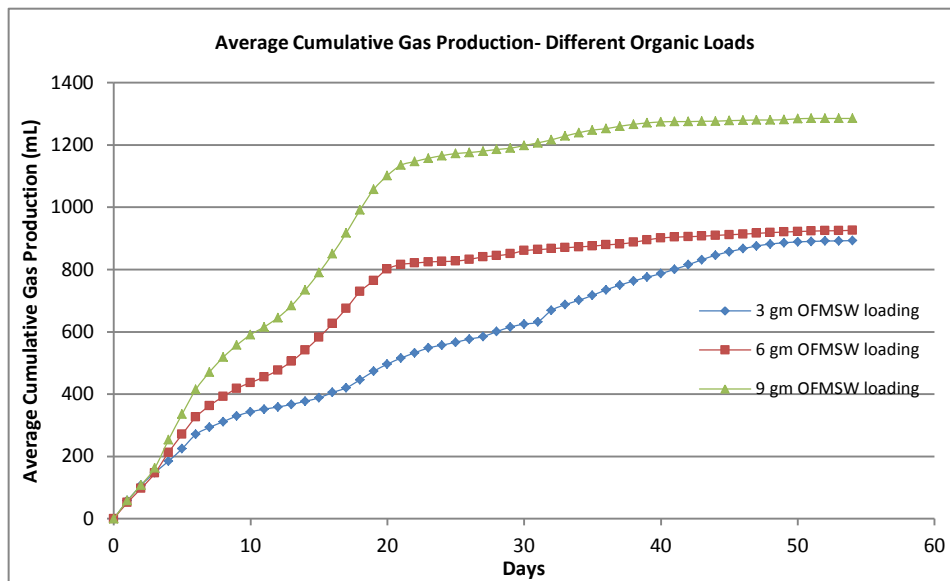


Fig. 1 Average cumulative gas production for different organic loading- BMP tests- Phase 1

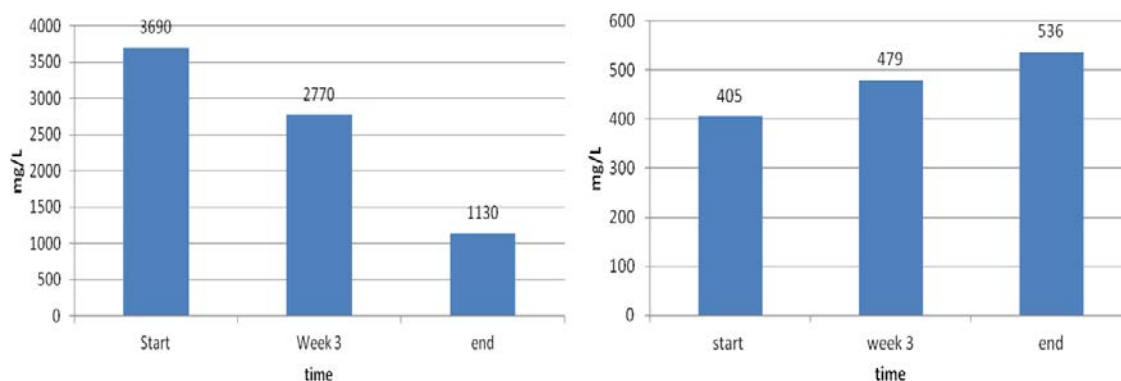


Fig. 2 COD (left) and Ammonia (right) at the start, after 3 weeks and completion

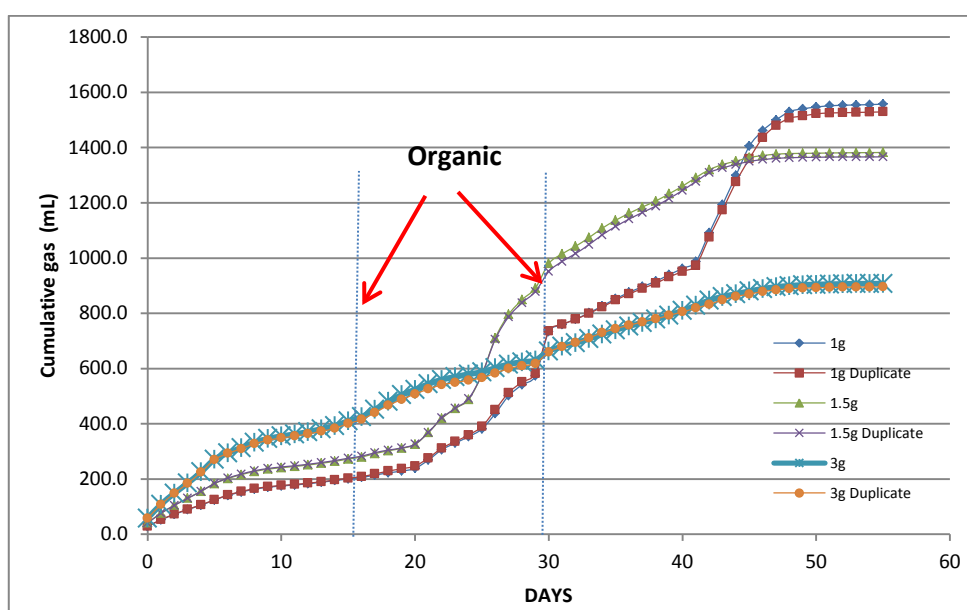


Fig. 3 Cumulative gas production for distributed organic waste loading - Phase 2

ASSESSING URBAN WATER SUPPLY SYSTEM IN NORTHEASTERN IN THAILAND: WATER QUALITY AND AUTHORITY ORGANIZATION

Oranee Roongrueang¹, Pensupa Wirikitkhul², Jareeya Yimrattanabavorn³ and Sudjit Karuchit⁴

^{1,2}Master student, ^{3,4}Assistant Professor, School of Environmental Engineering, Institute of Engineering, Suranaree Univ. of Technology, 111 University Ave., Muang District, Nakhon Ratchasima, Thailand 30000.

ABSTRACT

Providing safe water supply is one of important public health priorities. The water quality of water supply is closely associated with human health. The aim of this study was to assess the quality of water in the urban water supply systems and their authority organization to assess the existing performance of water supply system and their organization. The sampling locations were covered of 4 cities namely, Nakhon Ratchasima (Korat), Chaiyaphum, Buriram and Surin provinces. The total of 13 samples site locations of urban water supply system which owned by provincial and municipal waterworks authority. Water samples of each sampling site locations were collected from water resource, storage tank and household taps water and analyzed for various parameters. The results showed the water quality of urban water supply system had met water quality standards in parameter turbidity, TSS, TDS, Nitrate and total coliform except colour, iron due to the retention time of sedimentation process is not the proper. And there were problem with residual chlorine at storage tank and household tap water which were lower than standard limit and might affect with population health. There were no difference between the performance of provincial and municipal waterworks authority. The outcome of this study can support improvement of urban water supply system and their authority organization

Keywords: Urban water supply system, Water quality, Authority organization, Thailand

INTRODUCTION

Access to safe water supply is a basic concern for human health and health protection. According to the World Health Organization (WHO), a concentration of microorganisms, parasites or substances posing a possible risk to human health has to be prevented [1]. The water quality of water supply is closely associated with human health. If the water supply was contaminated by pollutants and microorganisms, it would affect with water qualities and affect the health of the population. Thus, water supply system and authority organization are obliged to monitor water quality for human consumption. The water qualities need to meet standard, which is why quality of water resource and tap water of water supply system should be assess to state their aspect of problems. Water supply in urban area is challenged by increasing population. In this study, the sampling locations were covered of 4 cities namely, Nakhon Ratchasima (Korat), Chaiyaphum, Buriram and Surin provinces. This region is covers more than one-third of the country which is called "Khorat plateau". The water supply consumption in this area has been seriously concerned because of the low level of rainfall intensity and long dry period in this area. This study is one of four sub-projects in research project "Study of Management Efficiency of Water Resources and Urban Water Supply

Systems in North-Eastern Region in Thailand". The main goal was thoroughly evaluating the existing urban water supply system in northeastern region of Thailand in term of the water resources, water quality, associated health risk and engineering aspect. The aim of this study was to assess the quality of water in the urban water supply systems and their authority organization to assess the existing performance of water supply system and their organization. The outcome of this study can support improvement of urban water supply system and their authority organization.

METHODS

Study Sites and Sampling

This study was carried out to collect water from urban water supply system in the lower northeastern of Thailand. The area covers of 4 provinces namely Nakorn Ratchasima (N), Chaiyaphum (C), Buriram (B) and Surin (S) provinces as shown in Fig 1. The urban water supply system was typically consisted of the coagulation-flocculation, sedimentation, filtration and disinfection systems. The water source of water treatment system was commonly taken from surface water. The water supply systems in northeastern Thailand are organized by two organizations: the provincial waterworks authority

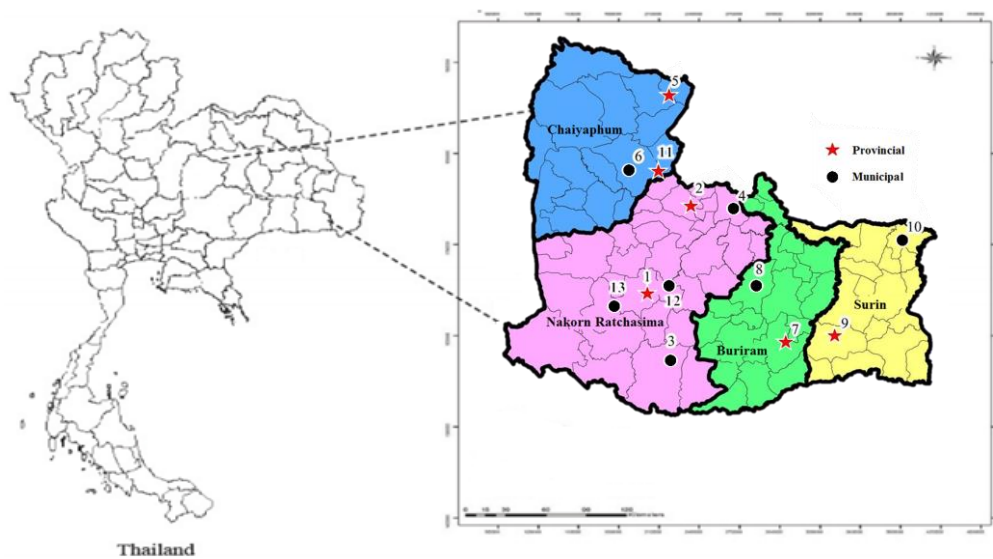


Fig. 1 Map of the study area and the sampling locations.

and the local authority. Thus, this study was focused on urban water supply system owned by provincial and municipal waterworks authority. The total of 13 samples site locations of urban water supply system were collected during dry period (January-April, 2016) and rainy period (July-October, 2016). The distribution of 13 sampling site locations was shown in Table 1.

Table 1 Sampling site locations of urban water supply system.

Study area	Authority organization		
	Provincial	Municipal	Total
Nakorn Ratchasima (N)	2	4	6
Chaiyaphum (C)	2	1	3
Buriram (B)	1	1	2
Surin (S)	1	1	2
Total	6	7	13

Analytical Methods

Water samples of each sampling site locations were collected from water resource, storage tank and household taps water. Water samples were analyzed for various parameters and analytical methods as shown in Table 2.

Table 2 Parameters and analytical methods.

Parameters	Analytical methods [2]	Parameters	Analytical methods [2]
Physical and Chemical quality		Physical and Chemical quality	
Turbidity	2130 B. Nephelometric Method	Nitrite, Nitrate	4500-NO ₂ ; NO ₃ B. Spectrophotometric
Colour	2120 D. Spectrophotometric Method	Fluoride	4500-F D. SPADNS Method
BOD	5210 B. 5-day BOD Test Method	Ammonia-N	4500-NH ₃ C. Titrimetric Method
Iron	3500-Fe B. Phenanthroline Method	TKN	4500-Norg Kjeldahl Method
Manganese	3500-Mn B. Persulfate Method	TDS, TSS	2540 C., D. Gravimetric Method
Hardness	2340 C. EDTA Titrimetric Method	Residual chlorine	4500-Cl B. Iodometric Method
Sulfate	4500-SO ₄ ²⁻ E. Turbidimetric Method	Biological quality	
Chloride	4500-Cl ⁻ B. Argentometric Method	Total Coliform	9222 B. Membrane Filter Method

Data Analysis

Water quality assessment

The results of water quality were checked with the guideline of World Health Organization (WHO) for water resources quality and standard of metropolitan waterworks authority for storage tank water quality and household tap water quality as shown in Table 3. The percentages of not exceed standard water sample were calculated by using the Eq. (1)

$$\% \text{Not exceed standard} = \frac{\text{Number of samples that were not exceed standard}}{\text{Total sample}} \times 100 \quad (1)$$

Statically analysis

The results of water quality of provincial and municipal waterworks authorities were analyzed, mean and standard deviation (SD) and analyzed variance with Independent Sample Test (2-tailed). SPSS Statistics Version 22.0

Table 3 Water quality standard.

Parameters	Units	Water quality standards	
		Surface water*	Tap water**
Physical and Chemical quality			
Turbidity	NTU	-	≤ 4
Colour	Pt-Co	≤ 300	≤ 15
DO	mg/L	≥ 4	-
BOD	mg/L	≤ 2	-
Nitrate	mg/L	≤ 5	≤ 50
Iron	mg/L	≤ 50	≤ 0.3
Manganese	mg/L	≤ 5	≤ 0.3
Hardness	mg/L	≤ 500	-
Chloride	mg/L	-	≤ 250
Ammonia nitrogen	mg/L	≤ 0.5	-
TDS	mg/L	≤ 1500	≤ 1500
Residual chlorine	mg/L	-	≥ 2
Biological quality			
Total Coliform	MPN/100 mL	≤ 20000	Not found

* : The guideline of World Health Organization (WHO).

** : Standard of metropolitan waterworks authority.

RESULTS AND DISCUSSION

Water Quality Assessment

Surface water resource quality

The results of surface water resource qualities were presented in Table 4. The results showed the parameters; turbidity, Iron, hardness, sulfate, chloride, TKN and ammonia-N met the guideline of WHO and not exceed standard value in 100% of samples. However, the parameters; colour, DO, manganese, nitrate, total coliform and BOD had number of samples that were limit exceed standard in range of 8-50% of samples. And all sampling site locations had surface water resource quality that were limit exceed standard of BOD about 50% of samples. These indicated that water resources of urban water supply were polluted due to wastewater, urban area and dense population. And Nakhon Ratchasima is the second largest cities in Thailand and had the poorest water resources among the other sampling cities.

Table 4 The percentage of water samples that were not exceed standard for water source.

Study area	Water quality of water source													Biological
	Physical		Chemical											
	Colour	Turbidity	DO	Iron	Mangnese	Hardness	Sulfate	Chloride	BOD ₅	Nitrate	Ammonia-N	TKN	Total Coliform	
N	91.7	100.0	83.3	100.0	91.7	100.0	100.0	100.0	58.3	91.7	100.0	100.0	83.3	
C	75.0	100.0	50.0	100.0	100.0	100.0	100.0	100.0	50.0	100.0	100.0	100.0	100.0	
B	100.0	100.0	75.0	100.0	100.0	100.0	100.0	100.0	50.0	100.0	100.0	100.0	100.0	
S	100.0	100.0	100.0	100.0	100.0	100.0	100.0	100.0	50.0	100.0	100.0	100.0	100.0	

Water quality of storage tank

As shown in Table 5, the water quality at storage tank had values of parameters TSS, TDS, nitrate and total coliform that met the standard of metropolitan waterworks authority in 100% of water samples. And the water quality of storage tank in Nakhon-Ratchasima also had limit exceed in parameters colour, turbidity, iron, manganese and residual chlorine. These results indicated that they might have the problem with the process of water treatment. These findings were supported by conclusion of the sub-research project that the retention time of sedimentation process is not the proper range [3].

Water quality of household taps water

As shown in Table 6, the water quality of household tap water had value of parameter turbidity, TSS, TDS, nitrate and total coliform that met the

standard of metropolitan waterworks authority in 100 % of samples. However they found more than 50% of water samples that had residual chlorine less than standard limit and had lower concentrations than at storage tank. These results indicated that the distribution system might have problems about leakage of piping. It was supported by conclusion of the sub-research project that found the amount of water loss from distribution system of water supply system were in range of 31-47% of water production [3]. These might affect with population health.

Table 5 The percentage of water samples that were not exceed standard for storage tank.

Study area	Water quality of storage tank								Biological
	Physical		Chemical						
	Colour	Turbidity	Iron	Manganese	TSS	TDS	Nitrate	Residual chlorine	
N	50.0	91.7	41.7	66.7	100.0	100.0	100.0	58.3	100.0
C	100.0	100.0	100.0	88.3	100.0	100.0	100.0	50.0	100.0
B	100.0	100.0	75.0	100.0	100.0	100.0	100.0	50.0	100.0
S	25.0	100.0	100.0	75.0	100.0	100.0	100.0	50.0	100.0

Table 6 The percentage of water samples that were not exceed standard for household tap water.

Study area	Water quality of household tap water								Biological
	Physical		Chemical						
	Colour	Turbidity	Iron	Manganese	TSS	TDS	Nitrate	Residual chlorine	
N	50.0	100.0	50.0	80.0	100.0	100.0	100.0	50.0	100.0
C	100.0	100.0	100.0	100.0	100.0	100.0	100.0	25.0	100.0
B	100.0	100.0	75.0	100.0	100.0	100.0	100.0	50.0	100.0
S	50.0	100.0	100.0	75.0	100.0	100.0	100.0	0.0	100.0

Efficiency of Water Supply System Plants

The efficiencies of water supply system were calculated by the reduction concentration of water qualities from water resource to storage tank. In Fig. 2, 3 and 4 shown the efficiency of urban water supply system in range of 76.6-95.8% for colour, 47.1-82.9% for iron and 0-68.5% for manganese. These results indicated that only Chaiyaphum urban water supply system had manganese removal efficiency higher than 50%, the others were lower than 25%. To assess the distribution system by comparison water qualities between storage tank and household tap water. In Fig. 5 shown increasing of

iron concentration from storage tank to household tap water. These result indicated that the distribution system of water supply system had problem. It was supported by conclusion of the sub-research project that they had a potential problems of leakage in water supply system and the maintenance of equipment [3]. The distribution system in many cities in Thailand are decade old. And numerous water contaminants has been reported in many cities in Pakistan, which could be the results of decade old cast iron pipes and mixing of sewerage water with portable water in poorly managed the water distribution system [4,5].

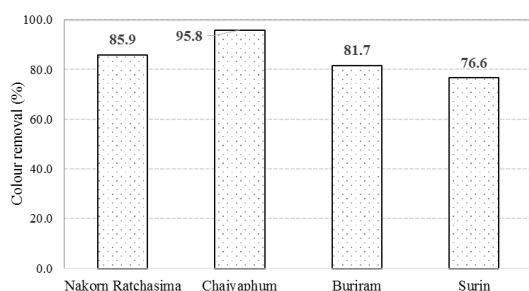


Fig. 2 Remove efficiency of urban water supply system for colour.

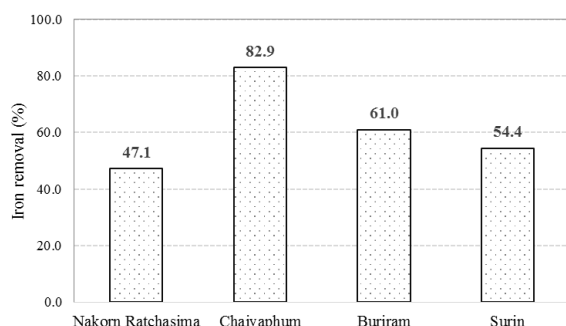


Fig. 3 Remove efficiency of urban water supply system for iron.

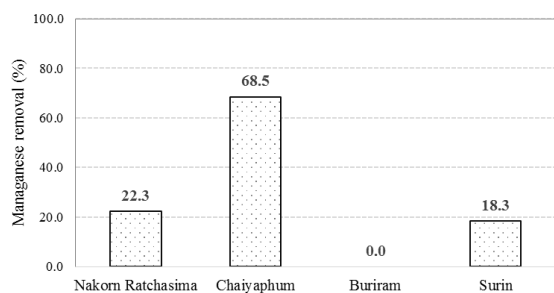


Fig. 4 Remove efficiency of urban water supply system for manganese.

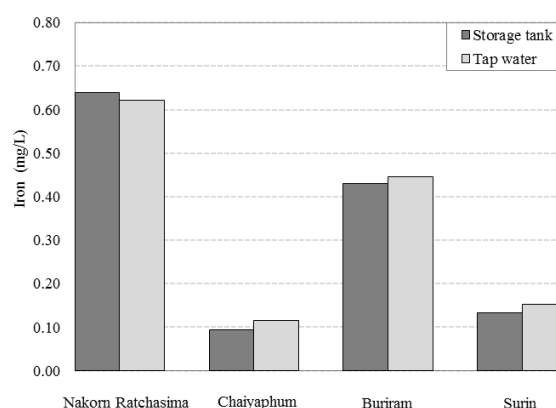


Fig. 5 The comparison of iron concentration between storage tank and household tap water.

The Authority Organization Comparison

To assess performance of the authority organization by comparison the water qualities of provincial and municipal waterworks authority by compared percentages of water samples that were not exceed standard level as show in Table 7 for water source, Table 8 for storage tank and Table 9 for household tap water. The data of water resource qualities were analyzed with Independent Sample Test (2-tailed) and presented the p-value, mean and SD of water qualities in Table 10. The results of p-values shown they had no significant in all parameters between the water resource qualities of provincial and municipal waterworks authority except sulfate parameter. However, they shown that many parameters had high SD values; these indicated that the data were fluctuating. And when considered of mean values, they shown that municipal authority waterworks had better water qualities than of provincial authority waterworks.

Table 7 The percentage of water samples that were not exceed standard for water source compared between Province and Municipal waterworks authority.

Authority organization	Water source												
	Physical		Chemical										Biological
	Colour	Turbidity	DO	Iron	Manganese	Hardness	Sulfate	Chloride	BOD5	Nitrate	Ammonia-N	TKN	Total Coliform
Provincial	90.0	100.0	100.0	100.0	100.0	100.0	100.0	100.0	50.0	100.0	100.0	100.0	90.0
Municipal	92.9	100.0	64.3	100.0	92.9	100.0	100.0	100.0	57.1	92.9	100.0	100.0	92.9

Table 8 The percentage of water samples that were not exceed standard for storage tank compared between Province and Municipal waterworks authority.

Authority organization	Storage tank							
	Physical		Chemical					Biological
	Colour	Turbidity	Iron	Manganese	TSS	TDS	Nitrate	Total Coliform
Provincial	66.7	100.0	75.0	75.0	100.0	100.0	100.0	50.0
Municipal	57.1	92.9	71.4	78.6	100.0	100.0	100.0	50.0

Table 9 The percentage of water samples that were not exceed standard for household tap water compared between Province and Municipal waterworks authority.

Authority organization	Household tap water							
	Physical		Chemical					Biological
	Colour	Turbidity	Iron	Manganese	TSS	TDS	Nitrate	Total Coliform
Provincial	80.0	100.0	70.0	90.0	100.0	100.0	100.0	40.0
Municipal	58.3	100.0	75.0	83.3	100.0	100.0	100.0	25.0

Table 10 The conclusion of data analysis with Independent Sample Test (2-tailed) of water source.

Parameter	Units	Water source				p-value	Result
		Provincial		Municipal			
		Mean	SD	Mean	SD		
Colour	Pt-Co	136.9	103.1	112.2	84.1	0.524	Non-sig.
Turbidity	NTU	12.2	14.0	9.8	10.5	0.629	Non-sig.
pH	-	6.9	0.6	7.1	0.3	0.225	Non-sig.
DO	mg/L	4.9	1.3	4.3	1.7	0.347	Non-sig.
Iron	mg/L	1.1	1.4	0.8	0.5	0.371	Non-sig.
Manganese	mg/L	0.7	0.7	1.0	2.4	0.681	Non-sig.
Hardness	mg/L	40.0	35.7	55.8	35.9	0.300	Non-sig.
Sulfate	mg/L	0.01	0.01	0.02	0.02	0.019	sig.
Chloride	mg/L	50.1	78.0	44.5	60.0	0.843	Non-sig.
TSS	mg/L	29.6	24.3	31.2	26.6	0.886	Non-sig.
TDS	mg/L	288.3	352.1	262.2	229.5	0.827	Non-sig.
BOD	mg/L	3.1	1.6	2.5	1.2	0.292	Non-sig.
Nitrate	mg/L	0.6	0.5	0.9	1.6	0.623	Non-sig.
TKN	mg/L	0.3	0.3	0.2	0.3	0.801	Non-sig.

Table 11 The conclusion of data analysis with Independent Sample Test (2-tailed) of storage tank.

Parameter	Units	Storage tank				p-value	Result
		Provincial		Municipal			
		Mean	SD	Mean	SD		
Colour	Pt-Co	18.8	16.8	13.8	11.5	0.383	Non-sig.
Turbidity	NTU	1.6	0.7	1.4	1.0	0.483	Non-sig.
pH	-	6.8	1.1	7.3	0.6	0.140	Non-sig.
DO	mg/L	5.8	1.1	5.6	1.5	0.737	Non-sig.
Iron	mg/L	0.4	0.4	0.4	0.6	0.732	Non-sig.
Manganese	mg/L	0.3	0.4	0.9	2.4	0.405	Non-sig.
Chloride	mg/L	28.2	24.3	50.9	61.2	0.241	Non-sig.
TSS	mg/L	27.6	34.0	22.4	25.5	0.656	Non-sig.
TDS	mg/L	125.2	65.8	217.3	244.0	0.218	Non-sig.
Nitrate	mg/L	0.7	0.6	1.1	1.8	0.402	Non-sig.
Residual chlorine	mg/L	0.5	0.6	0.7	1.2	0.582	Non-sig.

Table 12 The conclusion of data analysis with Independent Sample Test (2-tailed) of household tap water.

Parameter	Units	Household tap water				p-value	Result
		Provincial		Municipal			
		Mean	SD	Mean	SD		
Colour	Pt-Co	12.4	9.8	13.3	9.2	0.825	Non-sig.
Turbidity	NTU	0.9	0.4	1.2	0.7	0.208	Non-sig.
pH	-	7.2	0.5	7.2	0.4	0.933	Non-sig.
DO	mg/L	5.5	0.9	5.4	0.9	0.798	Non-sig.
Iron	mg/L	0.4	0.5	0.4	0.6	0.963	Non-sig.
Manganese	mg/L	0.1	0.2	0.9	2.6	0.378	Non-sig.
Chloride	mg/L	29.1	25.5	56.7	67.5	0.236	Non-sig.
TSS	mg/L	17.6	17.6	20.1	20.4	0.770	Non-sig.
TDS	mg/L	152.9	94.7	245.6	287.4	0.342	Non-sig.
Nitrate	mg/L	0.4	0.4	1.3	2.1	0.155	Non-sig.
Residual chlorine	mg/L	0.2	0.3	0.4	1.0	0.590	Non-sig.

The p-value, mean and SD of water qualities of storage tank and household tap water were analyzed by Independent Sample Test (2-tailed) and concluded in Table 11 and 12 respectively. The results of p-values shown they were no difference in all parameters of the water qualities at storage tank and household tap water between provincial and municipal waterworks authority. However, they had high SD values similar with water resources qualities and indicated that the data were fluctuating. On the other hand, when considered of mean values, they shown that provincial authority waterworks had better values than of municipal authority waterworks. These results indicated that the urban water supply system which authorized by municipal authority waterworks produced water qualities better than urban water supply system of provincial authority waterworks. However, the conclusion of the sub-research project was survey people satisfaction by using questionnaires; it was found that 83.43% of people were satisfied with the quality of water and the service of water supply authority organization [6].

CONCLUSION

In conclusion, the water quality of urban water supply system had met water quality standards in parameter turbidity, TSS, TDS, Nitrate and total coliform except colour, iron due to the retention time of sedimentation process is not the proper. And there were problem with residual chlorine at storage tank and household tap water which were lower than standard limit and might affect with population health. There were no difference between the performance of provincial and municipal waterworks authority. The outcome of this study can support improvement of urban water supply system and their authority organization.

ACKNOWLEDGEMENTS

This research was supported by Suranaree University of Technology.

REFERENCES

- [1] WHO, Guidelines for Drinking Water Quality, 4th ed. 2011.
- [2] APHA, AWWA, and WEF, Standard Methods for the Examination of Water and Wastewater, 22nd ed. American Public Health Association, 2012.
- [3] Racho P, Namgool S and Namseethan K, "Evaluation of the design and operation for water supply system in the Northeast", in Proc. 16th Conf. on National Environmental Engineering Conference, 2017.
- [4] Baig SA, Xu X, and Khan R, "Microbial water quality risks to public health: potable water assessment for a flood-affected town in northern Pakistan", J. of Rural and Remote Health, Vol. 12(3), Sep. 2012.
- [5] Khan K, Lu Y, Khan H, Zakir S, Ihsanullah, Khan S, Khan AA, Wei L, and Wang T, "Health risks associated with heavy metals in the drinking water of Swat, northern Pakistan", J. of Environmental Sciences, Vol. 25(10), Oct. 2013, pp. 2003-2013.
- [6] Racho P, Namseethan K and Namgool S, "Surviving-Oriented Evaluate of Urban Water Supply System in North-Eastern Region", in Proc. 16th Conf. on National Environmental Engineering Conference, 2017.

COMBINATION COAGULATION AND ADSORPTION PROCESSES FOR TREATING TEXTILE WASTEWATER IN HOUSEHOLD INDUSTRY

Tharika Kaenjun¹, Watcharapol Wonglertarak², Boonchai Wichitsathein³ and Jareeya Yimrattanabavorn⁴
¹Master student, ²Doctoral student, ^{3,4}Assistant Professor, School of Environmental Engineering, Institute of Engineering, Suranaree Univ. of Technology, 111 University Ave., Muang District, Nakhon Ratchasima, Thailand 30000.

ABSTRACT

Textile wastewater is a considerable source of environmental contamination due to its strong color, high pH and chemical oxygen demand (COD), and low biodegradability. The discharge of textile wastewater not only has diverse aesthetic effects, but such discharge can be carcinogenic, mutagenic and generally detrimental to our environment. Thus, textile wastewater should be removed completely before they are discharged into received water. Many methods have been reported for treating textile wastewater, among which coagulation and adsorption are widely used processes due to their relatively simple operation and low cost and suitable for household industry. The aim of this study was using the combination coagulation and adsorption processes to treat textile wastewater in household-scale industry. Coagulation performance and removal efficiencies in COD and color from four varies sources of textile wastewaters were investigated. The effluent from coagulation was treated with adsorption. The adsorption isotherm and removal efficiencies were investigated. The results showed the combination processes had the overall COD were in range of 72.9-93.8% and color removal efficiencies were in range of 70.6-98.5%. The results of coagulation study were found that in some cases of wastewater were effective in color removal but failed in COD removal, in another cases, had fail in color but were effective in COD removal efficiencies. The results showed varies of pH had much affected on color removal efficiencies more than COD removal efficiencies. The further experiments should be carried out to improve the combination removal efficiencies for application as suitable for textile household industry.

Keywords: Coagulation, Adsorption, Textile wastewater, household industry

INTRODUCTION

Textile wastewater is a considerable source of environmental contamination due to its strong color, high pH and chemical oxygen demand (COD), and low biodegradability. Due to toxic and carcinogenic effects of textile wastewater on living creatures and negative effects to photosynthetic activities of aquatic plants, removal of coloring agent, and chemical complex compounds in wastewater appears to be very important for human health and environment [1, 2]. Thus, textile wastewater should be removed completely before they are discharged into received water. Elimination of both dyes and COD in the textile wastewater by conventional wastewater treatment methods is very difficult. Conventional treatment methods such as biological, anaerobic microbial degradation, coagulation, adsorption and chemical oxidation, membrane separation process, electro-chemical are generally unsuccessful for the removal of wastewater containing dyes [2]. However, all of the methods suffered from one or another limitation. There is no single economically and technically viable method

to solve this problem and usually two or three methods have to be combination in order to achieve adequate level of color and COD removal [1]. Many methods have been reported for treating textile wastewater, among which coagulation and adsorption are widely used processes due to their relatively simple operation and low cost [3, 4] thus they are suitable for household industry. In this study the coagulation and adsorption processes were selected as combination to treat textile wastewater because of they were the most effective techniques for treatment textile wastewater and its simple design and low cost. The dyes of textile household industry can be classified as natural and synthetic which are complex organic molecules having groups such as azo, carbonyl, methane, nitro, quinoid, etc. [5]. The aim of this study was using the combination of coagulation and adsorption processes to treat textile wastewater in household industry. The performance of coagulation and adsorption processes were investigated in term of COD and color removal efficiencies. The outcome of this study could be applied to be used as the wastewater treatment process for textile household industry.

MATERIALS AND METHODS

The scope of this study was carried out to investigate wastewater treatment of textile household industry on the sub-district namely Pak Thong Chai, Pak Thong Chai district, this district is in the southern part of Nakhon Ratchasima Province, northeastern Thailand as shown in Fig.1. And it is a famous place to produce textile products especially Thai silk. There are many groups of household industry. Thus, in this study divided the group of textile household industries in two groups according with dye type. The dyes can be classified as natural and synthetic dye. The four sampling sites of textile household industries were selected; two sampling sites have used synthetic dyes in their process namely, Mudchada and Kayabatic. Another two sampling sites have used natural dyes in their process namely, Bandu-Yellow and Bandu-Red. The procedure of study is presented in Fig.2.



Fig. 1 The scope of this study namely Pak Thong Chai in the southern part of Nakhon Ratchasima Province.

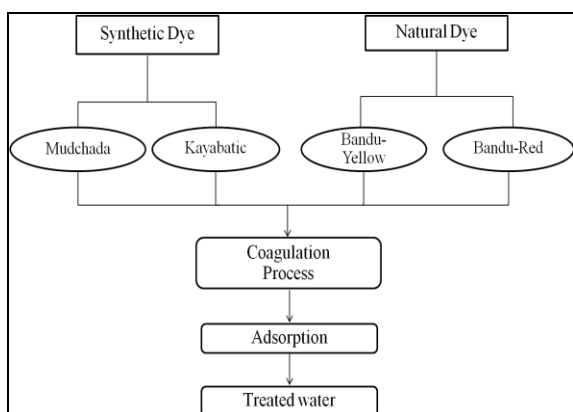


Fig. 2 The procedure of study.

The characteristics of wastewater and analytical methods

The study was carried out to collect raw wastewater from four sampling sites of textile household industries were Mudchada, Kayabatic, Bandu-Yellow and Bandu-Red. Wastewater samples were analyzed for various parameters and analytical methods as shown in Table 1.

Table 1 Parameter and analytical methods for wastewater.

Parameters	Unit	Analytical methods [6]
Physical and Chemical quality		
pH	-	pH Meter
Color	Pt-Co	2120 C. Spectrophotometric Method
COD	mg/L	5220 C. Closed Reflux, Titrimetric Method
TS	mg/L	2540 B. Total Solid Dried at 103-105° C
TDS	mg/L	2540 C. Total Dissolved Solid Dried at 180° C
TSS	mg/L	2540 D. Total Suspended Solid Dried at 180° C
TVS	mg/L	2540 E. Fixed and Volatile Solid Dried at 550° C
VSS	mg/L	2540 E. Fixed and Volatile Solid Dried at 550° C
VDS	mg/L	2540 E. Fixed and Volatile Solid Dried at 550° C

The coagulation process

The chemicals of coagulation

The coagulation-flocculation studies were carried out using the jar test method to determine the optimum pH range, suitable volume of polyaluminium chloride ($\text{Al}_2(\text{OH})_3\text{Cl}_3$ or PAC and polymer for each sampling wastewater.

The performance of coagulation process

The coagulation studies were carried out by use the optimum pH range, volume of PAC and polymer from chemical of coagulation study. Calculated COD and color removal efficiencies by using Eq. (1).

$$\% \text{Removal Efficiency} = \frac{(C_0 - C_e)}{C_0} \times 100 \quad (1)$$

The adsorption process

Adsorption isotherm

Adsorption isotherm studies were carried out at six different activated carbon (AC) mass (1, 2, 3, 4, 5 and 6 g.) which had Iodine was 1,015.30 mg/g. A series of 250 mL Erlenmeyer flask containing 200 mL of treated textile wastewater with coagulation process and required amount of AC mass were mixed using the shaker at constant agitation speed of 150 rpm. The sorbent was then separated by filtration. The filtration treated textile wastewater was measured color.

The performance of adsorption process

Batch adsorption experiments were performed as a function of varies pH (2, 4, 6, 8, 10, and 12). The conditions of batch experiment are shown in Table 2. A series of 250 mL Erlenmeyer flask containing 100 mL of treated textile wastewater with coagulation process, 2 g of AC mass and required varies of pH were mixed using the shaker at constant agitation speed of 150 rpm. The sorbent was then separated by filtration. The filtration treated textile wastewater was measured color. Influent and effluent of adsorption process were analyzed COD and color. Calculated COD and color removal efficiencies by using Eq. (1).

Table 2 The conditions of Batch adsorption experiments.

Factor	pH			
	Mudchada	Kayabatic	Bandu-Yellow	Bandu-Red
Mass (g)	2	3	2.5	3
Temperature (°C)	25	25	25	25
Volume of MB solution (mL)	100	100	100	100
Contact time (hour)	4,24	4,24	4,24	4,24
Agitation speed (rpm)	150	150	150	150
pH	2,4,6,8,10,12			

RESULTS AND DISCUSSION

Characteristics of Textile wastewater

As shown in Table 3, The results of raw wastewater characteristics were in wide range of COD from 2,872-84,624 mg/L, pH from 4.1-9.7 and color from 543-19,000 Pt-Co. The ratio of TDS/TS of all wastewater samples were in range of 0.8531-0.9842. These results indicated that raw wastewater contained dissolved solid more than 80%. And in Fig.3 showed the raw wastewater of synthetic dye group, Mudchada and Kayabatic had the ratio FDS/TS higher than the natural dye group of Bandu-Yellow and Bandu-Red. On the other hand, the natural dye group had the VDS/TS volatile dissolved solid higher than synthetic dye group. These indicated that raw wastewater of natural dye contains mainly organic substances which were in form of dissolved solids. The natural dye extracted from many kind of plants which are organic matter. Whereas the synthetic dye group contained mainly complex organic molecules having group such as azo, carbonyl, methane, nitro, quinoid, etc. [5]. These results similar with many researches [7] that reported wastewater from textile industries contains low biodegradability and had different types of dyes, which because of high molecular weight and complex structures.

Table 3 The characteristic of raw textile wastewater from household industry.

Parameter	Synthetic Dye		Natural Dye	
	Mudchada	Kayabatic	Bandu -Yellow	Bandu -Red
COD(mg/L)	2,872	2,733	84,614	10,708
pH	6.1	9.7	8.9	4.1
Color (Pt-Co)	543	9,671	51,867	5,650
TS(mg/L)	11,827	2,928	72,043	6,733
TSS(mg/L)	187	97	10,580	351
TDS(mg/L)	11,640	2,831	61,463	6,382
TVS(mg/L)	2,301	1,257	47,257	6,671
VSS(mg/L)	117	143	9,737	776
VDS(mg/L)	2,184	1,113	37,520	5,896
VS/TS	0.1946	0.4292	0.6559	0.9908
TDS/TS	0.9842	0.9670	0.8531	0.9479
VDS/TS	0.1847	0.3803	0.5208	0.8756

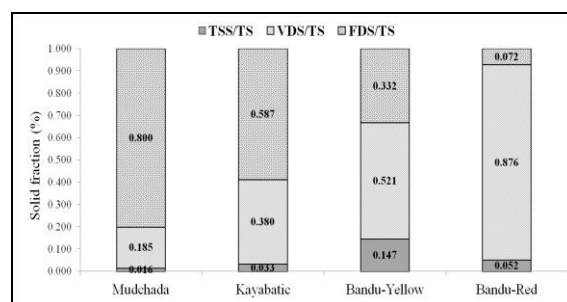


Fig. 3 The solid fraction of raw textile wastewater.

The coagulation process

The chemicals of coagulation

The results of coagulation studies were carried out to determine the chemicals and optimum pH for coagulation process. They were found the optimum pH were in range of 9 and 6 for synthetic dye group and for natural dye group respectively as shown in Fig 4 and the volume of PAC and polymer were 5 mL (Dosages PAC is 50,000 mg/L) and 0.4 mL (Dosages Polymer is 1,000 mg/L) for synthetic dye group and were 9 mL and 0.4 mL for natural dye group respectively as shown in Fig.5 and 6.

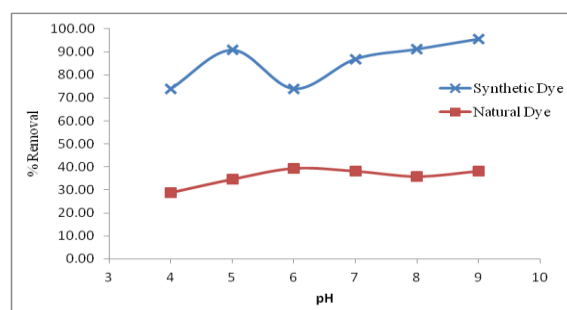


Fig. 4 The Results of coagulation studies to determine the optimum pH

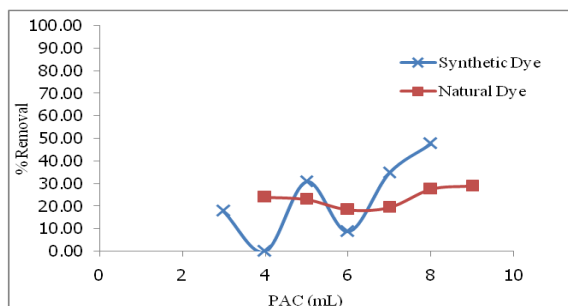


Fig. 5 The Results of coagulation studies to determine the optimum PAC.

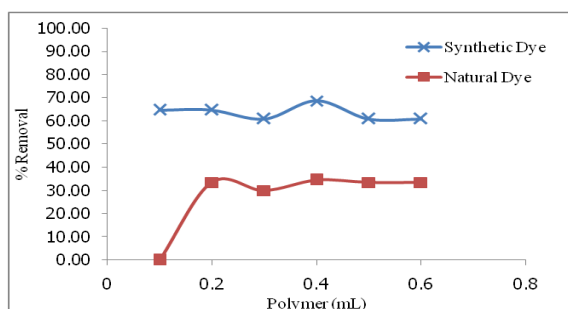


Fig. 6 The Results of coagulation studies to determine the optimum polymer.

Table 4 The conclusion of optimum conditions for coagulation process.

Sample		Optimum Condition		
		PAC (mL) ^a	Polymer (mL) ^b	pH
Synthetic Dye	Mudchada	5	0.4	9
	Kayabatic	5	0.4	9
Natural Dye	Bandu-Yellow	9	0.4	6
	Bandu-Red	9	0.4	6

^a Dosages PAC is 50,000 mg/L

^b Dosages Polymer is 1,000 mg/L

3.2.2 The performance of coagulation process

The results of optimum conditions for coagulation process as summarized in Table 4 were carried out to treated raw wastewater from four sampling sites for measuring the performance of coagulation process. The wastewater samples before and after treated by coagulation process were analyzed COD and color and calculated the removal efficiencies. The results of COD and color removal efficiencies of coagulation process were presented in Table 5 and Fig.7. They showed Mudchada and Bandu-Red had a same range of COD removal efficiencies were 44.44 and 46.86% respectively in the other hand, Kayabatic and Bandu-Yellow had similar range of COD removal efficiencies only 6.06 and 9.62 %. Whereas, the color removal efficiencies Kayabatic and Bandu-Yellow higher than Mudchada and Bandu-Red. And coagulation process showed none of color removal efficiencies from wastewater

of Bandu-Red. The mechanism of coagulation applied to decolorize wastewater is still not clear, color removal by coagulation is found in some cases very effective, in another cases however, has fail at all [8]. The efficiency of the coagulation-flocculation method depends on the raw wastewater characteristics, pH and temperature of the solution, the type and dosage of coagulants, and the intensity and duration of mixing [9].

Table 5 The results of COD and color removal efficiencies of coagulation process

Sample	Before Coagulation-Flocculation			After Coagulation-Flocculation			% Removal	
	pH	Color (Pt-Co)	COD (mg/L)	pH	Color (Pt-Co)	COD (mg/L)	Color	COD
Mudchada	9.0	473	7,067	6.9	333	3,755	29.58	46.86
Kayabatic	9.0	9,778	7,533	5.1	3,847	7,076	60.66	6.06
Bandu-Yellow	6.0	19,000	34,667	6.9	11,222	31,333	40.94	9.62
Bandu-Red	6.1	4,507	1,200	4.2	5,248	667	0.00	44.44

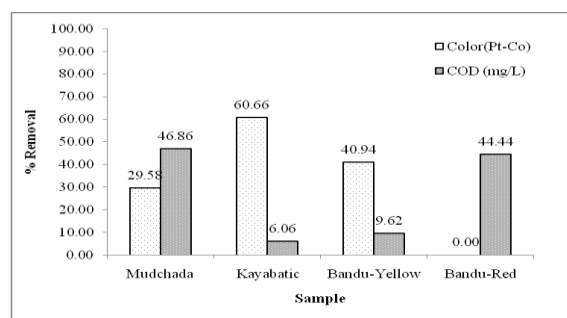


Fig. 7 The results of COD and color removal efficiency of coagulation process

The adsorption process

Adsorption isotherm

Langmuir and Freundlich isotherms are widely recognized and have been successfully applied to defining many adsorption equilibriums and evaluate adsorption equilibrium of dyes from effluent of coagulation. Therefore, dye adsorption data were analyzed by Langmuir and Freundlich Eq. (2) and (3), respectively;

$$\frac{C_e}{X} = \frac{C_e}{X_m} + \frac{1}{KX_m} \quad (2)$$

$$\log X = \log K_f + \frac{1}{n} \log C_e \quad (3)$$

Where K and X_m are Langmuir constants (L mg⁻¹) and maximum monolayer adsorption capacity (mg g⁻¹), respectively and Freundlich coefficients n and K_f are related to adsorption intensity and adsorption capacity, respectively. Isotherm coefficients of both models are given in Table 6. They were shown Freundlich isotherm are much closer to experimental

points than Langmuir isotherm. The coefficients of determination, R^2 of Freundlich isotherm were in range of 0.8583-0.9973 and R^2 of Langmuir isotherms were in range of 0.6791-0.9940. Mudchada had the highest adsorption capacity 1.39 Pt-Co/g.

Table 6 The constants of Langmuir and Freundlich isotherms for adsorption process.

Sample	Langmuir constant			Freundlich constant		
	q_{max} (Pt-Co/g)	K_L (L/g)	R^2	K_f (Pt-Co/g)	n	R^2
Mudchada	78.125	6.57×10^{-3}	0.9994	1.39	1.49	0.9973
Kayabatic	-31.95	-3.77×10^{-4}	0.9980	2.92×10^{-14}	0.21	0.9354
Bandu-Yellow	-212.77	-8.10×10^{-5}	0.6791	3.39×10^{-22}	0.16	0.8583
Bandu-Red	294.11	6.78×10^{-4}	0.9356	0.038	0.47	0.8770

3.3.2 The performance of adsorption process

Batch adsorption experiments were performed as a function of varies pH (2, 4, 6, 8, 10, and 12) in effluents after coagulation processes. Influent and effluent of adsorption process were analyzed COD and color. The Calculations of COD and color removal efficiencies were summarized in Fig.8 and 9 respectively. The results showed varies of pH had much affected on color removal efficiencies more than COD removal efficiencies. In table 7, the optimum condition and removal efficiencies for adsorption processes were selected and concluded the performance of adsorption processes by consideration of effluent characteristics and standard.

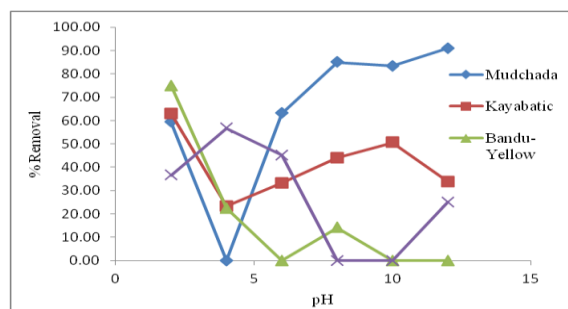


Fig.8 The performance of adsorption process in COD removal.

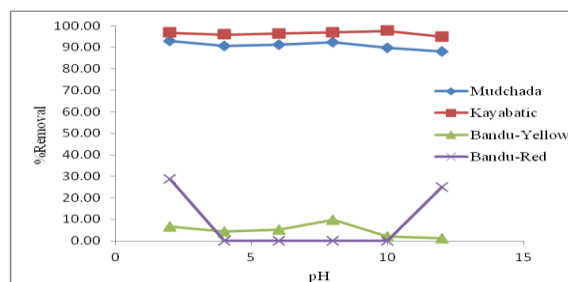


Fig. 9 The performance of adsorption process in color removal.

Table 7 The selected performance of COD and color removal efficiencies of adsorption process

Sample	Before Adsorption			After Adsorption			% Removal	
	pH	Color (Pt-Co)	COD (mg/L)	pH	Color (Pt-Co)	COD (mg/L)	Color	COD
Mudchada	8.0	67	4,337	8.4	10	333	85.00	92.32
Kayabatic	8.0	2,730	9,131	8.9	1,529	280	44.00	96.93
Bandu-Yellow	2.1	3,218	24,533	3.2	803	22,933	75.04	6.52
Bandu-Red	2.0	2,621	933	4.1	1,663	667	36.54	28.57

The performance of combination coagulation and adsorption processes

The conclusions of COD and color removal efficiencies for combination coagulation and adsorption processes are presented in Table 8. The overall removal efficiencies were calculated by selection optimum condition for coagulation and adsorption process under the characteristics of effluent and standard for textile effluent. The results showed the combination processes had the overall COD were in range of 72.9-93.8% and color removal efficiencies were in range of 70.6-98.5%. Although the performance of the combination processes obtained high removal efficiencies but the COD concentrations did not meet the standard for industry effluent. Our studies are going on to improve the removal efficiencies of this combination system such as using the other type of coagulants and optimum conditions for adsorption process.

Table 8 The conclusion of overall COD and color removal efficiencies for combination coagulation and adsorption processes

Sample	Influent			Effluent			% Over all removal efficiency	
	pH	COD (mg/L)	Color (Pt-Co)	pH	COD (mg/L)	Color (Pt-Co)	COD	Color
Mudchada	6.1	2,872	543	8.4	333	10	88.4	98.2
Kayabatic	9.7	2,733	9,671	8.9	280	1,529	89.8	84.2
Bandu-Yellow	8.9	84,614	51,867	3.2	22,933	803	72.9	98.5
Bandu-Red	4.1	10,708	5,650	4.1	667	1,663	93.8	70.6

CONCLUSION

In conclusion, the results showed the combination processes had the overall COD were in range of 72.9-93.8% and color removal efficiencies were in range of 70.6-98.5%. The results of coagulation study were found that in some cases of wastewater from Mudchada and Bandu-Yellow were effective in color removal but failed in COD removal, in another cases, wastewater from Kayabatic and Bandu-Red, had fail in color but were effective in COD removal efficiencies. The results showed varies of pH had much affected on color removal efficiencies more than COD removal efficiencies. The further experiments should be carried out to improve the combination removal efficiencies for application as suitable for textile household industry.

ACKNOWLEDGEMENTS

This research was supported by Suranaree University of Technology.

REFERENCES

- [1] C. Deepa, "A review of the textile industries wastewater treatment methodologies", *J. of Scientific & Engineering Research*, Vol. 7, Jan. 2016, pp. 392-403.
- [2] S.C.R. Santos, V.J.P. Vilar, R.A.R. Boaventura, "Waste metal hydroxide sludge as adsorbent for a reactive dye.", *J. of Hazard. Mater.*, Vol. 153, 2008, pp. 999-1008.
- [3] O. Gercel, A. Ozcan, A.S. Ozan, H.F. Gercel, "Preparation of activated carbon from a renewable bio-plant of *Euphorbia rigida* by H_2SO_4 activation and its adsorption behavior in aqueous solutions.", *J. of Applied Surface Science*, Vol. 253, Mar. 2007, pp. 4843-4852.
- [4] T. Chen, B.Y. Gao, Q.Y. Yue, "Effect of dosing method and pH on color removal performance and floc aggregation of polyferric chloride-polyamine dual coagulation in synthetic dyeing wastewater treatment", *J. of Colloids and Surfaces A: Physicochemical and Engineering Aspects*, Vol. 355, Feb. 2010, pp. 121-129.
- [5] F. Aci, M. Nebioglu, M. Arslan, M. Imamoglu, M. Zengin, M. Kucukislamoglu, "Preparation of activated carbon from sugar beet molasses and adsorption of methylene blue", *J. of Fresenius Environmental Bulletin*, Vol. 17, 2008, pp. 997-1001.
- [6] APHA, AWWA, and WEF, *Standard Methods for the Examination of Water and Wastewater*, 22nd ed. American Public Health Association, 2012.
- [7] A.K. Verma, R.R. Dash, P. Bhunia, "A review on chemical coagulation/flocculation technologies for removal of colour from textile wastewaters", *J. of Environmental Management*, Vol. 93, Jan. 2012, pp. 154-168.
- [8] M. Janeczko, S. Gaydarazhiev, "Removal of dyes from textile effluents by chemical coagulation", in *Proc 23rd Int. Conf. on International Mineral Processing Congress*, 2006, pp. 2163-2167.
- [9] P.W. Wong, T.T. Teng, N.A.R. Nik Norulaini, "Efficiency of the Coagulation-Flocculation Method for the Treatment of Dye Mixtures Containing Disperse and Reactive Dye", *J. of Water Quality Research Journal of Canada*, Vol. 42, 2007, pp. 54-62.

A COMPREHENSIVE METHOD OF EROSION RESISTANCE AND GROWTH PROMOTION FOR PISHA SANDSTONE

Zhishui Liang^{1,2}, Zhiren Wu³, Caiqian Yang¹, Mohammad Noori¹, Xiangyang Wu³, Hanbin Ge², Wenyi Yao⁴ and Peiqing Xiao⁴

¹ School of Civil Engineering, Southeast University, Nanjing 210096, China, ² Department of Civil Engineering, Meijo University, Nagoya, 468-8502, Japan, ³ School of the Environment and Safety Engineering, Jiangsu University, Zhenjiang 212013 China, ⁴ Key Laboratory of Soil and Water Loess Process and Control on Loess Plateau of MWR, Yellow River Institute of Hydraulic Research, 45 Shunhe Road, Zhengzhou 450003, China

ABSTRACT

Pisha sandstone is a special kind of soft rock that is severely eroded by wind, rainfall and gravity force, and the surface land is degraded resulted from the excessive human activities, and the vegetation coverage rate in this area is extremely low. In order to control it and develop new methods, the material components, nutrient content and the shear strength was studied and the field experiment used the new comprehensive method based on a kind of hydrophilic polyurethane (W-OH) was carried out. The results shows that in Pisha sandstone, the main minerals are quartz, feldspar, plagioclase, montmorillonite, illite, kaolinite, montmorillonite is the main cementitious material but is easy to expand when meets water. The nutrient content is low, organic matter, total nitrogen, total phosphorus, total potassium and available phosphorus belong to the six-level, available nitrogen is five-level and available potassium is four-level. In the field experiment, vegetation coverage rate of the control model was more than 95% after 4 months, and there was almost no shallow trench. The amount of sediment erosion was reduced by more than 90%, indicating that the effect of erosion prevention and promoting vegetation growth is significant. A demonstration project of 0.2 km² had been carried out in Odors in 2015 in this control model and a good result has been received, and the method has been widely accepted by local people and soil conservation bureau.

Keywords: Field experiment; Growth promotion; Mineral component; Sediment yield; Shear strength; Water and soil conservation

INTRODUCTION

Pisha sandstone is formed in Jurassic, Triassic and Cretaceous period [1]. It is widely distributed in an adjacent region close to Shanxi, Shaanxi and Inner Mongolia autonomous region in the Yellow River basin and Ordos Plateau (Fig. 1) [2], [3]. It is composed of a thick layer sandstone, arenaceous shale, and mudstone [4], [5]. The total area that Pisha sandstone underlies is approximately 16,700 km² [6], [7]. The Pisha sandstone has a low degree of diagenesis, poor bonded mechanism, and low compressive strength. As a result, it is extremely hard when it is dry but rapidly disintegrates when faced with water [7]-[9]. Due to the special properties of Pisha sandstone, in the condition of rainfalls, erosion occurs frequently in gullies and the erosion rate is considerably large [10]. The soil erosion modulus can reach about 3,000 ~ 4,000 t/(a·km²) on average according to the available statistical data. Coarse sediment (particle size > 0.05 mm) [11] derived from the Pisha sandstone area is the primary sediment [12] source of coarse sediment into the reaches of the Yellow River and accounts for 71.1% of the total coarse sediment yield (0.301 billion tons per year)

[13]. About half of the coarse sediment is deposited so that the lower reaches of the Yellow River has gained the reputation as the “Hanging River” [14]. Consequently, the Pisha sandstone area is called the most severe soil erosion region in both Loess Plateau and in the world [4], [5], [15].

From 1950s, the control measures for water and soil conservation in Pisha sandstone areas are mainly biological and engineering measures [16]. Among them, the biological measures are mostly applied, such as forest shelter belt, windbreak and sand fixation forest, slope protection plants, seabuckthorn flexible dam and so on [12], [15]. Engineering measures mainly include slope engineering, such as Terrance, level trench, scale-hole, intercepting ditch, protection engineering of gully head and channel engineering [7]. Nevertheless, there are some limitations for these measures and they cannot achieve the comprehensive goals of soil solidification, erosion resistance, vegetation growth promotion, and steep slope governance [14].

Recently, Pisha sandstone solidification and improvement combined with vegetation growth becomes a trend to protect and utilize this resource as well as controlling its adverse effects on the

environment [17]. Wu, et al. [18] studied a kind of hydrophilic polyurethane as a sand fixation agent. Su [19] analyzed the influence of EN-1 on engineering mechanical characteristics and simulated slope resistance to scour of Pisha sandstone weathered soil. Han et al., [20] proposed to compound soil with Pisha sandstone and aeolian sandy soil to improve the water retention characteristics. Li et al., [21] used Pisha sandstone via alkali activation process to produce a new raw structural material.

In order to develop a new efficient method to protect Pisha sandstone erosion, a novel hydrophilic polyurethane composite material (W-OH) was introduced [22] and based on it a new dual stereo configuration control model combined vegetation measures was proposed in the first time to protect Pisha sandstone. Actually, W-OH has been used on sand fixation to control desertification and to achieve ecological restoration [23]. In this paper the characteristics of Pisha sandstone and the reason for erosion were studied, and then the field experiment based on the comprehensive method was also carried out and the effect was evaluated in the following four months.

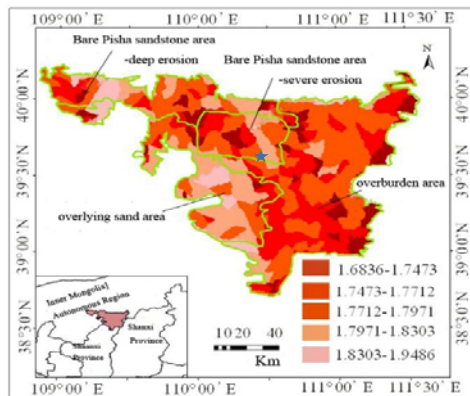


Fig. 1 Distribution of Pisha sandstone, ★ is experimental plot.

MATERIALS AND METHODS

Materials

Pisha sandstone was taken from the Erlaohu Gou in Ordos, Inner Mongolia Autonomous Region, China and it belongs to bare Pisha sandstone area. Horizontal stratified sampling method combining artificial and mechanical excavation [24] was used to get the samples with a bulk density ranging from 1.36 ~ 1.58 g/cm³, and a water content from 7.9 ~ 21.1%. The liquid limit (WL) is 32.2%, plasticity (IP) is 10.6, specific gravity (Gs) is 2.65, and the optimum water content (W_{op}) is 17%.

W-OH: a kind of hydrophilic polyurethane composite (produced by Toho Chemical Industry Co. Ltd.). This plyometric material doesn't contain any

heavy metal ion and has no harmful effect on vegetation and animals [23].

Methods

The mineral components were analyzed by X-ray method based on "transfer target polycrystalline X-ray diffraction method General" (JY / T 009-1996) by X-ray diffractometer (XRD-7000S, produced in Shimadzu Corporation).

Field experiment

In order to study the effect of the novel material and technology, the field experiment was conducted. The experimental field plot was selected in the middle of Erlaohu Gou in Inner Mongolia Ordos (110°36'2.74" E and 39°47'38.79" N, Fig. 1) and was constructed and monitored from May to October 2014. The topography in this area belongs to the transitional zone of Loess plateau and the Ordos plateau and typical bare Pisha sandstone area. The climate is arid and semi-arid temperate continental monsoon climate with cold winter, hot summer and there is more wind and sand in winter and spring. According to the meteorological data of Jungar Banner, the average annual rainfall is 400 mm, but the inter-annual change is large and the distribution is extremely uneven in one year (The total rainfall reached 250.2 mm in 2014). The largest months of rainfall are often concentrated from July to September, accounting for 70~80% of one year. Moreover, short-term heavy rainfall often occurs and the highest intensity rainfall can reach 80 mm per month. However, because of the harsh climate and sterile soil, the overall vegetation coverage rate is less than 30%.

Experimental design: The experimental slope in Erlaohu Gou with the height of approximately 43.5 m, vertical height of 29.9 m, and average gradient of 44.5° was chosen. According to the changes of slopes, the slope area was divided into three regions: consolidation & waterproof area, consolidation & growth promotion area and consolidation & green area. Moreover, a meteorological station, a water & sediment monitoring stations and a rainfall station were built to observed rainfall intensity, temperature, humidity, wind, sediments and other parameters.

In the top of slope, stereo configuration with trees, bushes, grass was established, and Chinese pine were planted, water drainage ditches were dug, and a cellar/tank was built to collect rainfall to make full use of. For the consolidation & waterproof area, the slope exceeded 60° and 8~10% W-OH solution was sprayed on the surface. However, in consolidation & growth promotion area, the slope was about 30~60°, the sprayed concentration of W-OH was about 4~5%, bushes and grass were planted and the micro irrigation systems were constructed to provide water for the vegetation. In respect to consolidation green

area with less than 30° slope, trees, bushes, and grass were planted. Last, at the bottom of the gully, two shunt barrels and collecting barrels were installed to collect rainfall erosion sediment and runoff. The barrels' height and diameter was 1 m, respectively. Between the shunt barrels and collecting barrels, nine tap holes with the same size were set up and the one in the middle was jointed with the collecting barrels through honeycomb dust.

RESULTS AND DISCUSSION

Mineral components in Pisha sandstone

From Table 1 it can be seen that the main minerals in Pisha sandstone includes quartz, feldspar, plagioclase, montmorillonite, illite, kaolinite, calcite, dolomite and hematite. In which, quartz, feldspar, plagioclase and hematite are primary minerals, accounting for about 70% ~80%, while montmorillonite, kaolinite, calcite and dolomite are secondary minerals from weathered primary minerals, therefore, Pisha sandstone is a kind of sandstone that has a low degree of rock diagenesis.

The characteristic of quartz is high strength, hardness and good performance for water resistance. It forms a strong skeleton of Pisha sandstone together

with feldspar and a bit amount of calcium carbonate. Montmorillonite (accounting for more than 15% for red Pisha sandstone, and approximately 10% for white one) is one kind of the common clay minerals and is the most important cementitious material in the matrix of Pisha sandstone. However, when it absorbs water, the volume will expand drastically, and the maximum volume expansion rate can be achieved approximately 400%, this is the main source of expansion in Pisha sandstone. Montmorillonite will gradually soften with producing enormous pressure and lose the bonding capacity after it absorbs water, resulting in destroy of the structure. Moreover, the crystal of montmorillonite is small and scaly, and it is hydrophilic, therefore, it is easy to be entrained by water, which is an important reason for the erosion of Pisha sandstone. Kaolinite, the product of feldspar and other silicate minerals, is an aqueous aluminosilicate. The properties of kaolinite are high water absorbability and strong plasticity, while once exposed to water, it will soften, inflate and lose the bonding capacity rapidly. Moreover, montmorillonite and kaolinite and other expansion of clay minerals will be easy to be weathered under certain conditions and decomposed in to silica and alumina in a long term in hot and humid conditions.

Table 1 Mineral components in Pisha sandstone

No.	Mineral contents /%								
	Quartz	Plagioclase	Feldspar	Montmorillonite	Illite	Kaolinite	Dolomite	Calcite	Hematite
1-1	38-43	25	20	5-10	1	2	1	2	-
1-2	28	30-35	15	15-20	1	2	1	1	1
1-3	23-28	20-25	20-25	10-15	2	3	1	10	-
1-4	25-30	10	10-15	20-25	3	4	1	15-20	1
1-5	35-40	25	15	10-15	1	2	1	5	-

Nutrient content

Table 2 Surface nutrient content of Pisha sandstone

		pH	Organic matter (%)	Total nitrogen (%)	Total phosphorus (%)	Total potassium (%)	Available nitrogen (mg/kg)	Available phosphorus (mg/kg)	Available potassium (mg/kg)
White	Maximum	10.04	0.78	0.054	9.5×10^{-6}	2.75×10^{-4}	53.8	0.31	78.5
	Minimum	8.91	0.17	0.017	3.5×10^{-6}	9.07×10^{-5}	42.4	0.10	55.2
	Average	9.51	0.44	0.026	6.6×10^{-6}	2.04×10^{-4}	47.9	0.20	62.8
	Range	>8.5	<0.60	<0.05	<0.040	<0.60	30-60	<3.0	40-85
	Grade	Six-level	Six-level	Six-level	Six-level	Six-level	Five-level	Six-level	Four-level
Red	Maximum	9.15	0.20	0.036	1.9×10^{-5}	2.42×10^{-4}	50.9	0.91	52.6
	Minimum	9.00	0.15	0.020	5.9×10^{-6}	9.22×10^{-5}	48.1	0.69	27.3
	Average	9.08	0.17	0.030	1.2×10^{-5}	1.67×10^{-5}	49.5	0.77	44.8
	Range	>8.5	<0.60	<0.05	<0.040	<0.60	30-60	<3.0	40-85
	Grade	Six-level	Six-level	Six-level	Six-level	Six-level	Five-level	Six-level	Four-level

It can be seen from Table 2 that both the red and white Pisha sandstone, the pH ranges from 8.91 to 10.04 and thus it is alkaline. The content of organic matter is approximately 0.15%-0.78%. The contents of total nitrogen, total phosphorus, total potassium, available nitrogen, available phosphorus and available potassium are in the range of 0.017%-0.054%, 3.5×10^{-6} -% 1.9×10^{-5} %, 9.07×10^{-5} -% 2.75×10^{-4} %, 0.10-0.91 mg/kg, 39.6-53.8 mg/kg and

27.3-80.8 mg/kg. According to the six-level classification of soil nutrient content grading table in our nation, pH, organic matter, total nitrogen, total phosphorus, total potassium and available phosphorus belong to the six-level, available nitrogen is five-level and available potassium is four-level, indicating that the overall nutrient content in Pisha sandstone is extremely low, resulting in difficult growth of vegetation.

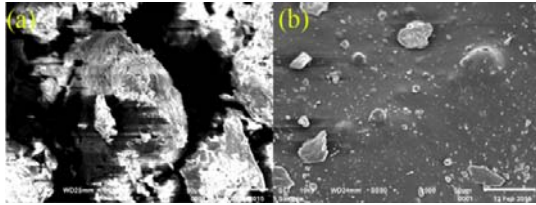


Fig. 2 The SEM images of red Pisha sandstone (a) Original Pisha sandstone particles; (b) Solidification layer on Pisha sandstone by spraying W-OH solution

As can be observed from Fig. 2, the original sandstone particles are discrete in SEM and the adhesion between particles is poor, so it is not stable and easy to become collapsible when meets water or wind. However, when W-OH solution was sprayed on the surface, a consolidation layer is formed and the particles are bonded together tightly. Thereby, the integrity is improved and the porosity is decreased significantly. Thereby, the Pisha sandstone particles cannot be easily destroyed in the condition of water, wind erosion or sunshine conditions.

The results of field experiment

The results and effects had been observed and studied in the following four months.

Sediment yield: after finishing constructing the experimental and control areas, on the second day it rained and lasted for 15 hours. The field observation showed that the consolidation & waterproof area and the consolidation & growth promotion area did not

change (Fig. 3a). The surface in consolidation green area had no obvious gully, and there was no Pisha sandstone particles in different barrels. However, in the control area, some shallow ridges appeared, indicating that the consolidation layer had a certain effect of anti-erosion.

Twenty days later, the surface in consolidation & waterproof area did not change and the consolidation layer remained completely, however, in the consolidation & vegetation promotion area a few small cracks appeared in some unsmooth places. As for the consolidation green area, the seeds began to sprout, seabuckthorn and Boston ivy began to grow new leaves, and green could be seen in some parts. Sediments of Pisha sandstone particles were found in difference barrels and it demonstrated that with the increase of rainfall and rainfall intensity, the sediment yield showed a trend of increase in both experimental and control areas (Table 3). When the rainfall reached 41.2 mm/h, the sediment yield of control area reached 1895.7 kg and the average unit loss was 11.8 kg/m². However, in the experimental area, the sediment yield was just 11.9 kg and the unit loss was 0.074 kg/m², the decreased rate was more than 99%. The results indicated that the consolidation layer had a significant effect on improving the performance of water, gravity, and wind erosion resistance of Pisha sandstone slopes. In addition, the sediment yield also had a direct relationship with the rainfall erosion force and the proportion of vegetation coverage.

Table 3 Results in experimental and control area during 7~8 month.

Date	7.1	7.22	7.28	8.2	8.12	8.22
Rainfall (mm)	16.4	8.6	23.2	35.6	20.6	34.4
Rainfall intensity I ₃₀ (mm/h)	26	4.4	15.6	41.2	26.8	20
Rainfall erosion force (MJ·mm/(ha·h))	94.8	9.43	77.2	373.3	131	133.3
Sediment yield in experimental area (kg)	8.6	0	1.8	11.9	0.4	1.6
Sediment yield in control area (kg)	216.1	42	27.3	1895.7	52.1	18.7
Reduced rate of sediment yield (%)	96.0	100	93.4	99.4	99.2	91.4

On the other hand, the consolidation layer in the consolidation & waterproof area stayed intact with a certain thickness, but in some places, a few cracks began to appear with the time going on (Fig. 3a). This indicated that under the effect of water and gravity erosion force, some changes on Pisha sandstone surface have taken place, leading to a minor damage in some places where the material was not sprayed uniformly. As time went by, the quantity of the grooves increased gradually, the width and depth also increased. By the end of August, there were 10 grooves in control area, 6 cm in width and 10~15 cm in depth on average. Some of them appeared across the entire growth promotion area. The monitoring results showed that the grooves appeared from the edge of the control area, of which depth increased with the rainfall intensity, and moved towards to the middle gradually, resulting in destruction or collapse of the entire slope. These were also one of the major forms of water erosion for slope.



Fig. 3 Comparison of experimental and control area. (a) a few cracks in consolidation and water proof area, (b) comparison with two plots in September, 2014

In the experimental area, where the amount of sprayed solution was small, the vegetation coverage was large even though the rainfall was heavy, but the slope surface showed a small erosion at the first time. However, as the vegetation coverage rate increased,

the gullies disappeared and vegetation played an important role on preventing weathered Pisha sandstone from further erosion.

Vegetation coverage rate: From Fig. 4 it could be seen that vegetation in growth promotion and green area grew fast and the vegetation coverage rate gradually increased. Three months later the rate reached 95%, and the height run up to 50~60 cm (Fig. 4b). However, the rate of the vegetation coverage was very slowly in the control area. It only occupied 8% with a height of 10 cm in average. Therefore, it was obvious that with the increase of the vegetation coverage rate, the surface roughness and permeability of Pisha sandstone could be enhanced to protect Pisha sandstone from water and wind erosion. This also indicated that material measure by W-OH combined with vegetation could have a significant effect on preventing Pisha sandstone from water, wind, and gravity erosion.

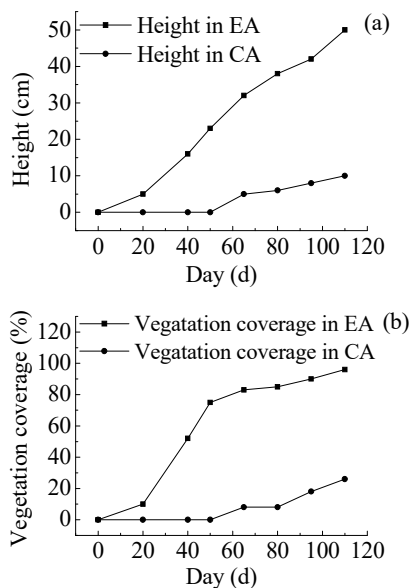


Fig. 4 Vegetation coverage and height in experimental and control area from May to September 2014

CONCLUSION

In order to develop the new comprehensive method to control Pisha sandstone erosion, the material components, nutrient content and the shear strength was studied and the field experiment based on a kind of hydrophilic polyurethane (W-OH) together with vegetation measure was carried out. The results shows that in Pisha sandstone, the main minerals are Quartz, feldspar, plagioclase, montmorillonite, illite, and kaolinite. Quartz, feldspar, plagioclase and hematite are primary minerals, and montmorillonite is the main cementitious material but it is easy to expand when meets water, leading the structural destroy of Pisha sandstone. organic matter, total

nitrogen, total phosphorus, total potassium and available phosphorus belong to the six-level, available nitrogen is five-level and available potassium is four-level, indicating that the overall nutrient content in Pisha sandstone is extremely low, resulting in difficult growth of vegetation. The experimental area was divided into three sections according to the slope gradients and vegetation coverage, consolidation & waterproof area, consolidation & growth promotion area and consolidation & green area. The new control method combining W-OH with vegetation was adopted. Four months later, the vegetation coverage rate reached more than 95%, and almost no shallow grooves were formed in the experimental area, but several deep grooves appeared and vegetation coverage was still less than 30% in the control area. The sediment yield in experimental area had been reduced by more than 95% compared with that in the control area. This new control method could reach the comprehensive efficiency of Pisha sandstone conservation both in water erosion resistance and ecological restoration. These results also indicated that combining materials with vegetation measures could be used as an efficient comprehensive method to protect water and soil from loss and erosion in the Pisha sandstone area.

ACKNOWLEDGEMENTS

This work is funded by the State Key Research Development Program of China (Grant No. 2017YFC0504505).

REFERENCES

- [1] Zhen, Q, Zheng, J, He, H, Han, F, & Zhang, X. Effects of pisha sandstone content on solute transport in a sandy soil. *Chemosphere*, Vol. 144, 2016, pp.2214-2220.
- [2] Ma, W & Zhang X. Effect of Pisha sandstone on water infiltration of different soils on the Chinese Loess Plateau. *Journal of Arid Land*, Vol. 8, No. 3, 2016, pp.331-340.
- [3] Ni, H, Zhang, L, Zhang, D, & Wu, X. Weathering of pisha-sandstones in the wind-water erosion crisscross region on the loess plateau. *Journal of Mountain Science*, Vol. 5, No. 4, 2008, pp.340-349.
- [4] Chen, W. The Pisha sandstone in Yellow River basin- non farming land and watch as picture scroll. *National Geography of China*, No. 3, 2012, pp.87-93. (in Chinese)
- [5] Martin M W, Jorge C R & Constantino M M. Late paleozoic to early Jurassic tectonic development of the high andean principal cordillera, El indio region, Chile (29-30°s). *Journal of South American Earth Sciences*, Vol. 12, No. 1, 1999, pp.33-49.

- [6] Wang, Y, Wu, Y, Kou, Q, Min, D, Chang, Y & Zhang, R. Definition of arsenic rock zone borderline and its classification. *Science of Soil & Water Conservation*, Vol. 5, No. 1, 2007, pp.14-18. (in Chinese).
- [7] Wang, Y, Wu, Y, Kou, Q & Li, M. Study on water and soil loss and control methods in Pisha sandstone. The Yellow River Water Conservancy Press, Zhengzhou, China, 2007. (in Chinese)
- [8] Li, C. Mineral composition and anti-erodibility of pisha sandstone. *Science of soil and water conservation*, Vol. 12, No. 2, 2015, pp.11-15. (in Chinese)
- [9] Guo, J, Shi Y & Wu L. Gravity erosion and lithology in Pisha sandstone in southern Inner Mongolia. *Journal of Groundwater Science and Engineering*, Vol. 3, No. 1, 2015, pp. 45-58.
- [10] Ziadat F M & Taimeh A Y. Effect of rainfall intensity, slope, land use and antecedent soil moisture on soil erosion in an arid environment. *Land Degradation & Development*, Vol. 24, No. 6, 2013, pp.582-590.
- [11] Xu, J, Wu, C, Lin, Y, Gao, Y, Zuo, Z & Yu, Q. Definition on source area of centralized coarse sediment in middle Yellow River., Vol. 20, No. 1, 2006, pp.6-14. (in Chinese).
- [12] Zhang K, Xu M & Wang Z. Study on reforestation with seabuckthorn in the Pisha Sandstone area. *Journal of Hydro-environment Research*, Vol. 3, No. 2, 2009, pp. 77-84.
- [13] Yang, F, Cao, M, Li, H, Wang, & Bi, C. Ecological restoration and soil improvement performance of the seabuckthorn flexible dam in the pisha sandstone area of northwestern china. *Solid Earth Discussions*, Vol. 6, No. 2, 2014, pp.2803-2842.
- [14] Xiao P, Yao W & Liu H. Research Progress and harnessing method of Soil and Water Loss in Pisha Sandstone Region. *Yellow River*. Vol. 36, No. 10, 2014, pp.92-94. (in Chinese).
- [15] Yang, F, Cao, M, Li, H, Wang, X. H & Bi, C. Simulation of sediment retention effects of the single seabuckthorn flexible dam in the pisha sandstone area. *Ecological engineering*, Vol. 52, No. 3, 2013, pp.228-237.
- [16] Li X, Yue G, S & Yu, Y. Research on Pisha-sandstone's anti-erodibility based on grey multi-level comprehensive evaluation method. *Journal of Groundwater Science and Engineering*, Vol. 4, No. 2, 2016, pp.103-109.
- [17] Liang Z, Wu Z, Yang C, Yao, W & Leng, Y. Mechanism of erosion resistance and vegetation promotion by W-OH in Pisha sandstone. *Journal of hydraulic engineering*, Vol. 47, No. 9, 2016, pp.1160-1166. (in Chinese).
- [18] Wu, Z, Gao, W, Wu, Z, Iwashita, K & Yang, C. Synthesis and characterization of a novel chemical sand-fixing material of hydrophilic polyurethane. *Journal of the Society of Material Science Japan*, Vol. 60, No. 7, 2011, pp.674-679.
- [19] Su T. Mechanism on scour resistance stability of EN-1 solidified slope in Pisha sandstone region. Doctoral dissertation, Northwest A&F University, Beijing, China, 2011. (in Chinese).
- [20] Han J, Liu Y & Luo L. Research on the core technology of remixing soil by soft rock and sand in the Maowusu sand land region. *China Land Science*, Vol. 26, No. 8, 2012, pp.87-94. (in Chinese).
- [21] Li C, Zhang T & Wang L. Mechanical properties and microstructure of alkali activated Pisha sandstone geopolymer composites. *Construction and Building Materials*, Vol. 68, No. 15, 2014, pp.233-239.
- [22] Liang Z, Wu Z, Yang C, Yao W & Deng, L. Study on water resistance, anti-erosion and UV durability of Pisha sandstone solidified body. *Yellow River*, Vol. 36, No. 8, 2016, pp.46-48. (in Chinese).
- [23] Wu, Z, Gao, W, Wu, Z, Iwashita, K & Li, R. New technology of desertification control and ecological restoration based on W-OH organic composite curing material. National seminar on water and soil conservation, Desertification control and ecological res-toration, 2009, pp.244-252. (in Chinese)
- [24] Yao W, Wu Z, Liu H, Xiao, P & Yang, C. Experimental research on the anti-Erosion and vegetation promotion for sandstone region in the Yellow River basin. *Yellow River*, Vol. 37, No. 1, 2015, pp. 6-10. (in Chinese).
- [25] Zeng Y, Qin F & Yue Y. Analysis on plant composition and diversity of hippophae forest in sandstone areas of Jungar Banner. *Northern Horticulture*, Vol. 37, No. 22, 2013, pp.98-101. (in Chinese)
- [26] Miao L, Zhong X & Yin Z. The relationship between strength and water content of expansive water content of expansive soil. *Rock and soil mechanics*, Vol. 20, No. 2, 1999, pp.71-75. (in Chinese)

PREPARATION AND EVALUATION BY ARTIFICIAL AGING TEST OF SiO_2 / FLUORINATED POLY-STYRENE-ACRYLATE COMPOSITE MATERIAL

Xiaoying Zhang¹, Dongya Yang, Wenya Wen², Hanqiang Yu², Xiangyang Wu^{1*}, Jicheng Xu^{2,3}, Qian Chen²

¹ School of the Environment and Safety Engineering, Jiangsu University, Zhenjiang 212013, China

² School of Chemistry and Chemical Engineering, Jiangsu University, Zhenjiang 212013, China

³ School of Chemical and Materials Engineering, Zhenjiang College, Zhenjiang 212003, China Road, Zhengzhou 450003, China

ABSTRACT

Recently, some heritages are suffering from varying degrees of physical, chemical and biological weathering damage. The aim of the project is the development of high hydrophobic and durability to provide protective coatings for stone. A series of SiO_2 -fluorinated poly-styrene-acrylate (SiO_2 /FPSA) composite emulsion was prepared with different content of 2,2,2-trifluoroethyl methacrylate content. The composite materials prepared by a semi-continuous emulsion polymerization process were characterized by various methods. The results exhibited that the SiO_2 /FPSA emulsion (S-5 emulsion) had satisfactory stability and low viscosity and surface tension, and SiO_2 /FPSA film (F-S-5 film) had excellent water resistance and acid/alkali resistance. Therefore, S-5 emulsion was chosen as the protect coating, and the effect of protect coating was evaluated by the artificial aging test. The artificial aging experiments such as freeze-thaw, acid aging and soluble salts tests of the SiO_2 /FPSA composite coating were investigated. The results indicated that SiO_2 /FPSA composite could be applied to the protective coatings for stone surface relics.

Keywords: Stone conservation; cultural heritage; composite; protective polymers

INTRODUCTION

The cultural heritage was created in a unique environment, promoting the development of modern civilization [1]. Recently, some heritages are suffering from varying degrees of physical, chemical and biological weathering damage [2]. Thus, the essential properties required to as protective agent could be summarized as follows: hydrophobic, permeability to water vapor, transparency, reversibility or possibility to re-treat the surface, durability [3-4]. The only way to preserve, as early as possible, is to investigate the new material or novel methodologies to resist these physical chemical and biological attacks. In summary, the protection of stone relics must be seriously.

Using of chemical materials to safeguard stone relics is a common method to avoid further weathering in outdoor conditions. Currently, most of organic materials have been attempted in the conservation of stones, such as acrylate, epoxies, silicones, fluorinated polymers, etc [5]. Recently years, acrylate and silicones or their mixtures have been widely used in the protection of stone relics. Fluorinated styrene-acrylate (or acrylate) copolymer has attracted a great deal of attention. Not only it is relatively low cost and environmental friendly, but also it contains the excellent properties of both fluorine and styrene-acrylate (or acrylate) copolymer.

At the same time, the increase in size of the particles could enhance mechanical properties of the films. Nano- SiO_2 possesses high hardness, and reasonable price among other nanoparticles.

The aim of this work is to prepare the core-shell SiO_2 -fluorinated poly-styrene-acrylate (SiO_2 /FPSA) composite emulsion. The composite materials prepared by a semi-continuous emulsion polymerization process were characterized by various methods. Performances of the satisfactory SiO_2 /FPSA were tested on calcites taken from Jiaoshan Steles Grove (China). The protective performances had been evaluated by the artificial aging tests, including freeze-thaw aging test, acid aging test and soluble salts aging test. The analysis revealed that the protective effects were satisfying.

EXPERIMENT

Materials

Styrene (St), ethyl acrylate (EA), methyl methacrylate (MMA), butyl methacrylate (BMA), acrylic acid (AA, 99.5%), 2,2,2-trifluoroethyl methacrylate (TFEMA), tetraethyl orthosilicate (TEOS), γ -methacryloxypropyl trimethoxysilane (KH-570), polyethylene p-octyl glycol phenylether (OP-10) and ethanol ($\text{C}_2\text{H}_5\text{OH}$) and sodium sulfate (Na_2SO_4) were all purchased from Sinopharm

Chemical Reagent Co., China. Sodium dodecyl sulfate (SDS) was obtained from Shanghai reagent factory, China. Potassium persulfate (KPS) was purchased from Tianjin Chemical Reagent Factory, China. Sodium hydrogen carbonate (NaHCO_3) was obtained from Shanghai Su Yi Chemical Reagent Co., China. Ammonia ($\text{NH}_3 \cdot \text{H}_2\text{O}$) was provided by Shanghai Pilot Chemical Co., China. All reagents were used without any further purification.

Preparation of modified the nano-SiO₂

Nano-SiO₂ particles were prepared by the well-known sol-gel process. Firstly, absolute ethanol, deionized water were introduced in a 250mL, three-neck, round-bottom flask heated to 30 °C under stirring. HCl was added into the reaction system and kept pH= 3; and TEOS was added into the solution and stirred at 30 °C for 3 h. Then it started with stirring a mixture of silica sol and KH-570 at 60 °C for 6 h under constant stirring. Finally, the KH-570-modified nano-SiO₂ was obtained. The synthetic route of nano-SiO₂ was shown in Fig. 1.

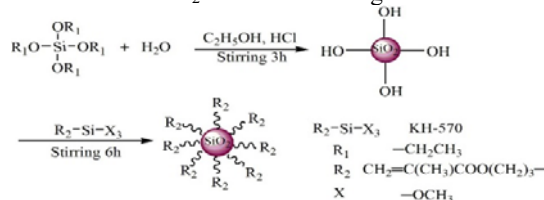


Fig. 1 The synthetic route of nano-SiO₂

Preparation of SiO₂-fluorinated poly-styrene-acrylate (SiO₂/FPSA) composite emulsion

SiO₂/FPSA composite emulsions were prepared by a semi-continuous emulsion polymerization process. A certain amount of water, 30 g of the monomer mixture and emulsifier (50 wt%, relative to the whole emulsifier level), polyethylene p-octyl glycol phenylether (OP-10) and sodium dodecyl sulfate (SDS) (at weight ratio of OP-10/SDS = 2:1) were pre-emulsified.

Seed emulsion polymerization was carried out in a 250 mL four-necked glass reactor. The initial charge in the reactor was water, the rest of the emulsifier, NaHCO_3 as buffer, the monomer pre-emulsified mixture (9 g) and varying contents of TFEMA. When the flask was heated to the reaction temperature, the second charge, part of the initiator solution was added. The reaction was held at 75 °C for 30 min, after which the rest of the pre-emulsified mixture was added into the reactor drop wise for about 2–3 h. The rest of initiator solution was then added to the system. Then, the mixture was kept at 90 °C for two more hours to completely polymerize all the monomers; and then cooled down to room temperature. Finally, the

emulsion was neutralized with $\text{NH}_3 \cdot \text{H}_2\text{O}$ to pH = 7–8.

Varying the contents of TFEMA (0, 2%, 4%, 6%, 8%, and 10%, based on total monomers), and the addition of nano-SiO₂ was 3%, a series of SiO₂-fluorinated poly-styrene-acrylate (SiO₂/FPSA) composite emulsion were prepared and named as S-2, S-3, S-4, S-5, S-6 and S-7, respectively, while pure styrene-acrylate emulsion was named as S-1 (PSA). The synthetic route of SiO₂-fluorinated poly-styrene-acrylate (SiO₂/FPSA) is shown in Fig. 2.

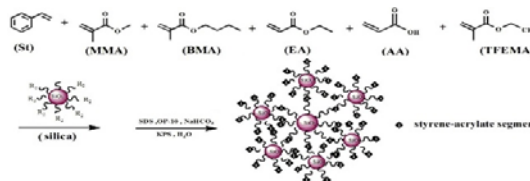


Fig. 2 The synthetic route of SiO₂-fluorinated poly-styrene-acrylate

All SiO₂/FPSA emulsions (S-1, S-2, S-3, S-4, S-5, S-6 and S-7) were poured into the poly(tetrafluoroethylene), and the SiO₂/FPSA films were obtained by drying for 6 days at room temperature and labeled as F-S-1, F-S-2, F-S-3, F-S-4, F-S-5, F-S-6 and F-S-7, respectively.

Characterization

The procedures for the measurements of the films were briefly described as follows: The dried films prepared (20×20 mm²) were soaked in deionized water or 5% NaOH or 5% H₂SO₄ solution at room temperature after being weighted (Original weight recorded as m_1). After 24 h, the liquid remaining on the films surface was then wiped with filter paper and weighed again (the weight was denoted as m_2). The water absorption (or swelling degree), ω , was calculated by as follows (1):

$$\omega = \frac{m_2 - m_1}{m_1} \times 100\% \quad (1)$$

The contact angles of water on SiO₂/FPSA composite films were measured with a commercial CAM200 optical system (KSV Instruments, Finland) by the sessile drop method with a micro-syringe at 25 °C. More than 3 contact angles were averaged to get a reliable value for each sample.

To investigate the morphology of the film and stone, scanning electron microscopy (SEM) micrographs were taken with a field emission scanning electron microscope (S-4800, Hitachi Corp., Tokyo, Japan) at a voltage of 15.0 kV. The samples were diluted with deionized water, dropped onto silicon wafer and dried at room temperature.

Artificial ageing test

To evaluate the performance of the protective material, artificial aging experiments were performed. Samples “A”, “C” and “E” were treated by the prepared emulsions; and samples “B”, “D” and “F” were blank samples. All stone samples were obtained from the hillside near the Moya stone inscriptions for consistency and smoothed with abrasive paper.

Freeze - thaw aging test

First, the stone samples “A” and “B” were soaked in distilled water for 8 hours. Then, the stone samples “A” and “B” were moved to the freezing chamber, and freezing period lasts for 16 hours at $-10\text{ }^{\circ}\text{C}$. Finally, samples “A” and “B” were removed from the freezing chamber, and transferred to an oven about $80\text{ }^{\circ}\text{C}$. The multiple cycles were performed.

Acid aging test

The stone samples “C” and “D” were immersed in H_2SO_4 solution ($\text{pH}=1$) in 72 h, observing the changes in the stone samples.

Soluble salts aging test

The stone samples “E” and “F” were immersed in $0.5\text{ mol/L Na}_2\text{SO}_4$ solution about 8 h. Then both samples were natural weathering at room temperature for the salt crystallization. The multiple cycles were carried out.

RESULTS AND DISCUSSION

Some properties of SiO_2/FPSA Films

Water absorption or swelling degree data are also listed in Table 1. Water absorption or swelling degree is another important indicator of stone protective material. A good protective material must have excellent hydrophobicity and good acid or alkali resistance. Compared with F-S-1 film (PSA film), the F-S-2, F-S-3, F-S-4, F-S-5, F-S-6, and F-S-7 films (SiO_2/FPSA films) present the satisfactory result in water absorption. The introduction of the fluorinated monomer improved the hydrophobic properties of the copolymer. The water contact angles are also shown in Fig. 3, reflecting an increase of hydrophobic with the increasing of the TFEMA content. The water contact angle for F-S-1 film is 52.71° . However, the water contact angle becomes 75.70° for F-S-6 film. The surface of SiO_2/FPSA film includes a large of low surface energy fluorinated groups. The fluorinated groups are an important factor to lead to a good performance in water resistance. Additionally, the existence of hydrophobic Si-O-Si also leads to films with lower water absorption. Meanwhile, the similar change can be found in swelling degrees (5.0% H_2SO_4 solution) or swelling degrees (5.0% NaOH solution). Therefore, SiO_2/FPSA films have excellent water resistance and acid / alkali resistance.

Table 1 The properties of SiO_2/FPSA films

Sample	F-S-1	F-S-2	F-S-3	F-S-4	F-S-5	F-S-6	F-S-7
Water absorption (%)	33.30	23.06	17.71	15.65	9.43	10.05	11.76
Swelling degree (5.0% H_2SO_4 solution)	17.63	9.45	8.74	8.23	7.24	7.28	7.21
Swelling degree (5.0% NaOH solution)	10.15	11.16	11.23	9.71	9.51	9.65	9.47
Water contact angle ($^{\circ}$)	52.71	65.46	69.22	69.83	72.63	75.70	75.43

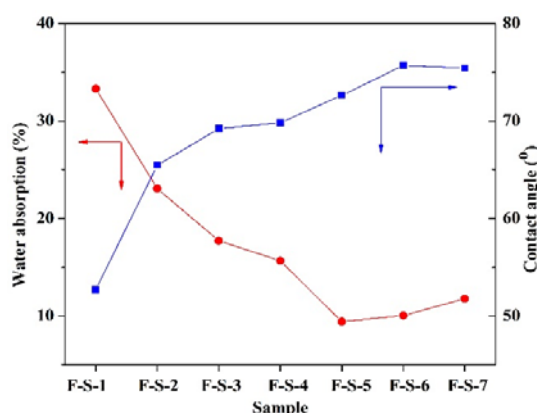


Fig. 3 The water absorption and water contact angle of the SiO_2/FPSA films

SEM analysis

SEM images of the fracture surface of F-S-1 (a), F-S-2 (b) and F-S-5 (c) films are shown in Fig. 4. The surface of the PSA (F-S-1) film is relatively flat and smooth. However, there are small waves on the surface of SiO_2/PSA film with adding 3 wt% SiO_2 (F-S-5 (b) film), indicating that the introduction of SiO_2 particles made the surface become rough. Furthermore, when simultaneously introducing SiO_2 and TFEMA (F-S-5 (c) films), there were many ripples on the surface, indicating between inorganic and organic phases formed interwoven network structure. The stone sample is observed by SEM analysis to investigate the morphology of stone and

SEM images are shown in Fig. 5. As can be seen from Fig. 5, the structure of stone sample is relatively loose and there are some pits and cracks on the surface. These results indicate that stone samples have been severely damaged.

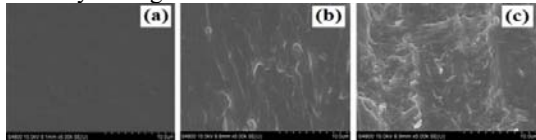


Fig. 4 SEM images of F-S-1 (a), F-S-2 (b) and F-S-5 (c)

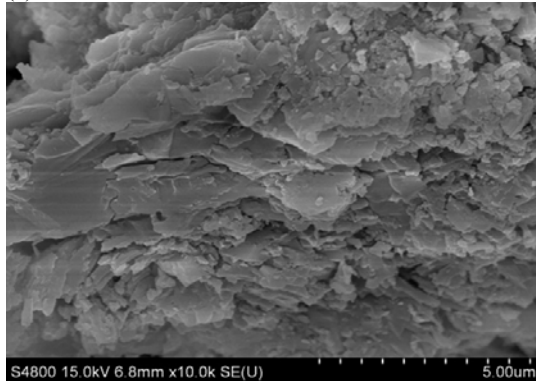


Fig. 5 SEM image of the stone sample

Freeze - thaw aging test

The images of freeze-thaw aging test after different cycles are illustrated in Fig. 6. It can be seen from Fig. 4, after 10 cycles, the letter “B” has blurred on the sample “B”; and after 15 cycles, the sample “B” begins to appear little cracks. After 20 cycles, there are obvious cracks on the surface of the sample “B”; however, the sample “A” has almost no change.

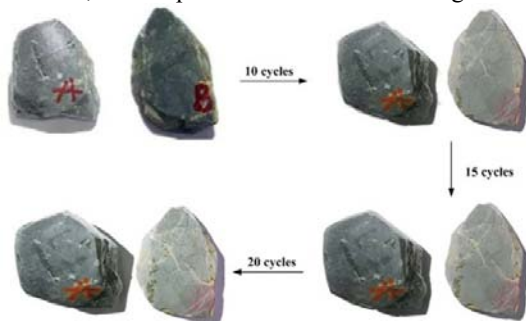


Fig. 6 The images of freeze-thaw aging test after different cycles

Acid aging test

As shown in Fig. 7, after acid aging test, both stone samples mass is reduced in varying degrees. This can be attributed to the reaction of sulfuric acid and calcium carbonate. There are still fluctuations in the sample “C” mass, but the rate has been significantly reduced, indicating markedly improved acid resistance.

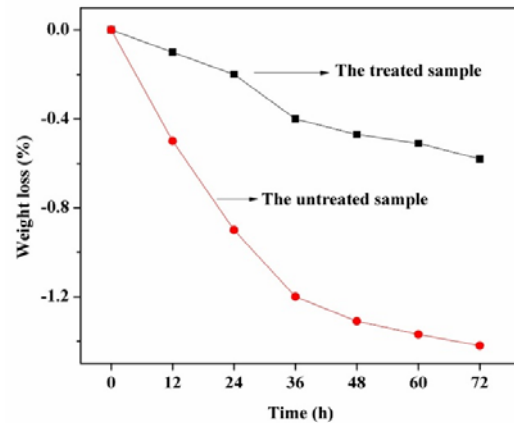


Fig. 7. The weight loss of stone sample in acid aging test

Soluble salts aging test

Soluble salts are considered to be the key deteriorating element of stone relics. The images of soluble salts aging test are shown in Fig. 8. As can be seen from Fig. 8, the untreated stone surface has taken place significant changes. However, there is no remarkable change on the treated stone surface. Compared to the treated stone sample “E”, the untreated stone sample “F” has cracks and pits after 15 cycles. That is to say, SiO_2/FPSC composite materials succeeded to reduce salt accumulation phenomena. This can be attributed to SiO_2/FPSC composite materials developed a network structure in the stone voids, effectively preventing the formation of crack, further weathering.

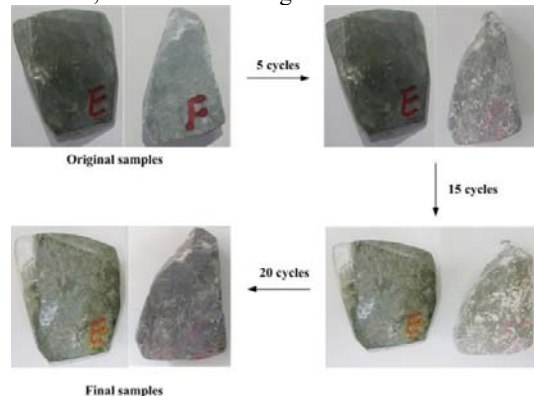


Fig. 8 The images of soluble salts aging test

CONCLUSION

The uniform core-shell SiO_2/FPSC composite materials were successfully prepared. The resulting SiO_2/FPSC composite emulsions exhibited higher hydrophobic property. Thus, SiO_2/FPSC composite materials can be used for the conservation of the stone relics.

ACKNOWLEDGEMENTS

This project was supported by the Innovation Program for Graduate Education of Jiangsu Province (SJLX_0477), Society Development Fund of Zhenjiang (SH2014074 and SH2013020), Zhenjiang College Scientific Research Team (ZJCKYTD07) and Sponsored by Qing Lan Project (2012-2015).

REFERENCES

- [1] Abbott A. Rescuers of Europe's cultural heritage struggle for funding. *Nature*, Vol. 414, 2001, pp. 572-572.
- [2] Zhang H, Liu Q, Liu T, Zhang BJ. The preservation damage of hydrophobic polymer coating materials in conservation of stone relics. *Prog Org Coat*, Vol. 76, 2013, pp. 1127-1134.
- [3] Varas MJ, de Buergo MA, Fort R. The influence of past protective treatments on the deterioration of historic stone facades - A case study, *Studies Conserv*, Vol. 52, 2007, pp. 110-124.
- [4] Pecchioni E, Gomez Ubierna M, Cagnini A, Galeotti M, Fratini F, Porcinai S. Ancient and new repair mortars for conservation: Application to the case of san leonardo pulpit (Florence, Italy). *Int J Archit Herit*, Vol. 8, 2014, pp. 556-580.
- [5] Tsakalof A, Manoudis P, Karapanagiotis I, Chrysoulakis I, Panayiotou C. Assessment of synthetic polymeric coatings for the protection and preservation of stone monuments. *J Cult Herit*, Vol. 8, 2007, pp. 69-72.

STUDY ON OUTDOOR THERMAL ENVIRONMENT OF CAMPUS BASED ON GIS

Minxue Zheng¹, Shanwei Li¹ and Hongxiao Liu¹

¹School of Environment and Safety Engineering, Jiangsu University, China

ABSTRACT

In recent years, the campus population and the buildings of Jiangsu University have increased and the pattern of the micro-city has preliminarily formed. The data of outdoor thermal environment of campus based on Geographic Information System (GIS) has found that the average temperature difference of outdoor temperature in space distribution in Jiangsu University is about 1°C. Five different underlying surfaces have a great influence on the outdoor thermal environment of campus, and the daily variation of temperature showed an inverted "V" single peak curve. The daily variation of temperature on the concrete road (direct sunlight) is approximately 4°C above that of the grassland at the time of 14:00. The temperature of the concrete road (direct sunlight) is higher than that of the concrete road (shadows), and the temperature difference between them is about 1°C. At the same time, five suggestions have been proposed for the improvement of outdoor thermal environment in Jiangsu University according to the results.

Keywords: Heat Island Effect, Outdoor Thermal Environment, Spatial Change, Underlying Surface, GIS

INTRODUCTION

Urban heat island effect, whose temperature is higher than that of outer suburbs, reduces the comfortability of the manufacture and life of people, that endangers the health and even life of human [1, 2]. With the warming of global, the influences of urban heat island effect on lives of people have become increasingly apparent. The rapid development of urban has accelerated the aggravation of urban heat island [3]. In recent years, the enrollment of Jiangsu University continues to expand, and the campus construction develops rapidly. The campus covers an area of 1,880,000 m². Among them, all types of building area hold more than 1,280,000 m², and nearly 50 thousand students are in school. With the increases of the campus population and buildings, the pattern of micro-city has preliminarily formed. Surface temperature change of different underlying surfaces is an important factor to improve urban heat island effect [4]. Accompanied by the increasingly obvious urbanization and huge development of the university campus, reducing the heat island effect has become an important topic to improve the learning and living environment of students, and create a comfortable outdoor environment [5, 6].

DATA MONITORING AND RESEARCH METHODS

Data Monitoring Methods

In this study, the Japanese advanced portable

carbon dioxide measuring instrument (model C2D-W02TR) was adopted to measure the outdoor temperature and relative humidity of the campus of Jiangsu University. GIS was used to analyze and study the distribution characteristics of outdoor thermal environment in campus.

The research object is the whole area of campus in Jiangsu University, which is in east longitude 119°30'~119°31'30"E, and north latitude 32°11'40"~32°12'50"N. The campus area was divided into 30 measuring area with each 300m*300m as a measuring unit. A position with marked facility of each measuring unit was chosen as a measuring point for measuring the latitude and longitude to ensure that each measurement was performed at the same location (Fig. 1 and Fig. 2). All the measuring points were measured in three time periods at 7:00-8:00 in the morning, 10:00-11:00 at noon and 17:00-18:00 at evening for three times a week. The underlying surfaces of the measuring points were divided into 4 categories, such as grassland, lake, concrete and marble road to discuss the temperature and relative humidity changes of different underlying surfaces.

Data Analysis Method

In this work, Microsoft Excel 2013 software was used to database establishment, data collection and analysis. GRASS and GMT software were used to visualize the temperature spatial distribution data, which directly and quantitatively reflected the temporal and spatial distribution characteristics of temperature in the campus.

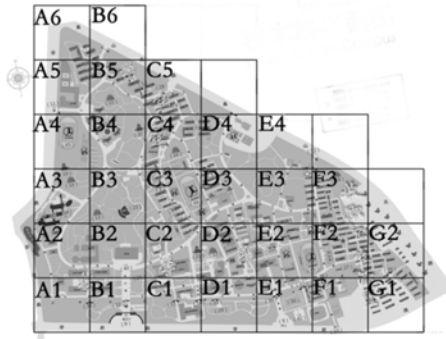


Figure 1 Area division of campus outdoor temperature measurement.

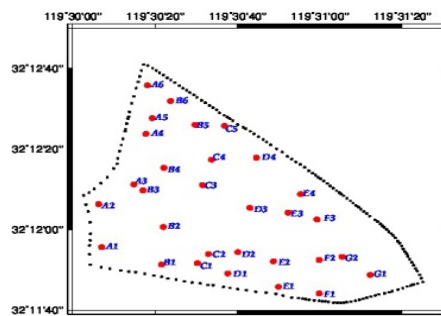


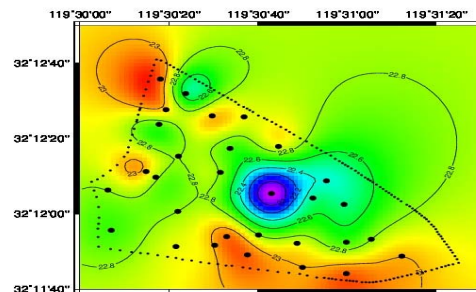
Figure 2 Point distribution of campus outdoor temperature measurement.

TEMPORAL AND SPATIAL DISTRIBUTION CHARACTERISTICS OF TEMPERATURE

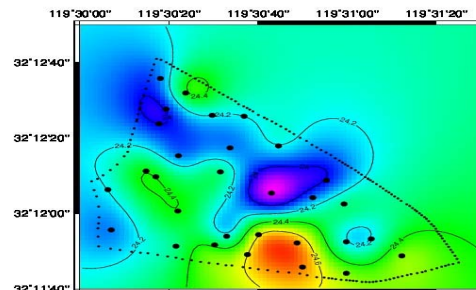
As shown in Figure 3, the temperature difference of the average temperatures among morning, noon and evening is about 1°C. The lowest temperatures of morning, noon and evening was concentrated near the round covers in front of the auditorium (D3). This measuring point is at the crossroads with good ventilation, where a lawn is in the front and is sheltered by tall trees. The trees can block shortwave radiation of the sun and absorb long-wave radiation of the ground. The highest temperature in the morning appeared in sixth canteen corner of Jiangsu University (A6) and the main entrance in front of the Mechanical College (C2). The highest temperature at noon was under a ladder of Sanjiang Floor Front Gate (E2). The highest temperature in the evening was at the entrance to the auditorium (D2). Except for the factors of the concrete surface, tall buildings and poor ventilation in these places, the influences of the traffic and population also contributed to the high temperature. So the temperature is higher in the areas with lots of population and traffic, such as canteen and accommodation areas. The temperature was low in the areas with plentiful vegetation cover and

a small quantity of population such as Thorpe plum. The temperature in the morning has bigger variation than that at noon and in the evening, which might be related to the sunshine, the wind speed, the underlying surface and the surrounding environment.

A



B



C

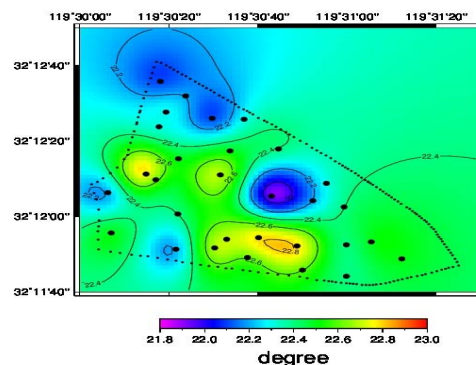


Fig. 3 Temperature distribution in time interval (A: morning; B: noon; C: evening).

As shown in Figure 4, the low temperature region was centered near the round covers in front of the auditorium (D3), near the lawn opposite the Valentine Valley (E3) and the yellow road in front of expert floor (E4). At these places, trees not only can reduce the outdoor wind speed, making the heat accumulation phenomenon appeared, but also can remove a large amount of short-wave radiation by reflection and transmission through their leaves to decrease the surrounding ambient air temperature. The high temperature region was distributed in the middle of the round altar opposite the Three Hill building (D1), at the entrance to the lecture hall (D2), in the roadside of Jiangsu University (E1), and under the stairs at the main entrance of Sanjiang building (E2). The minimum temperature was 22.5°C and the maximum temperature was 23.5°C. The average temperature difference was about 1°C. In this study, 300m*300m is a measurement unit, and the lowest and the highest temperature regions were only 1 to 2 measurement unit intervals. That is to say, in the range of 300m to 600m, the temperature has already changed 1°C. It shows that there was a more obvious heat island effect on the campus of Jiangsu University.

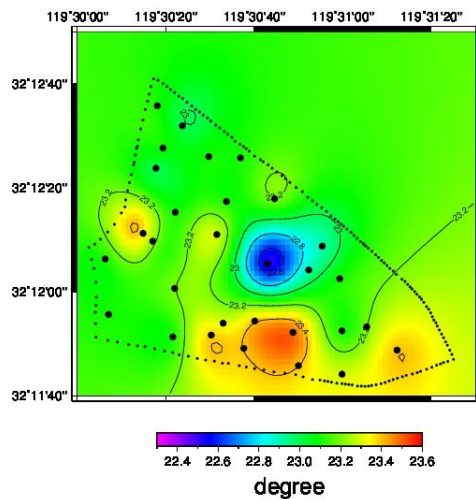


Fig. 4 Spatial distribution of the mean temperature.

In order to further investigate the effect of heat island effect, we select five measurement points to study the influences of different underlying surfaces according to the results of figure 4. Grassland (E3), riverside (F2), marble road (E2), concrete road with (C5) and without (C4) shadow were chosen for

studying the changes of the temperature and relative humidity around their surrounding environments.

CHARACTERISTICS OF TEMPERATURE AND RELATIVE HUMIDITY AT DIFFERENT UNDERLYING SURFACES

Daily Variation Of Temperature At Different Underlying Surfaces

As shown in Figure 5, temperatures of five different underlying surfaces in one day presented inverted "V" single peak curves. The temperatures were low in the morning and evening, which was high in the afternoon at about 16:00. The main reason is that the study area is located in the south, and the sunshine period is longer in spring. So that the endothermic and exothermic reached the balance at 16:00, when the temperature was the highest. It also found that the temperature of grassland is the lowest, while the temperature of the concrete road (direct sunlight) is the highest. The temperature of the concrete road under the shadow is lower than that of the concrete road with direct sunlight. The temperature difference between them is about 1°C. Because tree canopy tends to reduce surface temperature in the shade and thus reduces storage and convection of heat. Shading by trees can remove a large amount of incoming short wave radiation by reflection and transmission through their leaves. Therefore, the surface and air temperature can be lower in the shade of trees than in surrounding unshaded areas. So one way to mitigate urban heat island thereby reduce human heat stress is to increase vegetation cover in urban areas as vegetation can provide evatranspiration cooling and shading benefits as well as other ecosystem services.

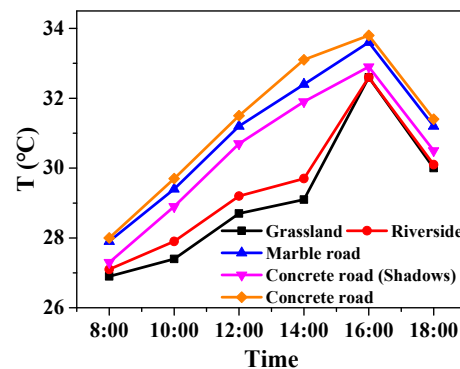


Fig. 5 Daily variation of temperature at different underlying surfaces.

Daily Variation Of Relative Humidity At

Different Underlying Surfaces

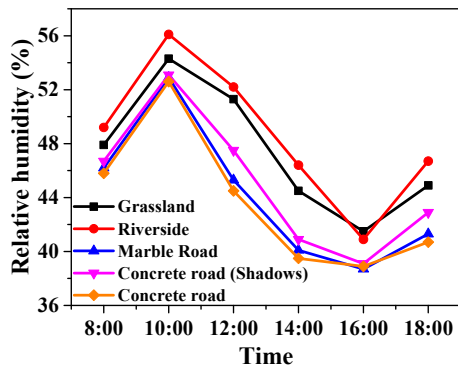


Fig. 6 Daily variation of relative humidity at different underlying surfaces.

As shown in Figure 6, the highest values of air relative humidity for five different underlying surfaces all appeared at 10:00, while the lowest values appeared at 16:00. Trees release water vapour to the air from leaf stomata during photosynthesis, which is known as transpiration. Leaf transpiration and soil water evaporation are all contributed to the air humidity. The relative humidity of the air changed at the beginning of 8:00 in the morning. It risen first, then dropped, and finally continued to rise following the sine curve. Although the trend of the curve changes in the same trend, there are obvious differences in the influence of the different underlying surfaces on relative humidity. For example, the relative humidity of hardened roads were lower than those at the riverside and the grassland.

The Relationship Between Temperature and Relative Humidity

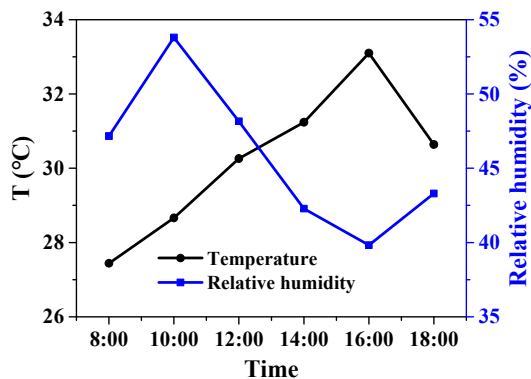


Fig. 7 Daily variation of mean temperature and mean relative humidity.

The temperatures and relative humidity of different underlying surfaces were numerical averaged. As shown in Figure 7, the peak temperature was at 16:00, when the relative humidity was at the lowest level. It is because that in the morning, the temperature and the relative humidity of the air rise with the increase of the solar radiation. After that, the temperature of the air continues to rise due to persistent solar radiation, while the relative humidity of the air decreases gradually and reaches a critical point at 16:00. Then, the radiation of sun weakened and the temperature began to decrease, while the relative humidity of the air gradually rose. According to the results, the temperature is negatively related to the relative humidity. Transpiration can mediate latent heat loss during the conversion of liquid water to vapour, thereby resulting in the cooling of the leaf and the surrounding environment.

CONCLUSION

In this work, the outdoor temperature, relative humidity and other environmental parameters of Jiangsu University campus were tested. GIS technology was used to study the distribution characteristics of campus thermal environment and the influences of different underlying surfaces on campus thermal environment.

According to the temperature spatial distribution map of Jiangsu University, the distance between the low and the high temperature region were about 300m ~ 600m and the temperature difference was 1°C. So that the heat island effect is more obvious.

The daily variation of the temperature of five different underlying surfaces showed inverted "V" single peak curves. The temperature was low in the morning and evening and high in the afternoon. At 14:00, the temperature difference between the grassland and the concrete road (direct sunlight) was about 4°C.

The temperature and the relative humidity showed a trend that the temperature was rising while the relative humidity was decreasing obviously. The temperature was negatively correlated with the relative humidity.

The temperature of concrete road with direct sunlight was obviously higher than that of concrete road with shadow, and the temperature difference between them was about 1°C. It means that trees play an important role in regulating the temperature.

The temperature is higher with abundant of population and traffic, such as canteens, playgrounds and bathrooms.

OUTLOOK

According to the conclusions, we forward five specific suggestions for improving the outdoor thermal environment in Jiangsu University:

The protection of the existing grassland is an effective way to mitigate the heat island effect. Therefore, the management system of campus vegetation should be perfected as soon as possible.

Recently, our school is on the remediation of the Yudai River Basin. Widening the river channel and increasing the drainage area could effectively reduce the outdoor temperature of the campus.

In summer, the temperature in the places with a small number of vegetation coverage and lots of people, such as the library is high. Sprinkling water could be used to increase the humidity of the air and decrease the temperature, which can provide a comfortable learning environment for students.

Tall shrubs should be planted in the areas with direct sunlight, which can increase the shadow area, and thus effectively decrease the temperature.

Students should be encouraged to instill the idea of environmental protection into all aspects of daily life. This is a long-term and meaningful work, which can directly reduce the anthropogenic heat emission and weaken the campus heat island effect.

ACKNOWLEDGEMENTS

The atmospheric parameter measuring instrument used in this project is provided by Nagoya Industry University of Japan.

REFERENCES

- [1] S. Zhong, Y. Qian, C. Zhao, R. Leung, H.L. Wang, B. Yang, J.W. Fan, H.P. Yan, X.Q. Yang, D.Q. Liu, Urbanization-induced urban heat island and aerosol effects on climate extremes in the Yangtze River Delta region of China, *Atmos Chem Phys*, 17 (2017) 5439-5457.
- [2] M. Palme, L. Inostroza, G. Villacreses, A. Lobato-Cordero, C. Carrasco, From urban climate to energy consumption. Enhancing building performance simulation by including the urban heat island effect, *Energ Buildings*, 145 (2017) 107-120.
- [3] W.F. Li, Q.W. Cao, K. Lang, J.S. Wu, Linking potential heat source and sink to urban heat island: Heterogeneous effects of landscape pattern on land surface temperature, *Sci Total Environ*, 586 (2017) 457-465.
- [4] J.Q. Chen, H. Wang, H.Z. Zhu, Analytical approach for evaluating temperature field of thermal modified asphalt pavement and urban heat island effect, *Appl Therm Eng*, 113 (2017) 739-748.
- [5] R.C. Estoque, Y. Murayama, S.W. Myint, Effects of landscape composition and pattern on land surface temperature: An urban heat island study in the megacities of Southeast Asia, *Sci Total*

Environ, 577 (2017) 349-359.

- [6] D.C. Zhou, L.X. Zhang, L. Hao, G. Sun, Y.Q. Liu, C. Zhu, Spatiotemporal trends of urban heat island effect along the urban development intensity gradient in China, *Sci Total Environ*, 544 (2016) 617-626.

DEGRADATION OF FAMOTIDINE IN WATER WITH Ag-ZnO UNDER UV LIGHT IRRADIATION

Md. Ashraful Islam Molla^{1,*}, Ikki Tateishi¹, Mai Furukawa¹, Hideyuki Katsumata¹, Tohru Suzuki², Satoshi Kaneco^{1,2}

¹Department of Chemistry for Materials, Graduate School of Engineering, Mie University, Japan

²Mie Global Environment Center for Education & Research, Mie University, Japan

ABSTRACT

Ag-doped ZnO photocatalysts were successfully synthesized at different Ag contents (0–15 wt%) through simple, effective, high yield and low cost mechanochemical combustion technique. The addition of silver acetate to zinc acetate and oxalic acid mixture was performed for mechanochemical technique. The photocatalytic performance of different prepared photocatalysts was evaluated by the degradation of Famotidine (FMT) under UV irradiation. The photodegradation rate increased with increasing the Ag contents from 0 to 10%, and it was 2.1 times better than undoped ZnO on 90 min. The photocatalytic degradation of FMT with Ag-doped ZnO was affected by degradation parameters such as calcination temperature, calcination time and doping concentrations. The Ag-doped ZnO demonstrated higher activity due to small particles size, large surface area, and reduction of electron-hole recombination. The trapping test with different scavengers proved it that the oxidation of FMT occurred with the reactive species of $\bullet\text{O}_2^-$, $\bullet\text{OH}$ and h^+ . In these species, $\bullet\text{O}_2^-$ radical was the main reactive species in the photodegradation process.

Keywords: Famotidine, Photocatalytic Degradation, Ag/ZnO, UV Light Irradiation

INTRODUCTION

Famotidine (FMT) is a histamine H_2 -receptor antagonist used to treat peptic ulcers, gastroesophageal reflux, and conditions, where the stomach produces an excess of acid [1],[2]. It has been documented that 65~70% of the parent compound is found unchanged in the urine, when patients used the FMT [3]. It creates stable complexes with palladium, copper, cobalt and nickel. Previous research reports have proved the stability of FMT in the environment and water bodies [4]. Taking the above-mentioned issues into account, one can argue that FMT should be considered as persistent contaminants in an aqueous environment.

Zinc oxide (ZnO) is a wide band-gap (3.2 eV) semiconductor with large exciton binding energy of 60 meV at room temperature [5]. It is known as one of the important active photocatalysts due to its advantages, including the large initial rates of activity, many active sites with high surface reactivity, low price and environment safety [6]. However, ZnO have several disadvantages such as a rapid recombination of photoexcited electron and hole pairs which inhibits its photocatalytic efficiency. To improve the photocatalytic activity of ZnO, surface charge transfer processes should be enhanced and the recombination rate of electron and hole should be decreased. Several methods have been improved to reduce electron-hole recombination and increased the surface charge

transfer [7]–[12]. One of these methods is to dope transition metal into ZnO photocatalysts. Doping of transition metals into the ZnO lattice can lead to changes in the electrical, optical, and magnetic properties of ZnO. Besides, it reduces band gap energy of ZnO, improves charge separation between electron and hole by forming electron traps and, enhances photocatalytic activity of ZnO [13]. Different transition or noble metals such as Mn, Fe, Ni, Cu and Ag have been widely used for doping of ZnO. Among them, Ag is the cheapest noble metal and has potentials in industrial productions [14]–[16]. The wide band gap ZnO semiconductor shows only photo-absorption under UV irradiation whereas silver metal acts as electron sink, which effectively trapped photo-excited electrons from ZnO surface and preventing the recombination of electron-hole [17]. Also the silver metal nanoparticles were effectively trapped the photo-excited electrons from the ZnO surface and enhanced the hole generation [18],[19]. The photo-generated holes and metal trapped electrons have effectively produced the hydroxyl radicals and super oxide radicals. The generated hydroxyl and superoxide radicals are strong oxidant species which can degrade the FMT molecule.

In this study, the various proportions of Ag/ZnO nanocomposites were prepared by hydrothermal method. Furthermore, the photocatalytic activities of pure ZnO and Ag/ZnO nanophotocatalysts were investigated by degrading Famotidine in aqueous

medium under UV-light. It is found that the 10%Ag/ZnO photocatalyst exhibits excellent photocatalytic activity.

EXPERIMENTAL

Chemicals and Materials

Zinc acetate dehydrate (99.9%), oxalic acid dehydrate (98%), silver acetate (99%) and Famotidine (99%) were obtained from Wako Pure Chemical Industries, Ltd. and were used as received without further purification. Laboratory pure water was obtained from an ultrapure water system (Advantec MFS Inc., Tokyo, Japan) resulting in a resistivity >18 MΩ cm.

Preparation of Photocatalyst

In a typical synthesis, 2.195 g of zinc acetate dihydrate and 2.521 g of oxalic acid dihydrate were taken in agate mortar and the mixture was ground for 10 min in order to obtain a paste of zinc oxalate dihydrate and acetic acid. The existence of acetic acid was confirmed by its typical smell. The loss of acetic acid byproduct in the form of fumes became a driving force for the reaction. Silver acetate was added to the above paste as a source of silver, and the grinding process was continued for the next 10 min to obtain zinc oxalate–silver oxalate.

The Ag-doped zinc oxide crystallites were obtained by calcination of precursor powders at the temperature of 300–700 °C under an air atmosphere. The undoped ZnO was also synthesized by calcination of a paste of zinc oxalate and acetic acid for the comparison.

Photocatalytic Activity

The photocatalytic activities of Ag/ZnO were evaluated by the degradation of Famotidine under UV irradiation at ambient temperature. Typically, 30 mL of Famotidine solution, 10 mg of photocatalyst were added to a 35-mL Pyrex glass cell. The initial concentration of Famotidine in all experiments was 10 mg/L and the Famotidine solution containing the appropriate quantity of the photocatalyst powder was magnetically stirred before and during irradiation. Before irradiation, the photocatalyst suspension containing Famotidine was allowed to equilibrate for 30 min in the dark. The sample solution was irradiated with a Black lamp (365 nm) which was positioned on the side of the reaction cell. After the desired irradiation time, the photocatalyst was separated by the centrifugation. The amount of the remnant Famotidine in the aqueous solution was

measured using a high-performance liquid chromatograph (HPLC, GL-7400), equipped with a HITACHI L-3000 optical detector and an Inertsil ODS-3 column (GL Science, Japan). The elution was monitored at 276 nm. The mobile phase was a mixture of acetonitrile and water (1/1, v/v) and was pumped at a flow rate of 1.0 mL/min.

Detection of reactive oxygen species

The scavenging experiments of reactive oxygen species were similar to the photodegradation experiments. Three scavengers were selected, namely, *tert*-butyl alcohol (\bullet OH radical scavenger), *di*-ammonium oxalate monohydrate (hole scavenger) and ascorbic acid (\bullet O₂⁻ radical scavenger). Different quantity of *tert*-butyl alcohol, *di*-ammonium oxalate monohydrate [20] and ascorbic acid [21] were added into the FMT solution prior to addition of catalysts.

RESULTS AND DISCUSSION

Effect of Ag-doping Amount on the Photocatalytic Degradation of FMT

The influence of silver doping amounts on the photocatalytic FMT degradation was studied in the aqueous solution under UV light irradiation. The results are depicted in Fig. 1. The degradation rate increased with an increase in silver percentage up to 10 wt% in the composite, and exceeding this silver percentage photocatalytic activity decreased

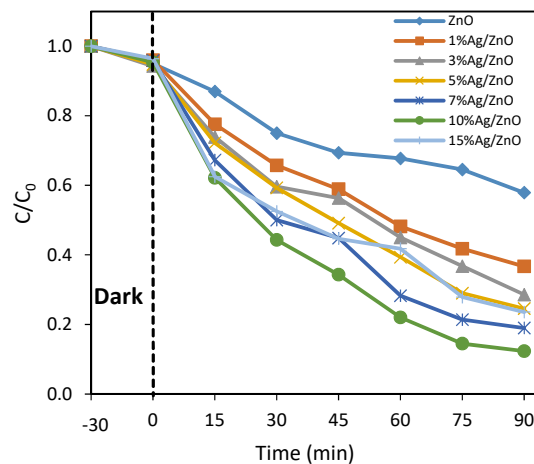


Fig. 1 Effect of Ag-doping amount on the photocatalytic degradation of Famotidine with Ag/ZnO under UV light irradiation. Calcination temperature 500 °C; calcination time 3 h.

The possible reason may be attributable to the tradeoff between the decrease in particle size and the deterioration in crystallinity for ZnO [22]. An optimal amount (10%) of silver doping into ZnO is

desirable for higher photocatalytic activity, which leads better charge separation at ZnO surface and efficient electron transfer to Ag metal. On the other hand, the higher percentage of silver shows higher negative charge on the silver surface, which effectively attracted positively charged holes from ZnO surface resulting in increased recombination rate [23]. Also, the higher percentage of silver masked the ZnO surface and affected the absorbance of UV light [24].

Effect of Calcination Temperature on the Photocatalytic Degradation of FMT

The photocatalytic FMT degradation with the Ag-doped ZnO was evaluated in the aqueous solution under UV light irradiation for 1 h. Figure 2 shows the effect of calcination temperature on the photocatalytic FMT degradation with undoped and doped ZnO materials. The oxides were sintered at different temperatures such as 300, 400, 500, 600 and 700 °C and were tested for their photocatalytic degradation of FMT. The optimum calcination temperatures for Ag-doped ZnO were 500 °C.

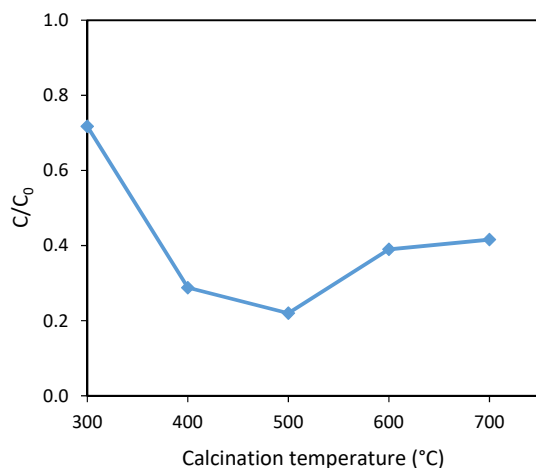


Fig. 2 Effect of calcination temperature on the photocatalytic degradation of Famotidine with Ag/ZnO under UV light irradiation. Calcination time 3 h; Ag doping 10wt %.

Above 500 °C, the photocatalytic FMT degradation decreased with the calcination temperatures. It was reported previously that the crystallite size of the oxides increased with increasing the calcination temperatures [25]-[28]. Therefore, the reason for the decrease in the photocatalytic FMT degradation may be due to the larger particle size of ZnO. The best material for the photocatalytic FMT degradation was the 10%Ag-doped ZnO, which was sintered at 500 °C.

Effect of Calcination Time on the Photocatalytic Degradation of FMT

The effect of calcination time on the photocatalytic FMT degradation using Ag-doped ZnO was investigated under UV light irradiation for 1 h. The results are illustrated in Fig. 3. As the calcination time increased up to 3 h, the photocatalytic FMT degradation with Ag/ZnO increased gradually. After the calcination time of 3 h, the photocatalytic FMT degradation turned from increase to decrease.

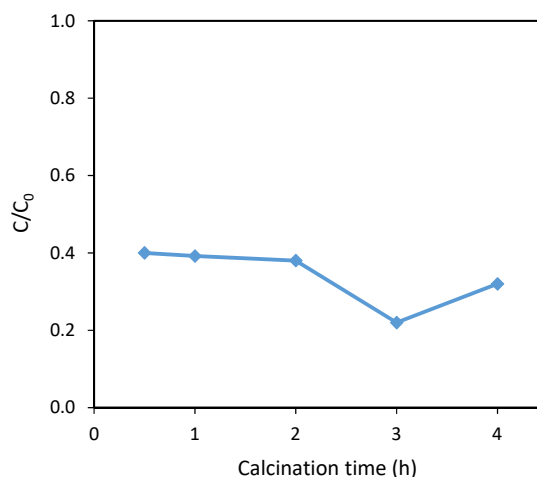


Fig. 3 Effect of calcination time on the photocatalytic degradation of Famotidine with Ag/ZnO under UV light irradiation. Ag doping 10wt %; calcination temperature 500 °C.

Role of the reactive species in the photocatalytic process

The role of the reactive species in the photocatalytic process was studied by using different quenchers. The quenchers used to scavenge the relevant reactive species were: *tert*-butyl alcohol ($\bullet\text{OH}$ radical scavenger), *di*-ammonium oxalate monohydrate (h^+ scavenger) and ascorbic acid ($\bullet\text{O}_2^-$ radical scavenger). The effect of different scavengers on the FMT degradation over Ag/ZnO heterojunction is presented in Fig. 4. It was observed that by using AO, TBA and AA as scavenger, the photocatalytic activity significantly reduced from 88% (no scavenger) to 18% (due to $\bullet\text{O}_2^-$), 33% (due to $\bullet\text{OH}$) and 46% (due to h^+), respectively. Hence, it was concluded that all the reactive species ($\bullet\text{O}_2^-$, $\bullet\text{OH}$ and h^+) contributed to the photodegradation process. In these species, $\bullet\text{O}_2^-$ was the main reactive species in the photodegradation process since worst photocatalytic activity was found by using AA as scavenger.

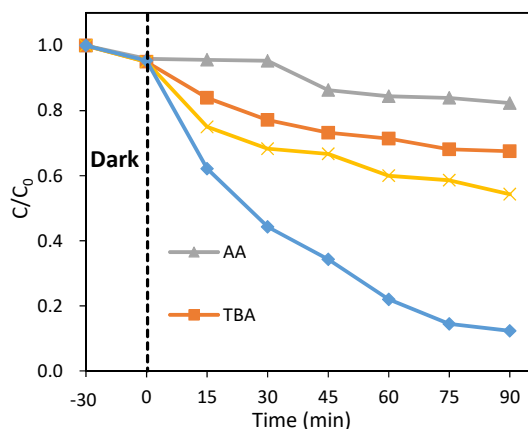


Fig. 4 Effects of different radical scavengers on the photocatalytic degradation of Famotidine with Ag/ZnO under UV light irradiation.

Mechanism

A plausible photocatalytic mechanism for the degradation of FMT in the presence of Ag/ZnO photocatalyst under UV light is illustrated in Fig. 5.

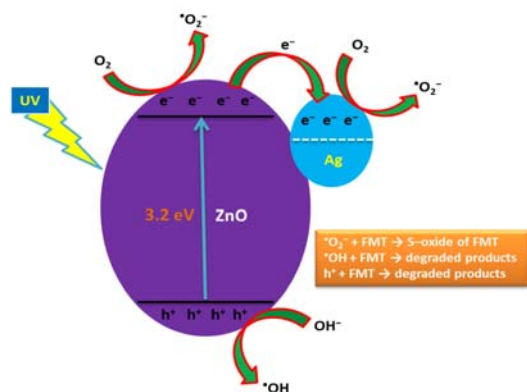


Fig. 5 The plausible photocatalytic mechanism for the photocatalytic degradation of FMT in the presence of Ag/ZnO under UV light irradiation.

Under UV irradiation of Ag/ZnO nanocomposite, the electrons are excited from valence band to the conduction band (CB) and the holes are generated at valence band (VB) of ZnO. Then the photo-excited electrons are transferred from the CB of ZnO to Ag metal nanoparticle because Ag metal act as electron sink. The silver trapped electrons react with surface adsorbed O_2 and produce superoxide radical [17],[29]. As well as the photo-induced holes can also readily react H_2O to generate hydroxyl radical. The generated hydroxyl and superoxide radicals are strong oxidant species which can degrade the FMT molecule. The silver metal incorporated in ZnO is responsible for reducing photo-induced electron-hole charge recombination and prolongs the lifetime of photo-excited electrons.

CONCLUSION

In summary, the Ag-doped ZnO was applied into the photocatalytic degradation of FMT in aqueous medium under UV light irradiation. The optimum calcination temperature and time were 500 °C and 3 h, respectively. The best Ag-doping amount was 10 wt%. The maximum photocatalytic activity for FMT degradation on Ag/ZnO was more than two times better compared with undoped ZnO. According to the investigation of the photocatalytic mechanism, the Ag/ZnO degradation of Famotidine under UV light irradiation could be attributed to the oxidation by $\bullet O_2^-$, $\bullet OH$ and h^+ radicals. Moreover, the $\bullet O_2^-$ radical was the main reactive species in the photodegradation process.

ACKNOWLEDGEMENTS

The present research was partly supported by Grant-in-Aid for Scientific Research (C) 15K00602 from the Ministry of Education, Culture, Sports, Science, and Technology of Japan. All experiments were conducted at Mie University.

REFERENCES

- [1] Hassan MA, Salem MS, Sueliman MS, Najib NM, "Characterization of famotidine polymorphic forms", *Int. J. Pharm.*, Vol. 149, 1997, pp. 227–232.
- [2] Mady FM, Abou-Taleb AE, Khaled KA, Yamasaki K, Iohara D, Taguchi K, Anraku M, Hirayama F, Uekama K, Otagiri M, "Evaluation of carboxymethyl-beta-cyclodextrin with acid function: improvement of chemical stability, oral bioavailability and bitter taste of famotidine", *Int. J. Pharm.*, Vol. 397, 2010, pp. 1–8.
- [3] Lee KW, Kayser SR, Hongo RH, Tseng ZH, Scheinman MM, "Famotidine and long QT syndrome", *Am. J. Cardiol.*, Vol. 93, 2004, pp. 1325–1327.
- [4] Karpin'ska J, Sokoł A, Kobieszko M, Starczewska B, Czyzewska U, Hryniewicka M, "Study on degradation process of famotidine hydrochloride in aqueous samples", *Toxicol. Environ. Chem.*, Vol. 92, 2010, pp. 1409–1422.
- [5] Lee KM, Lai CW, Ngai KS, Juan JC "Recent developments of zinc oxide based photocatalyst in water treatment technology: a review", *Water Res.* Vol. 88, 2016, pp. 428–448.
- [6] Lam SM, Sin JC, Abdullah AZ, Mohamed AR, "Degradation of wastewaters containing organic dyes photocatalysed by zinc oxide: a review", *Desalin. Water Treat.*, Vol. 41, 2012, pp. 131–169.
- [7] Siddhapara KS, Shah DV, "Study of photocatalytic activity and properties of

- transition metal ions doped nanocrystalline TiO₂ prepared by sol-gel method", *Adv. Mater. Sci. Eng.*, Vol. 2014, 2014, pp. 4462198.
- [8] Saleh R, Djaja NF, "UV light photocatalytic degradation of organic dyes with Fe-doped ZnO nanoparticles, *Superlattices Microstruct.*, Vol. 74, 2014, pp. 217–233.
- [9] Saleh R, Djaja NF, "Transition-metal-doped ZnO nanoparticles: synthesis, characterization and photocatalytic activity under UV light", *Spectrochim. Acta Part A: Mol. Biomol. Spectrosc.*, Vol. 130, 2014, pp. 581–590.
- [10] Kumar K, Chitkara M, Sandhu IS, Mehta D, Kumar S, "Photocatalytic, optical and magnetic properties of Fe-doped ZnO nanoparticles prepared by chemical route", *J. Alloys Compd.*, Vol. 588, 2014, pp. 681–689.
- [11] Deka S, Joy PA, "Synthesis and magnetic properties of Mn doped ZnO nanowires, *Solid State Commun.*, Vol. 142, 2007, pp. 190–194.
- [12] Viswanatha R, Sapra S, Gupta SS, Satpati B, Satyam PV, Dev BN, Sarma DD, "Synthesis and characterization of Mn-doped ZnO nanocrystals", *J. Phys. Chem. B*, Vol. 108, 2004, pp. 6303–6310.
- [13] Türkyılmaz SŞ, Güya N, Özacar M, "Photocatalytic efficiencies of Ni, Mn, Fe and Ag doped ZnO nanostructures synthesized by hydrothermal method: The synergistic/antagonistic effect between ZnO and metals", *J. Photochem. Photobiol. A: Chem.*, Vol. 341, 2017, pp. 39–50.
- [14] Hou XM, "ZnO/Ag heterostructured nanoassemblies: wet-chemical preparation and improved visible-light photocatalytic performance", *Mater. Lett.*, Vol. 139, 2015, pp. 201–204.
- [15] Yu CL, Zhou WQ, Zhu LH, Li G, Yang K, Jin RC, "Integrating plasmonic Au nanorods with dendritic like alpha-Bi₂O₃/Bi₂O₂CO₃ heterostructures for superior visible-light-driven photocatalysis", *Appl. Catal. B*, Vol. 184, 2016, pp. 1–11.
- [16] Feng WH, Wang B, Zheng ZY, Fang ZB, Wang ZF, Zhang SY, Li YH, Liu P, "Predictive model for optimizing the near-field electromagnetic energy transfer in plasmonic nanostructure-involved photocatalysts", *Appl. Catal. B*, Vol. 186, 2016, pp. 143–150.
- [17] Zheng Y, Chen C, Zhan Y, Lin X, Zheng Q, Wei K, Zhu J, "Photocatalytic activity of Ag/ZnO heterostructure nanocatalyst: correlation between structure and property", *J. Phys. Chem. C*, Vol. 112, 2008, pp. 10773–10777.
- [18] Xie W, Li Y, Sun W, Huang J, Xie H, Zhao X, "Surface modification of ZnO with Ag improves its photocatalytic efficiency and photostability", *J. Photochem. Photobiol. A*, Vol. 216, 2010, pp. 149–155.
- [19] Lee M-K, Kim TG, Kim W, Sung Y-M, "Surface plasmon resonance (SPR) electron and energy transfer in noble metal-zinc oxide composite nanocrystals", *J. Phys. Chem. C*, Vol. 112, 2008, pp. 10079–10082.
- [20] Katsumata H, Taniguchi M, Kaneco S, Suzuki T, "Photocatalytic degradation of bisphenol A by Ag₃PO₄ under visible light", *Catal. Commun.*, Vol. 34, 2013, pp. 30–34.
- [21] Su J, Zhu L, Geng P, Chen G, "Self-assembly graphitic carbon nitride quantum dots anchored on TiO₂ nanotube arrays: An efficient heterojunction for pollutants degradation under solar light", *J. Hazard. Mater.*, Vol. 316, 2016, pp. 159–168.
- [22] Ilican S, Yakuphanoglu F, Caglar M, Caglar Y, "The role of pH and boron doping on the characteristics of sol gel derived ZnO films", *J. Alloys Compd.*, Vol. 509, 2011, pp. 5290–5294.
- [23] Xu J, Chang Y, Zhang Y, Mab S, Qub Y, Xu C, "Effect of silver ions on the structure of ZnO and photocatalytic performance of Ag/ZnO composites", *Appl. Surf. Sci.*, Vol. 255, 2008, pp. 1996–1999.
- [24] Chai B, Wang X, Cheng S, Zhou H, Zhang F, "One-pot triethanolamine-assisted hydrothermal synthesis of Ag/ZnO heterostructure microspheres with enhanced photocatalytic activity", *Ceram. Int.*, Vol. 40, 2014, pp. 429–435.
- [25] Potti PR, Srivastava VC, "Comparative studies on structural, optical, and textural properties of combustion derived ZnO prepared using various fuels and their photocatalytic activity", *Ind. Eng. Chem. Res.*, Vol. 51, 2012, pp. 7948–7956.
- [26] Lu J, Zhang Q, Wang J, Saito F, Uchida M, "Synthesis of N doped ZnO by grinding and subsequent heating ZnO-urea mixture", *Powder Technol.*, Vol. 162, 2006, pp. 33–37.
- [27] Praserttham P, Silveston PL, Mekasuwandumrong O, Pavarajarn V, Phungphadung J, Somrang P, "A new correlation for the effects of the crystallite size and calcination temperature on the single metal oxides and spinel oxide nanocrystal", *Cryst. Growth Des.*, Vol. 4, 2004, pp. 39–43.
- [28] Li Y, Ma G, Peng S, Lu G, Li S, "Boron and nitrogen co-doped titania with enhanced visible-light photocatalytic activity for hydrogen evolution", *Appl. Surf. Sci.*, Vol. 254, 2008, pp. 6831–6836.
- [29] Zheng Y, Zheng L, Zhan Y, Lin X, Zheng Q, Wei K, "Ag/ZnO heterostructure nanocrystals: synthesis, characterization, and photocatalysis", *Inorg. Chem.*, Vol. 46, 2007, pp. 6980–6986.

ACCELERATING METHANE PRODUCT IN REACTION OF METHANOGENS ARCHAEA WITH COAL IN MUARA ENIM FORMATION

Ildo Muhary Putra, Muhammad Ihsan , T.J.L Tobing, Dio Rizqi Irawan, D.A.A. Putri
Geological Engineering, Sriwijaya University, Indonesia

ABSTRACT

Coal bed methane (CBM) is one of prospectus of renewable energy in the future, due to the many countries had coal deposit in the world. Indonesia has many potential deposit of coal and one of them is situated in South Sumatra with 183 tcf total potential. In 2025 Indonesia focuses to increase the invention and applicator of new and renewable energies until 17 % from total energy consumption. Therefore, exploration research were needed in order to enhance information related. Low volatile bituminous coal were selected due to its ability as a source rock for CBM. In this experiments, coal were mixed with methanogens from rumen liquid to initiate its reaction on methane gas production. Coal sample were collected from Muara Enim Formation, South Sumatera Basin, Indonesia. The coal, cattle rumen fluid and various water condition (fresh, brackish, and saline) were mixed into in vitro bottle culture by 1:4:5 proportions and incubated in 34°C for 30 days. Gas production and CH₄ concentration were collected every 5 days using gas gas springe and analyzed its composition by gas chromatography (GC) technique. The data tabulated and processed in descriptive statistics. The result showed that CBM generated from anaerobically fermentation were optimally obtained from brackish water.

Keywords: Coal Bed Methane (CBM), Bituminous Coal, Methanogens Archaea, Gas Chromatography (GC)

INTRODUCTION

The Exploitation of CBM was occurred in several country and successes to exploitation like USA, Canada, China, and other. This is causing the intensive research in related aspect with this resources. In Indonesia there are many basin that contain potential Methane gas as CBM, but still need the further related research. Coal Seam Gas (CSG) or Coal Bed Methane (CBM) has several dangerous in working coal mines and causing the greenhouse gas. Nevertheless it is source of energy in the place contains coal as the source rock and reservoir. One of it, using biological processing with methanogens bacteria. This processing was demonstrated in the early 1980s and now this research moving toward and apply in every coal from basin in Indonesia. The research has to do in enhancement coal bed methane in biological technique at Indonesia such as the coal sample from East Kalimantan by [1] that showed in the result is fit temperature for make sure the biological enhance coal bed methane optimally. So with [2] explanation the mechanism in forming of CBM for involving methanogens bacteria in laboratory experiment. The detail of coal analysis from coal rank, geochemical, and geology. In Indonesia showing the high potential to produce CBM.

Research location that contain sample of coal in South Sumatra Basin, Muara Enim Formation, In administration the site in Lahat regency toward to

southwest with distance between Palembang is 149 km. Sample location in pit of economical mining. This research focus into a coal sample in prospect seam which collected and analyses and react biologically to increasing the quantity of methane.

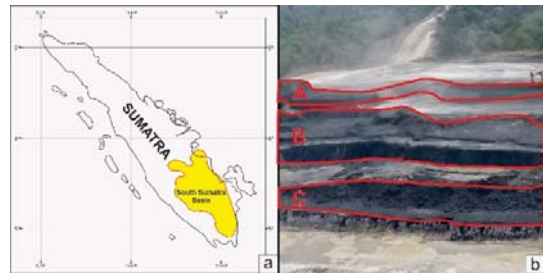


Fig.1 (a) Research area in South Sumatera basin and (b) Using seam B for research object

The aim of this research :

- To prove the activity of methanogens archaea in order to produce coal bed methane with laboratory experiment.
- To obtain the best water salinity condition to get the optimum production of CBM with several process of methanogen by using cow rumen.

AN OVERVIEW OF COAL GEOLOGY

Muara Enim Formation

According to [3] the South Sumatera basin is the big basin with Central Sumatra basin and identify by each sediment rock and separate by Tigapuluh mountain. The focus of research is toward Muara enim formation from late Miocene until Pliocene (10.2-1.65 Million years ago). From the calculation by [4] there are gas potential amount of 183 tcf in this formation. Muara enim formation have 18 coal seams but not all of it so important and named. A few of this coal bed are thin and not widely continuous with low rate economical to be mine. The significant layer gives an important status, Keladi layer as base of Muara enim formation. Shallower layer is niNu with top border in Muara enim formation. Middle layer from base of Muara enim formation there are Petai, Suban, Mangus, Burung, Benuang, Kebon, Babat/Benakat and Enim. In this area the Niru and Lematang layer is not developed. Mangus, Suban, and Petai are splitted in two, which named upper (A1) and lower (A2) of Mangus seam, Upper (B1) and lower (A2) Suban seams and upper (C1) and lower (C2) Petai seams (Fig.3). The common nomenclature using A1, A2, B1, B2, C1, C2. The thickness of this formation is 450-750 meters [5]. In general the depositional environment are from tropical delta

CBM Controls

The level or rank of coal from thermal maturity describe as the moisture of coal, vitrinite reflectance and another measuring. Entity from gas can be save into coal as fit as the coal rank. The porosity of coal seam characteristic by two things. There are well-defined and almost uniformly distributed network of natural fracture (cleats) and a coal matrix containing a highly heterogeneous porous structure between the cleats (coal bed reservoirs and their Co2 sequestration).

Coal bed methane forming in several process in coalification there are changing vegetation in chemical until become coal involving transformation biology complex and molecule structure in cell into chemical fragment. The product in this production sorption into high pressure coal.

In geometry CBM came from geology and biology processes during million of years or geology time scale. This process change the vegetation into several rank of coal with characteristic each other (Fig.4) such as lignite sub bituminous-bituminous-antracite-graphite.

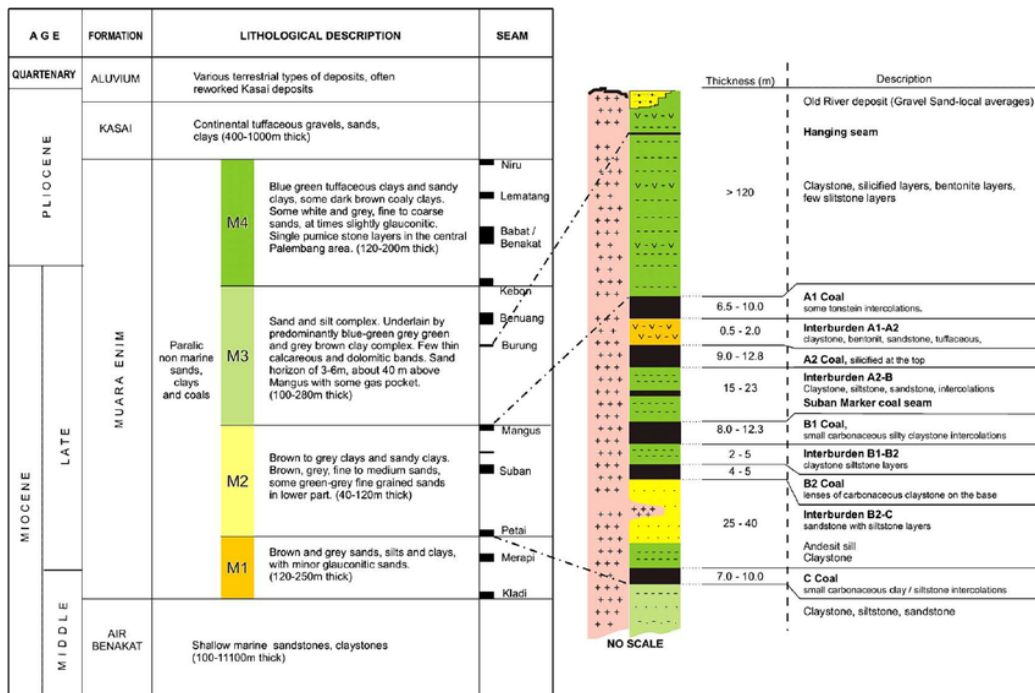


Fig. 3 Stratigraphy Muara enim formation as coal bearing formation [6]

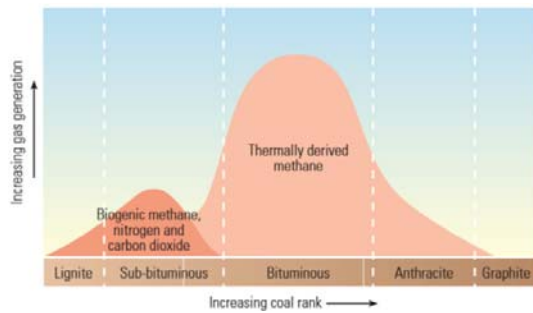


Fig.4 Coal rank [5]

Tabel 1. Proximate and Maceral Analysis

Component	Value	Remark
Total Moisture	16.12	Proximate
Inherent Moisture	8.14	Analysis
Ash Content	5.61	
Volatile Matter	43.6	
Fixed Carbon	42.65	
Total Sulfur	0.23	
Calory Value		
Ar	5976.24	
Adb	6556.4	
Daf	7519.26	
RD	1.31	
ID	1.27	
HGI	58.5	
Vitrinite	90.40%	Maceral
Liptinite	4.21%	Analysis
Inertinite	3.28%	
Other Minerals	2.04%	

Using low volatile bituminous coal, there are fit capacity to save the CBM as adsorbent function

Methanogens Archaea

Methanogens is a different group in organism which can be found in anaerobic environment, for example in mud accumulation, plant trees, rumen and black mud sediment. Methane is metabolism organic product which using carbon dioxide and hydrogen. In methanogenesys process with using Co₂ and H₂ for digest the organic material and convert into methane gas in anaerobic condition under the land. With the infiltration by protozoa,

fungi, methanogenic , archaea, and bacteriofag to help variation function in microbial ecosystem [7]. There are three main substrate to produce methanogens ; CO₂, the materials compound that produce metyl group or acetate [8]. Archae can adapt in many anaerobic environment, it can be found in the rumen gastrointertinal tract of ruminants.

Using Indicator Total Dissolve Solid (TDS) that contain of water with classification in many salinity, Fresh (0-1.000 ppm), brackish (1,000-10.000 ppm), saline (10.000-100.000) and brine (more than 100.000 ppm) [9]. In this research is using fresh, brackish and saline condition water salinity.

MATERIALS & METHOD

From many seams in Muara enim formation, we are choosing Suban seam which knowing as B seam. The Information from primary by collected in field site and laboratory analysis, and secondary data from literature in any reference. To understanding the characteristic of coal is needed to determine by geochemistry test by proximate and maceral test. Coal collect by channel sampling where to do it must in fresh layer and get in three point, top bottom and middle, then mix equally. The coal getting crush into powder using hammer, then getting heat in the oven with temperature 150⁰C for 10 Minutes to decrease the moisture of coal/ The rumen liquid get from cattle from animal husbandry and filtering it using gauze to hold the another macro substrate, adding water conditions (fresh, brackish and salty) with proportions 1:4:5. Incubated with incubator with temperature 34⁰C because the optimum temperature for in vitro reaction in batch culture according [1] pretend in 30 days and take the gas contain every 5 days using venoject capsule before laboratory analysis with chromatography gas.

In this occupation gas chromatography can determine the volume of quantity gas , so can read the CH₄ content.

Processes to forming Coal bed methane from massive coal related with fermentation. Occur in three degradation steps :

1. Hydrolisis process

p process from long chain compound into short chain compound with ingredient mass. This biomass such as cellulose, hemiselulose and other extractive product like protein, carbohydrate and lipid. This process involving the extracellular enzyme activity, there are Celolitic, amylase protease and lipase. This is occur while polisacaride became monosacaride and protein become peptide and amino acid [2]

2. Acidic Process

Present of bacteria producing acid which changing

the organic molecule complex like protein became amino acids, carbohydrate became simple compound like sugar, fat became length chain of acid and then divided into volatile fatty acid (VFA) as shown in (Fig.5). The fermentation of carbon dioxide producing VFA as main product for energy resources. So the use of Carbon for growth and retain the life living of organism community [2]

3. Methanogenesis process

With the aim to produce methane using acidic ion process which using CO_2 and H_2 to produce methane gas. Decomposition of Acid organic substance by methanogenic bacteria to produce CH_4 into two ways. First, with fermentation acetate acid became methane and CO_2 as shown in (Fig.6). Second, with reduction of CO_2 became methane using hydrogen gas of acid that producing from another bacteria [2].

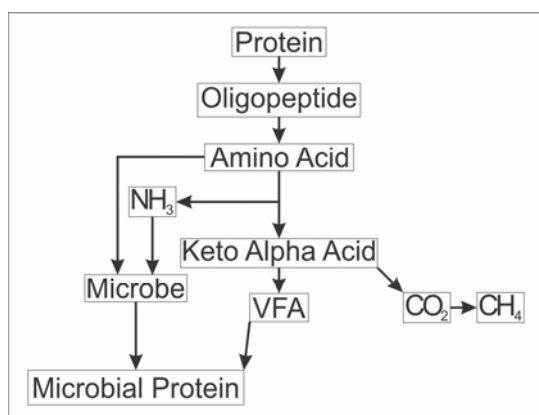


Fig. 5 Protein degradation in rumen

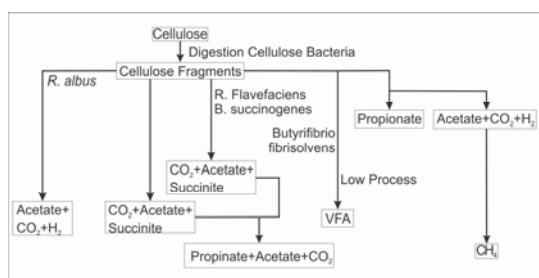


Fig. 6 Cellulose fermentation until producing VFA and CH_4

To get the methane gas as product in anaerobic reaction is needed the activity any rene creature like protozoa, fungi, methanogenic, bacteriofag together for chemical reaction and biological process in batch culture.

RESULT & DISCUSSION

Result

It's clearly that the path of graph show the top production in water salinity condition of brackish,

medium production in fresh water and minimum product CBM by saline water. The ability of this bacteria to adapt in fit salinity water condition and then expand to produce with his function as producer methane with some reaction in matrix of coal and not fit with brine water to adapt and producing methane gas.

From plotting at laboratory analysis graph, showing the plots of fluctuated or CBM producing top production is in the 20 days and then decreasing in time but it still producing some CH_4 , we can see in Fig. (7). According research before in [2] using 34°C temperature degree which the best condition which able for ruminal bacteria to live, growth and produce in Microcosm jar and to resist the enzymatic structure from bacteria.

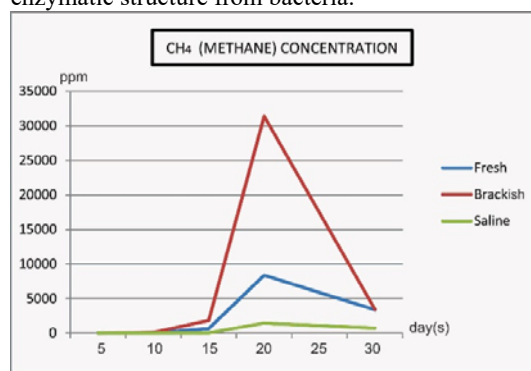


Fig. 7 The Quantity of methane according gas chromatography

The phases that happened in graphic:

1. Lag phase

With observation in under batch condition growing is zero. Log phase defined as transmission to exponential phase whereas first population had double itself [10]. There are adaptation phase from cell in culture condition. The length of this phase is depends on several factor because it control by medium type, and initial inoculums size.

2. Exponential phase

Observe in batch system in exponential phase. Characterize by the raised growth, because the development is too fast which makes it able to growth in batch culture. During this phase, accelerating of total amount of cells is increasing according the time. This conditions can be explain by progression geometric theory $2^0, 2^1, 2^2, 2^3, \dots, 2^n$.

3. Dead phase

Characterized by losing the cell that culturing condition, although the dead of many cell in condition, some bacteria still doing metabolism and growing to produce the methane product.

Discussion

There are many prospect seams in Muara enim formation that can be analysis and syntheses with microbial process to accelerating methane product in coal. Concern with several aspect such as thickness, quantity, outcrop condition and other. Hope the next research get more valuable data with the diversity seams an can be show for consideration.

Conclusion

This research using the laboratory analysis in anaerobic reaction the coal, rumen liquid and adding diversity of water formations (fresh, brackish and saline) and to make the result equally in chart to find the maximum condition in producing coal bed methane (CBM) in microcosm environment can be the initiator before application in large scale system [11]. In this capacity to producing its gas with several mechanism with biological enhance coal bed methane is able for accelerate quantity of methane gas and other gas product with change the substrate in anaerobic condition. Naturally the forming of coal happened in wet environment and calm water condition. Nevertheless there are some factor the influence the conversion microbial bacterial into methane gas, there are salinity, PH, nutrition, trace metal and coal surface area/bioavailability. This method can be pioneer in develop the new and renewable resources as mix energy that happened in microbiology process.

ACKNOWLEDGEMENTS

Thanks for participation partner from association of Geological Engineering. This research opportunity from facilitation gives to us by Arfan abrar PHD in animal feed and nutrition laboratory, Animal Science, Sriwijaya University with assistant laboratory. For the moral value, supporting, and correction by Steve nalendra and proof reading by Ardiansyah.

REFERENCE

- [1] Nazar MA, et al, "Accelerating Methana Production in Reaction Between Methanogen Bacteria And Coal : A Pilot Project For Optimizing Biologically Enhanced Coal Bed Methane". Proceedings of Indonesia Petroleum Association, IPA13-SE-126
- [2] Kusutyani K. and Kosasih, "Rumen medium for enhance coal bed methane producing" Center of Research and Developed Oil and Gas Technology. (LEMIGAS). M&E, Vol.13, No.1. (In Bahasa Indonesia).
- [3] Decoster GL, 1974, The Geology of The Central and South Sumatra Basin. Proceedings of the Indonesia Petroleum Association, Fourth Annual Convention
- [4] Balkin HE, et al. "Geochemistry and Petrology of Selected coal Samples from Sumatera , Kalimantan, Sulawesi , and Papua, Indonesia". International Journal of Coal Geology 77 (2009) 260-268.
- [5] Stevens SH & Sani K, "Coalbed methane potential of Indonesia: preliminary evaluation of a new natural gas source", Proceedings of Indonesian Petroleum Association, IPA01-G-063, 2001, pp. 727-738.
- [6] Endar BB, Nurhandoko, et al, "Rock Physics Study of Coal Bed Methane Reservoir Rock: Case Study of Muara enim Coal, Proceedings of Indonesian Petroleum Association , IPA12-G-157, 2012.
- [7] Morgavi DP, et al, "Microbial Ecosystem and Methanogenesis in Ruminants". Animal (2010) 4:7, pp1024-1036 The Animal Consortium 2010 doi:10.1017/S1751731110000546.
- [8] Liu Y & Whitman WB, Methabolic, phylogenetic, and ecological diversity of the methanogenic archaea. Annals of the New York Academic of Science 1125, 171-189.
- [9] Gorrel HA 1958. Classification of Formation Waters Based on Sodium Chloride Content, Bull. American Association of Petroleum Geologists, vol 42., p. 2513
- [10] Yates G T , and Smotzer T (2007) On the lag phase and initial decline of microbial growth curves . J. Theoret. Biol. 244 , 511 – 517 .
- [11] Strapoc D, et al, "Methanogenic Microbial Degradation of Organic Matter in Indiana Coal Beds. AAPG Annaul Convention, San Antonio, Texas, April 20-23 , 2008.
- [12] Bahrani A, et al, "Coalbed methane reservoirs and their Co2 sequestration potential", International of Oil, Gas, Petrochemical and Power Plant.
- [13] Candra A "Potential Evaluation of Coal Bed Methana Based on the Grade and Quantity of The Coal In the Mangus Seam, Muara enim Formation, Nibung Region, South Sumatera Basin. Proceedings of Indonesian Petroleum Association, IPA13-SG-051.
- [14] Doefert BN, et al, "Methanolobus zinderi sp. Nov., a Methylootropic methanofen isolated from a deep subsurface coal seam". International Journal of Systematic and Evolutionary Microbiology (2009) 59, 1064-1069.
- [15] Fallgren PH, et ,al, "Comparison of Coal Rank for Enhanced Biogenic Natural Gas Production". International Journal of Coal Geology 115 (2013) 92-96.
- [16] Hasmina A, Sutriyono, A., Hastuti, E.W.D, "Gas Content Appraisal of Shallow Seam in the South Palembang Basin, South Sumatera".

- International Journal Of Geomate 2017. Vol.12, Issue 33, pp. 45-52.
- [17] Kazi MH, "Production of Methane From Coal Through Bacterial Culture and Its Role For Sustainable Energy and Environment Protection. IA-ICENSUSA-150037-3247
 - [18] Maier RM, "Bacterial Growth, Book Chapter 3. Ch003-P370619.indd
 - [19] Nyemenim AR, et al. "Enhanced Coal bed Methane in Nigeria : Onyeama Coal bed". IJRET: International Journal of Research in Engineering and Technology .eISSN: 2319-1163| pISSN 2321-7308.
 - [20] Ollivier B, et al, "Methanocalculus halotolerans gen. nov., sp. nov., Isolated From An Oil-Producing Well". International Journal of Systematic Bacteriology (1998) 48, 821- 828.
 - [21] Permana AK, 2007, Coal Characteristics of Sarolangun – Pauh Region: Implication for Coalbed Methane Potential. Bandung: Jurnal Sumber Daya Geologi Vol 18 No. 6, Hal. 351–60.
 - [22] Pratiwi R, et al, "Structural Geology And Tectonism Influence in Predicting Coalbed Methane Potential of Seam Pangandang-A, In 'DIPA' Field, South Sumatera Basin". Proceedings of Indonesian Petroleum Association, IPA14-G-247.
 - [20] Pujibroto A, "Organic Petrology and Geochemistry of Bukit Asam Coal, South Sumatera, Indonesia". Research Online University of Wollongong thesis Collections.
 - [21] Rifai, 2010. "Effect of Cellulolytic Bacteria Isolate from Buffalo's rumen in Diverent wood". Minithesis, Husbandary Faculty, Bogor agriculture Institute (in Bahasa Indonesia).
 - [22] Schlumberger, 2009 Oilfield Review Summer: 21, no. 2.
 - [23] Wattimury PS, Amijaya, H, Hafsari, SW, "A Modelling of CO₂ Injection Based on Sensitivity Study To Improve The Coal Bed Methane (CBM) Production Profile In 'RAY' Field, South Sumatera Basin Indonesia. IPA Proceedings of Indonesian Petroleum Association, IPA13-E-006.
 - [24] Ziemiński K, & Frac M, "Methane Fermentation Processes as Anaerobic Digestion of Biomass: Transformations, Stages and Microorganisms. African Journal of Biotechnology Vol. 11(18), pp. 4127-4139, 1 March 2012.

A POST-LIQUEFACTION STUDY AFTER THE 2014 CHIANG RAI EARTHQUAKE AT TUNG-FAH-PAH VILLETTE IN CHIANG RAI, THAILAND

Sethapong Sethabouppha¹, Suriyah Tongmunee², Chollachai Kamtawai³ and Jittanan Kawilanan⁴
^{1,2}Faculty Members; ^{3,4}Graduate Students, Department of Civil Engineering,
Chiang Mai University, Thailand

ABSTRACT

A post-liquefaction study at a remote village was conducted after the 6.3 M_L 2014 Chiang Rai Earthquake. Site surveying, aerial map study, standard penetration test were conducted and found that the subsoil at this site was easily liquefied because the village was lying within abandon river channel with very loose sand layer from the depth of approximately 1.5 to 6 meters underneath the cohesive soil at the surface. Four liquefaction potential assessment methods commonly used in the United States and in Japan were examined. The calculation revealed that all four method yield slightly different factor of safety against liquefaction but can still be considered reliable. The calculation also showed that this site can still be re-liquefied if a strong earthquake strikes again.

Keywords: Earthquake, Soil Liquefaction, Post-Liquefaction Evaluation, Liquefaction Potential, Liquefaction Susceptibility

INTRODUCTION

The 6.3 M_L earthquake [1] which struck Chiang Rai Province (the northern-most province of Thailand - Figure 1) in the evening of May 5, 2014 was the first one that caused soil liquefaction in the recent history of earthquakes in Thailand. Soil Liquefaction has never been a significant issue in the country's earthquake concern since most earthquakes in this country were relatively small. Since that day, it is believed that stronger earthquakes are possible in the future. Learning about soil liquefaction starting with its affecting factors and potential assessment are important. It is the first step toward preventing liquefaction damages.

Learning from a case history is one of the most effective ways. Thus, a study was conducted in order to achieve two main objectives:

- 1) Understanding the conditions of factors affecting soil liquefaction at a selected site which liquefaction occurred during the Chiang Rai Earthquake in 2014.
- 2) Finding the most appropriate method to assess liquefaction potential in Thailand for the future.

THE 2014 CHIANG RAI EARTHQUAKE

As previously described in the introduction, Chiang Rai is a province located at the most northern point of Thailand. To the north are Myanmar and Laos where strong earthquakes

occurred frequently. Within the area of Chiang Rai Province, there are four groups of active faults almost all over the area. Mae Chan - Chiang Saen Fault is the one that most people are concerned about because there was a tale that very strong earthquakes occurred at night causing an ancient city of Yonok to become submerged underground (possibly by liquefaction phenomena). There is an evidence of a large lake in Chiang Saen District supporting that this tale was possibly true.



Figure 1 the location of Chiang Rai Province.
(<https://th.wikipedia.org>)

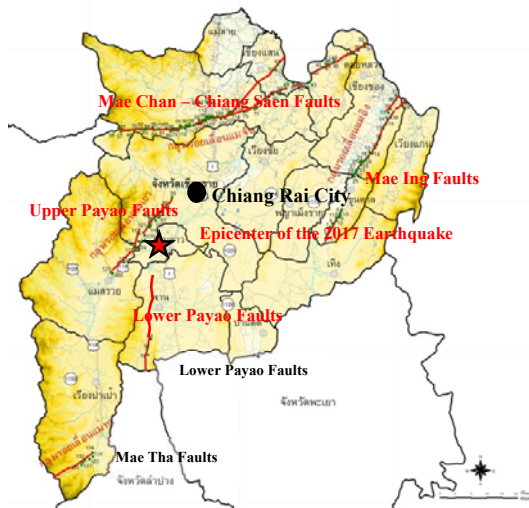


Figure 2 Chiang Rai Province and active faults.
(modified from www.dmr.go.th)

As seen in the figure, there are four active faults lying all over the area. Therefore, preparing for earthquake in the future is necessary. Preparation activities should include liquefaction study.

THE STUDY PROGRAM

The study of earthquake-induced liquefaction has just been around 50-60 years. However, it is widely known that there are three major factors affecting the phenomenon: soil type of sand, saturation of the sand layer, and strong vibration. It was interesting to see the combination of these three factors at liquefaction sites.

To obtain the answer and conclusion for the objectives indicated above, a program of study was designed that a study should be conducted at a liquefaction site. The study should include three main activities.

- 1) Site visit for investigating evidences of liquefaction and the environment suitable for liquefaction to occur,
- 2) Subsoil investigation by standard penetration test (SPT) to obtained the soil type and density; and
- 3) verifying liquefaction potential assessment methods.

SELECTED SITE: TUNG-FAH-PAH VILLAGE

Tung-Fah-Pah Village is located approximately 25 km southwest of the epicenter of the 2014 Chiang Rai Earthquake as shown in Figure 3. Most liquefaction sites caused by this earthquake were within 15 km around the epicenter.

The reason for selecting this village as the case study site was **that** this is the farthest site of liquefaction caused by this earthquake. Most liquefaction sites were within 15 km from the

epicenter.



Figure 3 Location of Tung-Fah-Pah Village and the epicenter of the 2014 Chiang Rai Earthquake.
(modified from www.google.com)

Evidences of Soil Liquefaction

There were plenty of evidences indicating that liquefaction occurred here in the village as shown in the following figures.



Figure 4 (a) Ground cracking occurred all over the village (this picture was taken at the primary school of the village,) (b) Pure sand appeared at the bottom of the cracks.



Figure 5 Fine sand ejected through ground cracks.

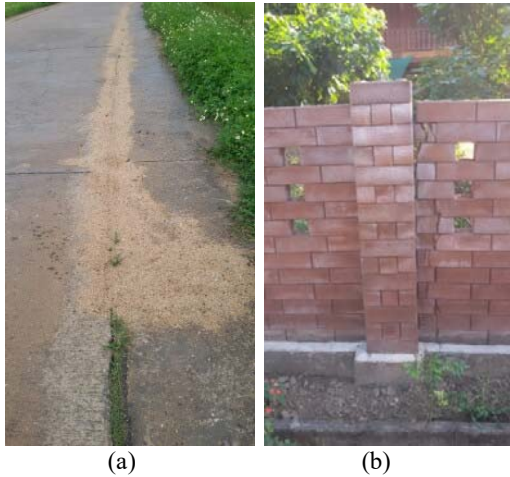


Figure 6 (a) Sand ejected through the joints of concrete pavement, (b) Separation of a wall made from interlocking bricks due to ground settlement.



Figure 7 Liquefied sand was ejected from the bed of this pond like a fountain of about 3-meter high (from interviewing an eye-witness.)



Figure 8 Sand injected into wells of several houses replacing the groundwater.

STANDARD PENETRATION TEST

After the first site visit, standard penetration test (SPT) was conducted at four locations in the village. Boreholes marked as BH-2, BH-3, and BH-5

located within 3 meters from the wells filled with the injected sand. Borehole BH-4 was at the primary school front yard (see Figure 12 for their locations). Figure 9 demonstrates SPT *N*-values, and Figure 10 shows the grain size distributions of the soil sample taken from the boreholes.

All 4 SPT boreholes yield very identical soil layers. The top layer was cohesive soil from the ground surface down to the depth of approximately 1.2 m, the gravel layer was from approximately 6-7 m downward, between top cohesive soil layer and the gravel layer was a layer of loose to medium sand which was expected to undergo liquefaction. (The liquefaction analysis will be shown later.)

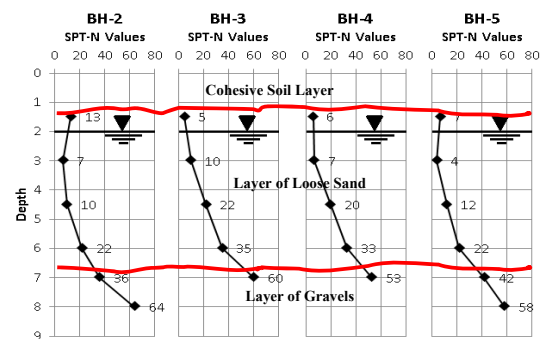


Figure 9 SPT *N*-values from all 4 boreholes.

An interesting finding obtained from the SPT investigation was the sand taken from the liquefied layer has “gap-graded” distribution as shown in Figure 10. However, when look at Figure 11 which shows the grain size distribution of the fine sand found on the ground (Figure 4) and in those wells (Figure 8) it shows that these injected sand particles may be those missing from the curves shown in Figure 10. This means sand particles of a certain size were ejected from the liquefied loose sand layer.

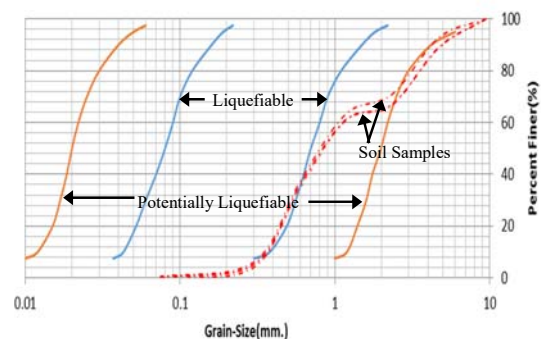


Figure 10 Grain size distribution of the sand samples taken from boreholes by SPT sampler.

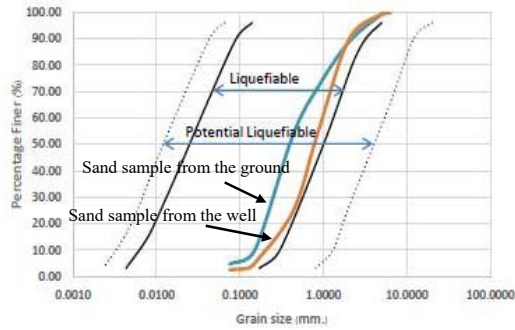


Figure 11 Grain size distribution of the sand found on the ground in Figure 4 and found in the well in Figure 8.

SITE ANALYSIS

There is another issue that should be addressed in this study. It was very interesting to find out why this site liquefied easily while other villages nearby and within closer distances did not have any

significant sign of liquefaction. This issue can be easily explained by 1) an aerial photo of the village's landscape as shown in Figure 12. The village was situated in the area with traces of abandoned rivers which can be liquefied easily [2], especially a group of houses was in the area of a so called "the island" which indicates that it was surrounded by water, 2) the sand layer should be saturated when earthquake struck because the groundwater at the time of the earthquake was at only 1.0-1.2 m below the ground surface and the area around the village wall filled with water as the farmer grew their off-season rice farm, 3) the distance of approximately 25 km from the epicenter was not surprise because this conforms to Figure 13 showing the earthquake of 6.3 Richter's magnitude can cause liquefaction at sites farther than 25 km, and 4) at this distance the peak ground acceleration was still high enough assuming this earthquake conformed to the relationship shown in Figure 14.



Figure 12 Aerial view of Tung-Fah-Pah Village. (modified from www.google.com)

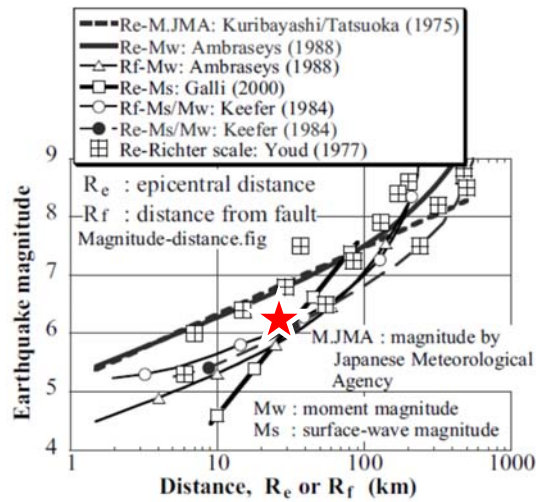


Figure 13 Maximum distance from epicenters to liquefaction sites. [3]

LIQUEFACTION POTENTIAL EVALUATION

Due to the availability of SPT test the following methods of liquefaction potential evaluation were studied.

1. Method proposed by NCEER 1996 [4]. This method was modified from the original Seed and Idriss' method first proposed in 1971.
2. Method proposed by Boulanger and Idriss in 2014 [5]. This method has been modified from the prior with some correcting factors.
3. Method proposed by Iwasaki in 1990 [6]. This one was the most commonly used in Japan as it appears in the Japanese Highway Bridge Code. The method relies heavily on D_{50} of the subsoil particles which can be obtained from grain size distribution curves.
4. Method proposed by Iwasaki in 1996 which has been revised from the 1990 version by adding the effect of SPT N -value [6].

Those four methods are similar in the stress-based approach but the major differences between them are criteria, equations, correcting factors and some input data. Details of those four methods can be found in the indicated references.

Another important factor was the ground acceleration at the site. For this study, there was no ground acceleration record available. Therefore, the relationship between peak acceleration versus epicenter distance as shown in Figure 14 should be helpful. From the distance of about 25 km, ground acceleration of 0.15g, 0.20g, and 0.25g were used in the calculation.

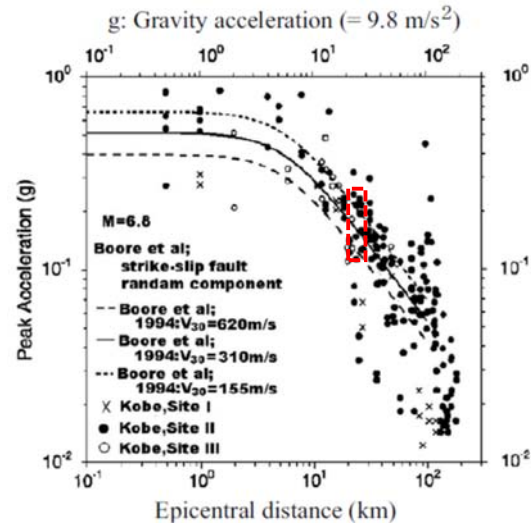


Figure 14 Relationship between peak ground acceleration versus distance from earthquake epicenter. [7]

Result

Figure 15, 16, 17 and 18 show values of the factor of safety against liquefaction of soil layers at BH-2, BH-3, BH-4 and BH-5, respectively. Following are the analysis of the results.

- 1) Those four methods are reasonably reliable since all of them indicated liquefaction had occurred. In these figures, some factor of safety numbers shown here are slightly more than 1.0 because they were calculated by using post-liquefaction SPT surveying.
- 2) Those three methods other than Iwasaki version 1990 yielded very close factor of safety values except when the SPT N -values reached 20 (see Figure 16 and 17 at the elevation below -3.5 m along with SPT N -values in Figure 9).

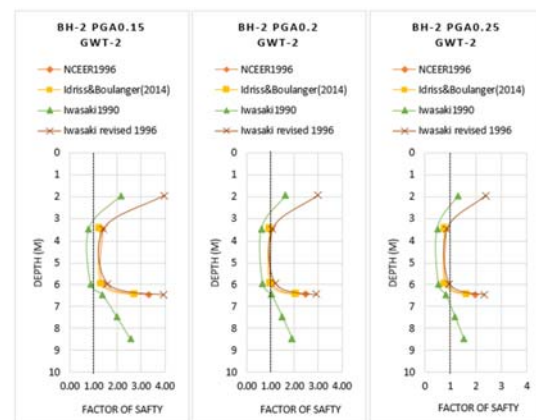


Figure 15 Factor of safety against liquefaction, BH-2

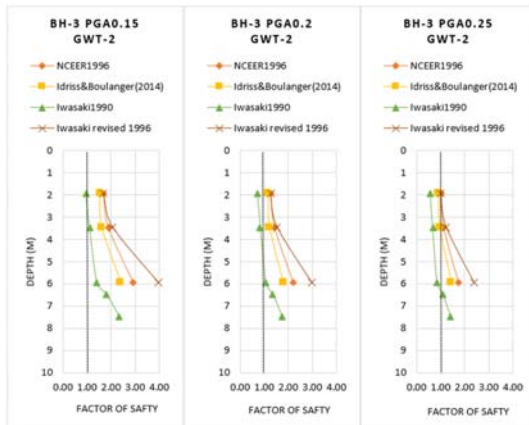


Figure 16 Factor of safety against liquefaction, BH-3

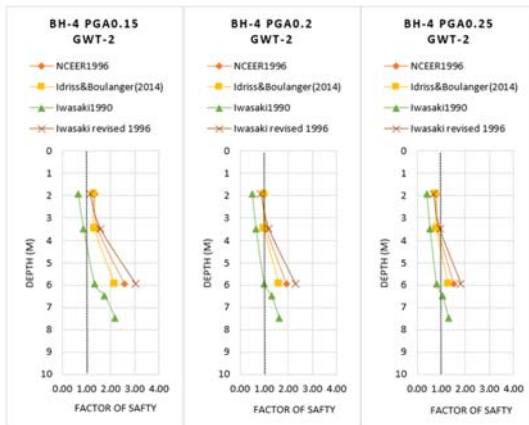


Figure 17 Factor of safety against liquefaction, BH-4

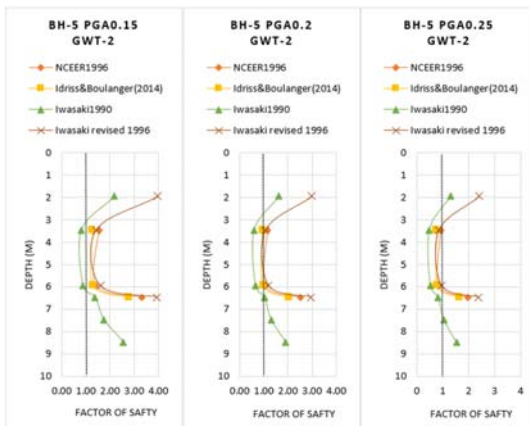


Figure 18 Factor of safety against liquefaction, BH-5

CONCLUSION

Two main conclusions can be made from this study.

- 1) The site of Tung-Fah-Pah Village was perfect for liquefaction. The village was

situated on the area of abandoned rivers with loose sand layer at a shallow depth of 1.2 m. The soil was saturated because the rice field was filled with water and it rained a lot before the earthquake.

- 2) Among those four, Iwasaki's method version 1990 was the most conservative while the 2014 Boulanger and Idriss' method may be more reasonable.

ACKNOWLEDGEMENTS

The authors would like to express the appreciation to Chiang Mai University and the Government Office at Chiang Rai for the research funding.

REFERENCES

- [1] Thai Meteorological Department, "Report on the 2014 Chiang Rai Earthquake" (in Thai), available at <http://www.earthquake.tmd.go.th>.
- [2] Wakamatsu, K., "Evaluation of Liquefaction Susceptibility Based on Detailed Geomorphological Classification". Proc., Technical Papers of Annual Meeting, Architectural Institute of Japan, B, 1992, pp.1443-1444.
- [3] Towhata, I., Geotechnical Earthquake Engineering, Verlag Berlin Heidenburg: Springer, 2008.
- [4] Youd, T. L., & Idriss, I. M., " Liquefaction Resistance of Soils: summary report from the 1996 NCEER and 1998 NCEER/NSF Workshops on Evaluation of Liquefaction Resistance of soils. Geotechnical and Geoenvironmental Engineering, 2001, 127(4), 297-313.
- [5] Boulanger, R. W., and Idriss, I. M., CPT AND SPT Based Liquefaction Triggering Procedure, Davis: University of California, 2014.
- [6] Technical Committee for Earthquake Geotechnical Engineering, T., ISSMGE. "Manual for Zonation on Seismic Geotechnical Hazards" (Revised Version): The Japanese Geotechnical Society, 1999.
- [7] Joyner, W.B., and Boore, D.M., Recent "Developments in Strong-motion Attenuation Relationships", UJNR 28th Joint Meeting of United States-Japan Panel on Wind and Seismic Effects, NIST SP904, Gaithersburg, 1996, pp.101-115.

PRESENCE STATE OF TRACE ELEMENTS IN THE OHTAKIGAWA RIVER WATERSHED FROM THE FOOT OF Mt. ONTAKE

*Akiko Usami¹, Megumi Nobori², Akihiko Yagi¹, Eiji Iwatsuki¹

¹Faculty of Engineering Aichi Institute of Technology (AIT), JAPAN,

²Mie Prefectural Center of Constructional Technology, JAPAN

ABSTRACT

This paper is aimed at understanding the influence of Mt. Ontake volcanic activity on the water quality of the Ohtakigawa River watershed. For this purpose, various properties of trace elements are investigated. The Ohtakigawa, which flows along the southern foot of Mt. Ontake, has several tributaries such as Nigorigawa River, Shirakawa River, Shimokurosawa River, and Uguigawa River. Seven sampling stations were selected in the four tributaries (four points) and the Ohtakigawa (three points). Filtration of samples was carried out with teflon filter paper (PTFE, 0.5 μ m, ϕ 47mm), and the samples were separated into dissolved and suspended matters. Trace elements contained in them were analyzed by using the ICPE. The concentrations of the trace elements were high in the following order: the Nigorigawa (6.16mg L⁻¹), the Ohtakigawa after the confluence of the Nigorigawa (1.92mg L⁻¹ and 0.88mg L⁻¹), and the others (0.06-0.70mg L⁻¹). This result indicates that among the four tributaries, the Nigorigawa plays a predominant role for the change in the water quality of the Ohtakigawa.

Keywords: trace elements, Mt. Ontake, volcanic activity, Ontake Landslide, Ohtakigawa River watershed

INTRODUCTION

Mt. Ontake (altitude 3,076m) is located across Nagano Prefecture and Gifu Prefecture. Mt. Ontake often has shown large volcanic activities since the prehistoric age. Recently the Western Nagano Prefecture earthquake (M6.8) occurred on September 14, 1984, and the volcano erupted on September 27, 2014.

Volcanic activities affect surrounding rivers

and change their water quality and biota. The Ohtakigawa River flows on the southern side of Mt. Ontake and is strongly influenced by volcanic eruptions. The river has many tributaries (Fig. 1). The Nigorigawa River, which is one of the tributaries of the Ohtakigawa, remarkably differs in pH, electric conductivity, and biota from other tributaries [1], [2]. The water quality of the Ohtakigawa changes at the junction with the Nigorigawa [3], [4].

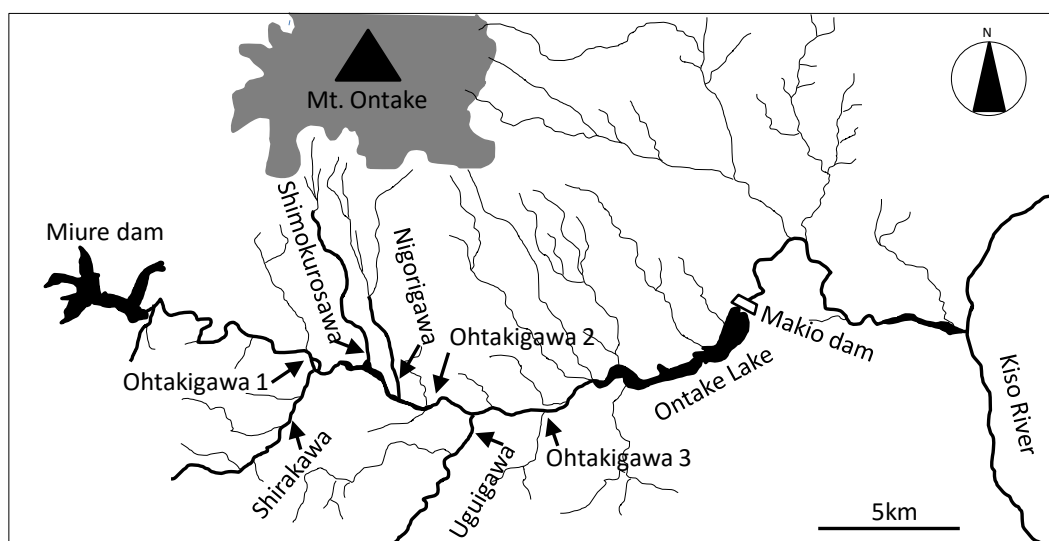


Fig. 1 Map of the locations of sampling stations in the Ohtakigawa watershed.

It is one of the most important topics to provide useful information to recover the river environment damaged owing to the influence of the volcanic eruption. In this paper, we investigate trace elements in water of the Ohtakigawa and tributaries of the Ohtakigawa to clarify the formation process of water quality of the Ohtakigawa.

METHODS

Study site

Figure 1 shows a map of sampling stations. We select seven stations as the sampling stations. They consist of four stations for the tributaries of the Ohtakigawa (the Shirakawa, Shimokurosawa, Nigorigawa, and Uguigawa) and three stations for the Ohtakigawa. We call the three stations in the Ohtakigawa as the Ohtakigawa 1, Ohtakigawa 2, and Ohtakigawa 3 stations, respectively. The Ohtakigawa 1 station is located before the joining of the Shirakawa, the Ohtakigawa 2 station is located after the junction with the Nigorigawa, and the Ohtakigawa 3 station is located after the confluence of the Uguigawa.

Observations were conducted three times on October 10 in 2015, September 17, and October 29 in 2016.

Sampling and analysis

Dissolved oxygen (DO)

DO was measured by a DO meter (input electrode type, fluorescence method, HACL Inc., turned electrode type).

Trace elements

Samples were filtered. Filtration was carried out with teflon filter paper (PTFE, 0.5 μ m, ϕ 47mm), and the samples were separated into dissolved and suspended matters.

The filtrate samples were added to aqua regia (HNO₃:HCl=1:3), and the suspended particle matter on the teflon filter was decomposed in aqua regia. Trace elements contained in them are analyzed and nine element species: Na, Mg, Al, Si, S, K, Ca, Mn, and Fe are measured by using the ICPE.

RESULTS

Figure 2 shows the concentrations of the nine element species. They have the similar tendency that the concentrations are high in the following order: at the Nigorigawa, at the Ohtakigawa 2, at the Ohtakigawa 3, and at the other stations. For

example, the concentration of Al is 0.70mg L⁻¹ at the Ohtakigawa 1 station, 1.92mg L⁻¹ at the Ohtakigawa 2 station, 0.88mg L⁻¹ at the Ohtakigawa 3 station. In the tributaries, it is 6.16mg L⁻¹ at the Nigorigawa station and 0.06-0.10mg L⁻¹ at the stations of the other tributaries.

In addition, the concentration of S, which has the influence on the change in pH, is observed. The S concentration is 4 μ g L⁻¹ at the Ohtakigawa 1 station, 30 μ g L⁻¹ at the Ohtakigawa 2 station, 20 μ g L⁻¹ at the Ohtakigawa 3 station, 83 μ g L⁻¹ at the Nigorigawa station, and 0-1 μ g L⁻¹ at the other stations, and it is observed that pH is low (5.4-6.0) at the Nigorigawa, the Ohtakigawa 2, and the Ohtakigawa 3 stations and is high (6.4-6.8) at the other stations. Therefore, it is confirmed that sulfuric acid causes the lowering in pH in the Nigorigawa and in the Ohtakigawa after the confluence of the Nigorigawa.

Next, the component compositions at the seven stations are investigated. Figure 3 shows the rates of the trace elements at the sampling stations. At the Ohtakigawa 1, the Shirakawa, the Shimokurosawa, and the Uguigawa stations, Si (37-47%), Ca (18-26%), and Na (11-23%) are the main components. As minor components, Al, Fe, and Mn account for 1-5%, 5-15%, and 0-1%, respectively. At the Nigorigawa, the Ohtakigawa 2, and the Ohtakigawa 3 stations, the rate of Si (16-25%) decreases compared with that at the above four stations. However the rates of Ca (17-22%) and Na (17-18%) show hardly change. By contrast, the rates of Al, Fe, and Mn increase to 3-5%, 22-31%, and 6-7%, respectively.

It is on the confluence point with Nigorigawa that the rates of Al, Fe, and Mn drastically increase. Therefore, it has been clarified that the water quality in the Ohtakigawa is affected dominantly by the Nigorigawa newly from analyzing the component compositions.

Finally, the maintenance process of dissolved matters is explained. In many circumstances, Al, Fe, and Mn exist as suspended matters, since they have a low redox potential. In this investigation, however, at the three stations which show high concentrations in Fig. 2, namely, at the Nigorigawa, the Ohtakigawa 2, and the Ohtakigawa 3 stations, Al, Fe, and Mn are detected mainly as dissolved matters. The dissolved oxygen level is 90-92%, quite high, thus clearly the water of the three stations is not under the reduction state. In contrast, pH indicates low values (5.4-6.0) at the three stations. Thereby it is found that the dissolved matters are maintained by the acidic environment.

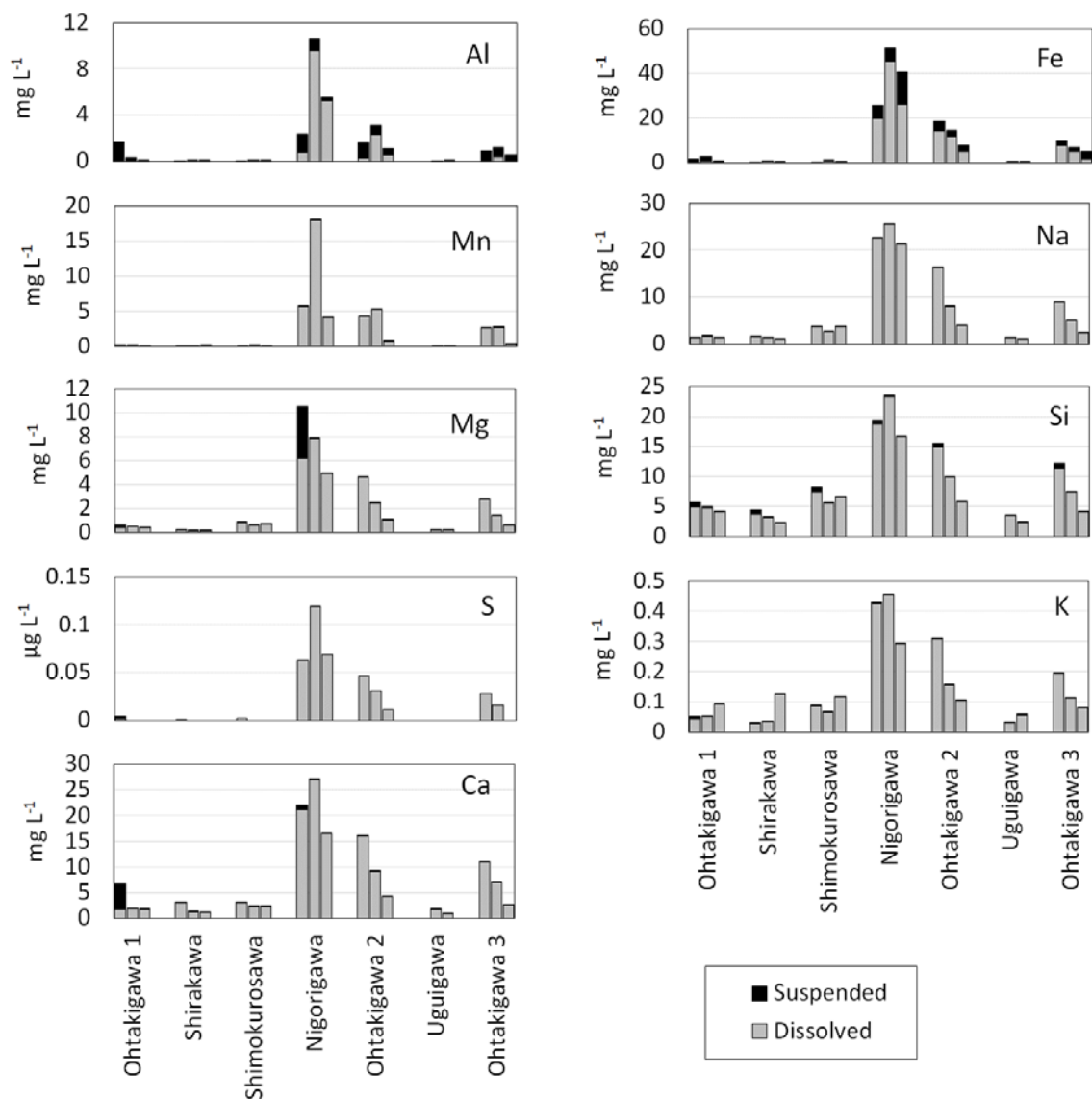


Fig. 2 Concentrations of suspended and dissolved trace elements at the sampling stations.

CONCLUSIONS AND DISCUSSION

In this work, it has been found that the Nigorigawa and the Ohtakigawa after the junction of the Nigorigawa have the anomalous water quality that the water is acidified, and the concentrations of Al, Fe, and Mn as dissolved matters are high. Consequently, it has been confirmed that the water quality in the Ohtakigawa is significantly affected by the Nigorigawa.

Now it is discussed that how the anomalous water quality is formed in the Nigorigawa. There are enormous sediment of erupted materials in the Nigorigawa basin [5], and large amounts of Al and

Fe are contained in the erupted materials [6]. Asami et al. reported that owing to the erupted materials injected into the river, pH was decreased to 2.5 [4]. This implies that the anomalous water quality in the Nigorigawa has been formed by the erupted materials.

Until now, only the dissolved matters of trace elements have been focused on. However, investigation on the precipitation of the trace elements is also an important issue, if the influence of the erupted materials on biota is discussed in the future. Trace elements are precipitated as pH recovers to the neutral state. Now it is predicted that the precipitation of the trace elements already has been accumulated in the Nigorigawa and

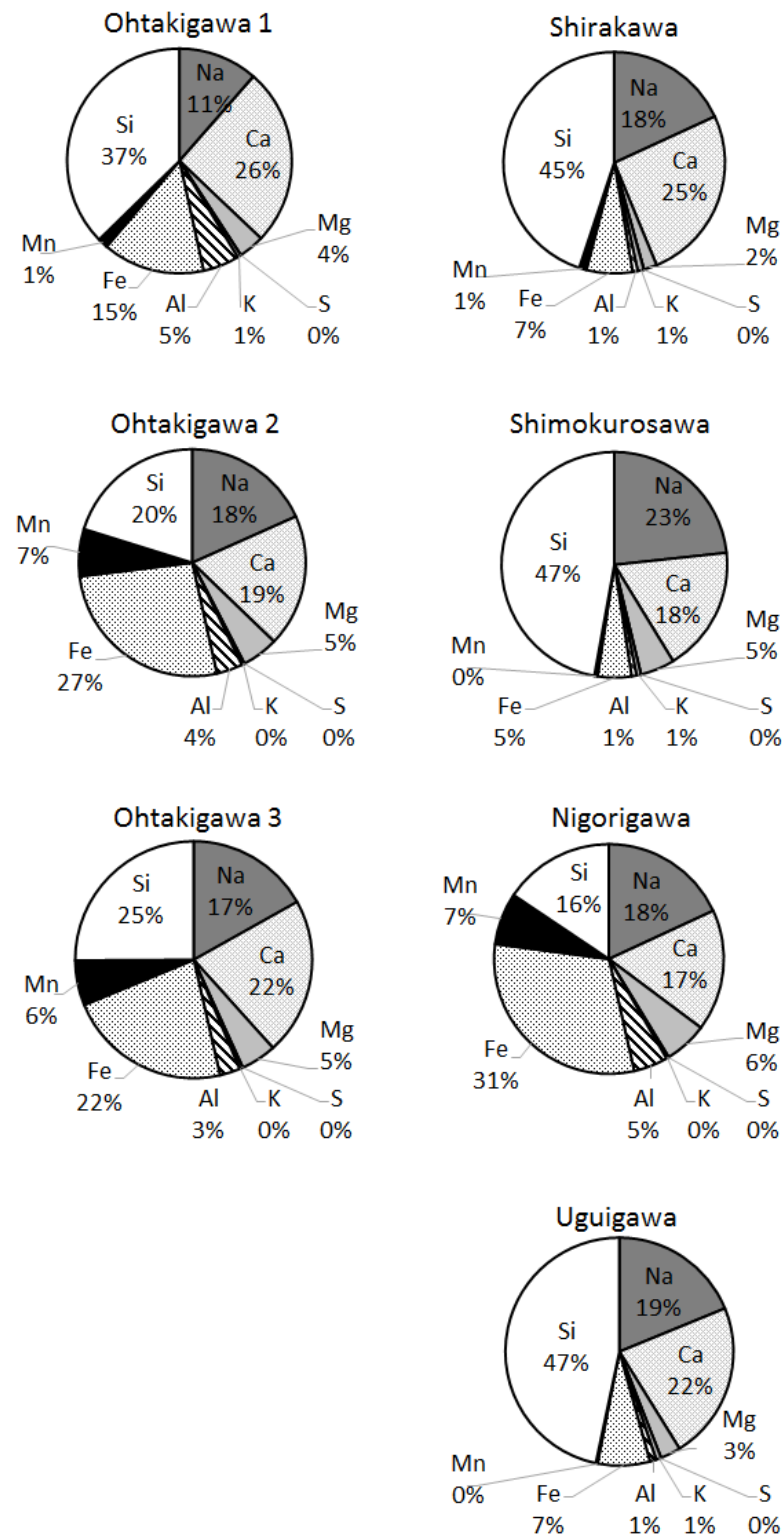


Fig. 3 Rates of trace elements at the sampling stations.

Ohtakigawa. This prediction is based on the following two facts. The one is that pH in the Nigorigawa varies seasonally, as reported by Asami

et al. [4], and the other is that the acid water in the Nigorigawa is clearly diluted by joining to the Ohtakigawa. It would be one of the most important

research topics to investigate in what way the precipitation of the trace elements affects attached organism and organism feeding on it.

ACKNOWLEDGEMENTS

The authors thank Takashi TASHIRO of Nagoya University, Tomomasa TANIGUTHI of Mie University, Kentaro NOZAKI of Sugiyama Jogakuen University, Yoshitaka MATHUMOTO of National Institute of Technology, Toyota College, and Yukio ONODA of the Aqua Restoration Research Center for cooperation in the field survey and valuable suggestions. They thank students of Aichi Institute of Technology for their helping in this work. The analysis in this work is performed on “ICPE-9000” (SIMADZU) which supported by 2012 Ministry of Education Private University Research Facilities Maintenance costs subsidies.

REFERENCES

- [1] Nozaki K. “Autumn and winter periphyton biomass in the Ohtakigawa River watershed 1 year after the 2014 eruption of Mount Ontake, central Japan”, *Rikunomizu (Limnology in Tokai Region of Japan)*, Vol.74, 2016, pp. 13-21.
- [2] Onoda Y. and Kayaba Y. “Comparison of fish fauna in a river that received pyroclastic flow from the volcanic eruption of Mt. Ontake in 2014 with that in neighboring rivers”, *Rikunomizu (Limnology in Tokai Region of Japan)*, Vol.74, 2016, pp. 23-28.
- [3] Taniguchi T. “Special feature: Effects of the 2014 Mount Ontake eruption on inland waters”, *Rikunomizu (Limnology in Tokai Region of Japan)*, Vol.74, 2016, pp. 1-3 (in Japanese).
- [4] Asami K. et al. “A study on the water environment of around Mt. Ontake after eruption (140927) (5)”, *Book of abstracts in The Study Meeting of the Association of Japanese Geographers Spring 2017*, pp. 100107 (in Japanese).
- [5] Kusano S. et al. “H26 Ontakesan hunka ni tomonau nigorigawa ni okeru dosha idou jittai”, *JSECE (Japan Society of Erosion Control Engineering) Publication No. 81*, 2017, pp. B-412-B-413.
- [6] Yamada N. and Kobayashi T. “Geology of the Ontakesan district. With Geological Sheet Map at 1: 50,000”, *Geological Survey of Japan*, 136p., 1988, pp. 122-127 (in Japanese).

ASSESSMENT ON THE AEROSOLS VARIATION DURING THE INTENSE HAZE EVENT OF JUNE 2013 OVER MALAYSIA BY UTILIZING THE SATELLITE REMOTE SENSING AND GROUND-BASED MEASUREMENT.

Nur Atiqah Aainaa Abd Latiff¹, and Takashi Machimura²

^{1,2} Division of Sustainable Energy and Environmental Engineering,
Graduate school of Engineering, Osaka University

ABSTRACT

The rapidly occurrence of forest fires in Southeast Asia and associated biomass burning, has contributed obviously to the problem of trans-boundary haze and the dispersion of pollutants in the region. Atmospheric pollutants, such as particulate matter in the atmosphere, have received extensive attention, mainly because of their adverse effect on people's health. In 2013, Malaysia experienced an intense haze episodes with high concentration of aerosols were recorded and degrading the local air quality and reduce the visibility. This paper aim is to analyze the spatio-temporal variation of aerosols concentration during intense haze event in 2013 over Malaysia by using remote sensing data and ground-based measurement. The air quality data across Malaysia was assessed based on PM₁₀ concentration which provided by Malaysia Department of Environment (MDOE) and the spatial view of aerosols optical depth (AOD) data from satellites (Terra Moderate-resolution Imaging Spectroradiometer (MODIS)). The environmental parameters including temperature, rainfall, and wind speed were obtained from NOAA's National Climatic Data Center (NCDC) while an additional information about the occurrence of active fires in surrounding region were retrieved from MODIS Active Fire Data was retrieved from NASA/LANCE – FIRMS. In June 2013, the PM₁₀ value were recorded high in few stations over the Peninsular Malaysia with the highest PM₁₀ was recorded in the Bukit Rambai Station from 21st until 23rd of June with more than 400 µg/m³. Low wind speed and low mixing depth, together with the absence of rainfall persisted during this hazy condition. The PM₁₀ were began cleared with the increase of wind speed starting 26th of June with the rainfall also contributed to disperse the haze from the atmosphere. The sources and destination of aerosols are identified via the HYSPLIT trajectory model, revealing that aerosols during June 2013 are mainly originated from the west and southwest area (Sumatera, Indonesia).

Keywords: Haze, Air quality, Remote sensing, Aerosols, Malaysia

INTRODUCTION

Haze situation is generally defined as the existence of fine particles with 0.1–1.0 µm in diameter range dispersed in highly concentrated portion at the atmosphere which reducing the horizontal visibility, giving the atmosphere a characteristic opalescent appearance [1][2]. This particles which are of respirable sizes, are of concern because of their negative effect on health, as well as their other environmental impacts [3][4][5][6].

In Malaysia, haze phenomenon have been plaguing almost every year since 1980's. The recent haze event was in 2013 which severely weakened regional horizontal visibility as thick smoke blanketed Peninsular Malaysia and Singapore. Extensive biomass burning from the land and forest clearing process in some places in neighboring country had resulting in trans-boundary haze which degrading the air quality in Peninsular Malaysia [3][7][8][9][10]. Therefore, this study aimed to provide a spatio-temporal assessment on aerosols concentration during intense haze event in 2013 over Malaysia by using remote sensing data and ground-

based measurement. Particularly emphasize on PM₁₀ as the aerosols and pollutant indicator. Other metrological parameters such as, surface wind speed and direction, rainfall amount, hotspot, temperature and visibility were also analyzed. Meanwhile, HYSPLIT backward trajectories were assessed to tack the pollutant transport during haze episode in 2013.

DATA AND METEOROLOGICAL DATA

Air Quality and Meteorological Data

Daily PM₁₀ concentration for 2013 were acquired from Malaysian Department of Environment (MDOE). Meanwhile, the metrological parameters such as rainfall amount, temperature, wind speed, and visibility were gathered from NOAA's National Climatic Data Center (NCDC). Thirteen monitoring stations were considered in this analysis of the aerosol properties located all over Peninsular Malaysia and East Malaysia (Fig. 1). The station locations represent highly urbanised or industrialised areas (Kuching and Sultan Abdul Aziz International Airport (SAAIA)),

moderately urbanised/industrialised areas (Kota Kinabalu, Setiawan, Bukit Rambai), high traffic areas (Johor Bahru), coastal areas (Sultan Ismail Petra Airport (SIP), Kuantan, Tawau, Sandakan, Labuan) and a rural/unurbanised site (Sibu, Limbang). Daily mean composites of wind vector were computed over the Southeast Asia region. In this region, it strategically depicts the tropospheric flow patterns where; it covers Malaysia and other neighboring countries. The maps were constructed from NCEP/NCAR Reanalysis Product developed by NOAA-ESRL9



Fig. 1 Map of the 13 monitoring stations over Malaysia which the air quality and meteorological data were obtained.

Active Fire and Hotspot Data

In order to do the analysis on the occurrence of active fires in Sumatra, the active fire and hotspot data were used and obtained from the Moderate Resolution Imaging Spectroradiometer (MODIS) from the Terra and Aqua satellite. MODIS Active Fire Data acquired from the NASA/LANCE – FIRMS website to monitor the distribution of hotspots within the Sumatera area. A polygon area was outlined which includes Riau ($0^{\circ} 32' N$, $101^{\circ} 27' E$) and Jambi ($1^{\circ} 35' S$, $103^{\circ} 36' E$) province in Sumatra. Only hotspot counts with confidence level higher than 30% were included in this study.

Aerosol Optical depth (AOD)

Aerosol Optical Depth (AOD) from Terra satellite on Moderate-resolution Imaging Spectroradiometer (MODIS AOD) was used in this study to analyse the spatial distribution of aerosols during the haze episode in 2013 over Malaysia. In general, the MODIS aerosol data are retrieved twice daily; in the morning from MODIS on Terra platform and in the afternoon (on Aqua platform) at 10×10 km spatial resolution [13]. Seven channels between 0.47 and $2.13 \mu m$ (calibrated and geolocated reflectance level 1B data) are used to retrieve aerosol properties [13][14]. AOD data that were used in this study was

the level 2 data and it represent the first level of MODIS aerosol retrieval. These data had been revised frequently and widely being used to retrieve AOD with high accuracy of 0.05 ± 0.2 [14][15].

RESULTS AND DISCUSSION

PM₁₀ Variation in Malaysia during the 2013 Intense Haze

Daily PM₁₀ concentration at 13 selected air quality monitoring stations and the daily average of wind speed are presented in Fig. 2, from which can be seen that the PM₁₀ peak occurred in June 2013, which started on 20th of June and keep increased until 25th of June 2013. The highest PM₁₀ was recorded in the Bukit Rambai Station from 21st until 23rd of June (PM₁₀ concentration more than $400 \mu g/m^3$). PM₁₀ concentration were also recorded high in few other stations mainly over Peninsular Malaysia which are; Bukit Rambai, Singapore, SAAIA and Setiawan. In addition, high concentration of PM₁₀ during this period indicating high level of haze and air pollution over Malaysia during the dry season in 2013. As been shown in Fig.2, the haze episode were started from the southern region and move to the north of Peninsular Malaysia. Besides that, the daily average wind speed were recorded low and initially shown a low mixing depth in the atmosphere during the hazy period in June 2013.

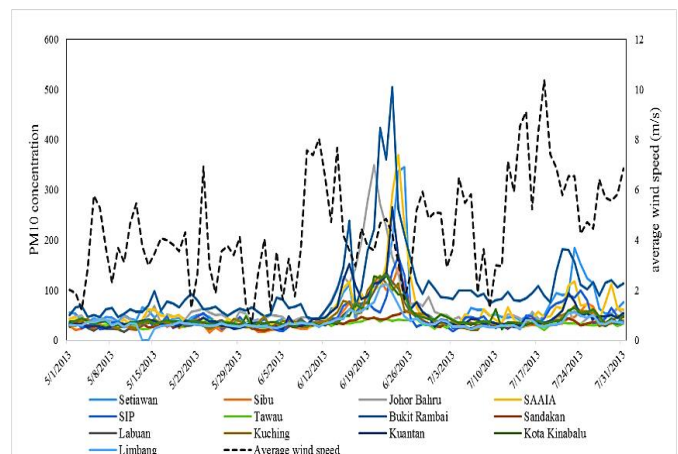


Fig. 2 Variation of PM₁₀ concentration at 13 monitoring stations over Malaysia and the daily average wind speed within three consecutive month (May until July) in 2013.

In the Fig. 3a) and 3b) illustrates the variation of daily surface wind speed and rainfall amount together with the PM₁₀ concentration for the period of May until July 2013. The wind speed were relatively low for each four stations within 20th of June until 25th of June 2013, while the daily temperature were

increased up to 36.11oC with the absences of rainfall. Hence, low wind speed with lack of rainfall which introduced to low mixing depth that worsened the condition during these intense haze episodes. The persistent supply of haze particles from its sources coupled with the surface inversion associated with the dry situation, light surface winds, and the nature of the topography resulted in the haze particles being trapped in Peninsular Malaysia.

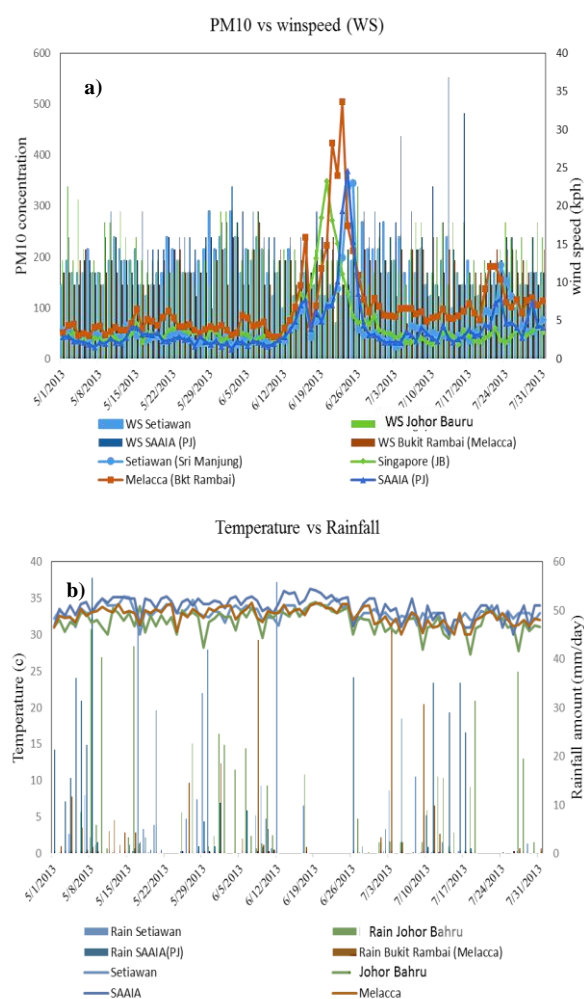


Fig. 3 The daily variations at four selected stations for a) PM₁₀ concentration and surface wind speed, and b) temperature and rainfall amount within May until July

The mixing depths and the wind speeds are relatively low, which also indicate to inefficient ventilation in the atmosphere. Thus, this condition was intensified with high temperature and less rainfall that may related with the southwest monsoon season. As shown in the Fig. 4, the wind direction maps show a weakening of the regional wind over Southeast Asia mainly at Malaysia and Indonesia area from 20th until 24th of June 2013. Generally, the southwest monsoon season flow was strengthened by a south to north pressure gradient, with northern hemisphere having a

lower surface pressure than southern hemisphere. The pressure gradient is a consequence of the temperature contrast between the northern and southern hemisphere due to seasonal variations. Moreover, during the haze period (June 2013) equatorial trade winds above the western Pacific weakened to a lesser extent. Since the effects of northeasterly trade winds were offset by the stronger southwesterly monsoonal flow, the northeasterly flow was essentially suppressed. The resulting southwesterly flow brought relatively less rainfall from the Straits of Melaka to the west coast of Peninsular Malaysia. Less rainfall in the west coast and southern part of Malaysia resulted in surging PM₁₀ concentrations at this area.

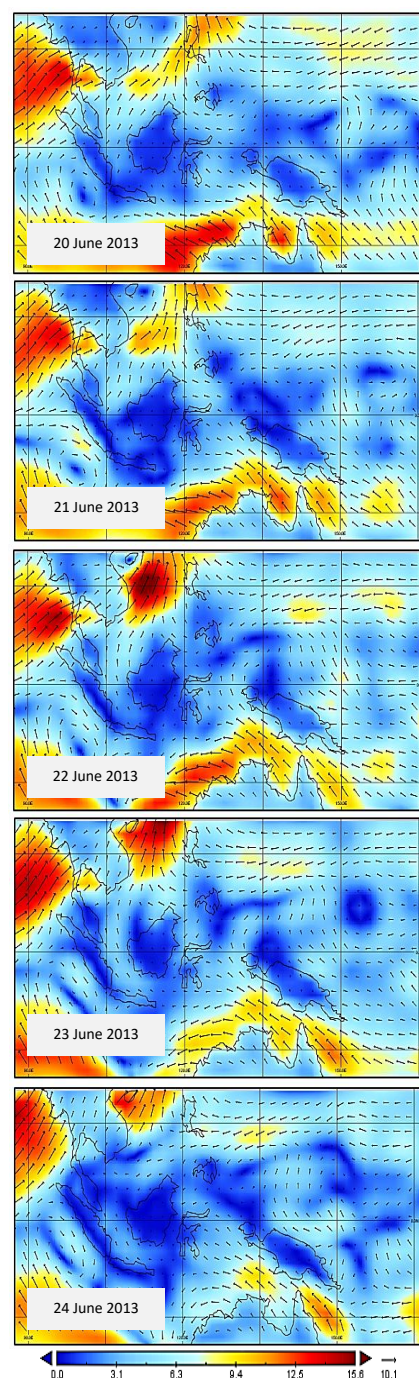


Fig. 4 Daily wind direction map at 10m over Southeast Asia region for the period of 20th until 24th of June 2013.

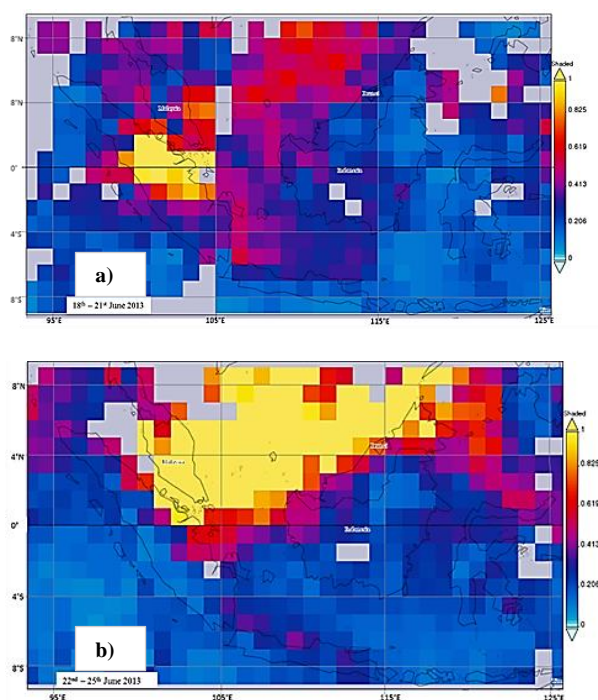


Fig. 5 The four day time average map of Terra Modis AOD during the intense haze a) 18th – 21st June 2013 and b) 22nd – 25th June 2013.

Spatial distribution of AOD during the intense haze in 2013 over Southeast Asia region were displayed in the Fig.5. The AOD distribution map were plotted based on high PM₁₀ concentration day as shown in Fig. 2. Based on Fig. 5(a), the AOD reaches maximum value particularly along the Sumatera Island. According to previous study, southwest monsoon will inducing wind circulation that blow the wind from south to north which may related to trans-boundary pollution happen during this period [2][3]. As shown in Fig. 5(b) the AOD distribution were moved towards Peninsular Malaysia and South China Sea region. This finding is justified by the result of that been presented in Fig. 6(b) the HYSPLIT trajectory model that ran during the hazy period in June 2013.

According to MODIS satellite observation the hotspot counts in Fig. 6 show a prominent peak on 19 June 2013 with more than 3000 hotspot were found over Sumatera, Indonesia on that particular date. This situation can be attributed to the existence of biomass burning activity that occurred in the Riau Province which had been reported by [1]. Therefore, biomass burning in surrounding area had indicate on the increasing of PM₁₀ concentration in Peninsular Malaysia during June 2013 [9][10][11]. As the biomass burning activities in Sumatra were detected

on 19th of June 2013, the meteorological effects were not immediately shown on Peninsular Malaysia. Long-range trans-boundary haze across the Straits of Melaka was further delayed by lower southwesterly wind speeds during the monsoon season. The HYSPLIT backward trajectories in Fig. 6, shown that the polluted substance were brought up to Peninsular Malaysia from 21st until 24th June 2013 were mainly from Sumatera within 24 hours.

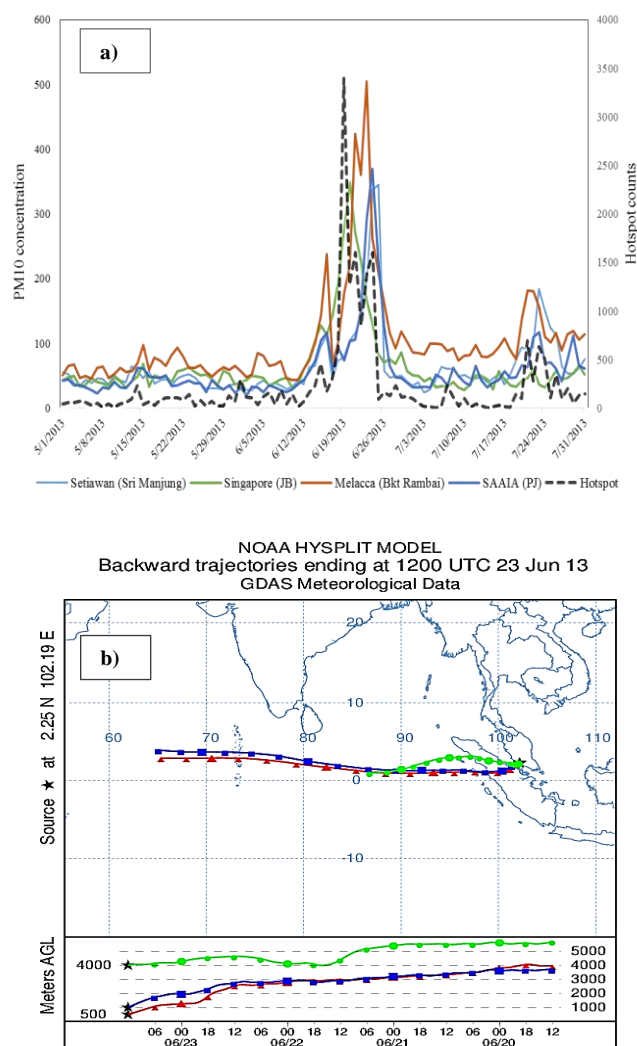


Fig. 6 a) The hotspot counts in Sumatera and PM₁₀ concentration from May until July 2013 and b) 5 days backward trajectories ending on 23rd of June 2013 which ends at the Bukit Rambai station. .

Impact of June 2013 Haze Episode on Malaysia

Visibility deprivation is a proxy measurement of polluted atmosphere. Poor visibility may cause by scattering and absorption of solar radiation of particles and gaseous pollutants [4][5][6]. The visibility in Malaysia were recorded poor during the 20th until 25th of June 2013 as it dropped until less

than 2 km compared to during non-polluted day with visibility more 10km. Thus, these hazy condition has given a huge impact toward the economy and health crisis to the surrounding community not only in Malaysia but also in Singapore and Indonesia.

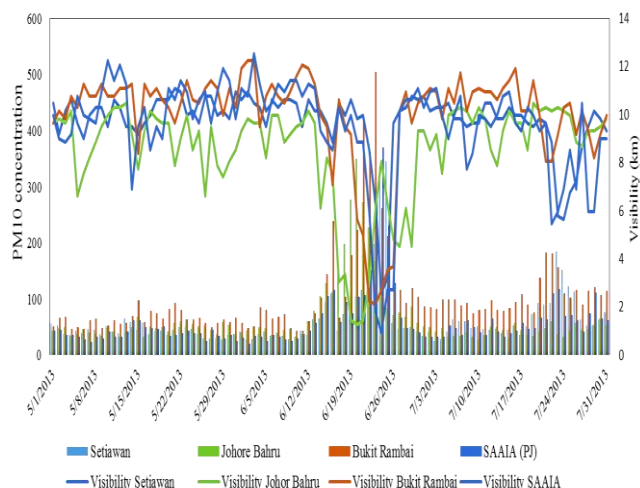


Fig. 7 Relationship of PM_{10} concentration and visibility over four stations in Peninsular Malaysia

CONCLUSION

This study had analyzed the spatio-temporal variation on PM_{10} concentration during intense haze condition in 2013 by utilizing all source of data including remote sensing data and ground-based data. In this study comprised with numerous parameters such as hotspot, rainfall amount, temperature, visibility, HYSPLIT trajectories, surface wind speed and direction via PM_{10} as the aerosols indicator. This assessment found that, during 2013 the highest peak of PM_{10} concentration started on 20th until 24th of June 2013 and were detected high at four stations over Peninsular Malaysia; Bukit Rambai, Singapore, SAAIA and Setiawan station. This condition coupled with low wind speed and less rainfall amount which relatively causing to low mixing depth and inefficient ventilation to the atmosphere. Haze episode in 2013 also occurs during the southwest monsoon season where; the wind flow southwesterlies and the pollutant substance were transported from Sumatera, Indonesia to Peninsular Malaysia. Thus, these trans-boundary haze were proved by the hotspot count in Sumatera, which were recorded high on 19th of June 2013 (more than 3000 counts). Trajectory modeling with HYSPLIT showed that smoke fire moves from Sumatera area towards the Peninsular Malaysia. A decline in air quality also affecting towards the decreasing in visibility. Hence, these situation may slow down the economy and disturb community health in the surrounding area.

ACKNOWLEDGEMENTS

We would like to thank the Malaysian Department of Environment for providing us a complete air quality data for our further study on Malaysian environment. We also gratefully acknowledge Moderate-resolution Imaging Spectroradiometer (MODIS) Terra AOD products data, NOAA's National Climatic Data Center (NCDC), MODIS Active Fire Data from NASA/LANCE – FIRMS and the HYSPLIT trajectory model that we used in this study.

REFERENCES

- [1] Malaysian Meteorological Service, "Report on air quality in Malaysia as monitored by the Malaysian Meteorological Service 1994", MMS Technical Note, No. 55, 1995.
- [2] Cheang B K, Leong C P, Ooi S H, and Tusin A M, "Haze episode October 1991", Malaysian Meteorological Service Information Paper no. 2, 1991.
- [3] Anwar A, Juneng L, Othman M R and Latif M T, "Correlation between hotspots and air quality in Pekanbaru, Riau,
- [4] Indonesia in 2006–2007", Sains Malaysiana 2010, Vol. 39, pp. 169–74.
- [5] Heil A and Goldammer J G, "Smoke-haze pollution: a review of the 1997 episode in Southeast Asia", J. of Regional Environment Change, Vol. 2, 2001, pp. 24–37.
- [6] Latha K M and Badarinath K V S, "Black carbon aerosols over tropical urban environmental case study" J. of Atmospheric Research, Vol. 69, 2003, pp. 125–33.
- [7] Han S, Bian H, Zhang Y, Wu J, Wang Y, Tie X, Li Y, Li X and Yao Q, "Effect of aerosols on visibility and radiation in spring 2009 in Tianjin", J. of China Aerosol and Air Quality Research, 2012, Vol. 12, pp. 211–217.
- [8] Jones D S, "ASEAN and transboundary in Southeast Asia", Asia Europe J. 2006, Vol. 4, pp. 431–446.
- [9] Andreae M O, Jones C D and Cox P M, "Strong present-day aerosol cooling implies a hot future", Nature, 2005, pp. 435 1187–1190.
- [10] Anderson I P and Bowen M R, "Fire zones and the threat to the wetlands of Sumatra, Indonesia forest fire prevention and control project", 2000.
- [11] Lestari R K, Watanabe M, Imada Y, Shioyama H, Field R D, Takemura T and Kimoto M, "Increasing potential of biomass burning over Sumatra, Indonesia induced by anthropogenic tropical warming", Environment Research Letter, 2014, Vol. 9, pp. 104010.

- [12] Vadrevu K P, Lasko K, Giglio L and Justice C, “Analysis of Southeast Asian pollution episode during June 2013 using satellite remote sensing datasets”, *J. of Environmental Pollution*, 2014, Vol. 195, pp. 245–56.
- [13] Kunii O, Kanagawa S, Yajima I, Hisamatsu Y, Yamamura S, Amagai T and Ismail I T “The 1997 haze disaster in Indonesia: its air quality and health effects”, *Archives of Environmental Health* 2002, Vol. 57, pp. 16–22.
- [14] Kaufman Y J, Tanre D, Remer L A, Vermote E F, Chu A, Holben B N, “Operational remote sensing of tropospheric aerosol over land from EOS moderate resolution imaging spectroradiometer”, *J. of Geophysical Research*, 1997, Vol. 102, pp. 17,051-17,067
- [15] Li X, Zhao X, Kahn R, Mishchenko M, Remer L, Lee K H, Wang M, Laszlo I, Nakajima T, Maring H, “Uncertainties in satellite remote sensing of aerosols and impact on monitoring its long term trend: a review and perspective”, *J. of Ann. Geophys.*, 2009, Vol. 27, pp. 2755-2770.
- [16] Levy R C, Remer L A, Dubovik O, “Second generation algorithm for retrieving aerosol properties over land from MODIS spectral reflectance”, *Journal of Geophysical Research*, 2007, Vol. 112

MAT FOUNDATION DESIGN REFERENCE FOR METRO MANILA, PHILIPPINES

Jonathan R. Dungca¹, Raynold Y. Pua², Raynold, Nelson Que³,
Anne Kristine M. Sangalang⁴, Ayran Nicole Tan⁵

¹²³⁴⁵Civil Engineering Department, De La Salle University – Manila, 2401 Taft Avenue, Manila, Philippines

ABSTRACT

To design mat foundations, there are certain values which are required for calculations and analyses, one of which would be the vertical modulus of subgrade reaction. It can be obtained through various deterministic tests such as the Plate Load Test. On the other hand, the study calculated this factor through the use of Standard Penetration Test (SPT) results by using four different methods. Comparative study and validation were also performed to confirm the most recommendable method to be used to compute for the soil spring constant, given the limitations of the SPT results, by correlation of this parameter to the California Bearing Ratio (CBR) test results. Through this, the study considered and used the equation formulated by Bowles to calculate for the vertical modulus of subgrade reaction. Then, a Geographic Information Systems (GIS) software was utilized to generate maps of these values by the method of ordinary kriging. These maps presented the locations with the predominantly high and low values of the soil spring constant. They were also used to create a digitized reference of the values of the vertical modulus of subgrade reaction for the design of mat foundations for preliminary design through the use of Visual Basic Applications 2010

Keywords: mat foundation, modulus of subgrade reaction, standard penetration test foundation design reference

INTRODUCTION

With the on-going modernization of the society, more technologically and competitively complex structures are being developed and constructed throughout the Metropolis. Civil engineers are faced with the constant dilemma of ensuring the safety and structural stability of any structure being designed, whether simple or complex. Before all the other safety and stability considerations, the design of foundations is the basic concern when designing any structure. Foundations are best known to be among the primary elements in any structure that provide structural stability. However, the design of any foundation would require the attainment of geotechnical parameters that necessitate extensive analysis and exploration of the soil where the structure would be built.

With a land area of approximately 619.5 square kilometers, Metro Manila covers a large portion of Luzon. Greater coverage means greater variation in the types of soils that are considered in the design of various structures. Along with the change of the soil types comes the adjustment in the foundation requirements, where despite the possibility of constructing exactly the same buildings in two different locations, the surrounding conditions will dictate what type of foundation design would be required.

Among those parameters greatly affected by changing soil conditions is the modulus of subgrade reaction, k , also known as the soil spring constant.

In the different models used to analyze soil, the soil

spring constant is used as a quantity that simplifies and generalizes its behavior. Imaginary springs are positioned continuously beneath the structure and a constant value, k , is generated [1]. The dilemma now is that the soil spring constant is not unique for specific types of soils [1] and is affected by various factors such as the depth of the foundation and dimensions of the mat foundation being considered such as its base width which will be considered as a variable in this paper. Therefore, the soil spring constant for a given type of soil cannot be generalized with a specific range unlike other parameters such as density, porosity, and the like. A soil test, specifically the Plate Load Test, can be used to determine such a geotechnical parameter; however, with the limited budget most constructions face, engineers are forced to theoretically propose or estimate conservative values for these to pursue their design.

Mat foundation is a specific type of shallow foundation that is commonly used when the loading on the ground is aimed to be spread throughout an area in consideration. Mat foundations are very useful because it controls differential settlement which causes additional moments in structures thus affecting its stability. Because mat foundations are designed to cover a large area with a slab, it helps in creating uniform settlement along the entire mat. To be able to design a mat foundation fit for a particular soil, there are specific soil parameters that should be obtained through the help of soil reports.

There have been some similar studies related to this research [2]-[8], however, there is not one dedicated to the estimation of subgrade reaction to be used for the

design of mat foundations for Metro Manila.

This study aims to generate a design reference for mat foundations through the computation of the soil spring constants of the various locations in Metro Manila through Standard Penetration Test (SPT) borehole logs.

METRO MANILA

The National Capital Region, also referred to as Metropolitan Manila, is the country's leading urban region and is considered as the centre for the Philippines' economy, politics and culture. The region is highly urbanized, providing jobs for a huge percentage of the country's population. Metro Manila is heart of the country's finance, commerce and industrial development. Within its borders lie the largest economic hub of the country, which is Makati. Other leading business districts which strive to be among the country's best districts are also within NCR, these are Eastwood in Quezon City, Bonifacio Global City in Taguig and Manila Reclamation Area in Manila. Because of this, a huge amount of structures are built to fit the economy and the lifestyle of Metro Manila. Design data concluded from soil conditions are required for majority, if not all, of the structures that are built in the region.

Metropolitan Manila is bordered by different provinces and water systems which help the region become prosperous. The provinces of Bulacan and Rizal are situated on the north and east of the region respectively. On the south-west lies the province of Cavite while on the south is Laguna. Water systems also envelop the region, these are Manila Bay on the west and Laguna de bay on the south-east.

Out of all the regions in the Philippines it is the only one that is subdivided into 17 government units, with no provinces where in 16 are cities and one is a municipality. The 16 cities include: Caloocan, Las Pinas, Malabon, Manila, Marikina, Makati, Mandaluyong, Muntinlupa, Navotas, Paranaque, Pasig, Pasay, Quezon, San Juan, Taguig and Valenzuela. Pateros is the only municipality in the region. The city sums up to a total of 63.6 square kilometres of land area with Quezon City as the largest and Navotas City as the smallest.

According to the data and maps provided by the Bureau of Mines and Geosciences, the entire region is divided into two major stratifications. These are Quaternary Alluvium and the Guadalupe formation.

The quaternary alluvium soils are consisted of deposited sediments from nearby water systems such as the Manila bay and Laguna de bay. These include detrital deposits composed of mostly silt, sand and gravel. The locations in the Metropolitan that are found on the coasts or along water systems are those that are consisted mainly of Quaternary Alluvium. These include Pasay City, Manila City, Paranaque and parts of Las Pinas on the west while there are Muntinlupa, Marikina,

Portions of Taguig and Pasig on the east.

The Guadalupe tuff formation (GF) is a series of soil classifications that is comprised of rock or tuffaceous materials distributed along Quezon City, Makati, Mandaluyong, parts of Pasig, and Rizal. It is divided into two members namely the Alat Conglomerate and the Diliman Tuff due to their differences in composition and structure. The Alat Conglomerate, the lower member of the formation, is generally composed of conglomerates, mudstones and sandstones. This member is located along the lowland hills of eastern Bulacan and southern Nueva Ecija. A predominant rock type in the GF member is conglomerate which is massive and poorly sorted with well- rounded pebbles. Cemented by coarse grained, calcareous, sandy matrix are small boulders of underlying rocks. It also contains mudstone which is medium to thin bedded with some varied characteristics of softness, stickiness, siltiness and tuffaceousness.

The Diliman tuff (the upper member) is made up of tuffs, pyroclastic breccias and tuffaceous sandstones. This member of the Guadalupe Formation consists of vitric tuffs and welded pyroclastic breccias . It also contains minor fine to medium grained tuffaceous sandstone. Some dark mafic minerals and pumice materials are spread out in the tuff matrix. The Diliman tuff stretches from Quezon city to the southern parts of Metro Manila, namely Pasig, Makati and Rizal province. [9].

METHODOLOGY

In designing foundations, geotechnical parameters can be acquired by various soil exploration methods. In the case of mat foundations, the geotechnical parameters that need to be considered are the modulus of subgrade reactions and the bearing capacity of the soil varying in a certain depth. In attaining these variables, plate load test should be performed, but due to availability and cost, the researchers utilized the Standard Penetration Test (SPT) values to derive the modulus of subgrade reactions. This value is significant because aside from that it is the basis of good foundation design, conservative assumptions of one of the factors for foundation design can also be avoided.

Borehole logs and other soil data from all the 16 cities and 1 municipality of Metro Manila were obtained. Soil data from some cities and municipalities surrounding Metro Manila including Rizal, Cavite, Laguna and Bulacan were also obtained for the proper interpolation of data. Data from soil tests such as the SPT and Borehole tests from government agencies, structural firms, and geotechnical firms were gathered by the researchers. A total of 809 borehole data were collected for the study, 776 of which are found within the Metropolitan and 33 are located on areas or provinces bordering around NCR. Factors such as the type of soil tested, undrained shear strength, and the N-values were extracted from these data. Further

computations were performed to estimate other soil parameters such as bearing capacity, settlement, and Modulus of Elasticity.

The obtained N-Values were corrected using Eq. 1, standardizing it into the N₆₀ value.

$$N_{60} = (5/3) (C_N C_E C_B C_R C_S) \quad (1)$$

where:

N₆₀ = Corrected SPT blow counts;

C_E = Energy Effect depending on hammer type;

C_B = Correction factor for borehole diameter;

C_R = Correction factor for rod length;

C_S = Correction factor for type of samplers;

C_N = Effective overburden pressure coefficient.

Certain parameters that are required for the determination of the Modulus of Subgrade Reaction are the base (width) of the lot area being considered and the flexural rigidity of the materials that will be used for the foundation. Since the base width is a value that is constantly changing and is dependent on the area to be constructed as well as the design of the structural engineer, the authors have deemed it to be a variable along with the values of the flexural rigidity. With the values of N₆₀, modulus of elasticity (Es), Poisson's ratio (v), and base as a variable, the study calculated the modulus of subgrade reactions through four methods. The first method is by using the definition of the soil spring constant which is a ratio between the applied pressure and the settlement (Se) created by such a pressure. In this study, the soil spring constant was computed through dividing the ultimate bearing capacity (Qu) by the settlement of the corresponding soil; both the bearing capacity and settlement were computed using values that were obtained from the SPT and borehole data. The second method was through a standard equation proposed by Vesic[10] which is usually used in the industry to estimate the value of the soil spring constant. This equation incorporates N-values to estimate elastic constants such as the Modulus of Elasticity of the soil and Poisson's ratio which are required by the said standardized equation.

The third method is the use of Empirical Equations provided by other researches performed by Moayed and Naeini [11] for gravely soils incorporating N60-values and Ou [12] for sandy and clayey soils incorporating N60-values and undrained shear strength (Su), respectively. The fourth, and last method, is the estimation by Bowles [13] that modifies the definition by limiting the settlements at certain values, particularly 25 mm.

From these four methods, a comparative study was conducted by comparing the outcomes of modulus of subgrade reactions from the different methods to conclude which of these is the most appropriate result. The value chosen from the different methods was mapped for the various cities and locations in Metro Manila.

As for the validation of the result, there can be different deterministic tests that could compute for the value of the Modulus of Subgrade Reaction. Plate Load Test is widely used to acquire actual values of the soil spring constant [14]. In this test, a load is applied to the plate in increments depending on the design load. Loading continuously applied until the change in settlement is significantly reduced to a specified amount. However, many researches also claim the inaccuracy of this test because of the size of the samples and the equipment being used. Other than this, there are issues regarding the availability of the equipment. According to the research of Thornton [15], another method that can be used to estimate the value of the soil spring constant is through the CBR test [16].

The CBR results used in this study were obtained from geotechnical companies that performed the actual CBR testing in various locations in Metro Manila. The collection of CBR data was geared towards the representation of different cities around the National Capital Region, wherein CBR data were collected for each city in Metro Manila. Out of the original 16 data points, only 13 data points were used in the study. This was due to the fact that the other CBR data were collected at shallow depths that are less than one (1) meter from the natural ground surface. This is not within the range of depths that are used in the study. Furthermore, there are many external factors that may affect the soil conditions at such a shallow depth and this may not provide accurate results for the modulus of subgrade reaction.

Using the equation formulated by Thornton [15] through the correlation of the CBR test results to the soil spring constants, values of the vertical modulus of subgrade reaction were computed. The results were concluded based on the nearness of the values (from the four methods) to the value obtained using the CBR test. This was done through the help of the statistical method of t-test analysis. A graph was also generated to present the differences of the values visually.

Since the aim of this paper is to provide a design reference for mat foundations, the values of spring constants calculated was plotted out onto the map of Metro Manila. To provide values for places where there are not enough available data, the Kriging method for optimal interpolation was performed so that a map of the values will be generated [17]. This is the reason why soils in places outside Metro Manila were analyzed as well, to provide reliable interpolation of the values. The said contour maps were generated for every 1m layer interval and were done with the help of a Geographic Information System software.

MAT FOUNDATION REFERENCE

With the aim of this study to generate a map by choosing the most recommendable method of obtaining the values of the modulus of subgrade reaction. To do so,

a simple comparison of the values obtained for all four methods of computations of the modulus of subgrade reaction was performed.

The first method is by definition. The soil spring constant (k) is defined as the ratio between the soil pressure(q) applied on the soil and the settlement (δ) produced by such an applied soil pressure, mathematically represented as:

$$k=q/\delta \quad (2).$$

The second method is estimation of k through standard equations. Different standard equations are readily available for the computation of the Modulus of Subgrade reaction. The same comparisons were performed by the Sadrekarimi & Akbarzad [18]. They compared the resulting values with each other and have concluded that the equation provided by Vesic [10] provided the most accurate variable. The value of the soil spring constant in this method can be computed by:

$$k = \frac{0.65E_s}{(1-\nu_s^2)} \sqrt{\frac{B^4E_s}{EI}} \quad (3);$$

where:

E_s = Modulus of Elasticity of the soil (kPa);

EI = Flexural Rigidity of Mat (kN-m²);

B = Slab width (m);

ν_s = Poisson's Ratio.

The third method Estimation of k through empirical equations. The research by Moayed & Naeini [19] uses the N -values obtained from the Standard Penetration test and correlated it with the plate load test to be able to derive an equation that represents the relationship between the standard $N_{1,60}$ value (blow counts corrected to 60% hammer energy and overburden pressure) and k . Once the value of the $N_{1,60}$ was obtained, it was statistically correlated to the results of the plate load test on the same soil sample and a relationship was determined by Eq. (4):

$$\text{For Gravelly Soil:} \\ k= 3.143 (N1)_{60}^{0.489} \quad (4).$$

The derivation of Eq. (4) only focuses on gravelly soils and the other soil types were delimited in the study performed by Moayed & Naeini [19]. Because of this, the empirical formula provided by Ou [20] would be helpful in the estimation of the values of the Modulus of Subgrade Reaction for clayey and sandy soils. These equations are as follows:

$$\text{For Clayey Soil: } k = 40 - 50 s_u \quad (5);$$

$$\text{For Sandy Soil: } k = 70 - 100 N \quad (6);$$

where:

k in (t/m³);

s_u = undrained shear strength (t/m²) and;

N = SPT N -values.

The fourth method is k through estimation of Bowles [13]. It is a variation of the estimation of the modulus of subgrade reaction by definition. The only difference is

that the author chose to limit the settlement to certain structurally acceptable values such as 25 mm, 20 mm, 12 mm and the like. The value of the modulus of subgrade reaction can be obtained through the equation shown below:

$$k = 40(SF)(q_u) \quad (7);$$

where:

SF = factor of safety;

q_u = ultimate bearing capacity.

A screening of individual values per layer was done to compare the results obtained for all four methods of calculation for the soil spring constant. This is to provide a better understanding on how the values turned out as they have and what factors may have played roles for such an outcome to occur.

With the individual analyses of the methods for the computation of the Modulus of Subgrade reaction, the method by Bowles and by definition provided the most recommendable values. Contrary to what the authors expected, the most conservative estimation of the modulus provided the value closest to the actual k values as shown in the validation through CBR testing. This may be because of the fact that both the Bowles and computation by definition are limited to existing soil specific data and required minimal assumptions. One of the methods used in this study, the computation by standard equation, required too many parameters majority of which are basic design data that are usually assumed. An example of this would be the Poisson's ratio. Perhaps this method can be best used if only a theoretical analysis of the modulus would be done. As for the empirical methods, these calculations resulted to very low values and has a high per cent difference from the site-specific k values obtained from the validation. This may be because these are obtained from correlations with the Plate load test, which as claimed by various literature is unreliable for obtaining the modulus of subgrade reaction. Because of all these reasons, the authors have mapped only the values obtained through the Method of Bowles.

Despite the lack of uniqueness among the values of the modulus of subgrade reaction, there are some general trends in the values that can be observed for each level of soil stratum. One trend is that the values of the modulus of subgrade reaction increases as the depth increases. This is due to the fact that as the depth of the analysis increases, it approaches the rock formation further. As the rock formation is reached, the soil becomes more compact and dense that it would have greater resistance to forces acted upon the soil as compared to the previous layers. This greater resistance is manifested by the increase in the values of the Modulus of subgrade reaction.

Shown in Figure 1 is the map generated by the study from the collected data for depths 1 meter from the ground surface to 4 meters. It can be seen from Figure 1 and Figure 2 that the values of the modulus of subgrade

reaction are high where the depth of the rock formation is shallow.

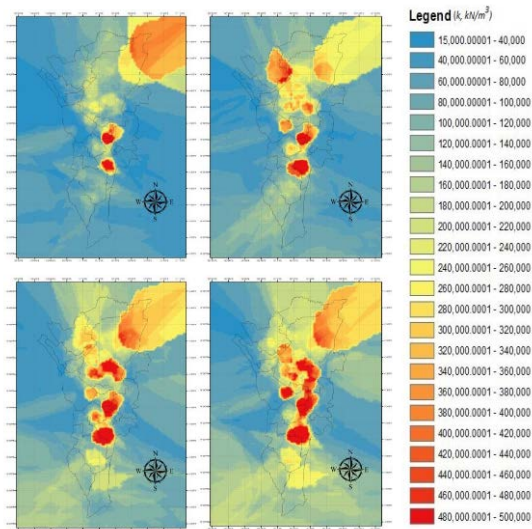
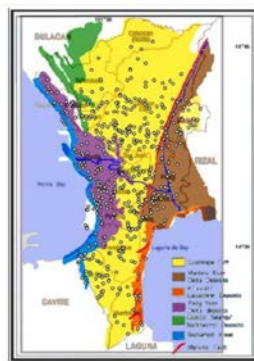


Fig. 1 Map of Metro Manila with values of modulus of subgrade reaction (all values are in kN/m^3) using Bowles [13]



- Yellow = Guadalupe Tuff;
- Brown = Marikina River Delta Deposits;
- Orange = Alluvial / Lacustrine Deposits;
- Violet = Pasig River Delta Deposits;
- Green = Coastal Swamp / Backswamp Deposits;
- Blue = Reclaimed Area; and
- Red Line = Marikina Fault / Valley Fault System

Fig. 2 Geologic Map of Metro Manila [21]

Another trend is that it is evident that the results are highly affected by the soil compositions of a particular region. Some areas, particularly where the upper layers of soil are composed of tuffaceous material, have observably higher values for the modulus of subgrade reaction compared to other areas where the rock layers are at a greater depth. The high values of the modulus of subgrade reaction are underlain by the Guadalupe Tuff and the low values are underlain by alluvial, delta deposits. It can also be observed in the comparison of the two maps (Figure 1 and Figure 2) that there is a sudden change in the values of the modulus of subgrade reaction (from dark red suddenly changed to blue) in areas that are divided by or are passed by the West Valley fault systems.

Areas where the values of the modulus are highest would be for the cities of Mandaluyong, Makati, Paranaque and Quezon City or all those cities that are away from the large basins or bodies of water and are underlain by the Guadalupe tuff formation. This is because through time, continuous deposition of soils on locations near the bodies of water have compacted the soil strata of those places found at the middle of the region. As expected also, the values of the subgrade reaction decrease as data points approach the large bodies of water particularly the Manila bay and the Laguna de bay. These cities that are nearest the bodies of water stated previously, are Manila, Pasay, Navotas and Muntinlupa. The decrease in the values of the modulus may explained by the soils found in these locations which are locations are mainly made up of silt and clay materials, or generally alluvial deposits. Furthermore, the values of the modulus of subgrade reaction increases again once the data points are moving away from large bodies of water and into mountainous areas and even the central part of the region. These trends can be seen in Figure 1 which is a sample map of the values of the modulus of subgrade reaction using the method suggested by Bowles.

CONCLUSION

The design of mat foundations considers the resistance of the soils to any force applied onto it. The study has limited the study depths from 2 to 6 meters because any deeper than this would not be recommendable for the construction of mat foundations. To assess such a resistance from the soil, the final output of the study has been to compute for the values of the modulus of subgrade reaction which are determined through borehole logs collected all over the region. These borehole logs were collected from different private testing companies, city government offices and national government offices in Metro Manila. However, certain places in Metro Manila are not yet as fully represented in this study. The cities of Caloocan, Valenzuela, Muntinlupa, and the Municipality of Pateros are among those that have data points that represent only around 60% of the total area. The calculation of the Modulus of subgrade reaction were performed through an excel program wherein soil properties, SPT N-values, and RQD were used to obtain information that would lead to the estimation of the k values.

The locations in Metro Manila that provided the low values of the Modulus of subgrade reaction are Manila, Pasay, Navotas, and Muntinlupa, which could be attributed to the type of soil layers underlain in these cities which is mainly composed of loose silty sand and clay materials. It could be because of the large bodies of water that are bordering these locations such as Manila Bay and Laguna de Bay which can be considered as a good source of sand, silt, and clay deposits in the area. It could be safe to claim that the modulus of subgrade reaction has significantly low values if the areas are

located in these cities and may not be recommendable for the use of mat foundations.

On the other hand, cities such as Mandaluyong, Paranaque, Makati, and Quezon provided significantly high values of the modulus of subgrade reaction. This may be attributed to the tuffaceous material from the Guadalupe tuff formation that is underlying these cities. Soils within the Guadalupe tuff formation are highly dense compared to other soils within Metro Manila and the rock formation is at very shallow depths. Because of these, computed settlements were small and the allowable bearing capacity is of a remarkable value making the modulus of subgrade reaction significantly high. It is for these locations where the use of mat foundations is recommendable.

REFERENCES

- [1] Daloglu, A & Vallabhan, G. (2000). Values of k for Slab on Winkler Foundation. *Journal of Geotechnical and Geoenvironmental Engineering*, 126(), pp. 462 – 471.
- [2] Dungca J. R. (1997). Liquefaction Potential Map of Manila (Masteral Thesis, De La Salle University, Philippines).
- [3] Dungca J. R. and Chua R. A. D., “Development of a Probabilistic Liquefaction Potential Map for Metro Manila”, *International Journal of GEOMATE*, Vol. 11, Issue 25, Sep. 2016, pp. 2461-2467.
- [4] Dungca J. R., Concepcion I., Limyuen M.C.M, See T. O. and Vicencio M. R., “Soil Bearing Capacity Reference for Metro Manila”, *International Journal of GEOMATE*, Vol. 12, Issue 32, Apr 2016, pp. 5-11.
- [5] Dungca J. R. and Macaraeg C. J., “Development of a Reference for Seismic Amplification: The Case of Metro Manila”, 19th Congress of International Association for Bridge and Structural Engineering, Stockholm, Sweden Sep. 2016.
- [6] Saldivar – Sali, A. (1992). An Earthquake Risk Analysis of Metro Manila from a Foundation Engineering Perspective. *Journal of the Geological Society of the Philippines*, 50, 287 – 289.
- [7] Guevarra E., Santos, J., Sy, Hazel (1999). *Data Aid for the Design of Foundation in Las Pinas City. Manila- De La Salle University Press.* Codilla, M., de Castro, A., Palanca, R. (2007). *Basic Geotechnical Characterization of Malabon and Navotas Subsoil.* Manila: DLSU Press.
- [8] Mustafa, K. (1995). *Evaluation of Soil Bearing Capacities in San Mateo, Rizal.*
- [9] Hosono, T., Siringan, F., Yamanaka, T., Umezawa, Y., Onodera, S., Nakano, T., & Taniguchi, M. (2010). Application of multi-isotope ratios to study the source and quality of urban groundwater in Metro Manila, Philippines. *Applied Geochemistry*, 25(6), 900–909.
- [10] Vesic, A.B. [1961]. “Beams on elastic subgrade and Winkler’s hypothesis”, *Proc. 5 th. Int. Conf. on Soil Mech. Found. Engrg.*, Paris, p.p. 845-50.
- [11] Moayed, R. & Janbaz, M. (2008). Foundation Size Effect on Modulus of Subgrade Reaction in Clayey Soil. *Electric Journal of Geotechnical Engineering*, 13
- [12] Ou, C.Y. & Lai, C.H. (1994). Finite-element analysis of deep excavation in layered sandy and clayey soil deposits. *Canadian Geotechnical Journal*, 31(2), pp. 204- 214
- [13] Bowles, J. E. (1987), *Elastic foundation settlements on sand deposits, Journal of Geotechnical Engineering, ASCE*, **113**, No. 8, pp. 846–860.
- [14] ASTM 1994. Test method for bearing capacity of soil for static load on spread footings, D 1194-94, Annual Book of ASTM Standards, 4.08. American Society for Testing and Materials, West Conshocken, PA.
- [15] Thornton, Sam I. *Correlation of Subgrade Reaction with CBR, Hveem Stabilometer, or Resilient Modulus.* Arkansas State Highway and Transportation Department. Little Rock, Arkansas. (1983).
- [16] ASTM D1883-16, Standard Test Method for California Bearing Ratio (CBR) of Laboratory-Compacted Soils, ASTM International, West Conshohocken, PA, 2016, www.astm.org.
- [17] E.H. Isaaks, R.M. Srivastava. *An Introduction to Applied Geostatistics*, Oxford University Press, New York (1989)
- [18] Sadrekarimi, J. & Akbarzad, M. (2009). Comparative Study of Methods of Determination of Coefficient of Subgrade Reaction. *Electronic Journal of Geotechnical Engineering*, 14, pp. 1-14.
- [19] Moayed, R. & Janbaz, M. (2008). Foundation Size Effect on Modulus of Subgrade Reaction in Clayey Soil. *Electric Journal of Geotechnical Engineering*, 13.
- [20] Ou, C.Y. & Lai, C.H. (1994). Finite-element analysis of deep excavation in layered sandy and clayey soil deposits. *Canadian Geotechnical Journal*, 31(2), pp. 204- 214.
- [21] Bureau of Mines and Geosciences, 1981. *Geology and Mineral Resources of the Philippines*, 1 (Geology). Ministry of Natural Resources, Manila.

PERFORMANCE OF ANN MODEL IN PREDICTING THE BEARING CAPACITY OF SHALLOW FOUNDATIONS

Mozaher Ul Kabir¹, Syed Shadman Sakib², Istiakur Rahman³, Md. Sirajul Arefin⁴, Hossain Md. Shahin⁵
^{1,2,4}Student, Islamic University of Technology, Bangladesh; ³Lecturer, Islamic University of Technology, Bangladesh; ⁵Professor, Islamic University of Technology, Bangladesh

ABSTRACT

This study deals with the performance of the Artificial Neural Networks (ANNs) for predicting the ultimate bearing capacity of shallow foundations on cohesion less soil. Footing geometry and other soil parameters from cone penetration tests (CPT) were the input variables considered to have the most significant impact on bearing capacity predictions. The application of Artificial Neural Network was carried out through the following steps considering total 100 sets of data. Firstly for training, 89 sets of data were used to determine a relation between input variables and the bearing capacity of the soil. For testing and validation, the other 11 data sets were used. The performance of the model was evaluated by comparing the results with conventional bearing capacity equations. High coefficients of correlation, low root mean squared errors (RMSE) and low mean absolute errors (MAE) were the indications to confirm that the ANN based model predicts with much perfection.

Keywords: ANNs, Bearing Capacity, RMSE, MAE.

INTRODUCTION

Every foundation setup requires satisfying two imperative criteria: ultimate bearing capacity of confinement and limiting settlement of foundations. Of these two criteria, a complete bearing capacity of confinement is managed by shearing nature of the soil and is evaluated by the theories of Terzaghi [1], Meyerhof [2], Vesic [3] and others. The explanation behind an extensive part of as far as possible theories is the most remote point adjust procedure. As far as possible in this manner got are affirmed through lab considers by different researchers. In any case, the trial looks at are generally done on tinier measured models, which are significantly cut back models stood out from real field footings. In this way, various authorities (e.g., [4, 5]) have prompted that one should be amazingly vigilant while extrapolating disclosures of examinations driven on little footings that have a width of several inches, to the broad evaluated footings. The clarification behind this is credited to the extension in shearing strain along the slip line with the development in width of the foundation and the extent of mean grain size of the soil and the adjust width [6]. For extensive scale establishments on dense sand, shearing strains demonstrate significant variety along the slip line and the normal assembled point of shearing resistance along the slip line is littler than the greatest estimation of the angle of shearing resistance (ϕ_{max}) gotten via plane strain shear tests. Henceforth, an option technique is required that gives better gauges of bearing capacity.

In the most recent two decades a few analysts have created successful demonstrating instruments. One of them is Artificial Neural Networks (ANNs) methodology. In the current past, ANNs have been connected to numerous geotechnical designing issues, including the expectation of the bearing capacity of footings, settlement forecasts, liquefaction and stability of slopes [7]. The real preferred standpoint of ANNs is that they can be used effectively as and when new information end up noticeably accessible that wipes out the requirement for a researcher to reanalyze the old and new information, use the old outline helps or conditions and additionally propose new conditions [8]. This paper shows the relevance of ANNs method in building up a compelling nonlinear model for anticipating a definitive bearing capacity of shallow foundations on cohesion less soils. The database, which comprises of load test aftereffects of extensive scale footings and smaller estimated demonstrate footings, is utilized to create and check the ANN model. This paper additionally goes for a broad assessment of the ANN model with Regression based models for ultimate bearing capacity using in total 100 sets of field data and evaluates their benefits and restrictions. The execution of these models is then contrasted and the most regularly utilized bearing capacity speculations.

DEVELOPMENT OF ULTIMATE BEARING CAPACITY MODEL

The data used for testing and validation of the ANN model were gathered from literatures, which incorporate load test data on real sized foundations and in addition the associated data regarding the footing and soil. From the 100 field data collections, 47 are from load tests on large scale footings and 50 are from small shallow footings. Of the 47 large scale footing data, 24 were reported by Muhs and Weiß [12], 11 by Weiß [13], 5 by Muhs et al. [14], 2 by Muhs and Weiß [15], 5 by Briaud and Gibbens [16].

One of the more vital initiative in the model improvement for the estimation of bearing capacity of shallow foundation is distinguishing proof of parameters that influence the bearing capacity, for which a portion of the conventional bearing limit techniques [1-3] are analyzed. In spite of the way that the bearing limit esteems gotten through these techniques vary impressively, the fundamental type of condition is the same for every one of the strategies, which is as per the following for establishments in cohesionless soil:

$$q_u = \gamma D N_q S_q d_q + 0.5 \gamma B N_\gamma S_\gamma d_\gamma$$

where B – width of footings, D – profundity of footings, γ – unit weight of sand (underneath or more the establishment level), N_q , N_γ – bearing capacity factors, S_q , S_γ – shape factors and d_q , d_γ – depth factors. Among the parameters identified with the footings, the principle factors influencing the bearing capacity are its width (minimum horizontal measurement, B), length of footing (L), shape (square, rectangular and round) and depth of the foundation (D). The depth of the foundation has the best impact on the bearing capacity among all the physical properties of the foundation [5]. The fundamental parameters with respect to the soil (sand) are its angle of shearing resistance and the unit weights from above and beneath the water table, if introduce. There are some different factors, for example, compressibility and thickness of the soil layer underneath the establishment that add to a lesser degree. Of the considerable number of properties of a soil, the edge of shearing resistance has most noteworthy impact on the bearing capacity, which increments with the relative thickness of the soil. The bearing capacity is straightforwardly corresponding to the unit weight of the soil and is affected by the area of water table.

In light of above discussion, the five input parameters used for the model advancement are width of footing (B), depth of footing (D), ratio of length and width (L/B), unit weight of sand (γ) and

angle of shearing resistance (ϕ). Extreme bearing capacity (q_u) is the single yield variable.

ANN model Development:

In this study feed-forward multilayer perceptron (MLP) is utilized; the portrayal of which can be found in numerous publications [9, 10]. The dataset was arbitrarily separated into three subsets: training and testing. 70% (or 63 cases) of the information was set for training the model, 15% (or 13 cases) was utilized for training, while the staying 15% (or 13 cases) was utilized for testing the execution of the proposed ANN based model. Using an trial-and-error strategy, the optimum number of hidden layers in the model was resolved which concluded by using ten hidden layer. Because of five input and one output variable; five node were used in the input layer and one in the output layer. A typical way to deal with problem of over fitting is early stopping. This approach includes monitoring the generalization error and stopping training when the minimum validation error is observed. Be that as it may, some care is required when to stop, since the

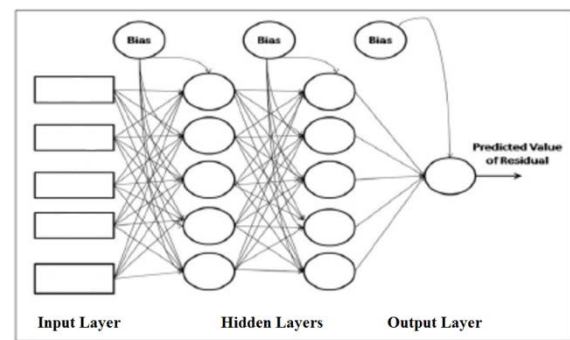


Fig. 1. Architecture of ANN model.

approval mistake surface may have local minima or long flat regions preceding a steep drop-off. To minimize these constraints Mackay [11] proposed the use of Bayesian back propagation neural networks which minimizes a combination of squared errors and weights and after that decides the correct combination, in order to create a network which sums up well. This procedure is called Bayesian regularization. In the Bayesian structure, the weights and the biases of the network are assumed to be random variables with indicated appropriation of distribution. The regularization parameters are identified with the unknown variances related with the distribution. These parameters are then evaluated using statistical techniques. In the present investigation, the Levenberg– Marquardt algorithm is utilized under the Bayesian network.

Multiple-regression analysis

To develop a relationship between the single dependent variable, q_u and one or more independent variables c_i , h_i and B , multiple-regression is used, the prediction of q_u is accomplished by the following equation:

$$q_u = w_1c_1 + w_2c_2 + w_3c_3 + w_4c_4 + w_5h_1 + w_6h_2 + w_7h_3 + w_8B + b$$

where w_i are the regression weights and are processed in a way that limits the aggregate of the squared deviations. Here b is the y axis intercept. Multiple-regression is associated with multiple correlation coefficient, which is the variance of the dependent variable explained collectively by all of the independent variables. A multiple-regression model was obtained using StataSE 12

Source	SS	df	MS	Number of obs = 89		
Model	19083512.9	5	3816702.58	F(5, 83) = 41.41		
Residual	7649780	83	92166.0241	Prob > F = 0.0000		
Total	26733292.9	88	303787.42	R-squared = 0.7138		
				Adj R-squared = 0.6966		
				Root MSE = 303.59		

Bearingcapc	Coef.	Std. Err.	t	P> t	[95% Conf. Interval]	
B	42.20546	94.93179	0.44	0.658	-146.61	231.021
Depth	1976.073	221.3357	8.93	0.000	1535.845	2416.301
LB	-27.58137	18.34084	-1.50	0.136	-64.06055	8.897815
unitw8	-21.22461	14.02371	-1.51	0.134	-49.1172	6.667982
angleoffriction	86.464	10.51894	8.22	0.000	65.54226	107.3857
_cons	-2833.27	466.6629	-6.07	0.000	-3761.444	-1905.097

Fig. 2. Output result from StataSE 12 for MLR model.

The following formulas, using the MLR technique, were found to offer the best fitting:

$$q_u = 1976.073D + 86.464h - 2833.27$$

where q_u (kPa) is the bearing capacity, s (m), h (deg) is the angle of friction.

Performance Evaluations & Results

Here the performance is being evaluated by assessing the degree to which model simulations match the actual output. The assessment was performed in the current study with various goodness-of-fit or correlation statistics. The values of performance indices or measures for the three models are summarized in Table 2. The correlation statistic (R), which evaluates the linear correlation between the actual and predicted ultimate bearing capacity, is good for all the models, for calibration as well as validation data. The model efficiency that

evaluates the performance of the model in predicting the ultimate bearing capacity values away from the mean is found to be more than 98% for calibration and validation data for the ANNs model was close to where it was first referenced.

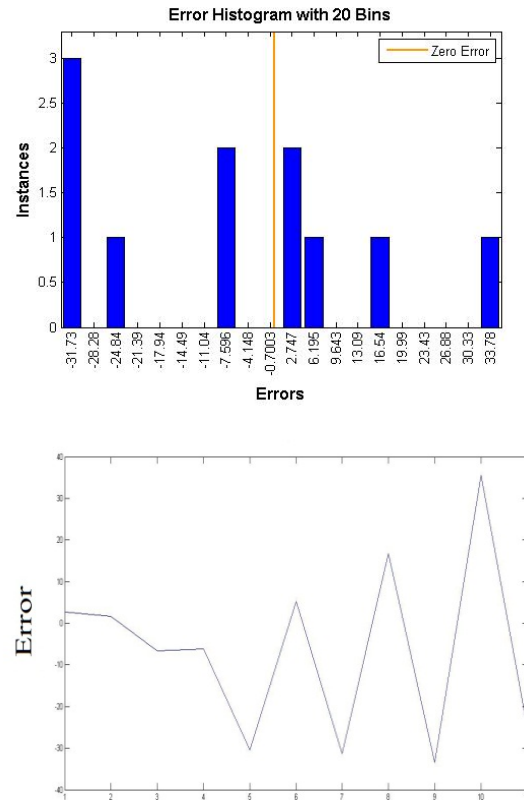
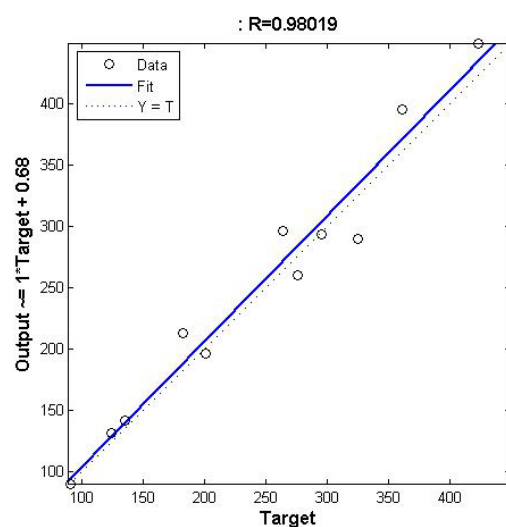


Fig. 2. Distribution of prediction error across different error thresholds.



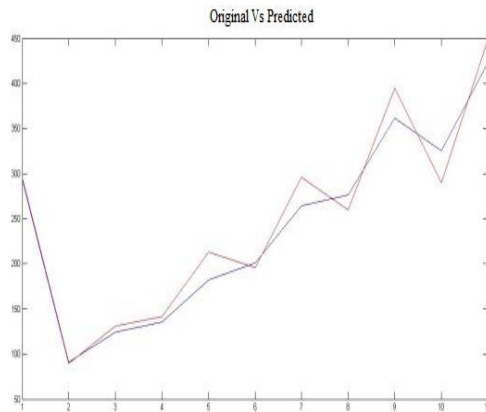
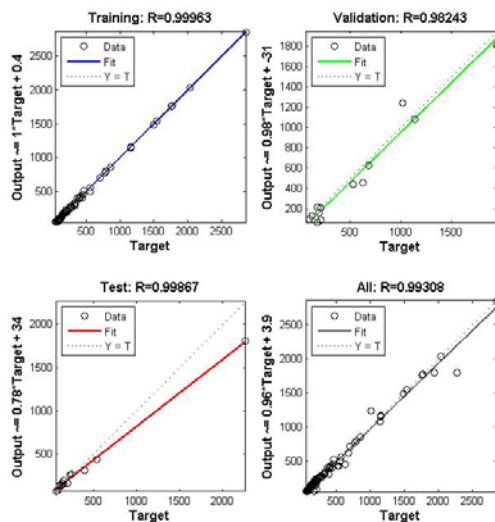


Fig. 3. Measured vs. predicted ultimate bearing capacity values.

Table 2
Performance evaluation & comparison

Performance index	ANN	MLR	Meyerhof
R^2	0.98019	0.7138	0.648



CONCLUSION

Artificial neural networks (ANNs) and the multi-linear regression model (MLR) were used to predict the bearing capacity of circular shallow footings on cohesion less soil. The artificial neural network model serves as a simple and reliable tool for the bearing capacity of shallow foundations in clay soil. The results produced high coefficients of correlation for the training and testing data of 0.99308 and 0.98019 respectively which has much more higher perfection then MLR model. Nevertheless this study deals that having some known parameters we can easily be able to have idea about the ultimate bearing capacity through the ANN model.

REFERENCES

- [1] Terzaghi K. Theoretical soil mechanics. New York: John Wiley & Sons; 1943.
- [2] Meyerhof GG. Some recent research on the bearing capacity of foundations. Can Geotech J 1963;1(1):16–26.
- [3] Vesic AS. Analysis of ultimate loads of shallow foundations. JSMFD, ASCE 1973;99(1):45–73.
- [4] De Beer EE. The scale effect on the phenomenon of progressive rupture in cohesionless soil. Proc. of the 6th int. con. on soil mech. and found. engg. vol. 2. 1965. p. 13–7.
- [5] Meyerhof GG. The bearing capacity of sand. PhD thesis, University of London; 1950.
- [6] Steinfelt JS. Scale effect on bearing capacity factor N_c . Proc. of the 9th international conference on soil mechanism and foundation engineering. vol. 1. 1977. p. 749–52.
- [8] Shahin MA, Maier HR, Jaksa MB. Artificial neural network applications in Geotechnical Eng. Austr Geomech 2001;36(1):49–62.
- [8] Pande GN, Shin H-S. Artificial intelligence v. equations. Proc ICE Civil Eng 2004;157(1):43–6.
- [9] Zurada JM. Introduction to artificial neural systems. Jaico Publishing House; 2003.
- [10] Fausett LV. Fundamentals of neural networks: architectures, algo-rithms and applications. Englewood cliffs (NJ): Prentice-Hall; 1994.
- [11] Mackay DJC. Bayesian methods for adaptive models. PhD thesis, California Institute of Technology; 1991.
- [12] Muhs H, Weiß K. Untersuchung von Grenztragfähigkeit und Setzungsverhalten flachgegründeter Einzelfundamente im ungleichförmigennichtbindigen Boden. Deutsche Forschungsgesellschaft fu r Bodenmechanik (DEGEBO), Berlin. HEFT 69, 1971.
- [13] Weiß K. Der Einfluß der Fundamentform auf die Grenztragfähigkeit flachgegründeter Fundamente. Deutsche Forschungsgesellschaft fu r Bodenmechanik (DEGEBO), Berlin. HEFT 65, 1970.
- [14] Muhs H, Elmiger R, Weiß K. Sohlreibung und Grenztragfähigkeit unter lotrecht und schräg belasteten Einzelfundamenten. Deutsche Forschungsgesellschaft fu r Bodenmechanik (DEGEBO), Berlin. HEFT 62, 1969.
- [15] Muhs H, Weiß K. Inclined load tests on shallow strip footings. Proceedings of the 8th international conference on soil mechanism and foundation engineering. vol. II. 1973. p. 173–9.
- [16] Briaud JL, Gibbens R. Behavior of five large spread footings in sand. ASCE J Geotech Geoenviron Eng 1999;125(9):787–96.

DEVELOPMENT OF THE TRADITIONAL LOCAL WISDOM INNOVATION USING COCONUT SHELL FOR STRESS RELAXING MASSAGE

Peerada Damapong¹, Pongmada Damapong¹, Wichai Eungpinichpong², and Thanarat Sripongngam³

¹College of Allied Health Science Suan Sunandha Rajabhat University, Bangkok 10300, Thailand

²Research Center in Back, Neck, and Other Joint Pain, and Human Performance, Faculty of Associated Medical Sciences, KhonKaenuniversity, KhonKaen 40002, Thailand

³Department of Health and Sport Science, Faculty of Education, Mahasarakham University, Thailand

ABSTRACT

This study was the research and development for developing innovation of coconut shell and studying the effectiveness of wisdom of the local doctor on using coconut shell for stress-relieving massage. The research and development was divided into 3 phases; Phase 1 – Developing innovation, Phase 2 – Testing innovation in patients with stress and cervicogenic headache, and 60 volunteers were selected by using Self-Stress Assessment (SSA) which they were treated by getting 10-minute of coconut shell massage for 5 days, then they were assessed before and after the treatment and Phase 3 – Concluding the effectiveness of innovation. The measurement instruments were Self-Stress Assessment (SSA), Visual Analog Scale (VAS), Cervical Range of Motion (CROM), Tissue Hardness Meter and Algometer, and Heart Rate Variability (HRV).

The findings revealed that; Phase 1 – the innovation of coconut shell for stress-relieving massage had occurred, Phase 2 - tested the innovation of coconut shell for stress-relieving massage in 60 volunteers and Phase 3 – effectiveness of the innovation, after they were treated by getting coconut shell massage, the level of cervicogenic headache was decreased with 0.95 level of significance ($P<0.05$), the cervical range of motion was increased with 0.95 level of significance ($P<0.05$), the tissue hardness meter and algometer compared before and after of the treatment were increased with 0.95 level of significance ($P<0.05$), and SDNN (Standard Deviation of Normal to Normal) and HRV value from the heart rate variability after the treatment was increased with 0.95 level of significance ($P<0.05$). In consequence, coconut shell for stress-relieving massage could relieve the stress and cervicogenic headache, and affected to the better change of relative variables in patients with stress as the appropriate and effective innovation for self-stress relief

Keywords: Local wisdom, Traditional innovation, Effectiveness, Stress relaxing massage

INTRODUCTION

Stress is the most common mental health issue in all ages, it is the physical, mental and behavioral reactions of people to the internal and external stimulators which might be a person, emotion, circumstance or environment. If a person is not adaptable when faces up the pressure, the stress would occur and affects to unbalance the living. Nowadays, the society has changed rapidly in economy, society and culture, and people have to face up many issues from the economic competition that affects to their physical and mental health. From the study of World Health Organization (WHO) which it has studied the circumstance or painfulness affecting to the stress and mental health in 21 countries around the world revealed that witnessing violence 21.8%, experiencing interpersonal violence 18.8%, accidents 17.7%, exposure to war 16.2%, trauma to a loved one 12.5% [1]. It should be careful for the treatment in patients with stress, especially the monitoring system to protect a self-injury and

suicide [2].

The wisdom of local people or local medicine, the passing on knowledge and experience of living, health treatment and disease treatment which a massage is one of the local wisdom for health treatment. Thai massage is not only for disease treatment but also for health treatment. A health massage is treated for freshness, stress relief and beautiful body [3]. From the past, the local people or local doctor has applied the existing materials in their house for self-massage, disease treatment and health treatment such as using coconut shell for foot massage in patients with the foot pain, analgesia in foot, inflammation of heel and for stress-relieving massage.

Samut Songkhram, Thailand is a province with a large number of coconut which the coconut shell is normally found in all houses and is developed as the innovation for stress-relieving

massage and disease treatment. In consequence, the researcher has studied the developing innovation and studying the effectiveness of wisdom of the local doctor on using coconut shell for stress-relieving massage in Samut Songkhram province.

OBJECTIVE

1. To develop the innovation from coconut shell for health treatment.
2. To study the effectiveness of wisdom of the local doctor on using coconut shell for stress-relieving massage

MATERIALS AND METHODS

Design

This study was the research and development.

The study was approved by the Ethics Review Committee for Research Involving Human Subjects, Mahasarakham University (number 273/2557).

Subjects

The sample groups were 60 patients at the age of 18 years old and above who were selected by using the Self-Stress Assessment (SSA) of Department of Mental Health (DMH) and were treated by getting coconut shell massage.

Measurement Instruments

The measurement instruments were Self-Stress Assessment (SSA), Visual Analog Scale (VAS), Cervical Range of Motion (CROM), Tissue Hardness Meter and Algometer, and Heart Rate Variability (HRV).

Intervention

The volunteers who were selected would get 10-minute of coconut shell massage for 5 days and they were assessed before and after the treatment.

Statistical Analysis

In this research, the descriptive statistic was used to describe the characteristic of volunteers; mean and standard deviation. Additionally, the paired t-test was used to analyze the variables compared before and after of the treatment with 0.95 level of significance ($P < 0.05$).

RESULTS

The findings of Phase 1 – Developing innovation of coconut shell for stress-relieving massage; from the study of coconut shell, principles of medical physics, anatomy and physiology for

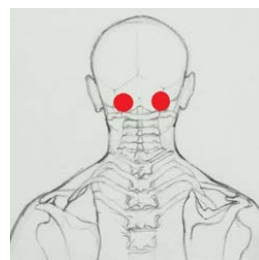
designing and developing innovation revealed that a prototype of the innovation of coconut shell had occurred, tested and developed the innovation for 2 times. (Figures 1 and 2)

The findings of Phase 2 and Phase 3 revealed that most of 60 volunteers were female (71.70%), most of the age was 59 – 61 years (40.00%), most of the marital status was married (75.00%), most of the occupation was agriculturist (53.40%) and most of them were not have the



congenital disease (73.30%).

Figure 1: A prototype of the innovation of coconut



shell.

Figure 2: The massage points of coconut shell for stress relaxing massage.

Assessing the level of cervicogenic headache by using Visual Analog Scale (VAS) before and after treating by coconut shell massage in the 5th day revealed that the level of cervicogenic headache was decreased with 0.95 level of significance ($P < 0.05$).

Assessing the cervical range of motion; cervical flexion, cervical extension, cervical left lateral flexion and cervical right lateral flexion compared before and after of the treatment by coconut shell massage in the 5th day revealed that all the cervical range of motions were increased with 0.95 level of significance ($P < 0.05$).

Assessing the pressure pain threshold (kg/cm^2) compared before and after of the treatment by coconut shell massage in the 5th day revealed that the pressure pain threshold was increased with 0.95 level of significance ($P < 0.05$).

Assessing the tissue hardness before and after treating by coconut shell massage in the 5th

day revealed that the tissue hardness was increased with 0.95 level of significance ($P < 0.05$).

The findings of heart rate variability from the study of Time Domain Analysis; SDNN, RMS-SD and the study of Frequency Domain Analysis; LF, HF, LF/HF compared before and after of the treatment by coconut shell massage in the 5th day revealed that SDNN, RMS-SD and LF, HF, LF/HF value were increased with 0.95 level of significance ($P < 0.05$). (Figure 3)

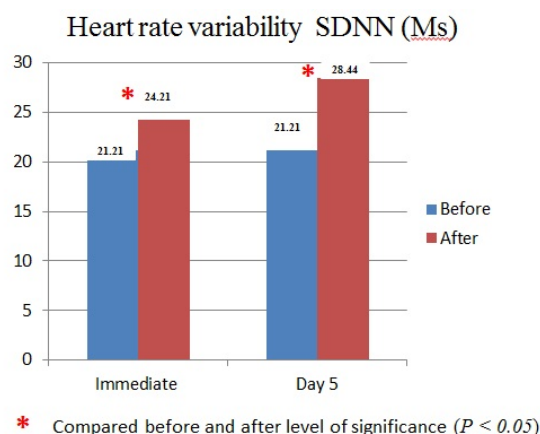


Figure 3: Heart rate variability by SDNN

DISCUSSION

The findings of the level of pain revealed that VAS value was decreased with the level of significance, it was consistent with the study of Peerada Damapong et al.[4], Effectiveness of Court-Type Traditional Thai Massage in Patients with Chronic Tension-Type Headache: A Pilot Study which revealed that the level of headache was decreased with 0.95 level of significance ($P < 0.05$).

Effects of a decrease of the level of pain by coconut shell massage could be described as the physiological effect that massage was the pressure through skin and muscle which affected to increase the circulation of blood and lymph. Additionally, the increased blood circulation might be an effect of stimulating the sympathetic nervous system; when the circulation of blood and lymph were increased, the vascular and excretory system were also increased that affected to decrease the inflammation, edema and pain [5].

The findings of assessing the cervical range of motion revealed it was decreased with 0.95 level of significance which the volunteers were treated by coconut shell massage and affected to a relief of the cervical muscle, an increase of blood circulation and cervical range of motion, it was consistent with the study of Eungpinichpong et al.[6] in 2000, Therapeutic Effects of Traditional Thai Massage on

Patients with Cervical Spondylosis: Comparison of Therapeutic Effects of Non-Steroidal Anti-Inflammatory Drug and Traditional Thai Massage which the findings of 8 weeks study revealed that cervical flexion, cervical extension, cervical left lateral flexion and cervical right lateral flexion after treating by Thai massage were increased and could be described that Thai massage would stretch the muscle, decrease the muscle fascia and increase the muscle flexibility.

Effects of the increase of the pressure pain threshold, it was consistent with the study of Peerada Damapong et al.[7], Short-Term Effects of Court-Type Traditional Thai Massage on Pressure Pain Threshold and Pain Intensity in Patients with Chronic Tension-Type Headache which revealed that after the volunteers were treated by Court-Type Traditional Thai Massage for assessing the pressure pain threshold, it was increased with 0.95 level of significance ($P < 0.05$).

Effects of the decrease of the tissue hardness, it was consistent with the study of Zheng et al.[8], Therapeutic Evaluation of Lumbar Tender Point Deep Massage for Chronic Non-Specific Low Back Pain which revealed that the pressure pain threshold and tissue hardness were increased with 0.95 level of significance ($P < 0.05$).

Effects of the increase of the heart rate variability compared before and after of the treatment by coconut shell massage revealed that SDNN, RMS-SD and LF of CTTM value were increased with the level of significance which indicated that after treating by Royal Thai Massage, the stress of patients was decreased (more relief); SDNN value was increased, the variance of myocardial function to the parasympathetic nervous system was increased, then the stress was decreased. It was consistent with the study of Toro-Velasco et al. [65], Immediate Effects of Head and Neck Massage on Changing of Heart Rate Variability (HRV), Mood States, and Pressure Pain Thresholds (PPTs) in Patients with Chronic Tension-Type Headache which revealed that HRV time interaction had changed with the level of significance. Additionally, it was consistent with the study of Peerada Damapong et al. [9], A Randomized Controlled Trial on the Effectiveness of Court-Type Traditional Thai Massage versus Amitriptyline in Patients with Chronic Tension-Type Headache which had assessed the Heart Rate Variability (HRV) before and after the treatment in patients with tension-type headache revealed that after treating by Thai massage, the heart rate variability had changed which indicated that the parasympathetic nervous system was increased ($P < 0.05$). In consequence, the innovation of coconut

shell for stress-relieving massage could increase the parasympathetic nervous system and affected to relieve the stress.

CONCLUSION

The findings of developing innovation and studying the effectiveness of wisdom of the local doctor on using coconut shell for stress-relieving massage revealed that; The decrease of Current visual analog scale (CVAS) with the level of significance, nevertheless, the other variables were consistently such as the increase of cervical range of motion after treating by coconut shell massage which affected to a relief of the cervical muscle and an increase of blood circulation. The increase of pressure pain threshold with the level of significance after treating by coconut shell massage. The decrease of tissue hardness with the level of significance indicated that coconut shell massage could decrease the muscle tone. The decrease of heart rate variability compared before and after of the treatment revealed that SDNN, RMS-SD, LF and LF/HF were increased with the level of significance which indicated that after treating by coconut shell massage, the stress of volunteers was decreased (more relief). In consequence, coconut shell massage could relieve the stress and cervicogenic headache, and increase the parasympathetic nervous system which affected to relieve the stress in patients, and decrease the variables which related to the cervicogenic headache and stress for the better change.

ACKNOWLEDGEMENTS

This study was supported by the Office of the Higher Education Commission : OHEC. This publication has been supported by Suan Sunandha Rajabhat University, Bangkok, Thailand.

REFERENCES

[1]. Stein, D.J., Chiu, W.T., Hwang, I., Kessler, R.C., Sampson, N., Alonso, J., Borges, G., Bromet, E., Bruffaerts, R., de Girolamo, G., Florescu, S., Gureje, O., He, Y., Kovess-Masfety, V., Levinson, D.,

Matschinger, H., Mneimneh, Z., Nakamura, Y., Ormel, J., Posada-Villa, J., Sagar, R., Scott, K.M., Tomov, T., Viana, M.C., Williams, D.R., Nock, M.K. Cross-national analysis of the associations between traumatic events and suicidal behavior: findings from the WHO World Mental Health Surveys. *PLoS One*. 2010 May 13;5(5):e10574.
 [2]. Damapong, P. and Damapong, P. (2016). Model Development for Outbreak of Dengue Fever Surveillance System in District Level. *International Journal of GEOMATE*. 11(27): 2777-2781.
 [3]. The Foundation for the Promotion of Thai Traditional Medicine Ayurved School, *Traditional massage (Court-type Thai traditional massage)*. 2005, Bangkok: Pickanesprinting
 [4]. Damapong, P. Kanchanakhan, N. Eungpinichpong, W., and Damapong, P (2015). Effectiveness of court-type traditional thai massage in patients with chronic tension-type headache: a pilot study. *J Health Res*. 29(5): 351-356.
 [5]. Eungpinichpong, W., *Therapeutic Thai Massage*. 2008, Bangkok: Chonromdek publishing house.
 [6]. Eungpinichpong, W., et al., *Therapeutic effects of traditional Thai massage on patients with cervical spondylosis: comparison of therapeutic effects of non-steroidal anti-inflammatory drug and traditional Thai massage*. *KKU Research Journal* 2000. 2: p. 5-7.
 [7]. Damapong, P. Kanchanakhan, N. Eungpinichpong, W., Putthapitak, P, and Damapong, P., Short-Term Effects of Court-Type Traditional Thai Massage on Pressure Pain Threshold and Pain Intensity in Patients with Chronic Tension-Type Headach. *International Journal of GEOMATE*. vol. 11, no. Dec., 2016..
 [8]. Zheng, Z., et al., *Therapeutic evaluation of lumbar tender point deep massage for chronic non-specific lowback pain*. *JTCM*, 2012. 32(4): p. 534-537.
 [9]. Damapong, P. Kanchanakhan, N. Eungpinichpong, W., Putthapitak, P, and Damapong, P., (2015). A Randomized Controlled Trial on the Effectiveness of Court-Type Traditional Thai Massage versus Amitriptyline in Patients with Chronic Tension-Type Headache. *Evid Based Complement Alternat Med*. 2015(2015): 12 pages.

SHORT-TERM EFFECTS OF THE AROMATHERAPY TO REDUCE STRESS IN THE ELDERLY

Pongmada Damapong¹, Peerada Damapong¹ and Kanyamanee Koomhangsung¹

¹College of Allied Health Science, Suan Sunandha Rajabhat University, Bangkok 10300, Thailand

ABSTRACT

This research was aimed to study the effects of stress treatment by inhaling the aromatherapy of lavender essential oil. It was a quasi-experimental research; the populations of this research were the elderly people in Wat Khok Ket Health Promoting Hospital, Plai Phong Phang Sub-district, Amphawa District, Samut Songkhram Province. The data was compiled using the questionnaire for the level of stress assessment to select 40 participants; 20 for the experimental group and 20 for the control group, by using random samples method. The experimental group was treated by inhaling the aromatherapy of lavender essential oil; the volunteers would lie down and inhale the essential oil from the kiln in 10 minutes for 3 days and the control group would receive a common suggestion. Both of 2 groups were assessed by using the HRV (Heart Rate Variability) before and after the experiment for comparing their results. The statistics for data analysis were percentage, mean and standard deviation, paired t-test and t-test.

As to the research result, the SDNN (Standard Deviation of Normal to Normal) and HRV score of the experimental group before and after the experiment had a differentiation with 0.95 level of significance ($P < 0.05$). Additionally, the SDNN and HRV score of the experimental group after the experiment were more than the control group with 0.95 level of significance ($P < 0.05$).

The findings revealed that using the aromatherapy could treat the stress; in consequence, inhaling the aromatherapy of lavender essential oil is a choice for the stress treatment.

Keywords: Short-term effects, Aromatherapy, Stress, Elderly

INTRODUCTION

Nowadays, stress becomes a significant issue of mental health in all ages which affects to the body systems; the nervous and brain system, endocrine system and immune system. The person who has a high stress would affect to the gastric disease, hypertension, coronary disease, insomnia and tension-type headache [1]. From the study of a trend of Thai population revealed that the elderly people tended to increase rapidly which they had the regressive changes, some of them were forced and affected to their physical and mental health, and the stress had occurred. From the report of Thai people's mental health of Department of Mental Health and National Statistical Office of Thailand 2008 – 2010 revealed that the elderly people had the lowest score of mental health compared with the other ages [2] and the health care of the elderly people should have a monitoring system for the health administration to monitor the unexpected symptoms [3]. In consequence, having a good health should have the stress management or stress treatment which the aromatherapy is a choice for the stress treatment by using the natural aroma or essential oil as it affected to the nervous system, relieve the stress and anxiety, relieve or stimulate the

better physical, mental and health balance.

From the information of this issue, the research had studied the stress and effects of reducing stress by inhaling the aromatherapy of lavender essential oil from the kiln in the elderly people, and brought the research result for defining a guideline of reducing stress of the elderly people.

OBJECTIVE

General Objective

To study the effects of aromatherapy on reducing stress of the elderly people.

Specific Objective

1. To study the heart rate variation of the elderly people who was treated by inhaling the aromatherapy of lavender essential oil.

2. To compare the effects of aromatherapy on reducing stress of the elderly people in the experimental group and the control group.

MATERIALS AND METHODS

Design

This research was the quasi-experimental research which conducted in Wat Khok Ket Health Promoting Hospital, Plai Phong Phang Sub-district, Amphawa District, Samut Songkhram Province.

Subjects

The sample groups were 40 elderly people at the age of 60 years old and above who were selected with the moderate level by the questionnaire for the level of stress assessment; 20 for the experimental group and 20 for the control group.

Assessment

Both of 2 groups were assessed by using the HRV before and after the experiment for comparing their results. (Figures 1)

Measurement Instruments

The data was compiled using the Suanprung Stress Test-20 (SPST-20) of Department of Mental Health and the HRV.



Figure 1: Assessed by using the HRV before and after the experiment.

Intervention

The experimental group was treated by inhaling the aromatherapy of lavender essential oil; the volunteers would lie down and inhale the essential oil from the kiln in 10 minutes for 3 days and the control group would receive a common suggestion. (Figures 2)



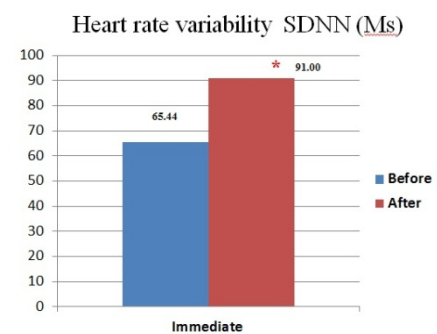
Figure 2: Aromatherapy of lavender essential oil.

Statistical Analysis

The researcher had conducted the experiment by announcing for the elderly people as volunteer, selecting 40 volunteers by the questionnaire for the level of stress assessment; 20 for the experimental group and 20 for the control group, using random samples method by drawing and signing an agreement of the 3 days experiment participation, assessing before the experiment by the HRV after assessing before the experiment of the experimental group who was treated by the aromatherapy for 10 minutes, and the control group would receive a common treatment and assessed by the HRV after the experiment immediately. The research was conducted for 3 days and assessed before and after the experiment immediately in each process.

RESULTS

The findings revealed that; in the experimental group: most of them were female 75% and male 25% and in the control group: most of them were female 90% and male 10%, most of the age was 60 – 65 years old: 35% in the experimental group and 40% in the control group. The findings of using the aromatherapy in relieve the stress by the HRV revealed that SDNN, LF (Low Frequency) and HF (High Frequency) scores from before and after the experiment immediately had increased with 0.95 level of significance ($P < 0.05$). (Figures 3)



* Scores from before and after the experiment immediately had increased with 0.95 level of significance ($P < 0.05$) within experimental group.

Figure 3: Heart rate variability by SDNN within experimental group.

Additionally, the comparison between the experimental group and the control group revealed that SDNN of HRV score after the experiment had

increased with 0.95 level of significance ($P < 0.05$). (Figures 4)

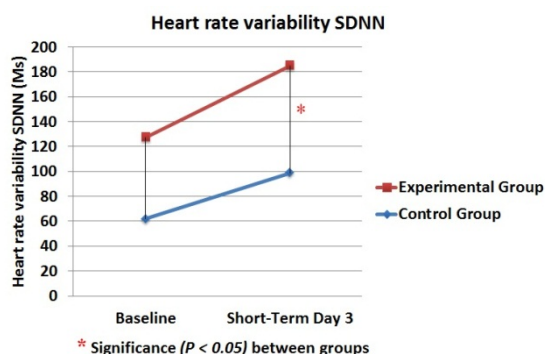


Figure 4: Heart rate variability by SDNN between groups

DISCUSSION

The findings revealed that after the experiment, the experimental group who was treated by the aromatherapy had SDNN of HRV score increasingly which affected to the parasympathetic nerve and stress reduction. It was consistent with the study of Waraporn Yammeesri [4], the study of effects of aromatherapy in relieving stress of patients in the Intensive Care Unit (ICU), Chiang Rai Prachanukroh Hospital revealed that the patient who was treated by the aromatherapy had the physical changes of relief; reducing in heart rate, breathing rate and mean coronary pressure. Buckle, [5] which had studied the patient after operating without the respirator but remaining in the ICU compared with applying 2 types of the aromatherapy for the physical changes; Lavender A (*Lavendula Angustifolia*) and Lavender B (*Lavendula Burnatii*), it was revealed that 2 types of lavender had affected to the physical changes; reduce the breathing rate, relieve the stress. Additionally, it was consistent with the study of Peerada Damapong and team, the study of short-term effects of court-type traditional Thai massage on pressure pain threshold and pain intensity in patients with chronic tension-type headache [6] which the findings revealed that the aromatherapy could reduce the stress of the elderly people.

CONCLUSION

As to the findings and the research which they were consistent with the study of essential oil in reducing stress of the elderly people, the assessment of the HRV revealed that SDNN, LF and HF scores from before and after the experiment immediately of the experimental group and the comparison between the experimental group and the control group had increased with 0.95 level of significance ($P < 0.05$), it showed that after the volunteers were treated by the essential oil, they had less stress (more relief). Nevertheless, inhaling the essential oil could reduce the stress and increase the parasympathetic nerve which affected to reduce the stress of the volunteers and the better changes of variables that related to the stress of the elderly people.

ACKNOWLEDGEMENTS

This study was supported by the Suan Sunandha Rajabhat University, Bangkok, Thailand.

REFERENCES

- [1]. Ward TN, Levin M, Philips JM. Evaluation and management of headache in the emergency department. *Med Clin North Am* 2001; 85: 971–84.
- [2]. National Statistical Office of Thailand. Statistic Data. (2012). Executive Summary: The Report of Thai People's Mental Health 2010. Searched on 2 October 2016. Searched from http://service.nso.go.th/nso/nsopublish/themes/theme_2-4-10.html
- [3]. Damapong, P. and Damapong, P. (2016). Model Development for Outbreak of Dengue Fever Surveillance System in District Level. *International Journal of GEOMATE*. 11(27): 2777-2781.
- [4]. Waraporn Yammeesri. (2004). Effects of Aromatherapy in Relieving Stress of Patients in the Intensive Care Unit (ICU). Master of Nursing in Adult Nursing, Graduate School, Chiang Mai University.
- [5]. Buckle, J. (1993). Aromatherapy. *Nursing Times*, 89(20), 32-35
- [6]. Damapong, P. Kanchanachan, N. Eungpinichpong, W., and Damapong, P., Short-Term Effects of Court-Type Traditional Thai Massage on Pressure Pain Threshold and Pain Intensity in Patients with Chronic Tension-Type Headach. *International Journal of GEOMATE*. vol. 11, no. Dec., 2016..

IMMEDIATE EFFECTIVENESS OF TRADITIONAL THAI MASSAGE ON CERVICAL RANG OF MOTION WITH CHRONIC TENSION-TYPE HEADACHE

Chamiporn Kongmong¹ and Peerada Damapong¹

¹College of Allied Health Science, Suan Sunandha Rajabhat University, Bangkok 10300, Thailand

Abstract

This research was aimed to assess the immediate effectiveness of Thai traditional massage on cervical range of motion in patients with tension-type headache. The data was compiled using the quasi-experimental research design; the populations of this research were 30 patients with tension-type headache, the assessment was before and after receiving the 45-minute of Thai traditional massage. The results were assessed immediately after the intervention which consisted of the increased cervical range of motion after receiving the Thai traditional massage while a significant difference was occurring ($P < 0.05$). In conclusion, Thai traditional massage would relieve the muscle tension by reducing its pain and increase the cervical range of motion.

Keywords: Immediate effectiveness, Traditional Thai Massage, Cervical Rang of Motion, Chronic Tension-type headache

INTRODUCTION

The tension-type headache is the most common type of headache, it could continue for few days, a week or a month which is disturbing, causes the uncomfortable and it could be stable. However, it is not harmful but it comes and it goes. It probably occurs in patients with Episodic Tension-Type Headache (ETTH) or Echronic Tension-Type Headache (CTTH). Otherwise, it is an effect from continue using the painkiller for a long time, so the aim of treatment is to use less medicine or change to the non-pharmacologic treatment especially the treatment by Thai traditional massage as it is from the various methods.

The tension-type headache is the pain above the eyes, ears and around the head or might be on the upper back [1]. Nowadays, most of the tension-type headache is the Tension-Type Headache (TTH) which consists of; pressure pain threshold on the temple or forehead occurring on 2 sides of the head and might be on the occiput or cervical area, and the intenseness is in the low to moderate level that patients can spend the day normally [2]. The factors of this Tension-Type Headache (TTH) consist of; stress, anxiety, sadness, insanitary motion and hardworking of the cervical muscle which affect to the contracture of cervical and scalp muscle [2]. The treatment is divided into 2 types; 1) Pharmacologic treatment and 2) Non-pharmacologic treatment due to continue using the medicine for a long time which could cause it to be

more chronic tension-type headache. Therefore, the aim of treatment of the chronic tension-type headache is to emphasize on decreasing a volume of using the medicine or change to the non-pharmacologic treatment are the safe methods for reducing a risk state from the pharmacological effect or painkiller addiction [3] which there are various methods. Nevertheless, the treatment by Thai traditional massage becomes a key role [4] to protect the tension-type headache systematically for monitoring the unexpected tension-type headache or illness [5].

The Thai traditional massage is one of the treatments for the muscular pain [6]. The massage is divided into 2 types; the royal massage and general massage, which are different technics [7]. The aims of massage are for; the better blood circulation, relieve the muscle tension, increase the cervical range of motion, extend the capillary, increase the elimination from cell to the vein system and the better urine which would reduce the pain from the arrearage of the chemical substance from cell function and affected to decrease the hypertension.

In consequence, this research was aimed to study the immediate effects of Thai traditional massage on cervical range of motion in patients with tension-type headache as the guideline for the treatment choice and affirm its treatment result to be more accepted.

MATERIALS AND METHODS

Design

This research was the quasi-experimental research design which the cervical range of motion assessment was conducted in the Department of Traditional Thai Medicine, Bamnet Narong Hospital, Bamnet Narong District, Chaiyaphum Province, Thailand

Subjects

The sample groups were 30 patients at the age of 18-65 years old with chronic tension-type headache, at the level 4 of VAS score by the criteria of chronic tension-type headache of International Headache Society: IHS[2]

Assessment

This research was the cervical range of motion assessment.

Measurement Instruments

In this research, the Visual Analog Scale (VAS) was used to assess the level of the tension-type headache which was a straight line with 10 centimeters long. The volunteers would mark the levels of the tension on the straight line; the left hand side was no tension (VAS = 0) and the right hand side was the highest tension (VAS = 10) which represented to the level of the tension-type headache before and after the treatment immediately, and the results were recorded as centimeter. Additionally, the Cervical Range Of Motion (CROM) was used to assess the cervical range of motion; cervical flexion, cervical extension, cervical left lateral flexion, cervical right lateral flexion, in a week before the treatment, before and after the treatment immediately, and the results were recorded as degree.

Intervention

The volunteers were treated by getting 45-minute of Thai traditional massage which was the pressure threshold; shoulder muscle, cervical muscle, front head and back head.

Statistical Analysis

In this research, the descriptive statistic was used to describe the characteristic of volunteers; mean and standard deviation. Additionally, the paired t-test was used to analyze the variables as

objected by conducting the result analysis immediately in the first day of the assessment.

RESULTS

The findings of the general information of 30 volunteers revealed that; most of them were female (86.70%), most of the age was 37 – 50 years old (43.30%), most of the marital status was married (86.70%) and most of them have no chronic disease (83.30%), most of the tension-type headache was 15 times per month or more (100%), most of the tension duration was 30 minutes - 1 hour (60.00%) and the level of tension-type headache in 24 hours last week was 6.26 ± 1.17 .

The assessment of the level of tension-type headache by the Visual Analog Scale (VAS) before and after the treatment immediately revealed that the VAS score was decreased with 0.95 level of significance ($P < 0.05$).

The assessment of the cervical range of motion; cervical flexion, cervical extension, cervical left lateral flexion, cervical right lateral flexion before and after the treatment immediately revealed that the immediate cervical range of motion was increased with 0.95 level of significance ($P < 0.05$) (Table 1).

Table 1 Comparison of the outcome measures between baseline (pre-test) and post-test assessments in Cervical range of motion (degree) (paired t-tests).

Outcome	Baseline	Immediate	P-value
	(Mean \pm SD)	(Mean \pm SD)	
Cervical flexion	52.94 \pm 9.27	58.16 \pm 10.55	<0.05
Cervical extension (%)	60.22 \pm 7.37	64.38 \pm 8.15	<0.05
Cervical left lateral flexion	37.49 \pm 6.0	43.94 \pm 6.98	<0.05
Cervical right lateral flexion	36.22 \pm 6.49	41.27 \pm 7.83	<0.05
mean \pm SD			

Note: CTTM is court-type traditional Thai massage. NA is not available. $P < 0.05$ is statistically significant differences from baseline.

DISCUSSION

The findings of the immediate cervical range of motion assessment were different in each motion with 0.95 level of significance ($P < 0.05$) which was increased more than 5 degrees. In consequence, it was different in the clinical significance that the volunteers were treated the Thai traditional massage would have a relief of muscle, shoulder muscle, cervical muscle, better blood circulation and affected to the better cervical range of motion.

The findings were consistent with the study of Kruapanich et al.[8], the study of Thai traditional massage (TTM) group compared with a napping with the episodic tension-type headache after the treatment for volunteers of the TTM group, the cervical range of motion was increased with 0.95 level of significance ($P < 0.05$); cervical flexion, cervical extension, cervical left lateral flexion, cervical right lateral flexion. Additionally, the comparison of each TTM group revealed that it had more cervical range of motion than who had a relief with 0.95 level of significance ($P < 0.05$) of all cervical range of motion at after 3-week, 6-week follow-up after the final treatment in TTM group. Besides, it was consistent with the study of Sooktho et al.[9], the study of effectiveness of Thai traditional massage in patients with chronic tension-type and migraine headache compared with the group immediately at after 3-week, 6-week follow-up after the final treatment, the group who were treated by getting Thai traditional massage had a better cervical range of motion than the sham ultrasound group. Moreover, it was consistent with the study of Puusjarvi et al. [10], the finding revealed that cervical range of motion was increased in the 3 and 6 phase. Lastly, it was consistent with the study of Eungpinichpong et al.[11] in 2000, the study of therapeutic effects of Thai traditional massage on patients with cervical spondylosis: comparison of therapeutic effects of non-steroidal anti-inflammatory drug and Thai traditional massage for 8 weeks, it revealed that after the treatment by Thai traditional massage; cervical flexion, cervical extension, cervical left lateral flexion, cervical right lateral flexion were increased as traditional Thai massage by stretching the muscle would decrease its tension and increase the cervical range of motion.

CONCLUSION

As the findings and the research which were consistent with the study of the cervical range of motion was increased after its studies, revealed that Thai traditional massage would increase the cervical range of motion due to Thai traditional massage had decreased its tension and increased the cervical range of motion [63] which affected to increase the cervical range of motion in all direction. In addition, there was a difference between before and after the treatment by Thai traditional massage which the pressure threshold on muscle and in-depth had affected to stimulate the peripheral receptor to react directly on those areas to be treated [64] that would decrease its tension and increase the cervical range of motion.

ACKNOWLEDGEMENTS

This study was supported by the National Research Council of Thailand. This publication has been supported by Suan Sunandha Rajabhat University, Bangkok, Thailand.

REFERENCES

- [1] Ward TN, Levin M, Philips JM. Evaluation and management of headache in the emergency department. *Med Clin North Am* 2001; 85: 971–84.
- [2] Olesen J. The International Classification of the Headache Disorder. 2nd ed. Application to practice. Denmark: Copenhagen Univ. Funct Neurol 2005; 20: 61-8
- [3] Ahonenv E, Hakumäki M, Mahlamäki S, etal. Effectiveness of acupuncture and physiotherapy on myogenic headache: a comparative study. *A cupunct Electrother Res* 1984; 9: 141–50
- [4]. Damapong, P. Kanchanakhan, N. Eungpinichpong, W.,and Damapong, P., Short-Term Effects of Court-Type Traditional Thai Massage on Pressure Pain Threshold and Pain Intensity in Patients with Chronic Tension-Type Headach. *International Journal of GEOMATE*.vol. 11, no. Dec., 2016..
- [5]. Damapong, P. and Damapong, P. (2016). Model Development for Outbreak of Dengue Fever

Surveillance System in District Level. International Journal of GEOMATE. 11(27): 2777-2781.

[6] T. P. Broh, Utilization of Thai traditional massage at the Institute of Thai Traditional Medicine [M.S. thesis], Department for Development of Thai Traditional and Alternative Medicine, Ministry of Public Health, Mahidol University, Bangkok, Thailand, 2004.

[7] Z Ayurved Thamrong School Center of Applied Thai Traditional Medicine Faculty of Medicine Siriraj Hospital Mahidol University, Traditional Massage (Court-Type Thai Traditional Massage) Massage Point, Mahidol University, Bangkok, Thailand, 2014.

[8] Kruapanich, C., et al., *The immediate effect of Traditional Thai massage for reducing pain on patients related with Episodic tension-type headache.*, in *Master of Science Thesis in Physical Therapy*. KhonKaen university. 2010.

[9]. Sooktho S, Chatchawan U, Eungpinichpong W, Tiamkao S. Therapeutic Effectiveness of Traditional Thai Massage on Patients with Chronic-Tension Type Headache And Migraine. Master of Science Thesis in Physical Therapy. Khon Kaen: The graduate school, Khon Kaen university; 2012.

[10]. Abbott, J.H., *Mobilization with movement applied to the elbow affects shoulder range of movement in subjects with lateral epicondylalgia*. Manual Therapy, 2001. 6(3): p. 170-177.

[11]. Puustjarvi, K., O. Airaksinen, and P.J. Pontinen, *The effects of massage in patients with chronic tension headache*. Acupunct Electrother Res, 1990. 15(2): p. 159-62.

Authors Index

A

A.B Sambah	653
A.B.K.T. Piumali	345
A.M.N Alagiyawanna	345
AUNG AUNG SOE	148
Abdul Hakam	222
Abdul Hakam	218
Abdul Hakam	499
Abdul Hakam	494
Abdul Halim Abdul Latiff	700
Abdul Halim Abdul Latiff	678
Abdul Naser Abdul Ghani	821
Abdulla Omarov	383
Abu Bakar Sambah	577
Abu Bakar Sambah	706
Adrian McCallum	298
Adrian McCallum	304
Adrian McCallum	315
Afshin Asadi	28
Agnes Garciano	588
Ahmad Amirul Faez	66
Akihiko Naganuma	206
Akihiko Taira	255
Akihiko Yagi	805
Akihisa Nakahashi	361
Akira Kondo	634
Akira MITSUMORI	269
Alexander Rubinstein	333
Alexis M. Fillone	660
AlfanJauhari	706
Ali Alnedawi	355
Ali Murtaza Rasool	60

Ali Nisari Tabrizi	184
Alsidqi Hasan	72
Alvin Lal	640
Amin Esmail Khalil	678
Amorn Chaiyasat	505
Amorn Chaiyasat	839
Andy Fourie	72
Anoop Aujayeb	108
Anthony Shun Fung Chiu	114
Ariya Aruninta	694
Arul Arulrajah	2
Arul Arulrajah	96
Asel Tulebekova	383
Asemgul Moldazhanova	383
Askar Zhussupbekov	383
Atchariya Saengthongthip	90
Atsuko Sato	167
Atsushi Yashima	78
Aung Kyaw Soe	713
Avirut Chinkulkijniwat	108
Ayaka Oya	275

B

Badhrulhisham Abdul Aziz	72
Bambang Istijono	222
Barrios Gonzalo	234
Barry KASSAMBARA	755
Bernardo A. Lejano	411
Bernardo A. Lejano	417
Bernardo A. Lejano	464
Bernardo A. Lejano	435
Bithin Datta	640

Authors Index

Bithin Datta	725	Cynthia Debby Heriyani	339
Bithin Datta	732		
Bithin Datta	775	D	
Boonchai Wichitsathein	912	D.A.A. Putri	939
Boonlert Archevarapuprok	866	D.G.R Wiadnya	653
Boontida Uapipatanakul	839	DR. K K GANGULY	511
Bujang B.K.Huat	28	Daeyoung Lee	373
		Daisuke Komori	84
C		Dang Thi Thanh Huyen	127
C. S. Kalpage.	666	Dang Thi Thanh Huyen	477
Caiqian Yang	918	Defrian Marza Arisandi	577
Charlle Sy	114	DefrianMarzaArisandi	706
Chatchai Ponchio	849	Dilip Kumar Roy	725
Chatchai Ponchio	854	Dong Daicho	361
Chatchai Ponchio	858	Dong Hyun Kim	133
Chatchai Ponchio	863	Dongmin Kim	373
Chaweewan Denpaiboon	275	Dongya Yang	924
Chayanon Hansapinyo	281	Dr. Wanchai Teparaksa	293
Chayanon Hansapinyo	531	Dr.Neelima Satyam D	367
Chee-Loong Wong	827		
Cheerawit Rattanapan	790	E	
Cheerawit Rattanapan	713	Edward Ephrem T. Codilla II	160
Cheerawit Rattanapan3	738	Emmanuel Bastian Pelaez	453
Cherdsak Suksiripattanapong	429	Erica Elice Saloma Uy	447
Cheryl Lyne C. Roxas	435	Erica Elice Saloma Uy	441
Cheryl Lyne C. Roxas	464	Erika Ueno and Hiroyuki Ii	878
Chia-Yun Wei	228		
Chinnapat Buachart	531	F	
Chinnapat Buachart	281	Fauzan	494
Chollachai Kamtawai	945	Fauzan	405
Clare Olver	564	Fauzan	499
Claudia Lovina A N	405	Fauzan Sahdi	72

Authors Index

Febrin A Ismail	494	Hirohisa Muto	206
Febrin Anas Ismail	405	Hirokazu Abe	564
Febrin Anas Ismail	499	Hiroki Kitagawa	623
Firman Farid Muhsoni	653	Hiroki Kohmori	593
Fuad	577	Hiroki Nishiwaki	896
Fumitake Nishimura	690	Hiromi Suda	805
Fusanori Miura	577	Hiroshi Kono	684
		Hiroshi Takebayashi	599
G		Hiroto Akimoto	249
G.B. Herath	666	Hiroyuki Hashida	178
G.M.P. Kumara	611	Hiroyuki Ii	623
Gicheol Lee	178	Hiroyuki Ii	890
Gulshat Tleulenova	383	Hiroyuki Ii	896
Guntur	577	Hiroyuki Ii	684
		Hiroyuki Nagahama	845
H		Hiroyuki Shimogaki	684
H.B. Ng	399	Hiryuki Ii	872
HamidTeennejad	184	Ho Cho	255
Hanan Elsawahli	810	Homayoon GANJI	755
Hanbin Ge	918	Hong-Da Chou	228
Hania Arif	794	Hongxiao Liu	929
Hanqiang Yu	924	Hongyang Cheng	558
Heka P Andriani	218	Hossain Md Shahin	351
Hide Sakaguchi	255	Hossain Md. Shahin	246
Hideki MAEDA	269		
Hidenori TANAKA	483	I	
Hidenori YOSHIDA	617	ISHIGURO Satoru	744
Hidenori Yoshida	628	ISLAM Mohammad Raihanul	744
Hideto Ohmori	571	ITO Ryoei	744
Hidetoshi NISHIOKA	269	ITO Tetsu	744
Hideyuki Katsumata	934	Idawati Ismail	470
Hikari Shimadera	634	Ignacio Fructuoso Solís Quispe	287

Authors Index

Ikki Tateishi	934	Jonathan Rivera Dungca	447
Ildo Muhary Putra	939	José Carlos Solís Tito	287
Ilyas AKRAM	148	Junichiro Takeuchi	884
Ivan Gratchev	133	Jutaporn Tanok	90
Ivan Syed	525	Jyunji Uno	684
J		K	
Jaksada Thumrongvut	429	K. Kawamoto	345
James Matthew L. De Jesus	411	Kakuta Fujiwara	78
Jareeya Yimrattanabavorn	912	Kali Prasad Nepal	355
Jareeya Yimrattanabavorn	906	Kanokwan Rudisirisak	672
Jeremy Stephens	133	Karin Kandananond	389
Jicheng Xu	924	Karlygash Borgekova	383
Jim Shiau	36	Katsuhiro Shibano	249
Jin Ishii	694	Katsuya Suzuki	249
Jinichi Koue	634	Kazuhei Kikuchi	845
Jirat Teparaksa	293	Kazuhiro Ishimaru	178
Jiro KUWANO	148	Kazuhiro KANEDA	240
Jiro Kuwano	60	Kazunori Nakashima	423
Jittanan Kawilanan	945	Kazunori Nakashima	719
Joel G. Galupino	605	Kazuya Itoh	234
Joel Galupino	114	Kazuya Itoh	249
John Tri Hatmoko	339	Kazuya Itoh	154
John Yeaman	315	Keiichi Toda	599
John Yeaman	298	Keiichiro SHIBATA	617
John Yeaman	304	Keiichiro Shibata	628
Jon Arnel S. Telan	102	Keiji Okumura	178
Jonathan Dungca	114	Keisuke Kase	571
Jonathan R. Dungca	605	Keita Sugito	321
Jonathan R. Dungca	102	Keita Sugito	327
Jonathan R. Dungca	160	Ken Kawamoto	127
Jonathan Rivera Dungca	441	Ken Kawamoto	477

Authors Index

Ken Kawamoto	611	M.I.M. Mowjood	666
Ken Kawamoto	666	Mahdi Miri Disfani	96
Kenichiro Nakarai	212	Mai Furukawa	934
Kennedy K.	902	Maki Oyagi	805
Kenta Eguchi	212	Maki Oyagi	647
Kenta Fukagawa	694	Makoto Takemoto	546
Kentaro Uemura	142	Mamoru Kawasaki	488
Kentaro Uemura	234	Mario Edisson Quilli Apaza	287
Khondoker Istiak Ahmad	246	Mary Ann Q. Adajar	43
Kiyoshi Numakami	249	Mary Ann Q. Adajar	49
Ko Hashimoto	172	Masaaki Hanaoka	571
Koichi Nagao	142	Masaaki Takahashi	647
Koji WATANABE	269	Masaaki Tanaka	805
Kota Kono	361	Masami Matsui	584
Kousuke Takahama	78	Masamichi AOKI	240
Kouta Katagishi	546	Masamitsu Fujimoto	275
Krister Ian Daniel Roquel	660	Masanobu Taniguchi	872
Kritika Trakoolngam	137	Masanori Shimomura	200
Kyle Solomon D. Pineda	417	Masato Kikuchi	571
Kyoichi OKAMOTO	770	Masato Takenaka	599
		Masatsugu Kiko	546
L		Masayuki Fujihara	884
Lanh Si Ho	212	Masayuki KODA	263
Lessandro Estelito Garciano	588	Masnun Abrar	246
Lucie Mynarzova	458	Md Amanul Hasan	525
Luky Handoko	339	Md. Al Imran	423
		Md. Aminul Islam	36
M		Md. Ashraful Islam Molla	934
M Sofian Asmirza	494	Melvyn Leong	96
M Sofian Asmirza	218	Menglim Hoy	2
M. Azizul Moqsud	66	Michael S. Hayford	775
M. Mahmudi	653	Michiko Masuda	690

Authors Index

MiladGhannadzadehKermani	184	Nattapong Damrongwiriyanupap	429
Miller DL. Cutora	43	Navid Khayat	377
Minoru Morioka	212	Nawawi Chouw	234
Minoru YAMANAKA	269	Nguyen Hoang Giang	127
Minxue Zheng	929	Nguyen Hoang Giang	477
Miroslav Mynarz	458	Nguyen Van Tuan	127
Mohammad Noori	918	Nguyen Van Tuan	477
Mohammad Reza Atrchian	184	Nicanor R. Roxas Jr	660
Mohammadjavad Yaghoubi	96	Niphawarn Kangkun	863
Mohammed Khachi Hatem	188	Nittaya Ngowattana	672
Moises Carl Caneca	453	Nobuo Fukushima	361
Muhammad Abdur Rahman	351	Nobutaka Hiraoka	234
Muhammad Ihsan	939	Noel Lester C. Gozum	102
Muqdad Al-Juboori	732	Noriko Otsuka	564
Muzamir Hasan	66	Noriyuki Okano	55
Myint Win Bo	96	Norsuzailina Mohamed Sutan	72
		Nuanlaor Kiama	858
N		Nur Aqilah Ahmad Faisal	821
N.H Priyankara	345	Nurfarhana Aisya Anuar	700
NAGAOKA Seiya	744	Nurulhuda Nadziri	470
Nahathai Chotklang	790	Nutchanon Siri	531
Nair A	902	Nuzaihan Aras Agus Salim	821
Najumuddin Anjum	782		
Naoaki Suemasa	142	O	
Naoaki Suemasa	154	OKAJIMA Kenji	744
Naoaki Suemasa	234	Oleg Kupervasser	333
Naoaki Suemasa	249	Oranee Roongrueang	906
Naomasa Honda	194	Orapin Laosee	713
Naomichi Matsumoto	628	Orapin Laosee	790
Naotaka Kikkawa	234		
Naozo FUKUDA	269	P	
Nattapong Damrongwiriyanupap	395	Pattranit Thongthep	849

Authors Index

Peiqing Xiao	918	Ryohta Takatoku	234
Pensupa Wirikitkhul	906	Ryoichi Fukagawa	275
Perayos Khangkhun	552	Ryoichi Fukagawa	321
Pervaiz Ahmad Naseri	782	Ryoichi Fukagawa	327
Phang Biao Yu	66	Ryoichi Fukagawa	361
Piti Pratomkhum	281	Ryota ISHII	488
Pramet Kaewmesri	866		
Preeyaporn Chaiyasat	839	S	
Premkamol Thuennadee	137	Saad Farhan Ibrahim	188
Primprapa Sangjun	505	Sachie Takeuchi.	647
Prinya Chindaprasirt	395	Sakonwan Hanjitsuwan	395
Prinya Chindaprasirt	429	Sakonwan Hanjitsuwan	429
Punthila Janthaphat	738	Sangsan Wongchairattana	395
		Sao-Jeng Chao	228
Q		Sartaj M.	902
Qian Chen	924	Satakhun Detphan	429
		Sato Shinji	815
R		Satoru Kawasaki	423
Rafiqul A. Tarefder	525	Satoru Kawasaki	719
Rajeshwar Goodary	108	Satoru OHTSUKA	240
Ratamane Nuntasarn	90	Satoru Ueda	890
Raymond Venneker	827	Satoshi Chiba	647
Renan Ma. Tanhueco	588	Satoshi Kaneco	934
Richard M. De Jesus	453	Satoshi Matsumura	546
Rio Sandi	405	Satoshi SUGIMOTO	269
Riyadh Al-Ameri	355	Seiichi Ishida	200
Rolando Orense	234	Sethapong Sethabouppha	945
Roman Yavich	333	Shahid Iqbal	794
Roodheer Beeharry	108	Shakerullah Hashimi	782
Rosilawati Zainol	810	Shanwei Li	929
Ruchuon Wanna	552	Shigemitsu Hatanaka	429
Runglawan Rachan	2	Shigeo Honma	538

Authors Index

Shingo Asamoto	611	T	
Shinya Hiramatsu	571	T. Saito	345
Shinya Inazumi	172	T. Saito M. Nagamori	666
Shinya Inazumi	178	T.J.L Tobing Dio Rizqi Irawan	939
Shinya Tsukada	764	Tadaomi Eguchi	172
Shinya Tsukada	750	Tadashi Chuman	178
Shohei Namiki	546	Taichi Hyodo	546
Shota NISHIOKA	617	Taijiro Fukuyama	571
Shuichi Kuwahara	172	Takaaki Okamoto	599
Shun Habara	249	Takahiro Tamura	584
Shunsuke Shimada	142	Takamitsu KAJISA	755
Shunsuke Shimada	154	Takamitsu Kajisa	782
Shunsuke Takiura	154	Takamitsu Sasaki	154
Shusaku Shiiba	571	Takamitsu Sasaki	142
Sindy Harvi Amalia	499	Takashi Nakayama	55
Sinin Hamdan	470	Takashi Saito	611
Sirapong Sooktawee	866	Takashi Sasaki	212
Siriluk Namwong	839	Takashi TOYAMA	770
Siska Apriwelni	499	Takatoshi Hondo	55
Siti Hanggita Rachmawati	36	Takaya KOGURE	148
Siti Noor Linda Taib	72	Takayuki Hirao	546
Sohei Itaya	55	Takayuki Shuku	558
Somsak Wongsawass	713	Takefumi Kurose	564
Sota Ikeda	684	Takeshi Kodaka	206
Soumik Nafis Sadeek	246	Takuma Kubohara	623
Sudjit Karuchit	906	Tam Weng Long	66
Suksun Horpibulsuk	96	Tanakorn Phoo-ngernkham	395
Suksun Horpibulsuk	2	Tanakorn Phoo-ngernkham	429
Sultan Al Shafian	246	Tarmizi Ismail	827
Sumiyati Gunawan	339	Taufika Ophiyandri	222
Suriyah Tongmune	945	Taze Jared Abubo	588
Swathi Priyadarsini Putti	367	Terry Lucke	19

Authors Index

Teruo Arase	593	U	
Teruo Arase	584	Udayagee Kumarasinghe	666
Teruo Nakai	351	Usa Humphries	866
Tetsuo Morita	750		
Tetsuo Morita	764	V	
Tetsuo Okano	593	Vatanavongs Ratanavaraha	108
Tetsuoh Shiota	593	Victor Carlo F. Torres	102
Tetsuya Ohmura	488	Vitalii Sarychev	333
Tetsuya Okano	321		
Tetsuya Okano	327	W	
Thapthai Chaithong	84	WATANABE Ken	744
Tharika Kaenjun	912	Wan Suzita Wan Ibrahim	810
Kumari Nawarathna T.H.	719	Warayuth Sajomsang	839
Thomas Larkin	234	Wataru Kawase	690
Tachapattaworakul Suksaroj T.	738	Watcharapol Wonglertarak	912
Timothy Scott Y. Uytengsu	102	Watcharapong Nareejun	854
Ting Wee Kiet	72	Weerawat Ounsaneha	790
Tohru Suzuki	934	Weerawat Ounsaneha	738
Tomoe KOMORIYA	770	Wenya Wen	924
Tomohiro TANIKAWA	240	Wenyi Yao	918
Tomohito Matsuo	634	WildanAlfarizi	706
Tomoko Miyagawa	564	Wincent Nicole K. Pabilona	49
Tomonori Ishigaki	127	Wonlee Nounmusig	800
Tong Ton Kien	127	Worsak Kanok-Nukulchai	281
Tong Ton Kien	477		
Toshihiro Hayashi	167	X	
Toshiki Nishimura	684	Xiangyang Wu	918
Toshinori Sakai	10	Xiangyang Wu	924
Tran Thi Viet Nga	127	Xiaoying Zhang	924
Tran Thi Viet Nga	477		
Tsuyoshi Tanaka	142	Y	
Tsuyoshi Tanaka	249	Y. Sakamoto	666

Authors Index

Y.Y. Zheng	399	Zulkifli Yusop	827
Yasushi Furugaichi	249	and Satoshi Anzai	84
Yoshiaki Kikuchi	546		
Yoshifumi Taguchi	121		
Yoshihito Kurazumi	694		
Yoshinobu Kashihara	599		
Yoshitaka Yanagihara	249		
Yoshiya Touge	84		
Yoshiyuki Uchikawa	584		
Yota Togashi	55		
Yu Fujiwara	10		
Yuan Zhang	249		
Yue Huang	395		
Yugo Isobe	127		
Yuji Yamakage	815		
Yuji Yamashita	684		
Yukihiro Morikawa	255		
Yukimasa Takemoto	647		
Yukio Uchida	172		
Yuko Ishida	275		
Yukoh Hasunuma	142		
Yusuke Tadano	200		
Yuta Mitobe	84		
Yuta Yamanaka	78		
Yuto Sukegawa	84		
Yuuya KATSUDA	269		
Z			
Zabihullah Mahdi	538		
Zakaria Hossain	36		
Zhiren Wu	918		
Zhishui Liang	918		

GEOMATE 2018

Eighth International Conference on

Geotechnique, Construction Materials & Environment

20-22 November 2018

Kuala Lumpur, MALAYSIA

- The "International Journal of GEOMATE" is a Scientific Journal of the GEOMATE International Society that encompasses a broad area in Geotechnique, Construction Materials and Environment.
- The key objective of this journal is to promote interdisciplinary research from various regions of the globe.
- The editorial board of the journal is comprised of extensively qualified researchers, academicians, scientists from Japan and other countries of the world.
- It is peer-reviewed Journal that is published quarterly till 2015 and now monthly. All articles published in this journal are available on line.
- Contributors may download the manuscript preparation template for submitting paper or contact to the Editors-in-Chief

[editor@geomatejournal.com].

ISSN: 2186-2990

DOI: <http://dx.doi.org/10.21660/geomate>



Scopus

EBSCO

CENGAGE Learning

U GIF GLOBAL IMPACT FACTOR



VOLUME 00
Issue 00
Month, Year

International Journal of GEOMATE

(Geotechnique, Construction Materials and Environment)



Tsu, Japan

THE GEOMATE INTERNATIONAL SOCIETY

<http://www.geomatejournal.com/>